ICF13

Beijing (China)

2013

Vol. C

The interphase elasto-plastic damaging model

Giuseppe Giambanco[1,*], Giuseppe Fileccia Scimemi[1], Antonino Spada[1]

[1] Department of Civil, Environmental, Aerospace and Materials' Engineering, University of Palermo, 90128, Italy
* Corresponding author: giuseppe.giambanco@unipa.it

Abstract Heterogeneous materials present a mechanical response strongly dependent on the static and kinematic phenomena occurring in the constituents and at their joints. In order to analyze this kind of materials it is a common practice to distinguish a macroscopic length scale of interest from a mesoscopic one, where the mesoscopic length scale is of the order of the typical dimensions of the constituents. At the mesoscopic level the interaction between the units is simulated by mean of apposite mechanical devices. Among these devices is popular the zero thickness interface model where contact tractions and displacement discontinuities are the primary static and kinematic variables respectively. However, in heterogeneous materials the response also depends on joint internal stresses as much as on contact stresses. The introduction of internal stresses brings to the interphase model or an enhancement of the classical zero-thickness interface. With the term 'interphase' we shall mean a layer separated by two physical interfaces from the bulk material or a multilayer structure with varying properties and several interfaces. Different failure conditions can be introduced for the physical interfaces and for the joint material. The interphase model has been implemented in an open-source research-oriented finite element analysis program for 2D applications. Numerical simulations are provided to show the main features of the model.

Keywords Interphase element, Damage, Elastoplasticity, Finite element

1. Introduction

The mechanical response of all those structures that are constituted by heterogeneous materials is dependent by different static and kinematic phenomena occurring in each constituent and at their joints. Material degradation due to nucleation, growth and coalescence of microvoids and microcracks is usually accompanied by plastic deformations as decohesion and sliding that cause strain softening and induced anisotropy.

The mesoscopic approach is by now the most diffused technique to understand this kind of materials, because it overcomes the problems associated with the strong simplifications that have to be introduced when the macroscopic approach is applied. In particular, with the mesoscopic approach all the material constituents are modelled individually and their interactions are regulated by using appropriate devices able to reproduce the inelastic phenomena that usually occur at the physical interfaces. In literature, these mechanical devices are generally called contact elements, normally distinguished between link elements, thin layer elements and zero-thickness interface elements (ZTI). In the last decades interface elements have been applied in several engineering applications due to their simple formulation and to their easiness to be implemented in finite element codes [1-10].

The interface constitutive laws are expressed in terms of contact tractions and displacement discontinuities which are considered as generalized joints strains. In order to model the nonlinear behaviour caused by plastic deformations and damage evolution the constitutive laws of the interface elements are formulated making use of concepts borrowed by theory of Plasticity and Continuum Damage Mechanics.

In many cases the structural response depends also on internal stresses and strains within the joint. It is sufficient to think to the fracture that appears in the middle of masonry blocks caused by the horizontal tangential contact stresses between the mortar and the block when a masonry assembly is subjected to a pure compressive load. These tangential stresses cannot be captured by the classical ZTI model. Therefore, the usual assumption used in zero-thickness interface elements, where the response is governed by contact stress components, may require a correction by introducing the

effect of the internal stresses into the analysis. This enhancement of the ZTI is known as interphase model, for the first time proposed by Giambanco and Mròz [11].
The interphase element has been formulated by authors as a new contact element and introduced in a scientific oriented finite element code. Patch tests have been carried out in elasticity to investigate the numerical performance and convergence of the element. All the results are shown in the paper written by Giambanco el al. [12]. In particular, in that paper is shown how strategies such as the Reduced Selective Integration or the Enhanced Assumed Strain methods are necessary to avoid shear locking effects of the element.
In this work the interphase element is implemented for nonlinear applications by introducing separate limit conditions for the joint bulk material and for the physical interfaces. In particular the damage mechanics theory is used to simulate the formation and propagation of fractures in the bulk material. The elastoplastic limit condition of Mohr-Coulomb type with a tensile cut-off is adopted to describe the decohesion process of the interfaces. The contact strains are subdivided in an elastic and a plastic part. The overall model is thermodynamically consistent and the flow rules are derived by applying the Lagrangian method. With the aim to show the effectiveness of the model the interphase constitutive laws have been implemented in an open-source research-oriented finite element analysis program for 2D applications and by using the Selective Reduced Integration.
The paper is organized as follows. In Section 2 the general assumptions of the model are reported and the expression of the Helmholtz free energy is furnished. In Section 3 the state equations and the flow rules are determined on the base of the thermodynamically consistent theory. Section 4 is finally dedicated to numerical applications in order to show the effectiveness of the proposed model.

2. General assumptions and Thermodynamics.

Let us consider, in the Euclidean space $\Re^3$ referred to the orthonormal frame $(O,\mathbf{i_1},\mathbf{i_2},\mathbf{i_3})$, a structure formed by two adherents Ω^+, Ω^- connected by a third material Ω in contact with the two bodies by means of the two physical interfaces Σ^+ and Σ^- respectively, as in Fig. 1.

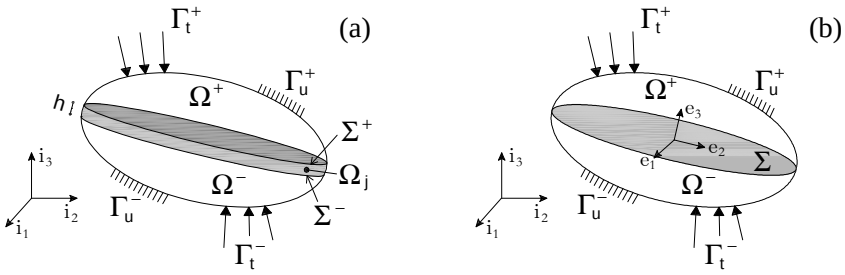

Figure 1. (a) Mechanical scheme of a third body interposed between two adherents;
(b) Interphase mechanical scheme.

It is assumed that the thickness h of the joint is small if compared with the characteristic dimensions of the bonded assembly.
The boundary of the two adherents is divided in the two parts $\Gamma_u^{\pm}$ and $\Gamma_t^{\pm}$, where kinematic and loading conditions are specified respectively.
The joint interacts with the two adherents through the following traction components:

$$\mathbf{t}^{\pm} = t_1^{\pm}\mathbf{e}_1 + t_2^{\pm}\mathbf{e}_2 + t_3^{\pm}\mathbf{e}_3 \tag{1}$$

which can be considered as the external surface loads for the joint.

In Eq. (1) $\mathbf{e}_1$, $\mathbf{e}_2$ and $\mathbf{e}_3$ are the unit vectors of the local reference system, with $\mathbf{e}_3$ oriented along the normal to the middle surface Σ and directed towards the adherent Ω^+.
The joint can be regarded as an interphase model. It is assumed that the fibers inside the interphase and directed along $\mathbf{e}_3$ are maintained rectilinear during the deformation process. In view of this hypothesis the interphase displacement field $\mathbf{u}$ can be easily obtained from the displacement $\mathbf{u}^+$ and $\mathbf{u}^-$ of the interfaces Σ^+ and Σ^-, thus

$$\mathbf{u}(x_1, x_2, x_3) = \left(\frac{1}{2} + \frac{x_3}{h}\right)\mathbf{u}^+\left(x_1, x_2\right) + \left(\frac{1}{2} - \frac{x_3}{h}\right)\mathbf{u}^-\left(x_1, x_2\right) \tag{2}$$

with x_1, x_2 and x_3 the Cartesian coordinates in the orthonormal frame $\left(O, \mathbf{e}_1, \mathbf{e}_2, \mathbf{e}_3\right)$.
Since the thickness of the joint is generally small if compared to the characteristic dimensions of the adherents, we can assume the strain state $\boldsymbol{\varepsilon}$ uniform along the $\mathbf{e}_3$ direction and given by:

$$\boldsymbol{\varepsilon}(x_1, x_2) = \frac{1}{h}\int_{-h/2}^{h/2} \nabla^s \mathbf{u}\left(x_1, x_2, x_3\right) dx_3 \tag{3}$$

Substituting the Eq. (2) we have:

$$\boldsymbol{\varepsilon}(x_1, x_2) = \frac{1}{2h}\left(\left[\mathbf{u}\right] \otimes \mathbf{n} + \mathbf{n} \otimes \left[\mathbf{u}\right]\right) + \frac{1}{2}\nabla^s\left(\mathbf{u}^+ + \mathbf{u}^-\right) \tag{4}$$

where $\left[\mathbf{u}\right] = \mathbf{u}^+ - \mathbf{u}^-$, $\mathbf{n}$ is the unit normal vector to the interphase plane and ∇^s is the symmetric gradient operator defined as $\nabla^s = \frac{1}{2}\left(\nabla + \nabla^T\right)$.
Let us note that in the interphase model the joint curvatures generated by displacement field (2) and the related flexural effect are neglected.
Equilibrium equations are derived by applying the principle of virtual displacements (PVD) that asserts that the external work produced by the contact tractions equals the internal work developed in the joint. According to the hypothesis of a constant strain state, by applying the divergence theorem and assuming that $\Sigma = \Sigma^+ = \Sigma^-$, the PVD leads to the following local equilibrium relations of the interphase model:

$$\mathbf{t}^+ - \boldsymbol{\sigma}\cdot\mathbf{n} + \frac{h}{2} div\boldsymbol{\sigma} = \mathbf{0}; \quad \mathbf{t}^- + \boldsymbol{\sigma}\cdot\mathbf{n} + \frac{h}{2} div\boldsymbol{\sigma} = \mathbf{0} \quad on\ \Sigma, \tag{5}$$

$$\mathbf{m}\cdot\boldsymbol{\sigma} = \mathbf{0} \quad on\ \Gamma. \tag{6}$$

The basic kinematical hypotheses are the additive decomposition of total strain in the internal (*i*) and contact (*c*) parts and, for the contact strain only, a further decomposition in elastic (*e*) and inelastic (*p*) parts:

$$\boldsymbol{\varepsilon} = \boldsymbol{\varepsilon}^i + \boldsymbol{\varepsilon}^c \tag{7}$$

$$\boldsymbol{\varepsilon}^c = \boldsymbol{\varepsilon}^{ce} + \boldsymbol{\varepsilon}^{cp} \tag{8}$$

with

$$\boldsymbol{\varepsilon}^i = \mathbf{A}\boldsymbol{\varepsilon}\mathbf{A} \tag{9}$$

being $\mathbf{A} = \mathbf{I} - \mathbf{n}\otimes\mathbf{n}$ the unit second order tensor.
In order to comply with thermodynamic requirements, the interphase Helmholtz free energy is introduced in the following form:

$$\Psi\left(\boldsymbol{\varepsilon}^i, \boldsymbol{\varepsilon}^c, \boldsymbol{\varepsilon}^{cp}, \boldsymbol{\omega}, \xi_d, \xi_p\right) = \Psi^i\left(\boldsymbol{\varepsilon}^i, \boldsymbol{\omega}, \xi_d\right) + \Psi^c\left(\boldsymbol{\varepsilon}^c, \boldsymbol{\varepsilon}^{cp}, \xi_p\right) + \Psi^{i,c}\left(\boldsymbol{\varepsilon}^i, \boldsymbol{\varepsilon}^c, \boldsymbol{\varepsilon}^{cp}, \boldsymbol{\omega}\right); \tag{10}$$

where Ψ^i and Ψ^c represent the free energies related to the internal and contact parts of the strain state respectively and Ψ^{ic} is the mixed term of the free energy which takes into account the co-presence of the contact and internal strains. ξ_d and ξ_p are the damage and plastic internal variables, respectively.

The principle considered for developing the constitutive laws is that damage occurs in the bulk material, therefore the damage tensor $\boldsymbol{\omega}$ appears in the two terms of the total free energy that are functions of the internal strains also. In this way the constitutive model takes into account the onset of microvoids and fractures along the thickness of the joint. On the other hand, debonding of the joint from the adherents, sliding and fractures developing on surfaces parallel to the middle plane of the interphase are modelled using elastoplasticity and the inelastic contact strains $\boldsymbol{\varepsilon}^{cp}$ are the related internal variables.

In this work a single scalar damage variable ω governs the loss of stiffness of the bulk material. It ranges from 0 to 1, with the inferior and superior limits having the meaning of a pristine and a fully damaged bulk material, respectively.

The explicit expression of the components of the free energy is given below:

$$\Psi^i = \frac{1}{2}(1-\omega)\left[\lambda \operatorname{tr}^2\left(\boldsymbol{\varepsilon}^i\right) + 2\mu\,\boldsymbol{\varepsilon}^i : \boldsymbol{\varepsilon}^i\right] - h_d\left[\xi_d + \ln\left(1-\xi_d\right)\right] \tag{11}$$

$$\Psi^c = \frac{1}{2}\left[\lambda \operatorname{tr}^2\left(\boldsymbol{\varepsilon}^c - \boldsymbol{\varepsilon}^{cp}\right) + 2\mu\left(\boldsymbol{\varepsilon}^c - \boldsymbol{\varepsilon}^{cp}\right) : \left(\boldsymbol{\varepsilon}^c - \boldsymbol{\varepsilon}^{cp}\right)\right] + \frac{1}{2}h_p\xi_p^2 \tag{12}$$

$$\Psi^{i,c} = (1-\omega)\lambda \operatorname{tr}\left(\boldsymbol{\varepsilon}^{\mathrm{i}}\right)\operatorname{tr}\left(\boldsymbol{\varepsilon}^{\mathrm{c}} - \boldsymbol{\varepsilon}^{\mathrm{cp}}\right) \tag{13}$$

where λ and μ are the Lamè's constants, h_d is a material parameter which governs the softening response associated to the damage onset and growth, and h_p is a material parameter specifying isotropic hardening/softening interface response.

3. State equations and flow rules.

In order to derive the interphase constitutive equations, the second principle of thermodynamics, taking into account also the balance equation (first principle) can be applied in the form of the Clausius-Duhem inequality. This inequality for isothermal purely mechanical evolutive process reads as

$$D = \boldsymbol{\sigma} : \dot{\boldsymbol{\varepsilon}} - \dot{\Psi} \geq 0 \tag{14}$$

where D is the interphase dissipation (for unit surface) or net entropy production.

From the assumed form of the Helmholtz free energy (Eq. 10) its general rate has the following expression:

$$\begin{aligned}\dot{\Psi} = &\left(\frac{\partial \Psi^i}{\partial \boldsymbol{\varepsilon}^i} + \frac{\partial \Psi^{i,c}}{\partial \boldsymbol{\varepsilon}^i}\right) : \dot{\boldsymbol{\varepsilon}}^i + \left(\frac{\partial \Psi^c}{\partial \boldsymbol{\varepsilon}^c} + \frac{\partial \Psi^{i,c}}{\partial \boldsymbol{\varepsilon}^c}\right) : \dot{\boldsymbol{\varepsilon}}^c + \left(\frac{\partial \Psi^c}{\partial \boldsymbol{\varepsilon}^{cp}} + \frac{\partial \Psi^{i,c}}{\partial \boldsymbol{\varepsilon}^{cp}}\right) : \dot{\boldsymbol{\varepsilon}}^{cp} + \\ &+ \left(\frac{\partial \Psi^i}{\partial \omega} + \frac{\partial \Psi^{i,c}}{\partial \omega}\right) : \dot{\omega} + \frac{\partial \Psi^i}{\partial \xi_d}\dot{\xi}_d + \frac{\partial \Psi^c}{\partial \xi_p}\dot{\xi}_p\end{aligned} \tag{15}$$

Particularizing Eq. (14) for a purely elastic incremental deformation process ($\dot{\boldsymbol{\varepsilon}}^{cp} = \mathbf{0}$, $\dot{\omega} = \dot{\xi}_d = \dot{\xi}_p = 0$), assuming the decomposition of the stress state similar to that used for the strain state

$$\boldsymbol{\sigma} = \boldsymbol{\sigma}^i + \boldsymbol{\sigma}^c, \qquad \text{being} \qquad \boldsymbol{\sigma}^i = \mathbf{A}\boldsymbol{\sigma}\mathbf{A} \tag{16}$$

and considering the adopted expressions of the free energy parts (Eq. 11-13), the elastic stress-strain equations can be derived, thus

$$\sigma^i = (1-\omega)\left\{\lambda\left[\operatorname{tr}\left(\boldsymbol{\varepsilon}^i\right) + \operatorname{tr}\left(\boldsymbol{\varepsilon}^c - \boldsymbol{\varepsilon}^{cp}\right)\right]\mathbf{A} + 2\mu\boldsymbol{\varepsilon}^i\right\} \tag{17}$$

$$\sigma^c = \lambda\left[(1\text{-}\omega)\operatorname{tr}\left(\boldsymbol{\varepsilon}^i\right) + \operatorname{tr}\left(\boldsymbol{\varepsilon}^c - \boldsymbol{\varepsilon}^{cp}\right)\right](\mathbf{I}-\mathbf{A}) + 2\mu\left(\boldsymbol{\varepsilon}^c - \boldsymbol{\varepsilon}^{cp}\right) \tag{18}$$

$$\chi_p = h_p \xi_p \tag{19}$$

$$\chi_d = h_d \frac{\xi_d}{1-\xi_d} \tag{20}$$

$$\zeta = \frac{1}{2}\left[\lambda \operatorname{tr}^2\left(\boldsymbol{\varepsilon}^i\right) + 2\mu\,\boldsymbol{\varepsilon}^i : \boldsymbol{\varepsilon}^i\right] + \lambda \operatorname{tr}\left(\boldsymbol{\varepsilon}^i\right)\operatorname{tr}\left(\boldsymbol{\varepsilon}^c - \boldsymbol{\varepsilon}^{cp}\right) \tag{21}$$

where χ_p and χ_d are the static variables conjugate of the internal variables ξ_p and ξ_d respectively, and ζ the thermodynamic force conjugate of the damage variable ω.

Making use of the elastic strain-stress equation and of the previous positions, the final expression of the instantaneous dissipation is obtained:

$$D = \boldsymbol{\sigma}^c : \dot{\boldsymbol{\varepsilon}}^{cp} - \chi_p \dot{\xi}_p - \chi_d \dot{\xi}_d + \zeta\dot{\omega} \geq 0\,. \tag{22}$$

In order to regulate the activation of each dissipative mechanism, two different yield functions are defined in the space of the proper static variables, namely:

$$\Phi_p\left(\boldsymbol{\sigma}^c, \chi_p\right) \leq 0, \qquad \Phi_d\left(\zeta, \chi_d\right) \leq 0 \tag{23}$$

where Φ_p is the classical plastic yield function specifying the elastic contact domain assumed convex and Φ_d is the damage activation function also assumed convex.

The activation of each dissipation mechanism can be effectively described by a variational formulation which is represented by the generalized principle of maximum intrinsic dissipation:

$$\max_{\boldsymbol{\sigma}^c, \chi_p, \chi_d, \zeta} \left(\boldsymbol{\sigma}^c : \dot{\boldsymbol{\varepsilon}}^{cp} - \chi_p \dot{\xi}_p - \chi_d \dot{\xi}_d + \zeta\dot{\omega}\right) \tag{24}$$

subject to the constraints (Eq. 23). The Kuhn-Tucker conditions of the maximum constrained problem provide the plastic and damage evolution laws of the interphase:

$$\dot{\boldsymbol{\varepsilon}}^{cp} = \dot{\lambda}_p \frac{\partial \Phi_p}{\partial \boldsymbol{\sigma}^c}; \quad \dot{\omega} = \dot{\lambda}_d \frac{\partial \Phi_d}{\partial \zeta} \tag{25}$$

$$-\dot{\xi}_p = \dot{\lambda}_p \frac{\partial \Phi_p}{\partial \chi_p}; \quad -\dot{\xi}_d = \dot{\lambda}_d \frac{\partial \Phi_d}{\partial \chi_d} \tag{26}$$

$$\Phi_p\left(\boldsymbol{\sigma}^c, \chi_p\right) \leq 0, \quad \dot{\lambda}_p \geq 0, \quad \dot{\lambda}_p \Phi_p\left(\boldsymbol{\sigma}^c, \chi_p\right) = 0 \tag{27}$$

$$\Phi_d\left(\zeta, \chi_d\right) \leq 0, \quad \dot{\lambda}_d \geq 0, \quad \dot{\lambda}_d \Phi_d\left(\zeta, \chi_d\right) = 0 \tag{28}$$

being $\dot{\lambda}_p$ and $\dot{\lambda}_d$ the plastic and damage multiplier, respectively.

In the present study the elasto-plastic convex domain is defined by the intersection of the classical Mohr-Coulomb bilinear function with a tension cut-off:

$$\Phi_{p1}\left(\boldsymbol{\sigma}^c, \chi_p\right) = \left|\boldsymbol{\tau}^c\right| + \sigma^c \tan\varphi - c_0\left(1-\chi_p\right) \tag{29}$$

$$\Phi_{p2}\left(\boldsymbol{\sigma}^c, \chi_p\right) = \sigma^c - \sigma_0\left(1-\chi_p\right) \tag{30}$$

where $\boldsymbol{\tau}^c$ and σ^c are the tangential stress vector and the normal stress component of the contact stresses, φ is the friction angle, c_0 and σ_0 the cohesion and tensile strength of the virgin interfaces.

The two yield functions are depicted in Fig. 2. The following four zones can be distinguished:

I elastic zone: $\Phi_{p1} < 0, \quad \Phi_{p2} < 0$

II plastic activation in shear: $\Phi_{p1} = 0, \quad \Phi_{p2} < 0$

III plastic activation in tension: $\Phi_{p1} < 0, \quad \Phi_{p2} = 0$

IV plastic activation in tension and shear (corner): $\Phi_{p1} = 0, \quad \Phi_{p2} = 0$.

The damage activation function is linear and the first activation occurs when the thermodynamic force reaches the relative threshold value ζ_0:

$$\Phi_d\left(\zeta, \chi_d\right) = \zeta - \zeta_0\left(1-\chi_d\right) \tag{31}$$

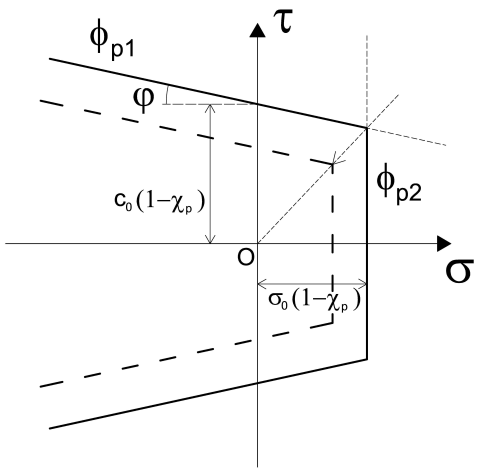

Figure 2. Plastic yield conditions represented in the stress space.

4. Numerical applications.

The interphase model presented in Sections 2 and 3 has been implemented in an open-source research-oriented finite element analysis program for 2D applications. With the aim to run a step-by-step integration, flow rules given in rate form were rewritten as discrete laws. The implicit backward-Euler difference method was applied to obtain results within the time step

$[t_n, \ t_{n+1}] \subset [0, \ T]$. In particular the nonlinear solution at time t_{n+1} has been calculated by means of an elastic prediction – plastic and/or damaging correction procedure. The interphase element has four nodes and zero-thickness. The integration of the stiffness matrix has been solved by applying the Reduced Selective Integration method, that is two Gauss are used for the integration in the direction normal to the interphase plane while one Gauss point is used in the tangential one.
The numerical applications presented in this work regard uniaxial compression and diagonal compression tests on masonry specimens. All numerical examples have been carried out under the hypothesis of plane stress state.

4.1. Uniaxial compression tests on masonry.

Uniaxial compression tests have been carried out to assess the performance of the interphase element. A brick-mortar-brick system uniformly compressed (Fig. 3) has been considered with the aim to show the formation of damage in the bulk material when the stiffness of the bricks is lower than that one of mortar. In this case, in fact, the bricks tend to expand more than the mortar in the horizontal direction because of the Poisson effect, but the higher stiffness of the mortar opposes to this displacement. The bricks are therefore subjected to compressive stresses while the mortar to tensile ones along the x-axis.

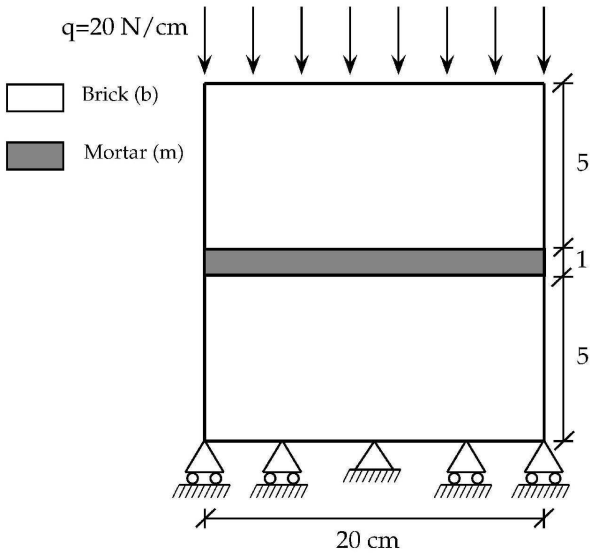

Figure 3. Uniaxial compression test on a masonry block.

The parameters used for tests are reported in Table 1, while the results are shown in Fig. 4. The numerical test has been performed under displacement control. In this paper the results obtained with a load multiplier equal to 3 and for a FE model with 80 interphase elements are reported in terms of stresses along the mortar layer.

Table 1. Parameters used for compression test.

E_{brick}	500 MPa	ν_{brick}	0.3
E_{mortar}	15000 MPa	ν_{mortar}	0.2
c_0	4.5 MPa	φ	30°
σ_0	1.0 MPa	h_p	1
ζ_0	0.001 MPa	h_d	0.0025 MPa

The diagrams depicted in Fig. 4 clearly show the points were the damage nucleation takes place. The first fracture forms in the middle of the layer and grows during the following steps. As a consequence, a redistribution of stresses takes place in the two parts on sides of the fracture. When the thermodynamic force in another Gauss point or group of Gauss points overcomes the threshold value a new fracture appears symmetrically with respect to the middle of the mortar joint. On the other hand, while σ_x stresses suddenly fall down and tend to zero, the σ_z values are little influenced by fracture. This is due to the fact that damage affects only internal and mixed terms of the free energy.

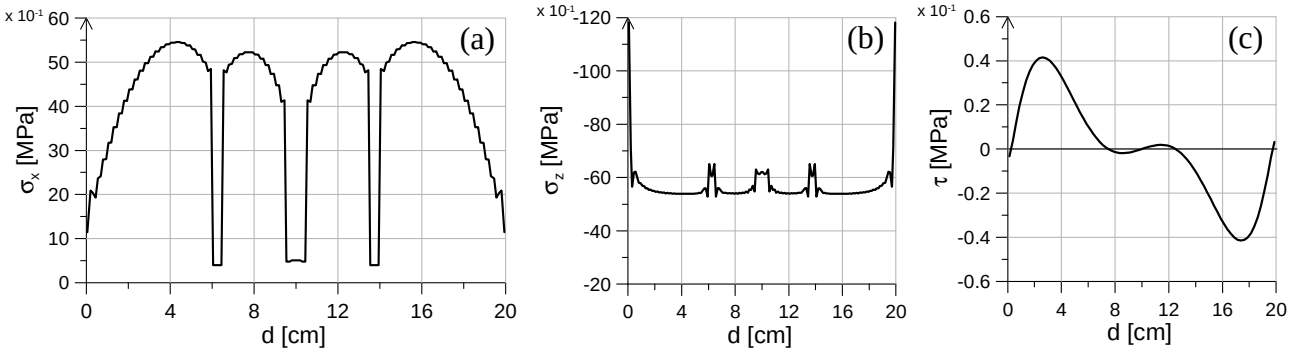

Figure 4. Uniaxial compression test on a masonry block: results at a load multiplier equal to 3. (a) normal stresses along x-axis; (b) vertical stresses; (c) tangential stresses.

4.2. Diagonal compression tests on masonry.

Diagonal compression numerical tests have been carried out on a masonry panel and compared with the experimental results obtained in laboratory. With reference to Fig. 5, the specimen is made up of four courses of sandstone blocks with calcium-cement mortar. It has a squared shape with a length of 67 cm for each side. A single block is 33 cm long and 16 cm high. The mortar layer has a thickness of 1 cm. A total number of 256 plane stress 2D solid elements and 72 interphase elements has been used to create the finite element model.

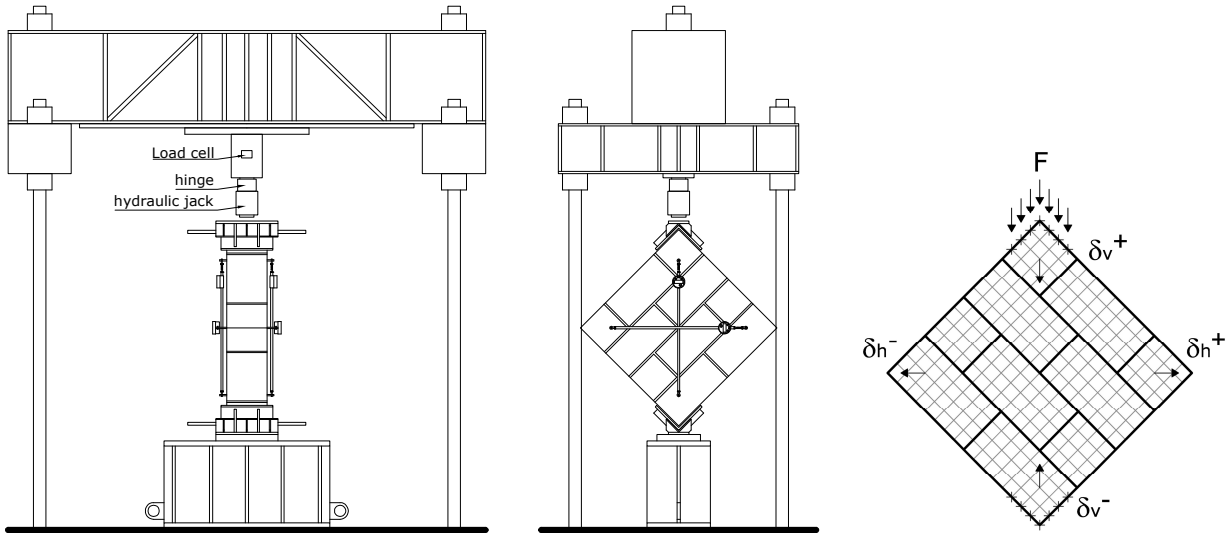

Figure 5. Diagonal compression test on a masonry panel. Experimental setup and finite element model.

The mechanical variables for blocks and mortar and the parameters used for the finite element model are reported in Table 2.

Table 2. Parameters used for diagonal compression test.

E_{brick}	11141.67 MPa	ν_{brick}	0.25
E_{mortar}	37000 MPa	ν_{mortar}	0.14
c_0	5.0 MPa	φ	35°
σ_0	1.0 MPa	h_p	0.04
ζ_0	$1 \cdot 10^{-5}$ MPa	h_d	0.001 MPa

The test has been run with 400 steps under displacement control. At each step the values of the total vertical load F and the displacement discontinuities $\delta h = \delta h^+ + \delta h^-$ and $\delta v = \delta v^+ + \delta v^-$, in horizontal and vertical direction respectively, have been evaluated and reported in the load-displacement curves of Fig. 6. A good agreement has been obtained with experimental results.

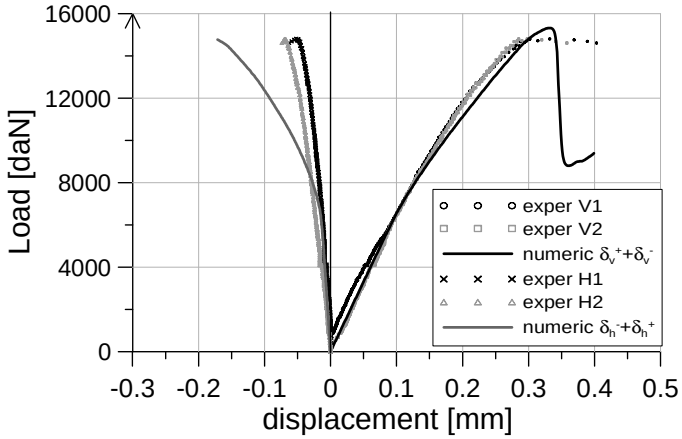

Figure 6. Load-displacement curves: comparison between numerical and experimental results.

Fig. 7 finally shows a comparison between the collapse experimental and numerical configurations. A very good agreement can be observed, even if the numerical model is not able to simulate the fracture inside the blocks because an elastic behavior was chosen for bricks.

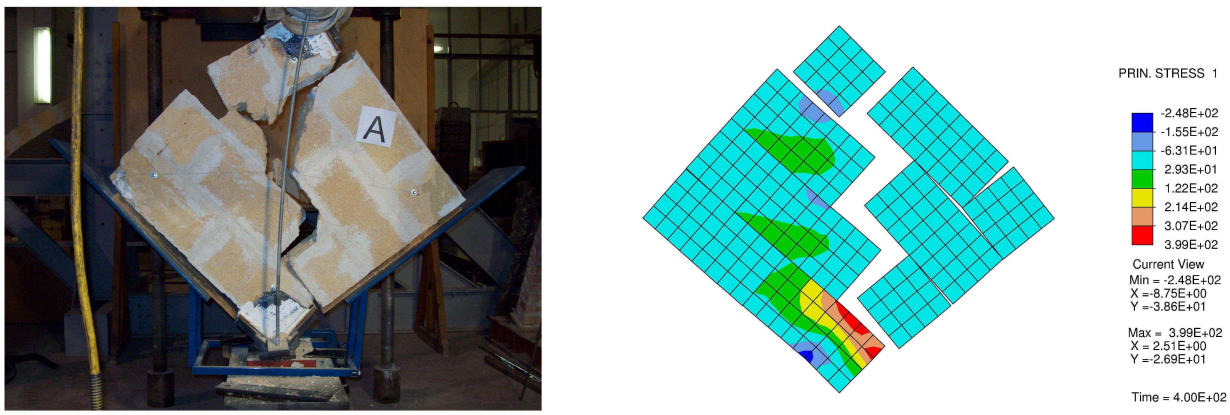

Figure 7. Comparison between numerical and experimental collapse configurations.

5. Conclusions.

The present paper deals with the mesomodelling of heterogeneous structures by means of interphase elements, that can be considered as an enhancement of the common interface elements. The possibility to distinguish internal and external contact stresses and strains permits to introduce separate failure conditions for the bulk material and for contact tractions. In particular an isotropic

damage model has been used to model the nonlinear response of the bulk material, while an elastoplastic bilinear domain governs the evolution of plasticity for contact tractions. The interphase model has been written in the framework of a thermodynamically consistent theory. State equations and flow rules have been derived and rewritten in a discrete form to be suitable to be used for finite element implementation. Two numerical applications on masonry structural elements have been conducted. In particular a compression test and a diagonal test have been carried out.
Ongoing and future efforts are devoted to the introduction of plastic activation functions on the physical interfaces between mortar and block, and to the possibility to introduce a new damage model to catch horizontal fractures also.

Acknowledgements

The authors acknowledge the financial support given by the Italian Ministry of Education, University and Research (MIUR) under the PRIN09 project 2009XWLFKW_005 , “A multiscale approach for the analysis of decohesion processes and fracture propagation”.

References

[1] G. Giambanco, S. Rizzo, R. Spallino, Numerical analysis of masonry structures via interface models. Comput. Methods Appl. Mech. Engrg., 190 (2001) 6493-6511.
[2] G. Alfano, E. Sacco, Combining interface damage and friction in a cohesive-zone model. Int. J. Numeric. Methods Engrg., 68 (2006) 542-582.
[3] I. Einav, G. T. Houlsby, G. D. Nguyen, Coupled damage and plasticity models derived from energy and dissipation potentials. Int. J. Solids Struct., 44 (2007) 2487-2508.
[4] M. R. Salari, S. Saeb, K. J. William, S. J. Patchet, R. C. Carrasco, A coupled elastoplastic damage model for geomaterials. Comput. Methods Appl. Mech. Engrg., 193 (2004) 2625-2643.
[5] P. B. Lourenco, J. Rots, Multisurface interface model for analysis of masonry structures. Journal Engrg. Mech., 123 (7) (1997) 660-668.
[6] A. Spada, G. Giambanco, P. Rizzo, Damage and plasticity at the interfaces in composite materials and structures. Comput. Methods Appl. Mech. Engrg., 198 (2009) 3884-3901.
[7] G. Alfano, M. A. Crisfield, Finite element interface models for the delamination analysis of laminated composite: mechanical and computational issues. Int. J. Numer. Meth. Engrg., 50 (2001) 1701-1736.
[8] K. William, I. Rhee, B. Shing, Interface damage model for thermomechanical degradation of heterogeneous materials. Comput. Methods Appl. Mech. Engrg., 193 (2004) 3327-3350.
[9] H. R. Lofti, P. B. Shing, Interface model applied to fracture of masonry structures. J. Struct. Eng. (ASCE), 120 (1) (1994) 63-80.
[10] F. Parrinello, B. Failla, G. Borino, Cohesive-frictional interface costitutive model. Int. J. Solids and Structures, 46 (2009) 2680-2692.
[11] G. Giambanco, Z. Mroz, The interphase model for the analysis of joints in rock masses and masonry structures. Mechanica, 36 (1) (2011) 111-130.
[12] G. Giambanco, G. Fileccia Scimemi, A. Spada, The interphase element. Comp. Mech., 50 (3) (2012) 353-366.
[13] E. Sacco, F. Lebon, A damage-friction interface model derived from micromechanical approach. Int. J. Solids and Structures, 49 (26) (2012) 3666-3680.

The damage evolution of 2D-Woven-C/SiC composite under tension loading

Min-ge Duan[1,2], Fei Xu[1,*], Zhong-bin Tang[1]

[1] School of Aeronautics, Northwestern Polytechnical University, Xi'an, 710072, China
[2] State Key Laboratory of Explosion Science and Technology, Beijing Institute of Technology, Beijing, 100081, China
* Corresponding author: fay.xu@nwpu.edu.cn

Abstract A meso-numerical model is set up to investigate the damage evolution of 2D woven C/SiC based on RVE(representative volume element) because the woven composite has a periodic in-plane structure. Periodic boundary conditions are imposed to the model. Three material models for the fibers, the matrix, and the yarn/matrix interface are considered. Basic damage modes and their evolutions are observed in the simulation. Firstly, the matrix is damaged at the global applied stress around 50Mpa, which agrees well with the tests. The stress/strain relation obtained from the meso-numerical model can represent the behavior of the 2D woven C/SiC under tension loading. Secondly, the void in the matrix plays an important role. The bundle/matrix interface is essential to investigate the interface debonding.
Keywords 2D-C/SiC composites, RVE, damage mechanisms

1. Introduction

C/SiC, as one of the most promising high temperature structural materials for its performance, such as low coefficient of thermal expansion, excellent thermal shock resistance, abrasion resistance, and high specific strength/modulus, has been applied in structures such as air-breathing engines, hot-gas valves and aerospace thermal structures. Consequently, the mechanical properties of the C/SiC has been an active research field for several decades. Both experimental studies and macro- or micromechanical methods have been used to obtain the mechanical properties of the C/SiC[1-13,20].

In experimental studies, the mechanical characterization of the C/SiC were studied by classical strain measurements, ultrasonic method, AE(acoustic emission) technique , infrared thermography and microstructural observations under the load of uniaxial tension[1-6], compression[1,5], in-plane shear[7], tension fatigue[8,9], thermal fatigue[10,11] and low-velocity impact[12]. Based on the expensive experiments, the damage modes found by microstructural observations are: matrix cracking, transverse bundle cracking, bundle/matrix and inter-bundle debonding, fiber cracking, ply delamination, bundle splitting and matrix wear. The damage evolution or development mention in the former studies are all deduced from the possible damage modes, which can only reflect the overall damage event and the detailed mechanical behavior of the constituents identification is beyond the detection. Fortunately, it is possible to identify detailed mechanical behavior of the constituents in FEM. However, there is not so much study on C/SiC with simulation method as experiment method. The prediction of the stiffness tensor has been carried out with FEM[13]. While, little work was done on the prediction of damage evolution and the strength[4].

Recently, simulation of plain woven fabrics based on photomicrograph measurement and idealized sinusoidal representation of the weave structure has been successfully applied to determine their mechanical properties by taking the advantages of their inherent periodicity of woven fabric architecture[14-19] at mesoscale in-plane. Both elastic moduli [14,15], damage[16] and fracture[18] behavior of the woven fabrics have been successfully predicted for the case of two-phase heterogeneous materials without considering the fiber-matrix interface using FEM by RVE (representative volume elements). While, it has been confirmed that interface obviously has great

influence on the macroscopic behavior, the toughness and strength of CMCs[20]. Interfaces are very narrow regions between matrix and fibers and are responsible for a variety of key properties, because of its significance role of stress transfer between fibers and matrix[20-23]. Recently, CZM(cohesive zone model) is being increasingly used in describing interfacial debonding and separation[23]. It was first proposed to analyze brittle fracture, and developed to model debonding of inclusions, crack growth processes in elastic-plastic solids, delamination process in composites subjected to low velocity impacts and so on. It is not so easy to simulate the bundle/matrix interface, because the mechanical properties of the interface is very difficult to obtain and the geometry of the interface in woven fabrics is curved surface.

The aim of the present contribution is to introduce the interface into the RVE model in terms of CZM, and to analyze the damage evolution in 2D woven C/SiC with the damage behavior of different constituents identified clearly. This paper is organized as follows: firstly, the geometry model and boundary conditions are presented. Next, the meso-model was outlined with the description of material models of matrix, fiber yarns and interface-matrix interface. Then, the damage of different constituents was predicted based on elastic model. In the last but one section, the damage initiation and evolution are described with different damage modes identified. Finally, conclusions are summarized in the final sections.

2. RVE and periodic boundary conditions

2D woven C/SiC is plain weave fabrics, which are formed by weaving of yarns, as shown in Fig. 1. The black yarn are in X(longitudinal) direction and the grey yarn are in Z(transverse) direction.

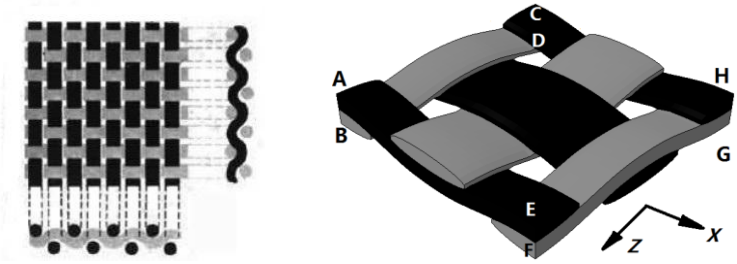

Figure 1. Sketch of 2D plain weave single lamina(left) and its RVE without matrix(right)

In order to modeling the fabric-reinforced laminates using FEM, the representative volume elements (RVE) of the respective configurations are chosen. The RVE is the repeated element that can represent the whole composite fabric structure by a periodical array. Then characteristics of the macrostructure composites can be represented by the RVE with a certain proper boundary conditions. And the data points are fit to a sinusoidal function of the form[15]:

$$f(x) = a\sin(bx + c) + d \qquad (1)$$

where, a, the amplitude of the yarn curve is 0.125mm; b=2π /1.8≈3.49, and 1.8 is the pitch of the yarn path curve in millimeters; d, the offset depicted is ±0.125mm; c is the phase adjusting factor.

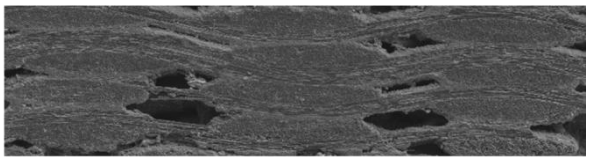

Figure 2. The photomicrograph of the 2D plain weave C/SiC

Fig. 2. is the photomicrograph of the 2D plain weave C/SiC by SEM. According to the micrograph the geometry of the fiber yarns is determined, AB=0.25mm, AE=AD=1.8mm, with the woven hole in the square of 0.2mm×0.2mm.

The periodic boundary conditions meets the requirement of displacement periodicity and continuity of the proper boundary conditions, which implies that no separation or overlap will be found between neighboring of RVEs. Each RVE in the composites has the same deformation mode. As stated by Z.Xia[18], the periodic conditions on the boundary ∂V is

$$u_i = \bar{\varepsilon}_{ik} x_k + u_i^* \tag{2}$$

where, $\bar{\varepsilon}_{ik}$ are the average strains, u_i^* is the periodic part of the displacement components on the boundary surfaces and it is related to the applied global loads. Aboudi has developed a unified micromechanical theory based on the study of interacting periodic cells, and its boundary conditions, plane-remains-plane, were applied to the RVE models in the normal traction loading conditions.

Now based on these the proper boundary conditions are the planes ABFE and CDGH keeps plane during the loading in x direction on EFHG plane. The ABCD plane keeps zero displacement in X direction. And to avoid the rigid motion, the displacement components of the center point of the ABCD plane are assumed to be zero.

3. The meso-model

In the model, RVE that used to investigate the 2D woven C/SiC under tension loading, is shown in Fig. 3. The matrix, fiber and the yarn/matrix interface are taken into account with their specific damage behavior.

(a) Matrix (b) Interface (c) Fiber bundles

Figure 3. The RVE model and its constituents

3.1. Matrix

The elastic constants for the matrix material SiC: Young's modulus E, Poisson's ratio v are found to be E=430Gpa, v=0.3. The brittle cracking material constitutive in ABAQUS is chosen to describe the damage and failure behavior of the isotropic brittle matrix. The failure stress and displacement are 200Mpa and 0.02mm, respectively. In order to consider void in matrix, the elastic constants is assumed to reduced to 10% of the original matrix, and the model with void is shown in Fig. 3(a), the small squares in the RVE is the void region.

3.2. Fiber yarns

The fiber bundles in C/SiC is regarded as transverse isotropic materials. And the properties are listed in Table 1.

Table 1. The mechanical properties of the fiber yarns

E_1(Gpa)	E_2(Gpa)	v_{12}	v_{23}	G_{12}(Gpa)	G_{23}(Gpa)	σ_f(Mpa)	ε_f
220	13.8	0.2	0.18	9	4.8	800	1.5%

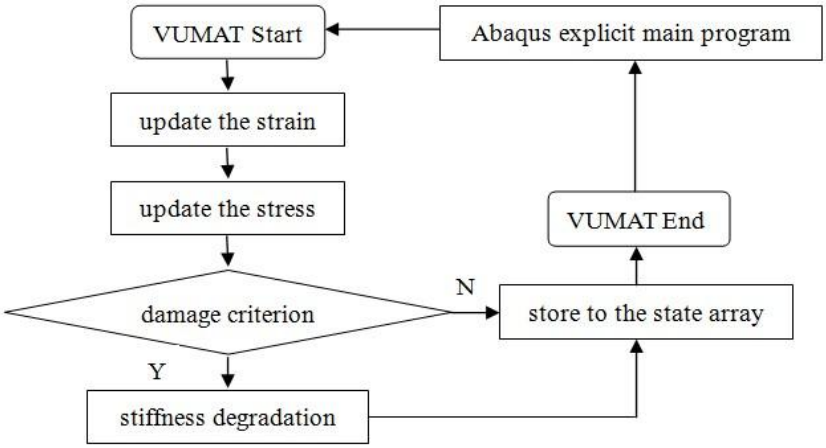

Figure 4. The flow chart for the VUMAT

To study the damage process, the damage model is introduced to the fiber yarns with VUMAT by Fortran, and the flow chart is shown in Fig. 4. Here the maximum stress criterion and linear stiffness degradation are chosen as the damage initiation criterion and damage evolution law of the fiber yarns.

3.3. Yarn/matrix interface

The interface zone plays a key role in the mechanical behavior of composite materials. Its properties can be influenced by different fiber coatings such as PyC, BN or SiC and its thickness. And the most important mechanism for improving the toughness of CMCs is the crack deflection along the interface after the initiation of the matrix cracking. In this meso-level FEM model, the inner-yarn interface is not considered, and fiber bundles is simplified as transversely isotropy.
In this work, bilinear models both for normal and tangential separation is used to simulate the response of the yarn/matrix interfacial zone. The curve of normal and tangential tractions with respect to δ_n and δ_t are shown in Fig.5, where σ_{max} and τ_{max} are the interface normal and tangential strength, are 200Mpa and 150Mpa respectively; δ_{max} is the interface characteristic length parameter; δ_n and δ_t denote the non-dimensional normal and tangential displacement respectively.

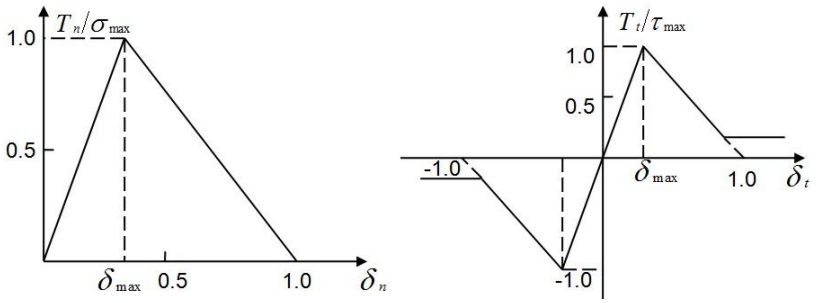

Figure 5. The curve of normal(left) and tangential(right) tractions with respect to δ_n and δ_t

In the FE model, CZM was realized by either cohesive element or cohesive behavior and maximum stress criterion was used to predict the damage initiation in Abaqus/explicit, and detailed constitutive model for the CZM can be found in the help documentation[24].

4. The result analysis

4.1. The mesh sensibility and validation

Firstly, in order to get accurate results, the mesh sensibility was studied with mesh size 10um, 30um and 50um in the quarter model. The result of the overall force-displacement response and the mises contour are shown in Fig.6. The overall force-displacement response shows very small difference. The mises contour pictures corresponding to the loading of 1.12×10^{-3}mm for 10um, 30um and 50um are listed from left to right(white means 0Mpa, and black grey means 200Mpa, and black means exceeding 200Mpa), the maximum stress in matrix is between 203.3Mpa and 208.7Mpa, while it is 250.8Mpa and 273.1Mpa for the yarns, which shows little difference. So, 50um was accepted for its time-efficiency.

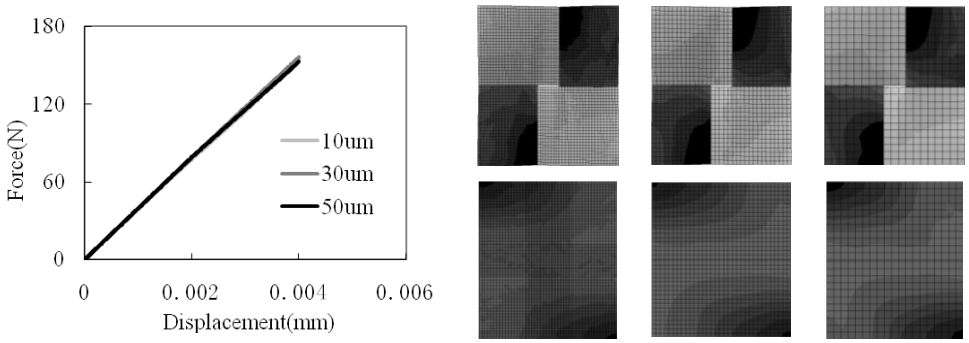

(a) Overall force-displacement (b) The mises contour

Figure 6. The effect of mesh size

The prediction of the elastic modulus is about 75Gpa. And the elastic modulus from experiments is almost between 70Gpa[10,11] and 81.2Gpa[3]. Furthermore, the damage in RVE initiates at the stress about 53Mpa in the matrix, which agrees well with the initial proportional limit of the composites[3], around 50Mpa.

4.2. The damage prediction

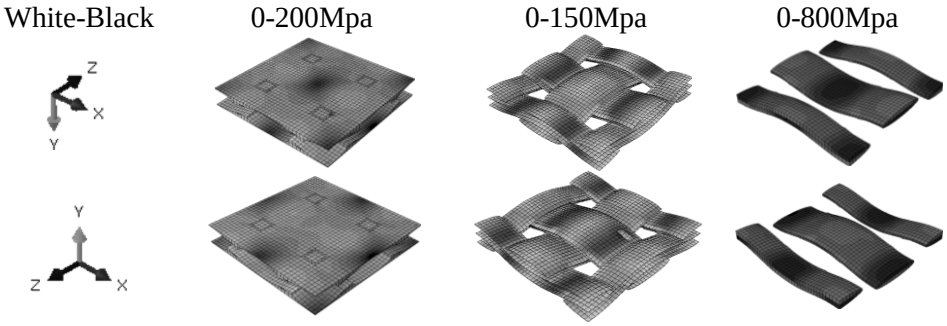

Figure 7. The mises contour of matrix(5th step)/interface/fibers(37th step)

From the elastic RVE model, the matrix is probably damaged first at the thinnest region that close to the yarns, the damage of the yarns will initiate at the woven point, and the interface is easy to get damaged at the region of woven edge, shown in black in Fig. 7.
When the stress in matrix reaches the strength, the average stress in the RVE is about 53Mpa. When the stress in the yarns reaches the strength, the average stress in the RVE is about 330Mpa,

corresponding to strain about 0.005 in Fig. 8 of the grey curve, higher than the failure stress of the composites, which indicates the limitation of the elastic model. So the damage models are introduced to the constituents of the C/SiC, and the corresponding stress-strain curve compared with no damage model is shown in Fig .8. The detailed damage process of the three constituents are shown in subsequent sections.

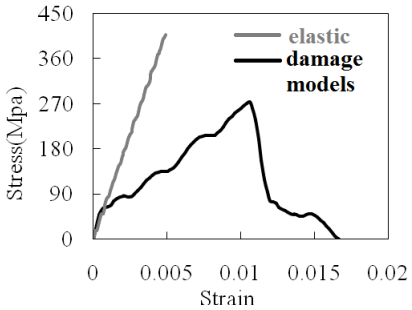

Figure 8. The stress-strain curve

4.3. The matrix damage evolution

The brittle cracking was introduced to matrix for its brittleness in fracture process. Fig. 9 shows the damage initiation and propagation process of the matrix in terms of STATUS, which represents the state of the element (1.0 means the element is active, shown in white; and 0.0 means the element is inactive, shown in black). It is found that the damage first occurs at the thinnest region close to the yarns in loading directions as predicted in the elastic model. In the upper(Y+) matrix, the damage initiates at the edge center of the RVE, while in the lower(Y-) matrix, it initiates at the center of the RVE. Then, the damage propagates in Z direction, vertical to loading. And the damage first runs through the Z direction in the lower matrix at the strain of 2200$\mu\varepsilon$, while it happens to the upper matrix at the strain of 2600$\mu\varepsilon$. The damage has already run through the cross section of the RVE at the strain of 2600$\mu\varepsilon$.

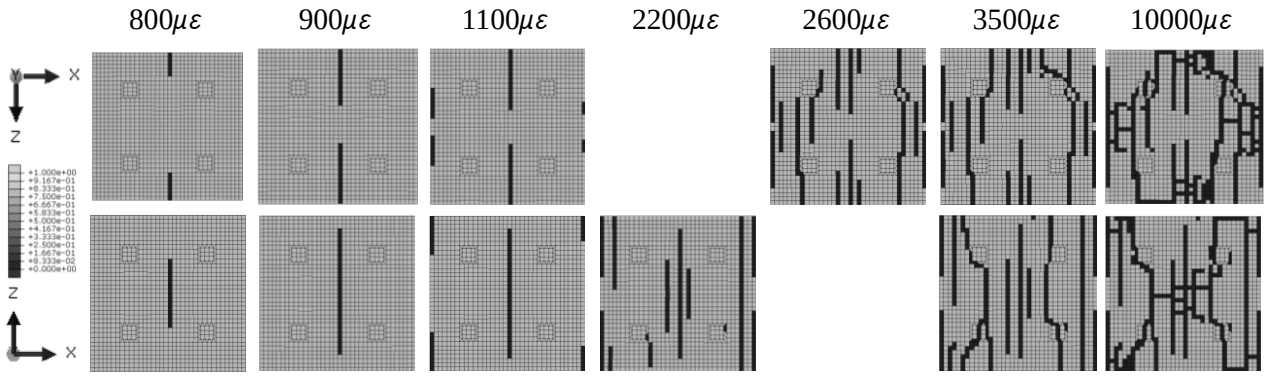

Figure 9. The damage process of the matrix

4.4. The fiber damage evolution

The simulation of fiber damage was introduced by VUMAT in Abaqus, which aims at investigating the possible damage process of fiber bundle damage. Fig. 10 shows the damage initiation and propagation process of the matrix in terms of STATUS. It is found that the damage first occurs at the weaving center of the yarns in loading directions as predicted in the elastic model. Then, the damage propagates in Z direction, vertical to loading. And the damage first runs through the Z direction in longitudinal yarns at the strain of 5800$\mu\varepsilon$, while it happens to the center yarns in

longitudinal at the strain of 6000$\mu\varepsilon$.

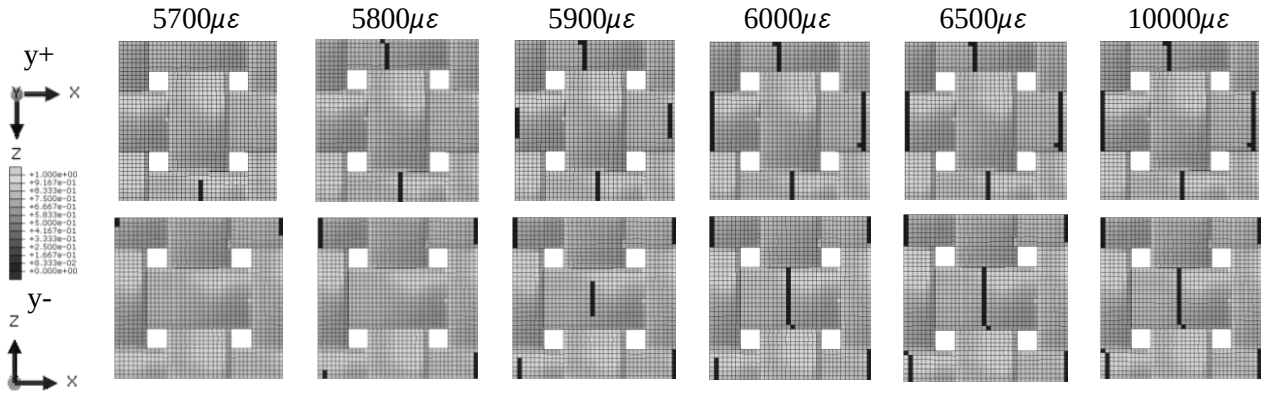

Figure 10. The damage process of the fiber bundle

4.4. The yarn/matrix interface damage evolution

The CZM was introduced to the RVE by cohesive element in Abaqus, which aims at investigating the possible damage process of yarn/matrix interface.

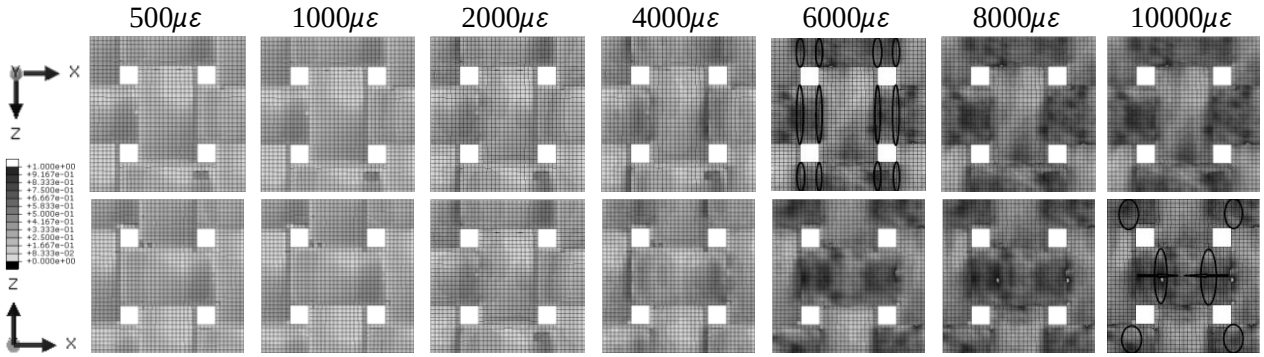

Figure 11. The damage process of the interface

Fig. 11 shows the damage initiation and propagation process of the interface in terms of MAXSCRT(0.0 means no damage occurs, shown in white grey; and 1.0 corresponding to failure, shown in black grey). It is found that the damage initiates at the weaving edge of the interface around the yarns in longitudinal direction as shown in the MAXSCRT contour of 6000$\mu\varepsilon$, then it spread to the weaving point of the RVE in longitudinal(X) direction, marked with circles and arrows. The interface around yarns in transverse(Z) direction get damaged at the strain of 10000$\mu\varepsilon$, later than it in longitudinal direction.

4.6. The effect of the void in matrix

The porosity in C/SiC may have great influence on the damage initiation, evolution. So, the RVE with void in matrix is investigated. From the photomicrograph of the 2D plain weave C/SiC, it can be found that the void in matrix is mainly around the weaving gap between yarns, so the mechanical properties of the matrix in this region, showing as four small rectangles in the matrix (the volume is about 6% of the whole volume of the RVE) is reduced to 10%. The result of the matrix damage evolution is shown below in Fig. 12. The damage of the matrix initiates around the void, which differs from the damage evolution in matrix without void compared with Fig. 8. And it is also found that the through damage in the model with void comes earlier than that without void. So the void in

matrix plays an important role in the damage evolution.

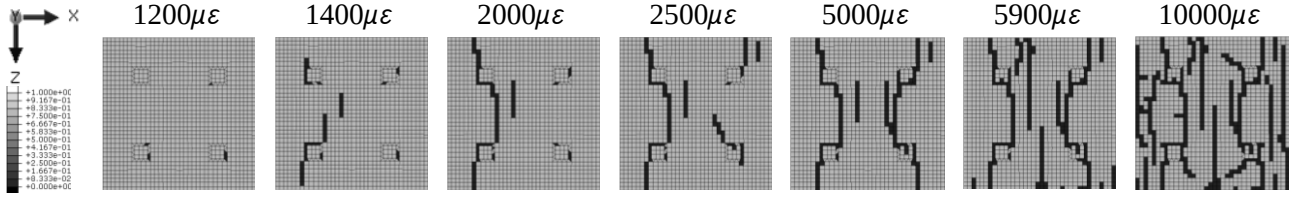

Figure 12. The damage process of the matrix with void

5. Conclusions

This paper focuses on the 2D plain woven C/SiC, and the conclusions are as follows:
1) The geometry model of RVE is established based on the photomicrograph of the 2D plain weave C/SiC by SEM with the yarn/matrix interface successfully introduced. And the damage models for the matrix, yarn/matrix interface and yarns are considered.
2) The established meso-level FEM is able to describe mechanical behavior of different constituents in the plain-woven C/SiC. Especially, the damage initiates in the matrix at the overall stress about 50Mpa, which agrees well with the experiments.
3) The damage of the matrix initiates near the void and spreads in transverse directions, and spreads through the section of the RVE; the damage of the fiber begins at the very region of the weaving point in longitudinal yarns and spreads in transverse direction; the damage of the yarn/matrix occurs near the weaving edge and spreads both in transverse and longitudinal directions.
4) The void in the matrix has great influence on the damage initiation and evolution of the matrix in the RVE model. It is found that the damage of the matrix without void initiates near the yarn in Z direction at the thin region of the matrix, while the damage of the matrix with void initiates around the void.

Acknowledgements

This work is supported by the Open Foundation provided by the State Key Laboratory of Explosion Science and Technology (KFJJ12-14M), the Natural Science Foundation of China (90916027), and the Natural Science Fund for Young Scholars of China (11102168).

References

[1] C. Gerald, G. Laurent, B. Stephane, Development of damage in a 2D woven C/SiC composite under mechanical loading: I. mechanical characterization. Composites Science and Technology, 56 (1996) 1363–1372.
[2] E.B. Rachid, B. Stephane, C. Gerald, Development of damage in a 2D woven C/SiC composite under mechanical loading: II. ultrasonic characterization. Composites Science and Technology, 56 (1996) 1373–1382.
[3] M. Hui, L.F. Cheng, L.T. Zhang, Y.D. Xu, Z.X. Meng, C.D. Liu, Damage evolution and microstructure characterization of a cross-woven C/SiC composite under tensile loading. Journal of the Chinese ceramic society, 35 (2007) 137–143. (in Chinese)
[4] C.P. Yang, G.Q. Jiao, B. Wang, Tensile damage behavior of 2D-C-SiC composite. Journal of Aeronautical Materials, 30 (2010) 87–92. (in Chinese)
[5] G.Y. Guan, G.Q. Jiao, Z.G. Zhang, Uniaxial macro-mechanical property and failure mode of a 2D-woven C/SiC composite. Acta Material Composite Sinica, 22 (2005) 81–86. (in Chinese)
[6] M.D. Wang, C. Laird, Characterization of microstructure and tensile behavior of a cross-woven C-SiC composite. Acta mater, 44 (1996) 1371–1387.

[7] G.Y. Guan, G.Q. Jiao, Z.G. Zhang, In-plane shear fracture characteristics of plain-woven C/SiC composite. Mechanical Science and Technology, 24 (2005) 515–521.(in Chinese)
[8] M.D. Wang, C. Laird, Tension-tension fatigue of a cross-woven C/SiC composite. Material Science and Engineering, A230(1997) 171–182.
[9] C.D. Liu, L.F. Cheng, X.G. Luan, B. Li, J. Zhou, Damage evolution and real-time non-destructive evaluation of 2D carbon-fiber/SiC-matrix composites under fatigue loading. Material Letters, 62 (2008) 3922–3924.
[10] M. Hui, L.F. Cheng, L.T. Zhang, X.C. Luan, J. Zhang, Behavior of two-dimensional C/SiC composites subjected to thermal cycling in controlled environments. Carbon, 44 (2006) 121–127.
[11] M. Hui, L.F. Cheng, Damage analysis of 2D C/SiC composites subjected to thermal cycling in oxidizing environments by mechanical and electrical characterization. Material Letters, 59 (2005) 3246–3251.
[12] L.J. Yao, Z.S. Li, Y.Q. Cheng, X.Y. Tong, Damage behavior of 2D C/SiC composites under low velocity impact. Journal of Inorganic Materials, 25(2010)311-314. (in Chinese)
[13] Y.J. Chang, Study on damage constitutive model and mechanical properties of C/SiC composite. PhD thesis, Northwestern Polytechnical University, Xi'an, 2008. (in Chinese)
[14] E.J. Barbero, J. Trovillion, J.A. Mayugo, K.K. Sikkil, Finite element modeling of plain weave fabrics from photomicrograph measurement. Composites Structures, 73 (2006)41–52.
[15] E.J. Barbero, T.M. Damiani, J. Trovillion, Micromechanics of fabric reinforced composites with periodic microstructure. International Journal of Solids and Structures, 42 (2005) 2487–2504.
[16] E.J. Barbero, P. Lonetti, K.K. Sikkil, Finite element continuum damage modeling of plain weave reinforced composites. Composites: Part B, 37 (2006)137–147.
[17] H. Ismar, F. Schroter, F. Streicher, Modeling and numerical simulation of the mechanical behavior of woven SiC/SiC regarding a three-dimensional unit cell. Computational Materials Science, 19 (2000) 320–328.
[18] S.I. Haan, P.G. Charalambides, M. Suri, A specialized finite element for the study of woven composites. Computational Mechanics, 27 (2001) 445–462.
[19] Z. Xia, Y. Zhang, F. Ellyin, A unified periodic boundary conditions for representative volume elements of composites and applications. International Journal of Solids and Structures, 40 (2003) 1907–1921.
[20] J.F. Despres, M. Monthioux, Mechanical properties of C/SiC composites as explained from their interfacial features. Journal of the European Ceramic Society, 15 (1995) 209–224.
[21] R.R. Naslain, The design of the fiber-matrix interfacial zone in ceramic matrix composites. Composites: Part A, 29A (1998) 1145–1155.
[22] P.C. Yang, G.Q. Jiao, Effects of interface on tensile properties of fiber reinforced ceramic matrix composite. Acta Material Composite Sinica, 27 (2010) 116–121. (in Chinese)
[23] N. Chandra, H. Li, C. Shet, H. Ghonem, Some issues in the application of cohesive zone models for metal-ceramic interfaces. International Journal of Solids and Structures, 39 (2002) 2827–2855.
[24] ABAQUS documentation.

Structure of micro-crack population and damage evolution in concrete

Andrey P Jivkov[1,*]

[1] School of Mechanical, Aerospace and Civil Engineering, The University of Manchester, Manchester M13 9PL, UK
* Corresponding author: andrey.jivkov@manchester.ac.uk

Abstract Tensile behaviour of concrete is controlled by the generation and growth of micro-cracks. A 3D lattice model is used in this work for generating micro-crack populations. In the model, lattice sites signify solid-phase grains and lattice bonds transmit forces and moments between adjacent sites. The meso-scale features generating micro-cracks are pores located at the interfaces between solid-phase grains. In the model these are allocated to the lattice bonds with sizes dictated by an experimentally determined pore size distribution. Micro-cracks are generated by removal of bonds when a criterion based on local forces and pore size is met. The growing population of micro-cracks results in a non-linear stress-strain response, which can be characterised by a standard damage parameter. This population is analysed using a graph-theoretical approach, where graph nodes represent failed bonds and graph edges connect neighbouring failed bonds, i.e. coalesced micro-cracks. The evolving structure of the graph components is presented and linked to the emergent non-linear behaviour and damage. The results provide new insights into the relation between the topological structure of the population of micro-cracks and the macroscopic response of concrete. They are applicable to a range of quasi-brittle materials with similar dominant damage mechanisms.

Keywords Concrete porosity; Lattice model; Cracking graphs; Macroscopic damage

1. Introduction

The mechanical behaviour of quasi-brittle materials, such as concrete, graphite, ceramics, or rock, emerges from underlying microstructure changes. At the engineering length scale it can be described with continuum constitutive laws of increasing complexity combining damage, plasticity and time-dependent effects [1-4]. In these phenomenological approaches the damage represents reduction of the material elastic constants. From the microstructure length scale perspective damage is introduced by the nucleation and evolution of micro-cracks. While the population of micro-cracks formed under loading could be sufficiently well captured by various continuum damage models, the latter cannot help to understand the effects of the population on other important physical properties of the material. In many applications the quasi-brittle materials have additional functions as barriers to fluid transport via convection/advection and/or diffusion. It is therefore important to take a mechanistic view on the development of damage by modelling the evolution of micro-crack population, which can inform us about changes in the transport properties. Such a mechanistic approach needs to account for the material microstructure in a way corresponding to the mechanism of micro-crack formation [5]. Micro-cracks typically emerge from pores in the interfacial transition zone between cement paste and aggregate in cement-based materials [6].

Discrete lattice representation of the material microstructure seems to offer the most appropriate modelling strategy for analysis of micro-crack populations. This is a meso-scale approach, where the material is appropriately subdivided into cells and lattice sites are placed at the centres of the cells. Discrete lattices allow for studies of distributed damage without constitutive assumptions about crack paths and coalescences that would be needed in a continuum finite element modelling. The deformation of the represented continuum arises from the interactions between the lattice sites. These involve forces resisting relative displacements and moments resisting relative rotations between sites. Two conceptually similar approaches have been proposed to link local interactions to continuum response. In the first one, the local forces are related to the stresses in the continuum cell, e.g. [7, 8]. In the second one, the interactions are represented by structural beam elements, the stiffness coefficients of which are determined by equating the strain energy in the discrete and the

continuum cell, e.g. [9, 10]. In both cases explicit relations between local and continuum parameters can be established for regular lattices [11], but the only isotropic material that can be represented in 3D is a material with zero Poisson's ratio. A bi-regular lattice that can represent all materials of practical interest has been proposed recently [12]. This lattice, currently formed by beams clamped at sites, is used in the current work together with microstructure data for concrete obtained with X-ray computed tomography. Failure models based on microstructure data and the new lattice have been previously used for modelling tensile and compressive behaviour of cement [13] and the compressive behaviour of concrete under various complex loading conditions [14]. This work makes a step into developing our understanding of the micro-crack population and its relation to macroscopic damage.

Most of the work relating micro-crack populations to elastic moduli follows the fundamental paper [15], where analytical statistical derivation of the relation was provided. We follow the interpretation given in [16], in which the damage is measured as a relative change of the elastic modulus and related to micro-crack population via

$$D = 1 - \frac{E}{E(0)} = \frac{\beta}{N_T} \sum_{c \geq 1} c^3 N(c), \tag{1}$$

where c is some measure of micro-crack size, $N(c)$ is the number of micro-cracks of size c, N_T is the total number of sites capable of nucleating micro-cracks, and β is a scaling parameter reported as 0.47π for cracks in a 2D medium. Eq. (1) is our point of comparison for the simulations performed with the lattice model for various tensile loading cases. In the current work we are interested in testing the range of applicability of Eq. (1) and understanding the reasons for deviation from this rule, should such occur, by explicitly analysing the micro-crack population growth.

2. Model and method

2.1. The site-bond model

The lattice model used in this work is illustrated in Fig. 1. The unit cell, shown in Fig. 1(a) is a truncated octahedron – a solid with six square and eight regular hexagonal boundaries. The 3D space can be compactly tessellated using such cells, with each cell representing a material meso-scale feature, e.g. grain, in an average sense. This representation is supported by physical and statistical arguments [12]. A discrete lattice is formed by placing sites at the centres of the cells and connecting each site to its 14 nearest neighbours; example is shown in Fig. 4(b). The lattice contains two types of bonds. Bonds denoted by B_1 are normal to square boundaries and form orthogonal set. For convenience this set is coincident with the global coordinate system and B_1 are referred to as principal bonds. Bonds denoted by B_2 are normal to hexagonal boundaries. The hexagons lie on the octahedral planes with respect to the selected system, hence B_2 are referred to as octahedral bonds.

Figure 1. Lattice illustration: (a) Unit cell showing the site with 14 coordinating bonds: six principal, B_1, and eight octahedral, B_2; (b) Discrete lattice of beam elements.

If the spacing between sites in the principal directions is denoted by L, bonds B_1 have length $L_1 = L$, and bonds B_2 have length $L_2 = \sqrt{3}\ L\ /\ 2$. Presently, the bonds are represented by structural beam elements of circular cross sections, with R_1 and R_2 denoting the radii of beams B_1 and B_2, respectively. The beams are clamped at the lattice sites. The two types of beams have identical modulus of elasticity, E_b, and Poisson's ratio, ν_b. With this setup, it has been previously shown that by calibrating four parameters: R_1 / L, R_2 / L, E_b, and ν_b, the lattice can produce a large class of isotropic elastic materials with Poisson's ratios of practical interest [12]. The reference material in this work is a concrete with $E = 46$ GPa and $\nu = 0.27$, for which the calibration, assuming isotropic elasticity, yields $R_1 / L = 0.2$; $R_2 / L = 0.32$; $E_b = 90$ GPa; and $\nu_b = 0.4$ [14]. The commercial software Abaqus [17] with Euler-Bernoulli beam formulation has been used for the calibration and the analyses reported in this work. The behaviour of the beams is linear elastic.

2.2. Pore distribution and failure criterion

Microstructure data for the reference material was obtained using X-ray Computed Tomography as reported in [14]. The pore size distribution was obtained by segmentation of reconstructed 3D images. The studied regions of interest had dimensions of 1700 x 1200 x 1200 voxels with a voxel size of ca. 15 μm, allowing for a minimum detectable pore radius of ca. 15 μm. The number of pores measured experimentally was $n \approx 41500$. The measured pore radii, c_i, were used to construct a cumulative probability distribution (CPD) with standard median ranking, where for pore radii ordered as $c_1 \leq c_2 \leq \ldots \leq c_n$, the cumulative probability for pores with radii less than c_i is given by $F(c < c_i) = (i - 0.3) / (n + 0.4)$. The CPD for the reference material is shown in Fig. 2(a), where the minimum and maximum pore radii are also depicted. The CPD is used to assign pore sizes to the lattice bonds. For each bond a uniformly distributed random number $0 \leq r < 1$ is generated and the assigned pore radius is calculated from $c = F^{-1}(r)$. This ensures that the distribution of pore sizes in the model comes from the same population as in the experiment. A fragment of the model with distributed pores is given in Fig. 2(b). The cell size, L, is calculated such that the volume of all distributed pores divided by the volume of the cellular structure equals the material porosity, which is ca. 5% for the reference material. The pore sizes shown are to scale with the sketched cellular structure. With respect to the cellular structure pores reside at cell boundaries, i.e. interfaces between grains. The lattice bonds are also depicted (diameters not to scale) in order to show that pores reside at bond centres.

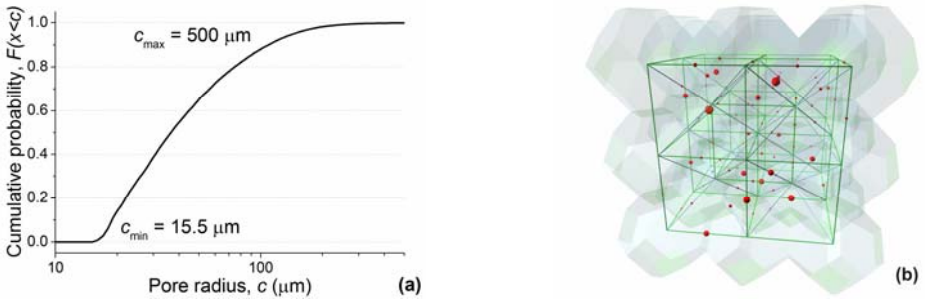

Figure 2. Pore distribution: (a) Cumulative probability of pore radii in the concrete; (b) Segment of model illustrating pores distributed to cell boundaries and corresponding. Pore sizes are to scale with the cell size.

Damage in the lattice model is introduced by removal of bonds. Propensity for bond failure is measured by the parameter

$$\Pi = \frac{N}{N_f} + \frac{|S|}{S_f} + \frac{|T|}{T_f} + \frac{|M|}{M_f}, \tag{2}$$

where N and S are the normal and shear forces in the beam; T and M are the twisting and bending moments; N_f, S_f, T_f, and M_f are critical values. N is positive for tension and negative for compression. S and M are obtained from the values in the two directions normal to the beam axis using the square root of squares rule. Eq. (2) provides an interaction between the different forces that allows for failure when $\Pi \geq 1$ under the combined action of normal and shear stresses [18, 14]. Taking only the first and fourth term was previously used in criteria with no account for shear, e.g. [19]. The second and third term allow for shear failure similarly to [10]. The failure parameters N_f, S_f, T_f, and M_f can be related [18]. For a beam of circular cross section of radius R, the tensile failure stress is $\sigma_f = N_f / (\pi R^2)$. The maximum bending stress is $\sigma_{max} = 4M / (\pi R^3)$, which equals σ_f when $M_f = N_f R / 4$. Similarly, the shear failure stress is $\tau_f = S_f / (\pi R^2)$. The maximum torsion stress is $\tau_{max} = 2T / (\pi R^3)$, which equals τ_f when $T_f = S_f R / 2$. Thus Π requires two material parameters: σ_f and τ_f. Noting that for quasi-brittle materials typically $1 \leq \tau_f / \sigma_f \leq 2$ [18], in this work $\tau_f = 2\sigma_f$ is used, representing more brittle materials.

The tensile failure strength of a bond, σ_f, is related to the size of the pore assigned to the bond. The relation used here is simpler than in the previous work [14] and based on the assumption that σ_f is the beam remote stress for which the average stress in the beam ligament outside the pore attains a critical value σ_0. Thus

$$\sigma_f = \sigma_0 \left[1 - \left(\frac{c}{R} \right)^2 \right], \tag{3}$$

where c and R are the pore and beam radii, respectively, and σ_0 can be interpreted as the tensile strength of the material without a defect. With this setup and the choice $\tau_f = 2\sigma_f$ the failure model requires a calibration of a single parameter, σ_0, against experimental stress-strain curve. However, since the beams behaviour is linear elastic, the choice of σ_0 would affect only the calculated macroscopic stresses but not the order in which damage (beam failures) would evolve in the system. Because the interest here is investigating the evolution of damage, σ_0 = 1 MPa is used for the calculations, noting that macroscopic stress response can be simply scaled by another value of σ_0.

2.3. Load cases and solution

A model of size ($20L$, $20L$, $20L$) was used. The lattice contained 17261 sites and 113260 bonds: 49260 B_1 and 64000 B_2. The coordinate system (X_1, X_2, X_3) was coincident with B_1, so that the boundary planes $X_1 = 0$, $X_1 = 20L$, $X_2 = 0$, $X_2 = 20L$, $X_3 = 0$, $X_3 = 20L$ contained 21×21 sites (nodes). Boundary conditions normal to each plane were only applied. Thus U_i and F_i denote displacements and forces of nodes on plane with normal X_i, while other displacements and rotations on this plane were unconstrained. Table 1 shows the conditions on planes $X_1 = 20L$, $X_2 = 20L$, and $X_3 = 20L$ for the analysed cases. Additionally, $U_1 = 0$ on $X_1 = 0$; $U_2 = 0$ on $X_2 = 0$; $U_3 = 0$ on $X_3 = 0$, apply to all.

Table 1. Boundary conditions for loading cases.
Values given in bold denote applied conditions. A stands for values obtained from finite element analyses.

Case	U_1	U_2	U_3	F_1	F_2	F_3	Note
C1	$\boldsymbol{d_1}$	A	A	A	**0**	**0**	Uniaxial unconfined extension
C2	$\boldsymbol{d_2}$	$\boldsymbol{d_2}$	A	A	A	**0**	Plane stress
C3	$\boldsymbol{d_3}$	$\boldsymbol{d_3}$	**0**	A	A	A	Plane strain
C4	$\boldsymbol{d_4}$	**0**	**0**	A	A	A	Uniaxial confined extension

For cases where nodal reaction forces were determined from analysis, the macroscopic stress in the

respective direction was calculated as the ratio between the total reaction force and the boundary area, i.e. $\sigma_i = \Sigma F_i / 400L^2$. For the cases where nodal displacements were determined from analysis, the macroscopic strain in the respective direction was calculated as the ratio between the average displacement and the model length, i.e. $\varepsilon_i = \Sigma U_i / (21^2 \times 20L)$.

The evolution of damage was simulated by failure of bonds, controlled by an in-house code, and repetitive solution for equilibrium performed by Abaqus with constant applied displacements. The values of $\boldsymbol{d_i}$ were selected so that the strain energy density in the system prior to damage was one for the four cases for the purpose of comparison. At each step the in-house code obtains the forces and moments in all bonds and calculates the propensity for failure, Π, for each bond. The bond with maximum Π is then removed and the updated lattice is solved for equilibrium. This leads to redistribution of forces for the continuous damage evolution. The magnitudes of Π at which consecutive failures occurred can be used to cut-back the applied strain and resulting stress and obtain a macroscopic stress-strain response. The focus of this work is not on determining the stress-strain response, but on the relation between damage and crack population. To this end we define four damage parameters, measuring the relative changes of the hydrostatic stress and the three components of the stress deviator by:

$$D_H = 1 - \frac{\sigma_H}{\sigma_H(0)}; \quad D_i = 1 - \frac{S_i}{S_i(0)}, \quad \textit{where} \quad S_i = \sigma_i - \sigma_H, \, i = 1,2,3 . \tag{4}$$

Note that for isotropic deformation and damage these parameters must be equal and equivalent to the damage parameter defined via relative reduction of Young's modulus or shear modulus.

2.4. Crack population analysis

A bond failure is thought of as a micro-crack nucleation, specifically as a separation between the adjacent cells in the cellular structure along their common face. Initially, the micro-cracks may be dispersed in the model reflecting the random distribution of pore sizes and the low level of interaction due to force redistribution. Interaction and coalescence may follow as the population of micro-cracks increases. The structure of the failed surface can be represented with a mathematical graph, where graph nodes represent failed faces and graph edges exist between failed faces with common triple line in the cellular structure, i.e. where two micro-cracks formed a continuous larger crack. Generally, the graph of a failed surface is a disconnected set of sub-graphs or components, some of which could be single nodes as at the start of damage evolution, while others could be connected sets representing larger micro-cracks as the coalescence develops. For the analysis, nodes are equipped with weights equal to the failed face areas. Edges are equipped with weights equal to the shortest path along connected faces between their centres.

The components of a failed surface graph are sorted into sets according to their areas $A_1 < A_2 \ldots < A_k$, so that each set contains N_i disconnected components of area A_i. The linear size of a component is approximated with the square root of its area so that the moment of the crack population is formed using (compare to Eq. (1))

$$M = \frac{1}{A_T} \sum_{i=1}^{k} A_i^{3/2} N_i , \tag{5}$$

where A_T is the total area of the faces in the cellular structure. This can in principle be replaced with a linear measure to conform to Eq. (1). A realistic choice is to use the component diameter which is the maximal shortest path between component's nodes calculated with the weighted edges. The process, however, is computationally expensive and does not lead to noticeable changes in the

results for the cases analysed here. Eq. (5) is used after each failure event to calculate the evolution of the moment with damage. In addition, the maximal component is monitored. This is the largest connected cracked surface.

3. Results and discussion

Figure 3 shows the results of the evolution of the damage parameters defined by Eq. (4) as functions of the moment of crack population defined by Eq. (5). Recall that a damage parameter, based on the relative change of the Young's modulus equals the damage parameters based on the individual stress components, deviatoric and hydrostatic, when the material remains macroscopically isotropic. In this case the same damage parameter describes the relative change of the shear modulus. The results for the cases of uniaxial extension, unconfined (a) and confined (d), show equality of the four damage parameters (approximate in case 4). This suggests that microscopic isotropy is maintained during damage evolution and the results reproduce very closely the linear relation predicted by the theory and given by Eq. (1). Interestingly, an estimate for the slope of the linear function from the figures is about 1.5, which is very close to the value of β reported in relation to Eq. (1).

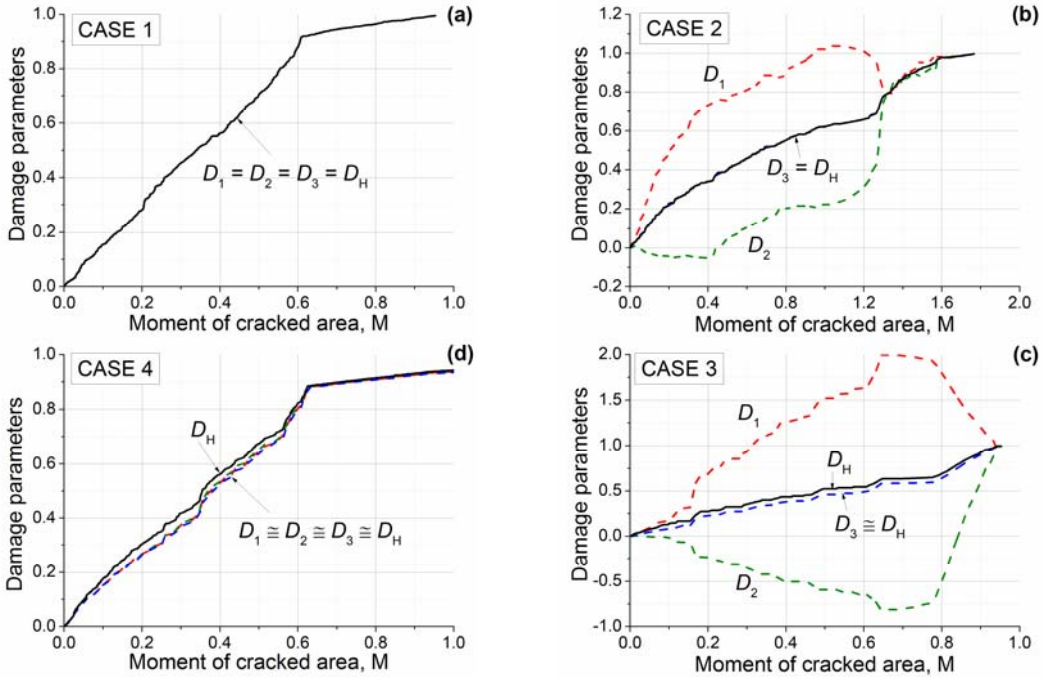

Figure 3. Damage parameters relation to crack population moment.

In the cases of plane stress (b) and plain strain (c), however, the development of damage is radically different, illustrating the development of damage-induced anisotropy. In this case the damage parameter D_i represents the relative reduction of the longitudinal shear modulus in direction X_i. Note that this is not the shear modulus relating shear stress to shear strain. In both plane cases, the evolution of D_1 suggest that the system undergoes transition into negative longitudinal shear resistance, quite more pronounces in the plane strain case (c), while the shear resistance in direction X_2 increases from its initial value. This behaviour may seem unusual, but it is not impossible for anisotropic materials. The bounds for Poisson's ratios in such materials calculated in [20, 21] allow for negative longitudinal shear moduli with the values recorded here. The results merely show that extreme anisotropy has been developed in the material with the evolution of micro-crack population under the two plane cases. The development of the hydrostatic damage is also affected in these cases, as it cannot be described as a linear function of the cracked area moment.

To understand what causes the anisotropy in the plane cases the structure of the crack population needs to be studied in more detail. This requires a single damage parameter; an appropriate choice is the relative reduction of the strain energy density in the system, $D = 1 - W / W(0)$, which is found to be approximately equal to the damage parameter defined via the relative reduction of the hydrostatic stress in all cases, see Fig. 4(a). The development of the maximal graph component, i.e. the main crack, with damage is shown in Fig. 4(b) with the ratio between the area of the maximal component, A_m, to the total cracked area, A. It is clear that the main crack becomes dominant very early in the development of damage (at damage less than 1%) and its relative area grows nearly exponentially for all cases. It seems therefore sufficient to examine the structure of the maximal component as the damage develops.

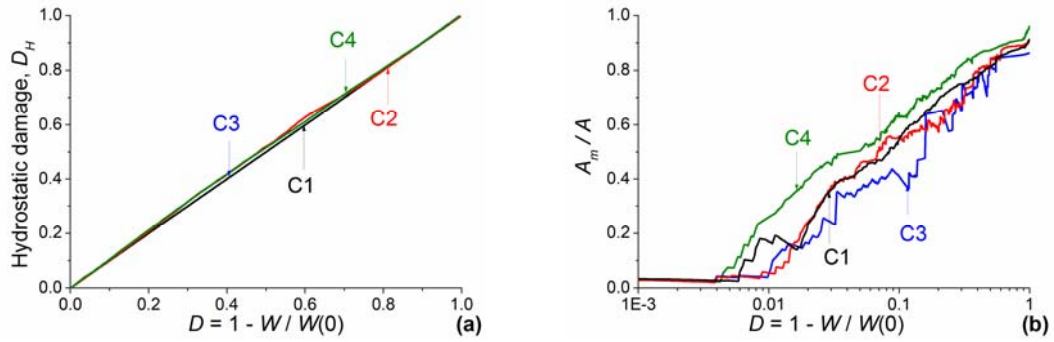

Figure 4. Hydrostatic damage (a) and relative area of main crack (b) development with damage defined as relative reduction of strain energy density.

Figure 5 shows the development of the maximal component area, split into the areas of surfaces normal to the three principal axes, A_1, A_2, A_3, and the surfaces formed on octahedral planes, A_4. All areas are normalised with the total areas of the corresponding boundaries in the cellular structure. In the cases of uniaxial extension, unconfined (a) and confined (d), the development of the main crack involves creation of surfaces normal to the applied load and on octahedral planes. Although there is a difference between the two cases in the rates of creation of normal and octahedral surfaces, the overall balance results in isotropic damage, see Fig. 3(a),(d).

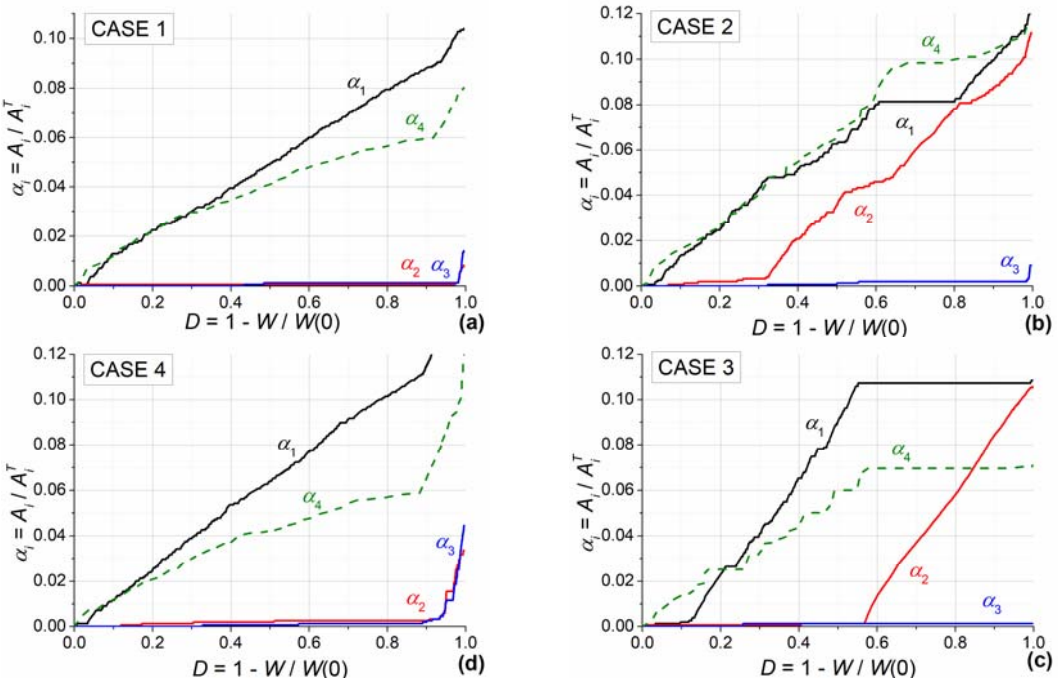

Figure 5. Structure of maximal graph component with damage.

In the plane stress (b) and plane strain (c) cases, the development of the main crack follows very different patterns. The parallel increase of normal to the first loading axis and octahedral surfaces in plane stress, Fig. 5(b), seems to be responsible for the immediate development of damage-induced anisotropy, which after that appears to be moderated by the development of surfaces normal to the second loading axis. The constraint in plane strain, Fig. 5(c), leads to a delayed but rapid increase of surfaces normal to the first loading axis together with a lower rate of creation of octahedral surfaces. This appears to delay substantially the development of cracked surfaces normal to the second loading axis and results in significantly higher anisotropy.

It should be noted that the structure-damage relations reported here were found qualitatively independent of the random assignment of pores in the lattice model as well as of the shape parameter of the pore distribution. This has been confirmed by a number of simulations with different shape of distribution and random assignments. One parameter that may affect the outcomes is the shear to normal strength ratio; this is a subject of ongoing work. It is further understood that the outcomes reported here are principally related to the selected lattice connectivity. However, the detail to which the surface topography can be studied is higher than the detail allowed by models based on cubic lattices. One unknown in the analysis is whether the crack development in the lattice is energetically equivalent to the development of continuum cracks. This question remains to be addressed in a future work. The current observations suggest that a common, constraint independent, damage evolution law might not be feasible to achieve. In such case it seems that a lattice-based analysis might be necessary as a sub-modelling approach to inform the behaviour of finite elements in a continuum model.

The last question of interest in this work is related to the use of the weakest-link statistics for global failure predictions. It was suggested in [16] that weakest-link should be applied to the population of micro-cracks in the system. However, from the simulations performed here it is evident that a single crack, the maximal connected component of the cracked surface, becomes rapidly dominating the behaviour, Fig. 4(b), with few much smaller components disconnected from the main crack. This does not allow for invoking the weakest-link as a descriptor of final failure.

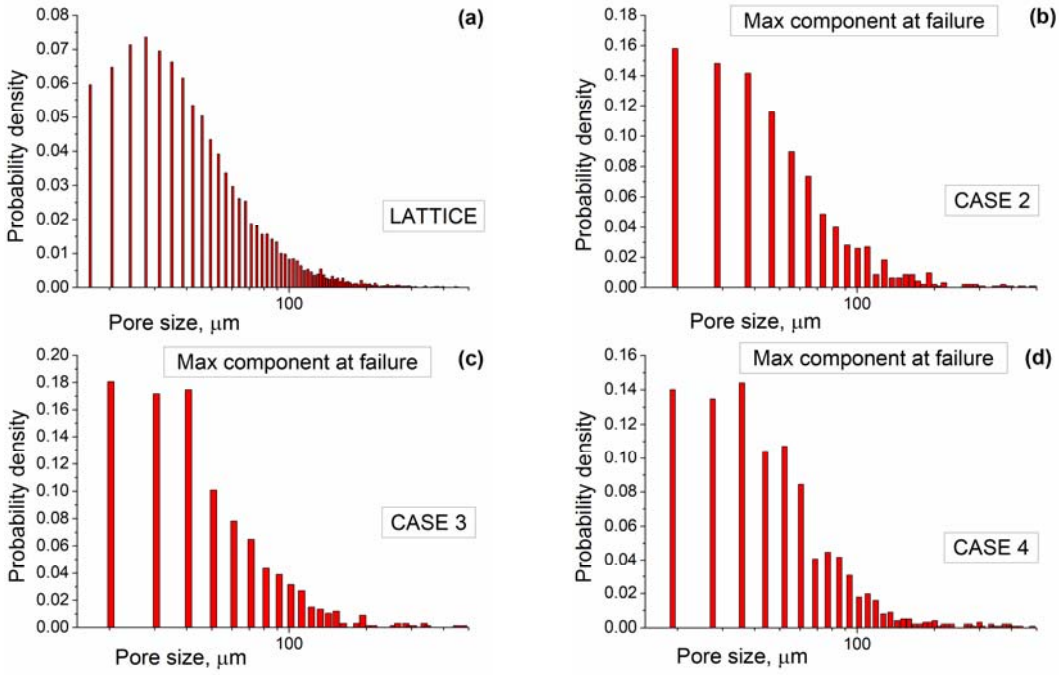

Figure 6. Probability density of pore sizes in the lattice (a) and in the maximal component at failure for three loading cases (b)-(d). Results obtain with the same distribution given by (a).

Another approach would be to base the weakest-link statistics on the microstructure information, in this case the size distribution of crack-initiation features, the pores. This is similar to the approach used in the modelling of cleavage fracture, where second-phase particles are considered to be cleavage initiators. In order to show whether this is a realistic approach, a comparison is made between the probability density of pore sizes distributed in the lattice and pore sizes contained in the maximal component at failure. The results are shown in Fig. 6 for the pores in the entire lattice (a) and three of the loading cases as depicted. The results shown correspond to one and the same random assignment of pore sizes. Evidently, the probability density of the pores belonging to the final fracture surface is different from the lattice distribution and depends on the loading mode. While the initial damage may start at one and the same location in the system, the nature of loading develops the main crack in different ways and the final failure cannot be described as a weakest-link event using the statistics of the sizes of the failure initiation sites. This makes it difficult to derive a load-independent, purely micro-structure based relation between the macroscopic damage and the probability of failure. The outcome supports further the suggestion that macroscopic failure analysis needs to be performed with an underlying lattice-based analysis of local micro-crack propagation.

4. Conclusions

- A microstructure-informed strategy for analysis of damage evolution in quasi-brittle materials was presented, whereas damage results from the formation, growth and interaction of a population of micro-cracks.
- It was demonstrated that in cases of non-uniaxial extension, such as plane stress or plane strain found ahead of a main crack, the micro-crack population development was responsible for elastic anisotropy with extreme variations of longitudinal shear moduli.
- It was shown that the damage-induced anisotropy was a complex function of the crack population structure. A load-independent damage evolution law might not be achievable and explicit analysis of crack population development, e.g. using a lattice model, might be necessary to complement continuum finite element analysis of failure.
- It was shown that the maximal connected component of the crack population, i.e. the largest crack, became dominant very early in the process of macroscopic damage and controlled the ultimate failure. The analysis if this component suggested that the global failure could not be treated as a weakest-link event.
- The graph-theoretical approach to the analysis of micro-crack populations showed significant potential to reveal the underlying topological structure of the cracked surface. Further work is required to link the topological structure to a measure for global probability of failure.

Acknowledgements

The author is grateful to EPSRC for the support for this work via grant EP/J019763/1, as well as to BNFL for the endowment allowing his continuous research.

References

[1] G. Pijaudier-Cabot, Z.P. Bazant, Nonlocal damage theory. J Eng Mech 113 (1987) 1512-1533.

[2] J.W. Ju, On energy-based coupled elastoplastic damage theories: constitutive modelling and computational aspects. Int J Solids Struct 25 (1989) 803-833.

[3] P. Grassl, M. Jirasek, Damage-plastic model for concrete failure. Int J Solids Struct 43 (2006) 7166-7196.
[4] J. Cervenka, V. Papanikolaou, Three dimensional combined fracture-plastic material model for concrete. Int J Plasticity 24 (2008) 2192–2220.
[5] H.S. Wong, M. Zobel, N.R. Buenfeld, R.W. Zimmerman, Influence of the interfacial transition zone and microcracking on the diffusivity, permeability and sorptivity of cement-based materials after drying. Mag Concr Res 61 (2009) 571-589.
[6] K.L. Scrivener, A.K. Crumbie, P. Laugesen, The interfacial transition zone (ITZ) between cement paste and aggregate in concrete. Interface Sci 12 (2004) 411–421.
[7] Z.P. Bazant, B.H. Oh, Microplane model for progressive fracture of concrete and rock. J Eng Mech 111 (1985) 559-582.
[8] G. Cusatis, Z.P. Bazant, L. Cedolin, Confinement-shear lattice CSL model for fracture propagation in concrete. Comp Meth Appl Mech Eng 195 (2006) 7154-7171.
[9] D.V. Griffiths, G.G.W. Mustoe, Modelling of elastic continua using a grillage of structural elements based on discrete element concepts. Int J Numer Meth Eng 50 (2001) 1759-1775.
[10] C.S. Chang, T.K. Wang, L.J. Sluys, J.G.M. van Mier, Fracture modeling using a micro structural mechanics approach - I. Theory and formulation. Eng Fract Mech 69 (2002)1941-1958.
[11] Y. Wang, P. Mora. Macroscopic elastic properties of regular lattices. J Mech Phys Solids 56 (2008) 3459-3474.
[12] A.P. Jivkov, J.R. Yates, Elastic behaviour of a regular lattice for meso-scale modelling of solids. Int J Solids Struct 49 (2012) 3089–3099.
[13] A.P. Jivkov, M. Gunther, K.P. Travis. Site-bond modelling of porous quasi-brittle media. Mineral Mag 76 (2012) 94-99.
[14] A.P. Jivkov, D.L. Engelberg, R. Stein, M. Petkovski, Pore space and damage evolution in concrete. Eng Fract Mech (2013) accepted.
[15] B. Budiansky, R.J. O'Connell, Elastic moduli of a cracked solid. Int J Solids Struct 12 (1976) 81-97.
[16] W.A. Curtin, H. Scher, Time-dependent damage evolution and failure in materials. I. Theory. Phys Rev B 55 (1997) 12038-12050.
[17] ABAQUS 6.11, DS Simulia Corp., 2011.
[18] Y. Wang, S. Abe, S. Latham, P. Mora, Implementation of particle-scale rotation in the 3D-lattice solid model. Pure Appl Geophys 163 (2006)1769-1785.
[19] E. Schlangen, J.G.M van Mier, Experimental and numerical analysis of micromechanisms of fracture of cement-based composites. Cement Concr Compos 14 (1992) 105-118.
[20] A.N. Norris, Extreme values of Poisson's ratio and other engineering moduli in anisotropic materials. J Mech Mater Struct 1 (2206) 793–812.
[21] C.Y. Guo, L.T. Wheeler, Extreme Lamé compliance in anisotropic crystals. Mat Mech Solids 14 (2009) 403-420.

Meso-scale features and couple stresses in fracture process zone

Craig N Morrison[1, 3,*], Andrey P Jivkov[2, 3], John R Yates[3]

[1] Nuclear FiRST Doctoral Training Centre
[2] Research Centre for Radwaste and Decommissioning
[3] Modelling and Simulation Centre
Dalton Nuclear Institute, The University of Manchester, Manchester, M13 9PL, UK
* Corresponding author: craig.morrison-2@postgrad.manchester.ac.uk

Abstract Generalized continuum theories such as couple stress theory have the potential to improve our understanding of material deformation and fracture behaviour in areas where classical continuum theory breaks down at, for example, the length scale of meso-scale features within the fracture process zone. The couple stress theory considers not only relative displacements between these features but also relative rotations, introducing a natural length scale. A model has been developed of a low stiffness matrix containing suitably situated high stiffness particles to simulate the presence of defects at the meso-scale. This has been used to assess the descriptive potential of a novel consistent couple stress theory. The model has been subjected to a set of displacement fields selected to produce strain energies with varying contributions from the coupled stresses. The results demonstrate the effect of particle size to spacing ratio on the elastic energies. These can be used to evaluate the couple stress constant as well as validate the constant experimentally for specific materials.

Keywords: generalized continuum; meso-scale defects; FE analysis; strain-curvature energy; size effect

1. Introduction

Analysis of materials at engineering length scales is based upon assumptions of classical continuum behaviour. This is adequate for most macro-scale analyses but, when considering smaller length scales where cracks, notches and defects introduce stress concentrations, the material microstructure is known to have a significant impact on material behaviour [1]. Local approaches, which incorporate mechanistic understanding of material failure behaviour at the length scale of their relevant features, are beneficial for linking microstructures to macroscopic responses [2]. However, the widely used weakest link (WL) assumption has been challenged as a realistic method of modelling size effects in cleavage [3] and quasi-brittle fracture [4] as a result of failing to account for the interaction processes during failure.

Discrete methods have shown promise for modelling materials undergoing such fracture. Lattice models consist of nodes connected into a lattice via springs [5], beams [6] or other discrete elements with the properties of these connections allowing a micro structurally informed response. Lattice modelling differs in principle from previous local approach models by using a statistically parallel system, where loads are redistributed upon the breaking of a single bond, rather than the ultimate failure seen in WL systems. This is considered to be a closer representation of the interaction and coalescence of micro-cracks and flaws, which characterize quasi-brittle materials such as graphite [7] and cement-based materials [8]. The work presented here explores aspects of the site-bond model developed by Jivkov and Yates [9] and used for studies of damage evolution from distributed porosity in cements [10]. Work on this model has shown that evaluating the stiffness coefficients of the bonds using strain energy equivalence between the discrete model and a classical continuum creates an indeterminate problem. Use of a generalized continuum theory, such as couple stress theory, offers a possible solution to this indeterminacy.

In couple stress theory (CST) each point within the continuum has three additional degrees of freedom, point rotations. These are associated with couple stresses as the classical (force) stresses are associated with strains. A general CST was proposed early in the 20th century by the Cosserat brothers [11]. It went largely unnoticed until the 1960s when a desire to understand the mechanisms behind micro-crack growth for more accurate crack assessment rejuvenated interest. One branch of CSTs considers point micro-rotations to be independent of the macro-rotations; the rotations derived from the displacement gradient [12, 13]. These are known as micropolar theories or Cosserat models with free rotations [14]. While such a view appears to be well suited for use with discrete lattice methods, it is difficult to establish a link between a continuum and a discrete representation of a material containing features that are following the deformations of the bulk. For such situations it is more plausible to assume that the micro-rotations are equal to the macro-rotation. This assumption led to a branch of CSTs known as Cosserat models with constrained rotations [14, 15]. Initially, these were based on couple stresses work-conjugate to the macro-rotation gradient. As a consequence, the spherical part of the couple stress tensor remained undetermined. Recently, Hadjesfandiari and Dargush [16] proposed a consistent CST using true kinematic quantities to remove the indeterminacy of the couple stress tensor.

The consistent CST [16] naturally introduces a length parameter. This is of key importance for the local material behaviour. But the calibration of the CST requires that the length parameter is physically related to the material microstructure; the sizes and distances between characteristic features that disturb the symmetry of the stresses. We report on work in progress investigating whether a medium with features can be used to calculate bond responses to bending and torsion in the discrete model [9] and if this can be used to calibrate the consistent CST.

2. Theory and model

2.1 Generalised continuum

The kinematics of a material point under small deformation is given by the displacement gradient, Eq. (1), where comma denotes differentiation, rounded parenthesis denotes symmetric part and square parenthesis denotes skew symmetric part of the tensor. The symmetric (strain tensor e_{ij}) and the skew symmetric (rotation tensor ω_{ij}) parts are given by Eq. (2) and Eq. (3), respectively. The right hand side of Eq. **Error! Reference source not found.** gives the rotation tensor as a vector using the permutation tensor.

$$u_{i,j} = u_{(i,j)} + u_{[i,j]} \tag{1}$$

$$u_{(i,j)} = e_{ij} = \frac{1}{2}\left(u_{i,j} + u_{j,i}\right) \tag{2}$$

$$u_{[i,j]} = \omega_{ij} = \frac{1}{2}\left(u_{i,j} - u_{j,i}\right) = \epsilon_{jik}\omega_k \tag{3}$$

In classical continuum mechanics, the elastic potential depends solely on the strain tensor. In generalised continuum, additional potential is carried by the gradient of the rotation vector, Eq. (4). The symmetric part of this gradient, χ_{ij} in Eq. (5), represent “pure” twists, and the skew symmetric part, κ_{ij} in Eq. (6), represent “pure” curvatures, which can be given by a vector as shown with the right-hand size.

$$\omega_{i,j} = \omega_{(i,j)} + \omega_{[i,j]} \tag{4}$$

$$\omega_{(i,j)} = \chi_{ij} = \frac{1}{2}\left(\omega_{i,j} + \omega_{j,i}\right) \tag{5}$$

$$\omega_{[i,j]} = \kappa_{ij} = \frac{1}{2}\left(\omega_{i,j} - \omega_{j,i}\right) = \epsilon_{jik}\kappa_k \tag{6}$$

Generally, the energy potential of the rotation gradient leads to a non-symmetric force stress tensor, σ_{ji}, Eq. (7), and the introduction of a couple stress tensor, μ_{ji}, Eq. (8). When the force stress is taken as work conjugate to the strain tensor, and the couple stress is taken as work conjugate to the gradient of the rotation, the symmetric part of the couple stress tensor becomes indeterminate.

$$\sigma_{ji} = \sigma_{(ji)} + \sigma_{[ji]} \tag{7}$$

$$\mu_{ji} = \mu_{(ji)} + \mu_{[ji]} \tag{8}$$

Hadjesfandiari and Dargush [16] suggested a solution to this problem by demonstrating that the entire rotation gradient does not have energy potential, only the curvature tensor, Eq. (6). Thus the deformation energy consists of the work done by the force stress on the strain and the work done by the couple stress on the pure curvature. The symmetric part of the rotation gradient, Eq. (5), has no forces associated with it, which solves the problem of the indeterminate spherical part of the rotation gradient. For an isotropic material, the elastic potential is given by [16]:

$$W(\varepsilon,\kappa) = \frac{1}{2}\lambda\,(\varepsilon_{kk})^2 + \mu\,\varepsilon_{ij}\varepsilon_{ij} + 8\eta\,\kappa_i\kappa_i \tag{9}$$

where λ and μ are Lamé parameters and η is a material couple stress constant.

According to this theory, a homogeneous displacement field, such as hydrostatic compression Eq. (10), does not introduce rotations and hence curvatures.

$$u_1 = x_1 \qquad u_2 = x_2 \qquad u_3 = x_3 \tag{10}$$

A displacement field producing pure twist, Eq. (11), introduces rotations, Eq. (12), but no true curvatures[16]:

$$u_1 = -\theta x_2 x_3 \qquad u_2 = \theta x_1 x_3 \qquad u_3 = 0 \tag{11}$$

$$\omega_1 = -\frac{1}{2}\theta x_1 \qquad \omega_2 = -\frac{1}{2}\theta x_2 \qquad \omega_3 = \theta x_3 \tag{12}$$

A displacement field corresponding to pure bending of a beam, Eq. (13), introduces non-zero rotations, Eq. (14), that result in a single non-zero curvature, Eq. (15), [16]:

$$u_1 = -\frac{1}{R}x_1 x_3 \qquad u_2 = -\frac{\nu}{R}x_2 x_3 \qquad u_3 = \frac{\nu}{2R}\left({x_2}^2 - {x_3}^2\right) - \frac{1}{2R}{x_1}^2 \tag{13}$$

$$\omega_1 = \frac{\nu x_2}{R} \qquad \omega_2 = \frac{x_1}{R} \tag{14}$$

$$\kappa_3 = \frac{1-\nu}{2R} \tag{15}$$

where ν is Poisson's ratio and R is the radius of curvature of the beam central axis.

2.2 Discrete site-bond model

The site-bond model [9] uses a discrete lattice, based on a regular tessellation of material space into truncated octahedral cells, Fig. 1(a). The lattice derives from the cellular structure when material particles, attached to cell centres, interact via deformable bonds. The bond properties relate to their ability to transfer shear and axial forces as well as torsion and bending moments to satisfy the six degrees of freedom of each site. A site requires 14 bonds to connect it to its neighbours, Fig. 1(b): six bonds of length $2L$ ($2L$ is the cell size) in principal directions (through square faces), and eight bonds of length $\sqrt{3}L$ in octahedral directions (through hexagonal faces). Development of this model involves bond representations with six independent elastic springs resisting three relative

displacements and three relative rotations between sites. This yields four spring types with axial, K_n, shear, K_s, twisting, K_t, and bending, K_b, stiffness [17], which could, in general, be different for principal and octahedral directions.

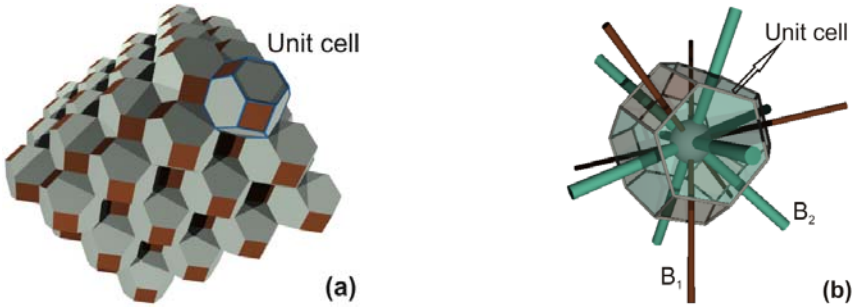

Figure 1. Cellular representation of material (a); and unit cell with bonds (b).

2.3 FE model of elastic continuum with rigid particles

For our investigation, we use a finite element model of a cube of an elastic material surrounding a truncated octahedral cell of size $2L$. The material has a unit modulus of elasticity and Poisson's ratio $\nu = 0.375$. Rigid cubic particles are introduced in the cube, so that one particle, P0, is positioned in the centre of the cell, while others are positioned outside the cell in the principal and octahedral directions as shown in Fig. 2. Three different loading conditions are used: (H) hydrostatic compression; (T) pure twist; and (B) pure bending. These are applied via displacement fields on the cube surfaces; examples for pure twist and pure bending are given in Fig. 3. In all cases we calculate elastic energies, Ω, within the unit cell surrounding the central particle. With no particles present, the cell elastic energy is given by the classical continuum solution, since no features exist to disturb stress symmetry. The displacement magnitudes for the three loading cases are selected so that Ω without particles is the same, Ω_0.

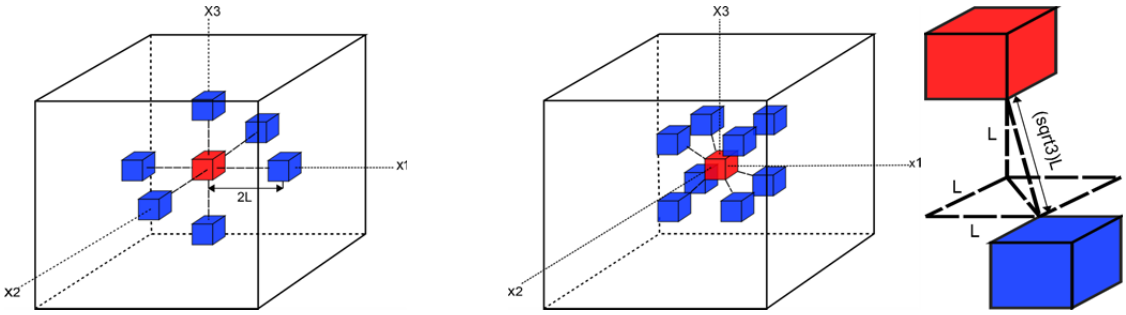

Figure 2. Particle additions in the principal (left) and octahedral (right) directions.

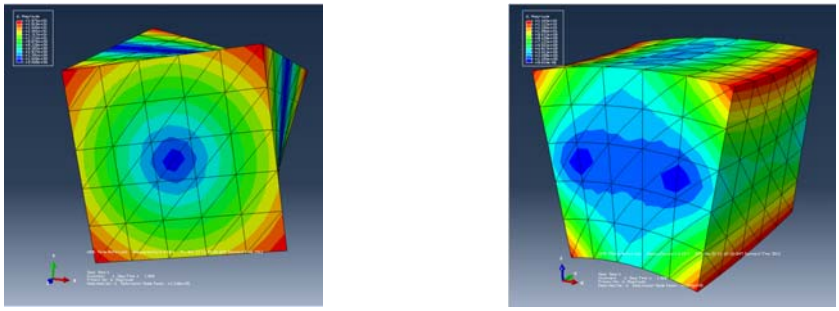

Figure 3. Displacement maps for the loading cases of pure twist (left) and pure bending (right).

To link the cell energies to kinematic quantities we calculate particle translations and rotations using three unit vectors, $\mathbf{n}_1$, $\mathbf{n}_2$ and $\mathbf{n}_3$ normal to three orthogonal faces of a particle, see Fig. 4. After deformation these vectors remain orthogonal as the particles are rigid, given with $\mathbf{t}_1$, $\mathbf{t}_2$ and $\mathbf{t}_3$ in Fig. 4. The coordinates of these, arranged in columns, form the transformation matrix, $\mathbf{T}$, for the particle. The particle motion can be represented by a single rotation, θ given by Eq. (16), around a normalized axis, α given by Eq. (17). The components of the rotation vector for a particle are calculated by Eq. (18). The relative rotations between central and any other particle are expressed in the coordinate system defined by the particular pair using the corresponding transformation.

$$\theta = cos^{-1}\left(\frac{trace\,(\mathbf{T})-1}{2}\right) \tag{16}$$

$$\alpha = \frac{1}{2\sin(\theta)}\begin{bmatrix} T_{32}-T_{23} \\ T_{13}-T_{31} \\ T_{21}-T_{12} \end{bmatrix} \tag{17}$$

$$\omega_i = \theta \times \alpha_i, \quad i = 1,2,3 \tag{18}$$

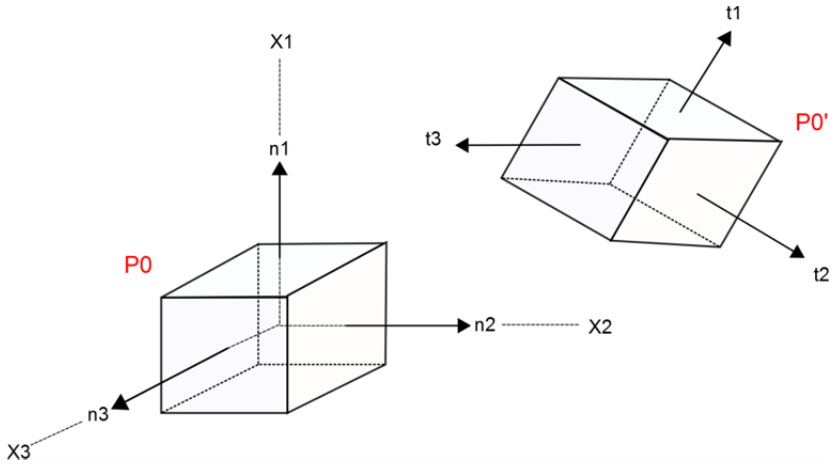

Figure 4. Orthogonal vectors, ($\mathbf{n}_1$, $\mathbf{n}_2$, $\mathbf{n}_3$) and ($\mathbf{t}_1$, $\mathbf{t}_2$, $\mathbf{t}_3$) describing the orientation of P0 before and after deformation respectively.

3. Results and Discussion

For the particle arrangement used (a central particle and all 14 particles of the site-bond model) we have used four different particle sizes relative to the cell size in order to investigate the effect of cell to particle size ratio, λ. The ratios are 3 (large particles), 4, 6, and 12 (small particles).

In the case of hydrostatic loading no rotations of particles were observed and the relative displacements between P0 and any principal or octahedral particle were only axial, conforming to Eq. (10). In the site-bond model these relative displacements should be resisted by axial springs with stiffness coefficients K_n^p and K_n^o, respectively. The relative axial displacements were found independent of λ, scaling with the applied displacements. The cell energies were found to be dependent on λ, as shown in Figure . For small particles, λ = 12, the cell energy approached Ω_0; the presence of particles has negligible effect. The cell energy and displacements from this case can be used to calibrate a linear combination of K_n^p and K_n^o. Note, that in general this case is not sufficient for calibrating stiffness coefficients separately. However, the particle size effect appears to be very

small, suggesting that the two stiffness coefficients could be assumed equal and given from the continuum solution, following [17] for example.

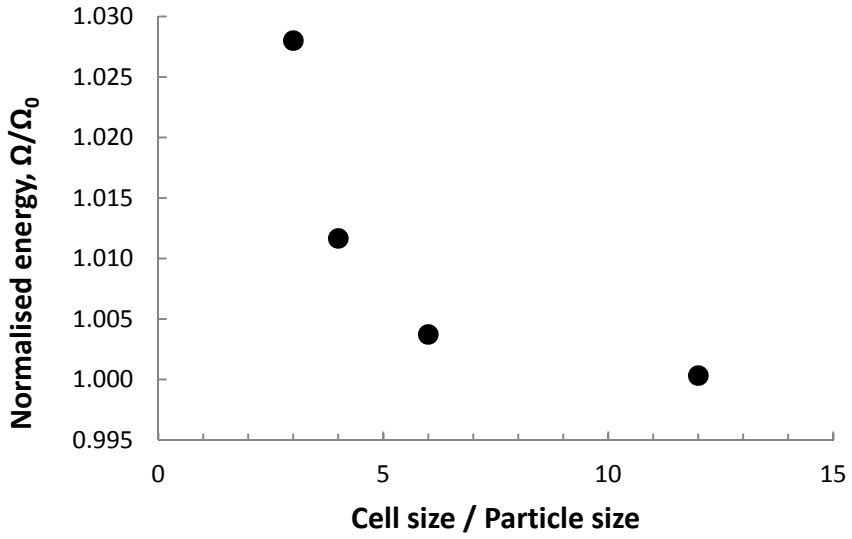

Figure 5. Normalised cell energy vs size ratio under hydrostatic compression.

In the case of pure twist the cell energies were found to be dependent on λ, Fig. 6. While this is similar to the case of hydrostatic compression the effect of particle size is substantially larger. All relative displacements between P0 and the principal particles were zero, conforming to Eq. (11). The relative displacements between P0 and octahedral particles were zero axial and non-zero transversal, again conforming to Eq. (11). This means that the only activated linear springs in the site-bond model are the shear springs in octahedral direction with stiffness K_s^o.

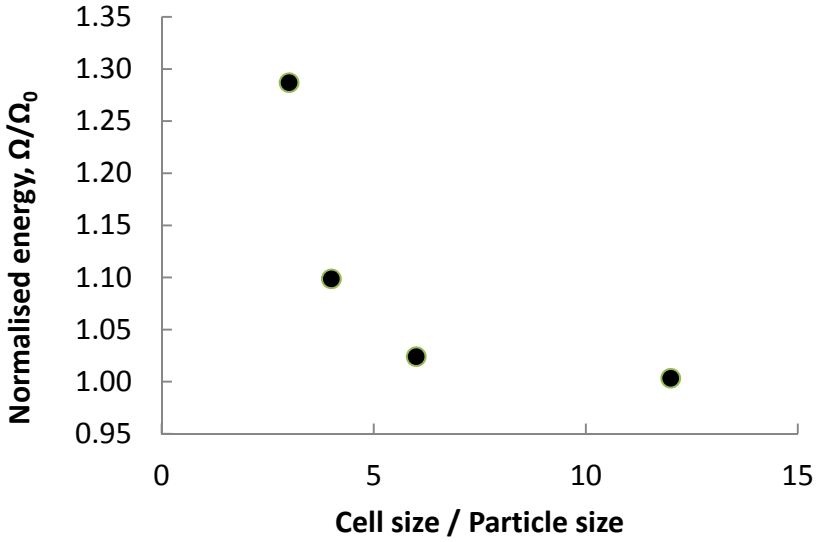

Figure 6. Normalised cell energy vs size ratio under pure twist

The calculated relative rotations between P0 and the particles in the two directions are shown in Fig.

7. The non-zero relative rotations between P0 and principal particles were twists as expected from Eq. (12) and the magnitude shown in Fig. 7 is the twist of the particle in direction X1. It is seen that this is 3-4 orders of magnitude smaller that the relative rotations between P0 and octahedral particles. The latter were found to be bend-type rotations only, conforming to Eq. (12), and suggesting that the only moment springs activated are the bending springs in the octahedral direction with stiffness K_b^o. The magnitudes of the bend-rotations of octahedral particles were found nearly independent of particle size. These results suggest that for the case of pure twist, the elastic strain energy is accumulated in the shear and bending springs in the octahedral direction only, and one can calibrate a linear combination of K_s^o and K_b^o, which should depend on the cell to particle size ratio. From this perspective the results support the analytical derivations in [16], where pure twists do not contribute to the elastic energy. From here, it can be speculated that the torsion springs in the principal directions could be omitted from the site-bond model, i.e. $K_t^p = 0$. This should be supported by considering other cases with curvature-free displacement fields which introduce twists of principal particles according to the theory.

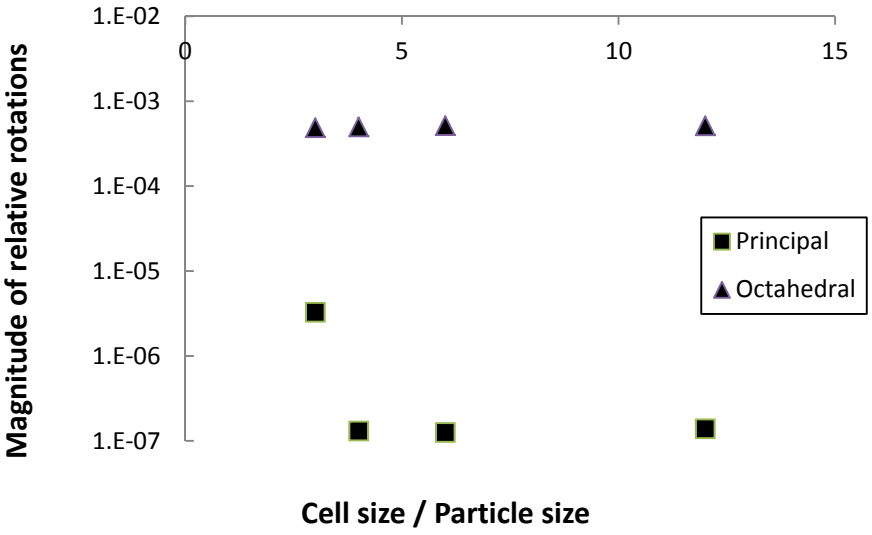

Figure 7. Relative rotation vs size ratio under pure twist

The cell energy dependence on λ for the case of pure bending is shown in Fig. 8. The effect of particle size is smaller than in the case of pure twist, but not negligible. The relative displacements between P0 and the octahedral particles were non-zero axial and tangential, conforming to Eq. (13). The relative displacements between P0 and the principal particles also conform to theory with non-zero axial for particles in X2, non-zero tangential for particles in X1 and zero displacements of particles in X3. This means that the activated linear springs in the site-bond model would be axial and shear springs in all octahedral directions with stiffness coefficients K_n^o and K_s^o, and axial and shear springs in two principal directions with stiffness coefficients K_n^p and K_s^p.

The calculated relative rotations of the particles are shown in Fig. 9. The only non-zero relative rotation of principal particles was found to be the bend-type rotation of the particles in X1, conforming to Eq. (14). However, this relative rotation was found at least an order of magnitude

smaller than the magnitude of the relative rotation between P0 and octahedral particles. The latter contains twist and bend components, suggesting an activation of both the torsion and bending springs in the octahedral direction with stiffness coefficients K_t^o and K_b^o. The much smaller rotation of the principal particles can be used to approximate the kinematics and assume zero rotation of principal particles. Thus the elastic energy is taken by the linear springs in all directions and the torsion and bending spring in the octahedral direction, allowing for calibration of a linear combination of K_n^o, K_s^p, K_n^o, K_s^o, K_t^o and K_b^o, which should depend on the cell to particle size ratio. As in the case of pure twist it can be speculated that the bending springs in the principal direction can be omitted, i.e. $K_b^p = 0$, but this needs to be supported by considering other displacement fields introducing bend-type rotations of principal particles. It can be further speculated, that the torsion stiffness in the octahedral direction should be zero, i.e. $K_t^o = 0$. This could be deduced from the theoretical requirement that pure twists have no energy potential, but requires further investigation. If these were shown to be true, the bending case would provide a calibration for the linear combination of K_n^o, K_s^p, K_n^o, K_s^o, K_b^o.

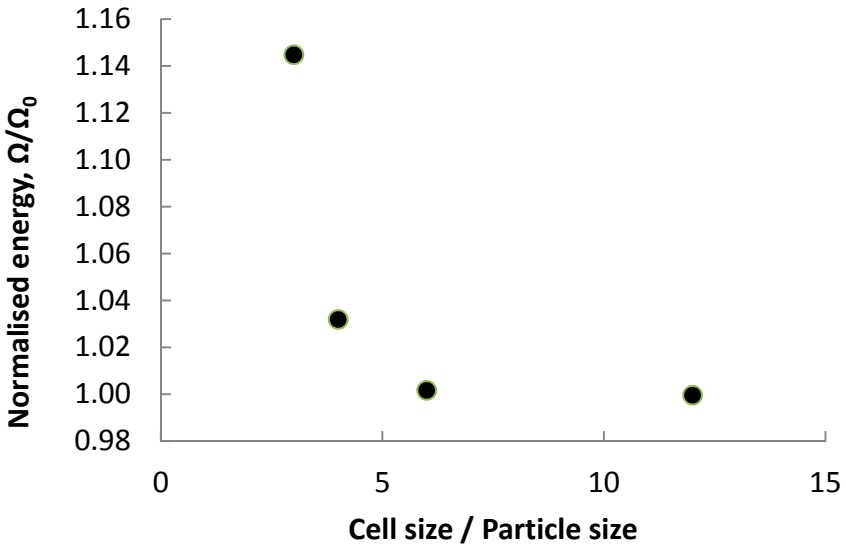

Figure 8 . Normalised cell energy vs size ratio under pure bending

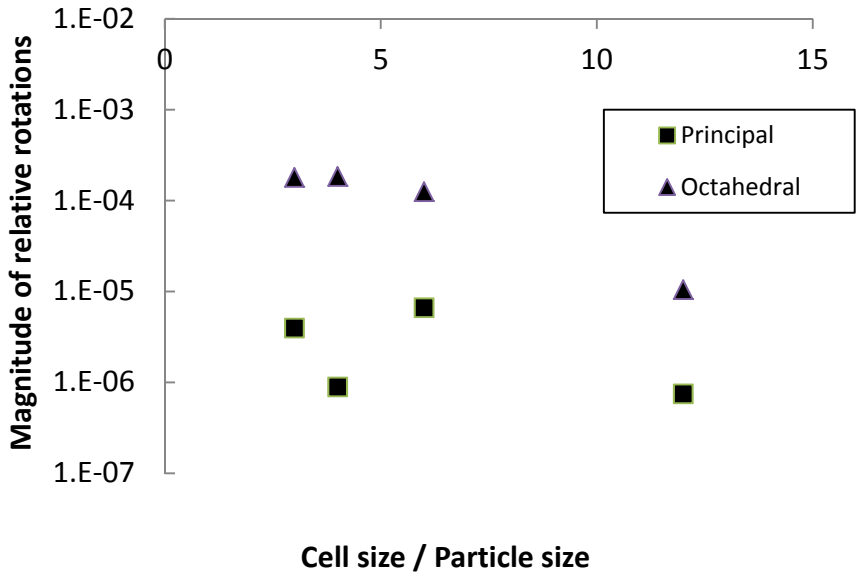

Figure 9. Relative rotation vs size ratio under pure bending

From the three cases considered in this work, it is clear that a separation between all required stiffness coefficients is not possible. However, there is a good indication that the site-bond model should not contain torsion springs and possibly bending springs in the principal directions. One way to check this is pure twist along the octahedral axis, which theoretically should provide twist and bend rotations of all particles. If this proves to be the case, the elastic energy of the continuum with features should be taken by the deformations of the remaining springs. Additional loading cases are necessary to determine the stiffness coefficients of these springs. If these are determined from curvature-free loading cases alone, a good strategy for the calculation of the coupled-stress constant can be proposed. The site-bond model with constants calibrated from curvature-free loading cases can be subjected to a case introducing curvature energy according to theory, for example pure bending, and any excess of energy between the site-bond model and classical continuum should be attributed to curvature energy.

4. Conclusions

- We have proposed a methodology for calibrating the spring constants of a special lattice model using a micromechanical model of a material containing features.
- The comparison of the results with the consistent couple-stress theory suggests that some of the possible moment springs in the lattice could be omitted, reducing the complexity and increasing the correspondence between continuum couple-stress theory and discrete representation.
- We have demonstrated that in all loading cases considered there is an effect of the distance to size ratio of the features, which must be taken into account when calibrating the constants. This suggests that actual microstructure data needs to be used for calibrating the site-bond model.
- The loading cases considered were not sufficient for complete determination of the spring constants of the discrete model. Further work is necessary with loading cases that provide different linear combinations of activated springs' kinematics.

- There is the potential that the lattice model, if fully calibrated with curvature-free loading cases, can provide a means of determining the couple-stress constant for a material with given microstructure properties such as average particle size and distance.

Acknowledgements

The support from EPSRC, via Nuclear FiRST Doctoral Training Centre, to Morrison, from EPSRC via grant EP/J019763/1 and BNFL to Jivkov, and from EDF R+D to Yates is gratefully acknowledged.

References

[1] G.B. Sinclair, A.E. Chambers, Strength size effects and fracture mechanics: What does the physical evidence say? Eng Fract Mech 26 (1987) 279-310.
[2] J. Lemaitre, Local approach of fracture. Eng Fract Mech 23 (1986) 523–537.
[3] A.P. Jivkov, D.P.G. Lidbury, P. James, Assessment of Local Approach Methods for Predicting End-of-Life Toughness of RPV Steels. In Proc. PVP2011 (2011) paper 57546, Baltimore, Maryland.
[4] Z.P. Bažant, S.-D. Pang, Activation energy based extreme value statistics and size effect in brittle and quasibrittle fracture. J Mech Phys Solids 55 (2007) 91–131.
[5] A. Pazdniakou, P.M. Adler, Lattice Spring Models. Transp Porous Med 93 (2012) 243–262.
[6] E. Schlangen, E. Garboczi, Fracture simulations of concrete using lattice models: computational aspects. Eng Fract Mech 57 (1997) 319–332.
[7] N.N. Nemeth, R.L. Bratton, Overview of statistical models of fracture for nonirradiated nuclear-graphite components. Nucl Eng Design 240 (2010) 1–29.
[8] P. Grassl, D. Grégoire, L. Rojas Solano, G. Pijaudier-Cabot, Meso-scale modelling of the size effect on the fracture process zone of concrete. Int J Solids Struct 49 (2012) 1818–1827.
[9] A.P. Jivkov, J.R. Yates, Elastic behaviour of a regular lattice for meso-scale modelling of solids. Int J Solids Struct 49 (2012) 3089–3099.
[10] A.P. Jivkov, M. Gunther, K.P. Travis. Site-bond modelling of porous quasi-brittle media. Mineral Mag 76 (2012) 94-99.
[11] F. Cosserat, E. Cosserat, Theory of Deformable Bodies. A. Hermann et Fils, Paris, 1909.
[12] R.D. Mindlin, Micro-structure in linear elasticity. Arch Ration Mech An 16 (1964) 51–78.
[13] W. Nowacki, Theory of Asymmetric Elasticity. Pergamon Press, Oxford, 1986.
[14] M. Garajeu, E. Soos, Cosserat Models Versus Crack Propagation. Math Mech Solids 8 (2003) 189–218.
[15] R.A. Toupin, Theories of elasticity with couple-stress. Arch Ration Mech An 17 (1964) 85-112.
[16] A.R. Hadjesfandiari, G.F. Dargush, Couple stress theory for solids. Int J Solids Struct 48 (2011) 2496–2510.
[17] Y. Wang, P. Mora, Macroscopic elastic properties of regular lattices. J Mech Phys Solids 56 (2008) 3459–3474.

Virtual Crack Closure Technique Based on MSIM Method

Feng Su [1, 2], Jie Wu [1, 2, *], Yongchang Cai [1, 2]

[1] State Key Laboratory for disaster reduction in Civil Engineering, Tongji University, Shanghai, China 200092;
[2] Key Laboratory of Geotechnical and Underground Engineering of Ministry of Education, Tongji University, Shanghai, China 200092;
* Corresponding author: jiee.wu@gmail.com

Abstract The virtual crack closure technique is applied to the calculation of stress intensity factor (SIF) in the framework of meshless Shepard interpolation method (MSIM). In the MSIM interpolation, the Shepard shape functions are used for the partition of unity and the local cover functions are separately constructed for the nodes on the boundary and inside the domain. There are three desirable properties in the MSIM including the completeness property, the delta property which lead to easy boundary treat and the low computational expense of the shape function. In the virtual crack closure technique, the assistant finite element mesh is added beside the crack tips, and the SIFs are calculated naturally and effectively near the tips by using the MSIM. Numerical result for a star-shaped crack in a square plate is reported to demonstrate the correctness and robust of the present method.

Keywords Meshless Shepard interpolation method, Partition of unity method, Virtual crack closure technique, Stress intensity factor

1. Introduction

Calculating of parameters such as stress intensity factor, J integral and strain energy release rate are always highly important but not well addressed in fracture mechanics, and lots of efforts have been devoted by the researchers and engineers in recent years. Analytic solutions for some particular structural components have been proposed and expressed as functions, line graft or tables, which can be referred in some handbooks compiled for the engineers [1-3]. However, the limited number of analytic solutions is far from the satisfaction of the need in the real world. The numerical calculations for the parameters in fracture mechanics become necessary in term of the realistic when considering the dramatically development of the hardware and software of computers [4-9].

J integral was proposed by Rice in 1969 and was introduced into the element free Galerkin method by Brighenti [7]. This method is attractive for the calculation of SIF because of its completeness of theory, high accuracy and path-independent integration. But the inappropriate determination of the radius of the integration circle may degrade the accuracy of J integral when dealing with problems involving short crack segment such as broken cracks and crack tips near the boundaries.

Virtual crack closure technique (VCCT) requires only 2 parameters (the nodal force and displacement near the crack tip) which can be obtained naturally in the FEM method to evaluate the SIF and, besides, the calculation results are often reliable and not effected by the small length of crack tips. Consequently, it is paid increasingly more attention by the researchers. However, at present, the VCCT is always carried out in the framework of the FEM, which is unavoidably encountered with the mesh refinement. More details about VCCT can refer to [10].

To alleviate this drawback, the meshless Shepard interpolation method (MSIM) [11] is used to model the discontinuous stress field near the crack and stress singularity near the crack tips and then, the stress and displacement results are used by the VCCT to evaluate the SIF. The time consuming remeshing process is unnecessary in this method and makes the simulation much more reliable and possessing high accuracy. Details of meshless simulation of discontinuous model and the determination of the SIF are provided. In the end, the method described here is used to analyze a square plate with a star-shape crack. The results obtained by the present method are compared with

reference solutions available showing the implementation effectively to model the discontinuous and to evaluate the SIF.

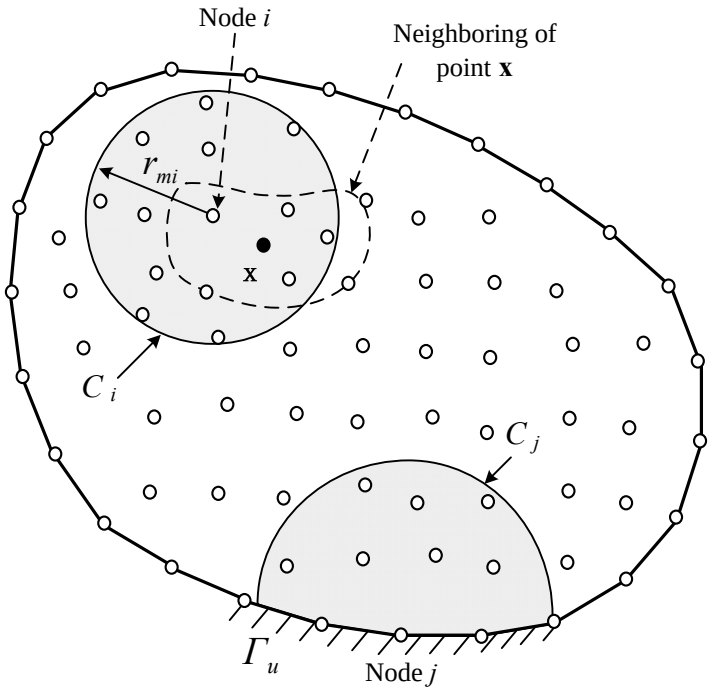

Figure 1. Discrete model of domain Ω

2. The PU-based meshless Shepard interpolation

Consider a two-dimensional domain Ω, and let Ω be discretized by N scattered nodes as shown in Fig. 1. For each node i, a circle cover (subdomain)

$$C_i = \{\mathbf{x} \in \Omega : \|\mathbf{x} - \mathbf{x_i}\| \le r_{mi}\}, \quad (1)$$

is attached. Here, r_{mi} is the radius of the cover C_i. The displacements associated with the node i are denoted by (u_{i0}, v_{i0}).

For a given point X($X \in \Omega$), based on the PU concept, a new interpolation $u^h(X)$ at X can be defined by

$$u^h(X) = \sum_{i-1}^{n} \emptyset_i^0(x)\, u_i^i(X) \quad (2)$$

where n is the total number of neighboring nodes where the position of point $\mathbf{X}$ located in the cover support. $u_i^l(\mathbf{x})$ are the cover interpolations defined on the cover of node i.

In MSIM, the interpolations are constructed separately for the nodes on the essential boundary or in the domain.. $\phi_i^0(\mathbf{x})$ is the Shepard function or zeroth-order function

$$\phi_i^0(\mathbf{x}) = \frac{w_i(\mathbf{x})}{\sum_{i=1}^{n} w_i(\mathbf{x})} \quad (3)$$

where $w_i(\mathbf{x})$ is the weight function associated with node i.

The Shepard function $\phi_i^0(\mathbf{x})$ in Eq. (3) satisfies the delta property if weight function is singular at $\mathbf{x} = \mathbf{x}_i$. The weight function[12] adopted here is

$$w_i(\mathbf{x})=\begin{cases}\dfrac{d_{mi}^2}{d_i^2+\varepsilon}\cos^2\left(\dfrac{\pi d_i}{2d_{mi}}\right), & d_i \le d_{mi}\\ 0 & d_i > d_{mi}\end{cases} \tag{4}$$

where $d_i=\|\mathbf{x}-\mathbf{x}_i\|$ is the Euclidian distance between the point $\mathbf{x}$ and node $\mathbf{x}_i$, and ε is a small number to avoid the numerical difficulty resulting from the singularity at nodes.

On each cover C_i, a local approximation is first expressed as

$$u_i^l(\mathbf{x}) = \mathbf{P}^{\mathrm{T}}(\mathbf{x})\mathbf{a}(\mathbf{x}) = \sum_{k=1}^{m} p_k(\mathbf{x})a_k \tag{5}$$

where m is the number of terms in the basis, $\mathbf{p}^{\mathrm{T}}(\mathbf{x})=[1,x,y,xy.....]$ are the nominal basis functions, a_i is their coefficients. Here, the bilinear basis $\mathbf{p}^{\mathrm{T}}(\mathbf{x})=[1,x,y,xy]$ is used as an example to introduce the construction of the MSIM interpolation.

2.1 Cover interpolation for the nodes not located on the essential boundary

For the typical node i not located on the essential boundary, the local cover approximation is directly taken as

$$u_i^l(\mathbf{x}) = u_i^{\ln}(\mathbf{x}) = a_{1i} + a_{2i}x + a_{3i}y + a_{4i}xy \tag{6}$$

Let the cover function at the node i satisfy the condition

$$u_i^{\ln}(x_i) = a_{1i} + a_{2i}x_i + a_{3i}y_i + a_{4i}x_iy_i = u_{i0} \tag{7}$$

Hence,

$$a_{1i} = u_{i0} - a_{2i}x_i - a_{3i}y_i - a_{4i}x_iy_i \tag{8}$$

Substituting Eq. (8) into Eq. (3) leads to

$$u_i^{\ln}(\mathbf{x})=u_{i0}+a_{2i}(x-x_i)+a_{3i}(y-y_i)+a_{4i}(xy-x_iy_i) = \overline{\mathbf{\Psi}}^i\mathbf{T}_x^i \tag{9}$$

where

$$\overline{\mathbf{\Psi}}^i(\mathbf{x})=[\Psi_1^i \quad \Psi_2^i \quad \Psi_3^i \quad \Psi_4^i]=[1 \quad x-x_i \quad y-y_i \quad xy-x_iy_i] \tag{10}$$

$$\mathbf{T}_x^i=[u_{i0} \quad a_{2i} \quad a_{3i} \quad a_{4i}]^T \tag{11}$$

Similarly, the y-displacement interpolation $v_i^{\ln}(x_i)$ is given by

$$v_i^{\ln}(\mathbf{x})=v_{i0}+b_{2i}(x-x_i)+b_{3i}(y-y_i)+b_{4i}(xy-x_iy_i) = \overline{\mathbf{\Psi}}^i\mathbf{T}_y^i \tag{12}$$

where

$$\mathbf{T}_y^i=[v_{i0} \quad b_{2i} \quad b_{3i} \quad b_{4i}]^T \tag{13}$$

Eq. (9) and (12) can be rewritten in the form

$$\mathbf{u}_i^{\ln}(\mathbf{x})=\begin{Bmatrix}u_i^{\ln}(\mathbf{x})\\ v_i^{\ln}(\mathbf{x})\end{Bmatrix}=\mathbf{\Psi}^i\mathbf{T}^i \tag{14}$$

where

$$\mathbf{\Psi}=\begin{bmatrix}1 & 0 & x-x_i & 0 & y-y_i & 0 & xy-x_iy_i & 0\\ 0 & 1 & 0 & x-x_i & 0 & y-y_i & 0 & xy-x_iy_i\end{bmatrix} \tag{15}$$

$$\mathbf{T}=[u_{i0} \quad v_{i0} \quad a_{2i} \quad b_{2i} \quad a_{3i} \quad b_{3i} \quad a_{4i} \quad b_{4i}]^T \tag{16}$$

(u_{i0},v_{i0}) are the nodal displacement of node i, $(a_{2i},b_{2i},a_{3i},b_{3i},a_{4i},b_{4i})$ are the extra freedoms of cover C_i. From Eq. (14), we observe that

$$\mathbf{u}_i^{\ln}(x_i, y_i) = \begin{Bmatrix} u_{i0} \\ v_{i0} \end{Bmatrix} \tag{17}$$

It means that the cover function of the node i is interpolated in terms of nodal displacements (u_{i0}, v_{i0}).

2.2 Cover interpolation for the nodes located on the essential boundary

For a typical node j located on the essential boundary, suppose that there M nodes in the support of cover C_j (Fig. 1). At the local cover C_j, a discrete error norm is defined as

$$u_j^{lb}(\mathbf{x}) = \overline{\mathbf{\Phi}}^j(\mathbf{x})\mathbf{u}_0^j = \sum_{k=1}^{M} \overline{\Phi}_k^j(\mathbf{x}) u_k \tag{18}$$

where

$$\overline{\mathbf{\Phi}}^j(\mathbf{x}) = [\Phi_1^j(\mathbf{x}) - \Phi_1^j(\mathbf{x}_j), \ \cdots, \ 1 + \Phi_j^j(\mathbf{x}) - \Phi_j^j(\mathbf{x}_j), \ \cdots, \ \Phi_M^j(\mathbf{x}) - \Phi_M^j(\mathbf{x}_j)] \tag{19}$$

x_j is the coordinate of node j.

Similarly, the y-displacement interpolation $v_j^{lb}(\mathbf{x})$ is given by

$$v_j^{lb}(\mathbf{x}) = \mathbf{\Phi}^j(\mathbf{x})\mathbf{V}_0^{\ j} = \sum_{k=1}^{M} \Phi_k^j(\mathbf{x}) v_k \tag{20}$$

where

$$\mathbf{V}_0^j = \begin{bmatrix} v_{10} & v_{20} & \cdots & v_{M0} \end{bmatrix} \tag{21}$$

Eq. (18) and (20) can be rewritten in the form

$$\mathbf{u}_j^{lb}(\mathbf{x}) = \begin{Bmatrix} u_j^{lb}(\mathbf{x}) \\ v_j^{lb}(\mathbf{x}) \end{Bmatrix} = \mathbf{\Phi}_*^j \mathbf{D}^j \tag{22}$$

where

$$\mathbf{\Phi}_*^j = \begin{bmatrix} \overline{\Phi}_1^j & 0 & \cdots & \overline{\Phi}_M^j & 0 \\ 0 & \overline{\Phi}_1^j & \cdots & 0 & \overline{\Phi}_M^j \end{bmatrix} \tag{23}$$

$$\mathbf{D}^j = \begin{bmatrix} u_{10} & u_{10} & u_{20} & u_{20} & \cdots & \cdots & u_{M0} & u_{M0} \end{bmatrix} \tag{24}$$

Substituting Eq. (14) and (22) into Eq. (2) leads to

$$u^h(\mathbf{x}) = \sum_{i=1}^{n} \phi_i^0(\mathbf{x}) u_i^l(\mathbf{x}) = \sum_{i=1}^{n_1} \phi_i^0(\mathbf{x}) u_i^{\ln}(\mathbf{x}) + \sum_{j=1}^{n_2} \phi_j^0(\mathbf{x}) \left(\sum_{k=1}^{M} \overline{\Phi}_k^j(\mathbf{x}) u_k \right) \tag{25}$$

where $n = n_1 + n_2$ is the total number of neighboring nodes where the position point $\mathbf{x}$ located in the cover support, n_1 denotes the node set not on the essential boundary, n_2 denotes the node set located on the essential boundary. The MSIM possesses the delta property and preserves the completeness of the field up to the order of the basis. The proof of these properties can be referred to [11].

3. The application of virtual crack closure technique in MSIM

Virtual crack closure technique (VCCT) is proposed by Rybicki and Kanninen [10] mainly dealing with two dimensional problems. In this method, the strain energy release rate for the crack propagation is always calculated based on the FEM analysis results. Here, taking a finite crack body as an example, the basic concept of virtual crack closure technique will be briefly introduced.

The length of crack is a, and the propagation length is Δa. When the quadrangle mesh is employed,

the stain energy release rate of the crack could be calculated by

$$G_I \cong \frac{F_{y1}\Delta v_{3,4}}{2B\Delta a} \tag{26a}$$

$$G_{II} \cong \frac{F_{x1}\Delta u_{3,4}}{2B\Delta a} \tag{26b}$$

where, F_{x1} and F_{y1} are the node forces (X direction, Y direction, respectively) belonging to node 1. $\Delta v_{3,4}$ and $\Delta u_{3,4}$ are the Y direction displacement and X direction displacement between node 3 and 4, respectively.

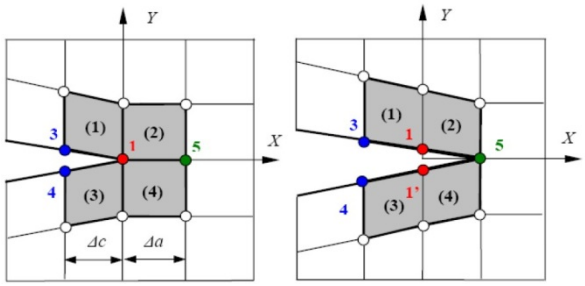

Figure 2. Illustration of calculating the strain energy release rate by the VCCT

Due to the fact that the virtual crack closure technique is always implemented in the framework of FEM, the remeshing during the simulation of crack propagation are unavoidably encountered. To solve this problem, the virtual crack closure technique will be introduced into MSIM in this section. Both the advantages of the two methods will be maintained to make the evaluation of the SIFs much more efficient. The progress will be carried out mainly in the following steps:

1) Construction of meshless numerical model;
2) Calculation of the displacement of the nodes based on the MSIM;
3) Setting the assistant mesh near the crack tip in order to calculate the nodal force
4) Constructing the global stiffness matrix of the assistant mesh and calculating the displacement of the node in the assistant mesh based on the MSIM.
5) Getting the nodal force near the crack tip by $F_e = K_e a_e$, where F_e is the assistant nodal force, K_e is the global stiffness matrix of the assistant mesh, a_e is the displacement vector of the assistant nodes.

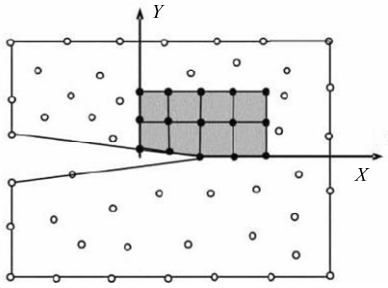

Figure 3. The assistant mesh employed in the MSIM to evaluate the nodal force

4. A case study on a finite plate with star-shaped crack

In this section, a star-shaped crack in a square plate subjected to bi-axial tension as shown in Fig.4 will be examined. The analysis is treated as plate strain problem, and the plate size is taken to be W = 2.0, and the bi-axial tension to be unity. The material constants are the Young's modulus

$E = 1 \times 10^7$ and the Poisson's ratio $\nu = 0.3$. The SIF of node A and B are calculated by both of the linear basis function and the enriched basis function with virtual crack closure technique. A meshless model is constructed as shown in Fig.5. The influence of crack geometry on the SIFs is also investigated by varying W/a (e.g.0.1W, 0.3W, 0.5W, 0.7W).

The normalized stress intensity factors at tips A and B are defined as $F_I^A = K_I^A / \sigma\sqrt{\pi a}$, $F_I^B = K_I^B / \sigma\sqrt{\pi a}$, $F_{II}^B = K_{II}^B / \sigma\sqrt{\pi a}$. The comparison between the calculation results and the reference solutions available [13] are demonstrated in Table 1. From this table, the excellent agreement of the computed SIF results and the reference solutions can be easily seen.

Table 1. Normalized SIFs comparison for a star-shaped crack

a/W	θ	*	MSIM(linear basis)	RE（%）	MSIM(enriched basis)	RE（%）
	F_I^A	0.751	0.736	-1.998	0.754	-0.533
0.1	F_I^B	0.769	0.758	-1.430	0.766	-0.391
	F_{II}^B	0.000	0.000	0.000	0.000	0.000
	F_I^A	0.793	0.778	-2.031	0.789	-0.504
0.3	F_I^B	0.798	0.786	-1.253	0.795	-0.376
	F_{II}^B	0.002	0.002	0.000	0.002	0.000
	F_I^A	0.886	0.868	-1.891	0.883	-0.456
0.5	F_I^B	0.926	0.912	-1.511	0.922	-0.432
	F_{II}^B	0.018	0.0176	-2.122	0.018	0.000
	F_I^A	1.097	1.084	-1.485	1.102	0.339
0.7	F_I^B	1.237	1.218	-1.536	1.233	-0.323
	F_{II}^B	0.059	0.058	-1.724	0.0586	-0.678

*Daux et al. (2000)

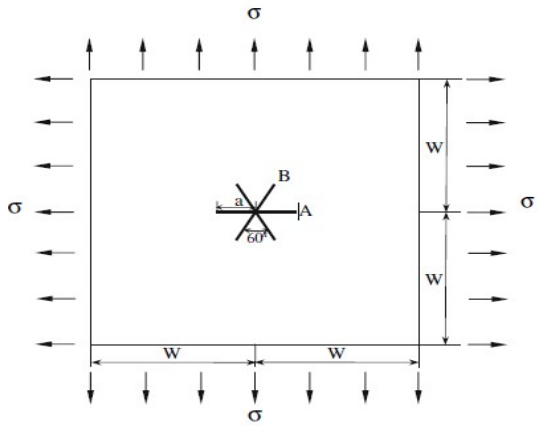

Figure 4. A star-shaped crack in a square plate under bi-axial tension

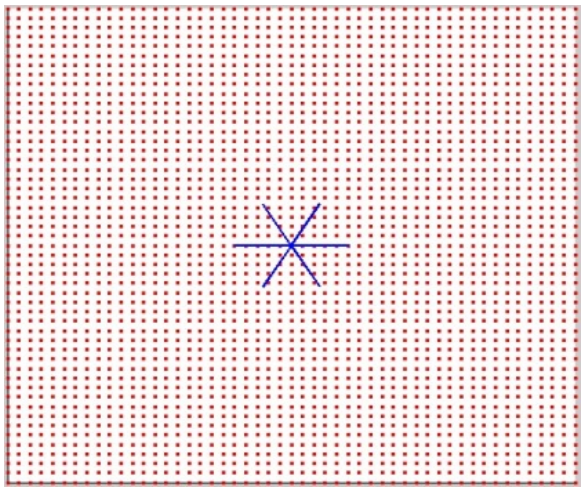

Figure 5. The meshless model of a star-shaped crack in a square plate

5. Conclusions

The application of virtual crack closure technique into the MSIM is presented in this paper. The remeshing and the refinement near the crack tips can be avoided in the present method, and as a result, it makes the evaluation of the SIF much easier and more efficient. The virtual crack closure technique is based on the stress analysis using the MSIM for discontinuous model here, however other meshless methods are equally viable, e.g., the element-free Galerkin method (EFG), and the meshless local-Petrov Galerkin method (MLPG). The numerical results indicate that the present method effectively calculates the SIF near the crack tips and possess a high accuracy.

Acknowledgements

The authors gratefully acknowledge the support of Program for New Century Excellent Talents (NCET-12-0415), the National Science and Technology Support Program (2011BAB08B01), and the Fundamental Research Funds for the Central Universities.

References

[1] Rooke D. P., Cartwright D.J. Compendium of stress intensityfactors[M]. London: Her Majesty’s Stationary Office, 1976
[2] Tada H., Paris P. C., Irwin G. R. The stress factor hand book [M]. Hellertown: Del Research Corporation, 1985
[3] Murakami Y. Stress intensity factors handbook[M]. New York: Pergamon, 1987
[4] Shahani A.R., Habibi S.E. Stress intensity factors in a hollow cylinder containing circumferential semi-elliptical crack sub-jected to combined loading[J]. International Journal of Fatigue, 2007, 29(1):128- 140
[5] Zhou W.Y., Xiao H.T.. Three dimension discontinuous displacement method and the strongly singular and hypersing ular integrals[J]. Acta Mechanica Sinica, 2002, 34(4): 645-651
[6] Citatella R., Perella M. Multiple surface crack propagation: numerical simulations and experimental tests[J]. Fatigue Fract Engng Mater Struct, 2005, 28(1/2): 135-148
[7] Brighenti R. Application of the element-free Galerkin meshless method to 3-D fracture mechanics problems[J]. Engineering Fracture Mechanics, 2005, 72(18):2808 - 2820
[8] Chihdar Y., Alireza C., Tomblin J.S. Strain energy release rate determination of prescribed cracks in adhesively-bonded single-lap composite joints with thick bondlines [J]. Composites: Part B, 2008, 39(5): 863 - 873.
[9] Rosa M., Freitas D.M. Characterisation of the edge crack torsion (ECT) test for the measurement of the mode III interlaminar fracture toughness[J]. Engineering Fracture Mechanics, 2009, 76(18): 2799 -2809.
[10] Rybicki E F, Kanninen M F. A finite element calculation of stress intensity factors by a modified crack closure integral. Engineering Fracture Mechanics, 1977, 9: 931-938
[11] Cai Y.C., Zhu H.H. A PU-based meshless Shepard interpolation method satisfying delta property [J].

Engineering Analysis with Boundary Elements, 2010, 34(1): 9-16.
[12] Lancaster P., Salkauskas K. Surfaces generated by moving least squares methods [J]. Mathematics of Computation, 1981, 37(2): 141-158
[13] Daux C., Moes N., Dolbow J., Sukumar N., Belytschko T. Arbitrary branched and intersecting cracks with the extended finite element method. Computer Methods in Applied Mechanics and Engineering, 2000, 48:1741- 1760.

I/II Mixed Mode Fracture in Graphene

Bin Zhang*, Lanjv Mei

[1] State Key Laboratory of Mechanics and Control of Mechanical Structures, and College of Aerospace Engineering, Nanjing University of Aeronautics and Astronautics, Nanjing 210016, China
* Corresponding author: beenchang@nuaa.edu.cn

Abstract Nanoscale fracture of pre-cracked graphene under coupled in-plane opening and shear mechanical loading in far-field is investigated by extensive molecular dynamics simulations. Under opening-dominant loading, zigzag edge cracks grow self-similarly. Otherwise, complex mechanical stresses concentrated in the vicinity of crack tip can manipulate the direction of crack initiation changing by 30° (or multiples of 30°) to the original crack line. Toughness determined from obtained critical stress intensity factors 2.63 ~ 3.38 nN $Å^{-3/2}$ is relatively low, which demonstrates graphene is intrinsically brittle opposite to its exceptional high strength at room temperature. Graphene is easier to break along zigzag direction. Torn edges are in either zigzag or armchair manner, while zigzag edges are observed prevalently, and armchair edges are formed occasionally under particular loading conditions. Crack kinking is related to the proportion of opening and shear components of loading, and topological defects frequently appear at turning points. Our theoretical results indicate that cracking of graphene has a dependence on local mechanical stresses, edge energy and dynamic effects, which provide a possible way to regulate the edge structure of graphene.

Keywords Graphene, Crack kinking, Stress intensity factor, Molecular dynamics

1. Introduction

Graphene, as an atomic monolayer of graphite, is extensively studied after successful laboratory exfoliation [1], and it has attracted significant attention from the scientific community for its remarkable mechanical and electrical properties that are currently being explored for a number of applications including nanoelectromechanical systems, nano-electronics, *etc*. Recent mechanical experiments have shown that graphene is the strongest material measured hitherto with an elastic modulus of 1.0 TPa [2], which exceeds those of any previously existing materials. Rafiee et al. also reported that graphene as reinforcement has extraordinary effectiveness to resist fracture and fatigue in composites [3]. However, Hashimoto et al. [4] have provided a direct experimental evidence for the existence of defects in graphene layers. The extraordinary mechanical properties can be affected by the presence of defects that cause a more reduction of the strength. The existing works have treated defects in graphene as cracks that can initiate fracture.

The research on fracture of graphene can date back to the simulations conducted by Omeltchenko et al. [5], in which a notched graphite sheet was loaded uniaxial tension and then underwent cleavage. However, that retention of the cutoff function of early version potential makes the quantitative aspects of results questionable. Recently, Belytschko et al. [6-8] carried out series of theoretical researches on the fracture of pre-cracked graphene under uniaxial tensile loading. The critical stress intensity factors under pure opening loading were obtained for zigzag and armchair cracks, while the propagation direction was manually specified. Lu et al. [9] also investigated fracture of graphene nano-ribbons (GNRs) under uniaxial tension. Furthermore, shear deformation plays an important role in the wrinkling and rippling behavior of graphene, which, in turn, controls charge carrier scattering and electron mobility [10]. It is even possible to modulate the graphene energy-gap from 0.0 to 0.9 eV by combining shear deformations with uniaxial strains [11]. In point

of fact, mixed-mode fracture inevitably occurred during the tearing of graphene sheets from graphite or other substrates to obtain free-standing sheets or narrow ribbons [12]. In [5], multiple crack branched sprouting off the primary crack front, thus tilted cracks were actually under mixed tensile and shear loading. Besides theoretical studies, Kim et al. [13] presented investigations on tears in suspended monolayer graphene membranes by high-resolution transmission electron microscopy (HRTEM). However, radiation damage by electron-beam energy and applied dose cannot be neglected for light element materials due to the limitations of HRTEM [14]. It is still a challenge to observe experimentally the cracking of graphene under pure mechanical loading without electromechanical coupling effects.

Thus far, complex mechanical loading is rarely considered in previous works on fracture in graphene. Here we will show our extensive molecular dynamics (MD) simulations on nanoscale fracture of graphene under coupled opening and in-plane shear loading of far-field (I/II mixed-mode fracture). A boundary layer model embedded with a straight crack along either zigzag (ZZ) or armchair (AC) edge is applied with complex stresses by a displacement boundary governed by crack-tip asymptotic solution. The modified second-generation reactive empirical bond-order (REBO) potential [15] is used by shifting the cut-off distance and removing cut-off function to avoid unphysical dramatic increase in the interatomic force. The evolution of atomically cleaving of graphene is then revealed without manually specified direction of crack propagation.

2. Methodology and model

The well established REBO potential for hydrocarbons has been widely used [5, 9, 16-18] to specifically describe the interatomic interaction of carbon atoms lattices and nonlocal effects via an analytic function, Lennard-Jones 6-12 potential was used to mimic the nonbonding interatomic interaction, and the potential can correctly describe the bond breaking and switching between carbon atoms. In REBO potential, two cutoff distances 1.7 Å and 2.0 Å are initially set for a smooth transition of cutoff function from 1 to 0 to limit the range of covalent interactions as the interatomic distance increases. However, as noted in several previous studies [19, 20], such a cutoff function generates spurious bond forces near the cutoff distance, which will lead to unphysical results due to discontinuity in the second derivative of the cutoff function. This artifact defect shall be avoided in the study of graphene fracture. In this study, the cutoff function is taken to be 1.0 within a cutoff distance of 1.92 Å [21] and zero otherwise, as suggested by the developers [19]. It was found that the numerical results up to fracture of GNRs are unaffected if the cutoff distance is within 1.9 Å to 2.2 Å [9].

A size-reduced model containing a small circular-shaped domain cut from the crack tip is utilized to model semi-infinite cracks in real graphene. A reasonable domain size is chosen so that its outer boundary falls in the *K*-dominant zone, which can make all-atom simulations computationally efficient. We consider an initially straight crack subject to in-plane opening and shear loading characterized by the local stress intensity factor (SIF) K field. Two prevalent cracks with orientations along ZZ or AC edges are chosen in Figure 1. Two or three rows of atoms are removed to generate cracks in our models, and the distance between two crack surfaces is big enough to

avoid self sealing, especially in pure shear case. The length of crack is more than 10 times lattice spacing to avoid unphysical Griffith fracture stress and flaw insensitiveness [22]. A total of around 4000 carbon atoms in our disk models with a radius r = 60Å are initially relaxed until the energy of the system is fully minimized for a specified temperature. The thickness of graphene is assumed to be 3.335Å under plane stress condition. Hereafter our results are divided by 3.335Å to make connection of a two-dimensional lattice with a three-dimensional solid.

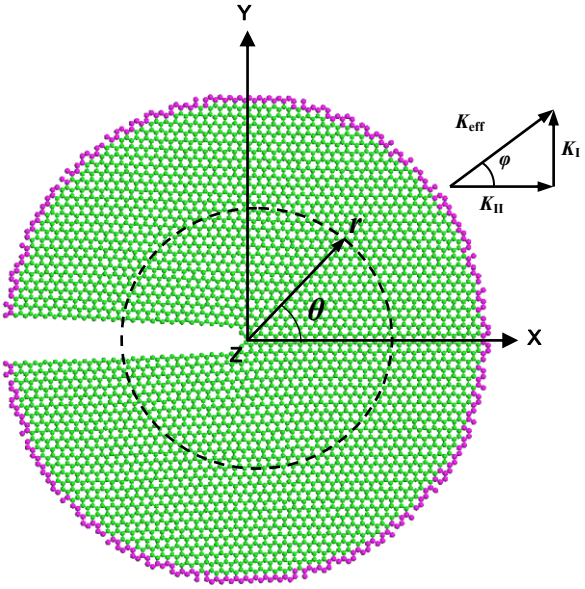

Figure 1. Boundary layer MD model and coordinates. A pre-existing straight crack along zigzag edge is embedded in a two-dimensional graphene lattice (green). The outer boundary layer (pink atoms) is subject to displacement loadings.

Williams [23] has given the asymptotic expansion of the displacement field around the crack tip in an isotropic linear elastic body. At a given SIF K^{app} applied by far-field loadings, the crack-tip asymptotic solution is as [24]

$$u_{\text{x}} = \frac{1+v}{E}\sqrt{\frac{r}{2\pi}}\left[K_{\text{I}}^{app}\cos\frac{\theta}{2}\left(k-1+2\sin^2\frac{\theta}{2}\right)+K_{\text{II}}^{app}\sin\frac{\theta}{2}\left(k+1+2\cos^2\frac{\theta}{2}\right)\right], \tag{1}$$

$$u_{\text{y}} = \frac{1+v}{E}\sqrt{\frac{r}{2\pi}}\left[K_{\text{I}}^{app}\sin\frac{\theta}{2}\left(k+1-2\cos^2\frac{\theta}{2}\right)-K_{\text{II}}^{app}\cos\frac{\theta}{2}\left(k-1-2\sin^2\frac{\theta}{2}\right)\right]. \tag{2}$$

where radius r and polar angle θ are defined in Figure 1, u_{x} and u_{y} are displacements in X and Y directions, respectively. Young's modulus E is 1.0 TPa [2], and Poisson's ratio v is 0.165 [25], and $k = (3\text{-}v)/(1+v)$ for plane stress here. $K_{\text{I}}^{\text{app}}$ and $K_{\text{II}}^{\text{app}}$ are SIF components specified by opening and shear stresses. Phase angle φ (loading mixed parameter or equivalent crack angle) is defined as $\varphi = \tan^{-1}(K_{\text{I}}^{\text{app}}/K_{\text{II}}^{\text{app}})$, and an effective SIF at the initial crack length is evaluated as $(K_{\text{eff}}^{\text{app}})^2 = (K_{\text{I}}^{\text{app}})^2 + (K_{\text{II}}^{\text{app}})^2$, see Figure 1. Therefore the far field behavior of pristine graphene is assumed to be well-represented by the solution since the singularity decreases apart from the crack tip. The boundary condition is similar to a suspended graphene spanning a hole in the TEM grid.

Mixed-mode loading in classical fracture mechanics is then imposed by initially assigning all atoms in the displacement field given by the crack-tip asymptotic solution of a specified initial $K_{\text{eff}}^{\text{app}}$. In Figure 1, atoms (pink) on the outer boundary layer are held fixed, while all the other atoms (green) are set free, and the atomic configuration is then relaxed. Then we implement the deformation-control method by applying displacement increments gradually to the fixed boundary layer separately every 500 MD steps. At each applied loading, the statically equilibrium lattice structure is calculated to minimize the total energy by the limited memory BFGS geometry optimization algorithm [26], thereby local energy minimum configurations are obtained. The velocity-Verlet time stepping scheme is used with a time step 1.0 fs at predominantly 300K with a Berendsen thermostat, and this yields a strain rate 0.0002 ps^{-1} primarily. We note that MD simulations are often sensitive to the temperature control and the loading rate, thus our results mainly provide a qualitative understanding of the fracture mechanisms.

3. Results and discussion

The energy-balance criterion by Griffith is the fundamental fracture criterion for brittle continua, which states that a crack meets the critical growth condition when the net change in the total energy of the system vanishes upon crack extension by an infinitesimal distance [27]. Using the relationship between the critical SIF of Griffith K_{th}^{c} and the energy release rate (twice of the surface energy density γ_s) for linear elastic materials, one has $K_{\text{th}}^{\text{c}} = (2E\gamma_s)^{1/2}$ [24]. Since E is assumed isotropic for graphene, K_{th}^{c} will be mainly determined by γ_s. By use of γ_s = 1.041 eV/Å and 1.091 eV/Å [28, 29] for ZZ and AC cracks, we get K_{th}^{c} = 3.162 nN $\text{Å}^{-3/2}$ and 3.238 nN $\text{Å}^{-3/2}$, respectively.

Table 1. Effective critical stress intensity factors $K_{\text{eff}}^{\text{c}}$ (nN $\text{Å}^{-3/2}$) of zigzag and armchair cracks in graphene under far-field loading at various phase angles φ.

φ		0°	15°	30°	45°	60°	75°	90°	90°	90°	90°	90°	90°
$K^{\text{c}}_{\text{eff}}$	ZZ	3.06	2.75	2.63	2.90	3.15	3.02	3.05	3.16[a]	4.21[b]	2.64[c]	6.0[d]	10.32[e]
	AC	2.87	3.30	3.28	2.87	2.78	2.85	3.38	3.24[a]	3.71[b]			

[a] Critical stress intensity factor of Griffith K_{th}^{c}; [b] Ref. 6; [c] Ref. 7; [d] Ref. 5; [e] Ref. 30.

In Table 1 and Figure 2, our results show that the effective critical SIF $K_{\text{eff}}^{\text{c}}$ of I/II mixed-mode loading falls in the range between 2.63 nN $\text{Å}^{-3/2}$ and 3.38 nN $\text{Å}^{-3/2}$ varying with φ, relatively low compared to steel, which reveals that graphene is brittle at 300K opposing its ultrahigh strength. As the difference of geometric chiral angle between AC and ZZ edges is 30°, similar trends for $K_{\text{eff}}^{\text{c}}$ are observed if φ is shifted by 30°, see Figure 2. $K_{\text{eff}}^{\text{c}}$ along ZZ edges are slightly lower indicating smaller toughness, thus graphene is easier to break along ZZ direction. For ZZ cracks under pure opening tension (φ = 90°), our $K_{\text{eff}}^{\text{c}}$ are reasonable with theoretical K_{th}^{c}, and compared with available reported datum, Table 1, the discrepancy may be due to different crack models [5, 7] and potentials [6, 30].

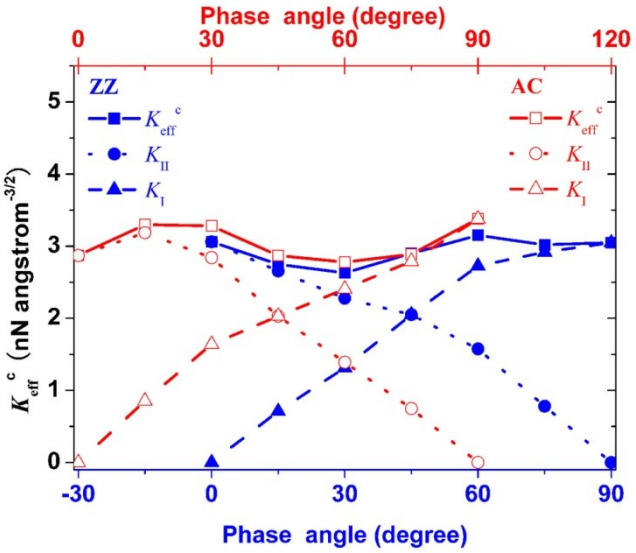

Figure 2. Effective critical stress intensity factors K_{eff}^{c} of graphene cracks, ZZ in blue and AC in red, changing with phase angles φ of far-field loading. K_I and K_{II} are opening and shear components of K_{eff}^{c}.

Up to now, no single criterion in classical continuum mechanics can give satisfactory predictions for crack initiation direction under all loading conditions. All existing criteria predict that a crack under mode II (in-pane shear, $\varphi = 0°$) loading propagates along about a 70° direction with respect to the original crack line. However, a mode II crack either propagates in mode I (opening, $\varphi = 90°$) or mode II, depending on material properties and load magnitudes [31].

Continuum criteria seem to lose efficacy in predicting direction of crack initiation in graphene. In Figure 3a-f, our results show that ZZ cracks initiate in the direction of an angle $\beta = 120°$ deviating from the original edge when in-plane shear loading is prevailing, β maintains unchanged till $\varphi = 60°$ and fresh edges are in zigzag (blue). Further increasing φ will induce the transition of β. At $\varphi = 65°$, β changes to 150°, and fresh edges are in armchair (red). This configuration coincides with the prediction that zigzag-armchair junctions with an angle of 150° would be more stable [32, 5]. Once $\varphi > 65°$, opening loading becomes dominant, crack grows self-similarly along original direction and fresh edges are in zigzag again.

For AC cracks in Figure 3g-l, initiation angle $\beta = 90°$ at $\varphi = 0°$, new crack tips nucleate prior to initial tip, and fresh edges are in zigzag. At $\varphi = 26.5°$, propagating direction changes to $\beta = 120°$, and fresh edges are in armchair. When $\varphi > 26.5°$, β transforms to 150° and keeps unchanged till $\varphi = 90°$, and fresh edges are in zigzag again.

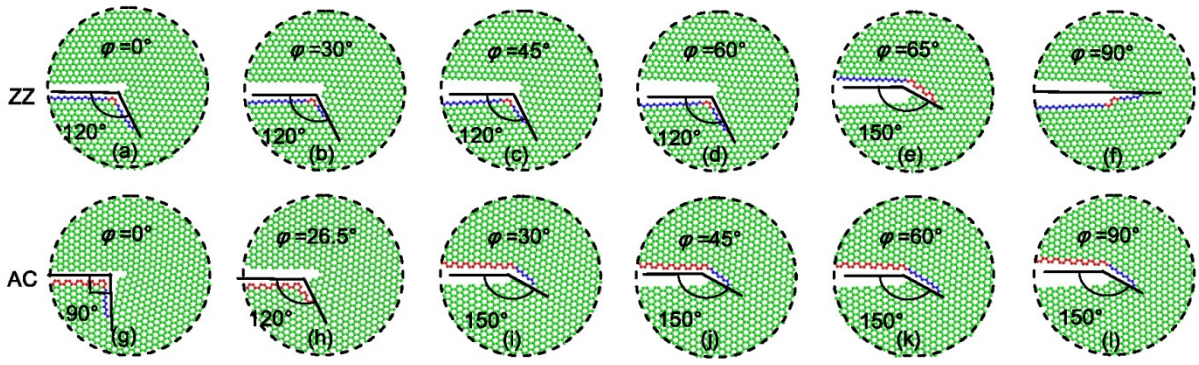

Figure 3. Insets (r = 30Å, cut from the whole models in Figure 1) of crack initiation in flawed graphene (green) under I/II mixed-mode loading. (a)-(f) ZZ cracks initiation at phase angle φ = 0°, 30°, 45°, 60°, 65°, 90°, and (g)-(l) AC cracks at φ = 0°, 26.5°, 30°, 45°, 60°, 90°, correspondingly.

Fresh edges exhibit mostly in zigzag, and armchair edges are formed during the transition of propagating direction. Under loading $K_{\text{eff}}^{\text{app}}$ = 3.21 nN Å$^{-3/2}$ at φ = 65° in Figure 3e, zigzag crack (blue) kinks and armchair edge (red) is formed. In Figure 3h, armchair crack (red) turns its direction with 120° followed by armchair edge (red) under $K_{\text{eff}}^{\text{app}}$ = 3.25 nN Å$^{-3/2}$ at φ = 26.5°. This is similar to experimental tears kinking within graphene membrane under complex mechanical stress applied by circular boundary of the Quantifoil holey carbon TEM grid [13].

With the increasing of complex loading, the stress concentrated around crack tip morphs the hexagonal carbon rings into deformed shapes. Once the bonds at the tip rotated or broken, the hexagonal symmetry of the graphene lattice is destroyed with the formation and motion of topological defects, which leads to crack kinking. The dynamic effect of a fast fracture in MD simulations can also cause kinking, while branching is not observed. Further crack extension would proceed by alternating sequence of bond breaking or rotation.

Graphene edges are of particular interest since their orientation determines the electronic properties. Crack extension with the formation of fresh edges is mainly caused by local high strain concentrated around crack tips. Our simulations demonstrate that torn edges maintain straightness and clean in either zigzag or armchair direction, in Figure 3, and can change directions by 30° or multiples of 30°, in Figure 3, coincided with experiments [13]. Under pure opening loading (φ = 90°), the growth of zigzag cracks is self-similar whereas armchair cracks advance in an irregular manner, consistent with previous reports [6]. The direction of crack growth changes definitely under coupled opening and shearing stresses and edges interconvert between ZZ and AC. Cracks preferably grow along zigzag directions in agreement with previous theoretical simulations [9, 12]. By Griffith criterion, this suggests lower edge energy in ZZ opposed to AC, which is coincided with simulations by empirical potentials [28, 29, 33]. More abundant ZZ edges appeared may be due to lower edge energy, somewhat local residual stresses and dynamic fracture effects. Experiments also showed long-term stability [34] of ZZ edges, and more ZZ edges were initially formed at high temperatures [35]. In [13], the initial torn edges were along ZZ direction under pure mechanical stress during the graphene transfer process, while heating and chemical effects, knock-on sputtering induced by electron irradiation in TEM inevitably influenced crack extension stimulated afterwards.

Another experiment [36] also confirmed that the zigzag edge is more stable than the armchair edge, although the opposite has been predicted theoretically by *ab initio* calculations which depend strongly on the choice of the density functional among different DFT calculations yielding dramatically different values in quantitative scattering.

During our simulations, total energy at each strain level is minimized for each equilibrium lattice structure. The kinematic energy changes slightly while potential energy increases gradually since the temperature is coupled with a thermostat. Energy jumps are infrequently observed, thus lattice-trapping effects are negligibly small for long-range potentials we used. Undoubtedly, temperature and strain rate can quantitatively affect K^c that increases slightly with increase of strain rates while decreases with temperature. At high temperature beyond 1000K, fracture shows plastic behaviors opposite to brittle at room temperature, the crack edges are reconstructed, fresh surfaces are bridged with carbon chains, and formation and motion of defects and vacancies appear frequently.

4. Concluding remarks

In summary, graphene embedded with pre-existing zigzag or armchair crack under complex mechanical stresses is studied by extensive molecular dynamics simulations based on the modified REBO potential. An asymptotic expansion of the displacement field in the region of crack tip is adopted to apply loading combined with in-plane opening and shear stresses. The critical effective stress intensity factors are obtained in the range of 2.63 nN $Å^{-3/2}$ to 3.38 nN $Å^{-3/2}$ varied with the phase angle of far-field loading, the predicted low toughness indicates that strong graphene is absolutely brittle at room temperature. The direction of crack initiation is also dependent on the phase angle, and changes by 30° (or multiples of 30°) to the original crack line. Straight cracks with zigzag edges grow self-similarly when opening loading is dominant, or else kinking occurred. Torn edges of fresh cracks are along either zigzag or armchair edge, while zigzag edges are more preferable. Fresh armchair edges are formed occasionally under particular stress conditions. Our theoretical results show that graphene cracking prefers along zigzag edges concerning with its lower toughness and complex mechanical stress in dynamic fracture.

Acknowledgements

The author gratefully acknowledges supports from Newton International Fellowship (NF080039) and Newton Alumni Follow-On of UK's Royal Society hosted by University of Glasgow and Newcastle University, and Aeronautical Science Foundation of China (2012ZF52074), NSFCs (10602023 and 11232007), the Fundamental Research Funds for the Central Universities, the Program for Changjiang Scholars and Innovative Research Team (IRT0968) and National Basic Research Program (973, 2011CB707602) of China.

References

[1]. K.S. Novoselov, A.K. Geim, S.V. Morozov, D. Jiang, Y. Zhang, S.V. Dubonos, I.V. Grigorieva, and A.A. Firsov, Electric field effect in atomically thin carbon films. Science, 306(5696) (2004) 666 -669.

[2]. C. Lee, X. Wei, J.W. Kysar, and J. Hone, Measurement of the elastic properties and intrinsic strength of

monolayer graphene. Science, 321(5887) (2008) 385 -388.

[3]. M.A. Rafiee, J. Rafiee, I. Srivastava, Z. Wang, H. Song, Z. Yu, and N. Koratkar, Fracture and fatigue in graphene nanocomposites. Small, 6(2) (2010) 179-183.

[4]. A. Hashimoto, K. Suenaga, A. Gloter, K. Urita, and S. Iijima, Direct evidence for atomic defects in graphene layers. Nature, 430(7002) (2004) 870-873.

[5]. A. Omeltchenko, J. Yu, R.K. Kalia, and P. Vashishta, Crack front propagation and fracture in a graphite sheet: a molecular-dynamics study on parallel computers. Phys Rev Lett, 78(11) (1997) 2148-2151.

[6]. M. Xu, A. Tabarraei, J.T. Paci, J. Oswald, and T. Belytschko, A coupled quantum/continuum mechanics study of graphene fracture. Int J Fracture, 173(2) (2012) 163-173.

[7]. S. Zhang, T. Zhu and T. Belytschko, Atomistic and multiscale analyses of brittle fracture in crystal lattices. Phys Rev B, 76(9) (2007) 094114.

[8]. S. Huang, S. Zhang, T. Belytschko, S.S. Terdalkar, and T. Zhu, Mechanics of nanocrack: fracture, dislocation emission, and amorphization. J Mech Phys Solids, 57(5) (2009) 840-850.

[9]. Q. Lu, W. Gao and R. Huang, Atomistic simulation and continuum modeling of graphene nanoribbons under uniaxial tension. Mod Simul Mater Sci Eng, 19 (2011) 054006.

[10]. M.I. Katsnelson and A.K. Geim, Electron scattering on microscopic corrugations in graphene. Phil Trans R Soc A, 366(1863) (2008.) 195-204.

[11]. G. Cocco, E. Cadelano and L. Colombo, Gap opening in graphene by shear strain. Phys Rev B, 81(24) (2010) 241412.

[12]. D. Sen, K.S. Novoselov, P.M. Reis, and M.J. Buehler, Tearing graphene sheets from adhesive substrates produces tapered nanoribbons. Small, 6(10) (2010) 1108-1116.

[13]. K. Kim, V.I. Artyukhov, W. Regan, Y. Liu, M.F. Crommie, B.I. Yakobson, and A. Zettl, Ripping graphene: preferred directions. Nano Lett., 12(1) (2012) 293-297.

[14]. J.C. Meyer, F. Eder, S. Kurasch, V. Skakalova, J. Kotakoski, H.J. Park, S. Roth, A. Chuvilin, S. Eyhusen, G. Benner, A.V. Krasheninnikov, and K. U., 14. Phys Rev Lett, 108(19) (2012) 196102.

[15]. D.W. Brenner, O.A. Shenderova, J.A. Harrison, S.J. Stuart, B. Ni, and S.B. Sinnott, A second-generation reactive empirical bond order (rebo) potential energy expression for hydrocarbons. J Phys Cond Mat, 14 (2002) 783.

[16]. B. Zhang and W. Guo, Cracking diamond anvil cells by compressed nanographite sheets near the contact edge. Appl Phys Lett, 87 (2005) 051907.

[17]. B. Zhang, Y. Liang and H. Sun. Structural phase transition and failure of nanographite sheets under high pressure: a molecular dynamics study. Journal of Physics: Condensed Matter, 19 (2007) 346224.

[18]. B. Zhang, L.Mei and H. F Xiao. Nanofracture in graphene under complex mechanical stresses. Applied Physics Letters, 101(12) (2012) 121915

[19]. O.A. Shenderova, D.W. Brenner, A. Omeltchenko, X. Su, and L.H. Yang, Atomistic modeling of the fracture of polycrystalline diamond. Phys Rev B, 61(6) (2000) 3877.

[20]. T. Belytschko, S.P. Xiao, G.C. Schatz, and R. Ruoff, Atomistic simulations of nanotube fracture. Phys Rev B, 65 (2002) 235430

[21]. R. Grantab, V.B. Shenoy and R.S. Ruoff, Anomalous strength characteristics of tilt grain boundaries in graphene. Science, 330(6006) (2010) 946-948.

[22]. H. Gao, B. Ji, I.L. J A Ger, E. Arzt, and P. Fratzl, Materials become insensitive to flaws at nanoscale: lessons from nature. Proc Natl Acad Sci USA, 100(10) (2003) 5597.

[23]. M.L. Williams, On the stress distribution at the base of a stationary crack. J Appl Mech, 24(1) (1957) 109-114.

[24]. T.L. Anderson, Fracture mechanics: fundamentals and applications. 2 ed, CRC Press, Boca Raton, FL, 1991

[25]. O.L. Blakslee, D.G. Proctor, E.J. Seldin, G.B. Spence, and T. Weng, Elastic constants of compression-annealed pyrolytic graphite. J Appl Phys, 41(8) (1970) 3373-3382.
[26]. D.C. Liu and J. Nocedal, On the limited memory bfgs method for large scale optimization. Math Program, 45(1) (1989) 503-528.
[27]. A.A. Griffith, The phenomena of rupture and flow in solids. Philos Trans R Soc London Ser A, 221 (1921) 163-198.
[28]. Q. Lu and R. Huang, Excess energy and deformation along free edges of graphene nanoribbons. Phys Rev B, 81(15) (2010) 155410.
[29]. P.S. Branicio, M.H. Jhon, C.K. Gan, and D.J. Srolovitz, Properties on the edge: graphene edge energies, edge stresses, edge warping, and the wulff shape of graphene flakes. Mod Simul Mater Sci Eng, 19 (2011) 054002.
[30]. S.S. Terdalkar, S. Huang, H. Yuan, J.J. Rencis, T. Zhu, and S. Zhang, Nanoscale fracture in graphene. Chem Phys Lett, 494(4) (2010) 218-222.
[31]. J. Qian and A. Fatemi, Mixed mode fatigue crack growth: a literature survey. Eng Fract Mech, 55(6) (1996) 969-990.
[32]. M. Engelund, J.A. F U Rst, A.P. Jauho, and M. Brandbyge, Localized edge vibrations and edge reconstruction by joule heating in graphene nanostructures. Phys Rev Lett, 104(3) (2010) 036807.
[33]. V.B. Shenoy, C.D. Reddy, A. Ramasubramaniam, and Y.W. Zhang, Edge-stress-induced warping of graphene sheets and nanoribbons. Phys Rev Lett, 101(24) (2008) 245501.
[34]. Ç. Ö. Girit, J.C. Meyer, R. Erni, M.D. Rossell, C. Kisielowski, L. Yang, C.H. Park, M.F. Crommie, M.L. Cohen, S.G. Louie, and Others, Graphene at the edge: stability and dynamics. Science, 323(5922) (2009) 1705-1708.
[35]. X. Jia, M. Hofmann, V. Meunier, B.G. Sumpter, J. Campos-Delgado, J.M. Romo-Herrera, H. Son, Y.P. Hsieh, A. Reina, J. Kong, and Others, Controlled formation of sharp zigzag and armchair edges in graphitic nanoribbons. Science, 323(5922) (2009) 1701-1705.
[36]. Y.C. Cheng, H.T. Wang, Z.Y. Zhu, Y.H. Zhu, Y. Han, X.X. Zhang, and U. Schwingenschl O Gl, Strain-activated edge reconstruction of graphene nanoribbons. Phys Rev B, 85(7) (2012) 073406.

Fracture initiation and size effect in V-notched structures under mixed mode loading

Pietro Cornetti[1,*], **Alberto Sapora**[1], **Alberto Carpinteri**[1]

[1] Department of Structural, Building and Geotechnical Engineering, Politecnico di Torino, Torino, 10124, Italy
* Corresponding author: pietro.cornetti@polito.it

Abstract In asserting structural safety it is of paramount importance to be able to evaluate the loading capacity of notched components, where stresses concentrate and can trigger cracks leading to a catastrophic failure or to a shortening of the assessed life of the structure. Restricting the analysis to brittle materials, we apply the Finite Fracture Mechanics criterion to address the problem of a V-notched structure subjected to a mixed-mode loading, i.e. we provide a way to determine the direction and the load at which a crack propagates from the notch tip and express the critical conditions in terms of the generalized stress intensity factors plus a suitable definition of the notch mode mixity. Weight functions of the stress intensity factors for V-notch emanated cracks available in the literature allow us to implement the fracture criterion proposed in an almost completely analytical manner: the determination of the critical load and the direction of crack growth is reduced to a minimization-under-constraint problem. We then highlight the size effect for a V-notched structure under mixed-mode loading and the differences between the structural behaviours of cracked and notched geometries.

Keywords sharp notches, mode mixity, size effect, finite fracture mechanics

1. Introduction

The development of suitable fracture criteria for brittle (isotropic or orthotropic) materials containing V-notches or multi-material interfaces is a problem of primary concern in order to control fracture onset phenomena taking place in mechanical components, composite materials and electronic devices. As well-known, the singularity of the stress field in the vicinity of the notch tip makes the problem non-trivial.

Concerning re-entrant corners in homogeneous media subjected to mode I loadings, since the pioneering paper by Carpinteri [1] a good correlation has been found between the critical value of the generalized stress intensity factor (i.e. the generalized fracture toughness) and the failure loads. Theoretical models to relate the generalized fracture toughness to material tensile strength, fracture toughness and re-entrant corner amplitude have been set by a number of researchers, e.g. [2-5].

Fewer contributions are available for what concerns mixed mode loading conditions [6-8]. Here we provide the generalization of the results obtained by Carpinteri et al. [5] to mixed mode problems. The proposed approach (as well as the ones previously cited) is based on the assumption that the region around the corner dominated by the singular stress field is large compared to intrinsic flaw sizes, inelastic zones or fracture process zone sizes. This hypothesis is the analogous of small-scale yielding in Linear Elastic Fracture Mechanics (LEFM).

While in LEFM there is a direct connection between the Stress Intensity Factors (SIFs) and the strain energy release rate (i.e. Irwin's relationship), this relation is missing in the case of notches, so that correlating fracture initiations with critical values of the stress intensity [1] could appear questionable. However, the recently introduced Finite Fracture Mechanics (FFM) criterion has shown this is not the case [4,5]. In fact, under the assumption of a finite crack extension at fracture initiation, it is possible to prove a relation between the Generalized Stress Intensity Factors (GSIFs) and the energy released when a crack appears at the V-notch tip.

2. Stress intensity factors for a V-notch emanated crack

Let us consider a re-entrant corner in an infinite homogeneous elastic medium with a polar coordinate system (r,ϑ) centred at the V-notch tip (see Fig.1a). After Williams, the asymptotical stress field is given by:

$$\sigma_{rr} = \frac{K_I^*}{(2\pi r)^{1-\lambda_I}} f_{rr}^{I}(\vartheta,\omega) + \frac{K_{II}^*}{(2\pi r)^{1-\lambda_{II}}} f_{rr}^{II}(\vartheta,\omega) \tag{1a}$$

$$\sigma_{\vartheta\vartheta} = \frac{K_I^*}{(2\pi r)^{1-\lambda_I}} f_{\vartheta\vartheta}^{I}(\vartheta,\omega) + \frac{K_{II}^*}{(2\pi r)^{1-\lambda_{II}}} f_{\vartheta\vartheta}^{II}(\vartheta,\omega) \tag{1b}$$

$$\tau_{r\vartheta} = \frac{K_I^*}{(2\pi r)^{1-\lambda_I}} f_{r\vartheta}^{I}(\vartheta,\omega) + \frac{K_{II}^*}{(2\pi r)^{1-\lambda_{II}}} f_{r\vartheta}^{II}(\vartheta,\omega) \tag{1c}$$

where K_I^* and K_{II}^* are the GSIFs in mode I (symmetrical) and mode II (anti-symmetrical) loading conditions respectively, λ_I and λ_{II} are the well-known Williams' eigenvalues and the functions f_{ij} are the angular shape functions (i.e. the eigenvectors). Both eigenvalues and eigenvectors depend on the notch opening angle ω. Note that the definition of the GSIFs is somewhat arbitrary, depending on the choice of the normalization factor, here taken equal to $(2\pi)^{1-\lambda_i}$ as in [2] but equal to 1 or to $\sqrt{2\pi}$ in other papers (e.g. [7] and [3], respectively). As we shall see later, the advantage of such a choice is that the critical value of the mode I GSIF continuously varies from the material tensile strength to the material fracture toughness as the re-entrant corner amplitude diminishes from 180° (flat edge) to 0° (cracked plate).

In order to apply the FFM criterion, we need to evaluate the energy necessary for the abrupt appearance of a finite length crack at the notch tip. This quantity can be easily computed if the SIFs K_I and K_{II} of a crack at the notch vertex are known. To this aim, we begin noticing that, if the crack occurs within the GSIFs dominated stress field, the SIFs depend only on the GSIFs, crack direction ϑ, crack length a and notch opening angle ω (see Fig.1b). A straightforward application of the Π-theorem (as well as the principle of effect superposition) shows that this dependency must take the following form [9]:

$$K_I = \mu_{11}(\vartheta,\omega)\, K_I^* a^{\lambda_I - 1/2} + \mu_{12}(\vartheta,\omega)\, K_{II}^* a^{\lambda_{II} - 1/2} \tag{2a}$$

$$K_{II} = \mu_{21}(\vartheta,\omega)\, K_I^* a^{\lambda_I - 1/2} + \mu_{22}(\vartheta,\omega)\, K_{II}^* a^{\lambda_{II} - 1/2} \tag{2b}$$

In case of pure mode I loaded V-notches, the emanated crack grows along the notch bisector ($\vartheta = 0$); hence K_{II} is zero and K_I simplifies into [10]:

$$K_I = \mu_{11}(\omega) K_I^* a^{\lambda_I - 1/2} \tag{3}$$

While the dimensionless μ_{ij} parameters can be found tabulated with great accuracy for a crack, i.e. for $\omega = 0°$ [11], their values for a generic notch opening angle ω are not available. Nevertheless, they can be obtained by exploiting the results provided in [12], where the SIFs for a pair of forces per unit thickness (either normal or tangential) acting on the faces of a V-notch emanated crack are given. Beghini et al. [12] evaluated such SIFs for several ω and ϑ values by proper finite element computations and provided accurate analytical expressions of the SIFs. From such expressions and by the principle of effect superposition the coefficients μ_{ij} can be obtained analytically [13].

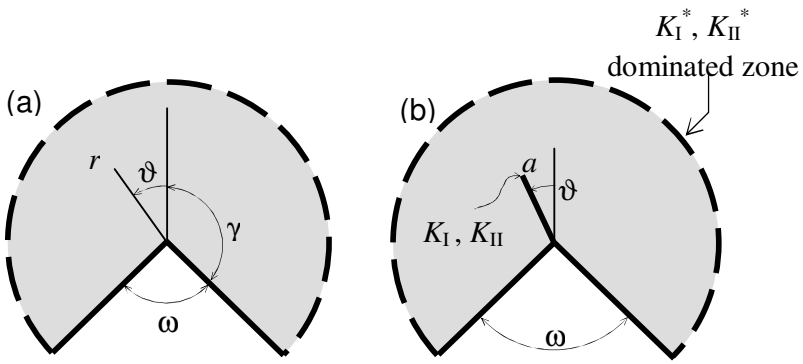

Figure 1. Polar reference system at the tip of a V-notch (a); V-notch emanated crack within the GSIFs dominated stress field region (b).

3. Coupled criterion

It is well known that both strength criteria and LEFM fail in predicting the failure load causing fracture propagation from a V-notch. In fact, the stress field given by eqn (1) is singular and strength criteria provide a vanishing failure load. On the other hand, the SIFs provided by eqn (2) vanish as the crack length a tends to zero and, consequently, LEFM provides an infinite failure load. These shortcomings can be overcome by resorting to Finite Fracture Mechanics [4,14], which couples the stress and energy approaches. Following the FFM approach proposed by Cornetti et al. [14], a crack propagates by a finite crack extension Δ if the following two inequalities are satisfied:

$$\begin{cases} \int_0^{\Delta} \mathcal{G}(a)\, \mathrm{d}a \geq \mathcal{G}_c\, \Delta \\ \int_0^{\Delta} \sigma_{\vartheta\vartheta}(r)\, \mathrm{d}r \geq \sigma_u\, \Delta \end{cases} \tag{4}$$

where σ_u is the material tensile strength and $\mathcal{G}_c$ is the fracture energy, related to the material fracture toughness by the well-known relation $\mathcal{G}_c = K_{Ic}^2 / E'$, where $E' = E / (1-\nu^2)$, E being the Young's modulus and ν the Poisson's coefficient.

The FFM criterion (4) can be regarded as a coupled Griffith-Rankine non-local failure criterion: the former inequality is an energy balance, whereas the latter is an (average) stress requirement for crack to propagate. It means that fracture is energy driven, but a sufficiently high stress field must act at the crack tip to trigger crack propagation. It is worth observing that, in the present case (which is the usual one, i.e. a positive geometry), the strain energy release rate function $\mathcal{G}(a)$ is monotonically increasing since the SIFs increase along with the crack length (see eqns (2)) while the stress $\sigma_{\vartheta\vartheta}(r)$ is monotonically decreasing with the distance r (see eqns (1)) from the notch tip (as far as both the modes provide a stress singularity, i.e. for a notch opening angle less than about 102.6°). This means that the lowest failure load (i.e. the actual one) is attained when the two inequalities are substituted by the two corresponding equations. In fact the first inequality is satisfied for crack steps larger than a threshold value, thus providing a lower bound for the set of admissible Δ-values; on the contrary, the second inequality is satisfied for crack advancements smaller than a certain value, thus providing an upper bound. For low load values, the upper bound is smaller than the lower bound and, consequently, the set of admissible Δ-values is empty. As the

external load increases, the upper bound increases and the lower bound decreases till a load value is met (i.e. the failure load) for which both conditions are strictly fulfilled. Therefore, we conclude stating that the system (4) reverts to a system of two equations in two unknowns: the crack advancement Δ and the corresponding (minimum) failure load, represented by the values K_{If}^{*} and K_{IIf}^{*} of the GSIFs in critical conditions, implicitly embedded in the functions $\sigma_{\vartheta\vartheta}$ and $\mathcal{G}$. Exploiting the well-known Irwin's relationship in plane strain and mixed mode, the system (4) becomes:

$$\begin{cases} \int_0^{\Delta} \left[K_{\mathrm{I}}^2(a) + K_{\mathrm{II}}^2(a)\right] \mathrm{d}a = K_{\mathrm{Ic}}^2 \, \Delta \\ \int_0^{\Delta} \sigma_{\vartheta\vartheta}(r) \, \mathrm{d}r = \sigma_{\mathrm{u}} \, \Delta \end{cases} \tag{5}$$

It is worth observing that the failure load estimate provided by the system (5) does depend on the crack propagation direction ϑ (see Fig.1b). Among all the possible directions, the actual one will be the direction ϑ_c providing the minimum failure load. Upon substitution of the SIFs eqns (2) into the first equation of the system (5) and integrating between 0 and Δ, we get:

$$\overline{\mu}_{11}\Delta^{2\lambda_{\mathrm{I}}}(K_{\mathrm{I}}^{*})^2 + \overline{\mu}_{12}\Delta^{\lambda_{\mathrm{I}}+\lambda_{\mathrm{II}}}K_{\mathrm{I}}^{*}K_{\mathrm{II}}^{*} + \overline{\mu}_{22}\Delta^{2\lambda_{\mathrm{II}}}(K_{\mathrm{II}}^{*})^2 = K_{\mathrm{Ic}}^2\Delta, \tag{6}$$

where, for the sake of simplicity, we have introduced the angular functions:

$$\overline{\mu}_{11} = \frac{\mu_{11}^2 + \mu_{21}^2}{2\lambda_{\mathrm{I}}}, \quad \overline{\mu}_{12} = 2\frac{\mu_{11}\mu_{12} + \mu_{21}\mu_{22}}{\lambda_{\mathrm{I}} + \lambda_{\mathrm{II}}}, \quad \overline{\mu}_{22} = \frac{\mu_{12}^2 + \mu_{22}^2}{2\lambda_{\mathrm{II}}} \tag{7}$$

Equation (6) highlights that the variation in the elastic energy is a quadratic function of the GSIFs. Equation (6) can be found also in Yosibash et al. [7], where it was derived in a different way, i.e. by directly computing coefficients of the quadratic form by suitable path independent integrals of the stress and displacement fields before and after the appearance of the finite crack advancement.

Upon substitution of the stress field represented by eqn (1) into the second equation of the system (5) and integrating between 0 and Δ, we get:

$$\overline{f}_{\vartheta\vartheta}^{\,\mathrm{I}} \, \Delta^{\lambda_{\mathrm{I}}} K_{\mathrm{I}}^{*} + \overline{f}_{\vartheta\vartheta}^{\,\mathrm{II}} \, \Delta^{\lambda_{\mathrm{II}}} K_{\mathrm{II}}^{*} = \sigma_{\mathrm{u}}\Delta \tag{8}$$

where, for the sake of simplicity, we have introduced the angular functions:

$$\overline{f}_{\vartheta\vartheta}^{\,\mathrm{I}} = \frac{f_{\vartheta\vartheta}^{\mathrm{I}}}{\lambda_{\mathrm{I}}(2\pi)^{1-\lambda_{\mathrm{I}}}}, \quad \overline{f}_{\vartheta\vartheta}^{\,\mathrm{II}} = \frac{f_{\vartheta\vartheta}^{\mathrm{II}}}{\lambda_{\mathrm{II}}(2\pi)^{1-\lambda_{\mathrm{II}}}} \tag{9}$$

4. Failure load, crack deflection and mode mixity

Under pure mode I loading condition, for symmetry reason the crack propagates along the notch bisector, i.e. $\vartheta_c = \vartheta_{Ic} = 0$. Upon substitution of eqns (6) and (8), limited to the mode I contributions, into the system (5), we get:

$$\begin{cases} \overline{\mu}_{11}\Delta^{2\lambda_I}(K_I^*)^2 = K_{Ic}^2\Delta \\ \overline{f}_{\vartheta\vartheta}^{\,I}\,\Delta^{\lambda_I}K_I^* = \sigma_u\Delta \end{cases} \tag{10}$$

The system (10) is readily solved, yielding the crack advancement Δ_c and the critical value K_{Ic}^* of the mode I GSIF K_I^* under pure mode I loading, i.e. the generalized fracture toughness [5]:

$$K_{Ic}^* = \xi(\omega)\,K_{Ic}^{2(1-\lambda_I)}\sigma_u^{2\lambda_I-1} = \xi(\omega)\,\sigma_u\,l_{ch}^{1-\lambda_I}\text{, with }\ \xi(\omega) = \lambda_I^{\lambda_I}\left[\frac{2(2\pi)^{2\lambda_I-1}}{\mu_{11}^2(\vartheta=0,\omega)}\right]^{1-\lambda_I} \tag{11}$$

where $l_{ch} = (K_{Ic} / \sigma_u)^2$ is the Irwin length. Note that, since ξ is equal to unity for ω equal to 0 or π, the generalized fracture toughness equals the fracture toughness for a cracked geometry and the tensile strength for a flat edge.

In the case of mixed mode loading, the critical values of the GSIFs can be obtained by substituting eqns (6) and (8) into the system (5):

$$\begin{cases} \left(\dfrac{K_I^*}{K_{Ic}^*}\right)^2 = \dfrac{\delta}{\xi^2\left(\overline{\mu}_{11}\delta^{2\lambda_I} + \overline{\mu}_{12}\delta^{\lambda_I+\lambda_{II}}\tan\psi + \overline{\mu}_{22}\delta^{2\lambda_{II}}\tan^2\psi\right)} \\ \dfrac{K_I^*}{K_{Ic}^*} = \dfrac{\delta}{\xi\left(\overline{f}_{\vartheta\vartheta}^{\,I}\,\delta^{\lambda_I} + \overline{f}_{\vartheta\vartheta}^{\,II}\delta^{\lambda_{II}}\tan\psi\right)} \end{cases} \tag{12}$$

where the mode I GSIF has been normalized with respect to the generalized fracture toughness K_{Ic}^*, the finite crack advancement with respect to l_{ch} ($\delta = \Delta / l_{ch}$) and ψ is the mode mixity, defined as:

$$\psi = \arctan\frac{K_{II}^*\,l_{ch}^{\lambda_{II}-\lambda_I}}{K_I^*} \tag{13}$$

The system (12) can be recast as:

$$\begin{cases} \dfrac{K_I^*}{K_{Ic}^*} = \dfrac{\delta}{\xi\left(\overline{f}_{\vartheta\vartheta}^{\,I}\,\delta^{\lambda_I} + \overline{f}_{\vartheta\vartheta}^{\,II}\delta^{\lambda_{II}}\tan\psi\right)} \\ \delta - \dfrac{\left(\overline{f}_{\vartheta\vartheta}^{\,I}\,\delta^{\lambda_I} + \overline{f}_{\vartheta\vartheta}^{\,II}\delta^{\lambda_{II}}\tan\psi\right)^2}{\overline{\mu}_{11}\delta^{2\lambda_I} + \overline{\mu}_{12}\delta^{\lambda_I+\lambda_{II}}\tan\psi + \overline{\mu}_{22}\delta^{2\lambda_{II}}\tan^2\psi} = 0 \end{cases} \tag{14}$$

The technique of Lagrange multipliers can now be exploited to solve eqn (14). In fact, eqn (14) can be interpreted as a constrained minimization problem, since, once the geometry, material and loading are fixed (i.e. ω and ψ are given), the actual crack advancement Δ_c and crack orientation ϑ_c are the ones that minimize the first equation, i.e. the dimensionless failure load K_{If}^* / K_{Ic}^*, under the constraint represented by the second equation. Once the critical value K_{If}^* of the mode I GSIF is determined, the corresponding critical value K_{IIf}^* of the mode II GSIF is provided by eqn (13).

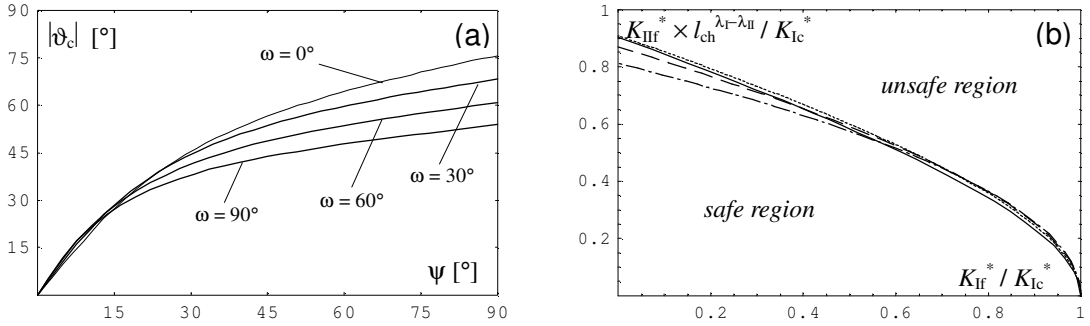

Figure 2. Crack deflection vs. mode mixity for different notch opening angle (a); safety domains in the GSIFs plane for different notch opening angles: continuous line, $\omega = 90°$; dotted line, $\omega = 60°$; dashed line, $\omega = 30°$; dot-dashed line, $\omega = 0°$ (b).

The values of the crack orientation angle are plotted in Fig. 2a vs. the mode mixity ψ for different notch opening angle ω. On the other hand, the critical values of the GSIFs can be plotted in the (K_I^*, K_{II}^*) plane for a given notch opening angle ω and varying the mode mixity ψ. In this way we obtain a curve delimiting a safety region, i.e. points lying in this domain correspond to admissible stress states, whereas points lying outside correspond to failure. It is convenient to plot the results in a dimensionless form: the mode I GSIF is normalized with respect to the generalized fracture toughness K_{Ic}^*, whereas the mode II GSIF is normalized with respect to $K_{Ic}^* \times l_{ch}^{\lambda_I-\lambda_{II}}$. The safety domains are plotted in Fig. 2b for different ω values and in Fig. 3 for $\omega = 90°$. If the external loads are increased proportionally, the ratio between the GSIFs keeps constant. It means that in the (K_I^*, K_{II}^*) plane, the loading curve is represented by a straight line starting from the origin. Furthermore, in the dimensionless plane, the angle between the loading path and the horizontal axis is exactly ψ.

According to the brittleness assumption, failure is attained suddenly when the straight line crosses the curve delimiting the safety domain, point A (Fig. 3). Apart from substitution of the SIFs with the GSIFs, this behaviour strictly resembles what occurs in the classical crack branching problem. Indeed, the crack branching problem is a particular case of the present one. However there is a substantial difference with respect to the crack kinking problem: if $\omega > 0°$, the mode mixity ψ depends also on the material brittleness through l_{ch} (see eqn (13)) and not only on the loading, i.e. on the GSIFs ratio. For a given K_{II}^* / K_I^* ratio, the slope of the loading line will diminish for brittle materials (low l_{ch}), while will increase for less brittle materials (high l_{ch}): in other words, whatever is the GSIF ratio, the failure point migrates towards point B (pure mode I failure) as material brittleness increases, whereas it moves towards point C, if the brittleness decreases (within a certain range, otherwise, as explained in the following section, the asymptotic approach does not hold any more).

As clearly shown by eqn (13), the effect of the material on the mode mixity increases as the notch opening increase. In fact, for larger ω, the gap between the Williams eigenvalues λ_{II} and λ_I grows. On the other hand, for a vanishing notch opening angle, both λ_{II} and λ_I tend to 1/2 and the effect of the material vanishes. This material dependence is valid also for the orientation of the V-notch emanated crack, see Fig. 2a: as brittleness increases, l_{ch} diminishes, ψ diminishes and the crack deflection ϑ_c tends to zero, i.e. the V-notch emanated crack tends to propagate in mode I along the bisector. On the other hand, for less brittle material, the crack deflection is higher under the same GSIFs ratio. Once more, it is worth emphasizing the fundamental difference with respect to the crack case, where the angle of the crack kinking depends only on the (dimensionless) SIFs ratio, i.e. is the same independently of the material.

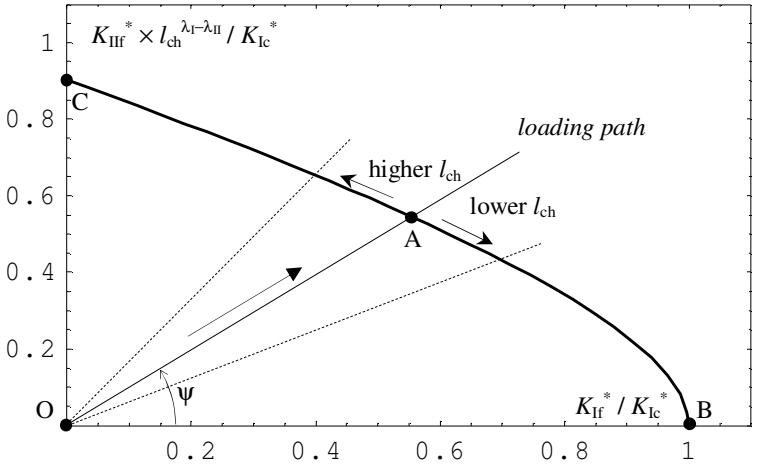

Figure 3. Resistance domain in the GSIFs plane ($\omega = 90°$): points lying beneath the thick curve correspond to admissible stress states and vice-versa.

In Fig. 2b we plotted the safety domains for different notch opening angles ω. It is evident that all the curves are similar. Of course, this fact does not imply that the failure load does not vary with ω, since the physical dimensions as well as the shape functions defining the GSIFs vary along with ω. It simply shows that the transition from mode I to mode II fracture is approximately the same for all the notch amplitudes.

5. Size effect and mode mixity

The introduction of a physical length against which to scale the notch tip GSIFs enables further aspects of the solution to be drawn out, such as the influence of a V-notch on the so-called size effect. Hence let us consider a set of self-similar geometries as the ones drawn in Fig. 4. Dimensional analysis allows us to write directly:

$$K_I^* = f_I(\omega, a/b)\,\sigma\, b^{1-\lambda_I}\,, \quad K_{II}^* = f_{II}(\omega, a/b)\,\sigma\, b^{1-\lambda_{II}} \tag{15}$$

where σ is the nominal stress, b is a characteristic size of the structure and f_I, f_{II} are shape factors depending on the geometry, here synthetically defined by the notch opening angle ω and relative notch depth a/b.

Now let us focus our attention to the size effect on the nominal stress at failure σ_f. If only either the mode I or the mode II GSIF is different from zero, failure will occur whenever the corresponding GSIF reaches K_{Ic}^* or K_{IIc}^*, respectively (the latter value being given by the intercept with the vertical axis in Fig. 3). Hence, according to eqn (15), the logarithm of the nominal stress at failure is given by [1]:

$$\ln\sigma_f = \ln\left[\frac{K_{Ic}^*}{f_I(\omega, a/b)}\right] - (1-\lambda_I)\ln b \qquad \text{or} \qquad \ln\sigma_f = \ln\left[\frac{K_{IIc}^*}{f_{II}(\omega, a/b)}\right] - (1-\lambda_{II})\ln b \tag{16}$$

It means that in a bi-logarithmic plot the strength vs. size curve is a straight line with (negative) slope equal to either $(1-\lambda_I)$ or $(1-\lambda_{II})$, see Figs. 5a,b. Since $\lambda_{II} > \lambda_I$, the size effect is stronger under mode I than under mode II loadings.

On the other hand, in the case of mixed mode loadings, we have to substitute both eqns (15) into the stress condition (8) for crack propagation. Accordingly, we get:

$$\frac{\sigma_f}{\sigma_u} = \frac{1}{f_I(\omega, a/b)\left[\overline{f}^{\,I}_{\vartheta\vartheta}\Big/\delta^{1-\lambda_I}\right] s^{-2(1-\lambda_I)} + f_{II}(\omega, a/b)\left[\overline{f}^{\,II}_{\vartheta\vartheta}\Big/\delta^{1-\lambda_{II}}\right] s^{-2(1-\lambda_{II})}} \tag{17}$$

where we introduced the brittleness number s as [15]:

$$s = \frac{K_{Ic}}{\sigma_u\sqrt{b}} = \sqrt{\frac{l_{ch}}{b}} \tag{18}$$

The terms in square brackets in eqn (17) show a modest variation with the size, so that the terms in round brackets dominate. It means that, for large sizes and/or brittle materials, the first addend at the denominator (i.e. mode I) prevails; on the other hand, for small sizes and/or less brittle materials, the second addend at the denominator (i.e. mode II) does govern the problem. The presence of the brittleness number s in (17) highlights that the transition from mode I- to mode II-governed failure depends both on size and material brittleness. Thus we conclude that the size effect for a V-notched structure under mixed mode loading is represented by a curve with two slant asymptotes in the bilogarithmic plot (see Fig. 5c): the right one with slope $(1-\lambda_I)$, the left one with slope $(1-\lambda_{II})$. This is a general trend, i.e. independent of the geometry and fracture criterion adopted.

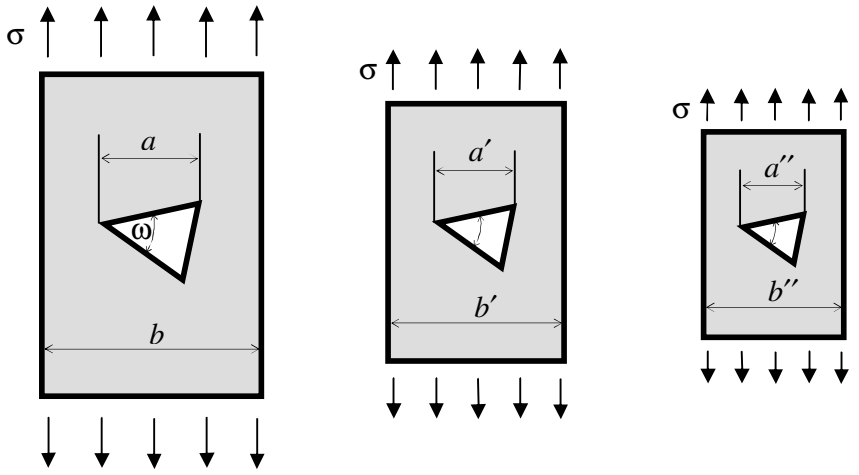

Figure 4. Self-similar specimens with a re-entrant corner of amplitude ω.

It is worth observing that the analysis of the mode mixity leads to the same conclusion. In fact substitution of eqns (15) into eqn (13) provides:

$$\psi = \arctan\left[\frac{f_{II}(\omega, a/b)}{f_I(\omega, a/b)} \quad s^{2(\lambda_{II}-\lambda_I)}\right] \tag{19}$$

Equation (19) clearly shows that, except in the crack case ($\lambda_I = \lambda_{II} = 1/2$), the mode mixity does not depend only on the shape factors, but also on the brittleness number, i.e. on the structural size. In fact, whatever is the ratio between f_{II} and f_I (provided they are both different from zero), for sufficiently large sizes the mode mixity will always tend to zero (i.e. pure mode I), whereas it will tend to $\pi/2$ for vanishing sizes (i.e. pure mode II).

While the large-size asymptote is always physically meaningful, the small-size asymptote could become only theoretical if mode II prevails for sizes too small for the asymptotic approach to hold true. In fact, when the finite crack extension is not negligible with respect to the other geometrical dimensions (e.g. for very small sizes), disregarding higher order terms in the asymptotic stress field is not acceptable. Similarly to LEFM, the asymptotic approach to V-notched structures leads to an infinite strength for vanishing sizes, i.e. to a result that, within the present coupled Rankine-Griffith criterion and under constant remote tensile stresses (see Fig. 4), must be regarded as physically unacceptable.

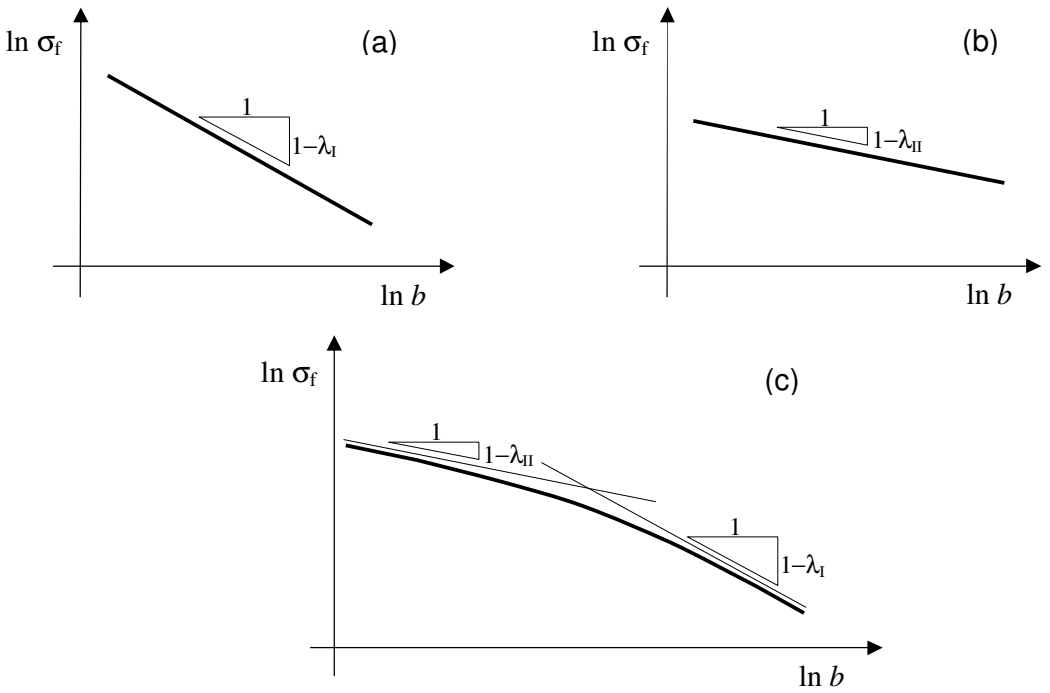

Figure 5. Size effect on nominal stress at failure: (a) pure mode I loading; (b) pure mode II loading; (c) mixed mode loading.

6. Conclusions

In the present paper we applied the FFM criterion provided in Cornetti et al. [14] to determine the critical load in V-notched structures under combined Mode I and Mode II loadings. With respect to simple Mode I loadings [5], the mixed mode problem is more complex since, beyond the failure load, also the direction of the crack onset at the re-entrant corner tip is unknown. Nevertheless, exploiting suitable weight functions for the SIFs of a V-notch-emanated crack [12], we were able to formulate the model as a standard minimization-under-constraint problem and to solve it by means of the Lagrange multiplier technique. A comparison with a broad set of experimental data (for both the failure load and the crack orientation) can be found in the recently published paper [16].

In mixed-mode loading cases, we showed that our model is able to explain the growing relevance of the mode II contribution for increasing material lengths l_{ch}, while it is negligible if l_{ch} tends to zero. Nevertheless, since the present approach is based on the asymptotic stress field, it yields accurate results only for sufficiently small l_{ch} values (with respect to the other geometrical dimensions). If this condition is not met, it is necessary to consider further terms in the stress field asymptotic expansions [17] or to tackle the problem numerically [18].

References

[1] A. Carpinteri, Stress-singularity and generalized fracture toughness at the vertex of re-entrant corners. Engineering Fracture Mechanics, 26 (1987) 143-155.
[2] A. Seweryn, Brittle fracture criterion for structures with sharp notches. Engineering Fracture Mechanics 47 (1994) 673-681.
[3] P. Lazzarin, R. Zambardi, A finite-volume-energy based approach to predict the static and fatigue behavior of components with sharp V-shaped notches. International Journal of Fracture 112 (2001) 275-298.
[4] D. Leguillon, Strength or toughness? A criterion for crack onset at a notch. European Journal of Mechanics A/Solids 21 (2002) 61-72.
[5] A. Carpinteri, P. Cornetti, N. Pugno, A. Sapora, D. Taylor, A finite fracture mechanics approach to structures with sharp V-notches. Engineering Fracture Mechanics 75 (2008) 1736-1752.
[6] A. Seweryn, S. Poskrobko, Z. Mroz, Brittle fracture in plane elements with sharp notches under mixed-mode loading. Journal of Engineering Mechanics-ASCE 123 (1997) 535-543.
[7] Z. Yosibash, E. Priel, D. Leguillon, A failure criterion for brittle elastic materials under mixed-mode loading. International Journal of Fracture 141 (2006) 291-312.
[8] F.J. Gómez, M. Elices, F. Berto, P. Lazzarin, Fracture of V-notched specimens under mixed mode (I + II) loading in brittle materials. International Journal of Fracture 159 (2009) 121-135.
[9] J. Li, X.B. Zhang, Crack initiation prediction for V-notches under mixed-mode loading in brittle materials. Journal of the Mechanics of Materials and Structures 1 (2006) 1385-1404.
[10] N. Hasebe, J. Iida, A crack originating from a triangular notch on a rim of a semi-infinite plate. Engineering Fracture Mechanics 10 (1978) 773-782.
[11] S. Melin, Accurate data for stress intensity factors at infinitesimal kinks. Journal of Applied Mechanics 61 (1994) 467-470.
[12] M. Beghini, L. Bertini, R. Di Lello, V. Fontanari, A general weight function for inclined cracks at sharp V-notches. Engineering Fracture Mechanics 74 (2007) 602-611.
[13] P. Cornetti, A. Sapora, A. Carpinteri, Mode mixity and size effect in V-notched structures. International Journal of Solids and Structures 50 (2013) 1562-1582.
[14] P. Cornetti, N. Pugno, A. Carpinteri, D. Taylor, Finite fracture mechanics: a coupled stress and energy failure criterion. Engineering Fracture Mechanics 73 (2006) 2021-2033.
[15] A. Carpinteri, Static and energetic fracture parameters for rocks and concrete. Materials and Structures 14 (1981) 151-162.
[16] A. Sapora, P. Cornetti, A. Carpinteri, A Finite Fracture Mechanics approach to V-notched elements subjected to mixed-mode loading. Engineering Fracture Mechanics 97 (2013) 216–226.
[17] C.Z. Cheng, Z.R. Niu, N. Recho, Effect of non-singular stress on the brittle fracture of V-notched structure. International Journal of Fracture 174 (2012) 127-138.
[18] J. Hebel, R. Dieringer, W. Becker. Modelling brittle crack formation at geometrical and material discontinuities using a finite fracture mechanics approach. Engineering Fracture Mechanics 77 (2010) 3558-3572.

Three-parameter approaches for three-dimensional crack-tip stress fields

Chongmin She[1,*], Junhua Zhao[2], Wanlin Guo[1,*]

[1] State Key Laboratory of Mechanics and Control of Mechanical Structures, Nanjing University of Aeronautics and Astronautics, Nanjing 210016, P. R. China
[2] Institute of Structural Mechanics, Bauhaus-University Weimar, 99423 Weimar, Germany
* Corresponding authors: cmshe@nuaa.edu.cn, wlguo@nuaa.edu.cn

Abstract Two three-parameter descriptions for the three-dimensional (3D) crack-tip stress fields have been introduced. The three-parameter solution K-T-T_z is developed to describe the linear elastic crack-tip stress state, and the J-Q_T-T_z is to elastic-plastic crack-tip field. The conventional two-dimensional solutions such as K, K-T, HRR and the extended J-Q description which considers the in-plane constraint modification can hardly provide satisfied description for the three-dimensional crack front fields, especially for the out-of-plane stress near the crack front. It is shown that a consideration of the out-of-plane constraint and use of the three-parameter description is necessary and efficient to predict the 3D stress fields near the crack front.

Keywords Fracture mechanics, Three-dimensional stress field, Out-of-plane stress constraint

1. Introduction

The complicated three-dimensional (3D) stress fields near the crack front play a vital role in the strength of materials [1], and control the initiation and propagation of cracks [2]. The character of the stress fields near the crack front has long been extensively studied. The classical linear elastic and elastic–plastic fracture mechanics are based on the theory stemming from the one singular term of asymptotic expression and its amplitude the stress intensity factor (SIF, K) [3] and HRR solution [4, 5], respectively. Then more accurate two-parameter approaches, such as K–T [6], J–T [7], J–Q [8, 9] and J–A_2 [10, 11], have been developed to describe the crack-tip field. These approaches have been applied successfully in engineering designs though they are limited to describe the effect of the in-plane constraint on the crack-tip field and fracture toughness. In fact, fracture toughness depends on the 3D out-of-plane stress level near the crack front also [12]. It is well known that fracture toughness depends highly on the thickness of the test specimen until a threshold thickness, beyond which the toughness does not decrease further. The toughness at this thickness is called plane strain fracture toughness. It is less than the fracture toughness of thinner plates and is a material property. So the variable fracture toughness is inconvenient in the engineering applications if the 3D out-of-plane stress level is not considered accurately.

In order to describe the out-of-plane stress level, the out-of-plane stress constraint factor T_z was introduced by Guo [13-15], the factor is defined as

$$T_z = \frac{\sigma_{33}}{\sigma_{11}+\sigma_{22}}, \qquad (1,\ 2,\ 3)=(x,\ y,\ z) \text{ or } (r,\ \theta,\ z) \tag{1}$$

where r, θ, x and y are coordinates in the conventional polar and Cartesian systems with origin at the crack tip and z is the third coordinate (parallel to the crack front) in both systems. The corresponding coordinate system and a normal sheet element of a through-straight crack are shown in Fig.1. In the state of plane stress, T_z=0. In the state of plane strain, T_z changes from the Poisson's ratio v of the linear elastic material to 0.5 for elastic-perfectly plastic material.

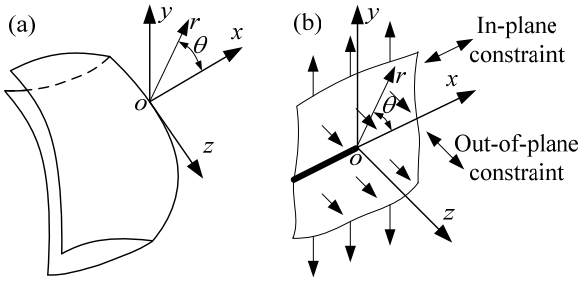

Fig. 1 The coordinate system and a normal sheet element of a through-straight crack.

The out-of-plane constraint factor T_z plays an important role in the determination of fracture toughness of a structural element. The effect of Tz on 3D crack-front fields and fracture toughness were systematically studied by Guo, then the 3D two-parameter principles of K–T_z, J–T_z have been proposed [12-16]. Combining with the in-plane constraint T or Q, the 3D three-parameter principles of K-T-T_z and J-Q_T-T_z have also been proposed [13-15, 17-22].

In this paper, the recent researches on the 3D three-parameter principles of K-T-T_z and J-Q_T-T_z are emphasisly summarized. The comparisons of the three-parameter principles with two-parameter and one-parameter principles are presented.

2. Three-parameter principle K–T–T_z for the linear elastic material

Based on the SIF K, the more accurate two-parameter approach K–T was proposed by Williams [6] for linear elastic material. For the 3D crack case, the three-parameter principle K-T-T_z was developed by Guo [13-15, 17-19] based on the K-T approach, which can be expressed as

$$\begin{cases} \sigma_{ij} = \dfrac{K}{\sqrt{2\pi r}} f_{ij}(\theta) + T\delta_{1i}\delta_{1j} \\ \sigma_{zz} = T_z(\sigma_{ii} + \sigma_{jj}) \end{cases} \qquad (i,\ j) = (x,\ y),\ (r,\ \theta) \text{ or } (1,\ 2) \tag{2}$$

where T is the T-stress,

$$f_{11}(\theta) = \cos\frac{\theta}{2}\left(1 - \sin\frac{\theta}{2}\sin\frac{3\theta}{2}\right) \tag{3}$$

$$f_{22}(\theta) = \cos\frac{\theta}{2}\left(1 + \sin\frac{\theta}{2}\sin\frac{3\theta}{2}\right) \tag{4}$$

$$\tau_{12}(\theta) = \cos\frac{\theta}{2}\sin\frac{\theta}{2}\cos\frac{3\theta}{2} \tag{5}$$

The three-parameter principle K-T-T_z can describe not only the in-plane constraint by T but also the out-of-plane stress constraint by T_z. Then the crack-tip stress fields described by the principle K-T-T_z for the typical cracks such as through-the-thickness crack, quarter elliptical corner crack, semi-elliptical surface crack and embedded elliptical crack are discussed. The geometry of a plate with a quarter elliptical crack under uniform tension is presented in Fig.2, the corresponding FE mesh is shown in Fig.3. The 3D singular elements with four mid-side nodes at the quarter points are used around the crack front to simulate the inverse square root singularity at the crack tip. The FE model in Fig.3 can be used to simulate the semi-elliptical surface crack and embedded elliptical

crack by altering the corresponding displacement boundary conditions.

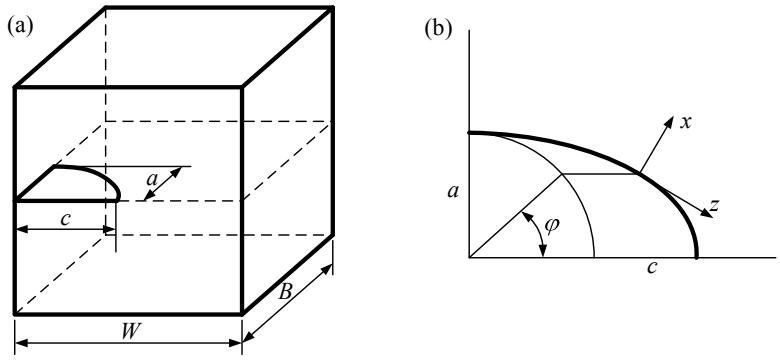

Fig.2 Geometry of a plate with a quarter elliptical crack under uniform tension. (a) The 3D geometry model. (b) Cracks with different a/c and the local rectangular coordinate system.

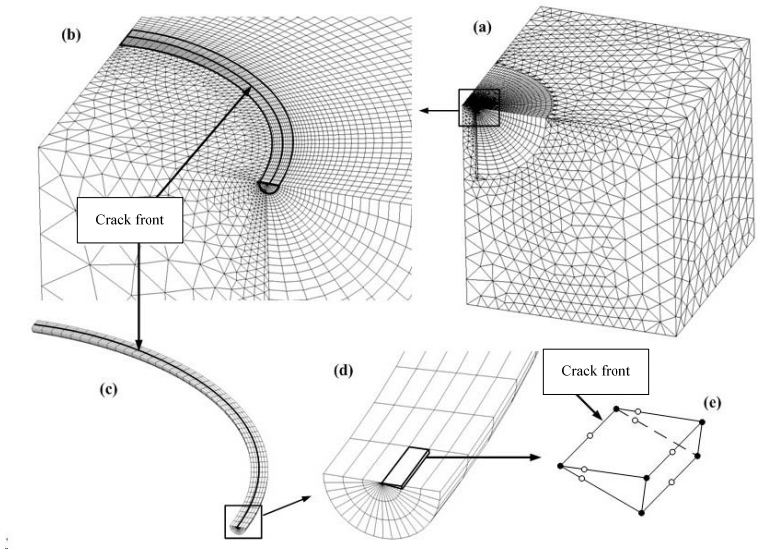

Fig.3 FE model of the quarter elliptic corner crack

The comparisons of the three-parameter principle K-T-T_z with the FE results are presented in Fig. 4.

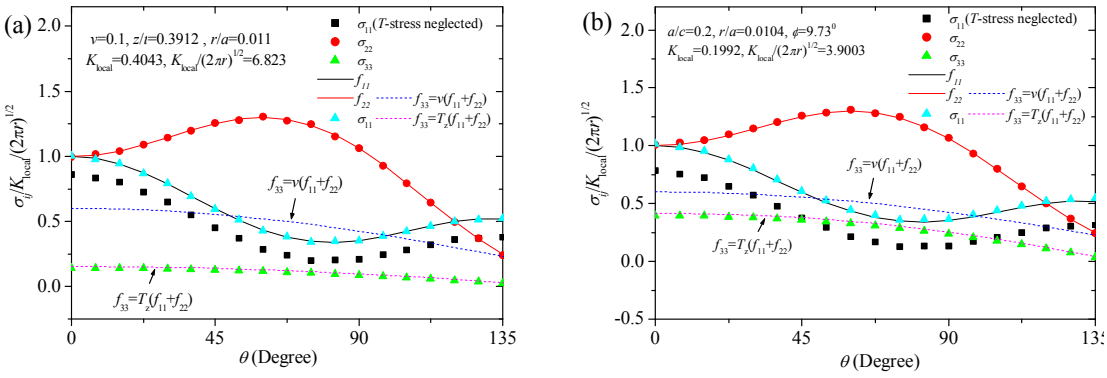

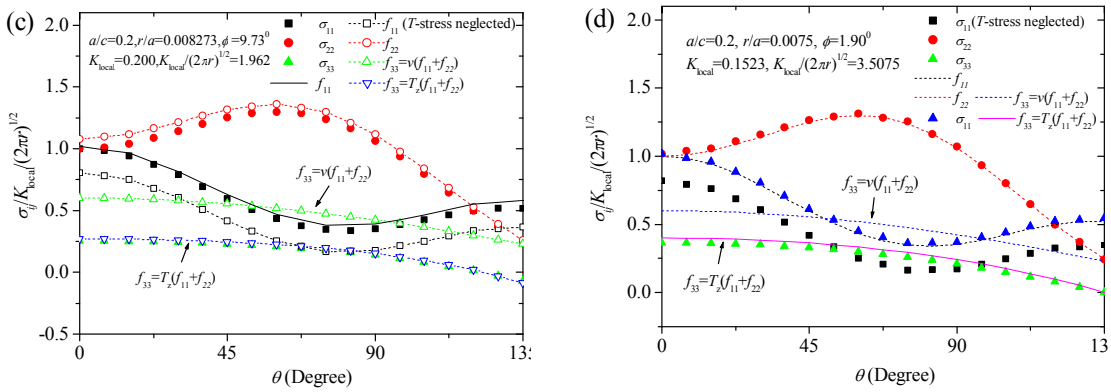

Fig.4 The angular distributions of stress components normalized by the local stress intensity factors in a normal plane of the quarter-elliptical corner crack front line. (a) through-the-thickness straight crack, (b) semi-elliptical surface crack, (c) quarter elliptical corner crack, (d) embedded elliptical crack.

As shown in Fig. 4, the angular distributions of stress components in a normal plane of various crack front lines are given in the local Cartesian coordinates. It can be seen that σ_{22} is in good agreement with f_{22}, while the differences between σ_{11} and f_{11} are great if the T-stress is neglected. When the T-stress is considered, the differences will become very small. In addition, the differences between σ_{33} and f_{33} for the plane strain state ($\nu(f_{11}+f_{22})$) are great. If the T_z factor is considered in f_{33}, f_{33} will be in good agreement with σ_{33}.

3. Three-parameter principle J–Q_T–T_z for the elastic-plastic material

The HRR stress components can be expressed as

$$\left(\sigma_{ij},\sigma_m,\sigma_e\right)=Kr^{-\frac{1}{n+1}}\left(\tilde{\sigma}_{ij}\left(\theta\right),\tilde{\sigma}_m\left(\theta\right),\tilde{\sigma}_e\left(\theta\right)\right) \tag{6}$$

where

$$K=\left(\frac{J}{\alpha\sigma_0\varepsilon_0 I\left(n\right)}\right)^{\frac{1}{n+1}} \tag{7}$$

σ_0 is the yield stress.

By considering the effects of geometry and size on crack-tip constraint, O'Dowd and Shih [8, 9] found that the near-tip stress field is governed by the two parameters of J and Q as follows:

$$\sigma_{ij}=\left(\frac{J}{\alpha\sigma_0\varepsilon_0 I\left(n\right)r}\right)^{\frac{1}{n+1}}\tilde{\sigma}_{ij}\left(\theta\right)+Q_{ij}\delta_{ij}\left(\frac{r}{J/\sigma_0}\right)^{\lambda}\sigma_0 \tag{8}$$

The first term is the HRR solution ($|\theta|<\pi/2$), Q is a function of the stress triaxiality achieved ahead of the plane strain cracks. The λ is set to zero, then Q_{rr}=$Q_{\theta\theta}$ and Q_{ij} is the form

$$Q_{ij}=\frac{\sigma_{ij}-\sigma_{ij}\big|_{HRR}}{\sigma_0} \qquad (\theta=0^{\circ},\ r=2J/\sigma_0) \tag{9}$$

The *J*-*Q* solution can effectively describe the influence of the in-plane stress parameters when the radial distances ($r/(J/\sigma_0)$) are relatively small, while the approach can hardly characterize it very well with the increase of $r/(J/\sigma_0)$ and strain hardening exponent n. On the other hand, it can hardly give a proper description of Von Mises equivalent stress σ_e because it seldom considers the out-of-plane stress constraint, so Guo and his collaborators proposed two 3D three-parameter principles of *K*-*T*-T_z and *J*-*Q*-T_z, combining with the in-plane constraint *T* or *Q*, for linear elastic and elastic-plastic materials.

Further researches by Guo [13-15, 20-22] show that I( ) is the function of n and T_z,

$$K=\left(\frac{J}{\alpha\sigma_0\varepsilon_0 I\left(n,T_z\right)}\right)^{\frac{1}{n+1}} \tag{10}$$

where

$$\begin{aligned} I\left(n,T_z\right)=\int_{-\pi}^{\pi}\{&\frac{n}{n+1}\tilde{\sigma}_e^{n+1}\cos\theta-\sin\theta\left[\tilde{\sigma}_{rr}\left(\tilde{u}_\theta-\frac{\partial\tilde{u}_r}{\partial\theta}\right)-\tilde{\sigma}_{r\theta}\left(\tilde{u}_r+\frac{\partial\tilde{u}_\theta}{\partial\theta}\right)\right]\\ &-\cos\theta\left[n\left(s-2\right)+1\right]\left(\tilde{\sigma}_{rr}\tilde{u}_r+\tilde{\sigma}_{r\theta}\tilde{u}_\theta\right)\}d\theta, \end{aligned} \tag{11}$$

$$\tilde{u}_r=\frac{\tilde{\sigma}_e^{\,n-1}}{n\left(s-2\right)+1}\left(d_1\tilde{\Phi}+d_2\frac{\partial^2\tilde{\Phi}}{\partial\theta^2}\right), \tag{12}$$

$$\tilde{u}_\theta=\frac{1}{n\left(s-2\right)}\left(2d_s\tilde{\sigma}_e^{\,n-1}\frac{\partial\tilde{\Phi}}{\partial\theta}-\frac{\partial\tilde{u}_r}{\partial\theta}\right), \tag{13}$$

$$\frac{\partial\tilde{u}_r}{\partial\theta}=\frac{1}{n\left(s-2\right)+1}\left[\frac{\partial\left(\tilde{\sigma}_e^{\,n-1}\right)}{\partial\theta}\left(d_1\tilde{\Phi}+d_2\frac{\partial^2\tilde{\Phi}}{\partial\theta^2}\right)+\tilde{\sigma}_e^{\,n-1}\left(d_1\frac{\partial\tilde{\Phi}}{\partial\theta}+d_2\frac{\partial^3\tilde{\Phi}}{\partial\theta^3}\right)\right], \tag{14}$$

$$\frac{\partial\tilde{u}_\theta}{\partial\theta}=\tilde{\sigma}_e^{\,n-1}\left(d_3\tilde{\Phi}+d_4\frac{\partial^2\tilde{\Phi}}{\partial\theta^2}\right)-\tilde{u}_r. \tag{15}$$

The d_i is the function of T_z and n, $\tilde{\Phi}=\tilde{\Phi}\left(\Phi\right)$, which is same as that in HRR solution.

The Eq.(8) can be modified

$$\sigma_{ij}=\left(\frac{J}{\alpha\sigma_0\varepsilon_0 I\left(n,T_z\right)r}\right)^{\frac{1}{n+1}}\tilde{\sigma}_{ij}\left(\theta,T_z\right)+Q_{Tij}\delta_{ij}\left(\frac{r}{J/\sigma_0}\right)^{\lambda}\sigma_0 \tag{16}$$

where

$$Q_{Tij} = \frac{\sigma_{ij} - \sigma_{ij}\big|_{J-T_z}}{\sigma_0} \qquad (\theta=0^{\circ} \text{ and } r=2J/\sigma_0) \tag{17}$$

Combining Eq.(9), the relationship between Q_{Tij} and Q_{ij} is

$$Q_{Tij} = Q + \frac{\sigma_{ij}\big|_{HRR} - \sigma_{ij}\big|_{J-T_z}}{\sigma_0} \tag{18}$$

The comparisons of the three-parameter solution J–Q_{T}–T_{z} with the solutions of J-Q and HRR are shown in Fig.5. It is shown that the three-parameter approach J–Q_{T}–T_{z} can describe the 3D stress fields effectively.

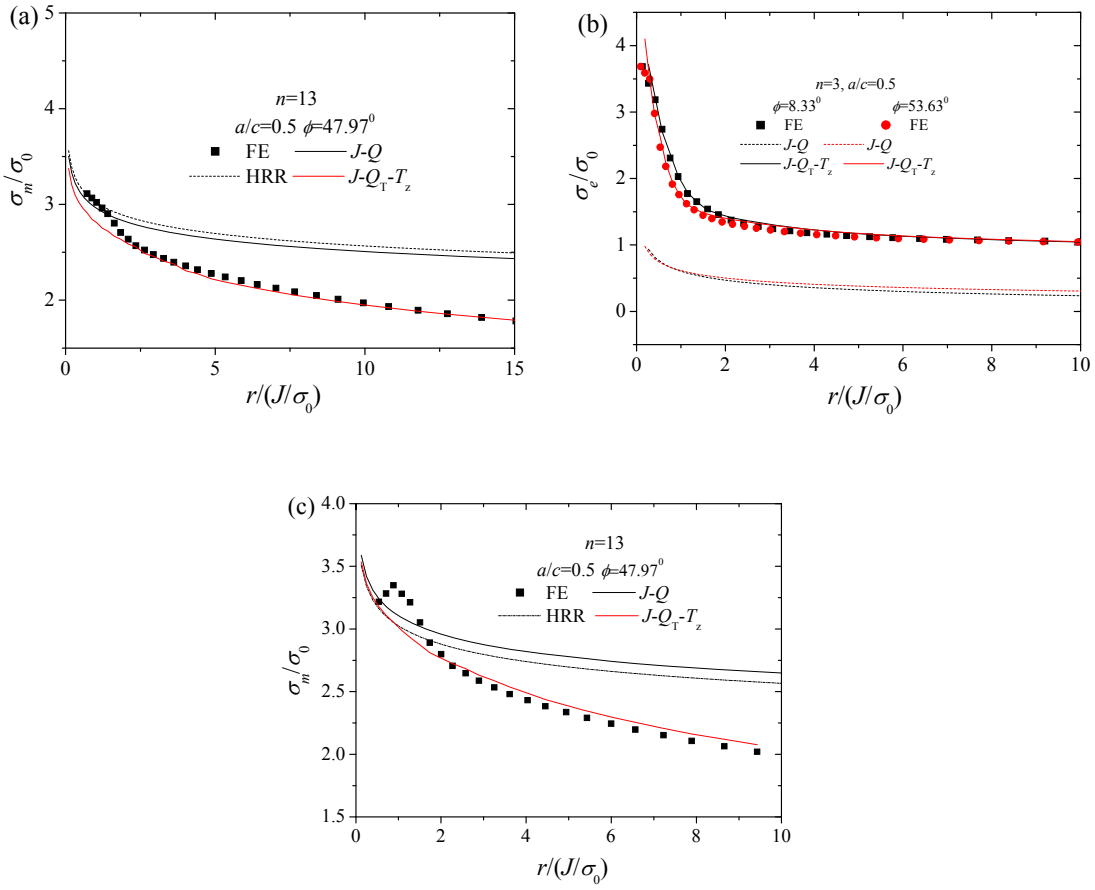

Fig.5 The radial distributions of the stress components. (a) Mean stress for a semi-elliptical surface crack, (b) Von Mises equivalent stress σ_{e} for a quarter elliptical corner crack, (c) Mean stress for an embedded elliptical crack.

4. Conclusions

Two three-parameter descriptions for the three-dimensional (3D) crack-tip stress fields have been introduced. The three-parameter solution K–T–T_z is developed to describe the linear elastic crack-tip stress state, and the J–Q_T–T_z is to elastic-plastic crack-tip field. The comparisons of the three-parameter solutions K–T–T_z, J–Q_T–T_z with the corresponding two-parameter solutions K-T, J–Q and single-parameter solutions K and HRR are presented. It is shown that the three-parameter approaches K–T–T_z, J–Q_T–T_z can describe the 3D stress fields effectively.

Acknowledgments

The work is supported by the Fundamental Research Funds for the Central Universities (No. NS2012126), Aviation Science Foundation Project (No. 2010ZA52005), Natural Science Foundation of China (No.50805079).

References

[1] D.M., Clatterbuck, D.C., Chrzan, J.W., MorrisJr., The influence of triaxial stress on the ideal tensile strength of iron. Scripta Mater. 49 (2003) 1007–1011.
[2] W., Guo, Recent advances in three-dimensional fracture mechanics. Key Eng. Mater. 183 (2000) 193–198.
[3] G.R., Irwin, Fracture. Handbuch der Physik, 6. Springer-Verlag, Heidelberg, 1958, pp. 551–590.
[4] J.W., Hutchinson, Singular behavior at the end of a tensile crack in a hardening material. J. Mech. Phys. Solids 16 (1968) 13–31.
[5] J.R., Rice, G.F., Rosengren, Plane strain deformation near a crack tip in a power-law hardening material. J. Mech. Phys. Solids 16 (1968) 1–12.
[6] M.L., Williams, On the stress distribution at the base of a stationary crack. J. Appl. Mech. 24 (1957) 109–114.
[7] C., Betegon, J.W., Hancock, Two-parameter characterization of elastic–plastic crack tip fields. J. Appl. Mech. 58 (1991) 104–113.
[8] N.P., O'Dowd, C.F., Shih, Family of crack-tip fields characterized by a triaxiality parameter—I. Structure of fields. J. Mech. Phys. Solids 39 (1991) 989–1015.
[9] N.P., O'Dowd, C.F., Shih, Family of crack-tip fields characterized by a triaxiality parameter—II. Fracture applications. J. Mech. Phys. Solids 40 (1992) 939–963.
[10] Y.C., Li, Z.Q., Wang, High-order asymptotic field of tensile plane-strain nonlinear crack problems. Sci. Sin. A 29 (1986) 941–955.
[11] Y.J., Chao, S., Yang, M.A., Sutton, On the fracture of solids characterized by one or two parameters: theory and practice. J. Mech. Phys. Solids 42 (1994) 629–647.
[12] C., She, W., Guo, The out-of-plane constraint of mixed-mode cracks in thin elastic plates. International Journal of Solids and Structures 44 (2007) 3021–3034.
[13] W., Guo, Elastoplastic three-dimensional crack border field—I. Singular structure of the field. Eng. Fract. Mech. 46 (1993) 93–104.
[14] W., Guo, Elastoplastic three-dimensional crack border field—II. Asymptotic solution for the field. Eng. Fract. Mech. 46 (1993) 105–113.
[15] W., Guo, Elastoplastic three-dimensional crack border field—III. Fracture parameters. Eng. Fract. Mech. 51 (1995) 51–71.
[16] J., Zhao, W., Guo, C., She, B., Meng. Three dimensional K-Tz stress fields around the

embedded center elliptical crack front in elastic plates. Acta Mech Sinica 22 (2006) 148–155.
[17] J., Zhao, W., Guo, C., She. The in-plane and out-of-plane stress constraint factors and K-T-Tz description of stress field near the border of a semi-elliptical surface crack. International Journal of Fatigue 29 (2007) 435–443.
[18] J., Zhao, W., Guo, Three-parameter K-T-Tz characterization of the crack-tip fields in compact-tension-shear specimens. Engineering Fracture Mechanics 92 (2012) 72–88.
[19] C., She, J., Zhao, W., Guo, Three-dimensional stress fields near notches and cracks. Int J Fract 151 (2008) 151–160.
[20] J., Zhao, W., Guo, C., She. Three-parameter approach for elastic–plastic fracture of the semi-elliptical surface crack under tension. International Journal of Mechanical Sciences 50 (2008) 1168–1182.
[21] J., Zhao, Three-parameter approach for elastic–plastic stress field of an embedded elliptical crack. Engineering Fracture Mechanics 76 (2009) 2429–244.
[22] J., Zhao, Three-parameter research on three-dimensional fracture for macrostructures. Ph.D thesis, Nanjing university of Aeronautics and Astronautics, 2008.

In-situ Observation of Mixed Mode Fatigue Crack Growth Behavior in Heat Affected Zone of a Welded Joint

Ming-Liang Zhu*, De-Qiang Wang, Fu-Zhen Xuan, Shan-Tung Tu

Key Laboratory of Pressure Systems and Safety, Ministry of Education, East China University of Science and Technology, Shanghai 200237, China
* Corresponding author: mlzhu@ecust.edu.cn

Abstract In-situ scanning electron microscope (SEM) observations of fatigue crack growth behavior in heat affected zone (HAZ) of a welded joint were performed with CTS (Compact-Tension-Shear) specimens under mixed-mode loading conditions in vacuum. Results showed that mode I fatigue behavior in the HAZ was influenced by local microstructure anisotropy and the 'zigzag' mode crack profile tended to deviate into the lower strength weld metal. With increasing the mixity of mode I/II loadings, fatigue crack growth rate was decreased with significant crack branching. Shear and branch cracks were competitive along the crack path, and fatigue cracks were often initiated from grain boundary and the interface of lath martensites. The cracks tended to orient themselves into a pure mode I condition. Three existing models were discussed with respect to their capabilities to predict crack direction under various loading conditions.

Keywords in-situ SEM, fatigue crack growth, crack growth path, mixed-mode loading, heat affected zone

1. Introduction

Generally, the various loading types in actual practices are often idealized as being mode I, mode II and mode III based on linear elastic fracture mechanics. Majority of crack growth investigations under both static and cyclic loadings were concentrated on single-mode loading mode such as the mode-I load condition. Unfortunately, single-mode loading seldom occurs in practice, and many service failures occur from cracks subjected to mixed mode loadings which involve more than one crack-tip mode. Even in pure mode I cyclic testing, any deviation of crack path or alternation of external loading direction would lead to combinations of mode II deformation in crack growth process.

Under mixed mode loading conditions, it was of importance to consider the evolution of crack growth direction. Several criteria for crack growth path prediction such as maximum tangential stress (MTS) criterion by Erdogan and Sih [1], minimum strain energy density (SED) criterion by Sih [2], the criterion of energy release rates by Nuismer [3], and the criterion of Richard [4], have been proposed and well documented in [4-6]. However, all these concepts were based on the isotropic material and limited to the linear elastic fracture mechanics [5]. Another issue in combined loading mode was the crack growth rate. Unlike the conventional stress intensity factor range ΔK in pure mode I fatigue, many parameters have been proposed to correlate mixed mode fatigue crack growth (FCG) rates. For example, Tanaka [7] and Yan [8] suggested the effective stress intensity factor range ΔK_{eff}, Patel and Pandey [9] insisted the strain energy density factor range ΔS, while Socie et al [10] proposed the equivalent strain intensity factor for small cracks.

Moreover, the fatigue thresholds [11, 12], crack closure [13, 14], microstructure [15] and loading path [16, 17] influences under mixed mode loading conditions have been investigated. While cracks were observed to propagate in homogeneous materials as widely reported, complications associated with the mixed mode fatigue crack behavior in heterogeneous microstructures, i.e., the gradient microstructures in the heat-affected-zone (HAZ), were far less well understood. In this case, the effect of microstructure anisotropy on crack growth morphology needed to be elucidated.

In the present work, mixed mode (I+II) FCG experiments were performed on an in-situ stage equipped in SEM by using CTS (Compact-Tension-Shear) specimens developed by Richard [18]. The effect of external loading angle on the crack growth rate and crack growth direction was analyzed in terms of local microstructure gradient in the HAZ. The crack growth direction was finally predicted on the basis of the existing models.

2. Materials and experiments

2.1. Materials and specimens

The material studied was the HAZ of a welded joint. The base material of the welding joint was a NiCrMoV type steel. It was undergone quenching and tempering heat treatment, and the resultant tensile strength and yield strength were 835.5 and 938 MPa, respectively. The weldment was formed by submerged arc welding (SAW) technique using filler metal of the 2.5%Ni low alloy steel. The HAZ, which had a width of about 3 mm, included three micro-zones, i.e., fully quenched-tempered zone (FQTZ), partially quenched-tempered zone (PQTZ) and tempered zone (TZ) [19]. The microstructures mainly included tempered martensites and bainites with martensite/bainite constituents altered in the HAZ.

In order to prepare CTS specimen for in-situ observation, standard three-point bending samples with a/W ratio of 0.5 and the thickness B of 16 mm were firstly machined from the welded joint. The initial notch in the sample was located in the FQTZ of the HAZ, with a distance of 120 μm to the fusion line. The samples were then pre-cracked under pure mode I loading at a stress ratio of 0.1 with a sinusoidal waveform to form a crack length of about 2 mm. Subsequently, relatively smaller specimens with a thickness of about 0.5 mm were prepared for in-situ tests. Fig. 1 shows the shape and dimensions of the CTS specimens.

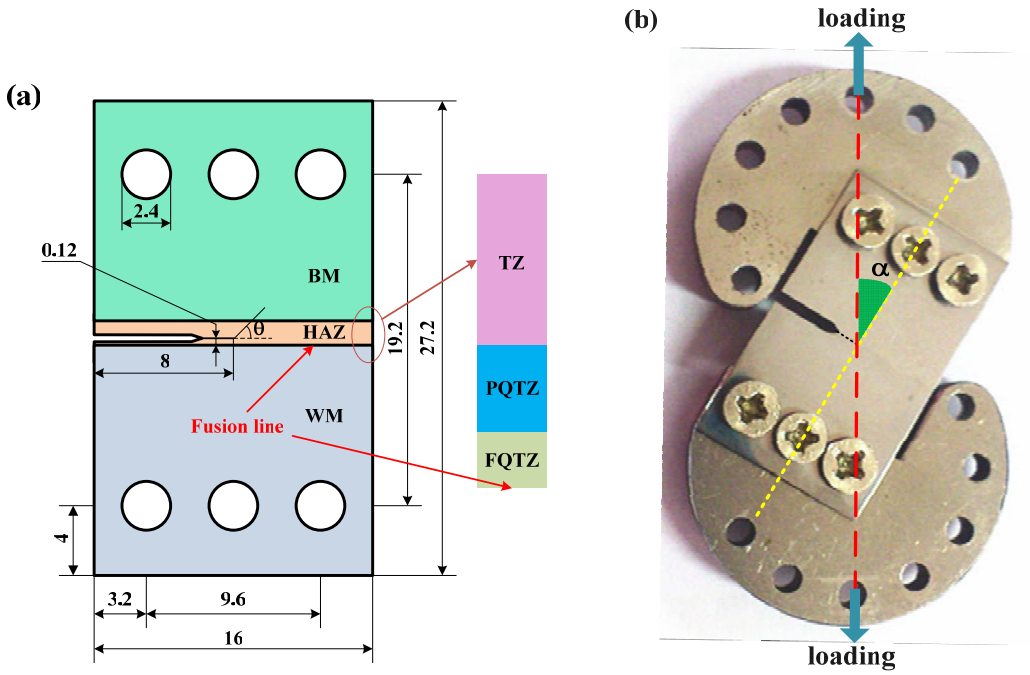

Figure 1. The shape and dimensions of the CTS specimens (a) and the loading device for mixed mode tests (b)

2.2. Fatigue experiments

Before the in-situ fatigue experiments, the CTS specimens were grounded, polished and finally

etched. Constant amplitude fatigue tests using triangular waveform with a load ratio of 0.1were performed on a loading stage equiped in the SEM in vacuum environment (9×10^{-4}–9×10^{-3} Pa). The frequency was as low as 0.03 Hz. The various values of $\Delta K_I/\Delta K_{II}$ could be achieved by changing the external loading angle α. As shown in Fig. 1b, the line of application of force F extends at an angle α to the longitudinal axis of the specimen. Depending on the size of angle α, mixed mode loadings occur at $0<\alpha<90°$. It is obvious that pure mode I loading corresponds to the α equaling to zero, whereas the α at 90° stands for the pure mode II loading. After the crack extended for a given length (less than 10 μm), the experiments were intermitted to measure crack length, record the cyclic numbers and characterize the crack morphology as well. For various loading angles, the initial mixed mode fatigue crack growth parameters, which was calculated by the Eqs. (1) - (3) developed by Richard [17], are listed in Table.1. In Eq. (3), the material parameter α_1 is set to 1.155.

$$K_{\mathrm{I}} = \frac{F\sqrt{\pi a}}{WB}\cdot\frac{\cos\alpha}{1-a/W}\cdot\sqrt{\frac{0.26+2.65\cdot\dfrac{a}{W-a}}{1+0.55\cdot\dfrac{a}{W-a}-0.08\cdot\left(\dfrac{a}{W-a}\right)^2}} \tag{1}$$

$$K_{\mathrm{II}} = \frac{F\sqrt{\pi a}}{WB}\cdot\frac{\sin\alpha}{1-a/W}\cdot\sqrt{\frac{-0.23+1.40\cdot\dfrac{a}{W-a}}{1-0.67\cdot\dfrac{a}{W-a}+2.08\cdot\left(\dfrac{a}{W-a}\right)^2}} \tag{2}$$

$$\Delta K_{\mathrm{eff}} = \frac{K_{\mathrm{I}}}{2}+\frac{1}{2}\sqrt{K_{\mathrm{I}}^2+4\left(\alpha_1 K_{\mathrm{II}}\right)^2} \tag{3}$$

Table 1. Initial mixed mode FCG parameters in the FQTZ of the HAZ

α	a_0/W	ΔK_I (MPa·m$^{1/2}$)	ΔK_{II} (MPa·m$^{1/2}$)	$\Delta K_I/\Delta K_{eff}$
0	0.5451	35.27	0	1
30°	0.5449	30.46	7.95	0.92
60°	0.5476	17.75	13.82	0.65

3. Results

3.1. *a*-*N* relationship

Fig. 2 shows the changes of crack extension as a function of cyclic numbers. It is observed that the crack extends slowly first and then become faster at all of the loading angles. However, with the decreasing of $\Delta K_I/\Delta K_{eff}$, which meant the reduced contribution of mode I loading, the crack extension was also decreased. Nevertheless, due to the proximity of the $\Delta K_I/\Delta K_{eff}$ values at α of zero and 30°, the corresponding crack extension values were also close and even converged to each other eventually. This indicated that the load mixity dependence of crack growth behavior located mainly in the initial crack growth process.

3.2. Fatigue crack growth rate d*a*/d*N*

Fig. 3 indicates the FCG rate da/dN at various loading angles. It is worth noting that the da/dN at α of zero and 30° are similar to each other but larger than those of the α of 60°. It is also worth noting that the evolution of da/dN for pure mode I loading fluctuates with the crack length, i.e., the delay and acceleration phases alternates. This reflected the influence of local microstructures. Whereas for

mixed mode of fatigue, the da/dN are tended to increase along with the crack length at both α of 30° and 60°. In this case, the important issue is that whether the local microstructures still have a large influence or are there other factors that should be considered. The roles of ΔK_{I} and ΔK_{II} in the mixed mode crack growth also need to be elucidated.

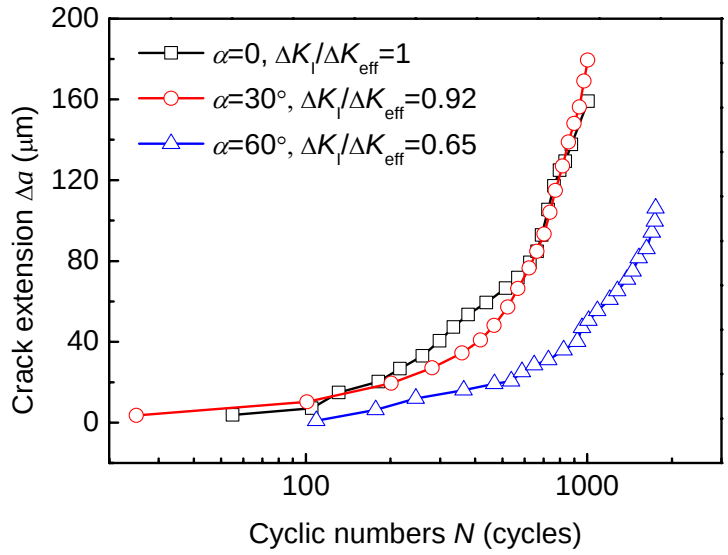

Figure 2. The crack extension Δa versus cyclic numbers N at different loading angles

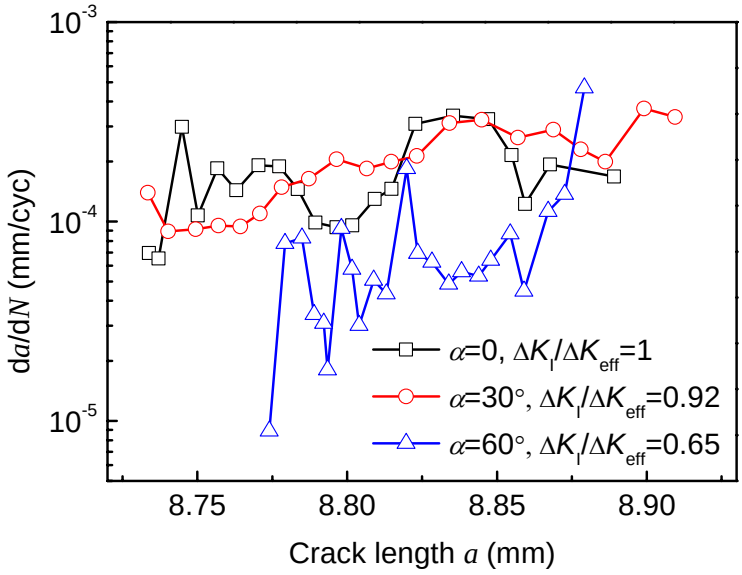

Figure 3. Fatigue crack growth rates at different loading angles

3.3. Crack growth path deflection

Fig. 4 presents the macro-crack profile at various loading angles. For mode I loading, as shown in Fig. 4a, crack deflected for about 21° from the initial pre-crack and then fluctuated, and the resultant crack path was quite tortuous. When load mode was superimposed with mode II loading at α of 30° (Fig. 4b), the initial angles of branch cracks was increased to 27°. Under this angle, crack extended for about 150 μm, after which the crack was further deviated to an angle of about 45° in

the final stage of growth of 40 μm. With the ΔK_{II} further increased, i.e., α equals 60° in Fig. 4c, the initial branch cracks deflected about 52°. The crack extension values along the crack path in the X and Y-axis directions are depicted in Fig. 5. By linear fitting of the data, the deflection angles were consequently calculated to be 25° and 50° at α of 30° and 60°, respectively. This agreed well with the work reported by Kim [20] who obtained similar values in a rail steel.

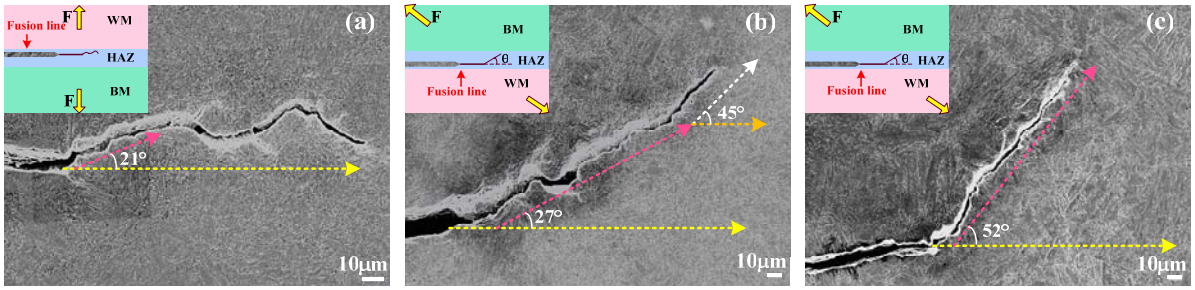

Figure 4. Macro-crack growth path at various loading angles: (a) α = 0, (b) α = 30°, and (c) α = 60°

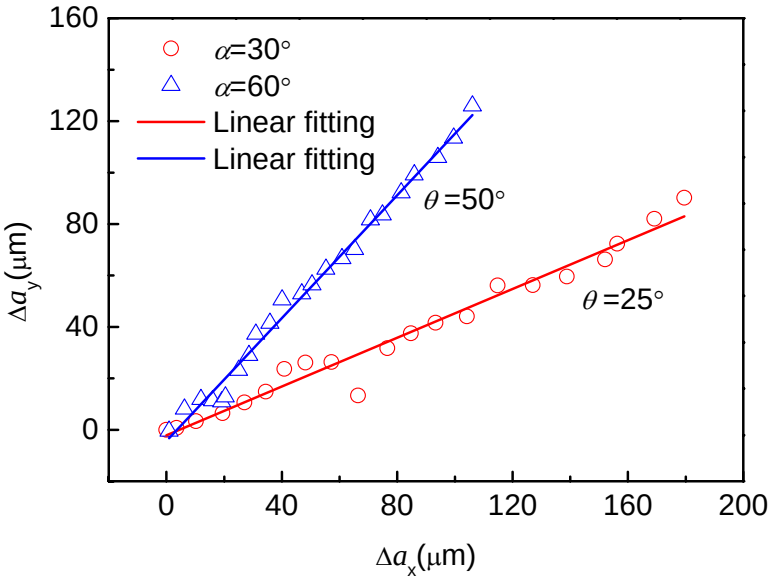

Figure 5. Fatigue crack extension in mixed mode loading conditions

4. Discussion

4.1. Influence of loading angle on FCG

Fig. 6 shows the FCG under pure mode I loading. At the end of the pre-crack, the crack propagated with two branches, as illustrated in Fig. 6b. One of the branch crack (lower side of the pre-crack) stopped growth after initiation along the grain boundary, whereas the other branch crack deflected at an angle of 21° and propagated to become the main crack. The competition between the two branch cracks to form the main crack was observed at *N* around 513 cycles in Fig. 6c. Though the original main crack continued growing forward, the lower side branch crack grew with a higher rate in a transgranular mode, and finally produced the main crack (Fig. 6d). In this process, it seemed that the crack tended to orient itself into a pure mode I condition at which the crack path was normal to the external loading direction.

The alternation of the main crack was also observed when *N* was around 727 cycles, as shown in

Figs. 6e and f. In this case, the main crack was finally formed by propagating the short branch crack and the non-propagation of the original main crack (the lower side branch crack in Fig. 6e). With the crack length increasing, as indicated in Fig. 6g, the slanted crack was again prone to return to the pure mode I trajectory, producing multiple bifurcations along the curved crack path. The bifurcated cracks were often located at grain boundaries and martensite lath interfaces. It is worth noting that the overall crack path propagated with serious local deviations, showing a 'zigzag' mode.

It is inferred that the significant changes of crack orientation is due to the highly anisotropic microstructures at the crack tip and the gradient strength distribution in the HAZ. It is generally accepted that the crack path is governed by the plastic behavior of the crack tip [21]. Accordingly, the cracks would orient themselves into the materials with lower strength values. Therefore, it is reasonable that the crack path is tended to deflect into the weld metal, which has lower strength than the PQTZ in the HAZ.

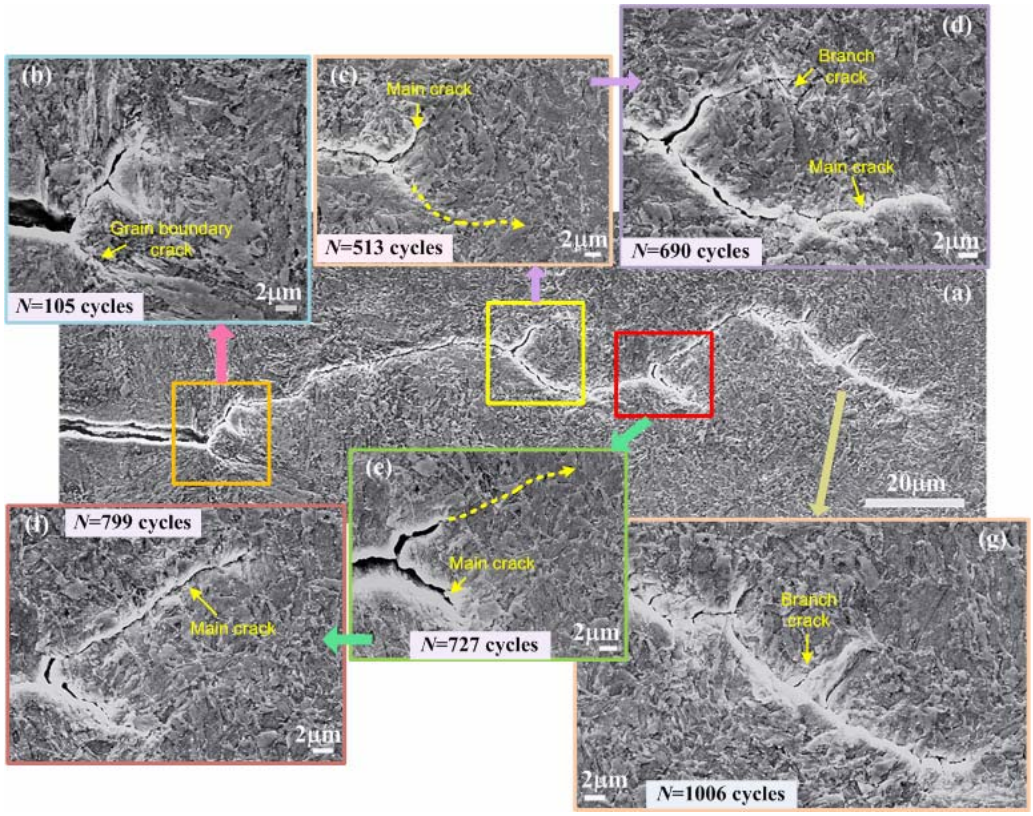

Figure 6. Fatigue crack growth morphology in pure mode I loading

Fig. 7 presents the FCG path at a loading angle of 30°. In Fig. 7a, the crack direction changed immediately from the initial pre-crack orientation with an angle of 27°. Crack bifurcations and shear cracks coexisted along with the main crack, which was resulted from the contribution of mode I and II components. As a result, the mode I component would drive the branch crack for a long length to a mode I crack direction. This was evidenced by formation of main crack based on the original branch crack in Fig. 7b. Tong et al. [22] reported that the formation and propagation of mode I branch cracks were of decisive importance for fatigue failures under combined loadings. It is also observed that the crack tip in Fig. 7a is branched along the grain boundary when N is increased to 622 cycles. On the other hand, the mode II component also contributed to FCG. With the formation of the grain boundary cracks at crack tip in Fig. 7b, a damage area containing many micro-cracks whose direction were almost parallel to the main crack was also formed, as shown in Fig. 7c. This was arisen from the shear deformation under mode II component in the mixed mode

loading.

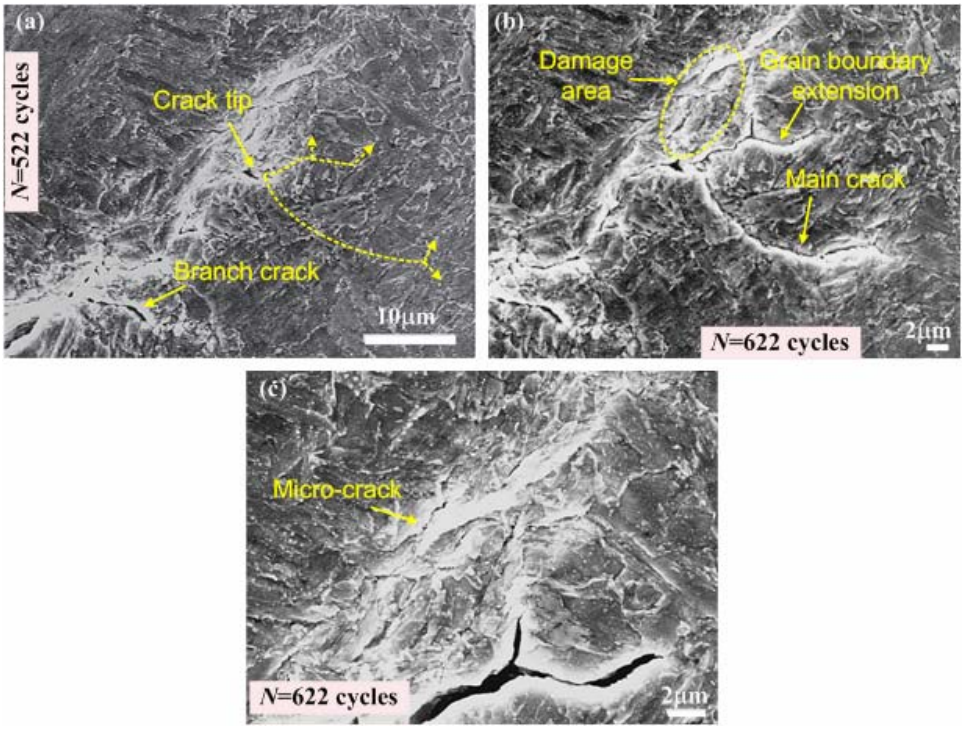

Figure 7. Fatigue crack growth path at a loading angle of 30°

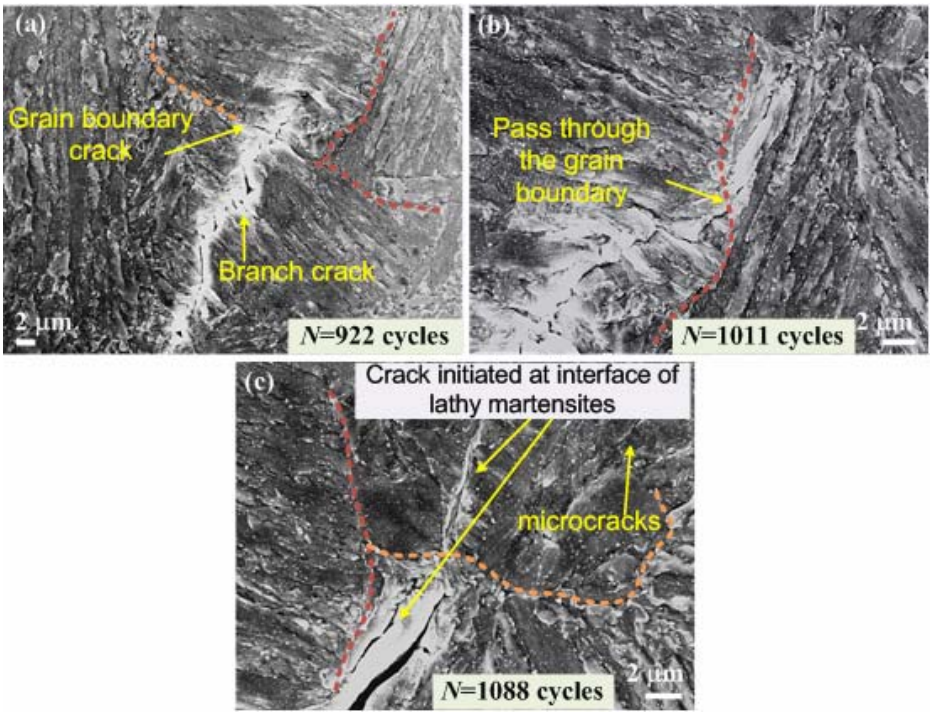

Figure 8. Fatigue crack growth path at a loading angle of 60°

The FCG behavior at a loading angle of 60° is illustrated in Fig. 8. It is observed in Fig. 8a that the crack extends transversely among the lathy martensites and propagates directly through the grain boundaries. In this process, crack bifurcated along the lath interfaces and grain boundaries. The passing through of the crack into the grain boundary was also observed in Fig. 8b, and then the crack extended along the interface of the lathy martensites. Therefore, it can be concluded that the interfaces of lathy martensites and the grain boundary are potential crack initiation sites. With the

increasing of cyclic numbers, one crack was formed again along the interface of the lathy martensites in the nearby grains, as can be seen in Fig. 8c. This would provide an easy path for the crack passing through the grain boundary since the cyclic plastic deformation has been extended to this area.

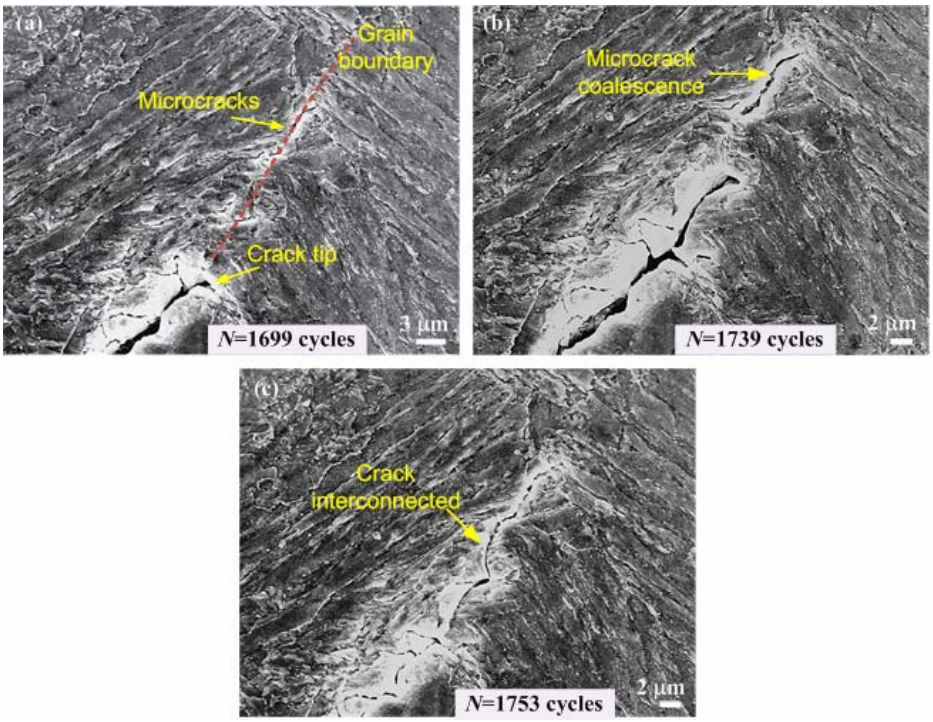

Figure 9. Coalescence of micro-cracks on the grain boundaries at the loading angle of 60°

Moreover, the damage area was dependent on the d*a*/d*N*, i.e., the higher the FCG rate, the larger the damage area. This is supported by the results in Fig. 9a, where a large number of micro-cracks has been formed at a distance about 30 μm in front of the main crack tip. Both branch and shear micro-cracks were occurred on the grain boundary. With the fatigue life increased to 1739 cycles, some micro-cracks were coalesced with each other, resulting in relatively longer cracks. Finally, all the micro-cracks were interconnected to form the main crack at N of 1753 cycles. The interconnection of grain boundary cracks increased the FCG rate considerably, which was plotted in Fig. 3. By comparing with the crack path at the loading angles of 30° and 60°, it can be observed that the length of branch cracks at α of 30° are longer and more shear micro-cracks at α of 60°. This was related to the branch versus shear crack competition in the mixed mode loading conditions.

4.2. Prediction of crack growth deflection angles

The initial deflection angles of FCG were predicted based on the SED criterion [2] in Eq. (4), the MTS criterion [1] in Eq. (5) and the criterion of Richard [4] in Eq. (6). In Eqs. (4) - (6), K_I and K_{II} are the mode I and II components, ν is Poisson's ratio, θ_0 is the critical deflection angles, and β is the angle between external loading and the crack surface. In this work, ν is set as 0.3, and the corresponding results are shown in Table 2. It is obvious that compared with the experimental data, all the predicted deflection angles for α of 30° and 60° are higher than the experimental data. Fortunately, the calculation based on MTS model was close to the experiments. Thus, the MTS criterion is suitable to predict crack growth direction in the HAZ under combined loadings. Nevertheless, all of the criteria cannot estimate the deflection of crack growth direction under pure mode I loading. This can be ascribed to the limitation of the models to homogeneous materials, and thus results in the disparities of crack deflection angle in mode I loading.

$$2(1-2\nu)\sin(\theta_0-2\beta)-2\sin\left[2(\theta_0-\beta)\right]-\sin 2\theta_0=0,\beta\neq 0 \tag{4}$$

$$K_{\mathrm{I}}\sin\theta_0+K_{\mathrm{II}}(3\cos\theta_0-1)=0 \tag{5}$$

$$\theta_0=\mathrm{m}\left[155.5°\frac{|K_{\mathrm{II}}|}{|K_{\mathrm{I}}|+|K_{\mathrm{II}}|}\right]-83.4°\left[\frac{|K_{\mathrm{II}}|}{|K_{\mathrm{I}}|+|K_{\mathrm{II}}|}\right]^2 \tag{6}$$

Table 2. Prediction of crack growth deflection angles based on different models

α	Minimum strain energy density (SED) criterion [2]	Criterion of Richard [4]	Maximum tangential stress (MTS) criterion [1]	Experiment
0	0	0	0	21°
30°	35°	28.6°	26.2°	25°
60°	55.26°	52.1°	48.98°	50°

5. Conclusions

In this study, the growth behavior of fatigue cracks in the HAZ of a welded joint under mixed mode loading conditions were studied by utilizing CTS specimens. The FCG morphology was characterized by in situ SEM observations in vacuum. The main conclusions are listed as follows.

(1) Mode I fatigue behavior in the HAZ was influenced by local microstructure anisotropy and the gradient distribution of material strength. The crack growth path tended to deflect into the lower strength weld metal, showing a “zigzag” mode.
(2) With the increasing of mixity in mode I/II fatigue loadings, FCG rate in the HAZ was decreased whereas the initial angles for crack branching were increased. Shear and branch cracks were competitive along the crack path, and fatigue crack was often initiated from grain boundary and the interface of lath martensites. Eventually the cracks tended to orient themselves into a pure mode I direction.
(3) The initial branch crack direction was predicted based on existed models, and calculation from the MTS criterion showed comparable agreement with experimental data.

Acknowledgements

The authors are grateful for the supports provided by National Natural Science Foundations of China (51205131) and the Natural Science Foundation of Shanghai (12ZR1442900). Ming-Liang Zhu would also appreciate the support from Chen Guang project (12CG33) by Shanghai Municipal Education Commission and Shanghai Education Development Foundation.

References

[1] F. Erdogan, G.C. Sih, On the Crack Extension in Plates Under Plane Loading and Transverse Shear, J Basic Eng, 85 (1963) 519-525.
[2] G.C. Sih, Mechanics of Fracture Initiation and Propagation, in, Kluwer, The Netherlands, 1991.
[3] R.J. Nuismer, An energy release rate criterion for mixed mode fracture, Int J Fract, 11 (1975) 245-250.
[4] H.A. Richard, M. Fulland, M. Sander, Theoretical crack path prediction, Fatigue Fract Eng Mater Struct, 28 (2005) 3-12.
[5] J. Qian, A. Fatemi, Mixed mode fatigue crack growth: A literature survey, Eng Fract Mech, 55 (1996) 969-990.

[6] A.K. Soh, L.C. Bian, Mixed mode fatigue crack growth criteria, Int J Fatigue, 23 (2001) 427-439.
[7] K. Tanaka, Fatigue crack propagation from a crack inclined to the cyclic tensile axis, Eng Fract Mech, 6 (1974) 493-507.
[8] Y. Xiangqiao, D. Shanyi, Z. Zehua, Mixed-mode fatigue crack growth prediction in biaxially stretched sheets, Eng Fract Mech, 43 (1992) 471-475.
[9] A.B. Patel, R.K. Pandey, Fatigue crack growth under mixed mode loading, Fatigue Fract Eng Mater Struct, 4 (1981) 65-77.
[10] D.F. Socie, C.T. Hua, D.W. Worthem, Mixed mode small crack growth, Fatigue Fract Eng Mater Struct, 10 (1987) 1-16.
[11] J.P. Campbell, R.O. Ritchie, Mixed-mode fatigue-crack growth thresholds in Ti-6Al-4V at high frequency, Scripta Mater, 41 (1999) 1067-1071.
[12] Y. Liu, S. Mahadevan, Threshold stress intensity factor and crack growth rate prediction under mixed-mode loading, Eng Fract Mech, 74 (2007) 332-345.
[13] P. Lopez-Crespo, A. Shterenlikht, J.R. Yates, E.A. Patterson, P.J. Withers, Some experimental observations on crack closure and crack-tip plasticity, Fatigue Fract Eng Mater Struct, 32 (2009) 418-429.
[14] A.M. Abdel Mageed, R.K. Pandey, Studies on cyclic crack path and the mixed-mode crack closure behaviour in Al alloy, Int J Fatigue, 14 (1992) 21-29.
[15] J.P. Campbell, R.O. Ritchie, Mixed-mode, high-cycle fatigue-crack-growth thresholds in Ti-6Al-4V: Role of bimodal and lamellar microstructures, Metall and Mat Trans A, 32 (2001) 497-503.
[16] M. Feng, F. Ding, Y. Jiang, A study of loading path influence on fatigue crack growth under combined loading, Int J Fatigue, 28 (2006) 19-27.
[17] M. Sander, H.A. Richard, Experimental and numerical investigations on the influence of the loading direction on the fatigue crack growth, Int J Fatigue, 28 (2006) 583-591.
[18] H.A. Richard, K. Benitz, A loading device for the creation of mixed mode in fracture mechanics, Int J Fract, 22 (1983) R55-R58.
[19] M.-L. Zhu, F.-Z. Xuan, Correlation between microstructure, hardness and strength in HAZ of dissimilar welds of rotor steels, Mater Sci Eng A, 527 (2010) 4035-4042.
[20] J.-K. Kim, C.-S. Kim, Fatigue crack growth behavior of rail steel under mode I and mixed mode loadings, Mater Sci Eng A, 338 (2002) 191-201.
[21] J.R. Yates, M. Zanganeh, R.A. Tomlinson, M.W. Brown, F.A.D. Garrido, Crack paths under mixed mode loading, Eng Fract Mech, 75 (2008) 319-330.
[22] J. Tong, J.R. Yates, M.W. Brown, The formation and propagation of mode I branch cracks in mixed mode fatigue failure, Eng Fract Mech, 56 (1997) 213-231.

Experimental Determination of Mode II Fracture Resistance in Asphalt Concretes

M.R. Ayatollahi[1,*], Sadjad Pirmohammad[1]

[1] School of Mechanical Engineering, Iran University of Science and Technology, 16846, Iran
* Corresponding author: m.ayat@iust.ac.ir

Abstract This paper presents a test set-up using semi-circular bend (SCB) specimen for measuring pure mode-II fracture toughness of asphalt concretes. Three-point bend fracture tests were performed on the SCB specimens at low temperature. The results showed that this set-up could be used for conducting mode-II fracture tests on hot mix asphalt (HMA) specimens. Linear elastic fracture mechanics (LEFM) concept was used to study the fracture behavior of cracked asphalt concrete. Mode-II critical stress intensity factor, K_{IIc}, was calculated using the fracture load measured from the three-point bend tests. In addition to pure mode-II tests, similar tests were carried out for pure mode-I loading. Results showed that mode-II critical stress intensity factor was higher than that of pure mode-I loading.

Keywords Asphalt concrete, Critical stress intensity factor, Low temperature, Pure mode-II fracture.

1. Introduction

Cracking at low temperatures is one of the major sources of deterioration in asphalt concretes imposing significant costs on the pavement rehabilitation agencies annually. There are many causes for crack nucleation on asphalt pavement surface such as the temperature fluctuation and the traffic load induced from vehicle wheels. Good understanding of cracking mechanism could be helpful for reducing those costs.

Asphalt concrete is a temperature dependant material that may fall within a category of materials that are defined as brittle or quasi-brittle at low temperatures. Many researchers have studied fracture behavior of hot mix asphalt (HMA) mixtures at low temperatures (e.g. see [1-3]). Linear elastic fracture mechanics (LEFM) is a reliable approach to investigate fracture behavior of brittle materials. In LEFM, the stress intensity factor, K, is a fundamental parameter characterizing the fracture phenomenon from the crack tip. This parameter has been used by many researchers (e.g. see [4-6]) for cracks in asphalt concrete mixtures.

In the recent decades, many researchers have studied the fracture behavior of asphalt concretes under pure mode-I (opening mode) loading (see e.g. [4-7]). The temperature cycling is one of the main causes of mode-I cracking in asphalt pavements. In some cases such as reflective cracks, the crack extension is known to take place under a combination of mode-I and mode-II loading. Similarly, according to the research performed by Ameri et. al. [8], the traffic load induced by vehicle wheels at top down cracks (TDC) also results in mixed mode I-II loading. Therefore, it is important to investigate the behavior of cracked asphalt concretes under pure mode-I, pure mode-II, and mixed mode I-II loading conditions. In particular, pure mode-II fracture in asphalt concretes has been rarely studied in the past.

In this research, the semi-circular bend (SCB) specimens, prepared from the cylindrical samples were utilized for conducting three-point fracture tests under pure mode-II loading. In addition to the mode-II tests, fracture tests were performed for mode-I loading as well and the critical stress

intensity factors were calculated and compared.

2. Specimen geometry and material

While HMA behavior is strongly affected by temperature, at subzero temperatures, its mechanical behavior is often considered to be brittle or quasi-brittle. Hence, linear elastic fracture mechanics (LEFM) concept is adoptable for investigating the fracture behavior of HMA mixtures at low temperatures. Generally, the cracked asphalt concrete pavement may experience three main modes of fracture, mode-I, mod-II, and mode-III. Among these three modes, mode-I and mode-II are predominant modes of crack propagation in asphalt concrete pavements containing reflective or top-down cracks.

Several test specimens such as single edge notched beam (SENB), disk-shaped compact tension (DC-T), semi-circular bend (SCB) and so on, have been used in the past by many researchers to study the fracture behavior of asphalt concretes. In this research, an improved SCB specimen was employed to conduct the experiments. For this purpose, first several cylindrical samples (130 mm in height, 150 mm in diameter) were prepared using superpave gyratory compactor (SGC) in the laboratory. These samples were sliced into several disks of 32 mm thick by means of a water-cooled masonry sawing machine. Each disk was then halved to obtain semi-circular shaped specimens. At the next stage, an artificial edge crack (20 mm in length) was generated within the specimen utilizing a water-cooled cutting machine with a very thin blade. The width of generated crack was 0.3 mm.

According to the finite element simulations performed by Ayatollahi [9], in a SCB specimen of radius 75 mm containing an edge crack of length 20 mm, pure mode-II loading is achieved when the edge crack distance is 16 mm from the middle of the specimen (see Fig. 1). S_1 and S_2 are the left and right hand side distances of the lower fixtures from the middle of the specimen, respectively. For pure mode-II loading, the values of S_1 and S_2 were found from the FE analysis to be 50mm and 20 mm respectively.

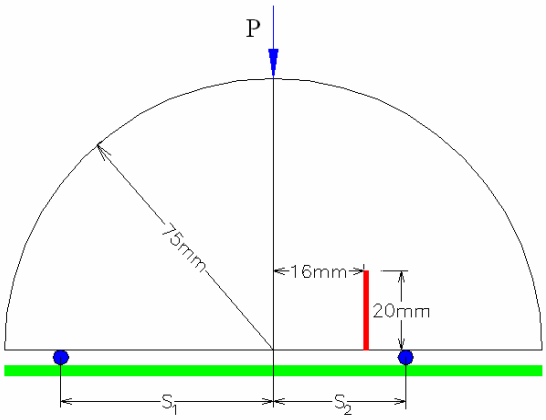

Figure 1. Test specimen used for pure mode-II fracture tests

The asphalt concrete used to prepare the cylindrical samples was similar to the one which is widely used in Iran pavement systems. Aggregate gradation of the HMA mixtures used in this study (as described in Table 1) is within the range of the recommendations by Iran Highway Asphalt Paving

Code (IHAPC). The air void of all mixtures was 4 percent. Asphalt binder with penetration grade of 60/70 was utilized for preparation of the cylindrical samples.

Table 1. HMA aggregate gradation

Sieve size (mm)	Requirements		Percent passing
	Min	Max	
19	100	100	100
12.5	90	100	95
9	67	87	77
4.75	44	74	59
2.36	28	58	43
1.18	20	46	33
0.5	13	34	23
0.3	5	21	13
0.15	4	16	9.5
0.075	2	10	8.4

3. Fracture tests and results

Three-point bend fracture tests were conducted on the SCB specimens under pure mode-II loading at -20°C. To achieve this temperature, the SCB specimens were first put into a freezer with the fixed temperature of -20°C for 4 hours. Then the tests were immediately carried out using a universal testing machine and a three-point bend fixture (as shown in Fig. 2). The displacement rate of the upper fixture was set to a constant value of 3 mm/min. In the first stage, the conventional round-tip supports were used to load the specimens. However, some of the tests were not successful. Because, the crack growth initiated from the lower and right hand side fixture and not from the crack tip (see Fig. 3).

To avoid crack initiation from undesirable locations, the lower fixtures were modified such that instead of applying the bottom loads in the concentrated points (as was the case in the first set-up) the loads were applied as distributed forces. Several finite element analyses were performed to find the width of distributed load (i.e. the magnitude of b in Fig. 4) in order to provide pure mode-II loading. Fig. 5 shows a typical mesh used in the finite element analyses. The appropriate value for the parameter b was eventually found to be 4 mm. The conventional fixtures used in the first set-up were replaced with the second set-up, and the mode-II fracture tests were repeated. By this modification, the crack extension in all the specimens took place from the crack tip (see Fig. 6). Therefore, the pure mode-II fracture test was successfully simulated experimentally using the SCB specimen. The fracture tests were also performed under pure mode-I loading and at -20°C using the same three-point test set-up. However, for this type of loading, the crack was generated in the middle of the specimen with symmetric loading supports of $S_1=S_2=50$ mm (see Fig. 1). Fig. 7 shows sample of the load-load line displacement curves recorded from the mode-I and mode-II fracture tests. In order to increase the reliability of the experimental results, four SCB specimens were tested for each mode of loading. As

shown in Fig. 7, the load increases linearly and then suddenly drops to zero. Therefore, one may suggest that the asphalt concrete failure was due to brittle fracture with negligible nonlinear deformation. Considering the area under the load-load line displacement curve, Fig. 7 shows that the asphalt mixture needs higher energy to fracture under mode-II loading than under mode-I loading.

Figure 2. Three point test set-up

Figure 3. Fracture test using first set-up

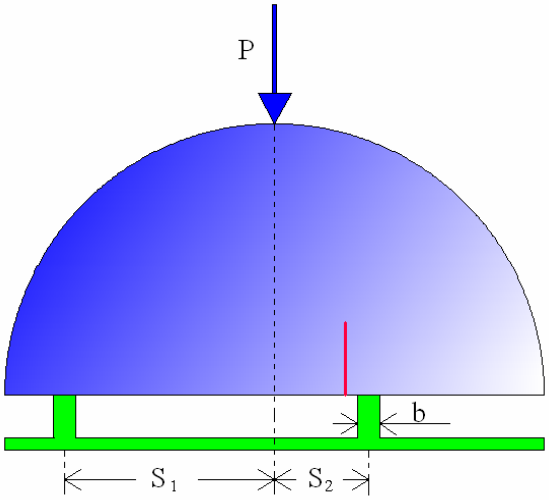

Figure 4. Three-point test (second set-up)

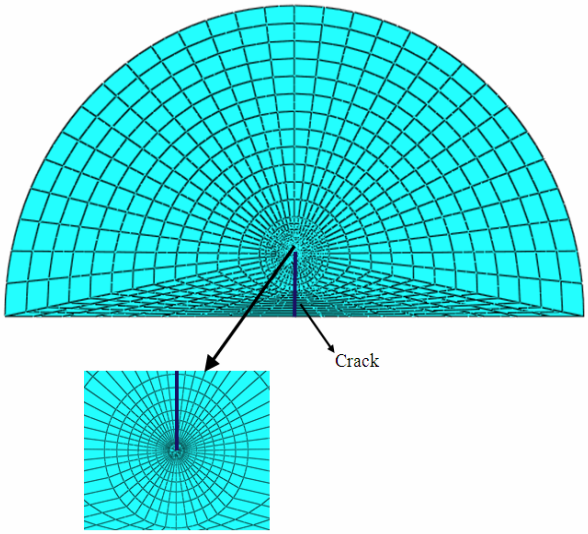

Figure 5. The finite element mesh

The fracture resistance in cracked specimens is often described by the values of critical stress intensity factors. The mode-I and mode-II critical stress intensity factors, K_{Ic} and K_{IIc} can be written for the SCB specimen in terms of the experimentally obtained fracture load P_{cr} as:

$$K_{Ic} = Y_I \frac{P_{I_{cr}}}{2Rt}\sqrt{\pi a} \qquad K_{IIc} = Y_{II} \frac{P_{II_{cr}}}{2Rt}\sqrt{\pi a} \tag{1}$$

The fracture load P_{cr} is obtained for each mode of loading from the maximum load recorded in the fracture tests. Y_I and Y_{II} are mode-I and mode-II geometry factors which were obtained from finite element analyses as 3.73 and 2.25, respectively. The specimen radius and thickness R, t, and the crack

length *a* are 75 mm, 32 mm, and 20 mm respectively.

Figure 6. Fracture test using second set-up

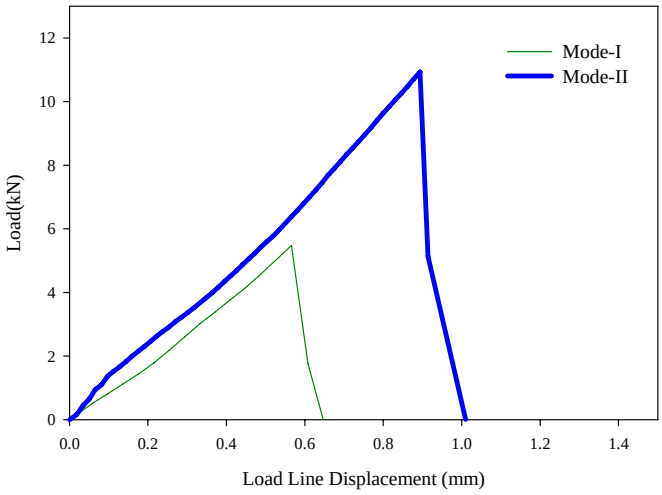

Figure 7. Load vs LLD at -20°C

Table 2. Average experimental results for mode-I and mode-II loading

Mode of loading	$P_{cr}(kN)$	Critical stress intensity factor $(MPa.\sqrt{m})$
Pure mode-I	5.3	1.03
Pure mode-II	11.2	1.3

The critical stress intensity factors (K_{Ic} and K_{IIc}) were calculated from Eq. 1 for each test conducted under mode-I or mode-II loading conditions. Table 2 shows the average values of P_{cr}, K_{Ic} and K_{IIc} obtained for asphalt samples. According to this Table, the critical stress intensity factor under pure mode-II loading is about 26% higher than that under pure mode-I loading. In other words, when a cracked asphalt concrete is under pure mode-II loading, its resistance against brittle fracture at low temperatures is more than that of mode-I loading. Moreover, the mode-II fracture load in the asphalt SCB specimens is more than twice the mode-I fracture load (see Table 2). While the crack extension in mode-I fracture tests took place along the pre-crack direction, all the mode-II cracks kinked out of the initial plane (see Fig. 6). This is mainly because the maximum tensile stress around the crack tip is no longer along the crack line when a cracked specimen like SCB is subjected to pure mode-II loading conditions [10].

4. Conclusion

In this paper, a suitable procedure was suggested for conducting fracture experiments on cracked asphalt concretes under pure mode-II loading and at low temperatures. The modified SCB specimens used for the experiments can be produced conveniently by a gyratory compactor or by coring from an existing asphalt pavement. The specimen can be used both for pure mode-I tests and for pure mode-II tests. The mode-I and mode-II tests were performed successfully on an asphalt mixture sample at -20^{o}C. The results showed that both the fracture load and the critical stress intensity factor obtained from the mode-II experiments were considerably higher than those obtained from the mode-I experiments.

References

[1] D.A. Anderson, D.W. Christensen, R. Dongre, M.G. Sharma, J. Runt, P. Jordhal, Asphalt Behavior at Low Temperatures, Publication No. FHWA-RD-88-078, RHWA, US Dept. of Transportation, 1990.

[2] B. Buttlar, Reflective crack relief interlayers. OMP Brown Bag Seminar Series, 2007.

[3] X. Li, M.O. Marasteanu, Using semi-circular bending test to evaluate low temperature fracture resistance for asphalt concrete. Exp. Mech., 50 (2007) 867-876.

[4] J.M.M. Molenaar, A.A.A. Molenaar, Fracture toughness of asphalt in the semicircular bend test. In. 2nd Eurasphalt and Eurobitume Congress, Barcelona, Spain, (2000).

[5] X. Li, M.O. Marasteanu, Evaluation of the low temperature fracture resistance of asphalt mixtures using the semi circular bend test. Asphalt Paving Technology: Association of Asphalt Paving Technologists-Proceedings of the Technical Sessions, 73 (2004) 401-426.

[6] R. Dongre, M.Cl. Sharma, D.A. Anderson, Development of fracture criterion for asphalt mixes at low temperatures. Transp. Res. Rec., 1228 (1989) 94-105.

[7] S.A Tekalur, A. Shukla, M. Sadd, K.W. Lee, Mechanical characterization of a bituminous mix under quasi-static and high-strain rate loading. Constr. Build. Mater., 23 (2008) 1795-1802.

[8] M. Ameri, A. Mansourian, M. Heidary-Khavas, M.R.M. Aliha, M.R. Ayatollahi, Cracked asphalt pavement under traffic loading – A 3D finite element analysis. Eng. Fract. Mech., 78 (2011) 1817-1826.

[9] M.R. Ayatollahi, Investigation of Mixed Mode Fracture in Asphalt Concretes Due to the Traffic Loads, Research Report, Project Code: 88B5T2P28(RP), Transportation Research Institute, Iran Ministry of Roads and Transportation, 2011.

[10] M.R. Ayatollahi, M.R.M Aliha, On determination of mode II fracture toughness using semi-circular bend specimen. Int. J. Solids Struct., 43 (2006) 5217–5227.

A New Test Method for High-Temperature Fracture of Alloys and Some Corresponding Results

Shaoqin Zhang[1,2,*], Wanlin Guo[2,*], He Li[1], Huihua Zhang[1], Ying Deng[1], Qiong Wu[1], Qinghui Xiao[1], Peng Zhou[1]

[1] Key Laboratory of Nondestructive Testing, Ministry of Education, Nanchang HangKong University, Nanchang 330063, China
[2] State Key Laboratory of Mechanics and Control of Mechanical Structures, Nanjing University of Aeronautics and Astronautics, Nanjing 210016, China
* Corresponding author: shaoqinzhangniat@yahoo.com.cn, wlguo@nuaa.edu.cn

Abstract A moiré interferometry-based experimental method is first introduced for high-temperature, mixed-mode fracture testing. The method allows real-time observation of surface deformation of cracked specimens and crack-tip plastic zone at elevated temperatures. Based on the moiré fringe patterns captured real time through image acquisition system, important fracture parameters, such as the crack open displacement, the crack initiation load, the ultimate load, etc., can be determined. With these data, the stress intensity factor, load bearing capacity, fracture ductility, strain, and stress fields near the crack-tip can be obtained. The method has been successfully applied to investigate pure mode I, I-II mixed-mode fracture performance of high temperature alloys. Furthermore, some significant thickness effects achieved by the group of researchers on the mixed-mode fracture performance of TC11 titanium alloy at high temperatures are cited and briefly introduced. Finally, three dimensional finite element simulations are performed for the tensile-shearing specimens at an elevated temperature. Simulation results are in agreement with measurements.

Keywords Moiré interferometry, High temperature, Mixed mode fracture, Thickness effect

1. Introduction

In industrial fields, such as aerospace, petrochemical, and dynamic transportation, there is a growing demand for high-temperature structural materials. The rising demand makes the issues of reliability design, failure analysis, and safety evaluation for high-temperature structures increasingly important [1-5]. The performance of engineering materials, especially metal materials, is always sensitive to temperature. At an elevated temperature, internal molecular motion aggravating, phase changing, cavity and micro crack emerging in materials make their fracture property significantly different from that at room temperature [3]. With the field of fracture still in development, high-temperature behavior remains one of the unresolved fundamental issues [6]. A better understanding of the fracture behavior is important. High-temperature components, such as engine turbine and blade, steam boiler and pipeline, and steam turbine bear complex loading at high temperatures. Therefore, mixed-mode fracture testing of materials from room to high temperature is necessary.

By far, the research on two-dimensional (2D) cracks of single and mixed modes under room temperature (RT) becomes better and approaches perfection day by day. However, most of the previously conducted analytical and numerical investigations in fracture mechanics were focused on 2D or axisymmetric geometries, although three-dimensional (3D) effects were often acknowledged. The stress state near an actual crack tip is always 3D, and the meaning of the results obtained within the 2D theories and their relation to the actual 3D stress distribution is still not fully understood [7].

3D effects increasingly drew attention in recent years from material experiments in laboratories to the real structure [6-8]. Experiments have shown that some damages or failure characteristic quantities, which are regarded as material constants, indeed are related to the structural geometry [5]. A large number of theoretical analysis, experimental investigations, and numerical computations reveal significant 3D effects such, as the thickness effect [9-14]. 3D fracture theory, founded in consideration both of in-plane and out-plane constraints, has made important progress [15-18]. The research on mixed-mode cracks gradually progresses from the 2D hypothesis to the 3D assumption [19-21]. Comparatively, research mainly focuses on the cracks of ideal mode I, 2D problems, theoretical analysis, and numerical computations. Experimental investigations, especially observations and measurements of real 3D fracture of mixed-mode cracks under high temperature, are very limited. There is no complete analytic solution for 3D fracture problems due to mathematical difficulties. Research on 3D fracture problem of mixed-mode cracks under high temperature still needs to be done. The existing theoretical fracture models have many weaknesses and are not verified by experiment and practical use [5]. In a conceptual paper on the past and future development of fracture mechanics, Erdogan [6] identifies 3D effects, high-temperature behaviors, computational methods, and experimental methods as the areas where further intensive research is needed.

A new fracture experimental technique based on the moiré interferometry is introduced in this study, by which I-II mixed-mode fracture phenomenon could be surveyed and recorded when temperature is high (say at least several hundreds of degrees in Celsius). Finite through-thickness cracked specimens are employed in tests under the coupling of thermal environment and mixed-mode loading. Displacement field moiré fringes around the crack are recorded. This experimental method was successfully used in investigation of fracture properties of high-temperature alloys. Several specific thickness effects at high temperatures are revealed based on the experimental results.

2. High-temperature, mixed-mode fracture test

2.1. Experimental setup and procedures

High-temperature moiré interferometry system has been successfully used in investigation of crack growth of pure mode I [22-24]. The same is employed in this present mixed-mode fracture research. The tensile-shearing specimen dimensions and mixed-mode loading fixture are given in Ref. [25]. A special orthogonal diffraction grating with high temperature resistance is chosen and fabricated on a highly polished surface of a specimen by photoetching and chemical etching [26]. Two sets of grid lines of the orthogonal grating are parallel to and perpendicular to the crack, respectively. A rotatable U-V mirror set [27] is invented for the purpose of the mixed-mode fracture experiment. The mirror set is designed to rotate by the same angle when angle β existed between loading direction and crack perpendicular, as shown in Figure 1. Consequently, the displacements normal to the crack (Mode I) and parallel to the crack (Mode II) were effectively separated, ensuring that moiré fringes corresponding to the u-displacement and v-displacement always are parallel and perpendicular to the crack at any I-II mixed-mode loading. The fracture testing procedure based on moiré interferometry at elevated temperature, including preparations of specimens, fabrication of specimen grating, heating, maintenance of temperature, and loading until fracture, is detailed in Ref.

[25].

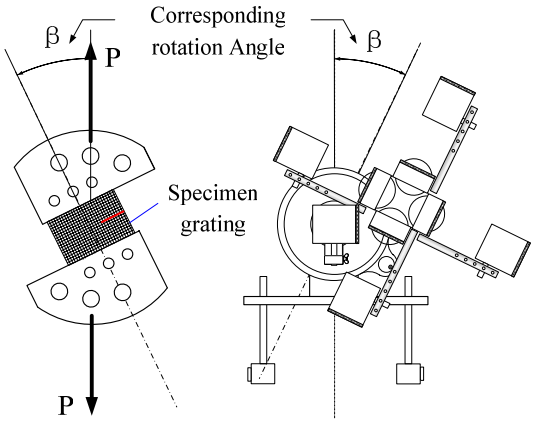

Figure 1: Mixed-mode fracture test fixture and corresponding arrangement of U-V mirror set

2.2. Evaluation of fracture parameters

Typical moiré fringes seen during the test are illustrated in Figure 2. The fringes tend to be closer to each other and move towards the crack tip with the load. Once the load increases, a small dark spot appears around the crack tip on the surface. This means a plastic zone forms and develops as the load increases. The crack mouth open displacement (COD), which is the relative displacement of point A and B in Figure 2, is measured using a v-displacement field moiré fringes based on the principle of moiré interferometry. Special image processing techniques, such as smoothing, filtering, and refining, are used to reproduce the moiré fringe for counting the number of fringes and reproducing the profile of plastic zone. The stress intensity factors K_I, K_{II}, K_{eff} are determined based on load, loading angle, and crack length when the fracture test is finished [25]. Load-COD curves and K_{eff}-COD curves then can be drawn.

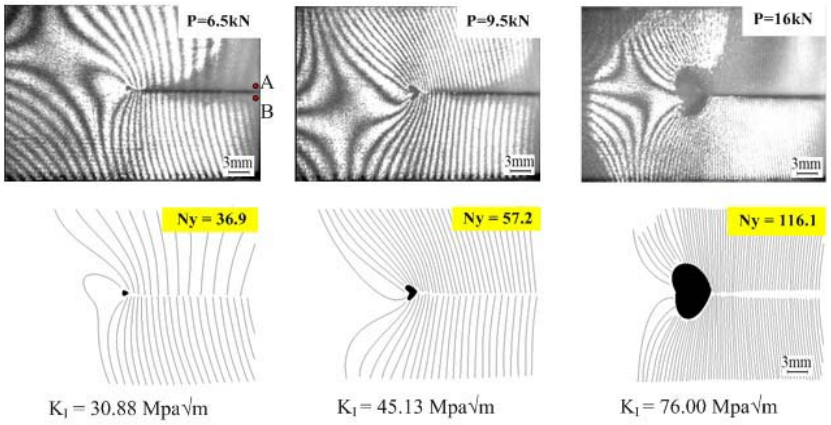

Figure 2: Representative moiré fringe patterns during the test and reproduced images

2.3. Measurement of crack initiation angle

From 2D fracture mechanics, the crack initiation angle is usually defined as the included angle between the initiation orientation and the original crack orientation at half-thickness (middle) plane. The included angle is the one between the flat region B and the pre-cracked plane A in Figure 3. It is an important parameter for mixed-mode fracture but is often difficult to measure. To obtain the angle, as a common methodology, the specimen is first cut into two separate parts from the middle plane, and then the angle is measured [19]. However, it does not work well for metallic material and thin samples. The following method is employed to measure the initiation angle. First, a CCD

camera is used to take photographs of the profile of the fractured specimens, as shown in Figure 3 (c). Subsequently, the profile photographs are processed as computer image files. The most important step in this procedure is accurately determining and drawing the tangent line at the beginning of the crack growth path at the middle thickness and the pre-crack line. Finally, the initiation angle is obtained by measuring the angle between the two lines. Based on the above mentioned scheme, the initiation angle of the specimen in Figure 3 is 27.7°. Using the same method, the included angle between the pre-cracked plane and the pre-notched plane (e.g., 5.5° in Figure 3(c)), which is the machining error and which should be distinguished from the initiation angle, also can be recorded.

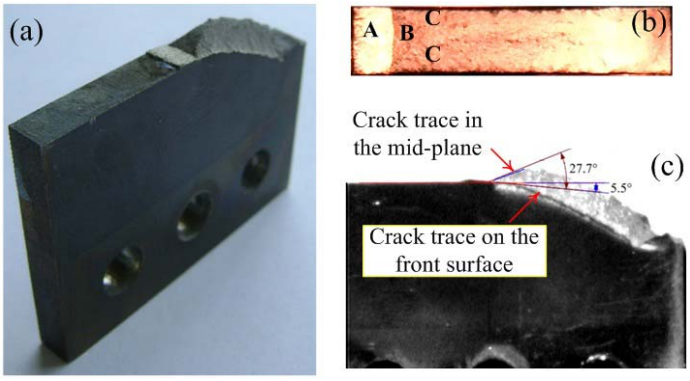

Figure 3: Representative macro pictures of the fracture surface with characteristic regions. A is the fatigue pre-crack, B is the flat fracture region, and C is the shear lip.

3. Fracture test on TC11 titanium alloy material

Mixed-mode fracture experiments are conducted on TC11 titanium alloy specimens with varied thicknesses at RT and elevated temperature. The experiments are conducted using the newly developed testing technology, which is based on high-temperature moiré interferometry. Some results are very unusual and remarkable.

3.1. Experimental results at elevated temperature [25]

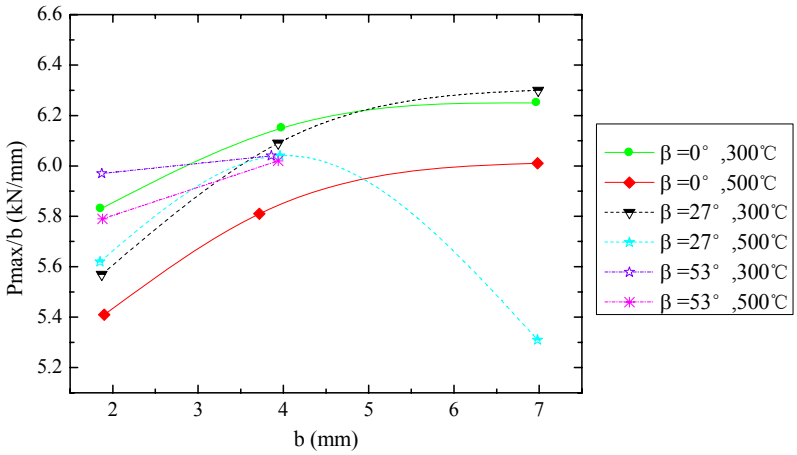

Figure 4: Load capacity versus thickness b and loading angles β at high temperatures (reproduced from Ref. [25])

Figure 4 illustrates the average results for the specimens in the same thickness group at an elevated

temperature. It shows that in addition to some individual cases, the loading capacity increases with the specimen thickness. This observation is contrary to common knowledge. Increasing temperature enhances the fracture load capacity for thick specimens, but reduces it for thin specimens. Detailed analysis is given in Ref. [25]. When fracture toughness is examined, K_{effi} (the stress intensity factor corresponding to the crack initiation load P_i) with loading angle β and specimen thickness b appears at high temperatures, as shown in Figure 5. Effects of thickness existed in K_{effi}, although regularity is not obvious. These results again confirm the complex coupled effects of thickness and temperature in the mixed-mode fracture of the alloy.

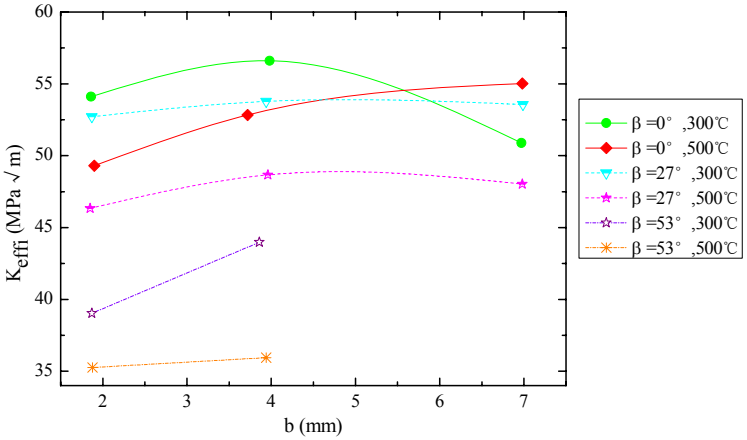

Figure 5: Results of K_{effi} versus thickness b and loading angles β at high temperatures (reproduced from Ref. [25])

The thickness effect is significantly coupled with the temperature effect in mixed-mode fracture of TC11 alloy, which is important for the development of 3D fracture theory under complex loading and temperature conditions. Why did this happen? Is this the peculiarity of titanium alloy or is this a shared property of metals or alloys? To answer the questions, further studies on fracture mechanism of high-temperature fracture should be conducted.

3.2. Qualitative comparison with finite element data

To compare the test results with the numerical solutions, specimens with the same dimensions as in the experiment are modeled using the finite element (FE) software ANSYS. In the 3D simulation, the Ramberg-Osgood constitutive relation [28] is adopted to represent the material nonlinearity. The corresponding parameters are determined through fitting of experimental data. Accordingly, the stress-strain relation is expressed as

$$\varepsilon = \frac{\sigma}{120000} + 9.9879\times10^{38}\left(\frac{\sigma}{120000}\right)^{19.9578} \tag{1}$$

at RT, and

$$\varepsilon = \frac{\sigma}{98000} + 9.089\times10^{11}\left(\frac{\sigma}{98000}\right)^{6.6095} \tag{2}$$

at 500℃.

The contours of Mises stress on the front surface at 500℃ are plotted in Figure 6, where the domain bounded by red lines conforms to the visual region of moiré fringe. In Figure 7, moiré fringe of the same specimen from the tests also is presented. In the first row of Figures 6 and 7, the same load is

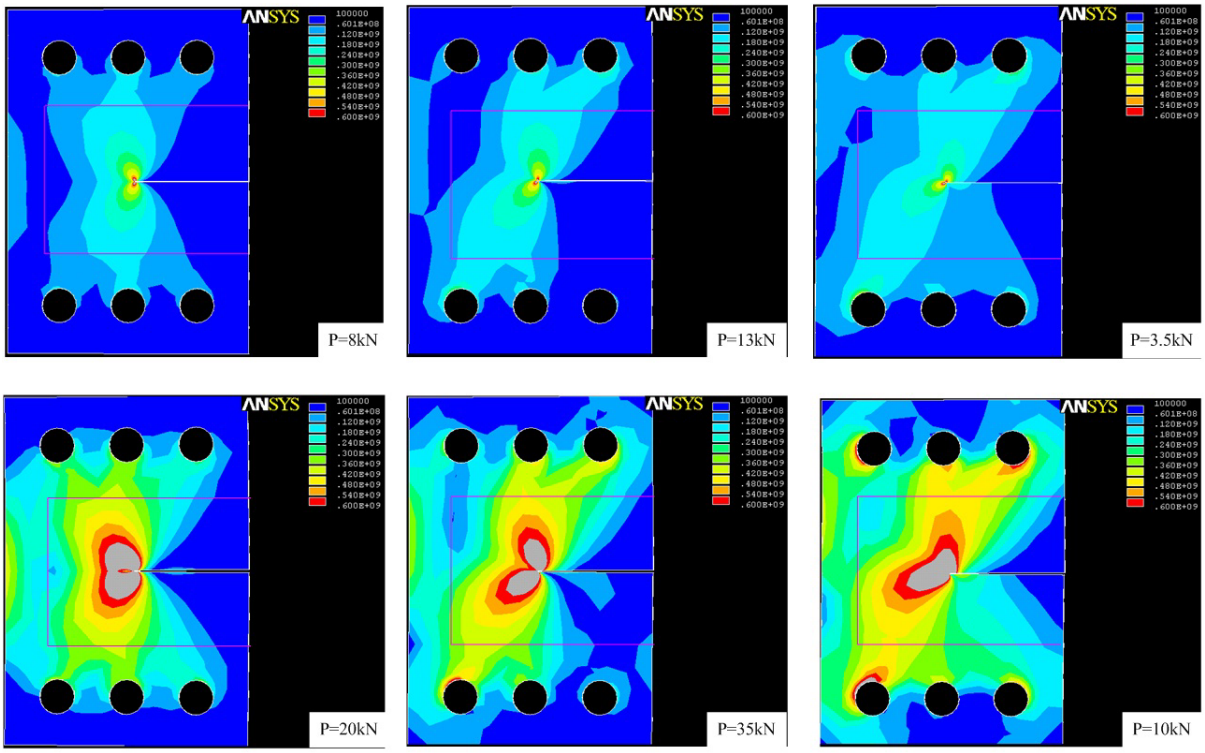

(a) b=4mm, 500℃, β=0° (b) b=7mm, 500℃, β=27° (c) b=2mm, 500℃,β=53°

Figure 6: ANSYS non-linear FE results (stress field and plastic zone on the front surface) at 500℃

considered. However, there are different exists in the second row, where the load is the maximum value before fracture in Figure 6 and the value under which the last clear moiré fringe is obtained in Figure 7. Based on Figures 6 and 7, numerical results apparently agree well with the experimental data. The displacement fields on the specimen surface by the moiré interferometry are invalid due to the existence of crack tip plasticity and out-plane deformation. As an amendment, the 3D FE simulation is a powerful auxiliary tool in the computation during late loading period, and the corresponding details will be described in future work. The hybrid experimental-numerical procedure [29] is believed to be an effective technique in the fracture analysis and prediction area.

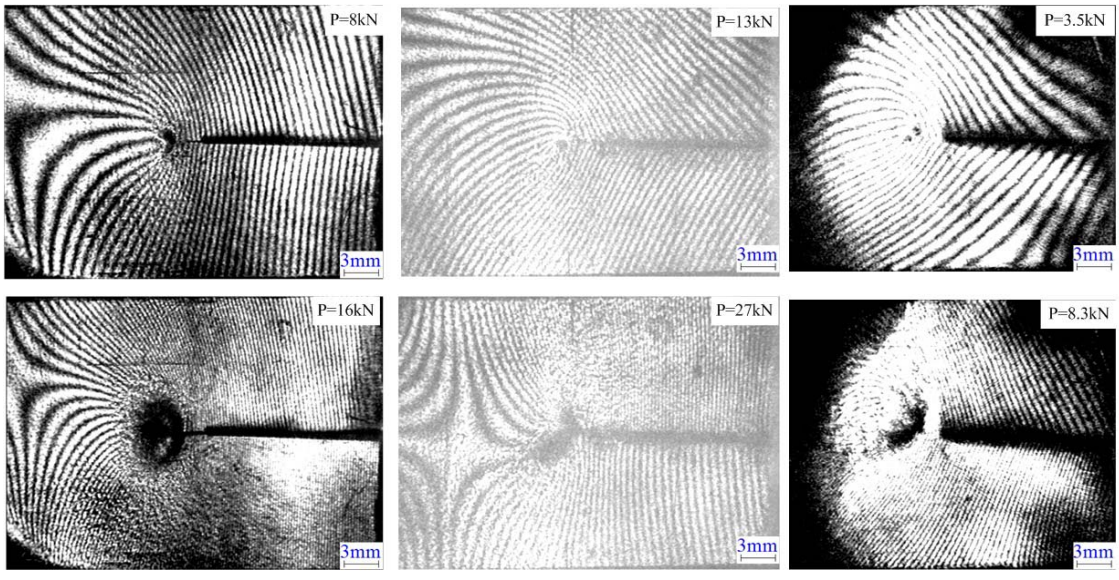

(a) *b*=4mm, 500℃, β=0° (b) *b*=7mm, 500℃, β=27° (c) *b*=2mm, 500℃, β=53°

Figure 7: Corresponding experimental results (displacement field and plastic zone on the front surface)

4. Conclusions

In the present paper, the newly developed fracture test equipment, techniques, and methodology based on moiré interferometry are presented in detail. Through real-time observation of fracture process around the crack tip and image acquisition of the moiré fringe at different loads, the magnitude of elastoplastic deformation and corresponding fracture parameters are extracted using the wave-front interference principle. In the test of TC11 finite specimen with through-thickness crack under mixed mode I-II loading, the duration from the beginning of loading to the ultimate fracture of specimen is relatively short, thereby causing difficulty in the determination of crack initiation moment. Moreover, no stable crack growth process is involved prior to the occurrence of unstable crack propagation. Concerning the common fracture mechanism on crack initiation, and the stable and unstable growth of metallic material, further investigation should be conducted to tell whether the size of crack tip plasticity zone on the surface can be adopted as a characteristic quantity of fracture. At the same time, the anomalous thickness effect of TC11 titanium alloy is reported, and the essence of this phenomenon is waiting to be uncovered.

Acknowledgements

The present work was supported by the National Natural Science Foundation of China (Grant nos. 61163048 and 11002066), the Aviation Science Foundation of China (Grant no. 2012ZF56027), and the Scientific Research Foundation of Key Laboratory of Nondestructive Testing, Ministry of Education (Grant no. ZD201129007).

References

[1] G.C. Sih, S. Tu, Z. Wang, Multiscaling Associated with structural and material integrity under elevated temperature. East China University of Science and Technology Press, Shanghai, 2006.

[2] Z. Wen, Z. Yue, Fracture behaviour of the compact tension specimens of nickel-based single crystal superalloys at high temperatures. Mat Sci Eng A, 456(2007) 189-201.

[3] S. Tu, F. Xuan, G. Wang, Recent progress in high temperature mechanical behavior of materials and structures. Chinese Journal of Solid Mechanics, 31(2010) 679-695.

[4] H. Shi, X. Ma, T. Yu, Some new progresses on the research of creep and fatigue behaviors of high temperature structural materials. Chinese Journal of Solid Mechanics, 31(2010) 696-715.

[5] S. Tu, F. Xuan, W. Wang, Some critical issues in creep and fracture assessment at high temperature. Acta Metallurgica Sinica, 45(2009) 781-787.

[6] F. Erdogan, Fracture mechanics. Int J Solids Struct, 37(2000) 171-183.

[7] A. Kotousov, Fracture in plates of finite thickness. Int J Solids Struct, 44 (2007) 8259-8273.

[8] W. Guo, Three-dimensional analyses of plastic constraint for through-thickness cracked bodies. Engng Fract Mech, 62 (1999) 383-407.

[9] T. Nakamura, D.M. Parks, Three-dimensional crack front fields in a thin ductile plate. J Mech Phys Solids, 38(1990) 787-812.

[10] X.M. Kong, N. Schluter, W. Dahl, Effect of triaxial stress on mixed-mode fracture. Engng Fract Mech, 52(1995) 379-388.

[11] H. Yuan, W. Brocks, Quantification of constraint effects in elastic-plastic crack front fields. J Mech Phys Solids, 46(1998) 219-241.

[12] Y.R. Arun, R. Narasimhan, An experimental investigation of constraint effects on mixed mode

fracture initiation in a ductile aluminirm alloy. Acta Mater, 47(1999) 1587-1596.

[13] Y. Kim, X.K. Zhu, Y.J. Chao, Quantification of constraint on elastic–plastic 3D crack front by the J–A2 three-term solution. Engng Fract Mech, 68 (2001) 895-914.

[14] S. Mahmoud, K. Lease, The effect of specimen thickness on the experimental characterization of critical crack-tip-opening angle on 2024-T351 alumimum alloy. Engng Fract Mech, 70(2003) 443-456.

[15] W. Guo, Elastoplastic three dimensional crack border field-I: Singular structure of the field. Engng Fract Mech, 46(1993) 93-104.

[16] W. Guo, Elastoplastic three dimensional crack border field-II: Asymptotic solution of the field. Engng Fract Mech, 46(1993) 105-113.

[17] W. Guo, Elastoplastic three dimensional crack border field-III: Fracture parameters. Engng Fract Mech, 51 (1995) 51-71.

[18] W. Guo, C. She, J. Zhao, B. Zhang, Advances in three-dimensional fracture mechanics. Key Engineering Materials, 312(2006) 27-34.

[19] H.R. Dong, W. Guo, Investigation on the experimental method for three-dimensional mixed mode fracture. Chinese Journal of Experimental Mechanics, 17(2002) 497-503.

[20] H.R. Dong, W. Guo, Mechanism Analysis of Thickness Effect on Mixed Mode I/II Fracture of LC4-CS Aluminum Alloy. Acta Metallurgica Sinica Letter, 3(2004) 255-262.

[21] D.J. Smith, T.D. Swankie, M.J. Pavier, M.C. Smith, The effect of specimen dimensions on mixed mode ductile fracture. Engng Fract Mech, 75(2008) 4394-4409.

[22] D.K. Tran, A.S. Kobayashi, K.W. White, Crack growth in alumina at high temperature. Engng Fract Mech, 68(2001) 149-161.

[23] B. Kang, X. Liu, C. Cisloiu, K. Chang, High temperature moiré interferometry investigation of creep crack growth of inconel 783 environment and β phase effects. Mat Sci Eng A, 347(2003) 205-213.

[24] X. Liu, B. Kang, W. Carpenter, E. Barbero, Investigation of the crack growth behavior of inconel 718 by high temperature moiré interferometry. J Mater Sci, 39(2004) 1967-1973.

[25] S. Zhang, W. Guo, H. Li, Y. Deng, Experimental investigation of three-dimensional mixed-mode fracture of a titanium alloy at room and elevated temperatures. Sci China Technol Sci, 54(2011) 2760-2767.

[26] H. Li, C.H. Yan, R.Z. Li, et al, Measuring elastic modulus and Poisson ratio for high-temperature materials by moiré inerferometry. Chinese J Mech Strength, 26(2004): 302-306.

[27] H. Li, S. Zhang, Y. Deng, Y. Wang, A removable system for in-plane displacement measuring based on moiré interferometry. Invention Patent, ZL200910115552.6.

[28] C.F. Shih, Small-scale yielding analysis of mixed mode plane strain crack problem. ASTM-STP 1974, 187-210.

[29] M.A. Sutton, M.L. Boone, F. Ma, J.D. Helm, A combined modeling-experimental study of the crack opening displacement fracture criterion for characterization of stable crack growth under mixed mode I/II loading in thin sheet materials. Engng Fract Mech, 66(2000) 171-185.

On Mixed-Mode Fracture

Christopher Harvey[1], Liangliang Guan[1], Huimin Xie[2], Simon Wang[1,*]

[1] Department of Aeronautical and Automotive Engineering, Loughborough University, Loughborough, LE11 3TU, UK
[2] Department of Engineering Mechanics, Tsinghua University, Beijing 100084, China
* Corresponding author: s.wang@lboro.ac.uk

Abstract This paper reports the authors' recent work on mixed-mode fracture in fiber-reinforced laminated composite beams and plates. The work considers the so-called one-dimensional fracture which propagates in one-dimension and consists of only mode I and mode II fracture modes. Fracture interfaces are assumed to be either rigidly or cohesively bonded. Analytical theories are developed within the contexts of both classical and first-order shear deformable laminated composite theories. When a rigid interface is assumed for brittle fracture, there are two sets of orthogonal pure modes in classical theory, and there is only one set of orthogonal pure modes in shear-deformable theory. A mixed-mode fracture is partitioned by using these orthogonal pure modes. The classical and shear deformable partitions can be regarded as either lower or upper bound partitions for 2D elasticity, and hence approximate 2D elasticity partition theories are developed by 'averaging' the classical and shear deformable partitions. When cohesively bonded interfaces are assumed for adhesively joined interfaces, the classical and shear deformable theories give the same pure modes. Approximate partition theories are also developed for 2D elasticity. Numerical investigations demonstrate excellent agreement with the corresponding analytical theories. Experimental data considered shows that the failure locus is strongly linear.

Keywords Composite, Energy release rate, Failure locus, Mixed-mode fracture, Orthogonal pure modes

1. Introduction

Delamination is a major concern in the application of laminated composite materials. Although it occurs often together with other fracture modes such as fiber breakage, matrix cracking and intra-laminar cracking, pure delamination is always an important research topic which provides insight and understanding of lamina interfacial mechanics, and it often occurs in one-dimensional delamination. A delamination is called one-dimensional when its crack front propagates only in one direction. Familiar examples are through-width delamination in laminated composite beams, circular ring shape delamination in laminated composite plates and shells, etc., as shown in Fig. 1. A distinct feature of one-dimensional delamination is that it usually consists of only the mode I and mode II fracture modes without any mode III. The study of one-dimensional delamination is of great importance for several reasons. It is the most fundamental problem in the fracture mechanics of materials. It is often used in experimental tests, such as the double cantilever beam (DCB), end-loaded split (ELS) and end-notched flexure (ENF) tests, to obtain the critical energy release rate (ERR) or toughness of a lamina interface in either pure mode I or mode II delamination. In the case of a mixed mode, it is often used to investigate delamination propagation criteria. Moreover, many practical cases of delamination in structures made of fiber-reinforced laminated composites can be approximated as one-dimensional. For example, the separation of stiffeners and skins in stiffened plate or shell panels made of laminated composite materials can be approximated as one-dimensional through-width delamination, and the separation of two material layers in laminated composite plates and shells in a drilling process can be approximated as one-dimensional circular ring-type delamination, etc.

Because of its importance, one-dimensional delamination has attracted the attention of many researchers including many of the world leaders in the areas of fracture mechanics and composite materials. The primary goal is to develop analytical theories to determine pure delamination modes

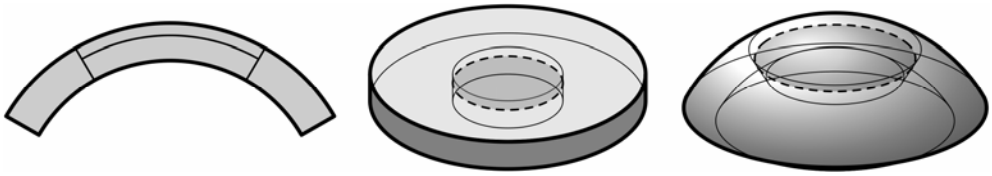

Figure 1. Some examples of one-dimensional fracture.

and then to partition a mixed mode into pure modes. Delamination propagation criteria can then be established by using the partition together with experimental data. The through-width delamination in a DCB made of isotropic material with rigidly bonded interface can be considered to be the 'simplest' one-dimensional delamination. Although it seems to be a straightforward matter to determine the pure modes and to partition a mixed mode, it has been proved to be an extremely complex and sophisticated problem. There has been a lot of confusion on the matter during the last 25 years. Ref. [1] may be the earliest work on the 'simplest' problem by Williams. A mixed-mode partition theory [1] was developed based on classical beam theory. Ref. [2] reported a combined numerical and analytical theory by Schapery and Davidson based on combined classical beam theory and 2D elasticity. It disagrees with the Williams' theory [1] and concludes that classical beam theory does not provide quite enough information to obtain an analytical decomposition of the mixed-mode ERR into its opening and shearing mode components. Hutchinson-Suo reported their work in Ref. [3] in which the mixed-mode ERR is calculated based on the classical beam theory but the partition of ERR is calculated based on stress intensity factors from 2D elasticity. Their theory [3] agrees well with the theory in Ref. [2] and claims that Williams' theory [1] contains conceptual errors. To respond to this claim, Williams reported some experimental work in Ref. [4] showing that Williams' theory [1] is in a better agreement with the test results than Hutchinson-Suo theory [3]. This has caused a lot of confusion, which has affected many academic researchers and design engineers until today. A great deal of research effort has been made during the last two decades to resolve the confusion. Among many others, the following significant works are referenced here. Ref. [5] reported a mixed-mode partition theory for laminated composite beams with rigidly bonded interface based on first-order shear-deformable beam theory, which gives different mixed-mode partitions to those from Williams' theory [1] and the Hutchinson-Suo theory [3]. The same theory as that in Ref. [5] was derived in Refs. [6, 7] but these are based on classical beam theory, which caused yet more confusion. Recently, the authors have developed analytical theories for one-dimensional delamination in laminated composite beams and plates by using a novel methodology [8–13]. All the confusion is explained. This paper reports some of the major results in Refs. [8–13].

2. Partition of mixed-mode fracture in laminated composite beams and plates with rigid interfaces

The mechanics of delamination depend on the mechanical properties of lamina interfaces. A lamina interface is considered to be a rigid interface when the interface separation is negligible before an existing delamination propagates. Otherwise, it is considered to be a non-rigid interface or as it often called, a cohesively bonded interface. Bare-bonded interfaces in the conventional manufacturing process from glass or carbon fiber epoxy pre-pregs are typical rigid interfaces because of their brittleness. While cohesively bonded interfaces are typical non-rigid interfaces which are achieved by adding adhesive layers between bare plies when manufacturing components.

2.1. Laminated composite DCBs

A laminated composite DCB with a delamination of length a is shown in Fig. 2 (a). The interface stresses in Fig. 2 (b) only show the sign convention rather than any representative distribution.

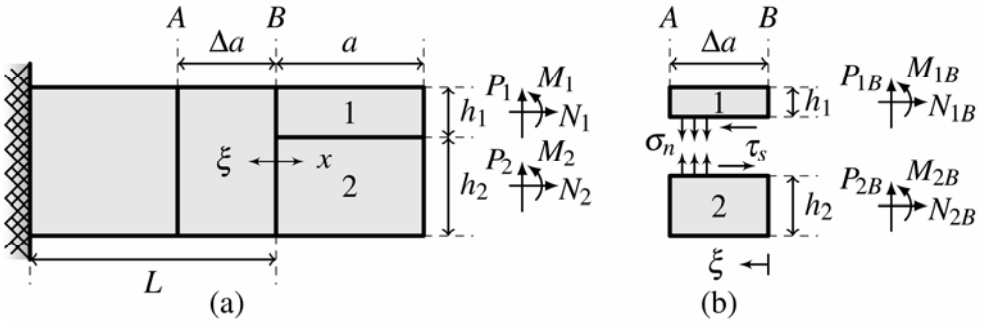

Figure 2. A laminated composite DCB and its loading conditions. (a) General description. (b) Details of the crack influence region Δa.

2.1.1. Classical beam partition theory

Using the constitutive relation in classical laminated composite beam theory, the ERR at the crack tip at location B, G is

$$G = \frac{1}{2b^2}\left(\frac{M_{1B}{}^2}{D_1^*} + \frac{M_{2B}{}^2}{D_2^*} - \frac{M_B{}^2}{D^*} + \frac{N_{1B}{}^2}{A_1^*} + \frac{N_{2B}{}^2}{A_2^*} - \frac{N_B{}^2}{A^*} - \frac{2B_1 M_{1B} N_{1B}}{B_1^*} - \frac{2B_2 M_{2B} N_{2B}}{B_2^*} + \frac{2B M_B N_B}{B^*} \right) \quad (1)$$

where subscript 'B' indicates loads at the crack tip at location B, for example, M_{1B} is the bending moment on the top sub-laminate at the crack tip. These loads are shown in Fig. 2 (b). Other quantities in Eq. (1) are

$$A_i^* = A_i - B_i^2/D_i \quad , \quad B_i^* = B_i{}^2 - A_i D_i \quad , \quad D_i^* = D_i - B_i^2/A_i \quad (2)$$

The range of subscript i is 1 and 2, which again refers to the upper and lower sub-laminates respectively. For the intact laminate, the subscript i is dropped. A, B and D are the equivalent extensional, coupling and bending stiffness of the DCB respectively.

A novel methodology to partition mixed-mode ERR G in Eq. (1) arises from the fact that G is of quadratic form and non-negative definite in terms of the crack tip bending moments M_{1B} and M_{2B}, and the crack tip axial forces N_{1B} and N_{2B}. An analogy of this is the positive definite kinetic energy of a vibrating structure, to which individual modal energies are attributed by using modal analysis from orthogonal natural vibration modes. A hypothesis is then made that the total ERR in a mixed-mode delamination can be partitioned into pure mode components by using orthogonal pure modes. There are two sets of fundamental orthogonal pure modes. The first set corresponds to zero relative shearing displacement just behind the crack tip (mode I) and zero crack tip opening force ahead of the crack tip (mode II). The second set corresponds to zero relative opening displacement just behind the crack tip (mode II) and zero crack tip shearing force (mode I). It is simple to derive the zero relative displacement modes first and then to find the zero force modes by applying orthogonality through Eq. (1). An alternative and more complex derivation considers the interface stresses. If the mode vector form is $\{M_{1B}, M_{2B}, N_{1B}, N_{2B}\}^T$, then the first set of fundamental orthogonal pure modes, referred to as the $\{\theta, \beta\}$ set, are found to be

$$\{\varphi_{\theta_1}\} = \begin{Bmatrix} 1 \\ \theta_1 \\ 0 \\ 0 \end{Bmatrix} \quad , \quad \{\varphi_{\theta_2}\} = \begin{Bmatrix} 1 \\ 0 \\ \theta_2 \\ 0 \end{Bmatrix} \quad , \quad \{\varphi_{\theta_3}\} = \begin{Bmatrix} 1 \\ 0 \\ 0 \\ \theta_3 \end{Bmatrix} \quad , \quad \{\varphi_{\beta_1}\} = \begin{Bmatrix} 1 \\ \beta_1 \\ 0 \\ 0 \end{Bmatrix} \quad , \quad \{\varphi_{\beta_2}\} = \begin{Bmatrix} 1 \\ 0 \\ \beta_2 \\ 0 \end{Bmatrix} \quad , \quad \{\varphi_{\beta_3}\} = \begin{Bmatrix} 1 \\ 0 \\ 0 \\ \beta_3 \end{Bmatrix} \quad (3)$$

with

$$\theta_1=\frac{\left(B_2^2-A_2D_2\right)\left(B_1+h_1A_1/2\right)}{\left(B_1^2-A_1D_1\right)\left(B_2-h_2A_2/2\right)}\ ,\ \theta_2=-\frac{B_1+h_1A_1/2}{D_1+h_1B_1/2}\ ,\ \theta_3=\frac{\left(B_1+h_1A_1/2\right)\left(B_2^2-A_2D_2\right)}{\left(D_2-h_2B_2/2\right)\left(B_1^2-A_1D_1\right)} \tag{4}$$

$$\beta_1=-\frac{D_2^*\left(D_1^*+D_1^*\theta_1-D^*\right)}{D_1^*\left(D_2^*+D_2^*\theta_1-D^*\theta_1\right)}\ ,\ \beta_2=\frac{\theta_2\left(\frac{h_2}{2D^*}-\frac{B_1}{B_1^*}+\frac{B}{B^*}\right)+\frac{1}{D_1^*}-\frac{1}{D^*}}{\theta_2\left(\frac{Bh_2}{B^*}-\frac{1}{A_1^*}+\frac{1}{A^*}+\frac{h_2^2}{4D^*}\right)-\frac{h_2}{2D^*}+\frac{B_1}{B_1^*}-\frac{B}{B^*}}\ ,$$

$$\beta_3=\frac{\theta_3\left(\frac{h_1}{2D^*}-\frac{B}{B^*}\right)-\frac{1}{D_1^*}+\frac{1}{D^*}}{\theta_3\left(\frac{Bh_1}{B^*}+\frac{1}{A_2^*}-\frac{1}{A^*}-\frac{h_1^2}{4D^*}\right)-\frac{h_1}{2D^*}+\frac{B}{B^*}} \tag{5}$$

The second set of fundamental orthogonal pure modes, referred to as the $\{\theta',\beta'\}$ set, has the same format as that of the first set in Eq. (3), but with

$$\theta_1'=-1\ ,\ \theta_2'=\frac{\beta_2'\left(\frac{h_2}{2D^*}-\frac{B_1}{B_1^*}+\frac{B}{B^*}\right)+\frac{1}{D_1^*}-\frac{1}{D^*}}{\beta_2'\left(\frac{Bh_2}{B^*}-\frac{1}{A_1^*}+\frac{1}{A^*}+\frac{h_2^2}{4D^*}\right)-\frac{h_2}{2D^*}+\frac{B_1}{B_1^*}-\frac{B}{B^*}}\ ,$$

$$\theta_3'=\frac{\beta_3'\left(\frac{h_1}{2D^*}-\frac{B}{B^*}\right)-\frac{1}{D_1^*}+\frac{1}{D^*}}{\beta_3'\left(\frac{Bh_1}{B^*}+\frac{1}{A_2^*}-\frac{1}{A^*}-\frac{h_1^2}{4D^*}\right)-\frac{h_1}{2D^*}+\frac{B}{B^*}} \tag{6}$$

$$\beta_1'=\frac{D_2^*}{D_1^*}\ ,\ \beta_2'=-\frac{A_1}{B_1}\ ,\ \beta_3'=-\frac{B_2^*}{D_1^*B_2} \tag{7}$$

Any four fundamental pure modes from either the first set or the second set can be used to partition a mixed mode. The partitions are given below.

$$G_{IE}=c_{IE}\left(M_{1B}-\frac{M_{2B}}{\beta_1}-\frac{N_{1B}}{\beta_2}-\frac{N_{2B}}{\beta_3}\right)\left(M_{1B}-\frac{M_{2B}}{\beta_1'}-\frac{N_{1B}}{\beta_2'}-\frac{N_{2B}}{\beta_3'}\right) \tag{8}$$

$$G_{IIE}=c_{IIE}\left(M_{1B}-\frac{M_{2B}}{\theta_1}-\frac{N_{1B}}{\theta_2}-\frac{N_{2B}}{\theta_3}\right)\left(M_{1B}-\frac{M_{2B}}{\theta_1'}-\frac{N_{1B}}{\theta_2'}-\frac{N_{2B}}{\theta_3'}\right) \tag{9}$$

where

$$c_{IE}=G_{\theta_1}\left[\left(1-\frac{\theta_1}{\beta_1}\right)\left(1-\frac{\theta_1}{\beta_1'}\right)\right]^{-1}\ ,\ c_{IIE}=G_{\beta_1}\left[\left(1-\frac{\beta_1}{\theta_1}\right)\left(1-\frac{\beta_1}{\theta_1'}\right)\right]^{-1} \tag{10}$$

and

$$G_{\theta_1}=\frac{1}{2b^2}\left[\frac{1}{D_1^*}+\frac{\theta_1^2}{D_2^*}-\frac{\left(1+\theta_1\right)^2}{D^*}\right]\ ,\ G_{\beta_1}=\frac{1}{2b^2}\left[\frac{1}{D_1^*}+\frac{\beta_1^2}{D_2^*}-\frac{\left(1+\beta_1\right)^2}{D^*}\right] \tag{11}$$

The partitions in Eqs. (8) and (9) use both sets of orthogonal pure modes. The partition theory in Ref. [1] only gives the $\{\theta_1',\beta_1'\}$ pure modes correctly. The partition theories derived in Refs. [6,7] is equivalent to using only the first set of pure modes to partition a mixed-mode. The methodologies used in Refs. [6,7] are not able to find the second set of pure modes. The partitions are easily reduced for isotropic materials. With a thickness ratio $\gamma=h_2/h_1$ now introduced, they are

$$G_{IE} = c_{IE}\left(M_{1B} - \frac{M_{2B}}{\beta_1} - \frac{N_{1Be}}{\beta_2} \right)\left(M_{1B} - \frac{M_{2B}}{\beta_1'} \right) \tag{12}$$

$$G_{IIE} = c_{IIE}\left(M_{1B} - \frac{M_{2B}}{\theta_1} - \frac{N_{1Be}}{\theta_2} \right)\left(M_{1B} - \frac{M_{2B}}{\theta_1'} - \frac{N_{1Be}}{\theta_2'} \right) \tag{13}$$

where c_{IE} and c_{IIE} are still given by Eq. (10) and $N_{1Be} = N_{1B} - N_{2B}/\gamma$. The pure mode relationships are now as follows:

$$\theta_1 = -\gamma^2 \ , \ \theta_2 = -\frac{6}{h_1} \ , \ \beta_1 = \frac{\gamma^2(3+\gamma)}{1+3\gamma} \ , \ \beta_2 = \frac{2(3+\gamma)}{h_1(\gamma-1)} \text{ for } \gamma \neq 1 \ , \ \beta_2 = 1 \text{ for } \gamma = 1 \tag{14}$$

$$\theta_1' = -1 \ , \ \theta_2' = -\frac{6(1+\gamma)}{h_1(1+\gamma^3)} \ , \ \beta_1' = \gamma^3 \tag{15}$$

The isotropic G_{θ_1} and G_{β_1} for use in Eq. (10) are

$$G_{\theta_1} = \frac{24\gamma}{Eb^2h_1^3(1+\gamma)} \ , \ G_{\beta_1} = \frac{72\gamma(1+\gamma)}{b^2Eh_1^3(1+3\gamma)^2} \tag{16}$$

2.1.2. Shear deformable beam partition theory

In the absence of crack tip shear forces, the total ERR G in a mixed-mode fracture is still given by Eq. (1) within the context of the first order shear deformable laminated composite beam theory. However, the two sets of fundamental orthogonal pure modes now coincide at the first set, i.e. the $\{\theta, \beta\}$ set and the partitions of the total G are given by

$$G_{IT} = c_{IT}\left(M_{1B} - \frac{M_{2B}}{\beta_1} - \frac{N_{1B}}{\beta_2} - \frac{N_{2B}}{\beta_3} \right)^2 \ , \ G_{IIT} = c_{IIT}\left(M_{1B} - \frac{M_{2B}}{\theta_1} - \frac{N_{1B}}{\theta_2} - \frac{N_{2B}}{\theta_3} \right)^2 \tag{17}$$

where

$$c_{IT} = G_{\theta_1}\left(1 - \frac{\theta_1}{\beta_1} \right)^{-2} \ , \ c_{IIT} = G_{\beta_1}\left(1 - \frac{\beta_1}{\theta_1} \right)^{-2} \tag{18}$$

When crack tip shear forces P_{1B} , P_{2B} are present, the following two terms need to be added to the mode I ERR in Eq. (17):

$$G_P = \frac{(H_1P_{2B} - H_2P_{1B})^2}{2b^2H_1H_2(H_1+H_2)} \ , \ \alpha_{\theta_1}\Delta G_{\theta_1 P} = \frac{\alpha_{\theta_1}}{b^2}\left(\frac{P_{1B}}{H_1} - \frac{P_{2B}}{H_2} \right)\left[\frac{H_1H_2}{H_1+H_2}\left(\frac{1}{D_1^*} + \frac{\theta_1^2}{D_2^*} - \frac{(1+\theta_1)^2}{D^*} \right) \right]^{1/2} \tag{19}$$

where H_1 and H_2 are the through-thickness shear stiffnesses and

$$\alpha_{\theta_1} = \frac{M_{2B}\beta_2 + N_{1B}\beta_1 - M_{1B}\beta_1\beta_2}{\beta_2(\theta_1 - \beta_1)} + \frac{N_{2B}\beta_1}{\beta_3(\theta_1 - \beta_1)} \tag{20}$$

In the case of layered isotropic DCBs, these partitions reduce to

$$G_{IT} = c_{IT}\left(M_{1B} - \frac{M_{2B}}{\beta_1} - \frac{N_{1Be}}{\beta_2} \right)^2 \ , \ G_{IIT} = c_{IIT}\left(M_{1B} - \frac{M_{2B}}{\theta_1} - \frac{N_{1Be}}{\theta_2} \right)^2 \tag{21}$$

The mode I contribution from crack tip shear forces reduces to

$$G_P = \frac{(\gamma P_{1B} - P_{2B})^2}{2b^2h_1k^2G_{xz}\gamma(1+\gamma)} \ , \ \alpha_{\theta_1}\Delta G_{\theta_1 P} = \frac{4\sqrt{3}\alpha_{\theta_1}(\gamma P_{1B} - P_{2B})}{b^2h_1^2(1+\gamma)(k^2G_{xz}E)^{1/2}} \tag{22}$$

2.1.3. 2D elasticity partition theory

One averaged partition theory is obtained by averaging the classical and shear deformable partitions. This partition has been found to give an excellent approximation to the partition from 2D elasticity. The mode I and II components of the ERR from the averaged partition theory denoted by G_I and G_{II} respectively. They are

$$G_I = \left(G_{IE} + G_{IT}\right)/2 + G_P + \alpha_{\theta_1}\Delta G_{\theta_1 P} \quad , \quad G_{II} = \left(G_{IIE} + G_{IIT}\right)/2 \tag{23}$$

2.1.4. Local and global partition theories

When ERR is calculated right at the crack tip, i.e. using an infinitesimally small region around the crack tip, it is called a local calculation. When it is calculated using a finite small region, it is called a global calculation. In terms of the finite element method (FEM), an infinitesimally small region means one element length in a very fine mesh, whilst a finite small region means multiple element lengths. When global ERR calculation is used, the above three local partition theories, i.e. the classical, shear-deformable and 2D partition theories give the same partitions as that of the local classical partition theory. That is, the classical partition theory unifies the three theories in a global partition. The differences between the three local theories arise from the differences of the crack tip stresses in the three theories. However, the global distribution of interfacial stresses is governed by the classical beam and plate theory.

2.2. Clamped-clamped laminated composite beams

A clamped-clamped composite laminated beam with a symmetric delamination is considered. The loads P_1 and P_2 are applied at the mid-span. The pure mode I mode in the first set of orthogonal pure modes in classical beam theory, i.e. the $\{\theta, \beta\}$ set, is given by

$$P_2/P_1 = \theta_P = -B_2^*\left(2B_1 + h_1A_1\right)/\left[B_1^*\left(2B_2 - h_2A_2\right)\right] \tag{24}$$

Its orthogonal pure mode II mode $P_2/P_1 = \beta_P$ is too complex to be presented here algebraically. The second set of orthogonal pure modes in classical beam theory, i.e. the $\{\theta', \beta'\}$ set is given by

$$\theta'_P = P_2/P_1 = -1 \quad , \quad P_2/P_1 = \beta'_P = D_2^*/D_1^* \tag{25}$$

Within the context of shear deformable beam theory, the expressions for $P_2/P_1 = \theta_P$ pure mode I and $P_2/P_1 = \beta_P$ pure mode II are too complex to be presented here algebraically. However, when the through-thickness shear effect is not excessively large, they are very close to those in classical beam theory.

2.3. Clamped circular layered isotropic plates

A clamped circular layered isotropic plate with a central delamination and central loads P_1 and P_2 are considered. The first set of orthogonal pure modes in classical plate theory are found to be

$$P_2/P_1 = \theta_P = \theta_1 \quad , \quad P_2/P_1 = \beta_P = \beta_1 \tag{26}$$

where θ_1 and β_1 are given in Eq. (14). The corresponding ERRs are given by

$$G_{\theta_P} = 3P_1^2\gamma\left(1-\nu^2\right)/\left[2Eh_1^3\pi^2\left(1+\gamma\right)\right] \quad , \quad G_{\beta_P} = 9P_1^2\gamma\left(1-\nu^2\right)\left(1+\gamma\right)/\left[2Eh_1^3\pi^2\left(1+3\gamma\right)^2\right] \tag{27}$$

The second set of pure mode I and II modes are the same as those in Eq. (15). In the first order shear deformable plate theory, the first set of pure modes is approximately pure and the second set disappears.

3. Partition of mixed-mode fracture in layered isotropic DCBs with non-rigid interfaces

3.1. Classical beam partition theory

The mode I ERR G_{IE} is considered first. The interface normal stress σ_n is found to be

$$\sigma_n = -Eh_1^3\gamma^3/\left[3(1+\gamma)^3\right]\left[\overline{w}^{(4)} + 3(1-\gamma)/(2h_1\gamma)\overline{u}^{(3)}\right] \tag{28}$$

where $\overline{w} = \overline{w}_1 - \overline{w}_2$ and $\overline{u} = \overline{u}_2 - \overline{u}_1$ are the relative opening and shearing displacements at interface. The mode I ERR is then found by using *J*-integral.

$$G_{IE} = \lim_{da\to 0}\left\{\frac{1}{da}\int_0^{da}\int_0^{\overline{w}}\sigma_n d\overline{w}dx\right\} = \int_0^{\overline{w}_B}\sigma_{nB}d\overline{w}_B \tag{29}$$

Substituting Eq. (28) into Eq. (29) gives

$$G_{IE} = G_{IE}^L + (1+3\gamma)/[b(1+\gamma)^3](P_{2B} - \beta_1 P_{1B})\overline{w}_B^{(1)} \tag{30}$$

The first term $G_{IE}^L = G_{IT}$ in Eq. (20) and the $\overline{w}_B^{(1)}$ in the second term is the relative crack tip rotation. It is seen that Eq. (30) is not completely analytical due to the second term. It is more important to note that the second set of orthogonal pure modes is not present. The mode II ERR can be considered similarly. The interface shear stress τ_s is found to be

$$\tau_s = \tau_{sP} + \tau_{s\sigma} + \tau_{s\overline{u}} \tag{31}$$

with

$$\tau_{sP} = 3\left(\gamma^2 P_{1B} + P_{2B}\right)/\left[2bh_1\gamma(1+\gamma)\right] \ , \ \tau_{s\sigma} = 3(1-\gamma)/(2h_1\gamma)\int_0^x \sigma_n dx \ , \ \tau_{s\overline{u}} = Eh_1\gamma\overline{u}^{(2)}/\left[4(1+\gamma)\right] \tag{32}$$

The mode II ERR G_{IIE} is then calculated by using *J*-integral.

$$G_{IIE} = G_{IIE}^L + \int_0^{\overline{u}_B}\tau_{sP}d\overline{u}_B \tag{33}$$

The first term $G_{IIE}^L = G_{IIT}$ in Eq. (20) and the second term can be calculated for a given cohesive law.

3.2. Shear deformable beam partition theory

It is simple to verify that the mode II ERR G_{IIT} remains the same as the G_{IIE} in Eq. (33). However, the mode I ERR G_{IT} needs reconsideration. The governing equation for the interface normal stress σ_n is

$$\sigma_n^{(2)} - \lambda^2\sigma_n = \alpha\left(\overline{w}^{(4)} + 3(1-\gamma)/(2h_1\gamma)\overline{u}^{(3)}\right) \tag{34}$$

where $\lambda = (1+\gamma)/(\gamma h_1)\left(3k^2G_{xz}/E\right)^{1/2}$ and $\alpha = k^2G_{xz}h_1\gamma/(1+\gamma)$. By using the method of parameter variation, the solution to Eq. (34) is found.

$$\begin{aligned}\sigma_n = {} & c_1e^{\lambda x} + c_2e^{-\lambda x} + \alpha\left[\lambda^2\overline{w} + \overline{w}^{(2)} + 3\overline{u}^{(1)}(1-\gamma)/(2h_1\gamma)\right] \\ & + \alpha\lambda^3/2\left(e^{\lambda x}\int_0^x \overline{w}e^{-\lambda x}dx - e^{-\lambda x}\int_0^x \overline{w}e^{\lambda x}dx\right) + 3\alpha\lambda^2(1-\gamma)/(4h_1\gamma)\left(e^{\lambda x}\int_0^x \overline{u}e^{-\lambda x}dx + e^{-\lambda x}\int_0^x \overline{u}e^{\lambda x}dx\right)\end{aligned} \tag{35}$$

The two integration constants c_1 and c_2 are determined using the conditions $\sigma_n(\Delta a) = \sigma_n^{(1)}(\Delta a) = 0$.

$$c_1 = -\alpha\lambda^3/2\int_0^{\Delta a}\overline{w}e^{-\lambda x}dx - 3\alpha\lambda^2(1-\gamma)/(4h_1\gamma)\int_0^{\Delta a}\overline{u}e^{-\lambda x}dx \tag{36}$$

$$c_2 = \alpha\lambda^3/2\int_0^{\Delta a}\overline{w}e^{\lambda x}dx - 3\alpha\lambda^2(1-\gamma)/(4h_1\gamma)\int_0^{\Delta a}\overline{u}e^{\lambda x}dx \tag{37}$$

Then, mode I ERR is found using *J*-integral.

$$\begin{aligned} G_{IT} &= -\int_0^{\overline{w}_B}\lambda^2 M_{nm}/b\,d\overline{w}_B + \alpha\left(\overline{w}_B^{(1)}\right)^2/2 + 3\alpha(1-\gamma)/(2h_1\gamma)\int_0^{\overline{w}_B}\overline{u}_B^{(1)}d\overline{w}_B \\ &= \int_0^{\overline{w}_{B\sigma_I}}\sigma_I d\overline{w}_B + \sigma_I\left(\overline{w}_B - \overline{w}_{B\sigma_I}\right) + \alpha\left(\overline{w}_B^{(1)}\right)^2/2 \end{aligned} \tag{38}$$

Note that the first term in Eq. (38) is calculated from a given interface cohesive law with $\sigma_I = -\lambda^2 M_{nm}/b + 3\alpha(1-\gamma)/(2h_1\gamma)\overline{u}_B^{(1)}$ in which

$$M_{nm} = (1+3\gamma)/(1+\gamma)^3\left(\beta_1 M_{1B} - M_{2B}\right) + h_1\gamma^2(1-\gamma)/[2(1+\gamma)^3]N_{1Be} \tag{39}$$

and

$$\overline{u}_B^{(1)} = -\left(6\gamma^2 M_{1B} + 6M_{2B} + \gamma^2 h_1^2 N_{1Be}\right)/\left(Eb h_1^2\gamma^2\right) \tag{40}$$

In the case of a rigid interface the first two terms in Eq. (40) disappear and the third term reduces to $G_{IT}^L = G_{IT}$ in Eq. (20). For a non-rigid interface the first term in Eq. (38) is calculated based on the given cohesive law and the second and third terms are not able to be determined analytically. However, for most of practical engineering problems with hard interfaces the third term in Eq. (38) can be replaced by G_{IT} in Eq. (20). Therefore, $\overline{w}_B$ in Eq. (38) can be calculated by using a given interface cohesive law and the following:

$$G_{IT}^L = \int_{\overline{w}_{B\sigma_I}}^{\overline{w}_B}\left(\sigma_{nB} - \sigma_I\right)d\overline{w}_B \tag{41}$$

Therefore, the second term in Eq. (38) is found and the mode I ERR G_{IT} for a hard interface is obtained analytically.

3.3. 2D elasticity partition theory

A DCB under crack tip bending moments M_{1B} and M_{2B} is considered here. Refer to Ref. [12] for general loading conditions. By using the two sets of fundamental orthogonal pure modes, i.e. $\{\theta, \beta\}$ in Eq. (14) and $\{\theta', \beta'\}$ in Eq. (15), approximate orthogonal pure mode I and mode II modes are

$$\theta_N(k_{er}) = \theta_{N2} + 1/2(\theta_{N1} - \theta_{N3})\log k_{er} + 1/2(\theta_{N1} - 2\theta_{N2} + \theta_{N3})(\log k_{er})^2 \tag{42}$$

$$\beta_N(k_{er}) = \beta_{N2} + 1/2(\beta_{N1} - \beta_{N3})\log k_{er} + 1/2(\beta_{N1} - 2\beta_{N2} + \beta_{N3})(\log k_{er})^2 \tag{43}$$

where $k_{er} = k/E$ is the ratio of interface stiffness to Young's modulus. θ_{N1}, θ_{N2}, θ_{N3}, β_{N1}, β_{N2}, β_{N3} are functions of the two sets of fundamental orthogonal pure modes. Detailed expressions for them are given in Ref. [12]. A mixed mode can be partitioned using this pair of pure modes.

4. Numerical and experimental assessments

The partition theories presented above have been extensively validated by using FEM simulations and in general excellent agreement has been observed [8–13]. Here, one example is presented for an isotropic DCB with non-rigid interface. The geometric dimensions of the DCB are length $L = 110$ mm, width $b = 1$ mm, total thickness $h_1 + h_2 = 2$ mm and crack length $a = 10$ mm. The material Young's modulus is $E = 1$ GPa. The loading conditions are $M_{1B} = 1$ Nm and $M_{2B} = 0$. Mixed-mode partitions from the present 2D elasticity theory and Abaqus FEM are recorded in Table 1 for various thickness ratios γ and interface stiffness to Young's modulus ratios k_{er}. An

excellent agreement is observed between the analytical and FEM results. Note that G_I / G in Table 1 is a percentage.

Table 1. Comparison between present 2D elasticity partition theory and FEM results.

		Analytical ($\times 10^6$ N/m)					FEM ($\times 10^6$ N/m)				
γ	k_{er}	0.1	0.5	1	5	10	0.1	0.5	1	5	10
1	G_I	3.000	3.000	3.000	3.000	3.000	3.029	3.029	3.028	3.024	3.022
	G_I / G	57.14	57.14	57.14	57.14	57.14	57.66	57.60	57.79	58.59	59.22
3	G_I	45.30	43.75	42.99	42.18	40.17	45.12	44.09	43.48	41.47	40.29
	G_I / G	95.87	92.59	90.98	89.26	85.01	94.72	92.71	91.56	87.96	85.97
5	G_I	159.7	154.9	152.0	148.6	139.7	159.0	156.4	154.7	148.6	144.7
	G_I / G	99.05	96.06	94.24	92.16	86.61	97.80	96.39	95.50	92.44	90.59
7	G_I	381.9	371.5	364.3	355.8	332.0	380.7	375.4	371.8	358.2	349.1
	G_I / G	99.65	96.94	95.06	92.83	86.63	98.59	97.46	96.72	94.07	92.40
9	G_I	748.0	728.9	714.5	697.0	647.6	746.3	736.6	729.8	703.7	686.0
	G_I / G	99.83	97.29	95.36	93.03	86.43	98.92	97.95	97.30	94.92	93.39

One example of experimental assessments is also presented here. Since the specimens in the tests were manufactured without adhesive layers [4] the laminar interfaces are considered to be rigid. Five partition theories, i.e. Williams theory [1], Suo-Hutchinson theory [3], Wang-Harvey classical, shear deformable and 2D theories, are assessed in Fig. 3. Although the Suo-Hutchinson and Wang-Harvey 2D partition theories are considered to be most accurate, the Wang-Harvey classical theory agrees the best with experimental data. It is suggested that the propagation of mixed-mode delamination on rigid interfaces is governed by the global partition as the global partitions of shear deformable and 2D partition theories are the same as the classical partitions.

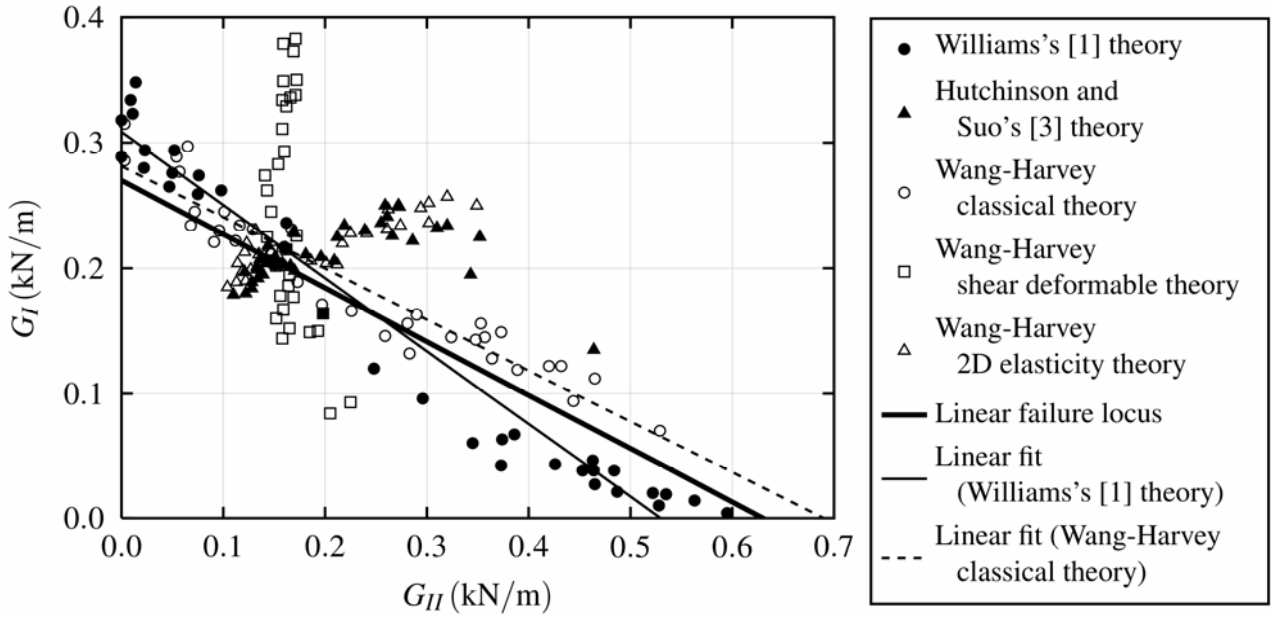

Figure 3. A comparison of various partition theories and the linear failure locus for epoxy-matrix/carbon-fiber composite specimens.

5. Conclusions

The present work discovers the most fundamental fracture modes – the two sets of orthogonal pure modes. A mixed-fracture mode can be superimposed or partitioned by these most fundamental pure modes. The two sets co-exist in classical laminated composite beams and plates and coincide in shear deformable beams and plates for rigid interfaces. When non-rigid interfaces considered the two sets coincide in both classical and shear deformable theories. By using these two sets of pure modes, a mixed-mode can also be partitioned based on 2D elasticity theory. The novel methodology is rooted in the mechanics of material and operated by a powerful mathematical method. It is capable of studying delamination in curved laminated composite beams and shells as well. It is also capable of studying general and buckling driven delamination consisting of all opening, shearing and tearing modes.

References

[1] J.G. Williams, On the calculation of energy release rates for cracked laminates. Int J Fract Mech, 36 (1988) 101–119.
[2] R.A. Schapery, B.D. Davidson, Prediction of energy release rate for mixed-mode delamination using classical plate theory. Appl Mech Rev, 43 (1990) S281–S287.
[3] J.W. Hutchinson, Z. Suo, Mixed mode cracking in layered materials. Adv Appl Mech, 29 (1992) 63–191.
[4] M. Charalambides, A.J. Kinloch, Y. Wang, J.G. Williams, On the analysis of mixed-mode failure. Int J Fracture, 54 (1992) 269–291.
[5] Z. Zou, S.R. Reid, P.D. Soden, S. Li, Mode separation of energy release rate for delamination in composite laminates using sublaminates. Int J Solids Struct, 38 (2001) 2597–2613.
[6] D. Bruno, F. Greco, Mixed mode delamination in plates: a refined approach. Int J Solids Struct, 38 (2001) 9149–9177.
[7] Q. Luo, L. Tong, Calculation of energy release rates for cohesive and interlaminar delamination based on the classical beam-adhesive model. J Compos Mater, 43 (2009) 331–348.
[8] S. Wang, C.M. Harvey, A theory of one-dimensional fracture. Compos Struct, 94 (2012) 758–767. Also a plenary lecture at the 16th international conference on composite structures (ICCS-16), 28–30th June 2011, Porto, Portugal.
[9] C.M. Harvey, S. Wang, Experimental assessment of mixed-mode partition theories. Compos Struct, 94 (2012) 2057–2067.
[10] S. Wang, C.M. Harvey, Mixed mode partition theories for one dimensional fracture. Eng Fract Mech, 79 (2012) 329–352. Also a plenary lecture at the 8th international conference on fracture and strength of solids (FEOFS 2010), 7-9th June 2010, Kuala Lumpur, Malaysia.
[11] C.M. Harvey, S. Wang, Mixed-mode partition theories for one-dimensional delamination in laminated composite beams. Eng Fract Mech, 96 (2012) 737–759.
[12] S. Wang, C.M. Harvey, Partition of mixed modes in double cantilever beams with non-rigid elastic interfaces. Eng Fract Mech (under review).
[13] C.M. Harvey, Mixed-Mode Partition Theories for One-Dimensional Fracture. PhD Thesis. March 2012, Loughborough University, UK.

Coupled fracture mode associated with anti-plane loading of cracks and notches

Filippo Berto[1], Paolo Lazzarin[1], L.Pook[2], A. Kotousov[3]

[1]Department of Management and Engineering, University of Padua, Stradella San Nicola 3 , 36100, Vicenza, Italy
[3]School of Mechanical Engineering, The University of Adelaide, South Australia, SA 5005, Australia; e-mail: Andrei.Kotousov@adelaide.edu.au
[2]21 Woodside Road, Sevenoaks TN13 3HF, UK

* Corresponding author: berto@gest.unipd.it

Abstract The purpose of this paper is to investigate by means of the 3D Finite Element method a coupled fracture mode generated by anti-plane loading of a straight through-the-thickness crack in a linear elastic plate. This coupled fracture mode represents one of three-dimensional phenomena, which are currently largely ignored in numerical simulations and failure assessment of structural components weakened by cracks. It arises due to the boundary conditions on the plate free surfaces, which negate the transverse shear stress components corresponding to classical mode III. Instead, a new singular stress state in addition to the well-known 3D corner singularity is generated. This singular stress state (or coupled fracture mode) can affect or contribute significantly to the fracture initiation conditions. The coupled singular mode exists even if the applied anti-plane loading produces no singularities ($K_{III} = 0$). In this case there is a strong thickness effect on the intensity of the coupled fracture mode.

Keywords Crack, anti-plane loading, coupled fracture mode, 3D modelling

1. Introduction

The first systematic study on the three-dimensional stress states of a through-the-thickness crack subjected to mode I loading was conducted in Refs [1-4]. Accurate studies on three-dimensional stress distributions in front of cracks have been carried out in those references, extending Williams' two-dimensional eigenfunction expansions [5] to the three-dimensional case, and in [6] four distinct harmonic functions have been used to solve the problem according to Papkovich-Neuber's method.
Utilising a variational principle, a system of simplified governing equations has been derived [1-4] for the extension and bending deformations of an elastic plate with a through-the-thickness crack and investigated the three-dimensional stress states surrounding the crack tip. One important result from this work is that the area of the three-dimensional stress state around the crack tip spreads in the plane direction to the distance of approximately half of the plate thickness. Beyond this distance the stress state follows the classical plane stress solution. Many experimental studies conducted in the past including those carried out in [7] who applied an optical technique confirmed this fundamental result.
Another interesting three-dimensional effect, which was first presented in [8], is the disappearance of the in-plane singularity at a point when a corner front (crack front) intersects a free surface. At this point a new three-dimensional corner singularity develops instead. The problem of a vertex (corner) singularity is now well documented in a number of articles in the last thirty years (see, among the others, Refs [9-17]). This problem was recently re-examined in [18] with reference to fatigue crack growth. In this paper, the effect of a free surface on fatigue crack behaviour was investigated experimentally and numerically for relatively thick specimens, where the solutions provided in [8] for semi-infinite space can be applied. In [9] it was underlined that the 3D corner

singularity in cracked plates, which usually can be neglected for mode I loading, should be taken into consideration for mixed mode loadings. However, despite all these studies the role of the corner singularities in fatigue and fracture phenomena remains largely unknown.

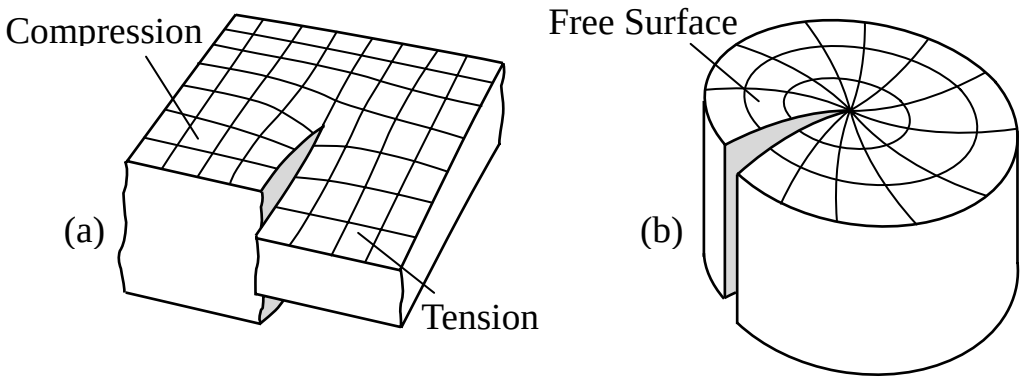

Fig.1 Generation of coupled fracture modes due to Poisson's effect and redistribution of stresses on free surfaces when a crack is subjected to shear (a) and anti-plane loading (b)

One more three-dimensional effect, which the two-dimensional numerical and analytical solutions are incapable to predict or analyse, is the existence of the coupled fracture modes. To illustrate these coupled fracture modes let us consider a through-the-thickness crack loaded in shear or anti-plane loading. In these cases additional local fracture modes are generated due to Poisson's effect and/or the redistribution of stresses on the free surfaces as illustrated: in Fig. 1 (a) – mode II loading and (b) – mode III loading in the case of a zero notch angle [16]. In many papers (see among others Refs [19, 20]) it was highlighted that modes II and III cannot exist independently and the presence of one of these modes always generates a coupled singular state.

The coupled modes induced by the primary modes II and III for through-the-thickness cracks have been known for a rather long period of time but the first systematic studies for semi-infinite cracks were conducted numerically using a careful FE modelling in [10, 21]. Recently the first coupled fracture mode (see Fig. 1a), which was called the out-of-plane or K_O-mode, was investigated for finite geometries representing welded joints as well as for sharp and round notches of arbitrary opening angle. It was demonstrated that the K_O-mode has many interesting and previously unknown features, which can influence mixed-mode fracture, crack initiation and fatigue growth phenomena.

A recent experimental and numerical study has been performed to investigate the fatigue crack growth tests in mixed-mode 2 + 3 on maraging steel and Ti-6Al-4V. The 3D evolutions of the crack fronts -measured by SEM after interrupted tests- have been analyzed [22]. A 3D finite element model of tested specimens has been prepared, with a refined mesh around the crack front. It has been shown that the profiles of stress intensity factors and energy release rate vary along the crack front. In particular due to the coupled Mode 2 and Mode 3 loadings K_2, K_3 and G have been found with an asymmetrical profile. When the inclination angle of the crack plane relative to the horizontal axis surface is equal to 45° the energy release rate is ten times higher near one free surface than on the other inducing a strong asymmetry in crack growth and showing the non

negligible effects of the coupled modes.

One of these interesting features is a coupling of this mode with the non-singular terms at shear loading. It means, if a crack is loaded in shear with $K_{II}= 0$, the intensity of the coupled K_0- mode can be different from zero. At such loading the intensity of the out-of-plane mode is finite and capable of initiating brittle fracture [23, 24]. The latter result and other three-dimensional features are in contradiction with the classical two-dimensional view on fracture, which states that brittle fracture can only be initiated with non-zero stress intensities of primary fracture modes (conventional mode I, II and III).

Important features of the out-of-plane singular mode were revealed in a careful three-dimensional numerical study of typical welded lap joint geometry [25] aimed to investigate the contribution of this mode to the overall stress state in the close vicinity of the slit/notch tip. The extension of the present study to sharp and blunt notches under mode II loading has been recently made by the present authors [26, 27].

In contrast to mode II loading, the coupled mode corresponding to mode III loading is much less investigated and there were no systematic studies focusing on the investigation of this mode except many remarks in literature on the coupled nature of modes II and III as well as the influence of this coupled mode on fracture appearance, crack path and crack initiation [19, 20]. The aim of this paper is to investigate this coupled mode using the Finite Element method and provide numerical estimates of the possible contribution of this mode to brittle fracture.

In the beginning of the present paper, a numerical technique based on FE method is developed and validated for the investigation of the coupled mode associated with the anti-plane loading. Because this mode is localised in the close vicinity of the crack tip, a careful meshing is required in order to avoid large numerical errors in this region. Further, a systematically study of this mode is carried out focusing on the effect of Poisson's ratio on the stress intensity of this mode, which also varies along the crack front. It is also demonstrated that similar to the K_0-mode, a non-singular mode III loading ($K_{III}=0$) is capable of generating the coupled singular stress state along the crack front. In this case, a strong scale effect exists and the intensity of the coupled mode strongly depends on the thickness of the plate.

2. Approach

2.1 Geometry

Because the coupled singular modes are local modes and spread to the distance of approximately half of the plate thickness as explained in the Introduction, the problem geometry is truncated to a disk with such dimensions which avoid the effect of the finite boundaries on the stress state of the coupled mode as well as the influence of bending stresses. The antisymmetric boundary conditions are utilised to further simplify the geometry. The final geometry is shown in Fig. 2 and appropriate displacement boundary conditions corresponding to anti-plane loading were applied on the cylindrical surface. The origin of the Cartesian coordinate system (x,y,z) is located at the crack tip, at the mid-surface where x direction was chosen to be the direction of the crack bisector.

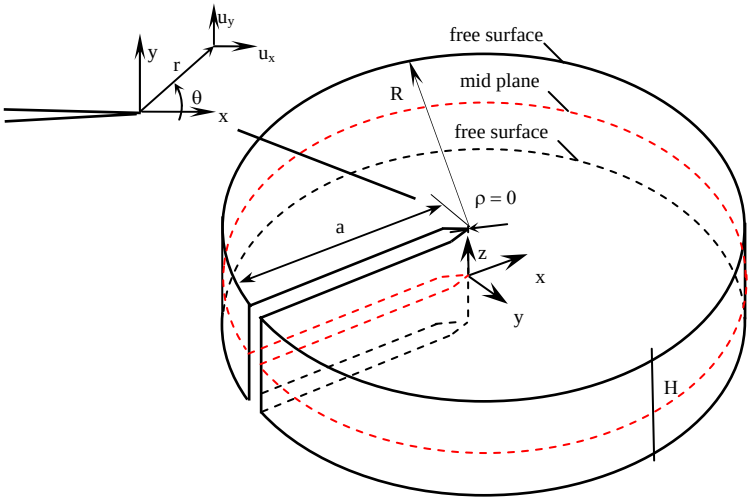

Figure 2. Geometry of the plate and coordinate system with z=0 in the mid-plane

2.2 Boundary Conditions

The displacement boundary conditions are applied to the outer cylindrical edge of the plate. In the beginning the out-of-plane displacement field corresponding to the first singular term in the asymptotic expansion of the stress field, which is valid far from the crack tip (model boundaries), was prescribed as follows:

$$w = u_z = \frac{2K_{III}}{\mu}\sqrt{\frac{r}{2\pi}}\sin\frac{\phi}{2} \tag{1}$$

$$u_x = 0$$

$$u_y = 0$$

where μ is the shear modulus. It is linked to Young's modulus by a well-known relationship:

$$\mu = \frac{E}{2(1+\nu)} \tag{2}$$

In further numerical examples Young's modulus was set at 200×10^9 Pa. However, the numerical results to be presented in the following sections can be easily rescaled for other values of mechanical properties, loading or plate thickness.

2.3 Validation

As highlighted in the Introduction section due to complexity of the numerical analysis and interpretation of the computational results there were almost no works investigating this singular mode. However, the three-dimensional effects, specifically the coupling of fracture modes II and III, were often recognised and acknowledged in many papers on stress analysis of cracked structural components, fracture and fatigue. A comparison of the present results obtained with ANSYS 11 and those published in [11] in terms of the ratio of the induced to applied stress intensity factors K_{II}^{C}/K_{III} as a function of the position along the crack front, z/H, are shown in Fig.3, demonstrating a good agreement. Description of all parameters of the modelling is given in [10] and the definition of the stress intensity factor of the coupled mode K_{II}^{C} will be provided in the next Section.

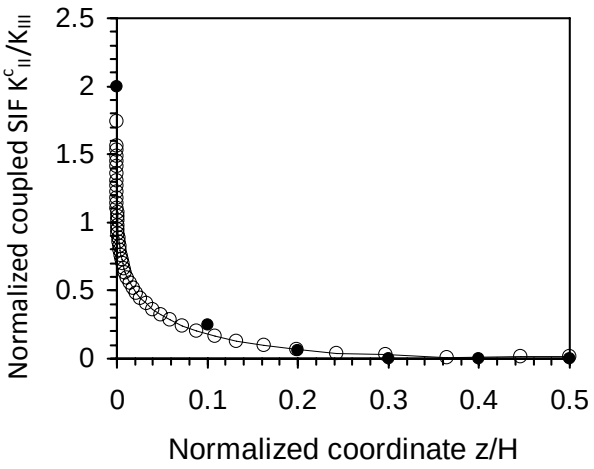

Fig.3 Comparison of the present FE calculations and published results: line is the current numerical results and filled circles are data from [11]

3. Numerical Results

3.1 Stress State

First, the results for the out-of-plane shear stress components along the bisector line for different distances from the crack tip are considered. The results can also be represented in non-dimensional form; however, the non-dimensional results are sometimes difficult to relate to practical situations. Therefore in the following computational examples, if it is not specified separately, the applied remote stress intensity factor, K_{III}= 1 MPa$\sqrt{m}$, Poisson's ratio ν=0.3 and the thickness of the plate, H= 40 mm.

The intensity of the computed stress component τ_{yz} defined similar to the classical definition of the stress intensity factor for mode II in plane problems of elasticity as

$$K_{III}(z) = \sqrt{2\pi}\lim_{x\to 0}\tau_{yz}(z)x^{1-\lambda_{III}} \qquad (3)$$

can be obtained using a standard log-log regression analysis of the stress distribution. The singular power describes the asymptotic rate at which the stress components increase as the crack tip is approached. As expected, the stress field everywhere has been found to have a degree of singularity

λ_{III}= 0.5. This value remains constant from the crack tip until the external radius is reached.
It has been found that the in-plane shear stress components associated with the coupled mode change in a wider range from zero at the mid-plane as expected to values of the same order as the applied stress intensity factor. In contrast, the out-of-plane shear stresses associated with the applied K_{III} mode do not significantly change across the thickness and the maximum shear stresses take place at the mid-plane of the plate decreasing smoothly towards the free surfaces. As mentioned above, the results were obtained for the above specified conditions (applied stress intensity factor, material properties and plate thickness) and can be easily rescaled or represented in a dimensionless form if necessary.

3.2 Stress Intensity Factors

The stress intensity factor of the coupled mode can be defined similar to mode II, or as

$$K_{II}^{C}(z)=\sqrt{2\pi}\lim_{x\to 0}\tau_{xy}(z)x^{1-\lambda_{II}} \qquad (4)$$

In general there are many similarities between the coupled mode and mode II corresponding to the shear loading of a crack. However there are some essential differences between these two singular modes. The coupled mode is a local mode, which is concentrated in the vicinity of the plate free surfaces. It is generated due to the boundary conditions, which negate the out-of-plane shear stress components corresponding to the applied mode. For this coupled fracture mode the effect of Poisson's ratio is rather small in comparison with the coupled mode generated by mode II loading [14]. The coupled modes rapidly decay with distance from the crack tip as it will be demonstrated later in this paper.
The distributions of the local intensities of mode III, $K_{III}(z)$ associated with the applied antisymmetric loading and $K_{II}^{C}(z)$, associated with the coupled mode are shown in Fig. 4. As it can be seen from this figure the coupled mode is localised in the close vicinity of the free surfaces and propagates into the thickness to the distance of approximately 0.2 H. There is a significant drop in the intensity of the applied mode in the precincts of the free surface. In the very close vicinity of the free surface the intensity of both modes is approaching to zero. As it was mentioned in the Introduction, at a point where a corner front (crack front) intersects a free surface the applied and coupled modes disappear and a new type of singularity, 3D corner singularity, develops instead. Consequently, the numerical results could be not very accurate in the vicinity of this location [10].

4. Anti-plane Loading with K_{III} = 0 and Scale Effect

4.1 Coupled Mode due to Anti-plane Loading

For an elastic plate with a crack, the possible contribution of higher order terms of the classical Williams' solution [28] to the fracture initiation was discussed with reference to a plane elastic problem in [29-31]. As discussed in Ref. [30] in some cases of practical interest, the contribution of the higher order stress terms to the stress state in the vicinity of the crack tip (in addition to the stress intensity factors and the T-stress) is not negligible. A set of equations has been proposed for accurately describing the crack tip stress components particularly for those cases where the mode I and mode II stress intensity factors used in combination with the T-stress component, are unable to capture with satisfying precision the complete stress field ahead the crack tip. In this session an

accurate analysis of mode III higher order (non-singular) terms on the induced mode II is carried.

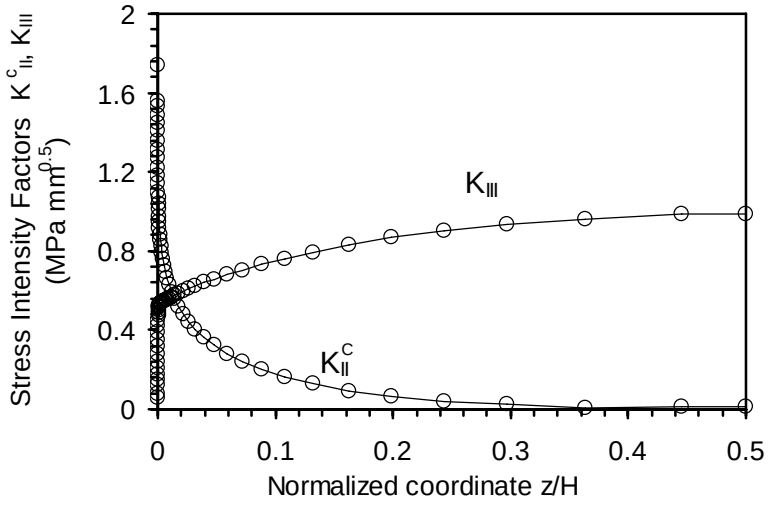

Fig. 4. Distribution of the stress intensity factors (mode III and the coupled mode) along the plate thickness, at a distance x = 0.05 mm from the crack tip.

The out-of-plane displacement, w, beyond the area of 3D effects (this 3D area is confined within a cylinder with the axis of symmetry along the crack front and radius equal to half of the plate thickness) can be expressed as [29]:

$$w = \sum_{n=0}^{\infty} \frac{r^{n+\frac{1}{2}}}{\mu} C_n \sin\left(\frac{1}{2} - n\right)\phi \tag{5}$$

with

$$C_0 = K_{III}^{\infty}\sqrt{\frac{2}{\pi}} \tag{6}$$

The previous results are related to the case when $C_0 \neq 0$ or $K_{III} \neq 0$ and all other terms in the asymptotic expansion (5) are zero ($C_n \equiv 0$ at $n = 1,2...\infty$). In Fe simulations the corresponding displacement boundary conditions far from the crack tip were applied to avoid effect of the finite boundaries of the FE model. In the following analysis the situation when a through-the-thickness crack loaded with $C_0 = K_{III} = 0$ is considered. It will be demonstrated that such a loading of a through-the-thickness crack is capable of inducing the singular coupled singular mode, the same as for the leading term in the asymptotic expansion of the two-dimensional displacement/stress field. It suggests that this coupled singular mode has a potential to cause fracture. In contrast, the classical two-dimensional theory of brittle fracture states that fracture by crack propagation is impossible due to the absence of the energy release rate when K_{III}=0.

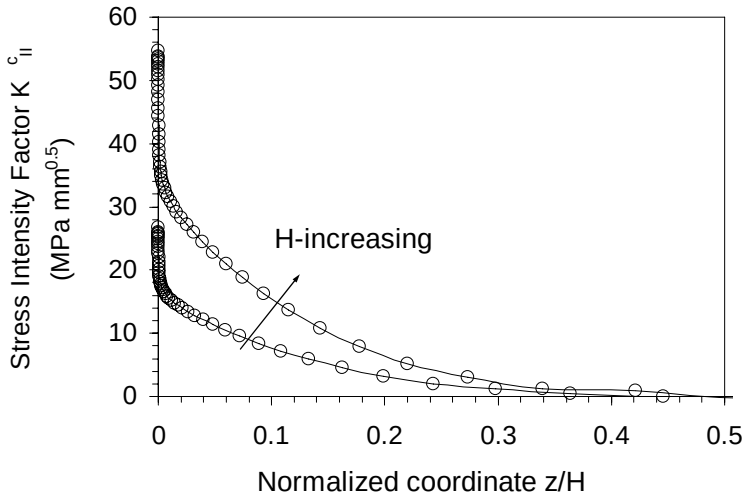

Fig.5. Effect of the thickness on the intensity of the coupled mode at distance x/H= 0.02 (a);

Consider the first non-singular term in the asymptotic expansion. Set its value C_1=1 MPa/$\sqrt{m}$ corresponding to n=1 in Eq. (5). Such loading produces no singularities corresponding to the applied antisymmetric loading, i.e. $K_{III} = 0$, which is also valid in the area of 3D effects (very close to the crack tip). The results of the FE calculations are presented in Fig.5, which reveals that a non-zero stress intensity of the coupled mode does exist at such loading. The latter effect has many implications for failure assessment. In particular, it indicates that brittle failure by crack propagation is possible even the intensity of the primary load (2D stress intensity factor) is close to zero $(K_{III} \approx 0)$.

It is interesting that the non-singular loading reveals a strong scale effect of deterministic nature, which can be also found from dimensionless considerations. Indeed, due to the localised nature of the coupled mode, its intensity has to be a linear function of the applied intensity, or $K_{II}^{C} \approx C_1$.

5. Conclusion

Below the most important findings of this work will be summarised:

a) Anti-plane loading of a through the thickness crack leads to generation of a singular stress state (or a coupled fracture mode), which has the similar singular behaviour as classical mode II. However there are some essential differences between these modes. The coupled mode is a local mode, which is concentrated in the vicinity of the plate free surfaces and is generated due to the Poisson's effect and boundary conditions, which negate the out-of-plane shear stress components corresponding to the applied mode. The coupled mode rapidly decays with distance from the crack tip. The local nature of the coupled modes means that the obtained results for the truncated geometry are applicable to other finite geometries provided that there is no interaction between the boundary conditions and the area of 3D effects.

b) The intensity of the primary (applied) anti-plane mode in the vicinity of the crack tip is moderately affected by Poisson's ratio. In contrast, the intensity of the coupled mode is largely unaffected by Poisson's ratio.

c) The singular coupled mode can be induced by, so called, non-singular anti-plane loading with $K_{III} = 0$. In this case a strong thickness effect is found and confirmed by FE calculations. The

intensity of the coupled mode decays (increases) with the decrease (increase) of the plate thickness as a power function. When several anti-plane non-singular terms are applied to the crack in an elastic plate the scale effect can be rather complicated. The influence of the higher terms on the stress intensity of the coupled mode depends on the number of the asymptotic mode, n, and this influence is more significant for the higher mode numbers.

All these theoretical findings, specifically the effects of Poisson's ratio and plate thickness on the stress intensities, have direct implications to the failure initiation conditions for cracks stressed in mode III. These findings demonstrate essential differences between classical two-dimensional considerations and 3D Fracture Mechanics. For example, the generation of the coupled singular mode at anti-plane loading with $K_{III} = 0$ indicates that contrary to the classical 2D theories, fracture under such loading conditions can be initiated due to the induced singular coupled modes. Such fracture is likely to take place close to free surfaces. It is also recognised that much work needs to be done to understand the contribution of the coupled modes to fracture initiation and fatigue.

Finally, all Finite Element results of the current study can be re-scaled to make these available for assessment of comparative studies. The only reason as to why it has been used particular values was to provide some physical feeling for the results of our finite element study.

References

[1] R.J. Hartranft, and G.C. Sih, Effect of plate thickness on the bending stress distribution around through cracks, J. Math. Phys., 47 (1968) 276–291.

[2] R.J. Hartranft, G.C. Sih, The use of eigenfunction expansions in the general solution of three-dimensional crack problems. J. Math. Mech., 19 (1969) 123–138.

[3] R.J. Hartranft, G.C. Sih, An approximate three-dimensional theory of plates with application to crack problems, Int. J. Eng. Sci., 8 (1970) 711-729.

[4] G.C. Sih, A review of the three-dimensional stress problem for a cracked plate, Int. J. Fract. Mech., 7 (1971) 39–61.

[5] M.L. Williams, The Bending Stress Distribution at the base of a stationary crack, ASME J. Appl. Mech., 28 (1961) 78–82.

[6] M.K. Kassir, and G.C. Sih. Application of Papkovich-Neuber potentials to a crack problem, Int. J. Solids Struct., 9 (1973) 643–654.

[7] Y. Kawagishi, M. Shozu, Y. Hirose, Experimental evaluation of stress field around crack tip by caustic method, Mech. Mater., 33 (2001) 741-757.

[8] J.P. Benthem, State of stress at the vertex of a quarter-infinite crack in a halfspace, Int. J. Solids Struct., 13 (1977) 479–92.

[9] Z.P. Bazant, L.F. Estenssoro, Surface singularity and crack propagation, Int. J. Solids Struct., 15 (1979) 405–26.

[10] L.P. Pook, A note on corner point singularities, Int. J. Fract., 53 (1992) R3–R8.

[11] L.P. Pook Some implications of corner point singularities, Eng. Fract. Mech., 48 (1994) 367–378.

[12] Z.H. Jin, R.C. Batra, A crack at the interface between a Kane-Mindlin plate and a rigid substrate, Eng. Fract. Mech., 57 (1997) 343-354.

[13] C. She, W. Guo, The out-of-plane constraint of mixed-mode cracks in thin elastic plates, Int. J. Solids Struct., 44 (2007) 3021–3034.

[14] A. Kotousov, Fracture in plates of finite thickness, Int. J. Solids Struct., 44 (2007) 8259-8273.
[15] A. Kotousov, P. Lazzarin, F. Berto, S. Harding, Effect of the thickness on elastic deformation and quasi-brittle fracture of plate components, Eng. Fract. Mech., 77 (2010) 1665-1681.
[16] A. Kotousov, Effect of plate thickness on stress state at sharp notches and the strength paradox of thick plates, Int. J. Solids Struct., 47 (2010) 1916-1923.
[17] P. Yu , C. She, W. Guo, Equivalent thickness conception for corner cracks, Int. J. Solids Struct., 47 (2010) 2123-2130.
[18] P. Hutar, L. Náhlík, Z. Knésl, The effect of a free surface on fatigue crack behaviour. Int. J. Fatigue, 32 (2010) 1265-1269.
[19] L.P. Pook, On fatigue crack path, Int. J. Fatigue, 17(1995) 5–13.
[20] A.J. Pons, A. Karma, Helical crack-front instability in mixed-mode fracture. Nature, 464 (2010) 85-89.
[21] T. Nakamura, D.M. Parks, Antisymmetrical 3-D stress field near the crack front of a thin elastic plate. Int. J. Solids Struct., 25 (1989) 1411-1426.
[22] V. Doquet, Q.H. Bui, G. Bertolino, E. Merhy, L. Alves, 3D shear-mode fatigue crack growth in maraging steel and Ti-6Al-4V. Int. J. Fract., 165 (2010) 61-76.
[23] F. Berto, P. Lazzarin, A. Kotousov, On the presence of the out-of-plane singular mode induced by plane loading with KII = KI = 0. Int. J. Fract., 167 (2011) 119-126.
[24] F. Berto P. Lazzarin, A. Kotousov, On higher order terms and out of plane singular mode , Mech. Mater., 43 (2011) 332-341.
[25] S. Harding, A. Kotousov, P. Lazzarin, F. Berto, Transverse singular effects in V-shaped notches stressed in Mode II. Int. J. Fract., 164 (2010) 1-14.
[26] F. Berto, P. Lazzarin, S. Harding, A. Kotousov, Out-of-plane singular stress fields in V-notched plates and welded lap joints induced by in-plane shear load conditions. Fatigue Fract. Eng. Mater. Struct., 34 (2011) 291-304.
[27] F. Berto, P. Lazzarin, A. Kotousov, L.P. Pook, Induced out-of-plane mode at the tip of blunt lateral notches and holes under in-plane shear loading, Fatigue Fract. Eng. Mater. Struct., 35 (2012) 538-555.
[28] M.L. Williams, On the stress distribution at the base of a stationary crack, J. Appl. Mech., 24 (1957) 109-114.
[29] A. Seweryn, K. Molski, Elastic stress singularities and corresponding generalized stress intensity factors for angular corners under various boundary conditions, Eng. Fract. Mech., 55 (1996) 529-556.
[30] K. Ramesh, S. Gupta, A.A. Kelkar Evaluation of stress field parameters in fracture mechanics by photoelasticity-revisited, Eng. Fract. Mech., 56 (1997) 25-45.
[31] Q.Z. Xiao, B.L. Karihaloo, X.Y. Liu, Direct determination of SIF and higher order terms of mixed mode cracks by a hybrid crack element. Int. J. Fract., 125 (2004) 207-225.

Numerical Solutions of Second Elastic-Plastic Fracture Mechanics Parameter in Test Specimens under Biaxial Loading

Ping Ding[1], Xin Wang[1,*]

[1] Department of Mechanical and Aerospace Engineering, Carleton University,
Ottawa, Ontario, K1S 5B6, Canada
*Corresponding author: xwang@mae.carleton.ca

Abstract Extensive finite elements analyses have been conducted to obtain solutions of constraint parameter A, which is the second parameter in a three-term elastic-plastic asymptotic expansion for crack-tip field, for test specimens under biaxial loading. Three mode I plane-strain test specimens, *i.e.* single edge cracked plate (SECP), centre cracked plate (CCP) and double edge cracked plate (DECP) were studied. The crack geometries analysed include shallow to deep cracks, and the biaxial loading ratios analysed are 0.5 and 1.0. Solutions of parameter A were obtained for materials following the Ramberg-Osgood power law with hardening exponents of n=3, 4, 5, 7 and 10. Remote tension loading were applied which covers deformation range from small-scale to large-scale yielding. Based on the finite element results of constraint parameter A, crack-tip constraint effect for cracked specimens under biaxial loading is analysed. Using the relationships between A and other two commonly-used second fracture parameters, Q and A_2, the present solutions for A can be used to calculate parameters Q and A_2.

Keywords elastic-plastic fracture, second fracture parameter, biaxial loading, solutions, constraint effect

1. Introduction

In classical elastic-plastic fracture mechanics (EPFM), one-parameter approach, which describes the HRR fields [1, 2] based on J-integral [3], usually can work well for high constraint cases. For low constraint cases, under high loading conditions, the dominance of J-integral will be lost, and the one-parameter approach of J-integral will not be appropriate any more.

Two-parameter approaches have been developed to overcome the limitation of the EPFM one-parameter approach, in which a second fracture mechanics parameter is introduced to characterize the constraint effect besides the load-related parameter J-integral. Several commonly-used two-parameter approaches are, J-T [4-6], J-Q [7, 8] and J-A_2 (J-A) [9-12] approaches, where constraint parameter A is a different normalizing form of A_2 [11, 12].

Determination of J-integral and second fracture mechanics parameter, T, Q and A_2 (A), is precondition of application of J-T, J-Q and J-A_2 (A) approaches. In the early development of EPFM, J-integral solutions have been well established. The solutions of constraint parameter T-stress have also been well established in the literature. Currently, numerical method, such as finite element analysis (FEA) method, is the main method for the determination of constraint parameters Q and A_2 (A). For example, Nikishkov *et al*. [12] suggested an algorithm which determines solutions of A using a least squares procedure based on the finite element analysis results. Although with high accuracy, numerical method is a time-consuming way to obtain solutions of parameters. Correspondingly, understanding of constraint effect near crack-tip is limited because of the scarcity of solutions of constraint parameter A_2 (A) and Q.

In previous works of authors [13, 14], extensive finite element analyses were conducted to obtain solutions of parameter A for several typical two-dimensional (2D) plane-strain specimens under uniaxial loading conditions. Biaxial loading cases are of equal theoretical and engineering practical significance as uniaxial loading cases. Many researchers have focused their investigations on biaxial loading cases, for example, the results reported by Pop *et al*. [15] and Méité *et al*. [16]. In the present work, solutions for A will be obtained for biaxial loading cases for three mode I crack plane-strain specimens, single edge cracked plate (SECP), center cracked plate (CCP) and double edge cracked plate (DECP). In this work, extensive finite element analyses will be carried out for SECP, CCP and DECP cracked specimens under biaxial loading conditions with biaxial loading

ratios λ=0.5, 1.0, to determine numerical solutions of constraint parameter *A* through a least squares fitting method suggested by Nikishkov *et al*. [12]. Using the obtained numerical solutions of constraint parameter, *A*, constraint effect near crack-tip of specimens is analyzed. Numerical solutions for constraint parameter *A* under biaxial loading conditions obtained in this work can be used to estimate other two commonly-used constraint parameters A_2 and *Q* conveniently by the relationships between *A* and A_2, *Q* presented in authors' previous paper [13].

2. Theoretical background

2.1. *J-A* approach

As mentioned in introduction section, *J-A* two-parameter approach of elastic-plastic fracture mechanics, which is suggested by Nikishkov *et al*. [11, 12], is an alternate format of *J*-A_2 approach developed by Yang *et al.* [9, 10]. In these two formats of the approach, both the constraint parameter *A* and A_2 are the magnitude of the second term in a three-term series expansion of crack-tip stress fields. In this paper, the *J-A* format is used.

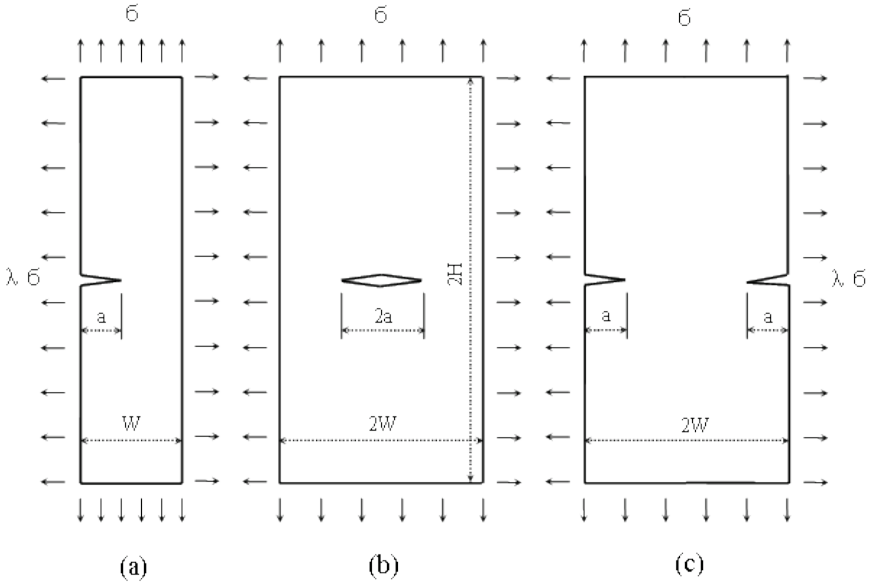

Figure 1. Cracked specimens under biaxial loading: (a) SECP, (b) CCP, (c) DECP

Considering a two-dimensional elastic-plastic specimen containing a mode I crack under plane strain condition, if the elastic-plastic behavior of the specimen material described by deformation theory of plasticity follows the Ramberg-Osgood relationship, the uniaxial stress-strain curve can be described as:

$$\frac{\varepsilon}{\varepsilon_0}=\frac{\sigma}{\sigma_0}+\alpha\left(\frac{\sigma}{\sigma_0}\right)^n \tag{1}$$

where α is a material coefficient, *n* is the hardening exponent ($n > 1$), $\varepsilon_0=\sigma_0/E$, *E* is Yong's modulus, σ is the stress applied on the remote end of specimen, and σ_0 is the material yield stress.

Table 1. Comparison of constraint parameter *Q* for CCP under *a/W*=0.5, *n*=10, λ=0.5

$\log(J/(a\sigma_0))$	-2.900	-2.491	-2.256	-2.074	-1.855	-1.593	-1.299	-0.991
Q_{SSY} [Ref.]	-0.2107	-0.3553	-0.4822	-0.5711	-0.6497	-0.7690	-0.8223	-0.9315
Q_{SSY}	-0.2196	-0.3714	-0.4849	-0.5763	-0.6758	-0.7790	-0.8739	-0.9815
Diff. (%)	4.232	4.526	0.558	0.923	4.003	1.299	6.274	5.376

In the *J-A* two-parameter approach suggested by Nikishkov *et al*. [11, 12], for the hardening exponent $n \geq 3$ and under plane-strain conditions, the three-term asymptotic solution expression for

stress field near the crack-tip in an elastic-plastic material is given as:

$$\frac{\sigma_{ij}}{\sigma_0} = A_0 \bar{r}^s \bar{\sigma}_{ij}^{(0)}(\theta) - A\bar{r}^t \bar{\sigma}_{ij}^{(1)}(\theta) + \frac{A^2}{A_0} \bar{r}^{2t-s} \bar{\sigma}_{ij}^{(2)}(\theta) \tag{2}$$

In Eq. (2), $\sigma_{ij}(\theta)$ are stress components, σ_r, σ_θ and $\sigma_{r\theta}$ in a polar coordinate system with origin at the crack-tip; $\bar{\sigma}_{ij}^{(0)}(\theta), \bar{\sigma}_{ij}^{(1)}(\theta)$ and $\bar{\sigma}_{ij}^{(2)}(\theta)$ are normalized angular stress functions. The dimensionless radius $\bar{r}$ is defined as $\bar{r} = r/(J/\sigma_0)$, where J is the J-integral at the crack-tip. Power t is an eigenvalue depending on the hardening exponent n of Ramberg-Osgood relation, and power $s=-1/(n+1)$. The polynomial coefficient A_0 is defined as [11], $A_0=(\alpha\varepsilon_0 I_n)^{-1/(n+1)}$, where I_n is a scaling integral only depending on n, see Refs. [1, 2]. Nikishkov [11] has proposed a computational algorithm to determine the values of normalized angular functions $\bar{\sigma}_{ij}^{(0)}(\theta)$, $\bar{\sigma}_{ij}^{(1)}(\theta)$, $\bar{\sigma}_{ij}^{(2)}(\theta)$, asymptotic power t, and scaling integral I_n. The three-term expansion in Eq. (2) for the crack-tip stress (displacement) fields is controlled by two parameters, the magnitude of the first term (J-integral) and a second parameter (A) controlling the second and third term.

2.2. Numerical method for determining of constraint parameter

The application of J-A (A_2) two-parameter approach depends on the determination of the load-related parameter J and constraint parameter A (A_2). The solutions of J-integral (including analytical, numerical and approximate solutions) have been well established in the literature, such as the numerical solution of J suggested by Moran and Shih [17], which has been adopted in the commercial code ABAQUS [18] utilized in the present research.

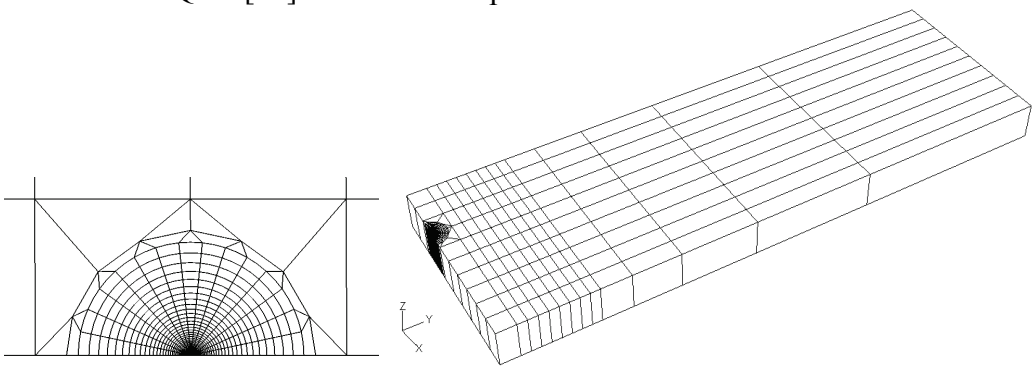

Figure 2. Typical FEA mesh, $a/W = 0.3$

Based on some stress component with corresponding finite element solutions at one or several locations (points) within the plastic zone, Yang *et al*. [9, 10] determine the A_2 values by matching a three-term expansion on crack-tip stress field. It is called the "*point match*" method by some researchers. Also based on FEA results, Nikishkov *et al*. [12] suggest a "*fitting method*" to determine parameter A values through a three-term expansion expressed by Eq. (2). In the present work, the proposed least square fitting method is utilized to obtained numerical solutions of constraint parameter A. See refs. [12] and [13] for more details about the procedure of the fitting method.

3. Finite element analysis, results and discussion

3.1. Material model and properties

The material model for finite element analyses carried out in the present work is the deformation theory of plasticity. Ramberg-Osgood power-law strain hardening relation is applied in finite element code ABAQUS [18], which is used in the present FEA.

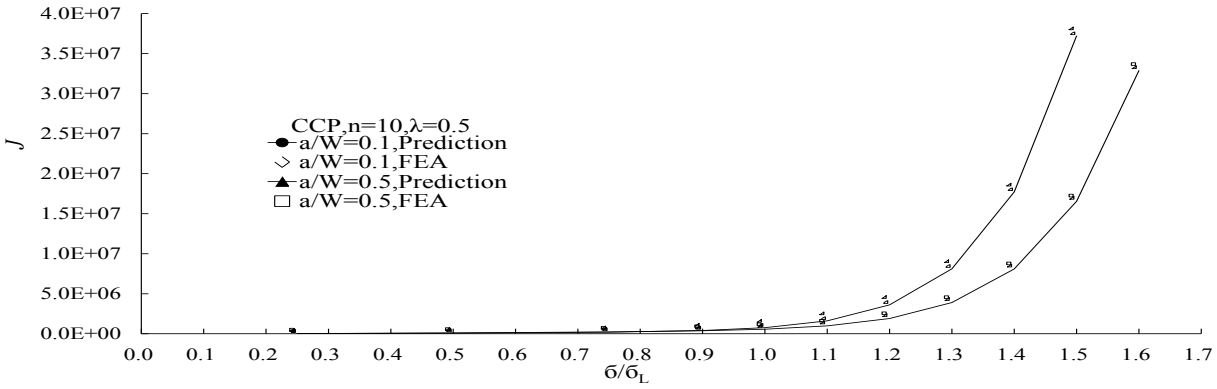

Figure 3. Comparisons of *J*-integral, CCP

Material properties used for all the analyses are specified as follows, yield stress $\sigma_0=4.0\times10^8$ *Pa*, elasticity modulus $E=2.0\times10^{11}$ *Pa*, Poisson ratio $\upsilon=0.3$, material coefficient $\alpha=1.0$, and hardening exponent n=3, 4, 5, 7 and 10. The used material properties cover a wide range of both high and low strain hardening behaviors.

3.2. 2D cracked models and FEA procedure

Three typical cracked specimens under biaxial loading (shown in Figure 1), *i.e.* single edge cracked plate (SECP), center cracked plate (CCP) and double edge cracked plate (DECP), are studied through finite element analysis method. Due to the symmetry of the specimens, only a half of the SECP or a quarter of the CCP or DECP structure is modeled in the finite element analyses. A typical three-dimensional (3D) finite element mesh used for all three specimen models is illustrated in Figure 2. Total 1196 elements are included in the mesh and element type is assigned as 20-node quadratic hybrid brick with linear pressure, reduced integration [18]. Element radial sizes of finite element mesh are varied according to a geometric progression. The value for geometry size ratio of height over width, *H/W*, is 3.0. This 3D mesh is utilized to simulate 2D plane strain conditions with an additional boundary condition, the displacement in the model thickness direction $u_z=0$. Finite element analyses for all three specimens (SECP, CCP and DECP) are carried out with two values of biaxial loading ratio, $\lambda=\sigma_x/\sigma_y=0.5$, and 1.0 (see Figure 1). The external loads applied on the remote end of the specimens are normalized by yield stress σ_0, *i.e.* σ/σ_0.

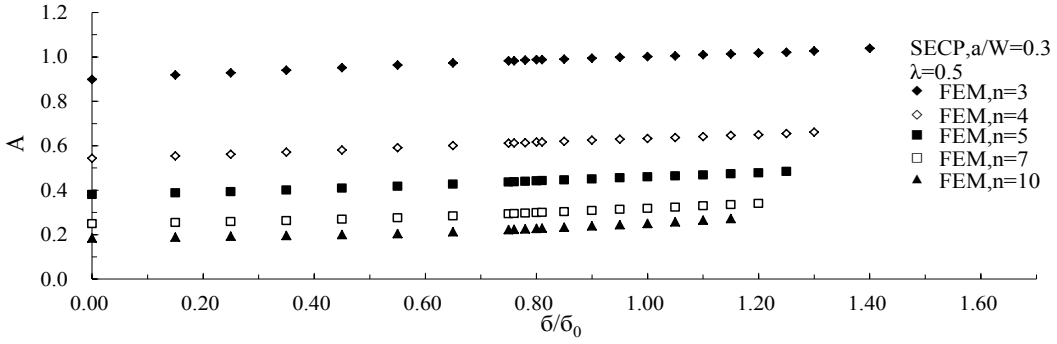

Figure 4. FEA solutions of constraint parameter *A* for SECP, *a/W*=0.3, λ=0.5

The fitting area to calculate the values of parameter *A* from FEA results by a least square fitting method suggested by Nikishkov *et al*. (see [12, 14]) is set as $1.5 \le \bar{r} \le 3$ and $0^0 \le \theta \le 45^0$, and the opening stress, σ_θ, is set as the stress component used for the least square fitting process.

Verifications of the used finite element model (mesh) and succedent fitting process for *A* values determination are carried out through comparison of solutions for two fracture parameters, load-related parameter *J*-integral and constraint parameter *Q* (*J*-*Q* approach). The comparison is based on *J*-integral estimation formulas and solutions of parameter *Q* for CCP specimen under

biaxial loading reported in the literature.

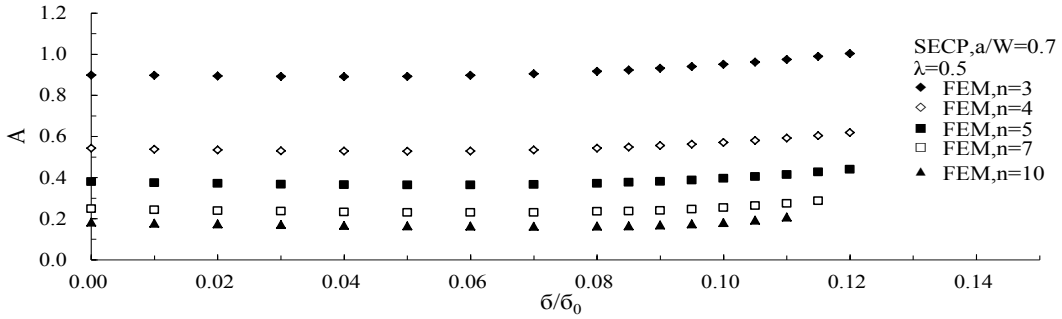

Figure 5. . FEA solutions of constraint parameter A for SECP, a/W=0.7, λ=0.5

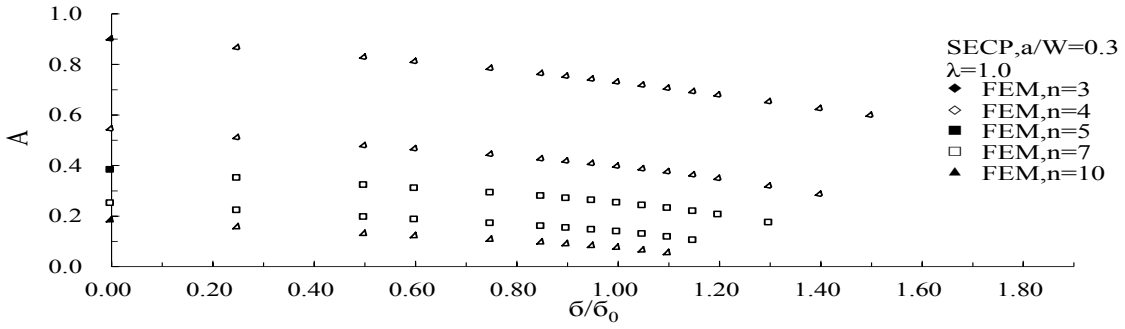

Figure 6. . FEA solutions of constraint parameter A for SECP, a/W=0.3, λ=1.0

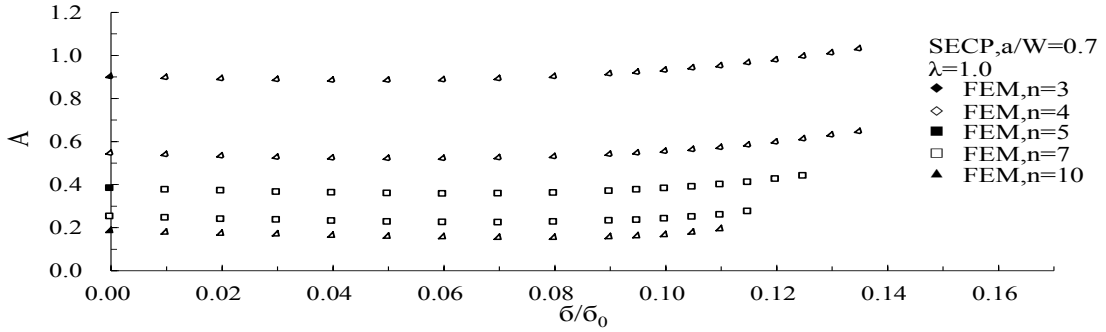

Figure 7. . FEA solutions of constraint parameter A for SECP, a/W=0.7, λ=1.0

For the purpose of comparison, finite element analysis for CCP specimen is carried out with hardening exponent n=10 for biaxial loading ratio λ=0.5 and geometry ratio a/W=0.1, 0.5. The values for J-integral from finite element analysis are compared with those obtained from EPRI estimation formulas of J [19]. Figure 3 shows the comparison results for a/W=0.1 and 0.5. It can be found that the J-integral values from FEA are very close to those from the estimation formulas. Based on the results of finite element analysis, constraint parameter A can also be obtained by using the fitting method proposed by Nikishkov *et al*. [12]. Through relationship between A and Q presented in authors' previous paper [13], the obtained solutions for A are converted to values of Q. Then determined Q values are compared with those reported by O'Dowd *et al.* [19]. It is found that, for both relative crack length a/W=0.1 and 0.5, Q solutions from the preset FEA results are close to those obtained by O'Dowd *et al.* [19]. As a numerical example, data comparison between Q values from FEA as well as A-Q relationship and those presented by O'Dowd *et al* [19] for the CCP under n=10 with a/W=0.5 and λ=0.5 is shown in Table 1.

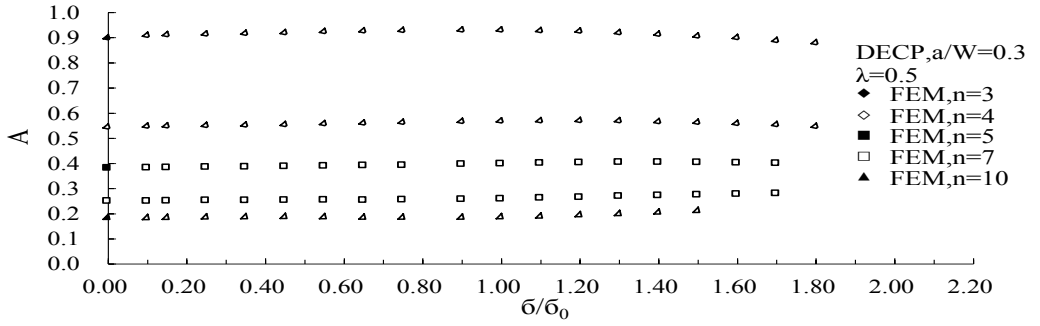

Figure 8. . FEA solutions of constraint parameter *A* for DECP, *a/W*=0.3, λ=0.5

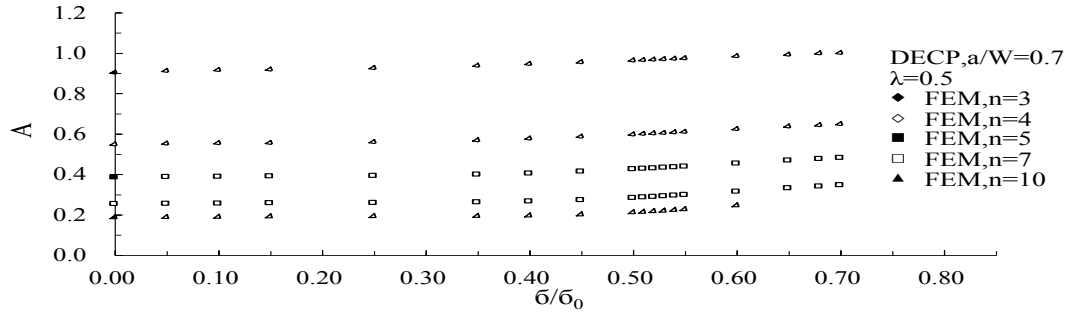

Figure 9. . FEA solutions of constraint parameter *A* for DECP, *a/W*=0.7, λ=0.5

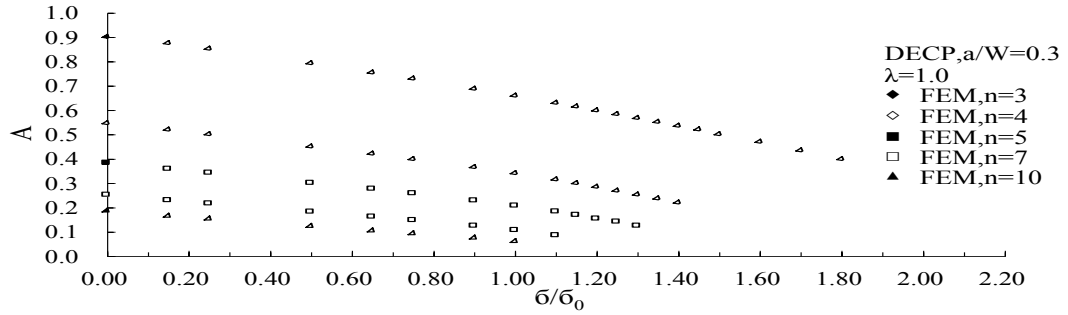

Figure 10. . FEA solutions of constraint parameter *A* for DECP, *a/W*=0.3, λ=1.0

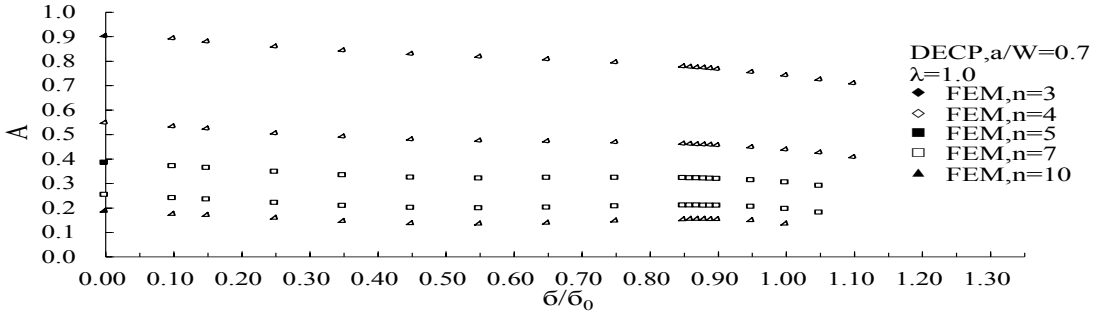

Figure 11. . FEA solutions of constraint parameter *A* for DECP, *a/W*=0.7, λ=1.0

3.3. FEA results

In the present work, a wide range of finite element analyses for three typical specimens (SECP, CCP and DECP) under biaxial loading are completed. Based on the FEA results, numerical solutions of constraint parameter *A* are determined by using the fitting method suggested by Nikishkov *et al*. [12].

The research of Chao and Zhu [20] on 2D plane strain models shows that the size requirement for ductile fracture initiation under J-A_2 dominant conditions is $a\sigma_0/J > 6$ for the shallow cracked cases or $b\sigma_0/J > 11$ for deep cracked cases, where a is the crack length and b is the remaining ligament. In the present finite element analyses (FEA), the highest load levels are those corresponding to the values mentioned above. In addition, Chao and Zhu [20] also argue that, for deep crack cases, a value of $b\sigma_0/J$ around 30 corresponds to fully plastic condition, while for shallow cracks, values of $a\sigma_0/J \leq 50$ already nearly correspond to the fully plastic deformation.

Table 2. FEA results for SECP specimen under λ=0.5

a/W	0.1						0.3				
σ/σ_0	n=3	n=4	n=5	n=7	n=10	σ/σ_0	n=3	n=4	n=5	n=7	n=10
0.250	0.91524	0.55153	0.38552	0.25194	0.18600	0.150	0.91848	0.55422	0.38785	0.25432	0.18828
0.500	0.92583	0.55861	0.39022	0.25514	0.18820	0.250	0.92787	0.56120	0.39339	0.25847	0.19307
0.750	0.93635	0.56870	0.39808	0.25894	0.18998	0.350	0.93984	0.57046	0.40079	0.26298	0.19567
0.900	0.93816	0.57312	0.40230	0.26189	0.19169	0.450	0.95082	0.58010	0.40830	0.26851	0.19989
1.000	0.93815	0.57465	0.40464	0.26473	0.19350	0.550	0.96266	0.59058	0.41728	0.27570	0.20481
1.100	0.93624	0.57543	0.40646	0.26701	0.19586	0.650	0.97216	0.60094	0.42667	0.28420	0.21255
1.200	0.93422	0.57461	0.40738	0.26909	0.19841	0.750	0.98224	0.61135	0.43656	0.29347	0.22260
1.300	0.92749	0.57367	0.40708	0.27057	0.20102	0.760	0.98243	0.61224	0.43751	0.29452	0.22376
1.400	0.92144	0.57114	0.40649	0.27139	0.20346	0.780	0.98498	0.61374	0.43951	0.29626	0.22521
1.450	0.91770	0.56776	0.40569	0.27165	0.20471	0.800	0.98738	0.61595	0.44135	0.29836	0.22766
1.500	0.91686	0.56569	0.40371	0.27184	0.20520	0.810	0.98750	0.61664	0.44223	0.29939	0.22884
1.600	0.90796	0.56079	0.40124	0.27086	0.20712	0.850	0.98972	0.62004	0.44594	0.30331	0.23291
1.700	0.89741	0.55511	0.39682	0.26981	0.20857	0.900	0.99387	0.62480	0.45027	0.30814	0.23877
1.800	0.89022	0.54923	0.39370	0.26909	0.21073	0.950	0.99752	0.62919	0.45497	0.31297	0.24481
1.900	0.88251	0.54524	0.39123	0.26969		1.000	1.00097	0.63260	0.45915	0.31797	0.25032
2.000	0.87144	0.54097	0.39000	0.27253		1.050	1.00410	0.63700	0.46394	0.32345	0.25702
2.100	0.86730	0.53830	0.39109			1.100	1.00960	0.64135	0.46831	0.32895	0.26489
2.200	0.85850	0.53831	0.39465			1.150	1.01256	0.64566	0.47320	0.33449	0.27227
2.300	0.85574	0.53960	0.40008			1.200	1.01744	0.64968	0.47739	0.34043	
2.400	0.85089	0.54220	0.40819			1.250	1.02045	0.65409	0.48381		
2.500	0.84605	0.54595	0.40777			1.300	1.02606	0.66051			
						1.400	1.03790				
a/W	0.5						0.7				
σ/σ_0	n=3	n=4	n=5	n=7	n=10	σ/σ_0	n=3	n=4	n=5	n=7	n=10
0.050	0.90776	0.54631	0.38146	0.24915	0.18447	0.010	0.89720	0.53809	0.37467	0.24350	0.17829
0.100	0.91152	0.54799	0.38246	0.25035	0.18470	0.020	0.89423	0.53474	0.37177	0.23876	0.17434
0.150	0.91955	0.55268	0.38576	0.25173	0.18561	0.030	0.89173	0.53033	0.36724	0.23706	0.17199
0.200	0.93053	0.56034	0.39127	0.25422	0.18691	0.040	0.89061	0.52866	0.36531	0.23293	0.16760
0.250	0.94523	0.57130	0.39853	0.25971	0.18961	0.050	0.89235	0.52783	0.36371	0.23065	0.16503
0.290	0.95976	0.58280	0.40750	0.26493	0.19437	0.060	0.89697	0.52928	0.36403	0.22991	0.16382
0.320	0.97212	0.59245	0.41527	0.27163	0.20003	0.070	0.90474	0.53483	0.36613	0.23019	0.16289
0.350	0.98591	0.60372	0.42555	0.28017	0.20751	0.080	0.91638	0.54304	0.37198	0.23524	0.16446
0.380	1.00133	0.61660	0.43649	0.29048	0.21678	0.085	0.92330	0.54792	0.37719	0.23715	0.16544
0.400	1.01265	0.62591	0.44562	0.29848	0.22604	0.090	0.93138	0.55575	0.38172	0.24035	0.16915
0.420	1.02430	0.63620	0.45449	0.30771	0.23951	0.095	0.94057	0.56281	0.38760	0.24638	0.17440
0.440	1.03745	0.64737	0.46606	0.32072		0.100	0.95116	0.57116	0.39635	0.25400	0.18140
0.450	1.04403	0.65423	0.47252	0.32716		0.105	0.96122	0.58068	0.40441	0.26322	0.19312
0.460	1.05195	0.66160	0.47764	0.33425		0.110	0.97422	0.59175	0.41412	0.27427	0.20781
0.470	1.05901	0.66752	0.48483	0.34231		0.115	0.98931	0.60421	0.42753	0.28745	
0.480	1.06637	0.67394	0.49279			0.120	1.00308	0.61856	0.44058		
0.490	1.07404	0.68244	0.50135								
0.500	1.08353	0.69169	0.50789								
0.510	1.09180	0.69890	0.51741								

According to the above criteria, the external load ratios (σ/σ_0) used here to determine numerical solutions for parameter A from FEA for the three specimens cover the deformation range from small-scale yielding (SSY) to large-scale yielding (LSY). For example, for SECP with a/W=0.7

(deep crack), the values of $b\sigma_0/J$ at maximum loads are within 54-64 and 38-62 for λ=0.5 and λ=1.0, respectively. For the SECP with a/W=0.3 (shallow crack), the values of $a\sigma_0/J$ at maximum loads are around 4 and within 4-8 for λ=0.5 and 1.0, respectively.

Table 3. FEA results for SECP specimen under λ=1.0

a/W	0.1					0.3					
σ/σ_0	n=3	n=4	n=5	n=7	n=10	σ/σ_0	n=3	n=4	n=5	n=7	n=10
0.100	0.87886	0.52283	0.36139	0.23252	0.16637	0.250	0.86428	0.50841	0.34846	0.22094	0.15636
0.150	0.87193	0.51733	0.35721	0.22864	0.16388	0.500	0.82627	0.47641	0.32046	0.19371	0.12998
0.200	0.86218	0.50929	0.35109	0.22374	0.16031	0.600	0.80984	0.46398	0.30834	0.18463	0.12093
0.250	0.85161	0.49880	0.34068	0.21418	0.15242	0.750	0.78229	0.44228	0.29016	0.16935	0.10651
0.350	0.82909	0.47963	0.32432	0.20187	0.13979	0.850	0.76195	0.42490	0.27680	0.15829	0.09611
0.500	0.79407	0.45111	0.30062	0.18177	0.12125	0.900	0.75108	0.41559	0.26863	0.15116	0.08927
0.600	0.77063	0.43254	0.28539	0.16720	0.10688	0.950	0.73967	0.40585	0.25995	0.14343	0.08173
0.750	0.73304	0.40275	0.25903	0.14895	0.09111	1.000	0.72792	0.39549	0.25051	0.13646	0.07483
0.850	0.70541	0.37904	0.24150	0.13336	0.08086	1.050	0.71585	0.38461	0.24033	0.12657	0.06438
0.900	0.69224	0.36832	0.23012	0.12645	0.07315	1.100	0.70320	0.37306	0.22917	0.11525	0.05330
0.950	0.67725	0.35462	0.22064	0.11689	0.06747	1.150	0.69053	0.36099	0.21703	0.10185	
1.000	0.66360	0.34334	0.20847	0.10631	0.05870	1.200	0.67721	0.34673	0.20361		
1.050	0.64850	0.32933	0.19825	0.09724		1.300	0.65063	0.31715	0.17182		
1.100	0.63293	0.31458	0.18450	0.08444		1.400	0.62324	0.28424			
1.150	0.61916	0.30239	0.16985	0.06920		1.500	0.59711				
1.200	0.60332	0.28683	0.15454								
1.250	0.58730	0.27077	0.13766								
1.300	0.57114	0.25416									
1.400	0.53570	0.21928									
1.500	0.50197	0.18206									
1.600	0.46465										
a/W	0.5					0.7					
σ/σ_0	n=3	n=4	n=5	n=7	n=10	σ/σ_0	n=3	n=4	n=5	n=7	n=10
0.050	0.89539	0.53593	0.37253	0.24163	0.17648	0.010	0.89473	0.53599	0.37287	0.24197	0.17685
0.100	0.88733	0.52721	0.36488	0.23443	0.17060	0.020	0.88944	0.53067	0.36825	0.23572	0.17150
0.150	0.88333	0.52205	0.35942	0.22926	0.16424	0.030	0.88477	0.52430	0.36202	0.23258	0.16777
0.200	0.88231	0.51950	0.35476	0.22375	0.15827	0.040	0.88147	0.52076	0.35844	0.22695	0.16194
0.250	0.88454	0.52020	0.35377	0.21954	0.15259	0.050	0.88117	0.51803	0.35517	0.22317	0.15793
0.300	0.89055	0.52282	0.35431	0.21939	0.14867	0.060	0.88350	0.51901	0.35378	0.22090	0.15523
0.350	0.89971	0.52851	0.35893	0.22101	0.14978	0.070	0.88898	0.52136	0.35405	0.21952	0.15264
0.380	0.90671	0.53415	0.36306	0.22482	0.15137	0.080	0.89831	0.52735	0.35806	0.22293	0.15239
0.400	0.91272	0.54037	0.36806	0.22831	0.15571	0.090	0.91089	0.53800	0.36607	0.22799	0.15500
0.420	0.91989	0.54386	0.37220	0.23301	0.16182	0.095	0.91888	0.54394	0.37266	0.23134	0.15918
0.440	0.92651	0.55243	0.37959	0.23953		0.100	0.92830	0.55118	0.37852	0.23782	0.16529
0.450	0.93211	0.55492	0.38148	0.24372		0.105	0.93908	0.55960	0.38576	0.24612	0.17609
0.460	0.93605	0.56045	0.38644	0.24899		0.110	0.94889	0.56956	0.39663	0.25629	0.19288
0.470	0.94035	0.56369	0.39208	0.25838		0.115	0.96294	0.58105	0.40683	0.27180	
0.480	0.94748	0.57034	0.39848	0.26546		0.120	0.97548	0.59448	0.42219		
0.490	0.95240	0.57420	0.40189			0.125	0.99333	0.60988	0.43656		
0.500	0.95775	0.57854	0.40964			0.130	1.00926	0.62795			
						0.135	1.02745	0.64357			

The obtained numerical solutions of A for biaxial loading ratios λ=0.5 and 1.0 and relative crack lengths a/W=0.1, 0.3, 0.5, 0.7 are listed in Tables 2-3, 4-5 and 6-7 for the SECP, CCP and DECP specimens, respectively. Typical numerical solutions for parameter A for a/W=0.3, 0.7 are presented in Figures 4-5 (λ=0.5) and Figures 6-7 (λ=1.0) for the SECP specimen as well as Figures 8-9 (λ=0.5) and Figures 10-11 (λ=1.0) for DECP specimen.

3.4. Discussions on FEA results and constraint effect

Examining the solutions of A obtained from FEA results for the SECP, CCP and DECP specimens under biaxial loading, it is found that, the curve shape similarity observed by Nikishkov *et al*. [12]

not only appear in the cases of uniaxial loading and external loading ratio σ/σ_L (σ_L, limit load of specimen) but also in the cases of biaxial loading and loading normalization, σ/σ_0, see Figure 4-7 for example.

Table 4. FEA results for CCP specimen under λ=0.5

a/W	0.1					0.3					
σ/σ_0	n=3	n=4	n=5	n=7	n=10	σ/σ_0	n=3	n=4	n=5	n=7	n=10
0.500	1.03293	0.64948	0.46887	0.32352	0.25390	0.250	0.98134	0.60644	0.43267	0.29277	0.22469
0.700	1.07906	0.68806	0.50129	0.34936	0.27751	0.500	1.05796	0.66917	0.48450	0.33539	0.26464
0.900	1.11904	0.71974	0.52744	0.36991	0.29557	0.750	1.12909	0.73037	0.53563	0.37581	0.30014
1.000	1.13527	0.73370	0.53894	0.37836	0.30237	0.900	1.16595	0.76170	0.56335	0.39798	0.31924
1.200	1.15529	0.75361	0.55608	0.39210	0.31170	1.000	1.18836	0.77990	0.58012	0.41203	0.33108
1.500	1.16895	0.76686	0.56621	0.39975	0.31748	1.100	1.20084	0.79773	0.59419	0.42491	0.34168
1.800	1.16139	0.75712	0.56246	0.39239	0.31165	1.200	1.21286	0.80829	0.60522	0.43449	0.35199
2.000	1.13246	0.74272	0.54581	0.38135	0.30277	1.300	1.22667	0.81872	0.61313	0.44234	0.36159
2.100	1.11699	0.73432	0.53681	0.37501	0.29808	1.400	1.22663	0.82549	0.62225	0.44924	0.37116
2.200	1.09825	0.71748	0.52619	0.36777	0.29321	1.450	1.22873	0.82394	0.62381	0.45351	0.37509
2.300	1.08745	0.70466	0.51373	0.35901	0.28309	1.500	1.22943	0.82773	0.62419	0.45429	0.37893
2.400	1.06267	0.68221	0.49896	0.34764	0.27633	1.550	1.22865	0.83059	0.62359	0.45407	0.37497
2.450	1.04035	0.67860	0.49075	0.34698		1.600	1.22625	0.82498	0.62134	0.45371	0.38314
2.500	1.03254	0.66464	0.48187	0.33447		1.650	1.22214	0.82517	0.62323	0.45807	0.39281
2.600	1.01409	0.64474	0.46421			1.700	1.21616	0.82321	0.62016	0.44720	0.39826
2.700	0.97462	0.62172				1.750	1.20833	0.81313	0.61771	0.46113	0.40449
						1.800	1.21234	0.81012	0.59436	0.45637	0.41530
a/W	0.5					0.7					
σ/σ_0	n=3	n=4	n=5	n=7	n=10	σ/σ_0	n=3	n=4	n=5	n=7	n=10
0.100	0.94657	0.57838	0.40893	0.27252	0.20548	0.050	0.94003	0.57410	0.40565	0.27004	0.20336
0.150	0.96767	0.59526	0.42335	0.28498	0.21745	0.100	0.97886	0.60394	0.43006	0.28991	0.22255
0.250	1.01066	0.63010	0.45229	0.30762	0.23933	0.150	1.01980	0.63643	0.45724	0.31137	0.24264
0.350	1.05770	0.66699	0.48260	0.33321	0.26171	0.250	1.11106	0.71061	0.51835	0.36082	0.28602
0.450	1.10582	0.70680	0.51559	0.35931	0.28520	0.350	1.19965	0.79269	0.59128	0.42146	0.34039
0.550	1.15103	0.74722	0.55041	0.38757	0.31005	0.400	1.24116	0.83100	0.62637	0.45712	0.37568
0.650	1.19119	0.78594	0.58557	0.41778	0.33689	0.450	1.28136	0.86873	0.66098	0.49110	0.41489
0.750	1.23122	0.82265	0.61827	0.44734	0.36587	0.460	1.28455	0.87745	0.66976	0.49773	0.42362
0.850	1.25716	0.85287	0.64612	0.47604	0.39809	0.470	1.29303	0.88141	0.67470	0.50429	0.43117
0.900	1.27272	0.86516	0.65953	0.48757	0.41343	0.480	1.30103	0.89001	0.68317	0.51077	0.43860
0.950	1.28575	0.87540	0.66842	0.49850	0.42643	0.490	1.30828	0.89773	0.68769	0.51719	0.44600
1.000	1.29677	0.88340	0.67961	0.50783	0.44074	0.500	1.31593	0.90135	0.69194	0.52353	0.45333
1.050	1.30484	0.89560	0.68895	0.51551	0.45175	0.510	1.31719	0.90949	0.70028	0.52982	0.45925
1.100	1.31050	0.89834	0.69041	0.51172	0.46758	0.550	1.34438	0.93362	0.72286	0.55120	0.48569
1.150	1.31258	0.90536	0.69556	0.53219	0.48279	0.580	1.36147	0.94855	0.73659	0.56478	0.50540
1.200	1.32147	0.90225	0.70169	0.54275		0.600	1.37217	0.95601	0.74623	0.57506	0.50833
						0.620	1.37384	0.96127	0.75475	0.58194	
						0.640	1.38217	0.97261	0.75650	0.57980	
						0.660	1.39806	0.98232	0.76824	0.59876	

By analyzing the numerical solutions of parameter *A* for three cracked specimens (see Tables 2-7, Figures 4-11), several dependencies have been found. First, it is found that, for any specific specimen geometry (*a/W*) of some cracked body (SECP, CCP or DECP), generally the maximum external loading ratios (σ/σ_0), which are determined by the criteria suggested by Chao and Zhu [20], increase with decreasing of hardening coefficient *n*.

In addition, the effects of crack geometry, hardening exponent (*n*) and biaxial loading ratio (λ) on parameter *A* (constraint level) are also observed. For uniaxial loading cases (λ=0.0) investigated in a previous work of authors [13], it has been shown that *A* values gradually increase with external loading. The results in the current work show that, with smaller biaxial loading ratio (λ=0.5), the parameter *A* follows a general decreasing trend with increasing external loading for shallow crack geometries (*e.g.* *a/W*=0.1 for SECP and CCP, *a/W*=0.1, 0.3 for DECP). Decreased values for parameter *A* indicate the increasing constraint level. For the cases with bigger biaxial loading ratio (λ=1.0), a decreasing trend of parameter *A* appears not only for those shallowest cracks but also for cracks with larger depth and even fairly deep cracks (*e.g.* *a/W*=0.3 for SECP, 0.3, 0.5 for CCP, 0.5,

0.7 for DECP). On the other hand, generally, a deep crack is not sensitive to the variation of the λ value, except in the case of DECP. For example, for SECP, with λ value increasing from 0.5 to 1.0, the trend of *A* curves for *a/W*=0.3 (shallow crack) changes from increasing to decreasing (see Figure 4 and Figure 6), while that for *a/W*=0.7 (deep crack) almost keeps no change (see Figure 5 and Figure 7).

Table 5. FEA results for CCP specimen under λ=1.0

a/W	0.1					0.3					
σ/σ_0	n=3	n=4	n=5	n=7	n=10	σ/σ_0	n=3	n=4	n=5	n=7	n=10
0.500	0.89279	0.53665	0.37503	0.24536	0.18130	0.500	0.91158	0.55164	0.38764	0.25670	0.19110
0.750	0.87398	0.52211	0.36309	0.23732	0.17650	0.750	0.90119	0.54687	0.38453	0.25403	0.19075
0.900	0.85974	0.51059	0.35378	0.23024	0.17073	0.900	0.89260	0.53934	0.37876	0.25124	0.18810
1.000	0.84974	0.50165	0.34734	0.22645	0.16867	1.000	0.88388	0.53271	0.37344	0.24757	0.18544
1.200	0.82588	0.48414	0.33109	0.21159	0.15611	1.200	0.86152	0.51500	0.35847	0.23465	0.17641
1.400	0.79886	0.46125	0.31191	0.19430	0.13836	1.300	0.84798	0.50381	0.34851	0.22595	0.16850
1.500	0.78414	0.44974	0.30024	0.18333	0.12928	1.400	0.83435	0.49110	0.33705	0.21513	0.15796
1.700	0.75316	0.42327	0.27812	0.16285	0.10628	1.500	0.81667	0.47705	0.32418	0.20261	0.14473
1.900	0.71719	0.39497	0.25383	0.14332	0.08701	1.600	0.79928	0.46145	0.30956	0.18870	0.12943
2.100	0.67310	0.36392	0.22880	0.12295	0.07116	1.700	0.77977	0.44471	0.29429	0.17382	
2.250	0.63545	0.33786	0.20833	0.10738	0.06048	1.800	0.75775	0.42657	0.27752	0.15722	
2.300	0.62310	0.32864	0.20185	0.10326	0.05819	1.900	0.73375	0.40695	0.25987		
2.400	0.59669	0.30860	0.18622	0.09313		2.000	0.70638	0.38399	0.24039		
2.500	0.56789	0.28749	0.17001	0.08243		2.100	0.67493	0.36126			
						2.200	0.64552				
a/W	0.5					0.7					
σ/σ_0	n=3	n=4	n=5	n=7	n=10	σ/σ_0	n=3	n=4	n=5	n=7	n=10
0.150	0.92731	0.56293	0.39591	0.26173	0.19560	0.020	0.91750	0.55434	0.38870	0.25562	0.19002
0.250	0.94008	0.57296	0.40354	0.26788	0.20128	0.050	0.92701	0.56345	0.39655	0.26195	0.19615
0.350	0.95237	0.58435	0.41347	0.27599	0.20909	0.080	0.94209	0.57458	0.40569	0.26987	0.20313
0.450	0.96587	0.59477	0.42278	0.28397	0.21564	0.100	0.95152	0.58162	0.41110	0.27409	0.20682
0.550	0.97609	0.60460	0.43141	0.29068	0.22245	0.120	0.96133	0.58941	0.41727	0.27917	0.21165
0.650	0.98365	0.61287	0.43900	0.29739	0.22770	0.150	0.97688	0.60129	0.42727	0.28709	0.21988
0.750	0.98812	0.61906	0.44531	0.30295	0.23276	0.180	0.99285	0.61442	0.43815	0.29533	0.22757
0.800	0.98985	0.62150	0.44737	0.30518	0.23472	0.200	1.00380	0.62312	0.44522	0.30168	0.23244
0.850	0.99025	0.62319	0.44922	0.30709	0.23698	0.220	1.01481	0.63209	0.45263	0.30755	0.23784
0.900	0.98949	0.62396	0.45041	0.30859	0.23838	0.250	1.03259	0.64629	0.46423	0.31652	0.24565
0.920	0.98942	0.62418	0.45089	0.30906	0.23877	0.270	1.04286	0.65555	0.47222	0.32281	0.25105
0.930	0.98763	0.62363	0.45059	0.30919	0.23914	0.280	1.04963	0.66082	0.47647	0.32620	0.25416
0.940	0.98931	0.62443	0.45123	0.30928	0.23916	0.290	1.05454	0.66546	0.48050	0.32960	0.25676
0.950	0.98723	0.62383	0.45089	0.30952	0.23905	0.300	1.06127	0.67082	0.48454	0.33284	0.25996
1.100	0.98060	0.61937	0.44883	0.30853	0.24025	0.350	1.08686	0.69490	0.50622	0.35042	0.27532
1.200	0.96946	0.61318	0.44308	0.30531	0.23882	0.400	1.11401	0.72094	0.52818	0.36947	0.29217
1.300	0.95729	0.60259	0.43585	0.29999	0.23579	0.450	1.13808	0.74526	0.55133	0.38980	0.31163
1.400	0.93431	0.58766	0.42178	0.28988	0.23386	0.500	1.15667	0.76722	0.57125	0.41117	0.33520
1.450	0.92294	0.57975	0.41574	0.28653	0.22748	0.540	1.17207	0.78207	0.58696	0.42791	0.35614
1.500	0.90961	0.56595	0.40578	0.28015	0.22326	0.570	1.18153	0.79379	0.59996	0.44119	0.37169
1.550	0.89519	0.55579	0.39827	0.27265		0.600	1.18951	0.80087	0.60980	0.45302	0.38818
1.600	0.88749	0.54476	0.39138	0.25768		0.620	1.19964	0.80759	0.61426	0.45920	0.40008
1.650	0.87294					0.650	1.20579	0.81690	0.62560	0.47051	0.41449
						0.700	1.21008	0.82964	0.63574	0.48499	
						0.750	1.21750	0.83818	0.64569	0.49148	

As for the effect of hardening exponent (*n*), with the increase of the biaxial loading ratio λ, decreasing trend of *A* curves appears earlier (under smaller external loading) or is more significant for cases with smaller *n* values than that for cases with bigger *n* values. For example, for DECP, the trend of the *A* curves for *a/W*=0.3 changes from increasing to decreasing as λ increases from 0.5 to 1.0 (see Figures 8 and 10 as well as Tables 6 and 7), but the curve for *n*=3 decreases more quickly than that for *n*=10 (see Figures 10 and Table 7).

Table 6. FEA results for DECP specimens under λ=0.5

a/W	0.1					0.3					
σ/σ_0	n=3	n=4	n=5	n=7	n=10	σ/σ_0	n=3	n=4	n=5	n=7	n=10
0.150	0.90737	0.54685	0.38224	0.24968	0.18406	0.100	0.90818	0.54679	0.38187	0.24907	0.18328
0.250	0.91158	0.54958	0.38434	0.24954	0.18362	0.150	0.91077	0.54809	0.38272	0.24964	0.18426
0.450	0.91661	0.55176	0.38502	0.25097	0.18526	0.250	0.91332	0.54994	0.38431	0.25151	0.18576
0.650	0.92183	0.55453	0.38650	0.25036	0.18286	0.350	0.91581	0.55120	0.38497	0.25171	0.18676
0.800	0.92350	0.55846	0.38904	0.25207	0.18261	0.450	0.91898	0.55328	0.38644	0.25232	0.18717
0.900	0.92404	0.55951	0.39042	0.25231	0.18207	0.550	0.92276	0.55630	0.38841	0.25332	0.18683
1.000	0.92281	0.55986	0.39114	0.25285	0.18237	0.650	0.92587	0.55910	0.38993	0.25278	0.18533
1.100	0.91969	0.55978	0.39137	0.25287	0.18183	0.750	0.92773	0.56158	0.39163	0.25428	0.18495
1.200	0.91664	0.55808	0.39106	0.25291	0.18259	0.900	0.92889	0.56526	0.39526	0.25590	0.18511
1.300	0.91133	0.55569	0.39007	0.25310	0.18236	1.000	0.92894	0.56735	0.39783	0.25800	0.18644
1.400	0.90467	0.55211	0.38811	0.25245	0.18210	1.100	0.92694	0.56796	0.40010	0.26100	0.18924
1.500	0.89569	0.54713	0.38449	0.25125	0.18167	1.200	0.92502	0.56908	0.40195	0.26447	0.19433
1.600	0.88816	0.54103	0.38036	0.24910	0.18155	1.300	0.91854	0.56778	0.40363	0.26817	0.19935
1.700	0.87634	0.53350	0.37532	0.24657	0.18074	1.400	0.91268	0.56469	0.40386	0.27134	0.20534
1.800	0.86651	0.52693	0.37039	0.24319	0.17890	1.500	0.90479	0.56190	0.40302	0.27421	0.21158
1.900	0.85595	0.51778	0.36420	0.23931	0.17728	1.600	0.89916	0.55791	0.40105	0.27645	
2.000	0.84454	0.51006	0.35776	0.23568	0.17673	1.700	0.88761	0.55272	0.39962	0.27887	
2.100	0.83298	0.50128	0.35187	0.23310		1.800	0.87853	0.54614	0.39536		
2.200	0.82121	0.49443	0.34718	0.23264		1.900	0.86295	0.53798	0.39186		
2.300	0.81263	0.48848	0.34429			2.000	0.85140	0.53106			
2.400	0.80199	0.48358	0.34293			2.100	0.84044	0.52425			
2.500	0.79129	0.47979									
2.600	0.78375	0.47724									
a/W	0.5					0.7					
σ/σ_0	n=3	n=4	n=5	n=7	n=10	σ/σ_0	n=3	n=4	n=5	n=7	n=10
0.150	0.91213	0.54967	0.38424	0.25152	0.18575	0.050	0.90756	0.54713	0.38246	0.24982	0.18460
0.250	0.91537	0.55176	0.38630	0.25296	0.18823	0.100	0.91131	0.54896	0.38365	0.25101	0.18524
0.350	0.92087	0.55515	0.38849	0.25473	0.18914	0.150	0.91350	0.55048	0.38552	0.25269	0.18811
0.450	0.92621	0.55914	0.39048	0.25557	0.18958	0.250	0.92076	0.55507	0.38757	0.25433	0.18911
0.550	0.93263	0.56450	0.39434	0.25664	0.18947	0.350	0.93280	0.56356	0.39414	0.25718	0.18980
0.650	0.93932	0.57156	0.40038	0.26070	0.19044	0.400	0.94105	0.57144	0.40002	0.26099	0.19214
0.750	0.94625	0.58013	0.40872	0.26762	0.19572	0.450	0.95005	0.58115	0.40893	0.26817	0.19751
0.800	0.94794	0.58492	0.41389	0.27244	0.20114	0.500	0.95887	0.59267	0.42054	0.27911	0.20770
0.850	0.95095	0.58934	0.41932	0.27876	0.20698	0.510	0.96088	0.59506	0.42304	0.28158	0.21009
0.900	0.95329	0.59420	0.42516	0.28572	0.21520	0.520	0.96283	0.59756	0.42566	0.28417	0.21276
0.920	0.95461	0.59628	0.42726	0.28844	0.21833	0.530	0.96481	0.60010	0.42834	0.28693	0.21570
0.940	0.95575	0.59727	0.42972	0.29143	0.22230	0.540	0.96671	0.60269	0.43112	0.29050	0.21966
0.950	0.95501	0.59886	0.43069	0.29296	0.22428	0.550	0.96864	0.60531	0.43396	0.29343	0.22287
1.050	0.95901	0.60715	0.44230	0.30817		0.600	0.97945	0.61862	0.44863	0.30978	0.24169
1.100	0.95830	0.61053	0.44644	0.31548		0.650	0.98736	0.63150	0.46353	0.32651	
1.150	0.95977	0.61315	0.45130	0.32235		0.680	0.99393	0.63871	0.47106	0.33586	
1.200	0.95740	0.61509	0.45563	0.32872		0.700	0.99604	0.64316	0.47639	0.34215	
1.250	0.95773	0.61597	0.45938	0.33408							

Based on the observations represented above, it can be concluded that, (1) in general, constraint level in crack-tip fields increases with the increase of biaxial loading ratio, λ; (2) the constraint level for materials with smaller values of hardening exponent *n* increases more with increased biaxial loading ratio; (3) the constraint level for shallow cracks rises more with increase of biaxial loading ratio; (4) comparing SECP and CCP specimens, an increase of biaxial loading ratio raises the constraint level of DECP more.

4. Conclusions

In this paper, numerical (finite element) solutions for the constraint parameter *A* for three plane strain mode I specimens, SECP, CCP and DECP, under biaxial load have been obtained based on the extensive finite element analyses of specimen crack-tip fields.

Table 7. FEA results for DECP specimens under λ=1.0

a/W	0.1						0.3				
σ/σ_0	n=3	n=4	n=5	n=7	n=10	σ/σ_0	n=3	n=4	n=5	n=7	n=10
0.150	0.86925	0.51533	0.35529	0.22685	0.16266	0.150	0.87254	0.51647	0.35567	0.22672	0.16228
0.250	0.84806	0.49772	0.34026	0.21168	0.14827	0.250	0.84930	0.49767	0.33986	0.21364	0.15104
0.500	0.78679	0.44669	0.29733	0.17643	0.11728	0.500	0.78991	0.44755	0.29760	0.17940	0.12105
0.650	0.74962	0.41600	0.27248	0.15509	0.09888	0.650	0.75172	0.41771	0.27370	0.15879	0.10214
0.750	0.72289	0.39416	0.25184	0.14370	0.08746	0.750	0.72614	0.39540	0.25541	0.14475	0.09047
0.900	0.68110	0.35892	0.22231	0.12096	0.06931	0.900	0.68443	0.36244	0.22572	0.12207	0.07298
1.000	0.65233	0.33357	0.20057	0.10054	0.05484	1.000	0.65589	0.33742	0.20404	0.10436	0.05877
1.100	0.62156	0.30469	0.17667	0.07855		1.100	0.62717	0.31193	0.18046	0.08248	
1.150	0.60835	0.29324	0.16211			1.150	0.61160	0.29698	0.16595		
1.200	0.59283	0.27797	0.14712			1.200	0.59593	0.28166	0.15098		
1.250	0.57732	0.26237	0.13066			1.250	0.58020	0.26597	0.13868		
1.300	0.56184	0.24644				1.300	0.56443	0.24989	0.12144		
1.350	0.54324	0.23021				1.350	0.54865	0.23344			
1.400	0.52774	0.21371				1.400	0.53291	0.21662			
1.450	0.51192	0.19698				1.450	0.51725				
1.500	0.49678					1.500	0.49766				
1.800	0.40071					1.600	0.46654				
1.900	0.36851					1.700	0.43085				
						1.800	0.39539				
a/W	0.5						0.7				
σ/σ_0	n=3	n=4	n=5	n=7	n=10	σ/σ_0	n=3	n=4	n=5	n=7	n=10
0.150	0.87424	0.51821	0.35734	0.22834	0.16451	0.100	0.88853	0.52789	0.36562	0.23577	0.17097
0.250	0.85134	0.49955	0.34149	0.21579	0.15266	0.150	0.87517	0.51917	0.35853	0.23019	0.16620
0.350	0.82888	0.48056	0.32587	0.20241	0.14183	0.250	0.85440	0.49999	0.34298	0.21630	0.15487
0.500	0.79558	0.45179	0.30169	0.18284	0.12336	0.350	0.83843	0.48690	0.32904	0.20342	0.14223
0.650	0.76040	0.42457	0.27963	0.16356	0.10690	0.450	0.82472	0.47563	0.31904	0.19605	0.13322
0.750	0.73700	0.40661	0.26290	0.15092	0.09652	0.550	0.81355	0.47025	0.31567	0.19398	0.13129
0.850	0.71251	0.38709	0.24703	0.13889	0.08753	0.650	0.80264	0.46755	0.31802	0.19668	0.13503
0.950	0.68765	0.36495	0.23096	0.12676	0.07590	0.750	0.79021	0.46407	0.31850	0.20183	0.14366
1.000	0.67356	0.35483	0.21976	0.12006	0.07036	0.850	0.77393	0.45752	0.31708	0.20500	0.14922
1.050	0.65937	0.34459	0.21074	0.10979		0.860	0.77172	0.45652	0.31663	0.20504	0.15020
1.100	0.64599	0.33115	0.20129	0.10092		0.870	0.76927	0.45543	0.31606	0.20495	0.15023
1.150	0.63102	0.32000	0.18807	0.09070		0.880	0.76820	0.45447	0.31541	0.20483	0.15019
1.200	0.61733	0.30549	0.17686	0.07515		0.890	0.76556	0.45323	0.31467	0.20457	0.15003
1.300	0.58549	0.27751	0.14798			0.900	0.76281	0.45187	0.31387	0.20437	0.15008
1.400	0.55166	0.24273				0.950	0.75103	0.44386	0.30871	0.19984	0.14562
1.500	0.51534	0.20277				1.000	0.73702	0.43410	0.29979	0.19153	0.13142
1.600	0.47414					1.050	0.72000	0.42111	0.28561	0.17653	
1.700	0.43161					1.100	0.70436	0.40281			

Through analyzing numerical solutions of constraint parameter *A*, several dependencies (mainly on the constraint effect) for 2D cracked models under biaxial loading are founded. They are:
(1) generally, the maximum external loading ratio (σ/σ_0) for which a valid solution can be obtained increases with decreasing hardening coefficient *n*;
(2) in general, the constraint level in crack-tip fields increases with an increase of biaxial loading ratio, λ;
(3) the constraint level for materials with smaller values of hardening exponent *n* rises more with increased biaxial loading ratio;
(4) the constraint level for shallow cracks increases more than for deep cracks with an increase of biaxial loading ratio;
(5) compared with SECP and CCP specimens, a higher biaxial loading ratio increases the constraint level of DECP more.
All numerical solutions for constraint parameter *A* under biaxial loading obtained in this work can be utilized to predict corresponding values for other two commonly-used constraint parameters A_2 and *Q* by the relationships between *A* and A_2, *Q* presented in an previous paper of authors [13].

Acknowledgements

The authors gratefully acknowledge the financial supports from the Natural Sciences and Engineering Research Council (NSERC) of Canada and Ontario Centres of Excellence (OCE). Thanks also go to Hibbit, Karlsson and Sorensen, Inc. for making ABAQUS available under an academic licence to Carleton University.

References

[1] J.W. Hutchinson, Singular behaviour at the end of a tensile crack in a hardening material. *Journal of the Mechanics and Physics of Solids*, Vol. 16 (1968) 13–31.

[2] J. R. Rice, G.F. Rosengren, Plane strain deformation near a crack tip in a power law hardening material. *Journal of the Mechanics and Physics of Solids*, Vol. 16 (1968) 1–12.

[3] J.R. Rice, A path independent integral and the approximate analysis of strain concentration by notches and cracks. *Journal of Applied Mechanics*, Vol. 35 (1968) 379–386.

[4] C. Betegon, J.W. Hancock, Two parameter characterization of elastic-plastic crack-tip fields. *Journal of Applied Mechanics*, Vol. 58 (1991) 104–110.

[5] A.M. Al-Ani, J.W. Hancock, *J*-dominance of short cracks in tension and bending. *Journal of the Mechanics and Physics of Solids*, Vol. 39 (1991) 23–43.

[6] Z.Z. Du, J.W. Hancock, The effect of non-singular stress on crack-tip constraint. *Journal of the Mechanics and Physics of Solids*, Vol. 39 (1991) 555–567.

[7] N.P. O'Dowd, C.F. Shih, Family of crack-tip fields characterized by a triaxiality parameter – I. Structure of fields. *Journal of the Mechanics and Physics of Solids*, Vol. 39 (1991) 989–1015.

[8] N.P. O'Dowd, C.F. Shih, Family of crack-tip fields characterized by a triaxiality parameter – II. Fracture applications. *Journal of the Mechanics and Physics of Solids*, Vol. 40 (1992) 939–963.

[9] S. Yang, Higher order asymptotic crack tip fields in a power-law hardening material, Ph.D. Dissertation, University of South Carolina, USA, 1993.

[10] S. Yang, Y.J. Chao, M.A. Sutton, Higher-order asymptotic fields in a power-law hardening material. *Engineering Fracture Mechanics*, Vol. 45 (1993) 1–20.

[11] G.P. Nikishkov, An algorithm and a computer program for the three-term asymptotic expansion of elastic-plastic crack tip stress and displacement fields. *Engineering Fracture Mechanics*, Vol. 50 (1995) 65–83.

[12] G.P. Nikishkov, A. Bruckner-Foit, D. Munz, Calculation of the second fracture parameter for finite cracked bodies using a three-term elastic-plastic asymptotic expansion. *Engineering Fracture Mechanics*, Vol. 52 (1995) 685–701.

[13] P. Ding, X. Wang, Solutions of the second elastic-plastic fracture mechanics parameter in test specimens. *Engineering Fracture Mechanics*, Vol. 77 (2010) 3462-3480.

[14] P. Ding, X. Wang, An estimation method for the determination of the second elastic-plastic fracture mechanics parameters. *Engineering Fracture Mechanics*, Vol. 79 (2012) 295-311.

[15] O. Pop, M. Méité, F. Dubois, J. Absi, Identification algorithm for fracture parameters by combining DIC and FEM approaches. *International Journal of Fracture*, Vol. 170 (2011) 101–114.

[16] M. Méité, O. Pop, F. Dubois, J. Absi, Characterization of mixed-mode fracture based on a complementary analysis by means of full-field optical and finite element approaches. *International Journal of Fracture*, Vol. 180 (2013) 41–52.

[17] B. Moran, C.F. Shih, A general treatment of crack tip contour integrals. *International Journal of Fracture*, Vol. 35 (1987) 295-310.

[18] ABAQUS Manual, Version 6.6, Hibbitt, Karlsson & Sorensen, Inc., Pawtucket, RI, 2006.

[19] N.P. O'Dowd, O. Kolednik, V.P. Naumenko, Elastic-plastic analysis of biaxially loaded center -cracked plates. *International Journal of Solids and Structures*, Vol. 36 (1999) 5639-5661.

[20] Y.J. Chao, X.K. Zhu, *J*-A_2 characterization of crack-tip fields: Extent of *J*-A_2 dominance and size requirements. *International Journal of Fracture*, Vol. 89 (1998) 285–307.

Experimental and numerical analysis of mixed mode fracture

Octavian POP[1,*], Mamadou Méité[1], Frédéric Dubois[1], Joseph Absi[2]

[1] GEMH, Université de Limoges, Centre Universitaire de Génie Civil, 19300 Egletons
[2] GEMH, Université de Limoges, IUT du Limousin, Département GM, 87000 Limoges
* Corresponding author: ion-octavian.pop@unilim.fr

Abstract Based on the global approach and the experimental measurements by digital image correlation, the presented study proposes a coupling between these two approaches in order to evaluate energy release rate. The proposed formalism allows calculating the energy release rate fracture parameters without considering the elastic parameters of material. The experimental analysis is realized using the specimens made in PVC isotropic material and Douglas fir (orthotropic material) under different mixed mode loadings. The loading under displacement control is applied using the Arcan system. From experimental data optimized by an adjustment procedure, the kinematic state in the crack tip vicinity is evaluated through the crack opening relative displacement factors. In parallel the stress state in vicinity of the crack tip is evaluated by a numerical analysis. This analysis is performed using the finite elements method and the integral invariant Mtheta, in order to evaluate the stress intensity factors. The finite element analysis is based on the reproduction of experimental test in terms of specimen geometry, experimental boundaries conditions and loading configurations. Then the energy release rate can be estimated by coupling of these two factors calculated without considering the material elastic parameters. Moreover, this method allows defining the local mechanical behavior.

Keywords Fracture mechanics, Mixed Mode, Experimental, Numerical, Digital Image Correlation

1. Introduction

Cracked structures are most often subjected to complex loadings in mixed-mode configurations that can lead to a catastrophic collapse of the structure and modify their mechanical behavior. In this case in order to avoid structural behavior, it is necessary to evaluate fracture process parameters and local mechanical behavior. Within this field of study, several numerical investigations have been carried out in the literature for the purpose of characterizing crack tip parameters through use of the energy method for mixed-mode configurations [1-4], for isotropic and orthotropic media. At present, these efficient techniques require an explicit knowledge of material properties; for orthotropic cases in particular, the complete compliance tensor is needed. In this context, our study proposes a new formalism that allows uncoupling the fracture parameter identification relative to material elastic properties.

Based on Digital Image Correlation (DIC) and a Finite Element Method (FEM), the fracture parameter identification can be performed from the kinematic and stress distributions in the crack tip vicinity. The complementarity of these two approaches distinguishes the calculation of energy release rates relative to opening and shear modes from the calculation of local material elastic proprieties.

According to our approach, DIC is employed to measure the displacement field evolution for the specimens made from a rigid Polyvinyl Chloride polymer and Douglas fir loaded under mixed-mode configurations. The application of such an experimental technique enables capturing both strong and weak kinematic discontinuities in the crack tip vicinity so as to characterize Crack Relative Displacement Factor (CRDF) [5-9]. The iterative Newton-Raphson method is then coupled with DIC to provide not only the real crack tip position needed for an accurate CRDF determination, but also the comprehensive raw dataset optimized through Williams' asymptotic series expansion solution.

The evaluation of stress distribution is realized using a finite element model. The model is based on experimental sample geometry and experimental boundary conditions. According to the Mq

method, Stress Intensity Factor (SIF) is defined by introducing a mixed-mode separation algorithm. For isotropic as for orthotropic configurations, stress distribution into the crack tip domain is assumed to be unaffected by elastic properties [5-7].
By aggregating the results of CRDF yielded by experimental DIC and SIF, as given by a numerical FEM, the prediction of an accurate energy release rate can be proposed. Fracture mode separation is also analyzed by establishing mode I and mode II energy release rates for mixed-mode loading conditions as well as plane configurations.

2. Experimental material and methods

The experimental evaluation of has been performed for several mixed-mode ratios. As shown in Figure 1, the experimental set-up involves an electromechanical press fitted with an LVDT displacement transducer and a load cell. The specimen geometry is a single-edge notched sample made from Polyvinyl Chloride (PVC) for the isotropic case and Douglas fir in the orthotropic case. The specimen dimensions are $208 \times 44 \times 10\,\text{mm}^3$ for the PVC specimen and $210 \times 50 \times 10\,\text{mm}^3$ with a notch length equal to $75\,\text{mm}$. The various mixed-mode loading configurations are applied thanks to Arcan fixtures that allow imposing a number of different mixed-mode ratios defined by the angle between force direction and crack orientation. The test is run under a displacement control with an imposed velocity of the cross-head equal to 0.1 mm/s.

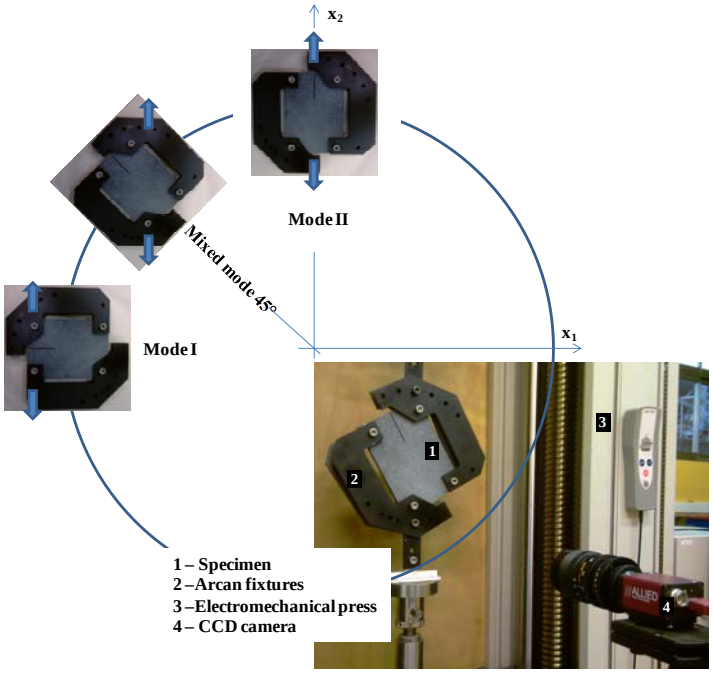

Figure 1. Experimental setup

Concerning measurement devices, the displacement field evolution is recorded on the specimen surface using an 8-bit CCD camera (1392 × 1040 pixel²). The image capture is performed at a rate of 1 frame per second and synchronized with the electromechanical press data (force and displacement). According to the DIC principle, a black-and-white speckled pattern is projected onto the specimen surface [10, 11]. The principle of this full-field method is based on a comparison between two images acquired during the test, one before deformation and the other after. The displacement field can then be obtained by comparing the reference image with the deformed image [10, 11]. The displacement fields, as presented in the present paper, are limited to 2D measurements. 3D effects are neglected (out-of-plane of crack lips or shear buckling induced by the specimen thickness), and plane stress state has been assumed.

2.1. Crack Relative Displacement Factor evaluation from experimental measurement

The experimental evaluation of CRDFs has been performed from the experimental measurements by DIC. The displacement data output by the DIC method are typically affected by experimental noise. It proves quite difficult to accurately analyze stress and strain fields from raw displacement data; moreover, real deformation fields of the crack tip and its location are difficult to obtain with precision from DIC [5-7, 11-14]. Consequently, the crack tip parameters predicted directly using raw experimental displacement data are inaccurate [5-7]. An adjustment procedure has thus been derived to avoid these difficulties.
Then, once the experimental displacement has been calculated, the adjustment procedure based on a nonlinear iterative Newton-Raphson is performed between the Williams' series forms (1) and the experimental data. By taking measurement boundary conditions (e.g. specimen geometry and symmetry, crack orientation) into account, this adjustment procedure is also able to consider a rigid body motion, crack tip localization and its orientation as unknowns. These parameters are then used to adjust the displacement fields.

$$\begin{aligned} u^1 &= \sum_{c=1}^{N} A_1^c \, r^{(c/2)} \, f_c(k,j) + A_2^c \, r^{(c/2)} \, g_c(k,j) + T_1 - R \cdot x_2 \\ u^2 &= \sum_{c=1}^{N} A_1^c \, r^{(c/2)} \, l_c(k,j) + A_2^c \, r^{(c/2)} \, z_c(k,j) + T_2 + R \cdot x_1 \end{aligned} \tag{1}$$

Where:

$$\begin{aligned} f_c &= k - \cos\left(\frac{c}{2}-1\right)j - \cos\left(\frac{c}{2}+1\right)j \\ g_c &= (-1)^c \sin\left(\frac{c}{2}-1\right)j - \sin\left(\frac{c}{2}+1\right)j \\ l_c &= k \sin\left(\frac{c}{2}-1\right)j - \sin\left(\frac{c}{2}+1\right)j \\ z_c &= k \cos\left(\frac{c}{2}-1\right)j + \cos\left(\frac{c}{2}+1\right)j \end{aligned} \tag{2}$$

The adjusted experimental field now allows defining a physical and local interpretation. The kinematic state of crack lips can in fact be identified using Crack Relative Displacement Factor $K_a^{(e)}$(CRDF) [5-9], which denote the relative opening and shear displacements of crack lips. Thanks to developments offered by Dubois, the kinematic state in the crack tip vicinity can be defined using Crack Relative Displacement Factors (CRDFs). At a very short distance x from the crack tip, the relative opening displacement $[u]_1$ and shear displacement $[u]_2$ are defined as follows (see Figure 2):

$$[u]_1 = K_2^{(e)} \sqrt{\frac{x}{2\pi}} \quad and \quad [u]_2 = K_1^{(e)} \sqrt{\frac{x}{2\pi}} \tag{3}$$

By combining Eqs. (1) with (3), we can now provide, in the crack tip vicinity, a mathematical interpretation of CRDF, such that:

$$K_1^{(e)} = 2\mu A_1^1 (k+1)\sqrt{2\pi} \quad and \quad K_2^{(e)} = 2\mu A_2^1 (k+1)\sqrt{2\pi} \tag{4}$$

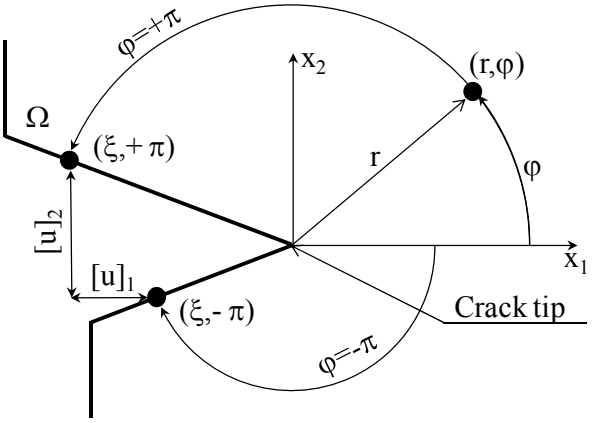

Figure 2. Relative displacements of crack lips

In Eqs. (1), (2), (3) and (4), (r, j) are the polar coordinates, k is the constant of Kolossov, A_a^c are the weighting coefficients relative to opening mode (α=1) and shear mode (α=2) and (T_1, T_2, R) are the rigid body motions.

From Eqs. (4), the CRDF can be determined without an explicit knowledge of the material elastic properties. Moreover, this initial step aims to accurately characterize the kinematic state of the crack.

2.2. Stress Intensity Factor evaluation from numerical analysis

In fracture mechanics, the stress state definition in the crack vicinity is expressed in terms of Stress Intensity Factor (SIF) $K_a^{(s)}$. As previously mentioned, the experimental test is conducted under displacement control, while the numerical model is loaded by imposing an equivalent force. In this case, SIF amplitude depends solely on model geometry, crack length and the force loading value. The definition of these factors implies developing a classical finite element model (Figure 3).

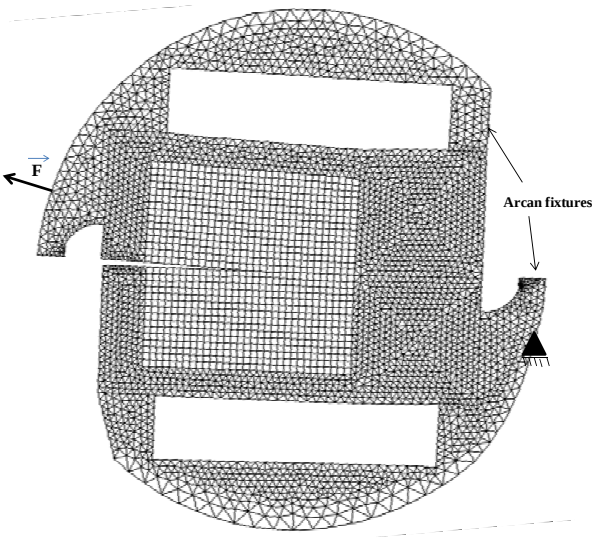

Figure 3. Finite element model

Note that the boundary conditions implemented in the finite element model have not integrated the experimental flaws, in terms of rigid body motion and crack tip orientation. Let's recall that these parameters have already been integrated into the optimized displacement fields obtained from the adjustment procedure described above. According to the finite element approach, we therefore place ourselves in an "ideal" test configuration.

In mixed-mode configurations, SIF calculations are often performed by implementing Mq method (Figure 4). The Mq-integral is an energy parameter established in order to analyze crack growth in a mixed-mode fracture by isolating various fracture modes, such as opening and shear, through a pseudo-potential that combines real displacements and kinematically admissible auxiliary displacements.

$$M\theta = \frac{1}{2} \cdot \int_V \left(\left(\sigma_{ij}\right)_{real} \cdot \left(u_{i,k}\right)_{aux} - \left(\sigma_{ij,k}\right)_{aux} \cdot \left(u_i\right)_{real} \right) \cdot \theta_{k,j} \cdot dV \tag{5}$$

The relationships between the stress tensor and the displacement vectors require introducing orthotropic elastic properties. By imposing an external force loading however, we can assume that SIF are not really influenced by elastic properties. Given these conditions, we have opted for an arbitrary elastic property rated '∼'.

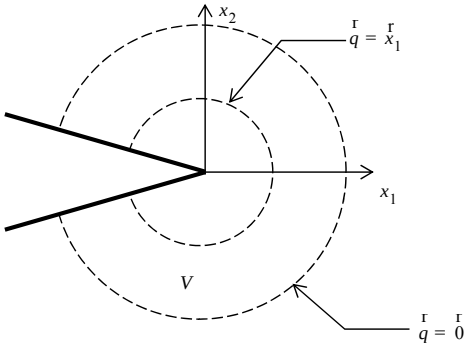

Figure 4. Integral domain

2.3. New formalism of energy release rate

The coupling between the kinematic and stress approaches allows calculating an energy release rate by the surrounding elastic proprieties. This coupling also serves to identify the actual reduced elastic compliance leading to the Young's modulus determination. Now, by replacing virtual displacements by real displacements, it has been shown that the Mq integral is mistaken for the energy release rate G [15]. More precisely, thanks to the superposition principle, in letting ${}^{real}K_a^{(s)}$ and ${}^{aux}K_a^{(s)}$ be the real and virtual Stress Intensity Factor, respectively, we can adopt the following expression:

$$Mq\left(\vec{u},\vec{v}\right) = \sum_a C_a \frac{{}^{real}K_a^s \times {}^{aux}K_a^s}{8} \tag{6}$$

where C_a is the reduced elastic compliance that allows defining local behavior in terms of Stress

Intensity Factor and Crack Relative Displacement Factor, such that:

$$K_{\alpha}^{\varepsilon} = C_{\alpha} \cdot {}^{real}K_{\alpha}^{\sigma} \tag{7}$$

Equation (6) yields a physical interpretation for Mq in the Stress Intensity Factor definition, i.e.:

$${}^{u}K_1^{(s)} = \frac{8?Mq\begin{cases}{}^{u}K_1^{(s)} & 1,\ {}^{v}K_2^{(s)} = 0\\ 0, & {}^{v}K_2^{(s)} = 1\end{cases}}{C_1} \text{ and } {}^{u}K_2^{(s)} = \frac{8?Mq\begin{cases}{}^{u}K_1^{(s)} & 0,\ {}^{v}K_2^{(s)} = 1\\ 0, & {}^{v}K_2^{(s)} = 1\end{cases}}{C_2} \tag{8}$$

For orthotropic media, these arbitrary reduced elastic compliance functions are defined by the following equations:

$$\overset{\circ}{C}_1 = \sqrt{\frac{\overset{\%}{a}_{11}\overset{\%}{a}_{22}}{2}}?\sqrt{\sqrt{\frac{\overset{\%}{a}_{22}}{\overset{\%}{a}_{11}}}\frac{2\overset{\%}{a}_{12}+\overset{\%}{a}_{33}}{2\overset{\%}{a}_{11}}} \text{ and } \overset{\circ}{C}_2 \quad \sqrt{\frac{\overset{\%}{a}_{11}\overset{\%}{a}_{11}}{2}}\sqrt{\sqrt{\frac{\overset{\%}{a}_{22}}{\overset{\%}{a}_{11}}}\frac{2\overset{\%}{a}_{12}+\overset{\%}{a}_{33}}{2\overset{\%}{a}_{11}}} \tag{9}$$

Where:

$$\overset{\%}{a}_{11} = \frac{1}{\overset{\circ}{E}_L};\ \overset{\%}{a}_{12} = -\frac{\overset{\%}{n}_{RL}}{\overset{\circ}{E}_R} = -\frac{\overset{\%}{n}_{LR}}{\overset{\circ}{E}_L};\ \overset{\%}{a}_{22} = \frac{1}{\overset{\circ}{E}_R};\ \overset{\%}{a}_{33} = \frac{1}{\overset{\circ}{G}_{LR}} \text{ in plane stress} \tag{10}$$

$$\overset{\%}{a}_{11} = \frac{1-\overset{\%}{n}_{LT}?\overset{\%}{n}_{TL}}{\overset{\circ}{E}_L};\ a_{12} = -\frac{\overset{\%}{n}_{RL}\quad\overset{\%}{n}_{RL}?\overset{\%}{n}_{TL}}{\overset{\circ}{E}_R};\ a_{22} = \frac{1\quad\overset{\%}{n}_{RT}\ \overset{\%}{n}_{TR}}{\overset{\circ}{E}_R};\ \overset{\%}{a}_{33} = \frac{1}{\overset{\circ}{G}_{LR}} \text{ in plane strain} \tag{11}$$

In which $\overset{\circ}{E}$ and $\overset{\%}{n}$ are the arbitrary elastic orthotropic properties of material.

In the case of isotropic material the arbitrary reduced elastic compliance functions are defined by:

$$\overset{\circ}{C}_a = \frac{\overset{\%}{k}+1}{\overset{\circ}{m}} \tag{12}$$

Where m is the Lamé coefficient given by :

$$\overset{\circ}{m} = \frac{\overset{\circ}{E}}{2?\left(1\quad\overset{\%}{n}\right)} \tag{13}$$

And:

$$\begin{aligned} k &= 3-4\,n \text{ in plane strain} \\ k &= \frac{3-n}{1+n} \text{ in plane stress} \end{aligned} \tag{14}$$

Now, in assuming a plane stress state, by substituting Equation (7) into the classical energy release rate expression, we obtain a new formalism:

$$G_a = \frac{{}^{real}K_a^{(s)} \times K_a^{(e)}}{8} \qquad a = 1;2 \tag{15}$$

In Eq. (15) G_{α} represents the portion of opening and shear modes in terms of energy release rate.

Next, using the numerical values of CRDFs and SIFs calculated above, the energy release rate can be estimated from Equation (15) independently of the material's elastic proprieties.

3. Results

In the case of rigid Polyvinyl Chloride polymer and Douglas fir the Figure 5 highlights a comparison between the experimental and analytical deformations after adjustment procedure.

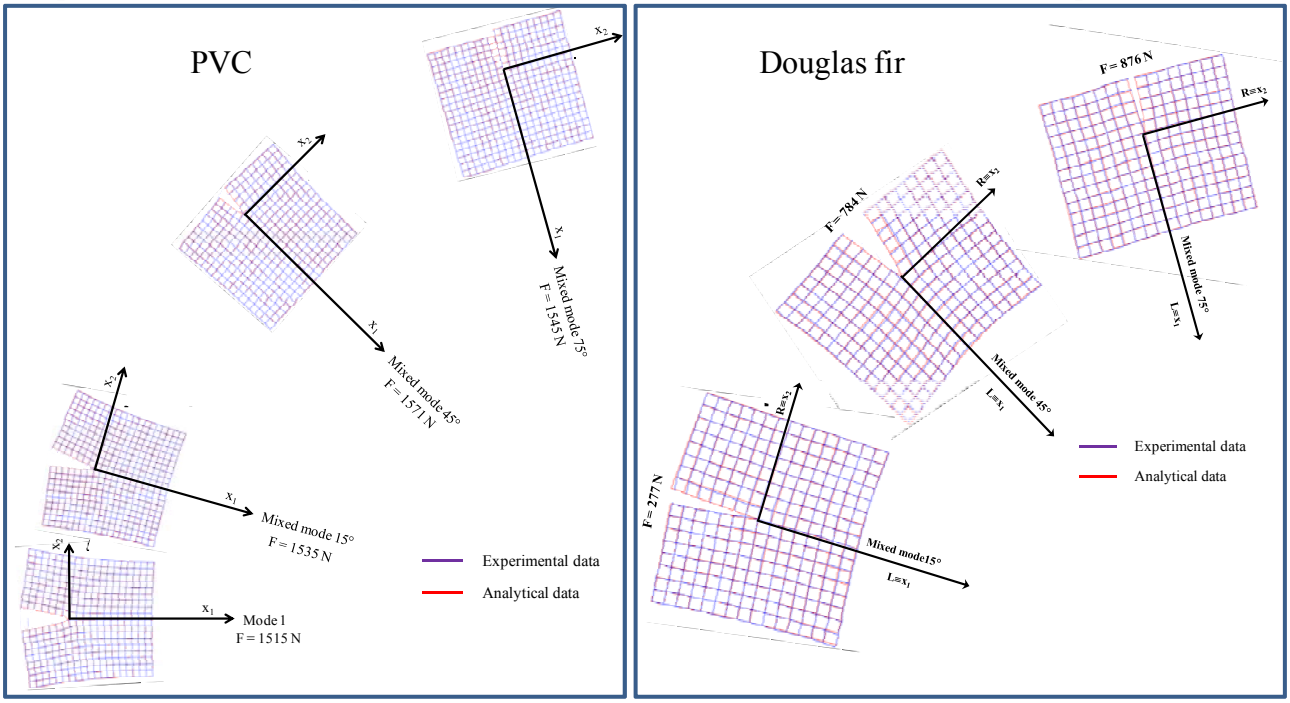

Figure 5. Results of the adjustment procedure

As is shown in Figure 5, the adjustment procedure allows obtaining an optimized displacement fields without experimental noises. Moreover, the adjustment procedure allows estimating the rigid body motion and the crack tip orientation. These parameters are essential to adjust the experimental conditions in order to obtain the specific mixed mode boundary conditions definite by the analytical expressions of displacement fields corresponding to mixed mode loading. Note that the representation of displacements fields shown in Figure 5 take into account these parameters.

According to Equations (4), the $K_a^{(e)}$ values are calculated from optimized displacement fields using the values of A_1^1, A_2^1 and k values. Then the Stress Intensity Factor can be evaluated from a FE analysis via the integral invariant Mq.

According to Equation (15), the energy release rate can be predicted by combining a kinematic approach (given by experimental testing) with a static approach (using numerical modeling) through determining CRDF and real SIF, respectively. The results of these energy release rate predictions are provided in Table 1 for isotropic case and Table 2 for orthotropic case. Not only does this method allow deducing the energy release rate, but moreover the use of the Mq-integral allows separating this energy for each part of both the opening and shear modes.

Table 1: Isotropic case

b	Force (N)	$K_1^{(\varepsilon)}$ ($m^{1/2}$)	$K_2^{(\varepsilon)}$ ($m^{1/2}$)	$K_1^{(\sigma)}$ ($MPa \cdot m^{1/2}$)	$K_2^{(\sigma)}$ ($MPa \cdot m^{1/2}$)	G_1 (J/m²)	G_2 (J/m²)
0°	1515	$5.03 \cdot 10^{-3}$	0	1.63	0	1025	0
15°	1535	$2.04 \cdot 10^{-3}$	$3.44 \cdot 10^{-4}$	0.66	0.11	168	5
45°	1571	$2.34 \cdot 10^{-3}$	$9.80 \cdot 10^{-4}$	0.76	0.32	222	39
75°	1545	$5.49 \cdot 10^{-4}$	$9.51 \cdot 10^{-4}$	0.18	0.31	10	37

Table 2: Orthotropic case

b	Force (N)	$K_1^{(\varepsilon)}$ ($m^{1/2}$)	$K_2^{(\varepsilon)}$ ($m^{1/2}$)	$K_1^{(\sigma)}$ ($MPa \cdot m^{1/2}$)	$K_2^{(\sigma)}$ ($MPa \cdot m^{1/2}$)	G_1 (J/m²)	G_2 (J/m²)
0°	245	$2.08 \cdot 10^{-3}$	0	0.45	0	116	0
15°	277	$5.95 \cdot 10^{-4}$	$1.43 \cdot 10^{-4}$	0.14	0.11	10.5	2.02
45°	748	$1.35 \cdot 10^{-3}$	$7.43 \cdot 10^{-4}$	0.32	0.59	54	55.2
75°	876	$6.91 \cdot 10^{-4}$	$6.58 \cdot 10^{-4}$	0.16	0.52	14.2	42.9

4. Conclusion

This work has presented an original coupling between Digital Image Correlation and Finite Element Analysis, making it possible to characterize both the mechanical and energy states in the crack tip vicinity.

Based on Dubois' developments, the kinematic state in the crack tip vicinity is evaluated using the Crack Relative Displacement Factors calculated from experimental measurements output by DIC. In parallel with this step, the stress distribution is evaluated by a finite element analysis according to the Mq method. The coupling of these two approaches allows distinguishing and calculating the energy release rates corresponding to opening and shear modes. The originality of this coupling procedure lies in the possibility of calculating the energy release rate independently of material elastic properties. Furthermore, our formalism allows evaluating local elastic properties via the elastic compliance correlated with Crack Relative Displacement Factors and Stress Intensity Factors.

In terms of follow-up work, crack initiation and propagation can be studied in greater depth thanks to this new technique, thus leading to a better understanding of all phenomena governing the crack tip growth process.

References

[1] B. Budiansky, J.R Rice, Conservation laws and energy release rate. Journal of Applied Mechanics, 400 (1973) 201-203.
[2] A.G. Hermann, On energy release rates for a plane crack. Journal of Applied Mechanics, 48, (1981) 525-528.
[3] L.B. Freund, Stress-intensity factor calculations based on a conservation integral. International of Journal of Solids and Structures, 14 (1978) 241-250.
[4] J.H. Chang, A.J. Chien, Evaluation of M-integral for anisotropic elastic media with multiple

defects. International Journal of Fracture, 114 (2002) 267-289.

[5] F. Dubois, M. Méité, O. Pop, J. Absi, Characterization of timber fracture using the Digital Image Correlation technique and Finite Element Method. Engineering Fracture Mechanics (2012). doi.org/10.1016/j.engfracmech.2012.07.008.
[6] O. Pop, M. Meite, F. Dubois, J. Absi, Identification algorithm for fracture parameters by combining DIC and FEM approaches. International Journal of Fracture, 170 (2011) 101-114.
[7] M. Méité, O. Pop, F. Dubois, J. Absi, Characterization of mixed-mode fracture based on a complementary analysis by means of full-field optical and finite element approaches. International Journal Fracture, (2012). DOI: 10.1007/s10704-012-9794-z.
[8] F. Dubois, C. Chazal, C. Petit, Viscoelastic crack growth process in wood timbers: an approach by the finite element method for mode I fracture. International Journal Fracture; 113 (2002) 367–88.
[9] F. Dubois, C. Petit, Modeling of the crack growth initiation in viscoelastic media by the Gθ integral. Engineering Fracture Mechanics, 72 (2005) 2821–2836.
[10] M.A. Sutton, W.J. Wolters, W.H. Peters, W.F. Ranson, S.R. McNeil, Determination of Displacements Using an Improved Digital Correlation Method, Image and Vision Computating, 1 (1983) 133-139.
[11] J. Réthoré, S. Roux, F. Hild, Optimal and noise-robust extraction of Fracture Mechanics parameters from kinematic measurements. Engineering Fracture Mechanics 78 (2011) 1827-1845.
[12] K. Machida, Y. Suzuki, Examination of the accuracy of the singular stress fields near a crack tip by Digital Image Correlation. Key Engineering Materials, 321 (2006) 32–37.
[13] S. Yoneyama, T. Ogawa, Y. Kobayashi, Evaluating mixed-mode stress intensity factors from full-field displacement obtained by optical methods. Engineering fracture mechanics, 74 (2007) 1399–1412.
[14] M. Méité, O. Pop, F. Dubois, J. Absi, Evaluation of mixed-mode integral invariant for polymer material trough the couple experimental-numerical Process. 14th International Conference on Experimental Mechanics (ICEM14), Poitiers, 2010.
[15] R. Moutou Pitti, F. Dubois, C. Petit, N. Sauvat, Mixed mode fracture separation in viscoelastic orthotropic media: numerical and analytical approach by the Mθv –integral. International Journal of Fracture, 145 (1997) 181–193.

Cracks under Mixed Mode loading: Questions and solutions for isotropic and graded materials

Hans. A. Richard[1], Britta Schramm[1,*], Alexander Eberlein[1], Gunter Kullmer[1]

[1] Institute of Applied Mechanics, University of Paderborn, 33098 Paderborn, Germany
* Corresponding author: schramm@fam.upb.de

Abstract In reality cracks often initiate and grow due to mixed mode loading. This paper deals with questions about stable and unstable crack growth and the crack growth direction under multi-axial loading conditions. For homogeneous materials many criteria and experimental confirmations exist. This paper shows a selection of these solutions and some experimental investigations. In practice innovative manufacturing and application-oriented products considering lightweight construction gain increasingly in importance. In this context structures with graded material properties are produced. However there does not exist many concepts for these graded materials. Within this paper fracture and fatigue criteria and experimental findings are presented. In particular the $TSSR^B$-concept is used for the determination of crack growth in fracture mechanical graded materials.

Keywords Mixed Mode, fracture criteria, isotropic materials, graded materials, TSSR-concept

1. Introduction

If the two basic fracture modes (Mode I and Mode II) temporarily or permanently occur in combination, as indicated in Fig. 1, local plane Mixed Mode loading conditions at cracks can be observed.

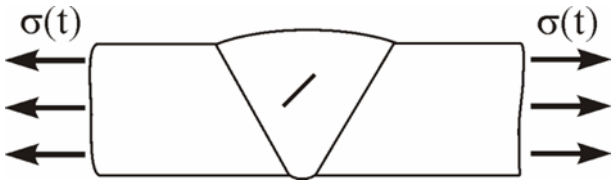

Figure 1. Mixed Mode loaded crack in a welded structure

For a fail-safe dimensioning it is important to know among other things if such a crack is able to grow, how fast and whereto does the crack grow and when unstable crack growth occurs. Answers can be found using crack propagation concepts which will be briefly described in the following chapter. An extensive description can be found in [1, 2].

2. Crack growth in isotropic and homogeneous materials

An isotropic and homogeneous structure is defined by fracture mechanical and elastic material properties which are independent of place and direction, i.e. they are the same for the whole structure. With regard to the subsequent consideration of fracture criteria for graded materials and their complexity only 2D-concepts will be regarded within this paper.

2.1. Concepts for two-dimensional Mixed Mode crack growth

In the following two theoretical concepts are presented which enable the determination of unstable crack growth. Information about further crack propagation concepts for 2D and 3D Mixed Mode situations can be found in [1-5].

2.1.1. Concept according to Erdogan and Sih

The concept of the maximum tangential stress (MTS) by Erdogan and Sih [4, 5] enables the determination of the crack growth direction as well as the start of unstable crack propagation on the basis of the tangential stress σ_φ, presented in Eq. (1).

$$\sigma_\varphi = \frac{K_I}{\sqrt{2\pi r}}\cos^3\frac{\varphi}{2} - \frac{K_{II}}{\sqrt{2\pi r}}\frac{3}{2}\sin\varphi\cdot\cos\frac{\varphi}{2} \tag{1}$$

The concept assumes that the crack propagates in the direction $\varphi_{0,MTS}$ which is perpendicular to the maximum tangential stress $\sigma_{\varphi max}$. Eq. (2) defines the kinking angle $\varphi_{0,MTS}$ according to the MTS-concept which depends on the loading condition.

$$\varphi_{0,MTS} = -\arccos\left(\frac{3K_{II}^2 + K_I\sqrt{K_I^2+8K_{II}^2}}{K_I^2+9K_{II}^2}\right) = -\arccos\left[\frac{3\left(\frac{K_{II}}{K_I}\right)^2 + \sqrt{1+8\left(\frac{K_{II}}{K_I}\right)^2}}{1+9\left(\frac{K_{II}}{K_I}\right)^2}\right] \tag{2}$$

The crack grows unstable if $\sigma_{\varphi max}$ reaches a material limit value $\sigma_{\varphi c}$ or if a maximum comparative stress intensity factor K_{Vmax} (Eq. 3), determined by the tangential stress σ_φ (Eq. 1), reaches the fracture toughness K_{IC}.

$$K_{Vmax} = \lim_{r\to 0}\left(\sigma_{\varphi max}\sqrt{2\pi r}\right) = \lim_{r\to 0}\left(\sigma_\varphi(\varphi_0)\sqrt{2\pi r}\right) = \cos\frac{\varphi}{2}\left(K_I\cos^2\frac{\varphi_0}{2} - \frac{3}{2}K_{II}\sin\varphi_0\right) \tag{3}$$

Eq. (4) shows the criterion for unstable crack growth.

$$K_{Vmax} = K_{IC} \tag{4}$$

Due to cyclic loading the tangential stress σ_φ (Eq. 1) is transformed to the cyclic tangential stress $\Delta\sigma_\varphi$ (Eq. 5) with the cyclic stress intensity factors ΔK_I and ΔK_{II}.

$$\Delta\sigma_\varphi = \frac{\Delta K_I}{\sqrt{2\pi r}}\cos^3\frac{\varphi}{2} - \frac{\Delta K_{II}}{\sqrt{2\pi r}}\frac{3}{2}\sin\varphi\cdot\cos\frac{\varphi}{2} \tag{5}$$

Fatigue crack growth starts if the cyclic comparative stress intensity factor $\Delta K_{Vmax}=\Delta\sigma_\varphi\sqrt{2\pi r}$ reaches the Threshold value ΔK_{th}. In case of cyclic loading unstable crack growth occurs if $K_{Vmax} = K_{IC}$ (Eq. 4) or if $\Delta K_{Vmax} = \Delta K_{IC} = K_{IC}\cdot(1-R)$, with the stress ratio $R = \sigma_{min}/\sigma_{max} = K_{min}/K_{max}$.

2.1.2. Concept according to Richard

The general fracture concept of Richard [1, 5, 6] is very practical and adaptive and can be used for different materials. The concept is based on a comparative stress intensity factor K_V. This value depends on the stress intensity factors K_I and K_{II} (Eq. 6).

$$K_V = \frac{1}{2}K_I + \frac{1}{2}\sqrt{K_I^2 + 4(\alpha_1 K_{II})^2} \tag{6}$$

The material parameter α_1 depends on the ratio of the fracture toughness of Mode I K_{IC} and the fracture toughness of Mode II K_{IIC}. If α_1 is set to 1.155 an excellent approximation of the fracture limit curve of the maximum tangential stress criterion is obtained. Unstable crack growth occurs as soon as K_V exceeds the fracture toughness K_{IC} for Mode I.

Furthermore the concept also enables the determination of the kinking angle φ_0 (Eq. 7), with

$\varphi_0<0$ for $K_{II}>0$, $\varphi_0>0$ for $K_{II}<0$ and K_I always larger than 0.

$$\varphi_0 = \mu\left[A\frac{|K_{II}|}{|K_I|+|K_{II}|} + B\left(\frac{|K_{II}|}{|K_I|+|K_{II}|}\right)^2 \right] \tag{7}$$

In this empirical formula the parameters have to be set to: A = 155,5° and B = -83,4°.

2.2. Comparison of the theoretical concepts and experimental findings

Experimental determined kinking angles φ_0 for different almost isotropic materials (for example PMMA, Araldit B, PVC, AlZnMgCu) are shown in Fig. 2. The kinking angle doesn't depend on the material. However the K_{II}/K_I-ratio is important. Furthermore the kinking angles determined by different fracture criteria (for example Erdogan and Sih, Richard) are presented in dependency of the Mixed Mode ratio $K_{II}/(K_I+K_{II})$. It can be seen that these crack propagation criteria are able to predict the crack kinking angle for isotropic and nearly isotropic material sufficiently exact [7]. For more information about experimental investigations see [5, 8].

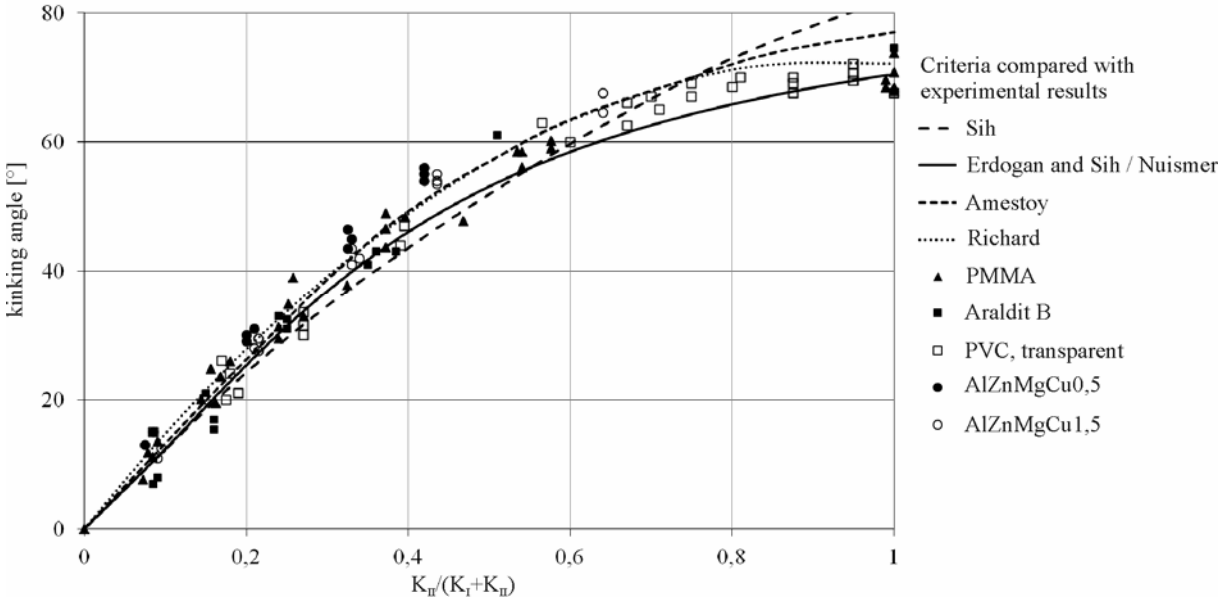

Figure 2. Kinking angle from criteria for 2D Mixed Mode cracks in comparison to experimental data

Fig. 3 shows aluminum alloy specimens which vary in their rolling direction. The specimen in Fig. 3a was rolled in crack direction, in Fig. 3b diagonal and in Fig. 3c perpendicular to the crack direction. After the production and rolling process these specimens were investigated experimentally. The resulting kinking angles φ_0 of these anisotropic structures are presented in Fig. 4. The results show that the crack propagation concepts are not able to predict the kinking angles of the rolled aluminum alloy specimens very well. The concepts are not able to consider the predominant direction due to the rolling process.

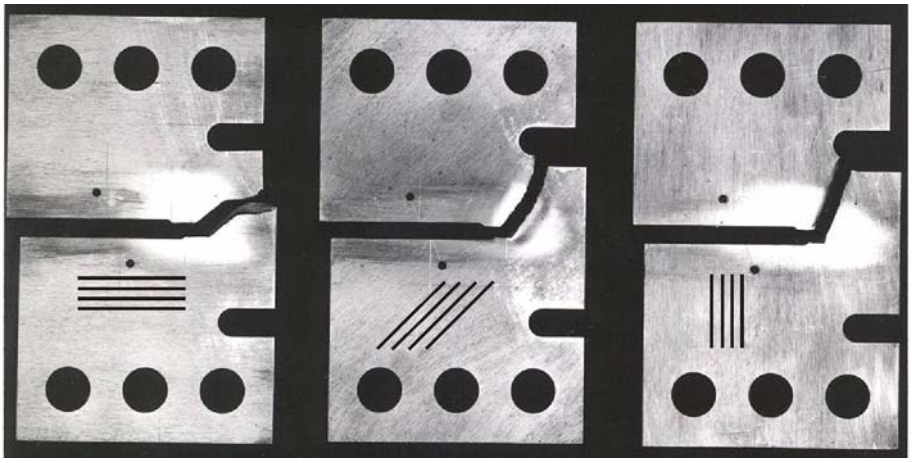

a) b) c)

Figure 3. Aluminum alloy specimens with special rolling direction: a) in crack direction, b) diagonal, c) perpendicular to the crack direction

These results lead to the knowledge that the presented concepts are able to predict the crack growth behavior very well as long as the structure is a homogeneous and isotropic one. For the description of materials with a graded property, for example in form of the shown predominant direction, other concepts have to be used considering the influence of the material gradation. Therefore hypotheses describing Mixed Mode crack growth in graded materials are presented in the following contribution.

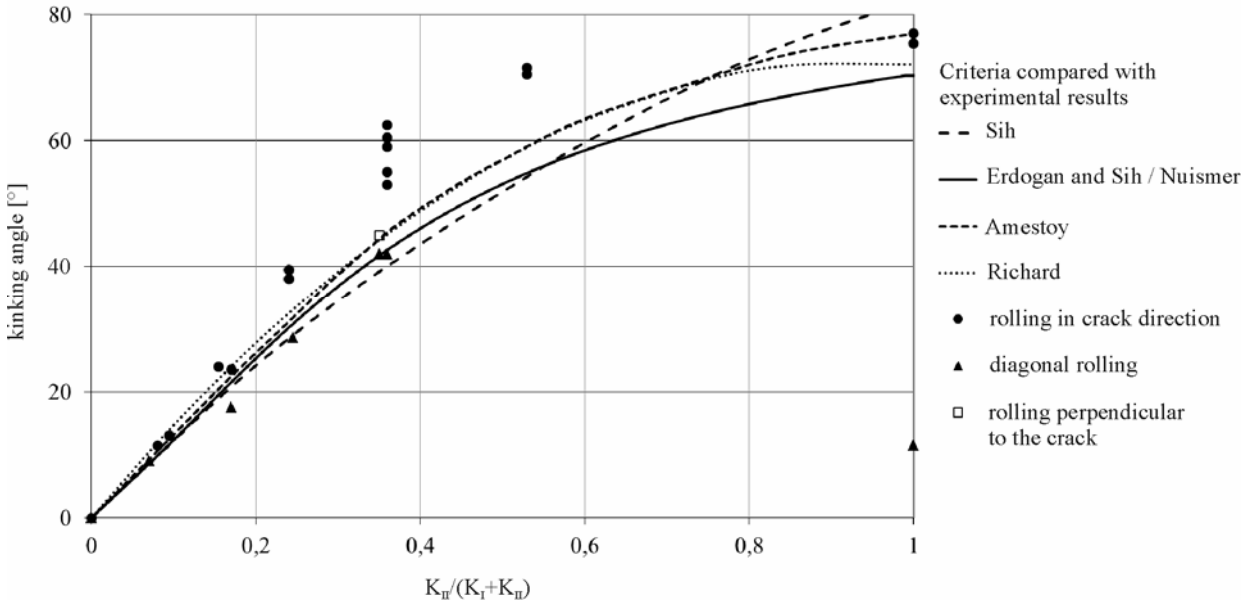

Figure 4. Kinking angle from criteria in comparison to experimental data of a rolled aluminium alloy specimens for 2D Mixed Mode cracks

3. Crack growth in functional graded materials

In technical practice innovative manufacturing and application-oriented products, considering lightweight construction, gain increasingly in importance. In this context functional graded materials and structures take a special position. Due to the fact that these materials possess an application matched functional gradation they are able to meet different local demands such as

among other things absorbability, abrasion and fatigue of structures. The material gradation has a remarkable influence on the crack propagation behavior which is why the development of appropriate concepts is important. The material gradation can be realized by different properties. On the one hand the gradation can be defined by different fracture mechanical properties, on the other side by differences in the elastic parameters. Furthermore a combination of the fracture mechanical gradation and the elastic gradation is imaginable. The following considerations deal with a fracture mechanical gradation.

3.1. Influence of a fracture mechanical material gradation on crack propagation

A fracture mechanical material gradation exists for example within the flanged shaft, Fig. 5a, which is used as a demonstrator object by the collaborative research centre Transregio 30 with the title "functionally graded materials in industrial mass production". Besides the development and manufacturing of these innovative materials another important task is the characterization of the mechanical properties of these materials regarding the remarkable influence of the gradation on the fracture mechanical behavior and hence on the life time of such a graded structure [9]. Due to a thermo-mechanical production process the unformed region of the shaft shows ferritic-perlitic base material of the heat treatable steel 51CrV4, whereas the formed flange consists of a martensitic structure. Fig. 5b clarifies that the fracture mechanical properties of these microstructures (i.a. Threshold value $\Delta K_{th,}$ fracture toughness K_{IC}, crack velocity da/dN) differ extremely from each other. The elastic properties (Young's modulus E, Poisson's ratio ν) are not affected by the production process. Furthermore there is a defined distinctive transition zone between the mentioned microstructures which is neglected in this contribution.

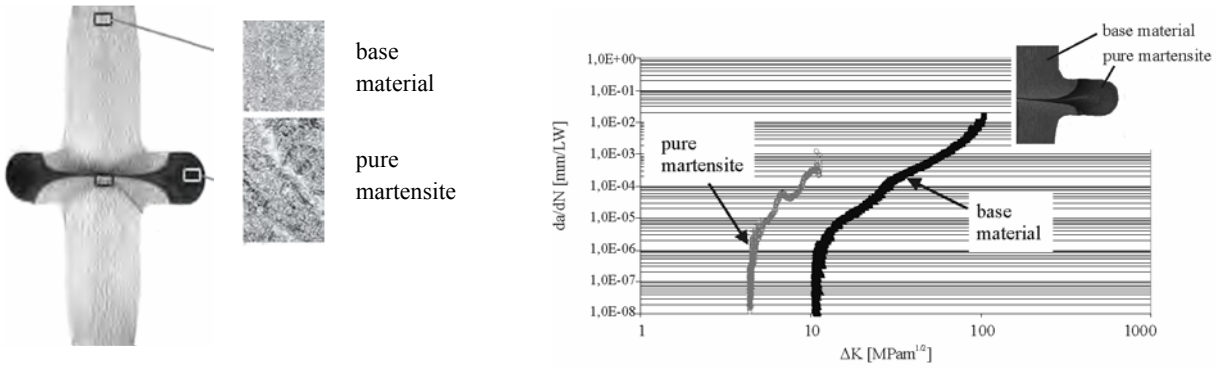

a) b)

Figure 5. a) Metallographic micrograph of the flanged shaft [9], b) crack velocity curves for the steal 51CrV4 with different microstructures [10]

3.1.2. Influence on the limits of fatigue crack growth

Fig. 6 shows the correlation between cyclic stress $\Delta\sigma$ and crack length a in dependency of a fracture mechanical gradation for a Griffith crack (geometry factor Y = 1) [10, 11]. Below the Threshold value curves a crack is not able to grow, whereas the unstable crack growth is above the fracture limit curves. The region of stable fatigue crack growth is between both material curves.

The crack starts in base material and reaches the martensitic microstructure at the crack length a = 6mm. It can be seen that the region of stable fatigue crack growth is more distinctive for the base material than for martensite. Furthermore there is no real overlapping at the transition, hence the

crack becomes unstable immediately after reaching the martensitic structure.

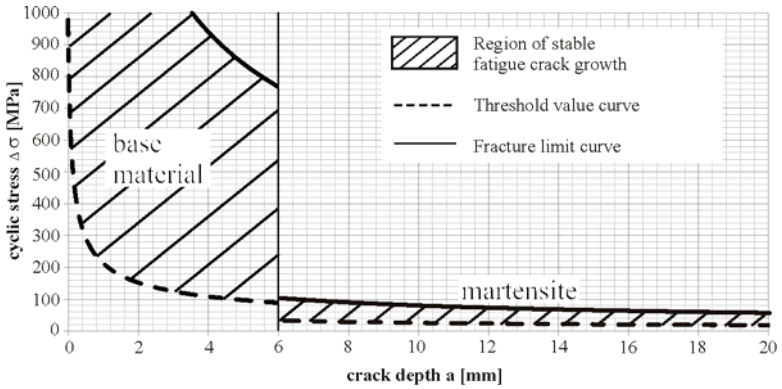

Figure 6. Δσ-a-diagram for a fracture mechanical gradation with a sharp transition at crack length a = 6mm

3.1.3. Influence on the crack growth velocity

Fig. 7a shows schematic crack velocity curves for two materials characterized by different fracture mechanical properties [10, 11]. At the beginning crack growth is starting within material 2. At reaching the other material a change to the crack velocity curve of material 1 occurs. Hence, the crack grows faster and reaches the fracture toughness much earlier as if it grows further within material 2. The worst imaginable case is that at the change to curve 1 the cyclic stress intensity factor ΔK is already larger than the cyclic fracture toughness ΔK_{C1} of material 1 leading to the immediate failure of the structure. In Fig. 7b the gradation is oriented opposite. The crack starts in the material with the worse fracture mechanical properties, material 1, and reaches material 2 afterwards. Due to the change the crack velocity slows down and more load cycles are tolerated until final fracture. At the best crack arrest occurs if the cyclic stress intensity factor ΔK is smaller than the Threshold value ΔK_{th2} of material 2 at the material change. As can be seen, a positive or a negative impact on the prospective lifetime is connected with the gradation constellation.

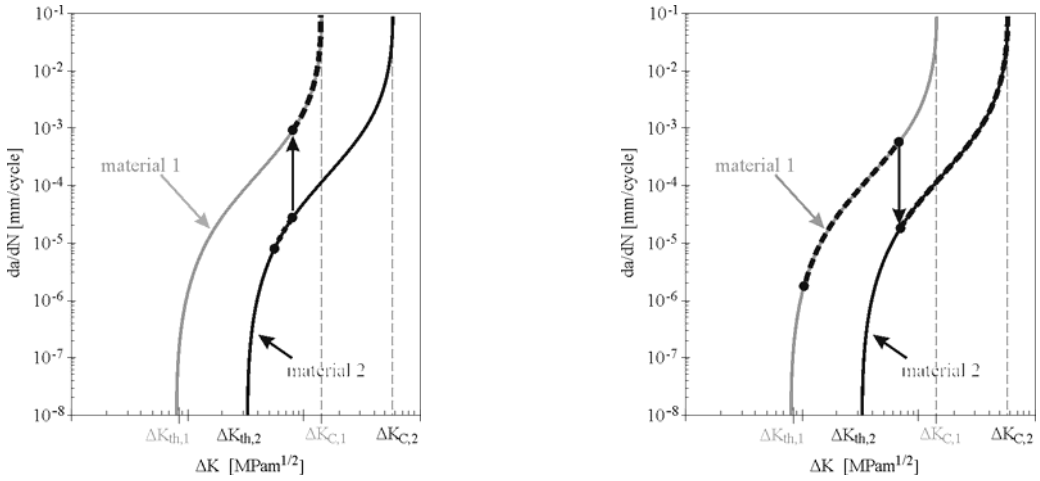

Figure 7. Schematic crack velocity curves:
a) transition from material 2 to material 1, b) transition from material 1 to material 2

3.2. TSSR^B-concept for the prediction of crack propagation in fracture mechanical graded materials

The new developed TSSR^B-concept enables the prediction of the start and the direction of the crack propagation as well as the determination of unstable crack growth in fracture mechanical graded materials [10, 11, 12]. Fig. 8 shows a crack-afflicted structure which is loaded periodically resulting in a pure Mode I loading solution. Furthermore the structure consists of two materials whose fracture mechanical properties differ from each other. The presented gradation angle $\varphi_M = 30°$ defines the position of the material transition in relation to the crack tip. The crack could kink by the kinking angle $\varphi_{0,MTS}$ which depends on the stress situation and can be determined by a crack propagation concept for homogeneous and isotropic materials (for example the MTS-concept of Erdogan and Sih). Another imaginable kinking angle is the gradation angle φ_M itself, due to the fact that the crack strives to take the way of least resistance.

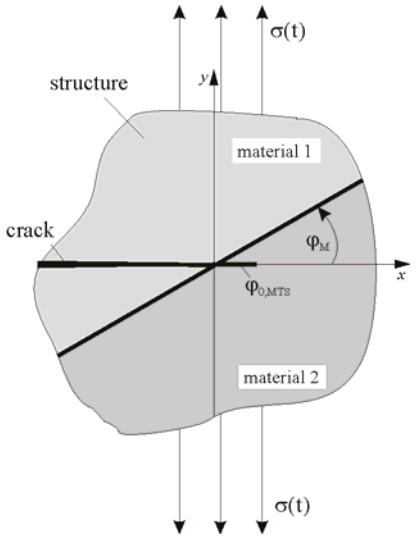

Figure 8. Fracture mechanical graded structure with gradation angle $\varphi_M = 30°$

The occurrence of fatigue crack growth as well as the entrant kinking angle φ_{TSSRB} can be determined by the TSSR^B-concept. This concept is based on the assumption that stable crack growth starts, when the cyclic tangential stress $\Delta\sigma_\varphi$ (Eq. 5) reaches a material limit value $\Delta\sigma_{\varphi,th}$ or rather when a cyclic comparative stress intensity factor ΔK_V, determined by the means of the cyclic tangential stress $\Delta\sigma_\varphi$, reaches the Threshold value curve $\Delta K_{th}(\varphi)$. This material function depends on the coordinate φ and consists of the values $\Delta K_{th,material1}$ and $\Delta K_{th,material2}$ for the different regions, see Eq. (8). Similarly the material functions $\Delta K_C(\varphi)$ and $K_C(\varphi)$ can be defined in dependency of the gradation angle φ_M.

$$\Delta K_{th}(\varphi) \begin{cases} \Delta K_{th,material1} & \varphi_M \le \varphi \le \varphi_M + 180° \\ \text{for} & \\ \Delta K_{th,material2} & \varphi_M - 180° < \varphi < \varphi_M \end{cases} \tag{8}$$

The determination of the start and the direction of fatigue crack growth is shown in Fig. 9a. The first intersection of the stress function $\Delta\sigma_\varphi\sqrt{2\pi r}$ with the material function $\Delta K_{th}(\varphi)$ (Eq. 8) identifies the occurrence and the corresponding direction of crack growth, whereas the intersection of the stress function $\Delta\sigma_\varphi\sqrt{2\pi r}$ with the material function $\Delta K_C(\varphi)$ defines the occurrence of final failure of

the structure. For static loading the occurrence of unstable crack growth can be predicted using the material function $K_C(\varphi)$.
At first it is assumed that the crack is not able to grow resulting in a stress function without point of contact with the material function $\Delta K_{th}(\varphi)$. Subsequently the cyclic load will be increased until the corresponding stress function has a contact with the material function. At this point the crack is able to grow. Furthermore the point of contact defines the kinking angle φ_{TSSRB} due to the loading situation and the material gradation.

3.2.1 Mode I loading in a graded material

As a special case of a Mixed Mode loading at first a pure Mode I situation is considered. In Fig. 9a a single Mode I ($\Delta K_{II} = 0$) is considered leading to the reduced stress function $\Delta\sigma_\varphi\sqrt{(2\pi r)}$, see Eq. (9), derived from Eq. (5).

$$\Delta\sigma_\varphi\sqrt{2\pi r} = \Delta K_I \cos^3\frac{\varphi}{2} \tag{9}$$

The point of contact can be found at the polar coordinate $\varphi_M = 30°$ resulting in the kinking angle $\varphi_{TSSRB} = \varphi_M = 30°$. First experimental investigations considering the same loading condition and the same gradation angle φ_M confirm this theoretical concept (Fig. 9b). In spite of pure Mode I the crack kinks due to the material gradation. For the further crack propagation the kinked crack evokes a Mixed Mode loading situation.

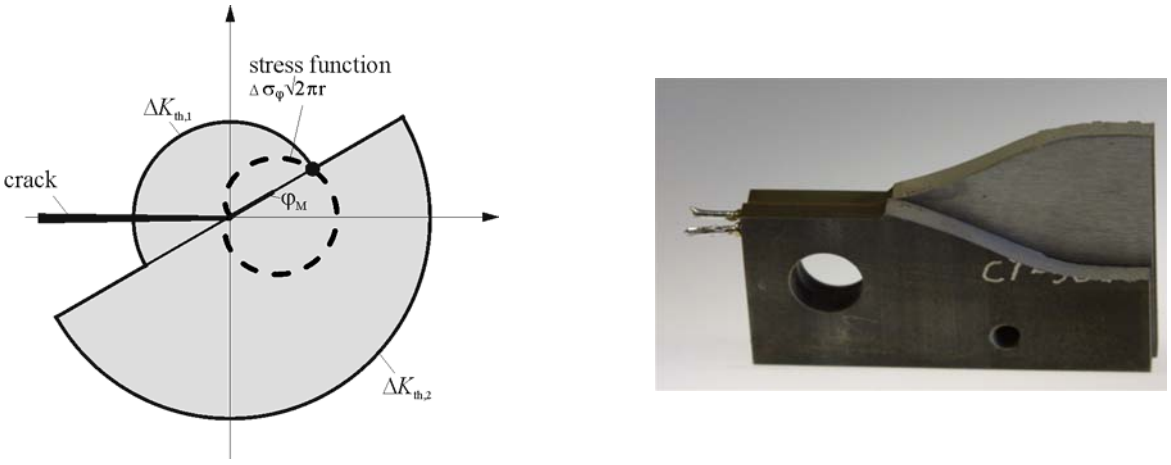

a) b)

Figure 9. a) Point of contact for the determination of occurrence and direction of fatigue crack growth for a Mode I loaded crack, b) experimental confirmation of the TSSR^B-concept

3.2.2 Mixed Mode loading in a graded material

The TSSR^B-concept can also be used for a Mixed Mode loading situation. Thereby the Mixed Mode ratio V, see Eq. (10), defines the combination of the pure loading cases Mode I and Mode II. Fig. 10 shows the stress functions $\Delta\sigma_\varphi\sqrt{(2\pi r)}$ (Eq. 11) for a Mixed Mode ratio V = 0,23, see also Eq. (5).

$$V = \frac{K_{II}}{K_I + K_{II}}. \tag{10}$$

$$\Delta\sigma_{\varphi}\sqrt{2\pi r} = \Delta K_{I}\cos^{3}\frac{\varphi}{2} - \Delta K_{II}\frac{3}{2}\sin\varphi\cdot\cos\frac{\varphi}{2}. \tag{11}$$

The structure in Fig. 10a and Fig. 10b possess different gradation angles φ_M. This difference in the gradation angle φ_M leads to a different kinking angle φ_{TSSRB} due to the loading condition and the material gradation. In Fig. 10a the gradation angle φ_M is 30°. The point of contact is at this coordinate leading to the kinking angle $\varphi_{TSSRB} = \varphi_M = 30°$. In Fig. 10b the structure possesses the gradation angle $\varphi_M = 60°$. Here the point of contact can be found at the coordinate with the largest stress. Hence the kinking angle $\varphi_{0,MTS} = -30°$ due to the loading condition, according to the MTS-concept of Erdogan and Sih, defines the kinking angle φ_{TSSRB} in this case.

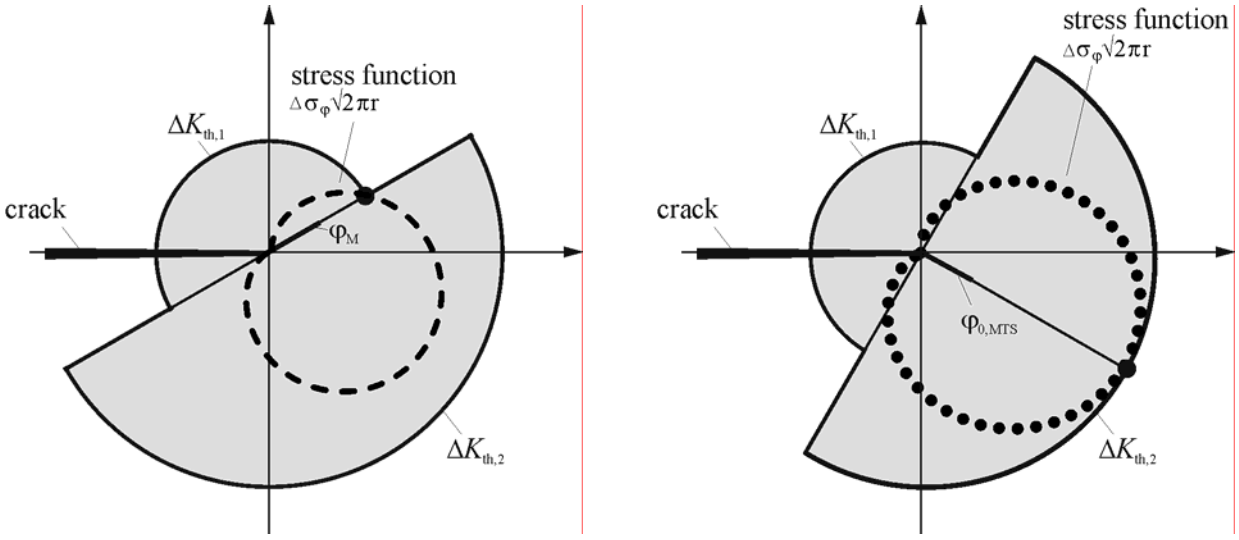

Figure 10. Occurrence and direction of fatigue crack growth for Mixed Mode loading in a fracture mechanical graded material: a) gradation angle $\varphi_M = 30°$, b) gradation angle $\varphi_M = 60°$.

In graded materials the crack propagation direction depends on the Mixed Mode loading situation and the material gradation. Which crack growth occurs can be determined with the TSSR^B-concept. Furthermore the concept enables the determination of the starting of fatigue crack growth and of unstable crack growth.

4. Conclusion

Using the presented TSSR^B-concept crack propagation as well as the direction of crack growth can be determined in fracture mechanical graded materials. By comparing the stress function $\Delta\sigma_{\varphi}\sqrt{2\pi}r$ with the material functions $\Delta K_{th}(\varphi)$, $\Delta K_C(\varphi)$ and $K_C(\varphi)$ the occurrence, the direction as well as the start of unstable fatigue crack growth and the start of unstable failure due to static loading can be determined. Furthermore this concept can also be modified for the application for an elastic material gradation as well as for the combination of a fracture mechanical and elastic material gradation.

Acknowledgements

This contribution is based on investigations of the collaborative research centre SFB/TR TRR30, which is kindly supported by the German research funding organisation (DFG).

References

[1] H.A. Richard, M. Fulland, M. Sander, Theoretical crack path prediction. In: Fatigue and Fracture of Engineering Materials and Structures 28 (2005) 3-12.
[2] H.A. Richard, F.G. Buchholz, G. Kullmer, M. Schöllmann, 2D- and 3D-Mixed Mode Fracture Criteria. In: F.G. Buchholz, H.A. Richard, M.H. Aliabadi (Eds.): Advances in Fracture Mechanics, Trans Tech Publications, Zürich, 2003, pp. 251-260.
[3] H.A. Richard, N.-H. Schirmeisen, A. Eberlein, Experimental investigations on mixed-mode-laded cracks. In: CD-Rom Proceedings of 4th International Conference on Crack Paths (2012) Gaeta, Italy.
[4] F. Erdogan, G.C. Sih, On the crack extension in plates under plane loading and transverse shear. In: Journal of Basic Engineering 85 (1963) 519-525.
[5] H.A. Richard, Bruchvorhersagen bei überlagerter Normal- und Schubbeanspruchung von Rissen. VDI-Verlag, Düsseldorf, 1985.
[6] H.A. Richard, Safety estimation for construction units with cracks under complex loading. In: International Journal of materials & Product Technology, 3 (1988) 326-338.
[7] H.A. Richard, Some theoretical and experimental aspects of mixed mode fractures. In: Valluri, S.R. et al. (Eds.) Advances in Fracture Research, Pergamon Press, Oxford, 1984, pp. 3337-3344.
[8] H.A. Richard, Major aspects of Mixed-Mode problems. In: CD-Rom Proceedings of ICF10 (2001) Honolulu, USA.
[9] K. Steinhoff, H.J. Maier, D. Biermann, Functionally Graded Materials in Industrial Mass Production, Verlag Wissenschaftliche Scripten, Auerbach, 2009.
[10] B. Schramm, H.A. Richard, Einfluss einer funktionalen Gradierung auf die Rissausbreitung. In: DVM-Bericht 244, Deutscher Verband für Materialforschung und – prüfung e.V., Berlin, 2012, pp. 201-210.
[11] H.A. Richard, B. Schramm, Influence of a functional gradation on crack propagation in real structures. In: Proceedings of the 19th Conference on Fracture (ECF19), Kazan, 2012.
[12] B. Schramm, H.A. Richard, M. Steigemann, M. Specovius-Neugebauer, Influence of a fracture mechanical gradation on crack propagation. Proceedings of 1st International Conference on Thermo-Mechanically Graded Materials, Wissenschaftliche Scripten, Auerbach, 2012, pp. 169-174.

A CMOD-Based Hybrid Approach to Determine Fracture Resistance Curve

Wuchao Yang[1], Xudong Qian[1,*]

[1] Department of Civil and Environmental Engineering, National University of Singapore, Singapore 117576, Singapore
* Corresponding author: qianxudong@nus.edu.sg

Abstract This study proposes a hybrid approach that relies both on the numerically computed and on the experimentally measured load (P) versus the crack-mouth opening displacement (CMOD) relationships to derive the fracture resistance curve (J-R curve) for the mixed-mode I and II fracture specimen. The CMOD-based hybrid approach utilizes a single experimental specimen with a growing crack and multiple finite element (FE) models, each with a different crack depth. The experimental procedure measures the P-CMOD curve from a standard fracture specimen with a growing crack. The intersections between the experimental P-CMOD curve and the numerical P-CMOD curves from multiple FE models dictate the CMOD levels to compute the strain energy (U). This approach simplifies the J-R curve test for the single-edge-notched bend, SE(B), specimen by eliminating the multiple unloading and reloading procedures in determining the variation of the compliance during the test. This method also provides an alternative simple measurement of the J-R curves for mixed-mode I and II specimens. The validation procedure shows accurate predictions of the J-R curves for both SE(B) specimens and mixed-mode I and II specimens.

Keywords mixed-mode fracture, fracture resistance, J-R curve, hybrid approach.

1. Introduction

The traditional load-line displacement (LLD) based incremental method has become widely implemented as a convenient experimental method to determine the fracture resistance curve, namely the J-R curve, for the SE(B) specimen, as recommended by the testing standards [1, 2]. The measurement of the specimen compliance at the each unloading and reloading procedure leads to a direct evaluation of the crack extension (Δa). The area under the load versus the LLD curve corresponding to different crack lengths allows the calculation of the energy release rate, J-value [3]. However, the measurement of the LLD for the SE(B) specimen requires extreme effort to prevent the potential errors introduced by the indentation at the loading point and the deformation of the testing frame [4]. In addition, the fracture toughness tests for the mixed-mode I and II specimens face critical challenges such as the calculation of the J-value and the determination of Δa [5]. The evaluation of the bending strain energy, which contributes to the J-value, depends on the current crack size (a_i) which cannot be determined via the traditional compliance approach for mixed-mode I and II specimens due to the unknown crack path prior to the test. Therefore, the experimental determination of the fracture resistance curve for both pure mode I SE(B) specimen and the mixed-mode I and II specimen requires a simplified and accurate approach based on the readily measurable quantities from the tests.

This study proposes a hybrid, numerical and experimental approach to determine the fracture resistance curve based on the readily measureable load versus CMOD (or Δ) relationship for SE(B) specimen (CMOD-hybrid approach). This research also extends the same approach to determine the fracture resistance for the mixed-mode I and II specimens. The J-value is derived from the variation in the total strain energy (including the bending and shear strain energy) with respect to the change in the crack depth, using the P-Δ curve measured from a single experimental specimen and P-Δ curves computed from multiple FE models with different crack sizes. The comparison of the fracture resistance curve obtained using the CMOD-hybrid approach with those obtained from the experimental results for both the SE(B) specimens and mixed-mode I and II specimens confirms the accuracy of the proposed CMOD-hybrid approach.

2. The CMOD-Based Hybrid Approach

The fundamental principle underlying the hybrid numerical and experimental approach remains similar to that of the conventional, multiple-specimen experimental approach proposed by Begley and Landes [6]. The procedure in the CMOD-hybrid approach follows similarly the hybrid approach, which relies on the *P*-LLD relations, proposed by the authors [7, 8], as illustrated in Figure 1. The numerical analyses of the hybrid approach generate a series of *P*-Δ curves from large-deformation, elastic-plastic analyses of multiple FE specimens with the same geometry, dimension and material, but different crack sizes. The experimental part of the hybrid approach produces the *P*-Δ curve for a fracture specimen with a growing crack.

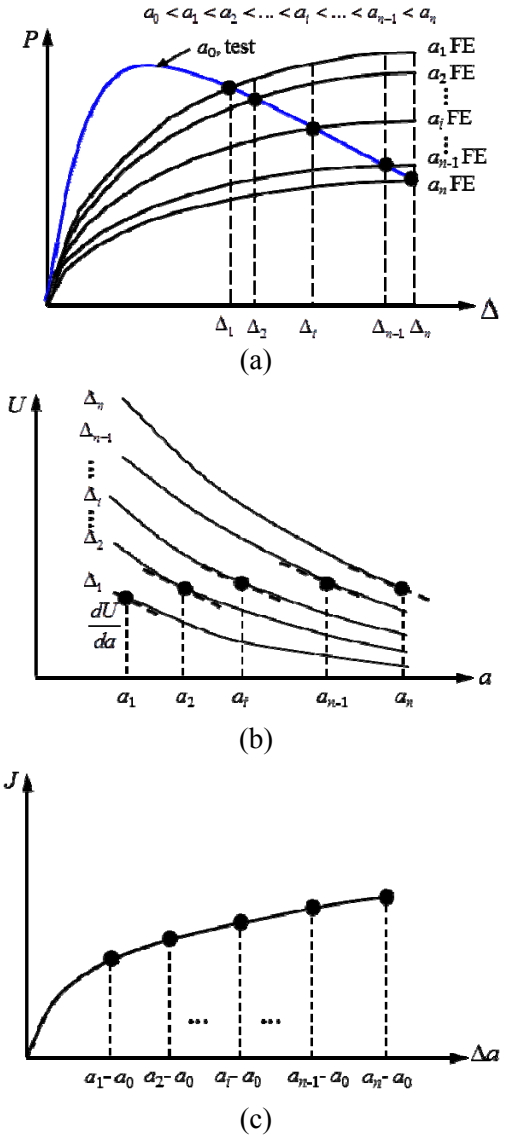

Figure 1. Schematic description for the proposed CMOD-based hybrid approach to determine the ductile fracture resistance.

Figure 1a illustrates the *P*-Δ curve obtained from the experimental specimen with the initial crack depth of a_0 and those obtained from the FE models with crack sizes ranging from a_1 to a_n. The intersection point between the experimental *P*-Δ curve and the numerical *P*-Δ curve defines a common loading and CMOD level in the FE specimen with a stationary crack and the experimental specimen with a growing crack. The crack extension (Δa_i) in the experimental specimen assumes a

value of ($a_i - a_0$) at the intersection of the test P-Δ curve and the numerical P-Δ curve computed from the FE model with a crack size of a_i. Since the crack size of the FE model equals the current crack size in the experimental specimen, the energy release rate calculated from the multiple FE specimens, using the same approach as the conventional multiple-specimen experimental approach, represents the J-value in the experimental specimen with the corresponding crack size.

The CMODs corresponding to the intersection points between the experimental curve and the numerical curves, *i.e.*, Δ_1 to Δ_n in Figure 1a, define the CMOD levels to compute the strain energy U for each crack depth. The evaluation of the strain energy U from the P-Δ curve becomes the primary step in applying the CMOD-based hybrid approach. Since the strain energy for the SE(B) specimen dissipates mainly through the rotation of the crack plane, the strain energy U equals the bending strain energy in the mode I SE(B) specimen. Based on the J-integral calculation proposed by Tohgo and Ishii [9], the bending strain energy for SE(B) specimen follows,

$$U_I = \int M d\theta \,. \tag{1}$$

Equation (1) also represents the mode I strain energy in mixed-mode I and II specimens. In such mixed-mode specimens, the shear strain energy follows,

$$U_{II} = \int F_V d\delta_V \,, \tag{2}$$

where, F_V is the shear force on the crack plane, and δ_V corresponds to the relative shear displacement between two crack planes. For the SE(B) specimens, the shear force remains zero and the bending moment M derives from equilibrium principles. The rotation of the crack plane, θ, depends on the current crack length,

$$\theta_i = \frac{\text{CMOD}}{a_{i-1} + r_p(W - a_{i-1})}, \tag{3}$$

where r_p represents the plastic rotation factor and equals 0.44 as suggested in ASTM E1820 [1] for SE(B) specimens, a_{i-1} corresponds to the crack depth determined at the previous intersection point between the experimental P-Δ curve and that obtained from the FE analysis, as demonstrated in Figure 1a.

Figure 1b illustrates the schematic variation of the strain energy with respect to the crack depth, calculated from multiple FE models. To facilitate the calculation of the energy release rate from the FE models, the hybrid approach utilizes a regression analysis to derive approximate polynomial functions in terms of the crack size, a, to describe the strain energy variations shown in Figure 1b. The solid circles in Figure 1b indicate the displacement level where the energy release rate calculated from multiple FE models equals (theoretically) the energy release rate in the experimental fracture specimen with a growing crack. The J-values at these solid circles are computed from Eq. (4),

$$J = -\frac{1}{B}\frac{dU}{da}. \tag{4}$$

Figure 1c sketches the J-values calculated at these solid circles with respect to the corresponding crack extensions. Tohgo and Ishii [9] separated the J-value for mixed-mode I and II specimens as,

$$J_T = J_I + J_{II} \,, \tag{5}$$

where, J_I and J_{II} correspond to the energy release rate contributed by the bending and shear deformation of the crack plane, respectively.

3. Validation on SE(B) Specimen

This section presents the validation of the proposed CMOD-based hybrid approach based on the

fracture resistance test results for the SE(B) specimens made of aluminum alloy (Al-alloy) 5083 H-112 reported by the authors [5]. The Al-alloy has a Young's modulus E of 69 GPa, with a Poisson's ratio of $\upsilon = 0.3$, the yield stress of $\sigma_y = 243$ MPa and the ultimate stress of $\sigma_u = 347$ MPa. Figure 2a presents the uniaxial stress-strain curves for the aluminum alloy material obtained from the axial tension test.

Figure 2a sketches the geometry of the SE(B) specimen. The total thickness of all the SE(B) specimen equals $B = 18$ mm, with the net-thickness after side-grooving equal to 80% of the total thickness, or $B_N = 0.8B$. The width of the specimen, W, equals to 36 mm, while the span over width, S/W, has a constant ratio of 4 for all SE(B) specimens. The CMOD or Δ is measured by the crack opening displacement gauge mounted at the mouth of the crack. The initial crack depth over the width ratios, a_0/W, equal 0.222 and 0.513 for the Al-alloy SE(B) specimens. The SE(B) specimen with a relatively shallow crack depth ($a_0/W \approx 0.2$) represents a fracture specimen with low crack-front constraints, while the deep crack ($a_0/W \approx 0.5$) corresponds to a high crack-front constraint condition complying with the ASTM E-1820 requirement [1].

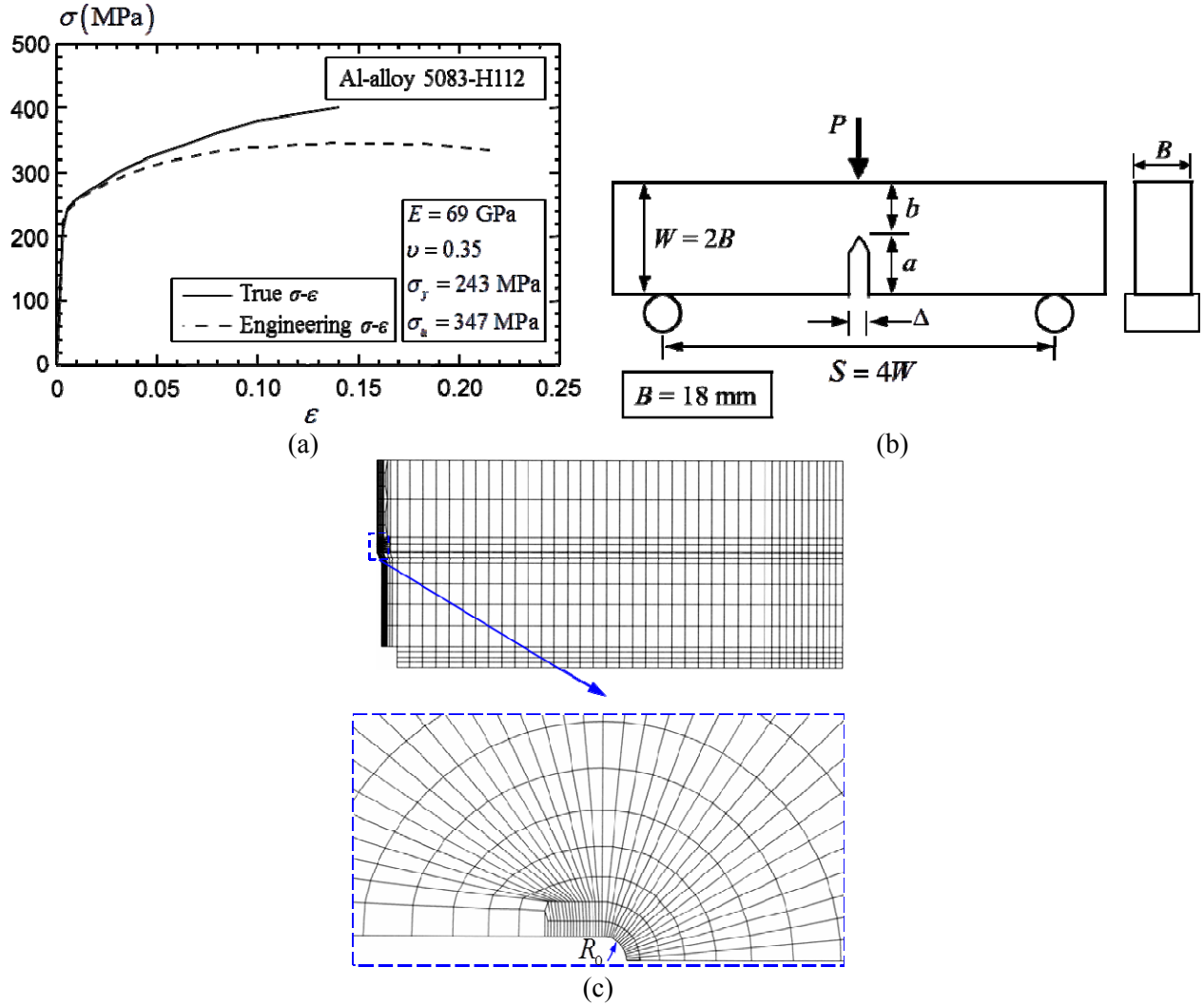

Figure 2. (a) Uniaxial stress-strain curves for the aluminum alloy material; (b) geometric configuration of the SE(B) specimen; and (c) the typical FE mesh for the SE(B) specimen.

Figure 2c shows a typical, half FE model for the Mode I SE(B) specimens, built from 3D 8-node brick elements. The FE model consists of one-layer of elements in the thickness direction, with all nodes in the FE model constrained against the out-of-plane displacement to represent the

plane-strain condition. The presence of a plane of symmetry enables a half model, with the displacement degree of freedom for all nodes on the plane of symmetry constrained in the direction normal to that plane. The crack-tip contains a focused mesh with an initial root radius of R_0 = 25 μm to facilitate numerical convergence under large deformations, as shown in Figure 2b. The total number of nodes in the FE models with different crack depths varies from 2000 to 3000, with the number of elements ranging from 1000 to 1500. The numerical computation in this study utilizes the FE research code, WARP3D [10].

For the Al-alloy SE(B) specimen with a_0/W = 0.222, this study generates thirteen FE models to compute the strain energy at thirteen different crack extensions (Δa_i), as summarized in Table 1. For the deep cracked SE(B) specimen with a_0/W = 0.511, the validation utilizes twelve FE models with various crack lengths to represent twelve different crack extensions (Δa_i), as shown in Table 1.

Table 1. The crack size in the FE models for the two SE(B) specimens made of Al-alloy 5083 H-112.

a_0/W	a_0 (mm)	Crack extensions (mm)					
		Δa_1	Δa_2	Δa_3	Δa_4 to Δa_{11}	Δa_{12}	Δa_{13}
0.222	8.0	0	0.2	0.5	1 to 4.5 @ 0.5 mm increment	5	5.5
0.511	18.5	0	0.2	0.6	1.2 to 5.4 @ 0.6 mm increment	6	-

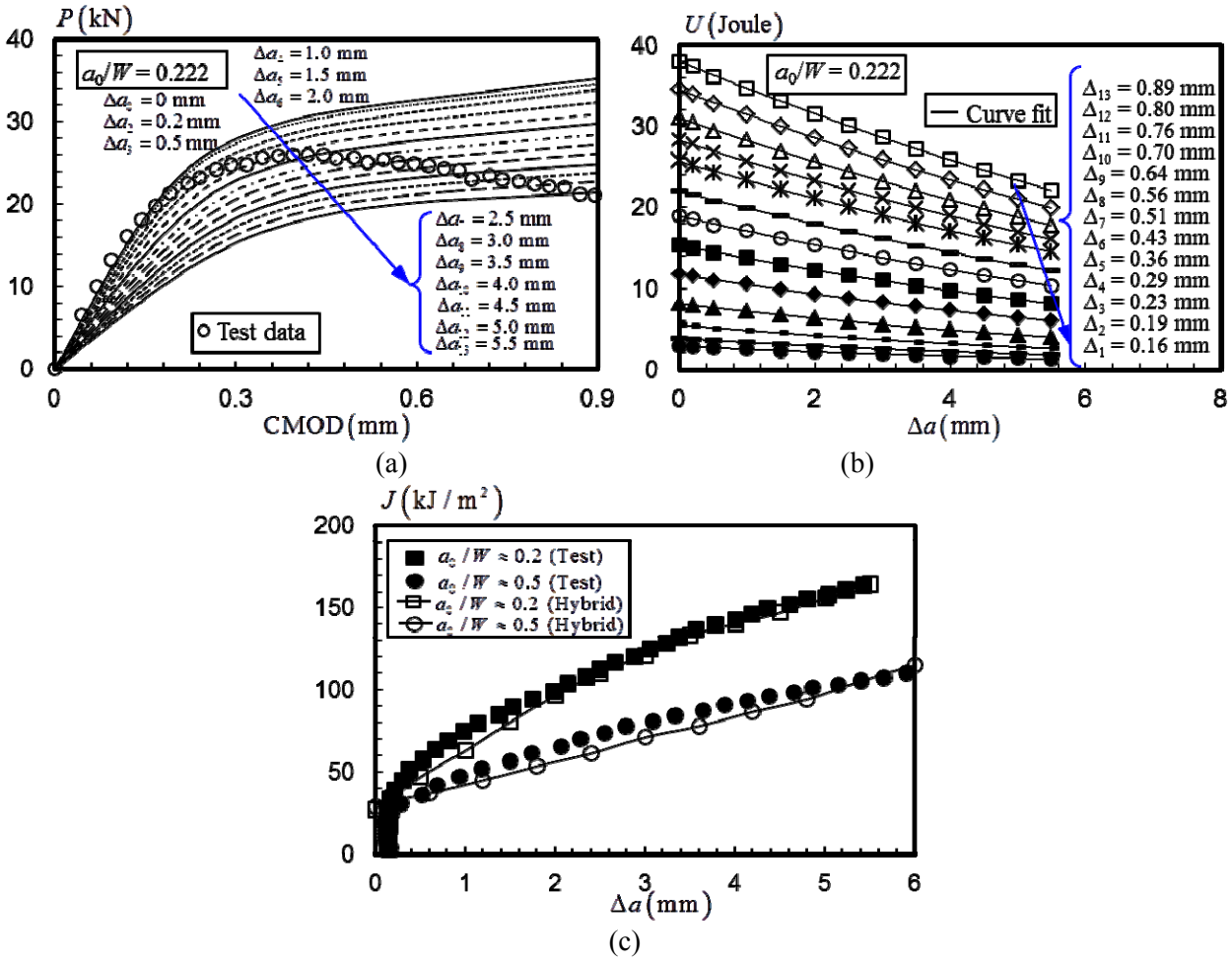

Figure 3. (a) P-Δ curve for SE(B) specimen with a_0/W=0.222; (b) U-Δa curves for SE(B) specimen with a_0/W=0.222; and (c) comparison of the J-R curves measured in the test and those derived from the CMOD-based hybrid approach for both shallow and deep cracked SE(B) specimens.

Figures 3a shows the P-Δ relationships for the experimental specimen of a_0/W = 0.222 with a growing crack indicated by the discrete circular symbols. The good agreement between the test data and the FE results at the zero crack extension, Δa = 0, confirms the boundary conditions of the FE models. In addition, the numerical P-Δ curve computed from the FE model with the same crack size as the experimental specimen at the end of the fracture test intersects with the test P-Δ curve at the end of the measured history. Figure 3b shows the strain energy U versus the crack extension evaluated from the P-Δ curves for the shallow cracked SE(B) specimen. The U value is computed at varied CMOD levels (Δ_i), which correspond to the intersections between the experimental and numerical P-Δ curves. The discrete symbols in Figure 3b represent the strain energy value computed from the FE model with the corresponding initial crack lengths $a_0+\Delta a_i$. The solid lines in Figure 3b correspond to the second-order polynomial functions derived from the regression analysis.

The J-value corresponding to each crack extension, Δa_i, can be derived from Eq. (4), using the first-order derivative of the fitted polynomial for the strain energy U (at the corresponding Δ_i) with respect to the crack depth. This leads to a J-R curve schematically shown in Figure 1c. The determination of the J-R curve by the CMOD-based hybrid approach for the SE(B) specimen with a_0/W = 0.511 follows the same procedures described in Figure 3a and 3b. Figure 3c compares the experimental J-R curves with those determined from the CMOD-based hybrid method for SE(B) specimens with two crack depth ratios, a_0/W = 0.222 and 0.511. The J-R curves obtained from the CMOD-based methods agree closely with the test results for both the shallow-crack and the deep-crack SE(B) specimens. This validates both the applicability and the accuracy of the CMOD-based hybrid method in determining the J-R curves for SE(B) specimens.

4. Validation on the Mixed-Mode Specimens

The verification of the hybrid method on the determination of the J-R curves utilizes two mixed-mode Al-alloy 5083 H-112 specimens reported by the authors [5, 11], the mode I dominant specimen AM1 (mode-mixity $\beta_{eq} = \tan^{-1}(K_I/K_{II}) = 75^o$) and the mode II dominant specimen AM5 ($\beta_{eq} = \tan^{-1}(K_I/K_{II}) = 20^o$) [5].

Figure 4a and 4b shows the typical FE models for the two mixed-mode specimens, AM1 and AM5. The geometrical configurations and the orientation of the crack planes follow exactly the test procedures described by the authors [5, 11]. Figure 4c and 4d illustrates the close-up view of the region around the crack tips for AM1 and AM5, respectively. The crack path deviates by 20^o from the original crack plane in the mode I dominant specimen AM1 and by 9^o from the original crack plane in the mode II dominant specimen AM5. The multiple FE models have varied crack lengths of $a_0+\Delta a_i$ along the crack directions observed from the tests, which have been summarized in Table 2. The verification of the CMOD-based hybrid approach on the mixed-mode specimens includes eight and six FE models with different crack sizes for the mode I dominant AM1 and the mode II dominant specimen AM5, respectively, as shown in Table 2. The crack tips for both specimens are simulated with an initial root radius of 25 μm to facilitate the convergence of the large-deformation analysis, similar to the method shown in the Figure 2c. The element type, boundary conditions and the calculation procedures follow similarly the methods described by Qian and Yang [7]. The material properties of the elements remain the same as those shown in Figure 2a.

Figure 5a and 5b show the M-θ curves and the F_V-δ_V relationships computed from the FE models listed in Table 2. The circles in Figure 5a and 5b represent the test results for AM1. Figure 5c and 5d illustrate the mode I strain energy U_I versus Δa curves and the mode II strain energy U_{II} versus Δa curves evaluated from the FE results at varied deformation levels listed in Table 2. The symbols

in Figure 5c and 5d represent the strain energy evaluated at different deformation levels (θ_i or δ_{Vi}) as listed in Table 2. The solid lines correspond to the fitted second-order polynomial functions, which are utilized to determine the first-order derivatives at various crack extensions.

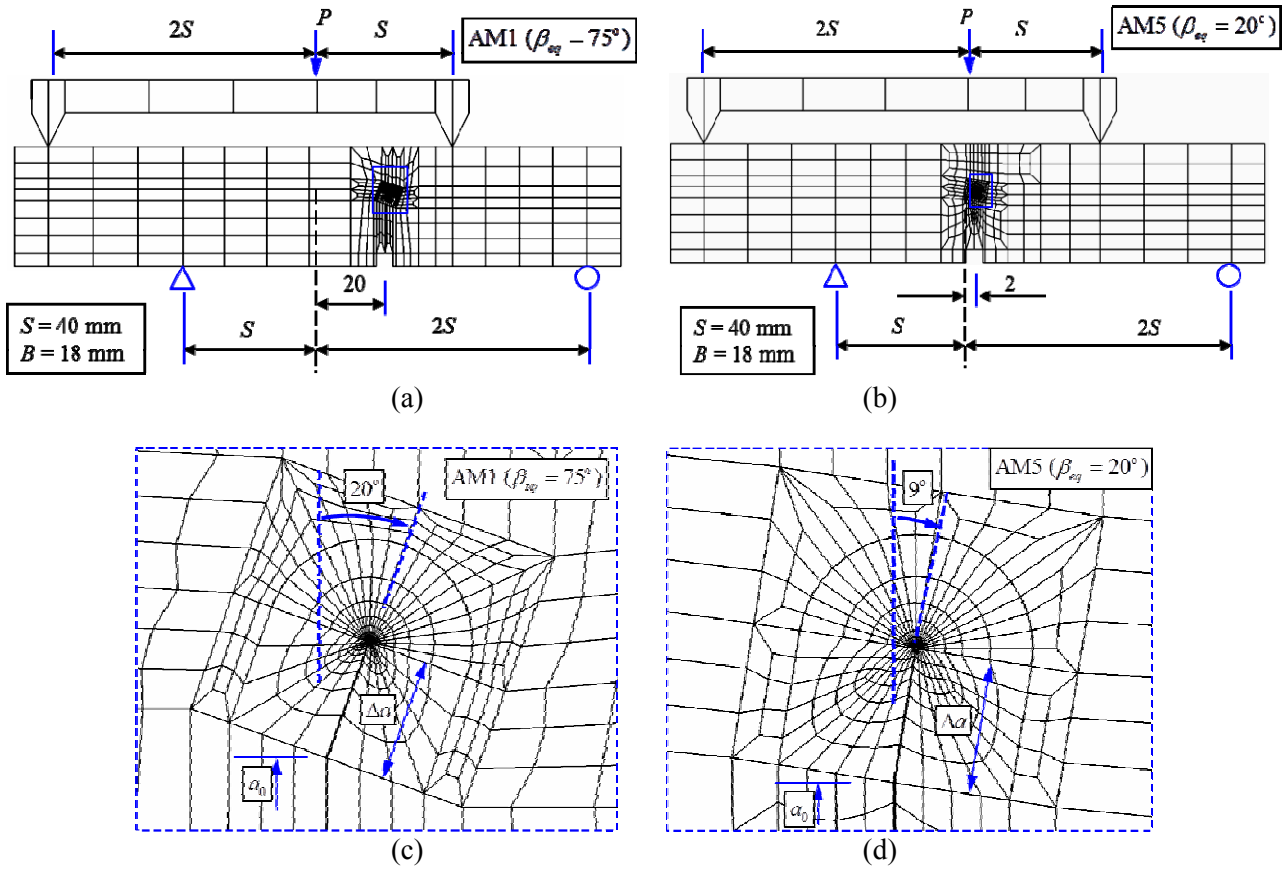

Figure 4. Typical FE models for the mixed-mode specimens made of Al-alloy 5083 H-112: (a) global FE model of the Mode I dominant specimen AM1; (b) global FE model of the Mode II dominant specimen AM5; (c) a close-up view around the crack tip for AM1; and (d) a close-up view around the crack tip for AM5.

Table 2. FE models for the mixed-mode I and II specimens made of Al-alloy 5083 H-112.

Specimen	Crack Parameters	FE models								
		$i = 0$	$i = 1$	$i = 2$	$i = 3$	$i = 4$	$i = 5$	$i = 6$	$i = 7$	$i = 8$
AM1 (Mode I dominant)	Δa (mm)	0	0.1	0.3	0.7	1.7	2.7	3.7	4.7	5.7
	θ (rad)	-	0.0247	0.0288	0.0356	0.06	0.0816	0.0924	0.106	0.115
	δ_V (mm)	-	0.052	0.09	0.159	0.273	0.486	0.588	0.672	0.749
AM5 (Mode II dominant)	Δa (mm)	0.15	0.5	1.0	2.0	3.0	3.9	4.5	-	-
	θ (rad)	-	0.017	0.019	0.021	0.022	0.023	0.024	-	-
	δ_V (mm)	-	0.604	0.731	0.911	1.050	1.233	1.412	-	-

Figure 6 compares the fracture resistance curves obtained from the hybrid approach and the test for AM1. Both the J_I-Δa and J_{II}-Δa hybrid results agree well with the test data at small crack extension, *i.e.*, $\Delta a < 1$ mm, as shown in Figure 6a. Figure 6a also shows that the hybrid approach leads to slightly lower J_I-Δa curve when $\Delta a > 1$ mm, due to the combined mode I dominant and mode II dominant fracture failure across the thickness of the specimen [11]. In general, the good agreement between the total J versus Δa curves determined using the hybrid approach and that obtained from

the test confirms the applicability of the hybrid method in predicting the fracture resistance for the Mode I dominant specimen AM1.

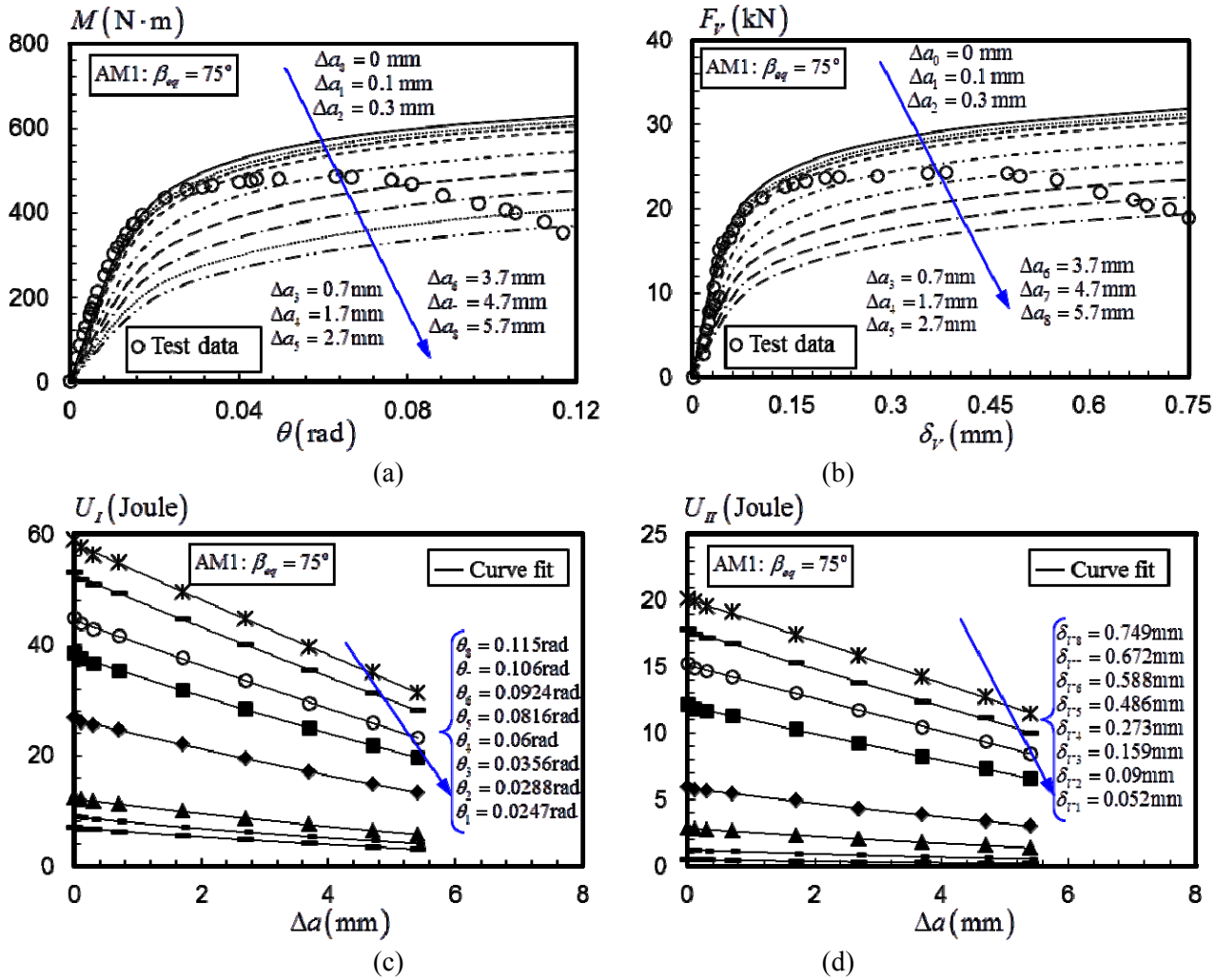

Figure 5. Determination of the strain energy for the Mode I dominant specimen, AM1: (a) The moment-rotation curves computed from multiple FE models; (b) the shear force versus shear deformation computed from multiple FE models; (c) the Mode I strain energy versus the change in the crack size; and (d) Mode II strain energy versus the change in the crack size.

Figures 6c and 6d compare the *J-R* curves reproduced from the hybrid approach and those obtained from the test for mode II dominant specimen, AM5. Very close agreement between the results obtained from these two methods is observed when $\Delta a < 1$ mm, as shown in Figure 6c and 6d. As $\Delta a > 1$ mm, the hybrid approach yields slightly lower (conservative) *J-R* curves.

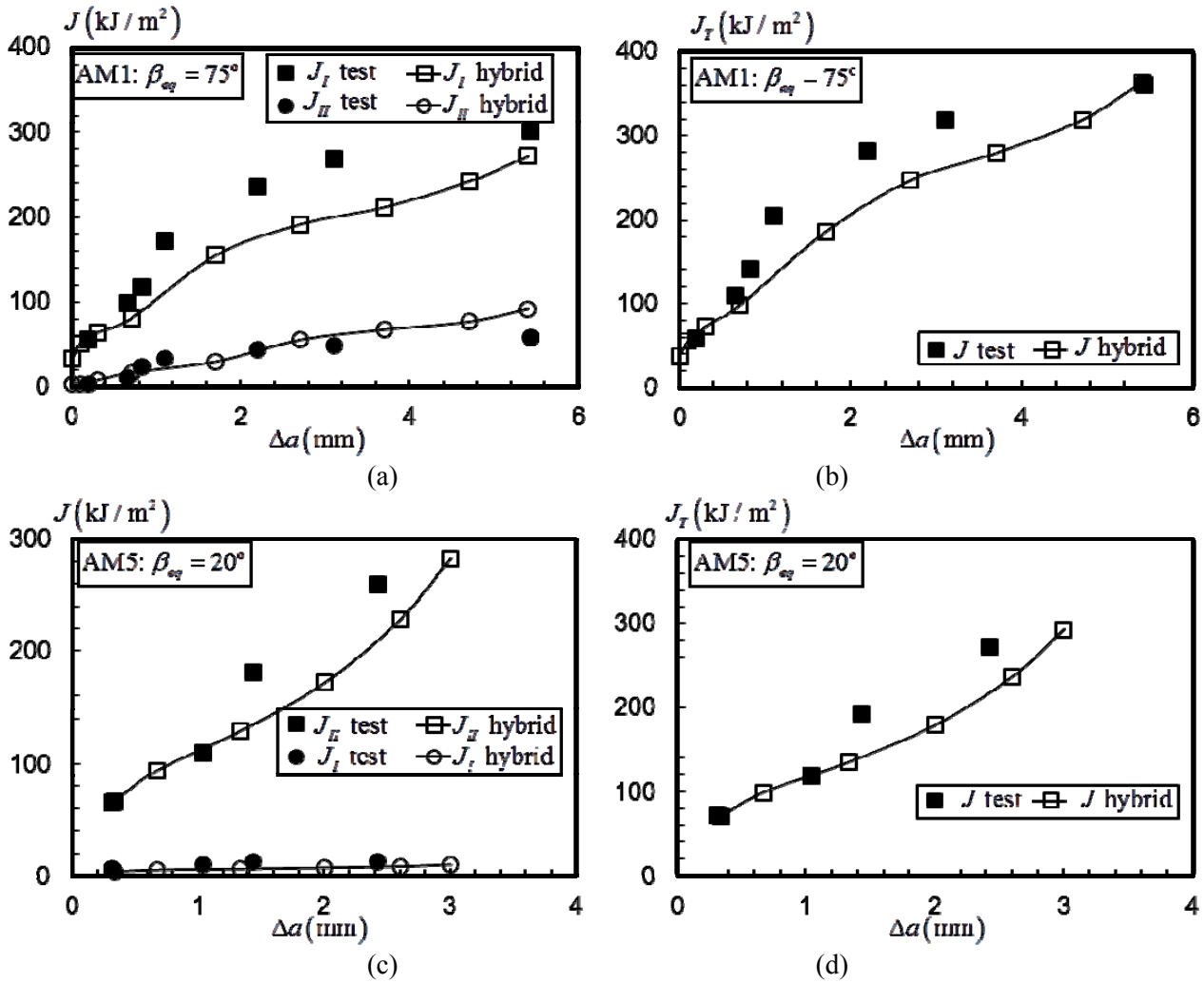

Figure 6. Verification for the mixed-mode specimen: (a) the Mode I and Mode II fracture toughness versus the crack extensions for AM1; (b) the total fracture toughness versus the crack extension curves for AM1; (c) the Mode I and Mode II fracture toughness versus the crack extensions for AM5; and (d) the total fracture toughness versus the crack extension curves for AM5.

5. Summary and Conclusions

The proposed CMOD-based hybrid method relies on a single experimental *P*-Δ curve and multiple numerical *P*-Δ curves to derive the fracture resistance curve for both the SE(B) specimen and the mixed-mode I and II specimen. The CMOD-based hybrid method simplifies the *J*-*R* curve testing procedure by eliminating the multiple unloading and reloading sequences, required to determine the specimen compliance and hence the crack size. The current CMOD-based hybrid method removes the dependence on the LLD, which requires careful instrumentation to prevent possible errors introduced by the indentation at the loading point. The close agreement between the *J*-*R* curves derived from the CMOD-based hybrid approach and those determined from the tests validates the proposed hybrid approach for both the SE(B) specimens and the mixed-mode I and II specimens.

References

[1] American Society for Testing and Materials, Standard test method for measurement of fracture toughness. ASTM E1820-11. West Conshohocken, PA, United States, 2011.
[2] International Standard Organization. Metallic Materials-Unified Method of Test for the

Determination of Quasistatic Fracture Toughness. International Standard ISO 12135, International Organization for Standardization, 2002.
[3] X. K. Zhu, J. A. Joyce, Revised incremental J-integral equations for ASTM E1820 using crack mouth opening displacement, J Test Eval, 37 (2009) 205-214.
[4] J. A. Joyce, Manual on elastic-plastic fracture: laboratory test procedures. West Conshohocken, PA, United States, American Society for Testing and Materials, 1996.
[5] X. Qian, W. Yang, Initiation of Ductile Fracture in Mixed-mode I and II Aluminium Alloy Specimens. Eng Fract Mech, 93 (2012) 189-203.
[6] J. A. Begley, J. D. Landes, The J-integral as a fracture criterion. ASTM STP 514 (1972) 1-20.
[7] X. Qian, W. Yang, A hybrid approach to determine fracture resistance for mode I and mixed mode I and II fracture specimens. Fatigue Fract Eng Mater Struct. 34 (2011) 305-320.
[8] X. Qian, W. Yang, A Hybrid Approach To Determine Ductile Fracture Resistance. Procedia Engineering. 10 (2011) 319-24.
[9] K. Tohgo, H. Ishii, Elastic plastic fracture-toughness test under mixed-mode I-II loading. Eng Fract Mech, 41 (1992) 529-40.
[10] A. Gullerud, K. Koppenhoefer, A. Roy, S. RoyChowdhury, M. Walters, B. Bichon, K. Cochran, A. Carlyle, R. H. Jr. Dodds. WARP3D: 3-D dynamic nonlinear fracture analysis of solids using parallel computers and workstations. Structural Research Series (SRS) 607 UILU-ENG-95-2012 University of Illinois at Urbana Champaign.
[11] W. Yang, X. Qian, The fracture resistance curve over the complete mixed-mode I and II range for aluminium alloys. Eng Fract Mech, 96 (2012) 209-225.

Simulation of fracture and fatigue damage in stainless steel 304 using a cohesive zone model

Huan Li, Huang Yuan*

Department of Mechanical Engineering, University of Wuppertal, Germany.
* Corresponding author: h.yuan@uni-wuppertal.de

Abstract In the present paper a cohesive zone model coupled with monotonic and cyclic damage mechanisms for simulating elastic-plastic fracture and fatigue crack growth is introduced and applied for investigating failure processes in compact tension specimens. Fracture and fatigue crack tests are conducted on the compact tension C(T) specimen made of stainless steel 304 to study crack growth behavior under fracture and low cycle fatigue loading condition associated with severe elastic-plastic deformations. A good agreement between the prediction and the experimental result is obtained from the present simulations. It confirms that the suggested cohesive model in conjugation with the nonlinear damage evolution equations is applicable for describing the material degradation behavior of stainless steel 304 under both monotonic and cyclic loading with large plastic deformations.

Keywords Cohesive model, damage evolution, low cycle fatigue, elasto-plastic growth, crack growth rate

1. Introduction

Fatigue crack in industrial components are often subjected to heavy cyclic loading, and it is important to predict the fatigue crack growth behavior under higher stress fields. In low cycle metal fatigue problems, e.g. under loading conditions with maximum stresses beyond yield stress, specimens fail in small numbers of loading cycles.

Comparing with Paris' law, Walker model and Forman model or any other kinds of stress intensity factor based models, the cohesive model is more advantageous and gives the possibility to analyze the fatigue propagation behavior under severe plastic loading conditions, since the characterization of the cohesive zone model is generally applicable for inelastic materials [1-7]. Furthermore, it becomes possible to describe crack nucleation and propagation uniformly by the cohesive model.

Originally, the cohesive zone model was introduced to describe the fracture process zone ahead of the crack-tip by Dugdale [8] and Barenblatt [9]. In the last twenty years, the cohesive modeling has been applied in simulating monotonic fracture process for diverse materials and has also been verified by experimental results [10-13]. For the fatigue failure analysis, the loading history dependent development of material degradation has to be taken into account under cyclic loading. Establishing a physical solid cohesive model for finite fatigue life is under intensive investigation in many research groups worldwide [2, 3, 14-17].

In the present study, the fatigue crack propagation experiments have been conducted using compact tension C(T) of type 304 stainless steel associated with large plastic deformations. A cohesive model coupled with damage for prediction of fracture and fatigue behavior is introduced for elastic-plastic crack propagation associated with both normal and shear displacements of the crack surface. Both rupture damage and cyclic damage accumulation are considered in the damage evolution equations. The numerical results agree with experimental data and reproduce the high

fatigue crack propagation rate. The present analysis is limited to a two-dimensional configuration by the plane strain assumption.

2. Experimental arrangement

2.1. Material and specimens

The material used in the present investigation comes with 304 austenitic stainless steel cylindrical bars with a 200mm diameter. The mechanical properties were obtained through tensile test performed on cylindrical specimen of 6mm diameter and about 70mm gauge length. The C(T) specimens were fabricated following the ASTM E399. The dimensions of C(T) specimen are illustrated in Figure 1(a). The material curves are shown in Figure 1(b).

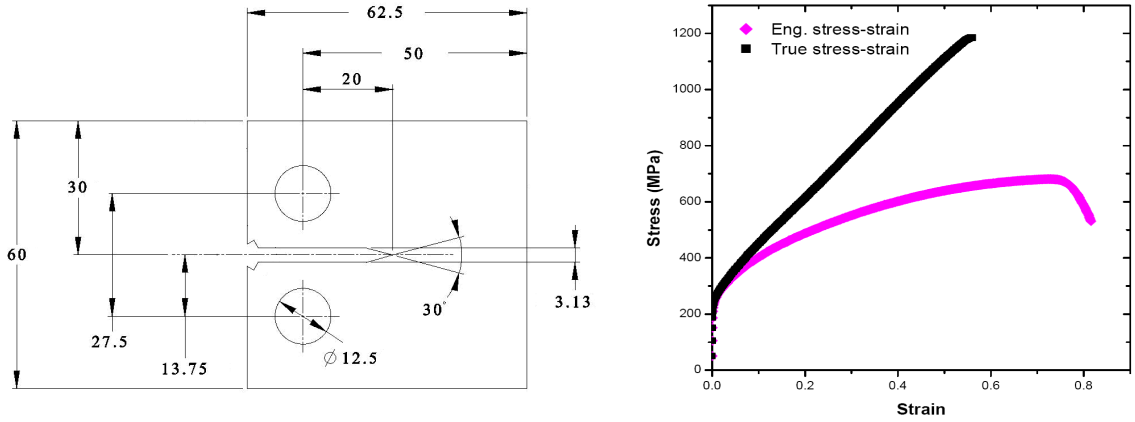

(a) (b)

Figure 1. (a) Dimensions of C(T) specimen, the thickness is 12.5mm. (b) Engineering and true stress-strain curves for the stainless 304 steel.

2.2. Experimental apparatus and conditions

The configuration of clevis used for C(T) specimen is based on ASTM E647. All fatigue pre-cracks of the specimens were generated under mode I loading using high frequency testing machine at a loading frequency of approx. 90 Hz. The fracture test was conducted to determine the plane strain fracture toughness of the stainless steel 304. Fatigue loading during the crack growth process was carried out in a MTS servo-hydraulic testing machine.

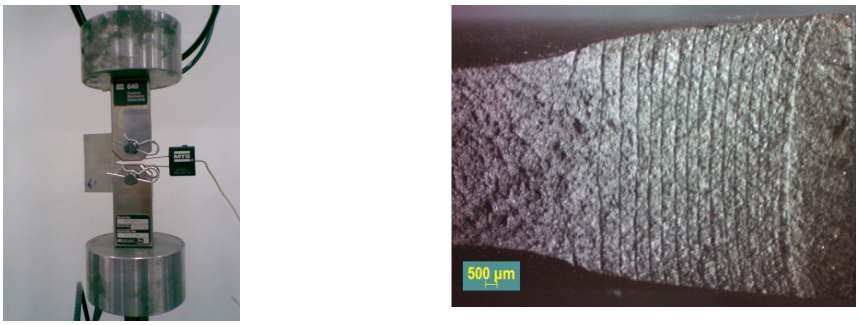

(a) (b)

Figure 2. (a) The compliance method and (b) beachmarks on the fracture surface for CT specimen.

The tests were performed in air at room temperature with sine waveform at a frequency of 8 Hz. The fatigue crack growth rate was measured by using the compliance method and also creating beachmark to record the crack front as displayed in Figure 2.

3. Cohesive zone model

3.1. Kinematics and constitutive relation under quasi-static and cyclic loading

Taking the principle of virtual work of the boundary value problem into account, the weak form of the equilibrium equation without body forces can be written as

$$\int_V \boldsymbol{\sigma} : \delta\boldsymbol{\varepsilon} \mathrm{d}V + \int_S \mathbf{T} \cdot \delta\boldsymbol{\Delta} \mathrm{d}S = \int_{\partial V} \mathbf{T}' \cdot \delta\mathbf{u} \mathrm{d}s \tag{1}$$

with $\boldsymbol{\sigma}$ as the Cauchy stress tensor, $\mathbf{T}'$ denotes the external traction vector and $<\delta\boldsymbol{\varepsilon}, \delta\boldsymbol{\Delta}, \delta\mathbf{u}>$ are the admissible displacement fields. The cohesive traction $\mathbf{T}$ is taken to have the following form,

$$\mathbf{T} = T_s\mathbf{s} + T_n\mathbf{n} = \frac{T}{\Delta}(\xi^2\Delta_s\mathbf{s} + \Delta_n\mathbf{n}), \tag{2}$$

where T_s and T_n are the cohesive traction components in shear and normal direction, respectively. Following the Ortiz et al. [1] and Ural et al. [17], the effective displacement jump Δ is a scalar parameter defined as

$$\Delta = \sqrt{\xi^2\Delta_s^2 + \Delta_n^2}, \tag{3}$$

where $\Delta_s = |\boldsymbol{\Delta}_s|$ and Δ_n are the displacement jumps in shear and normal directions and ξ weights the shear displacement jump over normal one. T is a scalar effective traction relates to the effective displacement jump Δ in the process zone where a crack may arise. The formulation of T used in the present study refers to a coupled damage model defined as

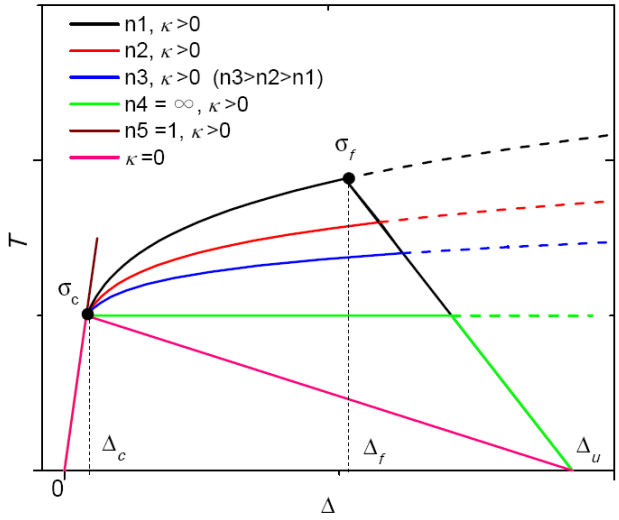

Figure 3. Illustration of the cohesive zone model under monotonic loading.

$$\Delta = \begin{cases} \dfrac{T}{\sigma_c}\Delta_c + \kappa\left(\dfrac{T}{\sigma_c}\right)^n & 0 \le \Delta \le \Delta_f \\ -\dfrac{T}{\sigma_f}\left(\Delta_u - \Delta_f\right) + \Delta_u & \Delta_f < \Delta \le \Delta_u \end{cases}, \tag{4}$$

where Δ_c is the onset of the displacement jump associated with initiation of the cohesive zone hardening, σ_c refers to the initial cohesive strength of the process zone corresponding to Δ_c and Δ_u is the final displacement jump which mirrors the complete loss of stress carrying capacity when the traction equals to zero. κ is a parameter which has the same unit as the displacement jump and n is the hardening exponent. Δ_f is the value of displacement jump after which the initiation of damage begins and the corresponding cohesive strength is σ_f, the effects of these parameters are shown in Figure 3. For the application of Eq. (4), the inequality must be satisfied that

$$T \le C(D) = \sigma_f(1-D), \tag{5}$$

where D is a scalar variable representing the overall damage in materials and C is identified with the cohesion as the function of the damage. The monotonic cohesive law is insufficient and the cyclic damage should be taken into account in the constitutive description. Should the cohesive model be applied for both fracture and fatigue crack growth, the material damage depends on both monotonic loading and loading cycles, i.e.

$$\frac{\mathrm{d}D}{\mathrm{d}t} = \dot{D} = \dot{D}_s + \dot{D}_c \tag{6}$$

with D_s for damage under monotonic loading and D_c for damage under cyclic loading. Obviously, both damage variables have to be expressed in evolution equations.

Under the monotonic loading condition, Eq. (4) denotes inelastic behavior of the material in the cohesive zone and Eq. (5) implies that the degradation of the material strength for $\Delta < \Delta_f$. For $\Delta > \Delta_f$, the damage grows and assumes to be expressed in a linear function of the displacement increment [17],

$$D_S = \frac{\Delta - \Delta_f}{\Delta_u - \Delta_f} \tag{7}$$

under monotonic loading condition.

For fatigue, the material should be damaged even under the cohesive strength, σ_f. The damage evolution equation proposed by Ural et al. [17] is used to characterize fatigue process reads

$$\dot{D}_c = \begin{cases} \alpha D_c(T-\beta C)\dot{\Delta} & T-\beta C > 0, \dot{\Delta} > 0 \\ \gamma D_c(T-\beta C)\dot{\Delta} & T-\beta C < 0, \dot{\Delta} < 0 \\ 0 & (T-\beta C)\dot{\Delta} < 0 \\ \dot{\lambda} & T = C, \dot{\Delta} > 0 \end{cases}, \tag{8}$$

where α and γ are two difference material constants used to conduct the damage accumulation during the reloading and unloading under the given conditions, respectively. The parameter β is adopted to denote the fatigue threshold in conjunction with the current cohesion C. The rate form of λ is a free variable is defined to represent the damage growth rate at a random stress state associated with the second equation of Eq. (4).

Following the suggestion in [17], the unloading and reloading paths of the present study can be

described in the incremental form as

$$\dot{T} = F(D)\dot{\Delta} \quad \text{with} \quad F(D) = \frac{\sigma_f(1-D)}{D(\Delta_u - \Delta_f) + q\Delta_c} \quad \text{and} \quad q = \frac{\sigma_f}{\sigma_c}. \tag{9}$$

The equation above indicates that the unloading/reloading stiffness the cohesive zone, $F(D)$, varies with D from σ_c/Δ_c for no damage (D=0) to zero for D=1.
The total damage in terms of a loading history should be the sum of the monotonic damage and cyclic damage

$$\dot{D} = \dot{D}_s + \dot{D}_c = \frac{\dot{\Delta}}{\Delta_u - \Delta_f} + \dot{D}_c \tag{10}$$

3.2. Implementation of cohesive element into ABAQUS

The commercial software ABAQUS[18] allows the user to define a new element conveniently, via the interface UEL. The formulation of the cohesive element is referred to the ABAQUS theoretical manual. We have to provide the cohesive element stiffness, the residual nodal force vector and derive the cohesive traction and displacement jump according to the cohesive law. These variables are needed to calculate the virtual work generated by the cohesive zone such that the internal work equals to the external virtual work for every kinematically admissible displacement field in accordance with Eq. (1). As illustrated in Figure 4, a four node cohesive element is defined in two dimensional x-y coordinates. The nodal displacement vector corresponding to 4 nodes is defined by

$$\mathbf{u} = [u_i, v_i]^{\mathrm{T}} \qquad i = 1, 2, 3, 4 \tag{11}$$

with u and v as nodal displacements in x and y direction, respectively. Then the local displacement jump vectors $\boldsymbol{\Delta}$ are written using the shape functions and the nodal displacement as

$$\boldsymbol{\Delta} = \begin{bmatrix} \Delta_s \\ \Delta_n \end{bmatrix} = \boldsymbol{\alpha}\mathbf{B}\mathbf{u} \tag{12}$$

with $\mathbf{B}$ as the matrix about the shape functions,

$$\mathbf{B} = \begin{bmatrix} -N_1 & 0 & -N_2 & 0 & N_2 & 0 & N_1 & 0 \\ 0 & -N_1 & 0 & -N_2 & 0 & -N_2 & 0 & N_1 \end{bmatrix}, \tag{13}$$

where N_1=(1-s)/2 and N_2=(1+s)/2 are linear interpolation functions in the intrinsic coordinate system and $\boldsymbol{\alpha}$ is the rotation matrix denoted by

$$\boldsymbol{\alpha} = \begin{bmatrix} \cos\theta & \sin\theta \\ -\sin\theta & \cos\theta \end{bmatrix}. \tag{14}$$

The cohesive element stiffness matrix and the traction force term are given by

$$\begin{aligned} \mathbf{K}^e &= \int_e \mathbf{B}^{\mathrm{T}}\mathbf{D}\mathbf{B}\mathrm{d}A = \frac{l_e}{2}\int_{-1}^{1} \mathbf{B}^{\mathrm{T}}\mathbf{D}\mathbf{B}\mathrm{d}s, \\ \mathbf{T}^e &= \int_e \mathbf{B}^{\mathrm{T}}\mathbf{T}\mathrm{d}A = \frac{l_e}{2}\int_{-1}^{1} \mathbf{B}^{\mathrm{T}}\mathbf{T}\mathrm{d}s, \end{aligned} \tag{15}$$

where l_e is the length of the element , $\mathbf{T}$ is the traction vector based on the Eq. (2) and $\mathbf{D}$ is the

material Jacobian matrix denoted as

$$\mathbf{D} = \begin{bmatrix} \dfrac{dT_s}{d\Delta_s} & \dfrac{dT_s}{d\Delta_n} \\ \dfrac{dT_n}{d\Delta_s} & \dfrac{dT_n}{d\Delta_n} \end{bmatrix}. \tag{16}$$

During the implementation, the matrices of Eq. (15) should be transformed to *x*-*y* coordinates according to Eq. (14).

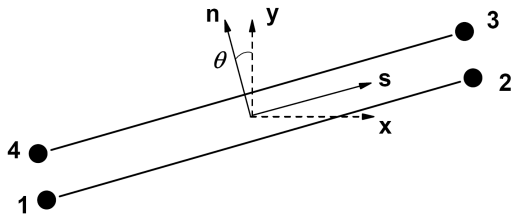

Figure 4. Illustration of a cohesive element

4. Results and discussion

4.1. Crack growth under monotonic loading

C(T) specimens were tested to determine cohesive parameters under monotonic loading. The load-displacement curve was recorded in the experiment. In computations the finite element mesh of the potential damage zone ahead of the crack tip is refined and the minimal element size is about 0.4mm. In the process of numerical simulation, cohesive elements are placed at the symmetric line of the mesh with zero thickness. The rest of region is occupied by the conventional four nodal elements under the plane strain assumption. The initial crack length is around 29mm. The stainless steel is described by the J_2 plasticity for simplicity.

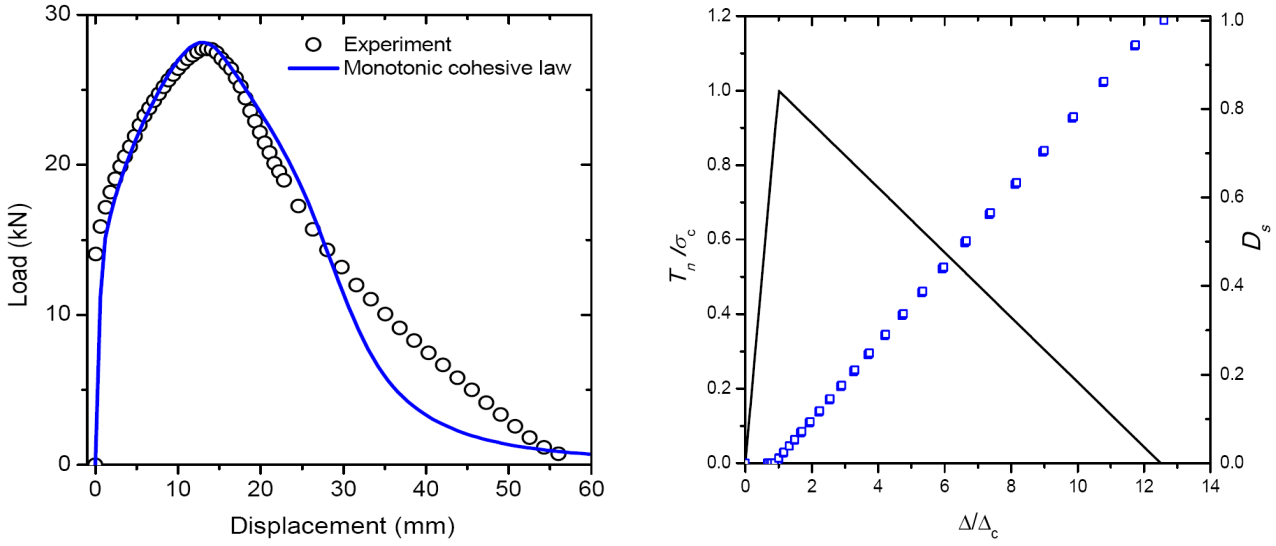

(a) (b)

Figure 5. Computational prediction of monotonic crack growth in a C(T) specimen. (a) Comparison between the simulation and the test result. (b) Cohesive response of a ruptured element during the crack propagation.

As mentioned in the previous sections, Eq. (4) shows the bilinear behavior if κ=0 under the monotonic loading and the initial cohesive strength of $\sigma_c=\sigma_f$ =1100MPa associated with $\Delta_c=\Delta_f$ =0.2mm. Computational simulation based on the cohesive zone model according to Eq. (4) is shown in Figure 5(a) for monotonic fracture. It confirms that the final displacement jump Δ_u=2.5mm gives a reasonable prediction in comparing with the experiment. This kind of the cohesive law is popular in simulation of quasi-brittle material failure. Figure 5(b) illustrates the cohesive response of a ruptured element along crack path, the static damage evolution of the element can be seen additionally and this result should be imagined according to Eq. (7) or Eq. (10).

4.2. Crack growth under cyclic loading

The crack growth under cyclic loading case is conducted within elasto-plastic region in this section. Considering the cyclic damage equation as mentioned in Eq. (8), the damage accumulation depends on the current cohesive traction and the increment of the displacement jump corresponding to the loading history. We use the concept of the loading cycles to capture the evolution of damage and predict the fatigue life. By recording the crack growth length, Δa, the fatigue crack growth rate can be determined by $\Delta a/\Delta N$. Since the global loading behavior of the C(T) specimen is represented by the amplitude of the stress intensity factor, ΔK, the numerical simulation by using the cohesive element can be verified through the experimental da/dN vs. ΔK curve.

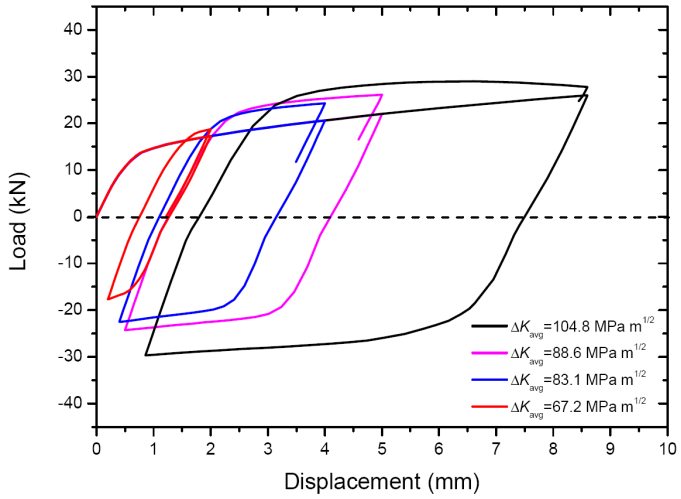

Figure 6. Four loading amplitudes for the CT specimen as a function of load line displacement.

As shown in Figure 6, four different loading amplitudes were performed under the displacement control at the loading ratio R=0.1. Because the stainless steel 304 is a cyclic instable material which associates the stress variation as a function of loading cycles, the average stress amplitude ΔK_{avg} is used to express the loading level during the crack growth process. The specimen dimensions and mesh configurations for the fatigue simulation are the same as those for the fracture test. The material parameters for the damage evolution are α=0.00053, β=0.15 and γ=0.0 combined with the monotonic cohesive law which has been determined from the fracture simulation. The damage growth process in an element ahead of the crack-tip is displayed in Figures 7, 8 and 9 under the conditions with ΔK_{avg}=83.1MPa m$^{1/2}$ and ΔK_{avg} =104.8 MPa m$^{1/2}$, respectively. In the figures, the traction and displacement jump are non-dimensionalized by σ_c and Δ_c, respectively. The negative displacement jump associated the compression of the crack surface is constrained by introducing a

penalty equation for contact. Comparing the amplitudes, the higher loading level results in a faster material degradation (Figure 7) and so shorter fatigue life (Figure 8). Actually, ΔK_{avg}=104.8 MPa $m^{1/2}$ asymptotically approaches the plain strain toughness K_c of 133MPa $m^{1/2}$ at the loading ratio R=0.1, larger amount of damage accumulation is coincident with that caused by the fracture loading. In Figure 8, the traction against the loading segment (half cycle) is illustrated in both loading and unloading path, no damage growth is assumed in the unloading path including the compression in terms of Eq. (8), as shown in Figure 9. In order to verify the simulation results, the popular crack growth law proposed by Erdogan et al. [19] is used to consider all ranges of cyclic crack growth which is given by

$$\frac{\mathrm{d}a}{\mathrm{d}N}=\frac{C(\Delta K-\Delta K_{\mathrm{th}})^{n}}{(1-R)K_{c}-\Delta K}, \tag{17}$$

where the fracture toughness of K_c=133MPa $m^{1/2}$, the threshold value of ΔK_{th} is 7.5MPa $m^{1/2}$ and material constants C=$10^{-5.578}$ and n=2.697 for correlating the experimental data. The computational result together with the experiment are compared in Figure 10, the prediction gives a better agreement with the test, especially in the region III of fatigue crack growth.

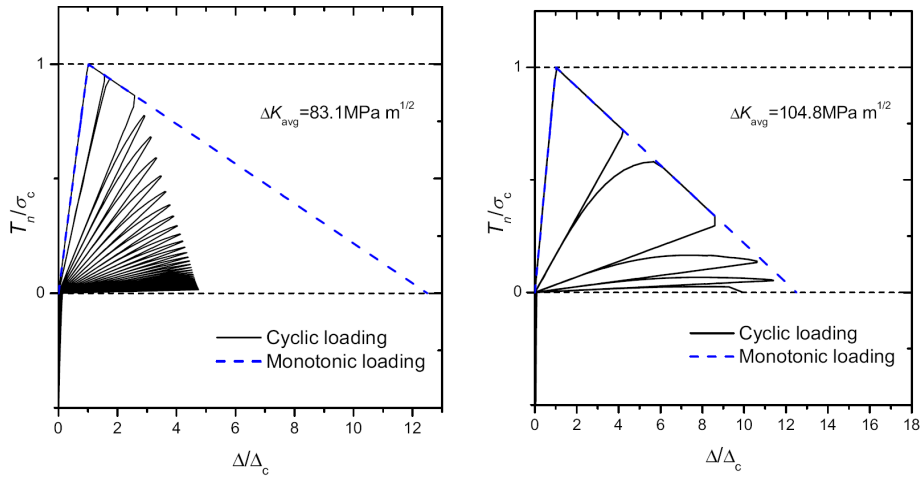

Figure 7. The traction vs. displacement jump curves in a cohesive element for ΔK_{avg}=83.1MPa $m^{1/2}$ and ΔK_{avg}=104.8MPa $m^{1/2}$.

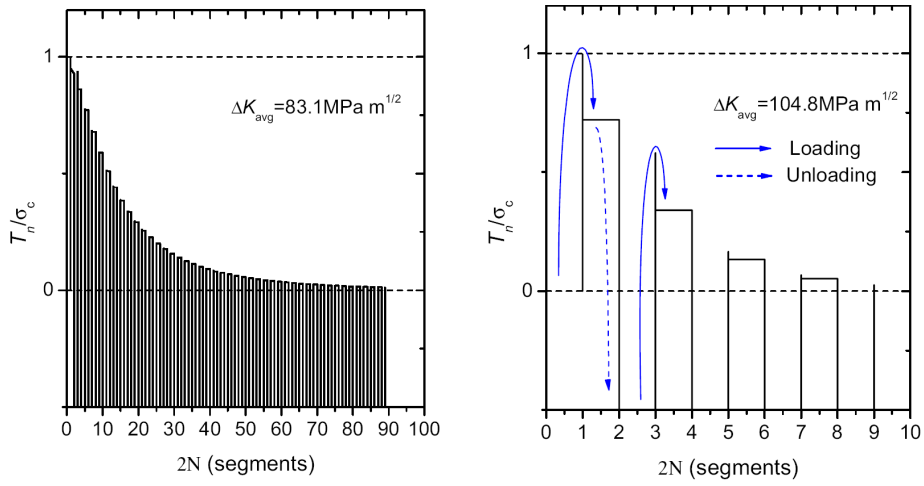

Figure 8. The traction vs. loading segements curves for ΔK_{avg}=83.1MPa $m^{1/2}$ and ΔK_{avg}=104.8MPa $m^{1/2}$.

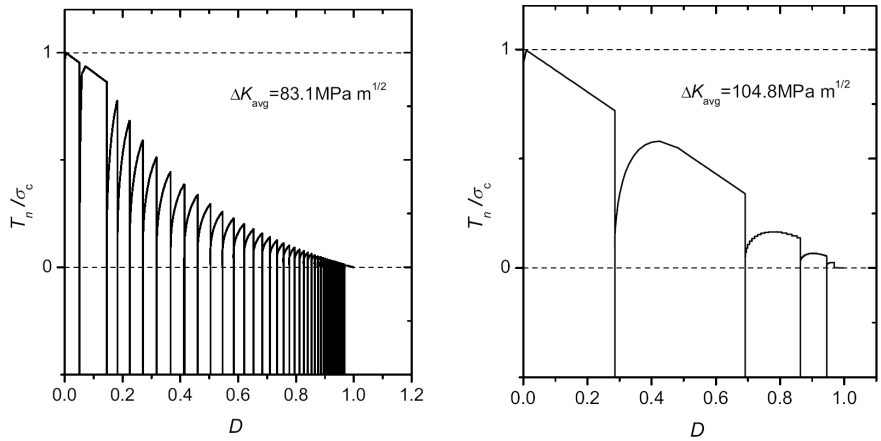

Figure 9. The traction vs. damage evolution curves for ΔK_{avg}=83.1MPa m$^{1/2}$ and ΔK_{avg}=104.8MPa m$^{1/2}$.

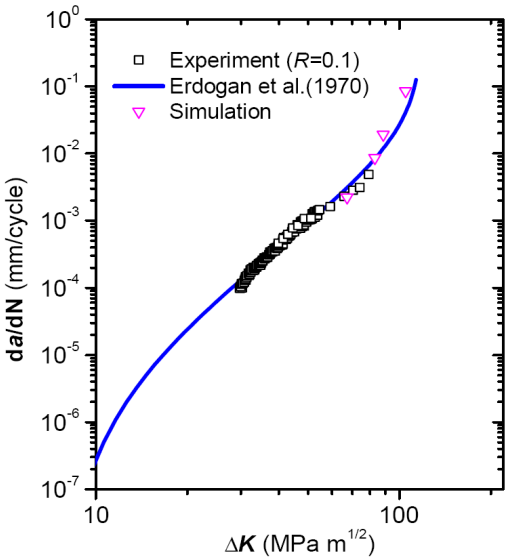

Figure 10. Comparison between the numerical simulation and the experimental data.

5. Concluding remarks

In the present paper a cohesive zone model in conjunction with monotonic damage and cyclic fatigue damage was investigated based on experimental tests, to create a unified fatigue crack growth model for both elastic and elastic-plastic fatigue crack growth.

In simulations the initial cohesive strength and the corresponding displacement jump are defined based on the true stress-strain relationship so that the cohesive zone does not affect the compliance of the specimen before damage initiation. The penetration of the crack surface under compression is prevented using the contact formulation. The first results confirm that the present cohesive zone model coupled with monotonic and cyclic damage evolution is suitable to describe fracture and fatigue crack growth of stainless steel 304 with severe plastic deformations.

In addition, the present computations reveal that the damage evolution in the low stress level and the material compression process could not be properly described need further improvement. More extensive studies on the cohesive model and the damage evolution equation may provide further understanding of ductile fatigue damage under more complex loading conditions.

Acknowledgements

The authors thank financial support of the German Science Foundation (DFG) under the contact number YU119/8-1.

References

[1] Ortiz M., Pandolfi A., Finite-deformation irreversible cohesive elements for three-dimensional crack-propagation analysis. International Journal for Numerical Methods in Engineering, 44 (1999) 1267-82.

[2] Xu Y., Yuan H., Computational modeling of mixed-mode fatigue crack growth using extended finite element methods. International Journal of Fracture, 159 (2009) 151-65.

[3] Xu Y., Yuan H., Computational analysis of mixed-mode fatigue crack growth in quasi-brittle materials using extended finite element methods. Engineering Fracture Mechanics, 76 (2009) 165-81.

[4] Wells G.N., Sluys L.J., A new method for modelling cohesive cracks using finite elements. International Journal for Numerical Methods in Engineering, 50 (2001) 2667-82.

[5] de Borst R., Numerical aspects of cohesive-zone models. Engineering Fracture Mechanics, 70 (2003) 1743-57.

[6] Freed Y., Banks-Sills L., A new cohesive zone model for mixed mode interface fracture in bimaterials. Engineering Fracture Mechanics, 75 (2008) 4583-93.

[7] Krull H., Yuan H., Suggestions to the cohesive traction–separation law from atomistic simulations. Engineering Fracture Mechanics, 78 (2011) 525-33.

[8] Dugdale D.S., Yielding of steel sheets containing slits. Journal of the Mechanics and Physics of Solids, 8 (1960) 100-4.

[9] Barenblatt G.I., The Mathematical Theory of Equilibrium Cracks in Brittle Fracture, in: H.L. Dryden T.v.K.G.K.F.H.v.d.D., Howarth L. (Eds.), Advances in Applied Mechanics, Elsevier, 1962, pp. 55-129.

[10] Xu X.P., Needleman A., Numerical simulations of fast crack growth in brittle solids. Journal of the Mechanics and Physics of Solids, 42 (1994) 1397-434.

[11] Yuan H., Lin G., Cornec A., Verification of a Cohesive Zone Model for Ductile Fracture. Journal of Engineering Materials and Technology, 118 (1996) 192-200.

[12] Cornec A., Scheider I., Schwalbe K.-H., On the practical application of the cohesive model. Engineering Fracture Mechanics, 70 (2003) 1963-87.

[13] Scheider I., Schödel M., Brocks W., Schönfeld W., Crack propagation analyses with CTOA and cohesive model: Comparison and experimental validation. Engineering Fracture Mechanics, 73 (2006) 252-63.

[14] Yang B., Mall S., Ravi-Chandar K., A cohesive zone model for fatigue crack growth in quasibrittle materials. International Journal of Solids and Structures, 38 (2001) 3927-44.

[15] Roe K.L., Siegmund T., An irreversible cohesive zone model for interface fatigue crack growth simulation. Engineering Fracture Mechanics, 70 (2003) 209-32.

[16] Xu Y., Yuan H., On damage accumulations in the cyclic cohesive zone model for XFEM analysis of mixed-mode fatigue crack growth. Computational Materials Science, 46 (2009) 579-85.

[17] Ural A., Krishnan V.R., Papoulia K.D., A cohesive zone model for fatigue crack growth allowing for crack retardation. International Journal of Solids and Structures, 46 (2009) 2453-62.

[18] ABAQUS Version 6.10, ABAQUS Inc., Pawtucket, U.S.A., 2010.

[19] Erdogan F., Ratwani M., Fatigue and fracture of cylindrical shells containing a circumferential crac. Int J Fract, 6 (1970) 379-92.

The effect of thickness on components of the non-singular T-stress under mixed mode loading

Yury G. Matvienko[1,*], Alexander S. Chernyatin[1], Igor A. Razumovsky[1], Hui-Ji Shi[2], Zhao-Xi Wang[2,3]

[1] Mechanical Engineering Research Institute of the Russian Academy of Sciences, 101990, Russia
[2] Department of Engineering Mechanics, Tsinghua University, 100084, China
[3] Suzhou Nuclear Power Research Institute, 215004, China
* Corresponding author: ygmatvienko@gmail.com

Abstract. Distributions of the singular (K_I, K_{II}) and the non-singular (T_{xx}, T_{zz}) terms along the 3D crack front are analyzed for the case of mixed (mode I and II) loading. Relations between the singular, non-singular terms and specimen thickness are calculated in the specimen middle plane for different values of the mixity parameter. The values of the mixity parameter are varied through 1 (pure mode I), 0.75, 0.5, 0.25–0 for pure mode II. It is shown that the increase of thickness in 8 times influences on values of K_I , K_{II} and T_{zz} . The strong effect of thickness and mixed mode loading conditions on the T_{zz}-stress is observed. At the same time, there is not the effect of thickness on the non-singular T_{xx} at the same loading conditions.

Keywords T-stress, Mixed mode, In-plane and out-of-plane constraint, Specimen thickness

Introduction

The development of modern fracture mechanics is closely related to the formation of two-parameter approaches and criteria, which introduce and nonsingular components of the stress field at the crack tip, such as the T-stress. Primarily it is due to the fact that the fracture toughness of structural materials shows a significant effect of the specimen geometry and thickness, load conditions, etc. (e.g. [1, 2]). The results of analytical and numerical calculations show that stress fields in the vicinity of the crack tip, in many cases, are strongly dependent on the non-singular terms of the stress field [3, 4]. Introduction of an additional parameter, namely, the nonsingular T_{xx}-stress in the criteria allows to eliminate the above-mentioned effects [5, 6]. It should be noted that the T_{xx}-stress describes in-plane constraint. In contrast to the T_{xx}-stress, out-of-constraint is connected with the T_{zz}-stress. However, investigation of joint influence of the nonsingular T-stress (T_{zz} and T_{xx}) terms on the fracture mechanics parameters is not carried out yet.

Present paper deals with numerical analysis of three-dimensional stress fields in the vicinity of through-thickness crack tip under mixed mode (I + II) loading. The combined effect of thickness on the effective stress intensity factor and T-stress terms are discussed.

Statement of the problem

An analysis of 3D stress field in the vicinity of the crack front is performed on the CCCD-specimen with the thorough-thickness crack of arbitrary space orientation. The specimen is loaded by 2 compressive forces acting in the vertical direction (Fig. 1). This configuration of the specimen is very suitable to create different conditions of mixed loading [7].

Finite element method is employed to estimate the 3D stress field in the vicinity of crack front. The orientation of the crack plane with respect to the disk can be arbitrary, since it is determined by both the angle α (Fig. 1) and the other two spatial angles. Changing the combination of angles can provide almost any relationship between the magnitudes of the K_I, K_{II}, K_{III}. The geometrical parameters of the model are given in dimensionless form, namely, $b=B/R$, $l=a/R$ (Fig. 1). Note that the developed procedure for the construction of the model allows taking into account the spatial symmetry of the problem and getting the best mesh in terms of accuracy and speed of calculation.

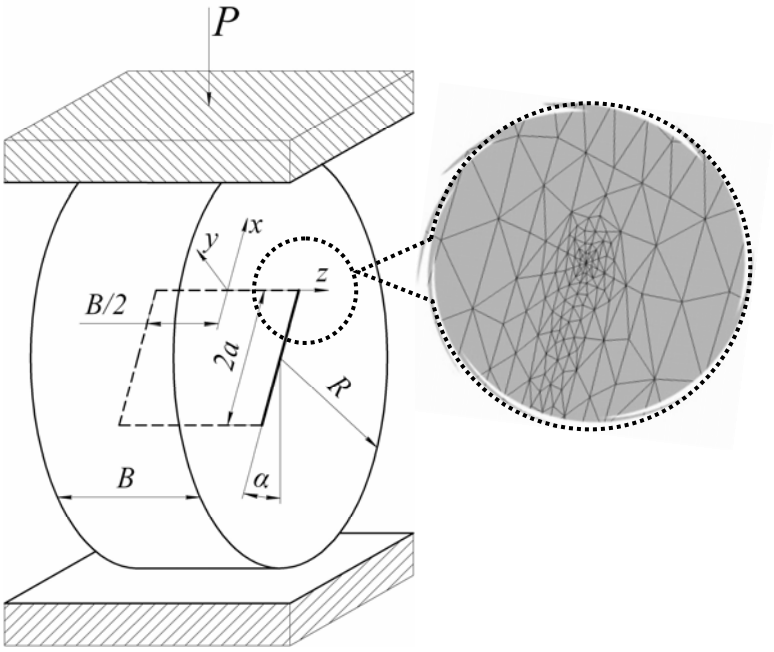

Figure 1. Model of the CCCD-specimen

The stress field in the vicinity of the crack tip of mixed type (I+II) can be represented in the form [8]:

$$\sigma_{xx} = \frac{1}{\sqrt{2\pi r}}\left[K_I \cos\frac{\theta}{2}\left(1-\sin\frac{\theta}{2}\sin\frac{3\theta}{2}\right) - K_{II}\sin\frac{\theta}{2}\left(2+\cos\frac{\theta}{2}\cos\frac{3\theta}{2}\right)\right] + T_{xx},$$

$$\sigma_{yy} = \frac{1}{\sqrt{2\pi r}}\left[K_I \cos\frac{\theta}{2}\left(1+\sin\frac{\theta}{2}\sin\frac{3\theta}{2}\right) + K_{II}\sin\frac{\theta}{2}\left(\cos\frac{\theta}{2}\cos\frac{3\theta}{2}\right)\right],$$

$$\sigma_{xy} = \frac{1}{\sqrt{2\pi r}}\left[K_I \sin\frac{\theta}{2}\left(\cos\frac{\theta}{2}\cos\frac{3\theta}{2}\right) + K_{II}\cos\frac{\theta}{2}\left(1-\sin\frac{\theta}{2}\sin\frac{3\theta}{2}\right)\right], \quad (1)$$

$$\sigma_{zz} = \frac{2\nu}{\sqrt{2\pi r}}\left[K_I \cos\frac{\theta}{2} - K_{II}\sin\frac{\theta}{2}\right] + T_{zz},$$

$$T_{zz} = E\varepsilon_{zz} + \upsilon T_{xx}.$$

where x is the direction formed by the intersection of the plane normal to the crack front and the crack plane, y is the direction orthogonal to the crack plane, z is the direction orthogonal to x and y directions (tangent to crack front); r and θ are the in-plane polar coordinates in plane $x0y$. Here, E and ν are the elastic modulus and Poisson's ratio, respectively.

The value of the angle α and the corresponding parameters M_e, which characterize loading mode mixity, for the specimen under consideration are shown in Table 1. Note that in the case of mode I crack (K_{II}=0) M_e=1, in the case of mode II crack (K_I=0) M_e=0.

$$M_e = \frac{2}{\pi} arctg\left(\frac{K_I}{K_{II}}\right) \quad (2)$$

Table 1. The mixity parameter and crack orientation

α, º	0	5	10,5	18	27
M_e	1	0,75	0,5	0,25	0

Determination of K_I, K_{II}, T_{xx}, T_{zz}

The evaluation of the stress intensity factor (SIF) is based on the well-known approach that includes the calculating of the SIF in a number of points (at varied *r*) using relations obtained from Eq. (1):

$$K_I = \sqrt{\frac{\pi r}{2}}\left(2\sigma_{xx}|_{\theta=0} - \sigma_{xx}|_{\theta=-\pi} - \sigma_{xx}|_{\theta=+\pi}\right), \quad K_{II} = \sqrt{\frac{\pi r}{8}}\left(\sigma_{xx}|_{\theta=-\pi} - \sigma_{xx}|_{\theta=+\pi}\right) \tag{3}$$

and extrapolation of the obtained values of the SIFs to the point r=0.

The computational procedure considers the nodes of the finite element mesh as the calculation points, but the nodes are located at some small distance from the crack front. To obtain the distribution of the SIF along the crack front, this procedure is used for a number of planes (x0y) orthogonal to the crack front. Their location is characterized by local coordinate *s* along the front and starts from the center of the crack front.

To assess the accuracy of the values of SIF, the comparison of magnitudes of the *J*-integral, calculated as contour integral (Eq. 4a) and based on the known relationship (Eq. 4b), has been done.

$$J = \int_{\Gamma}\left(W(x,y)dx - \sigma_{ij}n_j\frac{du_i}{dy}ds\right) \tag{4a}$$

$$J = \frac{1-\upsilon}{E}\left[K_I + K_{II} + (1+\upsilon)K_{III}\right] \tag{4b}$$

The calculation of the T_{xx}- and T_{zz}-stress is performed using the stresses in the points on the crack surface:

$$T_{xx} = \frac{1}{2}\left[\sigma_{xx}|_{\theta=-\pi} + \sigma_{xx}|_{\theta=+\pi}\right], \quad T_{zz} = \frac{1}{2}\left[\sigma_{zz}|_{\theta=-\pi} + \sigma_{zz}|_{\theta=+\pi}\right] \tag{5}$$

The determination of T_{xx} T_{zz} is similar to the procedure for SIF including extrapolation to the point r=0.

The special macros that carry out the automatic computation of the SIF, *J*-integral and T-stresses (on referred above relations) along the crack front are created in ANSYS environment.

Estimation of the accuracy of the numerical model and computational procedures is based on comparison of the calculated values of the SIF and the T-stresses with one presented in [7] for the CCCB-specimen in case of R=50 mm, b=0,8, l=1/3. Comparison of the results shows that there is good coincidence and only in some cases the relative difference is close to 10%.

Discussion of the results

The results of distribution of the SIF and the T-stress along the crack front for different mixed mode loading conditions are summarized in Fig. 2 and 3. To study the effect of specimen thickness on T_{zz}-stress, the compressive load was adjusted so that the T_{xx}-stress was remained approximately constant at variation of the specimen thickness (b= 0,2; 0,4; 0,8 and 1,6) at constant l=1/3 (for the corresponding values of mixity parameter M_e).

The increase of the specimen thickness is 8 times greatly reduces (in absolute value) the T_{zz}-stress (up to 75% at M_e=0,25), whereas the value of T_{xx} is virtually unchanged (Table 2). The predicted results are consistent with the data of numerical calculations [6]. Thus, magnitudes of the T_{zz}- stress have significant correlation with thickness of the specimen and allows taking into account the level of the out-of-constraint which should be included into assessment of the fracture toughness of full-scale structures.

Table 2. The effect of thickness on the SIF and T-stresses for M_e=0,25

b	K_I, MPa·m^{0,5}	K_{II}, MPa·m^{0,5}	T_{xx}, MPa	T_{zz}, MPa
0,2	0,105	0,252	-2,691	-0,309
0,4	0,104	0,255	-2,681	-0,206
0,8	0,099	0,254	-2,647	-0,121
1,6	0,087	0,246	-2,581	-0,079

To reflect mixed mode loading conditions, an effective SIF (K_{eff}) is introduced into consideration as follows

$$K_{eff} = \sqrt{K_I^2 + K_{II}^2} \qquad (6)$$

There are dependence of K_{eff} on T_{xx} and T_{zz} in the middle plane of the crack front (s=0) for varied parameters M_e at different thickness (b=0,2; 0,4; 0,8; 1,6) of the specimen and constant value of l=1/3 (Fig. 2 and 3).

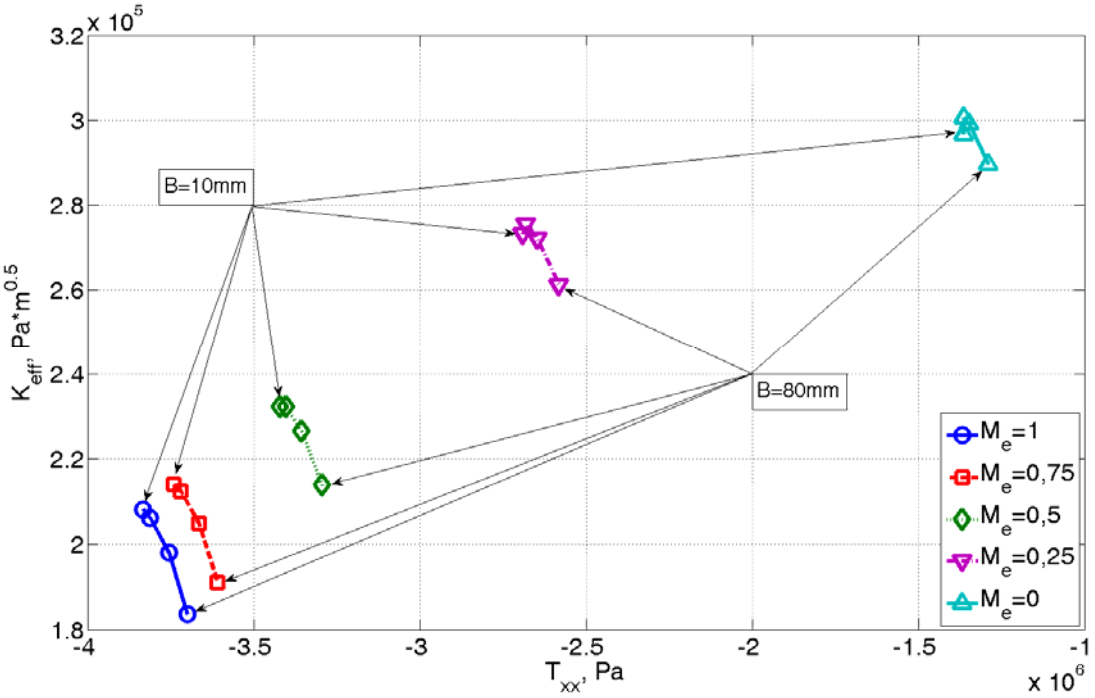

Figure 2. The effect of T_{xx}, M_e and thickness on K_{eff} at s=0

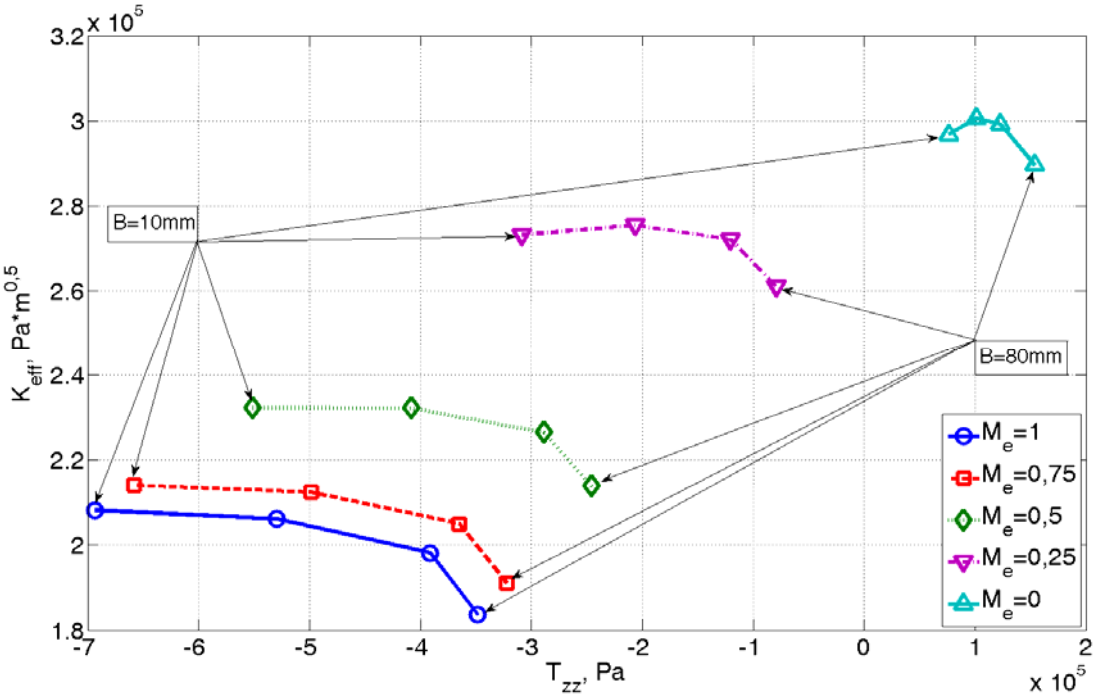

Figure 3. The effect of T_{zz}, M_e and thickness on K_{eff} at s=0 at s=0

Conclusions

The three-dimensional stress field ahead of the through-thickness crack under mixed mode (I+II) loading conditions is analyzed. The in-plane and out-of-plane constraint effect are discussed by means of the non-singular terms, namely, T_{xx}-stress and T_{zz}-stress, respectively. The distribution of the singular and non-singular terms along the crack front has been predicted. The significant effect of specimen thickness on the T_{zz}-stress in the middle plane of the crack front has been observed.

Acknowledgements

The authors acknowledge the support of the Russian Foundation of Basic Research (Grant N 12-08-91158-NSFC_a).

References

[1] S. Liu, Y.J. Chao, Variation of fracture toughness with constraint, International Journal of Fracture, 124 (2003) 113–117.
[2] X.K. Xhu, Y.J. Chao. Specimen size requirements for two-parameter fracture toughness testing, International Journal of Fracture, 135 (2005) 117–136.
[3] V.F. González-Albuixech, E. Giner, J. Fernández-Sáez, A. Fernández-Canteli, Influence of the t_{33}-stress on the 3-D stress state around corner cracks in an elastic plate, Engineering Fracture Mechanics, 78 (2011) 412–427.
[4] Yu.G. Matvienko, V.N. Shlyannikov, N.V. Boychenko, In-plane and out-of-plane constraint parameters along a three-dimensional crack-front stress field under creep loading, Fatigue and Fracture of Engineering Materials and Structures, 36 (2013) 14–24.
[5] H.M. Meliani, Yu.G. Matvienko, G. Pluvinage, Two-parameter fracture criterion ($K_{\rho,c}$-$T_{ef,c}$)

based on notch fracture mechanics, International Journal of Fracture, 167 (2011) 173-182.
[6] T. Meshii, T. Tanaka, Experimental T_{33}-stress formulation of test specimen thickness effect on fracture toughness in the transition temperature region, Engineering Fracture Mechanics, 77 (2010) 867–877.
[7] M.R.M. Aliha, M.R. Ayatollahi, D.J. Smith, M.J. Pavier, Geometry and size effects on fracture trajectory in a limestone rock under mixed mode loading, Engineering Fracture Mechanics, 7 (2010) 2200–2212.
[8] T. Nakamura, D.M. Parks, Determination of elastic T-stress along three-dimensional crack fronts using an interaction integral, International Journal of Solids and Structures, 29 (1992) 1597–1611.

Experiments on cracks under spatial loading

Hans A. Richard[1,*], Alexander Eberlein[1], Nils-H. Schirmeisen[2]

[1] Institute of Applied Mechanics, University of Paderborn, 33100, Germany
[2] WINDMOELLER & HOELSCHER KG, Lengerich, 49525, Germany
* Corresponding author: richard@fam.upb.de

Abstract

The basic loading cases (Mode I, Mode II and Mode III) of cracks are generally defined by the near-field solutions for the stress distribution at the crack front. Cracks, whose stress near fields are symmetric due to geometry and/or loading of the structure, are called Mode I-cracks. In case of spatial loaded cracks the stress fields near the crack tip are unsymmetrical. The fracture mechanical treatment of such Mixed-Mode-loaded cracks is consequently more complicated as of pure Mode I-loaded cracks.

For experimental investigations of 3D-Mixed-Mode-loaded cracks the CTSR-specimen (Compact-Tension-Shear-Rotation-specimen) will be proposed. The CTSR-specimen with the corresponding loading device enables the generation of pure Mode I, pure Mode II, pure Mode III and several combinations of the three basic fracture modes.

In this paper the CTSR-specimen, the loading device and various experimental results for fracture and fatigue loading situations are illustrated. Furthermore these results will be compared with existing fracture criteria for 3D-Mixed-Mode-problems.

Keywords

3D-Mixed-Mode, fracture, fatigue, CTSR-specimen

1. Introduction

In real structures fracture processes are in many cases of a three dimensional character. Different defects, e.g. pre-cracks, which often exist in materials and structures, may experience complex loading conditions. Cracks under complex loading are subjected to a superposition of the three basic fracture modes I, II and III. In this case cracks tend to kink and/or twist, Fig. 1.

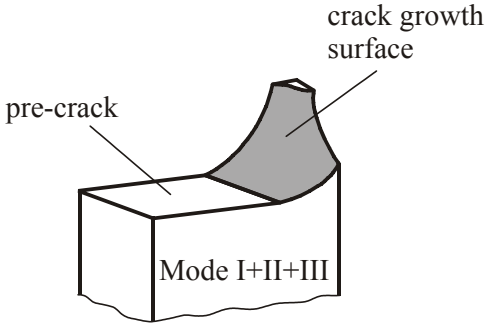

Figure 1. Crack screwing under combined loading

For static loading the stress field near the crack front (Eq. 1) here is not only defined by the stress intensity factor K_I, but also by K_{II} and K_{III}. In this case the calculation of a comparative stress intensity factor K_V is important (Eq. 2) [1].

$$\sigma_{ij} = \frac{1}{\sqrt{2\pi \cdot r}} \cdot \left[K_I \cdot f_{ij}^{I}(\varphi) + K_{II} \cdot f_{ij}^{II}(\varphi) + K_{III} \cdot f_{ij}^{III}(\varphi) \right] \tag{1}$$

$$K_V = \frac{K_I}{2} + \frac{1}{2} \cdot \sqrt{K_I^2 + 5{,}336 \cdot K_{II}^{\ 2} + 4 \cdot K_{III}^{\ 2}} \tag{2}$$

In this regard the fatigue crack growth then is governed by the cyclic stress intensity factors ΔK_I, ΔK_{II} and ΔK_{III} respectively the cyclic comparative stress intensity factor ΔK_V, which can be derived from Eq. 2:

$$\Delta K_V = \frac{\Delta K_I}{2} + \frac{1}{2} \cdot \sqrt{\Delta K_I^2 + 5{,}336 \cdot \Delta K_{II}^{\ 2} + 4 \cdot \Delta K_{III}^{\ 2}} \tag{3}$$

The *K*-concept for spatial Mixed-Mode-loading is based on the fact that unstable crack growth occurs, if the comparative stress intensity factor K_V reaches the fracture toughness value K_{IC} for Mode I. In case of fatigue crack growth the crack is propagable, if the cyclic comparative stress intensity factor ΔK_V for spatial Mixed-Mode-loading reaches or exceeds the threshold value ΔK_{th}. Both contexts can be illustrated clearly in a K_I-K_{II}-K_{III}-diagram, Fig. 2.
Unstable crack growth will occur, if a local loading condition along the crack front reaches a point on the fracture limit surface. Fatigue crack growth or stable crack growth develops, if points characterizing the local crack front loading conditions are lying between the threshold and the fracture limit surfaces.

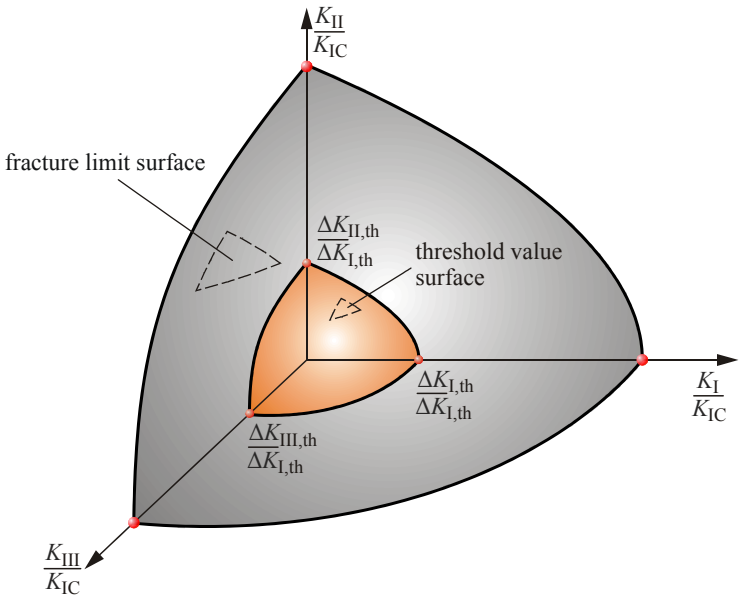

Figure 2. Fatigue crack growth limits at spatial Mixed-Mode-loading

Precisely because the fracture mechanical treatment of such three dimensional Mixed-Mode-loaded cracks is very complicated compared to pure Mode I-loaded cracks, the prediction of the above mentioned 3D-fracture-process is not yet well understood.
In addition there is a shortage of experimental investigations and findings regarding general spatial Mixed-Mode-fracture in order to compare the correlation between the experimental results and

existing fracture criteria for 3D-Mixed-Mode-loading conditions. Experimental investigations on spatial Mixed-Mode-loading are also necessary, in order to get a solid basis, on which, on the one hand, the existing fracture criteria for 3D-Mixed-Mode could be enhanced, on the other hand, new fracture criteria or hypotheses including the desired understanding could be established.

2. Mixed-Mode-criteria for 3D-loading conditions

For a complete prediction of crack growth behavior under combined loading not only the crack growth direction is required, but also the determination of comparative stress intensity factors, like K_V or ΔK_V, see Eq. 2 and Eq. 3.
Compared to characteristic fracture mechanical values, e.g. threshold value or fracture toughness value, conclusions could be drawn on crack growth behavior.
In this purpose some criteria for characterizing the crack growth under spatial Mixed-Mode-loading were established:

- Crack growth criterion by POOK [2-4]
- σ_1'-criterion by SCHÖLLMANN et al. [5, 6]
- Criterion by DHONDT [7]
- 3D-criterion by RICHARD [1]

A comparison of these criteria is given in e.g. [1].

3. Experiments on cracks under general loading

In order to understand the 3D-fracture-process completely not only further theoretical, but also experimental investigations have to be performed. Currently several types of specimens are available for experimental investigations of fatigue crack growth and fracture under various Mixed-Mode-loading conditions [8-17]. None of these specimens enables investigating the full range of all basic fracture modes or any combinations thereof.
But the AFM-specimen with the corresponding loading device and the so-called CTSR-specimen (Compact-Tension-Shear-Rotation-specimen) in combination with the special loading device fulfill these high requirements. Some of the experimental results of both specimen types are shown below.

3.1. Experiments on AFM-specimen

As already mentioned the AFM-specimen, developed by RICHARD, allows the investigation of crack problems under general loading conditions by using a simple uniaxial testing machine [18]. In the past experiments under static load were performed in order to determine the fracture limit surface and the crack deflection angles φ_0 and ψ_0 [19], see Fig. 3.
For fatigue tests this loading device is less suitable, due to its high weight and deformation. Only low test frequency, which leads to high test duration, can be realised for fatigue experiments. Making use of this background the CTSR-specimen (Fig. 4a) with the corresponding loading device (Fig. 4b) was developed.

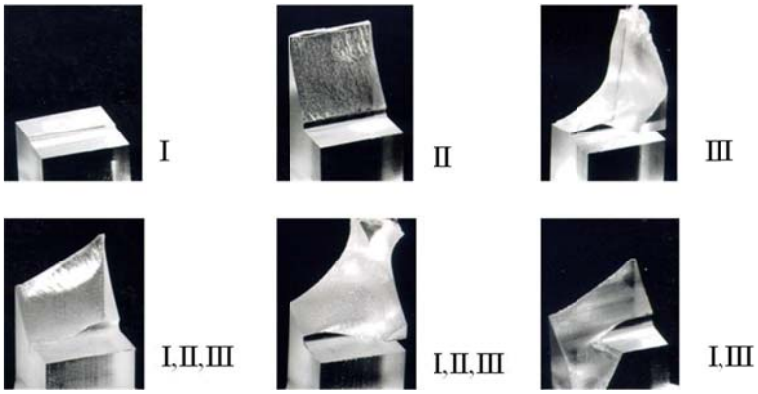

Figure 3. Crack growth direction under different loading conditions

3.2. Experiments on CTSR-specimen

This concept was developed especially for investigating Mixed-Mode-loaded cracks under cyclic loading. The loading device is designed in a way, with which any ratio of Mode I to Mode II/Mode III can be generated by the adjustment of the loading angle α (see Fig. 5). Furthermore, the ratio of Mode II- or Mode III-load can be set by rotating the so-called turret inside the loading device (see Fig. 6).

a)

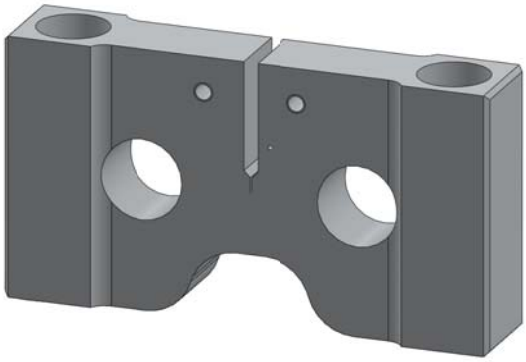

b)

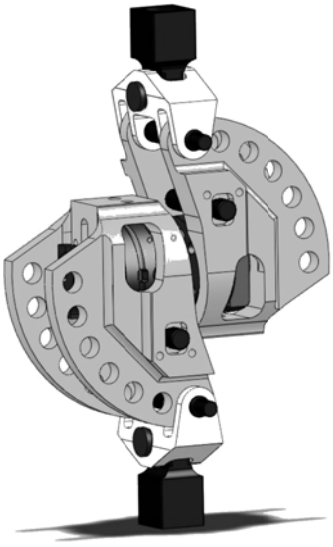

Figure 4. a) CTSR-specimen
b) Loading device for CTSR-specimen

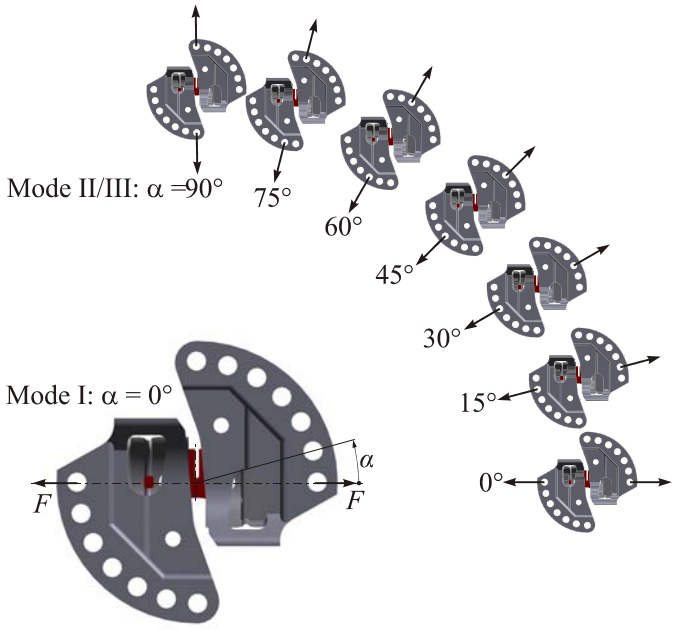

Figure 5. Setting of the ratio of Mode I to Mode II/Mode III

The superposition of Mode I, Mode II and Mode III takes place by the adjustment of both angles α and γ. Thereby the load line of action always passes through the center of the specimen.

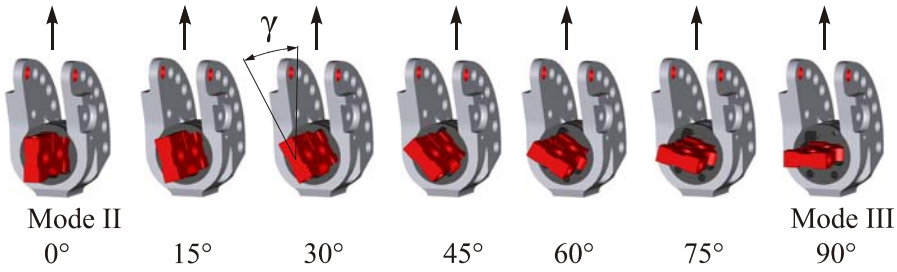

Figure 6. Setting of the ratio of Mode II- or Mode III-load

In this paper some experimental results on CTSR-specimen will be presented. On the one hand experiments on PMMA have been performed, in order to determine the fracture limit surface (cf. Fig. 2) for this material. On the other hand fatigue tests were performed on an EN AW-7075-T651 aluminium alloy, in order to identify the threshold value surface. The results of both experiment types are illustrated and discussed in the next chapter.

4. Results of experimental investigations

Figure 7 illustrates the measured fracture toughness values for PMMA material under several Mixed-Mode-loading combinations.

The fracture toughness values K_{IIIC} for pure Mode III-loading, measured on CTSR-specimen, exhibits a significant variation in comparison with the 3D-criterion by RICHARD. The resulting values for Mode III are around factor 2.7 above the hypothesis. Similar significant variations have already been observed on other specimen, e.g. [15]. Furthermore it is noticeable, that the difference between measured K_C values and the hypothesis decreases with decreasing Mode III-ratio. The

values are very close to the criterion as soon as there is no Mode III-loading. The same trend can be observed by the comparison with other criteria, mentioned in this paper. All these criteria are conservative.

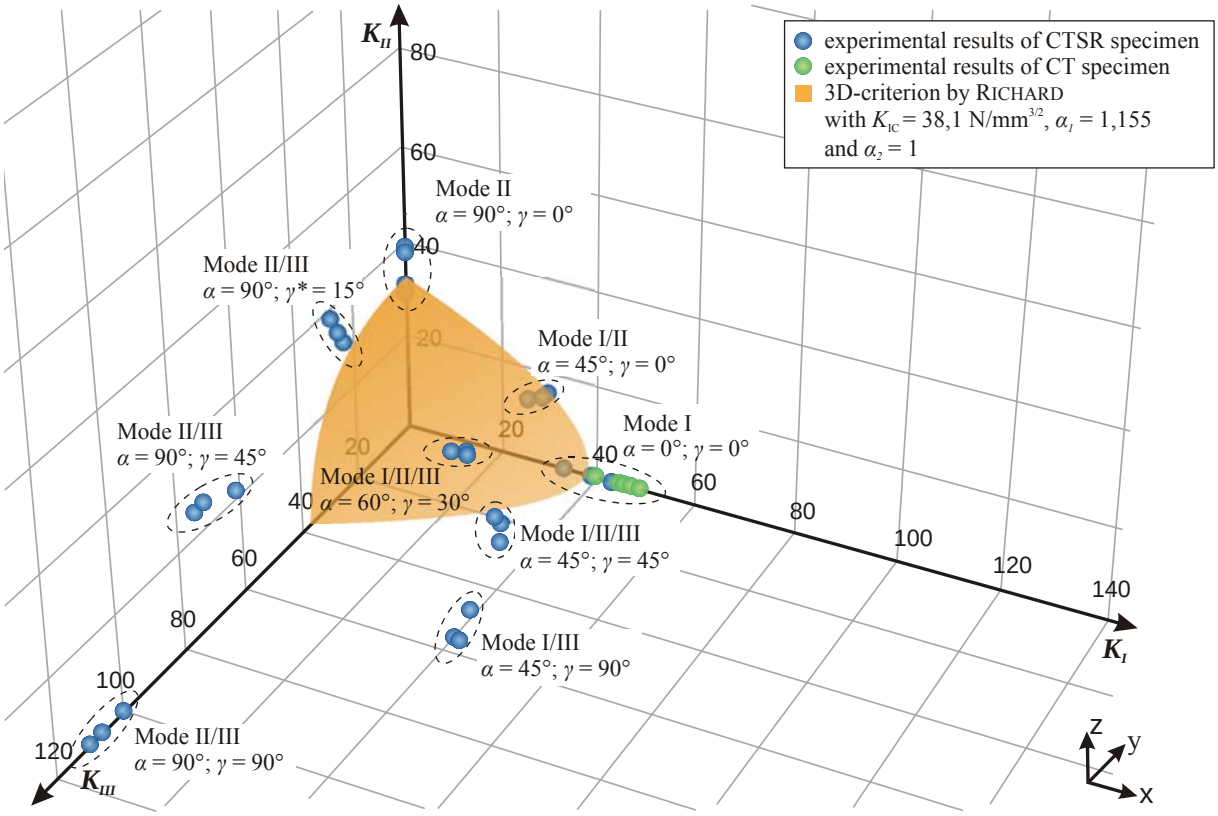

Figure 7. Comparison of experimental results with 3D-criterion by Richard

Due to these results and the significant difference to the hypothesis, an approximation of the 3D-criterion by Richard on the fracture toughness values for PMMA material is proposed. In Figure 8 the approximation of the criterion by RICHARD is shown. Here the α_2 parameter was changed to 0.36. This approximation is still conservative, but agrees very well with the experimental results.

In addition, fatigue tests on an EN AW-7075-T651 aluminium alloy were performed. The experimentally measured threshold values for different Mixed-Mode-loading conditions are pictured in Figure 9. Compared to the threshold value surface by RICHARD the experimentally determined threshold values depict also a significant variation under pure Mode III-loading. Here the $\Delta K_{III,th}$ values are around factor 2.2 above the hypothesis.

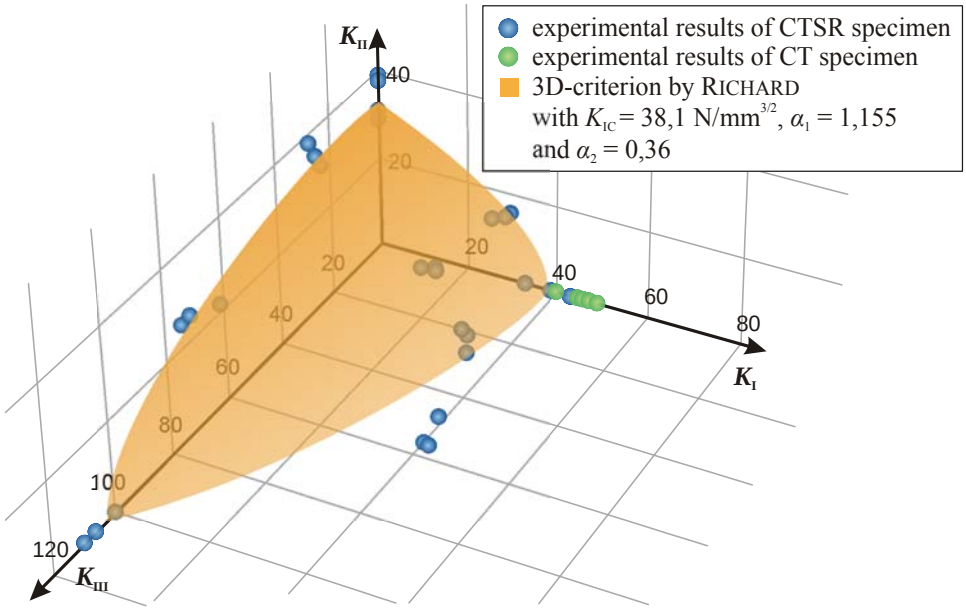

Figure 8. Approximation of the 3D-criterion by Richard on experimental results

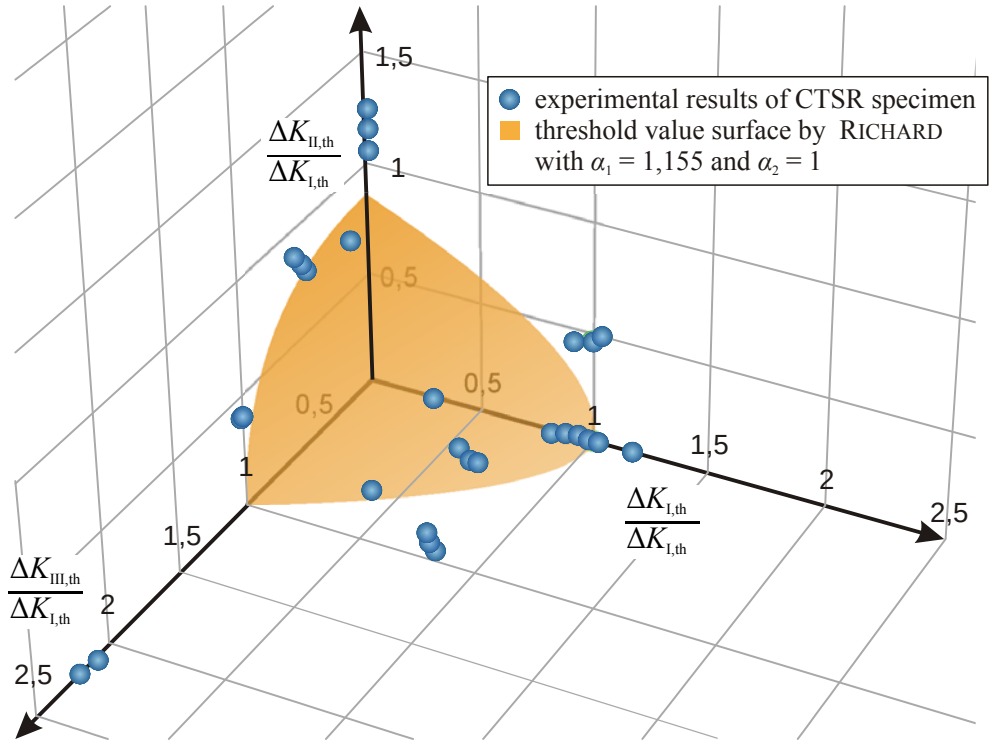

Figure 9. Threshold values for several Mixed-Mode-loading conditions

Moreover, for a complete description of crack growth behavior under general Mixed-Mode-loading the crack kinking and twisting angles were established by using an optical 3D-scanner. In order to prove the reliability of the criteria the determined crack deflection angles φ_0 and ψ_0 were compared with the predictions of the criteria. The comparison of the crack kinking angle φ_0 is shown in barycentric coordinates in Figure 10.

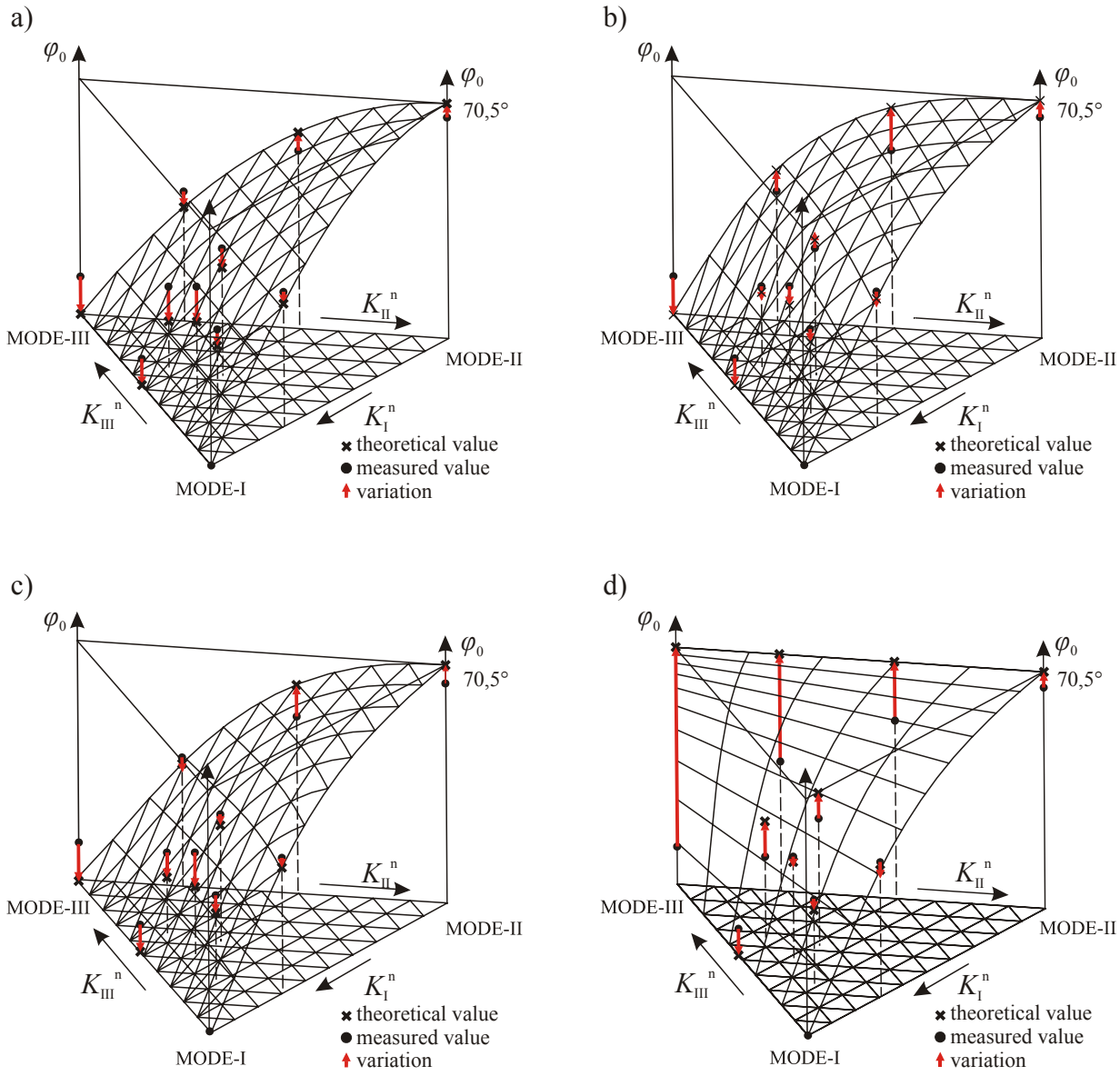

Figure 10. a) Comparison of kinking angle with criterion by RICHARD
b) Comparison of kinking angle with criterion by SCHÖLLMANN et al.
c) Comparison of kinking angle with criterion by DHONDT
d) Comparison of kinking angle with criterion by POOK

The measured crack kinking angle φ_0 coincides very well with the predictions of the hypotheses by RICHARD as well as by SCHÖLLMANN et al. and by DHONDT (see Fig. 10a-c). The maximal deviation here one finds at pure Mode III-loading. In Comparison with the predictions of the criterion by POOK the real crack kinking angle differs considerably from its predictions as soon as Mode III-loading part occurs (Fig. 10d).
The measurement results of the crack twisting angle ψ_0 exhibit also a very well agreement with the criterion by RICHARD as well as by SCHÖLLMANN et al. (Fig. 11a, 11b). The predictions of the criteria by DHONDT and by POOK show the greatest deviations from the real crack twisting angle (Fig. 11c, 11d).

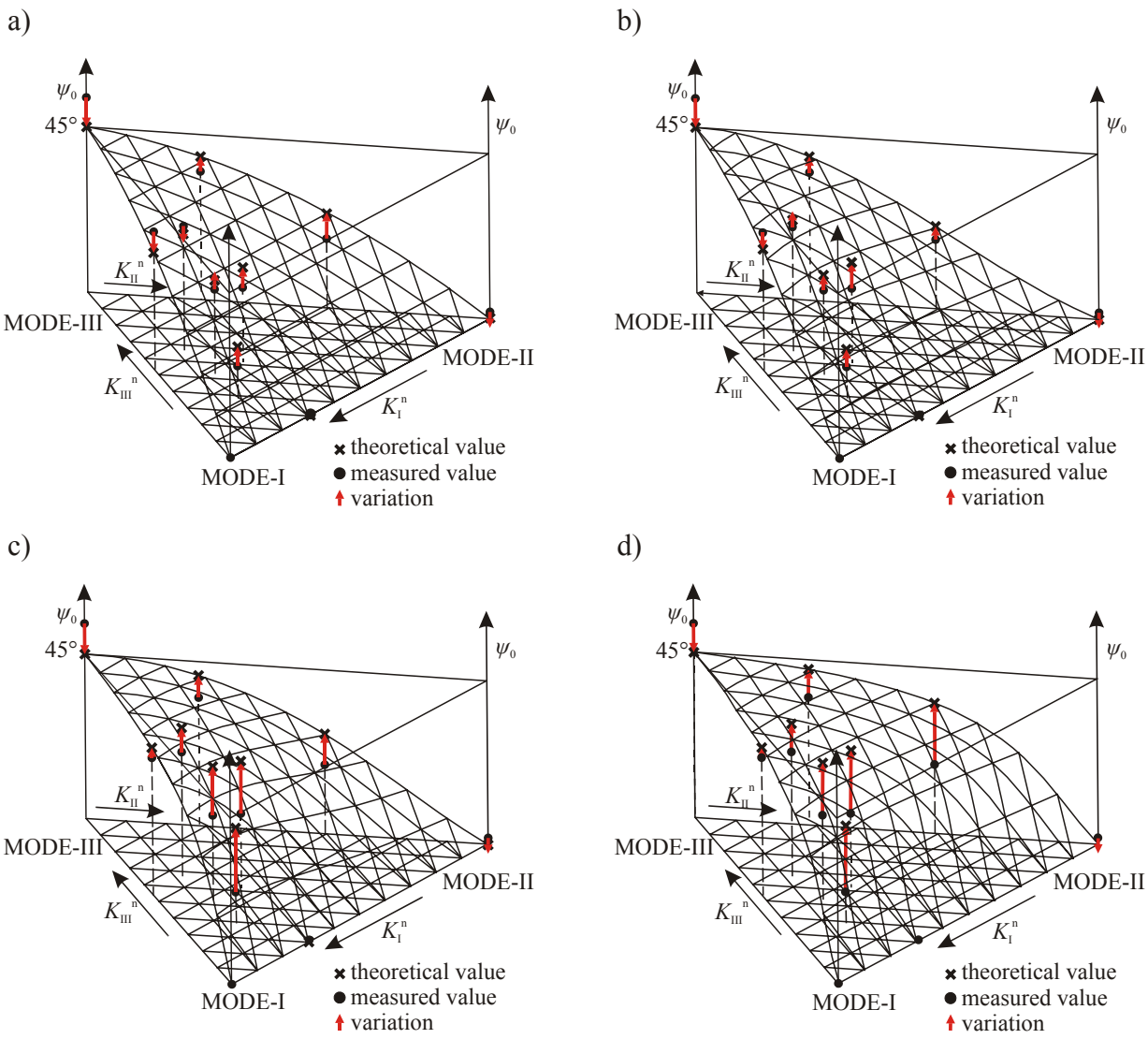

Figure 11. a) Comparison of twisting angle with criterion by RICHARD
b) Comparison of twisting angle with criterion by SCHÖLLMANN et al.
c) Comparison of twisting angle with criterion by DHONDT
d) Comparison of twisting angle with criterion by POOK

5. Conclusion

In this paper the suitability for experimental investigations under 3D-Mixed-Mode-loading conditions of the CTSR-specimen in combination with its loading device was presented.
The experimental results show obviously higher threshold and fracture toughness values for high Mode III-loading ratios than by criteria predicted. The most exactly predictions indicate the criteria by RICHARD and by SCHÖLLMANN et al.
These criteria give the best predictions regarding the crack kinking and twisting angle. Due to their exactness of predictions, they should be implemented in numerical calculation programs.

References

[1] H.A. Richard, M. Fulland, M. Sander, Theoretical crack path prediction, in: FFEMS 28 (2005), 3-12.
[2] L.P. Pook, Elasto-Plasticity, Thin Sheet and Micromechanism Problems, In: Fracture and Fatigue: Radon, J.C. (Ed.) Pergamon Press, Oxford, 1980, pp. 143-153.
[3] L.P. Pook, Multiaxial Fatigues, in: Miller, K.J., Brown, M.W. (Eds.), ASTM STP853, American Society for Testing and Materials, Philadelphia, 1985, pp. 249-263.
[4] L.P. Pook, Linear elastic fracture Mechanics for engineers: theory and application, WIT press, Southampton, 2000.
[5] M. Schöllmann, G. Kullmer, M. Fulland, H.A. Richard, A New Criterion for 3D Crack Growth under Mixed-Mode (I+II+III) Loading, in: Proc. of 6th Int. Conf. of Biaxial/Multiaxial Fatigue & Fracture, Vol. 2, 2001, 589-596.
[6] M. Schöllmann, H.A. Richard, G. Kullmer, M. Fulland, A new criterion for the prediction of crack development in multiaxially loaded structures, in: Int. J. Frac. 117 (2002) 129-141.
[7] G. Dhondt, A new Three-Dimensional Fracture Criterion, in: Key Engineering Materials 251-252 (2003), 209-214.
[8] H.A. Richard, Bruchvorhersage bei überlagerter Normal- und Schubbeanspruchung von Rissen, VDI-Verlag, Düsseldorf, 1985.
[9] F. Erdogan, G.C. Sih, On the crack extension in plates under plane loading and transverse shear, in: Journal of Basic Engineering 85 (1963) 519-527.
[10] H.A. Richard, A new compact shear specimen, in: Int. J. Fracture 17 (1981) R105-R107.
[11] H.A. Richard, K. Benitz, A loading device for the creation of mixed mode in fracture mechanics, in: Int. J. Fracture 22 (1983) R55-R58.
[12] L.P Pook, The fatigue crack direction and threshold behaviour of mild steel under mixed mode I and III loading, in: International Journal of Fatigue 7 (1985) 21-30.
[13] B.S.S.C. Rao, M. Srinivas, S.V. Kamat, Effect of temperature on fracture toughness of Timetal 834 titanium alloy under mode I and mixed mode I/III loading, in: Metallurgical and Materials Transactions A 39A (2008) 1340-1349.
[14] F.-G. Buchholz, H. Wang, J. Lin, H.A. Richard, 3D finite element analysis of different test specimens for investigations on mixed mode I, II and III fracture, in: S. Idelsohn , E. Onate, E. Dvorkin (Eds.), Computational Mechanics, CIMNE, 1998, pp. 1-21.
[15] J.C.W. Davenport, D.J. Smith, A study of superimposed fracture modes I, II and III on PMMA, in: Fatigue and Fracture of Engineering Materials and Structures 16 (1993) 1125-1133.
[16] D. Hull, The effect of mixed mode I/III on crack evolution in the brittle solids, in: Int. J. Frac. 70 (1995) 59-79.
[17] L.P. Pook, A finite element analysis of the angle crack specimen, in: H.P. Rossmanith, K.J. Miller (Eds.), Mixed-Mode Fatigue and Fracture, ESIS 14, Mechanical Engineering Publications, London, 1993, pp. 285-302.
[18] H.A. Richard, Praxisgerechte Simulation des Werkstoff- und Bauteilverhaltens durch überlagerte Zug-, ebene Schub- und nichtebene Schubbelastung von Proben, VDI-Verlag, Düsseldorf, 1983, 269-274.
[19] H.A. Richard, M. Kuna, Theoretical and experimental study of superimposed fracture modes I, II and III, in: Eng. Frac. Mech. 35 (1990) 949-960.

Constraint Effect in Fracture: Investigation of Cruciform Specimens using the J-A_2 Method

Larry Sharpe[1], Yuh Chao[2,*]

[1] Department of Mechanical Engineering University of Tennessee, Knoxville, TN, USA
[2] College of Material Science and Engineering, Tianjin University, Tianjin, China
* Corresponding author: chao@sc.edu

Abstract
The structural integrity of cracked mechanical components can be assessed using the fracture toughness material property. The fracture toughness of a particular component is often dependent upon the component geometry as well as the nature of loading (e.g. uniaxial or biaxial loading). This dependence is interpreted as the constraint effect in fracture. Various methods have been developed to investigate the constraint effect, including the two parameter J-A_2 method. The J-A_2 method is a more accurate representation of the stress fields near the crack tip, as additional terms from the well-known HRR series solution are included. The current study applies the J-A_2 method to fracture toughness data of cracked cruciform specimens subjected to uniaxial and biaxial stresses. The J-A_2 results of the cruciform specimens are compared to those of other plane strain specimens described by ASTM standards, including three point bend and compact tension, to determine if loss of constraint exists. Finite element models of each specimen were analyzed to determine the A_2 parameter used to quantify the level of constraint based on geometry and loading. The results reveal loss of constraint for shallow cracked specimens when compared to deep cracked specimens, and also that uniaxial loading results in loss of constraint when compared to biaxial loaded specimens. In summary, the J-A_2 method appears to be a viable tool to predict failure including the consideration of the constraint effect.

Keywords fracture, constraint, biaxial, cruciform

1. Introduction

A material's fracture toughness is used to determine the structural integrity of mechanical components containing cracks. Materials used in nuclear reactor pressure vessels (RPV), including A533B and A508, are of particular interest. RPVs can be subjected to conditions close to equibiaxial loading during extreme temperature gradients experienced during pressurized thermal shock (PTS).

Based on such biaxial loading, it is possible that traditional methods used to determine material properties may not provide accurate results. Widely used industry standards [1, 2] used to calculate material properties related to fracture toughness utilize specimens subjected to uniaxial loading, e.g., three point bend (3PB) and compact tension (CT) specimens. Therefore, the question arises regarding whether or not a "biaxial effect" exists for loading conditions similar to that of RPVs.

Much research has been conducted in recent years to determine how component geometry and applied loading affect fracture toughness. The industry standards mentioned previously typically use deep cracked (high constraint) specimens to determine the fracture toughness. But it is known that shallow cracked (low constraint) specimens exhibit higher fracture toughness, resulting in a "constraint effect" in fracture.

The current study uses a two-parameter method to quantify the constraint of a variety of specimens and also to predict failure of specimens of biaxial loads. The J-A_2 method has been applied to experimental data published by the Fraunhofer Institute for Mechanics. Fraunhofer conducted fracture toughness testing on 3PB and cruciform specimens, with the cruciform specimens subjected to biaxial loads. Such experimental data can be used to determine if the J-A_2 method can be used as a tool to i) predict failure of mechanical components of different constraints and ii) quantify the constraint due to loading and geometry.

2. J-A_2 Two Parameter Method

The stress distribution ahead of the crack tip described by the well-known HRR solution [3, 4] is

$$\sigma_{ij} = \sigma_0 \left(\frac{J}{\alpha \varepsilon_0 \sigma_0 I_n r} \right)^{1/n+1} \tilde{\sigma}_{ij}(\theta, n), \qquad (1)$$

where σ_0 is a reference (or yield) stress, $\varepsilon_0 = \sigma_0 / E$ is a reference (or yield) strain, E is Young's modulus, α is a material constant, and n is the strain-hardening exponent. The integration constant I_n and the dimensionless angular functions of stresses $\tilde{\sigma}_{ij}$ depend on the strain-hardening exponent. Equation 1 is the first term of a series solution. Further, the HRR solution described by Equation 1 is defined by only one parameter, the J-integral, which is related to the energy release rate around the crack tip during loading. As shown in Figure 1, the stress field as described by the HRR solution is valid as $r \to 0$. In theory, the stress approaching the crack tip increases asymptotically to infinity, meaning a component subjected to such stress would fail under very small loads.

In practice, this is typically not the case, especially with materials exhibiting elastic-plastic behavior. The HRR solution does not consider large deformations or blunting of the crack and is only valid for small strains as $r \to 0$. An example of the actual stress field near the crack tip is also shown in Figure 1. Ritchie, et al. [5] determined that cleavage fracture actually occurs at some critical distance (r_c) when the stress at that location exceeds the critical stress (σ_c) and this failure criterion is often referred to as the RKR model.

Clearly, the single term HRR solution can overestimate the actual stress ahead of the crack tip. As a result, various procedures have been developed to include additional terms from the series expansion. Yang et al. [6, 7] and Chao et al. [8] developed an asymptotic crack-tip solution using three terms of the series solution from which the HRR solution is derived. The *J-A_2* procedure uses two parameters to better define the stress ahead of the crack tip. The *J*-integral is representative of the magnitude of the applied loading, while the A_2 term is used to describe the constraint at the crack tip based on the loading and specimen geometry.

The procedure begins by using the Ramberg-Osgood power-law relationship for a strain-hardening material for a Mode I crack under plane strain conditions. The Ramberg-Osgood equation relating uniaxial strain ε to the uniaxial stress σ in tension is

$$\frac{\varepsilon}{\varepsilon_0} = \frac{\sigma}{\sigma_0} + \alpha \left(\frac{\sigma}{\sigma_0} \right)^n . \qquad (2)$$

Eq. 2 can be rewritten in general terms by applying the J_2 deformation theory of plasticity

$$\frac{\varepsilon_{ij}}{\varepsilon_0} = (1+\nu)\frac{\sigma_{ij}}{\sigma_0} - \nu\frac{\sigma_{kk}}{\sigma_0}\delta_{ij} + \frac{3}{2}\alpha\left(\frac{\sigma_e}{\sigma_0}\right)^{n-1}\frac{s_{ij}}{\sigma_0}, \qquad (3)$$

where ν is the Poisson's ratio, δ_{ij} is the Kronecker delta, s_{ij} is the deviatoric stress, and σ_e is the von Mises effective stress defined as $\sigma_e = \sqrt{3\,s_{ij}s_{ij}/2}$. The asymptotic stress field can then be expressed as

$$\frac{\sigma_{ij}}{\sigma_0} = A_1\left[\left(\frac{r}{L}\right)^{s_1}\tilde{\sigma}_{ij}^{(1)}(\theta,n) + A_2\left(\frac{r}{L}\right)^{s_2}\tilde{\sigma}_{ij}^{(2)}(\theta,n) + A_2^{\,2}\left(\frac{r}{L}\right)^{s_3}\tilde{\sigma}_{ij}^{(3)}(\theta,n)\right], \qquad (4)$$

The angular stress functions and the stress power exponents are functions solely of the hardening exponent and are independent of the applied load and any material properties. The characteristic length, L, in Equation 4 is typically assigned one of the primary dimensions of the specimen under investigation; possibilities include the crack length, the specimen width, the specimen thickness, or even unity. For the current study, L = 1 mm for all cases. The parameters A_1 and s_1 from Equation 4 are related to the HRR solution (Eq. 1) by

$$A_1 = \left(\frac{J}{\alpha\varepsilon_0\sigma_0 I_n L}\right)^{-s_1}, \quad s_1 = -\frac{1}{n+1}, \qquad (5)$$

Comparing Eq. 4 and 1, it can be seen that the first term of the two-parameter equation (Eq. 4) is the same as the HRR solution (Eq. 1). Further, the additional stress power exponents can be calculated using $s_3 = 2s_2 - s_1$ for $n \geq 3$. Thus, the final stress power exponent, s_2, can be calculated numerically.

An apparent application of the J-A_2 method is to use the two parameters to predict failure of flawed components. Chao et al. [9] described the development of Material Failure Curves by plotting J-integral values versus the absolute value of A_2 (J vs. $|A_2|$), as A_2 is always a negative value. Using a modified version of Equation 4,

$$\frac{\sigma_c}{\sigma_0} = A_1\left[\left(\frac{r_c}{L}\right)^{s_1}\tilde{\sigma}_{ij}^{(1)}(\theta,n) + A_2\left(\frac{r_c}{L}\right)^{s_2}\tilde{\sigma}_{ij}^{(2)}(\theta,n) + A_2^{\,2}\left(\frac{r_c}{L}\right)^{s_3}\tilde{\sigma}_{ij}^{(3)}(\theta,n)\right], \qquad (6)$$

the aforementioned critical stress (σ_c) and corresponding critical radial distance (r_c) from the RKR model are substituted and J and A_2 can be determined and plotted. According to the RKR model, the location where failure initiates, r_c, occurs in the range of 2-4 grain diameters ahead of the crack. This equates to 0.12mm to 0.24mm for A533B, or $1 < r/(J/\sigma_0) < 5$ where $r/(J/\sigma_0)$ is the normalized radial distance ahead of the crack. Once σ_c and r_c have been determined, the critical values can be used in Equation 6 to plot a Material Failure Curve as shown in the left portion of Fig. 1.

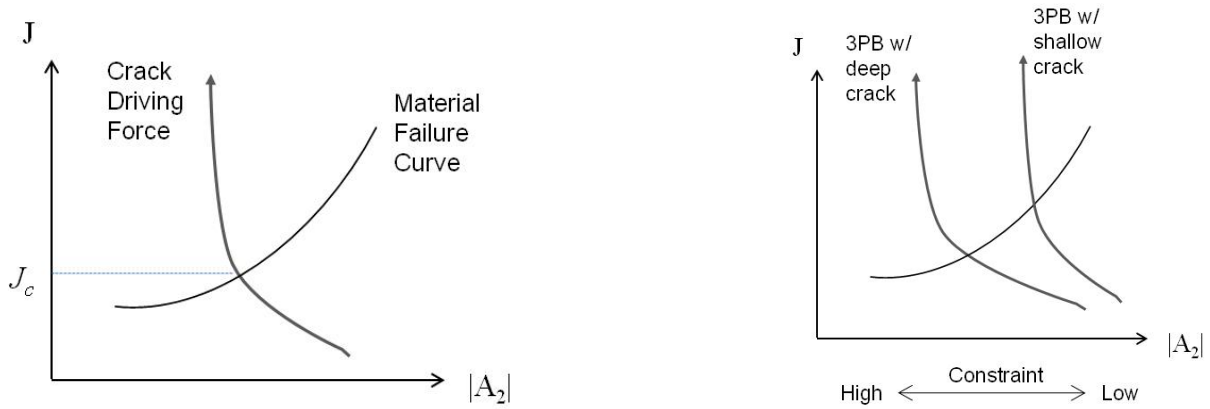

Figure 1. J vs. $|A_2|$ with Material Failure Curve and Crack Driving Force curve (left) and comparison of constraint levels (right)

The J vs. $|A_2|$ plot can be used to predict failure of components when the Crack Driving Force curve is added. The Crack Driving Force curve is a plot of multiple (J, $|A_2|$) pairs at any applied load, not just at the critical values. The intersection of the Material Failure Curve and the Crack Driving Force defines the critical J value (J_c) at which cleavage fracture will occur and can be used to predict the load at failure.

The J vs. $|A_2|$ plot can also be used to determine the constraint effect of specimens with different geometries and loading configurations. An example is shown in right diagram of Fig. 1. Crack Driving Force curves for 3PB specimens are shown on the J vs. $|A_2|$ plot. Specimens with deep cracks are high constraint specimens and typically exhibit lower fracture toughness than shallow cracked specimens. It should be noted that constraint is a relative term. A_2 provides a quantitative measure of constraint, although the magnitude of A_2 is of little value. The A_2 value of one specimen is simply compared to the A_2 value of other specimens to determine if there exists "loss of constraint" or, rather, an increase in fracture toughness.

3. Fraunhofer Experimental Data

3.1. Background

A set of published results to which the J-A_2 method could be applied were found in journal articles [10, 11] published by a team of researchers from the Fraunhofer Institute for Mechanics of Materials. These specimens and results presented in the article will be hereinafter referred to as the "Fraunhofer" specimens and results.

The goal of the Fraunhofer research was to determine the fracture toughness of a variety of cracked specimens. Specimens were tested over a wide range of lower shelf temperatures. Many trials with 3PB, C(T), and cruciform specimens were conducted at -85°C. The Fraunhofer cruciform specimen is shown below in Fig. 2. The cross sectional area of the small-scale cruciform arms

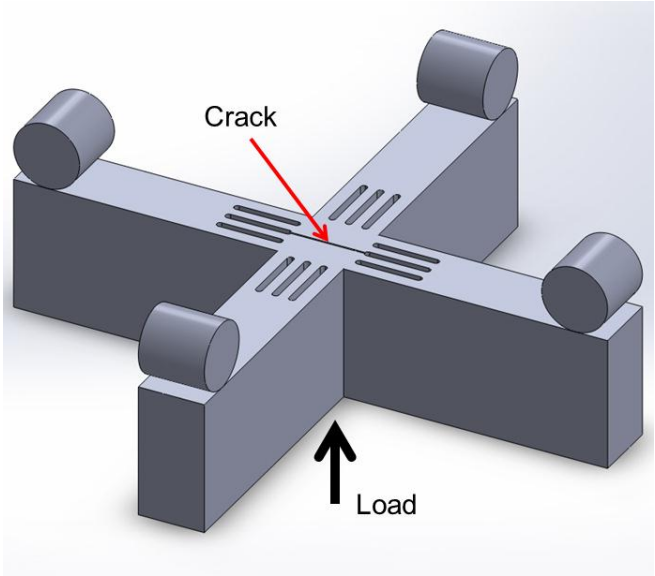

Figure 2. Fraunhofer cruciform specimen with five-point bending to simulate biaxial loading of crack

is only 10 mm x 20 mm (B = 10 mm and W = 20 mm). The distance between the roller supports in the five point bending test rig is 80 mm, while the overall dimensions of the specimen are 90 mm x 90 mm.

Also, smaller scale 3PB specimens are incorporated as well. The Fraunhofer study used pre-cracked Charpy test specimens rather than standard 3PB specimens specified in ASTM E1921 [2]. The 3PB specimens contained shallow cracks (a/W = 0.18). Standard 1T-C(T) specimens (a/W = 0.5) were also tested. Testing of such small specimens is completed in an effort to determine if the fracture toughness results are applicable to much larger scale components, including reactor pressure vessels.

3.2. Material Properties

The Fraunhofer specimens were machined from a section of A508 Class 2 steel, commonly used to fabricate reactor pressure vessels. Material properties for A508 were obtained from another recent study conducted by Scibetta et al. [12]. The researchers provided the following equation to correct the yield stress (in MPa) based on temperature (T, in degrees Celsius)

$$\sigma_{YS} = 398 + 45.2\exp(-0.01413\,T) \tag{7}$$

In addition, Scibetta et al. [12] also presented a temperature correction for E (in GPa) again where the temperature is in degrees Celsius,

$$E = 207 - 0.06\,T \tag{8}$$

Thus, at -85°C, the yield stress and Young's modulus were determined to be 550 MPa and 212.1 GPa, respectively. Poisson's ratio was assumed to be 0.3 as typical with many steels.

The Fraunhofer study [11] provided true stress vs. true strain curves for the material. A curve fitting procedure was used to determine the strain hardening exponent necessary for the elastic-plastic finite element analysis using the Ramberg-Osgood equation. The strain hardening exponent was determined to be n = 8. The angular stress functions and the stress power exponents

necessary to solve the two-parameter J-A_2 equation (Eq. 4) are provided in tables developed by Chao et al. [13].

3.3. Finite Element Analysis Models

The FEA models developed using Abaqus [14] for the 3PB and 1T C(T) specimens are shown below in Fig. 3.

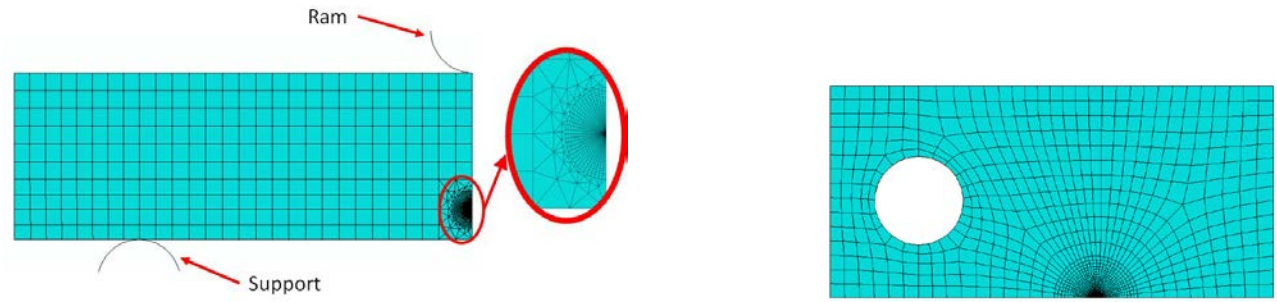

Figure 3. FEA mesh for Fraunhofer 3PB specimen (left) and 1T C(T) specimen (right).

Both meshes are composed mostly of eight node CPE8R quadratic plane strain elements, The extremely fine mesh around the crack tip includes elements with width of 0.001mm necessary to capture A_2 within the range of $1 < r/(J/\sigma_0) < 5$. The innermost ring of elements at the crack tip is comprised of eight node wedge elements with collapsed nodes at the tip to allow for blunting of the crack and large scale deformation.

The Fraunhofer cruciform is a small scale specimen. The overall dimensions are 90 mm x 90 mm. The specimen is machined with a shallow crack such that the crack depth ratio a/W = 0.08. The cruciform is tested in a five point bending configuration. In addition, two of the roller supports can be adjusted to allow for varying biaxiality ratios. However, only 1:1 biaxial loading was tested at the -85°C test temperature.

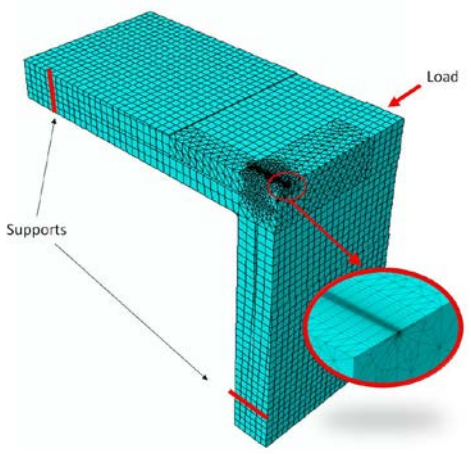

Figure 4. FEA mesh for Fraunhofer cruciform specimen

The cruciform specimen mesh shown in Fig. 4 contains 20,174 elements composed mostly of 20 node quadratic hexahedral C3D20R 3-D stress elements with a focused mesh around the crack tip. Elements in the focused mesh region are as small as 0.001 mm in order to capture the stress field in the region of cleavage fracture as defined by the RKR model. The average fracture toughness (J_c)

of the Fraunhofer biaxial cruciform specimens was determined to be 85.7 N/mm.

3.4. J-A_2 Method Applied to Fraunhofer Test Data

Loads were applied to the 3PB and C(T) FEA models until the J_c values presented in Table 1 were achieved. The stress (obtained from FEA output) perpendicular (i.e., $\theta = 0°$) to the crack front at a node ahead of the crack tip, along with radial position, r, of the node and J_c, can be substituted into Equation 4 to solve the quadratic equation for A_2 at each node. Again, according to the RKR model, fracture typically initiates within the range $1 < r/(J/\sigma_0) < 5$. Thus, A_2 was calculated at each node within this range and the average was tabulated. For this study, the average was actually taken approximately for the range $2 < r/(J/\sigma_0) < 5$ i.e., the first few nodes adjacent to the crack tip were neglected for the average A_2 calculation. The A_2 results are also summarized in Table 2 in the form of (J_c, A_2) pairs.

Table 1. (J_c, A_2) pairs for the 3PB and C(T) specimens

J_c is in N/mm, A_2 is unitless	
	-85°C
3PB shallow (a/W = 0.18)	(54.2, -0.392)
1T-C(T) (a/W = 0.5)	(13.1, -0.260)

Next, using the (J_c, A_2) pair for the 3PB specimen, and substituting the published value of σ_c = 1830 MPa [15, 16], Equation 6 can be used to solve for the fracture initiation location r_c, which is 0.104 mm for both specimens, a value which is in agreement with other published results. A study conducted by Wang et al. [17] focused on the determination of the fracture initiation location and they determined that, for temperatures in this range, r_c lies within the range of 0.1 mm to 0.25 mm. Additional evidence of an appropriate range of r_c values was found in [18], in which dozens of data points for the similar A508 material yielded 0.05 mm < r_c < 0.25 mm. Substituting r_c and σ_c into Equation 5, the Material Failure Curve can be plotted.

The FEA models are processed with incremental loads to determine a range of J values above and below J_c such that the Crack Driving Force curves for each specimen can be determined. The Material Failure Curve and Crack Driving Force curves are then plotted on the same J vs. $|A_2|$ plot. As the loading increases, the applied J increases from zero. And, therefore, referring to Figure 2, points on the plot above and left of the Material Failure Curve indicate fracture has occurred. Crack Driving Force curves, as shown in Figure 3, are indicative of each specimen's constraint and can be used to determine if the desirable "loss of constraint" occurs, i.e., fracture toughness increases due to geometry and/or loading conditions. The J vs. $|A_2|$ plot for the specimens is shown in Fig. 5. The triangles are actual data points obtained from the Fraunhofer study.

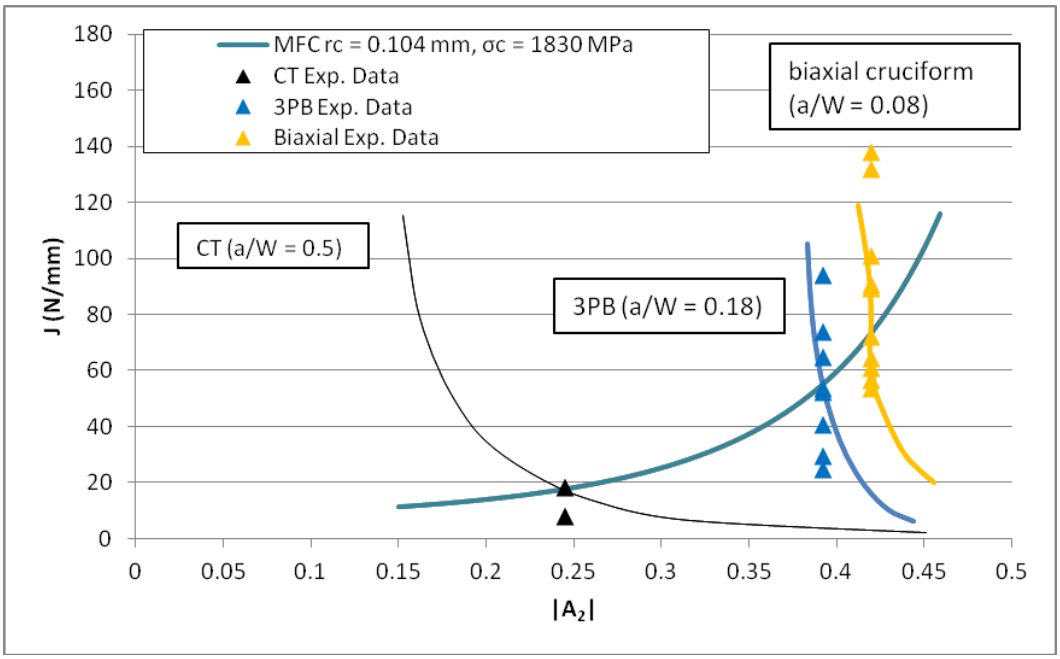

Figure 5. Material Failure Curve and Crack Driving Force curves for the Fraunhofer specimens (A508 material) at -85°C

4. Discussion of Results

The results presented in Fig. 5 reveal that the two parameter J-A_2 method does have the potential to i) predict failure, and ii) quantify constraint. The 3PB and biaxial cruciform specimens reveal significant loss of constraint when compared to the high constraint C(T) specimen. The biaxial cruciform exhibits higher fracture toughness (lower constraint) than the 3PB specimen. This may be attributed to the fact that the crack depth of the biaxial cruciform (a/W = 0.08) is more than twice as shallow as the 3PB specimen (a/W = 0.18), which may have overshadowed the biaxial effect. This supports the findings of Lidbury et al. [19] of a shallow crack effect.

Fig. 5 also shows the experimental fracture toughness data [10, 11] added to the Crack Driving Force curves in the form of the triangular symbols. The experimental fracture toughness data has been added at the $|A_2|$ values corresponding to the predicted critical $|A_2|$ to be compared with the Crack Driving Force curves. The average values of the experimental fracture toughness for all three specimens lies near the intersection of the MFC and the specimen CDFs. The constraint effect of each of the specimens can also be quantified and compared using the Crack Driving Force curves. The Crack Driving Force curves in Fig. 5 for the biaxial loading lies to the right of the 3PB specimen, meaning some loss of constraint and increased fracture toughness based on the loading and geometry.

For the purposes of comparing the fracture toughness values, a similar FEA and J-A_2 analysis of a uniaxial cruciform was conducted as part of the current investigation. The supports in the FEA model on the cruciform arms parallel to the crack, i.e., the horizontal arms shown in Fig. 2, were removed to simulate uniaxial loading. The same procedure was followed to develop the Crack Driving Force curve for the theoretical uniaxial cruciform specimen, which is shown as the red curve in Fig. 6. Clearly, the uniaxial cruciform specimen exhibits significant loss of constraint (increased fracture toughness) compared to the biaxial cruciform specimen.

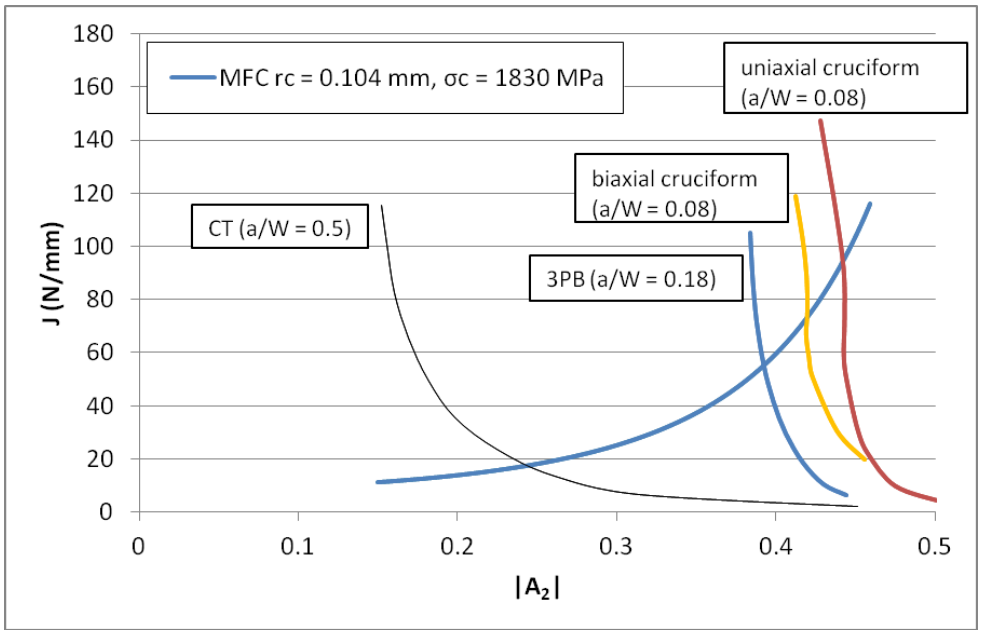

Figure 6. Crack Driving Force curve for theoretical uniaxial cruciform specimen indicated by the red curve (A508 material at -85°C)

The fracture toughness (J_c indicated by the intersection of the MFC and CDF) of the uniaxial cruciform specimen is estimated to be around 92 N/mm, while the fracture toughness of the biaxial cruciform is approximately 75 N/mm. In addition, the 3PB specimen has a slightly deeper crack than the cruciform specimens, therefore its fracture toughness is much less. The uniaxial specimen shows slightly greater loss of constraint (higher fracture toughness) when compared to biaxial specimens. This agrees with findings published by AREVA [20] related to RPV integrity assessment.

5. Conclusion

The two parameter J-A_2 method has been applied to experimental data obtained from testing A508B 3PB, C(T), and small scale cruciform specimens. The J-A_2 method shows great potential for use to predict failure in structural components and also to quantify the constraint effect due to varying loading and geometry. However, additional work is necessary to continue examination of the method. The current study utilized a small amount of data available from the literature. Future work will involve searching for larger available fracture toughness results necessary to conduct further evaluation of the J-A_2 method.

References

[1] ASTM, Standard E399-08, Linear-Elastic Plane-Strain Fracture Toughness K_{Ic} of Metallic Materials. *Annual Book of ASTM Standards,* ASTM International.
[2] ASTM, Standard E1921-11, Standard Test Method for Determination of Reference Temperature, To, for Ferritic Steels in the Transition Range. *Annual Book of ASTM Standards,* ASTM International.
[3] Hutchinson, J.W., 1968. Singular Behavior at the End of a Tensile Crack Tip in a Hardening Material. *J. Mech. Phys. Solids* 16 (1): 13-31.

[4] Rice, J.R., and Rosengren, G.F., 1968. Plane Strain Deformation Near a Crack Tip in a Power-Law Hardening Material. *J. Mech. Phys. Solids* 16 (1): 1-12.
[5] Ritchie, R.O., Knott, J.F., and Rice, J.R., 1973. On the Relationship Between Tensile Stress and Fracture Toughness in Mild Steel. *Journal of the Mechanics and Physics of Solids*, Vol. 21: 395-410.
[6] Yang, S., Chao, Y.J., and Sutton, M.A., 1993. Higher Order Asymptotic Crack Tip Fields in a Power-Law Hardening Material. *Engineering Fracture Mechanics* 45 (1): 1-20.
[7] Yang, S., Chao, Y.J., and Sutton, M.A., 1993. Complete Theoretical Analysis for Higher Order Asymptotic Terms and the HRR Zone at a Crack Tip for Mode I and Mode II Loading of a Hardening Material. *Acta Mechanica* 98 (1): 79-98.
[8] Chao, Y.J., Yang, S., and Sutton, M.A., 1994. On the Fracture of Solids Characterized by One or Two Parameters: Theory and Practice. *Journal of the Mechanics and Physics of Solids* 42 (1): 629-647.
[9] Chao, Y.J. and Ji, W., 1995. Cleavage Fracture Quantified by J and A2. *Constraint Effects in Fracture Theory and Applications: Second Volume.* ASTM STP 1244, Mark Kirk and Ad Bakker, Eds., American Society for Testing and Materials, Philadelphia, PA.
[10] Hohe, J., Hebel, J., Friedmann, V., and Siegele, D., 2007. Probabilistic failure assessment of ferritic steels using the master curve approach including constraint effects. *Engineering Fracture Mechanics* 74: 1274-1292.
[11] Hohe, J., Luckow, S., Hardenack, V., Sguaizer, Y., and Siegele, D., 2011. Enhanced fracture assessment under biaxial external loads using small scale cruciform bending specimens. *Engineering Fracture Mechanics* 78: 1876-1894.
[12] Scibetta, M., Schuurmans, J., and Lucon, E., 2008.Experimental Study of the Fracture Toughness Transferability to Pressurized Thermal Shock Representative Loading Conditions. *Journal of ASTM International* 5 (9): 1-14.
[13] Chao, Y.J. and Zhang, Li, 1997. *ME-Report 97-1: Tables of Plane Strain Crack Tip Fields: HRR and Higher Order Terms*. Department of Mechanical Engineering, University of South Carolina.
[14] Abaqus, 2010. *Abaqus/CAE User's* Manual. Version 6.10.
[15] Ritchie, R.O., Server, W.L., and Wullaert, R.A., 1979. Critical Fracture Stress and Fracture Strain Models for the Prediction of Lower and Upper Shelf Toughness in Nuclear Pressure Vessel Steels. *Metallurgical Transactions A* 10A: 1557-1570.
[16] Bates, R.C., 1987. Micromechanical Modeling for Prediction of Lower Shelf, Transition Region, and Upper Shelf Fracture Properties. *Fracture Mechanics: Microstructure and Micromechanisms (Papers presented at the 1987 ASM Material Science Seminar)* 1: 131-168.
[17] Wang, Z.X., Li, H.M., Chao, Y.J., and Lam, P.S., 2008. *Prediction of Characteristic Length and Fracture Toughness in Ductile-Brittle Transition (PVP2008-61608).* 2008 ASME Pressure Vessels and Piping Division Conference, Chicago, Illinois.
[18] Hohe, J., Hebel, J., Friedmann, V., and, Siegele, D., 2007. Probabilistic failure assessment of ferritic steels using the master curve approach including constraint effects. *Engineering Fracture Mechanics* 74 (1): 1274-1292.
[19] Lidbury, D. P. G., Sherry, A. H., Bass, B. R., Gilles, P., Connors, D., Eisele, U., Keim, E., Keinanen, H., Wallin, K., Lauerova, D., Marie, S., Nagel, G., Nilsson, K., Siegle, D., Wadier, Y., 2006. Validation of constraint-based methodology in structural integrity of ferritic steels for nuclear reactor pressure vessels. *Fatigue and Fracture of Engineering Materials & Structures* 29: 829-849.
[20] Keim, E., RPV integrity assessment using advanced fracture mechanics tools and multi scale modeling. *Regional workshop on Structural Integrity on LWR, Belo Horizonte, Brazil, 23-26 June 2009.*

Fracture analysis in plane piezoelectric media using hybrid finite element model

Hui Wang[1], Qing-Hua Qin[2,3*],

[1]Department of Engineering Mechanics, Henan University of Technology, Zhengzhou 450001, China
[2]Department of Mechanics, Tianjin University, Tianjin, 300072, China
[3]Research School of Engineering, Australian National University, ACT 0200, Australia
[*] Corresponding author: qinghua.qin@anu.edu.au

Abstract A two-dimensional electroelastic fracture analysis is performed on a plane piezoelectric material by the finite element model based on fundamental solution approximation. In the present element model, the fundamental solution of the piezoelectric problem is employed to construct the intra-element fields to make the final stiffness equation containing element boundary integrals only. Solving the stiffness equation can yield nodal displacement and electric potential, which are in turn used to evaluate the stress intensity factor and electric intensity factor by way of extrapolation techniques. Numerical results are provided to show the accuracy of the present method.

Keywords Piezoelectric materials, Crack, Stress intensity factor, Hybrid finite element method, Fundamental solution.

1. Introduction

Fracture analysis of piezoelectric materials is important for enhancing our understanding on the effect of the coupling properties on their fracture or damage behavior [1,2]. Because of complicated inherent coupling between electric and mechanical behaviors in piezoelectric solids, numerical simulation techniques have been widely employed for the fracture analysis of piezoelectric materials under complicated electric and mechanical load conditions. For example, finite element method [3, 4], boundary element method [5, 6], hybrid Trefftz finite element method [7,8], meshless methods [9], and virtual boundary integral method [10] have been developed for solving crack problems of piezoelectric materials.

In the paper, the hybrid finite element method developed recently by Wang and Qin [11-14] is extended to the case of cracked piezoelectricity. Different to other hybrid methods like the Trefftz finite element method [15-18], the basic idea of the proposed finite element model is the use of the novel interpolation kernels composed of fundamental solutions (or Green's functions) inside the multi-edge element to achieve the purpose of analytical satisfaction of governing equations of the problems of interest, and then the element stiffness equation which includes element boundary integrals only are formed for solving the electroelastic behavior.

In this work, the hybrid finite element method is extended for solving the piezoelectric problems. Using the fundamental solutions of piezoelectric problems, the intra-element displacement and electric potential fields are constructed. A modified variational functional is introduced to produce the linkage between intra-element and boundary fields. The minimization of the functional yields the stiffness matrix equation. As a result, the nodal displacements and electric potential can be determined by solving the linear stiffness equation. In the fracture analysis, the present hybrid finite element model is used to determine the displacement and electric potential distribution in the vicinity of the crack tip and then the stress and electric intensity factors can be obtained using the extrapolation technique [19].

2. Basic equations

For the transversely isotropic piezoelectric material, if the *x*-*y* plane is considered as the isotropic plane and the polarizing direction is assumed along the *z*-direction, one can employ either *x*-*z* or *y*-*z* plane to study the piezoelectric behavior. Here a plane piezoelectric media in the *x*-*z* plane is considered. In the absence of body forces and body electric charges, the equilibrium equations are given by [20]

$$\sigma_{ij,j} = 0, \qquad D_{i,i} = 0 \tag{1}$$

where $\sigma_{ij}(i, j = x, z)$ and D_i are stress tensor and electric displacement in the *i*-direction, respectively.

With plane strain assumption ($\varepsilon_{yy} = \varepsilon_{xy} = \varepsilon_{yz} = E_y = 0$), the constitutive equations in the *xz* system can be expressed as

$$\begin{Bmatrix} \sigma_{xx} \\ \sigma_{zz} \\ \sigma_{xz} \end{Bmatrix} = \begin{bmatrix} c_{11} & c_{13} & 0 \\ c_{13} & c_{33} & 0 \\ 0 & 0 & c_{44} \end{bmatrix} \begin{Bmatrix} \varepsilon_{xx} \\ \varepsilon_{zz} \\ 2\varepsilon_{xz} \end{Bmatrix} - \begin{bmatrix} 0 & e_{31} \\ 0 & e_{33} \\ e_{15} & 0 \end{bmatrix} \begin{Bmatrix} E_x \\ E_z \end{Bmatrix}$$
$$\begin{Bmatrix} D_x \\ D_z \end{Bmatrix} = \begin{bmatrix} 0 & 0 & e_{15} \\ e_{31} & e_{33} & 0 \end{bmatrix} \begin{Bmatrix} \varepsilon_{xx} \\ \varepsilon_{zz} \\ 2\varepsilon_{xz} \end{Bmatrix} + \begin{bmatrix} \kappa_{11} & 0 \\ 0 & \kappa_{33} \end{bmatrix} \begin{Bmatrix} E_x \\ E_z \end{Bmatrix} \tag{2}$$

where ε_{ij} and E_i denote the strain tensor and electric field in the *i*-direction, respectively. c_{ij}, e_{ij} and κ_{ij} stand for two dimensional material elastic, piezoelectric and dielectric coefficients. For the case of plane stress, the constitutive equation can be obtained similarly [20].

The remaining elastic strain-displacement and electric field-potential relations are given by

$$\varepsilon_{ij} = \frac{1}{2}(u_{i,j} + u_{j,i}), \qquad E_i = -\phi_{,i} \tag{3}$$

where u_i and ϕ are elastic displacement in the *i*-direction and electric potential, respectively.

The following boundary conditions are admissible on the boundary of the piezoelectric medium

$$\begin{aligned} u_i &= \overline{u}_i \quad \text{or} \quad t_i = \sigma_{ij} n_j = \overline{t}_i \\ \phi &= \overline{\phi} \quad \text{or} \quad D_n = D_i n_i = \overline{D}_n \end{aligned} \tag{4}$$

in which the components with an over bar denote specified values, and n_i is the *i*-component of outward unit normal vector.

3. Stress and electric intensity factors for plane piezoelectric crack

Now let us consider a crack embedded in an infinite plane piezoelectric solid, the origin of the local coordinate system is at the crack tip to be analyzed. Along the crack surface, the traction and normal electric displacement are free. According to Sosa's work [19] based on Lekhnitskii theory, the displacement components and electric potential along the upper crack surface near the crack tip can be written as

$$\begin{Bmatrix} u_x \\ u_z \\ \phi \end{Bmatrix} = \sqrt{\frac{2r}{\pi}} \,\mathrm{Re} \begin{bmatrix} \sum_{j=1}^{3} p_j \Lambda_{j1} & -\sum_{j=1}^{3} p_j \Lambda_{j2} & -\sum_{j=1}^{3} p_j \Lambda_{j3} \\ \sum_{j=1}^{3} q_j \Lambda_{j1} & -\sum_{j=1}^{3} q_j \Lambda_{j2} & -\sum_{j=1}^{3} q_j \Lambda_{j3} \\ \sum_{j=1}^{3} \lambda_j \Lambda_{j1} & -\sum_{j=1}^{3} \lambda_j \Lambda_{j2} & -\sum_{j=1}^{3} \lambda_j \Lambda_{j3} \end{bmatrix} \begin{Bmatrix} \mathrm{K_I} \\ \mathrm{K_{II}} \\ \mathrm{K_E} \end{Bmatrix} \tag{5}$$

where K_I,K_{II},K_E are respectively stress and electric intensity factors and r is the distance from the crack tip. In Eq. (5), the coefficients p_i, q_i, λ_i and Λ_{jk} can be found in Sosa's work [19].

From Eq. (5), it can be seen that the accuracy of displacement and electric potential can affect the results of stress and electric intensity factors. Therefore, developing new numerical approaches to achieve high accuracy of displacements and electric potential is important. The obtained numerical results below demonstrate that the proposed hybrid finite element formulation can serve for this purpose.

4. Hybrid finite element formulation

Consider a 2D electro-mechanical coupling problem, the energy functional used for constructing the proposed finite element model is given by

$$\Pi_e = \frac{1}{2}\int_{\Omega_e}(\sigma_{ij}\varepsilon_{ij} + D_i E_i)\mathrm{d}\Omega - \int_{\Gamma_t}\overline{t}_i\tilde{u}_i\mathrm{d}\Gamma - \int_{\Gamma_D}\overline{D}_n\tilde{\phi}\mathrm{d}\Gamma + \int_{\Gamma_e}t_i(\tilde{u}_i - u_i)\mathrm{d}\Gamma + \int_{\Gamma_e}D_n(\tilde{\phi}-\phi)\mathrm{d}\Gamma \quad (6)$$

in which $\tilde{u}_i$, $\tilde{\phi}$ and u_i, ϕ are the displacement components and electric potential respectively defined along the element boundary and inside the element domain.

In the present hybrid finite element model, the intra-element fields like displacement and electric potential inside the element can be approximated using the combination of the fundamental solution at different source points (the fundamental solution can be derived by either Lekhnitskii's formalism [21, 22] or Stroh's formalism [5]):

$$\begin{Bmatrix} u_x \\ u_z \\ \phi \end{Bmatrix} = \mathbf{N}_e\mathbf{c}_e \quad (\mathbf{x}\in\Omega_e, \mathbf{y}_{sk}\notin\Omega_e) \quad (7)$$

where

$$\mathbf{N}_e = \begin{bmatrix} u^*_{x1}(\mathbf{x},\mathbf{y}_{s1}) & u^*_{x2}(\mathbf{x},\mathbf{y}_{s1}) & u^*_{x3}(\mathbf{x},\mathbf{y}_{s1}) & \cdots & u^*_{x1}(\mathbf{x},\mathbf{y}_{sn_s}) & u^*_{x2}(\mathbf{x},\mathbf{y}_{sn_s}) & u^*_{x3}(\mathbf{x},\mathbf{y}_{sn_s}) \\ u^*_{z1}(\mathbf{x},\mathbf{y}_{s1}) & u^*_{z2}(\mathbf{x},\mathbf{y}_{s1}) & u^*_{z3}(\mathbf{x},\mathbf{y}_{s1}) & \cdots & u^*_{z1}(\mathbf{x},\mathbf{y}_{sn_s}) & u^*_{z2}(\mathbf{x},\mathbf{y}_{sn_s}) & u^*_{z3}(\mathbf{x},\mathbf{y}_{sn_s}) \\ \phi^*_1(\mathbf{x},\mathbf{y}_{s1}) & \phi^*_2(\mathbf{x},\mathbf{y}_{s1}) & \phi^*_3(\mathbf{x},\mathbf{y}_{s1}) & \cdots & \phi^*_1(\mathbf{x},\mathbf{y}_{sn_s}) & \phi^*_2(\mathbf{x},\mathbf{y}_{sn_s}) & \phi^*_3(\mathbf{x},\mathbf{y}_{sn_s}) \end{bmatrix} \quad (8)$$

is the interpolation matrix and

$$\mathbf{c}_e = [c_{11} \quad c_{21} \quad c_{31} \quad \cdots \quad c_{1n_s} \quad c_{2n_s} \quad c_{3n_s}]^{\mathrm{T}} \quad (9)$$

is the unknown coefficient vector. $u^*_{ij}(\mathbf{x},\mathbf{y}_{sk})$ and $\phi^*_j(\mathbf{x},\mathbf{y}_{sk})$ are induced displacement fundamental solutions at field point $\mathbf{x}$ due to a unit concentrated point load applied in the j-direction ($j=1,2$) and unit electric charge ($j=3$) at source point $\mathbf{y}_{sk}$ $(i=x,z;\ k=1,2,\cdots,n_s)$.

Whilst, the frame displacement and electric potential over the element boundary can be defined by

$$\begin{Bmatrix} \tilde{u}_x \\ \tilde{u}_z \\ \tilde{\phi} \end{Bmatrix} = \tilde{\mathbf{N}}_e\mathbf{d}_e \quad (10)$$

where $\tilde{\mathbf{N}}_e$ is the matrix of shape functions which is that same as those used in the conventional finite element method and boundary element method. $\mathbf{d}_e$ stands for the vector of the nodal displacements and electric potential.

Applying the Gauss theorem to the functional (6) and making use of the intra-element fields (7) and frame fields (10) yields

$$\Pi_e = -\frac{1}{2}\mathbf{c}_e{}^{\mathrm{T}}\mathbf{H}_e\mathbf{c}_e + \mathbf{c}_e{}^{\mathrm{T}}\mathbf{G}_e\mathbf{d}_e - \mathbf{d}_e{}^{\mathrm{T}}\mathbf{g}_e \tag{11}$$

where

$$\begin{aligned}\mathbf{H}_e &= \int_{\Gamma_e}\mathbf{Q}_e^{\mathrm{T}}\mathbf{N}_e \mathrm{d}\Gamma \\ \mathbf{G}_e &= \int_{\Gamma_e}\mathbf{Q}_e^{\mathrm{T}}\tilde{\mathbf{N}}_e \mathrm{d}\Gamma \\ \mathbf{g}_e &= \int_{\Gamma_t}\tilde{\mathbf{N}}_e^{\mathrm{T}}\bar{\mathbf{t}}\mathrm{d}\Gamma + \int_{\Gamma_D}\tilde{\mathbf{N}}_e^{\mathrm{T}}\bar{\mathbf{D}}\mathrm{d}\Gamma\end{aligned} \tag{12}$$

In Eq. (12), the matrix $\mathbf{Q}_e$ is a coefficient matrix in terms of intra-element traction and electric displacement induced by intra-element fields, that is

$$\begin{Bmatrix} t_x \\ t_z \\ D_n \end{Bmatrix} = \mathbf{Q_e c_e} \tag{13}$$

which can be derived from the assumed displacement and electric potential (7).

With the stationary condition of the functional (11), we finally have

$$\mathbf{G}_e{}^{\mathbf{T}}\mathbf{H}_e{}^{-1}\mathbf{G}_e\mathbf{d}_e = \mathbf{g}_e \tag{14}$$

and

$$\mathbf{c}_e = \mathbf{H}_e^{-1}\mathbf{G}_e\mathbf{d}_e \tag{15}$$

5. Numerical example

In this section, to investigate the performance of the present hybrid finite element formulation for the simulation of piezoelectric fracture behavior, a plane piezoelectric prism under uniform tension is considered with an embedded central crack and traction- and electric charge-free conditions are assumed along the crack surface (see Figure 1). Due to symmetry of the problem, only one quarter of the prism modeled, i.e. the shaded domain in Figure 1. The proper symmetrical mechanical boundary conditions should be applied along the symmetric lines x=0 and z=0 and the electric potential along the symmetric line z=0 is assumed to be zero. The plane strain case is assumed here and the PZT-4 material used in the computation has the following material constants [22]

$$c_{11} = 12.6\times10^{10}\,\mathrm{Nm}^{-2},\ c_{12} = 7.78\times10^{10}\,\mathrm{Nm}^{-2},\ c_{13} = 7.43\times10^{10}\,\mathrm{Nm}^{-2}$$

$$c_{33} = 11.5\times10^{10}\,\mathrm{Nm}^{-2},\ c_{44} = 2.56\times10^{10}\,\mathrm{Nm}^{-2}$$

$$e_{15} = 12.7\mathrm{Cm}^{-2},\ e_{31} = -5.2\mathrm{Cm}^{-2},\ e_{33} = 15.1\mathrm{Cm}^{-2}$$

$$\kappa_{11} = 6.464\times10^{-9}\,\mathrm{C/Nm},\ \kappa_{33} = 5.622\times10^{-9}\,\mathrm{C/Nm}$$

Firstly, to verify the present algorithm and show the accuracy of displacements and electric potential, the case without the crack is taken into consideration and the analytical results can be found in [22]. In the computation, thirty 8-node quadrilateral elements are used for the present hybrid finite element model (see Figure 2a). The results of displacements and electric potential at specific points are tabulated in Table 1, from which it's found that the numerical results from the proposed algorithm are in good agreement with the analytical results. Thus, the developed hybrid finite model can produce highly accurate displacement and electric potential results, which are important for the evaluation of stress intensity factors by displacement and electric potential extrapolation technique in the following analysis.

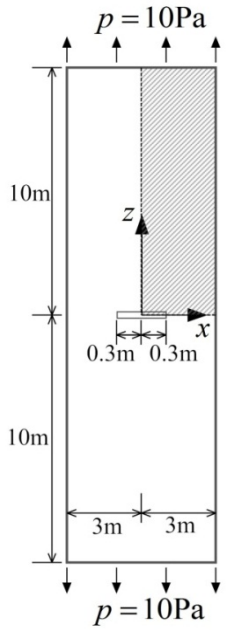

Figure 1 Geometry and boundary conditions of the piezoelectric prism with a central crack

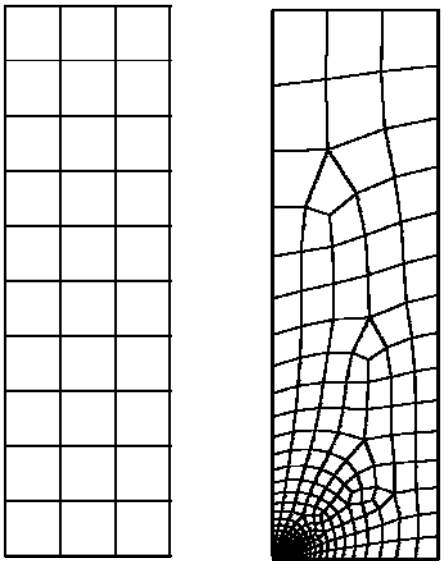

(a) (b)

Figure 2 Mesh configurations: (a) without central crack (b) with central crack

Table 1 Comparison of the numerical results by the present algorithm and the analytical solutions

Position	Analytical solutions			Numerical results		
	u_x	u_z	ϕ	u_x	u_z	ϕ
(2, 0)	-0.7222E-10	0	0	-0.7222E-10	0	0
(3, 0)	-1.0832E-10	0	0	-1.0832E-10	0	0
(0, 5)	0	3.915E-10	1.2184	0	3.915E-10	1.2184
(0,10)	0	7.829E-10	2.4367	0	7.829E-10	2.4367

Next, fracture analysis of the prism is considered and the corresponding mesh configuration is shown in Figure 2b, in which total 287 piezoelectric quadrilateral elements are used. The numerical results for crack is tabulated in Table 2, from we can find the displacement variation along the upper surface of the crack, also the corresponding electric displacement stress intensity factors $K_E \times 10^{-6} (Cm^{-3/2})$ can be evaluated by Eq. (5). The average value of it is 28.753.

Table 2 Variations of displacement and Stress intensity factor near the crack tip

r	0.01	0.02	0.03	0.04	0.05
u_x	-20.326E-12	-19.262E-12	-18.442E-12	-17.817E-12	-17.031E-12
u_z	17.901E-12	25.352E-12	31.050E-12	35.792E-12	39.651E-12
ϕ	0	0	0	0	0
$K_E \times 10^{-6}$	28.793	28.834	28.834	28.784	28.521

6. Conclusions

In the paper, a new hybrid finite element formulation is present for performing fracture analysis of piezoelectric media using fundamental solution approach. The hybrid piezoelectric element established in the present method contains element boundary integrals only. Numerical verification is conducted by analysing electroelastic behavior of plane piezoelectric prism without any internal crack. It is found that the developed hybrid finite model can produce relatively high accurate displacement and electric potential results. Subsequently, the fracture analysis is performed by considering a central crack in the piezoelectric prism and the corresponding electric displacement stress intensity factors is evaluated by using the extrapolation technique in the vicinity of crack tip.

References

[1] Q.H. Qin, Y.W. Mai, S.W. Yu, Effective moduli for thermopiezoelectric materials with microcracks. Int J Fracture, 91 (1998) 359-371.
[2] Q.H. Qin, Y.W. Mai, BEM for crack-hole problems in thermopiezoelectric materials. Eng Fract Mech, 69 (2002) 577-588.
[3] A. Benjeddou, Advances in piezoelectric finite element modeling of adaptive structural elements: a survey. Computers & Structures, 76 (2000) 347-363.
[4] C.Y. Cao, A. Yu, Q.H. Qin, A new hybrid finite element approach for plane piezoelectricity with defects. Acta Mechanica, 224 (2013) 41-61.
[5] E. Pan, A BEM analysis of fracture mechanics in 2D anisotropic piezoelectric solids. Engineering Analysis with Boundary Elements, 23 (1999) 67-76.
[6] Q.H. Qin, M. Lu, BEM for crack-inclusion problems of plane thermopiezoelectric solids. Int J Numer Meth Eng, 48 (2000) 1071-1088.
[7] Q.H. Qin, Solving anti-plane problems of piezoelectric materials by the Trefftz finite element approach. Computational Mechanics, 31 (2003) 461-468.
[8] H.T. Wang, K.Y. Sze, X.M. Yang, Analysis of electromechanical stress singularity in piezoelectrics by computed eigensolutions and hybrid-trefftz finite element models. Computational Mechanics, 38 (2006) 551-564.
[9] J. Sladek, V. Sladek, C. Zhang, F. Garcia-Sanchez, M. Wunsche, Meshless local Petrov-Galerkin method for plane piezoelectricity. Computers, Materials & Continua, 4 (2006) 109-117.
[10] W.A. Yao, H. Wang, Virtual boundary element integral method for 2-D piezoelectric media. Finite elements in analysis and design, 41 (2005) 875-891.
[11] H. Wang, Q.H. Qin, Hybrid FEM with Fundamental Solutions as Trial Functions for Heat Conduction Simulation. Acta Mechanica Solida Sinica, 22 (2009) 487-498.
[12] H. Wang, Q.H. Qin, Fundamental-solution-based hybrid FEM for plane elasticity with special elements. Computational Mechanics, 48 (2011) 515-528.
[13] H. Wang, Q.H. Qin, Special fiber elements for thermal analysis of fiber-reinforced composites. Engineering Computations, 28 (2011) 1079-1097.
[14] H. Wang, Q.H. Qin, Boundary integral based graded element for elastic analysis of 2D functionally graded plates. European Journal of Mechanics - A/Solids, 33 (2012) 12-23.
[15] H. Wang, Q.H. Qin, Matlab and C programming for Trefftz finite element methods, CRC Press, New York, 2008.
[16] Q.H. Qin, The Trefftz finite and boundary element method, WIT Press, Southampton, 2000.

[17] Q.H. Qin, Variational formulations for TFEM of piezoelectricity, International Journal of Solids and Structures, 40 (2003) 6335-6346.
[18] Q.H. Qin, Trefftz finite element method and its applications. Appl Mech Rev, 58 (2005) 316-337.
[19] H. Sosa, Plane problems in piezoelectric media with defects. International Journal of Solids and Structures, 28 (1991) 491-505.
[20] Q.H. Qin, Fracture mechanics of piezoelectric materials, WIT press, Southampton, 2001.
[21] X.L. Xu, R.K.N.D. Rajapakse, On a plane crack in piezoelectric solids. International Journal of Solids and Structures, 38 (2001) 7643-7658.
[22] H.J. Ding, G.Q. Wang, W.Q. Chen, A boundary integral formulation and 2D fundamental solutions for piezoelectric media. Computer Methods in Applied Mechanics and Engineering, 158 (1998) 65-80.

Thermo-elastic analysis of a cracked substrate bonded to a coating using the hyperbolic heat conduction theory

Zengtao Chen[1,*], **Keqiang Hu**[1]

[1] Department of Mechanical Engineering, University of New Brunswick, Fredericton NB E3B 5A3, Canada
* Corresponding author: ztchen@unb.ca

Abstract In this paper, the dynamic thermal stresses around a crack in a substrate bonded to a coating are obtained using the hyperbolic heat conduction theory. Fourier and Laplace transforms are applied and the hyperbolic heat conduction and thermo-elastic crack problems are reduced to solving singular integral equations. The crack kinking phenomenon under thermal loading is investigated by applying the criterion of maximum hoop stress. Numerical results show that the hyperbolic heat conduction parameters, the material properties and the geometric size of the composite have significant influence on the dynamic stress field. It seems that high temperature loading on the surface may lead to crack kinking away from the surface and low temperature loading may cause crack kinking toward the coating. Moreover, the hyperbolic heat conduction theory may give more conservative results than that the Fourier's heat conduction theory.

Keywords Cracked Substrate, Coating, Hyperbolic heat conduction, Singular integral equations, Crack kinking

1. Introduction

High-rate heat transfer has become a major concern in modern industries especially in material processing, such as the pulsed laser heat and ultrasonic waves, and accurate heat conduction analysis is of great importance for the material and structural integrity. Investigation of the temperature and stress fields is essential to the safety design of the composite structures under severe temperature loading. The Fourier heat conduction model, although give sufficient accuracy for many engineering applications, implies infinite thermal wave propagation speed, and renders ineffective at the very small length and time scales associated with small-scale systems [1]. Consideration of the hyperbolic heat conduction model becomes important if irreversible physical processes, such as crack or void initiation in a solid, are involved in the process of heat transport. In these cases, the hyperbolic heat conduction model should be used [2].

Inherent defects in materials such as dislocations and cracks may disturb the temperature distribution when thermal loading is applied, and singularities may be developed in the neighborhood of discontinuities. The singular behavior of temperature gradient around crack tip has been studied based on the classical Fourier heat conduction model [3]. Some investigations on crack problems in thermo-elastic materials have been made using the hyperbolic heat conduction model. The problem of a finite crack in a material layer under transient non-Fourier heat conduction was investigated by Wang and Han [4] and the problem of an interface crack in layered composite media under applied thermal flux was studied using the hyperbolic heat conduction theory [5]. A thermo-elastic analysis of a cracked substrate under a thermal shock was given in Chen and Hu [6] based on the hyperbolic heat conduction theory; and based on the same theory the transient temperature and thermal stresses around a partially insulated crack in a thermoelastic strip under a temperature impact were obtained [7]. The transient temperature field around a thermally insulated crack in a substrate bonded to a coating has been obtained by using the hyperbolic heat conduction model [8].

The thermo-elastic problem of a cracked substrate bonded by a coating under transient thermal loading is studied in this paper using the hyperbolic heat conduction model. Fourier and Laplace transforms are employed to reduce the problem to solving singular integral equations. The asymptotic fields around the crack tip are obtained in an explicit form and Laplace inversion is applied to get the dynamic temperature and stress fields. The crack kinking phenomenon is investigated by applying the criterion of maximum hoop stress.

2. Statement of the problem and basic equations

Consider a thermoelastic substrate containing a crack of length $2c$ parallel to the interface between the substrate and the coating, as shown in Figure 1. The composite is initially at certain temperature and the free surface of the coating $y=-h=-(a+b)$ is suddenly heated to by a temperature change T_0. The crack surfaces are assumed to be thermally insulated.

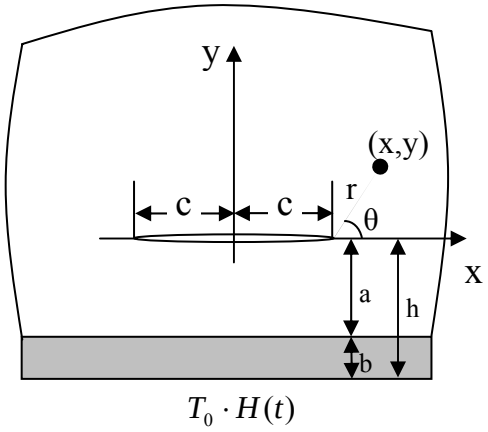

Figure 1. Crack geometry and coordinates.

2.1. Heat conduction equations

In the heat-transfer situations include extremely high temperature gradients, extremely large heat fluxes or extremely short transient durations, the Fourier's law may be modified to a relation of the type [9],

$$q+\tau\frac{\partial q}{\partial t}=-k\cdot\nabla T \tag{1}$$

where q is the heat flux, T is the temperature, k is the thermal conductivity of the material, ∇ is the spatial gradient operator, and τ is the so-called relaxation time. The local energy balance equation with vanishing heat source follows:

$$-\nabla q=\rho C\cdot\frac{\partial T}{\partial t} \tag{2}$$

where ρ and C are the mass density and the specific heat capacity, respectively. Incorporating Eq. (1) with Eq. (2) leads to the hyperbolic heat conduction equation for the substrate and the

coating,

$$d_i \cdot \nabla^2 T^{(i)} = \partial T^{(i)} / \partial t + \tau_i \, \partial^2 T^{(i)} / \partial t^2 , \qquad (i = 1,\ 2) \tag{3}$$

where ∇^2 is Laplace's differential operator, τ_i, $d_i = k_i / (\rho_i C_i)$ and k_i $(i = 1,\ 2)$ are the relaxation times, the thermal diffusivities and the thermal conductivities of the substrate and the coating, respectively. It is noted that here and afterwards the subscript "$i = 1,\ 2$" denote the quantities of the substrate and the coating, respectively.

By introducing the dimensionless variables

$$\bar{T} = T / T_0 , \quad \bar{t} = t d_0 / c^2 \tag{4}$$

where T_0 is the reference temperature and d_0 is the reference thermal diffusivity, the governing equations (3) have the following dimensionless forms:

$$\nabla^2 T^{(i)} = \frac{\partial T^{(i)}}{\partial t} \frac{d_0}{d_i} + \frac{\tau_i d_0^2}{c^2 d_i} \frac{\partial^2 T^{(i)}}{\partial t^2} , \qquad (i = 1,\ 2) \tag{5}$$

It is noted that here and afterwards, the hat "$\bar{}$" of the dimensionless variables is omitted for simplicity. The hyperbolic heat equation (5) is subjected to the following boundary and initial conditions in dimensionless forms

$$T(x,-h) = T_0 ,\ T(x,-a^+) = T(x,-a^-) ,\ k_1 \frac{\partial T(x,-a^+)}{\partial y} = k_2 \frac{\partial T(x,-a^-)}{\partial y} , \quad (|x| < \infty ,\ t > 0) \tag{6}$$

$$\begin{aligned} &\partial T(x,0) / \partial y = 0 ,\ (|x| < c) \\ &T(x,0^+) = T(x,0^-) ,\ \partial T(x,0^+) / \partial y = \partial T(x,0^-) / \partial y ,\ (|x| \geq c) \end{aligned} \tag{7}$$

It should be noted that the relaxation time (τ) for most engineering materials are of the order of $10^{-14} - 10^{-6}$ s and the thermal diffusivity $10^{-8} - 10^{-3}$ m^2/s, and therefore the Fourier parabolic heat conduction model can give good results. Experiments have shown that some special materials may have thermal relaxation time up to the order of 10s, which are important materials to work as thermal insulators [10]; in this case it is necessary to take into account the effect of the relaxation time and use the hyperbolic heat conduction model. Other applications of hyperbolic heat conduction model are in the area of transient thermal disturbance with small length and time scales.

2.2. Thermal-elastic field equations

The equilibrium equations, the strain-displacement relations, the compatibility equation and the constitutive law of plane stress thermoelasticity can be expressed as follows,

$$\partial \sigma_x / \partial x + \partial \sigma_{xy} / \partial y = 0 , \ \ \partial \sigma_{xy} / \partial x + \partial \sigma_y / \partial y = 0 \tag{8}$$

$$\varepsilon_x = \partial u/\partial x, \quad \varepsilon_y = \partial v/\partial y, \quad \varepsilon_{xy} = (\partial u/\partial y + \partial v/\partial x)/2 \tag{9}$$

$$\partial^2 \varepsilon_x/\partial y^2 + \partial^2 \varepsilon_y/\partial x^2 = 2\partial^2 \varepsilon_{xy}/\partial x \partial y \tag{10}$$

$$\varepsilon_x = (\sigma_x - \nu\sigma_y)/E + \alpha T, \ \varepsilon_y = (\sigma_y - \nu\sigma_x)/E + \alpha T, \ \varepsilon_{xy} = (1+\nu)\sigma_{xy}/E \tag{11}$$

where E, ν and α are Young's modulus, Poisson's ratio and the coefficient of linear thermal expansion, respectively.

Let $U(x, y)$ be the Airy stress function, then the stresses can be expresses in terms of U as

$$\sigma_x = \partial^2 U/\partial y^2, \quad \sigma_y = \partial^2 U/\partial x^2, \quad \sigma_{xy} = \partial^2 U/\partial x \partial y \tag{12}$$

Substitution of Eq. (12) into (10) and (11) leads to

$$\nabla^2 \nabla^2 U + E \cdot \nabla^2 (\alpha T) = 0 \tag{13}$$

By introducing the following dimensionless quantities

$$\bar{U} = U/(E\alpha c^2 T_0), \ \bar{\sigma}_{ij} = \sigma_{ij}/(E\alpha T_0), \ \bar{\varepsilon}_{ij} = \varepsilon_{ij}/(\alpha T_0), \ (\bar{u}, \ \bar{v}) = (u, \ v)/(\alpha c T_0) \tag{14}$$

the governing equations (13) can be rewritten in the following dimensionless forms:

$$\nabla^2 \nabla^2 U + \nabla^2 (T) = 0 \tag{15}$$

The mechanical boundary conditions can be expressed as

$$\sigma_{xy}(x,-a^+) = \sigma_{xy}(x,-a^-), \ \sigma_y(x,-a^+) = \sigma_y(x,-a^-), \ \sigma_{xy}(x,-h) = \sigma_y(x,-h) = 0, \quad (|x| < \infty) \tag{16}$$

$$\sigma_{xy}(x,0) = \sigma_y(x,0) = 0, \quad (|x| < c) \tag{17}$$

$$\sigma_{xy}(x,0^+) = \sigma_{xy}(x,0^-), \ \sigma_y(x,0^+) = \sigma_y(x,0^-), \ u(x,0^+) = u(x,0^-), \ v(x,0^+) = v(x,0^-), \ (|x| \geq c) \tag{18}$$

3. Temperature field

Apply Laplace transform to Eqs. (5):

$$\begin{aligned} T^{(i)*}(x, y, p) &= L\left(T^{(i)}(x, y, t)\right) = \int_0^\infty T^{(i)}(x, y, t) \exp(-pt) dt \\ T^{(i)}(x, y, t) &= L^{-1}\left(T^{(i)*}(x, y, p)\right) = \frac{1}{2\pi i} \int_{Br} T^{(i)*}(x, y, p) \exp(pt) dp \end{aligned} \tag{19}$$

where Br stands for the Bromwich path of integration, and assume the composite is at rest in the beginning, we have:

$$\nabla^2 T^{(i)*} = A_i p T^{(i)*} + B_i p^2 T^{(i)*}, \quad (i = 1, \ 2) \tag{20}$$

where $A_i = d_0/d_i$ and $B_i = \tau_i d_0^2/c^2 d_i$ $(i = 1, \ 2)$.

Following the procedure in Chen and Hu [8], the temperature field in the Laplace domain satisfying the boundary condition and regularity condition can be expressed as

$$T^{(1)*}(x,y,p)=\int_{-\infty}^{\infty}E_1(\xi)\exp(ry)\exp(-ix\xi)d\xi+W(y),\qquad (y\geq 0) \tag{21}$$

$$T^{(1)*}(x,y,p)=\int_{-\infty}^{\infty}\left[E_2(\xi)\exp(ry)+E_3(\xi)\exp(-ry)\right]\exp(-ix\xi)d\xi+W(y)\quad (-a\leq y\leq 0) \tag{22}$$

$$T^{(2)*}(x,y,p)=\int_{-\infty}^{\infty}\left[D_1(\xi)\exp(ny)+D_2(\xi)\exp(-ny)\right]\exp(-ix\xi)d\xi+V(y)\quad (-h\leq y\leq -a) \tag{23}$$

where $E_i(\xi)=E_i(\xi,p)$ ($i=1,2,3$) and $D_j(\xi)=D_j(\xi,p)$ ($j=1,2$) are unknowns to be determined, and

$$W(y)=W(y,p)=f\cdot\exp(-qy),\ V(y)=V(y,p)=C_1^0\cdot\exp(my)+C_2^0\cdot\exp(-my) \tag{24}$$

$$q=\sqrt{A_1p+B_1p^2},\ m=\sqrt{A_2p+B_2p^2},\ r=\sqrt{\xi^2+A_1p+B_1p^2},\ n=\sqrt{\xi^2+A_2p+B_2p^2} \tag{25}$$

Constants C_1^0, C_2^0 and f can be obtained from the boundary conditions. As the unknown functions are dependent, all other unknown functions can be expressed by only one independent unknown function, for example $D_1(\xi)$, as follows

$$D_2(\xi)=-D_1(\xi)/\exp[2n(a+b)] \tag{26-1}$$

$$E_1(\xi)=[\lambda_2(\xi)-\lambda_1(\xi)]D_1(\xi),\ E_2(\xi)=\lambda_1(\xi)D_1(\xi),\ E_3(\xi)=\lambda_2(\xi)D_1(\xi) \tag{26-2}$$

$$\lambda_1(\xi)=\exp(ra)(\alpha_1+\alpha_2)/2,\ \lambda_2(\xi)=\exp(-rh)(\alpha_1-\alpha_2)/2 \tag{26-3}$$

$$\alpha_1=[1-\exp(-2nb)]/\exp(na),\ \alpha_2=nk_2[1+\exp(-2nb)]/[rk_1\exp(na)] \tag{26-4}$$

Introduce the temperature density function as

$$\phi(x)=\phi(x,p)=\partial T^{(1)*}(x,0^+,p)/\partial x-\partial T^{(1)*}(x,0^-,p)/\partial x \tag{27}$$

It is clear from the boundary conditions (27) that

$$\int_{-c}^{c}\phi(t)dt=0,\quad \phi(x)=0\quad (|x|\geq c) \tag{28}$$

Substituting (21) and (22) into (27) and using Fourier inverse transform, we can get

$$D_1(\xi)=\frac{1}{i4\pi\lambda_1\xi}\int_{-c}^{c}\phi(s)\exp(is\xi)ds \tag{29}$$

Substituting (21) and (22) into (7) and applying the relation (29), we get the singular integral equation for $\varphi(t)=\phi(ct)$ as follows

$$\int_{-1}^{1}\varphi(t)[1/(t-x)+K(x,t)]dt=2\pi qf,\quad (|x|<1) \tag{30}$$

where the kernel function $K(x,t)$ is given as

$$K(x,t)=\int_0^{\infty}[1-R(\xi/c)]\sin[\xi(x-t)]d\xi \tag{31}$$

and $R(\xi) = r(\lambda_1 - \lambda_2)/\lambda_1\xi$. The singular integral equation (30) under the single-valuedness condition in (28) has the following form of solution [11]:

$$\varphi(x) = \Psi(x)\Big/\sqrt{1-x^2}\,, \qquad |x| < 1 \tag{32}$$

where $\Psi(x)$ is a bounded and continuous function. From the condition (28), it is clear that $\Psi(x)$ is an odd function of x, i.e., $\Psi(-x) = -\Psi(x)$.

Function $\Psi(x)$ can be solved numerically, as detailed in Chen and Hu [8], and function $D_1(\xi)$ can be calculated by using the Chebyshev quadrature for integration as

$$D_1(\xi) \cong \frac{c}{4\pi\xi\lambda_1}\sum_{i=1}^{n} w_i \Psi(x_i)\sin(c\xi x_i) \tag{33-1}$$

$$w_i = \pi/n\,,\ \ x_i = \cos[(2i-1)\pi/2n], \quad i = 1,2,...,n \tag{33-2}$$

By substituting Eq. (33) into (21)-(23) the temperature in the Laplace domain can be obtained. The temperature in the time domain can be determined by applying the Laplace inverse transform.

4. Thermal stress field

Considering the temperature expressions (21-23), the general solution of the Airy function satisfying the regular condition at infinity can be expressed as

$$U^* = \int_{-\infty}^{\infty}[(A_1 + A_2 y)\exp(|\xi|y) + G_{11}(\xi)\exp(-ry)]\exp(-ix\xi)d\xi - W(y,p)/q^2 \qquad (y \ge 0) \tag{34}$$

$$\begin{aligned} U^* = &\int_{-\infty}^{\infty}[(B_1 + B_2 y)\exp(|\xi|y) + (B_3 + B_4 y)\exp(-|\xi|y)]\exp(-ix\xi)d\xi \\ &+ \int_{-\infty}^{\infty}[G_{21}(\xi)\exp(ry) + G_{22}(\xi)\exp(-ry)]\exp(-ix\xi)d\xi - W(y,p)/q^2 \end{aligned} \qquad (-a \le y \le 0) \tag{35}$$

$$\begin{aligned} U^* = &\int_{-\infty}^{\infty}[(C_1 + C_2 y)\exp(|\xi|y) + (C_3 + C_4 y)\exp(-|\xi|y)]\exp(-ix\xi)d\xi \\ &+ \int_{-\infty}^{\infty}[G_{31}(\xi)\exp(my) + G_{32}(\xi)\exp(-my)]\exp(-ix\xi)d\xi - V(y,p)/m^2 \end{aligned} \qquad (-h \le y \le -a) \tag{36}$$

where B_i, C_i ($i = 1-4$), A_1 and A_2 are unknowns to be determined, and $G_{ij}(\xi)$ $(i = 1-3,\ j = 1,2)$ are known functions determined from the boundary conditions.

Denote the jumps of displacement across the plane $y = 0$ by $\langle u\rangle$ and $\langle v\rangle$,

$$\langle u\rangle = u(x,0^+,p) - u(x,0^-,p),\ \ \langle v\rangle = v(x,0^+,p) - v(x,0^-,p) \tag{37}$$

Following the procedure in Jin and Noda [12] and introducing two dislocation density functions $f_j(x)$ ($j = 1,\ 2$) as

$$f_1(x) = f_1(x, p) = \partial\langle u\rangle/\partial x, \quad f_2(x) = f_2(x, p) = \partial\langle v\rangle/\partial x \tag{38}$$

By applying the boundary conditions (16-18), it can be shown that $f_i(x)$ $(i = 1,\ 2)$ satisfy the following singular integral equations:

$$\int_{-c}^{c} f_1(t)[1/(x-t) + M_{11}(x,t)]dt + \int_{-1}^{1} f_2(t)M_{12}(x,t)dt = U_1(x) \tag{39-1}$$

$$\int_{-c}^{c} f_1(t)M_{21}(x,t)dt + \int_{-1}^{1} f_2(t)[1/(x-t) + M_{22}(x,t)]dt = U_2(x) \tag{39-2}$$

where functions $U_i(x),\ M_{ij}(x,t)$ $(i, j = 1,2)$ are known functions. Functions $f_j(x)$ $(j = 1,\ 2)$ also need to satisfy the single-valuedness conditions

$$\int_{-c}^{c} f_j(x)dx = 0, \qquad (j = 1,\ 2) \tag{40}$$

The solution of the integral Eqs. (39), $f_j(x)$ $(j = 1,\ 2)$, can be expressed as follows

$$f_j(ct) = F_j(t, p)\Big/\sqrt{1-t^2}, \qquad (j = 1,\ 2) \tag{41}$$

and the singular integral equations can be reduced to solving a system of algebraic equations in terms of $F_1(t, p)$ and $F_2(t, p)$, see [6, 7].

Following the procedure in Chen and Hu [9], the stress intensity factors (SIFs) $K_1^*(p)$ and $K_2^*(p)$ are obtained as

$$K_1^*(p) = -\sqrt{\pi c}F_2(1, p)/4, \quad K_2^*(p) = -\sqrt{\pi c}F_1(1, p)/4 \tag{42}$$

and the dynamic singular stresses near the crack tip are

$$\sigma_y(r,\theta,t) = \sqrt{\frac{c}{2\pi r}}\left\{K_1(t)\cos\left(\frac{\theta}{2}\right)\left[1+\sin\left(\frac{\theta}{2}\right)\sin\left(\frac{3\theta}{2}\right)\right] + K_2(t)\sin\left(\frac{\theta}{2}\right)\cos\left(\frac{\theta}{2}\right)\cos\left(\frac{3\theta}{2}\right)\right\} \tag{43}$$

$$\sigma_{xy}(r,\theta,t) = \sqrt{\frac{c}{2\pi r}}\left\{K_1(t)\sin\left(\frac{\theta}{2}\right)\cos\left(\frac{\theta}{2}\right)\cos\left(\frac{3\theta}{2}\right) + K_2(t)\cos\left(\frac{\theta}{2}\right)\left[1-\sin\left(\frac{\theta}{2}\right)\sin\left(\frac{3\theta}{2}\right)\right]\right\} \tag{44}$$

$$\sigma_x(r,\theta,t) = \sqrt{\frac{c}{2\pi r}}\left\{K_1(t)\cos\left(\frac{\theta}{2}\right)\left[1-\sin\left(\frac{\theta}{2}\right)\sin\left(\frac{3\theta}{2}\right)\right] - K_2(t)\sin\left(\frac{\theta}{2}\right)\left[2+\cos\left(\frac{\theta}{2}\right)\cos\left(\frac{3\theta}{2}\right)\right]\right\} \tag{45}$$

where the dynamic SIFs $K_1(t)$ and $K_2(t)$ are given by

$$K_1(t) = L^{-1}\left(K_1^*(p)\right), \quad K_2(t) = L^{-1}\left(K_2^*(p)\right) \tag{46}$$

and (r,θ) are the polar coordinates measured from the crack tip defined by

$$r^2 = (x-c)^2 + y^2, \quad \tan(\theta) = y/(x-c) \tag{47}$$

The hoop and shear stresses at an angle θ near the crack tip can be obtained in terms of the polar coordinates (r,θ) as

$$\begin{aligned} \sigma_{\theta\theta}(r,\theta) &= \sigma_y(r,\theta)\cos^2\theta + \sigma_x(r,\theta)\sin^2\theta - \sigma_{xy}(r,\theta)\sin 2\theta \\ \sigma_{r\theta}(r,\theta) &= \sin 2\theta\left[\sigma_y(r,\theta) - \sigma_x(r,\theta)\right]/2 + \sigma_{xy}(r,\theta)\cos 2\theta \end{aligned} \tag{48}$$

The hoop stress intensity factor and shear stress intensity factor associated with the hoop and shear stresses at an arbitrary angle θ can be defined as:

$$K_{\theta\theta} = \lim_{r\to 0}\left(\sqrt{2r}\sigma_{\theta\theta}\right), \quad K_{r\theta} = \lim_{r\to 0}\left(\sqrt{2r}\sigma_{r\theta}\right) \tag{49}$$

5. Numerical results and discussion

The effect of the thickness of coating b/c on the dynamic SIFs is shown in Figure 2 when the geometry of the cracked substrate is $a/c = 1$, the material properties are $k_1 = k_2 = 1$, $\nu = 0.4$ and $\tau_1 = 1$, $\tau_2 = 0.5$ and the boundary temperature condition $T_0 = +1$. The SIFs oscillate and increase in magnitude till they reach the peak values and oscillate for some time before approaching their static values. The magnitude of the peak value decreases as the size ratio b/c increases, which indicates that a thicker coating may decrease the magnitude of SIF.

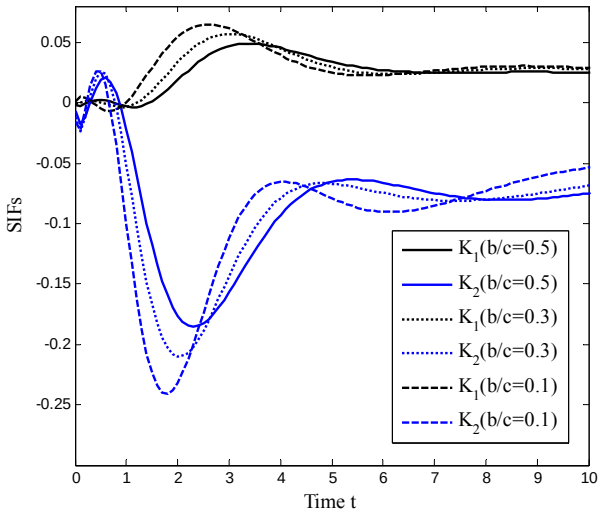

Figure 2. Effect of b/c on the dynamic SIFs when $a/c = 1$.

Figure 3 exhibits the variation of the dynamic SIFs with different thermal relaxation times τ_1 and τ_2 when $k_1 = k_2 = 1$, $\nu = 0.4$, $a/c = 1$, $b/c = 0.5$ and $T_0 = +1$. The results based on the Fourier heat conduction is the special case when $\tau_1 = \tau_2 = 0$, which shows that the dynamic SIF increases smoothly to reach the peak values and then decrease to the static values. The oscillating feature of the dynamic SIFs is observed when the hyperbolic heat conduction theory is applied, and as the relaxation time of the coating decreases the magnitude of the dynamic SIF decreases. This conclusion indicates that the structure safety design based on the hyperbolic heat conduction theory may lead to more conservative design than Fourier's heat conduction theory.

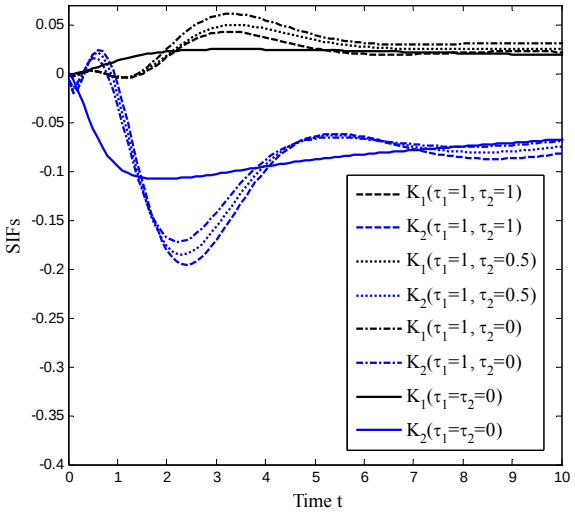

Figure 3. Effect of relaxation time on dynamic SIFs.

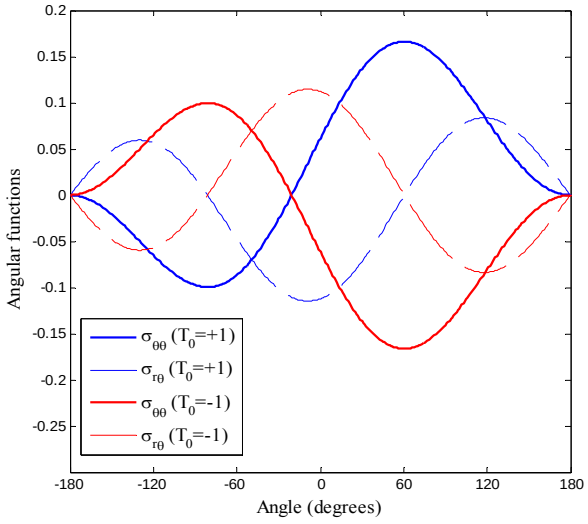

Figure 4. Angular functions of the normalized hoop stresses and shear stresses at a time instant.

The angular functions of the normalized dynamic hoop stresses $\sigma_{\theta\theta}\sqrt{2\pi r/c}$ and shear stresses $\sigma_{r\theta}\sqrt{2\pi r/c}$ at a specific time instant $t=3.0$ are displayed in Figure 4 when $a/c=1$, $b/c=0.1$, $k_1=k_2=1$ and $\nu=0.4$. The maximum hoop stress criterion is used to study crack kinking in this paper. It is shown that when the hoop stress reaches the maximum value, the shear stress is zero. When the temperature loading on the surface of the coating is positive, the maximum hoop stress appears at the angle $\theta=+60$ degrees, which indicates that the crack may kink in this direction; when a negative temperature is applied on the coating surface, the hoop stress reaches the maximum value at the angle $\theta=-70$ degrees, which means that the crack may kink toward the coating in this direction. It seems that high temperature loading on the surface may lead to crack kinking away

from the surface and low temperature loading may cause the crack to kink toward the coating.

6. Conclusions

The transient thermal stresses around a crack in a substrate bonded to a coating have been obtained using the hyperbolic heat conduction theory. Integral transform method is applied and the hyperbolic heat conduction and thermo-elastic crack problem are reduced to solving singular integral equations. The crack kinking phenomenon is investigated by applying the criterion of maximum hoop stress. Numerical results show that the hyperbolic heat conduction parameters, the material properties and the geometric size of the composite have significant influence on the dynamic stress field. Hot or cold temperature loadings may lead to different crack kinking directions. The results predicted by the hyperbolic heat conduction model are more conservative than that by the Fourier's heat conduction model.

References

[1] M.H. Babaei, Z.T. Chen, Transient hyperbolic heat conduction in a functionally graded hollow cylinder. J Thermophys Heat Transfer, 24 (2010) 325-330.
[2] M. Naji, M. Al-Nimr, T. Darabseh, Thermal stress investigation in unidirectional composites under the hyperbolic energy model. Int J Solids Struct, 44 (2007) 5111-5121.
[3] D.Y. Tzou, Characteristics of thermal and flow behavior in the vicinity of discontinuities. Int J Heat Mass Transfer, 35 (1992): 481-491.
[4] B.L. Wang, J.C. Han, A crack in a finite medium under transient non-Fourier heat conduction. Int J Heat Mass Transfer, 55 (2012) 4631-4637.
[5] B.L. Wang, J.C. Han, Non-Fourier heat conduction in layered composite materials with an interface crack. Int J Eng Sci, 55 (2012) 66-75.
[6] Z.T. Chen, K.Q. Hu, Thermo-elastic analysis of a cracked half-plane under a thermal shock impact using the hyperbolic heat conduction theory. J Therm Stresses, 35 (2012) 342-362.
[7] K.Q. Hu, Z.T. Chen, Thermoelastic analysis of a partially insulated crack in a strip under thermal impact loading using the hyperbolic heat conduction theory. Int J Eng Sci, 51 (2012) 144-160.
[8] Z.T. Chen, K.Q. Hu, Hyperbolic heat conduction in a cracked thermoelastic half-plane bonded to a coating. Int J Thermophys, 33 (2012) 895-912.
[9] J.D. Achenbach, Wave propagation in elastic solids, North-Holland, 1973.
[10] Y.M. Ali, L.C. Zhang, Relativistic heat conduction. Int J Heat Mass Transfer, 48 (2005) 2397-2406.
[11] F. Erdogan, Complex function technique, in: A.C. Eringen (Editor), Continuum Physics. Vol. 2, Academic Press, New York, 1975, pp. 523-603.
[12] Z.-H. Jin, N. Noda, An internal crack parallel to the boundary of a nonhomogeneous half plane under thermal loading. Int J Eng Sci, 31 (1993) 793-806.

Numerical simulations of thermo-electro-magnetic phenomena in YBCO films subjected to strains

Jing Xia and You-He Zhou*

Department of Mechanics and Engineering Sciences, Lanzhou University, 730000, People's Republic of China
* Corresponding author: zhouyh@lzu.edu.cn

Abstract Due to thermal contractions, tensions and electromagnetic forces, YBCO coated conductors in high-temperature superconductors apparatuses are subjected to mechanical strains. The strains cause the degradation of the critical current densities and influence thermo-electro-magnetic features in the conductors. Based on the dynamic process of thermo-electro-magnetic interaction, we report the results of numerical simulation of thermo-electro-magnetic phenomena in an infinite YBCO film subjected to a uniform in-plane strain in an alternating external magnetic field parallel to the sample surface. The numerical simulation shows the distributions of magnetic induction, electric intensity, current density and temperature in the film and their dependences on the uniform strain. The AC loss in the film is also calculated. We find that whether the magnetic field fully penetrates the superconductor is the key factor to influence the feature of AC loss. When the magnetic field cannot fully penetrate the superconductor the loss rises with increasing strain. When the magnetic field can fully penetrate the superconductor the feature is just opposite.

Keywords YBCO film; thermo-electro-magnetic phenomenon; strain

1. Introduction

The second-generation high-temperature superconductors consisting of a YBCO film deposited on a metallic substrate, referred to as YBCO coated conductors, are promising materials for power applications, such as cables, fault-current limiters and transformers. During the past several years impressive development is being made for the conductors. Very high critical current densities of $2.5-3.0\ \mathrm{MA\,cm^{-2}}$ at $77\ \mathrm{K}$ have been reached in long conductor lengths [1]. Due to thermal contractions, tensions and electromagnetic forces, the coated conductors in high-temperature superconductors apparatuses are subjected to mechanical strains. The strains cause the degradation of the critical current densities and influence thermo-electro-magnetic features in the conductors. But it is impossible to avoid the strains. The effects of strains on the critical current densities have been reported by many researches. However, researches investigating the effects of strains on the other thermo-electro-magnetic features are relatively less. Osami Tsukamoto and his partners have done a series of studies on the AC losses in coated conductors subjected to strains [2-6]. But they have not studied the details of thermo-electro-magnetic phenomena in the coated conductors, such as the distributions of magnetic induction, temperature, electric intensity and current density.

In this paper, we propose an approach to investigate the thermo-electro-magnetic features in an infinite YBCO film subjected to a uniform strain in an external AC magnetic field parallel to the surface of film. The approach is based on numerically solving the coupled magnetic and heat diffusion equations associated with the intrinsic nonlinear behaviors of $\rho(B,T,\varepsilon)$, $J_c(T,B,\varepsilon)$, $c(T)$, etc., from which the details of thermo-electro-magnetic phenomena in the film and their dependences on the strain are obtained.

2. Mathematical model and numerical analysis method

We consider an infinite YBCO film in yz plane with thickness $2d$ in x direction subjected to a uniform strain ε in y direction and an external magnetic field $\mathbf{B}_{ex}$ parallel to the sample

surface in z direction (see Fig. 1).

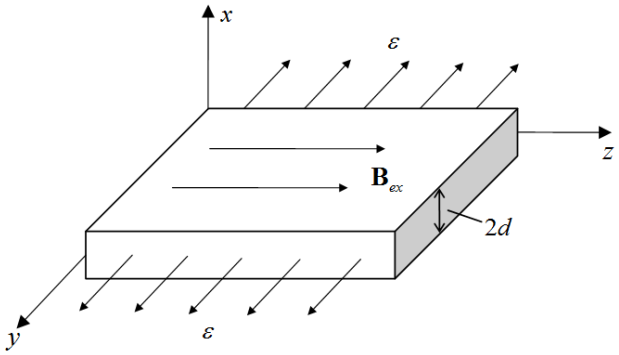

Figure 1. Sketch of the model.

The YBCO film is modeled as a slab, at which the distributions of the z component of magnetic induction $B(x,t)$, the y component of electric intensity $E(x,t)$, and the current density $J(x,t)$ are governed by the Maxwell equations

$$\frac{\partial B}{\partial x}+\mu_0 J=0, \tag{1}$$

$$\frac{\partial B}{\partial t}+\frac{\partial E}{\partial x}=0, \qquad -d\le x\le d. \tag{2}$$

Here, $\mu_0=4\pi\times10^{-7}$ N A^{-2} is the permeability of free space. Considering the $E-J$ relation of superconductor can be assimilated with that of normal conductor, i.e.,

$$E=\rho(B,T,\varepsilon)J, \tag{3}$$

where $\rho(B,T,\varepsilon)$ stands for the effective electric resistance, hence Eqs. (1) and (2) can be reduced into the form

$$\frac{\partial}{\partial x}\left(\rho(B,T,\varepsilon)\frac{\partial B}{\partial x}\right)-\mu_0\frac{\partial B}{\partial t}=0, \qquad -d\le x\le d. \tag{4}$$

The temperature $T(x,t)$ is satisfied with one-dimensional Fourier's heat conducting equation

$$\frac{\partial}{\partial x}\left(\kappa\frac{\partial T}{\partial x}\right)-c(T)\frac{\partial T}{\partial t}+W=0, \qquad -d\le x\le d, \tag{5}$$

in which κ represents the thermal conductivity, $c(T)$ is the heat capacity, and $W=EJ$ indicates the heat source intensity. After the YBCO film is cooled to the temperature of the coolant in the zero magnetic field (i.e., the external magnetic field is equal to zero), the boundary and initial conditions of the magnetic field and the temperature field can be written as

$$x=\pm d: \qquad B(x,t)=B_{ex}(t), \tag{6}$$

$$x=\pm d: \qquad \kappa\frac{\partial T}{\partial x}=\pm h(T)(T-T_0), \tag{7}$$

$$t=0: \qquad B(x,t)=0, \qquad T(x,t)=T_0, \tag{8}$$

where $h(T)$ is the heat transfer coefficient, T_0 denotes the temperature of the coolant, and $B_{ex}(t)$ stands for the external magnetic field. Here, we apply a sinusoidal field $B_{ex}(t)=B_0\sin 2\pi ft$.

At the temperature zone of liquid nitrogen, a power law $E=E_c(J/J_c)^{U_0/kT}$ is reasonable for describing electromagnetic constitutive relation of the high-temperature superconductor, where J_c is the critical current density defined by the reference electric field E_c, U_0 denotes the activation energy and k is the Boltzmann constant [7]. According to Eq. (3), the effective electric resistance

ρ is given by

$$\rho(B,T,\varepsilon)=\frac{E_c}{J_c}\left|\frac{J}{J_c}\right|^{U_0/kT-1}. \tag{9}$$

The present research on the activation energy indicates that the energy is dependent on the local temperature and magnetic field, and it is explicitly expressed by [8]

$$U_0(T,B)=U_{00}[1-(T/T_c)^4][1-B/B_{c2}(T)], \tag{10}$$

where U_{00} denotes the barrier height in the zero magnetic field at 0 K, T_c is the critical temperature, and $B_{c2}(T)=B_{c2}(0)[1-(T/T_c)^2]$ stands for the upper critical magnetic field.

For the samples of YBCO, the dependence of the critical current density on strain $J_c(\varepsilon)$ is given by fitting the experimental data with relation [9, 10]

$$J_c(\varepsilon)=J_c(\varepsilon=0)(1-a|\varepsilon|^{2.2}), \tag{11}$$

in which a is the fitting parameter. After the temperature and magnetic field dependence of critical current density is taken into account [11, 12], i.e.,

$$J_c(T,B)=J_{c0}[1+(T/T_c)^2]^{-1/2}[1-(T/T_c)^2]^{5/2}\frac{B^*}{|B|+B^*}, \tag{12}$$

we can get the temperature, magnetic field and strain dependence of critical current density, i.e.,

$$J_c(T,B,\varepsilon)=J_{c0}[1+(T/T_c)^2]^{-1/2}[1-(T/T_c)^2]^{5/2}(1-a|\varepsilon|^{2.2})\frac{B^*}{|B|+B^*}, \tag{13}$$

where the parameter J_{c0} is the critical current density when the temperature, magnetic field and strain are equal to zero, and B^* is a phenomenological parameter.

Consequently, the system with thermo-electro-magnetic interaction can be described by the initial-boundary problem of Eqs. (4)-(8). It is hard to solve the nonlinear coupling problem analytically, so we propose a numerical code by means of the finite difference method and iteration to solve it.

3. Results and discussions

In this section, thermo-electro-magnetic phenomena in the YBCO film subjected to a uniform strain in an external magnetic field parallel to the sample surface at the temperature zone of liquid nitrogen are displayed by the numerical results which are obtained from the essential equations in the previous section. We investigate the distributions of magnetic induction, temperature, electric intensity and current density in the film and their dependences on the uniform strain. Two situations are taken into account. One is that the magnetic field does not fully penetrate the YBCO film. The other one is that the magnetic field fully penetrates the YBCO film. In addition, the AC loss in the film is calculated. In the numerical analysis, we select the parameters in their possible regions given in literatures [9, 13-18]: $a=9900$, $J_{c0}=6.4\times10^{11}$ A m^{-2}, $2d=0.8\times10^{-6}$ m, $T_c=92$ K, $T_0=76$ K, $B_{c2}(0)=200$ T, $U_{00}/kT_0=54$, $B^*=0.3$ T, $E_c=10^{-4}$ V m^{-1}, $h=1$ J m^{-2} s^{-1} K^{-1}, $\kappa=4$ J m^{-1} s^{-1} K^{-1}, $c(T)=2.02\times10^2T^2-7.82\times10^{-3}T^4$ (J K^{-1} m^{-3}). The external magnetic field frequency f is selected as 50 Hz.

3.1. The magnetic field does not fully penetrate the YBCO film

Fig. 2 shows the distributions of the z component of magnetic induction $B(x,t)$, temperature

$T(x,t)$, the y component of electric intensity $E(x,t)$ and current density $J(x,t)$ in the YBCO film at $\varepsilon = 0.2\%$ and $B_0 = 0.001$ T. The curves at different times in a magnetization period T^{cycle} are displayed. When the external magnetic field amplitude B_0 is applied to 0.001 T, the magnetic field cannot fully penetrate the film. From Fig. 2(a), one sees that the magnetic field penetration depth increases with increasing external magnetic field. When $t = T^{cycle}/4$, the external magnetic field gets to the maximum. After the time, the external magnetic field decreases gradually. The magnetic induction in the film near the surface decreases with that. However, the magnetic field penetration depth does not decrease. This is because the pinning force hinders flux lines from moving out of the superconductor. After $T^{cycle}/2$, the external magnetic field increases in the opposite direction. When $t = 3T^{cycle}/4$ the external magnetic field gets to the maximum in the negative direction. The distribution of magnetic induction in the film at this time is just opposite compared with that when $t = T^{cycle}/4$, which means the distributions at the two times have the same values, however, their directions are opposite. The distributions of magnetic induction at $T^{cycle}/2$ and T^{cycle} have the same feature. Fig. 2(b) illustrates the temperature at every position in the film is the same during the magnetization period. Due to the AC loss in the film, the temperature of the film increases with time. But the increments of temperature are slight. From Fig. 2(c), one sees that the distributions of electric intensity are antisymmetrical about the middle layer of the film. At the surface of the film, the values of electric intensity at $T^{cycle}/2$ and T^{cycle} are larger than those at $T^{cycle}/4$ and $3T^{cycle}/4$. This is because the external magnetic field sweep rate $|dB_{ex}/dt|$ at $T^{cycle}/2$ and T^{cycle} is faster than that at $T^{cycle}/4$ and $3T^{cycle}/4$, the vortex electric intensities generated are larger. The current density has the same direction with the electric intensity, so the distributions of electric intensity are also antisymmetrical about the middle layer of the film (see Fig. 2(d)).

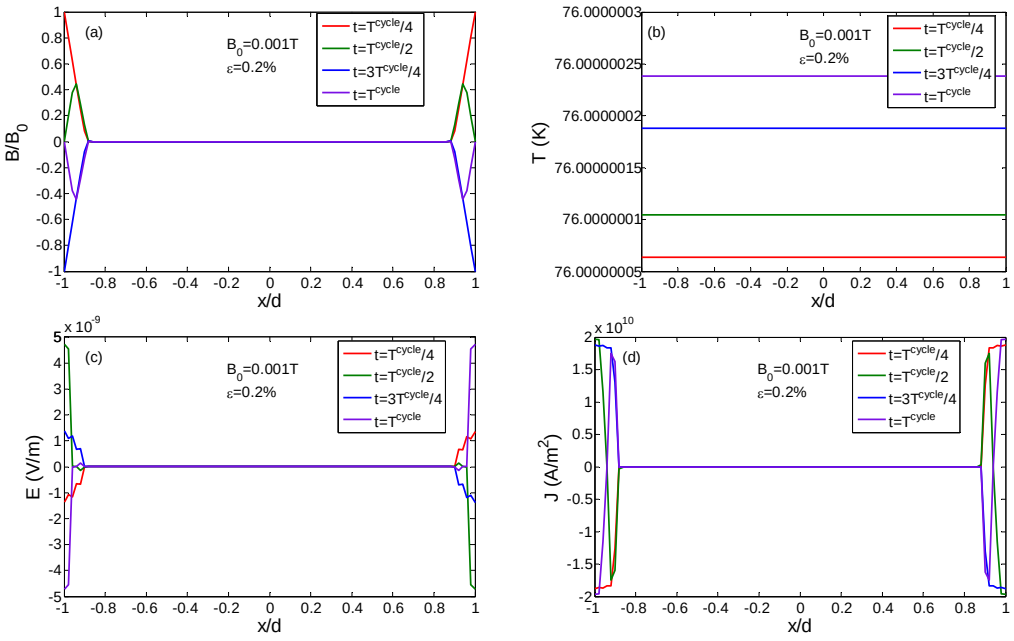

Figure 2. The distributions of the z component of magnetic induction $B(x,t)$, temperature $T(x,t)$, the y component of electric intensity $E(x,t)$ and current density $J(x,t)$ in the YBCO film at $\varepsilon = 0.2\%$ and $B_0 = 0.001$ T. In Fig. 2(a), the magnetic induction B is normalized by the external magnetic field amplitude B_0.

Fig. 3 demonstrates the dependences of the distributions of magnetic induction, temperature, electric intensity and current density on the uniform strain under the situation that the magnetic field does not fully penetrate the film. We find that their dependences on the strain are slight. Fig. 3(a) shows the distributions of magnetic induction at $\varepsilon = 0\%, 0.2\%, 0.4\%$ when the time is equal to $T^{cycle}/4$. One sees that the magnetic induction in the superconducting film increases slightly when the strain increases. According to Eq. (13) the critical current density J_c decreases with increasing strain ε, so the pinning force decreases with increasing strain. When the pinning force decreases, it is easier for the flux lines to move into the superconductor. So the magnetic induction in the film increases. However, the increment is slight, which indicates the effect of strain on the pinning force is very small when the magnetic field does not fully penetrate the film. From Fig. 3(b) and Fig. 3(c), one sees that the strain almost has no effect on the distributions of temperature and electric intensity. The three curves at $\varepsilon = 0\%, 0.2\%, 0.4\%$ superpose. Fig. 3(d) illustrates the current density in the film near the surface decreases with increasing strain. At the deeper position in the film, the feature is opposite. We need to point out that only the range of reversible strain is considered in our simulations. When the strain exceeds the irreversible strain limit ε_{irr} ($\varepsilon_{irr} = 0.5\%$ in this paper), cracks begin to appear in the superconductor, which result in the irreversible degradation in critical current density [9]. This is not permitted in applications [10, 19, 20].

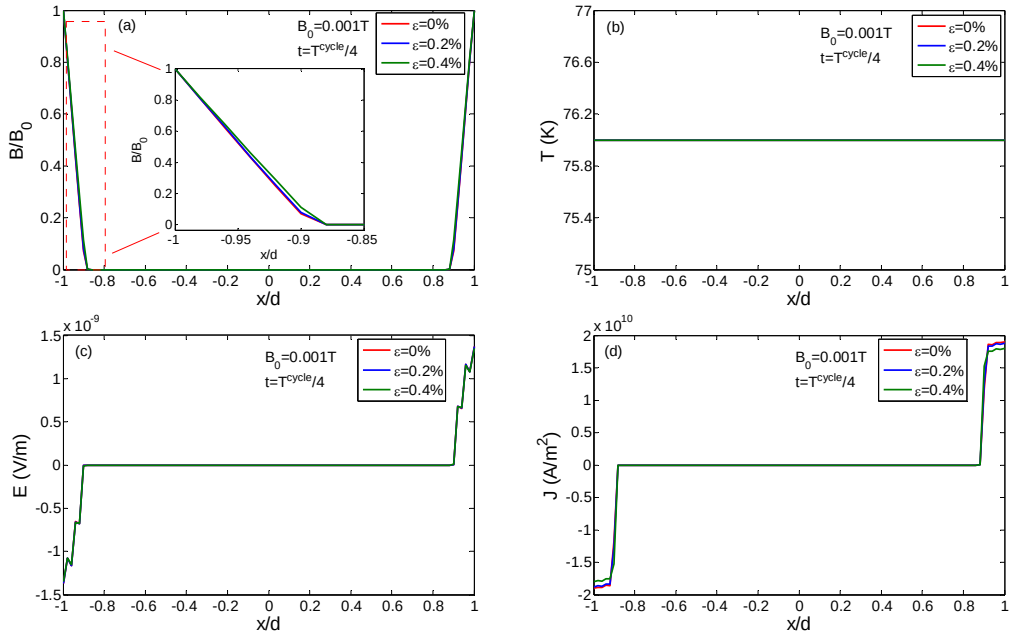

Figure 3. The dependences of the distributions of magnetic induction, temperature, electric intensity and current density on the uniform strain when $B_0 = 0.001$ T. In Fig. 3(b) and Fig. 3(c), the three curves at $\varepsilon = 0\%, 0.2\%, 0.4\%$ superpose.

3.2. The magnetic field fully penetrates the YBCO film

Fig. 4 shows the distributions of magnetic induction, temperature, electric intensity and current density in the YBCO film at different times when $\varepsilon = 0.2\%$ and $B_0 = 0.02$ T. When the external magnetic field amplitude B_0 is applied to 0.02 T, the magnetic field can fully penetrate the film. The features of the evolutions of these distributions with time are similar to those when the magnetic field cannot fully penetrate the film. From Fig. 4(a), one also sees that after $T^{cycle}/4$ although the external magnetic field decreases, the magnetic induction in the film closed to the

middle layer increases. According to this phenomenon, we can deduce the pinning force in the film closed to the middle layer reduces during the decrease of external magnetic field (Fig. 2(a) illustrates the same feature).

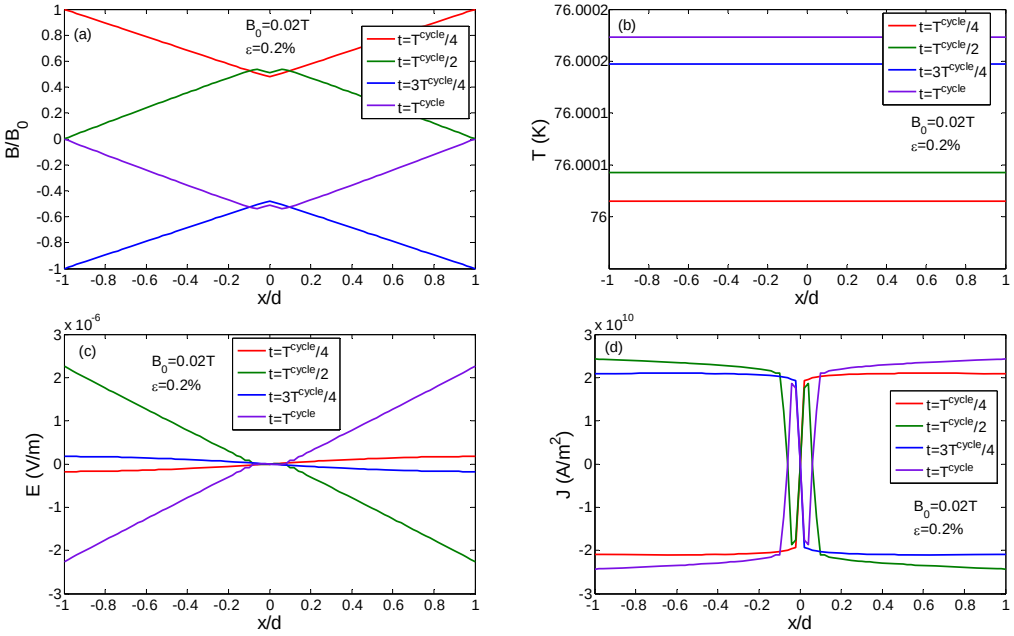

Figure 4. The distributions of magnetic induction, temperature, electric intensity and current density in the YBCO film at $\varepsilon = 0.2\%$ and $B_0 = 0.02$ T.

Fig. 5 demonstrates the dependences of the distributions of magnetic induction, temperature, electric intensity and current density on the uniform strain under the situation that the magnetic field fully penetrates the film. It is found that the effects of strain on these distributions are more obvious than those when the magnetic field does not fully penetrate the film in the range of reversible strain. When the strain increases the AC loss in the film decreases, which results in the decrease of temperature in the film (see Fig. 5(b)). Fig. 5(c) and Fig. 5(d) indicate that the larger the strain is, the smaller the electric intensity and current density are. This feature is different from that when the magnetic field does not fully penetrate the film.

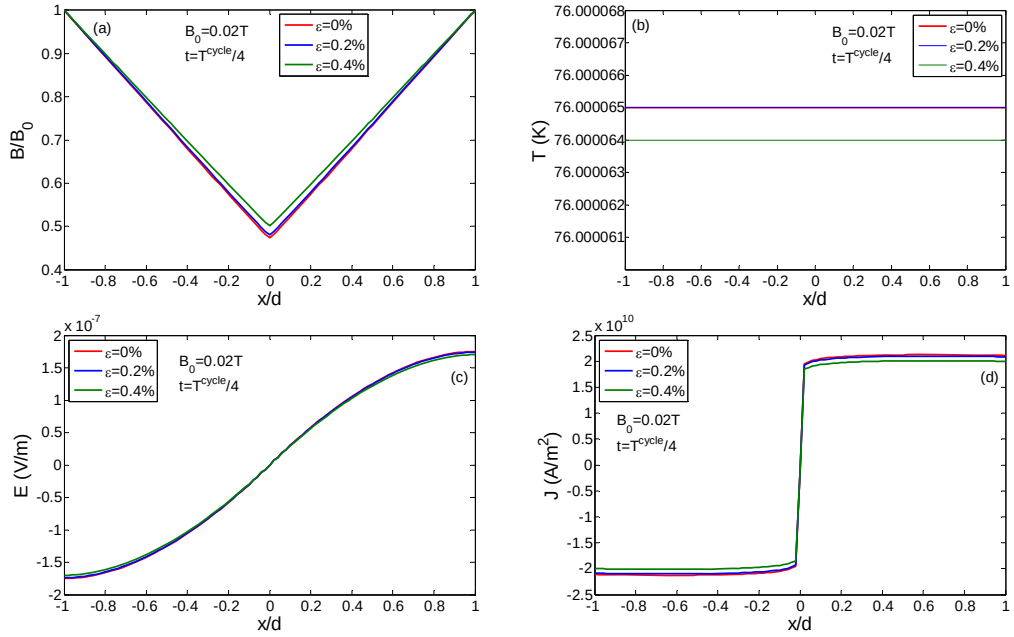

Figure 5. The dependences of the distributions of magnetic induction, temperature, electric intensity and

current density on the uniform strain when $B_0 = 0.02$ T. In Fig. 5(b), the red line and blue line superpose.

3.3. The AC loss in the YBCO film

After $E(x,t)$ and $J(x,t)$ in the YBCO film are numerically obtained, AC loss per unit volume per cycle Q is obtained by the following formula

$$Q = \frac{1}{2d}\int_{T^{\text{cycle}}} \mathrm{d}t \int_{-d}^{d} EJ\mathrm{d}x. \tag{14}$$

Fig. 6 shows curves of the AC loss Q versus the uniform strain ε at different external magnetic field amplitudes. It is interesting to find that when the magnetic field cannot fully penetrate the superconducting film ($B_0 = 0.001$ T), the loss rises with increasing strain. However, the feature is opposite when the magnetic field can fully penetrate the film ($B_0 = 0.02$ T).

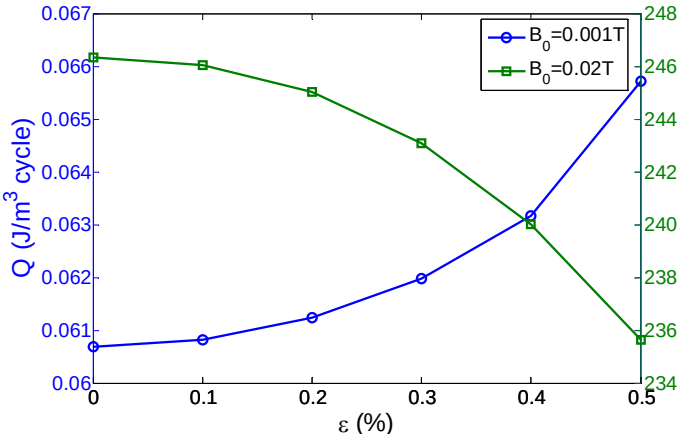

Figure 6. Curves of the AC loss Q versus the uniform strain ε when $B_0 = 0.001$ T and $B_0 = 0.02$ T.

4. Conclusions

By solving the nonlinear coupled equations of magnetic and heat diffusions numerically, we study thermo-electro-magnetic phenomena in an infinite YBCO film subjected to a uniform in-plane strain in an alternating external magnetic field parallel to the sample surface. The distributions of magnetic induction, temperature, electric intensity and current density in the film are investigated at different times under two situations. In one of the situations the magnetic field does not fully penetrate the film and in the other one the magnetic field does. In addition, we investigate the effects of the uniform strain on those distributions. It is found that the effects of the uniform strain are small in the range of reversible strain. At last, the AC loss in the film is reported. We find that whether the magnetic field fully penetrates the superconductor is the key factor to influence the feature of AC loss. When the magnetic field cannot fully penetrate the superconductor the loss rises with increasing strain. When the magnetic field can fully penetrate the superconductor the feature is just opposite.

Acknowledgments

This work was supported by the Fund of Natural Science Foundation of China (Grant No. 11032006; 11121202). We would like to thank Dr Xiaobin Yang for the help on procedure working in this paper.

References

[1] V. Selvamanickam, Y. Chen, X. Xiong, Y. Xie, X. Zhang, Y. Qiao, J. Reeves, A. Rar, R. Schmidt, K. Lenseth, Progress in scale-up of second-generation HTS conductor. Physica C, 463-465 (2007) 482-487.

[2] O. Tsukamoto, A. Kataoka, K. Ohmatsu, AC transport current loss characteristics of REBCO coated conductors subjected to bending strains. IEEE Trans Appl Supercond, 16 (2006) 89-92.

[3] A. Kataoka, O. Tsukamoto, S. Sekizawa, Y. Kawano, N. Kashima, S. Nagaya, Y. Iijima, T. Saitoh, AC transport current loss characteristics of YBCO coated conductors subjected to bending strains. IEEE Trans Appl Supercond, 17 (2007) 3171-3174.

[4] S. Mitsui, T. Uno, S. Maruyama, Y. Nakajima, T. Takao, O. Tsukamoto, AC transport current loss characteristics of copper-stabilized YBCO subjected to repeated mechanical stresses/strains. IEEE Trans Appl Supercond, 20 (2010) 2184-2189.

[5] T. Uno, T. Ojima, S. Mitsui, T. Takao, O. Tsukamoto, AC magnetization losses in copper-stabilized YBCO coated conductors subjected to repeated mechanical stresses. IEEE Trans Appl Supercond, 21 (2011) 3257 - 3260.

[6] O. Tsukamoto, H. Suzuki, Z. Li, M. Ciszek, N. Kashima, S. Nagaya, AC losses in YBCO conductors subjected to tensile stresses. Cryogenics, 47 (2007) 418-424.

[7] E. Zeldov, N.M. Amer, G. Koren, A. Gupta, R.J. Gambino, M.W. McElfresh, Optical and electrical enhancement of flux creep in $YBa_2Cu_3O_{7-\delta}$ epitaxial films. Phys Rev Lett, 62 (1989) 3093-3096.

[8] R. Griessen, Resistive behavior of high-T_c superconductors: Influence of a distribution of activation energies. Phys Rev Lett, 64 (1990) 1674-1677.

[9] D.C. van der Laan, J.W. Ekin, Large intrinsic effect of axial strain on the critical current of high-temperature superconductors for electric power applications. Appl Phys Lett, 90 (2007) 052506.

[10] D.C. van der Laan, J.W. Ekin, J.F. Douglas, C.C. Clickner, T.C. Stauffer, L.F. Goodrich, Effect of strain, magnetic field and field angle on the critical current density of $YBa_2Cu_3O_{7-\delta}$ coated conductors. Supercond Sci Technol, 23 (2010) 072001.

[11] R. Griessen, W. Hai-hu, A.J.J. Van Dalen, B. Dam, J. Rector, H.G. Schnack, S. Libbrecht, E. Osquiguil, Y. Bruynseraede, Evidence for mean free path fluctuation induced pinning in $YBa_2Cu_3O_7$ and $YBa2Cu_4O_8$ films. Phys Rev Lett, 72 (1994) 1910-1913.

[12] M.J. Qin, X.X. Yao, Ac susceptibility of high-temperature superconductors. Phys Rev B, 54 (1996) 7536-7544.

[13] D.C. van der Laan, J.W. Ekin, Dependence of the critical current of $YBa_2Cu_3O_{7-\delta}$ coated conductors on in-plane bending. Supercond Sci Technol, 21 (2008) 115002.

[14] M.K. Wu, J.R. Ashburn, C.J. Torng, P.H. Hor, R.L. Meng, L. Gao, Z.J. Huang, Y.Q. Wang, C.W. Chu, Superconductivity at 93 K in a new mixed-phase Y-Ba-Cu-O compound system at ambient pressure. Phys Rev Lett, 58 (1987) 908-910.

[15] M. Polak, E. Demencik, L. Jansak, P. Mozola, D. Aized, C.L.H. Thieme, G.A. Levin, P.N. Barnes, Ac losses in a YBa2Cu3O7-x coil. Appl Phys Lett, 88 (2006) 232501.

[16] E. Pardo, F. Grilli, Numerical simulations of the angular dependence of magnetization AC losses: coated conductors, Roebel cables and double pancake coils. Supercond Sci Technol, 25 (2012) 014008.

[17] C. Uher, A.B. Kaiser, Thermal transport properties of $YBa_2Cu_3O_7$ superconductors. Phys Rev B, 36 (1987) 5680-5683.

[18] K.-H. Müller, C. Andrikidis, Flux jumps in melt-textured Y-Ba-Cu-O. Phys Rev B, 49 (1994) 1294-1307.

[19] D.C. van der Laan, H.J.N. van Eck, B. ten Haken, H.H.J. ten Kate, J. Schwartz, Strain effects in high temperature superconductors investigated with magneto-optical imaging. IEEE Trans Appl Supercond, 13 (2003) 3534-3539.

[20] M. Sugano, S. Machiya, K. Osamura, H. Adachi, M. Sato, R. Semerad, W. Prusseit, The direct evaluation of the internal strain of biaxially textured YBCO film in a coated conductor using synchrotron radiation. Supercond Sci Technol, 22 (2009) 015002.

J-integral Calculation of Nonlinear Fracture for Colloidal Soft Material

Hongyan Wang, Jun Lei, Qingsheng Yang *

Department of Solid Mechanics, Beijing University of Technology, 100124, China
* Corresponding author: qsyang@bjut.edu.cn; Tel & Fax: 86-10-67396333

Abstract J-integral of nonlinear fracture for the colloid soft material is calculated by the finite element method in this paper. The J-integral is based on the concept of conservation of energy, hardly depending on the crack-tip stress singularity. Therefore, the fracture of colloidal soft material could be characterized by the J-integral. In this paper, a limited area near the crack tip replacing the integral loop is used to calculate J-integral value. J-integral within one unit is approximated by summation of the formulas related with gauss points. Such repeatedly, J-integral corresponding to integral path is calculated. Effect of different loading conditions and crack lengths on J-integral of PVA-H nonlinear fracture mainly is emphasized. This study shows that the J-integral can effectively characterize the nonlinear fracture of colloidal soft material.

Keywords PVA-H, Fracture, J-integral, Finite element method

1. Introduction

The wide use of hydrogels in the biomedical field is getting more and more frequent in recent years, and enormous potential in the tissue engineering is showed for the swelling and indissolvable features in the water. Especially, polyvinyl alcohol hydrogel (PVA-H) is a very promising material. A few studies have confirmed that the biomechanical properties of the polyvinyl alcohol hydrogel are similar to that of the articular cartilage, which is based on the good biocompatibility and is able to be a partial substitute for the articular cartilage, delay or prevent the occurrence of traumatic osteoarthritis. So PVA-H has become an alternative material with great promise in a clinical context [1-2]. However, after implantation into the human body PVA-H will appear wearing and cracks which can impact its function as well as what articular cartilage damage seriously affects. Therefore, the study of the PVA-H fracture characteristics is obviously important, but few international scholars research on the aspect at present.

Although the mechanical constitutive relation of the PVA-H is complicated, a relatively simple elastic-plastic theory model is adopted to research PVA-H material by simplifying the relation in this paper. On linear elasticity or small range yield condition, PVA-H crack tip energy release rate is evaluated by J-integral fracture criterion which is commonly used to deal with nonlinear fracture problem. The J-integral is based on the concept of conservation of energy, hardly depending on the crack-tip stress singularity and treating specially for the unit at the crack tip. Hence, J-integral can effectively characterize the nonlinear fracture of PVA-H material.

In this paper, aiming at PVA-H as articular cartilage repair material, the energy release rate of PVA-H crack tip is calculated by finite element method. J values of the crack tip under different loading conditions and different integration paths are obtained, also in consideration of the impact of the crack length on the J-integral.

2. Theoretical model

Polyvinyl alcohol aqueous solution gel can be made into polyvinyl alcohol hydrogel elastomer by repeated freezing-melting method. In 2007, Pan et al. [3] obtained the PVA-H curves of the stress and instant tensile modulus with changing strain through five freezing-melting cycles (see Fig.1). PVA gel is a kind of viscoelastic material, whose stress-strain relationship has typical viscoelastic properties. Taking the modulus-strain relationship into consideration, it is known that the tensile modulus of PVA gel is significantly various in different strain range. When strain range is 0 ~ 100%, PVA gel whose tensile modulus is essentially unchanged has elasticity characteristic, so its stress-strain shows a good linear relationship. In 100 ~ 250% strain, PVA tensile modulus increases up to 4 times with the increment of strain. In this range, PVA gel demonstrates typical viscoelastic character, whose stress-strain relationship is distinctly nonlinear.

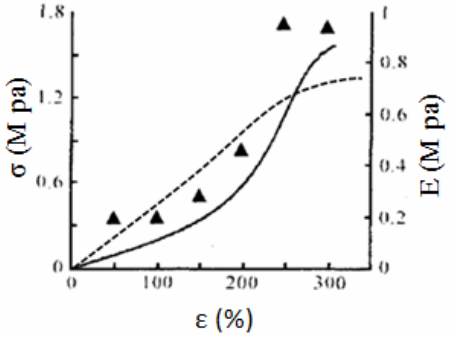

Fig.1 Stress-strain, modulus-strain and simplified stress-strain characteristic of PVA hydrogel
—: tension strength ▲: tension modulus ----: simplified stress-strain

Rice [4] introduced the J integral theory to analyze the crack behavior in an elastic body. This theory can quantitatively describe stress-strain field intensity of elastic materials with a crack, which has clear definition and strict theoretical basis. Consider a homogeneous plate containing a penetrating crack. There is no external force near the crack tip, but tension stress acting on the homogeneous plate produces 2D stress-strain field around the crack. J integral is defined as

$$J=\int_{\Gamma}\left(\text{wdy-T}\frac{\partial U}{\partial x}ds\right) \tag{1}$$

Where Γ loop shown in Fig.2 is around the crack tip, which starts from the crack lower surface and ends at the upper surface (counterclockwise direction), w is the strain energy density of the plate, T is the force vector acting on micro arc, and U is the displacement on Γ loop.

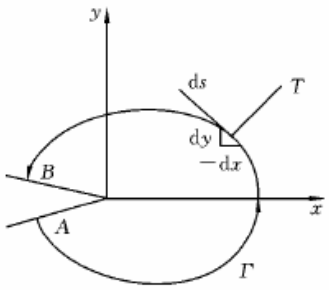

Fig.2 Schematic of the J-integral path

Rice [4] proved the path-independence of the J integral in the case of linear and nonlinear elastic material. Eq. (1) is not suitable for numerical calculation, because of not only the infeasibility of calculating stress and strain on Γ loop but the results are not always compatible when integral circuit is very close to the crack tip. Therefore, Shih [5] and Raju et al. [6] proposed the equivalent integral area method to compute J-integral by numerical calculation. A limited area near the crack tip replacing the integral loop is used to calculate J-integral value. According to divergence theorem,

Eq. (1) translates into

$$J=\int_A \left(\sigma_{ij} \frac{\partial u_j}{\partial x_1} - \omega \delta_{1i} \right) \frac{\partial q}{\partial x_i} dA \tag{2}$$

For 2D crack analysis, Eq. (2) can be divided into

$$J=\int_A \left[\left(\sigma_{xx} \frac{\partial u}{\partial x} + \tau_{xy} \frac{\partial v}{\partial x} - \omega \right) \frac{\partial q}{\partial x} + \left(\tau_{xy} \frac{\partial u}{\partial x} + \sigma_{yy} \frac{\partial v}{\partial x} \right) \frac{\partial q}{\partial y} \right] dA \tag{3}$$

In order to easily calculate the integral numerically, function q(x, y) must have a certain value on each node of the integral area. Shih etc. proofed that the J integral is not sensitive to the assumption form of q(x, y), i.e., q(x, y) can be arbitrarily selected [5]. But the boundary values of the integral area are strictly prescribed. For example, q = 1on the internal boundary, then q=0 on the external boundary for a plane problem. Equivalent integral area method is very convenient in finite element analysis, surely becoming the common tools calculating J integral.

In this paper, the plane stress four node unit calculating the J integral of the PVA-H crack tip is used, which is corresponding to standard CPS4 in ABAQUS. Using the gauss integral method, J-integral within one unit is approximated by summation of the formulas related with gauss points, i.e.

$$\bar{J} \approx I(r_1,s_1)+I(r_2,s_2)+I(r_3,s_3)+I(r_4,s_4) \tag{4}$$

In which

$$I(r,s)=\left[\left(\sigma_{xx} \frac{\partial u}{\partial x} + \tau_{xy} \frac{\partial v}{\partial x} - \omega \right) \frac{\partial q}{\partial x} + \left(\tau_{xy} \frac{\partial u}{\partial x} + \sigma_{yy} \frac{\partial v}{\partial x} \right) \frac{\partial q}{\partial y} \right] \det(J^e) \tag{5}$$

$$r=\left\{ -\frac{1}{\sqrt{3}}, \frac{1}{\sqrt{3}}, \frac{1}{\sqrt{3}}, -\frac{1}{\sqrt{3}} \right\}, \quad s=\left\{ -\frac{1}{\sqrt{3}}, -\frac{1}{\sqrt{3}}, \frac{1}{\sqrt{3}}, \frac{1}{\sqrt{3}} \right\}$$

Thus, J integral of PVA-H corresponding to one unit is obtained. Such repeatedly, J values of all units covering integral area are calculated. By determining J integral of different integral paths, whether the J integral of nonlinear fracture of PVA-H depends on the integral loop near the crack tip or not is given. Moreover, the influence of loadings and crack lengths on the J integral of nonlinear fracture of PVA-H is obtained by changing different loadings and crack lengths.

2. Determination of J integral

Figure 3 shows a center crack in a limited plate subjected to tension stress. It has a span 2H=400mm, a width 2W=200mm, a thickness B=1mm and the length of the crack a=20mm. Tensile modulus of PVA-H material is various as different manufacture method. According to the results given by Gao etc. [7], PVA-H with the following material properties is considered

$$E=10\text{Mpa}, \quad \nu=0.49, \quad \sigma_s=4.47\text{Mpa}$$

Where E is the elastic modulus, ν is the Poisson ratio, σ_s is the tensile strength.

According to the asymmetry, the finite element model of a quarter PHV-H plate is shown in Fig.4 by ABAQUS pretreatment with transverse 100 division and vertical 200 division. Then all the information including geometric and material properties of the model extracted from ABAQUS is input into the FORTRAN input data file. The units from 1 to 20 are free, and the twenty-first node is the crack tip. Hence, y direction displacement of the right nodes of the crack tip and x direction displacement of the left boundary nodes is restrained, then the upper boundary nodes are applied by tensile load σ =0.1Mpa.

Equivalent integral area (gray section) including 8*2 units near the crack tip is selected shown in

Fig.5. J value of nonlinear fracture of PVA-H by FORTRAN program is given as J= 0.065082349N/mm.

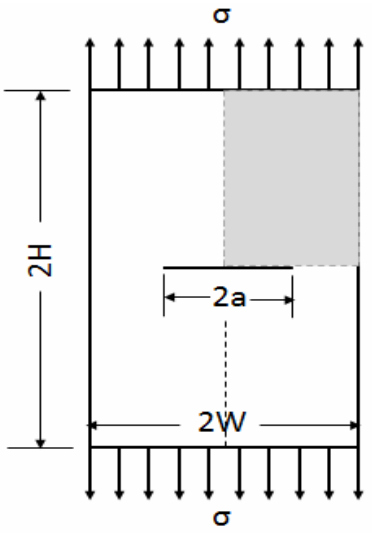

Fig.3 A center crack in a limited plate subjected to tension stress.

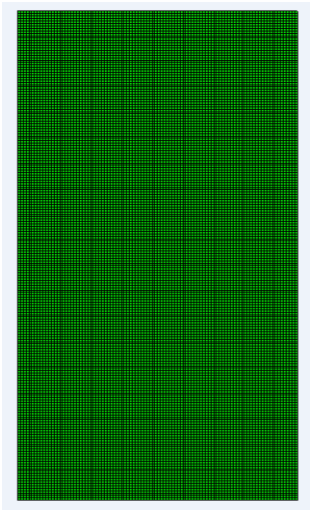

Fig.4 PHV-H plate finite element model

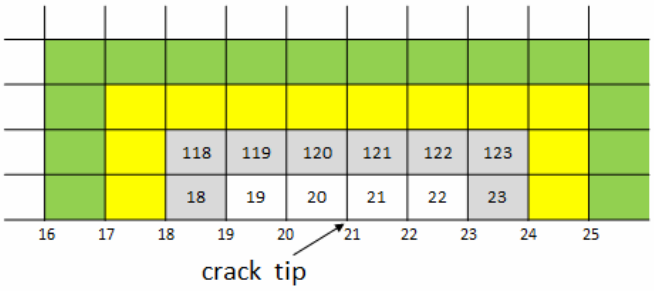

Fig.5 Equivalent integral area

Change tensile load σ , respectively, σ = 0.1、0.4、0.7、1.0、1.5 and 2.0Mpa. The calculated J integral values by FORTRAN in equivalent integral area are plotted in Fig.6. It shows that the J integral of nonlinear fracture of PVA-H increases as the increment of the applied loading, approximately, for square relation.

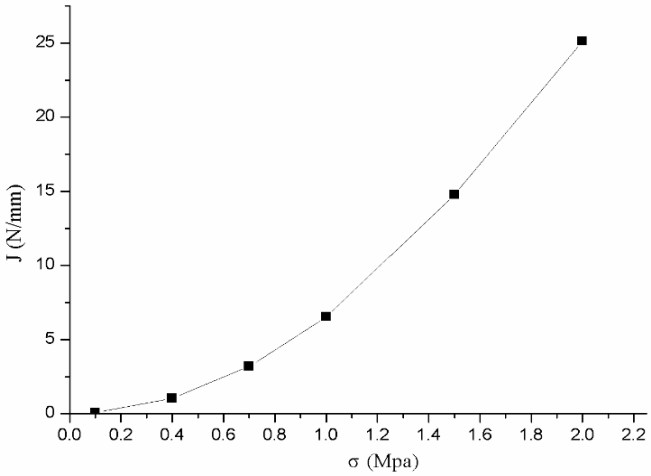

Fig.6 J-σ curve under different loadings

Each layer starting from the third layer outside of the crack tip is taken as integral path. The largest number of units of the layer is 24*2. Fig.7 plots the J-integral by FORTRAN in equivalent integral area against different integral paths under different loadings. It shows J integral in a certain loading remains unchanged as the increment of the chosen integral units, namely the J integral of nonlinear fracture of PVA-H is independent on the integral path. The result is found in very nice agreement with path-independent of the J integral in the case of linear and nonlinear elastic materials proved by Rice. Moreover, the bigger the applied loading, the greater the J integral value in the same integral path.

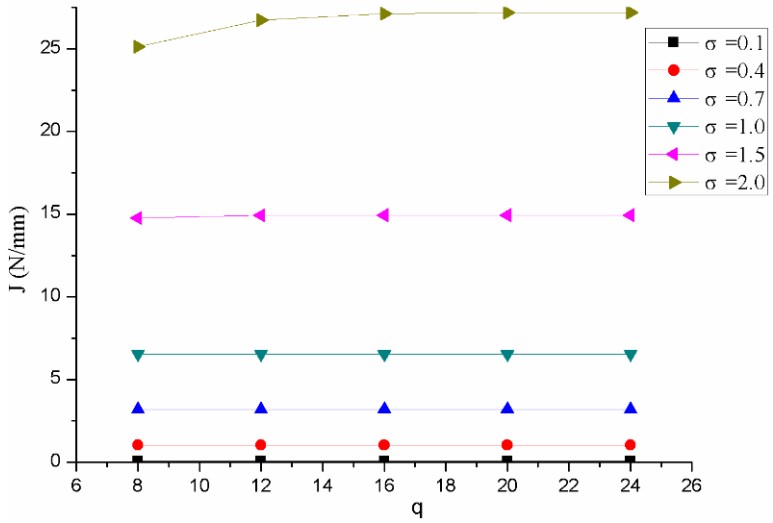

Fig.7 J curves for different integral paths under different loadings

In order to get the influence of the crack length on the J integral of nonlinear fracture of PVA-H, the location of the crack tip is changed from the eighteenth to the twenty-four node and the crack length ranges from 34 mm to 46 mm. The equivalent integral area is similar to that of Fig.5 (gray section). When the crack tip moves one unit length to the left or to the right, correspondingly, the equivalent integral area also moves a unit length to the left or to the right for guaranteeing the area covering 8*2 units. Change the tensile load, respectively, σ = 0.1、0.4、0.7、1.0、1.5 and 2.0Mpa. The calculated J values by FORTRAN in equivalent integral area are shown in Fig.8. It shows that J integral value at the crack tip increases linearly along with the PVA-H crack length increasing. It is clear that J integral or energy release rate of nonlinear fracture of PVA-H is severely affected by the crack length.

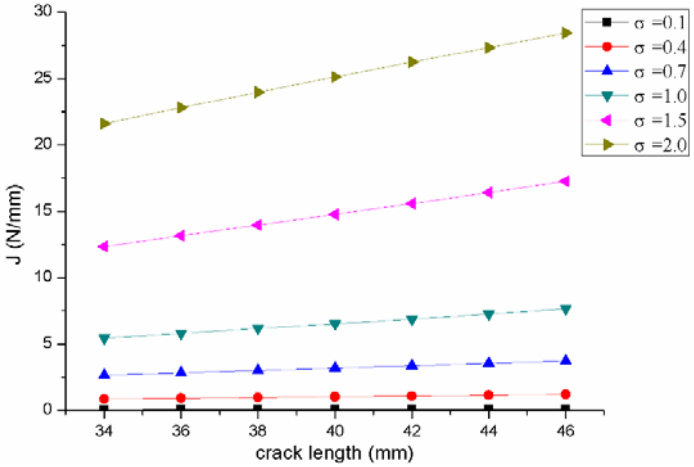

Fig.8 Effect of crack length on J-integral under different loadings

3. Conclusin

In this work, J-integral of nonlinear fracture for the colloid soft material with a center crack is calculated by the finite element method. When the integral circuit is very close to the crack tip, using the equivalent integral area method simulates J integral numerically. Through the divergence theorem, a limited area near the crack tip replacing the integral loop is used to calculate J-integral value. The PVA-H colloid soft material is simplified to elastic plastic model. J-integral within one unit is approximated by the gauss integral method. By summing for the J values of all units, J integral of the equivalent integral area corresponding to integral path is derived. Change integral path and calculate J integral of PVA-H colloid soft material in different integral path. The results can be summarized as follows:

(1) J integral of nonlinear fracture of PVA-H in a certain loading is independent on the integral path. Path-independent of the J integral obtained by Rice is proved once again by numerical method.

(2) The bigger the applied loading, the greater the J integral value of nonlinear fracture of PVA-H in the same integral path, approximately, for square relation.

(3) J integral value at the crack tip increases linearly along with the PVA-H crack length increasing. It is obvious that J integral or energy release rate of nonlinear fracture of PVA-H is severely affected by the crack length.

In the future, the above conclusions will provide certain theoretical guidance for PVA hydrogel as articular cartilage repair materials.

Acknowledgements

This work is supported by the Natural Science Foundation of China under Grant No. 11002006 and the German Research Foundation (DFG) under the project number ZH 15/6-1 and ZH 15/6-3, which are gratefully acknowledged.

References

[1] Gu ZQ, Xiao JM, Zhang XH. Biomed Mater Eng, 1998, 8(2): 75-81.

[2] S.M. Malmonge. Int J Artif Organs, 2001, 24(3): 119-122.

[3] Y.S. Pan, D.S. Xiong, X.L. Chen. Mechanical and Swelling Properties of Polyvinyl Alcohol Hydrogel. POLYMER MATERIALS SCIENCE AND ENGINEERING. 2007, 23(6): 228-231.

[4] J.R. Rice. A path independent integral and the approximate analysis of strain concentration by notches and cracks. Journal of Applied Mechanics, 1968, 35: 379-186.

[5] B. Moura, C.F. Shih. A treatment of crack tip contour integrals. International Journal of Fracture, 1987, 35: 295-310.

[6] K.N. Shivakumar, I.S. Raju. An equivalent domain integral method for three-dimensional mixed-mode fracture problem. Engineering Fracture Mechanics, 1992, 42: 935-959.

[7] F. Gao, Y. Jiang, B.F. Zeng. Advance in Polyvinyl alcohol hydrogel replacing articular cartilage. Foreign medical bone in science. 2004, 25(1): 41-43.

Pre-kinking analysis of a mixed-mode crack in a magnetoelectroelastic layer

Keqiang Hu[1,*], **Zengtao Chen**[1]

[1] Department of Mechanical Engineering, University of New Brunswick, Fredericton NB E3B 5A3, Canada
* Corresponding author: ckhu@unb.ca, keqianghu@163.com

Abstract A mixed-mode crack in a magnetoelectroelastic layer under in-plane mechanical, electric and magnetic loadings is considered for electrically and magnetically impermeable crack surface conditions. Fourier transforms are applied to reduce the mixed-boundary-value problem of the crack to a system of singular integral equations. The asymptotic fields near the crack tip are obtained in an explicit form and the corresponding field intensity factors are obtained. The exact solution for a crack in an infinite magnetoelectroelastic material can be recovered if the width of the layer tends to infinity. The crack kinking phenomenon is investigated by applying the criterion of maximum hoop stress intensity factors. The results show that the size of the layer and the electric and magnetic loadings have significant effects on the singular field distributions around the crack tip, and the hoop stress intensity factors are influenced by the material parameters, the electric loadings and the geometric size ratios.

Keywords Mixed-mode crack, Magnetoelectroelastic layer, Singular integral equations, Crack kinking, Hoop stress intensity factor

1. Introduction

In the recent decade, effect, magentoelectroelastic materials can be used in intelligent structures as sensors, actuators and transducers Owing to the unique magneto-electro-mechanical coupling effect. In the recent decade, there is a growing interest among researchers in solving fracture mechanics problems in magnetoelectroelastic media.

Crack initiation behavior in magnetoelectroelastic composite under in-plane deformation was investigated by Song and Sih [1]. Gao et al. [2] developed an exact treatment on the crack problems in a magnetoelectroelastic solid subjected to far-field loadings. Qin [3] obtained 2D Green's functions of defective magnetoelectroelastic solids under thermal loading, which can be used to establish boundary formulation and to analyze relevant fracture problems. The moving crack problem in an infinite size magnetoelectroelastic body under anti-plane shear and in-plane electro-magnetic loadings has recently been solved by Hu and Li [4] whose results predicted that the moving crack may curve when the velocity of the crack is greater than a certain value. The dynamic response of a penny-shaped crack in a magnetoelectroelastic layer was studied by Feng et al. [5]. Boundary element method was developed by Rojas-Díaz et al. [6] to study crack problem in linear magnetoelectroelastic materials under static loading conditions. Wang and Mai [7] discussed the different electromagnetic boundary conditions on the crack-faces in magnetoelectroelastic materials, which possess coupled piezoelectric, piezomagnetic and magnetoelectric effects. Zhong and Li [8] gave a magnetoelectroelastic analysis for an opening crack in a piezoelectromagnetic solid. Zhou and Chen [9] analyzed a partially conducting mode I crack in piezoelectromagnetic materials. Zhao and Fan [10] proposed a strip electric-magnetic breakdown model in magnetoelectroelastic medium to study the nonlinear character of electric field and magnetic field on fracture of magnetoelectroelastic materials. The problem of a planar magnetoelectroelastic

layered half-plane subjected to generalized line forces and edge dislocations is analyzed by Ma and Lee [11]. Li and Lee [12] established real fundamental solutions for in-plane magnetoelectroelastic governing equations and studied collinear unequal cracks in magnetoelectroelastic materials. An embedded mixed-mode crack in a functionally graded magnetoelectroelastic infinite medium has been studied by Rekik et al. [13]. Recently, the pre-curving analysis of a crack in a magnetoelctroelastic strip under in-plane dynamic loading has been conducted by Hu and Chen [14] and the same authors [15] also studied the anti-plane problem of a magnetoelectroelastic strip sandwiched between elastic layers. The mode III crack crossing the magnetoelectroelastic bimaterial interface under concentrated magnetoelectromechanical loads was investigated by Wan et al. [16].

To the best knowledge of the authors, the mixed-mode crack in a magnetoelectroelastic layer with finite width under in-plane magneto-electro-elastic loadings has not been reported in the literature. This problem is solved in this paper. Fourier transforms are applied to reduce the mixed-boundary-value problem to a system of singular integral equations which can be solved numerically. The asymptotic fields near the crack tip are obtained in an explicit form and the corresponding field intensity factors are determined. The crack kinking phenomena is investigated by applying the criterion of maximum hoop stress intensity factors. The coupling magneto-electro-elastic effects on the crack-tip fields are investigated and the finite size effects on the dynamic fracture properties are discussed.

2. Problem statement and method of solution

Consider a transversely isotropic, linear magnetoelectroelastic material and denote the rectangular coordinates of a point by (x, y, z). The constitutive equations can be written as

$$\begin{Bmatrix}\sigma_{xx}\\ \sigma_{zz}\\ \sigma_{xz}\end{Bmatrix}=\begin{bmatrix}C_{11} & C_{13} & 0\\ C_{13} & C_{33} & 0\\ 0 & 0 & C_{44}\end{bmatrix}\begin{Bmatrix}\partial u_x/\partial x\\ \partial u_z/\partial z\\ \partial u_x/\partial z+\partial u_z/\partial x\end{Bmatrix}+\begin{bmatrix}0 & e_{31}\\ 0 & e_{33}\\ e_{15} & 0\end{bmatrix}\begin{Bmatrix}\partial\phi/\partial x\\ \partial\phi/\partial z\end{Bmatrix}+\begin{bmatrix}0 & h_{13}\\ 0 & h_{33}\\ h_{15} & 0\end{bmatrix}\begin{Bmatrix}\partial\varphi/\partial x\\ \partial\varphi/\partial z\end{Bmatrix}$$

$$\begin{Bmatrix}D_x\\ D_z\end{Bmatrix}=\begin{bmatrix}0 & 0 & e_{15}\\ e_{31} & e_{33} & 0\end{bmatrix}\begin{Bmatrix}\partial u_x/\partial x\\ \partial u_z/\partial z\\ \partial u_x/\partial z+\partial u_z/\partial x\end{Bmatrix}-\begin{bmatrix}\lambda_{11} & 0\\ 0 & \lambda_{33}\end{bmatrix}\begin{Bmatrix}\partial\phi/\partial x\\ \partial\phi/\partial z\end{Bmatrix}-\begin{bmatrix}d_{11} & 0\\ 0 & d_{33}\end{bmatrix}\begin{Bmatrix}\partial\varphi/\partial x\\ \partial\varphi/\partial z\end{Bmatrix} \tag{1}$$

$$\begin{Bmatrix}B_x\\ B_z\end{Bmatrix}=\begin{bmatrix}0 & 0 & h_{15}\\ h_{31} & h_{33} & 0\end{bmatrix}\begin{Bmatrix}\partial u_x/\partial x\\ \partial u_z/\partial z\\ \partial u_x/\partial z+\partial u_z/\partial x\end{Bmatrix}-\begin{bmatrix}d_{11} & 0\\ 0 & d_{33}\end{bmatrix}\begin{Bmatrix}\partial\phi/\partial x\\ \partial\phi/\partial z\end{Bmatrix}-\begin{bmatrix}\mu_{11} & 0\\ 0 & \mu_{33}\end{bmatrix}\begin{Bmatrix}\partial\varphi/\partial x\\ \partial\varphi/\partial z\end{Bmatrix}$$

where u_x, u_z are components of the displacement vector, ϕ and φ are the electric and magnetic potentials, respectively; $C_{11}, C_{13}, C_{33}, C_{44}$ are elastic constants, e_{15}, e_{31} are piezoelectric constants, h_{15}, h_{31} are piezomagnetic constants, $\lambda_{11}, \lambda_{33}$ are dielectric permittivities, and d_{11}, d_{33} are

electromagnetic constants; σ_{ij}, D_i and B_i ($i, j = x, z$) are components of stress, electric displacement and magnetic induction, respectively.

We study an electrically and magnetically impermeable crack of length $2c$ in a magnetoelectroelastic layer of width $h_1 + h_2$, with the poling direction perpendicular to the crack plane, as shown in Fig. 1. Uniform normal stress P_0 and in-plane electric field E_0 and magnetic field H_0 are applied on the cracked layer. Symmetry conditions can be applied and then it is necessary to consider only the region ($x \geq 0,\ -h_2 \leq z \leq h_1$).

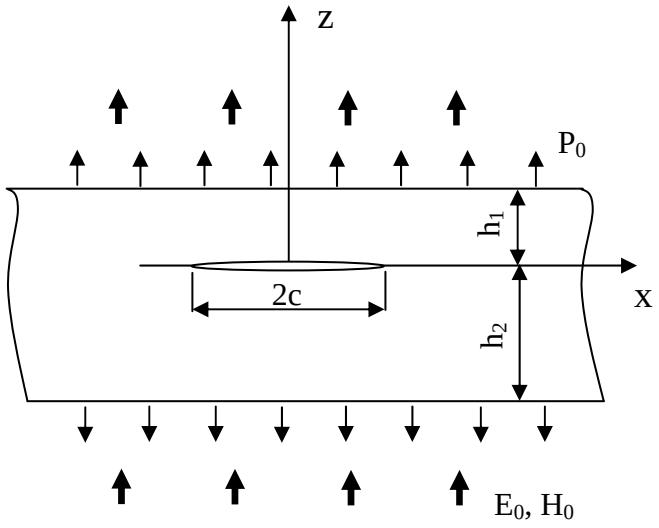

Figure 1. A cracked magnetoelectroelastic layer under in-plane magnetoelectromechanical loadings

Under the assumption of plane strain, the governing equations take the form

$$\begin{aligned}
&C_{11}u_{x,xx} + C_{44}u_{x,zz} + (C_{13} + C_{44})u_{z,xz} + (e_{31} + e_{15})\phi_{,xz} + (h_{31} + h_{15})\varphi_{,xz} = 0\\
&(C_{13} + C_{44})u_{x,xz} + C_{44}u_{z,xx} + C_{33}u_{z,zz} + e_{15}\phi_{,xx} + e_{33}\phi_{,zz} + h_{15}\varphi_{,xx} + h_{33}\varphi_{,zz} = 0\\
&(e_{31} + e_{15})u_{x,xz} + e_{15}u_{z,xx} + e_{33}u_{z,zz} - \lambda_{11}\phi_{,xx} - \lambda_{33}\phi_{,zz} - d_{11}\varphi_{,xx} - d_{33}\varphi_{,zz} = 0\\
&(h_{31} + h_{15})u_{x,xz} + h_{15}u_{z,xx} + h_{33}u_{z,zz} - d_{11}\phi_{,xx} - d_{33}\phi_{,zz} - \mu_{11}\varphi_{,xx} - \mu_{33}\varphi_{,zz} = 0
\end{aligned} \tag{2}$$

The boundary conditions on the layer surfaces and the impermeable crack faces are:

$$\sigma_{zz}(x, h_1) = \sigma_{zz}(x, -h_2) = P_0 \qquad (0 \leq x < \infty) \tag{3}$$

$$\sigma_{zx}(x, h_1) = \sigma_{zx}(x, -h_2) = 0 \qquad (0 \leq x < \infty) \tag{4}$$

$$E_z(x, h_1) = E_z(x, -h_2) = E_0 \qquad (0 \leq x < \infty) \tag{5}$$

$$H_z(x, h_1) = H_z(x, -h_2) = H_0 \qquad (0 \leq x < \infty) \tag{6}$$

$$\sigma_{zz}(x,0)=0,\ \ \sigma_{zx}(x,0)=0 \qquad (0\le x<c) \tag{7}$$

$$D_z(x,0)=0,\ \ B_z(x,0)=0 \qquad (0\le x<c) \tag{8}$$

The continuity conditions for the physical quantities across the crack plane are:

$$\sigma_{zx}(x,0^+)=\sigma_{zx}(x,0^-),\ \ \sigma_{zz}(x,0^+)=\sigma_{zz}(x,0^-), \qquad (x\ge c) \tag{9}$$

$$D_z(x,0^+)=D_z(x,0^-),\ \ B_z(x,0^+)=B_z(x,0^-), \qquad (x\ge c) \tag{10}$$

$$u_x(x,0^+)=u_x(x,0^-),\ \ u_z(x,0^+)=u_z(x,0^-), \qquad (x\ge c) \tag{11}$$

$$\phi(x,0^+)=\phi(x,0^-),\ \ \varphi(x,0^+)=\varphi(x,0^-), \qquad (x\ge c) \tag{12}$$

Fourier transforms are then applied on Eq. (2) and the solutions may be expressed as

$$u_{iz}^{(n)}(x,z)=\sum_{j=1}^{4}\Omega_{ij}\int_0^\infty\left[A_j^{(n)}(\xi)\cosh(\gamma_j\xi z)+B_j^{(n)}(\xi)\sinh(\gamma_j\xi z)\right]\cos(\xi x)d\xi+T_i z \qquad (i=1-3) \tag{13}$$

$$u_x^{(n)}(x,z)=-\sum_{j=1}^{4}a_j\gamma_j\int_0^\infty\left[A_j^{(n)}(\xi)\sinh(\gamma_j\xi z)+B_j^{(n)}(\xi)\cosh(\gamma_j\xi z)\right]\sin(\xi x)d\xi \tag{14}$$

where $u_{1z}=u_z,\ u_{2z}=\phi,\ u_{3z}=\varphi,\ \Omega_{1j}=1,\ \Omega_{2j}=b_j,\ \Omega_{3j}=d_j,\ \mathrm{T}_j\ (j=1,2,3)$ are constants and $a_j,\ b_j,\ d_j \quad (j=1-4)$ are known functions defined in Appendix A, $A_j^{(n)}(\xi),\ B_j^{(n)}(\xi),\ (n=1,2;\ j=1,2,3,4)$ are unknowns to be determined and the superscripts (1), (2) denote the fields quantities in the upper $0\le y\le h_1$ and lower parts $-h_2\le y\le 0$ of the cracked magnetoelectroelastic layer (as shown in Fig. 1), respectively.

The roots γ_j $(j=1-4)$ are determined from solving the following characteristic equation:

$$\begin{vmatrix} C_{11}-C_{44}\gamma^2 & (C_{13}+C_{44})\gamma & (e_{31}+e_{15})\gamma & (h_{31}+h_{15})\gamma \\ (C_{13}+C_{44})\gamma & C_{33}\gamma^2-C_{44} & e_{33}\gamma^2-e_{15} & h_{33}\gamma^2-h_{15} \\ (e_{31}+e_{15})\gamma & e_{33}\gamma^2-e_{15} & \lambda_{11}-\lambda_{33}\gamma^2 & d_{11}-d_{33}\gamma^2 \\ (h_{31}+h_{15})\gamma & h_{33}\gamma^2-h_{15} & d_{11}-d_{33}\gamma^2 & \mu_{11}-\mu_{33}\gamma^2 \end{vmatrix}=0 \tag{15}$$

It is noted that the eighth-order characteristic equation (15) has eight roots which occur in pairs with the same magnitude but opposite signs, and for complex roots, the roots always appear in conjugate pairs. In the expressions (13, 14), the roots γ_j $(j=1-4)$ are chosen as $\mathrm{Re}(\gamma_j)>0$ by requiring a positive internal energy for the system to be in a steady state.

The expressions for the stresses, electric displacement and magnetic induction can be obtained as follows:

$$\sigma_{ix}^{(n)}=-\sum_{j=1}^{4}V_{ij}\int_0^\infty\xi\left[A_j^{(n)}(\xi)\cosh(\gamma_j\xi z)+B_j^{(n)}(\xi)\sinh(\gamma_j\xi z)\right]\sin(\xi x)d\xi \qquad (i=1-3) \tag{16}$$

$$\sigma_{iz}^{(n)} = \sigma_{i0} - \sum_{j=1}^{4} U_{ij} \int_0^\infty \xi \left[A_j^{(n)}(\xi) \sinh(\gamma_j \xi z) + B_j^{(n)}(\xi) \cosh(\gamma_j \xi z) \right] \cos(\xi x) d\xi \quad (i = 1-4) \tag{17}$$

where

$$\begin{aligned} &\sigma_{1x} = \sigma_{zx},\ \sigma_{2x} = D_x,\ \sigma_{3x} = B_x;\ V_{1j} = f_j,\ V_{2j} = s_j,\ V_{3j} = t_j \\ &\sigma_{1z} = \sigma_{zz},\ \sigma_{2z} = D_z,\ \sigma_{3z} = B_z,\ \sigma_{4z} = \sigma_{xx};\ U_{1j} = g_j,\ U_{2j} = m_j,\ U_{3j} = n_j,\ U_{4j} = q_j \\ &\sigma_{10} = P_0,\ \sigma_{20} = e_{33}T_1 - \lambda_{33}T_2 - d_{33}T_{33},\ \sigma_{30} = h_{33}T_1 - d_{33}T_2 - \mu_{33}T_3,\ \sigma_{40} = C_{13}T_1 + e_{31}T_2 + h_{31}T_3 \end{aligned} \tag{18}$$

and the coefficients are defined as:

$$\begin{aligned} &f_j = C_{44}(a_j\gamma_j^2 + 1) - e_{15}b_j - h_{15}d_j,\ g_j = (C_{13}a_j + e_{33}b_j + h_{33}d_j - c_{33})\gamma_j \\ &q_j = (C_{11}a_j + e_{31}b_j + h_{31}d_j - c_{13})\gamma_j,\ m_j = (e_{31}a_j - \lambda_{33}b_j - d_{33}d_j - e_{33})\gamma_j \\ &n_j = (h_{31}a_j - d_{33}b_j - \mu_{33}d_j - h_{33})\gamma_j,\ s_j = e_{15}(a_j\gamma_j^2 + 1) + \lambda_{11}b_j + d_{11}d_j \\ &t_j = h_{15}(a_j\gamma_j^2 + 1) + d_{11}b_j + \mu_{11}d_j \end{aligned} \tag{19}$$

From the boundary conditions (3-10), the unknown functions $B_j^{(1)}(\xi)$, $A_j^{(2)}(\xi)$, $B_j^{(2)}(\xi)$ $(j = 1-4)$ can be expressed by the four independent unknowns $A_j^{(1)}(\xi)$ $(j = 1-4)$ as

$$B_j^{(1)}(\xi) = \sum_{i=1}^{4} R_{ji}^{(1)}(\xi, h_1) A_i^{(1)}(\xi) \tag{20}$$

$$A_j^{(2)}(\xi) = \sum_{i=1}^{4} T_{ji}(\xi, h_1, h_2) A_i^{(1)}(\xi) \tag{21}$$

$$B_j^{(2)}(\xi) = \sum_{i=1}^{4} R_{ji}^{(2)}(\xi, h_2) A_i^{(2)}(\xi) = \sum_{i=1}^{4} Q_{ji}(\xi, h_1, h_2) A_i^{(1)}(\xi) \tag{22}$$

where $R_{ji}^{(1)}(\xi, h_1)$, $T_{ji}(\xi, h_1, h_2)$ and $R_{ji}^{(2)}(\xi, h_2)$ are known functions.

Introduce the auxiliary functions $\Phi_i(x)$ $(i = 1-4)$ such that

$$\begin{Bmatrix} \Phi_1(x) \\ \Phi_2(x) \\ \Phi_3(x) \\ \Phi_4(x) \end{Bmatrix} = \frac{\partial}{\partial x} \begin{Bmatrix} u_x^{(1)}(x,0^+) - u_x^{(2)}(x,0^-) \\ u_z^{(1)}(x,0^+) - u_z^{(2)}(x,0^-) \\ \phi^{(2)}(x,0^+) - \phi^{(1)}(x,0^-) \\ \varphi^{(2)}(x,0^+) - \varphi^{(1)}(x,0^-) \end{Bmatrix} \tag{23}$$

By applying the solutions (13, 14) and using the Fourier inverse transform, the unknowns can be obtained as

$$\begin{Bmatrix} A_1^{(1)}(\xi) \\ A_2^{(1)}(\xi) \\ A_3^{(1)}(\xi) \\ A_4^{(1)}(\xi) \end{Bmatrix} = -\frac{2}{\pi\xi} \begin{bmatrix} Y_{11}(\xi) & Y_{12}(\xi) & Y_{13}(\xi) & Y_{14}(\xi) \\ Y_{21}(\xi) & Y_{22}(\xi) & Y_{23}(\xi) & Y_{24}(\xi) \\ Y_{31}(\xi) & Y_{32}(\xi) & Y_{33}(\xi) & Y_{34}(\xi) \\ Y_{41}(\xi) & Y_{42}(\xi) & Y_{43}(\xi) & Y_{44}(\xi) \end{bmatrix} \begin{Bmatrix} \int_0^c \Phi_1(s)\cos(s\xi)ds \\ \int_0^c \Phi_2(s)\sin(s\xi)ds \\ \int_0^c \Phi_3(s)\sin(s\xi)ds \\ \int_0^c \Phi_4(s)\sin(s\xi)ds \end{Bmatrix} \tag{24}$$

where $Y_{ij}(\xi)$ $(i, j = 1-4)$ are known functions. Satisfaction of the mixed boundary conditions (7, 8) on the crack face plane leads to the simultaneous singular integral equations

$$\begin{aligned}
&\int_{-1}^{1}\left\{\kappa_{i1}(s,x)\Psi_1(s)+\sum_{j=2}^{4}\left[\frac{U_{ij}^0}{s-x}+\kappa_{ij}(s,x)\right]\Psi_j(s)\right\}ds=-\pi\sigma_{i0}, \quad (i=1-3)\\
&\int_{-1}^{1}\left\{\left[\frac{U_{41}^0}{x-s}+\kappa_{41}(s,x)\right]\Psi_1(s,p)+\sum_{j=2}^{4}\kappa_{4j}(s,x)\Psi_j(s)\right\}ds=0
\end{aligned} \tag{25}$$

where $\Psi_i(s)=\Phi_i(cs)$, and $\kappa_{ij}(s,x)$ $(i=1-4)$ are known kernel functions, the constants U_{ij}^0 are defined as $U_{ij}^0=\lim_{\xi\to\infty}U_{ij}(\xi)$, and $U_{ij}(\xi)$ are known functions. The functions $\Psi_i(s)$ $(i=1-4)$ satisfy the single-valuedness condition:

$$\int_{-1}^{1}\Psi_i(s)ds=0, \quad (i=1-4) \tag{26}$$

The solution of $\Psi_i(s)$ may be expressed as

$$\Psi_i(s)=H_i(s)\Big/\sqrt{1-s^2} \tag{27}$$

where $H_i(s)$ $(i=1-4)$ are new unknowns to be solved.

The singular integral equations can be solved numerically as [17], [18]:

$$\begin{aligned}
&\sum_{i=1}^{n}A_i\left\{[\kappa_{m1}(x_k,s_i)]H_1(s_i)+\sum_{j=2}^{4}\left[\frac{U_{mj}^0}{s_i-x_k}+\kappa_{mj}(x_k,s_i)\right]H_j(s_i)\right\}=-\pi\sigma_{m0}, \quad (m=1-3)\\
&\sum_{i=1}^{n}A_i\left\{\left[\frac{U_{41}^0}{x_k-s_i}+\kappa_{41}(x_k,s_i)\right]H_1(s_i)+\sum_{j=2}^{4}[\kappa_{4j}(x_k,s_i)]H_j(s_i)\right\}=0
\end{aligned} \tag{28}$$

where,

$$\begin{aligned}
&s_i=\cos\left[\frac{(i-1)\pi}{n-1}\right], \quad (i=1,2,...,n); \quad x_k=\cos\left[\frac{(2k-1)\pi}{2(n-1)}\right], \quad (k=1,2,...,n-1)\\
&A_i=\frac{\pi}{2(n-1)}, \quad (i=1,n); \quad A_i=\frac{\pi}{(n-1)}, \quad (i=2,3,...,n-1)
\end{aligned} \tag{29}$$

For $h_1,\ h_2\to\infty$, $\kappa_{ij}(s,x)=0$ and from (25) the exact solution can be obtained as

$$\Psi_1(s)=0,\ \Psi_i(s)=c_i s\Big/\sqrt{1-s^2} \qquad (i=2-4) \tag{30}$$

where c_i $(i=2-4)$ are constants related to U_{ij}^0.

3. Asymptotic fields near the crack tip

Once the functions $H_j(s)$ ($j=1-4$) are obtained from solving the algebraic equations (28), following the procedure in Li and Lee [19], the asymptotic solutions of the magnetoelectroelastic fields near the crack tip can be obtained by introducing a polar coordinate system (r,θ) with the origin at the right crack tip as

$$r=\sqrt{(x-c)^2+z^2},\quad \theta=\tan^{-1}[z/(x-c)] \tag{31}$$

The hoop and shear stresses at an angle θ near the right tip of the crack are obtained from the following relations in terms of the polar coordinates (r,θ)

$$\begin{aligned}\sigma_{\theta\theta}(r,\theta)&=\sigma_{zz}(r,\theta)\cos^2\theta+\sigma_{xx}(r,\theta)\sin^2\theta-\sigma_{xz}(r,\theta)\sin 2\theta\\ \sigma_{r\theta}(r,\theta)&=\sin 2\theta[\sigma_{zz}(r,\theta)-\sigma_{xx}(r,\theta)]/2+\sigma_{xz}(r,\theta)\cos 2\theta\end{aligned} \tag{32}$$

Define the hoop stress intensity factor and shear stress intensity factor associated with the hoop and shear stresses at an arbitrary as angle θ as [20]:

$$K_{\theta\theta}=\lim_{r\to 0}\left(\sqrt{2r}\sigma_{\theta\theta}\right),\quad K_{r\theta}=\lim_{r\to 0}\left(\sqrt{2r}\sigma_{r\theta}\right) \tag{33}$$

The hoop and shear stress intensity factors can be obtained as:

$$K_{\theta\theta}^{(n)}=\sqrt{c}\sum_{j=1}^{4}\left\{\begin{array}{l}H_1(1)Y_{j1}^0\left[(-1)^n\Lambda_{1j}(\theta)\left(g_j\cos^2\theta+q_j\sin^2\theta\right)-\Lambda_{2j}(\theta)f_j\sin 2\theta\right]\\ +\sum_{k=2}^{4}H_k(1)Y_{jk}^0\left[(-1)^n\Lambda_{1j}(\theta)f_j\sin 2\theta+\Lambda_{2j}(\theta)\left(g_j\cos^2\theta+q_j\sin^2\theta\right)\right]\end{array}\right\} \tag{34}$$

$$K_{r\theta}^{(n)}=\sqrt{c}\sum_{j=1}^{4}\left\{\begin{array}{l}H_1(1)Y_{j1}^0\left[(-1)^n\Lambda_{1j}(\theta)\sin 2\theta\left(q_j-g_j\right)/2+\Lambda_{2j}(\theta)f_j\cos 2\theta\right]\\ +\sum_{k=2}^{4}H_k(1)Y_{jk}^0\left[\Lambda_{2j}(\theta)\sin 2\theta\left(g_j-q_j\right)/2-(-1)^n\Lambda_{1j}(\theta)f_j\cos 2\theta\right]\end{array}\right\} \tag{35}$$

where $0\le\theta\le\pi$ when $n=1$ for the upper part and $-\pi\le\theta\le 0$ when $n=2$ for the lower part of the cracked layer, respectively; $Y_{ij}^0=\lim_{\xi\to\infty}Y_{ij}(\xi)$, and the angular functions $\Lambda_{1j}(\theta)$ and $\Lambda_{2j}(\theta)$ ($j=1-4$) are defined as

$$\Lambda_{nj}(\theta)=\sqrt{\frac{\sqrt{\cos^2(\theta)+\left[\gamma_j\sin(\theta)\right]^2}+(-1)^n\cos(\theta)}{2\left[\cos^2(\theta)+\left[\gamma_j\sin(\theta)\right]^2\right]}}\qquad (n=1,2) \tag{36}$$

By setting the angle θ equal to zero, the common expressions for the Mode-I and Mode-II stress intensity factors can be recovered

$$K_I=K_{\theta\theta}|_{\theta=0}=\sqrt{c}\sum_{j=1}^{4}g_j\sum_{k=2}^{4}Y_{jk}^0H_k(1),\quad K_{II}=K_{r\theta}|_{\theta=0}=\sqrt{c}H_1(1)\sum_{j=1}^{4}f_jY_{j1}^0 \tag{37}$$

In this paper the criterion of maximum hoop stress intensity factors is applied to predict the crack kinking phenomena. It is noted that the applied electric and magnetic loadings and material properties have influence on the singular field near the crack tip, as shown in Eqs. (18), (25), (34), and (35).

4. Numerical results and discussions

For the magneto-electrically impermeable crack problem, the crack-tip fields are dependent on the remote mechanical, electrical and magnetic loading. To study the effect of magneto-electro-elastic interaction, the electric and magnetic loading parameters are introduced as:

$$L_E = e_{33}E_0/P_0, \quad L_H = h_{33}H_0/P_0 \tag{38}$$

The material constants used in the numerical calculation are selected as $BaTiO_3$-$CoFe_2O_4$ composite [21]:

$$\begin{aligned}
&C_{11} = 22.6\times10^{10}(\mathrm{N/m^2}),\ C_{13} = 12.4\times10^{10}(\mathrm{N/m^2}),\ C_{33} = 21.6\times10^{10}(\mathrm{N/m^2})\\
&C_{44} = 4.4\times10^{10}(\mathrm{N/m^2}),\ e_{15} = 5.8\ (\mathrm{C/m^2}),\ e_{31} = -2.2\ (\mathrm{C/m^2}),\\
&e_{33} = 9.3\ (\mathrm{C/m^2}),\ h_{15} = 275\ (\mathrm{N/Am}),\ h_{31} = 290.2\ (\mathrm{N/Am})\\
&h_{33} = 350\ (\mathrm{N/Am}),\ \lambda_{11} = 56.4\times10^{-10}(\mathrm{C^2/Nm^2}),\ \lambda_{33} = 63.5\times10^{-10}(\mathrm{C^2/Nm^2})\\
&\mu_{11} = 29.7\times10^{-5}(\mathrm{Ns^2/C^2}),\ \mu_{33} = 6.35\times10^{-5}(\mathrm{Ns^2/C^2})\\
&d_{11} = 5.367\times10^{-12}(\mathrm{Ns/VC}),\ d_{33} = 2737.5\times10^{-12}(\mathrm{Ns/VC})
\end{aligned} \tag{39}$$

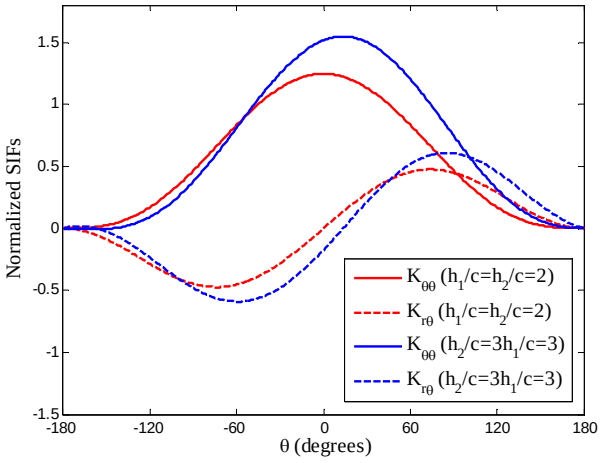

Figure 2. Normalized SIFs versus angle θ when $L_E = +0.5,\ L_H = -0.3$.

The variation of the normalized hoop and shear stress intensity factors (normalized by $P_0\sqrt{c}$) with angular position θ are displayed in Fig. 2. Without loss of generality, the applied stress is taken as $P_0 = 4.2$ MPa, and the magnitudes of the electric and magnetic loading parameters are chosen as $L_E = +0.5,\ L_H = -0.3$. The maximum hoop stress intensity factor (HSIF) occurs at $\theta = 0$ when the crack locates on the central plane of the layer, which indicates that the crack has a tendency to propagate along its original plane when the criterion of the maximum hoop stress

intensity factor is applied. When $h_1 \neq h_2$, the maximum HSIF occurs at $\theta \neq 0$, which indicates that the crack has a tendency to deviate from its original plane. When the HSIFs reach the maximum, the magnitude of the SSIF is zero.

5. Concluding remarks

A mixed-mode crack in a magnetoelectroelastic layer under in-plane mechanical, electric and magnetic loadings is studied for impermeable crack surface conditions. Fourier transforms are applied to reduce the mixed-boundary-value problem of the crack to a system of singular integral equations. Asymptotic fields near the crack tip are obtained explicitly and the corresponding field intensity factors are defined. The analytic solution of the degenerated case for a cracked infinite magnetoelectroelastic solid is recovered when the width of the layer tends to infinity. The crack kinking phenomena is investigated by applying the criterion of maximum hoop stress intensity factors.

Appendix A

$$\mathrm{T}_1 = \left(P_0 + e_{33}E_0 + h_{33}H_0\right)/C_{33}, \quad \mathrm{T}_2 = -E_0, \quad \mathrm{T}_3 = -H_0 \tag{A.1}$$

$$\begin{Bmatrix} a_j \\ b_j \\ d_j \end{Bmatrix} = \begin{bmatrix} C_{11} - C_{44}\gamma_j^2 & e_{31} + e_{15} & h_{31} + h_{15} \\ (C_{13} + C_{44})\gamma_j^2 & e_{33}\gamma_j^2 - e_{15} & h_{33}\gamma_j^2 - h_{15} \\ (e_{31} + e_{15})\gamma_j^2 & \lambda_{11} - \lambda_{33}\gamma_j^2 & d_{11} - d_{33}\gamma_j^2 \end{bmatrix}^{-1} \begin{Bmatrix} C_{13} + C_{44} \\ C_{33}\gamma_j^2 - C_{44} \\ e_{33}\gamma_j^2 - e_{15} \end{Bmatrix} \tag{A.2}$$

References

[1] Z.F. Song, G.C. Sih, Crack initiation behavior in a magnetoelectroelastic composite under in-plane deformation. Theor Appl Fract Mech, 39 (2003) 189-207.

[2] C.F. Gao, K. Hannes, B. Herbert, Crack problems in magnetoelectroelastic solids. Part I: exact solution of a crack. Int J Eng Sci, 41 (2003) 969-981.

[3] Q.H. Qin, 2D Green's functions of defective magnetoelectroelastic solids under thermal loading. Eng Anal Bound Elem, 29 (2005) 577-585.

[4] K.Q. Hu, G.Q. Li, Constant moving crack in a magnetoelectroelastic material under anti-plane shear loading. Int J Solids Struct, 42 (2005) 2823-2835.

[5] W.J. Feng, E. Pan, X. Wang, Dynamic fracture analysis of a penny-shaped crack in a magnetoelectroelastic layer. Int J Solids Struct, 44 (2007) 7955-7974.

[6] R. Rojas-Diaz, F. Garcia-Sanchez, A. Saez, C. Zhang, Fracture analysis of magnetoelectroelastic composite materials. Key Eng Mater, Advances in Fracture and Damage Mechanics VI, 348-349 (2007) 69-72.

[7] B.-L. Wang, Y.-W. Mai, Applicability of crack-face electromagnetic boundary conditions for fracture of magnetoelectroelastic materials. Int J Solids Struct, 44 (2007) 387-398.

[8] X.C. Zhong, X.F. Li, Magnetoelectroelastic analysis for an opening crack in a piezoelectromagnetic solid. Eur J Mech A/Solids, 26 (2007) 405-417.
[9] Z.G. Zhou, Z.T. Chen, Fracture mechanics analysis of a partially conducting mode I crack in piezoelectromagnetic materials. Eur J Mech A/Solids, 27 (2008) 824-846.
[10] M.-H. Zhao, C.-Y. Fan, Strip electric-magnetic breakdown model in magnetoelectroelastic medium. J Mech Phys Solids, 56 (2008) 3441-3458.
[11] C.-C. Ma, J.-M. Lee, Theoretical analysis of generalized loadings and image forces in a planar magnetoelectroelastic layered half-plane. J Mech Phys Solids, 57 (2009) 598-620.
[12] Y.D. Li, K.Y. Lee, Collinear unequal crack series in magnetoelectroelastic materials: Mode I case solved via new real fundamental solutions. Eng Fract Mech, 77 (2010) 2772-2790.
[13] M. Rekik, S. El-Borgi, Z. Ounaies, An embedded mixed-mode crack in a functionally graded magnetoelectroelastic infinite medium. Int J Solids Struct, 49 (2012) 835-845.
[14] K.Q. Hu, Z.T. Chen, Pre-curving analysis of an opening crack in a magnetoelectroelastic strip under in-plane impact loadings. J Appl Phys, 112, (2012) 124911.
[15] K.Q. Hu, Z.T. Chen, Dynamic response of a cracked magnetoelectroelastic layer sandwiched between two elastic layers. ZAMM Z Angew Math Mech, (2012) 1-12 DOI10.1002/zamm. 201200105.
[16] Y.P. Wan, Y.P. Yue, Z. Zhong, The mode III crack crossing the magnetoelectroelastic biomaterial interface under concentrated magnetoelectromechanical loads. Int J Solids Struct, 49 (2012) 3008-3021.
[17] P.S. Theocaris, N.I. Ioakimidis, Numerical integration methods for the solution of singular integral equations. Quart Appl Math, 35 (1977) 173-183.
[18] F. Delale, F. Erdogan, Effect of transverse shear and material orthotropy in a cracked spherical cap. Int J Solids Struct, 15 (1979) 907-926.
[19] X.F. Li, K.Y. Lee, Three-dimensional electroelastic analysis of a piezoelectric material with a penny-shaped dielectric crack. J Appl Mech, 71 (2004) 866-878.
[20] A. Azhdari, S. Nemat-Nasser, Hoop stress intensity factor and crack-kinking in anisotropic brittle solids. Int J Solids Struct, 33 (1996) 2023-2037.
[21] W.Y. Tian, R.K.N.D. Rajapakse, Fracture analysis of magnetoelectroelastic solids using path independent integrals. Int J Fract, 131 (2005) 311-335.

Three-dimensional annular saturated crack propagation in ultralow permeability rock under wave & electro-magneto-thermo-elastic fields

BoJing Zhu[1,2*],YaoLin Shi[1] ,TianYou Fan[3]

[1] Key Laboratory of Computational Geodynamics of CAS, University of Chinese Academy of Sciences, Beijing 100049, CHINA

[2] Rock Mechanics Laboratory, University of Durham, Durham DH1 3LE, UK

[3] Beijing Institute of Technology, Beijing 100081,CHINA

* Corresponding author: cynosureorion@ucas.ac.cn (B.J.Zhu)

Abstract: This contribution presents a new theory with lattice Boltzmann & finite element & hypersingular integral equation (LB-FE-HIE) to explore the three-dimensional pore-network cracks transient hydrofacturing-liquefaction in tight sandstone (3D PC-TH-TS) under seismic waves & electro-magneto-thermo-elastic fields through intricate theoretical analysis and numerical simulations. First, the 3D PN-TH-TS problem is reduced to solving a set of coupled LB-FE-HIEs by using the Green functions and distribution functions, in which the unknown functions are the extended pore-network cracks displacement discontinuities. Then, the behavior of the extended displacement discontinuities at the pore-network cracks surface terminating at the solid-liquid film interface are analyzed through extended dynamic hypersingular integral main-part analysis method of LB-FE-HIEs. Closed formed solutions for the extended singular dynamic stress, the extended dynamic stress intensity factor and the extended dynamic energy release rate near the dislocations interface are provided. Last, the tight sandstone sample from the Ordos Basin Triassic formation is selected, the fluid-solid coupled digital rock physical modeling is established, and the simulations of 3D PC-TH-TS process is presented on the parallel CPU-GPU platform. The hydrofacturing-liquefaction varying with the amplitude, frequency and constituting time of earthquake wave is obtained. The relationship between the tight sandstone pore-network cracks transient propagation-evolution and the maximum tight sandstone fracturing-liquefaction stress criteria is explored.

Keywords Hydrofracturing-liquefaction, tight sandstone, lattice Boltzmann method, finite element method, hypersingular integral equation, seismic wave & electro-magneto-thermo-elastic fields, parallel CPU-GPU technology.

1. Introduction

Hydrofracturing-liquefaction mechanism is the basic theory for understanding the in-situ stress measurement, the petroleum-gas (nature gas and shale gas)-geothermic develop, and the earthquake evaluation and mechanism exploration. With the complex and challenge of this issue, the mechanism of dynamic Hydrofracturing-liquefaction is still not clear even a lot of fundamental and landmark achievements have been obtained in this field since the last century 60's. The oscillation singularity of dynamic stress wave as well as stress oscillation singularity index of pore-network cracks transient Hydrofracturing-liquefaction (PC-TH) fluid pore-solid sketch interface under seismic wave & electro-magneto-thermo-elastic fields (SW&EMTE) makes it much more difficult than the unsaturated cased of the ordinary cracks, for in this process, including fluid transient undrained process, fluid transient compression and expansion process, physical properties of tight

stone varying with PC-TH propagation process and tight stone transient failure with the liquefaction process (the liquefaction process time is around 10E-5s).

The mode I stress intensity factor for a constant velocity semi-infinite crack moving in a fluid-saturated porous medium with finite height is calculate[1]. The linear elastic solid with cavities containing nonviscous compressible fluid is explored[2], and the abnormally high fluid pressure in the cavities affects is analyzed. The mode I crack in an elastic fluid-saturated porous solids is studied[3], and relatively closed-form asymptotic solution near the crack tip is obtained. Extended horizontal cracks in a vertical column of saturated sand is explored [4], and the theory is good qualitative agreement with the experimental findings. The interaction of a normally incident time-harmonic longitudinal plane wave with a circular crack imbedded in a porous medium is considered [5], and the problem is formulated in dual integral equations for the Hankel transform of the wave field. The formation mechanism of "water film" (or crack) in saturated sand is analyzed theoretically and numerically[6]. The cracks in fluid-saturated two-phase medium is explored [7] by finite element method. A circular crack imbedded in a porous medium under a normally incident time-harmonic longitudinal plane wave is studied by second kind single Fredholm integral equation[8]. A finite element algorithm is presented for the numerical modeling of cohesive fracture in a partially saturated porous media[9]. The saturated cracks in 4% porosity Fontainebleau sandstone fro an effective mean pressure ranging from 2 to 95MPa under high ultrasonic frequencies, Vp/Vs, ratio is explored [10]. The narrow distribution of cavities permeability model is devised combining the hydraulic radium and percolation concepts [11]. But this problem is far from solved for complex relationship between fluid states, physical properties of tight sandstone and ultra high temperature-pressure (UHTP). There are four differences between classical porous medium and tight sandstone. First, the pore/void size is located at atom-molecular-pico-nano scale level, the fluid viscous (as function of UHTP), the effects of boundary layer, and the unsteady fluid flow (eddy flow and turbulent flow) can not be neglected; Second, when the P-T conditions are high enough, the water role in the rock/mineral includes free-supercritical-constitutional state, the fluid flow particles are composed of four components [H2O, H+, (OH)-, (H3O)+]. Third, the micro pore is composed of four types [multi-grain gap, polycrystalline space, crystal space and crystal internal space] and the deformation of the micro-structure had to be considered; Last, the fluid flow permeability and diffusion include intermolecular collisions and diffusion (Fick's laws of diffusion), molecular collisions with interface (Knudsen diffusion), molecular and interfacial adhesive and viscous flow (Darcy and Forchheimer flow). With the scale decrease, the surface stress component became domain, the effect of the body stress component reducing, and the classical N-S equation is no longer applies.

In this work, based on the previous work on saturated dislocation transient propagation-evolution in olivine structure under ultra-high temperature and pressure (UHTP)[12], and general solutions of extended displacement (elastic displacement, electrical potential, magnetic potential and thermal potential) given in the previous work[13, 14], the three-dimensional pore-network crack transient Hydrofracturing-liquefaction in tight sandstone (3D PC-TH-TS) under seismic waves & electro-magneto-thermo-elastic fields is studied by using lattice Boltzmann & finite element & hypersingular integral equation (LB-FE-HIE) on parallel GPU-CPU environment.

First, the 3D PN-TH-TS problem is reduced to solving a set of LB-FE-HIEs coupled with extended boundary integral equations by using the Green functions and distribution functions, in which the

unknown functions are the extended pore-network cracks displacement discontinuities. Then, the behavior of the extended displacement discontinuities around the pore-network cracks surface terminating at the solid-liquid film interface are analyzed by the extended hypersingular integral main-part analysis method of LB-FE-HIEs. Analytical solutions for the extended singular dynamic stresses, the extended dynamic stress intensity factors and the extended dynamic energy release rate near the dislocations front are provided. Thrid, the tight sandstone sample from the Ordos Basin Triassic formation is selected and different tomography resolution data is obtained by X-ray CT digital technology, the fluid-solid coupled porous medium physical modeling is established, and the relatively Hydrofracturing-liquefaction numerical modelling of tight sandstone is obtained for the first time. Last, The simulations of 3D PC-TH-TS process is presented, the hydrofacturing-liquefaction varying with the amplitude, frequency and time of earthquake wave is obtained. The relationship between the tight sandstone pore-network cracks transient propagation-evolution and the maximum tight sandstone fracturing-liquefaction stress criteria is explored.

2. Basic equations

Here summation from 1 to 3(1 to 6) over repeated lowercase (uppercase) subscripts is assumed, and a subscript comma denotes the partial differentiation with respect to the coordinates. The ultralow permeability tight sandstone (UPTS) consists of six constituents, i.e. the particles of solid skeleton (the 1st component), bound liquid film (the 2nd component), static pore-liquid (the 3rd component, free state water), dynamic pore-liquid I (the four component, free state water), dynamic pore-liquid II (the five component, supercritical state water) and dynamic pore-liquid III (the 6th component, constitutional state water [H+, (OH)-, (H3O)+]. The governing equations and constitutive relations of UPTS under EMTE field can be expressed as [15, 16],

$$A_L \tau^L_{ij,j} + B_L + \Sigma_{iJ,i} + f_J = 0 \tag{1}$$

where

$$A_L = \begin{cases} 1-(1-\alpha)\kappa & L=1 \\ \phi_2^P & L=2 \\ \phi_3^P & L=3 \\ \phi_4^P & L=4 \\ \phi_5^P & L=5 \\ \phi_6^P & L=6 \end{cases} \qquad B_L = \begin{cases} \left[(1-\kappa)\rho_1 + \alpha\kappa\rho_2\right]\ddot{U}(x_i,t)_{1i} - \sum_{N=1}^{5}\left\{v_N\delta_N^2\chi^{-1}\chi_N^{-1}\left[\dot{U}(x_i,t)_{(N+1)i} - \dot{U}(x_i,t)_{Ni}\right]\right\} & L=1 \\ \phi_2^P\rho_2\ddot{U}(x_i,t)_{2i} - \sum_{N=2}^{5}\left\{v_N\delta_N^2\chi^{-1}\chi_N^{-1}\left[\dot{U}(x_i,t)_{(N+1)i} - \dot{U}(x_i,t)_{Ni}\right]\right\} & L=2 \\ \phi_3^P\rho_3\ddot{U}(x_i,t)_{3i} - \sum_{N=3}^{5}\left\{v_N\delta_N^2\chi^{-1}\chi_N^{-1}\left[\dot{U}(x_i,t)_{(N+1)i} - \dot{U}(x_i,t)_{Ni}\right]\right\} & L=3 \\ \phi_4^P\rho_4\ddot{U}(x_i,t)_{4i} - \sum_{N=4}^{5}\left\{v_N\delta_N^2\chi^{-1}\chi_N^{-1}\left[\dot{U}(x_i,t)_{(N+1)i} - \dot{U}(x_i,t)_{Ni}\right]\right\} & L=4 \\ \phi_5^P\rho_5\ddot{U}(x_i,t)_{5i} - v_5\delta_5^2\chi^{-1}\chi_5^{-1}\left[\dot{U}(x_i,t)_{6i} - \dot{U}(x_i,t)_{5i}\right] & L=5 \\ \phi_6^P\rho_6\ddot{U}(x_i,t)_{6i} + v_6\delta_6^2\chi^{-1}\chi_6^{-1}\dot{U}(x_i,t)_{6i} & L=6 \end{cases}$$

$U(x_i,t)_{i1}, U(x_i,t)_{i2}, U(x_i,t)_{i3}, U(x_i,t)_{i4}, U(x_i,t)_{i5}$ and $U(x_i,t)_{i6}$ denote the components of displacements of drained porous solid frame, the components of displacements of drained bound liquid film, denote the components of displacements of the static pore-liquid, the components of displacements of the dynamic pore-liquid I, the components of displacements of the dynamic pore-liquid II, and the components of displacements of the dynamic pore-liquid III respectively; ρ_L, v_{NL}, χ, χ_{NL} and δ_L denote density, viscosity, intrinsic permeability, relative permeability and volume fractions of L th component of ultra-low permeability porous rock respectively; κ, α, ϕ_2^P, ϕ_3^P, ϕ_4^P, ϕ_5^P and ϕ_6^P represent macro porosity of ultra-low permeability rock, fraction occupied by bound liquid film, the connected porosity of bound liquid film, the connected porosity of static pore-liquid part, the connected porosity of dynamic pore-liquid I, II and III respectively. In addition, the extended stress displacement matrix tensor and the extended body load vector, $\sum_{iJ}$ and f_J, are defined respectively as

$$\sum_{iJ}=\begin{cases}\sigma_{ij} & J=j=1,2,3\\ D_i & J=4\\ B_i & J=5\\ \vartheta_i & J=6\end{cases}\qquad f_J=\begin{cases}f_j & J=j=1,2,3\\ -f_e & J=4\\ -f_m & J=5\\ -f_\vartheta & J=6\end{cases}\tag{2}$$

The combined constitutive equation is written as

$$\sum_{iJ}=E_{iJKl}Z_{Kl}\tag{3}$$

where the EMTE constant matrix tensor and the extended strain field matrix tensor, E_{iJKl} and Z_{Kl}, take the form

$$E_{iJKl}=\begin{bmatrix}C_{iJKl} & -\Pi_{iJ} & 0\\ 0 & 0 & -\lambda_{iJ}\end{bmatrix}\qquad Z_{Kl}=[\ U^s_{K,l}\quad \Upsilon_{,l}\ ]^T\tag{4}$$

The extended elastic stiffness tensor, the extended thermal stress constants tensor and the extend elastic displacement vector, C_{iJKl}, Π_{iJ} and U_K, are defined as

$$C_{iJKl}=\begin{cases}c_{ijkl} & J,K=1,2,3\\ e_{lij} & J=1,2,3;K=4\\ e_{ikl} & J=4;K=1,2,3\\ d_{lij} & J=1,2,3;K=5\\ d_{ikl} & J=5;K=1,2,3\\ -g_{il} & J=4;K=5 or J=5;K=4\\ -\in_{il} & J,K=4\\ -\mu_{il} & J,K=5\end{cases}\quad \Pi_{iJ}=\begin{cases}\iota_{ij} & J=1,2,3;K=6\\ \varsigma_{il} & J=4;K=6\\ \eta_{il} & J=5;K=6\end{cases}\quad U^s_K=\begin{cases}u^s_i & K=1,2,3\\ \phi^s_4 & K=4\\ \varphi^s_5 & K=5\\ \Upsilon^s_6 & K=6\end{cases}\tag{5}$$

σ_{ij}, D_i, B_i, ϑ_i, f_i, f_e, f_m , f_ϑ, c_{ijkl}, e_{lij}, d_{lij}, $\in_{il}$, g_{il}, μ_{il}, ι_{ij}, ς_{il}, η_{il}, λ_{ij}, u^s_i, ϕ^s_4, φ^s_5 and Υ^s_6 are defined in [14]. The drained porous solid frame and the drained bound liquid film have the same displacement and pressure; The static pore-liquid, the dynamic pore-liquid I have the same displacement; The pressure of saturated porous solid frame is the sum of static pore-liquid, dynamic pore-liquid I, dynamic pore-liquid II and dynamic pore-liquid III components pressure. The seismic wave displacement in ultra-low permeability porous rock can be written as

$$U(x_i,t)_{iL}=\Phi^1(x_i,t)_{iL,i}+\varepsilon_{ijk}\Phi^2(x_i,t)_{jL,k}$$

where

$$\Phi(x_i,t)^\alpha_{iL}=-A^\alpha_i E(\omega t)\left\{\delta_{3i}\begin{bmatrix}E(-2\omega^\alpha_L x_1x_2x_3\sin\theta^\alpha_{1L}\cos\theta^\alpha_{2L})+E(-2\omega^\alpha_L x_1x_2x_3\cos\theta^\alpha_{1L}\sin\theta^\alpha_{2L})\\ +E(-2\omega^\alpha_L x_1x_2x_3\cos\theta^\alpha_{1L}\cos\theta^\alpha_{2L})+E(-2\omega^\alpha_L x_1x_2x_3\sin\theta^\alpha_{1L}\sin\theta^\alpha_{2L})\end{bmatrix}\right\}$$
$$\begin{bmatrix}+E(-2\omega^\alpha_L x_3\cos\angle(x_3,x_2)^\alpha_{pL})+E(-2\omega^\alpha_L x_3\cos\angle(x_3,x_1)^\alpha_{pL})\end{bmatrix}$$
$$\times\begin{bmatrix}E(\omega^\alpha_L x_1\sin\angle(x_3,x_2)^\alpha_{pL})+E(\omega^\alpha_L x_2\sin\angle(x_3,x_1)^\alpha_{pL})+E(2\omega^\alpha_L x_1x_2\sin\theta^\alpha_{1L}\cos\theta^\alpha_{2L})+E(2\omega^\alpha_L x_1x_2\cos\theta^\alpha_{1L}\sin\theta^\alpha_{2L})\\ +E(2\omega^\alpha_L x_1x_2\cos\theta^\alpha_{1L}\cos\theta^\alpha_{2L})+E(2\omega^\alpha_L x_1x_2\sin\theta^\alpha_{1L}\sin\theta^\alpha_{2L})\end{bmatrix}$$

$$\theta^\alpha_{1L}=\begin{cases}\angle(x_3,x_2)_{pL}+\angle(x_3,x_1)_{pL} & \alpha=1\\ \angle(x_3,x_2)_{pL}-\angle(x_3,x_1)_{pL} & \alpha=2\end{cases},\ \theta^\alpha_{2L}=\begin{cases}\angle(x_3,x_2)_{sL}+\angle(x_3,x_1)_{sL} & \alpha=1\\ \angle(x_3,x_2)_{sL}-\angle(x_3,x_1)_{sL} & \alpha=2\end{cases},\ \omega^\alpha_L=\begin{cases}\omega/v^L_P & \alpha=1\\ \omega/v^L_S & \alpha=2\end{cases},\ E()=e^{i()}$$

v^1_P, v^2_P, v^3_P, v^4_P, v^5_P and v^6_P denote the P-wave velocity in drained porous solid frame, drained bound liquid film, static pore-liquid, dynamic pore-liquid I, dynamic pore-liquid II and dynamic pore-liquid III respectively; v^1_S, v^2_S, v^3_S, v^4_S, v^5_S and v^6_S denote the P-wave velocity in drained porous solid frame, drained bound liquid film, static pore-liquid, dynamic pore-liquid I, dynamic pore-liquid II and dynamic pore-liquid III respectively; $\angle(x_3,x_2)_{pL}$, $\angle(x_3,x_1)_{pL}$, $\angle(x_3,x_2)_{sL}$ and $\angle(x_3,x_1)_{sL}$ denote the P-wave incidence angle between x_3 and x_2 axes, the P-wave incidence angle between x_3 and x_1 axes, the S-wave incidence angle between x_3 and x_2 axes and the S-wave incidence angle between x_3 and x_1 axes in the L th component of ultra-low permeability porous rock

respectively. If we defined that solid skeleton component and liquid components are parallel and subjected to the same strain, the time-dependent rigidity modulus components G_L of ultra-low permeability porous rocks can be defined as

$$G_L = (1-f)G_0 + \alpha f (v_s^L \varepsilon_L^{-2})_{,t}$$

f, α, ε_L^{-2} and G_0 represent macro-porosity of ultra-low permeability porous rocks, fraction occupied by bound liquid film, non-dimensional parameter (linked fluid viscosity, bulk modulus, density and permeability) of L th component of ultra-low permeability porous rock, and rigidity modulus of solid grains.

3.LB-FE-HIE for 3D PC-TH-TS under seismic wave & electro-magneto-thermo-elastic fields

3.1 Lattice Boltzmann & finite element (LB-FE) coupled modeling

It is shown in the Fig 1, The LB-FE coupled modeling for tight sand porous media is established. The finite element method is using to analyze solid sketch part of the porous tight sand (the strain/strain rate-stress/stress rate-temporal spatial solid sketch structure-macro strength) (Fig1D, 1E); D3Q27 lattice Boltzmann method is using to analyze fluid pore part of the porous tight sand (fluid stress-viscous-density-time-bulk strain) (Fig 1F); LB-FE coupled modeling can deal with interface stress-strain between solid sketch and fluid pore (surface of pore-network cracks) (Fig 1C). In our work, the three-dimensional 20 node arbitrary hexahedral element (3D-20 Hexahedral element) is defined for the solid sketch part of the porous tight sand, and the three-dimensional 27 particle arbitrary hexahedral node (D3Q27) is defined for the fluid pore part of the porous tight sand; if the element is located at the surface of the pore-network cracks, then we defined that each D3Q27 node has the same physical meaning as one arbitrary node of 3D-20 Hexahedra element (Fig 1G,1H and 1I), the distribution function of lattice Boltzmann and the shape function in finite element can be linked through intricate theoretical formulation, and the LB-FE coupled fluid pore-solid sketch porous modeling can be established, the theoretical derivation can be written as follows,The equation of shape function for 3D-20 Hexahedra isoparametric element is defined as

$$N_k = \begin{cases} \prod_{i=1}^{3}(1+x_{ik}x_i)\left(\sum_{i=1}^{3}x_{ik}x_i - 2\right) & k = 1 \sim 8 \\ 2\prod_{i=1}^{3}(1+x_1^2) & k = 9 \sim 12 \\ 2(1-x_2^2)(1+x_{ik}x_1)(1+x_{3k}x_3) & k = 13 \sim 16 \\ 2(1-x_3^2)(1+x_{1k}x_1)(1+x_{3k}x_3) & k = 16 \sim 20 \end{cases} \tag{6}$$

The relatively stiffness matrix for 3D-20 Hexahedra isoparametric element is defined as

$$[K] = \int_{-1}^{1}\int_{-1}^{1}\int_{-1}^{1}[B]^T[D][B]\lfloor J \rfloor dx_1 dx_2 dx_3 \tag{7}$$

where

$$[B_K] = \begin{bmatrix} \frac{\partial N_K}{\partial \xi_1} & 0 & 0 \\ 0 & \frac{\partial N_K}{\partial \xi_2} & 0 \\ 0 & 0 & \frac{\partial N_K}{\partial \xi_3} \\ \frac{\partial N_K}{\partial \xi_2} & \frac{\partial N_K}{\partial \xi_1} & 0 \\ 0 & \frac{\partial N_K}{\partial \xi_1} & \frac{\partial N_K}{\partial \xi_2} \\ \frac{\partial N_K}{\partial \xi_3} & 0 & \frac{\partial N_K}{\partial \xi_1} \end{bmatrix} \quad [D] = \frac{E(1-v)}{(1+v)(1-2v)}\begin{bmatrix} 1 & A_1 & A_2 & 0 & 0 & 0 \\ A_1 & 1 & A_1 & 0 & 0 & 0 \\ A_2 & A_1 & 1 & 0 & 0 & 0 \\ 0 & 0 & 0 & A_2 & 0 & 0 \\ 0 & 0 & 0 & 0 & A_2 & 0 \\ 0 & 0 & 0 & 0 & 0 & A_2 \end{bmatrix} \quad [J] = \begin{bmatrix} \frac{\partial \xi_1}{\partial x_1} & \frac{\partial \xi_2}{\partial x_1} & \frac{\partial \xi_3}{\partial x_1} \\ \frac{\partial \xi_1}{\partial x_2} & \frac{\partial \xi_2}{\partial x_2} & \frac{\partial \xi_3}{\partial x_2} \\ \frac{\partial \xi_1}{\partial x_3} & \frac{\partial \xi_1}{\partial x_3} & \frac{\partial \xi_1}{\partial x_3} \end{bmatrix} \quad A_1 = \frac{v}{1-v} \quad A_2 = \frac{1-2v}{2(1-v)}$$

The extended equivalent stress and tension for 3D-20 Hexahedra isoparametric element is defined as

$$\{R\}_{volume} = \int_{-1}^{1}\int_{-1}^{1}\int_{-1}^{1}[N]^T\{p\}|J|dx_1dx_2dx_3 \tag{8}$$

$$\{R\}_{surface} = \iint_{A_{x_1x_2}}[N]^T\{\bar{p}\}\Big|_{x_1=1}dA \tag{9}$$

Take the distribution function of D3Q27 LB node[17] into the shape function of 3D-20 Hexahedra element, the LB-FE modeling can be established to analyze the fluid-solid coupled porous structure problem.

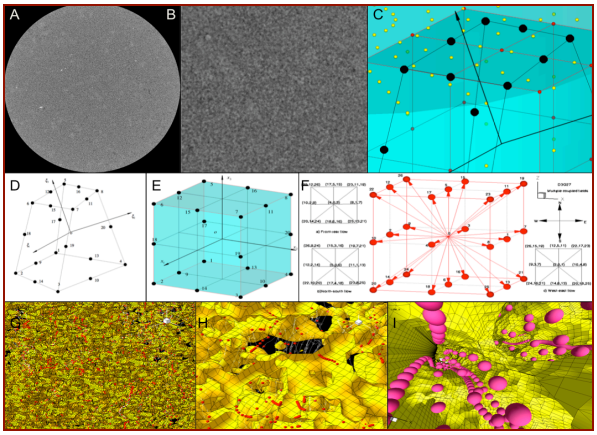

Fig 1. The lattice Boltzmann & finite element fluid-solid coupled modeling
Fig 1A. Cross-section of rock CT scan digital data, Fig 1B. Cross-section of digital rock, Fig 1C. LBM & FEM fluid-solid coupled modelling
Fig 1D, Sketch of 20 nodes FEM cell, Fig 1E. Sketch of 20 nodes isoparametric FEM cell, Fig 1F Sketch of D3Q27 LBM grid point
Fig 1G. Micro structure of tight rock (Scale I), Fig 1H. Micro structure of tight rock (Scale II), Fig 1I Micro structure of tight rock (Scale III)

3. 2 LB-FE-HIE for 3D PC-TH-TS under seismic wave & electro-magneto-thermo-elastic fields

Using Micro XCT-400 CT system, the high resolution data are obtained, the 3D virtual digital rock are reestablished, and the LB-FE-HIE physical model are constructed; The threshold is arrange from 78~100, the interior geometry structure at low level scales translate from the pix RGB color into the cell-mesh-grid model, the initial/boundary conditions, the physical/chemical parameters of rock and water, and the low level scales geometry pore-solid structure can be defined.

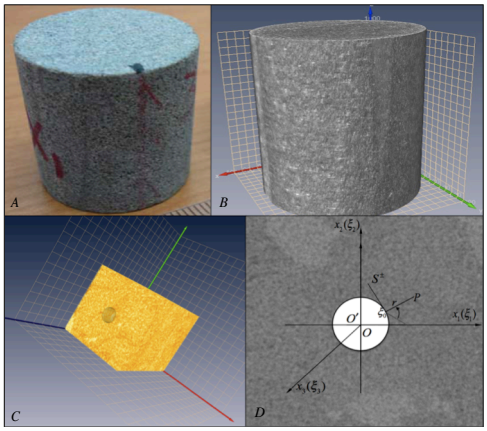

Fig 2. The tight sandstone transient hydrofracturing-liquefaction lattice Boltzmann & finite element fluid-solid coupled modelling
Fig 2A. Sample of tight sandstone, Fig 2B. Virtual digital rock sample of tight sandstone
Fig 2C, A circle drilling in the tight sandstone, Fig 1D. Sketch of transient hydrofracturing-liquefaction in the tight sandstone

Fig 2. shows the PC-TD-TS LB-FE-HHIE coupled modeling, the diameter and the length of the core samples are equal to 5cm and 10cm respectively; the resolution of cross-section and the interval between cross-sections are equal to 10μm. The general model was formulated by utilizing an automatic local amplification grid technique, and the initial LB-FE-HIE physical model is equal to 1024×1024×1024 pixels, which does not include the extended variables. Applying function in references [18, 19] to the initial virtual digital rock modeling, we can obtained the random LB-FE-HIE modeling (decreasing the computational scale in parallel CPU-GPU environment). The pore/void size is located at atom-molecular-pico-nano scale level, the fluid viscous (as function of

pressure-temperature), the effects of boundary layer, and the unsteady fluid flow (eddy flow and turbulent flow) had to be considered. The water role in the rock includes free state, supercritical state and constitutional state; the fluid flow particles are composed of four components [H2O, H+, (OH)-, (H3O)+]. The micro pore is composed of four kinds [multi-grain gap, polycrystalline clearance, crystal space and crystal internal clearance] and the deformation of the microstructure had to be considered. The fluid flow permeability and diffusion include intermolecular collisions and diffusion (Fick's laws of diffusion); molecular collisions with interface (Knudsen diffusion), molecular and interfacial adhesive and viscous flow (Darcy flow and Forchheimer flow). With the scale decrease, the surface stress component became domain, the effect of the body stress component reducing, and the classical N-S equation is no longer applies. The more detailed introduction can be found elsewhere in the literature[20-23].

Consider the tight sandstone containing a random three-dimensional transient hydrofacturing-liquefaction crack as shown in Fig.2D. A fixed global rectangular Cartesian system x_i (i=1,2,3) is chosen. Assume that the pore-network crack S ($S^+ \bigcup S^-$) is subjected to remote the seismic wave mechanical loads $p_j(P,Q,t)$, the seismic wave electrical loads $q(P,Q,t)$, the seismic magnetic loads $b(P,Q,t)$ and the thermal loads $\rho(P,Q,t)$, respectively. The local rectangular Cartesian system ξ_i are chosen, the stochastic flaws are assumed to be in the $\xi_1\xi_2^i$ plane and normal to the ξ_3 axis. Using the EMTE form of the Somigliana identity, the extended displacement vector, $U_I(p)$, at interior point $p(x_1,x_2,x_3)$ is expressed as

$$U_I(p)=\int_{S^+}(U_{IJ}(p,q)T_J(q)-T_{IJ}(p,q)U_J(q))ds(q)-\int_{\Gamma}(T_{IJ}(p,q)U_J(q)+U_{IJ}(p,q)T_J(q))ds(q)+\int_{\Omega}U_{IJ}(p,q)f_J(q)ds(q) \tag{10}$$

where Ω is the domain occupied by the EMTE-CMCs, Γ is the external boundary, $T_J(q)$ is the extended elastic tractions on boundaries, $U_{IJ}(p,q)$ and $T_{IJ}(p,q)$ are the fundamental solutions. Using constitutive Equation (10), the corresponding extended stresses tensor, Σ_{IJ}, is expressed as

$$\Sigma_{IJ}(p)=-\int_{S^+}S_{KiJ}(p,q)\tilde{U}_K(q)ds(q)+\int_{\Gamma}(D_{KiJ}(p,q)T_K(q)-S_{KiJ}(p,q)U_K(q))ds(q)+\int_{\Omega}D_{KiJ}(p,q)f_K(q)ds(q) \tag{11}$$

The kernels functions, S_{KiJ} and D_{KiJ}, are as follows:

$$S_{KiJ}(p,q)=-E_{iJMn}T_{MK,n}(p,q) \qquad D_{KiJ}(p,q)=-E_{iJMn}U_{MK,n}(p,q) \tag{12}$$

The hypersingular integral equations can be obtained as

$$\sum_{i=1}^{5}\rho_i^2t_i^2\sum_{m=3}^{6}\tilde{u}_{m,1}=\int_{S^+}\left(\frac{c_{44}^2D_0s_0^2(\delta_{\bar{\alpha}\bar{\beta}}-3r_{,\bar{\alpha}}r_{,\bar{\beta}})+(\delta_{\alpha\beta}-3r_{,\alpha}r_{,\beta})\sum_{i=1}^{5}\rho_i^2t_i^2}{r^3}\hat{K}\,\tilde{u}_{\beta}+\frac{3r_{,\alpha}\sum_{i=1}^{5}\lambda_{33}s_i^2t_i}{r^4}\tilde{u}_6\right)ds+\int_{S^+}K_{\alpha i}\tilde{u}_i\,ds=-p_{\alpha} \tag{13}$$

$$\sum_{n=3}^{5}\sum_{i=1}^{5}\rho_i^mt_i^t\sum_{m=3}^{6}\tilde{u}_{m,2}+\int_{S^+}\left(\frac{r_{,\alpha}\sum_{i=1}^{5}A_i^{\Upsilon}t_i^2\rho_i^1}{r^2}\tilde{u}_{\alpha}+\frac{\sum_{n=3}^{5}\sum_{i=1}^{5}\rho_i^mt_i^t}{r^3}\tilde{u}_n+\frac{3\lambda_{3\alpha}r_{,\alpha}\sum_{i=1}^{5}s_i^2\lambda_i^{\vartheta}\rho_i^m}{r^4}\tilde{u}_6\right)ds+\int_{S^+}K_{mi}\tilde{u}_i\,ds=-p_m \tag{14}$$

$$\sum_{i=1}^{5}A_i^{\Upsilon}\lambda_{3\beta}t_i^2\tilde{u}_{\alpha,\alpha}+\int_{S^+}\left(\frac{(\delta_{\alpha\beta}-3r_{,\alpha}r_{,\beta})\sum_{i=1}^{5}A_i^{\Upsilon}\lambda_{3\beta}t_i^2}{r^2}\tilde{u}_{\beta}+\frac{3\lambda_{3\alpha}r_{,\alpha}\sum_{i=1}^{5}A_i^{\Upsilon}s_i^2\lambda_i^{\vartheta}\lambda_{33}\rho_i^6}{r^4}\tilde{u}_6\right)ds+\int_{S^+}K_{6i}\tilde{u}_i\,ds=-p_6 \tag{15}$$

where $p_i^{\hat{i}}$, $p_4^{\hat{i}}(q^{\hat{i}})$, $p_5^{\hat{i}}(b^{\hat{i}})$ and $p_5^{\hat{i}}(\rho^{\hat{i}})$ can obtained from the solution for the loads of the solids.

4. Dynamic stress, dynamic stress intensity factors and energy release rate near the dislocations front

In order to investigate the singularity of the dislocations front, consider a local coordinate system defined as $x_1\ x_2\ x_3$. The x_1-axis is the tangent line of the dislocation front at point q_0, x_2-axis is the internal normal line in the dislocation plane, and x_3-axis is the normal of the dislocation. Then, the extended displacement discontinuities of the dislocation surface near a dislocation front point q_0 can be assumed as

$$[\ \tilde{u}_i^{\hat{I}}(q)\quad \tilde{\phi}^{\hat{I}}(q)\quad \tilde{\varphi}^{\hat{I}}(q)\quad \tilde{\Upsilon}^{\hat{I}}(q)\ ] = g_k^{\hat{I}}(q_0)\xi_2^{\lambda_k} \qquad 0 < Re(\lambda_k) < 1 \tag{16}$$

where $g_k(q_0)$ and λ_k represent non-zero constants and singular index, respectively. The dynamic stress intensity factors are defined as

$$K_1^{\hat{I}} = \lim_{r\to 0}\sqrt{2r}\sigma_{33}^{\hat{I}}(r,\theta)\Big|_{\theta=0}, K_2^{\hat{I}} = \lim_{r\to 0}\sqrt{2r}\sigma_{32}^{\hat{I}}(r,\theta)\Big|_{\theta=0}, K_3^{\hat{I}} = \lim_{r\to 0}\sqrt{2r}\sigma_{31}^{\hat{I}}(r,\theta)\Big|_{\theta=0} \tag{17}$$

$$K_4^{\hat{I}} = \lim_{r\to 0}\sqrt{2r}D_3^{\hat{I}}(r,\theta)\Big|_{\theta=0}, K_5^{\hat{I}} = \lim_{r\to 0}\sqrt{2r}B_3^{\hat{I}}(r,\theta)\Big|_{\theta=0}, K_6^{\hat{I}} = \lim_{r\to 0}\sqrt{2r}\vartheta_3^{\hat{I}}(r,\theta)\Big|_{\theta=0} \tag{18}$$

where r is the distance from point p to the dislocation front point q_0, the dynamic stress around the dislocation front can be expressed as follows

$$\sigma_{13}^{\hat{I}} = c_{44}^2 D_0 s_0^2 \frac{\pi g_1^{\hat{I}}}{\sqrt{rr_0}}\cos\frac{\theta_0}{2} \tag{19}$$

$$\begin{aligned}\sigma_{23}^{\hat{I}} = \sum_{i=1}^{5}\frac{\pi}{\sqrt{rr_i}}\{&g_6^{\hat{I}}\lambda_{33}[15\lambda_{33}s_i^2\cot\theta_i(3\cos\frac{\theta_i}{4}-3\sin^2\frac{\theta_i}{2}\cos\frac{\theta_i}{2}-\frac{1}{4}\sin^2\theta_i\cos\frac{3\theta_i}{2})-\frac{2\lambda_{33}}{r^2r_i^2}\sin^{-1}\frac{\theta_i}{2}\\ &+\frac{\lambda_{32}}{2rr_i\sin\theta}(2\cos^{-1}\frac{\theta_i}{2}-3\cos\frac{\theta_i}{2}-\cos\frac{5\theta_i}{2})]+\rho_i^2\pi\cos\frac{\theta_i}{2}(t_2g_2+4\sum_{m=3}^{5}t_i^m g_m^{\hat{I}})\}\end{aligned} \tag{20}$$

$$\begin{aligned}\dot{\sigma}_{3n}^{\hat{I}} = \sum_{i=1}^{5}\rho_i^n s_i\pi[&\frac{1}{\sqrt{rr_i}}(t_i^2 g_2^{\hat{I}}\cot\theta_i\cos^{-1}\frac{\theta_i}{2}+6\cot\frac{\theta_i}{2}\sum_{m=3}^{5}t_i^m g_m^{\hat{I}})+g_6^{\hat{I}}s_i\lambda_i^{\vartheta}\sqrt{rr_i}\cot\theta_i\cos\frac{\theta_i}{2})]\\ &+2\pi A_i^{\Upsilon}\mathfrak{t}_{33}[\sqrt{rr_i}\cos\frac{\theta_i}{2}(g_2^{\hat{I}}\cot\theta_i+\sum_{m=3}^{5}t_i^m g_m^{\hat{I}})+\frac{s_i^2\lambda_{33}\lambda_i^{\vartheta}g_6^{\hat{I}}}{\sqrt{rr_i}}\cos\frac{\theta_i}{2}],n=3-5\end{aligned} \tag{21}$$

$$\begin{aligned}\vartheta_3^{\hat{I}} = \sum_{i=1}^{5}\frac{A_i^{\Upsilon}\pi}{\sqrt{rr_i}}&[\cos\frac{\theta_i}{2}(\lambda_{32}+4\lambda_{33}s_i^2)\sum_{m=2}^{5}t_i^m g_m^{\hat{I}}+\frac{4\lambda_{32}t_i^2 g_2^{\hat{I}}s_i^2\lambda_i^{\vartheta}}{3}(2\lambda_{32}\cos\frac{\theta_i}{2}+\frac{3\lambda_{33}}{r^2r_i^2}\sin^{-1}\frac{\theta_i}{2})\\ &15rr_i g_6^{\hat{I}}\lambda_{32}s_i^2\lambda_i^{\vartheta}\cot\theta_i(3\cos\frac{\theta_i}{4}-6\cos\frac{\theta_i}{2}\sin^2\frac{\theta_i}{2}-\frac{1}{4}\sin^2\theta_i\cos\frac{3\theta_i}{2})(2s_i^2\lambda_{33}+\frac{\lambda_{32}}{rr_i\sin\theta_i})]\end{aligned} \tag{22}$$

The extended singular stresses, $\dot{\sigma}_{3n}^{\hat{I}} = [\ \sigma_{33}^{\hat{I}}\quad D_3^{\hat{I}}\quad B_3^{\hat{I}}\ ]$, can be rewritten as

$$\sigma_{13}^{\hat{I}} = K_3^{\hat{I}}\cos\frac{\theta_0}{2}/\sqrt{2rr_0} \tag{23}$$

$$\hat{\sigma}_{n3}^{\hat{I}} = [\quad \sigma_{23}^{\hat{I}}\quad \sigma_{33}^{\hat{I}}\quad D_3^{\hat{I}}\quad B_3^{\hat{I}}\quad \vartheta_3^{\hat{I}}\quad] = (K_1^{\hat{I}}f_{n1}+K_2^{\hat{I}}f_{n2}+K_4^{\hat{I}}f_{n4}+K_5^{\hat{I}}f_{n5}+K_6^{\hat{I}}f_{n6})/\sqrt{2r}, n=2-6 \tag{24}$$

where the coefficient functions f_{IJ} are listed in [14]. Other extended singular stresses near point q_0 can also be obtained by use of above method. $K_2^{\hat{I}}$ is coupled with $K_3^{\hat{I}}$ and $K_6^{\hat{I}}$, $K_1^{\hat{I}}$ is coupled with $K_4^{\hat{I}}$, $K_5^{\hat{I}}$ and $K_6^{\hat{I}}$. The energy release rate can be obtained and expressed as followings,

$$\frac{dW}{dV} = 2\sqrt{2r}S = \frac{K_n^2}{2\sqrt{2r}}\left(\frac{a_{3n}^2}{E}+\frac{a_{1n}^2+a_{2n}^2}{\tilde{\mu}}+\frac{a_{4n}^2+a_{5n}^2+a_{6n}^2}{E'}\right) \tag{13}$$

$$W = U_s + U_k + U_f \tag{14}$$

5. Numerical simulation and discussion

A tight sandstone core samples from the Ordos Basin Triassic formation of China which include multi pore-network cracks is selected, the rock depth, the diameter, the length, the density, the confining pressure, the pore stress and the temperature are defined as 862.76~864.36m, 25.4mm, 25~30mm, 2.359~2.426g/cm3, 0~200MPa, 0~10MPa, 35~45 °C respectively, the more detail parameters of the tight sandstone core sample are shown in Tab.1.

Tab.1. Mineral composition, porosity and matrix density of the tight sandstone samples

Sample Number	Direction	Mineral composition(volume percent)					Porosity (%)	Density (g/cm^3)
		Quarzt	Feldspar	Rock debris	Mica	Heavy placer mineral		

	X1	24.34	63.05	8.17	3.73	0.71	8.216	2.368
S1	Y1	23.05	63.16	9.98	3.63	0.18	6.744	2.359
	Z1	28.66	61.36	7.95	0.16	1.87	6.992	2.379
	X2	33.33	57.43	9.24	-	-	6.252	2.426
S2	Y2	27.93	61.39	10.68	-	-	6.822	2.384
	Z2	23.42	56.32	12.08	8.18	-	7.649	2.379
	X3	34.05	57.93	7.83	-	0.19	7.017	2.374
S3	Y3	29.14	58.48	11.43	-	0.95	7.333	2.379
	Z3	26.36	58.53	13.56	-	1.55	6.918	2.382

5.1 Hydrofacturing-liquefaction process varying with the frequency of earthquake wave

The pore-network cracks transient hydrofacturing-liquefaction as function of the frequency of the earthquake wave is shown in Fig. 3. At the fixed amplitude and constituting time, the dynamic fluid stress act on the tight sandstone as electromagnetic wave and stress wave, at the range of 10Hz～100Hz, the surface of pore-network cracks do not appear liquefaction phenomena, even the surface of pore-net-work cracks began propagation and hydrofacturing phenomena appears; with the frequency increasing, when it reach to 200Hz～300Hz, the hydrofacturing phenomena is domain and some pore-network cracks zone of the tight sandstone appear hydrofacturing-liquefaction phenomena, and the constituting time and amplitude decreasing with the frequency increased, the constituting time is around 10E-5s and no draining phenomena appears during hydrofacturing-liquefaction process..

When the frequency is lower than 10Hz, the dynamic fluid stress act on the tight sandstone as quasi-static pore hydrostatic stress, and accompanying draining phenomena in the hydrofacturing failure progress; the maximum tight sandstone fracturing-liquefaction stress is the criteria which leading the hydrofacturing failure.

In general, the low frequency part of the earthquake wave act on the tight sandstone as static/quasi-static style, when the maximum principle stress is reach to the tight sandstone strength criteria, the pore-network cracks begin propagation and accompanying with draining process, no liquefaction appearing for do not reach the maximum micro tight sandstone structure strength limit; the dynamic stress released sharply with the distance between the surface of cracks, we defined it as crack surface frequency earthquake wave or near-field (around the crack surface) frequency earthquake wave.

The high frequency part of the earthquake wave act on the tight sandstone as transient electromagnetic wave and stress wave, the constituting time is very short and no draining accompanied in the whole process; the high frequency energy reach the maximum micro tight sandstone structure strength limit and destroy the tight micro pore-network structure in 10E-5s (Non-connected pore throat destruction); when the frequency is exceed to 400Hz, the electromagnetic wave can leading pore stress oscillation sharply and make the transient liquefaction appear in the whole tight sandstone zone, without draining and hydrofacturing process.

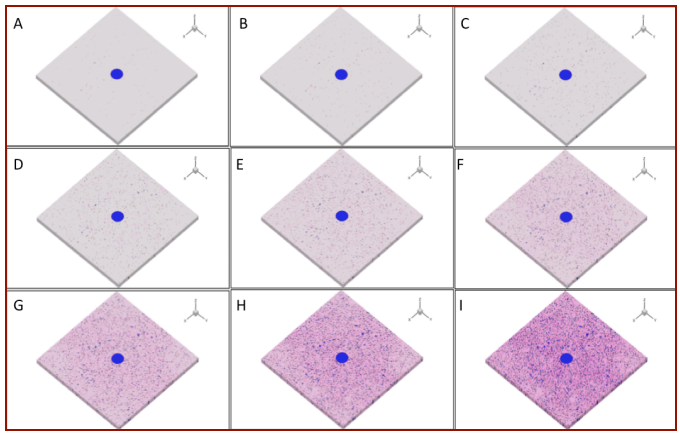

Fig 3. The transient hydrofracturing-liquefaction process as function of frequency of earthquake wave
Fig3A. Frequency is 10Hz, Fig3B. Frequency is 50Hz, Fig3C. Frequency is 100Hz
Fig3D. Frequency is 200Hz, Fig3E.Frequency is 250Hz, Fig3F. Frequency is 300Hz
Fig3G. Frequency is 400Hz, Fig3H. Frequency is 450Hz, Fig3I. Frequency is 500Hz

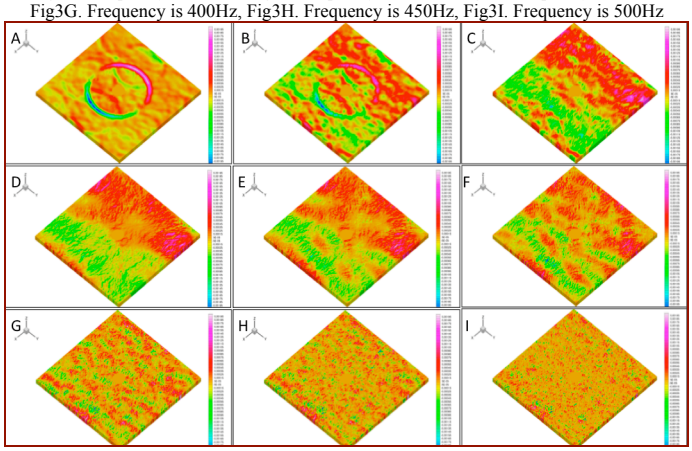

Figure 4. Dynamic stress in x direction as function of frequency at undrained state under earthquake wave
Fig4A. Frequency is 10Hz, Fig4B. Frequency is 50Hz, Fig4C. Frequency is 100Hz
Fig4D. Frequency is 200Hz, Fig4E. Frequency is 250Hz, Fig4F. Frequency is 300Hz
Fig4G. Frequency is 400Hz, Fig4H. Frequency is 450Hz, Fig4I. Frequency is 500Hz

The dynamic stress in x and y direction as function of frequency at undrained state are shown in the Fig.4 and Fig.5, the low frequency dynamic stress destroy the structure closed to the surface of the pore-network cracks, the high frequency dynamic stress destroy the structure far from the pore-network cracks surface. The low frequency earthquake wave have little energy than frequency part, with the distance (far from the front of the crack) increased, their effect to the structure of the tight sandstone decreased sharply; while the high frequency carry major energy of the earthquake wave, their effect distance to the tight sandstone can reach the whole zone. All these results are consisted with the observation data in tight sandstone liquefaction process in nature earthquake[25-28].

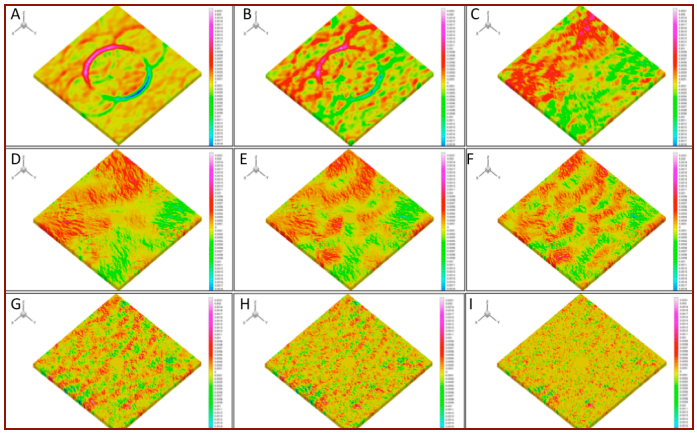

Figure 5. Dynamic stress in y direction as function of frequency at undrained state under earthquake wave

Fig5A. Frequency is 10Hz, Fig5B. Frequency is 50Hz, Fig5C. Frequency is 100Hz
Fig5D. Frequency is 200Hz, Fig5E. Frequency is 250Hz, Fig5F. Frequency is 300Hz
Fig5G. Frequency is 400Hz, Fig5H. Frequency is 450Hz, Fig5I. Frequency is 500Hz

The transient liquefaction process as function of frequency of the earthquake wave are plotted in Fig.6, when the frequency of the earthquake is higher than 1250Hz, the electromagnetic wave energy make the fluid volume in the three-dimensional pore-network cracks changed sharply, let the dynamic stress in the three-dimensional pore-network cracks surface (solid sketch interface) exceed the solid sketch part strength criteria in 10E-5s, the liquefaction in the micro tight sandstone zone appears in 10E-5s and propagates to the whole domain zone of the tight sandstone in 10E-5s, only seldom higher strength components in the tight sandstone can keep macro-structure (the white zone in the Fig 6D).

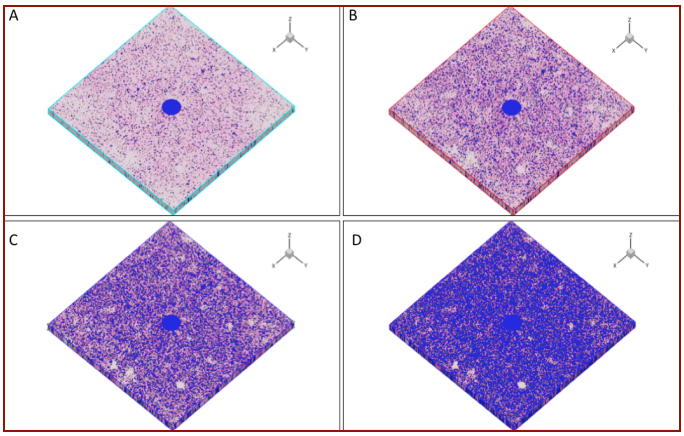

Fig 6. The transient liquefaction process as function of frequency of the earthquake wave
Fig6A. Frequency is 500Hz, Fig6B Frequency is 750Hz, Fig6C. Frequency is 1000Hz, Fig6D Frequency is 1250Hz

5.2 Hydrofacturing-liquefaction process varying with the amplitude of earthquake wave

The pore-network cracks hydrofacturing-liquefaction process as function of the amplitude of the earthquake wave is shown in the Fig. 7, at the fixed constituting time and frequency of the earthquake condition, when the amplitude is arrange at 0.01GPa~0.03GPa, the surface of the pore-network cracks begin propagate, the hydrofracturing around the big pore-network cracks fronts appear, and the liquefaction phenomena do not happen; with the amplitude of the earthquake increased, when it reach to 0.05GPa~0.07GPa, the coupled hydrofacturing-liquefaction begin at most of the pore-network cracks fronts; when the amplitude of the earthquake is exceeded to 0.07GPa~0.1GPa, the pore-network cracks propagate sharply and the hydrofacturing-liquefaction happen in the whole tight sandstone zone, only seldom components micro structure do not failure(white zone in Fig7E, 7F).

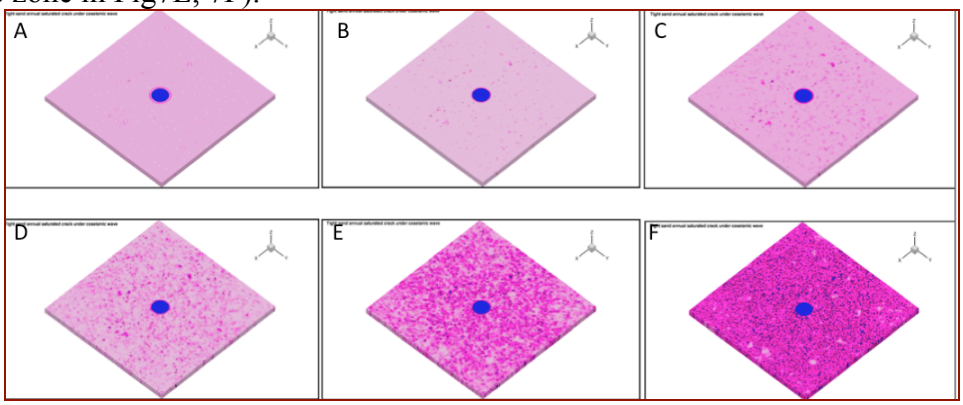

Fig 7. The cracking propagating process variation as the AM of the earthquake wave
Fig7A. AM of earthquake wave is 0.01GPa, Fig7B AM of earthquake wave is 0.03GPa, Fig7C AM of earthquake wave is 0.05GPa
Fig7D. AM of earthquake wave is 0.07GPa, Fig7E AM of earthquake wave is 0.09GPa, Fig7F AM of earthquake wave is 0.1GPa

The distribution of dynamic stress in x and y direction as function of amplitude of the earthquake are shown in the Fig.8 and Fig 9, respectively. When the amplitude arrange at 0.01GPa~0.03GPa, the electromagnetic wave and stress wave propagation far in the tight sandstone, for the whole tight

sandstone structure remains intact, low earthquake energy consumed in the spreading process; When the amplitude of the earthquake reach to 0.05GPa~0.07GPa, with the pore-network cracks propagation, the non-connected pore throats in the tight sandstone are destroyed quickly, most of the earthquake energy are used to providing the surface energy of the pore-network cracks interface, the electromagnetic wave and stress wave propagation distance decrease with the amplitude increasing; When the amplitude of the earthquake is exceeded to 0.07GPa~0.1GPa, the vase majority non-connected pore throats in the tight sandstones are destroyed and the whole tight sandstone structure instability and failure, the propagation media of the electromagnetic wave and stress wave translate from solid (tight porous structure) to fluid (liquefaction sandstone structure), their spreading distance decreased sharply.

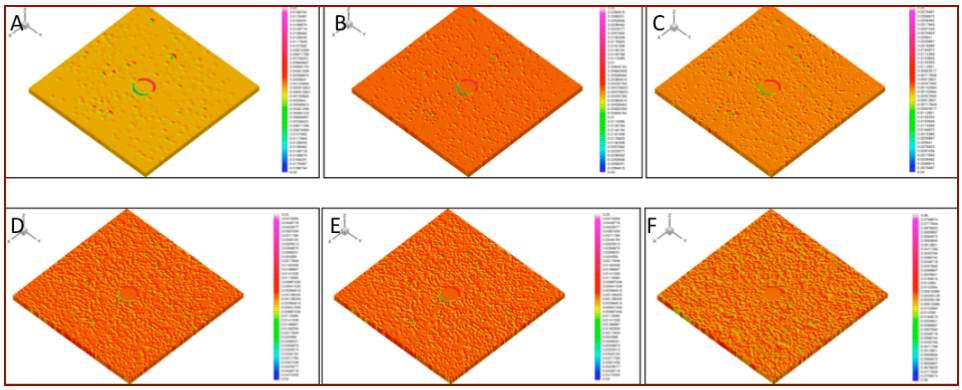

Figure 8. Dynamic stress in x direction variation as function of time at undrained state under earthquake
Fig8A. AM of earthquake wave is 0.01GPa, Fig8B AM of earthquake wave is 0.03GPa, Fig8C AM of earthquake wave is 0.05GPa
Fig8D. AM of earthquake wave is 0.07GPa, Fig8E AM of earthquake wave is 0.09GPa, Fig8F AM of earthquake wave is 0.1GPa

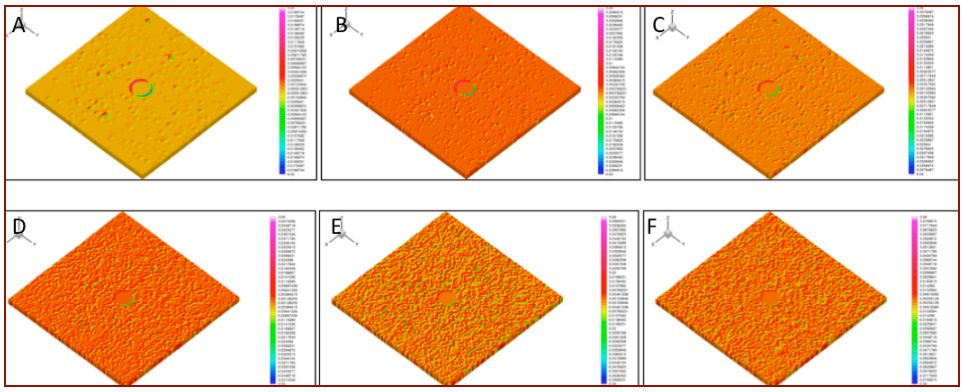

Figure 9. Dynamic stress in y direction variation as function of time at undrained state under earthquake wave
Fig9A. AM of earthquake wave is 0.01GPa, Fig9B AM of earthquake wave is 0.03GPa, Fig9C AM of earthquake wave is 0.05GPa
Fig9D. AM of earthquake wave is 0.07GPa, Fig9E AM of earthquake wave is 0.09GPa, Fig9F AM of earthquake wave is 0.1GPa

In general, both high frequency and amplitude of the earthquake wave are the main factors which lead to the pore-network cracks transient Hydrofracturing-liquefaction process; high frequency of electromagnetic wave and stress wave make the porous and permeability of the tight sandstone changed sharply in 10E-5s which lead the strength criteria of the tight sand stone decrease; high amplitude of the electromagnetic wave and stress wave make the dynamic pore stress in the tight sandstone changed sharply in 10E-5s which lead the maximum principle stress increased to the macro tight sandstone strength criteria; all these leading to pore-network cracks propagation, local area hydrofacturing-liquefaction, and the eventual entire region liquefaction occurred. All these results are consisted with the nature earthquake liquefaction observation data [28, 29].

At practice drilling project, with the hydro-pressure increasing, the pore stress in the tight sandstone is reach to the maximum principal stresses and the sandstone begin failure, this stage is a static/quasi-static process which including the drained propagation; once the tight sandstone begin rupture, this means that the micro pore-network cracks begin propagation, the pore stress will spreading as stress wave way, the stage is transient process and the drained propagation do not happen. The results well consisted with the practical observation data and can well explain why

secondary hydrofacturing stage maximum principal stress reduced.

6. Conclusions

In this work, an novel intricate theoretical analysis and numerical simulations methods (LB-FE-HIE) is proposed by the author to explore the three-dimensional pore-network cracks transient hydrofacturing-liquefaction in tight sandstone under seismic wave & electro-magneto-thermo-elastic field. The conclusion can be drawn as follows.

1. The problem is reduced to solving a set of coupled lattice Boltzmann & finite element & hypersingular integral equations by using the Green functions and distribution functions.

2. The behavior of the extended displacement discontinuities around the pore-network cracks surface terminating at the solid-liquid film interface is analyzed. Analytical solutions for the extended singular dynamic stresses, the extended dynamic stress intensity factors and the extended dynamic energy release rate near the dislocations front are provided.

3.The tight sandstone sample from the Ordos Basin Triassic formation is selected and the fluid-solid coupled digital rock physical modeling is established. The simulations of 3D PC-TH-TS process is presented, the hydrofacturing-liquefaction varying with the amplitude, frequency and time of earthquake wave is obtained, the results are consisted with the nauture earthquake observation data and practical drilling project observation data.

4. The relationship between the tight sandstone pore-network cracks transient propagation-evolution and the maximum tight sandstone fracturing-liquefaction stress criteria is explored, which are useful to guide the in-situ stress measurement in practical drilling project and are helpful to understand the liquefaction mechanismu of earthquake.

Acknowledgements

The work was supported by National Natural Science Foundation of China (NOD0408/4097409), Chairmen Foundation of UCAS [A](D0408/4097409) and Deep exploration in China-Sinoprobe-04 (0819011A90).

References

[1] Fan TY. Propagating Semi-Infinite Crack in Fluid-Saturated Porous-Medium of Finite Height. Theor Appl Fract Mec 1991;16:237.

[2] Kachanov M, Tsukrov I, Shafiro B. Materials with fluid-saturated cracks and cavities: Fluid pressure polarization and effective elastic response. Int J Fracture 1995;73:R61.

[3] Loret B, Radi E. The effects of inertia on crack growth in poroelastic fluid-saturated media. J Mech Phys Solids 2001;49:995.

[4] Cheng CM, Tan QM, Peng FJ. On the mechanism of the formation of horizontal cracks in a vertical column of saturated sand. Acta Mech Sinica 2001;17:1.

[5] Galvin RJ, Gurevich B. Interaction of an elastic wave with a circular crack in a fluid-saturated porous medium. Appl Phys Lett 2006;88.

[6] Lu XB, Zheng ZM, Wu YR. Formation mechanism of cracks in saturated sand. Acta Mech Sinica 2006;22:377.

[7] de Borst R, Rethore J, Abellan MA. A numerical approach for arbitrary cracks in a fluid-saturated medium. Arch Appl Mech 2006;75:595.

[8] Galvin RJ, Gurevich B. Scattering of a longitudinal wave by a circular crack in a fluid-saturated

porous medium. Int J Solids Struct 2007;44:7389.
[9] Barani OR, Khoei AR, Mofid M. Modeling of cohesive crack growth in partially saturated porous media; a study on the permeability of cohesive fracture. Int J Fracture 2011;167:15.
[10] Wang XQ, Schubnel A, Fortin J, David EC, Gueguen Y, Ge HK. High Vp/Vs ratio: Saturated cracks or anisotropy effects? Geophys Res Lett 2012;39.
[11] Sarout J. Impact of pore space topology on permeability, cut-off frequencies and validity of wave propagation theories. Geophys J Int 2012;189:481.
[12] B.J.Zhu, C.Liu, Y.L.Shi, X.Y.Liu. Saturated dislocations transient propagation–evolution in olivine structure under ultra high-coupled thermal-force fields. Theor Appl Fract Mec 2012;58:9.
[13] Zhu BJ, Qin TY. Hypersingular integral equation method for a three-dimensional crack in anisotropic electro-magneto-elastic bimaterials. Theoretical and Applied Fracture Mechanics 2007;47:219.
[14] Bojing Z, Taiyan Q. Application of hypersingular integral equation method to three-dimensional crack in electromagnetothermoelastic multiphase composites. Int J Solids Struct 2007;In Press, Accepted Manuscript.
[15] Aboudi J. Micromechanical analysis of fully coupled electro-magneto-thermo-elastic multiphase composites. Smart Materials & Structures 2001;10:867.
[16] Perez-Aparicio JL, Sosa H. A continuum three-dimensional, fully coupled, dynamic, non-linear finite element formulation for magnetostrictive materials. Smart Materials & Structures 2004;13:493.
[17] H.H.Cheng, Y.C.Qiao, C.Liu, Y.B.Li, B.J.Zhu, Y.L.Shi, D.S.Sun, K.Zhang, W.R.Lin. Extended hybrid pressure and velocity boundary conditions for D3Q27 lattice Boltzmann model. Applied Mathematical Modelling 2012;36:2031.
[18] Ma J, Wu K, Jiang Z, Couples GD. An implementation for lattice Boltzmann simulation in low-porosity porous media. Phys Rev A 2010;E 81, 056702.
[19] Jiang Z, Wu K, Couples G. The Impact of Pore Size and Pore Connectivity on Single-Phase Fluid Flow in Porous Media. Advanced Engineering Materials. 2010;doi: 10.1002/adem.201000255.
[20] Zhu B, Cheng H, Qiao Y, Liu C, Shi Y, Zhang K, Sun D, Lin W. Porosity and permeability evolution and evaluation in anisotropic porosity multiscale-multiphase-multicomponent structure. Chinese Sci Bull 2012;57:320~327.
[21] Dmitriev NM. Surface porosity and permeability of porous media with a periodic microstructure. fluid Dynamics 1995;30:64~69.
[22] C.Y K, J.D F, J.L.A C. Image analysis determination of stereology based fabric tensors. Geotechnique 1998 48:515~525.
[23] Koo J, Kleinstreuer C. Liquid flow in microchannels: experimental observations and computational analyses of microfluidics effects. JOURNAL OF MICROMECHANICS AND MICROENGINEERING 2003:568~579.
[24] Qin TY, Tang RJ. Finite-Part Integral and Boundary-Element Method to Solve Embedded Planar Crack Problems. Int J Fracture 1993;60:373.
[25] Wang CY. Liquefaction beyond the near field. Seism. Res. Lett. 2007;78:512.
[26] Popescu R. Finite element assessment of the effects of seismic loading rate on soil liquefaction. Canadian Geotech. J 2002;29:331.

[27] Ghosh B, Madabhushi SPG. A numerical investigation into effects of single and multiple frequency earthquake motions. Soil Dynamics and Earthquake Engineering 2003;23:691－704.
[28] Kilb.D., J.Gomberg, P.Bodin. Aftershock triggerinig by complete Coulomb stress changes. J.Geophys.Re 2002;107:doi:10.1029/2001JB000202.
[29] Ishihara K. Soil Behavior in Earthquake Geotechnics,. Oxford: Clarendon Press. 1996:350.

Interaction between an Annular Crack and the Imperfect Interface in Magnetoelectroelastic Layers

Yansong Li*, Longjiang Bian, Jun Li

College of Civil Engineering, Hebei University of Engineering, Handan 056038, China
*Corresponding author: liyshbue@163.com

Abstract The interaction between an annular crack and the interface is of practical significance. The interface, which is imperfect with the assumption that it is mechanically compliant and magnetoelectrically weakly conducting. For a mechanically compliant interface tractions are continuous but displacements are discontinuous across the imperfect interface. For a magnetoelectrically weakly conducting interface the normal electric displacement and magnetic induction are continuous but the electric and magnetic potentials are discontinuous across the interface. Such a problem is investigated by the method of singular integral equation in the present work. The field intensity factors and energy release rate are derived. Numerical results reveal the effects of electric or magnetic loadings, material parameters and interfacial imperfection on crack propagation and growth. The results seem useful for design of the magnetoelectroelastic composite structures and devices of high performance.

Keywords Annular crack, Imperfect interface, Energy release rate, Magnetoelectroelastic materials, Fracture mechanics

1. Introduction

Magnetoelectroelastic materials, which are composed of a piezoelectric and piezomagnetic phase, not only have original piezoelectric and piezomagnetic properties but also exhibit a remarkable magneto-electric coupling effect that is not present in the constituents. Such composites have found increasing applications in several engineering fields such as magnetic field probes, electronic packaging, hydrophones, medical ultrasonic imaging and in general as transducers, sensors and actuators. Micromechanics modeling to predict and estimate the material properties of piezoelectric/piezomagnetic composites was presented [1-3].

These magnetoelectroelastic materials are generally brittle; therefore cracks inevitably form during the manufacturing process and subsequent handling. For that reason, it is of great importance to study the fracture behavior of such composites and its influence on the coupled response. Recently, research on fracture mechanics of magnetoelectroelastic materials has drawn increased interest. Most of the achievements are made on the anti-plane and in-plane crack problem [4-8]. For the axisymmetric crack in magnetoelectroelastic materials, some progress has also been made. Studies related to penny-shaped or annular cracks can be found in the literature [9-11].

When two dissimilar materials bonded together, it is difficult to guarantee them to be perfectly bonded. Some interfacial models, i.e. spring-like model, are presented. Meguid and Wang [12] dealt with the interaction of crack and imperfect interface when dynamic antiplane shear waves are applied. a crack situated at the imperfect interface has been considered by Lenci [13], who found only the logarithmic stress singularity near the crack tips. Instead of the usual traction-free crack surface condition, Udea et al. [14] applied the spring-like imperfect interface condition to reconsider the corresponding antiplane shear problem, and found that the stress singularity at the crack tips is no longer an inverse square-root singularity, but a singularity of power law governed by the interface parameters. Zhong et al. [15] investigated the elastostatic problem of a mode-I crack embedded in a bimaterial with an imperfect interface.

This paper aims at analyzing the interaction of an annular crack and an imperfect interface. The interface, which is imperfect with the assumption that it is mechanically compliant and magnetoelectrically weakly conducting. For a mechanically compliant interface tractions are continuous but displacements are discontinuous across the imperfect interface. For a magnetoelectrically weakly conducting interface the normal electric displacement and magnetic induction are continuous but the electric and magnetic potentials are discontinuous across the interface. Using the Hankel transform technique, the associated mixed-boundary value problem is reduced to a singular integral equation. Numerical results are presented. The influences of interfacial imperfection on energy release rates near the crack tips are analyzed in detail.

2. Formulation of the problem

As shown in Fig. 1, two dissimilar magnetoelectroelastic materials bonded with an imperfect interface. For convenience, they are marked with material I and material II, which occupy the region $-h_2 < z < h_1$ and region $h_1 < z < h_1 + h_3$ respectively. An annular crack with the outer radius *b* and inner radius *a* perpendicular to the poling axis is situated in the magnetoelectroelastic material I and occupies the region $a \le r \le b$, $z = 0$. And the crack width *c* is introduced with $c = b - a$.

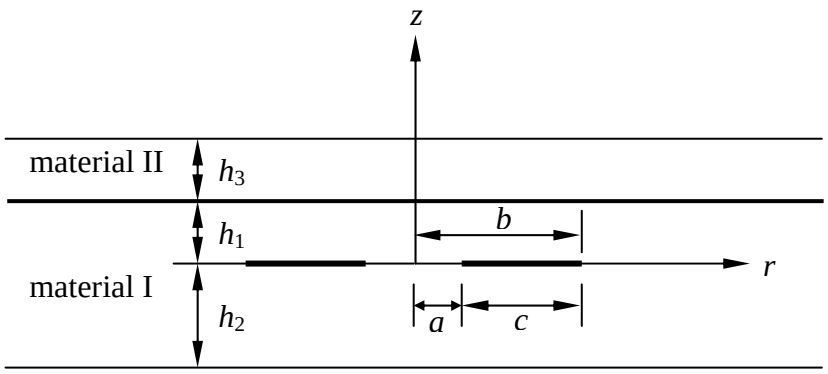

Figure 1. Configuration of the annular and imperfect interface in bonded magnetoelectroelastic layers

The boundary conditions for the magnetoelectrically impermeable annular crack and mechanically compliant and magnetoelectrically weakly conducting interface conditions are set as

$$\sigma_{rzI}^{(1)}(r,0) = \sigma_{rzI}^{(2)}(r,0) = p_1(r),\ \sigma_{zzI}^{(1)}(r,0) = \sigma_{zzI}^{(2)}(r,0) = p_2(r),\ (a < r < b) \tag{1}$$

$$D_{zI}^{(1)}(r,0) = D_{zI}^{(2)}(r,0) = p_3(r),\ B_{zI}^{(1)}(r,0) = B_{zI}^{(2)}(r,0) = p_4(r),\ (a < r < b) \tag{2}$$

$$u_{rI}^{(1)}(r,0) = u_{rI}^{(2)}(r,0),\ u_{zI}^{(1)}(r,0) = u_{zI}^{(2)}(r,0),\ (0 \le r \le a, b \le r < \infty) \tag{3}$$

$$\phi_I^{(1)}(r,0) = \phi_I^{(2)}(r,0),\ \psi_I^{(1)}(r,0) = \psi_I^{(2)}(r,0),\ (0 \le r \le a, b \le r < \infty) \tag{4}$$

$$\sigma_{rzI}^{(1)}(r,0) = \sigma_{rzI}^{(2)}(r,0),\ \sigma_{zzI}^{(1)}(r,0) = \sigma_{zzI}^{(2)}(r,0),\ (0 \le r \le a, b \le r < \infty) \tag{5}$$

$$D_{zI}^{(1)}(r,0) = D_{zI}^{(2)}(r,0), B_{zI}^{(1)}(r,0) = B_{zI}^{(2)}(r,0), (0 \le r \le a, b \le r < \infty) \tag{6}$$

$$\sigma_{rzI}^{(2)}(r,-h_2) = 0,\ \sigma_{zzI}^{(2)}(r,-h_2) = 0,\ D_{zI}^{(2)}(r,-h_2) = 0, B_{zI}^{(2)}(r,-h_2) = 0\ (0 \le r < \infty) \tag{7}$$

$$\sigma_{rzI}^{(1)}(r,h_1) = \sigma_{rzII}(r,h_1),\ \sigma_{zzI}^{(1)}(r,h_1) = \sigma_{zzII}(r,h_1), \tag{8}$$

$$D_{zI}^{(1)}(r,h_1) = D_{zII}(r,h_1),\ B_{zI}^{(1)}(r,h_1) = B_{zII}(r,h_1),\ (0 \le r < \infty) \tag{9}$$

$$u_{rI}^{(1)}(r,h_1) - u_{rII}(r,h_1) = \beta_1 \sigma_{rzII}(r,h_1),\ u_{zI}^{(1)}(r,h_1) - u_{zII}(r,h_1) = \beta_2 \sigma_{zzII}(r,h_1), \tag{10}$$

$$\phi_{rI}^{(1)}\left(r,h_1\right)-\phi_{rII}\left(r,h_1\right)=\beta_3 D_{zII}\left(r,h_1\right),\ \psi_{rI}^{(1)}\left(r,h_1\right)-\psi_{rII}\left(r,h_1\right)=\beta_4 B_{zII}\left(r,h_1\right),\ \left(0\le r<\infty\right) \tag{11}$$

$$\sigma_{rzII}\left(r,h_1+h_3\right)=0,\ \sigma_{zzII}\left(r,h_1+h_3\right)=0,\ D_{zII}\left(r,h_1+h_3\right)=0,B_{zII}\left(r,h_1+h_3\right)=0\ \left(0\le r<\infty\right) \tag{12}$$

where the superscripts (1) and (2) denote the upper and lower of the magnetoelectroelastic material I, respectively; $p_1(r)$, $p_2(r)$, $p_3(r)$ and $p_4(r)$ are the given amplitude of the applied loadings. β_1, β_2, β_3 and β_4 are interface parameters, respectively.

For the axisymmtric problem, the government equations of magnetoelectroelastic material are

$$c_{11}\left(\frac{\partial^2 u_r}{\partial r^2}+\frac{1}{r}\frac{\partial u_r}{\partial r}-\frac{1}{r^2}\right)+c_{44}\frac{\partial^2 u_r}{\partial z^2}+\left(c_{13}+c_{44}\right)\frac{\partial^2 u_z}{\partial r\partial z}+\left(e_{31}+e_{15}\right)\frac{\partial^2 \phi}{\partial r\partial z}+\left(f_{31}+f_{15}\right)\frac{\partial^2 \psi}{\partial r\partial z}=0, \tag{13}$$

$$\begin{aligned}&\left(c_{13}+c_{44}\right)\left(\frac{\partial^2 u_r}{\partial r\partial z}+\frac{1}{r}\frac{\partial u_r}{\partial z}\right)+c_{44}\left(\frac{\partial^2 u_z}{\partial r^2}+\frac{1}{r}\frac{\partial u_z}{\partial r}\right)+c_{33}\frac{\partial^2 u_z}{\partial z^2}\\&+e_{15}\left(\frac{\partial^2 \phi}{\partial r^2}+\frac{1}{r}\frac{\partial \phi}{\partial r}\right)+e_{33}\frac{\partial^2 \phi}{\partial z^2}+f_{15}\left(\frac{\partial^2 \psi}{\partial r^2}+\frac{1}{r}\frac{\partial \psi}{\partial r}\right)+f_{33}\frac{\partial^2 \psi}{\partial z^2}=0,\end{aligned} \tag{14}$$

$$\begin{aligned}&\left(e_{15}+e_{31}\right)\left(\frac{\partial^2 u_r}{\partial r\partial z}+\frac{1}{r}\frac{\partial u_r}{\partial z}\right)+e_{15}\left(\frac{\partial^2 u_z}{\partial r^2}+\frac{1}{r}\frac{\partial u_z}{\partial r}\right)+e_{33}\frac{\partial^2 u_z}{\partial z^2}\\&-\varepsilon_{11}\left(\frac{\partial^2 \phi}{\partial r^2}+\frac{1}{r}\frac{\partial \phi}{\partial r}\right)-\varepsilon_{33}\frac{\partial^2 \phi}{\partial z^2}-g_{11}\left(\frac{\partial^2 \psi}{\partial r^2}+\frac{1}{r}\frac{\partial \psi}{\partial r}\right)-g_{33}\frac{\partial^2 \psi}{\partial z^2}=0,\end{aligned} \tag{15}$$

$$\begin{aligned}&\left(f_{15}+f_{31}\right)\left(\frac{\partial^2 u_r}{\partial r\partial z}+\frac{1}{r}\frac{\partial u_r}{\partial z}\right)+f_{15}\left(\frac{\partial^2 u_z}{\partial r^2}+\frac{1}{r}\frac{\partial u_z}{\partial r}\right)+f_{33}\frac{\partial^2 u_z}{\partial z^2}\\&-g_{11}\left(\frac{\partial^2 \phi}{\partial r^2}+\frac{1}{r}\frac{\partial \phi}{\partial r}\right)-g_{33}\frac{\partial^2 \phi}{\partial z^2}-\mu_{11}\left(\frac{\partial^2 \psi}{\partial r^2}+\frac{1}{r}\frac{\partial \psi}{\partial r}\right)-\mu_{33}\frac{\partial^2 \psi}{\partial z^2}=0,\end{aligned} \tag{16}$$

The generally solutions of the equations above mentioned are

$$u_r\left(r,z\right)=\sum_{j=1}^{8}\int_0^\infty a_{1j}\exp\left(\rho\lambda_j z\right)A_j\left(\rho\right)J_1\left(\rho r\right)d\rho, \tag{17}$$

$$u_z\left(r,z\right)=\sum_{j=1}^{8}\int_0^\infty a_{2j}\exp\left(\rho\lambda_j z\right)A_j\left(\rho\right)J_0\left(\rho r\right)d\rho, \tag{18}$$

$$\phi\left(r,z\right)=\sum_{j=1}^{8}\int_0^\infty a_{3j}\exp\left(\rho\lambda_j z\right)A_j\left(\rho\right)J_0\left(\rho r\right)d\rho, \tag{19}$$

$$\psi\left(r,z\right)=\sum_{j=1}^{8}\int_0^\infty a_{4j}\exp\left(\rho\lambda_j z\right)A_j\left(\rho\right)J_0\left(\rho r\right)d\rho, \tag{20}$$

where $A_j\left(\rho\right)\left(j=1,2,\mathrm{L}\ ,8\right)$ are unknown functions to be determined and $J_i\left(i=0,1\right)$ are i th order Bessel functions of the first kind. The constants $\left\{a_{1j},a_{2j},a_{3j}\right\}$ and parameters λ_j are constant related to material parameters.

3. The derivation of the integral equations

A set of new unknown functions are now introduced

$$d_1\left(r\right)=\frac{1}{r}\frac{\partial}{\partial r}\left\{ru_{rI}^{(1)}\left(r,0\right)-ru_{rI}^{(2)}\left(r,0\right)\right\}, \tag{21}$$

$$d_2(r)=\frac{\partial}{\partial r}\left\{u_{zI}^{(1)}(r,0)-u_{zI}^{(2)}(r,0)\right\}, \tag{22}$$

$$d_3(r)=\frac{\partial}{\partial r}\left\{\phi_I^{(1)}(r,0)-\phi_I^{(2)}(r,0)\right\}, \tag{23}$$

$$d_4(r)=\frac{\partial}{\partial r}\left\{\psi_I^{(1)}(r,0)-\psi_I^{(2)}(r,0)\right\}. \tag{24}$$

In the annular crack shown in Fig. 1, physical considerations require that

$$\left[u_r^{(1)}(r,0)-u_r^{(2)}(r,0)\right]\to 0\text{, for } r\to a,b\text{,} \tag{25}$$

$$\left[u_z^{(1)}(r,0)-u_z^{(2)}(r,0)\right]\to 0\text{, for } r\to a,b\text{,} \tag{26}$$

$$\left[\phi_I^{(1)}(r,0)-\phi_I^{(2)}(r,0)\right]\to 0 \text{ for } r\to a,b\text{.} \tag{27}$$

$$\left[\phi_I^{(1)}(r,0)-\phi_I^{(2)}(r,0)\right]\to 0 \text{ for } r\to a,b\text{.} \tag{28}$$

Therefore, the unknown function defined by Eq. (10) must satisfy the following conditions

$$\int_a^b r d_1(r)\,dr=0, \tag{29}$$

$$\int_a^b d_2(r)\,dr=0, \tag{30}$$

$$\int_a^b d_3(r)\,dr=0, \tag{31}$$

$$\int_a^b d_4(r)\,dr=0. \tag{32}$$

Substitute Eqs. (17)-(20) into boundary conditions Eqs. (1)-(12) and using Eqs. (21)-(24), one obtains

$$\frac{1}{\pi}\mathbf{M}\int_a^b\frac{1}{s-r}\mathbf{F}(s)\,ds+\frac{1}{\pi}\int_a^b\mathbf{Q}\mathbf{F}(s)\,ds=\mathbf{\Gamma}(r), \tag{33}$$

where

$$\mathbf{M}=\begin{bmatrix} M_{11} & 0 & 0 & 0\\ 0 & M_{22} & M_{23} & M_{24}\\ 0 & M_{32} & M_{33} & M_{34}\\ 0 & M_{42} & M_{43} & M_{44}\end{bmatrix}, \tag{34}$$

$$\mathbf{Q}=\boldsymbol{\kappa}\mathbf{M}+\pi\int_0^\infty\rho s\mathbf{J}_{10}(\rho r)\left[\mathbf{K}(\rho)-\mathbf{M}\right]\mathbf{J}_{01}(\rho s)\,d\rho, \tag{35}$$

$$M_{ij}=\lim_{\rho\to\infty}K_{ij}(\rho), \tag{36}$$

with $K_{ij}(\rho)$ can be found in Appendix A. And

$$\boldsymbol{\kappa}=diag\left[\kappa_{11}(r,s),\kappa_{22}(r,s),\kappa_{22}(r,s),\kappa_{22}(r,s)\right], \tag{37}$$

$$\kappa_{11}(r,s)=\left[\frac{2rM_1(r,s)}{s^2-r^2}-\frac{1}{s-r}\right], \tag{38}$$

$$\kappa_{22}(r,s)=\left[\frac{2sM_2(r,s)}{s^2-r^2}-\frac{1}{s-r}\right], \tag{39}$$

and

$$M_1(r,s)=\begin{cases}\dfrac{s}{r}E(s/r), & s<r,\\ \dfrac{s^2}{r^2}E(r/s)-\dfrac{s^2-r^2}{r^2}K(r/s), & s>r,\end{cases} \tag{40}$$

$$M_2(r,s)=\begin{cases}\dfrac{r}{s}E(s/r)+\dfrac{s^2-r^2}{rs}K(s/r), & s<r,\\ E(r/s), & s>r.\end{cases} \tag{41}$$

Introducing two non-dimensional variables η and ξ

$$s=(b-a)\eta/2+(b+a)/2, \tag{42}$$

$$r=(b-a)\xi/2+(b+a)/2. \tag{43}$$

Eq. (33) becomes

$$\frac{\mathbf{M}}{\pi}\int_{-1}^{1}\frac{\mathbf{G}(\eta)}{\eta-\xi}d\eta+\frac{1}{\pi}\int_{-1}^{1}\bar{\mathbf{Q}}(\xi,\eta)\mathbf{G}(\eta)d\eta=\mathbf{L}(\xi), \tag{44}$$

where

$$\mathbf{G}(\eta)=\mathbf{F}\left(\frac{b-a}{2}\eta+\frac{b+a}{2}\right), \tag{45}$$

$$\bar{\mathbf{Q}}(\eta,\xi)=\frac{b-a}{2}\mathbf{Q}\left(\frac{b-a}{2}\eta+\frac{b+a}{2},\frac{b-a}{2}\xi+\frac{b+a}{2}\right), \tag{46}$$

$$\mathbf{L}(\xi)=\Gamma\left(\frac{b-a}{2}\xi+\frac{b+a}{2}\right). \tag{47}$$

4. The solution of integral equations

So far, the Cauchy singular integral Eq. (44) and the single-valued conditions Eqs. (29)-(32) have been derived. By using the numerical method of Erdogan and Gupta [16], a system of linear algebraic equations can be obtained

$$\frac{1}{n}\sum_{l=1}^{n}\left(\frac{\mathbf{M}}{\eta_l-\xi_m}+\bar{\mathbf{Q}}(\eta_l,\xi_m)\right)\mathbf{R}(\eta_l)=\mathbf{L}(\xi_m), \tag{48}$$

$$\frac{1}{n}\sum_{l=1}^{n}diag\left(\left(\frac{b-a}{2}\right)\eta_l+\frac{b+a}{2},1,1,1\right)\mathbf{R}(\eta_l)=0, \tag{49}$$

where $\mathbf{R}(\eta)=\sqrt{1-\eta^2}\mathbf{G}(\eta)$, and n is the number of the discrete points of $\mathbf{R}(\eta_l)$ between -1 and +1. The discrete values of ξ_m and η_l are the roots of the Chebyshev polynomials of the first and second kind, respectively:

$$\xi_m=\cos(m\pi/n),\quad m=1,2,\mathrm{L}\ n-1, \tag{50}$$

$$\eta_l=\cos\left[(2l-1)\pi/2n\right],\quad l=1,2,\mathrm{L}\ n. \tag{51}$$

One may solve Eqs. (48) and (49) numerically to get the solutions of $\mathbf{R}(\eta_l)$, which can be further used to determine the stress intensity factor (SIF).

5. Field intensity factors and energy release rates

The field intensity factors (FIFs) including mode-I and mode-II stress intensity factors (SIFs) and electric displacement intensity factor (EDIF), which characterize magnitudes of stress, electric displacement respectively, of the outer and inner crack tips can be deduced

$$\mathbf{K}_b = \left\{ K_{\mathrm{II}b} \quad K_{\mathrm{I}b} \quad K_{\mathrm{D}b} \quad K_{\mathrm{B}b} \right\}^T = -\sqrt{\pi\left(b-a\right)/2}\mathbf{M}\mathbf{R}\left(1\right) \tag{52}$$

and

$$\mathbf{K}_a = \left\{ K_{\mathrm{II}a} \quad K_{\mathrm{I}a} \quad K_{\mathrm{D}a} \quad K_{\mathrm{B}a} \right\}^T = \sqrt{\pi\left(b-a\right)/2}\mathbf{M}\mathbf{R}\left(-1\right) \tag{53}$$

The energy release rates (ERRs) of the outer and inner crack tips can be derived as

$$G_\upsilon = \frac{1}{4}\mathbf{K}_\upsilon^{\mathrm{T}}\mathbf{M}^{-1}\mathbf{K}_\upsilon, \quad \left(\upsilon = b, a\right) \tag{54}$$

6. Numerical results

For the numerical examples, magnetoelectroelastic composite $BaTiO_3$-$CoFe_2O_4$ are used as materials I and II. For simplicity, only the loading case of $\Gamma\left(r\right) = \left\{0 \quad -\sigma_0 \quad -D_0 \quad -B_0\right\}^{\mathrm{T}}$ is considered. Also, D_0 and B_0 are determined by the load combination parameters $\lambda_D = D_0 c_{33}/\left(\sigma_0 e_{33}\right)$ and $\lambda_B = D_0 c_{33}/\left(\sigma_0 f_{33}\right)$. The numerical results are plotted in Figs. 2-5, where ERRs, G_b and G_a, are normalized by G_0, which can be expressed as

$$G_0 = \frac{\pi}{8}\Lambda_{22}\sigma_0^2 c, \tag{55}$$

where Λ_{22} is the element of matrix $\mathbf{\Lambda}$, and

$$\mathbf{\Lambda} = \mathbf{M}^{-1}. \tag{56}$$

Figs. 2 and 3 show the effects of β_1 and β_2 on the normalized ERRs of the outer and inner crack-tips. From Fig. 2, it is clear that the normalized ERRs increase with increasing β_1. Similar phenomena can be observe in Fig. 3. This means that increasing β_1 and β_2 will promote the crack propagation or growth.

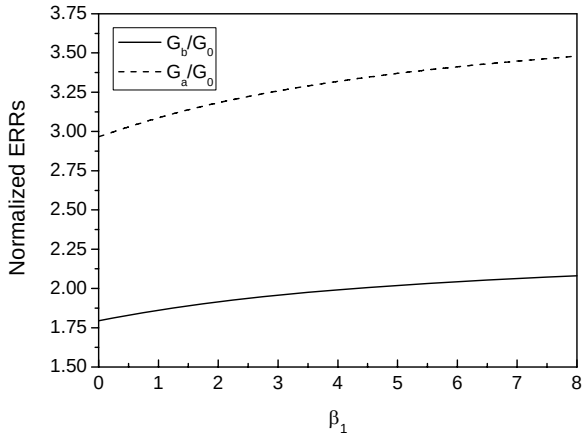

Figure 2. The effect of β_1 on the normalized ERRs of the outer and inner crack tips of an annular crack

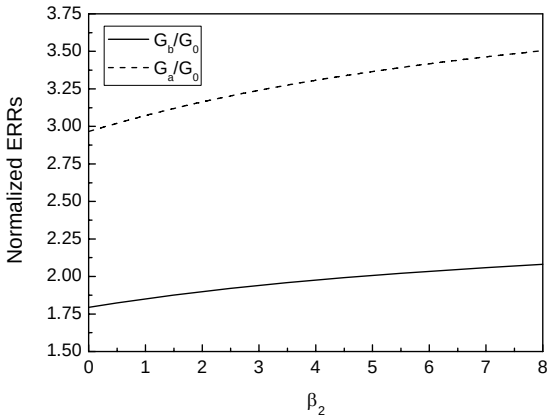

Figure 3. The effect of β_2 on the normalized ERRs of the outer and inner crack tips of an annular crack

The effects of β_3 and β_4 on the normalized ERRs are plotted in Figs. 4 and 5. From these figures, one knows that the normalized ERRs are almost independence of β_3 and β_4.

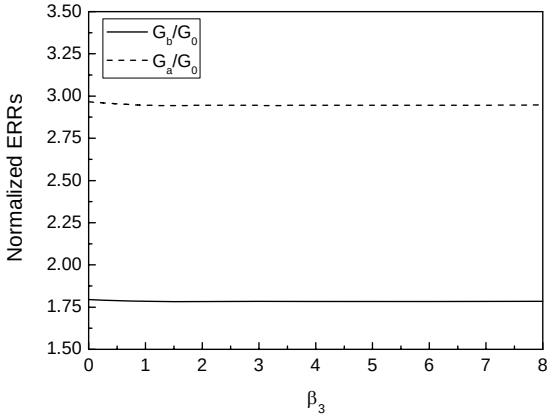

Figure 4. The effect of β_3 on the normalized ERRs of the outer and inner crack tips of an annular crack

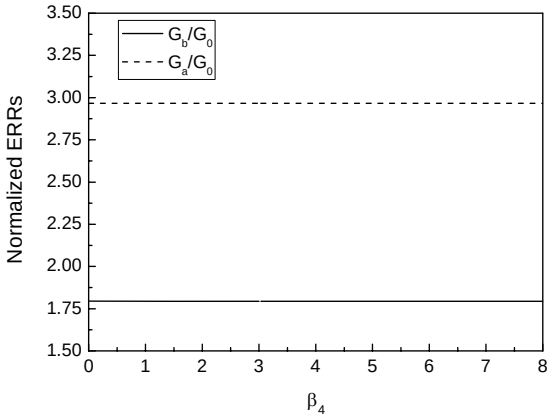

Figure 5. The effect of β_4 on the normalized ERRs of the outer and inner crack tips of an annular crack

From Figs. 2-5, one can also know that the fracture parameters ERR of the inner crack tip of the annular crack are always larger than those of the outer one.

7. Conclusions

In this paper, the interaction of an annular crack and an imperfect interface in bonded magnetoelectroelastic layers is investigated. The interface, which is imperfect with the assumption that it is mechanically compliant and magnetoelectrically weakly conducting. Using the Hankel transform technique, the associated mixed-boundary value problem is reduced to a singular integral equation, which are further reduced to a system of algebraic equations. Finally, the field intensity factor and energy release rate are determined and numerically solved. The following conclusions may be drawn:

(i) Different interfacial parameters have different influences on the propagation and growth of the annular crack. Increasing β_1 and β_2 can promote the crack propagation or growth. However, the effects of β_3 and β_4 on energy release rates are very small.

(ii) The energy release rates of the inner crack tip of the annular crack are always larger than those of the outer one.

Appendix A

The matrix $\mathbf{K}(\rho)$ can be expressed as

$$\mathbf{K}(\rho)=\frac{1}{\rho}\begin{bmatrix} \sum_{j=1}^{8}\frac{H_{17j}\Delta_{21j}(\rho)}{\Delta(\rho)} & -\sum_{j=1}^{8}\frac{H_{17j}\Delta_{22j}(\rho)}{\Delta(\rho)} & -\sum_{j=1}^{8}\frac{H_{17j}\Delta_{23j}(\rho)}{\Delta(\rho)} & -\sum_{j=1}^{8}\frac{H_{17j}\Delta_{24j}(\rho)}{\Delta(\rho)} \\ \sum_{j=1}^{8}\frac{H_{18j}\Delta_{21j}(\rho)}{\Delta(\rho)} & -\sum_{j=1}^{8}\frac{H_{18j}\Delta_{22j}(\rho)}{\Delta(\rho)} & -\sum_{j=1}^{8}\frac{H_{18j}\Delta_{23j}(\rho)}{\Delta(\rho)} & -\sum_{j=1}^{8}\frac{H_{18j}\Delta_{24j}(\rho)}{\Delta(\rho)} \\ \sum_{j=1}^{8}\frac{H_{19j}\Delta_{21j}(\rho)}{\Delta(\rho)} & \sum_{j=1}^{8}\frac{H_{19j}\Delta_{22j}(\rho)}{\Delta(\rho)} & \sum_{j=1}^{8}\frac{H_{19j}\Delta_{23j}(\rho)}{\Delta(\rho)} & \sum_{j=1}^{8}\frac{H_{19j}\Delta_{24j}(\rho)}{\Delta(\rho)} \\ \sum_{j=1}^{8}\frac{H_{20j}\Delta_{21j}(\rho)}{\Delta(\rho)} & \sum_{j=1}^{8}\frac{H_{20j}\Delta_{22j}(\rho)}{\Delta(\rho)} & \sum_{j=1}^{8}\frac{H_{20j}\Delta_{23j}(\rho)}{\Delta(\rho)} & \sum_{j=1}^{8}\frac{H_{20j}\Delta_{24j}(\rho)}{\Delta(\rho)} \end{bmatrix},$$

where $\Delta(\rho)$ is the determinant of the coefficient matrix $\mathbf{H}$, whose elements can be expressed as H_{ij} with i th row and j th column; $\Delta_{kj}(\rho)(k=21,22,23,24)$ are, respectively, the corresponding algebra cofactors. The components of $\mathbf{H}$ are given by

$$H_{1j}=\left(c_{44II}\lambda_{jII}a_{1jII}-c_{44II}a_{2jII}-e_{15II}a_{3jII}-f_{15II}a_{4jII}\right)\exp\left(\rho\lambda_{jII}\left(h_1+h_3\right)\right),H_{1(j+8)}=0,H_{1(j+16)}=0,$$

$$H_{2j}=\left(c_{13II}a_{1jII}+c_{33II}\lambda_{jII}a_{2jII}+e_{33II}\lambda_{jII}a_{3jII}+f_{33II}\lambda_{jII}a_{4jII}\right)\exp\left(\rho\lambda_{jII}\left(h_1+h_3\right)\right),H_{2(j+8)}=0,H_{2(j+16)}=0,$$

$$H_{3j}=\left(e_{31II}a_{1jII}+e_{33II}\lambda_{jII}a_{2jII}-\varepsilon_{33II}\lambda_{jII}a_{3jII}-g_{33II}\lambda_{jII}a_{4jII}\right)\exp\left(\rho\lambda_{jII}\left(h_1+h_3\right)\right),H_{3(j+8)}=0,H_{3(j+16)}=0,$$

$$H_{4j}=\left(f_{31II}a_{1jII}+f_{33II}\lambda_{jII}a_{2jII}-g_{33II}\lambda_{jII}a_{3jII}-\mu_{33II}\lambda_{jII}a_{4jII}\right)\exp\left(\rho\lambda_{jII}\left(h_1+h_3\right)\right),H_{4(j+8)}=0,H_{4(j+16)}=0,$$

$$H_{5j}=0,H_{5(j+8)}=0,H_{5(j+16)}=\left(c_{44I}\lambda_{jI}a_{1jI}-c_{44I}a_{2jI}-e_{15I}a_{3jI}-f_{15I}a_{4jI}\right)\exp\left(-\rho\lambda_{jI}h_2\right),$$

$$H_{6j}=0,H_{6(j+8)}=0,H_{6(j+16)}=\left(c_{13I}a_{1jI}+c_{33I}\lambda_{jI}a_{2jI}+e_{33I}\lambda_{jI}a_{3jI}+f_{33I}\lambda_{jI}a_{4jI}\right)\exp\left(-\rho\lambda_{jII}h_2\right),$$

$$H_{7j}=0, H_{7(j+8)}=0, H_{7(j+16)}=\left(e_{31I}a_{1jI}+e_{33I}\lambda_{jI}a_{2jI}-\varepsilon_{33I}\lambda_{jI}a_{3jI}-g_{33I}\lambda_{jI}a_{4jI}\right)\exp\left(-\rho\lambda_{jI}h_2\right),$$

$$H_{8j}=0, H_{8(j+8)}=0, H_{8(j+16)}=\left(f_{31I}a_{1jI}+f_{33I}\lambda_{jI}a_{2jI}-g_{33I}\lambda_{jI}a_{3jI}-\mu_{33I}\lambda_{jI}a_{4jI}\right)\exp\left(-\rho\lambda_{jI}h_2\right),$$

$$H_{9j}=\left(c_{44II}\lambda_{jII}a_{1jII}-c_{44II}a_{2jII}-e_{15II}a_{3jII}-f_{15II}a_{4jII}\right)\exp\left(\rho\lambda_{jII}h_1\right),$$

$$H_{9(j+8)}=-\left(c_{44I}\lambda_{jI}a_{1jI}-c_{44I}a_{2jI}-e_{15I}a_{3jI}-f_{15I}a_{4jI}\right)\exp\left(\rho\lambda_{jI}h_1\right), H_{9(j+16)}=0,$$

$$H_{10j}=\left(c_{13II}a_{1jII}+c_{33II}\lambda_{jII}a_{2jII}+e_{33II}\lambda_{jII}a_{3jII}+f_{33II}\lambda_{jII}a_{4jII}\right)\exp\left(\rho\lambda_{jII}h_1\right),$$

$$H_{10(j+8)}=-\left(c_{13I}a_{1jI}+c_{33I}\lambda_{jI}a_{2jI}+e_{33I}\lambda_{jI}a_{3jI}+f_{33I}\lambda_{jI}a_{4jI}\right)\exp\left(\rho\lambda_{jI}h_1\right), H_{10(j+16)}=0,$$

$$H_{11j}=\left(e_{31II}a_{1jII}+e_{33II}\lambda_{jII}a_{2jII}-\varepsilon_{33II}\lambda_{jII}a_{3jII}-g_{33II}\lambda_{jII}a_{4jII}\right)\exp\left(\rho\lambda_{jII}h_1\right),$$

$$H_{11(j+8)}=-\left(e_{31I}a_{1jI}+e_{33I}\lambda_{jI}a_{2jI}-\varepsilon_{33I}\lambda_{jI}a_{3jI}-g_{33I}\lambda_{jI}a_{4jI}\right)\exp\left(\rho\lambda_{jI}h_1\right), H_{11(j+16)}=0,$$

$$H_{12j}=\left(f_{31II}a_{1jII}+f_{33II}\lambda_{jII}a_{2jII}-g_{33II}\lambda_{jII}a_{3jII}-\mu_{33II}\lambda_{jII}a_{4jII}\right)\exp\left(\rho\lambda_{jII}h_1\right),$$

$$H_{12(j+8)}=-\left(f_{31I}a_{1jI}+f_{33I}\lambda_{jI}a_{2jI}-g_{33I}\lambda_{jI}a_{3jI}-\mu_{33I}\lambda_{jI}a_{4jI}\right)\exp\left(\rho\lambda_{jI}h_1\right), H_{12(j+16)}=0,$$

$$H_{13j}=\left[a_{1jII}/\rho-\beta_1\left(c_{44II}\lambda_{jII}a_{1jII}-c_{44II}a_{2jII}-e_{15II}a_{3jII}-f_{15II}a_{4jII}\right)\right]\exp\left(\rho\lambda_{jII}h_1\right),$$

$$H_{13(j+8)}=-\left(a_{1jI}/\rho\right)\exp\left(\rho\lambda_{jI}h_1\right), H_{13(j+16)}=0,$$

$$H_{14j}=\left[a_{2jII}/\rho-\beta_2\left(c_{13II}a_{1jII}+c_{33II}\lambda_{jII}a_{2jII}+e_{33II}\lambda_{jII}a_{3jII}+f_{33II}\lambda_{jII}a_{4jII}\right)\right]\exp\left(\rho\lambda_{jII}h_1\right),$$

$$H_{14(j+8)}=-\left(a_{2jI}/\rho\right)\exp\left(\rho\lambda_{jI}h_1\right), H_{14(j+16)}=0,$$

$$H_{15j}=\left[a_{3jII}/\rho-\beta_3\left(e_{31II}a_{1jII}+e_{33II}\lambda_{jII}a_{2jII}-\varepsilon_{33II}\lambda_{jII}a_{3jII}-g_{33II}\lambda_{jII}a_{4jII}\right)\right]\exp\left(\rho\lambda_{jII}h_1\right),$$

$$H_{15(j+8)}=-\left(a_{3jI}/\rho\right)\exp\left(\rho\lambda_{jI}h_1\right), H_{15(j+16)}=0,$$

$$H_{16j}=\left[a_{4jII}/\rho-\beta_4\left(f_{31II}a_{1jII}+f_{33II}\lambda_{jII}a_{2jII}-g_{33II}\lambda_{jII}a_{3jII}-\mu_{33II}\lambda_{jII}a_{4jII}\right)\right]\exp\left(\rho\lambda_{jII}h_1\right),$$

$$H_{16(j+8)}=-\left(a_{4jI}/\rho\right)\exp\left(\rho\lambda_{jI}h_1\right), H_{16(j+16)}=0,$$

$$H_{17j}=0, H_{17(j+8)}=\left(c_{44I}\lambda_{jI}a_{1jI}-c_{44I}a_{2jI}-e_{15I}a_{3jI}-f_{15I}a_{4jI}\right),$$

$$H_{17(j+16)}=-\left(c_{44I}\lambda_{jI}a_{1jI}-c_{44I}a_{2jI}-e_{15I}a_{3jI}-f_{15I}a_{4jI}\right),$$

$$H_{18j}=0, H_{18(j+8)}=\left(c_{13I}a_{1jI}+c_{33I}\lambda_{jI}a_{2jI}+e_{33I}\lambda_{jI}a_{3jI}+f_{33I}\lambda_{jI}a_{4jI}\right),$$

$$H_{18(j+16)}=-\left(c_{13I}a_{1jI}+c_{33I}\lambda_{jI}a_{2jI}+e_{33I}\lambda_{jI}a_{3jI}+f_{33I}\lambda_{jI}a_{4jI}\right),$$

$$H_{19j}=0, H_{19(j+8)}=\left(e_{31I}a_{1jI}+e_{33I}\lambda_{jI}a_{2jI}-\varepsilon_{33I}\lambda_{jI}a_{3jI}-g_{33I}\lambda_{jI}a_{4jI}\right),$$

$$H_{19(j+16)}=-\left(e_{31I}a_{1jI}+e_{33I}\lambda_{jI}a_{2jI}-\varepsilon_{33I}\lambda_{jI}a_{3jI}-g_{33I}\lambda_{jI}a_{4jI}\right),$$

$$H_{20j}=0, H_{20(j+8)}=\left(f_{31I}a_{1jI}+f_{33I}\lambda_{jI}a_{2jI}-g_{33I}\lambda_{jI}a_{3jI}-\mu_{33I}\lambda_{jI}a_{4jI}\right),$$

$$H_{20(j+16)}=-\left(f_{31I}a_{1jI}+f_{33I}\lambda_{jI}a_{2jI}-g_{33I}\lambda_{jI}a_{3jI}-\mu_{33I}\lambda_{jI}a_{4jI}\right),$$

$$H_{21j}=0, H_{21(j+8)}=a_{1jI}/\rho, H_{21(j+16)}=-a_{1jI}/\rho,$$

$$H_{22j}=0, H_{22(j+8)}=a_{2jI}/\rho, H_{22(j+16)}=-a_{2jI}/\rho,$$

$$H_{23j}=0, H_{23(j+8)}=a_{3jI}/\rho, H_{23(j+16)}=-a_{3jI}/\rho,$$

$$H_{24j}=0, H_{24(j+8)}=a_{4jI}/\rho, H_{24(j+16)}=-a_{4jI}/\rho,$$

where $j=1,2,\mathrm{L}\ ,8$.

Acknowledgements

The authors wish to acknowledge the support from the Natural Science Fund of China (11072160).

References

[1] Y. Benveniste, Magnetoelectric effect in fibrous composites with piezoelectric and piezomagnetic phases. Phys Rev B, 51 (1995) 16424–16427.
[2] J. Aboudi, Micromechanical analysis of fully coupled electro-magneto-thermo-elastic multiphase composites. Smart Mater Struct, 10 (2001) 867–877.
[3] S. Priya, R. Islam, S.X. Dong, D. Vehland, Recent advancements in magnetoelectric particular and laminate composites. J Electroceram, 19 (2007) 149–66.
[4] J.X. Liu, X.L. Liu, Y.M. Zhao, Green's functions for anisotropic magnetoelectroelastic solids with an elliptical cavity or a crack. Int J Eng Sci, 39 (2001) 1405–1418.
[5] C.F. Gao, H. Kessler, H. Balke, Crack problems in magnetoelectroelastic solids. Part I: exact solution of a crack. Int J Eng Sci, 41 (2003) 969–981.
[6] G.C. Sih, Z.F. Song, Piezomagnetic and piezoelectric poling effects on mode I and II crack initiation behaviour of magnetoelectroelastic materials composite. Theor Appl Fract Mech, 40 (2003) 161–186.
[7] B.L. Wang, Y.W. Mai, Applicability of the crack-face electromagnetic boundary conditions for fracture of magnetoelectroelastic materials. Int J Solids Struct, 44 (2007) 387–398
[8] X.F. Li, G.L. Liu, K.Y. Lee, Magnetoelectroelastic field induced by a crack terminating at the interface of a bi-magnetoelectric material. Philo Mag, 89 (2009) 449–463.
[9] W.J. Feng, E. Pan, X. Wang, Dynamic fracture analysis of a penny-shaped crack in a magnetoelectroelastic layer. Int J Solids Struct, 44 (2007) 7955–7974.
[10] M.H. Zhao, F. Yang, T. Liu, Analysis of a penny-shaped crack in a magneto-electro-elastic medium. Philo Mag, 86 (2006) 4397–4416.
[11] Y.S. Li, Y.Y. Jiang, J.H. Ren, Z.Y. Cai, An annular interfacial crack between dissimilar magnetoelectroelastic layers. Smart Mater Struct, 20 (2011) 085011.
[12] S.A. Meguid, X.D. Wang, Wave scattering from cracks and imperfectly bonded inhomogeneities in advanced materials. Mech Mater, 31 (1999) 187-195.
[13] S. Lenci, Analysis of a crack at a weak interface. Int J Fract, 108 (2001) 275-298.
[14] S. Ueda, S. Biwa, K. Watanabe, R. Heuer, C. Pecorari, On the stiffness of spring model for closed crack. Int J Eng Sci, 44 (2006) 874-888.
[15] X.C. Zhong, X.F. Li, K.Y. Lee, Analysis of a mode-I crack perpendicular to an imperfect interface. Int J Solids Struct, 46 (2009) 1456-1463.
[16] F. Erdogan, G.D. Gupta, On the numerical solution of singular integral equations. Quart Appl Math, 29 (1972) 525–539.

Numerical simulations of interface cracks in layered magnetoelectroelastic solids under dynamic loadings

Michael Wünsche[1,*], Chuanzeng Zhang[1], Jan Sladek[2], Vladimir Sladek[2]

[1] Chair of Structural Mechanics, University of Siegen, D-57068 Siegen, Germany
[2] Institute of Construction and Architecture, Slovak Academy of Sciences, 84503 Bratislava, Slovakia
* Corresponding author: wuensche@bauwesen.uni-siegen.de

Abstract In this paper, transient dynamic crack analysis in two-dimensional, layered, anisotropic and linear magnetoelectroelastic solids is presented. For this purpose, a time-domain boundary element method (BEM) is developed. The layered magnetoelectroelastic solids are modeled by the multi-domain BEM formulation. The time-domain dynamic fundamental solutions for homogeneous and linear magnetoelectroelastic solids are applied in the present BEM. The spatial discretization of the boundary integral equations is performed by a Galerkin-method, while a collocation method is implemented for the temporal discretization of the arising convolution integrals. An explicit time-stepping scheme is obtained to compute the discrete boundary data including the generalized crack-opening-displacements (CODs). To show the effects of the interface, the material combinations and the dynamic loading on the intensity factors, numerical examples are presented and discussed.

Keywords transient dynamic crack analysis, linear magnetoelectroelastic solids, impact loading, interface-cracks, dynamic intensity factors.

1. Introduction

Magnetoelectroelastic materials offer many possibilities for advanced engineering structures due to their inherent coupling effects between mechanical, electrical and magnetic fields [3]. Important applications of magnetoelectroelastic materials are layered or laminated composites because they can be optimized to satisfy the high-performance requirements according to different in-service conditions. Beside cracks inside homogeneous domains, one of the most dominant failure mechanisms in layered or laminated composites is the interface failure. Interface cracks or interface debonding may be induced by the mismatch of the mechanical, electric, magnetic and thermal properties of the material constituents during the manufacturing process and the in-service loading conditions. Although the dynamic crack analysis in homogenous magnetoelectroelastic solids have been investigated by several authors (e.g., [5,6,7,9]) the corresponding investigation of interface cracks in layered magnetoelectroelastic solids is rather limited due to the problem complexity.
In this paper, an interface crack analysis in two-dimensional, layered and linear magnetoelectroelastic solids under impact loading is presented. For this purpose, a time-domain boundary element method (BEM) is developed. The layered magnetoelectroelastic solids are modeled by the multi-domain BEM formulation. The time-domain dynamic fundamental solutions for homogeneous and linear magnetoelectroelastic solids are applied in the present BEM. The spatial discretization of the boundary integral equations is performed by a Galerkin-method, while a collocation method is implemented for the temporal discretization of the arising convolution integrals. An explicit time-stepping scheme is obtained to compute the discrete boundary data including the generalized crack-opening-displacements (CODs). Since the asymptotic crack-tip field for an interface crack between two dissimilar anisotropic and linear magnetoelectroelastic materials shows different kinds of oscillating and non-oscillating singularities [1], which makes an implementation of a special crack-tip element somehow cumbersome, only standard elements are used at the crack-tips. For the accurate computation of the dynamic intensity factors the numerical error is minimized by a displacement-based extrapolation technique. To show the effects of the

interface, the material combinations and the dynamic loading on the intensity factors, numerical examples are presented and discussed.

2. Problem formulation

Let us consider a piecewise homogeneous, layered and linear magnetoelectroelastic solid with an interface crack as shown in Figure 1.

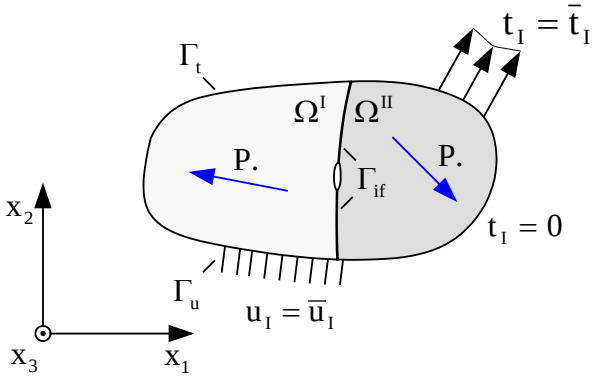

Figure 1. A cracked piecewise homogeneous and linear magnetoelectroelastic solid

In the absence of body forces, free electric charges, magnetic induction sources and applying the quasi-static assumption for the electric and magnetic fields, the cracked solid satisfies the generalized equations of motion

$$\sigma_{iJ,i}(\mathbf{x},t) = \rho^{\varsigma}\delta^{*}_{JK}\ddot{u}_K(\mathbf{x},t), \quad \delta^{*}_{JK} = \begin{cases} \delta_{JK}, J,K = 1,2 \\ 0, \text{otherwise} \end{cases}, \tag{1}$$

the constitutive equations

$$\sigma_{iJ}(\mathbf{x},t) = C^{\varsigma}_{iJKl}u_{K,l}(\mathbf{x},t), \tag{2}$$

where the generalized displacements, the generalized stresses and the generalized elasticity matrix C_{iJKl} for a homogenous domains Ω^{ζ} (ζ=1,2,…,N) are defined by

$$u_I = \begin{cases} u_i, I = 1,2 \\ \varphi, I = 4 \\ \phi, I = 5 \end{cases}, \quad \sigma_{iJ} = \begin{cases} \sigma_{iJ}, J = 1,2 \\ D_i, J = 4 \\ B_i, J = 5 \end{cases}, \quad C_{iJKl} = \begin{cases} c_{ijkl}, \ J,K = 1,2 \\ e_{lij}, \ J = 1,2, \quad K = 4 \\ h_{lij}, \ J = 1,2, \quad K = 5 \\ e_{ikl}, \ J = 4, \quad K = 1,2 \\ -\varepsilon_{il}, \ J,K = 4 \\ -\beta_{il}, \ J = 4, \quad K = 5 \\ h_{ikl}, \ J = 5, \quad K = 1,2 \\ -\beta_{il}, \ J = 5, \quad K = 4 \\ -\gamma_{il}, \ J,K = 5 \end{cases}, \tag{3}$$

the initial conditions

$$u_i(\mathbf{x}, t = 0) = \dot{u}_i(\mathbf{x}, t = 0) = 0, \tag{4}$$

the boundary conditions

$$t_I(\mathbf{x},t) = \bar{t}_I(\mathbf{x},t), \quad \mathbf{x} \in \Gamma_t, \tag{5}$$

$$u_I(\mathbf{x},t) = \bar{u}_I(\mathbf{x},t), \quad \mathbf{x} \in \Gamma_u, \tag{6}$$

and the continuity conditions on the interface without debonding

$$u_I^I(\mathbf{x},t) = u_I^{II}(\mathbf{x},t), \quad \mathbf{x} \in \Gamma_{if}, \tag{7}$$

$$t_I^I(\mathbf{x},t) = -t_I^{II}(\mathbf{x},t), \quad \mathbf{x} \in \Gamma_{if}. \tag{8}$$

In Eqs. (1)-(8), u_i, φ, Φ, σ_{ij}, D_i, B_i are the mechanical displacements, the electric potential, the magnetic potential, the mechanical stresses, the electric displacements and the magnetic inductions; ρ, c_{ijkl}, ε_{ij}, γ_{ij}, e_{ijk}, h_{ijk} and β_{ij} denote the mass density, the elasticity tensor, the dielectric permittivity tensor, the magnetic permittivity tensor, the piezoelectric tensor, the piezomagnetic tensor and the magnetoelectric tensor, respectively. Further, Γ_{if} is the interface between the homogenous domains Ω^{ζ} (ζ=1,2,…,N), Γ_t and Γ_u stand for the external boundaries where the generalized tractions t_I and the generalized displacements u_I are prescribed. The interface cracks are considered as free of mechanical stresses, electric displacements and magnetic inductions

$$\sigma_{iJ}(\mathbf{x} \in \Gamma_{c^+}, t) = \sigma_{iJ}(\mathbf{x} \in \Gamma_{c^-}, t) = 0, \tag{9}$$

where $\Gamma_{c\pm}$ are the two crack-faces. The generalized crack-opening-displacements (CODs) are defined by

$$\Delta u_I(\mathbf{x},t) = u_I(\mathbf{x} \in \Gamma_{c+}, t) - u_I(\mathbf{x} \in \Gamma_{c-}, t). \tag{10}$$

A comma after a quantity represents spatial derivatives while a dot over the quantity denotes time differentiation. Lower case Latin indices take the values 1 and 2 (elastic), while capital Latin indices take the values 1, 2 (elastic), 4 (electric) and 5 (magnetic).

3. Time-domain boundary integral equations

To solve the initial-boundary value problem, a spatial Galerkin-method is implemented, where the time-domain BIEs are treated in a weighted residual sense. The generalized time-domain displacement and traction BIEs can be written as

$$\int_\Gamma \psi(\mathbf{x})\, u_J(\mathbf{x},t)\, d\Gamma_x = \int_\Gamma \psi(\mathbf{x}) \int_\Gamma \left[u_{IJ}^G(\mathbf{x},\mathbf{y},t) * t_I(\mathbf{y},t) - t_{IJ}^G(\mathbf{x},\mathbf{y},t) * u_I(\mathbf{y},t) \right] d\Gamma_y d\Gamma_x, \tag{11}$$

$$\int_\Gamma \psi(\mathbf{x})\, t_J(\mathbf{x},t)\, d\Gamma_x = \int_\Gamma \psi(\mathbf{x}) \int_\Gamma \left[v_{IJ}^G(\mathbf{x},\mathbf{y},t) * t_I(\mathbf{y},t) - w_{IJ}^G(\mathbf{x},\mathbf{y},t) * u_I(\mathbf{y},t) \right] d\Gamma_y d\Gamma_x, \tag{12}$$

where ψ is the weighting function, an asterisk " * " denotes the Riemann convolution, $u_{IJ}^G(\mathbf{x},\mathbf{y},t)$, $t_{IJ}^G(\mathbf{x},\mathbf{y},t)$, $v_{IJ}^G(\mathbf{x},\mathbf{y},t)$ and $w_{IJ}^G(\mathbf{x},\mathbf{y},t)$ are the generalized displacement, traction and higher-order traction fundamental solutions. It should be mentioned that the dynamic time-domain fundamental solutions for homogeneous, anisotropic and linear magnetoelectroelastic solids are not available in an explicit form. In the two-dimensional case they can be expressed by a line integral over the unit-circle [4,9].

4. Numerical solution algorithm

A solution procedure is presented in this section to solve the time-domain BIEs (11) and (12) numerically. The procedure uses a Galerkin-method for the spatial discretization and a collocation method for the temporal discretization. A sub-domain technique is utilized, which divides the layered piecewise homogenous solid into two or several sub-domains with homogeneous material properties and to each sub-domain the time-domain BIEs (11) and (12) are applied. In the following, some details of the numerical solution algorithm are described. For the spatial discretization, the crack-faces, the external boundary of each homogeneous sub-domain and the interfaces are discretized by linear elements. Linear shape functions are also used for the temporal discretization in the present analysis. Since the asymptotic crack-tip field in the case of an interfacial crack between two dissimilar magnetoelectroelastic materials shows different oscillating and non-oscillating singularities in the generalized stress field, which makes an implementation of a special crack-tip element quite cumbersome, only standard elements are applied at the crack-tips. The strongly singular and hypersingular boundary integrals can be computed analytically by special

techniques. By using linear temporal shape-functions, time integrations can also be performed analytically. Only the line integrals over the unit-circle arising in the regular parts of the dynamic fundamental solutions have to be computed numerically by the standard Gaussian quadrature.
After temporal and spatial discretizations and considering the initial conditions the following systems of linear algebraic equations can be obtained for each sub-domain Ω^{ζ} (ζ=1,2,…,N)

$$\mathbf{C}_{\zeta}\,\mathbf{u}_{\zeta}^{\mathrm{K}} = \mathbf{U}_{\zeta}^{\mathrm{S}}\,\mathbf{t}_{\zeta}^{\mathrm{K}} - \mathbf{T}_{\zeta}^{\mathrm{S}}\,\mathbf{u}_{\zeta}^{\mathrm{K}} + \mathbf{T}_{\zeta}^{\mathrm{S}}\,\Delta\mathbf{u}_{\zeta}^{\mathrm{K}} + \sum_{\mathrm{k}=1}^{\mathrm{K}}\left[\mathbf{U}_{\zeta}^{\mathrm{D;K-k+1}}\,\mathbf{t}_{\zeta}^{\mathrm{k}} - \mathbf{T}_{\zeta}^{\mathrm{D;K-k+1}}\,\mathbf{u}_{\zeta}^{\mathrm{k}}\right], \tag{13}$$

$$\mathbf{D}_{\zeta}\,\mathbf{t}_{\zeta}^{\mathrm{K}} = \mathbf{V}_{\zeta}^{\mathrm{S}}\,\mathbf{t}_{\zeta}^{\mathrm{K}} - \mathbf{W}_{\zeta}^{\mathrm{S}}\,\mathbf{u}_{\zeta}^{\mathrm{K}} + \mathbf{W}_{\zeta}^{\mathrm{S}}\,\Delta\mathbf{u}_{\zeta}^{\mathrm{K}} + \sum_{\mathrm{k}=1}^{\mathrm{K}}\left[\mathbf{V}_{\zeta}^{\mathrm{D;K-k+1}}\,\mathbf{t}_{\zeta}^{\mathrm{k}} - \mathbf{W}_{\zeta}^{\mathrm{D;K-k+1}}\,\mathbf{u}_{\zeta}^{\mathrm{k}}\right]. \tag{14}$$

By invoking the continuity conditions (7) and (8) on the interface Γ_{if} and the crack-face boundary conditions (9) on Γ_{c^+} and Γ_{c^-}, and by considering the boundary conditions (5) and (6), Eqs. (13) and (14) can be summarized and recast into the following system of linear algebraic equations

$$\mathbf{x}^{\mathrm{K}} = (\mathbf{C}^{1})^{-1}\left[\mathbf{D}^{1}\,\mathbf{y}^{\mathrm{K}} + \sum_{\mathrm{k}=1}^{\mathrm{K-1}}(\mathbf{B}^{\mathrm{K-k+1}}\,\mathbf{t}^{\mathrm{k}} - \mathbf{A}^{\mathrm{K-k+1}}\,\mathbf{u}^{\mathrm{k}})\right], \tag{15}$$

where $\mathbf{y}^{\mathrm{K}}$ is the vector of the prescribed boundary data, $\mathbf{x}^{\mathrm{K}}$ represents the vector of the unknown boundary data, $\mathbf{A}^{\mathrm{k}}$, $\mathbf{B}^{\mathrm{k}}$, $\mathbf{C}^{1}$ and $\mathbf{D}^{1}$ are the system matrices. Eq. (15) can be computed time-step by time-step.

5. Intensity factors for an interfacial crack

The intensity factors for an interface crack between two dissimilar anisotropic and linear magnetoelectroelastic materials can be computed from the generalized crack-opening displacements (CODs)

$$\Delta\mathbf{u}(\mathrm{r}) = (\mathbf{H}+\overline{\mathbf{H}})\sqrt{\frac{\mathrm{r}}{2\pi}}\left[\frac{\mathrm{K}\mathrm{r}^{\mathrm{i}\varepsilon_1}\mathbf{w}}{(1+2\mathrm{i}\varepsilon_1)\cosh(\pi\varepsilon_1)} + \frac{\overline{\mathrm{K}}\mathrm{r}^{-\mathrm{i}\varepsilon_1}\overline{\mathbf{w}}}{(1-2\mathrm{i}\varepsilon_1)\cosh(\pi\varepsilon_1)} + \frac{\mathrm{K}_4\mathrm{r}^{-\varepsilon_2}\mathbf{w}_4}{(1-2\varepsilon_2)\cos(\pi\varepsilon_2)} + \mathrm{K}_5\mathbf{w}_5\right], \tag{16}$$

where $\mathrm{K}=\mathrm{K}_1+\mathrm{i}\mathrm{K}_2$, is the complex stress intensity factor, K_4 is the electric displacement intensity factor and K_5 is the magnetic induction intensity factor, ε_1 and ε_2 are the bimaterial constants, an overbar denotes the complex conjugate and i stands for the imaginary unit. The complex Hermitian matrix **H** is defined by

$$\mathbf{H} = \mathbf{Y}_{\mathrm{I}} + \overline{\mathbf{Y}}_{\mathrm{II}}, \quad \mathbf{Y}_{\mathrm{I}} = \mathrm{i}\mathbf{A}_{\mathrm{I}}\mathbf{B}_{\mathrm{I}}^{-1}, \quad \mathbf{Y}_{\mathrm{II}} = \mathrm{i}\mathbf{A}_{\mathrm{II}}\mathbf{B}_{\mathrm{II}}^{-1}, \tag{17}$$

where the subscripts I and II indicate the two layers. The matrices **A** and **B** are computed from the eigenvalue problem as shown in [1,2]. The two bimaterial constants ε_1 and ε_2 as well as the eigenvectors **w**, $\mathbf{w}_4$ and $\mathbf{w}_5$ are determined by the eigenvalue problem

$$\mathbf{D}^{-1}\mathbf{W}\mathbf{w} = -\mathrm{i}\beta\mathbf{w}, \tag{18}$$

with **D**=Re(**H**) and **W**=Im(**H**) being the real and the imaginary part of the matrix **H**. The eigenvalue β is either real or purely imaginary and related to the bimaterial constants by

$$\varepsilon_1 = \frac{1}{2}\ln\frac{1-\beta}{1+\beta}, \qquad \varepsilon_2 = \frac{1}{2}\ln\frac{1-\mathrm{i}\beta}{1+\mathrm{i}\beta}. \tag{19}$$

As shown by Eq. (16) the generalized crack-opening-displacements (CODs) in the crack-tip vicinity of interface cracks between two dissimilar linear magnetoelectroelastic materials show $\mathrm{a}\mathrm{r}^{1/2\pm\mathrm{i}\varepsilon}$-oscillating behavior and additionally a non-oscillating $\mathrm{r}^{1/2\pm\varepsilon}$-behavior. A similar behavior is known for interface cracks between two dissimilar piezoelectric materials [8]. This makes an implementation of special spatial crack-tip shape functions rather difficult. For this reason, only standard linear elements near the tips of interface cracks are used in this analysis. To minimize the numerical errors, a displacement-based extrapolation technique is applied to calculate the dynamic intensity factors from the numerically computed generalized crack-opening-displacements (CODs).

6. Numerical examples

In this section, numerical examples are presented and discussed to show the effects of the coupled fields, the interface, the material combinations and the dynamic loading on the dynamic intensity factors (IFs). The following loading parameters are introduced in order to measure the intensity of the electric and magnetic loading

$$\chi^{e}=\frac{e_{22}^{I}}{\varepsilon_{22}^{I}}\frac{D_0}{\sigma_0},\quad \chi^{m}=\frac{h_{22}^{I}}{\gamma_{22}^{I}}\frac{D_0}{\sigma_0}, \tag{20}$$

where σ_0, D_0 and B_0 are the mechanical, electric and magnetic loading amplitudes. For convenience of the presentation, the real part K_1 and the imaginary part K_2 of the complex dynamic stress intensity factors as well as the electric displacement intensity factor K_4 and the magnetic induction intensity factor K_5 of the interface crack are normalized by

$$K_1^{*}(t)=\frac{K_1(t)}{K_0},\quad K_2^{*}(t)=\frac{K_2(t)}{K_0},\quad K_4^{*}(t)=\frac{e_{22}^{I}}{\varepsilon_{22}^{I}}\frac{K_4(t)}{K_0},\quad K_5^{*}(t)=\frac{h_{22}^{I}}{\gamma_{22}^{I}}\frac{K_5(t)}{K_0}, \tag{21}$$

with $K_0=\sigma_0\sqrt{\pi a}$ and a is the half-length of an internal interface crack.

In the example we consider a central interface crack of length 2a in a rectangular, layered, anisotropic and linear magnetoelectroelastic plate with the poling direction normal to the interface crack as shown in Figure 2.

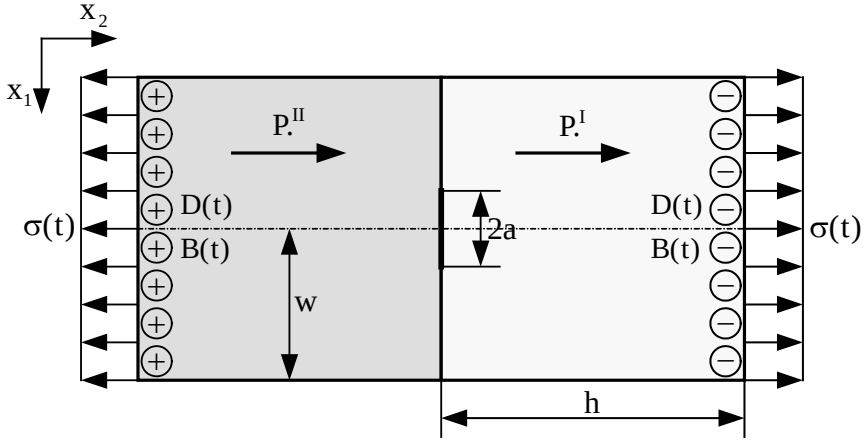

Figure 2. An interface crack in a rectangular layered magnetoelectroelastic plate

The cracked plate is subjected to an impact tensile loading $\sigma(t)=\sigma_0 H(t)$, an impact electric loading $D(t)=D_0 H(t)$ and an impact magnetic loading $B(t)=B_0 H(t)$, where H(t) denotes the Heaviside step function. The geometry is determined by h=20.0mm, w=10.0mm and 2a=4.8mm. The spatial discretization of the external boundary and the interface is performed by an element-length of 1.0mm. Each crack-face is approximated by 20 elements and a normalized time-step of $c_L\Delta t/h=0.05$ is chosen, where c_L is the quasi-longitudinal wave velocity. Numerical calculations are carried out for $BaTiO_3$-$CoFe_2O_4$ composite, with $BaTiO_3$ being its piezoelectric phase and $CoFe_2O_4$ its piezomagnetic phase. The magnetoelectroelastic material for the domain I has the constants

$$C_{11}=226.0\,\mathrm{GPa},\quad C_{12}=125.0\,\mathrm{GPa},\quad C_{22}=216.0\,\mathrm{GPa},\quad C_{66}=44.0\,\mathrm{GPa},$$
$$e_{16}=5.8\,\mathrm{C/m^2},\quad e_{21}=-2.2\,\mathrm{C/m^2},\quad e_{22}=9.3\,\mathrm{C/m^2},$$
$$h_{16}=275.0\,\mathrm{N/(Am)},\quad h_{21}=290.2\,\mathrm{N/(Am)},\quad h_{22}=350.0\,\mathrm{N/(Am)},$$
$$\varepsilon_{11}=56.4\,\mathrm{C^2/(GNm^2)},\quad \varepsilon_{22}=63.5\,\mathrm{C^2/(GNm^2)},$$
$$\beta_{11}=0.005367\,\mathrm{N/(GAV)},\quad \beta_{22}=2.7375\,\mathrm{N/(GAV)},$$
$$\gamma_{11}=297.0\,\mathrm{N/MA^2},\quad \gamma_{22}=83.5\,\mathrm{N/MA^2}, \tag{22}$$

while for domain II the material constants

$$C_{11} = 260.0\,GPa\,,\quad C_{12} = 150.0\,GPa\,,\quad C_{22} = 248.0\,GPa\,,\quad C_{66} = 45.0\,GPa\,,$$
$$e_{16} = 2.3\,C/m^2\,,\quad e_{21} = -0.9\,C/m^2\,,\quad e_{22} = 3.7\,C/m^2\,,$$
$$h_{16} = 440.0\,N/(Am)\,,\quad h_{21} = 464.2\,N/(Am)\,,\quad h_{22} = 560.0\,N/(Am)\,,$$
$$\varepsilon_{11} = 23.0\,C^2/(GNm^2)\,,\quad \varepsilon_{22} = 25.9\,C^2/(GNm^2)\,,$$
$$\beta_{11} = 0.0028\,N/(GAV)\,,\quad \beta_{22} = 2.0\,N/(GAV)\,,$$
$$\gamma_{11} = 473.0\,N/MA^2\,,\quad \gamma_{22} = 127.6\,N/MA^2\,, \tag{23}$$

are applied. The numerical results of the present time-domain BEM obtained for different loading combinations and the application of material (22) for both layers are presented in Figure 3. This special case is equal to an interior crack inside a homogenous magnetoelectroelastic plate and the intensity factors are given in [9]. The normalized dynamic intensity factors for the interface crack are shown in Figure 4.

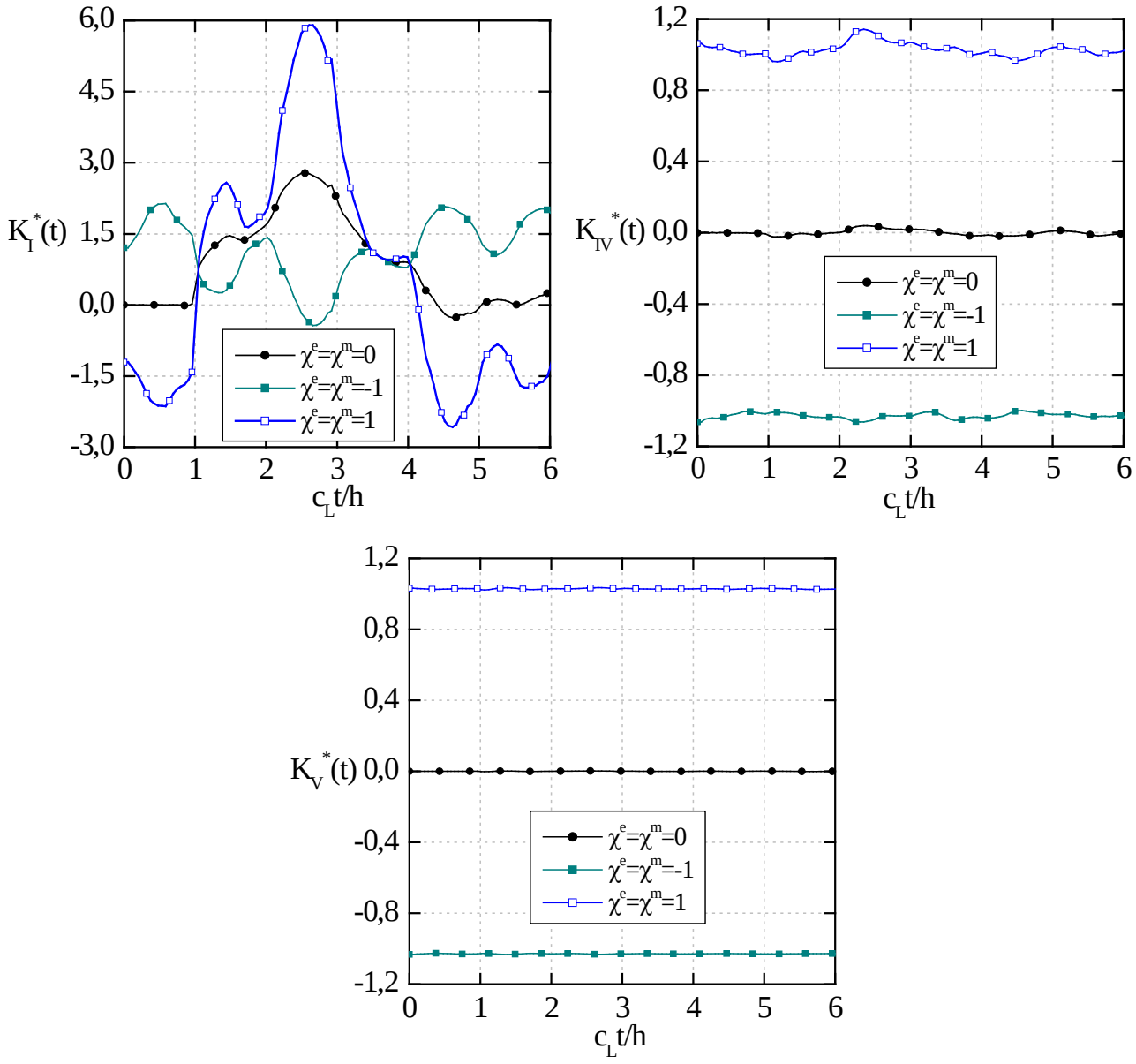

Figure 3. Normalized dynamic intensity factors for an interior crack subjected to different loadings

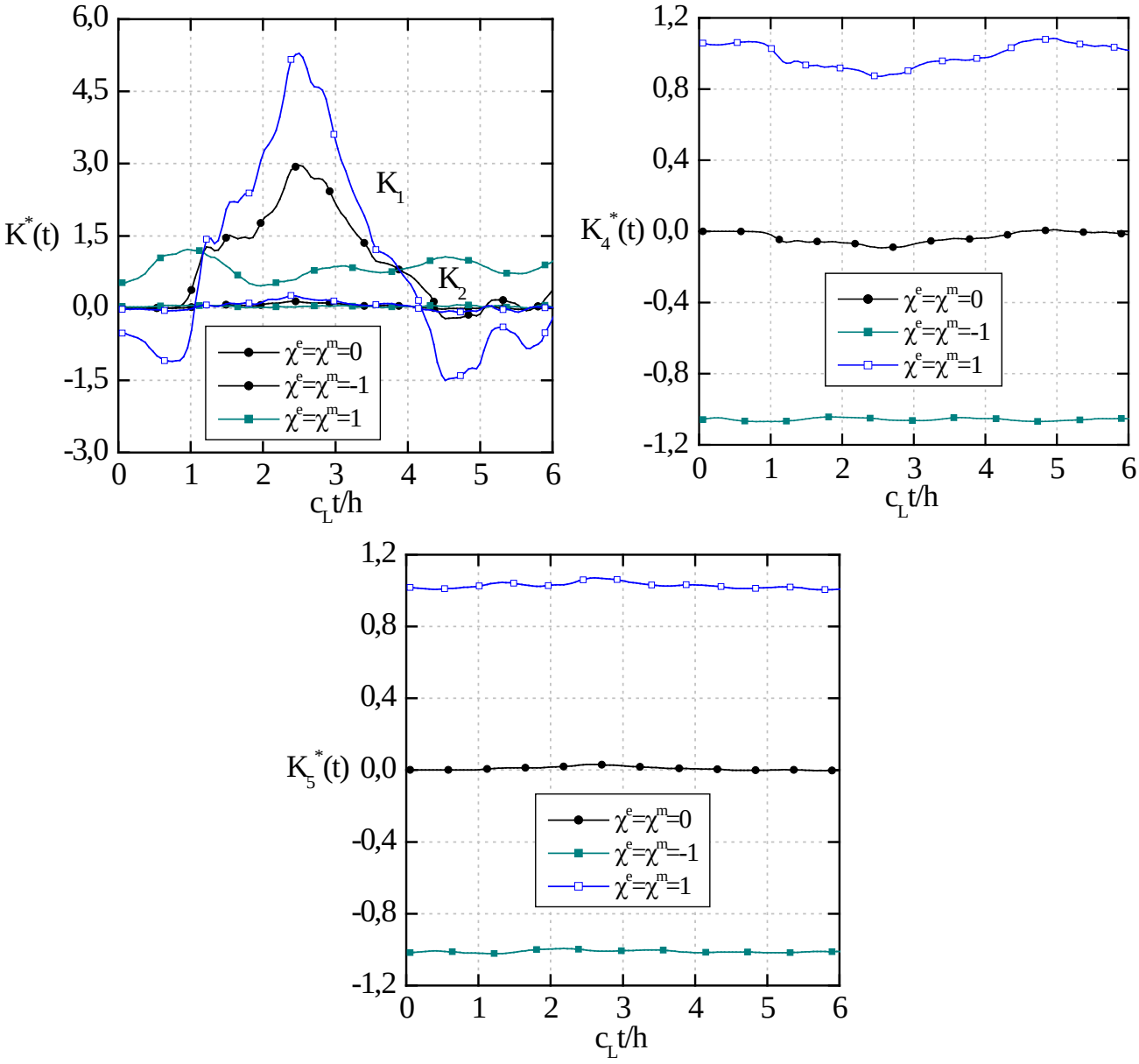

Figure 4. Normalized dynamic intensity factors for an interface crack subjected to different loadings

The normalized dynamic mode-I, mode-IV and mode-V intensity factors for an interior crack in a homogenous magnetoelectroelastic plate as well as the real part of the complex intensity factor, the electrical displacement intensity factor and the magnetic induction intensity factor for the interface crack obtained by the present TDBEM have a similar global behavior. The mode-II intensity factors vanish, since no shear stress components are induced for all applied loadings in the case of a transversely isotropic material behavior. In contrast, the crack opening and sliding modes I and II are coupled each other for the interface crack and therefore the imaginary part of the complex intensity factor is unequal zero. It can be observed that, when an electric and magnetic impact is applied, the normalized dynamic mode-I stress intensity factor and the complex stress intensity factor start from a non-zero value at t=0. This is due to the quasi-static assumption on the electromagnetic fields, which implies that the cracked magnetoelectroelatic plate is immediately subjected to an electromagnetic wave and therefore the crack opens at t=0. In contrast, the elastic waves induced by the mechanical impact need some time to reach and excite the crack, as clearly observed for the case $\chi^e=\chi^m=0$. It should further be mentioned here, that the applied electric and

magnetic loading may lead to a physically meaningless crack-face intersection in different time ranges for the case $\chi^e=\chi^m=1$. This requires an advanced iterative solution procedure for the crack-face contact analysis which is not considered in this work. The peak values of the normalized dynamic intensity factors decrease with increasing electric and magnetic loading amplitudes.

Acknowledgements

This work is supported by the German Research Foundation (DFG) under the project number ZH 15/14-1 and by the Slovak Science and Technology Assistance Agency registered under the number APVV-0014-10. The financial support is gratefully acknowledged.

References

[1] C.-F. Gao, P. Tong, T.-Y. Zhang, Interfacial crack problems in magneto-electroelastic solids. International Journal of Engineering Science, 41 (2003) 2105-2121.
[2] C. Fan, Y. Zhou, H. Wang, M. Zhao, Singular behaviors of interfacial cracks in 2D magnetoelectroelastic bimaterials. Acta Mechanica Solida Sinica, 22 (2009) 232-239.
[3] C.W. Nan, Magnetoelectric effect in composite of piezoelectric and piezomagnetic phases. Phys. Rev. B, 50 (1994) 6082-6088.
[4] R. Rojas-Díaz, A. Sáez, F. García-Sánchez, Ch. Zhang, Time-harmonic Green's functions for anisotropic magnetoelectroelasticity. International Journal of Solids and Structures, 45 (2008) 144-158.
[5] R. Rojas-Díaz, F. García-Sánchez, A. Sáez, E. Rodríguez-Mayorga, Ch. Zhang, Fracture analysis of plane piezoelectric/piezomagnetic multiphase composites under transient loading. Computer Methods in Applied Mechanics and Engineering, 200 (2011) 2931-2942.
[6] J. Sladek, V. Sladek, P. Solek, E. Pan, Fracture analysis of cracks in magneto-electro-elastic solids by the MLPG. Computational Mechanics, 42 (2008) 697-714.
[7] J. Sladek, V. Sladek, P. Stanak, Ch. Zhang, M. Wünsche, An interaction integral method for computing fracture parameters in functionally graded magnetoelectroelastic composites. Computer, Materials and Continua, 23 (2011) 35-68.
[8] Z. Suo, C.M. Kuo, D.M. Barnett, J.R. Willis, Fracture mechanics for piezoelectric ceramics. Journal of the Mechanics and Physics of Solids, 40 (1992) 739-765.
[9] M. Wünsche, A. Sáez, F. García-Sánchez, Ch. Zhang, Transient dynamic analysis of cracked magnetoelectroelastic solids by a time-domain BEM. European Journal of Mechanics - A/Solids, 32 (2012) 118-130.

Micromechanical modelling of advanced ceramics

Patricia Alveen[1,*], Declan McNamara[1], Declan Carolan[1], Neal Murphy[1], Alojz Ivanković[1]

[1] School of Mechanical and Materials Engineering, University College Dublin, Ireland
* Corresponding author: Patricia.Alveen@ucdconnect.ie

Abstract

Advanced ceramics comprise a class of new materials finding increased application used in extreme conditions, such as high speed turning of aerospace alloys and rock drilling. Their high hardness makes them suitable for these applications, however their lower toughness means that premature failure due to fracture and chipping is still a major issue. Typically, they are composed of micron-sized particles of a primary hard phase together with a ceramic or metallic matrix.

A combined experimental-numerical method was used to investigate the role of microstructure on the fracture of these advanced ceramics. In particular, the effect of grain size and matrix content was examined. Representative finite volume (FV) microstructures were created using Voronoi tessellation. The cohesive zone parameters for the FV model were found experimentally using an adapted Three-Point-Bend (TPB) fracture toughness test method [1]. Image analysis was carried out on actual representative microstructures and compared to the FV microstructures to ensure that they were statistically similar.

It was found that the underlying microstructure significantly affects the fracture toughness of the advanced ceramic. Furthermore, it was found that by altering the microstructural parameters in the numerical model, such as grain size and binder content, it is possible to specify material improvements.

Keywords Advanced ceramics, microstructure, Voronoi tessellation, cohesive zone model

1. Introduction

In this study, we examine a two-phase ceramic structure composed of stiff hard particles together with a softer ceramic matrix material. Carolan et al [1, 2] have shown that the strength and toughness of polycrystalline materials are affected by both the grain size and matrix content. Therefore it is desirable to be able to virtually optimise these parameters to be able to produce stronger or tougher materials for specific applications. Current methods adopt a so-called "trial-and-error" approach to the design of new materials, which is both costly and time consuming. Hence, it is beneficial to be able to specify improvements to materials numerically. By specifying materials virtually, the influence of individual material parameters on the microstructural scale can easily be investigated and altered to change bulk material properties. In order to better model and predict material behaviour, the first step is the ability to produce statistically representative microstructures.

A number of authors [7–10] have generated finite element meshes directly based on actual microstructural images. In this work, however, a representative synthetically generated geometry is

produced, which is then compared to a real microstructure. Numerous studies have been carried out to produce numerical microstructures using Voronoi tessellation [11–13], with an emphasis on investigating stress distributions in plasticity [14–17] and fracture [18–20]. However there is little in the literature to show that numerical microstructures are actually representative of the real microstructures they were created to replace. This is important, especially in the case of fracture problems, where the morphology of a grain boundary interface is of added importance in initiating fracture. The present work attempts to produce numerical microstructures and subsequently compare them to these real microstructures to prove that they are statistically representative.

2. Synthetic microstructure generation

Voronoi tessellation was used to generate the geometrical model of the microstructure. It is a commonly used method for the generation of numerical microstructures of ceramic [19, 20] and metallic [11, 16, 21, 22] materials in both two- and three-dimensions. The Voronoi tessellation algorithm produces a random structure, which is representative of a polycrystalline material. A periodic microstructure was generated with periodic boundary conditions. To generate a dual interpenetrating phase microstructure, typical of some advanced ceramics, the Voronoi tessellation is applied. Each Voronoi tile is then reduced in area around the circumcentre of the tile until the desired area fraction of the second interpenetrating phase is reached, as shown in Figure 1.

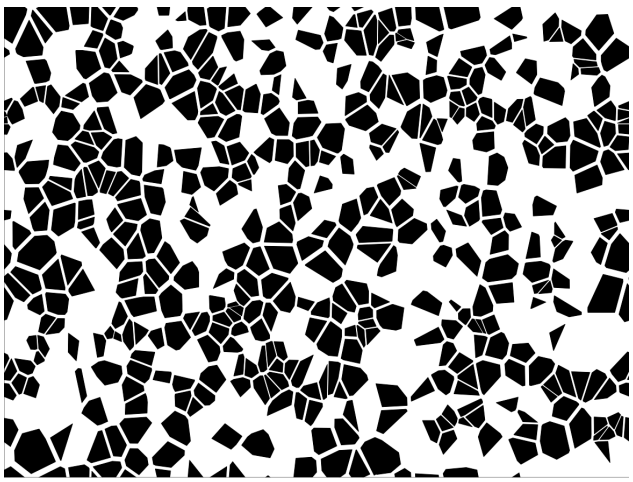

Figure 1: Numerically generated microstructure with 50% primary phase.

3. Results

3.1 Comparison of real and numerical microstructures

Grain size distribution, aspect ratio, percentage matrix agglomerations (MA) and percentage primary phase were obtained through image analysis. Matrix agglomerations are large regions containing no primary phase. From the image analysis it was found that the two real microstructures being investigated had an average areal primary phase content of 50.5% and 47.2% respectively. Four synthetic microstructures were generated for comparison, as shown in Figure 2. The generated microstructures all had a particle content in the range of 49-54%, which was close to the real

microstructures investigated. The percentage matrix agglomerations with respect to matrix phase content was calculated for the two real microstructures and was found to have an average value of 57.5% and 45.9% respectively. The two synthetic microstructures with matrix agglomerations, Figures 2b and 2d, had matrix agglomerations of 52.6% and 52.3% respectively.

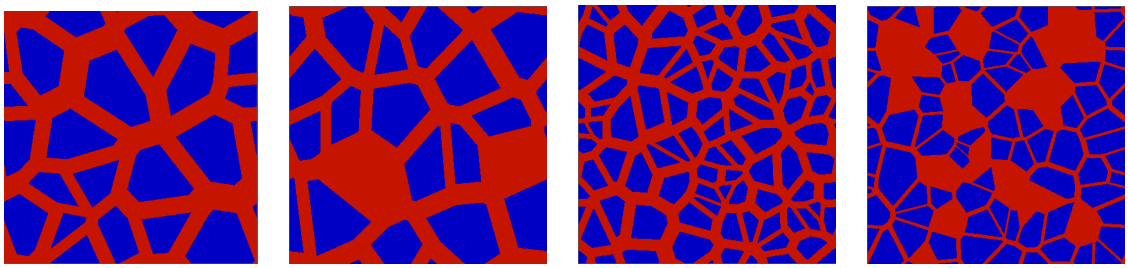

(a) 5×5 grains (b) 5×5 grains with MA (c) 10×10 grains (d) 10×10 grains with MA

Figure 2: Numerical microstructures used for finite volume

Grain size distribution, percentage particle phase and aspect ratio were obtained for both the numerical and corresponding real microstructures. A comparison between the two confirms that the numerical model is a good representation of the real microstructure, see Figures 3a and 3d. The grain size distribution of both the real and the numerical microstructure follow a log-normal distribution with a greater number of small grains, see Figure 3b and 3e. The real microstructure has a higher percentage of these small grains than its numerical counterpart due to small fragmented grains. However, it is not thought that these small fragments affect the mechanical properties of the bulk material. The aspect ratio of the real and the numerical microstructures show excellent agreement, as shown in Figure 3c and 3f. Visually it was also observed that the numerical microstructure resembled the real microstructure.

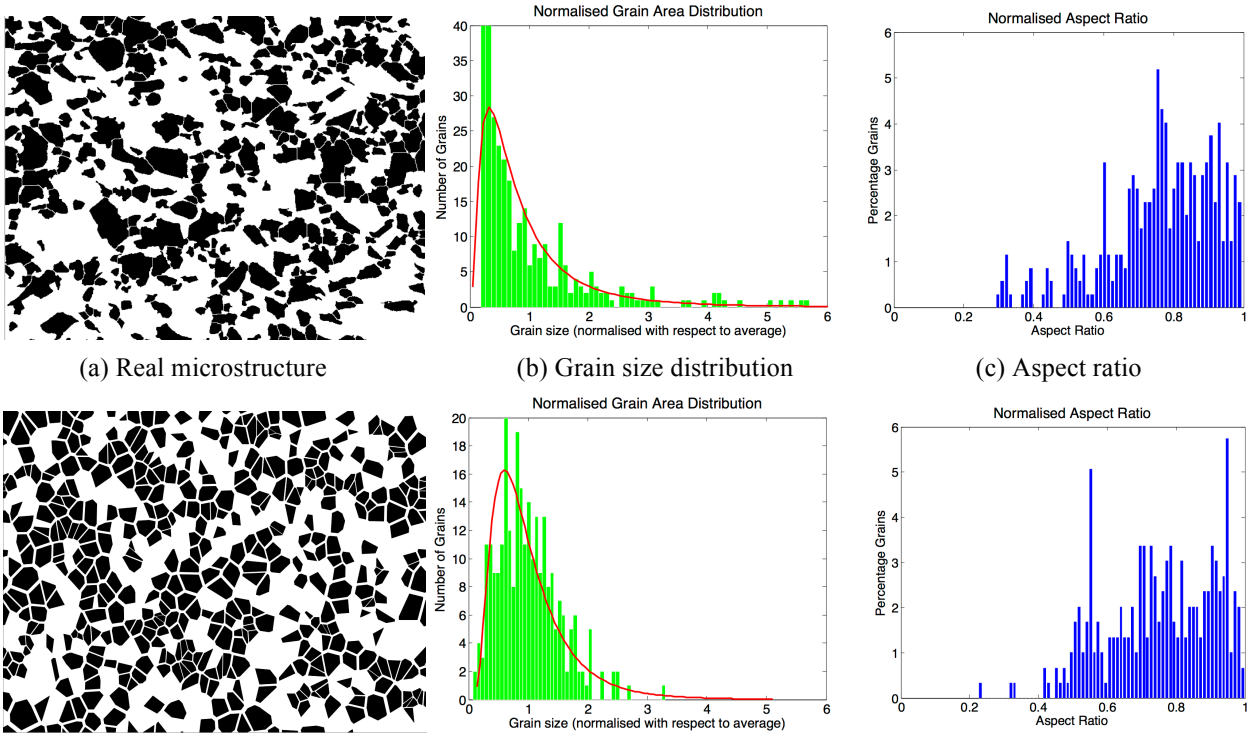

(a) Real microstructure (b) Grain size distribution (c) Aspect ratio

(d) Numerical microstructure (e) Grain size distribution (f) Aspect ratio

Figure 3: Comparison of real (a,b,c) and numerical (d,e,f) microstructures in terms of grain size distribution and aspect ratio.

3.2 Finite volume stress analysis

Finite volume based stress analysis was carried out on the four generated microstructures using OpenFOAM 1.6-ext [23]. Each generated microstructure was 100×100μm in size with approximately 50% particulates, but with varying grain sizes and matrix agglomerations, as shown in Figure 2. The simulations were 2-dimensional and plane strain was specified in the third direction. The Young's modulus and Poisson's ratio for the grains are 800 GPa and 0.1 respectively, while for the matrix material E = 300 GPa and ν = 0.1 were chosen for illustration. Both the particulates and matrix were treated as linear elastic over the course of the simulation. It should be noted that the elastic constants picked for each phase are not representative of any particular material.

The microstructures were subjected to a normal traction rate of 10 MPa/s in the y-direction for a total loading time of 10 seconds, while cyclic boundary conditions were applied in the x-direction, see Figure 4. The cyclic boundary conditions ensure that both material and displacement distribution are continuous from right to left. Furthermore, the 10×10 grain microstructures were increased to 200×200μm to investigate size effects.

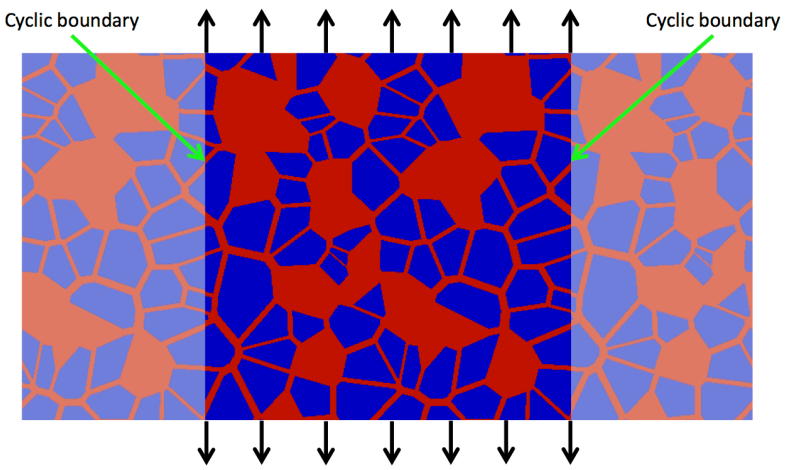

Figure 4: Generated microstructure with periodic boundary conditions subjected to a fixed traction

3.3 Effective elastic properties

The Young's Modulus value of a multiphase material depends on the properties of the individual phases. The upper and lower bounds for the elastic properties of the microstructures can be found using the Hashin-Shtrikman method from Eq. (1) and (2). The Hashin-Shtrikman bounds can be applied to transversely isotropic composites with arbitrary phase geometry [24–26].

$$k_l = k_2 + \frac{m_1}{\frac{1}{k_1-k_2}+\frac{m_2}{k_2+\mu_2}}, \quad k_u = k_1 + \frac{m_2}{\frac{1}{k_2-k_1}+\frac{m_2}{k_1+\mu_1}} \tag{1}$$

$$\mu_l = \mu_2 + \frac{m_1}{\frac{1}{\mu_1-\mu_2}+\frac{m_2(k_2+2\mu_2)}{2\mu_2(k_2+\mu_2)}}, \quad \mu_u = \mu_1 + \frac{m_2}{\frac{1}{\mu_2-\mu_1}+\frac{m_1(k_1+2\mu_1)}{2\mu_1(k_1+\mu_1)}} \tag{2}$$

Where *l* and *u* represent the upper and lower bounds respectively, k is the bulk modulus, μ is the shear modulus, m is the volume fraction and *1* and *2* represent the two phases in the material.

$$E = \frac{9k_i\mu_i}{3k_i+\mu_i} \tag{3}$$

$$\nu = \frac{3k_i-2\mu_i}{6k_i+2\mu_i} \tag{4}$$

The upper and lower bounds for the Young's modulus and Poisson's ratio can then be calculated from Eq. (3) and (4) respectively [21], by letting i equal u and l from Eq. (1) and (2). Using the Hashin-Shtrikman method the Young's modulus bounds for 50% particulates was found to be 459.9-480.6 GPa (Table 1).

The Eshelby-Mori-Tanaka approach [27–29] for determining the elastic properties of composites containing randomly oriented inclusions was also employed in the current work. Using this approach, and treating the inclusions as circular, i.e. an aspect ratio of one, the ratio of bulk modulus, k, and shear modulus, μ of a composite material to that of the matrix can be written as:

$$\frac{k}{k_m} = \frac{1}{1+V_f p} \tag{5}$$

$$\frac{\mu}{\mu_m} = \frac{1}{1+V_f q} \tag{6}$$

where k_m, μ_m and V_f are the bulk modulus of the matrix, shear modulus of the matrix and volume fraction of the inclusion respectively, and p and q are parameters derived from the Eshelby tensor and defined in Tandon and Weng [27]. Using the Eshelby-Mori-Tanaka method, the Poisson's ratio was found to be 0.114 for all the microstructures.

The effective stress, σ^e, and strain, ε^e, were found by averaging the local stress and strain in each cell using Eq. (7) and (8) [30]. This is known as homogenisation.

$$\sigma^e = \frac{1}{V_\Omega}\int_{V_\Omega} \sigma \, dV \tag{7}$$

$$\varepsilon^e = \frac{1}{V_\Omega}\int_{V_\Omega} \varepsilon \, dV \tag{8}$$

Where V_Ω is the total volume of integration. These values were then used to calculate the effective Young's Modulus E^e from

$$E^e = \frac{1}{\varepsilon^e_{yy}}[\sigma^e_{yy} - \nu^e(\sigma^e_{xx} + \sigma^e_{zz})] \tag{9}$$

where the effective Poisson's ratio, ν^e, is

$$\nu^e = \frac{\sigma^e_{xx}}{\sigma^e_{yy} + \sigma^e_{zz}} \tag{10}$$

The effective Young's modulus, $E_{Eq.9}$ of the microstructures is as shown in Table 1. The Poisson's ratio was found to be 0.112 for all the microstructures. The Young's modulus was also determined by calculating the average tractions and strains on the loading boundaries. Using these values the stress, σ, and strain, ε, and hence the Young's Modulus, E, could be calculated by:

$$\sigma^e = \frac{F_1}{L_1 t} \tag{11}$$

$$\varepsilon^e = \frac{u_1}{L_2} \tag{12}$$

$$E^e = \frac{\sigma^e}{\varepsilon^e} \tag{13}$$

Where F_1 is the loading force on the prescribed boundary, L_1 and L_2 are the width and height of the specimen, t is the thickness of the specimen and u_1 is the displacement of the sample along the loading direction. The Young's modulus value calculated using Eq. (13), was found to be higher than the value calculated using the average volumes (Table 1).

Table 1: Elastic properties of numerical microstructures where $E_{Eq.9}$ is calculated using the homogenisation method in Eq. (9), $E_{Eq.13}$ is calculated using the load-displacement method in Eq. (13), E_{EMT} is calculated using the Eshelby-Mori-Tanaka method, and E_{HS} is calculated using the Hashin-Shtrikman method

Microstructure	V_f	$E_{Eq.9}$ **(GPa)**	$E_{Eq.13}$ **(GPa)**	E_{EMT} **(GPa)**	E_{HS} **(GPa)**
5×5	0.5	463.2	475.9	462.1	459.6 - 480.6
10×10	0.5	463.3	476.3	462.1	459.6 - 480.6
5×5 with MA	0.49	459.7	472.4	457.7	455.3 - 476.1
10×10 with MA	0.54	485.1	498.6	484.7	477.4 - 499.8
10×10 (200×200μm)	0.5	463.3	476.3	462.1	459.6 - 480.6
10×10 with MA (200×200μm)	0.54	485.1	498.6	484.7	477.4 - 499.8

The Young's modulus value for the two microstructures with no matrix agglomerations was found to be very similar using all the methods for calculating the Young's modulus. This suggests that the Young's modulus is not affected by the grain size. It was also observed that increasing the specimen size to 200×200μm did not change the Young's modulus value showing that it is not size dependent. Furthermore, the matrix agglomerations were not found to affect the Young's modulus values. Only the volume fraction of particles was found to make a difference.

It was found that the load-displacement method consistently gave higher results than both the Eshelby-Mori-Tanaka and the homogenisation methods. The load-displacement values were found to lie close to the upper bounds of the Hashin-Shtrikman limits. The homogenising was found to give realistic values for Young's modulus and Poisson's ratio, and these values were found to be in good agreement with the Eshelby-Mori-Tanaka method. Both these values tend to lie close to the lower bound of the Hashin-Shtrikman limits.

Figures 5a and 5b plot the distribution of Von-Mises equivalent strain for a 5×5 and 10×10 microstructure with no matrix agglomerations. Figures 5c and 5d plot the distribution of Von-Mises

equivalent stress for the same two microstructures. Similarly Figures 6a and 6b plot the Von-Mises equivalent strain for a 5×5 and 10×10 microstructure with matrix agglomerations and Figures 6c and 6d plot the corresponding Von-Mises stresses. From Figure 5 it may be observed that the distribution of local stress and strain does not vary significantly between the two microstructures, showing that stress and strain are not size dependent. However, when comparing Figure 5 and 6, it can be observed that the matrix agglomerations do affect the local distribution of stress and strain in the microstructure, with higher stress and strain being detected near the agglomerations. The highest stresses are seen in the hard phase at the phase interface, while the highest strains are seen in the more compliant matrix phase. This shows that matrix agglomerations in the microstructure act as stress concentration factors. Carolan has previously observed this effect in the context of dynamic fracture of advanced ceramics [31].

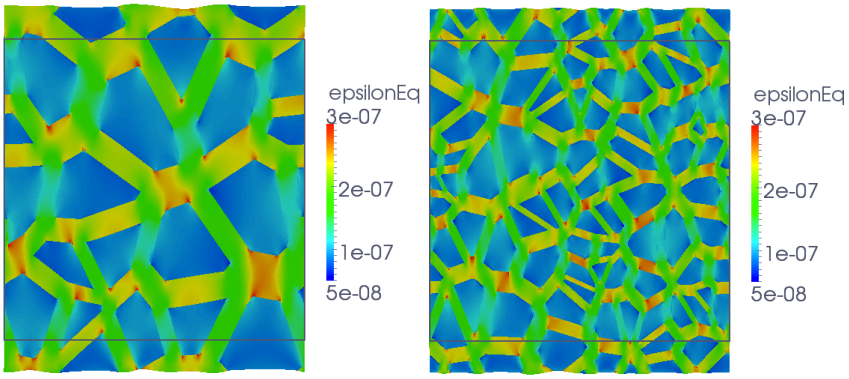

(a) 5x5 grains strain (b) 10x10 grains strain

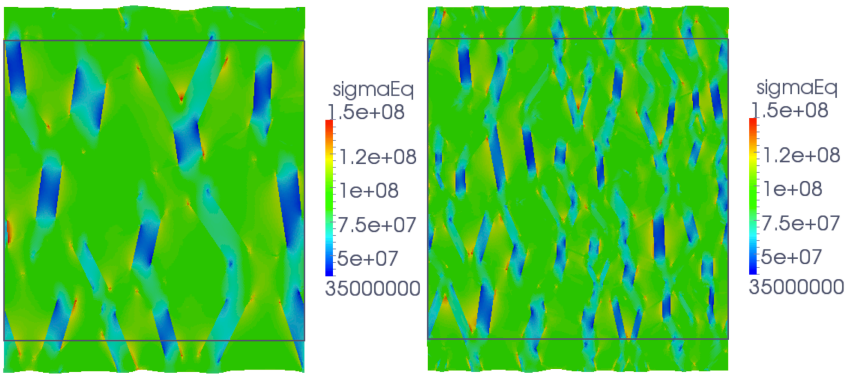

(c) 5×5 grains stress (d) 10×10 grains stress

Figure 5: Strain and stress distribution in the numerical microstructures with no matrix agglomerations subjected to a normal traction of 100 MPa. The deformation of the microstructure is magnified by a factor of 1000.

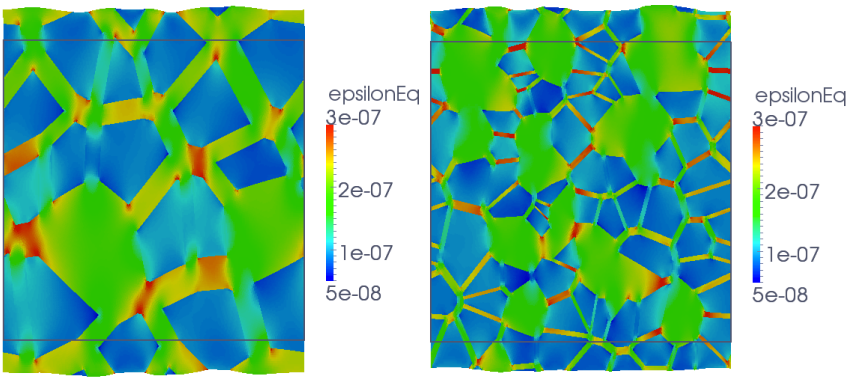

(a) 5×5 grains strain (b) 10×10 grains strain

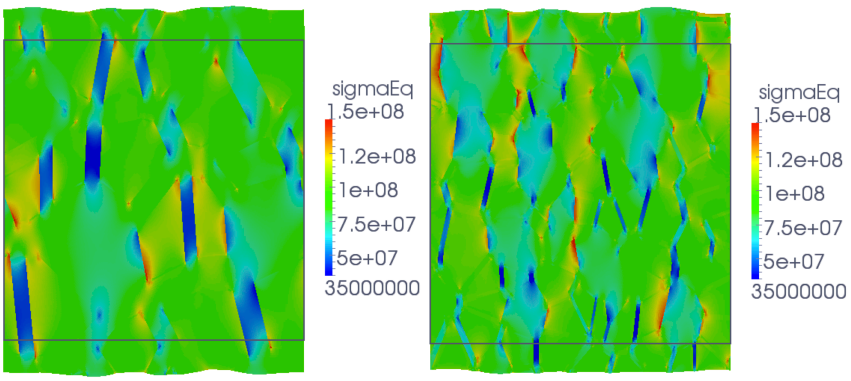

(c) 5×5 grains stress (d) 10×10 grains stress

Figure 6: Strain and stress distribution in the numerical microstructures with matrix agglomerations subjected to a normal traction of 100 MPa. The deformation of the microstructure is magnified by a factor of 1000.

4. Conclusion

The purpose of this paper was to develop statistically representative numerical models of advanced ceramic microstructures. The microstructures were generated using the Voronoi tessellation algorithm and subsequently altered to add a specified percentage primary inclusion phase and secondary phase matrix agglomerations to the microstructure. In the current paper it has been shown that the Voronoi Tessellation technique is a good method for the production of synthetic microstructures. The synthetic microstructures were compared to true microstructures and were found to be statistically representative in terms of grain size distribution, aspect ratio and agglomeration of a second phase material.

Using the numerically generated microstructures, Finite Volume analysis was carried out to investigate the stress and strain distributions in the microstructures and hence calculate the effective Young's modulus and Poisson's ratio. It was observed that the higher strains occur in the more compliant second phase material. This was more prevalent when there were agglomerations of the second phase material. Furthermore, it was observed that the presence of matrix agglomerations act as a stress concentration factor. Hence, the interface between particulates and a matrix agglomeration is likely to be the source of failure. This emphasises the need for accurate representation of microstructures in a numerical model.

The current paper presents a useful and implementable tool for investigating the effect of microstructural parameters on the microscopic stress distribution in a polycrystalline material. It is intended that the work will be extended to include other types of advanced ceramic material including single-phase ceramic as well as complex structures containing many different phases. Future work will concentrate on comparing the bulk elastic predictions with experimentally determined values for a range of advanced ceramics. It is also intended to extend the predictive capabilities of the models to capture strength and fracture behaviour.

Acknowledgements

The authors would like to thank Element Six Ltd., Enterprise Ireland and the Irish Research Council for providing financial support for this research.

References

[1] D. Carolan, P. Alveen, A. Ivanković, N. Murphy. Effect of notch root radius on fracture toughness of polycrystalline cubic boron nitride. Eng. Fract. Mech., 78 (2011) 2885-2895

[2] D. Carolan, A. Ivanković, N. Murphy. Thermal shock resistance of polycrystalline cubic boron nitride. J. Eur. Ceram. Soc., 32 (2012) 2581–2586

[3] J.J. Friel, J.C. Grande, D. Hetzner, K. Kurzydlowski, D. Laferty, M.T. Shehata, V. Smolej, G.F. Van-der Voort, L. Wojnar. Practical Guide to Image Analysis. ASM International, 2000.

[4] J.C. Russ. The Image Processing Handbook. CRC Press, 2nd edition, 1995.

[5] W.S. Rasband. ImageJ. U.S. National Institute of Health, Bethesda, Maryland, USA, http://imagej.nih.gov/ij/, 1997-2012.

[6] MATLAB. Image Processing Toolbox. The MathWorks Inc., Natick, Massachusetts.

[7] S.A. Langer, E.R. Fuller Jr., W.C. Carter. OOF: An Image-Based Finite-Element Analysis of Materials Microstructures. Comput. Sci. Eng., May/June (2001) 15–23

[8] V.R. Coffman, A.C.E. Reid, S.A. Langer, G. Dogan. OOF3D: An image-based finite element solver for materials science. Math. Comput. Simul. (2012) (http://dx.doi.org/10.1016/j.matcom.2012.03.003)

[9] A.C.E. Reid, S.A. Langer, R.C. Lua, V.R. Coffman, S. Haan, R.E. García. Image-based finite element mesh construction for material microstructures. Comput. Mater. Sci., 43(4) (2008) 989-999

[10] M. Huang, Y. Li. X-ray tomography image-based reconstruction of microstructural finite element mesh models for heterogeneous materials. Comput. Mater. Sci., 67 (2012) 63–72

[11] M. Nygårds, P. Gudmundson. Three-dimensional periodic Voronoi grain models and micromechanical FE-simulations of a two- phase steel. Comput. Mater. Sci., 24 (2002) 513–519

[12] M. Kühn, M.O. Steinhauser. Modeling and simulation of microstructures using power diagrams: Proof of the concept. Appl. Phys. Lett., 93 (2008) 034102

[13] L. Madej, L. Rauch, K. Perzynski, P. Cybulka. Digital Material Representation as an efficient tool for strain inhomogeneities analysis at the micro scale level. Archives of Civil and Mechanical Engineering, XI(3) (2011) 661–679

[14] P Zhang, D Balint, J Lin. An integrated scheme for crystal plasticity analysis: Virtual grain

structure generation. Comput. Mater. Sci., 50 (2011) 2854–2864

[15] P. Zhang, M. Karimpour, D. Balint, J. Lin, D. Farrugia. A controlled Poisson Voronoi tessellation for grain and cohesive boundary generation applied to crystal plasticity analysis. Comput. Mater. Sci., March (2012) 2–7

[16] R. Dobosz, M. Lewandowska, K.J. Kurzydlowski. FEM modelling of the combined effect of grain boundaries and second phase particles on the flow stress of nanocrystalline metals. Comput. Mater. Sci., 53(1) (2012) 286–293

[17] M. Danielsson, D.M. Parks, M.C. Boyce. Micromechanics, macromechanics and constitutive modeling of the elasto-viscoplastic deformation of rubber-toughened glassy polymers. J. Mech. Phys. Solids, 55(3) (2007) 533–561

[18] H.D. Espinosa, P.D. Zavattieri. A grain level model for the study of failure initiation and evolution in polycrystalline brittle materials. Part I: Theory and numerical implementation. Mech. Mater., 35 (2003) 333–364

[19] D.H. Warner, J.F. Molinari. Micromechanical finite element modeling of compressive fracture in confined alumina ceramic. Acta Mater., 54(19) (2006) 5135–5145

[20] T. Zhou, C. Huang, H. Liu, J. Wang, B. Zou, H Zhu. Crack propagation simulation in microstructure of ceramic tool materials. Comput. Mater. Sci., 54 (2012) 150–156

[21] H. Li, K. Li, G. Subhash, L.J. Kecskes, R.J. Dowding. Micromechanical modeling of tungsten-based bulk metallic glass matrix composites. Mater. Sci. Eng., A, 429 (2006) 115–123

[22] Y. Wang, L. Shuhua, P. Xiao, J. Zou. FEM simulations of tensile deformation and fracture analysis for CuW alloys at mesoscopic level. Comput. Mater. Sci., 50 (2011) 3450–3454

[23] H. Weller, G. Tabor, H. Jasak, C. Fureby. A tensorial approach to CFD using object oriented techniques. Computers in Physics, 12 (1998) 620– 631

[24] Z. Hashin, S. Shtrikman. A variational approach to the theory of the elastic behaviour of multiphase materials. J. Mech. Phys. Solids, 11 (1963) 127–140

[25] P. Wall. A comparison of homogenization, Hashin-Shtrikman bounds and the Halpin-Tsai equation. Applications of Mathematics, 42 (1997) 245–257

[26] Z. Hashin. On elastic behaviour of fibre reinforced materials of arbitrary transverse phase geometry. J. Mech. Phys. Solids, 13 (1965)119–134

[27] G. P. Tandon and G. J. Weng. Average stress in the matrix and effective moduli of randomly oriented composites. Compos. Sci. Technol., 27 (1986) 111–132

[28] T. Mori and K. Tanaka. Average stress in matrix and average elastic energy of materials with misfitting inclusions. Acta Metall., 21 (1973) 571– 574

[29] J.D. Eshelby. The determination of the elastic field of an ellipsoidal inclusion, and related problems. Proc. R. Soc. London, Ser. A, 241 (1957) 376–396

[30] X. Chen, Y. Mai. Micromechanics of rubbertoughened polymers. J. Mater. Sci., 33 (1998) 3529–3539

[31] D.Carolan, Mechanical and fracture properties of polycrystalline cubic boron nitride as a function of rate and temperature, PhD Thesis, University College Dublin, 2011.

Experimental Investigation on Deformation and Failure of Rock under Cyclic Indentation

Hao Zhang[1], Haipeng Song[1], Yilan Kang [1,*], Ganyun Huang[1]

[1] Tianjin Key Laboratory of Modern Engineering Mechanics, School of Mechanical Engineering, Tianjin University, Tianjin 300072, People's Republic of China

[*] Correspondence. E-mail: tju_ylkang@tju.edu.cn

Abstract Indentation induced cracking may have widely encountered in rock engineering, such as drilling and cutting process. It is significant to investigate the deformation and failure process for further understanding the failure mechanism of rock under cyclic indentation. In the present work, we have experimentally investigated the deformation fields on the sample surface via digital image correlation (DIC) technique. It has been found that the force-indentation displacement exhibits hysteresis during the loading-unloading cycles. The energy dissipation and the displacement field in the samples during the process has been analyzed. Furthermore, a median crack has been observed to nucleate running almost parallel to the loading axis when indentation force amounts to a critical value. Experimental analysis reveals that local tensile strain dominates the crack nucleation of rock and the shear strain has an effective influence on crack propagation. In unload-reloading process, crack behavior closure and re-opening is clearly observed by DIC technique. By the displacement distribution along the crack surface, crack opening displacement (COD) and stress intensity factor can be calculated for further fracture analysis.

Keywords Rock, Cyclic indentation, Digital image correlation, Deformation and failure

1. Introduction

Rock fragmentation induced by mechanical tools is an effective technique in mining and civil engineering. Rock cutting by various bits, such as drilling bit, rolling cutter, could be simplified as the cyclic indentation process [1]. Knowledge on deformation and failure process of rock is an important basis for the study of rock failure mechanisms. Therefore, it is necessary to experimentally investigate the damage and fragmentation of rock during cyclic indentation.

Many experimental tests have been conducted in the past decades to investigate the fragmentation of rock. Damage pattern which consists of inelastic zone and a region of multiple cracks is observed in rock under indentation [2]. Laboratory tests, simulating the disk cutter action at the tunnel face by means of an indenter, were carried out to explore the influence of the lateral confinement acting on the rock failure [3]. Acoustic emission (AE) and electronic speckle pattern interferometry (ESPI) techniques were used to detect the events of microcrack nucleation [4]. Numerical methods, such as the finite element method (FEM) [5], rock failure process analysis of two dimensions (RFPA2D) [6], have been developed to simulate the fragmentation process in rocks under indentation. Repeated loading–unloading conditions are widely encountered in practical excavation and drilling engineering. However, affects of cyclic loading on indentation-induced failure remains unclear.

In this work, cyclic indentation tests have been conducted to investigate the deformation and damage evolution of Yunnan sandstone. During the loading-unloading process, images of rock specimens have been sequently captured, from which deformation fields can be obtained by digital image correlation (DIC) processing. Displacement and apparent strain fields calculated by DIC, are

used to analyze the deformation, crack initiation, propagation during cyclic loading tests.

2. Experimental setup

Indentation tests were conducted on Yunnan sandstone plates with a dimension of 150×100×25 mm. Its surface was painted with randomly artificial speckle.Loading system includes electric universal machine (CSS-44100), indenter(diameter Φ=20 mm) and the fixture on which the specimen is mounted. During experiments, the load cell moved down and up with a constant velocity of 0.06 mm/min, the displacements, loads and time from the load cell, were continuously recorded during the experiment.

CCD camera with 1004×1003 pixels, a Matrox meteor Ⅱ image capture, a frame grabber and two white lights are used to capture images of the specimen. The observed area of specimen surface is 57×57mm. Sequential images were captured by a digital image system at a rate of 1 frame/s. Digital image correlation (DIC) is a powerful tool to measure the full field displacement distribution on the surface of specimens [7-9]. Then the displacement field can be used to derive the strain field by smoothing difference with numerical methods [10].Deformation information of specimen surface obtained by DIC, is used to characterize the damage and fracture process of rock.

3. Experiment

Samples of Yunnan sandstone were subjected to increasing-amplitude cyclic indentation experiments to investigate the evolution of deformation and fracture as rock approaches failure. The typical Load-displacement and Load-time curves are shown in Fig.1. The peak load of the first cycle is 10 kN (~30% peak load) and is increased by 5 kN in the subsequent cycles until the sample failed. The loading curves are usually not coincidence with the unloading curves and hence they form hysteresis loops which indicate that residual displacement develops.

The residual deformation exists not only at end of each cycle, but virtually at any load level during loading-unloading stage. It can be verified upon examining the load-displacement curves during different loading cycles but at the same load level. For instance, Fig.2 shows that during cycle 1 and 2 at the same load of 5 kN, the loading and unloading points A01, A11, B01, B11 are not coincident with each other on the load-displacement curves. To look into the displacement field in the indented sample, Fig.3 demonstrates DIC contours corresponding to points A01, A11, B01 and B11 designated in Fig. 2. One may find that the sequence of the severity of the vertical deformation at those points are A01, A11, B01 and B11, which is in good agreement with overall force-indenter displacement curves, but the horizontal displacement field at those points seems not to follow that simple sequence.

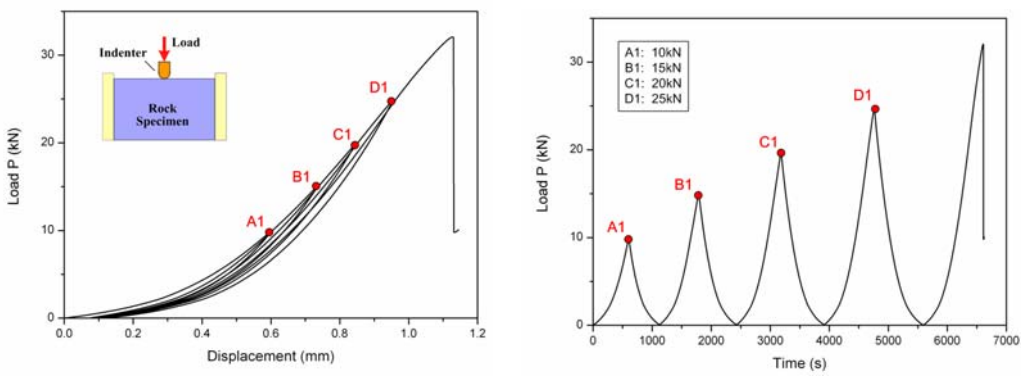

(a) (b)

Fig.1 Load-displacement and load-time curves of cyclic indentation tests.

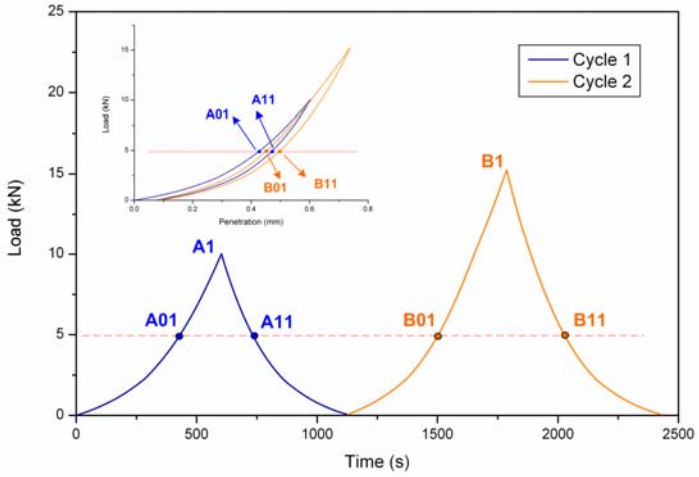

Fig.2 Mechanical response in the first two cycles

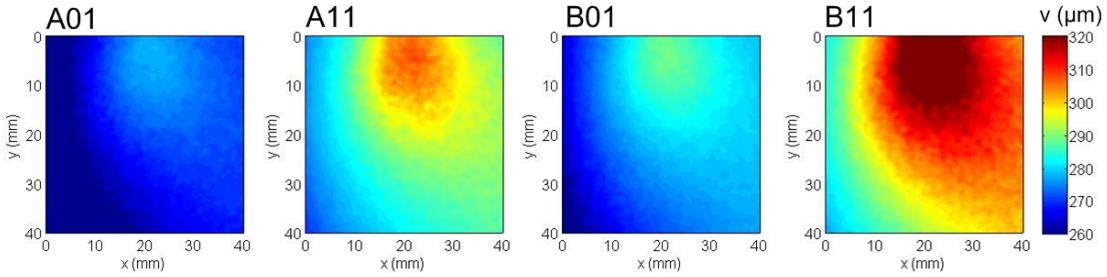

Fig.3 Vertical displacement fields at selected points with the same load P=5 kN.

It is well known that when the indentation force attains at a critical value, crack will nucleate and propagate in the sample that may lead to the final failure. By using the DIC technique, apparent strains at final stage of loading-unloading cycle are presented in Fig.4.Upon reloading to point D01 with load P=20 kN, tensile strain appears beneath the indenter and its maximum magnitude is about 0.6% located in the local region (Fig.5 D01 ε_x). Apparent shear strains were recognized by the contrast of red and blue regions, indicating concentration of shear strains in the central part of the specimen.

At D1 for load P=25 kN, the tensile strain concentrates in a very narrow belt, the value is far larger than those at other load level. Giving the sharp gradient of displacement, it can be concluded that a

crack has nucleated there. During the unloading period the peak of apparent strain is lower Fig.5 D2). It indicates that no additional new crack appears but only the existed crack begins to close. The value of ε_x is smallest at point D2 (load=0kN).

With increased subsequent loading, the crack develops both in length and opening. The significant increase was found in D21 (Load=25kN), apparent strains at the crack surfaces were obviously greater than D1. Afterwards, on continuous development of the cracking, the fracture eventually went through the specimen. After the test, it was observed that the crack identified by DIC developed along the path of the final failure.

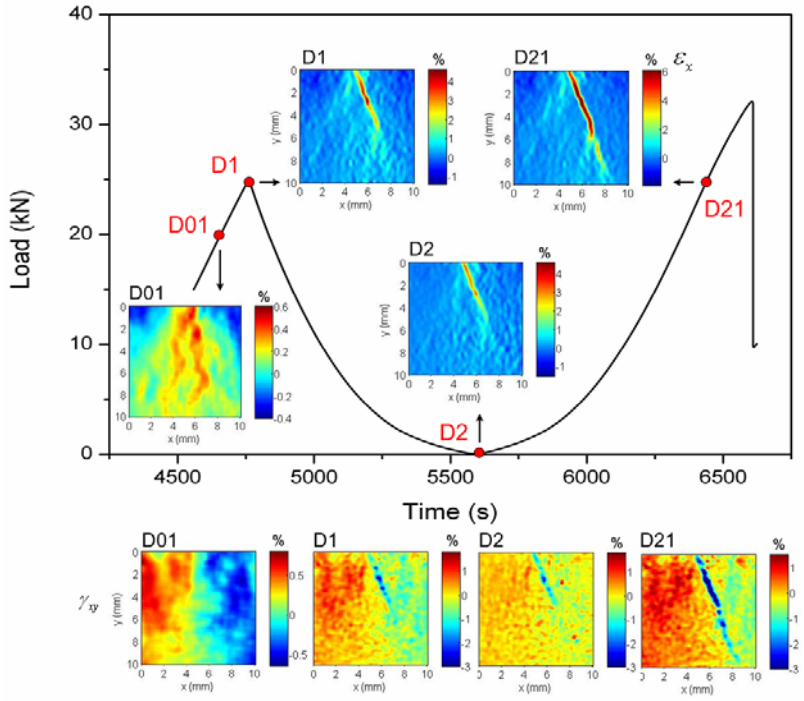

Fig.4 Distribution of the apparent strains ε_x and γ_{xy} during the final unloading and reloading stage

4. Conclusion

Cyclic indentation tests have been conducted in conjunction with the nondestructive technique of DIC to study the deformation and failure of rock samples. It has been found that DIC is an efficient method in tracing the deformation behavior and identifying the onset of the crack in rock.

By analysis of the experimental results, it has been detected that tensile strains concentrate beneath the indenter just before cracking, and a crack nucleates when the indentation load exceeds a critical value. The closure and propagation of the crack during unloading-reloading can be well described by the apparent strain fields.

Acknowledgements

This work was supported by the National Basic Research Program of China (No.2013CB035402) and National Natural Science Foundation of China (NSFC, Grant No.11127202 and No.11072170).

References

[1] Chiaia B. Fracture mechanisms induced in a brittle material by a hard cutting indenter. Int J Solids Struct. 2001;38:7747-68.
[2] Pang SS, Goldsmith W. Investigation of crack formation during loading of brittle rock. Rock Mechanics and Rock Engineering. 1990;23:53-63.
[3] Innaurato N, Oggeri C, Oreste PP, Vinai R. Experimental and Numerical Studies on Rock Breaking with TBM Tools under High Stress Confinement. Rock Mech Rock Eng. 2007;40:429-51.
[4] Chen LH, Labuz JF. Indentation of rock by wedge-shaped tools. Int J Rock Mech Min Sci. 2006;43:1023-33.
[5] Carpinteri A, Invernizzi S. Numerical analysis of the cutting interaction between indenters acting on disordered materials. Int J Fract. 2005;131:143-54.
[6] Wang S, Sloan S, Liu H, Tang C. Numerical simulation of the rock fragmentation process induced by two drill bits subjected to static and dynamic (impact) loading. Rock Mech Rock Eng. 2011;44:317-32.
[7] Zhang H, Huang G, Song H, Kang Y. Experimental investigation of deformation and failure mechanisms in rock under indentation by digital image correlation. Eng Fract Mech. 2012;96:667-75.
[8] Kang Y-L, Zhang Z-F, Wang H-W, Qin Q-H. Experimental investigations of the effect of thickness on fracture toughness of metallic foils. Mater Sci Eng: A. 2005;394:312-9.
[9] Wang H-W, Kang Y-L, Zhang Z-F, Qin Q-H. Size effect on the fracture toughness of metallic foil. Int J Fract. 2003;123:177-85.
[10] Pan B, Qian K, Xie H, Asundi A. Two-dimensional digital image correlation for in-plane displacement and strain measurement: a review. Measure Sci Tech. 2009;20:062001.

Investigation of the fracture behavior of tungsten at the micro scale

Nicola J. Schmitt[1,*], Christoph Bohnert[1,2], Christoph Eberl[1,3], Ruth Schwaiger[1], Sabine M. Weygand[2], Oliver Kraft[1]

[1)] Institute for Applied Materials (IAM), Karlsruhe Institute of Technology (KIT), Hermann-von-Helmholtz-Platz 1, 76344 Eggenstein-Leopoldshafen (Germany)

[2)] Faculty of Mechanical Engineering and Mechatronics (MMT), Karlsruhe University of Applied Sciences, Moltkestr. 30, 76133 Karlsruhe (Germany)

[3)] Fraunhofer Institute for Mechanics of Materials (IWM), Wöhlerstraße 11, 79108 Freiburg (Germany)

*Corresponding author: nicola.schmitt@kit.edu

Abstract Tungsten promises great potential in very high temperature applications due to its very high melting point. Yet its brittleness, far above room temperature, limits its application. Investigations have already shown that fracture toughness of polycrystalline tungsten strongly depends on microstructural characteristics like grain size and shape, and texture. To gain a better insight into the basic mechanisms, fracture toughness experiments are carried out at the micro-scale. First experiments focus on the influence of the crystal orientation with respect to cracking. Here, we report on micro bending tests on free standing, notched, single crystal micro cantilevers. With respect to the {110}<1$\bar{1}$0> crack system, the beam axis was normal to the {110} crystal plane.

Keywords Tungsten, fracture toughness, crystal orientation, micro bending experiments

1. Introduction

Tungsten is a very promising material for power generation due to its outstanding properties at high temperatures such as high strength, high Young's modulus, and of course its high melting point. A huge drawback, though, is its brittleness and high brittle-to-ductile temperature which limits the use of tungsten significantly. Therefore, several studies have already been carried out to investigate the fracture behavior and to provide suitable remedies.

An extensive study of the fracture toughness of tungsten single crystals had been carried out by Riedle and Gumbsch [1-3]. They considered the influence of crystal orientation, loading rate, and temperature on the fracture behavior. Furthermore, studies on the fracture behavior of polycrystalline tungsten were reported by Gludovatz et al. [4], who investigated pure polycrystalline tungsten as well as doped tungsten to gain different microstructures at various temperatures. Experiments on pure rolled polycrystalline tungsten were carried out by Rupp and Weygand [5]. They observed the influence of different grain boundary orientations on the fracture behavior. All those investigations showed that fracture toughness in single crystal and commercial polycrystalline tungsten strongly depend on microstructural characteristics and loading conditions. However, most studies were carried out at the macro-scale with few exceptions such as Wurster et al. [6] who studied the fracture behavior of single crystalline tungsten at the micro-scale.

The aim of this study is to observe the fracture behavior of tungsten at the micro-scale to deepen the insight into the fracture behavior of tungsten on a micromechanical basis. For this, free standing single crystal bending cantilevers with a typical dimension of 20 µm in width and 40 µm in height have been manufactured and tested using a nanoindenter. To investigate the influence of different crack systems, experiments will be carried out with differently oriented beams. Further experiments

on bi-crystals will be conducted in situ using the SEM to see the influence of grain boundary. Here, we report on the development of the testing procedure as well as first results for beams that are oriented to induce fracture in the {110}<1$\bar{1}$0> crack system. The investigations are accompanied by crystal plasticity simulations [7] addressing the interplay of cracking and plastic deformation at small scale.

2. Experimental

Tungsten single crystals with 3 mm in width and height and 5 mm in length were used for the manufacturing of the free-standing micro bending beams. The samples were aligned in a specific crystal orientation.

At the scale the experiments are conducted, the standard geometry and procedure of the ASTM E 399-90 for the determination of the fracture toughness does not apply, the plastic zone is too large relative to the cantilever dimensions. Also, no standardized testing device is available to conduct standard fracture toughness tests at this length-scale. Therefore, a new specimen geometry was developed which is shown in Figure 1. The geometry is a result of the available manufacturing and testing conditions. To design the experiment close to the standard test, the relations of width, length, and height are derived from the ASTM E 399-90 for standard fracture toughness tests. As the samples are going to be tested with a nanoindenter free-standing cantilevers were chosen. The length of the cantilevers is roughly 160 µm, the width is 33 µm and the height is 40 µm. At this scale the focused ion beam (FIB, FEI Company, Nova 200 NanoLab) is an accurate and nearly inevitable tool, yet at the targeted dimensions it is rather time consuming and inefficient. Therefore, the basic cantilevers were carved by a micro electrical discharge machining (µ-EDM) process. The actual width of the gage section width is thinned to 20 µm and the notch is cut to a depth of 20 µm at a distance of 50 µm from the shoulder using a focused ion beam (FIB). The radii between the bulk material and the cantilever are roughly 20 µm which can be realized reliably by µ-EDM. Due to the manufacturing process, however, the geometry varies from the design dimensions, and the size and shape of each individual beam is inspected by scanning electron microscopy (SEM).

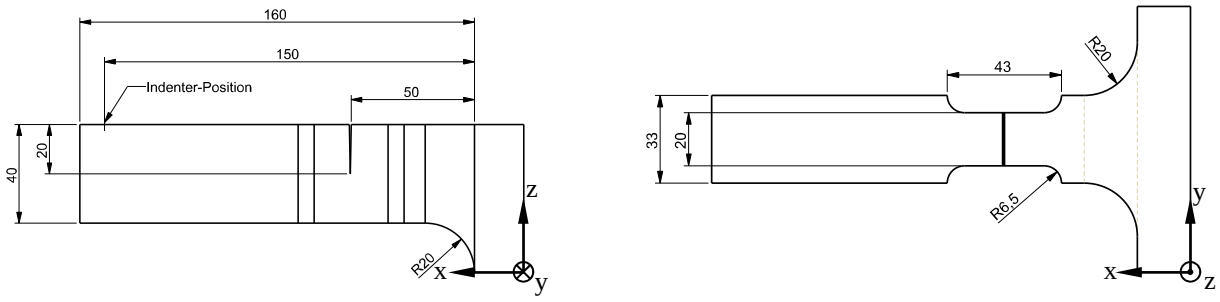

Figure 1. Developed free standing micro bending beam geometry as a result of manufacturing and testing restrictions.

In the first preparation step, the samples were mechanically polished using a Struers TriPod polishing fixture and Allied diamond lapping foils (9 µm, 6 µm, 3 µm, 1 µm, 0.5 µm). This results in an almost plane surface and sharp edges. This is necessary, as the bending cantilevers will be

carved from the edges of the single crystals. Rounded edges would lead to cantilevers with decreasing thickness.

A custom-built specimen holder based on a goniometer was used to align the samples accurately for the µ-EDM process. First, a thin plate with the thickness of the cantilevers was prepared by a horizontal cut parallel to the polished surface. Afterwards, every single cantilever was carved from the thin plate by vertical cuts.

Due to the heat input and the re-deposition of molten material, the µ-EDM process results in a rather rough surface of the micro cantilevers. Also micro-cracks and changes of the microstructure may be possible. The µ-EDM exposed surfaces did not yield a diffraction pattern when investigated by electron backscatter diffraction (EBSD). However, EBSD investigations on a beam cross-section after EDM showed that less than 1 µm beneath that modified layer the EBSD pattern indicates no orientation changes, with respect to the initial material. Thus, we conclude that the beams remain single crystalline after the EDM process.

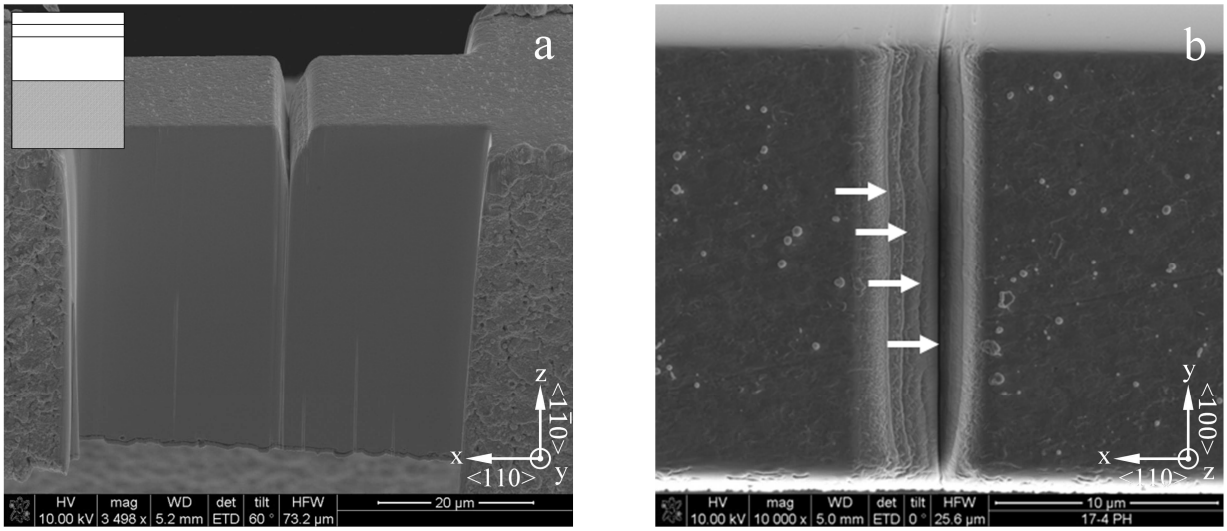

Figure 2. SEM micrographs showing the introduced notch which is cut with the ion beam perpendicular to the surface. The SEM micrograph 2a shows the cleaned gage section and the notch from the side. The insert shows a schematic cross-section of the notch. The SEM micrograph 2b shows a top-view. The arrows show the individual millings steps for 5, 3, 1 µm and the line milling mode.

To minimize the influence of µ-EDM processing, FIB was used to polish the gage sections of the cantilevers. Successive cutting from the surface towards the middle of the beam by FIB was conducted to remove the damage layer, to machine the necessary dimensions, and to smoothen the surface of the beam. For all milling steps an acceleration voltage of 30 kV was used. To remove the main part of the material relatively high gallium ion currents of 5 to 20 nA were applied. In order to reduce the influence of the gallium ions in the material the last cleaning steps were carried out by lower gallium ion currents of 1 to 3 nA. Finally, a notch was cut from the top surface with a depth of approximately 8 µm. For the notches a current of 1 nA was used. In order to gain a deep and sharp notch the machining process was carried out in several milling steps. The steps were

successively narrowed from 5 to 3 and 1 µm and as a last milling step, the final notch was introduced using the line milling mode. The ion beam was always perpendicular to the surface. Figure 2 shows the notch shape.

The successive milling process of the gage section showed that the µ-EDM induced micro-cracks. However, they never reached deeper than 3 µm. Therefore, the milling process was adjusted such that roughly 4 µm of the material was removed to exclude the influence of micro-cracking on the fracture behavior. Figure 3 shows a typical surface of a micro-cantilever which was treated by µ-EDM, micro-cracks can be observed.

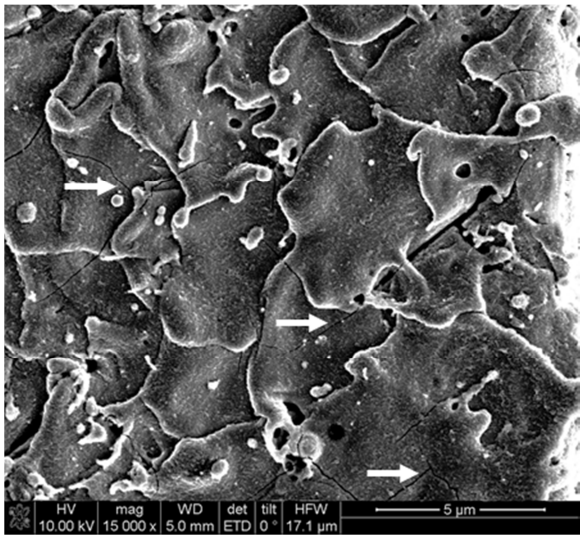

Figure 3. The rough surface of the micro cantilever as a result of the µ-EDM process. Micro cracks in the surface can be observed. The white arrows highlight some of the micro cracks.

For the bending experiments two commercially available nanoindentation systems were used (MTS, Nano Indenter XP and Agilent Technologies, G200). The indenter tip was used to bend the cantilever at a defined distance to the notch. Then, a holding segment of 10 seconds was applied before unloading. For all experiments a Berkovich tip was used. Afterwards the broken cantilevers were investigated by scanning electron microscopy (SEM).

3. Results and Discussion

The force-displacement curves shown in Figure 4 belong to two beams that are oriented to induce fracture in the $\{110\}\langle 1\bar{1}0\rangle$ crack system. The cantilevers were displaced to 12 µm (blue curve) and 15 µm (green curve) at a distance of about 120 µm from the notch. As the maximum displacement is reached, the holding segment follows and the maximum load is held constant. The curve shows clearly an elastic-plastic transition but no abrupt load drop which would be indicative of brittle fracture. Interestingly, a large deflection takes place during the hold segment. Presumably this is caused by an increasing crack length over time which in turn is correlated to an increasing ΔK under constant load. Since this is a rather peculiar behavior, it will be investigated further by

changing the loading sequence of the test.

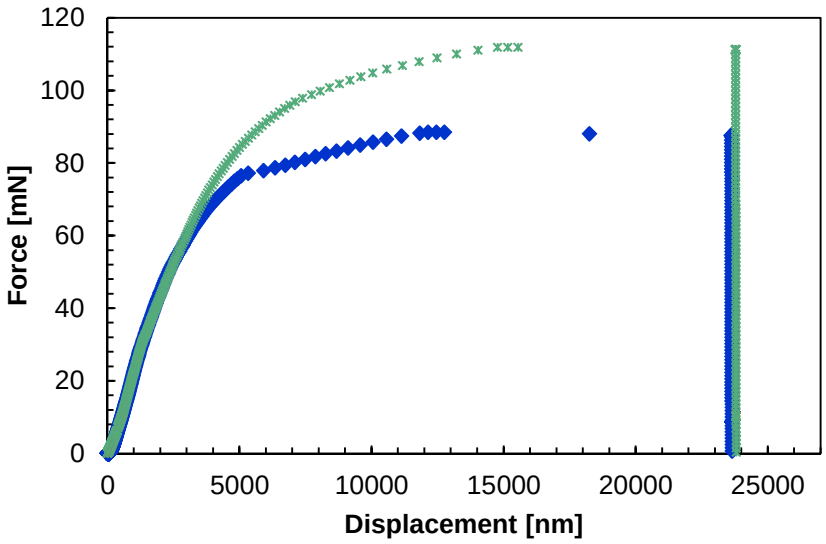

Figure 4. Two force-displacement curves of two notched beams. One beam was loaded to a displacement of 12 µm (blue curve) the other one to 15 µm (green curve) (Figure 5a). With respect to the {110}<1$\bar{1}$0> crack system, the beam axis was normal to the {110} crystal plane for both notched beams.

The curves show a rather ductile behavior, however, an investigation of the fractured surface indicates partially brittle failure. Figure 5a shows the fractured beams and Figure 5b and c the surface of the broken cantilevers. It clearly shows brittle cleavage in the middle of the beam, while at the upper edges signs of plastic deformation are seen.

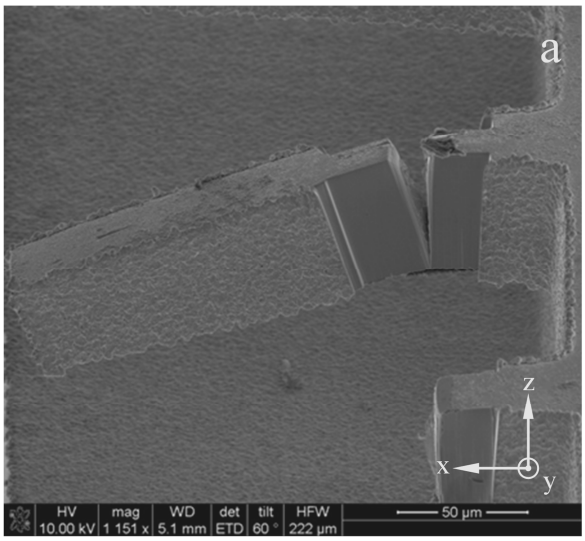

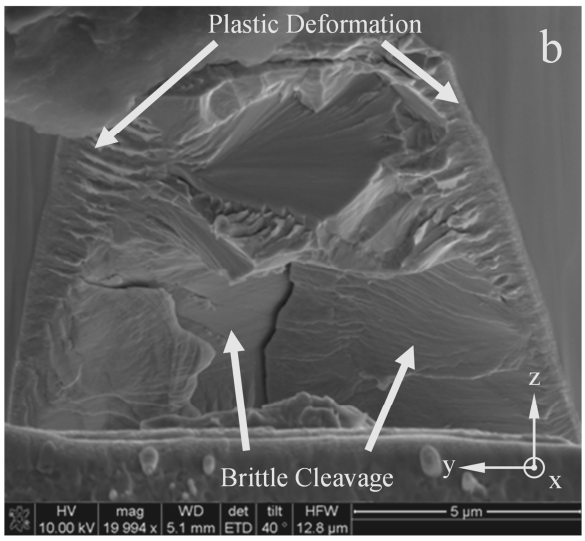

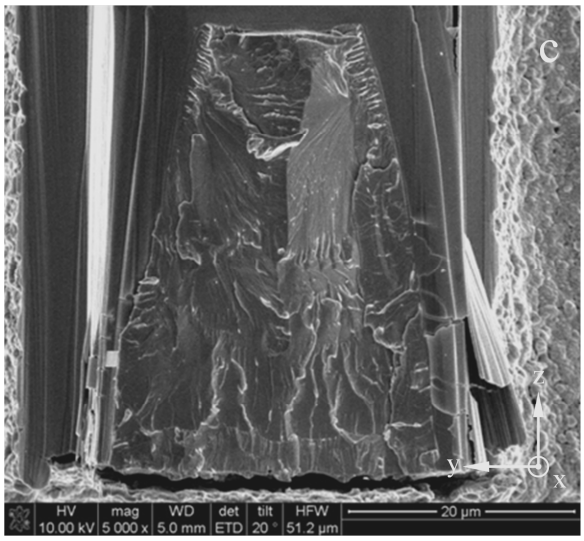

Figure 5. a) Post-test overview of beam 1 and 2. b) Cleavage surface of beam 1 which was deflected 12 µm under displacement control and fractured further under constant load. The beam did not fail completely. c) Cleavage surface of beam 2 which was displaced 15 µm. It fractured completely during the holding segment

The fracture toughness cannot be calculated following the ASTM E 399-90 as it does not apply at this small scale. Also, it is not trivial to determine the weight function for this geometry. Therefore, we take a simplistic approach to estimate the fracture toughness by looking at an energy relation. Equation (1) relates the fracture toughness K_Q and the energy release rate G_Q were E is Young's modulus [8].

$$K_Q^2 = G_Q \cdot \mathrm{E}, \tag{1}$$

Thereby G_Q can be calculated after [9]:

$$G_Q = \frac{d(W - U_{el})}{dA}, \tag{2}$$

Here, W is the work of the external forces, U_{el} the elastically stored energy and dA the change of the area of the crack which is taken here to be the entire fracture plane. As the elastically stored energy U_{el} is subtracted from the external forces W, the shape modification energy only remains. To gain the work of the external forces, the load-displacement curve was integrated. For the elastically stored energy, the area enclosed by Hook's' straight line and the curve at the maximum displacement was calculated. For the calculation of the size of the fracture plane the program ImageJ was used. Therefore, the fracture surface, depicted in an SEM Image, was enclosed by a polygon. The resulting surface area was calculated by the program in dependence of the SEM magnification. With this calculation, values of the fracture toughness K_Q = 31 MPa·m$^{1/2}$ and 35 MPa·m$^{1/2}$ were obtained when including the displacement during the hold segment. These values are quite high and can be only considered as an upper bound. For a lower bound, a second value was calculated neglecting the holding segment. Thereby, values for the fracture toughness K_Q of 6.7 MPa·m$^{1/2}$ and 5.9 MPa·m$^{1/2}$

were obtained. These values are pretty low compared to data of Gumbsch and Riedel [1,3] of 12.9 ± 2.1 MPa·m$^{1/2}$ for the fracture toughness of the {110}<1$\bar{1}$0> crack system. However, the experiments are not completely comparable as different sample dimensions and loading conditions were used. As shown in Figure 5, for our small samples, it is seen that the plastic zone size is large relative to the sample dimensions. Therefore, we would rather expect a larger value than the one reported by Riedel and Gumbsch. This also confirms the need to improve the test method. Errors in the fracture surface analysis cannot account for the large difference.

Improvements in the manufacturing process, testing conditions and also analysis are currently in progress. For instance, the surface of the basic material can be treated by µ-EDM. This would lead to sharper edges. Therefore, cantilevers with decreasing cross sections along the axis will be avoided, compared to the polishing with the Struers TriPod and diamond lapping foils. Also, a wedge tip will be used instead of the Berkovich tip in order to avoid slipping and other effects related to the point loading.

Most importantly, another notch geometry will be tested. As it is not possible to introduce a sharp crack via fatigue at this specimen dimension, a Chevron notch geometry will be tested in the future. This should lead to a more controlled crack propagation as the resistance against crack propagation will increase with increasing crack propagation. An example of the FIB machined Chevron notch geometry is shown in Figure 6. For fabrication, the specimen was tilted so that the ion beam cut the specimen at an angle of about 30°. The middle of the width of the specimen, where the notch should be placed, was marked by FIB. From this mark, the notch was cut under the given angle, then the specimen was rotated by 180° and the second part of the notch was milled.

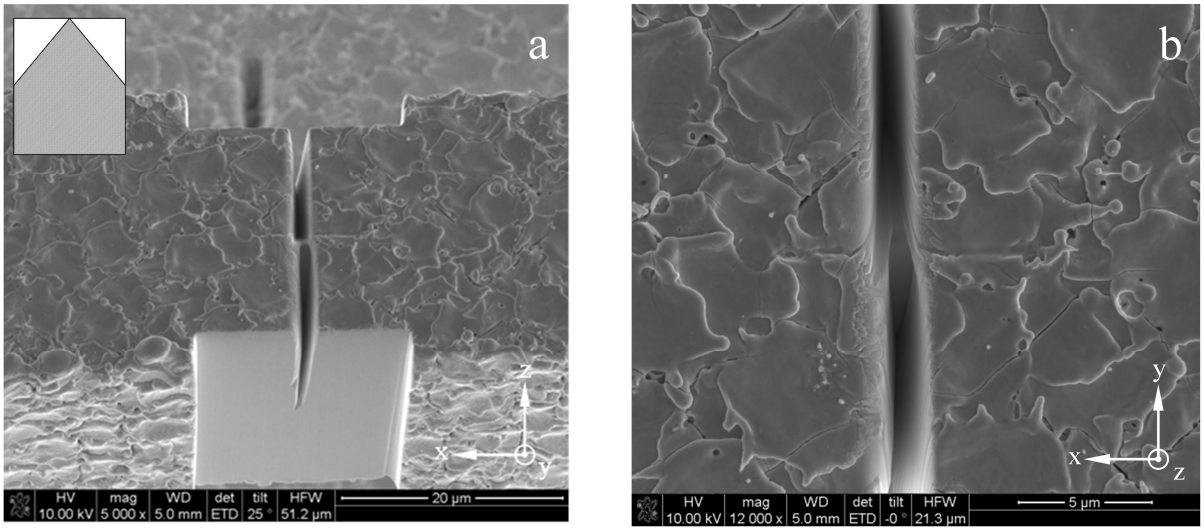

Figure 6. The introduced Chevron notch. The SEM micrograph 6a shows the cleaned gage section and the notch from the side. The insert shows a schematic cross-section of the Chevron notch. The SEM micrograph 6b shows the top-view.

4. Summary

The fracture toughness of single crystalline tungsten for the {110}<1$\bar{1}$0> crack system at the micro scale has been investigated. Free-standing single crystal micro cantilevers were manufactured by µ-EDM followed by surface cleaning and cutting a notch by FIB. The micro cantilevers were tested with a nanoindenter. The cantilever axes were aligned with the normal direction of the {110} crystal plane, while the loading direction was parallel to the <1$\bar{1}$0> direction. The force-displacement curves show a rather elastic-plastic behavior, whereas the observation of the fracture surface reveals ductile features at the edges of the crack surface and brittle ones in the middle. The K_Q values were estimated via an energy relation. The estimated values were in a range between 5.9 and 35 MPa·m$^{1/2}$ as the lower and upper limits. Further improvements of the test method will be made in the future including optimizing the beam shape, testing method as well as the notch shape. Furthermore, the investigations will be extended towards other crack systems as well as bi-crystals and in situ experiments in the SEM.

Acknowledgements

The authors thank Christoph Ruhs and the Institute of Production Science of the Karlsruher Institute of Technology for the implementation of the µ-EDM process.
Also, thank goes to the Landesgraduiertenförderung of the state of Baden-Württemberg in the framework of the Promotionskolleg on ”Gefügestrukturanalyse und Prozessbewertung” for their financial support.

References

[1] P. Gumbsch, Brittle fracture and the brittle-to-ductile transition of tungsten. J Nucl Mater 2003; 323:304-12.
[2] J. Riedel, Bruchwiderstand in Wolfram-Einkristallen: Einfluss der kristallographischen Orientierung, der Temperatur und der Lastrate. Reihe 18 – Nr. 184: Düsseldorf: VDI Verlag; 1990.
[3] J. Riedel, P. Gumbsch, H. Fischmeister, Cleavage anisotroy in tungsten single crystals. Phys Rev Lett 1996;76:3594-7
[4] B. Gludovatz, S. Wurster, A. Hoffmann, R. Pippan, Fracture toughness of polycrystalline tungsten alloys. Int J of Refrac Met and Hard Mat 2010;28:674-678
[5] D. Rupp, S. M. Weygand, Experimental investigation of the fracture toughness of polycrystalline tungsten in the brittle and semi-brittle regime. J Nucl Mater 2009;386-388:591-593
[6] S. Wurster, C. Motz, R. Pippan, Characterization of the fracture toughness of micro-sized tungsten single crystal notched specimens. Philos Mag 2012;92:1803-1825
[7] C. Bohnert, S. M. Weygand, N. J. Schmitt, O. Kraft, Numerical Investigation of the Fracture Behavior of Tungsten at the Micro scale, ICF13th International Conf. on Frature, Beijing, 2013
[8] J. Rösler, H. Harders, M. Bäker, Mechanisches Verhalten der Werkstoffe. B. G. Teubner Verlag/GWV Fachverlage GmbH, Wiesbaden 2003
[9] H. Blumenaue, G. Pusch, Technische Bruchmechanik, WILEY-VCH Verlag GmbH & Co. KgaA, Weinheim 2001

Prediction Model of Cleavage Fracture Toughness of Ferrite Steel

Kazuki Shibanuma[1,*], Shuji Aihara[1], Motoyuki Matsubara[2], Hiroyuki Shirahata[3], Tsunehisa Handa[4]

[1] Department of Systems Innovation, The University of Tokyo, Tokyo 113-8656, Japan
[2] Hanshin Plant, Kubota Corporation, Hyogo 660-0857, Japan
[3] Oita R&D Lab., Nippon Steel & Sumitomo Metal Corporation, Oita 870-0992, Japan
[4] Joining & Strength Research Department, JFE Steel Corporation, Chiba 260-0835, Japan
* Corresponding author: shibanuma@fract.t.u-tokyo.ac.jp

Abstract A numerical model to quantitatively predict a cleavage fracture toughness in ferrite-cementite steel is proposed based on a microscopic fracture initiation process of three stages; (I) formation of fracture origin by cementite cracking, (II) propagation of the cementite crack into ferrite matrix, and (III) propagation across ferrite grain boundary. The fracture condition of Stage (I) is formulated as a ratio of cementite cracking based on experimental results of a tensile testing with notched specimens and SEM observation. Stage (II) and Stage (III) conditions are formulated based on a concept of fracture stress criterion. In the numerical model, an active zone is divided into finite volume elements. Ferrite grains and cementite particles are assigned based on their distributions into each volume element. Strain and stress at each volume element are calculated by a macroscopic FEA. Fracture is assumed to initiate at the time when the fracture conditions of the all stages are satisfied in any one of the volume elements. The model is validated by three point bend testing with notched specimens. The predicted values of fracture toughness show good agreement with the experimental results. Therefore, the effectiveness of the proposed model is found out.
Keywords Cleavage fracture, Fracture toughness, Multiscale, Fracture stress, Ferrite

1. Introduction

In order to prevent brittle fracture in steel structures, it is critically important to predict fracture toughness by clarification of crack initiation mechanism.

It is widely known that fracture appearance transition temperature of Charpy impact testing changes linearly with reciprocal of the square root of grain size [1]. The reason is, however, not clarified completely. It is also known that the fracture toughness depends on the size of brittle phase such as cementite [2]. In addition, several formulations to evaluate the influence of microstructures including the size of ferrite grain and brittle phase are proposed by Almond *et al*. [3], Petch [4] and Bingley [5]. However, there remains a problem to improve their accuracy.

The cleavage fracture of steel is generally interpreted by the weakest-link mechanism differently from the yielding and the work hardening. Scatter in the fracture toughness is therefore essential. This is a principal reason of the difficulty to quantify the influence of microstructures on fracture toughness. A formulation to evaluate the variation of fracture toughness was proposed by Beremin [6] based on the weakest-link theory. It was, however, based on the concept of the macroscopic continuum mechanics and thus was not able to clarify the relationship between the variation of the fracture toughness and microstructures.

In the present paper, a numerical model is proposed to quantitatively predict the influence of microstructures on the fracture toughness of ferrite-cementite steels, based on the formulation of the cleavage fracture initiation process.

2. Formulation of Cleavage Fracture Initiation Process

2.1. Process of fracture initiation

We assume that the process of cleavage fracture initiation in ferrite-cementite steels is composed of three stages; (I) formation of fracture origin by cementite cracking, (II) propagation of the crack in cementite into the ferrite matrix and formation of a cleavage crack, and (III) propagation of the cleavage crack across ferrite grain boundary. Schematic view of this process is shown in Fig. 1. It is assumed that a macroscopic brittle fracture occurs if fracture conditions of all the above stages are satisfied. In the following section, the fracture conditions of respective stages are formulated.

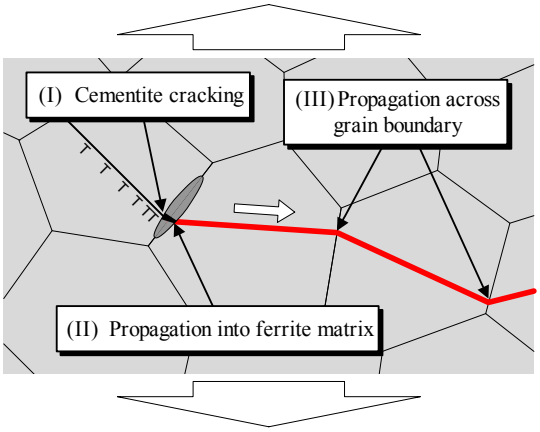

Fig. 1 Three stages of cleavage fracture initiation process

2.2. Formulations of fracture conditions

Stage (I). Formation of fracture origin by cementite cracking

We quantify the influencing factors on the cementite cracking based on experimental facts.

Test steels with various sizes of ferrite grains and cementite particles were produced and tensile testing with a circumferential notched round bar specimen was performed. The test steels were produced by laboratory scale vacuum melting and rolling. Two types of chemical compositions are employed, as shown in Table 1. It can be regarded that their compositions are practically the same except for carbon concentration. Seven types of steels were produced whose sizes of ferrite grains and cementite particles were systematically changed by combinations of controlled rolling, controlled cooling, normalizing and annealing processes. Definitions of symbols relating to the sizes of ferrite grains and cementite particles are shown in Table 2. Grain sizes of the steels were measured as area equivalent diameter by EBSD observation [7]. In addition, cementite particle thickness was measured as minor axis of approximated ellipse by FE-SEM observation of the microstructure etched by nital and an image analysis [8]. Representative values of ferrite grain size

Table 1 Chemical compositions of test steels [mass%]

Symbol	C	Si	Mn	P	S	Al	N
10	0.10	0.06	0.49	< 0.002	0.0005	0.010	0.0011
5	0.05	0.05	0.48	< 0.002	0.0003	0.010	0.0014

Table 2 Symbols of steels

Cementite size	**Ferrite grain size**		
	Large	Medium	Small
Large	10LL	-	5SL
Medium	10LM	10MM	-
Small	10LS	-	10SS / 5SS

Table 3 Representative values of grain size and cementite particle thickness and yield stress at room temperature

Symbol		10LL	10LM	10LS	10MM	10SS	5SL	5SS
Ferrite grain diameter [$\times 10^{-3}$ mm]	Average	57	63	58	38	16	27	23
	Max	218	226	229	104	47	67	45
Cementite thickness [$\times 10^{-3}$ mm]	99%max	0.83	0.41	0.24	0.43	0.20	0.66	0.20
	Max	1.87	1.02	0.66	1.21	0.49	1.15	0.44
Yield stress at room temperature [MPa]		161	170	171	215	247	213	248

and cementite particle thickness, together with yield stress at room temperature are shown in Table 3.

Quasi-static tensile test using circumferential notched round bar specimens was conducted. The specimen configuration is shown in Fig. 2. After tensile strain was applied, the specimen was unloaded and cementite cracking was observed. Extensometer gauge displacement at unloading was determined so that the maximum principal plastic strain at the minimum cross section is equal to 0.4. The displacement was estimated by a preliminary elasto–plastic FEA. An example of the numerical results is described as Fig. 3. The results show that the maximum principal plastic strain and stress change in the axial direction but are almost constant on each transverse cross section.

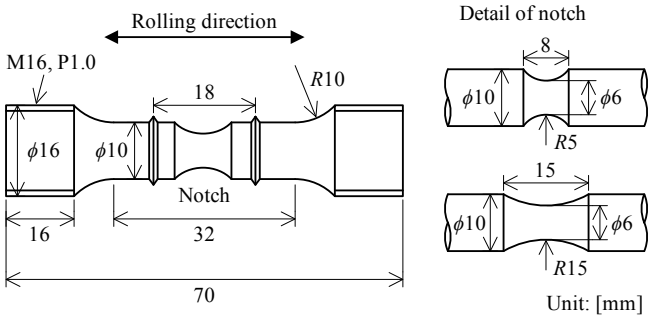

Fig. 2 Configuration of circumferential notched round bar specimen

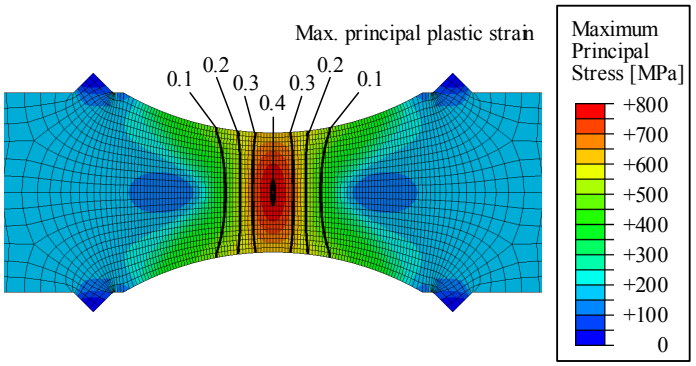

Fig. 3 Strain and stress distributions in circumferential notched round specimen (10MM, $R = 15$ mm, -80°C)

The unloaded specimen was cut in the axis direction. The maximum principal plastic strain and stress are assumed constant along the transverse direction on the cut surface. The cracked cementite was measured by scanning the surface in the transverse direction by SEM observation after polishing and etching. The applied strain can be varied by changing the scanning location in the axial direction.

The numbers of the cracked cementite particles were measured for the steels and conditions of temperature and strain. An example of the SEM images of the cracked cementite is shown in Fig. 4. Results of dependence of the number of the cracked cementite on the maximum principal plastic strain and the temperature for 10LM steel are shown in Fig. 5. The number of the cracked cementite is almost in proportion to the principal plastic strain. The results also show that the lower temperature makes the larger number of the cementite cracking.

The cementite cracking might be regarded as stress-controlled fracture. However, the stress applied to a cementite particle is controlled by the applied strain of the ferrite matrix. It can be understood that the larger deformation resistance of ferrite matrix makes the larger applied stress in the cementite particle. Furthermore, total number of the cementite particles must be proportional to carbon content if cementite size distribution remains unchanged.

Now, it may be rationalized that the number of cracked cementite particles is normalized by a parameter η, which is defined as a product of the applied maximum principal stress $\sigma_{\max}$ (normalized by Young's modulus E) and mass fraction of carbon r_C as

$$\eta = \frac{\sigma_{\max}}{E} r_C \tag{1}$$

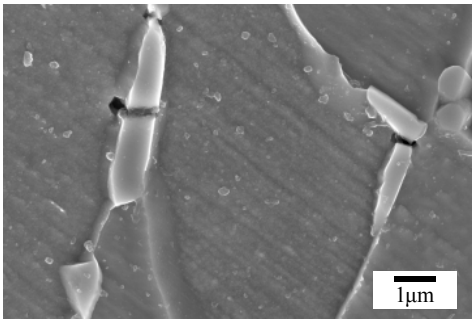

Fig. 4 SEM image of cracked cementite (10LM, $\varepsilon_p = 0.2$)

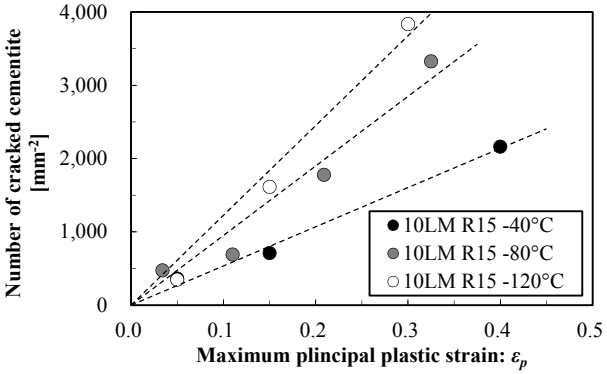

Fig. 5 Dependence of the number of cementite cracking on plastic strain and temperature

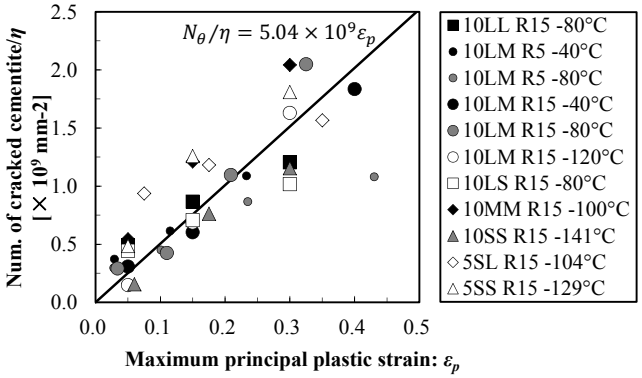

Fig. 6 Number of cracked cementite normalized by applied maximum principal stress and mass fraction of carbon

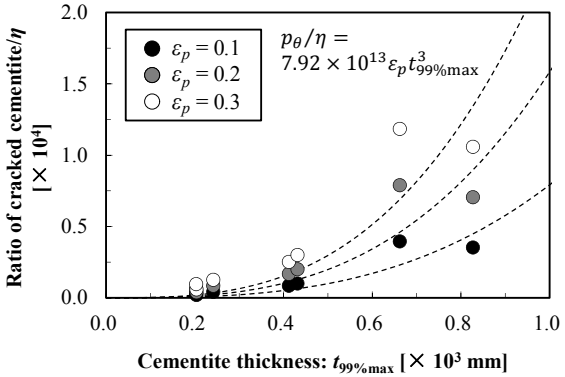

Fig. 7 Ratio of cementite cracking normalized by applied maximum principal stress and mass carbon content

Results of all the tests are shown in Fig. 6. Although a data scatter is found, the number of the cracked cementite particles mig ht be approximated as

$$\frac{N_\theta}{\eta} = 5.04 \times 10^9 \varepsilon_p \tag{2}$$

where N_θ is the number of the cracked cementite particles per unit area (1 mm^2) and ε_p is the maximum principal plastic strain. It is noted that N_θ/η is independent from the cementite particle thickness distribution.

A ratio of cementite cracking p_θ is defined as the number of the cracked cementite particles divided by the number of the all cementite particles per unit area. It is found that the ratio of the cementite cracking is higher in the steel with larger cementite size. Plots of p_θ/η related to $t_{99\%\max}$ (unit: mm) of each steel (see Table 3) are shown in Fig. 7. By fitting the relationship between p_θ/η and $t_{99\%\max}$, we obtain

$$\frac{p_\theta}{\eta} = 7.92 \times 10^{13} \varepsilon_p t_{99\%\max}^3 \tag{3}$$

as indicated by the lines in Fig. 7.

As a generalization of Eq. (3), the ratio of cementite cracking for arbitrary cementite particle thickness t (unit: mm) is expressed as

$$p_\theta = 7.92 \times 10^{13} \eta \varepsilon_p t^3 \quad (4)$$

Stage (II). Propagation of crack in cementite into ferrite matrix

Local fracture stress required for a propagation of a cementite crack into ferrite matrix was formulated by Petch [4]. We assume a fracture condition of Stage (II) as

$$\sigma_n \geq \sigma_{F\theta\alpha} \quad (5)$$

σ_n is a maximum normal stress on the {100}-plane of the ferrite grain because it is known that a cleavage fracture surface in a BCC polycrystal including ferrite-cementite steel are generally formed on a {100}-plane [9]. σ_n is calculated as

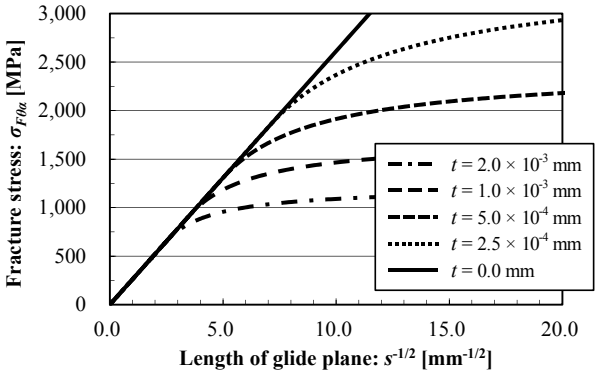

Fig. 8 Dependence of fracture stress $\sigma_{F\theta\alpha}$ on grain size d and cementite particle thickness t

$$\sigma_n = \max_{m=1,2,3} (\mathbf{n}_m)^T \cdot \boldsymbol{\sigma} \cdot \mathbf{n}_m \quad (6)$$

where $\mathbf{n}_m$ is a normal vector of the m-th {100}-plane and $\boldsymbol{\sigma}$ is a applied stress tensor.

$\sigma_{F\theta\alpha}$ in Eq (5) is the fracture stress of Stage (II) originally formulated by Petch [4] as

$$\sigma_{F\theta\alpha} = \begin{cases} \dfrac{4E\gamma_{\theta\alpha}}{\left(1+\dfrac{1}{\sqrt{2}}\right)(1-\nu^2)k_y\sqrt{s}} & (t_\theta < c_c) \\ \sqrt{\dfrac{4E\gamma_{\theta\alpha}}{\pi(1-\nu^2)t_\theta} - \dfrac{k_y^2 s}{8\pi^2 t_\theta^2}} - \dfrac{k_y\sqrt{s}}{2\sqrt{2}\pi t_\theta} & (t_\theta \geq c_c) \end{cases} \quad (7)$$

where ν is a Poisson's ratio. The definition of $\sigma_{F\theta\alpha}$ is slightly modified from the original one by replacing a ferrite grain diameter with a length of the dislocation line s. k_y is a locking parameter in the Hall-Petch law and is assumed to equal 20.7 MPa mm$^{1/2}$ based on our preliminary test. $\gamma_{\theta\alpha}$ is effective surface energy and is given as 10 J/m^2 [4]. c_c is critical cementite particle thickness defined as

$$c_c = \frac{\left(1+\dfrac{1}{\sqrt{2}}\right)(1-\nu^2)k_y^2 s}{8\pi E\gamma_{\theta\alpha}} \quad (8)$$

$\sigma_{F\theta\alpha}$ is derived from a comparison of the sum of energy release rate of the crack and piled-up dislocation energy with the effective surface energy. The dependence of $\sigma_{F\theta\alpha}$ on s and t is shown in Fig. 8.

Stage (III). Propagation of cleavage crack across ferrite grain boundary

We assume fracture condition of propagation of a cleavage crack across ferrite grain boundary as

$$\sigma_n \geq \sigma_{F\alpha\alpha} \quad (9)$$

where σ_n can be calculated by the equation same as that for Stage (II), i.e. Eq. (6). On the other

hand, $\sigma_{F\alpha\alpha}$ is local fracture stress for Stage (III) formulated based on the Griffith theory, as

$$\sigma_{F\alpha\alpha} = \sqrt{\frac{\pi E \gamma_{\alpha\alpha}}{(1-\nu^2)D}} \tag{9}$$

where D is a diameter of cleaved surface formed in Stage (II) and $\gamma_{\alpha\alpha}$ is an effective surface energy for a cleavage crack in a ferrite grain to propagate across grain boundary. It is assumed that $\gamma_{\alpha\alpha}$ depends on temperature because plastic deformation below cleavage fracture surface changes with temperature [10]. Temperature dependence of $\gamma_{\alpha\alpha}$ is thus assumed based on the experimental results by San Martin and Rodriguez-Ibabe [11], as shown in Fig. 9. Although the figure shows steep increase at temperature higher than -70°C, the present study employs the value of $\gamma_{\alpha\alpha}$ in the temperature range lower than -80°C.

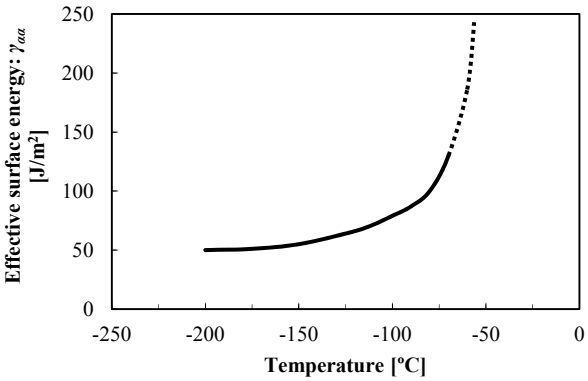

Fig. 9 Effective surface energy for across grain boundary [11]

3. Development of Numerical Model

Considering the fracture conditions of the three stages described in the previous section, a numerical model of the cleavage fracture initiation of ferrite-cementite steels is developed. Procedures of the modeling are described as follows.

(a) A domain where the cleavage fracture initiation is possible to occur is defined as an active zone.
(b) The active zone is divided by cubic volume elements of the same size. It is noted that the size of the volume elements must be larger than the maximum grain size. A schematic view of the volume element is shown in Fig. 10.
(c) Ferrite grains are assigned at random in each volume element based on ferrite grain size distribution until sum of the volume of the assigned grains reaches that of the elemental volume. At the same time, crystallographic orientation of each grain is determined at random.
(d) Cementite particles are assigned in each volume element based on cementite particle thickness (minor axis) distribution. The shape of the cementite is approximated as a prolate spheroid.
(e) Macroscopic elasto-plastic FEA is performed based on true stress-strain curve and stress tensor and a maximum principal plastic strain at each volume element are evaluated at each step time. In the calculation, step time increments are defined for the evaluation of the cleavage fracture initiation at the same time.
(f) The cleavage fracture initiation process based on the three stages is evaluated in each volume element for a time step as following (g) ~ (k).
(g) For Stage (I), cracked cementite particle distribution is evaluated based on Eq. (4) by using the distribution of cementite particle thickness in the volume element.
(h) For the stage (II), first, two ferrite grains (Grain A and Grain B) adjacent to the respective cracked cementite obtained in [g] are selected at random. Grain A and Grain B are used for the evaluation of σ_n in Eq. (6) and $\sigma_{F\theta\alpha}$ in Eq. (7), respectively. Assuming the location of the each cementite particle on the boundary of Grain B, the length of dislocation line s is determined. Then, the evaluation of fracture condition of Stage (II) is carried out based on Eq. (5) for all the combinations of the ferrite grains and the cracked cementite particles. If the fracture condition is satisfied, a cleavage crack is assumed to form in Grain A and the cleaved

grain is excluded in following time steps.

(i) In the case that Stage (II) is satisfied, Stage (III) is then evaluated. First, an additional grain (Grain C) is selected at random. Then, $\sigma_{F\alpha\alpha}$ and σ_n in Eq. (8) are respectively calculated by using Grain A and of Grain C, and the fracture condition of Stage (III) is evaluated.

(j) Cleavage fracture is assumed to be initiated at the time when the fracture condition of Stage (III) is satisfied in any one of the volume elements. That is a "weakest link" assumption in this model.

(k) If the fracture is not initiated, the calculations of (f) ~ (j) are carried out for the next time step.

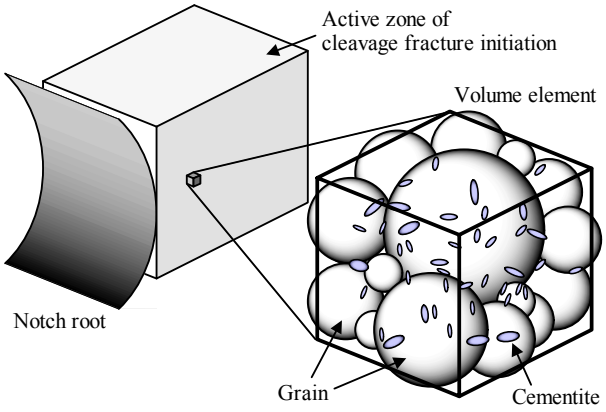

Fig. 10 Modeling of volume element

4. Simulation of Fracture Toughness Testing

4.1 Experiment

Three point bending test using notched specimens was conducted. The specimen was machined from the steels 10LL, 10LS, 5SL and 5SS, which were used in Section 2.2. Configuration of the specimen is shown in Fig. 11. Test temperature was changed between -150°C and -80°C. Loading rate was 1 mm/min. Notch opening displacement was measured by a clip gauge attached to the edge of the notch.

Quasi-CTOD is introduced as a parameter to evaluate the fracture toughness. The quasi-CTOD is calculated by simply applying the CTOD estimation formula [12], as

$$\delta = \frac{K^2(1-\nu^2)}{2\sigma_Y E} + \frac{r_p(W-a)V_p}{r_p(W-a)+a+z} \tag{9}$$

where K is a stress intensity factor, σ_Y is a yield stress at a test temperature, r_p is the rotation factor (= 0.4), W is the width of the specimen (= 20 mm), a is the notch depth (= 7 mm), z is the distance of the notch opening gauge location above the specimen surface (= 0 mm), V_p is plastic component of the notch opening displacement. It is noted that the quasi-CTOD does not represent physical crack tip opening displacement but just represents intensity of deformation at the notch root. Critical values of the quasi-CTOD are used for a validation of the developed model.

4.2 Model conditions

In the procedure (a), the active zone is defined as a rectangular parallelepiped whose side lengths are 1.6 mm, 1 mm and 20.0 mm in respective directions of the width, the axis and the thickness of the specimen, based on the preliminary observation of the fracture initiation points.

The size of each volume element in the procedure (b) is also defined as a rectangular parallelepiped. The side lengths are 0.2 mm, 0.167 mm and 0.2 mm in the respective directions. This is nearly equivalent to the size of a sphere whose diameter is 0.25 mm. The number of the volume elements is 6,000 in the active zone as a result.

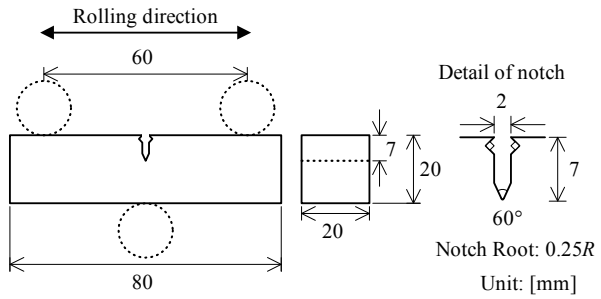

Fig. 11 Configuration of three point-bend specimen

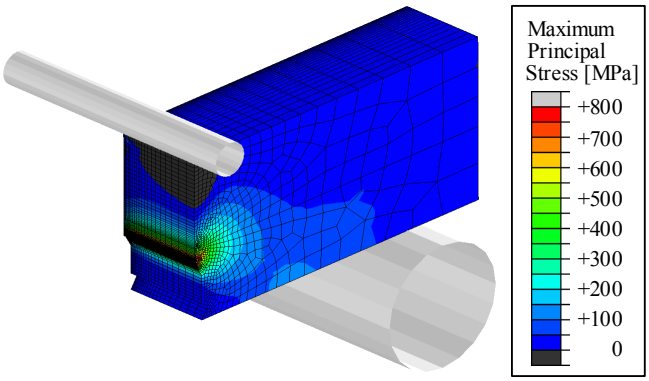

Fig. 14 Mesh division and stress distribution in FEA (10LL, -120°C)

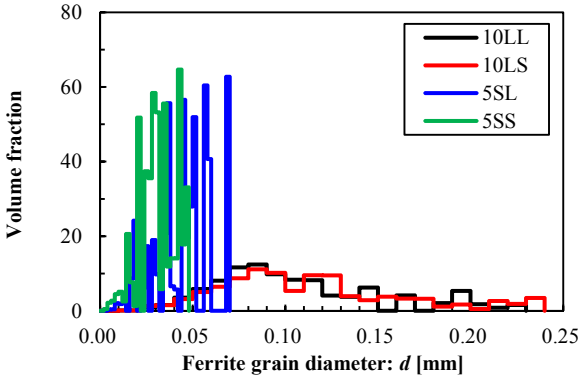

(a) Ferrite grain diameter

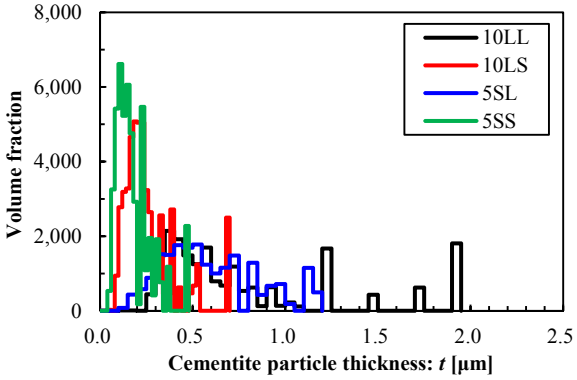

(b) Cementite particle thickness

Fig. 13 Distributions of ferrite grain diameter and cementite particle thickness

In the procedures (c) and (d), The ferrite grains and the cementite particles are assigned at random in each volume element based on their distributions shown in Fig. 13.

A quarter-symmetry finite element model is used to obtain stress and strain distributions in the active zone in the procedure (e). Displacement is applied by the jig. The mesh division and an example of the calculated stress distribution are shown in Fig. 14.

4.3 Results and discussions

Comparisons of the experimental results and the prediction values of the critical quasi-CTOD are shown in Fig. 15. The predicted values show good agreements with the experimental results in all the steels. The variation of the predicted critical values under the same conditions is derived from the stochastic nature of the developed model, i.e., the toughness scatter is derived from the statistical size distributions of ferrite grains and cementite particles. It is obviously found that the transition curve of the critical quasi-CTOD is shifted to lower temperature for finer ferrite grain steel. In addition, the same tendency is found for smaller cementite particle steel.

In the results of the respective steels, the predicted values reproduce the tendency that lower temperature makes lower values of the critical quasi-CTOD. The predicted values at high temperature are evaluated with high accuracy. On the other hand, the results at low temperature are underestimated in some cases. As causes of this result, an excessive cementite cracking in Stage (I) and accuracies of the effective surface energies $\gamma_{\theta\alpha}$ in Stage (II) and $\gamma_{\alpha\alpha}$ in Stage (III) might be

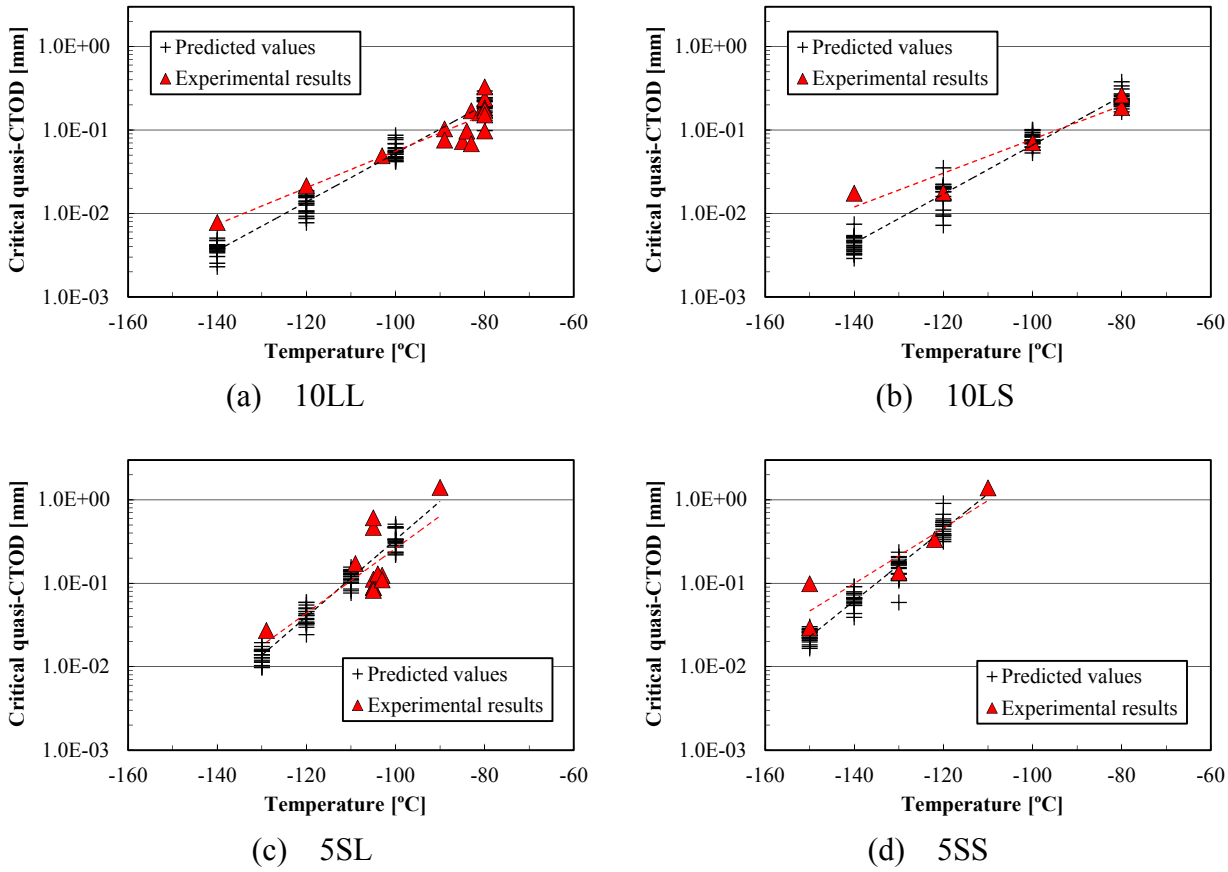

Fig. 15 Comparison between experimental and numerical results of critical quasi-CTOD

pointed out. In order to improve this problem, modification of the formulation of the ratio of the cementite cracking considering the shape of the cementite particles, and quantitative and accurate estimations of $\gamma_{\theta\alpha}$ and $\gamma_{\alpha\alpha}$ must be required. The maximum differences of the transition temperatures between the experimental results and the predicted values is however 15°C. Based on the aforementioned results, the validation and the effectiveness of the proposed model are found out.

5. Conclusions

A numerical model to quantitatively evaluate a cleavage fracture initiation in ferrite-cementite steel was developed. The model is based on the microscopic fracture process of the three stages; (I) formation of fracture origin by cementite cracking, (II) propagation of the cementite crack into ferrite matrix and formation of a cleavage crack, and (III) propagation of cleavage crack across ferrite grain boundary.

The fracture conditions of respective stages were formulated. The fracture condition of Stage (I) is formulated as a ratio of cementite cracking based on experimental results of a tensile testing with notched specimens and SEM observation using steels with various ferrite and cementite sizes. The fracture conditions of Stage (II) and Stage (III) were formulated based on the concept of the fracture stress.

In the development of numerical model, an active zone is defined and divided into volume elements. Ferrite grains and cementite particles are assigned based on their distributions into each volume

element. Strain and stress at each volume element are evaluated by macroscopic FEA. Cleavage fracture is assumed to initiate at the time when the fracture conditions of the all stages are satisfied in any one of the volume element.

The developed model was validated by three point bend testing of notched specimens using steels with various ferrite and cementite sizes. The numerical predicted values of fracture toughness show good agreement with the experimental results for all cases. It is therefore concluded that the proposed model is effective to predict the fracture toughness of ferrite-cementite steels.

Acknowledgements

Part of the present work was funded by the Fundamental Research Developing Association Shipbuilding Offshore. The authors would like to thank the members of the forum of the Iron and Steel Institute of Japan for their valuable discussions.

References

[1] W.C. Leslie, The Physical Metallurgy of Steels, Mcgraw-Hill College, 1981.
[2] D.A. Curry, J.F. Knott, Effects of microstructure on cleavage fracture stress in steel. Metal Science, 12 (1978) 511-514.
[3] E.A. Almond, D.H. Timbres, J.D. Embury, The influence of second phase particles on fracture. Proceedings of the International Conference on Fracture, 2 (1969) 253-265.
[4] N.J. Petch, The influence of grain boundary carbide and grain size on the cleavage strength and impact transition temperature of steel. Acta Metallurgica, 34 (1986) 1387-1393.
[5] M.S. Bingley, Effect of grain size and carbide thickness on impact transition temperature of low carbon structural steels. Materials Science and Technology, 17 (2001) 700-714.
[6] F.M. Beremin, A local criterion for cleavage fracture of a nuclear pressure vessel steel. Metallurgical and Materials Transactions A, 14 (1983) 2277-2287.
[7] OIM Data Collection User's Manual, TexSEM Laboratories, 2007.
[8] W.S. Rasband, ImageJ, U. S. National Institutes of Health, Bethesda, Maryland, 2011, http://rsb.info.nih.gov/ij/.
[9] A.S. Tetelman, A.J. McEvily, Jr. Fracture of Structural Materials, John Wiley & Sons, Inc., New York, 1967.
[10] Tsann Lin, A.G. Evans, R.O. Ritchie, Stochastic modeling of the independent roles of particle size and grain size in transgranular cleavage fracture. Metallurgical and Materials Transactions A, 18 (1987) 641-651.
[11] J.I. San Martin, J.M. Rodriguez-Ibabe, Determination of energetic parameters controlling cleavage fracture in a Ti-V microalloyed ferrite-pearlite steel. Scripta Materialia, 40 (1999) 459-464.
[12] BS 7448: Part 1, Fracture Mechanics Toughness Tests, Part 1, Method for Determination of K_{Ic}, Critical CTOD and Critical J Values of Metallic Materials, British Standard Institution, 1991.

Investigation of grain-scale surface deformation of a pure aluminium polycrystal through kinematic-thermal full-field coupling measurement

X.G. Wang*, J.F. Witz, A. El Bartali, P. Dufrénoy, E. Charkaluk

Laboratoire de Mécanique de Lille - CNRS UMR 8107, Boulevard Paul Langevin,
59655 Villeneuve d'Ascq cedex, France
* Corresponding author: xiaogang.wang@ed.univ-lille1.fr

Abstract This is a study of plastic strain localization, temperature evolution, surface roughening and of the origin of these phenomena in polycrystals. First, a review on different techniques of coupled kinematic-thermal measurements is given, and the two-face set-up, after several technical improvements, was employed in our work. Thanks to this integrated optical system, the full-field strain and temperature of the aluminium oligocrystal specimen were measured simultaneously during a tensile test. And the coupled data was further proceeded by following some particular methodologies, namely the Lagrangian thermography and the crystallography-based field projection. The surface profile of the deformed specimen was measured by interferometric profilometer, which showed clearly that the specimen had been suffered a strong out-of-plane deformation during the test. This out-of-plane effect was highlighted in the temperature field as well as in the strain field, which brought considerable affections on the measurement precisions of temperature and in-plane strain. Further data analysis shows that the heterogeneity of the out-of-plane deformation is closely associated with the crystallographic structure of the material, and reveals that the grain boundaries and grain interactions during the deformation play an important role in the process of deformation, temperature and surface profile evolutions.

Keywords Strain heterogeneity, Out-of-plane deformation, Infrared thermography, Digital image correlation, Coupled measurement

1. Introduction

The polycrystalline metal is an aggregate of grains having a distribution of crystallographic orientations. During an applied mechanical loading, according to the different orientations and the influences from neighboring grains, some grains are submitted to a more important deformation than others, leading to local heterogeneous plasticity [1]. As known that when the metal is plastically deformed, a certain part of strain energy will be dissipated as heat, and the left will remain in the material. The latter, conventionally called stored energy, is associated with microstructure changes of material and was regarded as a sensitive indicator of damage evolution [2]. As a consequence, the study on "heat source" (or stored energy) needed to be linked with the material plasticity and microstructure evolution, and an experimental energy balance was expected to be built based on a full-field measurement of strain and temperature.

Nowadays the full-field optical measurement techniques, due to its advantages in non-contact, full-field and scalability, become more and more popular. Among these techniques, DIC (Digital Image Correlation) and IRT (InfraRed Thermography) have attracted increasingly attentions, which can provide the full-field measurements of strain and temperature, respectively. The heterogeneity feature of the plastic strain occurring on polycrystal was well characterized by DIC [3, 4], as well as the heterogeneous temperature field observed by IRT [5–7]. For promoting a better understanding of heat source, a coupled kinematic-thermal measurement becomes a necessary.

Recently, this anticipated coupled measurement has been realized, and it exists actually several different techniques, which can be classified according to their experimental set-ups: namely two-face measurement [8, 9], single-face measurement [10, 11] and one-shot measurement [12, 13]. In this paper we will also present our novel two-face measurement system, with its improvements in aspects of synchronization and spatial alignment.

Beyond these advances in aspects of technique, the research interest in this field appeared a noteworthy tendency: a transformation from macroscale to microscale [14, 15]. At the same time the role and importance of the microstructure were highlighted, which gave birth to a new methodology: microstructure-based full-field analysis [16, 17]. This method was applied on a polycrystalline material made of grown but still relatively small grains in the work [16]. Recently, some more simple and well-defined crystallographic structures, such as oligocrystal and bi-crystal, were tested [9, 11]. That certainly simplified the thermomechanical behavior of the material and thus facilitated a microstructure-based analysis.

In this work the studied material is a pure oligocrystal aluminium specimen with a single layer of coarse grains. It will undergo a plastic deformation in a tensile test, being measured in real time by the fully-coupled optical system, which thus provides the strain and temperature fields. The surface profile of the deformed specimen will be also measured after the test by interferometric profilometer. The various data will be treated in Lagrangian coordination system and be projected on a crystallographic base followed by the results analysis and discussions.

2. Coupled kinematic-thermal measurement

2.1. Review of techniques

To our knowledge, it exists actually four different experimental techniques that have been developed in the last few years for achieving the combined kinematic-thermal field measurements. Among them, each technique has its advantages and disadvantages, regarding on the studied material, measurement scale and expected precision. Nevertheless, it is important to note that IRT and DIC usually have contrast technique restraints, in particular on choosing the surface coatings for the specimen. IRT generally prefers a uniform coating with a very high emissivity, such as carbon black, thus an accurate infrared measurement can be conducted. On the contrast, DIC requires a very heterogeneous coating, such as speckled painting, for the purpose of tracking material points that should differ widely in gray levels. Several ways of achieving such a coupling are presented here.

1) Two-face measurement

Each imaging device (IR and visible camera) observes one face of the specimen [8, 9]. The main advantage of this set-up is that each technique has the flexibility to choose the surface coating for its own good without special constraints. This is very important concerning the measurement precision for each technique. The disadvantage of this set-up lies in the fact: for a thin, flat specimen being studied on a macroscale, it is assumed that the two faces of the specimen show virtually the same thermomechanical behaviors. But if thermal and kinematic fields are sought for comparison at the microstructural scale, this technique requires the microstructure to be the same on both faces.

2) Single-face measurement

Both IR and visible cameras observe the same face of the specimen. Two kinds of the experimental set-up can be found:

a) Introducing an angle between the IR and visible cameras [11]. Generally this kind of set-up needs a correction of the image distortions introduced by the inclination of the camera with respect to the normal direction to the specimen surface. This angle should be as small as possible, but still restricted by the physical volumes of the cameras.

b) Introducing a dichroic mirror [10]. The dichroic mirror, thanks to its filtering properties,

transmits the IR radiations towards the IR camera placed in the front of the specimen, and reflects the rest of the radiations towards the CCD camera located on the other side. This set-up can solve the image distortion problem, but the mirror may also introduce some experimental bias due to the transmission and reflection [16].

A common problem for the single-face measurement is the coating for the specimen surface, which is desired to be heterogeneous in the visible vision and be homogeneous in the IR vision. A special coating developed in the work [10] meets such a characteristic.

3) One-shot measurement

A single IR camera is used to measure both kinematic and thermal fields on the same surface of the specimen. In other words, the IR images will be treated not only for IRT but also for DIC. This technique, called "one-shot measurement", was recently developed in [12, 13]. The main advantage of this technique is that it needs neither synchronization nor spatial matching, thus any temporal/spatial bias between the kinematic and thermal fields can be avoided. However, the main problem with this method is that the DIC precision will be inevitably lowered as the IR camera cannot provide a comparable high-resolution sensor array as the visible camera. A decrease in performance should be also found in IRT because of a wide variation in emissivity on the surface coating, which serves for the point tracking of DIC.

After an overview on the available techniques, the two-face measurement was chosen in this study for two reasons: 1) a high requirement on the measurement precision; 2) the oligocrystal specimen used in this work exhibits a quasi-identical microstructure on the two faces.

2.2. Developments on "two-face" measurement

In order to perform a precise and reliable two-face measurement, the two cameras should be firstly synchronized, and then a spatial alignment should be achieved on the two kinds of images produced by the IR and visible cameras, respectively.

2.3.1. Synchronization

The digital camera for DIC technique adopted in this work is the Elphel network camera (Elphel 353), and the IR camera is the FLIR Titanium camera (SC7000). As there is no commercial trigger box available for synchronizing these two cameras, a micro-controller (Arduino Mega 2560) was thus employed for triggering them from external.

The working principle of the micro-controller is to trigger the two cameras, by sending two periodic pulse signals, so as to command them function at the same moment. It is important to note that each camera has a time delay (the time period from receive the signal to take the image), which should be considered in the controlling program in order to assure that they take images on exactly the same moment.

The time delay of FLIR camera was given by the manufacturer, which was as low as 2.8 μs. The time delay of Elphel camera, however, was unknown, and thus needed to be tested. To this end, a special free-fall test was designed in order to estimate this time delay. In this test, the two cameras observed the same zone on a background, a small object was dropped from the air to pass this common zone, and a position difference, due to the time delay, thus appeared in the two captured images. According to the distance and velocity, the time delay can be estimated.

The results showed that the measured time delay of Elphel camera was 2.65 ms with a slight

deviation. After considering each time delay of the two cameras in the trigger program, the coupled measurement system can be synchronized.

2.3.2. Reference target

In the experimental set-up of the two-face measurement, the two cameras are placed face-to-face, each measures one face of the specimen. To set the two cameras observing on the same zone of the specimen is difficult, not to mention adjusting them perfectly perpendicular to the specimen surfaces. As a result, a spatial matching on the obtained IR and visible images cannot be reached.

In order to solve this problem, a special target of reference was developed. This target was a perforated metal plate, with around 20 holes through the thickness and randomly distributed. Thus the target has two identical faces and the holes form a special pattern.

Before the test the two faces of the target will be observed by IR and visible cameras, respectively. Thus it offers two visions of the target: one in IR image and the other in visible image. Each of them will be correlated to the analytical model of the target, and further to be deformed by the estimated transformation functions so as to reach the spatial matching with the analytical model.

Figure 1. shows an example of the overlay of the targets from IR and visible images: (a) before spatial correction; (b) after spatial correction. It shows clearly that the unmatched holes in image (a) are superposed in image (b) after the spatial correction. The transformation functions applied in this example are an affine transformation plus a B-spline transformation.

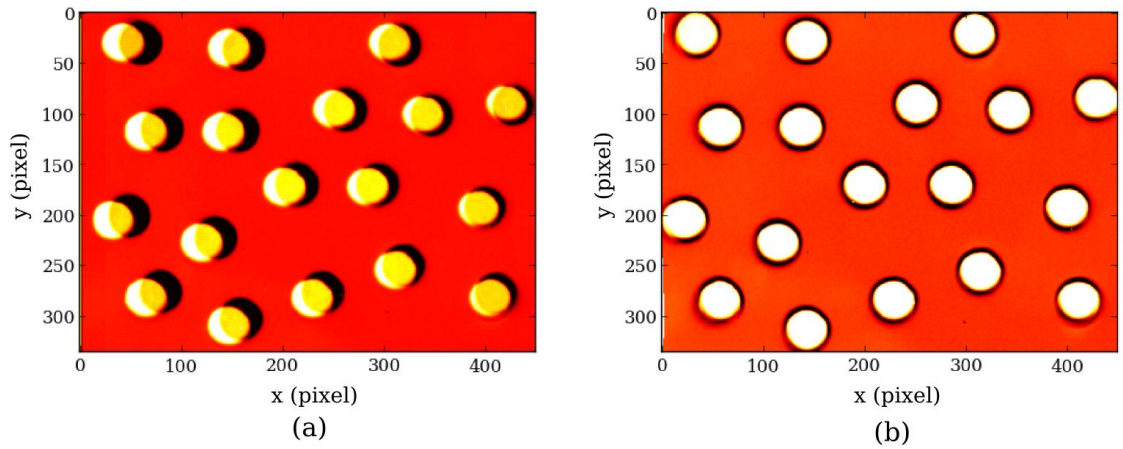

Figure 1. Overlay of the IR and visible images: (a) before spatial correction (b) after spatial correction

An affine transformation in Elastix is defined as:

$$T_\mu(x) = A(x-c)+t+c \tag{1}$$

where A is a matrix, c is the center of rotation and t the translation vector. The matrix A has no restrictions that means the image can be translated, rotated, scaled, and sheared.

B-splines are often used as a parameterization:

$$T_\mu(x) = x + \sum_{x_k \in N_x} p_k \beta^3\left(\frac{x-x_k}{\sigma}\right) \tag{2}$$

with x_k the control points, $\beta^3(x)$ the cubic multidimensional B-spline polynomial, p_k the B-spline

coefficient vectors, σ the B-spline control point spacing, and N_x the set of all control points within the compact support of the B-spline at x.

Since the two cameras are always fixed during the test and the target is placed at the same position as the specimen, so the correlation functions should be applicable for the specimen. Hence, the spatial alignment of the two faces of the specimen can be realized thanks to the reference target.

3. Experimental procedure

3.1. Specimen preparation

An oligocrystal specimen that contains only about ten grains in a single layer was prepared. The average size of the grains can attain 15 mm in diameter, and the thickness of the specimen is 1.5 mm. This type of oligocrystal specimen was prepared by the strain-annealing method [18, 19], from a very pure aluminium (purity 99.99%). The preparation of the oligocrystal specimens, following the strain-annealing method, required three steps.

1. Specimens cut from the original metal sheet were annealed at 545 ℃ for 1 h. This first annealing allows removing of the residual stresses resulting from the manufacturing process.

2. Annealed specimens were then stretched by around 3.5% longitudinal strain which corresponds to the ‘‘critical strain” value necessary to obtain, after a second annealing of re-crystallization, maximum grain size.

3. Stretched specimens were finally annealed at 545 ℃ for 1 h.

Concerning the two-face measurement, one important issue here is the identity of the crystallographic features of the two faces of the specimen. This point can be checked by overlapping the grain boundaries from the two faces. Figure 2. shows the grain textures of the two faces (face A for visible measurement and face B for IR measurement) and the overlay of the grain boundaries. The overlapping effect is, on the whole, satisfactory, in particular for the big grains in the middle.

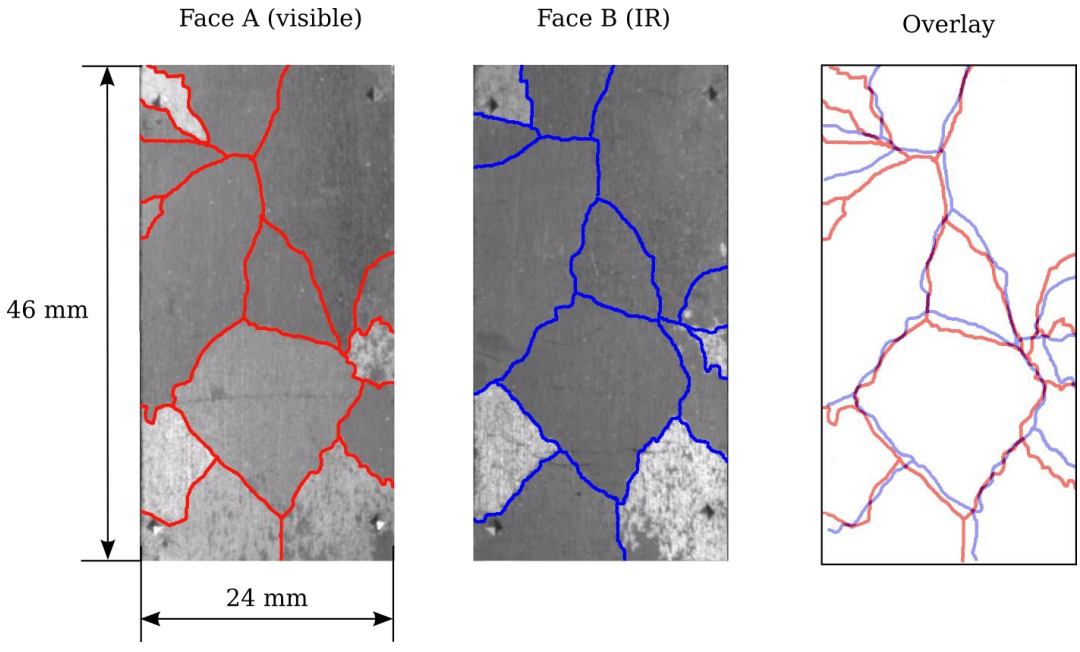

Figure 2. Grain textures of the two faces and the overlay of the grain boundaries

3.2. Test and measurements

Before the tensile test, an in-situ calibration was carried out in order to calibrate the IR camera, and the reference target was also measured in advance.

The tensile test was performed at room temperature and at a constant crosshead velocity of 1 mm/s. Strain and temperature were measured simultaneously by the two-face measurement system. The experimental set-up is shown in Figure 3. In the IR aspect, there was an enclosed box between the camera and the specimen for isolating the influences from environment; and for strain measurement a light made of LEDs was adopted to illuminate the specimen.

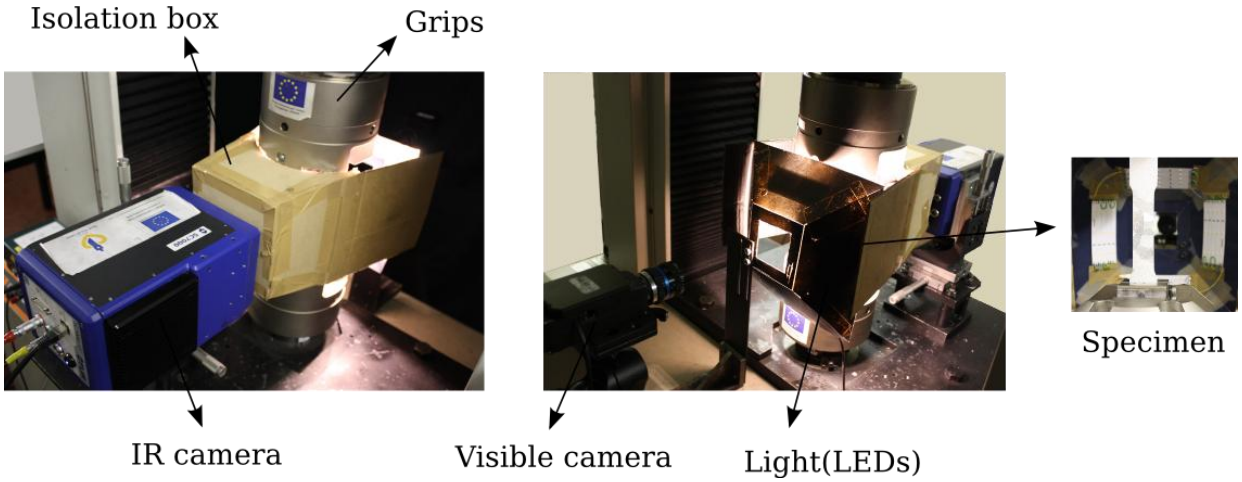

Figure 3. Experimental set-up of the two-face measurement system

The surfaces of the specimen were treated by depositing speckled painting for face A (strain measurement) and carbon black for face B (temperature measurement). Visible images were recorded by Elphel camera at 20 Hz with a resolution of 1712 × 1552 pixels. And IR images were recorded by FLIR Titanium camera at a frequency of 100 Hz with a resolution of 472 × 368 pixels.

It is important to note that there is an apparent difference in the sampling frequency for the two cameras, one is 5 times lower than the other. This is owing to our strategy on the parameter setting, as the sampling frequency was considered a priority for IR camera and the spatial resolution for visible camera. In this case, the two cameras were not synchronized in a strict sense, but the micro-controller guarantees that each visible image has a temporal corresponding IR image.

After the tensile test, the deformed specimen was measured by interferometric profilometer (Wyko NT1100) that provided the surface profiles of the two faces. Four marks on each face (see Figure 2) are the landmarks for the spatial alignment with the measured full-field strain and temperature.

3.3. Data treatment

First of all, the spatial alignment of IR and visible images was realized thanks to the reference target. Then, due to the fact that the visible camera has a lower sampling frequency, the visible images were interpolated linearly in order to produce the same number of images to the IR images. At this step, a data coupling, spatially and temporally, was done.

DIC technique was realized by Elastix [20], an open source software. B-spline transformation was applied as the correlation function with a final deformation grid 32 × 32 pixels following a

multi-resolution strategy. IR images were proceeded by converting original Digital Level (DL) to temperature through a so-called Quantitative Infrared Thermography (QIRT) procedure [16]. In this procedure, a N points Non-Uniformity Correction (NUC) was applied in order to eliminate the radiometric artifacts [21].

During the tensile test, as the two cameras were always fixed and the specimen had been displaced, thus the data recorded is in Euler coordination system. Since DIC provides the displacement information of the specimen and the kinematic-thermal data have been coupled, thus all IR images can be deformed so as to return to the initial coordination. This method is called Lagrangian thermography [10, 16]. The interest of performing Lagrangian Thermography is to follow the temperature evolution of each physical point of material, which is not evident when the material points are in the movement.

Another special data treatment was applied is so-called crystallography-based full-field projection proposed by Seghir [16]. In this method, the strain, temperature and profile data were projected on a crystallographic base: the data were fitted as polynomials in units of individual grains. Thus the hypothesis made here is the physical discontinuity of polycrystal because of grain boundaries.

5. Results and discussions

5.1. Out-of-plane deformation and its influences on measurement

The first noticeable phenomenon found in the results is that the specimen has suffered a strong out-of-plane deformation during the tensile test, as shown by Figure 4, the surface profiles of the deformed specimen. The two faces shows almost the same statistic results: the surface roughness average is about 70 µm, but the maximum height of the surface reaches around 700 µm regarding a thickness of 1.5 mm for the specimen. It is also interesting to notice that the two faces show a profile pattern similar and in opposite signs.

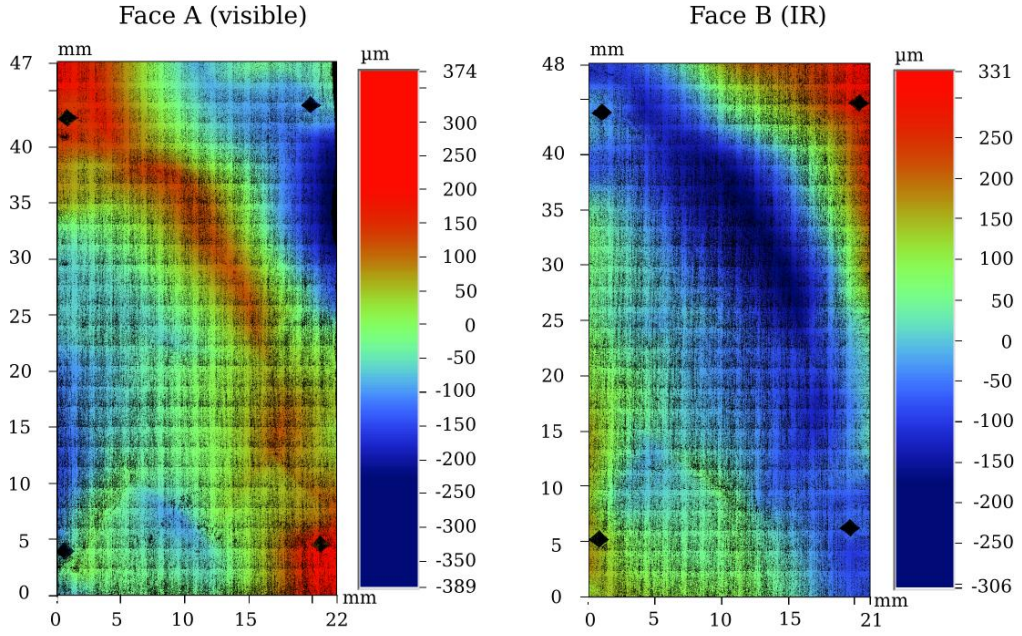

Figure 4. Surface profiles of the deformed specimen

This type of out-of-plane deformation has considerable influences on the in-situ full-filed measurements. For a 2D in-plane DIC system adopted in this work, the out-of-plane deformation brought inevitably errors on the image correlation. Figure 5(a). shows an error map (or residual

image) of DIC calculation for the last visible image (i.e., the final state of the deformed specimen). The special pattern observed in this residual image reflects the out-of-plane deformation, which changed the gray levels of the material points during the test in the light of the reflection effect.

Concerning IRT, the non-plane surface of the specimen will change the apparent emissivity of the surface coating due to the varied incidence angles with respect to the IR camera [22]. The apparent emissivity can be changed and re-distributed heterogeneously corresponding to the deformed shape of the specimen. Figure 5(b). shows the temperature field of the specimen in the final state, derived from the last IR image after proceeding Lagrangian thermography. Comparing to Figure 5(a), a similar pattern can be remarked, globally and in some zones particular. This is due to the fact that the two faces of the specimen showed a very similar profile feature and the optical reflection effect influenced the two optical measurements, DIC and IRT, almost in the same way.

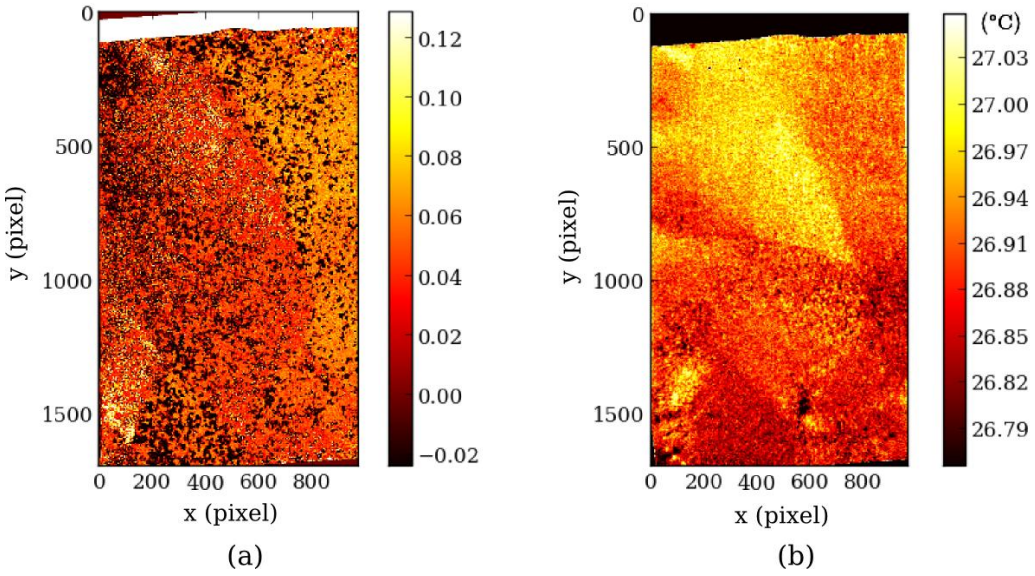

Figure 5. Reflection effects caused by out-of-plane deformation demonstrated by:
(a) Residual image of DIC (b) Temperature field

Nevertheless, it is worthy to mention that this type of artifact due to reflection is not so important regarding the absolute errors it may introduce, but its influences can be much magnified when a relatively homogeneous strain or temperature field is involved. This is what happened in this test, especially for the temperature field, as aluminium has a very high thermal conductivity.

5.2. Out-of-plane deformation and microstructure

For oligocrystal specimen, because of the difference in crystallographic orientations, the grains were subjected to the stresses of different levels during the uniaxial tensile test. This stress heterogeneity led to a heterogeneous deformation process. In this process, grain boundaries, as the interfaces of different grains, played an important role.

Comparing the surface profiles in Figure 4. with the initial grain texture in Figure 2, it is not difficult to find out that the most marked relieves, where the profile changes most abruptly, coincide with the grain boundaries. This point can be better investigated in the projection of full-filed measurements on a crystallographic base.

Figure 6. shows the projection results of the strains (E_{xx}, E_{yy}) and temperature at the final state of the specimen during the deformation. The interpolation, through second-degree polynomial fitting, was applied for each grain according to the grain texture provided by Figure 2.

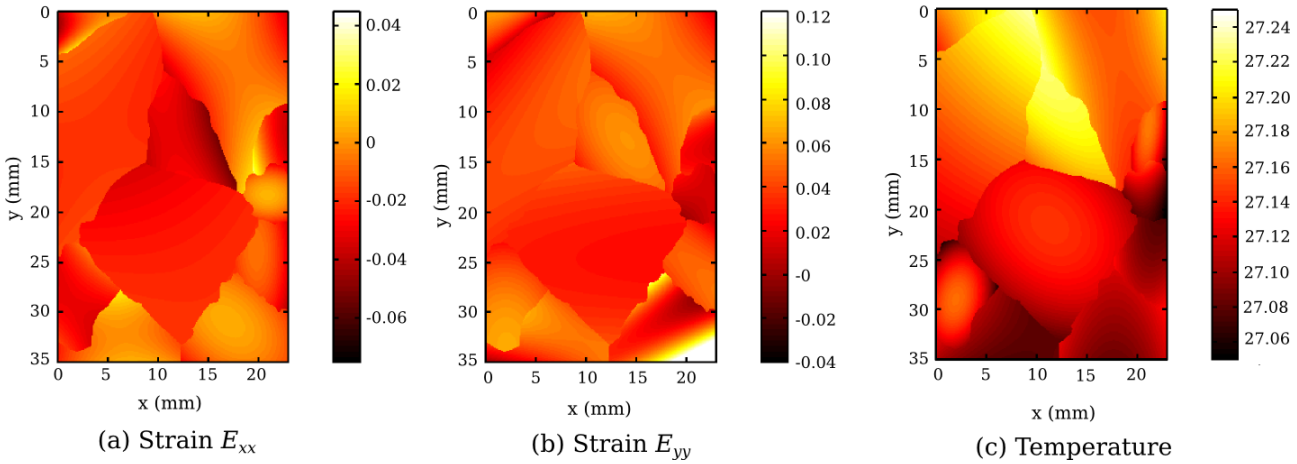

(a) Strain E_{xx} (b) Strain E_{yy} (c) Temperature

Figure 6. The crystallography-based projection from the full-field measurements of: (a) Strain E_{xx} (b) Strain E_{yy} (c) Temperature

Both strain and temperature fields in Figure 6. demonstrate a heterogeneity, where the discontinuity of the grain boundaries is remarkable. This heterogeneity is mainly due to the out-of-plane deformation that is closely linked with the microstructure of the material. Nevertheless, a further analysis cannot be conducted unless the optical reflection effects can be quantified. This is one of the perspective studies in the near future.

Another work undergoing is the study on the thermomechanical behavior of nickel single crystal by using the two-face measurement system. One of the greatest interests on studying single crystal is to establish a quantitative relationship between the stored energy, stress-strain state and microstructural changes of the slip systems that are activated.

5. Conclusions

1. An overview of technique possibilities of coupled kinematic-thermal measurement was given, and several advances in technique have been achieved in this work for building an advanced two-face measurement system.

2. An aluminium oligocrystal specimen was measured during a monotonic deformation by the coupled optical system, which showed an important out-of-plane deformation. This kind of out-of-plane deformation has considerable affections on the optical measurements.

3. Further investigation shows that the heterogeneity of the out-of-plane deformation is closely associated with the microstructure of material, and reveals that the grain boundaries and grain interactions during the deformation play an important role in the process of deformation, temperature and surface profile evolutions.

References

[1] J. Lemaitre, J.L. Chaboche. Mechanics of Solid Materials, Dunod, Paris, 1988.
[2] M.P. Luong. Fatigue limit evaluation of metals using an infrared thermographic technique. IMechanics of Materials, 28(1998) 155–163.
[3] G. Besnard, F. Hild, S. Roux. “Finite-Element” Displacement Fields Analysis from Digital Images: Application to Portevin-Le Châtelier Bands. Experimental Mechanics, 46(2006), 789–803.

[4] A. El Bartali, V. Aubin, S. Degallaix, Surface observation and measurement techniques to study the fatigue damage micromechanisms in a duplex stainless steel. International Journal of Fatigue, 31 (2009) 2049–2055.
[5] A. Chrysochoos, H. Louche. An infrared image processing to analyse the calorific effects accompanying strain localisation, International Journal of Engineering Science, 38(2000) 1759–1788.
[6] H. Louche, A. Chrysochoos. Thermal and dissipative effects accompanying Lüders band propagation. Materials Science and Engineering: A, 307(2001), 15–22.
[7] T. Boulanger, A. Chrysochoos, C. Mabru, A. Galtier. Calorimetric analysis of dissipative and thermoelastic effects associated with the fatigue behavior of steels, International Journal of Fatigue, 26(2004), 221–229.
[8] A. Chrysochoos, B. Berthel, F. Latourte, S. Pagano, B. Wattrisse, B. Weber. Local Energy Approach to Steel Fatigue. Strain, 44(2008), 327–334.
[9] C. Badulescu, M. Grédiac, H. Haddadi, J.D. Mathias, X. Balandraud, H.S. Tran. Applying the grid method and infrared thermography to investigate plastic deformation in aluminium multicrystal. Mechanics of Materials, 43(2011), 36–53.
[10] L. Bodelot, L. Sabatier, E. Charkaluk, P. Dufrénoy. Experimental setup for fully coupled kinematic and thermal measurements at the microstructure scale of an AISI 316L steel. Materials Science and Engineering: A, 501(2009), 52–60.
[11] A. Saai, H. Louche, L. Tabourot, H.J. Chang. Experimental and numerical study of the thermo-mechanical behavior of Al bi-crystal in tension using full field measurements and micromechanical modeling. Mechanics of Materials, 42(2010), 275–292.
[12] A. Maynadier, M. Poncelet, K. Lavernhe-Taillard, S. Roux. One-shot Measurement of Thermal and Kinematic Fields: InfraRed Image Correlation (IRIC). Experimental Mechanics, 52(2012), 241–255.
[13] M.L.Silva, G. Ravichandran. Combined thermoelastic stress analysis and digital image correlation with a single infrared camera. Journal of Strain Analysis and Engineering Design, 46(2011), 783–793.
[14] L. Bodelot, E. Charkaluk, L. Sabatier, P. Dufrénoy. Experimental study of heterogeneities in strain and temperature fields at the microstructural level of polycrystalline metals through fully-coupled full-field measurements by Digital Image Correlation and Infrared Thermography. Mechanics of Materials, 43(2011), 654–670.
[15] D. Delpueyo, M. Grédiac, X. Balandraud, C. Badulescu. Investigation of martensitic microstructures in a monocrystalline Cu-Al-Be shape memory alloy with the grid method and infrared thermography. Mechanics of Materials, 45(2012), 34–51.
[16] R. Seghir. Experimental and numerical investigation of thermomechanical couplings and energy balance in metallic polycrystals. Ph.D. thesis, Ecole Centrale de Lille, 2012.
[17] R. Seghir, J.F. Witz, L. Bodelot, E. Charkaluk, P. Dufrénoy. A thermomechanical analysis of the localization process at the microstructure scale of a 316L stainless steel, Procedia Engineering, 10(2011), 3596–3601.
[18] H.C.C. Carpenter, C. Elma. The production of single crystals of aluminium and their tensile properties. Proceedings of the Royal Society A, 100(1921), 329–353.
[19] J. Philibert, A. Vignes, Y. Bréchet, P. Combrade. Métallurgie: du minerai au matériau, Edition Masson, Paris, 1998.
[20] http://elastix.isi.uu.nl/
[21] M. Poncelet, J.F. Witz, H. Pron, B. Wattrisse. A study of IRFPA camera measurement errors: radiometric artefacts. Quantitative InfraRed Thermography Journal, 8(2011), 3–20.
[22] G. Gaussorgues. Infrared Thermography, Chapman & Hall, London, 1994.

Experimental Study on Propagation Rule of Semi-elliptical Surface Crack in Steel Plate Strengthened with FRP under Cyclic Bending Load

Zhao Chuanyu[1], Huang Peiyan[1,2]*, Feng Fajuan[1], Zhou Hao[1]

[1] School of Civil and Transportation, South China University of Technology, Guangzhou 510640, China

[2] State Key Laboratory of Subtropical Construction Science, South China University of Technology, Guangzhou 510640, China

* Corresponding author: pyhuang@scut.edu.cn

Abstract: Strengthening steel structures containing semi-elliptical surface crack with fiber reinforced polymer (FRP) can delay crack propagation, and increase the service life of structures. In this paper, carbon fiber laminate (CFL), which has independent intellectual property, was adopted to strengthen X80 steel plate containing a 3D semi-elliptical surface crack, and based on this study object, the surface crack propagation rule in the specimens was studied by experimental method under cyclic bending loads. The results show that 3D semi-elliptical surface crack propagation rates in the crack length direction and crack depth direction can be described by corresponding Paris equation for the specimens strengthened with CFL, the constant coefficients in Paris equation can be obtained by fitting the data from fatigue crack propagation experiments, and stress intensity factor of the surface crack in steel plate strengthened with CFL can be obtained by numerical calculation with FEM.

Keywords：3D surface crack, fiber reinforced polymer (FRP), fatigue crack growth, beach-mark, stress intensity factor (SIF)

1. Introduction

Surface crack is a common defect in oil and gas pipelines, offshore oil platform, aviation mechanical and other steel structures [1,2]. Such kind of crack is easy to propagation and results in shortage of service life, especially can bring catastrophic results. So many researchers have done a lot of studies on surface crack [3,4]. In order to improve service life of structures which contain surface crack, some researchers propose to strengthen structures with fiber reinforced polymer (FRP), and have studied the strengthening method and strengthening effect [5,6]. Liu et al [7] discussed the fatigue lives and stress intensity factors of steel plate containing through crack strengthened with FRP, and their results indicate that fatigues lives of steel plates strengthened with FRP can increase 1.3 times than that of non-strengthened steel plates, and stress intensity factors can be reduced by 28%~60%. Tsai and Shen [8] studied the aluminum alloy plate containing through crack strengthened by FRP, and their results show that two face sides strengthening can delay crack propagation obviously, and fatigue lives can increase 2.6 times than non-strengthened plates. C.C.LAM's studies [9] show that stress intensity factors of through crack can be reduced by 54% in steel pipe after strengthening by FRP. However, the research for propagation rule of the semi-elliptic surface crack in steel structure strengthened with FRP has not yet been reported. For this reason, in this article, propagation behavior of the three dimensional semi-elliptic surface crack

in X80 steel plate strengthened with carbon fiber laminate (CFL) [10] was experimentally studied, and the stress intensity factor of the surface crack was computed by FEM method.

2. Fatigue crack propagation experiments

2.1 Specimens and pre-cracking

Specimens are made of X80 steel, which is a kind of high strength pipe steel. The size of steel plate was: length H=110mm, width W=70mm, thickness B=8mm. The mechanical properties were: yield strength $\sigma_{0.2}$=522MPa, Young' modulus E_s=200GPa and Poisson's ratio ν_s=0.3. In the surface centre of the specimen, an artificial semi-elliptical crack starter is machined by electrical discharge machining, show in figure 1(a), and fatigue pre-cracking is carried out on testing system by three-point bending method. The maximum load P_{max} of prefabricated fatigue crack can be calculated with the following equation [11] :

$$P_{max} = k\frac{2\sigma_{0.2}B^2W}{3S} \tag{1}$$

Where, S is the span of the specimen, and k is set to 1.0 for pre-cracking, and 0.5 for crack propagation. If the fatigue crack cannot be initiated by crack starter under current load after several ten thousand cycles, the current load should be increase by 10% of the maximum load. The stress ratio for pre-cracking is $R=P_{min}/P_{max}$=0.1. Crack size for pre-cracking is approximately following the empirical equation:

$$\frac{a_0}{B}+\frac{a_0}{c_0}=1\pm 0.1 \tag{2}$$

Where, a_0 and c_0 is initial depth and initial length of the surface crack. Based on Eq.(2), initial crack depth a_0 can be estimated by observation and controlling initial crack length approximately to $2c_0$.

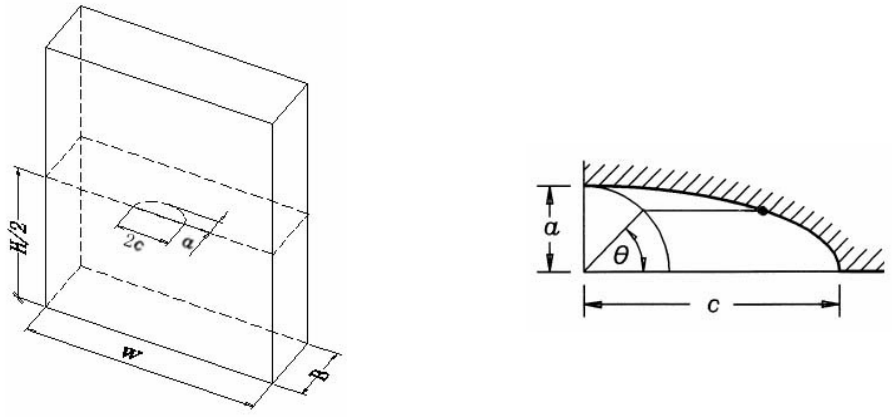

(a) Non-strengthened specimen (b) Parametric angle for the crack

Figure 1. Steel plate specimen with a semi-elliptical surface crack

After pre-cracking, CFL was bonded on the crack front side surface of the steel plate as shown in figure 2. The CFL has length H=90mm, width W=70mm, thickness t_f=0.2mm, Young' modulus E_f=230GPa and Poisson's ratio ν_f=0.25. After 5~7 days for adhesive to solidify, then the specimens

can be used in fatigue crack propagation experiments.

Six specimens were tested in the studies. Three non-strengthened specimens were symbolized by S1, S2 and S3, and three strengthened specimens were symbolized by SC1, SC2 and SC3.

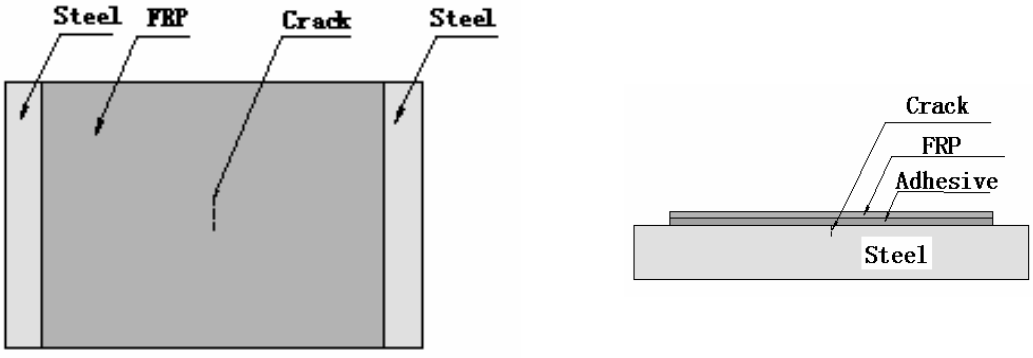

(a) Plane view (b) Section view

Figure 2. Strengthened specimen

2.2 Experimental method

The test was carried out on electro-hydraulic servo dynamic and static testing machine which produced by Changchun Institute of Testing Machine. The testing data, such as load, time, strain, and corresponding fatigue loading cycles, are recorded automatically. Fatigue loads applied by force control mode with sinusoidal wave, and a frequency of 15 Hz and a stress ratio of 0.1. P_{max} and P_{min} denote the peak load and volley load respectively, corresponding to N cycles applied on the specimen. The non-strengthened specimens were applied to the maximum load, $P_{max,}$ as 8.0kN, and the strengthened specimens as 9.5kN.

For the measurement of crack depth and length, beach-mark method was used to obtain beach-mark boundary, as shown in figure 3. After a certain number of cycles of normal propagation, reduce the applied load to 2/3 of normal propagation load to slow down the propagation rate, then a clear striation will appear following the slow propagation. And repeating above procedures, more of striation, the beach-mark can be obtained. Based on this beach-mark, crack depth, a, and length, 2c, which is corresponding to a certain number of cycles, N, can be easily measured, and then a~N curves and c~N curves, and fatigue crack propagation rate, da/dN and dc/dN, can be easily obtained.

(a) Non-strengthened specimen S1

(b) Strengthened specimen SC1

Figure 3. Beach-mark on fracture surface of the specimens

3. Propagation rates of 3D surface crack

Three non-strengthened specimens（S1, S2, S3）and three strengthened specimens（SC1, SC2, SC3）were tested in fatigue crack propagation experiments by adopting experimental method in the above Chapter 2, and fatigue crack propagation curves (a～N curves) of each specimen were obtained.

Based on the research results from the other metal materials, we assume that the propagation rates, da/dN and dc/dN (mm/cycles), of the surface crack in X80 steel plate strengthened with CFL and non-strengthened specimens all can be described by Paris formula [11] as,

$$\frac{dc}{dN} = C_L(\Delta K_c)^{m_L} \tag{3}$$

$$\frac{da}{dN} = C_D(\Delta K_a)^{m_D} \tag{4}$$

Where, C_L, C_D, and m_L, m_D were material constants, ΔK_c and ΔK_a (MPa·m$^{1/2}$) were the amplitude values of the stress intensity factors of the surface crack ($\Delta K=K_{max}-K_{min}$), whereas the stress intensity factor K can be calculated by Newman-Raju formula [2] for the non-strengthened specimens, but for the strengthened specimens, it has need to use the FEM [12].

Based on the test data obtained from the non-strengthened specimens S1, S2 and S3, and strengthened specimens SC1, SC2 and SC3, the relationship of ΔK_c and dc/dN, ΔK_a and da/dN were obtained and shown in figure 4 and figure 5.

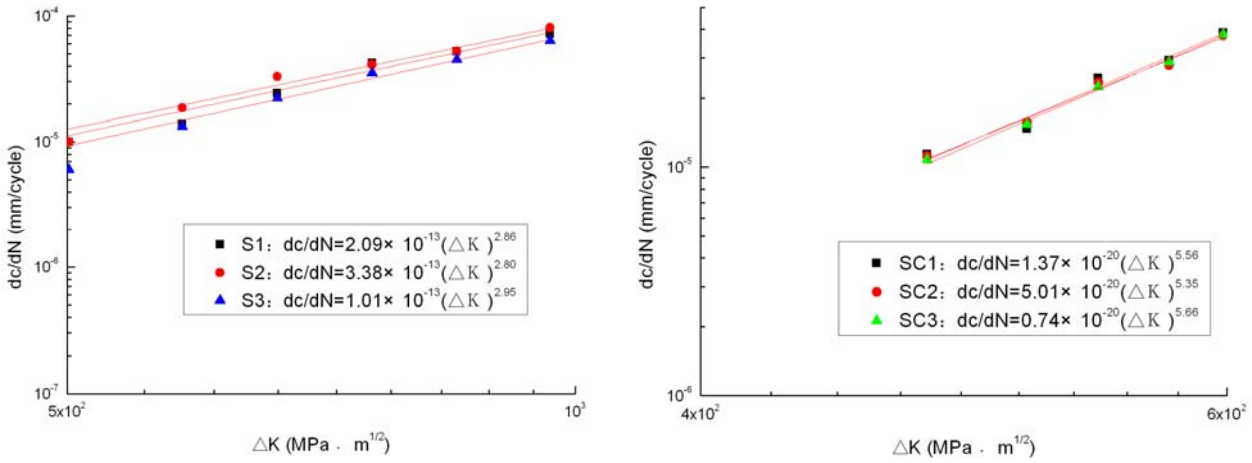

(a) non-strengthened specimens (b) strengthened specimens

Fig.4 Relationship between ΔK_c and dc/dN

Fitting the data to Eq.(3), the average of C_L, and m_L were determined, and the fatigue crack propagation equations in crack length direction for non-strengthened and strengthened specimens were as follows:

$$\frac{dc}{dN} = 2.16\times10^{-13}(\Delta K_c)^{2.87}, \text{ for non-strengthened specimens} \tag{5}$$

$$\frac{dc}{dN} = 2.37\times10^{-20}(\Delta K_c)^{5.52}, \quad \text{for strengthened specimens} \tag{6}$$

In surface crack length direction, the above two equations show that strengthened with CFL can change the crack propagation coefficient C and the index m in Paris law. The crack propagation coefficient C decreases, while the crack propagation index m increases.

In surface crack depth direction, there is no obvious regularity for the relationship of ΔK_a and da/dN for the non-strengthened specimens, shown in figure 5(a). This may be because the position of neutral axis in the non-strengthened specimens has been changing as crack propagation in depth direction, and this change has a great effect on propagation rate. But the relationship of ΔK_a and da/dN for the strengthened specimens agrees well with Paris law as shown in figure 5(b). This is because the position of neutral axis in the strengthened specimens became more stable than that of the non-strengthened specimens.

Fitting the data to Eq.(4), the average of C_D, and m_D were determined, and the fatigue crack propagation rate equation in crack depth direction for the strengthened specimens was as follows:

$$\frac{da}{dN} = 4.28\times10^{-7}(\Delta K_a)^{0.66} \tag{7}$$

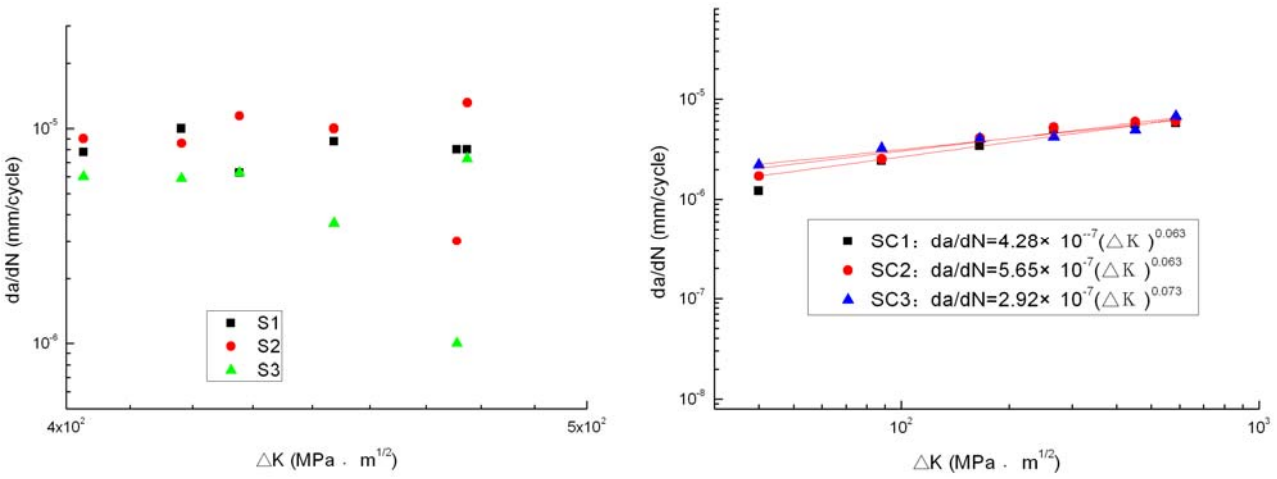

(a) Non-strengthened specimens (b) Strengthened specimens

Figure 5. Relationship between ΔK_a and da/dN for strengthened specimens

4 Conclusions

A method of combination of experiment and numerical analysis was applied to study the 3D semi-elliptical surface crack propagation rule in non-strengthened and strengthened steel plate with carbon fiber laminate (CFL), and the main results are as follows:

1) Strengthening with CFL can reduce fatigue crack propagation rate, and increase fatigue life of the specimen.

2) 3D semi-elliptical surface crack propagation rate in crack length direction can be described by corresponding Paris equation. The constant coefficients in Paris equation can be obtained by fitting the data from fatigue crack propagation experiments, and stress intensity factor can be obtained by numerical calculation with FEM.

3) Beach-mark method was a better way to obtain data like the change of crack size in fatigue

surface crack propagation.

4) Crack propagation rule in crack depth direction in non-strengthened specimens do not accord with Paris law, while after strengthened with CFL, the crack propagation rule go back to accord with Paris law. The mechanism to be further discussed.

Acknowledgments

The project is supported by National Natural Science Foundation of China (No.51078145 and No.11132004) and Guangdong Province Natural Science Foundation of China (No.9251064101000016).

References

[1] A.T. Diamantoudis, GN Labeas, Stress intensity factors of semi-elliptical surface cracks in pressure vessels by global-local finite element methodology. Eng Fract Mech, 72(2005) 1299-1312.

[2] I.S. Raju, J.C. Newman, Stress-intensity factors for internal and external surface cracks in pipes. J Press Vess-T ASME, 104(1982)293-298.

[3] F.Ndiri, C.L.Tan, R.T.Fenner, Three-dimensional analyses of surface cracks in pressurized thick-walled cylinders. International Journal of Pressure Vessels and Piping, 10(1982)159-167.

[4] TVRS Umamaheswar, R. Singh, Modeling of a patch repair to a thin cracked sheet. Engineering Fracture Mechanics, 62(1999)267–89.

[5] X.L. Zhao, Zhang L. State-of-the-art review on FRP strengthened steel structures. Eng Struct, 29(2007)1808–1823.

[6] S.C. Jones, S.A. Civjan, Application of fiber reinforced polymer overlays to extend steel fatigue life. Journal of Composites for Construction, 7(2003)331–338.

[7] H.B. Liu, X.L. Zhao, Riadh Al-Mahaidi. Boundary element analysis of CFRP reinforced steel plates. Composite Structures, 91(2009) 74-83.

[8] G.C. Tsai, S. B. Shen, Fatigue analysis of cracked thick aluminum plate bonded with composite patches. Composite Structures, 64(2004)79-90.

[9] C.C.LAM, J.J.CHENG, C.H.YAM. Finite element study of cracked steel circular tube repaired by FRP patching. Procedia Engineering, 14(2011)1106-1113.

[10] P.Y. Huang, J.C Zeng, Application of Carbon Fiber Laminate. Chinese Patent No. ZL200410026742.8, China Patent Administration, 2006.

[11] American Society for Testing and Materials AI. ASTM designation: E647. Standard test method for measurement of fatigue crack growth rates. In: Annual book of ASTM standards, ASTM International, 2001.

[12] C.Y. Zhao, P.Y. Huang, H. Zhou, X.H. Zheng, Numerical Analysis of K_I of Semi-elliptical Surface Crack in Steel Structure Strengthened with FRP under tensile load. Applied Mechanics and Materials, 137(2012)42-49.

Numerical Analysis of K_I of Semi-elliptical Surface Crack in X80 Steel Plate Strengthened with FRP under Tensile Load

Zheng Xiaohong[1], Huang Peiyan[1,2]*, Zhao Chuanyu[1], Zhou Hao[1]

[1] School of Civil and Transportation, South China University of Technology, Guangzhou 510640, China
[2] State Key Laboratory of Subtropical Construction Science, South China University of Technology, Guangzhou 510640, China
* Corresponding author: pyhuang@scut.edu.cn

Abstract: Semi-elliptic surface crack is the common defect in metal structures. To ensure the structural integrity and security, the new material such as fiber reinforced polymer (FRP) was adopted for strengthening and repairing. In this paper, three dimensional semi-elliptic surface crack in X80 steel tension specimen strengthened with carbon fiber laminate (CFL) was studied, and numerical analysis was undertaken by Abaqus finite element software to study the stress intensity factor (SIF, K_I) of the surface crack for CFL reinforcement effect. The results shown that, strengthening by CFL reduced the stress intensity factors of semi-elliptical surface crack significantly; Crack shape ratio *a/c* and crack relative depth *a/B* had a great effect on stress intensity factors of strengthened specimen; An expression for calculating stress intensity factors of semi-elliptic surface crack under strengthening condition was obtained by adopting MATLAB software.

Keywords: surface crack, fiber reinforced polymer (FRP), stress intensity factor (SIF), numerical analysis

1. Introduction

With the development of society, the steel structure has been widely used in all kinds of engineering construction, such as oil and gas pipelines, bridges, marine oil platform and so on. In the process of long-term use, it will inevitably produce some defects in steel structure, such as surface crack, under the influence of environmental conditions and external load. Surface crack propagation will bring a lot of potential safety problems to engineering facilities. In recent years, scholars from home and abroad carried out a number of studies [1,2], and to the strengthening with crack repair technology have also made some progress [3-8]. Edberg et al [3] made some experimental studies to research the properties of I-font section steel beam strengthened with FRP using several different kinds of reinforcement scheme, the results show that the stiffness of the steel after strengthening increased by 23%, the ultimate bearing capacity increased by 42%. Nicholas G.Tsouvalis et al [4] conducted experiment and the finite element method to study the steel structures strengthened with composite. The results show that the bonded composite materials can effectively reduce crack propagation rate, the fatigue life of specimen increased by 74% or more. However, the research for stress intensity factor of the semi-elliptic surface crack in steel structure strengthened with FRP has not yet been reported. For this reason, in this paper, three dimensional semi-elliptic surface crack in X80 steel tension specimen strengthened with carbon fiber laminate (CFL) [9] was studied, and numerical analysis was undertaken by Abaqus finite element software to study the stress intensity factor (SIF, K_I) of the surface crack for CFL reinforcement effect.

2. Finite element model

Research object in this paper was the 3D semi-elliptical surface crack in the center of the rectangle X80 steel plate. The steel plate was strengthened with carbon fiber laminate (CFL) in front side invented by this research group [9], and was subjected to uniform tension load of 100MPa on both ends, shown in Figure.1 and Figure.2. Where, the size of X80 steel plate was: length

H=90mm, width W=70mm, thickness B=8mm, Young' modulus E_s=206GPa and Poisson's ratio ν_s=0.3. The CFL has length H=90mm, width W=70mm, thickness t_f =0.2, 0.4, 0.6, 0.8, 1.0mm, Young' modulus E_f =230GPa and Poisson's ratio ν_f =0.25. Surface crack shape ratio a/c=0.4, 0.6, 0.8, and relative depth a/B=0.1, 0.2, 0.3.

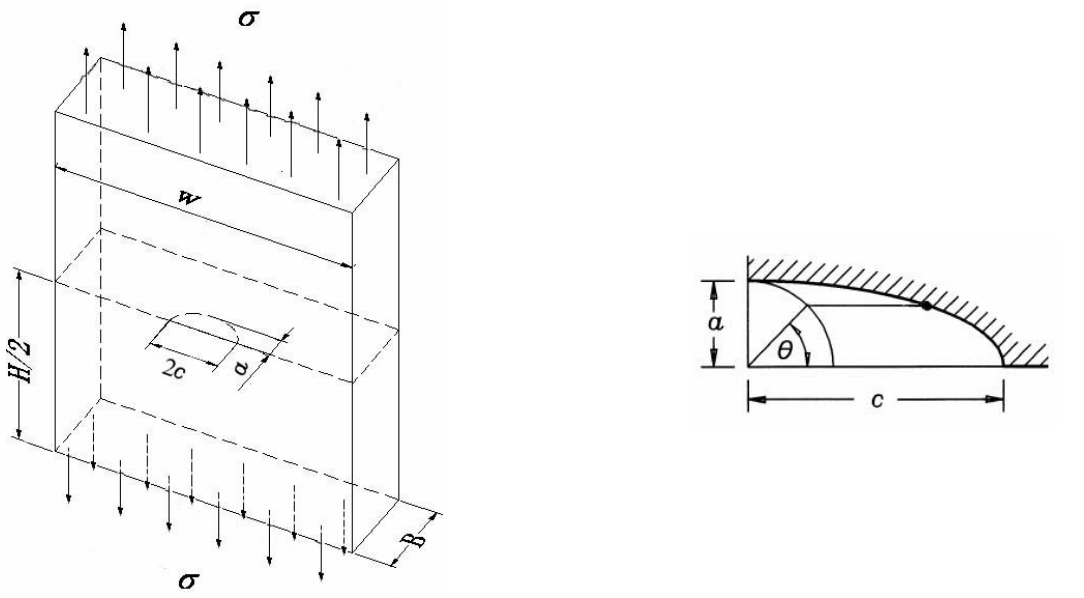

(a) Steel plate with surface crack (b) Parametric angle for the crack

Figure 1. Steel plate with surface crack under tensile load

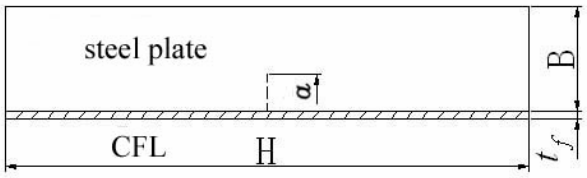

Figure 2. Steel plate strengthened with CFL

Finite element software Abaqus was used to establish the model for calculating the stress intensity factor of the semi-elliptical surface crack in different strengthening conditions. Due to symmetry of the analysis object, only one-quarter of the steel plate was analyzed. Two symmetrical surfaces of the model were restricted by symmetrical boundary conditions. In this analysis model, to avoid incompatible situations between CFL elements and crack front elements in front side strengthening, in the same time, to make the results comparable, steel plate and CFL were meshed using the three-dimensional elements. Around the crack tip area, a total of 11 layers elements were created. The first layer was wedge elements, and other 10 layers were hexahedral elements, there were totally 132 elements, shown in Figure. 3(a). Along the semi-elliptical curve, 20 equal parts were divided, which means there were 20 groups of elements and totally 2640 elements in the crack tip, shown in Figure. 3(b). The whole finite elements model was shown in Figure. 3(c), and there were totally 25932 elements.

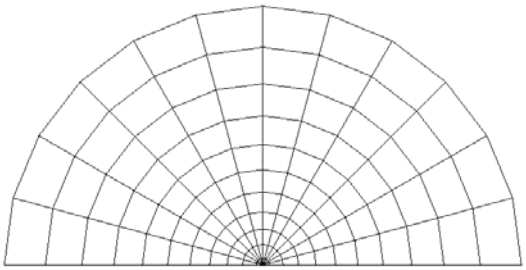

(a) crack front

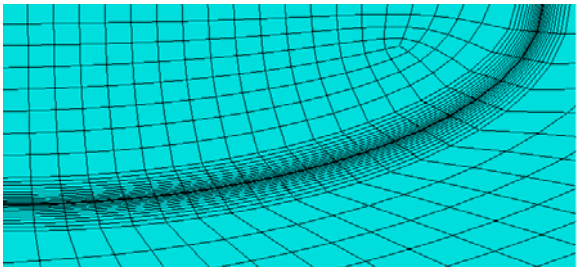

(b) crack surface

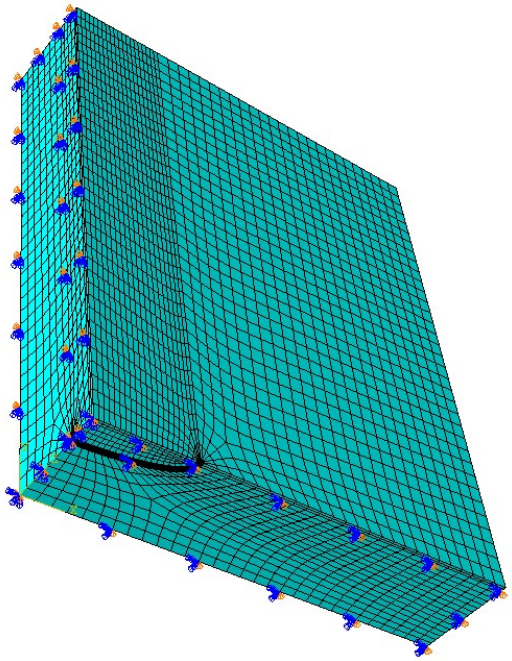

(c) whole model

Figure 3. Meshes of the FEM model

3. SIF of 3D surface cracks

3.1 SIF of crack in non-strengthened steel plate

Finite element analysis for stress intensity factor (SIF, K_I) of 3D semi-elliptical surface crack in non-strengthened steel plate was compared with that obtained by the Newman-Raju equation to prove the effectiveness of the FEM method in this paper.

For finite element calculation, due to 11 layers of elements were meshed at the crack tip, the corresponding SIF obtained by contour J-integration at every point in front of the crack. Generally, the calculated values of the inside layer had a larger fluctuation, compared with that of the outer layer. In default situations, the results were outputted by the software Abaqus from the inner layer. Therefore, at least 6 SIFs were obtained at each point in front of the crack to insure the accuracy. The relatively stable value of the outer layer was selected as the final SIF.

SIF of three a/c ratios and three raletive deepth a/B of the surface crack were calculated using the above FEM method and Newman-Raju equation were shown in Figure.4. From this Figureure, the finite element analysis results agreed well with that of the Newman-Raju equation in generally, the average relative error is less than 3%.

The minimum relative error was 0.38% when $\theta = 90^{\circ}$. There was a larger error near $\theta = 0^{\circ}$ especially when the crack was shallower (*a*/*B* is smaller) and flatter (*a*/*c* is smaller). The maximum relative error was 7.8% when *a*/*B*=0.1, *a*/*c*=0.4 and $\theta = 0^{\circ}$. When the crack was shallower, flatter and the centrifugal angle was smaller (*a*/*B*, *a*/*c*, θ was smaller), the relative error was larger. This was caused by the default conditions that the whole model was in plane strain state during the finite element analysis. However, it was in fact in plane stress state near the surface of the steel plate which caused greater relative error around $\theta = 0^{\circ}$ and also caused larger relative error when *a*/*B* and *a*/*c* were smaller. The results show that the above method of calculating the SIF of 3D surface cracks in steel plates using Abaqus was effective and available.

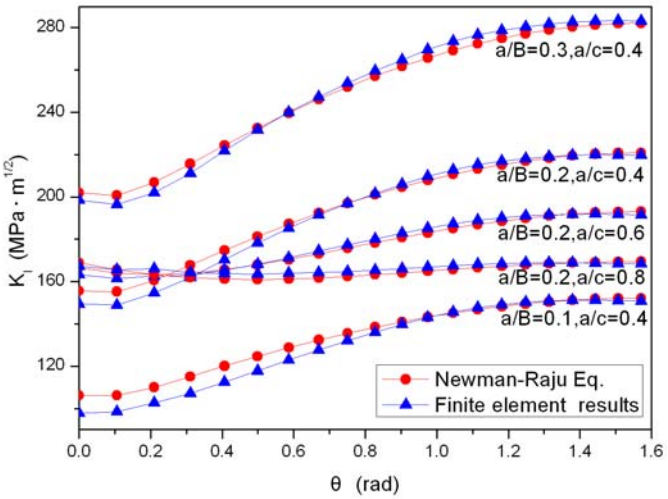

Figure 4. Computing values of K_I by FEM and Newman-Raju Eq.

3.2 SIF of crack in steel plate strengthened with FRP

In front surface strengthening (shown in Figure.2), the calculation values of SIF of 3D surface crack with t_f=0, 0.2, 0.4, 0.6, 0.8, 1.0 when a/B＝0.2，a/c＝0.6 were listed in Figure.5. This Figure shown that the SIF generally decreased by 21% in front surface strengthening compared with that of non-strengthening (t_f=0). As shown in Figure.5, the strengthening effect decreased as the angle changing from 0°to 90°, such as the reduction of stress intensity factor was the most (54.9%) when t_f = 0.2 and θ=0°, and the stress intensity factor to reduce small (20.6%) when θ=90°. This is because that the displacement between the upper and the underside of the crack was restricted by the CFL bonded to the surfaces. Therefore, the closer distance to the surface of the steel was, the better effect of the reinforcement was otained, where, the SIF on the surface of the steel was reduced most. Furthermore, the decreasing degree of SIF became smaller as the increasing of the thickness of CFL. That means overabundance of FRP caused material waste. The calculation values of SIF of the surface crack by FEM had the same properties when the shape and relative depth changed.

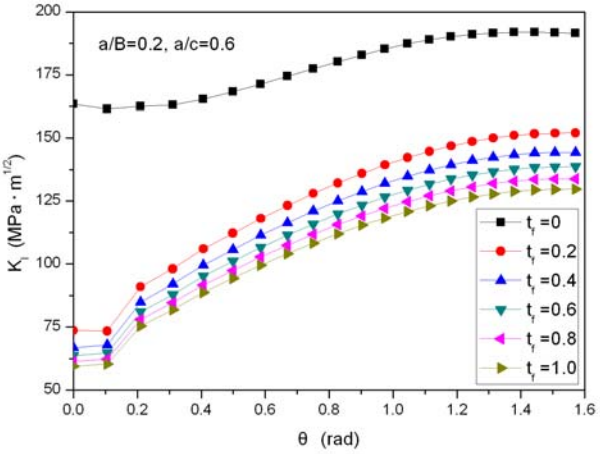

Figure 5. Computing values for K_I

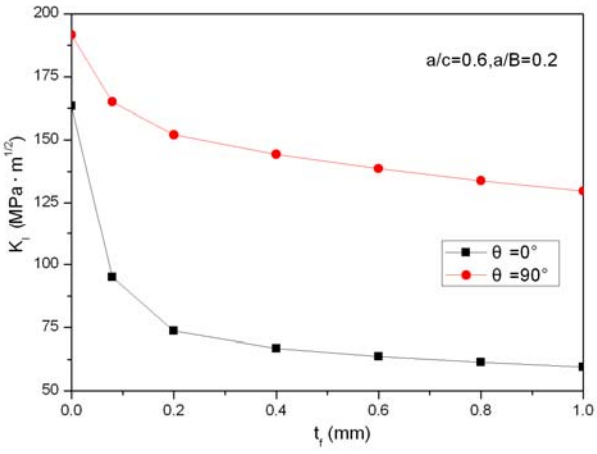

Figure 6. Relationship between K_I and t_f

The strengthening effect was lowest when θ=90°. For safety (conservative) considerations, the series was chosen as the calculation reference values in strengthening design. Therefore, functions of SIF and different thickness of CFL when θ=90° were simulated as:

$$K_{I,\theta=90^o} = K_0 - 2.49t_f^{0.29} \qquad \left(t_f \geq 0, \theta = 90°\right) \tag{1}$$

Where, K_I was the stress intensity factor (SIF), which unit was MPa·m$^{1/2}$; t_f was the thickness of FRP which unit was mm; K_0 was the stress intensity factor without strengthening (t_f=0).

The SIF was gradually decreasing as the increasing of the thickness of CFL in front surface strengthening from Figure.6, and becoming flat after $t_f \geq 0.6mm$.

3.3 Effect of crack parameters on K_I

3.3.1 Effect of *a/c*

To discuss the effect of crack shape ratio *a/c* on K_I, the relative depth *a/B* was supposed to be invariable in FEM analysis. The curves of K_I in front side strengthening were listed in Figure. 7 when t_f=0.2*mm*, *a/B*=0.2，*a/c*=0.4, 0.6 0.8. The strengthening effect was better from Figure.7, while *a/c* was larger, the effect was weaker. For example, strengthening effect was 26.1% when θ=90° and *a/c*=0.4, and that was 20.6% and 16.1% when *a/c*=0.6 and *a/c*=0.8 respectively as shown in Figure.8. It can be considered as *a/B* was invariant, *a/c* was larger, *c* was lower, and the interaction region between FRP and surface crack was shorter, the function of FRP was smaller.

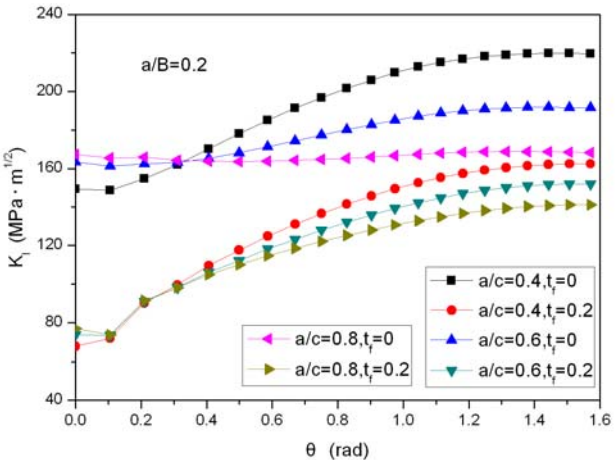

Figure 7. Effect of *a/c* on K_I

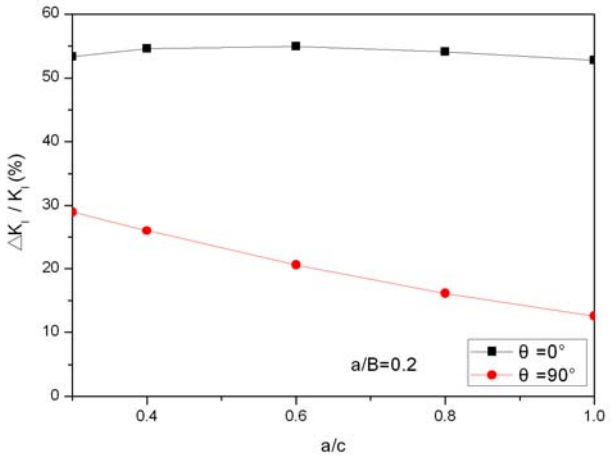

Figure 8. Effect of *a/c* on K_I for θ=90° and θ=0°

3.3.2 Effect of *a/B*

To discuss the effect of the relative depth *a/B* on K_I, the shape ratio *a/c* was supposed to be invariable for FEM analysis. The curves of K_I in front strengthening were listed in Figure. 9 when t_f =0.2, *a/c*=0.4，and *a/B* was equal to 0.1, 0.2 and 0.3. The strengthening effect in front side strengthening was better, while *a/B* was larger, the effect was weaker. As shown in Figure.10, the reinforcement effect can be reduced when *a/B*<0.3 and θ=90°, but the reinforcement effect will increase when *a/B* >0.3 and θ=90°. For example, the effect of reinforcement was 32.1%, 26.1%, 24.8%, 25.9% and 28.1% when *a/B* was equal to 0.1, 0.2, 0.3, 0.4 and 0.5 respectively near θ=90°. It was because that the increasing of the crack depth caused further distance from CFL to the crack

tip, and the resistance to crack development was weaker when the CFL was bonded to the front side surface.

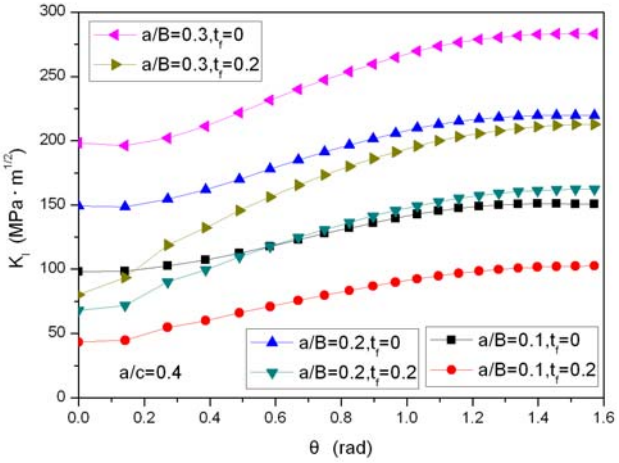

Figure 9. Effect of *a/B* on K_I

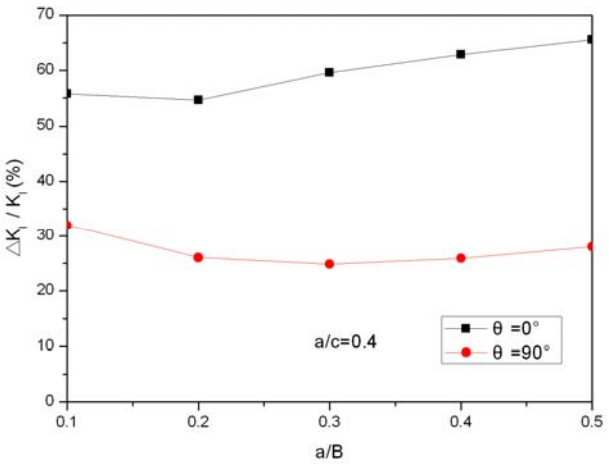

Figure 10. Effect of *a/B* on K_I for θ=90° and θ=0°

4. Expression for K_I

In order to facilitate the calculation of SIF for the 3D semi-elliptical surface crack in the center of the rectangle steel plate strengthened with FRP, and very convenient for engineering application, based on the analysis results of a large number of finite element calculation, the mathematical software Matlab was used to fit the calculation expression of SIF, and get the expression as follows:

$$K_I = \sigma \cdot F\left(\frac{a}{c}, \frac{a}{B}, t_f, \theta\right) \tag{2}$$

Where, σ is tensile stress acted on the ends of the steel plate, and

$$\begin{aligned} F\left(\frac{a}{c}, \frac{a}{B}, t_f, \theta\right) = {} & 0.4 + 0.23 \cdot p + q \cdot (4.96 - 10.09 \cdot t + 4.24 \cdot r) + t^2 \cdot (6.44 \cdot q - 0.39) + 0.44 \cdot r^2 \\ & + p \cdot q \cdot r \cdot (27.35 \cdot t - 6.82) + t \cdot r^2 \cdot (3.11 \cdot q - 0.82 \cdot p) - p \cdot q \cdot t \cdot r \cdot (26.09 \cdot t + 17.35 \cdot r) \\ & + t^2 \cdot r^2 \cdot (0.66 \cdot p - 6.4 \cdot q + 22.01 \cdot p \cdot q) \end{aligned} \tag{3}$$

Where, $p = a/c$, $q = a/B$, $t = \ln(1 + t_f^{0.25})$, $r = \sin\theta$, $0 < a/c < 1.0$, $0 < a/B < 1.0$, $2c/W \le 0.5$, $0^\circ \le \theta \le 90^\circ$.

Comparing the calculating values by equations (2) and (3) with the data from FEM, it is shown that the average error is within 3% and the fitting result is reasonable.

5. Conclusions

Finite element software Abaqus was applied to study the stress intensity factors (SIF) of 3D semi-elliptical surface crack in rectangle steel plate strengthened with CFL, and the strengthening effects were discussed. The conclusions were as follows:

(1) Front side strengthening reduced the stress intensity factors of 3D semi-elliptical surface crack significantly, but the increasing amplitude of strengthening effects decreased gradually with increasing of thickness of CFL.

(2) Crack shape ratio *a/c* had a great effect on front side strengthening, and its effect decreased with the increasing of *a/c*.

(3) Crack relative depth *a/B* also had some effect on front side strengthening. The strengthening effect decreased with the increasing of *a/B*. The strengthening effect can be reduced when $a/B<0.3$ and $\theta=90°$, but the strengthening effect will increase when $a/B>0.3$ and $\theta=90°$.

(4) An expression for calculating the stress intensity factors of semi-elliptic surface crack under strengthening condition was proposed by adopting MATLAB software.

Acknowledgments

The project is supported by National Natural Science Foundation of China (No. 51078145 and No. 11132004) and Guangdong Province Natural Science Foundation of China (No.9251064101000016).

References

[1] X.B.Lin, R.A.Smith, Numerical analysis of fatigue growth of external surface cracks in pressurized cylinders. Pres.Ves.& Piping, 71(1997)293-300.

[2] Hadi Khoramishad, Majid Reza Ayatollahi, Finite element analysis of a semi-elliptical external crack in a buried pipe. Transactions of the Canadian Society for Mechanical Engineering, 33(2009) 399-409.

[3] Edberg W, Mertz D, Gillespie Jr J, Rehabilitation of Steel Beams Using Composite Materials. Proceedings of the Materials Engineering Conference, Materials for the New Millenium, New York, NY:ASCE, 1(1996)502-508.

[4] Nicholas G.Tsouvalis, Lazarus S.Mirisiotis, Dimitris N.Dimou, Experimental and numerical study of the fatigue behaviour of composite patch reinforced cracked steel plates. International Journal of Fatigue, 31(2009)1613-1627

[5] P.Y. Huang, XP. Zhou, C. Zhao, Some Key Mechanical Problems on FRP Sheet Applied in Civil Engineering. Journal of South China University of Technology, 30(2002):101-105.

[6] X.L. Zhao, L. Zhang, State-of-the-art review on FRP strengthened steel structures. Engineering Structures, 29(2007) 1808-1823.

[7] L.Briottet, R.Batisse, G.de Dinechin, et al, Recommendations on X80 steel for the design of hydrogen gas transmission pipelines. International Journal of Hydrogen Energy, 11(2012) 9423-9430.

[8] Kent A. Harries, Andrew J. peck, Elizabeth J. Abraham, Enhancing stability of structural steel sections using FRP. Thin-Walled Structures, 47(2009) 1092-1101.

[9] P.Y. Huang, J.C. Zeng, Application of Carbon Fiber Laminate. Chinese Patent No. ZL200410026742.8, China Patent Administration, Beijing, 2006

A Self-consistent Model in the Local Residual Stress Evaluation of 316H Stainless Steel

Jianan Hu[1,*], Bo Chen[2], David Smith[2], Peter Flewitt[3], Alan C.F. Cocks[1]

[1] Department of Engineering Science, University of Oxford, OX1 3PJ, UK
[2] Department of Mechanical Engineering, University of Bristol, BS8 1TR, UK
[3] IAC, University of Bristol, BS8 1TR, UK
* Corresponding author: jianan.hu@eng.ox.ac.uk

Abstract The residual stresses in materials have a considerable effect on the mechanical properties, including creep and failure behaviour. Due to elastic and plastic anisotropy, differently oriented grains will exhibit different mechanical responses for a given macroscopic stress, leading to a variation of stresses within the grains. Experimental studies of meso-scale residual stress evolution can be used to validate crystal based plasticity and hardening models. In this paper, a self-consistent model and a simple multi-bar system are employed to determine how the evolution of the residual stress field depends on the constitutive assumptions for the individual grains. This framework has been used to evaluate data for the lattice strain evolution in 316H stainless steel measured from neutron diffraction experiments. A suitable model is identified, which captures the macroscopic response of the material and explains the way in which the meso-scale residual stresses evolve. The good agreement achieved between the self-consistent model and experiment demonstrates that this model reasonably reflects the mechanical physics of 316H stainless steel, and may help improve our understanding of the influence of the residual stress on the fracture and failure behaviour.

Keywords Residual stress, Self-consistent model, 316H stainless steel, Neutron diffraction

1. Introduction

Residual stresses developed within grains of a polycrystalline material have a considerable effect on material properties, including load carrying capacity, creep and crack initiation and propagation [1]. Thus, understanding the distribution and the evolution of residual stresses is vital to assessing the performance of engineering components. Elastic and plastic anisotropy of the differently oriented grains results in a variation in the mechanical response of different grains and the development of meso-scale intragranular residual stresses [2,3], i.e. the stresses within the grains. The development of these residual stresses depends on the detailed flow, hardening and recovery laws for the different slip systems in the body. A number of techniques have been developed for measuring residual stresses (or residual elastic strains) in a body. Neutron diffraction can provide information about the residual elastic strains in different families of grains within the bulk of a polycrystalline sample. Availability of the data offers the opportunity to identify the most appropriate forms of constitutive relationships for the individual grains, which can then be used to predict the evolution of residual stresses and the macroscopic material response under complex thermo-mechanical loading histories.

Various models have been proposed or developed to predict quantitative and qualitative features of the elastic-plastic behaviour of polycrystalline materials, such as Taylor model [4], which assumes that all grains experience identical strain, but elastic anisotropy plays no role. Self-consistent models which employ solutions of the classical Eshelby inclusion problem [5,6], have been employed extensively to describe the structure-property relationship of materials. Examples of this approach are given by Kroner [7], and Budiansky and Wu [8] to describe the effect of misfit strain on plastic deformation. However, the inclusion is simplified as being elastically isotropic and with the same properties as the matrix. Self-consistent models, suggested by Hill [9] and Hutchinson [10],

incorporate a more elaborate description of single crystal behaviour for calculating the stresses and strains in the individual grains, but with no physical description of work hardening. The physical characterization of work hardening is discussed by Kocks and Mecking [11], based on dislocation multiplication and the evolution of dislocation density. Lagneborg's dislocation link length model [12] provides a more detailed description of the dislocation structure and evolution of the structure based on Orowan bowing [13] and recovery of the dislocation structure.

In this paper, a self-consistent model is developed to consider both elastic and plastic anisotropy of the polycrystalline grains. A hardening model is described based on Lagneborg's dislocation link length model. A simplified multi-bar representation of the polycrytsal is also described. Both these models are used to predict the elastic-plastic responses and the development of meso-scale residual stresses of a Type 316H stainless steel under uniaxial tensile loading. These models are validated using elastic lattice strain and residual lattice strain data obtained by the neutron diffraction technique. A detailed description and explanation of the experiment is presented in the companion paper [14]. The ability of these models to capture the observed response is discussed.

2. Formulation of the self-consistent model

In the self-consistent approach, each individual grain of a polycrystalline material, is regarded as a spherical inclusion in an infinite homogeneous matrix with the average macroscopic properties [7,8]. The purpose of the Eshelby based deformation model is to establish the relationship between the local individual grain-scale responses and the polycrystal aggregate response.

2.1. Model of elasticity

Eshelby obtained the solution for the elastic field of a misfitting (with a stress-free transformation strain ε^t) ellipsoidal homogeneous inclusion embedded in an infinite isotropic matrix of the same elastic constants. The total strain in the inclusion is linked by the transformation strain and a 6th-order tensor S^i relating the final constrained inclusion shape to the original shape mismatch between the matrix and the inclusion, and is only dependent on the geometry of the inclusion and Poisson's ratio of the medium [5,15]. For an inhomogeneity (a single inhomogeneous grain in the model) with different elastic constants containing a transformation strain ε^{ta}, its elastic field can be simulated by an equivalent homogeneous inclusion with a properly chosen transformation strain ε^{t*}. Given a macroscopically applied stress σ, the relationship between the real transformation strain in the inhomogeneity and the virtual transformation strain in the equivalent inclusion can be derived as

$$\varepsilon^{ta}+\left[\left(C^a\right)^{-1}-\left(C^i\right)^{-1}\right]T\sigma=\left[\left(C^a\right)^{-1}C^i\left(I-S^i\right)+S^i\right]\varepsilon^{t*} \tag{1}$$

where C^a, C^i are respectively the stiffness matrices of the grain and the surrounding matrix. T is the orientation matrix of the grain described by the three Euler angles. I is the unity matrix. If the deformation is fully elastic, i.e. $\varepsilon^{ta}=0$, ε^{t*} can be solved and the relationship between the applied stress and the grain stress and strain can be established

$$\sigma^a=\left\{\left\{\left[I-\left(S^i\right)^{-1}\right]^{-1}\left(C^i\right)^{-1}-\left(C^a\right)^{-1}\right\}^{-1}\left[\left(C^a\right)^{-1}-\left(C^i\right)^{-1}\right]+I\right\}T\sigma=H^aT\sigma \tag{2}$$

$$\varepsilon^a=\left\{\left(C^i\right)^{-1}+\left\{\left[\left(C^a\right)^{-1}-\left(C^i\right)^{-1}\right]^{-1}\left(C^a\right)^{-1}C^i\left(S^i\right)^{-1}-C^i\right\}^{-1}\right\}T\sigma=K^aT\sigma \tag{3}$$

where $H^a=\left\{\left[I-\left(S^i\right)^{-1}\right]^{-1}\left(C^i\right)^{-1}-\left(C^a\right)^{-1}\right\}^{-1}\left[\left(C^a\right)^{-1}-\left(C^i\right)^{-1}\right]+I$ and

$$K^a = \left(C^i\right)^{-1} + \left\{\left[\left(C^a\right)^{-1} - \left(C^i\right)^{-1}\right]^{-1}\left(C^a\right)^{-1} C^i \left(S^i\right)^{-1} - C^i\right\}^{-1}$$

2.2. Model of plasticity

The expression of the transformation strain in the grain has been considered to be the plastic misfit strain between the grain and the matrix in the same coordinate [7,8]

$$\varepsilon^{ta} = \varepsilon^p - T^{-T} E^p \tag{4}$$

where ε^p is the local plastic strain in the grain and E^p is the polycrystal plastic strain obtained by the volume average over all the grains with possible orientations. In Eq. (1), if $\varepsilon^{ta} \neq 0$, i.e. the material is plastically deformed, a relationship between ε^{t*} and the real plastic misfit strain ε^{ta} can be obtained by macroscopically unloading the sample (i.e. setting $\sigma = 0$). Further, the residual stress in the grain (X^a) can be derived as a function of the plastic misfit strain ε^{ta}

$$X^a = C^i\left(I - S^i\right)\left(\left(C^a\right)^{-1} C^i S^i - \left(C^a\right)^{-1} C^i - S^i\right)^{-1} \varepsilon^{ta} \tag{5}$$

2.3. Crystal based plasticity model

Plastic deformation is the glide of dislocations on multiple slip systems [11,16]. Following the classical crystal plasticity model [16,17], the shear strain rate ($\dot{\gamma}^\beta$) of a slip system β ($\beta = 1 \sim m$, m: total number of slip systems) is related to the resolved shear stress (RSS, τ^β) and the critical resolved shear stress (CRSS, τ^β_{crss}) of the corresponding slip system by the power-law relationship

$$\dot{\gamma}^\beta = \dot{\gamma}_0 \left|\frac{\tau^\beta}{\tau^\beta_{crss}}\right|^t \mathrm{sgn}(\tau^\beta) \tag{6}$$

where $\dot{\gamma}_0$ is a reference shear strain rate and t is the rate sensitivity exponent. As $t \to \infty$ this constitutive response of each slip system is consistent with rate-independent deformation [17]. In the computations here a value of t=600 is used to provide a response that is essentially rate independent for the timescales employed in the simulations. If $\overline{n}^\beta(n_1^\beta, n_2^\beta, n_3^\beta)$ is the normal direction and $\overline{s}^\beta(s_1^\beta, s_2^\beta, s_3^\beta)$ is one of the slip directions associated with the slip system β, the shear strain rate $\dot{\gamma}^\beta$ on this slip system provides a contribution to the plastic strain rate given by:

$$\dot{\overline{\varepsilon}}^\beta = sym(\dot{\gamma}^\beta \overline{n}^\beta \otimes \overline{s}^\beta) = \theta^\beta \dot{\gamma}^\beta \tag{7}$$

where θ^β is the Schmid factor of the slip system, which also links the RSS with the stress of each individual grain [16,17]. The total plastic strain rate is the sum of $\dot{\overline{\varepsilon}}^\beta$ over all the slip systems

$$\dot{\varepsilon}^p = \sum_\beta \dot{\overline{\varepsilon}}^\beta = \sum_\beta \theta^\beta \dot{\gamma}^\beta \tag{8}$$

The controlling parameters for slip are the CRSS and the hardening law. The initial CRSS is assumed to be the same on all slip systems and it is taken to evolve as [9]

$$\dot{\tau}^i_{crss} = \sum_j h^{ij} \left|\dot{\gamma}^j\right| \quad \text{with} \quad h^{ij} = h\left(q + (1-q)\delta^{ij}\right) \tag{9}$$

where h^{ij} is the rate of strain hardening on slip system i due to a shearing on slip system j [16]. The summation is over all active slip systems. h is the hardening coefficient dependent on the previous deformation history and q is a factor determining the degree of latent hardening: q=0 provides only self-hardening, q=1 represents Taylor hardening, and q>1 gives stronger latent hardening. For latent hardening, the range of q has been reported to be $1<q<1.4$ [17,18]. As for the coefficient h, the specific form needs to be given by the physical hardening model.

2.4. Dislocation link length based hardening model

The strain hardening effect is physically characterized by the motion of mobile dislocations. The dislocation link length model originally proposed by Lagneborg [12] offers a reasonable illustration of such an effect. A dislocation link is defined as the segment between two pinning points (dislocation junctions or other obstacles). The hardening behaviour is characterized by the evolution of the distribution of dislocation link lengths associated with a particular slip system.

2.4.1. The structure of dislocation link distribution

In the model, the dislocation structure can be described as a population of dislocation links with spacing occurring as a spectrum of lengths, i.e. a 3D dislocation network [12]. The distribution of link lengths in the network is described by an instantaneous distribution function $\phi(\lambda)$, defined such that $\phi(\lambda)d\lambda$ equals the number of links per unit volume with lengths between λ and $\lambda + d\lambda$. The detailed form of the distribution function can be expressed as [19,20]

$$\phi(\lambda) = A\lambda^2 e^{-B\lambda^2} \tag{10}$$

where *A* and *B* are two constants which evolve during deformation. A typical distribution is shown in Fig. 1(a), as a truncated Weibull distribution. λ_{th} is the threshold or the current maximum link length on a slip system, directly related to the current CRSS on the corresponding system.

$$\lambda_{th} = \frac{\alpha G b}{\tau_{crss}} \tag{11}$$

where α is a dimensionless constant determining the strength of an obstacle, *G* is the shear modulus and *b* is the value of Burgers vector. The truncation in Fig. 1(a) indicates that no links longer than the threshold links can exist in the complex network without recovery. Thus the total number (*N*) per unit volume and the total density (ρ) of dislocation links can be expressed as

$$N = \int_0^{\lambda_{th}} \phi(\lambda) d\lambda \qquad \text{and} \qquad \rho = \int_0^{\lambda_{th}} \lambda\phi(\lambda) d\lambda = N\bar{\lambda} \tag{12}$$

where $\bar{\lambda}$ is the average link length, or mean free path of dislocation motion [12,21,22]. Meanwhile, a constant volume boundary condition is required and expressed as [12,21]

$$\int_0^{\lambda_{th}} c\lambda^3 \phi(\lambda) d\lambda = 1 \tag{13}$$

where *c* is a geometric constant close to 1.

2.4.2. The dislocation unzipping movement

In Lagneborg's model, dislocation motion is described as long waiting times at the obstacles and occasional spurtlike movements of dislocation links between obstacles [12]. Thus at any instant, all the dislocations in the network can be considered as immobile and held up at obstacles. At a certain stress, dislocation links with the threshold length will be released and become mobile. They overcome the obstacles and then continue to glide and sweep out an area before being blocked and partitioned into shorter links by adjacent obstacles in the network, which become immobile again (Fig. 1b). If the area swept out by each released dislocation link is *s*, the shear strain rate is [12,22]

$$\dot{\gamma} = bs\dot{N}_m \tag{14}$$

where $\dot{N}_m$ is the release rate of mobile links, which is related to the current value of CRSS and its rate of increase. The expression of *s* is complicated and not reproduced here. The Orowan bowing [13] process was assumed in Lagneborg's original model, where the released links expand to circular loops and the area is assumed to be $4\pi\bar{\lambda}^2$. However, such encircling movement is often the characterization for strong obstacles (large α) and the spatial distribution of obstacles is always a

random array for a wide range of strengths [23]. A consecutive release process (Fig. 1c) is observed for weak obstacles (such as forest dislocations), which is commonly referred to as an unzipping mechanism [23]. Although it describes a release process by links with various lengths besides the threshold one, it is assumed that this does not influence the activation criterion of the release process in the model, but only offers a greater sweeping area than the original Orowan bowing process. The sweeping area in the model is assumed to be a circular arch and the averaged distance a link can reach is proportional to $\overline{\lambda}$ but needs to be determined by fitting with experimental data.

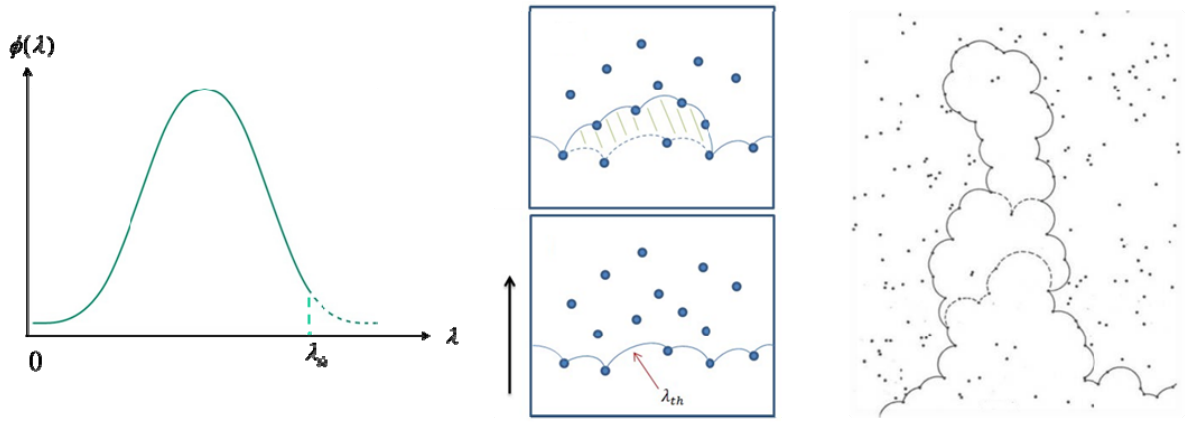

(a) (b) (c)

Figure 1. (a) Truncated Weibull dislocation distribution; (b) A schematic diagram of the kinetic motion of dislocation links before and after release, where the solid points are obstacles, e.g. dislocation junctions on other slip planes; (c) Unzipping movement of a dislocation which glides on a slip plane [23]

The evolution of the dislocation distribution function updates two state variables in the model: (1) the local threshold link length; (2) the global dislocation density. The dislocation multiplication is described by the generation and disappearance of links, which can be separated into different stages such as release, expansion and cut. The detailed model derivation for the structure evolution is not shown here. Finally, the relationship between the shear strain rate and the CRSS rate of increase on a single slip system can be derived from Eq. (14) as

$$\dot{\gamma} = f(\tau_{crss}, \rho, \dot{\rho})\dot{\tau}_{crss} \tag{15}$$

Compared with Eq. (9), $1/f(\tau_{crss}, \rho, \dot{\rho}) = h$ is the hardening coefficient. In the simulation, a simple linear hardening is considered, which is given by an assumption that the total unzipped link length in a slip system and the link length at which the distribution function has the maximum value are proportional to the threshold link length. The model gives a range of linear hardening coefficients obtained by the variation of different parameters such as the obstacle strength α. However, the coefficient as a whole is treated as a fitting parameter in the simulation, but its value must lie within a physical range for this model to hold.

3. A simplified multi-bar system

A simplified and straightforward 1D multi-bar system which captures the general structure of the self-consistent model was established. The general structure the system is shown in Fig. 2. Taking an face centred cubic (fcc) material as an example, all the thick bars (with the properties of single cubic grains with their specific orientation and with equal cross-sectional area) are representative components of the isotropic polycrystal and their average response gives the polycrystal behaviour. The small bar in the system represents a grain family, which does not influence the averaged behaviour of the system since its cross-sectional area is negligible. Therefore, this system demonstrates the framework of the basic structure of a self-consistent model, a single grain

embedded in an infinite matrix with the averaged isotropic property, despite the difference that the geometric feature requires equal strain for all the bars which is similar to a Taylor model.

The elastic anisotropy for the multi-bar system is determined such that each bar has a different Young's modulus along the loading direction related to the individual orientation. Whilst for the plastic anisotropy, the classic 1D incremental plasticity model of isotropic hardening [24] is used, where the strain hardening effect is characterised by a plastic modulus defined as the instantaneous slope of the stress-strain curve after micro-yielding. For the multi-bar system, the assumption of linear hardening of each grain is described by an orientation-dependent bilinear response [24] and the plastic modulus serves as the hardening coefficient of this system.

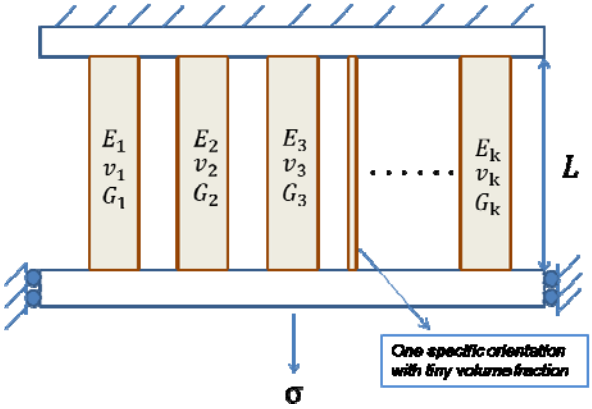

Figure 2. A schematic diagram of the multi-bar system

4. Model evaluation

4.1. Neutron diffraction experiment

To validate the self-consistent model, the lattice strain evolution, especially the residual lattice strain in different crystallographic planes of a fcc material of ex-serviced 316H stainless steel was measured using neutron diffraction (ND) combined with in-situ tensile deformation on the ENGIN-X instrument at the ISIS pulsed neutron facility, Rutherford Appleton Laboratory. A schematic diagram of the experimental setup is shown in Fig. 3.

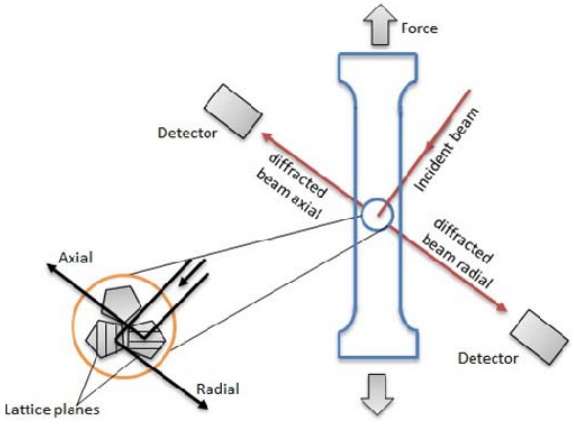

Figure 3. Schematic diagram of neutron diffraction experiment

The incident beam directed at a specimen consists of a polychromatic spectra with a continuous range of wavelengths, which enables the recording of many lattice planes in each measurement. The loading direction is horizontal and at 45^{o} to the incident beam. Two detectors are positioned to

allow simultaneous measurement of lattice spacing both parallel (axial) and perpendicular (radial) to the loading direction. The lattice strain measured for each plane represents the average value of the elastic strain within a family of grains which are oriented such that a specific {*hk*l} plane diffracts to the detector. For example, in the axial direction, a specific {*hk*l} lattice strain indicates the average axial elastic strain over the grains located in the gauge volume with their {*hk*l} plane normal parallel to the loading axis. The complete description of the experiment and the full range of measurement are presented in Ref [14].

4.2. Simulation of the experimental results

4.2.1. Macroscopic behaviour and parameter identification

In the present calculations, no lattice rotation or texture development was incorporated due to the small plastic deformation [25]. The property of the matrix was initially undetermined and was solved by iteration from the average response of all the grains. This then served as the standard for the selection of the number of bars in the multi-bar system. The latent hardening factor q was pre-set as 1, i.e. the hardening on all slip systems were equal, which is reasonable in the current framework since the expansion and partition of dislocation links may generate equal obstacles for all slip planes. The effect of different values of q was considered elsewhere [26]. The fitting process was to initially make the macroscopic stress-strain response of the self-consistent model resemble the actual measured macroscopic behaviour of the sample and then to use the refined parameters to predict the macroscopic behaviour of the multi-bar model and the microscopic behaviours of the local grain family in both models. The fitting parameters are listed in Table 1 together with the single crystal elastic constants of the fcc material 316H stainless steel. The calculated macroscopic stress-strain responses are shown in Fig. 4, with the results obtained by both the self-consistent and multi-bar models.

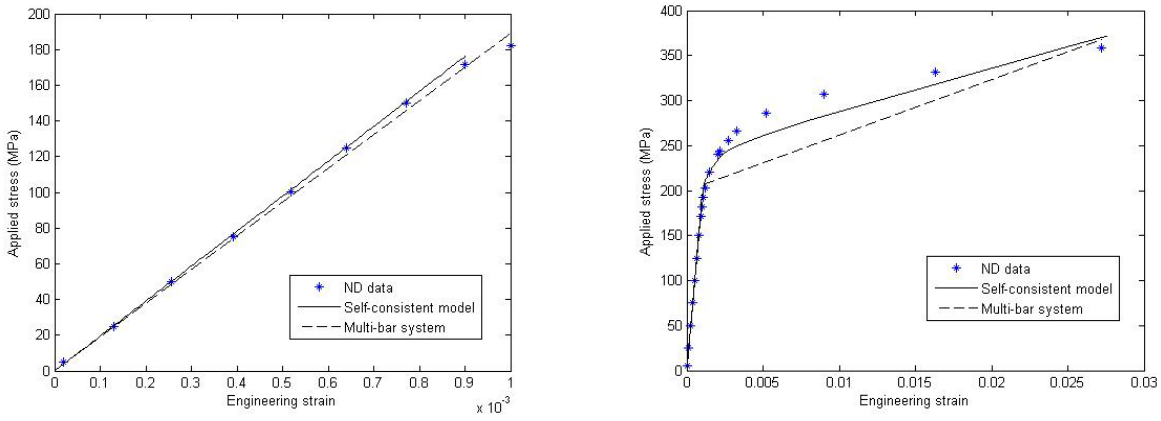

(a) (b)

Figure 4. Macroscopic polycrystal stress-strain response of 316H stainless steel under uniaxial tension at room temperature; (a) the elastic region; (b) the whole region. (ND=neutron diffraction)

Table 1. Material parameters of 316H stainless steel used in the simulation

C_{11} (GPa)	C_{12} (GPa)	C_{44} (GPa)	$\dot{\gamma}_0$	t	τ_{crss0} (GPa)	b (m)	q	h *(MPa)*
198	125	122	5e-6	600	82	2.5e-10	1	370

4.2.2. The grain family and the Young's modulus

The family of grains contributing to the reflection of a certain crystallographic plane in neutron diffraction has one uniform orientation along the measurement direction. The averaged response of

this grain family can be determined either by averaging the responses of all the members or by considering the family as a whole with an averaged transversely isotropic property. In the present simulation, the results of two representative grain families {220} and {111} with the aggregate normal along the axial direction were considered. The diffraction elastic constants were measured in the experiment, in which the Young's modulus was defined as the slope of the applied stress over the elastic lattice strain [2,3]. The experimental measurement and the model prediction results for the two grain families are listed in Table 2, where the theoretical value and model prediction of the physical Young's modulus is also presented as a further validation of the model.

Table 2 Measurement and prediction of the Young's modulus of {220} and {111} grain family

Grain family	**{220}**	**{111}**
Diffraction Young's modulus (GPa)	209.1±15.8	225.3±11.9
Self-consistent model prediction	210.8	241.8
Physical Young's modulus (GPa) [27]	196	285
Self-consistent model prediction	225.1	285.1

4.2.3. The residual lattice strain

The results of axial elastic lattice strain evolution during loading, together with the predictions of the self-consistent (blue solid line) and multi-bar (blue dash line) models are demonstrated in Fig. 5. At each unloading step, the residual axial elastic lattice strain for the grain families was measured and was then plotted against the macroscopic residual plastic strain (shown in Fig. 6 with the model prediction). Good agreement is observed between the experimental data and the prediction of self-consistent model, while the quality of the prediction of multi-bar model is a mixture.

From the figures, although multi-bar model gives a poorer prediction than the self-consistent model, both of the models capture the major trend of the experimental data, particularly the transition that occurs in both the lattice strain and the residual lattice strain evolution upon micro-yielding. In addition, the two models predict that both grain families have an initially increasing residual lattice strain evolution, which is when the surrounding matrix yields (or some grains in the matrix yield) before each grain family. The subsequently decreasing residual lattice strain is when all the grains deform plastically, which is reflected in the difference in the plastic misfit strains in Eq. (4).

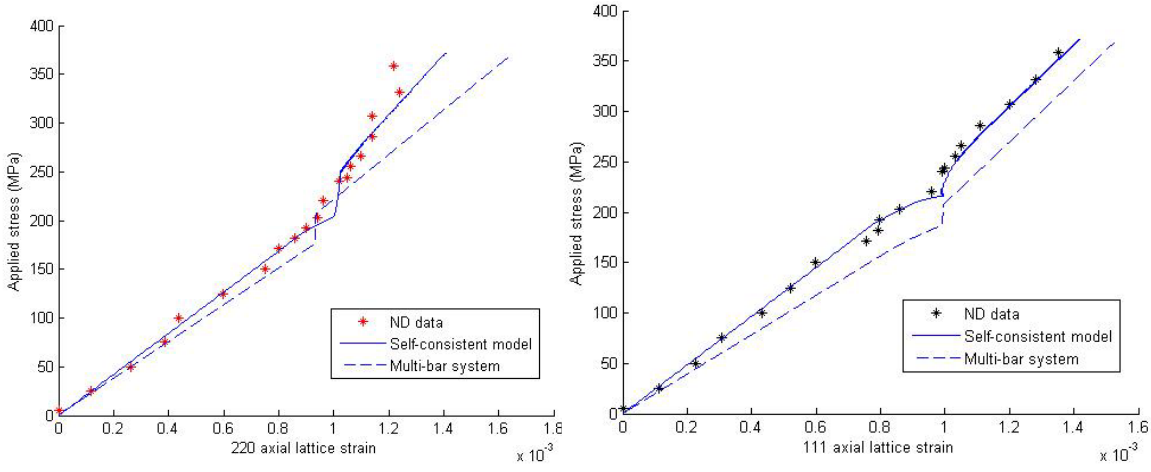

(a) (b)

Figure 5. Neutron diffraction (ND) measurement and model prediction results of the applied stress vs axial lattice strain upon loading (a) {220} grain family; (b) {111} grain family.

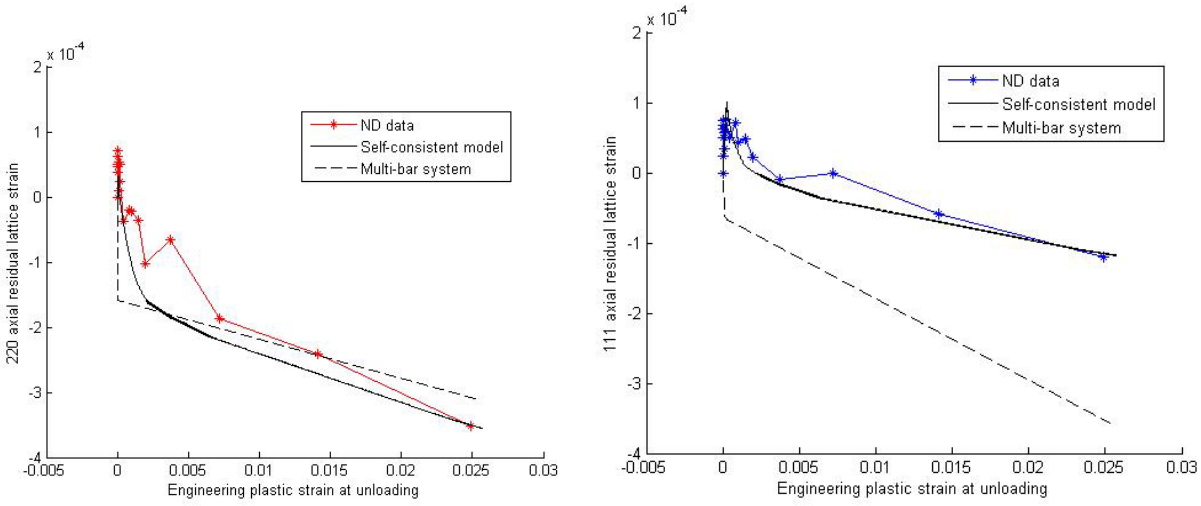

(a) (b)

Figure 6. Neutron diffraction (ND) measurement and model prediction results of the axial residual lattice strain vs the engineering plastic strain at unloading. (a) {220} grain family; (b) {111} grain family.

5. Discussion and conclusion

The mechanical features of {220} and {111} grain families have been discussed in [2,3]. From the results, the linear hardening assumption is acceptable and permits only one parameter, the hardening coefficient *h* to be used. The oscillation of the residual elastic lattice strain at relatively small plastic strain region in the measurement is expected to be a result of a combination of experimental error and the complex interaction between grains. Since the self-consistent model only considers the interaction between one single grain and the whole matrix, such oscillations cannot be predicted by the model. The poorer predictions from the multi-bar system in Fig. 5-6 may result from the identical strain for all the bars, regardless of their stiffness and hardening responses. Despite the same applied stress and yield stress with those in the self-consistent model, the multi-bar system may display a different mechanical response, especially the accumulation of residual elastic lattice strain. Such a discrepancy demonstrates that the identical strain assumption may not be acceptable for the local residual lattice strain evaluation.

A self-consistent model for polycrystal deformation is established with specific emphasis on the elastic and plastic anisotropy. The self-consistent scheme includes the elastic-plastic interaction between the grains which are regarded as spherical inclusions in an infinite homogeneous matrix with the averaged polycrystal response. A simplified multi-bar system is introduced which captures the basic structure of the self-consistent model. The models predictions were compared with the neutron diffraction measurements of elastic lattice strains in grain families within an ex-serviced 316H stainless steel polycrystal subjected to uniaxial tensile loading. The good agreement between the measured and calculated lattice strains validates the self-consistent model.

Acknowledgements

ISIS is acknowledged for the provision of beamtime at Beamline ENGIN-X. The authors also wish to acknowledge the financial support from EDF Energy.

References

[1] O. Kwon, B. Pathiraj, K.M. Nikbin, Effect of residual stress in creep crack growth analysis of cold bent tubes under internal pressure, Int J Pres Ves Pip, 78(2001) 343-350.
[2] B. Clausen, T. Lorentzen, T. Leffers, Self-consistent modelling of the plastic deformation of f.c.c

. polycrystals and its implications for diffraction measurements of internal stresses, Acta Mater, 22 (1998) 3087-3098.
[3] M.R.Daymond, P.J. Bouchard, Elastoplastic deformation of 316 stainless steel under tensile load ing at elevated temperatures, Metall Mater Trans A, 37 (2006) 1863–1873.
[4] G.I. Taylor, Plastic strain in metals, J Inst Metals, 62(1938) 307-325.
[5] J.D. Eshelby, The determination of the Elastic Field of an Ellipsoidal Inclusion and Related Prob lems. Proc R Soc Lond A, 241 (1957) 376–396.
[6] P.J. Withers, W.M. Stobbs, O.B. Pedersen, The application of the Eshelby method of internal stress determination to short fibre metal matrix composites, Acta Metall, 37(1989) 3061-3084.
[7] E. Kroner, On the plastic deformation of polycrystals, Acta Metall, 9(1961) 155-161.
[8] B. Budiansky, T.T. Wu, Theoretical prediction of plastic strains of polycrystals, Proc. 4th Congr Appl Mech, 1962 1175-1185.
[9] R. Hill, Generalized constitutive relations for incremental deformation of metal crystals by multislip, J Mech Phys Solids, 14(1966) 95-102.
[10] J.W. Hutchinson, Elastic-plastic behaviour of polycrystalline metals and composites, Proc Roy Soc Lond A, 319 (1970) 247-272.
[11] U.F. Kocks, H. Mecking, Physics and phenomenology of strain hardening: the FCC case, Progress in Materials Science, 48(2003) 171-273
[12] R. Lagneborg, B.H. Forsen, A model based on dislocation distributions for work-hardening and the density of mobile and immobile dislocations during plastic flow, Acta Metall, 21(1973) 781-790.
[13] E. Orowan, The creep of metals, J West Scotland Iron Steel Inst, 54(1946-1947) 45-96.
[14] B. Chen, D.J. Smith, P.E.J. Flewitt, S.Y. Zhang, Measurement of internal stress and internal resistance resulting from creep of Type 316H stainless steel, 13th Int. Conf. Fract., Beijing, (2013).
[15] T. Mura, Micromechanics of Defects in Solids, Martinus Nijhoff Publishers, 1982.
[16] R.J. Asaro, A. Needleman, Texture development and strain hardening in rate dependent polycrystals, Acta Metall, 33(1985) 923-953.
[17] J.W. Hutchinson, Bounds and self-consistent estimates for creep of polycrystalline materials, Proc R Soc Lond. A 348(1976) 101-127.
[18] C.A. Bronkhorst, S.R. Kalidindi, L. Anand, Polycrystalline plasticity and the evolution of crystallographic texture in fcc metals, Phil Trans R Soc Lond A, 341(1992) 443-477.
[19] L. Shi, D.O. Northwood, On dislocation link length statistics for plastic deformation of crystals, Phys Stat Sol A, 137(1993) 75-85.
[20] B.S. Wang, F.Y. Sun, Q.E. Meng, W.C. Xu, An approach to theoretical function of dislocation link length distribution in metal, Acta Metall A, 5(1992) 314-317.
[21] A.J. Ardell, M.A. Przystupa, Dislocation link length statistics and elevated temperature deformation of crystals, Mech Mater, 3(1984) 319-332.
[22] O. Ajaja, A dislocation network model of recovery-controlled creep, J Mater Sci, 21(1986) 3351-3356.
[23]A.J.E.Foreman, M.J. Makin, Dislocation movement through random arrays of obstacles, Philos Mag, 14 (1966) 911-924.
[24] J.C. Simo, T.J.R. Hughes, Computational inelasticity, Springer-Verlag, New York, 1998.
[25] B. Clausen, Characterization of polycrystal deformation, PhD thesis, Riso National Laboratory, Roskilde, Denmark, 1997.
[26] D.F. Li, N.P.O. Dowd, On the evolution of lattice deformation in austenitic stainless steels—The role of work hardening at finite strains, J Mech Phys Solids, 59(2011) 2421-2441.
[27] G.E. Dieter, Mechanical Metallurgy, McGraw-Hill Book Co., New York, 1986.

Fracture Toughness of SE(B) Specimens of Steel in the Presence of Splitting

Pablo J. Lara Melcher, Enrique M. Castrodeza*

Laboratory of Fracture Mechanics, Department of Metallurgical and Materials Engineering, COPPE/Federal University of Rio de Janeiro, P.O. Box 68505, 21941-972, Rio de Janeiro, RJ, Brazil

*castrode@metalmat.ufrj.br

Abstract

Instabilities (pop-ins) in load-displacement records of fracture tests could be originated from small unstable crack growth in the main crack plane, as usual in welded joints, or from delamination of the ligament (splitting), as in some rolled steels. According to the standards, no matter the origin of the instability the fracture toughness need to be reported at the first significant pop-in. In most cases this treatment greatly penalizes the fracture toughness of the material. In that way a question arose: What would be the fracture toughness of a material featuring splitting if the specimen were not suffered split? To answer this question several test were made in rolled steels showing and not pop-ins from splitting. It is being now proposed that the change in the system energy associated to splitting instabilities could be neglected, the records corrected by adding the load drop caused by the split to the points on the right, and the toughness calculated at the maximum load. The results (for the magnitude of the instabilities we faced) showed that maximum load CTOD from corrected records and from records of the same material without pop-ins by splitting are statistically equivalent.

Keywords: Pop-in, Split-Out, Fracture Toughness, Rolled Steel.

1. Introduction

Pop-ins in load-displacement records of fracture tests are not always related to unstable crack growth and arrest in the main plane of the crack. Sometimes these instabilities are related to delamination (or splitting) of the ligament. This behavior could be present in some rolled steels and is related to some metallurgical characteristics of the material like crystallographic texture, elongated inclusions, banded microstructure, and/or central segregation, among others [1]-[3]. The origin of splitting is related to the stress triaxiality ahead of the crack-tip [2] [2] and the low toughness of the materials in the rolling plane, which can cause delaminations in the ligament in a plane perpendicular to the main crack one. An example of this behavior is shown in Figure 1.

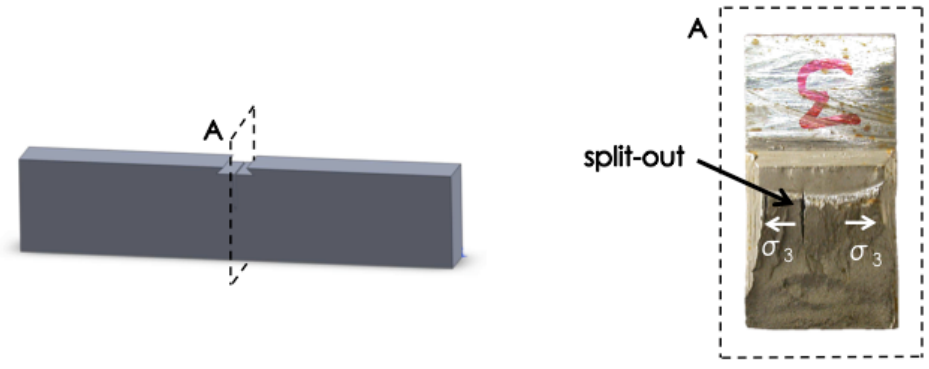

Figure 1. SE(B) specimen of rolled steel showing delamination (splitting) in the ligament.

When a split-out happens, one instability (pop-in) in the load-displacement records appears. Facing this kind of instabilities the standards have similar approaches, as shown in Table 1 [5]-[9].

Table 1. Excerpts of international standards on pop-ins caused by delaminations.

Standard	Excerpt
BS7448 part 1	Splits and delaminations can result in pop-ins with no arrested brittle crack extension in the plane of the fatigue precrack.
BS7448 part 2	Pop-in can be caused by an arrested crack running perpendicular to the plane of the fatigue precrack; this is sometimes referred to as a 'split'. The fracture toughness at pop-in caused by a split needs to be reported. However, the assessment of the structural significance of the split is outside the scope of this standard.
ASTM E1290 ASTM E1820	If the pop-in is attributed to an arrested unstable brittle crack extension in the plane of the fatigue precrack, the result must be considered as a characteristic of the material tested.
DS EN ISO 15653	Pop-in can be caused by an arrested crack running perpendicular to the plane of the fatigue precrack. This is sometimes referred to as a "split". The fracture toughness at pop-in caused by a split shall be reported, but might not characterize the fracture toughness of the material for the intended crack orientation. A different specimen and crack plane orientation might be necessary to characterize the fracture toughness of the material in the plane of the split. Assessment of the structural significance of a split is outside the scope of this International Standard.

As can be seen from Table 1, the standards do not offer alternative methodologies for fracture toughness evaluation when splitting occurs and the toughness basically needs to be calculated and reported at the first significant instability. The lack of alternatives for toughness evaluation in the presence of splitting could greatly penalize the toughness of the tested material, especially when the instabilities occur at the first stages of the test. Facing this scenario a question arose: What would be the fracture toughness of a material featuring splitting if the specimen were not suffered split? Or, in another words: It could be possible to estimate the fracture toughness of a material from a specimen that shows splitting? A possible answer to these questions was the main objective of the work and the results of our research follow.

2. Experimental

Fracture tests were performed on SE(B) specimens of rolled and accelerated cooled CLC DH36 ferritic steels (W=26 mm), as well as on conventional rolled API X65 and X70 steels (W=40 mm). The specimens were machined according to the ASTM 1820 standard in the LT orientation. The specimens were tested in an Instron 1332 servo-hydraulic testing machine with a 250 KN load cell, under displacement control and at different (low) temperatures. The specimens were submerged in an instrumented alcohol-cooled bath and the temperature was maintained at the nominal value with an accuracy of ±2°C. Load, crack mouth opening displacement and load line displacement were recorded. Additionally, on DH36 steels unloading compliance technique was applied for R-curves evaluation. J-Integral values and J-R curves were calculated according to the ASTM E1820 standard [8] and CTOD values were calculated according to the BS 7440 part 1 standard [5].

3. Results and Discussion

Figure 2a and 2b presents P-LLD and P-CMOD records of one test specimen of DH36 steel tested at –50°C. These records are representative of the behavior of specimens of the same steel at this temperature. As can be seen, the records show a pop-in caused by splitting. Figure 3 presents the J-R curve of this specimen. From Figure 2 it is possible to see that the pop-in occurred between the 5th and the 6th cycle in a total of 26 unloading-reloading cycles. The segment between the 5th and the 6th points in the J-R curve is pointed out by the arrow in Figure 3. It is interesting to observe that, without the help of the arrow, the position of the pop-in it is almost impossible to be identified in the J-R curve. In other words, there is no evidence of crack growth in the main plane of the crack associated to the split.

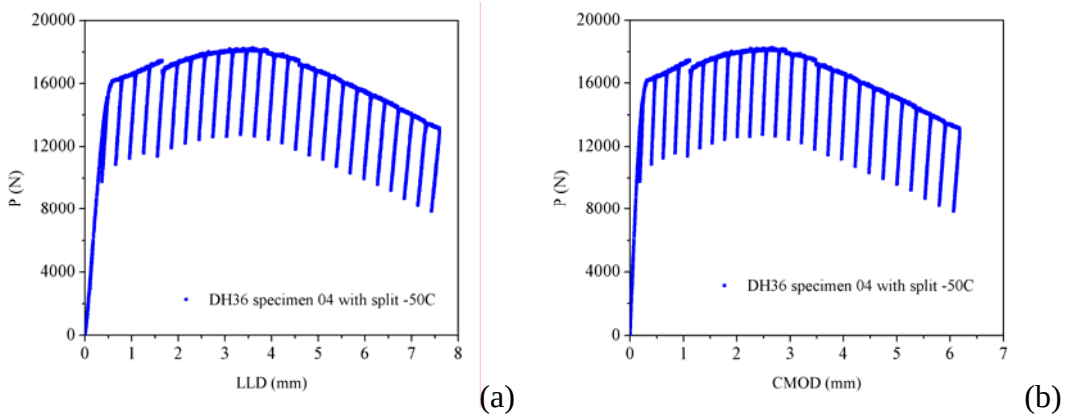

Figure 2. Experimental records of DH36 specimen 04 tested at -50°C. a) load vs. load line displacement; b) load vs. crack mouth opening displacement.

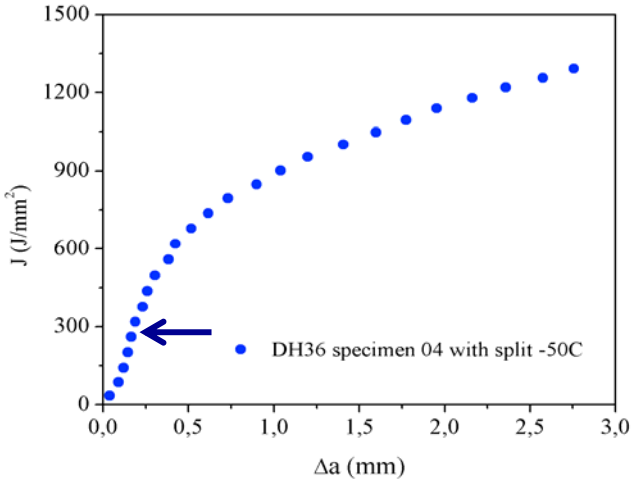

Figure 3. J-R curve of DH36 specimen 04 tested at -50°C.

This result shows that the change in the system energy associated to the pop-in caused by splitting could be almost completely related to the split formation itself and not to crack growth in the main plane of the crack. This idea is schematically shown in Figure 4, where the lower curve is represented in dots because its shape is still unknown. Being the energy change associated to

splitting independent of the main crack growth the effect of the pop-in by splitting on the fracture toughness of the material could be neglected. But, how to neglect the effect of splitting in the records? We think that this could be done through corrections of the experimental records. Several corrections were analyzed, being adding the load drop during the instability to the points on the right part of the records (that is, after split-out) the straightforward one. After corrected, the record are ready to be analyzed through standard methodologies and the fracture toughness calculated at the maximum load point or at the main crack instability one.

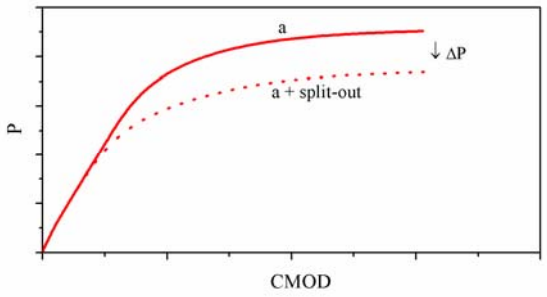

Figure 4. Scheme of the energy changes during a pop-in caused by splitting.

In a work on materials with delaminations Pisarski *et al.* [10] concluded that: "*when there is no significant loading perpendicular to the thickness direction, the pop-in can be ignored. Assuming that ductile behavior is indicated during the rest of the test, maximum load fracture toughness can be used to characterize toughness in the intended crack plane.*" We agree with this approach but we think that for improving the fracture toughness evaluation and for maintaining the equivalence among elastic-plastic methodologies, corrections of load-displacement records could still be necessary. The convenience of correcting load-displacement records was analyzed from a semi-hypothetical record, as follows.

Figure 5 presents modified P-LLD and P-CMOD records from the SE(B) specimens whose original records are shown in Figure 2. The unloading-reloading sequences are not shown here for clarity. The magnitude of the original load drop (approximately 4% of the load at the instability point) was now intentionally exaggerated by the addition of load drops of 10% and 20% as pop-ins. Additionally a corrected record was also added to the figure. When the fracture toughness at points A, B (as suggested by Pisarski), and C was calculated some controversial results were found. That is exemplified in Table 2, where J-Integral and CTOD values at points A, B and C are presented.

By comparing the results shown in Table 2 it is possible to see that $CTOD_A \approx CTOD_B \approx CTOD_C$ but $J_A < J_B < J_C$. Going further, when CTOD and J-Integral values are calculated at the beginning of each unloading-reloading sequence and the results plotted as J vs. CTOD (Figure 6), it is possible to see that J-Integral and CTOD values maintain linear proportionality before splitting in all records, as well as after splitting in the corrected record, but does not maintain the original proportionality after splitting in the uncorrected records. As can be shown, an increasing in the load drop in the pop-ins caused by splitting increases the deviation of J-CTOD pairs from its original equivalence. As far as we can understand, that effect is caused by taking into account in J-Integral calculations a change in the system energy that is not associated to crack growth in the pre-cracking plane and that did not substantially affected the main crack length nor the crack tip opening displacement. The load drop in such a kind of pop-ins is clearly associated to the creation of a crack in a plane perpendicular to the main crack one. The proposed correction to load-displacement records

featuring instabilities by splitting resolves this issue, being J-Integral and CTOD values continuously equivalent. Obviously, small splits produced small load drops in the load-displacement records and the effect on the J-CTOD equivalence is much less perceptible, but always existent.

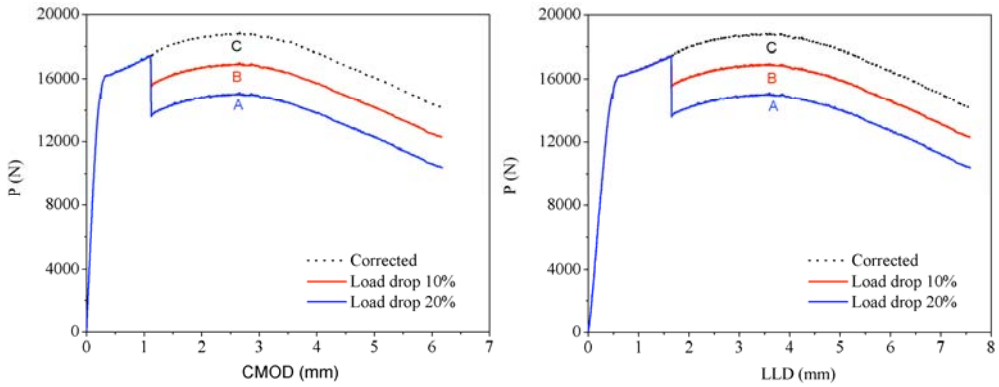

Figure 5. Semi-hypothetical P-CMOD and P-LLD records of a specimen of DH36 steel. The load drops at the instability were intentionally exaggerated.

Table 2. J-Integral and CTOD values calculated at points A, B, and C from the records shown in Figure 5.

Point	CTOD [mm]	J-Integral [J/mm^2]
A	0.623	513.33
B	0.624	546.27
C	0.628	590.63

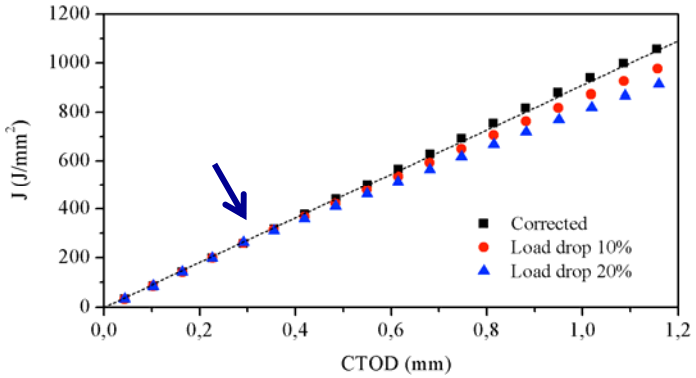

Figure 6. J-CTOD curves calculated from the records of Figure 5. The arrow indicates the position of splitting between the 5th and 6th unloading-reloading sequence.

The proposed correction of the load-displacement records has now been justified and the results of the whole experimental program will be now presented. When tested from room temperature to -30ºC the specimens of DH36 steel do not showed pop-ins. The specimens of this steel randomly showed pop-ins in the range from -40ºC to -58ºC. In all the cases the instabilities were associated to splitting. Almost 50% of the API X65 specimens showed splitting and mostly of API X70

specimens showed splitting at -20ºC. In most cases the splitting occurred before the attainment of maximum load plateau. Figures 7a, 7b and 7c show typical P-CMOD records with pop-ins of API X-65, API X-70 and DH36 steels, respectively (the unloading-reloading sequences of DH36 tests were removed from the records for clarity), as well as the corrected records. Figure 8 shows a comparison between the corrected records of Figure 7 and P-CMOD records of the same materials without split.

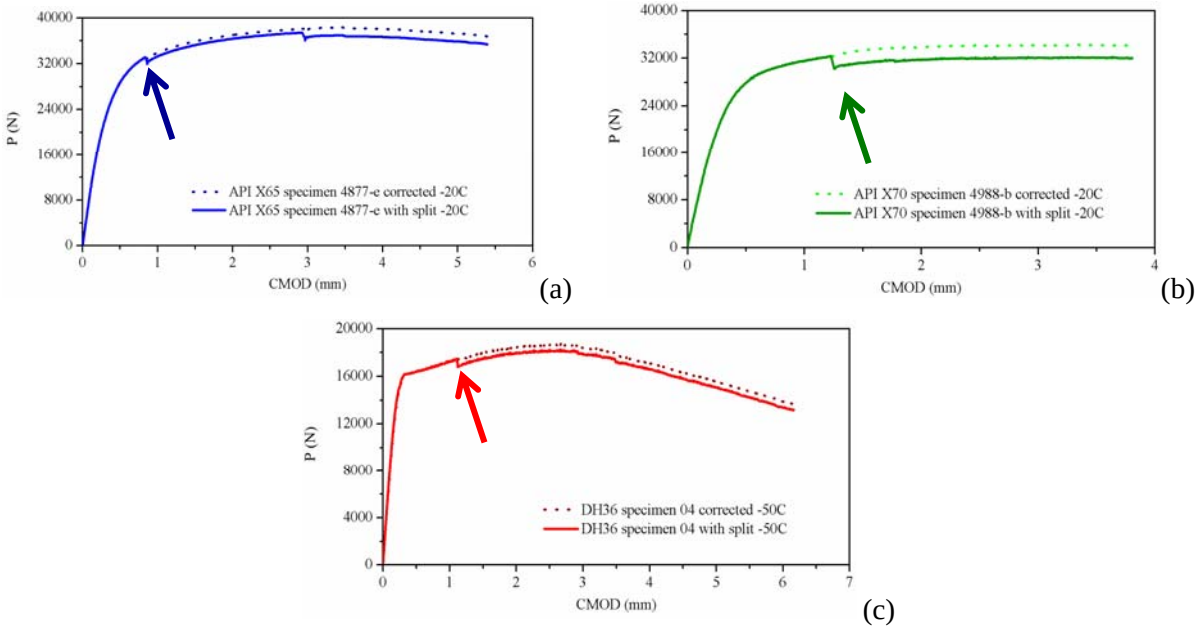

Figure 7. Original and corrected P-CMOD records of specimens featuring splitting. a) API X65, b) API X70, and c) DH36.

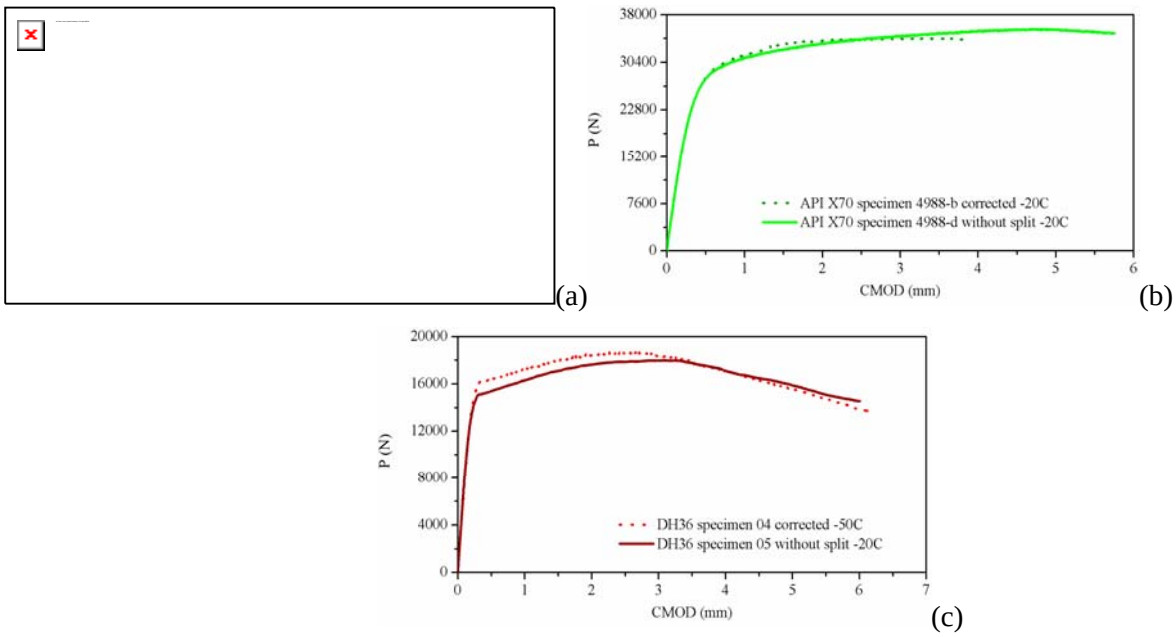

Figure 8. Corrected P-CMOD records and records from specimens of the same materials without splitting. a) API X65, b) API X70, and c) DH36.

Table 3 shows individual CTOD values of DH36 specimens calculated from the original and corrected P-CMOD records, as well as from specimens without splitting. Table 4 shows individual CTOD values of API X65 specimens, and Table 5 shows the same kind of data for API X70 specimens.

Table 3. Fracture toughness of SE(B) specimens of DH36 steel.

Specimen	Temp. (ºC)	Splitting	CTOD pop-in (mm)	CTOD max load (mm)	CTOD corrected (mm)
1	RT	No	--	0.663	--
3	-50	Yes	0.707	--	0.764
4	-50	Yes	0.284	--	0.723
5	-20	No	--	0.833	--
6	-20	No	--	0.688	--
7	-40	Yes	0.720	--	0.780
8	-40	No	--	0.707	--
9	-40	No	--	0.763	--
10	-50	No	--	0.775	--
11	-30	No	--	0.663	--
12	-30	No	--	0.800	--
13	-30	No	--	0.774	--
14	-30	No	--	0.692	--
15	-58	Yes	0.645	--	0.711
16	-55	Yes	0.588	--	0.675
17	-58	Yes	0.385	--	0.526
18	-55	Yes	0.248	--	0.591
19	-55	No	--	0.739	--
20	-55	Yes	0.670	--	0.737

Table 4. Fracture toughness of SE(B) specimens of API X65 steel.

Specimen	Temp. (ºC)	Splitting	CTOD pop-in (mm)	CTOD max load (mm)	CTOD corrected (mm)
4877-a	-20	No	--	0.882	--
4877-b	-20	No	--	0.796	--
4877-c	-20	No	--	0.918	--
4877-d	-20	Yes	0.698	--	0.962
4877-e	-20	Yes	0.166	--	0.815

Table 5. Fracture toughness of SE(B) specimens of API X70 steel.

Specimen	Temp. (ºC)	Splitting	CTOD pop-in (mm)	CTOD max load (mm)	CTOD corrected (mm)
4988-a	-20	Yes	0.714	--	0.863
4988-b	-20	Yes	0.254	--	0.744
4988-c	-20	Yes	1.089	--	1.201
4988-d	-20	No	--	1.104	--
4988-e	-20	Yes	0.793	--	0.963
6006T 01	-20	Yes	0.435	--	0.921
6006T 02	-20	Yes	0.256	--	0.592
6006T 03	-20	Yes	0.336	--	0.888
6006T 05	-20	Yes	0.262	--	0.791
6006T 07	-20	No	--	0.798	--
6006T 10	-20	Yes	0.791	--	0.910
6006T 11	-20	Yes	0.302	--	0.798

The mean and standard deviation of the different types of calculated CTOD are shown in Table 6, which also includes the minimum CTOD value of each set of specimens calculated according to the BS standard [5]. The mean values of DH36 steel were divided in two temperature ranges. One range going from room temperature to -30 ºC, in which no one of the specimens showed splitting, and another from -40 to -58 ºC.

Table 6. Minimum and mean CTOD values of the tested specimens.

Steel	Temp. (ºC)	Minimum CTOD (mm)	CTOD pop-in (mm)	CTOD max load (mm)	CTOD corrected (mm)
DH36	RT to -30	0.663	--	0.730 ±0.070	--
DH36	-40 to -58	0.248	0.531 ±0.194	0.746 ±0.030	0.688 ±0.088
API X65	-20	0.166	0.432 ±0.376	0.865 ±0.063	0.889 ±0.104
API X70	-20	0.254	0.523 ±0.299	0.951 ±0.216	0.867 ±0.159

A statistical analysis on the results of Table 6 using Student's t-tests [11] reveals, with 95% of confidence, that there is no statistical difference between CTOD values from corrected records and the CTOD values from specimens without splits. This result indicates that it could be possible to estimate the main crack fracture toughness of the analyzed steels from SE(B) specimen showing splitting, with reasonable accuracy. This was achieved through the proposed modification of the experimental records, based on the idea that the change in the system energy due to splitting is mainly associated to the creation of the split itself and can be neglected for the main crack toughness evaluation.

4. Conclusion

Based on the presented results and discussion it is possible to conclude:

Splitting in SE(B) specimens of DH36 steel did not influence the main crack length measured by the unloading compliance technique. As a result, the change in the system energy associated to the instability was totally related to the split creation itself.

The fracture toughness associated to the main crack of a specimen featuring splitting could be estimated, with reasonable accuracy, through the proposed correction of the original load-displacement records. The proposed correction consists in removing the load drop at instabilities associated to splitting.

J and CTOD values calculated from the modified records kept its equivalence along the entire test. When calculated from non-corrected load-displacement records of specimens featuring instabilities by splitting the J-CTOD equivalence deviates beyond the instability point.

The fracture toughness of SE(B) specimens of the same material showed no statistical differences when calculated from specimens featuring splitting and modified records or from specimens without splitting.

Acknowledgements

The authors gratefully acknowledge to PEMM/COPPE/Federal University of Rio de Janeiro by the financial support, to CAPES for the scholarship of Pablo Lara Melcher, and to the Eng. Wagner Duarte Flores and Usiminas for the DH36 steel samples.

References

[1] T. Tanaka, Controlled rolling of steel plate and strip. International Materials Reviews, Vol. 26, No. 1 (1981) 185-212.

[2] B.L. Bramfitt, A.R. Marder, A Study of the Delamination Behavior of a Very Low-Carbon Steel, Metallurgical Transactions A., Vol. 8A, (1977) 1263-1273.

[3] Y. Kimura, T. Inoue, F. Yin, K. Tsuzaki, Delamination Toughening of Ultrafine Grain Structure Steels Processed Through Tempforming at Elevated Temperatures, ISIJ International, Vol. 50, No. 1 (2010) 152-161.

[4] J. Perez Ipiña, I. Korin, Effects of divider orientation split-out on fracture toughness. Fatigue & Fracture of Engineering Materials & Structures, Vol. 36, issue 3 (2013) 242-253.

[5] BS 7448-1 (1991) (Incorporating Amendment No. 1 and Corrigendum No. 1) Fracture mechanics toughness tests - Part: 1 Method for the determination of KIc, critical CTOD and critical J values of metallic materials. 2002, BSI, 389 Chiswick High Road, London, United Kingdom.

[6] BS 7448-2 (1997) Fracture mechanics toughness tests - Part: 2 Method for the determination of KIc, critical CTOD and critical J values of welds in metallic materials. BSI, 389 Chiswick High Road, London, United Kingdom.

[7] ASTM E1290 (2008) Standard test method for crack-tip opening displacement (CTOD) fracture toughness measurement. ASTM International, West Conshohocken, PA 19428–2959, United States.

[8] ASTM E1820 (2011) Standard test method for measurement of fracture toughness. ASTM International, West Conshohocken, PA 19428–2959, United States.

[9] BS EN ISO 15653 (2010) Metallic materials. Method of test for the determination of quasistatic fracture toughness of welds. BSI, 389 Chiswick High Road, London, United Kingdom.

[10] H.G. Pisarski, R. Hammond, K. Watt, Significance of splits and pop-ins observed during fracture toughness testing of pipeline steel, Proceedings of IPC 2008, 7th International Pipeline Conference, Calgary, Alberta, Canada, 2008, ASME, Paper IPC 2008-64676.

[11] R. Liman Ott, M. T. Longnecker, An Introduction to Statistical Methods and Data Analysis, Brooks-Cole, Cengage Learning, Canada, 2010.

Local approach of fracture on semi-crystalline polymers: contribution of X-ray laminography technique

Lucien Laiarinandrasana[1,*], Thilo F. Morgeneyer[1], Henry Proudhon[1], Lukas Helfen[2], Jacques Besson[1]

[1] Centre des Matériaux, Mines ParisTech, Evry Cedex 91003, France
[2] European Synchrotron Radiation Facility (ESRF), Grenoble Cedex 38043, France
* Corresponding author: Lucien.Laiarinandrasana@mines-paristech.fr

Abstract Damage mechanisms in a PolyAmide 6 semi-crystalline polymer were characterized by using Synchrotron Radiation Laminography technique on CT like specimen. Damage appeared as multiple penny shaped crazes. The maximum damage occurred at mid-thickness and located at a small distance from the notch root. An attempt was made to apply local approach of fracture concept thanks to finite element analysis using damage-based constitutive model. FE simulation successfully captured the aforementioned micro-mechanisms of crack initiation, by void coalescence. Further work is carried out to determine the crack dimension corresponding to the maximum net stress: the criterion being used for the global approach of fracture.

Keywords Polymers, X-ray laminography, Local approach of fracture, Finite element

1. Introduction

The use of fracture mechanics concepts for polymers is subjected to controversial discussions. It is often reported that many requirements are not fulfilled to obtain fracture mechanics characteristics such as the toughness. For instance, plane strain conditions together with tunneling effect (curved crack front), crack advance measurement, crack initiation/growth determination…are more difficult to obtain for polymers than in metallic materials. In the recent years, growing interest for X-ray tomography technique was observed. Indeed, this is a non destructive method allowing for construction of digital image in 3D. Therefore, virtual cuts and local observations of the microstructure can easily be carried out. The present contribution aims at highlighting the crack initiation concept from CT like specimen on a semi-crystalline polymer: PolyAmide 6 (PA6). The evolution of the microstructure during an increasing load could be observed thanks to laminography technique. The local coalescence of voids at mid-thickness was evidenced. The increase in macroscopic net stress was computed by Finite Element (FE) analysis, with a dedicated damage based model. The crack initiation criterion at macroscopic scale, based on the maximum net stress, was then assessed in terms of critical size of the principal damage within the microstructure.

2. Experimental procedure

2.1. Material - Specimen

The material of interest is a PolyAmide 6 (PA6) [1], selected among several semi-crystalline polymers. Indeed, for this polymer void morphology and distribution were already studied [2] for axi-symmetrically notched specimens, together with a dedicated constitutive model for FE analysis. In the present work, the approach consisted of application of the local approach of fracture which takes the damage evolution in the microstructure into account. Here a novel technique, known as laminography is utilized [3]. The method takes advantage of the Synchrotron Radiation Tomography (non destructive and 3D reconstructed images) but applied to plate like specimen. In situ test is carried out on CT like specimen. The geometry is described in fig.1a. The specific dimensions were: thickness B = 2mm, width W = 40mm, crack depth ratio a/W = 0.5, notch root

radius ρ = 250µm, half height H/2 = 20mm. For the following FEA (section 3), figs.1b-c respectively illustrate the CT specimen overall meshing and refined meshes (25µm) in the vicinity of the crack tip.

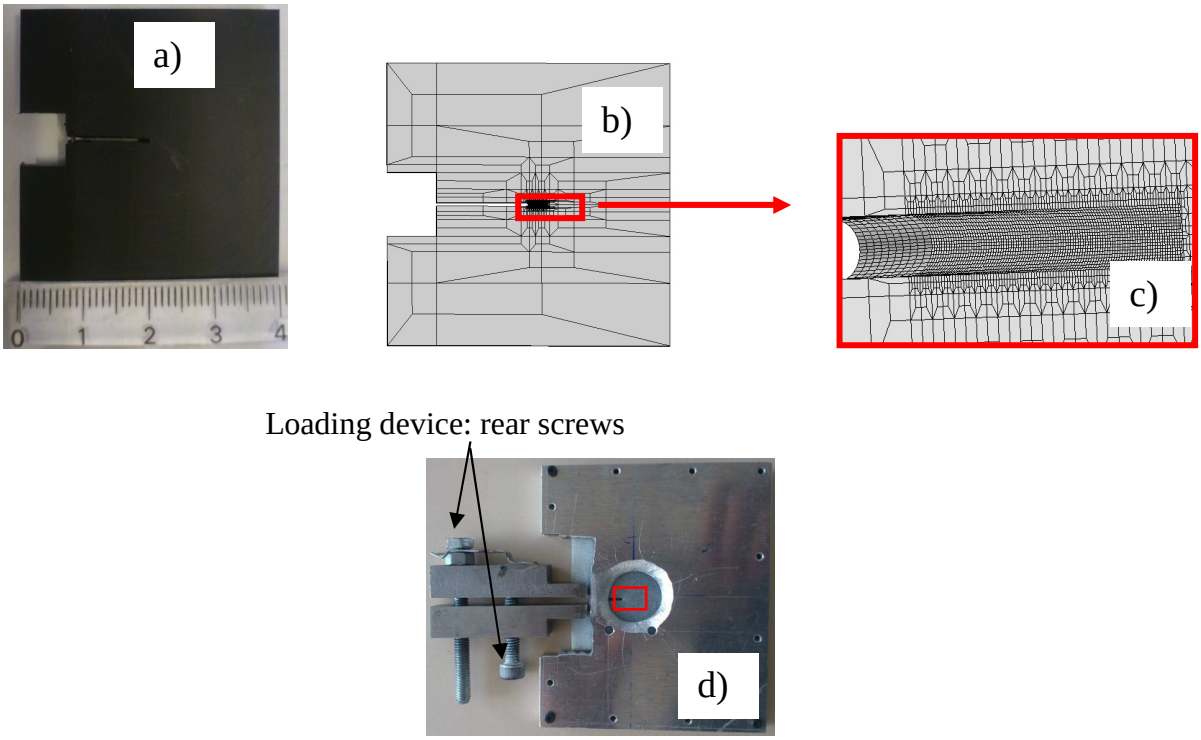

Figure 1. CT specimen geometry with the experimental setup: a) CT specimen sketch; b) Overall view of the sample meshing; c) Fine meshing near the notch root (mesh size 25µm); d) Experimental setup.

The experimental setup is presented in fig.1d. The CT specimen was inserted between two aluminum plates to avoid buckling in the compressive part of the remaining ligament. The opening displacement is applied thanks to the turns of both rear screws. A circular window was designed within the anti-buckling aluminum system allowing for inspection of the region near the notch root, at the macroscopic scale (pictures), as well as at the microscopic scale (laminography scans).

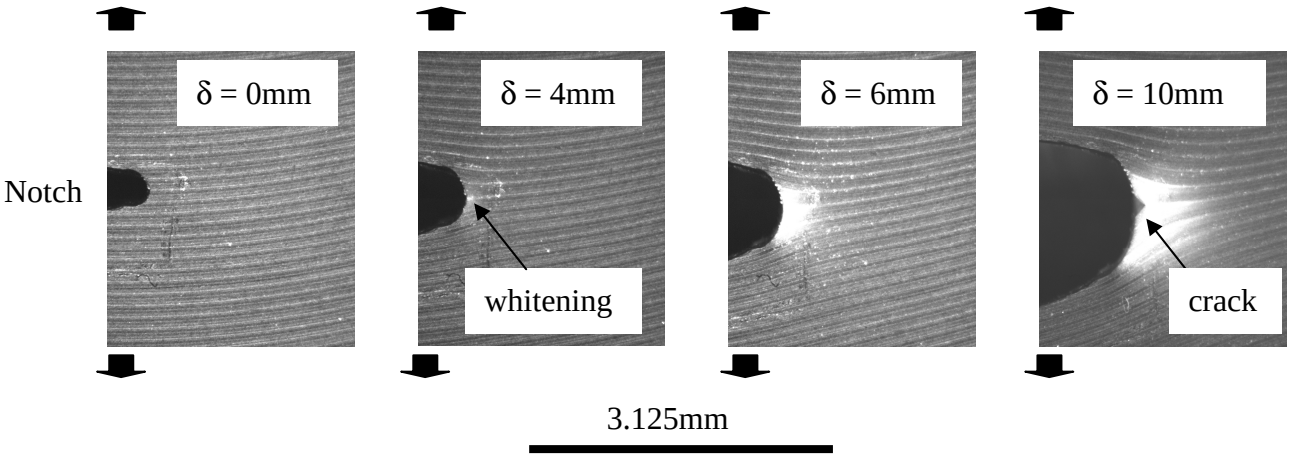

Figure 2. Evolution of the geometry observed at the external face of the CT specimen. Black arrows indicate the loading direction.

Stepwise loading was applied between laminography observations. Fig.2 shows a series of pictures made at the side view of the specimen before the laminography scans. The corresponding applied displacement δ is indicated in each viewgraph, starting from the initial material without any deformation, up to δ = 10 mm. For this latter, a crack is visible at the external surface of the sample. For δ = 4mm, a localized whitening at the notch root is observed. Being the first event appearing at the surface, it was considered that this corresponded to an internal crack initiation. For δ = 6mm, whitening is spreading out, surrounding the notch root. It should be mentioned that no scan was done between δ = 6mm and 10mm. Moreover, the present experimental setup was not equipped with a load cell. The load level was therefore estimated by using FEA with a dedicated constitutive model.

2.2. Laminography technique

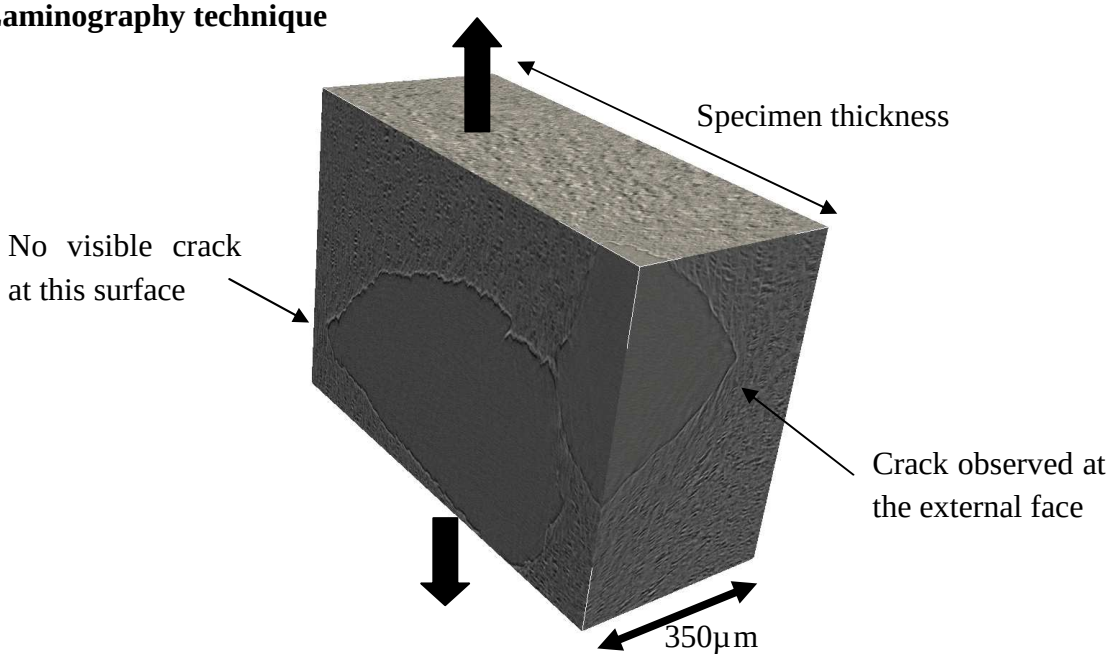

Figure 3. Volume corresponding to δ = 10mm: two cracks through the thickness

Synchrotron Radiation Laminography (SRL) technique is detailed elsewhere [3]. It has already been applied on both metallic and laminate composite materials. To the authors' best knowledge, it is the first time that this technique is utilized for semi-crystalline polymer investigations. To this end, for each value of the applied opening displacement δ the whole experimental setup (fig.1c) was mounted on adapted sample support of the laminography device at the ID19 beamline of the European Synchrotron Radiation Facility (ESRF) in Grenoble (France). The scanned volume was about 1 mm^3, with a voxel size of 0.7µm. Fig.3 shows a trough thickness microstructure around the crack tip in 3D. Apart from multiple crazes observed within the whole volume, two large cracks were evidenced. One of them appeared at the surface (fig.2, δ = 10 mm) whereas the opposite face did not show any crack. Attention is now paid on the scans corresponding to δ = 4mm and δ = 6mm to observe the microstructure, especially at mid-thickness.

Fig.4 illustrates such views in 3D where the plane at mid-thickness is shown in forefront. Multiple penny shaped crazes [2, 4] were observed around the notch root. These features could be linked to the whitening observed at the macroscopic scale.

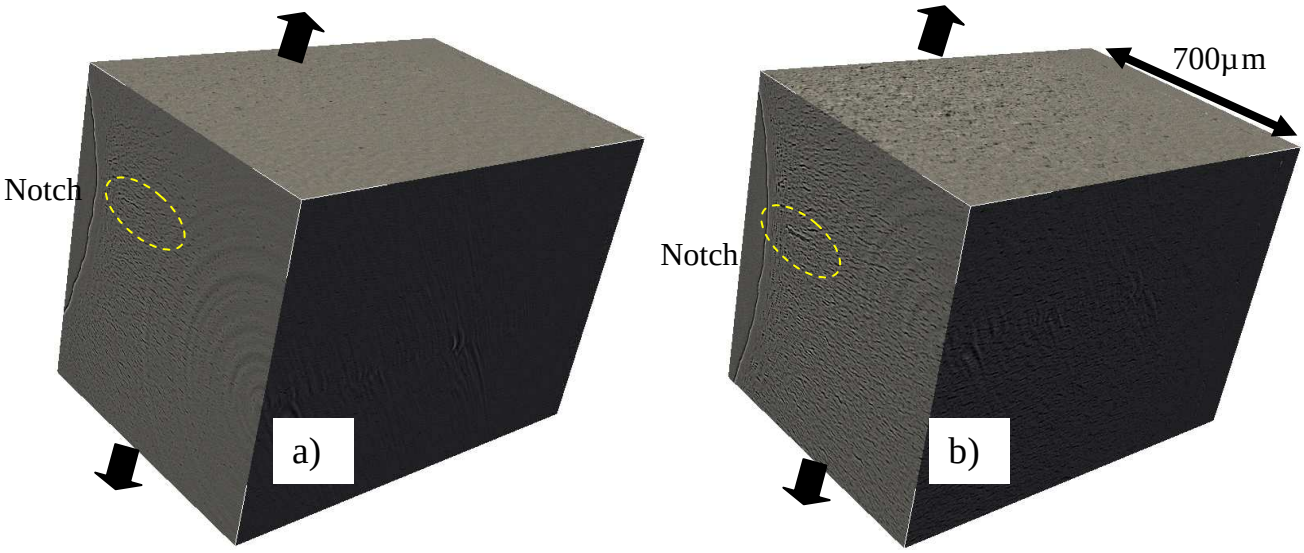

Figure 4. Observations at mid-thickness plane: a) δ = 4mm; b) δ = 6mm

A significant damage, surrounded by the dashed lines was evidenced at mid-thickness, located at a small distance (~100µm) from the initial notch root.

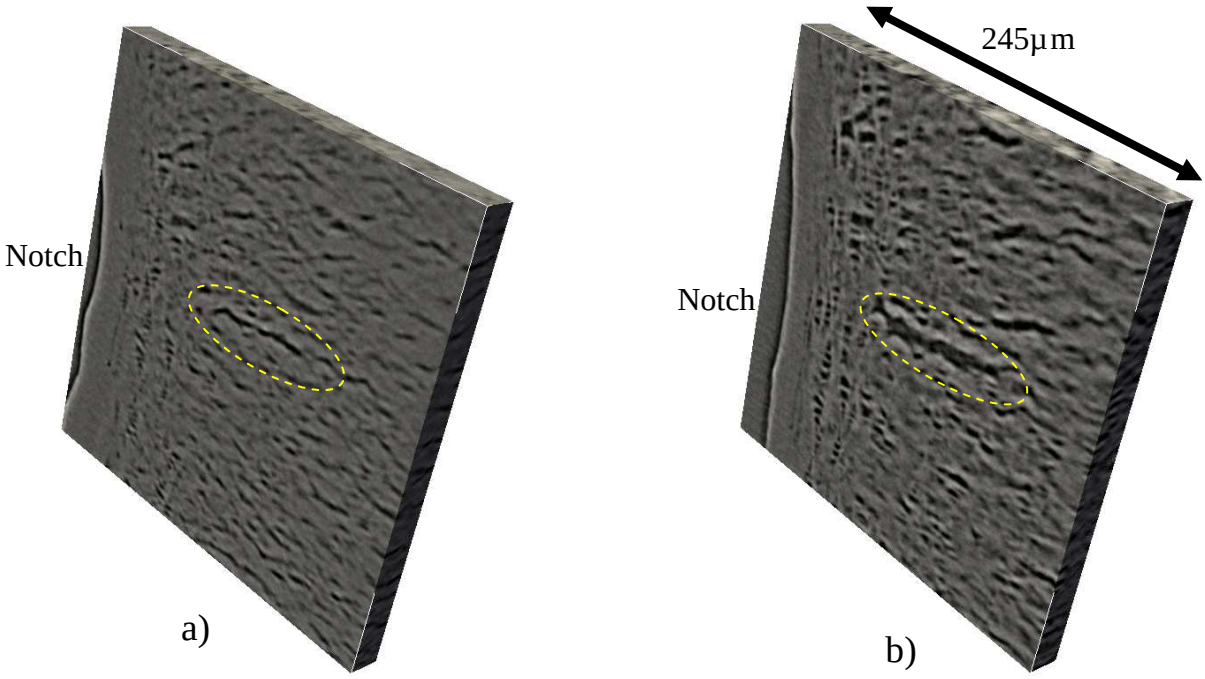

Figure 5. Maximum damage at mid-thickness surrounded by dashed lines: a) δ = 4mm; b) δ = 6mm

Fig.5 details the morphology and the size of this damage. To this end, a 19µm thick slice of PA6 scan was extracted and analyzed for both δ values. It was observed that the damage consisted of crazes (presence of fibrils within the voids) aligned (coalesced) following the crack remaining ligament plane. This damage increased in height from δ =4mm to 6mm. Its average values of the characteristic dimensions were summarized in Table 1.

Table 1. Characteristic dimensions of the damage located at mid-thickness

	δ = 4mm	δ = 6mm
Length	60µm	90µm
Height	5µm	10µm
Width	20µm	30µm

3. Finite element modeling

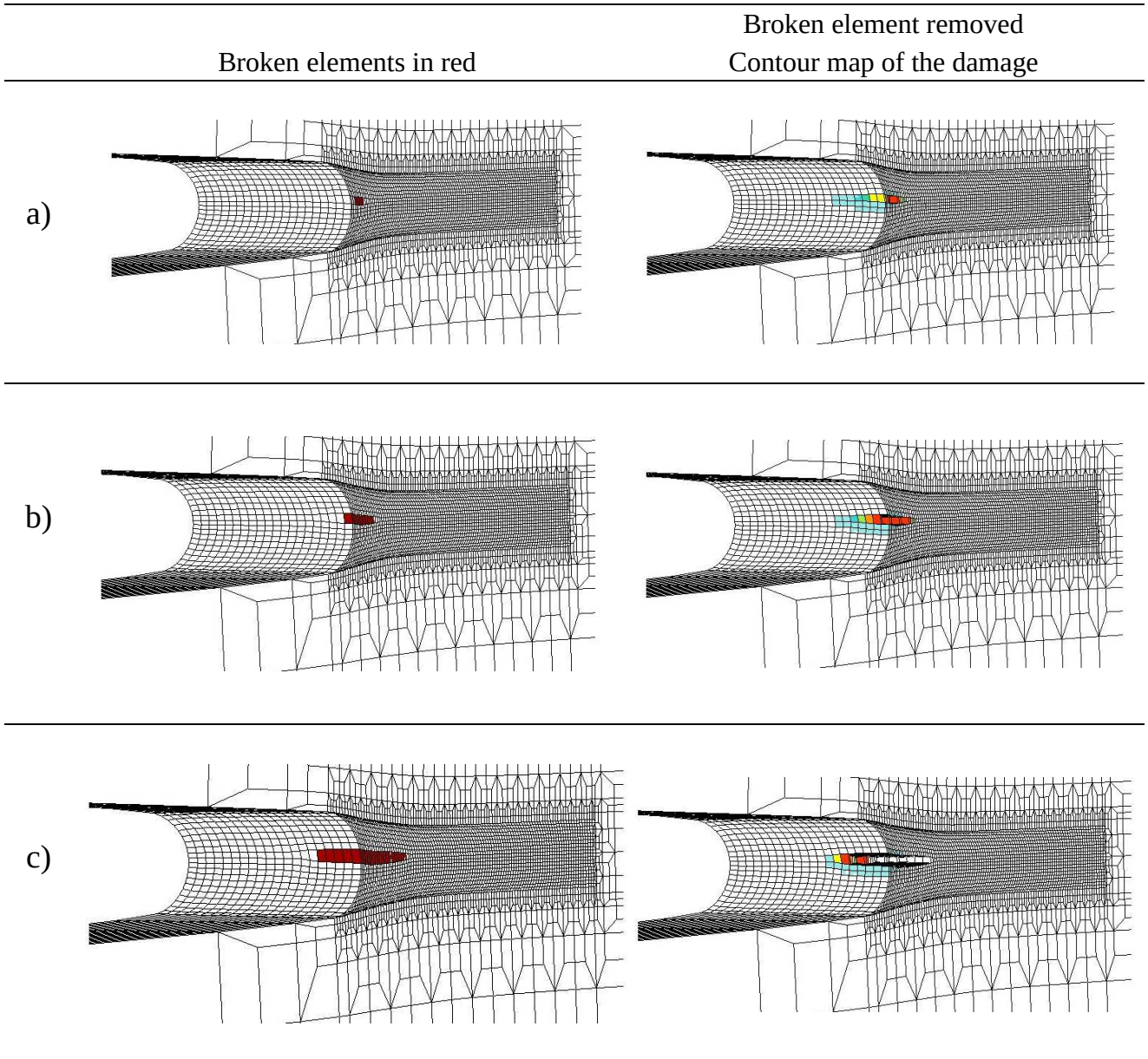

Figure 6. FE simulations of the crack initiation by using damage based constitutive model.

The local approach of fracture requires FE computation with a damage based constitutive model to better assess the stress/strain tensors distribution within the material. For the PA6 under study, a multi-mechanisms model was proposed [5-6] where the void volume fraction is considered as an internal variable. By using the same damage based model, simulation of laminography CT test was

carried out. A procedure of “kill/remove element” was applied when a critical porosity value was reached within this element. The following analyses focus on the refined meshes (fig. 1c) in the vicinity of the notch root. Constant mesh size of 25µm was set for 2.5mm along the ligament.

Fig.6 summarizes the evolution of damage (broken element) during the increasing load. The forefront face corresponds to the plane at mid-thickness. The first column of deformed meshes shows the broken elements in red. The second column illustrates the contour map of the void volume fraction over the deformed mesh where the broken elements were removed.
Fig.6a shows that four elements simultaneously broke for the first time (length ~100µm; width ~25µm). They appeared at mid-thickness and located at 3 elements away from the notch root (distance ~75µm). These characteristic values correspond to those of δ = 6mm. Fig.6b indicates that broken elements propagate into two opposite directions: ahead of and back to the notch root. The width seems to remain constant (one element size). Fig.6c evidences that the broken elements propagates through the thickness as well, but did not reach the external surface. These latter steps were not observed with SRL technique since no scan was done between δ = 6mm and δ = 10mm when the crack appeared at the external face. However, although fine tuning of damage parameters is still ongoing, these figures demonstrate that the FE analysis with the damage based model was able to reproduce the micro-mechanisms of crack initiation. At present time, computation is still running to obtain the configuration where the crack reaches the external surface.
Next investigation consists of using FE modelling to estimate the load evolution during the crack propagation. The aim is to determine the crack size allowing the crack initiation criterion at the macroscopic scale to be reached (maximum load). To this end, in fig.7 the load divided by the net section of the remaining ligament is plotted as a function of the applied opening displacement.

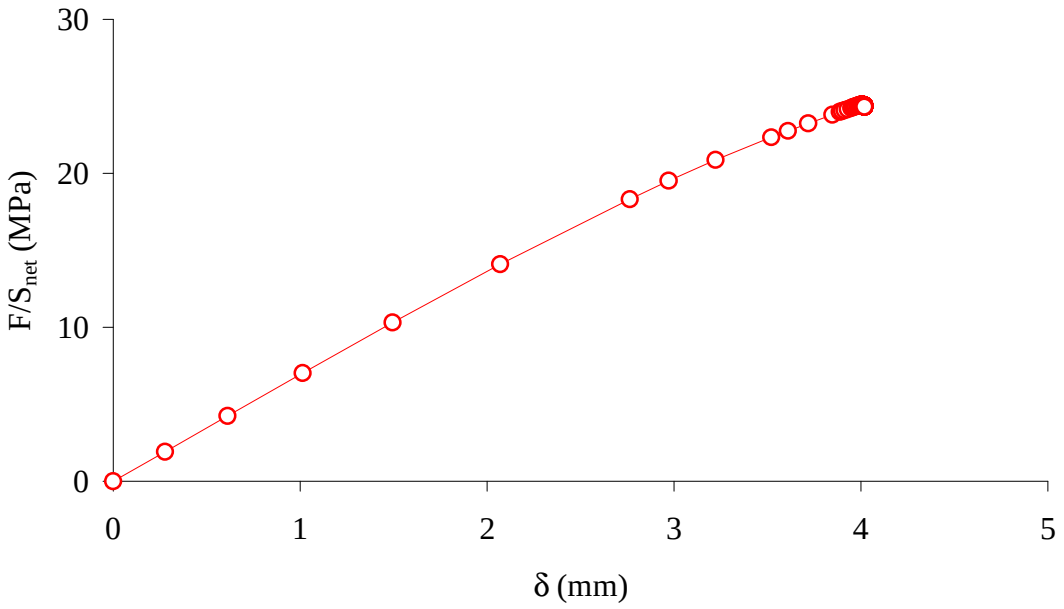

Figure 7. Net stress as a function of the opening displacement by FE analysis

Contour maps presented in fig.6 correspond to the last loading steps of the numerical simulations ($\delta \geq$ 4mm). The first results shown at this stage indicate that although a non linearity appears in the last part of the plot (fig.7), the net stress is still increasing. The maximum net stress is not yet reached. Final results will be shown later.

5. Conclusion

The micro-mechanisms of damage and crack initiation were investigated thanks to Synchrotron Radiation Laminography (SRL) technique. In situ tests were carried out on CT-like specimen. The local coalescence of voids leading to crack initiation occured at mid-thickness of the specimen located at a small distance from the initial notch root. Finite Element analysis, with a damage based constitutive model was able to capture the location of the crack initiation, as well as the damage mechanisms observed by SRL. The evolution of the macroscopic net stress was also computed by FEA. At present time, the crack initiation criterion based on the maximum net stress has not still been reached. Computation is still ongoing to compare this criterion with the critical size of the crack at the microscopic scale.

References

[1] L. Laiarinandrasana, T.F. Morgeneyer, H. Prodhoun, C. Regrain, Damage of semicrystalline Polyamide 6 assessed by 3D X-Ray Tomography: from microstructural evolution to constitutive modeling. Journal of Polymer Science Part B: Polymer Physics, 48 (2010) 1516-1525.

[2] L. Laiarinandrasana, T.F. Morgeneyer, H. Proudhon, F. N'guyen, E. Maire, Effect of multiaxial stress state on morphology and spatial distribution of voids in deformed semi-crystalline polymer assessed by X-ray tomography. Macromolecules, 45 (2012) 4658-4668.

[3] T.F. Morgeneyer, L. Helfen, H. Mubarak, F. Hild, 3D digital volume correlation of Synchrotron Radiation Laminography images of ductile crack initiation: an initial feasibility study. Experimental Mechanics, DOI 10.1007/s11340-012-9660-y. Published on line 15 August 2012.

[4] L. Laiarinandrasana, H.A. Cayzac, T.F. Morgeneyer, H. Proudhon, Modelling of damage distribution and orientation assessed by X-ray tomography technique on semicrystalline polymers. Proceedings of the 15th International Conference on Deformation Yield and Fracture of Polymers, 1-5 April 2012, Rolduc Abbey, Kerkrade, The Netherlands.

[5] K. Saï, L. Laiarinandrasana, I. Ben Naceur, J. Besson, M. Jeridi, G. Cailletaud, Multi-mechanism damage-plasticity model for semi-crystalline polymer: Creep damage of notched specimen of PA6. Materials Science and Engineering A 528 (2011) 1087–1093.

[6] H.A. Cayzac, K. Saï, L. Laiarinandrasana, Damage based constitutive relationships in semi-crystalline polymer by using multi-mechanisms model. *Submitted to International Journal of Plasticity (2013)*

Micro-scale Testing to Evaluate the Fracture Characteristics of Quasi-brittle Materials

Dong Liu[1,2*], Peter Heard[1] and Peter E J Flewitt[1,3]

[1]Interface Analysis Centre, University of Bristol, Bristol, BS2 8BS, UK
[2]Department of Mechanical Engineering, University of Bristol, Bristol, BS8 1TR, UK
[3]School of Physics, HH Wills Laboratory, University of Bristol, Bristol, BS8 1TL,
* Corresponding author: dong.liu@bristol.ac.uk

Abstract In this paper micro-scale testing techniques have been implemented on two types of quasi-brittle material: pile grade A (PGA) graphite and air-plasma sprayed yttria (7 wt.%) stabilized zirconia (APS-YSZ). One approach uses a force measurement system within a FEI Helios Dualbeam FIB/SEM workstation, which allows the fracture characteristics and mechanical properties of the two materials to be evaluated and correlated with local microstructural features. In addition for PGA graphite, disc-compression and trench-probe methods have been applied. Hence the initiation, propagation of the cracks and the corresponding deformation can be recorded and investigated. For the APS-YSZ, micro-scale cantilevers have been fabricated using FIB and a load-recording probe has been applied in-situ. The fracture toughness, flexural strength and the cracking path are analysed. Interpretation of these tests has contributed to the understanding of the macro-scale quasi-brittle mechanical behaviour of the two materials.

Keywords Pile grade A graphite, Air-plasma-sprayed yttria stabilized zirconia, Disc compression, Micro-scale cantilever testing

1. Introduction

Pile Grade A (PGA) graphite used for a wide range of applications, including nuclear reactor core, is often cited as a classic example of a brittle material because failure, in tension, is associated with small strains. It has been recognised that these graphites are multiphase, polygranular, aggregate structures and have features similar to other aggregate materials such as concrete [1, 2]. However, attempts to characterise the fracture behaviour of graphite by linear elastic fracture mechanics methods have been largely unsuccessful. Observations of graphite fracture show that elastic strain energy may be dissipated by the formation of distributed micro-cracks and their formation may be responsible for non-linearity in the rising load-displacement curve [3, 4]. A typical example is shown by the load-displacement response for bend geometry specimens, Fig. 1. There is no evidence that polygranular, aggregate graphites can be plastically deformed. Hence, the change in compliance together with any deviation from an initial linear shape of the load-displacement curve, Region II in Fig. 1, can be attributed to micro-cracking. Progressive softening is also observed in some specimens post the peak load, Region III. This type of load-displacement behaviour is a characteristic of quasi-brittle materials [2]. Air-plasma-sprayed (APS) yttria (7 wt.%) stabilized zirconia (YSZ) has been applied widely in thermal barrier coating systems (TBC) to isolate metallic components from the high temperature environmental gas in crucial parts of engines. APS produces TBC with a splat microstructure, moderate porosity and compliance, and low thermal conductivity. For example, APS-YSZ coatings on turbine blades are normally 150 to 300 μm thick sustaining a temperature difference up to 300 °C. Due to manufacturing, the APS-YSZ splat microstructure contains defects, pores and unmelted particles. These internal microstructures result in non-linear brittle behaviour of the coatings.

To understand the macro-scale mechanical behaviour of these types of quasi-brittle materials, micro-scale testing samples an appropriate small volume of material and localised microstructure to characterise initiation and propagation of micro-cracks. This paper considers micro-scale tests undertaken by the research group at the University of Bristol, UK [2, 4-6].

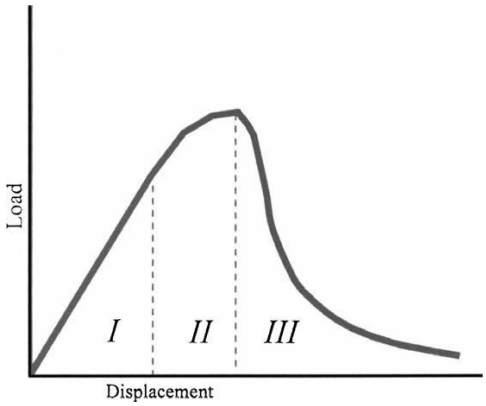

Fig.1 A characteristic bend geometry load-displacement curve for a quasi-brittle material, region I is linear, region II is non-linear, region III is post peak softening.

2. Experiments

2.1. Materials

Cylindrical PGA test specimens were made by trepanning 12 mm diameter rods extracted from bulk virgin PGA graphite reactor core bricks. These were sliced into 6 mm thick cylinders using a South Bay Technology Inc. Model 650 low speed diamond wheel saw with deionised water as coolant. The diamond saw produced smooth high-quality surfaces suitable for subsequent microscopic examination. The brick extrusion direction was diametrically across the flat surfaces of the cut cylinders. The extrusion direction was marked on the edges of the cylinders for reference during compression testing.

For testing of APS-YSZ specimens, samples manufactured by Praxair Surface Technologies Ltd with a curved geometry designed to simulate key features of coated blade were used. Each comprised a Superalloy substrate (CMSX4) with air plasma sprayed (APS) 7 wt.% Y_2O_3-stabilised ZrO_2 (YSZ) applied onto an Amdry 995 bond coat deposited using high velocity oxygen fuel (HVOF) [7]. The thickness of the TBC varied with position around the specimen from 130 µm to 230 µm. A typical cross-section of the TBC system is shown in Fig. 2a. The YSZ which is ~200 µm thick comprises lameller splats, micro-scale air pores and defects. The interfaces, YSZ-TBC/TGO and TGO/BC, are undulating with a variable thickness of TGO. In this present work, the focus was on the APS-YSZ material in as-coated condition, and the specimens are tapered to reveal the interfaces, Fig. 2b. Micro-cantilever specimens with the size of ~2×2×10 µm are created at preferred locations of this coating as shown in Fig. 2b.

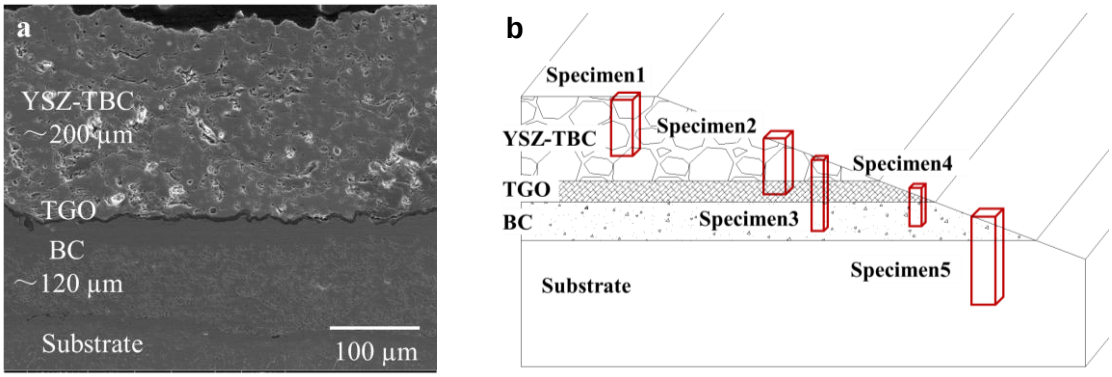

Fig. 2 The TBC system (a) typical cross-section for specimen that has been oxidised for 100 hours at 925°C and (b) creation of micro-cantilever specimen at preferred locations on tapered surface.

2.2 Testing methods

Controlled cracking was introduced in the quasi-brittle specimens using appropriate methods. Each method allowed specimens to be subsequently examined under load.

2.2.1 Disc compression method

Compression testing of the cylindrical graphite specimens was done using a Deben compression/tensile stage (MicroTest 2000 model, Gatan Ltd., Abingdon, Oxon, UK), Fig. 3. The unit is capable of operation externally or within a scanning electron microscope or focused ion beam (FIB) workstation. The stage can be operated at compression speeds of between 0.033 and 0.4 mm/min, with a load cell giving force measurements up to a maximum of 2 kN. The cylindrical graphite specimens were loaded into the compression tester such that the direction of the compressive load was along a diameter of the flat face of the cylinders, chosen here to be the extrusion direction of the graphite. This provided a tensile load normal to the direction of the applied load so that cracks would be induced in the plane parallel to the load direction. Load-displacement curves were recorded whilst observing the surface of the specimen by optical microscopy or focused ion beam imaging.

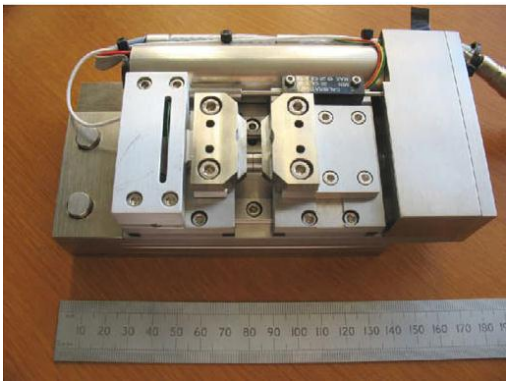

Fig. 3 Compression tester applied in micro-scale mechanical testing.

2.2.2 Trench-probe loading method

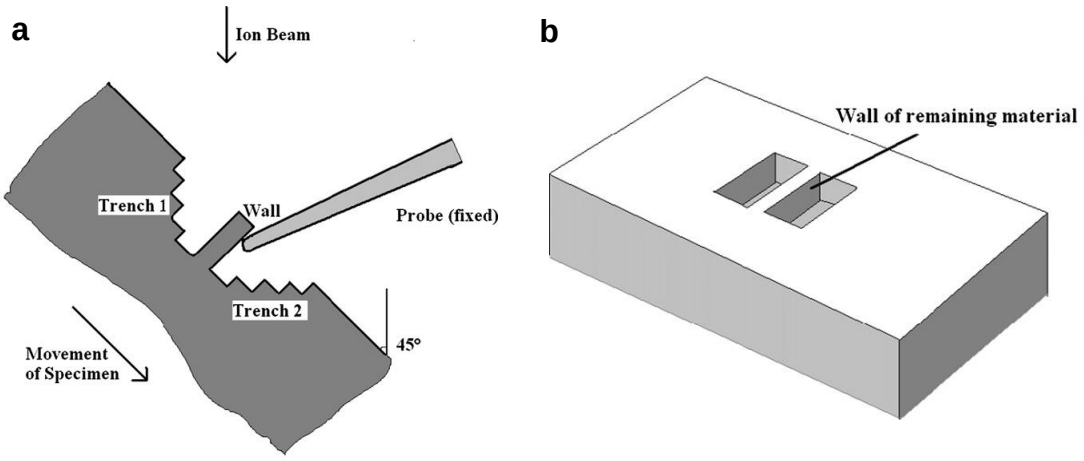

Fig. 4 (a) Schematic of the trench-probe method for applying a force to a prepared wall of material 35 μm long within the FIB; (b) the thin wall of residual materials created between the two trenches.

The trench-probe method provided a means of applying a small, progressive, localised force to a prepared region of a ‘wall’ specimen of graphite whilst it was under observation in the FIB workstation, Fig. 4. For this, a sharpened steel probe (tip radius 5 μm approximately) was attached to the end of a spare gas injector on the instrument. The retractable probe was aligned to be in the centre of the field of view, so that it could be used to push on a prepared part of the specimen, Fig. 4a. Local deformation and cracking could be studied at high resolution within chosen regions of a specimen, Fig. 4b.

2.2.3 Micro-cantilever beam bending method

The experimental arrangement for the mechanical property testing was a combination of a FEI Helios NanoLab 600i Dualbeam workstation and a compact force measurement system supplied by Kleindiek which allowed in-situ loading and force readout, Fig. 5a. The dualbeam workstation provided ion beam milling and in-situ SEM imaging. Before commencing the measurements, a calibration of the force sensor was carried out by loading a standard spring embedded in the system to provide the resistance conversion references and zero the load reading. Details of the force measurement system and the cantilever specimen preparation are described elsewhere [8, 9]. A typical set up of in-situ loading of a cantilever beam using the force measurement probe is shown in Fig. 5b.

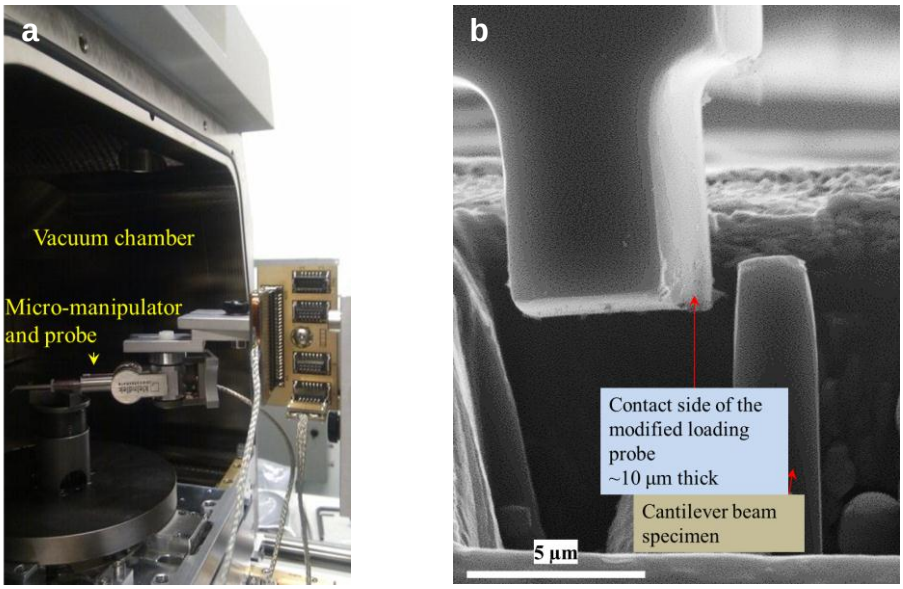

Fig. 5 (a) Installation of the FMS into the dualbeam FIB vacuum chamber. Side-view showing the FMS in the middle of the stage (b) SEM image showing loading the micro-cantilever specimen.

3. Results

3.1 Load and displacement

3.1.1 PGA graphite in compression

PGA graphite has a complex structure of filler particles interspersed within a matrix which consists of small flour particles and the graphitised pitch together with porosity. When examined at high resolution in the FIB, the two areas have very distinct microstructures. Filler particles (Fig. 6a left hand side) are solid with isolated shrinkage (Mrozowski) cracks. The matrix areas (Fig. 6a right hand side) are dominated by the presence of lamellar graphite. This is believed to be the graphite residue of the mesophase produced during the graphitisation of the pitch. Serial sections of the

region shown in Fig. 6a and in other similar areas reveal that the porosity in such regions is interconnected.

The load-displacement curve resulting from compression of a cylindrical PGA specimen is shown in Fig. 6b. Compression proceeded at a rate of 0.1 mm/min. Displacement and load measurements were recorded at 500 ms intervals. The initial region, up to 0.1 mm displacement, had a relatively low slope, characteristic of a ‘‘bedding-in” region in which the specimen accommodated to the compression clamps. A linear region was observed between 0.2 and 0.3 mm displacement, in which elastic deformation occurred. Beyond this point the curve became non-linear with a gradually reducing compliance, until peak force was reached. After the maximum force, failure was gradual with force reducing slowly with displacement.

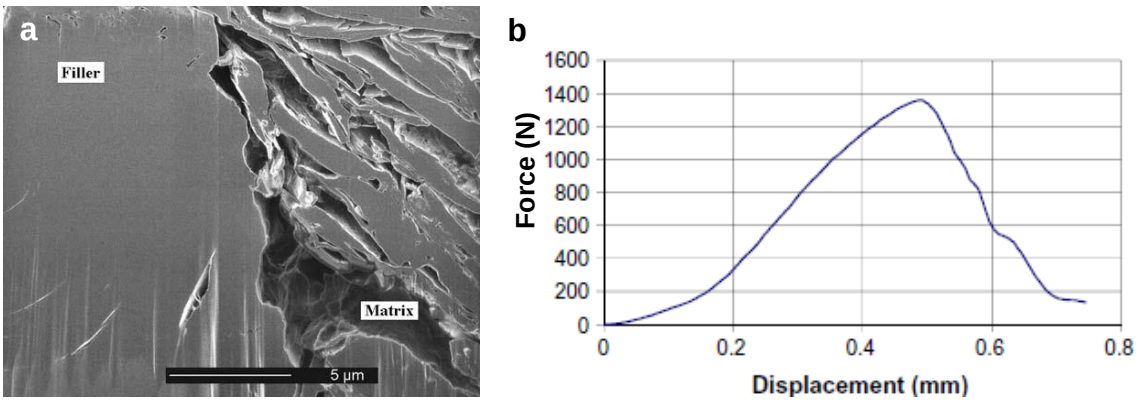

Fig. 6 (a) Microstructure of virgin PGA graphite revealed by FIB sectioning and imaging; (b) Load-displacement curve from compression of a cylindrical PGA specimen.

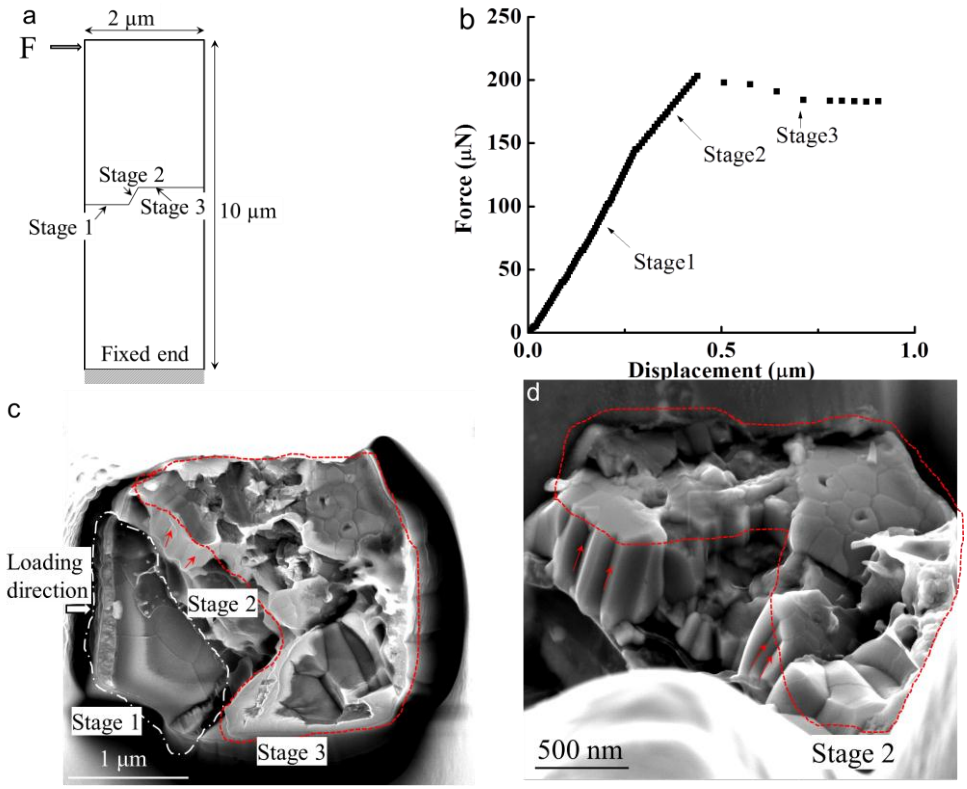

Fig. 7 A cantilever specimen containing a surface breaking flaw. (a) Schematic of the loaded specimen. (b) Force-deflection curve. (c) Surface of brittle fracture (the arrow indicates the load direction). (d) Side view of the fractured surface revealing vertical steps along the grains [6].

3.1.2 APS-YSZ in bending

In the case of a typical cantilever specimen, the force-deflection curve, Fig. 7b, containd three distinct stages 1 to 3. During stage 1 there was elastic deflection and at the end of this stage (~150 μN) the gradient changed. Stage 2 reached a maximum at ~200 μN. This was followed by a period of stable deflection as cracks propagated during stage 3. Examination of the final fracture surface, Fig. 7c, revealed the initial pre-existing flaw. There was evidence for some crack extension during stage 2 and then mainly inter-granular brittle fracture in stage 3, Fig. 7d. The elastic modulus calculated from the first linear part of the loading curve gave a value of ~35±5 GPa which is within the range of macroscopic values of 10 to 100 GPa [10-13]. Fracture toughness can be derived from the maximum load to be ~ 5.30 MPa·$m^{1/2}$ which is at the higher end of the macroscopic range of values, 0.7 to 5 MPa·$m^{1/2}$ [14-16].

3.2 Crack initiation and propagation

3.2.1 Disc compression

The compression method was used on a PGA graphite specimen within the FIB work station. Compression proceeded until fine cracking was observed at a pre-peak load at the top surface of the specimen. Sites were then chosen for FIB trenching, generally at positions across the observed cracks close to the crack tip, or ahead of the crack tip. The specimen was then tilted to 45° for high-resolution imaging of the cut face to observe sub-surface detail. Compression was resumed, increasing the load by small increments, realigning the specimen to centre the region of interest in the field of view and recording images. Force increments of 40 N were used and FIB images were captured at 8000× magnification, giving a horizontal field of view of 38 μm. Fig. 8 shows, optical images Fig. 8a and b and FIB images Fig. 8c and d, of the cut face of the specimen at compression loads of: (c) 497 N, and (d) 830 N respectively. The arrows in Figs. 8c and d mark the position of a crack forming and developing in the bulk of the graphite, within a filler particle. After crack formation, the two halves slide across each other.

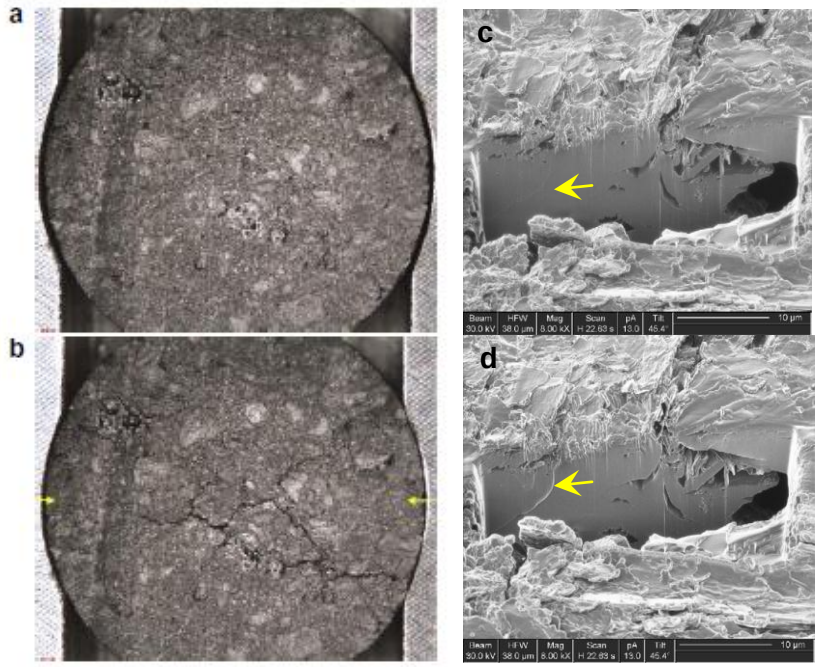

Fig. 8 Optical image of PGA specimen: (a) before compression and (b) after 0.55 mm compressive displacement showing macro-cracking (displacement is horizontal, as shown by arrows). FIB images of PGA specimen under (c) 560 N and (d) 830 N compression. Arrows show developing micro-crack.

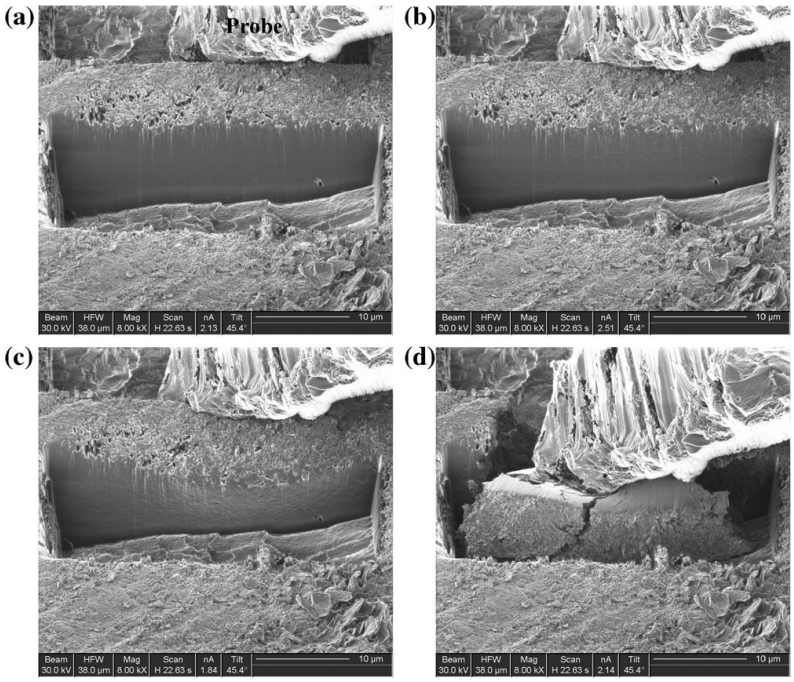

Fig. 9 Deformation of virgin PGA graphite filler using the trench-probe method. (a) Prior to loading (probe marked). (b) Showing onset of texturing. (c) Just prior to failure. (d) Just after failure.

3.2.3 Trench probe method

The trench-probe method was used to study the cracking of the individual components of the graphite microstructure such as filler particles or matrix. The method was used first on a virgin PGA specimen. Fig. 9 shows a sequence of FIB images of a region containing a filler particle recorded during testing. Fine undulations appeared at the cut surface of the specimen as it deformed, Fig. 9b, similar to those previously observed in deformed graphite. Failure occurred suddenly after considerable deformation, Fig. 9c, and the rapid movement of the probe at failure indicated that significant energy had been stored in the probe during deformation, which was released upon failure. In this case cracks formed at the mid position and ends of the loaded wall micro-specimen, Fig. 9d. The crack path was irregular and branched. Further measurements were undertaken on radiolytically oxidised PGA where twinning was observed and the cracking pattern was modified by the increase porosity within the material [5].

3.2.4 Micro-scale cantilever bending

Fig. 10a showed a typical cantilever beam created in APS-YSZ with a pre-existed external flaw (~0.1 μm) which is visible at one end of the splat boundary. The top of the beam is ~2 μm × 2 μm and a slight taper is present so that the base of the beam is ~2.2 μm × 2.2 μm. The force-deflection curve is shown in Fig. 10b and fracture occurred when the force reached ~301 μN. The fractured surface revealed an amorphous phase at the splat boundary which was in contact with the upper half of the beam before fracture, Fig. 10c. A detailed check of the fractured surface gave an equivalent crack area of 2 μm ×1 μm. In this figure, the large grains of YSZ (~0.8 μm in length) could be observed which were different from the upper side of the beam, where there were grains of sub-micrometre size. The tensile stress at fracture was ~3.6 GPa, and the elastic modulus of this particular beam was calculated to be ~43 GPa [6].

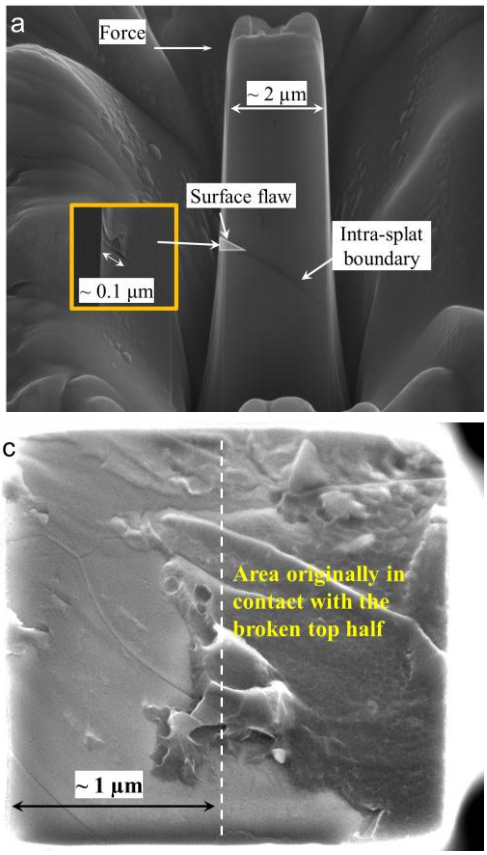

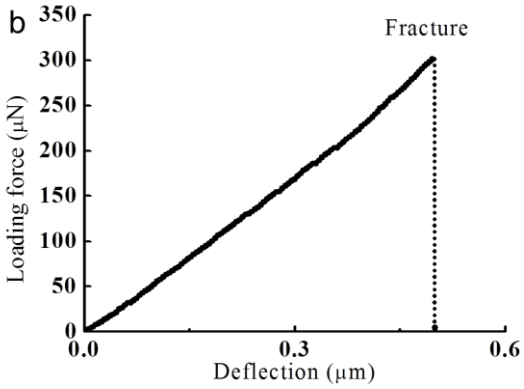

Fig. 10 A specimen created within APS-TBC. (a) Dimensions and a pre-existing flaw on the side of the cantilever with a size of ~0.1 µm as shown in insert. (b) Force-deflection curve. (c) Microstructure, dimensions of the fractured surface and the area which was in contact with the top half of the cantilever.

4. Discussion

Despite the widespread use of polygranular graphite for example for the construction of the gas cooled reactor cores in the UK reactor plant, there remain issues relating to the detailed understanding of the fracture processes at the micro-scale. Similar issues are associated with APS-YSZ as thermal barrier coatings. Here, the range of mechanical test methods assisted with understanding of the micro-scale mechanical fracture behaviour of these quasi-brittle materials.

The load-displacement curve, Fig. 6b, obtained for the compression disc test showed initial 'bedding' of the specimen to a load of about 300 N. There followed a short linear range where the material behaved elastically, prior to the onset of non-linearity. The ion milled section sequence, Figs. 8c and d, showed that as the load was increased to 560 N, Fig. 8c, a micro-crack formed and the feature became enhanced when the load reached 830 N, Fig. 8d. This sequence provides evidence that micro-cracks initiate and propagate prior to peak load to accommodate specimen displacement. At peak load and beyond, micro-cracks link to form the dominant macro-cracks shown in Fig. 6. Moreover Figs. 9a and 9b provided limited evidence for micro-cracking on the flank of a macro-crack. When interrupted post peak load, Figs. 9c and 9d showed that the macro-cracks follow an irregular path similar to that observed previously in the flexural test specimens of fractured un-irradiated PGA graphite [4]. The macro-cracks follow a path dominated by the direction of the applied tensile stress and the microstructure.

Two novel test procedures have been adopted to load graphite specimens combined with high-resolution imaging to investigate further the micro-cracking pre-peak load and macrocracking post peak load with respect to the microstructure of unirradiated PGA graphite. The disc compression test method provides the capability to view the surface of the small disc specimens when subject to a given load and under a progressively increasing applied load. The former is

important since, when using X-ray tomographic imaging of loaded and cracked, notched compact geometry unirradiated Gilsocarbon graphite specimens, Hodgkins et al. [3] observed closure of both the micro-and macro-cracks when the load was removed. This makes examination of cracking extremely difficult even when using high-resolution imaging techniques, for example focused ion beam imaging, unless a load is applied. The use of ion beam milling to produce surfaces normal to the specimen surface has provided the opportunity, for both test methods, to correlate surface and sub-surface microstructure and crack morphology. Fig. 6a provides a measure of the quality of such a milled surface in un-irradiated graphite.

One of the advantages of the in-situ micro-scale cantilever testing approach is the ability to record the specimen image at high resolution continually throughout the entire loading process. This enables the deflection of the cantilever at the loaded point to be captured and measured at the same time as the incremental loading force. This feature is especially important in the case of APS-TBC with its heterogeneous microstructure where the connecting ligaments fail. If the mechanical properties of these local ligaments can be mapped and incorporated into finite element analysis, the microstructural feature that promote failure can be identified with the potential for the manufacturing of the coatings to be improved. One of the challenges of this approach lies in that the manufacture of the beams is found to be more difficult in APS-YSZ than in homogeneous materials such as silicon due to changes in the milling or sputtering rate of the ion beam. It has been shown elsewhere that the complex local morphology leads to a varied milling rate resulting in a significant non-uniformity at the base [8, 9].

5. Conclusions

It may be concluded from this micro-scale investigation that: (i) The diametral compression of small disc specimens provides a useful tool for examining crack formation in quasi-brittle materials such as polygranular reactor core graphite, particularly when supported by focused ion beam milling and imaging. (ii) Micro-cracks in virgin PGA graphite have been confirmed to precede macro-crack formation. The micro-cracking accommodates the non-linearity in the load-displacement curves prior to the peak load. Such cracks have been observed at loads which are as low as 30% of the peak load. (iii) Micro-cantilever testing in APS-YSZ was found to produce comparable mechanical properties and fracture toughness with conventional macro-scale testing. This demonstrates that more insights into the fracture mechanics can be provided by the micro-scale testing.

Acknowledgement

We would like to acknowledge the support of The Energy Programme, which is a Research Councils UK cross council initiative led by EPSRC and contributed to by ESRC, NERC, BBSRC and STFC, and specifically the Supergen initiative (Grants GR/S86334/01 and EP/F029748). Additionally, we would like to thank Magnox Ltd. for funding and permission to publish this work.

References

[1] E. Schlangen and E. J. Garboczi, Fracture simulations of concrete using lattice models: Computational aspects, Eng. Fract. Mech., 57 (1997) 319-332.
[2] A. Hodgkins, T. J. Marrow, M. R. Wootton, R. Moskovic and P. E. J. Flewitt, Fracture behaviour of radiolytically oxidised reactor core graphites: a view, Mater. Sci. Technol., 26 (2010) 899-907.
[3] A. Hodgkins, T.J. Marrow, P. Mummery, B. Marsden and A. Fok, X-Ray tomography observation of crack propagation in nuclear graphite, Mater. Sci. Technol., 22 (2006) 1045-0151.
[4] P. J. Heard, M. R. Wootton, R. Moskovic and P. E. J. Flewitt, Crack initiation and propagation in pile grade A (PGA) reactor core graphite under a range of loading conditions, J. Nucl. Mater., 401 (2010) 71-77.
[5] P. J. Heard, M. R. Wootton, R. Moskovic and P. E. J. Flewitt, Deformation and fracture of irradiated polygranular pile grade A reactor core graphite, J. Nucl. Mater., 418 (2011) 223-232.
[6] D Liu and P. E. J. Flewitt, The measurement of mechanical properties of thermal barrier coatings by micro-cantilever tests, Key. Eng. Mat., 525-526 (2013) 13-16.
[7] D. Liu, The role of thermal exposure and substrate curvature on the residual stresses and mechanical properties in environmental and thermal barrier coating systems, PhD thesis, University of Bristol, 2012.
[8] J. E. Darnbrough, S Mahalingam and P. E. J. Flewitt, Micro-scale cantilever testing of linear elastic and elastic-plastic materials, Key. Eng. Mat., 525-526 (2013) 57-60.
[9] D. Liu and P. E. J. Flewitt, The Measurement of Mechanical Properties of Thermal Barrier Coatings by Micro-cantilever Tests Key Engineering Materials, Key. Eng. Mat. (2012) 13-16.
[10] K. W. Schlichting, N. P. Padture, E. H. Jordan and M. Gell, Failure modes in plasma-sprayed thermal barrier coatings, Mater. Sci. Eng. A-Struct., 342 (2003) 120-130.
[11] E. Rybicki, J. Shadley, Y. Xiong and D. J. Greving, A Cantilever Beam Method for Evaluating Young's Modulus and Poisson's Ratio of Thermal Spray Coatings, J. Therm. Spray. Tech., 4 (1995) 377-383.
[12] J. A. Thompson and T. W. Clyne, The Effect of Heat Treatment on the Stiffness of Zirconia Top Coats in Plasma-Sprayed TBCs, Acta. Mater., 49 (2001) 1565-1575.
[13] F. Tang and J. M. Schoenung, Evolution of Young's modulus of air plasma sprayed yttria-stabilized zirconia in thermally cycled thermal barrier coatings, Scripta Mater., 54 (2006) 1587-1592.
[14] A. Rabiei and A. G. Evans, Failure mechanisms associated with the thermally grown oxide in plasma-sprayed thermal barrier coatings, Acta. Mater., 48 (2000) 3963-3976.
[15] Y. Yamazaki, S. I. Kuga and T. Yoshida, Evaluation of interfacial strength by a instrumented indentation method and its application to an actual TBC vane, Acta Metall. Sin. (Engl. Lett.), 24 (2011) 109-117.
[16] D. Di Maio and S. G. Roberts, Measuring fracture toughness of coatings using focused-ion-beam-machined microbeams, J. Mater. Res. , 20 (2005) 299-302.

Micro-cutting tests: a new way to measure the fracture toughness and yield stress of polymeric nanocomposites

Hongjian Wang[1], Li Chang[1*], Lin Ye[1], and Gordon. J. Williams[1, 2]

[1]Aero, Mechanical and Mechatronics Engineering Department, University of Sydney, Sydney, Australia
[2]Mechanical Engineering Department, Imperial College London, South Kensington Campus, London, UK
* Corresponding author: li.chang@sydney.edu.au

Abstract

The fracture toughness, G_c, of pure epoxy and epoxy nanocomposites with 10 wt% nano-rubber and 10 wt% nano-silica particles, was determined using an orthogonal cutting method on a CNC machine. The cutting forces were measured by a multi-axis dynamometer, and depths of cut were precisely controlled from 30 μm to 120 μm. High speed cutting tools with three rake angles of 10º, 20º, and 30º were used for the cutting. The fracture results of pure epoxy and 10 wt% nano-silica epoxy composite determined by the cutting test has the same order of magnitude as which determined by the standard compact tension test. However, for 10 wt% nano-rubber epoxy, a much lower G_c value was measured due to the interaction between the plastic zone size of the crack tip and the magnitude of cutting depth. The results have indicated that orthogonal cutting could be an alternative approach to traditional LEFM testing for brittle polymeric nanocomposites. The specimen preparation and testing procedures would be greatly simplified compared with current fracture test technologies.

Keywords: Orthogonal cutting, fracture toughness, polymer nanocomposites

1. Introduction

The accurate estimation of fracture toughness for ductile, yet tough polymers remains to be a challenging task in material science. Traditional LEFM testing is affected by the blunting of the crack tip during crack propagation, which results in over-estimation of the toughness results. Recent research carried out by Patel et al. [9, 10] has proposed that orthogonal cutting may be a suitable method for measuring the strain energy release rate, G_c, for such polymers. The theory was initiated by Atkins [1-3, 5] who pointed out that the fracture energy in the orthogonal cutting process should be equally important as the plastic work and frictional loss, and that the critical fracture energy during cutting be equivalent to the cutting energy extrapolated to the zero depth of cut. Subsequently, Williams [9] developed a more sophisticated orthogonal cutting model by taking Tresca yield criterion and Coulomb friction of the workpiece material into account. A linear relationship between the cutting energy and the cutting depth with the inclusion of the constant global fracture energy, G_c, has been deduced. The new theory has been verified by the testing of some typical high toughness but low strength engineering polymers. The cutting experiment gives valid toughness results for these materials.

It is expected that this marvel fracture testing technique will also be applicable for a variety of engineering polymers, in particular, such as tough, yet brittle polymeric composites, thin polymeric film and micro-fabricated materials. The method will greatly simplify the preparation of testing specimens and avoid the limit of size requirements in the standard fracture toughness test. Our work has been focused on employing the orthogonal cutting method to measure fracture toughness of brittle amorphous epoxy and its nano-modified composites (10 wt% nano-rubber and 10 wt% nano-silica epoxies). The cutting experiment was performed on a rigid CNC machine where the depth of cut can be precisely controlled within few hundreds of microns. At this range of cutting depth, the cut material behaved sufficient plasticity. Continuous chipping process and steady-state cutting force signals were observed. The cutting condition satisfied Williams' notion of cutting

tough, yet ductile polymers. Hence, the same analytical method can be used in the cutting data analysis.

2. Analysis

2.1 Orthogonal Cutting with Consideration of Fracture Energy

A schematic representation of the orthogonal cutting model developed by Williams et al. [9] is illustrated in Fig. 1 (a), where a tool with a single cutting edge of rake angle α is driven at a constant velocity V to remove a chip of thickness h_c and width b from a testing material. The force relationship of the model may be considered by treating the chip as an isolated system. During a steady-state cutting process, the chip is hold by two equal and opposite resultant forces F and F' under equilibrium condition. F' is generated by the tool which acts on the back surface of the chip; F is due to the reaction of the testing material being cut which exerts on the base of the chip. F' may be resolved into a friction force S and its normal component N along the chip back surface. S is responsible for the work expended in fraction as the chip slides over the tool rake face. On the other hand, F may be resolved into a shear force F_s and a compressive force F_n on the base of the chip. The base of the chip can be considered as a shear plane, of a shear angle φ, where shear yielding of the testing material take places. The shear force F_s is then responsible for the work expended in plastic deformation of the testing material. [7-9]

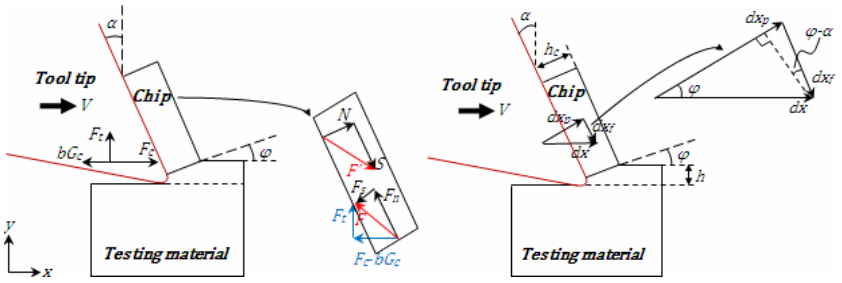

Figure 1. Schematic diagrams of orthogonal cutting (a) force relationship of the cutting system and (b) geometrical relationship of displacements of forces during cutting.

From another standpoint, the resultant force, F, may also be decomposed into F_c-bG_c along the tool moving direction and F_t which is perpendicular to the tool moving direction. F_c is the cutting force delivered from the tool which is responsible for the total work dissipated in the cutting process. F_t arises from the existence of F_c, which is described as a transverse force to maintain the steady-state during cutting process. G_c is considered as the global fracture energy reserved in the testing material. Furthermore, bG_c is modelled as a reaction force towards the cutting direction to prevent the material from separation, where b represents the width of cut. [9, 10]

2.2 An Energy-based Approach to Determine the Fracture Energy

In the orthogonal cutting system as illustrated in Fig.1 (a), the total cutting energy delivered by the tool is considered to be completely dissipated into the plastic work of the chip, the frictional loss due to tool-chip interaction and the fracture work of the testing material [9], where

$$dU_{diss} = dU_{plast} + dU_{frict} + dU_{fract} \tag{1}$$

In force-displacement relation, Eq. (1) becomes

$$F_c dx = F_s dx_p + S dx_f + bG_c dx \tag{2}$$

where dx represents the incremental displacement of tool movement. The corresponding displacements owing to F_s and S, dx_p and dx_f, respectively, can be derived based on the geometrical relationship as shown in Fig. 1 (b) [9]

$$dx_f = \frac{\sin\varphi}{\cos(\varphi-\alpha)}dx \tag{3}$$

$$dx_p = \frac{\sin\alpha}{\cos(\varphi-\alpha)}dx \tag{4}$$

Considering force equilibrium of the chip, the friction force on the tool-chip interface may be expressed as

$$S = (F_c - bG_c)\sin\alpha + F_t\cos\alpha \tag{5}$$

On the other hand, the shear force on the shear plane can be modelled in accordance with Tresca yielding criterion. It is assumed that the shear plane is formed at a critical shear stress which is half of the yield strength of the testing material [9], thus,

$$F_s = \frac{\sigma_Y}{2}\frac{bh}{\sin\varphi} \tag{6}$$

where $bh/\sin\varphi$ is the effective area of the shear plane.

Substituting Eq. (3) to (6) into (2), we have

$$\frac{F_c}{b} - \frac{F_t}{b}\tan\varphi = \frac{\sigma_Y}{2}(\tan\varphi + \frac{1}{\tan\varphi})h + G_c \tag{7}$$

Thus, the fracture energy, G_c, induced by the cutting process can be determined from the linear plot of F_c/b-$(Ft/b)\tan\varphi$ versus $(\tan\varphi+1/\tan\varphi)h$ data [9, 10], where

$$\tan\varphi = \frac{\cos\alpha}{\frac{h_c}{h} - \sin\alpha} \tag{8}$$

and h_c represents the chip thickness.

3. Experimental

3.1 Cutting Experiment Set-up

Cutting tests were carried out on a hydraulic driven rigid CNC machine (Minini Junior 90 M286). A customised tool post and a sample holder were made to cope with orthogonal cutting. The cutting forces were measured by a multi-component dynamometer (Kistler 9257B). The cutting force signals were recorded by an digital oscilloscope (Agilent 54621A) and the data were processed in Excel. A set of high speed cutting tools (Cobalt M42), of rake angles 10º, 20º and 30º and clearance angle 4º, were used in the experiment. The tools were sharpened with tip radii less than 5μm.

3.2 Testing Materials

A diglycidyl ether of bisphenol A (DGEBA) epoxy resin, Araldite-F (Ciba-Geigy, Australia), cured using piperidine (Sigma-Aldrich, Australia) with a ratio of 100:5 (epoxy/piperidine), was used as the base material. For two epoxy nanocomposites, one has 10 wt% SiO_2 nanoparticle produced from Nanopox XP 22/0616 resin (Hanse-Chemie AG, Germany), which consists of well dispersed silica nanoparticles (40 wt%) with an average particle size of 20 nm, while the other has 10 wt% spherical rubber particle produced from a bisphenol master batch resin with 25 wt% well dispersed rubber nanoparticles of 100 nm in size (Kaneka Corporation, Japan). [6, 11] For the cutting experiment, the testing materials were prepared into approximately 5mm thick rectangular blocks.

The values of fracture toughness G_c and yielding stress σ_Y of the testing materials have been determined from conventional compact tension and tensile tests [6, 11], where the CT test followed ASTM D5045 while the tensile test followed ASTM D638.

3.3 Cutting Test Method

The testing material and tool were firmly gripped on the sample holder and tool post, respectively. Cutting started with first a few thin sectioning of the testing material in order to flatten the cut surface. Subsequently, consecutive cutting operation was performed with a speed of *1 mm/s* and the depths of cut were varied from 30μm to 120μm. After each cut, the chip was collected for further measurement.

4. Results and Discussion

4.1 Cutting Results for Pure Epoxy and Epoxy Nanocomposites

Cutting results are presented for pure epoxy and two epoxy nanocomposites. Cutting forces F_c and F_t, and chip thickness h_c are measured for a range of cutting depths h. The data are evaluated by Eq. 7, as shown in Fig. 2.

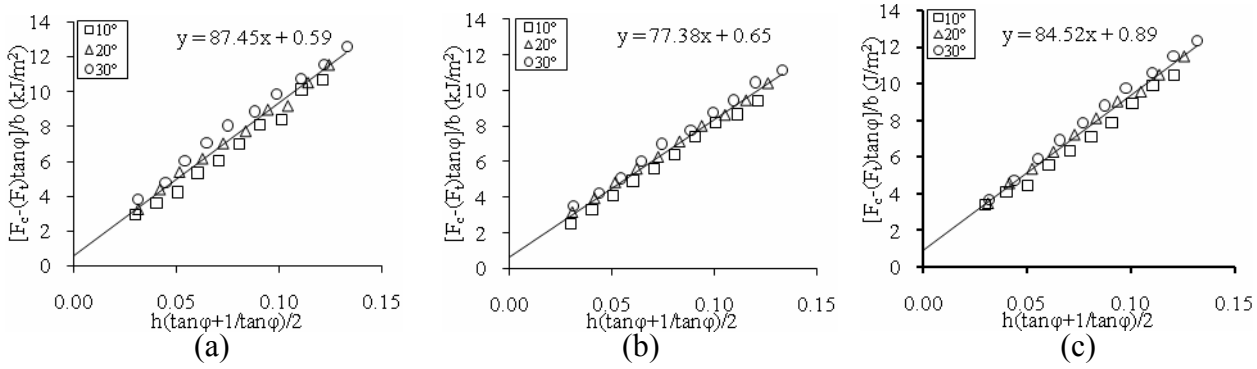

Figure 2. Cutting results for (a) pure epoxy with specimen width b=5.57*mm*, (b) 10% nano-rubber epoxy with specimen width b=5.04*mm*, and (c) 10% nano-silica epoxy with specimen width b=5.40*mm*. The cutting velocity was at *1 mm/s*. The legend shows the rake angle in degrees.

Table 1. Yield stress and fracture toughness for epoxy and its nanocomposites [6, 11].

		Pure epoxy		10% nano-rubber epoxy		10% nano-silica epoxy	
Method	Testing rate	$\sigma_Y(MPa)$	$G_c\,(kJ/m^2)$	$\sigma_Y(MPa)$	$G_c\,(kJ/m^2)$	$\sigma_Y(MPa)$	$G_c\,(kJ/m^2)$
Cutting test	1mm/s	87.46±2.47	0.59±0.21	77.38±1.25	0.65±0.09	84.52±1.73	0.89±0.15
CT test	1mm/min	--	0.28±0.25	--	1.93±0.1	--	0.69±0.05

Tensile test	5mm/min	42.1±2.6	--	37.6±0.8	--	46.5±1.1	--

The linear regression analysis has been shown in the plots of F_c/b-$(F_t/b)\tan\varphi$ versus $(\tan\varphi+1/\tan\varphi)h$ data. The gradient gives the yield stress, σ_Y, which was deduced in accordance with Tresca yield criterion, and the y-intercept is the fracture energy, G_c, of the testing material induced by cutting. The σ_Y and G_c determined from the cutting test are compared with those determined from standard compact tension and uni-axial tensile tests, as listed in Tab. 1.

4.2 Results Discussion

The compact tension test gives G_c values of 0.28±0.25 kJ/m^2, 1.93±0.1 kJ/m^2 and 0.69±0.05 kJ/m^2 for pure epoxy, 10% nano-rubber epoxy and 10% nano-silica epoxy, respectively. Cutting test gives higher G_c results for pure epoxy and 10% nano-silica epoxy, but within reasonable limits. The cause of discrepancy is attributed to the complication in the estimation of depth of cut, h. Since the tool cannot be perfectly sharp, the lower portion of the tool tip may result in a ploughing of the testing material during the cutting process. Thus, the measurements of the cutting depth were overestimated by the size of δ, as shown in Fig. 3 (b).

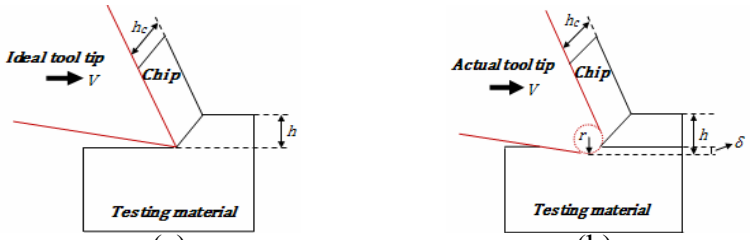

Figure 3. Schematics of orthogonal cutting with (a) an ideal sharp tool, and (b) an actual tool with a tip radius r.

Assuming that half size of the tip radius contributes to the ploughing process, the fracture energy that was over estimated by ploughing could be approximated by

$$G' = \delta\sigma_Y \tag{9}$$

where the tool tip radius used in the experiment was around 5μm; σ_Y is the yield stress determined from the cutting test. [4] Hence, the actual fracture energy induced by cutting for pure epoxy becomes

$$G_c = 0.59kJ/m^2 - \frac{2.5\times 87.46}{1000}kJ/m^2 \approx 0.37kJ/m^2 \tag{10}$$

and also, for 10% nano-silica epoxy

$$G_c = 0.89kJ/m^2 - \frac{2.5\times 84.52}{1000}kJ/m^2 \approx 0.68kJ/m^2 \tag{11}$$

which are in good agreement with the results derived from the compact tension test.

The cutting test gives 0.65±0.09 kJ/m^2 for the G_c value of 10% nano-rubber epoxy. The result is about 3 times lower than that given by the compact tension test. In this particular case, the cutting result is most likely affected by the crack tip plastic zone size of the testing material. The estimated plastic zone size in the compact tension test for 10% nano-rubber epoxy is about 190μm, which is

far above the nominal depth of cut for the cutting test: 30μm to 120μm. Thus, the plastic zone size induced by cutting is confined and the measured G_c value is much more conservative.

Finally, it is noticed that cutting method always determines high values of yield stress compared with those determined from the tensile test. This has been ascribed to large strain and high strain rate on the shear plane during the chip formation process [9].

5. Conclusion

The fracture toughness of epoxy and its epoxy nanocomposites with 10 wt% rubber and silica nanoparticle has been measured by use of an orthogonal cutting method. The cutting method has been proven as a valid way to characterise the G_c of ductile and moderately tough polymeric materials [10]. This work expands the applicability of the method to brittle and tough amorphous polymer and its nanocomposites. It is believed that with the careful examination of the cutting quantities and the material property, orthogonal cutting could become an alternative approach to easily determine the fracture toughness of a wide variety of engineering polymers.

Reference

[1] Atkins AG. Modelling metal cutting using modern ductile fracture mechanics: quantitative explanations for some longstanding problems. International Journal of Mechanical Sciences. 2003;45(2):373-396.

[2] Atkins AG. Toughness and cutting: a new way of simultaneously determining ductile fracture toughness and strength. Eng Fract Mech. 2005;72(6):849-860.

[3] Atkins AG, Vincent JFV. An Instrumented Microtome for Improved Histological Sections and the Measurement of fracture Toughness. J Mater Sci Lett. 1984;3(4):310-312.

[4] Blackman BRK, Hoult TR, Patel Y, Williams JG. Tool sharpness as a factor in machining tests to determine toughness. Eng Fract Mech;101(0):47-58.

[5] Ericson ML, Lindberg H. Design and potential of instrumented ultramicrotomy. Polymer. 1997;38(17):4485-4489.

[6] Liu HY, Wang GT, Mai YW, Zeng Y. On fracture toughness of nano-particle modified epoxy. Compos Pt B-Eng. 2011;42(8):2170-2175.

[7] Merchant E. MECHANICS OF THE METAL CUTTING PROCESS .1. ORTHOGONAL CUTTING AND A TYPE-2 CHIP. J Appl Phys. 1945;16(5):267-275.

[8] Merchant ME. MECHANICS OF THE METAL CUTTING PROCESS .2. PLASTICITY CONDITIONS IN ORTHOGONAL CUTTING. J Appl Phys. 1945;16(6):318-324.

[9] Patel Y, Blackman BRK, Williams JG. Determining fracture toughness from cutting tests on polymers. Eng Fract Mech. 2009;76(18):2711-2730.

[10] Patel Y, Blackman BRK, Williams JG. Measuring fracture toughness from machining tests. Proc Inst Mech Eng Part C-J Eng Mech Eng Sci. 2009;223(12):2861-2869.

[11] Zhang J, Deng S, Ye L. Roles of rigid nano-particles and CTBN rubber in toughening DGEBA epoxies with different cross-linking densities. ACUN 6. Melbourne; 2012.

Mixed-mode crack initiation at the edge of Cu/Si interface in nanoscale components

Yabin Yan[1,*], Kohei Kishimoto[2], Takashi Sumigawa[2], Takayuki Kitamura[2]

[1]Institute of Structural Mechanics, China Academy of Engineering Physics, Mianyang 621900, China
[2] Department of Mechanical Engineering and Science, Kyoto University, Kyoto 606-8501, Japan
* Corresponding author: yanyabin@gmail.com

Abstract The crack initiation behavior under the mixed-mode at the edge of a Cu/Si interface in nanoscale components has been investigated by a novel torsion method using a double nano-cantilever specimen consisting of a 20-nm-thick Cu layer and a Si substrate. By using this nano-cantilever torsion method, the shear stress is applied to the Cu/Si interface with the nanoscale stress concentration through the transverse arm. The mode mixity, which is the ratio of the shear stress to the normal stress, can be precisely controlled by changing the loading position. During the experiment, the crack is successfully initiated at the Cu/Si interface edge for various mode mixities by the developed method. The detailed stress fields along the Cu/Si interface at the critical loads for crack initiation are analyzed by the finite element method, and the stress concentration region near the interface edge in all specimens is within the scale of 100 nm. The critical normal stress and maximum shear stress at crack initiation have a circular relation.

Keywords Nanoscale, Mixed-mode, Crack initiation, Interface, Torsion test

1. Introduction

Micro- and nano-mechanical systems and electronic devices consist of dissimilar components, of which size is on the nanometer scale. Since intrinsic bi-material interfaces are inevitably introduced into these devices, deformation mismatch between the dissimilar materials induces a stress concentration at the interface. Thus, the interface is one of the potential sites of fracture [1–3].

Since the stress concentration region is proportionally scaled down for the shrinkage of component size, the stress concentration region at the interface edge is confined to the nanoscale in advanced devices [4–5]. On the other hand, as the state of internal stress is complex in micro-devices, the interface cracking usually takes place under a mixed-mode due to asymmetric loading across the interface and the difference in elastic properties [6]. Thus, to ensure the reliability of these devices, it is important to investigate the mixed-mode fracture criterion under a nanoscale stress concentration. Many investigations for various mode mixities have been conducted for macroscale materials [7], and they revealed that the critical normal and shear stresses for the interface fracture exhibit an elliptical relationship [7]. However, due to the difficulty in handling and applying effective loads to nanoscale specimens, conventional methods [8–11] cannot be applied in fracture experiments of nanoscale components. Recently, although the interfacial crack initiation by nanoscale stress concentration has been experimentally studied by a bending method using a straight nano-cantilever [12–14], the normal stress dominated the crack initiation at the interface edge, *i.e.*, mode-I fracture. It is thus necessary to develop a suitable method for performing mixed-mode fracture experiments on nanoscale components and to investigate the criterion in the mixed-mode due to the nanoscale stress concentration.

In this study, we develop a nano-cantilever torsion method and use it to perform crack initiation experiments for the interface between 20-nm-thick copper (Cu) film and silicon (Si) substrate under a 100-nm-scale stress concentration with different mode mixities.

2. Experiments

2.1. Tested material

The nano-cantilever torsion specimen is cut from a multi-layered material, *i.e*. silicon/copper/silicon nitride ($Si/Cu/Si_3N_4$). A Si(100) wafer surface is cleaned by inverse sputtering to remove the native oxide layer and then a 20-nm-thick Cu layer is deposited by radio-frequency magnetron sputtering in a 0.67 Pa argon atmosphere. An approximately 1000-nm-thick silicon nitride (SiN) layer is subsequently deposited by the same method without breaking the vacuum. This study focuses on the interface between the Cu layer and the Si substrate.

2.2. Nano-cantilever torsion specimen

Figure 1 schematically illustrates the nano-cantilever torsion specimen used to investigate the mixed-mode cracking at the Cu/Si interface edge in the present study. As shown in Fig. 1(a), the nano-cantilever torsion specimen is a three-dimensional bent structure in the shape of "⊐" that has three arms (see top view of specimen in Fig. 1(b)). The Cu/Si interface is located at arm ①. The load is applied to the SiN layer in arm ③ by a diamond loading tip to stress the Cu/Si interface by a torque and bending moment transferred through arm ②. In addition, to eliminate the strong stress singularity at the sharp corner of the rectangular cross-section of arm ① and obtain a controllable mild concentrated stress field, the inner corner is rounded by focused ion beam (FIB) processing, as shown in the cross-sectional view of Fig. 1(a). Three specimens with different size are prepared and their scales are summarized in the table of Fig. 1(a).

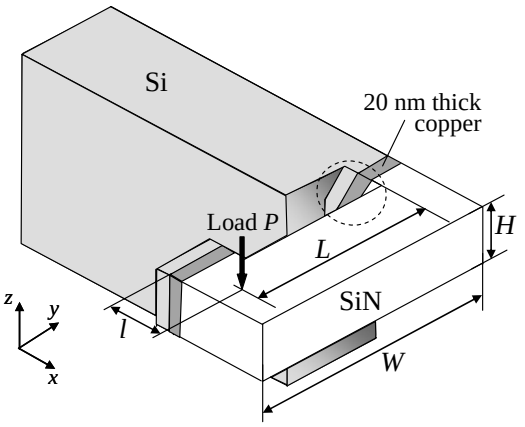

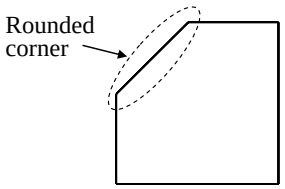

Cross section of arm ①

Specimen No.	*L*	*l*	*W*	*H*
T1	2075	657	2879	760
T2	2850	600	1661	656
T3	2391	115	2915	584

(a)

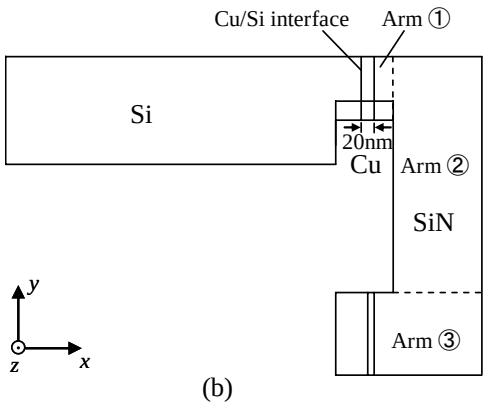

(b)

Figure 1 (a) Schematic illustration of a nano-cantilever torsion specimen with 20-nm-thick Cu thin film and its dimensions. (b) Top view of specimen. The dimensions in the table are given in nanometers.

Figure 2 schematically illustrates the procedure used to fabricate the nano-cantilever torsion specimen. As it has three-dimensional shape, the process is much more complex than that for previous straight-cantilever specimen. Before the sample fabrication, passivation layers of gold (Au) and carbon (C) are formed on the SiN layer to protect the specimen from damage during processing. After a cubic block with the side length of about 10 μm is cut from the multi-layered material by a focused ion beam (FIB) (JEOL Ltd., SMI9200) (Fig. 2(a)), it is picked up by a glass probe manipulator (Fig. 2(b)) and is carefully glued to the flat top of a gold (Au) wire with a diameter of 0.25 mm (Fig. 2(c)). The block is thinned in the *y*-direction (Fig. 2(d)) and an L-shaped extension that includes multilayer Si/Cu/SiN is formed (Fig. 2(e)). After thinning the L-shaped extension in the *z*-direction to form a cantilever (Fig. 2(f)), the inner middle part of the long arm of the L-shaped cantilever is cut to expose the inner Cu/Si interface edge (Fig. 2(g)). The inner corner of the upper edge of the Cu/Si interface is rounded (Fig. 2(h)). Finally, the Au and C layers are removed. The gallium (Ga) ion beam energy is set to 30 kV and the beam current is controlled between 5 pA and 5 nA depending on the fabrication precision.

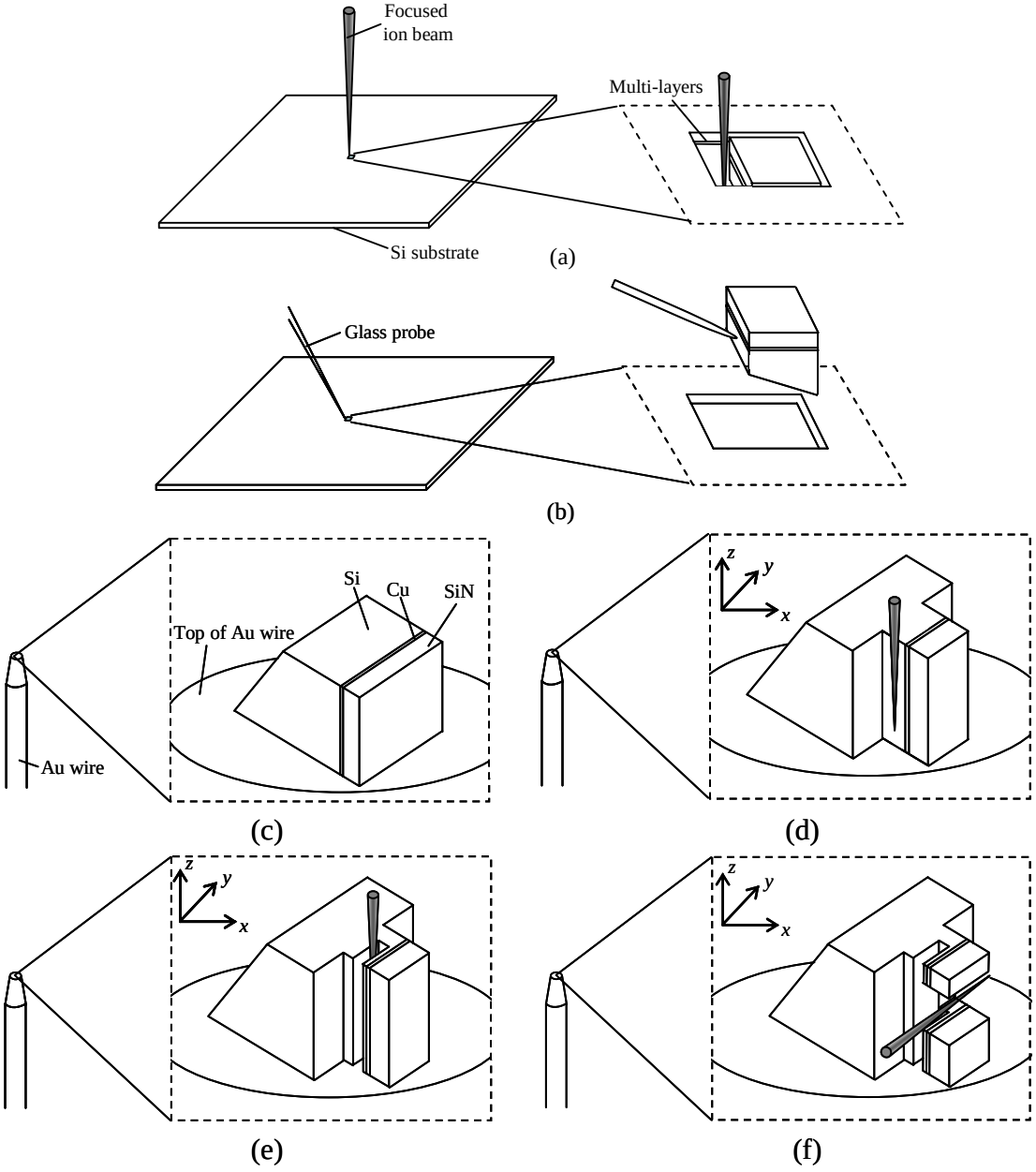

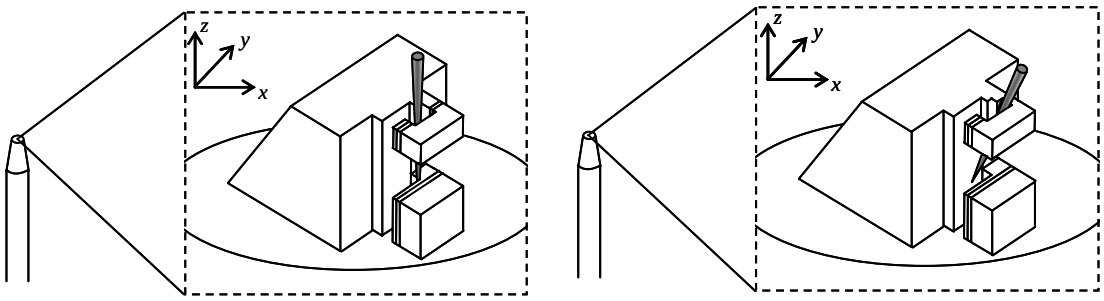

(g) (h)

Figure 2 Schematic illustrations of the procedure used to prepare nano-cantilever torsion specimen. (a) A block is cut from a multi-layered material by FIB. (b) The block is manipulated using a glass probe. (c) The block is mounted on the top of an Au wire. (d)–(h) The shape of the nano-cantilever torsion specimen is fabricated.

Figure 3 shows a scanning electron microscopy (SEM) micrograph of a nano-cantilever torsion specimen. It reveals that there is no damage on the Cu/Si interface edge before the experiment.

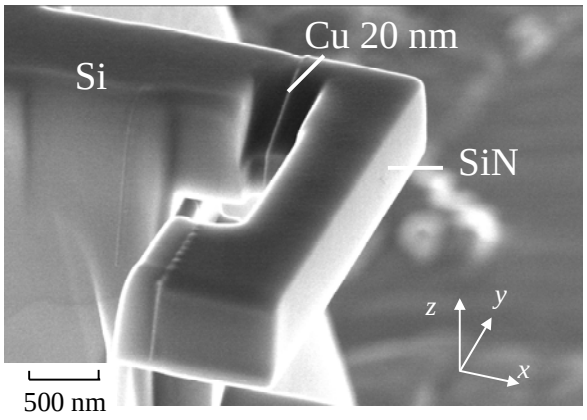

Figure 3 SEM image of a nano-cantilever torsion specimen (T1).

2.3. Loading apparatus

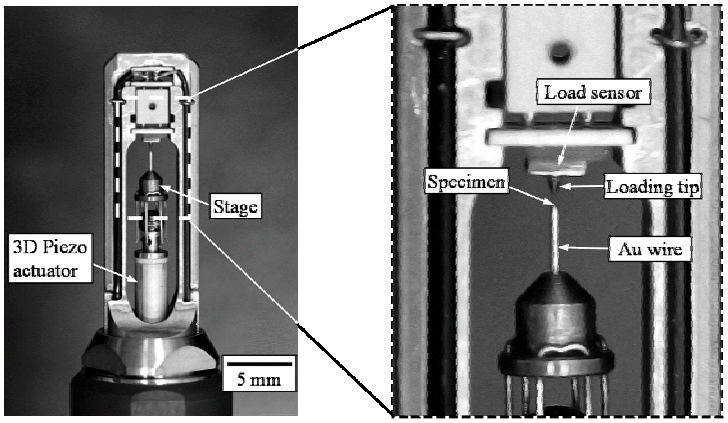

Figure 4 Mechanical loading apparatus used in the mixed-mode interface cracking experiments of nanoscale specimen.

Figure 4 shows the minute mechanical loading apparatus (Nanofactory Instruments AB, SA2000N) used in this study. The apparatus, which consists of a movable sample stage and a diamond loading tip with a load sensor, is built into a transmission electron microscopy (TEM) holder. The gold wire

with a nano-cantilever torsion specimen mounted on top is attached to the sample stage, which is actuated three-dimensionally by a piezoelectric actuator. The load resolution of the sensor is 0.1 μN and the alignment resolution of the piezoelectric actuator in each direction is approximately 1 nm.

3. Analytical procedure

To inquire the stress distribution along the Cu/Si interface at crack initiation, elasto-plastic analysis is performed by the finite element method (FEM) using the commercial software, ABAQUS. Figure 5 shows typical finite element meshes for specimen T1. The configuration of the simulation model is reconstructed using three-dimensional computer-aided design (CAD) software on the basis of 3D analysis of SEM and TEM micrographs. The area near the free edge of the Cu/Si interface, where the stress concentration is expected, is carefully divided into fine meshes. A perfect constraint condition is imposed on the back and bottom ends.

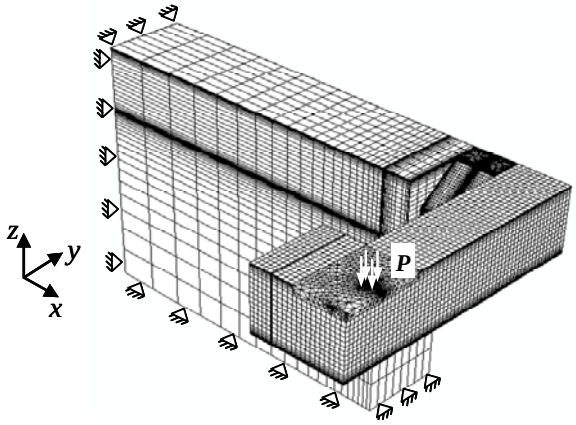

Figure 5 Typical finite element meshes for numerical analysis (specimen T1)

Because the Si substrate is a single crystal, it was treated as an orthotropic elastic material. The Young's modulus of the SiN layer which affects the stress distribution along the Cu/Si interface is measured by an indentation test. Table 1 lists the elastic constants of the component materials.

Table 1 Elastic constants of materials

Material	Young's modulus (GPa)		Poisson's ratio
Cu	129		0.34
SiN	197		0.27
Au	78		0.44
C	400		0.30
	C_{11} (GPa)	C_{12} (GPa)	C_{44} (GPa)
Si	167.4	65.23	79.57

Since the yield stress of the Cu layer is much lower than the Si substrate (σ_y > 3.4 GPa [15]) and the SiN layer (σ_y > 8.4 GPa [16]), only the Cu layer is subjected to elasto-plastic deformation during these experiments. The constitutive relation has been experimentally obtained in a previous study [13], and is given by:

$$\sigma = \begin{cases} 129000\varepsilon & \text{for } \sigma \le 765\ \text{MPa} \\ 3316\varepsilon^{0.332} & \text{for } \sigma \ge 765\ \text{MPa} \end{cases} \quad (1)$$

where σ and ε are the von Mises stress and strain, respectively.

In addition, the residual stresses introduced during processing are measured experimentally (760 MPa for Cu layer; –290 MPa for SiN layer) [13] and are taken into account in the FEM analysis. After corresponding residual stresses are uniformly imposed on Cu and SiN layers respectively, they are relaxed by the FEM calculation.

4. Results and discussion

Figure 6 shows the loading curve (*P*–*t*) obtained for specimen T1 and TEM micrographs of the specimen at three specific loading levels (A, B, and C). As shown in Fig. 6(a), after the loading tip hits the SiN layer at point A, the applied load, *P*, increases monotonically up to a peak magnitude of 49.9 μN (point B), after which it abruptly decreases (point C). Figure 6(b) clarifies that no crack initiation is recognized before the peak load while the specimen has an interface crack after. That is to say, the crack initiates at point B at the top edge of the Cu/Si interface and instantly propagates along the interface. A magnified image of the Cu/Si interface edge after crack initiation (at point C) indicates that no dissimilar material remains on either delaminated surface, which confirms the pure interface cracking. Similar behavior is also observed in the other specimens. Thus, the peak load for crack initiation, P_C, is defined as the critical load. Table 2 lists the magnitude of P_C, which shows that it depends greatly on the specimen geometry.

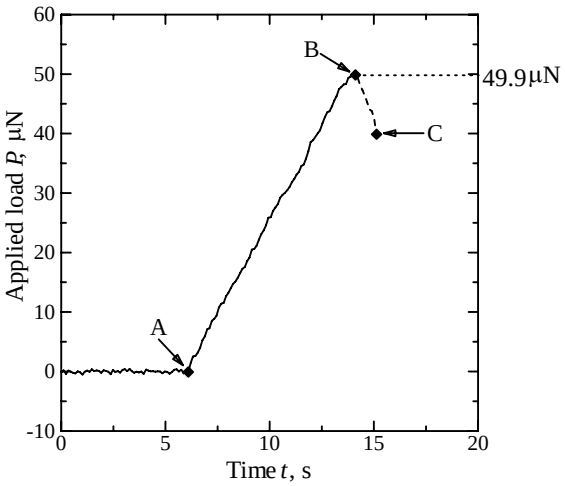

(a)

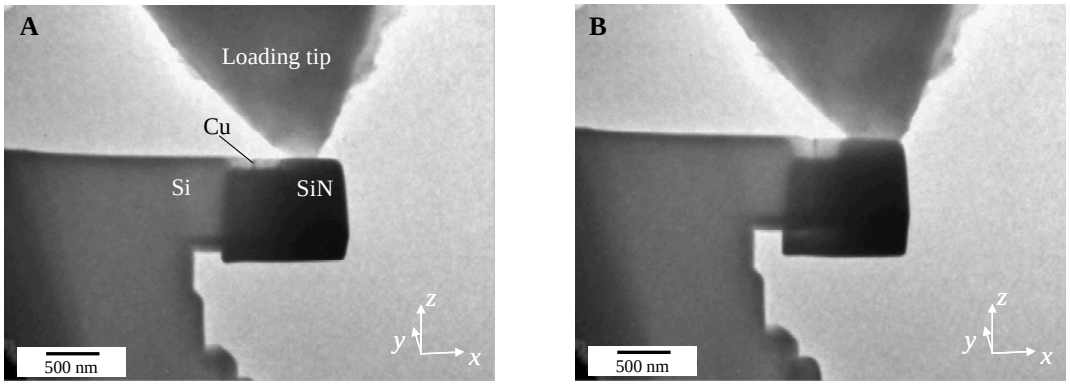

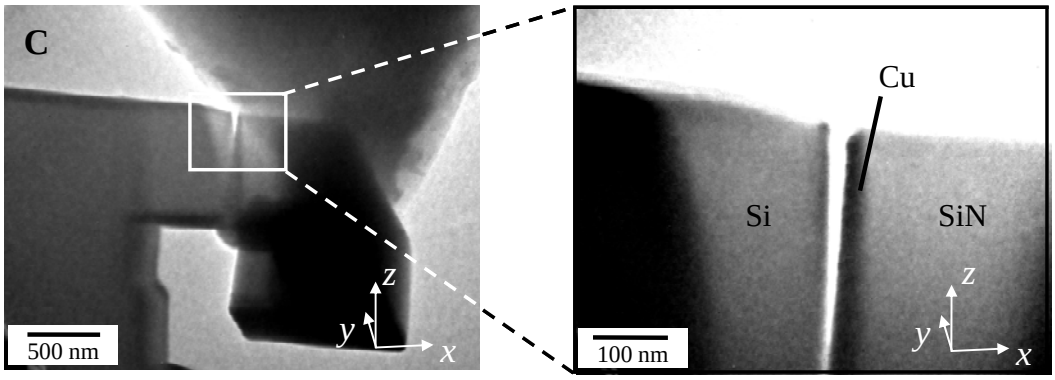

(b)

Figure 6 (a) Load–time relationship and (b) *in situ* observations of interfacial fracture of specimen T1.

Table 2 Critical load, P_C, for crack initiation at interface edge

Specimen No.	Critical load, P_C, μN
T1	49.9
T2	25.6
T3	12.0

Figure 7 shows the distribution of shear stress τ_{xy} on the Cu/Si interface of a nano-cantilever torsion specimen, T1. It shows that the stress concentrates at the adjacent area of the rounded inner corner and its size is in the scale of 100 nm. Similar stress distribution on the Cu/Si interface is also found in other specimens. Thus, we set the origin, *O*, on the rounded corner to be the site of crack initiation. Since the stress is almost constant within the area of 50 nm away from the origin (the area in the dashed circle in Fig. 7(b)), we take the *r*-axis along the loading direction.

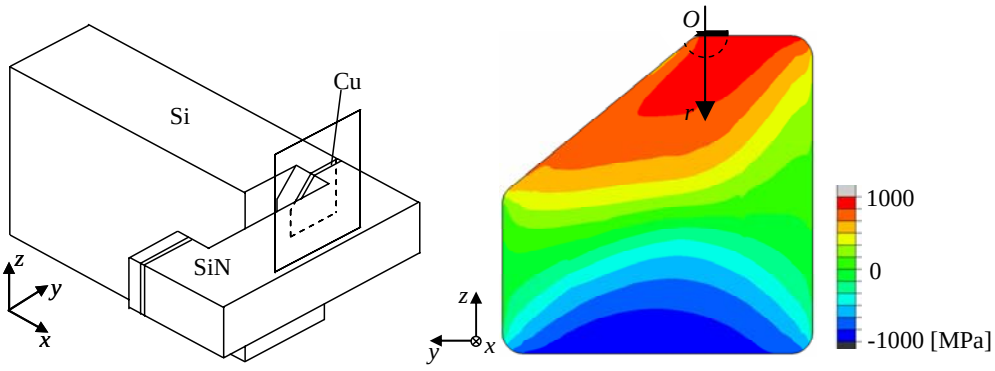

(a) (b)

Figuer 7 Distribution of shear stress τ_{xy} on the Cu/Si interface of a nano-cantilever torsion specimen.

Since FEM analysis on stress distribution of the Cu/Si interface indicates that the shear stress τ_{xy} concentrates at the site of crack initiation and much larger than other shear stress components, following discussions focus on the shear stress τ_{xy} and the normal stress σ_{xx}. Figure 8 shows the distributions of the normal and shear stresses, σ_{xx} and τ_{xy}, on the Cu/Si interface along the *r*-axis at the critical loads for crack initiation in different specimens. For comparison, the critical interfacial stress distribution of a straight-cantilever specimen (A1) is referred in Fig. 8(a). In straight-cantilever specimen A1 (Fig. 8(a)), the normal stress is two orders of magnitude larger than the shear stress, which indicates that the normal stress dominates crack initiation at the Cu/Si interface edge. Figures 8(b)–(d) reveal that with changing the loading position, *i.e.*, the magnitude of *L*/*l*, different ratios of the shear stress to the normal stress are realized. In specimen T1, the shear

stress is comparably large with the normal stress (Fig. 8(b)), and a larger ratio of shear stress to normal stress is achieved in specimen T2 (Fig. 8(c)). In specimen T3, the shear stress is 10 times larger than the normal stress (Fig. 8(d)). It should be noted that the stress concentrated area is about 100 nm in all specimens. These indicate the success of the nano-cantilever torsion method for conducting fracture experiments under different mode mixities with the nanoscale stress concentration.

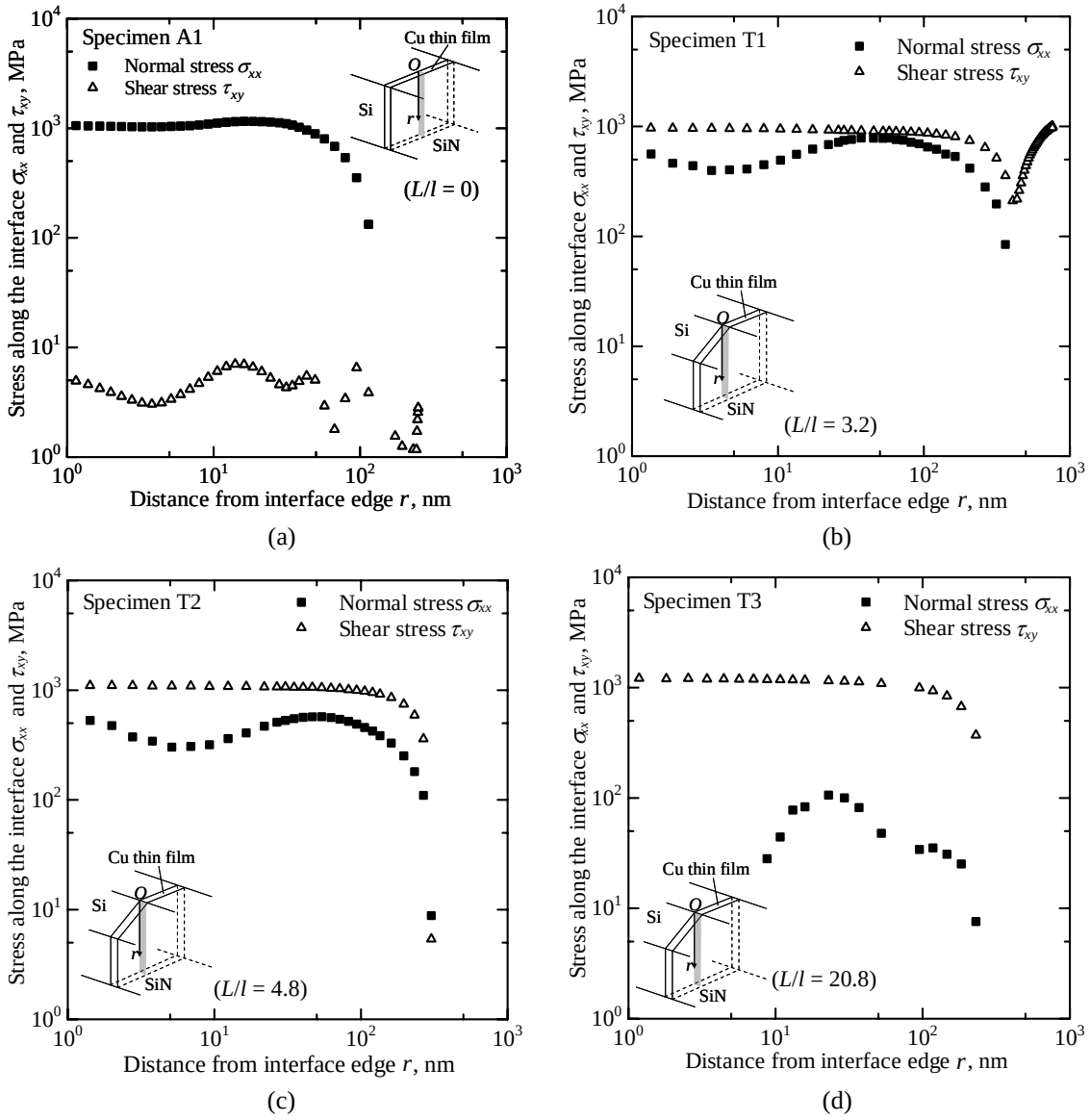

Figure 8 Critical stress distributions at crack initiation on the Cu/Si interface near the edge of (a) straight-cantilever bending specimen and (b)–(d) nano-cantilever torsion specimens.

Since both torsion and bending moments are applied to the Cu/Si interface with the nano-cantilever torsion method, the relation between the maximum shear stress and the normal stress is discussed to extract the mixed-mode fracture criterion of interfacial cracking. Here, it should be noted that the magnitude of maximum shear stress is almost same with that of τ_{xy} because of the domination of τ_{xy} for crack initiation compared with other shear stress components. On the other hand, a previous experimental study [14] revealed that the concentrated stress field of 30 nm from the edge of the Cu/Si interface dominates crack initiation at the edge of interface between the 20-nm-thick Cu layer and the Si substrate. Thus, the averages of the normal and the maximum shear stresses over the area of 30 nm away from the interface edge are used to represent the dominant stress components for

crack initiation; they are denoted by σ_{mc} and τ_{mc}, respectively. Figure 9 shows the plot of the normal stress σ_{mc} versus the maximum shear stress τ_{mc} for all four specimens (A1, T1, T2, and T3). In the straight-cantilever specimen A1, τ_{mc}/σ_{mc} is nearly zero, indicating the domination of normal stress for the crack initiation at the interface edge. In the nano-cantilever torsion specimens, *i.e.*, T1, T2, and T3, τ_{mc}/σ_{mc} is 1.6, 2.5, and 19, respectively, which shows that the crack is initiated at the interface edge with different mode mixities. By fitting the experimental results with the least-squares method, an elliptical relation that is commonly used for macroscopic materials and a circular relation between the σ_{mc} (MPa) and τ_{mc} (MPa) are obtained and respectively depicted in Eqs. (2) and (3):

$$\left(\sigma_{mC}/1106\right)^2+\left(\tau_{mC}/1129\right)^2=1 \tag{2}$$

As shown in Fig. 9, by calibrating with experimental results (circle points), the circular relation (red dash line) gives simple correspondence.

$$\sigma_{mC}{}^2+\tau_{mC}{}^2=1143^2 \tag{3}$$

This indicates that the mixed-mode fracture criterion for interfacial cracking in nanoscale components simply exhibits a circular relation between the critical normal stress and maximum shear stress.

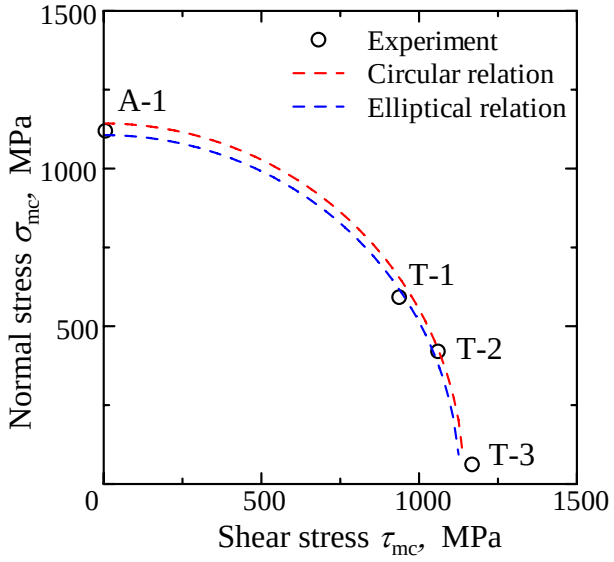

Figure 9 Critical relation of interfacial cracking under the mixed-mode.

5. Conclusions

In order to investigate the mixed-mode crack initiation due to the nanoscale stress concentration at the edge of the Cu/Si interface, we developed a methodology and conducted the fracture experiments using novel nano-cantilever torsion specimens with the interface between a 20-nm-thick Cu layer and a Si substrate. The results are summarized below:

(1). A novel nano-cantilever torsion method was developed that can apply the shear stress to the Cu/Si interface for crack initiation at the interface edge. The ratio of the critical shear stress to the normal one at crack initiation, *i.e.*, the mode mixity, could be controlled by varying the loading position. FEM analysis revealed that the concentrated stress region near the interface edge was within the scale of 100 nm in all specimens.

(2). In the nano-cantilever torsion specimens, the crack was successfully initiated from the edge of the Cu/Si interface under different ratios of the critical shear stress to the normal stress. The corresponding critical load was measured by in situ TEM observations on the cracking.

(3). The mixed-mode fracture criterion for interfacial cracking in nanoscale components is represented by a circular relation between the critical normal stress and maximum shear stress.

References

[1] D.B. Bogy, Two edge-bonded elastic wedges of different materials and wedge angles under surface tractions. J Appl Mech, 22 (1971) 377–386.
[2] E.D., Reedy, T.R. Guess, Comparison of butt tensile strength data with interface corner stress intensity factor prediction. Int J Solids Strcut, 30 (1993) 2929–2936.
[3] X.J. Fan, H.B. Wang, T.B. Lim, Investigation of the underfill delamination and cracking in flip-chip modules under temperature cyclic loading, IEEE Trans Compon Pack Technol, 24 (2001) 84–91.
[4] T. Kitamura, T. Shibutani, T. Ueno, Crack initiation at free edge of interface between thin films in advanced LSI. Engng Fract Mech, 69 (2002) 1289–1299.
[5] T. Kitamura, H. Hirakata, T. Itsuji, Effect of residual stress on delamination from interface edge between nano-films. Engng Fract Mech, 70 (2003) 2089–2101.
[6] J.W. Hutchinson, Z. Suo, Mixed mode cracking in layered materials. In: J.W. Hutchinson, T.Y. Wu (Eds), Advances in Applied Mechanics, Academic Press, Cambridge, 1992, pp. 65-187.
[7] C.T. Sun, Z.H. Jin, Fracture Mechanics, Academic Press, Oxford, 2011.
[8] M.T. Laugier, An energy approach to the adhesion of coatings using the scratch test. Thin Solid Films, 117 (1984) 243–249.
[9] J. Salem, F. Seqeda, Influence of ion bombardment and intermediate layer on the adherence of gold to oxide substrates. J Vac Sci Technol, 18 (1981) 149–152.
[10] A.J. Kinloch, C.C. Lau, J.G. Williams, The peeling of flexible laminates. Int J Fract, 66 (1994) 45–70.
[11] Q. Ma, H. Fujimoto, P. Flinn, V. Jain, F. Adibi-Rizi, F. Moghadam, et al. Quantitative measurement of interface fracture energy in multi-layer thin film structures. In: Materials research society symposium proceeding, 391 (1995) 91–96.
[12] H. Hirakata, Y. Takahashi, D.V. Truong, T. Kitamura, Role of plasticity on interface crack initiation from a free edge and propagation in nano-component. Int J Fract, 145 (2007) 261–271.
[13] T. Sumigawa, T. Shishido, T. Murakami, T. Iwasaki, T. Kitamura, Evaluation on plastic deformation property of copper nano-film by nano-scale cantilever specimen. Thin solid films, 518 (2010) 6040–6047.
[14] T. Sumigawa, T. Shishido, T. Murakami, T. Kitamura, Interface crack initiation due to nano-scale stress concentration. Mat Sci Engng A-Struct, 527 (2010) 4796–4803.
[15] W.D. Nix, Mechanical properties of thin films. Metall Mater Trans, 20 (1989) 2217–2245.
[16] K.S. Lee, S. Wuttiphan, X.Z. Hu, S.K. Lee, B.R. Lawn, Contact-induced transverse fractures in brittle layers on soft substrates: a study on silicon nitride bilayers. J Am Ceram Soc, 81 (1998) 571–580.

Fracture toughness and toughening mechanisms of unsaturated polyester-based clay nanocomposites

Mushtaq T. Albdiry[1 *], Belal F. Yousif[1], and Harry Ku[1]

[1]**Centre of Excellence in Engineered Fibre Composites (CEEFC), Faculty of Engineering and Surveying, University of Southern Queensland, Toowoomba 4350, QLD, Australia.**

Mushtaq.Albdiry@usq.edu.au

Abstract

In this study, the role of nanoclay particles (MMT) on the micro- and nano-scale deformation and fracture behaviour of a crosslink unsaturated polyester (UPE)-based nanocomposites is presented. Nanocomposites from well-dispersed MMT and UPE are prepared by a combination of mechanical stirrer and ultrasonication process. Fracture toughness represented by critical stress intensity factor (K_{Ic}) based on linear elastic fracture mechanics (LEFM) and compact tension (CT) configuration is evaluated. Morphological characteristics for all nanocomposites are examined by using TEM, and the fracture surface and the toughening mechanisms of materials are identified by SEM analysis. The morphological characterization showed an intercalation/ partially exfoliation structure of UPE/MMT nanocomposite with a moderate enhancement in fracture toughness in nanocomposite. The UPE/ 3 wt. % clay nanocomposite had the highest K_{Ic} by a 61 % improvement over the neat UPE. The incorporation of clay nanofiller into the crosslink UPE demonstrated a shift in toughening mechanism from a highly brittle fracture for the UPE into shear bands and particles' debonding and decohesion for nanocomposites.

Keywords fracture toughness; toughening mechanisms; unsaturated polyester; clay nanocomposites.

1. Introduction

In general, polymer-clay nanocomposites (PCNs) properties are directly dependent on the state of nanoparticles dispersion in the polymeric matrix, whether it is immiscible, intercalated or exfoliated nanocomposites [1-3]. The exfoliated/intercalated nanostructure and the strong interaction between clay nanolayers and polymer chains play a role in constraining the mobility of polymer matrix and delay the crack initiation and propagation and consequently induce reasonable mechanical strength and toughness [4, 5]. Fracture toughness is a critical mechanical property which characterizes the resistance of a material to crack propagation or to fracture. The toughness of materials is directly dependent on the energy dissipation, or on the energy absorbed in fracturing the part.

Unsaturated thermoset polyester resin (UPE) is one of the most used thermosetting polymers in different industrial applications due to its good mechanical properties and low cost and density [6]. However, the brittleness of this class of materials because of a radical polymerisation process between unsaturated prepolymer and styrene is one of their major drawbacks [7]. Hence numerous studies have been done on the introduction of second phase particles in them in order to control the toughness of thermoset polymers. For instance, Evora et al. [8] embedded small loadings of TiO_2 nanoparticles in the unsaturated polyester resin. The presence of the particles had the greatest effect on fracture toughness and tensile strength. Baskaran et al. [9] found that the fracture toughness of UPE resin has improved when 5 wt. % of Alumina (Al_2O_3) particles was added. Moreover, the investigation of the fracture behaviour and toughening mechanisms were done on the introduction

of multiwall carbon nanotubes in unsaturated polyester [10, 11], and halloysite nanotubes (HNTs) in epoxy [12]. It was found that the use of nanopatricles with polymers are effectively increased their fracture toughness without sacrificing other properties such as strength, modulus and glass transition temperature.

As a result of the abovementioned works, several toughening mechanisms have been observed in polymers filled by micro- and nano-particles such as multiple craze-like banding with dilatation (dilation) [13]. Crack-pinning mechanism while the crack front bows out between the filler particles and remains pinned at the particles [14]. Microcracking mechanism is another mechanism in which the toughness increases due to the incorporation of rubber or nano-scale particles into polymers [7]. Localized shear yielding (or shear banding) mechanism which is a narrow zone of intense shearing strain forming due to a material instability i.e. corresponding to an abrupt loss of homogeneity of deformation. However, increase in tendency to shear yield in nanocomposites may cause an increase in energy absorption prior to fracture [15]. Also, there is a massive shear-banding mechanism which occurs due to the reduction in yield stress by the stress concentration of the compliant nano-scale or rubber particles that facilitate shear yielding. Additionally, particle bridging (rigid particles) mechanism in which a rigid or ductile particle plays as a bridging particle that applies compressive traction in the crack wake and the ductile particle deforms plastically in the material surrounding the crack tip, which provides additional crack shielding. The particle bridging provides most of the improvements in toughness since it remain intact for some distance behind the crack-front [16]. In this study, the attempt is made to investigate the relationship between well-dispersed structure nanocomposites and the fracture behaviour of unsaturated polyester (UPE), and to understand to what extent clay particles can inhabit crack initiation, crack growth, and then enhance the fracture toughness of the networked UPE.

2. Experimental setup

2.1 Materials and nanocomposites preparation

Organoclay platelets (MMT, Cloisite® 30B, provided by Southern Clay Products, Inc. via Jim Chambers & Associates, Australia) were introduced into unsaturated polyester resin (UPE, AROPOL®-1472PLSE, Nupol, Australia having 45 % styrene) at different amounts (1, 3, 5, 7, and 9 wt. %). Nanocomposites from MMT/UPE were prepared by means of high shear mixing followed by sonication (agitation) to drive the air bubbles off. After mixing, the catalyst Methyl Ethyl Ketone Peroxide (MEKP/Butanox-M50) was added to the mixture at 2 % of UPE weight and stirred manually for 1 min as per the instructions of the supplied company. Later, the mixture was poured in a special plastic moulds having the fracture specimens geometry, and cured at room temperature for 24 h and post cured at 60°C for 2h followed by 90°C for 2h following an increment rate of 10°C/30 min.

2.2 Morphological characterization

Transmission electron microscope (TEM) was used to observe the dispersion of clay layers in the UPE polymer resin. Ultra-thin sections of approximately 70 nm in thickness were cut by diamond knife from the nanocomposites at room temperature and examined using a JEOL (JEM-1010) TEM instrument at an acceleration voltage of 100KV. Scanning Electron Microscope (SEM, Philip XL-30)

was utilized to identify the failure modes and toughening mechanism. SEM observations were carried out on the fracture surfaces of compact tension fracture specimens after sputter coating with a thin layer of platinum to increase electric conductivity.

2.3 Fracture mechanisms study

The stress intensity factor (K_{Ic}) and the strain energy release rate (G_{Ic}) of the cured neat UPE and the UPE/nanocomposites were evaluated using the compact tension (CT) configurations. The CT fracture specimens were prepared according to ASTM D5045 as shown in **Fig. 1**. A pre-crack was generated by tapping a fresh razor blade into the notch tip with a drop weight to maintain an accurate K_{Ic} values. 5 mm/min is adapted as loading rate and the following relationships are used to measure the K_{Ic}:

$$K_{Ic} = \frac{P_Q}{BW^{1/2}} \cdot f\left(\frac{a}{W}\right) \tag{1}$$

$$f\left(\frac{a}{W}\right) = \frac{\left(2+\frac{a}{W}\right)\left\{0.886+4.64\left(\frac{a}{W}\right)-13.32\left(\frac{a}{W}\right)^2+14.72\left(\frac{a}{W}\right)^3-5.6\left(\frac{a}{W}\right)^4\right\}}{\left(1-\frac{a}{W}\right)^{3/2}} \tag{2}$$

Where P_Q is the load determined from the load-displacement curve, B the specimen thickness. The calculated K_{Ic} values were checked against: B, a, (W-a) > 2.5 $(K_{Ic}/\sigma_y)^2$ (3)

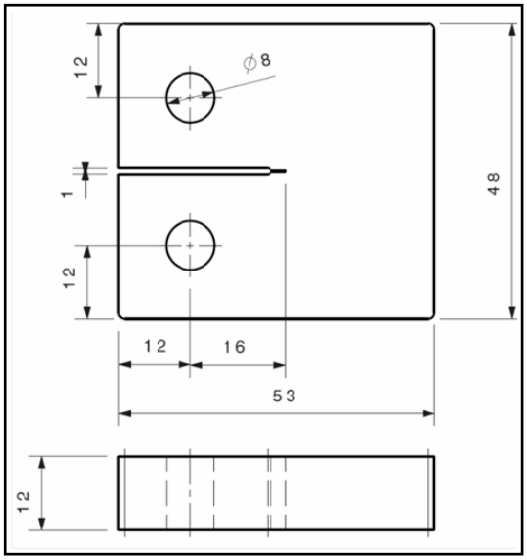

Fig.1 Dimension of the compact tension (CT) specimen.

3. Results and discussion

3.1 Morphology

Fig. 2 shows representative TEM micrographs of the cured unsaturated polyester (UPE) filled by different nanoclay loadings. From the figure, it can be noticed that a good dispersion of clay layers in the polymeric matrix with a plausible intercalation between nanoclay and the polymer chains has achieved by using direct high shear mixing and sonication. However, several agglomerates of micro-particles with thickness of 100 nm or greater are created at higher nanoclay loadings can also

be seen in **Fig. 2c**. The appearance of these clusters are attributed to the structure of clay that composed of platelets with an inner octahedral layer surrounded by two silicate tetrahedral layers and because of the natural state of clay which exists as stacks of many platelets at several hundred nanometres long and wide separated by an interlayer distance of ~1-3 nm [5, 17].

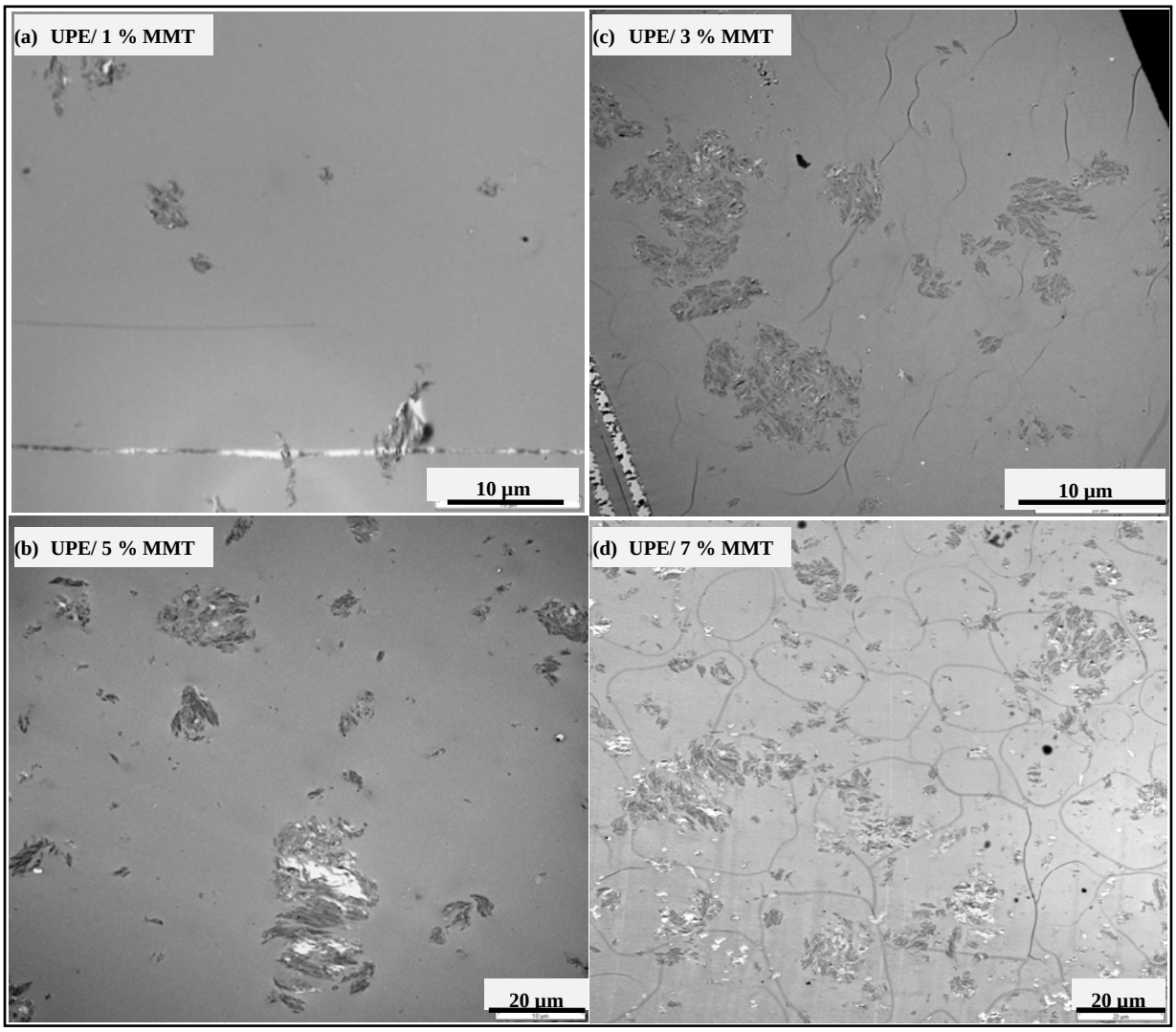

Fig. 2 TEM photomicrographs of UPE filled by different clay nanocomposites.

3.2 Fracture toughness and mechanism

Fig. 3 shows a set of typical load-crack opening displacement (COD) curves obtained from the CT fracture tests for the cured neat unsaturated polyester (UPE) and UPE filled by different contents of 3 wt. % and 5 wt clay nanocomposites. It can be found that all samples have undergone unstable crack propagation with s straight line when the maximum load is reached due to the high crosslink density of the UPE and its prone to fast fracture. Meanwhile, the UPE- based 3 wt. % MMT nanocomposites manifested their ability to carry higher loads with lesser displacements (COD) whereas the addition of 5 wt % MMT showed lower loads with higher displacements compared to the neat UPE resin.

The fracture toughness values (K_{Ic}) versus different clay loadings (1-9 wt. %) with respect to the

neat resin value were illustrated in **Fig. 4**. The magnitudes of K_{Ic} of the modified UPE have modestly improved after nanoclay platelets were incorporated where the introduction of 3 wt % MMT content showed the highest K_{Ic} value by 61% higher than the neat UPE. However, these values have decreased at higher nanofiller contents due to the appearance of clay aggregates and the weak interaction between clay layers and polymer resin thereof with the increase of clay contents. These results are in conformance with these reported in the literature [18]. A comparison of different studies where K_{Ic} values have been obtained is addressed in **Table 1.** From the table, it can be noted that the incorporation of even low levels of nanoparticle into unsaturated polyester resin resulted in noticeable changes in fracture toughness of the produced materials over the neat resin due to the presence of nanoparticles.

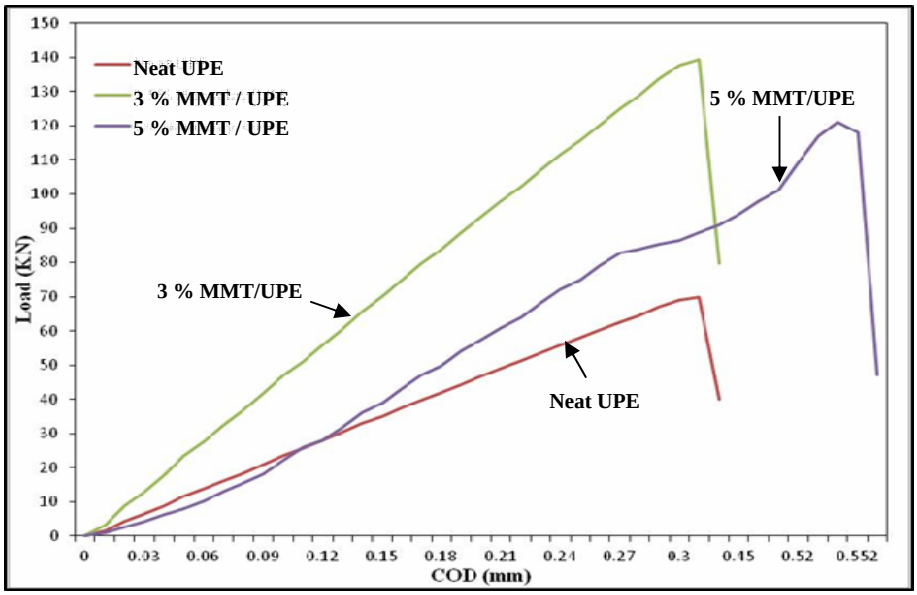

Fig. 3 Typical load vs. crack opening displacement (COD) curves.

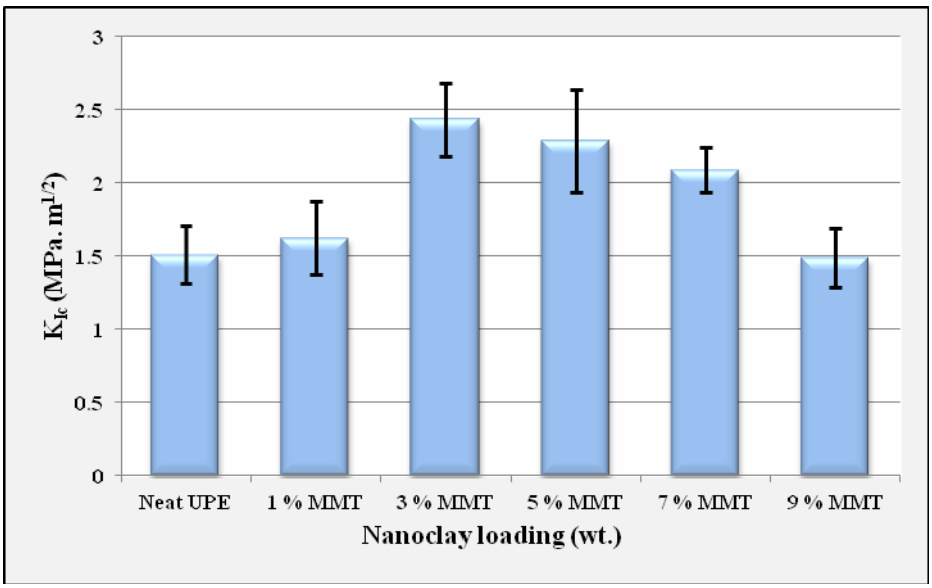

Fig. 4 Fracture toughness of the neat UPE and the UPE/MMT nanocomposites

Table 1 Fracture toughness for different nanoparticles-filled unsaturated polyester (UPE)

Materials	**K_{IC} (MPa $m^{1/2}$) {test specimen type }**	**Comments and Reference**
UPE/ 3 wt. % MMT	2.435 [1.51: Neat UPE] {CT}	The current study
UPE/ 1 wt.% TiO_2	0.85 [0.5: Neat UPE] {SENB}	Direct ultrasonification method, [8]
UPE / 40 % Bamboo fibre	1.2 [0.5: Neat UPE] {CT}	Laminating lay-up process, [19]
UPE / 1 wt. % Alumina	1.42 [1: Neat UPE] {SENB}	Prepared using direct mixing approach, [20]

CT: Compact tension, SENB: Single-edge notched bending,

The fracture modes and toughening mechanisms in the thermosetting unsaturated polyester (UPE) toughened by clay nanomaterials ruptured at ambient temperature are identified by using SEM analysis as shown in **Fig. 5.** The SEM micrograph (**Fig. 5a**) showed the failure mechanism of the fracture surface of the neat UPE is a highly brittle failure mode without crazing. However, the introduction of clay particles into the networked UPE resin associated with better absorbing of energy, leading to localized shear yielding. Similarly, the authors in [21] referred to the appearance of isolated shear bands as an energy absorption mechanism accompanied with better plastic deformation in the failure mode of polymer having a second phase. Furthermore, the addition of nanofiller into the UPE resin resulted in particle pinning of the crack (**Fig. 5c**) leaving behind tail-like structure. SEM image (**Fig. 5d**) of the fracture surface of UPE-5 wt. % clay nanocomposite depicts various crack propagation directions on the cleavage surface. The direction of crack advancement is from top to bottom with an irregular curved path. Further clay nanoparticles (> 5 wt. % MMT) incorporation into the crosslink UPE resin accompanied with mixed failure mechanism represented by cleavage and void-coalescence as shown in **Fig. 5 e and f**.

Additionally, in order to fully understand the nano-effect of clay particles on the fracture surface of UPE/clay nanocomposite, SEM images with different magnifications (**Fig. 6**) for the fracture surface of UPE- 3 wt % MMT nanocomposite were taken. This sample was chosen because of its relative higher fracture toughness. **Fig. 6a** illustrates the fracture topography at low magnification, showing the crack-initiation and crack-propagation zones. Another SEM view (**Fig. 6b**) at low magnification, showing the first zone of crack growth (zone 2A), in which the formation of microcracks can be noted. The tearing of the connected material (the particle-matrix interface) and decohesion occurred at the weakest locations in zone 2A (**Fig. 6c**) [22]. Comparatively, zone 2B (**Fig. 6d and e**), showing a similar flat cleavage along the fracture planes. The intergranular fracture mechanism or decohesion can also be observed in zone 2c (**Fig. 6f**).

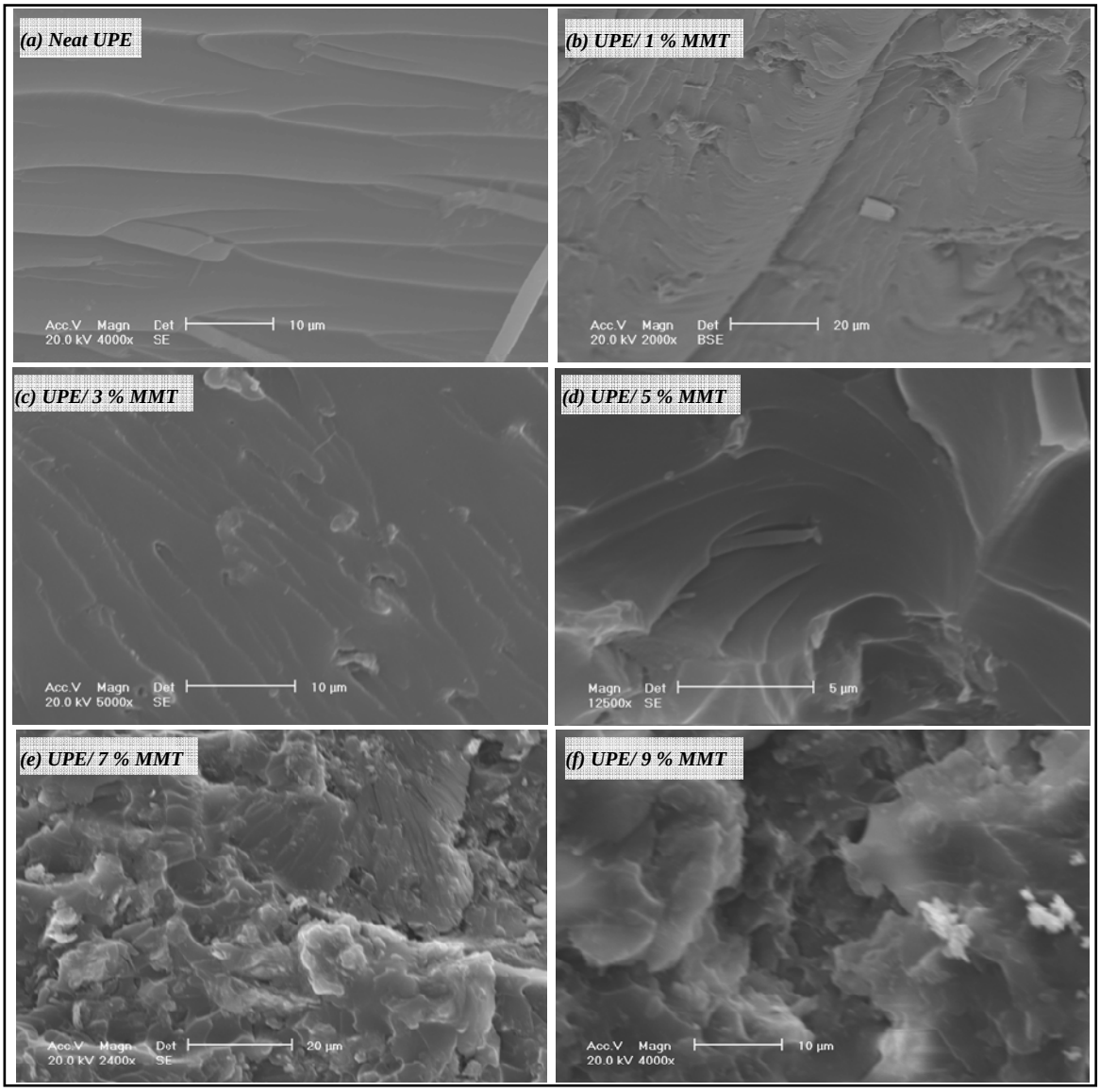

Fig. 5 SEM micrographs showing the failure mechanisms of the fracture surface obtained from the compact tension specimens of the neat UPE and the UPE-filled by different clay nanocomposites.

Conclusion

The nano-effect of clay nanoparticles on the fracture toughness and toughening mechanisms of fully crosslink thermoset unsaturated polyester (UPE) was experimentally investigated in this study. The morphological characterization was described by using TEM examination and the failure modes of the fracture surfaces of compact tension samples ruptured at room temperature was also identified by using SEM analysis. An intercalation structure with a uniform dispersion of UPE/clay nanocomposites prepared by direct high shear mixing and sonication process were observed. The incorporation of MMT into UPE resin induced higher fracture toughness where nanocomposites containing UPE and 3 wt. % MMT showed a higher stress intensity factor (K_{Ic}) by a 61 % increase over the neat UPE. The role of nanofiller on the deformation mechanism demonstrated a shift from

highly brittle fracture mode without crazing for the neat UPE into shear yielding deformation mechanism with plausible energy absorption for nanocomposites.

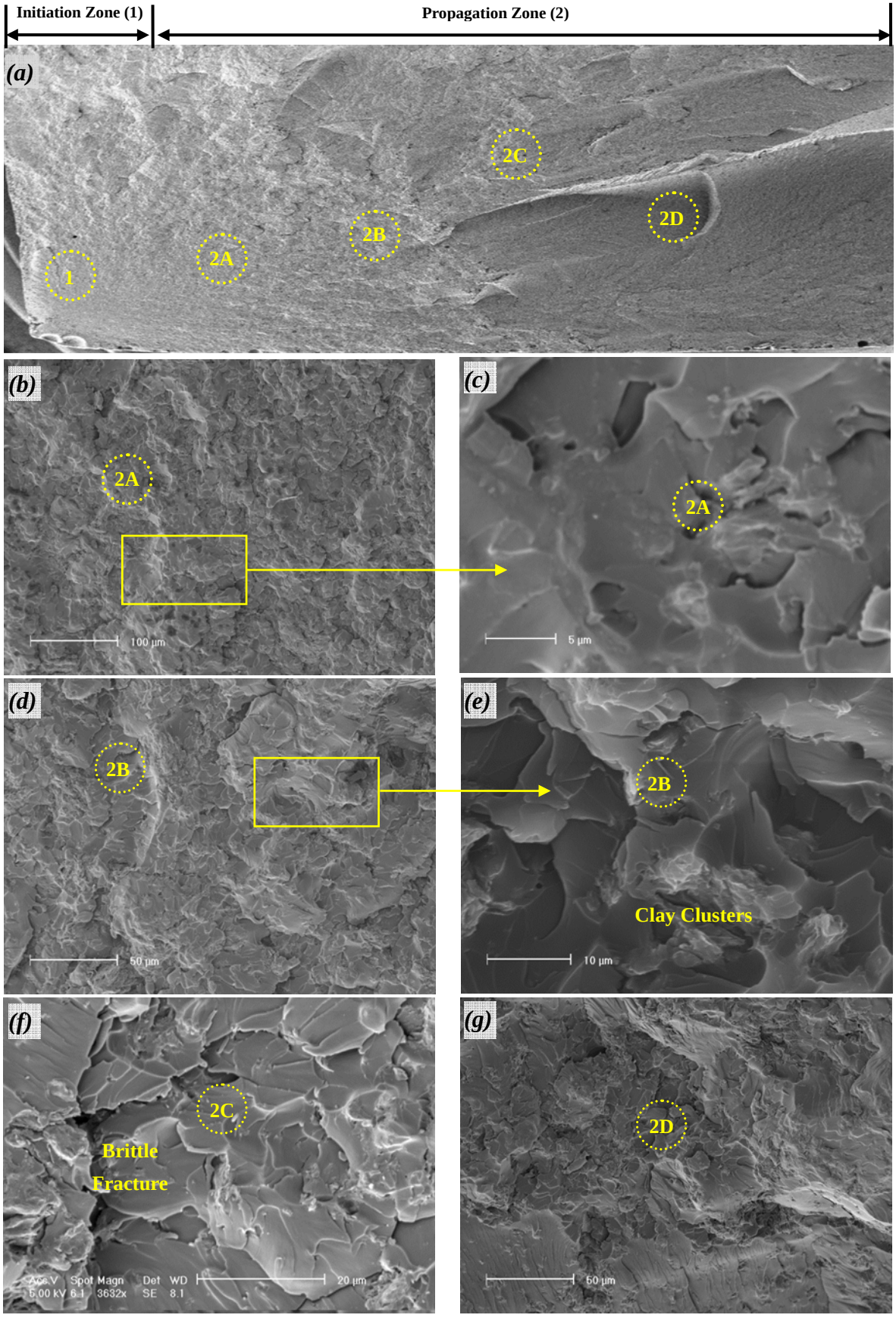

Fig. 6 SEM micrographs of the fracture surface of UPE-3 wt. % clay nanocomposites ruptured at room temperature showing initiation and different crack propagation zones.

References

[1] Chinellato AC, Vidotti SE, Hu G-H, Pessan LA. Compatibilizing effect of acrylic acid modified polypropylene on the morphology and permeability properties of polypropylene/organoclay nanocomposites. Composites Science and Technology 2010; 70 : 458–65.

[2] Utracki LA. Clay-Containing Polymeric Nanocomposites. Shrewsbury, GBR: Smithers Rapra, 2004.

[3] Koo JH. Polymer Nanocomposites Processing, Characterization, and Applications. OH, USA : McGraw-Hill Professional Publishing, ; 2006.

[4] Albdiry M, Yousif B, Ku H, Lau K. A critical review on the manufacturing processes in relation to the properties of nanoclay / polymer composites. J Compos Mater. 2012; In press, DOI: 10.1177/0021998312445592: 1-23.

[5] Okamoto M. Polymer/Layered Silicate Nanocomposites 2003.

[6] Pascault J-P, Sautereau H, Verdu J, Williams RJ. Thermosetting Polymer. New York: Marcel Dekker, Inc.; 2002.

[7] Arends CB. Polymer Toughening. New York: Marcel Dekker Inc.; 1996.

[8] Evora VMF, Shukla A. Fabrication, characterization, and dynamic behavior of polyester/TiO2 nanocomposites. Materials Science and Engineering A 2003;361:358–66.

[9] Baskaran R, Sarojadevi M, Vijayakumar CT. Unsaturated polyester nanocomposites filled with nano alumina. J Mater Sci 2011;46:4864–71.

[10] Vera-Agullo J, Glória-Pereira A, Varela-Rizo H, Gonzalez JL, Martin-Gullon I. Comparative study of the dispersion and functional properties of multiwall carbon nanotubes and helical-ribbon carbon nanofibers in polyester nanocomposites. Composites Science and Technology 2009;69:1521–32.

[11] Seyhan AT, Tanoglu M, Schulte K. Tensile mechanical behavior and fracture toughness of MWCNT and DWCNT modified vinyl-ester/polyester hybrid nanocomposites produced by 3-roll milling. Materials Science and Engineering A 2009; 523 : 85–92.

[12] Deng S, Zhang J, Ye L, Wu J. Toughening epoxies with halloysite nanotubes. Polymer. 2008; 49: 5119–27.

[13] Cotterell B, Chia JYH, Hbaieb K. Fracture mechanisms and fracture toughness in semicrystalline polymer nanocomposites. Engineering Fracture Mechanics. 2007;74:1054-78.

[14] Zhao Q, Hoa SV. Toughening Mechanism of Epoxy Resins with Micro/Nano Particles. J Compos Mater. 2007; 41(2) : 201-19.

[15] Akbari B, Bagheri R. Deformation mechanism of epoxy/clay nanocomposite. Eur Polym J. 2007; 43.

[16] Peters ST. Handbook of Composites. England. : Chapman & Hall, Cambridge University Press, ; 1998

[17] Krishnamoorti R, Vaia RA. Polymer Nanocomposites Synthesis, Characterization, and Modeling. ACS Symposium Series 804. Washington, DC, USA: American Chemical Society; 2002.

[18] Quaresimin M, Salviato M, Zappalorto M. Fracture and interlaminar properties of clay-modified epoxies and their glass reinforced laminates. Engineering Fracture Mechanics. 2012;81:80-93.

[19] Wong KJ, Zahi S, Low KO, Lim CC. Fracture characterisation of short bamboo fibre reinforced polyester composites. Materials and Design 2010;31:4147–54.

[20] Zhang M, Singh RP. Mechanical reinforcement of unsaturated polyester by AL2O3 nanoparticles. Materials Letters 2004;58:408– 12.

[21] Srivastava I, Koratkar N. Fatigue and Fracture Toughness of Epoxy Nanocomposites. JOM. 2010; 62(2).

[22] Brooks CR, Choudhury A. Failure Analysis Engineering Materials. New York: McGraw-Hill Companies Inc.; 2002.

Interlaminar Fracture Toughness and Fatigue Delamination Growth of CF/EP Composites with Matrices Modified by Nano-silica and CTBN rubber

Jianing Zhang[1], Shiqiang Deng[1], Lin Ye[1,*] Zhong Zhang[2]

[1] Center for Advanced Materials Technology, School of Aerospace, Mechanical and Mechatronic Engineering, The University of Sydney, NSW 2006, Australia
[2] National Centre for Nanoscience and Technology,100190 Beijing, PR China
* Corresponding author: lin.ye@sydney.edu.au

Abstract Experimental investigations were conducted to characterize mode I interlaminar fracture and fatigue delamination growth behaviors of carbon fiber-reinforced epoxy (CF/EP) laminates with modified epoxy matrices using nano-silica particles, a reactive CTBN liquid rubber and a hybrid of nano-silica particles and CTBN liquid rubber. The CF/EP composites were fabricated using unidirectional carbon fibre and a DGEBA epoxy by means of a vacuum resin infusion technique. The mode I interlaminar fracture toughness (G_{IC}) of the CF/EP laminates was increased significantly after the additives were incorporated in the matrices, especially for the laminates containing the hybrid particles of nano-silica and CTBN liquid rubber. Furthermore, nano-silica and CTBN liquid rubber were also found to effectively improve the fatigue performance of the CF/EP laminates by noticeably decreasing the fatigue crack propagation rates, particularly for the laminate with the matrices modified by the hybrid of nano-silica and CTBN liquid rubber. The results confirm that the enhancement in the fracture toughness due to the incorporation of the nanoparticles to the epoxy matrices has been partially transferred into the improvement of the interlaminar fracture resistance of the CF/EP composites, under both static and cyclic loadings.

Keywords Interlaminar fracture, fatigue delamination growth, nano-silica, CTBN liquid rubber

1. Introduction

Interlaminar fracture toughness and delamination growth resistance play a major role in determining long-term service life of carbon fibre-reinforced epoxy (CF/EP) composite structures. A large number of research efforts have been carried out to improve interlaminar properties of CF/EP composite laminates, including the use of toughened matrices, stitching, Z-pining, etc [1-7]. Toughened epoxy matrices can normally result in high interlaminar fracture toughness and delamination growth resistance [8-11]. Recently, nano-sized silica particles produced by a sol-gel process and CTBN liquid rubber have been reported to significantly increase the toughness of epoxies and also the mode I interlaminar fracture toughness for carbon fiber reinforced epoxy composites [12]. As a result of the unique combination of the additives, the hybrid epoxy matrices may also improve the interlaminar fatigue crack growth resistance of CF/EP composites.

The present paper presents the experimental results of a study in exploring the role of silica nano-particles and CTBN liquid rubber in the epoxy matrices of CF/EP composites. Mode I interlaminar fracture toughness and fatigue delamination growth rate are evaluated and possible mechanisms are discussed.

2. Experimental

2.1. Materials

A DGEBA epoxy (Araldite-F, Huntsman) was used for the study. Piperidine was used as hardener for curing the epoxy. The modifiers for the epoxy were a SiO_2 nano-particle dispersed epoxy (Nanopox XP, Nanoresins, Germany) and a CTBN liquid rubber (Hycar CTBN 1300X13). Nanopox

XP consists of surface-modified silica nano-particles (40 wt%) with an average particle size of 20nm. T300 unidirectional carbon fibre fabrics (FGI Fibre Glass International, Australia) were used.

2.2. Fabrication of CF/EP composites

The CF/EP composites were fabricated from the unidirectional carbon fibre fabric using a vacuum assisted resin infusion molding (VARIM) process. Neat epoxy and modified epoxies with 10 wt% silica nano-particles and/or 10 wt% rubber were premixed at 80^{o}C and later used in VARIM. Piperidine was added at a ratio of 5:100 (hardener/epoxy) in weight. The laminates consisted of 20 unidirectional carbon fiber layers. A polyimide thin film (50 μm in thickness and 120 mm in length) was inserted between the 10th and 11th layers at one end of the laminate, to serve as a "pre-crack" for the interlaminar fracture tests. Two loading blocks of 20 mm in width were bonded to up and bottom sides of one end of the specimen for load applying.

2.3. Mechanical tests

Double cantilever beam (DCB) specimens (dimensions of 20 mm in width, 240 mm in length, 4 mm in thickness and 50 mm in initial "pre-crack" length) were prepared for the interlaminar fracture tests of the laminates under static and fatigue loadings. For static testing on an Instron 5567 universal testing machine, a displacement rate of 1 mm/min was used. Mode I interlaminar fracture toughness (G_{IC}) of unidirectional CF/EP composites was determined by the Modified Beam Theory (MBT) Method, according to ASTM D5528,

$$G_{IC} = \frac{3P\delta}{2b(a+|\Delta|)} \tag{1}$$

Where b is the specimen width, P is the applied load, δ is the displacement of the load-point and $|\Delta|$ is the modification of actually measured crack length a. Two values of G_{IC} were defined, namely G_{IC} (init.), at the point when the delamination was observed visually to propagate from the pre-crack tip, and G_{IC} (prop.), the plateau value of the resistance curve (R-curve).
The fatigue tests were carried out on an MTS-810 servo-hydraulic machine in reference to ASTM D6115 to measure the interlaminar delamination growth rate. During fatigue testing, the displacement ratio (R) of the minimum to the maximum displacements was kept constant (R = 0.1), and a cyclic frequency of 1 Hz was adopted. At least 3 specimens were tested for each group starting from the maximum cyclic strain energy release rate at the peak of displacement cycle being 60% of mode I interlaminar fracture toughness measured from quasi-static tests of the corresponding CF/EP laminates. The maximum cyclic strain energy release rate can be calculated from:

$$G_{\mathrm{Im}ax} = \frac{3P_{\max}\delta_{\max}}{2b\left(a+|\Delta|_{av}\right)} \tag{2}$$

Where $P_{\max}$ is the maximum cyclic load, $\delta_{\max}$ is the maximum value of cyclic displacement, $|\Delta|_{av}$ is the average value of $|\Delta|$ from static tests. The crack length was determined by visual observation during the crack propagation. The corresponding number, N, of fatigue cycles required to generate delamination growth in the CF/EP laminates were recorded during the fatigue tests, thus allowing the crack growth rate, da/dN, to be calculated.

3. Results and discussion

3.1. Interlaminar fracture toughness

Typical curves of mode I interlaminar growth resistance as a function of crack length (R-curves) under static loading are shown in Figure 1 for CF/EP laiminates with unmodified and modified matrices. The corresponding mode I interlaminar fracture properties are shown in Table 1. It can be seen that both G_{IC} (init.) and G_{IC} (prop.) increased after the epoxy matrix was modified. The presence of 10 wt% nano-silica particles or 10 wt% CTBN rubber, showed a significant effect on the interlaminar fracture toughness, leading to increases in both G_{IC}(init.) and G_{IC}(prop.). The combined use of the nano-silica particles and the CTBN rubber with the epoxy, to form a "hybrid" epoxy matrix, gives a further enhancement to the fracture toughness, with the maximum values of 649 J/m^2 for G_{IC} (init.) and 1323 J/m^2 for G_{IC} (prop.) being recorded.

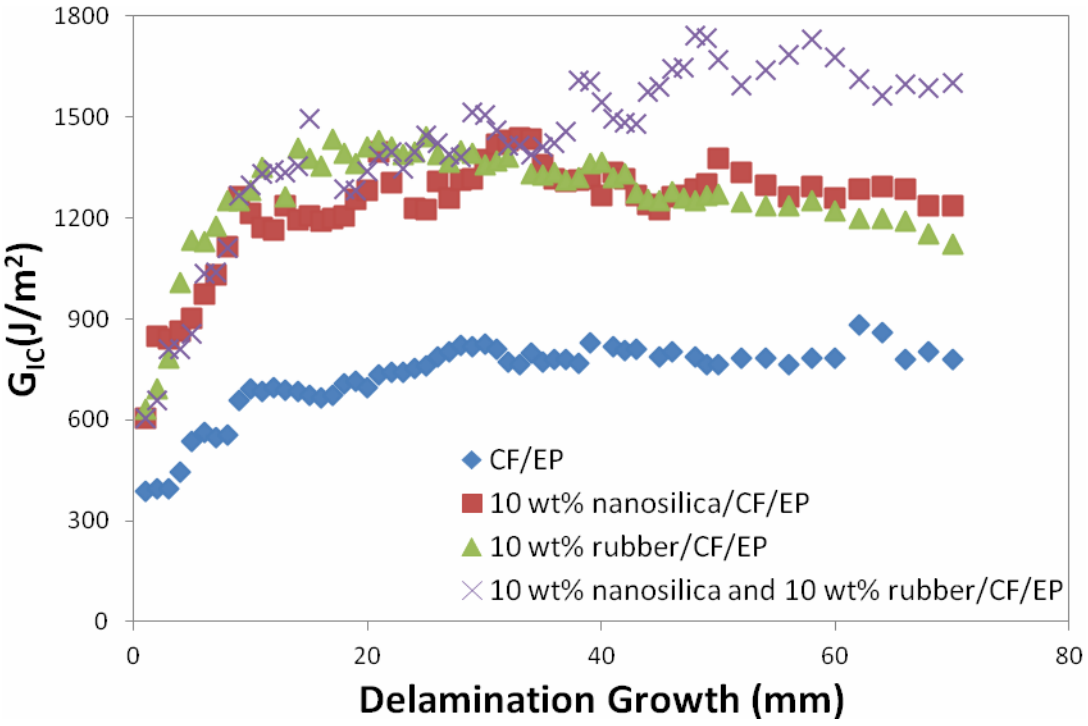

Figure 1 Typical R-curves for mode I interlaminar fracture of CF/EP laminates

Table 1. Mode I interlaminar fracture properties of CF/EP laminates

Laminates	G_{IC} (init.)[J/m^2]	G_{IC}(prop.)[J/m^2]
CF/EP	389±20	741±70
10 wt% nano-silica/CF/EP	602±4	1130±93
10 wt% rubber/CF/EP	629±31	1256±37
10 wt% nano-silica and 10 wt% rubber/CF/EP	649±112	1323±101

3.2. Fatigue delamination resistance

The crack growth rate (da/dN) versus delamination length curves are shown in Figure 2 for CF/EP laminates with unmodified and modified matrices. The results show that the fatigue delamination resistance in composite laminates with the matrix modified by nano-silica, CTBN rubber and the hybrid of these additives was greatly improved. Generally, the rate of delamination propagation was initially high and then decreased as the delamination growth because of reduced strain energy release rate under the constant peak displacement. In particular, the CF/EP composite laminate with the matrix modified by the hybrid of 10wt% nano-silica and 10 wt% rubber have the slowest delamination growth rate, being about almost two orders lower than that of the laminates with the neat epoxy at the early stage of delamination growth.

As shown in Figure 3, the da/dN-G_{Imax} curve characterized the relationship between delamination growth rates and the maximum delamination energy (G_{Imax}) used for different group of CF/EP laminate specimens. It can be seen that the plots for the four groups of CF/EP laminates show the same trend, i.e., a high growth rate corresponds to a high G_{Imax}. Furthermore, it requires higher G_{Imax} for the same delamination growth rate for the CF/EP laminates with modified matrices. Particularly, the CF/EP laminate with the matrix modified by the hybrid of 10 wt% nano-silica and 10 wt% rubber, requires the highest G_{Imax} for the same delamination growth rate, compared with other three groups of CF/EP laminates without modification, with 10 wt% nano-silica or 10 wt% rubber, respectively.

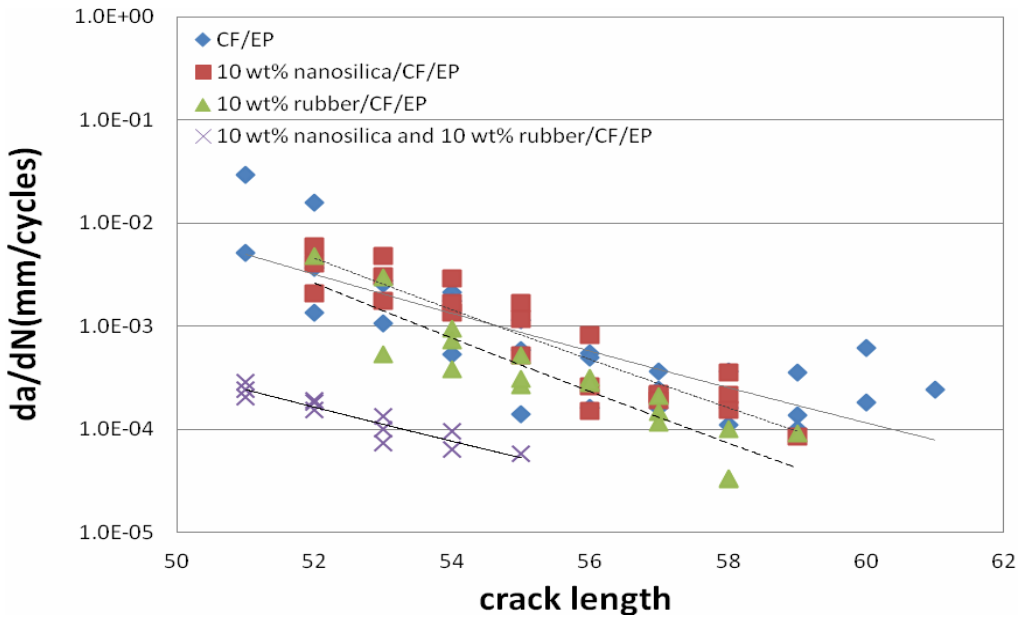

Figure 2 Propagation rate versus delamination length under cyclic fatigue for the CF/EP laminates

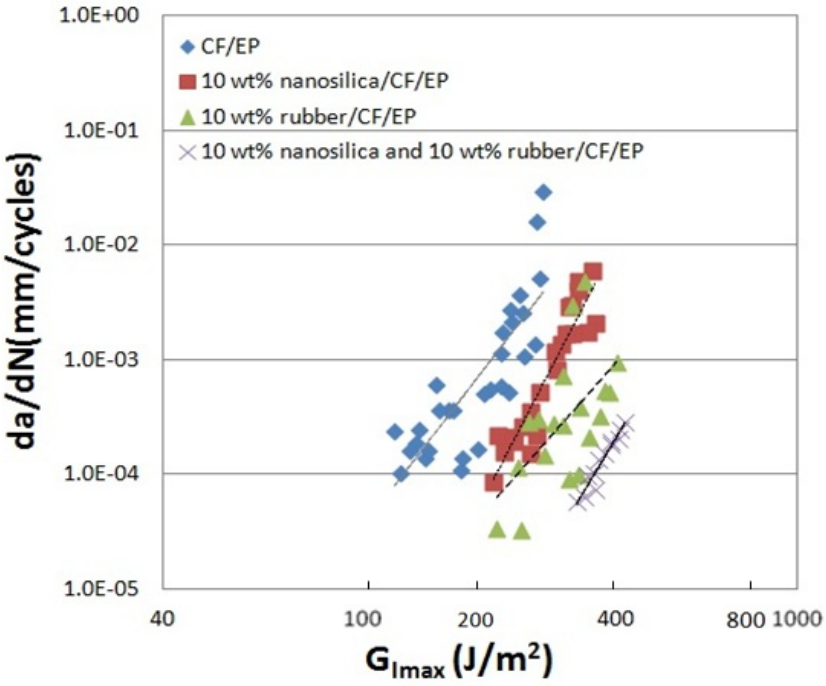

Figure 3 Propagation rate versus G_{Imax} under cyclic fatigue for the CF/EP laminates

SEM photographs in Figure 4 show the morphology of fracture surfaces in the initial region of crack growth for the fatigue delamination growth in CF/EP laminates. For the neat epoxy laminate, in Figure 4 (a), exposed fibres can be seen being completely stripped of matrix resin, indicating an interfacial failure in the unmodified CF/EP laminate. However, more matrix resin remains on the exposed fibre surfaces in the 10 wt% nano-silica modified CF/EP laminate, in Figure 4 (b), showing better adhesion at fibre-matrix interface. The same phenomenon were also reported by Tang et al [9], who investigated mode I and II interlaminar fracture toughness in CF/EP laminated modified with nano-silica particles under static loading. The increasing fatigue delamination resistance for 10 wt % nano-silica CF/EP laminates can be attributed to the toughening mechanisms in the matrix induced by nano-silica ahead of delamination tip. It was observed that the plastic void growth around the nano-silica particles makes a contribution to the fracture energy of the epoxy modified by nano-silica during the delamination propagation, reported by Hsieh et al [12]. Enhanced plastic deformation can also be observed for the matrix modified with 10 wt% rubber, as shown in Figure 4(c), indicating shear flow of the matrix resin due to the increased ductility. The hybrid matrix containing both 10 wt% nano-silica and 10 wt% rubber presented a rougher matrix surface that may be resulted from a synergistic effect of plastic void growth and shear yielding mechanisms, which correlates well with the highest delamination growth resistance under both static and cyclic loading.

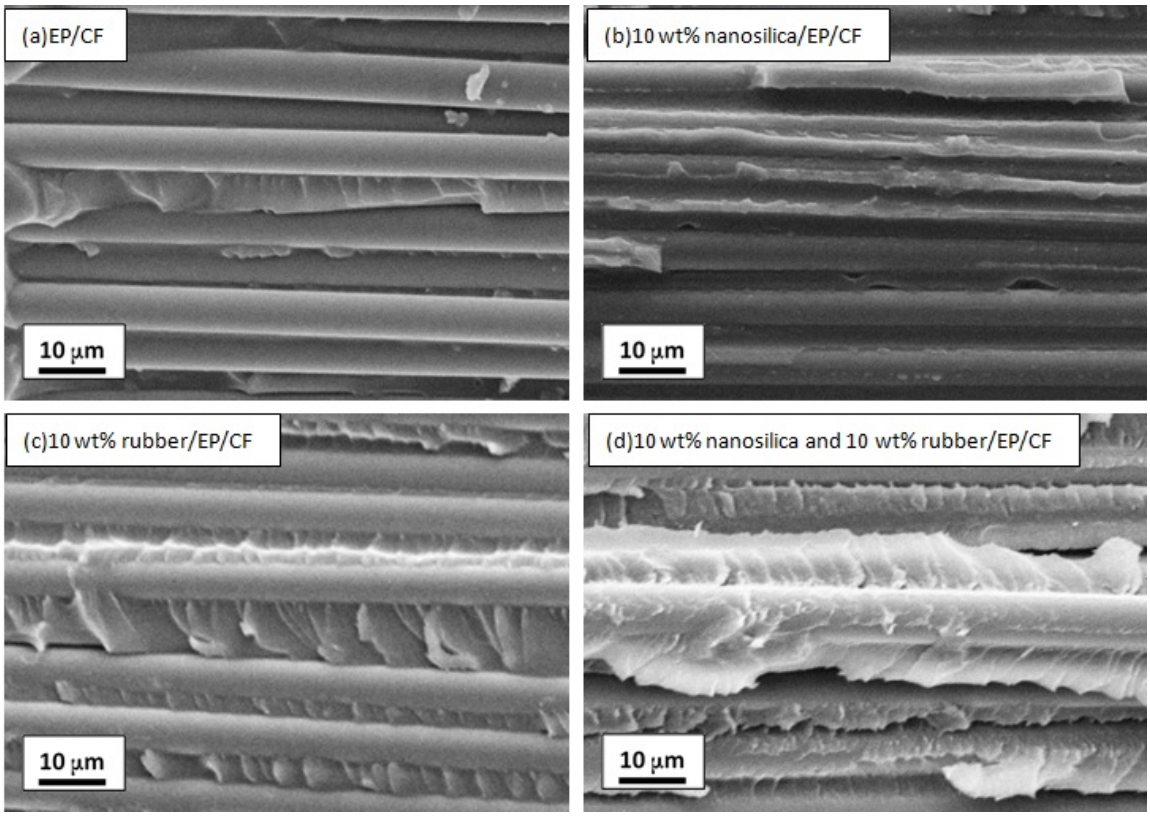

Figure 4 SEM photographs of fracture surfaces for fatigue tested CF/EP laminates

4. Conclusions

(1) The mode I interlaminar fracture toughness of CF/EP laminates under static loading was significantly improved after the epoxy matrix was modified with 10 wt% nano-silica particles or 10 wt% CTBN rubber. In particular, for the CF/EP laminate with the matrix modified by the hybrid of 10 wt% nano-silica and 10 wt% rubber, the interlaminar fracture toughness was further improved.

(2) The fatigue delamination growth resistance of the CF/EP laminates was also improved after the matrix was modified by nano-silica and/or CTBN rubber. It was observed that the CF/EP laminate with the matrix modified by the hybrid of 10 wt% nano-silica and 10 wt% rubber achieved the highest resistance to fatigue delamination growth, attributed to the synergistic contribution of toughening mechanisms induced by nano-silica particles and CTBN rubber, respectively.

References

[1] Y. Zeng, H.Y. Liu, Y.W. Mai, X.S. Du, Improving interlaminar fracture toughness of carbon fibre/epoxy laminates by incorporation of nano-particles. Compos Part B-Eng, 43 (2012) 90-94.

[2] K.A. Dransfield, L.K.Jain, Y.W. Mai, On the effect of stitching in CFRPs-I. Mode I delamination toughness. Compos Sci Technol, 58(1998) 815-827.

[3] Q. An, A.N. Rider, E.T. Thostenson, Electrophoretic deposition of carbon nanotubes onto carbon-fiber fabric for production of carbon/epoxy composites with improved mechanical properties, Carbon, 50 (2012) 4130-4143.

[4] N. Ghafari-Namini, H. Ghasemnejad, Effect of natural stitched composites on the crashworthiness of box structures, Mater Design, 39 (2012) 484-494.

[5] F. Mujika, G. Vargas, J. Ibarretxe, J.D. Gracia, A. Arrese, Influence of the modification with MWCNT on the interlaminar fracture properties of long carbon fiber composites, Compos Part B-Eng, 43(2012) 1336-1340.
[6] P. Robinson, S. Das, Mode I DCB testing of composite laminates reinforced with z-direction pins: a simple model for the investigation of data reduction strategies. Eng Fract Mech, 71 (2004) 345-364.
[7] A.P. Mouritz, P. Chang and M.D. Isa, Composites: aerospace structural design comsiderations, J Aerosp Eng, 24 (2011) 425-432.
[8] Y. Ye, H. Chen, J. Wu, C.M. Chan, Interlaminar properties of carbon fiber composites with halloysite nanotube-toughened epoxy matrix, Compos Sci Technol, 71(2011) 717-723.
[9] Y. Tang, L. Ye, D. Zhang, S. Deng, Characterization of transverse tensile, interlaminar shear and interlaminate fracture in CF/EP laminates with 10 wt% and 20 wt% silica nanoparticles in matrix resins, Compos Part A-Appl S, 42(2011) 1942-1950.
[10] D. Zhang, L. Ye, S. Deng, J. Zhang, Y. Tang, Y. Chen, CF/EP composite laminates with carbon black and copper chloride for improved electrical conductivity and interlaminar fracture toughness, Compos Sci Technol, 72 (2012) 412-420.
[11] N. Hu, Y. Li, T. Nakamura, T. Katsumata, T. Koshikawa, M. Arai, Reinforcement effects of MWCNT and VGCF in bulk composites and interlayer of CFRP laminates, Compos Part B-Eng, 43 (2012) 3-9.
[12] T.H. Hsieh, A.J. Kinloch, K. Masania, J.S. Lee, A.C. Taylor, S. Sprenger, The toughness of epoxy polymers and fibre composite modified with rubber microparticles and silica nanoparticles, J Mater Sci, 45 (2010) 1193-1210.

Evaluation on the Factors Influencing Thermal-stress-induced Growth of Sn Nanowires

Yuan Li[1,*], Kentaro Miura[1], Shien Ri[2], Masumi Saka[1]

[1] Department of Nanomechanics, Tohoku University, Sendai 980-8579, Japan
[2] National Institute of Advanced Industrial Science and Technology, Tsukuba 305-8568, Japan
* Corresponding author: liyuan@ism.mech.tohoku.ac.jp

Abstract By employing a multilayer thin film structure composed of thermally oxidized Si substrate and sputtered Sn film, a series of thermal annealing experiments are carried out to challenge the synthesis of Sn nanowires following thermal-stress-induced method. The effects of two vital influencing factors, i.e., surface morphology of Sn film and annealing conditions, are explored systematically. For Sn films with either isolated islands or voids in grain boundaries, there is no any change on surface morphology after annealing. Such behavior can be attributed to the existence of gaps among islands or voids in grain boundaries, which make it difficult to generate sufficient stress to grow Sn nanowire. On the other hand, for Sn films with dense grains or coalescent islands, the occurrence of hillocks or whiskers after annealing at high temperature indicates that the proper control of surface morphology of Sn film and thermal annealing conditions may grow Sn nanowires with large aspect ratio.

Keywords Atomic migration, Influencing factors, Metallic nanowire, Thermal stress

1. Introduction

The study of Sn nanowires has been motivated by the attractive properties of bulk Sn including excellent ductility, electrical conductivity, resistance to corrosion, and its extensive application in electronics industry. Recent experimental studies [1-6] have shown that Sn nanowires have unique superconductivity and magnetic properties, which indicates their potential application in superconductors. Moreover, vertical arrays of Sn nanowires have been expected to be ideal anode materials for lithium rechargeable batteries with improved cycling life and high power capabilities [7-9]. In addition, oxidation of Sn nanowires has provided an alternative method to prepare sensitive SnO_2 nanowires for gas sensors [10]. Such exciting applications and the reliability evaluation (e.g., thermal instability [11]) have promoted the development of various strategies to grow Sn nanowires.

Several template-assisted synthesis methods have been attempted, in which Sn nanowires have been grown inside the nanochannels of anodized aluminum oxide or track etched polycarbonate membrane by electrodeposition using an aqueous solution containing Sn^{2+} ions [1, 2], and by solidification of the molten Sn injected with gas pressure [12] or hydraulic pressure [13]. Although the above template-assisted methods have offered the advantages of predefined morphology and size controllability, there still exist extrinsic shortcomings such as the troublesome template removal and possible chemical contamination [14]. Besides, successful growth of Sn nanowires following vapor-solid mechanism has also been reported by employing a noncatalytic and template-free vapor transport process [3]. In this case, the source of Sn vapor is required, which is obtained by ultra-high temperature (i.e., 973K) heating of Sn. Additionally, Xiao *et al*. [15] have grown Sn nanowires using thermal-stress-induced method by annealing a Si-Sn nanocomposite film in vacuum.

In this study, the same mechanism (i.e., thermal-stress-induced method) is employed to challenge the growth of Sn nanowires by using a multilayer thin film structure following thermal annealing in ambient environment. The effects of two vital influencing factors including surface morphology of

Sn film and annealing conditions are explored systematically.

2. Fundamentals and Experiments

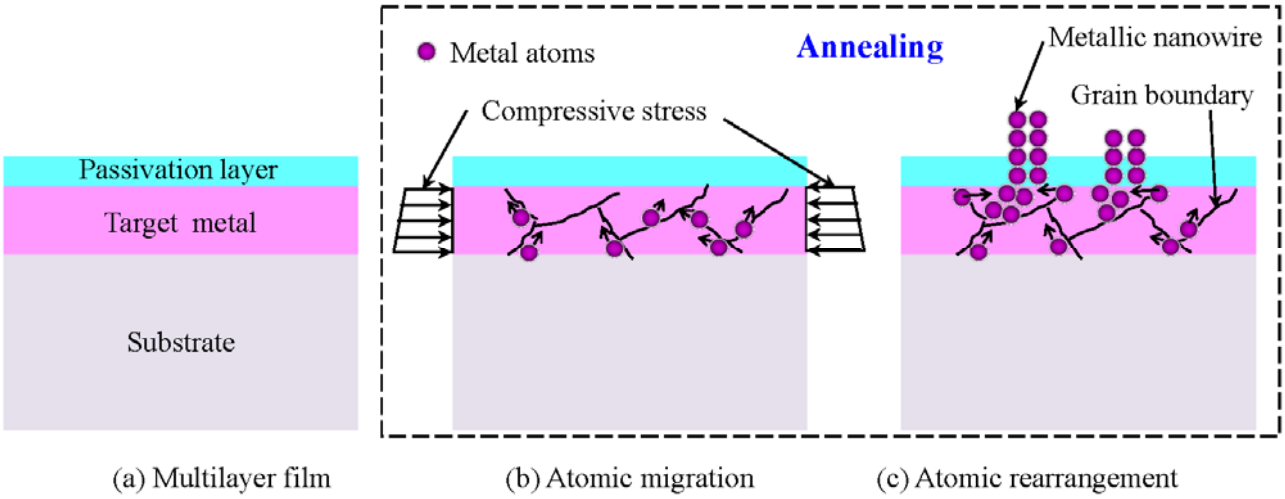

Fig. 1 Schematic thermal-stress-induced growth of metallic nanowires from a multilayer film

The mechanism of the present thermal-stress-induced growth of metallic nanowire using a multilayer is schematically illustrated in Fig. 1. A multilayer film shown in Fig. 1(a) is composed of three layers from top to down: passivation layer (e.g., natural oxide layer of Sn), target metal (e.g., Sn) and substrate (e.g., thermal oxidized Si). Because of the significant mismatch in the coefficient of thermal expansion (CTE) between target metal and substrate (α_{Sn} = 23.5×10^{-6}/K; α_{Si} = 7.6×10^{-6}/K [16]), the compressive thermal stress will be induced in target metal film during thermal annealing. Taking into account of material and geometrical singularities of the target metal film, the resulted local compressive stress gradient drives atoms migrating from more compressive areas to less compressive ones in the form of grain boundary diffusion and surface diffusion as shown in Fig. 1(b). With the accumulation of migrated atoms, the compressive stress gradient is generated between the interface of target metal/passivation layer and the free surface of passivation layer. Once the pressure resulted by the accumulated atoms attains a critical value, weak spots in the passivation layer will be broken and metallic nanowire will be formed through the rearrangement of metallic atoms. Based on the above growth mechanism, the similar multilayer thin film structure has been employed to fabricate various metallic nanowires, such as Cu [17], Bi [18], Ag [19], Al [20].

In the present work, a multilayer thin film structure for grow Sn nanowires are prepared. The Sn thin films are deposited on a 280μm-thick thermally oxidized Si wafer by radio frequency (RF) sputtering with an Ar flow of 20sccm and pressure of 5mTorr. The substrate temperature during sputtering is controlled to be room temperature (R.T.) by water cooling to assure thermal stress as high as possible in the following thermal annealing. By varying the RF power and sputtering time, a series of multilayer thin film structures are prepared in which the sputtered Sn films have different surface morphologies.

By using the obtained multilayer thin films, thermal annealing experiments are carried out at 473~503K for 2h in ambient environment. By observing the surface morphologies of the as-sputtered Sn films and the annealed ones using a scanning electron microscope (SEM), the effects of two vital influencing factors, including surface morphology of the as-sputtered Sn film and annealing conditions, are investigated.

3. Results and Discussion

3.1 Surface Morphologies of As-sputtered Sn Films

As a representative, the cross-sectional image of the prepared multilayer thin film is observed in Fig. 2 by using transmission electron microscope (TEM), in which the Sn film is sputtered at 20W and 240s. According to SEM observations, the surface morphologies of as-sputtered Sn films can be categorized into three representative sets, which are related to different RF power P and sputtering time t. For the films shown in Fig. 3 which are sputtered at RF power of 50W with sputtering rate of 1.5nm/s from 30s to 60s, the isolated island structure is clearly observed in each case. Moreover, the

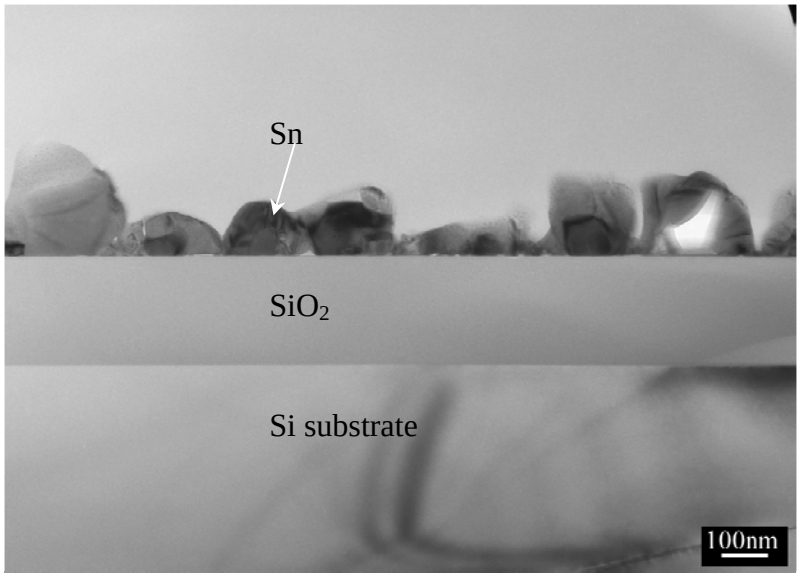

Fig. 2 Cross-sectional TEM image of the multilayer thin film (P=20W, t=240s)

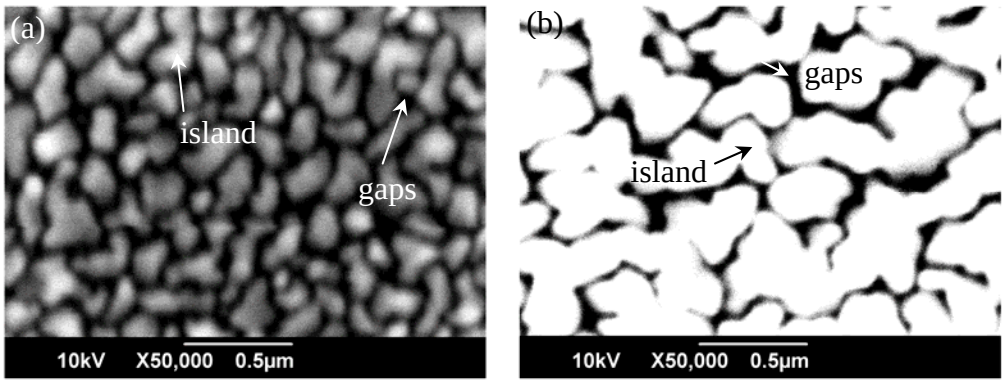

Fig. 3 Surface morphologies of Sn films with isolated island structure
(a) P=50W, t=30s; (b) P=50W, t=60s

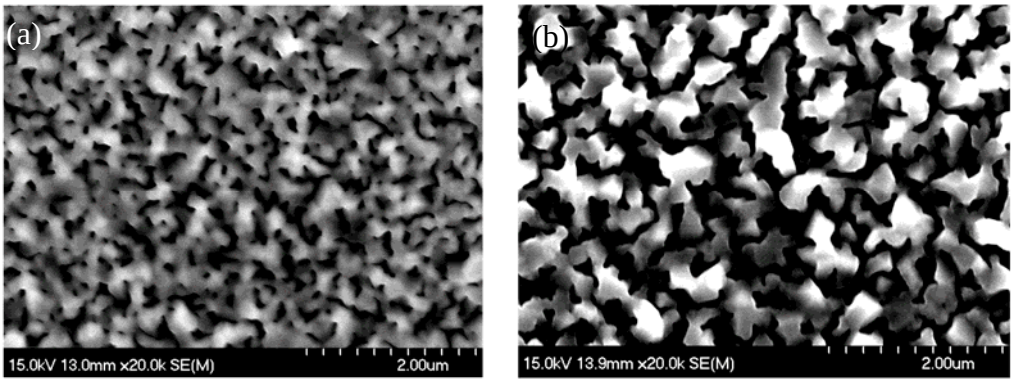

Fig. 4 Surface morphologies of Sn films with coalescent island structure
(a) P=50W, t=90s; (b) P=20W, t=240s

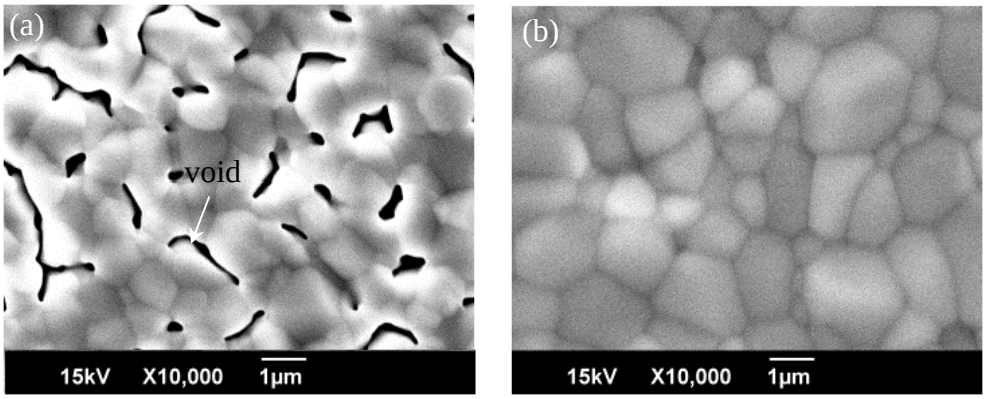

Fig. 5 Surface morphologies of Sn films with clear grains
(a) P=300W, t=125s; (b) P=300W, t=500s

size of island increases as the sputtering time increases. However, when the sputtering time increases to 90s, the isolated islands begin to coalesce with each other as shown in Fig.4 (a). This structure with coalescent islands is very similar with that in Fig. 4(b) sputtered at RF power of 20W for 240s with sputtering rate of 0.5nm/s. For films in Fig. 5 which are sputtered at RF power of 300W for 125~500s with sputtering ratio of 4nm/s, grain boundaries can be clearly observed. Interestingly, by comparing Fig. 5(a) and Fig. 5(b), it is found that with the sputtering time increases and the corresponding increasing film thickness, the voids at the grain boundaries decrease and finally vanish.

3.2 Surface Morphologies of Annealed Sn Films

The surface morphologies of the above as-sputtered Sn films after annealing at 473~503K for 2h are given in Fig. 6. Significant changes on the surface morphologies are only observed for Sn films which are sputtered under the following three conditions: (I) P=50W, t=90s (Fig. 6(a)); (II) P=20W, t=240s (Figs. 6(b, d)); (III) P=300W, t=500s (Fig. 6(c)). At the annealing temperature of T=473K, large numbers of hillocks shown are observed on the films sputtered at the above three cases (i.e., Figs. 6(a~c)) while no any change is found on the other films. When the annealing temperature is increased up to T=503K, large numbers of whiskers with various shapes are only observed on the film sputtered at P=20W (Fig. 6(d)). The representative images of hillock or whisker are shown in in Fig. 7. These distinctive differences can be discussed as below: for the sputtered Sn films with

isolated islands or voids in grain boundaries, it is difficult to result in stress concentration because of the existence of gap or voids. On the other hand, for Sn films with dense grains or coalescent islands, it is possible to induce thermal stress during the annealing with consideration of material and geometrical singularity. It should be noted that for the former (i.e., Sn film with dense grains) with thickness in micro-scale, the part of internal stress is released by recrystallization during the formation of grains. However, for the latter (i.e., Sn film with coalescent islands) with thickness in nanoscale, the induced thermal stress is much higher than that in the former.

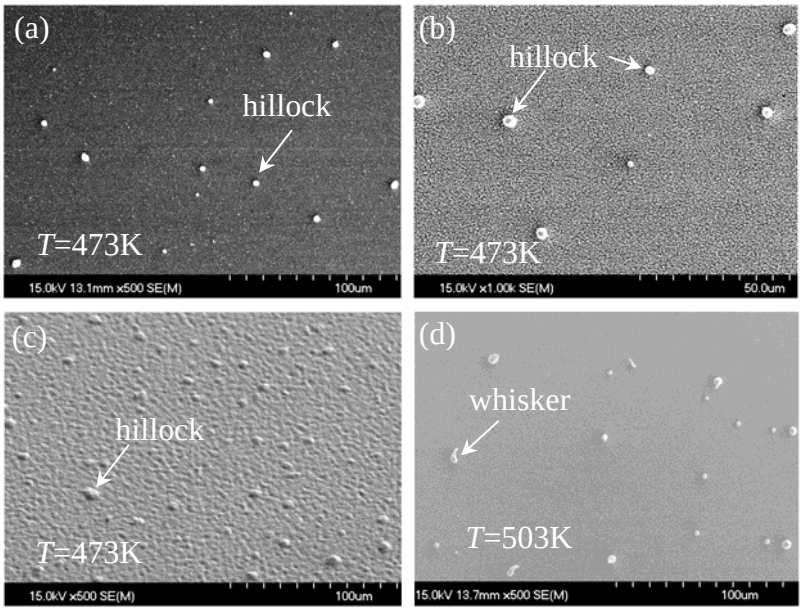

Fig. 6 Surface morphologies of annealed Sn films
(a) P=50W, t=90s; (b,d) P=20W, t=240s; (c) P=300W, t=500s

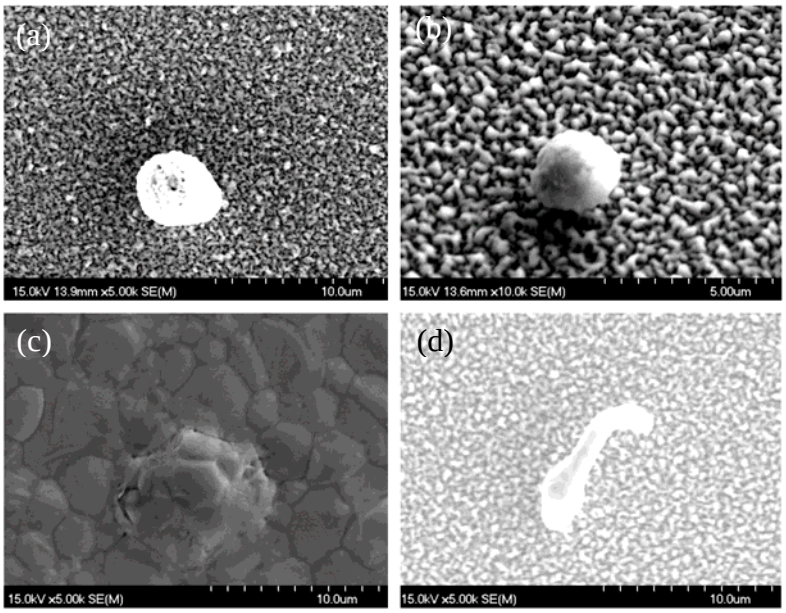

Fig. 7 Representative hillock or whisker in annealed Sn films
(a) P=50W, t=90s; (b,d) P=20W, t=240s; (c) P=300W, t=500s

4. Conclusions

By employing a multilayer thin film structure composed of thermally oxidized Si substrate and sputtered Sn film, a series of thermal annealing experiments are carried out to challenge the growth of Sn nanowires using thermal-stress-induced method. The effects of two vital influencing factors, i.e., surface morphology of Sn film and annealing conditions, are explored systematically. For Sn films with either isolated island structure or voids in grain boundaries, there is no any change on surface morphology after annealing. Such behavior can be attributed to the existence of gaps among islands or voids in grain boundaries, which make it difficult to generate sufficient stress to make Sn nanowires grow. On the other hand, for Sn films with dense grains or coalescent islands, the occurrence of hillocks or whiskers after annealing indicates that the proper control of surface morphology of Sn film and annealing conditions may grow Sn nanowires with large aspect ratio.

Acknowledgements

The authors are grateful to be partly supported by the Grand-in-Aid for Challenging Exploratory Research (No. 23656076) and Tohoku Leading Women's Jump Up Project for 2013 (J110002183, J110002158, J120000428) from the Ministry of Education, Culture, Sports, Science and Technology (MEXT) of Japan.

References

[1] M. Tian, J. Wang, J. Snyder, J. Kurtz, Y. Liu, P. Schiffer, T.E. Mallouk, and M. Chan, Synthesis and characterization of superconducting single-crystal Sn nanowires. Appl. Phys. Lett., 83 (2003) 1620-22.

[2] M. Tian, J. Wang, J. Kurtz, Y. Liu, and M. Chan, Dissipation in quasi-one-dimensional superconducting single-crystal Sn nanowires. Phys. Rev. B, 71 (2005) 104521.

[3] Y. Hsu, and S. Lu, Vapor-solid growth of Sn nanowires: growth mechanism and superconductivity. J. Phys. Chem. B, 109 (2005) 4398-403.

[4] L. Jankovic, D. Gournis, P. Trikalitis, I. Arfaoui, T. Cren, P. Rudolf, M. Sage, T. Palstra, B. Kooi, J. Hosson, M. Karakassides, K. Dimos, A. Moukarika, and T. Bakas, Carbon nanotubes encapsulating superconducting single-crystalline tin nanowires. Nano Lett., 6 (2006) 1131-35.

[5] N. Tombros, L. Buit, I. Arfaoui, T. Tsoufis, D. Gournis, P. Trikalitis, S. Molen, P. Rudolf, and B. Wees, Charge transport in a single superconducting tin nanowire encapsulated in a multiwalled carbon nanotube. Nano Lett., 8 (2008) 3060-64.

[6] E. Gordon, A. Karabulin, V. Matyushenko, V. Sizov, and I. Khodos, The electrical conductivity of bundles of superconducting nanowires produced by laser ablation of metals in superfluid helium. Appl. Phys. Lett., 101 (2012), 052605.

[7] A. Whitehead, J. Elliott, and J. Owen, Nanostructured tin for use as a negative electrode material in Li-ion batteries. Journal of Power Sources, 81-82 (1999) 33-38.

[8] J. Kim, S. Khanal, M. Islam, A. Khatri, and D. Choi, Electrochemical characterization of vertical arrays of tin nanowires grown on silicon substrates as anode materials for lithium rechargeable microbatteries. Electrochemistry Communications, 10 (2008) 1688-90.

[9] A. Kamali, and D. Fray, Tin-based materials as advanced anode materials for lithium ion batteries: a review. Rev. Adv. Mater. Sci., 27 (2011) 14-24.

[10] A. Kolmakov, Y. Zhang, G. Cheng, and M. Moskovits, Detection of CO and O_2 using tin oxide nanowire sensors. Adv. Mater., 15 (2003) 997-1000.

[11] H. Sun, J. Yu, and J. Song, Size-dependent thermal instability and melting behavior of Sn nanowires. Appl. Phys. Lett., 91 (2007), 173106.

[12] C. Huber, T. Huber, M. Sadoqi, J. Lubin, S. Manalis, and C. Prater, Nanowire array composites. Science, 263 (1994) 800-02.

[13] C. Chen, Y. Bisrat, Z. Luo, R. Schaak, C. Chao, and D. Lagoudas, Fabrication of single-crystal

tin nanowires by hydraulic pressure injection. Nanotechnology, 17 (2006) 367-74.
[14] Y. Xia, P. Yang, Y. Sun, Y. Wu, B. Mayers, B. Gates, Y. Yin, F. Kim, and H. Yan, One dimensional nanostructures: synthesis, characterization, and applications. Adv. Mater., 15 (2003) 353-89.
[15] X. Xiao, A. Sachdev, D. Haddad, Y. Li, B. Sheldon, and S. Soni, Stress-induced Sn nanowires from Si-Sn nanocomposite coatings. Appl. Phys. Lett., 97 (2010) 141904.
[16] E.A. Brandes, and G.B. Brook (Eds.), Smithells Metal Reference Book (7th Edition) Butterworth-Heinemann, Oxford, 1992.
[17] M. Saka, F. Yamaya, and H. Tohmyoh, Rapid and mass growth of stress-induced nanowhiskers on the surfaces of evaporated polycrystalline Cu films. Scripta Materialia, 56 (2007) 1031-34.
[18] W. Shim, J. Ham, K. Lee, W. Jeung, M. Johnson, and W. Lee, On-film formation of Bi nanowires with extraordinary electron mobility. Nano Lett., 9 (2009) 18-22.
[19] H. Tohmyoh, M. Yasuda, and M. Saka, Controlling Ag whisker growth using very thin metallic films. Scripta Materialia, 63 (2010) 289-92.
[20] M. Chen, Y. Yue, and Y. Ju, Growth of metal and metal oxide nanowires driven by the stress-induced migration. J. Appl. Phys., 111(2012)104305.

Toughness Enhancement in Nanocomposite Thermosets with Application to Carbon-Epoxy System

Catalin Radu Picu[1], Dan Mihai Constantinescu[2,*], Marin Sandu[2], Dragoş Alexandru Apostol[2], Ioana Cosmoiu[2]

[1] Department of Mechanical, Aerospace, and Nuclear Engineering, Rensselaer Polytechnic Institute, Troy 12180, USA
[2] Department of Strength of Materials, University POLITEHNICA of Bucharest, Bucharest 060042, Romania
* Corresponding author: dan.constantinescu@upb.ro

Abstract Neat epoxy and epoxy-based nanocomposites were subjected to monotonic uniaxial and fracture toughness testing. Samples of epoxy filled with 0.1wt% multi-wall carbon nanotubes (MWNT) and of epoxy filled with 0.1wt% graphene platelets (GPL) were considered. The nanoscale inclusions were used in the as-received state. The processing procedure involved sonication and high-speed mixing followed by degassing and curing. Traction tests were performed with ASTM-type specimens using both an Epsilon extensometer and the digital image correlation method (DIC). DIC was performed using an ARAMIS system and the entire length of each specimen was analyzed. The stress-strain behavior of these materials was essentially identical. However, the toughness of MWNT was even 50% higher than that of neat epoxy. The toughness of GPL-filled epoxy was only marginally larger than that of the neat matrix. These observations are attributed to the crack bridging effect of the MWNT.

Keywords Nanocomposites, Fracture toughness, Digital image correlation, Crack bridging

1. Introduction

Polymer nanocomposites have emerged as important structural materials, competing with neat polymers and classical composites. These materials exhibit a combination of exceptional properties which usually cannot be achieved in standard composites. Some of the most studied systems are nanocomposite thermosets, that is polymers filled with nanoparticles and various forms of nano-carbon (carbon nanotubes, graphene, graphene platelets, etc.).

In [1], [2], GPL and MWNT-epoxy composites with various weight fractions (0 to 0.5wt%) were prepared, and were tested under monotonic, cyclic (fatigue) and creep conditions. It was observed that the addition of GPL and MWNT has a marginal effect on the stress-strain curve at all strain rates investigated. However, GPL reduces the creep rate at elevated temperatures, especially in the transient creep regime [1]. Both MWNT and GPL lead to a dramatic reduction of crack growth rate under fatigue conditions [2].

Epoxy-based nanocomposites with 0.1wt% MWNT were subjected to monotonic uniaxial and fracture toughness testing on single-edge notched (SEN) specimens [3]. SEM analyses were performed to study the fracture surfaces and the effect of fillers on crack propagation. For dispersing the MWNT in the epoxy resin special equipment is needed. A high energy sonicator was used, Sonics VCX-750 (US), characterized by a generator with 750 W output, a 20 kHz convertor and a temperature controller. For mechanical mixing, a shear mixer Thinky ARE-250 (Japan) with maximum rotation speed of 2000 rpm was used.

In this work we study the mechanical properties of epoxy-based composites in which the additives are multiwall carbon nanotubes (MWNT) and graphene platelets (GPL), in separate materials, at 0.1wt% filling fraction. The nanocomposites were subjected to monotonic uniaxial and fracture toughness testing on single-edge notched (SEN) specimens. SEM analyses were performed to study the fracture surfaces and the effect of fillers on crack propagation.

2. Traction testing

Uniaxial tension tests were performed with ASTM-type specimens using both an Epsilon extensometer and the digital image correlation method (DIC). The testing speed was 1.5 mm/min which corresponds to an initial strain rate of approximately 10^{-3} s^{-1}; DIC was performed using an ARAMIS system and the entire length of each specimen was analyzed. The ultimate tensile stress was in the range 50 to 55 MPa and the elongation at failure about 3-4.5%. The Young's modulus is in the range 2300 to 2600 MPa. No significant difference was observed between MWNT and GPL-filled epoxy samples in this type of test.

For a pure epoxy specimen failure is typically brittle, and may initiate from a corner of the specimen, probably due to a local defect (Fig. 1). On the fracture surface the SEM analysis shows striations on a radial direction converging towards the fracture initiation area.

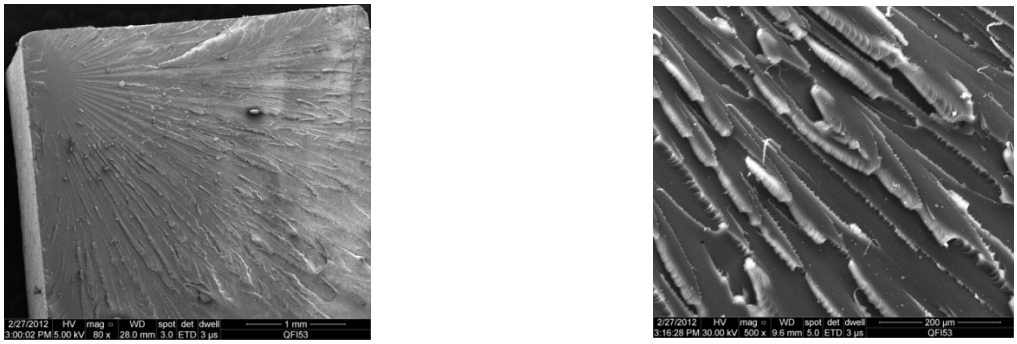

Figure 1. Fracture surface of a fractured pure epoxy specimen analyzed by SEM.

As an example, just before failure, for a MWNT filled epoxy, the maximum von Mises strain is 7.26 % due to a local stress raiser effect (Fig.2).

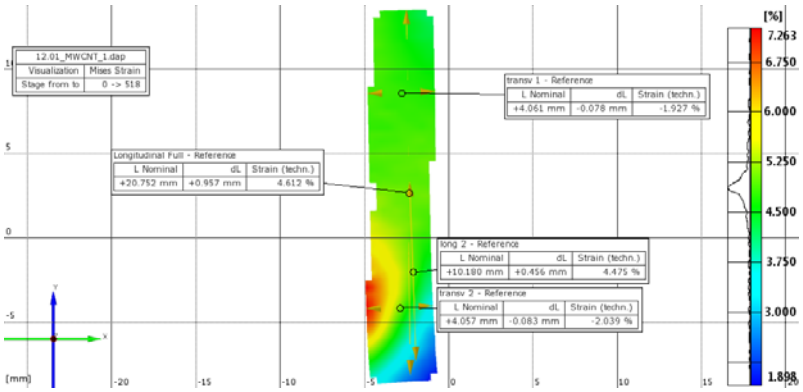

Figure 2. von Mises strains obtained experimentally for a MWNT specimen

We show in Fig. 3 the von Mises strains (from DIC) for a GPL epoxy specimen tested in uniaxial tension, just before unstable crack propagation was observed. The maximum von Mises strain is now 2.6% in the area where failure initiates.

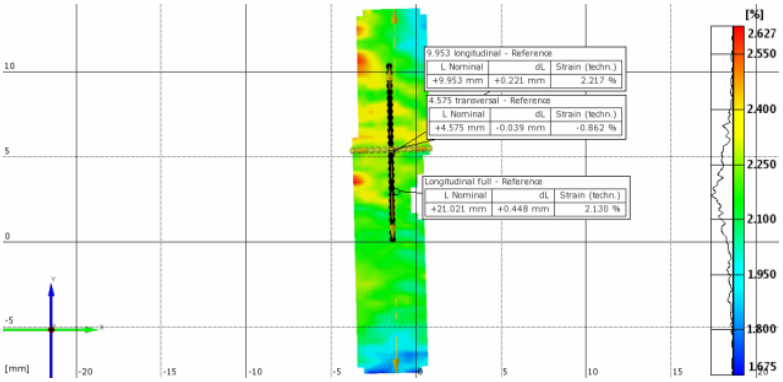

Figure 3. von Mises strains in a GPL specimen

3. Fracture toughness evaluation

The fracture toughness evaluation was performed using SEN specimens. Notches were cut with a fine saw and then sharpened with a razor blade. The total length of the crack was 1.3 mm. The DIC was used to monitor the local Mises strains at the tip of the crack up to failure. The crack area was masked to prevent obtaining spurious strains due to the relative movement of the crack flanks. Fig. 4 shows the von Mises strains in a MWNT nanocomposite specimen in the last frame before unstable crack propagation. The maximum strain is 2.4% and the failure was brittle.

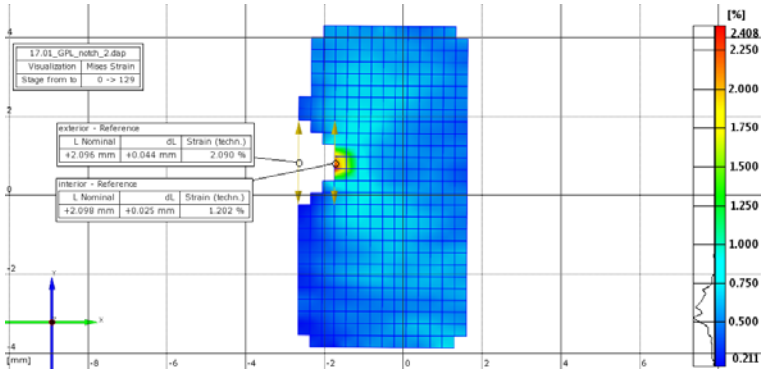

Figure 4. von Mises strains before failure in a MWNT SEN specimen; the crack area is masked

Analyzing by SEM the fracture surface of a MWNT SEN specimen (Fig. 5) it can be observed that fracture phenomena at the initial crack front are different than those observed in specimens from pure epoxy. Fibers of material are pulled-out, this being a common feature. These fibers are not necessarily associated with the MWNT and have diameters much larger than those of MWNT.

By observing in more detail the fracture surface (Fig. 6), one can notice that the MWNT were pulled out during the major crack propagation process, and can be seen on the crack surface. The measured diameters of the nanotubes are in between 30-45 nm.

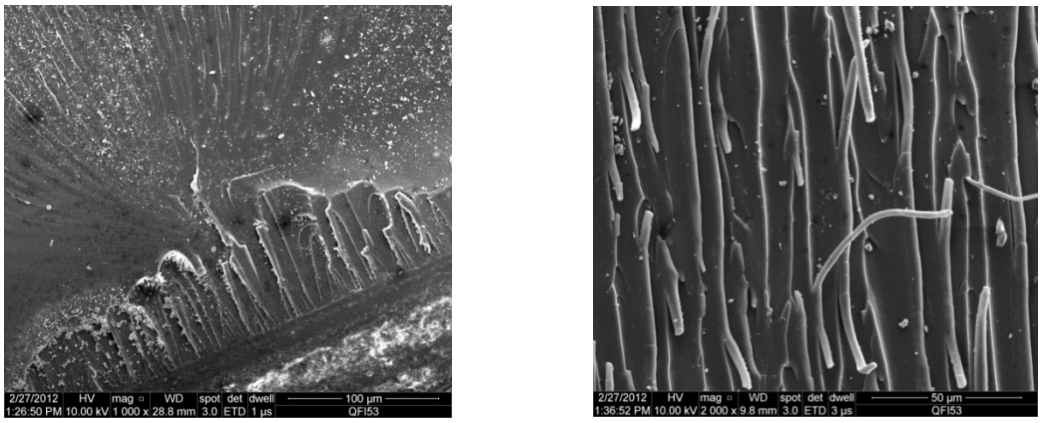

Figure 5. Fracture surface analyzed by SEM for a MWNT-epoxy SEN specimen

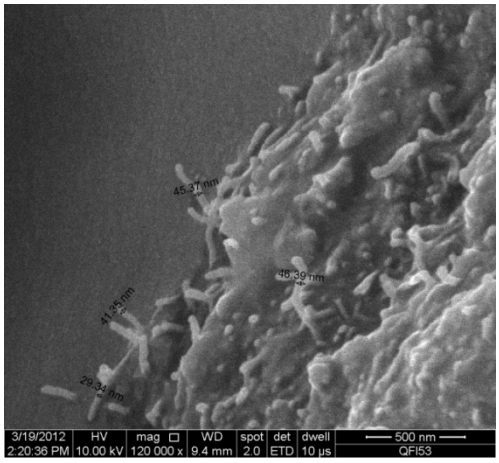

Figure 6. Fracture surface of a MWNT-epoxy sample showing MWNT pull-out.

In GPL-epoxy, both isolated and clustered platelets are observed. The distribution of cluster sizes is rather broad. These are observed on the crack surface, as seen in Fig. 7 (right). It is also observed that the initiation of crack propagation from the front of the artificially cut crack (Fig. 7 left) takes place at the site of a GPL cluster, which indicates that the clusters reduce the measured fracture toughness.

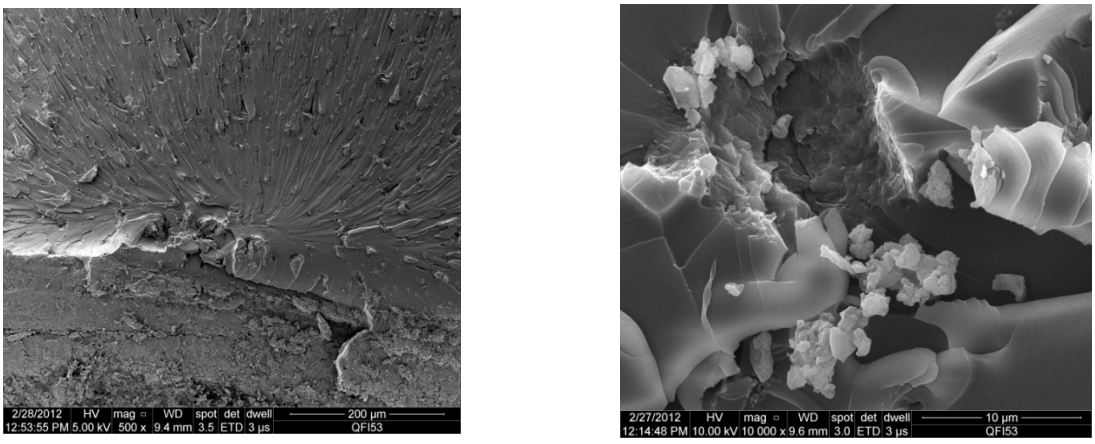

Figure 7. Fracture surface of GPL-epoxy SEN specimen

The fracture toughness is represented in Fig. 8 in the case of pure epoxy and both GPL-epoxy and MWNT-epoxy in the cases when good dispersion and insufficient dispersion are achieved. Clearly a good dispersion of the nanoparticles is essential to improve the critical fracture toughness of the material. However, an insufficient dispersion leads to no increase of the toughness, as one would expect.

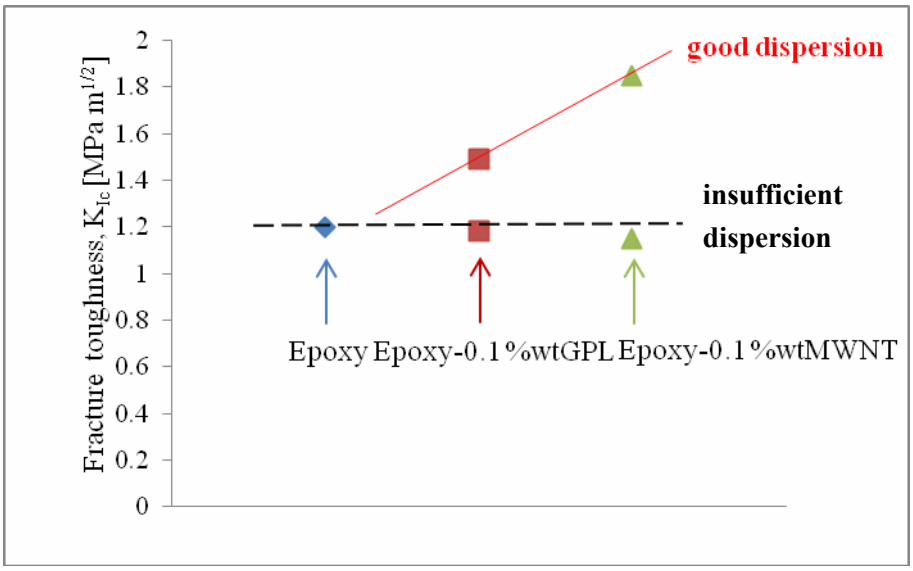

Figure 8. Critical fracture toughness values for pure epoxy and epoxy mixed with 0.1wt% graphene platelets (GPL) and with 0.1wt% carbon nanotubes (MWNT)

4. Conclusion

An adequate dispersion of the MWNT may lead to an increase of the fracture toughness of 80%. Smaller increases were obtained with GPL, even at similar dispersion quality. In the preliminary studies it was observed that the nanotubes increase the toughness through a *crack bridging* mechanism which is well-known in the case of standard composites with fibers of μm and mm dimensions. The results concerning the importance of good dispersion of nanofillers confirm observations of other research groups.

Acknowledgements

This work has been supported by a grant of the Romanian National Authority for Scientific Research, CNCS – UEFISCDI, project number PN-II-ID-PCE-2011-3-0120, contract 293/2011.

References

[1] A. Zandiatashbar, R.C. Picu, N. Koratkar, Control of epoxy creep using graphene. Small, (2012) DOI:10.1002/smll.201102686

[2] W. Zhang, R.C. Picu, N. Koratkar, Suppression of fatigue crack growth in carbon nanotube composites. Appl Phys Lett, 91 (2007) 193109.

[3] D.M. Constantinescu, C.R. Picu, D.A. Apostol, M. Sandu, Evaluation of the fracture toughness of MWNT and GPL epoxy nanocomposites, in: Proceedings of the 29th Danubia-Adria Symposium on Advances in Experimental Mechanics, Belgrade, Serbia, September 26-29, 2012, pp. 122-123.

Improvement of interlaminar mechanical properties of CARALL based on nanofiller interface reinforcement and other fabrication techniques

Huiming Ning[1], Yuan Li[2] and Ning Hu[1,*]

[1]Department of Mechanical Engineering, Chiba University, 1-33 Yayoi-cho, Inage-ku, Chiba 263-8522, Japan
[2]Department of Nanomechanics, Tohoku University, 6-6-01 Aramaki-Aza-Aoba, Aoba-ku, Sendai 980-8579, Japan
* Corresponding author: huning@faculty.chiba-u.jp

Abstract: Improvement of interlaminar mechanical properties in carbon fiber aluminum laminates (CARALL) fabricated by carbon fiber reinforced plastic (CFRP) layers combined with aluminum alloy layers was studied. Various toughing methods including acid etching treatment and patterned structure manufacturing on the surfaces of aluminum alloy layers, and addition of nanofiller, i.e., VGCF, to the interface of CFRP and aluminum alloy through powder method, were employed to improve the mechanical properties of CARALL. Experimental results of double cantilever beam (DCB) tests indicated the improvement on the interlaminar mechanical properties of Mode-I fracture from much higher critical load P_c and fracture toughness G_{IC} when using the acid etching treatment and VGCF addition. The acid etching treatment sample with VGCF 20 g/m^2 possesses the highest G_{IC}, which is 41 times higher than that of the sample without any treatment. The patterned structure manufacturing on the surfaces of aluminum alloy layers can further improve the fracture properties of CARALL without adding VGCF. While VGCF was included in CARALL specimens, the patterned structure manufacturing has a minor effect on the Mode-I interlaminar mechanical properties. Crack propagation and fracture surface have also been observed to interpret the improvement mechanism.

Keywords: Carbon fiber aluminum laminates (CARALL), vapor grown carbon fiber (VGCF), fracture toughness, interlaminar mechanical properties.

1. Introduction

Carbon fiber aluminum laminates (CARALL) are a kind of FML (fiber metal laminates) materials which are hybrid composite structures based on thin sheets of metal alloys and plies of fiber reinforced polymeric (FRPs) materials combining the advantages of metallic materials and fiber reinforced matrix systems. Metallic materials are for instance isotropic, have a high bearing strength and impact resistance and are easy to repair, while fiber reinforced matrix systems have excellent fatigue characteristics and high strength and stiffness. The fatigue and corrosion problems of metallic materials and the low bearing strength, impact resistance and reparability of fiber reinforced matrix systems can be overcome by the combination [1]. Nevertheless, laminates, and CARALL is no exception, have some disadvantages as well. Due to the combination of different materials, new failure mechanisms are introduced. One of such a mechanism is delamination, which can have serious consequences for the overall stiffness of the material, especially in those cases where compressive or shear loadings are dominate. The relatively weak bonding between metal/polymer interfaces still remains a problem to be solved.

In order to solve this problem, surface treatment methods (e.g. acid treatment, anodizing, and

patterned structure manufacturing etc.) were employed by many researches to improve the interface mechanical properties of FMLs [2-7]. Kim *et al.* [3] systematically investigated the influence of surface morphology on the adhesion strength of a CFRP/Steel bond by incorporating micro-periodic line patterned surface on the metal substrate. They pointed out that the major source of strength enhancement caused by metal surface topography modification in polymer/metal bonded joints is the transition from interfacial to cohesive failure. Nano- and micro-scale surface treatment effects on adhesion strength improvement for CFRP/aluminum interfaces were investigated by Jang *et al*. [6]. Micro-scale line pattern was made on the aluminum surface by using conventional photolithography and acid etching. Anodizing process was employed to create uniform nano-porous morphology across the whole line pattern region on the aluminum specimen. The results showed that the specimen with nano-scale morphology in micro-scale line pattern resulted in the highest maximum load bearing capacity compared with that of only with micro-scale line pattern.

With excellent mechanical properties, nanofillers (carbon nanotubes (CNTs), nanoclays, vapor grown carbon fiber (VGCF), etc.) are considered as ideal reinforcement candidates to the matrix or the interface of laminate composite to improve its mechanical properties. For instance, Jen *et al.* [8] observed that the incorporation of 1.0 wt.% SiO_2 nanoparticles into interfaces among CFRP plies resulted in the increase of the overall in-plane tensile strength and stiffness of CFRP, but little improvement in fatigue behavior. A prepared VGCF paste interlayer was inserted into the interface between two $[0^o]_7$ CFRP sublaminates by Arai *et al.* [9], and revealed that the Mode-I fracture toughness was enhanced by 50%. However, till now, there has been no report about using nanofillers as the reinforcement for FML. The combined effects of various toughing methods (e.g. acid etching treatment, patterned structure manufacturing, addition of nanofiller) have not been well explored.

In this study, various toughing methods including acid etching treatment and patterned structure manufacturing on the surfaces of aluminum alloy layers, and addition of nanofiller (i.e., VGCF) to the interface of CFRP and aluminum alloy through powder method, were employed to improve the interlaminar mechanical properties of CARALL. The area density of VGCF varies at 0, 10, 20, and 30g/m^2 at the interface. The results of DCB tests demonstrate that this new hybrid CARALL with acid etching treatment and 20g/m^2 VGCF addition possess the highest Mode-I interlaminar fracture toughness. While the patterned structure manufacturing on the surfaces of aluminum alloy layers only has an improvement effect on the Mode-I interlaminar mechanical properties when VGCF was not dispersed into the laminate interfaces. Crack propagation and fracture surface observations of specimens using optical microscopy have also been carried out to study the toughening mechanism of the hybrid CARALL.

2. Experiments

2.1 Fabrication of specimens

To systematically investigate the effects of different toughing technologies, as shown in Table 1, 9 kinds of CARALL specimens have been fabricated in an autoclave for 3h at curing temperature of 130℃. The producing process was schematically shown in Fig. 1. The CFRP prepregs (TOHO

TENAX Co., Ltd, Japan), one commercial aluminum alloy AL2017 (TOHO Hitetsu-Kinzoku Co., Ltd, Japan) and VGCF (Showa Denko K.K, Japan) were used, where the details of the physical and mechanical properties were given in Table 2, where "A" denotes the acid-treatment, and "G" denotes patterned structure manufacturing with grooves. All of the specimens except the first kind CARALL were treated by acid etching process. In the acid etching process, the aluminum alloy layers were socked in 1mol/l nitric acid for 24h to increase their surface roughness. In addition to acid etching treatment, the aluminum alloy layers of the last four kinds of specimens were also processed with small grooves which were vertical to the fiber direction of the CFRP laminates. The dimensions of the grooves were shown in Fig. 2. Moreover, in some specimens, three different contents of VGCF, as the reinforcement for interface, were dispersed at the interface of unidirectional CFRP laminates and the aluminum alloy layers during the hand lay-up process,

Table 1. Specimen list

Specimens	Acid treatment	Grooved	VGCF
CARALL	—	—	—
A-CARALL	○	—	—
A-CARALL(10)	○	—	10 [g/m^2]
A-CARALL(20)	○	—	20 [g/m^2]
A-CARALL(30)	○	—	30 [g/m^2]
A-G-CARALL	○	○	—
A-G-CARALL(10)	○	○	10 [g/m^2]
A-G-CARALL(20)	○	○	20 [g/m^2]
A-G-CARALL(30)	○	○	30 [g/m^2]

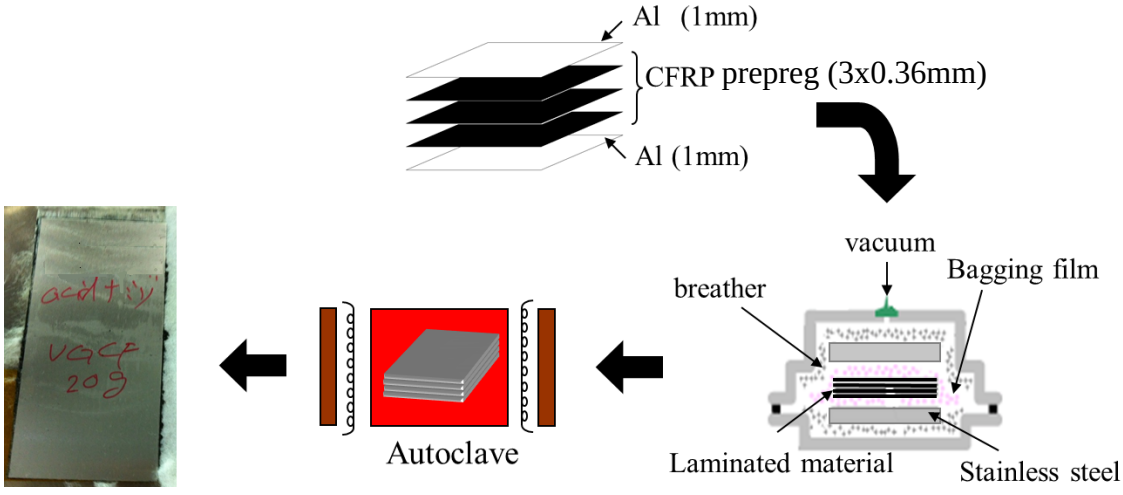

Figure 1. Schematic illustration of specimen fabrication process

Table 2. Physical and mechanical properties of CFRP prepregs, AL2017 and VGCF

CFRP prepreg		VGCF	
Young's modulus (Fiber direction)	116.8GPa	Diameter	150nm
Young's modulus (Transverse direction)	8.83GPa	Length	10-20mm
CF content	63%	Aspect ratio	10-500
AL2017		Density	2.0g/cm^3
Young's modulus	80GPa	Young's modulus	273-760GPa
Tensile strength	375MPa	Tensile stress	2700-3500MPa

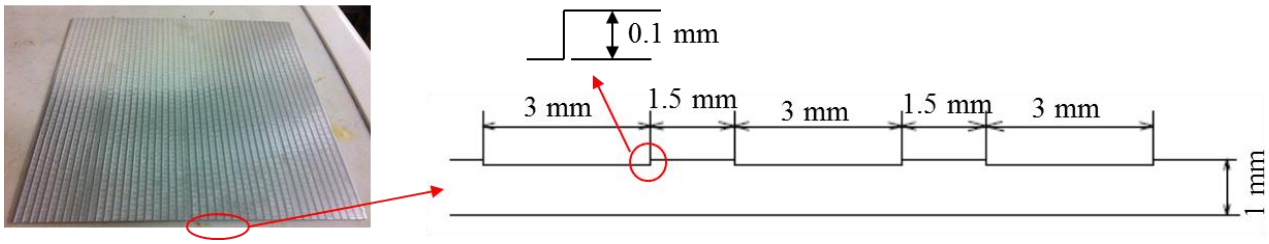

Figure 2. Dimensions of the grooves on the aluminum alloy layer

where a simple and newly-developed fabrication technology with low production cost, i.e., *powder method* [10], was employed.

2.2 DCB test procedure

In order to evaluate the Mode-I interlaminar fracture toughness, DCB tests have been carried out using a universal material testing machine at 25^{o}C by referring to Japanese Industrial Standards (JIS) K7086 [11]. Two specimens for each type of laminate with different toughing treatments were cut from the fabricated panels, where mark lines were painted on side surface for crack length measurement. The dimensions of specimens were schematically depicted in Fig. 3. Tensile loads

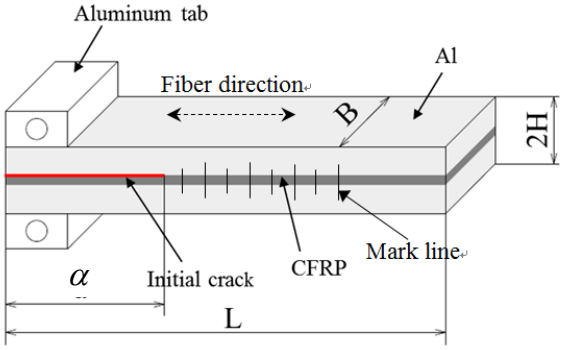

Length L=125mm; Width B=20mm; Height H=2.36mm~
Initial crack length *a*=45mm
Figure 3. Specimen for DCB tests

were applied at two aluminum tabs at one end of the specimen by using special apparatus through universal joints at a crosshead speed of 0.5mm/min. As given in Ref. [11], G_{IC} at the initial stage of crack growth and fracture resistance G_{IR} during crack propagation process can be calculated as a function of the crack growth, which is obtained by visually measuring the side surface of specimen. First, the relationship between the crack length a, and the compliance of load-COD (crack opening displacement) curve λ, are expressed in the following equation,

$$\frac{a}{2H} = \alpha_1 (B\lambda)^{\frac{1}{3}} + \alpha_0 \tag{1}$$

$$\lambda = \frac{\delta}{P} \tag{2}$$

Here δ and P stand for COD and the applied force respectively, α_0, α_1 are the fitted coefficients obtained from the experimental relation between a and λ. Then, by using the compliance method of homogeneous isotropic materials in classical fracture mechanics, G_{IC} and G_{IR} can be evaluated as follows,

$$G_{IC} = \frac{3}{2(2H)} \left(\frac{P_C}{B} \right)^2 \frac{(B\lambda_0)^{\frac{2}{3}}}{\alpha_1} \tag{3}$$

$$G_{IR} = \frac{3}{2(2H)} \left(\frac{P_R}{B} \right)^2 \frac{(B\lambda)^{\frac{2}{3}}}{\alpha_1} \tag{4}$$

where P_C is the critical load at the initialization of crack growth, and P_R the load during crack growth process, which can be obtained from load-COD curves.

3. Results and discussion

3.1 Mode-I interlaminar fracture toughness

Typical load-COD curves were plotted in Fig. 4, which shows the comparison of four representative types of specimens, i.e., CARALL, A-CARALL, A-CARALL(20), and A-G-CARALL. Critical loads at crack growth P_C for various types of specimens, which are obtained from peaks loads in Fig. 4, were shown in Fig. 5. From Figs. 4 and 5, it can be found that P_C of A-CARALL, A-CARALL(20), and A-G-CARALL were higher than that of base CARALL, which indicates the reinforcement effect of acid etching treatment, patterned surface manufacturing and VGCF interlayer. The highest P_C occurs in the case of A-CARALL(20), which is about 12 times higher than that of the base CARALL laminates and 4 times higher than that of the A-CARALL specimen.

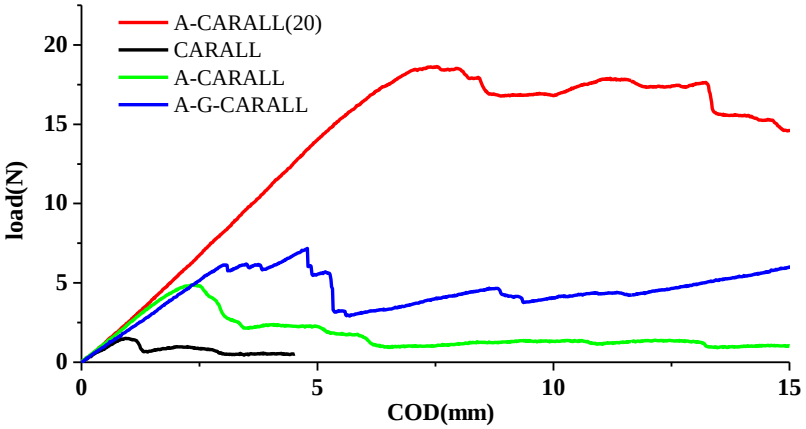

Figure 4. Comparison of load-COD curves for four kinds of specimens

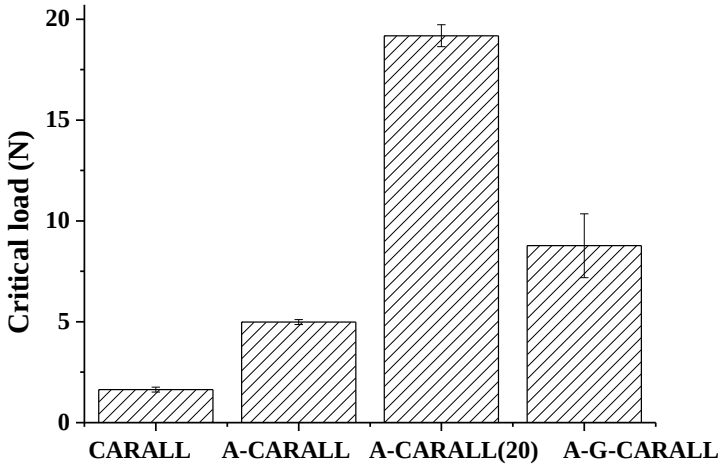

Figure 5. Critical load P_C for four kinds of specimens

Based on the load-COD curves of all fabricated samples and Eqs. (3-4), Mode-I fracture toughness G_{IC} and fracture resistance G_{IR} were demonstrated in Figs. 6 and 7 respectively. Note that G_{IR} was obtained by averaging the G_{IR} values of 5 points within the range of increment of crack length from 20 mm to 40 mm. For better understanding of the results from Figs. 6 and 7, two different situations were discussed. In the first situation, no VGCF was added into the specimens. In this case, it can be found from Figs. 6 and 7 that G_{IC} and G_{IR} were increased greatly for the A-CARALL and A-G-CARALL specimens. This indicates that the acid etching treatment can enhance the interlaminar mechanical properties of hybrid CARALL effectively. Without the addition of VGCF(0g/m^2), the higher G_{IC} and G_{IR} of A-G-CARALL compared to that of A-CARALL demonstrates that the patterned surface manufacturing in the acid treatment aluminum alloy layers can further improve the interlaminar mechanical properties of hybrid CARALL. Therefore, in the case of no nanofiller, the optimal toughing technique was the combination acid treatment and patterned surface manufacturing. In the other situation, VGCF interlayer was included in the specimens. In this case, we can see from Figs. 6 and 7 that the G_{IC} of A-CARALL and A-G-CARALL specimens were both improved significantly with the addition of VGCF. In particular, the specimens with VGCF 20g/m^2 loading have the highest fracture toughness which is of approximate 41 times higher G_{IC} than that of the pure CARALL specimen. However, as VGCF

content increases above 20g/m^2, the fracture toughness tends to decrease. By increasing the VGCF content to 30g/m^2, the G_{IC} of these specimens are approximate one half of the 20g/m^2 specimens. Moreover, it is easy to find that although the patterned surface can improve the interlaminar mechanical properties of A-CARALL composite without VGCF addition, however, when VGCF was added into the specimens, the G_{IC} of A-G-CARALL is all lower than that of A-CARALL except A-G-CARALL(30) specimen. This indicates that the improvement effects of VGCF addition for A-W-CARALL were lower than A-CARALL specimens. Therefore, in this case, the optimal toughing method was acid treatment combined with 20g/m^2 VGCF or 10g/m^2 VGCF. Note that the G_{IC} of A-CARALL(20) is only slightly higher than A-CARALL(10), however, the VGCF loading is two times of A-CARALL(10). As for G_{IR}, the trend of results was almost the same as that of G_{IC}, except for the result of A-G-CARALL(20). G_{IR} of the specimens increases with the addition of VGCF, passes through a peak value (for A-CARALL at 20g/m^2 loading, for A-G-CARALL at 10g/m^2 loading), and then decreases.

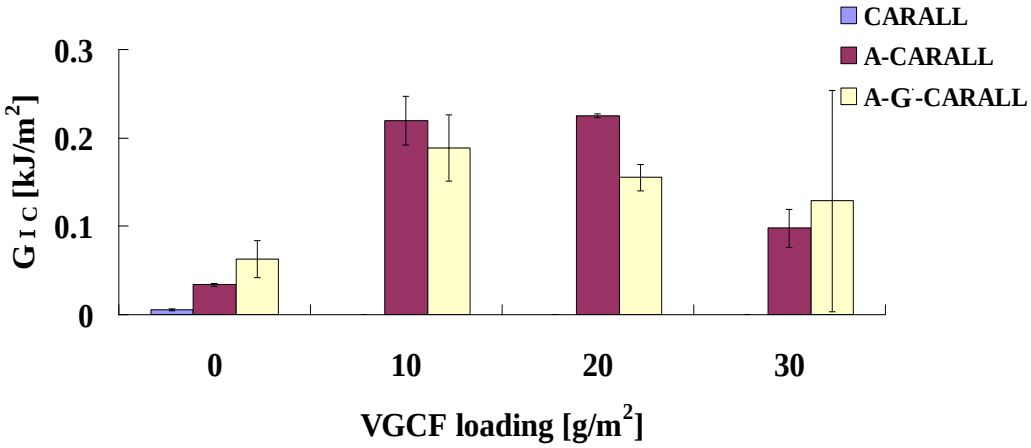

Figure 6. Comparison of G_{IC} for various specimens

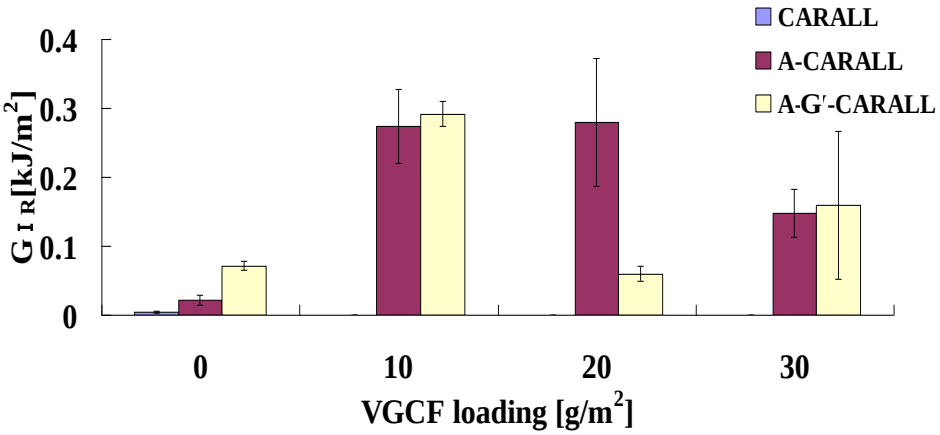

Figure 7. Comparison of G_{IR} for various specimens

3.2 Crack path and fracture surface observations

To uncover the relevant toughening mechanisms involved, the following experimental observations have been conducted.

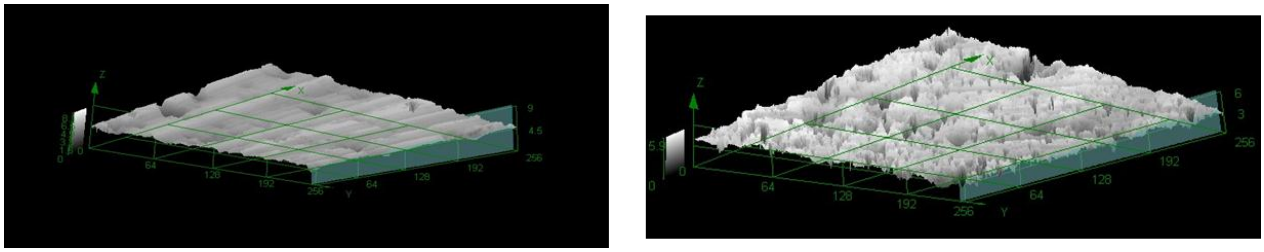

Figure 8. Surface morphology of the aluminum layers (a) before and (b) after acid etching treatment

For the first case, no VGCF was added into the specimens. Figure 8 describes the surface morphology of the aluminum layers before and after acid etching treatment respectively. It can be found that the acid etching treatment have produced a rough surface on the aluminum plate which consist of many small holes, grooves. The average diameter is about 18μm and the depth is approximately 2-5μm. When a liquid epoxy resin is applied to the rough surface, it conforms to the rough surface and tends to fill up the irregularities of the substrate surface such as microgrooves, holes. Consequently, mechanical interlock forms after the epoxy resin is cured. Due to the formed mechanical interlock, cohesive failure of the epoxy resin occurs near the interface as the epoxy is peeled away from the substrate, resulting in the crack path deviating from the interface. Such deviation of crack path away from the interface usually results in the increase of fracture surface area and requires additional energy associated with the crack propagation within the polymer. Moreover, cohesive failure, caused from the molecular decohesion of the polymer resin, expends larger energy for crack propagation than interfacial failure [4]. Furthermore, plastic energy dissipation in the bulk polymer material is effectively-induced during the crack growth in the polymer region rather than during the crack growth at the interface. Therefore, the acid etching treatment can effectively enhance the interface strength. As for the patterned structure manufacturing, the crack path deflected at the position of patterned grooves as shown in Fig. 9. Therefore, more cohesive failure occurred and more fracture surface formed during the crack propagation which explains the improvement of G_{IC} and G_{IR} compared to that of A-CARALL specimen.

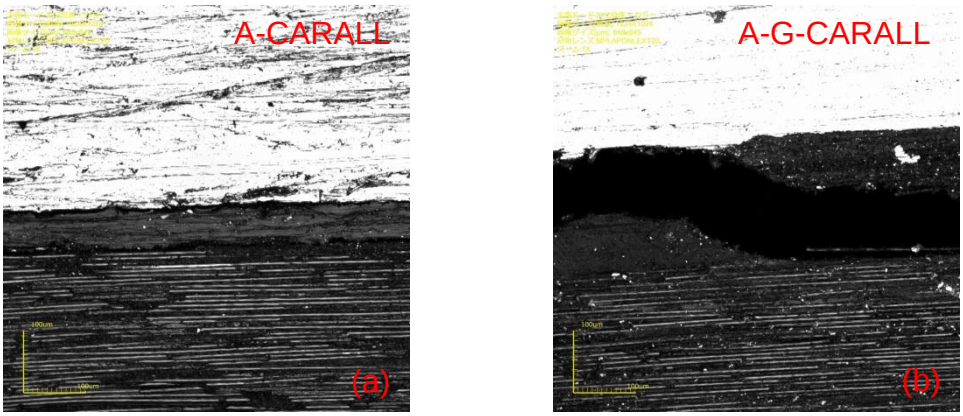

Figure 9. Crack propagation of A-CARALL and A-G-CARALL speimens

Figure 10 shows the fracture surface of three kinds of specimens which also confirm the aforementioned explanation. It can be found from Fig. 10(b) that there is more residual epoxy resin

on the fracture surface of A-CARALL specimen compared to CARALL specimen which indicates the more cohesive failure occurred in the A-CARALL specimen. Therefore, the fracture toughness of A-CARALL is higher than that of CARALL. From Fig. 10(c) we can see there are some fractured carbon fibers in the groove position which play a "bridging" role to resist the delamination propagation. Moreover, there is more cohesive failure than the A-CARALL specimen due to the existence of patterned grooves. This may explain the higher G_{IC} of A-G-CARALL than that of A-CARALL.

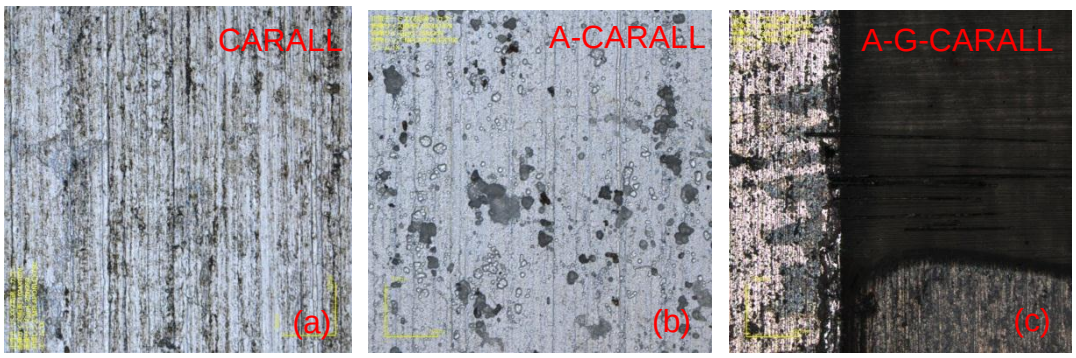

Figure 10. Fracture surface of (a) CARALL, (b) A-CARALL, (c) A-G-CARALL

For the second case, VGCF were included in the specimens. It can be found from Fig. 11(a) that almost all of the fracture surface were covered with residual epoxy resin and fractured fiber due to the proper addition of VGCF. This indicates that a lot of cohesive failure and "bridging" effect occurred on the fracture interface of A-CARALL(10) specimen. Therefore the fracture toughness was increased significantly compared with that of no VGCF. This is the same for Fig. 11(b), compared to A-G-CARALL, the residual epoxy resin and fractured fibers were left not only on the groove position but also on the flat part. This indicates that the flat part on the fracture surface of A-G-CARALL(10) was also contribute to the improvement of fracture toughness, which explains the enhancement of G_{IC} compared to A-G-CARALL specimens.

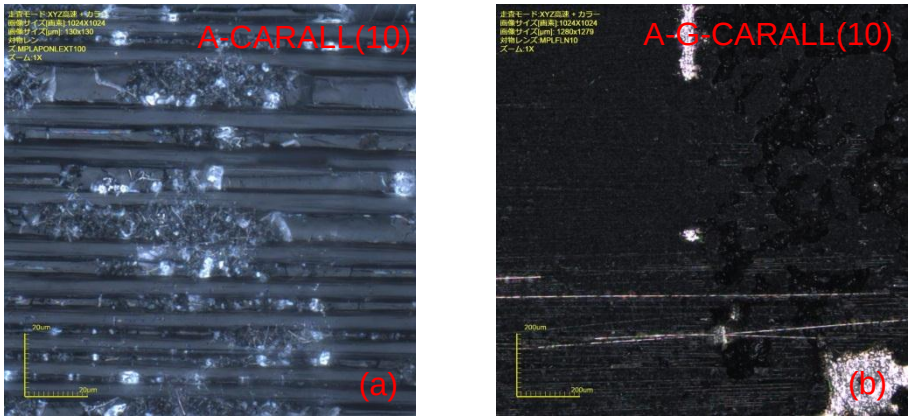

Figure 11. Fracture surface of (a) A-CARALL(10), (b) A-G-CARALL(10)

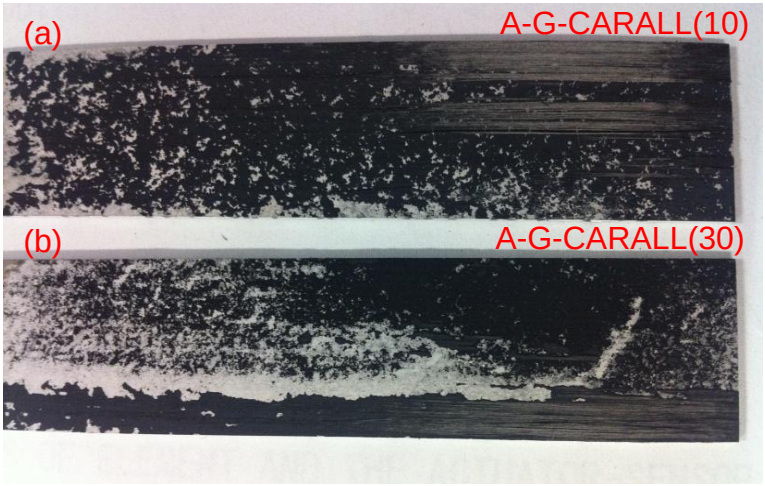

Figure 12. VGCF dispersion condition of (a) A-G-CARALL(10), (b) A-G-CARALL(30)

From the above analysis, it reveals that the incorporation of proper content of VGCF at interface of the hybrid CARALL results in the enhancement of interlaminar fracture toughness. However, the overdose of VGCF in the interface of CFRP and aluminum alloy layer may cause the decrease of its fracture toughness. This may be explained by Fig. 12, which shows that the dispersion of VGCF on the A-G-CARALL(10) specimen is better than that of the A-G-CARALL(30) specimen. The VGCF agglomerate condition of A-G-CARALL(10) specimens was not so severe. However, when the VGCF area density reaches to 30 g/m^2, as shown in Fig. 12(b), the fracture surface containing some large defects caused by insufficient dispersion of VGCF can be seen clearly, which implies its lower fracture toughness.

4. Conclusions

In this study, we systematically investigated the effects of various toughing methods on the mode-I fracture toughness of hybrid CARALL. The following conclusions can be made:

1. When there is no VGCF addition, by carrying out DCB tests, the critical load and Mode-I fracture toughness of hybrid CARALL have been verified to be improved with acid etching treatment. And the patterned surface manufacturing on the aluminum alloy layers can further enhance the fracture toughness and resistance based on the acid etching treatment.
2. The fracture toughness of A-CARALL and A-W-CARALL was improved significantly by adding controlled amount of VGCF into the interface of CFRP and aluminum layer. However, the improvement was less for A-W-CARALL compared to that of A-CARALL. This indicates that, when VGCF was dispersed into the hybrid CARALL, the patterned surface may have a negative effect.
3. The reinforcement and toughening effects of VGCF interlayer depend on the area density of VGCF, which do not certainly increase as the addition amount of VGCF increases. The fracture toughness of the specimen first increases with the addition of VGCF, passes through a peak value, and then decreases. From the previous results, at least for the fabrication method described in this work, the best value of VGCF area density at the interface is 20 g/m^2.

References

[1] P.Y. Chang, P.C. Yeh, J.M. Yang, Fatigue crack initiation in hybrid boron/glass/aluminum fiber metal laminates. Materials Science and Engineering: A, 496 (2008) 273-280.

[2] Q. Yao, Modeling and characterization of interfacial adhesion and fracture. PhD thesis, Georgia Institute of Technology, USA, (2000).

[3] I.H. Yun, W.S. Kim, K.H. Kim, J.M. Jung, J.J. Lee, H.T.Jung, Highly enhanced interfacial adhesion properties of steel-polymer composites by dot-shaped surface patterning. Journal of Applied Physicals, 109 (2011) 074302.

[4] W.S. Kim, I.H. Yun, J.J. Lee, H.T. Jung, Evaluation of mechanical interlock effect on adhesion strength of polymer-metal interfaces using micro-patterned surface topography. International Journal of Adhesion & Adhesives, 30 (2010) 408-417.

[5] Q. Yao, J. Qu, Interfacial versus cohesive failure on polymer-metal interfaces in electronic packaging-effects of interface roughness. Journal of Electronic Packaging, 124 (2002) 127-134.

[6] C.J. Jang, W.S. Kim, H.C. Kim, J.J. Lee, J.W. Jeong, Study on the nano and micro surface morphology effects on interfacial strength of adhesively bonded biomaterials. Procedia Engineering, 10 (2011) 2585-2590.

[7] Jr. E.D. Reedy, N.R. Moody, J.A. Zimmerman, X. Zhou, M.S. Kennedy, W.M. Mook, D.F. Bahr, Effect of nanoscale patterned interfacial roughness on interfacial toughness. Sandia National Laboratories Report, USA, (2007).

[8] R.M.H. Jen, Y.C. Tseng, C.H. Wu, Manufacturing and mechanical response of nanocomposite laminates. Composites Science and Technology, 65 (2005) 775-779.

[9] M. Arai, Y. Noro, K. Sugimoto, M. Endo, Mode I and mode II interlaminar fracture toughness of CFRP laminates toughened by carbon nanofiber interlayer. Composites Science and Technology, 68 (2008) 516-525.

[10] Y. Li, N. Hori, M. Arai, N. Hu, Y.L. Liu, H. Fukunaga, Improvement of interlaminar mechanical properties of CFRP laminates using VGCF. Composites: Part A, 40 (2009) 2004-2012.

[11] JIS K 7086-1993. Testing methods for interlaminar fracture toughness of carbon fiber reinforced plastics. Tokyo: Japan Standards Association, (1993).

Structure and Magnetic Properties of Perovskite $LaFeO_3$ Nanocrystals Synthesized Via Reverse Micelle Technique

Abdullah A. Saad[1*], Wasi Khan[1], Pooja Dhiman[2], A. H. Naqvi[1], M. Singh[2]

[1]Centre of Excellence in Materials Science (Nanomaterials), Department of Applied Physics, Z.H. College of Engg. & Tech., Aligarh Muslim University, Aligarh 202 002, U.P., India

[2] Department of Physics, Himachal Pradesh University, Shimla-171 005, India

* Corresponding author: abdullah_talha2004@yahoo.com

Abstract Orthorhombic structure perovskite $LaFeO_3$ (LFO) nanoparticles (NPs) were prepared by reverse micelles method. The control of particle size was achieved by varying the water to surfactant molar ratio. The dried precipitate was transformed to pure $LaFeO_3$ phase by calcinations at 750 ºC. The average particle size was found to increase with increase in water to surfactant ratio(R). The nanostructure properties were studied by using contact mode of atomic force microscopy (AFM), X-ray diffraction (XRD) and scanning electron microscopy (SEM) equipped with energy dispersive X-ray spectrometer (EDS) techniques. These techniques led themselves very well to investigate the structure of NPs and to find out properties and structure on surface of LFO. At room temperature the magnetic properties (M–H) were measured using a vibrating sample magnetometer (VSM) with a maximum magnetic field of 20 kOe.

Keywords Reverse micelle, Nanoparticles, XRD, Magnetization

1. Introduction

Reverse micelles, or water-in-oil microemulsions, incorporate a variety of solutes. The distribution of the solute between the surrounding solvent and the micelles can be described in terms of a partition constant based on a two pseudophases model that can be expanded to three pseudophases in micelles with high water to surfactant mole ratios. In these systems, two partition constants can be defined, one between the external solvent and the micellar interface, and other between the external solvent and the inner water pool [1]. The perovskite structures with general formula ABO_3 have been formed by mixed oxides of rare earth elements and d transition metals. Lanthanum ferrite ($LaFeO_3$) has orthorhombic symmetry perovskite structure (a= 8.135 Å, b= 6.040 Å, and c= 8.540 Å) and an antiferromagnetic insulator with Nell temperature T_N = 750K [2]. These materials are interesting for catalytic applications due to the extensive range of elemental compositions that can be prepared as crystalline structures [3]. The molecular structure of the surfactant affects the size of micelle water pools and is it common in some surfactant systems to use a co-surfactant to produce a larger range of micelle sizes, such as CTAB, NP4 and NP7. It has been shown that using this combination also improves solubilization and overall micelle stability when compared to the corresponding single surfactants [4]. By using reverse micelles, we have been able to control the size and partially the shape of metallic copper particles. Recently we observed that the reducing agent plays an important role in the control of particle size and in the final oxidation state at the surface.

2. Experimental

$LaFeO_3$ NPs were prepared using reverse micelle technique. A quaternary system of iso-octane/CTAB/n-buty alcohol/water was selected in this RM process. In this process we used two

kinds of RM solutions namely RM1 and RM2. For first solutionRM1contained (5 wt %) an aqueous solution of an equimolar mixture (0.1M) of ($La(No_3)_3.6H_2O$) and ($Fe(No_3)_3.9H_2O$), CTAB as a surfactant (7.5 wt%), n-buty alcohol as a co-surfactant (7.5 wt%) and iso-octane as oil (30 wt%). The stirring was continued for 30 min resulting in a stable reverse micelle (RM1). While RM2 contained the same constituent as RM1 except that the aqueous solution was NaOH (0.1 M) instead of ($La(No_3)_3.6H_2O$) and ($Fe(No_3)_3.9H_2O$) was prepared under similar conditions. These two reverse micelles were mixed under constant stirring and a brown color solution was obtained. In addition ammonium NH_3 was slowly added to adjust the PH and stirred 24 h on a magnetic stirrer. The resulting precipitate was separated from the surfactant and a polar solvent by centrifugation and washing it one time by ethanol and three times by distilled water. The precipitate was dried in an oven at 80 ºC for 6 h to obtain $LaFeO_3$ powder and heated at 750 ºC for 6 h in air.

The crystal structure was investigated by X-ray diffraction (Rigaku, Japan, Miniflex-II) using Cu-K_α radiation (λ= 1.5418 Å) in 2θ range from 20º to 80º. A scanning electron microscope (JEOL JSM-6510LV) equipped with an energy dispersive spectrometer (EDS) was used to check the morphology and particle size. The atomic force microscopy (Veeco-contact mode) was used to examine the morphology and the surface roughness. Room temperature magnetic measurements (M–H) were measured using a vibrating sample magnetometer (VSM) with a maximum magnetic field of 20 kOe.

3. Results and discussions

The X-ray diffraction (XRD) pattern of $LaFeO_3$ nanopowders calcined at 750 ºC is shown in Fig. 1.

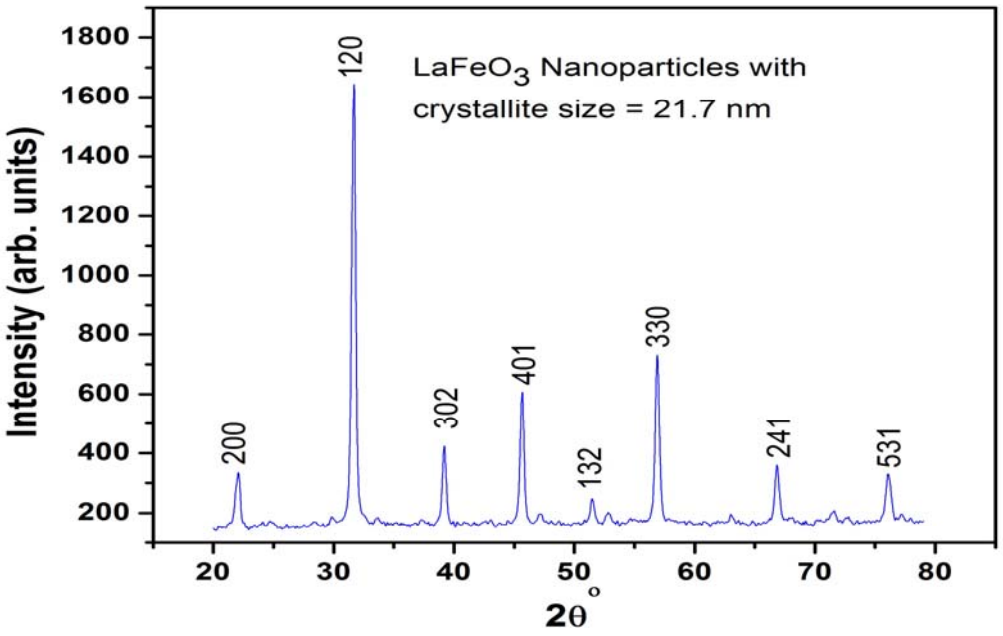

Figure 1. XRD pattern of the LFO NPs.

The position of the all peaks confirmed the high crystallinity and perovskite structure of the NPs and no other impurity peaks were detected in the XRD patterns. Furthermore, the products of the

three samples were observed in orthorhombic perovskite structure with space group Pbnm, which is well consistent with the standard JCPDS card of perovskite $LaFeO_3$ (JCPDS88-0641) [5] and lattice parameters were found a= 8.135 Å, b= 6.040 Å, and c= 8.540 Å. The average of crystallite size using the most intense peak (120) at angle 2θ~33° was estimated from the XRD pattern by using Debye–Scherer's formula.

The AFM images of $LaFeO_3$ standard roughness, two and three dimensions have shown in Fig. 2. The Fig. 2a, 2b and 2c are displayed the standard roughness of $LaFeO_3$ NPs, where R_a is the roughness average, R_p is the maximum height of the profile above the mean line, R_t is the maximum peak to valley height the profile and R_{pm}, R_{tm} are the mean values more representative of the entire profile. Fig. 2d and 2e are shown the uniform grains of $LaFeO_3$ NPs surface morphology. Actually, a homogeneous surface was formed and the grains were observed in different area. The AFM images for two and three dimensions reveal grains with size of few tens nanometers, that is meaning that the micron sized grains consisted of an agglomeration of small grains.

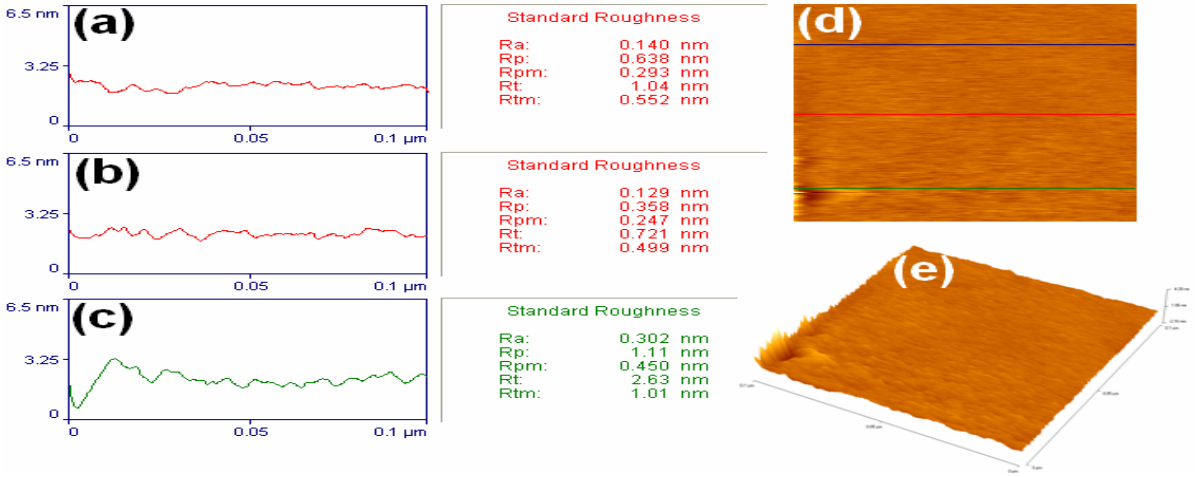

Figure 2. (a, b and c) the standard roughness area of $LaFeO_3$ NPs, (d) two dimensions AFM image for $LaFeO_3$ and (e) three dimensions AFM image for the same.

SEM image of $LaFeO_3$ NPs is displayed in Fig. 3a. The surface morphology of NPs reveals the uniform grains, which displays that the complete incorporation of $LaFeO_3$ as supported by XRD analysis. In addition the EDS analysis also confirms the presence of La, Fe and O elements in good stoichiometric as displayed in the Fig. 3b.

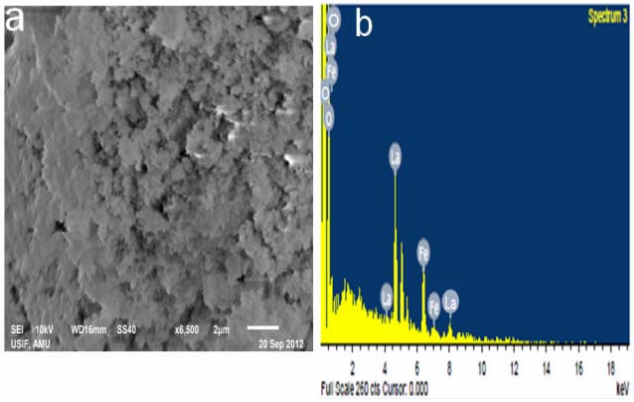

Figure 3. a) SEM image of the LFO NPs b) EDS microstructure of LFO NPs spectrum for the same.

The magnetization hysteresis (M-H) loops measured at room temperature of $LaFeO_3$ with maximum applied field of 20 kOe as displayed in Fig. 4. We can see that the magnetization of $LaFeO_3$ NPs is 0.136(emu/gm). The plot of the magnetization indicting that the ferromagnetic behavior was observed on the $LaFeO_3$ NPs.

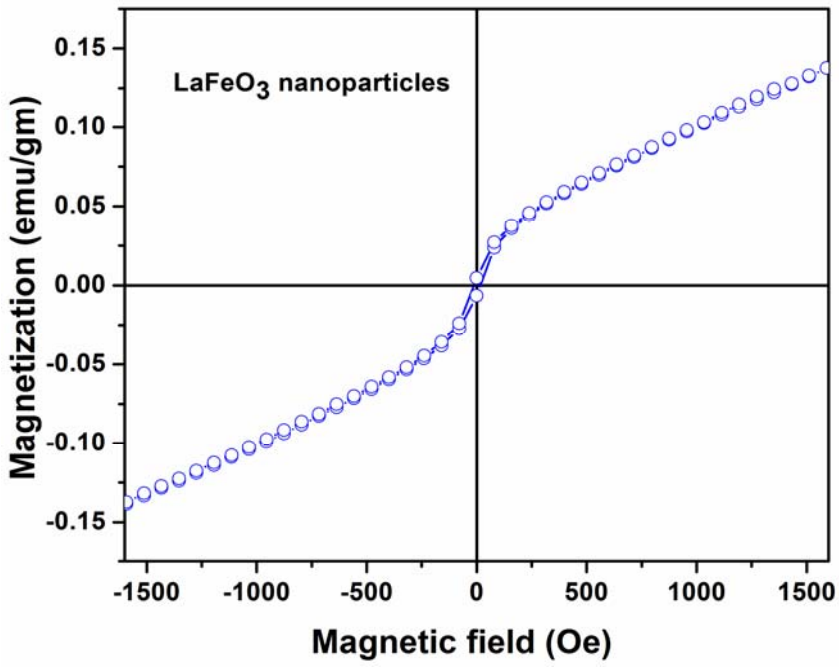

Figure 4. Magnetization versus field for $LaFeO_3$ NPs.

In summary, the $LaFeO_3$ NPs were successfully prepared by reverse micelle method, orthorhombic perovskite structure and phase conformation was confirmed by X-ray diffraction. Ferromagnetic behavior was observed in the $LaFeO_3$ NPs.

Acknowledgements

Authors are greatly thankful to the Council of Science & Technology (CST), Govt. of UP for financial support in form of Centre of Excellence in Materials Science (Nanomaterials) and DST, Govt. of India for M. Tech. Programme under Nanomission. The first Author is also greatly thankful to Albayda University, Republic of Yemen for providing him scholarship.

References

[1] J. J. Silber, A. B. E. Abuinb, E. Lissib, Interactions of small molecules with reverse micelles. Advances in Colloid and Interface Science, 82 (1999) 189-252.

[2] H. Falcon, E. A. Goeta, G. Punt, R. E. Carbonio, Crystal structure refinement and stability of $LaFe_xNi_{1-x}O_3$ solid solutions. J. Solid State Chem., 133 (1997) 379-385.

[3] M. Wallim, N. Cruise, U. Klement, A. Palmqvist, M. Skoglundh, Preparation of Mn, Fe and Co based perovskite catalystsusing microemulsions. Collids surf. A. Physicochem. Eng., 238 (2004) 27-35.

[4] M. A. Michaels, S. Sehrwood, M. Kidwell, M. J. Allsbrook, S. A. Morrison, S. C. Rutan, E. E. Carpenter, Quantitative model for prediction of hydrodynamic size of nonionic reverse micelles. J. Colloid and Interface Science, 311 (2007) 70–76.

[5] D. Wang, M. Gong, Surface and shape anisotropy effects in $LaFeO_3$ nanoparticles. J. Appl. Phys., 109 (2011) 114304.

Cap Effect on Pull-out Behavior of CNT in CNT-reinforced Nanocomposites

Ning Hu[1,*], Yuan Li[2], Sen Liu[1]

[1] Department of Mechanical Engineering, Chiba University, Chiba 263-8522, Japan
[2] Department of Nanomechanics, Tohoku University, Sendai 980-8579, Japan
* Corresponding author: huning@faculty.chiba-u.jp

Abstract Systematic atomic simulations based on molecular mechanics are carried out to investigate the pull-out behavior of carbon nanotubes (CNTs) in CNT-reinforced nanocomposites. In contrast with open-ended CNT, capped CNT is incorporated into the current computational model to explore the effect of the CNT cap for the first time. Two common cases are discussed: the pull-out of a whole CNT from a polymer matrix in a CNT/Polymer nanocomposite, and the pull-out of the broken outer walls against the intact inner walls of a CNT (i.e., sword-in-sheath mode) in a CNT/Alumina nanocomposite. By analyzing the obtained relationship between energy increment and pull-out displacement, a set of simple empirical formulae is proposed to predict the corresponding pull-out force from the nanotube diameter. The obtained pull-out force agrees well with experimental measurement. Moreover, the much higher pull-out force in the case of capped CNT than that of open-ended CNT implies a great contribution of the CNT cap to the interfacial properties of CNT-reinforced nanocomposite. This finding provides valuable insight into designing nanocomposites with desirable mechanical properties.
Keywords Carbon nanotube, Nanocomposites, Mechanical properties, Pull-out behavior

1. Introduction

To date, many experiments have demonstrated that the pull-out of carbon nanotubes (CNT) from a matrix is a common critical phenomenon, as seen from observation of fractured surfaces of CNT-reinforced nanocomposites. CNT pull-out can be further divided into the following two categories: one is the pull-out of a whole CNT from a matrix [1-3] and the other is the pull-out of the broken outer walls against the intact inner walls embedded in matrix (the so-called sword-in-sheath mode) [4,5]. The reduced load carrying capability of CNT due to the above two representative pull-out modes may be detrimental to the overall mechanical properties of bulk nanocomposites, such as stiffness and strength [6]. Thus, the continuously increasing demand for nanocomposites with significant mechanical properties provokes a thorough investigation of this pull-out behavior with the hope of finding effective methods to improve the interfacial properties between CNTs and the matrix as desired.

Direct pull-out experiments [7-11] have been carried out in which the interfacial shear strength of CNT-reinforced nanocomposites was calculated by dividing the measured pull-out force by the embedded lateral area of CNT. On the other hand, various theoretical models [12, 13] based on continuum mechanics have also been developed to predict the interfacial shear strength. Moreover, atomic simulations [14, 15] have also provided an alternative method to predict the interfacial shear strength with the approach of potential energy variation.

However, to the best of our knowledge, there is no any systematical study about the effect of CNT's unique capped structure on CNT pull-out in CNT-reinforced nanocomposites, although this cap has a great influence on the pull-out of the outer walls against the inner walls of a multi-walled carbon nanotube (MWCNT) (i.e., interfacial sliding among nested walls in a MWCNT) [16-23]. It should be noted that the pull-out force of the outer wall against the inner walls in a MWCNT itself consists of the van der Waals (vdW) force and the frictional force between the walls. The frictional force may become significant when referring to the defects or chemical cross-linking [17-19]. On the other hand, for the perfect CNT, the vdW force will be dominant. In our previous experimental study [21] plus computational effort, due to very high quality of MWCNT, the frictional effect among the walls is very small as verified by the experimental evidences. Moreover, no direct quantitative comparison between the numerical pull-out forces and experimental data has been

reported to date since the existing numerical values are generally much (at least from 10 to several hundreds of times) lower than the existing experimental data. We have simulated the pull-out process of an open-ended CNT in detail based on molecular mechanics (MM) for CNT/Polymer [14] and CNT/Alumina nanocomposites [15]. As a continuous work, here, we investigate the pull-out behavior of a capped CNT in the above two nanocomposites *for the first time*. By carrying out a series of MM pull-out simulations, the detailed variation of systematic energy increment during the pull-out process is obtained. A set of empirical formulae is, therefore, proposed to predict the corresponding pull-out forces with good consistence of existing experimental data.

2. Pull-out simulation of a capped CNT in CNT/Polymer Nanocomposite

The pull-out of a whole CNT from various polymer matrices has been clearly observed from fractured surfaces in various CNT/Polymer nanocomposites [1-3], which may imply comparatively weak interfaces between CNT and polymer matrices. To understand the inherent characteristics of this pull-out behavior, we have analyzed, in detail, the pull-out process of an open-ended CNT from a polyethylene (PE) polymer matrix in our previous work [14]. It has been concluded that the corresponding pull-out force is independent of nanotube length and nanotube chirality, but proportional to nanotube diameter. Moreover, we have also demonstrated [20, 21] that the CNT capped structure significantly affects the pull-out behavior of the outer walls against inner walls in a MWCNT in the sword-in-sheath mode based on massive quantitative comparisons between the MM results and experimental data.

Based on the above outcomes, to investigate the effect of the cap on CNT pull-out behavior, three capped single walled carbon nanotubes (i.e., SWCNTs(5,5), (10,10), (12,12)), which are of the same length of 2.46nm, but different diameters, are incorporated into the PE matrix, respectively. The construction of the simulation cell is described elsewhere in detail [14], in which only vdW interactions between CNT and matrix are modeled without considering the chemical bonds or mechanical cross-links.

The pull-out of the above three capped SWCNTs based on MM are carried out in a similar way with previous works [14, 15]. The pull-out process of the capped SWCNT(5,5) is schematically described in Fig. 1 as a representative example, where a prescribed displacement on the CNT is applied on its axial direction. Note that a much smaller displacement increment, Δx_1 of 0.01nm, than that of the 0.2nm in previous simulations [14] is adopted in the present simulation in order to explore the cap effect in a more detailed way.

It should be noted that the quasi-static characteristics of MM simulations yield a considerable improvement in the computational efficiency compared to that of traditional molecular dynamics (MD) simulations since the velocity components of the individual atoms within the system are ignored. In other words, the MM method is insensitive to the effects of thermal instability and kinetic excitation, and can therefore be expected to provide an accurate representation of the low

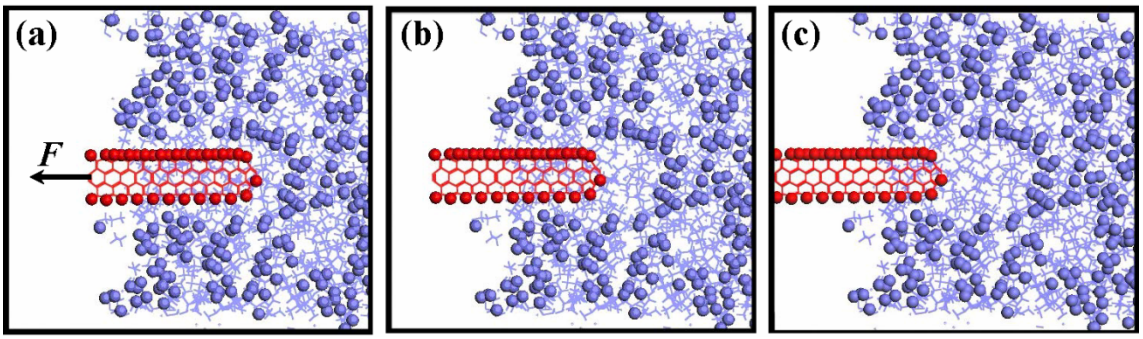

Figure 1. Pull-out process of SWCNT (5,5) from PE matrix

strain rate deformation of nano-scale materials.

The present results for the relationship between nanotube diameter and energy increment between two consecutive pull-out steps are shown in Fig. 2a for the three SWCNTs, where D_o is the nanotube diameter. It can be seen that for each SWCNT, the energy increment, ΔE, between two consecutive pull-out steps (referred to as *energy increment* hereafter for simplicity) increases rapidly to a peak value at a specified displacement (labeled as Stage-1 in Fig. 2a), then remains steady with continued pull-out (labeled as Stage-2 in Fig. 2a). Finally, ΔE decreases quickly and arrives at a comparatively flat stage (labeled as Stage-3 in Fig. 2a). After entering Stage-3, to save computational cost, the simulation stops without further pull-out once the energy increment becomes stable. It can be seen that this trend is surprisingly consistent with that of the pull-out of outer walls against the inner walls in a capped MWCNT [21]. Moreover, the maximum energy increment in Stage-2 (i.e., $\Delta E_{\max}$) increases with nanotube diameter.

The relationship between the maximum energy increment, $\Delta E_{\max}$ in Stage-2, and nanotube diameter D_o can be fit into a quadratic function (see Fig. 2b), as follows:

$$\Delta E_{\max} = 2.72 D_o^{\,2} - 3.65 D_o + 4.67 \tag{1}$$

in which $\Delta E_{\max}$ and D_o are in the units of kcal/mol and nm, respectively. In view of that the energy increment is equal to the work done by the pull-out force, the maximum pull-out force with the unit of nN, for the case of a capped SWCNT, can be evaluated as

$$F_{\mathrm{SWCNT}} = 1.89 D_o^{\,2} - 2.54 D_o + 3.25 \tag{2}$$

For the pull-out of a whole open-ended MWCNT from PE matrix [14], it is believed that only the outer three walls have an effect on the variation of energy increment during the pull-out process. The reason can be explained as follows: from the outermost wall to the innermost wall, the distance between the inner walls of the CNT and the pull-out interface increases gradually. The longer the distance is, the weaker the vdW interaction. Therefore, since the cut-off distance of the vdW interaction is around 0.95nm and the wall spacing of MWCNT is 0.34nm, the pull-out of a whole MWCNT with more than 3 walls can be simplified as that of a triple walled carbon nanotube (i.e., TWCNT) composed of the outermost three walls of the MWCNT. From MM simulations, the corresponding pull-out force is found to be approximately about 1.2 times of that of a SWCNT composed solely of the outermost wall of the MWCNT.

On this basis, for the pull-out of a whole capped MWCNT from PE matrix, we can approximately revise the above formula of the pull-out force as

$$F_{\mathrm{MWCNT}} = \lambda (1.89 D_o^{\,2} - 2.54 D_o + 3.25) \tag{3}$$

in which F_{MWCNT} and D_o are in the units of nN and nm, respectively. Note that the coefficient λ indicates the effect of the wall number, which is 1.0 for SWCNT and 1.2 for MWCNT.

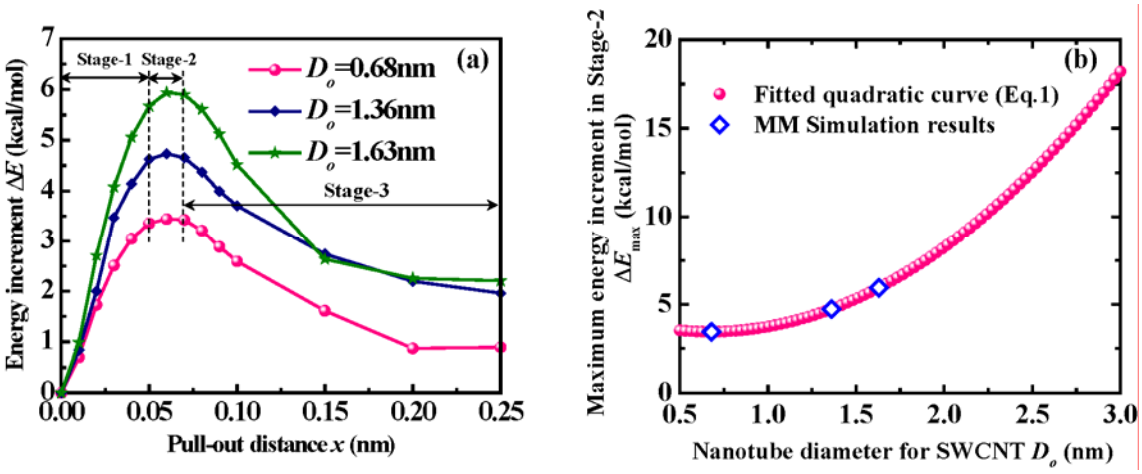

Figure 2. Energy increment during pull-out of SWCNT from PE matrix, (a) Energy increment ΔE versus pull-out displacement x; (b) Maximum energy increment in Stage-2 $\Delta E_{\max}$ versus nanotube diameter D_o

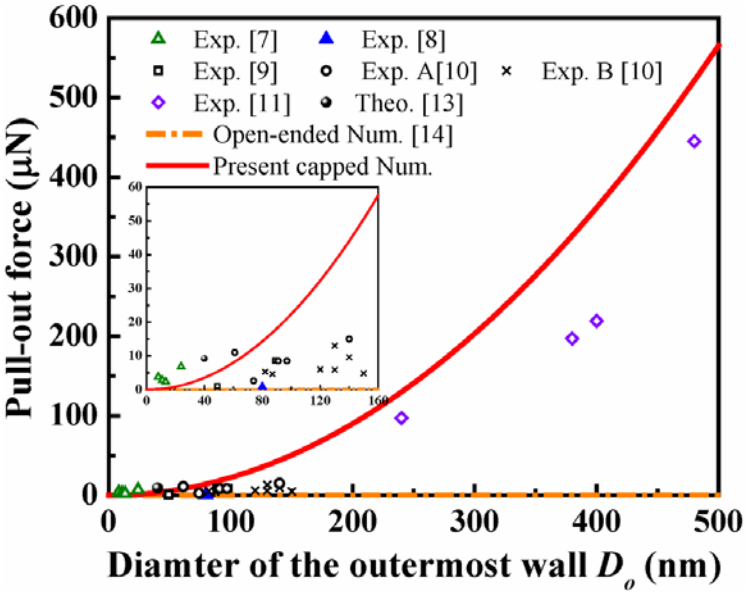

Figure 3. Comparison of experimental [7-11], theoretical [13] and present numerical pull-out forces in CNT/Polymer nanocomposites

Obviously, as given in Fig. 3, this predicted pull-out force for the capped MWCNT is much larger than that for open-ended CNT [14], which indicates the significant contribution of the CNT cap to the maximum pull-out force. Moreover, the predicted pull-out forces using the present method in Eq. (3) are also compared with the experimental results [7-11] in Fig. 3, in which the effect of polymer matrix type is ignored. It is found that the predicted values can comparatively effectively reflect the most of the experimental data (e.g., over 80%) very well, since it is very difficult to accurately match all experimental data at the nano-scale because of the difference of materials, fabrication conditions, test methods and etc. For example, Cooper *et al.* [7] attempted a drag-out configuration of a MWCNT bridging a hole in a CNT/Epoxy nanocomposite by loading the nanotube at its center. This set-up is analogous to a cable with two fixed ends and a center loading, in which the necessary force is obviously much higher than that during axial pull-out. On the other hand, the pull-out force measured by Barber *et al.* [8] is found to be much weaker than our predicted value. It can be explained by sample preparation, where their CNT is pushed into the molten polyethylene-butene thin film. Another set of pull-out tests are carried out using fractured specimens under tensile loading [9-11]. The small discrepancy can be attributed to the interface damage between CNT and matrix caused by tensile fracture, which can be positively recovered by the hot pressing method (Exp. A [10] in Fig.3) when compared to an untreated specimen (Exp. B [10] in Fig.3). It should be noted that there is large data scattering, even within the same research group. This scattering is probably due to the difficulty of nano-manipulation and precise measurement during these experiments.

The theoretical value calculated by multiplying the predicted interfacial shear strength [13] and the embedded lateral area of CNT is also incorporated into Fig. 3. Note that the adopted interfacial shear strength is predicted from experimental measured data using expansion of the classical Kelly-Tyson force balance method [22].

The above comparison validates the effectiveness of the proposed empirical formulae and further highlights the great contribution of the CNT cap to the pull-out force and interfacial properties of CNT/Polymer nanocomposites.

3. Pull-out Simulation of a Capped CNT in CNT/Alumina Nanocomposite

It has been experimentally reported that the sword-in-sheath mode is a common fracture mode for CNT/Alumina nanocomposites [4, 5]. The detailed process, as illustrated in Fig. 4, can be

summarized as follows [5]: initially, tensile stress leads to matrix crack formation and partial debonding. Then, as the displacement increases, some outer walls of the MWCNT break. The intact inner walls are then pulled away, leaving a fragment of the broken outer walls in the matrix (or the broken outer walls are pulled out against the intact inner walls). It should be noted that there are two pull-out interfaces, in contrast with the case of CNT/Polymer nanocomposites: one is between the outermost wall and the matrix, and the other is between the nested walls in the MWCNT. This observation indicates that this pull-out behavior, corresponding to the sword-in-sheath mode in CNT/Alumina nanocomposite, can be assumed to be the superimposition of the pull-out of the broken outer walls (Fig. 4b, I, left) against the matrix (Fig. 4b, I, right), and the pull-out of the broken outer walls (Fig. 4b, II, left) against the intact inner walls. By further decomposing the CNT into open-ended and capped components, the pull-out of the broken outer walls against the intact inner walls (Fig. 4b) can be divided into the pull-out of the open-ended component (Fig. 4b, II-O) and the pull-out of the capped component (Fig. 4b, II-C). It should be noted that the effect of the matrix (left) on the pull-out of the broken outer walls against the intact inner walls can be ignored, as the reported number of broken walls is about 10 or more [4], indicating a much longer distance from the matrix to the pull-out interface than the cut-off distance of the vdW interaction. The corresponding pull-out force for each part is discussed in the following:

(I)*Pull-out of broken outer walls against matrix*

As the number of the broken outer walls is usually more than 3, the model can be simplified as the pull-out of a TWCNT from alumina matrix. The corresponding energy increment for each pull-out step with constant displacement Δx_I of 0.2nm and the pull-out force can be predicted by [15]

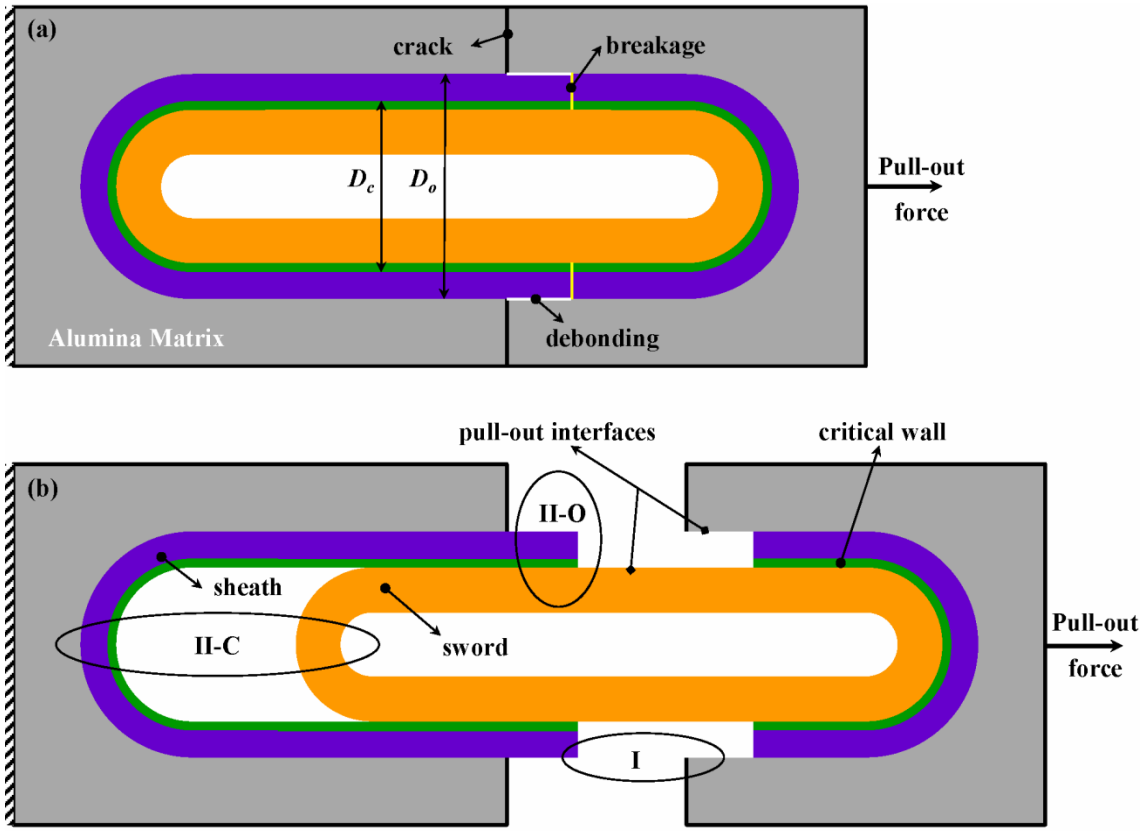

Figure 4. Schematic of CNT pull-out with sword-in-sheath mode in tensile tests of CNT/Alumina nanocomposites

$$\Delta E_{\mathrm{I}} = 58.26 D_o + 6.50$$
$$F_{\mathrm{I}} = \frac{\Delta E_{\mathrm{I}}}{\Delta x_{\mathrm{I}}} = 2.03 D_o + 0.23 \tag{4}$$

where D_o is the diameter of the outmost wall.

(II-O) ***Pull-out of open-ended component of broken outer walls against open-ended component of intact inner walls***

As the number of inner walls and outer walls are usually more than 3, the model can be simplified as the pull-out of a MWCNT with 5 walls, which consists of the immediate outer wall at the pull-out interface (the critical wall) in Fig. 4 and the two neighboring walls on each side [21]. The corresponding energy increment for each pull-out step with a constant displacement $\Delta x_{\mathrm{II\text{-}O}}$ of 0.2nm and the pull-out force can be therefore predicted by [21]

$$\Delta E_{\mathrm{II\text{-}O}} = 37.56 D_c - 10.5$$
$$F_{\mathrm{II\text{-}O}} = \frac{\Delta E_{\mathrm{II-O}}}{\Delta x_{\mathrm{II-O}}} = 1.31 D_c - 0.37 \tag{5}$$

where D_c is the diameter of the critical wall as shown in Fig. 4.

(II-C) ***Pull-out of capped component of broken outer walls against capped component of intact inner walls***

The corresponding energy increment for each pull-out step with a considerably smaller constant displacement of $\Delta x_{\mathrm{II\text{-}C}}$=0.01nm and the pull-out force can be predicted by [21]

$$\Delta E_{\mathrm{II-C}} = 1.29 \times (2.09 D_c^2 - 2.15 D_c + 0.94)$$
$$F_{\mathrm{II-C}} = \frac{\Delta E_{\mathrm{II-C}}}{\Delta x_{\mathrm{II-C}}} = 1.29 \times (1.45 D_c^2 - 1.49 D_c + 0.65) \tag{6}$$

In view of the above discussions, for the pull-out of a capped MWCNT from alumina matrix in a sword-in-sheath mode, the corresponding pull-out force can be assumed to be the sum of the above three parts (i.e., Eq. (4) for part I, Eq. (5) for part II-O, and Eq. (6) for part II-C):

$$F = F_{\mathrm{I}} + F_{\mathrm{II-O}} + F_{\mathrm{II-C}} = 1.87 D_c^2 - 0.61 D_c + 2.03 D_o + 0.7 \tag{7}$$

Note that the units of diameter and force are nm and nN, respectively.

The obtained relationship between nanotube diameter and the predicted pull-out force is shown in Fig. 5, which indicates that the pull-out force increases with wall diameters (D_o and D_c in Fig. 4) of both the outermost wall and the critical wall. The reason can be attributed to the atom number at both pull-out interfaces increases with the wall diameters. The larger the wall diameters, the stronger the vdW interaction needed to be overcome during the pull-out.

The results, without considering the effect of CNT cap, are also given in Fig. 5 based on the formula of

$$F^* = F_{\mathrm{I}} + F_{\mathrm{II-O}} = 2.03 D_o + 1.31 D_c - 0.14 \tag{8}$$

Obviously, the predicted pull-out force for capped MWCNTs is much larger than that for open-ended MWCNT, which indicates the significant effect of the CNT cap.

As of yet, it is impossible to carry out the corresponding experiment (Fig. 4) to validate the above proposed formula. Nevertheless, the present authors, e.g., Yamamoto *et al.* [5], have performed a series of MWCNT pull-out tests using an *in situ* SEM on fractured composite specimens by conducting bending tests, which strongly suggest that the broken outer walls of the MWCNT and the intact inner walls are completely pulled away, leaving the companion fragment of the outer walls in the alumina matrix. This process can be schematically illustrated in Fig. 6. It can be found that there is only one pull-out interface, in contrast with that in Fig. 5. By using the above

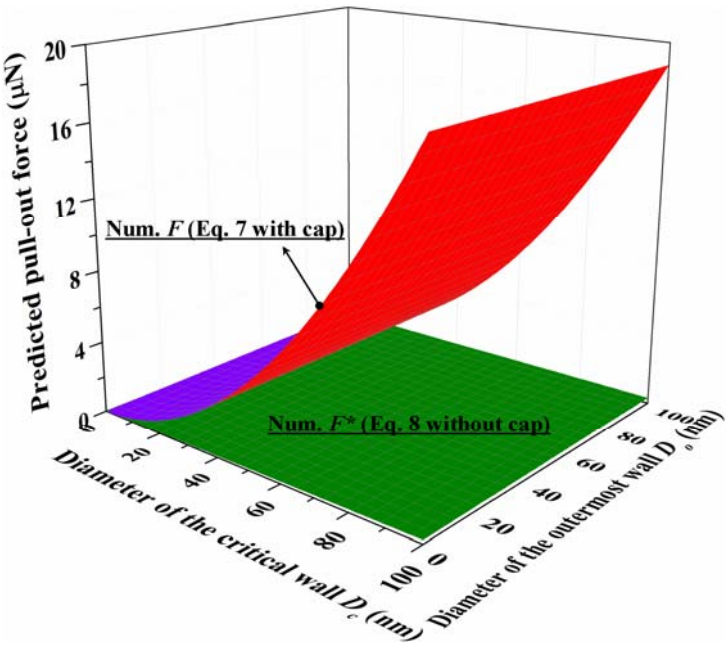

Figure 5. Comparison of numerical pull-out forces for capped and open-ended CNTs in CNT/Alumina nanocomposites

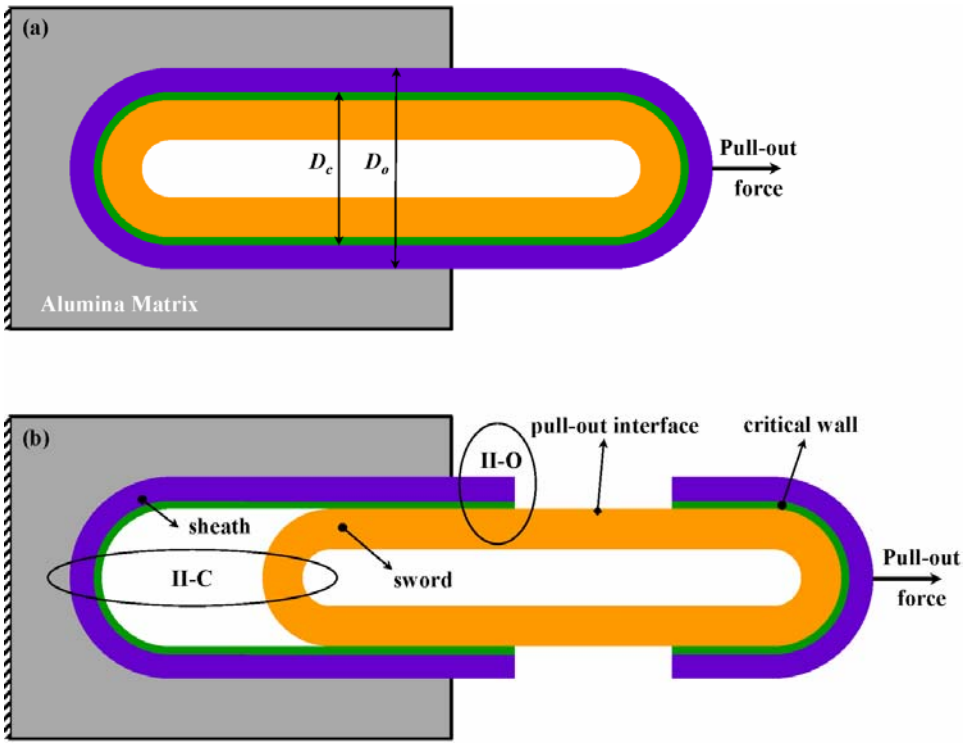

Figure 6. Schematic process of direct CNT pull-out experiment using fractured CNT/Alumina nanocomposite specimens [5]

method, the corresponding pull-out force should be composed only of part-II:

$$F^{**} = F_{\mathrm{II}} = F_{\mathrm{II-O}} + F_{\mathrm{II-C}} = 1.87D_c^{\,2} - 0.61D_c + 0.47 \qquad (9)$$

Note that both Eqs. (7) and (9) are dominated by $D_c^{\,2}$ and there is no big difference between F for the problem in Fig. 4 and F^{**} for the problem in Fig. 6. The present predicted pull-out forces by Eq. (9) are compared with the only one experimental value [5] obtained by directly performing CNT pull-out tests from CNT/Alumina nanocomposites in Table 1 and Fig. 7. Note that the diameter of the critical wall is calculated from the outermost wall and the number of broken walls observed in

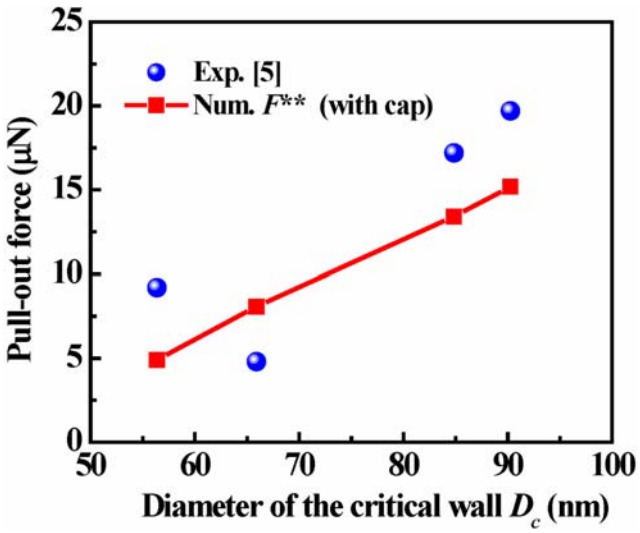

Figure 7. Comparison of experimental [5] and numerical pull-out forces in CNT/Alumina nanocomposites

Table 1 Comparison of experimental [5] and numerical pull-out forces in CNT/Alumina nanocomposites

D_o (nm)	Number of broken outer walls	D_c (nm)	Pull-out force (μN)	
			Experimental [5]	Numerical F** (Eq. (9))
71	15	65.9	4.8	8.08(+68%)
72	46	56.36	9.2	5.91(-36%)
93	24	84.84	17.2	13.41(-22%)
94	11	90.26	19.7	15.18(-23%)

experiments, with the assumption that the wall distance between MWCNT walls is 0.34nm. Obviously, there is good consistency between the experimentally measured pull-out forces and the numerical predictions by neglecting large data scattering resulted by great difficulties in nano-manipulation and precise measurement. The results suggest that the above analysis method is feasible and that the proposed empirical formula can approximately predict the pull-out force.

4. Conclusions

The present work incorporates, for the first time, a capped CNT into a computational model to investigate its pull-out behavior in CNT-reinforced nanocomposite. By using pull-out simulations based on MM, a set of simple and empirical formulae is proposed to predict the corresponding pull-out force, which has been validated by experimental results. The significant contribution of the CNT cap to the pull-out force is confirmed, which deepens the understanding of the interfacial properties of CNT-reinforced nanocomposites and provides a valuable guideline to design ideal materials with desirable interfacial properties.

Acknowledgements

The authors are grateful to be partly supported by the Grand-in-Aid for Scientific Research (No. 22360044) and Tohoku Leading Women's Jump Up Project for 2013 (J120000428) from the Ministry of Education, Culture, Sports, Science and Technology (MEXT) of Japan. The contribution of computational resources by Prof. C.B. Fan (Beijing Institute of Technology, China) is greatly appreciated by the authors.

References

[1] C. Bower, R. Rosen, L. Jin, J. Han, O. Zhou, Deformation of carbon nanotubes in nanotube-polymer composites. Appl. Phys. Lett. 74(1999) 3317- 3319.
[2] P.M. Ajayan, L.S. Schadler, C. Giannaris, A. Rubio, Single-walled carbon nanotube-polymer composites: strength and weakness. Adv. Mater. 12(2000) 750-753.
[3] N. Hu, Y. Li, T. Nakamura, T. Katsumata, T. Koshikawa, M. Arai, Reinforcement effects of MWCNT and VGCF in bulk composites and interlayer of CFRP laminates. Compos. Part B 43 (2012) 3-9.
[4] G. Yamamoto, M. Omori, T. Hashida, H. Kimura, A novel structure for carbon nanotube reinforced alumina composites with improved mechanical properties. Nanotech. 19(2008) 315708.
[5] G. Yamamoto, K. Shirasu, T. Hashida, T. Takagi, J.W. Suk, J. An, R.D. Piner, R.S. Ruoff, Nanotube fracture during the failure of carbon nanotube/alumina composites. Carbon 49(2011) 3709-3716.
[6] R.E. Gorga, K. Lau, K. Gleason, R. Cohen, The importance of interfacial design at the carbon nanotube/polymer composite interface. J. Appl. Polym. Sci. 102(2006) 1413–1418.
[7] C.A. Cooper, S.R. Cohen, A.H. Barber, H.D. Wagner, Detachment of nanotubes from a polymer matrix. Appl. Phys. Lett. 81(2002) 3873-3875.
[8] A.H. Barber, S.R. Cohen, S. Kenig, H.D. Wagner, Measurement of carbon nanotube-polymer interfacial strength. Appl. Phys. Lett. 82(2003) 4140-4142.
[9] F. Deng, Investigation of the interfacial bonding and deformation mechanism of the nano composites containing carbon nanotubes. Tokyo University, PhD Dissertation, 2008.
[10] T. Tsuda, T. Ogasawara, F. Deng, N. Takeda, Direct measurements of interfacial shear strength of multi-walled carbon nanotube/PEEK composite using a nano-pullout method. Comp. Sci. Tech. 71(2011) 1295-1300.
[11] M.P. Manoharan, A. Sharma, A.V. Desai, M.A. Haque, C.E. Bakis, K.W. Wang, The interfacial strength of carbon nanofiber epoxy composite using single fiber pullout experiments. Nanotech. 20(2009) 295701.
[12] H.D. Wagner, Nanotube-polymer adhesion: a mechanics approach. Chem. Phys. Lett. 361(2002) 57-61.
[13] S.Y. Fu, Z.K. Chen, S. Hong, C.C. Han, The reduction of carbon nanotube (CNT) length during the manufacture of CNT/polymer composites and a method to simultaneously determine the resulting CNT and interfacial strengths. Carbon 47(2009) 3192-3200.
[14] Y. Li, Y. Liu, X. Peng, C. Yan, S. Liu, N. Hu, Pull-out simulations on interfacial properties of carbon nanotube-reinforced polymer nanocomposites. Comput. Mater. Sci. 50(2011) 1854-1860.
[15] S. Liu, N. Hu, G. Yamamoto, Y. Cai, Y. Zhang, Y. Liu, Y. Li, T. Hashida, H. Fukunaga, Investigation on CNT/alumina interface properties using molecular mechanics simulations. Carbon 49(2011) 3701–3704.
[16] G.A. Shen, S. Namilae, N. Chandra, Load transfer issues in the tensile and compressive behavior of multi-walled carbon nanotubes. Mater. Sci. Eng. A 429(2006) 66-73.
[17] Z. Xia, W.A. Curtin, Pullout forces and friction in multiwall carbon nanotubes. Phys. Rev. B 69(2004) 2333408.
[18] W. Guo, W. Zhong, Y. Dai, S. Li, Coupled defect-size effects on interlayer friction in multiwalled carbon nanotubes. Phys. Rev. B 72(2005) 075409.
[19] A. Kis, K. Jensen, S. Aloni, W. Mickelson, A. Zettl, Interlayer forces and ultralow sliding friction in multiwalled carbon nanotubes. Phys. Rev. Lett. 97(2006) 025501.
[20] Y. Li, N. Hu, G. Yamamoto, Z. Wang, T. Hashida, H. Asanuma, C. Dong, T. Okabe, M. Arai, H. Fukunaga, Molecular mechanics simulation of the sliding behavior between nested walls in a

multi-walled carbon nanotube. Carbon 48(2010) 2934-2940.
[21] G. Yamamoto, S. Liu, N. Hu, T. Hashida, Y. Liu, C. Yan, Y. Li, H. Cui, H. Ning, L. Wu, Prediction of pull-out force of multi-walled carbon nanotube (MWCNT) in sword-in-sheath mode. Comput. Mater. Sci. 60(2012) 7–12.
[22] A. Kelly, W.R. Tyson, Tensile properties of fibre reinforced metals: copper/tungsten and copper/molybdenum. J. Mech. Phys. Solids 13(1965) 329-350.

Deformation and Failure of Graphene Sheet and Graphene-Polymer Interface

Mingchao Wang[1], Cheng Yan[1,*], Ning Hu[2]

[1] School of Chemistry, Physics and Mechanical Engineering, Science and Engineering Faculty, Queensland University of Technology, 2 George Street, GPO Box 2434, Brisbane, Australia
[2] Department of Mechanical Engineering, Chiba University, Inage-ku, Chiba, Japan
* Corresponding author: c2.yan@qut.edu.au

Abstract With a monolayer honeycomb-lattice of sp^2-hybridized carbon atoms, graphene has demonstrated exceptional electrical, mechanical and thermal properties. One of its promising applications is to create graphene-polymer nanocomposites with tailored mechanical and physical properties. In general, the mechanical properties of graphene nanofiller as well as graphene-polymer interface govern the overall mechanical performance of graphene-polymer nanocomposites. However, the strengthening and toughening mechanisms in these novel nanocomposites have not been well understood. In this work, the deformation and failure of graphene sheet and graphene-polymer interface were investigated using molecular dynamics (MD) simulations. The effect of structural defects on the mechanical properties of graphene and graphene-polymer interface was investigated as well. The results showed that structural defects in graphene (e.g. Stone-Wales defect and multi-vacancy defect) can significantly deteriorate the fracture strength of graphene but may still make full utilization of corresponding strength of graphene and keep the interfacial strength and the overall mechanical performance of graphene-polymer nanocomposites.

Keywords Graphene, structural defect, fracture strength, graphene-polymer interface, load transfer

1. Introduction

Graphene has attracted increasing research effort since its discovery [1], largely due to its excellent electrical, mechanical and thermal properties. For example, graphene has high electron mobility (25000 cm^2/Vs) at room temperature [1], anomalous quantum Hall effect [2], extremely high Young's modulus (~1TPa) and fracture strength (~130 GPa) [3] and superior thermal conductivity (5000 $Wm^{-1}K^{-1}$) [4]. These exceptional properties make graphene an ideal candidate as reinforcement in functional and structural polymer composites. For instance, graphene-polymer composite has a electrical conductivity of ~0.1 Sm^{-1} when adding only 1 v% graphene [5]. Poly(acrylonitrile) with 1 wt% functionalized graphene obtains a remarkable shift in glass transition temperature of over 40 °C [6]. More significantly, the composites show notable improvement in fracture strength and toughness, buckling and fatigue resistance [7-12].

Graphene can be produced via chemical vapour deposition (CVD) [13], mechanical exfoliation [14], chemical reduction of graphene oxide sheets [15], etc. It has been confirmed the properties of graphene can be modified by chemical functionalization [16-18]. However, both material production processes and chemical treatment may introduce structural defects in graphene, such as Stone-Wales (S-W) type defects (nonhexagonal rings generated by reconstruction of graphene lattice) [19], single and multiply vacancies, dislocation like defects, carbon adatoms, or accessory chemical groups. Recently, Gorjizadeh et al. [20] demonstrated that the conductance decreases in defective graphene sheets. Pei et al. [21, 22] studied the influence of functionalized groups on mechanical properties of graphene. Furthermore, it is still not well understood the underlying strengthening and toughening mechanisms of graphene-polymer nanocomposites and the influence of defective graphene on them. Further study is much required. Due to the nano-scale dimensions, it is difficult to accurately evaluate the properties of graphene sheets via experiment. Alternatively, molecular dynamics (MD) method has been widely utilized to investigate carbon-based nanomaterials [23-27]. In this work, we present a MD investigation on the fracture strength of graphene with structural defects (S-W defect and multi-vacancy defect) and interfacial behaviour of

graphene-polymer nanocompsites. Our results are helpful for a better understanding of the design and performance of graphene-polymer nanocomposites.

2. Models and Methods

To simulate a monolayer graphene sheet, a MD model (42.6 Å × 49.2 Å) was built that consists of 800 carbon atoms. As confirmed by Zhao et al. [28], the possible model size effect on mechanical properties can be largely neglected when the diagonal length is over 5 nm. Therefore, the diagonal length of our model was chosen as 6.51 nm. The model was firstly relaxed to a minimum energy state with the conjugate gradient energy minimization. Then, Nose-Hoover thermostat [29, 30] was employed to equilibrate the graphene sheet at a certain temperature with periodic boundary conditions (PBCs). The adaptive intermolecular reactive bond order (AIREBO) potential [31] implemented in the software package LAMMPS [32], was used to simulate covalent bond formation and bond breaking. Such AIREBO potential has successfully simulated and predicted mechanical properties of carbon-based materials, i.e. fullerene, carbon nanotube and graphene.

In order to prepare the atomistic structures of graphene-polymer nanocomposite for simulation, a two-dimensional (2D) periodic model of polyethylene (PE) layer independent of graphene nanofiller was established. The polymer system consists of 25 PE molecules, with each molecule (CH_3-(CH2-CH2)$_{59}$-CH_3) composed of about 60 monomers. All the PE chains were prepared by commercial software Material Studio developed by Accelrys Inc. Then, two types of graphene-PE unit cells were constructed by stacking two PE layers with single graphene sheet (Case 1) and single defective graphene sheet (Case 2). To investigate the interfacial characteristics of graphene-PE nanocomposite, an ab initio force filed polymer consistent force field (PCFF) [33, 34] was employed with the effective open-source code LAMMPS [32]. The interfacial interaction has been widely investigated in carbon-based materials and polymer-matrix nanocomposites [35-41]. To obtain the equilibrated structure of such unit cell, the model was first put into a constant-temperature, constant-pressure (NPT) ensemble for 250 ps by fixing the graphene with temperature of T=100 K, pressure of P=1 atm and time step of Δt=1 fs after initial energy minimization (stage 1). Then, the unit cell model was further equilibrated for 250 ps with the same NPT ensemble and time step (stage 2). For the pull-out simulation of graphene from PE matrix, the displacement increment along the x axis of Δx=0.001 Å was applied. During such process, graphene nanofiller were fixed while PE matrix was relaxed to equilibrate the whole dynamic system.

3. Results and Discussion

3.1 Effect of Stone-Wales (S-W) on Fracture Strength

Due to the short-ranged covalent bonding between carbon atoms, bond rotation and bond breaking are two basic deformation mechanisms in graphene. In this study, we considered two types of S-W defects, namely S-W_1 and S-W_2, which are caused by 90° rotation of C-C bonds in different directions, as shown in Figure 1(a). Figure 1(b) showed corresponding stress-strain curves at different temperatures (300 K~900 K). In terms of true (Cauchy) stress, fracture strengths along armchair and zigzag directions at 300 K are 104 and 127 GPa, respectively. These values are in good agreement with experiment results $\sigma_f \approx$130 GPa [3], as well as previous atomistic simulation results [26, 28].

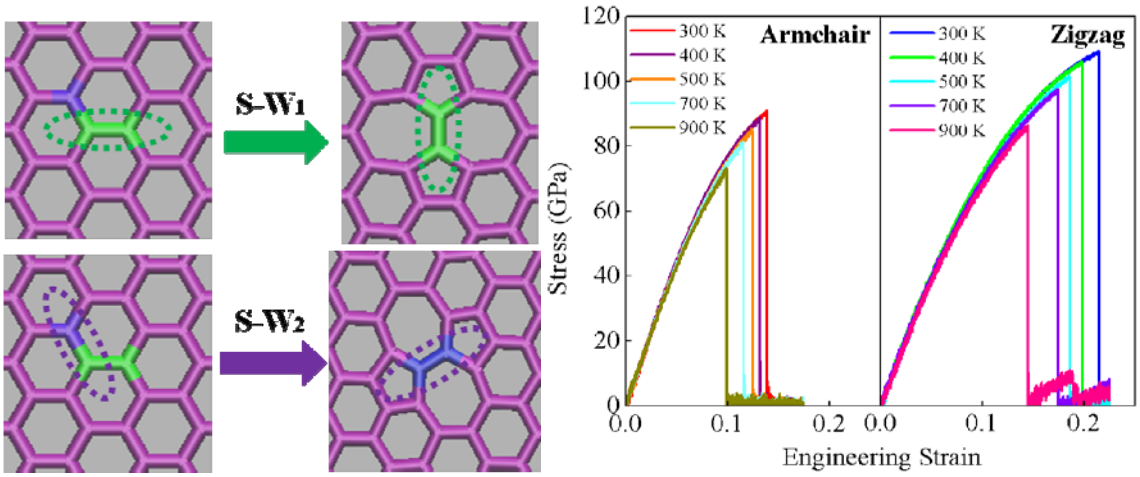

Figure 1. (a) Atomistic models of S-W_1 and S-W_2 defects. (b) Stress-strain curves of pristine graphene sheet under uniaxial tension along armchair and zigzag directions at different temperatures (300~900 K).

Our MD simulation results demonstrated that both S-W defects and temperature could significantly deteriorate the fracture strength of graphene. Figure 2 showed the fracture strength of graphene with S-W defects at different temperatures (300 K ~ 900 K). Under zigzag loading, the average strength loss caused by S-W_1 and S-W_2 was 16.26% and 41.30%, respectively. Under armchair loading, the average loss of facture strength by S-W_2 defect was about 15.75%. For S-W_1, however, fracture strength increased when temperature was above 600 K (C point in Figure 2(a)). This was attributed to the healing of S-W_1 defect with increasing temperature. As shown in Figure 2(b), at 600 K, the S-W_1 defect was stable. At 700 K, however, the S-W_1 defect was healed by 90° rotation of C-C bond. As mentioned above, mechanical strain could lower the healing energy barrier E_{eb}^{-}. Therefore, according to the kinetic rate of the healing of S-W defects (ν),

$$\nu = af_0 \exp^{-E_{eb}^{-}/kT} \quad (1)$$

Where f_0 is attempt frequency (about 10^{13}/s); k is the Boltzmann's constant and a is the lattice spacing $a = \sqrt{3}r_0$, where $r_0 = 1.42$ Å is the C-C bond length. From Eq. 1, the healing of S-W_1 defect became easier with increase of mechanical strain and temperature, consistent with the MD simulation.

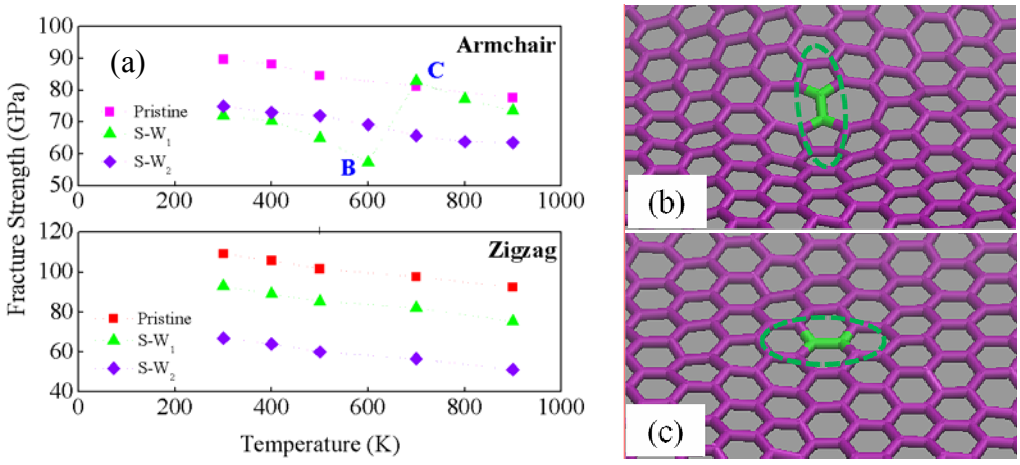

Figure 2. (a) Fracture strength of pristine, S-W_1 and S-W_2 defected graphene versus temperature under armchair and zigzag loading conditions. (b-c) Configuration change in the pre-existing S-W_1

defect from point B (b) (at 600 K) to point C (c) (at 700 K) highlighted in (a).

3.2 Effect of Vacancy Defect on Fracture Strength

In the temperature range of 300~900 K, the fracture strength of graphene sheet with vacancy was evaluated under tension along the armchair direction. The simulation model with 1, 2, and 3 vacancies is shown in Figure 3(a). Figure 3(b) showed the fracture strength σ_f for the graphene sheets with different vacancy number at temperatures 300 K, 500 K, and 900 K. It can be seen that fracture strength decreases with increasing temperature as well as the number of vacancy. For the sheet with 3 vacancies, the fracture strength loss was 37.3%, 40.2% and 42.4%, corresponding to 300, 500 and 900 K, respectively. Therefore, atomic scale defect such as vacancy does play a critical role in dictating the mechanical performance of graphene.

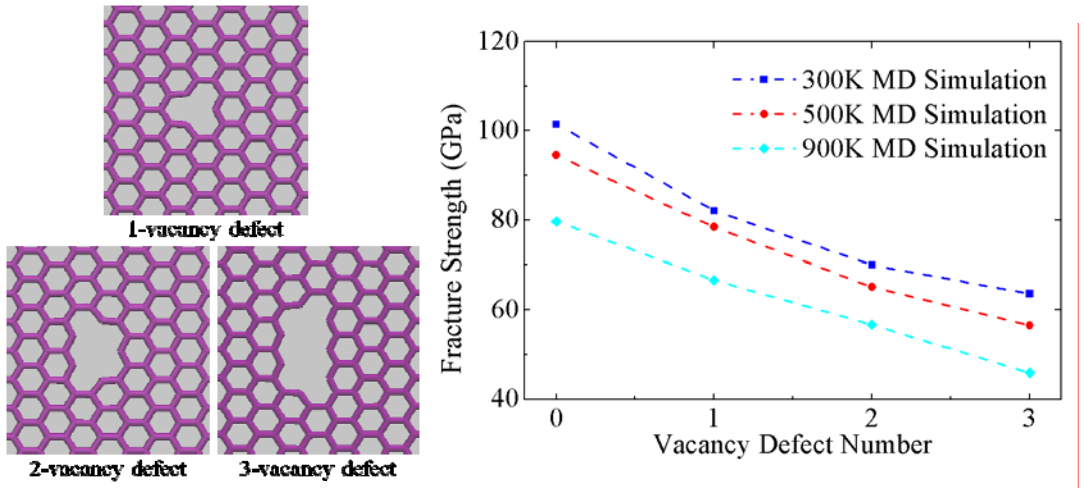

(a) **(b)**

Figure 3. (a) Three types of vacancy defect. (b) Fracture strength of defective graphene sheet versus the number of vacancy defect.

3.3 Interfacial Behaviour of Graphene-PE Nanocomposites

To study the interfacial behavior of graphene-PE nanocomposites, MD simulation of pull-out test was carried out by pulling out the graphene nanofiller from PE matrix. In particular, interfacial shear force (ISF) can govern the effectiveness of load transfer during pull-out process. On the basis of the expressions $f_{ISF} = -\partial E_{\text{int}} / \partial X$, f_{ISF} can be calculated in terms of the given E_{int}-X curve. As shown in Figure 4(a), f_{ISF}-X curve can also be divided into three stages. It can be found that the Stage I and Stage III had approximately the same range of X_I=X_{III}=1.0 nm, which was close to the cut-off distance of vdW interaction. At Stage I, the magnitude of f_{ISF} rose quickly in all cases. The increase of f_{ISF} can be attributed to the newly formed surface of graphene (outside part). Then, f_{ISF} went through a long and approximate platform at Stage II. This was because that the length of the effective newly formed surface kept at 1 nm from the pull-out end, thus leading to constant f_{ISF}. Finally, it decreased to the value similar to that at first beginning until complete pull-out. At all three stages, the values of f_{ISF} varied periodically with the variation of X, largely due to the inhomogeneous distribution of PE structures in the interfacial area. The effect of structural defect on f_{ISF} was considered as well. However, the effect of structural defects on f_{ISF} is unobvious, which might be beneficial for application of graphene-polymer nanocomposites. Then, pull-out stress could be calculated in the expression as σ_p=f_{ISF}/A_{eff}, where A_{eff} is the effective cross section of graphene sheet, A_{eff}=Wt with W=50 Å the width of graphene sheet and t=3.44 Å the sheet thickness.

According to Figure 4, the maximum pull-out stress $\sigma_p^{\max}$ in both cases was about 0.87 GPa, much lower than fracture strength of pure graphene and defective graphene, namely $\sigma_p^{\max} / \sigma_f = 1$. Therefore, in the pratical applications of graphene-polymer nanocomposites, graphene nanofiller could be full utilized even with structural defects on its surface. However, increasing the utilization of fracture strength of graphene deserves further investigation in future.

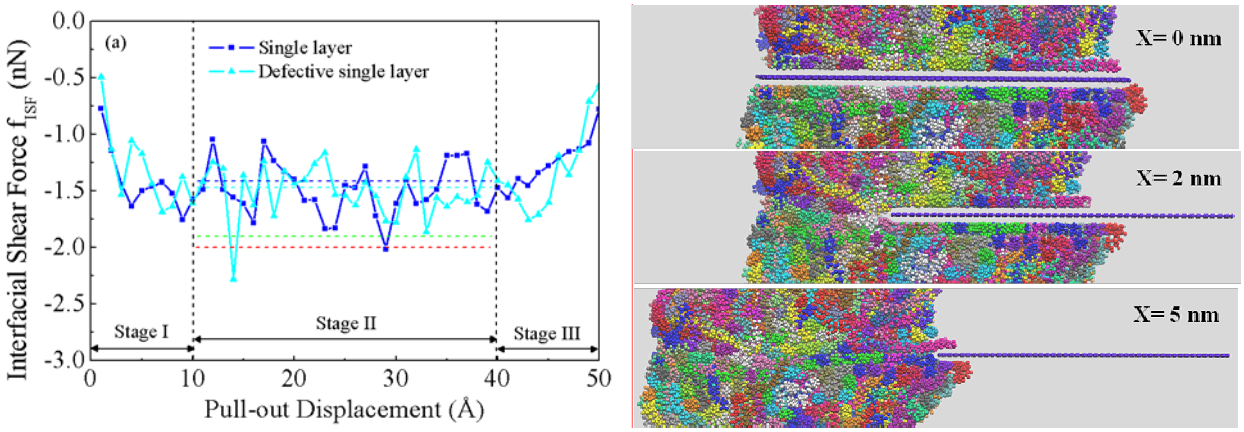

(a) (b)

Figure 4. (a) Interfacial shear force f_{ISF} versus pull-out displacement X in Case 1 (pure graphene sheet) and Case 2 (defective graphene sheet). (b) Snap shots of graphene pull-out from PE matrix in Case 1.

4. Conclusions

Deformation and failure of graphene sheet and graphene-polymer interface was investigated using MD simulations. Calculation results showed that the fracture strength of graphene is dependent on both structural defects and temperature. Structural defects in graphene (e.g. Stone-Wales defect and multi-vacancy defect) can remarkably damage the fracture strength of graphene. As for the interfacial behaviour of graphene-polymer nanocomposites, it was shown that the value of ISF vary at each end of the graphene nanofiller within the range of 1 nm, while keep approximately constant (ISF) and zero (ISS) at middle stage. Particularly, ISF is independent of the pre-existing vacancy defect in graphene. Furthermore, graphene nanofiller could be full utilized even with structural defects owing to much lower pull-out stress. The study of the mechanical performance of defective graphene and graphene-polymer interface sheds light on the better understanding of design and application of graphene-polymer nanocomposites.

References

[1] K. S. Novoselov, A. K. Geim, S. V. Morozov, D. Jiang, Y. Zhang, S. V. Dubonos, I. V. Grigorieva and A. A. Firsov, Electric field effect in atomically thin carbon films. Science, 306 (2004) 666.

[2] Y. Zhang, Y.-W. Tan, H. L. Stormer and P. Kim, Experimental observation of the quantum Hall effect and Berry's phase in graphene. Nature (London), 438 (2005) 201.

[3] C. Lee, X. Wei, J. W. Kysar and J. Hone, Measurement of the elastic properties and intrinsic strength of monolayer graphene. Science, 321 (2008) 385.

[4] A. A. Balandin, S. Ghosh, W. Bao, I. Calizo, D. Teweldebrhan, F. Miao and C. N. Lau, Superior Thermal Conductivity of Single-Layer Graphene. Nano Lett, 8 (2008) 902.

[5] S. Stankovich, D. A. Dikin, G. H. B. Dommett, K. M. Kohlhaas, E. J. Zimney, E. A. Stach, R. D.

Piner, S. T. Nguyen and R. S. Ruoff, Graphene-based composite materials. Nature, 442 (2006) 282.
[6] RamanathanT, A. A. Abdala, StankovichS, D. A. Dikin, M. Herrera Alonso, R. D. Piner, D. H. Adamson, H. C. Schniepp, ChenX, R. S. Ruoff, S. T. Nguyen, I. A. Aksay, R. K. Prud'Homme and L. C. Brinson, Functionalized graphene sheets for polymer nanocomposites. Nat Nanotechnol, 3 (2008) 327.
[7] M. A. Rafiee, J. Rafiee, Z. Z. Yu and N. Koratkar, Buckling resistant graphene nanocomposites. Appl Phys Lett, 95 (2009) 223103.
[8] M. A. Rafiee, J. Rafiee, Z. Wang, H. Song, Z.-Z. Yu and N. Koratkar, Enhanced mechanical properties of nanocomposites at low graphene content. ACS Nano, 3 (2009) 3884.
[9] X. Zhao, Q. Zhang, D. Chen and P. Lu, Enhanced Mechanical Properties of Graphene-Based Poly(vinyl alcohol) Composites. Macromolecules, 43 (2010) 2357.
[10] M. A. Rafiee, J. Rafiee, I. Srivastava, Z. Wang, H. H. Song, Z. Z. Yu and N. Koratkar, Fracture and Fatigue in Graphene Nanocomposites. Small, 6 (2010) 179.
[11] M. A. Rafiee, W. Lu, A. V. Thomas, A. Zandiatashbar, J. Rafiee, J. M. Tour and N. A. Koratkar, Graphene nanoribbon composites. ACS Nano, 4 (2010) 7415.
[12] I. Srivastava, R. J. Mehta, Z.-Z. Yu, L. Schadler and N. Koratkar, Raman study of interfacial load transfer in graphene nanocomposites. Appl Phys Lett, 98 (2011) 063102.
[13] P. R. Somani, S. P. Somani and M. Umeno, Planer nano-graphenes from camphor by CVD. Chem Phys Lett, 430 (2006) 56.
[14] A. A. Green and M. C. Hersam, Solution phase production of graphene with controlled thickness via density differentiation. Nano Lett, 9 (2009) 4031.
[15] V. Singh, D. Joung, L. Zhai, S. Das, S. I. Khondaker and S. Seal, Graphene based materials: Past, present and future. Prog Mater Sci, 56 (2011) 1178.
[16] F. OuYang, B. Huang, Z. Li, J. Xiao, H. Wang and H. Xu, Chemical functionalization of graphene nanoribbons by carboxyl groups on Stone-Wales defects. J Phys Chem C, 112 (2008) 12003.
[17] D. W. Boukhvalov and M. I. Katsnelson, Chemical functionalization of graphene. J Phys-Condens Mat, 21 (2009) 344205.
[18] M. Wu, X. Wu, Y. Gao and X. C. Zeng, Materials design of half-metallic graphene and graphene nanoribbons. Appl Phys Lett, 94 (2009) 223111.
[19] A. J. Stone and D. J. Wales, Theoretical-studies of icosahedral C60 and some related species. Chem Phys Lett, 128 (1986) 501.
[20] N. Gorjizadeh, A. A. Farajian and Y. Kawazoe, The effects of defects on the conductance of graphene nanoribbons. Nanotechnology, 20 (2009) 015201.
[21] Q. X. Pei, Y. W. Zhang and V. B. Shenoy, Mechanical properties of methyl functionalized graphene: a molecular dynamics study. Nanotechnology, 21 (2010) 115709.
[22] Q. X. Pei, Y. W. Zhang and V. B. Shenoy, A molecular dynamics study of the mechanical properties of hydrogen functionalized graphene. Carbon, 48 (2010) 898.
[23] Y. Li, Y. Liu, X. Peng, C. Yan, S. Liu and N. Hu, Pull-out simulations on interfacial properties of carbon nanotube-reinforced polymer nanocomposites. Comp Mater Sci, 50 (2011) 1854.
[24] G. Yamamoto, S. Liu, N. Hu, T. Hashida, Y. Liu, C. Yan, Y. Li, H. Cui, H. Ning and L. Wu, Prediction of pull-out force of multi-walled carbon nanotube (MWCNT) in sword-in-sheath mode. Comp Mater Sci, 60 (2012) 7.

[25] Alamusi, N. Hu, B. Jia, M. Arai, C. Yan, J. Li, Y. Liu, S. Atobe and H. Fukunaga, Prediction of thermal expansion properties of carbon nanotubes using molecular dynamics simulations. Comp Mater Sci, 54 (2012) 249.
[26] M. C. Wang, C. Yan, L. Ma, N. Hu and M. W. Chen, Effect of defects on fracture strength of graphene sheets. Comp Mater Sci, 54 (2012) 236.
[27] M. C. Wang, C. Yan, L. Ma and N. Hu, Molecular dynamics investigation on edge stress and shape transition in graphene nanoribbons. Comp Mater Sci, 68 (2013) 138.
[28] H. Zhao, K. Min and N. R. Aluru, Size and Chirality Dependent Elastic Properties of Graphene Nanoribbons under Uniaxial Tension. Nano Lett, 9 (2009) 3012.
[29] W. G. Hoover, Canonical dynamics: Equilibrium phase-space distributions. Phys Rev A, 31 (1985) 1695.
[30] S. Nosé, A unified formulation of the constant temperature molecular dynamics methods. J Chem Phys, 81 (1984) 511.
[31] S. J. Stuart, A. B. Tutein and J. A. Harrison, A reactive potential for hydrocarbons with intermolecular interactions. J Chem Phys, 112 (2000) 6472.
[32] S. Plimpton, Fast parallel algorithms for short-range molecular dynamics. J Comput Phys, 117 (1995) 1.
[33] H. Sun, Ab initio characterizations of molecular structures, conformation energies, and hydrogen-bonding properties for polyurethane hard segments. Macromolecules, 26 (1993) 5924.
[34] H. Sun, S. J. Mumby, J. R. Maple and A. T. Hagler, An ab Initio CFF93 All-Atom Force Field for Polycarbonates. J Am Chem Soc, 116 (1994) 2978.
[35] I. Yarovsky and E. Evans, Computer simulation of structure and properties of crosslinked polymers: application to epoxy resins. Polymer, 43 (2002) 963.
[36] T. C. Clancy and T. S. Gates, Modeling of interfacial modification effects on thermal conductivity of carbon nanotube composites. Polymer, 47 (2006) 5990.
[37] M. Naito, K. Nobusawa, H. Onouchi, M. Nakamura, K.-i. Yasui, A. Ikeda and M. Fujiki, Stiffness- and Conformation-Dependent Polymer Wrapping onto Single-Walled Carbon Nanotubes. J Am Chem Soc, 130 (2008) 16697.
[38] J. Lee, V. Varshney, J. S. Brown, A. K. Roy and B. L. Farmer, Single mode phonon scattering at carbon nanotube-graphene junction in pillared graphene structure. Appl Phys Lett, 100 (2012) 183111.
[39] L. Hu, T. Desai and P. Keblinski, Determination of interfacial thermal resistance at the nanoscale. Phys Rev B, 83 (2011) 195423.
[40] S. Yang, S. Yu, W. Kyoung, D.-S. Han and M. Cho, Multiscale modeling of size-dependent elastic properties of carbon nanotube/polymer nanocomposites with interfacial imperfections. Polymer, 53 (2012) 623.
[41] E. Zaminpayma and K. Mirabbaszadeh, Interaction between single-walled carbon nanotubes and polymers: A molecular dynamics simulation study with reactive force field. Comp Mater Sci, 58 (2012) 7.

Stress Concentration based on Non-linear Motion Equations and its Application for Non-destructive Detection of Plate

Jianhua Xiao[1,*], **Jingjing Wang**[1]

[1] Measurement Institute, Henan Polytechnic University, Jiaozuo 454000, China
* Corresponding author: jhxiao@hpu.edu.cn

Abstract For a plate with large deformation, where the possible fracture will be initiated is an important problem. It is true that the defects or voids of material usually are the initial positions. However, the more important problem is the local defect (fatigue-fracture) caused by the global deformation of medium, as this problem is very common in practical engineering. For this purpose, two sets of non-linear motion equations of deformation established in rational mechanics frame are used to study this problem. The stress concentration problem is defined as: for a given deformation, how the stresses are distributed to meet the motion equations under the cost of fatigue-fracture within the plate. The motion equations show that the local curvature is the main cause of fatigue-fracture. Taking the local deformation curvature as a parameter function, the stress transportation solution is obtained. The result shows that: for plate bending, the stress is varied in exponential law with the path-integral of local curvature of plate. In non-destructive detect, when the pressure wave data are recorded in an array, they can be used to inverse the intrinsic local curvature of target medium region. Then, the "inversed" local curvature can be used to predict the potential fatigue-cracking initiation region.

Keywords Nondestructive detect, Stress concentration, Stress transportation, Non-linear motion equation, Large deformation

1. Introduction

Stress concentration usually is addressed by the irregular boundary problems [1-3]. As a simple example, for a plate with small hole, the stress around hole will be increased rapidly when the in-plane stretching is increased. To express the effects of stress concentration, a factor (defined as maximum stress over name stress) is introduced. Its shortage is that the voids geometry features are required. Then, taking the voids as boundary, the motion equations are used to calculate the factor based on theoretic solutions. The crack tip field theory is fully developed along this theoretic line. Hence, it is understandable that many researchers focus on their attention upon micro-scale phenomena. However, based on experiences, we usually have no ad-hoc information about where the defects exist. What we want to know is where the fatigue-fracture will be initiated? The micro-scale structure description has little help on this topic. Generally, for uniform continuum, the stress concentration phenomena can be attributed to the cause of the defects of micro-scale structures. For a plate with arbitral deformation, the real fatigue-fracture frequently appears in the highest curvature position or the position inherited with large scale deformation or singularity. On phenomenon sense, the defects or voids of material were produced by the macro deformation in space-time domain.

Recently, how the macro deformation alters the microstructures of material is raised as an important problem for fracture mechanics. The dual scale or multiscale viewpoint is proposed to answer how the macro deformation causes the microstructure instability [4-6]. To answer this question, the first problem is returned to the question about where the stress will be concentrated. This problem may be answered by formulating related motion equations.

For this purpose, two sets of non-linear motion equations of deformation [7] established in rational

mechanics frame [8] are used to study this problem. One set of equations corresponds to linear momentum conservation, and another set of equations corresponds to angular momentum conservation. Then, the fatigue-fracture is initiated by local asymmetrical stress (which is related with local curvature [9]), although it may be very small comparing with the symmetrical stress. Hence, the research is looking for the "omitted" items in classical mechanics.

In this research, the stress concentration problem is defined as: for a given deformation, how the stresses are redistributed to meet the motion equations under the cost of fatigue-fracture within the plate. The motion equations show that the local curvature is the main cause of fatigue-fracture (in classical plate stability problem, the local curvature plays the similar role in von Karman equations [10]). Taking the local deformation curvature as a parameter function, the stress transportation solution is obtained. The result shows that: for plate bending, the stress is varied in exponential law with the path-integral of local curvature of plate.

For bending with harmonic local curvature, the integral along any path tends to be small, then, there is no stress concentration potential. However, for bending with monotone local curvature, the integral along any path tends to be large. Then, referring to a given stress position (as the path-integral starting point), the stress concentration will appear at the positions with maximum of path integral. In non-destructive detect, when the pressure wave data at different frequencies are recorded in an array, they can be used to inverse the intrinsic local curvature of target medium region. Then, the "inversed" local curvature can be used to predict the potential fatigue-cracking initiation region.

2. General Equations for Large Deformation

For large deformation, the deformation tensor (defined by displacement gradient) was introduced by Truesdell [11] and is named as a two-point tensor. Viewing that the base vector transformation for commoving dragging coordinator (natural coordinator) uniquely defines the deformation between initial configuration and current configuration, Chen Zhida [8, 12] established a new formulation for rational mechanics. This theoretic formulation is based on point-set transformation and is briefed as following. For a set of co-moving dragging coordinators defined in continuum, a material point is coordinated as (x^1, x^2, x^3). For initial configuration, the base vector is expressed as $(\overset{0}{\rho}\overset{}{g}_1(x), \overset{0}{\rho}\overset{}{g}_2(x), \overset{0}{\rho}\overset{}{g}_3(x))$. For current configuration, the base vector is expressed as $(\overset{}{\rho}\overset{}{g}_1(x), \overset{}{\rho}\overset{}{g}_2(x), \overset{}{\rho}\overset{}{g}_3(x))$. Then, the differential distance vector between two material points is expressed as: $d\overset{0}{\rho}\overset{}{s}_0(x) = dx^i \overset{0}{\rho}\overset{}{g}_i(x)$ (here and after repeating index summation convention is applied for $i = 1,2,3$) for initial configuration; $d\overset{}{\rho}\overset{}{s}(x) = dx^i \overset{}{\rho}\overset{}{g}_i(x)$ for current configuration (here and after, repeat index summation convention is used).

For large deformation, the deformation tensor $F_j^i(x)$ (the coordinator dependence x will be omitted below and after) is defined by base vector transformation equation (point-sets group transformation):

$$\overset{}{\rho}\overset{}{g}_i = F_i^{\ j} \overset{0}{\rho}\overset{}{g}_j = (\delta_i^j + u^j\big|_i)\overset{0}{\rho}\overset{}{g}_j . \tag{1}$$

Where, u^j is displacement field defined in initial configuration, the covariant derivative $\big|_i$ is performed in initial gauge field.

The Cauchy strain tensor is defined as:

$$\varepsilon_i^j = F_i^j - \delta_i^j = u^j\big|_i . \tag{2}$$

For simple idea isotropic elastic continuum, the stress tensor is defined as a mixture tensor $\sigma_i^j(\overset{0}{g}_i \otimes \overset{0}{g}_j)$ [7-9] through constitutive equations:

$$\sigma_i^j = \lambda\varepsilon_k^k\delta_i^j + 2\mu\varepsilon_i^j . \tag{3}$$

In engineering sense, the stress tensor component σ_i^j is explained as the surface force acting on current face $\overset{0}{g}_i$ in the direction $\overset{0}{g}_j$. In fact, this engineering interpretation is widely used in mechanics textbooks about stress tensor σ_{ij} (a kind of logic weakness on the sense that which one index represents surface or which one represents direction). For this mixture stress definition, the physical components of stress tensor are defined as $\tilde{\sigma}_i^j = \frac{\sqrt{g^0_{(jj)}}}{\sqrt{g_{(ii)}}}\sigma_i^j$. Surely, the stress symmetry in engineering stress sense does not mean the stress is symmetrical in intrinsic sense.

Then, as logic consequence, the stress differential for large deformation is:

$$\sigma_i^j\big|_k = \frac{\partial\sigma_i^j}{\partial x^k} + \sigma_i^l\Gamma_{lk}^j - \sigma_l^j\tilde{\Gamma}_{ik}^l . \tag{4}$$

Where, the connection Γ_{jk}^i is defined in initial configuration; $\tilde{\Gamma}_{jk}^i$ is defined in current configuration. Without losing generality [7], taking the initial configuration in standard rectangular coordinator system to make a simplification that $\Gamma_{jk}^i = 0$, it can be simplified as:

$$\sigma_i^j\big|_k = \frac{\partial\sigma_i^j}{\partial x^k} - \sigma_l^j\frac{\partial\varepsilon_i^l}{\partial x^k} \quad . \tag{5}$$

It shows that the non-linear items for large deformation are mainly originated from strain gradient and large stress. In resent years, the role of strain gradient has been studied extensively.

In rational mechanics of Chen formulation [7-9], the motion equations are classified into two categories as: covariant form and anti-variant form. In deformation mechanics, they must be satisfied at the same time. Generally speaking, the anti-variant force corresponds to linear momentum conservation and the covariant force corresponds to angular momentum conservation.

For large deformation with body force $\overset{\nu}{f} = f^i\overset{0}{g}_i$ in local standard rectangular coordinator system, the anti-variant form of motion equation (linear momentum conservation) is:

$$\frac{\partial\sigma_j^i}{\partial x^j} - \sigma_l^i\frac{\partial\varepsilon_j^l}{\partial x^j} = f^i . \tag{6}$$

The covariant form of motion equation (angular momentum conservation) is:

$$\frac{\partial\sigma_i^j}{\partial x^j} - \sigma_l^j\frac{\partial\varepsilon_i^l}{\partial x^j} = f^j F_i^j . \tag{7}$$

In von Karman elastic shell theory the item $-\frac{\partial\varepsilon_j^l}{\partial x^j} = -\frac{\partial^2 u^l}{\partial x^j\partial x^j}(l=3, i, j=1,2)$ is related with the curvature of shell or plate. So, the Eq.6 should be viewed as von Karman equation. Following this curvature interpretation, it is concluded that: for high stress deformation, the curvature produced by deformation must be taken into consideration.

3. Geometrical Equations for Plate Bending

For simplicity, the initial configuration of central plan is taking as standard rectangular coordinator system (x^1, x^2). Hence, the plate is described as a two dimension manifold. The thickness direction

is taken as coordinator (x^3). In this research, the plate bending problem is described by unit-orthogonal transformation of base vector as:

$$\overset{\rho}{g}_i = R_i^j \overset{\rho}{g}_j^0 . \tag{8}$$

Where, for plate bending, based on Chen's S+R additive decomposition of deformation tensor [7-9], the tensor R_i^j is defined as:

$$R_i^j = \delta_i^j + \sin\Theta \cdot L_i^j + (1-\cos\Theta) L_k^j L_i^k . \tag{9}$$

Where, the Θ is local whole rotation in average sense (local curvature) [12], and the tensor L_i^j is the rotation direction.

The related items are expressed by the displacement fields as:

$$L_1^3 = -L_3^1 = \frac{1}{2\sin\Theta}\left(\frac{\partial u^3}{\partial x^1} - \frac{\partial u^1}{\partial x^3}\right) = L_2 , \tag{10-1}$$

$$L_3^2 = -L_2^3 = \frac{1}{2\sin\Theta}\left(\frac{\partial u^2}{\partial x^3} - \frac{\partial u^3}{\partial x^2}\right) = L_1 , \tag{10-2}$$

$$L_2^1 = -L_1^2 = \frac{1}{2\sin\Theta}\left(\frac{\partial u^1}{\partial x^2} - \frac{\partial u^2}{\partial x^1}\right) = 0 , \tag{10-3}$$

$$\sin\Theta = \frac{1}{2}\sqrt{\left(\frac{\partial u^3}{\partial x^1} - \frac{\partial u^1}{\partial x^3}\right)^2 + \left(\frac{\partial u^2}{\partial x^3} - \frac{\partial u^3}{\partial x^2}\right)^2} . \tag{10-4}$$

For plate bending, as the gauge tensor is invariant, the geometrical conditions [7-9] are obtained as:

$$\frac{\partial u^1}{\partial x^1} = -(1-\cos\Theta)(L_2)^2 , \tag{11-1}$$

$$\frac{\partial u^2}{\partial x^2} = -(1-\cos\Theta)(L_1)^2 , \tag{11-2}$$

$$\frac{1}{2}\left(\frac{\partial u^1}{\partial x^2} + \frac{\partial u^2}{\partial x^1}\right) = -(1-\cos\Theta)(1-L_1 L_2) , \tag{11-3}$$

$$\frac{\partial u^3}{\partial x^3} = -(1-\cos\Theta) , \tag{11-4}$$

$$\frac{1}{2}\left(\frac{\partial u^1}{\partial x^3} + \frac{\partial u^3}{\partial x^1}\right) = 0 , \tag{11-5}$$

$$\frac{1}{2}\left(\frac{\partial u^2}{\partial x^3} + \frac{\partial u^3}{\partial x^2}\right) = 0 . \tag{11-6}$$

Combining Eqs.10 and Eqs.11, it is easy to find out that: all $\varepsilon_j^i = \frac{\partial u^i}{\partial x^j}$ are non-zeros, and the plate bending is completely determined by three independent quantities: $\Theta(x), L_1(x)$, and $L_2(x)$. Note that for small Θ, the $(1-\cos\Theta) \approx \frac{1}{2}\Theta^2$ is higher order smaller. The corresponding Cauchy stress components are defined by Eq.3. In engineering, the effective stresses (which contain non-linear effects) are used as a convention. In this research, the effective stress fields in the plate are studied by motion equations to study stress concentration problem.

4. Effective Stress Concentration for Plate Bending

Letting $\frac{\partial \varepsilon_j^l}{\partial x^j} = \kappa^l$ ($l = 1,2,3$) as local curvature functions, based on Eq.6, the anti-variant motion

equations are rewritten as:

$$\frac{\partial \sigma_j^i}{\partial x^j} - \sigma_j^i \kappa^j = f^i \tag{12}$$

As the plate bending is dominated by out-plan displacement u^3 measured by central plane coordinator (commoving dragging coordinator system), by Eqs.10 and Eqs.11, the curvature functions can be approximated as:

$$\kappa^3 = \frac{\partial^2 u^3}{\partial x^1 \partial x^1} + \frac{\partial^2 u^3}{\partial x^2 \partial x^2} = \frac{\partial (L_2 \sin\Theta)}{\partial x^1} + \frac{\partial (L_1 \sin\Theta)}{\partial x^2} \tag{13-1}$$

$$\kappa^1 = -\frac{\partial^2 u^3}{\partial x^1 \partial x^3} = \frac{\partial (L_2 \sin\Theta)}{\partial x^3} \tag{13-2}$$

$$\kappa^2 = -\frac{\partial^2 u^3}{\partial x^2 \partial x^3} = \frac{\partial (L_1 \sin\Theta)}{\partial x^3} \tag{13-3}$$

By these equations, the local curvature functions are the gradient of global bending curvature. In classical plate theory, the κ^1 and κ^2 are taken as linear function about thickness and are explained as curvature variation along thickness direction.

For fatigue-fracture problems, as the deformation is given, so the effective stress is varied to meet the motion equations.

Observing Eq.3, the effective stress field $\tilde{\sigma}_j^i$ can be defined by the following equation:

$$\frac{\partial \tilde{\sigma}_j^i}{\partial x^j} = \frac{\partial \sigma_j^i}{\partial x^j} - \sigma_j^i \kappa^j = f^i \tag{14}$$

Then the effective stresses meet classical motion equations. Omitting the derivatives of curvature functions (as first order approximation), one simple form solution for effective stress is:

$$\tilde{\sigma}_j^i(x) = \sigma_j^i(x) \cdot \exp(-\int_{x_0}^{x} \kappa^l dx^l) \tag{15}$$

Where, the x_0 is a reference point waiting to be determined by boundary conditions and loads. This solution means that: local effective stress is redistributed by the path-integral of global curvature functions. Therefore, stress concentration may appear somewhere. Based on Eq.3, for the effective stress, the constitutive equation is:

$$\tilde{\sigma}_i^j = (\lambda \varepsilon_k^k \delta_i^j + 2\mu \varepsilon_i^j) \cdot \exp(-\int_{x_0}^{x} \kappa^l dx^l) \tag{16}$$

It says that: for effective stress, the elasticity parameters are exponentially varied with the path-integral of curvature functions. In engineering mechanics, the increased elasticity is named as hardening and the decreased elasticity is named as softening. Then, by the above equations, the effective elasticity of bending plate has both effects. In engineering sense, the effective elasticity is varied by bending deformation significantly.

To make its meaning clear, the thickness effects can be expressed as:

$$\tilde{\sigma}_j^i(x)\Big|_{x^3} = \tilde{\sigma}_j^i(x)\Big|_{x^3=0} \cdot \exp(-\int_0^{x^3} \kappa^3 dx^3) \tag{17}$$

It shows that the effective stresses are exponentially distributed on thickness direction. In classical plate theory, the linear approximation is assumed.

It shows that: the effective stress on central plan parallel surface is exponentially varied with path-integral of curvature along thickness direction. So, the effective stress will concentrated on one surface parallel to central plan. If the local curvature is big enough, the fatigue-fracture may be initiated as surface cracking parallel to central plan (surface sliding or buckling). In some researches [13-15], the thickness direction stress concentration effects are studied under the terms distension or post-buckling). The above equation shows that, for given curvature, the plate thickness is limited by stress concentration effects along thickness direction.

Similarly, taking the effective stress at some potions as reference, the scale effects can be expressed

as effective stress transportation along plan directions as:

$$\tilde{\sigma}_j^i(x)\Big|_{x^1} = \tilde{\sigma}_j^i(x)\Big|_{x_0^1} \cdot \exp(-\int_{x_0^1}^{x^1} \kappa^1 dx^1) \tag{18-1}$$

$$\tilde{\sigma}_j^i(x)\Big|_{x^2} = \tilde{\sigma}_j^i(x)\Big|_{x_0^2} \cdot \exp(-\int_{x_0^2}^{x^2} \kappa^2 dx^2) \tag{18-2}$$

They show that: the effective stresses on central plan parallel surface are exponentially varied with path-integral of curvature along scale directions. So, the effective stress will concentrated on one side. If the local curvature is big enough, the fatigue-fracture may be initiated as surface cracking line (surface fracture). Therefore, for given curvatures, the plate scale is limited by stress concentration effects along plan directions.

For spatial harmonic bending with spatial frequencies (k_1, k_2, k_3), $\kappa^i = \kappa_0^i \sin(k_1 x^1 + k_2 x^2 + k_3 x^3)$, the path-integral values depends its corresponding spatial scales $(1/k_1, 1/k_2, 1/k_3)$. Therefore, multi-scale effects are very significant [4-6] for stress concentration phenomenon or fracture problems. This explains why microstructure analysis is always dominating the theoretic development about fatigue-fracture mechanism.

For forward problems of non-destructive detect, the central plan bending functions $\Theta(x)$, $L_1(x)$, and $L_2(x)$ are measured directly. Then, the curvature functions can be calculated by Eqs.13. In this case, the stress concentration effects can be evaluated by the Eqs.18.

For inverse problems of non-destructive detect, when the effective stress data can be acquitted, the Eqs.18 can be used to estimate the curvature functions. By the estimated curvatures, the potential fatigue-fracture positions can be predicted.

For supersonic wave methods, a lot of technology to get effective elasticity is available. By Eq.16, the effective elasticity for wave (incremental deformation [16]) is determined as:

$$\Delta\tilde{\sigma}_i^j = \lambda(\Delta\varepsilon_k^k)\delta_i^j + 2\mu(\Delta\varepsilon_i^j)] \cdot \exp(-\int_{x_0}^{x} \kappa^l dx^l) \tag{19}$$

So, as the original elasticity is known parameter, the curvature functions can be inversed. Therefore, stress concentration effects can be predicted.

5. Stress Concentration Caused by Load

Usually, the typical plate bending is produced normal loading (defined by $f^1 = f^2 = 0$). By subtracting Eq.6 and Eq.7, the asymmetrical stress motion equations are obtained as:

$$\frac{\partial(\sigma_1^3 - \sigma_3^1)}{\partial x^3} = f^3 \sin\Theta \cdot L_2 + (\sigma_l^j \frac{\partial \varepsilon_1^l}{\partial x^j} - \sigma_l^1 \frac{\partial \varepsilon_j^l}{\partial x^j}), \tag{20-1}$$

$$\frac{\partial(\sigma_2^3 - \sigma_3^2)}{\partial x^3} = -f^3 \sin\Theta \cdot L_1 + (\sigma_l^j \frac{\partial \varepsilon_2^l}{\partial x^j} - \sigma_l^2 \frac{\partial \varepsilon_j^l}{\partial x^j}), \tag{20-2}$$

$$\frac{\partial(\sigma_3^1 - \sigma_1^3)}{\partial x^1} + \frac{\partial(\sigma_3^2 - \sigma_2^3)}{\partial x^2} = (\sigma_l^j \frac{\partial \varepsilon_3^l}{\partial x^j} - \sigma_l^3 \frac{\partial \varepsilon_j^l}{\partial x^j}). \tag{20-3}$$

Where, the approximation $R_i^j \approx \delta_i^j + \sin\Theta \cdot L_i^j$ is applied. By Eq.3 and Eqs.11, the non-symmetrical stress components are σ_1^3, σ_3^1, σ_2^3, and σ_3^2. They are expressed as:

$$\sigma_1^3 = -\sigma_3^1 = 2\mu L_2 \sin\Theta, \tag{21-1}$$

$$\sigma_3^2 = -\sigma_2^3 = 2\mu L_1 \sin\Theta. \tag{21-2}$$

So, letting: $w_i = (\sigma_l^j \frac{\partial \varepsilon_i^l}{\partial x^j} - \sigma_l^i \frac{\partial \varepsilon_j^l}{\partial x^j})$, the asymmetrical stress motion equations are rewritten as:

$$4\mu\frac{\partial(L_2\sin\Theta)}{\partial x^3}=f^3\sin\Theta\cdot L_2+w_1 \tag{22-1}$$

$$-4\mu\frac{\partial(L_1\sin\Theta)}{\partial x^3}=-f^3\sin\Theta\cdot L_1+w_2 \tag{22-2}$$

$$-4\mu\frac{\partial(L_2\sin\Theta)}{\partial x^1}+4\mu\frac{\partial(L_1\sin\Theta)}{\partial x^2}=w_3 \tag{22-3}$$

Where, the third motion equation is used to determine the whole bending along plan direction.
Referring to the solutions $(L_2\sin\Theta)\big|_{f^3=0}$ at central plan for $f^3=0$, the body force caused asymmetrical stresses concentration in thickness direction are obtained as:

$$\sigma_1^3\big|_{f^3}=[\sigma_1^3\big|_{f^3=0}+\frac{1}{2}\int_0^{x^3}w_1\exp(-\int_0^{x^3}\frac{f^3}{4\mu}dx^3)dx^3]\cdot\exp(\int_0^{x^3}\frac{f^3}{4\mu}dx^3) \tag{23-1}$$

$$\sigma_2^3\big|_{f^3}=[\sigma_2^3\big|_{f^3=0}-\frac{1}{2}\int_0^{x^3}w_2\exp(-\int_0^{x^3}\frac{f^3}{4\mu}dx^3)dx^3]\cdot\exp(\int_0^{x^3}\frac{f^3}{4\mu}dx^3) \tag{23-2}$$

It shows that: the local body force (load) will cause local asymmetrical stress concentration along thickness direction with exponential law about thickness. If the local curvature at free load is big enough, the load-caused stress concentration will be significant for thick plate. Then, fatigue-fracture may be initiated.
It also shows that, at local load position, the asymmetry stress and non-linear effects will be very significant for thick plate bending, where wrinkling [17] may be produced.

6. Stress Concentration for Kirchhoff Approximation

The bending momentum motion equations, as the results of Kirchhoff approximation theory of plate, are widely used in engineering. How to estimate the stress redistribution caused by thickness and global curvature is a practical problems. As many linear results are well-known, how the non-linear behaves will be exposed in this section.
Using the approximation $R_i^j\approx\delta_i^j+\sin\Theta\cdot L_i^j$, for the typical plate bending produced by normal loading (defined by $f^1=f^2=0$), the Eq.12 will be used to obtain the bending momentum motion equations in Kirchhoff approximation. Letting $\sigma_{ij}=\frac{1}{2}(\sigma_j^i+\sigma_i^j)$, the plate bending momentums M_{ij} $(i,j=1,2)$ in Kirchhoff plate theory are defined as:

$$M_{ij}=\int_{-D/2}^{D/2}\sigma_{ij}x^3dx^3 \tag{24-1}$$

Where, D is plate thickness. Noting that, by Eqs.11 and Eq.3, $\sigma_{13}=\sigma_{31}=0$ and $\sigma_{23}=\sigma_{32}=0$, so, the Kirchhoff assumption is automatically satisfied. The load vector components are defined as:

$$Q_1=\frac{1}{2}\int_{-D/2}^{D/2}f^3\sin\Theta\cdot L_2\cdot x^3dx^3 \tag{24-2}$$

$$Q_2=\frac{1}{2}\int_{-D/2}^{D/2}f^3\sin\Theta\cdot L_1\cdot x^3dx^3 \tag{24-3}$$

$$q_3=\frac{1}{2}\int_{-D/2}^{D/2}f^3\cdot x^3dx^3 \tag{24-4}$$

By Eqs.20, omitting the non-linear items, the following approximations are obtained:

$$\frac{1}{2}\frac{\partial(\sigma_1^3-\sigma_3^1)}{\partial x^3}=\frac{1}{2}f^3\sin\Theta\cdot L_2, \tag{25-1}$$

$$\frac{1}{2}\frac{\partial(\sigma_2^3-\sigma_3^2)}{\partial x^3}=-\frac{1}{2}f^3\sin\Theta\cdot L_1, \tag{25-2}$$

$$\frac{1}{2}\frac{\partial(\sigma_3^1-\sigma_1^3)}{\partial x^1}+\frac{1}{2}\frac{\partial(\sigma_3^2-\sigma_2^3)}{\partial x^2}=0. \tag{25-3}$$

By Eqs.21, it is easy to identify that the above equations can be rewritten as:

$$Q_1=\int_{-D/2}^{D/2}\frac{\partial\sigma_1^3}{\partial x^3}x^3dx^3=-\int_{-D/2}^{D/2}\frac{\partial\sigma_3^1}{\partial x^3}x^3dx^3 \tag{26-1}$$

$$Q_2=\int_{-D/2}^{D/2}\frac{\partial\sigma_3^2}{\partial x^3}x^3dx^3=-\int_{-D/2}^{D/2}\frac{\partial\sigma_2^3}{\partial x^3}x^3dx^3 \tag{26-2}$$

Then, the Eqs.12 is rewritten as:

$$\frac{\partial M_{11}}{\partial x^1}+\frac{\partial M_{12}}{\partial x^2}-Q_1-\frac{1}{2}\int_{-D/2}^{D/2}\sigma_j^1\kappa^j x^3dx^3=0 \tag{27-1}$$

$$\frac{\partial M_{21}}{\partial x^1}+\frac{\partial M_{22}}{\partial x^2}+Q_2-\frac{1}{2}\int_{-D/2}^{D/2}\sigma_j^2\kappa^j x^3dx^3=0 \tag{27-2}$$

$$\frac{\partial Q_1}{\partial x^1}-\frac{\partial Q_2}{\partial x^2}+\frac{1}{2}\int_{-D/2}^{D/2}\frac{\partial\sigma_3^3}{\partial x^3}x^3dx^3-\frac{1}{2}\int_{-D/2}^{D/2}\sigma_j^3\kappa^j x^3dx^3=q_3 \tag{27-3}$$

Omitting the non-linear items and letting $\sigma_{33}=0$, they can be combined as the classical linear bending momentum equation [10]:

$$\frac{\partial^2 M_{11}}{\partial x^1\partial x^1}+2\frac{\partial^2 M_{12}}{\partial x^1\partial x^2}+\frac{\partial^2 M_{22}}{\partial x^2\partial x^2}=q_3 \tag{28}$$

This research shows that the classical linear bending momentum equation is the logic results of two sets of motion equations for unit orthogonal deformation (defined by Eq.8). It makes this research soundness.

For plate bending, the non-linear bending momentum equation is:

$$\begin{aligned}&\frac{\partial^2 M_{11}}{\partial x^1\partial x^1}+2\frac{\partial^2 M_{12}}{\partial x^1\partial x^2}+\frac{\partial^2 M_{22}}{\partial x^2\partial x^2}\\&-\frac{1}{2}\frac{\partial}{\partial x^1}\left(\int_{-D/2}^{D/2}\sigma_j^1\kappa^j x^3dx^3\right)-\frac{1}{2}\frac{\partial}{\partial x^2}\left(\int_{-D/2}^{D/2}\sigma_j^2\kappa^j x^3dx^3\right)\\&+\frac{1}{2}\int_{-D/2}^{D/2}\frac{\partial\sigma_3^3}{\partial x^3}x^3dx^3-\frac{1}{2}\int_{-D/2}^{D/2}\sigma_j^3\kappa^j x^3dx^3=q_3\end{aligned} \tag{29}$$

Only taking the effects of the asymmetrical stress components σ_1^3, σ_3^1, σ_2^3, and σ_3^2 into consideration, the Eq.29 is approximated as:

$$\begin{aligned}&\frac{\partial^2 M_{11}}{\partial x^1\partial x^1}+2\frac{\partial^2 M_{12}}{\partial x^1\partial x^2}+\frac{\partial^2 M_{22}}{\partial x^2\partial x^2}\\&-\frac{1}{2}\frac{\partial}{\partial x^1}\left(\int_{-D/2}^{D/2}\sigma_3^1\kappa^3 x^3dx^3\right)-\frac{1}{2}\frac{\partial}{\partial x^2}\left(\int_{-D/2}^{D/2}\sigma_3^2\kappa^3 x^3dx^3\right)\\&-\frac{1}{2}\int_{-D/2}^{D/2}\sigma_1^3\kappa^1 x^3dx^3-\frac{1}{2}\int_{-D/2}^{D/2}\sigma_2^3\kappa^2 x^3dx^3=q_3\end{aligned} \tag{30}$$

In non-destructive detect, the Eq.28 is assumed as precondition determined by manufacture or working condition. Therefore, the stress redistribution caused by non-linear items can be studied by introducing the effective load, which is defined as:

$$\tilde{q}_3 = q_3 + \frac{1}{2}\frac{\partial}{\partial x^1}(\int_{-D/2}^{D/2}\sigma_3^1\kappa^3 x^3 dx^3) + \frac{1}{2}\frac{\partial}{\partial x^2}(\int_{-D/2}^{D/2}\sigma_3^2\kappa^3 x^3 dx^3) + \frac{1}{2}\int_{-D/2}^{D/2}\sigma_1^3\kappa^1 x^3 dx^3 + \frac{1}{2}\int_{-D/2}^{D/2}\sigma_2^3\kappa^2 x^3 dx^3 \quad (31)$$

By this way, the fatigue-fracture initiation position can be predicted by calculating the effective load. Based on previous results (Eqs.13, Eqs.21, and Eqs.31), each items of effective load can be obtained. As a first approximation, on the thickness direction, the local whole rotation angle variation can be expressed as:

$$\Theta(x^3) = \Theta + (\Theta)^2 x^3 \quad (32)$$

Then, for small Θ (defined on central plan) and small thickness ($-D/2 \le x^3 \le D/2$), the following equation can be used to simplify the asymmetrical stress in Eq.31.

$$\sin\Theta(x^3) \approx \sin\Theta + (\Theta)^2 x^3 \quad (33)$$

Furthermore, omitting the higher order infinitesimals, the following approximations are obtained:

$$\frac{1}{2}\frac{\partial}{\partial x^1}(\int_{-D/2}^{D/2}\sigma_3^1\kappa^3 x^3 dx^3) \approx -\frac{(D)^3}{12}\cdot\mu\cdot\frac{\partial[(\Theta)^2 L_2\kappa^3]}{\partial x^1} \quad (34\text{-}1)$$

$$\frac{1}{2}\frac{\partial}{\partial x^2}(\int_{-D/2}^{D/2}\sigma_3^2\kappa^3 x^3 dx^3) \approx \frac{(D)^3}{12}\cdot\mu\cdot\frac{\partial[(\Theta)^2 L_1\kappa^3]}{\partial x^2} \quad (34\text{-}2)$$

$$\frac{1}{2}\int_{-D/2}^{D/2}\sigma_1^3\kappa^1 x^3 dx^3 \approx \frac{(D)^3}{12}\cdot\mu\cdot(\Theta)^2\cdot L_2\kappa^1 \quad (34\text{-}3)$$

$$\frac{1}{2}\int_{-D/2}^{D/2}\sigma_2^3\kappa^2 x^3 dx^3 \approx -\frac{(D)^3}{12}\cdot\mu\cdot(\Theta)^2\cdot L_1\kappa^2 \quad (34\text{-}4)$$

As a simple example, for simple bending $\frac{\partial u^3}{\partial x^1} \approx \Theta$, $L_2 = 1$, $L_1 = 0$, $\kappa^3 \approx \frac{\partial\Theta}{\partial x^1}$, $\kappa^1 \approx (\Theta)^2$, the effective load is simplified as:

$$\tilde{q}_3 = q_3 + \frac{(D)^3}{12}\cdot\mu\cdot\{(\Theta)^4 - \frac{\partial}{\partial x^1}[(\Theta)^2\frac{\partial\Theta}{\partial x^1}]\} \quad (35)$$

It shows that the local whole rotation in average sense (local curvature) has significant effects. Here, the stress concentration is expressed by effective load variation. Hence, it can be used in forward problems to predict possible fatigue-fracture initiating positions.

6. Conclusions

For large deformation, such as plate bending, the linear momentum conservation equations and angular momentum conservation equations are used to study the stress concentration problems. The research shows that, for plate bending, the dominate Cauchy stresses are asymmetrical. The symmetrical stress components are higher order smaller. By requiring both sets of motion equations are satisfied, the classical bending momentum linear motion equation is obtained as a linear approximation.

Based on the linear momentum conservation equations, the stress concentration caused by bending curvature functions is studied by introducing effective stress transportation solutions. The results show that: the effective stresses on central plan parallel surface are exponentially varied with path-integral of curvature along scale directions. The effective stresses on thickness direction are exponentially varied with the path-integral of curvature functions. The scale effects are very significant. As the effective stresses can be detected by many non-destructive methods, the curvature functions can be estimated. For supersonic wave method, the effective elasticity can be detected and used to estimate the curvature functions. Hence, the fatigue-fracture initiating position

can be predicted.

Based on the angular momentum conservation equations, the stress concentration caused by local load on thickness direction is studied. The results show that: the local body force (load) will cause local asymmetrical stress concentration along thickness direction with exponential law about thickness.

Finally, the effective load caused by local bending curvature is introduced to estimate the stress concentration as effective load variation. For simple bending, an explicit formula is given. It shows that the local rotation in average sense (local curvature) has significant effects. This equation can be easily used for non-destructive inverse problems.

References

[1] C.C. Osgood, Fatigue Design, Wiley-Interscience, New York, 1970
[2] S. Suresh, Fatigue of Materials (2ed.), Cambridge University Press, Cambridge,1998
[3] Z.B. Kuang, F.S. Ma, Crack Tip Fields, Xian Jiaotong University Press, Xian, 2001 (in Chinese)
[4] G.C. Sih, Crack tip mechanics based on progressive damage of arrow: Hierarch of singularities and multiscale segments, Theo. App. Fracture Mechanics. 51 (2009) 11-32
[5] G.C. Sih, B. Liu, Mesofracture mechanics: a necessary link. Theo. & App. Fracture Mechanics. 37 (2001) 371-395
[6] G.C. Sih, Anomalies of momoscale notion of failure in contrast to multiscale character of failure for physical processes, in: S.T. Tu, Z.D. Wang, G.C. Sih (Eds.), From Failure to Better Design Manufacture and Construction, East China University of Science and Technology Press, Shanghai, 2012, pp. 1-7
[7] Jianhua Xiao, Fatigue-fracture mechanism under larger stress and strain conditions, in: S.T. Tu, Z.D. Wang, G.C. Sih (Eds.), From Failure to Better Design Manufacture and Construction, East ChinaUniversity of Science and Technology Press, Shanghai, 2012, pp. 129-134
[8] Zhida Chen, Rational Mechanics, Chongqing Press, Chongqing, 2000 (in Chinese)
[9] Jianhua Xiao, Geometrical field description of fatigue-fracture caused by high temperature or its gradient, in: G.C. Sih, S.T. Tu, and Z.D. Wang (Eds.), Multi-scaling Associated with Structural and Material Integrity under Elevated Temperature, East China University of Science and Technology Press, Shanghai, 2006, pp. 211-216
[10] C.Y. Chia, Nonlinear Analysis of Plates, McGraw-Hill, New York, 1980
[11] Truesdell, C., The Mechanical Foundation of Elasticity and Fluid Mechanics, Gordon and Breach Science Pub. Inc., New York, 1966.
[12] Chen Zhida. Limit rotation expression in non-linear field theory of continuum, Applied Mathematics and Mechanics 7 (1986) 959-968. (In Chinese)
[13] A. DiCarlo, P. Podio-Guidugli, W.O. Williams. Shell with thickness distension. Int. J. Solids and Structures. 38 (2001) 1201-1225,
[14] S. Knoche, Jan Kierfeld. Buckling of spherical capsules. Phy. Rew. E 84 (2011) 046608
[15] D. Vella, A. Ajdari, A. Vaziri, A. Boudaoud. Wrinkling of pressurized elastic shells. PRL. 107 (2011) 174301
[16] M.A. Biot, Mechanics of Incremental Deformations, John Wiley & Sons Inc, New York, 1965
[17] D. Vella, A. Ajdari, A. Vaziri, A. Boudaoud. Wrinkling of pressurized elastic shells. PRL. 107 (2011) 174301

Based on Micromechanical Damage of Q345 Specimen's Acoustic Emission Quantitative Assessment in Tensile Process

ZHANG Ying[1*], WANG Zi-xing[1], ZHOU Jun-peng[1], LIU Ai-ling[1]

[1] Department of Mechanical Science and Engineering, Northeast Petroleum University, Daqing 163318, China
* Corresponding author: aezy163@163.com

Abstract To further reveal the mesomechanical damage behavior of the plastic material, quantitative evaluation the micromechanical damage state of material use acoustic emission characteristic parameters. Based on the Gurson-Tvergaard-Needleman micromechanical damage model, establish the quantitative evaluation model of acoustic emission cumulative hits, taking void growth ratio as the damage variable. Taking steel Q345 notched bar specimens tensile process as example, using acoustic emission testing technology, get the AE information from yield to fracture process. Using ABAQUS finite element analysis software, analyze the meso-damage process during tensile process of steel Q345 notched bar specimens, and get the numerical solution of meso-damage parameters. Based on AE testing and Finite Element Simulation, get the quantitative evaluation formula of void growth ratio based on AE cumulative hits N during Q345 steel notched bar specimens tensile process. Result shows that, in the tensile process of Q345 steel from yield to fracture damage, the function relationship of N and V_G is divided into two stage, linear damage stage and nonlinear damage stage, and when the N reaches 128, the material is at the transition state from linear damage stage to nonlinear damage stage. This critical transition area value could be used as steel Q345 damage fracture of acoustic emission recognition feature and safety evaluation threshold value.

Keywords Acoustic emission, Void growth ratio, Cumulative hits, Gurson-Tvergaard-Needleman model, steel Q345

1. Introduction

Acoustic emission refers to the material or components rapid release of strain energy and the transient stress wave phenomenon when stress exceeds yield stress into the irreversible stage of plastic deformation or crack initiation, growth and fracture. There is consistent correspondence relationship between acoustic emission and material interior damage. Acoustic emission cumulative hits directly correspond to different material damage state and the new damage must be accompany with the release of stress wave, which is the basis fundamental to the direct measurements and modeling of acoustic emission[1-3].Generally micro-void nucleation, growth and coalescence is a typical mechanism of microstructure damage and failure for metal plastic material. Gurson-Tvergaard-Needleman (GTN) model[4-6]is regard as a significant progress in meso-damage mechanics. Because it was well descript the metal plastic damage in the process of plastic deformation caused by the evolution of micro-voids and had been developed and applied in many fields[7,8]. Based on voids nucleation controlled by the stress triaxiality and equivalent plastic strain, Zheng Changqing[9]proposed the concept of critical void ratio V_{GC}.V_{GC} is an micromechanics parameters which built on the micro-void damage mechanism when metals got into the plastic deformation, and it contacts the meso-damage parameters and macro-mechanical behavior. The variation of void growth ratio V_G directly reflects the damage state of the materials. Therefore, established the relationship between the characteristics parameters of acoustic emission and the void growth ratio can be deeply understanding the macroscopic and micromechanics behavior in the process of metal plastic damage, and achieving quantitative evaluation materials micromechanical damage state used acoustic emission testing technology.

This paper from micro-void damage mechanisms of metal plastic materials, used acoustic emission testing the steel Q345 round notch specimen in tensile process, obtained of material's release of the stress wave from yielding to the fracture process. Using ABAQUS analyzed the changes of steel Q345 round bar notched specimen micromechanics parameters in tensile fracture process, obtained

numerical solution of void growth ratio in different damage states. Based on acoustic emission testing result, establish acoustic emission characteristics parameters of tensile process and quantitative evaluation formula of void growth ratio, in order to achieve Q345 quantitative evaluation of micro-damage state.

2.The relationships between AE and material micro-damage parameters

2.1. GTN model

Based on the previous work, Gurson researched the response under the axisymmetric triaxial stress state in limited large matrix of cylindrical or spherical with void. He constructed material damage yield function to describe the effect of micro-void damage to the metal plastic deformation behavior. After further amended to the Gurson model by Tvergaard and Needleman[5,6], the model's prediction accuracy has greatly improved[8,10].The GTN model yield function φ is expressed as follows:

$$\phi = (\frac{\sigma_{eq}}{\sigma_s})^2 + 2fq_1 \cosh(q_2 \frac{3\sigma_m}{2\sigma_s}) - (1+q_3 f)^2 = 0 \tag{1}$$

Where q_1, q_2, q_3,is revision coefficient; σ_{eq} is Misses stress; σ_m is macro hydrostatic stress; σ_s is flow stress of the base material in the unit; f is the percentage of void volume. In GTN model damage variable is considering as isotropic, which comprises two parts:

$$f = (f)_{growth} + (f)_{nucleation} = (1-f)\varepsilon_{ij}^{p} + A\langle R_\sigma \rangle \eta^p \tag{2}$$

Assumed the nucleation void mechanism by strain controlled and the void follows normal distribution. The voids nucleation intensity function A is expressed as:

$$A = \frac{f_N}{hs_N\sqrt{2}} \exp\left[-\frac{1}{2}(\frac{\eta^p - \varepsilon_N}{s_N})^2\right] \tag{3}$$

where $(f)_{\text{growth}}$ indicates the void-volume fraction caused by the void growth;$(f)_{\text{nucleation}}$ is the void-volume fraction caused by the nucleation of a void; ε_{ij}^{p} is macroscopic plastic strain rate tensor; R_σ is stress triaxiality ($R_\sigma=\sigma_m/\sigma_{eq}$); η^p is equivalent plastic strain of the matrix material; $\langle x \rangle$ Macauley operator; f_N for the nucleation of micro-voids volume percentage of the two-phase particles; h is material constants; S_N is void nucleation average strain standard; ε_N is void nucleation average strain.

2.2. The relationships between AE and material damage

The emergence and development of inside damage (micro-cracks and micro-voids) in the metal plastic material generates the acoustic emission, so there is inevitable relation between acoustic emission parameters and material damage variable. C.A.Tang etal.[11] obtain damage model which based on damage mechanics theory characterized by AE parameters, the relationship was written as:

$$D = \frac{A_d}{A} = \frac{N}{N_m} \tag{4}$$

Where the damage variable D represents the damage state of the material, Kachanov defined it as ratio of the instant all the area of the bearing surface defects A_d and sectional area when initial nondestructive; N_m is the total number of acoustic emission cumulative hits when material entire cross section A destructed, N is the instant acoustic emission cumulative hits.

Base on the microcosmic architectural feature, Gurson proposed that make the void-volume percentage f as a micro-mechanical damage variable for metal-plastic material. Zheng Changqing[9]

used an electron microscope to observe micro-void nucleation, growth, and coalescence of plastic deformation when metal stretching, necking as well as instability in the fracture process. Combined experiment and numerical simulation and analyzed the relations between the strain and stress, make the fracture strain ε_f and stress triaxiality $R_{\sigma 0}$ as critical void growth ratio V_{GC} when material fractured. Micromechanics fracture criterion was $V_G \geq V_{GC}$,V_G is the void growth ratio under the conditions of forcing. For notched specimen was the following relationship:

$$V_G = \varepsilon_p \exp(1.5R_\sigma) \tag{5}$$

Where ε_p is the equivalent plastic strain. The nucleation of micro-void controlled by the triaxiality stress and equivalent plastic strain. Also they were the function of void growth ratio V_G. The void growth ratio is the micromechanics parameters which establish on the micro-voids growth and coalescence in metal plastic materials. It is the bridge of contacting microscopic damage characteristic and micromechanics parameter. The change of V_G directly reflected the material damage of macro-micro state changes in real time, so make the void growth ratio V_G as the new damage variable of material deterioration state.

Considering formula (4) and (5), the void growth ratio V_G and acoustic emission cumulative hits N can be used as parameters which describe the damage state of the metal plastic materials. Therefore established the quantitative evaluation of the formula between the void growth ratio and acoustic emission cumulative hits:

$$V_G = f(N) \tag{6}$$

According to the formula (6), used the acoustic emission testing technology obtained the Q345 notched bar specimen's information in tensile process. Using ABAQUS finite element analysis software to obtained the numerical solution of void growth ratio in different damage state. Then establish quantitative evaluation formula between the acoustic emission characteristics parameters and void growth ratio when steel Q345 in stretch process. Finally realized use acoustic emission quantitative evaluation the material's microscopic damage state.

3. Steel Q345 notched specimen tensile process acoustic emission testing experiment

3.1. The Steel Q345 notched specimen size and mechanical properties

The size of Steel Q345 tensile specimen is shown in Figure 1. There are eight specimens, numbering from#1 to #8.

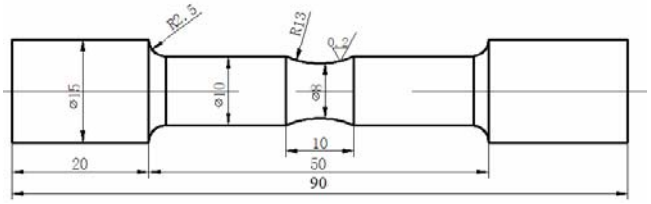

Fig.1 The shape and size of notched tensile specimens

Experiment mechanical properties and chemical composition of the steel Q345 are shown in Table 1.

Table 1 Steel Q345 mechanical properties and chemical composition

mechanical properties						chemical composition %				
σ_s	σ_b	E	γ	Ψ	Φ	C	Mn	Si	P	S
MPa	MPa	GPa		%	%					
408	533	200	0.3	4.58	60.58	0.17	1.42	0.019	0.020	0.031

3.2. Experimental equipment and methods

The tensile test was on the SANS electronic universal testing machine, adopted displacement loading, axial tensile in constant speed, loading rate was 0.3mm/min. Acoustic emission data acquisition system was the U.S. PAC PCI-2 acoustic emission system, and the sensor was WD broadband sensor, the frequency range of 100~1000kHz. The preamplifier was PAC2/4/6 produced in PAC. The sensors were installed at the end of the specimen, and coupled by vacuum grease. To calibrated the sensitivity of each channel used HB pencil(Φ=0.5mm) breaking signals as sound simulate source. In order to collect the acoustic emission signal that generated from material's microscopic damage during tensile stretched, need to lower the threshold value. In order to testing the experiment environment, environmental noise and electromagnetic noise of AE signal distribution levels under no-load operation, finally set threshold value is 30dB. Acoustic emission testing system parameter settings were shown in Table 2.

Table 2 Acoustic emission detection system parameter settings

Parameter category	Setting value	Parameter category	Setting value
Threshold value /dB	30	Peak definition time PDT/μs	200
Sampling rate /MB	2	Hits definition time HDT/μs	600
Sampling length /K	4	Hits lockout time HLT/μs	1000

3.3. Experimental results and analysis of acoustic emission testing

Table 3 shows the results of eight specimens' acoustic emission testing experimental. It listed axial displacements and acoustic emission cumulative hits and corresponding mean value of separately yield point B and yield end point C, tensile strength point D and breaking point E. Studies[11,12] indicated that acoustic emission cumulative hit can reflect the changes in the material damage state, so selected the acoustic emission cumulative hits combined with the amplitude to analyze different damage stage of Steel Q345 in tensile process. The amplitude of the #1 specimen's AE vs. the cumulative hit vs. stress increases with the experiment time is shown in Figure 2.

Table3 Steel Q345 axial tensile displacement and acoustic emission cumulative hitting statistics

		1#	2#	3#	4#	5#	6#	7#	8#	average
B	displacement /mm	1.79	0.98	1.86	2.28	1.91	1.92	1.82	1.76	1.79
	Accumulate strike count	20	23	18	24	20	22	19	22	21
C	displacement /mm	2.24	2.10	2.06	2.61	2.45	2.31	1.96	2.43	2.28
	Accumulate strike count	104	99	110	103	100	107	104	109	104.50
D	displacement /mm	4.33	4.45	4.01	4.45	4.66	4.51	4.41	4.57	4.42
	Accumulate strike count	148	150	165	150	160	162	150	160	155.62
E	displacement /mm	6.15	5.49	6.21	6.25	5.99	5.39	5.53	6.03	5.88
	Accumulate strike count	157	160	176	156	164	171	162	171	164.63

Figure 2 shows Steel Q345 tensile damage process is divided into four phases, i.e., AB, BC, CD, and DE, respectively corresponding to the elastic deformation stage, the yield phase, strengthening phase and necking stages of the specimen. (1) The elastic deformation stage (0~320s, 0~408MPa). There are few acoustic emission signals in the stage and acoustic emission cumulative hit change is also very small. Amplitude are less than 35dB, most of the which are from mechanical noise caused by the loaded the initial specimen two ends of the fixture bite and friction; (2) Yield stage (321~496s, 408~432MPa),which are also known as the stage of plastic flow. After the specimen entering this phase, the acoustic emission signal was significantly increased, and then the acoustic emission yield effect appears. Signal amplitude between 30~54dB, the cumulative hit - time curve

appears apparent inflection in the vicinity of the point B, and rapid raised. The micro-voids generally nucleation at lower strain in the vicinity of the inclusions or second phase particles itself broken, or produced in the detachment of the inclusions and matrix interface[9,13].This stage acoustic signal reflects the sensitive to metal plastic material micro-voids nucleation process; (3) strengthening stage (497~931s, 432~533MPa). The specimen was in the uniform state of strain and begun to produce plastic deformation, the damage of micro-void continued to develop. The amount of AE signals reduced significantly and accompanied by a little amount of high-amplitude signal, the amplitude range between 30~55dB. The curve of accumulation hits vs. time rising trend was becoming slowly;(4) Necking stage(932~1230s,533~441MPa).When the stress reaches to the point D, since strength increase insufficient to compensate for size contraction caused by the work hardening, resulting in the phenomenon of necking. Since then, the deformation of the material became non-uniform. In this stage the amount of acoustic emission signals continued to reduce, the amplitude below 50dB, the curve of cumulative hits substantially in the horizontal direction.
Based on the above analysis, the acoustic emission amplitude and the slope of cumulative hits have obvious stage characteristics from yielding to plastic deformation then to the stages of the fracture process of steel Q345. The relationship between simulation and experiment with the load and time curve were fit well, which illustrates the changes of acoustic emission cumulative hits can reflect the different processes of the development of material damage state.

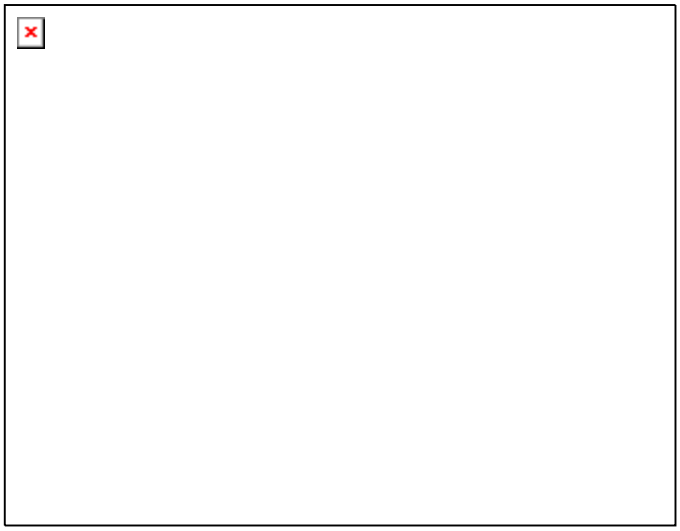

Fig.2 Accumulated hit-amplitude-stress vs. time for specimen 1.

4 The tensile process micro-damage of Steel Q345 notched specimen: simulation and analysis

4.1 The establishment of the Steel Q345 notched micro model and parameter selection

The voids growth ratio VG of Steel Q345 notched specimen are obtained with numerical simulation method in tensile process. Take GTN as the micro-damage model, using the ABAQUS finite element analysis software, we analyzed Steel Q345 notched specimen and observed micro-damage evolution, then obtain the numerical solution of the micro-damage parameters. Voids growth ratio V_G is a function of the stress triaxiality and equivalent plastic strain, so using the finite element software ABAQUS/Explicit can calculate stress triaxiality, equivalent plastic strain, void volume percent distribution and changes with the load in notched specimen. First, modeling of the notched specimen, due to the geometric axis of the specimen, took the modeling of the test piece of 1/4

which shown in Fig.3. The element type is CAX4R. Meshing principle is that the more close to the notched root the meshing was more dense, the minimum mesh size of the front notched is about 80μm. The number of nodes of the model was 496, the number of units was 328. The boundary conditions are consistent to the former experimental conditions, loading mode is displacement loading. Loading amount of displacement of eight specimens at the point B~E which listed in Table 2 is displacement average. Choice of the steel Q345 GTN model parameters are as follows: q_1=1.5，q_2=1.0，q_3=2.25，f_N=0.02，S_N=0.1，ε_N=0.25.

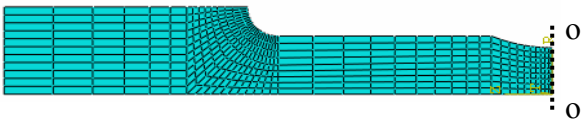

Fig.3 1/4 finite element model of notched tensile specimens

4.2 The numerical simulation results and analysis

Figure 4 is a numerical simulation proceeds that steel Q345 axial tensile stress-displacement curve compared with the specimen 1 of the experimental curves. The highest stress point D and the yield point B obtained by the numerical simulation agree with the experiment results, which are proved the GTN model parameter selected reasonable. These can truly reflect the macro-mechanics and micro-mechanics behavior of Steel Q345 axial tensile experiment. Figures 5~7 are respectively different loading stage of model notched o-o, they are the curves of stress triaxiality R_σ, equivalent plastic strain ε_p and the void volume percentage f versus x. x represents the specimen o-o surface center (x=0mm) to the distance of the notched root(x=4mm). To express the micro-damage parameters changes with the loading clearly, the middle of the loading process should select appropriately. Concluded from Fig.5, the R_σ of the specimen notched center is bigger than the value of the root of the specimen and the maximum R_σ always at the center of the specimen during the loading stage, and increasing with the loading. Fig.6 and Fig.7, ε_p and f change similar with x, but in the loading process they change different with R_σ , and can be divided into two stages. Stage I: Hardening stage (B~D point), the stage is the material yield and enhanced stage, ε_p and maximum f appear at the root of the notched, and they rise with the loading increase. Stage II: Necking stage (D~E point). When the material loaded to the strength limit point D, for the influence of R_σ intensified, ε_p at the middle of the specimen change greater than the growth of the roots. Micro voids move from the notched root to the core part. After plastic zone extends to the core part, stress triaxiality at the core part is much larger than the value of the root, ε_p and f at the core part of the specimen is far greater than the value, which lead to the occurrence of fracture of the specimen from the core part.

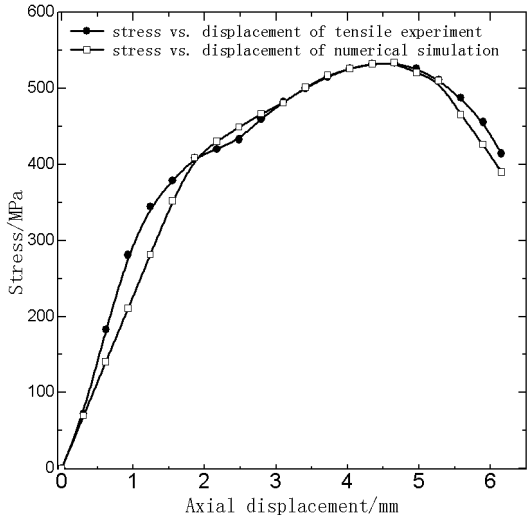

Fig.4 Numerical simulation and experimental results

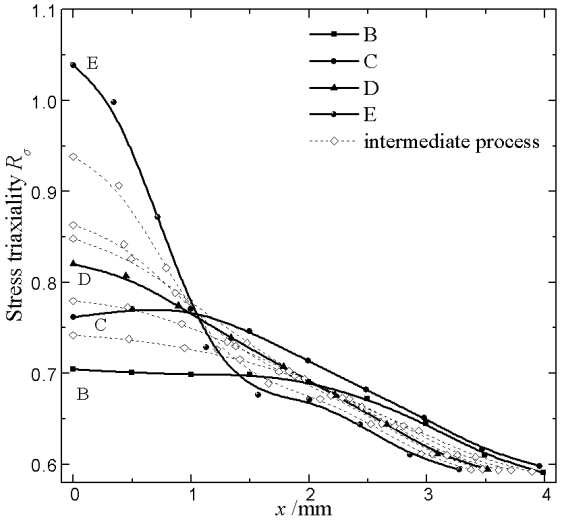

Fig.5 Distribution of Rσ on notch tip

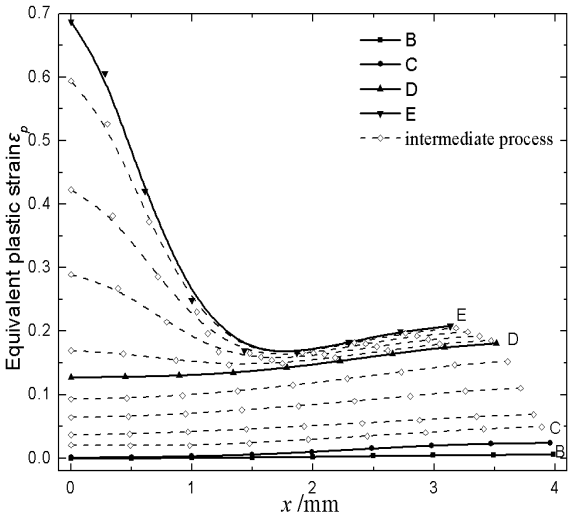

Fig.6 Distribution of εp on notch tip

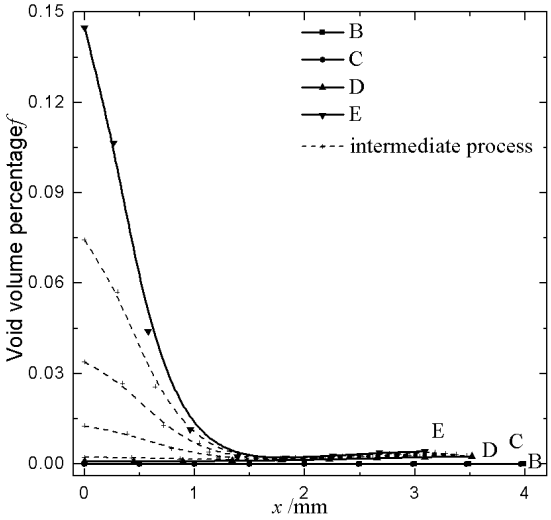

Fig.7 Distribution of f on notch tip

4.3 The numerical simulation of Steel Q345 notched specimen voids growth ratio

Concluded from the simulation results, the final fracture first occurs at o-o surface, so R_σ and ε_p at point B~E which located at model integrator x=0 from o-o surface, and select the appropriate middle point in the loading process. According to equation (6), the numerical simulation results of steel Q345 notched specimens in tensile process are showed in Table 4.

Table 4 Table of voids growth ratio calculation

	stress triaxiality	equivalent plastic strain	voids growth ratio
B	0.704	0	0
C	0.762	0.00104	0.00326
D	0.820	0.128	0.437
E	1.22	0.687	4.29

5. The quantitative evaluation formula between AE cumulative hits and the void growth ratio VG

Selecting the critical point B~E in the tensile process, so do the intermediate process in the loading process, the acoustic emission of each point in the cumulative hit average and numerical simulation of the void growth ratio V_G are showed in Figure 8. From Figure 8, the relationship between $\overline{N}$ and

V_G can be divided into two stages:
Stage I: point B~D, steel Q345 is in the yielding and hardening process. This stage is an important period of the material within the nucleation and growth of micro-voids, the void growth and acoustic cumulative hit are linear growth, and the growth trend is relatively slow. Therefore, this stage is defined as the stage of the linear damage of the material. By numerical fitting:

$$V_{G\,\mathrm{I}} = 0.0021\overline{N} - 0.109 \qquad (7)$$

Where $21 \leqslant \overline{N} \leqslant 155$.
Stage II: point D~E, steel Q345 is in the necking stage. This is the development of late damage, micro-void confluence occur in the material internal. With the cumulative hit increases, void growth ratio is increasing rapidly. Contrast to stage I, this stage increase evidently in exponential form. Therefore, the stage is defined as a nonlinear damage stage. By numerical fitting:

$$V_{G\,\mathrm{II}} = 0.058(\overline{N} - 153.05)^{1.75} \qquad (8)$$

Where $155 \leqslant \overline{N} \leqslant 164$.

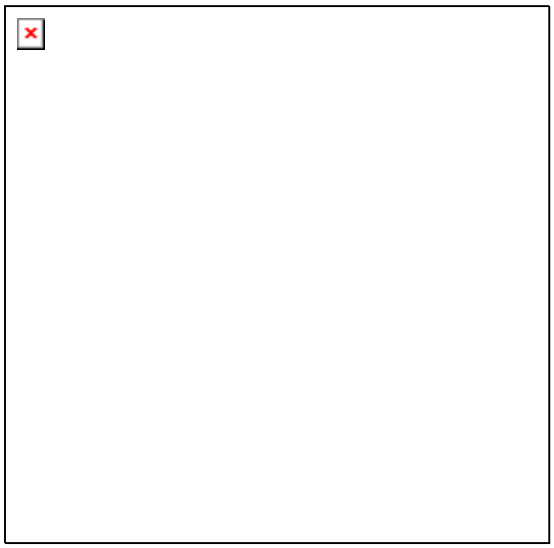

Fig.8 The diagram of AE average cumulative hit vs. void growth ratio

The intersection point F (147.28, 0.26) was obtained by simultaneous the equation (7) and (8), it revealed that steel Q345 notched specimen begins to transform from linear damage stage to nonlinear damage stage. Taking the uniformity of experimental material , the micro-voids distribution and mechanical noise impact in acoustic emission testing experimental process into consideration, the safety factor n range was 0.9~0.95. Material transform from linear damage to the next stage, the critical acoustic emission cumulative hits take $[N^*]=N_F \times n$. When n=0.9, acoustic emission cumulative hit is 128, which can be taken as the critical value of steel Q345 notched specimen in plastic damage. This is the evident to certify the transformation of steel Q345 notched specimen from linear damage stage to nonlinear damage stage.

6. Conclusions

(1) The meso-damage mechanism of metal-plastic material is micro-void nucleation, growth and coalescence. Steel Q345 notched specimen in tensile process shows that AE and micro-voids of metal plastic material have the consistent corresponding relationships, which the changing of AE cumulative hits directly corresponds with the different damage stage of material.
(2) Based on the micro-void damage theory of metal plastic materials, the micromechanics parameters of void growth ratio V_G is the bridge with which combined micromechanical

characteristics and macro mechanical parameters. The changes of V_G directly reflects the state of deterioration of the material. Applying GTN model to calculate the changes of V_G on tips of Steel Q345 notched specimen combined with AE testing experiment, and finally established the quantitative evaluation formulas between acoustic emission cumulative hits and void growth ratio.

(3) The quantitative evaluation formulas between acoustic emission cumulative hits and void growth ratio can be divided into two parts: linear damage stage and nonlinear damage stage. From the function of cumulative hits and void growth ratio, when the acoustic emission cumulative hits is larger than 128, the steel Q345 damage transform from linear damage stage to nonlinear damage stage.

References

[1] Wang Huijing, Lin Zhe, Zhao Deyou. Application and prospect of acoustic emission technology in engineering structural damage monitoring [J]. Journal of Vibration and Shock, 2007, 26(6): 157—191. (in Chinese)

[2] D.E. Lee, I. Hwang, C.M.O.Valente, J.F.G. Oliveira, etal. Precision manufacturing process monitoring with acoustic emission[J]. International Journal of Machine Tools and Manufacture, 2006,46(2):176—188.

[3] C. Ennaceur, A. Laksimi, C.Herve, etal. Monitoring crack growth in pressure vessel steel by the acoustic emission technique and the method of potential difference[J]. International Journal of Pressure Vessels and Piping, 2006,83(1):197—204.

[4] Gurson A L. Continuum Theory of Ductile Rupture by Void Nucleation an Growth: Part I—Yield Criteria and Flow Rules for Porous Ductile Media[J]. Transactions of ASME: Journal of Engineering Materials and Technology,1977, 8(1):1—15.

[5] Tvergaard V, Needleman A. Analysis of the Cup–Cone Fracture in a Round Tensile Bar[J]. Acta Metal, 1984, 32(1):157—169.

[6] Needleman A, Tvergaard V. Numerical Modeling of the Ductile-brittle Transition[J]. International Journal of Fracture, 2000, 101 (1/2):73—97.

[7] M. Abbasi, B. Bagheri, M. Ketabchi, D.F. Haghshenas. Application of response surface methodology to drive GTN model parameters and determine the FLD of tailor welded blank[J]. Computational Materials Science,2012, 53 (12):368—376.

[8] CHAE D, KOSS D A. Damage accumulation and failure of HS-LA-100 steel[J]. Materials Science and Engineering, 2004,A366(2) : 299—309.

[9] Zheng Changqing, Zhou Li, Zhang Keshi. Micromechanical research and application for the ductile fracture of metal. [M]. Beijing: National Defense Industry Press, 1995.(in Chinese)

[10] KIM J, GAO Xiaosheng, SRIVAT SANT .Modeling of void growth in ductile solids effects of stress triaxiality and initial porosity[J]. Engineering Fracture Mechanics, 2004, 71 (6):379—400.

[11] Tang C A，Xu X H. Evolution and propagation of material defects and Kaiser effect function[J]. Journal of Seismological Research,1990,13(2):203—213.

[12] Long Xianhai, Yang Nengjun, Wang Hangong. Fracture mechanism for 30CrMnSi steel based on acoustic emission technology [J] Materials Engineering, 2011,20(1):17—22.(in Chinese)

[13] Zhu Hongping, Xu Wensheng, Chen Xiaoqiang, Xia Yong. Quantitative concrete-damage evaluation by acoustic emission information and rate-process theory [J] Engineering Mechanics, 2008, 25 (1): 186—191. (in Chinese)

[14] Xu Jinquan. Strength of materials science. [M]. Shanghai: Shanghai Jiaotong University Press, 2009:133-135.(in Chinese)

Some Statistical Parameters of Acoustic Emission Signals in Porous Iron under Static Loading

Andrey A. Lependin[1,*], Victor V. Polyakov[1], Aleksandr V. Egorov[1]

[1] Physics department of Altay State University, Barnaul 656049, Russian Federation
* Corresponding author: andrey.lependin@gmail.com

Abstract Acoustic Emission (AE) method is based on detection of ultrasonic signal due to the process of plastic deformation and fracturing of a loaded material. In this paper two characteristics of the AE signal, distributions of time intervals between successive pulses and amplitude distributions of these pulses were obtained. Samples were made of the porous iron with a porosity in the range P=0.05-0.25. This class of materials can be considered as a model to study the influence of geometry of the inhomogeneous medium and percolation effects (due to changing of porosity) on the processes of deformation and fracture, and therefore the behavior of the various parameters of acoustic emission. Registered signals were broadband in a range of frequencies from 100 to 800 kHz. Consideration of amplitude distributions of AE signals showed that it is possible to identify two groups of AE pulses - low-amplitude and high-amplitude in the recorded signals. The first group corresponds to the plastic deformation of the compact sites of the material, and the latter one is usually generated by large plastic shears and crack propagation. It was showed that they have scaling with exponents vary with changes in porosity. Obtained distributions can be perceived as indirect evidence of self-organized processes occurring in porous metallic materials.

Keywords acoustic emission, plastic deformation, amplitude distribution, fracture

1. Introduction

Acoustic emission (AE) method is successfully used for nondestructive testing purposes. It is well developed for homogeneous metallic materials. New types of materials such as sintered powder metals or composites with high degree of heterogeneity have many potential mechanisms of ultrasonic emission. Therefore it is very important to understand how and when these mechanisms activate, and to be able to estimate their parameters.

Usually only some basic characteristics of acoustic emission process are used for AE diagnostics [1]. These characteristics are kinetic, such as rate or AE event count, and energy (energy of AE signal and energy of discrete events). But AE process in heterogeneous material is a complex phenomenon, with many mechanisms interacting with each other. Not without reason there are many synergetic and/or fractal theories of plastic deformation and fracturing of materials. For this kind of processes some new integral parameters of AE signal can be introduced.

In this paper two of such complex or integral parameters of AE were considered. First is well known. It is an amplitude distribution of AE signal. In heterogeneous materials this parameter has complex behavior. It is closely associated with second parameter - distribution of time intervals between successive AE events.

2. Materials and samples

As an example of material with highly heterogeneous structure porous metals were used. They can be considered as heterophase media with ultimately different properties of the two phases (solid framework and pores) [2].

Samples for acoustic emission tests were made of an iron powder obtained by spraying in air

(PZhRV2 grade). They were prepared by pressing to a preset porosity followed by sintering at 1500 K for 2.5 h in vacuum. The samples had the standard shape for tensile tests with a rectangular working part of 3X3 mm cross section. Their porosity varied within P=0.05-0.25. During static loading of these samples AE signals were recorded, and thereafter were digitally processed [3]. First, digital band-pass filtering with cutoff frequencies 100 and 800 kHz was done. Events with amplitudes under preassigned threshold (~0.2 V) were not taken into succeeding calculations.

3. Amplitude distributions

Amplitude distributions for extracted events were calculated. An example of such distribution is presented on Fig.1. Logarithmic scale was used. We can see two amplitude ranges. Dependence of amplitude rate in these ranges can be written as $n(u) \sim u^{-h}$, where h is an exponent coefficient. Amplitude of AE events is closely related to the size of the AE sources. Of course, inhomogeneity of material, reflection of acoustic waves on sample surfaces can change amplitudes of AE events, but qualitative dependence of amplitude distributions cannot be changed dramatically. So we see that there were two groups of AE events. First group of events with low amplitudes can be attributed to plastic deformation of material. From [4] we know that such type of deformation cause AE emission with frequent and low bursts. Second group of events with high amplitudes is related to nucleation and propagation of microcracks, originated from the pores [2, 4]. There's an amplitude threshold between two groups. This threshold didn't change for every sample in our setting. So we can use it for discrimination of AE events with different mechanisms.

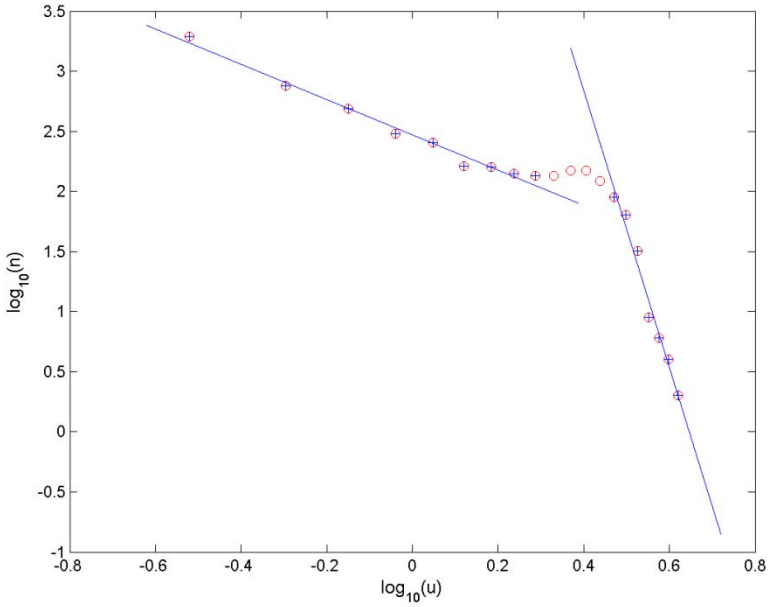

Figure 1. An example of amplitude distribution (P=0.09).

On Fig.2 the values of exponent coefficients for different samples were showed. The exponent coefficient of high amplitude events were changed for different values of porosity, while the other group of events had the same coefficients regardless of porosity. As we can see, for samples with porosity near percolation threshold (P~0.1 for porous iron [2, 5]) there was a large spread of coefficients for high amplitude AE events. It can be explained by the fact, that the structure of porous space varies from sample to sample and scale range of AE sources varies greatly respectively. For some samples isolated pores were prevailed, and for others pores form "infinite" clusters [5]. Plastic flow in compact regions of porous metal doesn't change and therefore there's no

dependence of low amplitude coefficients on porosity.

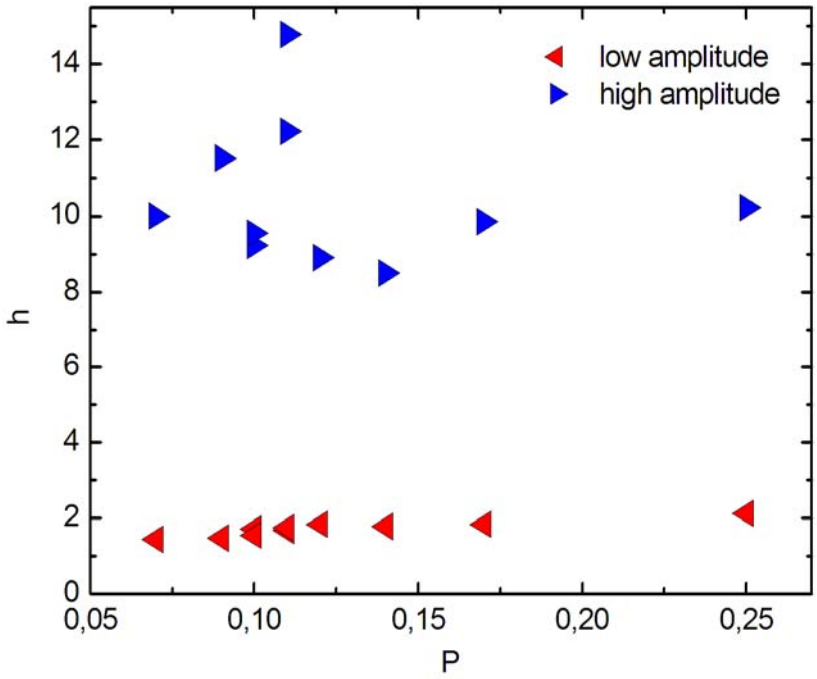

Figure 2. Exponent values of amplitude distributions for different porosities.

4. Distributions of time intervals between AE events

The next step of our work was calculation of distributions of time intervals. This parameter has a great advantage over other AE parameters, because it does not depend on peculiarities of acoustic wave propagation. Time intervals between registered AE bursts and corresponding AE events in media are the same. Also time intervals between AE events give more information about kinetic characteristics of AE process than usual parameters such as AE event count. There is only one difficulty in applying this parameter. Time distribution for all AE events takes into account all the processes that are responsible for the emission of acoustic waves. The structure of such distribution can be too intricate. To overcome this difficulty the following approach had been proposed.

All AE events had been divided into two groups according to the amplitude. Time intervals were calculated not for successive events but for successive events in one group. Fig.3 illustrates this idea. For low amplitude events with $U_{discr} < U < U_{threshold}$, where $U_{threshold}$ corresponds to amplitude threshold between "low" and "high" groups and U_{discr} was a preassigned threshold above, a distribution $w_{low}(\Delta t^{low})$ was calculated. And for high amplitude AE events with $U_{threshold} < U$ a distribution $w_{high}(\Delta t^{high})$ was obtained. These distributions had the same scaling form:

$$w_{low}(\Delta t^{low}) \sim (\Delta t^{low})^{-a_{low}}, \quad (1)$$

$$w_{high}(\Delta t^{high}) \sim (\Delta t^{high})^{-a_{high}} \quad (2)$$

Values of exponents a_{low} and a_{high} are showed in Fig.4. As we see from this figure, all exponents for low and high amplitude events were in two "bands" or value intervals.

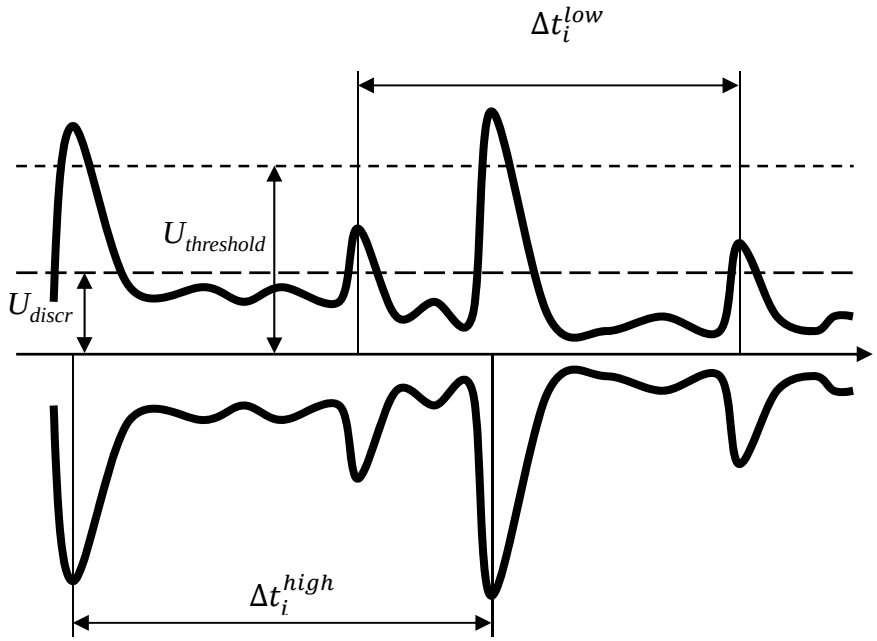

Figure 3. Explanation of the method of finding time interval distributions.

A theoretical approach for the self-organization of defects in material [6, 7] can be used to understand these experimental results. Low amplitude events strongly correlated with each other. Their exponents had higher values than for high amplitude events. Therefore “low” events and sources of acoustic emission in compact sites of porous material respectively were strongly correlated with each other. On the contrary, in the case of high amplitudes, correlation of events was weaker. The ensembles of microcracks emit acoustic waves synchronous and relatively independent of each other.

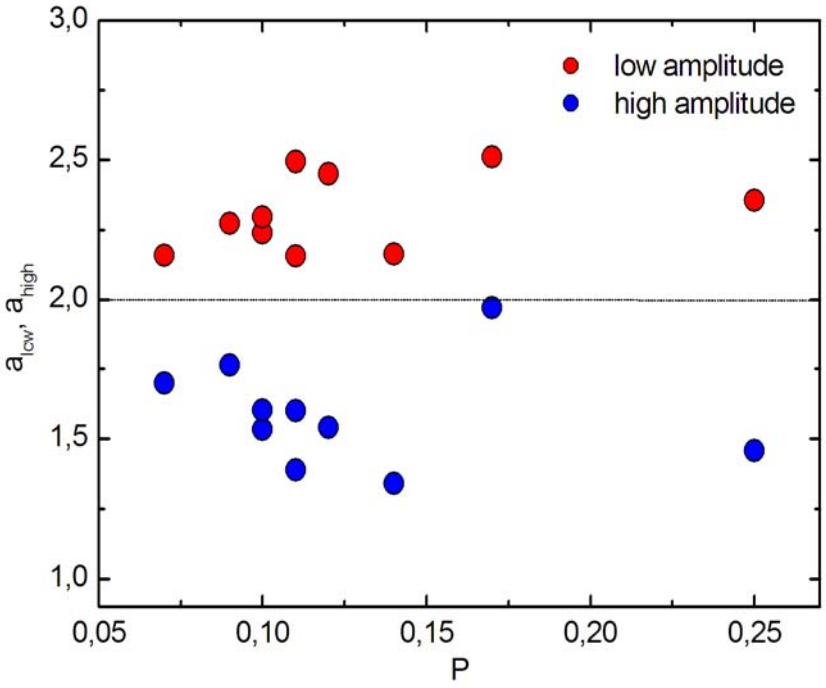

Figure 4. Exponent values of time intervals distributions for different porosities

5. Conclusion

The modified method of AE signal processing based on separate estimation of AE parameters for different groups of events was proposed. It was shown, that for the acoustic emission in porous metallic materials two groups of events and respectively two groups of AE sources can be identified. The first group was characterized by low amplitudes and the second had high amplitudes. They had different behavior of exponents for amplitude and time interval distributions. Proposed approach can be used for the development of nondestructive testing methods applied to inhomogeneous materials.

References

[1] V. A. Greshnikov and V. I. Drobot, Acoustic Emission. Its Use for Testing Materials and Parts [in Russian], Standartov, Moscow 1976.
[2] V. V. Polyakov, A. V. Egorov, A. A. Lependin, Modeling plastic deformation and fracture of porous materials, Technical Physics Letters, 31, Issue 2 (2005) 140-142.
[3] A. V. Egorov, V. V. Polyakov, E. A. Gumirov, A. A. Lependin, Recording Acoustic Emission Signals by the Modified Oscillation Method, Instruments and Experimental Techniques. 48, Issue 5 (2005) 667-670.
[4] O. V. Gusev, Acoustic Emission in the Deformation of Single Crystals of Refractory Metals [in Russian], Nauka, Moscow, 1982.
[5] B.I. Shklovski, A.L. Efros, Percolation theory and conductivity of strongly inhomogeneous media, Sov. Phys. Usp. 18 (1975) 845–862.
[6] V S Ivanova, Synergetics: Strength and Fracture of Metallic Materials, International Science Publishing, Cambridge, 1998.
[7] D. L. Turcotte, Fractals and Chaos in Geology and Geophysics, Cambridge University Press, Cambridge, 1997.

Models for Microcracks Extension and Damage Evolution Based on Acoustic Emissions

Wang Li* MAO Yuanchun Ye Jinsheng Yang Jianhui Rui Dahu
Department of Civil Engineering of Henan Polytechnic University, Jiaozuo, 454000, China
* Corresponding author: wlcjwh@163.com

Abstract In the paper, aiming to build models of microcracks extension and damage evolution in the phase of microcracks evolution based on number series of microdefects nucleation, we firstly built a relation formula between accumulated number series of microdefects nucleation and microcracks size, which we called the crack growth model(CGM), by means of the fractal statistical method. Then, we set up a damage evolution model based on growing microcrack size which is determined by microdefects nucleation number series, which we called the damage evolution model(DEM).The statistical analysis on the microcracks evolution in a gradually fractured rock plate shows that the predictive crack size growth by CGM and damage evolution by DEM are in good accord with the measured values. Based on the fact that a microdefect nucleation is accompanied with a acoustic emission(AE), the two models maybe become good methods to predict microcrack growth and damage evolution by use of AE series.
Keywords fractal; microcrack; rough surface; microdefect; damage evolution; acoustic emission

1. Introduction

The research[1,2] shows that in the early stage of damage evolution, the evolution mechanism of microcrack system is microdefects random nucleation and growth in limited size. Microdefect nucleation means the embryo defects in inhomogeneous material extends by tension strain and grows into a microdefect which is the smallest size in microcrack system. In the macro stress field, microdefects nucleate at the inhomogeneous positions which are uniformly distributed in the materials. The microdefect size can be as small as a grain size. Then with the distribution of microdefects nucleation approaching saturation, microdefects nucleation take place closely next to the existing cracks under controlling of the macro shear stress field, which is called as microcrack growth. The microcracks in the larger deformation bands take the superiority of prior growth and in return they can stir up more microdefects nucleation at their two ends and grow into larger-scale microcracks. So the size distribution in the microcrack system is non-uniform. The connection of larger-sized microcracks brings about macro crack nucleation, which marks the end of microcracks system evolution .

In the following, based on the fact that microdefects nucleate in clustering arrange without overlapping and grow into microcrack, we establish the microcrack growth model based on ANMDN series.

2. The number of microdefects in single microcrack

As is well-known, the crack surface is rough, according to the fractal theory, the fractal area $A_T(\delta)$ could be calculated as[3]

$$A_T(\delta) = A_T \delta^{2-D_s} \tag{1}$$

In which A_T is the apparent area; D_s is the fractal dimension of the rough surface; δ is the measure size, its minimum is the grain size δ_c（Xie,1994）[4].So, on the surface of a penny-shaped crack with apparent diameter c, the number of grains n_d is calculated as

$$n_d \frac{\pi}{4}\left(\frac{\delta}{c}\right)^2 = \frac{\pi}{4}\left(\frac{c}{c}\right)^2 (\frac{\delta}{c})^{2-D_s} \quad (2)$$

Reduction to

$$n_d(c) = \left(\frac{\delta}{c}\right)^{-D_s} \quad (3)$$

For a penetrating crack in a two-dimensional plate, $D_s = d_f$. Here d_f is the fractal dimension of the crack line. The fracture mechanism of the fractal crack line was known as intergranular fracture, transgranular fracture, and coupling fracture of them. And the fractal dimensions d_f can be obtained by theoretical calculation（Xie,1988）[5]. For example, the crystallite size of marble is $\delta_c = 10^{-2} cm$, in tensile condition, the three kinds of fractal dimensions in theory are $d_f = 1.26$,1.365 and 1.30, and the measured values are $d_f = 1.18,1.31,1.29$. For a embedding crack in three dimensional condition, D_s is valued approximately as[6,7]

$$1 + \max(d_f^x,\ d_f^y) = D_s < d_f^x + d_f^y \quad (4)$$

In which, d_f^x and d_f^y represents respectively the mean value of fractal dimensions on fracture lines in x-direction and y-direction. So, if $d_f = 1.3$, then $D_s = 1 + d_f = 2.3$.

3The microcracks growth model based on ANMDN

At a certain time t, the parameters of the microcracks system are marked as

$$\Omega(t) = \left[c_{\min} \le c \le c_{\max},\ D_c,\ N(\delta),\ N_0(c_{\max}),\ N(c),\ N_d\right] \quad (5)$$

Here $c_{\min}$ represents the minimum microcrack size, in theory, can be valued as crystal grain size; $c_{\max}$ represents at time t the maximum crack size; D_c represents the fractal dimension of crack size scale-frequency distribution; $N(\delta)$ represents the total number of cracks with size no less than δ; $N(c)$ represents the total number of cracks with size no less than c; $N_0(c_{\max})$ represents the total number of cracks with maximum size $c_{\max}$; N_d represents the accumulated number of microdefects nucleation(ANMDN).

According to that the crack size-frequency distribution is fractal(Peng & Xie,1989[8]; Xie & Gao,1991[9]), at time t, we have the equation

$$N(c) = N_0(c_{\max})\left(\frac{c}{c_{\max}}\right)^{-D_c} \quad (6)$$

So in $\Omega(t)$， the number of microcracks with size in $c \sim dc + c$ is

$$N(c-dc)-N(c)=N_0(c_{\max})\left[\left(\frac{c-dc}{c_{\max}}\right)^{-D_c}-\left(\frac{c}{c_{\max}}\right)^{-D_c}\right]$$
$$=\frac{N_0(c_{\max})}{c_{\max}^{-D_c}}[(c-dc)^{-D_c}-(c)^{-D_c}] \quad (7)$$

Use Tailor series expansion

$$(c-dc)^{-D_c}=c^{-D_c}+(-D_c)c^{-D_c-1}(-dc)+\frac{1}{2}(-D_c)(-D_c-1)c^{-D_c-2}(-dc)^2+\Lambda$$
$$\approx c^{-D_c}+(-D_c)c^{-D_c-1}(-dc) \quad (8)$$

Substituting Eq.(8) into Eq.(7) we have

$$N(c-dc)-N(c)=\frac{N_0(c_{\max})}{c_{\max}^{-D_c}}D_c c^{-D_c-1}dc \quad (9)$$

Substituting in Eq.（3）we have the total number of microdefects nucleation that compose all the micro cracks with size in $c\sim dc+c$ in $\Omega(t)$

$$[N(c-dc)-N(c)]n_d(c)=\frac{N_0(c_{\max})}{c_{\max}^{-D_c}}D_c c^{-D_c-1}\left(\frac{\delta}{c}\right)^{-D_s}dc \quad (10)$$

Further, we have

$$[N(c-dc)-N(c)]n_d(c)=\frac{N_0(c_{\max})D_c\delta^{-D_S}}{c_{\max}^{-D_c}}c^{D_s-D_c-1}dc \quad (11)$$

So, the total number of all the micro defects nucleation in $\Omega(t)$ is

$$N_d(t)=\int_{\delta_c}^{c_{\max}}[N(c-dc)-N(c)]n_d(c)=\int_{\delta_c}^{c_{\max}}\frac{N_0(c_{\max})D_c\delta^{-D_S}}{c_{\max}^{-D_c}}c^{D_s-D_c-1}dc \quad (12)$$

Integration of Eq.(12) is

$$N_d(t)=\frac{N_0(c_{\max})D_c\delta^{-D_S}}{(D_s-D_c)}\left(\frac{c_{\max}^{D_s-D_c}-\delta^{D_s-D_c}}{c_{\max}^{-D_c}}\right) \quad (13)$$

From Eq.(6), if at time t, the total number of all the micro cracks $N(\delta)$ is known in $\Omega(t)$, then, $N_0(c_{\max})$ can be determined

$$N_0(c_{\max})=N(\delta)\left(\frac{\delta}{c_{\max}}\right)^{D_c} \quad (14)$$

Substituting Eq.(14) into Eq.(13), we have relation $N_d\sim c_{\max}$

$$N_d(t)=\frac{N(\delta)D_c}{(D_s-D_c)}\left[1-\left(\frac{c_{max}}{\delta}\right)^{D_s-D_c}\right] \quad (15)$$

From which, the maximum crack size should be expressed as

$$c_{max}=\delta\left(1-\frac{N_d(t)(D_s-D_c)}{N(\delta_c)D_c}\right)^{-(D_s-D_c)} \quad (16)$$

In which the parameters D_c , $N(\delta_c)$, N_d need to be obtained from the AE series.

4 Damage evolution model based on ANMDN series

The purpose of studying the microcracks system is to answer how the microcracks growth in material will affect the macroscopic mechanical properties. In statistical meso-scopic damage mechanics[1], a series of damage functions are used to describe the macro-effects caused by microcracks. The m-th order damage function is defined as（Bai & Xia,1991[10],Xia,1995[1]）

$$D_m(t,\sigma)=\int_0^\infty n(c,t;\sigma)c^m dc \tag{17}$$

Here c is the linear size of microcrack; $n(c,t;\sigma)$ represents in macro stress field σ , at time t , the number density of microcracks with size c . The zero-th order damage function, D_0 represents the total number effect of microcracks; The1st order damage function, D_1 represents the total size effect of microcracks; The second order damage function, D_2 represents the reduced load bearing area and D_3 is proportional to the volume occupied by the microcracks.

In the stage of microcracks evolution, the size of the microcracks is small and their spatial distribution is uniform and sparse[2], which is approximately thought to be suitable for mean field model[1], therefore the damage effects by microcracks on macro mechanical properties are isotropous. So in three dimensional conditions, we define the damage variable as

$$D=K\frac{D_3}{V} \tag{18}$$

In which V represents macro element volume with linear size L ; K is correction factor. Adopting the form of Eq.(17), we have

$$D=K\frac{\int_0^\infty n(c,t;\sigma)c^3 dc}{V} \tag{19}$$

In which $0<D<1$. Adopting the form of Eq.(9), $n(c,t;\sigma)dc$ takes the form of

$$n(c,t;\sigma)dc=\frac{N_0(c_{\max})}{c_{\max}^{-D_c}}D_c c^{-D_c-1}dc \tag{20}$$

Substituting Eq.(20) in Eq.(19), we have

$$D=K\frac{1}{V}\int_{c_{\max}}^{\delta}\frac{N_0(c_{\max})}{c_{\max}^{-D_c}}D_c c^{2-D_c}dc \tag{21}$$

Use $V=L^3$, and integrating, then

$$D=K\frac{N_0(c_{\max})D_c}{(3-D_c)}\left[\left(\frac{\delta}{L}\right)^3\cdot\left(\frac{\delta}{c_{\max}}\right)^{-D_c}-\left(\frac{c_{\max}}{L}\right)^3\right] \tag{22}$$

Substituting in Eq.（14）and put it in order, we have

$$D = K\frac{N(\delta)D_c}{(3-D_c)}\left[1-\left(\frac{c_{\max}}{\delta}\right)^{3-D_c}\right]\left(\frac{\delta}{L}\right)^3 \tag{23}$$

In which $c_{\max}$ is determined by the total number of microdefects, so, substituting in Eq.（16）,we have

$$D = K\frac{N(\delta)D_c}{(3-D_c)}\left[1-\left(1+\frac{N_d(t)(D_s-D_c)}{N(\delta)D_c}\right)^{-(D_s-D_c)(3-D_c)}\right]\left(\frac{\delta}{L}\right)^3 \tag{24}$$

Which is the damage evolution equation. The parameters $N(\delta)$, $N_d(t)$ and $D_c(t)$ are needed to be obtained from AE series.

In two dimensional condition, the material volume is written as $V = hL^2$, in which h represents the thickness of the plate. Substitute $V = hL^2$ in Eq.(21),we have another form of damage model

$$D = K\frac{N(\delta)D_c}{(3-D_c)}\left[1-\left(1+\frac{N_d(t)(D_s-D_c)}{N(\delta)D_c}\right)^{-(D_s-D_c)(3-D_c)}\right]\left(\frac{\delta}{L}\right)^2\cdot\frac{\delta}{h} \tag{25}$$

5 Test

Now, use the AE data in literature[28] to test the validity of the model proposed in the paper. $L = 50mm$, $\delta_c = 10^{-2}cm$, $D_s = 2.3$ The series of AE number per 400 seconds is

$$N_{AE}(t) = \{57\ \ 52\ \ 45\ \ 29\ \ 41\ \ 41\ \ 25\ \ 30\ \ 60\ \ 52\ \ 63\ \ 83\ \ 83\ \ 80\}、$$

Here we assume the total micro cracks number increases as a rule of

$$N(\delta_c,t) = N_\delta^i(t) = N_{AE}^i(t) = N_{AE}(t)/exp(n/5) \tag{26}$$

The evolution of the size of the maximum cracks and damage of sample according to the paper shows as figure 1.

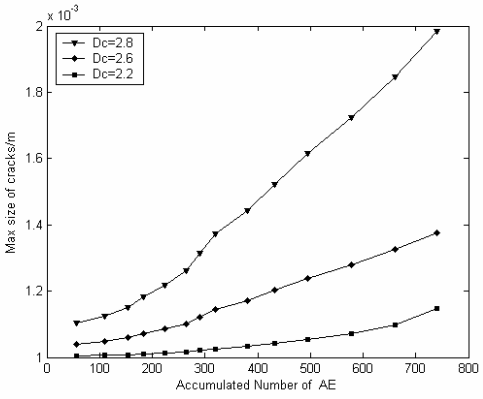

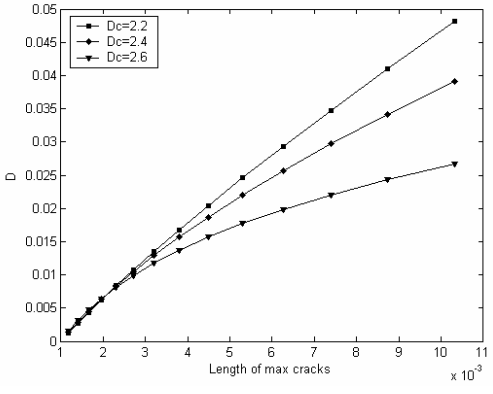

（a） （b）

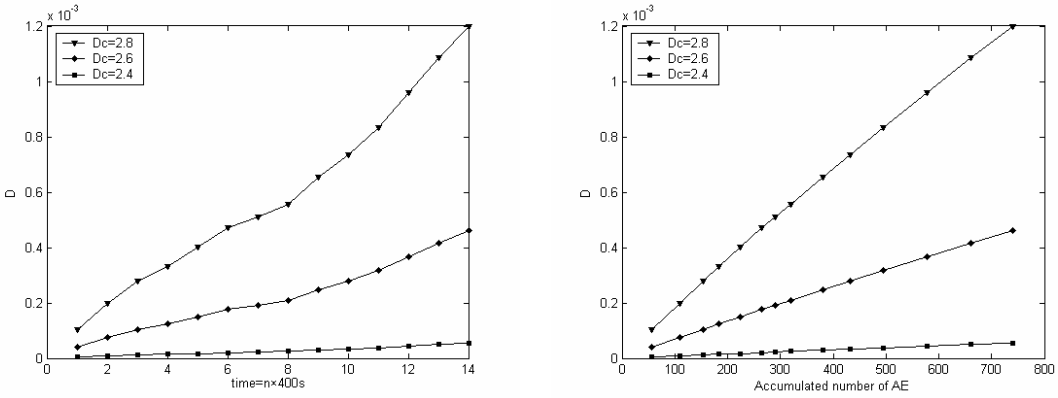

（c） （d）

Fig.4 The preliminary test of the model

6 Conclusions

In the paper, based on the idea of the microcrack formed by microdefects nucleation gathered in line without overlapping, and the fractal statistics relations between the number of microdefects nucleation and microcrack size, we established the microcrack growth model and elasticity damage model based on accumulated microdefects nucleation number. They are needed to be proved effective in predicting microcrack size growth and damage evolution using AE accounts series. In practical use, some problems needed to be resolved: (1) How to get $N(\delta,t)$, the total number of cracks with size no less than δ. A likely workable way is to detach the isolated nucleation AE accounts from the accumulated AE accounts, the isolated nucleation number represents $N(\delta,t)$;(2) How to get the microcrack size scale-freqiency fractal dimension $D_c(t)$ from the AE series. The fractal dimension of seismic magnitude-frequency distribution in AE series has been researched [11-13], the next work is to establish the relationship of the two kinds of fractal dimensions; (3) How to identify the microcrack evolution stage from the AE series. It needs to identify the macro Nucleation from the AE series, so the AE characters of macro Nucleation should be specially researched; (4) in engineering catastrophe monitoring, AE location is necessary to determine L, the size of the rock element. In the end, we need to note that the damage model in the paper is multiscaled with the rock element size L, microdefect size δ and macro crack nucleation size.

Acknowledgements

This work was supported by National natural science foundation of China(41172317/D0218) and foundation of Henan provincial key discipline of engineering mechanics.

References

[1] Xia, M.F., Han, W.S., Ke, F.J., et al. Statistical meso-scopic damage mechanics and damage evolution induced catastrophe. ADVANCES IN MECHANICS, 1995, 25(1):1-40

[2] Wang, L., Li, S.B.. Numerical simulation of damage pattern growth in quasi-brittle materials.

ENGINEERING MECHANICS,2011,28(4):238-245
[3] Wang, J.A., Xie, H.P., Tian, X.Y., et al. Direct fractal measurement of fracture surfaces. Journal of University of Science and Technology Beijing ,1999,21(3):6-9
[4] Xie, H.P., Feng, Z.G., Chen, Z.D.. On star product fractal surfaces and their dimensions. Applied Mathematics and Mechanics, 1999,20(11):1101-1106
[5] Niu, Z.R., Shi, X.J.. Statistical theory of rock fractal fracture. ACTA FEOPHYSICA SINICA, 1992,35(5):595-603
[6] Xie, H.P., Chen, Z.D.. Fractal geometry and fracture of rock. ACTA MECHANICA SINICA, 1988,20(3):264-271
[7] Zhou, H.W., Xie, H.P., Kwasniewski, M.A.. Fractal dimension of rough surface estimated by the cubic covering method. TRIBOLOGY, 2000,20(6):455-459
[8] Peng, C.B., Chen, Y.. On the fractal structure of earthquakes. EARTHQUAKE RESEARCH IN CHINA, 1989,5(2):19-26
[9] Xie, H.P., Gao, F.. The fractal features of the damage evolution of rock materials. *Chinese Journal of Rock Mechanics and Engineering* , 1991,10(1):74-82
[10] Bai, Y.L., Ke, F.J., Xia, M.F.. Formulation of statistical evolution of microcracks in solids. ACTA MECHANICA SINICA,1991,23(3):290-298
[11] Lv, P.L., Wu, K.T., Jiao, Y.B., et al. The experimental study of acoustic emission during creep of rocks. ACTA, SEISMOLOGICA SINICA, 1991,13(1):104-112
[12] Chen, Y.. Discussion on some scientific issues in earthquake prediction. EARTHQUAKE RESEARCH IN CHINA,1988,4(2):1-8
[13] Geng, N.G.. The development of b-value simulated experiments and the beging of b-value simulated experiments in China. ACTA SEISMOLOGICAL SINICA, 1986,8(3):330~333

An Efficient A-FEM for Arbitrary Cracking in Solids

Qingda Yang[1,*], Wei Liu[1,2], and Xian-Yue Su[2]

[1] Dept. of Mechanical and Aerospace Engineering, University of Miami, Coral Gables, FL 33124. USA
[2] Dept. of Mechanics & Aerospace Engineering, Peking University, Beijing 100871, China
* Corresponding author: Tel: +1 305-284-3221; Email: qdyang@miami.edu

Abstract In this paper a new augmented finite element method (A-FEM) that can account for multiple, intra-elemental discontinuities in heterogeneous solids has been derived. It does not need the extra DoFs as in the extended finite element method (X-FEM), or the additional nodes as in the phantom node method (PNM). The new A-FEM employs four internal nodes to facilitate the calculation of subdomain stiffness and the crack displacements due to an intra-elemental discontinuity. It is shown that through a novel efficient solving algorithm the displacement DoFs associated with the internal nodes can be solved analytically as functions of the regular nodal DoFs for any piece-wise linear cohesive laws, which leads to a fully-condensed elemental equilibrium equation that is mathematically exact. The new formulation permits repeated elemental augmentation to include multiple interactive cracks within a single element, enabling a unified treatment of the evolution from a weak discontinuity, to a strong discontinuity, and to multiple intra-element discontinuities, all within a single element that employs standard DoFs only. The new A-FEM's capability in high-fidelity simulation of interactive cohesive cracks in homogeneous and heterogeneous solids has been demonstrated through several numerical examples. It has been demonstrated that the new A-FEM achieved more than two orders of magnitude improvement in numerical accuracy, efficiency, and robustness, compared to the X-FEM.

Keywords Augmented FEM, Extended FEM, Fracture, Cohesive model, Numerical simulation

1. Introduction

High-fidelity numerical simulation to the progressive damage evolution in complex heterogeneous materials such as composites remains a significant challenge despite decades of intensive research [1]. Heterogeneity poses special problems with the accurate prediction of local stress and strain fields, which can vary strongly with local material features; and with predicting cracks and localized damage bands, which can appear during damage evolution not only on the material boundaries, but also on other surfaces that cannot be specified *a priori*. The material heterogeneity issue cannot be resolved adequately by mainstream formulations of conventional materials/structures modeling, owing to the complex interaction between fiber tow architecture and constituent materials heterogeneity. One challenge is that many complex composites such as textiles are heterogeneous on the same scale as that of the features of the structures, which negates the common strategy of homogenizing the material properties in simulations. Furthermore, the structure will generally be subject to non-periodic mechanical and thermal loads, including spatial and temporal peaks.

The above challenges require the establishment of numerical modeling platforms that can deal with structural level performance with microscopic level resolution so that arbitrary local damage evolution, from their nucleation stage and coupled evolution to structurally critical dimensions, can be faithfully predicted. Traditional material degradation types of continuum mechanics based approaches are not likely to meet the challenges because the critical damage coupling information is lost during the homogenization process [2, 3]. Currently there are several promising methods that can deal with the material heterogeneity and the associated progressive damage issues. For example, the Peridynamics method [4, 5]. However, this method remains extremely computational intensive and its fidelity in dealing with complex material heterogeneity in 3D textiles has yet to be demonstrated. Another important class of numerical methods is the partition-of-unity based finite element methods (PUFEM[6], including the extended finite element method (X-FEM) [7-9] and the phantom node method (PNM) [10-14]. These methods are relatively mesh-independent and

computationally efficient when dealing with individual cracks. However, with these methods, tracing the evolution of complex fracture surfaces of multiple cracks quickly becomes extremely tedious and numerically burdensome [8, 15, 16].

Therefore, it is beneficial to seek numerical methods that can account for arbitrary discontinuities with less numerical burden for tracing complex crack surfaces. In this regard the embedded discontinuity FEM with internal DoFs is very promising [17-20]. This approach seeks to enrich the elemental strain field so that the discontinuity in strains or in displacements across a discontinuity can be represented. The additional DoFs associated with the crack displacements are then fully condensed at elemental level [19, 21]. However, this method suffers from possible stress locking because in many cases the assumed deformation modes are not permissible with the sub-domain element deformation modes. Furthermore, construction of an enhanced or augmented element with embedded multiple cracks to permit arbitrary crack merging and bifurcation becomes extremely tedious and difficult.

It is therefore highly desired to develop new finite element methods that can deal with discrete cracks without the need of introducing additional DoFs or nodes, so that the numerical burden for tracing crack surfaces can be minimized. In this paper, we present a new augmented finite element method (A-FEM) that can account for 1) intra-element material heterogeneity and 2) repeated elemental augmentation to enable multiple, interactive intra-element discontinuities. These capabilities are crucial to high-fidelity simulations of heterogeneous materials such as composites. In addition, we report a novel and efficient solving algorithm for elemental condensation that provides analytical solutions to the local equilibrium equations with embedded piece-wise linear cohesive crack like discontinuities. It will be demonstrated that the A-FEM empowered by the new condensation algorithm can provide orders of magnitude improvement in numerical efficiency, accuracy and robustness.

2. New A-FEM for Arbitrary, Multiple Cracking in Heterogeneous Solids

2.1 A-FE Formulation with Single Crack

Without the loss of generality, we choose the 4-node quadratic plane element to illustrate the augmented finite element scheme. The physical element with regular nodes 1, 2, 3, and 4 is severed by a cohesive crack (a strong discontinuity) or a bi-material interface (weak discontinuity) where the tractions are continuous but displacements are not. Figure 1 shows the two possible cut configurations. Instead of introducing two nodes with DoFs representing the assumed deformation modes (constant or linear) as in literature [19, 20], here we introduce 4 internal nodes (node No. 5, 6, 6' and 5' in Fig 1 (b & c)) with regular displacement DoFs so that the displacement jump is simply the difference between the respective node-pairs. As will be seen shortly this novel formulation allows us to derive accurate elemental equilibrium equations without the need to assume deformation modes, and more importantly, it offers the great advantage of permitting multiple intra-element discontinuities.

The internal nodes also facilitate the stiffness calculation of the sub-domains so that the equilibrium of the entire element can be expressed in general as the following.

$$\begin{bmatrix} [\mathbf{L}_{11}^{+}] & [\mathbf{L}_{12}^{+}] \\ [\mathbf{L}_{21}^{+}] & [\mathbf{L}_{22}^{+}] \end{bmatrix} \begin{Bmatrix} \mathbf{d}_{\text{ext}}^{+} \\ \mathbf{d}_{\text{int}}^{+} \end{Bmatrix} = \begin{Bmatrix} \mathbf{F}_{\text{ext}}^{+} \\ \mathbf{F}_{\text{int}}^{+} \end{Bmatrix} \quad (\text{for } \Omega^{+}); \quad \begin{bmatrix} [\mathbf{L}_{11}^{-}] & [\mathbf{L}_{12}^{-}] \\ [\mathbf{L}_{21}^{-}] & [\mathbf{L}_{22}^{-}] \end{bmatrix} \begin{Bmatrix} \mathbf{d}_{\text{ext}}^{-} \\ \mathbf{d}_{\text{int}}^{-} \end{Bmatrix} = \begin{Bmatrix} \mathbf{F}_{\text{ext}}^{-} \\ \mathbf{F}_{\text{int}}^{-} \end{Bmatrix} \quad (\text{for } \Omega^{-}) \quad (1)$$

where $\{\mathbf{d}_{\text{ext}}^{+}, \mathbf{d}_{\text{int}}^{+}\}^{\text{T}}$ and $\{\mathbf{d}_{\text{reg}}^{-}, \mathbf{d}_{\text{int}}^{-}\}^{\text{T}}$ are DoFs of the external or regular nodes and the internal nodes in the two subdomains, respectively. $\{\mathbf{F}_{\text{ext}}^{+}, \mathbf{F}_{\text{int}}^{+}\}^{\text{T}}$ and $\{\mathbf{F}_{\text{ext}}^{-}, \mathbf{F}_{\text{int}}^{-}\}^{\text{T}}$ are the nodal forces associated with regular and internal nodes; $[\mathbf{L}_{ij}^{+}]$ and $[\mathbf{L}_{ij}^{-}]$ $(i, j = 1, 2)$ are the stiffness sub-matrices of respective domains, which can be easily obtained with standard or subdomain integration schemes. The internal force arrays come from the integration of cohesive stresses along the crack surfaces, and,

due to stress continuity across the cohesive crack, $\mathbf{F}_{\text{int}}^{+} = \mathbf{F}_{6'5'}^{+} = -\mathbf{F}_{\text{int}}^{-} = -\mathbf{F}_{65}^{-}$. Note that, irrespective the cut configurations in Figure 1 (b) or (c), the internal displacements are always $\mathbf{d}_{\text{int}}^{+} = \mathbf{d}_{6'5'}; \mathbf{d}_{\text{int}}^{-} = \mathbf{d}_{65}$.

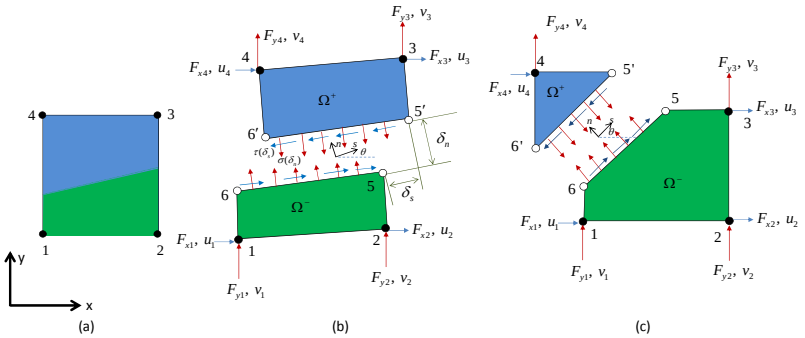

Figure 1 Illustration of the element augmentation from a regular element with possible different material domains (a), to an A-FE with two rectangular sub-domains (b), or to an A-FE with one triangular sub-domain and one pentagon sub-domain (c).

For the piece-wise linear cohesive laws shown in Figure 2, the cohesive stresses as functions of crack displacements can be written as

$$\begin{aligned} &\sigma(\delta_n) = \hat{\sigma}^{(i-1)} + \alpha_n^{(i)}(\delta_n - \delta_n^{(i-1)}) \qquad (\delta_n \subset [\delta_n^{(i-1)}, \delta_n^{(i)}] \qquad (i = 1,2,\cdots 4) \\ &\tau(\delta_s) = \text{sgn}(\delta_s)\left[\hat{\tau}^{(j-1)} + \alpha_s^{(j)}\left(|\delta_s| - \delta_s^{(j-1)}\right)\right] \quad (|\delta_s| \subset [\delta_s^{(i-1)}, \delta_s^{(i)}] \quad (j = 1,2,\cdots 4) \end{aligned} \tag{2}$$

where sgn(·) is a sign function, and |·| denotes absolute value; $\sigma(\delta_n)$ and $\tau(\delta_s)$ are normal and tangential tractions along the cohesive crack; δ_n and δ_s are normal and tangential crack displacement; the superscripts *i* and *j* denote the linear segment number as labeled in Figure 2. $\hat{\sigma}^{(i)}$ and $\hat{\tau}^{(j)}$, $\delta_n^{(i)}$ and $\delta_s^{(j)}$, $\alpha_n^{(i)}$ and $\alpha_s^{(j)}$ are the characteristic stresses, crack displacements, and slopes (Fig 2), and $\hat{\sigma}^{(0)} = \hat{\tau}^{(0)} = 0$ and $\delta_n^{(0)} = \delta_s^{(0)} = 0$.

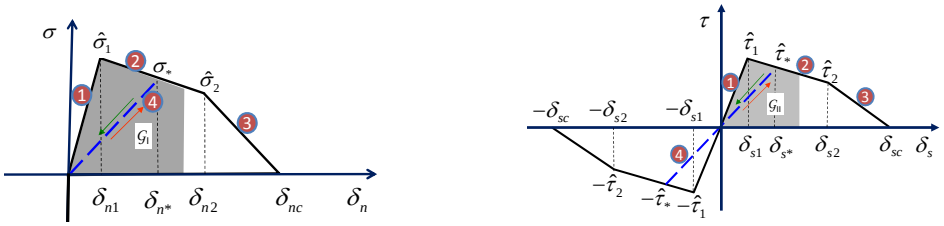

(a) mode I cohesive law (b) mode II cohesive law

Figure 2 Mixed-mode cohesive model with piece-wise linear traction-separation laws used in this study

The propagation criterion used for the cohesive crack is one that has been widely used and validated in literature [22, 23]

$$\mathcal{G}_{\text{I}}^{*} / \Gamma_{\text{I}} + \mathcal{G}_{\text{II}}^{*} / \Gamma_{\text{II}} = 1 \tag{3}$$

where $\mathcal{G}_{\text{I}}^{*}$ and $\mathcal{G}_{\text{II}}^{*}$ are the energy dissipations at which the cohesive failure occurs (shaded areas in Fig 2), and Γ_{I} and Γ_{II} are the <u>total</u> areas under the pure opening and pure shear traction-separation laws.

With the above piece-wise linear cohesive law, the cohesive stresses between the two pairs of internal nodes 5-5' and 6-6' are known. The internal force arrays $\mathbf{F}_{65}$ and $\mathbf{F}_{6'5'}$ are the cohesive stresses integrated over the crack surfaces and transfer them into global coordinates,

$$\mathbf{F}_{65} = -\mathbf{F}_{6'5'} = l_e^{\theta}(\mathbf{S}_0 + \boldsymbol{\alpha}\{\Delta\mathbf{d}_{66'}, \Delta\mathbf{d}_{55'}\}^{\text{T}}) \tag{4}$$

where $\Delta\mathbf{d}_{6'6} = \mathbf{d}_{6'} - \mathbf{d}_6$ and $\Delta\mathbf{d}_{5'5} = \mathbf{d}_{5'} - \mathbf{d}_5$. $\mathbf{S}_0$ and $\boldsymbol{\alpha}$ are the matrices determined by the characteristic cohesive stresses and slopes. Substituting Eqn (4) to Eqn (1) the following is derived

$$\begin{Bmatrix}\mathbf{d}_{6'5'}\\ \mathbf{d}_{65}\end{Bmatrix}=\begin{bmatrix}-l_{e1}\mathbf{A}^{-1}\left(\mathbf{I}-l_{e1}\boldsymbol{\alpha}(\boldsymbol{\Psi}_{22}^{-})^{-1}\right) & \mathbf{0}\\ \mathbf{0} & l_{e1}\mathbf{B}^{-1}\left(\mathbf{I}-l_{e1}\boldsymbol{\alpha}(\boldsymbol{\Psi}_{22}^{+})^{-1}\right)\end{bmatrix}\begin{Bmatrix}\mathbf{S}_0\\ \mathbf{S}_0\end{Bmatrix}+\begin{bmatrix}-l_{e1}\mathbf{A}^{-1}\boldsymbol{\alpha}(\boldsymbol{\Psi}_{22}^{-})^{-1}\mathbf{L}_{21}^{-} & -\mathbf{A}^{-1}\mathbf{L}_{21}^{+}\\ -\mathbf{B}^{-1}\mathbf{L}_{21}^{-} & -l_{e1}\mathbf{B}^{-1}\boldsymbol{\alpha}(\boldsymbol{\Psi}_{22}^{+})^{-1}\mathbf{L}_{21}^{+}\end{bmatrix}\begin{Bmatrix}\mathbf{d}_{ext}^{-}\\ \mathbf{d}_{ext}^{+}\end{Bmatrix} \tag{5}$$

where $\boldsymbol{\Psi}_{22}^{+}=\mathbf{L}_{22}^{+}+l_{e1}\boldsymbol{\alpha};\boldsymbol{\Psi}_{22}^{-}=\mathbf{L}_{22}^{-}+l_{e1}\boldsymbol{\alpha};\mathbf{A}=\boldsymbol{\Psi}_{22}^{+}-l_{e1}{}^{2}\boldsymbol{\alpha}(\boldsymbol{\Psi}_{22}^{-})^{-1}\boldsymbol{\alpha};\ \mathbf{B}=\boldsymbol{\Psi}_{22}^{-}-l_{e1}{}^{2}\boldsymbol{\alpha}(\boldsymbol{\Psi}_{22}^{+})^{-1}\boldsymbol{\alpha}$, and $\mathbf{I}$ is the identity matrix. Substituting Eqn (5) it into Eqn (1) the full condensed equilibrium is obtained,

$$\begin{bmatrix}\mathbf{L}_{11}^{-}-\mathbf{L}_{12}^{-}\mathbf{B}^{-1}\mathbf{L}_{21}^{-} & -l_{e1}\mathbf{L}_{12}^{-}\mathbf{B}^{-1}\boldsymbol{\alpha}(\boldsymbol{\Psi}_{22}^{+})^{-1}\mathbf{L}_{21}^{+}\\ -l_{e1}\mathbf{L}_{12}^{+}\mathbf{A}^{-1}\boldsymbol{\alpha}(\boldsymbol{\Psi}_{22}^{-})^{-1}\mathbf{L}_{21}^{-} & \mathbf{L}_{11}^{+}-\mathbf{L}_{12}^{+}\mathbf{A}^{-1}\mathbf{L}_{21}^{+}\end{bmatrix}\begin{Bmatrix}\mathbf{d}_{ext}^{-}\\ \mathbf{d}_{ext}^{+}\end{Bmatrix}=\begin{Bmatrix}\mathbf{F}_{ext}^{-}\\ \mathbf{F}_{ext}^{+}\end{Bmatrix}-\begin{bmatrix}l_{e1}\mathbf{L}_{12}^{-}\mathbf{B}^{-1}\left(\mathbf{I}-l_{e1}\boldsymbol{\alpha}(\boldsymbol{\Psi}_{22}^{+})^{-1}\right) & 0\\ 0 & -l_{e1}\mathbf{L}_{12}^{+}\mathbf{A}^{-1}\left(\mathbf{I}-l_{e1}\boldsymbol{\alpha}(\boldsymbol{\Psi}_{22}^{-})^{-1}\right)\end{bmatrix}\begin{Bmatrix}\mathbf{S}_0\\ \mathbf{S}_0\end{Bmatrix} \tag{6}$$

Elemental Condensation Algorithm

Eqn (6) is nonlinear due to the nonlinearity from the cohesive laws. In the literature, Newton-Raphson method [19, 20] (or its modified variants) has been used to solve this equation iteratively. However, our novel derivation above has yielded an explicit expression between the displacements of the internal nodes and those of the external nodes, i.e., Eqn (5). We have proved that, for any piece-wise linear cohesive laws, $\mathbf{d}_{6'5'}$ and $\mathbf{d}_{65}$ can be uniquely determined with mathematical exactness through a very simple yet efficient algorithm. The algorithm solves Eqn (5) by consistent check between trial cohesive slopes and the resulted crack displacements. Once Eqn (5) is solved, the matrices $[\boldsymbol{\beta}]$, $[\mathbf{K}_{22}^{+}]$, and $[\mathbf{K}_{22}^{-}]$ are all determined and elemental equilibrium of Eqn (6) is determined with mathematical rigor. This novel way of solving the crack displacements has never been reported in literature and we later show that it leads to orders of magnitude improvement on numerical efficiency.

2.2 A-FE Formulation with Two Interactive Cracks

In such a case, there are altogether three basic cracking configurations as shown in Fig 3(a), Fig 3(b) and Fig3(c), where l_{e1} is the first crack length and l_{e2} is the second crack length. The second crack intersects and cuts the first crack into two segments with length γl_{e1} (left) and $(1-\gamma)l_{e1}$ (right). Despite the different crack configurations in Figure 3, the internal DoF and force arrays can be arranged in a unified way as below.

$$\mathbf{d}_{\text{int}}^{+}=\mathbf{d}_{6'5'};\ \mathbf{d}_{\text{int}}^{r-}=\mathbf{d}_{58'7'};\ \mathbf{d}_{\text{int}}^{l-}=\mathbf{d}_{786}\qquad \mathbf{F}_{\text{int}}^{+}=\mathbf{F}_{6'5'};\ \mathbf{F}_{\text{int}}^{r-}=\mathbf{F}_{58'7'};\ \mathbf{F}_{\text{int}}^{l-}=\mathbf{F}_{786} \tag{7}$$

This enables a unified expression for the equilibrium of all three subdomains as follows

$$\begin{cases}\begin{bmatrix}\mathbf{L}_{11}^{+} & \mathbf{L}_{12}^{+}\\ \mathbf{L}_{21}^{+} & \mathbf{L}_{22}^{+}\end{bmatrix}\begin{Bmatrix}\mathbf{d}_{ext}^{+}\\ \mathbf{d}_{6'5'}\end{Bmatrix}=\begin{Bmatrix}\mathbf{F}_{ext}^{+}\\ \mathbf{F}_{6'5'}\end{Bmatrix} & \text{(a)}\\ & \text{(b)}\end{cases}\quad(\text{for }\Omega^{+})$$

$$\begin{cases}\begin{bmatrix}\mathbf{L}_{11}^{r-} & \mathbf{L}_{12}^{r-}\\ \mathbf{L}_{21}^{r-} & \mathbf{L}_{22}^{r-}\end{bmatrix}\begin{Bmatrix}\mathbf{d}_{ext}^{r-}\\ \mathbf{d}_{58'7'}\end{Bmatrix}=\begin{Bmatrix}\mathbf{F}_{ext}^{r-}\\ \mathbf{F}_{58'7'}\end{Bmatrix} & \text{(c)}\\ & \text{(d)}\end{cases}\quad(\text{for }\Omega^{r-}) \tag{8}$$

$$\begin{cases}\begin{bmatrix}\mathbf{L}_{11}^{l-} & \mathbf{L}_{12}^{l-}\\ \mathbf{L}_{21}^{l-} & \mathbf{L}_{22}^{l-}\end{bmatrix}\begin{Bmatrix}\mathbf{d}_{ext}^{l-}\\ \mathbf{d}_{786}\end{Bmatrix}=\begin{Bmatrix}\mathbf{F}_{ext}^{l-}\\ \mathbf{F}_{786}\end{Bmatrix} & \text{(e)}\\ & \text{(f)}\end{cases}\quad(\text{for }\Omega^{l-})$$

Here, the sub-matrices ($\mathbf{L}_{ij}^{l-}, \mathbf{L}_{ij}^{r-}$, and $\mathbf{L}_{ij}^{+}$ $(i, j = 1, 2)$) are the stiffness matrices of the subdomains Ω^{+}, $\Omega^{r-}$and Ω^{l-}, respectively. To integrate the cohesive stress along the three cohesive crack segments into respective internal nodal forces, the first order Gaussian Integration scheme was used on each of the three cracked segments. The integration points are at the center of each crack

segment as indicated in Figure 3(b) by the solid dots labeled by I, II, and III.

The relation between these cohesive stresses and the internal nodal displacements is

$$\begin{cases} \left\{\tau_{\mathrm{I}}^{(i)}, \sigma_{\mathrm{I}}^{(j)}\right\}^{\mathbf{T}} = \boldsymbol{\sigma}_{0\mathrm{I}} + \boldsymbol{\alpha}_{0\mathrm{I}}\mathbf{R}_1\left((1-\gamma/2)\mathbf{d}_{6'} + (\gamma/2)\mathbf{d}_{5'}\right) - \boldsymbol{\alpha}_{0\mathrm{I}}\mathbf{R}_1\left(\mathbf{d}_6 + \mathbf{d}_8\right)/2 \\ \left\{\tau_{\mathrm{II}}^{(k)}, \sigma_{\mathrm{II}}^{(l)}\right\}^{\mathbf{T}} = \boldsymbol{\sigma}_{0\mathrm{II}} + \boldsymbol{\alpha}_{0\mathrm{II}}\mathbf{R}_1\left((1-\gamma/2)\mathbf{d}_{6'} + (1+\gamma/2)\mathbf{d}_{5'}\right) - \boldsymbol{\alpha}_{0\mathrm{II}}\mathbf{R}_1\left(\mathbf{d}_5 + \mathbf{d}_{8'}\right)/2 \\ \left\{\tau_{\mathrm{III}}^{(m)}, \sigma_{\mathrm{III}}^{(n)}\right\}^{\mathbf{T}} = \boldsymbol{\sigma}_{0\mathrm{III}} + \boldsymbol{\alpha}_{0\mathrm{III}}\mathbf{R}_2\left(\mathbf{d}_{7'} + \mathbf{d}_{8'}\right)/2 - \boldsymbol{\alpha}_{0\mathrm{III}}\mathbf{R}_2\left(\mathbf{d}_7 + \mathbf{d}_8\right)/2 \end{cases} \tag{9}$$

where

$$\boldsymbol{\sigma}_{0\mathrm{I}} = \begin{Bmatrix} \hat{\tau}^{(i)} - \alpha_s^{(i)}\delta_s^{(i)} \\ \hat{\sigma}^{(j)} - \alpha_n^{(j)}\delta_n^{(j)} \end{Bmatrix}; \quad \boldsymbol{\sigma}_{0\mathrm{II}} = \begin{Bmatrix} \hat{\tau}^{(k)} - \alpha_s^{(k)}\delta_s^{(k)} \\ \hat{\sigma}^{(l)} - \alpha_n^{(l)}\delta_n^{(l)} \end{Bmatrix}; \quad \boldsymbol{\sigma}_{0\mathrm{III}} = \begin{Bmatrix} \hat{\tau}^{(m)} - \alpha_s^{(m)}\delta_s^{(m)} \\ \hat{\sigma}^{(n)} - \alpha_n^{(n)}\delta_n^{(n)} \end{Bmatrix}$$

$$\boldsymbol{\alpha}_{0\mathrm{I}} = \mathrm{Diag}[\alpha_s^{(i)}; \alpha_n^{(j)}]; \quad \boldsymbol{\alpha}_{0\mathrm{II}} = \mathrm{Diag}[\alpha_s^{(k)}; \alpha_n^{(l)}]; \quad \boldsymbol{\alpha}_{0\mathrm{III}} = \mathrm{Diag}[\alpha_s^{(m)}; \alpha_n^{(n)}];$$

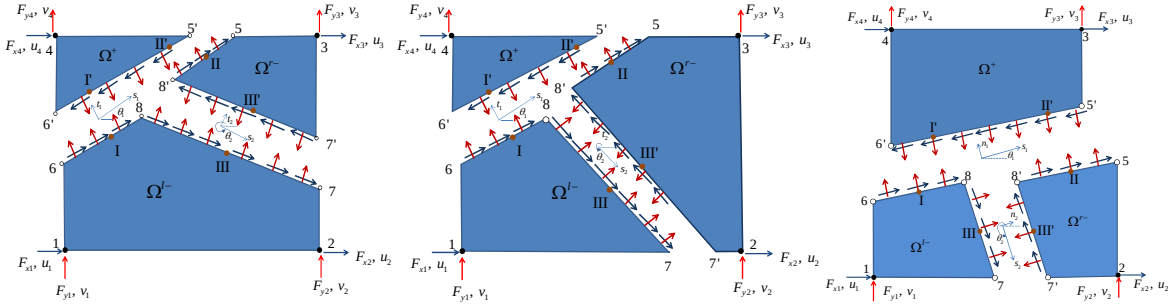

(a) (b) (c)

Figure 3 Illustration of a 2D A-FE with two intra-elemental cracks (3 subdomains)

The internal forces, $\{\mathbf{F}_{6'5'}\}$, $\{\mathbf{F}_{58'7'}\}$, and $\{\mathbf{F}_{786}\}$, integrated from the cohesive stresses along the respective crack lengths are

$$\begin{cases} \mathbf{F}_{6'5'} = \mathbf{T}_{\mathbf{R}}^{+}\left\{\tau_{\mathrm{I}}^{(i)}, \quad \sigma_{\mathrm{I}}^{(j)}, \quad \tau_{\mathrm{II}}^{(k)}, \quad \sigma_{\mathrm{II}}^{(l)}\right\}^{\mathbf{T}} \\ \mathbf{F}_{786} = \mathbf{T}_{\mathbf{R}}^{l-}\left\{\tau_{\mathrm{I}}^{(i)}, \quad \sigma_{\mathrm{I}}^{(j)}, \quad \tau_{\mathrm{III}}^{(m)}, \quad \sigma_{\mathrm{III}}^{(n)}\right\}^{\mathbf{T}} \\ \mathbf{F}_{58'7'} = \mathbf{T}_{\mathbf{R}}^{r-}\left\{\tau_{\mathrm{I}}^{(k)}, \quad \sigma_{\mathrm{I}}^{(l)}, \quad \tau_{\mathrm{III}}^{(m)}, \quad \sigma_{\mathrm{III}}^{(n)}\right\}^{\mathbf{T}} \end{cases} \tag{10}$$

where $\mathbf{T}_{\mathbf{R}}^{+}$, $\mathbf{T}_{\mathbf{R}}^{l-}$, and $\mathbf{T}_{\mathbf{R}}^{r-}$ are the respective integration matrices:

$$\mathbf{T}_{\mathbf{R}}^{+} = -\frac{1}{2}\begin{bmatrix} \gamma(2-\gamma)l_{e1}\mathbf{R}_1^{\mathbf{T}} & (1-\gamma)^2 l_{e1}\mathbf{R}_1^{\mathbf{T}} \\ \gamma^2 l_{e1}\mathbf{R}_1^{\mathbf{T}} & (1-\gamma^2)l_{e1}\mathbf{R}_1^{\mathbf{T}} \end{bmatrix};$$

$$\mathbf{T}_{\mathbf{R}}^{l-} = \frac{1}{2}\begin{bmatrix} \mathbf{0} & l_{e2}\mathbf{R}_2^{\mathbf{T}} \\ \gamma l_{e1}\mathbf{R}_1^{\mathbf{T}} & l_{e2}\mathbf{R}_2^{\mathbf{T}} \\ \gamma l_{e1}\mathbf{R}_1^{\mathbf{T}} & \mathbf{0} \end{bmatrix}; \quad \mathbf{T}_{\mathbf{R}}^{r-} = \frac{1}{2}\begin{bmatrix} (1-\gamma)l_{e1}\mathbf{R}_1^{\mathbf{T}} & \mathbf{0} \\ (1-\gamma)l_{e1}\mathbf{R}_1^{\mathbf{T}} & -l_{e2}\mathbf{R}_2^{\mathbf{T}} \\ \mathbf{0} & -l_{e2}\mathbf{R}_2^{\mathbf{T}} \end{bmatrix} \tag{11}$$

Substituting Eqn (9) into (10) and then Eqn (8), the internal crack displacements can be derived as

$$\begin{Bmatrix} \mathbf{d}_{6'5'} \\ \mathbf{d}_{786} \\ \mathbf{d}_{58'7'} \end{Bmatrix} = \begin{bmatrix} \mathbf{Y}_7 & \mathbf{Y}_8 & \mathbf{Y}_9 \\ \mathbf{Y}_4 & \mathbf{Y}_5 & \mathbf{Y}_6 \\ \mathbf{Y}_1 & \mathbf{Y}_2 & \mathbf{Y}_3 \end{bmatrix}\begin{Bmatrix} \mathbf{S}_1 \\ \mathbf{S}_2 \\ \mathbf{S}_3 \end{Bmatrix} + \begin{bmatrix} \mathbf{X}_{13} & \mathbf{X}_{14} & \mathbf{X}_{15} \\ \mathbf{X}_{10} & \mathbf{X}_{11} & \mathbf{X}_{12} \\ \mathbf{X}_7 & \mathbf{X}_8 & \mathbf{X}_9 \end{bmatrix}\begin{Bmatrix} \mathbf{d}_{ext}^{l-} \\ \mathbf{d}_{ext}^{r-} \\ \mathbf{d}_{ext}^{+} \end{Bmatrix} \tag{12}$$

where $\mathbf{S}_1 = \mathbf{T}_{\mathbf{R}}^{+}\left\{\boldsymbol{\sigma}_{0\mathrm{I}}, \boldsymbol{\sigma}_{0\mathrm{II}}\right\}^{\mathbf{T}}$, $\mathbf{S}_2 = \mathbf{T}_{\mathbf{R}}^{l-}\left\{\boldsymbol{\sigma}_{0\mathrm{I}}, \boldsymbol{\sigma}_{0\mathrm{III}}\right\}^{\mathbf{T}}$, $\mathbf{S}_3 = \mathbf{T}_{\mathbf{R}}^{r-}\left\{\boldsymbol{\sigma}_{0\mathrm{II}}, \boldsymbol{\sigma}_{0\mathrm{III}}\right\}^{\mathbf{T}}$;

$$\mathbf{X}_1 = \mathbf{L}_{22}^{+} - \boldsymbol{\alpha}_{11}; \qquad \mathbf{X}_2 = \mathbf{L}_{22}^{l-} - \boldsymbol{\alpha}_{22} - \boldsymbol{\alpha}_{21}(\mathbf{X}_1)^{-1}\boldsymbol{\alpha}_{12};$$

$$\mathbf{X}_3 = -\boldsymbol{\alpha}_{21}(\mathbf{X}_1)^{-1}\boldsymbol{\alpha}_{13} - \boldsymbol{\alpha}_{23}; \qquad \mathbf{X}_4 = -\boldsymbol{\alpha}_{31}(\mathbf{X}_1)^{-1}\boldsymbol{\alpha}_{12} - \boldsymbol{\alpha}_{32};$$

$$\mathbf{X}_5 = \mathbf{L}_{22}^{r-} - \boldsymbol{\alpha}_{33} - \boldsymbol{\alpha}_{31}(\mathbf{X}_1)^{-1}\boldsymbol{\alpha}_{13}; \qquad \mathbf{X}_6 = \mathbf{X}_5 - \mathbf{X}_4(\mathbf{X}_2)^{-1}\mathbf{X}_3$$

$$\mathbf{X}_7 = (\mathbf{X}_6)^{-1}\mathbf{X}_4(\mathbf{X}_2)^{-1}\mathbf{L}_{21}^{l-}; \qquad \mathbf{X}_8 = -(\mathbf{X}_6)^{-1}\mathbf{L}_{21}^{r-};$$

$$\mathbf{X}_9 = (\mathbf{X}_6)^{-1}\left(\mathbf{X}_4(\mathbf{X}_2)^{-1}\boldsymbol{\alpha}_{21} - \boldsymbol{\alpha}_{31}\right)(\mathbf{X}_1)^{-1}\mathbf{L}_{21}^{+}$$

$$\mathbf{X}_{10} = -(\mathbf{X}_2)^{-1}\left(\mathbf{X}_3\mathbf{X}_7 + \mathbf{L}_{21}^{l-}\right); \qquad \mathbf{X}_{11} = -(\mathbf{X}_2)^{-1}\mathbf{X}_3\mathbf{X}_8;$$

$$\mathbf{X}_{12} = -(\mathbf{X}_2)^{-1}\left(\mathbf{X}_3\mathbf{X}_9 + \boldsymbol{\alpha}_{21}(\mathbf{X}_1)^{-1}\mathbf{L}_{21}^{+}\right) \qquad \mathbf{X}_{13} = (\mathbf{X}_1)^{-1}\left(\boldsymbol{\alpha}_{13}\mathbf{X}_7 + \boldsymbol{\alpha}_{12}\mathbf{X}_{10}\right);$$

$$\mathbf{X}_{14} = (\mathbf{X}_1)^{-1}\left(\boldsymbol{\alpha}_{13}\mathbf{X}_8 + \boldsymbol{\alpha}_{12}\mathbf{X}_{11}\right); \qquad \mathbf{X}_{15} = (\mathbf{X}_1)^{-1}\left(-\mathbf{L}_{21}^{+} + \boldsymbol{\alpha}_{13}\mathbf{X}_9 + \boldsymbol{\alpha}_{12}\mathbf{X}_{12}\right)$$

$$\mathbf{Y}_1 = (\mathbf{X}_6)^{-1}\left(\boldsymbol{\alpha}_{31} - \mathbf{X}_4(\mathbf{X}_2)^{-1}\boldsymbol{\alpha}_{21}\right)(\mathbf{X}_1)^{-1}; \qquad \mathbf{Y}_2 = -(\mathbf{X}_6)^{-1}\mathbf{X}_4(\mathbf{X}_2)^{-1};$$

$$\mathbf{Y}_3 = (\mathbf{X}_6)^{-1} \qquad \mathbf{Y}_4 = (\mathbf{X}_2)^{-1}\left(\boldsymbol{\alpha}_{21}(\mathbf{X}_1)^{-1} - \mathbf{X}_3\mathbf{Y}_1\right);$$

$$\mathbf{Y}_5 = (\mathbf{X}_2)^{-1}\left(\mathbf{I} - \mathbf{X}_3\mathbf{Y}_2\right); \qquad \mathbf{Y}_6 = -(\mathbf{X}_2)^{-1}\mathbf{X}_3\mathbf{Y}_3;$$

$$\mathbf{Y}_7 = (\mathbf{X}_1)^{-1}\left(\mathbf{I} + \boldsymbol{\alpha}_{13}\mathbf{Y}_1 + \boldsymbol{\alpha}_{12}\mathbf{Y}_4\right); \qquad \mathbf{Y}_8 = (\mathbf{X}_1)^{-1}\left(\boldsymbol{\alpha}_{13}\mathbf{Y}_2 + \boldsymbol{\alpha}_{12}\mathbf{Y}_5\right);$$

$$\mathbf{Y}_9 = (\mathbf{X}_1)^{-1}\left(\boldsymbol{\alpha}_{13}\mathbf{Y}_3 + \boldsymbol{\alpha}_{12}\mathbf{Y}_6\right)$$

$$\boldsymbol{\alpha}_{11} = \frac{1}{2}\mathbf{T}_{\mathbf{R}}^{+}\begin{bmatrix}(2-\gamma)\boldsymbol{\alpha}_{0\mathrm{I}}\mathbf{R}_1 & \gamma\boldsymbol{\alpha}_{0\mathrm{I}}\mathbf{R}_1 \\ (1-\gamma)\boldsymbol{\alpha}_{0\mathrm{II}}\mathbf{R}_1 & (1+\gamma)\boldsymbol{\alpha}_{0\mathrm{II}}\mathbf{R}_1\end{bmatrix}; \qquad \boldsymbol{\alpha}_{12} = \frac{1}{2}\mathbf{T}_{\mathbf{R}}^{+}\begin{bmatrix}\mathbf{0} & -\boldsymbol{\alpha}_{0\mathrm{I}}\mathbf{R}_1 & -\boldsymbol{\alpha}_{0\mathrm{I}}\mathbf{R}_1 \\ \mathbf{0} & \mathbf{0} & \mathbf{0}\end{bmatrix};$$

$$\boldsymbol{\alpha}_{13} = \frac{1}{2}\mathbf{T}_{\mathbf{R}}^{+}\begin{bmatrix}\mathbf{0} & \mathbf{0} & \mathbf{0} \\ -\boldsymbol{\alpha}_{0\mathrm{II}}\mathbf{R}_1 & -\boldsymbol{\alpha}_{0\mathrm{II}}\mathbf{R}_1 & \mathbf{0}\end{bmatrix}; \qquad \boldsymbol{\alpha}_{21} = \frac{1}{2}\mathbf{T}_{\mathbf{R}}^{l-}\begin{bmatrix}(2-\gamma)\boldsymbol{\alpha}_{0\mathrm{I}}\mathbf{R}_1 & \gamma\boldsymbol{\alpha}_{0\mathrm{I}}\mathbf{R}_1 \\ \mathbf{0} & \mathbf{0}\end{bmatrix};$$

$$\boldsymbol{\alpha}_{22} = \frac{1}{2}\mathbf{T}_{\mathbf{R}}^{l-}\begin{bmatrix}\mathbf{0} & -\boldsymbol{\alpha}_{0\mathrm{I}}\mathbf{R}_1 & -\boldsymbol{\alpha}_{0\mathrm{I}}\mathbf{R}_1 \\ -\boldsymbol{\alpha}_{0\mathrm{III}}\mathbf{R}_2 & -\boldsymbol{\alpha}_{0\mathrm{III}}\mathbf{R}_2 & \mathbf{0}\end{bmatrix}; \qquad \boldsymbol{\alpha}_{23} = \frac{1}{2}\mathbf{T}_{\mathbf{R}}^{l-}\begin{bmatrix}\mathbf{0} & \mathbf{0} & \mathbf{0} \\ \mathbf{0} & \boldsymbol{\alpha}_{0\mathrm{III}}\mathbf{R}_2 & \boldsymbol{\alpha}_{0\mathrm{III}}\mathbf{R}_2\end{bmatrix};$$

$$\boldsymbol{\alpha}_{31} = \frac{1}{2}\mathbf{T}_{\mathbf{R}}^{r-}\begin{bmatrix}(1-\gamma)\boldsymbol{\alpha}_{0\mathrm{II}}\mathbf{R}_1 & (1+\gamma)\boldsymbol{\alpha}_{0\mathrm{II}}\mathbf{R}_1 \\ \mathbf{0} & \mathbf{0}\end{bmatrix}; \qquad \boldsymbol{\alpha}_{32} = \frac{1}{2}\mathbf{T}_{\mathbf{R}}^{r-}\begin{bmatrix}\mathbf{0} & \mathbf{0} & \mathbf{0} \\ -\boldsymbol{\alpha}_{0\mathrm{III}}\mathbf{R}_2 & -\boldsymbol{\alpha}_{0\mathrm{III}}\mathbf{R}_2 & \mathbf{0}\end{bmatrix};$$

$$\boldsymbol{\alpha}_{33} = \frac{1}{2}\mathbf{T}_{\mathbf{R}}^{r-}\begin{bmatrix}-\boldsymbol{\alpha}_{0\mathrm{II}}\mathbf{R}_1 & -\boldsymbol{\alpha}_{0\mathrm{II}}\mathbf{R}_1 & \mathbf{0} \\ \mathbf{0} & \boldsymbol{\alpha}_{0\mathrm{III}}\mathbf{R}_2 & \boldsymbol{\alpha}_{0\mathrm{III}}\mathbf{R}_2\end{bmatrix}$$

Finally, by substituting Eqn (12) into expressions (a, c, e) in Eqn (8) to eliminate the internal nodal displacements, the fully condensed elemental equilibrium equation is obtained as

$$\begin{bmatrix}\mathbf{L}_{11}^{l-} + \mathbf{L}_{12}^{l-}\mathbf{X}_{10} & \mathbf{L}_{12}^{l-}\mathbf{X}_{11} & \mathbf{L}_{12}^{l-}\mathbf{X}_{12} \\ \mathbf{L}_{12}^{r-}\mathbf{X}_7 & \mathbf{L}_{11}^{r-} + \mathbf{L}_{12}^{r-}\mathbf{X}_8 & \mathbf{L}_{12}^{r-}\mathbf{X}_9 \\ \mathbf{L}_{12}^{+}\mathbf{X}_{13} & \mathbf{L}_{12}^{+}\mathbf{X}_{14} & \mathbf{L}_{11}^{+} + \mathbf{L}_{12}^{+}\mathbf{X}_{15}\end{bmatrix}\begin{Bmatrix}\mathbf{d}_{ext}^{l-} \\ \mathbf{d}_{ext}^{r-} \\ \mathbf{d}_{ext}^{+}\end{Bmatrix} = \begin{Bmatrix}\mathbf{F}_{ext}^{l-} \\ \mathbf{F}_{ext}^{r-} \\ \mathbf{F}_{ext}^{+}\end{Bmatrix} - \begin{bmatrix}\mathbf{L}_{12}^{l-}\mathbf{Y}_4 & \mathbf{L}_{12}^{l-}\mathbf{Y}_5 & \mathbf{L}_{12}^{l-}\mathbf{Y}_6 \\ \mathbf{L}_{12}^{r-}\mathbf{Y}_1 & \mathbf{L}_{12}^{r-}\mathbf{Y}_2 & \mathbf{L}_{12}^{r-}\mathbf{Y}_3 \\ \mathbf{L}_{12}^{+}\mathbf{Y}_7 & \mathbf{L}_{12}^{+}\mathbf{Y}_8 & \mathbf{L}_{12}^{+}\mathbf{Y}_9\end{bmatrix}\begin{Bmatrix}\mathbf{S}_1 \\ \mathbf{S}_2 \\ \mathbf{S}_3\end{Bmatrix} \quad (13)$$

Note that Eqn (12) and Eqn (13) share the same matrices $\mathbf{X}_p$ (p = 1, 2, …15), $\mathbf{Y}_q$ (q = 1, 2,…9),), and $\boldsymbol{S}_r$ (r = 1, ..3), which are all functions of the characteristic cohesive stresses ($\boldsymbol{\sigma}_{0\mathrm{I}}, \boldsymbol{\sigma}_{0\mathrm{II}}$, and $\boldsymbol{\sigma}_{0\mathrm{III}}$) and the cohesive stiffnesses ($\boldsymbol{\alpha}_{0\mathrm{I}}, \boldsymbol{\alpha}_{0\mathrm{II}}$, and $\boldsymbol{\alpha}_{0\mathrm{III}}$) (Eqn 9). The same elemental condensation procedure in section 2.1 applies to Eqn (12) and, once the solution is found, $\mathbf{X}_p$, $\mathbf{Y}_q$, $\boldsymbol{S}_r$ are all established. Substituting them into Eqn (13) the fully condensed elemental equilibrium is then satisfied with mathematical exactness.

3. A-FEM Simulated 4PSB Test and Compared with X-FEM

In this section, the capabilities of the proposed A-FEM is first evaluated by simulating the crack propagation in a 4-point shear beam (4PSB) test reported in [24]. The problem has been simulated

by Moes and Belytschko in [7] using the X-FEM with a non-structured triangular mesh. The numerical model setup used in [7] is reproduced in Figure 4(a). The geometry dimensions are: b = 200 mm; l/b = 4; a/b = 0.2; c/b = 0.4; $l_1 = l_2$ = 20 mm; t = 100 mm.

As in [7], the maximum principal stress criterion was used for crack initiation and the cohesive parmaeters for the concrete material are identical to those used in [7].

To investigate the mesh sensitivity of the present A-FEM, the problem was analyzed by five different structured meshes with characteristic mesh size of h = 2, 4, 8, 13.3, and 20 mm (the total elements are 10760, 2849, 1094, 640, and 410, respectively), and two unstructured meshes with h ~ 4, 8, and 15 mm (total elements 4062, 1333, and 463, respectively). The two finer meshes (h = 2 and 4 mm) are the typical of those used in literature [21, 25], while the larger meshes (8, 13.3, and 20 mm) are used in this study to explore the mesh limit of the present A-FEM. The unstructured meshes of ~ 4, 8, and 15 mm were intended to check the mesh sensitivity and the robustness of the new A-FEM. Five of the discretized models (structured h = 2, 8, and 20 mm meshes and unstructured h ~ 8 and 13 mm meshes) under deformed states are shown in Figure 4 (b, c, d, e, f) with the crack trajectories roughly following the center lines of the white bands.

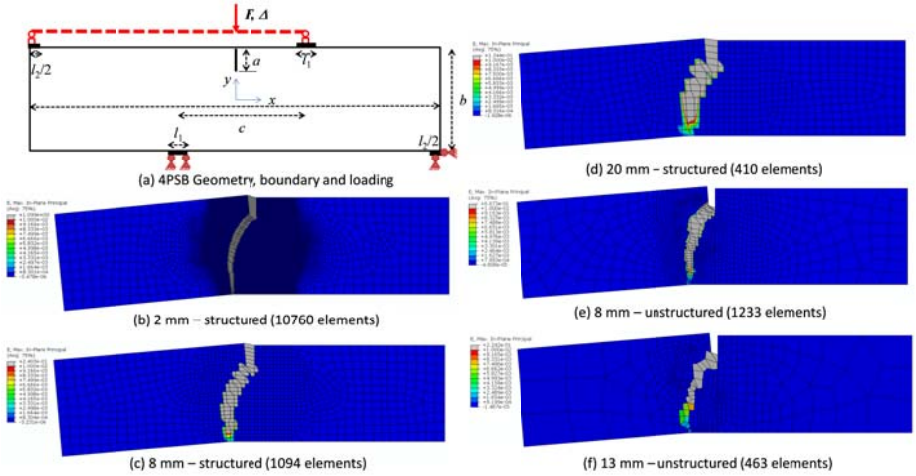

Figure 4 (a) Numerical models and simulated crack paths for structured 2mm (b), 8 mm mesh (c), and 20 mm mesh (d), and unstructured 8 mm (e) and 15 mm (f) meshes.

3.1 Mesh Sensitivity

The simulated load-displacement curves are plotted in Figure 5(a). The X-FEM prediction obtained by Moes and Belytschko [7], which used a triangular mesh of h ~ 3 mm, was superimposed on this plot for comparison (the dashed line). All curves exhibit a strong snap-back behavior. In this study, the strong snap-back behavior was captured using the arc-length method available in ABAQUS (Option RIKS).

The A-FEM computed load-displacement results are very consistent with the X-FEM result obtained in [7]. In particular, the load-displacement curves obtained with smaller mesh sizes (i.e., h = 2 mm, 4 mm, and 8 mm) are almost identical with the X-FEM results. For the larger meshes, i.e., h = 13.3 mm and 20 mm, the curves deviates mildly the finer mesh curves due to increases in initial stiffness. The systematic increase of initial stiffness with the increase of mesh sizes is largely due to the inherent numerical inaccuracy associated with the 4-node plane elements. This clearly demonstrates the mesh insensitivity of the present A-FEM.

Figure 5(b) summarizes the crack trajectories predicted by the five simulations with structured meshes. The crack paths are all very consistent and close to the experimental curve, despite they were obtained with vastly different mesh sizes. The predicted crack trajectories with the three unstructured meshes are also very consistent with those in Fig 5(b), which further demonstrates the mesh objectivity of the new A-FEM.

The insensitivity of the A-FEM to mesh structures is further demonstrated in Fig. 5(c) and Fig.

5(d). These plots compare the load-displacement curves (Fig 6c) and crack trajectories (Fig 6d) obtained with three structured meshes (4, 8 , and 13 mm) (solid lines) and those computed with unstructured meshes of similar mesh sizes (broken lines). The two sets of results are basically indistinguishable.

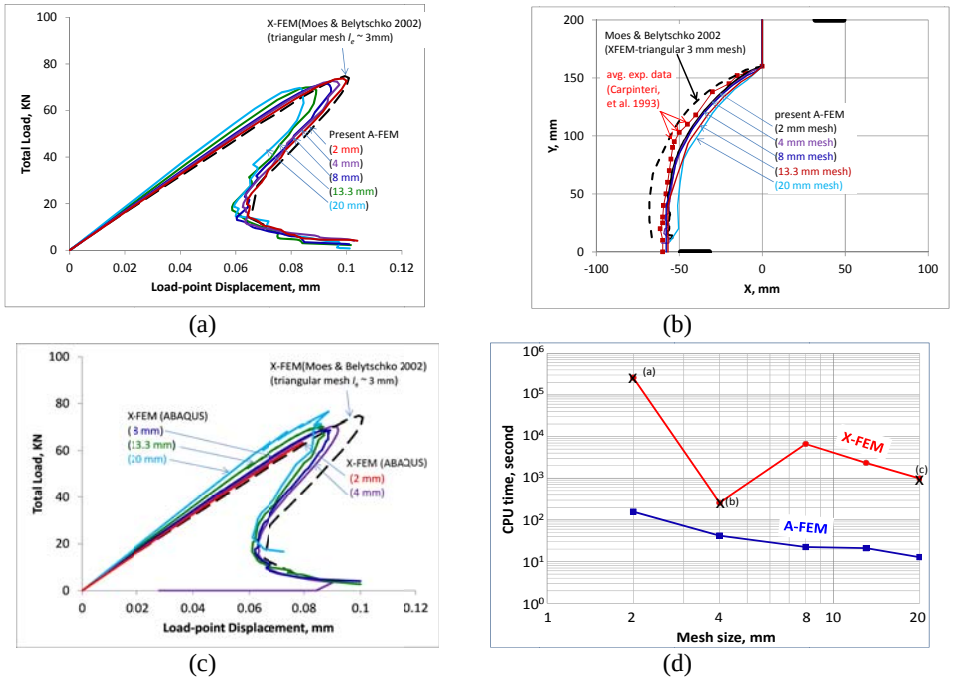

Figure 5 A-FEM simulated load-displacement curves (a) and crack trajectories (b) with the five meshes as compared to the X-FEM results and experimental results. (c) X-FEM predicted load-displacement curves compared with the A-FEM predictions. (d) Comparison of the CPU time (right vertical axis), and the numerical error (left axis) as function of mesh sizes

3.2 Numerical Efficiency and Stability as Compared to X-FEM in ABAQUS(v6.10)

In this section, the numerical accuracy, efficiency, and stability of the new A-FEM is compared against the X-FEM results obtained with ABAQUS (v6.10). Comparisons were carried out for the structure meshes only because the X-FEM failed to obtain converged solutions for any of the unstructured meshes. The meshes, boundary conditions, and loading are exactly the same as those used in previous section. All simulations were run on a Dell precision M4600 (x64 bit) mobile workstation with Intel Core i7–2860 QM CPU @ 2.5 GHz and with 8 GB of RAM.

The XFEM (ABAQUS) simulated load-displacement curves are plotted in Figure 5(c). The XFEM had enormous difficulty in completing these simulations. For the 2 mm mesh, the simulation proceeded with such a small incremental size (10^{-6} ~ 10^{-8} mm) that it had to be terminated at the displacement of 0.08 mm after 72 CPU hours of running. For the 4 mm mesh, a sudden strong snap back resulted from an incorrectly predicted crack path occurred at the displacement of 0.09 mm after the peak (Fig 5c). For the 20 mm mesh, the simulation diverged at the displacement of 0.072 mm (after snap back). For the rest cases (i.e., 8 mm and 13.3 mm mesh), the simulations were able to finish and the XFEM curves captures the peak loads and snap-back behavior reasonably well and they are close to the A-FEM results in Figure (5c).

Figure 5(d) compares the computational cost in terms of CPU time (in seconds) as functions of the mesh size. The CPU time corresponds to the point that when the displacement reached 0.1 mm (after snap-back). For the 2 mm, 4 mm, and 20 mm mesh, the X-FEM simulations were aborted due to the reasons discussed above. In these cases, the CPU times at the aborting points were taken and such data points were indicated by the X in Fig 5(d). From Figure 5(d), it is concluded that the

present A-FEM empowered by the novel condensation procedure, is at least 2 orders of magnitude more efficient than the X-FEM.

4. CONCLUSIONS

In this paper, an elemental augmentation procedure has been established to derive the augmented finite elements (A-FEs) that can accurately account for arbitrary intra-element cracks and their interaction without the need for additional external DoFs as in X-FEM or extra nodes as in PNM. It has been demonstrated that the new formulation makes it much easier in handling the multiple crack interaction problems including crack coalescence or bifurcation, since it does not require complex numerical algorithms to track the complex crack fronts.

The new A-FEM formulation does not need to assume deformation modes for elemental displacement enrichment as in the embedded discontinuity method either. Instead, it introduces internal node-pairs with normal displacements as internal nodal DoFs, which are eventually condensed at elemental level. With the proposed formulation, the crack displacements become natural outcomes of the elemental equilibrium consideration. The advantage is multi-fold. First, it enables a unified treatment of both weak and strong discontinuities. Second, for strong discontinuities with piece-wise linear constitutive relations, the new A-FEM formulation ensures an exact solution (in the piece-wise linear limit) to the condensed elemental equilibrium, which greatly improves the numerical accuracy, stability, and efficiency. Third, the unique A-FEM formulation makes it straightforward to repeat the augmentation procedure within an element to include multiple intra-element cracks, which is very powerful in dealing with multiple crack interaction problems because such augmented elements do not need extra external DoFs or nodes.

A novel elemental condensation algorithm that can provide analytical solution to local equilibrium has also been developed. The novelty in this algorithm is that, instead of assuming trial crack displacements and iterating for elemental equilibrium such as in the Newton-Raphson method, it starts with trial cohesive segments in the cohesive laws and finds the analytical solution (in piece-wise linear sense) to the elemental equilibrium through a simple consistency check. For piece-wise linear cohesive laws with only a small number of possible stiffness segments, this algorithm is very efficient.

Through the numerical examples, it has been demonstrated that the new A-FEM method, empowered by the new elemental condensation algorithm, achieved very significant improvements in numerical accuracy, efficiency, and stability. In particular, through a rigorous comparison study on a 4-point shear beam test, it has been found that the present A-FEM achieved an improvement in numerical efficiency by more than two orders of magnitude as compared to the X-FEM in ABAQUS. The A-FEM's capabilities in high-fidelity simulations of interactive cohesive cracks in heterogeneous solids have also demonstrated through the coupled debonding/kinking processes frequently observed in fiber-reinforced polymer matrix composites

Acknowledgements

Q. D. Yang acknowledges the support from the Air Force Office of Scientific Research (Dr. Ali Sayir) and NASA (Dr. Anthony Calomino) under the National Hypersonics Science Center for Materials and Structures (AFOSR Contract No. FA9550-09-1-0477). W. Liu and X. Y. Su wish to acknowledge the support from the China Scholarship Council and NSFC (Contract No. 11232001).

References

1. Cox, B.N. and Q.D. Yang, *In Quest of Virtual Tests for Structural Composites.* Science, 2006. **314**: p. 1102-1107.
2. Talreja, R., *Mulitscale modeling in damage mechanics of composite materials.* Journal of Material Science, 2006. **41**: p. 6800-6812.
3. Van de Meer, F.P. and L.J. Sluys, *Continuum Models for the Analysis of Progressive Failure in*

Composite Laminates. Journal of Composite Materials, 2009. **43**: p. 2131-2156.
4. Ha, Y.D. and F. Bobaru, *Studies of dynamic crack propagation and crack branching with peridynamics.* International Journal of Fracture, 2010. **162**: p. 229-244.
5. Silling, S.A., *Reformulation of Elasticity Theory for Discontinuities and Long-Range Forces.* Journal of the Mechanics and Physics of Solids, 2000. **48**: p. 175-209.
6. Babuška, I. and J.M. Melenk, *The partition of unity method.* International Journal for Numerical Methods in Engineering, 1997. **40**: p. 727-758.
7. Moës, N. and T. Belytschko, *Extended finite element method for cohesive crack growth.* Engineering Fracture Mechanics, 2002. **69**: p. 813-833.
8. Daux, C., et al., *Arbitrary branched and intersecting cracks with the extended finite element method.* International Journal for Numerical Methods in Engineering, 2000. **48**: p. 1741-1760.
9. Huynh, D.B.P. and T. Belytschko, *The extended finite element method for fracture in composite materials.* International Journal for Numerical Methods in Engineering, 2009. **77**: p. 214-239.
10. Song, J.H., P.M.A. Areias, and T. belytschko, *A method for dynamic crack and shear band propagation with phantom nodes.* Inter. J. Numer. Meth. Engng, 2006. **67**: p. 868-893.
11. Remmers, J.C., *Discontinuities in Materials and Structures -- A Unifying Computational Approach*, 2006, Delft University.
12. Hansbo, A. and P. Hansbo, *A finite element method for the simulation of strong and weak discontinuities in solid mechanics.* Computer Methods in Applied Mechanics and Engineering, 2004. **193**: p. 3523-3540.
13. Fang, X.J., et al., *High-Fidelity Simulations of Multiple Fracture Processes in a Laminated Composites in Tension.* Journal of the Mechanics and Physics of Solids, 2011. **59**: p. 1355-1373.
14. Ling, D.S., Q.D. Yang, and B.N. Cox, *An augmented finite element method for modeling arbitrary discontinuities in composite materials.* International Journal of Fracture, 2009. **156**: p. 53-73.
15. Budyn, E.R.L., *Multiple crack growth by the extended finite element method[D]*. 2004, Northwestern University: Evanston, Illinois.
16. Holl, M., S. Loehnert, and P. Wriggers, *An adaptive multiscale method for crack propagation and crack coalescence.* Inter. J. Numer. Meth. Engng, 2012. **in press**(DOI: 10.1002/nme.4373).
17. Alfaiate, J., G.N. Wells, and L.J. Sluys, *On the use of embedded discontinuity elements with crack path continuity for mode-I and mixed-mode fracture.* Engineering Fracture Mechanics, 2002. **69**: p. 661-686.
18. Sluys, L.J. and A.H. Berends, *Discontinuous failure analysis for mode-I and mode-II localization problems.* Int. J. Solids Struct., 1998. **35**: p. 4257–4274.
19. Linder, C. and F. Armero, *Finite elements with embedded branching.* Finite Elements in Analysis and Design, 2009. **45**: p. 280-293.
20. Dias-da-Costa, D., et al., *Towards a generalization of a discrete strong discontinuity approach.* Computational methods in Applied Mechanics and Engineering, 2009. **198**: p. 3670-3681.
21. Linder, C. and F. Armero, *Finite elements with embedded strong discontinuities for themodeling of failure in solids.* International J. Numer. Meth. Engng, 2007. **72**: p. 1391-1433.
22. Yang, Q. and M.D. Thouless, *Mixed mode fracture of plastically-deforming adhesive joints.* International Journal of Fracture, 2001. **110**: p. 175-187.
23. Yang, Q.D. and B.N. Cox, *Cohesive Models for damage evolution in laminated composites.* International Journal of Fracture, 2005. **133**(2): p. 107-137.
24. Carpinteri, A., et al., *Is mode II fracture energy a real material property?* computers and structures, 1993. **48**(3): p. 397-413.
25. Dias-da-Costa, D., et al., *An embedded formulation with conforming finite elements to capture strong discontinuities.* Int. J. Numer. Meth. Engng, 2012. **in press, DOI: 10.1002/nme.4393**.

Analysis of resistance cracking process on the experiment of meso and macroscopic of quasi-brittle materials

Wang Limin[1,*)], Xu Shilang[2)], Wang Haiying[3)] , Zhang Donghuan[4)]

1) Department of Science, Qingdao Technological University, Qingdao Shandong 266033, China;
2) Constructure Engineering School of Zhejiang University, Hangzhou Zhejinag 310058 China;
3) Institute of Mechanics，Chinese Academy of Sciences，Beijing 100190 China;
4) School of Transportation and Vehicle Engineering, Shandong University of Technology, Zibo 255049
* Corresponding author: wanglimin@qtech.edu.cn

Abstract: Engineering materials such as cast iron and concrete are quasi-brittle materials, and there is a fracture process zone in front of opening crack and it exist micro and macro defect and energy dissipation. The damage development area is simplified into fictitious crack, and its action stress distribution and opening displacement or deformation are along the cohesive crack. In order to investigate the constitutive relation of cohesive crack opening displacement and its stress distribution in quasi brittle materials, cast iron and concrete were used to test their fracture process by electronic equipment and micro view experiment facility. Through the analytical method of applied mathematics and mechanics, the material deformation stress constitutive relations were gotten for the cohesive crack. The theoretical calculation and test results are basically in agreement with each other. From the fracture criterion of Double K and the mechanics model of cohesive crack, the bearing capacity of structure with crack was estimated in this present paper.

Key Words: Quasi brittle materials; constitutive relation of cohesive crack; mesoscopic damage; fracture process testing; inverse problem

Engineering materials such as cast iron or concrete, not same as carbon steel and other reinforcement materials, its stress and deformation or constitutive behavior shows softening characteristics when stress or strain reaches a certain value. So them are classified to the quasi brittle materials. Those materials fracture phenomenon has attracted many scholars research. Hillerborg etc presented virtual crack model for concrete fracture based on the Dugdal-Barenblatt elastic-plastic fracture model, also other researchers have double parameters, equivalent crack, double K fracture model and size effect model ad so on[1-4]. In fact, this kind of material, its fracture process zone or a fuzzy damage crack area has action force each other when external load exerting among the area. If the strip area was named fictitious crack of being not completely separate, and it has bridging role on resistance crack opening. The cohesive force must be put along the fictitious crack segment. The mechanics behavior of those quasi-brittle materials will be analyzed in the present paper by combining cohesive crack model with macro and mesoscopic experiment investigation.

1. The cohesive crack model

As shown in Fig.1，a model of cohesive crack has been formed with both segments. One is completely opening crack segment without any force, and the other is the cohesive crack segment with stress distribution showing the fracture process damage area. The damage region was regarded as part of crack, the cohesive stress distribution express the interaction of material media. The medium outside of damage or cohesive crack is regarded as a linear elastic medium. The cohesive crack tip point is named as

the origin of rectangular coordinate, and the direction of level axis is for right. As the length of cohesive crack segment is indicated to '**b**', and the coordinate '**x**' to be the position of some point, then the follow polynomial express the opening displacement distribution of cohesive crack.

$$U(x)=\frac{4b}{E\pi}\sum_{n=1}^{N}c_n\left(\frac{x}{b}\right)^{n-1/2} \qquad (0\le x\le b) \qquad (1)$$

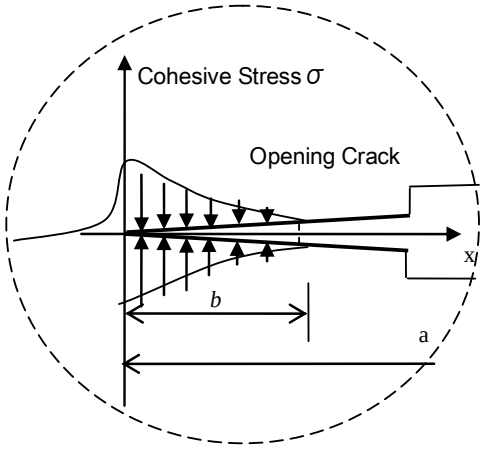

Figure 1. The cohesive crack model with cohesive stress and opening displacement in front of smooth crack

The Crack Opening Displacement or $\tilde{U}$ can be regarded as the superposition of both an opening displacement or V_K coursed by load P far from crack tip and a closing displacement done by the cohesive stress σ along crack together. Then, an integral equation was been formed with the unknown function σ being of cohesive stress distribution, based on the superposition principle of stress and deformation of the solid structure.

$$\int_0^b \tilde{G}(\xi,x)\sigma(\xi)d\xi=V_K(P,x)+\tilde{U}(x,u) \qquad (0\le x\le b) \qquad (2)$$

Here, $\tilde{G}(\xi,x)$ is a Green function about the displacement of point x by unit force at ξ point. The solution of equation was been worked out, and the formula of cohesion stress distribution is as follows [5].

$$\sigma(x)=\frac{K_I}{\sqrt{2\pi(b-x)}}+\frac{-1}{2\pi\sqrt{b}}\sum_{n=1}^{N}c_n\sqrt{\frac{1}{b-x}}\sum_{r=0}^{n-1}\left(\frac{x}{b}\right)^{n-r-1}\frac{2^{-2r}(2r)!}{(r!)^2}+\frac{1}{\pi\sqrt{b}}\sum_{n=2}^{N}c_n\sqrt{b-x}\sum_{r=0}^{n-2}\frac{2^{-2r}(n-r-1)(2r)!}{(r!)^2}\left(\frac{x}{b}\right)^{n-r-2} \qquad (0\le x\le b) \qquad (3)$$

Here, E is Young's elastic modulus of matrix materials for plane stress state. For the plane strain state the $E/(1-\nu^2)$ will be instead of the E, and ν is Poisson's ratio. The $c_i(i=1,2,...,N)$ is undetermined parameter with stress dimension. The K_I is the crack stress intensity factor by far field load P.

2 Experiment of micro detection and electronic measurement

2.1 The micro detection of iron and concrete

For the fracture process zone of quasi brittle material, its resistance part of crack opening is an area reflecting the characteristics of material nonlinear mechanical behavior. For the strip area with damage or plastic deformation, its microscopic characteristics are also complicated with load changing [6,7]. As shown in Figure 2, it is the microstructure morphology for cast iron or concrete. The status pictures of graphite piece in cast iron were shown in Fig2 (a, b) before and after loaded on the specimen. The former are not stress action in the pictures, and the latter shows the graphite flake being open or taking shape of crack in ferrite. As the area still has connection force among, this just be the mesoscopic experimental evidence of existing cohesive stress along virtual crack. Of course, the crack deformation of material with graphite flake will increase along with the increasing of load. The micro appearance of concrete were shown in Fig 2 (c, d), the interface crack between cement and stone being in picture 'c' and cracks in cement base doing in picture 'd'. The cracks existing in media is the increasing cause of deformation or strain.

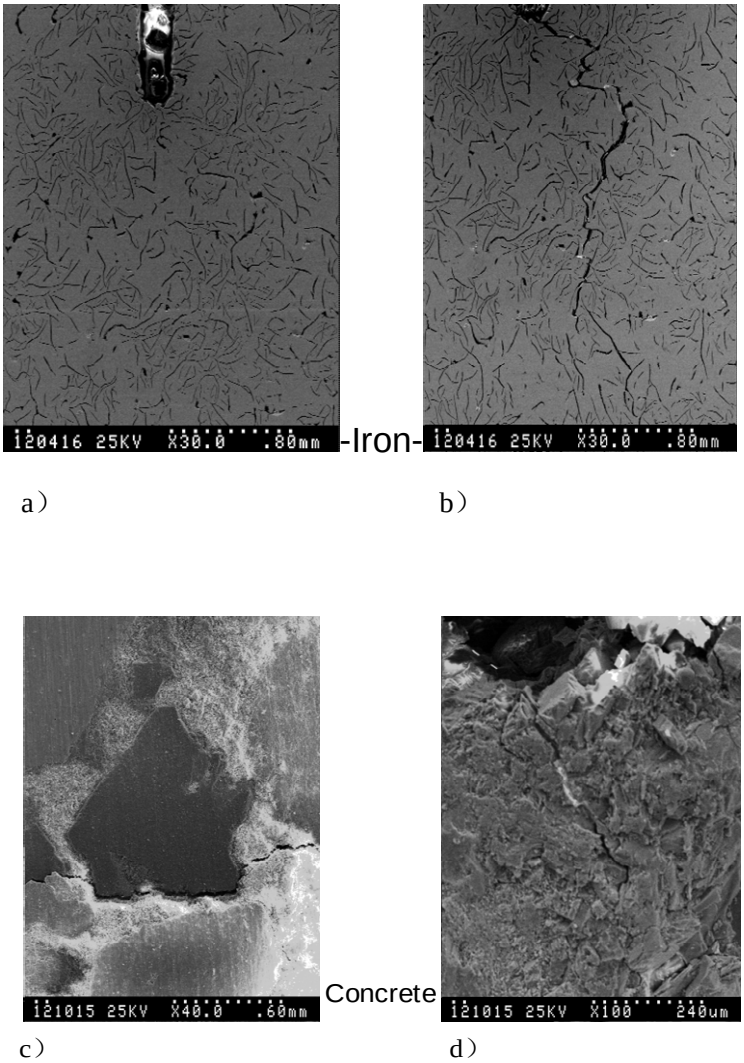

Figure 2. Electron microscopy (sem) surface images of Iron (a,b) and Concrete (c,d).

2.2 The fracture process test of materials

The specimen of iron and concrete with prefabricated crack were tested by three point bending or wedge splitting loading way, as shown in Fig 3. In order to record the process of crack ligament deformation, a few pieces of strain gauges were been pasted on front of prefabricated crack. Only, were the both sides of a strain gauge just posted at the materials surface in case of preventing the gauge film early to be pulled apart [8].

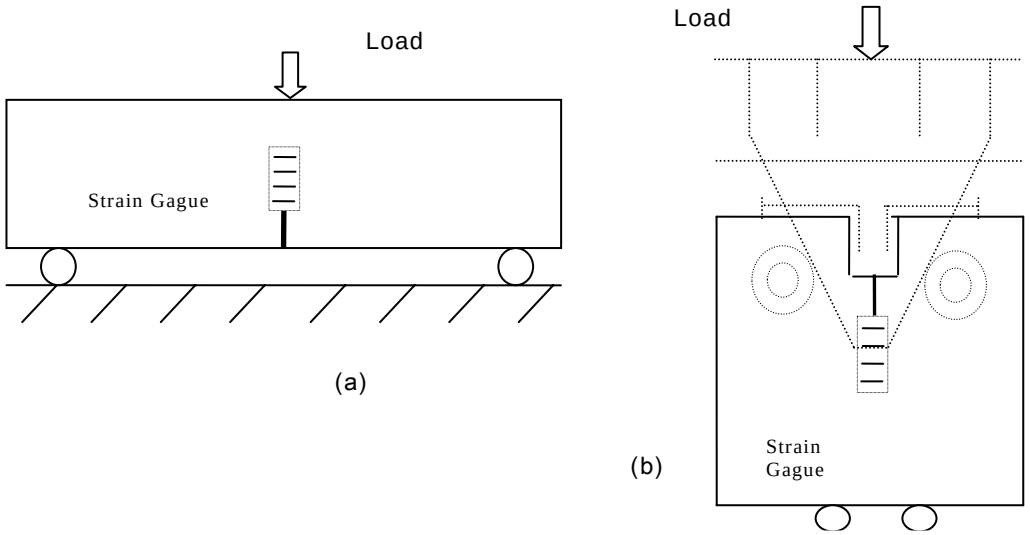

Figure 3. The experiment device of fracture process: a) Iron loaded by three point bending; b) Concrete loaded by wedge splitting pull

As shown in Fig 4, it is the deformation distribution of specimen ligament of iron or concrete under different load. The deformation is the relative displacement between its two sides of a gauge posted on materials ligament. In Fig 4 (i), the experimental curves are for cast iron specimen by the loading of three-point bending. The appearance size are respectively 'Length * Thick * High = 300 * 50 * 65 (mm*mm* mm), and loaded span is 260 mm, prefabricated crack length 5 mm. In Fig 4 (ii), the experiment curves are for concrete by loading of wedge splitting pull. The appearance size is that 'Wide*High*Thick=500*520*150(mm*mm*mm)' and the prefabricated crack length is about 120 mm.

Of course, the cohesive crack deformation distribution can be seen from the graphs of test on fracture process zone. Obviously, no matter what kind of material, it is the deformation changing with the load increasing.

3 The constitutive relation of cohesive stress and opening displacement of fictitious crack

From above formula (1) and (3) for the cohesive crack model, the simple calculation equations can be worked out. As the 'N'is selected to be 2 in Eq(1,3), the distribution of cohesive stress or opening displacement of virtual crack can be expressed as following.

$$u(x) = \frac{8K_I}{3E}\left(\frac{x}{b}\right)^{3/2}\sqrt{\frac{2b}{\pi}} \qquad (4a)$$

$$\sigma(x) = \frac{K_I \sqrt{2}}{b} \sqrt{\frac{b-x}{\pi}} \tag{4b}$$

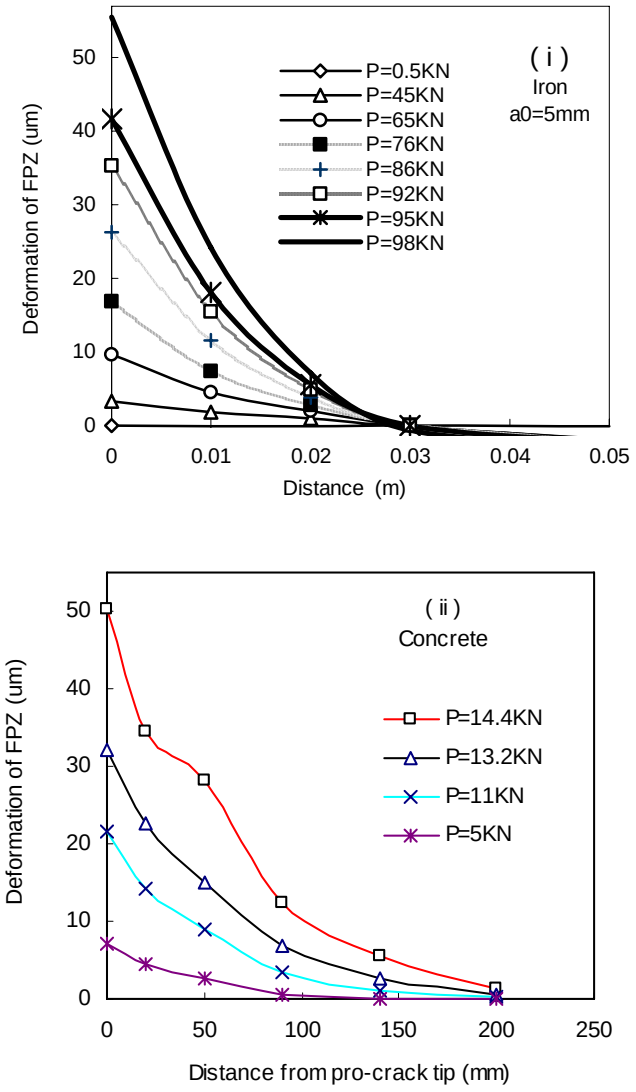

Figure 4. The deformation distribution along the crack ligament of （i）iron（ii）concrete under different load

If the coordinate x is taken away from Eq 4 (a,b), the constitutive equation of fictitious crack can be worked out between cohesive stress and opening displacement of cohesive crack. Refering to Fig 3 and 4, the displacement distribution can be calculated from the cast iron test data in Ref [8] through above Eq 4 (a). In Fig 5, the theoretical curve is compared with the experimental results of iron specimen, and the calculation curve is basely consistent with experiment data. In Fig 6, it is the constitutive relation curves between the cohesion stress and crack opening displacement for concrete specimens under different load. There is a little difference about concrete constitutive relation between different loading condition, but it also be consistent with reference early results [9,10].

4 The bearing capacity estimate of structure with crack

As the fracture process zone length changing with variable load in experiment specimen, the quantitative relationship of its loading and damage zone length can be worked out according to the fracture criterion of Double-K and the theoretical analysis results of cohesive crack [9]. For fracture specimen configuration such as three-point bending beam with crack, the equation can be written as followings.

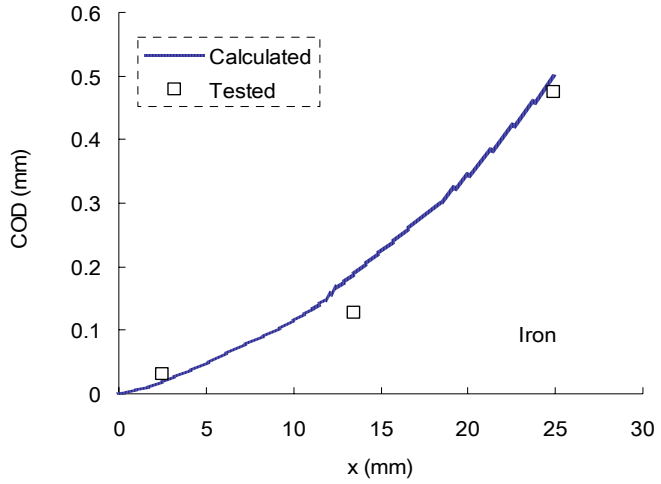

Figure 5. The compare of theory curve of cast iron cohesive crack opening displacement with experimental data

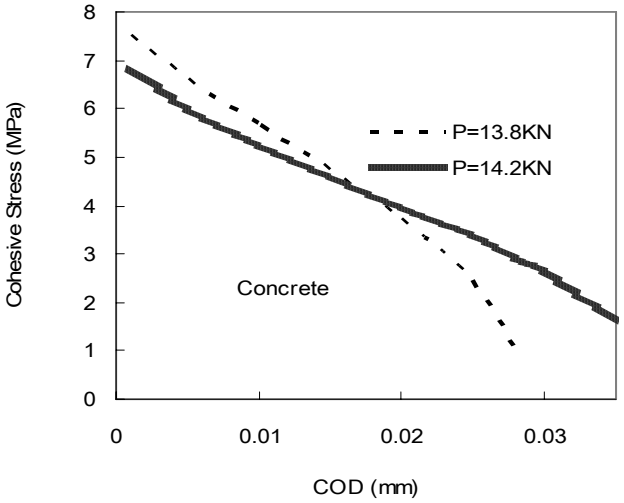

Figure 6. The constitutive relation between cohesive stress and opening displacement of cohesive crack for concrete being under different load

$$P=\frac{2Bh^{2}\left(k_{0}+\eta\sqrt{\frac{b}{2\pi}}\right)\left(1+2\frac{a_{0}+b}{h}\right)\left(1-\frac{a_{0}+b}{h}\right)^{3/2}}{3s\sqrt{a_{0}+b}\left[1.99-\frac{a_{0}+b}{h}\left(1-\frac{a_{0}+b}{h}\right)\left(2.15-3.93\frac{a_{0}+b}{h}+2.7\left(\frac{a_{0}+b}{h}\right)^{2}\right)\right]} \quad (4)$$

Where, k_0 is the stress intensity factor of initiation crack; and a_0 is for the

prefabricated crack length. Refer to Fig 3, the symbol *s* and *h* are span and high respectively. Regarding to the specimens with pre-crack length 5mm and 20 mm, the changing length of damage zone respectively with loading was shown in Fig 7 for iron materials [8]. Continuous curve is the theoretical calculation value, and scatter icons indicate experimental test results. From the figure it can be seen that theories values are in good agreement with experiment, and the maximum bearing capacity value of structure with cracked can be estimated from the curve peak.

5 Conclusion

(1) Through nonlinear crack model analysis, both the cohesive stress distribution and opening displacement of fictitious crack can be calculated by analytical equation.

(2) Regarding the cohesive crack model, specimen of cast iron or concrete was observed or tested in order to investigate the mechanics behavior of quasi-brittle materials. And its theoretical calculation is consistent with experimental observation.

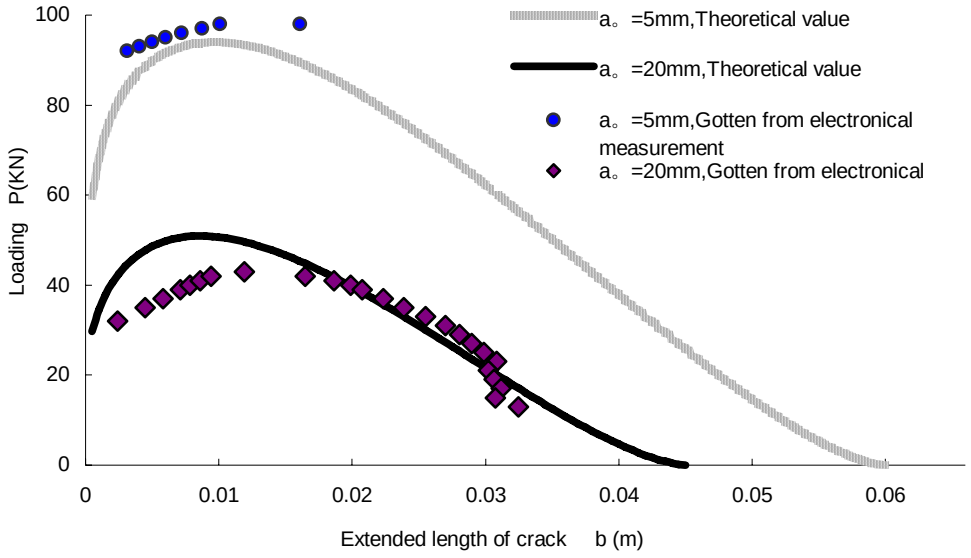

Figure 7. The relation between the loading of three point bending beam with crack and the length of extended crack for iron material

Acknowledgements

This work was supported by the National Natural Science Foundation of China (Grant Nos. 10272068，50438010，11172311) and the Shandong Natural Science Foundation (Grant No. Y2006A29). Thanks for (Institute of Mechanics, Chinese Academy of Sciences) Mr. Li Duanyi's help regarding mesoscopic experiment of materials.

Reference

[1] Xu Shilang Concrete fracture mechanics (in Chinese). Beijing: Science Press, 2010

[2] Jenq Y S, Shah S P. Two parameters fracture model for concrete, Journal Engineering Mechanical,ASCE,1985,111(10)：l227～l241

[3] Karlhaloo B L and Nallathambi P. Effective crack model for the determination of fracture toughness of concrete.Engineering Fracture Mechanics, 1990,35(4/5)：637～645
[4] Bazant Z P and Chen E P. Scaling of structural failure, Applied Mechanics Review.1997,50(10):593～627
[5] Wang Limin, Xu Shilang, Zhao Xiqiang. Analysis on cohesive crack opening displacemen considering the strain softening effect, Science in China-G, 2006, 49(1)：88～101
[6] Feng Xiqiao,Yu Shouwen. Quasi-brittle material mesoscopic damage mechanics (in Chinese). Beijing: higher education press, 2002
[7] ZhangYan, Zhang Ziming. Material micromechanics (in Chinese). Beijing: science press, 2008
[8] Wang Limin Sun Mingyuan, et al. Electronical measurement of incision iron specimens' fracture proceeding and calculation of the structure bearing capacity (in Chinese). Acta Metall Sinica, 2008, 44(7): 853-858
[9] Xu Shilang and Reinhardt H W. Determination of double-K criterion for crack propagation in quasi-brittle fracture.Part I ,II and III, International Journal of Fracture,1999,98(2):111～193
[10] Horii H and Ichinomiya T.Observation of fracture process zone by laser spec technology and governing mechanism in fracture of concrete. International Journal of Fracture,1991,51(1):19～29

Matched asymptotic expansions in an elastic-creeping material : a new view on the Hui-Riedel equation.

Radhi ABDELMOULA[1,*] Gilles DEBRUYNE[2] , Jia LI[1]

[1] Paris XIII University, LSPM ,*Avenue J.B. Clément 93430 Villetaneuse, France*
[2] LaMSID-EDF-CEA, *1 avenue du Gal de Gaulle 92141 Clamart, France*

* Corresponding author: *, radhi.abdelmoula@univ-paris13.fr*

Abstract

The work deals with the asymptotic stress-strain field around a crack tip, steadily propagating in a viscous material for antiplane conditions. A solution of this problem has been offered by Hui and Riedel, but with some unexpected features. In particular, the solution generally leads to an autonomous crack growth (independent on the loading state). This problem is revisiting here, using a multiscale asympotic analysis. Small scale yielding and low crack velocity are assumed. A small parameter ε, proportional to the crack growth rate, is introduced to switch from the inner solution (close to the crack tip) to the outer one (far field), using an asymptotic expansion of the solution. The outer solution is equivalent to the non linear elastic HRR field at the first order for ε=0, while the viscosity appears at the second order. Close to the crack tip, the viscous effects arise at the first order and the corresponding asymptotic field is governed the elastic field associated to the crack velocity, while the non linear term, corresponding to the nonlinear elasticity emerges at the second order . This is a basic difference with the Hui-Riedel solution where the two scale orders are merged. The matching conditions allow to link the far and close fields, and to correct the paradox whereby the crack velocity should not depend to the far field governed by the loading (except for perfect plasticity ($n \to \infty$) where the solution remains autonomous).

Keywords Hui-Riedel solution, creep, steadily growing crack, singularity, matched asymptotic expansions.

1. Introduction

An antiplane asymptotic solution for a steadily slowly growing crack in an elastic-non linear viscous medium has been suggested by Hui and Riedel [1]. A power law creep is considered. For uniaxial tension, the Norton law has the following form :

$$\dot{\varepsilon} = \frac{\dot{\sigma}}{\mu} + B\sigma^n \quad (1)$$

For $n > 3$ some paradox events arise, in particular the solution is autonomous, independent on the remote loading (this phenomenon is described by Bui as an analogy to the “soliton” in non linear waves problems [2]). Some authors have corrected this paradox, but with substantive changes to the law or introducing a threshold [3,4]. Keeping the original Norton law, a new antiplane shear analysis is offered here, using a matched asymptotic expansion method. Higher expansion terms of the stress function will allow to connect the « inner solution » (near the viscous crack tip) to the « outer solution » (corresponding to the far HRR field).

2. Initial problem formulation.

Figure 1 shows the crack, embedded inside the body Ω, located in the (x,z) plane at y=0. The stress and strain tensors in antiplane conditions are :

$$\tau_i = \sigma_{3i}, \gamma_i = 2\varepsilon_{3i}, \quad i = 1,2 \quad (2)$$

The equivalent stress is introduced as $\tau_e = (\tau_1^2 + \tau_2^2)^{1/2}$, so that the material law is (with $\bar{B} = \sqrt{3}^{(n+1)} B$) :

$$\dot{\gamma}_i = \frac{\dot{\tau}_i}{\mu} + \bar{B}\tau_e^{n-1}\tau_i, \quad i = 1,2 \quad (3),$$

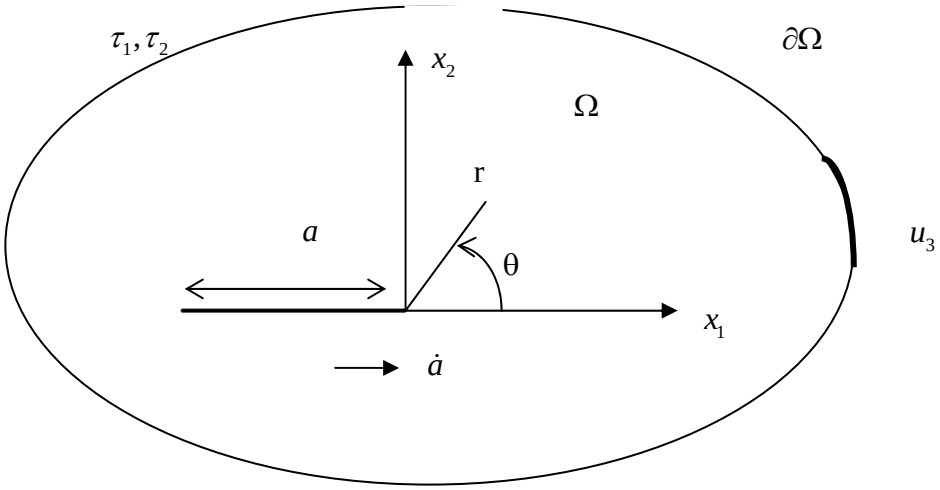

Figure 1 Crack steadily moving with velocity $\dot{a}$ under shear load in mode III.

The equilibrium equations are $\nabla_i \tau_i = 0$, where the summation convention holds. The stress function is then introduced, so that the previous equation is automatically fulfilled :

$$\tau_1 = -\frac{\partial \Psi}{\partial x_2}, \quad \tau_2 = \frac{\partial \Psi}{\partial x_1} \quad (4)$$

The crack is assumed to grow steadily so that in the moving coordinate system the fields remain constant, which involves :

$$\frac{\partial \Psi}{\partial t} = -\dot{a}\frac{\partial \Psi}{\partial x_1} \quad (5)$$

Using the compatibility of the strain rates, the following equation holds everywhere inside the body Ω :

$$-\frac{\dot{a}}{\mu}\frac{\partial \Psi}{\partial x_1}\Delta\Psi + \bar{B}\nabla_i(\tau_e^{n-1}\nabla_i\Psi) = 0 \quad (6)$$

3. Rescaling the problem.

Dimensionless variables will be used now ($\bar{x}_1 \equiv x_1 / a, \bar{x}_2 \equiv x_2 / a, \bar{\Psi}(\bar{x}_1, \bar{x}_2) \equiv \Psi / \mu$). Furthermore, a small parameter $\varepsilon = \frac{\dot{a}}{\bar{B} a \mu^n}$ is introduced, so that the Hui-Riedel relation may be written as :

$$-\varepsilon\,\Delta\frac{\partial \bar{\Psi}}{\partial \bar{x}_1} + \nabla_i\left[\bar{\tau}_e^{n-1}\nabla_i\bar{\Psi}\right] = 0 \quad (7)$$

with the boundary conditions : $\frac{\partial \bar{\Psi}}{\partial \bar{x}_1} = 0, \quad -1 < \bar{x}_1 < 0, \bar{x}_2 = 0$ on the crack lips and $\tau_i(\partial\Omega) = \tau_0$ for the remote loading. Henceforth, the bar will be removed from all the following notations, to lighten the notations. The key ideas are firstly to distinguish two observation scales (the fields in the crack tip vicinity and the far fields), secondly to expand the stress function at higher orders for each scale, and finally to match these asymptotic expansions. This method has been already applied for instance in elastic-plastic materials [5] or for a series of cracks in the frame of elasticity [6,7].

4. Asymptotic expansions of the stress function.

It is supposed that the stress function is asymptotically expanded, and that each i^{th} expansion term is weighed by the parameter ε^{α_i}.

Far from the crack tip, $r >> \varepsilon$ in Ω_o, the expansion will be designed by “outer”, in the vicinity of the crack tip in Ω_i, it will be called “inner”.

4.1. Outer expansion

It is assumed that the stress function may be expanded as :

$$\Psi(x_1, x_2) = \varepsilon^{\alpha_1}\Psi^{(1)}(x_1, x_2) + \varepsilon^{\alpha_2}\Psi^{(2)}(x_1, x_2) + \varepsilon^{\alpha_3}\Psi^{(3)}(x_1, x_2) + \ldots \quad (8)$$

Developing with the previous relation the equivalent stress, we find that :

$$\tau_e^{n-1} = \varepsilon^{\alpha_1(n-1)}(\nabla_i\Psi^{(1)}.\nabla_i\Psi^{(1)} + 2\varepsilon^{\alpha_{2-}\alpha_1}\nabla_i\Psi^{(1)}.\nabla_i\Psi^{(2)} + \varepsilon^{2(\alpha_{2-}\alpha_1)}\nabla_i\Psi^{(2)}.\nabla_i\Psi^{(2)} + ...)^{(n-1)/2} \quad (9)$$

The Taylor expansion of the previous expression is then :

$$\tau_e^{n-1} = \varepsilon^{\alpha_1(n-1)}\sigma^{(1)} + \varepsilon^{\alpha_{2+}\alpha_1(n-2)}\sigma^{(2)} + \varepsilon^{2\alpha_{2+}\alpha_1(n-3)}\sigma^{(3)} + O(\varepsilon^{\alpha_3+\alpha_1(n-2)}) \quad (10)$$

where $\sigma^{(1)}, \sigma^{(2)}, \sigma^{(3)}$ are functions depending on $\nabla_i\Psi^{(1)}, \nabla_i\Psi^{(2)}, n$. Using the relation (10), the equilibrium equation is therefore in Ω_o :

$$\begin{aligned} &-\Delta\frac{\partial}{\partial x_1}(\Psi^{(1)} + \varepsilon^{\alpha_{2-}\alpha_1}\Psi^{(2)} + \varepsilon^{\alpha_{3-}\alpha_1}\Psi^{(3)} + ...) + \\ &\varepsilon^{\nu}\nabla_i\left((\sigma^{(1)} + \varepsilon^{\alpha_{2-}\alpha_1}\sigma^{(2)} + \varepsilon^{2(\alpha_{2-}\alpha_1)}\sigma^{(3)} + ...)\nabla_i(\Psi^{(1)} + \varepsilon^{\alpha_{2-}\alpha_1}\Psi^{(2)} + ...)\right) = 0 \end{aligned} \quad (11)$$

where $\nu = \alpha_1(n-1) - 1$.

The first term in the relation (11) is relative to the viscous behaviour near the crack tip. The second term relative to the non linear behaviour far from the crack tip must be dominant here. Thus :

$$\nu = \alpha_1(n-1) - 1 < 0, \quad \forall n \geq 1 \quad (12)$$

The outer equilibrium equation at the first order is then :

$$\nabla_i\left(\sigma^{(1)}\nabla_i\Psi^{(1)}\right) = 0 \quad (13)$$

The following terms order is $\varepsilon^{\alpha_{2+}\alpha_1(n-2)-1}$ It is assumed now that :

$$\alpha_2 + \alpha_1(n-2) - 1 = 0 \quad (14)$$

This assumption will be explained in a next section, and justified by matching considerations. Therefore, the final equilibrium for the outer expansion, at the first order is :

$$-\Delta\frac{\partial}{\partial x_1}\Psi^{(1)} + \nabla_i\left(\sigma^{(1)}\nabla_i\Psi^{(2)} + \sigma^{(2)}\nabla_i\Psi^{(1)}\right) = 0 \quad (15)$$

with $\sigma^{(1)} = \left\|\nabla\ \Psi^{(1)}\right\|^{n-1}, \sigma^{(2)} = (n-1)\left\|\nabla\ \Psi^{(1)}\right\|^{n-3}\nabla_i\Psi^{(1)}\nabla_i\Psi^{(2)}$

4.2. Inner expansion

In the neighbouring of the crack tip, a new variable designed as : $y_i = \frac{x_i}{\varepsilon^{\beta}}$ is used as a microscope focal. This variable change is one of the clue to explain the paradox of the autonomous solution (in the original analysis $\beta = 1$). The inner expansion is then assumed as :

$$\Psi(x_1, x_2) = \varepsilon^{\beta_1}\varphi^{(1)}(y_1, y_2) + \varepsilon^{\beta_2}\varphi^{(2)}(y_1, y_2) + \varepsilon^{\beta_3}\varphi^{(3)}(y_1, y_2) + ... \quad (16)$$

The equilibrium equation in Ω_i is :

$$-\varepsilon^{\delta}\Delta\frac{\partial}{\partial y_1}(\varphi^{(1)}+\varepsilon^{\beta_2-\beta_1}\varphi^{(2)}+\varepsilon^{\beta_3-\beta_1}\varphi^{(3)}+...)+ \\ \nabla_i\left((\tau^{(1)}+\varepsilon^{\beta_2-\beta_1}\tau^{(2)}+\varepsilon^{2(\beta_2-\beta)}\tau^{(3)}+...)\nabla_i(\varphi^{(1)}+\varepsilon^{\beta_2-\beta_1}\varphi^{(2)}+...)\right)=0 \quad (17)$$

where $\delta=\beta\,(n-2)+\beta_1(1-n)+1$. We claim that :

$$\delta=\beta\,(n-2)+\beta_1(1-n)+1<0 \quad (18)$$

In fact, this parameter cannot be positive, otherwise the relation (17) would be the same as equ. (13) at the first order (note that in the Hui-Riedel analysis $\delta=0$). At the order ε^{δ}, the equilibrium condition holds :

$$-\Delta\frac{\partial}{\partial y_1}\varphi^{(1)}=0, \quad in\ \Omega_i \quad (19)$$

Transferring the expression (19) into (17), the remaining terms are of order 1 and $\varepsilon^{\delta+\beta_2-\beta_1}$. Both of them must be considered, otherwise the solution regress to the HRR field or to the solution of (19). Therefore :

$$\delta+\beta_2-\beta_1=0 \quad (20)$$

Finally, at the first order the inner equilibrium equation is (with $\tau^{(1)}=\left\|\nabla\ \varphi^{(1)}\right\|^{n-1}$) :

$$-\Delta\frac{\partial}{\partial y_1}\varphi^{(2)}+\nabla_i\left(\tau^{(1)}\nabla_i\varphi^{(1)}\right)=0, \quad in\ \Omega_i \quad (21)$$

It may be noticed that at the micro-scale, contrary to the macroscopic scale, the Laplace operator is relative to the second term of the stress function expansion and the non linear term is relative to the first one. Starting from now, it is necessary to solve the equations (15) and (21).

5. Stress functions solutions

5.1. Singularity analysis

From the equation (13), the singular HRR field emerges with :

$$\Psi^{(1)}(x_1,x_2)=K_1 r^s f_1(\theta)+more\ regular\ terms, \quad (22)$$

with $s=\dfrac{n}{n+1}$, and where K_1 will be clarified in a further section. Injecting the expression (22)

inside the complete equilibrium equation (15) allows to compute the second term $\Psi^{(2)}$:

$$\Psi^{(2)}(x_1, x_2) = K'_1 r^s f_1(\theta) + K_2 r^t f_2(\theta) + \textit{more regular terms} \quad (23)$$

the exponent t is deduced from s, so that :

$$t = \frac{n-2}{n+1} \quad (24)$$

A HRR field with higher order terms has been established for far fields. To clarify the fields close to the crack tip, it is necessary to use matching conditions.

5.2. Matching outer and inner expansions.

For the inner expansion, equilibrium equations (19) and (21) have only free stress boundary conditions on the crack lips, and no outer boundary conditions since Ω_i is unbounded. The matching conditions will substitute to these latter, and involve that in the overlapping area, the inner expansion matches the outer one for small ε values. The asymptotic matching principle will then applied [8]. The first outer term (respectively the first inner term) is rewriting in inner variable (resp. outer variable), with $r = \varepsilon^\beta \rho$ (resp. $(y_1 = \frac{x_1}{\varepsilon^\beta}, y_1 = \frac{x_1}{\varepsilon^\beta})$, and the relation (22) becomes :

$$\Psi^{(1)}(x_1, x_2) = K_1 \varepsilon^{\alpha_1} \varepsilon^{\beta s} \rho^s f_1(\theta) + ... = \varepsilon^{\alpha_1} \varphi^{(1)}(x_1 / \varepsilon^\beta, x_2 / \varepsilon^\beta) + ... \quad (25)$$

$\forall \varepsilon$, which leads to the supplementary relation :

$$\beta_1 = \alpha_1 + \beta s \quad (26)$$

When $\varepsilon \to 0, \rho \to \infty$, the first order matching holds :

$$\varphi^{(1)}(y_1, y_2) \square K_1 \rho^s f_1(\theta) \quad (27)$$

Let's tackle now the resolution of (19).

$$\varphi^{(1)}(y_1, y_2) = K_1 \rho^s f_1(\theta) + \tilde{\varphi}(y_1, y_2) \quad (28)$$

where $\tilde{\varphi}(y_1, y_2)$ is of order $\rho^p, \; p < s, \; for \; \rho \to \infty$

Moreover, the classical solution of linear elasticity is valid for the relation (19) :

$$\hat{\varphi}(y_1, y_2) = K_{III} \rho^{1/2} \sin\frac{\theta}{2} \quad (29)$$

Inserting the first term of (28) into (19) :

$$\zeta(y_1, y_2) = \Delta \frac{\partial \rho^s f_1(\theta)}{\partial y_1} \quad (30)$$

and reporting (28),(29),(30) in (19), the function $\tilde{\varphi}(y_1, y_2)$ may be found, solving the problem :

$$\begin{cases} -\Delta \dfrac{\partial \tilde{\varphi}}{\partial y_1} = K_1 \zeta \ in \ \Omega_i, \\ \dfrac{\partial \tilde{\varphi}}{\partial y_2} = 0, \forall y_1 \in]-\infty, 0[, \\ \tilde{\varphi} \to \hat{\varphi} \ for \ |y| \to \infty \end{cases} \quad (31)$$

Using the same way as in (25), the expansions second terms are matched :

$$\Psi(x_1, x_2) = K_1 \varepsilon^{\alpha_1} \varepsilon^{\beta_1} \rho^s f_1(\theta) + \varepsilon^{\alpha_2} \varepsilon^{\beta s} \rho^s f_1(\theta) + . = \varepsilon^{\beta_1} \varphi^{(1)}(x_1 / \varepsilon^{\beta}, x_2 / \varepsilon^{\beta}) + \varepsilon^{\beta_2} \varphi^{(2)}(x_1 / \varepsilon^{\beta}, x_2 / \varepsilon^{\beta}) \quad (32)$$

and the supplementary condition holds :

$$\alpha_2 = \alpha_1 - \frac{1}{2}\beta + \beta s \quad (33)$$

5.3. Complementary matching using path-independent integrals.

The problem unknowns are $(\alpha_1, \alpha_2, \beta_1, \beta_2, \beta)$ and considerations about dominant terms at each scale allow us to determine four relations (14,19,27,33). The missing relation will be built up starting from energy considerations. It is well known that for HRR fields [9,10] the crack-tip fracture behaviour may be characterized by a Γ path-independent line integral, where Γ is a line circumscribing the crack tip :

$$J = \int_{\Gamma} (\omega n_1 - \sigma . n \frac{\partial u}{\partial x_1}) \, ds \quad (34)$$

where ω is the material strain energy density and n the outer normal to the line Γ. For a steadily moving crack under creep conditions, a similar path-independent has been offered [11,12] :

$$C^* = \int_{\Gamma} (\omega n_1 - \sigma . n \frac{\partial u}{\partial y_1}) \, ds \quad (35)$$

Developing the two integrals, respectively for the far and the near crack tip fields, the following relations hold :

$$\begin{cases} J = \varepsilon^{(n+1)\alpha_1} K_1^{n+1} I \\ C^* = \varepsilon^{2\beta_1 - \beta} K_{III}^2 \end{cases} \quad (36)$$

In the transition area, the integral values have to coincide, so that :

$$2\beta_1 - \beta = (n+1)\alpha_1 \quad (37)$$

5.4. Summary of the results.

The equations (14,19,27,33,35) may be summarized :

$$\begin{cases} \delta - \beta_1 + \beta_2 = 0 \\ \alpha_2 + \alpha_1(n-2) - 1 = 0 \\ \beta_1 = \alpha_1 + \beta s, \qquad with \quad s = \dfrac{n}{n+1} \\ \alpha_2 = \beta_2 - \beta p, \qquad with \quad p = \dfrac{n+2}{n+1} \\ 2\beta_1 - \beta = (n+1)\alpha_1 \end{cases} \quad (38)$$

with $\delta = \beta\,(n-2) + \beta_1(1-n) + 1 < 0$

which leads to the solutions :

$$\begin{cases} \beta = \beta_1 = \dfrac{(n+1)}{(n-1)} \\ \alpha_1 = \dfrac{1}{(n-1)} \\ \alpha_2 = \dfrac{1}{(n-1)} \\ \beta_2 = \dfrac{n+3}{(n-1)} \end{cases} \quad (39)$$

The parameter β depends on the hardening coefficient. For $\beta = 1$, no zoom is available (this is the case of the Hui-Riedel analysis) so that the connection between the remote fields and the viscous fields is impossible (unless $n < 3$). When $n \to \infty$ (perfect plasticity), $\beta \to 1$, there is no matching again, and therefore an autonomous solution, but in an asymptotic way, which is natural because the material yields without supplementary loading.

6. Conclusions and outlines.

The matched asymptotic expansion method affords to connect the H.R.R. far fields and the fields near a crack tip steadily moving under creep conditions, as described in the Hui-Riedel analysis. The space variable magnifying designed by ε^{β} allows to adjust the viscous dominant area size with respect to the crack velocity and the material properties. The Hui-Riedel analysis is a particular case where no zoom is used ($\beta = 1$). A significant work remains to achieve a complete solution setting up. A further step in the analysis is to used this scaling method with the time variable, so as to break the assumption $\frac{\dot{a}}{B\mu^{n}} << 1$. The study must be also completed by the angular functions resolve.

References

1. C.Y. Hui, H. Riedel, The asymptotic stress and strain field near the tip of a growing crack under creep conditions, Int. J. of Fracture Vol. 17, N° 4, pp. 409-425, 1981.
2. H.D. Bui, Fracture Mechanics, Inverse problems and solution, Springer Verlag 2006.
3. W. Yang, L.B. Freund, An analysis of antiplane shear crack growth in a rate sensitive elastic-plastic material, Int. J. of Fracture, 30, pp. 157-174, 1986.
4. T.C. Chang, C.H. Popelar, G.H. Staab, Creep crack growth in an elastic-creeping material. Part I: mode III, Int. J. of Fracture, 33, pp. 17-30, 1987.
5. T.M. Edmunds, J.R. Willis, Matched asymptotic expansions in nonlinear fracture Mechanics_I. Longitudinal shear of an elastic perfectly-plastic specimen, J. Mech. Phys. Solids, Vol 24, pp. 205-223, 1976.
6. R. Abdelmoula, J.-J. Marigo, The effective behaviour of a fiber bridged crack, Journal of the Mechanics and Physics of Solids, Volume 48, Issue 11, Pages 2419-2444, 2000.
7. D. Leguillon, R. Abdelmoula, Mode III near and far fields for a crack lying in or along a joint, International Journal of Solids and Structures, Volume 37, Issue 19, Pages 2651-2672, 2000.
8. M. Van dyke, Perturbation Methods in Fluid Mechanics. Academic Press, New York, 1964.
9. J.W. Hutchinson, Singular behaviour at the end of a tensile crack in a hardening material, J. Mech. Phys. Solids, Vol 16, pp. 13-31, 1968.
10. J.R. Rice, G.F. Rosengren, Plane strain deformation near a crack tip for a power law hardening material, J. Mech. Phys. Solids, Vol 16, 1968.
11. R. Riedel, Fracture at high temperatures. Springer-Verlag, 1987.
12. G.A. Webster, R.A. Ainsworth, High temperature component life assessment. Chapman & Hall, 1994.

The Mechanical Fracture Characterization of Non-Linear Flexible Ceramics Using Digital Image Correlation

Younes Belrhiti [1, 2], Ion Octavian Pop [1*], Pascal Doumalin [3], Jean Christophe Dupre [3], Thomas Auer[4], Dietmar Gruber[4], Harald Harmuth[4], Marc Huger [1, 2], Thierry Chotard [1, 2]

[1] GEMH, CEC, Université de Limoges 12 rue Atlantis, 87068 Limoges Cedex, France

[2] SPCTS UMR CNRS 7315, CEC, 12 rue Atlantis, 87068 Limoges Cedex, France

[3] Institut Pprime, CNRS, Université de Poitiers, 11 Boulevard Marie et Pierre Curie, 86962 Futuroscope Chasseneuil Cedex, France

[4] Chair of Ceramics, University of Leoben, 8700 Leoben, Austria

* Corresponding author: ion-octavian.pop@unilim.fr

Abstract During their application, refractory materials are submitted to several thermal shock attacks. That is why; improving their thermal shock resistance has a great importance and can enhance their lifetime. This characteristic is directly related to strains to rupture.

The non-linear mechanical behavior which characterizes specific developed ceramics, and is a consequence of their micro-cracked microstructure, leads to the increase of their strain to rupture level. This limit allows a better resistance to thermal shock solicitations.

Magnesia spinel materials are good candidates to characterize such non-linear mechanical behavior dependent on their microstructure. This non linearity is due to the presence of micro-cracks network. Indeed, mechanical behavior can vary from a fragile one to a large non-linear one according to the degree of micro-cracking present within the material.

In this paper, to investigate the crack propagation and the non-linear mechanical behavior of this material, wedge splitting test was used and coupled to digital image correlation technique. Results underline the influence of the addition of spinel on the non-linear mechanical behavior by comparing the non-linear mechanical behavior of magnesia spinel with pure magnesia. Besides, results clarified also the crack propagation mechanisms which are specific to these heterogeneous materials.

Keywords Magnesia spinel, Flexibility, Digital image correlation, Crack branching

1. Introduction

Due to their properties, pure magnesia and magnesia spinel materials showed a great interest for commercials and researchers [1-4]. Pure magnesia bricks are known by their resistance to corrosion and their relatively low thermal shock resistance. Besides, the incorporation of spinel improves the thermal shock resistance and can extend to three times longer service life of cement rotary kiln. Indeed, the addition of spinel, leads to a better adaptability of the material to severe solicitations generated during high and quick temperature variations. Even if their process of elaboration can affect the economy, but they still preferable to magnesia chromite refractories which have nearly the same properties such as their high resistance against thermal shock damage, erosion and corrosion but are not recommended due to the toxicity of waste refractories containing chrome.

The behavior of magnesia spinel is related to their microstructure and especially to the difference

between the thermal expansion of magnesia and spinel which is behind the development of micro-cracks around the spinel grains and can prevent crack propagation generated by thermal shock [5-6]. Moreover, their microstructure induces a significant non-linear stress-strain mechanical behavior allowing a high strain to rupture, high fracture energy and as a consequence improves their thermal shock resistance. It has been reported that micro-cracking caused by the addition of spinel reduces both strength and stiffness, and affect the fracture behavior [7]. Both the knowledge of the mechanisms initiating such behavior and the possibility to characterize those in the best accurate way are essential.

From these considerations, this study is a part of a work aiming to understand the relationship between microstructure and the non-linear mechanical behavior of magnesia-spinel materials and compared to pure magnesia materials.

The fracture characterization is done using wedge splitting test (WST) which affords stable crack propagation [8-11].

To assess to strain fields on the surface of the material, digital image correlation (DIC) technique has been chosen. This full-fields practical and effective tool for quantitative deformation measurement of a planar sample surface is now widely accepted and commonly used in the field of experimental mechanics. This non-contact optical method directly provides full-fields strains by comparing the digital images of the sample's surface obtained before and during deformation [12-14]. Using DIC, the propagation of the crack was studied thanks to kinematic fields approach in terms of strains. It allows highlighting the "crack branching" phenomenon due to the particularity of the microstructure of magnesia spinel materials.

2. Experimental

2.1. Materials

Pure magnesia and magnesia 15%-spinel (MSp) used in this study were elaborated from different grain distribution of industrial magnesia with low iron content (fines<0.1 mm ; 0-1 mm ; 1-3 mm ; 3-5 mm) and additional sub-stoichiometric spinel (1-3 mm) in the case of MSp. Spinel grains replaced the same content of magnesia aggregates having the same size.

Their elaboration was done using a maximum pressure of 140MPa and a maximum firing temperature of 1600°C.

Due to the thermal expansion mismatch existing between the magnesia matrix ("the whole material excepting spinel inclusions") and the spinel inclusions (α_{MgO}=13.3 x 10^{-6} K^{-1} and $\alpha_{MgAl2O4}$=8.9 x 10^{-6} K^{-1}), it appears that there are some micro-cracks around the spinel inclusions. These micro-cracks appear during the cooling stage of the process conferring the material a "thermally damaged" character [.

2.2. Wedge Splitting Test

A more recent and widely accepted test, which has been used frequently for materials with coarse microstructures, is the method patented by Tschegg under the name "wedge splitting test". This technique is being used by a numerous research centers and universities, as well as by

manufacturers of refractories.

As shown in figure 1a the WST consists of opening a crack using a wedge. The principle of this test is to apply a vertical force (F_v) received from the device which is transformed in a much higher horizontal force (F_H) causing a symmetrical opening mode of the crack (Fig.1b). Samples were equipped with a groove in order to apply the splitting load and a starter notch. The specimen geometry and dimensions are illustrated in fig.1a.

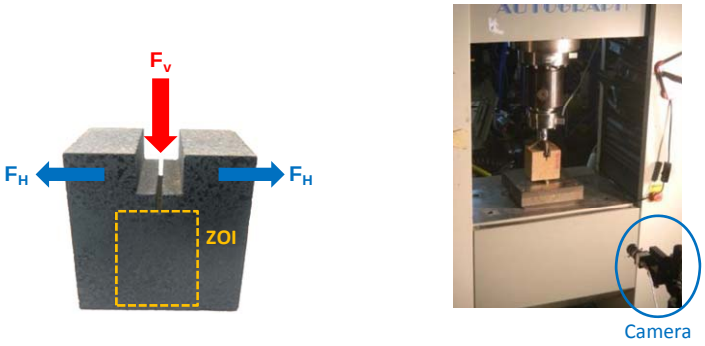

- a - **- b -**

Figure 1: The principle of wedge splitting test with sample's geometry (a) and image acquisition setup (b).

Since the thermal shock resistance of these materials has to be improved, the brittleness of these materials has to be reduced and the deformation before cracking has to be higher by modifying the microstructure of the refractory. In fracture mechanics, the fracture energy is one parameter that characterizes the fracture strength of the material.

Then, from the experimental data in terms of load-displacement, the specific fracture energy $\mathbf{G}_f$ ($N.m^{-1}$) is defined as the mean work per unit of projected fracture area required to propagate a crack, and represented by the sum of distinct energies consumed during the crack propagation process. $\mathbf{G}_f$ is calculated using equation (1).

$$G_F = \frac{1}{A} \cdot \int_0^{\delta_{max}} F_H \cdot d\delta_H \qquad (1)$$

Where A is the crack area, F_H is the horizontal force and δ_H is the horizontal deformation. This specific fracture energy is calculated for δ values from zero up to the displacement δ_{max} corresponding to 10% of the maximum load.

The horizontal force (F_H) is calculated from the vertical force (F_v) neglecting any friction effects using the equation (2).

$$F_H = \frac{F_v}{2 \cdot \tan(\alpha / 2)} \qquad (2)$$

Where α is the wedge angle, which was 19.5° in this investigation. The fact that (F_H) is much higher than (F_v) reduces the load applied on the machine's frame and storing less elastic energy in it and helping the propagation of the crack.

Another mechanical property of material estimate from the WST is the nominal notched tensile

strength (σ_{NT}), which represents the stress at the point of beginning of rupture, is calculated by the equation (3).

$$\sigma_{NT} = \frac{6 \cdot y \cdot F_{H,max}}{b \cdot h^2} + \frac{F_{H,max}}{b \cdot h} \quad (3)$$

Where b (mm), h (mm) are sample's dimensions and y (mm) is the distance between $F_{H,max}$ and the middle of h.

In addition to the experimental setup, a 8-bits CMOS camera (1600 x 1900 pixels^2) used to record images is placed in front of the speckled surface in order to perform optical measurements thanks to digital image correlation (Fig 1b). This will stress crack growth during mechanical tests and the strain state around the crack tip. The acquisition frequency was 1 image per second.

2.3. Digital image correlation

The damage level neighborhood to the crack tip and the crack advancement are estimated from the strain cartographies obtained by digital image correlation (DIC). This full fields optical method is based on the analysis of successive digital images of a same sample during a mechanical test. The displacement fields are obtained by measuring the degree of similarity of series of subsets between the image corresponding to an unloaded state and the deformed image recorded during the test. The zone of interest, on which the calculation is done, is represented in figure 1a. Each pixel of these images stores a grey level value due to a pattern at the surface. To avoid ambiguities in the similarity process a random distribution of grey levels can be used called speckle pattern. This pattern can be the natural texture of the specimen surface or artificially made by spraying black and/or white paints. As an example for sample's surface preparation, a black opaque paint layer is deposited on the surface of sample then dried. After that, white speckles will be carefully projected on using spray paint.

The used DIC process consists in calculating displacements and strains on specific points several subsets which constitute a grid. The principle of this technique is explained in figure 2

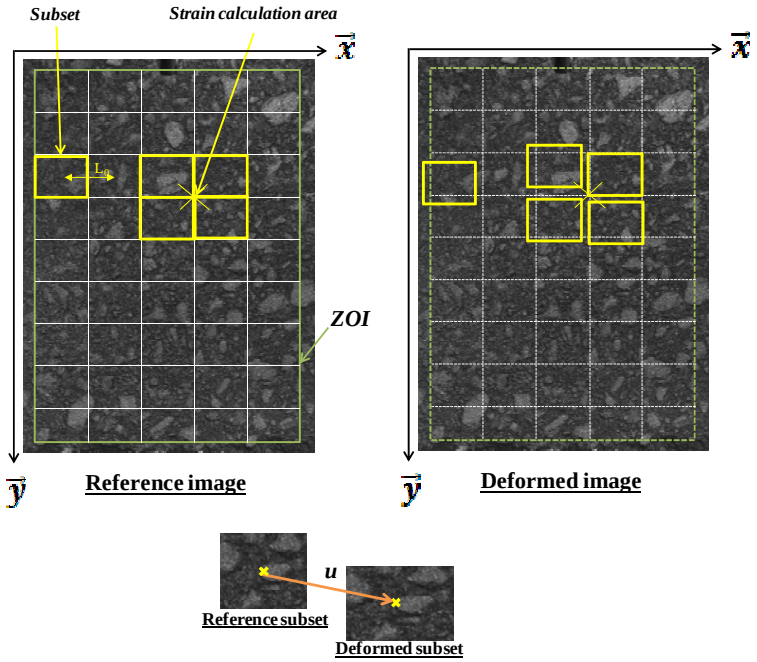

Figure 2: The principle of digital image correlation

3. Results

3.1. Mechanical properties

Figures 3, 4 represent the non-linear load-deflection curves of pure magnesia and magnesia spinel materials obtained by wedge splitting test.

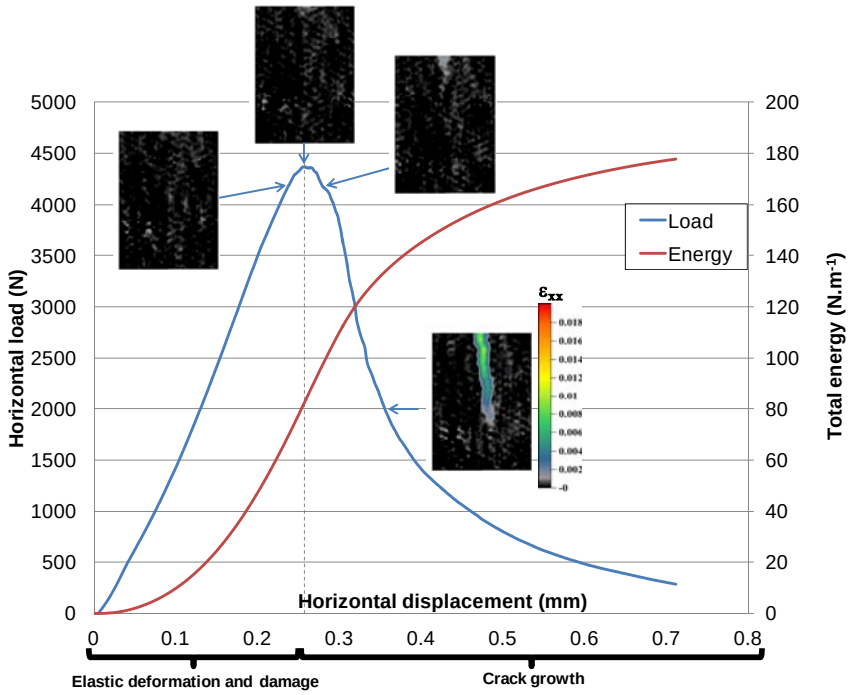

Figure 3: Horizontal load-displacement curve and total energy of pure magnesia material obtained thanks to

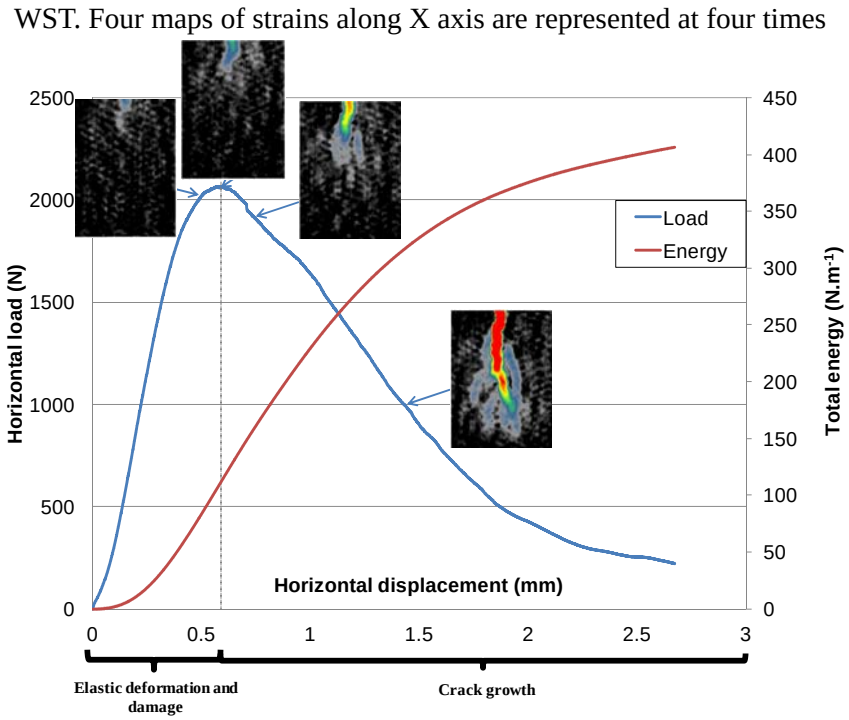

Figure 4: Horizontal load-displacement curve and total energy of magnesia spinel material obtained thanks to WST. Four maps of strains along X axis are represented at four times

The pure magnesia material presents a non-linear behavior (rather small) before the peak with a significant post-peak region and a high strain to rupture. It exhibits a much higher maximum load corresponding to the crack initiation, a lower strain at the peak, and a thinner peak due to a smaller post-peak region in comparison with MSp. This behavior is not common at room temperature for homogeneous ceramic materials. A possible explanation of this behavior is the coarse grain size (1-3 mm and 3-5 mm) distribution of this material which was reported to potentially improve fracture and thermal shock resistance of magnesia refractories.

Besides, load-deflection curve of magnesia spinel presents a non-linear mechanical behavior up to the peak with a significant post-peak region and residual strain when unloading. Moreover, the increase of spinel content seems mainly to lower the maximum load but does not influence so much the end of the post-peak region since it is close to pure magnesia. By considering the very beginning of this curve, the addition of spinel, and therefore, the thermal damage introduction, allows to enhance the non-linearity of the mechanical behavior. This material has a higher strain and a low mechanical resistance in comparison with pure magnesia; this can be explained by the higher volume of microcracks in the case of magnesia spinel developed during cooling and toughening mechanisms occurring around the crack, especially in the following wake region, which may increase the resistance to crack propagation. The higher volume of microcracks in the case of magnesia spinel is due to the difference between the thermal expansion coefficient of magnesia (α_{MgO}=13.3 x 10^{-6} K^{-1} and $\alpha_{MgAl2O4}$=8.9 x 10^{-6} K^{-1}) which leads to the apparition of microcracks around the grain of spinel.

In the two cases, the mechanical behavior of these materials is characterized by three phases, one corresponding to the elastic behavior, a second one characterized by the elastic behavior coupled

with damage (elastoplasticity), and the last one corresponding to the crack growth.
Only the main macrocrack can be detected by the naked eye, but the early apparition of the macrocrack, as well as all the stressed microcracks pre-existing around the middle plane, is not really visible. That is why; digital image correlation has been used in order to obtain the strain fields so as to analyze the crack propagation and the presence of damage process.
Thanks to digital image correlation, the evolution of the strains along X-axis has been represented for different instants corresponding to different loading states (fig 3, 4). These maps correspond to the zone of interest defined in figure 1a .According to DIC principle, this area is subdivided using subsets of 32 x 32 pixels^2 with a gap of 8 x 8 pixels^2 and a scale factor of 0.067295 mm/pixels. In the two materials, we notice before reaching $F_{H,max}$ the development of the damage zone in the neighbor of the crack tip. The initiation and the propagation of the crack take place after this critical load ($F_{H,max}$). Due to the higher ductile behavior of magnesia spinel, the damaged zone in the neighbor of the crack tip is larger than the case of pure magnesia. Besides, this zone is developing and moving with the crack tip advancement. This confirms the complexity of crack growth in heterogeneous materials which feature many physical mechanisms such as crack branching phenomenon.
Nominal notched tensile strength and specific fracture energy for each sample have been calculated thanks to the equations (2) and (3) and represented in Table 1.

Table 1: Nominal notched tensile strength and specific fracture energy values

	σ_{NT} (MPa)	G_F (N.m^{-1})	G_F/σ_{NT} (mm) x 10^{-3}
Pure MgO	14.36	206.50	14.39
	14.38	182,00	12,66
MgO-15% spinel	6.65	361.00	54.25
	6.75	396.00	58.63

These intrinsic fracture parameters introduced in table 1 stress the nominal notched tensile strength shows that mechanical resistance decreases whereas the energy stresses that the fracture resistance increases with the increase of the spinel rate. The ratio G_F/σ_{NT} indicates the brittleness of the material: the more brittle material is, the lower value of the ratio is.
Figures 10 and 11 represent also the evolution of the total energy during the test. The total energies are deduced from the total area under the horizontal load-displacement curves obtained by wedge splitting test divided by the section of fracture and represent the sum of the elastic energy and dissipated one. The curves confirm that during the test, the total energy is higher in the case of magnesia-15% spinel than pure magnesia. The dissipated energy is mainly due to the dense network of microcracks created during the test.

4. Conclusion

The impact of microstructure on the mechanical behavior has been clarified. Indeed, studying mechanical behavior is important to have an idea on the thermal shock resistance of materials. In

this paper, mechanical behavior of magnesia spinel products were analyzed and compared to pure magnesia. The difference between mechanical behaviors of these materials is due to the development of the network of micro-cracks in the case of magnesia-spinel materials. This is a consequence of the thermal expansion mismatch between magnesia and spinel grains. To study the mechanisms of micro-cracking and the influence of damage on the non-linearity, wedge splitting test has been used and coupled to digital image correlation. Indeed, by the calculation of mechanical properties such as nominal notched tensile strength and fracture energy in addition to the measurement of strain fields, the influence of the addition of spinel is clarified. In fact, it was confirmed that the addition of spinel influences clearly mechanical properties and the non-linearity of the mechanical behavior due to the presence of high level of damage induced by micro-cracks as shown thanks to digital image correlation. This microstructure optimization allows an increase of strain to rupture, which is considered as a key parameter for improving thermal shock resistance of refractories.

Acknowledgements

This work is a part of a global research program engaged through collaboration between the University of Leoben (Austria) and GEMH ENSCI (Limoges, France) thanks to the F.I.R.E network. The authors are thankful to RHI AG for having provided the materials.

References

[1] WD Kingery. Factors Affecting Thermal Stress Resistance of Ceramic Materials. Journal of the American Ceramic Society, 38(1955) 3–15.
[2] DPH Hasselman. Elastic Energy at Fracture and Surface Energy as Design Criteria for Thermal Shock. Journal of the American Ceramic Society, 46(1963) 535–540.
[3] DPH Hasselman. Unified Theory of Thermal Shock Fracture Initiation and Crack Propagation in Brittle Ceramics. Journal of the American Ceramic Society, 52(1969) 600–604.
[4] C Aksel, B Rand, FL Riley, PD Warren. Thermal shock behaviour of magnesia–spinel composites. Journal of the European Ceramic Society, 24(2004) 2839-2845.
[5] R Grasset-Bourdel, A Alzina, M Huger, D Gruber, H Harmuth, T Chotard. Influence of thermal damage occurrence at microstructural scale on the thermomechanical behaviour of magnesia–spinel refractories. Journal of the European Ceramic Society, 32(2012) 989-999.
[6] C Aksel, B Rand, FL Riley, PD Warren. Mechanical properties of magnesia-spinel composites. Journal of the European Ceramic Society, 22(2002) 745-754.
[7] C Aksel, RW Davidge, PD Warren, FL Riley. Mechanical Properties of Model Magnesia-Spinel Composite Materials. Key Engineering Materials, 132-136(1997) 1774-1777.
[8] I Löfgren, H Stang, JF Olesen. The WST method, a fracture mechanics test method for FRC. Materials and Structures, 41(2007) 197-211.
[9] H Harmuth, K Rieder, M Krobath, E Tschegg. Investigation of the nonlinear fracture behaviour of ordinary ceramic refractory materials. Materials Science and Engineering: A, 214(1996) 53-61.
[10] XZ Wang, ZC Xu, Z Bi, H Wang. Experimental Investigation on Relative Crack Length For Fracture Toughness of Concrete. Advanced Materials Research,146-147(2010) 1524-1528.

[11] E Brühwiler, FH Wittmann. The wedge splitting test, a new method of performing stable fracture mechanics tests. Engineering Fracture Mechanics, 35(1990) 117-125.
[12] B Wattrisse, A Chrysochoos, J-M Muracciole, M Némoz-Gaillard. Analysis of strain localization during tensile tests by digital image correlation. Experimental Mechanics, 41(2001) 29-39.
[13] TC Chu, WF Ranson, MA Sutton. Applications of digital-image-correlation techniques to experimental mechanics. Experimental Mechanics, 25(1985) 232-244.
[14] Y Belrhiti, A Gallet-Doncieux, A Germaneau, P Doumalin, JC Dupre, A Alzina, P Michaud, O Pop, M Huger, T Chotard. Application of optical methods to investigate the non-linear asymmetric behavior of ceramics exhibiting large strain to rupture by four-points bending test, 32(2012) 4073-4081.

On fracture toughness J_{IC} testing of martensitic stainless steels

Jianqiang Chen[1,*], Yves Verreman[1], Jacques Lanteigne[2]

[1]École Polytechnique de Montréal, C.P.6079, succ. Centre-ville, Montréal (Québec), Canada H3C 3A7

[2]Hydro-Québec, Institut de Recherche, 1800, boul. Lionel-Boulet, Varennes (Québec), Canada, J3X 1S1

* Corresponding author: jianqiang.chen@polymtl.ca

Abstract The objective of this research is to determine the best conditions to measure the fracture toughness of an ASTM A-743 grade CA-6NM stainless steel used in hydraulic turbine runners. The tests are performed on 12.7 mm and 25.4 mm thick compact tension (CT) specimens. Experimental results show that only the thicker specimen gives a valid test according to ASTM E1820 standard. However, very close crack initiation J_{IC} values are obtained with thinner specimens provided they are side-grooved. Thickness effect is exhibited both on the resistance curve *J-Δa* and the crack front during the stable crack propagation.
This paper is documented with both macroscopic and microscopic descriptions of fracture surfaces in the stable crack extension region.

Keywords J_{IC} fracture toughness, CA-6NM steel, CT specimen, thickness constraint effect

1. Introduction

The use of high-strength martensitic stainless steels in hydraulic turbine runners allows reduction in weight and cost of some components such as rotors, pumps and compressors. Designers take advantage of the high strength of these steels, which are also very little sensitive to corrosion and to cavitation damage [1-3]. Conventional turbine runners design is based on a so-called static stress design approach, which limits the Von Mises stress at operating condition to a prescribed fraction of the material yield stress (eg. $\sigma_e < 1/3\ \sigma_{YS}$). However, this approach does not guarantee reliability of runners as many other variables other than static stress can cause failure [4-5]. Welding blades, crown and band together unavoidably involves the presence of weld defects. It is not possible to detect accurately or size all defects with non-destructive inspection during the turbine runners manufacturing process, and due to economic reasons they cannot all repaired. Moreover, some defects can possibly be tolerated based on Fracture Mechanics assumptions for the whole runner lifetime (70 years). Hence, to determine a maximum allowable defect size, accurate knowledge of material properties and in particular fracture toughness need to be evaluated.

Measurement of fracture toughness K_{IC} is based on Linear-Elastic Fracture Mechanics (LEFM) [6-7]. It has been extensively used for high-strength and relatively brittle materials such as metals used in the aerospace industry and ceramics. However, the low carbon martensitic stainless steels used in hydraulic turbine runners manufacturing are in the range of immediate-strength and high toughness engineering materials. In order to get a valid K_{IC} test under small-scale yielding and plane-strain conditions, the required specimen can be as big as 300 mm in thickness for a compact tension specimen which is difficult to be tested in a common laboratory. Moreover, it is also impossible to fabricate steel in such dimension with homogeneous metallurgical properties (microstructure and texture) through the whole thickness. In this case, an alternative J_{IC} test method based on Elastic-Plastic Fracture Mechanics (EPFM) can be used [8-9]. J_{IC} test can be performed on a relatively small laboratory specimen. This testing method, firstly developed for the engineering materials used in nuclear power plants, is based on Rice's *J*-integral concept [10].

The objective of the present work is to determine the best conditions to measure the fracture

toughness of ASTM A-743 grade CA-6NM stainless steel used in hydraulic turbine runners. For this purpose, fracture toughness J_{IC} tests are performed on smooth and side-grooved compact tension (CT) specimens of different thicknesses. Tests are carried out based on ASTM E1820 guide lines [11]. The investigated material and the experimental technique are first presented. Results of mechanical tests are analyzed and compared; fractographic examinations are also made in the crack growth regions in order to interpret the fracture mechanisms of the tested steel.

2. Material studied

The experimental material studied in this work is a low carbon CA-6NM steel (13Cr-4Ni martensitic stainless cast steel). Table 1 gives the chemical composition limits of the tested material as required by ASTM A-743 standard [12]. Heat treatment consisted of austenitizing at 955 ^{o}C followed by air cooling. Then, a tempering was performed between 565^{o}C and 620^{o}C allowing the fresh martensite to temper, giving rise to a beneficial softening corresponding to reduce hardness but increase ductility. The resulting microstructure is mainly tempered martensite with about up to 15% reformed austenite. The basic mechanical properties have been characterized in an early study [1]. For brevity, only tensile properties are given here. The measured yield strength σ_{YS} is 763 MPa, the tensile strength σ_{TS} is 837 MPa and the elongation is 27%. All measured mechanical properties meet ASTM A-743 standard requirements.

Table 1. Chemical composition limits of tested steel (wt.%)

	C	Mn	Si	S	P	Cr	Ni	Mo
CA-6NM	0.03	0.57	0.37	0.02	0.02	12.68	4.03	0.67
ASTM A-743	0.06 max	1.0 max	1.0 max	0.03 max	0.04 max	11.5-14.0	3.5-4.5	0.4-1.0

3. Mechanical testing

Standard compact tension (CT) specimen according to the recommendations of ASTM designation E1820 is used. The geometry of J_{IC} test specimen (Figure 1) allows the measurement of load line displacement (LLD) by means of an extensometer. One 12.7 mm thick smooth specimen without side grooves was first tested. Then five side-grooved specimens were tested: two specimens with B = 12.7 mm (*B/W =1/4)* and three specimens with B = 25.4 mm (*B/W =1/2)*. Side grooves have each a depth of 10% of the gross thickness B. As the tested material is in a cast condition, there is no need to orientate it during machining. All tests were carried out at room temperature using partial unloading compliance method on a servo-hydraulic testing machine. The tests followed the guide-lines of the ASTM E1820 standard for the fracture toughness determination from a single specimen.

For the fatigue pre-cracking, two different procedures were assessed. First, four specimens were pre-cracked prior to the side-grooving operation as recommended by E1820 standard. The crack growth was followed by an optical microscope on specimen polished surfaces. Secondly, two other specimens were pre-cracked after the side-grooving operation, side grooves were machined at the same time as the specimens. In this case, the pre-cracking is monitored by a COD gage using elastic-compliance method. For all specimens, the pre-crack length is about 5 mm, providing an a_0/W value of 0.55. During pre-cracking, the loading ΔK is kept to 12 MPa$\sqrt{m}$ in order to limit the plastic zone size.

During the experiments, the specimens are subjected to about 20 loading/unloading cycles. The

unloading ratio is 10 % of actual maximum load. A representative experiment is shown in Figure 2 for a 12.7 mm thick side-grooved specimen. After the final unloading, the specimen was marked by heat tinting (450^{o}C for 1 hour). The initial and final crack lengths a_0, a_f are measured at 9 equally spaced locations on the broken specimens.

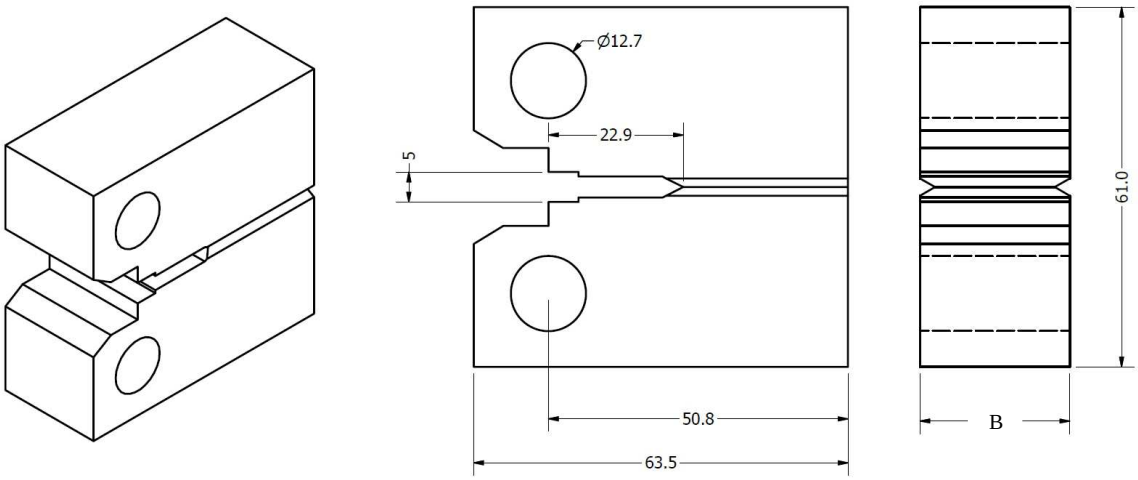

Figure 1. Compact tension J_{IC} specimen with side grooves (dimensions in mm); specimen gross thickness B is 12.7 mm or 25.4 mm; the side groove depth is $0.1B$ at each side.

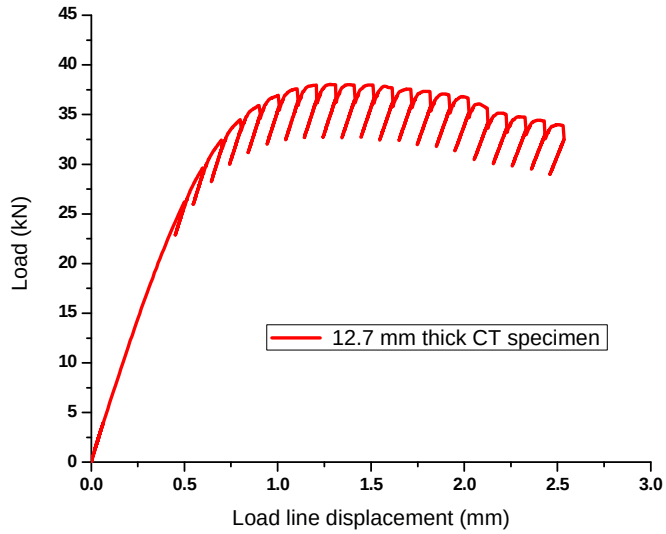

Figure 2. Load – load line displacement curve (10% unloading)

4. Results and discussion

4.1 Results

4.1.1 J_{IC} testing

Figure 3 shows a representative *J-Δa* curve obtained from the previous 12.7 mm thick side-grooved specimen. The blunting line is calculated from material tensile properties as following,

$$J = 2\sigma_Y \Delta a \tag{1}$$

$$\text{and} \quad \sigma_Y = \frac{\sigma_{YS} + \sigma_{TS}}{2}$$

The data points lie between the 0.15 mm offset line and 1.5 mm offset line parallel to the blunting line ($J = 2\sigma_Y \Delta a$) are used for regression line fitting. They can be represented by a power-law expression $J = A(\Delta a)^b$. The intersection point between the regression line and 0.2 mm offset line gives a candidate value J_Q which becomes J_{IC} provided that the validity requirements are satisfied.

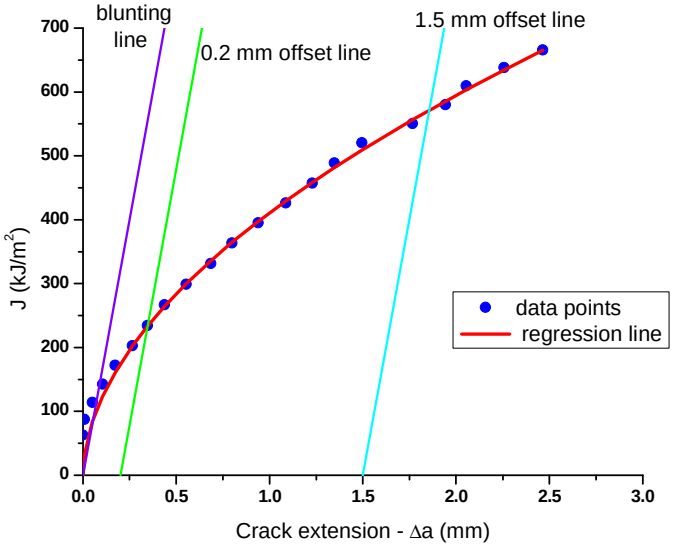

Figure 3. *J-Δa* curve for the 12.7 mm thick CT specimen

Then, K_{IC} can be estimated by

$$K_{IC} = \sqrt{\frac{EJ_Q}{(1-\nu^2)}} \tag{2}$$

where E is Young's modulus of the steel tested and ν is Poisson's ratio.

Table 2 gathers all test results on both 12.7 mm and 25.4 mm thick side-grooved specimens. For the smooth specimen (B = 12.7 mm) which was firstly assessed in the present study, no valid data point is found due to an extremely steep *J-Δa* curve. There is no intersection between the regression line and 0.2 mm offset line. So the testing result is not given here.

Table 2. Testing results of J_Q for CA-6NM steel

Specimen thickness (mm)	Test	J_Q (kJ/m^2)	dJ/da (MPa)	K_{IC} (MPa$\sqrt{m}$)
12.7	CT_05in_1	232	220	230
	CT_05in_2	280	210	252
25.4	CT_1in_1	256	128	241
	CT_1in_2	255	133	240
	CT_1in_3	286	124	255

As shown in Figure 4, there is little difference at the beginning of crack extension between 12.7 mm and 25.4 mm thick side-grooved specimens. Similar fracture initiation toughness J_Q values can be

obtained on both specimens. However, in the following crack growth region (Δa > 0.5 mm), thin specimen gives a steeper *J-Δa* curve and exhibits higher load carrying capacity than the thick sample. The tearing moduli *dJ/da*, which is more representative of crack propagation, is much higher for thin specimens than thick specimens (see Table 2).

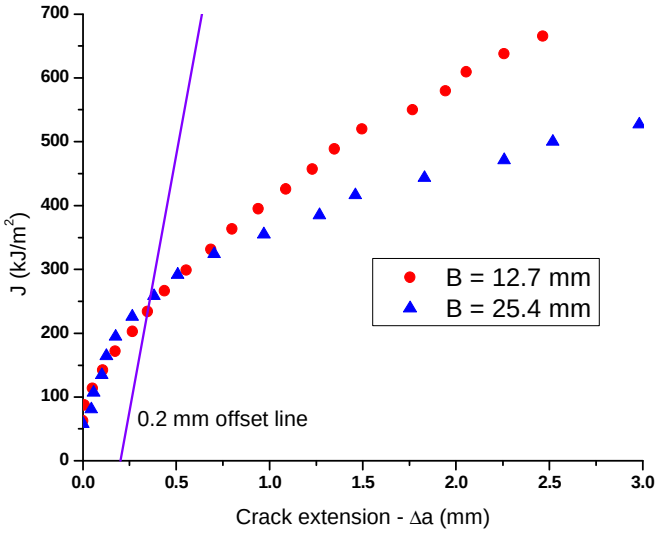

Figure 4. Effect of specimen thickness on *J-Δa* curve

4.1.2 Fractography

Fracture surfaces are firstly examined at the macroscopic scale on both 12.7 mm and 25.4 mm thick samples (see Figure 5). In the 12.7 mm thick smooth specimen (Figure 5a), strong crack tunneling is observed. There are no crack growths at both side surfaces of specimen while the crack advances more than 2 mm in the center section of the specimen. In the 12.7 mm thick side-grooved specimen (Figure 5b), crack tunneling is less pronounced, but the crack grows again faster in the center section of the specimen than near the specimen surfaces. As it is stated in section 9.1 of E1820 standard, such a test cannot be valid due to the strong crack front curvature. In the 25.4 mm thick side-grooved specimen (Figure 5c), crack grows with the same rate at the center of the specimen as at the two side surfaces. The crack extension front is nearly straight, and the test is valid according to E1820 standard. In the final ductile tearing (white part of Figure 5), we can also see that there is stronger lateral contraction in the thin specimen than in the thick one.

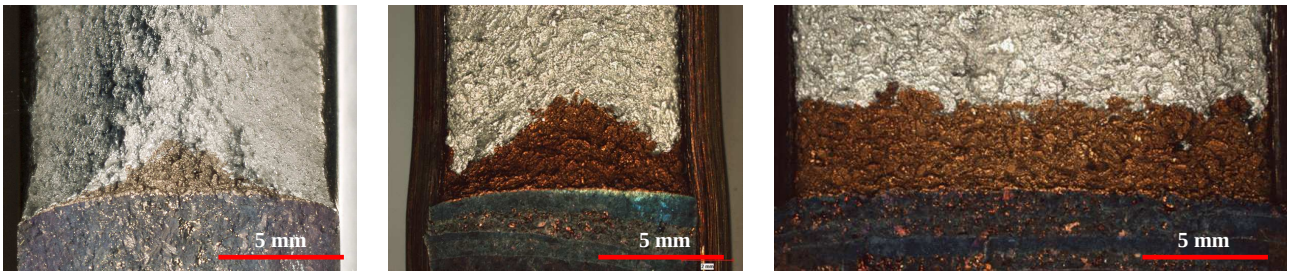

(a) (b) (c)

Figure 5. Fracture surface of broken specimens: (a) 12.7 mm thick smooth specimen, (b) 12.7 mm thick side-grooved specimen, (c) 25.4 mm thick side-grooved specimen. Crack front at the end of stable propagation was marked by heat tinting.

In order put into evidence the fracture mechanisms at microscopic scale, one 25.4 mm thick

side-grooved specimen was marked under fatigue instead of heat tinting after the final unloading. Broken sample was observed using scanning electron microscopy. In the stable crack extension region (Figure 6) void growth mechanism is dominant. Very large dimples can be seen, their size being about 20 μm. At a higher magnification (Figure 6b), the presence of inclusions in the bottom of dimples is clearly visible. It can be interpreted by the high stress triaxiality (plane-strain state) which triggers a fast void growth leading to formation of large dimples [13].

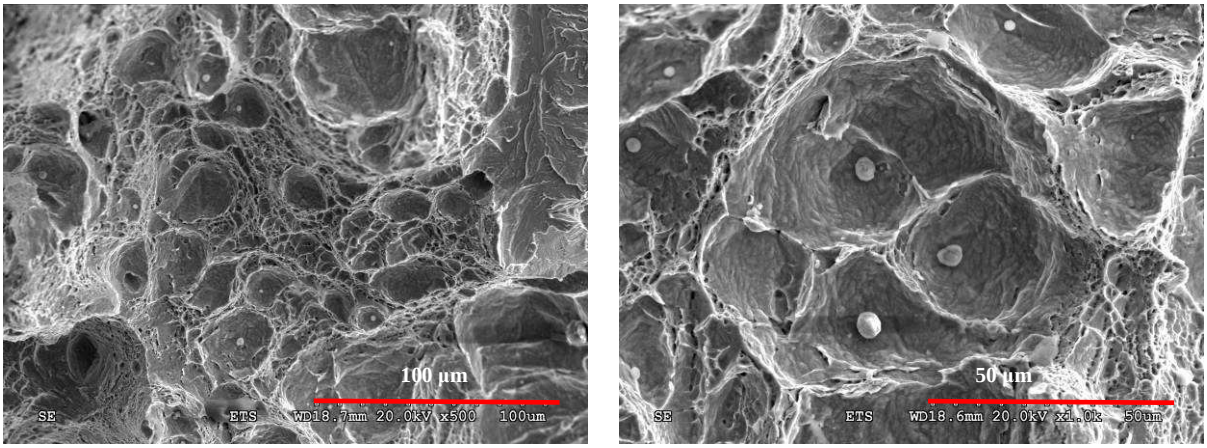

(a) (b)

Figure 6. SEM micrography of a broken specimen in the stable crack growth region

4.2 Discussion

4.2.1 Constraint effects

From the present study, experimental results show that the crack extension behavior is related to the variation of stress triaxiality across the specimen thickness. In 12.7 mm thick smooth specimen, strong crack tunneling is observed because of relatively low stress triaxiality and constraint level across the whole specimen thickness. And final fracture by ductile tearing or shearing can be seen on broken surfaces. In 12.7 mm thick side-grooved specimen, lateral constraint is increased by side grooving operations, and flat ductile fracture is observed. But the specimen is not thick enough to get a full constraint across the thickness and which caused a final curved crack front. In 25.4 mm thick side-grooved specimen, a perfectly straight crack front is obtained after stable crack extension. Because the side grooves promote practically uniform plane strain constraint along the crack front [14]. Similar results were reported in [15-18] for CT and SENB testing with various smooth and side-grooved specimen sizes.

Our investigations also show that the variation of stress triaxiality or thickness constraint leads to changes on the shape of *J-Δa* resistance curve after certain amount of crack extension. The slope of the *J-Δa* curve for the thin specimen is significantly steeper than the corresponding value for the thick specimen. In other words, thin specimen exhibits higher load carrying capacity (*dJ/da*) than thick specimen. It is known that the lateral constraint and average stress triaxiality increases with increasing specimen thickness. For thick specimen, the high stress triaxiality reduces the apparent ductility of the material by a faster void growth mechanism which is predominant as shown in Figure 6 in the previous section. While for thin specimen, the average stress triaxiality is lower and the lateral contraction is less constrained during the loading, so a relatively steeper resistance curve is generated.

4.2.2 Side-grooves and fatigue pre-cracking

Side-grooved specimen is recommended by E1820 when the compliance method of crack size prediction is used. One objective of using side-grooved specimen is to create a straight crack front to reduce the number of tests invalided by curved crack front. In this study, 0.2B side-grooved specimens were used after having an invalid test with a smooth specimen. In order to produce nearly straight fatigue pre-crack fronts, the pre-cracking is suggested to be performed prior to the side-grooving operations by E1820. However, this procedure is time consuming. The specimen needs to be polished on two surfaces in order to monitor the crack length with an optical microscope and the pre-cracked specimens have to be returned to the machine shop for side grooves machining. Moreover, the fatigue pre-cracking front is not straight. The crack grows faster in the center section of the specimen than near the specimen surfaces even with low pre-cracking load (ΔK = 12 MPa$\sqrt{m}$ in present work). As shown in Figure 7a, the crack measured on the specimen surfaces by microscopy is shorter than the real average crack length measured on the broken surface. This curvature probably results from slower crack growth under plane stress condition.

As mentioned earlier, two specimens with side grooves machined before the pre-cracking operations were also prepared. The crack growth is followed by a COD gage with the elastic compliance method. Experiments show a good agreement between calculated crack length by elastic compliance and the measured crack length on final broken specimens. With this procedure, polished surfaces are no longer needed and the side grooves are machined at the same time as the specimen itself. Time and machining cost can be saved. For the fatigue pre-cracking, due to a relative constant constraint level across the thickness, an approximately straight crack front is produced (Figure 7b).

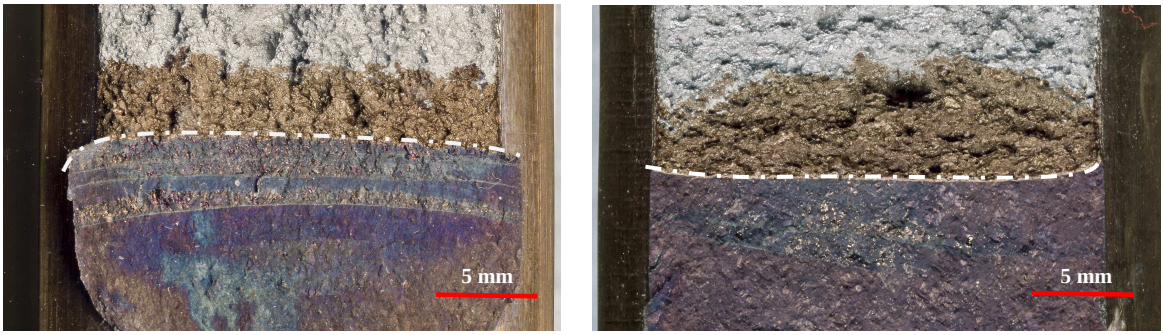

(a) (b)

Figure 7. (a) Fatigue pre-cracking performed before side grooves operation and (b) fatigue pre-cracking performed after side grooves operation. White dashed line: fatigue pre-cracking front.

5. Conclusions

J_{IC} fracture toughness testing was performed on CA-6NM martensitic stainless steel, the following conclusions are drawn:

1. Due to high toughness of the material, side-grooved specimen must be used in order to get a valid test according to ASTM E1820. Side grooves can prevent the development of crack tunneling and to maintain a relatively straight crack growth.
2. Crack growth exhibits a thumb-nail front for both 12.7 mm thick side-grooved CT specimens. It cannot be valid per ASTM standard due to the significant curvature of final crack front.

3. Valid tests are obtained with 25.4 mm thick side-grooved CT specimens with a straight crack extension front.
4. Both thin and thick specimens give very close *J* values at crack initiation (0.2 mm offset line). So, thin specimen can also be used if only crack initiation toughness is required. It is recommended that thicker specimen should be used if the plane strain *J*-resistance curve is required.
5. Side grooves can be machined before the pre-cracking; it can reduce the preparation time and machining delay and it gives a straight pre-cracking crack front. No significant difference was found on the fracture toughness testing as recommended by ASTM E1820 (pre-cracking before side grooving).
6. Fractography analysis shows that the void growth from inclusions is dominant in the crack extension region; large dimples are observed which can be explained by the high stress triaxiality of specimen.

Nomenclature

a	Crack length (mm)	b_0	Uncracked ligament length (mm)
Δa	Crack extension (mm)	σ_{YS}	Yield stress (MPa)
B	Specimen gross thickness (mm)	σ_{TS}	Ultimate tensile stress (MPa)
B_N	Specimen net thickness (mm)	E	Young's Modulus (GPa)
W	Specimen width (mm)	ν	Poisson's ratio
K	Stress intensity factor (MPa$\sqrt{m}$)	J	J-integral (kJ/m^2)
K_{IC}	Fracture toughness (MPa$\sqrt{m}$)	J_Q	Fracture toughness (kJ/m^2)

Acknowledgements

The authors thank Alstom Power Hydro, Hydro-Québec and National Research Council of Canada for financial support. The authors also wish to thank Carlo Baillargeon, Technologist at Hydro-Québec, for his experimental assistance in this study.

References

[1] J. Lanteigne, M. Sabourin, T. Bui-Quoc, D. Julien, The characteristics of the steels used in hydraulic turbine runners, 24th Symposium on hydraulic machinery and systems, Foz do Iguassu (2007).
[2] W.P. Casas, S.L. Henke, N. Novicki, Fracture toughness of CA6NM alloy, quenched and tempered, and of its welded joint without PWHT, Welding International 23 (2009), pp. 166–172.
[3] P. Blimes, C. Llorente, J. Perez Ipina, Toughness and Microstructure of 13Cr4NiMo high-strength steel welds, Journal of Materials Engineering and Performance 9(6) (2000) 609–615.
[4] M. Sabourin, B. Papillon, L. Mathieu, D. Julien, Francis runner fabrication process corner stone of power plant reliability , HydroVision, Montréal (2004).
[5] M. Sabourin, D. Bouffard, F. Paquet, Life prediction of hydraulic runner using fracture mechanics analysis, WaterPower XV, Chattanooga (2007).
[6] ASTM E399-09, Standard test method for linear-elastic plane-strain fracture toughness K_{IC} of metallic materials, American Society for Testing and Materials, 2009
[7] T.L. Anderson, Fracture Mechanics, Fundamentals and Applications, CRC Press, Taylor & Francis Group, 2005

[8] J.A. Begley, J.D. Landes, The J-integral as a fracture criterion, Fracture toughness, ASTM STP 514, American Society for Testing and Materials, 1972, pp. 1-23
[9] J.D. Landes, H. Walker, G.A. Clarke, Evaluation of estimation procedures used in J-integral testing, in: ASTM STP 668, American Society for Testing and Materials, 1979, pp. 266-287
[10] J.R. Rice, A path independent integral and the approximate analysis of strain concentration by notched and cracks, Journal of Applied Mechanics 35 (1968) 379–386.
[11] ASTM E1820-11, Standard test method for measurement of fracture toughness, American Society for Testing and Materials, 2011.
[12] ASTM A743-06, Standard specification for castings, iron-chromium, iron-chromium-nickel, corrosion resistant, for general application, American Society for Testing and Materials, 2006
[13] J.R. Rice, D.M. Tracy, On the ductile enlargement of voids in triaxial stress fields, Journal of Mechanics and Physics of Solids 17 (1969), pp. 210–217.
[14] C.F. Shih, H.G. deLorenzi, W.R. Andrews, Elastic compliance and stress-intensity factors for side-grooved compact specimens, International Journal of Fracture 13 (1977), pp. 544–548.
[15] E. Roos, U. Eisele, H. Silcher, Effect of stress state on the ductile fracture behavior of large-scale specimens, ASTM STP 1171, American Society for Testing and Materials, 1993, pp.41-63.
[16] P.S. Lam, Y. J. Chao, X.K. Zhu, R.H. Sindelar, Determination of constraint-modified J-R curves for carbon steel storage tanks, Journal of Pressure Vessel Technology 125 (2003) 136–143.
[17] X. K. Zhu, J.A. Joyce, Review of fracture toughness (G, K, J, CTOD, CTOA) testing and standardization, Engineering Fracture Mechanics 85 (2012) 1-46.
[18] B. Tanguy, T.T Luu, G. Perrin, A. Pineau, J. Besson, Plastic and damage behavior of a high strength X100 pipeline steel: Experiments and modeling, International Journal of Pressure Vessels and Piping 85 (2008) 322–335.

Numerical Modeling and Analysis of Dynamic Crack Propagation in Rubber

Elsiddig Elmukashfi[1,*], **Martin Kroon**[1]

[1] Department of Solid Mechanics, Royal Institute of Technology, Osquars backe 1,
SE-100 44 Stockholm, Sweden
* Corresponding author: elsiddig@kth.se

Abstract Dynamic crack propagation in rubber is modeled and analyzed numerically using the finite element method. The problem of a suddenly initiated crack at the center of stretched sheet is studied under plane stress conditions. A nonlinear finite element analysis using implicit time integration scheme is used. The bulk material behavior is described by finite-viscoelasticity theory and the fracture separation process is characterized using a cohesive zone model with a bilinear traction-separation law. Hence, the numerical model is able to model and predict the different contributions to the fracture toughness, i.e. the surface energy, viscoelastic dissipation, and inertia effects. The separation work per unit area and the cohesive strength has been parameterized, and their influence on the separation process has been investigated. A steadily propagating crack is obtained and the corresponding crack tip position and velocity history as well as the steady crack propagation velocity are evaluated and compared with the experimental data. A minimum threshold stretch of 3.0 is required for crack propagation. The numerical model is able to predict the dynamic crack growth such that the strength and the surface energy vary with the crack speed.
Keywords rubber, crack, viscoelasticity, cohesive zone, dynamic fracture

1. Introduction

Elastomers are important materials in many engineering applications; consequently a wide variety of elastomeric materials is used in several products, e.g., tires, springs, dampers, gaskets, bearings, oil seals, etc. Fracture mechanics in elastomers is of great importance in the design process and it is fundamental in some applications such as adhesion technology, elastomers wear, etc.

Dynamic crack propagation in rubber-like materials has been investigated both theoretically and experimentally but the field is relatively undeveloped compared with brittle materials [8, 12, 21, 28]. Generally, the dynamic fracture in rubber shows remarkable deviation from the dynamic fracture theories for brittle materials, e.g. the cracks propagate at speeds greater than the speed of sound without branching and at high stretch levels oscillatory crack propagation results.

The fracture energy of rubber is the sum of different contributions [20, 22, 23]: the surface energy required to create new crack surfaces, the energy dissipated in the viscoelastic processes around the crack tip, and the inertia effects that contribute in the case of dynamic fracture. Furthermore, the separation process is accompanied with a viscoelastic dissipation process to which takes place in the crack tip vicinity [2].

The theoretical treatment of the problem of crack propagation in rubber-like solid reveals that the region around the crack tip can be divided into three different zones, determined by the relaxation spectrum, as shown in Fig. 1a [10]. These regions are: glassy region occurs at the closest to the crack tip, rubbery region occurs far from the crack tip, the viscous dissipation region that is located between these two regions. Depending on the relaxation spectrum and crack propagation velocity, the glassy and viscous dissipation regions may vanish, e.g. in the case of carbon-filled natural rubber glassy zones are not expected to exist, while viscous dissipation is expected.

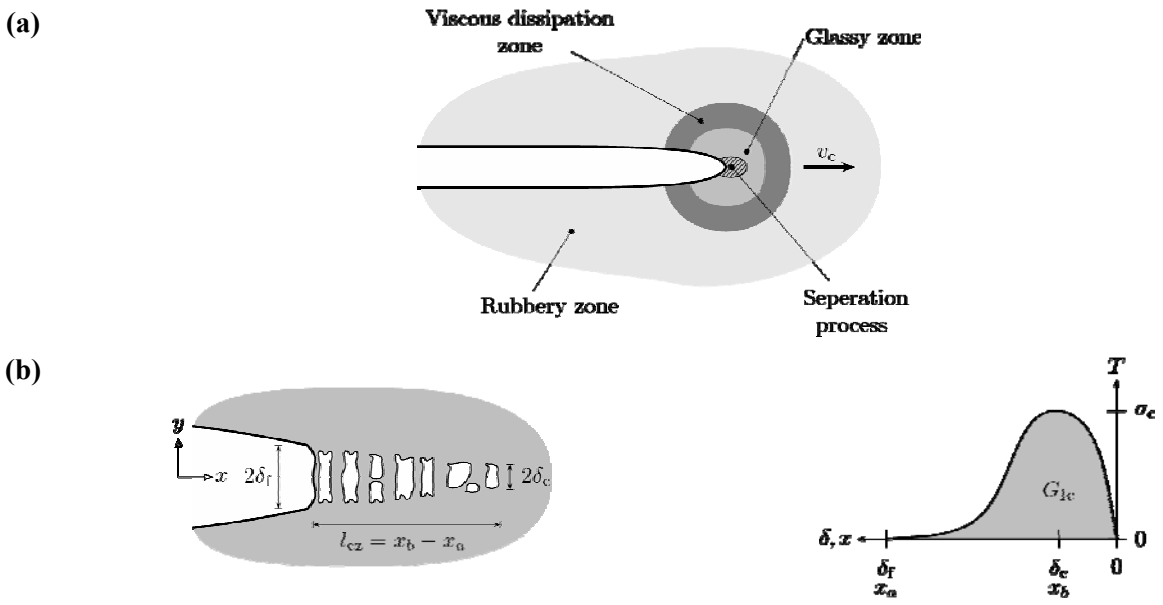

Figure 1. The fracture processes around a crack propagating in rubber with a speed v_c : **a** the different zones around the propagating crack tip determined by the viscoelastic behavior; and **b** the cohesive process zone and its traction-separation law ($T-\delta$). G_{Ic} is the fracture energy, l_{cz} is the length of the cohesive zone, δ_c is the critical displacement, δ_f is the failure displacement, and σ_c is the cohesive strength.

One way to give a quantitative description of the contribution from the different fracture-associated processes is to use the cohesive zone theories. The cohesive zone modeling approach was originally proposed by Dugdale and Barenblatt [9, 11] to simulate the fracture process and was later implemented in a finite element environment [3]. A cohesive zone model describes the fracture process in the crack tip vicinity as a gradual surface separation process, such that the normal and shear forces at the interface resist separation and relative sliding. Several cohesive zone models have been introduced in the literature including rate-dependent and independent models and have been successfully used in both quasi-static and dynamic crack growth problems [1, 4, 13, 27].

The purpose of the present study is to model as well as to analyze the dynamic crack propagation in rubber. The problem of a suddenly initiated crack at the center of stretched sheet is analyzed using finite element method, and plane stress conditions are assumed to prevail. A nonlinear finite element analysis using implicit time integration scheme is used. The bulk material behavior is described by finite-viscoelasticity theory. The fracture separation process is modeled using a cohesive zone model with a bilinear traction-separation law. A parametric study is performed over a range of cohesive zone properties, i.e. cohesive strength and energy, and the steady crack propagation velocity is calculated and compared with crack speeds obtained in experiments. The problem is formulated in Section 2, and the numerical analysis is provided in Section 3. A discussion is presented in Section 4.

2. Problem formulation

2.1. Geometry

Consider a thin rectangular sheet of rubber with the initial dimensions $2W_0$ (width), $2H_0$ (height), and B_0 (thickness), as shown in Fig. 2a. The sheet is initially unloaded, and the Cartesian material coordinates X_I, $I = 1,2,3$, are used to describe the reference configuration. Plane stress conditions are assumed to prevail, such that the $X_1 - X_2$-plane is the plane of stresses. The sheet is first subjected to a stretch λ in the X_2-direction at low rate of loading, such that inertia effects are

ignored. The deformation is assumed to be defined by the motion $\mathbf{x}=\boldsymbol{\chi}(\mathbf{X},t)$, where the Cartesian coordinates x_i, $i=1,2,3$, are defined in the deformed configuration, as shown in Fig. 2b. The position vectors in material and spatial coordinates are defined as $\mathbf{X}=X_i\mathbf{e}_i$ and $\mathbf{x}=x_i\mathbf{e}_i$, respectively, such that the two coordinates possess the same origin and the same set of orthogonal basis vectors $\mathbf{e}_i$, $i=1,2,3$. The displacement vector is defined as $\mathbf{u}=\mathbf{x}-\mathbf{X}$, and the first Piola-Kirchhoff traction vector $\mathbf{T}$ is defined as force per unit undeformed area. After the required extension has been achieved, a crack of length $2a$ is initiated at the center of the deformed sheet parallel to x_1-direction. Thereafter, the crack propagates dynamically and symmetrically along a path defined by $x_2=0$.

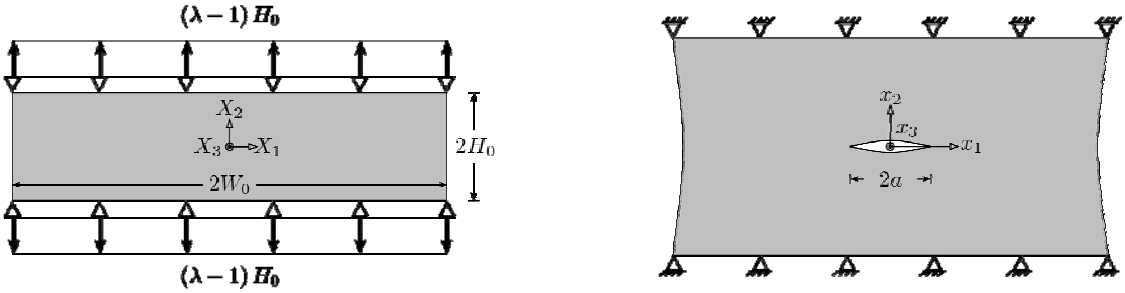

(a) **(b)**

Figure 2. The geometry of the thin rectangular rubber sheet: **a** the reference configuration; and **b** the current configuration.

Considering the symmetry of loading and geometry, only a half portion of the sheet, defined by $X_1\geq 0$, is modeled. The crack propagation is then studied over a length of Δa in the deformed configuration. The time scale is defined according to the following: the sheet is loaded quasi-statically for $t<0$, and at $t=0$, the crack is initiated. The boundary conditions applied for the whole period of time are defined according to

$$X_1=0: u_1=0, T_2=0, \tag{1}$$

$$X_1=W_0: T_1=T_2=0, \tag{2}$$

$$X_2=\pm H_0: u_1=0, u_2=\pm(\lambda-1)\cdot H_0. \tag{3}$$

The initial crack is located at $0\leq X_1\leq a_0$, $X_2=0$. Note that a pertains to the deformed configuration, while a_0 pertains to the reference configuration. The crack starts to propagate immediately after the initiation process, i.e. for $t>0$. The propagation process is determined by a cohesive law. Assuming that the crack tip position is defined as $\mathbf{x}_{\text{tip}}=x_{\text{tip}}\mathbf{e}_1$, the crack tip velocity is then determined as

$$v_{\text{tip}}=\frac{dx_{\text{tip}}}{dt}, \tag{4}$$

implying that the crack propagates in the X_1-direction, i.e. $\mathbf{v}_{\text{tip}}=v_{\text{tip}}\mathbf{e}_1$ and d/dt is the time derivative taken with respect to spatial coordinates.

2.2. Constitutive models

2.2.1. The finite-strain viscoelasticity model

The mechanical behavior of rubber-like materials is characterized by finite elasticity theory, i.e. hyperelasticity, for the quasi-static response. Further, the dynamic response is often characterized by viscoelasticity theory. The finite-strain viscoelasticity implementation in ABAQUS [14] is based on a local additive split of the stress tensor into initial and non-equilibrium parts [15]. The initial part

follows the finite-strain constitutive equations while the non-equilibrium part determines the viscous response.

Consider a deformation that is defined by the deformation gradient $\mathbf{F}$ and the associated Jacobian J. The deformation gradient is decomposed into volume changing (dilatational) part $J^{2/3}\mathbf{I}$ and volume preserving (distortional) part $\overline{\mathbf{F}} = J^{1/3}\mathbf{F}$. The initial free strain energy function, that determines the initial stress part, can be written in the decoupled form

$$\Psi = \Psi_{\text{vol}}(J) + \Psi_{\text{iso}}(\overline{\mathbf{F}}), \tag{5}$$

where $\Psi_{\text{vol}}(J)$ is the volumetric part and $\Psi_{\text{iso}}(\overline{\mathbf{F}})$ is the isochoric part. The total strain energy, including the viscous response, can be written using a generalized Maxwell model (Prony series) as

$$\Psi = k_R(t)\cdot\Psi_{\text{vol}}(J) + g_R(t)\cdot\Psi_{\text{iso}}(\overline{\mathbf{F}}), \tag{6}$$

where $k_R(t)$ and $g_R(t)$ are the Prony series dimensionless relaxation moduli.

In this context, an isotropic and incompressible hyperelastic material is considered, i.e. $J = 1$. Hence, the volumetric part of the strain energy function is then expressed in terms of a hydrostatic pressure p.

$$\Psi_{\text{vol}} = p(J-1), \tag{7}$$

The isochoric part of the strain energy function is defined by the Ogden model for incompressible materials [25], which reads

$$\Psi_{\text{iso}} = \sum_{p=1}^{M}\frac{\mu_p}{\alpha_p}\left(\lambda_1^{\alpha_p} + \lambda_2^{\alpha_p} + \lambda_3^{\alpha_p} - 3\right), \tag{8}$$

where the λ_i, $i = 1,2,3$, are the principal stretches, μ_p and α_p are material parameters that fulfill the condition $\mu_p\alpha_p > 0$ (no summation) and the shear modulus μ_p is defined by $\mu = \sum_{p=1}^{M}\mu_p\alpha_p$.

Further, the volumetric response is assumed to be purely elastic such that the viscoelastic response is determined by the isochoric response, i.e. $k_R(t) = 1$. The total strain energy function, including the viscoelastic response, can be written in the decoupled form

$$g_R(t) = 1 - \sum_{i=1}^{N}\overline{g}_i^P\left(1 - e^{-t/\tau_i}\right), \tag{9}$$

where N, $\overline{k}_i^P$, $\overline{g}_i^P$ and τ_i are material constants. The model includes N Maxwell elements, i.e. series combinations of spring and dash-pot.

2.2.2. The cohesive zone model

The constitutive response for the cohesive surface is modeled in terms of the relationship between the traction and the displacement jump across the surface. The traction-separation law (TSL) is a physically based or a phenomenological model that can be obtained from a free energy density function, ϕ, as

$$\mathbf{T} = \mathbf{T}(\boldsymbol{\Delta}) = \frac{\partial\phi}{\partial\boldsymbol{\Delta}}, \tag{10}$$

where $\mathbf{T}$ is a first Piola-Kirchhoff traction vector, and $\boldsymbol{\Delta}$ is the displacement jump vector between two initially coincident points which are defined in three different directions the normal (n) direction, and the two shear directions (s and t) with respect to the cohesive surface.

In this work, a bilinear traction-separation law is used, and only the opening mode fracture (mode I) is considered. For this reason, only the constitutive behavior in the normal direction is controlled, see Fig. 3. The material parameters of the bilinear traction-separation law are K_{n} (the initial elastic

or penalty stiffness), $\delta_{\mathrm{n}}^{\mathrm{c}}$ (the critical normal separation), $\delta_{\mathrm{n}}^{\mathrm{f}}$ (the failure separation), and σ_{c} (the cohesive strength in the normal direction).

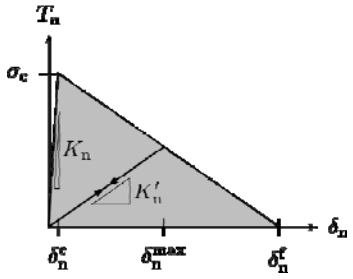

Figure 3. The bilinear traction-separation law

The cohesive element behavior in ABAQUS [14] is based on the characterization of the damage process as the degradation of the material stiffness. The initial behavior is assumed to be linear elastic and is active until damage is initiated. When damage is initiated, the material stiffness decreases and the rate of degradation is defined by the damage evolution law. A scalar damage variable, d, that determines the stiffness degradation, is used, which evolves monotonically from 0 to 1, i.e. from an undamaged to a fully damaged state. The irreversible bilinear traction-separation law is then written as

$$T_{\mathrm{n}} = \begin{cases} K_{\mathrm{n}}\delta_{\mathrm{n}} & \text{if } \delta_{\mathrm{n}} \le \delta_{\mathrm{n}}^{\mathrm{c}}, \\ (1-d)\cdot K_{\mathrm{n}}\delta_{\mathrm{n}} & \text{if } \delta_{\mathrm{n}} \ge \delta_{\mathrm{n}}^{\mathrm{c}}, \end{cases} \tag{11}$$

where the linear elastic unloading behavior after damage onset is determined by the degraded stiffness $K_{\mathrm{n}}' = (1-d)\cdot K_{\mathrm{n}}$. The damage variable, d, for linear softening is determined as

$$d = \frac{\delta_{\mathrm{n}}^{\mathrm{f}}\left(\delta_{\mathrm{n}}^{\max} - \delta_{\mathrm{n}}^{\mathrm{c}}\right)}{\delta_{\mathrm{n}}^{\max}\left(\delta_{\mathrm{n}}^{\mathrm{f}} - \delta_{\mathrm{n}}^{\mathrm{c}}\right)}, \tag{12}$$

where $\delta_{\mathrm{n}}^{\max}$ is the maximum value of the displacement attained during the loading history, see Fig. 3. A maximum nominal stress criterion is used to predict damage initiation, i.e. damage is assumed to be initiated when the maximum nominal stress reaches a critical level $T_{\mathrm{n}} \ge \sigma_{\mathrm{c}}$.

3. Numerical analysis

3.1 Estimation of material parameters

A carbon-black-filled natural rubber material is considered here and its physical and chemical properties are illustrated in [5, 10]. This material has been studied extensively [5-7].

Experimental data from a uniaxial tensile test for the carbon-black filled natural rubber [3] has been used to estimate the parameters in the Ogden strain energy function. The Cauchy (true) stress, σ, in the uniaxial test is defined by

$$\sigma = \sum_{p=1}^{M} \mu_p \left(\lambda^{\alpha_p} - \lambda^{-(1/2)\alpha_p}\right), \tag{13}$$

where λ is the stretch in the uniaxial tension direction. Using a nonlinear least squares method, the Cauchy stress in Eq. (13) is fitted to the uniaxial tension data and two sets of parameters are found to be sufficient, see Fig. 3. The parameter values are shown in Table 1.

Table 1. The Ogden strain energy function parameters ($M = 2$)

p	μ_p [MPa]	α_p [-]
1	1.639	2.724
2	0.088	0.004

Free retraction test experimental data [5] is used to estimate the model parameters in the

viscoelasticity model. Maxwell model with one element has been used, i.e. $N=1$. The relaxation time for rubber is experimentally found to be of the order of $1.0\,\mathrm{s}$ at ambient temperatures [19, 26], and therefore we assumed a relaxation time of $\tau_1 = 1.0\,\mathrm{s}$. (The viscoelastic response of the rubber material is much slower than the rapid processes that we are considering in the present dynamic crack propagation analysis, so the exact value of τ_1 is irrelevant.) The associated relative stiffness, g_1^P, then has to be determined from the experimental data from the retraction tests.

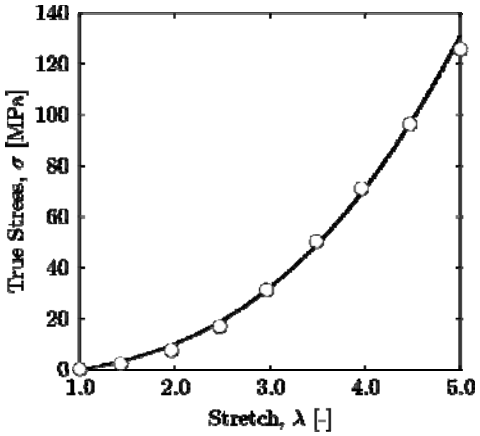

Figure 4. Comparison between the uniaxial true stress-stretch data ('∘') [5] and Ogden material model ($M=2$)

In the free retraction experiment, we consider a thin rectangular strip of rubber with initial dimensions $L_1 = 250\,\mathrm{mm}$, $L_2 = 10\,\mathrm{mm}$ and $L_3 = 0.5\,\mathrm{mm}$, see Fig. 5a (i). The strip is stretched quasi-statically to a certain stretch, λ_0, and then one end is released as shown in Fig. 5a (ii). Consequently, the released end undergoes retraction at a relatively high speed which depends on the initially imposed stretch as well as the material parameters.

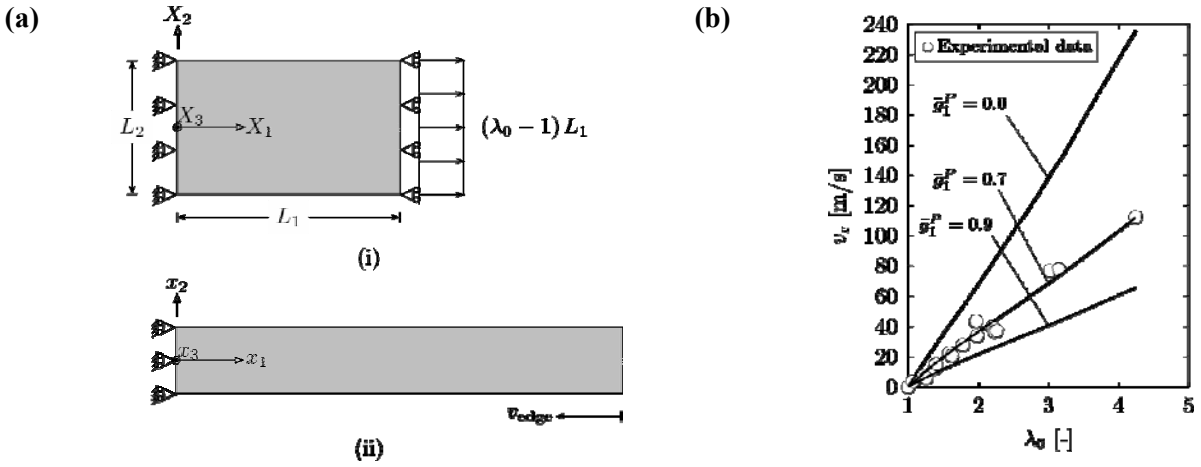

Figure 5. The free retraction experiment: **a** the geometry of the rubber specimen used in the free retraction experiments (i) the reference configuration; and (ii) the current configuration; **b** the predicted retraction speeds for different viscoelastic properties compared with the experimental data [7]. The dashed, full, and dotted lines represent different values of the relative stiffness ($g_1^P = 0.0, 0.7,$ and 0.9), respectively.

The initial-boundary value problem for the free retraction experiment is analyzed using a two-dimensional plane stress finite element model. A nonlinear dynamic analysis, using an implicit time integration scheme, is performed using the finite element code ABAQUS [14], and the free edge steady retraction velocity, v_r, is computed and fitted to the data from the retraction velocity tests, see Fig. 5(b) using different values of the relative stiffness, g_1^P. The parameter values obtained for the Maxwell model are shown in Table 2 below.

Table 2. Prony series coefficients

i	$\bar{g}_i^p$	τ_i
1	0.7	1.0

3.2 Numerical implementation

The initial-boundary value problem described in Sec. 2 is numerically solved using the finite element code ABAQUS [14]. A nonlinear quasi-static analysis is used for the initial loading, and a nonlinear dynamic analysis, using implicit time integration, is used for the crack propagation analysis.

The rubber material is modeled using finite-strain viscoelasticity as described in Sec. 2.2.1 and the material parameters in Tables 1 and 2 are used.

The fracture separation process is modeled using the cohesive zone model that is described in Sec. 2.2.2. The cohesive zone parameters, the cohesive strength and cohesive energy, are material parameters that determine the length of the process zone together with the other material properties [3, 17]. They are not easily measurable, and they are often estimated using experimental data of a known problem setup. The cohesive strength is directly related to the tensile strength of the material while the cohesive energy may be estimated on the basis of fracture mechanics experiments as the work needed for fracture. However, in such estimates, both the actual surface energy and additional dissipative work are included. In this work the cohesive energy is equal is assumed to be total fracture energy. The cohesive strength is chosen to be $\sigma_c = 30\,\text{MPa}$ and then the experimental data are fitted using variable fracture energy.

A high value of the initial stiffness K_n is often assumed in order to avoid ill-conditioning and to reduce the changes of the structure compliance due to the presence of the compliance of the cohesive elements. Therefore, the initial stiffness is assumed to be $K_n = 2.67\times10^6\,\text{MPa}$ such that a stiff behavior is obtained prior to damage initiation without risking the numerical instabilities.

The geometry of the thin rectangular sheet in Fig. 2 is discretized, and a typical finite element mesh is shown in Fig. 6. Due to symmetry, only one half of the specimen is analyzed. The initial dimensions are taken as $W_0 = 75\,\text{mm}$, $H_0 = 5\,\text{mm}$, and $B_0 = 0.5\,\text{mm}$ [6]. The initial crack is assumed to be $2a_0 = 10\,\text{mm}$, and the crack propagation is studied over a length of $\Delta a = 50\,\text{mm}$. Note that Δa pertains to the deformed configuration, while Δa_0 pertains to the reference configuration. The 4-node bilinear plane stress element CPS4 and 4-node two-dimensional linear cohesive element COH2D4 are used in the discretisation. The cohesive elements are inserted along the crack propagation path, i.e. along $X_2 = 0$, and the bulk elements are defined elsewhere. The top and bottom faces of the cohesive elements are tied to the adjacent bulk plane stress elements, implying that three cohesive elements are attached to two bulk elements, see Fig. 6b. The cohesive elements are modeled with zero initial thickness in the reference configuration, and consequently the top and bottom faces and nodes coincide. The mesh comprises 27207 elements, of which 25506 are bulk elements and 1701 are cohesive elements. A cohesive element length of $l_{ce} = 0.025\,\text{mm}$ is used.

The element death/birth technique is adopted to model crack initiation. The initial crack domain is discetized using cohesive elements, and therefore they have been removed at the instant of crack initiation, i.e. at $t = 0$.

The problem is solved for different values of the initial stretching, i.e. $\lambda = [2.0, 4.0]$. The relative normal separation displacement, Δu_2, between each pair of initially coincident nodes in the interface ($X_2 = 0$) is computed and recorded during the analysis. The crack tip position, x_{tip}, is

defined by $\Delta u_2 = \delta_{\mathrm{n}}^{\mathrm{c}}$, and the crack tip velocity is determined using forward differencing of Eq. (14) of the smoothed cohesive crack tip position data, $\bar{x}_{\mathrm{tip}}$, (using Savitzky-Golay smoothing filter).

$$v_{\mathrm{tip}}^{n} = \frac{\bar{x}_{\mathrm{tip}}^{n+1} - \bar{x}_{\mathrm{tip}}^{n}}{\Delta t_n}, \tag{14}$$

where indices n and $n+1$ denote variable values at time instants t_n and t_{n+1}, respectively, and $\Delta t_n = t_{n+1} - t_n$ is the time increment. Further, the steady crack velocity, v_{c}, is computed by taking the average velocity over the steady propagation period.

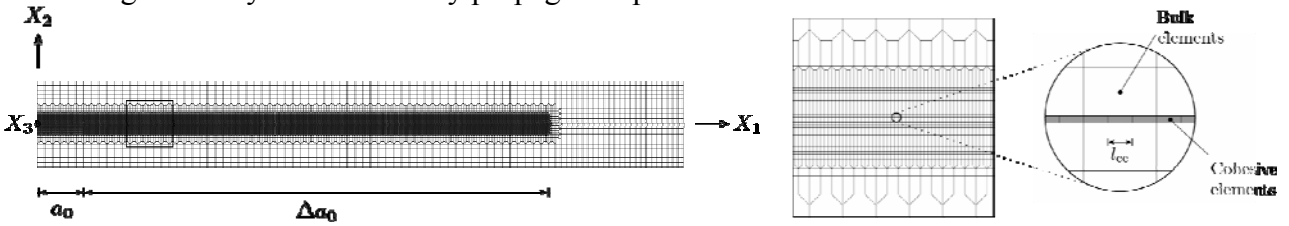

Figure 6. The finite element mesh of the thin rectangular sheet of rubber: **a** the mesh of the whole geometry; and **b** mesh details along the middle of the sheet where the cohesive elements are inserted along the crack propagation path

3.3 Numerical results

Several analyses have been performed for different combinations of stretch and cohesive zone properties. The cohesive crack tip position and velocity, as well as the steady crack propagation velocity, have been obtained for all the combinations.

Typical crack propagation results, including the cohesive crack tip position and velocity results, are shown in Figs. 8a and 8b. At $t = 0$, the crack is initiated such that it propagates immediately after the initiation, i.e. typically within less than $1\,\mathrm{ms}$, at low velocity and continues propagating with a slow acceleration, see in Fig. 8b. After approximately $1.5\,\mathrm{ms}$, the crack velocity approaches a transition region wherein the crack starts to accelerate rapidly and the velocity increases to high velocity levels. Then, after about $1.83\,\mathrm{ms}$, the crack tip velocity reaches a plateau region, where steady crack propagation occurs. Different cohesive properties virtually yield the same type of behavior. Stationary crack propagation was obtained for all sets of cohesive properties, provided that the crack was able to get started. There was a threshold stretch, λ_{th}, below which the initial crack was immediately arrested and no propagation occurred.

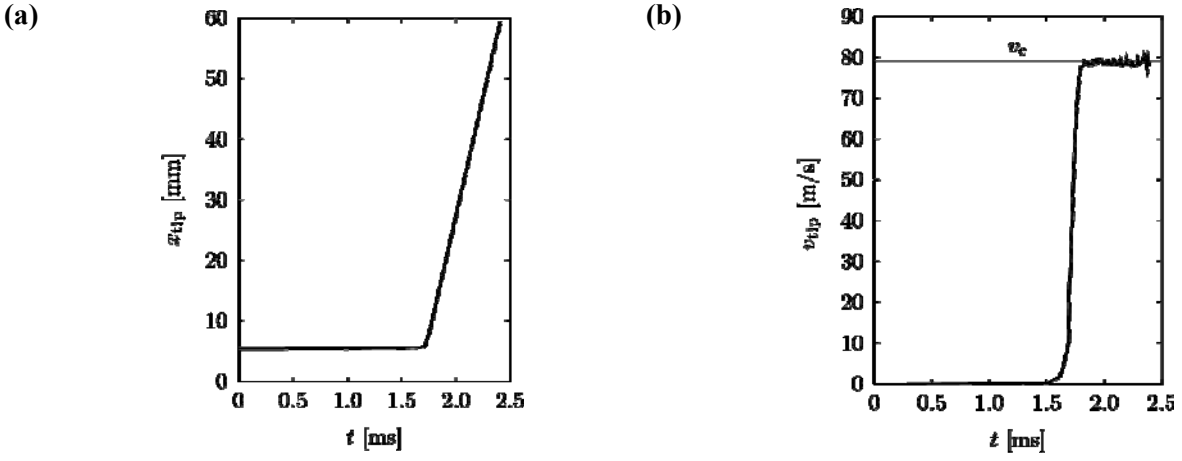

Figure 8. Crack propagation results for $\lambda = 4.0$, $\sigma_{\mathrm{c}} = 60\,\mathrm{MPa}$ and $G_{\mathrm{Ic}} = 20\,\mathrm{KJ/m^2}$: **a** crack tip position x_{tip} vs time t; and **b** crack tip velocity v_{tip} vs time t.

The numerical predictions of the steady crack propagation velocity are compared with the experimental data [6], as shown in Fig. 9. The numerical threshold stretch differs for the different cohesive properties, such that its minimum value, $\lambda_{th} = 3.0$, occurs for $\sigma_c = 60\,\text{MPa}$ and $G_{Ic} = 20\,\text{KJ/m}^2$. For low stretches, the model clearly overestimates the crack speeds from the experimental data. However, by using different cohesive properties, the numerical model is able to predict the crack speeds from the experiments, at least in the high stretch regime ($\lambda \geq 3.5$).

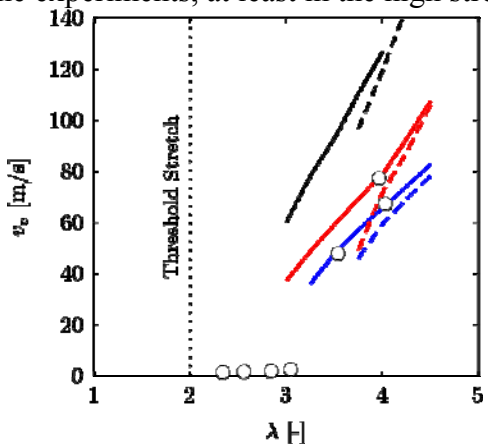

Figure 9. Comparison between numerical predictions of the steady crack propagation velocity and experimental data ('o') [4]. The black, red and blue lines indicate simulations with the cohesive strengths 30,60,90 MPa , respectively, and the full and dashed lines indicate simulations with cohesive energies 20,40 KJ/m^2, respectively.

4. Discussion and concluding remarks

In the present analysis, the contribution from viscoelastic dissipation in the bulk material to the total work of fracture is negligible. This is due to the fact that the crack propagation process is very rapid in comparison with the relaxation time of the rubber material.

In the analyses, the main properties of the cohesive law, i.e. the cohesive energy and the cohesive strength, were varied to enable a prediction of the experimentally obtained crack speeds. The analyses indicate that the effective fracture energy of the rubber material at hand is to be found roughly in the range $20-40\,\text{KJ/m}^2$, and the cohesive strength is expected to be approximately $30-90\,\text{MPa}$. We emphasize that this estimate of the fracture energy should not be taken as the actual surface energy required to create new crack surface at the very crack tip. Rather, this estimate should be taken as a value that contains the actual surface energy but also significant amounts of dissipation associated with damage processes in the vicinity of the crack tip. Strictly speaking, this would be dissipation that takes place in the bulk material surrounding the crack tip, which is not really accounted for by the continuum viscoelasticity model adopted for the bulk behavior.

Few experimental investigations have been concerned with characterization of high speed fracture of rubber, in which crack speed variation with fracture toughness has been experimentally measured under high strain or loading rate. Typical fracture toughness has been reported to be in the range $7-300\,\text{KJ/m}^2$ for the crack speed in the range $0.5-30\,\text{m/s}$ using pure shear and tensile strip specimens [12, 24]. It is also shown that a low fracture toughness of $30\,\text{KJ/m}^2$ can be measured at a crack speed of $30\,\text{m/s}$. Thus, the effective fracture energy reported in the literature shows good agreement with the values attained here.

References

[1] A Corigliano, M Ricci, Rate-dependent interface models: formulation and numerical applications. Int J Solids Struct, 38(2001) 547–76.

[2] AG Thomas, The development of fracture mechanics for elastomers. Rubber Chem Technol, 67(1994) G50–G60.
[3] A Hillerborg, M Modeer and PE Petersson, Analysis of crack formation and crack growth in concrete by means of fracture mechanics and finite elements. Cem Concr Res, 6(1976) 773–81.
[4] A Needleman, A continuum model for void nucleation by inclusion debonding. J Appl Mech, 54(1987) 525–531.
[5] AN Gent, HJ Kim, Tear strength of stretched rubber. Rubber Chem Technol, 51(1978) 35–44.
[6] AN Gent, P Marteny, Crack velocities in natural rubber. J Mat Sci, 17(1982) 2955–2960.
[7] AN Gent, P Marteny, The effect of strain upon the velocity of sound and the velocity of free retraction for natural rubber. J Appl Phys, 53 (1982) 6069–6074.
[8] CH Chen, HP Zhang, J Niemczura, K Ravi-Chandar, M Marder, Scaling of crack propagation in rubber sheets. EPL 96(2011) 36009
[9] DS Dugdale, Yielding of steel sheets containing slits. J Mech Phys Solids, 8(1960) 100–4.
[10] E Elmukashfi, M Kroon, Numerical analysis of dynamic crack propagation in rubber. Int J Fract, 177 (2012) 163–178.
[11] GI Barenblatt, The mathematical theory of equilibrium cracks in brittle fracture. Adv Appl Mech, 7(1962) 55–129.
[12] GJ Lake, CC Lawrence, AG Thomas, High-speed fracture of elastomers: Part I. Rubber Chem Technol, 73(2000) 801–817.
[13] GT Camacho and M Ortiz, Computational Modeling of Impact Damage in Brittle Materials. Int. J. Solids Struct., 33(1996) 2899–2938.
[14] Hibbit, Karlsson and Sorensen Abaqus: Theory and User's Manual. Inc., Pawtucket, RI, 2011.
[15] J.C. Simo, On a Fully Three-Dimensional Finite-Strain Viscoelastic Damage Model: Formulation and Computational Aspects. Comput Method Appl M, 60 (1987) 153–173.
[16] JD Ferry, RG Mancke, E Maekawa, Y Oyanagi, and RA Dickie, Dynamic Mechanical Properties of Cross-Linked Rubbers. I. Effects of Cross-Link Spacing in Natural Rubber. J. Phys. Chem., 68(1964) 3414–3418.
[17] JR Rice, Mathematical Analysis in the Mechanics of Fracture, in Fracture: An Advanced Treatise. H. Liebowitz, ed., Vol.2 (1968) 191–311.
[18] JR Rice, Mechanics of quasi-static crack growth. In: Proceedings of Eighth U.S. National Congress on Mechanics, (1978) 191–216.
[19] JS Bergström, MC Boyce, Constitutive modeling of the large strain time-dependent behavior of elastomers. J Mech Phys solids, 46 (1998) 931–954.
[20] PG de Gennes, Soft adhesives. Langmuir, 12(1996) 4497–4500.
[21] PJ Petersan, RD Deegan, M Marder, HL Swinney, Cracks in rubber under tension exceed the shear wave speed. Phys Rev Lett, 93(2004) 1–4.
[22] PNJ Persson, O Albohr, G Heinrich, H Ueba, Crack propagation in rubber-like materials. J Phys: Condens Matter, 17(2005) R1071–R1142.
[23] M Kroon, Steady-state Crack Growth in Rubber-like Solids. Int J Fract., 169 (2011)49–60.
[24] MS Hoo Fatt, L Chen, and AA Al-Quraishi, Fracture Parameters for Natural Rubber Under Dynamic Loading. Strain 47(2011) 505–518.
[25] RW Ogden, Large Deformation Isotropic Elasticity - On the Correlation of Theory and Experiment for Incompressible Rubberlike Solids, Proceedings of the Royal Society of London, Series A, Mathematical and Physical Sciences, 326(1972) 565–584.
[26] S Kawabata, H Kawai, Strain energy density functions of rubber vulcanizates from biaxial extension. Adv. Polym. Sci., 24 (1977) 89–124.
[27] V Tvergaard, Effect of fibre debonding in a whisker-reinforced metal. Mater Sci Engng, A 125(1990) 203–213.
[28] W Wang, Hyperelasticity, viscoelasticity, and nonlocal elasticity govern dynamic fracture in rubber. Phys Rev Lett, 95(2005) 1–4.

13th International Conference on Fracture
June 16-21, 2013, Beijing, China

Fracture of anisotropic materials with plastic strain-gradient effects

Brian Nyvang Legarth[1,*]

[1] Department of Mechanical Engineering, Solid Mechanics,
Technical University of Denmark, DK-2800, Denmark
* Corresponding author: bnl@mek.dtu.dk

Abstract A unit cell is adopted to numerically analyze the effect of plastic anisotropy on fracture evolution in a micro-reinforced fiber-composite. The matrix material exhibit size-effects and an anisotropic strain-gradient plasticity model accounting for such size-effects through a material length scale parameter is adopted. The fracture process along the fiber-matrix interface is modeled using a recently proposed cohesive law extension having an additional material length parameter. Due to the fiber-matrix fracture a sudden stress-drop is seen in the macroscopic stress-strain response which defines the failure strain of the composite. The effect of the two material length parameters on the failure strain of the composite is studied. For small values of the material length scale parameter conventional predictions are obtained. Larger values of the material length scale parameter result in corresponding larger failure strains, but only up to a material length scale parameter approximately equal to 15% of the reinforcement size. At this point, the failure strain becomes smaller again for further increasing values of the material length scale. It is shown that the cohesive length parameter monotonically affects the failure strain as a decreasing failure strain is predicted for smaller value of the material parameter.

Keywords Composite Materials, Strain-gradient plasticity, Debonding, Failure strain

1. Introduction

Failure mechanisms of fiber-reinforced composite materials are still a challenging topic due to the large number of failure modes compared to conventional homogeneous materials[1]. A unidirectional fiber-composite subjected to transverse tensile loading often fail by either matrix damage or microcracks evolving at the fiber-matrix interfaces. For longitudinal loading the most often seen failure modes are matrix and fiber cracking.

For a composite reinforced at the micron scale, two competing mechanisms affect the overall behavior: (I) interfacial failure reduces the strength and (II) strain-gradient effects enhance the strength. When analyzing such composites in general a full 3D analysis is required in order to fully represent the geometry, the loading and the boundary conditions. Such analyses are complicated and the computations become very time consuming when anisotropic plasticity and progressive debonding is to be accounted for. Thus, assuming a periodical distribution of the reinforcement allows for greatly simplified approaches.

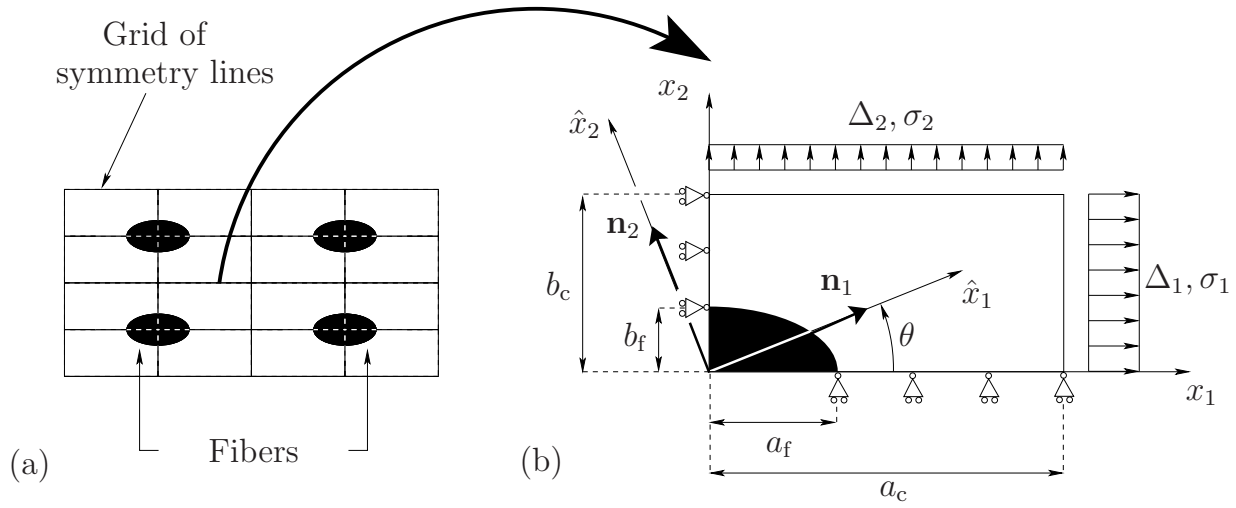

Figure 1. The plane strain cell model for the composite. (a) Periodically distributed fibers. (b) The cell used for modeling with initial dimensions, loads, supports and coordinate systems.

Here, a composite material having a periodical distribution of reinforcement is analyzed using a plane strain unit cell approach. Thus, the results presented in this study approximate a composite of rather long, almost aligned, stiff reinforcement which is subjected to a fixed stress state that is acting mainly in the transverse direction of the reinforcement. Fig. 1(a) shows the distribution of fibers and Fig. 1(b) shows the unit cell adopted here. The orthonormal basis, $\mathbf{n}_i$, of the principal axes of plastic anisotropy, $\hat{x}_i$, is defined by the angle θ, from from the global Cartesian coordinate system, x_i. The applied conventional boundary conditions are

$$\begin{array}{llllllll} \dot{u}_1 = 0, & \dot{T}_2 = 0 & \text{on} & x_1 = 0 & \text{and} & \dot{u}_1 = \Delta_1, & \dot{T}_2 = 0 & \text{on} \quad x_1 = a_c \\ \dot{u}_2 = 0, & \dot{T}_1 = 0 & \text{on} & x_2 = 0 & \text{and} & \dot{u}_2 = \Delta_2, & \dot{T}_1 = 0 & \text{on} \quad x_2 = b_c \end{array} \tag{1}$$

where u_i are the displacement components, Δ_1 and Δ_2 are displacement increment quantities on two sides of the cell, which are calculated such that the ratio of the average true stresses σ_2 and σ_1 remains fixed, $\sigma_2/\sigma_1 = \kappa$. These stresses are calculated as

$$\begin{aligned} \sigma_1 &= \tfrac{1}{b_c+\Delta b_c} \int_0^{b_c+\Delta b_c} [T_1]_{x_1=a_c+\Delta a_c}\, dx_2 \\ \sigma_2 &= \tfrac{1}{a_c+\Delta a_c} \int_0^{a_c+\Delta a_c} [T_2]_{x_2=b_c+\Delta b_c}\, dx_1 \end{aligned} \tag{2}$$

Here Δa_c and Δb_c denote the accumulated elongations of the cell sides whereas T_1 and T_2 are normal tractions. The corresponding average logarithmic strains are

$$\begin{aligned} \epsilon_1 &= \ln(1 + \Delta a_c/a_c) \\ \epsilon_2 &= \ln(1 + \Delta b_c/b_c) \end{aligned} \tag{3}$$

In this study, a micro-crack evolving at the fiber-matrix interfaces is analyzed for a two-phase composite material, where the matrix material exhibits size-effects. The higher-order strain-gradient plasticity model of Fleck and Hutchinson accounts for such size-effects and will be adopted here in the anisoropic version proposed by Legarth [2,3]. In this model a higher-order stress work-conjugate to the gradient of the effective plastic strain is introduced together with a material length scale parameter. The reinforcement is assumed to be much stiffer than the matrix material and will therefore be considered as perfectly stiff. As dislocations cannot penetrate into the perfectly elastic fiber they pile up

at the interface which corresponds to zero plastic deformations. Thus, zero plastic strain is imposed at the bonded part of the interface. This is known a higher-order boundary conditions. The fracture process along the fiber-matrix interface is modelled using a recently proposed cohesive law extension[4]. Hence, plasticity will affect the fracture process as both the average as well as the jump in plastic strain across the fiber-matrix interface are taking into account in this cohesive law. Using this extended cohesive law ensures stress-free crack faces after failure. The formulation used here only demands one additional interfacial cohesive zone parameter.

2. Material models

The material model used accounts for small elastic and finite plastic strain in an updated Lagrangian formulation in which the current configuration is taken as the reference configuration, i.e. $J = 1$ but $\dot{J} = \dot{\epsilon}_{kk}$ when J is the determinant of the metric tensor and the superposed dot denotes the time rate.

2.1 Higher order elasto-plastic constitutive model

The fibers are assumed to be purely elastic with a stiffness much larger than the elasto-plastic matrix material, which is assumed to obey the strain gradient model proposed by Fleck and Hutchinson [2]. Denoting the velocity field $\dot{u}_i$ the components of the second-order velocity gradient tensor, $\dot{e}_{ij}$, are determined by $\dot{e}_{ij} = \dot{u}_{i,j}$. The symmetric part of $\dot{e}_{ij}$ is the strain rate, $\dot{\epsilon}_{ij}$, and the antisymmetric part is the continuum spin tensor, $\dot{\omega}_{ij}$. Following the multiplicative decomposition of the deformation gradient into an elastic and a plastic part the kinematics of the material can be written as

$$\begin{aligned} \dot{\epsilon}_{ij} &= \tfrac{1}{2}(\dot{e}_{ij} + \dot{e}_{ji}) = \dot{\epsilon}^{\mathrm{e}}_{ij} + \dot{\epsilon}^{\mathrm{P}}_{ij} \\ \dot{\omega}_{ij} &= \tfrac{1}{2}(\dot{e}_{ij} - \dot{e}_{ji}) \end{aligned} \tag{4}$$

with $\dot{e}_{ij} = \dot{\epsilon}_{ij} + \dot{\omega}_{ij}$ and e and p denote the elastic and the plastic parts, respectively.

Plastic anisotropy is accounted for using the anisotropic version of the Fleck and Hutchinson model as suggested by Legarth [3]. Thus, the effective plastic strain, $\dot{E}^p$, is enriched by the gradients of the conventional effective plastic strain, $\dot{\epsilon}^{\,p}_{,i}$, and a material length scale parameter, l_*, as

$$\dot{E}^p = \sqrt{\frac{2}{3}\dot{\epsilon}^p_{ij}\dot{\epsilon}^p_{ij} + l_*^2\dot{\epsilon}^{\,p}_{,i}\,\dot{\epsilon}^{\,p}_{,i}} \qquad ; \qquad \dot{\epsilon}^p_{ij} = \dot{\epsilon}^p N^p_{ij} = \dot{\epsilon}^p \frac{\partial \Gamma}{\partial \sigma_{ij}} \qquad ; \qquad \dot{\epsilon}^p = \sqrt{\frac{2}{3}\dot{\epsilon}^p_{ij}\dot{\epsilon}^p_{ij}} \tag{5}$$

The work-conjugate effective stress is denoted σ_c and is given in Tab. 1 for the four posible cases of isotropy or anisotropy with and without strain gradient effects. Plastic anisotropy enters through the effective stress measure Γ whereas the higher-order stress, ρ_i, relates to the strain-gradient effects as the work-conjugate stress quantity to the gradient of the plastic strain rate, $\dot{\epsilon}^{\,p}_{,i}$. The work-conjugate stress quantity to the effective plastic strain rate, $\dot{\epsilon}^p$ is denoted q.

Two different anisotropic yield surfaces are adopted here, namely the classical anisotropic Hill yield surface [5] and the more recent non-quadratic proposal by Barlat et al. [6], here denoted Hill-48 and Barlat-91, respectively.

Table 1. Summary of the effective stress, σ_c, for different materials.

	Conventional materials $(l_* = 0, \rho_i = 0)$	Higher order materials $(l_* \neq 0, \rho_i \neq 0)$
Isotropic	$\rho_{i,i} = 0$	$\rho_{i,i} = q - \sigma_e$
$(\Gamma = \sigma_e)$	$\sigma_c = \sigma_e$	$\sigma_c = \sqrt{(\sigma_e + \rho_{i,i})^2 + l_*^{-2}\rho_i\rho_i}$
Anisotropic	$\rho_{i,i} = 0$	$\rho_{i,i} = q - \Gamma$
	$\sigma_c = \Gamma$	$\sigma_c = \sqrt{(\Gamma + \rho_{i,i})^2 + l_*^{-2}\rho_i\rho_i}$

Hill-48

For the case of plane strain conditions with $\sigma_{13} = \sigma_{23} = 0$ the yield surface of Hill is

$$\Gamma = \sqrt{\tfrac{3}{2(F+G+H)}\left[F(\hat{\sigma}_{22} - \hat{\sigma}_{33})^2 + G(\hat{\sigma}_{33} - \hat{\sigma}_{11})^2 + H(\hat{\sigma}_{11} - \hat{\sigma}_{22})^2 + 2N\hat{\sigma}_{12}^2\right]} \tag{6}$$

The Cauchy stresses, $\hat{\sigma}_{ij}$, refer to the principal axes of plastic anisotropy. For $F = G = H = 1$ and $N = L = M = 3$, Eq. (6) equals the isotropic Mises yield surface, σ_e.

Barlat-91

Barlat et al. [5] proposed the non-quadratic yield function

$$\Gamma \;\; = [S_1 - S_2]^d + [S_2 - S_3]^d + [S_1 - S_3]^d \tag{7}$$

where

$$\begin{aligned} S_1 &= 2\sqrt{I_2}\cos\left(\tfrac{\bar{\theta}}{3}\right) \\ S_2 &= 2\sqrt{I_2}\cos\left(\tfrac{\bar{\theta}-2\pi}{3}\right) \\ S_3 &= 2\sqrt{I_2}\cos\left(\tfrac{\bar{\theta}+2\pi}{3}\right) \end{aligned} \tag{8}$$

$$\begin{aligned} I_2 = \;& \tfrac{1}{3}\left[(\bar{f}\bar{F})^2 + (\bar{g}\bar{G})^2 + (\bar{h}\bar{H})^2\right] \\ & + \tfrac{1}{54}\left[(\bar{a}\bar{A} - \bar{c}\bar{C})^2 + (\bar{c}\bar{C} - \bar{b}\bar{B})^2 + (\bar{b}\bar{B} - \bar{a}\bar{A})^2\right] \\ I_3 = \;& \tfrac{1}{54}\left[(\bar{c}\bar{C} - \bar{b}\bar{B})(\bar{a}\bar{A} - \bar{c}\bar{C})(\bar{b}\bar{B} - \bar{a}\bar{A})\right] + \bar{f}\bar{g}\bar{h}\bar{F}\bar{G}\bar{H} \\ & - \tfrac{1}{6}\left[(\bar{c}\bar{C} - \bar{b}\bar{B})(\bar{f}\bar{F})^2 + (\bar{a}\bar{A} - \bar{c}\bar{C})(\bar{g}\bar{G})^2 + (\bar{b}\bar{B} - \bar{a}\bar{A})(\bar{h}\bar{H})^2\right] \end{aligned} \tag{9}$$

$$0 \leq \bar{\theta} = \arccos\left(\frac{I_3}{I_2^{3/2}}\right) \leq \pi \tag{10}$$

with

$$\begin{aligned} \bar{A} &= \hat{\sigma}_{22} - \hat{\sigma}_{33} \quad ; \quad \bar{F} = \hat{\sigma}_{23} \\ \bar{B} &= \hat{\sigma}_{33} - \hat{\sigma}_{11} \quad ; \quad \bar{G} = \hat{\sigma}_{31} \\ \bar{C} &= \hat{\sigma}_{11} - \hat{\sigma}_{22} \quad ; \quad \bar{H} = \hat{\sigma}_{12} \end{aligned} \tag{11}$$

For $\bar{\theta} = 0$ or $\bar{\theta} = \pi$ in Eq. (10) the derivatives in Eq. (5) are singular. For these particular cases Eq. (7) reduces to

$$\Gamma = 2 \cdot 3^d I_2^{\frac{d}{2}} \qquad \text{for } \bar{\theta} = 0 \quad \text{or} \quad \bar{\theta} = \pi \tag{12}$$

which are then directly used to evaluate the strain increments. If the coefficients of anisotropy, $\bar{a}, \bar{b}, \bar{c}, \bar{f}, \bar{g}$ and $\bar{h}$, are chosen to be unity and the exponent to $d = 2$, this criterion reduces to the von Mises yield surface.

2.2 Higher-order cohesive model

The bi-axial loading on the unit cell, Fig. 1(b), will tend to cause both normal and tangential interfacial separation, u_n and u_t, respectively, at the fiber-matrix interface. The cohesive zone model proposed by Tvergaard[7] takes both types of separation into account and therefore this model may seem suitable for the present study. However, due to the existence of the higher order stress, ρ_i with the corresponding higher order tractions, $\rho_i n_i$ additional terms need to be included in order to have a conventional as well as higher order stress-free surface after debonding failure. Hence, a non-dimensional damage parameter is introduces as[4]

$$\lambda = \sqrt{\left(\frac{u_n}{\delta_n}\right)^2 + \left(\frac{u_t}{\delta_t}\right)^2 + l_*^2\left[\left(\frac{<\epsilon^p>}{l_A}\right)^2 + \left(\frac{[\epsilon^p]}{l_J}\right)^2\right]} \tag{13}$$

where $<\epsilon^p>$ is the average (subscript A) and $[\epsilon^p]$ is the half jump (subscript J) in plastic strain across the interface, respectively, whereas l_A and l_J are corresponding critical interfacial length scale parameters. For $\lambda \geq 1$ total separation have occurred. It is noted, that since the fiber is taken to be purely elastic in this study the average plastic strain across the fiber-matrix interface equals the jump, i.e. $<\epsilon^p>=[\epsilon^p]$. The corresponding tractions are

$$T_n = \frac{u_n}{\delta_n}F(\lambda)\,; \quad T_t = \alpha\frac{u_t}{\delta_t}F(\lambda)\,; \quad T_A = l_*^2\frac{\delta_n}{l_A^2}F(\lambda)<\epsilon^p>\,; \quad T_J = l_*^2\frac{\delta_n}{l_J^2}F(\lambda)[\epsilon^p] \tag{14}$$

with $\alpha = \delta_n/\delta_t$ and $F(\lambda) = \frac{27}{4}\sigma_{max}(1-2\lambda+\lambda^2)$ for $0 \leq \lambda \leq 1$. The maximum interfacial stress is denoted σ_{max}. For the numerical implementation, an incremental version of these tractions can be stated generally as

$$\begin{Bmatrix} \dot{T}_n \\ \dot{T}_t \\ \dot{T}_A \\ \dot{T}_J \end{Bmatrix} = \begin{bmatrix} a_{nn} & a_{nt} & a_{nJ} & a_{nA} \\ a_{tn} & a_{tt} & a_{tJ} & a_{tA} \\ a_{Jn} & a_{Jt} & a_{JJ} & a_{JA} \\ a_{An} & a_{At} & a_{AJ} & a_{AA} \end{bmatrix} \begin{Bmatrix} \dot{u}_n \\ \dot{u}_t \\ [\dot{\epsilon}^p] \\ <\dot{\epsilon}^p> \end{Bmatrix} \tag{15}$$

where the a-coefficients can be found from the cohesive law. Using this higher order cohesive law ensures that the debonded part of the fiber-matrix interface is stress free both in terms of the conventional stress, σ_{ij}, as well as the higher order stress, ρ_i.

3. Computational Method

The problem is solved incrementally by a finite element code based on the principle of virtual work. In the updated Lagrangian formulation the incremental form of the principle of virtual work is, see [3,5]

$$\begin{aligned} &\Delta t\int_V \left(\overset{\triangledown}{\varsigma}_{ij}\,\delta\dot{\epsilon}_{ij} - \sigma_{ij}(2\dot{\epsilon}_{ik}\delta\dot{\epsilon}_{kj} - \dot{e}_{kj}\delta\dot{e}_{ki}) + \left(\dot{q} - \dot{\Gamma}^{\varsigma}\right)\delta\dot{\epsilon}^{\mathrm{P}} + \overset{\vee}{\rho}_i\,\delta\dot{\epsilon}^{\mathrm{P}}_{,i}\right) dV \\ &+\Delta t\int_{S_I}\left(\dot{T}_n\delta\dot{u}_n + \dot{T}_t\delta\dot{u}_t + \dot{p}\delta[\dot{\epsilon}^{\mathrm{P}}] + \dot{q}\delta<\dot{\epsilon}^{\mathrm{P}}>\right) dS = \Delta t\int_S\left(\dot{T}_i\delta\dot{u}_i + \dot{\rho}_i n_i\delta\dot{\epsilon}^{\mathrm{P}}\right) dS \end{aligned} \tag{16}$$

Here, Δt is the time step, V the volume, $\overset{\triangledown}{\varsigma}_{ij}$ denotes the Jaumann rate of the Kirchhoff stress with $\dot{\Gamma}^{\varsigma} = N_{ij}^{\mathrm{P}}\,\overset{\triangledown}{\varsigma}_{ij}$ and $T_i = \sigma_{ij}n_j$ are the surface tractions on the surface S with

the unit outward normal n_i. Due to the updated Lagrangian formulation all integrations are carried out in the current deformed configuration. The Jaumann rate of the Kirchhoff stress entering the virtual work principle is

$$\overset{\triangledown}{\varsigma}_{ij}\,\Delta t = R_{ijkl}\left(\Delta\epsilon_{kl} - N^{\mathrm{P}}_{kl}\Delta\epsilon^{\mathrm{P}}\right) = \Delta\varsigma_{ij} - \Delta\omega_{ik}\sigma_{kj} - \sigma_{ik}\Delta\omega_{jk} \tag{17}$$

where R_{ijkl} are the isotropic elastic moduli determined by Young's modulus, E, Poisson's ratio, ν, and Kronecker's delta, δ_{ij}, as

$$R_{ijkl} = \frac{E}{1+\nu}\left(\frac{1}{2}(\delta_{ik}\delta_{jl} + \delta_{il}\delta_{jk}) + \frac{\nu}{1-2\nu}\delta_{ij}\delta_{kl}\right) \tag{18}$$

The finite element procedure adopted here follows the method used by de Borst and Pamin[8] for time-independent plasticity and Borg et al.[9] for viscoplasticity, where both the conventional displacement increments, $\mathbf{\Delta D}$, as well as the increments of the effective plastic strain rates, $\mathbf{\Delta}\dot{\epsilon}^{\mathrm{P}}$, appear as unknowns. However, they solved for $\mathbf{\Delta D}$ and $\mathbf{\Delta}\dot{\epsilon}^{\mathrm{P}}$ simultaneously, even though the system of equations decouples. Here, the numerical solution is obtained by decoupling the equations. In doing so, the stiffness matrices become symmetric, less sparse and more well conditioned, leading to a significantly improved computational time. Thus, the equations to solve are

$$\mathrm{K_e}\mathbf{\Delta}\mathrm{D} = \mathbf{\Delta}\mathrm{F}_1 + \mathbf{\Delta}\mathrm{F}_{1\mathrm{c}} \tag{19}$$

for the displacement increments and

$$\mathrm{K_p}\mathbf{\Delta}\dot{\epsilon}^{\mathrm{P}} = \mathbf{\Delta}\mathrm{F}_2 + \mathbf{\Delta}\mathrm{F}_{2c} \tag{20}$$

for the increments of the conventional effective plastic strain rate. Here 8 node isoparametric elements are used for both the displacements as well as the plastic strain field using the shape functions N and M, respectively, within the bulk material. Thus, the field of total strains within an element is bi-linear whereas the plastic strains vary parabolically. The local stiffness matrices and load vectors are

$$\begin{aligned}
\mathrm{K_e}^{NM} = \;& \int_V \left(E^N_{ij} R_{ijkl} E^M_{kl} + \sigma_{ij}\left(N^M_{k,j}N^N_{k,i} - 2E^M_{ik}E^N_{jk}\right)\right)\mathrm{d}V + \\
& \int_{S_I}\left(\{a_{nn}(Q^N_i n_i) + a_{nt}(Q^N_i t_i)\}(Q^M_i n_i) + \right. \\
& \left.\{a_{tn}(Q^N_i n_i) + a_{tt}(Q^N_i t_i)\}(Q^M_i t_i)\right)\mathrm{d}S
\end{aligned} \tag{21}$$

$$\begin{aligned}
\mathrm{K_P}^{NM} = \;& \int_V \left(\left(\tfrac{\dot{\epsilon}^{\mathrm{P}}}{\dot{E}^{\mathrm{P}2}}(m-1)q + \tfrac{\sigma_{\mathrm{c}}}{\dot{E}^{\mathrm{P}}}\right) M^M M^N \right. \\
& + l^2_* \tfrac{\dot{\epsilon}^{\mathrm{P}}_{,i}}{\dot{E}^{\mathrm{P}2}} q M^M M^N_{,i} + \tfrac{\dot{\epsilon}^{\mathrm{P}}}{\dot{E}^{\mathrm{P}2}}(m-1)\rho_i M^M_{,i} M^N \\
& \left. + l^2_* \tfrac{\dot{\epsilon}^{\mathrm{P}}_{,i}}{\dot{E}^{\mathrm{P}2}}\rho_k M^M_{,k} M^N_{,i} + \tfrac{\sigma_{\mathrm{c}}}{\dot{E}^{\mathrm{P}}} M^M_{,i} M^N_{,i}\right)\mathrm{d}V
\end{aligned} \tag{22}$$

$$\mathbf{\Delta}\mathrm{F}_1{}^N = \int_S \Delta T_i N^N_i \mathrm{d}S + \Delta t \int_V E^N_{ij} R_{ijkl} N^{\mathrm{P}}_{kl} \dot{\epsilon}^{\mathrm{P}} \mathrm{d}V \tag{23}$$

$$\begin{aligned}
\mathbf{\Delta}\mathrm{F}_2{}^N = \;& \int_S \Delta\rho_i n_i M^N \mathrm{d}S - \Delta t \int_V \left(\left(N^{\mathrm{P}}_{ij} R_{ijkl}(N^{\mathrm{P}}_{kl}\dot{\epsilon}^{\mathrm{P}} - \dot{\epsilon}_{kl})\right.\right. \\
& \left.\left. + \tfrac{\dot{\epsilon}^{\mathrm{P}}}{\dot{\epsilon}^m_0}\dot{E}^{\mathrm{P}m}\tfrac{\mathrm{d}g}{\mathrm{d}E^{\mathrm{P}}}\right) M^N + \dot{\epsilon}^{\mathrm{P}}_{,i}\,\dot{E}^{\mathrm{P}m}\tfrac{\mathrm{d}g}{\mathrm{d}E^{\mathrm{P}}}\tfrac{l^2_*}{\dot{\epsilon}^m_0} M^N_{,i}\right)\mathrm{d}V
\end{aligned} \tag{24}$$

where $E_{ij} = \frac{1}{2}\left(N_{i,j} + N_{j,i}\right)$ and m is the rate sensitivity parameter. The additional load vectors $\Delta\mathrm{F}_{1c}$ and $\Delta\mathrm{F}_{2c}$ resulting from the higher order cohesive zone are

$$\begin{aligned}
\mathbf{\Delta}\mathrm{F}_{1c}{}^N = \;& -\Delta t \int_{S_I}\left(\{a_{nJ}[\dot{\epsilon}^p] + a_{nA} < \dot{\epsilon}^p >\}(Q^N_i n_i) \quad + \right. \\
& \left.\{a_{tJ}[\dot{\epsilon}^p] + a_{tA} < \dot{\epsilon}^p >\}(Q^N_i t_i)\right)\mathrm{d}S
\end{aligned} \tag{25}$$

$$\begin{aligned}
\mathbf{\Delta}\mathrm{F}_{2c}{}^N = \;& -\Delta t \int_{S_I}\left(a_{Jn}\dot{u}_n + a_{Jt}\dot{u}_t + a_{JJ}[\dot{\epsilon}^p] + a_{JA} < \dot{\epsilon}^p > \quad + \right. \\
& \left. a_{An}\dot{u}_n + a_{At}\dot{u}_t + a_{AJ}[\dot{\epsilon}^p] + a_{AA} < \dot{\epsilon}^p >\right) R^N \mathrm{d}S
\end{aligned} \tag{26}$$

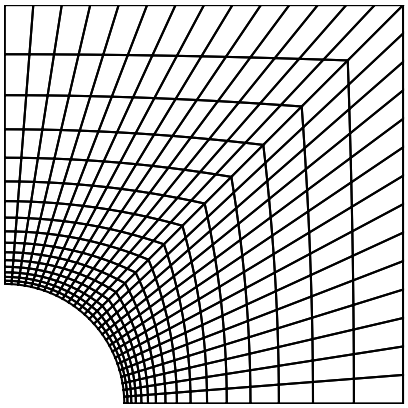

Figure 2. Example of mesh adopted.

Here, 6 node isoparametric elements with the shape functions Q and R for the displacement field and the plastic strain field, respectively, are used for the cohesive zone where the normal and tangential unit vectors are introduced as n_i and t_i, respectively. It noted that the incremental cohesive tractions, Eq. (15), depends on the rates of the displacement and the plastic strain, whereas the solution procedure outlined here solves for the rates of the displacement and the plastic strain increments, meaning that the higher order contributions from the cohesive law only enters through the load vectors, $\Delta \mathrm{F}_{1c}$ and $\Delta \mathrm{F}_{2c}$. The conventional part of the cohesive law also gives an stiffness contribution, Eq. (21). An example of a mesh used is shown in Fig. 2 for $\frac{a_f}{b_f} = \frac{a_c}{b_c} = 1$.

4. Results

Fig. 3 shows results for a load case with $\kappa = \frac{\sigma_2}{\sigma_1} = 0.5$ corresponding to bi-axial plane strain tension. The fiber volume fraction is $V_f = \frac{\pi a_f b_f}{4 a_c b_c}$, with $\frac{a_f}{b_f} = \frac{a_c}{b_c} = 1$. The initial yield stress is $\sigma_0/E = 0.003$, where E is Young's modulus. The coefficients of anisotropy using Hill-48 are $F = 0.7, G = 3.33, H = 1$ and $N = 9.6$ with $\theta = 0^o$ and $\sigma_{max} = 3\sigma_0$.

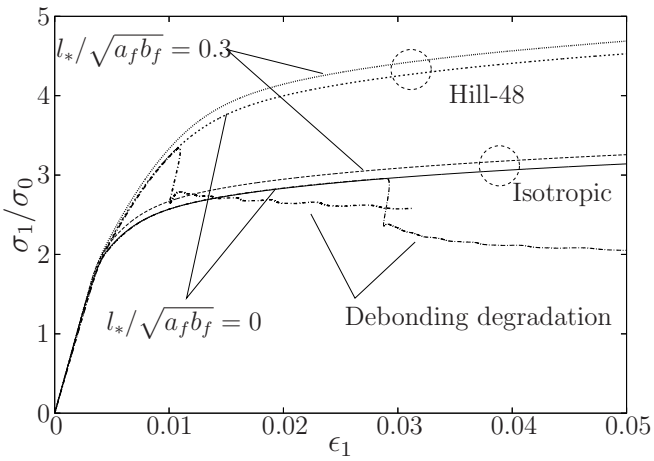

Figure 3. Bi-axial tension results, $\kappa = 0.5$, for isotropy and Hill-48 anisotropy. (a) Average stress-strain curves, Eqs. (2) and (3). (b) Contours of effective plastic strain for a conventional anisotropic material with debonding (c) Contours of effective plastic strain for a higher order anisotropic material without debonding.

For both isotropic and anisotropic behavior the effect of the material length scale parameter, l_*, is an increased load carrying capacity. A sudden stress drop occurs due to debonding which defines the failure strain of the composite, ϵ^f. In Fig. 4 this failure strain is plottet as function of the normalized material length scale parameter of the matrix material, $l_*/\sqrt{a_f b_f}$. It is seen, that the failure strain, ϵ^f, does not vary monotonically by the material length scale parameter, l_*, but reaches a maximum approximately for $l_*/\sqrt{a_f b_f} = 0.15$.

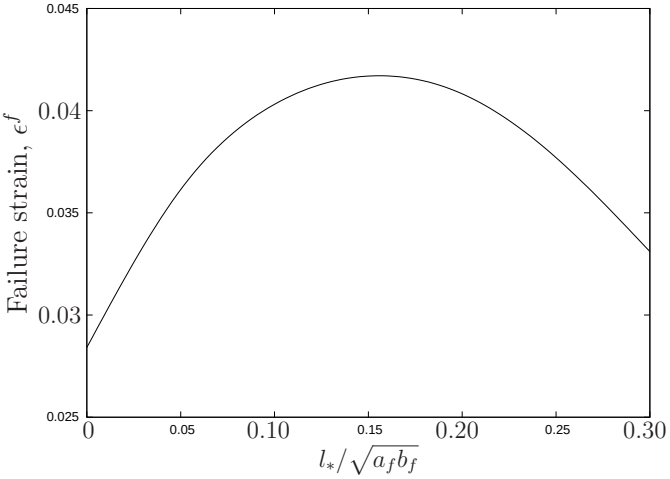

Figure 4. The failure strain as function of the material length scale parameter, l_*, normalized against the fiber radius, R. Isotropic results are shown for $\kappa = 0.5$.

On the other hand, a monotonic effect on the failure strain is found when studying the influence of the length scale parameter of the cohesive law, $l_A = l_J$ in Eq. (13). Fig. 5 shows the failure strain as function of the new cohesive length scale parameter, L_J, normalized against the matrix material length scale parameter, l_*. Both isotropic results as well as anisotropic results are shown using Hill-48 as well as Barlat-91. The coefficients of Barlat-91 are chosen such that the same plastic anisotropy as modeled by Hill-48 is reproduced. Thus, the two anisoropic results are directly comparable.

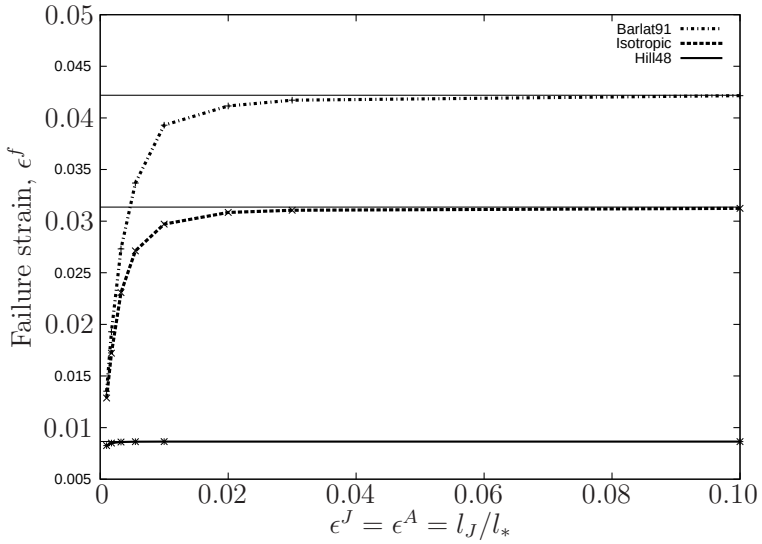

Figure 5. The failure strain as function of the cohesive length scale parameter, L_J, normalized by the matrix material length scale parameter, l_*. Isotropic as well as anisotropic results are shown for $\kappa = 0.5$.

Compared to isotopy, the failure strain is larger using Barlat-91 and smaller using Hill-48. However, a significant effect of $l_J/l_* = l_A/l_*$ is seen for decreasing values as the failure strain decreases as well. On the other hand, for increasing larger l_J-values the plastic behaviour of the cohesive law is supressed and conventional results are obtained as shown by the asymptotic lines. For the Hill material the effect is very small, as debonding failure occurs at a rather small plastic strain, see Fig. 3. Thus, the influence of plasticity in the cohesive law is limited.

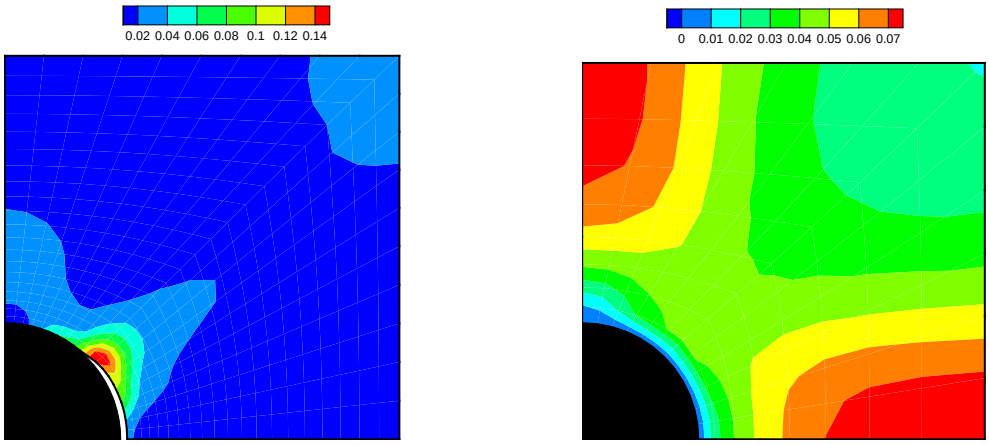

$\epsilon_1 = 0.02$

(a) (b)

Figure 6. Bi-axial tension results, $\kappa = 0.5$, for Hill-48 anisotropy at $\epsilon_1 = 0.02$. (a) Contours of effective plastic strain for a conventional anisotropic material with debonding (b) Contours of effective plastic strain for a higher order anisotropic material without debonding.

In Fig. 6(a) the micro-crack evolving at the fiber-matrix interface can be seen and the contours of the effective plastic strain shows severe strain with larger gradient at the crack-tip. Such large gradients are costly if strain-gradient effects are accounted for. Fig. 6(b) illustrates this for a case where a micro-crack has not evolved but the strain field is much more smooth. It can also be seen that the plastic strain near the fiber-matrix interface vanishes due to the imposed boundary conditions.

5. Conclusion

In conclusion, this study analyzes numerically the combined effects of plastic anisotropy, size-effects and debonding in a composite material. Debonding is seen as a sudden stress drop and plastic anisotropy highly affects the failure strain, while the size-effect is observed as an increased load carrying capacity. The material length scale of the cohesive law tends to reduce the failure strain of the composite, but as the parameter becomes sufficient large conventional results are predicted. This holds for both isotropic as well as anisotropic materials. The material length scale of the matrix material shows a non-monotonic effect on the failure strain such that a maximum failure strain is predicted for approximately a material length scale parameter of 15% of the fiber radius.

References

[1] Talreja R. Damage analysis for structural integrity and durability of composite materials, Fatigue Fract Engng. Mater. Struct., 29, 481-506, 2005.

[2] Fleck. N. A., Hutchinson, J. W.: A reformulation of strain gradient plasticity. J. of the. Mech. and Phys. of Solids, 49, 2245-2271, 2001.

[3] Legarth, B. N.: Strain-gradient effects in anisotropic materials. Model. and Sim. in Mater. Sci. and Eng. 15, S71-S81, 2007.

[4] Niordson, C. F.: Cohesive element for Fleck & Hutchinson 2001. Technical report, Technical University of Denmark, 2010.

[5] Hill, R.: A theory of the yielding and plastic flow of anisotropic metals. Proc. Royal Soc. London. A193, 281-297, 1948.

[6] Barlat, F., Lege, D.J. and Brem, J.C.: A six-component yield function for anisotropic materials. Int. J. Plast. 7, 693-712, 1991.

[7] Tvergaard, V.: Effect of fibre debonding in a whisker-reinforced metal. Mater. Sci. & Eng. A125, 203-213, 1990.

[8] Borg. U, Niordson, C. F., Fleck. N. A., Tvergaard, V.: A viscoplastic strain gradient analysis of materials with voids or inclusions. Int. J. Solids Struct, 43, 4906-4916, 2006.

[9] de Borst, R. Pamin, J.: Some novel developments in finite element procedures for gradient-dependent plasticity. Int. J. Num. Meth. Eng. 39(14), 2477-2505, 1996.

Acknowlegdment

This work was supported by the Danish Center for Composite Structures and Materials for Wind turbine (DCCSM), supported by The Danish Council for Strategic Research grant no: 09-067212.

Nonlinear fracture mechanics metal foams

Tian You Fan[1,*], Hai Yun Hu[1], Ling Yun Xie[1], Lin Feng Sun[1], Rui Ping Guo[2]

[1] School of Physics, Beijing Institute of Technology, Beijing, 100081, China
[2]The Academy of Equipment Command and Technology, Beijing, 101416, China

* Corresponding author: tyfan2006@yahoo.com.cn

Abstract Nonlinear fracture mechanics of metal foams is discussed. The equivalent continuum constitutive model is introduced first. Then we studied analytic solutions on plastic analysis based on generalized cohesive force model, approximate analytic solution of elasto-plastic analysis for central crack, single edge crack specimens in tension and bending, respectively. The finite element analysis is also conducted. In addition, the crack slowly growth and fast propagation are studied as well.Atthe end we proposed a fracture criterion on metal foam.

Keywords Cellular/foam material, Crack tip opening displacement, Analytic solution in closed foam, Approximate solutions, Finite element analysis

1. Introduction

Cellular/foam material, which is one of advanced materials, has become an important engineering material to date due to its lower density and higher specific strength and other excellent mechanical, thermal and acoustical behaviour. For engineering usage, the structural integrity requires materials to have sufficient strength and toughness. Hence the study of crack problems in the material is significant. It is well-known that the basis of deformation and fracture investigation is constitutive law for any engineering materials. Triantafilou and Gibson [1], Gibson et al [2], Deshpande and Fleck [3], Miller [4] and others carried on considerable studies in this respect. Based on the equivalent continuum model they put forward some new macroscopic parameters out of the conventional materials to describe the influence of the substructure, which is called cells. The existence of cells leads to unusual plasticity of metal foams, that is the plasticity dependent from volume deformation.Thus the effect of hydrostatic pressure or the average stress should be considered, and these quantities should be contained into the new constitutive equations in the so-called equivalent continuum model. With these constitutive equations, the elasto-plastic analysis for cellular/foam material can be done. The nonlinearity of the governing equations of the material makes it difficult to construct analytic solutions of boundary value problems. Fan and co-workers [5,6] paid attention to developing a generalized cohesive force model and making the problem being linearized for static crack and moving crack problems, and they developed an asymptotic analysis method by using singular perturbation procedure for slowly steady crack growth problem. Within the linearization regime, the complex analysis presents its particular role and in this paper we report one of the works. The application of conformal mapping helps us to construct some solutions of finite size crack specimens, and it may be useful to experimental investigation and engineering

application.

2. Overview in brief of equivalent continuum constitutive laws

The artificial cellular materials include metal, polymer and ceramic foams respectively. The first two foams display plasticity of dependent of volume deformation, so that the hydrostatic pressure p or the average stress σ_{m} must be taken into account in the constitutive law of the material. The yield/loading surface can be expressed by

$$\Phi = \hat{\sigma} - Y = 0 \tag{1}$$

where $\hat{\sigma}$ represents the generalized effective stress which will be discussed in the following, and if

$$Y = \sigma_{\mathrm{Y}} = \text{const} \tag{2}$$

in which σ_{Y} denotes the uniaxial tensile yield limit of the material, then equation (1) stands for an initial surface. Alternatively if

$$Y = Y(h) \tag{3}$$

where h is a parameter describing plastic deformation history, then equation (1) represents the evolution equation of yield/loading surface.

Triantafilou and Gibson [1] ("TG" to "abbreviated as the TG model" in the following) suggested that

$$\hat{\sigma} = \sigma_{\mathrm{e}} + 0.03\frac{\rho^*}{\rho_{\mathrm{s}}}\sigma_{\mathrm{m}} \tag{4}$$

where ρ^* denotes the density of foam, and ρ_{s} the density of cell wall of the foam, and

$$\sigma_{\mathrm{e}} = \left(\frac{3}{2}s_{ij}s_{ij}\right)^{1/2} \tag{5}$$

is the von Mises effective stress, and

$$s_{ij} = \sigma_{ij} - \frac{1}{3}\sigma_{kk}\delta_{ij} = \sigma_{ij} - \sigma_{\mathrm{m}}\delta_{ij} = \sigma_{ij} + p\delta_{ij} \tag{6}$$

the deviate stress tensor, in which σ_{ij} represents stress tensor, and $\sigma_{kk} = \sigma_{11} + \sigma_{22} + \sigma_{33} = 3\sigma_{\mathrm{m}} = -3p$, δ_{ij} the unit tensor. Substituting equation (4) into equation (1) obtains the TG yield/loading surface of foams.

Gibson, Ashby, Zhang and Triantafilou[2] ("GAZT" to "abbreviated as the GAZT model" in the following) put forward

$$\hat{\sigma} = \sigma_{\mathrm{e}} + 0.81\frac{\rho^*}{\rho_{\mathrm{s}}}\frac{\sigma_{\mathrm{m}}{}^2}{\sigma_{\mathrm{Y}}} \tag{7}$$

Substituting equation (7) into equation (1) leads to the GAZT yield/loading surface of cellular materials.

After the work of TG and GAZT the constitutive models of foams were studied by many other groups. Distinguished from the above models, researchers take other parameters, according to experiments, to describe the effect of cells rather than the

relative density ρ^* / ρ_s.

Deshpande and Fleck [3] ("DF" to "abbreviated as the DF model" in the following) define a plastic Poisson's ratio as

$$v^{\mathrm{p}} = -\frac{\dot{\varepsilon}_{11}^{\mathrm{p}}}{\dot{\varepsilon}_{22}^{\mathrm{p}}} \tag{8}$$

where $\dot{\varepsilon}_{11}^{\mathrm{p}}$ and $\dot{\varepsilon}_{22}^{\mathrm{p}}$ are plastic strain rates. In terms of equation (8) DF derived a parameter α to describe plasticity of dependent volume deformation

$$\alpha = 3\left(\frac{1/2 - v^{\mathrm{p}}}{1 + v^{\mathrm{p}}}\right)^{1/2} \tag{9}$$

where the value of α is in range $1 < \alpha < 2$. Further they suggested the generalized effective stress as follows

$$\hat{\sigma} = \left[\frac{1}{1 + (\alpha/3)^2}(\sigma_{\mathrm{e}}{}^2 + \alpha^2 \sigma_{\mathrm{m}}{}^2)\right]^{1/2} \tag{10}$$

It is evident that if $v^{\mathrm{p}} = 1/2$, then $\alpha = 0$, this corresponds to the plasticity of independent volume deformation, i.e., the classical plasticity.

The substitution of equation (10) into equation (1) yields the DF yield/loading surface.

There are other models of constitutive law for metal foams and polymer foams, but we do not list again.

By considering isotropic hardening, based on flow rule and the above yield/loading surfaces, one can obtain the corresponding constitutive equations, which can be expressed uniformly as follows

$$\dot{\varepsilon}_{ij} = \dot{\varepsilon}_{ij}^{\mathrm{e}} + \dot{\varepsilon}_{ij}^{\mathrm{p}} = \frac{1+v}{E}\dot{\sigma}_{ij} - \frac{v}{E}\dot{\sigma}_{kk}\delta_{ij} + \frac{\dot{\hat{\sigma}}}{H(\hat{\sigma})}\frac{\partial \Phi}{\partial \sigma_{ij}} \tag{11}$$

where $\dot{\varepsilon}_{ij}$ represents strain rate tensor, $\dot{\varepsilon}_{ij}^{\mathrm{e}}$ the elastic strain rate one, $\dot{\varepsilon}_{ij}^{\mathrm{p}}$ the plastic strain rate one, $\dot{\sigma}_{ij}$ the stress rate one, E and v the Young's modulus and Poisson's ratio, and $H(\hat{\sigma})$ the hardening modulus, which can be approximately calibrated through a simple stress-strain relation, e.g. $H(\hat{\sigma}) = \mathrm{d}\sigma / \mathrm{d}\varepsilon^{\mathrm{p}}$ represents the hardening modulus at the stress amplitude value as $\hat{\sigma}$, respectively. From equations (1) and (4), (7), (10) and (11), we have

$$\frac{\partial \Phi}{\partial \sigma_{ij}} = \begin{cases} \dfrac{3}{2}\dfrac{1}{\sigma_{\mathrm{e}}}s_{ij} + 0.09\dfrac{\rho^*}{\rho_{\mathrm{s}}}\delta_{ij}, \text{ TG model} \\ \dfrac{3}{2}\dfrac{1}{\sigma_{\mathrm{e}}}s_{ij} + 0.18\dfrac{\rho^*}{\rho_{\mathrm{s}}}\dfrac{\sigma_{\mathrm{m}}}{\sigma_{\mathrm{Y}}}\delta_{ij}, \text{ GAZT model} \\ \dfrac{1}{[1+(\alpha/3)^2]\hat{\sigma}}\left(\dfrac{3}{2}s_{ij} + 3\left(\dfrac{\alpha}{3}\right)\sigma_{\mathrm{m}}\delta_{ij}\right), \text{ DF model} \end{cases} \tag{12}$$

The form of rate $\dot{\hat{\sigma}}$ can be easily found from the previous definitions of generalized effective stresses.

Coupling the constitutive equation (11) and the deformation geometry equationsand equilibrium equationsand appropriate boundary conditions, the elasto-plastic analysis for the foam materials can be carried out.

3. Generalized cohesive force model and solution

Due to the nonlinearity of equations we can find that the elasto-plastic analysis of crack problems of metal foams is very difficult, the exact analytical solution is almost not available. But the application of some simple physical models can simplify the solving dramatically. It is well-known that the Dugdale model [7], or the Dugdale-Barenblatt model [7, 8], or the cohesive force model is very effective in the study of plastic fracture of conventional structural materials. A similar work is the so-called BCS model [9, 10]. We extend the Dugdale model for conventional structural materials into the foam materials, the statement is as follows.

3.1 Generalized cohesive force model for cellular/foam materials --plane strain state

Assume that an infinite plane of foam material with a Griffith crack subjected a uniform tension $\sigma^{(\infty)}$ at infinity, refer to Fig.1, in which the pulling stress $p=\sigma^{(\infty)}$, and the plastic zone around crack tip is with a narrow band type, whose length is denoted by d, but its value is unknown at moment to be determined.

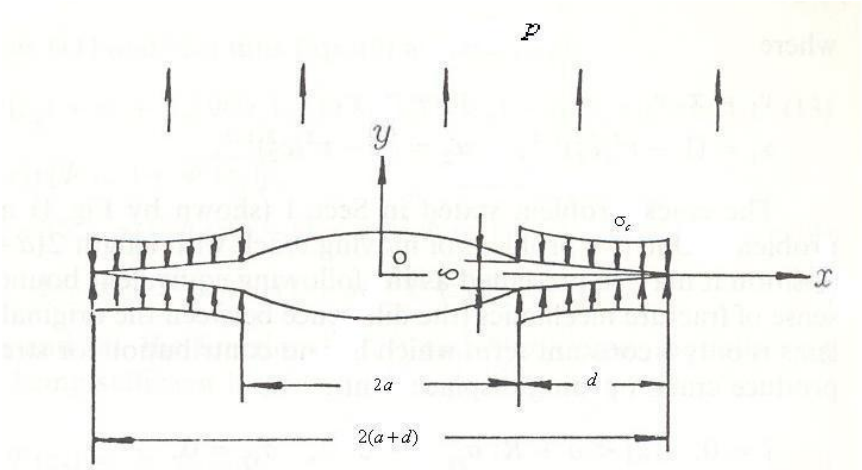

Fig. 1 The generalized cohesive force model for infinite specimen

According to the yield criteria of TG, GAZT, DF models respectively, the corresponding Dugdale plastic zone near the crack tip leads to

$$y=0,\ a<|x|<a+d:\ \sigma_{yy}=\beta\sigma_{\mathrm{Y}},\ \sigma_{xy}=0 \quad (13)$$

Based on the constitutive laws of listed by (11) with (4), (7), (10) respectively, where σ_{Y} represents the uniaxial tensile yield limit of foam materials, and the

parameter β describing cellular/foam materials behaviour and stress state, for plane stress case:

$$\beta=\begin{cases}\dfrac{1}{1+0.03\rho^{*}/\rho_{\mathrm{s}}}, & \text{TG model}\\ \dfrac{\left(1+1.44\rho^{*}/\rho_{\mathrm{s}}\right)^{1/2}-1}{1+0.03\rho^{*}/\rho_{\mathrm{s}}}, & \text{GAZT model}\\ \left[\dfrac{1+(\alpha/3)^{2}}{1+(2\alpha/3)^{2}}\right]^{1/2}, & \text{DF mod}\end{cases} \tag{14}$$

Though there is a new unknown quantity d , the nonlinear problems is linearized, so the equations are reduced to biharmonic equation:

$$\nabla^{2}\nabla^{2}U=0 \tag{15}$$

where $\partial^{2}U/\partial^{2}x=\sigma_{yy},\ \partial^{2}U/\partial^{2}y=\sigma_{xx},\ \partial^{2}U/\partial x\partial y=-\sigma_{xy}$ .The complex representations of U is the stress potential function, u_i the displacement vector and σ_{ij} is similar to that given in conventional structural materials.

The corresponding boundary conditions are

$$\begin{cases}\sqrt{x^{2}+y^{2}}\to\infty:\ \sigma_{yy}=\sigma^{(\infty)},\ \sigma_{xx}=\sigma_{xy}-0;\\ y=0,\ |x|<a:\ \sigma_{yy}=0,\ \sigma_{xy}=0;\\ y=0,\ a<|x|<a+d:\ \sigma_{yy}=\beta\sigma_{\mathrm{Y}},\ \sigma_{xy}=0\end{cases} \tag{16}$$

The linearization problem of cellular/foam materials is concluded to solve the boundary value problem.

Similar to the classical plastic fracture theory, the solutions are

$$d=a\left[\sec\left(\frac{\pi\sigma^{(\infty)}}{2\beta\sigma_{\mathrm{Y}}}\right)-1\right] \tag{17}$$

and

$$\delta_{\mathrm{t}}=\mathrm{CTOD}=\frac{8a\beta\sigma_{\mathrm{Y}}}{\pi E}\ln\sec\left(\frac{\pi\sigma^{(\infty)}}{2\beta\sigma_{\mathrm{Y}}}\right) \tag{18}$$

in which equation (17) determines the plastic zone size, and equation (18) gives the crack tip opening displacement (these two equations were first given by Fan et [5]), respectively. The both formulas contain the parameter β describing behaviour of foam materials. The variations of the crack tip opening displacement versus applied stress for different values of the new material constant α for DF model are shown in Figs. 2 in which the foam material constants $E=0.271\mathrm{GPa},\ \sigma_{Y}=0.811\mathrm{MPa}$.

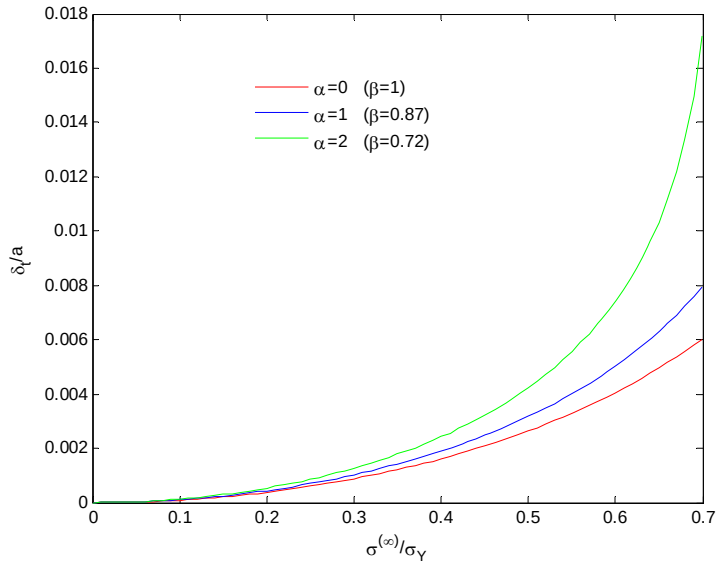

Fig. 2 Variation of values of δ_t versus applied stress for infinite specimen

3.2 Generalized cohesive force model for cellular/foam materials --plane strain state

The discussion is similar to Subsection 3.1, the only differences lie in that the boundary conditions (16) are replaced and the parameter β (given by (14)) is replaced by β' (given by the following (20))

$$y=0,\ a<|x|<a+d:\ \sigma_{yy}=\beta'\sigma_Y,\ \sigma_{xy}=0 \tag{19}$$

And

$$\beta'=\begin{cases}\dfrac{1}{1-2\nu+0.02(\rho^*/\rho_s)(1+\nu)}, & \text{TG model}\\ \dfrac{[(1-2\nu)^2+1.44(\rho^*/\rho_s)(1+\nu)^2]^{1/2}-(1-2\nu)}{0.72(\rho^*/\rho_s)(1+\nu)^2}, & \text{GAZT model}\\ \left[\dfrac{1+(\alpha/3)^2}{(1-2\nu)^2+(2\alpha/3)^2(1+\nu)^2}\right]^{1/2}, & \text{DF model}\end{cases} \tag{20}$$

The solutions are similar to those in Subsection 3.1, the only difference is that the parameter β should be replaced by β'

$$d=a\left[\sec\left(\frac{\pi\sigma^{(\infty)}}{2\beta'\sigma_Y}\right)-1\right] \tag{21}$$

$$\delta_t=\mathrm{CTOD}=\frac{8a\beta'\sigma_Y}{\pi E/(1-\nu^2)}\ln\sec\left(\frac{\pi\sigma^{(\infty)}}{2\beta'\sigma_Y}\right) \tag{22}$$

4. The development of the generalized cohesive force model

In the applications, the finite size specimens are particular important, which are discussed as following.

4.1 Central crack specimen of finite width

4.1.1 Plane stress state

The approximate analytic solution is obtained as follows

$$\delta_t = \mathrm{CTOD} = \left[\left(\frac{2W}{\pi a}\right)\tan\left(\frac{\pi a}{2W}\right)\right]\frac{8a\beta\sigma_Y}{\pi E}\ln\sec\left(\frac{\pi\sigma^{(\infty)}}{2\beta\sigma_Y}\right) \tag{23}$$

4.1.2 Plane strain state

The solution is

$$\delta_t = \mathrm{CTOD} = \left[\left(\frac{2W}{\pi a}\right)\tan\left(\frac{\pi a}{2W}\right)\right]\frac{8a\beta'\sigma_Y}{\pi E/(1-\nu^2)}\ln\sec\left(\frac{\pi\sigma^{(\infty)}}{2\beta'\sigma_Y}\right) \tag{24}$$

4.2 Single edge crack specimen with finite width

Another significant specimen is single edge crack specimen, shown as below:

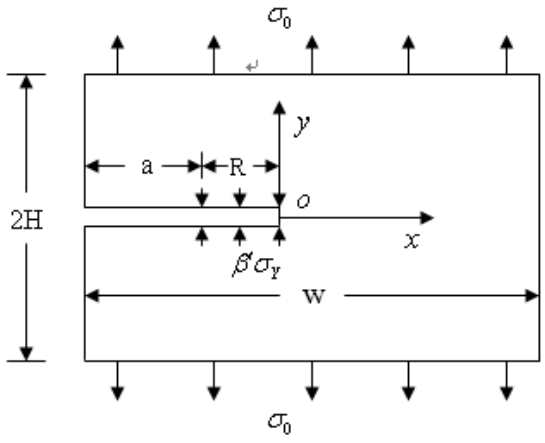

Fig. 3 Single edge crack specimen under tension

4.2.1 Plane stress state

The approximate analytic solution is obtained as follows

$$\delta_t = \mathrm{CTOD} = \frac{4}{\pi}\left[\left(\frac{2W}{\pi a}\right)\tan\left(\frac{\pi a}{2W}\right)\right]\frac{8a\beta\sigma_Y}{\pi E}\ln\sec\left(\frac{\pi\sigma^{(\infty)}}{2\beta\sigma_Y}\right) \tag{25}$$

In the derivation the conformal mapping

$$z = \omega(\zeta) = \frac{2W}{\pi}\arctan\left\{\sqrt{1-\zeta^2}\,\tan\left(\frac{\pi a}{2W}\right)\right\} - a \tag{26}$$

is used to transform region of the specimen at the physical plane (i.e., the $z-$plane) onto the upper half-plane at the mapping plane (i.e., the $\zeta-$plane).

4.2.2 Plane strain state

The solution for plane strain is

$$\delta_t = \mathrm{CTOD} = \frac{4}{\pi}\left[\left(\frac{2W}{\pi a}\right)\tan\left(\frac{\pi a}{2W}\right)\right]\frac{8a\beta'\sigma_Y}{\pi E}\ln\sec\left(\frac{\pi\sigma^{(\infty)}}{2\beta'\sigma_Y}\right) \tag{27}$$

The numerical results are shown in Fig.4.

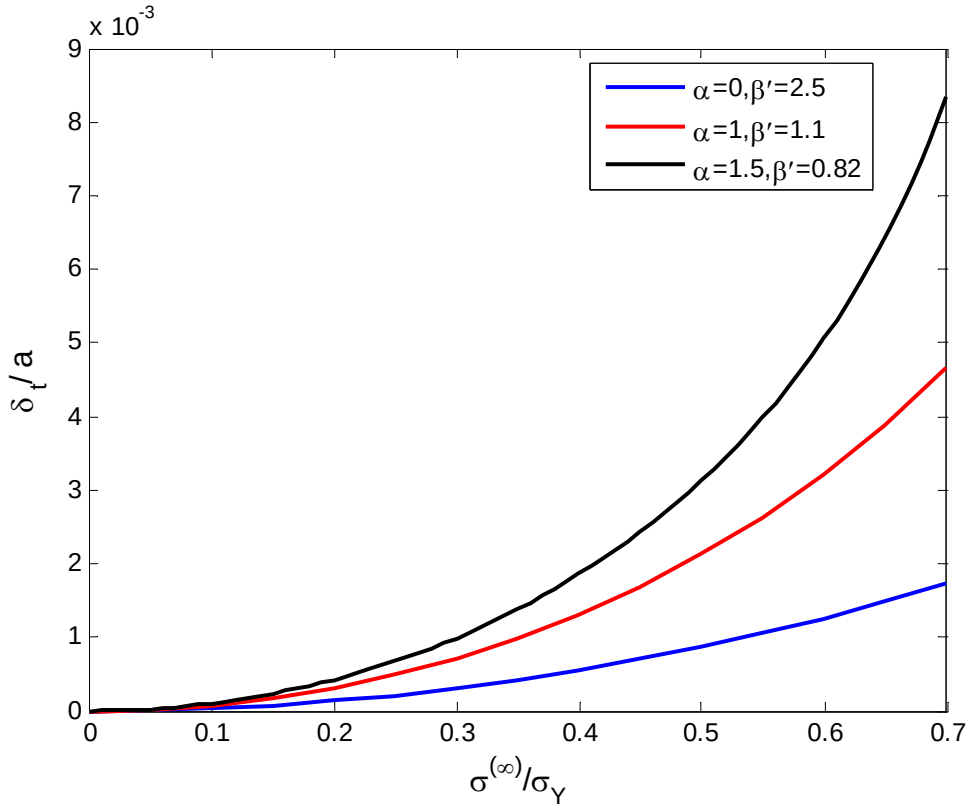

Fig.4Variation of values of δ_t versus applied stressfor finite specimen with a/W =0.3

4.3. Pure bending specimen of central crack

The pure bending specimen is significant in applications.

4.3.1 Plane stress state

The solution is

$$\delta_t = \text{CTOD} = \frac{8\boldsymbol{a}\beta\sigma_Y}{\pi \boldsymbol{E}} \ln \sec\left(\frac{\pi\sigma_N}{2\beta\sigma_Y}\right) \tag{28}$$

$$\sigma_N = 6\frac{M(a+d)}{BW^3} \tag{29}$$

in which M is bending moment, the a crack length, the W width of specimen, and

$$\boldsymbol{d} \approx \boldsymbol{a}\left[\sec\frac{\pi}{2\beta\sigma_Y}\left(6\frac{\boldsymbol{Ma}}{\boldsymbol{BW}^3}\right)-1\right] \tag{30}$$

the plastic zone size, and the others are the same defined before.

4.3.2 Plane strain state

The solution for plane strain is

$$\boldsymbol{d} \approx \boldsymbol{a}\left[\sec\frac{\pi}{2\beta'\sigma_Y}\left(6\frac{\boldsymbol{Ma}}{\boldsymbol{BW}^3}\right)-1\right] \tag{31}$$

and

$$\delta_t = \text{CTOD} = \frac{8\boldsymbol{a}\beta'\sigma_Y}{\pi \boldsymbol{E}/(1-\boldsymbol{\nu}^2)} \ln \sec\left(\frac{\pi\sigma_N}{2\beta'\sigma_Y}\right) \tag{32}$$

5. Finite element analysis

Analytic solutions also have their limitations, and numerical method is important as well. We list a part of numerical solutions conducted by finite element method.

5.1 Single edge crack under tension[14]

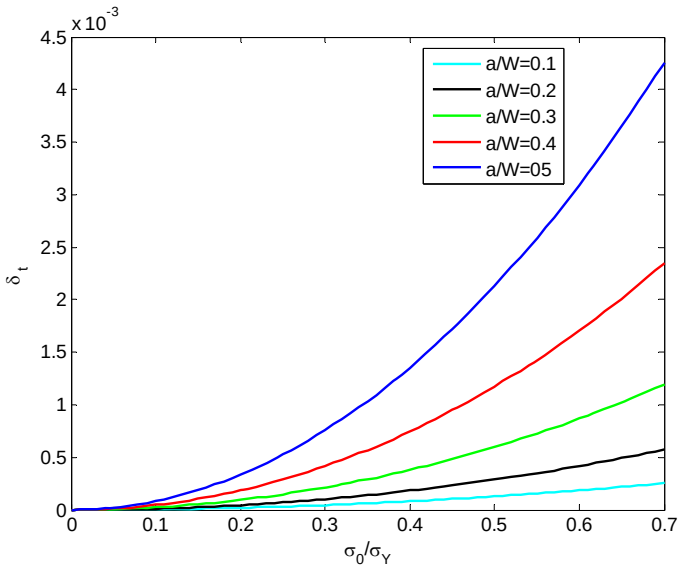

Fig. 5The CTOD of a finite size edge crack specimen of cellular/foam materials indifferent a/w

The comparison between Fig.4 and Fig.5 shows the analytic and numerical solutions are in good agreementwith each other.

5.2 Single edge crack under bending

The elasto-plastic analysis of metal foam in terms of finite element is carried out, the plastic zone around crack tip is shown in Fig.6.

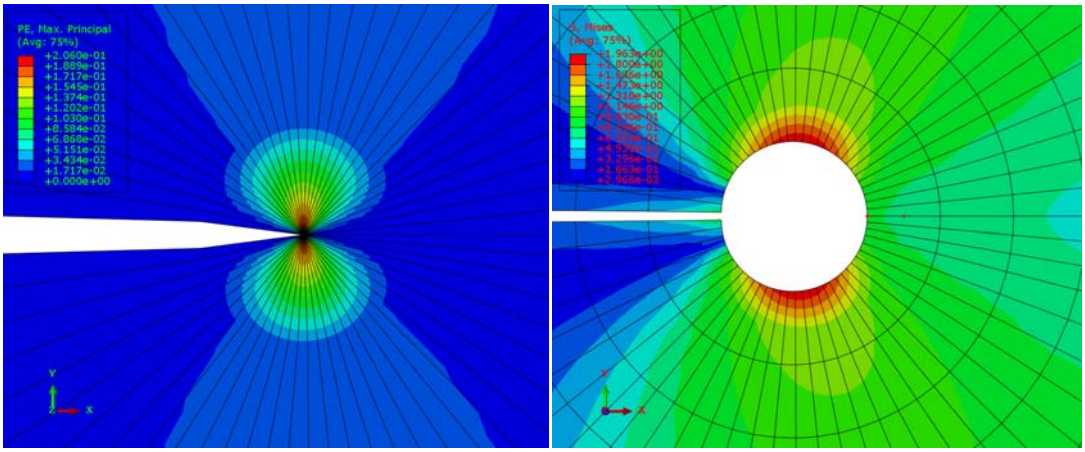

Fig.6The plastic zone around crack tip

6. Crack slowly growth

The crack growth in the metal foams is significant, we discussed two cases and introduce as below.

6.1 TG model [5,15]

In the analysis we developed the singular perturbation, see Fan et al [5]. The constitutive law for TG model is, refer to equations (15) and (16)

$$\dot{\varepsilon}_{ij} = \dot{\varepsilon}_{ij}^{\mathrm{e}} + \dot{\varepsilon}_{ij}^{\mathrm{p}} = \frac{1+\nu}{E}\dot{\sigma}_{ij} - \frac{\nu}{E}\dot{\sigma}_{kk}\delta_{ij} + \frac{\dot{\hat{\sigma}}}{H(\hat{\sigma})}\frac{\partial \Phi}{\partial \sigma_{ij}} = \frac{1+\nu}{E}\dot{\sigma}_{ij} - \frac{\nu}{E}\dot{\sigma}_{kk}\delta_{ij} + \dot{\Lambda} s_{ij}$$
$$\dot{\Lambda} = \frac{1}{H(\hat{\sigma})}\left\{\frac{9}{4}\frac{1}{\sigma_e^2}s_{kl}\dot{\sigma}_{kl} + 0.045\frac{\rho^*}{\rho_s}\sigma_m\right\} \tag{33}$$

The singular perturbation is taken as

$$\sigma_{ij} = \sigma_0 \xi^s \sum_{m=0}^{\infty} \sigma_{ij}^{(m)}(\theta)\xi^{-m}, \xi = \ln\frac{R}{r} \tag{34}$$

in which σ_0 denotes the yield stress in uniaxial tension, s a parameter to be determined, $\sigma_{ij}^{(m)}(\theta)$ the expansion coefficients, R the size of crack tip, and r the distance measured from crack tip.

The structure of the plastic zones around crack tip and the stress distribution are found by further analysis, but the results are omitted due to the limitation of space.

6.2 DF model[6]

The perturbation analysis and results are also constructed, but omitted due to the limitation of space.

7. Crack fast propagation[5]

Some approximate solutions for crack propagation in the material have been obtained as well but the discussions are omitted here.

8. Fracture criteria

Because the metal foams are plastic material, the fracture presents plastic behaviour, the fracture should be used the crack tip opening criterion rather than stress intensity factor criterion, i.e.,

$$\delta_t = \delta_t^c \tag{35}$$

in which δ_t^c is the critic value of δ_t, a material constant, measured by experimental tests. In the above the main attention of our analysis lies in the determination of the crack tip opening displacements for various specimens, because the quantity presents the fundamental importance in the plastic fracture analysis.

9. Conclusion and discussion

The above discussion gives a comprehensive introduction on the plasticity of metal foams, plastic fracture theory and some solutions for cracked specimens with infinite and finite sizes. These solutions are useful to the theoretical and experimental studies. In the work the complex analysis is developed.

Acknowledgement

This work is supported by the National Natural Science Foundation of China through grant 10972035.

Reference

[1] Triantafilou T V and Gibson L J, Constitutive modeling of elastic-plastic open-cell foams, J. Engng. Mech., (1990), 116, 2772-2778.
[2] Gibson L J, Ashby F M, Zhang J et al, Failure surface for cellular materials under multiaxial loads, Int. J. Mech. Sci.,(1989), 31, 635-643.
[3] Deshp and V and Fleck N A, Isotropic constitutive models for metallic foams, J. Mech. Phys. Solids, (2000), 48, 1253-1283.
[4] Miller R, A continuum plasticity model for the constitutive and indentation behaviour of foamed metals, Int. J. Mech., Sci., (2000), 42, 729-754.
[5] Fan T Y, Mai Y W, Guo R P et al, Continuum constitutive models and analytic solutions of crack problems of cellular materials, Journal of Materials andTechnology, (2003), 11, 94-114.
[6] Guo R P, Mai Y W, Fan T Y et al, Plane stress crack growing steadily in metal foams, Materials Science and Engineering A, (2004), 381, 292-298.
[7] Dugdale D S, Yielding of steel sheets containing slits, J MechPhys Solids, (1960), 32, 105-108.
[8] Barenblatt G I, The mathematical theory of equilibrium of cracks in brittle fracture,Advances in Applied Mechanics, (1962), 7, 55-129.
[9] Bilby B A , Cottrell A H and Swinden K H, The spread of plastic yield from a notch, Proc. R. Soc. A,(1963), 272 , 304-314.
[10] Bilby B A , Cottrell A H , Smith E et al, Plastic yielding from sharp notches, ibid, (1964), 279, 1-9.
[11] Fan T Y, Hu H Y and Tang Z Y, Central crack specimen of metal foams with finite size under tension, EngFractMech, (2013), 83, in press.
[12] Fan T Y and Wu Y L, Single edge crack specimen of metal foams with finite size under tension, Advances in Mathematical Physics, (2012), submitted.
[13] Fan T Y and Tang Z Y, Bending specimen of metal foams, Phil Mag, (2012), in reviewing.
[14] Xie L Y and Fan T Y, Finite element analysis of single edge crack specimen under tension of metal foams, Acta Mechanica Solida Sinica, (2012), in reviewing.
[15] Fan T Y,Foundation of Fracture Theory, Science Press, Beijing, 2003, in Chinese.

CRACK DELOPMENT AND DYNAMIC NATURE OF CRACK PROPAGATION IN STRUCTURES

Dr.Subhash Chanda,
Deptt. of physics, A.C College, Jalpaiguri,
West Bengal , India
Email address: dsc3din@yahoo.co.in

Abstract: This paper aims at finding the sources of crack development in modern structures at an elevated temperature and under severe vibrations due to excessive load magnitudes and also of ceismic vibrations. In the present paper attempts have been made for solving the problems relating to large amplitude vibrations of uniform elasto plastic plates and shells under both static and dynamic loads using the method of constant deflection contour lines[8-15]. Also, the effect of crack development and its propagation through the structures have been studied rigorously. The works in this field by numerous researchers are discussed shortly in the introduction and considering all the assumptions made by them after proper correction compatible with the boundary conditions, the present author tries to develop the equations with consideration of multi aspect crack generating factors and their impact on the time periods of nonlinear vibration of the structures and the results obtained for a crack structure are presented along with that of the non cracked structure.

I N T R O D U C T I O N

Modern structures are often subjected to severe vibrations and high temperatures. Sometimes the magnitudes of the applied forces or loads become very large, exceeding the elastic limit and brittle strength of the material used. Ceismic vibrations during earth quake, crashes and blasting of bombs etc. sometimes initiate the growth of fractures within the structures Also, if there exist any source of fracture like crystal defects, brittle disorder, imperfections etc within the structures (may or may not be visible from outsides), fracture will be developed and during the load variations in static cases or during vibrations in all dynamic cases and also during temperature elevation , the fractures have got dynamic character; i.e., crack begins to propagate through the structures causing a notable variation of the magnitude of the flexural rigidity of the material. Gradually, the crack developed within the structures causes a damage of the system due it its growth and dynamic nature. Griffith [1], Irwin[2], E. Erdogan [3], Orowan [4], G.I. Barenblatt [5], D.S, Dugdale [6], J. R. Wills [7] had made extensive researches on fracture mechanics. Some had attempted to explain the fracture character in structures assuming some sort of flaws within it. But all the works are based on some highly simplified hypothesis. To verify the flaw hypothesis, Griffith introduced an artificial flaw in his experimental specimens. The artificial flaw was in the form of a surface crack which was much larger than other flaws in a specimen. Irwin strategically partitioned the energy in two parts; the stored elastic strain energy which is released as a crack grows. This is the thermodynamic driving force for fracture and the dissipated energy which includes plastic dissipation and the surface energy also any other dissipative forces that may be at work.

The dissipated energy provides the thermodynamic resistance to fracture. The Stress Intensity Factor is given by the following equations.

$$G = G_I = \begin{cases} \dfrac{K_I^2}{E} & \text{plane stress} \\ \dfrac{(1-\nu^2)K_I^2}{E} & \text{plane strain} \end{cases}$$

where E is the Young's modulus, v is Poisson's ratio, and K_I is the stress intensity factor in mode I. Irwin also showed that the strain energy release rate of a planar crack in a linear elastic body can be expressed in terms of the mode I, mode II (sliding mode), and mode III (tearing mode) stress intensity factors for the most general loading conditions. Irwin adopted the additional assumption that the size and shape of the energy dissipation zone remains approximately constant during brittle fracture. This assumption suggests that the energy needed to create a unit fracture surface is a constant that depends only on the material. This new material property was given the name *fracture toughness* and designated G_{Ic}. Today, it is the critical stress intensity factor K_{Ic}, found in the plain strain condition, which is accepted as the defining property in linear elastic fracture mechanics.

By applying the theory of fracture mechanics one can study the propagation of cracks in materials. Fracture Mechanics uses methods of analytical solid mechanics to calculate the driving force on a crack and those of experimental solid mechanics to characterize the material's resistance to fracture. It applies the Physics of Stress and Strain, in particular the theories of elasticity and Plasticity, to the microscopic Crystallographic defects found in real materials in order to predict the macroscopic mechanical failure of bodies.A comparative study of the static and dynamic characteristics of the structure will provide a notice for of such a failure before hand . The prediction of crack growth is at the heart of the damage tolerance discipline. Still, by studying the static and dynamic characteristics of the structures and comparing the results with the standard results of the same structures without any crack, an estimation of the safety factor may be obtained with ease.

Derivation Of The Governing Differential Equations for A Non Cracked Structure

A shallow shell of uniform thickness `h ` is considered. Let the equation of the middle surface of the shell, referred to an orthogonal coordinate system (x,y,z), be given by

$$Z = (x^2 / 2 R_x) + (xy / R_{xy}) + (y^2 / 2 R_y) \qquad (1)$$

For a shallow shell $r = \sqrt{(x^2 + y^2)}$ considered small in comparison to the least of the radii of curvature, R_x , R_{xy} and R_y which are taken to constants.When the shell experiences axisymmetric free vibration the intersections of the deflected surface and the parallels z = constant yield contour lines of constant deflection. Application of D` Alembert`s principle to an element of the shell bounded by such a contour at any time τ and subsequent summation of the forces in the direction normal to the surface yields the following dynamical equations [1] :

$$\int V_n \, ds + \int\int [\rho h (\partial^2 w) / \partial \tau^2 + (N_x) / R_x + (N_y) / R_y + 2 (N_{xy}) / R_{xy}] \, dx \, dy = 0 \qquad (2)$$

where the transverse reaction forces $V_n = Q_n - \partial/\partial s(M_{nt})$ in absence of fractures, (2,a)

$V_n = Q_n - \partial/\partial s(M_{nt}) – f(a, G, K)$, the last term is due to fractures, (2,b)

represents the effect of the shearing force Q_n and the edge-rate of change of twisting moment M_{nt} along the contour C_u. According to Ilyushin`s theory of the elastic plastic deformation (1948), the bending moments M_x, M_y, M_{xy} and their shear forces Q_x, Q_y are given by the following relations:

$$M_x = -D(1-\nu)\{(\partial^2 w/\partial x^2) + \nu(\partial^2 w/\partial y^2)\} \quad (3)$$
$$M_y = -D(1-\nu)\{(\partial^2 w/\partial y^2) + \nu(\partial^2 w/\partial x^2)\}$$
$$M_{xy} = D(1-\nu)(1-\Omega)(\partial^2 w/\partial x \partial y)$$
$$Q_x = (\partial/\partial x)\{M_y\} - (\partial/\partial y)\{M_{xy}\}$$
$$Q_y = (\partial/\partial y)\{M_x\} - (\partial/\partial x)\{M_{xy}\}$$
$$Q_n = Q_x \cos\alpha + Q_y \sin\alpha$$

$$M_{nt} = M_{xy}(\cos^2\alpha - \sin^2\alpha) + (M_x - M_y)\sin\alpha\cos\alpha \quad (4)$$

Where, $\cos\alpha = (dy/ds)$ and $\sin\alpha = -(dx/ds)$.

Here, ρ, h and w are, respectivly, the mass density, the shell thickness and the deflection. Using the well known expressions for the moments and shearing forces and assuming that the membrane forces N_x, N_y and N_{xy} are given by

$$N_x = (\partial^2\Phi/\partial y^2),\quad N_y = (\partial^2\Phi/\partial x^2),\quad N_{xy} = -(\partial^2\Phi/\partial x\partial y) \quad (5)$$

Equation (2) finally reduces to:

$$(\partial^3 w/\partial u^3)\int(1-\Omega)R\,ds + (\partial^2 w/\partial u^2)\int(1-\Omega)F\,ds + (\partial w/\partial u)\int(1-\Omega)G\,ds$$
$$+ (\partial^2 w/\partial u^2)\int D[(\partial\Omega/\partial x)(\partial u/\partial x) + (\partial\Omega/\partial y)(\partial u/\partial y)]\sqrt{t}\,ds + (\partial w/\partial u)\int (D/\sqrt{t})[K(\partial\Omega/\partial x) + L(\partial\Omega/\partial y)]\,ds + \iint[\rho h (\partial^2 w/\partial\tau^2 (1/R_x)(\partial^2\Phi/\partial y^2) + (1/R_y)(\partial^2\Phi/\partial x^2) - 2/(R_{xy}\partial^2\Phi/\partial x\partial y]\,dx\,dy = 0 \quad (6)$$

Where R,F,G are given in Ref.13, $D = (E h^3/12(1-\nu^2))$,is the flexural rigidity.
Here, $\Omega = 0$ when $e \le 1$, the region is elastic ; when $e > 1$ the region is plastic. Also, $\Omega = \lambda[1 - (3/2e) + (1/2e^3)$

and $e^2 = (h^2/3e_s^2)[(\partial^2 w/\partial x^2)+(\partial^2 w/\partial y^2)+(\partial^2 w/\partial x\partial y)+(\partial^2 w/\partial x^2)(\partial^2 w/\partial y^2)$

$$= (h^2/3e_s^2)[M(\partial w/\partial u)^2 + N(\partial w/\partial u)(\partial^2 w/\partial u^2)(\partial w/\partial u) + t^2(\partial^2 w/\partial u^2) \quad \textbf{(7)}$$

in which e_s is the yield strain, ν is the poisson`s ratio, D is the flexural rigidity of the plate material, λ is a material constant .

Here, $M = [u_{,xx}^2 + u_{,yy}^2 + u_{,xx}u_{,yy} + u_{,xy}^2]$
$N = [2u_{,x}^2 u_{,xx} + 2u_{,y}^2 u_{,yy} + u_{,xx}u_{,y}^2 + u_{,x}u_{,yy} + 2u_{,x}u_{,y}u_{,xy}]$
$t^2 = (u_{,x}^2 + u_{,y}^2)$

Considering only the transverse vibration, we assume that

$$w = W(x,y)f(t) \quad (8)$$
$$\Phi = \Phi(x,y)f(t) \quad (9)$$

Equation (6) will now reduce to

$$[(\partial^3 W/\partial u^3)\int(1-\Omega)R\,ds + (\partial^2 W/\partial u^2)\int(1-\Omega)F\,ds + (\partial W/\partial u)\int(1-\Omega)G\,ds$$
$$+ (\partial^2 W/\partial u^2)\int D[(\partial\Omega/\partial x)(\partial u/\partial x) + (\partial\Omega/\partial y)(\partial u/\partial y)]\sqrt{t}\,ds + (\partial W/\partial u)\int(D/\sqrt{t})[K(\partial$$

$\Omega / \partial x) + L (\partial \Omega / \partial y)] ds] f(t) + \iint [\rho h W f``(t) + \{ (1/ R_x)(\partial^2 \Phi / \partial y^2) + (1 / R_y) (\partial^2 \Phi / \partial x^2) - 2 / (R_{xy} \partial^2 \Phi / \partial x \partial y \} f(t)] dx dy = 0$ (10)

Consequently, the condition for continuity of deformation reduces to

$\nabla^4 \Phi = \{ 12D (1 - \nu^2) \} / h^2 (1 - \Omega) [(1/ R_x)(\partial^2 \Phi / \partial y^2) + (1 / R_y) (\partial^2 \Phi / \partial x^2) - 2 / (R_{xy})$ (11)

This equation must hold over all points in the interior of the shell. After integration over the area and application of Greens theorem one obtains :

$(d^3\Phi/du^3) \int Rds + (d^2 \Phi/du^2) \int Fds + (d\Phi/du) \int Gds * 12D^2 (1 - \nu^2) / h^2 (1 - \Omega)(dW/du)$
$\int K_x (\partial u / \partial y)^2 + Ky (\partial u / \partial x)^2 / t^{½} ds = 0$ (12)

where K_x and K y denote curvatures at a point and K xy has been assumed to be zero in accordance with the shallowshell theory. Equations (11) and (13) are now the two basic equations for large amplitude vibration of shallow shell.

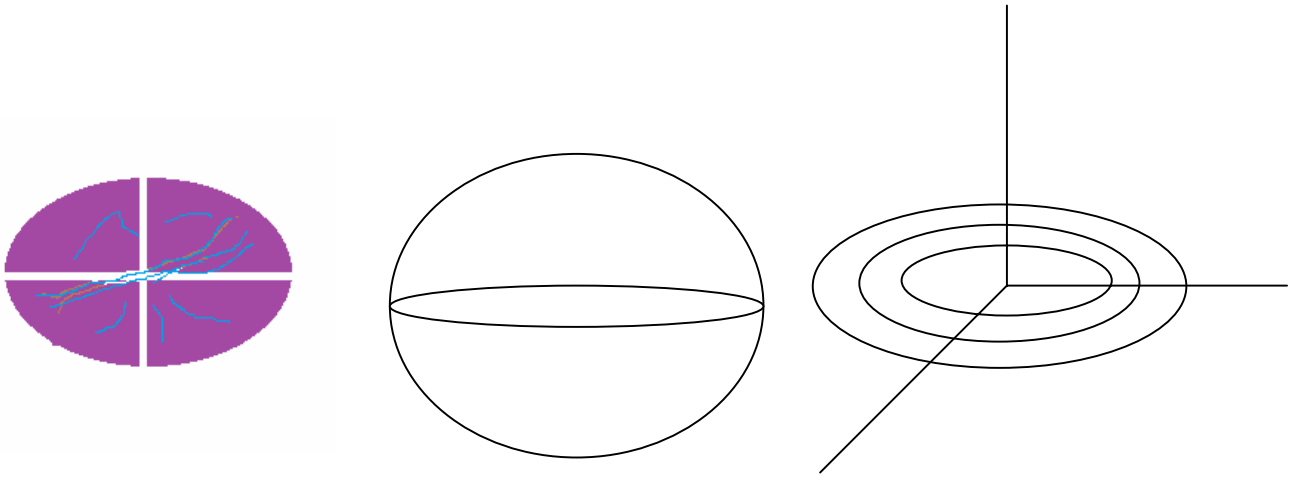

Internally Cracked shallow domes and isodeflection contour lines

Figure-I

ILLUSTRATION:

Let us now consider a clamped dome of non-zero curvature upon an elliptic base. For the first approximation under symmetry consideration we may write

$$u = 1 - x^2 / a^2 - y^2 / b^2 \quad (13)$$

Performing the contour integrations taken around the closed contour

$$u = 1 - x^2 / a^2 - y^2 / b^2$$

And the double integration extending over the ellipse

$$x^2 / a^2 + y^2 / b^2 = 1 - u \qquad (14)$$

Equation (11) in non dimensional form becomes

$$(1 - \Omega)(1 - u)(d^3W/du^3) - 2(1 - \Omega)(d^2W/du^2) - (d\Omega/du)[(1 - u)(d^2W/du^2) - 2P\{(1/a^4) + (1/b^4) + 2\nu/a^2b^2)(dW/du)] + (\rho h^2 \omega^2 P)/(2 D e_s a^2) - \{(E h \gamma)/D\}(d\Phi/du) = 0 \qquad (15)$$

where $P = (a^4 b^4)/(3a^4 + 2a^2b^2 + 3b^4)$, while equation (12) in non dimensional form will reduce to

$$(1 - u)(d^3\Phi/du^3) - 2(d^2\Phi/d^2u) + (1 - \Omega)\gamma(dW/du) = 0 \qquad (16)$$

with $\gamma = p(k_x/b^2 + k_y/a^2)$; $W = wh/e_s a^2$; $\Phi = \varphi/E e_s a^2$ (17)

(18)

METHOD OF SOLUTION

On substitution of the value of Ω into equations (16) & (17), one obtains

$$[(1 - u)(d^3W/du^3) - 2(d^2W/du^2)] Q_1 f(t) - [2M(d^2W/du^2)(dW/du) + N(d^2W/du^2)^2 N(d^3W/du^3)(dW/du) + 2t^2(d^3W/du^3)(dW/du)][(1 - u)(d^2W/du^2) - 2P_1(dW/du)Q_2 f^3(t) - (Eh\gamma/D) f(t)(d\Phi/d + (\rho h/(2 D e_s a^2) f``(t) = 0 \qquad (18)$$

and $$(1 - u)(d^3\Phi/du^3) - 2(d^2\Phi/d^2u) + Q_1\gamma(dW/du) = 0 \qquad (19)$$

Where, $Q_1 = [2e^3(1 - \lambda) + \lambda(3e^2 - 1)]/2e^3$; $Q_2 = (\lambda/4e^5)(e^2 - 1)$

$P_1 = P(1/a^4 + 1/b^4 + 2\nu/a^2b^2)$

Also, e^2 is given by

$$e^2 = \tfrac{1}{3}[M(dW/du)^2 + N(dW/du)(d^2W/du^2) + t^2(d^2W/du)^2] \qquad (20)$$

Suppose the shell is completely clamped along the boundary.

The boundary conditions are given by

$$W|_{u=0} = 0 = (dW/du)|_{u=0}$$
$$\Phi|_{u=0} = 0 = (d\Phi/du)|_{u=0}$$

To find an approximate solution, we assume the following trial solutions:

$$W = \Sigma a_j u^j \; ; \quad \Phi = \Sigma b_j u^j \qquad (21)$$

On substitution of these trial solutions in equations (16) & (18), we get the residuals R_1 & R_2 which, after the application of Galerkin`s procedure, yield the following results.

$$(\rho h^2 P)/(6 D e_s a^2) f``(t) = [(4/3) Q_1 a_2 + (Eh\gamma/2D) b_2] f(t) + [(4/5) M + (2/3) N - (32/5) M P_1 - 4 N P_1] Q_2 a_2^3 f^3(t) \qquad (22)$$

and $$b_2 = (3/8) Q_1 \gamma a_2 \qquad (23)$$

while the average value of `e` happens to be

$$e = a_2 \sqrt{[(1/a^4) + (1/b^4) + (2/a^2 b^2)]} \, (40/9) \qquad (24)$$

From equations (22) & (23), one obtains the following time differential equations in f(t):

$$f``(t) + \mu f(t) + \zeta f^3(t) = 0 \qquad (25)$$

where, $\mu = -(6 D e_s a_2 / \rho h^2 P) [(4/5) M + (2/3) N - (32/5) M P_1 - 4 N P_1] Q 2 a_2^3$

Since the series is rapidly converging hence considering the first few terms one may obtain the approximate value of the central deflection w* as

$$w^* = \Sigma_j a_j$$

The solution of equation (25) is given by

$$f(t) = a_0 \operatorname{Sin} [\mu t \{ 1 + (3/8) a_0^2 (\zeta/\mu) \} + \theta_0] \qquad (26)$$

The time periods of the non-linear and linear oscillations are

$T^* = 2\pi / [\mu \{ 1 + (3/8) a_0^2 (\zeta/\mu) \}]$ and $T = 2\pi/\mu$.

Thus $[T/T^*] = 1/\{ 1 + (3/8) a_0^2 (\zeta/\mu) \} \qquad (27)$

NUMERICAL RESULTS

Numerical results are computed both for circular and elliptic plates & shallow domes upon the circular & elliptic bases in the elastic and elastic plastic regions and these are presented in tables (1 – 4). The computations are made with different values of the shallowness parameter (2 γ / h) and material constant ν = 0.3. Dynamic responses of the elasto-plastic shells for moderately large amplitude are obtained from the same differential equations. Moreover, effect of crack / fractures are computed with the same equation only changing the term for Vn in equation (2,b) and making subsequent changes in other equations and the results are presented in the tables from (1-4, red coloured) .This is no doubt advantageous as such both static and dynamic behaviors are obtained simultaneously with least effort.

T A B L E - 1

Free vibrations of clamped plastic shallow shell with circular planform. First row results for without crack while the second row results[Red coloured] are with crack.
e >1 , a = b, ν = 0.3 ,λ =1

T*/T→

W*a_0→	0	0.5	1.0	1.5	2.0
2γ/=0	1.0000 , 1.0276	1.0256 1.0453	1.1111 1.0689	1.2903 1.3561	1.6666 1.7860
2γ/h=1	1.0000 1.0045	1.0184 1.0235	1.0778 1.0976	1.1940 1.2357	1.4063 1.5872
2γ/h=2	1.0000 1.0011	1.0099 1.0212	1.0411 1.1676	1.0975 1.2879	1.1874 1.3654
2γ/h=3	1.0000 1.0078	1.0056 1.0487	1.0230 1.1432	1.0532 1.1769	1.0985 1.1980
2γ/h=4	1.0000 1.0061	1.0037 1.0764	1.0149 1.1267	1.0345 1.1478	1.0621 1.1645
2γ/h=5	1.0000 1.0032	1.0024 1.0989	1.0095 1.1087	1.1215 1.1112	1.0390 1.1313

T A B L E -2

Free vibrations of clamped plastic shallow shell with elliptic planform . e >1 , a =2 b, ν = 0.3 ,λ = 1. First row results for without crack while the second row results[Red coloured] are with crack.

T*/T→

W*a_0→	0	0.5	1.0	1.5	2.0
2γ/h=0	1.0000 1.0087	1.0866 1.1432	1.4682 1.8760	2.5398 2.7890	4.6241 5.0023
2γ/h=1	1.0000 1.1123	1.0611 1.1564	1.2995 1.8709	2.0768 2.9556	2.2857 3.0986
2γ/h=2	1.0000 1.2345	1.0325 1.4532	1.1439 1.6750	1.3947 1.9870	2.6125 3.1012
2γ/h=3	1.0000 1.5680	1.0182 1.7690	1.0771 1.9080	1.1919 2.3240	1.4009 3.4532
2γ/h=4	1.0000 1.6730	1.0133 1.8750	1.0468 2.0021	1.1117 2.0234	1.2176 3.6700
2γ/h=5	1.0000 1.8870	1.0075 2.0222	1.0310 2.3421	1.0726 2.4562	1.1367 3. 7800

T A B L E - 3

Free vibrations of clamped elastic shallow shell with circular planform . e >1 , a = b, ν = 0.3 ,λ = 1. First row results for without crack while the second row results[Red coloured] are with crack. T*/T→

W*a_0→	0	0.5	1.0	1.5	2.0
2γ/=0	1.0000 1.0500	1.9582 2.1865	0.8513 2.5087	0.7179 3.1254	0.5887 3.2754
2γ/h=1	1.0000 1.0836	1.9695 2.3905	0.8880 2.6540	0.7789 3.2300	0.6646 3.4322
2γ/h=2	1.0000 1.1021	1.9831 2.5214	0.9355 2.8800	0.8657 3.3500	0.7840 3.4804
2γ/h=3	1.0000 1.1208	1.9903 2.7806	0.9623 2.9231	0.9189 3.5602	0.8645 3.7120
2γ/h=4	1.0000 1.1457	1.9936 2.9807	0.9751 3.0061	0.9457 3.6615	0.9074 3.8654
2γ/h=5	1.0000 1.1674	1.9960 3.0085	0.9838 3.0120	0.9645 3.7211	0.9385 3.9800

T A B L E - 4

Free vibrations of clamped elastic shallow shell with elliptic planform . e >1 , a = 2b, ν = 0.3 ,λ = 1 . First row results for without crack while the second row results[Red coloured] are with crack.

T*/T→

W*a_0→	0	0.5	1.0	1.5	2.0
2γ/=0	1.0000 1.0764	0.8778 2.3421	0.6423 2.3675	0.4436 3.1586	0.3098 3.4210
2γ/h=1	1.0000 1.0887	0.9085 2.4531	0.7130 2.4722	0.5247 3.4326	0.3883 3.4789
2γ/h=2	1.0000 1.0912	0.9479 2.6487	0.8200 2.7120	0.6692 3.6870	0.5323 3.7123
2γ/h=3	1.0000 1.1105	0.9697 2.7896	0.8888 2.8760	0.7805 3.8902	0.6667 3.9431
2γ/h=4	1.0000 1.1236	0.9808 2.9807	0.9276 3.0023	0.8507 3.9034	0.7622 3.9890
2γ/h=5	1.0000 1.1432	0.9865 3.0231	0.9480 3.0765	0.8902 3.9986	0.8203 4.0064

O B S E R V A T I O N S A N D C O N C L U S I O N S

It is observed that the results obtained for elastic shallow shells are in excellent agreement with those obtained in [4, 5].Also, the results for plastic shells based on circular and elliptic domes are in good agreement with those obtained in [4]. It is found in both the cases that the ratio of nonlinear to linear time periods become larger in case of plastic shell in comparison to those obtained in case of elastic shells and which is expected. This actually supports the application of the isodeflection contour lines method to analyse such problems. Inspite of that the method has some limitations. It heavily relies on the accuraqcy of the choice of the iso-deflection contour function u(x,y). The main advantage of the method lies in the fact that once the form of the function u (x,y) is chosen suitably the remaining task can be tackled with ease and accuracy. Numerical results [red coloured] obtained for the plates and shells in presence of fractures reveal the fact that due to reduction of the values of elastic constants reaction falls and some irregularities are observed when the cracks propagating through the specimen increasing their dimensions which is expected.

R E F E R E NC E S

1.Griffith, A. A. (1921), "The phenomena of rupture and flow in solids", *Philosophical Transactions of the Royal Society of London*, A **221**: 163–198, http://www.cmse.ed.ac.uk/AdvMat45/Griffith20.

2.E. Erdogan (2000) *Fracture Mechanics*, International Journal of Solids and Structures, 37, pp. 171–183.

3.Irwin G (1957), *Analysis of stresses and strains near the end of a crack traversing a plate*, Journal of Applied Mechanics 24, 361–364.

4.Orowan, E., 1948. *Fracture and strength of solids*. Reports on Progress in Physics XII, 185–232.

5. Willis, J. R. (1967), "A comparison of the fracture criteria of Griffith and Barenblatt", *Journal of the Mechanics and Physics of Solids* **15** (3): 151–162.
6. Dugdale, D. S. (1960), "Yielding of steel sheets containing slits", *Journal of the Mechanics and Physics of Solids* **8** (2): 100–104
7. Dugdale, D. S. (1960), "Yielding of steel sheets containing slits", *Journal of the Mechanics and Physics of Solids* **8** (2): 100–104

8. L.A.Pipes and L.R.Harvill,Mathematics for Engineers and Physicists, 3rd Edn., p –632, Mc Graw Hill, New York.

9. A.A.Ilyushin,1948 OGIZ,GITTL,Moscow,Leningrad, Plasticity.
10 . J. Mazumdar and R.K..Jain,1989, International Journal of Plasticity, vol.5, 463 –475.
Elastic Plastic analysis of plates of arbitrary shape –A new approach.

11. J.Mazumdar, P.K.Bhattacheryya, and M.M.Banerjee,1994, Elastic Plastic analysis of shallow shels- A New approach, accepted for presentation at the 4th Pan American Congress of Applied Mechanics, Buenos Aires, Argentina, Jan. 3-6,1995.
12 . R Jones and J. Mazumdar,1994, Transverse Vibrations of shallow shells by the method of constant deflection contours, J. Acoust.Soc. Am. Vol. 56, 1487-1492.
13 S.Chanda, 2003,Invited paper for 17th Int. Con. On structural mechanics in reactor technology , Static responses of elasto-plastic non-uniform plates of arbitrary shape.
14 J. Mazumdar and D. Bucco, 1978 Journal of Sound and Vibrationvol.57,323 – 331.Transverse vibration of visco elastic shallow shells.
15 . S.Chanda and M.M.Banerjee ,Large deflections of thin elastic plates of arbitrary shape placed on elastic foundation under both uniform load and concentrated load at the centre. European Journal of Mechanical Engineering, BSME.

Initiation and Interaction of a Pulse Beam of Xenon Ions with an Obstacle

Viktor A. Morozov[1*], Yuriy V. Petrov[1], Anton A. Lukin[1], Viktor M. Kats[1], Vladimir A. Bratov[1], Sergei I. Fedoseenko[1]**

[1] Saint-Petersburg state university, 7-9, Universitetskaya nab., Russia
*viktor.morozov@math.spbu.ru, **yp@yp1004.spb.edu

Abstract

The concept of creating intense pulsed ion beam from source based on cryogenic target of inert gases (Xe) irradiated by intense electrons beam from the cathode with explosive emission in the nanosecond range was realized.
The studies were conducted on the modernized experimental equipment consisting of a short high- voltage pulse generator GKVI-300, high-vacuum pumping system based on turbo-molecular pump TMN-1000M with the ability to hold pressure in research chamber $\sim 1 \cdot 10^{-6}$ Torr, Gifford-McMahon cryocoolers MSMR-110-3, 2/20 with closed He – cycle that provides cooling temperature T=20K and a gas injection system.
Gas xenon (Xe 4,8, with the percentage of xenon 99,9988%) was used as working gas It ffreezes to copper anode plate cooled to a temperature of 45-50 K.
As a test materials were selected D16 aluminum alloy and stainless austenitic steel 12X18H10T (cryogenic constructional steel) having wide practical application.
Micro-topography surface and X-ray photoelectron spectra of samples were obtained at an atomic force microscope Solver PRO-M and the electron spectrometer ESCALAB-5 (line Kα Al ($h\nu$=1486.6 eV)) .
The impact of short-pulsed ion beam on a sample of D16 alloy and stainless steel 12X18H10T leads to erosion of the surface in the form of separate craters, the depth of which depends on the hardness of the material and the number of pulses. Uniform over the surface area distribution of craters can be achieved when placed in front of target fine-mesh nets of a refractory metal such as molybdenum.
A numerical simulation of fracture of aluminum target by a beam of high-energy ions, the finite element method, corresponding flow through one grid was realized. The results are in good agreement with experimental data.

Keywords: ion beam, electron beam, erosion, cryogenic target, computational modeling

1. Introduction

Influence of powerful short-time beam of particles – photons, electrons, ions – on physical and mechanical properties of constructional materials represents a great interest, both with theoretical, and from the practical point of view. It gains special relevance in connection with the technogenic accident which have occurred recently, especially on nuclear power plants where the processes caused by fast particles are extremely important. Influence is capable to modify significantly physical and chemical and mechanical properties of materials. The knowledge of mechanisms of changes of properties is extremely necessary as for an estimation of possible changes under the influence of particles, and in connection with prospects of creation of new functional materials and changes of characteristics in the necessary direction. Studying of influence of the ions having high energy, on constructional materials very important. Radiation bunch processing everything is wider and more widely applied to modifying of near-surface layers of parts that allows to improve considerably their operational characteristics [1]. The particular interest represents research of influence of the short-time beam having a number of features in relation to influence on physical and mechanical characteristics. The large number of the designs, allowing to receive ionic bunches with various parameters [2] is so far developed. However they represent rather difficult devices that does them extremely expensive. In this regard in this work researches on creation of the source, allowing to receive short-time, about 10-100 nanoseconds, a beam of ions of the high power which design has to be most adapted for the available equipment are conducted.

2. Experimental techniques

The main idea based on creation of a source of ions, consists in the following. The generator of short high-voltage impulses of GKVI-300 allows to receive a short-time pulse beam of the electrons having high energy. This beam can be directed on a material containing atoms of the necessary grade. This leads to a number of processes (thermal heating, an electronic and stimulated desorption, cascade ionization) and at a surface of the anode is formed the plasma consisting of electrons and ions of a various charges. These ions, being positively charged, move in the direction, return to electrons beam. It is a so-called passive source of ions. In our case the version of the cryogenic passive anode which allows to receive unicomponent structure of an ionic bunch is chosen.
When developing a design a number of the moments was considered. First, it is necessary that issue of electrons which in available strong electric fields has explosive character, didn't lead to changes on a surface of the sample which is a part of cathode assembly. Therefore the cathode was made compound. It represented a ring in which the sample (fig.1) took place.

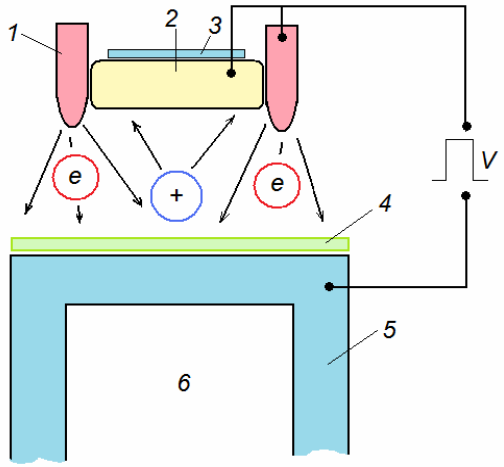

Fig. 1. Schematic image of a source of ions. 1 – cathod ring, 2 – a sample, 3 – a reflecting layer for registration of mechanical stress by an interferometric method, 4 - a layer of the condensed inert gas, 5 – the anode, 6 – the volume cooled by the cryorefrigerator.

Edges of a ring 1 have the pointed form and protrude from the sample 2. When giving a high-voltage impulse electron emission happens from a ring edge as such geometrical form provides the greatest intensity of electric field in this place. The sample thus doesn't participate in formation of an electronic beam. The back party of a sample is polished to mirror shine and serves as an informative mirror of the interferometer of Michelson by means of which shift of this surface is measured. Shift arises owing to impact on a sample of an ionic beam. In the ring cathode there are openings for leading of a laser beam of the interferometer.
The second important point belongs to an anode material. At impact of ions on a solid body it is important that there was no chemical interaction between ions and atoms of a material. Otherwise it can lead to change not only mechanical and structural properties, but also to change of a chemical composition. In this regard ions of inert atoms are the most suitable. As that xenon was chosen. The choice was dictated by possibility of condensation of this gas when cooling anode. For this purpose the anode was carried out in the form of a rod 5 cooled by system, consisting of compressor installation with the control and management block and a cooler. Such system allows to receive the xenon layer which thickness is defined by pressure of gas filled through a inlet valve and hold time on an anode surface. After achievement of a layer of the necessary thickness xenon is pumped out up to the pressure $\sim 10^{-6}$ Tor. Such

sequence of actions provides localization of a place of formation of ions. Ionization of atoms of xenon takes place only in close proximity to an anode surface. Besides, in high vacuum length of run of particles considerably exceeds an available interval between the anode and the cathode. It means that dispersion of ions in such conditions is negligible.

2.1. Experimental unit

Researches were conducted on the modernized experimental unit consisting of the generator of short high-voltage impulses of GKVI-300, the research camera which appearance is given on Fig. 2, high-vacuum pumping system, MCMP-110-3,2/20 Gifford-Makmagona cryorefrigerator with closed He – cycle providing temperature of cooling of $T_{coll}=20\ K$ and gases inlet system.

Fig. 2. Appearance of the research camera and gases inlet system .

Appearance of the block of a cooler and cooling head is given on Fig. 3.

(a)

(b)

Fig. 3. Appearance of the block of a cooler (a) and cooling head (b).

Air pumping from the research camera was carried out by means of the turbomolecular pump TMN-1000M, for the purpose of an exception of vapors of oil in it. Thus working pressure in the research camera made ~ $1 \cdot 10^{-6}$ Tor.

As studied constructional materials the aluminum alloy of D16 and stainless steel of an austenitic class 12X18H10T (steel constructional cryogenic), having broad practical application were chosen.

Samples represented disks with a diameter of 7 mm and 3 mm high. Flat surfaces of disks were ground and polished from two parties to mirror shine. The typical micrograph of a surface measured by means of a atomic force microscope Solver PRO-M, is given on Fig. 4. The average size of a roughness of a surface on a site with sizes of 100x100 microns didn't exceed 170 nanometers

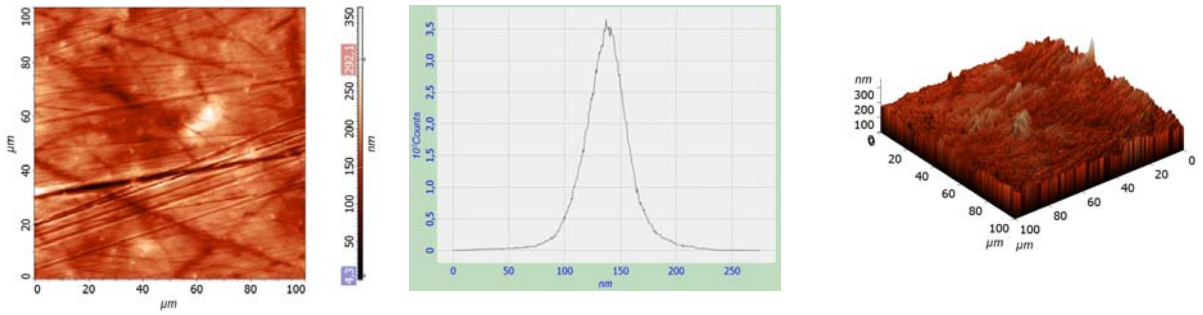

(a) (b) (c)

Fig. 4. Micrograph of a surface of a sample from D16 alloy: (a) - the two-dimensional image of a surface in brightness scale; (b) – average roughness of a surface; (c) – three-dimensional image of a surface.

When carrying out researches various options of placement of samples in the ring cylindrical cathode with explosive issue were used. This cathode took place in the removable cathode assembly shown on Fig. 5.

Fig. 5. Appearance of removable cathode assembly with explosive emission: 1 – ring cylindrical cathode; 2 – sample.

2.2. Parameters of an exciting pulse electronic beam

In the process of researches on studying of influence of intensive streams of ions of small duration on constructional materials the pulse heavy-current accelerator of electrons with average energy of electrons in a range 250 keV was used. Characteristic oscillograms of impulses of voltage and the current, measured at discharge on a cryotarget, are given in Fig.6. Amplitude of impulses of voltage made ~ 250 kV. Duration of impulses of voltage made ~ 40 nanoseconds. Assessment of amplitude of an impulse of current ~ 9.5 kA at distance the cathode anode ~ 5 mm.

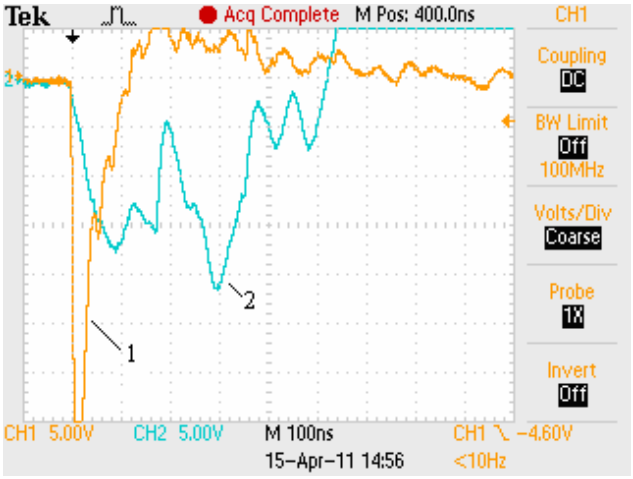

Fig. 6. Characteristic forms of oscillograms of impulses of current and voltage at direct release of an electronic beam on the cryotarget/anode from firm inert gas (Xe): 1 – voltage impulse (relative units), 2 – a current impulse (relative units).

2.3. Cryotarget/anode formation from firm inert gases (Xe)

As the working gas which is freezing condensing at cooling of a copper anode plate (Fig.3) up to the temperature of 45 - 50 K, was used gas xenon (Xe 4.8, with percentage of xenon 99,9988 %). At such temperature all gases, except for helium, hydrogen and neon are condensed. Freezing / xenon condensation on the cooled copper plate of the anode was conducted for filling in the research

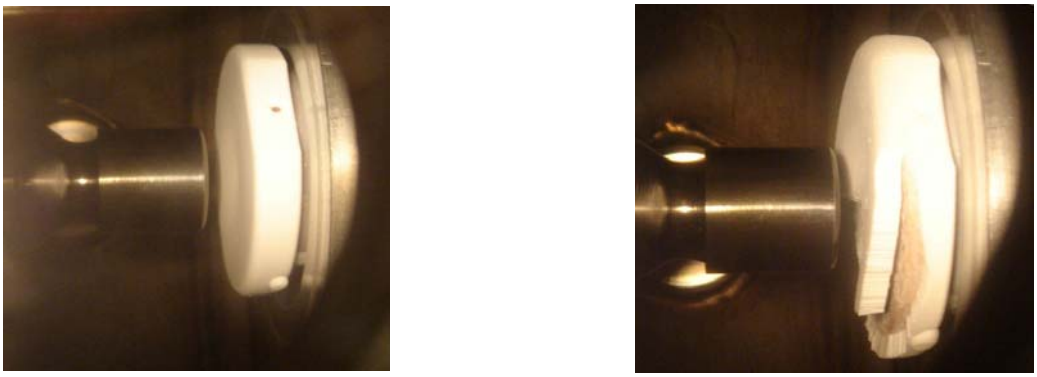

(a) (b)

Fig. 7. Cryotarget/anode photos with condensed layer of solid xenon: (a) – an initial layer; (b) – a type of a target after a splitting off.

camera xenon gas. The photo of a thin frozen layer of Xe is provided on Figs. 7(a).
At target radiation by a powerful high-voltage impulse of electrons in the center of a target the crater by diameter ~ 10 mm is formed. At repeated radiation such target needs to be restored, i.e. freez in the target center a new layer of Xe by a repeated blousing of xenon and to sustain necessary time (~ 10 min.). At rather thick layer of xenon in the process of discharge the splitting off of part of a layer, as shown in Figs is observed. 7. It is visible that the condensed layer of xenon possesses crystal structure. By a visual assessment thickness of a layer of xenon, frozen within 1 hour, made ~ 3 mm.

3. The experimental results

3.1. Radiation by an ionic bunch of samples from D16 alloy

At radiation by an ionic beam of samples from an alloy of D16 the following geometry of an arrangement of a sample in the cathode was used. Before a sample at distance of 1 mm the molybdenic grid with optical transparency of ~80% (3 lines/mm, thickness of Mo wire of 40 microns), welded on a ring from stainless steel 12X18H10T 1 mm thick was established. This sample was subjected to influence of five consecutive impulses of ions of Xe. Results of such impact are given in Fig.8.

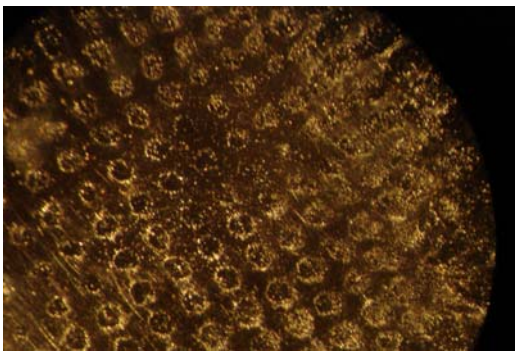

Fig. 8. The photo of a surface of a sample from an alloy of D16 subjected to influence of five impulses of ions of xenon through a molybdenic grid.

It is visible that on a surface of a sample accurately expressed regular relief from hollows (craters) and hills with approximately identical sizes is observed: width of hollows (craters) is equal ~ 180 microns, and width of hills ~ 160 microns. Thus distribution of intensity of a beam almost uniform on all area of a sample with primary concentration in the center of sample with a diameter about 3 mm, i.e. at the set configuration of cathodic knot is observed focusing of an ionic beam.
There is a probability of formation of craters at the expense of sample bombing by "spalls" microparticles from a firm xenon target which can arise because of a powerful irradiating impulse of electrons. To confirm or exclude such opportunity, experiment on sample radiation by an ionic bunch of xenon through an aluminum foil 10 microns thick was put. It was expected that in case of bombing by " spalls " microparticles of the xenon which is taking off from the cryotarget/anode with a huge speed, the aluminum foil will be punched and will contain a set of microopenings which can be registered by means of a nuclear and power microscope. As a result of such experiment the aluminum foil simply "exploded": the melted drop of a foil appeared on a sample surface, and on a copper plate of the anode drops of the melted aluminum were observed when defrosting target, as shown in Fig.9. The received result can be explained only with interaction of ions with an aluminum target, but not bombing by microparticles.

Fig. 9. The cryotarget/anode photo when defrosting after radiation of an aluminum foil (thickness of 10 microns) a powerful impulse of ions.

3.2. Radiation by an ionic beam of samples from stainless steel 12X18H10T

Experiments on radiation of samples were executed by a powerful pulse bunch of ions of xenon from stainless steel in the same geometry, as well as at impact on D16 alloy. Symmetric distribution of influence and the relief of a surface consisting of hollows and heights is here too observed, coincides with received earlier for samples from an aluminum alloy (Figs. 10).

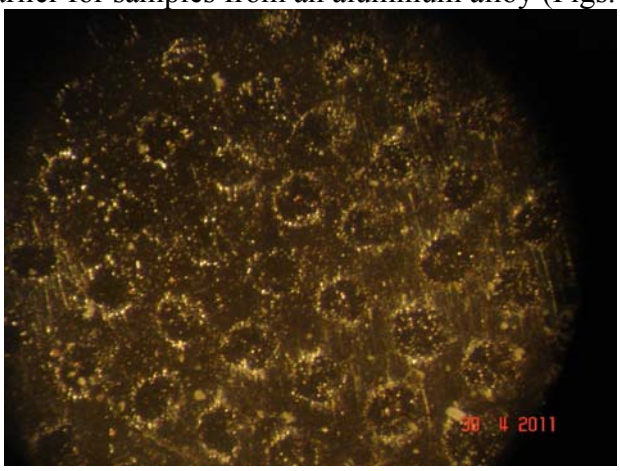

Fig.10. The photo of a surface of a sample from stainless steel 12X18H10T after radiation by a pulse beam of ions of xenon.

4. Numerical modeling of process of destruction of an aluminum sample

When carrying out experiment the bunch of ions was passed through a molybdenic grid with a cell size ~ 250x250μm^2. On an aluminum sample craters with sizes ~ 180 μm opposite to each cell of a grid are found. Let's consider the task corresponding to impact on a sample of a stream of ions, passing through one cell of a grid. In experiment it is possible to define the energy transferred to a sample by a stream, passing through one cell of a grid. Further, we replace impact of this stream on a sample with blow to a sample of the aluminum cylinder with a diameter of 60 microns and length corresponding to duration of influence (80-100 nanoseconds). Speed of the cylinder we choose from compliance of energy of the hammer of energy of a beam of the ions passing through one cell of a

molybdenic grid. When carrying out numerical modeling the developed approach [3-5], allowing to integrate criterion of incubation time into numerical schemes on the basis of a method of final elements was applied. For the solution of a task the finite element ANSYS [6] package was used.
The following parameters of a target, characteristic for aluminum were chosen: density – 2700 kg/m^3, the Young's modulus – 6.65•10^{10} Pa, Poisson's ratio – 0.34, critical stress on a gap – 3•10^8 Pa, the structural size – 15 microns, target thickness – 3 mm. The hammer material on properties corresponds to a target material. Diameter of the hammer – 60 microns, height – 90 microns. hammer speed at the time of the contact beginning – 650 m/s.
After completion of modeling the zone in which there was a material division was investigated. On a fig. 11 the type of a sample after completion of modeling is presented. On a fig. 12 on not deformed sample knots in which there was a destruction are noted.

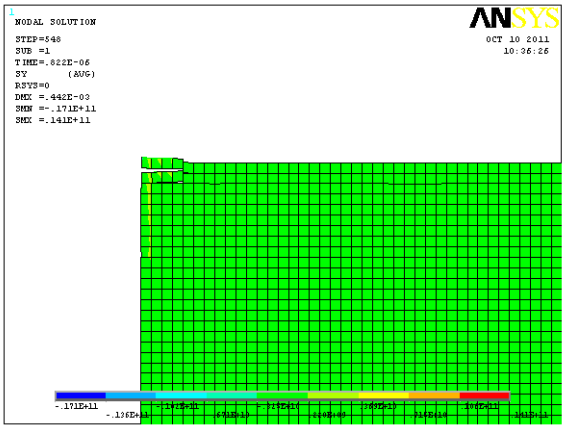

Fig. 11. Type of a sample after completion of modeling.

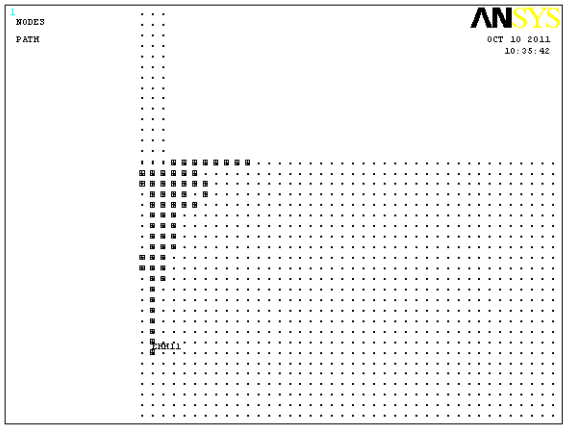

Figure 12. Node in which there was a destruction.

The size of the stamp formed on an irradiated surface, received as a result of numerical modeling coincides with observed in experiment. The received results speak about applicability of the developed approach for a prediction of destruction of the samples loaded by a stream of high-energy heavy ions.

5. Conclusion

On the basis of the conducted research on influence of intensive streams of ions (xenon) of small duration on physical and mechanical properties of constructional materials it is possible to draw the following conclusions:
1. The concept of creation of an intensive pulse source of ions on the basis of a cryotarget from solid inert gases (xenon) is realized at radiation by its powerful impulse of electrons from the cathode with explosive issue in the nanosecond range.
2. Impact of a short-time pulse ionic beam on samples from an alloy of D16 and stainless steel 12X18H10T leads to a surface erosion in the form of the separate craters which depth depends on the hardness of a material and quantity of impulses.
3. The measured parameters of craters on a surface of samples give the chance to formulate initial and boundary conditions in mathematical model for calculation of influence of intensive streams of ions of small duration on physical and mechanical properties of constructional materials.
4. Results of the carried-out numerical modeling of process of destruction of an aluminum target under the influence of a beam of high-energy ions by a method of final elements well coordinated with data of experiments.

References

[1] B.A.Kalin, Radiation beam technologies of processing of constructional material. Physics and Chemistry of Materials Treatment, 4 (2001) 5-16.

[2] V.M.Bystritsky, G.A. Mesyats, Ya.E.Krasik, Powerful pulse sources of ions, Physics of elementary particles and atomic nucleus, 22 (1991) 1171-1198.

[3] V. Bratov, Yu.Petrov, Application of incubation time approach to simulate dynamic crack propagation. International Journal of Fracture, 146 (2007) 53-60.

[4] V. Bratov, Yu. Petrov, Optimizing energy input for fracture by analysis of the energy required to initiate dynamic mode I crack growth, International Journal of Solids and Structures, 44 (2007) 2371-2380.

[5] V. Bratov, Yu.Petrov, Application of incubation time approach to description dynamic crack propagation. Doklady Akademii Nauk, 416 (2007) 624-626.

[6] ANSYS. User's Guide, Release 11.0 ANSYS Inc., Pennsylvania, USA, 2006.

Crack and fracture theory of liquid crystals and quasicrystals

Tian You Fan

School of Physics, Beijing Institute of Technology, Beijing, 100081,China

Corresponding author: tyfan2006@yahoo.com.cn

Abstract Liquid crystals and quasicrystals are fascinating phases of modern physics and chemistry, they are also important materials in current and potential applications. The liquid crystals belong to intermediate phase between fluids and solids in macroscopic sense, they present behaviour of anisotropic fluids, i.e., they behave both characters of conventional fluids and anisotropic elastic solids. The quasicrystals present unusual mechanical and physical properties due to the atomic arrangement being quite different from that of conventional crystals. To describe the mechanical behaviour of quasicrystals, one must introduce two different displacement fields, this leads to two different strain tensors and two stress tensors. This paper reports some results in the study on crack and fracture problems of liquid crystals and quasicrystals. The nonlinear fracture analysis is important for the both materials. However there is fundamental difficulty in the analysis due to lack of plastic constitutive equations for them. Some physical models and relevant mathematical methods are developed to overcome the difficulty, and some results have been obtained, which are of a development of fracture theory of conventional structural materials.

Keywords Liquid crystals, quasicrystal, crack, fracture

1. Introduction

Liquid crystals, in macroscopic sense, are anisotropic fluids. Therefore they belong to an intermediate phase between fluids and crystals. The mechanical behaviour of liquid crystals presents the character of both fluids and solids.

There are various types of liquid crystals, here we discuss the mechanics only for nematic, smectic and columnar liquid crystals.

Different from the behaviour of both fluids and solids, the deformation and motio of liquid crystals should be introduced a vector named director $\mathrm{n}=\left(n_x,n_y,n_z\right)$ apart from displacement vector $\mathrm{u}=\left(u_x,u_y,u_z\right)$ and velocity vector $V=\left(V_x,V_y,V_z\right)$.In addition, the constitutive equation of liquid crystals is different from either generalized Newton's equation or generalized Hooke's equation. For example, for the nematic liquid crystals, we have constitutive law [1]

$$\sigma_{ij} = \sigma_{ij}^{0} + \sigma_{ij}^{'}$$
$$\sigma_{ij}^{0} = -\Pi_{ik}\frac{\partial}{\partial x_j}n_k, \Pi_{ik} = \frac{\partial F}{\partial\left(\frac{\partial}{\partial x_i}n_k\right)} \tag{1}$$
$$\sigma_{ij}^{'} = -p\delta_{ij} + \mu\frac{1}{2}\left(\frac{\partial V_i}{\partial x_j} + \frac{\partial V_j}{\partial x_i}\right)$$

in which F is the free energy of the system, n_k the component of the director mentioned above, p the pressure, μ the fluid viscosity, V_i the component of velocity and δ_{ij} the unit tensor, respectively. The free energy consists of three parts: first one arising from bulk deformation (by the displacements), second one arising from deformation due to curvature, another arising from the coupling between distortion and curvature, i.e.,

$$F = F_e + F_c + F_{ec} \tag{2}$$

where

$$F_e = \frac{1}{2}C_{ijkl}\varepsilon_{ij}\varepsilon_{kl} \tag{3}$$

denotes the conventional elastic strain energy, or the Cauchy strain energy, C_{ijkl} the elastic constants, ε_{ij} the Cauchy strain tensor, and

$$F_c = \frac{1}{2}K_1(div(\mathbf{n}))^2 + \frac{1}{2}K_2(\mathbf{n}\cdot rot\mathbf{n}))^2 + \frac{1}{2}K_3(\mathbf{n}\times rot\mathbf{n}))^2 \tag{4}$$

the Frank energy due the curvature, and K_1, K_2, K_3 the modulia of Frank deformation, in addition

$F_{ec} =$ Deformation energy of coupling between Cauchy strain and Frank strain (5)

For the most cases F_{ec} can be omitted.

The equations of motion include the equations of momentum conservation,

$$\rho\left[\frac{\partial V_i}{\partial t} + (\mathrm{V}\cdot\nabla V_i)\right] = \frac{\partial\sigma_{ij}}{\partial x_j} \tag{6}$$

equation of mass conservation

$$\frac{\partial\rho}{\partial t} + div(\rho\mathrm{V}) = 0 \tag{7}$$

and equation of entropy conservation if there is no dissipation

$$\frac{\partial S}{\partial t} + div(S\mathrm{V}) = 0 \tag{8}$$

where ρ denotes the mass density of the matter, S the entropy. If there is dissipation the equation (8) should be changed, but the discussion is omitted here. From the above simple introduction, we can mind that the equations of the liquid crystals are quite complicated. Some detail for the solutions will be introduced later.

For smectic liquid crystals, the director stands for

$$\mathrm{n} = \left(\frac{\partial u_z}{\partial x}, \frac{\partial u_z}{\partial y}, 1\right) \tag{9}$$

where u_z is the displacement component in the direction normal to the layers of

smectics, and $u_x = u_y = 0$.

For columnar liquid crystals, the director stands for

$$\mathrm{n} = \left(\frac{\partial u_x}{\partial z}, \frac{\partial u_y}{\partial z}, 1 \right) \tag{10}$$

where u_x, u_y are the displacement components along the directions x, y respectively, and $u_z = 0$.

Quasicrystals belong to another fascinating phase of condensed matter, first observed in 1982[2]. Macroscopically their main feature is that there are two different displacement fields, one is the phonon field u, according to the terminology of physics, which is similar to the displacement field in the classical elasticity under the long-wave length approximation, the other is the phason field which is new concept out of the regime of the classical continuum mechanics. The introducing of the phason field results in a great challenge to the traditional continuum mechanics. This leads to two different strain tensors, one is the Cauchy strain tensor

$$\varepsilon_{ij} = \left(\frac{\partial u_i}{\partial x_j} + \frac{\partial u_j}{\partial x_i} \right) \tag{11}$$

another is the phason strain

$$w_{ij} = \frac{\partial w_i}{\partial x_j} \tag{12}$$

The constitutive equations are

$$\sigma_{ij} = C_{ijkl}\varepsilon_{kl} + R_{ijkl}w_{kl} \qquad H_{ij} = R_{klij}\varepsilon_{kl} + K_{ijkl}w_{kl} \tag{13}$$

in which σ_{ij} is the stress tensor associated with strain tensor ε_{ij}, H_{ij} the stress tensor associated with the strain tensor w_{ij}, C_{ijkl} the phonon elastic constants, K_{ijkl} the phason elastic constants, and R_{ijkl} the phonon-phason coupling elastic constants, respectively.

The equations of motion are as follows [39,40]

$$\rho \frac{\partial^2 u_i}{\partial t^2} = \frac{\partial \sigma_{ij}}{\partial x_j} \tag{14}$$

$$\kappa \frac{\partial w_i}{\partial t} = \frac{\partial H_{ij}}{\partial x_j} \tag{15}$$

where $\kappa = 1/\Gamma_w$, in which Γ_w the dissipation kinematics coefficient of phason field of the material defined by Lubensky et al [3]. It is evident that the equation (14) represents the wave propagation, while equation (15) represents diffusion. Because σ_{ij} and H_{ij} are coupled, the motion of quasicrystals is in coupled of wave propagation and diffusion.

The above equations are only an outlook of dynamics of liquid crystals and quasicrystals, this reveals that the mechanics of either liquid crystals or quasicrystalsis quite different from that of conventional fluids as well as elastic solids (or periodic crystals), so the solutions of them are quite different from those of classical fluid dynamics and elasticity.

2. Crack and fracture of liquid crystals

The mechanics of liquid crystals are studied by de Gennes et al [4], Oswald et al [5] etc, the main attention of theirs was paid to discuss the dislocation and disclination problems, but there are some questions of the classical solutions which may be paradoxes, this suggests that the mechanics of liquid crystals needs to develop further. Brostow et al [5] started to study the crack problems in polymer liquid crystals. Because liquid crystals including nematic, smectic and columnar ones, they can be classified as monomer liquid crystals (MLCs) irrespectively of the fact whether they can or cannot polymerize into polymer liquid crystals (PLCs) [6]. That classification is due to Samuski [7] and has been used by a number of authors [8, 9]. The present model applies to MLCs and nematic, smectic and columnar phase LCs in particular. For studying crack problems of liquid crystals one must develop mechanics of liquid crystals, including three-dimensional elasticity, plasticity and dynamics.

The problem of screw dislocation in smectic liquid crystals A or smectics A for simplicity is a longstanding puzzle, de Gennes [4], Kleman [10], Pershan [11] and Landau and Lifscitz [12] presented the solution, but which may be of mistake. Pleineer [13] pointed out the problem of the solution, but the mistake could not be corrected. This problem shows in the theoretical system of mechanics of liquid crystals there may be some difficulties, in which the incompatibility between governing equations and boundary conditions is one of puzzles. For example, in the smectics A, the final governing equation is if only analyzing dislocation

$$\left(\rho B^{'}\frac{\partial^2}{\partial z^2}-K_1\nabla^2\nabla^2\right)u_z=0 \tag{16}$$

which is a partial differential equation of fourth order, which needs two boundary conditions to determine solutions, but the authors of Refs [4,10-13] gave only one boundary condition, this leads to the incompatibility between governing equation and boundary conditions and is the reason of their mistakes. Fan and Li [14] develop the elasticity of the smectic liquid crystals, pay attention to create the well-conditional boundary value problem of governing equation of mechanics of liquid crystals. So that Fan and Li give a correct solution for the dislocation problem as

$$u_z=\frac{b}{2\pi}\left[1+D_1 r\sin\theta\right]\theta \tag{17}$$

in which

$$D_1=\frac{-\frac{8}{3}\pi\alpha}{\left(R_0+r_0\right)\left(\frac{\pi}{4}\alpha\beta+\frac{b^2K_1}{8\pi}\right)\ln\frac{R_0}{r_0}+\frac{\pi}{320}\alpha\gamma\left(R_0-r_0\right)} \tag{18}$$

where

$$\alpha=\left(\frac{b}{2\pi}\right)^4\rho_0 B^{'},\beta=2+\frac{32\pi^2}{3},\gamma=75-160\pi^2+256\pi^4 \tag{19}$$

in equations (15) and (19), $\rho_0 B^{'}$ represents the Young's modulus in direction z of the smectics A, the meaning of K_1 is one of Frank modulus mentioned above, b the magnitude of the Burgers vector of dislocation, r_0 the size of dislocation core, R_0 the size of the body containing the dislocation. The solution (17) modifies the mistake of the classical solution of de Gennes-Kleman-Pershan.

The well-conditional boundary value problem just can develop the work on crack in liquid crystals. As an example, a solution of plastic crack in one of smenctics A is found by Fan [15] based on the dislocation pile-up concept, the size of plastic zone around crack tip and crack tip opening displacement are determined, shown in Figs. 1 and 2.

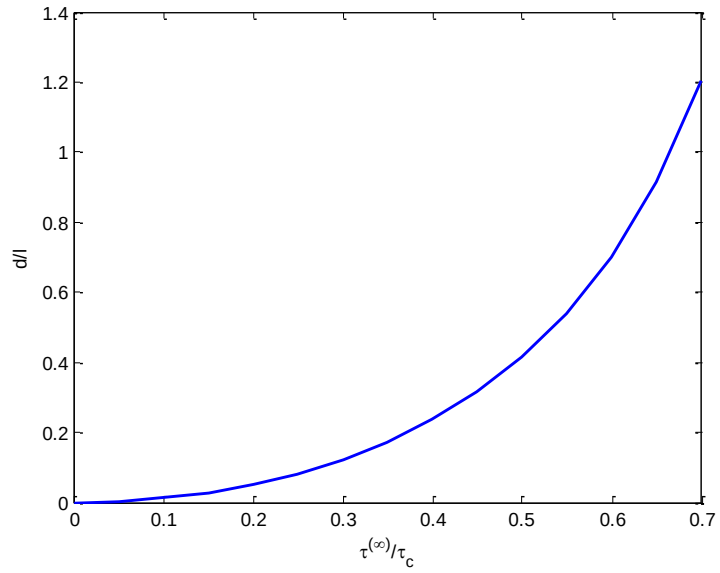

Fig.1 Variation of normalized plastic zone size with normalized applied stress

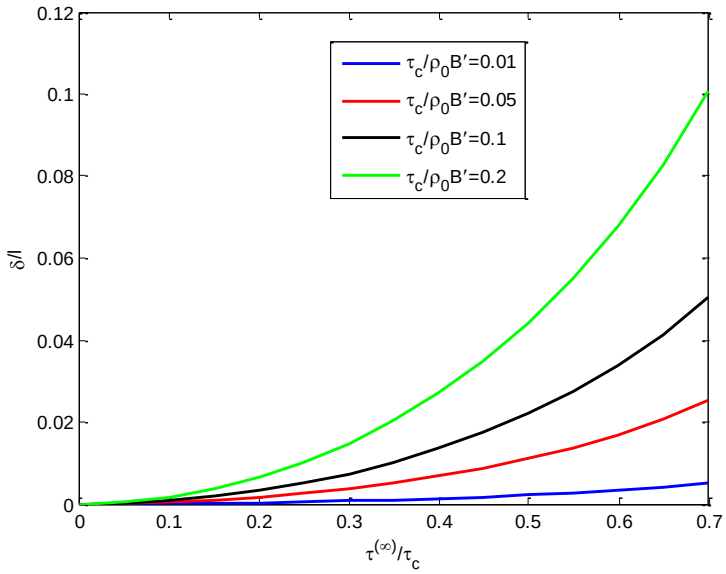

Fig.2 The variation of normalized crack tip opening displacement versus normalized applied stress

Other solutions for plastic crack in smectic A are obtained by Fan [16]. The three-dimensional elasticity of smectics B liquid crystals is studied by Fan [17], the governing equations are reduced to three generalized harmonic equations, and an elliptic disc-shaped crack problem is solved, an approximate analytic solution is constructed. Fan and Chen [18] studied the solution of plastic crack of columnar

liquid crystals, but the result is more complicated than those of smectic liquid crystals A.

Due to the unusual structure of stress field of liquid crystals leads to some difficulties of the crack problem, for example, in the smectics A

$$\sigma_{xx} = \sigma_{yy} = \boldsymbol{K}_1 \nabla^2 \frac{\partial \boldsymbol{u}}{\partial \boldsymbol{z}}, \sigma_{zz} = \rho_0 \boldsymbol{B}' \frac{\partial \boldsymbol{u}}{\partial \boldsymbol{z}}, \sigma_{zx} = \sigma_{xz} = -\boldsymbol{K}_1 \nabla^2 \frac{\partial \boldsymbol{u}}{\partial \boldsymbol{x}}$$

$$\sigma_{zy} = \sigma_{yz} = -\boldsymbol{K}_1 \nabla^2 \frac{\partial \boldsymbol{u}}{\partial \boldsymbol{y}}, \sigma_{xy} = \sigma_{yx} = 0$$

it is evident that between the stress components the stress singularities will be quite different .

Due to the space limitation, we do not list the other questions and other results on mechanics of liquid crystals.

3. Linear theory crack and fracture of quasicrystals

The mechanics of quasicrystals is developed by many scientists, in which the elasticity of the material is advanced for example, refer to Lubensky et al [3], Ding et al [19], Fan and Mai [20], Fan [21]. The systematical mathematical theory of elasticity of quasicrystals is developed by Chinese group [21]. The elasticity, plasticity and dynamics of icosahedral quasicrystals, the most important class of the material, are well studied in the work. By introducing displacement potential, the plane elasticity of icosahedral quaiscrystals is reduced to solve the sextuple harmonic equation [21,22,23]

$$\nabla^2\nabla^2\nabla^2\nabla^2\nabla^2\nabla^2 F(x,y) = 0 \tag{20}$$

From the equation we obtain the solution of a crack in icosahedral Al-Pd-Mn quasicrystals by the complex analysis of the Fourier analysis, which is given as follows

$$K_I^{\|} = \sqrt{\pi a}\, p \tag{21}$$

$$G_I = \frac{1}{2}\frac{\partial}{\partial a}[2\int_{-a}^{a}(\sigma_{yy}(x,0) \oplus H(x,0))(u_y(x,0) \oplus w_y(x,0))dx] = \frac{1}{2}(\frac{1}{\lambda+\mu} + \frac{c_7}{c_3})(K_I^{\|})^2$$

in which

$$c_3 = \mu(K_1 - K_2) - R^2 - \frac{(\mu K_2 - R^2)^2}{\mu K_1 - 2R^2}, c_7 = \frac{c_3 K_1 + 2c_1 R}{\mu K_1 - 2R^2}$$

$$c_1 = \frac{R(2K_2 - K_1)(\mu K_1 + \mu K_2 - 3R^2)}{2(\mu K_1 - 2R^2)}$$

The Fig. 3 shows the energy release rate variation and comparison between solutions of quasicrystals and crystals.

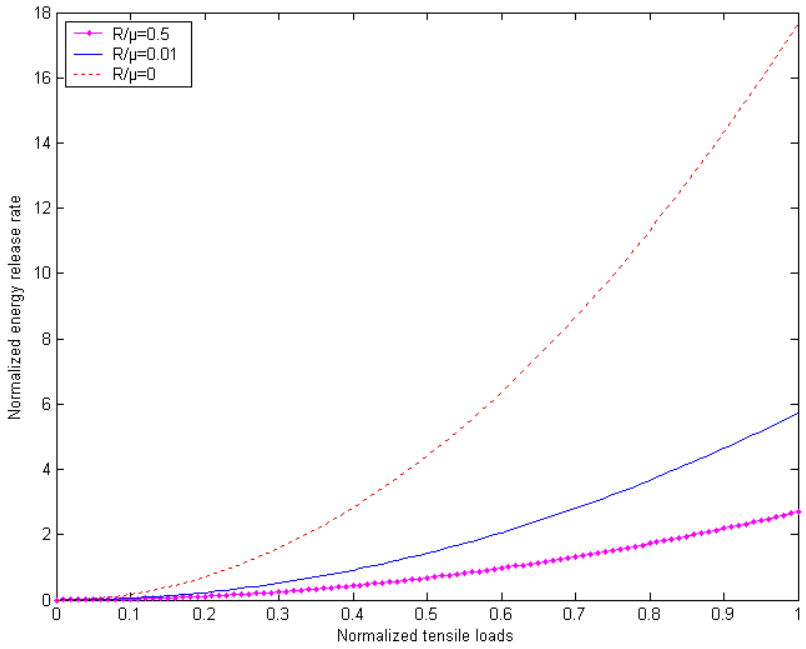

Fig.3 Influence of phason and phonon-phason coupling to the energy release rate

in which solution for crystals is also given. One can find that the solutions of quasicrystals and crystals are quite different each other (one corresponding to crystals is the case $R/\mu = 0$).

Other solutions can be found in Ref [21].

4. Nonlinear solutions of cracks of quasicrystals

Though there are people try to give some explanations on plastic deformation by using dislocation model and so on, the problem is substantively unsolved so far. Due to lack of enough experimental data in macroscopy, the constitutive equation of plasticity of quasicrystals has not been set up. This leads to difficulty doing stress analysis of the material. One can say that the study is in an infant stage. In spite of these difficulties, people pay effort to do some work as above pointed out, the experiments[24-33] reported in the above references provide some hints, which are beneficial for the stress analysis for plasticity and defects of the material. In the following some semi-phenomenological and semi-theoretical results are listed, they may provide a reference for the researchers in the community.

4.1 Generalized cohesive force model [34,35]

Due to lack of constitutive equation of plasticity of quasicrystals up to now, it may be a possible way that we draw the results of classical plasticity, classical dislocation theory and classical nonlinear fracture theory to study some relevant problems in quasicrystals. A useful model in classical elasto-plastic fracture theory is so-called Dugdale-Barenblatt model, the paper [34] extended it to plastic analysis of quasicrystals, and named it be generalized Dugdale-Barenblatt model, the classical work has been done by [34] and [35]. In terms of the model, we determined the size

of plastic zone around the crack tip of anti-plane problem of three-dimensional icosahedral quasicrystals

$$\delta_I = \lim_{x\to l} 2u_y(x,0) = \lim_{\varphi\to\varphi_2} 2u_y(x,0) = 2\left(\frac{1}{\lambda+\mu}+\frac{c_4}{c_2}\right)\cdot\frac{\sigma_s a}{\pi}\cdot\ln\sec\left(\frac{\pi}{2}\frac{p}{\sigma_s}\right) \qquad (22)$$

where

$$c_2 = \mu(K_1-K_2)-R^2-\frac{(\mu K_2-R^2)^2}{\mu K_1-2R^2},\quad c_4 = c_1 R+\frac{1}{2}c_2\left(K_1+\frac{\mu K_1-2R^2}{\lambda+\mu}\right) \qquad (23)$$

and

$$c_1 = \frac{R(2K_2-K_1)(\mu K_1+\mu K_2-3R^2)}{2(\mu K_1-2R^2)}$$

The curve drawn from（22）refer to Fig.4，which shows the effect of phason and phonon-phason coupling is significant.

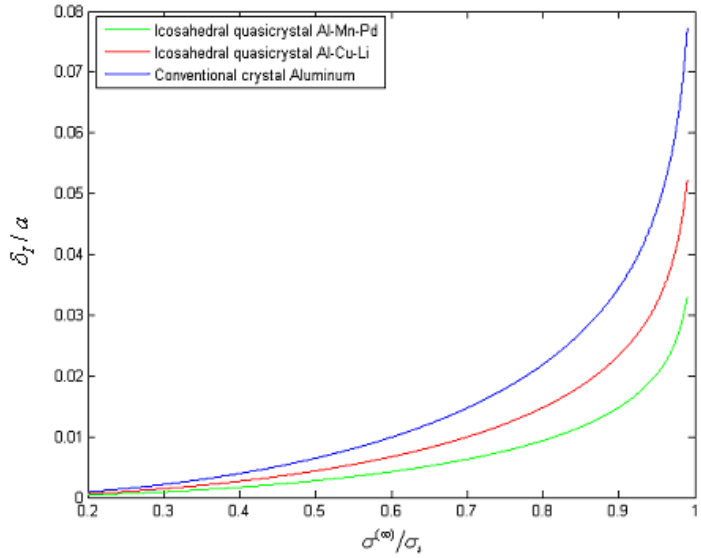

Fig. 4 Crack tip opening displacement versus applied stress for icosahedral quasicrystal [21]

4.2 Generalized continuum dislocations model [36]

We developed the continuous dislocation model [36], the results are identical to those given in Subsection 4.1.

4.3 Model based on generalized Eshelby energy-momentum tensor [37]

The generalized Dugdale-Barenblatt model and generalized continuum dislocation model, are quite different physically and mathematically, yield amazingly the complete identical solutions, we realized that there exist some inherent connection between the two models. Paper [37] gave a probe for the question. They proposed the generalized energy-momentum tensor of quasicrystals

$$G = Fn_1 - \sigma_{ij} n_j \frac{\partial u_i}{\partial x_1} - H_{ij} n_j \frac{\partial w_j}{\partial x_1} \tag{24}$$

and generalized integral of path independency

$$E = \int_\Gamma G d\Gamma \tag{25}$$

and found that they are the uniformly theoretical base of generalized Dugdale-Barenblatt model and generalized continuum dislocations model.The idea comes from the classical work of Eshelby [38] for crystals.

5. Dynamic solutions of cracks of quasicrystals

In the dynamic regime, the essential differences between phonons and phasons just can be profoundly revealed. However the problem presents fundamental difficulty because the mechanism of phason dynamics is not so clear so far.

Rocal and Lorman[39]and Fan et al [40]，suggested the dynamic equation set for quasicrystals (14) and (15).This is the simplest dynamic equation set of quasicrystals, which coupled deformation geometry equations and stress-strain relations and lead to.the final governing equations of elasto-dynamics (or call elasto-/hydro-dynamics)

$$\left.\begin{aligned}
&\frac{\partial^2 u_x}{\partial t^2} + \theta \frac{\partial u_x}{\partial t} = c_1^2 \frac{\partial^2 u_x}{\partial x^2} + (c_1^2 - c_2^2) \frac{\partial^2 u_y}{\partial x \partial y} + c_2^2 \frac{\partial^2 u_x}{\partial y^2} + c_3^2 \left(\frac{\partial^2 w_x}{\partial x^2} + 2 \frac{\partial^2 w_y}{\partial x \partial y} - \frac{\partial^2 w_x}{\partial y^2} \right) \\
&\frac{\partial^2 u_y}{\partial t^2} + \theta \frac{\partial u_y}{\partial t} = c_2^2 \frac{\partial^2 u_y}{\partial x^2} + (c_1^2 - c_2^2) \frac{\partial^2 u_x}{\partial x \partial y} + c_1^2 \frac{\partial^2 u_y}{\partial y^2} + c_3^2 \left(\frac{\partial^2 w_y}{\partial x^2} - 2 \frac{\partial^2 w_x}{\partial x \partial y} - \frac{\partial^2 w_y}{\partial y^2} \right) \\
&\frac{\partial^2 u_z}{\partial t^2} + \theta \frac{\partial u_z}{\partial t} = c_2^2 \left(\frac{\partial^2}{\partial x^2} + \frac{\partial^2}{\partial y^2} \right) u_z + c_3^2 \left(\frac{\partial^2 w_x}{\partial x^2} - \frac{\partial^2 w_x}{\partial y^2} - 2 \frac{\partial^2 w_y}{\partial x \partial y} + \frac{\partial^2 w_z}{\partial x^2} + \frac{\partial^2 w_z}{\partial y^2} \right) \\
&\frac{\partial w_x}{\partial t} + \theta w_x = d_1 \left(\frac{\partial^2}{\partial x^2} + \frac{\partial^2}{\partial y^2} \right) w_x + d_2 \left(\frac{\partial^2}{\partial x^2} - \frac{\partial^2}{\partial y^2} \right) w_z + d_3 \left(\frac{\partial^2 u_x}{\partial x^2} - 2 \frac{\partial^2 u_y}{\partial x \partial y} - \frac{\partial^2 u_x}{\partial y^2} + \frac{\partial^2 u_z}{\partial x^2} - \frac{\partial^2 u_z}{\partial y^2} \right) \\
&\frac{\partial w_y}{\partial t} + \theta w_y = d_1 \left(\frac{\partial^2}{\partial x^2} + \frac{\partial^2}{\partial y^2} \right) w_y - d_2 \frac{\partial^2 w_z}{\partial x \partial y} + d_3 \left(\frac{\partial^2 u_y}{\partial x^2} + 2 \frac{\partial^2 u_x}{\partial x \partial y} - \frac{\partial^2 u_y}{\partial y^2} - 2 \frac{\partial^2 u_z}{\partial x \partial y} \right) \\
&\frac{\partial w_z}{\partial t} + \theta w_z = (d_1 - d_2) \left(\frac{\partial^2}{\partial x^2} + \frac{\partial^2}{\partial y^2} \right) w_z + d_2 \left(\frac{\partial^2 w_x}{\partial x^2} - \frac{\partial^2 w_x}{\partial y^2} - 2 \frac{\partial^2 w_y}{\partial x \partial y} \right) + d_3 \left(\frac{\partial^2}{\partial x^2} + \frac{\partial^2}{\partial y^2} \right) u_z
\end{aligned}\right\} \tag{26}$$

where

$$c_1 = \sqrt{\frac{\lambda + 2\mu}{\rho}}, c_2 = \sqrt{\frac{\mu}{\rho}}, c_3 = \sqrt{\frac{R}{\rho}}, d_1 = \frac{K_1}{\kappa}, \ \mathrm{d}_2 = \frac{K_2}{\kappa}, d_3 = \frac{R}{\kappa} \tag{27}$$

Note that c_1, c_2 and c_3 represent speeds of elastic waves, while d_1, d_2 and d_3 are not wave speeds, which are diffusive coefficients of phasons.

The numerical analysis is given for the specimen shown in Fig.5 made of icosahedral quasicrystal. After finite difference treatment on equation set (26) and corresponding boundary and initial conditions, the dynamic stress intensity factor for initiation of crack growth is obtained and shown in Fig.6.In the computation this is a

simplest equation set of hydrodynamics of quasicrystals, which is simplified from the equations of Lubensky et al [3].

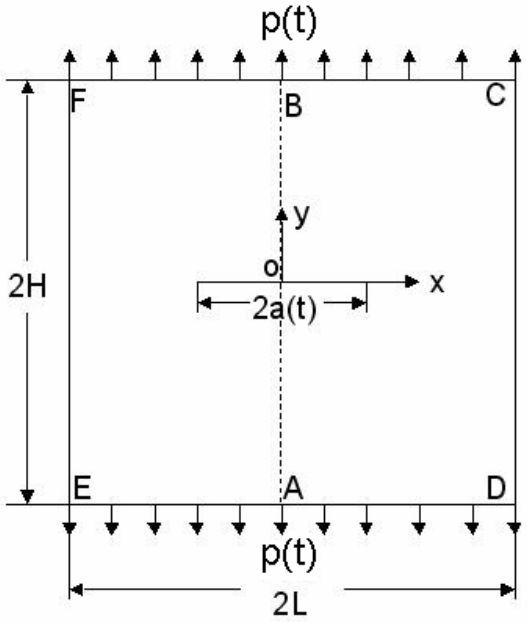

Figure 5 Sample containing a dynamic crack of two-dimensional quasicrystals

After finite difference treatment on equation set (26) and corresponding boundary and initial conditions, the dynamic stress intensity factor for initiation of crack growth is obtained and shown in Fig.6. In the computation

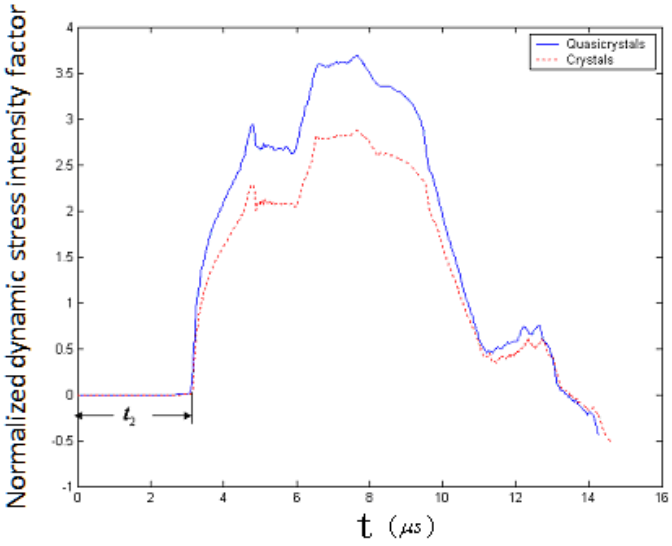

Figure 6 The dynamic stress intensity factor of rectangular specimen with a central crack of icosahedral Al-Pd-Mn quasicrystal under impact loading (for stationary crack)

the material is icosahedral Al-Pd-Mn quasicrystal with material constants：

$$\rho = 5.1\text{g/cm}^3, \lambda = 74.2, \mu = 70.4(GPa), K_1 = 72, K_2 = -37(MPa)$$

$$\Gamma_w = 1/\kappa = 4.8\times10^{-19}\text{m}^3\bullet\text{s/kg}=4.8\times10^{-10}cm^3\bullet\mu s/g$$

$R/\mu = 0.01$ for quasicrystal, and $R/\mu = 0$ for crystal. It is evident that the results between quasicrystal and crystal are quite large.

The dynamic stress intensity factor for fast crack propagation of the central specimen is illustrated in Fig.7, which comes from monograph [21].

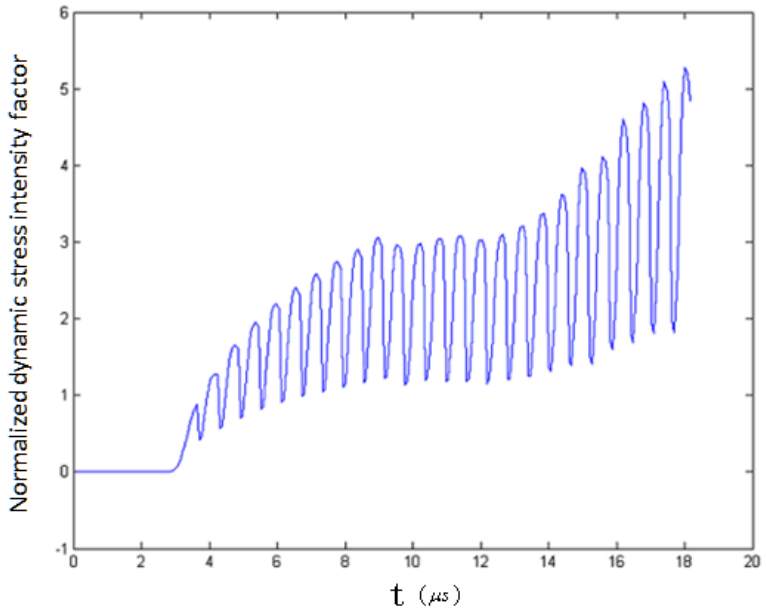

Figure 7 Dynamic stress intensity factor versus time of fast propagating crack in rectangular specimen with a central crack of icosahedral Al-Pd- Mn quasicrystal

The oscillation of the curve comes from the interference and reflection of waves, in which there are reasons come from numerical computation, it is needed doing further study.

6. Discussion and conclusion

The study of crack and fracture problems in liquid crystals is just begun, so it is in infant stage. The difficulty comes from some basic problems in the mechanics of liquid crystals, this also provides opportunity to gain the achievements in the field.

The linear elastic fracture theory of quasicrystals has been developed, the study of nonlinear and dynamic fracture theories of quasicrystals is also carried out, but faces some fundamental difficulties.

Because of many unsolved critical issues, the study is a fascinating research area of the materials science.

References

[1]M. Kleman and P. Oswald, Columnar discotic mesophases: elasticity, dislocations, instabilities, J Physique, 43(1982), 655-662.

[2]D. Shechtman, I. Blech, D. Gratias et al, Metallic phase with long-range orientational order and no translational symmetry, Phys Rev Lett, 53(1984), 1951-1953.

[3]T. C. Lubensky ,S Ramaswamy and J Toner, Hydrodynamics of icosahedral quaiscrystals, Phys. Rev. B, 32(1985), 7444-7452.
[4]P. G. de Gennes and P. Prost, The Physics of Liquid Crystals, Clarendon, London,1993, pp.387-680.
[5]P. Oswald and P. Pieranski, Smectic and Columnar Liquid Crystals, Taylor & Francis, London, 2006,pp.320-587.
[6]W. Brostow, A.M. Cunha, J. Quintanila et al, Macromol. Crack formation and propagation in molecular dynamics simulation of polymer liquid crystals, Macromol. Theory Simul.11 (2002), 308-314.
[7]E.T. Samulski, Macromolecular structure and liquid crystallinity, Faraday Discuss. Chem. Soc.,79(1985) ,7-20.
[8]W. Brostow, Properties of polymer liquid crystals: choosing molecular structures and blending, Polymer, 31(1990), 979-995.
[9]M. Hess, High Performance Polymers, in Performance of Plastics,Brostow W, ed , Hanser , Munich-Cincinnati, 2000, Ch. 21,
[10]M. Kleman, Linear theory of dislocations in a smectic A, J Physique, 35(1974), 595-600.
[11]P. S. Pershan, Dislocation effect in smectic-A liquid crystals, J Appl Phys, 45(1974), 1590-1599.
[12]L. D. Landau and M.E.Lifshitz, 1988, Theory of Elasticity, Pergamon, Oxford, pp.150-178.
[13]H. Pleiner, 1986, Dynamics of a screw dislocation in smectic A liquid crystals, Phil Mag A, 54(1986), 421-439.
[14]T.Y. Fan and X.F. Li, 2013, The stress s field and energy of screw dislocation in smectic A liquid crystals and on the mistakes of the classical solution, Chin Phys B, in press.
[15]T.Y. Fan, A plastic crack in a smectic liquid crystal A, Phil Mag Lett, 92(2012), 153-158.
[16]T Y Fan and Tang Z Y, 2012, A crack model of smectic liquid crystals, arXiv, 1211,7897.
[17]T.Y. Fan, 2011, Chin Phys B, An elliptic shaped crack in columnar liquid crystals, unpublished work.
[18]T. Y. Fan and W. Q. Chen, 2012, Plastic crack in smectic liquid crystals B, Physica B, submitted.
[19]D. H. Ding, W. G. Yang, R. H. Wang et al, Generalized elasticity theory of quasicrystals,1993, Phys Rev B,48(1993),7003-7006.
[20]T. Y. Fan and Y. W. Mai, Elasticity theory, fracture mechanics and some relevant thermal properties of quasicrystalline materials, Appl Mech Rev,57(2004), 235-334.
[21]T. Y. Fan, Mathematical Theory of Elasticity of Qusicrystals, Science Press, Beijing/Springer-Verlag, Heidelberg, 2010, pp.30-360.
[22]T. Y. Fan and L. H. Guo, Final governing equation of plane elasticity of icosahedral quasicrystals , Phys Lett A, 341(2005),215-218.
[23]T. Y. Fan, Z. Y. Tang, L. H. Li et al, The strict theory of complex variable function method for solving elasticity problems of quasicrystals, J Math Phys,54(2010), 053519.
[24]M. Feuerbacher and K. Urban, Platic behaviour of quasicrystalline materials, in : Quasicrystals, ed. by Trebin H R, Wiley Press, Berlin, 2003.
[25]D. Calliard, Dislocation mechanism and plasticity of quasicrystals: TEM observations in icosahedral Al-Pd-Mn, Materials Sci.Forum, 509(2006),49-56.

[26]B. Geyer, M. Bartisch, M. Feuerbacher et al, Plastic deformation of icosahedral Al-Pd-Mn single quasicrystals, I. Experimental results, Phil. Mag.A, 80(2000),1151-1164.
[27]U. Messerschmidt,M. Bartisch,B. Geyer et al, Plastic deformation oficosahedral Al-Pd-Mn single quasicrystals, II，Interpretation of experimental results, Phil. Mag.A, 80(2000),1165-1181.
[28]K. Urban and M. Wollgarten, Dislocation and plasticity of quasicrstals, Materials Sci. Forum, 150-151(1994), 315-322.
[29]M. Wollgarten et al, In-situ observation of dislocation motion in icosahedral Al-Pd-Mn single quasicrystals, Phil Mag Lett.,71(1995),99-105.
[30]M. Feuerbacher, B. Bartsch, B. Grushk et al, , Plastic deformation of decagonal Al-Ni-Co quasicrystals, Phil Mag Lett, 76(1997),396-375.
[31]U. Messerschmidt, M. Bartsch, M. Feuerbacher, et al, Friction mechanism ofdislocation motion in icosahedral Al-Pd-Mn single quasicrystals, Phil Mag A, 79(1999),2123-2135.
[32]P. Guyot and G. Canova, The plasticity of icosahedral quasicrystals, Phil. Mag. A, ,79(1999), 2815-2822.
[33]M. Feuerbacher, P. Schall, Y. Estrin et al, A constitutive model for quasicrystal plasticity, Phil Mag Lett, 81(2001),473-482
[34]T. Y. Fan and L. Fan,Plastic fracture of quasicrystals, Phil Mag , 88(2008), 523-535.
[35]W. Li, T. Y. Fan, Study on plastic analysis of crack in three-dimensional quasicrystal materials, Phil Mag, 89(2009),2823-2831.
[36]T. Y. Fan, H. R. Trebin, U. Messerschmidt et al, Plastic flow coupled with a Griffith crack in some one- and two-dimensional quasicrystals, J Phys: Condens Matter, 16(2004), 5229-5240.
[37]T. Y. Fan, L. Fan，Relation between Eshelby integral and generalized BCS and generalized DB models for some one- and two-dimensional quasicrystals, Chin Phys B,20(2011)，036102
[38]J. D. Eshelby, The continuum theory of dislocations in crystals, Solid State Physics (Ed. by Seits F et al), Vol. 3, Academic Press, New York, USA, 1956.
[39]S. B. Rochal and V. L. Lorman，Minimal model of the phonon-phason dynamics on icosahedral quasicrystals and its application for the problem of internal friction in the i-AlPdMn alloys, Phys Rev B, 66 (2002), 144204.
[40]T. Y. Fan, X. F. Wang, W. Li et al, Elasto-hydrodynamics of quasicrystals, Phil Mag, 89(2009),501-512.

Analysis of Failure Waves with an Elasto-statistical-brittle Model

Zhijie Jiang[1], Mengfen Xia[1], Haiying Wang[1,*]

[1] Institute of Mechanics, Chinese Academy of Sciences, 100190, China
* Corresponding author: why@lnm.imech.ac.cn

Abstract The origin and propagation mechanism of failure waves poses a challenge to our conventional understanding of dynamic failure. In this paper, the failure wave is attributed to the catastrophic rupture in brittle materials and an elasto-statistical-brittle (ESB) model is developed to describe the catastrophic behavior. In the ESB model, the disordered heterogeneity of brittle solids at mesoscopic scale is characterized with statistical description of the shear strength of mesoscopic units. The evolution of microdamage is controlled by the shear strength and the shear stress applied, and eventually induces catastrophic rupture in brittle materials. Considering the failure wave as a propagating boundary of catastrophic failure, the propagation of the failure wave is predicated with wave theory. Several predicted speeds of failure waves are in good agreement with experimental observations.

Keywords failure wave, wave speed, elasto-statistical-brittle model, catastrophic rupture, heterogeneity

1. Introduction

Shock induced delayed failure (the so called failure wave) in brittle materials has attracted extensive research in recent years [1-11]. This feature was first noted by Razorenov et al [2] as a small reload signal superimposed on rear surface velocity trace, suggesting the interaction of the release from the rear surface of the target with a moving front behind which the material undergoes a reduction of shock impedance. Further experiments [3] prove that the failure wave can be generated in glasses or ceramics at a stress near or below the HEL and the speed of failure wave does not correspond to any elastic wave. In addition, behind this wave, the longitudinal stress changes little but the transverse stress increases, indicating a decrease in shear strength, and spall tensile strength falls to essentially zero [4-6].

Several models have been proposed to address the origin of failure waves. However, a satisfactory explanation and description for the failure wave is still lacking. Clifton [7] assumes the failure wave as a propagating phase boundary. In his model, the square of the failure wave speed is proportional to the ratio of the jump in stress over the jump in strain. However, the available stress measurements clearly show that the failure wave causes either no change or small deduction in the longitudinal stress, but a large jump in the longitudinal strain. Feng [8] suggests that the propagation mechanism of failure front is a diffusive process. In his model, the failure front is not a mechanical wave, and the failure front speed is controlled by the stress deviator and dilated volume. To some extent, his simulation agrees with experiments, but the failure wave speed is disordered during the failure wave propagating. Moreover, his model assumes no changes in the longitudinal strain, which conflicts with experimental observations [9]. Kanel [2], Partom [10] and Espinosa [11] suppose the failure wave as a damage evolution process originating from the shocked surface. Hence, the predicted failure evolution behind the initial shock wave is independent of location instead of having an increasing time delay with propagation distance as observed experimentally. As a result, the simulations of the failure wave phenomenon based on this type of material model require the use of a nonphysical ‘‘failure wave’’, e.g. switching on a failure process cell by cell at an assumed successive sequence.

In this paper, we attribute the failure wave to a propagating catastrophe process in brittle materials. To describe catastrophic rupture in heterogeneous brittle materials, an elasto-statistical-brittle (ESB)

model is developed. Considering the failure wave as a propagating boundary of catastrophic failure, the critical condition to generate failure wave and the failure wave speed could be obtained from the law of conservation.

The paper is organized as follows: Section 2 describes the details of ESB model and Section 3 is the modelling of failure wave phenomenon. Numerical simulation and comparison with the experimental data are presented in Section 4. A summary is given in Section 5.

2. Elasto-statistical-brittle (ESB) MODEL

Generally speaking, the catastrophic failure of heterogeneous brittle materials under impact loading is resulted from the initiation, growth, and coalescence of microdamage, which is obviously controlled by the interactions of stress pulse with local material properties and microstructure. Hence, in the ESB model, we consider a macroscopic representative volume element (RVE) comprised of a great number of heterogeneous mesoscopic units. The heterogeneity of the mesoscopic units can be characterized by their shear strength. For instance, we assume their shear strength τ_c follows a statistiacal distribution $h(\tau_c)$. The Weibull distribution is often used in the field of failure analysis due to its flexibility. That is,

$$h(\tau_c) = \frac{m}{\eta}\left(\frac{\tau_c}{\eta}\right)^{m-1} \exp\left(-\left(\frac{\tau_c}{\eta}\right)^m\right) \tag{1}$$

where η and m are the scale parameter and shape parameter of Weibull distribution, respectively. The scale parameter η is proportional to the mean strength of mesoscopic units and the shape parameter m reflects the degree of material heterogeneity. Physically, a larger m implies a more homogeneous material. Fig. 1 shows the distribution of material shear strength with different heterogeneity index m.

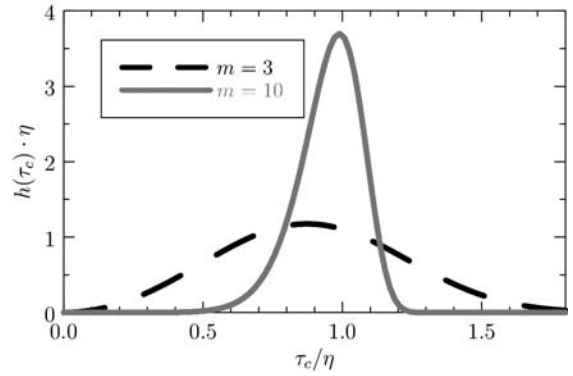

Figure 1. The distribution of material shear strength with different shape parameter m

If the applied shear stress on the mesoscopic unit τ_{meso} reaches its shear strength τ_c, the unit fails. Denote macroscopic damage of the RVE as D, which can be expressed as:

$$D = \int_0^{\tau_{meso}} h(\tau_c)\, d\tau_c = 1 - \exp\left(-(\tau_{meso}/\eta)^m\right) \tag{2}$$

We further assume that compared with intact unit, the breaking mesoscopic units can sustain less hydrostatic stress but no shear stress. This assumption physically means that the macroscopic damage causes reductions in both shear modulus and volumetric modulus of the material, and the latter degrades less than the former. That is,

$$\begin{aligned} G &= G_0(1-D) \\ K &= (1-\zeta D)K_0 \end{aligned} \tag{3}$$

where $\zeta < 1$, K_0 and G_0 are the volumetric modulus and shear modulus of intact material, respectively.

The material behavior at the macroscopic level can be written as

$$\sigma_{ij} = [1-\zeta+\zeta\exp(-(\tau_{meso}/\eta)^m)]K_0\theta\delta_{ij} + 2G_0\exp(-(\tau_{meso}/\eta)^m)(\varepsilon_{ij} - \frac{1}{3}\theta\delta_{ij}) \tag{4}$$

where ε_{ij} is the strain tensor, σ_{ij} the stress tensor, θ the volumetric strain. Provided small damage and mean field approximation, γ is the maximum shear strain of the macroscopic element. Hence,

$$\tau_{meso} = G_0\gamma\,. \tag{5}$$

Specifically, in uniaxial strain state($\varepsilon_x = \gamma \neq 0$, $\varepsilon_y = \varepsilon_z = 0$), the constitutive relation can be simplified as

$$\begin{aligned} \sigma_x &= [1-\zeta+\zeta\exp(-(G_0\varepsilon_x/\eta)^m)]K_0\varepsilon_x + \frac{4}{3}G_0\exp(-(G_0\varepsilon_x/\eta)^m)\varepsilon_x \\ \sigma_y &= [1-\zeta+\zeta\exp(-(G_0\varepsilon_x/\eta)^m)]K_0\varepsilon_x - \frac{2}{3}G_0\exp(-(G_0\varepsilon_x/\eta)^m)\varepsilon_x\,. \\ \tau_{xy} &= G_0\exp(-(G_0\varepsilon_x/\eta)^m)\varepsilon_x \end{aligned} \tag{6}$$

In order to show the response of material under impact, we normalize the constitutive relation and get the dimensionless constitutive relation as

$$\begin{aligned} \bar{\sigma}_x &= \frac{2(1+\nu)}{3(1-2\nu)}[1-\zeta+\zeta\exp(-\bar{\varepsilon}_x^{\,m})]\bar{\varepsilon}_x + \frac{4}{3}\bar{\varepsilon}_x\exp(-\bar{\varepsilon}_x^{\,m}) \\ \bar{\sigma}_y &= \frac{2(1+\nu)}{3(1-2\nu)}[1-\zeta+\zeta\exp(-\bar{\varepsilon}_x^{\,m})]\bar{\varepsilon}_x - \frac{2}{3}\bar{\varepsilon}_x\exp(-\bar{\varepsilon}_x^{\,m}) \\ \bar{\tau}_{xy} &= \bar{\varepsilon}_x\exp(-\bar{\varepsilon}_x^{\,m}) \end{aligned} \tag{7}$$

where ν is the Possion's ratio of the intact material, $\bar{\sigma}_{ii} = \sigma_{ii}/\eta$, $\bar{\varepsilon}_{ii} = G_0\varepsilon_{ii}/\eta$. Fig.2 plots the normalized stress-strain relationship with different parameters.

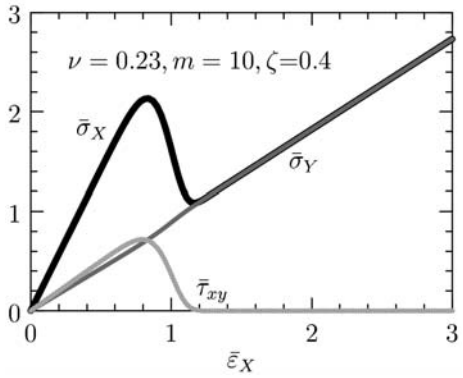

Figure 2. The simplified stress-strain relationship in uniaxial strain state

As Fig.2 shows, there exists a saddle point in the $\varepsilon_x - \sigma_x$ curve. Actually, the saddle point implies a catastrophic transition happening. As illustrated in Fig.3, when the longitudinal stress reaches σ_E, solids can not sustain any further compression, all of the meso-elements fail suddenly and the state directly jump from the unstable state A to the corresponding state B. In this process, the energy provided is used in fragmenting, thus, the longitudinal stress does not change.

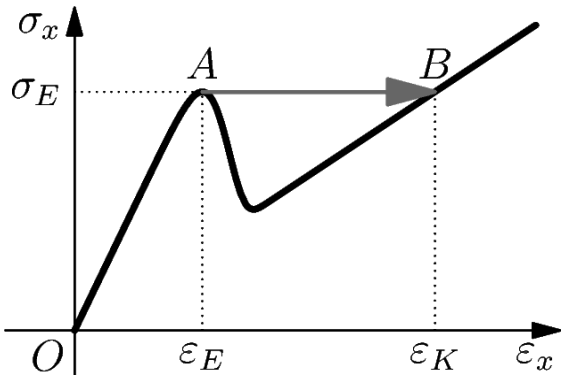

Figure 3. The catastrophic transition in ESB model

3. MODELLING OF THE FAILURE WAVE

In this section, we will analyze the origin of failure waves in a target plate described with a simplified ESB model.

Fig. 4 is the $x-t$ diagram of flyer plate and target plate. In the flyer plate, region 1 is in the initial state and region 4 in the final state. In the target plate, region 2 is the shocked region behind the elastic wave and region 3 is failed zone behind the failure wave. As the flyer plate and target plate do not split up, region 3 and region 4 have the same longitudinal stress and particle velocity.

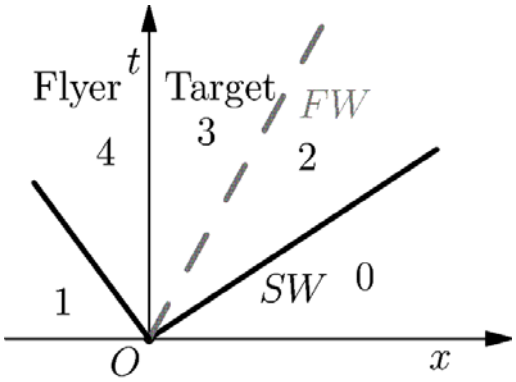

Figure 4. the $x-t$ diagram for waves

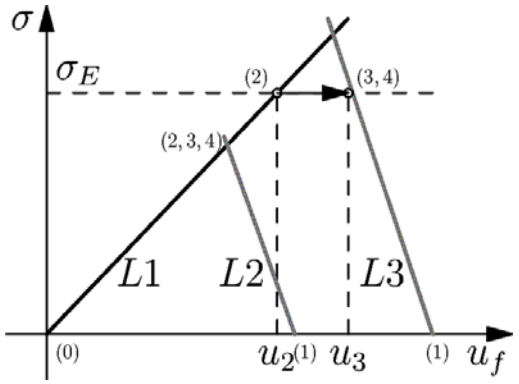

Figure 5. the $u-\sigma$ plane of plates system

Fig. 5 is the $u-\sigma$ plane of plates system. In the $u-\sigma$ plane, (u_2, σ_E) stands for region 2, and (u_3, σ_E) stands for region 3 and 4. L1 is the trajectory of states in flyer plate, and L2 is the trajectory of states of target subjected to low-velocity impact. When the impact loading is lower than the stress threshold σ_E, the catastrophic transition couldn't happen and there is no failure wave. However, if the stress state of target could exceed the stress threshold σ_E, as expressed by

L3 and L1, the catastrophic rupture happens and failure wave comes out.

Considering the law of conservation of mass, the failure wave speed can be obtained as,

$$C_{fw} = \frac{u_3 - u_2}{\varepsilon_3 - \varepsilon_2} = \frac{u_f - \rho_f \varepsilon_{fE} - \rho_t \varepsilon_2}{\varepsilon_3 - \varepsilon_2} \tag{8}$$

4. NUMBERICAL SIMULATION

In order to validate our theory, we simulate normal impact experiments on soda-lime glass specimens by copper plates. The properties of copper and soda-lime glass are summarized in Table 1.

Table 1 The properties of flyer plate materials [3]

Material	$C_L / km \cdot s^{-1}$	$\rho / kg \cdot m^{-3}$	ν
copper	4.560	8930	0.33
soda-lime glass	5.840	2490	0.23

Bourne et al. [3, 12] studied failure waves in soda-lime glass impacted with copper flyer. The results prove that the threshold stress to generate failure wave in soda-lime glass is 4.0 GPa. Therefore, in the simulation, we assume the threshold stress σ_E to be 4.0 GPa. In addition, since soda-lime glass is less heterogeneous, the shape parameter m is set as 10 and ζ as 0.4. The stress-strain relationship of soda-lime glass is presented in Fig. 6. As Fig. 6 shows, for soda-lime glass, the strain at the threshold stress is 0.0471 prior to the catastrophic rupture (ε_E) and 0.1330 after the catastrophic rupture (ε_K).With these parameters, we can calculate the speed of failure waves from Eq. (8).

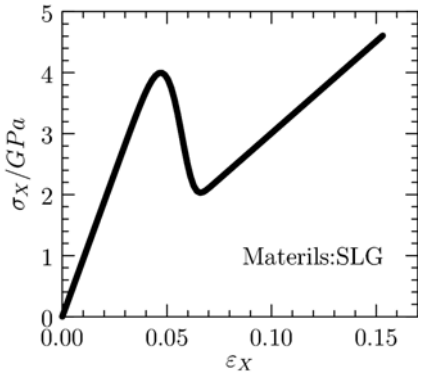

Figure 6. The response of soda-lime glass

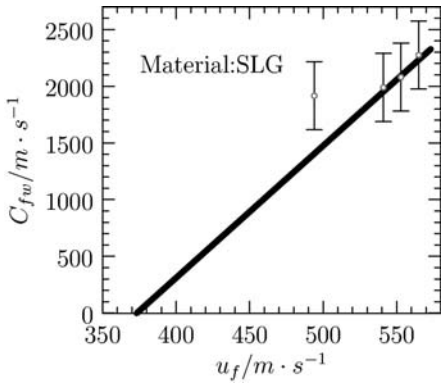

Figure 7. The relationship between u_f and C_{fw}

From Eq. (8), we obtain the relationship of failure wave speed vs. the impact velocity, as shown in Fig.7. It is obvious that, according to the ESB model, the speed of failure wave is linear with the impact velocity. In addition, Fig.7 demonstrates that the lowest impact velocity to generate the failure wave is 373.3 m/s, which approximately coincides with experimental observations [3, 12]. Table 2 quantitatively compares the speed of failure waves calculated with the ESB model with

experimental ones. Apparently, the model can basically replicate the experiments and the error is acceptable.

Table 2. Summary of Experimental data and the simulation results [3, 12]

Shot no.	Impactor	Target	Impact velocity u_f	C_{fw}(experimental)	C_{fw}(simulated)
98-01	copper	soda lime glass	494 m/s	1916 ± 300 m/s	1405 m/s
98-02	copper	soda lime glass	541 m/s	1989 ± 300 m/s	1952 m/s
98-03	copper	soda lime glass	553 m/s	2080 ± 300 m/s	2092 m/s
98-04	copper	soda lime glass	565 m/s	2275 ± 300 m/s	2232 m/s

5. SUMMARY

The origin and propagation of failure waves in brittle materials under impact loading have been investigated for many years. However, till now, failure waves cannot be well illustrated by any constitutive models. In this paper, the failure wave is attributed to the catastrophic rupture in brittle materials under impact loading. To describe the catastrophe behavior, an elasto-statistical-brittle (ESB) model is developed. In the ESB model, the shear strength of mesoscopic units follows a Weibull distribution, which reflects the heterogeneity of brittle solids. The evolution of microdamage is controlled by the shear strength and the shear stress applied, and induces reductions in shear modulus and volumetric modulus. Catastrophic rupture occurs when stress cannot be hold by the damaged material.

With the ESB model and wave theory, we predicted the failure waves in soda-lime glass impacted with copper plates. The critical impact velocity to generate the failure wave approximately coincides with experimental data. In addition, several predicted speeds of failure waves are in good agreement with experimental observations.

Acknowledgements

This work was supported by the National Natural Science Foundation of China (Grant Nos. 11172311, 11021262, 10932011).

References

[1] S. J. Bless and N. S. Brar, failure wave and their effects on penetration mechanics in glass and ceramics, in: Y. Horie(Eds.), Shock Wave Science and Technology Reference Library, Springer, New York, 2007, pp. 105-141.

[2] G. I. Kanel, S. V. Rasorenov and V. E. Fortov, The failure waves and spallations in homogeneous brittle materials, in: S. C. Schmidt, R. D. Dick and J. W. Forbes(Eds.), Shock Compression of Condensed Matter, Elsevier, New York, 1991, pp. 451-454.

[3] N. Bourne, J. Millett, Z. Rosenberg and N. Murray, On the shock induced failure of brittle solids, Journal of the Mechanics and Physics of Solids, 46(1998) 1887-1908.

[4] N. S. Brar, S. J. Bless and Z. Rosenberg, Impact-induced failure waves in glass bars and plates, Applied Physics Letters, 56(1991) 3396-3398.

[5] N. S. Brar, Z. Rosenberg and S. J. Bless, Spall strength and failure waves in glass, Journal De Physique IV, 1(1991) 639-644.

[6] H. D. Espinosa and Y. P. Xu, Micromechanics of Failure Waves in Glass: I, Experiments,

Journal of the American Ceramic Society, 80(1997) 2061-2073.

[7] R. J. Clifton, Analysis of Failure Waves in Glasses, Applied Mechanics Reviews, 46(1993) 540-546.

[8] R. Feng, Formation and propagation of failure in shocked glasses, Journal of Applied Physics, 87(2000) 1693-1700.

[9] Z. Rosenberg, N. K. Bourne and J. C. F. Millett, Direct measurements of strain in shock-loaded glass specimens, Journal of Applied Physics, 79(1996) 3971-3974.

[10] Y. Partom, Modeling failure waves in glass, International Journal of Impact Engineering, 21(1998) 791-799.

[11] H. D. Espinosa, Y. P. Xu and N. S. Brar, Micromechanics of Failure Waves in Glass: II, Modeling, Journal of the American Ceramic Society, 80(1997) 2074-2085.

[12] J. C. F. Millett and N. K. Bourne, Effect of internal strain on the propagation of failure in shock loaded soda-lime glass, Journal of Applied Physics, 95(2004) 4681-4685.

Fracture problem of the thin superconducting strip with transverse crack

Cun Xue, An He, Huadong Yong, Youhe Zhou*

Department of Mechanics and Engineering Sciences, School of Civil Engineering and Mechanics, Lanzhou University, Lanzhou, Gansu 730000, P.R. China

Key Laboratory of Mechanics on Disaster and Environment in Western China attached to the Ministry of Education of China

* Corresponding author: zhouyh@lzu.edu.cn

Abstract This paper presents the fracture behaviors in thin type-II superconducting strips with a transverse crack induced by the electromagnetic body force under a perpendicular applied field. Different from the longitudinal crack, the effect of the transverse crack on the current in the thin strip is considered. The Bean and Kim model of critical state are adopted to calculate the electromagnetic force. Based on the finite element method, the stress intensity factors of the transverse crack are obtained during one full cycle applied field (the field increasing process and decreasing process). Furthermore, the influences of the crack length on the stress intensity factors are also studied in this paper. Generally speaking, all the results are useful for understanding the critical state model and the fracture mechanism of high-temperature superconductors, which could provide a theoretical guide for the ITER CICC designer.

Keywords Thin superconducting strip, Bean model, Kim model, Transverse crack

1. Introduction

High-temperature superconductor (HTS) tapes have provided a wide range of engineering applications, such as ac power transmission cables [1, 2] and filters for wireless communication [3]. With the development of engineering applications, improvements on mechanical performances of HTS bulks in the presence of high magnetic fields have attracted considerable interest. The stress and the magnetostriction in bulk superconductors subjected to high magnetic fields were analyzed for various geometrical cases, critical state models, and magnetization conditions [4-7]. Cracks in samples can be explained by tensile stresses that occur during the magnetization process due to the stored flux density gradient and may exceed the tensile strength of the material [8]. In recent years, a multitude of theoretical analyses for the crack problem of long rectangular slabs and long cylinders under electromagnetic force have been achieved [9-11]. Owing to the strong demagnetization effects in the perpendicular geometry, the central crack in a thin superconducting strip was studied according to the Bean critical state model [12].

However, it is observed experimentally that the critical current density usually depends on the flux density in real materials. The body forces induced by flux-pinning and magneto-elastic behavior are significantly different in magnitude between the Kim model and Bean model in thin superconducting strip [13]. It is found that the magnetostrictive behavior for the Kim model is in much better agreement with experiment than that for the Bean model at low temperatures. The Kim model is chosen because it has been shown to fit well the $J_c\left(H_a\right)$ measured in thin YBCO films

[14]. Therefore, it is of great practical importance to investigate crack problem of HTS thin films for the Kim model. It is to be known that stress intensity factor is a good fracture criterion and can provide successful prediction for fracture behavior. Although the longitudinal crack problem was extensively studied, the influence of transverse crack on the transport current has not been considered for thin films in the literature. Our main aim of this paper is to study the fracture behaviors of transverse crack in a HTS thin film based on the framework of field-dependent critical current model [15]. Applying finite element method, the stress intensity factors of the transverse crack are obtained during one full cycle applied field (the field increasing process and decreasing process) for the Bean model and Kim model. The comparisons are made between the results from the transverse crack and the longitudinal crack. The influence of the crack length is also studied in this paper.

2. Basic equations

We consider a thin type-II superconducting strip with a transverse crack of length $2a$ in an applied perpendicular field. As shown in Figure 1 (a), the thin strip is located in the Cartesian coordinate system. The width and the thickness of the film is $2w$ and d, respectively. The film is assumed to be isotropic and infinite along the x axis. Different from the longitudinal crack, the effect of the transverse crack on the current distribution in the thin strip should be considered (see Figure 1 (b)).

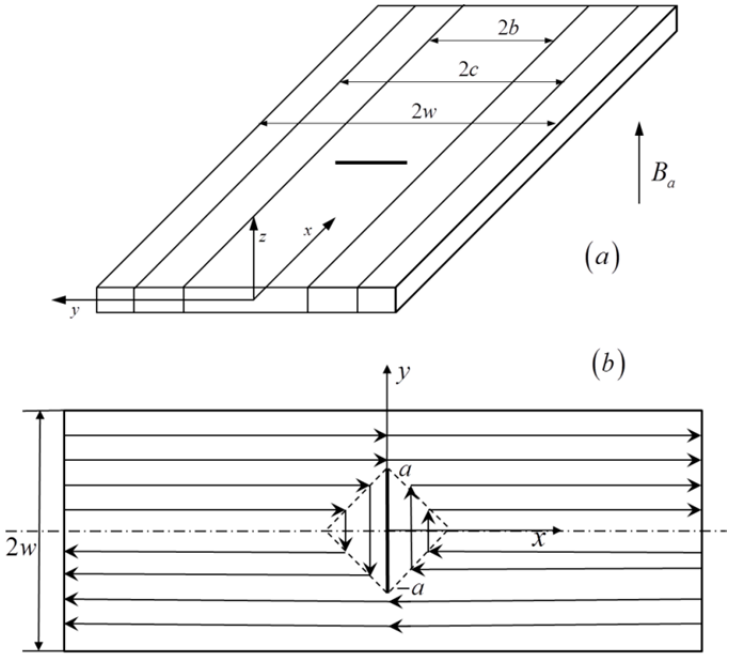

Figure 1. (a) A thin superconducting strip with a transverse crack in a perpendicular field. (b) The current distribution in the thin strip with a transverse crack.

When the superconducting strip is in a perpendicular field which exceeds the lower critical field B_{c1}, the flux and current starts to penetrate at the edge of the strip. Based on the critical state model, the shielding current density J is less than the critical current density J_c. Two classical critical

state models, Bean model and Kim model, are adopted to analyze this problem. For the Bean model, the critical current is constant, i.e. $J_c = J_{c0}$. The current density is dependent on the flux density in the Kim model, i.e.

$$\frac{J_c\left(B_z\left(y\right)\right)}{J_{c0}} = \frac{B_0}{B_0 + \left|B_z\left(y\right)\right|}, \tag{1}$$

where B_0 is a constant field that characterizes the degree of field dependence.

After ignoring the effect of the lower critical field, the current profile can be obtained by conformal mapping analytically for the Bean model [16]. When applied field increases from zero to a maximum B_{am}, the shielding current and penetrated flux are

$$J(y) = \begin{cases} \dfrac{2J_c}{\pi} \arctan \dfrac{y}{w}\sqrt{\dfrac{w^2 - b^2}{b^2 - y^2}}, & |y| < b \\ \dfrac{y}{|y|} J_c, & b < |y| < w \end{cases}, \tag{2}$$

$$B(y) = \begin{cases} 0, & |y| < b \\ B_f \arctan \mathrm{h} \dfrac{w}{|y|}\sqrt{\dfrac{y^2 - b^2}{w^2 - a^2}}, & b < |y| < w \end{cases}, \tag{3}$$

$$\tanh\left(\frac{B_a}{B_f}\right) = \frac{\left(a^2 - b^2\right)^{1/2}}{a}, \tag{4}$$

and the scaling field B_f is defined by

$$B_f = \frac{\mu_0 J_{c0} d}{\pi}, \tag{5}$$

where J_{c0} and μ_0 is the zero-field critical current and the permeability of free space, respectively.

When applied field decrease from the maximum B_{am} to $-B_{am}$, the current and penetrated flux can be obtained as

$$J\left(y, B_a, J_c\right) = J\left(y, B_{am}, J_c\right) - J\left(y, B_{am} - B_a, 2J_c\right), \tag{6}$$

$$B\left(y, B_a, J_c\right) = B\left(y, B_{am}, J_c\right) - B\left(y, B_{am} - B_a, 2J_c\right). \tag{7}$$

However, it can be found from the experimental results that the critical current density j_c is related to local flux density B. The results of magnetostriction in our preceding paper [13] also

that the Kim model is in better agreement with experiments than Bean model at low temperatures. Unfortunately, one cannot obtain the analytical solutions based on Kim model. However, for the applied magnetic field increased from zero to B_{am}, the profiles of current and flux density can be calculated numerically from the equations below [15]

$$J_x(y)=\begin{cases}-\dfrac{2}{\pi}y\sqrt{b^2-y^2}\displaystyle\int_b^w \frac{J_c\left(B_z(y')\right)dy'}{\left(y'^2-y^2\right)\sqrt{y'^2-b^2}}, & |y|<b\\ -\dfrac{y}{|y|}J_c\left(B_z(y)\right), & \mathrm{b}<|y|<w\end{cases}, \tag{8}$$

$$B_z(x)=B_f|x|\sqrt{x^2-b^2}\int_b^w \frac{J_c\left(B_z(x')\right)}{J_{c0}}\frac{dx'}{\left(x^2-x'^2\right)\sqrt{x'^2-b^2}},\ b<|x|\neq w, \tag{9}$$

$$B_a=B_f\int_b^w \frac{J_c\left(B_z(y')\right)}{J_{c0}}\frac{dy'}{\sqrt{y'^2-b^2}}. \tag{10}$$

When the applied magnetic field is increased from initial value B_{am} to B_a, the flux density changes in the outer regions ($c<|x|<w$) but is unchanged in the inner regions ($b<|x|<c$), and the central region ($|x|<b$) remains free of flux. Therefore, the distributions of current and flux density can be obtained by solving the following equations

$$J_x(y)=\begin{cases}\dfrac{2}{\pi}y\sqrt{c^2-y^2}\left[\begin{array}{l}\displaystyle\int_c^w \frac{J_c\left(B_z(y')\right)}{\left(y'^2-y^2\right)\sqrt{y'^2-c^2}}dy'\\ \displaystyle-\frac{2}{\pi}J_{c0}\int_b^c \frac{B_z(y')}{B_f}\frac{dy'}{\left(y'^2-y^2\right)\sqrt{c^2-y'^2}}\end{array}\right], & |y|<c\\ \dfrac{y}{|y|}J_c\left(B_z(y)\right), & \mathrm{c}<|y|<w\end{cases}, \tag{11}$$

$$B_z(y)=|y|\sqrt{y^2-c^2}\left[\begin{array}{l}\displaystyle-B_f\int_c^w \frac{J_c\left(B_z(y')\right)}{J_{c0}}\frac{dy'}{\left(y^2-y'^2\right)\sqrt{y'^2-c^2}}\\ \displaystyle+\frac{2}{\pi}\int_b^c \frac{B_z(y')}{\left(y^2-y'^2\right)\sqrt{c^2-y'^2}}dy'\end{array}\right],\ \mathrm{c}<|y|\neq w, \tag{12}$$

$$B_a=-B_f\int_c^w \frac{J_c\left(B_z(y')\right)}{J_{c0}}\frac{dy'}{\sqrt{y'^2-c^2}}+\frac{2}{\pi}\int_b^c \frac{B_z(y')}{\sqrt{c^2-y'^2}}dy'. \tag{13}$$

The body force (Lorentz force density) in the film is

$$\boldsymbol{f} = \boldsymbol{J} \times \boldsymbol{B}. \tag{14}$$

Because the thickness is very small compared with other two dimensions, this is a plane stress problem. For the symmetric model, it is convenient to analyze one quarter part of the film by means of finite element method. The famous virtual crack closure technique [17] is adopted to calculate the stress intensity factor, which can save our computational time and has high precision with fewer meshes. In our calculations, the Young's modulus and the Poisson's ratio equal to 125 GPa and 0.3, respectively.

3. Results and discussions

In this section, we will discuss the development of the stress intensity factor for applied field increasing to different maximum (B_f, $2B_f$, $3B_f$, $4B_f$) based on Bean model and Kim model. The crack length is the half of strip width. In addition, the crack length effect on the stress intensity factor is also discussed for applied field decreasing from $4B_f$ to B_f. The stress intensity factor is normalized by $K_0 = 1.2153\times10^6\,\mathrm{Pa}\cdot\mathrm{m}^{0.5}$ for applied field increasing to B_f with Kim model.

Figure 2 shows the development of the stress intensity factor in a full cycle applied field with maximum B_f. It can be found that the stress intensity factor is positive as applied field increases from zero to B_f. The depth of the penetrated flux has not reached the crack in this case. Therefore, all the body force is compressive and along y direction. The tensile stress along x direction induces positive stress intensity factor. The stress intensity factor for the Kim model is large than for the Bean model.

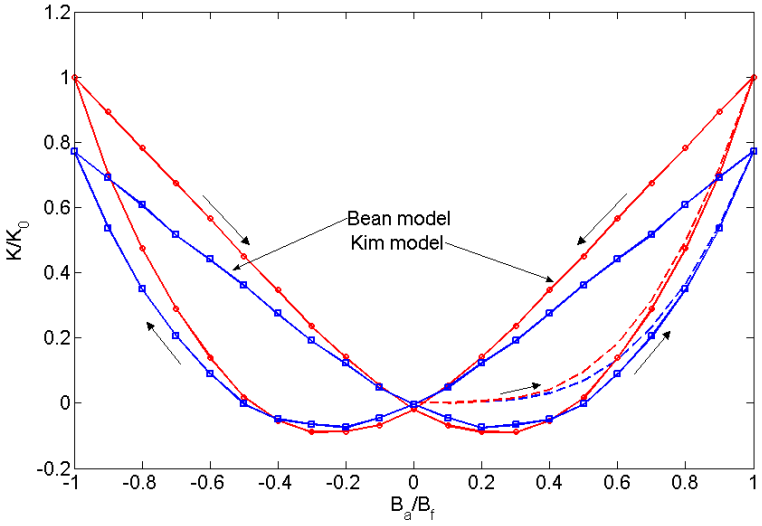

Figure 2. The development of the stress intensity factor in a full cycle applied field with maximum B_f.

If the applied field increases from zero to $2B_f$, the depth of the penetrated flux will reach the crack. The body force near the crack is along x direction in this case. Therefore, the stress intensity factor will decrease when applied field exceeds a certain value (see Figure 3). The value for the Kim model is less than for the Bean model since the filed dependence of J_c leads to a larger amount of penetration in a given applied field. The stress intensity factor increases firstly, and then decreases during the field decent. Moreover, it cannot recover zero when applied field decreases to zero because of remnant field.

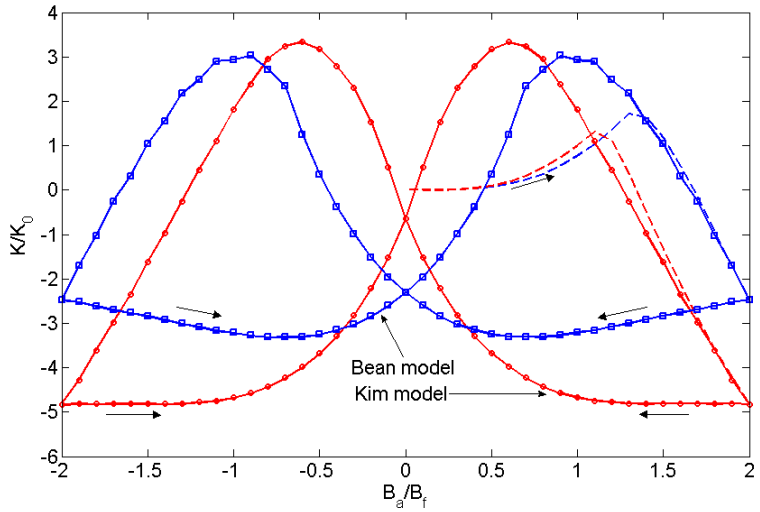

Figure 3. The development of the stress intensity factor in a full cycle applied field with maximum $2B_f$.

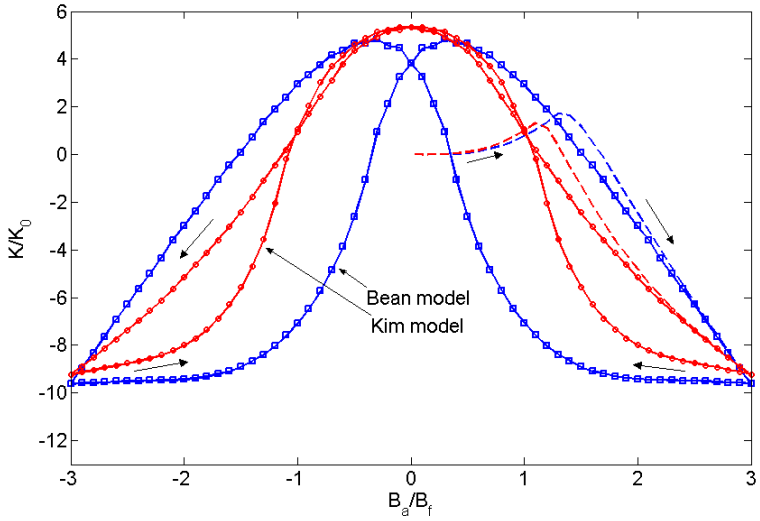

Figure 4. The development of the stress intensity factor in a full cycle applied field with maximum $3B_f$.

When applied field continue to increase, it can be found from Figure 4 that the stress intensity factor profiles is becoming complex. The development of the stress intensity factor during field decent is similar to Figure 3. However, different from Figure 3, the remnant stress intensity factor is positive when applied field decreases to zero. It is interesting that the stress intensity factor is maximal in the absence of applied field for the Kim model during field decent, and it is larger than for the Bean model.

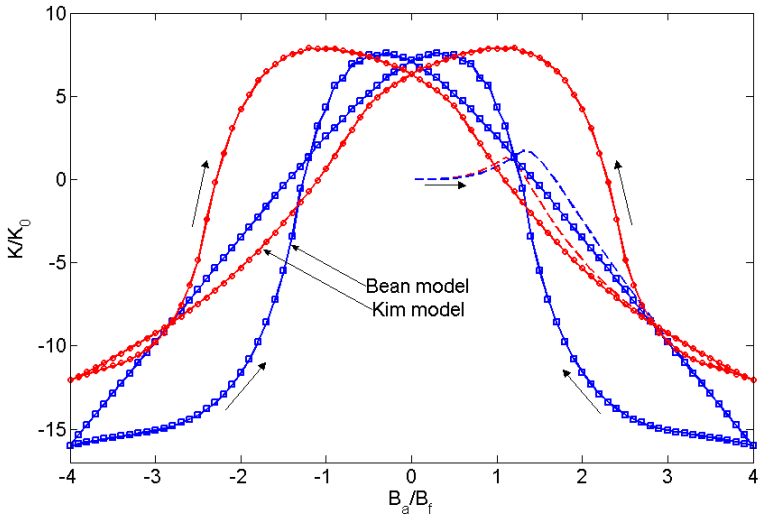

Figure 5. The development of the stress intensity factor in a full cycle applied field with maximum $4B_f$.

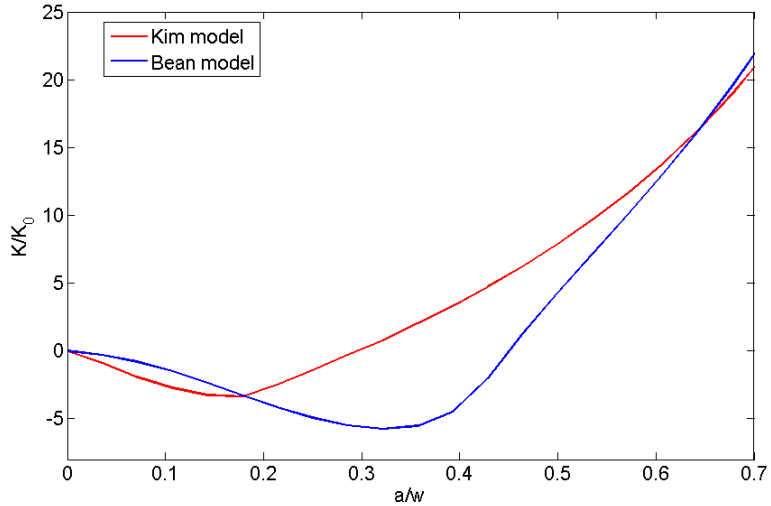

Figure 6. The stress intensity factor for different crack lengths in a perpendicular field which decreases from $4B_f$ to B_f.

Shown in Figure 5 is the development of the stress intensity as applied field increases to $4B_f$. In

this case, one can see that the stress intensity factor profiles become even more complex. The maximum of the stress intensity during field decent for both Bean model and Kim model is larger than that in Figure 4. Therefore, it is more dangerous in this case. Moreover, the decreasing field corresponding to the maximal stress intensity factor for the Kim model is greater than for the Bean model.

Finally we discuss the effect of crack length on the stress intensity factor for applied field decreasing from $4B_f$ to B_f. One can see from Figure 6 that the stress intensity factor firstly decreases as the crack length increases, and then increases when the crack length exceeds a certain value. The value for the Kim model is less than for the Bean model. The reason is that the depth of current change for the Kim model is larger than for Bean model. Moreover, Figure 6 demonstrates that it is more dangerous for large crack than for small crack.

4. Conclusions

The problem of thin superconducting strip with transverse crack in a perpendicular field is investigated in this paper. The Bean model and Kim model are adopted to analyze this problem. Different from the longitudinal crack, the transverse crack is more complex because of the effect of the transverse crack on the current. The results are useful for understanding the fracture mechanism of high-temperature superconductors, which could provide a theoretical guide for the ITER CICC designer.

Acknowledgements

This research was supported by the Fund of Natural Science Foundation of China (Nos. 11032006, 11121202 and 11202087), the Fundamental Research Funds for the Central Universities (lzujbky-2011-6) and Specialized Research Fund for the Doctoral Program of Higher Education under Grant 20110211120027. The authors gratefully acknowledge this support.

References

[1] S. Fleshler, L. T. Cronis, G. E. Conway, A. P. Malozemoff, T. Pe, J. McDonald, J. R. Clem, G. Vellego, P. Metra, Measurement of the ac power loss of (Bi, Pb)$_2$Sr$_2$Ca$_2$Cu$_3$O$_x$ composite tapes using the transport technique. Appl. Phys. Lett., 67 (1995) 3189.

[2] M. Suenaga, V. F. Solovyov, Q. Li, Z. Ye, H. J. Wiesmann, M. Iwakuma, M. Fukui, K. Toyota, F. Funaki, T. H. Johansen, D. V. Shantsev, J. R. Clem, AC losses in circular disks of thin $YBa_2Cu_3O_7$ films in perpendicular magnetic fields. J. Appl. Phys., 94 (2003) 502.

[3] G. B. Lubkin, Applications of high-temperature superconductors spproach the marketplace. Phys. Today, 48 (1995) 20.

[4] A. Nabialek, H. Szymczak, V. A. Sirenko, A. I. D'yachenko, Influence of the real shape of a sample on the pinning induced magnetostriction. J. Appl. Phys., 84, 3770 (1998).

[5] T. H. Johansen, Flux-pinning-induced stress and strain in superconductors: Long rectangular slab, Phys. Rev. B, 59 (1999) 11187.

[6] T. H. Johansen, Flux-pinning-induced stress and strain in superconductors: Case of a long circular cylinder. Phys. Rev. B, 60 (1999) 9690.

[7] T. H. Johansen, Flux-pinning-induced stress and magnetostriction in bulk superconductors.

Supercond. Sci. Technol., 13 (2000) R121.
[8] Y. Ren, R. Weinstein, J. Liu, R. P. Sawh, C. Foster, Damage caused by magnetic pressure at high trapped field in quasi-permanent magnets composed of melt-textured Y-Ba-Cu-O superconductor. Physica C, 251 (1995) 15.
[9] Y. H. Zhou, H. D. Yong, Crack problem for a long rectangular slab of superconductor under an electromagnetic force. Phys. Rev. B, 76 (2007) 094523.
[10] H. D. Yong, Y. H. Zhou, J. Zeng, Crack problem in a long cylindrical superconductor. J. Appl. Phys., 104 (2008) 113902.
[11] J. Zeng, Y. H. Zhou, H. D. Yong, Fracture behaviors induced by electromagnetic force in a long cylindrical superconductor. J. Appl. Phys., 108 (2010) 033901.
[12] H. D. Yong, Y. H. Zhou, Crack Problem for thin superconducting strip in a perpendicular magnetic field. IEEE Trans. Appl. Supercond., 22 (2012) 8400905.
[13] C. Xue, A. He, H. D. Yong, Y. H. Zhou, Magneto-elastic behaviour of thin type-II superconducting strip with field-dependent critical current. J. Appl. Phys., 2 (2013) 113.
[14] M. Suenaga, Q. Li, Z. Ye, M. Iwakuma, K. Toyota, F. Funaki, S. R. Foltyn, H. Wang, J. R. Clem, Thickness dependence of ac losses in circular disks of $YBa_2Cu_3O_7$ films in perpendicular magnetic fields. J. Appl. Phys., 95 (2004) 208.
[15] J. McDonald, J. R. Clem, Theory of flux penetration into thin films with field-dependent critical current. Phys. Rev. B, 53 (1996) 8643.
[16] E. H. Brandt, M. Indenbom, “Type-II-superconductor strip with cur-rent in a perpendicular magnetic field,” Phys. Rev. B, 48 (1993) 12893.
[17] E. F. Rybicki, M. F. Kanninen, A finite element calculation of stress intensity factors by a modified crack closure integral. Eng. Fract. Mech., 9 (1977) 931.

Fracture behaviors of thin superconducting films with field-dependent critical current density

An He, Cun Xue, Huadong Yong, Youhe Zhou*

Department of Mechanics and Engineering Sciences, School of Civil Engineering and Mechanics, Lanzhou University, Lanzhou, Gansu 730000, P.R. China

Key Laboratory of Mechanics on Disaster and Environment in Western China attached to the Ministry of Education of China

*Corresponding author: zhouyh@lzu.edu.cn

Abstract The fracture behaviors under electromagnetic force with field-dependent critical current density in thin superconducting film are investigated. Applying finite element method, the stress intensity factors of one central crack versus applied field and crack length are obtained for the exponential model, which was compared with the Bean model and Kim model. This work can offer good estimations and provide a basis for interpretation of cracking and mechanical failure of HTS thin films in numerous real situations.

Keywords Fracture behaviors, Superconducting film, Stress intensity factor, Exponential model

1. Introduction

High-temperature superconductor (HTS) tapes have provided a variety of engineering applications, such as ac power transmission cables [1, 2], filters for wireless communication [3]. With the development of engineering applications, major efforts are directed towards improvements on mechanical performances of HTS bulks in the presence of high magnetic field. During the past years, a series of investigations were devoted to the magneto-elastic behaviors induced by flux-pinning in bulk superconductors for different sample shapes, critical state models and magnetization processes [4-6]. For example, Johansen studied magnetostrictive behavior during the field activation processes, and revealed that the giant irreversible magnetostriction and internal stress could often lead to fatal cracking of the HTS bulks [7]. It is well established experimentally that when an HTS bulk traps large magnetic fields, the mechanical stability can be threatened by the tensile stress induced by flux-pinning [8]. Due to their low tensile strength of melt-processed HTS materials, micro-cracks and macro-cracks parallel to the $a-b$ plane were both observed in large grain bulk RE–Ba–Cu–O (RE: rare earth elements) superconductors [9, 10]. In recent years, many theoretical analyses for the crack problem of long rectangular slabs and long cylinders under electromagnetic force have been achieved [11-13]. Very recently, the central crack and interface crack problem of a thin superconducting strip were investigated by a field-independent J_c (the Bean model) [14, 15].

However, it is observed experimentally that the critical current density strongly depends on the flux density in real materials. The body forces induced by flux-pinning and magneto-elastic behavior are significantly different in magnitude between the Kim model and Bean model in thin superconducting strip [16]. It is found that Kim model is in much better agreement with experiment than Bean model at low temperatures. Furthermore, the exponential model, on the other hand, is one of the models that has been recently discussed in relation to the high-temperature superconductors [17-19]. Therefore, it is very worthwhile to investigate crack problem of HTS thin films for the exponential model. Since the superconducting materials are brittle, the stress intensity factor is a good fracture criterion and can provide successful prediction for fracture behavior. Our main purpose of this paper is to study the fracture behaviors in a HTS thin film with one central

longitudinal crack under electromagnetic force. Compared with the Bean model and Kim model, we investigate center-situated crack problem in an infinitely long superconducting film for the exponential model. The stress intensity factors at the crack tips are obtained by means of finite element method, which are discussed for different applied fields and crack lengths. In our calculations, the Young's modulus and the Poisson's ratio are assumed to be 125 GPa and 0.3 as adopted in Ref. [17].

2. Basic equations

In the present article, we consider a thin film with one central crack in a perpendicular applied magnetic field, and the film is located in the Cartesian coordinate system [see Fig. 1]. The width and the thickness of the film is $2w$ and d, respectively. The film is assumed to be isotropic and infinite along the x axis. Due to the symmetry of the problem, the current density has only a x component $J_x(y)$. Since the crack is parallel to the current, the disturbance of crack on the current and flux are negligible. The current density $J_x(y)$ and flux density $B_z(y)$ can be regarded as average value over the film thickness in case of $d << w$. Based on the theory of field-dependent current [20], for the applied magnetic field increasing from zero to B_{am}, the profiles of current and flux density can be calculated numerically from the equations below

$$J_x(y)=\begin{cases} -\dfrac{2}{\pi}y\sqrt{b^2-y^2}\displaystyle\int_b^w \frac{J_c\left(B_z(y')\right)dy'}{\left(y'^2-y^2\right)\sqrt{y'^2-b^2}}, & |y|<b \\ -\dfrac{y}{|y|}J_c\left(B_z(y)\right), & \mathrm{b}<|y|<w \end{cases}, \tag{1}$$

$$B_z(y)=B_f|y|\sqrt{y^2-b^2}\int_b^w \frac{J_c\left(B_z(y')\right)}{J_{c0}}\frac{dy'}{\left(y^2-y'^2\right)\sqrt{y'^2-b^2}},\ b<|y|\neq w, \tag{2}$$

$$B_a=B_f\int_b^w \frac{J_c\left(B_z(y')\right)}{J_{c0}}\frac{dy'}{\sqrt{y'^2-b^2}}, \tag{3}$$

and the scaling field B_f is defined by

$$B_f=\frac{\mu_0 J_{c0} d}{\pi}, \tag{4}$$

where J_{c0} and μ_0 is the zero-field critical current and the permeability of free space, respectively.

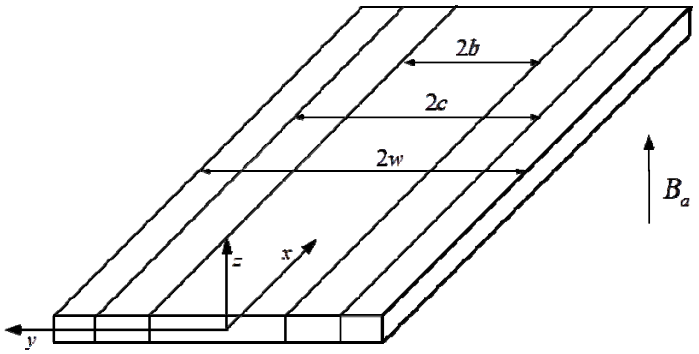

(a)

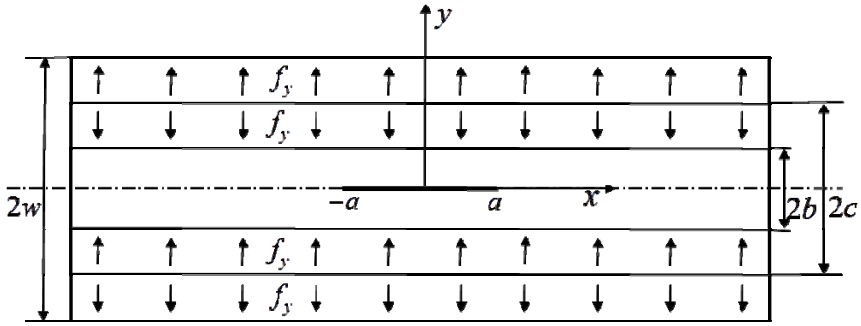

(b)

Figure 1. (a) Schematic of the superconducting thin film and coordinate system in a perpendicular applied field. The superconducting film subjected to the Lorentz force with one central crack.

When the applied magnetic field decreases from initial value B_{am} to B_a, the flux density changes in the outer region ($c<|x|<w$) but is unchanged in the inner region ($b<|x|<c$), and the central region ($|x|<b$) remains free of flux. Therefore, the distributions of current and flux density can be obtained by solving the following equations

$$J_x(y)=\begin{cases}\dfrac{2}{\pi}y\sqrt{c^2-y^2}\left[\begin{array}{l}\displaystyle\int_c^w\frac{J_c\left(B_z(y')\right)}{\left(y'^2-y^2\right)\sqrt{y'^2-c^2}}dy'\\ \displaystyle-\frac{2}{\pi}J_{c0}\int_b^c\frac{B_z(y')}{B_f}\frac{dy'}{\left(y'^2-y^2\right)\sqrt{c^2-y'^2}}\end{array}\right], & |y|<c\\ \dfrac{y}{|y|}J_c\left(B_z(y)\right), & c<|y|<w\end{cases}, \tag{5}$$

$$B_z(y)=|y|\sqrt{y^2-c^2}\left[\begin{array}{l}\displaystyle-B_f\int_c^w\frac{J_c\left(B_z(y')\right)}{J_{c0}}\frac{dy'}{\left(y^2-y'^2\right)\sqrt{y'^2-c^2}}\\ \displaystyle+\frac{2}{\pi}\int_b^c\frac{B_z(y')}{\left(y^2-y'^2\right)\sqrt{c^2-y'^2}}dy'\end{array}\right],\ c<|y|\neq w, \tag{6}$$

$$B_a=-B_f\int_c^w\frac{J_c\left(B_z(y')\right)}{J_{c0}}\frac{dy'}{\sqrt{y'^2-c^2}}+\frac{2}{\pi}\int_b^c\frac{B_z(y')}{\sqrt{c^2-y'^2}}dy'. \tag{7}$$

In the Bean model, the critical current density is constant in the film. While in reality the critical current density is dependent on the flux density $B_z(y)$, so the Kim model and the exponential model are respectively expressed as follows:

$$\frac{J_c\left(B_z(y)\right)}{J_{c0}}=\frac{B_0}{B_0+\left|B_z(y)\right|}, \tag{8}$$

$$\frac{J_c\left(B_z(y)\right)}{J_{c0}}=\exp\left(-\left|B_z(y)\right|/B_0\right), \tag{9}$$

where B_0 is a constant field that characterizes the degree of field dependence. The body force (Lorentz force density) in the film is

$$\boldsymbol{f}=\boldsymbol{J}\times\boldsymbol{B}. \tag{10}$$

The magneto-elastic problem of thin superconducting strip for the two different critical-state models

has been studied in our preceding paper [16]. In the field ascent stage, the body force remains zero in the central region and increases in magnitude along y-direction, but it is always negative, which means the film with crack is subjected to compressive stress. During the field descent branch, the body force has both negative value and positive value. Its peak value moves towards the middle of the film, and the peak value decreases as the maximum applied field decreases. Therefore, at the intermediate state of field reduction, the crack may be subjected to the largest tensile body force. Attention is limited to the crack problem of thin film in the field reduction. Fig. 2 shows the variations of body force for the three models with the applied field reduction. There is an important distinction between the three models. Thus, it's essential to take field-dependent $J_c(B)$ into account for studying the fracture behaviors of superconducting film. Because the thickness is very small compared with other two dimensions, this is a plane stress problem. Since the crack is parallel to the x axis, the effect of body forces f_x along the x direction at infinity can be neglected, i.e. $f_x = f_z = 0$. The body force along y axis becomes $f_y(y) = J_x(y)B_z(y)$. Due to the symmetry of the problem, it is convenient to analyze one quarter part of the film by means of finite element method.

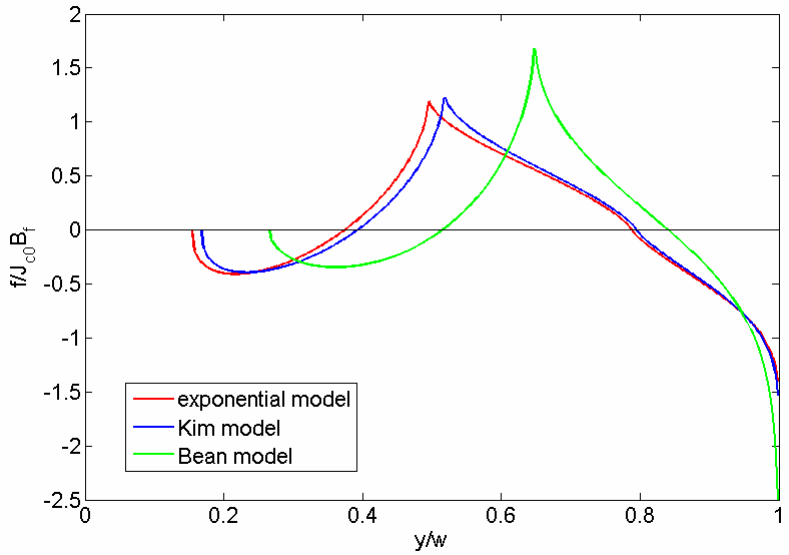

Figure 2. The variations of body force for the Bean model, Kim model and exponential model when the applied field decreases from the maximal value $2B_f$ to 0.

The stress intensity factor K is an important parameter in fracture mechanics, which determines whether the crack propagates or not. The crack would start to propagate the stress intensity factor K increases to the critical stress intensity factor K_{cr}. The critical stress intensity factor K_{cr} is material parameters, which is independent of the mechanical load and the applied field. Since the body force is perpendicular to the crack, only the mode I crack is considered in this paper and the energy release rate G_{II} is neglected. For the linear elastic fracture mechanics, the energy release rate is defined by

$$G = G_I = \lim_{\Delta a \to 0} \frac{1}{2d\Delta a} \int_0^{\Delta a} \sigma_{yy}(x)\Delta v(x)\,dx, \tag{11}$$

where Δa is the increment of the crack length at the crack front. In addition, $\sigma_{yy}(x)$ and $\Delta v(x)$ are the normal stress and the virtual crack opening displacement at the extension of the crack, respectively. Because this equation is complex in calculation, Rybicki and Kanninen [21] proposed

the famous virtual crack closure technique to calculate the energy release rate, which can save our computational time and has high precision with fewer meshes. Then the energy release rate can be obtained by

$$G \cong \frac{F_y \Delta v}{2d\Delta a}, \tag{12}$$

where F_y, Δa and Δv are the nodal force along y direction at the crack tip, the width of the mesh and the crack opening displacement at the node near the crack tip, respectively. The stress intensity factor K, one of the most important parameters in linear elastic fracture mechanics, reflects the singularity of the stress at the crack tip. The relationship between the stress intensity factor K and energy release rate G is given by

$$G = \frac{K^2}{E}. \tag{13}$$

3. Results and discussions

In this section, we discuss the crack problems of thin superconducting film with one central crack. The stress intensity factor is normalized by

$$K_0 = \sigma_0 \sqrt{a/\pi}, \tag{14}$$

where $\sigma_0 = \mu_0 J_{c0}^2 dw$. We mainly draw attention to the developments of stress intensity factor versus applied field and crack length for the three models.

Shown in Fig. 3 is the variation of K/K_0 for different critical state models when the applied field decreases from the initial value $2B_f$ to 0. It can be seen that the stress intensity factor firstly increases to the maximum value at a parameter field B_a^*, then decreases after it reaches peak value. Note that the superconducting film with crack is the most dangerous near the parameter field B_a^* during the field descent. What's more, although the profiles of stress intensity factor between the exponential model and the Kim model is nearly the same, it is not difficult to find that the maximum stress intensity factor and the corresponding parameter field B_a^* for the exponential model are larger than those for the Bean model and Kim model. These imply that the crack in the thin superconducting film will propagate more easily based on the results of the exponential model than that of the other two models. In addition, due to the trapped field, one can see obviously that the intensity factor cannot recover to zero even when the applied field decreases from B_{am} to zero.

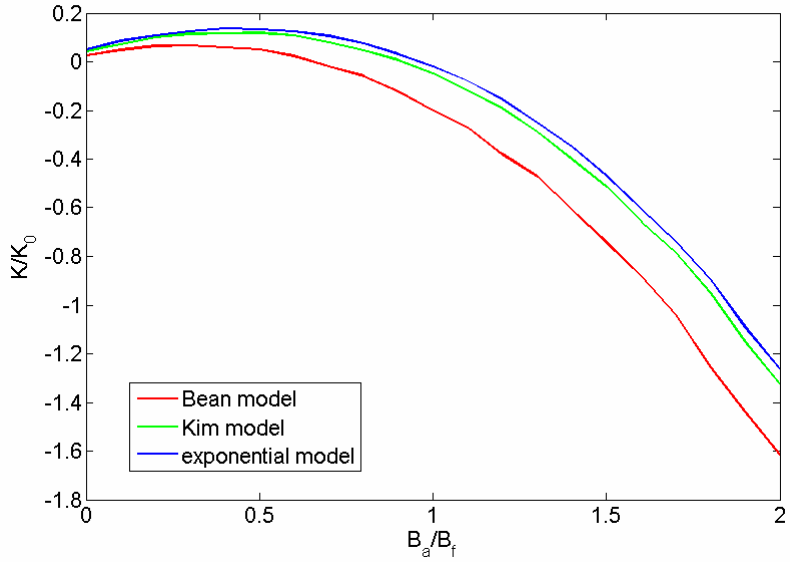

Figure 3. The stress intensity factors in the thin film with one central crack for the maximum field decreasing from $2B_f$ to 0.

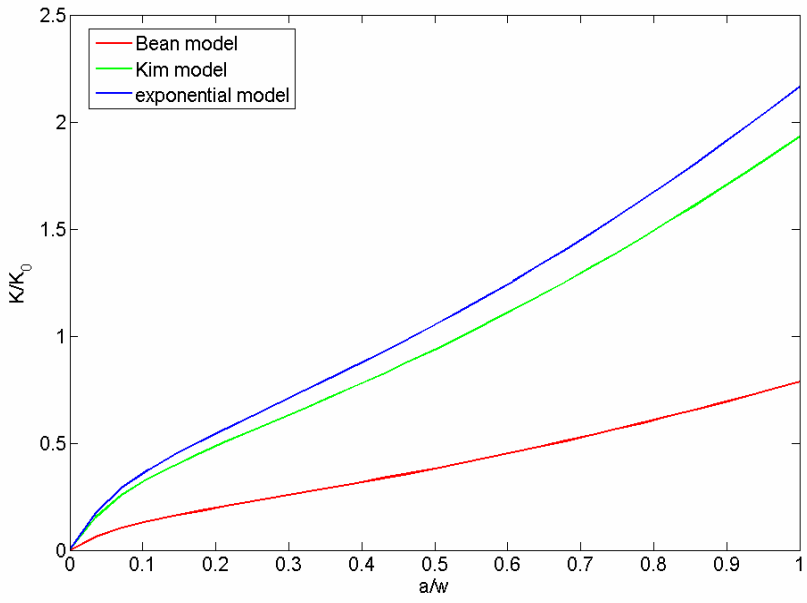

Figure 4. The stress intensity factors in the film with one central crack versus the crack length for the three models.

Fig. 4 shows the development of the stress intensity factor with respect to a/w for different critical state models. As anticipated, the stress intensity factor K increases as crack propagates, which indicates that the HTS film will have a tendency to break into pieces if the crack length increases to a critical value a_{cr}. One can tell the difference that the values derived from the exponential model increase more quickly than those from the other two models. That is to say, the effect of the crack length on stress intensity factor may be greater for the exponential model.

4. Conclusions

In this paper, we investigate the fracture behaviors induced by electromagnetic force with

field-dependent critical current in thin superconducting film. Applying finite element method, the stress intensity factors of one central crack versus applied field and crack length are obtained for different critical state models. From the comparison between the three models, it can be found that the magnitudes of the G and K are remarkably different. Thus the prediction of parameter field B_a^* corresponding to the overall maximum stress intensity factor, where the HTS thin film is the most dangerous, can be of practical importance. It is intended that these results presented in this paper may be useful for the interpretation of cracking and mechanical failure of HTS thin film in a number of real situations.

Acknowledgements

This research was supported by the Fund of Natural Science Foundation of China (Nos. 11032006, 11121202 and 11202087) and the Fundamental Research Funds for the Central Universities (lzujbky-2011-6) and Specialized Research Fund for the Doctoral Program of Higher Education under Grant 20110211120027. The authors gratefully acknowledge the support.

References

[1] S. Fleshler, L. T. Cronis, G. E. Conway, A. P. Malozemoff, T. Pe, J. McDonald, J. R. Clem, G. Vellego, P. Metra, Measurement of the ac power loss of (Bi, Pb)$_2$Sr$_2$Ca$_2$Cu$_3$O$_x$ composite tapes using the transport technique. Appl. Phys. Lett., 67 (1995) 3189.

[2] M. Suenaga, V. F. Solovyov, Q. Li, Z. Ye, H. J. Wiesmann, M. Iwakuma, M. Fukui, K. Toyota, F. Funaki, T. H. Johansen, D. V. Shantsev, J. R. Clem, AC losses in circular disks of thin $YBa_2Cu_3O_7$ films in perpendicular magnetic fields. J. Appl. Phys., 94 (2003) 502.

[3] G. B. Lubkin, Applications of high-temperature superconductors spproach the marketplace. Phys. Today, 48 (1995) 20.

[4] A. Nabialek, H. Szymczak, V. A. Sirenko, A. I. D'yachenko, Influence of the real shape of a sample on the pinning induced magnetostriction. J. Appl. Phys., 84, 3770 (1998).

[5] T. H. Johansen, Flux-pinning-induced stress and strain in superconductors: Long rectangular slab, Phys. Rev. B, 59 (1999) 11187.

[6] T. H. Johansen, Flux-pinning-induced stress and strain in superconductors: Case of a long circular cylinder. Phys. Rev. B, 60 (1999) 9690.

[7] T. H. Johansen, Flux-pinning-induced stress and magnetostriction in bulk superconductors. Supercond. Sci. Technol., 13 (2000) R121.

[8] Y. Ren, R. Weinstein, J. Liu, R. P. Sawh, C. Foster, Damage caused by magnetic pressure at high trapped field in quasi-permanent magnets composed of melt-textured Y-Ba-Cu-O superconductor. Physica C, 251 (1995) 15.

[9] P. Diko, Cracking in melt-processed RE-Ba-Cu-O superconductors. Supercond. Sci. Technol., 11 (1998) 68.

[10] P. Diko, G. Krabbes, Macro-cracking in melt-grown YBaCuO superconductor induced by surface oxygenation. Supercond. Sci. Technol., 16 (2003) 90.

[11] Y. H. Zhou, H. D. Yong, Crack problem for a long rectangular slab of superconductor under an electromagnetic force. Phys. Rev. B, 76 (2007) 094523.

[12] H. D. Yong, Y. H. Zhou, J. Zeng, Crack problem in a long cylindrical superconductor. J. Appl. Phys., 104 (2008) 113902.

[13] J. Zeng, Y. H. Zhou, H. D. Yong, Fracture behaviors induced by electromagnetic force in a long cylindrical superconductor. J. Appl. Phys., 108 (2010) 033901.

[14] H. D. Yong, Y. H. Zhou, Crack Problem for thin superconducting strip in a perpendicular magnetic field. IEEE Trans. Appl. Supercond., 22 (2012) 8400905.

[15] H. D. Yong, Y. H. Zhou, Interface crack between superconducting film and substrate. J. Appl. Phys., 110 (2011) 063924.
[16] C. Xue, A. He, H. D. Yong, Y. H. Zhou, Magneto-elastic behaviour of thin type-II superconducting strip with field-dependent critical current. J. Appl. Phys., 2 (2013) 113.
[17] H. Ikuta, K. Kishio, and K. Kitazawa, Critical state models for flux-pinning-induced magnetostriction in type-II superconductors. J. Appl. Phys., 76 (1994)4776
[18] K. Yamafuji, T. Fujiyoshi, K. Toko, T. Matsuno, T. Kobayashi, and K. Kishio, On the magnetic field dependence of critical current density in single crystals of high-T_c superconductors. Physica C, 226 (1994) 133.
[19] S. Senoussi, M. Oussena, G. CoIlin, and I. A. Campbell, Exponential *H* and *T* decay of the critical current density in $YBa_2Cu_3O_{7-\delta}$ single crystals. Phys. Rev. B, 37 (1998) 9792.
[20] J. McDonald, J. R. Clem, Theory of flux penetration into thin films with field-dependent critical current. Phys. Rev. B, 53 (1996) 8643.
[21] E. F. Rybicki, M. F. Kanninen, A finite element calculation of stress intensity factors by a modified crack closure integral. Eng. Fract. Mech., 9 (1977) 931.

Fracture of Low-dimensional Nanomaterials

Wanlin Guo*, Yufeng Guo, Chun Tang and Liangzhi Kou

State Key Laboratory of Mechanics and Control of Mechanical Structures and Key Laboratory for Intelligent Nano Materials and Devices of MOE, Institute of Nanoscience, Nanjing University of Aeronautics and Astronautics, Nanjing, 210016, China

* Corresponding author: wlguo@nuaa.edu.cn

Abstract We found different failure mechanisms and mechanical properties for single-walled carbon nanotubes (SWCNTs) when subjected to electric fields and that subjected to tensile load by quantum mechanics calculations. The electric field induced breaking in SWCNT begins from the outmost carbon atomic layers while the tensile load breaks the nanotube near its middle. When a tube is tensioned in an electric field, the critical tensile strength of the tube decreases significantly with increasing intensity of the electric field. It is interesting to be shown that a piece of graphene sheet formed by unwrapping the SWCNT can also be stretched up to 2.5% by applied electric field and fractured at it edges. We also studied the mechanical response and structural evolution of graphene with topological line defect under tensile strain by using first-principles calculations. We studied the superelongation and fracture of carbon nanotubes at high temperatures by molecular dynamics simulations, and found that the nearly simultaneous activation and wide distribution of a large number of defects near the elastic limit play a key role in impeding the formation of localized predominant instability and facilitating large tensile elongation of carbon nanotubes at high temperature.

Keywords Carbon nanotubes, mechanical and electric coupling, failure, quantum mechanics

Carbon nanotubes (CNTs), a novel form of carbon materials, have been recognized as particularly important nanoscopic systems. The exceptional mechanical properties of carbon nanotubes have been the subject of numerical experimental and theoretical studies. Electric field will impose significant influence on the electronic and structural properties of carbon nanotubes. Electric field induced failure of carbon nanotubes as well as the corresponding mechanisms are key issues for nanotube applications in nanoelectromechanical devices. By using semi-empirical quantum mechanical calculations as well as quantum-molecular dynamics techniques based on the Roothaan–Hall equations and the Newton motion laws, we [1] found different failure mechanisms and mechanical properties for single-walled carbon nanotubes (SWCNTs) when subjected to electric fields and that subjected to tensile load. The electric field induced breaking in SWCNT begins from the outmost carbon atomic layers while the tensile load breaks the nanotube near its middle. Electronic polarization and mechanical deformation induced by an electric field can significantly change the electronic properties of a SWCNT. Under electric field, the SWCNT can be stretched but the toughness is much lower than that under mechanical loading. When a tube is tensioned in an electric field, the critical tensile strength of the tube decreases significantly with increasing intensity of the electric field, as shown in Fig. 1.

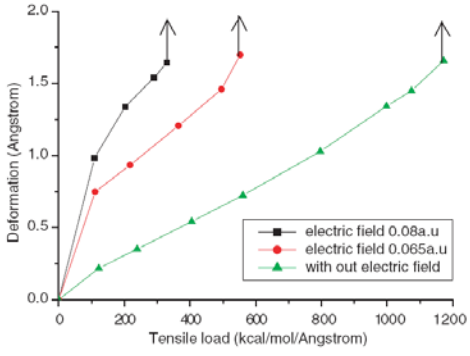

Figure 1. Deformation of SWCNTs versus the tensile load in the absence and presence of electric fields [1].

On the other hand, the mechanical behaviors and the electric and electronic properties of carbon nanotubes are always coupled with each other. By using Hartree-Fock and density functional quantum mechanics simulations, we [2] demonstrated a large axial electrostrictive deformation in short SWCNTs under electric field [Fig. 2 (a)]. The external field induced axial strains in armchair and zigzag tubes can be greater than 10% for a field strength within 1 V/Å. The corresponding volumetric and gravimetric work capacities of the SWCNTs are predicted to be three and six orders higher than those of the best known ferroelectric, electrostrictive, magnetostrictive materials and elastomers, respectively. Further study indicated the significant effect of axial electrostrictive deformation on the electronic properties of SWCNTs. It is also found that the band structures of SWCNTs change in electric fields and the change can be significantly enhanced by the electrostrictive deformation. The polarization of the orbital charge densities and the variation of the dipole moment are also enhanced by the electrostriction. The coupled mechanical and electrical behaviors of CNTs might lead to wider applications of nanotubes in nanoelectromechanical systems. It is interesting to be shown [2] that a piece of graphene sheet formed by unwrapping the single walled carbon nanotube can also be stretched up to 2.5% by applied electric field [Fig. 2 (b)].

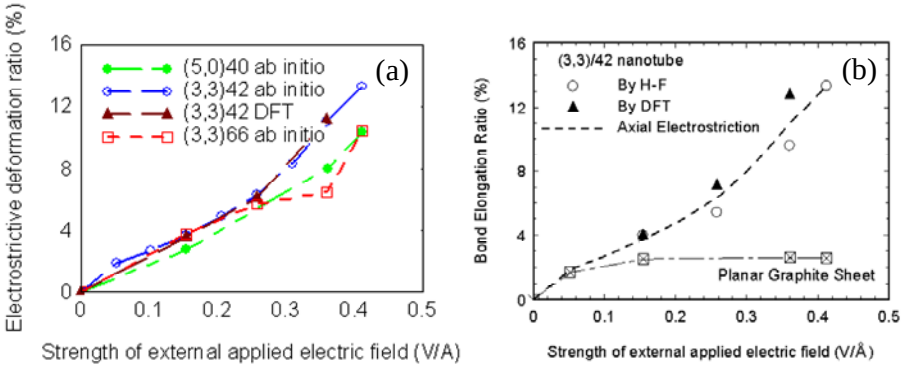

Figure 2. (a) Axial electrostrictive deformation ratio induced by external applied electric field in (3, 3) metallic single walled nanotubes of different lengths and a (5, 0) semi-metallic tube. (b) Average elongation ratios of the C-C bonds having a contribution to the deformation along the direction of the external electric field for the (3, 3)/42 tube and the corresponding single layer planar graphite sheet by unwrapping the nanotube. [2].

A recent experiment discovered that SWCNTs become superplastic and can accommodate extremely large plastic strains with a total elongation of 280% when being tensile loaded at high temperatures [3]. Similar ductile behaviors have been observed in individual double-walled and triple-walled carbon nanotubes at high temperatures above 2000 oC, with tensile elongation of 190% and diameter reduction of 90% [4]. However, several fundamental questions concerning the mechanism for superelongation of CNTs remain. By using molecular dynamics (MD) simulations, we [5] found that the nearly simultaneous activation and wide distribution of a large number of defects near the elastic limit play a key role in impeding the formation of localized predominant instability and facilitating large tensile elongation of carbon nanotubes at high temperature, as shown in Fig. 3. Intricate interplay between nanotube sizes and defect nucleation and motion determine the overall deformation pattern.

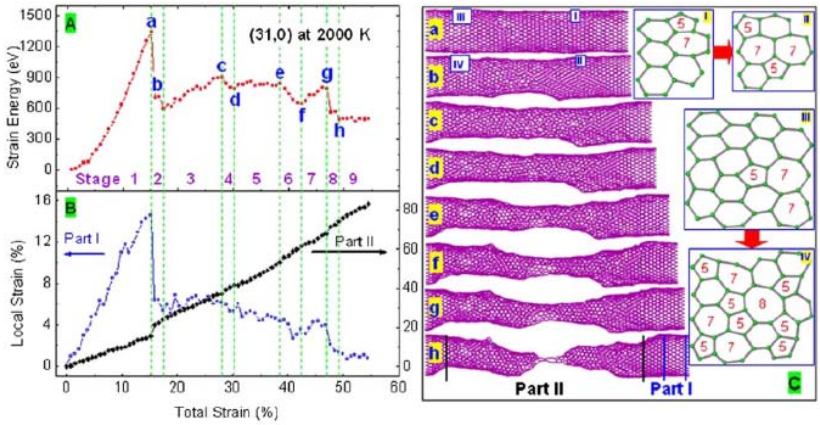

Figure 3. A (31,0) SWCNT subjected to tensile loading at 2000 K. The tube is 10.6 nm in length and 2.43 nm in diameter. (a) Strain energy. (b) Variation of local strain in two distinct parts of the tube: the elastic (part I) and plastic (part II) as shown in (c). (c) a–h: Selected snapshots of stretched SWCNT from the MD simulation; the insets show the 5-7-7-5 dipole and other defect formation and motion, and the rearrangement of local atomic structure during the deformation [5].

Graphene, a two-dimensional honeycomb carbon layer of sp2 hybridized carbon atoms, exhibits exceptional electronic, magnetic, optical and chemical properties. As the carbon-carbon bond is one of the strongest covalent bonds in the world, the mechanical behaviors of graphene have attracted enormous scientific interests from experimental and theoretical studies. We studied the mechanical response and structural evolution of graphene with topological line defect under tensile strain by using first-principles calculations, as shown in Fig. 4 [6]. It is seen that, before the strain reaches the critical value of about 12%, both bond lengths l1 and l2 increase monotonically with strain. It is interesting to note that when strain reaches about 4% the two bond lengths intersect. When the strain exceeds 12%, the two bond lengths experience an abrupt change: l1 suddenly increases while l2 sharply decreases. Such sudden variations of bond lengths induce significant redistribution of spin-polarized electrons at the defected part, which indicates that the magnetism of defected graphene can be tuned by strain.

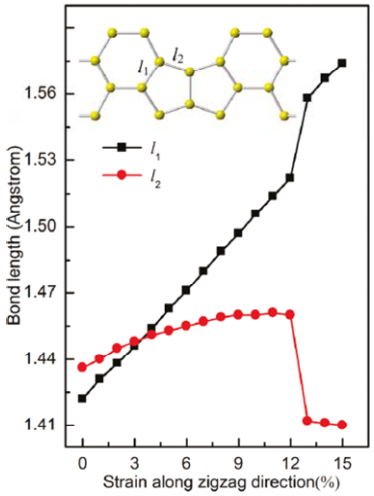

Fig. 4. Local bond length variation of defected graphene around the line defect region with strain [6].

References

[1] Y. F.Guo, W. L. Guo, Mechanical and electrostatic properties of carbon nanotubes under tensile loading and electric field. Journal of Physics D: Applied Physics, 36 (2003) 805-811.

[2] W. L. Guo, Y. F.Guo, Giant Axial Electrostrictive Deformation in Carbon Nanotubes. Physical Review Letters, 91 (2003) 115501.

[3] J. Y. Huang, S. Chen, Z. Q. Wang, K. Kempa, Y. M. Wang, S.H. Jo, G. Chen, M. S. Dresselhaus,

Z. F. Ren, Superplastic carbon nanotubes. Nature, 439 (2006) 281.
[4] J. Y. Huang, S. Chen, Z. F. Ren, Z. Q. Wang, K. Kempa, M. J. Naughton, G. Chen, M. S. Dresselhaus, Enhanced Ductile Behavior of Tensile-Elongated Individual Double-Walled and Triple-Walled Carbon Nanotubes at High Temperatures. Physical Review Letters, 98 (2007) 185501.
[5] C. Tang, W. L. Guo, C. F. Chen, Mechanism for Superelongation of Carbon Nanotubes at High Temperatures. Physical Review Letters, 100 (2008) 175501.
[6] L. Kou, C. Tang, W. Guo, C. Chen, Tunable Magnetism in Strained Graphene with Topological Line Defect ACS Nano, 5 (2011) 1012–1017.

Cracks formation in the vertical co-depositing colloidal crystal

Ding Lan[$], Yuren Wang*

Chinese Academy Science, Institute of Mechnices, National Microgravity Lab, Key Lab Microgravity, Beijing 100190, China

*Corresponding author: yurenwang@imech.ac.cn

[$] Email: landing@imech.ac.cn

Abstract: It is a cost-efficient approach to take the colloidal crystals (CCs) as template to fabricate three-dimensional photonic crystals. However, cracks occurring in the colloidal crystal synthesis process typically divided a colloidal crystal film into single crystalline domains of several tens of micrometers size, setting a major obstacle to the application of CCs template method. As a modified method, the co-deposition of microsphere and nanoparticles in CCs formation was put forward to reduce the formation of cracks. However, the physical mechanism of crack inhibition in co-deposition process was not well studied.

In this paper, we reported an in-situ observation study on the crack formation in the co-deposition process. It was found that the crack morphology has a large difference compared with that in the normal CCs template method. The cracks in normal CCs growth are usually formed and developed as parallel straight lines along the substrate surface in the growth direction. In contrary, the cracks present a pattern of regular triangular lattices in co-deposition. The crack morphology changes from CCs process to co-deposition process was considered to have a strong relationship to the gel formation in co-deposition procedure which can be ignored in the normal CCs growth. The corresponding physical model was developed and compared with the experimental results. The present study was helpful to give a deep insight into the crack formation mechanism in the colloidal spheres (CSs) assembling process.

Keywords：Crack, co-deposition, colloidal crystal

1. Introduction

Vertical self-depositing (VSD) method has proven to be highly-efficient for the synthesis of the colloidal crystals (CCs) which cannot be got by conventional top-down methods. The CCs are three-dimensional periodic structures formed from colloidal sub-microspheres. [1] The most remarkable property of the CCs is the photonic band gap (PGB)[2], which makes the CCs have great potential application in photonic crystals. At the same, the CCs can be as a template to get well-ordered, porous “inverse opal” structures for optical, electronic, and (bio) chemical application.[3] Such ordered, high surface area nanoporous solids are important for potential applications in fields from catalysis to tissue engineering, drug delivery, gas sensing, and filtration and PGB devices. Compared to conventional top-down process, this kind of bottom-up self-depositing method shows its low-cost and high-efficiency. However, during the deposition of the CCs, a number of defects such as cracks, domain boundaries and vacancies will be produced. Among them, the large length scale defects, cracks, will split the CCs into countless small domains, which make the practical applications of the CCs impossible.

In order to reduce or even eliminate cracks, researchers developed many growth methods of the CCs. van Blaaderen A. et al. [4] invented “colloidal epitaxy” to fabricate CCs. They made the slow sedimentation of CSs onto a patterned substrate (or template), which could direct the crystallization of bulk CCs, and permit tailoring of the lattice structure, orientation and size of the CCs.

Rudolf Zentel et al. [5] spread the colloidal suspension on the surface of the liquid substrate (gallium or

mercury) and the crystallization and drying of the CCs were finished at room temperature for about one day. In this way, they got crack-free CCs of a size of nearly a centimeter square. Norris et al. [6] found that the cracks could be avoided in fabricating adverse opals by sintering the silica spheres prior to assembly of the CCs. However, the methods mentioned above were too complicated, high cost and not reliable to produce crack-free CCs with large domains.

The co-depositing method was first used by Meng et al. [7] to fabricate ordered porous materials. Due to the co-assembly of the CSs and the ultrafine particles, such as TiO_2 or SiO_2, the researcher can get the CCs by a one-step process. With the water evaporation at the meniscus, the ultrafine particles were infiltrated into the voids of the CSs during the co-deposition. The following investigators went beyond the co-deposition of the binary particles and got crack-free colloidal films of centimeter square through co-assembly of the CSs and polymer precursors [8] or salt precursors [9]. The infiltrated materials could be as a sacrifice to be got rid of, and the large area CCs would be left.

In fact, cracking during drying of colloidal dispersion has been investigated for many years and made the model system for crack study [10-15]. In order to understand the mechanism of cracking, it is base to study the dying process and the crack morphology. Drying accompanies the whole process of the thin film formation and has very important effects on the quality and shape of the colloidal film. [16-19]Although through the co-depositing method researchers could improve the CCs' quality and get crack-free CCs of large domain, it is not clear whether there are differences between deposition of the CSs of single size and co-deposition of the binary particles. In this paper, we show the cracking process during the deposition of the CSs of 360nm and the binary deposition of the CSs (360nm) with the SiO_2 nanoparticles (7nm) by real time observation method. It is noteworthy that in spite of the same drying condition absolutely, the morphology of cracks is different from each other.

2. Experiment

The experimental set-up for the in-situ observation was shown in Fig. 1. A magnified schematic of the observed region is shown, as well as the image observed at the initial growth stage. To have a comprehensive understanding of the assembly process, large colloid spheres with the diameter of 3 micrometers were used for the observation of the initial assembly process. Cracks formation process by VSD was observed in a transparent glass cell and the inner temperature could be controlled. Polystyrene latex spheres (from Duke Scientific Corporation, California, USA) with 360nm diameter were used in this work. Polystyrene spheres were mono-dispersed in Milli-Q water with 0.1% volume fraction. The Silica nanoparticles with mean diameter of 7nm were used for co-deposition. A 4x1.5 mm rectangular, 1 mm thick glass substrate was inserted vertically into a semi-cylindrical glass growth cell. To guarantee good water wetting, the glass substrate and the growth cell walls were cleaned with detergent, followed by immersion in chromic acid for about 24 hours. Cleaned glass plates were kept in Milli-Q water for about 8 hours, and dried naturally in the clean room environment before experiments. The growth temperature was kept at 55 °C during the experiment. Mean water evaporation rate was about 0.19 grams/hour. A long working distance optical microscope (Questar QM100, USA) was used to carry out experimental observations. The crack growth process was recorded with a digital video recorder connected to the microscope camera.

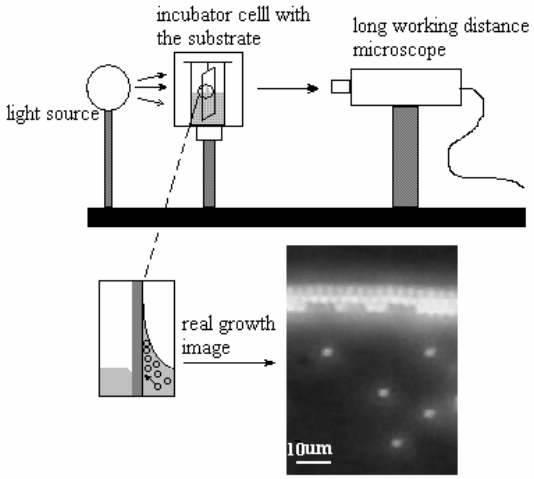

Figure 1. A schematic diagram of the experimental setup. A magnified schematic of the observed region is shown at the vicinity of the meniscus, as well as the image observed at the initial growing stage. Large colloid spheres with the diameter of 3 micrometers were used in the observation of the initial assembly process.

3. Results

The VSD experimental system of CSs is different from conventional colloidal suspension drying system [16-19]: a) it is capable of growing large-scale crystals from low particle concentration suspensions (0.1% volume fraction); b) without gel formation, the colloidal particles self-assemble to be a film by capillary forces and micro flow at the vicinity of the solvent menisci; c) a film with uniform thickness is formed of close-packed spheres. For the co-deposition, the CSs are close-packed orderly, and the nanoparticles infiltrate into the void among the CSs. [7]

Figure 2 shows the cracks of the colloidal films drying from the suspensions with different ratio of the CSs and silica nanoparticles. In all suspensions, the volume fraction of the CSs was 0.1%, and mixed the CSs with the silica nanoparticles in volume ratio of 5:0, 5:1, and 5:2. The line in fig.2 denotes the crack's tip and the arrows was the growth direction of the colloidal films. In fig.2a, the growth directions of the cracks and the colloidal film are same, the cracks are longitudinal. When the nanoparticles are added, the crack patterns change significantly (Fig. 2b, c). From fig. 2b, c, it is clear that the crack density has a relationship with the amount of the silica nanoparticles. There is higher crack density in fig. 2b. From the insets of the fig. 2, the directions of the crack also change with the addition of the nanoparticles.

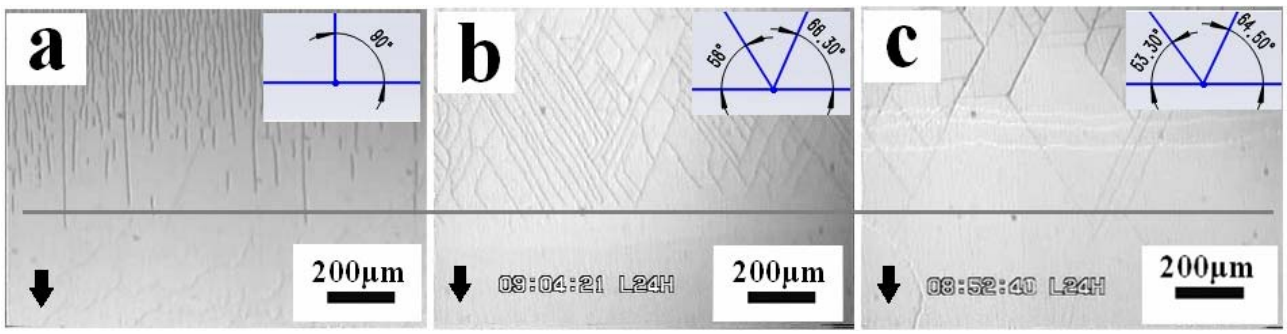

Figure 2 Different crack morphology drying from mixed suspension. The CSs with the silica nanoparticles in volume

ratio of a5:0 (a), 5:1(b), and 5:2 (c). The direction of the arrows is x axis. The insets show the angles between the cracks and x axis.

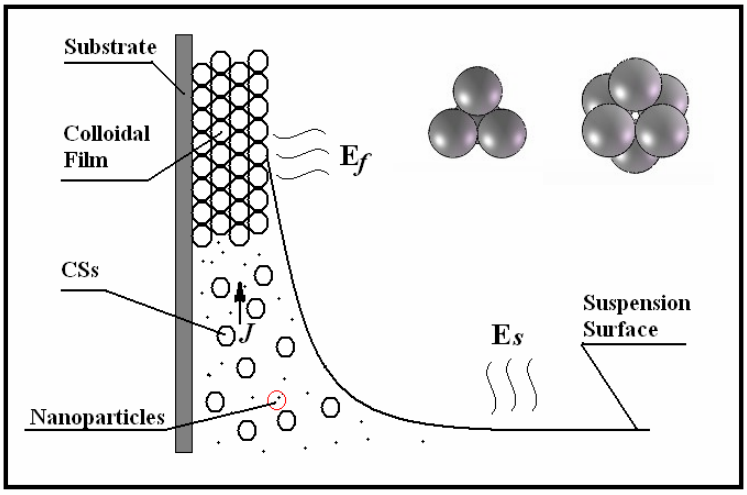

Figure 3 The VSD process of the CSs (or co deposition with nanoparticles) in meniscus region of the suspension. E_f and E_s are the evaporation of the colloidal film and the suspension respectively. J is the diffusive flux of the CSs (nanoparticles). Left inset is tetrahedral site. Right inset is octahedral site.

The VSD method (showed by Fig. 3) gets the colloidal film at the air-water-substrate interface from low-viscosity suspensions. The evaporation-driven flow makes the spheres or particles deposited in the meniscus. When the water reservoir is sufficiently large, the evaporation process does not significantly enrich the colloidal density. As the water evaporates, more substrate is exposed and coated colloidal film. The CSs or nanoparticles in suspension, within the solid-liquid-gas interface, are deposited on the substrate subject to interfacial forces. In this process, the thickness of the film can be adjusted by the concentration of the suspensions or by the descent speed of the suspension surface.

At the very beginning, the CSs and the silica nanoparticles are entrained toward the growth front at the same velocity, and the large spheres nucleate first in a close-packed network because of their higher volume fraction and larger size. With the evaporation and convective flow of the liquid medium through the pore space of the network, the nanoparticles can easily move and fill the voids of the fcc structure (formed by the CSs). From a simple geometric analysis indicated that, in the close-packed colloidal sphere arrays, two types of interstitial sites exist: the tetrahedral site and the octahedral site. One cubic unit cell contains four large spheres, eight tetrahedral voids, and four octahedral voids.

During the evaporation of the film, the strong particle wetting prevents the invasion of air into the colloidal film. With the sustained water loss, the nanomenisci will occur in the film interface, which create capillary the capillary tension to pull water through the network deposited by CSs (nanoparticles) to replace the lost by evaporation. For the wet film (no crack), the rate of fluid flow through (J) must balance the evaporation rate (E_f). The fig. 2a shows the directional cracks which indicate there is nearly uniaxial stress and the stress $\sigma_{xx} >> \sigma_{yy}$. When the nanoparticles were added into the suspension, the film stress state was changed into biaxial stress which leaded to a crack pattern of triangular lattices.

4. Conclusions

In summary, the comparison study of the crack formation during the VSD process with and without

nanoparticles. It was found that co-deposition lead to different crack morphology and decreased the crack density. In contrary, the cracks present a pattern of regular triangular lattices in co-deposition. The crack morphology changes from CCs process to co-deposition process was considered to have a strong relationship to the gel formation in co-deposition procedure which can be ignored in the normal CCs growth. This study indicates the co-VSD method is a cost-efficient approach to get single colloidal crystal of large domain.

5. Acknowledgements

This work was supported by the National Nature Science Foundation of China (Grand No. 11202209), National Program on Key Basic Research Project (2011CB710901).

6. References

[1] Jiang, P., Bertone, F., Hwang, K. S., Colvin, V. L., Single-crystal colloidal multilayers of controlled thickness. Chem. Mater. 11(1999)2132-2140.

[2] Dongbin; Liu Hongguang; Cheng Bingying et a1.; Visible and near-infrared silica colloidal crystals and photonic gaps．Phys．Rev．Lett．B，58, 1(1998)35-38.

[3] Imhof, A., Pine, D.J., Ordered macroporous materials by emulsion templating. Nature, 389(1997) 948-951.

[4] van Blaaderen, A., R. Ruel, P. Wiltzius, Template-Directed Colloidal Crystallization. Nature 385(1997) 321-324.

[5] Griesebock, B., M. Egen, R. Zentel, Large Photonic Films by Crystallization on Fluid Substrates." Chemistry of Materials, 10 (2002) 4023.

[6] Chabanov, A. A., Y. Jun, D. J. Norris. Avoiding Cracks in Self-Assembled Photonic Band-Gap Crystals, Applied Physics Letters, 18 (2004)3573-357.

[7] Meng Q.B., Gu Z.Z., Sato O., Fabrication of highly ordered porous structures, Applied Physics Letters, , 77, 26 (2000)4313-4315.

[8] Kanai, T. & Sawada, T. New route to produce dry colloidal crystals without cracks. Langmuir 25(2009) 13315–13317.

[9] Wang, L., Zhao, X. S. Fabrication of Crack-Free Colloidal Crystals Using a Modified Vertical Deposition Method, J. Phys. Chem. C, 111(2007)8538-8542.

[10]Skjeltorp, A.T., Meakin, P., Fracture in microsphere monolayers studied by experiment and computer simulation. Nature, 335(1988)424-426.

[11]Allain, C., Limat, L., Regular pattern of cracks formed by directional drying of colloidal suspensions, Phys.Rev.Lett., 74, 15(1995)2981-2984.

[12]Pauchard, L., Parisse, F., Allain, C., Influence of salt content on crack patterns formed through colloidal suspension desiccation, Phys. Rev. E., 59, 3(1999)3737-3740.

[13]Shorlin,K., de Bruyn, J., Graham, M., Morris, S., Development and geometry of isotropic and directional shrinkage-crack patterns, Phys. Rev. E., 61, 6(2000)6950-6957

[14] Tirumkudulu, M. S. and Russel, W. B.; Cracking in Drying Colloidal Films, Langmuir, 21(2005)4938-4948.

[15] Lee, W. P. and Routh , A. F., Why do drying films crack, Langmuir, 20(2004)9885-9888.

[16] Allain, C., Limat, L. Regular patterns of cracks formed by directional drying of a colloidal suspension. Physical Review Letters, 74(1995)2981–2984.

[17] Skjeltorp, A.T., Meakin, P. Fracture in microsphere monolayers studied by experiment and computer simulation. Nature (London), 335(1988)424–426.

[18] Lee, W.P.; Routh, A.F. Why do drying films crack? Langmuir, 20(2004)9885–9888.

[19] Tirumkululu, M.S.; Russel, W.B. Cracking in drying latex films.Langmuir, 21(2005)4938–4948.

Fracture of Metallic Ring Samples under Magnetic Pulse Shock Action

Viktor A. Morozov[1*], Yuriy V. Petrov[1], Anton A. Lukin[1], Viktor M. Kats[1], Svetlana A. Atroshenko[1], and Georgii D. Fedorovskii[1]**

[1] Saint-Petersburg state university, 7-9, Universitetskaya nab.,St. Petersburg, 199034, Russia

[*] viktor.morozov@math.spbu.ru, [**] yp@yp1004.spb.edu

Abstract

Metallic rings made of aluminum alloy are studied upon the application of a distributed radial load by a magnetic pulse technique. Two modifications of the magnetic pulse method were implemented on the basis of the GKVI-300 high voltage short pulse generator providing the formation of voltage pulses of 30-300 kV in amplitude. These two approaches making it possible to decrease the period of the harmonic load to 7,5 μs and 1 μs . Method to determine the instant of rupture of the ring from a flash arising at rupture with the help of a photo detector was developed and applied. Load signal and signal from the photo detector are displayed and saved with a digital oscilloscope.

Fracture stress value was estimated. It increased on load time shortens.

The surfaces of fracture of aluminum samples were investigated after the tests by optical microscope. It is shown, when the load time shortens, the ductile component of fracture declines and the samples fail in a more brittle manner.

Keywords: Magnetic Pulse Technique, Metallic Ring Samples, Dynamic Loading

1.Introduction

In the works of American authors [1-4], an original magnetic-pulse method is proposed for the tangential stretching thin metal rings up to destruction. The method allows them to achieve the radial velocities of ring expansion in the range of 80-200 m/s at strain rates of the order $10^4 s^{-1}$. The process of the formation of necks and fragmentation fixed using high-speed photography with high temporal and spatial resolution. It is shown that the destruction of the ring occurs in a time much less than the first period of the current oscillations in the ring. Fragmentation process takes less than 20 μs. The increase in the cross-section of the specimen significantly increases the deformation of localization start. Deformation of localization origin is independent of strain rate. An increase of deformation homogeneity takes place with increasing sample sizes.

The high-speed radial expansion of ring is analyzed in [5] in plane strain. The material behavior is ductile, deformation hardening takes into account also. Tensile tests of rings of aluminum alloy [6] with speeds $3 \cdot 10^3 - 2{,}3 \cdot 10^4 s^{-1}$ at pulse durations between 5 and 41 μs revealed the effect of the speed and size of the expanding rings on the deformation of an aluminum alloy. Loading rate below $2 \cdot 10^3 s^{-1}$ does not affect the deformation. Flow stress depends on the maximum strain rate and the size of the ring.

The work [7] shows the effect of pulse duration on the microstructure produced as a result of impact loading. The authors [8] have shown that the generation of dislocations and the formation of twins in copper alloy with low stacking fault energy depend on the pulse duration less than 0.3 μs. The main cause of hardening under the pulse duration of 0.5 μs is the twinning and slip contribution becomes more significant when pulse duration is large. Number of damage upon rings extension of aluminum alloy is independent of the ring radius and is proportional to its expansion rate as is shown in [9]. Paper [10] provides a method to represent the investigation of fragmentation in the rapidly expanding metal rings. A quick discharge system of the capacitor generates magnetic forces that accelerate the ring to the maximum radial velocity of about 200 m/s, which corresponds to the

peripheral strain rate at about $10^4 s^{-1}$ under fragmentation. The streak camera technique is used to record the movement of the rings. Experiments on the destruction and fragmentation were performed on the samples of OFHC copper and aluminum 1100-0. Thin rings have rapidly expanded in [11] using magnetic fields to study the effect of strain rate on the strain to failure of ductile metals. In the interval of studied expansion velocities (50 to 300 m/s), the experimental results showed that the plasticity of Al 6061 and OFHC Cu increases monotonically with increasing speed. In each case, the deformation of the specimen to the destruction is almost two times more at 300 m/s than in static conditions.
All peer-reviewed papers on the metal rings maximum tensile strain rate did not exceed $10^4 s^{-1}$. This paper presents the results of a study on the destruction of the metal ring samples of D16 aluminum alloy with a substantially reduced period of harmonic loading. Voltage of destruction was rated and it shows its increase with shortening of the loading duration. Short-term loading leads to dynamic recrystallization - the formation of new small grains. The method of determining when the sample breaks is developed and applied.

2. Technique of experiment and results

Figure 1 shows the loading scheme. The current flowing through the coil, in which the ring specimen is located coaxially, causes inductive current in it, and the interaction of these currents generates a force of repulsion between the solenoid and the ring.

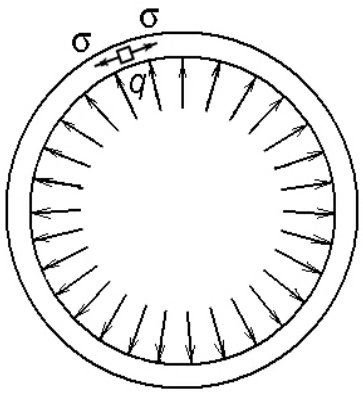

Fig. 1. Loading scheme of the sample (q- load, σ - tensile stress)

Two modifications of magnetic pulse method of loading were realized on the basis of short high-voltage pulse generator GKVI-300, which provides the formation of electrical voltages with amplitudes of 30 - 300 kV. Electrical block-schemes of the installation under the implementation of a sinusoidal load with a period of 7.5 μs (modification 1) and with a period of 1 μs (modification 2) are shown in Fig. 2 and 3, respectively.

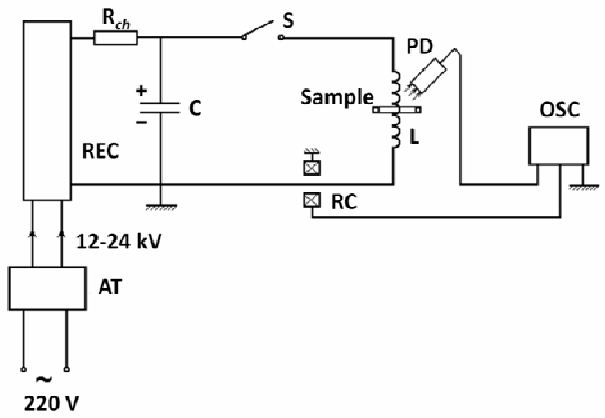

Figure 2. The block-scheme of the setup for sinusoidal electromagnetic load of period 7.5 μs: AT - autotransformer; REC - rectifier; R_{ch} - charge resistor; C - condenser; S - discharge; RC - Rogowski belt; L - coil (coil without core); Sample - sample (metal ring); PD - photodiode; OSC – oscilloscope

In testing of ring specimens with a period of sinusoidal current T = 7,5 μs (Fig. 2) the charge of capacitor (C) is carried out by rectifying device (REC) with variable voltage from 12 to 24 kV. Then the discharge of capacitor (C) was proceeded through the coil (L) with a high-voltage spark gap (S)

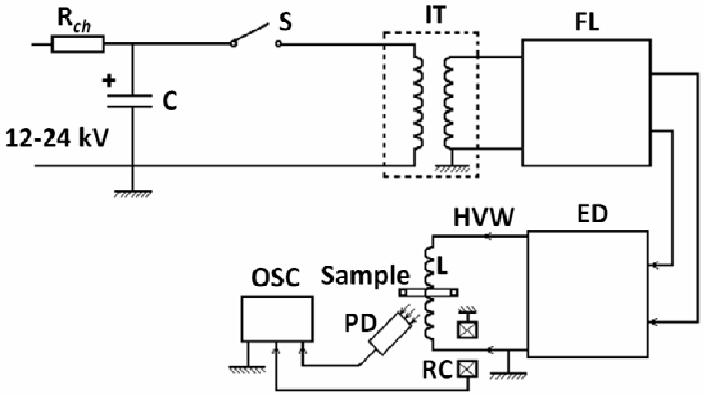

Fig. 3. The block-scheme of the setup for sinusoidal electromagnetic load of period 1 μs: IT - pulse transformer; FL - forming line; ED - output device; HVW - high-voltage electrode

The coil is made of copper wire 1mm in diameter, has 5 turns of the coil 25 mm in diameter. The current flowing through the coil, was measured by Rogowski coil (RC) and displayed on a digital oscilloscope (OSC), from which the information was recorded on an electronic bearer. When the ring (Sample), coaxially mounted on the middle of the coil (L) is broken, a spark is appeared, which permits record the time of the destruction of the sample using a photodiode (PD). More complex unit is used in the test samples, when current was passed through the coil with a period of the damped oscillations T = 1μs. Its block-scheme is shown in Fig. 3. With the help of a pulse transformer (IT) the voltage of sine wave signal increased in 10 times, compared with the above case (Fig. 3) and by forming line (FL), and an output device (ED) (Fig. 3) was supplied to the same coil. However, the period of the current oscillations is already a T = 1μs. Appearance of plants is shown in Fig. 4

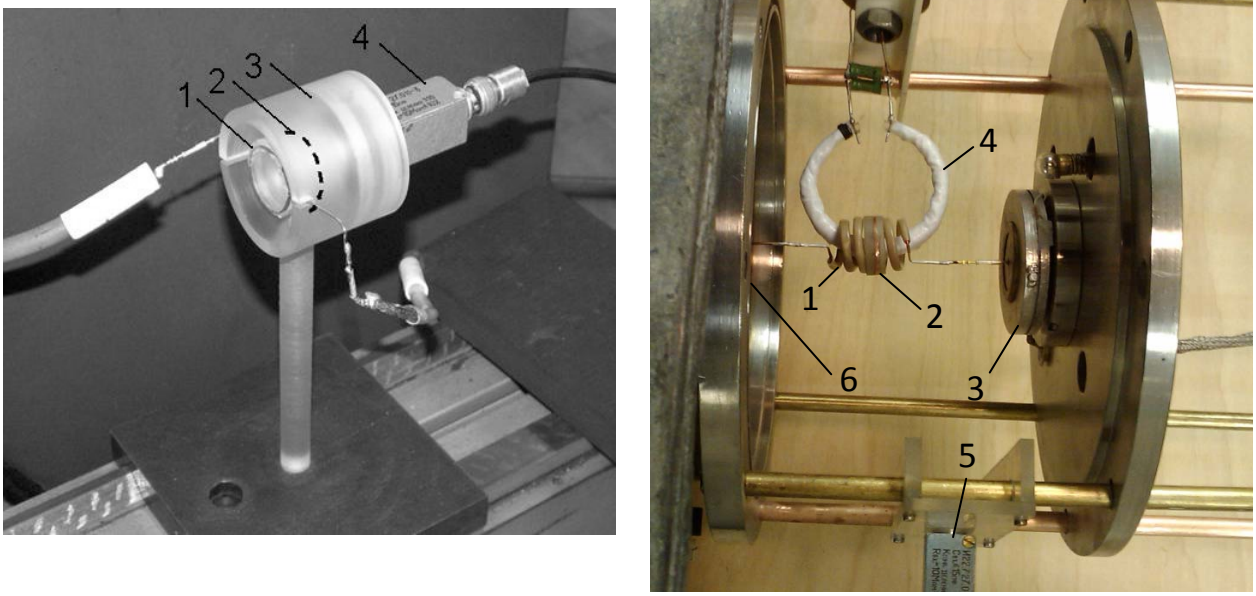

а б

Figure 4. Appearance of plants: a - at 7.5 μs (1 - solenoid, 2 - sample 3 - housing, 4 - photodiode), b - at 1 μs (1 - solenoid, 2 - sample 3 - Rogowski belt to measure the current in the coil 4 - Rogowski coil to measure the current in the ring, 5 - photodiode, 6 - output device).

The study of fracture surfaces of aluminum and copper samples after the test was carried out on an optical microscope Axio-Observer-Z1-M in a dark field, and study the structure of cross sections - in the bright field or polarized light. The structure has been studied in cross sections after appropriate etching. Grain size and the number of pores on the surface of cross sections were determined after etching. Microhardness was measured on a PMT-3 device with a load of 20g. Ring samples were tested from duralumin D16 brand with an inner diameter of 28 mm. The ring D16 had a thickness of 0.11 - 0.40 and a width of 0.5 - 1.0 mm, when they exposed to electric currents with a long period.

Fig. 5 shows the waveforms of current through the coil (2) and the signal from the photodiode (1) fixing the time of rupture of the sample for the two variants of tests: T = 7,5 μs and T = 1 μs.

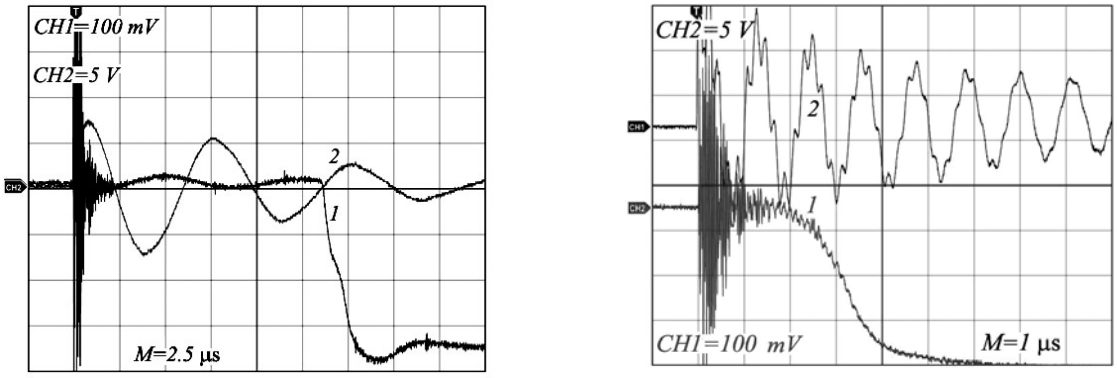

а б

Fig. 5. Waveform signal from the photodiode (1) and current from Rogowski belt (2), a - in the current period $T = 7.5$ μs; b - $T = 1$ μs. Sample size: b= 1.0, h=0,11 mm

3. Discussion of the results

Fig. 6 shows the samples in the initial (pre-test) state and after loading in different modes. The figure shows that failure occurs in one place for a period of change of the current 7,5 μs, and for the period of 1 μs, but in a shorter period can be seen multiple neck. When energy increases with the period of 7,5 μs the number of destruction fragments increases.

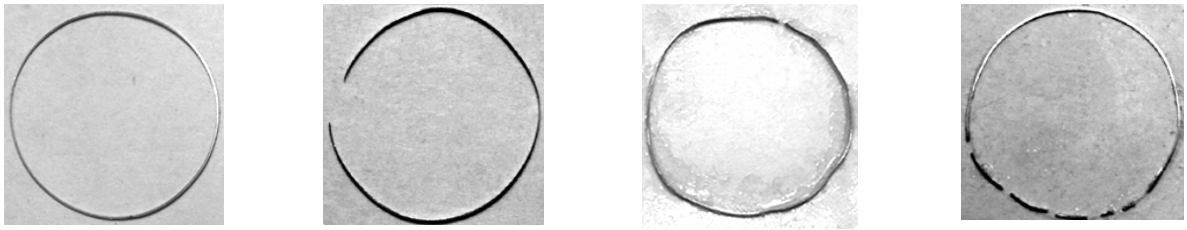

а б в г

Fig. 6. Photographs of aluminum samples: a - before loading; b - destruction at the threshold energy, T = 7,5 μs; c - the same at T = 1 μs; d - the destruction at an energy well above the threshold, T = 7,5 μs

Let us estimate the radial force acting on the ring from the side of the coil windings. Calculation scheme is shown in Fig. 7. Estimation of the force is held in the quasi-static approximation. It is believed that the main force is the Ampere force. The total force acting on the ring, adds together of the main force of the turns of the coil, which is located in the plane of the ring coaxially with it (Fig. 7) and on the side of turns. Calculations have shown that the main contribution is made to Ampere force by two side ring. From these considerations, the number of turns of the coil was chosen to be five.

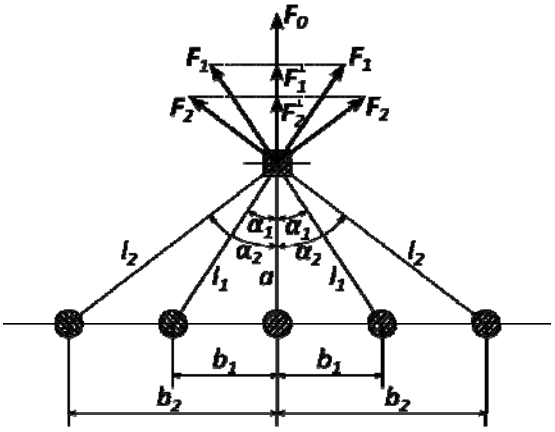

Figure 7. Scheme for calculation of the force acting on the ring

So the force acting on the ring will be

$$F(t) = F_0(t) + 2F_1^{\perp}(t) + 2F_2^{\perp}(t),$$

where

$$F_0(t) = \frac{\mu_0}{4\pi}\frac{2I_1(t)I_2(t)}{a}, \quad F_1^{\perp}(t) = F_1(t)Cos\alpha_1 = \frac{\mu_0}{4\pi}\frac{2I_1(t)I_2(t)}{l_1}Cos\alpha_1,$$

$$F_2^{\perp}(t) = F_2(t)Cos\alpha_2 = \frac{\mu_0}{4\pi}\frac{2I_1(t)I_2(t)}{l_2}Cos\alpha_2,$$

$\mu_0 = 4\pi 10^{-7} \frac{H}{m}$ - magnetic constant, $I_1(t)$ - the current in the loop coil, $I_2(t)$ - the current in the ring, a - the distance from the coil to the ring.

Distributed load acting on the inner surface of the ring,

$$q(t) = \frac{F(t)l}{S},$$

where l - length of the inner circumference of the ring, S = lc - area of the inner surface of the ring, c - the width of the ring.

Thus, $q(t) = \frac{F(t)}{c}$.

The tangential tensile stress (Fig. 1) can be calculated from the Laplace formula for thin shells:

$$\sigma(t) = \frac{q(t)R}{h},$$

where R - radius of the inner ring of the sample and h - its thickness.

In determining the tensile stress its pulsating value $\sigma(t)$ replaces averaged in the form of a rectangular pulse of amplitude σ_0 and duration equal to the time from the start of the current delivery in the coil until the breaking of the ring t_c (Fig. 8)

$$\int_0^{t_c} \sigma(t)dt = \sigma_0 t_c, \quad \sigma_0 = \frac{\int_0^{t_c} \sigma(t)dt}{t_c}.$$

Time recorded in the experiments

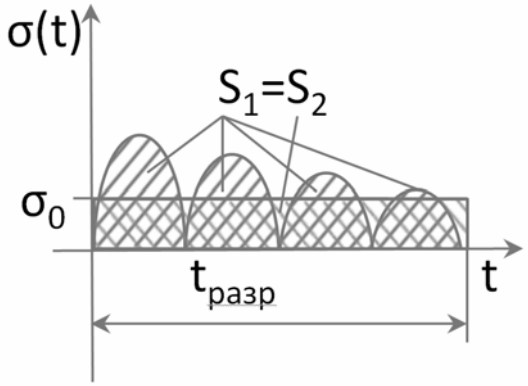

Fig. 8. Replacement scheme of ripple voltage: S_1 - the area under pulsed voltage, S_2 - the area under constant stress σ_0.

The following parameters of the device are used in made experiments and calculations: a = 3 mm, b_1 = 7.5 mm, b_2 = 15 mm.

Characteristics of the samples, the experimental conditions and results are summarized in Table 1, where T - the period of oscillation of the current in the coil; h - thickness of the ring; c - width of the ring; ∅ - ring diameter; U - capacitor charging voltage; σ_0 - tensile stress for rupture of the ring; τ - time to failure; W - energy of a charged capacitor; I - maximum amplitude of the current through the coil

Table 1. The experimental results

Material	T, μs	h, mm	c , mm	∅, mm	U, kv	σ_0 , MPa	τ, μs	W, J	I, A
Al	7,5	0,12	1,0	28	20	104	13,75	100	5700
Al	1	0,11	1,0	28	27	142	2,05	182	6000

Measurement results of ductile component in the fracture of aluminum samples are described in [12], which shows that the shortening of the current period the share of fiber in the fracture surface decreases monotonically, i.e. samples become more fragile.
In Table 2 and in the micrographs (Fig. 9) the results of microstructural studies is presented, where T - the period of oscillation of the current in the coil; S = hxb - section of the sample; D - grain size; n - number of pores in the area of 400 μm^2; HV - microhardness.

Table 2. Characteristics of the structure

Material	T, μs	$h \times b, \mu m^2$	D, μm	n, 1/400μm^2	HV, MPa
Al	7,5	$193{,}5 \times 10^3$	1,2	121	1318,6
Al	1	$68{,}4 \times 10^3$	3,0	70	639,1
Al initial		120 x10^3	4,6	53	720,4

Fig. 9 shows the structure of aluminum samples at initial state and after loading with different periods and different cross-section (scale factor).

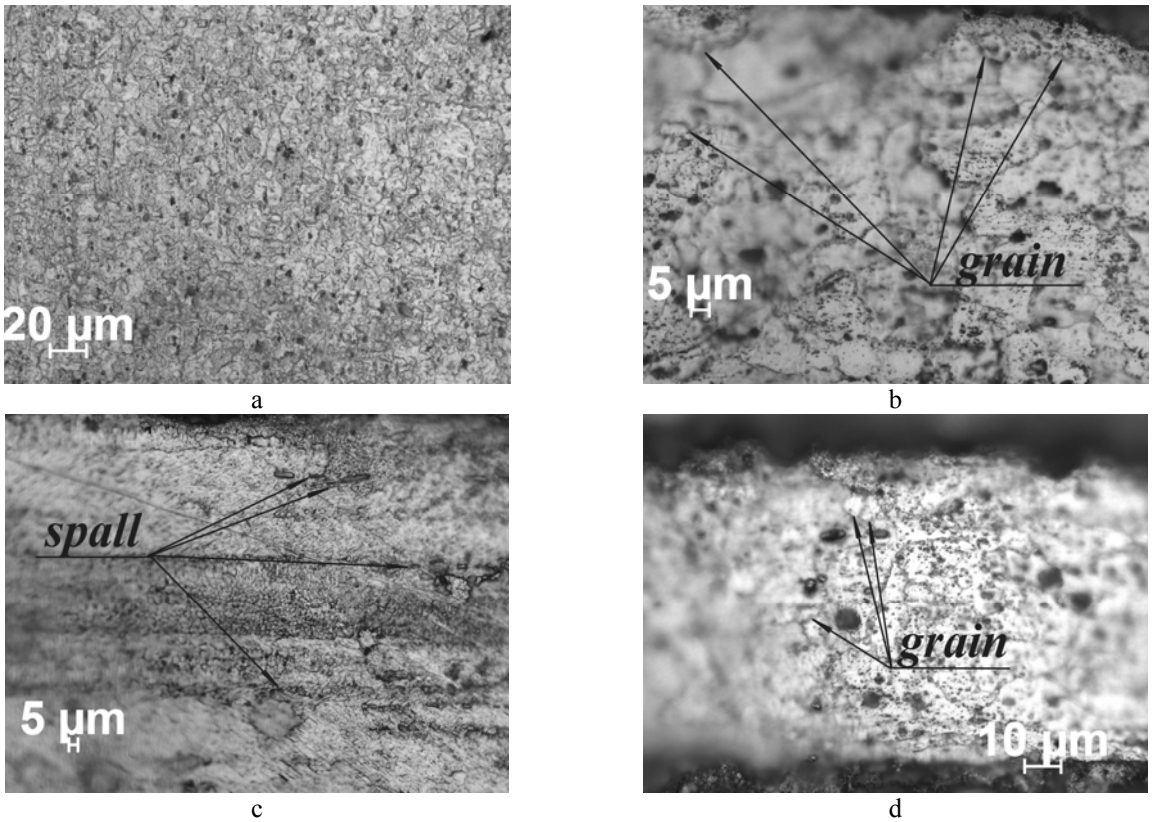

Figure 9. The structure of aluminum: (a) - in the initial state, (b) - after loading with the period T = 7,5 μs (S = 0,13 mm^2); (c) - after loading with the period T = 7,5 μs (S = 0, 19mm^2); (d) - after loading with the period T = 1μs (S = 0,07 mm^2), here the notation: spall - split, grain - recrystallized grains.

It is seen the dynamic recrystallization - the formation of new small grains for short-time loading. The highest degree of dynamic recrystallization is in the samples of aluminum with longer duration

of loading and a maximum cross-section (scale factor). Samples of aluminum after loading showed a greater tendency to pore formation with increasing loading period compared with initial state. In addition, with increasing loading duration the samples had the generation of multiple spallation (Fig. 9c).

4. Conclusion

1. It was developed and tested a magnetic pulse method of destruction and photographic registration moment of destruction for ring metalllic samples at much shorter pulses of loading.
2. It was proposed the evaluation method of the radial force acting on the ring, and the tensile stress at break of the ring.
3. The dynamic recrystallization, the formation of shear bands and multiple spallation were revealed using magnetic pulse loading of the ring samples.

5. References

[1] Zhang O. H., Ravi-Chandar K. Int. J. Fract. (2006) 142: 183.
[2] Zhang O. H., Ravi-Chandar K. International Journal of Fracture (2008) 150: 3.
[3] Zhang O. H., Liechti K.M., Ravi-Chandar K. Int. J. Fract (2009) 155: 101.
[4] Zhang O. H., Ravi-Chandar K. Int. J. Fract. (2010) 163: 41.
[5] S. Mercier, A. Molinari. International Journal of Impact Engineering 30 (2004) 403–419.
[6] A.E. Carden, P.E. Williams, R.R. Karpp Shock waves and high-strain-rate phenomena in metals // Editors: Meyers M.A. and Murr L.E. New York and London, Plenum Press, 1984, 1, 1.4, p.51.
[7] L.E. Murr Shock waves and high-strain-rate phenomena in metals // Editors: Meyers M.A. and Murr L.E. New York and London, Plenum Press, 1984, 3, 3.3, p.260.
[8] R.N/ Wright, D.E. Mikkola, S. LaRouche Shock waves and high-strain-rate phenomena in metals // Editors: Meyers M.A. and Murr L.E. New York and London, Plenum Press, 1984, 3, 3.12, p.353.
[9] G.V. Stepanov, Elasto-plastic deformation and destruction of materials at puls loading. Kiev, naukova dumka, 1991.
[10] D.E. Grady and D.A. Benson, Experimental Mechanics, 12, (1983) 393-400.
[11] M. Altynova , X. Hu , G.S. Daehn, Metall Trans A 27(1996) 1837–1844.
[12] V.A. Morozov, Yu.V. Petrov, A.A. Lukin, V.M. Katz, A.G. Udovik, S.A. Atroshenko, G.D. Fedorovskii, metal-ring stretching under magnetic-pulse shock action, Doklady Akademii Nauk, 2011 Vol. 439, N6, pp. 761-763.

On Kinetics of "Diffusion" Cracks and Delaminations

Ilya Nickolaevich Dashevskiy

A. Ishlinsky Institute for Problems in Mechanics, Russian Academy of Sciences, 119526, Russia
dash@ipmnet.ru

Abstract In the cracks contained in such materials as metals under the action of corrosive media, degrading polymers and ceramics (for example, HTSC-ceramics), gas-saturated rocks, etc., gas can be accumulated. For a penny-shaped crack in an unbounded elastic medium and for a thin penny-shaped delamination under the surface of a half-space, as well as for similar cracks-strips, in a new uniform way – on the basis of the energy approach and with the use of Clapeyron theorem – kinetic equations are derived describing the growth of specified defects under gas diffusion into them. The analysis of the reasons leading to identity of the equations named, allows (under some conditions) to extend the results obtained for these problems to a number of other important cases: cracks on the interface of an adhesive joint of two pliable half-spaces with different mechanical and diffusion properties (with the interface being permeable as well as impermeable), the account of anisotropy, etc. It is shown, that exactly the same reasons (and under the same restrictions) make it possible to extend to the same cases the results obtained earlier for growth laws of a penny-shaped crack in an unbounded elastic medium versus laws of gas inflow into it as well.

Keywords Kinetics, Diffusion, Cracks, Delaminations, Model

1. Introduction

One of the models of crack growth as a gas is accumulated in the crack according to the diffusion mechanism (in what follows, a "diffusion" crack), which, for example, is typical of the process of structural steel hydrogenizing, was formulated and justified in [1] (different approaches are represented, for example, in [2, 3, 4, 5]). Later, in [6, 7, 8, 9, 10], this model was developed and generalized in different directions. In what follows, we analyze the derivation of the kinetic equations for this model, which allows for better understanding of the role and the action mechanism of its principal factors and also for showing the directions of extrapolation of the earlier results to different cases.

2. Derivation of kinetic equations

Let obtain kinetic equations for a penny-shaped crack in an infinite elastic space and for a circular crack, which is a delamination from the boundary of the half-space under gas diffusion into them (Fig.1) in a uniform way.

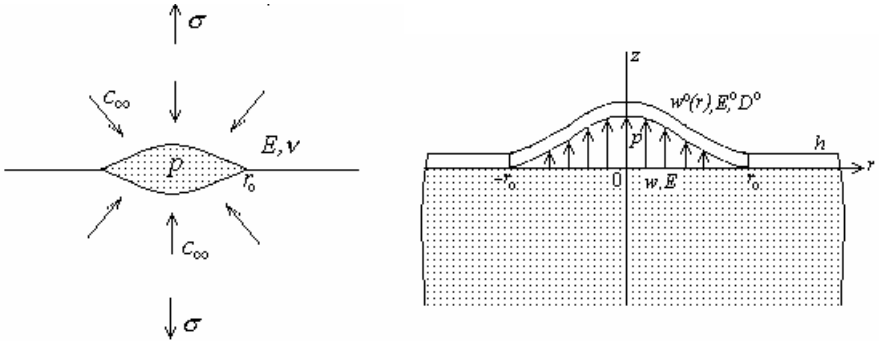

Fig.1.

First we derive expressions for the case of a gas influx into the crack. Since the problem on a

penny-shaped crack in infinite space is symmetric about the crack plane $z = 0$ ([6], p. 828), it suffices to consider the problem in the half-space $z \le 0$. We assume that the process is quasistationary ([1]; [9], p. 120) and take the axial symmetry of the problem into account. Then, for the unknown gas concentration $c(\rho, z, t)$, where ρ is the radial coordinate in the cylindrical system of coordinates, in the half-space $z \le 0$, we obtain the mixed problem from the theory of harmonic functions:

$$\Delta c = 0, \quad z \le 0; \qquad c|_{z=0} = 0, \quad \rho \le r(t);$$
$$\partial c/\partial z|_{z=0} = 0, \quad \rho > r(t); \qquad c|_{z=\infty} = c_\infty$$

where time t is a parameter. Subtracting the equilibrium state $c = c_\infty$, we obtain

$$\Delta c = 0, \quad z \le 0; \qquad c|_{z=0} = -c_\infty, \quad \rho \le r(t);$$
$$\partial c/\partial z|_{z=0} = 0, \quad \rho > r(t); \qquad c|_{z=\infty} = 0 \tag{1}$$

This mixed problem of potential theory is formally equivalent to the contact problem on the indenta-
tion of a rigid die, that is circular in cross-section and has a smooth bottom, in to an elastic isotropic half-space ([11], p. 385, formula (11.6.8) and later). Taking use of the solution of the latter contact problem we obtain for the density $q(\rho, t)$ of the gas diffusive flux into the crack

$$q(\rho,t) = -D\frac{\partial c}{\partial z}\bigg|_{z=0,\,\rho<r} = \frac{2c_\infty D}{\pi\sqrt{r^2-\rho^2}}$$

The total flux through the surface $z = -0$, $\rho < r$ is

$$Q_- = \int_0^r 2\pi\rho q(\rho,t)d\rho = 4c_\infty D\int_0^r \frac{\rho d\rho}{\sqrt{r^2-\rho^2}} = 4c_\infty Dr \tag{2}$$

For the delamination problem, the obtained quantity Q_- is simultaneously the total gas influx Q into the crack. But, for the case of a crack in infinite space gas influx goes through the lower and upper surfaces of the crack and is equal to

$$Q = Q_- + Q_+ = 2Q_- = 8c_\infty Dr \tag{3}$$

Combining Eq. 2 and Eq. 3, we write

$$Q = N\cdot 4c_\infty Dr \tag{4}$$

where N is the number of "gas transmitting" surfaces of the crack.
Taking into account the expression $Q/k = dn(t)/dt$, where k is the coefficient of gas recombination in the crack (in the case of hydrogen, $k = 2$, because, on the crack surface, the protons melted in the metal recover to the atomic hydrogen which, flowing inside the crack, recombines into molecular hydrogen) and $n(t)$ is the number of gas moles in the crack, we can rewrite Eq. 4 in the form

$$dn(t) = 4Nc_\infty Dr\, dt/k \tag{5}$$

From the equation of state for the ideal gas (the Mendeleev–Clapeyron equation), we have

$$pV = RTn(t) \tag{6}$$

where p is the gas pressure inside the crack and V is the crack volume.
Expressing $n(t)$ from Eq. 6 and substituting into Eq. 5, after the replacement $dt = dr/u$, we obtain

$$d(pV) = (4Nc_\infty DRT)rdr/(ku) \tag{7}$$

The Clapeyron theorem for linear media ([11], p. 160) implies that

$$U = pV/2, \quad pV = 2U \tag{8}$$

where U remains the elastic energy of the body.
We introduce G, which is the elastic energy release rate or the "crack-moving force" ([12], p. 71, formula (3.12) and further) or the "force of resistance to the crack propagation" ([11], p. 686) or the "energy flux towards the crack vertex", the "intensity of released elastic energy" ([3, pp. 28–30, p. 51), or the "strain energy release rate" ([13], p. 119). For a linearly elastic body, all these quantities, as well as the Γ-integral ([14], Chapter 1, Sec. 1), as well as the J-integral, coincide ([15], pp. 107–116). By definition ([12], pp. 73–74, formulas (3.21)–(3.23)), we write

$$G = \left.\frac{\partial U}{\partial S}\right|_p \tag{9}$$

where U is the elastic energy of the body and S is the crack area.
Under the axisymmetric extension of a penny-shaped crack, we have $dS = 2\pi rdr$, and

$$G = \left.\frac{\partial U}{\partial S}\right|_p = \frac{1}{2\pi r}\left.\frac{\partial U}{\partial r}\right|_p$$

If the dependence of U (or of V, which is the same in the linear case, as it follows from Eq. 8) on r is power-law, i.e.

$$U \sim r^m \tag{10}$$

then

$$\frac{1}{r}\frac{\partial U}{\partial r} = m\frac{U}{r^2}, \quad G = \frac{mU}{2\pi r^2}, \quad U = \frac{2\pi r^2 G}{m} \tag{11}$$

Substituting Eq. 11 into Eq. 8 and then into Eq. 7, we obtain

$$d(r^2G) = \frac{Nm}{2\pi k} c_\infty DRT \frac{d(r^2)}{u} \tag{12}$$

When a crack grows really, its propagation rate cannot be arbitrary, but, according to the kinetic diagram of static fracture strength at each time instant, is determined by the current value of the stress intensity factor on its contour or by the current energy release rate G. Thus, to derive the kinetic equation, we must assume in Eq. 12 that the the crack propagation rate u is the function of G determined by the kinetic diagram of static fracture strength, $u = u(G)$. This is that gives the desired kinetic equation, expressed in variables G и r, which, by the way, does not contain time t explicitly.

But what is the real, actual character of the dependences $U(r)$, $V(r)$? For a penny-shaped crack under internal pressure in an infinite body, we have $V = V(r, p, E, \nu)$, and it follows from dimension considerations that $V \sim r^3 p/E$ (the exact formulas see in ([16], p. 548, formula (10.131)). In this case $m = 3$, $N = 2$, and Eq. 12 becomes

$$d(r^2G) = \frac{3}{\pi} c_\infty DRT \frac{d(r^2)}{ku} \tag{13}$$

In the case of a thin parallel-to-the-boundary impenetrable delamination of thickness h from the half-space, the problem is reduced [9] to the problem of axisymmetric bending of a circular plate fixed on the boundary under the action of uniform pressure, $V = V(r, p, D_0)$, and it follows from dimension considerations that $V \sim r^6 p/D_0$ (the exact formula is ([9], Eq. 12)). Thus, here we have $m = 6$ and $N = 1$ and Eq. 12 becomes

$$d(r^2G) = \frac{6}{2\pi} c_\infty DRT \frac{d(r^2)}{ku} = \frac{3}{\pi} c_\infty DRT \frac{d(r^2)}{ku} \tag{14}$$

which coincides exactly with the similar Eq. 13.

3. Kinetic equation integral. Step-like kinetic diagram

Eq. 12 can be easily integrated

$$\ln\left(\frac{r}{r_0}\right) = \frac{1}{2} \int_{G_{SCC}}^{G} \frac{dG}{\dfrac{\alpha}{u(G)} - G}$$

$$\alpha = \frac{Nm}{2\pi k} c_\infty DRT$$

$$\begin{gathered} \text{When} \quad r \to \infty, \quad \ln(r/r_o)^2 \to \infty \quad \leftrightarrow \quad [\alpha/u(G) - G] \to 0 \\ G \to G_\infty: \quad u(G_\infty) = \alpha/G_\infty,\ u \to u_\infty = u(G_\infty) \end{gathered} \tag{15}$$

For metals and rocks kinetic diagram $u(G)$ is nearly step-like (Fig. 2). In this case it follows from Eq. 15 that

if $\alpha/G_{SCC} < u^*$, then $G_\infty = G_{SCC}$, $u_\infty = \alpha/G_{SCC}$,
if $\alpha/G_{SCC} > u^* \rightarrow u_\infty = u^*$, $G_\infty = \alpha/u^*$

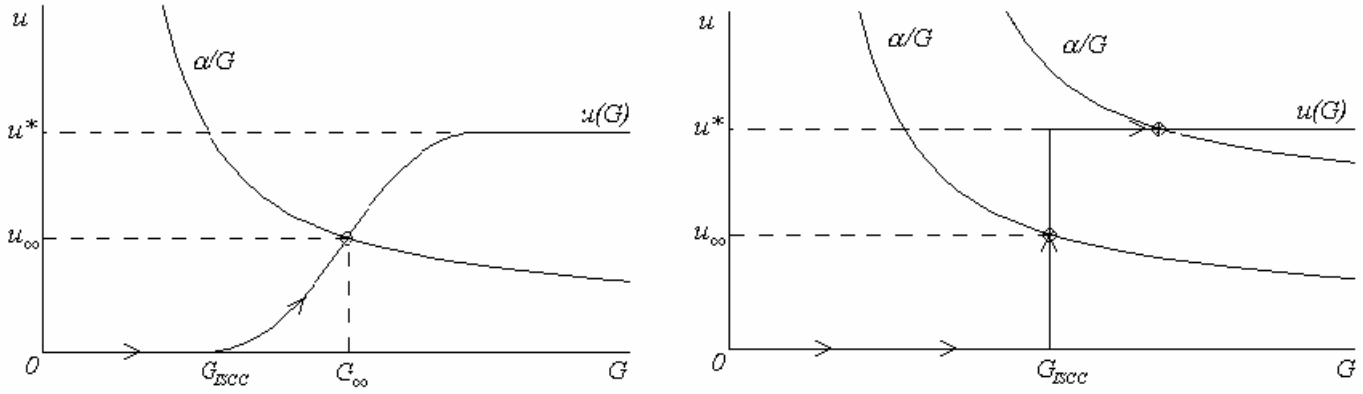

Fig. 2

4. Example: life-time evaluation of a massive piece of structural steel with a penny-shaped crack under hydrogenation

We use these results to analyze the kinetics of a penny-shaped crack in a bulk sample of low-carbon low-alloy steel in hydrogenation. We simulate a sample as infinite elastic medium and assume that the material has the $u(G)$ diagram of threshold type (which is close to reality).
The process of crack development consists of two stages: incubation period, t_i (gas accumulation in the stationary crack), followed by a period of growth (movement) t_m.
During the period of incubation, $r = r_0 = \text{const}$. Turning back in (2.16) from dr^2 to rdr, dividing both sides by r, substituting $k = 2$, substituting dr/u on dt, and r on r_0 and integrating, we obtain

$$G = 3c_\infty DRTt/(\pi r_0) \tag{16}$$

The incubation time is determined by the achievement of G its critical value G_{ISCC}, which gives

$$t_i = \pi r_0 G_{ISCC}/(3c_\infty DRT) \tag{17}$$

In the literature they give the values not for G_{ISCC}, but for the corresponding SIF K_{ISCC}, which is related to G_{ISCC} by the Irwin formula $G_{ISCC} = (1 - \nu^2)K^2_{ISCC}/E$. For the concentration c_∞ of the hydrogen dissolved in the metal the literature values given are for the so-called "weight parts" (the ratio of the weight of hydrogen per unit volume to the weight of the metal containing it), we denote this quantity by c^∞, while c_∞ has the dimension of mol/volume and is numerically equal to $c^\infty g$, where g is the steel density. Therefore, passing in Eq. 17 from G_{ISCC} to K_{ISCC} and from the c^∞ to c_∞ we finally obtain

$$t_i = \pi(1 - \nu^2)K^2_{ISCC} r_0/(3c^\infty g\, DRTE) \tag{18}$$

During the period of growth with the $u(G)$ diagram of threshold-type $G = const = G_{ISCC}$.

Substituting this into (2.16), substituting $k = 2$, dividing both sides by dr^2 and replacing c^∞ with c_∞ and G_{ISCC} with K_{ISCC}, we obtain

$$u = 3c_\infty DRT/(2\pi G_{ISCC}) = 3c^\infty gDRTE/[2\pi(1-\nu^2)K^2_{ISCC}] = const \quad (19)$$

$$t_i = r_0/(2u) \quad (20)$$

$$r = r_0 + (t - t_i)\cdot u = r_0 + t_m \cdot u \quad (21)$$

We assume room temperature $T = 273^0$K and use the default values for the universal gas constant $R = 8.31$ J/(mol·grad) = $8.32\cdot10^7$ erg /(mol·grad) ([17], p. 153 [18], p. 151) and typical values for density and elastic constants of low-alloy steel $g = 7.8$ g·cm^{-3} ([17], p. 40), $E = 2\cdot10^4$ kg·mm^{-2}, $\nu = 0.3$ ([17], p. 116). We also know that $D = 10^{-3}$ mm^{2}s^{-1} [19], $K_{ISCC} \cong 120$ kg·mm$^{-3/2}$ [20], and the values of c^∞ can reach 10^{-5} parts by weight [21]. In addition, we assume that the initial radius of the crack r_0 is equal to $r_0 = 10$ mm.

Table 1. The parameters values taken for calculations

T^0 [K]	R [J/(mole·K)]	g [g·cm^{-3}]	E [kG·mm^{-2}]	ν	D [mm^{2}c^{-1}]	K_{ISCC} [kG·mm$^{-3/2}$]	c^∞	r_0 [mm]
273	8.31	7.8	$2\cdot10^4$	0.3	10^{-3}	120	10^{-5}	10

Substituting these values in Eq. 19, we obtain

$u \cong 10^{-5}$ mm/s

Thus, the crack front velocity turned out to be of the order of 10^{-5} mm/s and according to Eq. 20, incubation time

$t_i = r_0/(2u) = 10$ mm/($2\cdot10^{-5}$ mm/s) = $5\cdot10^5$ s ≅ $1.5\cdot10^2$ h = 150 h ≈ 6 days and nights.

If the front crack after the start begins to move at a speed of about 10^{-5} mm/s, then the radius equal, for example, $r = 50$ mm, will be according to Eq. 21 achieved through

$t_m = (r - r_0)/u =$ (50–10) mm/(10^{-5} mm·s^{-1}) = $40\cdot10^5$ s ≅ $1.1\cdot10^3$ h ≈ 46 days and nights.

As can be seen from Eqs. 19-21, the values of durability can vary by orders of magnitude depending on the concentration of the gas in the metal.
In the case of the $u(G)$ diagram of general form, as well as in the presence of tensile stresses and taking into account a number of additional physical and physical-chemical factors [5] the range of possible values of life can range from several hours up to many hundreds of years.

5. Main assumptions and the scope of the equation obtained above

To specify the scope of the kinetic Eq. 12 and the results obtained from this equation earlier in [1, 6, 7, 8, 9], we list the assumptions used above in its derivation:
1. The medium is homogeneous and diffusively linear, see Eq. 5.

2. The gas is thermodynamically ideal (obeys the Mendeleev–Clapeyron equation of state), see Eq. 6.
3. The medium is mechanically linear, see Eq. 8.
4. The dependence of V , and hence of U, on r is power-law, see Eqs. 10, 11.

As to the last assumption, it follows from dimension considerations that, in any case, the expression for the volume V of the crack must have the form

$$V = r^3 \frac{p}{E} f(\frac{r}{h_i}, \nu_i)$$

where h_i are the problem parameters of dimension of length (except for r), ν_i are the dimensionless parameters (except for r/h_i), $f(r/h_i, \nu_i)$ is a function determined by the geometry and physics of the problem.

Thus, condition 4 means that either the problem does not contain any geometric parameters other than the crack dimensions (as in the case of an infinite homogeneous body) or all the parameters of dimension of length in the formula for the volume V are combined into a single factor (as in the case of delamination from the half-space).

On the one hand, this implies that all the main results must remain valid if the complication of the problem is not related to the appearance of new parameters of dimension of length. For example, these are (under some conditions) the following cases: cracks on the adhesion boundary between two compliant half-spaces with different mechanical but equal (close) diffusive properties (in the case of an impenetrable boundary, the diffusive properties can also be different); the case of taking the anisotropy into account; delamination from the membrane half-space; etc.

Since the argument in [8] is also based on the same assumptions 2–4, the results in [8] can be generalized (under the same conditions) to all problems where the above assumptions remain valid.

Acknowledgements

This research was partially supported by the RFBR under project No. 11-08-01243.

References

[1] R. V. Goldshtein, V. M. Entov, and B. R. Pavlovskii, “A Model of Hydrogen Cracks Propagation in Metal,” Dokl. Akad. Nauk SSSR **237** (4), 828–831 (1977) [SovietMath. Dokl.].

[2] V. V. Panasyuk, A. E. Andreikiv, and V. Z. Parton, *Foundations of FractureMechanics* (*Fracture Mechanics and Material Strength, Reference Book*, Vol. 1) (Naukova Dumka, Kiev, 1988) [in Russian].

[3] V. Z. Parton and E.M.Morozov, *Mechanics of Elastoplastic Fracture* (Nauka, Moscow, 1985) [in Russian].

[4] G. P. Cherepanov, *Mechanics of Brittle Failure* (Nauka, Moscow, 1974) [in Russian].

[5] V. I. Astaf’ev and L. K. Shiryaeva, *Damage Accumulation and Corrosion Cracking of Stressed Metals* (Izd-vo Samar. Univ., Samara, 1998) [in Russian].

[6] A. V. Balueva, “Spatial Problems of Crack Kinetics with the Gas Diffusion in Them Taken into Account,” Izv. Akad. Nauk.Mekh. Tverd. Tela, No. 6, 123–131 (1993) [Mech. Solids (Engl. Transl.)].

[7] A. V. Balueva and I. N. Dashevskii, Model of Growth of an Internal Gas-Filled Crack in a Material," Izv. Akad. Nauk.Mekh. Tverd. Tela, No. 6, 113–118 (1994) [Mech. Solids (Engl. Transl.)].
[8] A. V. Balueva and I. N. Dashevskii, "Qualitative Estimates of Growth of Gas-Filled Cracks," Izv. Akad. Nauk.Mekh. Tverd. Tela, No. 6, 122–128 (1995) [Mech. Solids (Engl. Transl.)].
[9] A. V. Balueva and I. N. Dashevskii, "Growth of Hydrogen Delaminations in Metals," Izv. Akad. Nauk.Mekh. Tverd. Tela, No. 1, 119–123 (1999) [Mech. Solids (Engl. Transl.)].
[10] I. N. Dashevskii, To the Kinetics of Diffusion Cracks, Mechanics of Solids, 2007, Vol. 42, No. 1, pp. 149–156.
[11] Yu. N. Rabotnov, *Mechanics of Deformable Solids* (Nauka, Moscow, 1979) [in Russian].
[12] K. Hellan, *Introduction to Fracture Mechanics* (McGraw-Hill, New York, 1984; Mir, Moscow, 1988).
[13] H. Liebowitz, Editor *Fracture. An Advanced Treastise*, Vol. 2, *Mathematical Fundamentals*, (Acad. Press, New *Fracture Toughness Testing and Its Applications, A Sympos. Presented at the Sixty-Seventh Annual Meeting, Chicago, Ill.: American Society for Testing and Materials (ASTM Special Technical Publications No. 381)* (ASTM, Chicago, 1964; Mir, Moscow, 1968)
[14] G. P. Cherepanov, *Mechanics of Fracture of Composite Materials* (Nauka, Moscow, 1983) [in Russian].
[15] V. I. Astaf'ev, Yu. N. Radaev, and L. V. Stepanova, *Nonlinear Fracture Mechanics* (Izd-vo Samar. Univ., Samara, 2001) [in Russian].
[16] I. N. Sheddon, *Fourier Trasnforms* (McGraw-Hill, New York, 1951; Izd-vo Inostr. Liter., Moscow, 1955).
[17] V.E. Kuzmichev, Laws and formulas of physics. Handbook. Kiev: Nauk. Dumka, 1989. 864 p. [in Russian]
[18] B.M. Yavorsky, A.A. Detlaf, Handbook of physics. M. GRFML, 1977. 944 p. [in Russian]
[19] P.V. Geld, R.A. Ryabov, Hydrogen in Metals and Alloys, Moscow, 1974. [in Russian]
[20] *C. Lang,* Kovove Materialy, v. 11, № 4, 358 (1973).
[21] *E. Sunami, V. Tanimura, G. Tenmyo.* Boshoku Gijutsu, v. 23, № 6, 281 (1974).

The elastic-plastic limit pressure of cylinder under internal pressure using a new yield criterion

Xiaoyu Liu [1], Zheng Yang [1,*], Shanshan Huang[1]

[1]Department of Civil Engineering, Xi'an Jiaotong University, Xi'an 710049, China
* zyang@mail.xjtu.edu.cn

Abstract Elastic-plastic limit pressure(EPLP) of closed-end cylinders under internal pressure is derived, using a new yield criterion that depends on stress triaxiality and Lode angle. The von Mises, Tresca, twin-shear and Drucker-Prager yield criterions are encompassed in the new yield criterion for the EPLP. The results reveal that, with the increasing of the parameters of stress triaxiality and Lode angle, the EPLP decreases for cylinder with fixed outer-to-inner radius ratio(k). As k increases, the EPLP increases when the parameters of stress triaxiality and Lode angle are certain value. The parameter of Lode angle is much more important than the parameter of stress triaxiality affecting the EPLP of cylinders. The new yield criterion with smaller parameters of stress triaxiality and Lode angle is used instead of the conventional von Mises, Tresca, twin-shear and Drucker-Prager yield criterions in design, it can lead to substantial saving the material required. While the new yield criterion with larger parameters of stress triaxiality and Lode angle is used in design, it can make the design more safe and reliable.

Keywords Closed-end cylinder, New yield criterion, Stress triaxiality, Lode angle

1. Introduction

Closed-end cylinders are used in engineering, as pressure vessels, nuclear reactors and capsules. It is important to know the EPLP of cylinders under internal pressure. A considerable amount of work has been done on the problem of elastic-plastic analysis in a closed-end cylinder under internal pressure[1-4]. However, when the conventional yield criterions are adopted to derive the EPLP, the Tresca[5] and von Mises[6] yield criterions ignore the effect of the intermediate principal stress and octahedral normal stress on yield, respectively. They lead to conservative predictions of limit pressures. Although the twin-shear[7] and Drucker-Prager[8] yield criterions overcome above deficiencies, they still ignore the effect of stress triaxiality and Lode angle on yield. By the view of equivalent stress, stress triaxiality and Lode angle, the von Mises yield criterion ignore the effect of stress triaxiality and Lode angle on yield, and the Tresca yield criterion also ignore the effect of stress triaxiality on yield. But the effect of stress triaxiality and Lode angle on yield have been confirmed[9-13]. Based on the von Mises, Tresca and Drucker-Prager yield criterions, a new yield criterion, which considers the effect of stress triaxiality and Lode angle on yield, is proposed and confirmed by experiments[9]. In this paper, the EPLP of closed-end cylinders under internal pressure, which are two important parameters in the design of closed-end cylinders, is determined using the new yield criterion. Important results concerning the influence of the EPLP determined with the new yield criterion on the design of closed-end cylinders under internal pressure are presented.

2. Determined the EPLP of closed-end cylinders under internal pressure using the new yield criterion

The new yield criterion, which considers the effect of stress triaxiality and Lode angle on yield, as follows,

$$\sigma_{\mathrm{yld}} = \sigma_{\mathrm{eq}}\left[1 - c_{\eta}\left(\eta - \eta_0\right)\right]\cdot\left[c_{\theta} + \left(c_{\mathrm{ax}} - c_{\theta}\right)\gamma\right]. \tag{1}$$

Where γ and c_{ax} are two parameters defined by

$$\gamma = \frac{\sqrt{3}}{2-\sqrt{3}}\left[\sec\left(\theta - \frac{\pi}{6}\right) - 1\right], \quad c_{ax} = \begin{cases} c_t & 0 \le \theta \le \dfrac{\pi}{6} \\ c_c & \dfrac{\pi}{6} < \theta \le \dfrac{\pi}{3} \end{cases}. \tag{2}$$

Where σ_{eq}, η and θ are equivalent stress, stress triaxiality and Lode angle, respectively. σ_{yld} is the yield stress. η_0, c_η, c_θ, c_t and c_c are material constants, this depends on which type of reference test is used to calibrate the relationship of stress-strain.

Let us consider a closed-end cylinder under an internal pressure p. The inner and outer radius of the cylinder are a and b, respectively. In elastic stage, the σ_{eq}, η and θ are determined with Lame solutions of the elastic stress distribution in cylindrical coordinates system[14] as follows,

$$\sigma_{eq} = \sqrt{3}\frac{\rho^2}{k^2-1}p, \eta = \frac{\sqrt{3}}{3}\frac{1}{\rho^2}, \theta = \frac{\pi}{6}. \tag{3}$$

Where $k=b/a$ and $\rho=b/r$ ($a \le r \le b$).

Yielding will appear at the inner surface of the closed-end cylinder at the elastic limit pressure(ELP) p_e. Substituting Eq. (3) into Eq. (1), the yield condition is satisfied at the inner surface $(\sigma_r)_{r=a}=-p_e$, the ELP obtained by the new yield criterion is

$$p_e = \sigma_{yld}\frac{\left(k^2-1\right)}{\sqrt{3}c_\theta k^2}\left[1 - c_\eta\left(\frac{\sqrt{3}}{3k^2} - \eta_0\right)\right]^{-1}. \tag{4}$$

Because θ is a constant ($\theta=\pi/6$), the effect of Lode angle on the ELP is equal to c_θ. The relationship of stress-strain is obtained from smooth round bar tensile test, therefore, η_0 is equal to 1/3. c_η represents the effect of stress triaxiality on material plasticity.

When the internal pressure exceeds p_e, a plastic zone will appear at the inner surface and spread toward the outer surface. The elastic-plastic boundary at any stage has radius r_y ($a \le r_y \le b$), in the elastic region ($r_y \le r \le b$), the radial stress is obtained from Lame's equations using the boundary condition $\sigma_r=0$ at $r=r_b$ as follows,

$$\sigma_r = \frac{1}{k_y^2-1}\left(1-\rho^2\right)p_y. \tag{5}$$

Where $p_y = \dfrac{\sigma_{yld}\cdot\left(k_y^2-1\right)}{\sqrt{3}c_\theta\cdot k_y^2}\left[1 - c_\eta\left(\dfrac{\sqrt{3}}{3}\dfrac{1}{k_y^2} - \dfrac{1}{3}\right)\right]^{-1}$ and $k_y = \dfrac{b}{r_y}$.

In plastic region, the material is assumed perfectly elastic-plastic, the equation of equilibrium is

$$\frac{d\sigma_r}{dr} + \frac{\sigma_r - \sigma_\theta}{r} = 0. \tag{6}$$

The cylinder is assumed at the plane strain condition, therefore, the longitudinal stress in the plastic region is

$$\sigma_z = \frac{1}{2}\left(\sigma_r + \sigma_\theta\right). \tag{7}$$

The σ_{eq}, η and θ are determined with Eq. (7), σ_r and σ_θ as follows,

$$\sigma_{eq}=\frac{\sqrt{3}}{2}(\sigma_\theta-\sigma_r),\ \ \eta=\frac{\sqrt{3}}{3}\frac{\sigma_\theta+\sigma_r}{\sigma_\theta-\sigma_r},\theta=\frac{\pi}{6}. \tag{8}$$

Substituting Eq. (8) into Eq. (1), we have

$$A=\sigma_\theta-B\sigma_r. \tag{9}$$

Where $A=\dfrac{2\sqrt{3}}{c_\theta}\dfrac{\sigma_{yld}}{3+\left(1-\sqrt{3}\right)c_\eta}$ and $B=\dfrac{3+\left(1+\sqrt{3}\right)c_\eta}{3+\left(1-\sqrt{3}\right)c_\eta}$.

When $c_\eta\neq0$, Substituting Eq. (9) into Eq. (6), then the boundary condition $(\sigma_r)_{r=a}=-p$ is satisfied, the stress distribution in the plastic region ($a\leq r\leq r_y$) is

$$\sigma_r=C\cdot r^{B-1}-\frac{A}{B-1},\sigma_\theta=B\cdot C\cdot r^{B-1}-\frac{A}{B-1}. \tag{10}$$

Where $C=\left(\dfrac{A}{B-1}-P\right)a^{-(B-1)}$.

According to the stress continuity of radial stress σ_r across $r=r_y$, it requires that

$$(\sigma_r)_{r=r_y}\text{ (elastic zone)}=(\sigma_r)_{r=r_y}\text{ (plastic zone)}. \tag{11}$$

Substituting the radial stress Eq. (5) for the elastic zone and the radial stress Eq. (10) for the plastic zone into Eq. (11), the relation of pressure p with plastic zone radius is obtained as follows

$$p=\frac{A}{B-1}+\left\{\frac{\sigma_{yld}\cdot\left(k_y^2-1\right)}{\sqrt{3}c_\theta\cdot k_y^2}\left[1-c_\eta\left(\frac{\sqrt{3}}{3}\frac{1}{k_y^2}-\frac{1}{3}\right)\right]^{-1}-\frac{A}{B-1}\right\}\left(\frac{r_y}{a}\right)^{-(B-1)}. \tag{12}$$

When r_y becomes equal to b, the closed-end cylinder is completely plastic, the plastic limit pressure(PLP) for closed-end cylinder is, therefore, obtained as

$$p_p=\frac{\sigma_{yld}}{c_\theta c_\eta}\left[1-k^{\frac{-2\sqrt{3}c_\eta}{3+\left(1-\sqrt{3}\right)c_\eta}}\right]. \tag{13}$$

When $c_\eta=0$, the PLP for closed-end cylinder also is obtained as follows,

$$p_p=\frac{2\sigma_{yld}}{\sqrt{3}c_\theta}\ln k. \tag{14}$$

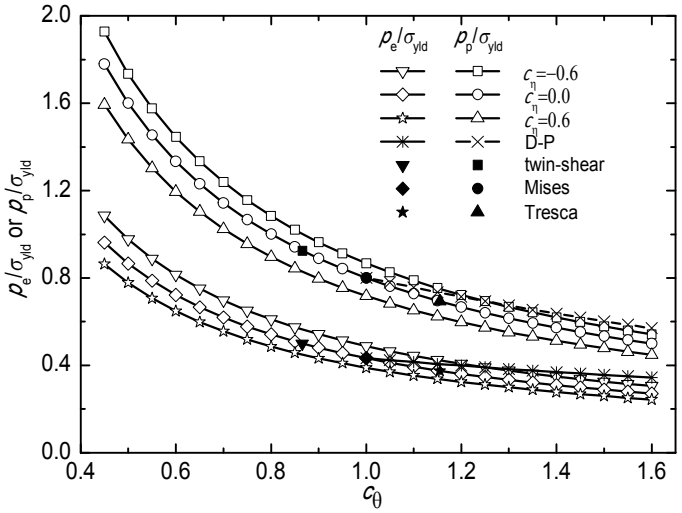

Fig.1 Relation of EPLP of closed-end cylinder under internal pressure with c_θ (k=2).

If the ratio of outer radius to the inner radius is 2(k=2), the relation of EPLP of closed-end cylinders under internal pressure with c_θ is illustrated in Fig.1. It can be seen that, the EPLP

calculated by von Mises, Tresca and twin-shear yield criterions equal these obtained by the new yield criterion when c_η=0 and c_θ=1, 2/√3 and √3/2, respectively. While $c_\eta \neq 0$, c_η=3(1-c_θ)/c_θ and c_θ>1, one will get the EPLP determined with Drucker-Prager. Therefore, it can be concluded that the von Mises, Tresca, twin-shear and Drucker-Prager yield criterions are encompassed in the new yield criterion for the EPLP. It is also found that, when c_η=0.0 and c_θ>√3/2, the EPLP is higher than those obtained by the von Mises, Tresca, twin-shear and Drucker-Prager yield criterions. When c_η=0.0 and c_θ<2/√3, the EPLP is lower than those obtained by conventional yield criterions. When c_θ is certain value, the EPLP in range of c_η<0.0 is larger than that at c_η=0.0, the EPLP in range of c_η>0.0 is smaller than that at c_η=0.0. c_θ is much more important than c_η affecting the EPLP of cylinder, similar conclusions are also found in earlier report[9, 15]. The EPLP decreases with the increasing of c_θ and c_η.

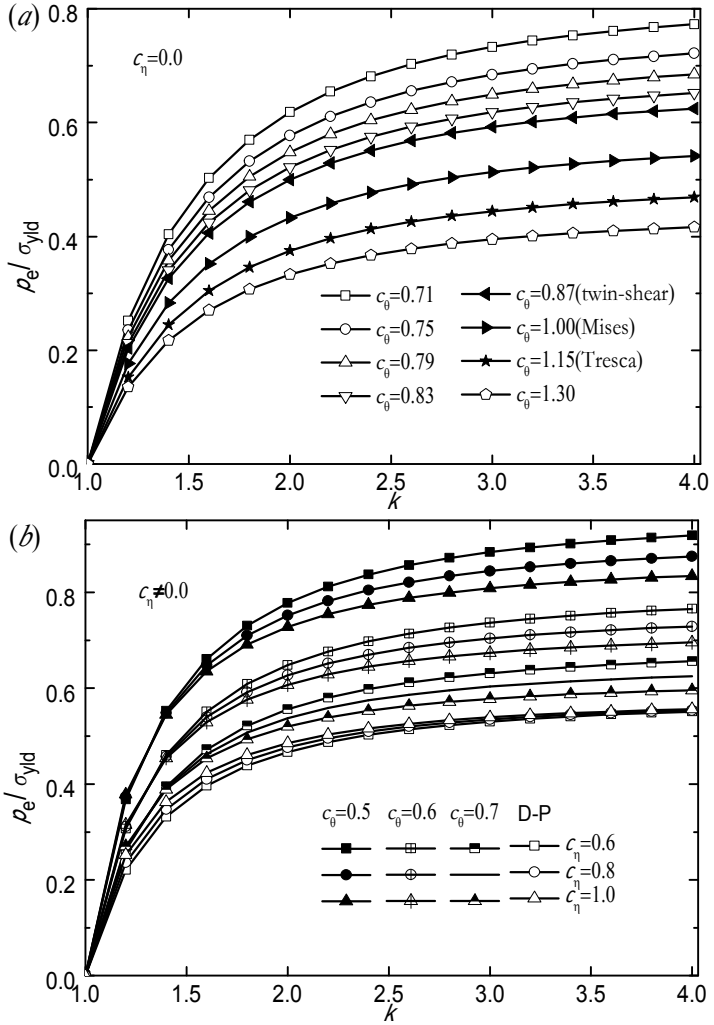

Fig.2 Relation of ELP of closed-end cylinders under internal pressure with k at c_η=0(*a*) and $c_\eta \neq 0$(*b*).

A number of the relations of EPLP with the ratio of outer radius to the inner radius, are shown in Fig. 2 and Fig. 3. In Fig.2 and Fig.3, the EPLP increases with the increasing of k, when c_θ and c_η are certain value. In Fig.2(*a*), when the effect of stress triaxiality on yield is ignored (c_η=0), it is worth noting that, if k approaches the value 3.0, the increase in the ELP is very small with the increasing of k. While the effect of stress triaxiality on yield is considered ($c_\eta \neq 0$), the increase in the ELP is also very small when $k \geq 2.5$, shown in Fig.2(*b*). From what I have mentioned above, we can see the new yield criterion with smaller c_θ and c_η is used instead of the conventional von Mises, Tresca, twin-shear and Drucker-Prager yield criterions in design, it can lead to substantial saving the material required. While the new yield criterion with larger c_θ and c_η is used in design, it can make

the design more safe and reliable.

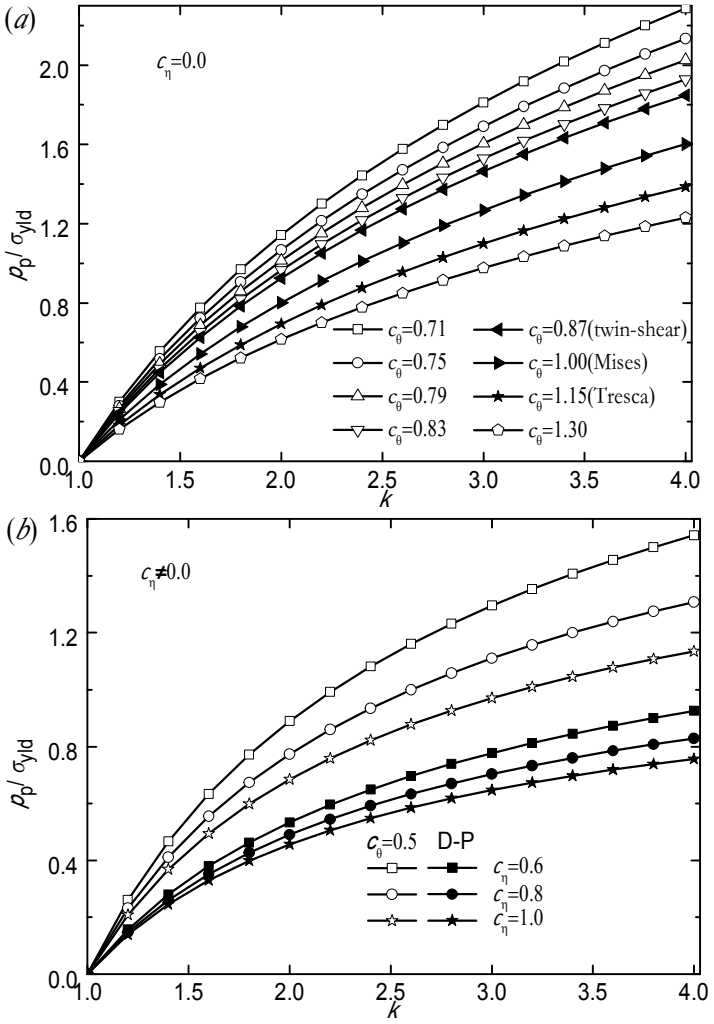

Fig.3 Relation of PLP of closed-end cylinders under internal pressure with k at c_η=0(a) and c_η≠0(b).

3. Summary

The EPLP of closed-end cylinders under internal pressure is derived using the new yield criterion that depends on stress triaxiality and Lode angle. The von Mises, Tresca, twin-shear and Drucker-Prager yield criterions are encompassed in the new yield criterion for the EPLP. The results reveal that, with the increasing of c_θ and c_η, the EPLP decreases for cylinder with fixed k. As k increases, the EPLP increases when c_θ and c_η are certain value. c_θ is much more important than c_η affecting the EPLP of cylinder, The new yield criterion with smaller c_θ and c_η is used instead of the conventional von Mises, Tresca, twin-shear and Drucker-Prager yield criterions in design, it can lead to substantial saving the material required. While the new yield criterion with larger c_θ and c_η is used in design, it can make the design more safe and reliable.

Acknowledgements

This work was financially supported by the National Natural Science Foundation of China (Grant No.50971098, 51271138) and the Scientific Research Starting Foundation for Returned Overseas Chinese Scholars, Ministry of Education, China (Grant No. 09-18).

References

[1] Turner LB. The elastic breakdown of materials submitted to compound stress. Engineering[J]. 1909, 87-169.

[2] Hill R, Lee EH and Tupper SJ. The theory of combined plastic and deformation with particular reference to a tube under internal pressure[J]. Proc. Roy. Soc. London A, 1947, 191: 278-303.
[3] Chakrabary J. Theory of Plasticity[M]. New York: McGraw-Hill, 1987:276-281.
[4] Ni XH, Liu XQ, Liu YT and Wang XS.Calculation of stable loads of strength-differential thick cylinders and spheres by the twin shear strength theory. Strength Theory : Application, Developments and Prospects for the 21st Century[J]. Yu MH and Fan SC eds. Science press. 1998: 1043-1046.
[5] Tresca H. Sur I'e coulement des corps solids soumis a de fortes pression[J]. Comptes Rendus hebdomadaires des Seances de l' Academie des Sciences, 1864: 59 ,754-758.
[6] von Mises R. Mechanik der festen Körper im plastisch deformablen Zustand. Nachrichten von der Königlichen Gesellschaft der wissenschaften zu Göettinger[J]. Mathematisch-Physikalische Klasse, 1913:582-592.
[7] Yu MH. Unified Strength Theory and Its Applications[M]. Germany: Springer Press, 2004: 36-38.
[8] Drucker DC, Prager W. Soil mechanics and plastic analysis for limit design[J]. Quart. Appl. Math. 1952, 10: 157-165.
[9] Bai Y, Wierzbicki T. A new model of metal plasticity and fracture with pressure and lode dependence[J]. Int J Plast, 2008, 24(6): 1071–1096.
[10] Richmond, O., Spitzig, W.A., . Pressure dependence and dilatancy of plastic flow[C]. In: Theoretical and Applied Mechanics, Proceedings of the 15th International Congress of Theoretical and Applied Mechanics, Toronto, Ont., Canada. North-Holland Publ. Co., Amsterdam, The Netherlands, 1980:377–386.
[11] Brownrigg, A., Spitzig, W.A., Richmond, O., Teirlinck, D., Embury, J.D. . The influence of hydrostatic pressure on the flow stress and ductility of a spherodized 1045 steel[J]. Acta Metallurgica, 1983,31 (8): 1141–1150.
[12] Spitzig, W.A., Richmond, O. The effect of pressure on the flow stress of metals[J]. Acta Metallurgica, 1984.32 (3): 457–463.
[13] Bao Y, Wierzbicki T. On fracture locus in the equivalent strain and stress triaxiality space[J]. International Journal of Mechanical Sciences, 2004, 46(1): 81–98.
[14] Johnson W, Mellor PB. Plascity for Mechanical Engineerings[M]. Lonton and New York: Van Nostrand Press, 1962: 296-305.
[15] Fengping Yang, Qin Sun and Wei Hu. Yield criterions of metal plasticity in different stress states[J]. Acta Metallurgica, 2009,22(2):123-130.

Finite Element Analysis on Burst Pressure of Steel Pipes with Corrosion Defects

N.A.Alang[1,*], N.A.Razak[1], K.A.Shafie'[1], A.Sulaiman[1]

[1] Corrosion and Fracture Focus Group, Faculty of Mechanical Engineering, University Malaysia Pahang, Malaysia.
* Corresponding author: azuan@ump.edu.my

Abstract The effect of metal loses due to corrosion on burst pressure of API X42 steel pipes was studied using nonlinear finite element (FE) method. The nonlinear finite element method coupled with stress modified critical strain (SMCS) model was used to predict the failure of the pipes. In this paper, the corrosion defects were simplified to rectangular shape. The procedure in determining the SMCS model parameters from tensile bars was systematically discussed. The effect of defects length, depth and width was investigated. The burst pressure estimated was then compared to available design codes of corroded pipelines. For validation, the results of burst pressure from FE were compared to experimental data. The depth of corrosion defects appears as the most influential parameter that affects the burst pressure of the pipes.

Keywords Burst Pressure, Corrosion Defects, Stress Modified Critical Strain, Stress Triaxiality

1. Introduction

In petrochemical industry, pipelines play an important role in transporting crude oil and gas. As in service duration increases, the pipelines are affected by corrosion mechanism which leads to fatal accident. Corrosions can occur in both internal and external surfaces of the pipelines. In general, corrosion would cause metal loss which lead to reduction of pipe thickness and consequently decreases its strength. The probability of pipe to burst then will increase. Therefore, failure due to corrosion defects has been a major concern in maintaining pipeline integrity [1]. There are several design codes used in practice to evaluate the remaining strength of corroded pipelines such as American Society of Mechanical Engineer (ASME) B31G [2], modified ASME B31G [2] and DNV-RP-F101 [3] codes. These codes were developed many years ago and used throughout the industry. ASME B31G and modified ASME B31G simplify a short longitudinal corrosion defect as a parabolic curve whereas long corrosion defect can be simplified to a rectangular shape. According to ASME B31G and DNV-RP-F101 codes, the failure of corroded pipelines is controlled by the defect size as well as the flow stress of the material. The DNV-RP-F101 code can be applied for both defect subjected to internal pressure loading only or internal pressure loading combined with longitudinal compressive stresses. However, the ASME B31G is limited to defect subjected to internal pressure only. DNV-RP-F101 design code equations also include the assessment of single and interacting defects and complex shaped defects. The input parameter of these codes include outer diameter of the pipe, D, wall thickness, t, yield strength of the material, σ_y or ultimate tensile strength, σ_u, the length of the defect, L and defect depth, d. The width, w was considered to have less effect on strength of corroded pipe and therefore this factor was avoided in all assessment equations [4]. The equations used to calculate the burst pressure, P_b based on these codes are expressed as:

$$P_b = \frac{2ts_f}{D} \tag{1}$$

For ASME B31G:

$$S_f = 1.1\sigma_y \left[\frac{1-\frac{2}{3}\left(\frac{d}{t}\right)}{1-\frac{2}{3}\left(\frac{d}{t}\right)/M}\right]; \quad M = (1+0.8\frac{L^2}{Dt})^{0.5} \tag{2}$$

For Modified ASME B31G:

$$S_f = (\sigma_y + 69)\left[\frac{1-0.85\left(\frac{d}{t}\right)}{1-0.85\left(\frac{d}{t}\right)/M}\right]; \quad M = \left[1+0.6275\frac{L^2}{Dt}-0.003375\left(\frac{L^2}{Dt}\right)\right]^{0.5} \tag{3}$$

For DNV-RP-F101:

$$S_f = (\sigma_y + 69)\left[\frac{1-0.85\left(\frac{d}{t}\right)}{1-0.85\left(\frac{d}{t}\right)/M}\right]; \quad M = \left[1+0.31\frac{L^2}{Dt}\right]^{0.5} \tag{4}$$

where M represents as bulging stress magnification factor.

A numbers of researchers [5-7] have studied the remaining strength of pipelines with corrosion defect using FE method together with stress based failure criterion and used to predict failure in the damage pipe. However, this leads to conservative results because stress based failure criterion relies on flow stress of the materials only. Other methods use strain based failure criterion including Gurson–Tvergaard–Needleman (GTN) model [8], void growth model (VGM) [9], continuum damage model (CDM) [10] and SMCS model [11]. However, a few issues need to be resolved in practical applications of these methods. For example, GTN models consist of relatively high number of parameters compare to SMCS and VGM models [12]. These GTN parameters are difficult to identify and calibrate which require a large number of FE and experimental work.

Oh et al [13] recently developed the SMCS model based on local criteria for API X65. The model was used to predict the burst pressure of pipes with gouge and corrosion defects. The study is limited to API X65 steel material and pipe outer diameter of 762 mm. The accuracy and validity of the model is well discussed and acceptable in wide range of defect geometries. Mathematically, SMCS is evaluated by Eq. (5) through Eq. (8), where the stress triaxiality, T is defined by the ratio of hydrostatic stress, σ_m and equivalent stress σ_e given by:

$$T = \frac{\sigma_m}{\sigma_e} = \frac{\sigma_1+\sigma_2+\sigma_3}{3\sigma_e} \tag{5}$$

$$\sigma_e = \frac{1}{\sqrt{2}}[(\sigma_1-\sigma_2)^2+(\sigma_3-\sigma_1)^2+(\sigma_2-\sigma_3)^2]^{\frac{1}{2}} \tag{6}$$

On the other hand, the equivalent strain ε_e is given by:

$$\varepsilon_e = \frac{\sqrt{2}}{3}\left[(\varepsilon_1-\varepsilon_2)^2+(\varepsilon_3-\varepsilon_1)^2+(\varepsilon_2-\varepsilon_3)^2\right]^{\frac{1}{2}} \tag{7}$$

where the σ_1, σ_2, σ_3 and ε_1, ε_2, ε_3 are the principle stresses and principle strain, respectively. The fracture strain ε_f is determined using the equation proposed by Rice and Tracey [9]:

$$\varepsilon_f = A\exp\left(-\frac{3\sigma_m}{2\sigma_e}\right) \tag{8}$$

Where A is the material constant found through an experiment.

In the present work, the effect of corrosion defect on burst pressure was investigated through an experimental and numerical works. The burst pressure of defective pipes was predicted using a three-dimensional nonlinear, homogeneous isotropic elasto-plastic material model with large deformation finite element model. The SMCS model was used in predicting the failure of the defective pipe. The FE analysis results then were compared to available design codes for pipelines assessment with single longitudinal corrosion defects. The model was validated by comparing the FE results with physical testing and subsequently extensive parametric studies were carried out.

2. Material and Experimental Procedure

Tensile Test The material used in this study was API X42 steel. The chemical compositions and mechanical properties of the material are tabulated in Table 1 and Table 2, respectively.

Table 1. Chemical composition of API X42 steel (%wt)

C	P	Mn	S	Si	Fe	CE
0.03	0.01	0.98	0.003	0.19	98.6	0.21

Table 2. Mechanical properties of API X42 steel at room temperature

Young Modulus, E (GPa)	Yield Strength, σ_y (MPa)	Tensile Strength, σ_u (MPa)
207	284.7	464.4

The detailed specimen dimensions used for uniaxial tensile test are shown in Fig. 1. The test was performed according to ASTM E08-08 [14]. The specimens were extracted in longitudinal direction from API X42 steel pipes with schedule of 120. An extensometer with gauge length of 25 mm was attached to the specimen in order to monitor the axial displacement of the material. A total of four specimens were tested for a given geometry.

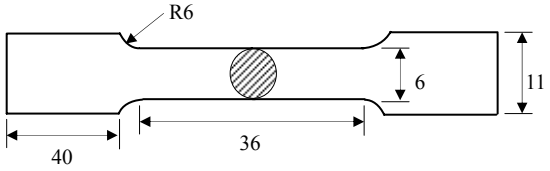

Figure 1. Smooth round tensile bar

Burst Pressure Test. Four API X42 steel pipes with different longitudinal artificial corrosion defect geometries were prepared. Detailed dimensions of the pipes with artificial corrosion defect are shown in Table 3. The defects on the pipe surface were machined using Computer Numerical Control (CNC) machine. The nominal outer diameter of the pipe is 60 mm. The overall length of the pipe was kept constant to be 600 mm. A schematic illustration of pipes with corrosion defect on its outer surface is shown in Fig. 2. The external thread with pitch of 2 mm was machined with 50 mm long on both ends of the defective pipes. The pipes were then attached to the cap with internal thread. The internal thread of the cap was machined with the same pitch of pipe thread. End of the pipes was sealed with aluminum O-rings to avoid leakage of the hydraulic oil when the pipes are pressurized. The cap has been covered by a solid cylinder to prevent the movement of the pipes in both transverse and longitudinal directions. Two solid cylinders were connected to each other using four threaded rods.

The defective pipe was internally pressurized by the oil using manual hydraulic pump. The pump was connected to the test rig through hydraulic line. Analog pressure gauge was attached between pump and defective pipe for pressure measurement. The oil was carefully pumped to the test rig to minimize the strain rate effect until the failure was detected on the pipe. During pressurization, the pipe was expanded and the localized bulge could be clearly seen in the weakest region. Detail experiment setup for the burst pressure testing is shown in Fig. 3a. The failure occurs on the principle plane direction. This is confirmed by observation on the failure pipe whereby the crack on defect is propagated in longitudinal direction. Figure 3b shows the API X42 steel pipe after performing the burst pressure test. The failure occurred at defective region where the minimum thickness of the pipe is placed. The maximum pressure which represents as the burst pressure was recorded and listed in Table 3.

Table 3. Effect of defect size on burst pressure

Case No.	Defect Dimension (mm)			Thickness, t (mm)	Burst Pressure (MPa)
	Length, *l*	Depth, *d*	Width, *w*		
EX1	49.7	4.1	13.7	5.80	54
EX2	49.8	3.5	13.9	5.60	61
EX3	69.7	4	17.3	5.55	46
EX4	50	4.5	14	5.62	44

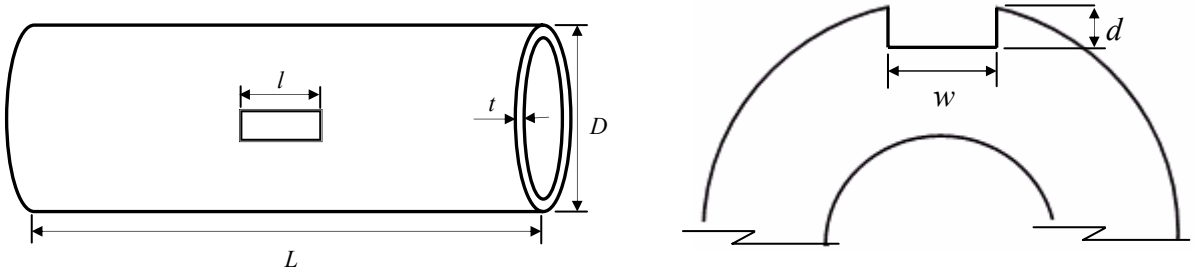

Figure 2. Schematic of pipes with corrosion defect

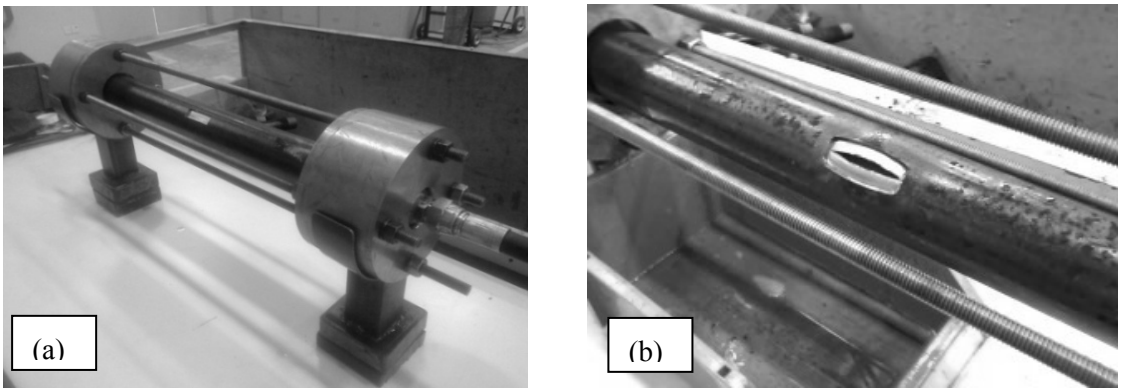

Figure 3. Experimental set up (a) Before Failure, (b) After Failure

3. Determination of SMCS Model Parameter

Remarking that the stress triaxiality for round bars is roughly $\sigma_m/\sigma_e \approx 1/3$. Substituting this value into Eq. (8), an approximate expression of the ratio of fracture strain ε_f is given by:

$$\frac{\varepsilon_f}{\varepsilon_f^*} = \frac{\exp\left(\frac{-3\sigma_m}{2\sigma_e}\right)}{\exp(0.5)} \tag{9}$$

where ε_f^* denotes the fracture strain obtained from tensile test of smooth round bar. The value of average fracture strain is $\varepsilon_f^* = 1.04$ and is shown in Fig 7. Thus, the ε_f for API X42 material used in this paper is proposed to be:

$$\varepsilon_f = 1.732\exp\left(-1.5\frac{\sigma_m}{\sigma_e}\right) \tag{10}$$

Figure 4 shows the failure curve proposed for API X42 steel pipes based on Eq. (10).

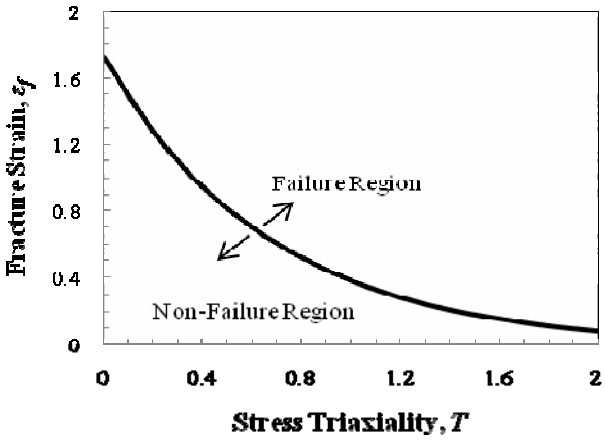

Figure 4. Failure curve for API X42 steel pipes

4. Validation of the Model

A 3-D nonlinear FE analysis was performed on experimental case studies listed in Table 3. The pipes with a rectangular artificial corrosion defects were modeled and eight node solid elements with reduced integration scheme are applied using commercial MSC PATRAN/MARC 2008r1 software. The material is modeled as an isotropic elasto-plastic material. Fig. 5 shows true stress strain data employed in FE analysis. The defective pipe with the same parameter used in experimental work was analyzed. A detailed finite element mesh applied on the models is shown in Fig. 6. Since the failure of the pipe was observed in defective region during the experiment, the FE mesh is designed sufficiently small around the defect area. The enlargement on the defective region is also shown in Fig. 6. Internal pressure was applied to the inner surface of the pipe. The boundary condition was applied at one end of the pipe to simulate the closed cap condition. The symmetrical condition was also applied for computational efficiency. The von Mises stress distribution on defect for pipe CS3 is shown in Fig. 7. At an applied pressure of 16 MPa, the pipe did not show any plastic deformation. However, at the onset of failure, the bulging on the defect can be clearly seen as shown in Fig. 7b. The reduction of pipe thickness at defective area was detected before the pipe started to burst.

To predict ductile failure of defective pipes made of API X42 steel pipes using the present approaches, the proposed Eq. (10) will be combined with detailed elasto-plastic FE analyses from which local stresses and strains are determined. For example, from the FE analysis, stress and strain data can be monitored as a function of pressure. Over the loading history, the stress triaxiality and equivalent strain were calculated using Eq. (5) to (7). Then, the equivalent strain to fracture or true fracture strain is estimated from Eq. (10). When the equivalent strain from the FE analysis equals to the fracture strain, failure is assumed to occur. The results of burst pressure from FE have been compared to experimental data and shown in Fig. 8. The percentage of the error for each case was also included. The maximum error between these two methods is 9%.

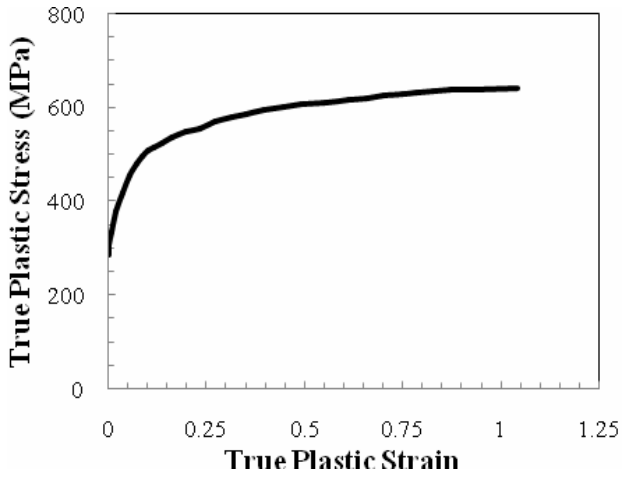

Figure 5. True plastic stress-strain data employed in FE analysis

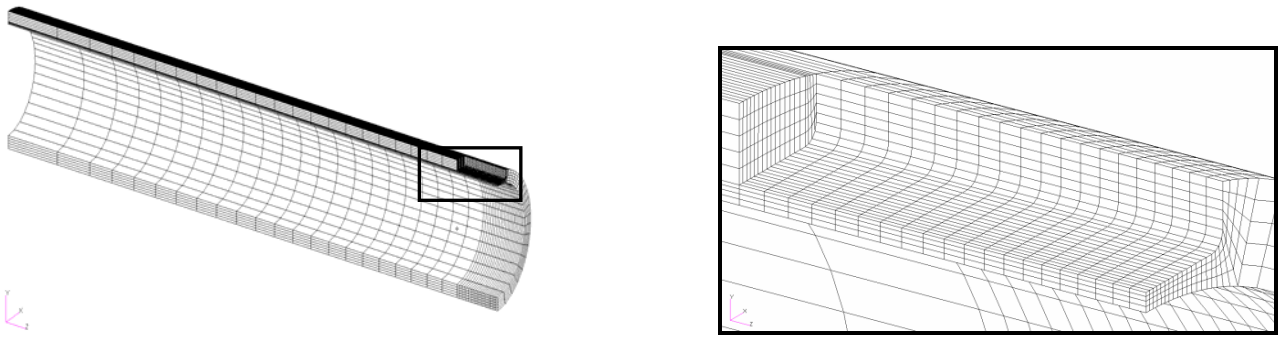

Figure 6. Detailed FE mesh of the model

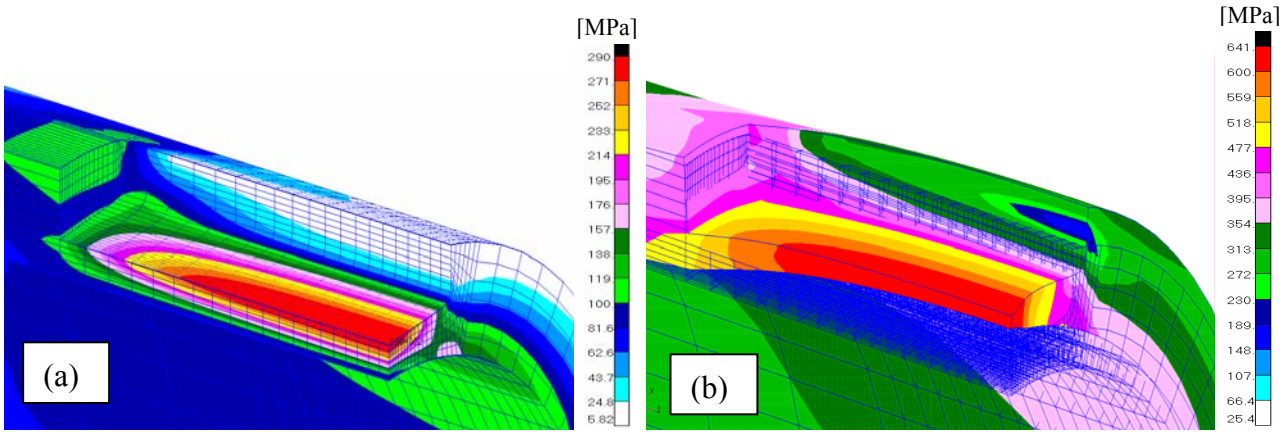

Figure 7. von Mises stress plots: (a) Internal pressure of 16 MPa, (b) Internal pressure of 64 MPa (Burst pressure)

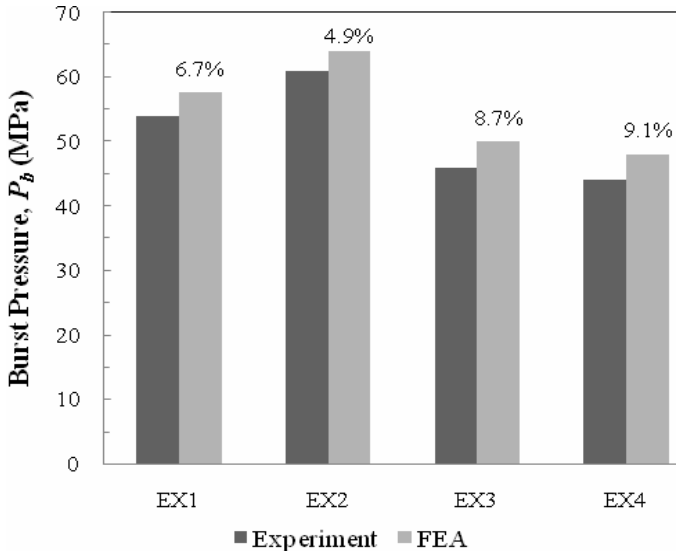

Figure 8. Comparison of burst pressure between experimental data and FE results

5. Parametric Study

The pipe with different defect depths, lengths and widths were simulated and the burst pressure for each case was predicted. In the present study, the totals of 10 cases represent by CS1 to CS10 were analyzed. The defect width, *t* depth, *d* and length, *l* for the case studies are summarized in Table 4. The wall thickness and outer diameter of the pipe are kept constant to be 6 mm and 60 mm, respectively.

Table 4. Different pipe sizes and defect dimensions

Case No.	Dimension (mm)			Failure Pressure (MPa)
	Length, *l*	Depth, *d*	Width, *w*	
CS1	50	3	14	83
CS2	50	3.5	14	72.4
CS3	50	4	14	64
CS4	50	4.5	14	52
CS5	50	3	10	83.2
CS6	50	3	6	84
CS7	50	3	4	84
CS8	30	3	14	88.4
CS9	40	3	14	86
CS10	60	3	14	81.6

Figure 9 shows the results of burst pressure predicted from FE analysis. The results of burst pressure calculated from ASME B31G, Modified ASME B31G and DNV-RP-F101 design codes for corroded pipelines were also included. Based on these three design codes, the failure of the pipelines is assume to occur when the stress developed in the pipes equal to or higher than the flow stress of the materials. Since the flow stress is always lower than the ultimate strength, the failure will be predicted before necking occurred. In contrast, SMCS model used in this paper predicted the failure based on the fracture strain of the materials. The parameter of the model is determined from fracture point during uniaxial tensile test, therefore necking of the material is allowed. Neglecting the increment of pressure from the onset of necking to fracture point causes the design codes to always give lower value in predicting the burst pressure. In general, the results of burst pressure calculated from these three design codes show lower values compared to FE. The results clearly show that ASME B31G design code gives lowest value of burst pressure in all cases studied. This is followed by modified ASME B31G and DNV-RP-F101 design codes except for cases CS3 and CS4 in which the modified ASME B31G appears as the most conservative compared to other codes. Referring to the FE results from Fig. 9a, the burst pressure slightly decreases as the length of defect increases from 30 mm to 60 mm. A similar pattern is shown by all design codes. In contrast, as the defect depths increase from 3 mm to 4.5 mm (50% to 75% of pipe thickness) as shown in Fig. 9b the burst pressure decreases significantly. The burst pressure drops higher than 13% as the depth of defect change even as small as 0.5 mm. In this respect, the defect depth appears as the main factor that governs the failure of the pipes. This observation is consistent with the fact that hoop stress is

dependent with the remaining effective thickness of the damage pipe as predicted in Eq. (1). The effect of defect width on burst pressure was also studied in this paper. Four different defect widths, *w* were simulated to investigate its effect on burst pressure. The results are summarized in Fig. 9c. Eq. (2) to Eq. (4) do not include the parameter, *w*. It is due to the assumption that the burst pressure is not affected by the width of the defect [4]. The assumption has been confirmed by the FE results in which as the width increases from 4 mm to 14 mm, almost no changes on burst pressure was detected.

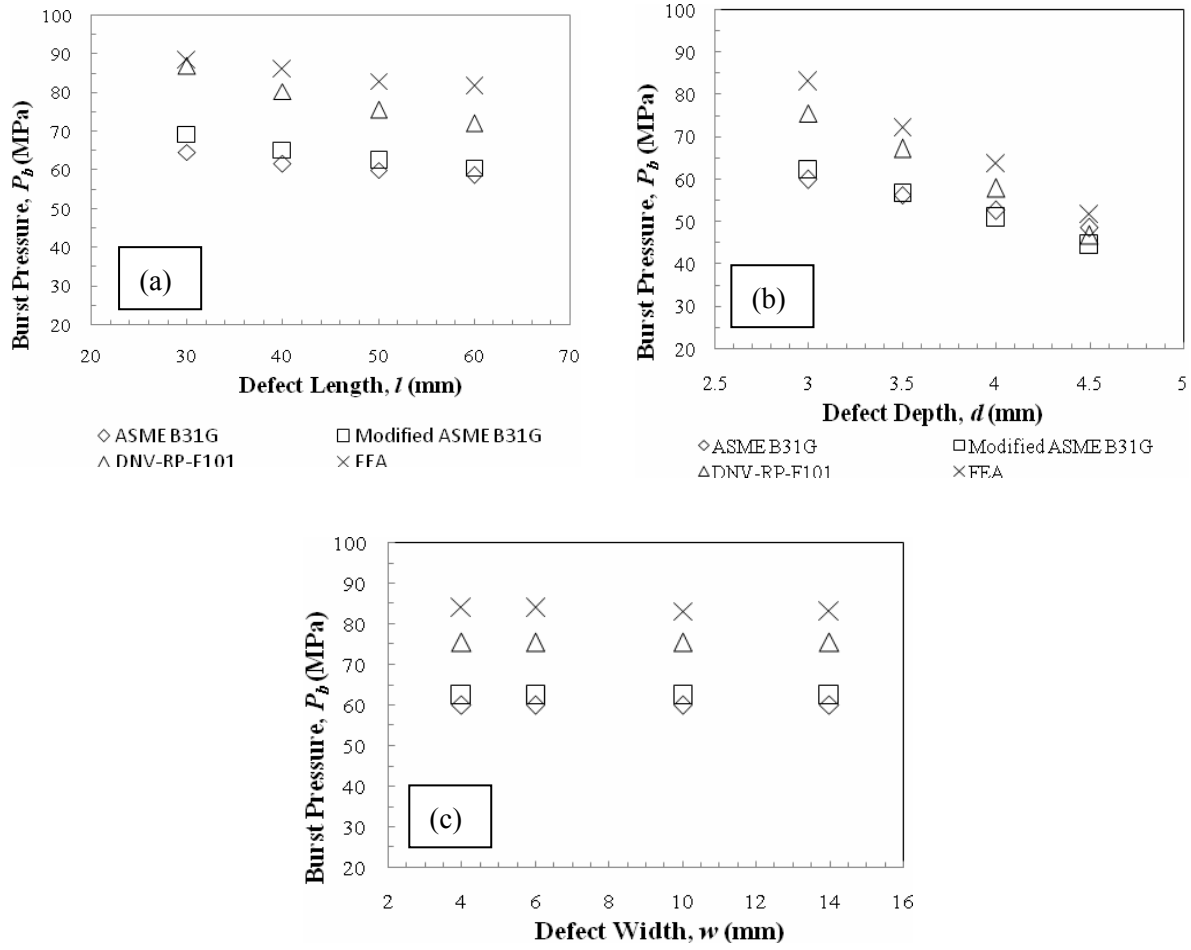

Figure 9. Effect on burst pressure (a) Defect length, (b) Defect depth, (c) Defect width

6. Conclusions

This paper has presented the effect of longitudinal corrosion defects on burst pressure of API X42 steel pipes. The results obtained are as follow:

1) The burst pressure of corroded pipelines is affected by the length and depth of the defects. The depth of corrosion defect is more influential parameter that would affect the burst pressure of pipes.

2) The width of the longitudinal corrosion defects affect insignificantly on burst pressure.

3) The FE results based on SMCS model always predict higher value of burst pressure compared to ASME B31G, Modified ASME B31G and DNV-RP-F101 design codes. ASME B31G is the most conservative design code.

Acknowledgments

The authors would like to express appreciation to all members of Corrosion and Fracture Focus Group (CFRAC) and Dr Hassan Ibrahim for their technical support. Not forgotten to the sponsors of the research, University Malaysia Pahang, Malaysia (RDU100312). Also a special appreciation is dedicated to Khairul Anwar Ibrahim for his contribution on simulation works.

References

[1] Y.K. Lee, Y.P. Kim, M.-W. Moon, 2005, The Prediction of Failure Pressure of Gas Pipeline with Multi Corroded Region, Materials Science Forum, 475-479, pp. 3323-3326

[2] ASME B31G-2009. Manual for Determining the Remaining Strength of Corroded Pipelines. A supplement to ASME B31 code for pressure piping. 2009.

[3] DNV Recommended Practice, RP-F101, 2010, Corroded pipelines, Det Norske Veritas.

[4] C.K. Oh, Y.J. Kim, J.H. Baek , W.-s. Kim, 2007, Ductile Failure Analysis of API X65 pipes with Notch-Type Defects using a Local Fracture Criterion, Int. J of Pressure Vessels and Piping 84, pp. 512–525

[5] Nasir Shafiq, Mokhtar Che Ismail, Chanyalew Taye, 2010, Burst Test Finite Element Analysis and Structural Integrity of Pipeline System, Hydrocarbon Asia's Engineering and Operations Convention. Kuala Lumpur, Malaysia

[6] T.A. Netto, U.S. Ferraz, S.F. Estefen, 2005, The Effect of Corrosion Defects on the Burst Pressure of Pipelines, Journal of Constructional Steel Research, 61, pp. 1185–1204

[7] L.Y. Xu, Y.F. Cheng, 2012, Reliability and Failure Pressure Prediction of Various Grades of Pipeline Steel in the Presence of Corrosion Defects and Pre-strain, International Journal of Pressure Vessels and Piping, 89, pp. 75-84

[8] A.L. Gurson, 1977, Continuum Theory of Ductile Rupture by Void Nucleation and Growth. Part 1-Yield Criteria and Flow Rules for Porous Ductile Media. J Eng Mater Tech, 1.

[9] J. R. Rice, D. Ai. Tracey, 1969, On the Ductile Enlargement of Voids In Triaxial Stress Fields, J. Mech. Phys. Solids, 17, pp. 201 -217.

[10] J.A Lemaitre, 1985, Continuous Damage Mechanics Model for Ductile Fracture, Journal of Engineering Material and Technology 107, pp.83-89

[11] J. W. Hancock and A.C. Mackenzie,1976, On The Mechanisms Of Ductile Failure In High-Strength Steels Subjected To Multi-Axial Stress-States, J. Mech. Phys. Solids, 24, pp. 147 - 169.

[12] C.K. Oh, Kim Y.J, J.H Baek , Y.P. Kim, W.-s. Kim, 2007, A phenomenological Model of Ductile Fracture for API X65 Steel, Int. Journal of Mechanical Sciences, 49, pp.1399-1412.

[13] C.K. Oh, Kim Y.J, Park JM, Baek JH, Kim WS.,2007, Development of Stress-Modified Fracture Strain for Ductile Failure of API X65 Steel, Int J Fract ,143,pp.119–33.

[14] ASTM Standard E8-08, 2008, Standard Test Method for Tension Testing of Metallic Material, American and Society for Testing and Materials.

13th International Conference on Fracture
June 16-21, 2013, Beijing, China

Critical Strain Based Ductile Damage Criterion and its Application to Mechanical Damage in Pipelines

Ming Gao, Ravi Krishnamurthy, Samarth Tandon, Udayasankar Arumugam
Blade Energy Partners, Houston, TX, USA

Abstract

Strain based assessment of mechanical damage in pipelines requires a failure criterion for cracking based on plastic damage. Several criteria have been proposed by industry codes such as B31.8 and in the literature. However, these criteria essentially are based on engineering decisions. In this paper, a plastic damage based criterion that combines material critical strain and triaxiality of stress is used. The theoretical aspect of the criterion, including early work by Hancock and Mackenzie on strain limit (i.e., reference failure strain), ε_f, for ductile failure is discussed. The experimental aspect of material's critical strain and its measurement using uniaxial tensile testing is described. An elastic-plastic finite element analysis is employed to calculate ductile failure damage indicator (DFDI), which can be used to describe the amount of accumulated plastic strain in the damage and its susceptibility to cracking. Its application to assessing mechanical damage in pipelines, including dent with gouge/crack, is presented. Examples are given to illustrate the effectiveness of the criterion for prediction of cracks in dents in pipelines.

Keywords: Mechanical Damage, Dent, Critical strain, Damage Model (DFDI), ASME B31.8

1 Introduction

Strain calculations have been used in the past to estimate the severity of mechanical damage in pipelines. ASME B31.8 2004 established an allowable strain in dents to be 6% [1] based on the experience of the likelihood cracking of cold bend and puncture in dents when material strain exceeds 12% [2]. Numerous studies of failure criteria involving limit states due to crack initiation in the metal forming industry have been conducted in the past [3-14]. However, none of them have been applied to the pipeline industry for integrity management of mechanical damage.

One of the criteria [7, 10,11] that involves critical strain and utilization of damage parameter, i.e., ductile failure damage parameter (DFDI), is adopted by the present study to calculate the amount of plastic damage in pipelines due to mechanical damage, where the critical strain is a material's property defined as the true strain at the onset of incipient crack measured from uni-axial tensile testing, and the DFDI is a damage parameter that is a function of triaxiality of stresses, equivalent strain, and material's critical strain. The onset of incipient crack in a ductile material due to plastic damage is given when DFDI $\geq$1.

In this paper, the theoretical background of plastic damage due to large deformations in ductile materials is presented first. The critical strain and its measurements using uniaxial tensile testing are described. Its application to evaluate mechanical damage including dents in pipelines is then

discussed. The finite element simulation of the denting process is then performed to calculate the cumulative plastic damage and presented as "ductile failure damage indicator" (DFDI). The results demonstrate that the DFDI method predicted well for the crack initiation in dent and can be utilized as a severity indicator and failure criterion for dent repair/mitigation. Finally, an approach proposed by Wang et al [18] that combined DFDI and signal recognition from MFL (magnetic flux leakage) in-line-inspection for evaluation of dent with corrosion/cracking/gouge is presented.

2 Background

As early as the 1960's, a damage relevant stress, i.e., critical stress σ_{cr}, was used as the state limit for sheet forming [7], and was later further developed by others [8,9]. These simplified stress criteria have proven to be very restrictive, as well as related to a special forming process [7,8]. Later, researchers tried to correlate plastic damage to the plastic work done during deformation, and proposed critical work, W_c, as a damage relevant term. However, for the same reasons, the concept of W_c may be suspicious, especially when it is applied to significant crack propagation in a tension bar [9].

Large plastic deformation of ductile materials involves initiation, growth and coalescence of microvoids to form cracks, known as "ductile plastic damage", and is the mechanism for ductile cracking, tearing, and rupture of ductile materials. Considerable effort has been made since the mid-1960's [3-6] to establish a frame work (failure criteria, for example) for studying conditions and variables associated with the failures.

In the late 1960's, McClintock [10] and Rice and Tracey [11] established the basic relation between growth of a void and imposed stress and strain from a tri-axial stress field using a micro mechanics approach. Hancock and Mackenzie [6] in the mid-70's followed Rice et al's work, and proposed a reference failure strain, ε_f, i.e., a strain limit for ductile failure:

$$\varepsilon_f = 1.65\varepsilon_o \exp(-\frac{3}{2}\frac{\sigma_m}{\sigma_{eq}}) \qquad (1)$$

where σ_m = average stress of three principle stresses in a tri-axial stress field, and σ_{eq} = equivalent von Mises stress. The ratio of σ_m/σ_{eq} represents the tri-axiality of the stress field, and ε_o is the critical strain of ductile materials for incipient crack, a material property measured by uniaxial tension testing.

Equation (1) indicates that the strain limit of a structural component, ε_f, is not a constant. It is a function of stress tri-axiality and the material's critical strain. Equation (1) defines a generalized strain limit, i.e., reference failure strain, for large plastic deformations subject to both uni-axial and multi-axial stress states. In the uni-axial tension condition, Equation (1) becomes $\varepsilon_f = \varepsilon_o$ i.e., the reference failure strain in the uni-axial tension is equal to its critical strain of the material. Equation 1 is derived from the concept that ductile failure results from initiation, growth and coalescence of voids on a micro scale, and formation of cracks during large plastic deformation. Given the established strain limit for ductile failure, the degree of plastic damage is defined as:

$$dD_i = \frac{d\varepsilon_{eq}}{\varepsilon_f} \qquad (2)$$

$$D_i = \int_0^{\varepsilon_{eq}} \frac{d\varepsilon_{eq}}{\varepsilon_f} \qquad (3)$$

Equation (2) shows that the plastic damage induced by each increment of the plastic strain, $d\varepsilon_{eq}$, involved in the deformation process is the ratio of the increment to the failure strain. Equation (3) is the integral of Equation (2), i.e., the total plastic damage for entire plastic deformation. D_i is the indicator of cumulative plastic damage during plastic deformation which has a general form of $D_i = D_i(\sigma_m / \sigma_{eq}, \varepsilon_{eq}, \dot{\varepsilon}_{eq})$, where σ_{eq} is the equivalent von Mises stress, and σ_m is the average stress. Its value ranges from 0 (undamaged) to 1 (rupture). By the definition, ductile failure will occur when $D_i \geq 1$, where D_i is the measure, or indicator, of ductile failure damage. A safe DFDI less than one (<1) would be appropriate to prevent failures.

Substituting Hancock et al's failure strain ε_f (Eq. (1)) into Equation (3), gives

$$D_i = \int_0^{\varepsilon_{eq}} \frac{\exp\left(\frac{3}{2}\frac{\sigma_m}{\sigma_{eq}}\right)}{1.65\varepsilon_o} d\varepsilon_{eq} = \frac{1}{1.65\varepsilon_o} \int_0^{\varepsilon_{eq}} \exp\left(\frac{3}{2}\frac{\sigma_m}{\sigma_{eq}}\right) d\varepsilon_{eq} \qquad (4)$$

Equation (4) relates the ductile failure damage indicator D_i, the stress tri-axiality (σ_m/σ_{eq}) and the material's critical failure strain ε_o. Various modifications of the reference failure strain ε_f, which lead to a better agreement with experiments for high stress tri-axialities, are available in the literature [12-14].

3 Critical Strain and its measurement

Critical strain is a material property and measured by uni-axial tension testing. The critical strain of a material, ε_o, is defined as the critical point of the true strain at which incipient crack occurs. To measure the critical strain of a material from a uniaxial tension testing, both engineering and true stress vs. strain curves in the necking (non-uniform elongation) regime are required.

For true stress and strain measurement in the necking (non-uniform elongation) regime, a series of images of the necking area needs to be recorded either on a time or displacement basis. The recorded images are used to determine the radius or the cross-section area of the neck for true stress and strain calculation using the following Equation [5] and to establish the relationship between true stress and true strain:

$$\sigma_{true} = \frac{P}{A}, \ \varepsilon_{true} = \varepsilon_o = 2\ln\frac{A_o}{A} = 2\ln\frac{r_o}{r} \qquad (5)$$

where A_o and r_o are the initial cross-section area and radius of the tensile specimen, respectively, and A and r are the smallest cross section area and radius of the neck at the time of the measurement, respectively.

For the onset point at which incipient crack occurs, cracking, it cannot be determined from the true stress and true strain data itself. It is determined from the second sharp knee on the engineering stress-strain curve or load-displacement curve [7], shown in Figure 1(a).

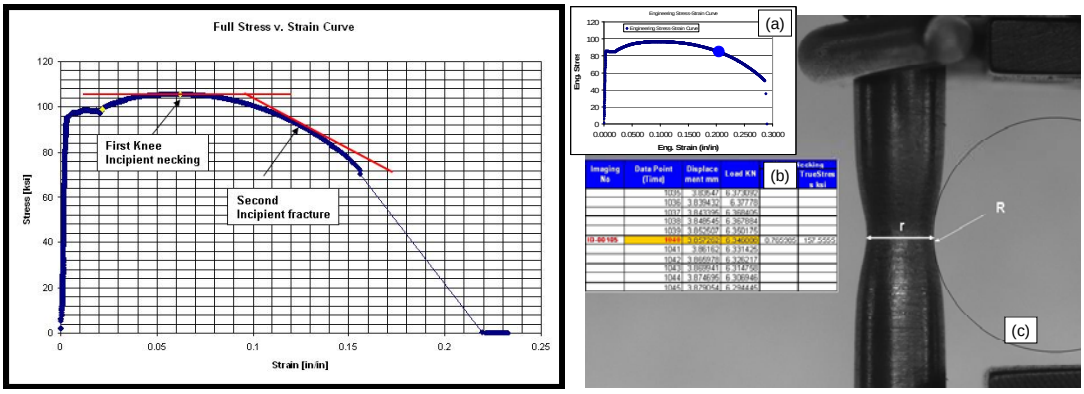

Figure 1: (a) A typical engineering Stress and Strain curve of LXS80, showing the second sharp knee related to the incipient crack (b) Typical image recorded by the video camera on a time-based sampling scheme. The insert shows the respective location of the image on the load-displacement curve

Using the identified onset point of incipient crack and the true strain and true stress curve, the critical strain can be determined by correlating the engineer strain at the onset point of incipient crack to the respective true strain. Efforts were made to develop a time-based switching and data acquisition system. The system consisted of three major components: a closed loop tensile test machine, a high resolution digital video camera, and a synchronized and data acquisition system for simultaneously sampling load-displacement data and image recording. The system provides a signal to trigger the video camera's "shutter" on and off for a given time interval and interfaces between the high resolution digital video camera and the tensile test machine. Each recorded image contains a time code that can be used to match a respective point on the load-displacement curve that was saved at the same time by the data acquisition system of the tensile testing machine. One of the recoded images that correspond to the point of the onset of incipient crack is the one corresponding to the critical strain that can be found from the true stress-strain curve. There is a possibility that no image could be matched with the onset point for critical strain calculation. However, this may be resolved either by interpolating the critical strain values obtained from two adjacent images that are across the onset point, or, more accurately, by establishing an engineering strain and true strain curve around the fracture incipient point and then using the curve-fit equation to calculate critical strain.

3.1 Determination of Crack-incipient from uniaxial tensile test

The information obtained from the synchronized system contains three sets of data: (1) load-displacement data directly obtained from the tensile test machine, (2) the time-based images recorded by the video camera, and (3) the time code for each image and corresponding load and displacement recorded by the synchronized data acquisition board. These three pieces of information were analyzed using the following methods to determine critical strain.

The crack-incipient point is a characteristic point on the load-displacement curve. This point can be diagnosed by a sharp knee in the engineering stress-strain curve or by a second knee in the $d\sigma/d\varepsilon$-ε curve as shown in (a) and (b) of Figure 2, respectively [7].

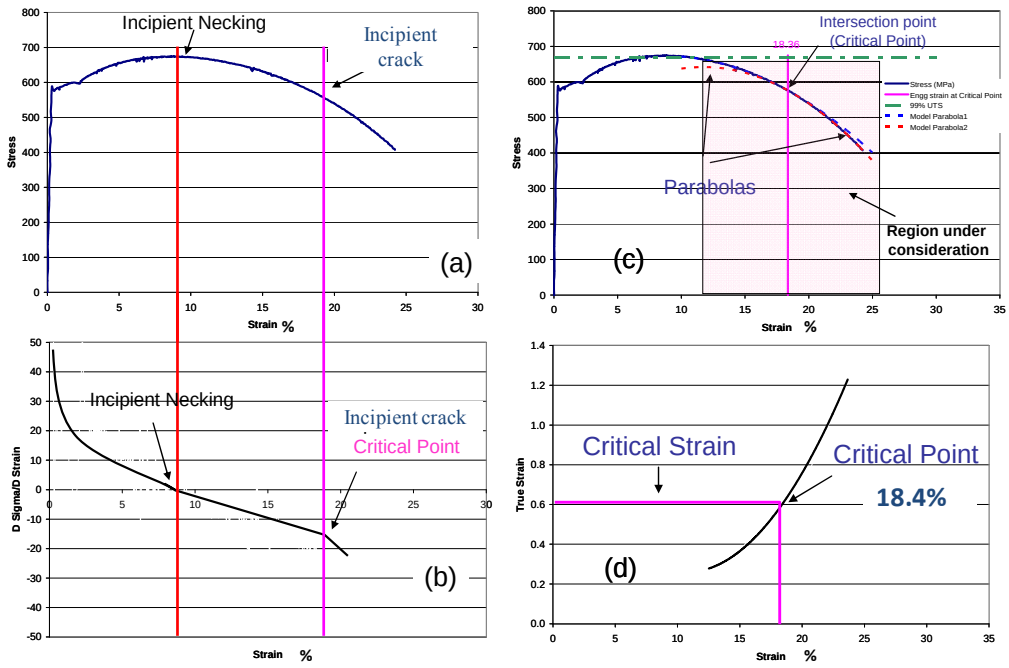

Figure 2: A composite figure showing (a) the engineering stress-strain (σ vs. ε) curve with the incipient necking and crack; (b) dσ/dε vs. ε plot – a knee shaped curve giving the incipient crack point which is the critical point; (c) the intersection of two parabolic curves derived from a mathematical best fit model for determination of critical point; and (d) the relationship between the true strain and engineering strain. The relationship is obtained from the synchronized camera system.

For the sharp knee diagnosis method from the engineering stress-strain curve, two parabolas are used to model the upper and lower portions of the curve [5]. The intersection of the two parabolas is the point that corresponds to the on-set point of incipient crack. For the "second knee" diagnosis method from the dσ/dε-ε curve, two straight lines are used to model the upper and lower portions of the dσ/dε-ε curve. Again the intersection of the two straight lines is the point corresponding to the crack incipient point.

These two diagnostic methods are equally applicable and should yield the same results. However, the data processing showed that because the "second knee" diagnosis method involves a derivative operation of σ with respect to ε from the experimental stress-strain data, which resulted in a large scattered band of the dσ/dε-ε curve, the uncertainty in linear regression for straight line modeling would be large. Therefore, the first method was adopted for the present study. The intersection of the parabolas was found by utilizing the "Method of Least Squares". Once the incipient point is determined, Figure 2(c) it may be used to calculate the critical strain by utilizing the curve fit equation between engineering and true strain, Figure 2(d).

4 Application of DFDI to Mechanical Damage

Dent or indentation in pipe is described as a permanent deformation of the pipe's circular cross section arising from external forces [1]. Depending on the severity of the dent or the amount of plastic deformation, crack(s) may be initiated in the dent. Ductile Failure Damage Indicator

(DFDI) can be utilized as a criterion to gage the severity of plastic damage in dents, and predict its susceptibility to cracking. To evaluate the effectiveness of this model, one case involving 2.7% OD bottom-side rock dent associated with 76% WT metal loss reported by a combo ILI tool (geometry + MFL) is studied. Elastic-plastic finite element modeling incorporating actual measured uni-axial tensile stress-strain curve from pipeline material and calculated critical strain is performed. More case studies involving dents associated with metal loss and plain dents can be found in Reference [21].

The pipe had an OD of 30in, nominal wall thickness of 9.5mm, Grade of X52, constructed in the year 1958 with depth of cover of 90cm, and was operating at 6,895 kPa (77% SMYS). The dent was 2.7% deep with length of 120mm, and width of 97mm, at a clock position of 6:15. Figure 3(a) shows the screenshot of the ILI reported dent deformation profiles in circumferential and axial direction, respectively.

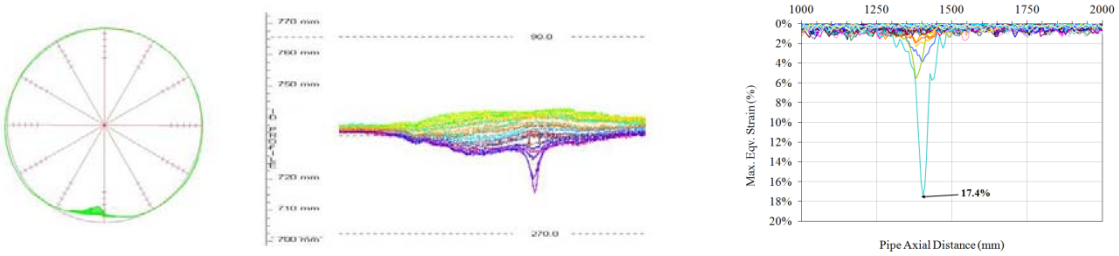

Figure 3: (a) Dent circumferential and axial profile (b) Strain profile using Blade's in-house dent strain software

From Figure 3(a), dent apex seemed sharp, suggesting the possibility of high strain at this location. Strain analyses was performed on this dent utilizing an in-house point-to-point strain analysis tool [17] using the strain equation recommended in the Reference [15, 16]. The calculated maximum equivalent strain (true strain) is 17.4%, which is located at the dent apex.

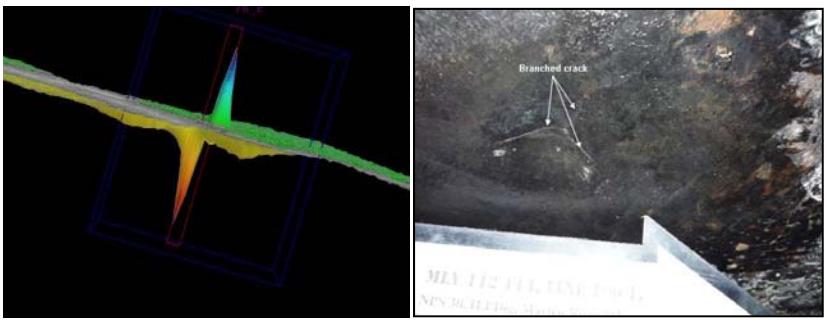

(a) **(b)**

Figure 4: (a) Equivalent strain distribution plot around and in the dent area, (b) Dent with branched crack in-ditch (OD)

A review of the MFL raw signal showed sharp and strong signal characteristics of magnetic flux leakage, seen in Figure 4(a), suggesting that the reported 76% WT metal loss is more likely

cracking or gouging rather than corrosion. The dent was excavated for further investigation. On excavation, it was found to be in contact with a rock. On the removal of the rock, it was found to be associated with three cracks originating near its apex, Figure 4(b). No leak was detected in the field, indicating the cracks were partially through-wall. Since the dent was associated with cracks, the pipe joint was cut out for further investigation. The dent was inspected from inside, which showed branched cracks at the same location as the OD cracks, but in ID surface of the dent apex. A 3D mapping [17] of the cracked dent geometry was conducted using a portable 3D LaserScan system. The axial and circumferential profiles were extracted at the ID surface. The strain analysis was performed using the profiles. The maximum equivalent strain in the dent was found to be 16%, located at its apex.

The measured ILI maximum equivalent internal strain was 17.4%, compared to LaserScan profile internal strain of 16%. The maximum equivalent strain value obtained from LaserScan is comparable to that obtained from ILI; however, this apparent consistency may not be true because the dent profile was significantly changed due to spring back (rebound) when the constraint (rock) of the dent was removed. A comparison of the dent profile before and after excavation is given in Figure 5. The measured dent depth after the rock was removed was ~1.4% OD, which is one half of the ILI-reported depth of 2.7% OD. In order to estimate the change in plastic strain due to rebounding, the high resolution LaserScan ID profile was scaled by a factor of 1.7 to match closely with the ILI data. The calculated maximum equivalent strain after scaling was 32.3%, about twice after rebounding.

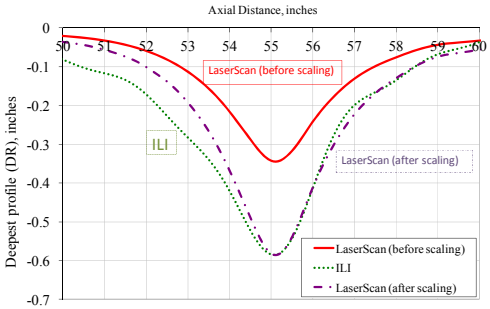

Figure 5: Change in dent ID profile before and after excavation, showing the dent had significantly rebounded.

An elastic-plastic finite element analysis (FEA) was performed using the scaled ID LaserScan profile of the cracked dent. The Critical strain was measured utilizing the procedure in Section 3. The measured value of the material critical strain was 51.2%. The maximum equivalent plastic strain based on FEA in the dent was 35.0%, located at the dent apex. DFDI values were calculated at each of the deformation nodes using the FEA result. The calculated maximum DFDI is 1.1, which is greater than 1.0, indicating that the dent is susceptible to cracking at its internal surface.

Figure 6(a) shows the maximum principal stress contour plot with the probable crack propagation direction, compared with the ID actual crack path, as shown in Figure 6(b). The FEA-predicted crack path is in good agreement with the observed actual crack pattern. FEA also showed a high reaction force associated with the dent, indicating a very high external force might have caused this dent deformation, possibly during construction.

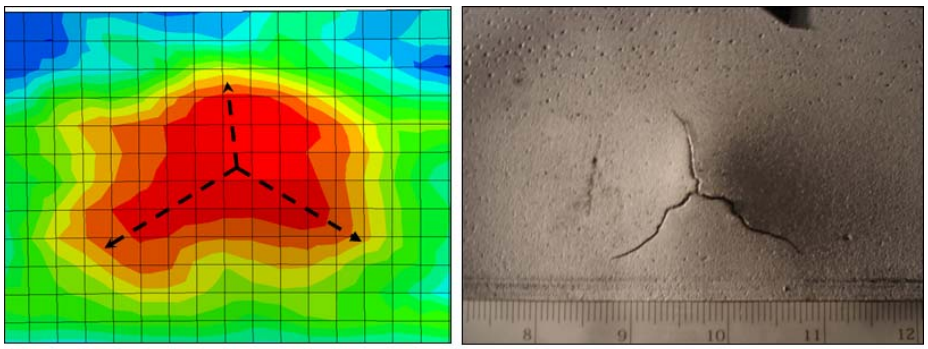

(a) Max principal stress plot with predicted crack path

(b) Actual crack path

Figure 6: Case-1: Color-coded contour plot of maximum principal stress plot (indicated probable crack path) vs. actual crack path (ID)

In summary, this case study showed a failure condition (cracking) of the dent by the plastic damage mode, and demonstrates its effectiveness of capturing critical dents i.e. dents with susceptibility to crack in pipeline which can pose an integrity threat. Inline inspection Magnetic Flux Leakage (MFL) signal data was also utilized as an added dimension in understanding whether the dent is associated with a crack. A combined approach, utilizing the DFDI model and MFL signal recognition to identify dent with corrosion/cracking/gouging is presented in the next section.

3 A combined approach for dent with Corrosion/cracking/gouging evaluation [18]

Current in-line inspection technologies (e.g., caliper/MFL or combo) for mechanical damage assessment can detect dent with metal loss but with limited ability. However, they are incapable of discriminating metal loss from corrosion, gouge and crack. Practical experience showed that, with the assistance of strain based dent analysis and strain limit damage criteria, detailed characterization of MFL signals could effectively facilitate to identify potential risk of dent with cracking and to discriminate between metal loss features of corrosion and cracking/gouging. Therefore, a dent assessment approach which combines the plastic damage model with MFL signal recognition was recently developed by Wang et al and some of the present authors [18]. The strain severity based criterion is used to assess dent susceptibility to cracking regardless if the dent was reported as plain dent or dent with metal loss. Only those dents that meet the strain criterion will be considered as a candidate for investigation of MFL signal characteristics to assure if the dent is associated with cracking/gouging. The flow chart shown in Figure 7 describes the combined approach used for the assessment.

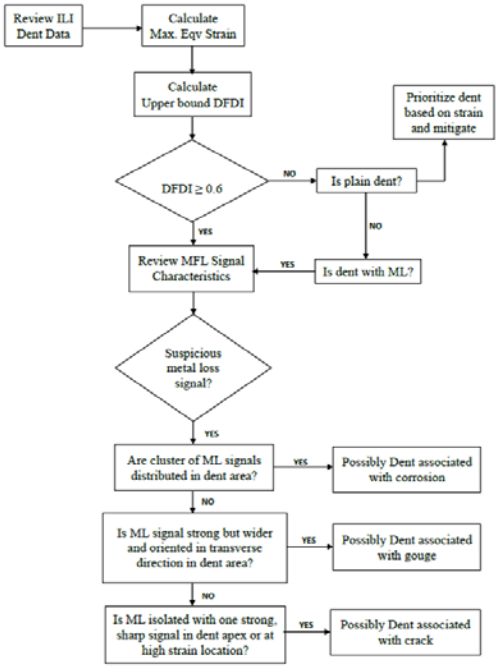

Figure 7: Flow chart – Procedure used in the combined assessment approach.

Using the above described procedure, case studies were performed to quantify the effectiveness of the approach for (1) identifying critical dents that are associated with cracking or gouging; and (2) the ability to discriminate the metal loss features of corrosion vs. cracking/gouging. Assessments were made using two recent in-line inspections which reported 4,823 dents in total. Among them, more than 150 dents were selected for assessment. Eight (8) dents were predicted to contain cracking or gouging. A total of fifteen (15) validation excavations, including the 8 predicted 'dent with crack' and 7 predicted 'dent without crack' were performed. All eight predictions were validated with excavations (true positive). Among them, two (2) were associated with through-wall cracks and were leaking during excavation, and the remaining 6 dents either contain surface cracks or gouges. The other seven (7) excavations showed no cracks or metal loss, i.e. true negative. The combined approach and its impact to integrity management of dents were successfully demonstrated with the case studies. The details of assessment approach, procedure, result and findings can be found in Reference [18] of this paper.

4 Summary

Critical strain based failure criterion, i.e., ductile failure damage indicator DFDI, can be applied to evaluate the severity of mechanical damage in pipelines for predicting susceptibility to cracking. Critical strain can be measured with uni-axial tensile testing and calculated using simplified mathematical model on uni-axial tensile full engineering and true stress-strain data recorded by synchronized data acquisition system. Finite element simulation demonstrated the effectiveness of the DFDI model for predicting cracks in dent. The study further demonstrates that the combined DFDI with MFL signal recognition approach can effectively identify potential risk of dent with cracking and to discriminate metal loss features between corrosion and cracking/ gouging.

References

1. B31.8 Gas Transmission and Distribution Piping System, 2004)
2. M.J. Rosenfeld, J.W. Pepper, K. Leewis, "Basis of the new criteria in ASME B31.8 for prioritization and repair of mechanical damage", Proceedings of IPC 2002, 4th International Pipeline Conference, IPC2002-27122, Sep 29-Oct 3, 2002, Calgary Alberta, Canada
3. A.L. Gurson, "Continuum Theory of Ductile Rupture by Void Nucleation and Growth. Part I: Yield Criteria and Flow Rules for Porous Ductile Media" Journal of Engineering Materials and Technology, v 99, n 1, Jan. 1977, pp. 2-15.
4. V. Tvergaard and A Needleman "Constitutive Relations for Creep in Polycrystals with Grain Boundary Cavitation" Acta Metallurgica, v 32, n 11, Nov, 1984, pp. 1977-1990.
5. J. A. Lemaitre:" A Continuous Damage Mechanics Model for Ductile Fracture", Journal of Engineering Materials and Technology, Vol. 107, 1985, pp. 83-89, and also in Mechanics of Solids Materials, Cambridge, MA, Cambridge University Press, 1990.
6. J. W. Hancock and A. C. Makenzie:"On the Mechanisms of Ductile Failure in High-Strength Steels Subject t Multi-Axial Stress-States", Journal of Mechanics and Physics of Solids, 24 (1976) pp.141-169.
7. F.D. Fischer, O. Kolednik, G.X. Shan and F.G. Rammerstorfer:"A Note on Calibration of Ductile Failure Damage Indicators", International Journal Fractures, V. 73, 1995, pp. 345-357.
8. F.B. Beremin, Metallurgical Transaction, 12A, 1981, pp. 723-731.
9. K. S. Zhang and C. Q. Zheng, Acta Mechanica Sinica, Vol. 7, 1991, pp. 243-250.
10. F. A. McClintock, J. Appl. Mech., Vol. 35, 1968, pp. 363
11. J. R. Rice and D. M. Tracy: "On the Ductile Enlargement of Voids in Triaxial Stress Fields", J. Mech. Phys. Solids, 1969, Vol 17, pp. 201-217.
12. P. J. Budden and M. R. Jones, Fatigue and Fracture of Engineering Materials and Structure, Vol. 14, 1991, pp. 469 and 482.
13. M. Zheng, X. Zheng and Z. J. Luo, International Journal of Fracture, Vol. 56, 1992, R61-R65.
14. T.-J Wang, International Journal of Fracture Vol.54, 1992, R23-R29.
15. M., Gao et al, "Strain-Based Models for Dent Assessment – A Review", IPC 2008, Paper No. 64565, 7th International Pipeline Conference, Calgary, Canada September 29-October 3, 2008.
16. S.A., Lukasiewicz, J.A., Czyz, C., Sun, S., Adeeb, "Calculation of Strains in Dents Based on High Resolution In-Line Caliper Survey", IPC2006, Paper No. 10101, 6th International Pipeline Conference, Calgary, Canada, September 25-29, 2006.
17. Blade Energy Partners, "A Point-to-Point Dent Strain Analysis using ILI and Laserscan dent profile data, User Instruction Manual", 2009.
18. R., Wang, R., Kania, U., Arumugam, M., Gao, "A Combined Approach to Characterization of Dent with Metal Loss", IPC2012, Paper 90499, 9th International Pipeline Conference, Calgary, Canada, September 24-28, 2012.

13th International Conference on Fracture
June 16-21, 2013, Beijing, China

API 579 G-factors for K Calculations and Improvements For Assessment of Crack-like Flaws in Pipelines

Shaikh Rahman, Ming Gao*, Ravi Krishnamurthy
Blade Energy Partners, Houston, TX, USA
Corresponding author: mgao@blade-energy.com

Abstract

API 579-1/ASME FFS-1 2007 gives a complete guideline of Fitness-For-Service (FFS) assessment of crack-like flaws in structural components based on the Failure Assessment Diagram (FAD) method. The assessment is carried out in FAD using a non-linear relationship between the load ratio (L_r) and the toughness ratio (K_r) where the toughness ratio (K_r) is defined as the ratio of the Mode I stress intensity factor (K_I) to the toughness of the material (K_{mat}). One of the methods for Mode I stress intensity factor (K_I) calculation in API 579-1/ASME FFS-1 2007 is FEA based, which correlates five influence coefficients, namely G_o to G_4, for K_I calculation. These influence coefficients are dimensionless and are tabulated for a range of two ratios; the wall thickness to the internal radius (t/R_i) and the flaw depth to the wall thickness (a/t) for infinite cracks and three ratios (crack depth to half crack length (a/c) besides a/t and t/R_i) for finite cracks. API 579-1/ASME FFS-1 2007 allows interpolation of the influence coefficients, Gs for intermediate values. Even though it is not explicitly mentioned about the method of interpolation, a linear interpolation is generally considered. Another possible method is explored here with the polynomial function fitted by the FEA data provided in the table given in API 579. A detail discussion on obtaining the influence coefficients for an intermediate value is outlined here. Case studies are provided to illustrate the advantages and disadvantages of the linear interpolation and the fitted polynomial function.

Keywords: Stress Intensity Factor, Influence Coefficients G_i, G Interpolation, FAD, Level 2 Limiting Pressure

1 Introduction

The Mode I Stress Intensity Factor (K_I) in API 579 is a fourth order polynomial function of (a/R_i) or (a/R_o) with applied internal pressure and pipe dimension. The solution is obtained from FEA work completed by T. L. Anderson Group [1]. According to API 579, the Mode I Stress Intensity Factors for the infinite length internal and external surface cracks in axial (longitudinal) direction are given by the following equations [2] respectively.

Internal axial infinite surface crack:

$$K_I = \frac{pR_o^2}{R_o^2 - R_i^2}\left[2G_o - 2G_1\left(\frac{a}{R_i}\right) + 3G_2\left(\frac{a}{R_i}\right)^2 - 4G_3\left(\frac{a}{R_i}\right)^3 + 5G_4\left(\frac{a}{R_i}\right)^4\right]\sqrt{\pi a}$$

External axial infinite surface crack:

$$K_I = \frac{pR_i^2}{R_o^2 - R_i^2}\left[2G_o + 2G_1\left(\frac{a}{R_o}\right) + 3G_2\left(\frac{a}{R_o}\right)^2 + 4G_3\left(\frac{a}{R_o}\right)^3 + 5G_4\left(\frac{a}{R_o}\right)^4\right]\sqrt{\pi a}$$

Where, p is the internal pressure, R_i and R_o are the internal and external radii respectively, a is the flaw depth and G_o to G_4 are the influence coefficients. This equation is valid for $0.0 \leq a/t \leq 0.8$ and $0.001 \leq t/R_i \leq 1.0$. The influence coefficients are given in Table C.10 and Table C.11 in API 579 document for infinite axial and circumferential cracks respectively. The table gives values of influence coefficients for various t/R_i and a/t. t/R_i is converted to R_i/t for the convenience in calculation performed in this work. R_i/t can also be readily converted to OD/t $[= 2(R_i/t + 1)]$ that is more common in tubular performance calculation in Oil and Gas Industry. For finite surface crack $\sqrt{\pi a}$ in the above two equations are replaced by $\sqrt{\pi a/Q}$. The influence coefficients for the finite crack are function of a/c in addition to a/t and t/R_i ratios. Therefore, for infinite crack, two interpolations and for finite crack, three interpolations are required to obtain the desired influence coefficients. It is mentioned in API 579 that "interpolation of the influence coefficients, G_i, may be used for intermediate values of t/R_i and a/t" but does not state explicitely how the interpolation should be performed, linearly or otherwise. The work described in this paper takes an attempt to explain if the linear interpolation is adequate or accurate enough for this purpose. The cubic polynomial interpolation is used for the comparative study.

2 Interpolation methods

2.1 Infinite Surface Crack

Table C.10 and Table C.11 in API 579 give the influence coefficients of infinite surface crack for axial and circumferential direction respectively. Figure 1 shows part of the Table C.10 and Table C.11 from API 579. The influence coefficients shown in these tables are function of t/R_i and a/t. Therefore, two interpolations are required to obtain the desired influence coefficients for a given pipe and crack dimensions.

Table C.10
Influence Coefficients For a Longitudinal Infinte Length Surface Crack in a Cylindrical Shell

t/Ri	a/t	Internal Crack					External Crack				
		G0	G1	G2	G3	G4	G0	G1	G2	G3	G4
0.001	0	1.12	0.682	0.5245	0.4404	0.379075	1.12	0.682	0.5245	0.4404	0.379075
	0.2	1.362669	0.775768	0.577169	0.475763	0.405555	1.362492	0.77543	0.577078	0.475707	0.40532
0.00333	0	1.12	0.682	0.5245	0.4404	0.379075	1.12	0.682	0.5245	0.4404	0.379075
	0.2	1.357654	0.772719	0.575074	0.47405	0.404119	1.357654	0.772836	0.57512	0.47405	0.404212
0.01	0	1.12	0.682	0.5245	0.4404	0.379075	1.12	0.682	0.5245	0.4404	0.379075
	0.2	1.355721	0.772039	0.574618	0.473607	0.403962	1.355914	0.772205	0.574709	0.473663	0.404056

Table C.11
Influence Coefficients For a Circumferential 360° Surface Crack in a Cylindrical Shell

t/Ri	a/t	Internal Crack					External Crack				
		G0	G1	G2	G3	G4	G0	G1	G2	G3	G4
0.001	0	1.12	0.682	0.5245	0.4404	0.379075	1.12	0.682	0.5245	0.4404	0.379075
	0.2	1.322217	0.749276	0.557422	0.459379	0.392453	1.322614	0.749276	0.557516	0.459436	0.392373
0.00333	0	1.12	0.682	0.5245	0.4404	0.379075	1.12	0.682	0.5245	0.4404	0.379075
	0.2	1.326772	0.756593	0.563926	0.464829	0.397395	1.327958	0.75694	0.564112	0.464942	0.397435
0.01	0	1.12	0.682	0.5245	0.4404	0.379075	1.12	0.682	0.5245	0.4404	0.379075
	0.2	1.328921	0.764758	0.572095	0.471607	0.403497	1.332125	0.754093	0.552893	0.446495	0.394324

Figure 1 – Partial Table C.10 and Table C.11 from API 579

Interpolation is performed in two steps using the following methodology:

- For a given pipe and crack geometry, a/t and t/R_i are calculated.
- The a/t and t/R_i are then used to identify the neighboring a/t and t/R_i in the table. There are two sets of influence coefficients for each t/R_i obtained from two neighboring a/t.
- First interpolation is performed for each t/R_i between the corresponding set of a/t for the desired a/t.

- The second and final interpolation is performed between those interpolated influence coefficients for the desired t/R_i.

The order of the interpolations (starting with a/t or t/R_i) is irrelevant. Linear interpolation requires two sets of data points surrounding the desired a/t or t/R_i. But for the cubic polynomial interpolation requires four sets of data points. In the subsequent sections a detail description is given with examples on how to perform the both interpolations and is shown the difference with respect to linear interpolation. Out of the five influence coefficients, the first one, G_o has the most influence in the stress intensity function. Therefore, the comparative analysis is performed on G_o alone.

2.1.1 Nature of nonlinearity

The influence coefficients are function of a/t and inverse of R_i/t. The nature of nonlinearity of the influence coefficients with a/t and R_i/t are discussed here starting with a/t.

Figure 2 shows the nature of non-linearity of all five influence coefficients for $R_i/t = 10$. The first influence coefficient shows the highest nonlinearity and the nonlinearity diminishes for the subsequent influence coefficients. It also shows a very good fit with cubic polynomial. For other R_i/t the cubic polynomial function will change. Figure 3a shows the first influence coefficient (G_o) for $R_i/t = 10$ and $R_i/t = 5$. It can be visually inferred from Figure 3a that linearity can be assumed between any two consecutive points without losing a considerable amount of accuracy. The effect of non-linearity on G_o can be observed from Figure 3b. Non-linearity reduces with lesser R_i/t as well as lesser a/t.

There are seven points identified in the Figure 3a. They are -

- Point A: a/t=0.6 and R_i/t=5
- Point B: a/t=0.6 and R_i/t=10
- Point C: a/t=0.8 and R_i/t=5
- Point D: a/t=0.8 and R_i/t=10
- Point E: a/t=0.7 and R_i/t=5. This is one of the two interpolated points obtained after the first interpolation.
- Point F: a/t=0.7 and R_i/t=10. This is one of the two interpolated points obtained after the first interpolation.
- Point X: a/t=0.7 and R_i/t=7. This is the final value after the second interpolation between points E and F.

Point A through Point D are obtained from Table C.10. The example discussed later uses these points and shows the differences in calculating G_o using cubic polynomial interpolation and linear interpolation. Next discussion is on the nonlinear nature of G_o with respect to R_i/t.

Figure 4a shows the nature of the nonlinearity of G_o with respect to R_i/t. It is observed from the earlier figures that the non-linearity reduces with decreasing a/t as well as with decreasing R_i/t. Even more interestingly, Figure 4a shows that the nonlinearity of G_o vanishes beyond a value of R_i/t. This value varies with variation of a/t. Assuming the maximum $R_i/t = 40$ after which the influence of R_i/t vanishes, Figure 4b shows a set of cubic polynomials of R_i/t for various a/t. These are not as good fit as we have seen earlier with cubic polynomial of a/t even though the maximum

of R_i/t is reduced down to 40. Improvement can be made in the curve fitting is to perform the curve fitting around the desired value. In explaining this, two piecewise curve fittings are performed and shown in Figure 5. Curve fittings with R_i/t from 1 to 10 (left in the figure) and from 10 to 40 (right in the figure) are considered in this figure.

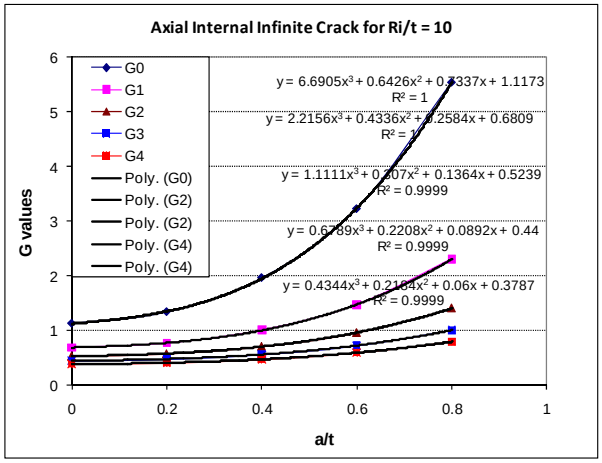

Figure 2 – Nonlinear behavior of the influence coefficients of the axial internal infinite surface crack for $t/R_i = 10$

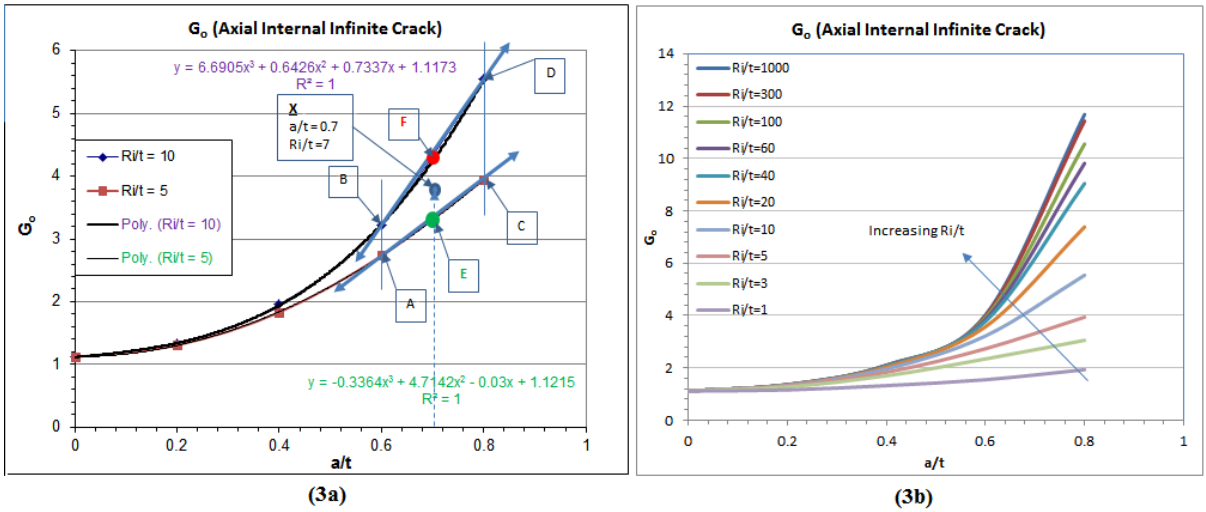

Figure 3 – (3a) First influence coefficient (G_o) for $t/R_i = 10$ and 5 and (3b) Effect of non-linearity in G_o with increasing R_i/t

Figure 6 shows the similar arrangement of points A through D described earlier along on the cubic curve fit between R_i/t of 1 to 10. It also shows the linear approximation lines. It can be clearly inferred from this figure that linearity can be assumed between two adjacent points as shown in the previous case.

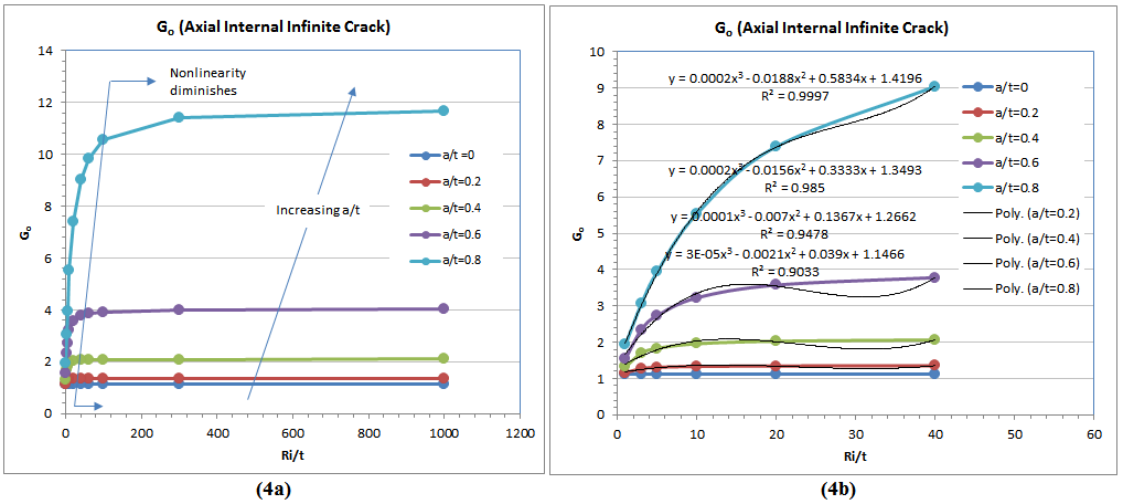

Figure 4 – (4a) The first influence coefficient (G_o) with respect to R_i/t and (4b) Nonlinear behavior of the first influence coefficient with respect to R_i/t

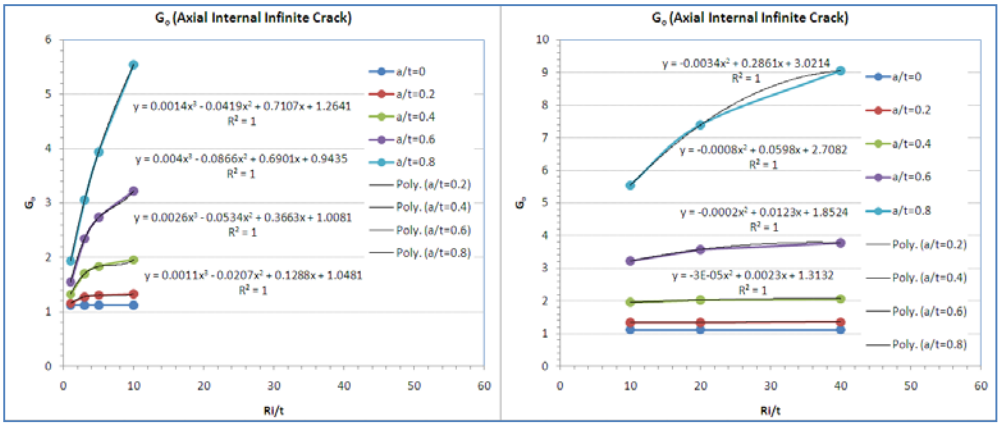

Figure 5 – Local cubic polynomial of the first influence coefficient with respect to R_i/t. (a) $R_i/t \leq 10$ (left figure) (b) $10 \leq R_i/t \leq 40$ (right figure)

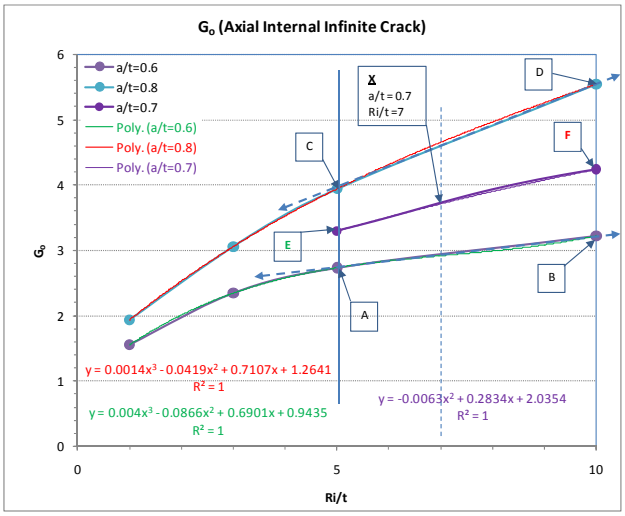

Figure 6 – First influence coefficient (G_o) for a/t = 0.6 and 0.8

Therefore, linearity between two adjacent a/t points and two R_i/t points can be assumed without losing much accuracy. Following example takes an attempt of quantifying the accuracy. The first influence coefficient (G_o) is selected because it has the most influence in stress intensity function (Equation is given at the beginning).

2.1.2 Example

Let us assume that the influence coefficients for a/t=0.7 and R_i/t=7 are needed for calculating stress intensity factor. Table 1 shows a portion of Table C.10 from API 579 for R_i/t of 10 and 5 and for a/t from 0 to 0.8. The values we are looking for are between R_i/t of 10 and 5 and a/t of 0.6 and 0.8. These values are marked in the table. As it is mentioned earlier that two interpolations are required. The first interpolation is performed for a/t = 0.7 that is in between a/t of 0.6 and 0.8. This yields two sets of influence coefficients; one for R_i/t = 10 and the other for R_i/t = 5. The next and final interpolation is performed for R_i/t = 7 that is in between R_i/t of 10 and 5. It is also important to note that the interpolations are performed between values of a/t and R_i/t that are adjacent to the desired values.

Table 1 – Influence coefficients for Axial Internal Infinite Crack

		Internal Crack				
Ri/t	a/t	G0	G1	G2	G3	G4
10	0	1.12	0.682	0.5245	0.4404	0.379075
10	0.2	1.332691	0.763153	0.569758	0.470495	0.401459
10	0.4	1.957764	1.002123	0.702473	0.556857	0.467621
10	0.6	3.223438	1.466106	0.953655	0.718048	0.585672
10	0.8	5.543784	2.300604	1.398958	1.000682	0.789201
5	0	1.12	0.682	0.5245	0.4404	0.379075
5	0.2	1.307452	0.753466	0.564298	0.466913	0.398757
5	0.4	1.8332	0.954938	0.676408	0.539874	0.454785
5	0.6	2.734052	1.28757	0.857474	0.656596	0.54072
5	0.8	3.940906	1.739955	1.10621	0.81823	0.661258

2.1.3 Interpolation between a/t

Following are couple of important notes that can be inferred from Figure 2:

- The first influence coefficient (G_o) is more nonlinear than other influence coefficients.
- For lesser a/t, the function is more linear than higher a/t.
- A linear behavior may be assumed between two adjacent a/t.

Figure 3 shows the first influence coefficients for R_i/t = 10 and R_i/t = 5. Two vertical straight lines are drawn between a/t = 0.6 and a/t = 0.8. Four points are identified on these two lines. The values of the points are given in Table 2 along with the values computed using cubic functions and the associated % difference. It is important to note that even at the known values of a/t and R_i/t the cubic functions yield difference even though the % difference are minor.

Table 2 – Values of four points used in the interpolations

Point	a/t	Ri/t	Go	Go using cubic function	% Difference
A	0.6	5	2.734052	2.727950	-0.22%
B	0.6	10	3.223438	3.234004	0.33%
C	0.8	5	3.940906	3.942351	0.04%
D	0.8	10	5.543784	5.541060	-0.05%

Next, we calculate G_o for a/t = 0.7 by using cubic polynomial function and by using linear interpolation method. Linear interpolation method uses the tabular values of G_o for a/t = 0.6 and a/t = 0.8. The points E and F in Figure 3 are the interpolated points for a/t = 0.7 for R_i/t = 5 and R_i/t = 10 respectively. Table 3 shows the values of points E and F by using cubic and linear interpolations. The % difference shown in the table indicate that the linear interpolation yields 1.27% and 2.36% higher G_o in reference to the cubic interpolated values. It is important to remember that the values using cubic functions associate with some difference.

Table 3 –Interpolation for a/t=0.7 between 0.6 and 0.8

Point	a/t	Ri/t	Go using cubic function	Go using linear function	% Difference
E	0.7	5	3.295073	3.337479	1.29%
F	0.7	10	4.240606	4.383611	3.37%

2.1.4 Interpolation between Ri/t

Figure 6 shows influence coefficient points A through F on R_i/t axis. A cubic curve fit is obtained for a/t=0.7. Since cubic polynomial interpolation requires four points to perform the calculation we calculated G_o for a/t=0.7 and R_i/t=20. Using the cubic polynomial function for a/t=0.7, G_o is calculated for R_i/t=7. Finally, linear interpolation is performed between Ri/t = 5 and 10 for Ri/t = 7 on a/t = 0.7. The final interpolated values for point X using cubic and linear interpolation are shown in Table 4. The overall % difference is 1.22% for linear interpolated value in reference to the cubic interpolated value.

Table 4 – Interpolation for Ri/t=7 between 5 and 10 at a/t=0.7

Point	a/t	Ri/t	Go using cubic function	Go using linear function	% Difference
E	0.7	5	3.295073	3.337479	1.29%
F	0.7	10	4.240606	4.383611	3.37%
	0.7	20	5.189129		
X	0.7	7	3.710500	3.755932	1.22%

2.1.5 Findings of the example

- Cubic interpolation introduces complexity in the calculation without improving much accuracy in the results.
- Besides computational complexity following are some comments and observations on cubic polynomial and curve fitting:
    - Cubic polynomial interpolation requires four consecutive points if local curve fitting is intended otherwise global curve fitting may be employed.
    - Global curve fitting introduces more difference in the interpolation.
    - Cubic polynomial function needs to be obtained for each set of Ri/t and a/t that will introduce complexity in the calculation and increase computation time.
- The % difference in reference to the cubic interpolation is reasonable if linear interpolation is performed.
- Similar arguments for linear interpolation on other influence coefficients can be made.

2.2 Finite Surface Crack

Figure 7 shows partial tables for influence coefficients of finite axial inside and outside surface cracks. Unlike the tables for infinite crack, these tables contain one more level of variable that is the ratio of crack depth to the half crack length (a/c). Hence, to obtain the desired influence coefficients, three interpolations are required.

Table C.12

Influence Coefficients For A Longitudinal Semi-Elliptical Surface Crack in A Cylinder - Inside Surface

t/Ri	a/c	a/t	Gi	A0	A1	A2	A3	A4	A5	A6
0	0.03125	0	G0	0.1965046	2.9373464	-5.2582823	7.4889153	-6.9282667	3.3673349	-0.6677966
		0	G1	0.005178	0.175028	2.771868	-4.6457154	4.6780502	-3.276809	0.9840994
		0.2	G0	0.208076	3.0112422	-5.1048701	7.6348715	-6.8347547	2.7940766	-0.3882688
		0.2	G1	0.0084834	0.2406767	2.4574292	-3.6452421	3.6142837	-2.8451814	0.9270638
0	0.0625	0	G0	0.2695332	2.1626001	-1.6551569	-1.2970208	4.5604304	-4.3163876	1.4010655
		0	G1	0.0138667	0.1827458	2.5749608	-3.9044679	3.3556301	-2.1772209	0.6420134
		0.2	G0	0.2845892	2.2264055	-1.454619	-1.5760719	5.1131083	-4.9485443	1.6207574
		0.2	G1	0.0199077	0.2210874	2.4642047	-3.5898625	3.1624039	-2.240378	0.6965751

Table C.13

Influence Coefficients For A Longitudinal Semi-Elliptical Surface Crack in A Cylinder - Outside Surface

t/Ri	a/c	a/t	Gi	A0	A1	A2	A3	A4	A5	A6
0	0.03125	0	G0	0.1965046	2.9373464	-5.2582823	7.4889153	-6.9282667	3.3673349	-0.6677966
0	0.03125	0	G1	0.005178	0.175028	2.771868	-4.6457154	4.6780502	-3.276809	0.9840994
0	0.03125	0.2	G0	0.208076	3.0112422	-5.1048701	7.6348715	-6.8347547	2.7940766	-0.3882688
0	0.03125	0.2	G1	0.0084834	0.2406767	2.4574292	-3.6452421	3.6142837	-2.8451814	0.9270638
0	0.0625	0	G0	0.2695332	2.1626001	-1.6551569	-1.2970208	4.5604304	-4.3163876	1.4010655
0	0.0625	0	G1	0.0138667	0.1827458	2.5749608	-3.9044679	3.3556301	-2.1772209	0.6420134
0	0.0625	0.2	G0	0.2845892	2.2264055	-1.454619	-1.5760719	5.1131083	-4.9485443	1.6207574
0	0.0625	0.2	G1	0.0199077	0.2210874	2.4642047	-3.5898625	3.1624039	-2.240378	0.6965751

Figure 7 – Partial Table C.12 and Table C.13 from API 579

Interpolation is performed using the following methodology:

- For a given pipe and crack geometry, t/R_i, a/c and a/t are calculated.
- The a/t a/c and t/R_i are then used to identify the neighboring a/t, a/c and t/R_i in the table. There are two sets of influence coefficients with the neighboring a/t for each t/R_i and a/c.
- First interpolation is performed for each t/R_i and a/c between the corresponding set of a/t for the desired a/t.
- The second interpolation is performed between those interpolated influence coefficients for the desired a/c for each t/R_i.
- Finally the third and final interpolation is performed for the desired t/R_i.

2.3 Effect of interpolation on limiting pressure prediction

In the earlier section, we discussed and showed in the example the differences in the influence coefficients when using the cubic polynomial interpolation instead of the linear interpolation. With the finite crack we will calculate Level 2 limiting pressure using both interpolation methods. Level 2 limiting pressure for a known crack is defined as the pressure at which the toughness ratio (K_r) equals to the toughness ratio calculated from the Level 2 FAD equation for the calculated load ratio (L_r). This is the maximum operation pressure beyond which the crack will be unacceptable for fitness for service according to Level 2 FAD. FAD is a relation between K_r and L_r, which is described as follows:

$$K_r = [1 - 0.14(L_r)^2]\{0.3 - 0.7e^{[-0.65(L_r)^6]}\} \quad for\ L_r \leq L_{r\,max}$$

Where, $L_{r\,max} = 1.25$ for Carbon Steels, $K_r = K_I/K_{mat}$ and $L_r = \sigma_{ref}/\sigma_{YS}$, K_I is the mode I stress intensity factor, K_{mat} is the materials fracture toughness, σ_{ref} is the reference stress, based on yield load and limit load solutions for the configuration of interest, and σ_{YS} is the yield strength of the material. Figure 8 shows the FAD using the above equation. If the assessment point lies inside the FAD, the structure is considered safe and the crack is acceptable for fit. The unacceptable crack is predicted when the assessment point falls outside the FAD.

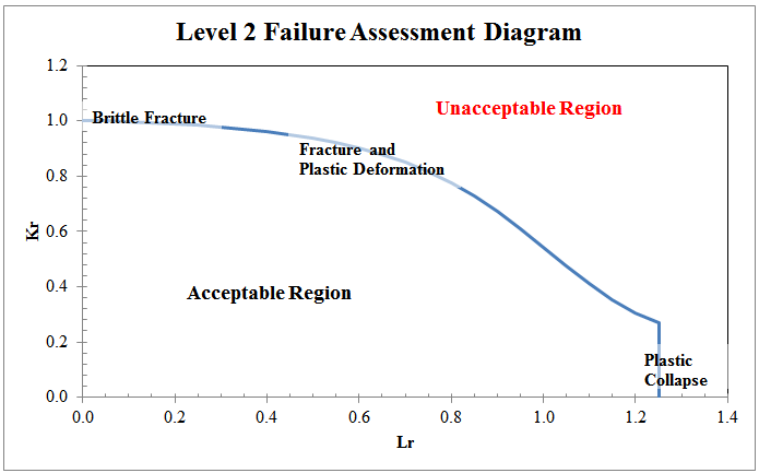

Figure 8 – FAD for Level 2 Assessment

Both K_I and σ_{ref} calculated for a given crack are function of operating pressure. The limiting pressure is that operating pressure at which the calculated K_r for the given crack equals to the K_r calculated from the above FAD equation. Therefore, a difference in K_I due to the use of linear instead of cubic interpolation method for estimating influence coefficients is carried in K_r calculation and there on to the limiting pressure prediction.

In this example, we choose a 914.4 mm (36 in.) X65 pipe with the wall thickness of 6.35 mm (0.25 in.) and 12.7 mm (0.50 in.). The internal pressure for this example is assumed as 4,356 kPa (70% SMYS). The cracks used in this example are defined as a/t varying from 0.1 to 0.8 and as a/c from 2 to 0.03125. Three material toughness values (20, 100 and 200 MPa√mm), K_{mat} are used in this example.

Figure 9 shows the percent difference in Level 2 limiting pressure versus the percent difference in K_r. The variation in K_r due to the use of interpolation method introduces a variation in limiting pressure for various crack dimensions. We can infer the following from the figure –

- The difference in limiting pressure is inversely varying with the difference in K_r.
- Difference in predicted limiting pressure diminishes with higher material toughness value. For a higher material toughness, the difference in limiting pressure is considerably lower than a lower material toughness value. It is also observed that with a higher toughness (i.e. K_{mat} = 200 MPa√mm) and shallower crack (i.e. a/t <0.4) the difference in limiting pressure is zero or negligible.

- The maximum difference in limiting pressure observed is less than 6%. However, it can be critical for a particular application. Therefore for a deep surface crack with low material toughness it is important to be cautious in predicting Level 2 limiting pressure.

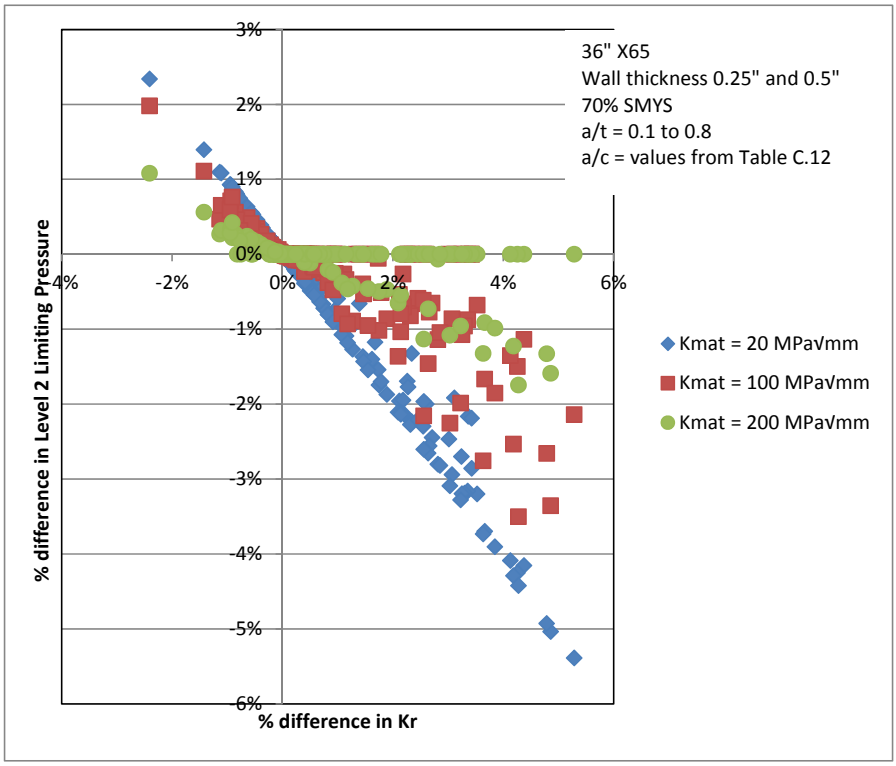

Figure 9 – Percent difference in the Level 2 limiting pressures

3 Conclusions

Even though the values of the influence coefficients given in the tables in API 579 fit with some cubic polynomial functions for a/t and also for R_i/t, the nonlinearity is found more in the first influence coefficient (G_o). For a/t equal or less than 0.4, the influence coefficients can be assumed linear. It is also concluded that shallower cracks (a/t <0.4) with a relatively high material toughness, the linear interpolation does not produce significant difference in predicting limiting pressure with respect to nonlinear interpolation. While for the deep surface cracks with low material toughness may be critical for a particular application and should require caution in predicting Level 2 limiting pressure. However the overall difference in K_I as well as in Level 2 limiting pressure by using the linear interpolation rather than the cubic polynomial interpolation is less than 6% which is reasonably within the acceptable error margin.

4 Reference

[1] Ted L. Anderson, et. al, Development of Stress Intensity Factor Solutions for Surface and Embedded Cracks in API 579, Bulletin 471, Welding Research Council, Inc. New York, NY, May 2002

[2] API 579-1/ASME FFS-1 2007 Fitness-For-Service, Equation C.175 and C.176.

Improved Exploitation of High-strength Steels in Pressure Vessel Design by Simulations Based on Damage Mechanics

Victoria Brinnel[1,*], Christian Schruff[1], Sebastian Münstermann[1]

[1] Department of Ferrous Metallurgy, RWTH Aachen University, Aachen D-52072, Germany
* Corresponding author: Victoria.Brinnel@iehk.rwth-aachen.de

Abstract Pressure vessels are subjected to regulation by European standards, which define design procedures and nominal material properties that are guaranteed by the steel producers. Over-conservative safety factors for materials with high yield-to-tensile ratios hinder the application of modern high-strength steels despite their excellent toughness and possible economic and ecologic benefits. Damage mechanics enable a more adequate failure description for these steels since they can consider ductile crack initiation as limit state. Such concepts should refer to nominal material characteristics to enhance their applicability in design procedures. A method is presented to correlate the nominal Charpy impact toughness to simulations with the Gurson-Tvergaard-Needleman-model (GTN). The resulting GTN parameters are used in cell model simulations to derive strain-based empirical failure criteria as nominal ductility measure for simulations on component level. A sensitivity study on the GTN parameter choice shows that the initial pore volume is the most relevant parameter, but other non-unique parameters also influence the failure prediction. The impact of the individual parameters is discussed. By the definition of a reliable calibration scheme for the GTN parameters this approach enables an identification of adequate lower bound failure criteria for high-strength steels in pressure vessels as a preliminary pressure vessel simulation demonstrates.

Keywords Strain-based Design, Pressure vessel, Damage mechanics, Damage curve

1. Introduction

In Europe, pressure vessels are subjected to regulation by the European Standard EN 13445, which contains the corresponding design rules. Additionally, the material requirements for pressure vessel steels are part of EN 10028. Therein, nominal material properties are defined, which specify minimum values for the mechanical properties. These have to be guaranteed by the steel producers and are often exceeded, especially by high quality steels. The nominal characteristics form the basis of the design process for pressure vessels. The required wall thickness is determined in dependence of the materials' nominal yield or tensile strength. The relevant design stress is specified in EN 13445 as the minimum of the yield strength divided by a safety factor of 1.5 or the tensile strength divided by 2.4. Therefore, the yield-to-tensile (Y/T) ratio determines the magnitude of the applied safety factor. From a Y/T-ratio of 0.625 on, the tensile strength with an increased safety factor of 2.4 is relevant for the design. Modern high strength steels are often characterised by such an increased Y/T-ratio, e.g. steel grade P500Q with Y/T = 0.85 and P690Q with Y/T = 0.9. By the application of the increased safety factor, only a poor exploitation of their load bearing capacity can be achieved. In this safety factor domain, the design stress is only 41% of the yield strength. Consequently, these rather expensive steel grades are rarely applied in pressure vessel design. However, their application would foster substantial economic and ecological benefits by e.g. thinner walls, which result in lower welding, energy and transportation cost.

The current safety factors are mainly based on experience and do not consider the actual failure behaviour [1]. Since EN 13445 requires brittle fracture to be excluded by the toughness requirements, an improved prediction of ductile crack initiation is needed. Hence, to improve the exploitation of high strength steels in pressure vessel design it is necessary to include a description of their ductility. The methods of damage mechanics are able to provide such predictions [2]. Although research on this field has been conducted for several decades, the methods of damage mechanics are not used regularly in industrial applications, let alone considered standard design procedures. One reason is that the application of damage mechanics models requires considerable

expertise and experience since most of these models are strongly dependent on the non-unique parameter selection and the mesh size [2, 3]. A requirement for a safe and reliable use of damage mechanics models in pressure vessel design are therefore standardised application guidelines. Moreover, newly developed design criteria should be transferable to the standards and therefore need to refer to the nominal material properties. Currently, only yield and tensile strength are considered. The nominal property related to ductility is the minimum Charpy impact toughness. For example, EN10028-6 requires a nominal Charpy impact toughness of 60 J at room temperature for P500Q. Münstermann and Schruff have developed a method to determine ductile failure criteria for high strength pressure vessel steels out of these nominal characteristics [4, 5], which is further explained and discussed in the following.

2. A method for strain-based pressure vessel design with respect to nominal material properties

The ductile failure mechanism of metallic materials consists of the nucleation and coalescence of voids, which form under plastic deformation at inclusions [2]. This process is described by the damage model of Gurson, Tvergaard and Needleman (GTN). It was established by Gurson in 1977 [6] and is based on a continuum mechanics description of a hollow sphere in surrounding homogeneous material. Tvergaard and Needleman optimised the shape of the yield surface by the introduction of empirical fitting parameters [7]. The GTN model consists of a modified von Mises flow potential (Eq.1), and functions for the description of void nucleation (Eq.2) and coalescence (Eq.3).

(1)

(2)

(3)

The flow potential is a function of the equivalent stress σ_v, the hydrostatic stress σ_1, the empirical fit parameters q_i and the effective void volume fraction f^*. The latter is defined out of the nucleation function until the critical void volume fraction f_c is reached. Then the void growth is accelerated by the factor κ to account for the effects of void interaction. The nucleation function considers the plastic equivalent strain ε^{pl}, the volume fraction of possible nucleation sites for secondary voids f_N, the characteristic strain for nucleation of secondary voids ε_N as well as the standard deviation S_N.
The micromechanical motivation is one of the main advantages of this model. Some of its parameters, such as the initial void volume fraction, can be determined in metallographic analyses [2, 8]. This simplifies the parameter selection. Therefore, the GTN model is suitable to predict the crack initiation of high strength pressure vessel steels and is employed in the discussed approach.

However, the computational implementation of GTN requires too many resources for large scale component simulation as pressure vessel modelling. Therefore, a simpler model has to be applied in the component simulation. Such a model is the damage curve established by Johnson and Cook [9]. Depending on the evaluation procedure it describes the characteristic strain at failure or crack initiation as a function of stress triaxiality η, which is the ratio of hydrostatic to equivalent stress, and three constants c_i (Eq.4).

(4)

The damage curve can either be calibrated by experiments or by unit cell simulations based on the GTN model [10]. The unit cell (Fig. 1a) consists of one axisymmetric element, which is subjected to loads in two directions. By changing the ratio of the applied loads, it is possible to create different triaxiality states. Since the developed design approach shall be transferable to the standards it should refer to the nominal properties. An experimental calibration of the damage curve is only possible for a specific material of a single producer. Consequently, it allows no general application in standard design procedures. A derivation via unit cell simulations is a more general approach and is therefore applied.
The main idea of this approach is to re-calibrate an experimentally derived GTN parameter set for a specific steel grade in simulated Charpy tests [5]. The aim is to meet the nominal Charpy energy required in the standard for this steel grade. Such a set consequently characterizes the minimum ductile crack resistance. With this calibrated parameter set it is possible to determine a lower bound damage curve (Fig. 1b) for the simulation of ductile failure in pressure vessels with regard to nominal material properties [4, 5].

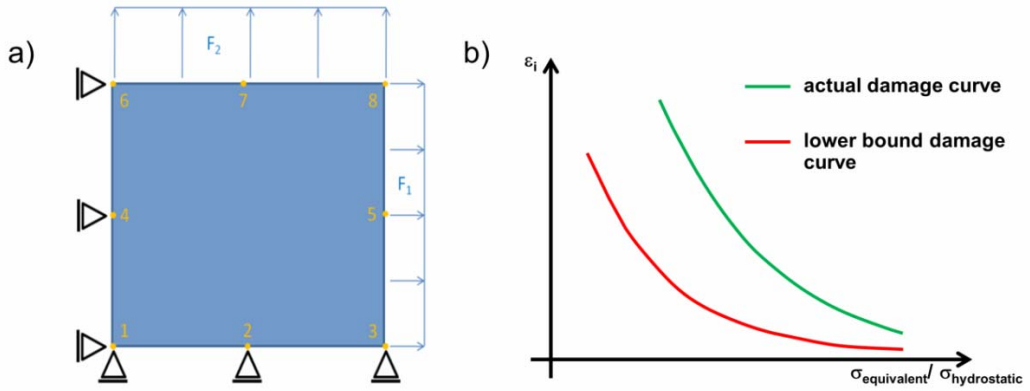

Figure 1. Schematic illustration of a) the axisymmetric unit cell and b) the damage curves.

The corresponding procedure based on [4, 5] consists of the following steps:

(1) Calibration of a suitable GTN parameter set and the corresponding mesh size for the selected material by metallography and an iterative optimisation process involving experimental and numerical results of notched round bar and fracture mechanics tests. Derivation of empirical functions for the materials strain rate and temperature dependence in an iterative process considering tensile tests at different temperatures and strain rates.
(2) Simulation of a Charpy impact toughness test with the determined values to validate the selection and the model and determine the corresponding friction value. Agreement between experimental and numerical results in overall energy and the course of the force-displacement curve shall be achieved.
(3) Derivation of the selected materials' damage curve via unit cell simulations with varying stress triaxiality according to [5, 10].
(4) Calibration of a lower bound GTN parameter set in the simulation of a Charpy impact test with the aim to meet the nominal Charpy impact toughness specified in the standard for the selected material.

(5) Derivation of the lower bound damage curve via unit cell simulations with varying stress triaxiality according to [5, 10].
(6) Application of the lower bound damage curve in burst simulations for pressure vessels.

The burst simulation based on the lower bound damage curve allows a prediction of the failure onset in pressure vessels under consideration of the nominal Charpy impact toughness. These simulations can be part of an approach to derive more adequate safety factors for high strength pressure vessel steels. However, this approach can also be easily transferred to other applications fields subjected to regulation, e.g. civil engineering.

3. Influence of the non-unique GTN parameter selection on the course of the damage curve.

The developed concept contains the required steps for the identification of suitable GTN parameter sets. However, this selection is well-known to be non-unique [3, 8, 11]. It is therefore necessary to investigate the influence of the GTN parameter selection on the derived damage curve, since it represents the failure prediction element in the developed concept. Therefore, a sensitivity analysis is conducted with a GTN parameter set determined for the steel P500Q.
The reference set is derived by metallography and the comparison of numerical and experimental results of notched round bars in a tensile test. The relevant mesh size is determined in comparison to results of Compact-Tension-tests. The parameter set is validated in the simulation of a Charpy test. Details of the calibration procedure can be found in [5]. Unit cell calculations are performed with this reference set at stress triaxialities of 0.5, 1.0, 1.5, 2.0 and 2.5. The strain corresponding to the maximum stress in the unit cell is selected as critical strain for the derivation of the damage curve. At low stress triaxialities the GTN model may fail to predict softening, consequently no point for the damage curve can be derived.
During the sensitivity analysis one parameter is varied in the unit cell simulations while the others are kept constant. The calculations are performed at the above mentioned five stress triaxialities. Table 1 shows the reference parameter set determined for steel grade P500Q and the selected values for variation, which were chosen in accordance with literature [3, 11]. For q_3 the common relation $q_3 = q_1^2$ was applied in accordance with [7]. The aim of the sensitivity analysis is a qualitative description of individual parameters' influence on the damage curve. This description can form the basis for a rule set for the parameter derivation in the investigated approach.

Table 1. Reference set and variations for GTN parameters of steel P500Q

Parameter	f_0	f_N	S_N	ε_N	f_c	κ	q_1	q_2
Reference value	0.00185	0.00215	0.4	0.12	0.015	1.1	1.5	1.0
Maximum value	0.01	0.015	0.6	0.3	0.05	6	2.5	1.5
Minimum value	0.0005	0.0005	0.1	0.05	0.005	1	1	0.5
Mean value	-	-	-	-	-	3	-	0.8

3.1. Results of the sensitivity analysis

3.1.1. Influence of f_0

The variation of the initial pore volume f_0 has a strong influence on the course of the damage curve, as can be seen in Fig. 2a. This effect increases with decreasing stress triaxiality. At a triaxiality of η=1, there is a maximum difference in critical strain of 34%. One reason for the strong impact of f_0 is that the initial pore volume influences the computation right from the beginning. This is also

shown in Fig. 2e, which displays the equivalent stress in the unit cell and the effective void volume as a function of the equivalent strain for two triaxialities of η=1 and η=2.5. f_0 can very well be correlated to the volume content of non-metallic inclusions [5] and therefore be determined in metallographic analyses.

3.1.2. Influence of the void nucleation parameters f_N, ε_N and S_N

The void nucleation function (Eq.3) is based on a Gaussian distribution function. It is influenced by the volume fraction of possible nucleation sites for secondary voids f_N, the characteristic strain for nucleation of secondary voids ε_N and the corresponding standard deviation S_N. Consequently, these parameters interact. The secondary void volume f_N has a clear influence on the course of the damage curve at low triaxialities (Fig. 2b), the maximum difference at η=1 is 12%. However, this impact is lower than the one of f_0 although the input variation was comparable. Figure 2c and Figure 2d show that ε_N and S_N only have a minor influence on the predicted failure strains. This is due to the value of f_N, which limits the influence of ε_N and S_N. For many materials, the magnitude of f_N can also be determined in metallographic analyses. For the reference set it was determined as the volume fraction of carbides in P500Q. The minor influence of ε_N and S_N holds therefore true for realistic values of f_N, but it increases for higher values of f_N.

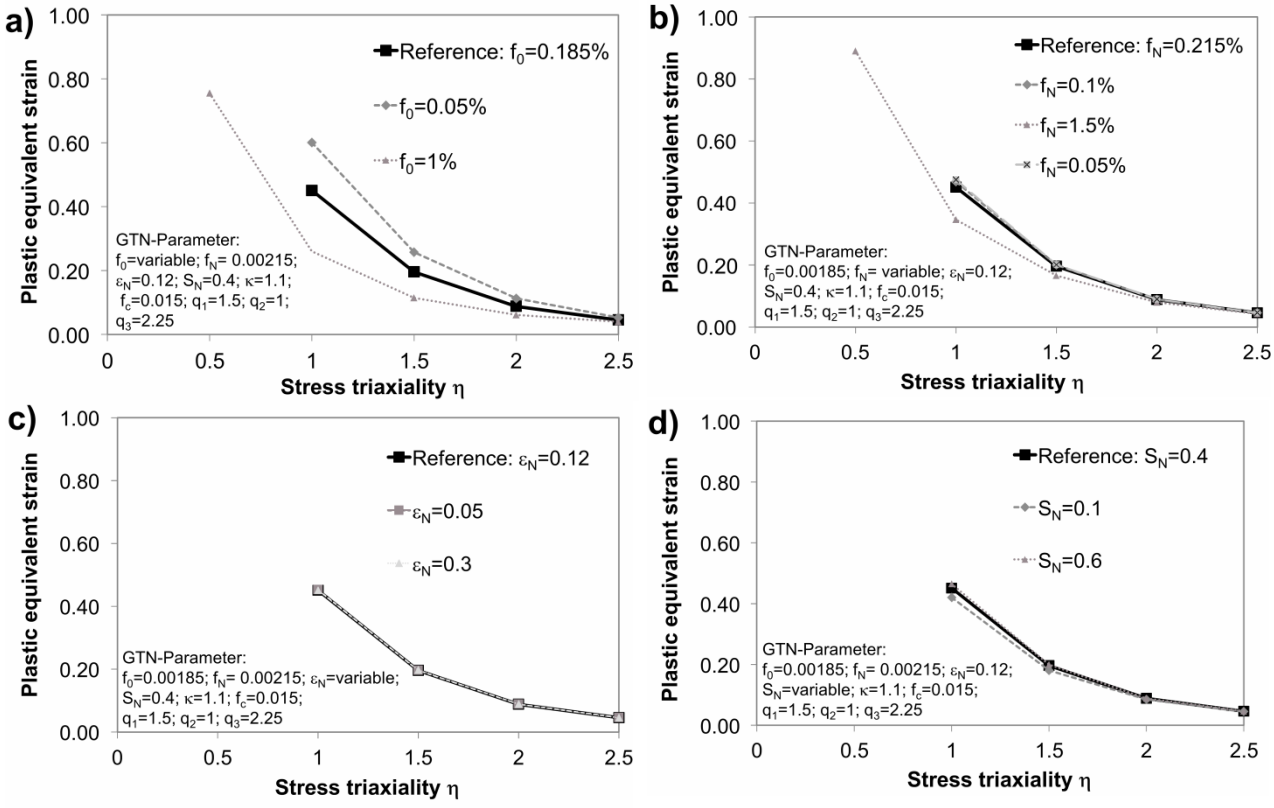

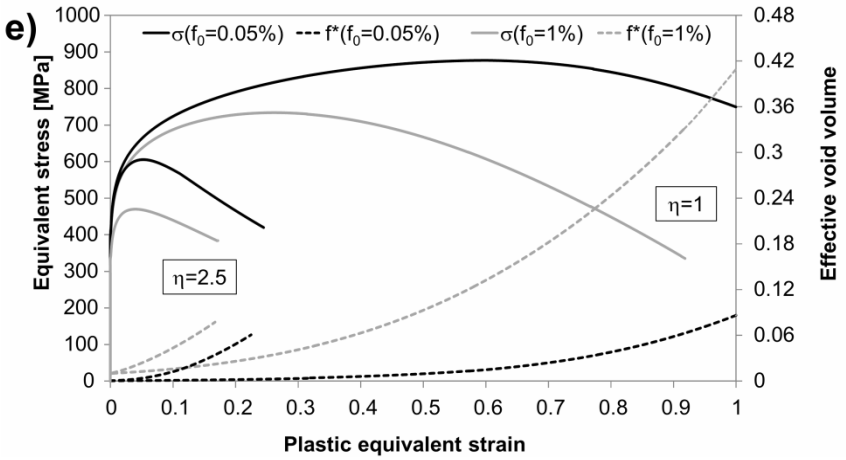

Figure 2. Damage curves under variation of a) f_0 b) f_N c) ε_N & d) S_N. Subfigure e) Equivalent stress and effective void volume as a function of the plastic equivalent strain under variation of f_0 for η=1 and η=2.5.

3.1.3. Influence of the void coalescence parameters f_c and κ

The void coalescence behaviour is implemented in the GTN model by an acceleration of void growth and nucleation. The critical void volume f_c determines the onset of acceleration, while the acceleration factor κ defines its magnitude. Therefore, f_c and κ have a crucial influence on the failure detection. Figure 3a displays the influence of κ on the damage curve. It is low with a maximum difference in critical strain of 6% at η=1. Figure 3c proves that there are significant differences in the corresponding stress-strain-curves. Since the strain at maximum stress is relevant for the derivation of the damage curve in this evaluation concept, κ only marginally impacts the damage curve. The value of f_c determines the onset of acceleration. With the currently calibrated low value of κ = 1.1 the influence of f_c on the damage curve is very small. It is therefore evaluated for an increased value of κ = 3. Figure 3b shows a significant influence of f_c on the damage curve for κ = 3, which is also reflected in the corresponding stress-strain-curves in Fig. 3c.

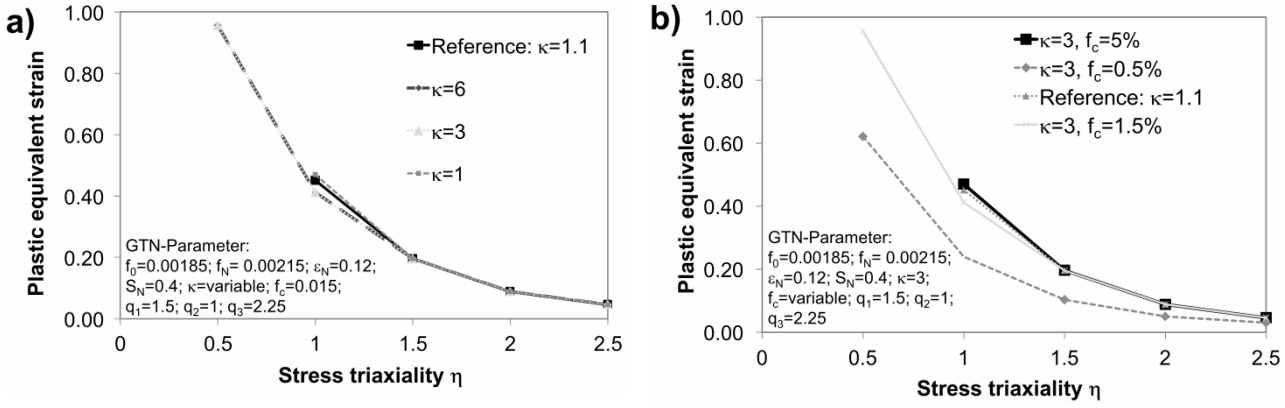

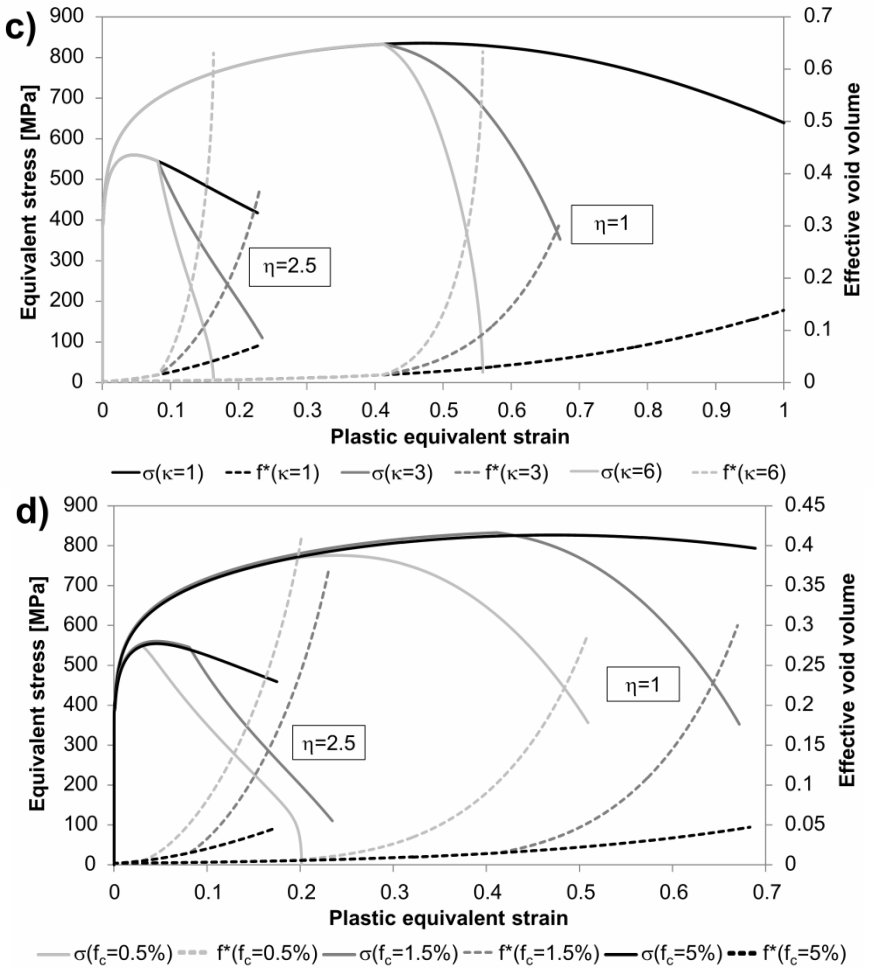

Figure 3. Damage curves under variation of a) κ b) f_c. Equivalent stress and effective void volume as a function of the plastic equivalent strain under variation of c) κ and d) f_c for η=1 and η=2.5.

3.1.4. Influence of the empirical fit parameters q_1 and q_2

The empirical fit parameters q_1 and q_2 have massive influence on the course of the damage curve, as can be seen in Fig. 4. The reason is that they directly change the shape of the yield surface. Contrary to most other parameters, the influence of q_2 is not decreasing with increasing triaxiality.

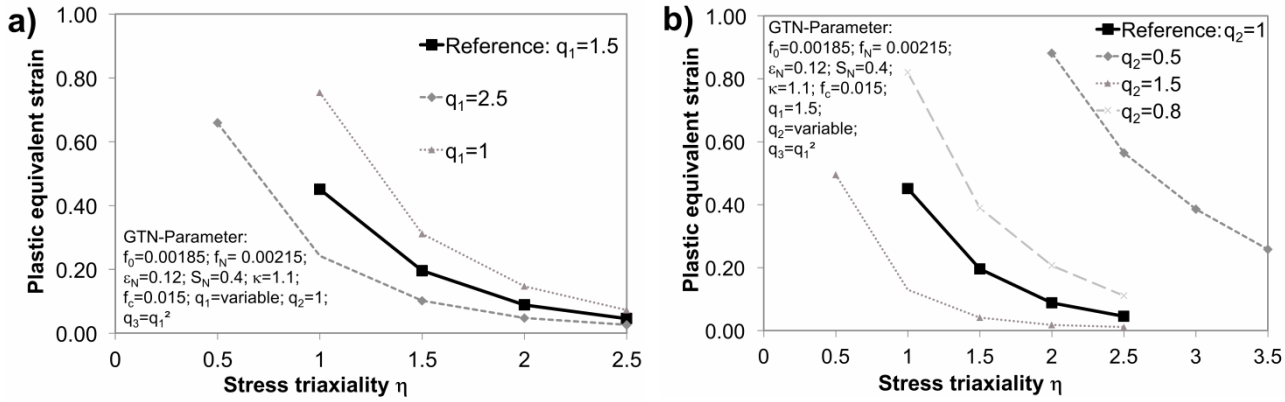

Figure 4. Damage curves under variation of a) q_1 and b) q_2.

3.1.5. Investigations on the uniqueness of the damage curve

The qualitative sensitivity analysis shows that the GTN parameter selection has a clear influence on

the course of the damage curve. The impact of the individual parameters varies and their interaction is non-linear. Therefore, it is possible to determine several different parameter sets that yield the same result, the solution is not unique. Since the lower bound damage curve is calibrated at Charpy simulations in this methodology, two parameter sets are determined that compute a similar impact toughness and force-displacement-curve. In version A, f_N and S_N were increased to f_N=0.01 and S_N=2. In version B f_0 is decreased to f_0=0.001, while f_N is increased to f_N=0.015. Figure 5 shows the damage curves for these parameter sets. A good agreement can be found at higher triaxialities but the maximum difference of critical strain is 8% at η=1. The damage curve of version A is identical to the reference damage curve. The increased f_N should affect the damage curve, but due to the high S_N the nucleation of secondary voids is distributed over a broad strain interval so that the actual influence of f_N is diminished. Consequently, an identical damage curve is produced. Considering the micromechanical motivation of the GTN model this parameter selection is not sensible. Although the version B parameter set has a similar force-displacement curve, the influence of the important void parameters f_0 and f_N affects the course of the damage curve at low triaxialities.

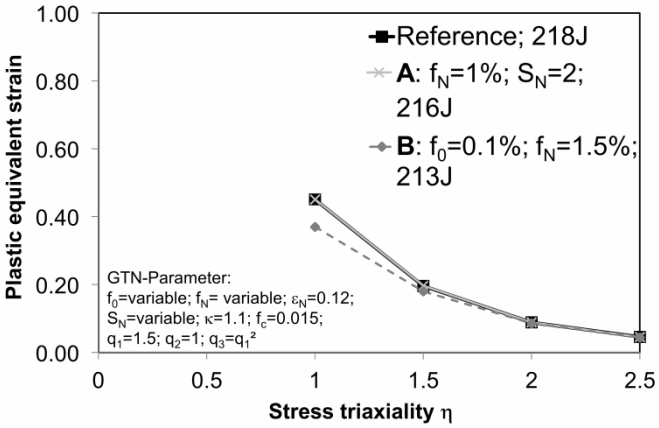

Figure 5. Damage curves for two parameter sets yielding a similar Charpy impact energy in simulation.

3.2. Discussion of the sensitivity analysis

The non-uniqueness of the GTN parameter selection may lead to identical damage curves resulting from different parameter sets if the interaction of individual parameters compensates their respective impacts. However, this is not always the case. Therefore, it is necessary to establish clear guidelines for the parameter derivation to ensure reproducible results. The guiding principle should be the micromechanical motivation of GTN. The basis for such a rule set is the performed sensitivity analysis. The impact and the consequences for the parameter derivation are discussed in the following for each variable.

Currently, the strain at maximum stress in the unit cell is considered as the crack initiation strain for the derivation of the damage curve. This enables a simple identification of the critical strain. This basic assumption needs to be considered during the GTN parameter calibration on tensile and fracture mechanics test. Consequently, the GTN parameter choice must ensure that in simulation of these samples the stress maximum of the failing element is correlated to the physical crack initiation measured in the experiment. An advantage of this criterion is that the mesh sensitivity of the results is reduced, since the mesh-dependence of the results begins with the onset of softening at the stress maximum [12].

The initial void volume fraction f_0 has a strong influence on the course of the damage curve. It can clearly be related to the microstructure of a material, since voids in many materials form at non-metallic inclusions at the onset of plastic deformation. f_0 has no direct interaction with other parameters but influences the whole computation from the beginning. Therefore, f_0 should be

considered as the main parameter for the derivation of the lower bound damage curve. The micromechanically based motivation behind this procedure is that steel grades of low ductility often exhibit an increased amount of inclusion resulting in a poor internal cleanness. If f_0 is used as the main or even single parameter for the derivation of the lower bound criteria, its strong influence on the damage curve also facilitates the derivation of unique damage curves, since its effects cannot be compensated easily.

The volume fraction of potential secondary voids, f_N, also has a significant influence on the course of the damage curve. However, it is lower than the impact of f_0. For some materials, the nucleation sites for secondary voids can also be correlated to metallographic results, such as the carbide volume fraction. Even if this is not possible, the order of magnitude of f_N should be chosen in a micromechanically sensible range. In the nucleation function, f_N interacts with ε_N and S_N, which only have a low impact on the damage curve for common values of f_N. Their impact is increased proportionally with f_N. Therefore, if the nucleation parameters are modified, matching magnitudes should be selected to avoid non-uniqueness due to interactions. Alternatively, the modification could be restricted to f_N.

The coalescence parameters f_c and κ have a strong influence on the stress-strain-curve of the unit cell, since they determine onset and magnitude of the accelerated void growth. Consequently, there is also a relevant interaction of these parameters. If the critical strain f_c is reached after the maximum stress, the choice of κ and f_c has only little influence on the damage curve. This is more likely for high triaxialities. Since the maximum is correlated to crack initiation, κ should have a minimum value clearly larger than unity to enable a rapid failure of the element. This also reduces the influence of κ on the maximum stress point and consequently the damage curve. A further aspect is that the area beneath the stress-strain-curve is a measure for the dissipated energy. This is important for the parameter calibration of f_c and κ in tensile and fracture mechanics test. Different studies show the dependence of f_c on the stress triaxiality [3]. If possible, it is therefore advantageous to calibrate f_c such that the critical value is reached after the stress maximum of the critical element. If f_0 is modified for the derivation of the lower bound damage curve, it may therefore also be necessary to adapt f_c and κ.

The empirical fitting parameters q_i have massive influence on the course of the damage curve. Different studies show that a calibration of these parameters can improve the agreement between simulation and experiment [3]. However, considering the acceptance of the method and the reliability of the result it is better to keep the standard literature values, especially since they are able to represent the failure behaviour.

The definition of a fixed calibration scheme with respect to the considered experimental results is currently under research. Such a scheme can help to foster the acceptance of damage mechanics and may also be transferred to other applications than pressure vessels.

4. Application example of the lower bound damage curve in a pressure vessel simulation

The concept of the lower bound damage curve was applied to a pressure vessel simulation. It is loaded with increasing internal pressure. The lower bound damage curve is applied as the failure criterion. The resulting critical pressure is compared to the one defined by the design formulae of the current standard EN 13445 in the procedure “Design by Formulae” (DBF). Figure 6a shows the model, which could be reduced to a quarter of the vessel due to symmetry. The vessel has a mean diameter of 2600 mm and a wall thickness of 50 mm. The lug has a diameter of 631 mm and a wall thickness of 72.5 mm. P500Q is assumed as the material for the pressure vessel. The lower bound damage curve is derived according to the above explained concept. The parameters according to Eq. 4 are c_1= 0.94, c_2 = 1.76 and c_3=0.01. However, due to missing data, temperature and strain rate

dependence are not yet considered. The results are therefore preliminary. Figure 6b shows the ductile damage criterion at the critical loading step, which highlights if the critical strain has been reached. The crack initiation takes place in the wall besides the lug. In this case, crack initiation happens in parallel with a plastic collapse.

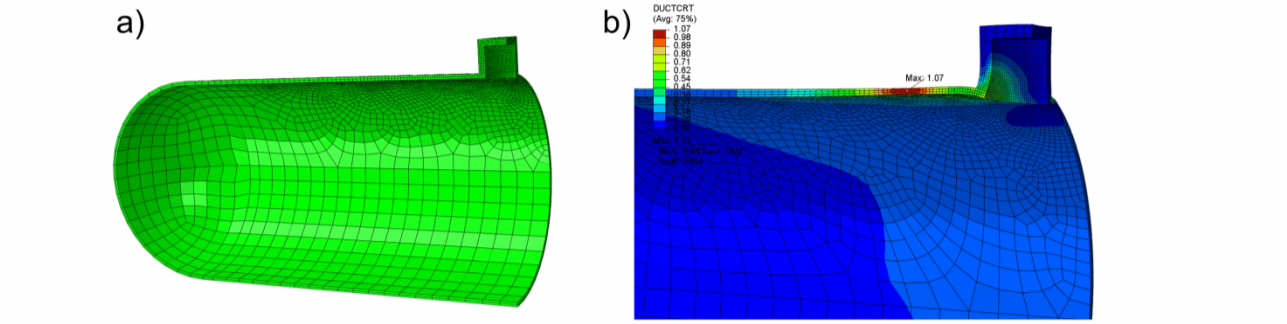

Figure 6. a) Quarter model of the pressure vessel b) Ductile crack initiation besides the lug

The internal pressure at failure is predicted to be 29.61 MPa. A design according to EN 13445 predicts a failure at a maximum pressure of 23.1 MPa. The damage curve concept can consequently be used to quantify unnecessary safety margins for high strength steels in pressure vessels.

5. Conclusions and Outlook

The nominal damage curve concept is a suitable approach to quantify unnecessary safety margins for high strength steels in pressure vessel design, which are included in the current European standard EN 13445. Its main advantage is that a failure prediction is possible under consideration of the nominal Charpy impact toughness by the application of the lower bound damage curve. Therefore, the materials ductility is considered in the design process. The application of this concept can help to derive more adequate safety factors for high strength steels. However, further research is necessary to ensure the safe application of this method. A sensitivity analysis shows that the course of the damage curve is influenced by the non-unique GTN parameter choice. Therefore, a calibration scheme with regard to the evaluated experimental results and considered nominal properties needs to be defined and is currently under research. Additionally, a modification of the applied GTN model towards a consideration of the third invariant of the stress tensor should be considered, since latest research shows that it has significant influence on the prediction of ductile fracture [2].

Acknowledgements

This research is granted by FOSTA (“Forschungsvereinigung Stahlanwendungen e.V.”) in projects P758 and P950.

References

[1] E. V. Chechin, A way to put an end to an unjustified overconsumption of plastic steels and alloys in industry, in: Proceedings of the 11th International Conference on Fracture, Torino, 2005

[2] A. A. Benzerga, J. Leblond, Ductile fracture by void growth to coalescence, in: H. Aref, E. van der Giessen (Eds.), Advances in Applied Mechanics (Volume 44), Elsevier, Amsterdam, 2010, pp.169-305.

[3] J. Kim, X. Gao, T. S. Srivatsan, Modeling of void growth in ductile solids: effects of stress triaxiality and initial porosity. Engineering Fracture Mechanics, 71 (2004) 379 – 400.
[4] C. Schruff, S. Münstermann, W. Bleck, D. Schäfer, M. Feldmann, P. Langenberg, Strain-based design approaches for unfired pressure vessels - an extension of the DBA methodology based on ductile failure locus criteria, in: Proceedings of the European Symposium on Pressure Equipment, Paris, 2010.
[5] S. Münstermann, C. Schruff, J. Lian, B. Döbereiner, V. Brinnel, B. Wu, Predicting lower bound damage curves for HSLA steels. Accepted for publication in Fatigue & Fracture of Engineering Materials & Structures, (2013).
[6] A. Gurson, Continuum theory of ductile rupture by void nucleation and growth: Part I - yield criteria and flow rules for porous ductile media. Journal of Engineering Materials and Technology, 99 (1997) 2 – 15.
[7] V. Tvergaard, A. Needleman, Analysis of the cup-cone fracture in a round tensile bar. Acta Metallurgica, 32 (1984) 157 – 169.
[8] N. Bonora, Identification and measurement of ductile damage parameters. The Journal of Strain Analysis for Engineering Design, 34 (1999) 463–478.
[9] G.R. Johnson, W.H. Cook, A constitutive model and data for metals subjected to large strains, high strain rates and high temperatures, in: Proceedings of the 7th International Symposium on Ballistics, The Hague, 1983, pp. 541 – 547.
[10] U. Weber, A. Mohanta, S. Schmauder, Numerical determination of parameterised failure curves for ductile structural materials. International Journal of Materials Research, 98 (2007) 1071–1080.
[11] Z. L. Zhang, A sensitivity analysis of material parameters for the Gurson constitutive model. Fatigue & Fracture of Engineering Materials & Structures, 19 (1996) 561–570.
[12] F. Reusch, Entwicklung und Anwendung eines nicht-lokalen Materialmodells zur Simulation duktiler Schädigung in metallischen Werkstoffen, Universität Dortmund, Dortmund, 2003.

Constitutive modeling and Computational Simulations of the external pressure induced buckling collapse of High Density Polyethylene (HDPE) liners

Patricia M. Frontini[1,*], **Federico Rueda**[1], **Juan P. Torres**[2]

[1] Instituto de Tecnología y Ciencia de Materiales, Universidad Nacional de Mar del Plata, B7608FDQ, Argentina
* Corresponding author: pmfronti@fi.mdp.edu.ar

Abstract The objective of this work is to evaluate the capability of an advanced constitutive model, namely the Three Network Model (TNM) of simulating the mechanical response of HDPE liners undergoing buckling collapse. In order to determine the input parameters for the model, a series of tensile and compressive uniaxial tests were conducted. Simulations were performed using Finite element modeling (FEM) analysis with the ABAQUS 6.10 package. The complex strain rate, temperature and pressure dependent mechanical response of HDPE was analyzed by modeling the dynamic event as an increasing volume of fluid entering the gap cavity between liner and host pipe, and a mathematical relationship between fluid flow rate and collapse pressure was proposed.

Keywords buckling collapse, constitutive modeling, HDPE liners, Finite Element modeling

1. Introduction

The use of polymers in the gas and oil transportation industry is nowadays widely spread. One of their main uses is as lining materials for oil and gas pipelines. These liners serve the function of providing internal protection of metallic tubes mainly in two different situations, namely: by providing enhanced corrosion resistance from aggressive chemical agents, and, in a rehabilitation technique for damage pipes known as relining, during which these structures are slip lined with a polyethylene liner that replaces the inoperative section of the tube [1]. However, there is a number of ways in which polymeric liners can fail in service after a certain time. The present study specifically concerns with the buckling collapse of liners induced by external pressure. This failure mode takes place by the combined action of two separate factors, these are: *i)* the permeation of oil derived gases through the liner wall for extended periods of time, and *ii)* the rapid decompression of pipelines that can occur during service stoppages or maintenance and inspection shutdowns [2].

Recently, a number of studies have been devoted to understand the underlying mechanisms that eventually lead to liner failure [3,4]. Material failure is associated with the phenomenon known as physical swelling. This occurs in liners when some organic components, such as the CO_2 and CH_4 dissolved in oil, penetrate into the polymer macromolecular chain network aided by the high pressure operating conditions, increasing the space between molecules and decreasing the intermolecular bonding. As this operation takes place, the migratory gases can permeate throughout the liner wall and gradually balance the pressure difference between the inside of the liner and the annular region consisting of the gap between the liner and the pipe wall. This permeation mechanism worsens recursively since permeation rate increases with the severity of swelling of the liner. Finally, buckling collapse occurs when the liner is intentionally decompressed and the external pressure built up by the confined gases in the annular region, generates a stress state in the liner that induces the radial buckling failure.

Currently, a number of analytical models that deal with the buckling collapse of metallic tubes under external pressure have been developed in the literature [5-7]. In all cases, the analytical solutions found are restricted to purely elastic or ideal elastoplastic behavior and cannot analyze the influence of geometrical or surface defects, so commonly generated during the manufacturing, storage, transport and installation stages. Moreover, they are only useful for obtaining a critical

pressure value and are not able to describe the whole deformation process. On the other hand, in [8], Rueda et al. developed a specific FEM model for the simulation of the buckling collapse of HDPE liners. In their work, they were able to simulate an overall buckling collapse situation by introducing hydrostatic fluid elements in the model to allow for hydraulic effects. For the description of material constitutive response, they used linear elastic, linear elastoplastic, and linear elastoplastic with strain hardening behavior. Their investigation served as the first step for the prediction of actual failure situations since it showed that the transient dynamic response could be effectively simulated by FEM analysis. However, the traditional constitutive models used in their work cannot account for the intrinsic strain-rate, pressure and temperature dependence of polymer mechanical behavior and therefore are not sufficient to reproduce the complex multiaxial stress response and rate-dependent deformation evolution that will take place during an actual rapid pipe depressurization situation. As a consequence, it remains to include into the analysis an advanced constitutive model capable of accounting for the intricate response of polymers.

Constitutive modeling of polymers is nowadays a well-established field with a large number of advances over the last 40 years. In this regard, one of the most successful developments has been the family of tridimensional constitutive models started by Boyce and coworkers [9-13], which brought together current theories of macromolecular physics with recent work in the fields of statistical mechanics, continuum mechanics, and computational mechanics. These models employ a constitutive framework intended to be general enough to capture material behavior over a wide range of loading conditions, in order to be appropriate for their use in FEM analysis. The original work of Boyce et al. [9] was concerned with the large viscoplastic deformation of amorphous polymers, such as polycarbonate (PC) and acrylic glass (PMMA). So far, this constitutive approach has been consecutively enhanced in order to include additional features of polymer deformation such as, strain induced anisotropy, rubber elasticity, thermo-mechanical coupling, high strain-rate testing and so on. Among these, a notable contribution was the Hybrid Model (HM) of Bergstrom et al. [14] which was designed for capturing the mechanical response of a semi-crystalline polymer: Ultra-high molecular weight polyethylene (UHMWPE). Following this, in [15], Bergstrom et al. developed the Three Network Model (TNM) which is a further refinement of the HM model to be more accurate and computationally efficient. For its pertinence regarding semi-crystalline thermoplastic polymers, the TNM model results in a suitable choice for modeling the mechanical response of HDPE liners. Therefore, the objective of the present work is the evaluation and validation of the TNM model, for its use in FEM assisted design to accurately predict the buckling failure in pipes in a varying range of temperature and loading-rate conditions.

2. Experimental

2.1. Uniaxial tensile and compression tests

For the calibration of the TNM material model, tensile and compression tests were performed on an Instron 4467 universal testing machine. Tensile and compression specimens were machined out from a supplied liner as indicated in Figure 1. In order to univocally determine the viscous parameters, the tests were carried out at 3 different strain-rates, corresponding to crosshead speeds of 1, 10 and 50 mm/min. Tensile tests were performed using a extensometer of 12.5mm gauge length. Compression tests were carried out employing specimens of approximately 10 mm in height and 5 mm in diameter according to 2:1 (height : diameter) ratio recommended in [16]. For a complete characterization of deformation evolution, both loading and unloading response was registered.

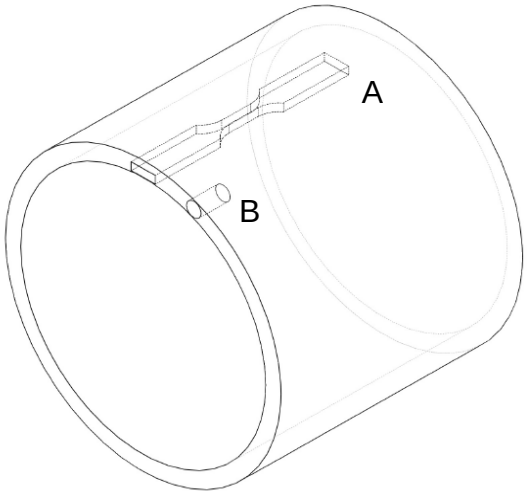

Figure 1. Tensile (A) and compression (B) specimens as obtained from the liner.

3. Computational efforts

3.1. Constitutive model

The main aspects of the TNM model constitutive framework will be described below, more details on the formulation can be found on the original works [14,15]. The TNM model consists of three networks acting in parallel as can be shown in the rheological representation (Fig.2)
The total deformation gradient of the assembly is decomposed into a thermal expansion component and a mechanical deformation component:

$$\mathbf{F}^{app} = \mathbf{F}\mathbf{F}^{th}$$

The mechanical deformation gradient of networks A and B are further decomposed into elastic and viscoplastic components:

$$\mathbf{F} = \mathbf{F}_n^e \mathbf{F}_n^v$$

Where *n* takes the value *A* and *B*, for networks *A* and *B* correspondingly. The Cauchy stress acting in networks A and B has the following form:

$$\boldsymbol{\sigma}_n = \frac{\mu_n}{J_n^e \overline{\lambda_n^{e*}}} \left[1 + \frac{\theta - \theta_0}{\hat{\theta}} \right] \frac{\mathcal{L}^{-1}\left(\overline{\lambda_n^{e*}} / \lambda_L \right)}{\mathcal{L}^{-1}\left(1/\lambda_L \right)} \mathrm{dev}\left[\mathbf{b}_n^{e*} \right] + \kappa \left(J_n^e - 1 \right) \mathbf{1}$$

Where, $J_n^e = \det[\mathbf{F}_n^e]$; $\mathbf{b}_n^{e*} = (J_n^e)^{-2/3} \mathbf{F}_n^e (\mathbf{F}_n^e)^{\mathrm{T}}$ is the Cauchy-Green deformation tensor; $\overline{\lambda}_n^{e*} = (\mathrm{tr}[\mathbf{b}_n^{e*}]/3)^{1/2}$ is the effective chain stretch and $\mathcal{L}^{-1}(x)$ is the inverse Langevin function.

The velocity gradient of networks A and B has the following form:

$$\dot{\mathbf{F}}_n = \dot{\chi}_n \mathbf{F}_n^{e-1} \frac{\mathrm{dev}[\boldsymbol{\sigma}_n]}{\tau_n} \mathbf{F}$$

Where:

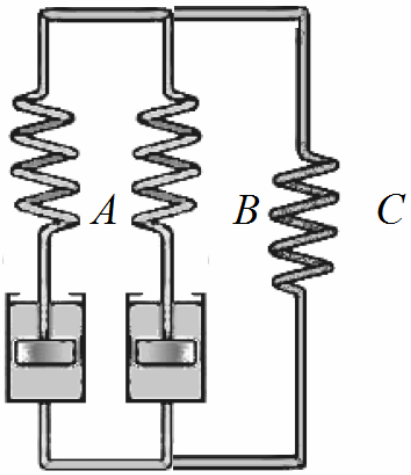

Figure 2. Rheological representation of the TNM constitutive model.

$$\dot{\gamma}_n = \dot{\gamma}_0 \left(\frac{\tau_n}{\hat{\tau}_n + aR(p_n)} \right)^{m_n} \left(\frac{\theta}{\theta_0} \right)^{n}$$

Here *R(x)* is the ramp function; p_n is the hydrostatic pressure; τ_n is the Fronebius norm of the deviatoric part of $\boldsymbol{\sigma}_n$.
The Cauchy stress acting in network C has the following form:

$$\boldsymbol{\sigma}_C = \frac{1}{1+q} \left\{ \frac{\mu_C}{J\lambda_{chain}} \left[1 + \frac{\theta - \theta_0}{\hat{\theta}} \right] \frac{\mathcal{L}^{-1}(\lambda_{chain}/\lambda_L)}{\mathcal{L}^{-1}(1/\lambda_L)} \mathrm{dev}\left[\mathbf{b}^* \right] + \kappa (J-1)\mathbf{1} + q \frac{\mu_C}{J} \left[I_1^* \mathbf{b}^* - \frac{2I_2^*}{3}\mathbf{I} - (\mathbf{b}^*)^2 \right] \right\}$$

Where $J = \det[\mathbf{F}]$; $\mathbf{b}^* = J^{-2/3}\mathbf{F}(\mathbf{F})^{\mathrm{T}}$ is the Cauchy-Green deformation tensor, and $\lambda_{chain} = (\mathrm{tr}[\mathbf{b}^*]/3)^{1/2}$
Finally, since they are in parallel, the three networks have equal mechanical deformation gradients and the total stress of the system is the sum of each network stress.

The TNM model was coded as a user material subroutine (UMAT/VUMAT) for ABAQUS and the constitutive parameters were determined using MCalibration software which uses a minimization algorithm based on the Nelder-Mead simplex method [17].

3.2. Liner-pipe system FEM model

The buckling collapse event was simplified assuming an ideal vacuum in the interior cavity of the liner and an increasing volume of fluid entering the liner-pipe cavity at a fluid flow rate *q*. This simplification has been made since this situation is easier to reproduce experimentally under controlled laboratory conditions. The event was simulated using ABAQUS/Implicit 6.10 for *q* values ranging from 10^{-5} to 10^{5} cm^3/s.

The thermoplastic liner was modeled as a planar bidimensional deformable solid (Fig.3a) using CPE8R elements and assuming plain strain, i.e. neglecting the effect of restraint at the liner ends. This assumption has proven to be valid for length to radius *L/R* values greater than 2 [18]. A small elliptical curvature was introduced in the upper part of the liner along the positive region of the

y-axis in order to induce single lob buckling (Fig.3b) in this region, which is the most critical failure mode and the most frequently observed in practice. Symmetry conditions were imposed with respect to the y-axis. The external metallic tube was assumed to be completely rigid in order to save CPU time. The fluid was modeled using F2D2 hydrostatic fluid elements and the depressurization event was modeled by imposing a fluid volume flux using the "fluid flux" option in ABAQUS/Implicit. These hydrostatic fluid elements are surface elements that cover the boundary of fluid containing cavity and provide the coupling between the deformation of the fluid-filled solid and the pressure exerted by the contained fluid on the solid surface defined as cavity boundary [19].

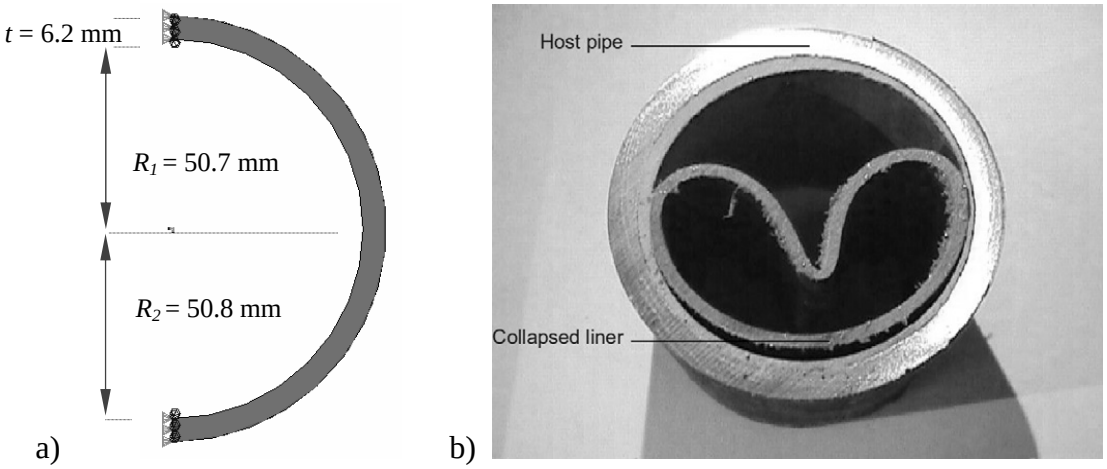

Figure 3. a) liner geometry and boundary conditions for the FEM model. b) single lob failure mode geometry

4. Results & Discussion

4.1. Uniaxial tensile and compression tests

Tensile and compression tests results are shown in Fig.5. In both cases, an initial time-independent elastic response can be observed. At a stress value of 5 MPa approximately the material enters the visco-elastoplastic regime, this region corresponds to the complex onset of different plastic flow mechanisms in the amorphous and semicrystalline domains of the thermoplastic material. In the constitutive model, the deformation gradients of the dashpots, which were at first negligible, start to flow at these stress values. Also in this regime, hardening is observed with increasing of strain rate, as expected. The material shows strain rate sensitivity both in tension and compression. Differences of approximately 30% in stresses are observed increasing 50 times the strain rate. Pressure dependency can be observed as the maximum stress achieved is higher in compression than in tension for equal deformation rates. A very good fit was obtained, with a R^2 (mean square difference) value of 1.5. The constitutive parameters obtained are presented in table 1.

4.1. FEM Simulations

Simulations predicted the buckling collapse pressure of the liner in all the range of q values. Fig 4 shows the final failure geometry in the simulations.

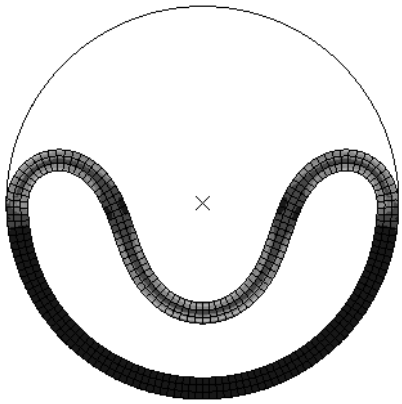

Figure 4. Final collapse geometry predicted by FEM simulations

Fig 6 shows the fluid pressure evolution as a function of fluid volume (V). Strain-rate dependency is manifested as it can be observed from the effect of increasing q values on fluid pressure, which are related to the speed at which the liner is accommodating deformation. Only at low values of V (up to V = 25 cm^3 approximately) a similar response can be observed for all q values, this is the initial elastic response which showed negligible strain-rate dependency as was noted in the tensile test results. In contrast, it can be seen that from V = 50 cm^3, higher q values lead to a more rapid increase in fluid pressure with fluid volume. This observation is consistent with the expected material stiffening as deformation rate increases (once in the visco-elastoplastic regime), meaning that, as the cavity is filled more rapidly, the liner can hold about the same volume of fluid at smaller deformations. This is done at the expense of the fluid high incompressibility, which therefore increases fluid pressure dramatically. Consequently, the maximum pressure attained, i.e. the collapse pressure, increases with q. Fig.7 shows the collapse pressure as a function of imposed flow rate. The logarithmic scale shows a potential relationship of the form $P_{max} = k.q^{RTF}$, where P_{max} is the collapse pressure, and *RTF* is a flow rate sensitivity exponent which ultimately characterizes the effect of material strain rate dependency on collapse pressure. The value of *RTF* is expected to be different for different materials, with *RTF* = 0 meaning a rate independent material. For the studied HDPE, the value of *RTF* obtained was approximately equal to 0.05. This factor can be of significant importance in the materials selection stage, when the values of expected depressurization velocities (v_{dep}) in service conditions are known. For this, a precise relationship between q and v_{dep} needs to be established. Furthermore, the possible influence of geometrical parameters such as the *t/D* ratio on the value of *RTF* still remains to be investigated.

Table 1. Constitutive parameters for the TNM model

Symbol	Name	Value
μ_A	Shear modulus of network A	40 MPa
λ_L	Chain locking stretch	1.02
$\hat{\theta}$	Temperature response of stiffness	-300 K
κ	Bulk modulus	2000 MPa
$\hat{\tau}_A$	Flow resistance of network A	2.07 MPa

a	Pressure dependence of flow	0.36
m_a	Stress exponential of network A	5.15
m_b	Stress exponential of network B	22.35
n	Viscosity parameter	40
$\hat{\tau}_B$	Flow resistance of network B	16.9 MPa
μ_{Bi}	Initial shear modulus of network B	259.3 MPa
μ_{Bf}	Final shear modulus of network B	60.51 MPa
μ_C	Shear modulus of network C	0.004 MPa
q	Relative contribution of I_2 of network C	zero

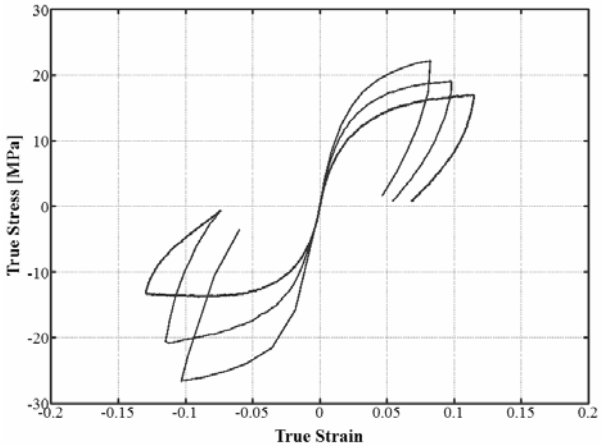

Figure 5. Uniaxial tensile and compression results at different cross-head speeds for HDPE.

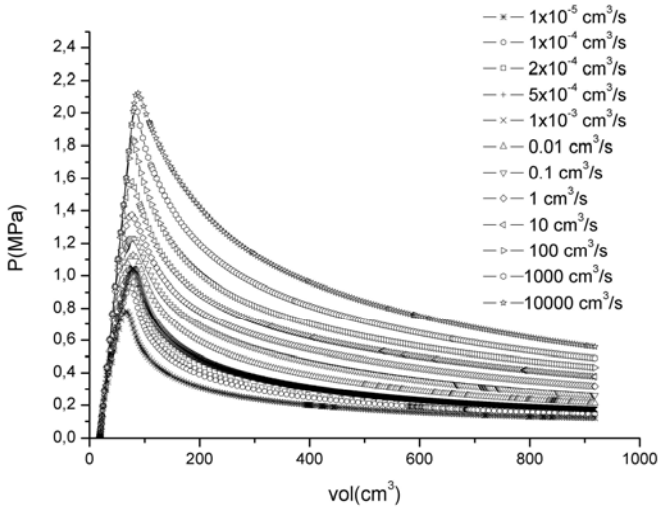

Figure 6. Evolution of fluid pressure, as a function of fluid volume in the liner-pipe cavity, for a wide range of fluid flow rates

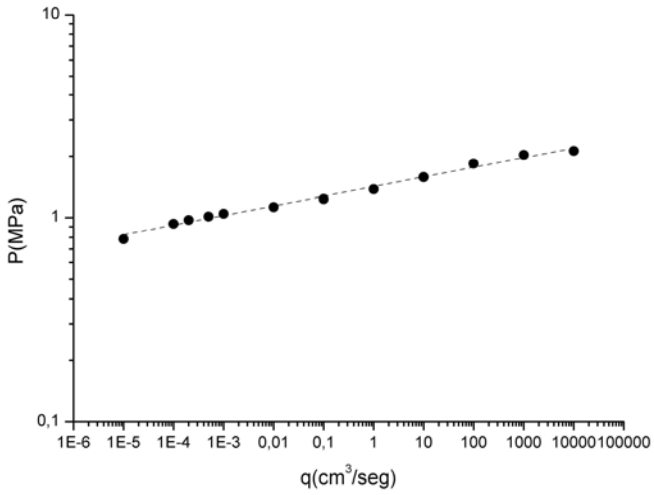

Figure 7. Collapse pressure as a function of imposed fluid flow rate.

5. Conclusion and forthcoming work

The external pressure-induced buckling collapse of thermoplastic liners was simulated using FEM analysis. The stress-strain response of the material and its intrinsic strain-rate and pressure dependency was modeled with the advanced TNM viscoelastic-viscoplastic model. Constitutive parameters were determined from tensile and compression stress-strain curves at different strain rates. The buckling failure event was simulated for a wide range of fluid flow rates. It was found that the material strain rate dependency has a significant effect on the collapse pressure P_{max} which leads to a potential relationship between P_{max} and q quantified by an exponent factor *RTF.* The value of *RTF* will vary with each material and quantifies the effect of strain rate dependency of the material on failure pressure. A forthcoming investigation will deepen the understanding of this factor and its dependence with the liner-pipe geometry. It also remains as future work to evaluate the prediction capability of the TNM model by comparing P_{max} FEM obtained values to empirical values determined under a controlled experimental setup.

References

[1] E. Engle, HR-370 Pipe rehabilitation with polyethylene pipe liners, 2003.
[2] Canadian Standards Association. CSA Z662-03 Oil and gas pipeline systems, 2003.
[3] B. Daniel, B.P. Lebsack, D.E. Hawn, R. Egner, Extending Liner Installation Lengths. United Pipeline Systems Inc., Corrosion, 2004 .
[4] NACE, RP0304-2004 liners for oilfield pipelines, 2004.
[5] D. Glock, Behavior of liners for rigid pipeline under external water pressure and thermal expansion. Der Stahlbau, 1977, pp. 212–217.
[6] S. Jacobsen, Buckling of circular rings and cylindrical tubes under external pressure. Water Power, 1974.
[7] KM. El-Sawy, Inelastic stability of tightly fitted cylindrical liners subjected to external uniform pressure. International Journal of Thin-Walled Structtures, 2001, pp.731–744.

[8] F. Rueda, J.L. Otegui, P.M. Frontini, Numerical tool to model collapse of polymeric liners in pipelines. Engineering Failure Analysis, 2011, pp. 24-34.
[9] M.C.Boyce, D.M. Parks, A.S. Argon, Large Inelastic Deformation of Glassy Polymers, Part I: Rate-Dependent Constitutive Model, Mechanics of Materials, 1988, pp. 15-33.
[10] E. M. Arruda, M. C. Boyce, A three-dimensional constitutive model for the large stretch behavior of rubber elastic materials, J. Mech. Phys. Solids. 1993, pp. 389–412.
[11] E. Arruda, M. Boyce, Effects of strain rate, temperature and thermo-mechanical coupling on the finite strain deformation of glassy polymers. Mech. Mater. 1995, pp. 193–212.
[12] J. S. Bergström, M. C. Boyce, Constitutive modeling of the large strain time-dependent behavior of elastomers. J. Mech. Phys. Solids, 1998, pp. 931–954.
[13] J. S. Bergström, M. C. Boyce, Large strain time-dependent behavior of filled elastomers, Mechanics of Materials, 2000, pp. 620–644.
[14] J. S. Bergström, C.M. Rimnac, S.M. Kurtz, An augmented hybrid constitutive model for simulation of unloading and cyclic loading behavior of conventional and highly crosslinked UHMWPE, Biomaterials, 2004, pp. 2171–2178
[15] J. S. Bergström, J.E. Bischoff, An Advanced Thermo-mechanical Constitutive Model for UHMWPE, International Journal of Structural Changes in Solids, 2010, pp. 31-39
[16] ASTM D0695-02A Test Method for Compressive Properties of Rigid Plastics.
[17] PolyUMod, A library of advanced used materials, Veryst Engineering LLC.
[18] S.R. Frost, A.M. Korsunsky, Wu Y-S, A.G. Gibson, 3-D Modeling of liner collapse. In: Conference NACE; 2000.
[19] Abaqus Analysis User´s Manual, 2010, Section 11.5.1, Dassault Systèmes, 2010.

Effects of Specimen Geometry and Mode Loading on Crack Growth Resistance Curves of X80 Pipeline Girth Welds

Claudio Ruggieri[1,*], **Leonardo L. S. Mathias**[1]

[1] Department of Naval Architecture and Ocean Engineering, University of São Paulo, 05508-030, Brazil
* Corresponding author: claudio.ruggieri@poli.usp.br

Abstract This work presents an investigation of the ductile tearing properties for a girth weld made of an API 5L X80 pipeline steel using experimentally measured crack growth resistance curves. Use of these materials is motivated by the increasing demand in the number of applications for manufacturing high strength pipes for the oil and gas industry including marine applications and steel catenary risers. Testing of the pipeline girth welds employed side-grooved, clamped SE (T) specimens and 3P bend SE(B) specimens with a weld centerline notch and varying crack sizes to determine the crack growth resistance curves based upon the unloading compliance (UC) method using a single specimen technique. Recently developed compliance functions and η-factors applicable for SE (T) and SE(B) fracture specimens are introduced to determine crack growth resistance data from laboratory measurements of load-displacement records.

Keywords *J*-Resistance Curves, Ductile Fracture, SE(T) Specimen, SE(B) Specimen, Crack Growth

1. Introduction

Fracture mechanics based approaches to describe ductile fracture behavior in structural components rely upon crack growth resistance (J-Δa) curves to characterize crack extension followed by crack instability of the material. These approaches allow the specification of critical crack sizes based on the predicted growth of crack-like defects under service conditions. Current standardization efforts now underway advocate the use of single edge notch tension SE(T) specimens to measure experimental *R*-curves more applicable to high pressure piping systems, including girth welds of marine steel risers.

The primary motivation to use SE(T) fracture specimens in defect assessment procedures for this category of structural components is the strong similarity in crack-tip stress and strain fields which drive the fracture process for both crack configurations. However, while now utilized effectively in fracture testing of pipeline girth welds, some difficulties associated with SE(T) testing procedures, including fixture and gripping conditions, raise concerns about the significance and qualification of measured crack growth resistance curves. While slightly more conservative, testing of shallow-crack bend specimens (which is a nonstandard SE(B) configuration) may become more attractive due to its simpler testing protocol, laboratory procedures and much smaller loads required to propagate the crack.

This work presents an investigation of the ductile tearing properties for a girth weld made of an API 5L X80 pipeline steel using experimentally measured crack growth resistance curves. Use of these materials is motivated by the increasing demand in the number of applications for manufacturing high strength pipes for the oil and gas industry including marine applications and steel catenary risers. Testing of the pipeline girth welds employed side-grooved, clamped SE (T) specimens and 3P bend SE(B) specimens with a weld centerline notch and varying crack sizes to determine the crack growth resistance curves based upon the unloading compliance (UC) method using a single specimen technique. Recently developed compliance functions and η-factors applicable for SE (T) and SE(B) fracture specimens are introduced to determine crack growth resistance data from laboratory measurements of load-displacement records

2. *J*-Resistance Curve Measurements Based on the UC Procedure

2.1. Evaluation Procedure of the *J*-Integral

Conventional testing programs to measure crack growth resistance ($J-\Delta a$) curves in metallic materials routinely employ the unloading compliance (UC) method based on a single specimen test. A widely used approach (which forms the basis of current standards such as ASTM E1820 [1]) to evaluate *J* with crack extension follows from an incremental procedure which updates J_e and J_p at each partial unloading point, denoted *k*, during the measurement of the load vs. displacement curve as

$$J^k = J_e^k + J_p^k \tag{1}$$

where the current elastic term is simply given by

$$J_e^k = \left(\frac{K_I^2}{E'}\right)_k \tag{2}$$

and the current plastic term follows an incremental formulation which is applicable to CMOD data in the form [2,3]

$$J_p^k = \left[J_p^{k-1} + \frac{\eta_{J-CMOD}^{k-1}}{b_{k-1}B_N}\left(A_p^k - A_p^{k-1}\right)\right]\left[1 - \frac{\gamma_{LLD}^{k-1}}{b_{k-1}}\left(a_k - a_{k-1}\right)\right] \tag{3}$$

in which factor γ_{LLD} is evaluated from

$$\gamma_{LLD} = \left[-1 + \eta_{J-LLD}^{k-1} - \left(\frac{b_{k-1}}{W\eta_{J-LLD}^{k-1}}\frac{d\eta_{J-LLD}^{k-1}}{d(a/W)}\right)\right] \tag{4}$$

In the above expressions, K_I is the elastic stress intensity factor for the cracked configuration, A_p is the plastic area under the load-displacement curve, B_N is the net specimen thickness at the side groove roots ($B_N = B$ if the specimen has no side grooves where *B* is the specimen gross thickness), *b* is the uncracked ligament ($b = W - a$, where *W* is the width of the cracked configuration and *a* is the crack length). In writing Eq. (2), plane-strain conditions are adopted such that $E' = E/(1-\nu^2)$ where *E* and ν are the (longitudinal) elastic modulus and Poisson's ratio, respectively. Factor η_J appearing in Eqs. (3) and (4) represents a nondimensional parameter which relates the plastic contribution to the strain energy for the cracked body and *J*. Figure 1 illustrates the essential features of the estimation procedure for the plastic component J_p. Here, we note that A_p (and consequently, η_J) can be defined in terms of load-load line displacement (LLD or Δ) data or load-crack mouth opening displacement (CMOD or *V*) data. For definiteness, these quantities are denoted η_{J-LLD} and η_{J-CMOD}.

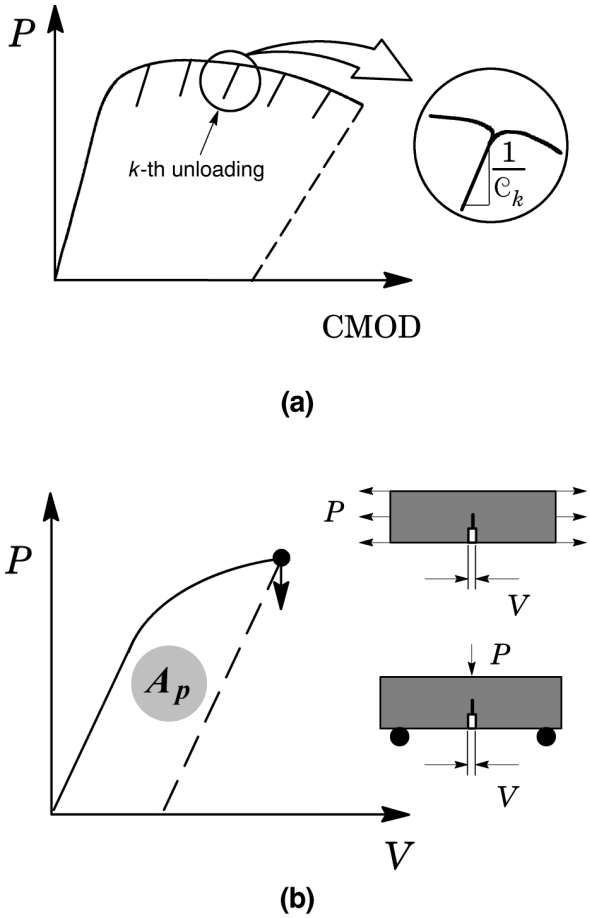

Figure 1. (a) Partial unloading during the evolution of load with crack mouth opening displacement (CMOD or *V*); (b) Definition of the plastic area under the load-displacement curve.

The incremental expression for J_p defined by Eq. (3) coupled with Eq. (4) contains two contributions: one is from the plastic work in terms of CMOD and, hence, η_{J-CMOD} and the other due to crack growth correction in terms of LLD by means of η_{J-LLD}. Evaluation of Eqs. (3) and (4) is relatively straightforward provided the two geometric factors, η_{J-CMOD} and η_{J-LLD}, are known. For the clamped SE(T) specimens with $H/W=10$ and the conventional SE(B) configuration utilized in this study, a convenient polynomial fitting of the results given by Cravero and Ruggieri [4], Ruggieri [5] and Donato and Ruggieri [6] provide the corresponding η-factor equations in the form

$$\eta_{J-CMOD}^{SET} = 1.067 - 1.767\frac{a}{W} + 7.808\left(\frac{a}{W}\right)^2 - 19.269\left(\frac{a}{W}\right)^3 + 15.295\left(\frac{a}{W}\right)^4 - 3.083\left(\frac{a}{W}\right)^5 \quad (5)$$

$$0.2 \le a/W \le 0.7$$

$$\eta_{J-LLD}^{SET} = -0.623 + 9.336\frac{a}{W} - 4.584\left(\frac{a}{W}\right)^2 - 47.963\left(\frac{a}{W}\right)^3 + 87.697\left(\frac{a}{W}\right)^4 - 44.875\left(\frac{a}{W}\right)^5 \quad (6)$$

$$0.2 \le a/W \le 0.7$$

$$\eta_{J-CMOD}^{SEB} = 3.650 - 2.111\frac{a}{W} + 0.341\left(\frac{a}{W}\right)^2 \qquad (7)$$

$$0.1 \le a/W \le 0.7$$

$$\eta_{J-LLD}^{SEB} = 0.020 + 18.086\frac{a}{W} - 72.256\left(\frac{a}{W}\right)^2 + 152.225\left(\frac{a}{W}\right)^3 - 159.769\left(\frac{a}{W}\right)^4 + 66.879\left(\frac{a}{W}\right)^5 \qquad (8)$$

$$0.1 \le a/W \le 0.7$$

2.2. Crack Extension Estimation

Current testing protocols to measure the crack growth resistance response using a single-specimen test are primarily based on the unloading compliance (UC) technique to obtain accurate estimates of the (current) crack length from the specimen compliance measured at periodic unloadings with increased deformation. Figure 1 illustrates the essential features of the method. The slope of the load-displacement curve during the *k*-th unloading defines the current specimen compliance, denoted C_k, which depends on specimen geometry and crack length. For the clamped SE(T) and SE(B) crack configurations analyzed here, the specimen compliance is most often defined in terms of normalized quantities expressed as [1,4]

$$\mu_{CMOD}^{SET} = \left[1 + \sqrt{EB_eC_{CMOD}}\right]^{-1} \qquad (9)$$

and

$$\mu_{CMOD}^{SEB} = \left[1 + \sqrt{\frac{EWB_eC_{CMOD}}{S/4}}\right]^{-1} \qquad (10)$$

where μ_{CMOD}^{SET} and μ_{CMOD}^{SEB} define the normalized compliances for the SE(T) and SE(B) specimens. In the above expressions, E is the longitudinal elastic modulus, C_{CMOD} denotes the specimen compliance defined in terms of crack mouth opening displacement ($C_{CMOD} = V/P$ where V is the CMOD and P represents the applied load) and the effective thickness, B_e, is defined by

$$B_e = B - \frac{(B - B_N)^2}{B} \qquad (11)$$

By measuring the instantaneous compliance during unloading of the specimen (see Fig. 1), the current crack length follows directly from solving the functional dependence of crack length and specimen compliance in terms of μ_{CMOD}. For the clamped SE(T) specimen and SE(B) configuration analyzed here, the corresponding compliance expressions follow from Cravero and Ruggieri [4] and ASTM E1820 [1] as

$$\left[\frac{a}{W}\right]_{SET} = 1.9215 - 13.2195\mu + 58.7080\mu^2 - 155.2823\mu^3 + 207.3987\mu^4 - 107.9176\mu^5 \quad (12)$$

$$0.1 \le a/W \le 0.7$$

$$\left[\frac{a}{W}\right]_{SEB} = 10.9997 - 3.9504\mu + 2.9821\mu^2 - 3.2141\mu^3 + 51.5164\mu^4 - 113.0310\mu^5 \quad (13)$$

$$0.1 \le a/W \le 0.8$$

3. Experimental Details

3.1. Material Description and Welding Procedures

The material utilized in this study was a high strength, low alloy (HSLA), API grade X80 pipeline steel produced as a base plate using a control-rolled processing route without accelerated cooling. The mechanical properties and strength/toughness combination for this material are mainly obtained by both grain size refinement and second-phase strengthening due to the small-size precipitates in the matrix. The 20-inch pipe with longitudinal seam weld from which the girth weld SE(T) and SE(B) specimens were extracted was fabricated using the UOE process.

The tested weld joint was made from the API X80 UOE pipe having thickness, $t_w = 19$ mm. Girth welding of the pipe was performed using the FCAW process in the 1G (flat) position with a single V-groove configuration in which the root pass was made by GMAW welding. The main weld parameters used for preparation of the test weld using the FCAW process are: i) number of passes 12 (including the root pass made by the GMAW process); ii) welding current 165 A; iii) welding voltage 23 V; iv) average heat input 1.5 kJ/mm. Mathias et al. [7] provide the tensile properties for the tested pipeline girth weld and base material which include: $\sigma_{ys}^{WM} = 715$ MPa, $\sigma_{uts}^{WM} = 750$ MPa, $\sigma_{ys}^{BM} = 609$ MPa, $\sigma_{uts}^{BM} = 679$ MPa. Here, σ_{ys} and σ_{uts} represent the material's yield stress and tensile strength, and WM and BM denote the weld metal and base plate. The degree of weld strength overmatch is ~18% so that mismatch effects on the measured crack growth resistance curves are very small.

3.2. Specimen Geometries

Unloading compliance (UC) tests at room temperature were performed on weld centerline notched SE(T) specimens with fixed-grip loading to measure tearing resistance curves in terms of $J - \Delta a$ data. The clamped SE(T) specimens have a fixed overall geometry and crack length to width ratio defined by $a/W = 0.4$, $H/W = 10$ with thickness $B = 14.8$ mm, width $W = 14.8$ mm and clamp distance $H = 148$ mm (refer to Fig. 2(a)). Here, a is the crack depth and W is the specimen width which is slightly smaller than the pipe thickness, t_w. UC tests at room temperature were also conducted on weld centerline notched SE(B) specimens with $a/W = 0.25$ with thickness $B = 14.8$ mm, width $W = 14.8$ mm and span $S = 4W$ (refer to Fig. 2(b)). Conducted as part of a collaborative research program conducted at University of São Paulo on structural integrity asssessment of marine steel catenary risers (SCRs), testing of these specimens focused on the

development of accurate procedures to evaluate crack growth resistance data for pipeline girth welds.

All specimens, including the SE(T) configuration, were precracked in bending using a three-point bend apparatus very similar to a conventional three-point bend test. After fatigue precracking, the specimens were side-grooved to a net thickness of ~85% the overall thickness (7.5% side-groove on each side) to promote uniform crack growth and tested following some general guidelines described in ASTM E1820 standard [1]. Records of load vs. crack mouth opening displacements (CMOD) were obtained for the specimens using a clip gauge mounted on knife edges attached to the specimen surface.

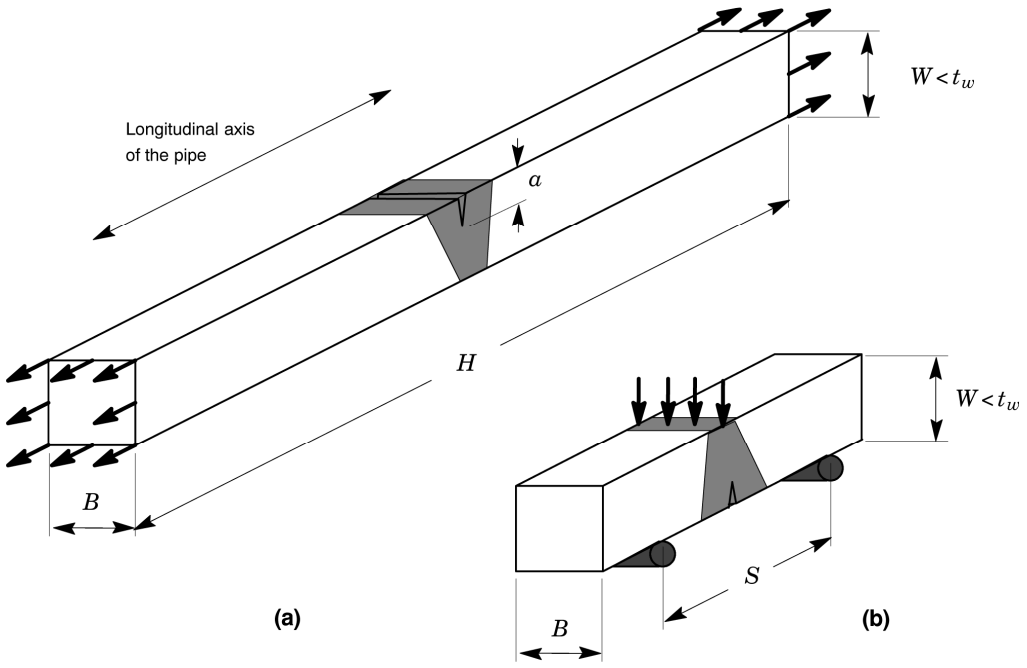

Figure 2.Geometry of tested fracture specimens with weld centerline notch. (a) Clamped SE(T) specimen with a/W = 0.4 and H/W = 10; (b) 3P SE(B) specimen with a/W = 0.25 and S/W = 4. All geometries follow (*BxB*) configuration

4. Crack Growth Resistance Curves

This section presents the crack growth resistance evaluated for the tested X80 pipeline girth weld based on laboratory measurements of load and CMOD for the clamped SE(T) specimens and the 3P bend SE(B) specimens with center notched welds. The geometrical features of each specimen type and the considered material properties were presented in the previous section. Figure 3 shows the measured load-displacement curve (*P vs.* CMOD) for both test specimens which clearly reveals the reduced test load for the SE(B) specimen compared with the SE(T) configuration.

Evaluation of the crack growth resistance curve follows from determining J and Δa at each unloading point of the measured load-displacement data. Based upon the previous results for the η-factors and compliance functions provided in previous Section 2, the present analysis employs η_{J-CMOD} and η_{J-LLD} to estimate the plastic component of the J-integral, J_p. Figures 4-5 present the measured crack growth resistance curves for the tested clamped SE(T) and 3P SE(B) specimens.

The significant features associated with these plots include: (1) The shallow-crack SE(B) specimen provides *R*-curves which exhibits levels of *J*-values which are comparable to the *J*-values corresponding to the deeply-cracked SE(T) specimen at a fixed amount of crack growth, Δa; (2) The value of the *J*-integral at onset of ductile tearing, J_{Ic}, is fairly independent of specimen geometry and loading mode.

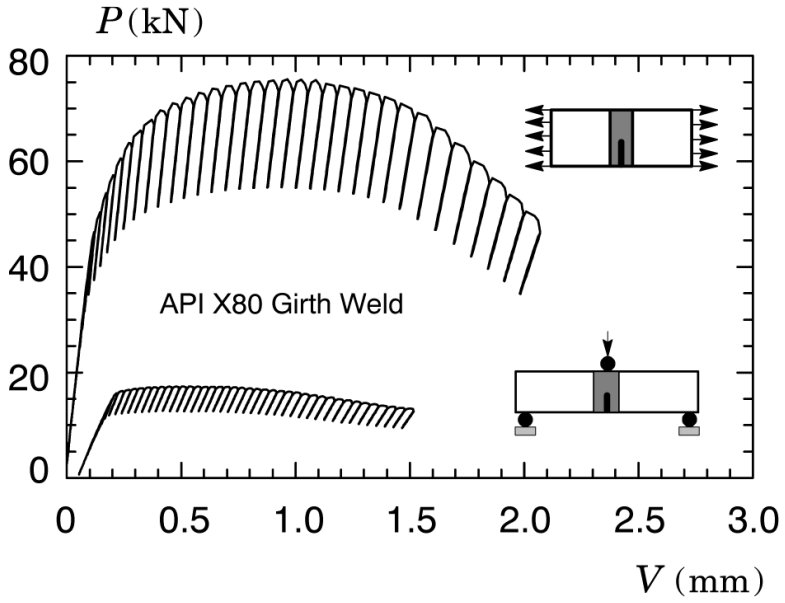

Figure 3. Measured load-CMOD curve for the tested X80 pipeline girth weld using clamped SE(T) specimens with $a/W = 0.4$ and 3P SE(B) specimens with $a/W = 0.25$.

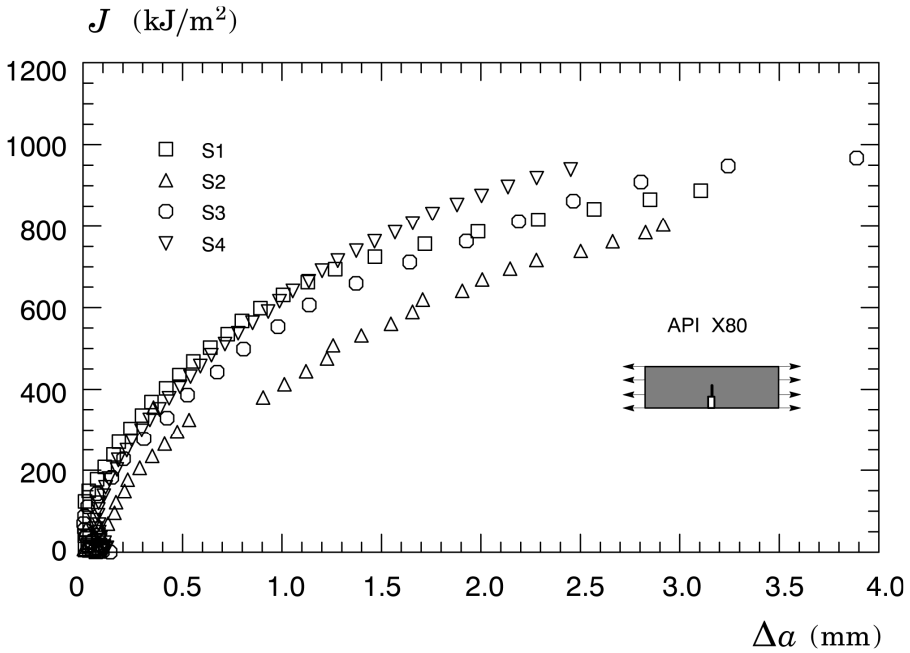

Figure 4. Experimental *R*-curves for tested clamped SE(T) specimens with $a/W = 0.4$

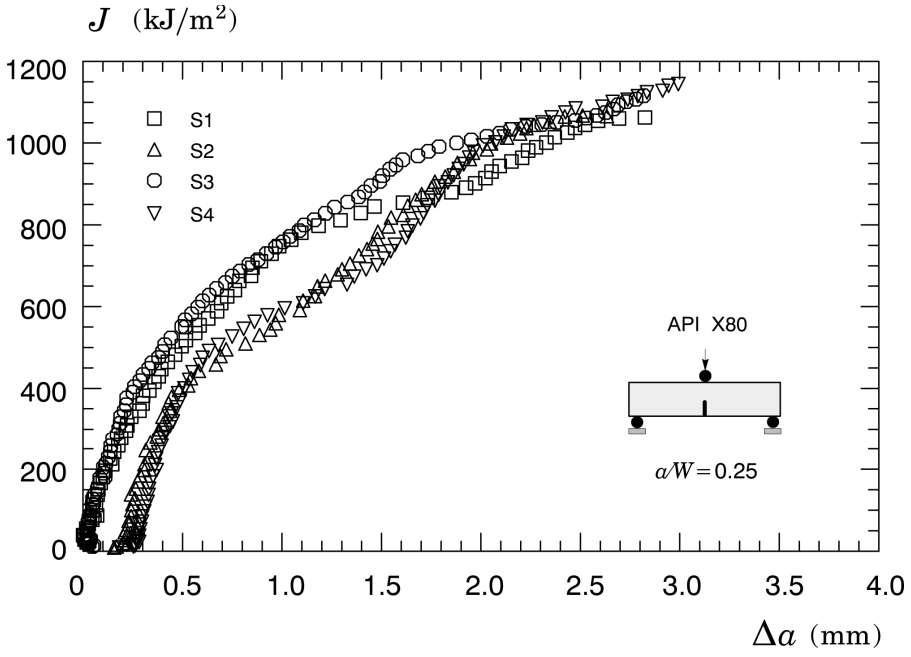

Figure 5. Experimental *R*-curves for tested SE(B) specimen with $a/W = 0.25$.

After testing, all specimens were subjected to heat tinting treatment (300°C for 30 min), and then air cooled before being broken apart. Table 1 shows a comparison of the predicted and estimated crack extension for the tested fracture specimens. For the SE(T) specimens, the deviation ($\Psi = \left|(a_{predicted} - a_{measured})/a_{measured}\right|$) is within 1.5~6.2% while for the SE(B) specimen, the accuracy is within 12~17%%. These results indicate that the UC procedure provides reasonable estimates of the final crack length for the SE(T) specimen. In contrast, crack length estimates for the SE(B) configuration display a somewhat larger deviation compared to the measured crack length; such behavior is mainly due to more severe crack front tunneling that occurred in these specimens.

Table 1. Crack length estimation based on UC procedure.

ID	a_0 (mm)	a_p (mm)		ψ (%)
		Measured	**Predicted**	
SE(B) Specimens				
S1	3.85	7.85	6.68	14.9
S2	4.15	8.21	7.15	12.9
S3	3.65	7.55	6.29	16.7
S4	3.72	7.82	6.53	16.4
SE(T) Specimens				
S1	5.66	8.84	8.76	0.9
S2	6.11	8.06	8.56	6.2
S3	6.29	9.78	9.20	5.9
S4	6.70	10.75	10.59	1.5

5. Concluding Remarks

This work presents an investigation of the ductile tearing properties for a girth weld made of an API 5L X80 pipeline steel using experimentally measured crack growth resistance curves ($J-\Delta a$ curves). Testing of the pipeline girth welds utilized side-grooved, clamped SE (T) specimens and 3P bend SE(B) specimens with a weld centerline notch to determine the crack growth resistance curves based upon the unloading compliance (UC) method using a single specimen technique. This experimental characterization provides additional toughness data which serve to evaluate crack growth resistance properties of pipeline girth welds using SE (T) and SE(B) specimens with weld centerline cracks. Additional work is in progress to further validate the use of shallow-crack SE(B) specimens as an alternative fracture specimen to measure crack growth properties for pipeline girth welds. Ongoing investigation also focuses on establishing robust correlations between *J* and CTOD for stationary and growing cracks in SE(T) and SE(B) fracture specimens.

Acknowledgements

This investigation is supported by Fundação de Amparo à Pesquisa do Estado de São Paulo (FAPESP) through Grant 2012/13053-2 and by the Brazilian Council for Scientific and Technological Development (CNPq) through Grant 304132/2009-8.

References

[1] American Society for Testing and Materials, Standard test method for measurement of fracture tough ness, ASTM E1820, 2011.
[2] S. Cravero, C. Ruggieri, Further developments in *J* evaluation procedure for growing cracks based on LLD and CMOD data, International Journal of Fracture, 148 (2007) 347-400.
[3] X. K. Zhu, B. N. Leis, J. A. Joyce, Experimentation estimation of *J-R* curves from load-CMOD record for SE(B) specimens, Journal of ASTM International, 5 (2008) JAI101532.
[4] S. Cravero, C. Ruggieri, Estimation procedure of *J*-resistance curves for SE(T) fracture specimens using unloading compliance, Engineering Fracture Mechanics 74 (2007) 2735-2757.
[5] C. Ruggieri, Further results in *J* and CTOD estimation procedures for SE(T) fracture specimens - Part I: Homogeneous materials, Engineering Fracture Mechanics 79 (2012) 245-265.
[6] G. H. B. Donato, C. Ruggieri, Estimation procedure for *J* and CTOD fracture parameters using three-point bend specimens, in: 6th International Pipeline Conference (IPC 2006), Calgary, Canada, 2006.
[7] L. L. S. Mathias, D. F. B. Sarzosa, C. Ruggieri, Effects of Specimen Geometry and Loading Mode on Crack Growth Resistance Curves of a High-Strength Pipeline Girth Weld, Manuscript in Preparation.

Comparison of different techniques for the monitoring of the Lüders bands development

J. Petit[1], D. Wagner[1], N. Ranc[2], G. Montay[3], M. François[3]

[1] LEME, EA4416, Université Paris Ouest, 92410 Ville d'Avray, France
[2] PIMM, CNRS, 151 Bd de l'Hôpital, 75013 Paris, France
[3] LASMIS, UMR CNRS 6279, University of Technology of Troyes, 10010 Troyes, France

In C-Mn and some low alloyed steels, the plastic deformation begins by a macroscopic heterogeneous strain which materializes into the propagation of a strain band along a tensile sample with a uniform cross-section. This band is named Lüders, or Piobert-Lüders, band and it is considered by some authors as a plastic wave. This particular strain localization, which goes through the length of the sample, is explained by an avalanche phenomenon which enables step by step to unfix the dislocations from their Cottrell's atmosphere. However, although its effects are well enough known, one knows much less its causes. In this paper, the travel of the Lüders band is monitored thanks to several techniques based on different physical principles: optical (speckle interferometry), thermal (infrared pyrometry) and acoustic (acoustic emission). The position of the band, its inclination, its propagation speed and the strain rate inside the band are the main points of comparison between each technique. They allow verifying some features about the propagation of the bands and giving some new assumptions about their formation and their development.

Keywords Lüders Band, Strain Localization, Infrared Thermography (IRT), Electronic Speckle Pattern Interferometry (ESPI), Acoustic Emission (AE), Tensile Test

1. Introduction

Plastic strain localization is a major problem in metalworking situations. In ductile metals, macroscopic plastic deformation heterogeneities such as Lüders bands [1-3], Portevin-Le Châtelier effect [4-6] or necking [7-10] can occur. Lüders bands and Portevin-Le Châtelier bands, in particular type A and type B, propagate in some metallic alloys for specific temperatures and strain rate conditions. This last localization phenomenon is described in many papers [11-14]. In ductile metals, the onset of necking is well referenced in literature and is particularly important for the characterization of the forming limit diagram [15-16].

Lüders bands propagation often occurs in hot-rolled low-carbon steels deformed or annealed at 300°C (static ageing). These bands are observed in ferritic phase of steels and form unaesthetic patterns on the material surface. They appear when the plastic deformation starts and disappear early. In uniaxial tensile test, Lüders bands propagate all along the gauge length of the specimen. Indeed, when interaction energy is strong between dislocations and solute atoms which can easily diffuse, like carbon and nitrogen atoms in iron, they gather around dislocations to form Cottrell's atmospheres. Dislocations are strongly anchored and a considerable stress is necessary to release them. Very often, this stress level is reached first in a point of the metal as the result of local effect of stress concentration, notably, in uniaxial tensile test, at the fillet radius with the specimen heads. Deformation remains localized in a narrow zone, corresponding to a Lüders band. The stress concentrations at the band front enable a gradual unlocking of the dislocations in the non-deformed part of the specimen. Thus, this process activates an avalanche that, from grain to grain, goes through all the polycrystal; there is band propagation [17-18]. Besides, the band propagates under a macroscopic stress, R_e^l, lower than the one, R_e^u, needed for initiation.

In order to go further concerning origins and activation modes understanding of this specific deformation mechanism, full-field measurements methods: Infrared Thermography (IRT) [19],

Electronic Speckle Pattern Interferometry (ESPI) and Acoustic Emission (AE) [3] are used, sometimes combined, and compared.

2. General experiments description

Lüders bands were studied during tensile test on two hot-rolled low-carbon steels: one S235 (0.16%wt Carbon) and one C35 (0.35%wt Carbon) according to the European standard. Both are centered cubic (cc) ferritic steels with pearlite. For the first one, propagation of the bands was followed by IRT. For the second one, propagation was followed by AE sole and by ESPI and AE simultaneously. Note that these two experiments were performed in two different laboratories, on two different tensile machines. One knows that the stiffness of the tensile machine can modify the Lüders bands generation and propagation. Here, machines are supposed stiff enough to have an insignificant influence on the Lüders bands behavior. In the future, coupling of the three investigation techniques is foreseen on the same machine.
Dog-bone like specimens with rectangular cross-section are used for the tests. The planar surfaces of the specimens are convenient for 2-D thermal and kinematics full-field measurements techniques and to fix acoustic sensors. The dimensions of the specimens are given on the Fig. 1. Although their influence was not studied here, curvature of the fillet radius are also reported.

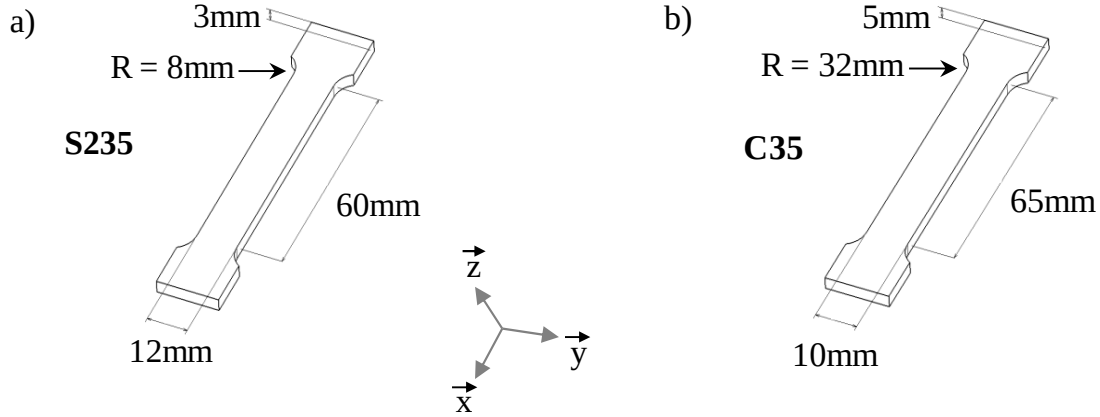

Figure 1. Scheme of the specimens: a) S235 and b) C35.

The initial microstructure of the as received materials is characterised by a grain size ranging between 10 and 15 µm for the S235 and 5 and 10 µm for the C35. The roughness of the S235 specimen is Ra / Rt ≈ 2.0 / 15 µm, the C35's one is Ra / Rt ≈ 5.3 / 35 µm.

3. IRT as Lüders bands following technique

3.1. Experimental procedure

Tests on the S235 steel were performed at 10 mm.min^{-1} on a hydraulic tensile machine with a 100 kN load cell. The stiffness of the machine is 156 kN.mm^{-1}. To characterize temperature increase due to the Lüders bands, specimens were placed in front of an infrared CCD camera. The camera model is a Cedip Silver Orion MW F/3 with InSb detectors. The size of the camera matrix and the spatial resolution are respectively about 320 x 256 pixels and 0.25 mm per pixel. The aperture time is fixed at 1000 µs. The refresh frequency of the camera is of 33 Hz, which corresponds to a duration between two pictures of 30.3 ms. Others acquisition parameters are given in Table 1. Under these conditions, the noise of the camera is about 25 mK. A calibration with a black body allows to deduce the links between the specimen surface temperature and the camera signal. In order to reduce the effect of the emmittance of the material surface, the samples were covered with black paint to get an emissivity close to 1.

Table 1. Acquisition parameters of the IRT device used during tensile test on the S235 steel.

Integration time	Frame rate	Bandwidth	Room temperature
1000 µs	33.33 Hz	3.7 - 4.8 µm	22.5°C

In most of metallic materials, during quasi-static tests at room temperature, plastic deformation goes with thermal energy dissipation, which is the result of dislocations movements inside grains. Another part, less important, of the mechanical energy brought to deform the sample is stored in the material. Thus, the temperature variation is related to the plastic deformation through the following relation [20]:

$$\rho c_p \dot{T} = \beta \underline{\underline{\sigma}} : \underline{\underline{\dot{\varepsilon}_p}} + \lambda \Delta T \quad (1)$$

where ρ is the density, c_p the specific heat, T the temperature, the symbol " $\dot{}$ " for the time derivative, β the Taylor-Quiney coefficient, $\underline{\underline{\sigma}}$ the stress tensor, $\underline{\underline{\dot{\varepsilon}_p}}$ the plastic deformation rate tensor, λ the thermal conductivity and the symbol Δ for the Laplacian.

More particularly, $\rho c_p \dot{T}$ represents the calorific power related to the atomic excitement. $\beta \underline{\underline{\sigma}} : \underline{\underline{\dot{\varepsilon}_p}}$ is the mechanical-thermal coupling term related to the dissipative thermal energy, which represents $100 \times \beta$ % of the energy creation inside the material; the other part corresponding to the stored energy. $\lambda \Delta T$ represents the thermal transfers by conduction.

During the Lüders band propagation and along an increment of plastic deformation, given the weak thermal conductivity of the S235 steel, the term $\lambda \Delta T$ in the Eq. 1 can be ignored such as the band propagation is adiabatic. Eq. 1 becomes:

$$\rho c_p dT = \beta \underline{\underline{\sigma}} : d\underline{\underline{\varepsilon_p}} \quad (2)$$

Consequently, if the constitutive law of the material is known, then the temperature variation is fully representative of the plastic deformation.

3.2. Thermal following of the Lüders band

The beginning of the tensile test (total strain under 10%) of the S235 steel followed by IRT is shown on Fig. 2. All the IRT images recorded during tensile test and shown in Fig. 2 were subtracted with the first image (0% of total strain) to get the temperature variation during the test. A constant scale with boundaries close to the max and the min values met through the 12 images sequence is chosen.

In the beginning of the tensile test, the temperature decreases. The associated homogeneous temperature variation is about -0.40°C until the upper yield stress R_e^u. Just before the upper yield stress (3rd image), a raising of the temperature corresponding to the beginning of the plastic deformation localization can be observed simultaneously near the two specimen edges. When stress is enough, a plastic deformation band, which makes growth the temperature on its way, leaves one side of the specimen to join the other one, deformation localization in the second edge fades; this phenomenon is typical of the Lüders band propagation.

On the 8th image, a second band is forming at the upper end of the specimen. But, this one will be rapidly absorbed by the main band. When the Lüders band stops, plastic deformation tends to become more and more homogeneous along the specimen.

The temperature recordings at the points 1, 2 and 3 (Fig. 2) show a sudden increase in the temperature when the band goes in front of the measurement point. After the band goes beyond each point, it can be remarked that the temperature remains constant, what means that neither elastic nor plastic strains take place; the specimen keeps the heat generated during the band passing.

Moreover, the amplitude of temperature reached after the band passing is observed to increase during the propagation, what means the properties of the Lüders band could change.

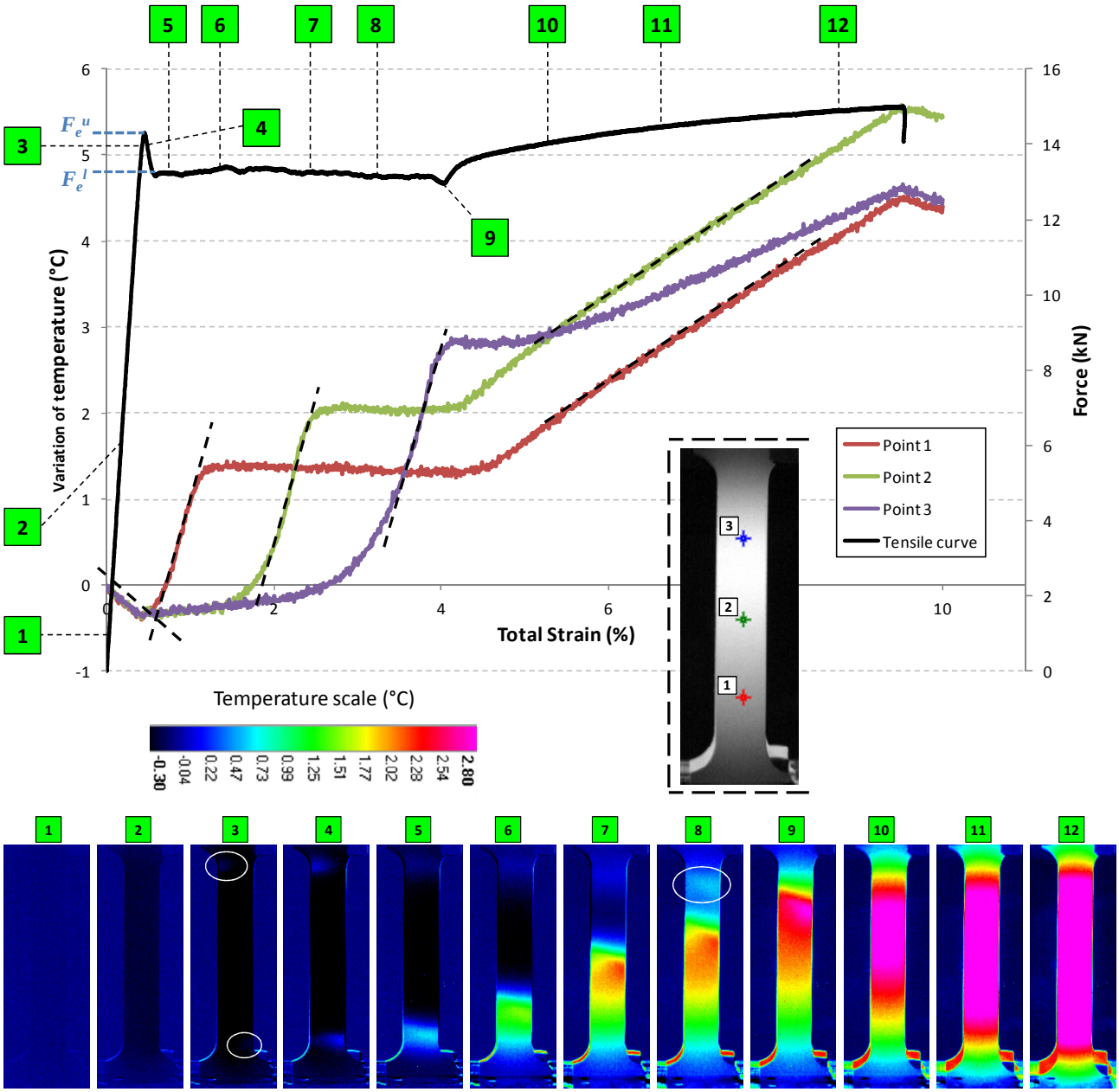

Figure 2. IRT maps obtained while the first 10% of total strain of a S235 steel. The tensile curve (black line) and the temperature evolution (red, green and blue lines) for three points placed on the specimen (see inset) are also depicted. The tensile forces F_e^u and F_e^l corresponding to the upper and lower yield stresses are showed on the tensile curve.

In order to be more sensitive to local variations of temperature on a short period, each image was subtracted with another one which arrives 0.6 s before. Fig. 3(a) shows the new type of obtained image. According to the IRT pictures, the velocity of the band propagation seems constant and approximately 24 times the crossbeam speed v_t. The inclination angle of the band varies hardly during propagation, it is mostly about 60° with respect to the tensile axis. For a given band position, temperature profiles of each line (Fig. 3) show maxima which don't superimpose, what proves the band is tilted.

The shape of the temperature profiles can be fitted by a Lorentz function, like proposed in [21], to deduce the maximum and the integral width of the band. It is found that the maximum is approximately 0.7°C and the integral width 11 mm. Both values strongly depend on the time

elapsed between the two subtracted images. In addition, this value is probably overestimated because of the conduction phenomenon which tends to spread the band.
It is also interesting to note the temperature profile associated to the line 3 on Fig. 3 presents a small negative hook to the rear of the band. This negative hook certainly corresponds to a tensile elastic stress which is higher in this zone than anywhere else. So, is it a consequence of the band propagation or does this tensile state contribute to the successive dislocations unpinning ? In addition, the temperature profile associated to the line 1 presents a small positive hook to the rear of the band. This one could correspond to an elastic compression state. By following this idea and by noticing that the temperature profile associated to the line 2 presents neither a negative nor a positive hook to the rear of the band, it can be assumed that the part of the specimen behind the band rotates.

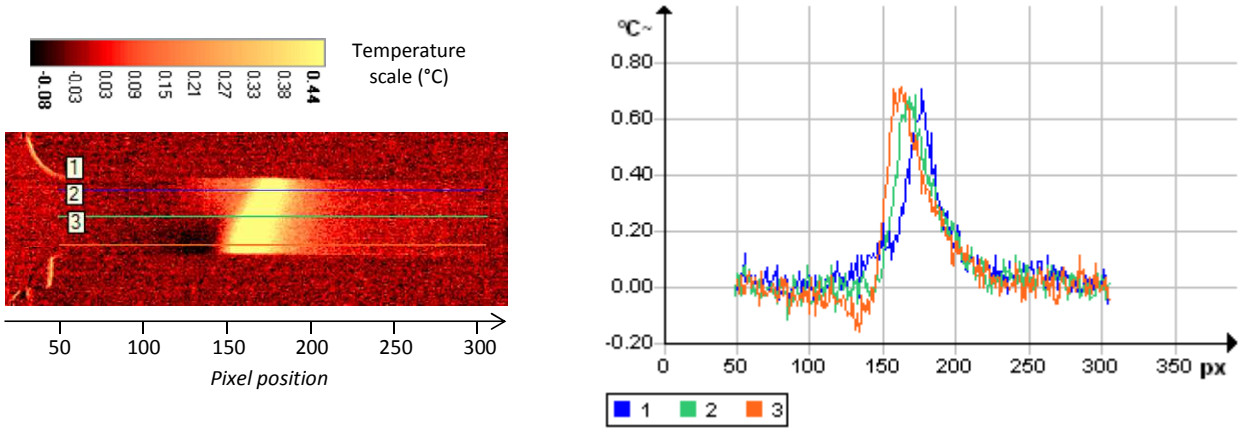

(a) (b)

Figure 3. (a) Typical recomputed image (differences between two original images separated of 0.6 s) obtained during Lüders band propagation in a S235 steel. (b) Temperature profiles along three lines uniformly distributed through the specimen width (see (a)).

Finally, after the Lüders band passing, when the deformation is homogeneous in the specimen (last images on Fig. 2), the temperature is about constant on the whole surface of the gauge length of the specimen and raises much slower than during Lüders band propagation.

4. ESPI and AE as Lüders bands following techniques

4.1. Experimental procedure

Tests on the C35 steel were performed on a 150 kN capacity tensile machine at different crossbeam speeds. The experimental setup, mainly including the speckle interferometer, the acoustic sensors and the tensile machine, is presented on Fig. 4. The theoretical principles of ESPI and AE can be found respectively in reference books [22, 23] and [24]. At the sample scale, ESPI offers a better resolution, one or two orders of magnitude, on material displacements than DIC (Digital Image Correlation) or photoelasticity. Nevertheless, after surface coating preparation, DIC gives direct access to two sensibility vectors without additional equipment [2]. When sample surface is coated with birefringent resin, photoelasticity, as for it, allows to reveal naked-eye Lüders bands [25].
In the present case, the speckle interferometer setup is an in-plane sensitive configuration, known as a Leendertz set-up, with a sensitivity vector $\vec{s}$ parallel to the tensile direction. Speckle patterns are recorded on a CCD camera (1280 pixels × 980 pixels, monochromatic, 8 bits) with a 5µm spatial resolution. One of the mirrors is mounted on a piezo-electric transducer generating optical path differences by translation; it enables to get the phase of the interference pattern at all pixels of the image and obtain a better resolution on measured displacements (~25 nm in practice).

Note that no preparation of the surface of the specimens was performed for ESPI measurements. The surfaces were sufficiently rough to generate the speckle patterns and not too much to keep the plane surface hypothesis and avoid a premature localization.

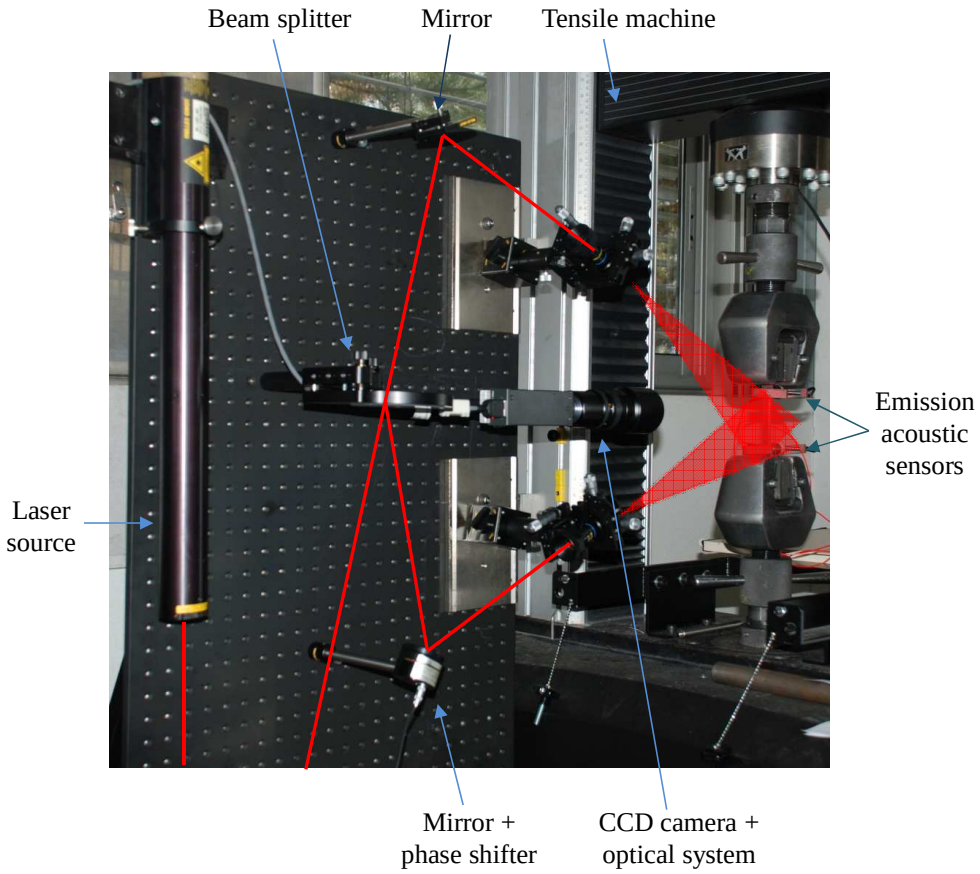

Figure 4. Experimental setup: in-plane speckle interferometer and micro-tensile machine. The laser beam path is schematized as a red line.

For AE measurements, two large-band (50 – 600 kHz) piezo-electric sensors were used. They convert acoustic signal into electric signal machine readable. These sensors are elastically maintained on the surface specimen with the same tension all along the test, Fig. 5. Because of the small size of the specimen heads, sensors are located near the fillet radius. To ensure the crossing of the acoustic wave between the specimen and the sensor, a coupling fluid (thixotropic gel) is inserted between both of them. The electric signal received by each sensor is amplified by a 40 dB pre-amplifier with a 1 MHz cut-off frequency, and then the electric signal is sent towards the acquisition card of the AEwin system (Euro Physical Acoustics). This latter gives intrinsic parameters related to the signals like amplitude, duration, energy, etc...

Many acoustic events do not come from the material been deforming, but they can come from the tensile machine working, slip of the sensors on the sample surface, micro-slips of the sample into the jaws, external noise… So, thanks to an acoustic events localization treatment, it is possible not to take into account those parasite events in the future analysis. The acoustic events localization requires at least two sensors set on the specimen and it enables to know, in our case, the position of the event sources along the gauge length of the specimen with an accuracy of about 5 mm. Given the small size of the specimens, the recorded signal for one acoustic event is a combination of the longitudinal wave, the transversal wave and possibly also some reverberated waves. For localization, longitudinal wave speed is considered, especially since the sensors are more sensible to this type of wave.

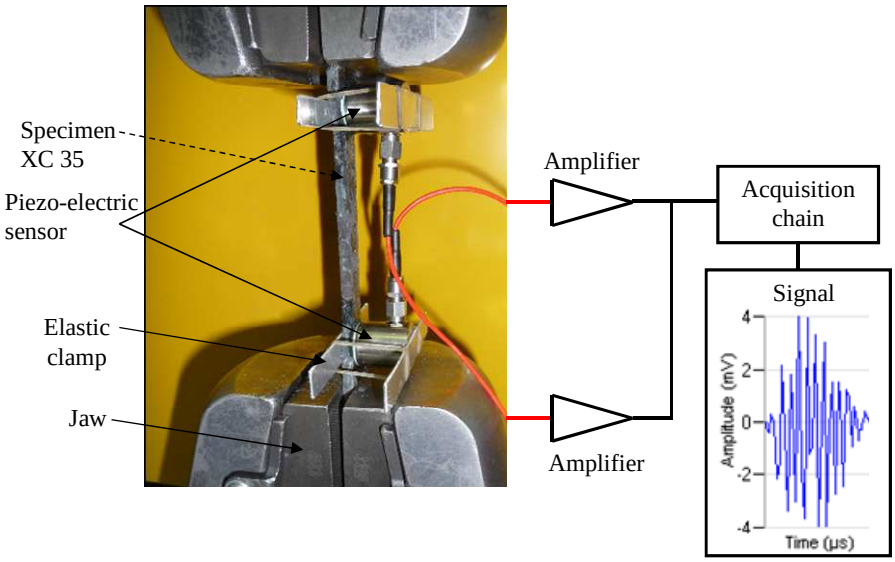

Figure 5. Scheme of the AE setup mounted on tensile specimen.

4.2. AE analysis

The Fig. 6, in a Event Amplitude versus Total Strain representation, shows all the detected events all along a tensile test performed at 0.5 mm.min^{-1}, with a signal amplitude higher than an arbitrary threshold (30 dB). It can be observed that until the disappearance of the Lüders band, a lot of events were detected. About 75% of the total acoustic activity corresponds to only 3% of the total strain, knowing that fracture occurs at 31.1% of the total strain. This observation is consistent with the fact of the band propagation produces a spectacular increase of the mobile dislocations density [26]. In the 5086-0 aluminium alloy [27], Baram also observed that deformation in the Lüders band region generated an high acoustic activity.

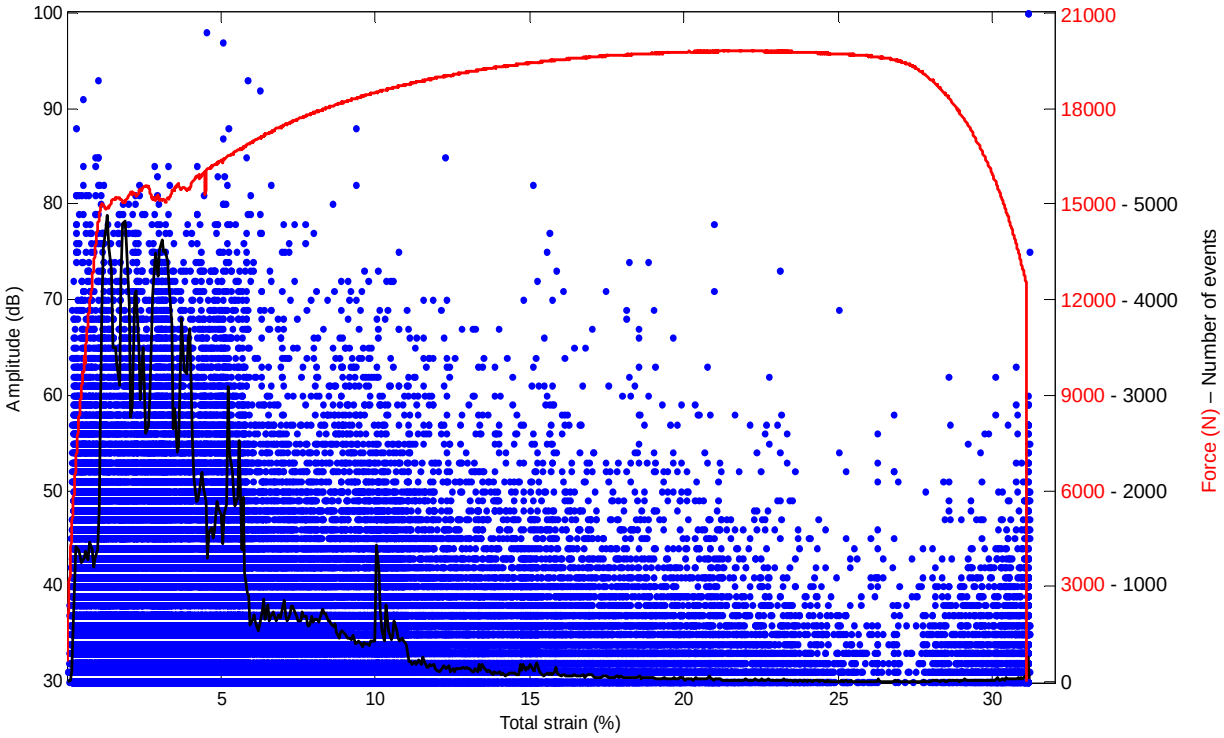

Figure 6. Amplitude versus Total Strain representation of the acoustic events recorded on the two sensors during tensile test of a C35 steel. The tensile curve (red line) and the number of events collected on a 5s time range (black line) are also depicted.

It can be highlighted that the number of events is very variable on a given short duration during the Lüders band propagation. AE activity shows important fluctuations and it can be remarked that this activity presents some intense local maxima when the tensile load presents local minima. Conversely, the AE activity presents some local minima when the tensile load presents maxima. Consequently, that means an important dislocation activity appears for each loading drop, as if each maximal local stress could unpin a lot of dislocations anchored in a certain neighborhood. This unpinning making fall down the stress, then it is necessarily to increase the tensile load again to set in motion dislocations fixed in a neighborhood adjacent to the previous one. That's why, during the reloading, the AE activity rapidly decreases because many less dislocations can move.

4.3. Localization treatment

Localization of the acoustic events along the gauge length of the specimen, Fig. 7, shows that the Lüders band propagation is followed with a good enough resolution, unlike the necking for example. As seen previously thanks to the IRT technique, strain localization occurs near both fillet radius at the end of the elasticity and then, a band with a high strain rate (= high density of events) propagates along the specimen.

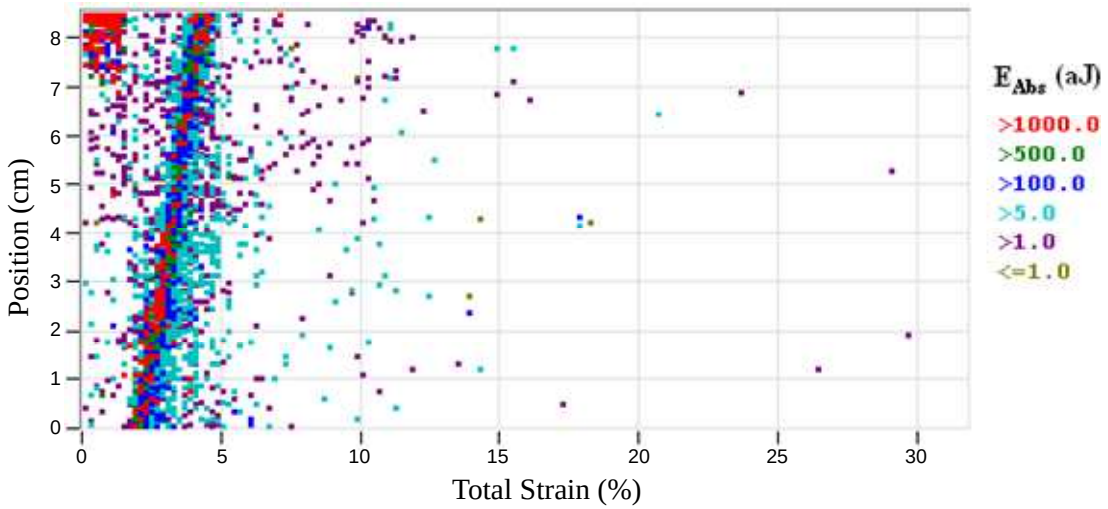

Figure 7. AE sources localization during tensile test on C35 steel.

Spatial distribution of the acoustic events is also correlated with their absolute energy. It can be observed that the most energetic events are localized at the band front. The reason is certainly due to a higher local dislocation activity, what is consistent with the dislocations avalanches which occur gradually at the band front. By keeping only events whose the absolute energy is higher than 500 aJ, a fortiori the most representative of the local strains, the standard deviation obtained on the Lüders band localization is less than 2 mm.

It can be noticed on Fig. 7, the band propagates at constant speed. This speed is about 40 times the crossbeam speed of the tensile machine. Others tests with a crossbeam speed varying between 0,02 and 1 $mm.min^{-1}$ on similar specimens led to the same result. Plekhov [28], in armco iron, finds also a linear dependence between the global deformation speed of the specimen and the propagation speed of the wave (Lüders band) where the plastic strains take place. In the SOLDUR 355 steel, Wattrisse [2] gets the same result.

4.4. AE – ESPI coupling results

To obtain good quality fringe patterns, crossbeam speed of the tensile machine was reduced to 0.02 $mm.min^{-1}$. All speckle patterns were saved manually, because of absence of automatic acquisition.

The Fig. 8 shows the very good correlation between both measurements techniques. As seen previously, at the beginning, plastic strains are localized in a fillet radius of the specimen (position between 0 and 1 cm). Then, when the stress is enough to activate gradually the slip systems in each grain of the gauge length of the specimen, deformation propagates at constant speed ($\approx 40 \times v_t$) by taking a localization band shape tilted of 58° with respect to the tensile axis.
It is interesting to note the inversion of the band inclination about half way (between fringe patterns 4 and 5 Fig. 8). This information can not be obtained with AE by using only two sensors. Thanks to the inclination angle measured on fringe patterns and the range of the AE zone along the specimen for a given total strain, it is possible to deduce the Lüders band width. This one is estimated to about 12 mm. Here, this value is not time dependent and about the same value was measured for different crossbeam speeds, in particular for the tests Fig. 7 (0.5 $mm.min^{-1}$) and Fig. 8 (0.02 $mm.min^{-1}$). Like for IRT, it is clear that Lorentz function applies on fringe patterns would give an integral band width depending on both the time elapsed to obtain these patterns and the crossbeam speed.
Fringes parallel to the tensile axis can be observed behind the band on several fringes patterns. These fringes, also parallel to the sensibility vector of the interferometer, show that the part of the specimen to the rear of the band rotates, as previously deduced by IRT. The same thing is more difficult to detect in front of the band, but these rotations can explain the AE activity outside of the band during its passing.

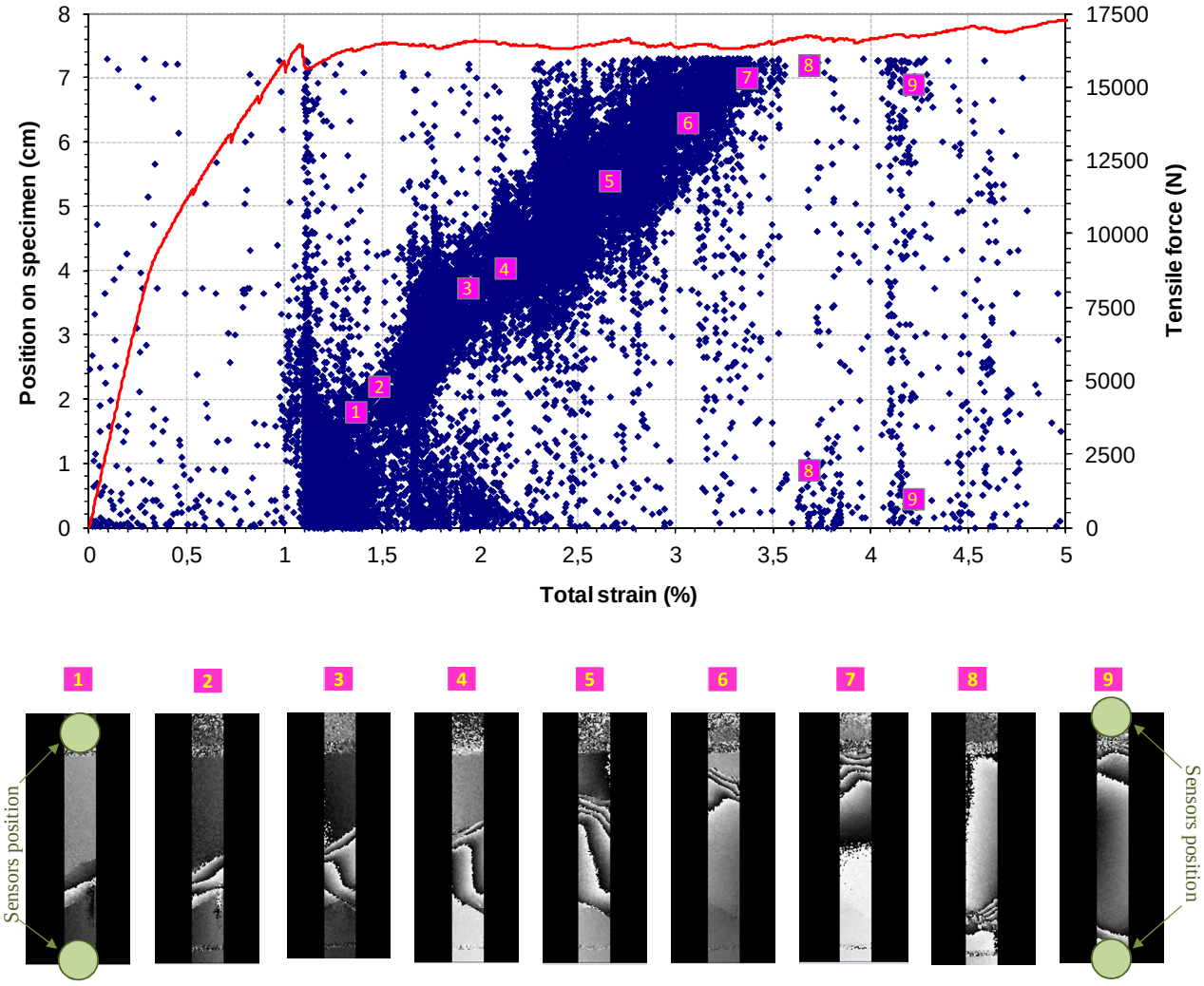

Figure 8. AE – ESPI coupling results collected while Lüders band propagation. The band position obtained by ESPI is reported on the AE data. A very good correlation is found between the two techniques.

Finally, by observing the evolution of the number of events on Fig. 6, one could think that the Lüders band propagates by jerks along the specimen, but according to ESPI results, the band propagation appears continuous. Indeed, it always exists a strain rate noticeably higher (presence of more close fringes) at the band front than in the rest of the specimen, on all fringe patterns, and it can be seen that the band front moves at constant speed from the ESPI pictures. However, jerky propagation of the band could not be measured if the break time or the slowing down of the band is less than the speckle patterns acquisition frequency.

5. Comparison and conclusion

The phenomenon of Lüders band propagation was investigated by three full-field measurements techniques: Infrared Thermography (IRT), Electronic Speckle Pattern Interferometry (ESPI) and Acoustic Emission (AE). Band features such as the ratio crossbeam speed / propagation velocity, inclination angle and band width were reported for a S235 steel by IRT and for a C35 steel by AE – ESPI coupling.

For the two materials, band propagation velocity is much higher than the crossbeam speed. Moreover, for the S235, the ratio crossbeam speed / propagation speed is more than the C35's one, what is consistent with a Lüders plateau greater in the case of the S235. In the two cases, it can be seen this ratio is approximately equal to the length of the plateau, *i.e.* data on S235 and C35 confirm the following equation given by Hähner [1]:

$$v_t = \varepsilon_p \times v_{BPL} \tag{4}$$

where v_t is the crossbeam speed, ε_p the plastic strain reached at the end of the Lüders plateau and v_{BPL} the Lüders band propagation velocity. This equation comes directly from an analysis of the propagation of the plastic front by assuming that the plastic strain is constant in the band and null outside, like shown in Fig. 9.

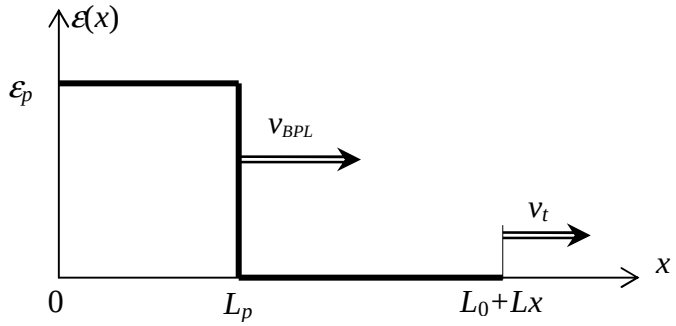

Figure 9. Scheme illustrating the propagation of the plastic front of a Lüders band.

So, the specimen elongation *Lx* would be only due to the propagation of the plastic front. AE measurements, Fig 7, confirm this hypothesis: there is only emission at the band front and, on each side of this front, there is a very weak acoustic activity, so no significant dislocation activity. When the length *Lp* travelled by the plastic front is equal to L_0+Lx (L_0: initial length of the specimen before the band apparition), the Lüders band crossed all the specimen and disappears.

The relation (4) was checked for the S235 at 10 mm.min^{-1} and for all experiments on C35 whatever the crossbeam speed between 0,02 mm.min^{-1} and 1 mm.min^{-1}, and it's found respectively : $\varepsilon_p = \frac{v_t}{v_{BPL}} \approx \frac{1}{24} = 4{,}1\%$ and $\varepsilon_p = \frac{v_t}{v_{BPL}} \approx \frac{1}{40} = 2{,}5\%$, what is close to the length of the experimental Lüders plateau on tensile curves (Fig. 2, Fig. 6 and Fig. 8). However, according to the temperature evolutions in front of the three points Fig. 2 and the relation Eq. 2, plastic strains inside the Lüders band could not be constant along the propagation and the modeling proposed in Fig. 9 would be unsuitable. More investigations have to be done.

For the two materials, the inclination angle with respect to the tensile axis is almost the same, 60° for the S235 and 58° for the C35. Nevertheless, this angle can vary and it was observed at the beginning of the test on the S235, the band was close to 90° and at half way of the band travel in the C35, the angle inverted, going from 58° to -58°.
Because of the movement of the band, it is difficult to measure a not time dependent band width. Yet, the AE – ESPI coupling allowed to introduce a way to determine a band width independently of the time and the crossbeam speed. But, accuracy of this method remains to define.
Concerning the band propagation, it was shown thanks to IRT, just behind the band, one part, the lower part for example, would be under purely elastic tensile stress while the other part, the upper part in this case, would be under purely elastic compressive stress. This particular mechanical state induces rotation of the part of the specimen located to the rear of the band. This assertion was confirmed by ESPI observations and, to a lesser extent, by AE.
Thanks to AE, important dislocations activity was observed during the Lüders band passing and correlation was found between the evolution of the dislocations activity and the tensile curve fluctuations. This serrated dislocations activity let think of a jerky propagation which seems in contradiction with ESPI and IRT (but on a different steel) measurements at the acquisition frequencies used. In fact, the bands determined by IRT and ESPI are obtained on time scales, relatively to the crossbeam speed, much smaller than the jerks measured by AE, what could explain the continuous aspect of the band get by IRT and ESPI, contrarily to the AE.
The following table, Table 2, summarizes the features of each technique and the measurements performed by.

Table 2. Technique features and possible Lüders band properties measurements.

Technique	**Type of propagation detected**	**Spatial resolution**	**Accuracy**	**Total strain rate (s^{-1})**	**Possibility of band inclination measurement**	**Possibility of band position estimation**	**Band velocity/ crossbeam speed ratio**
IRT	Continuous in S235 at 33Hz	0.25mm/pix	25mK on temperature	1.7×10^{-1}	Yes, 60° in S235	Yes	24
ESPI	Continuous in C35 at ~0.1Hz	5µm/pix	25nm on displacement 10^{-6} on strain	3×10^{-4} to 1.5×10^{-1}	Yes, 58°/-58° in C35	Yes	40
AE	Continuous but jerky at random time acquisition with a minimum interval of 2.10^{-5} s		±5mm on event localization		No with only 2 sensors	Yes	

At last, let's remind the two experiments were performed in two different laboratories, on two different tensile machines, with two different steels and at two different crossbeam speeds, what makes difficult the comparison between the techniques. Consequently, to refine this study, coupling of the three analysis techniques on the same material is being implemented.

References

[1] P. Hähner. Theory of solitary plastic waves – Part I: Lüders bands in polycrystals. *Applied Physics A Solids and Surfaces*, 1994, 58:41–48.

[2] B. Wattrisse, A. Chrysochoos, J.-M. Muracciole, M. Némoz-Gaillard : Kinematic manifestations of localisation phenomena in steels by digital image correlation. *Eur. J. Mech. A-Solids*, 20:189–211, 2001.
[3] O.A. Plekhov, O.B. Naimark, N. Saintier, T. Palin-Luc. Elastic–Plastic Transition in Iron: Structural and Thermodynamic Features. *Technical Physics*, 2009, 54(8):1141–1146.
[4] R. Shabadi, S. Kumar, H.J. Roven, E.S. Dwarakadasa. Characterisation of PLC and parameters using laser speckle technique. *MSEA*, 2004, 364:140–150.
[5] H. Neuhäuser, F.B. Klose, F. Hagemanna, J. Weidenmüller, H. Dierke, P. Hähner. On the PLC effect in strain-rate and stress-rate controlled tests–studies by laser scanning extensometry. *Journal of Alloys and Compounds*, 2004, 378:13–18.
[6] Q. Zhang, Z. Jiang, H. Jiang, Z. Chen, X. Wu. On the propagation and pulsation of Portevin-LeChatelier deformation bands: An experimental study with digital speckle pattern metrology. *Int. J. Plasticity*, 2005, 21:2150–2173.
[7] B. Guelorget, M. François, C. Vial-Edwards, G. Montay. Strain rate measurement by ESPI: A new look at the strain localization onset. *Mat. Science & Eng*., 2006, 415: 234–241.
[8] G. Montay, M. Francois, M. Tourneix, B. Guelorget, C. Vial-Edwards, I. Lira. Analysis of plastic strain localization by a combination of the speckle interferometry with the bulge test. *Opt. & Lasers Eng.*, 2007, 45:222–228.
[9] J. Petit, G. Montay, M. François. Localisation Phenomenon Investigation on SMATed Stainless Steel Samples by Speckle Interferometry. *Strain*, 2011, 47:363–371.
[10] P. Hogström, J.W. Ringsberg, E. Johnson. An experimental and numerical study of the effects of length scale and strain state on the necking and fracture behaviours in sheet metals. *International Journal of Impact Engineering*, 36 (2009) 1194–1203.
[11] F.B. Klose, F. Hagemann, P. Hähner, H. Neuhäuser. Investigation of the Portevin-Le Châtelier effect in Al-3wt.%Mg alloys by strain-rate and stress-rate controlled tensile tests. *MSEA*, 2004, 93:387–389.
[12] Z. Jiang, Q. Zhang, H. Jiang, Z. Chen, X. Wu. Spatial characteristics of the Portevin-Le Chatelier deformation bands in Al-4 at%Cu polycrystals. *MSEA*, 2005, 403:154–164.
[13] H. Dierke, F. Krawehl, S. Graff, S. Forest, J. Săchl, H. Neuhäuser. Portevin–LeChatelier effect in Al–Mg alloys: Influence of obstacles – experiments and modelling. *Computational Materials Science*, 2007, 39:106–112.
[14] N. Ranc, D. Wagner. Experimental study by pyrometry of Portevin–Le Châtelier plastic instabilities—Type A to type B transition. *MSEA*, 2008, 474(1–2):188–196.
[15] Z. Marciniak, K. Kuczyński. Limit strains in the processes of stretch-forming sheet metal. *Int. J. Mech. Sci.*, 1967, 9:609–620.
[16] R. Mahmudi. Plastic instability in equi-biaxial deformation of aluminium alloy sheet. *J. Mater. Process. Technol.*, 1996, 57:266–271.
[17] A.H. Cottrell. Report of the Bristol Conference on Strength Solids, *Phys. Soc. Lond.*, 1948, 30.
[18] W.G. Johnston and J.J. Gilman. *J. Appl. Phys*, 1959, 30:129.
[19] Louche, H., Chrysochoos, A. Thermal and dissipative effects of accompanying Lüders band propagation. *Materials Science and Engineering A*, 2001, 307(1-2):15-22.
[20] Chrysochoos, A., Louche, H. An infrared image processing to analyse the calorific effects accompanying strain localisation. *International Journal of Engineering Science*, 2000, 38:1759–1788.
[21] B. Guelorget, M. François, Guillaume Montay. Strain localization band width evolution by electronic speckle pattern interferometry strain rate measurement. *Scripta Materialia*, 2009, 60(8):647–650.
[22] R. Jones, C. Wykes. Holographic and Speckle Interferometry, 2nd edn. vol. 6, Cambridge Studies in Modern Optics, Cambridge University Press, Cambridge, 1989.
[23] G. Cloud. Optical Methods of Engineering Analysis, Cambridge University Press, NY, 1995.

[24] J. Roget. Essais non destructifs. L’émission acoustique. Mise en œuvre et application. AFNOR - CETIM, 1988.
[25] M. Grumbach, M. Prudhomme, Ph. Lemble. Lüders Bands Propagation At Steel Yield Point, Films. IRSID, 1962.
[26] P. Fleischmann, F. Lakestani, J.C. Baboux. Analyse Spectrale et Energétique d'une Source Ultrasonore en Mouvement – Application à l'Emission Acoustique de l'Aluminium soumis à Déformation Plastique. *Materials Science and Engineering*, 1977, 29:205–212.
[27] J. Baram, M. Rosen. Acoustic Emission Generated during the Tensile Testing of Aluminium Alloys. *Materials Science and Engineering*, 1979, 40: 21–29.
[28] O.A. Plekhov, O.B. Naimark, N. Saintier, T. Palin-Luc. Elastic–Plastic Transition in Iron: Structural and Thermodynamic Features. *Technical Physics*, 2009, 54(8):1141–1146.

Experimental investigations on the cyclic behavior and fatigue of extruded 2017 aluminum alloy

Abdelghani May[1,2], Lakhdar Taleb[2,*], Mohamed el Amine Belouchrani[1]

[1]Laboratoire Génie des Matériaux, EMP, BP 17 Bordj El-Bahri Algiers, Algeria
[2]INSA/GPM, BP 08 avenue de l'université, 76801 St Etienne du Rouvray Cedex, France
* Corresponding author: lakhdar.taleb@insa-rouen.fr

Abstract The present work is devoted to the study of the anisotropic behavior of an extruded aluminum alloy under cyclic loading in axial and shear directions at room temperature. First, we have studied the elastoplastic behavior through the evolution of the isotropic and kinematic hardening evaluated considering the stress-strain loops in axial and shear directions. Second, we have investigated the fatigue damage of the material in both directions. The observed lifetimes seem rather short regarding the elastic shakedown obtained at the steady state.

Keywords: Anisotropic behavior, Extruded alloys, isotropic and kinematic hardening, cyclic plasticity.

1. Introduction

Aluminum alloys are frequently selected for many applications where low density and high strength-to-weight ratios are required. Thus, 2XXX series are currently being used as the main structure in components which are often subjected to cyclic loading. Therefore, we devote this work to the investigation of mechanical anisotropy in the cyclic behavior of aluminum alloy through stress controlled tests.

Many authors focused their work on the influence of microstructural and metallurgical states on the behavior of age hardened aluminum alloys during cyclic loading [1-6]. Furthermore, the anisotropy of mechanical behavior in metallic alloys during monotonic deformation was investigated by several authors [7-9]. Firstly, this anisotropy was discussed only for rolled or extruded alloys, such as metal sheets. Achani et al. [10] characterized the plastic anisotropy of extruded aluminum alloys 7003 and 6063 by uniaxial tensile testing and disc compression tests, showing that the increase of flow stress is directional and most significant for orthogonal sequences. On the other hand, some authors [11, 12] observed a strong anisotropic flow behavior between the rolling and transverse direction of rolled aluminum alloys during uniaxial tests. Recently, other authors have studied the effect of plastic anisotropy on the mechanical behavior of a rolled aluminum alloy 7075 [13]. They stated that the crystallographic texture and grain morphology gave rise to a strong plastic anisotropy in the rolled aluminum plate; they observed that the effect of plastic anisotropy is less for notched than for smooth tensile tests. Recently, Saï et al. [14] have focused their work on modeling the cyclic behavior of aluminum alloys. They up-dated the multi-mechanism models to be applied to anisotropic materials such as 2017 aluminum alloy.

The fatigue behavior of aluminum alloys under stress control tests has also been investigated for many years [3, 15, 16]. It has been shown that a microstructure strengthened by nonshearable and hard particles is usually preferable to resist more at fatigue crack initiation [17]. Similarly, Malekjani et al. [18] demonstrated the beneficial effect of precipitates at the core of the sample on the fatigue life during cyclic loading. Furthermore, according to [19, 20], fatigue evolution is not accompanied by any apparent modification of either the form or the aspect of the test specimen. Flaceliere et al. [21] studied the effect of shakedown phase on cyclic behavior of polycrystalline materials. They stated that the hardening saturation effect at the beginning of the fatigue lifetime and damage-induced softening at the end of fatigue lifetime describe all the cyclic behavior during loading. Despite all these studies, aluminum alloy anisotropy and its influence on the evolution of the cyclic behavior is not yet well investigated. Therefore, we devote the present paper to the following investigations performed on a 2017 aluminum alloy at room temperature:

- Study of the mechanical anisotropy in cyclic behavior through the stress-strain responses.
- Investigation of the cyclic hardening using the concept of isotropic and kinematic hardenings and their dependence on the loading direction.
- Correlation between the rate of isotropic hardening, elastic shakedown and fatigue lifetime.

This article is composed of three parts. The first section is devoted to the description of our experimental procedure, while the second section presents the results obtained about the cyclic behavior and their discussions. In the last section, the results obtained concerning fatigue damage evolution will be discussed.

1. Experimental procedure

1.1 Material

All the investigations carried out in this study were performed at room temperature using a 2017 aluminum alloy. The chemical composition is given in Table 1.

Table 1. Chemical composition of the material used (wt %)

Cu	Mg	Mn	Fe	Si	Zn	Ni	Cr	Al
3.9 – 4.0	1.1 – 1.2	0.7 – 0.8	0.5 – 0.6	0.6 – 0.7	< 0.21	< 0.16	< 0.10	Bal.

It is well-known that the hardening of this alloy arises from Al_2Cu and Al_2CuMg precipitation, provided that particles are finely and densely distributed. However, these precipitations lead to heterogeneity phenomena of the material that can generate anisotropy in mechanical behavior.

1.2. Specimens and experimental device

All the specimens were machined from solid bars extruded in the axial direction and a tubular shaped sample with two massive heads is used; its gage length is 46 mm in the central part where an extensometer of 25 mm gage length is installed. In this zone, the outer and inner diameters are 20 mm and 17 mm, respectively (Fig. 1), making it possible to have relatively thin tubes.

To ensure the same microstructural state of the material all specimens were heat treated according to a T3 thermal cycle (Fig. 2). The tests were performed with a MTS axial-torsional servo-hydraulic machine, an extensometer was used to measure the axial and torsional displacements in the central area of the specimen. The gage length of the extensometer is 25 mm for the shearing tests and 12 mm in tension/compression tests.

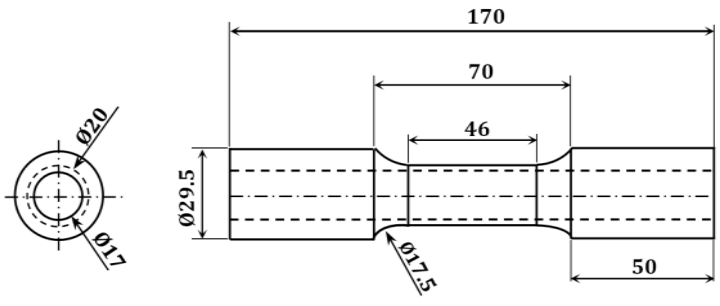

Figure 1. Geometry of the specimen used in the study

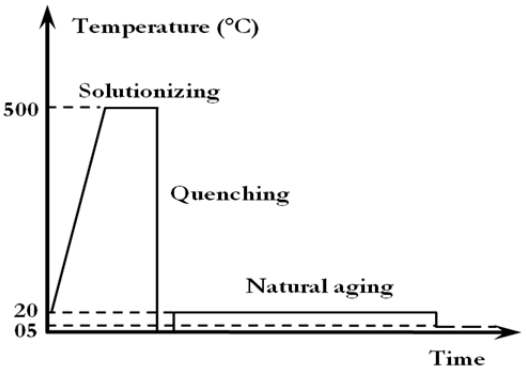

Figure 2. Sequences of the heat treatment applied to specimens

A permanent cooling of the specimen is applied during tests in order to remain close to room temperature and minimize the effect of heating due to the dissipation process observed under cyclic loading in the plastic domain.

1.3. Tests performed

Two types of stress-controlled tests were performed in this study. First, a cyclic tension-compression loading is applied with a zero mean stress (R = -1). In order to ensure a ‘‘perfect” uniaxial stress state, all the tests were performed under bi-axial controlled conditions, where the torque is set at zero (Fig. 3a). The second type is a cyclic shear tests applied with zero axial stress on six identical specimens (Fig. 3b). The applied frequency for both tests is 0.5 Hz during the first 400 cycles and 1 Hz after.

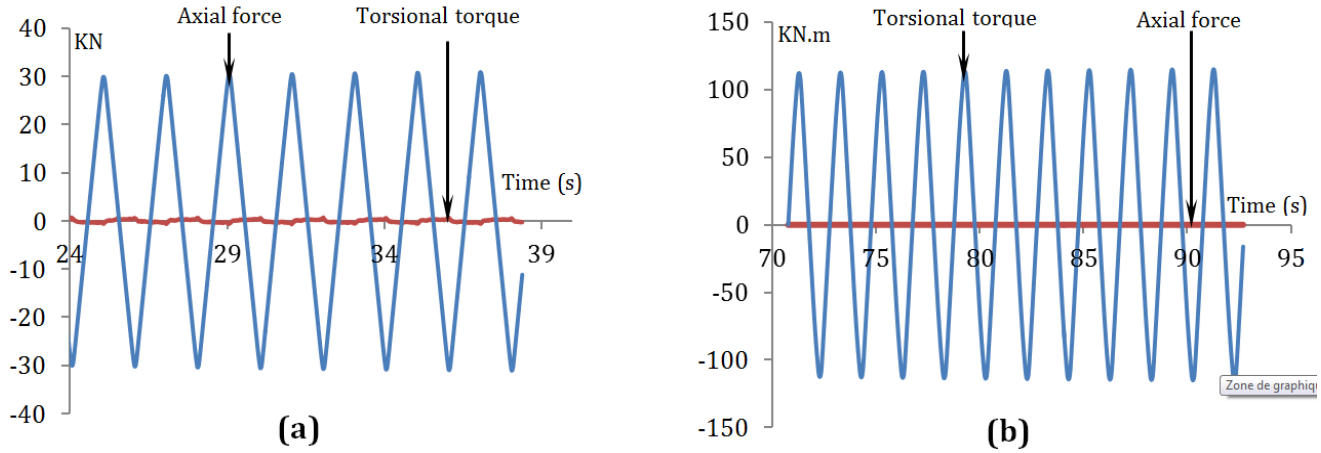

Figure 3. The two types of stress controlled tests performed in the study. (a) Cyclic tension-compression under zero shear stress; (b) Cyclic shearing stress under zero axial stress

The list of the tests performed in this study is shown in Table 2 where**:**

- σ_{zz} : is the maximum stress applied in tension – compression.
- $\sigma_{\theta z}$: is the maximum stress applied in shearing.
- σ^{eq} : is the equivalent maximum shearing stress using Von Mises criterion.

Note that the equivalent shearing amplitudes were calculated using Von Mises criterion.

Table 2. List of the tests performed in this study

Tension-compression tests		Shearing tests			
σ_{zz} (MPa)	Reference	Torque (N.m)	$\sigma_{\theta z}$ (MPa)	σ^{eq} (MPa)	Reference
240	ax240	80	98	170	sh80
260	ax260	90	110	190	sh90
280	ax280	100	122	211	sh100
300	ax300	110	136	235	sh110
320	ax320	120	148	256	sh120
340	ax340	130	160	277	sh130
360	ax360				

2. Results of the cyclic behavior

Before the analysis of the cyclic behavior, let us first see the evolution of lifetimes obtained under the axial and shear directions in Fig. 4.

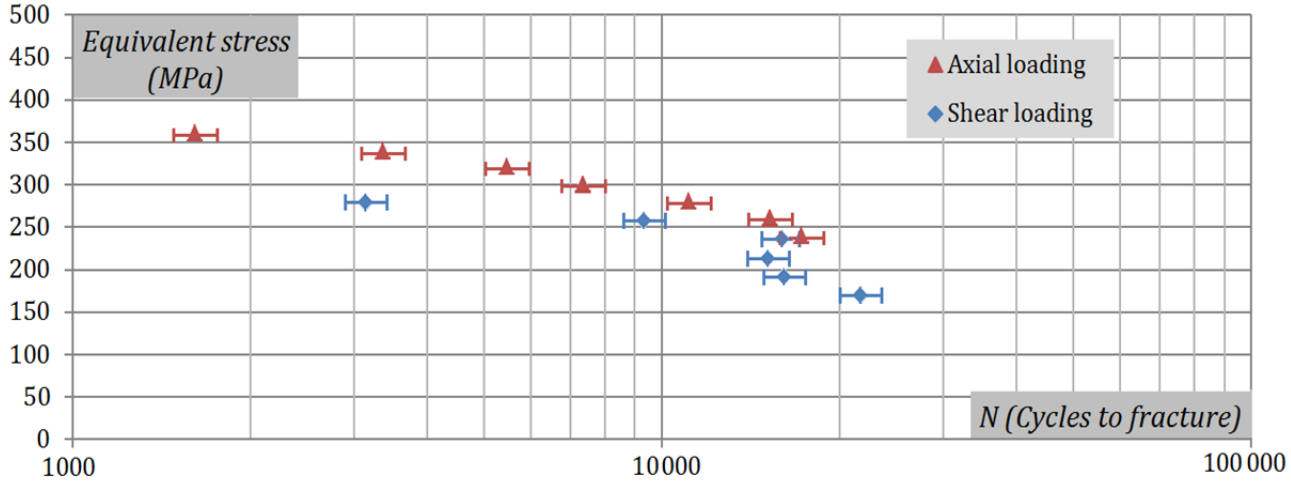

Figure 4. Wohler curve of a 2017 aluminum alloy for the axial and the shear loadings.

Note that each point of these curves represents the average result of at least two tests. Indeed, we have a more or less linear increase in the number of cycles to failure, when the applied maximum stress decreases. According to the two curves presented in Fig. 4, we can also remark anisotropy between the two directions in fatigue life. In fact, we notice a significant difference between lifetimes in axial and shear directions. Indeed, for the same equivalent stress amplitude, lifetime in the axial direction is higher compared to that in the shear direction. However, one can expect the opposite observation in case of strain control.

2.1. Test results under axial loading

To better represent the evolution of the stress-strain loops, we plot for each test and in the same graph the first and the stabilized loops. The first loop is taken when the maximum set-point stress is reached. The stabilized stress-strain loop is chosen at mid-life where the strain hardening does not evolve significantly. In Fig 5, we depict six graphs representing axial tests.

2.2. Test results under shear loading

In Fig. 6a, we depicted the equivalent stress versus the equivalent strain, where the maximum stress in Von Mises equivalence is 277 MPa. In this case, we have the plastic flow which remains high even in mid-life. However, in Fig. 5a, the maximum axial stress is 360 MPa, the plastic flow decreases gradually until it stops before mid-life and the behavior becomes almost elastic. This behavior suggests the anisotropy of the material between the axial and shear directions.
Such anisotropy appears also in the yield stress given in Table 3 where the axial elastic limit is 207 MPa while the equivalent shearing one is only 142 MPa. This behavior will be discussed in more details in the next section.

Table 3 Mechanical properties of the 2017 aluminum alloy determined from monotonic loading

Axial yield stress at 0.01%	Axial yield stress at 0.2%	Young's modulus E	Equivalent shear yield stress at 0.01%	Coulomb's modulus G
207 MPa	284 MPa	72 GPa	142 MPa	23.5 GPa

2.3. Discussion

To study the cyclic behavior of 2017 aluminum alloy in plasticity, we have to investigate the evolution of the elastic domain in the stress space which is usually represented by a translation of its center (kinematic hardening) and the expansion (isotropic hardening) of its size. In the case of isotropic material, the yield surface expands generally in a homogeneous manner all over the

directions. However, this behavior remains debatable for the majority of aluminum alloys under a high stress loading.
As it is not an easy task to identify the linear part of the stress–strain diagram and therefore the elastic domain, we have admitted a small equivalent plastic strain offset equal to 0.0001. The isotropic and kinematic hardening variables were evaluated in each cycle using the same formulation used in [22]**.** In Fig. 7, we show how the isotropic and kinematic cyclic hardening variables are estimated according to:

$$\begin{cases} |\sigma_{max} - X| - R - \sigma_y = 0 \\ |\sigma_{off} - X| - R - \sigma_y = 0 \end{cases} \text{ And since } \begin{cases} \sigma_{max} - X > 0 \\ \sigma_{off} - X < 0 \end{cases} \qquad \text{Then, } \begin{cases} R = \frac{\sigma_{max} - \sigma_{off}}{2} - \sigma_y \\ X = \frac{\sigma_{max} + \sigma_{off}}{2} \end{cases}$$

R and X represent a first approximation of the isotropic and kinematic hardening variables respectively; σ_{max} is the maximum equivalent stress reached in the considered cycle while σ_y is the initial elastic limit deduced from the first cycle. σ_{off} is the stress corresponding to 0.0001 of plastic strain offset obtained during the unloading (see Fig. 7a). In Fig. 7b, we depicted two experimental examples. The obtained results are given in Fig. 8 and Fig.9.
According to the results obtained under axial loadings, we note that the increase of R is slightly high during the first cycles, where the maximum stress set-point is reached (Fig. 8a); this progression seems to be less important after the 40 first cycles, which depends strongly on the maximum stress of each test. However, the X variable decreases in all the tests (Fig. 8b), especially when the maximal applied stress is slightly high.

The same work was done for shear loading; the obtained results are plotted in Fig. 9 which shows that shear loading leads to more kinematic hardening than the isotropic one when the maximum applied shear stress is relatively small. But when the shear stress is relatively high, we obtained a significant hardening for both isotropic and kinematic types.
Comparing the two types of the tests, we deduce once again a relatively significant anisotropy in cyclic behavior. In fact, the isotropic hardening increases cyclically in the two directions of the tests but more significantly in the axial one. Furthermore, kinematic hardening decreases in both directions but more significantly in the axial one.

The amount of anisotropy obtained in the two directions of loading can be attributed to the nature and the size of dispersed precipitates in the alloy. This anisotropy is even larger when the maximum stress is high, because of the increase in the resistance of the precipitates to the dislocation movements which become more and more dense.

Furthermore, we can notice that the evolution of isotropic hardening may be correlated with the evolution of the shakedown limit. In order to understand this relationship, we have to investigate the behavior of our material in shakedown phenomenon where the mechanical behavior becomes purely elastic. The plastic strain is used to estimate the shakedown occurrence. We assume that:
$\varepsilon = \varepsilon^e + \varepsilon^p$ where ε^e and ε^p are respectively the elastic and the plastic strains.
With this assumption, we estimate the plastic deformation at any point of the stress-strain loops. Then, we assume that shakedown state is reached when the plastic strain of a given cycle is less than 0.0001. This is a reasonable assumption, since beyond this limit, it becomes very difficult to assess both isotropic and kinematic hardening (R and X). The procedures presented in **Error! Reference source not found.** illustrate the method used to determine the occurrence of the shakedown phenomenon from the stress-strain loops and from the ε^p versus number of cycle curves. However, when the maximum stress is too high, the behavior may be different. Indeed, the plastic strain reaches a periodic stabilized limit state; this phenomenon is referred as plastic

shakedown.

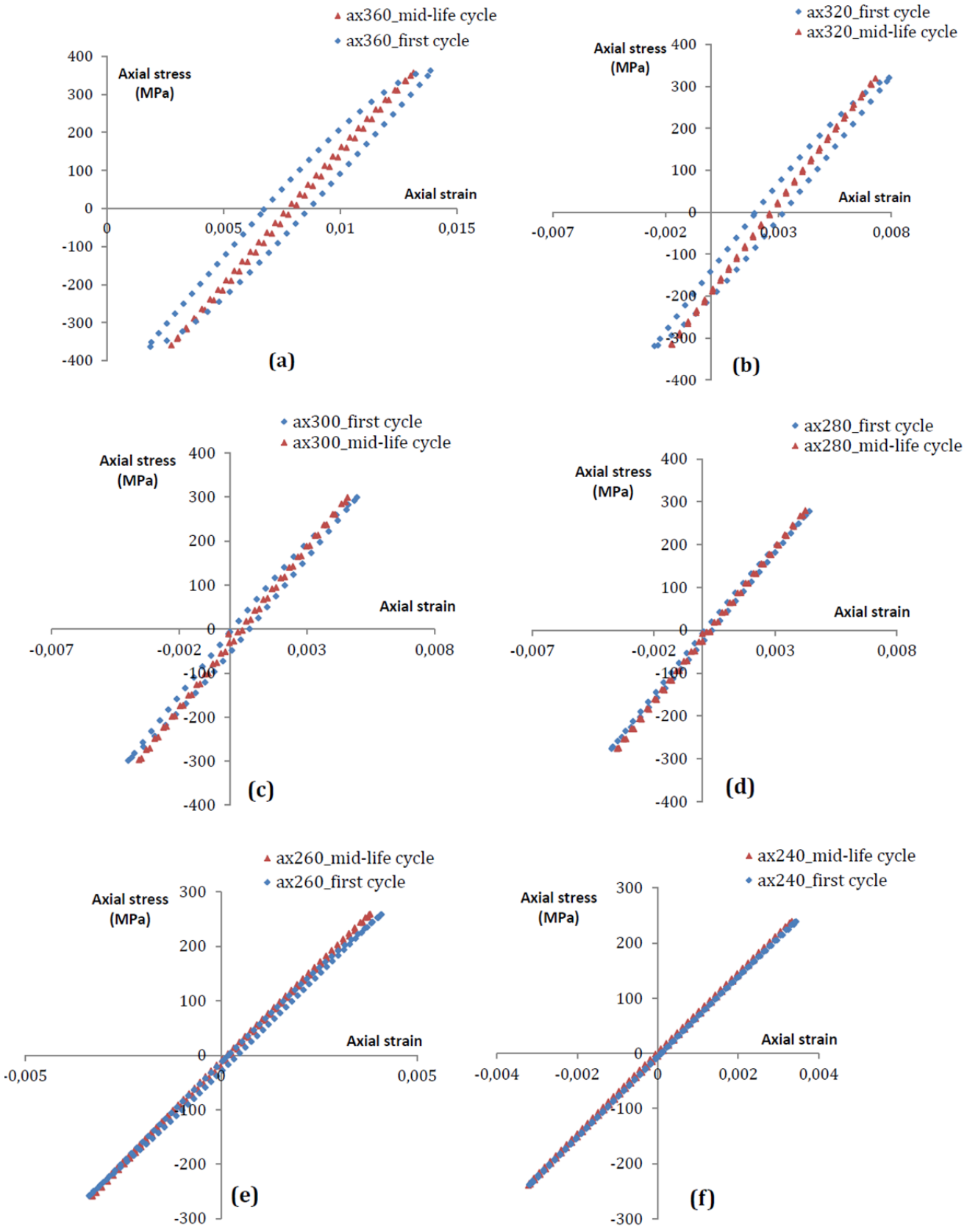

Figure 5. Axial stress–strain loops (first and mid-life cycles)

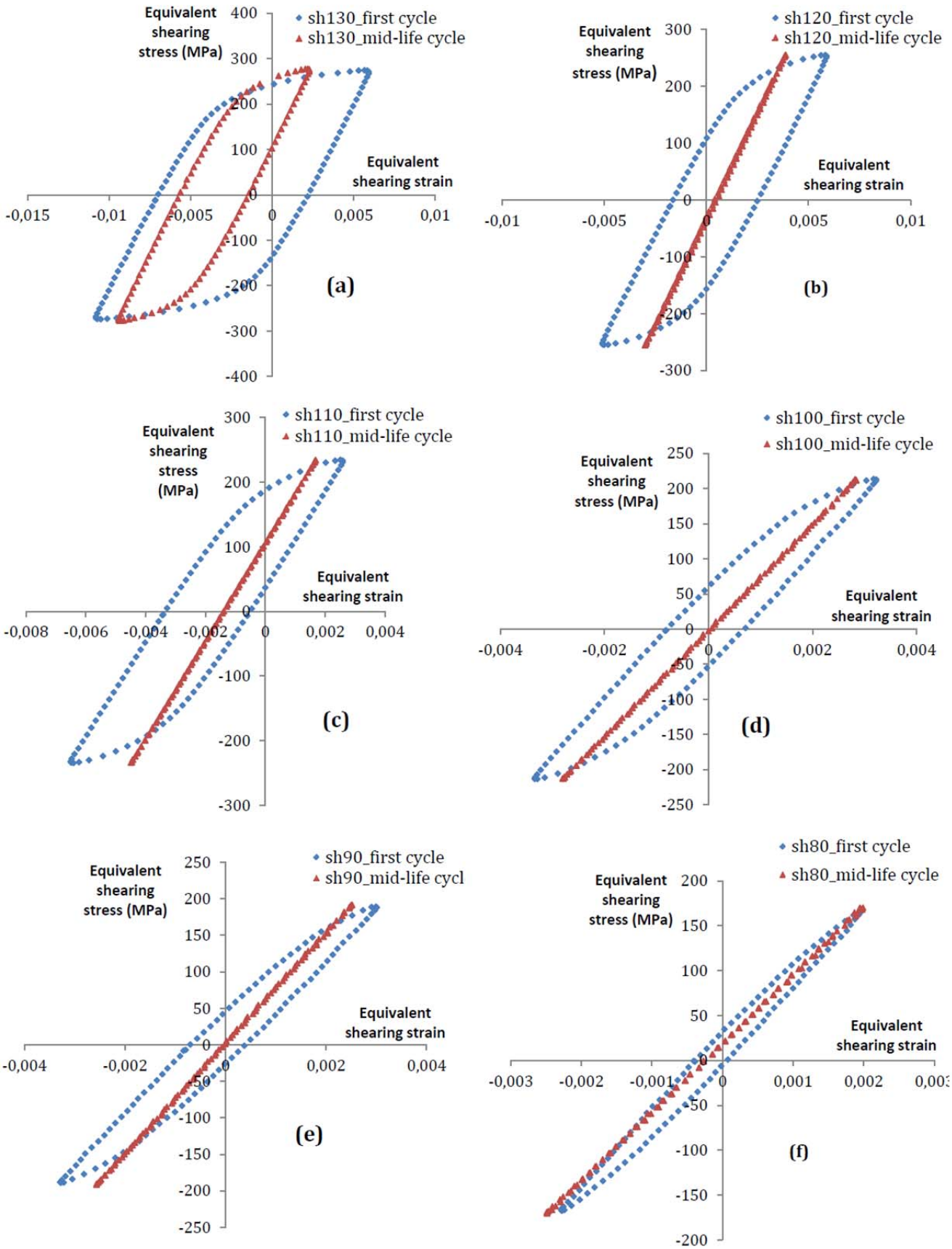

Figure 6. Results of the shear tests: Equivalent shearing stress ($\sqrt{3}\sigma_{\theta z}$) versus equivalent shearing strain ($2\varepsilon_{\theta z}/\sqrt{3}$) loops

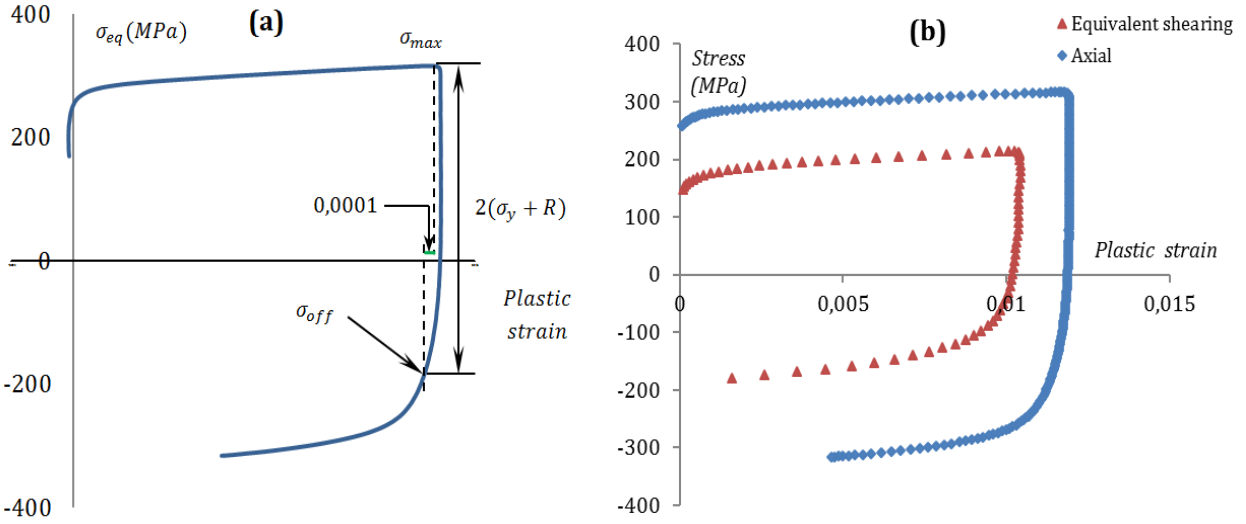

Figure 7. Evaluation of isotropic and kinematic hardenings: (a) Method of determining σ_{off} and σ_{max} (b) Experimental examples responses of the two test types performed in the present work

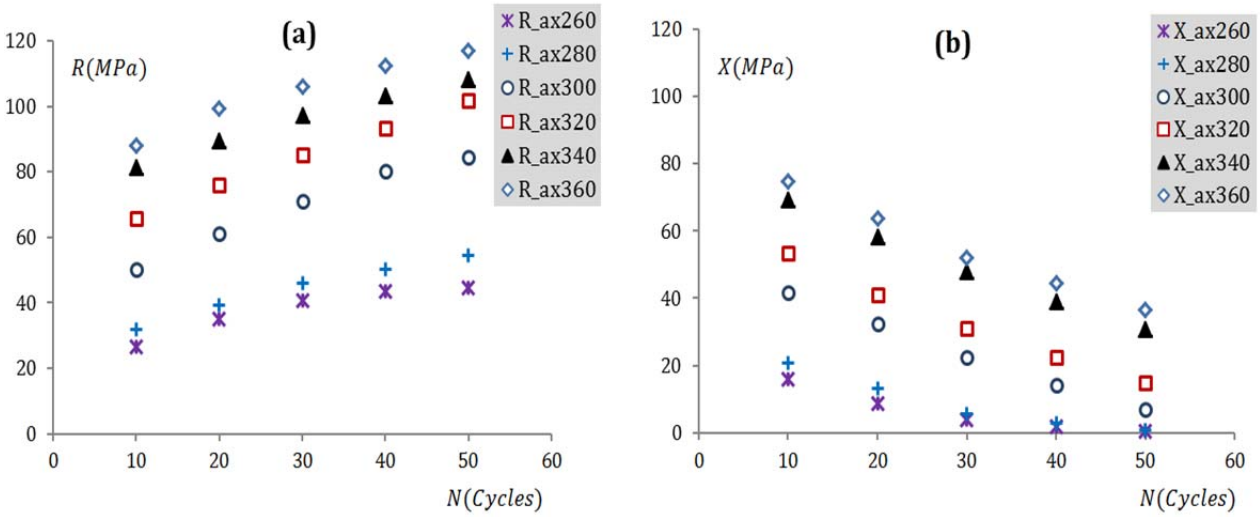

Figure 8. Evolution of cyclic hardening in axial loadings: (a) evolution of the variable R (pseudo isotropic hardening); (b) evolution of the variable X (pseudo kinematic hardening)

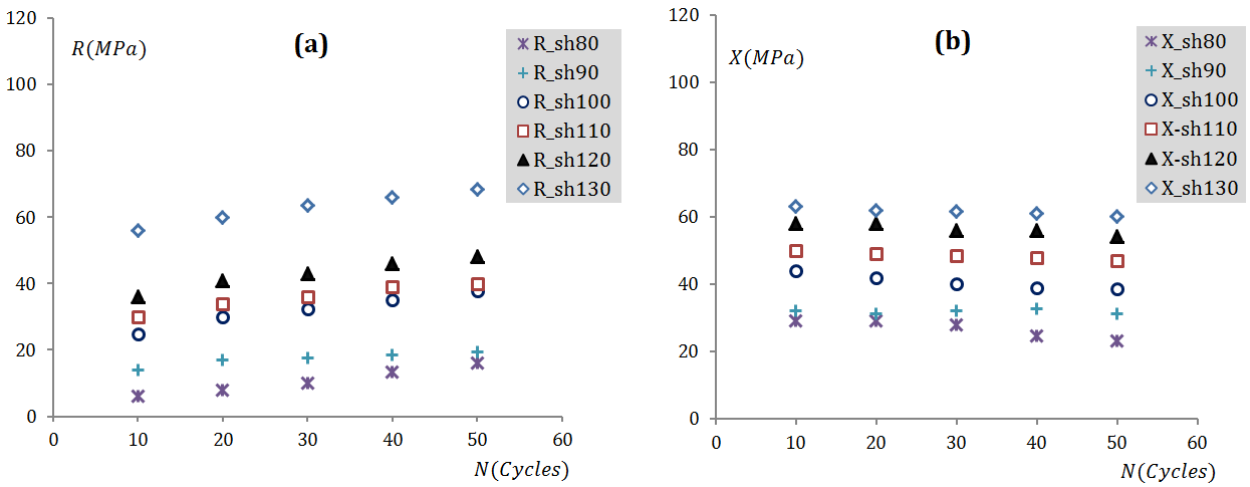

Figure 9. Evolution of cyclic hardening in shear loadings: (a) evolution of the variable R; (b) evolution of the variable X

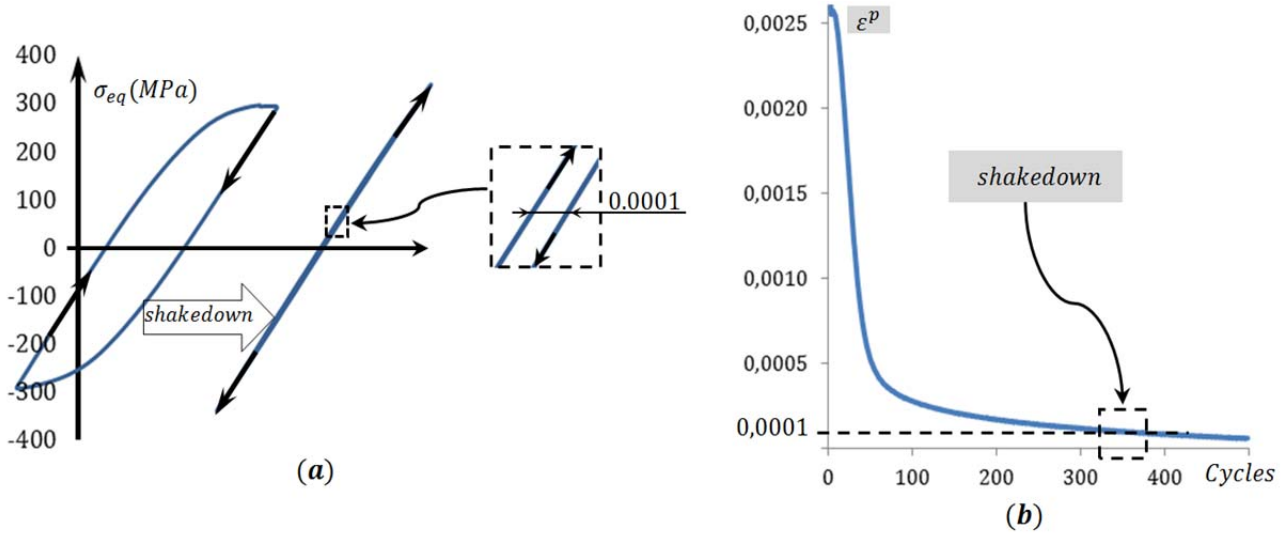

Figure 10. Evaluation of shakedown limit: (a) from the stress-strain loops; (b) from the plastic strain evolution

Following the previous method described in Fig. 10, we can easily evaluate the number of cycles corresponding to the elastic shakedown and the obtained results are given in Table 4. According to these findings and the results presented in Fig. 8 we deduce that a large increase of isotropic hardening leads to an early elastic shakedown despite the application of a high maximum stress. In other words, we can assert that a high isotropic hardening rate, found in the axial loadings, accelerates the shakedown limits.

Table 4. Evaluation of the number of cycles before the shakedown state

Test	ax240	ax260	ax280	ax300	ax320	ax340	ax360
Cycles to Shakedown	1st cycle	95th	77th	170th	320th	430th	>1400th

Under shear loading, elastic shakedown was also observed in the majority of the performed tests except in that of sh130, where the steady state is a closed elastic-plastic loop, but with very small accumulation of plastic deformation until final fracture. The obtained results for the shear loadings are summarized in Table 5.

Table 5. Evolution of the shakedown limit for the shearing tests

Test	sh80	sh90	sh100	sh110	sh120	sh130
Shakedown limit (Cycle)	180th cycle	390th	430th	800th	1600th	Plastic shakedown

According to these shakedown findings and the results presented in Fig. 9, we deduce the relationship between hardening and elastic shakedown in shear loading. Indeed, in these tests, the hardening rate (both isotropic and kinematic) is relatively low, leading to a very late shakedown.
The results presented in Table 5, confirm once again the anisotropic behavior of our alloy. Therefore, we deduce that elastic shakedown is quickly reached under axial loading but later in the shear one.
These results show that when the maximal stress is too high, the shakedown behavior is obtained after having a long time in plastic loading, which contributes largely to microstructural evolution of the specimen. Thus, the specimen breaks despite the elastic shakedown state is reached!

CONCLUDING REMARKS:

In the present work, the anisotropic behavior of a 2017 aluminum alloy is investigated through a stress controlled cyclic loading where two types of tests were performed. In the first one, seven tests using cyclic axial loading were done and in the second we have carried out six tests applying cyclic shear loading. The study is focused on the cyclic behavior as well as on the fatigue life: stress-strain loops, isotropic and kinematic hardenings and cyclic steady state were discussed.

The anisotropic behavior of our alloy is firstly deduced from the difference between the equivalent stress-strain loops obtained in the axial and shearing directions. The study of the cyclic behavior shows that isotropic hardening increases both in axial and shear directions, but more significantly in the axial one. On the other hand; isotropic hardening depends largely on the maximum amplitude of the loading for the two directions. Indeed, large stress amplitude generates a large amount of isotropic hardening which tends to grow during cyclic loading. The kinematic hardening decreases cyclically in both directions of loading, but more significantly in the axial tests where it tends to disappear very quickly. Furthermore, we can notice that the evolution of the isotropic hardening rate may be correlated with the evolution of the shakedown limit, where we can assert that a large isotropic hardening rate, found in the axial loadings, accelerates the shakedown limits. The same results obtained about shakedown limits allow us to conclude that the increase in maximum stress amplitude leads to a late elastic shakedown in the two directions of loading. Indeed, all the cycles done before elastic steady state, contribute largely to the nucleation of micro-voids causing microstructural evolution of the specimen and continue to grow despite the shakedown steady state. The anisotropy is also observed between the two directions in fatigue life as for the same equivalent stress amplitude, lifetime in the axial direction is higher compared to that in the shear direction. However, one can expect the opposite observation in case of strain control.

References

[1] J.B. Clark, Acta. Metall. 12 (1964) 1197-1201.
[2] C.T. Hahn, R. Simon, Eng. Fract. Mech. 5 (1973) 523-540.
[3] T.S. Srivatsan, E.J. Coyne Jr, Int. J. Fatigue. 8 (1986) 201-208.
[4] S.P. Ringer, K. Hono, Mater. Charact. 44 (2000) 101-131.
[5] R. Sadeler, Y. Totik, M. Gavgalı, I. Kaymaz, Mater. Des. 25 (2004) 439-445.
[6] T. Ludian, L. Wagner, Mater. Sci. Eng. A. 468–470 (2007) 210-213.
[7] R. Hill, J. Mech. Phys. Solids. 1 (1953) 271-276.
[8] F. Barlat, K. Lian, Int. J. Plast. 5 (1989) 51-66.
[9] H. Takahashi, H. Motohashi, S. Tsuchida, Int. J. Plast. 12 (1996) 935-949.
[10] D. Achani, O.S. Hopperstad, O.G. Lademo, J. Mater. Process. Technol. 209 (2009) 4750-4764.
[11] A.B. Lopes, F. Barlat, J.J. Gracio, J.F. Ferreira Duarte, E.F. Rauch, Int. J. Plast. 19 (2003) 1-22.
[12] N. Tardif, S. Kyriakides, Int. J. Solids. Struct. (2012) 00.
[13] M. Fourmeau, T. Børvik, A. Benallal, O.G. Lademo, O.S. Hopperstad, Int. J. Plast. 27 (2011) 2005-2025.
[14] K. Saï, L. Taleb, G. Cailletaud, Comput. Mater. Sci. 65 (2012) 48-57.
[15] T.B. Kermanidis, S.P. Pantelakis, D.G. Pavlou, Theor. Appl. Fract. Mech. 14 (1990) 43-47.
[16] Y. Murakami, K.J. Miller, Int. J. Fatigue. 27 (2005) 991-1005.
[17] E.A. Starke Jr, J.T. Staley, Prog. Aerosp. Sci. 32 (1996) 131-172.
[18] S. Malekjani, P.D. Hodgson, P. Cizek, I. Sabirov, T.B. Hilditch, Int. J. Fatigue. 33 (2011) 700-709.
[19] S.G. Pantelakis, P.V. Petroyiannis, K.D. Bouzakis, I. Mirisidis, Theor. Appl. Fract. Mech. 48 (2007) 68-81.
[20] A. May, M.A. Belouchrani, A. Manaa, Y. Bouteghrine, Proced. Eng. 10 (2011) 798-806.
[21] L. Flaceliere, F. Morel, A. Dragon, Int. J. Fatigue. 29 (2007) 2281-2297.
[22] L. Taleb, A. Hauet, Int. J. Plast. 25 (2009) 1359-1385.

13th International Conference on Fracture
June 16–21, 2013, Beijing, China

Ratchetting Behaviour of High Strength Rail Steel under Uniaxial and Biaxial Cyclic Loadings

Chung Lun Pun[1], Qianhua Kan[2], Peter Mutton[3], Guozheng Kang[2], Wenyi Yan[1,*]

[1] Department of Mechanical and Aerospace Engineering, Monash University, Clayton, VIC 3800, Australia
[2] School of Mechanics and Engineering, Southwest Jiaotong University, Chengdu, 610031, People's Republic of China
[3] Institute of Railway Technology, Monash University, Clayton, VIC 3800, Australia
* Corresponding author: wenyi.yan@monash.edu

Abstract An experimental study was carried out to investigate the cyclic deformation characteristic and ratchetting behaviour of a hypereutectoid high strength rail steel subjected to uniaxial and non-proportionally compression-torsion cyclic loadings. The cyclic deformation characteristic of the material was investigated under uniaxial symmetrical strain cycling. The uniaxial ratchetting was studied under asymmetrical stress cycling with different mean stresses and stress amplitudes and the multiaxial ratchetting was investigated under stress cycling with different axial stresses, equivalent stress amplitudes and non-proportional loading paths. It is shown that the responding stress amplitude decreases with cyclic number, i.e., the steel exhibits cyclic softening under uniaxial symmetrical strain cycling. The uniaxial ratchetting strain increases with mean stress and stress amplitude, but behaves differently under tension and under compression. The multiaxial ratchetting behaviour strongly depends not only on the axial stress and equivalent shear stress amplitudes but also on the non-proportional loading path. Additionally, the material reaches cyclic stabilization after a certain number of loading cycles under both uniaxial and multiaxial stress cyclings. These results can be applied to develop a reliable multiaxial cyclic plasticity model for investigating the degradation behaviour of the high strength rail steel under cumulative wheel-rail contact.

Keywords Ratchetting, high strength rail steel, non-proportionally multiaxial loading, cyclic loading.

1. Introduction

In the wheel/rail rolling contact process, the rail is subjected to a cyclic loading and the mechanical responses are more complicated than that exhibited under monotonic loading. The rail degradation modes, wear and rolling contact fatigue, are the result of the accumulation of plastic deformation, so called ratchetting, under severe wheel and rail contact cyclic loading. Generally, the response of an elastic-plastic material subjected to cyclic loading can be categorized into four different levels [1]. If the external load is high and above the plastic shakedown limit or ratchetting threshold, e.g., the contact load in a heavy haul line, new plastic deformation will occur and accumulate, i.e., ratchetting, under each cycle of loading. When the ratchetting strain reaches the ductility of the material, the material will failure at the local point [2], which corresponds to the initiation of wear and rolling contact fatigue, e.g., in the form of head checks in the rail head. Therefore, an investigation on plastic ratchetting in the rail head under cyclic loading is of paramount importance in the development of new rail steel and development of rail maintenance strategy in order to mitigate rail degradation.

To quantify the plastic ratchetting in the rail head accurately, a combined isotropic-kinematic hardening model, which reasonably describes the ratchetting behaviour, has to be applied to simulate the rolling contact between the wheel and the rail. Such models included that developed by Armstrong and Frederick [3] and the one modified by Chaboche [4, 5]. The application of these hardening models requires the calibration of some material properties, including basic mechanical parameters and nonlinear coefficients for nonlinear isotropic and kinematic hardening rules, from monotonic and cyclic tests. Examples of calibrating such parameters for ratchetting studies can be found in recent studies by Fedele et al. [6] and Broggiato et al. [7]. To correlate and calibrate the

material data for the ratchetting models, both uniaxial and multiaxial cyclic loading tests should be carried out. These testing methods have been widely applied to investigate the uniaxial and multiaxial ratchetting behaviour of materials, such as stainless steels and ordinary carbon steels, see [8-15]. It was found that different materials exhibit different ratchetting behaviours. Some experimental results of ratchetting behaviour of rail steels under uniaxial and multiaxial strain/stress cycling have also been reported in [16-21]. Four rail steels used in their studies exhibit different features from each other. Therefore, to accurately model the cyclic stress-strain behaviour of a specific material, it is essential to carry out carefully designed uniaxial and multiaxial cyclic loading tests in order to reveal its cyclic deformation characteristics.

In the case of wheel/rail contact, the cyclic compression-torsion test is one of the most appropriate methods to simulate the loading experienced by rail steel in the rail head due to rolling contact between the wheel and the rail. The objective of present study is to experimentally investigate the ratchetting behaviour of a high strength rail steel, which is currently used in heavy haul railways in Australia, under uniaxial and biaxial compression-torsion cyclic loadings at room temperature.

2. Experimental Setup

The material studied herein is a hypereutectoid rail steel with carbon content of 0.85%, which is currently used in heavy haul railways in Australia. Uniaxial cyclic tests were performed on the round solid specimens with test section diameter of 5 mm and length of 30mm, see Fig. 1a. Biaxial compression-torsion tests were performed on thin-walled tubular specimens with outside diameter of 16 mm, inside diameter of 13 mm, and length of 30mm in the test section, see Fig. 1b. All specimens were machined from the rail head of a new flat bottom rail which has the mass of 68 kilogram per metre. The hole in the tubular specimen was made by deep hole drilling operation.

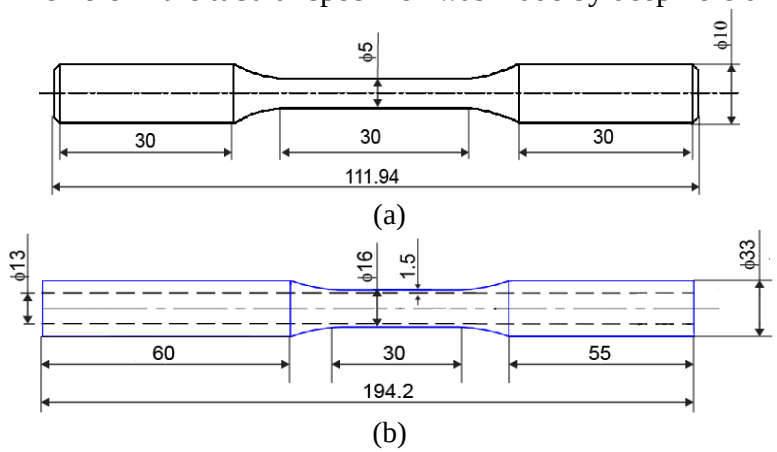

Figure 1. Drawing of (a) round solid specimen for uniaxial cycling tests; (b) thin-walled tubular specimen for biaxial compression-torsion stress cycling tests.

All tests were conducted at room temperature by employing a servo-valve controlled elector-hydraulic testing machine MTS809-250kN, which has the capacity to control axial force and torque independently. The testing process was controlled and the data were collected by a Teststar II control system. A tension-torsion extensometer with 25 mm gauge length and limit of axial strain of ±10% and shear angle of $\pm 5^{o}$ was employed to measure the axial elongation and torsional angle. Loading rates of strain cycling and stress cyclic were 0.2% s^{-1} and 200MPa s^{-1}, respectively. The total number of loading cycles in each case was 100.

The specimen was first tested under monotonic tensile test in order to obtain some basic mechanical parameters, such as, yield strength and ultimate tensile strength. Following the monotonic tensile test, the deformation behaviour of the specimen under symmetrical strain cycling was observed

from the relationship between the stress amplitude and the number of loading cycle. The maximum and minimum of axial stress σ_{max} and σ_{min} in each cycle was obtained from the collected experimental data and so the stress amplitude σ_a can be determined as,

$$\sigma_a = \frac{1}{2}(\sigma_{max} - \sigma_{min}) \tag{1}$$

After that, the ratchetting behaviour of the specimen under uniaxial and biaxial compression-torsion stress cycling with different mean stresses and stress amplitudes was studied. Under asymmetrical stress cycling, the maximum and minimum of axial strain ε_{max} and ε_{min} and the maximum and minimum of shear strain γ_{max} and γ_{min} in each cycle were obtained from the collected experimental data. Due to the unclosed hysteresis loop produced under asymmetric stress cycling, the axial ratchetting strain ε_r and torsional ratchetting strain γ_r are defined as:

$$\varepsilon_r = \frac{1}{2}(\varepsilon_{max} + \varepsilon_{min}) \tag{2}$$

$$\gamma_r = \frac{1}{2}(\gamma_{max} + \gamma_{min}) \tag{3}$$

Ratchetting strain rates are then defined as $d\varepsilon_r/dN$ and $d\gamma_r/dN$, i.e., the increment of ratchetting strains ε_r and γ_r per cycle. The ratchetting behaviour of the specimen under different loadings can be illustrated by the curve of ratchetting strain versus number of cycles. To investigate the influence of multiaxial loading path on the ratchetting behaviour of the material, five loading paths shown in Fig. 2 were adopted, where σ and $\sqrt{3}\tau$ represent the axial stress and the equivalent shear stress, respectively. In compression-torsion loading paths, the von Mises equivalent stress and strain can be determined as,

$$\sigma_{eq} = \sqrt{\sigma^2 + 3\tau^2} \tag{4}$$

$$\varepsilon_{eq} = \sqrt{\varepsilon^2 + \frac{\gamma^2}{3}} \tag{5}$$

where τ and γ represent the shear stress and shear strain and ε is the axial strain. Therefore, the equivalent shear stress and the equivalent shear strain under pure torsion can be defined as $\sqrt{3}\tau$ and $\gamma/3$, respectively.

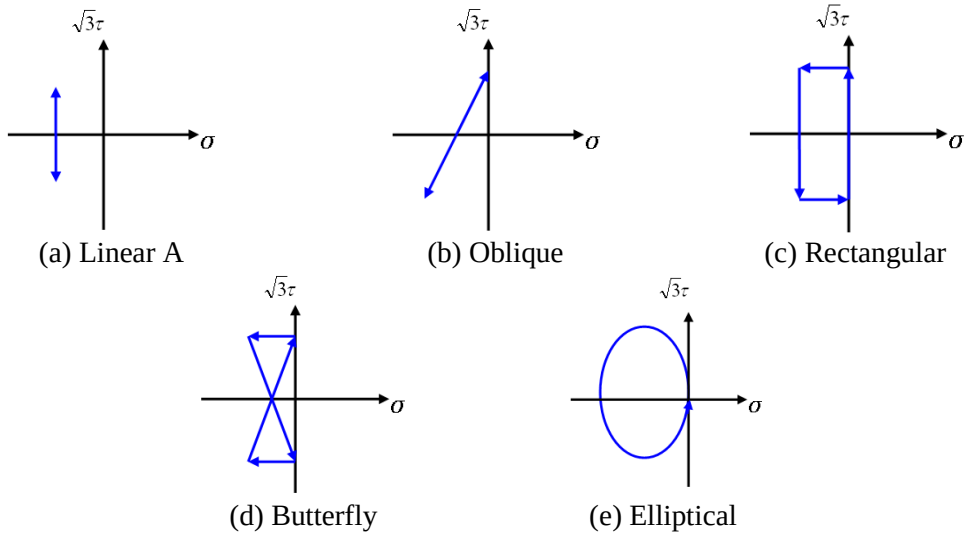

Figure 2. Loading paths for compression-torsion stress cycling.

3. Results

The tensile stress-strain curve for round solid specimen is shown in Fig. 3. The experimental results of elastic modulus E, nominal yield strength $\sigma_{0.2}$, ultimate tensile strength σ_b and elongation δ are 212 GPa, 910 MPa, 1384 MPa and about 12%, respectively.

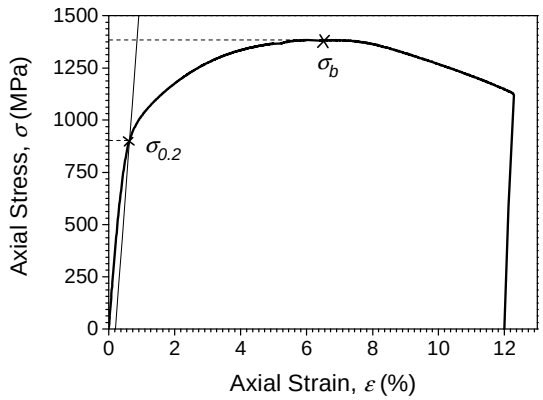

Figure 3. Monotonic tensile stress-strain curve of round solid specimen.

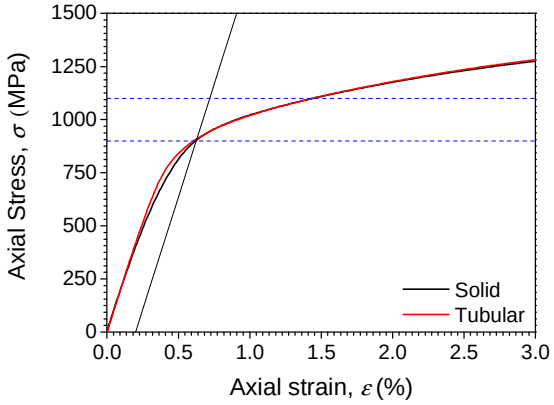

Figure 4. Comparison of mechanical responses from round solid and tubular specimens under monotonic tensile test.

To understand the effect of the specimen design on the measured mechanical properties, a monotonic tensile test was also performed on the tubular specimen. The stress-strain curves from the round solid and the tubular specimens are shown in Fig. 4. The comparison clearly shows that the measured curve of the tubular specimen agrees well with that of the solid specimen in the plastic region and both of them give the same nominal yield strength $\sigma_{0.2}$ of 910 MPa. The discrepancy in the elastic region is negligibly small. Based on the monotonic tensile stress-strain curves of the material, the peak stress applied in the uniaxial stress cycling and the multiaxial stress cycling was selected in the range of 910 MPa to 1100 MPa as illustrated by the dotted horizontal line in Fig. 4.

3.1 Uniaxial strain cycling

The specimen was tested under symmetrical strain cycling at room temperature with the strain amplitude of 0.8%. The cyclic hysteresis loop under uniaxial symmetrical strain cycling is shown in Fig. 5. The results clearly show that the size of the hysteresis loop decreases with the increase of number of cycles. To clearly identify the deformation behaviour of the material under uniaxial strain cycling, the curve of stress amplitude σ_a versus number of cycles N is shown in Fig. 6. It clearly illustrates that the material features cyclic softening remarkably over the first 10 cycles. The decreased rate of stress amplitude in the beginning stage is the largest and reaches a stable value after a certain number of cycles. Similar deformation behaviour was also found in ordinary carbon rail steel and heat-treated rail steel [19]. However, the cyclic softening of the hypereutectoid rail steel in current study is more remarkable.

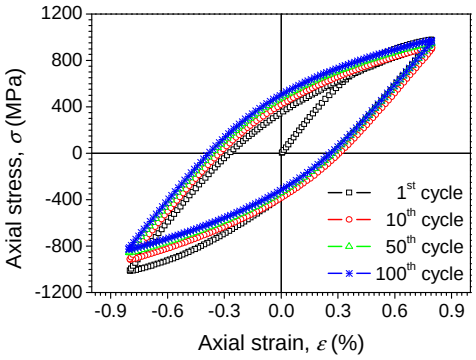

Figure 5. Cyclic hysteresis loops under uniaxial symmetrical strain cycling with strain amplitude of 0.8%.

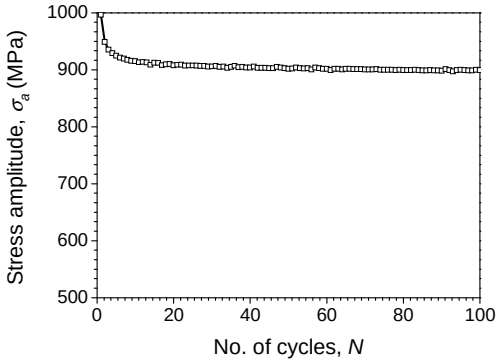

Figure 6. Diagram of stress amplitude σ_a versus number of loading cycle *N* under uniaxial symmetrical strain cycling with strain amplitude of 0.8%.

3.2 Uniaxial stress cycling

To observe the ratchetting behaviour of hypereutectoid rail steel under uniaxial asymmetrical stress cycling at room temperature, the material was tested with different mean stresses and stress amplitudes. Fig. 7a demonstrates the cyclic hysteresis loops of the specimen under an asymmetrical stress cycling with load condition of 200 ± 800 MPa. The results clearly show that ratchetting occurs under the asymmetrical stress cycling. The hysteresis loop becomes smaller and smaller at the beginning of cycling. After certain cycles, it almost keeps unchanged in the remaining cycles. Similar ratchetting behaviour can be found in the asymmetrical stress cycling with load condition of 200 ± 900 MPa and 100 ± 900 MPa as shown in Fig. 7b and 7c, respectively.

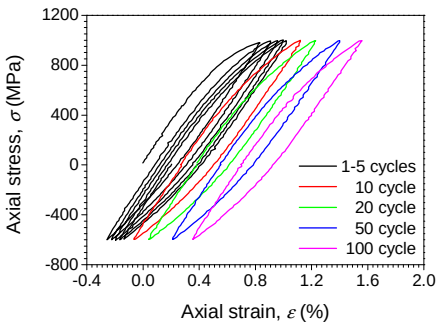

(a)

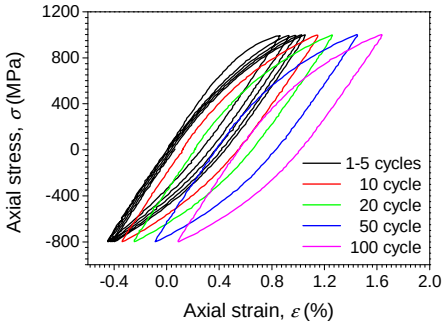

(b)

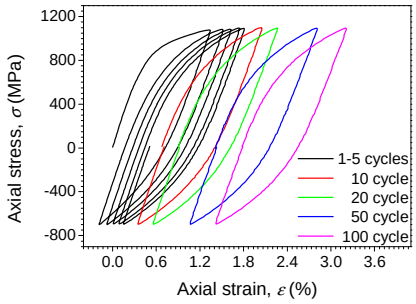

(c)

Figure 7. Cyclic hysteresis loops under asymmetrical stress cycling with load condition of (a) 200 ± 800 MPa; (b) 200 ± 900 MPa; (c) 100 ± 900 MPa.

To clearly illustrate the influence of stress amplitude on the ratchetting behaviour of the material, the axial ratchetting strain, which is determined by following Eq. (2), and the ratchetting strain rate versus number of cycles with different stress amplitudes are shown in Figs. 8a and 8b, respectively. The results clearly demonstrate that both ratchetting strain and ratchetting strain rate increase with stress amplitude. Furthermore, the axial ratchetting strain increases but the ratchetting strain rate decreases continuously with the increasing number of loading cycles. After about 10 cycles for σ_a = 800 MPa and about 15 cycles for σ_a = 900 MPa, the ratchetting strain rate becomes very small and almost remains constant over the remaining cycles.

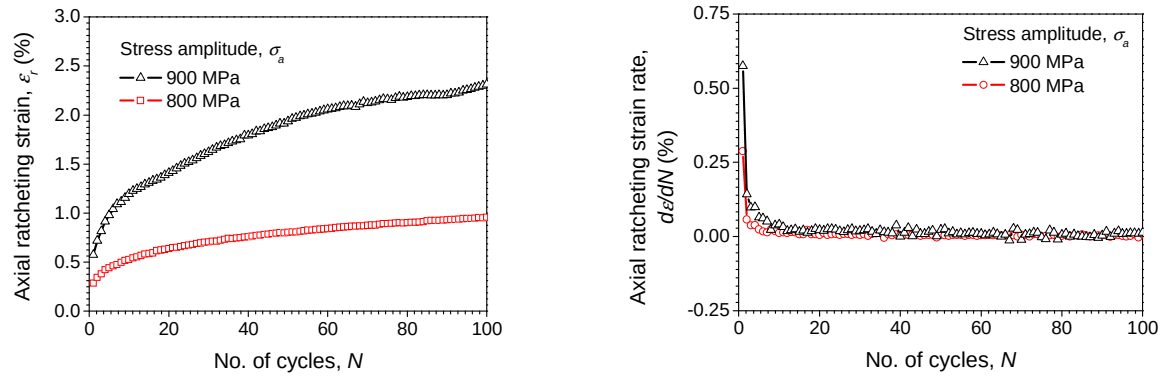

(a) (b)

Figure 8. (a) Axial ratchetting strain ε_r; (b) Axial ratchetting strain rate $d\varepsilon_r/dN$, versus number of cycles N with different stress amplitude σ_a while the mean stress σ_m is kept constant in all cases.

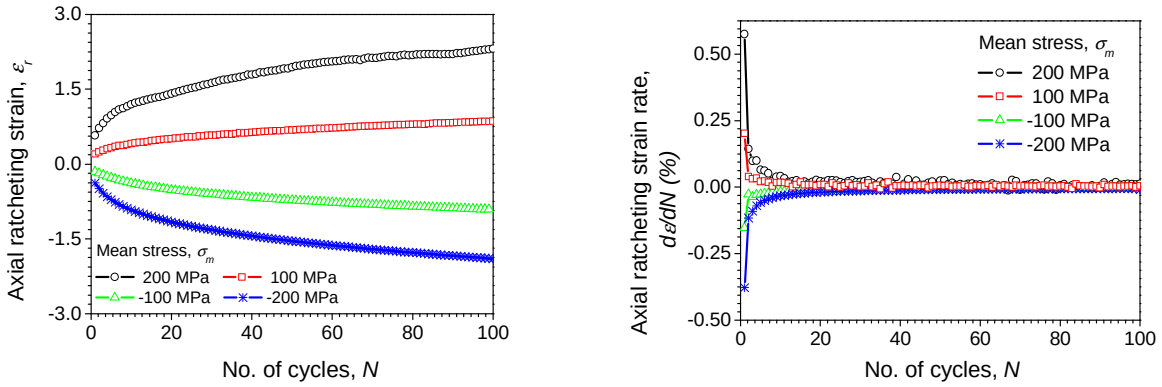

(a) (b)

Figure 9. (a) Axial ratchetting strain ε_r; (b) Axial ratchetting strain rate $d\varepsilon_r/dN$, versus number of cycles N with different mean stress σ_m while the stress amplitude σ_a is kept constant in all cases.

Figs. 9a and 9b show the ratchetting strain ε_r and the ratchetting strain rate $d\varepsilon_r/dN$ versus number of cycles N with different mean stresses. The results show that both ratchetting strain and ratchetting strain rate increase with the mean stress. After certain cycles, the ratchetting strain rate $d\varepsilon_r/dN$ becomes very small and remains constant over the remaining cycles. It is also found that the material requires more cycle to stabilize when the mean stress is higher. Additionally, the results indicate that negative mean stress does not provide a perfectly symmetrical result as the positive mean stress does. This means that the material has a slight difference in ratchetting behaviour under tension and under compression. Furthermore, both Figs 8b and 9b show that the axial ratchetting strain rate decreases with increasing number of loading cycles and becomes almost constant in the remaining cycles, which indicates that the ratchetting of the material is dominated by kinematic

hardening and so a cyclic stabilization is reached after certain number of cycles under uniaxial stress cycling.

3.3 Compression-torsion stress cycling

Under the loading paths shown in Figs 3a to 3e, the material was tested under compressive-torsional stress cycling with different mean stresses and stress amplitudes. The relation between ratchetting behaviour and non-proportionally multiaxial loading path is also discussed. Experimental results of two of the loading cases are shown in Fig 10a and 10b. The case shown in Fig. 11a is under symmetrical torsional stress cycling and the results clearly show that the axial ratchetting is the dominant while the torsional ratchetting is relatively small and can be neglected. The same evolution tendency of ratchetting strain can be found in the stress cycling under elliptical path as illustrated in Fig 11b, and the other three paths. Comparing Fig. 10a and 10b, it is found that the absolute value of ratcheting strain at 100 cycles for elliptical path is smaller than that for linear path (1.5% to 3.0%).

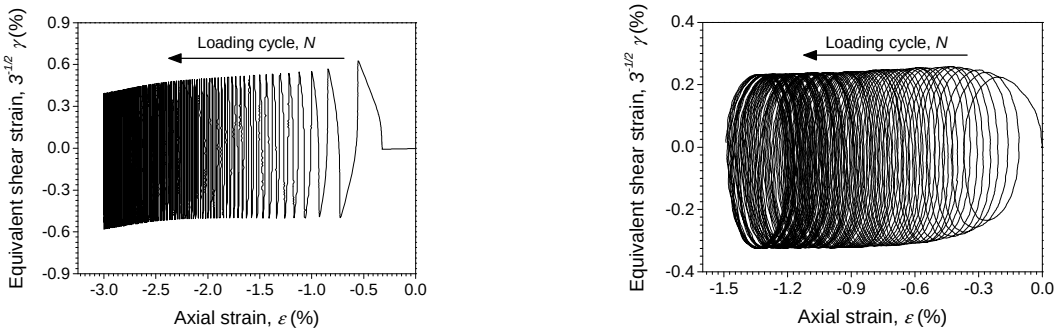

(a) (b)

Figure 10. Experimental results of equivalent shear strain $\gamma/\sqrt{3}$ versus axial strain, ε under (a) linear path; and (b) elliptical path with the same loading condition of σ_{eq} = 1019.8 MPa.

Figs. 11a and 11b demonstrate the influence of axial stresses on the ratchetting behaviour under linear path while the equivalent shear stress $\sqrt{3}\tau$ is kept constant as 0 ± 1000 MPa for all cases. The results show that ratchetting takes place when axial stress σ is high enough. Both axial ratchetting strain ε_r and axial ratchetting strain rate $d\varepsilon_r/dN$ increases with axial stress σ. Additionally, the ratchetting behaviour of the material depends on the equivalent shear stress amplitude under linear path, as shown in Figs. 12a and 12b. For all the cases, the axial stress σ and the mean equivalent shear stress $\left(\sqrt{3}\tau\right)_m$ are kept constant as -200 MPa and 0 MPa, respectively. The results indicate that both axial ratchetting strain ε_r and axial ratchetting strain rate $d\varepsilon_r/dN$ increases with the equivalent shear stress amplitude $\left(\sqrt{3}\tau\right)_a$.

The ratchetting behaviour of the specimen is significantly influenced not only by the axial stress and the equivalent shear stress amplitude but also by the non-proportional loading path as illustrated in Figs. 13a and 13b. For all cases, the applied equivalent stress σ_{eq} is kept constant as 1019.8 MPa. The results show that the non-proportional loading path influences not only the axial ratchetting strain ε_r but also the axial ratchetting strain rate $d\varepsilon_r/dN$. Among all the five loading paths, the elliptical path gives the lowest ratchetting strain and rate. When N is less than 65, the linear path gives the highest ratchetting strain. When N is larger than 65, the highest ratchetting strain is contributed by the rectangular path.

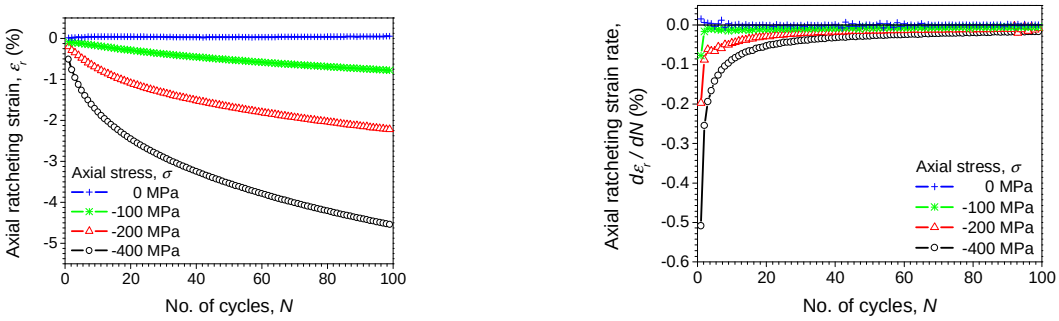

(a) (b)

Figure 11. (a) Axial ratchetting strain ε_r; (b) Axial ratchetting strain rate $d\varepsilon_r/dN$, versus number of cycles N under linear path with different axial stress σ while the equivalent shear stress $\sqrt{3}\tau$ is kept constant.

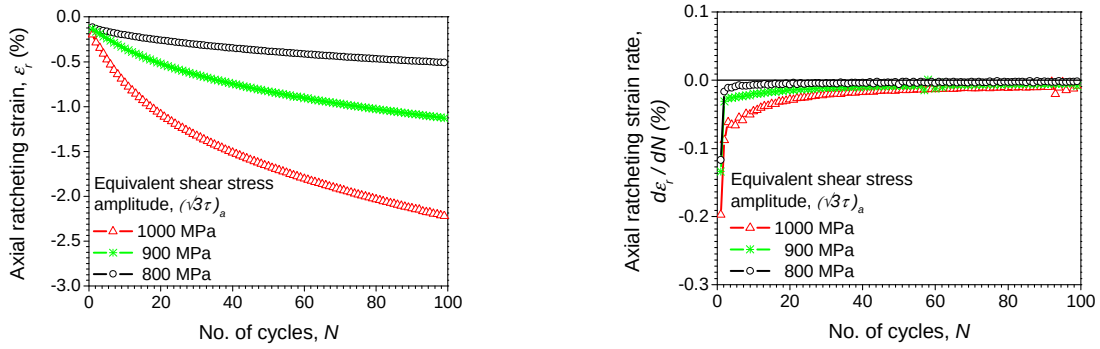

(a) (b)

Figure 12. (a) Axial ratchetting strain ε_r; (b) Axial ratchetting strain rate $d\varepsilon_r/dN$, versus number of cycles N under linear path with different equivalent shear stress amplitude $\left(\sqrt{3}\tau\right)_a$ while the axial stress is kept constant.

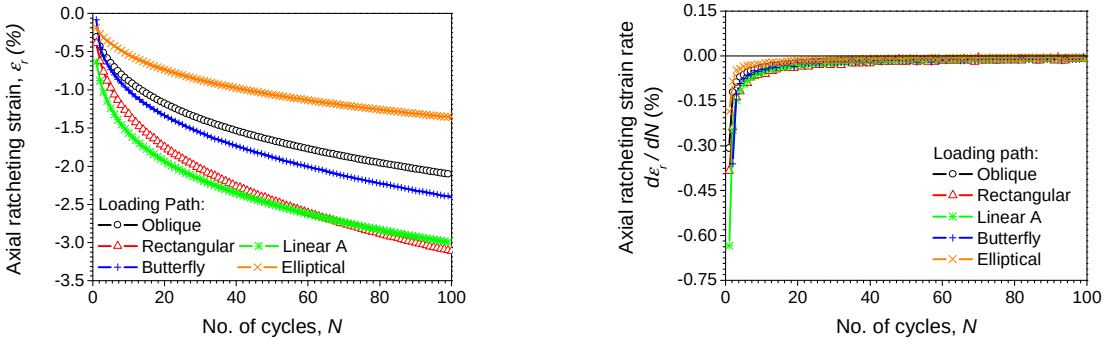

(a) (b)

Figure 13. (a) Axial ratchetting strain ε_r; (b) Axial ratchetting strain rate $d\varepsilon_r/dN$, versus number of cycles N with different non-proportional loading paths while the applied equivalent stress σ_{eq} is kept constant.

It is worth noting that Figs 11, 12 and 13 demonstrate that the axial ratchetting strain increases but its rate decreases continuously with increasing number of cycles. After a certain number of cycles, the axial ratchetting strain rate becomes very small and almost remains constant in the remaining cycles. Therefore, it can be concluded that the ratchetting of the material under multiaxial stress cycling is dominated by kinematic hardening and so a cyclic stabilization is reached after certain number of cycles, i.e. about 45 cycles when σ = -200 MPa in Fig 12b. It is also found that the increase of axial stress and equivalent shear stress lead to increase the required cyclic number to

reach cyclic stabilization of the material. Moreover, it is indicated from Fig 13a that the nonproportional additional hardening will restrain the ratchetting strain even under compression-torsion loading, which is consistent with [14] under tension-torsion loading. The elliptical path is more relevant to actual wheel/rail contact situations as the contact patch was often found to be elliptical in shape which implies that the relative weak ratchetting behaviour will occur in real wheel/rail rolling contact process. These features and their effects on ratchetting should be taken into account in cyclic constitutive model development in the future.

4. Conclusion

A hypereutectoid grade high strength rail steel, which is currently used in heavy haul operation in Australia, has been tested under uniaxial and compression-torsion cyclic loadings. The elastic modulus, nominal yield strength and ultimate tensile strength of the material are found as 212 GPa, 910 MPa and 1384 MPa, respectively. Under symmetrical strain cycling, the material exhibits cyclic softening at the start and then stabilizes quickly. Although this material's behaviour is similar to those found in the literature, the cyclic softening of the hypereutectoid rail steel is more remarkable.

Under uniaxial stress cycling, ratchetting behaviour strongly depends on mean stress and stress amplitude. Both ratchetting strain and ratchetting rate increase with mean stress and stress amplitude. The material stabilizes after certain number of loading cycles and the required number of cycles to reach cyclic stabilization also depends on mean stress and stress amplitude. It is found that the ratchetting of the material behaves slightly different under tension and compression.

Under multiaxial stress cycling, ratchetting is significantly influenced by axial stress, equivalent shear stress amplitude and non-proportional loading path. Both ratchetting and ratchetting strain rate increases with axial stress and equivalent shear stress amplitude. It is also found that kinematic hardening is dominant in the ratchetting of the material. It reaches cyclic stabilization after certain number of loading cycles and the required cyclic number is also influenced by the axial stress and equivalent shear stress amplitude. Among all the five studied loading paths, the elliptical loading path is more relevant to actual wheel/rail contact situations and it gives the lowest ratchetting strain and ratchetting strain rate.

Acknowledgements

The present work has been partly funded by an Australian Research Council Linkage Project (LP110100655) with support from Rio Tinto Iron Ore.

References

[1] A. Kapoor, K.L. Johnson, Plastic ratchetting as a mechanism of metallic wear. Proc R Soc Lond, A445 (1994) 367-384.
[2] A. Kapoor, A re-evaluation of the life to rupture of ductile metals by cyclic plastic strain. Fatigue Fract Engng Mater Struct 17 (1994) 201-219.
[3] P.J. Armstrong, C.O. Frederick, A mathematical representation of the multiaxial Bauschinger effect, CEGB Report RD/B/N731, Berkely Nuclear Laboratories, Berkely, UK, 1966.
[4] J.L. Chaboche, Time-independent constitutive theories for cyclic plasticity. Int J Plast 2 (1986) 149-188.
[5] J.L. Chaboche, Constitutive equations for cyclic plasticity and cyclic viscoplasticity. Int J Plast 5 (1989) 247-302.
[6] R. Fedele, M. Filippini, G. Maier, Constitutive model calibration for railway wheel steel through tension-torsion tests. Comput and Struct 83 (2005) 1005-1020.

[7] G.B. Broggiato, F. Campana, L. Cortese, The Chaboche nonlinear kinematic hardening model: calibration methodology and validation. Meccanica 43 (2008) 115-124.
[8] F. Yoshida, Uniaxial and biaxial creep-ratchetting behaviour of SUS304 stainless steel at room temperature. Int J Press Ves Pip 44 (1990) 207-223.
[9] T. Hassan, S. Kytriakides, Ratcheting in cyclically hardening and softening materials: I. Uniaxial behavior. Int J Plast 10(2) (1994) 149-184.
[10] T. Hassan, S. Kyriakides, Ratcheting in cyclically hardening and softening materials: II. Multiaxial behaviour. Int J Plast 10(2) (1994) 185-212.
[11] P. Delobelle, P. Robinet, L. Bocher, Experimental study and phenomenological modelization of ratchet under uniaxial and biaxial loading on an austenitic stainless steel. Int J Plast 11(4) (1995) 295-330.
[12] M. Mizuno, Y. Mima, M. Abdel-Karim, N. Ohno, Uniaxial ratchetting of 316FR steel at room temperature-- Part 1: Experiments. ASME J Eng Mater Technol 122(1) (2000) 29-34.
[13] G.Z. Kang, Q. Gao, X.J. Yang, Y.F. Sun, An experimental study on uniaxial and multiaxial strain cyclic characteristics and ratcheting of 316L stainless steel. J Mater Sci Technol 17(1) (2001) 219-223.
[14] G.Z. Kang, Q. Gao, X.J. Yang, Uniaxial and non-proportionally multiaxial ratcheting of SS304 stainless steel at room temperature: experiments and simulations. Int J Nonlinear Mech 39 (2004) 843-857.
[15] G.Z. Kang, Y.G. Li, J. Zhang, Y.F. Sun, Q. Gao, Uniaxial ratcheting and failure behaviors of two steels. Theor Appl Fract Mech 43 (2005) 199-209.
[16] A.F. Bower, Cyclic hardening properties of hard-drawn copper and rail steel. J Mech Phys Solids 37(4) 455-470.
[17] D.L. McDowell, On the path dependence of transient hardening and softening to stable states under complex biaxial cyclic loading. In: Desai, C.S., Gallagher, R.H. (Eds), Proceeding of International Conference on Constitutive Laws for Engineering Materials: Theory and Application, Univ Arizona, Tucson, AZ, 1983, pp. 125-131.
[18] D.L. McDowell, An evaluation of recent developments in hardening and flow rules for rate independent nonproportional cyclic plasticity. ASME J Appl Mech 54 (1987) 323-331.
[19] D.L. McDowell, Stress state dependence of cyclic ratchetting behaviour of two rail steels. Int J Plast 11(4) (1995) 397-421.
[20] G.Z. Kang, Q. Gao, X.J. Yang, Experimental study on the cyclic deformation and plastic flow of U71Mn rail steel. Int J Mech Sci 44 (2002) 1647-1663.
[21] G.Z. Kang, Q. Gao, Uniaxial and non-proportionally multiaxial ratcheting of U71Mn rail steel: experiments and simulations. Mech Mater 34 (2002) 809-820.

An extended cyclic plasticity model at finite deformations describing the Bauschinger effect and ratchetting behaviour

Yilin Zhu [1], Guozheng Kang [1,*], Qianhua Kan [1], Chao Yu [1]
Jun Ding [1]

[1] Department of Applied Mechanics and Engineering, Southwest Jiaotong University, Chengdu, 610031, China
* Corresponding author: Guozhengkang@126.com

Abstract A popular cyclic plasticity model at small deformations is extended to finite deformations for describing the Bauschinger effect and ratchetting behaviour by considering the combined isotropic and kinematic hardening rules. The model is based on the multiplicative decomposition of deformation gradient into elastic and inelastic parts. Following, a further multiplicative decomposition of inelastic part of deformation gradient into energetic and dissipative parts is adopted to extend the popular Ohno-Karim nonlinear kinematic hardening rule. Finally, numerical examples are carried out to validate the proposed model under strain controlled and stress controlled cyclic loadings.

Keywords Finite deformation, cyclic plasticity, ratchetting; kinematic hardening, Bauschinger effect

1. Introduction

In engineering applications, engineering components are usually subjected to complex cyclic loading. For instance, metal forming, mechanical cutting, wheel/rail contact in high speed railway and aero fasteners connection, etc. Cyclic plasticity models for describing Bauschinger effect and ratchetting behaviour of metals associated with cyclic loading have been one of the most popular research topic for solid mechanics in recent years. At small deformation regime, cyclic constitutive model research has reaped great achievements under the effort of numerous scholars [1-9]. The most popular model, which can describe Bauschinger effect and ratchetting behaviour, is Armstrong-Frederick kinematic model (shorted as A-F model) [1]. Even though the prediction of ratchetting behaviour by A-F model is too high relative to the actual situation, it is still widely applied in engineering analysis due to its solid physical background and concise theory system. And after then, there have been a lot of attempts to modify A-F model to improve predicting in ratcheting [2-9]. Ohno-Karim model, owing to the convenience of material parameters determination and the reasonable prediction in ratchetting, was widely adopted to simulate cyclic plastic behaviour of metal materials at present. The models were mostly constructed in the frame of small deformation.

It is must be noted that the deformation of structural components is finite and associated with finite rotation in practical modelling situations.. Cyclic constitutive models established at small deformation regime are no longer suitable for these circumstances due to without considering rotation effect. Recently, some constitutive models were extended from small deformation to finite deformation [10-24]. Among these models, two main strategies are followed. One class is hypo-elasticity theory which is developed by introducing a stress-like internal variable to model

kinematic hardening with the assumption that the stretching tensor is additively decomposed into the elastic part and plastic part. This theory requires adopting appropriate objective stress rate to establish the frame-indifference evolution equations. Alternatively, the other one is hyper-elasticity theory, in which the inelastic part is based on the standard Kröner multiplicative decomposition [25] and can be further multiplicatively decomposed into energetic and dissipative parts [15]. In hyper-elasticity theory, a strain-like internal variable is introduced to model kinematic hardening. The requirement of this strategy is to establish all evolution equations in the same configuration. For the first strategy, it has been shown that the rate form model for elastic response is integrable [18, 26] only in form of the logarithmic rate. Therefore, some unreasonable responses in elastic behaviour, such as shear oscillatory phenomenon and the nonzero work in a hysteretic loop, may appear. To avoid the nonzero work in elastic response, a continuum mechanical extension of A-F type kinematic hardening rule can be achieved naturally motivated by a typical rheological model description. However, as so far only A-F model is extended in both of the two strategies.

In the present work, the Ohno-Karim model is firstly extended from small deformations to finite deformations based on the hyper-elasticity theory. Some numerical examples were provided to display the prediction in Bauschinger effect and ratchetting behaviour under strain controlled and stress controlled cyclic loadings, respectively.

2. Continuum extension of Ohno-Karim model at finite deformations

2.1. Kinematic

In order to model the inelastic response of materials, the deformation gradient $\mathbf{F}$ may be classically multiplicatively decomposed as

$$\mathbf{F} = \mathbf{F}^e\mathbf{F}^p \tag{1}$$

where, $\mathbf{F}^p$ represents the local inelastic distortion of material due to “plastic mechanism”, and this local deformation carries the material from reference space ($\tilde{\mathrm{K}}$) to structure space ($\hat{\mathrm{K}}$); $\mathbf{F}^e$ represents the subsequent stretching and rotation, and it maps material element from structure space ($\hat{\mathrm{K}}$) to current space (K) (see Fig. 1) [25].

Following, $\mathbf{F}^p$ can be further multiplicatively decomposed into energetic part $\mathbf{F}^{pe}$ and dissipative part $\mathbf{F}^{pi}$ [15].

$$\mathbf{F}^p = \mathbf{F}^{pe}\mathbf{F}^{pi} \tag{2}$$

where, $\mathbf{F}^{pi}$ maps material element from reference space into intermediate configuration of kinematic hardening($\breve{\mathrm{K}}$); and $\mathbf{F}^{pe}$ maps material element from intermediate configuration($\breve{\mathrm{K}}$) into structure space(K) (see Fig. 4) [15, 24].
Three right Cauchy-Green tensors are given by

$$\mathbf{C} = \mathbf{F}^T\mathbf{F}, \quad \mathbf{C}^e = \mathbf{F}^{eT}\mathbf{F}^e = \mathbf{F}^{p-T}\mathbf{C}\mathbf{F}^{p-1}, \quad \mathbf{C}^{pe} = \mathbf{F}^{peT}\mathbf{F}^{pe} = \mathbf{F}^{pi-T}\mathbf{C}^p\mathbf{F}^{pi-1} \tag{3}$$

with

$$\mathbf{C}^p = \mathbf{F}^{pT}\mathbf{F}^p \tag{4}$$

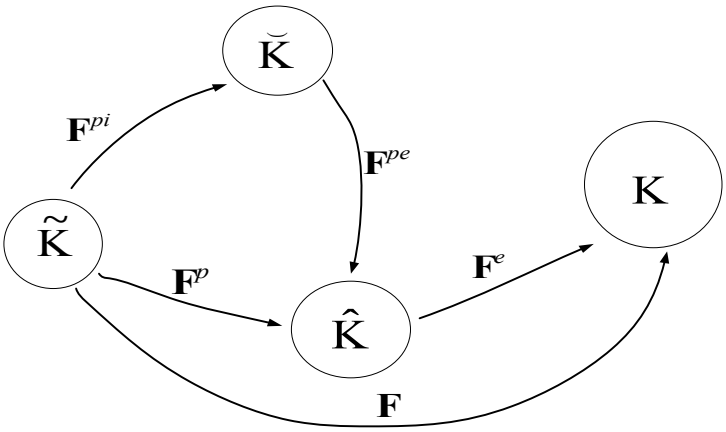

Figure 1. Elastic-inelastic decomposition of the kinematics deformation

2.2. Helmholtz free energy

Similar to the small deformation regime and based on the requirement of material objectivity, the Helmholtz free energy is additively decomposed into three parts

$$\psi = \psi^{e}\left(\mathbf{C}^{e}\right) + \psi^{kin}\left(\mathbf{C}^{pe}\right) + \psi^{iso}\left(p\right) \tag{5}$$

where ψ^{e} represents the standard energy associated with intermolecular interactions; ψ^{kin} is a defect-energy associated with plastic deformation; and $\psi^{iso}\left(p\right)$ represents the additional amount of stored energy related to isotropic hardening, where p is accumulated plastic strain.

2.3. Clausius-Duhem inequality

Inspired by the existing work [21, 23], we derive the constitutive equations of Ohno-Karim model in a continuum method in this paper. The derivation is based on the requirement of the Clausius-Duhem inequality.

For isothermal process, the reduced Clausius-Duhem inequality is

$$\mathbf{S} : \frac{1}{2}\dot{\mathbf{C}} - \dot{\psi} \geq 0 \tag{6}$$

where $\mathbf{S}$ is the second Piola-Kirchhoff stress tensor; $(:)$ represents the inner product of tensors.

For Ohno-Karim kinematic hardening rule, the kinematic free energy term is given by

$$\psi^{kin} = \sum_{i}^{N} \psi_{i}^{kin}\left(\mathbf{C}_{i}^{pe}\right)\left(N \geq 1\right) \tag{7}$$

with

$$\mathbf{C}_{i}^{pe} = \mathbf{F}_{i}^{pe^{T}}\mathbf{F}_{i}^{pe} \tag{8}$$

and

$$\mathbf{F}_{i}^{pe} = \mathbf{F}^{p}\mathbf{F}_{i}^{pi^{-1}} \tag{9}$$

Eq. (9) indicates that the form of multiplicative decomposition for $\mathbf{F}^{p}$ is not exclusive.

Combing Eq. (7) and Eq. (5), yields

$$\psi = \psi^{e}\left(\mathbf{C}^{e}\right) + \sum_{i}^{N} \psi_{i}^{kin}\left(\mathbf{C}_{i}^{pe}\right) + \psi^{iso}\left(p\right) \tag{10}$$

Substituting Eq. (10) into Eq. (6), the Clausius-Duhem inequality can be rewritten as

$$\mathbf{S}:\frac{1}{2}\dot{\mathbf{C}}-\frac{\partial\psi^{e}}{\partial\mathbf{C}^{e}}:\dot{\mathbf{C}}^{e}-\sum_{i}^{N}\frac{\partial\psi_{i}^{kin}}{\partial\mathbf{C}_{i}^{pe}}:\dot{\mathbf{C}}_{i}^{pe}-\frac{\partial\psi^{iso}}{\partial p}\dot{p}\geq 0 \tag{11}$$

According Eq. (3),

$$\dot{\mathbf{C}}^{e}=\dot{\mathbf{F}}^{p^{-T}}\mathbf{C}\mathbf{F}^{p^{-1}}+\mathbf{F}^{p^{-T}}\dot{\mathbf{C}}\mathbf{F}^{p^{-1}}+\mathbf{F}^{p^{-T}}\mathbf{C}\dot{\mathbf{F}}^{p^{-1}} \tag{12}$$

Furthermore, by adopting the two identities, gives

$$\dot{\mathbf{F}}^{p^{-1}}=-\mathbf{F}^{p^{-1}}\dot{\mathbf{F}}^{p}\mathbf{F}^{p^{-1}},\quad \dot{\mathbf{F}}^{p^{-T}}=-\mathbf{F}^{p^{-T}}\dot{\mathbf{F}}^{p}\mathbf{F}^{p^{-T}} \tag{13}$$

Combing Eq. (12) and Eq. (13), $\dot{\mathbf{C}}^{e}$ is derived as

$$\dot{\mathbf{C}}^{e}=-\mathbf{L}^{p^{T}}\mathbf{C}^{e}+\mathbf{F}^{p^{-T}}\dot{\mathbf{C}}\mathbf{F}^{p^{-1}}-\mathbf{C}^{e}\mathbf{L}^{p} \tag{14}$$

where $\mathbf{L}^{p}=\dot{\mathbf{F}}^{p}\mathbf{F}^{p^{-1}}$ is the plastic velocity gradient.

In the same process,

$$\dot{\mathbf{C}}_{i}^{pe}=-\mathbf{L}_{i}^{pi^{T}}\mathbf{C}_{i}^{pe}+\mathbf{F}_{i}^{pi^{-T}}\dot{\mathbf{C}}^{p}\mathbf{F}_{i}^{pi^{-1}}-\mathbf{C}_{i}^{pe}\mathbf{L}_{i}^{pi} \tag{15}$$

where $\mathbf{L}_{i}^{pi}=\dot{\mathbf{F}}_{i}^{pi}\mathbf{F}_{i}^{pi^{-1}}$ is the so called "inelastic" plastic velocity gradient.

Considering the symmetric property of tensor functions ψ^{e} and ψ_{i}^{kin} [23]

$$\frac{\partial\psi^{e}}{\partial\mathbf{C}^{e}}:\left(\mathbf{C}^{e}\mathbf{L}^{p}\right)=\left(\mathbf{C}^{e}\frac{\partial\psi^{e}}{\partial\mathbf{C}^{e}}\right):\mathbf{D}^{p} \tag{16a}$$

$$\frac{\partial\psi_{i}^{kin}}{\partial\mathbf{C}_{i}^{pe}}:\left(\mathbf{C}_{i}^{pe}\mathbf{L}_{i}^{pi}\right)=\left(\mathbf{C}_{i}^{pe}\frac{\partial\psi_{i}^{kin}}{\partial\mathbf{C}_{i}^{pe}}\right):\mathbf{D}_{i}^{pi} \tag{16b}$$

where $\mathbf{D}^{p}$ and $\mathbf{D}_{i}^{pi}$ are symmetric part of $\mathbf{L}^{p}$ and $\mathbf{L}_{i}^{pi}$, respectively.

Moreover

$$\mathbf{D}^{p}=\frac{1}{2}\mathbf{F}^{p^{-T}}\dot{\mathbf{C}}\mathbf{F}^{p^{-1}},\quad \mathbf{D}_{i}^{pi}=\mathbf{F}_{i}^{pi^{-T}}\dot{\mathbf{C}}^{p}\mathbf{F}_{i}^{pi^{-1}} \tag{17}$$

By Eqs. (14)- (17), the Clausius-Duhem inequality (11) yields the final form

$$\begin{aligned}&\left(\mathbf{S}-2\mathbf{F}^{p^{-1}}\frac{\partial\psi^{e}}{\partial\mathbf{C}^{e}}\mathbf{F}^{p^{-T}}\right):\frac{1}{2}\dot{\mathbf{C}}+\left(2\mathbf{C}^{e}\frac{\partial\psi^{e}}{\partial\mathbf{C}^{e}}-2\sum_{i}^{N}\mathbf{F}_{i}^{pe}\frac{\partial\psi_{i}^{kin}}{\partial\mathbf{C}_{i}^{pe}}\mathbf{F}_{i}^{pe^{T}}\right):\mathbf{D}^{p}\\&+2\sum_{i}^{N}\left(\mathbf{C}_{i}^{pe}\frac{\partial\psi_{i}^{kin}}{\partial\mathbf{C}_{i}^{pe}}:\mathbf{D}_{i}^{pi}\right)-\frac{\partial\psi^{iso}}{\partial p}\dot{p}\geq 0\left(N\geq 1\right)\end{aligned} \tag{18}$$

According to the Coleman-Noll procedure, the second Piola-Kirchhoff stress tensor can be defined as

$$\mathbf{S}=2\mathbf{F}^{p^{-1}}\frac{\partial\psi^{e}}{\partial\mathbf{C}^{e}}\mathbf{F}^{p^{-T}} \tag{19}$$

Furthermore, the so-called Mandel stress $\mathbf{M}$, kinematic Mandel stress $\mathbf{M}^{kin}$, back stress $\boldsymbol{\chi}$ and isotropic deformation resistance *R* are defined as follows:

$$\mathbf{M}=2\mathbf{C}^{e}\frac{\partial\psi^{e}}{\partial\mathbf{C}^{e}} \tag{20}$$

and

$$\mathbf{M}^{kin}=\sum_{i}^{N}\mathbf{M}_{i}^{kin} \tag{21}$$

with

$$\mathbf{M}_i^{kin} = 2\mathbf{C}_i^{pe}\frac{\partial \psi_i^{kin}}{\partial \mathbf{C}_i^{kin}} \tag{22}$$

and

$$\boldsymbol{\chi} = \sum_i^N \boldsymbol{\chi}_i \tag{23}$$

with

$$\boldsymbol{\chi}_i = 2\mathbf{F}_i^{pe}\frac{\partial \psi_i^{kin}}{\partial \mathbf{C}_i^{pe}}\mathbf{F}_i^{peT} \tag{24}$$

and

$$R = -\frac{\partial \psi^{iso}}{\partial p} \tag{25}$$

In general, R can be written in the Voce's exponential form

$$R = Q\left(1-\exp(-bp)\right) \tag{26}$$

where Q and b are nonnegative material parameters.

Finally, the Clausius-Duhem inequality reduces to the form

$$\left(\mathbf{M}-\boldsymbol{\chi}\right):\mathbf{D}^p + \sum_i^N \mathbf{M}_i^{kin}:\mathbf{D}_i^{pi} + R\dot{p} \geq 0 \tag{27}$$

The evolution equations of Ohno-Karim model can be given by

$$\mathbf{D}^p = \dot{\lambda}\frac{\partial F_y}{\partial \mathbf{M}} = \dot{\lambda}\frac{\mathbf{M}^D-\boldsymbol{\chi}}{\left\|\mathbf{M}^D-\boldsymbol{\chi}\right\|} \tag{28a}$$

$$\mathbf{D}_i^{pi} = u_i b_i \dot{\lambda}\mathbf{M}_i^{kin} + H\left(f_i\right)\frac{b_i}{c_i}\mathbf{M}_i^{kin}\left\langle \mathbf{D}^p:\mathbf{K}_i - u_i\dot{\lambda}\right\rangle \tag{28b}$$

$$\dot{p} = \sqrt{\frac{2}{3}}\dot{\lambda} \tag{28c}$$

with the yield function

$$F_y = \left\|\mathbf{M}^D-\boldsymbol{\chi}\right\| - \sqrt{\frac{2}{3}}\left(\sigma_y + R\right) \tag{29}$$

where the superscript D denotes the deviator of a tensor, i.e. $\mathbf{A}^D = \mathbf{A} - \frac{1}{3}tr\left(\mathbf{A}\right)\mathbf{1}$.

and the plastic multiplier $\dot{\lambda}$ is determined by the Kuhn-Tucker conditions

$$\dot{\lambda} \geq 0\,, \quad F_y \leq 0\,, \quad \dot{\lambda}F_y = 0\left(if\ F_y = 0\right) \tag{30}$$

In Eq. (28b), b_i and c_i are nonnegative kinematic parameters; H and $\left\langle\ \right\rangle$ are Heaviside function and Macauley operator, respectively; f_i represents the critical surface for i-th back stress which is defined by

$$f_i = \left\|\boldsymbol{\chi}_i\right\|^2 - \left(\frac{c_i}{b_i}\right)^2 \tag{31}$$

And forther more

$$\mathbf{K}_i = \frac{\boldsymbol{\chi}_i}{\left\|\boldsymbol{\chi}_i\right\|} \tag{32}$$

By the foregoing equations

$$
\begin{aligned}
&(\mathbf{M}-\boldsymbol{\chi}):\mathbf{D}^p+\sum_i^N \mathbf{M}_i^{kin}:\mathbf{D}_i^{pi}+R\dot{p}\\
&=\dot{\lambda}\left\|\mathbf{M}^D-\boldsymbol{\chi}\right\|+\dot{\lambda}\sum_i^N\left(u_i b_i+H(f_i)\frac{b_i}{c_i}\left\langle \mathbf{D}^p:\mathbf{K}_i-u_i\dot{\lambda}\right\rangle\right)\left\|\mathbf{M}_i^{kin}\right\|^2+R\sqrt{\frac{2}{3}}\dot{\lambda} \qquad (33)\\
&=\dot{\lambda}\left(F_y+\sqrt{\frac{2}{3}}\sigma_y\right)+\dot{\lambda}\sum_i^N\left(u_i b_i+H(f_i)\frac{b_i}{c_i}\left\langle \mathbf{D}^p:\mathbf{K}_i-u_i\dot{\lambda}\right\rangle\right)\left\|\mathbf{M}_i^{kin}\right\|^2
\end{aligned}
$$

Based on the foregoing statement, Eq. (33) is nonnegative can be obtained directly. Thus, the Clausius-Duhem inequality is satisfied.

However, it should be noted that the constitutive equations (19), (28) and (29) are not defined in the same configuration. The second Piola-Kirchhoff stress (Eq. (19)) is defined in the reference configuration; Eqs. (28a) and (28b) act in the structure configuration and the intermediate configuration of kinematic hardening, respectively; Eqs. (28c) and (29) are scalar equations [23]. In order to satisfy the basic requirement of constitutive model, the evolution equations (28a) and (28b) are transformed to the reference configuration, in the following. Obviously, the yield function is also rewritten in term of quantities defined in the reference configuration.

2.4. Representation in the reference configuration

It has been proved that the second Piola-Kirchhoff stress tensor is only the function of $\mathbf{C}$ and $\mathbf{C}^p$ [23], namely

$$\mathbf{S}=\tilde{\mathbf{S}}\left(\mathbf{C},\mathbf{C}^p\right) \qquad (34)$$

A new back stress tensor $\mathbf{X}_i$ defined as a pullback of $\boldsymbol{\chi}_i$ by $\mathbf{F}_i^p$, i.e.

$$\mathbf{X}_i=\mathbf{F}_i^{p^{-1}}\boldsymbol{\chi}_i\mathbf{F}_i^{p^{-T}}=2\mathbf{F}_i^{p^{-1}}\mathbf{F}_i^{pe}\frac{\partial\psi_i^{kin}}{\partial\mathbf{C}_i^{pe}}\mathbf{F}_i^{pe^T}\mathbf{F}_i^{p^{-T}}=2\mathbf{F}_i^{pi^{-1}}\frac{\partial\psi_i^{kin}}{\partial\mathbf{C}_i^{pe}}\mathbf{F}_i^{pi^{-T}} \qquad (35)$$

also is the function of $\mathbf{C}^p$ and $\mathbf{C}_i^{pi}$ only [23], namely

$$\mathbf{X}_i=\tilde{\mathbf{X}}_i\left(\mathbf{C}^p,\mathbf{C}_i^{pi}\right) \qquad (36)$$

It means that the back stress tensor $\mathbf{X}_i$ is defined in the reference configuration. Then, the total back stress is

$$\mathbf{X}=\sum_i^N\mathbf{X}_i \qquad (37)$$

Further, according to Eq. (17), it can be obtained that

$$\dot{\mathbf{C}}^p=2\mathbf{F}^{p^T}\mathbf{D}^p\mathbf{F}^p,\quad \dot{\mathbf{C}}_i^{pi}=\mathbf{F}_i^{pi^T}\mathbf{D}_i^{pi}\mathbf{F}_i^{pi} \qquad (38)$$

Thus, the evolution of $\dot{\mathbf{C}}^p$ and $\dot{\mathbf{C}}_i^{pi}$ have the form

$$\dot{\mathbf{C}}^p=2\dot{\lambda}\mathbf{F}^{p^T}\frac{\mathbf{M}^D-\boldsymbol{\chi}}{\left\|\mathbf{M}^D-\boldsymbol{\chi}\right\|}\mathbf{F}^p=2\dot{\lambda}\frac{\mathbf{Y}^D\mathbf{C}^p}{\sqrt{\mathbf{Y}^D:\mathbf{Y}^D}} \qquad (39a)$$

$$
\begin{aligned}
\dot{\mathbf{C}}_i^{pi}&=2\mathbf{F}_i^{pi^T}\left(u_i b_i\dot{\lambda}\mathbf{M}_i^{kin}+H(f_i)\frac{b_i}{c_i}\mathbf{M}_i^{kin}\left\langle \mathbf{D}^p:\mathbf{K}_i-u_i\dot{\lambda}\right\rangle\right)\mathbf{F}_i^{pi}\\
&=2\dot{\lambda}\left(u_i b_i+H(f_i)\frac{b_i}{c_i}\left\langle \mathbf{D}^p:\mathbf{K}_i-u_i\dot{\lambda}\right\rangle\right)\mathbf{Y}_i^{kin}\mathbf{C}_i^{pi}
\end{aligned} \qquad (39b)
$$

with

$$\mathbf{Y}=\mathbf{CS}-\mathbf{C}^{p}\mathbf{X}=\tilde{\mathbf{Y}}\left(\mathbf{C},\mathbf{C}^{p},\mathbf{C}_{i}^{pi}\right),\quad \mathbf{Y}_{i}^{kin}=\mathbf{C}^{p}\mathbf{X}_{i}=\tilde{\mathbf{Y}}_{i}^{kin}\left(\mathbf{C}^{p},\mathbf{C}_{i}^{pi}\right) \tag{40}$$

and

$$f_{i}=\left\|\boldsymbol{\chi}_{i}\right\|^{2}-\left(\frac{c_{i}}{b_{i}}\right)^{2},\quad \mathbf{K}_{i}=\frac{\boldsymbol{\chi}_{i}}{\left\|\boldsymbol{\chi}_{i}\right\|} \tag{41}$$

Clearly, all constitutive equations are represented in terms of the symmetric tensor $\mathbf{C}$, $\mathbf{C}^{p}$ and $\mathbf{C}_{i}^{pi}$ and the plastic multiplier $\dot{\lambda}$. And the yield function is

$$F_{y}=\sqrt{\mathbf{Y}^{D}:\mathbf{Y}^{D}}-\sqrt{\frac{2}{3}}\left(\sigma_{y}+R\right) \tag{42}$$

Kuhn-Tucker conditions are as following

$$\dot{\lambda}\geq 0,\quad F_{y}\leq 0,\quad \dot{\lambda}F_{y}=0\left(if\ F_{y}=0\right) \tag{43}$$

For numerical examples to be discussed in the follow section, the specific form of the second Piola-Kirchhoff stress and back stress can be given by the well-known neo-Hookean form [23], i.e.

$$\psi^{e}=\frac{\mu}{2}\left(tr\mathbf{C}^{e}-3\right)-\mu\ln\left(\sqrt{\det\mathbf{C}^{e}}\right)+\frac{\Lambda}{4}\left(\det\mathbf{C}^{e}-1-2\ln\left(\sqrt{\det\mathbf{C}^{e}}\right)\right) \tag{44a}$$

$$\psi_{i}^{kin}=\frac{c_{i}}{4}\left(tr\mathbf{C}_{i}^{pe}-3\right)-\frac{c_{i}}{2}\ln\left(\sqrt{\det\mathbf{C}_{i}^{pe}}\right) \tag{44b}$$

where μ and Λ are the Lamé constants, and c_i is the kinematic hardening parameter.

Thus, the corresponding constitutive relations for $\mathbf{S}$ and $\mathbf{X}_i$ are derived

$$\mathbf{S}=\mu\left(\mathbf{C}^{p^{-1}}-\mathbf{C}^{-1}\right)+\frac{\Lambda}{2}\left(\det\mathbf{C}\left(\det\mathbf{C}^{p}\right)^{-1}-1\right)\mathbf{C}^{-1} \tag{45a}$$

$$\mathbf{X}_{i}=\frac{c_{i}}{2}\left(\mathbf{C}_{i}^{pi^{-1}}-\mathbf{C}^{p^{-1}}\right) \tag{45b}$$

It should be noted that Ohno-Kairm model reduces to A-F model when $u_i=1$, and reduces to Ohno-Wang model when $u_i=0$ in Eq. (39b), respectively.

3. Numerical examples

The prediction ability and stability of A-F model at finite deformations had been investigated [21-23]. In this section, some numerical examples were carried out under strain controlled and stress controlled cyclic loadings, respectively.

The material parameters adopted is shown as table 1(parameters of Q and b are set to be zero as without considering isotropic hardening).

Table 1. Material parameters used in the proposed model

N=11, E=202GPa, v=0.33, σ_y=240MPa, Q=200, b=2.5, u_i=0.2;
$\zeta^{(1)}$=4000, $\zeta^{(2)}$=1052.6, $\zeta^{(3)}$=396.8, $\zeta^{(4)}$=200.4, $\zeta^{(5)}$=93.5, $\zeta^{(6)}$=50.1, $\zeta^{(7)}$=32.7, $\zeta^{(8)}$=22.9, $\zeta^{(9)}$=16.8, $\zeta^{(10)}$=12.6, $\zeta^{(11)}$=1.0;
$r^{(1)}$=1.29, $r^{(2)}$=4.83, $r^{(3)}$=6.39, $r^{(4)}$=5.42, $r^{(5)}$=25.3, $r^{(6)}$=30.8, $r^{(7)}$=67.7, $r^{(8)}$=66.7, $r^{(9)}$=65.6, $r^{(10)}$=111.4, $r^{(11)}$=5.0 (*MPa*).

It should be noted here

$$c_i = \frac{2}{3}\zeta_i r_i, \quad b_i = \zeta_i \tag{46}$$

The strain and stress at finite deformation modeling is logarithmic strain (true strain) and Cauchy stress, i.e.

$$\boldsymbol{\varepsilon} = \ln \mathbf{V}, \quad \boldsymbol{\sigma} = \frac{1}{\det \mathbf{F}} \mathbf{F}\mathbf{S}\mathbf{F}^T \tag{47}$$

with

$$\mathbf{V} = \mathbf{F}\mathbf{F}^T \tag{48}$$

3.1. Cyclic straining

3.1.1. Uniaxial tension-compression

In the section, Capacity of the proposed model describing Bauschinger effect is investigated. For finite deformation modeling, it can be controlled by

$$\mathbf{F} = \begin{vmatrix} 1+\Delta & 0 & 0 \\ 0 & e & 0 \\ 0 & 0 & e \end{vmatrix}, \quad S_{22} = S_{33} = 0 \tag{49}$$

where Δ is the applied load, and the unknown e can be determined through Eq. (49).

The stress-strain curves (1 cycle, with $\Delta: 0 \to 0.6487 \to 0 \to 0.3935 \to 0$) are shown as follows:

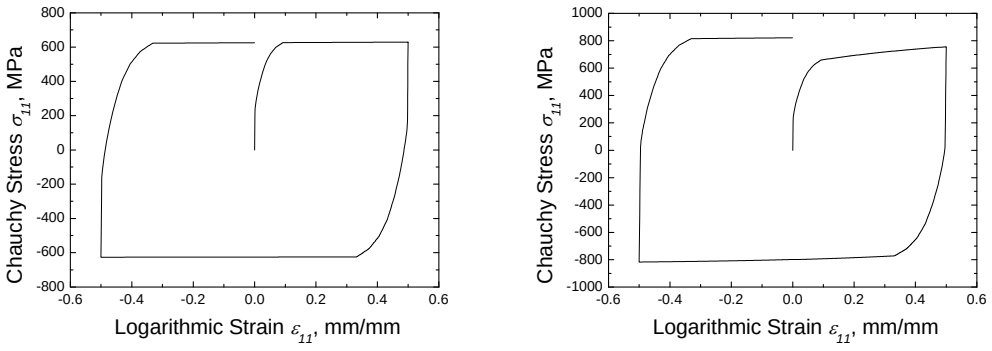

(a) (b)

Figure 2. Uniaxial tension-compression under cyclic straining: (a) without isotropic hardening, (b) with isotropic hardening.

Figure 2 shows the stress-strain curves in one loading cycle under strain controlled. It is found that Bauschinger effect in loading-unloading cycle is reasonably reproduced even though in a relative large strain regime (maximum strain is up to 64.87%). Comparing figure 2(a) and 2(b), it is shown that if isotropic hardening is considered, the strain hardening process can be well simulated.

3.1.2. Simple shear

When shear deformation is very large, shear oscillatory phenomenon will appear if the unreasonable finite deformation frame is adopted. It is very important to validate the prediction in shear deformation case for a developed model at finite deformations.

For simple shear case, deformation gradient can be expressed as

$$F = \begin{vmatrix} 1 & \lambda & 0 \\ 0 & 1 & 0 \\ 0 & 0 & e \end{vmatrix}, \quad S_{33} = 0 \tag{50}$$

where λ is the load, and the unknown e can be determined through Eq. (50).

The stress-strain curves (1 cycle, with $\lambda : 0 \to 0.5 \to 0 \to -0.5 \to 0$) are shown as follows:

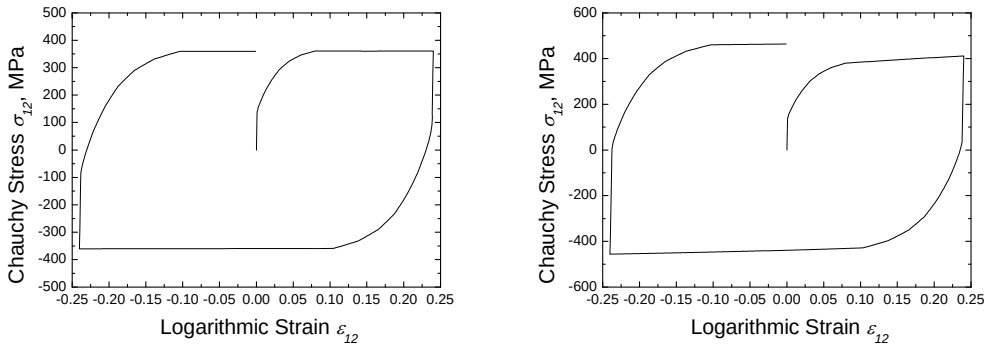

(a) (b)

Figure 3. Simple shear under cyclic straining: (a) without isotropic hardening, (b) with isotropic hardening.

It is shown from Figure 3 that no shear oscillatory phenomenon appears in simple shear case in a relative large strain regime, including with and without consider isotropic hardening cases.

3.2. Cyclic stressing

The prediction ability of ratchetting behaviour is investigated in this section. The loading cases are (150 ± 350)MPa and (100 ± 200)MPa for uniaxial tension-compression and simple shear cases, respectively. The stress-strain curves (10 cycles) are shown as follows:

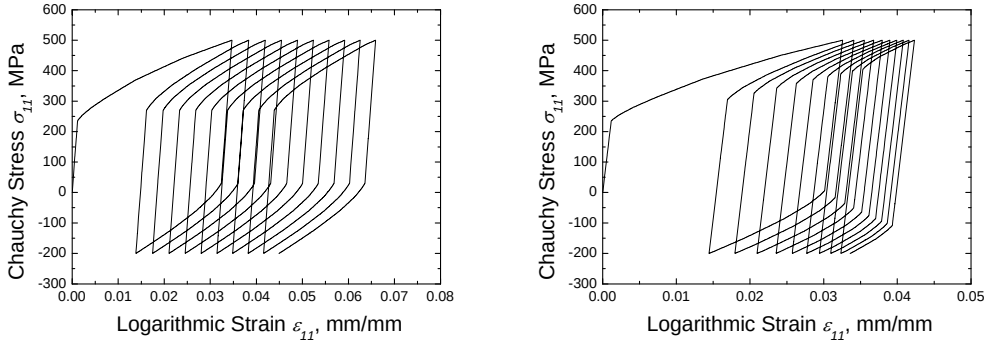

(a) (b)

Figure 4. Uniaxial tension-compression under cyclic stressing: (a) without isotropic hardening, (b) with isotropic hardening.

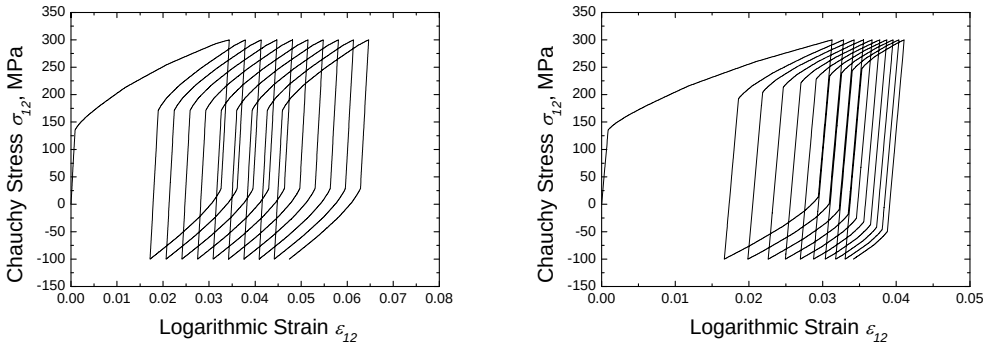

(a) (b)

Figure 5. Simple shear under cyclic stressing : (a) without isotropic hardening, (b) with isotropic hardening.

It is shown from Figure 4 that the presented model can reproduce ratchetting behaviour, regardless of uniaxial tension-compression or simple shear case. Moreover, the ratchetting strain exhibits a constant evolution rate without isotropic hardening; however, the evolution rate of ratchetting strain decreases as isotropic hardening is considered, which is a good agreement with constitutive models at small deformation [7].

4. Conclusions

Cyclic models at finite deformations were derived based on hyper-elastic theory. The deformation gradient is first additional multiplicatively decomposed into elastic and inelastic parts; inelastic part of deformation gradient is further decomposed into energetic and dissipative parts. Based on the frame of finite deformation, the cyclic constitutive model, combining isotropic hardening and Ohno-Karim nonlinear kinematic hardening rules, was proposed to describe Bauschinger effect and ratchetting behaviour. The proposed constitutive equations had been proven to satisfy Clausius-Duhem inequality. Tension-compression and simple shear simulations under cyclic stressing and straining were performed to validate the proposed model.

Acknowledgements

This work was supported by the Doctoral Innovation Funds of Southwest Jiaotong University (2013) and the Fundamental Research Funds for the Central Universities (SWJTU12CX044).

References

[1] C.O. Fredericka, P.J. Armstrong, A mathematical representation of the multiaxial Bauschinger effect. Tech. Rep. RD/B/N731, Berkeley Nuclear Laboratories, 1966.
[2] J.L. Chaboche, Time-independent constitutive theories for cyclic plasticity. Int. J. Plasticity, 2(1986) 149-188.
[3] J.L. Chaboche, Constitutive equations for cyclic plasticity and cyclic viscoplasticity. Int. J. Plasticity, 5(1998) 247-302.
[4] J.L. Chaboche, A review of some plasticity and viscoplasticity constitutive theories. Int. J.

Plasticity, 24(2008) 149-188.
[5] N. Ohno , J.D. Wang, Kinimatic hardening rules with critical state of dynamic recovery, Part I: Fornulation and basic features for ratchetting behavior. Int. J. Plasticity, 9(1993) 375-391.
[6] N. Ohno, J.D. Wang, Kinimatic hardening rules with critical state of dynamic recovery, Part II: Application to experiments of ratchetting behavior, Int. J. Plasticity, 9(1993) 391-403.
[7] M. Abdel-Karim, N. Ohno, Kinematic hardening model suitable for ratchetting with steady -state. Int. J. Plasticity, 16(2000) 225-240.
[8] M. Abdel-Karim, Numerical integration method for kinematic hardening rules with partial activation of dynamic recovery term. Int. J. Plasticity, 21(2005) 1303-1321
[9] G.Z. kang, N. Ohno, A. Nebu, Constitutive modeling of strain-range-dependent cyclic hardening. Int. J. Plasticity, 19(2003) 1801-1819.
[10] C. Tsakmakis, Kinematic hardening rules at finite plasticity, Part 1: a constitutive approach. Continuum Mech. Thermodynam, 8(1996) 215-231.
[11] C. Tsakmakis, Kinematic hardening rules at finite plasticity, Part 2: some examples. Continuum Mech. Thermodynam, 8(1996) 233-246.
[12] C. Tsakmakis, A. Willuweit, A comparative study of kinematic hardening rules at finite deformations. International Journal of Non-Linear Mechanics, 39(2004) 539-554.
[13] G. Lührs, On the numerical treatment of finite deformations in elastoviscoplasticity, Comput. Methods Appl. Mech. Engrg, 144(1997) 1-21.
[14] B. Svendsen, S. Arndt, D. Klingbeil, R. Sievert, Hyperelastic models for elastoplasticity with nonlinear isotropic and kinematic hardening at large deformation, Int. J. Solids Struct, 35 (1998) 3363-3389.
[15] A. Lion, Constitutive modelling at finite thermoviscoplasticity: a physical approach based on nonlinear rheological models. Int. J. Plasticity, 16(2000) 469-494.
[16] F. Mollica, K.R. Rajagopal, A.R. Srinivasa, The inelastic behavior of metals subject to loading reversal, Int. J. Plast, 17(2001) 1119-1146.
[17] L.J. Shen, Constitutive relations for isotropic or kinematic hardening at finite elastic–plastic deformations. Int. J. Solids Struct, 43(2006) 5613-5627.
[18] O.T. Bruhns, H. Xiao, A. Meyers, Self-consistent Eulerian rate type elasto-plasticity models based upon the logarithmic stress rate. Int. J. Plasticity, 15(1999) 479-520.
[19] O.T. Bruhns, H. Xiao, A. Meyers, Large simple shear and torsion problems in kinematic hardening elasto-plasticity with logarithmic rate. Int. J. Solids Struct, 38(2001) 8701-8722.
[20] H. Xiao, O.T. Bruhns, A. Meyers, A consistent finite elastoplasticity theory combining additive and multiplicative decomposition of the stretching and the deformation gradient. Int. J. Plasticity, 16(2000) 43-177.
[21] A.V. Shutov, R. Kreißig, Finite strain viscoplasticity with nonlinear kinematic hardening: Phenomenological modeling and time integration. Comput. Methods Appl. Mech. Engrg, 197 (2008) 2015-2029.
[22] W. Dettmer, S. Reese, On the theoretical and numerical modeling of Armstrong-Frederick kinematic hardening in the finite strain regime. Comput. Methods Appl. Mech. Engrg, 193 (2004) 87-116.
[23] I.N. Vladimirov, M.P. Pietryga, S. Reese, On the modelling of non-linear kinematic hardening at finite strains with application to springback-Comparison of time integration algorithms. Int. J. Numer. Meth. Engng 75(2008) 1-28.
[24] D.L. Henann, L. Anand, A large deformation theory for rate-dependent elastic-plastic materials with combined isotropic and kinematic hardening. Int. J. Plasticity, 25(2009) 1833-1878.
[25] E. Kröner, Allgemeine kontinuumstheorie der versetzungen und eigenspannungen. Archive for Rational Mechanics and Analysis 4(1960) 273-334.
[26] J.C. Simo, K.S. Pister, Remarks on rate constitutive equations for finite deformation problem: computational implications. Compt. Meth. Appl. Mech. Engng, 46(1984) 201-215.

Time dependent ratcheting-fatigue interactions of tempered 42CrMo steel: Experiments and constitutive model

Juan Zhang*, Haibo Luo, Guozheng Kang, Qianhua Kan

School of Mechanics and Engineering, Southwest Jiaotong University, Chengdu 610031, PR China
* Corresponding author: sarazj@126.com

Abstract The time dependent ratcheting behavior and fatigue failure, as well as their interaction were investigated by uniaxial cyclic stressing tests for tempered 42CrMo steel at room temperature. The effects of stress rates and peak stress hold on the ratcheting strain and final failure life were discussed. Then based on the experimental observations, a damage-coupled constitutive model was developed to simulate the whole-life ratcheting by employing a static recovery term in the nonlinear kinematic hardening rule. Comparing with the corresponding experimental results, it is shown that the developed model can describe the whole-life ratcheting behavior of the tempered 42CrMo steel reasonably.

Keywords Ratcheting, Low-cycle fatigue, Visco-plastic constitutive model, Damage, Tempered 42CrMo steel

1. Introduction

When the materials and structures are subjected to a stress-controlled cyclic loading with non-zero mean stress, ratcheting, a cyclic accumulation of inelastic deformation, will occur. Since ratcheting is a secondary deformation superposed on the primary cyclic stress–strain response and develops progressively during the cyclic loading, it is very important and should be addressed in the safety assessment and fatigue life estimation of the materials and structure components. Therefore, the ratcheting has been extensively studied in the last twenty years and many cyclic constitutive models were established to describe the ratcheting[1-8]. However, the referable literature focused mainly on the ratcheting deformation and its constitutive modeling, and the whole-life ratcheting and fatigue failure life were not addressed, since the number of applied cycles was relatively small there. The models do not consider any effect of fatigue damage on the ratcheting, and fail to simulate the whole-life ratcheting of the materials. It is necessary to discuss the ratcheting–fatigue interaction and simulate the whole-life ratcheting and fatigue failure life of the materials.

The low-cycle fatigue involving the ratcheting, i.e., ratcheting–fatigue interaction[9-11] has been investigated recently by some researchers due to its significance in the design and assessment of structure components. And a damage-coupled cyclic constitutive model was constructed by Kang et al.[12] to describe the whole-life ratcheting and predicting the failure life of the materials. It is proved that the simulated whole-life ratcheting behavior and predicted failure life of tempered 42CrMo steel are in a fairly good agreement with the experimental ones. However, the effects of some time-related factors, such as stress rate, hold-time, and so on, on the ratcheting behavior and fatigue failure are not involved in the referable literature. So in this work, the time dependent ratcheting behavior and fatigue failure, as well as their interaction were investigated. Firstly, the ratcheting behavior and low-cycle fatigue for tempered 42CrMo steel were investigated by uniaxial cyclic stressing tests at room temperature. The effects of stress rates and peak stress hold on the ratcheting strain and final failure life were discussed. Then based on the experimental observations, a damage-coupled constitutive model was developed to simulate the whole-life ratcheting by employing a static recovery term in the nonlinear kinematic hardening rule.

2. Experimental results and discussions

The material used in this work is 42CrMo steel. Its chemical composition is: C, 0.43%; Mn, 0.68%; Si, 0.27%; P, 0.014%; Cr, 1.11%; Ni, 0.05%; W, 0.01%; Mo, 0.17%; V, 0.01%; Ti, 0.004%; Cu, 0.03%; Fe, remained. The as-forged 42CrMo steel bars were tempered (tempering at 560℃ after heating at 850℃ for 1h and quenching in oil), and then were machined to be round, solid bar fatigue specimens with test section diameter of 10mm and gauge length of 30mm for uniaxial tests. The test machine was MTS809-250KN; the loading process was controlled and the experimental data were collected by Teststar control system attached to the machine. The axial strain was measured by a tensile extensometer, whose limited axial nominal strain was 50%. The specimens were tested under monotonic tension, uniaxial cyclic straining and uniaxial cyclic stressing at room temperature. To illustrate the ratcheting behavior more clearly, the variation of ratcheting strain ε_{r} (defined by Eq. (1)) with the number of cycles for each loading case of cyclic stressing, was obtained from the experimental data and is shown in the figures in this section. In this work, the ratcheting strain ε_{r} is defined as

$$\varepsilon_{\mathrm{r}} = \frac{1}{2}\left(\varepsilon_{\max} + \varepsilon_{\min}\right) \tag{1}$$

where $\varepsilon_{\max}$ is the maximum axial nominal strain in each cycle measured by the extensometer, and $\varepsilon_{\min}$ is the minimum. Meanwhile, in this work, the ratcheting true strain rate is defined as the increment of ratcheting strain after each cycle and denoted as $\mathrm{d}\varepsilon_{\mathrm{r}}/\mathrm{d}N$, where *N* means the number of cycles.

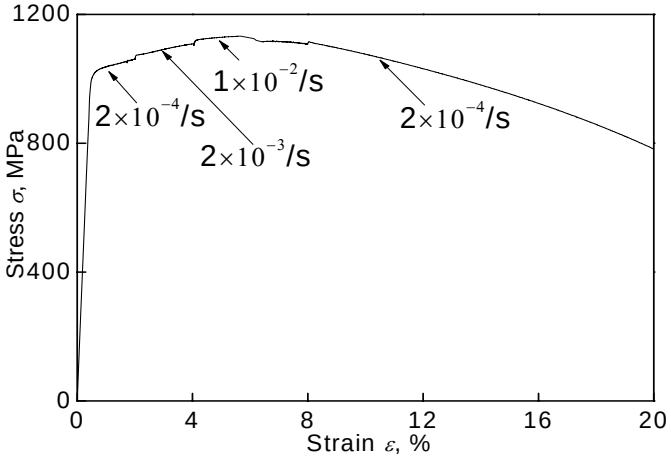

Figure 1. Monotonic tensile stress-strain curves with different straining rates

Monotonic tensile results of tempered 42CrMo steel at different straining rates are shown in Fig. 1. It is shown that the material exhibits rate-dependence at room temperature, and the responded stress at smaller strain rate is much lower than that at higher one.

2.1. Time-dependent strain cyclic features

The cyclic softening/hardening features of the material were investigated under the symmetrical axial cyclic straining (±0.6%) at different straining rates (0.2%/s and 0.04%/s). It can be seen from Fig. 2 that: (1) the material presents significant cyclic at two straining rates, (2) the cyclic softening behavior of the material is rate-dependent even at room temperature, i.e., responded stress amplitude at smaller straining rate is lower than that at higher one.

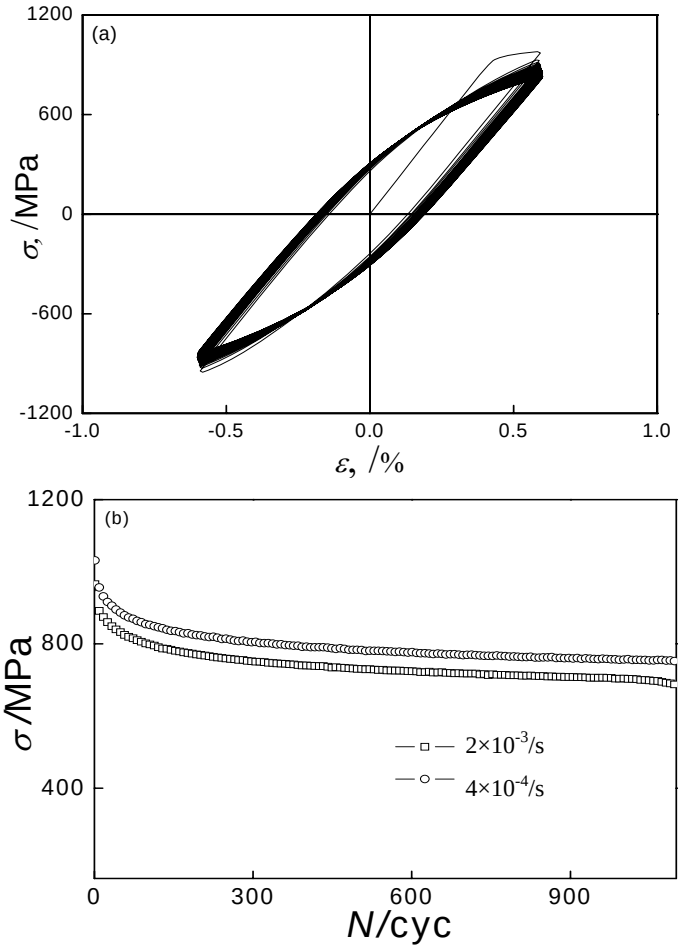

Figure 2. Results of symmetrical axial cyclic straining at different straining rates: (a) stress–strain curve at straining rate of 0.2%/s; (b) curves of stress amplitude vs. cyclic number at two straining rates

2.2. Time-dependent ratcheting-fatigue interactions

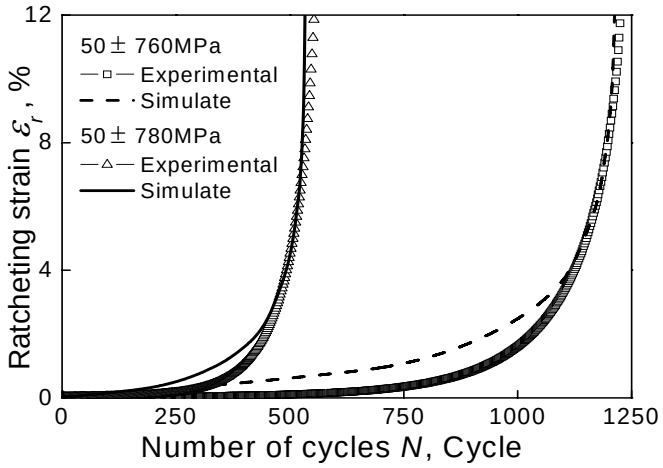

Figure 3. Experimental and simulated whole life ratcheting with different stress amplitude

Firstly, the specimens were tested by cyclic stressing with various nominal stress amplitudes, mean nominal stresses at the same stress rate till the failure occurred. The experimental results of ratcheting behavior of tempered 42CrMo steel at room temperature (shown in Fig.3 and Fig.4) is the same as that was observed in previous work[11]: (1) The evolution of ratcheting strain can be

divided as three stages regarding to the different ratcheting strain rates due to the cyclic softening feature of tempered 42CrMo steel, i.e., the first stage with decreasing ratcheting strain rate, the second stage with an almost constant rate and the third stage with quickly increasing rate. (2)When the stress amplitude or mean stress increases, the ratcheting strain ε_r increases correspondingly, and the first and second stages are ended and the third stage appears more quickly, causing the failure of the material within fewer cycles.

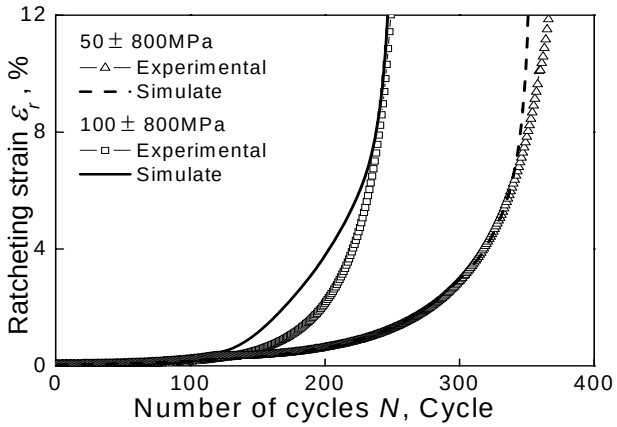

Figure 4. Experimental and simulated whole life ratcheting with different mean stress

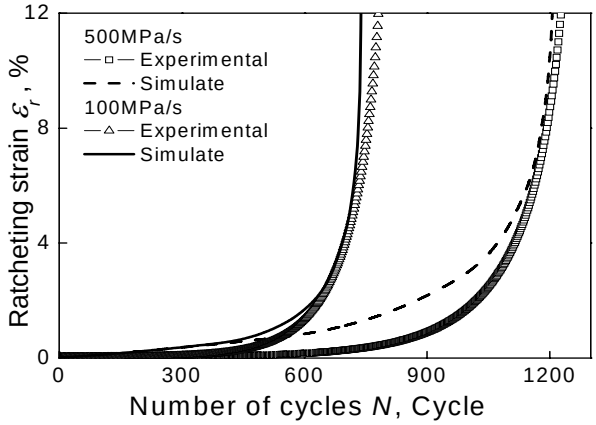

Figure 5. Experimental and simulated whole life ratcheting at different stress rate

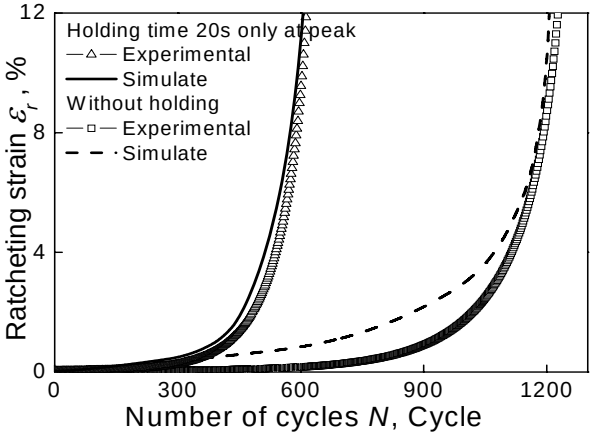

Figure 6. Experimental and simulated whole life ratcheting with and without peak stress holding time

Then the axial cyclic stressing tests were done with constant mean stress and stress amplitude (50 ± 760MPa) but at different stress rates (500 and 100MPa/s). The experimental result is shown in Fig.5. It can be seen that the effect of stressing rate on the ratcheting and fatigue life is remarkable. The evolution of ratcheting strain also can be divided as three stages at different stress rates, but the ratcheting strain ε_r increases with the increasing of stress rate, and the first and second stages are ended and the third stage appears more quickly at lower stress rate, causing the failure of the material within fewer cycles.

The effect of the peak stress hold in each cycle on ratcheting and fatigue life also was discussed under uni-stepped axial cyclic stressing test (50 ± 760MPa) at stressing rate of 500MPa/s. It is concluded from Fig. 6 that non-zero hold-time influences apparently the ratcheting and the fatigue life of the material. The ratcheting strain ε_r with peak stress holding is larger than that without peak stress holding. When the stress holds 20s at peak, the first and second stages of ratcheting are ended and the third stage appears more quickly, so the material fails within fewer cycles

3. Constitutive model and simulation

To describe the ratcheting–fatigue interaction of the tempered 42CrMo steel, Kang et al.[12] proposed a damage-coupled visco-plastic cyclic constitutive model. It has been verified their model could simulate the whole-life ratcheting and predict the fatigue failure life of the material reasonably. So in this work，the damage-coupled visco-plastic cyclic constitutive model proposed by Kang was used to describe the whole-life ratcheting of the material, except that a new nonlinear kinematic hardening rule was introduced to improve the description of time-dependent ratcheting behavior.

3.1. Damage-coupled constitutive model

The governing equations of the damage-coupled constitutive model are outlined as follows:

$$\varepsilon_{ij} = \varepsilon_{ij}^{e} + \varepsilon_{ij}^{vp} \tag{2}$$

$$\varepsilon_{ij}^{e} = \frac{1+\nu}{E}\left(\frac{\sigma_{ij}}{1-D}\right) - \frac{\nu}{E}\left(\frac{\sigma_{kk}\delta_{ij}}{1-D}\right) \tag{3}$$

$$\dot{\varepsilon}_{ij}^{vp} = \frac{3}{2}\frac{\dfrac{S_{ij}}{1-D} - \alpha_{ij}}{\left(\dfrac{S_{ij}}{1-D} - \alpha_{ij}\right)_{eq}}\left(\frac{\dot{\lambda}}{1-D}\right) \tag{4}$$

$$F_y = \left(\frac{S_{ij}}{1-D} - \alpha_{ij}\right)_{eq} - Q \tag{5}$$

$$\frac{\dot{\lambda}}{1-D} = \dot{p} = \left\langle \frac{F_y}{K} \right\rangle^{n} \tag{6}$$

$$(\frac{S_{ij}}{1-D}-\alpha_{ij})_{eq}=\sqrt{\frac{3}{2}\left(\frac{S_{ij}}{1-D}-\alpha_{ij}\right)\left(\frac{S_{ij}}{1-D}-\alpha_{ij}\right)} \quad (7)$$

In previous work[13], a new kinematic hardening rule with a static recovery term (based on the Ohno–Abdel-Karim equation[5]) provide a reasonable simulation to the time-dependent ratcheting of SS304 stainless steel. So in this work, the damage was introduced in the kinematic hardening rule with a static recovery term to describe the whole-life time-dependent ratcheting of tempered 42CrMo steel. The evolution law of nonlinear kinematic hardening rule is

$$\alpha_{ij}=\sum_{k=1}^{M}\alpha_{ij}^{(k)} \quad (8)$$

$$\dot{\alpha}_{ij}^{(k)}=\xi^{(k)}\left[\frac{2}{3}r^{(k)}(1-D)\dot{\varepsilon}_{ij}^{p}-\mu\alpha_{ij}^{(k)}\dot{\bar{\varepsilon}}^{p}-H(f^{(k)})(1-\mu)\alpha_{ij}^{(k)}\dot{\bar{\varepsilon}}^{p}\right]-\chi^{(k)}\left(\bar{\alpha}^{(k)}\right)^{m^{(k)}-1}\alpha_{ij}^{(k)} \quad (9)$$

The evolution law of isotropic hardening is

$$\dot{Q}=\gamma(Q_{\infty}-Q)\dot{\bar{\varepsilon}}^{p}=\gamma(Q_{\infty}-Q)\dot{p}(1-D) \quad (10)$$

In above equations, D is the damage variable. From the evolution feature of the damage during the stress cycling, it is concluded that the total damage presented in the stress cycling can be divided as two parts, i.e., elastic damage and plastic damage[12]:

$$D=D_{\mathrm{e}}+D_{\mathrm{p}} \quad (11)$$

The evolution rules of D_{e} and D_{p} are

$$\dot{D}_{e}=\left(\frac{\sigma_{eq}^{2}}{2E_{0}S_{e}(1-D)^{2}}\right)\dot{p} \quad (12)$$

$$\dot{D}_{p}=\left(\frac{\sigma_{eq}^{2}}{2E_{0}S_{p}(1-D_{p})^{2}}\right)\dot{p} \quad (13)$$

It can be seen that they have the same original form but different constants. When the plastic strain is very small, the macroscopic elastic damage is a main cause of the fatigue damage; however, when the plastic strain develops significantly due to the cyclic softening of the material, the plastic damage dominates the damage after certain cycles[12].

3.2. Simulations to whole life ratcheting

In the constitutive model, the material parameters relative to the evolution of elastic and plastic damages can be determined from the experimental results by the method mentioned in reference [12]. For simplicity, other material parameters are determined from the experiments without any fatigue damage considered. In this case, the procedure to determine the parameters is similar to that used by Kang[8]. The values of all material parameters used in the proposed damage-coupled constitutive model are listed in Table 1.

Table 1. Material parameters used in the constitutive model

M=10, E_0=213GPa, v=0.3, K=90MPa, n=10, Q_0=709.5MPa;
$\zeta^{(1)}=6060.6$, $\zeta^{(2)}=2020.2$, $\zeta^{(3)}=673.4$, $\zeta^{(4)}=303.3$, $\zeta^{(5)}=151.5$, $\zeta^{(6)}=75.7$, $\zeta^{(7)}=43.2$
$\zeta^{(8)}=28.8$, $\zeta^{(9)}=21.6$, $\zeta^{(10)}=17.3$; $r^{(1)}=203.5$, $r^{(2)}=26.4$, $r^{(3)}=13.6$, $r^{(4)}=1.8$, $r^{(5)}=2.1$,
$r^{(6)}=1.4$, $r^{(7)}=7.9$, $r^{(8)}=20.1$, $r^{(9)}=42.8$, $r^{(10)}=19.2$ (MPa);
$\gamma=0.2$, $\mu=0.15$, $Q_\infty=600$ MPa;
$\sigma_{-1}^{f}=419.6$ MPa, $A_1=7.4\times10^{-5}$, $A_2=2.2\times10^{-6}$, $A_3=8.16$, $A_4=-0.569$, $S_p=29$ MPa.

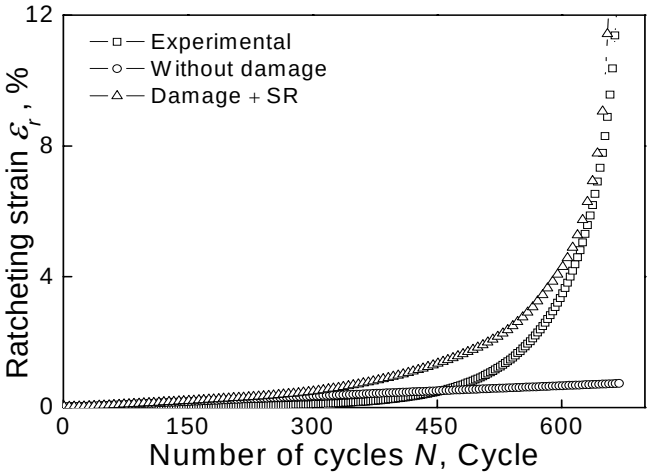

Figure 7. Experimental and simulated whole-life ratcheting by the model coupled with damage or not

The uniaxial whole-life time-dependent ratcheting behavior of tempered 42CrMo steel is simulated by the damage-coupled constitutive model. Fig. 7 shows the experimental and simulated results (50±780MPa, 500MPa/s) obtained by the damage-coupled model and the model with no damage, respectively. It is seen from Fig.7 that the constitutive model introducing damage gives a reasonable simulation for the whole-life ratcheting, especially for the accelerated increase of ratcheting strain at the end stage of cycling.

Figs. 3 and 4 provide some simulated results obtained by the model for some loading cases with various nominal stress amplitudes, mean nominal stresses at the same stress rate. It is shown that the simulated results are in fairly good agreement with the experimental ones and cyclic softening feature of the material on the ratcheting behavior are reasonably considered because of the introducing of damage.

Fig. 5 shows the simulated results of whole life ratcheting behavior at different stress rate, which loading condition is 50±760MPa. It is shown that the constitutive model proved good simulation to the effect of stress rate, and the ratcheting strain and ratcheting strain rate were increase with the decline of stress rate. Fig. 6 shows the simulated results of whole life ratcheting behavior with and without peak stress hold. It is shown that the simulated results are in fairly good agreement with the experimental ones. In one word, the developed constitutive model can describe the time dependent ratcheting reasonably since a static recovery term is introduced to the kinematic hardening rule.

4. Conclusions

(1) The tempered 42CrMo steel presents a rate-dependence under monotonic tension and uniaxial cyclic straining at room temperature. The variations of stress rate and peak stress hold-time have remarkable effect on the ratcheting behavior and low-cycle fatigue life.

(2) Based on the experimental results, a damage-coupled cyclic constitutive model is develops in the framework of continuum damage mechanics and unified visco-plasticity. In the model, the effects of cyclic softening feature and fatigue damage on the ratcheting are addressed by introducing the damage variable *D*. And the effects of stress rate and peak stress hold are simulated by employing a static recovery term in the nonlinear kinematic hardening rule. The model describes the whole-life ratcheting behavior of the material reasonably. The model describes the whole-life time dependent ratcheting behavior of the material reasonably.

Acknowledgements

The work was financially supported by the Fundamental Research Funds for the Central Universities (SWJTU11CX070).

References

[1] Chaboche, J.L., On some modifications of kinematic hardening to improve the description of ratcheting effects, Int. J. Plast., 7, (1991) 661–678.
[2] Ohno, N.,Wang, J.D., Kinematic hardening rules with critical state of dynamic recovery: I. Formulation and basic features for ratcheting behaviour, Int. J. Plast., 9, (1993)375–389.
[3] Ohno, N.,Wang, J.D., Kinematic hardening rules with critical state of dynamic recovery: II. Application to experiments of ratcheting behaviour, Int. J. Plast., 9, (1993) 390–403.
[4] Jiang, Y., Sehitoglu, H., Modeling of cyclic ratcheting plasticity, ASME J. Appl. Mech., 63, (1996) 720–733.
[5] Abdel-Karim, M., Ohno, N., Kinematic hardening model suitable for ratcheting with steady-state, Int. J. Plast., 16, (2000) 225–240.
[6] Bari, S., Hassan, T., An advancement in cyclic plasticity modeling for multiaxial ratcheting simulation, Int. J. Plast., 18, (2002) 873–894.
[7] Chen, X., Jiao, R., Modified kinematic hardening rule for multiaxial ratcheting prediction, Int. J. Plast., 20, (2004) 871–898.
[8] Kang, G.Z., A visco-plastic constitutive model for ratcheting of cyclically stable materials and its finite element implementation, Mech. Mater., 36, (2004) 299–312.
[9] Kwofie, S., Chandler, H.D., Low cycle fatigue under tensile mean stresses where cyclic life extension occurs, Int. J. Fatigue, 23, (2001) 341–345.
[10] Yang, X.J., Low cycle fatigue and cyclic stress ratcheting failure behavior of carbon steel 45 under uniaxial cyclic loading, Int. J. Fatigue, 27, (2005) 1124–1132.
[11] Kang, G.Z., Liu, Y.J., Uniaxial ratcheting and low-cycle fatigue failure of the steels with cyclic stabilizing or softening feature, Mater. Sci. Eng. A, 472 (1–2), (2008) 258–268.
[12] G.Z. Kang, Y.J. Liu, J. Ding, Q. Gao, Uniaxial ratcheting and fatigue failure of tempered 42CrMo steel: Damage evolution and damage-coupled visco-plastic constitutive model, Int. J. Plast., 25, (2009) 838–860.
[13] Q.H. Kan, G.Z. Kang, J. Zhang, Uniaxial time-dependent ratchetting: Visco-plastic model and finite element application, Theoretical and Applied Fracture Mechanics, 47, (2007) 133–144.

Grain size dependence of the yield stress for metals at quasistatic and dynamic loadings

Elijah N. Borodin[1,2*], Alexander E. Mayer[2], Polina N. Mayer[2]

[1]Institute of Problems of Mechanical Engineering RAS, 199178, Russia
[2]Department of Physics, Chelyabinsk State University, 454001, Russia
* Corresponding author: elbor7@gmail.com

Abstract
Micro mechanisms of plastic deformation and the defect structure evolution are sufficiently changing with the strain rate increase. It leads to non-monotonic relations between the macroscopic characteristics of metal strength or ductility and the structure parameters such as a grain size. Our simulations predict an inverse Hall-Petch relation for ultrafine-grained metals at extremely high strain rate (above $10^7 s^{-1}$). Mechanisms of the homogeneous nucleation of dislocations and the mechanical twining can effectively decrease the stresses at strain rates up to $10^9 s^{-1}$.

Keywords High strain rates plasticity, Ultrafine-grained materials, Inverse Hall-Petch relation, Grain boundary sliding

1. Introduction

Materials with ultrafine-grained structure (with the grain diameters of several tenth parts of micrometer), as well as nanocrystalline materials, are widely investigated both theoretically and experimentally for the last twenty years [1,2]. This goes in parallel with the development of experimental technic [3], and leads to discover and investigation of some new effects specific for these materials. One of them is an inverse Hall-Petch relation – the decrease of the yield stress at the grain size decrease. All observations of this effect can be divided on two parts: deformation at low strain rates - usually less than $10^{-1} s^{-1}$ [4-6], and the molecular dynamics simulation at extremely high strain rates - usually greater than $10^8 s^{-1}$ [7]. Preparation and experimental investigation of the nanocrystalline materials is very difficult. On the other hand, the molecular dynamics is very limited in application to macroscopic volumes of microcrystalline and coarse grained materials. It does not allow one to define directly the macroscopic characteristics of the material and to carry out simulations of deformation of the macroscopic volumes of substance with realistic strain rates.

For investigation of the internal defect structure influence on the macroscopic strength and ductility one can take some microscopic mechanisms proposed by theoretical investigations or molecular dynamics simulations and to include it in the modeling in the framework of continuum mechanics. Simulation results could be verified by comparison with experimental data. This way, supplemented by the procedure of averaging over the micro-volumes of substance, allows us to monitor the change of the defect structure and its influence on the strength parameters of different metals.

2. Yield strength at low strain rate

The yield strength σ_y is one of the key macroscopic parameters, which determines the strength of the material. It grows with the dislocation density ρ_D increase and the grain size d decrease, which are well-known effects in most polycrystalline metals and alloys. This dependences are expressed by the Taylor [8,9] and the Hall-Petch relations [10,11] for the barrier of dislocations gliding:

$$\sigma_y = \sigma_0 + \alpha G b \sqrt{\rho_D} + k_{HP} / \sqrt{d} \qquad (1)$$

Here σ_0 includes an influence of impurities and of the Pierls relief resistance for dislocation gliding; G is the shear modulus, b is the Burgers vector, k_{HP} is the Hall-Petch constant, which is a characteristic of the metal. This relation is exactly satisfied until the grain size in polycrystalline material is higher than 1 μm and at the low strain rates. Influence of the mechanical twinning on the resistance for dislocations gliding can be accounted in the form of the Hall-Petch relation with an average distance between the twins Δ instead of the grain size and with other constant k_{TW} [9].

If we introduce the volume fractions of the dislocations $R = b^2\rho_D$, the grain boundaries $\eta = 1-(1-\delta/d)^3 \approx 3\delta/d$ and the twins [12] $F = (1+\Delta/2e)^{-1}$ then the Eq. (1) takes the next form:

$$\sigma_y = \sigma_0 + k_1\frac{\sqrt{R}}{b} + k_2\frac{\sqrt{\eta}}{\sqrt{\delta}} + k_3\frac{\sqrt{F}}{\sqrt{e}}, \qquad (2)$$

were δ and e are the grain width and the twin width correspondently, which are almost constant for the material as well as the Burgers vector. Constants: $k_1 = \alpha Gb$, $k_2 \sim \sqrt{3}k_{HP}$, $k_3 \sim k_{TW}/\sqrt{2}$. As the volume fractions are less than unity, the yield stress is limited. Introduction of impurities apparently is the only way to the increase yield stress to the theoretical tensile strength value [13].

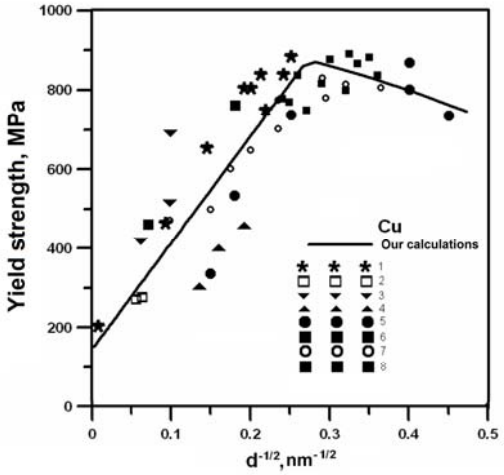

Figure 1 The grain size dependence of the yield strength for copper. Experimental data: 1 – [1], 2 – [17], 3 – [18], 4 – [19], 5 – [4], 6 – [20], 7 – [5], 8 – [6].

In microcrystalline metals ($d < 1$ μm), it is often observed the abnormal Hall-Petch relation with k_{HP} different from that in the coarse-grained crystal; as a result, slope of the Hall-Petch curve is changing [14]. Therefore, the yield stress does not achieve the value predicted from the Eq. (2). In many nanocrystalline materials with d lesser than 12 nm-15 nm an inverse Hall-Petch relation is observed: the yield strength decreases with the decrease of the grain size [4-6,15]. This effect is often related with the grain boundary sliding as an alternative mechanism of plasticity. As it was shown in [16], there is a barrier resistance stress y_b; it is equal to the doubled external stresses, which must be exceeded for initiating of the grain boundary sliding. It depends on the grain size.

$$y_b = 0.01\cdot\frac{G}{1-\nu}\left(1-\frac{\delta}{d}\right)^2, \qquad (3)$$

where ν is the Poisson ratio of the material, which is slightly varied for different metals. For activation of the grain boundary sliding one need to apply the stress exceeding $\sigma_y = 2y_b$; for copper and iron it is about 1GPa. Therefore, in ultrafine-grained and nanocrystalline materials the plastic

flow occurs only at high internal stresses. This model give a good fit with experimental results for different metals [16]. Fig. 1 presents the experimental observation points and the theoretical curve for copper in the Hall-Petch coordinates. One can see an existing of the maximum of the yield strength for grain size of about 12nm. Yield strength here is less than 1 GPa.

3. Yield strength at high strain rates

Micro mechanisms of plastic deformation and defect structure evolution are sufficiently changing with the strain rate increase. The high stain rate experiments demonstrate a deviation from the Hall-Petch relation even for ultrafine grained metals. At these deformation conditions we will define dynamical yield strength of the material through the maximal shear stresses, which is reached during the high-rate deformation. Dynamical yield stress not fully determined by the internal stresses from different obstacles as in the quasistatic deformation conditions. At extremely high strain rate (above 10^6 s^{-1}) it has a sufficiently dynamical nature and defined by dynamics properties of the dislocation and grains gliding, by the kinetics of the dislocation generation and annihilation. For the yield stress definition one must solve a full system of equation which describes the material plasticity as it was done in [21]. This system includes the equations for dislocation and grain boundary plasticity and the continuum mechanics equations.

3.1 Dislocation plasticity model

Theoretical description of the dislocation plasticity one can get using the model proposed in [22]. In monocrystalline metals, dislocations can glide along the limited numbers of slip planes; we shall numerate it by index β. Equation for plastic deformation caused by the dislocation glide [23] can be written as:

$$\frac{dw_{ik}^{D}}{dt} = -\frac{1}{2}\sum_{\beta}\left(b_i^{\beta}\, n_k^{\beta} + n_k^{\beta} b_i^{\beta}\right) V_D^{\beta}\, \rho_D^{\beta}\,. \tag{4}$$

Here b^{β} is the Burgers vector of dislocations, ρ_D^{β} is the scalar density of dislocation (their number per unit square) in glide plane with index β, V_D^{β} – velocity of dislocations. These parameters fully determine the plastic deformation of the coarse-grained crystals. Velocity of dislocation can be defined from the movement equation [22]:

$$\frac{m_0}{\left(1-\left(V_D^{\beta}/c_t\right)^2\right)^{3/2}}\frac{dV_D^{\beta}}{dt} = \left(F_D^{\beta} \pm \frac{b^{\beta}Y}{2}\right) - \frac{B(T)V_D^{\beta}}{\sqrt{1-\left(V_D^{\beta}/c_t\right)^2}}, \tag{5}$$

Here $F_D^{\beta} = S_{ik} b_i n_k$ is the Pitch-Keller force (it acts on the unit length of dislocation line from the external stresses), Y is the static yield stress of the material, which depends on the dislocation density, the grain size and the presence of different impurities [24]. m_0 is the field mass of dislocation, c_t is transverse sound velocity. The terms with sound velocity allows one to take into account an experimental fact that dislocation velocity is always limited above by the sound velocity. Coefficient of viscous friction $B(T)$ is temperature dependent [25,26]. Eq. (5) had demonstrated a good fit with experimental data for over barrier dislocation gliding at the high rate deformation [22].

For determination of the dislocation density one can write a kinetics equation in the next form [22]:

$$\frac{d\rho_D^{\beta}}{dt} = \frac{\eta}{\varepsilon_L}\frac{B\left(V_D^{\beta}\right)^2\rho_D^{\beta}}{\sqrt{1-\left(V_D^{\beta}/c_t\right)^2}} - k_a b\left|V_D^{\beta}\right|\left(\rho_D^{\beta}\right)^2 - \frac{\rho_D^{\beta}\left|V_D^{\beta}\right|}{d}. \tag{6}$$

Here the dislocation source (the first term in the Eq. (5)) has been recorded from the energy-wise consideration; $\eta = 0.1$ is a portion of dissipated power, which is spent on generation of new defects; the energy $\varepsilon_L = 8\text{э}B/b$ [25] is required for generation of new dislocations (per unit of length). Annihilation term (the second term in the Eq. (5)) was written similar to [27].

For nanocrystalline materials one has to take into account an additional term in the kinetic equation (5). Dislocation core are being delocalized in the disordered grain boundary material [28], when it reaches any grain boundary [29]. Therefore, dislocation in nanocristalline material has a lifetime, which is equal to the traveling time of dislocation through the grain $d/\left|V_D^\beta\right|$, where d is an average grain size. Corresponding additional term in the right-hand part of the kinetics equation (5) is the next: $-\rho_D^\beta \left|V_D^\beta\right| / d$. The proposed model was verified on the experiments at various high strain rate deformation conditions, including the shock wave propagation in metals [22,30]. Its application demonstrates a good fit with experimental data at minimum adjustable parameters.

3.2 Model for grain boundary sliding

The plastic deformation related with the grain boundary plasticity one can describe similar to the Maxwell model for a highly viscous liquid [31] with the exception of the barrier resistance stress y_b . It means that grain boundaries are elastically deformed during short intervals of time. But when the deformation ceases, shear stresses remain in them, although they are dumped in the course of time, so that after sufficiently long time almost no inertial stress remains in the boundaries, exception of y_b . Viscous force appears in the grain boundaries due to diffusion, which counteracts the sliding of the grains layers relative to each other; it can be characterized by a relaxation time τ . As a result, the plastic deformation caused by the grain boundary sliding can be written in the next form [16]:

$$\dot{w}_{ik}^{gb} = \frac{1}{2G}\sum_\alpha \tau_i^\alpha n_k^\alpha \frac{\Theta\left(\sigma_\tau^\alpha - y_b\right)}{\tau}, \tag{7}$$

where $\Theta(x)$ is a Heaviside function, index α numerates the possible shifting planes of the grains; normal vectors to these planes can be written as n_i^α . Stresses applied to corresponding plane are $\sigma_{ik} n_k^\alpha$ and the stress component, which acts in the tangent direction τ_i to the plane, is equal to the convolution product $\sigma_{ik} n_k^\alpha \tau_i$. We will denote τ_i^α as the direction of the tangent vector corresponding to the maximum shear stresses applied to this plane. Then the maximal shear stress acting on the layer of grains can be represented as $\sigma_\tau^\alpha = s_{ik} n_i^\alpha \tau_k^\alpha$, where s_{ik} is a deviator of stresses. Using a linear approximation, one can obtain the following expression for the relaxation time of grain boundary sliding [16] from data of the molecular dynamics simulation [32]:

$$\tau = \frac{dk_bT}{12Gb\nu_D V_s}\exp\left(\frac{U_s}{k_bT}\right) \tag{8}$$

Activation volume V_s can be estimated as $V_s \sim b^3$. Activation energy U_s has the same order as the activation energy of viscous flow in molten state of the metal [28].
Tensor of the full plastic deformation can be written as

$$w_{ik} = w_{ik}^D + w_{ik}^{gb} \tag{9}$$

4. Simulation results

4.1 Dislocation starvation

At increasing of the strain rate an over-barrier dislocation gliding occurs and the domination resistant force becomes a phonon drag to the gliding dislocations [23]. At the further increasing of the strain rate the main mechanism of strain hardening becomes the dislocation starvation - it is well known phenomena in the field of nanopillars and thin film modeling [33] at rapid deformation condition. A distinction between the bulk material and these nano-crystals is in the cause of the starvation. In nano-crystals there are no ordinary dislocation sources, and the plasticity is usually provided by several entered dislocations and by surface instabilities [33]. In the bulk materials there is relatively large dislocation density and active dislocation sources exist. But the maximal dislocation density can be estimated through critical stress for the Frank-Read sources activation:

$$\sigma_\tau = Gb/L_{FR} \,. \tag{10}$$

Here b $L_{FR} \sim 1/\sqrt{\rho_D}$ – a base of the Frank-Read source which has the same order as an inverse square root of the total dislocation density ρ_D. Then, for reasonable stresses $\sigma_\tau \sim 2$ GPa, the total dislocation density is limited by the value $\rho_D \sim 10^{16} m^{-2}$. On the other hand, the Orowan equation [24] gives:

$$\dot{\varepsilon} = \rho_D b V_D \,. \tag{11}$$

The dislocation velocity V_D can not exceeded the transverse sound velocity $c_t \approx 3000$ m/s. As a result, we obtain the maximal strain rate at which dislocations can theoretically provide the full relaxation of shear stresses: $\dot{\varepsilon} < 10^{10} s^{-1}$. In real metals sufficient part of dislocations consists of immobile dislocations, which is not contributing to plastic relaxation. Our calculations demonstrate that the dislocation starvation takes place already at $\dot{\varepsilon} > 10^7 s^{-1}$. Therefore, even in ultrafine crystals with the grain size of about hundreds of nanometers a sufficient deviation from the Hall-Petch relation takes place at high strain rates, and it is erroneously to extrapolate the molecular dynamics simulation results on microcrystalline material by experimental data obtained at low strain rate.

The dislocation mechanism of stress relaxation is very limited for the strain rates exceeding $10^9 s^{-1}$ because of a dislocation starvation. Figure 2 demonstrates the dislocation starvation in ultrafine-grained copper at the strain rate from $10^7 s^{-1}$ to $10^9 s^{-1}$.

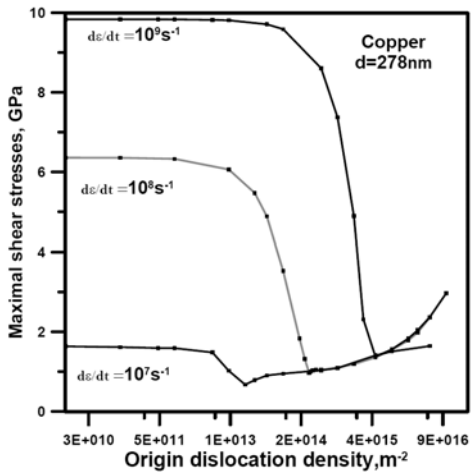

Figure 2 The dependence of the maximal shear stress on the origin dislocation density for copper at extremely high strain rates: 10^7-10^9 s^{-1}.

For origin dislocation densities below $10^{12}m^{-2}$ (an undeformed material) the yield stress is high and it is almost unchanged with the dislocation density decrease. One can see that there is an "optimal" dislocation density which corresponds to the lowest shear stress. It is proportional to the strain rate according to Orowan equation (11). Further increasing of the origin dislocation density results in the increase of the yield strength according to the Taylor hardening low (1). Increasing of the dislocation density during the deformation is almost absent if the origin dislocation density exceeds $10^{14}m^{-2}$, as it was demonstrated by our calculations with use of the Eq.(6) for dislocations kinetics.

4.2 An inverse Hall-Petch relation in ultrafine crystalline copper

Figure 3 presents dependence of the dynamical yield stress on the grain size (in the Hall-Petch coordinates) at strain rates from $2.4\cdot10^{8}s^{-1}$ to $3.5\cdot10^{8}s^{-1}$ with «not optimal» origin dislocation densities. In the coarse grained materials (grain size above 300μm) the Hall-Petch relation is observed.

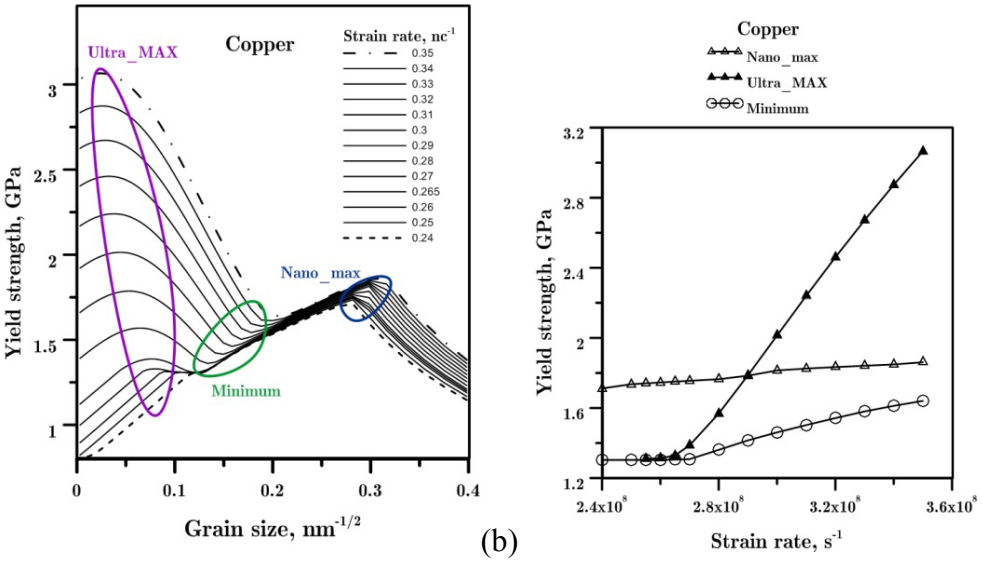

Figure 3 The dependence of the dynamic yield stress on the grain size at different strain rate (a) and on the strain rate at different grain size (b) for copper at extremely high strain rate.

The well-known inverse Hall-Petch relation is also observed for the grain size range <12 nm ($d^{-1/2}$~0.3). But the second maximum of the dynamic yield strength corresponding to the grain sizes of about of hundreds of nanometers appears in this situation. Our calculations demonstrate that at the strain rate above $10^{7}s^{-1}$, the ultrafine-grained copper is stronger to shifting than the nanocrystalline copper. Existence of additional maximum in the ultrafine-grain material is explained by the beginning of the grain boundary sliding and by its contribution into the plastic deformation rate. Figure 3(b) demonstrates a linear growth of the yield strength with increasing of the strain rate. Growth rate is maximal for the ultrafine crystalline metals.

4.3 Yield strength limitations

For all high strain rates the yield strength increases with the strain rate increase. But there are several mechanisms limiting this growth. The homogeneous nucleation dislocation must solve the problem of the dislocation starvation. It can be included as an additional dislocation source in the dislocation kinetics equation (6):

$$\frac{d\rho_D^G}{dt} = 2\pi c_t N, \quad \dot{N} = J_{GD} - \frac{N}{c_s\sqrt{\rho_D}}, \tag{12}$$

where N is a number of homogeneously nucleated dislocation per unit volume. We supposed here that the homogeneously nucleated dislocation loop becomes an ordinary dislocation if its diameter grows up to the mean distance between the dislocations. The nucleation rate of the dislocations per unit volume is equal to [34]:

$$J_{GD} = J_{GD}^0 \exp\left(-\frac{U_{GD} - \sigma_\tau V_{GD}}{kT} \right) \tag{13}$$

For copper activation volume $V_{GD} = 2.7 \cdot 10^{-28}$ m^3 , activation energy $U_{GD} = 4.67$ eV and the constant $J_{GD}^0 = 10^{14}$ s^{-1} [34]. Figure 4 demonstrates the dependence of the dynamic yield stress on the strain rate for different dislocation densities. One can see that homogeneously nucleation of dislocation effective for strain rate 10^8s^{-1}-10^9s^{-1}. After that efficiency of dislocation gliding mechanism achieve its theoretical limit.

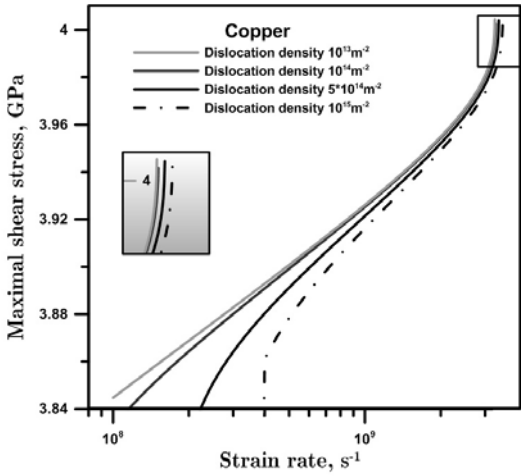

Figure 4 the dependence of the dynamic yield stress on the strain rate for different dislocation densities.

The twinning, as an additional mechanism of plasticity, has to limit the yield strength at extremely high-rate deformations. But our estimates show that efficiency of twinning mechanism is only a few times more than the efficiency of the dislocation plasticity. Therefore, it also decreases stresses in only limited range of the strain rates – less than 10^{10}s^{-1}.

4. Summary

The yield strength at low strain rate is limited and can be sufficiently increasing to theoretical tensile strength only by the way of impurities introduction. At the strain rates above 10^6s^{-1}, the ultrafine-grained metals have the maximum dynamical yield strength (instead of the nanocrystalline metals at the low strain rates). Abnormal and inverse Hall-Patch relations in the ultrafine grained copper were demonstrated by numerical simulations; dislocation starvation effect is related for its explanation. Analogous effect was detected experimentally in tantalum [35] and copper [36]. Mechanisms of the homogeneous nucleation of dislocation and the mechanical twinning effectively decrease the dynamical yield strength at the strain rates 10^8s^{-1}-10^9s^{-1}.

Acknowledgements

The study was supported by The Russian Foundation of Basic Research, project 12-02-31375/12 and by The Ministry of education and science of Russian Federation, project 14.B37.21.0384.

References

[1] M.A. Meyers, A. Mishra, D.J. Benson, Mechanical properties of nanocrystalline materials. Prog Mat Sci, 51 (2006) 427–556.
[2] D. Wolf, V. Yamakov, S.R. Phillpot, A. Mukherjee, H. Gleiter, Deformation of nanocrystalline materials by molecular-dynamics simulation: relationship to experiments? Acta Mater, 53 (2005) 1-40.
[3] Y.M. Wang, E.M. Bringa, J.M. McNaney, M. Victoria, A. Caro, A.M. Hodge, R. Smith, B. Torralva, B.A. Remington, C.A. Schuh, H. Jamarkani, M.A. Meyers, Deforming nanocrystalline nickel at ultrahigh strain rates. Appl Phys Lett, 88 (2006) 061917.
[4] G.W. Nieman, J.R. Weertman, R.W. Siegel, Mechanical behavior of nanocrystalline Cu and Pd. J Mater Res, 6 (1991) 1012-1027.
[5] P.G. Sanders, J.A. Eastman, J.R. Weertman //Acta Mater, 45 (1997) 4019-4025.
[6] G.E. Fougere, J.R. Weertman, R.W. Siegel, S. Kim, Dependent hardening and softening of nanocrystalline Cu and Pd. Scripta Metall Mater, 26 (1992) 1879-1883.
[7] J. Schiøtz, K.W. Jakobsen, A maximum in the strength of nanocrystalline copper. Science, 301 (2003) 1357-1359.
[8] G.I. Taylor, The mechanism of plastic deformation of crystals. Pt 1. Theoretical. Proc Roy Soc London, 145A (1934) 362-387.
[9] M.A. Meyers, K.K. Chawla, Mechanical Behavior of Materials, Cambridge University Press, New York, 2009.
[10] E.O. Hall, The deformation and ageing of mild steel: III discussion of results. Proc Phys Soc B, 64 (1951) 474-753.
[11] N.J. Petch, The cleavage strength of polycrystals. J Iron Steel Inst, 174 (1953) 25-28.
[12] R.L. Fullman Measurement of particle sizes in opaque bodies. Trans AIME, 197 (1953) 447-453.
[13] S. Ozerinc, K.Tai, N.Q. Vo, P.Bellon, R.S. Averback, W.P. King, Grain boundary doping strengthens nanocrystalline copper alloys. Scripta Mater, 67 (2012) 720-723.
[14] H. Conrad, K. Jung, Effect of grain size from millimeters to nanometers on the flows stress and deformation kinetics of Ag. Mater Sci Eng A, 391 (2005) 272-284.
[15] J. Schiøtz, F.D. Di Tolla, K.W. Jacobsen, Softening of nanocrystalline metals at very small grain sizes. Nature London 391, (1998) 561-563.
[16] E.N. Borodin, A.E. Mayer, A simple mechanical model for grain boundary sliding in nanocrystalline metals. Mater Sci Eng A, 532 (2012) 245-248.
[17] M. Haouaoui, I. Karaman, H.J. Maier, K.T. Hartwig, Microstructure evolution and mechanical behavior of bulk copper obtained by consolidation of micro- and nanopowders using equal-channel angular extrusion. Metall Mater Trans A, 35 (2004) 2935-2949.
[18] F. Ebrahimi, Q. Zhai, D. Kong, Deformation and fracture of electrodeposited copper. Scr Mater 39, (1998) 315-321.
[19] I.R. Suryanarayanan, C.A. Frey, S.M.L. Sastry, B.E. Waller, W.E. Buhro, Plastic deformation of nanocrystalline Cu and Cu–0.2 wt.% B. Mater Sci Eng A, 264 (1999) 210-214.
[20] Y.M. Wang, K. Wang, D. Pan, K. Lu, K.J. Hemker, E. Ma, Microsample tensile testing of nanocrystalline copper. Scr Mater, 48 (2003) 1581-1586.
[21] E.N. Borodin, A.E. Mayer, Yield strength of nanocrystalline materials under high-rate plastic deformation. Solid State Phys, 54 (2012) 808-815.
[22] V.S. Krasnikov, A.E. Mayer, A.P. Yalovets, Dislocation based high-rate plasticity model and its application to plate-impact and ultra short electron irradiation simulations. Int J Plast, 27 (2011) 1294–1308.
[23] A.M. Kosevich, Dynamical theory of dislocations. Sov Phys Uspekhi, 7 (1965) 837-854.
[24] J.P. Hirth, J. Lothe, Theory of dislocations, Wiley & Sons, New York, 1982.

[25] C. Kittel, Introduction to solid state physics, Wiley & Sons, New York, 2005.
[26] V.S. Krasnikov, A.Yu. Kuksin, A.E. Mayer, A.V. Yanilkin, Plastic deformation under high-rate loading: the multiscale approach. Solid State Phys, 52 (2010) 1386-1396.
[27] G.A. Malygin, Dislocation self-organization processes and crystal plasticity. Phys Usp, 169 (1999) 979–1010.
[28] V.N. Chuvildeev, Nonequilibrium Grain Boundaries in Metals: Theory and Application, Fizmatlit, Moscow, 2004.
[29] H.V. Swygenhoven, P.M. Derlet, A. Hasnaoui, Interaction between dislocations and grain boundaries under an indenter – a molecular dynamics simulation. Acta Mater, 52 (2004) 2251-2258.
[30] E.N. Borodin, A.E. Mayer, V.S. Krasnikov, Wave attenuation in microcrystal copper at irradiation by a powerful electron beam. Current Appl Phys, 11 (2011) 1315-1318.
[31] L.D. Landau, E.M. Lifshitz, Course of Theoretical Physics, Theory of Elasticity, Vol. 7, Pergamon, New York, 1986.
[32] H.V. Swygenhoven, A. Caro, Plastic behavior of nanophase metals studied by molecular dynamic. Phys Rev B, 58 (1998) 11246.
[33] J.R. Greer, J.Th.M. De Hosson, Plasticity in small-sized metallic systems: Intrinsic versus extrinsic size effect. Prog Mat Sci, 56 (2011) 654-724.
[34] G.E. Norman, A.V. Yanilkin Homogeneous nucleation of dislocations. Solid State Phys, 53 (2011) 1614-1619.
[35] S.V. Razorenov, G.I. Kanel, G.V. Garkushin, O.N. Ignatova, Resistance to dynamic deformation and fracture of tantalum with different grain and defect structures. Solid State Phys, 54 (2012) 790-797.
[36] E.F. Dudarev, A.B. Markov, G.P. Bakach, A.N. Tabachenko, S.D. Polevin, N.V. Girsova, O.A. Kashin, M.F. Zhorovkov, V.P. Rotshtein, Spall fracture of coarse- and ultrafine-grained FCC metals under nanosecond high-current relativistic beam irradiation. Russian Phys J, 52 (2009) 239–244.

Evolution of perturbations of temperature and dislocation density at high-rate shear deformation of pure metals and alloys

Alexander E. Mayer[1,*], Elijah N. Borodin[2,1], Polina N. Mayer[1], Yury V. Vorobyov[1], Dmitry A. Tikhonov[1]

[1] Department of Physics, Chelyabinsk State University, Chelyabinsk, 454001, Russia
[2] Institute of Problems of Mechanical Engineering RAS, St. Petersburg, 199178, Russia
* Corresponding author: mayer.al.evg@gmail.com, mayer@csu.ru

Abstract We have investigated numerically an evolution of initial perturbations of temperature or dislocation density in metals at high-rate deformation and its influence on the localization of plastic flow. A high-rate simple shear of micro-samples of pure metals and alloys, coarse-grained as well as nano-crystalline, has been simulated in two-dimensional geometry with use of the continuum mechanics supplemented by the dislocation plasticity and the grain-boundary sliding models. Perturbations of the temperature or dislocation density lead to restricted localization of the plastic deformation, but they can not initiate instability of the plastic flow as a self-sustained and increasing process. A more effective reason of the localization is the stress concentration, caused, for example, by boundary conditions. Rate of the plastic deformation is maximal in areas of the shear stress localization and it can be close to zero outside these areas. Heterogeneity of the grain sizes distribution through the sample can also lead to substantial localization of the plastic flow due to the grain size dependence of the dynamic yield strength.

Keywords High-rate plasticity, Localization, Temperature perturbation, Dislocations, Metals

1. Introduction

Localization of macroscopic plastic deformation is a widespread phenomenon in metals. It can be provoked by decrease of the material temperature, by increase of deformation rate or by decrease of grain size in polycrystalline metals. Localization of the plastic flow manifests themselves as an appearance of local areas with high plastic deformation values - up to several tens. This phenomenon is being researched intensively [1-6]. Heterogeneities in form of narrow bands arising at the high rate deformation are known as adiabatic shear bands. They are two-dimensional and almost flat formations, which boundaries are displaced, one relative to another, like in cracks of the 2nd or 3rd type, but material between the boundaries remains continuous. Thickness of the bands usually varies from ten to several hundreds of micrometers, while an extent of the bands varies from several millimeters up to several centimeters. Up to 90% of the whole plastic deformation of the material can be concentrated in the shear bands, as well as high shear deformation is observed in the neighborhood of the bands [3]. Shear bands have a complex structure of highly deformed material and can contain dislocation arrangements and nanocrystalline grains inside themselves [7]. Such bands were observed in metallurgical processes for a long time and were described first by H. Tresca [8]. A hard striker breaking through the metallic barrier is another example of practically important process, in which localization is well defined and it was observed rather long ago [9,10]. Localization substantially effects on the material strength as a whole relative to shear deformation.

First important point in explanation of the shear bands formation was made by C. Zener and J.H. Hollomon [11], which had proposed that a local temperature rise during the deformation leads to softening of the material, and that competition between the temperature softening and a strain hardening results in instability of the plastic flow (thermoplastic instability) and in the localization [1,3]. This viewpoint had been supported by many authors and until recently it often was seen as only one possible. But in a large number of materials revealing the localization, the plastic deformation results in inessential temperature increase, which is not enough for a substantial

softening of a uniformly deformed material [12,13]. High-speed infrared photography have shown, that even in the areas of the plastic flow localization the temperature rise does not exceed 10 K in iron [14], while in titanium it is about 100 K [15]. Therefore, the thermoplastic instability could not be a universal mechanism of the localization.

At high-rate deformation of pure metals (at the strain rates about 10^5-10^6 s^{-1} or higher) a temperature hardening came in the stead of the temperature softening [16,17]. It is caused by an increase with temperature of friction force, which acts on moving dislocation [17,18]. Dislocations move in an over-barrier mode in the pure metals at such strain rates, and the dynamic yield stress is determined by the friction force and by the dislocation density. The transition to the over-barrier mode, revealing in the temperature hardening, can by expected in alloys as well but at the even more high strain rates. In conditions of the temperature hardening the thermoplastic instability scenario can not be truth. It also puts a question about place of the temperature perturbations and other factors in initiation of the localization.

Localization is often attended by a substantial change of defects substructure [7]. While the thermoplastic instability is theoretically well described, an influence of the defect substructure on the localization process is investigated on the level of estimations only. Objective of the present work was to investigate possible instabilities of plastic flow with respect to initial perturbations of temperature or dislocations density or the grain size in polycrystalline metals. We numerically studded a simple shear of pure monocrystalline aluminum, nanocrystalline aluminum and aluminum alloy. It is known that the pure aluminum is not inclined to the localization [19], while the aluminum alloys reveal it [20,21]. The obtained results, at first, seemed to be strange, but, in truth, fully explainable.

2. Model and formulation of problem

Total plastic deformation of the polycrystalline metals is supposed to be a result of the combined action of two competing effects, namely, the dislocation motion and the sliding along the grain boundaries. According to this viewpoint, the plastic deformation tensor w_{ik} is represented by the sum $w_{ik} = w_{ik}^{\mathrm{D}} + w_{ik}^{\mathrm{gb}}$, where w_{ik}^{D} is the part of plastic deformation caused by the dislocation motion, and w_{ik}^{gb} is the part caused by the grain boundary sliding. The dislocation plasticity [22,23] and the grain boundary sliding [24-26] models are generalized on the two-dimensional Cartesian case (2D) and used here for determination of w_{ik}^{D} and w_{ik}^{gb} correspondently. Full model consists of continuum mechanics equations supplemented by the equations for dynamics and kinetics of dislocations and by the equations for time derivatives of w_{ik}^{D} and w_{ik}^{gb}.

2.1. Equations system

Here we write down the equations system to be solved numerically below:

$$\frac{1}{\rho}\frac{d\rho}{dt} = -\frac{\partial v_k}{\partial x_k}, \tag{1}$$

$$\rho\frac{dv_i}{dt} = \frac{\partial}{\partial x_k}\left(-P\cdot\delta_{ik} + S_{ik}\right), \tag{2}$$

$$\rho\frac{dU}{dt} = \left(P + \frac{S_{ik}^2}{4G} + \varepsilon_D\rho_D\right)\frac{1}{\rho}\frac{d\rho}{dt} + \frac{\partial}{\partial x_l}\left(\kappa\frac{\partial T}{\partial x_l}\right) + S_{ik}\frac{dw_{ik}}{dt} - \varepsilon_{\mathrm{D}}\frac{d\rho_{\mathrm{D}}}{dt}, \tag{3}$$

$$S_{ik} = 2G\left[u_{ik} - \frac{1}{3}u_{ll}\cdot\delta_{ik} - w_{ik} \right], \tag{4}$$

$$\frac{du_{ik}}{dt} = \frac{1}{2}\left[\frac{\partial v_i}{\partial x_k} + \frac{\partial v_k}{\partial x_i} \right] + \Omega_{ik}, \tag{5}$$

$$\frac{dw_{ik}^{\mathrm{D}}}{dt} = -\sum_{\beta} \frac{1}{2}\left(b_i^{\beta} n_k^{\beta} + b_k^{\beta} n_i^{\beta} \right) V_{\mathrm{D}}^{\beta} \rho_{\mathrm{D}}^{\beta} + \omega_{ik}, \tag{6}$$

$$\frac{m_0}{\left[1-\left(V_{\mathrm{D}}^{\beta}/c_{\mathrm{t}}\right)^2\right]^{3/2}} \frac{dV_{\mathrm{D}}^{\beta}}{dt} = \left(S_{ik} b_i^{\beta} n_k^{\beta} - \frac{bY}{2}\cdot \mathrm{sign}\left(S_{ik} b_i^{\beta} n_k^{\beta} \right) \right) - \frac{B\cdot V_{\mathrm{D}}^{\beta}}{\left[1-\left(V_{\mathrm{D}}^{\beta}/c_{\mathrm{t}}\right)^2\right]^{3/2}}, \tag{7}$$

$$\frac{d\rho_{\mathrm{D}}^{\beta}}{dt} = \frac{0.1}{\varepsilon_{\mathrm{D}}} \left\{ \frac{B\cdot\left(V_{\mathrm{D}}^{\beta}\right)^2}{\left[1-\left(V_{\mathrm{D}}^{\beta}/c_{\mathrm{t}}\right)^2\right]^{3/2}} + b\cdot Y\cdot\left|V_{\mathrm{D}}^{\beta}\right| \right\} \cdot \rho_D^{\beta} - k_a b\cdot\left|V_{\mathrm{D}}^{\beta}\right|\cdot\left(\rho_{\mathrm{D}}^{\beta}\right)^2, \tag{8}$$

$$\frac{dw_{ik}^{\mathrm{gb}}}{dt} = \frac{1}{2G\,\mathrm{T}} \sum_{\alpha} \tau_i^{\alpha} n_k^{\alpha} \left(S_{lm}\cdot\tau_l^{\alpha} n_m^{\alpha} - y_b \right) + \omega_{ik}^{\mathrm{gb}}. \tag{9}$$

where Eq. (1) is the continuity equation [27], Eq. (2) is the equation of motion, Eq. (3) is the energy conservation law, Eq. (4) is the generalized Hooke law [28] with accounting of the plastic strains w_{ik}, Eq. (5) is the equation for geometrical deformation u_{ik}, induced by a macroscopic motion of substance, Eq. (6) is the generalized Orowan equation [29] for the plastic strain w_{ik}^{D}, Eq. (7) and Eq. (8) are equations of dynamics and kinetics of dislocations [22]. Eq. (9) describes the grain boundary sliding [24-26], where T - relaxation time and y_b - threshold stress for sliding.

In the Eq. (1) – Eq. (9): ρ is substance density; $v_i = \{v_x, v_y, 0\}$ is velocity vector; $x_i = \{x, y, 0\}$ are the Cartesian coordinates; P is the pressure, which is determined from a wide-range equation of state $P = P(\rho, U)$ [30,31]; S_{ik} is the tensor of stress deviators, which characterizes the shear stresses; U is the part of internal energy, which corresponds to the state with zero stress deviators $S_{ik} = 0$ and with zero dislocation density $\rho_{\mathrm{D}} = 0$; T is the substance temperature, which also can be found from the wide-range equation of state $T = T(\rho, U)$; G is the shear modulus; κ is the heat conductivity coefficient; $\varepsilon_{\mathrm{D}} \approx 8\ \mathrm{eV}/b$ is the dislocation formation energy per unit length, where b is modulus of the Burgers vector of dislocation.

Tensors Ω_{ik}, ω_{ik}^{D} and $\omega_{ik}^{\mathrm{gb}}$ take into account the change of u_{ik}, w_{ik}^{D} and w_{ik}^{gb} correspondently due to substance rotation [32]. Indexes i,k,l,m numerate the space directions and run from 1 to 3; the summation rule is valid for dummy indexes; δ_{ik} is the bivalent mixed tensor. Index β numerates possible slip systems of dislocations, which is characterized by the Burgers vector b_i^{β} and by the normal to the slip plane n_i^{β}. Dislocation density in the corresponding slip system is designated as $\rho_{\mathrm{D}}^{\beta}$, velocity of these dislocations - V_{D}^{β}. Total density of dislocations can be obtained by summation $\rho_{\mathrm{D}} = \sum_{\beta} \rho_{\mathrm{D}}^{\beta}$. In the Eq. (7), Eq. (8): $c_{\mathrm{t}} = \sqrt{G/\rho}$ is the transverse sound speed of the material; $m_0 \approx 10^{-16}$ kg/m is the rest mass of the dislocations; Y is the static yield stress; k_a is the annihilation factor; B is the coefficient of phonon friction, it describes the

resistance to the dislocation motion. Index α numerates possible planes of grains sliding, which are characterized by the normal n_i^α; τ_i^α is the direction of maximal shear stresses in the α-plane.

Eqs (1)-(8) were solved numerically with use of the computer program CRS, written by A.E. Mayer. Sub-problem of the substance dynamics (Eqs (1)-(3)) were solved by a modification of the numerical method proposed by A.P. Yalovets [33]. All other equations were solved by Euler method with a varied time step.

2.2. Problem statement

Simple shear of 2D metallic sample with square cross-section is simulated (Fig. 1). One face of the sample ("lower" face, $y = 0$) is at rest $\vec{v}(y = 0) = 0$, while the opposite face ("upper" face, $y = L$) moves along the "lower" face with constant velocity $v_x(y = L) = L \cdot \dot{\varepsilon}$ and $v_y(y = L) = 0$, where L is a lateral length of the square, $\dot{\varepsilon}$ is a shear deformation rate. The length L must be chosen small enough to provide disturbance propagation through the sample during a characteristic time of deformation (an inverse value to $\dot{\varepsilon}$), therefore, inequality $L \le 10^{-2} \cdot c_t / \dot{\varepsilon}$ was required.

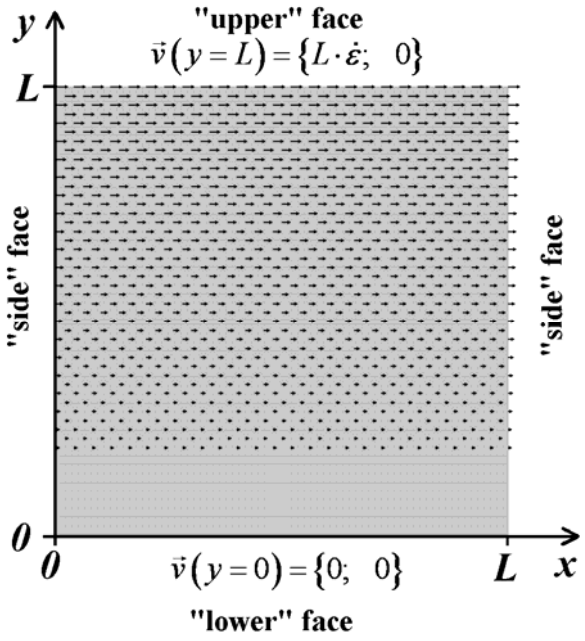

Figure 1. Initial state of the investigated 2D sample (initial velocity field is shown by little arrows).

Initial velocity was set linearly increasing from the "lower" face to the "upper" face: $v_x(x, y) = y \cdot \dot{\varepsilon}$, $v_y(x, y) = 0$, which corresponds to a uniform simple shear, thus, an initial shear rate was uniform along the sample. Two different problems were determined by boundary conditions on the "side" faces: constrained shear – at the forced movement of the "side" faces with velocity $v_x = y \cdot \dot{\varepsilon}$, $v_y = 0$; and free shear – at free surface condition on it.

Pure aluminum, aluminum-copper alloy and ultra-fine-grained aluminum were studied. The pure aluminum was characterized by the next expression for the static yield stress $Y_{\mathrm{Al}} = 2.2 \cdot 10^7 + 0.4Gb\sqrt{\rho_{\mathrm{D}}}$. This expression takes into account the strain hardening (second term in the right-hand part) in a Taylor relation form [34]. The aluminum-copper alloy was characterized by

another expression for the static yield stress $Y_{\mathrm{Al+Cu}} = 28.625 \cdot 10^7 - 2.425 \cdot 10^5 \cdot T + 0.4Gb\sqrt{\rho_{\mathrm{D}}}$. First and second terms of the last expression represent a critical stress, which is necessary for dislocation detachment from inclusion. This critical stress depends on temperature; presented expression was obtained from molecular-dynamics simulations by A. Kuksin and A. Yanilkin [34]. The main differences between the pure aluminum and the aluminum-copper alloy in our study were the higher value of $Y_{\mathrm{Al+Cu}}$ in comparison with Y_{Al}, and the decrease of $Y_{\mathrm{Al+Cu}}$ with temperature. All other parameters (equation of state, friction coefficient of dislocation movement) were supposed to be the same for both materials. For the ultra-fine-grained and nanocrystalline aluminum the yield stress was chosen in the next form: $Y_{\mathrm{Al}} = 2.2 \cdot 10^7 + 0.4Gb\sqrt{\rho_{\mathrm{D}}} + H/\sqrt{d}$, where d is the grain size, $H \approx 4.2\ \mathrm{GPa} \cdot \mathrm{nm}^{1/2}$ is the Hall-Petch coefficient for aluminum.

Plastic strain intensity W was used as indicator of the state of plastic strain. In the 2D case it can be written as, $W = \sqrt{(4/3) \cdot \left(w_{xx}^2 + w_{yy}^2 + w_{xx} \cdot w_{yy} + w_{xy}^2 \right)}$. Average value is determined as $\langle W \rangle = A^{-1} \int_A W \cdot dA$, where A is a cross-section of the sample (approximately $A \approx L^2$ during the shear). Deviation of the plastic deformation from its average value is numerically characterized by the root-mean-square deviation $\Delta W = \sqrt{A^{-1} \int_A \left(W - \langle W \rangle \right)^2 \cdot dA}$.

The considered strain rate was equal to $\dot{\varepsilon} = 10^5\ \mathrm{s}^{-1}$, which value is typical for the high-speed impact experiments [17]. The sample size L was chosen equal to $L = 100\ \mu\mathrm{m}$; the computational grid was 50x50 nodes. Initial perturbations were set in form of a narrow stripe ($4\ \mu\mathrm{m}$ width-way) parallel to *Ox* axis, which crosses the sample in its middle. In this stripe, either the initial temperature of substance was raised on ΔT, or the initial dislocation density was multiplied on factor $\left(1 + \Delta\rho_{\mathrm{D}} / \rho_{\mathrm{D}}\right)$, where ρ_{D} is an unperturbed value of the dislocation density, $\Delta\rho_{\mathrm{D}}$ is its perturbation; the value $\rho_{\mathrm{D}} = 10^7\ \mathrm{cm}^{-2}$ was used in calculations below. In nanocrystalline aluminum perturbation of the grain size was also investigated – grain size inside the stripe was set equal to d_1, which value is different from the grain size outside the stripe d.

3. Results and discussion

It was supposed, that if the specified perturbation is appropriate and enough for localization of plastic flow, then the upper half of the sample will plastically displace relative to the lower half at the free shear. But numerical experiments have shown that the initial perturbations of temperature or dislocation density influence on the localization of plastic flow only at the constrained shear mode. Therefore, we will consider results of the constrained shear at first.

Fig. 2 shows typical distributions of the plastic strain intensity for alloy and pure aluminum with initially perturbed temperature field. Raise of temperature in the alloy leads to decrease of the yield stress, and plastic deformation tends to be localized in the hot stripe (Fig. 2(a)). Constrained movement of the "side" faces suppresses total plastic shear along this stripe, therefore, the plastic deformation redistributes around the stripe, which, particularly, cause formation of arrowhead-like structures. Plastic deformation in vicinity of the hot stripe (aside from the arrowhead-like areas) is lower then the plastic deformation near the "upper" and "lower" faces. An inverse situation takes place for the pure aluminum (Fig. 2(b)). Rise of temperature increases the resistance to dislocations

motion and suppresses the plastic deformation inside of the hot stripe. For compensation of this effect, a more intensive plastic flow occurs in its vicinity. It can be treated as localization as well, not in the hot stripe, but around the stripe (around the perturbed area).

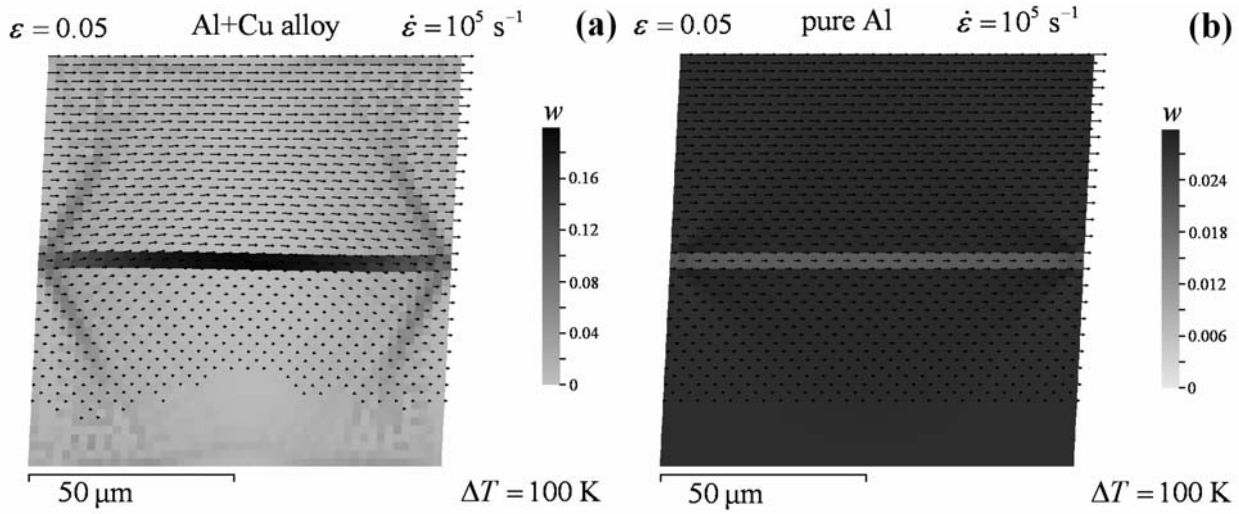

Figure 2. Distributions of the plastic strain intensity w in the aluminum-copper alloy (a) and in the pure aluminum (b) samples at the total deformation $\varepsilon = 0.05$. Initial temperature field was perturbed by narrow (4 μm) stripe with temperature raised on $\Delta T = 100$ K ; constrained shear.

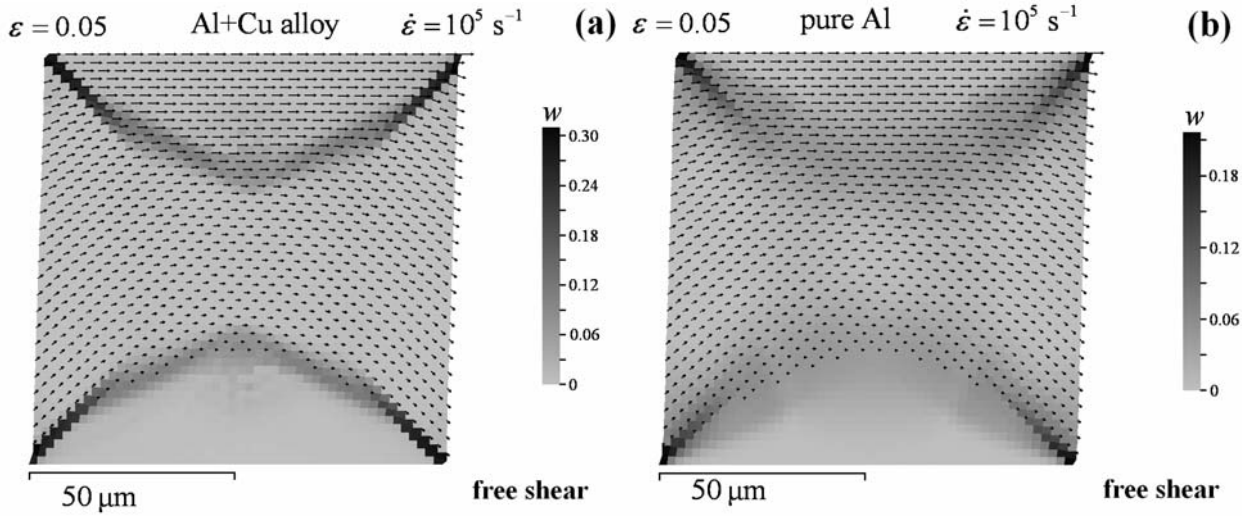

Figure 3. Distribution of the plastic strain intensity w in the aluminum-copper alloy (a) and in the pure aluminum (b) at the free shear are presented at the shear deformation $\varepsilon = 0.05$. Both in alloy and in the pure metal, localization begins along diagonals of the square.

Calculations show that substantial localization takes place only at ΔT above several tens or hundreds of K, while the plastic flow causes an increase of temperature on only about several K. These facts indicate that any random disturbance in temperature can not of itself lead to a self-sustained process of the connected temperature rise and temperature softening of the material. In other words, temperature perturbation can not initiate instability of plastic flow even in alloys. But pre-existing areas with substantially different temperature can in some degree localize the plastic flow around themselves both in alloys and in pure metals. The degree of localization in the pure metal is on an order of magnitude less than that in the alloy.

Increase of the initial dislocation density leads to a temporary softening of pure metal at dynamic

deformation, therefore, plastic deformation is higher in the perturbed stripe with the higher initial dislocation density and it is lower in the attached areas. This is a temporary effect, and it becomes lower with the increase of total deformation. It is explained by the fact that the dislocation density grows up, and the softening (a dynamical effect) is replaced by an increase of the yield stress with dislocation density (a strain hardening). In the case of alloy, the higher value of the yield strength causes an earlier transition to the strain hardening. As opposed to the temperature, the dislocation density changes substantially during the plastic flow. But it seems that the plastic flow instability can not be provoked by the dislocation density perturbation as well as in the temperature perturbation case. At the dislocation-induced softening the dislocation density growth diminishes the softening effect. At the strain hardening the "inverse" localization takes place, but more intensive plastic deformation around the perturbed area increases the dislocation density in this surroundings. It leads to an equalizing of the dislocation density and to a broadening of the involved area, it means, to delocalization. Meanwhile, an irregularity in the dislocations distribution leads to some localization of the plastic deformation, but this localization is restricted.

Much more localization takes place at the free shear (Fig. 3). Both in alloy and in the pure metal, localization begins along diagonals of the square. Region at rest near the "lower" face, region moving with constant velocity $\dot{L}$ near the "upper" face and a flowing central region appear as a result of development and intersection of the localization bands. In the alloy localization is stronger than in the pure metal. It must be emphasized, that the localization at free shear arises without any initial perturbation of the initial parameters. Moreover, any perturbation of temperature or dislocation density does not effect in this case.

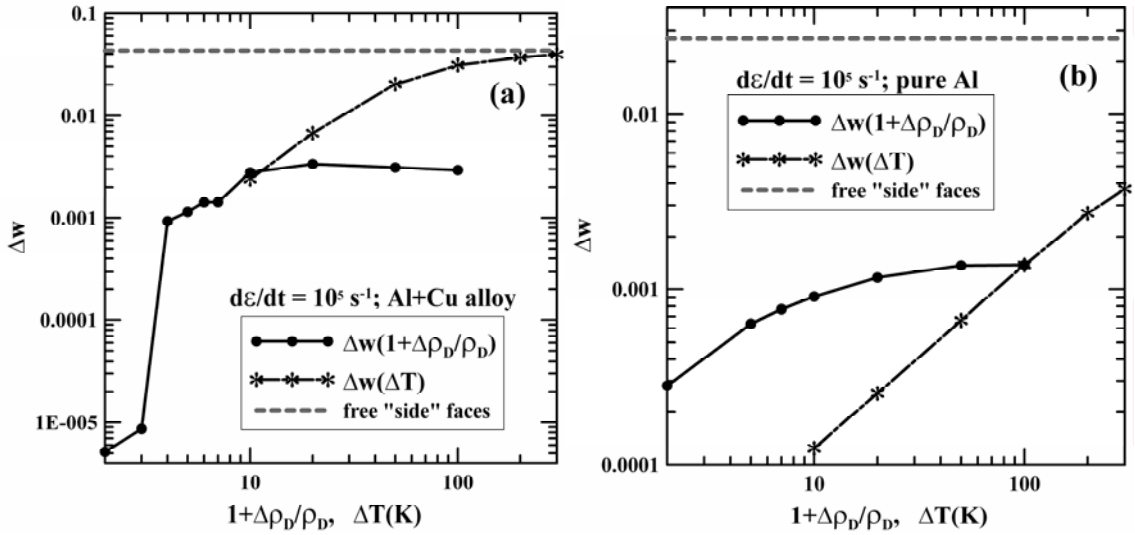

Figure 4. Comparison of the plastic flow localization degree in different situations. Aluminum-copper alloy (a) and pure aluminum (b), total strain is $\varepsilon = 0.05$. At the free shear the value of ΔW is constant.

Fig. 4 presents a comparison of the plastic flow localization degree produced by various initial perturbations of dislocation density or temperature at the constrained shear and the localization at the free shear. In the alloy, the temperature perturbations with $\Delta T > 10\,\mathrm{K}$ are substantially more effective than the dislocation density perturbation (Fig. 4(a)). At the temperature increase on $\Delta T \approx 300\,\mathrm{K}$ the degree of localization tents from bellow to the localization degree at the free shear. But it seems hardly probable that such high temperature drop can initially exist in the material. In the pure aluminum, the dislocation density perturbation is more effective from the viewpoint of the localization excitation than the temperature increase with $\Delta T < 100\,\mathrm{K}$ (Fig. 4(b)); but the free shear is much more effective than the both types of perturbations.

Perturbation of the grain size in ultra-fine-grained or nano-crystalline aluminum leads to substantial localization of the plastic flow at the "constrained" shear due to difference in the dynamical yield strength. Localization degree in nano-materials with the grain size $d < 100$ nm depends weakly on the perturbation value d_1 / d, therefore, localization in such materials has to arise at any arbitrary size distribution of the grains. But the localization degree is all the same less than it at the "free" shear; they become comparable only at the grain size $d < 10$ nm.

4. Conclusions

Summarizing, one can conclude that perturbation of both the temperature and the dislocation distribution, as well as of the grain size, can lead to restricted localization of the plastic flow. But they can not initiate the self-sustained process of the joint increase of corresponding parameter and of the localization degree, it means, they can not initiate the instability of plastic flow. Nonuniformity of acting stresses is the dominant factor of the localization of the plastic deformation. Therefore, the process of localization must substantially depend on the loading conditions and on the internal structure of the material (on the presence of inhomogeneities, pores, inclusions).

Acknowledgements

The study was supported by The Ministry of education and science of Russian Federation, project 14.B37.21.0384, and by The Russian Foundation of Basic Research, project 12-02-31375/12.

References

[1] Y. Bai, B.Dodd, Shear Localization: Occurrence Theories and Applications, Pergamon, Oxford, 1992.
[2] A.R. Shahan, A.K. Taheri,. Adiabatic shear bands in titanium and titanium alloys: a critical review. Mater Des, 14 (1993) 243–250.
[3] T. Wright, The Physics and Mathematics of Adiabatic Shear Bands, Cambridge University Press, Cambridge, 2002.
[4] C.A. Bronkhorst, E.K. Cerreta, Q. Xue, P.J. Maudlin, T.A. Mason, G.T. Gray III, An experimental and numerical study of the localization behavior of tantalum and stainless steel. Int J Plast, 22 (2006) 1304-1335.
[5] S.M. Walley, Shear localization: a historical overview. Met and Mat Trans A, 38 (2007) 2629-2654.
[6] M. Kobayashi, Analysis of deformation localization based on proposed theory of ultrasonic wave velocity propagating in plastically deformed solids. Int J Plast, 26 (2010) 107-125.
[7] Y. Xu, J. Zhang, Y. Bai, M.A. Meyers, Shear localization in dynamic deformation: microstructural evolution. Met and Mat Trans A, 39 (2008), 811.
[8] H. Tresca, On further applications of the flow of solids. Proc Inst Mech Eng, 30 (1878) 301–345.
[9] M.R. Staker, The relation between adiabatic shear instability strain and material properties. Acta Metall, 29 (1981) 683–689.
[10] E.A. Lyapunova, A.N. Petrova, I.G. Brodova, O.B. Naimark, M.A. Sokovikov, V.V. Chudinov, S.V. Uvarov, Morphology of multiscale defect structures and plastic strain localization during impact perforation of A6061 alloy targets. Techn Phys Lett, 38 (2012) 6-8.
[11] C. Zener, J.H. Hollomon, Effect of strain rate upon plastic flow of steel. J Appl Phys, 15 (1944) 22–32.
[12] A. Marchand, J. Duffy, An experimental study of the formation process of adiabatic shear bands in a structural steel. J Mech Phys Solids, 36 (1988) 251–283.
[13] D. Rittel, Z.G. Wang, Thermo-mechanical aspects of adiabatic shear failure of AM50 and

Ti6Al4V alloys. Mech Mater, 40 (2008) 629–635.
[14] O.A. Plekhov, O.B. Naimark, N. Saintier, T. Palin-Luc, Elastic-plastic transition in iron: Structural and thermodynamic features. Techn Phys, 54 (2009) 1141-1146.
[15] O. Plekhov, V. Chudinov, V. Leont'ev, O. Naimark, Experimental investigations of the laws of energy dissipation during dynamic deformation of nanocrystalline titanium. Techn Phys Lett, 35 (2009) 92-95.
[16] G.I. Kanel', S.V. Razorenov, K. Baumung, J. Singer, Dynamic yield and tensile strength of aluminum single crystals at temperatures up to the melting point. J Appl Phys, 90 (2001) 136-143.
[17] G.I. Kanel', V.E. Fortov, S.V. Razorenov, Shock waves in condensed-state physics. Phys Usp 50 (2007) 771-791.
[18] V.S. Krasnikov, A.Yu. Kuksin, A.E. Mayer, A.V. Yanilkin, 2010. Plastic deformation under high-rate loading: The multiscale approach. Phys Solid State, 52 (7), 1386-1396.
[19] J.M. Yellup, R.L. Woodward, Investigaion into the prevention of adiabatic shear failure in high strength armor materials. Res Mech 1 (1980) 41–57.
[20] R.W. Chen, K.S. Vecchio, Microstructural Characterization Of Shear Band Formation In Al-Li Alloys. J Phys IV C, 8 (1994) 459–464.
[21] Y.L. Bai, J. Bai, H.L. Li, F.J. Ke, M.F. Xia, Damage evolution, localization and failure of solids subjected to impact loading. Int J Impact Engng, 24 (2000) 685–701.
[22] V.S. Krasnikov, A.E. Mayer, A.P. Yalovets, Dislocation based high-rate plasticity model and its application to plate-impact and ultra short electron irradiation simulations. Int J Plast, 27 (2011) 1294-1308.
[23] V.S. Krasnikov, A.E. Mayer, Numerical investigation of the change of dislocation density and microhardness in surface layer of iron targets under the high power ion- and electron-beam treatment. Surf Coat Techn, 212 (2012) 79-87.
[24] E.N. Borodin, A.E. Mayer, V.S. Krasnikov, Wave attenuation in microcrystal copper at irradiation by a powerful electron beam. Current App Phys, 11 (2011) 1315-1318.
[25] E.N. Borodin, A.E. Mayer, Yield strength of nanocrystalline materials under high-rate plastic deformation. Phys Solid State, 54 (2012) 808-815.
[26] E.N. Borodin, A.E. Mayer, A simple mechanical model for grain boundary sliding in nanocrystalline metals. Mater Sci Eng A, 532 (2012) 245-248.
[27] L.D. Landau, E.M. Lifshitz, Course of Theoretical Physics, Vol. 6, Fluid Mechanics, Pergamon, New York, 1987.
[28] L.D. Landau, E.M. Lifshitz, Course of Theoretical Physics, Vol. 7, Theory of Elasticity, Pergamon, New York, 1986.
[29] A.M. Kosevich, Dynamical Theory of Dislocations. Sov Phys Uspekhi, 7 (1965) 837-854.
[30] S.N. Kolgatin, A.V. Khachatur'yants, Interpolation equations of state of metals. Teplofiz Vys Temp, 20 (1982) 90-94.
[31] V.E. Fortov, K.V. Khishchenko, P.R. Levashov, I.V. Lomonosov, Wide-range multi-phase equations of state for metals. Nucl Instrum Meth Phys Res A, 415 (1998) 604-608.
[32] M.L. Wilkins, Calculation of elastic-plastic flow, UCRL-7322, 1963.
[33] A.P. Yalovets, Calculation of flows of a medium induced by high-power beams of charged particles. J Appl Mech Tech Phys, 38 (1997) 137-150.
[34] T. Suzuki, S. Takeuchi, H. Yoshinaga, Dislocation Dynamics and Plasticity, Springer, Berlin, 1991.
[35] D. Ilnitski, V. Krasnikov, A. Kuksin, A. Mayer, A. Yanilkin, Dynamics and kinetics of dislocations in metals and alloys under dynamic loading, Proc. of the 6th Int. Conf. on Multiscale Materials Modeling (MMM2012), Singapore, 2012.

Texture evolution in Mg-Al and Mg-RE alloy during hot extrusion

Jie Dong [a], Jie Sun [a], Li Jin [a], Zhenyan Zhang [a] and Wenjiang Ding [a, b]

[a] *National Engineering Research Center of Light Alloy Net Forming, Shanghai Jiaotong University, Shanghai 200240, PR China*
[b] *Key State Laboratory of Metal Matrix Composite, Shanghai Jiaotong University, Shanghai 200240, PR China*

Abstract

The application of Mg alloys is greatly restricted because of their poor plasticity, which is closely related with the texture formed during hot forming. In this paper, the texture evolutions in Mg-Al and Mg-RE alloy during extrusion have been investigated. The results suggested that the texture of Mg alloy extrusion bar and tubes could be weakened by Ce addition with small content, but it does not work when Al is also exists. Thus, the Mg-RE alloys exhibit much higher tensile elongation and good yield symmetry. The mechanism of texture weakening by RE addition is due to the solute effect, which could surpass the twinning and activated non-basal slip.

Keywords: Texture, Mg-Al alloy, Mg-RE alloy, extrusion

1. Introduction

Deformation structures produced during high temperature extrusion of Mg rods recrystallize to produce a ring fiber texture with the c-axes of the grains perpendicular to the extrusion direction (ED) [1-2]. Such extrusions exhibit poor ductility and strong anisotropy [3] in their mechanical properties. Texture weakening or randomization is a desirable approach to get high ductility Mg alloys and a number of cases of weak or non-basal textures have been reported recently for Mg alloy sheets and extrusions [3-7]. Various authors have suggested that texture could be weakened via dynamical recrystallization during the processing with addition of Y, Ce and other rare earth elements. Mishra et. al [5] have shown that tensile ductility of extruded Mg-0.2wt% Ce is significantly enhanced due to texture randomization where the basal planes get oriented at 40~50° to the extrusion direction (ED) in the recrystallized microstructure.

Texture weakening in Mg alloy have been associated with various phenomena, including abnormal grain growth [8-9], particle-stimulated nucleation (PSN) [3, 6], particle pinning [10], solute drag [4], dynamic strain aging [11] and heterogeneous deformation leading to ease of shear band formation [6-7]. To clarify the effect of RE-element addition on the recrystallization texture after extrusion and to optimize the processing conditions for producing random texture in the Mg alloy extrusions, the microstructures of Mg-Ce and Mg-Al-Ce alloy tubes or rods have been investigated in this study. The approach for developing wrought Mg alloys with texture randomization and strengthening via alloying is discussed on the basis of the results.

2. Experimental

The materials studied in this work include nominally pure Mg (baseline), Mg-Ce, Mg-Al, and Mg-Al-Ce alloys. Unalloyed Mg and Mg alloy melts of about 100kg were prepared using commercially pure Mg ingots, pure aluminum and Mg-20%Ce master alloy in a steel crucible with SF6/CO2 protective cover gas. Billets of 75mm diameter and 230mm length were cast at about 700ºC into a permanent mold. The billets were preheated to 400 ºC for two hours and extruded in a Wellman Enefco™ 500-ton multipurpose vertical hydraulic press fitted with a circular die. Solid rods, approximately 15mm in diameter corresponding to an extrusion ratio (ER) of 25 were extruded using boron nitride lubricant at a billet speed of 10mm s^{-1} and air cooled.

Metallographic samples were prepared by standard methods, and the polished samples were etched in a solution containing 20ml glacial acetic acid, 50ml picric acid, 10ml methanol and 10ml deionized water. The polished samples were examined by the scanning electron microscope (SEM) and electron backscattered diffraction (EBSD) in a LEO™ 1450 SEM operating at 20kV fitted with a TSL™ EBSD camera [5]. The compositions of the particles in the Mg alloys were analyzed by electron probe microanalysis (EPMA). EBSD scans were obtained using beam step size of 2mm and a camera length of 18cm from an area approximately 1mm x 1mm and at least three different scans from the same sample were collected to ascertain the repeatability of the results. The inverse pole figure (IPF) map, image quality map with the twin boundaries outlined, and the (0001), (10-10), and (1-210) pole figures were processed with TSL OIM commercial software.

3. Results

The original microstructure including of AZ31 and AM30 alloy tubes are showed in Fig. 1, the IPF map in Fig. 1a and 1b show crystallization occurred during extrusion and the grain boundaries among majority grains are high angle grain boundaries with their misorientation higher than 15°, and average grain size is 50mm for AZ31 and 30mm for AM30. Pole figure shows ring basal texture with their c-axes perpendicular to extrusion direction(ED) in the two samples, but the majority grain orientations can be divided into two groups: one with their c-axes approximately parallel to the radial direction (Called the RD component) and the other with their c-axes approximately parallel to the tangential direction (Called the TD component), which is the typical extruded tube texture. And the max texture intensity is 5.704 and 5.051 for AZ31 and AM30, respectively.

The EBSD inverse pole figure (IPF) maps and corresponding (0001), (10-10), and (11-20) texture plots from as-extruded tubes of Mg-0.2Ce are shown in Figures 2(a) and (b). The differences in the texture between Mg-0.2Ce and AZ31, AM30 are evident from these figures. In the case of the Mg-0.2Ce tubes, the c-axes of the grains are not normal to the extrusion axis but make an angle about 45° to the extrusion axis, as is evident from the texture plot in Figure 2(b). This is similar to what has been reported in Mg-0.2Ce rods [10]. As the RD component shows clearly, the TD component seems to be very weak. Besides, the tensile curve of as-extruded tubes of Mg-0.2Ce tube is shown in Fig.2(c) compared with that of pure-Mg. It can be seen clearly that with the addition of 0.2%Ce the ductility enhances a lot.

With the addition of Ce and Al, the formability of the tubes and the macroscope of the tube are enhanced as showed in Fig. 3a. However, the deflection of the main texture seen in Mg-0.2Ce alloy did not occur in the case of Mg-3Al-0.5Ce alloy tube which can be seen in Fig.3 (b). The texture of Mg-3Al-0.5Ce is similar to that of AZ31. The tension and compression mechanical property are shown in Fig.3 (c). It can be seen that the strength of alloy increased a lot compared with Mg-0.2Ce but also exhibited the obvious yield asymmetry which can be seen widely in textured Mg alloys. And the elongation of Mg-3Al-0.5Ce alloy is about 20% which is lower than that of Mg-0.2Ce alloy.

The effects of RE addition on the texture of extrusion rod were also investigated in this study. The texture of pure-Mg, Mg-0.2Ce and Mg-3Al-0.2Ce alloy rods are shown in Fig.4 in a same reference frame to get a flagrant contrast. For the Mg-0.2%Ce alloy, the texture altered from typical

ring basal texture as showed in Fig. 4a, but for the Mg-3%Al-0.2%Ce alloy rod, the texture is similar with that in AZ31 or pure Mg rod.

Fig. 5 shows the backscattered electron micrographs along with the electron probe composition maps. The samples were taken from the longitudinal section (extrusion axis parallel to the sample plane). The results show that some particles in Mg-3%Al-0.2%Ce alloy have a composition close to $Mg_{17}Al_{12}$ phase an others with a composition close to $Al_{11}Ce_3$ are seen aligned along the ED [13]. By contrast, small intermetallic $Mg_{12}Ce$ phase particles [12] are distributed homogeneously in the Mg-0.2Ce alloy. In addition, the electron probe maps of individual element compositions in Fig. 5 suggest that, in the Mg-0.2Ce, the solute Ce is distributed in the matrix while there is no measurable solute Ce present in the matrix of the Mg-3%Al-0.2%Ce sample.

4. Discussion

Deformed Mg acquires a preferred orientation or texture because deformation occurs on the most favorably orientated slip or twinning systems that reorient the grains [14]. The ring basal texture and rolling basal texture are almost universal in extruded Mg rod [2, 4, 15] and rolled Mg sheet [15-17], respectively, because of the basal slip and {10-12}extension twinning [18-19] dominating the deformation process. Fig. 6 shows IPF and PF maps of AZ31 tube compressed at room temperature to true strain of: (a) 0.01 (b)0.09 (C) 0.18. The figure shows that the {10-12} extension twinning resulted in the orientation altered during compression, in which the [0001] of twins is parallel to compression axis. That is the reason why the textures in AZ31 and AM30 tubes show TD and RD component as showed in Fig. 1. These textures are retained through the recrystallization stage. In this study, the Mg-0.2 wt.% Ce alloy tube and rod exhibited non-basal texture after hot extrusion, e.g. the basal poles were rotated ~45° towards the extrusion direction (ED). A postulate is an idea that the deformation mechanism in Mg-0.2 wt.% Ce is different from that in pure Mg and AZ31, e.g. there is few twinning and more non-basal slip in Mg-Ce alloy system.

In earlier studies of relationship between particle simulated nucleation (PSN) and recrystallization texture in Mg alloys, the weakening of the texture of WE54 alloy[3, 6] with 4wt% RE was ascribed to particle simulated nucleation or PSN. More recent studies [4] of Mg-1 wt.% Y alloy have showed significant texture-randomization even though this alloy is expected to contain very few particles [20]. Increasing the Mn content (i.e. particle) in AZ31 does not lead to changes in the sheet texture [21]. PSN alone cannot explain the different texture in AZ31 and ME10 alloy although both alloys contain particles [22]. In this study, weak or non-basal texture in the Mg alloy with 0.2 wt.% Ce, addition, and typical ring basal texture in the Mg-3 wt.%-0.2 wt.% Ce alloys are observed. Microprobe analysis for those samples (Fig. 5) indicated that there are many particles in Mg-0.2 wt.% Ce and Mg-3 wt.%Al-0.2 wt.% Ce alloys. The results suggest that particles are not necessary for the texture randomization in magnesium.

Comparing the solute (Ce and Al) distribution in the Mg-0.2 wt.% Ce and Mg-3 wt.% Al-0.2 wt.% Ce (Fig. 5), Solute Ce is distributed in the magnesium matrix in Mg-0.2 wt.% Ce alloy, but Ce is exhausted by the $Al_{11}Ce_3$ particles and no solute Ce is found in the matrix in Mg-3 wt.%-0.2 wt.% Ce alloy. The difference suggests that Ce solute in the magnesium may be necessary for the texture randomization for the Mg-Ce alloys. Al solute does not affect the texture according to the microstructure in AZ31 alloy presented in Fig.1. The above results point to the fact that Mg alloys, which are solute-strengthened by Al addition will not benefit from texture modification for ductility enhancement but such addition can influence grain refinement in lean Al alloys when Al content is below solubility limit. Concurrent strengthening and texture modification in Mg alloys have been reported in Mg-Zn-Ce alloys where Zn-Ce intermetallics have not been reported [7, 24].

Solute drag is known to influence both the grain boundary mobility of different grain boundary or ientations [14] and the recrystallization kinetics [23]. In this study, the grain structures in Fig.2 show more equiaxed grains and higher grain aspect ratio in the alloys with Ce in solution. This is consistent with Ce solutes influencing the boundary mobility due to solute drag to influence texture. Al solutes in magnesium do not affect the texture evolution during the hot extrusion as solute drag effect could be

absent at the temperature/strain rate combination present during extrusion. In Mg-3 wt.%-0.2 wt.% Ce alloy, the Ce and Al are tied up in $Al_{11}Ce_3$ phase and no Ce solute is present in the alloy, leading to th e ring basal texture. The solute drag effect in Mg-RE alloy is discussed broadly however how the solut e RE works on the deformation modes or recrystallization behavior is still confusion.

5. Summary

The texture evolutions in Mg-Al and Mg-RE alloy during extrusion have been investigated. The results suggested that the texture of Mg alloy extrusion bar and tubes could be weakened by Ce addition with small content, but it does not work when Al also exists. Thus, the Mg-RE alloys exhibit much higher tensile elongation and good yield symmetry. The mechanism of texture weakening by RE addition is due to the solute effect, which could surpass the twinning and activated non-basal slip.

ACKNOWLEDGMENTS

This work was supported by National Natural Sciences Foundation of China (Grant Nos. 50901044 and 51271118) and Shanghai Rising-Star Program (B type) (Grant No. 12QB1403300)

References

[1] A. Styczynski, C. Hartig, J. Bohlen, D. Letzig, Scripta Materialia 2004, Vol. 50, pp. 943-947.
[2] L. Jiang, R. K. Mishra, A. A. Luo, A. K. Sachdev, S. Godet. Acta Materialia 2007, Vol. 55, pp. 3899-3910.
[3] E. A. Ball, P. B. Prangnell. Scripta Materialia 1994, Vol. 31, pp. 111-116.
[4] J. Bohlen, J. W. Senn, D. Letzig, S. R. Agnew, Acta Materialia 2007, Vol. 55, pp. 2101-2112.
[5] R. K. Mishra, P. R. Rao, A. K. Sachdev, A. M. Kumar, A. A. Luo. Scripta Materialia 2008, Vol. 59, pp. 562-565.
[6] L. W. F. Mackenzie, F. J. Humphreys, G. W. Lorimer.. Materials Science and Technology 2007, Vol. 3, pp. 1173-1179.
[7] L. W. F. Mackenzie, M. O. Pekguleryuz.. Scripta Materialia 2008, Vol.59, pp. 665-668.
[8] M. T. Perez-Prado, O. A. Ruano. Scripta Materialia 2003, Vol. 48, pp. 59-64.
[9] F. J. Humphreys. Acta Materialia 1997, Vol. 45, pp. 5031-5049.
[10] T. Laser, T. Ebeling, M.R. Nürnberg, D. Letzig, R. Bormann., Magnesium Technology, TMS (The Minerals, Metals & Materials Society), 2008, pp.283-288.
[11] L. Jiang, J.J. Jonas and R. Mishra, Materials Science and Engineering A, 2011 Vol. 528, pp. 6596– 6605
[12] L. L. Rokhlin. Magnesium Alloys Containing Rare Earth Metals, Published by Taylor & Francis, 2003.
[13] N.D. Saddock, A. Suzuki, K. Wu, S.C. Wildy, Y.A. Chang, T.M. Pollock, J. W. Jones, Magnesium Technology, TMS (The Minerals, Metals & Materials Society) 2005, pp. 121-126.
[14] F. J. Humphreys. Recrystallization and related annealing phenomena. Published by ELSECIER Ltd, 2004, pp. 67.
[15] Y. N. Wang, J. C. Huang. Materials Chemistry and Physics, 2003, Vol. 81, pp. 11-26.
[16] Q. Jin, S. Lim. Scripta Materialia 2006, Vol. 55, pp. 843-846.
[17] M. R. Barnett, M. D. Nave, C. J. Bettles. Materials Science and Engineering A 2004, Vol. 386, pp. 205-211.
[18] M. D. Nave, M. R. Barnett. Scripta Materialia 2004, Vol. 51, pp. 881-885.
[19] J. Bohlen, S. B. Yi, J. Swiostek, D. Letzig, H. G. Brokmeier, K. U. Kainer.. Scripta Materialia 2005, Vol. 53, pp. 259-264.
[20] S. R. Agnew, J. W. Renn, J. A. Horton, JOM, 2006, Vol. 58, pp. 62-69.

[21] T. Laser, M. R. Nürnberg, A. Janz, C. Hartig, D. Letzig, R. Schmid-Fetzer, Bormann R. Acta Materialia 2006, Vol. 54, pp. 3033-3041.
[22] N. Stanford, M. Barnett. Scripta Materialia 2008, Vol. 58, pp. 179-182.
[23] K Lücke, K Detert . Acta Metallurgica 1957, Vol. 5, pp. 628-637.
[24] A. A. Luo, R. K. Mishra, A.K. Sachdev, Scripta Materialia 64 (2011) 410 – 413

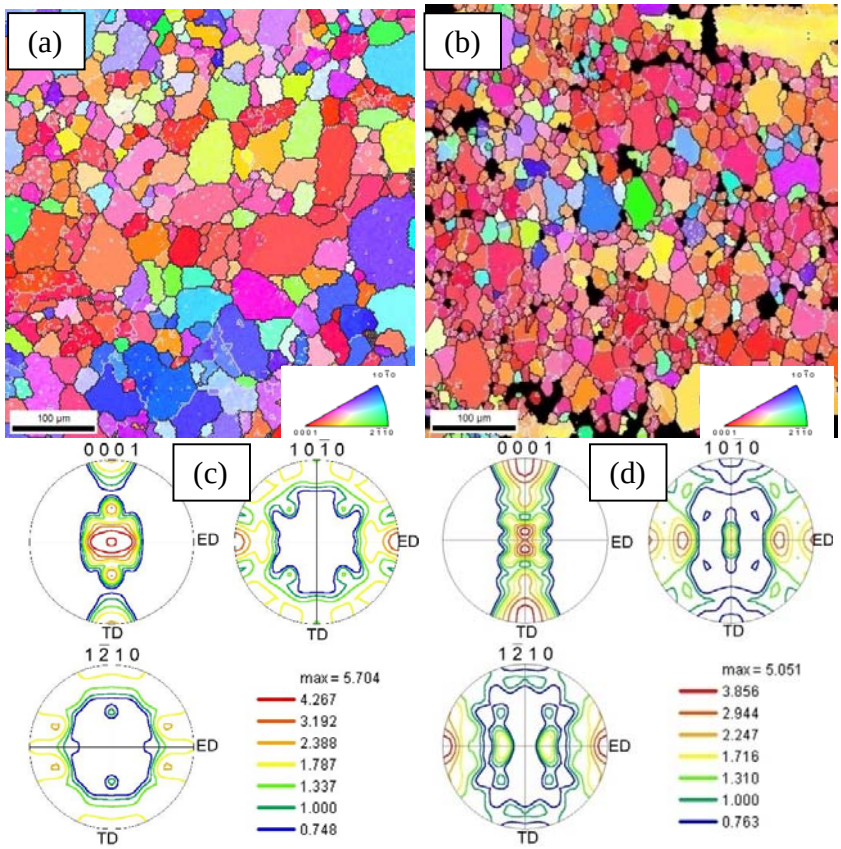

Fig.1 The microstructure and texture of the as-received AZ31and AM30 alloy tube. (a) PF map of AZ31, (b) IPF map AM30 (c) Pole figure of AZ31 (d) Pole figure of AM30.

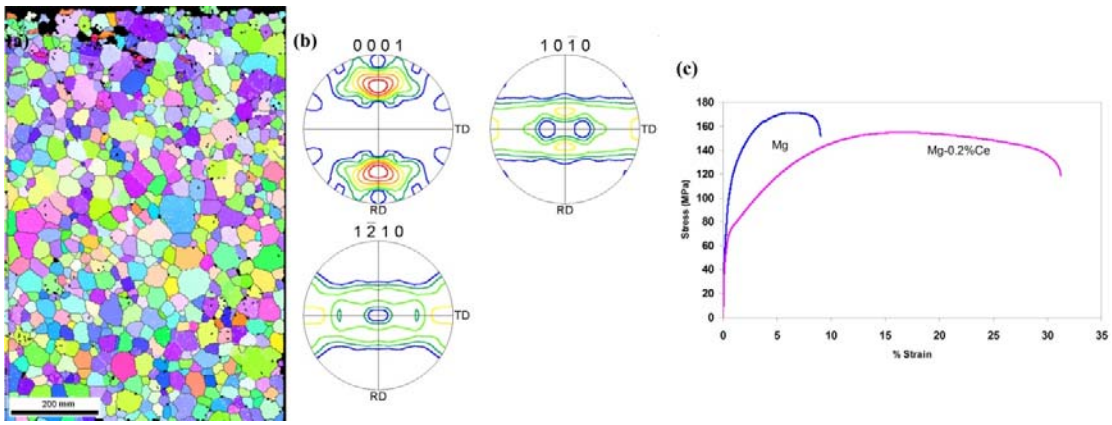

Fig.2 (a) IPF maps, (b) corresponding (0001), (10-10), and (11-20) texture plots, and (c) tensile curve of as-extruded tubes of Mg-0.2Ce tubes

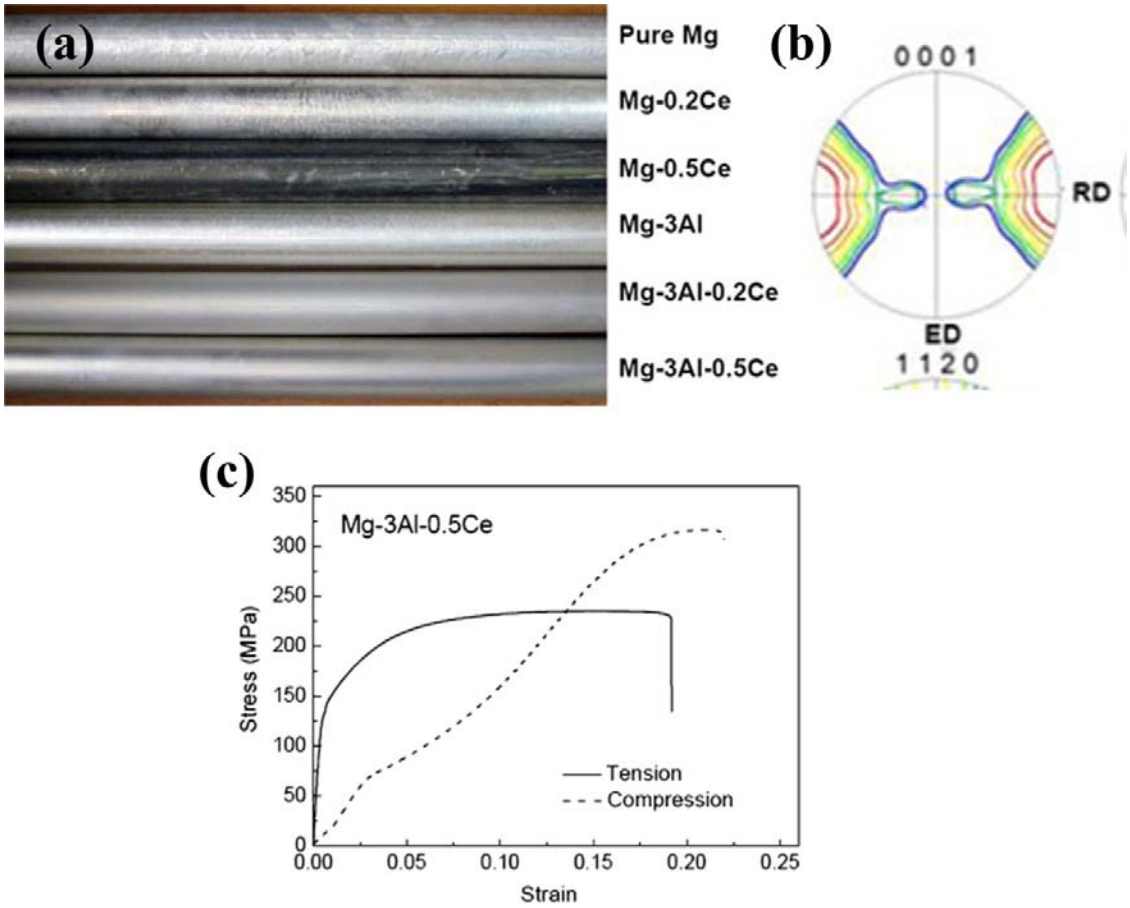

Fig. 3 Macroscope, texture and mechanical properties of Mg-Al and Mg-RE alloy tubes: (a) extruded tubes, (b) (0001) pole figure of Mg-3Al-0.5Ce alloy tube, (c) tensile and compression curve of Mg-3Al-0.5Ce alloy tube

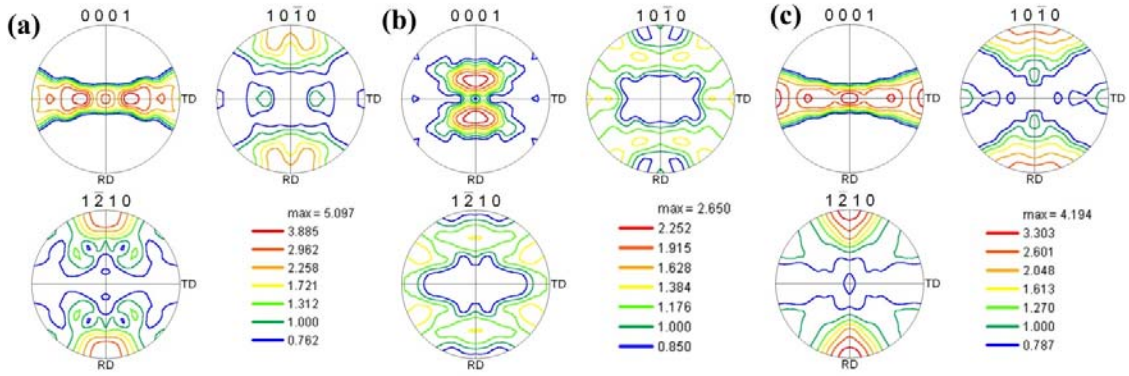

Fig. 4 (0001), (10-10) and (1-210) pole figures of Mg and alloys from the longitudinal section. TD refers to the tangential direction and ED to the extrusion direction. The sample surface normal is parallel to the radial direction: (a) unalloyed Mg, (b) Mg-0.2 wt.% Ce, (c) Mg-3 wt.% Al-0.2 wt.% Ce.

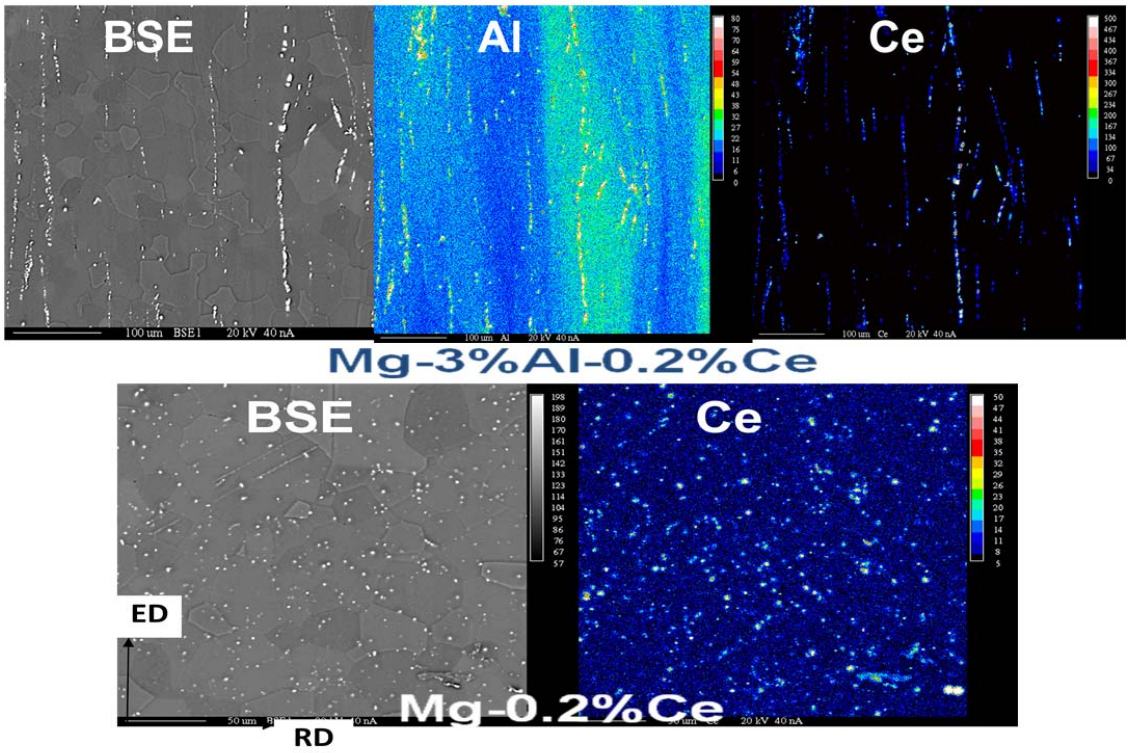

Fig. 5 Microprobe analysis showing the backscattered images and the element distribution maps for Mg-3Al-0.2Ce alloy and Mg-0.2 Ce alloy.

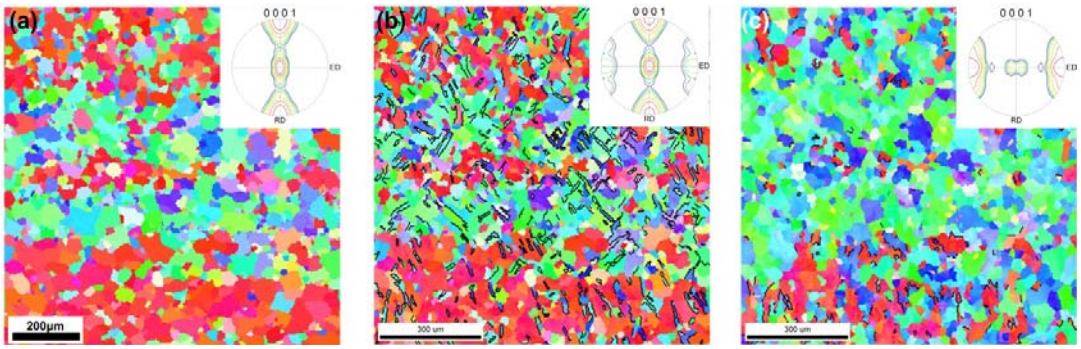

Fig.6 IPF and PF maps illustrating the microstructure and texture evolution of AZ31 tube compressed at room temperature to true strain of: (a) 0.01 (b)0.09 (C) 0.18 and the max intensity of texture is 9.8, 8.4 and 13.9 respectively.

A thermo-mechanically coupled cyclic plasticity model at large deformations considering inelastic heat generation

Qianhua Kan [1,*], Guozheng Kang [1], Wenyi Yan[2], Yilin Zhu [1], Han Jiang[1]

[1] Department of Applied Mechanics and Engineering, Southwest Jiaotong University, Chengdu, 610031, China

[2] Department of Mechanical and Aerospace Engineering, Monash University, Clayton, VIC3800, Australia

* Corresponding author: qianhuakan@yahoo.com.cn

Abstract In the process of inelastic deformation, cyclic accumulation of heat flux transferred from plastic work under cyclic loading results in an increased work temperature. The heat softening effects of material properties and external heat source will produce more plastic work. The fraction between plastic work and heat generation per unit volume can be introduced as a coupled source for thermal-mechanical analysis. Such coupling might be important in a simulation in which extensive inelastic deformation is accumulated fairly rapidly under cyclic loading and the mechanical properties are temperature dependent. To investigate the couple effect among temperature, stress and deformation under cyclic loading, a coupled thermo-mechanically cyclic plasticity model combined nonlinear isotropic hardening and kinematic hardening was established firstly in thermodynamics frame at large deformations. And then, the proposed model was implemented into finite element code ABAQUS by combining the user subroutine UMAT and UMATHT. Finally, some numerical results show the proposed model can capture thermal-induced necking in tensile loading, and the isotropic and kinematic hardening and thermal softening under cyclic loadings.

Keywords Inelastic heat generation, ratchetting, thermal softening, cyclic loading

1. Introduction

Elastic-plastic deformation behavior under cyclic loading has been investigated for some decades. Material models which describing macroscopic ratcheting response can be obtained within the framework of plasticity by combining the von Mises yield criterion with nonlinear kinematic hardening rules, e.g., the Armstrong-Frederick rule [1]. Some extended constitutive models of cyclic plasticity have been proposed to reasonably predict cyclic deformation behaviours of metal materials [2-6]. As a matter of fact, in the process of inelastic deformation, cyclic accumulation of heat flux transferred from plastic work under cyclic loading results in an increased work temperature. The thermal softening effect of material properties and external heat source will produce more plastic work The fraction between plastic work and heat generation per unit volume can be introduced as a source of coupling for thermal-mechanical analysis. However, the thermal effect induced by inelastic heat generation and its coupling with deformation were neglected in most ratcheting models. It is a reason that all the above-mentioned ratcheting models concern ratcheting in the context of small strains, the inelastic heat generation is neglectful small.

Recent experimental observation found that the ratchetting strain is up to 50% in the low-cycle fatigue [7], and thermo-elastic-plasticity coupling analysis in actual engineering application has attract attention [8]. So ratcheting problem without shakedown needs to be addressed on a consistent thermodynamic and large deformation frame. The thermo-mechanically coupled effect only in monotonic loading case has been modeled by the thermo-mechanically coupling constitutive models [9-16]. Therefore, a thermo-mechanically coupling cyclic plasticity constitutive model

needs to be established and make it available in commercial finite element packages, such as Abaqus for structural analysis.

In this work, a thermo-mechanically coupled cyclic plasticity model combined nonlinear isotropic hardening and kinematic hardening was established firstly in thermodynamics frame at large deformations. Further, the proposed model was implemented into finite element code ABAQUS by combining the user subroutine UMAT and UMATHT. Some numerical results were provided to validate the proposed model by simulating coupling thermo-mechanically behaviours under monotonic and cyclic loadings.

2. Thermo-elastic-plastic constitutive model

2.1. Deformation gradients

If the total deformation of materials is enough small, the thermal effect deriving from inelastic thermal generation is not significant. Therefore, the proposed model is derived at large deformation based on the hypoelastic-plastic theory. To separate recoverable and plastic contributions of the deformation gradient, the multiplicative decomposition of the deformation gradient is used [17]

$$\mathbf{F} = \mathbf{F}^r \mathbf{F}^p, \quad \mathbf{F}^r = \mathbf{F}^e \mathbf{F}^T \tag{1}$$

where $\mathbf{F}^r$ and $\mathbf{F}^p$ represents the thermo-elastic recoverable contribution and the plastic contribution of the total deformation gradient, respectively [18]. For metal materials, $\mathbf{F}^r$ describes the reversible distortion of the crystal, $\mathbf{F}^p$ describes irrecoverable deformation, for instance dislocation movements. Moreover, $\mathbf{F}^e$ and $\mathbf{F}^T$ are the elastic and thermal parts of the deformation gradient, respectively. For most metal materials, the elastic and thermal strains are small, and the multiplicative decomposition may be approximated by an additive decomposition of velocity gradient tensor $\mathbf{L}$ [16]

$$\mathbf{L} = \mathbf{L}^e + \mathbf{L}^T + \mathbf{L}^p \tag{2}$$

The rate of deformation tensor is the symmetrical part of velocity gradient tensor $\mathbf{L}$

$$\mathbf{D} = \frac{1}{2}(\mathbf{L} + \mathbf{L}^T) \tag{3}$$

2.2. Constitutive equations

Using the symmetric part of velocity gradient tensor in Eq. (2), the additive decomposition of the total rate of deformation tensor is expressed as

$$\mathbf{D} = \mathbf{D}^e + \mathbf{D}^p + \mathbf{D}^T \tag{4}$$

When we use the symmetric part of the velocity gradient with respect to current position and when the total elastic strain is always small compared to one. The rate of deformation decomposition is used in the form in almost all the inelastic constitutive models in finite element codes.

If only isotropic materials are considered, the elastic part of deformation rate can be given as

$$\mathbf{D}^e = \frac{1}{2G}\overset{\circ}{\tau} - \frac{v}{E}(tr\overset{\circ}{\tau})I \tag{5}$$

The thermal part of the rate of deformation tensor for isotropic materials can be expressed as

$$\mathbf{D}^T = \alpha \dot{T} \mathbf{I} \tag{6}$$

where α is thermal expansion coefficient and $\mathbf{I}$ is unit second order tensor.

At large deformation, an objective rate must be provided to state the objectivity of constitutive equations. The elastic stress-strain relation based on Jaumann objective rate can be written as

$$\overset{\circ}{\boldsymbol{\sigma}} = \mathbf{C}^e : \mathbf{D}^e = \mathbf{C}^e : (\mathbf{D} - \mathbf{D}^p - \mathbf{D}^T) \tag{7}$$

where $\overset{\circ}{\boldsymbol{\sigma}}$ is Jaumann rate of Cauchy stress, $\mathbf{C}^e$ is four order elastic tensor. Considering von Mises plasticity combined isotropic hardening and kinematic hardening and temperature dependent material properties, the yield function is expressed as a function of stress, temperature and equivalent plastic strain:

$$f = \bar{\sigma} - \sigma_y(\bar{\varepsilon}^p, T) \tag{8}$$

The equivalent stress can be defined as

$$\bar{\sigma} = \sqrt{1.5(\mathbf{s} - \boldsymbol{\alpha}) : (\mathbf{s} - \boldsymbol{\alpha})} \tag{9}$$

where $\boldsymbol{\alpha}$ is deviatoric back stress and the deviatoric part of stress tensor $\mathbf{s}$ is defined as

$$\mathbf{s} = \boldsymbol{\sigma} - \frac{1}{3} tr(\boldsymbol{\sigma}) \mathbf{I} \tag{10}$$

Associated plastic flow is used to derive the plastic part of deformation rate:

$$\mathbf{D}^p = \frac{\partial f(\mathbf{s} - \boldsymbol{\alpha})}{\partial \boldsymbol{\sigma}} \dot{\bar{\varepsilon}}^p = \dot{\bar{\varepsilon}}^p \mathbf{N} \tag{11}$$

where $\mathbf{N}$ is flow tensor of plastic strain and $\dot{\bar{\boldsymbol{\varepsilon}}}^p$ is the equivalent plastic rate defined as

$$\dot{\bar{\varepsilon}}^p = \sqrt{\frac{2}{3} \mathbf{D}^p : \mathbf{D}^p} \tag{12}$$

The isotropic hardening can be regarded as an increasing size in yield surface. In general, an exponential hardening is adopted to describe isotropic hardening with a threshold value as follows

$$\sigma_y(T) = \sigma_{y0}(T) + Q_{sa}(T)(1 - \exp(-b(T)\bar{\varepsilon}^p)) \tag{13}$$

where σ_{y0} is initial yield stress in the uniaxial loading at a reference temperature. The isotropic hardening parameters b and Q_{sa} are temperature dependent and can easily be calibrated by the uniaxial strain cycling at different temperatures.

A successful and popular approach is to introduce several back-stresses, where each back-stress is governed by the Armstrong-Frederick type of hardening rule. These models can be united in the following form:

$$\boldsymbol{\alpha}_i = \frac{2}{3} k_{1i}(T) \mathbf{D}^p - k_{2i}(T) \boldsymbol{\alpha}_i \dot{p}\,, \quad \boldsymbol{\alpha} = \sum_{i=1}^{M} \boldsymbol{\alpha}_i \tag{14}$$

where k_{1i} and k_{2i} are linear kinematic hardening coefficient and dynamics recovery coefficient for superposed M back stress components, respectively. Difference in Armstrong-Frederick typed models causes by different expressions in k_{1i} and k_{2i}. The accumulated plastic strain rate $\dot{p}$ is

equal to the equivalent plastic rate $\dot{\bar{\varepsilon}}^p$ according to J_2 plasticity.

According to the consistency condition, the differential form of Eq. (8) gives:

$$\dot{f} = \frac{\partial f}{\partial(\mathbf{s}-\boldsymbol{\alpha})} : \dot{\boldsymbol{\sigma}} - \frac{\partial f}{\partial(\mathbf{s}-\boldsymbol{\alpha})} : \dot{\boldsymbol{\alpha}} + \frac{\partial f}{\partial T}\dot{T} \tag{15}$$

Combining Eqs. (7), (11) and (15), the accumulated plastic strain rate can be obtained as:

$$\dot{p} = \frac{2G}{H(T)}\mathbf{N}:\mathbf{D} - \frac{1}{H(T)}(2G\alpha\mathbf{N}:\mathbf{I} + \frac{\partial\sigma_y(T)}{\partial T})\dot{T} \tag{15}$$

where G is shear modulus, H is defined as

$$H = 3G + k_{iso} + k_{kin} \tag{16}$$

where k_{iso} and k_{kin} represent isotropic hardening and kinematic hardening behaviours, respectively, and can be given as

$$k_{iso} = \frac{\partial\sigma_y(T)}{\partial\bar{\varepsilon}^p} \tag{17a}$$

$$k_{kin} = k_{1i}(T) - k_{2i}(T)\mathbf{N}:\boldsymbol{\alpha} \tag{17b}$$

Substituting Eq. (15) into Eq. (7) yields

$$\overset{\circ}{\boldsymbol{\sigma}} = \mathbf{C}^{ep} : (\mathbf{D} - \mathbf{I}\alpha\dot{T}) + \mathbf{C}^{e} : \mathbf{N}\frac{\partial\sigma_y(T)}{H(T)\partial T}\dot{T} \tag{18}$$

where $\mathbf{C}^{ep}$ is elasto-plastic modulus of continuum solids and defined as follows

$$\mathbf{C}^{ep} = \mathbf{C}^{e} - \frac{4G^2}{H}\mathbf{N}\otimes\mathbf{N} \tag{19}$$

2.3. Equation of energy balance

The material system must be in thermodynamic equilibrium. The local form of the first law of thermodynamics can be expressed as

$$\rho c_p\dot{T} = W^{pd} + \rho r - J\cdot div(\mathbf{q}) \tag{20}$$

where $J = \det\mathbf{F}$, c_p is specific heat and it is temperature dependent material parameter. $\mathbf{q}$ is thermal flux tensor, r is the internal thermal source, T is temperature. W^{pd} is the plastic dissipation term.

The latent stored energy for cold worked mild steel and copper was measured [18], which was assumed that the stored energy was a constant fraction of plastic work. However, subsequent experiment [19, 20] show it is dependent on the accumulated strain. Therefore, the heat generation is assumed as the rate of the plastic work multiplied by a function $\eta(p)$ related to calculated plastic strain:

$$W^{pd} = \eta(p)\cdot\boldsymbol{\sigma}:\mathbf{D}^p \tag{21}$$

According to Fourier's law, the heat conduction in the isotropic material can be expressed as

$$\mathbf{q} = -\mathbf{k}\partial_x T \tag{22}$$

The conductivity tensor $\mathbf{k}$ is assumed to be an isotropic tensor, that is related to a scalar material parameter K and $\mathbf{k} = K\mathbf{I}$.

Combining Eqs. (20), (21) and (22), the energy balance equation can be rewritten as

$$\rho c_p \dot{T} = \eta(p) \cdot \boldsymbol{\tau} : \mathbf{D}^p + \rho r + J \cdot div(\mathbf{q}) \tag{23}$$

The general form of three-type thermal boundary conditions are expressed as

$$\mathbf{q} : \mathbf{n} = -q_s\big|_{s1} + h(T_s - T_0)\big|_{s2} \tag{24}$$

$$T\big|_{s3} = T_s \tag{25}$$

These boundary conditions represent specified flux, convection and specified temperature on the respective parts of boundary, s_1-s_3. Here, h is the convection coefficient and $\mathbf{n}$ is the surface normal tensor.

2.4. Solution method

To solve thermo-mechanically coupling problem, coupled method and staggered method can be selected. The coupled method is more realistic even though it is computationally expensive due to involving handling of a large system of equations at every increment, which is necessary when a very large temperature gradient appears in an increment step. The staggered method have been improved to solve thermo-elasto-plastic problem [21], it is numerically convenient because it reduces the computational efforts significantly. In the work, the numerical treatment of coupled finite element analysis is based on the staggered solution scheme. The temperate fields are solved and as a known deformation field to apply in the deformation field, the temperature is updated as a common variable after iterating the two solutions until convergence. Moreover, a finite element implementation into finite element code, i.e., Abaqus, is also necessary for considering the thermal exchange with the around environment in thermo-mechanically coupled structural analysis. Based this purpose, the proposed model is implemented into Abaqus by combining user subroutine UMAT and UMATHT. The heat generation from plastic work is given by the heat generation rate RPL, which is related to plastic work and heat exchange factor η. The deformation and temperature fields are solved simultaneously at a reference temperature.

It is well known that the work done in a close loop is not exactly zero based on the hypoelastic-plastic frame. The stabilization with dissipated energy fraction option in the transient coupled temp-displacement analysis should be used to improve the convergence.

3. Numerical examples

3.1. Uniaxial tension

In this section, a numerical example was provided to simulate typical thermo-mechanically coupling effect. Thermally triggered necking of solid bar has been studied in literature [22], which is considered as a consequence of thermo-mechanically coupling. A 4-node axisymmetric thermally coupled quadrilateral element CAX4HT is used for coupled temperature-displacement analysis, the

finite element mesh is shown in Figure 1(a). To capture the necking process more accurately, a dense mesh is used nearby central section the specimen and ALE mesh technique is applied in the same place. The total length of the bar is 60mm, the length of work segment is 30mm, the radius of transition circular arc is 4mm and the radius of work segment is 4mm. Convection is applied on all free surfaces for a physically realistic simulation, the h is chosen to be 20000Wm^2/^{o}C, which is a generally used value [16]. For rail steel used here [24], the heat exchange factor η and its relation with accumulated plastic strain is not known. And then the factor η is simplified to be a constant value 0.9. For isotropic hardening, b and Q_{sa} are set to 0.25 and 100MPa. The upper end is fixed all freedoms and tensile velocity of 1mm/s is applied in the symmetrical plane. The surrounding temperature is assumed as room temperature 20^{o}C. The maximum allowable temperature change per increment is set to 10^{o}C. Total time 0.4s is used in the simulation and the automatic incrementation is used, the whole solution consist of 314 increment steps. Thermal-mechanical properties of the rail steel for the simulated specimen are given in Table 1. In the most quasi-static tension simulations, the increased temperature generated from plastic work is less than 100^{o}C, and then only part parameters are present here.

The equivalent stress, equivalent plastic strain and temperature were shown in Figure 1 (b), (c) and (d), respectively. It is found that necking can be reproduced successfully without any initial geometrical defect. Moreover, the temperature distribution is consistent with the equivalent plastic strain one, which shows that the temperature change causes by the plastic work. It must be noted that the isothermal analysis gives rise to a classical bifurcation problem, an initial defect must be introduced to trigger necking. However, the thermo-mechanically coupled problem is not a bifurcation problem, since inelastic heat generation gives rise to an increased temperature in the specimen and convection results in the non-homogeneous temperature distribution, which in combination with the thermal softening, triggers necking [23].

Table 1. Thermo-mechanical properties used in simulations [24]

T (℃)	E (GPa)	σ_y (MPa)	v	k_1 (GPa)	k_2	T (℃)	C_p (W/m-℃)	K (J/(Kg.C))	T(℃)	α (1e-6)
24	213	483	0.295	22.7	200	0	59.71	420	0	9.89
230	201	465.1	0.307	21.9	200	350	40.88	630	90	11.3

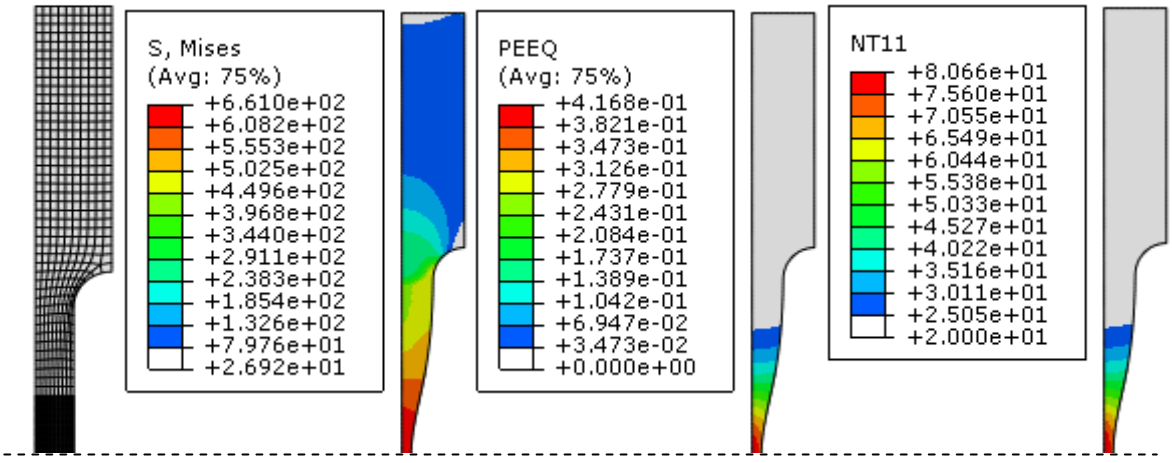

(a) (b) (c) (d)

Figure 1. Finite element simulations for necking of a circular bar with kinematic hardening model at time 0.4s: (a) the axisymmetrical finite element model with a symmetry plane (dot line); (b) the distribution of

equivalent von Mises stress; (c) the distribution of equivalent plastic strain; (d) the distribution of temperature

The thermo-mechanical coupling effect results in a significant thermal softening effect as shown in Figure 2. The load decreases with an increasing displacement when thermal-induced necking occurs. It is noted from Table 1 that the rail steel used in the simulation has a relative hardening parameter, which results in a flat plastic flow when applied displacement is less than 2mm.

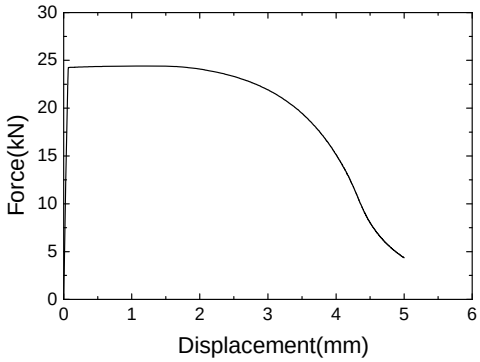

Figure 2. Force-displacement curve

3.2. Cyclic loading

In this example, thermo-mechanically coupling effect is investigated under cyclic stressing. An unsymmetrical stress cycling is applied in the symmetrical plane shown in Figure 1(a) and a total of 30 cycles were calculated. Figures 3(a) and (b) show the stress-strain curves located inside and outside nodes of central section of specimen, respectively. S22 and LE22 are Cauchy stress and logarithmic strain along Y direction, respectively. It is shown that the strain inside node of central section is much more than strain in outside node, which results in a large hysteresis loop in inside node of central section, i.e., more plastic work is done.

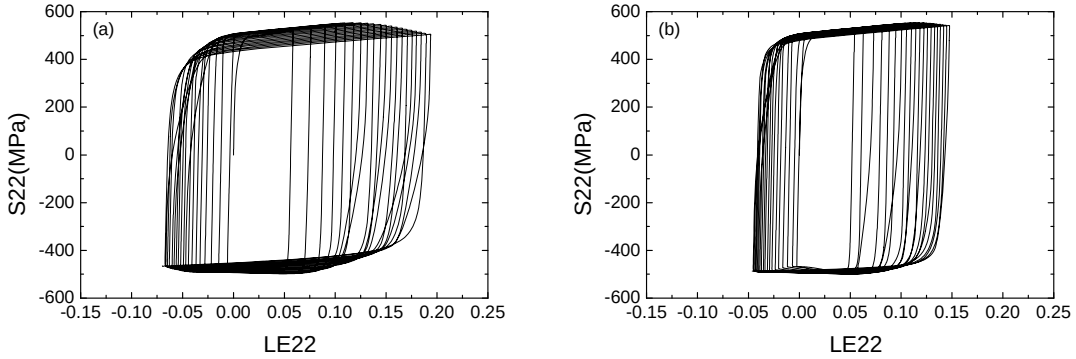

Figure 3. Stress-strain curves along loading direction: (a) inside node in central section; (b) outside node in central section.

Figures 4(a) and (b) show the accumulated plastic strain and temperature for inside and outside nodes in central section, respectively. It is found that more accumulated plastic strain appears in inside than outside nodes of central section. Corresponding, the temperature is higher for inside

node in central section due to conduction and convection. More accumulated plastic strain results in more inelastic heat generation; higher temperature result in more plastic strain due to thermal softening. It is the result the coupling among stress, deformation and temperature.

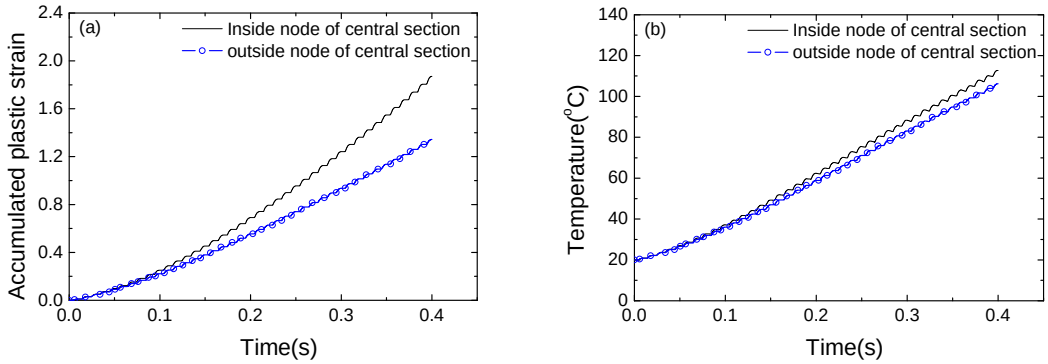

Figure 4. (a) accumulated plastic strain versus time and (b) temperature versus time located in different points.

For rail steel used here [24], the heat exchange factor η and its relation with accumulated plastic strain are not known. However, the influence of the heat exchange factor η on temperature field can be discussed by change the constant value of η, as shown in Figure 5. The total simulated time is limited within 0.1s. It is shown that isotropic hardening contributes more large thermal effect than isotropic hardening when the heat exchange factor η is fixed as 0.9. If only kinematic hardening is considered, the more temperature change occurs with the increased the heat exchange factor η at a fixed time. More important is that the temperature is accumulated with the increased loading cycle. It implies that the inelastic thermal generation can be neglected at a large cyclic number, e.g., low-cycle fatigue, even though the plastic strain is not significantly large.

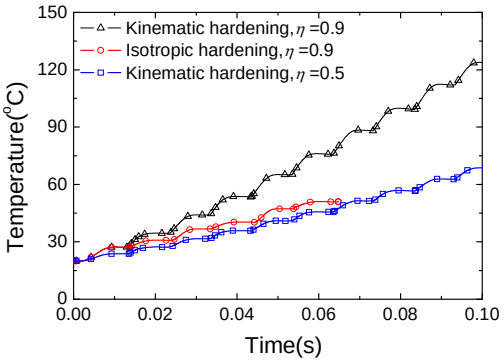

Figure 5. The curves of temperature versus time for isotropic hardening and kinematic hardening with different factors η

4. Conclusions

In the work, a thermo-mechanically coupling cyclic plasticity model with nonlinear isotropic and kinematic hardening was established at large deformations based on hypoelastic-plastic theory. The contribution of plastic dissipation to internal heat generation of materials was also addressed. The temperature dependent mechanical properties are employed. And then, the proposed model is

implemented into Abaqus by combining user subroutine UMAT and UMATHT. Transient coupled temperature-displacement finite element analysis was carried out to investigate thermo-mechanically coupled behaviours under monotonic and cyclic loadings. The thermally induced necking was reproduced without introducing any initial geometrical defect. The inelastic heat generation and, consequently, temperature are accumulated with an increased cyclic number, the interaction between deformation and thermal softening can be neglected, which should be addressed to constructing a more accurate model for predicting ratchetting at large cycles.

Acknowledgements

This work was financially supported by National Natural Science Foundation of China (11025210, 11202171) and the Fundamental Research Funds for the Central Universities (SWJTU12CX044).

References

[1] P.J. Armstrong, C.O. Frederick, A mathematical representation of the multiaxial Bauschinger effect. GEGB report RD/B/N731, Berkeley Nuclear Laboratories, 1966.

[2] J.L. Chaboche, G. Rousselier, On the plastic and viscoplastic constitutive equations. part I and II. J Press Vessel-T ASME 105(1983) 153-164.

[3] N. Ohno, J.D. Wang, Nonlinear kinematic hardening rule with critical state of dynamic recovery, part I: formulation and basic features for ratchetting behavior. Int J Plasticity 9(1993)3575-3590.

[4] M. Abdel-Karim, N. Ohno, Kinematic hardening model suitable for ratchetting with steady state. Int J Plasticity 16 (2000) 225-240.

[5] S. Bari, T. Hassan, Anatomy of coupled constitutive models for ratcheting simulations. Int J Plasticity 16(2000)381-409.

[6] X. Chen, R. Jiao, Modified kinematic hardening rule for multiaxial ratcheing prediction. Int J Plasticity 20(2004) 871-898.

[7] Y.J. Liu, G.Z. Kang, Q. Gao. Stress-based fatigue failure models for uniaxial ratchetting-fatigue interaction, Int J Fatigue 30(2008)1065-1073.

[8] L. Wu, Z.F. Wen, W. Li, X.S. Jin, Thermo-elastic-plastic finite element analysis of wheel-rail sliding contact. Wear 271 (2011) 437-443.

[9] F. Yoshida, T. Uemori, A model of large-strain cyclic plasticity describing the Bauschinger effect and workhardening stagnation. Int J Plasticity 18(2002)661-686.

[10] A.S. Khan, K.M. Jackson, On the evolution of isotropic and kinematic hardening with finite plastic deformation, part I: compression/tension loading of OFHC copper cylinders. Int J Plasticity 15(1999) 1265-1275.

[11] Z. Hu, Work-hardening behavior of mild steel under cyclic deformation at finite strains. Acta Metall. Mater. 42(1994)3481-3491.

[12] G. Jahonsson, M. Ekh, K. Runesson, Computational modeling of inelastic large ratcheting strains. Int. J. Plasticity 21(2005) 955-980.

[13] M. Wallin, M. Risinmaa, N.S. Ottosen, Kinematic hardening in large strain plasticity. Europ. J. Mech A/Solid 22(2003)341-356.

[14] G. Jahonsson, J. Ahlstr o¨m, M. Ekh, Parameter identification and modeling of large ratcheting strains in carbon steel, Comput Struc 84(2006)1002-1011.

[15] H. Xiao, O.T. Bruhns, A. Meyes, Thermodynamic laws and consistent Eulerian formulation of finite elastoplasticity with thermal effects. J Mech Phys Solids 55(2007)338-365.

[16] Y. Tadi Beni , M.R. Movahhedy, Consistent arbitrary Lagrangian Eulerian formulation for large deformation thermo-mechanical analysis, Mater Design 31(2010)3690-3702.
[17] E.H. Lee, Elastic-plastic deformation at finite strains. J Appl Mech 36 (1969)1-6.
[18] G. Taylor, H. Quinney, The latent energy remaining in a metal after cold working. Prog. Mater. Sci. A 143(1934)307-326.
[19] M. Bever, D. Holt, A. Tichener, The stored energy of cold work. Prog Mater Sci (1973)7.
[20] W. Oliferuk, W. Swiatnicki, M. Grabski, Rate of energy storage and microstructure evolution during the tensile deformation fo austenitic steel. Mater Sci Eng A 161(1993)55-63.
[21] P. Rosakis, A. Rosakis, G. Ravichandran, J. Hodowany, A thermodynamic internal variable model for the partition of plastic work into heat and stored energy in metals. J Mech Phys Solids 48(2000)581-607.
[22] J. Simo, F. Armero, Recent advances in the numerical analysis and simulation of thermoplasticity at finite strain. In: D. Besdo, E. Stein, Finite inelastic deformations- Theory and applications. Springer, Berlin, (1992)259-272.
[23] P. Ha˚kansson, M. Wallin, M. Ristinmaa, Comparison of isotropic hardening and kinematic hardening in thermoplasticity. Int J Plastcity 21(2005)1435-1460.
[24] T. Bradon, G. Jeff, A. B. Periman, Investigation of effects of sliding on wheel tread damage, Int Mech Engng Congress Exposition ASME, Nov 5-11, Orlando, Florida USA (2005)1-7.

Influence of Free Surface Roughening on Ductile Fracture Behavior Under Uni-axial Tensile State for Metal Foils

Tsuyoshi Furushima[1*], Hitomi Tsunezaki[1], Ken-ichi Manabe[1], Ming Yang[2], Sergei Alexandrov[3]

[1] Department of Mechanical Engineering, Tokyo Metropolitan University, 1-1 Minami-osawa, Hachioji, Tokyo 192-0397, Japan
[2] Institute for Problems in Mechanics, Russian Academy of Sciences, 101-1 Prospect Vernadskogo, 119526 Moscow, Russia
* Corresponding author: furushima-tsuyoshi@tmu.ac.jp

Abstract The metal foils indicate low level fracture strain compared with metal sheet. In this study, the free surface roughening is focused on to clarify the mechanism of ductile fracture for metal foils, since the ratio of surface roughness to thickness becomes larger compared with metal sheets. Materials used are pure copper and pure titanium foils and sheets with thickness of 0.05, 0.1, 0.3 and 0.5mm respectively. Free surface roughening and ductile fracture behavior are measured and observed under uni-axial tensile state. As a result, the surface roughening to thickness of metal foils with thickness of 0.05 and 0.1mm was larger than that of metal sheets with thickness of 0.3 and 0.5mm. To investigate the fracture behavior of metal foils, the fracture surface is observed by scanning electron microscope. For pure copper foils with thickness of 0.05 and 0.1mm, dimple pattern cannot be observed, while some dimples for metal sheets such as pure copper and pure titanium sheets with thickness of 0.3, 0.5mm and pure titanium foils with 0.05 and 0.1mm can be observed. As a result, the fracture type of metal foils divides broadly into two categories: existence dimple type for pure titanium and non-existence dimple for pure copper on fracture surface. In addition, the magnitude relation between the increase in ratio of surface roughness to thickness and strain hardening exponent *n* value would affect fracture strain level and existence or non-existence of dimple pattern on fracture surface.

Keywords Metal foil, Free surface roughening, Ductile fracture, Thickness

1. Introduction

Recently, micro metal forming process using metal foils is one of the promising approaches to fabricate micro stamping products such as micro shim, micro gasket, ultra thin valve for micro pump and parts for electric and medical devices. However, it is well known that the micro metal forming for metal foil with ultra thin thickness has problems on size effect. For example of the size effect, Fu reported that fracture strain decreases with decreasing thickness of specimen in uni-axial tensile test [1]. Thus, the metal foils in micro scale indicate different fracture behavior from metal sheet in macro scale. To clarify the fracture mechanism and to predict forming limit of metal foils are absolutely imperative for further development of micro metal forming.

In our previous report, we focused on free surface roughening phenomenon as one of factors related to fracture mechanism of metal foils. It is well known that surface roughness on free surface with non-contact tool situation increases with plastic deformation during metal forming process. An inhomogeneous model has been suggested for prediction of free surface roughening [2, 3]. Our experimental works reported that the ratio of surface roughness to thickness of copper foils with ultra thin thickness becomes large compared with that of conventional sheets [4]. Thus, the free surface roughening of copper foils may affect not only local problem such as accuracy of products and frictional condition but also global deformation behavior such as necking behavior which is onset of fracture. Furthermore, we reported that the forming limit of copper foils in stretching forming cannot be predicted by conventional ductile fracture criterion [5]. Moreover, unlike general metal sheets, dimple pattern on fracture surface cannot be observed of the copper foil. However, the previous reports dealt with limited materials such as copper alloy. The discussion about fracture

mechanism of metal foils was not insufficient.

In this study, we investigated the ductile fracture behavior and free surface roughening for not only pure copper foils but also various metal foils such as pure titanium foils. Influence of free surface roughening on ductile fracture behavior under uni-axial tensile state for metal foils was discussed experimentally.

2. Materials and experiment

Pure copper C1020-O and pure titanium TR270C-O foils and sheets with thickness t_0 of 0.05, 0.1, 0.3 and 0.5mm were used. The tensile test specimens were cut along the 0° to the rolling direction. In uni-axial tensile test, gage length was 10mm. A commercial tensile test machine was used for the tensile tests. Since a contact extensometer cannot be pasted for the metal foil, elongation was measured optically by using a video type non-contact extensometer. Tensile tests were conducted at room temperature and a strain rate of 1.6×10^{-3} /s. To get repeatability of experimental result, tensile tests were performed 3 times. After tensile test, fracture surface was observed by scanning electron microscope (SEM). To investigate effect of free surface roughening on ductile fracture behavior, the surface roughness was measured by confocal laser microscope. Until material fractures, surface roughness is measured at same area in five stages.

3. Results and discussion

3.1. Effect of thickness on fracture strain and free surface roughening behavior

Fig. 1 shows the effect of thickness on fracture strain obtained from uni-axial tensile test. Fracture strain decreases with decreasing thickness for all materials used as is the case in previous report [1]. In particular, the fracture strain of pure copper and pure titanium dramatically decrease from thickness of 0.3mm to 0.1mm. Thus, it is found that the thickness strongly affects fracture strain.

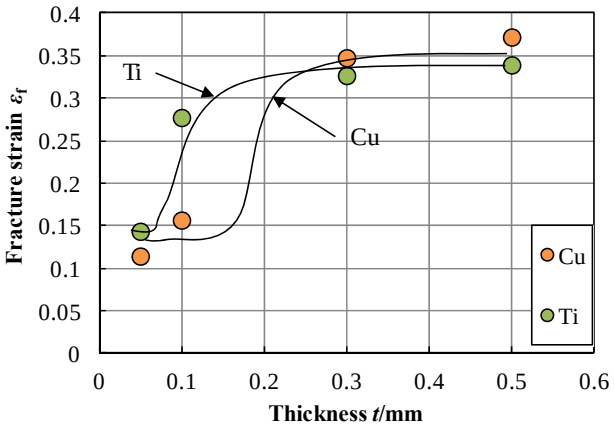

Figure 1. Effect of thickness on fracture strain in uni-axial tensile test

To clarify why the fracture strain significantly decrease with decreasing thickness, the free surface roughening on specimen surface during uni-axial tensile test was investigated. Here, we used ratio of maximum surface roughness to thickness Rz/t, because it is not always true that the surface roughness similarly decreases with decreasing thickness. The thickness t during deformation is calculated by assumption of volume constancy law and isotropic material. Fig. 2 shows the ratio of surface roughness to thickness Rz/t during uni-axial tensile test. The ratio of surface roughness to

thickness for each material linearly increases with increasing plastic strain. In addition, most important part is that the slope of ratio of surface roughness to thickness *Rz*/*t* is completely different between sheets (*t*=0.3 and 0.5mm) and foil (*t*=0.05 and 0.1mm). Particularly, the slope of evolution of *Rz*/*t* is changing significantly from thickness 0.3 to 0.1mm. As a result, it is supposed that the decrease in fracture strain has some connections with slope of relative free surface roughening *Rz*/*t*.

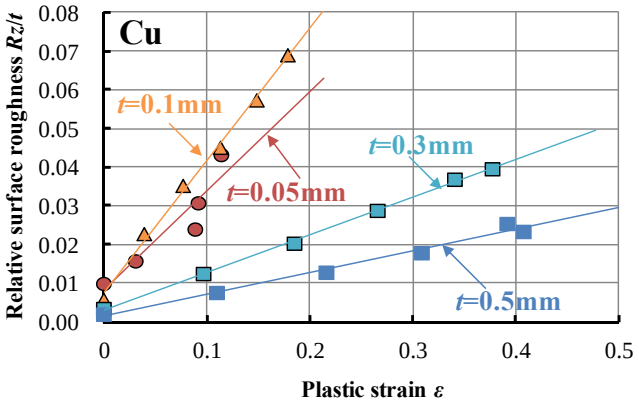

(a) Pure copper

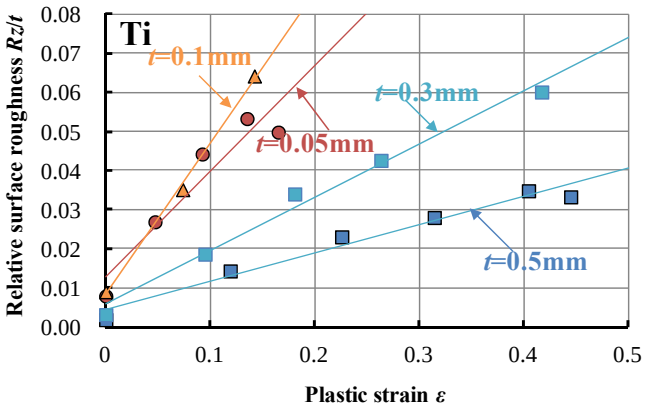

(b) Pure titanium

Figure 2. Evolution of ratio of surface roughness to thickness during uni-axial tensile deformation

3.2. Fracture surface observation

To clarify the reason why the fracture strain changes significantly between thicknesses of 0.1 and 0.3mm, the difference in fracture mode was investigated by observing fracture surface by SEM. Figs. 3 and 4 show the SEM images of fracture surface for pure copper and pure titanium foils and sheets.

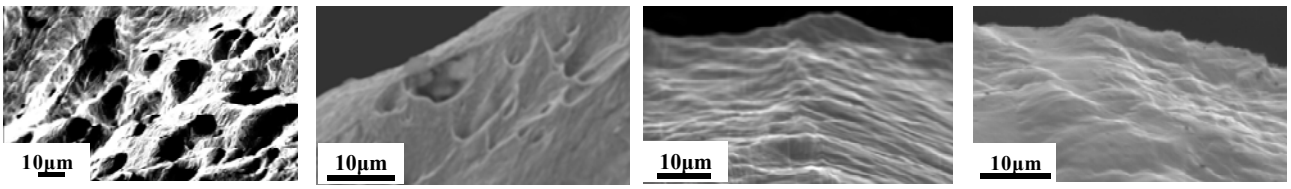

(a) *t*=0.5mm (b) *t*=0.3mm (c) *t*=0.1mm (d) *t*=0.05mm

Figure 3. SEM photographs of fracture surface for pure copper

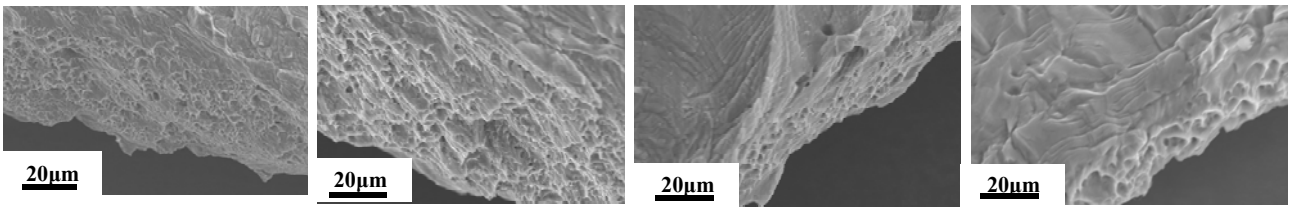

(a) t=0.5mm (b) t=0.3mm (c) t=0.1mm (d) t=0.05mm

Figure 4. SEM photographs of fracture surface for pure titanium

In Fig. 3, some dimples on the fracture surface can be observed for pure copper sheets with thicknesses of 0.3 and 0.5mm. Meanwhile, non-dimples were on fracture surface of copper foils with thicknesses of 0.05 and 0.1mm. Generally, it is known that nucleation and growth of voids during plastic deformation causes dimple pattern on the fracture surface. Therefore, for metal sheets with relatively thicker thickness of 0.3 and 0.5mm, ductile fracture is caused by nucleation and growth of voids. On the contrary, it can be guessed that the metal foils with relatively thinner thickness of 0.05 and 0.1mm were fractured by other mechanism except nucleation and growth of voids because of non-dimple pattern on the fracture surface. These results about the existence or non-existence of dimple pattern on fracture surface between metal foils and metal sheets had some connections with significantly change in fracture strain in Fig. 1 and free surface roughening in Fig. 2. In the previous study, it was confirmed that the deep depth of surface defect purposely fabricated on the tensile specimen causes fracture at early tensile deformation stage [6]. Therefore, it would be considered that the evolution of free surface roughness causes similar effect of surface defect on the specimen. Thus, the fracture would be due to free surface roughening rather than nucleation and growth of voids inside the material.

Meanwhile, the dimple pattern can be observed for pure titanium foils and sheets with thickness of 0.05, 0.1, 0.3 and 0.5mm as shown in Fig. 4. The difference in fracture surface for pure titanium between foil and sheet cannot be confirmed seen in pure copper. Thus, it is guessed that origination of ductile fracture is not generated by free surface roughening but void nucleation and growth cause ductile fracture for pure titanium foils similar to general metal sheet, regardless the slope of relative free surface roughening is large for pure titanium foils as shown in Fig. 2. From these results, there are two fracture type of metal foils: pure titanium type with dimple pattern and pure copper type with non-dimple pattern on fracture surface.

3.3. Discussion on ductile fracture mechanism of metal foils

As described in section 3.1 and 3.2, it is found that the fracture type of metal foils divides broadly into two categories: existence dimple type for pure titanium and non-existence dimple for pure copper on fracture surface. To consider difference between both fracture types occurs for metal foils, we are focusing on not only the relative free surface roughening behavior and fracture surface observation described above but also basic material properties obtained from uni-axial tensile test as shown in Table 1. Material properties such as strain hardening n, K, ε_0 for each material were obtained from swift type flow stress curve as shown in Eq. (1).

$$\sigma = K(\varepsilon_0 + \varepsilon)^n \tag{1}$$

In addition, we discuss necking behavior near fracture area as shown in Fig. 5. Generally, the occurrence of necking behavior is strongly related to strain hardening exponent n [7]. it is well known that the larger n value, the larger necking strain.

Table 1. Material properties obtained from uni-axial tensile test

Material	Thickness t [mm]	n	K [MPa]	ε_0
Pure copper	0.05	0.56	671.2	0.022
	0.1	0.54	602.6	0.026
	0.3	0.46	524	0.014
	0.5	0.44	509.6	0.012
Pure titanium	0.05	0.085	533	0.015
	0.1	0.16	521.7	0.0063
	0.3	0.38	616.8	0.07
	0.5	0.33	604.1	0.05

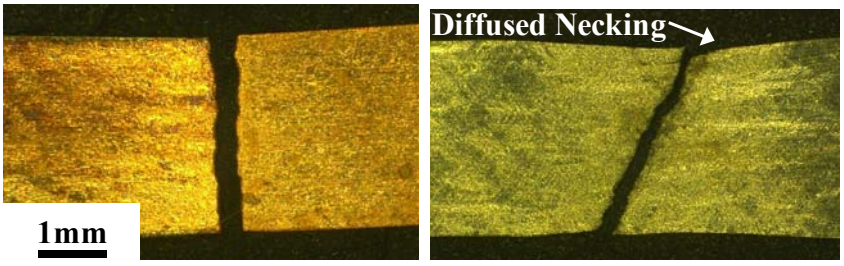

(a) Pure copper (b) Pure titanium

Figure 5. Photographs of necking area after uni-axial tensile test

The strain hardening exponent n value of pure copper foil with thickness of 0.05mm in Table 1 was 0.56, respectively, but n value of pure titanium foil with thickness of 0.05mm was 0.085. Thus, n value of pure titanium foil is smaller than that of pure copper foil. The fracture strain of pure copper foil with thickness of 0.05mm indicates very low value as shown in Fig. 1 in spite of large n value 0.56. Additionally, it can be observed that the tensile test specimen of pure copper foil was fractured vertically to the tensile direction without diffused necking as shown in Fig. 5 (a). From these result, it is considered that the increase in the ratio of surface roughness to thickness causes inhomogeneous thickness distribution, which would lead to origination of fracture as a fracture mechanism of metal foil with non-dimple type such as pure copper. Originally, the pure copper foil with thickness of 0.05mm is supposed to indicate large fracture strain due to large n value, but fracture occurred before diffused necking because of increasing the ratio of surface roughness to thickness during deformation. Thus, it is considered that the void nucleated by occurrence of diffused necking is not growing in the specimen, and then the dimple pattern on fracture surface of pure copper foils with thickness of 0.05 and 0.1mm cannot be observed.

Meanwhile, n value of pure titanium foil with thickness of 0.05mm is extremely low value of 0.085 as shown in Table 1. Thus, it is confirmed that the necking strain indicates low level and the fracture occurs obliquely to the tensile direction as shown in Fig. 5 (b) after diffused necking. As shown in Fig. 2, the relative free surface roughening of pure titanium foils with thickness of 0.05 and 0.1mm is large as well as that of pure copper foils. However, in case of pure titanium foils with lower n value, it is supposed that the fracture occurs by necking along with metal sheet before effect of free surface roughening becomes marked. As a fracture mechanism of pure titanium foil, the occurrence of necking with lower n value is initiative of fracture of foils compared with relative free surface roughening. Therefore, the dimple pattern on fracture surface which is generated by nucleation and growing of voids after necking of pure titanium foil can be observed.

From these results, fracture mechanism of metal foil can divide broadly into two categories by the magnitude relation between the increase in ratio of surface roughness to thickness and strain hardening exponent *n* value, which would affect fracture strain level and existence or non-existence of dimple pattern on fracture surface.

4. Conclusion

In this study, the ductile fracture behavior and free surface roughening for various metal foils such as pure copper and pure titanium foils was investigated experimentally to clarify the general fracture mechanism of metal foils. As a result, the fracture type of metal foils divides broadly into two categories: existence dimple type for pure titanium and non-existence dimple type for pure copper on fracture surface. In addition, the magnitude relation between the increase in ratio of surface roughness to thickness and strain hardening exponent *n* value would affect fracture strain level and existence or non-existence of dimple pattern on fracture surface.

Acknowledgements

This research was supported by RFBR and JSPS under the Russia-Japan Research Cooperative Program.

References

[1] M.F. Fu, W.L. Chan, Geometry and grain size effects on the fracture behavior of sheet metal in micro-scale plastic deformation. Mater. Des., 32 (2011) 4738-4746.
[2] Z. Zhao, R. Radovitzky, A. Cuitino, A study of surface roughening in fcc metals using direct numerical simulation. Acta Mater., 52 (2004) 5791–5804.
[3] T. Furushima, T. Masuda, K. Manabe, S. Alexandrov, Prediction of free surface roughening by 2D and 3D model considering material inhomogeneity. J. Solid Mech. Mater. Eng. 5 (2011) 978-990.
[4] T. Furushima, T. Masuda, H. Tsunezaki, S. Alexandrov, Free surface roughening and ductile fracture of metal foils in micro metal forming. in Proceedings of the 3rd Asian Symposium on Materials & Processing (ASMP 2012) (2012) CD-ROM.
[5] T. Furushima, T. Masuda, H. Tsunezaki, S. Alexandrov, Fracture prediction in micro sheet forming using ductile fracture criterion. Steel Res. Int., Special Edition (2012) 1183-1186.
[6] T. Hiroi, H. Nishimura, The influence of surface defects on the forming-limit diagram of sheet metal. J. Mater. Process. Technol. 72 (1997) 102-109.
[7] H. Swift, Plastic instability under plane stress. J. Mech. Phys. Solids, 1 (1952) 1-18.

A mechanism-based plastic model to simulate the mechanical properties in nanostructured bimodal metals

LinLi Zhu[1,*], Jian Lu[2]

[1] Department of Engineering Mechanics, School of Aeronautics and Astronautics, Zhejiang University, Hangzhou 310027, Zhejiang Province, China
[2] Department of Mechanical and Biomedical Engineering, City University of Hong Kong, Kowloon, Hong Kong, China
* Corresponding author: llzhu@zju.edu.cn

Abstract Engineering a bimodal grain size distribution in nanostructured materials has been proved to effectively achieve both higher strength and higher ductility. In these materials, large grains provide hardening ability and small grains provide larger yield stress. Accounting for the contributions of microcracks which nucleate in the nano/ultrafine grained phase and stop at the boundary of large grains during the plastic deformation, a mechanism-based plastic model is developed to describe the strength and ductility of the bimodal metals. The strain-based Weibull probability distribution function is utilized to predict the failure behavior of the bimodal metals. With the aid of the modified mean field approach, the stress–strain relationship can be derived by combining the constitutive relations of the nano/ultrafine grained phase and the coarse grained phase. Numerical results show that the proposed model can completely describe the mechanical properties of the bimodal metals, including yield strength, strain hardening and uniform elongation. The predictions are in good agreement with the experimental results. These results will benefit the optimization of both strength and ductility by controlling constituent fractions and the size of the microstructures in materials.

Keywords Bimodal grain size distribution, Strength, Strain hardening; Ductility, Weibull distribution

1. Introduction

Nanostructured and ultrafine-grained metallic materials have been observed to perform outstanding physical and mechanical properties. One of the most remarkable improvement is the superior mechanical strength compared to those of corresponding coarse-grained counterparts [1]. Therefore, these materials have been of significant interest and the key importance in designing lighter and stronger structures. So far, there have been several strategies to obtain the higher strengthening materials, including refining grain size, solid solution alloying and plastic straining [2], but these materials perform the disappointingly low tensile ductility. Due to this fact, the simultaneously higher strength and ductility in metals and alloys are expected and have emerged as the essentially challenging issue in the application of the nanostructured metals. In the past ten years, several alternative approaches are addressed to achieve the higher strength with keeping the high ductility, such as by generating the internal boundaries such as nanotwins in polycrystalline metals [3], or mixing the various sizes of microstructures in nanostructured materials [4-5].

The bimodal grain size distributions in nanostructured metals/alloys, which is considered as an effective approach to obtain the higher strength with good ductility, were first studied experimentally by Wang et al [4] and Tellkamp et al. [6] respectively. Their observations showed that such kind of nanostructured metals/alloys have higher strength and high ductility simultaneously. After these pioneering works, the subsequent various experiments and theoretical studies are carried out to investigate the mechanical performance in bimodal nanostructured metals and alloys [7-9]. These experiments demonstrated that the nanograins or ultrafine grains contribute

to the higher strength and the higher ductility is attributed to the coarse grains. For the fracture in bimodal metals/alloys, there exist some explanations to shed some lights into the possible mechanism of failure. The cavitations in nanograin/ultrafine phase, necking in coarse grains and shear localization are responsible for the fracture in bimodal metals [10-12]. Besides of that, the cavitations and microcracks play an important role in the improved ductility of the bimodal metals/alloys, which have been indentified further by the recent experiments [13]. The predictions of mechanical behaviors in bimodal metals/alloys have become a key issue to optimize the grain size distribution and the volume fraction of continents in bimodal metals/alloys for desiring the high strength and high ductility. So far, there are several works to develop the theoretical model for predicting the constitutive behavior and the failure properties of bimodal metals/alloys [14-15].

It has been demonstrated in experimental observations of tensile deformation in bimodal materials that the nanoscale voids or nano/microcracks lead to the modification of stress and strain for the plastic deformation. The objective of the present paper is to introduce the mechanism-based plastic model for bimodal metals in which the impacts of the microcracks generated during plastic deformation in bimodal materials on the mechanical properties are accounted for [16]. The bimodal copper is selected as an example to predict the corresponding mechanical behavior of bimodal metals. The weibull probability distribution of nan/microcracks is analyzed in the simulations. Numerical results show that the developed plastic model of bimodal metals can describe the mechanical properties of bimodal copper completely.

2. A Set Up of Model

The nanostructured metal with bimodal grain size distribution is considered as the composite metals consisting of the nanograined matrix phase and the course grained phase, as shown in Fig. 1. Since the grain boundaries have great contribution on the mechanical properties of nanocrystalline materials, the strain gradient in GBDPZs are involved in the proposed model to capture the effects of grain boundaries on the plastic deformation. Therefore, the mechanism-based strain gradient plasticity [17] is adopted here to describe the stress-strain response in each constituent of bimodal metals. A summary of the formulation is provided in the following. The strain rate $\dot{\boldsymbol{\varepsilon}}$ can be decomposed into its elastic and plastic parts,

$$\dot{\boldsymbol{\varepsilon}} = \dot{\boldsymbol{\varepsilon}}^{\mathrm{e}} + \dot{\boldsymbol{\varepsilon}}^{\mathrm{p}} \tag{1}$$

The elastic strain rate is obtained from the stress rate in the linear elastic relation as

$$\dot{\boldsymbol{\varepsilon}}^{\mathrm{e}} = \mathbf{M} : \dot{\boldsymbol{\sigma}} \tag{2}$$

where $\mathbf{M}$ is the elastic compliance tensor. The plastic strain rate is proportional to the deviatoric stress $\boldsymbol{\sigma}'$ based on the conventional J2-flow theory of plasticity, given as

$$\dot{\boldsymbol{\varepsilon}}^{\mathrm{p}} = \frac{3\dot{\varepsilon}^{\mathrm{p}}}{2\sigma_{\mathrm{e}}}\boldsymbol{\sigma}' \tag{3}$$

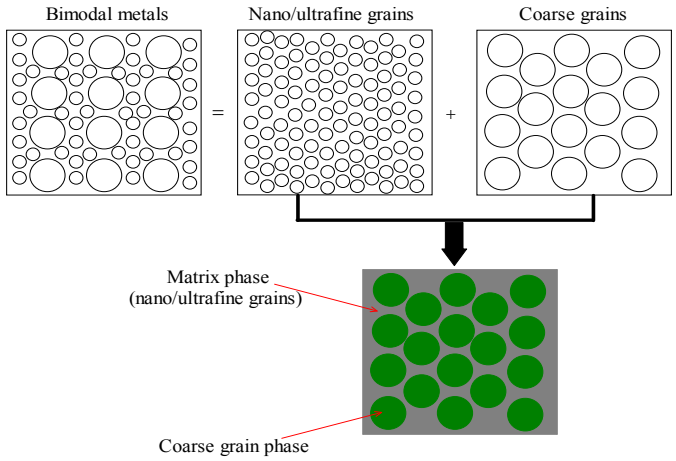

Fig. 1 Schematic drawings of bimodal grain size distributions in polycrystalline materials with assumption of the composite mixture model.

Here, $\sigma'_{ij} = \sigma_{ij} - \sigma_{kk}\delta_{ij}/3$ and $\sigma_e = \sqrt{3\sigma'_{ij}\sigma'_{ij}/2}$ is the von Mises equivalent stress. $\dot{\varepsilon}^p$ is the equivalent plastic strain rate which is determined by

$$\dot{\varepsilon}^p = \dot{\varepsilon}\left[\frac{\sigma_e}{\sigma_{flow}}\right]^{m_0} \tag{4}$$

in which $\dot{\varepsilon} = \sqrt{2\dot{\varepsilon}'_{ij}\dot{\varepsilon}'_{ij}/3}$ is the equivalent strain rate and $\dot{\varepsilon}'_{ij} = \dot{\varepsilon}_{ij} - \dot{\varepsilon}_{kk}\delta_{ij}/3$. m_0 is the rate-sensitivity exponent and σ_{flow} is the flow stress which will be addressed in the coming subsections for coarse grain and nano/ultrafine grains respectively. Eqs. (2)-(4) then establish the triaxial constitutive relation for the constituents in bimodal metals.

In the coarse grains, the surface-to-volume ratio of the grain boundaries is low enough to neglect its contribution on the plastic deformation. The primate deformation mechanism is dominated by the intragrain dislocation-mediated interaction which can be described by the Taylor evolution law. Thus the flow stress of the coarse grain can be expressed as

$$\sigma_{flow} = \sigma_0 + M\alpha\mu b\sqrt{\rho} + \sigma_b \tag{5}$$

Here, α, μ and M are the empirical constant, the shear modulus and the Taylor factor, respectively. σ_0 is the lattice friction stress and σ_b represents the back stress . ρ denotes the density of dislocations in grains which can be determined by the Kocks-Mecking's model [40]. According to Kocks and Mecking's model, the density of dislocations in the crystal interior obeys the evolution law with plastic strain, which allows for competition between accumulation and annihilation by dynamic recovery [18].

For the flow stress in the nano/ultrafined grains phase, the isotropic strain hardening is involved in the flow stress that is in consistency with the one in coarse grains described by Kocks-Mecking model, while the back stress with respect to the kinematic strain hardening is excluded in the nano/ultrafine grains phase. Then, the flow stress of the matrix phase can be expressed by

$$\sigma_{flow} = \sigma_0 + M\alpha\mu b\sqrt{\rho_I + \rho_{GB}} \tag{6}$$

in which the Taylor term in the flow stress is relevant to the dislocation densities in crystal interior and the GBDPZ. The density of dislocations in the GBDPZ can be expressed by

$$\rho_{GB} = \frac{n^{GB}\lambda^{GB}}{V_{Cell}} = k^{GB}\frac{\eta^{GB}}{b} \tag{7}$$

Here, $k^{GB} = 6d_{GBDPZ}/\phi^{GB}d_G$.

2.1. Impact of nano/microcracks

As the appearance of microcracks indicates, the number of dislocations stopped at the grain boundaries or around the cracks is increased. These dislocations pile up along the grain boundaries, impeding the movement of dislocations and ultimately resulting in back stress effects that must be taken into account during the plastic deformation in the nano/ultrafine-grained phase. Thus, the constitutive relation of the nano-grained phase will involve the back stress term in the flow stress expression. The flow stress in this phase is rewritten as

$$\sigma_{flow} = \sigma_0 + M\alpha\mu b\sqrt{\rho_I + \rho_{GB}} + \sigma_b^*, \tag{8}$$

where σ_b^* is the microcrack-induced back stress. The microcrack-matrix-effective-medium approach is utilized here to model the overall stress and strain in the nano/ultrafine-grained phase of the bimodal metals. The representative volume element (RVE) is often applied to account for the crack orientation statistics in the composite mechanics. The RVE boundary is subjected to tractions in equilibrium with a uniform overall stress of σ^∞ and the average strain in a solid with microcracks is consistent with regular and singular parts as

$$\overline{\boldsymbol{\varepsilon}} = \overline{\boldsymbol{\varepsilon}}^{\mathbf{m}} + \overline{\boldsymbol{\varepsilon}}^{\mathbf{c}}, \tag{9}$$

where $\overline{\boldsymbol{\varepsilon}}^{\mathbf{m}}$ and $\overline{\boldsymbol{\varepsilon}}^{\mathbf{c}}$ denote the matrix strain averaged over the RVE and the microcrack-induced variations in the overall average strain, respectively. If the matrix satisfies to be linear elastic, the matrix strain can be written as $\overline{\boldsymbol{\varepsilon}}^{\mathbf{m}} = \mathbf{M}^{\mathbf{m}} : \boldsymbol{\sigma}^\infty$. Because the microcracks generated during the plastic deformation of the bimodal metals are supposed to be parallel, the corresponding effective moduli are as follows:

$$E_1 = E_0[1 + \frac{16(1-v_0^2)}{3}\rho]^{-1}; G_{12} = G_0[1 + \frac{8(1+v_0)}{3(1-v_0/2)}\rho]^{-1}. \tag{10}$$

Please note from Eq.(15) that the effective moduli of the bimodal metals are associated with the density of microcracks in the materials. Experiments have revealed that the number of microcracks in the bimodal metals increased during the plastic deformation, suggesting that the density of microcracks in the bimodal metals is sensitive to the applied stress or strain. From this perspective, the strain-based Weibull distribution function with respect to the plastic strain is adopted here to character the number of microcracks. Thus the density of microcracks can be expressed as following

$$\rho = \rho_0 P(f_W) = \rho_0(1 - f_W(\varepsilon_p)) \tag{11}$$

Here, ρ_0 is a constant; $f_W(\varepsilon_p) = \exp(-(\varepsilon_p/\varepsilon_0)^m)$ is the strain-based Weibull distribution function in which ε_0 is the reference strain and m is the Weibull modulus.

2.2. Composite model

The composite model derived from the modified mean-field approach involves the Hill's recognition of a weakening constraint power for plastic deformation [19]. However, the flow stress in the following derivation is substituted by those in the nano/ultrafine-grained phase and the coarse-grained phase, respectively, both of which will be derived in the next section. Thus, the secant Young's modulus and secant Poisson ratio of the *i*th phase can be expressed by

$$E^{S(i)}=\frac{E^{(i)}}{1+\frac{E^{(i)}\varepsilon^{(i)}}{\sigma_{flow}^{(i)}}(\frac{\sigma_{11}^{(i)}}{\sigma_{flow}^{(i)}})^{\mathrm{m}_0-1}},\nu^{S(i)}=\frac{1}{2}-(\frac{1}{2}-\nu^{(i)}\frac{E^{S(i)}}{E^{(i)}}) \quad , \tag{12}$$

Throughout this paper the matrix will be indicated as phase 0 and coarse grains as phase 1. $E^{(i)}$ and $\nu^{(i)}$ denote the Young's modulus and the Poisson's ratio of the *i*th phase, respectively. The corresponding secant bulk and shear moduli of the *i*th phase are taken to satisfy the isotropic relations as $k^{S(i)}=E^{S(i)}/[3(1-2\nu^{S(i)})],\mu^{S(i)}=E^{S(i)}/[2(1+\nu^{S(i)})]$, respectively. Suppose that the composite is subjected to a boundary-displacement with a uniform strain $\overline{\boldsymbol{\varepsilon}}$, the relationship between the hydrostatic and deviatoric strains of the constituent phases and those of the composite are as follows [19]:

$$\begin{aligned}
&\varepsilon_{kk}^{(0)}=\frac{\alpha_0^s(\kappa_1-\kappa_0)+\kappa_0}{c_0\alpha_0^s(\kappa_1-\kappa_0)+\kappa_0}\overline{\varepsilon}_{kk},\varepsilon_{ij}^{(0)\prime}=\frac{\beta_0^s(\mu_1-\mu_0^s)}{c_0\beta_0^s(\mu_1-\mu_0^s)+\mu_0^s}\overline{\varepsilon}_{ij}^{\prime}-\frac{c_1\beta_0^s\mu_1}{c_0\beta_0^s(\mu_1-\mu_0^s)+\mu_0^s}\varepsilon_{ij}^{p(1)}\\
&\varepsilon_{kk}^{(1)}=\frac{\kappa_0}{c_0\alpha_0^s(\kappa_1-\kappa_0)+\kappa_0}\overline{\varepsilon}_{kk},\varepsilon_{ij}^{(1)\prime}=\frac{\mu_0^s}{c_0\beta_0^s(\mu_1-\mu_0^s)+\mu_0^s}\overline{\varepsilon}_{ij}^{\prime}+\frac{c_0\beta_0^s\mu_1}{c_0\beta_0^s(\mu_1-\mu_0^s)+\mu_0^s}\varepsilon_{ij}^{p(1)}
\end{aligned}, \tag{13}$$

where the mean stress components of the matrix phase and inclusions are given by

$$\begin{aligned}
&\sigma_{kk}^{(1)}=3\kappa_0\frac{\kappa_1}{c_0\alpha_0^s(\kappa_1-\kappa_0)+\kappa_0}\overline{\varepsilon}_{kk},\sigma_{ij}^{(1)\prime}=\frac{2\mu_0^s\mu_1[\overline{\varepsilon}_{ij}^{\prime}-(1-c_0\beta_0^s)\varepsilon_{ij}^{p(1)}]}{c_0\beta_0^s(\mu_1-\mu_0^s)+\mu_0^s}\\
&\sigma_{kk}^{(0)}=3\kappa_0\frac{\alpha_0^s(\kappa_1-\kappa_0)+\kappa_0}{c_0\alpha_0^s(\kappa_1-\kappa_0)+\kappa_0}\overline{\varepsilon}_{kk},\sigma_{ij}^{(0)\prime}=\frac{2\mu_0^s\{[\beta_0^s(\mu_1-\mu_0^s)+\mu_0^s]\overline{\varepsilon}_{ij}^{\prime}-c_1\beta_0^s\mu_1\varepsilon_{ij}^{p(1)}\}}{c_0\beta_0^s(\mu_1-\mu_0^s)+\mu_0^s}
\end{aligned}. \tag{14}$$

Here, f_i is the volume fraction of the *i*th phase and α and β are the components of Eshelby's tensor for spherical inclusions, as follows:

$$S_0^s=(\alpha_0^s,\beta_0^s),with\ \alpha_0^s=\frac{1+\nu_0^s}{3(1-\nu_0^s)},\beta_0^s=\frac{2(4-5\nu_0^s)}{15(1-\nu_0^s)}. \tag{15}$$

Therefore, the dilatational and deviatoric stresses and strains of the composite are connected by

$$\begin{aligned}
&\overline{\sigma}_{kk}=3\kappa_0\left[1+\frac{c_1(\kappa_1-\kappa_0)}{c_0\alpha_0^s(\kappa_1-\kappa_0)+\kappa_0}\right]\overline{\varepsilon}_{kk},\\
&\overline{\sigma}_{ij}^{\prime}=2\mu_0^s\left\{\left[1+\frac{c_1(\mu_1-\mu_0^s)}{c_0\beta_0^s(\mu_1-\mu_0^s)+\mu_0^s}\right]\overline{\varepsilon}_{ij}^{\prime}-\frac{c_1\mu_1}{c_0\beta_0^s(\mu_1-\mu_0^s)+\mu_0^s}\varepsilon_{ij}^{p(1)}\right\}
\end{aligned}. \tag{16}$$

To get an accurate description of the grain size-dependent local interaction and behavior in each phase, the grain size statistical distribution is frequently used to characterize the grain size distribution. Here, the grain size distribution in each phase is supposed to follow a Rayleigh

distribution with one parameter, instead of the log-normal distribution, for simplicity [20].

3. Numerical results and discussion

We now apply the developed models to predict the mechanical and failure behaviors of bimodal coppers, and then make comparisons with experimental results of bimodal coppers [4]. In the proposed composite mixture model, the matrix phase and coarse grain phase have equal elastic properties. These and other material parameters used in calculation are adopted in Ref [21]. For the sake of predicting the stress-strain relation of bimodal copper, the constitutive behavior in the matrix phase and coarse grain phase must be captured firstly. With the aid of the proposed constitutive relations, the stress-strain curves of matrix phase with average grain size as 300nm and coarse grain phase with mean grain size as 2μm are given in Fig.2a and Fig.2b respectively, by adopting the corresponding parameters. The corresponding experimental results are also plotted in Fig.2. Due to that the strain gradient is involved in the ultrafine or nanograins phase to describe the contribution of grain boundaries on the deformation mechanism, a reasonable value of strain gradient is provided to fit the experimental data. Note that the prediction can be in good accord with the measurements shown as in Fig.2a. For the coarse grain phase, the isotropic and kinetic strain hardening are both taken into account in the proposed constitutive relation and the calculated results can be agreeable very well with the experimental results (Seen in Fig.2b). After indentifying the constitutive relation in matrix phase and coarse grain phase, we then can simulate the stress-strain response in the framework of the proposed composite model involving the contributions of the microcracks. Fig.3 plots the predicted results based on the proposed model and the experimental data for bimodal copper are also reproduced in the figure. Here, the initial crack density ρ_0 is given as 0.04 and the Weibull modulus m as 10. It can be clearly noticed that the proposed model can capture very well the mechanical behavior in bimodal copper, the agreement between the simulations and the experiments is quite good not only in the yield stress but also in the strain hardening and the elongation at the ultimate strength.

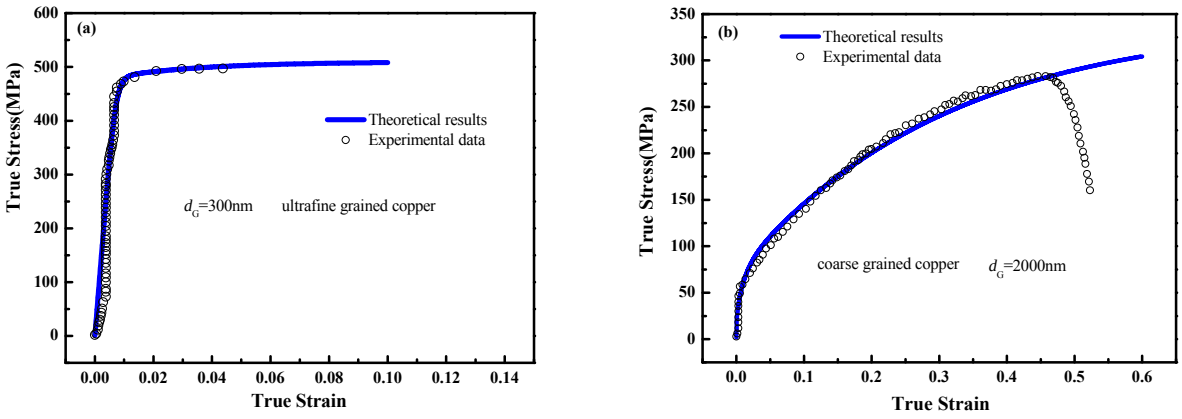

Fig. 2 Comparison of the stress-strain relationship between the experiments and theoretical results of coppers for the ultrafine/nanograins and the coarse grains

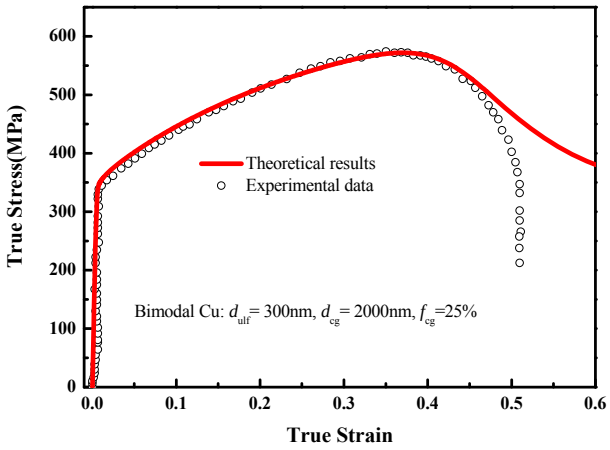

Fig. 3 Comparison of the stress-strain relationship between theoretical results and experiments for the bimodal Cu[8]

Owing to that the matrix grain dominates the high strength of the bimodal coppers and the inhomogeneous microstructures induces various mechanisms of strain hardening, we then further examined the dependence of the volume fraction of coarse grains on the mechanical response in bimodal copper. we plot the strength vs. uniform elongation with dependence of the volume fraction of coarse grains for the Weibull modulus as 3, 6 and 12 in Fig.4. It is worth to note from the figure that the strengths, including yield strength and ultimate strength, is weakened while the ductility is improved with the increment of the volume fraction of coarse grains. For the various Weibull modulus, the ductility increases with the increment of the Weibull modulus, and the slope of the curves for three different Weibull modulus are quite different with each other. It is also interesting to find from Fig.8 that the yield strength is independent on the Weibull modulus while the ultimate strength becomes smaller with decreasing the Weibull modulus.

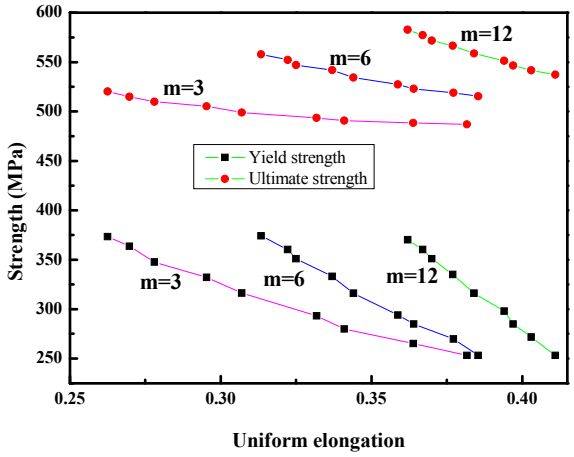

Fig. 4 Relationship between the strength and uniform elongation with different Weibull modulus for bimodal copper (d_{ulf}= 300nm, d_{cg}= 2000nm)

We further plot the curves of failure probability varied with the failure strain from the strain-based Weibull distribution function for the nanograined copper, coarse grained copper as well as bimodal coppers in Fig.5a. Inspired by the experimental observations, the characteristic strain ε_0 is adopted approximately as the measured uniform elongation. The Weibull modulus for the coarse grains and nano grains are determined by fitting the experimental results and the ones for bimodal cases are obtained by comparing with experiments. It can be found from the figure that the curves of bimodal cases are all located in the region surrounded by the curves of nanograins and coarse grains. The curves of bimodal copper with volume fraction of coarse grain as 45% and 83% in Li's measurements [9] are close to the one of the nano grains. It means that the failure properties of these two cases perform in an obvious brittleness comparable with nanocrystalline metals. The curve of the bimodal copper achieved by Wang et al [4], however, approaches the one of the coarse grains as well as the one with coarse grain fractions as 98% [9]. Under the same reference strain, the variability of the failure strain with a large Weibull modulus is less than the one with a small Weibull modulus, as shown in Fig. 9b. It means that, suppose the reference strain in the bimodal metal of $f_c = 0.45$ to be 30%, the limited measurements of corresponding case in Ref.[9] can be included in the reasonable failure probability which is determined by the sufficient data of measured samples.

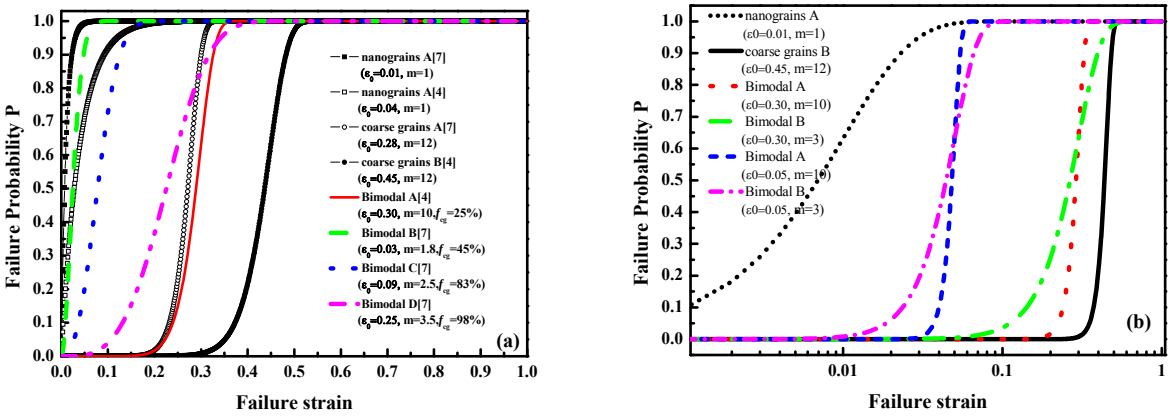

Fig. 5 The failure probability varied with failure strain with different Weibull modulus and a given volume fraction of coarse grain in bimodal copper.

4. Conclusion

In this paper, a micromechanics-based model, which has been developed in the previous authors' work, is introduced to investigate the mechanical behaviors of polycrystalline coppers with bimodal grain size distribution, accounting for the microcracks generated during plastic deformation.. Because of the appearance of the microcracks in the bimodal metals, the local mechanical properties are modified completely. After indentifying the related parameters in the developed model, the stress-strain response of the bimodal copper are predicted to make a comparison with the corresponding experimental results. The present numerical results reveal that the proposed micromechanical model can be utilized to describe the mechanical behavior of bimodal metals completely and successfully and to be expected to predict the mechanical properties such as the

yield stress and ductility. The predictions based on the proposed model are agreeable very well with the experimental data of bimodal copper. The results with respect to the Weibull modulus of microcrack density suggest that the bimodal metals will have good ductility with higher Weibull modulus which can be considered to be associated with the microstructures in the materials. The results in this paper will shed some lights on optimizing the distribution of microstructures and the grain size in polycrystalline materials to promise the achievement of higher strength and higher ductility in polycrstal metals or alloys.

Acknowledgements

The authors gratefully acknowledge the support received from Zhejiang Provincial Qianjiang Talent Program (Grant No. QJD1202012), the Grant of Educational Commission of Zhejiang Province of China (Grant No. Y201223476), the National Key Basic Research Program (Grant No. 2012CB932203), and the Research Grants Council of the Hong Kong Special Administrative Region of China under grants CityU8/CRF/08 and GRF/CityU519110, the Croucher Fundation CityU9500006.

References

[1] C.C. Koch, D.G. Morris, K. Lu, A Inoue, Ductility of nanostructured materials. Mater Res Soc Bull 24 (1999), 54-58.

[2] L. Lu, Y.F. Shen, X.H. Chen, L.H. Qian, K. Lu, Ultrahigh Strength and High Electrical Conductivity in Copper. Science, 304 (2004) 422-426.

[3] L. Lu, X. Chen, X. Huang, K. Lu, Revealing the Maximum Strength in Nanotwinned Copper. Science, 323(2009) 607-610.

[4] Y.M. Wang, M.W. Chen, F.H. Zhou, E. Ma, Extraordinarily high tensile ductility in a nanostructured metal. Nature, 419 (2002) 912-915.

[5] YH Zhao, T Topping, JF Bingert, et al., High Tensile Ductility and Strength in Bulk Nanostructured Nickel. Adv Mater, 20 (2008) 3028-3033.

[6] V.L. Tellkamp, A. Melmed, E.J. Lavernia, Mechanical behavior and microstructure of a thermally stable bulk nanostructured Al alloy. Metall Mater Trans A 32 (2001) 2335-2343.

[7] G. He, J. Eckert, W. Löser, L. Schultz, Novel Ti-base nanostructure-dendrite composite with enhanced plasticity. Nature Mat, 2 (2003) 33-37.

[8] B.Q. Han, J.Y. Huang, Y.T. Zhu, E.J. Lavernia, Strain rate dependence of properties of cryomilled bimodal 5083 Al alloys. Acta Mater 54 (2006) 3015-3024.

[9] Y.S. Li, Y. Zhang, N.R. Tao, K. Lu, Effect of thermal annealing on mechanical properties of a nanostructured copper prepared by means of dynamic plastic deformation. Scripta Mater 59 (2008) 475-478.

[10] G.J. Fan, H. Choo, P.K. Liaw, E.J. Lavernia, Plastic deformation and fracture of ultrafine-grained Al–Mg alloys with a bimodal grain size distribution. Acta Mater 54 (2006) 1759-1766.

[11] J. Das, A. Güth, H.J. Klau, et al., Effect of casting conditions on microstructure and mechanical properties of high-strength Zr73.5Nb9Cu7Ni1Al9.5 in-situ composites. Scripta Mater 49 (2003) 1189- 1195.

[12] B.Q. Han, Z. Lee, D. Witkin, et al., Deformation behavior of bimodal nanostructured 5083 Al

alloys. Metall Mater Trans A 36 (2005) 957-965.

[13] Z.H. Lee, V. Radmilovic, B. Ahn, et al., Tensile deformation and fracture mechanism of bulk bimodal ultrafine-grained Al-Mg alloy. Metall Mater Trans A 41 (2010) 795-801.

[14] R.Q. Ye, B.Q. Han, E.J. Lavernia, Simulation of deformation and failure process in bimodal Al alloys. Metall Mater Trans A 36 (2005) 1833-1840.

[15] S.P. Joshi, K.T. Ramesh, B.Q. Han, E.J. Lavernia, Modeling the constitutive response of bimodal metals. Metall Mater Trans A 37 (2006) 2397-2404.

[16] L. L. Zhu and J. Lu, Modeling the plastic deformation of nanostructured metals with bimodal grain size distribution. Int J Plasticity 30-31 (2012) 166-184.

[17] Y. Huang, S. Qu, K.C. Hwang, M. Li, H. Gao, A conventional theory of mechanism-based strain gradient plasticity. Int J Plasticity 20 (2004) 753-782.

[18] L. Capolungo, C. Jochum, M. Cherkaoui, J. Qu, Homogenization method for strength and inelastic behavior of nanocrystalline materials. Int J Plasticity 21 (2005) 67-82.

[19] G.J. Weng, The overall elastoplastic stress-strain relation of dual-phase metals. J Mech Phys Solid 38 (1990) 419-441.

[20] Y.J. Wei, L Anand, A constitutive model for powder-processed nanocrystalline metals. Acta Mater 55 (2007) 921-931.

[21] H.S. Kim, Y. Estrin, M.B. Bush, Plastic deformation behaviour of fine-grained materials. Acta Mater 48 (2000) 493-504.

Combined Self-Consistent and Mori-Tanaka Approach for Evaluation of Elastoplastic Property of Particulate Composites

Xianghe Peng[1,*], Ning Hu[1,2], Xuesong Long[1], Hengwei Zheng[1]

[1] Department of Engineering Mechanics, Chongqing University, Chongqing, 400044, China
[2] Department of Mechanical Engineering, Chiba University, 1-33 Yayoi, Inage-ku, Chiba, 263-8522, Japan
* Corresponding author: xhpeng@cqu.edu.cn

Abstract Suppose the particles in with volume fraction c in an RVE of a particulate composite are separated into two groups, with volume fractions $(1-\lambda^{-1})c$ and c/λ over the RVE, respectively, a combined self-consistent and Mori-Tanaka approach is proposed for the evaluation of the effective elastoplastic property of particulate composites. The particles in Group I and the original matrix form a fictitious matrix, and its mechanical property is determined with the self-consistent scheme. The RVE of the composite consists of the fictitious matrix and Group of particles, and its mechanical property is determined with the Mori-Tanaka scheme. The conventional Mori-Tanaka scheme and self-consistent scheme can be obtained as the two limit cases as λ =1 and λ =∞, respectively. The constitutive behavior of the particles in Group I is identical with that in Group II. The effective elastoplastic behavior of some typical particulate composites is evaluated, and the comparison with the experimental results demonstrates the validity of the proposed approach. The induced λ can serve as a parameter related to the actual property of composites and identified by experiment, for a more accurate evaluation of the effective elastoplastic property of particulate composites.

Keywords Particulate composite, Elastoplasticity, Effective property, Mean-field approach

1. Introduction

The overall property of a composite is governed by the properties of their constituents and the microstructures. In order to achieve the desired property of a composite, an appropriate approach for the evaluation of the overall property of the composites is essential. Many micromechanics approaches have been developed [1-8] and extensively used to evaluate the effective properties of composites. The homogenization approaches have also been developed for the evaluation of the elastoplastic or elastoviscoplastic properties of composites [9-11].

It has been shown that there might be a big gap between the effective properties of a composite obtained respectively with the conventional Mori-Tanaka scheme and the conventional self-consistent scheme [12]. Since both schemes are extensively used in the evaluation of the effective property of composites, a question one may ask is whether one can evaluate more accurately the effective property of a composite with the combination of these two schemes. A combined self-consistent and Mori-Tanaka approach was proposed by Peng et al [13] for the evaluation of the effective elastic property of particulate composites. It was shown that the conventional Mori-Tanaka scheme and self-consistent scheme can be obtained as the two limit cases of the approach. The effective elastic properties of some typical particulate composites were evaluated and compared with experimental results, and the satisfactory agreement between the computed and the experimental results demonstrates the validity of the proposed approach.

In this article, the combined self-consistent and Mori-Tanaka approach [13] is extended to the evaluation of elastoplastic properties of particulate composites. The effective elastoplastic responses of some typical particulate composites are analyzed and compared with experimental results.

2. Extension of Combined Self-consistent and Mori-Tanaka Approach

An RVE of a particulate composite consists of the matrix of mechanical property $\mathbf{L}^m$ and particles of mechanical property $\mathbf{L}^c$ with total volume fraction c. The particles are separated into two groups by introducing a parameter λ ($\lambda \geq 1$): Group I contains particles with total volume fraction $(1-\lambda^{-1})c$ over the RVE, and Group II contains particles with total volume fraction c/λ over the RVE. The effective elastoplastic property of the composite can be determined by two steps: in the first step, the particles in Group I are embedded in the original matrix to form the fictitious matrix (with equivalent particle volume fraction $\hat{c}$), and the elastoplastic property of the fictitious matrix, $\hat{\mathbf{L}}^m$, is determined with the self-consistent scheme; and in the second step, the particles in Group II are further distributed randomly in the fictitious matrix to form the RVE, and the effective elastoplastic property of the composite, $\bar{\mathbf{L}}$, is determined with the Mori-Tanaka scheme, the particle inclusions in Group II should be necessarily sufficient to meet the requirement of the application of the Mori-Tanaka scheme.

Suppose the volume of the RVE is V, the volume of the original matrix is $V_m = (1-c)V$ and the volume of the particle inclusions in Group I is $(1-\lambda^{-1})cV$, the volume of the fictitious matrix is $\hat{V}_m = V_m + (1-\frac{1}{\lambda})cV = (1-\frac{c}{\lambda})V$, and the equivalent volume fraction of the particles in the fictitious matrix is

$$\hat{c} = (1-\frac{1}{\lambda})cV \Big/ \left[(1-\frac{1}{\lambda})cV + (1-c)V\right] = \frac{\lambda-1}{\lambda-c}c\,. \tag{1}$$

In the first step, making use of the Hill's self-consistent scheme, the elastoplastic tensor of the fictitious matrix can be determined as follows by averaging the stress rate field over $\hat{V}_m$, i.e.,

$$\hat{\mathbf{L}}^m = (1-\hat{c})\mathbf{L}^m \cdot \mathbf{A}^m + \hat{c}\mathbf{L}^c \cdot \mathbf{A}^c\,, \tag{2}$$

where
$$\mathbf{A}^c = [\mathbf{L}^* + \mathbf{L}^c]^{-1} : [\mathbf{L}^* + \hat{\mathbf{L}}^m], \qquad \mathbf{A}^m = [\mathbf{L}^* + \mathbf{L}^m]^{-1} : [\mathbf{L}^* + \hat{\mathbf{L}}^m], \tag{3}$$

and
$$\mathbf{L}^* = \hat{\mathbf{L}}^m : \left(\mathbf{S}^{-1} - \mathbf{I}_4\right). \tag{4}$$

$\hat{\mathbf{L}}^m$ relates the stress rate $\dot{\hat{\boldsymbol{\sigma}}}^m$ and the strain rate $\dot{\hat{\boldsymbol{\varepsilon}}}^m$ of the fictitious matrix by

$$\dot{\hat{\boldsymbol{\sigma}}}^m = \hat{\mathbf{L}}^m : \dot{\hat{\boldsymbol{\varepsilon}}}^m\,, \tag{5}$$

and the stress rate and the strain rate in the original matrix and the particles are determined with

$$\begin{aligned} \dot{\boldsymbol{\varepsilon}}^c &= \mathbf{A}^c : \dot{\hat{\boldsymbol{\varepsilon}}}^m, & \dot{\boldsymbol{\sigma}}^c &= \mathbf{L}^c : \dot{\boldsymbol{\varepsilon}}^c, \\ \dot{\boldsymbol{\varepsilon}}^m &= \mathbf{A}^m : \dot{\hat{\boldsymbol{\varepsilon}}}^m, & \dot{\boldsymbol{\sigma}}^m &= \mathbf{L}^m : \dot{\boldsymbol{\varepsilon}}^m.\end{aligned}\,' \tag{6}$$

In the second step, making use of the Mori-Tanaka scheme and keeping in mind that the RVE of the material is composed of the fictitious matrix and the particle inclusions in Group II (with total volume fraction c/λ) and the domain for averaging strain (or stress) is $\hat{V}^m + \frac{c}{\lambda}V = V$, the

corresponding expression can easily be obtained as

$$\dot{\boldsymbol{\varepsilon}}^c = \tilde{\mathbf{A}}^c : \hat{\dot{\boldsymbol{\varepsilon}}}^m, \qquad \dot{\boldsymbol{\sigma}}^c = \mathbf{L}^c : \dot{\boldsymbol{\varepsilon}}^c, \tag{7}$$

where $$\tilde{\mathbf{A}}^c = [\tilde{\mathbf{L}}^* + \mathbf{L}^c]^{-1} : [\tilde{\mathbf{L}}^* + \hat{\mathbf{L}}^m], \quad \text{with} \quad \tilde{\mathbf{L}}^* = \hat{\mathbf{L}}^m : (\mathbf{S}^{-1} - \mathbf{I}_4), \tag{8}$$

$$\bar{\mathbf{L}} = \hat{\mathbf{L}}^m + \frac{c}{\lambda}\left(\mathbf{L}^c - \hat{\mathbf{L}}^m\right) : \tilde{\mathbf{A}}^c : \left[\left(1 - \frac{c}{\lambda}\right)\mathbf{I} + \frac{c}{\lambda}\tilde{\mathbf{A}}^c\right]^{-1}, \tag{9}$$

$$\bar{\dot{\boldsymbol{\sigma}}} = \bar{\mathbf{L}} : \bar{\dot{\boldsymbol{\varepsilon}}}, \tag{10}$$

$$\hat{\dot{\boldsymbol{\varepsilon}}}^m = \left[\left(1 - \frac{c}{\lambda}\right)\mathbf{I} + \frac{c}{\lambda}\tilde{\mathbf{A}}^c\right]^{-1} : \bar{\dot{\boldsymbol{\varepsilon}}}. \tag{11}$$

It can be seen easily by comparing Eq. (8) with Eqs. (3) and (4) that $\tilde{\mathbf{L}}^* = \mathbf{L}^*$ so that $\tilde{\mathbf{A}}^c = \mathbf{A}^c$, indicating that the response of the particles in Group I given by Eq. (6) is identical with that of the particles in Group II given by Eq. (7). This fact, on one hand, implies the consistency of the constitutive behavior of the two parts of the particles in the extended approach, and on the other hand, brings convenience to the corresponding analysis.

Eqs. (9) and (11) can be reduced to the results of the conventional Mori-Tanaka scheme if λ =1 (noticing that if λ=1, there would be no particles in the fictitious matrix), $\hat{\mathbf{L}}^m = \mathbf{L}^m$. If λ is sufficiently large so that $c/\lambda \to 0$ (implying that there would be no particles in Group II), one obtains $\bar{\mathbf{L}} = \hat{\mathbf{L}}^m$ (Eq. (9)), $\hat{\dot{\boldsymbol{\varepsilon}}}^m = \bar{\dot{\boldsymbol{\varepsilon}}}$ (Eq. (11)), so that $\hat{\dot{\boldsymbol{\sigma}}}^m = \bar{\dot{\boldsymbol{\sigma}}}$ (Eqs. (10) and (5), noticing that $\bar{\dot{\boldsymbol{\sigma}}} = \dot{\boldsymbol{\sigma}}^0$ in the Mori-Tanaka scheme), the extended approach is reduced to the conventional self-consistent scheme.

Thus, it is known that the conventional Mori-Tanaka scheme and the conventional self-consistent scheme can be obtained as the two limit cases of the proposed approach as λ=1 and λ=∞, and the variation of λ may provide the evaluation of the elastoplastic property varying between the result given by the Mori-Tanaka scheme and that given by the self-consistent scheme. In practical application, the introduced λ may serve reasonably as an adjustable parameter that can be associated with the actual properties of composites and determined by experiment. This is important because the mechanical properties of composites are affected by many factors such as compositions, microstructures, internal constraints, etc., and the fabrication of composites may inevitably involve various unexpected factors that also strongly affect the overall property of the composites. The effects of these factors could be comprehensively considered with λ.

3. Constitutive Model and Numerical Algorithm

3.1. Elastoplastic constitutive equation

Assuming both constituents of a composite are initially isotropic and plastically incompressible, in the case of isothermal and small deformation, the following incremental form of the elastoplastic relationship can be obtained [14]

$$\Delta\mathbf{s}(z) = A\Delta\mathbf{e}^p + \mathbf{B}(z_n)\Delta z \tag{12}$$

where **s** and $\mathbf{e}^p$ are deviatoric stress and plastic strain, respectively,

$$A = \sum_{r=1}^{3} k_r C_r \qquad \mathbf{B}(z_n) = -\sum_{r=1}^{3} k_r \alpha_r \mathbf{s}^{(r)}(z_n), \tag{13}$$

$$\Delta\mathbf{s}^{(r)}(z) = k_r(C_r\Delta\mathbf{e}^p - \alpha_r\mathbf{s}^{(r)}(z_n))\Delta z, \quad k_r = \frac{1-e^{-\alpha_r\Delta z}}{\alpha_r\Delta z}, \qquad z = z_n + \Delta z, \tag{14}$$

z is generalized time that is non-negative and increases monotonically during any plastic deformation in terms of the following definition

$$\Delta z = \frac{\Delta\zeta}{f(z)}, \qquad \Delta\zeta^2 = \Delta\mathbf{e}^p : \Delta\mathbf{e}^p, \tag{15}$$

$f(z)$ is a hardening function, C_r and α_r (r =1,2,3) are material constants. The deviatoric elastic relation is

$$\Delta\mathbf{e} - \Delta\mathbf{e}^p = \frac{\Delta\mathbf{s}}{2G} \tag{16}$$

where **e** is deviatoric strain tensor and G is shear modulus. The volumetric constitutive relation can be expressed as

$$tr(\boldsymbol{\sigma}) = 3Ktr(\boldsymbol{\varepsilon}) \qquad \text{or} \qquad tr(\Delta\boldsymbol{\sigma}) = 3Ktr(\Delta\boldsymbol{\varepsilon}), \tag{17}$$

where $\boldsymbol{\sigma}$ and $\boldsymbol{\varepsilon}$ are stress and strain tensors, respectively, and K is bulk modulus. Rewriting Eq. (15) as

$$\Delta z = \frac{\Delta\mathbf{e}^p}{f^2\Delta z} : \Delta\mathbf{e}^p \tag{18}$$

and making use of the following relationships

$$\Delta\mathbf{s} = \Delta\boldsymbol{\sigma} - \frac{1}{3}tr(\Delta\boldsymbol{\sigma})\mathbf{I}_2 \qquad \Delta\mathbf{e} = \Delta\boldsymbol{\varepsilon} - \frac{1}{3}tr(\Delta\boldsymbol{\varepsilon})\mathbf{I}_2, \tag{19}$$

where $\mathbf{I}_2$ is the identity tensor of rank two, the incremental constitutive equation can be derived from Eqs. (12), (16) and (17) as [14]

$$\Delta\boldsymbol{\sigma} = \mathbf{L} : \Delta\boldsymbol{\varepsilon}, \tag{20}$$

where

$$\mathbf{L} = 2G_p\mathbf{I}_4 + \left\{K - \frac{2}{3}G_p\right\}\mathbf{I}_2 \otimes \mathbf{I}_2 + \frac{(2G)^2}{(2G+A)^2 f^2(z)}\frac{1}{a}\mathbf{B}\otimes\frac{\Delta\mathbf{e}^p}{\Delta z}, \tag{21}$$

with $$G_p = \frac{GA}{2G + A}, \qquad a = 1 + \frac{\mathbf{B} : \Delta\mathbf{e}^p}{(A + 2G) f^2 \Delta z}. \tag{22}$$

If the particles are assumed linearly elastic, the constitutive relationship of the particles can easily be obtained as follows by ignoring the terms related to plastic deformation and noticing that for elastic material, A is sufficiently large and G_p tends to G (Eqs. (22) and (21))

$$\mathbf{L} = 2G\mathbf{I}_4 + \left\{K - \frac{2}{3}G\right\}\mathbf{I}_2 \otimes \mathbf{I}_2. \tag{23}$$

Eq. (20) can be specified as follows for the matrix and the particles in a particulate composite

$$\Delta\boldsymbol{\sigma}^m = \mathbf{L}^m : \Delta\boldsymbol{\varepsilon}^m \qquad \text{and} \qquad \Delta\boldsymbol{\sigma}^c = \mathbf{L}^c : \Delta\boldsymbol{\varepsilon}^c \tag{24}$$

3.2. Numerical Algorithm

For simplicity, we assume in the analysis that the particles are of spheres with identical size, if we further ignore the minor difference between the result obtained with anisotropic Eshelby tensor and that obtained with isotropic Eshelby tensor provided the plastic deformation is moderate [15], both the original matrix and the fictitious matrix can be approximated as overall isotropic, then the following Eshelby tensor for isotropic media is adopted in the analysis [10],

$$\mathbf{S} = a\,\mathbf{I}_2 \otimes \mathbf{I}_2 + b[\mathbf{I}_4 - \mathbf{I}_2 \otimes \mathbf{I}_2], \tag{25}$$

with $$b = \frac{2(4 - 5\nu)}{15(1 - \nu)}, \qquad a = 1 - b. \tag{26}$$

The analysis of the response of a composite material involves the constitutive behavior of the original matrix and that of the particles, which are determined with Eq. (6). For a stress-controlled process, the numerical algorithm for the analysis of the elastoplastic response of a two-constituent composite is stated as follows: For the prescribed particle volume fraction c and the parameter λ, $\hat{c}$ can be calculated with Eq. (1), and with the results obtained in the k-th iteration of the l-th increment of loading, such as $(\Delta\bar{\boldsymbol{\varepsilon}})_{(l)}^{(k)}$ and of the composite, $(\hat{\mathbf{L}}^m)_{(l)}^{(k)}$ of the fictitious matrix, $(\Delta\boldsymbol{\varepsilon}^m)_{(l)}^{(k)}$, $(\Delta\boldsymbol{\sigma}^m)_{(l)}^{(k)}$ and $(\mathbf{L}^m)_{(l)}^{(k)}$ of the matrix, and $(\Delta\boldsymbol{\varepsilon}^c)_{(l)}^{(k)}$, $(\Delta\boldsymbol{\sigma}^c)_{(l)}^{(k)}$ and $(\mathbf{L}^c)_{(l)}^{(k)}$ of the particles, in the following (k+1)th iteration, $(\mathbf{L}^*)_{(l)}^{(k+1)}$, $(\mathbf{A}^c)_{(l)}^{(k+1)}$ and $(\mathbf{A}^m)_{(l)}^{(k+1)}$ can be calculated with Eqs. (4) and (3) respectively, and then, keeping in mind $\tilde{\mathbf{A}}^c = \mathbf{A}^c$, $\bar{\mathbf{L}}_{(l)}^{(k+1)}$ of the composite can be immediately obtained with Eq. (9). Given the l-th increment of stress $(\Delta\boldsymbol{\sigma}^0)_{(l)}$, $(\Delta\bar{\boldsymbol{\varepsilon}})_{(l)}^{(k+1)}$ can be solved from Eq. (10), and $(\Delta\hat{\boldsymbol{\varepsilon}}^m)_{(l)}^{(k+1)}$ with Eq.(11), then $(\Delta\boldsymbol{\varepsilon}^m)_{(l)}^{(k+1)}$, $(\Delta\boldsymbol{\sigma}^m)_{(l)}^{(k+1)}$, $(\Delta\boldsymbol{\varepsilon}^c)_{(l)}^{(k+1)}$ and $(\Delta\boldsymbol{\sigma}^c)_{(l)}^{(k+1)}$ can be obtained with Eq. (6), the mechanical property of the matrix $(\mathbf{L}^m)_{(l)}^{(k+1)}$ and that of particles $(\mathbf{L}^c)_{(l)}^{(k+1)}$ can be updated with Eqs. (21) and (23), respectively, than the mechanical property of the fictitious matrix, $(\hat{\mathbf{L}}^m)_{(l)}^{(k+1)}$, can be calculated with Eq. (2). The iterative process continues until the following inequality is satisfied,

$$\delta = \frac{\left\| \Delta \bar{\boldsymbol{\varepsilon}}_{(l)}^{(k+1)} - \Delta \bar{\boldsymbol{\varepsilon}}_{(l)}^{(k)} \right\|}{\left\| \Delta \bar{\boldsymbol{\varepsilon}}_{(l)}^{(k+1)} \right\|} \le \delta_0 , \tag{27}$$

where δ_0 is the tolerant error and δ_0=0.0001 is used in computation. After superimposing the derived increments on the corresponding quantities up to that after the (l-1)th increment of loading, one obtains $(\boldsymbol{\sigma}^0)_{(l)}$ and $(\bar{\boldsymbol{\varepsilon}})_{(l)}$ of the composite, and then starts the computation for the next increment of loading.

3. Numerical Examples and Verification

The elastoplastic behavior of some typical particulate composite materials subjected to tensile/compressive loading is computed and compared with experimental results.

The material constants involved in the proposed approach includes elastic/elastoplastic material constants of each constituent and λ. For the composites consisting of purely elastic particles and elastoplastic matrix, the elastic property of each constituent is usually provided by material suppliers or can be determined with conventional test; and the plastic constants of the matrix can be identified with simple test (e.g., tensile test) of pure matrix; λ can then be identified by fitting simple testing result (e.g., σ-ε curve) of the composite.

The variation of the tensile response of an Al/Al_2O_3 composite with respect to the volume fraction of Al_2O_3 particles is computed and shown in Fig. 1. The material constants adopted are given in Table 1, in which the Al matrix is assumed elastoplastic and the Al_2O_3 particles are purely elastic. The elastic constants are adopted from [16]. The plastic constants of the matrix are identified with the empirical relation $\sigma = 130 \times \left[1 + \left(\varepsilon^p \right)^{0.2} \right]$ [16], and the hardening function $f(z)$ (in Eq.(15)) takes the following form

$$f(z) = d - (d-1)e^{-\beta z} \tag{28}$$

where d and β are material constants. It can be seen in Fig. 1 that the σ - ε curve of the Al matrix (c=0) computed with the obtained material constants can reasonably replicate the empirical σ-ε curve. The ultimate strength of the composite, σ_u, increases with the increase of c.

Table 1 Material constants of Al/Al_2O_3

Constituent	E (GPa)	ν	C_1/α_1, C_2/α_2, C_3/α_3 (MPa)	$\alpha_1, \alpha_2, \alpha_3$	d, β
Al	69	0.345	112, 25, 17.5	2500, 800, 200	1.25, 16
Al_2O_3	400	0.25	----------	----------	---------

The effective σ - ε curves of c=0.34 corresponding to different λ is shown in Fig.2(a), where the σ-ε curve is hoisted with the increase of λ, but all the curves lie between the two bounds determined respectively by λ=1 and $\lambda \to \square$. There is a remarkable gap between the σ-ε curves evaluated respectively with λ=1 and $\lambda \to \square$. The variation of σ_u against λ for c=0.34 is shown in Fig. 2(b), where the results given by the conventional Mori-Tanaka scheme and the conventional self-consistent scheme are independent of λ and serve as the lower and the upper bounds, respectively. The results given by the combined self-consistent and Mori-Tanaka approach starts from that obtained with Mori-Tanaka scheme, increases with λ, and approaches the asymptotic

value determined with self-consistent scheme. It can be seen that the experimental result also lies in the region bounded by the curve with λ=1 and that with λ=∞. It can be found that the σ-ε curve with λ=8 can well fit the experimental result. All the curves in Fig. 1 are computed with λ=8, the obtained results fit well the empirical results at c=0 and experimental results at c=0.34, and the curves obtained at different c seems reasonable.

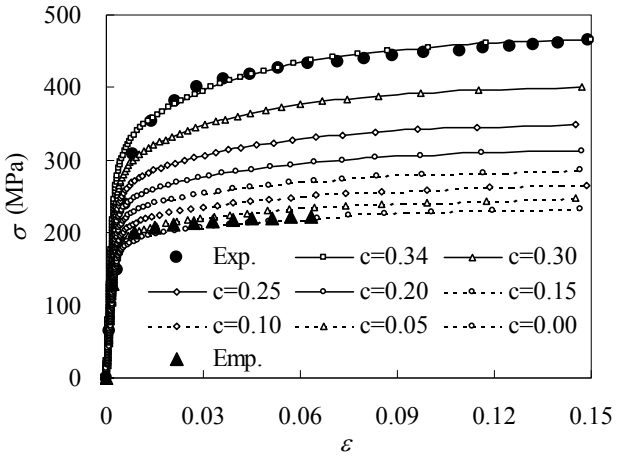

Fig. 1 Experimental and computational σ-ε curves of Al/Al_2O_3 composite

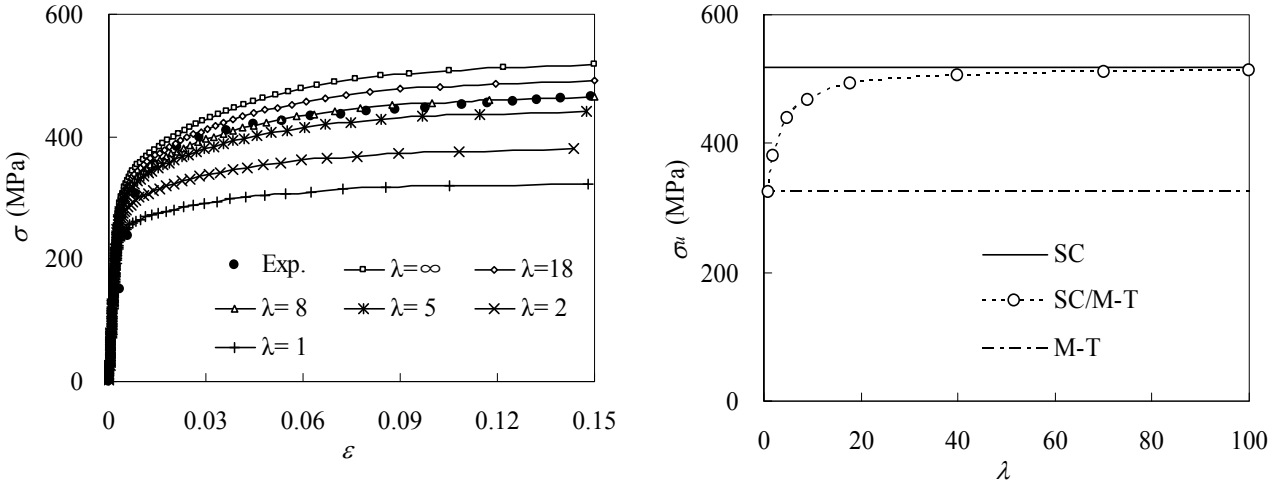

(a) Effective σ-ε curves of Al/Al_2O_3 composite using different λ (c=0.34)

(b) Variation of ultimate strength against λ (c=0.34)

Fig. 2 Effect of λ on σ-ε curves of Al/Al_2O_3 composite

It can be found in Fig. 2 that λ strongly affects the evaluated effective property of the composite. If λ changes between 1 and infinite, the evaluated effective property of the composite will change between the result determined by the Mori-Tanaka scheme and that by the self-consistent scheme, with the tendency definitely identical to that caused by the decrease of particle size, which was reported frequently and investigated extensively by many researchers [17-20]. It implies the possibility for the extended approach to describe implicitly and phenomenologically the size-effect of particulate composites. Suppose the volume of a RVE is fixed, given particle volume fraction c, the number of particle inclusions in the RVE, N, should reflect the size information of the particles. For instance, N should be a smaller value for larger particles, and vice versa. Suppose the particle volume fraction c is fixed in both Composite 1 and Composite 2, and the particles are of identical

spheres of diameter φ_1 in Composite 1 and diameter φ_2 in Composite 2, letting $N_1=\lambda_1 m$ for Composite 1 and $N_2=\lambda_2 m$ for Composite 2, where m is a constant related to the volume of RVE and the minimal number of particles required by the application of the Mori-Tanaka scheme, one can easily obtain the relation between λ_1 and λ_2 of the two composites as $\lambda_2=\left(\varphi_1/\varphi_2\right)^3\lambda_1$. It indicates that if λ_1 for the evaluation of the effective property of Composite 1 is fixed or fitted from experimental data, λ_2 for that of Composite 2 can be approximately estimated with the above relationship without necessity of being identified individually.

Fig. 3 shows the capability of the present approach in the description of the effective σ-ε relation of the composite consisting of Al356 (T4) matrix and 15% SiC particles. The material constants adopted are listed in Table 2, where it is assumed that the Al356 (T4) matrix is elastoplastic and the SiC particles are purely elastic. The elastic constants of the two constituents are the same as those used by Lloyd [17]. The plastic constants of the matrix are identified by fitting the empirical relation $\sigma=86+141.7\left(\varepsilon^p\right)^{0.365}$ given in [17]. It can be seen in Fig. 3 that the σ-ε curve of the matrix obtained by the extended approach (with c=0) agrees reasonably with that given by the empirical relation [17]. For c=0.15 and φ=16 μm, the effective σ-ε curve obtained with the extended approach using λ_{16} =1, corresponding to the result using the Mori-Tanaka scheme, can reasonably fit the experimental result. Experimental results show that, even if the volume fraction of particles keeps unchanged, the composite with smaller SiC particle inclusions (e.g., φ=7.5 μm) exhibits larger resistance against irreversible deformation. The effective σ-ε curve of the composites using $\lambda=\left(16/7.5\right)^3\lambda_{16}\approx 9.71$ is shown in Fig. 3 with solid line, which agrees reasonably with the experimental effective σ-ε curve. The effective σ-ε curve computed with the self-consistent scheme is also shown in Fig. 3 for comparison.

Table 2 Material constants of Alcoa X2080/SiC composite

Constituent	E (GPa)	v	C_1/α_1, C_2/α_2, C_3/α_3 (MPa)	$\alpha_1, \alpha_2, \alpha_3$	d, β
Al356 (T4)	70	0.33	72.14, 31.25, 18.0	7000, 800, 200	1.75, 30
SiC	490	0.17	----------	----------	--------

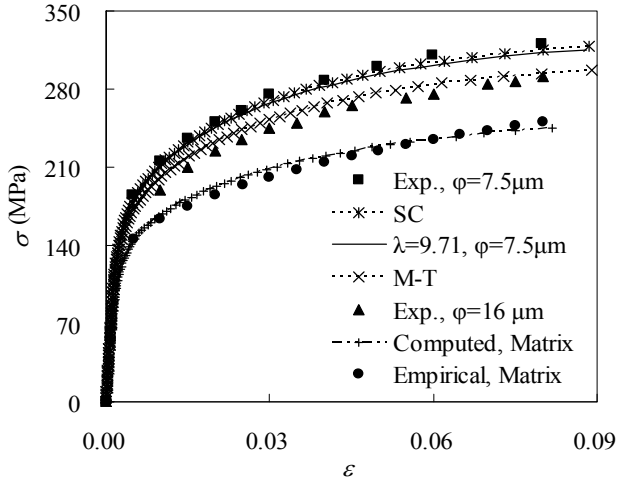

Fig. 3 Experimental and computational σ-ε curves of Al356/SiC composite

5. Conclusion and discussion

The combined self-consistent and Mori-Tanaka approach for the evaluation of the elastic

property of particulate composites [13] is extended to the evaluation of the elastoplastic property of particulate composites. Several examples are exhibited and compared with the experimental results. The following conclusion can be drown from the analysis:

(1) The comparison between the computed and the experimental results shows that the effective elastoplastic property of the composites can be satisfactorily evaluated with the extended approach by properly choosing the parameter λ, demonstrating the validity of the extended approach.

(2) The results given by the Mori-Tanaka scheme and the self-consistent scheme can be obtained as two bounds of that by the extended approach as the λ=1 and λ=∞, respectively, and the variation of λ between λ=1 and λ=∞ yields the results lying between the two bounds.

(3) The constitutive behavior of the particles outside of the introduced fictitious matrix is identical with that of the particles inside the fictitious matrix, indicating the consistency of the particle behavior in the combined approach.

(4) The introduced parameter λ can take into account comprehensively the effects of the factors such as microstructures (e.g., the size and shape of the inclusions), internal constraints (e.g., interfacial condition between different constituents), etc., as well as various unexpected factors during the fabrication of composites, which may strongly affect the overall property of the composites. In other words, λ can be associated with the actual property of composites and identified with experiment for a more accurate evaluation of the effective property of composites.

(5) The approach can describe implicitly the effect of particle size on the elastoplastic property of composites. With the help of the baseline experimental data of a composite with the particles of a specified size, the mechanical properties of composites with the same constituents but different size of particles could be estimated approximately with the proposed approach.

In this article we like to suggest a method parallel with the conventional mean-field schemes. In order to show more clearly the capability of the approach, we do not introduce other influencing factors, for example, higher-order gradients of deformation or isotropisation of tangent stiffness tensor, etc., to avoid blurring the advantages of the proposed approach.

It should be mentioned that, in the proposed approach with the increase of λ, the obtained effective elastoplastic response exhibits the tendency definitely identical with the size-effect phenomenon. Although it is known that “such effects cannot be included in the conventional inclusion-infinite matrix based Eshelby problem” [21], we are still interested in this capability. It can be accounted for with the difference between the assumptions used in the Mori-Tanaka scheme and in the self-consistent scheme. It is known that, although the Mori-Tanaka scheme involves the interaction between mediums, when any particle is added, the matrix is always considered as the original one without taking into account the existing reinforcement by other particles. Thus, in mathematics, the particles in an RVE can be assumed necessarily sufficient and randomly distributed, which implies relatively large size of the particle inclusions. However, in the conventional self-consistent scheme, the property of the matrix is assumed to be that after all the particle inclusions are added, which implies sufficiently large number of sufficiently small inclusions in the RVE. Since the proposed approach could adjust the property of the fictitious matrix (from that of the original matrix to that of the matrix with all particle inclusions being added) by adjusting λ, it should be able to describe the particle size effect to some extend. The introduced parameter λ can, on one hand, take into account averagely the enforcement in the fictitious matrix, and on the other hand, related to the ratio of the particle size to the reference particle size, which account for why it possesses the capability of

describing the relative “size-effect” of particulate composites.

Acknowledgements

The authors gratefully acknowledge the financial support to this work from NSFC under Grant Number 11272364.

References

[1] A. V. Hershey, The elasticity of an isotropic aggregate of anisotropic cubic crystals. J Appl Mech, 21(1954) 236–240.
[2] E. Kröner, Berechung der elastischen konstanten des vielkristalls aus den konstanten des einkristalls. Zeitschrift für Physik, 151(19584) 504–518.
[3] B. Budiansky, On the elastic moduli of some heterogeneous materials. J Mech Phys Solids, 13(1965) 223–227.
[4] R. Hill, A self-consistent mechanics of composite materials. J Mech Phys Solids, 13(1965) 213–222.
[5] T. Mori, K. Tanaka, Average stress in matrix and average elastic energy of materials with misfitting inclusions. Acta Metall, 21(1973) 571–574.
[6] S. Nemat-Nasser, M. Hori, Micromechanics: Overall properties of heterogeneous materials. Elsevier, North-Holland, 1993.
[7] R. M. Christensen, K. H. Lo, Solutions for effective shear properties in three phase space and cylinder model. J Mech Phys Solids, 27(1979) 315–330.
[8] Y. Huang, K. X. Hu, X. A. Wei, Chandra, A generalized self-consistent mechanics method for a composite with multi-phase inclusions. J Mech Phys Solids, 42(1994) 491–504.
[9] J. W. Hutchinson, Bounds and self-consistent estimates for creep of polycrystalline materials. Proc Royal Soc London. Series A, Math Phys Sci, 1976, 348(1652) 101–127.
[10] M. Berveiller, A. Zaoui, An extension of the self-consistent scheme to plastically flowing polycrystals. J Mech Phys Solids, 26(1979) 325–344.
[11] A. Molinari, G. R. Canova, S. Ahzi, A self consistent approach of the large deformation polycrystal viscoplasticity. Acta Metall, 35(1987) 2983–2994.
[12] R. M. Christensen, A critical evaluation for a class of micro-mechanical models. J Mech Phys Solids, 38(1990) 379–404.
[13] X. Peng, N. Hu, H. Zheng, H. Fukunaga, Evaluation of mechanical properties of particulate composites with a self-consistent and Mori-Tanaka approach. Mech Mat, 41(2009) 1288–1297.
[14] J. Fan, X. Peng, A physically based constitutive description for nonproportional cyclic plasticity. J Engng Mat Tech, 113(1991) 254-262.
[15] X. Peng X. Long, J. Fan, Micro-Macro Description for elastoplasticity of materials with lamellar microstructure using anisotropic Eshelby tensor, Mech Adv Mat Structs, 16(2009) 542-551.
[16] M. Kouzeli, D. C. Dunand, Effect of reinforcement connectivity on the elasto-plastic behavior of aluminum composites containing sub-micron alumina particles. Acta Mat, 51(2003) 6105–6121.
[17] D. J. Lloyd, Particle-reinforced aluminumand magnesiummatrix composite. Int Mat Rev, 39(1994) 1–23.
[18] K. Derrien, D. Baptiste, D. Guedra-Degeorges, J. Foulquier, Multiscale modeling of the damaged plastic behavior and failure of Al/SiCp composites, Int J Plasticity, 15(1999) 667-685.
[19] Y. Nakamura, M. Yamaguchi, M. Okubo, T. Matsumoto, Effects ofparticle size on mechanical and impact properties of epoxy resin filled with spherical silica. J Appl Polymer Sci, 45(1992) 1281–1289.
[20] P. Barai, G. J. Weng, The competition of grain size and porosity in the viscoplastic response of nanocrystalline solids. Int J Plasticity, 24(2008) 1380–1410.

[21] V. Marcadon, E. Herve, A. Zaoui, Micromechanical modeling of packing and size effects in particulate composites. Int J Solids Structs, 44(2007) 8213–8228.

Effect of Nanoparticle Modification on Composite Mode II Delamination

Ying Zeng[1,2*], Hong-Yuan Liu[1], Yiu-Wing Mai[1] , Xu-Sheng Du[1]

[1]Centre for Advanced Materials Technology (CAMT), The University of Sydney, 2006, Australia
[2]Structure Department, Shanghai Aircraft Design & Research Institute, 201221, China
* Corresponding author: zengying@comac.cn

Abstract The effect of nanoparticle modification on the interlaminar shear fracture behavior of carbon fibre/ epoxy laminates were studied by the End Notched Flexure (ENF) tests. The mode II fracture toughness was improved in the presence of these nanoparticles although nano-rubber was more effective compared to nano -silica. Examination of the fracture surfaces of composite laminates by scanning electron microscopy showed no debonding of nano-silica particles but some evidence of nano-rubber cavitation. Anti-Symmetric Four-Point Bending (ASFPB) tests of the nanoparticles modified epoxies was conducted and the results indicated that nano-silica was more effective in toughening bulk epoxy, but this high toughness could not be effectively transferred to mode II delamination in the composite laminates. Finite element analysis was performed to confirm the predominant Mode II stress state of the ASFPB test.

Keywords: Mode II delamination; carbon fibre composite; silica nanoparticles; rubber nanoparticles.

1. Introduction

Fiber laminates are widely used today for their outstanding strength-to-weight ratio. However, their interlaminar weakness is a major problem limiting their service applications. Hence, many past efforts have focused on increasing the interlaminar fracture resistance. Recently, nano-sized particles are found to improve the toughness of bulk epoxies [1-4] and this has stimulated many new research activities on the potential of incorporating these nanoparticles to increase the fracture toughness of composite laminates. Thus, previous studies on mode I double-cantilever-beam (DCB) delamination tests [5-6] showed that, with nanoparticle modification of the epoxy matrix, the mode I interlaminar fracture toughness of carbon fibre composites can be improved up to 150% and 27% by rubber and silica nanoparticles, respectively [6]. But in most practical situations, delamination often happens in a mixed mode I and mode II fracture. Hence, before studying the mixed mode problem, it is important to investigate whether the nanoparticles can also increase the mode II fracture resistance.

In this paper, we present recent findings on mode II toughness of carbon fibre/epoxy laminates and corresponding bulk epoxies, which are modified by different nanoparticles: (a) nano-silica and (b) nano-rubber. End Notched Flexure (ENF) tests [7] were conducted on these composite systems and their interlaminar toughness values, G_{IIC}, were evaluated. Corresponding bulk materials without carbon fibers were investigated by the Anti-Symmetric Four-Point Bending (ASFPB) test. Finite element analysis was applied to evaluate the stress state at the crack-tip based on the ASFPB experiments. Fracture surfaces of both ENF and ASFPB samples of different material systems were studied by Scanning Electron Microscopy (SEM) to examine their toughening mechanisms and possible interactions between fibers and nanoparticles. Comparison of mode I [6] and mode II toughness was made to quantitatively study the overall delamination resistance of the fiber laminates with different matrix formulations.

2 Experimental Method

2.1 Sample preparation

The processing of the composite laminates with different matrix systems (see Table 1) for mode II testing was identical to that used in our previous work on mode I delamination [6]. The composite laminates were fabricated from plain woven carbon fibres (168058ITL supplied by Inter-Turbine Advanced Logistics Pty Ltd, Australia) with a planar density of 203 g/m^2. The epoxy resin system included Araldite-F (diglycidyl ether of bisphenol A, DGEBA) and piperidine, both supplied by Sigma-Aldrich, where the piperidine was applied as a curing agent by the weight ratio of 100:5. Two types of nanoparticles were used: 40 wt% sol-gel nano-silica (Nanopox F400, Nanoresins AG, Germany) with ~20 nm SiO_2, and nano-rubber/bisphenol A (Kaneka Corporation, Japan) with 25 wt % of ~100 nm core-shell rubber in master batches.

Eighteen-ply laminates of ~270 mm^2 were prepared by the hand lay-up method. Precautions were taken to keep the fabrics well aligned and flat. A 0.2 mm thickness Kapton® polyimide film was inserted in the mid-plane of the laminates to act as the initial crack. The laminates were wrapped with bleeders and release film within a vacuum bag, and first vacuumed in a chamber for 20 min followed by curing in a hot-press at 120 ºC for 16 h. High curing temperature excursions for long durations were applied to ensure the resin was fully cured. A pressure of 250 kPa was applied during curing to maintain a uniform laminate thickness and a constant fiber volume fraction, which were 0.19 mm and 60±1%, respectively. 120x20 mm^2 ENF samples were finally cut from the square panels by a wet diamond saw.

The bulk materials prepared for ASFPB testing were the same as the matrices of the laminates. Material formulations were prepared by mixing plain DGEBA resin with required amounts of nano-silica or nano-rubber master batch. After adding the curing agent to the blend, the mixture was poured into a preheated mould for curing at 120 °C for 16 h identical to the laminates. A pre-crack was made under the requirements of the test on the middle of each specimen with a sharp blade.

Table 1 Matrix formulation of carbon fibre laminates

Material Code	Matrix Formulation by Weight Percentage (%)		
	Epoxy	Silica	Rubber
E* (control)	100	--	--
S6	94	6	--
S8	92	8	--
S10	90	10	--
S12	88	12	--
R6	94	--	6
R8	92	--	8
R10	90	--	10
R12	88	--	12

*E represents neat epoxy resin matrix.

2.2 Fracture toughness measurements

Three-point ENF tests

Standard 3-point ENF tests were performed in an Instron 5567 machine according to the Protocol for Interlaminar Fracture Testing No. 2 (1992) [7]. Fig. 1 shows the geometry and dimensions of the ENF sample. The initial crack length a is 25 mm and a/L = 0.5. The crack mouth opening displacement rate was 0.5 mm/min. 5 samples were tested for each matrix system and their load-displacement curves were recorded. The interlaminar toughness, G_{IIC}, was calculated according to

the protocol [7] by:

$$G_{IIC} = \frac{9a^2\delta P}{2b(2L^3+3a^3)} \cdot \frac{1-0.6099\times\left(\delta/L\right)^2}{1+0.3766\times\left(\delta/L\right)^2} \tag{1}$$

where δ and P are displacement and maximum force recorded at the load-point at fracture.

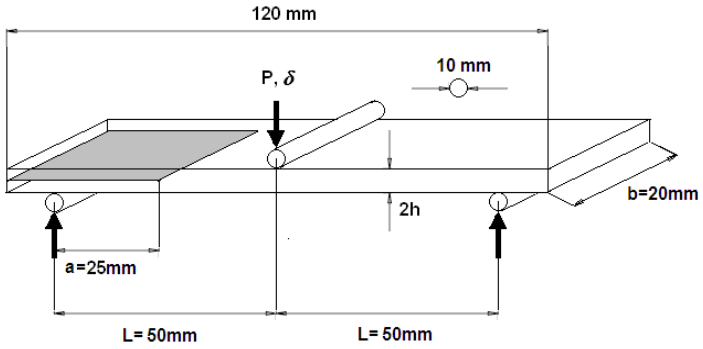

Figure 1. Dimensions of ENF specimen.

Four-point ASFPB tests

ASFPB tests were conducted on bulk materials with pre-cracked specimens, 90(L)x6(B)x16(W) mm^3, as shown in Fig. 2. The loading distance S_2/W = 0.75; S/W=3 was chosen and the pre-crack length was strictly limited to within $0.53 \le a/W \le 0.75$ based on previous studies [8-10] in order to provide a pure in-plane shear stress field around the crack-tip which would induce a high K_{II}/K_I ratio (over 20) [8]. Thus, it is reasonable to consider the ASFPB test as pure mode II fracture under such a geometric configuration since mode I fracture can be essentially neglected. Hence, according to [10], the mode II stress intensity factor can be calculated from:

$$K_{II} = F_{II}\tau_0\sqrt{\pi a} \tag{2}$$

where

$$F_{II} = -0.2915 + 6.33229\frac{a}{W} - 9.1199\left(\frac{a}{W}\right)^2 + 6.0570\left(\frac{a}{W}\right)^3$$

$$\tau_0 = \frac{P_1 - P_2}{WB} \quad P_1 = \frac{S_1}{S}P\,; \quad P_2 = \frac{S_2}{S}P$$

We assume $K_{IIC} \approx K_{II}$ when P is substituted with the maximum load at fracture. The tests were conducted on an Instron 5567 at a speed of 0.5 mm/min at the load-point.

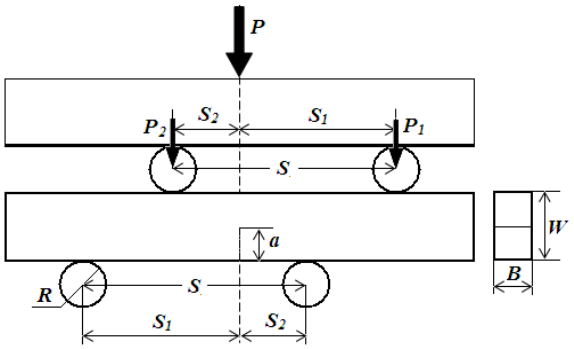

Figure 2. Dimensions of ASFPB specimen.

2.3 Finite Element Analysis (FEA)

The stress state for the mode II ASFPB test was simulated using ABAQUS. The geometry of the model is the same as the test sample, which is 90(L)x6(B)x16(W) mm^3. Since the ASFPB sample is symmetric to the central crack line, two parts were built and partially tied together to form a 10 mm crack. The loads, P_1 and P_2, were applied over contact areas, 2x6 mm^2 and 1x6 mm^2, respectively, aligned with the impressions left on the sample after the test. Young's modulus was chosen as 2.6 GPa to simulate the stress distribution, which was found insensitive to modulus verification within a small range (~10%) due to the plane strain feature of the FEA model. The average maximum load at fracture during the experiments (1200 N) was applied in the simulation study. Hence, the resultant stress distribution obtained in FEA should show the stress state at fracture initiation.

2.4 Microstructure analysis

The fracture surfaces of the fibre composites and the bulk samples were coated with a thin gold layer and examined by SEM (Zeiss ULTRA Plus SEM) at an accelerated voltage of 2 kV.

3 Results and Discussion

3.1 Carbon fiber laminates

Load-displacement curves of the ENF tests were recorded with an Instron 5567. The maximum load P and corresponding displacement δ from each load-displacement curve were substituted into Eq. (1) with the initial crack length a to obtain G_{IIC} for each specimen. According to the protocol [7], the crack length a is measured after the test by opening the sample. The average value of 4 samples was reported as the mode II fracture toughness of the corresponding material system.
In Fig. 3, calculated G_{IIC} values with standard deviations of nano-silica and nano-rubber modified fiber laminates are compared with their G_{IC} values [6]. In mode II fracture, the silica nano-particles are not as effective as they are in mode I, Fig. 3(a). G_{IIC} increases with increasing nano-silica loading until it reaches a maximum at 10 wt% silica, which is ~8% higher than the control. Further increase of silica loading lowers G_{IIC}. This trend is similar to the mode I results [6]. Mode II fracture toughness of nano-rubber modified fiber laminates are shown in Fig. 3 (b). Unlike silica, nano-rubber particles can improve G_{IIC} by as much as 43% higher than the control at 8 wt%. Again, higher nano-rubber loading cannot improve G_{IIC}; and at 12 wt%, G_{IIC} is even lower than the control. These results should be viewed with caution since at 12 wt% of nano-rubber or nano-silica uniform dispersion of these particles was difficult to achieve, which would lead to reduced toughness values. It is further noted that with pure epoxy matrix, G_{IC} of the composite laminates is ~54% lower than G_{IIC}. For silica modified epoxy matrix, the mode I delamination resistance G_{IC} is ~48-50% of the mode II delamination, G_{IIC}. However, the differences between G_{IC} and G_{IIC} of nano-rubber filled composites, R6, R10 and R12, are less than 10%. Indeed, G_{IC} of R12 is even slightly higher than G_{IIC}. Hence, nano-rubber modified composite laminates can provide superior mode I and mode II toughness, e.g., R8 and R10, which is not possible in nano-silica laminates.

3.2 Bulk materials

The mode II fracture toughness, G_{IIC}, of the bulk materials, which are the same as the matrix of the composites, was determined by the ASFPB tests. The results are listed in Table 2 with ±1standard deviation, where the K_{IIC} values were calculated using Eq. (2). To compare to the toughness of the corresponding fiber composites, the critical stress intensity factors K_{IIC} of bulk materials are converted to the fracture energy G_{IIC} (see Table 2) by:

$$G_{IIC} = \frac{(1-\mu^2)K_{IIC}^2}{E} \tag{3}$$

where μ is Poisson's ratio and E is Young's modulus. In the calculations, the values of Poisson's ratio of different material systems were obtained by the simple rule of mixture based on the density, Poisson's ratio and volume percentage of the epoxy and particles [4]. Note that the ratio of K_I/K_{II} at fracture is less than 4%, indicating that the ASFPS geometry is suitable for mode II toughness evaluation.

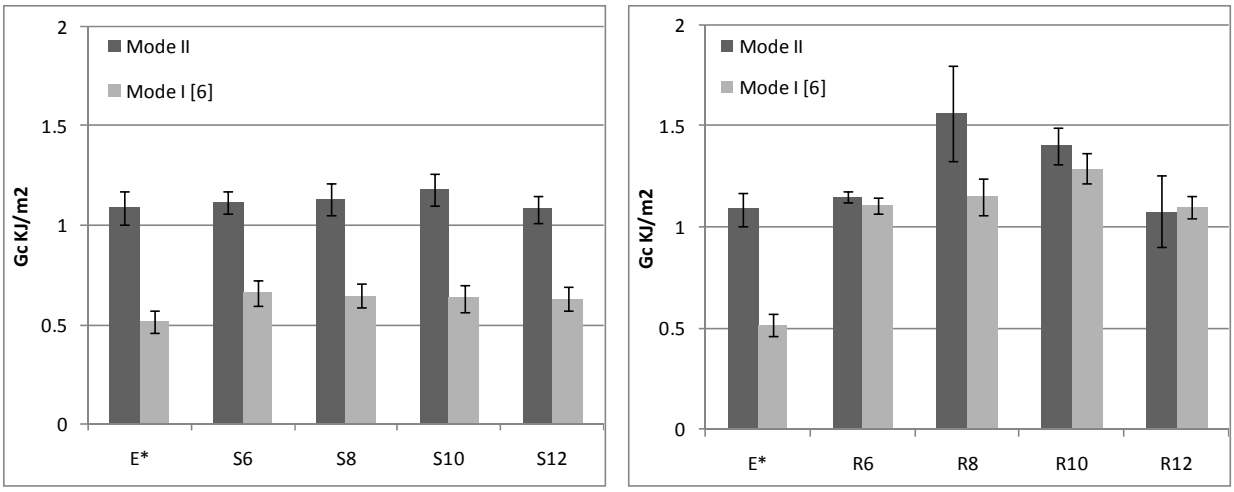

(a) Nano-silica modified system (b)Nano-rubber modified system

Figure 3 Comparisons between G_{IIC} and G_{IC} [taken from [6]] of nanoparticles modified composites.

Table 2. Mode II fracture toughness of the bulk material.

Material Code	K_{IIC} (MPa $\sqrt{m}$)	K_I/K_{II}	E (GPa) [4]	G_{IIC} (kJ/m^2)
E*	3.53 (±0.23)	0.031	2.86	3.82
S10	4.18 (±0.21)	0.044	3.14	4.88
R10	2.78 (±0.21)	0.035	2.30	2.95

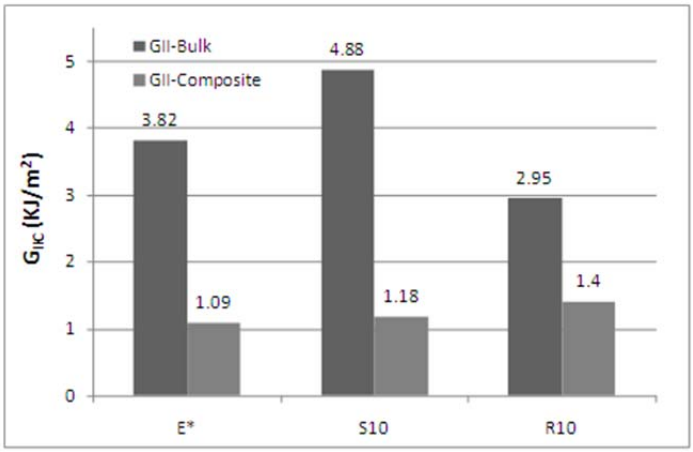

Figure 4. Comparison of G_{IIC} of bulk and composite laminates.

Figure 4 compares the mode II fracture toughness G_{IIC} of the bulk materials (neat epoxy and nanoparticle modified epoxy) and their fibre composite laminates. Notably, the fracture energy is improved by nano-silica modification in S10 as bulk; however, G_{IIC} of the S10 composite laminate is 76% less than that of the corresponding bulk materials. Thus, the toughness transfer efficiency in mode II of S10 is much lower than that in mode I [6], where the G_{IC} of fibre composite is more than 94% of the corresponding bulk. The nano-rubber filled epoxy has a higher transfer efficiency of ~50% from bulk to composite laminate, but the incorporation of rubber particles decreases the bulk G_{IIC} when compared to pure epoxy.

FEA was applied to understand the stress state of mode II ASFPB test. Figures 5(a)-(c) show the distributions of normal stresses, σ_x and σ_y, and shear stress, τ_{xy}, respectively. The crack tip stresses have been discussed in [11]. At fracture initiation, the crack-tip is subjected to a local tensile stress σ_x of ~5 MPa, (see Figure 5(a)), but the shear stress τ_{xy} is most dominant, which is ~30 MPa. The FEA results confirm that the samples failed primarily due to mode II fracture.

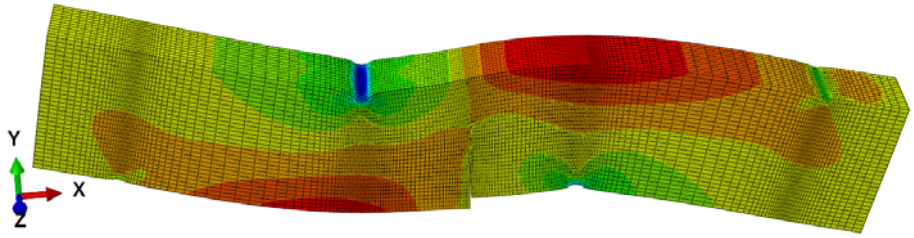

(a) Distribution of normal stress σ_x.

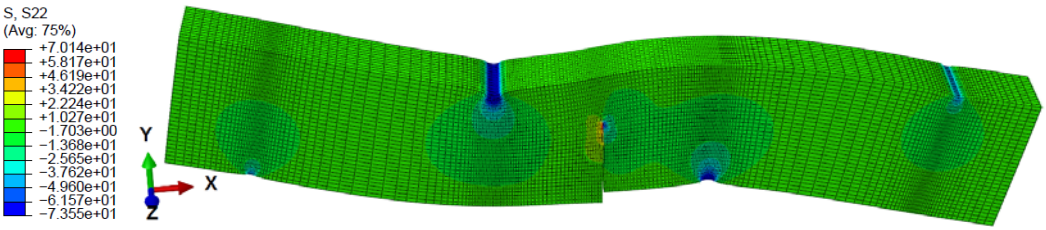

(b) Distribution of normal stress σ_y.

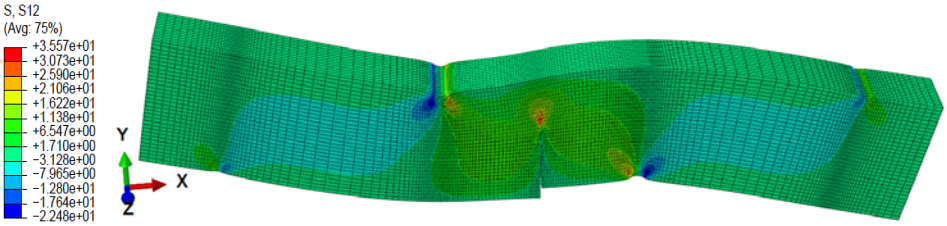

(c) Distribution of shear stress τ_{xy}

Figure 5 General stress distribution of mode II ASFPB specimen.

3.3 Fractograph study

Two matrix formulations were chosen to study the effects of nanoparticles on ENF tests: 10 wt% silica (S10) and 10 wt% rubber in epoxy (R10), in comparison with the control laminate (E*). In mode II fracture, there is good bonding observed between fiber and matrix for all composites and no separations can be seen in Figs. 6(a)-(c). However, obvious debonding between fibers and rubber modified matrix was observed in our previous study on mode I delamination [6] possibly due to the different fracture mode. Since the cracks are not open in mode II, fiber pullout from the matrix is difficult. Fig. 6(a) shows the fracture surface of the composite laminates, where silica nanoparticles

are evenly dispersed in the matrix. No particle debonding or pullout can be found in Fig. 6(a), where the nano-silica particles are well covered by epoxy. Since silica nanoparticle debonding is the major toughening mechanism in mode I [4-6], Fig. 6(a) therefore explains why the improvement of fracture toughness of these composites in mode II is not as remarkable when compared to the laminates with unmodified epoxy matrix. In contrast, nano-rubber particles in mode II fracture surface are observed to be well-dispersed in epoxy in Fig. 6(b). However, it is difficult to ascertain if the nano-rubber particles are cavitated, though some evidence exists when examined on much higher magnification. Another possible reason for the increase in toughness of R10 is the micro-voids introduced during processing of the laminates. When the rubber particles were added to epoxy, the viscosity of the resin was increased which made the resin flow between the fibres more difficult. More air bubbles and voids might form in the laminates. During delamination propagation, these voids may reduce the stress intensity at the crack tip and delay the delamination growth. However, further examination on the composite microstructure before and after testing are needed to prove the above hypothesis.

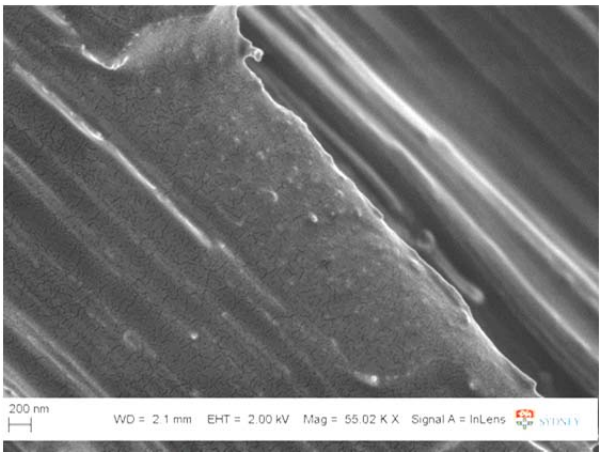

(a) Fracture surface of carbon fiber/S10 composite.

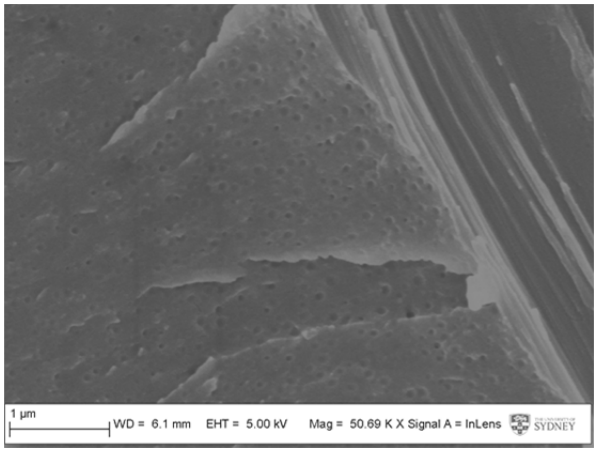

(b) Fracture surface of carbon fibre/R10 composite.

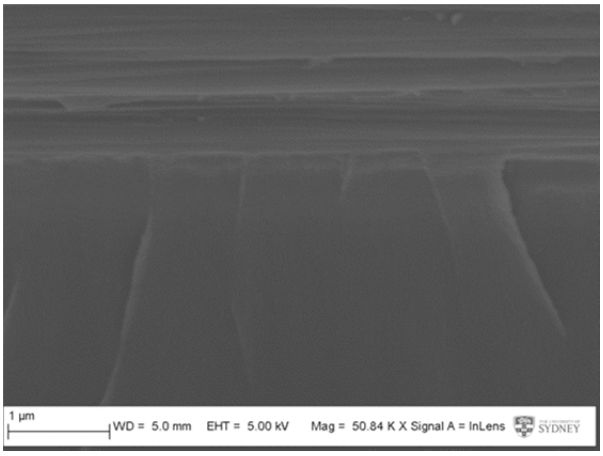

(c) Fracture surface of carbon fibre/E* composite.

Figure 6. Fractographs of ENF mode II specimens.

Figs. 7(a)-(c) show fracture surfaces of mode II ASFPB specimens of pure epoxy (E*), nano-rubber and nano-silica modified epoxies (R10 and S10) by optical microscopy under low magnification (x6) on the left side and high magnification (x750) by SEM on the right side. Pure epoxy shows typical brittle fracture characteristics in Fig. 7(a). Silica modified bulk epoxy shows the roughest surface; however, no typical silica debonding is observed in Fig. 7(b) even at higher resolution. In Fig. 7(c),

the rubber modified sample shows clear stress-whitened area in the center of the crack tip, indicating plastic deformation occurred during mode II fracture. R10 also possesses the smoothest near crack-tip region, which agrees with the test results where rubber modified epoxy shows the lowest G_{IIC}.

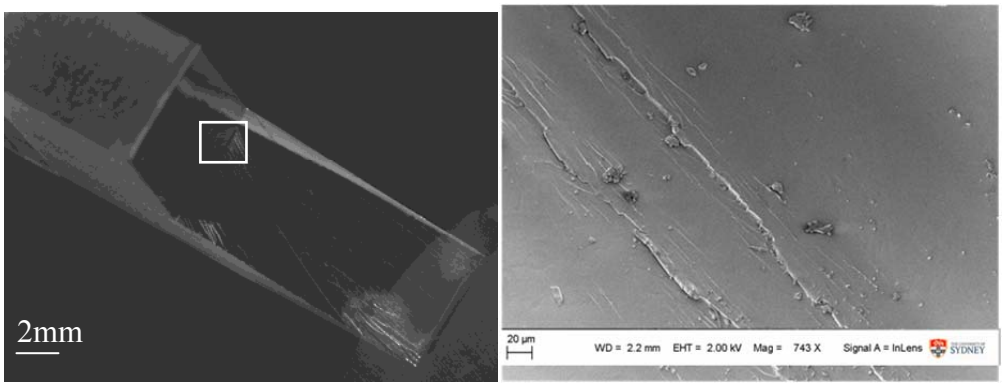

(a) Crack tip of E*.

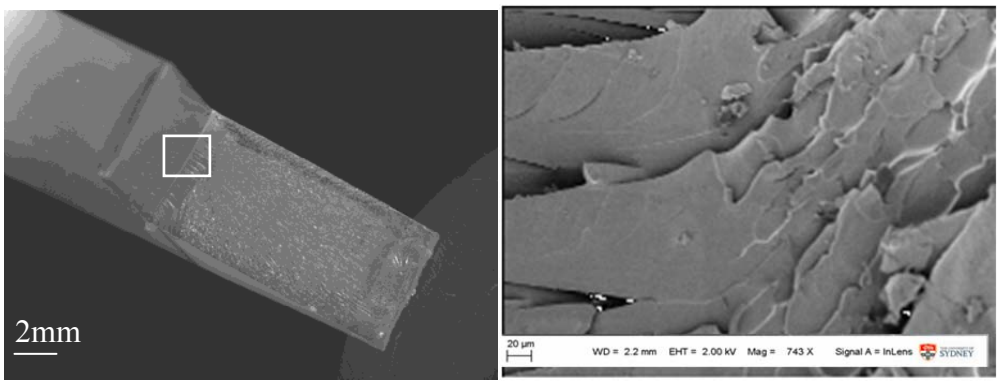

(b) Crack tip of S10.

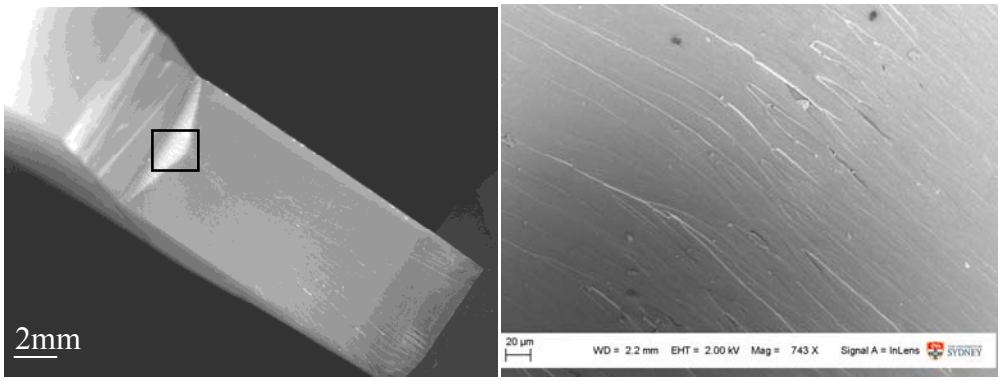

(c) Crack tip of R10.

Figure 7. Crack tip of bulk ASFPB specimens.

4 Conclusion

Mode II fracture behaviors of nanoparticles modified carbon fibre laminates have been studied by the ENF tests. Additional mode II ASFPB tests were also conducted on the nanoparticles modified bulk epoxies. From the results obtained we can conclude below:

(a) Nano-rubber modified epoxy is effective in enhancing the mode II toughness, G_{IIC}, of composite laminates depending on the particle loading. For example, R8 increases G_{IIC} by over 40% compared

to E*. By contrast, nano-silica modified epoxies are not as effective and only less than 8% improvement on G_{IIC} can be achieved.
(b) Mode II toughness G_{IIC} of nano-silica modified epoxy composite laminates are approximately twice the mode I toughness G_{IC} independent of the particle loading. The ratio of G_{IIC}/G_{IC} for nano-rubber modified epoxy composite laminates is much less.
(c) Nano-silica particles increase significantly G_{IIC} of the bulk epoxy; but this high toughness cannot be effectively transferred to the delamination toughness of the nano-silica modified epoxy composite laminates.
(d) Regarding the toughening mechanisms, silica particle debonding and rubber cavitation are not clearly shown by the SEM photos of mode II fracture surfaces, although thyeare the major toughening mechanisms in Mode I fracture of nanoparticle modified epoxy [6] and their fibre composites [4]. Further study will be conducted to identify the main reasons for the increase of G_{IIC} in S10 (bulk) and R10 (composites laminates).

Acknowledgements

Y Zeng would like to thank colleagues at the University of Sydney and the Shanghai Aircraft Design & Research Institute for their support and helpful discussions. H-Y Liu wishes to thank the Australian Research Council (ARC) for the support of this project through a Future Fellowship awarded to her (FT0992081, 2009-2013) tenable at the University of Sydney. Finally, the authors wish to acknowledge Nanoresin AG, Germany for the supply of nanosilica particles for this study.

References

[1] H. Zhang, L-C. Tang, Z. Zhang, K. Friedrich and S. Sprenger, Fracture behaviours of in situ silica nanoparticle-filled epoxy at different temperatures, Polymer, 2008, 49, 3816-3825.
[2] Y.L. Liang and R.A. Pearson, Toughening mechanisms in epoxy-silica nanocomposites (ESNs), Polymer, 2009, 50, 4895-4905.
[3] J-L. Tsai, H. Hsiao and Y-L. Cheng, Investigating mechanical behaviours of silica nanoparticle reinforced composites, Journal of Composite Materials, 2010, 44 (4), 505-524.
[4] H-Y. Liu, G-T. Wang, Y-W. Mai, Y. Zeng, On fracture toughness of nano-particle modified epoxy. Composites Part B: Engineering. 2011;42(8):2170-5.
[5] T.H. Hsieh, A.J Kinloch, K. Masania, J.S. Lee, A.C. Taylor and S. Sprenger, The toughness of epoxy polymers and fibre composites modified with rubber microparticles and silica nanoparticles, Journal of Material Science, 2010, 45, 1193-1210.
[6] Y. Zeng, H-Y. Liu, Y-W. Mai, X-S. Du. Improving interlaminar fracture toughness of carbon fibre/epoxy laminates by incorporation of nano-particles. Composites Part B: Engineering. 2012;43(1):90-4.
[7] Protocol for interlaminar fracture testing No.2, Mode II (ENF), 1992.
[8] M.R. Ayatollahi, S. Shadlou, M.M. Shokrieh. Fracture toughness of epoxy/multi-walled carbon nanotube nano-composites under bending and shear loading conditions. Materials & Design. 2011;32(4):2115-24.
[9] W. Araki, D. Asahi, T. Adachi, A. Yamaji. Time-temperature dependency of mode II fracture toughness for bisphenol A type epoxy resin. Journal of Applied Polymer Science. 2005;96(1):51-5.
[10] Y. Murakami, E.d. Pergamon. Stress Intensity Factors Handbook; Oxford, England, 1987; p 941
[11] H.S. Kim, P. Ma. Mode I and II fracture behaviour of rubber modified brittle epoxies. In: Ye L, Mai Y-W, editors. Polymer Blends and Polymer Composites1998. p. 179-86.

Variation in Thermal Conductivity of CFRP Plates due to Impact Damage

Mamoru Mizuno[1,*], Atsushi Ogawa[2], Garuda Fujii[1]

[1] Dept. Machine Intelligence and Sys. Eng., Akita Pref. Univ., Yuri-Honjo 015-0055, Japan
[2] Graduate student of Akita Pref. Univ., Yuri-Honjo 015-0055, Japan
* Corresponding author: mizuno@akita-pu.ac.jp

Abstract CFRP plates were subjected to impact loading by a drop-weight impact testing machine. Stacking sequence of the plates was [cloth/0°/90°/0°/90°/0°/cloth]. Dimension of the plates was 60 mm in length and width and 2mm in thickness. Then thermal conductivity of the plates in the thickness direction was measured by the static comparison method. Although it is difficult to measure the absolute value of thermal conductivity in general, reproducibility of the measurement was improved and variation from the initial value was discussed in the present paper. Distribution of the thermal conductivity due to impact damage on the plane was clarified as a function of distance from the impact point. On the other hand, the CFRP plates were cut by diamond saw and cross sections of the plates were observed by an optical microscope. Then length and number of delamination and transverse cracks were measured respectively on the photomicrographs. Distribution of damage such as delamination and transverse cracks on the plane was also clarified as a function of distance from the impact point. Finally, the relationship between variation in thermal conductivity and impact damage was clarified experimentally on the basis of the experimental measurements.

Keywords CFRP, Impact damage, Thermal conductivity, Delamination, Transverse crack

1. Introduction

Carbon fiber reinforced plastics (CFRP) have remarkable properties such as high strength-to-density ratio, tailor-made strength, etc. as well as advantages of polymers. Using the advanced properties, CFRP are utilized for many engineering structures and products of daily use. Especially, usage of CFRP for airplanes is increased recently from the viewpoint of weight reduction in order to save fuel consumption.

Considering the usage of CFRP in airplanes and automobiles, impact loading is unavoidable in their operations. For instance, bird strikes during flight, drop of tools during maintenance and collision during driving. Delamination, transverse cracks and debonding between matrix and fibers are well-known as internal damage of CFRP due to applied loading. When CFRP is fabricated by laminating prepreg sheets, impact loading causes internal damage such as delamination. Since internal damage causes reduction of mechanical properties and residual life, development of non-destructive inspections for CFRP [1–6] is important to guarantee reliability for structures.

Hammering tests among non-destructive inspections are often used practically for large-scale structures. The method of hammering tests is very simple and necessary tools are only hammers. However, the test results depend on experience of inspectors and only qualitative results are obtained. On the other hand, since X-ray inspections [3] and ultrasonic inspections [3] are precise methods, expensive equipments and special techniques are necessary and testing places are restricted. Non-destructive tests by infrared pulse thermography [4–6] are simple method, however, resolution to inspect internal damage is not so high.

Internal damage causes variation in material properties [7], so that internal damage can be inspected from the variation in material properties inversely. In practice, distribution of temperature is measured in non-destructive tests by infrared pulse thermography, and the distribution is caused by variation in thermal conductivity due to internal damage [8, 9]. In the present research, in order to

improve the resolution to inspect internal damage by infrared pulse thermography, assistance by numerical simulation is considered. Namely, if distribution of temperature in CFRP plates due to internal damage can be simulated, the internal damage could be predicted from the distribution of temperature by inverse analyses. For the numerical simulation, the relationship between thermal conductivity and internal damage is necessary. Accordingly, in the present paper, in order to investigate the relationship as a first step, CFRP plates are subjected to impact loading by a drop-weight impact testing machine, and variation in thermal conductivity from the initial value and internal damage such as delamination and transverse cracks are evaluated. Then the relationship between thermal conductivity and internal damage is clarified.

2. Experimental Methods

2.1. Drop-weight impact test

CFRP plates are used as specimens. Dimension of the plates is 60 mm in length and width and 2mm in thickness, and the stacking sequence is [cloth/0^o/90^o/0^o/90^o/0^o/cloth]. The CFRP plates are fixed in a drop-weight impact testing machine (Instron, CEAST9310) by the plate with a hole 40 mm across. A hemispherical tup falls on the center of specimens inside of the hole. Diameter of the tup is 12.6 mm. Three levels of impact energy are applied to specimens, and they are 5.1, 9.9 and 21.0 J. In the tests, drop height is fixed to 0.7 m and mass of weight is changed.

2.2. Measurement of thermal conductivity

Thermal conductivity of CFRP plates in the thickness direction is measured by the static comparison method [10]. Fig. 1 shows schematic diagram of the method. Self-making apparatus is used. In the static comparison method, a specimen and a reference sample whose thermal conductivity is known are placed in series. Then heat flow is given to the reference sample and specimen in series by a heater, and the difference in temperature ΔT_1 and ΔT_2 between both ends of specimen and sample is measured by thermocouples, respectively. The thermal conductivity of the specimen λ is evaluated relatively from the thermal conductivity of the reference sample λ_{ref} by using the ratio of the difference in temperature ΔT_1 and ΔT_2 and dimensions of specimen and sample [10].

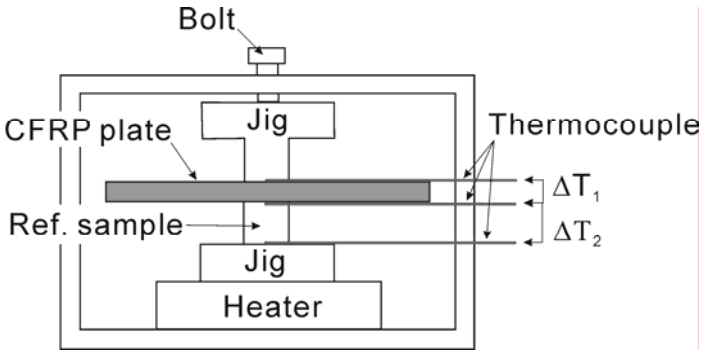

Figure 1. Schematic diagram of the static comparison method to measure thermal conductivity in the thickness direction of CFRP plates.

In order to improve reproducibility of measurement, the measurement is carried out in a vacuum vessel. The reference sample is selected so that thermal conductivity of the sample λ_{ref} is close to that of specimens. In the present paper, type 304 stainless steel (SUS304) is used as the reference

sample. The measurement is carried out in two cases. Namely, heat flow is given to specimen through reference sample, and heat flow is given to reference sample through specimen. The order of sequence for specimen and reference sample is changed. In the calculation of thermal conductivity λ, difference in temperature is necessary. However, if gradient of the relationship between difference in temperature and input electric power of heater is used instead of the difference in temperature, the reproducibility of measurement is improved [10].

Although it is difficult to measure the absolute value of thermal conductivity in general, reproducibility of the measurement could be improved. Since objectives of the present research are non-destructive inspection based on variation in material properties, the reproducibility is important because variation in material properties from their initial values is measured and discussed.

Fig. 2 shows positions of measuring thermal conductivity in specimens. Impact loading is applied to the center of specimens and the loading point is numbered 1. Thermal conductivity is measured at nine points (No. 1 through 9) as shown in the figure.

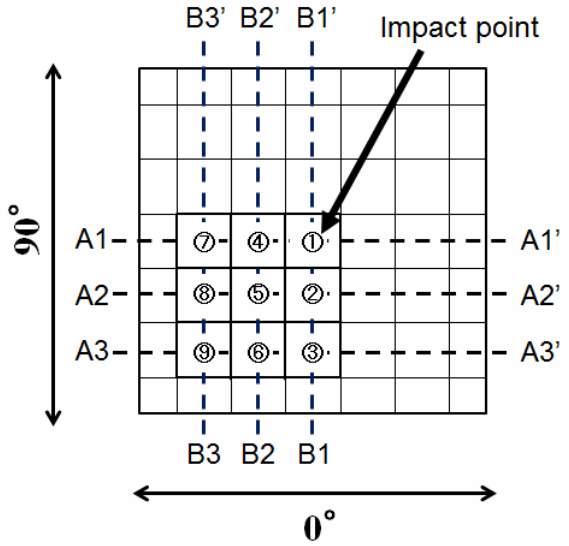

Figure 2. Positions of measuring thermal conductivity and observing cross sections.

2.3. Evaluation of internal damage

Specimens are cut in two directions as shown in Fig. 2. They are named A-direction and B-direction. A-direction coincides with 0^o which is orientation of fiber alignment directly under cloth layer. Three cross sections in each direction (for instance, A1-A1', A2-A2' and A3-A3' in A-direction) are observed by an optical microscope. Specimens are embedded in resin and they are cut by diamond saw for the observation. After cutting, cross sections are polished. A couple of specimens subjected to the same impact loading are prepared for observation in A-direction and B-direction. In order to evaluate internal damage due to impact loading, photographs of cross sections are captured into a personal computer, and length and number of delamination and transverse cracks are evaluated.

3. Experimental Results

Figs. 3 show distribution of thermal conductivity in a quarter of specimen subjected to impact energy of (a) 5.1J, (b) 9.9 J and (c) 21.0 J. Thermal conductivity is normalized by the initial value. Coordinate point of A1 and B1 is a position of impact loading. As shown in the figures, reduction of

thermal conductivity is the largest at the position of impact loading. Reduction of thermal conductivity in A-direction (measuring points of No. 4 and 7) is larger than that in B-direction (those of No. 2 and 3). They are caused by anisotropy of specimens. Stacking sequence of specimens is [cloth/0°/90°/0°/90°/0°/cloth] and internal damage is more significant at opposite side of impact point. The layer directly under cloth layer is important for damage development and anisotropy is caused by the orientation of fiber alignment in the layer.

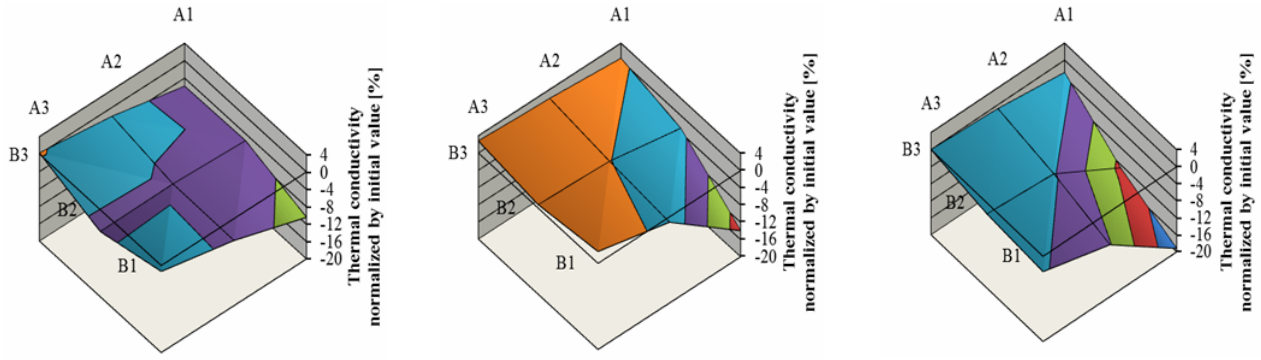

(a) 5.1 J (b) 9.9 J (c) 21.0 J

Figure 3. Distribution of thermal conductivity in a quarter of specimen subjected to impact energy of (a) 5.1J, (b) 9.9 J and (c) 21.0 J. Thermal conductivity is normalized by the initial value. The A1-B1 point is a position of impact loading.

Figs. 4 show photomicrographs of cross sections for specimens subjected to impact energy 21.0 J on (a) A1-A1' cross section and (b) B1-B1' cross section. As shown in the figures, delamination and transverse cracks are observed on the cross sections. Internal damage expands from impact point and it is significant near opposite side of impact point. By comparing both photomicrographs, anisotropy on internal damage is found clearly.

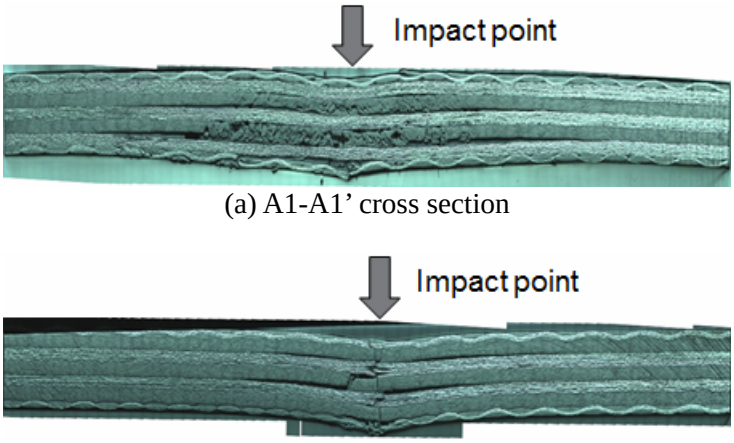

(a) A1-A1' cross section

(b) B1-B1' cross section

Figure 4. Photomicrographs of cross sections for specimens subjected to impact energy 21.0 J on (a) A1-A1' cross section and (b) B1-B1' cross section.

On the basis of photomicrographs, length and number of delamination and transverse cracks were measured. Figs. 5 show internal damage on each cross section of specimen subjected to impact energy of 21.0 J. Fig. 5(a) shows total length of delamination and transverse cracks plotted as internal damage, and Fig. 5(b) shows number of delamination and transverse cracks plotted as internal damage. In the figures, "fracture" means that damage is significant and it is difficult to

distinguish between delamination and transverse cracks. Internal damage reduces as position is apart from impact point, and internal damage in A-direction is larger than that in B-direction. It is also found that ratio of delamination to transverse cracks with respect to total length in Fig. 5(a) is about 9 to 1 at any positions while the ratio with respect to number in Fig. 5(b) is about 6 to 4.

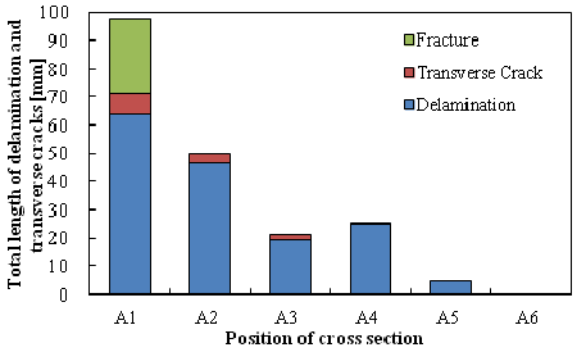

(a) Total length of delamination and transverse cracks

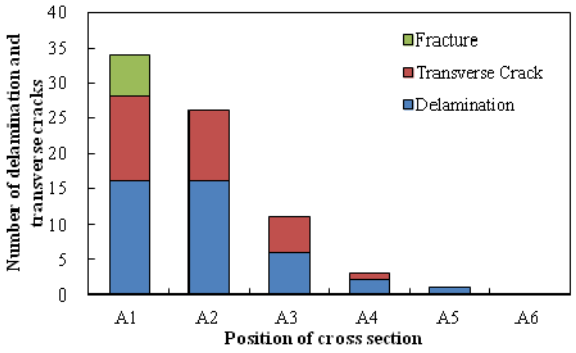

(b) Number of delamination and transverse cracks

Figure 5. Internal damage on each cross section of specimen subjected to impact energy of 21.0 J. (a) Total length and (b) number of delamination and transverse cracks are plotted as internal damage.

Figs. 6 show the relationship between thermal conductivity and internal damage. Thermal conductivity is normalized by the initial value. Total length and number of delamination and transverse cracks are adopted as internal damage. The total length and number of delamination and transverse cracks are summation of those in A-direction and B-direction, and the summation is carried out on the same area as thermal conductivity is measured. As shown in the figures, thermal conductivity reduces as internal damage increases. The relationship was clarified experimentally in the present research.

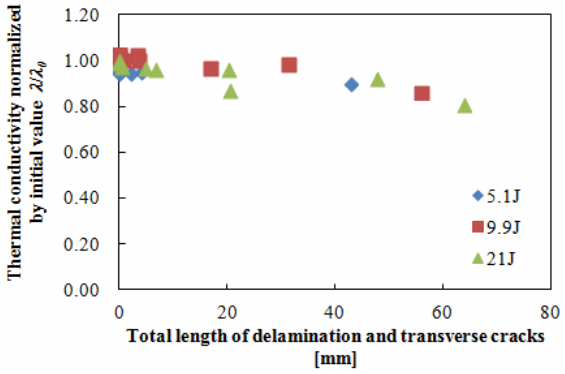

(a) Total length of delamination and transverse cracks

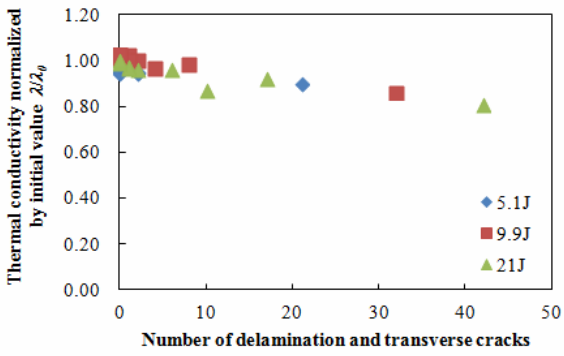

(b) Number of delamination and transverse cracks

Figure 6. Relationship between thermal conductivity and internal damage. (a) Total length and (b) number of delamination and transverse cracks are adopted as internal damage.

4. Concluding Remarks

The objectives of the present research are to improve the resolution of non-destructive inspection for CFRP by infrared pulse thermography. For the purpose of the improvement, assistance of numerical simulation is necessary. Therefore, in the present paper, in order to simulate distribution

of temperature due to variation in thermal conductivity on CFRP plates including internal damage, the relationship between thermal conductivity and internal damage due to impact loading was investigated experimentally.

Conclusions of the present paper are summarized briefly as follows:

(1) Distribution of thermal conductivity in the thickness direction on CFRP plates including impact damage was clarified, and it was indicated that the distribution depends on the level of impact energy.
(2) By observation of cross sections of CFRP plates, length and number of delamination and transverse cracks were measured as internal damage. The internal damage has anisotropy with respect to the fiber orientation directly under cloth layer, and it was found that the ratio of delamination to transverse cracks has constant value.
(3) By combining results of measurement for thermal conductivity with results of evaluation for internal damage such as length and number of delamination and transverse cracks, the relationship between thermal conductivity and internal damage was clarified experimentally.

As next steps, internal damage is described by a damage variable on the basis of the continuum damage mechanics [9, 11], and development of internal damage is formulated as an evolution equation of the damage variable as a function of impact energy and distance from impact point. Using the relationship between thermal conductivity and internal damage, variation in thermal conductivity is calculated by the damage variable and distribution of temperature is simulated by taking into account the development of internal damage. By utilizing inverse analyses, internal damage could be predicted inversely from distribution of temperature which is measured by infrared pulse thermography, in future.

References

[1] S. Wang, D. Wang, D.D.L. Chung and J.H. Chung, Method of sensing impact damage in carbon fiber polymer-matrix composite by electrical resistance measurement, J. Mater. Sci., 41 (2006) 2281–2289.
[2] N. Angelidis and P.E. Irving, Detection of impact damage in CFRP laminates by means of electrical potential techniques, Composites Sci. Tech., 67 (2007) 594–604.
[3] D.D. Symons, Characterisation of indentation damage in 0/90 lay-up T300/914 CFRP, Composites Sci. Tech., 60 (2000) 391–401.
[4] T. Sakagami and K. Ogura, New flaw inspection technique based on infrared thermal images under joule effect heating, JSME Int'l J., 37 (1994) 380–388.
[5] T. Sakagami, Nondestructive testing of structural materials by infrared thermography, J. Japan Welding Soc., 72 (2003) 251–255.
[6] J. Tashan and R. Al-mahaidi, Investigation of the parameters that influence the accuracy of bond defect detection in CFRP bonded specimens using IR thermography, Composite Struct., 94 (2012) 519–531.
[7] M.Y. Kashtalyan and C. Soutis, Mechanisms of internal damage and their effect on the behavior and properties of cross-ply composite laminates, Int'l App. Mech., 38 (2002) 641–657.
[8] K.K. Chawla, Composite Materials, Springer, New York, 1998.
[9] J. Skrzypek and A. Ganczarski, Modeling of Material Damage and Failure of Structures, Springer, Berlin, 1999.
[10] A. Ibe, H.T. Kaibe and O. Ohashi, Evaluation of thermal properties for thermoelectric materials by combination of steady and non-steady state methods, J. Mater. Sci. Soc. Japan, 40 (2003) 49–54.
[11] J. Lemaitre, A Course on Damage Mechanics, Springer-Verlag, Berlin, 1992.

Numerical simulation of the influence of particle clustering on tensile behavior of particle reinforced composites; Study of shape of the particles

Seyed.M.R. Rafieipour Alavi, Armin Abedini, Zengtao Chen*

Department of Mechanical Engineering, University of New Brunswick, Canada
*Corresponding author: ztchen@unb.ca

Abstract

This paper aims to investigate the influence of particle clustering on the tensile behavior of particle-reinforced composites composed of aluminum matrix and ceramic particles. Matrix was allowed to deform plastically, yet particles had only elastic deformation in a damage free process. By assuming a periodic microstructure, finite element simulations of a unit cell were carried out. The unit cells were modeled with different cluster densities as well as different particle aspect ratios. All particles were assumed to be oblate ellipsoids which were arranged linearly along the loading direction. Uniaxial stress-strain curves were gained through imposing gradual incremental displacements on the surface of the unit cell to the overall far-field strain of four percent. It was shown that clustering increases the plastic strain within ligaments between particles and promotes the strain hardening in the clustered region. Eventually, it causes a considerable increase in the level of the maximum principal stress in particles. The differences in stress-strain behavior among various composite models in macroscopic level were negligible.

Keywords: Particle-reinforced composites, Clustering, Finite Element Method (FEM)

1. Introduction

Dual-phase alloys and particle-reinforced composites are widely used in numerous areas such as automotive and aerospace industries. Dispersed particles improve mechanical properties of the matrix and lead to high strength composites. Several modelling methods have been proposed recently in order to predict mechanical behaviors of these composites. These modelling techniques can be split into two categories: analytical and finite elements methods. In general, analytical methods rely upon the equivalent inclusion method of Eshelby [1] and on their mean-field extensions [2]. There are a number of analytical modelling approaches proposed, such as the tangent-based [3] and secant-based [4] homogenization approaches, which have been relatively successful in terms of predicting non-linear behavior of composite materials. However, in terms of micro-structural details such as stress state within the particles, analytical approaches are not sufficiently accurate [5], because their formulations are based on different simplifying assumptions such as a homogeneous distribution of particles in the matrix [6]. Unlike the analytical approaches, FE techniques enable us to distinguish the influence of heterogeneous particle distribution, which is much more realistic than homogeneous particle distribution [7].

In the study conducted by Abedini et al. [8], the influence of particle clustering on mechanical behavior of particle-reinforced composites has been investigated quantitatively by using the method introduced by Thomson et al. [9] for multi-particle unit cells. Composite material is assumed to be composed of repeated multi-particle unit cells containing spherical particles. Morphology of different types of particle clustering has been investigated so that useful comparisons between different cluster severities and geometries can be made. This method has provided a good understanding of local stress state within particles in a cluster. Local stresses

within clusters have a significant role for the initiation of microvoids which can result in the earlier onset of damage. By taking advantage of the periodic symmetry, the particle field has been reduced to a single unit cell. Based upon FE analysis, Abedini et al. [8] has concluded that as the degree of clustering increases, the flow stress of the composite exhibits a slight increase. The objective of the present article is to perform a quantitative analysis of linear cluster arrangement within unit cell in uniaxial tension. According to Abedini et al.'s work [8], linear cluster morphology was highlighted among other morphologies as the most sensitive cluster type to various stress conditions. Unlike Abedini et al. [8], in the present study, ellipsoidal particles are modeled instead of spherical ones since based on Chawla and Chawla's [6] results, ellipsoidal particles simulate more realistic geometry comparing to spherical particles .

2. Model Description

2.1. Cluster Geometry

Due to the high sensitivity it indicates [8], linear cluster morphology has been considered. Figure 1 shows one-eighth of a single particle unit cell along with a linear particle arrangement in the cluster. Ellipsoidal particles aligned with loading axis were modeled in clusters with a variety of densities. Here in Figure 1 particles are not depicted in their spots , for the morphology is clearer in this way. Due to the symmetry, only one eighth of each unit cell has been modeled. Each unit cell of the cluster model contains three ellipsoidal particles within it.

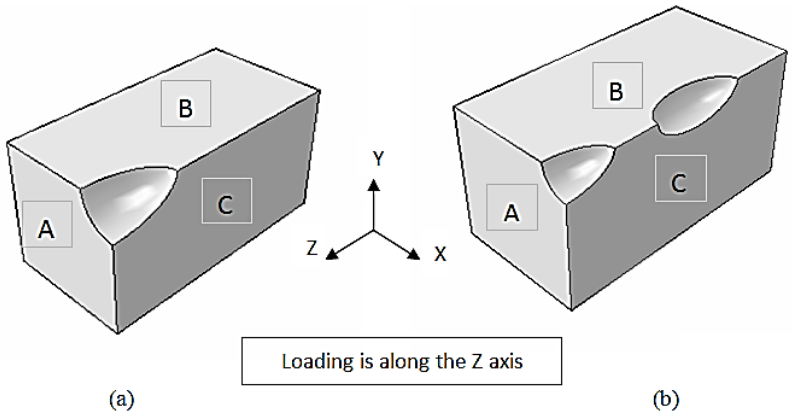

Figure 1- One eighth of unit cell for: (a) Single particle, (b) Linear cluster.

As displayed in Eq. 1, severity of a cluster is quantified through the variable *K* which is equal to the inter cluster spacing, *D*, relative to the inter particle spacing, *d*. The larger the value of *K*, the denser particle clustering is achieved.

$$K = \frac{D}{d} \tag{1}$$

Cluster densities of K = 18, 10, 6 and 3 were investigated along with aspect ratios of AR=2,3 for ellipsoids. The aspect ratio of the unit cell $\frac{L_1}{L_2}$ was assumed to be equal to the aspect ratio of the particles.

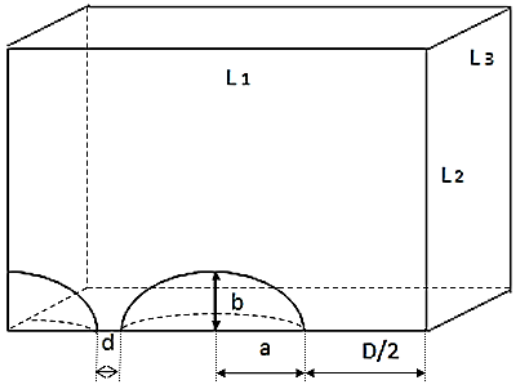

Figure 2 – One eighth of a unit cell along with symbol definitions, $AR = \frac{a}{b}$.

2.2. Boundary Conditions and Material Properties

In order to ensure that the periodic microstructure assumption is still valid, all of the planes of the unit cell are considered to remain planar and to maintain their initial orientation. Displacements along normal directions as well as rotations around all axes are restricted for all three planes of symmetry (planes A, B and C in Figure 1). Uniaxial tension was gained through imposing gradual incremental displacements on the side surface along the z axis to the overall strain of four percent. The small level of overall strain was chosen to support the assumption of damage free composite.

Three-dimensional FE models of particle-reinforced composite were simulated in order to predict the overall uniaxial tensile stress-strain response, local stress fields and local strain fields. Commercial FE software, ABAQUS, was used to perform the simulation. A typical FE mesh with eight-node linear brick elements was used, as is depicted in Figure 3. Each series of meshing was checked for mesh sensitivity, and distortion, which was pointed out through the ABAQUS mesh verification tool, which was found adequately negligible with a sufficiently refined mesh. All simulated particle-reinforced composites were composed of an aluminum matrix and ceramic particles.

It was assumed that the elastic-plastic matrix obeys the hardening rule represented in Eq. 2 :

$$\sigma = \sigma_y + K\varepsilon_p^n \tag{2}$$

Where ε_p and σ_y are the accumulated plastic strain and the initial yield stress, respectively and the values of constants, K and n, are shown in Table 1 along with other mechanical properties of the constituents.

The bonding between the matrix and particles was assumed to be perfect, and thermal residual stresses were not taken into account. Furthermore, the nucleation of voids by particle cracking or

interface separation was also not considered as the objective of this study is to investigate the influence of particle clustering on the material response before the onset of damage.

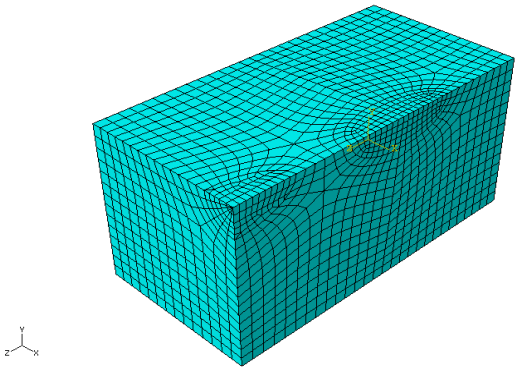

Figure 3- A typical FE mesh for the linear cluster model with *AR*=2 and *K*=3.

Table 1 – Material properties of each of the phases.

	E (GPa)	*Poisson's ratio*	σ_y (MPa)	*K* (MPa)	*n*
Aluminum	75	0.3	75	416	0.39
Ceramic	400	0.2	-	-	

3. Results and Discussion

3.1. Macroscopic Response

Overall mechanical behavior of the unit cells under uniaxial tension is reported in this section. Linear clusters containing ellipsoidal particles with different aspect ratios and levels of cluster densities have been studied and compared over the particle volume fraction of 0.01. These results are based on volumetrically averaged, macro stress values with respect to macro strain. Figures 5 and 6 indicate that as *K* increases (i.e., the cluster becomes denser), the flow stress in the unit cell increases slightly. However, these graphs represent almost the same behaviors in the elastic regime. Moreover, the difference between the largest and the smallest flow stress is so small (around 0.6%) that makes the effect of particle clustering on overall behavior of the unit cells negligible. Therefore, it is concluded that the higher particle clustering increases the work hardening to a very limited degree in the macroscopic scale. All FE results are in qualitative agreement with the results obtained by Abedini et al. [8] for spherical particles.

Another comparison also has been made to analyze clusters with the same clustering density but different particle aspect ratios. According to the definition of aspect ratio presented in Figure 2, spherical particles acquire *AR*=1. This comparison illustrates the influence of particle aspect ratio on the overall response of the composite. The results for ellipsoidal particles (with *AR*=2 and 3) are compared to the corresponding curves for spherical particles (*AR*=1) reproduced from Abedini et al [8]. Figures 7-9 depict overlapping curves of the same cluster density with different aspect ratios of particles. These diagrams show nearly identical curves in the elastic regime and a very limited scatter when plastic deformation becomes dominant. However, in all cases, it is observed that the stress-strain curves with greater particle aspect ratios lie slightly above other curves. It implies that longer oblate ellipsoidal particles make the composite slightly stronger.

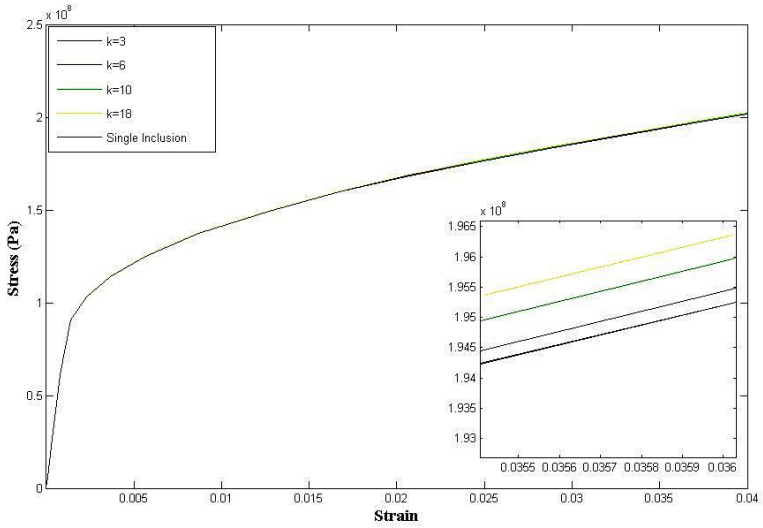

Figure 5-Overall behavior of the composite for the ellipsoidal particle linear cluster with *AR*=2 and different values of *K*.

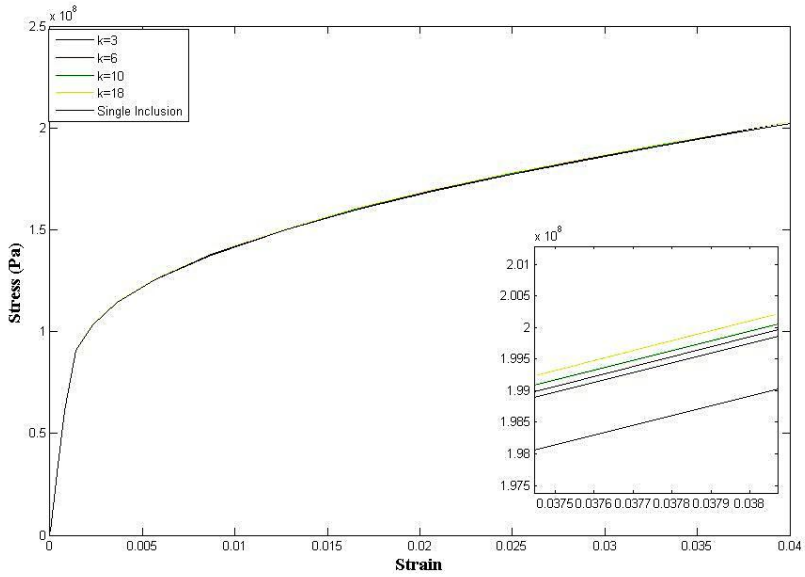

Figure 6-Overall behavior of the composite for the ellipsoidal particle linear cluster with *AR*=3 and different values of *K*.

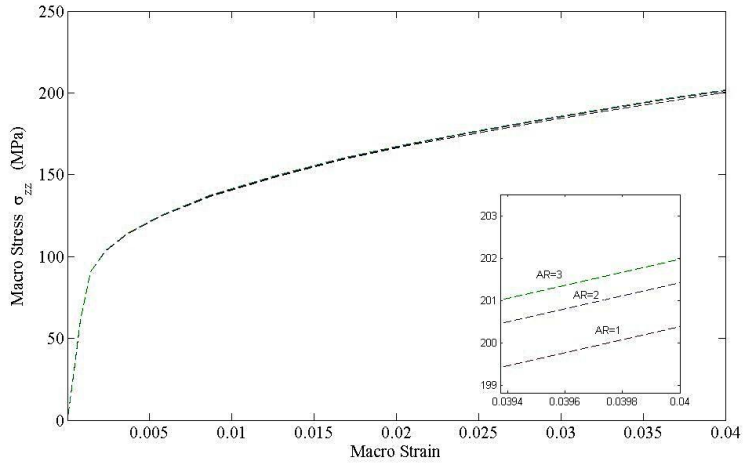

Figure 7- Overall behavior of composites for *AR*= 1,2,3 with a single inclusion within the cluster.

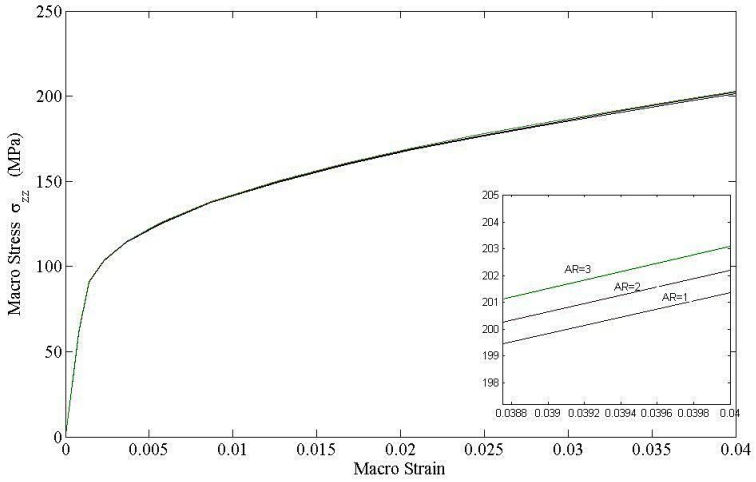

Figure 8- Overall behavior of composites for *AR*= 1,2,3 with a cluster ratio of *K*=10.

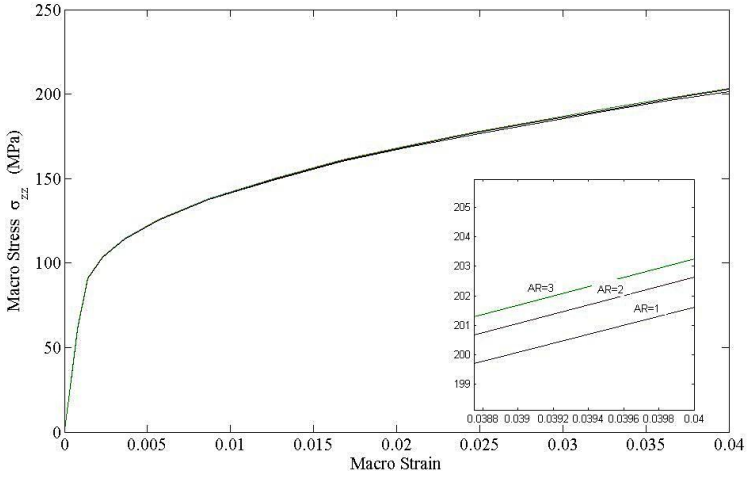

Figure 9- Overall behavior of composites for *AR*= 1,2,3 with a cluster ratio of *K*=18.

3.2. Microscopic Response

Although macroscopic response for the composite is important, it does not fully reveal why and how failure occurs in the heterogeneous material. Hence, microscopic response should be investigated since failure begins as a local event. Figures 10 and 11 show the results for volume averaged principal stress in the middle particle of the linear cluster model with respect to far-field strain. Unlike macroscopic responses that were not substantially influenced by cluster densities, Figures 10 and 11 evidently show a significant increase of the principal stress within the particle with increasing the particle clustering density. In other words, the smaller the space between particles, the greater stress is present in the particle. Also, single particle models show the smallest level of stress in comparison with all multi-particle cluster models. As expected, these trends are totally in agreement with the results for spherical particle(s) [8].

After the evaluation of the influence of the cluster density on averaged principal stress in the middle particle, the volumetrically averaged maximum principal stress in the middle particle of the linear cluster model with respect to far-field strain was investigated for models of the same cluster densities (K) and different ARs. Figures 12 and 13 depict the results. Curves representing the behavior of spherical particles (AR=1) are taken from Abedini et al.'s work [8]. According to Figures 12 and 13, as the aspect ratio increases in the composite, the larger maximum principal stress is imposed on the middle particle. Furthermore, the amount of stress experienced by the particle increases as the cluster density increases and this increase is more significant for the cluster models with higher aspect ratio particles.

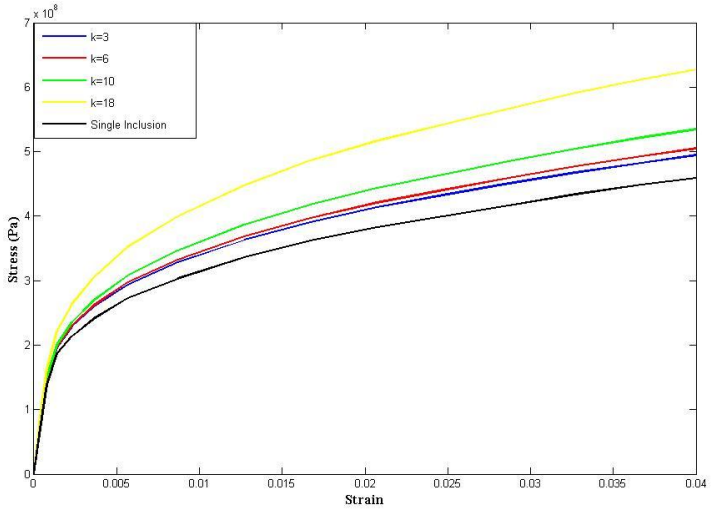

Figure 10- Microscopic behavior of middle ellipsoidal particle for linear cluster with AR=2 and different values of K.

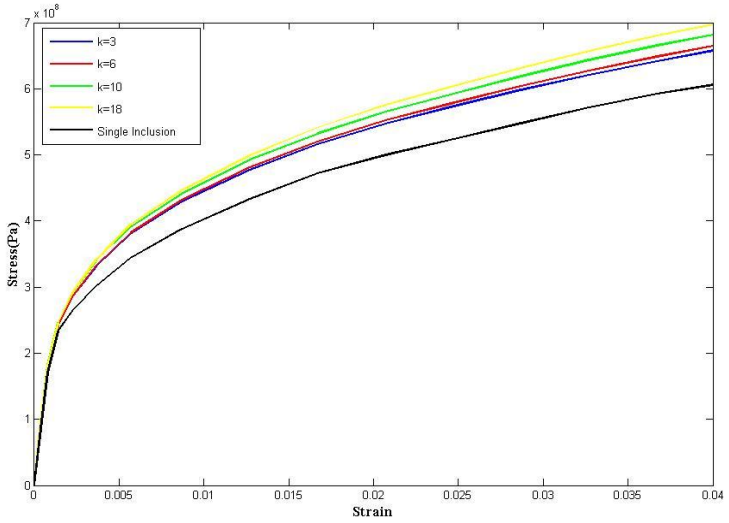

Figure 11- Microscopic behavior of middle ellipsoidal particle for linear cluster with *AR*=3 and different values of *K*.

The equivalent plastic strain is a direct measure of the level of plastic flow in the matrix. Higher plastic strain in a region causes more hardening, and, consequently, greater stress is transferred into the particles in the region. As Figure 14 indicates, the maximum equivalent plastic strain occurs in the space between particles. Since the maximum plastic strain takes place within clusters, it can be predicted that particle fracture (and consequently damage) is initiated from the clustered area which is in total agreement with experimental results available in the literature [9].

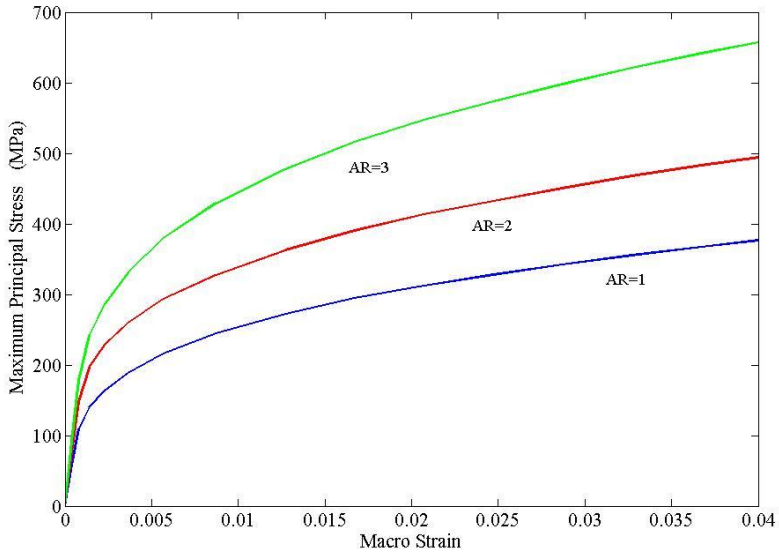

Figure 12- Mechanical behavior of the middle particle in linear cluster model of the composites with *AR*= 1,2,3 and *K*=3.

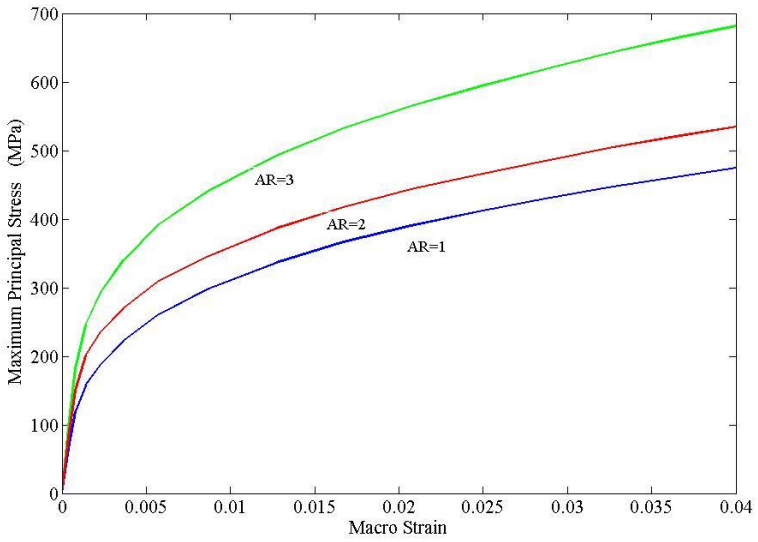

Figure 13- Mechanical behavior of the middle particle in linear cluster model of the composites with *AR*= 1,2,3 and *K*=10.

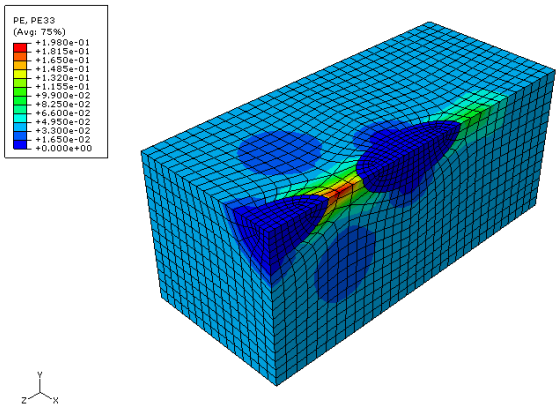

Figure 14-Contour plot of the maximum principal plastic strain in the FE model.

4. Conclusions

The traditional analytical and numerical approaches to predict the mechanical behavior of particle-reinforced composites are based on assuming homogeneous distribution of particles within the matrix; however, this assumption is not compatible with real composites. Finite elements simulation of uniaxial tension has been conducted considering particle clusters with different aspect ratios of the particles within the matrix and different densities of clusters. In the work conducted by Abedini et al. [8], linear cluster models were found to be the most sensitive particle clustering arrangement to cluster density variation compared to other cluster geometries. The current study was focused on the effect of linear clusters consisting of ellipsoidal particles on the mechanical behavior of particle-reinforced composites.

In both macro and micro scales, it was evident that increasing the cluster density leads to higher level of average stress experienced by the whole composite and the middle particle. However,

differences in macroscopic stress among different cluster densities were negligible for the same particle volume fraction. Furthermore, influence of particle aspect ratio was evaluated for models with same cluster densities (K), in macro and microscopic level. Models with higher aspect ratios demonstrated greater levels of stresses within individual particles, implying that a higher load is being transferred to the particles.

Results obtained from this research indicate that as cluster density increases, so does plastic strain in the ligament and this increase is more significant for the clusters with oblate particles. Therefore, it clearly justifies how an increase in cluster density and particle aspect ratio eventually increases stress both in micro and microscopic scale. All results obtained in this study are in good agreement with experimental and FE results available in the literature.

5. Acknowledgement

The present work was supported by the New Brunswick Innovation Foundation, the AUTO21 Network of Centres of Excellence, and the Natural Sciences and Engineering Research Council of Canada.

6. References

[1] J.D. Eshelby, The determination of the elastic field of an ellipsoidal inclusion, and related problems. Proc Roy Soc London A, 241 (1957) 376-369.

[2] R. Hill, A self-consistent mechanics of composite materials. J Mech Phys Solids, 13 (1965a) 213-222.

[3] R. Hill, Continuum micro-mechanics of elasto-plastic polycrystals. J Mech Phys Solids, 13 (1965b) 89-101.

[4] M. Berveiller, A. Zaoui, An extension of the self-consistent scheme to plasticity-flowing polycrystals. J Mech Phys Solids, 26 (1979) 325-344.

[5] O. Pierard, C. Gonzalez, J. Segurado, J. LLorca, I. Doghri, Micromechanics of elasto-plastic materials reinforced with ellipsoidal inclusions. Int J Solid Struct, 44 (2007) 6945-6962.

[6] N. Chawla, K.K. Chawla, Microstructure-based modeling of the deformation behavior of particle reinforced metal matrix composites. J Mater Sci, 41 (2006) 913-925.

[7] A. Ayyar, G.A. Crawford, J.J. Williams, N. Chawla, Numerical simulation of the effect of particle spatial distribution and strength on tensile behavior of particle reinforced composites. Comput Mater Sci, 44 (2008) 496-506.

[8] A. Abedini, C. Butcher, Z.T. Chen. Numerical simulation of the influence of particle clustering on tensile behavior of particle-reinforced composites. Submitted to J Comput Mater Sci (2012).

[9] P.B. Prangnell, S.J. Barnes, S.M. Roberts, P.J. Whiters, The effect of particle distribution on damage formation in particulate reinforced metal matrix composites deformed in compression. Mater Sci Eng A, 220 (1996) 41-56.

The Effect of Nano- and Micro-Fillers on the Strength and Toughness of PIR Foams Obtained From Renewable Resources

Janis Andersons[1,*], Ugis Cabulis[2], Uldis Stirna[2]

[1] Institute of Polymer Mechanics, University of Latvia, Riga LV-1006, Latvia
[2] Latvian State Institute of Wood Chemistry, Riga LV-1006, Latvia
* Corresponding author: janis.andersons@pmi.lv

Abstract Low-density rigid polyisocyanurate (PIR) foams obtained from renewable resources (with the polyol system comprising up to 80% of rapeseed oil esters) have been produced and tested for strength and fracture toughness in a range of foam density of importance for practical applications. In order to enhance the mechanical characteristics of the foams, the effect of several nano- and micro-fillers has been investigated experimentally. It is demonstrated that nano-fillers, such as organically modified nanoclays, carbon nanotubes, ZnO nanoparticles, increase both the strength and toughness of the foams whereas such micro-fillers as milled carbon fibers, while providing substantial increase in stiffness, have little effect on foam strength and toughness. Scaling models relating filled solid polymer properties to those of the filled foams have been considered and shown to have a predictive potential.

Keywords polymer foams, strength, toughness, nanoclay, carbon fibers

1. Introduction

Currently there is an increasing worldwide interest in modern technologies based on renewable raw materials. The introduction of plant components into polyurethane (PUR) systems meets all the aims of sustainable development and is an important challenge for chemical companies. Polyisocyanurates (PIRs) are synthesized using two basic components: polyols and isocyanates. In recent years, increasing interest from industry concerning polyols derived from renewable sources (different natural oils, such as rapeseed oil (RO), castor, soya, palm, sunflower oils, etc.) has been perceived. These natural ingredients can be successfully used to obtain different PIRs including porous composites. Moreover, the anticipated effects of progress in polymer materials should lead to the improvement of their properties and the reduction of their manufacturing cost. This is one of the reasons to carry on the research in the field of porous composites with the use of nano- and micro-fillers [1].

Rigid low-density closed-cell PIR foams are used primarily as a thermal insulation material in building construction and in the global appliances (refrigerators, freezers, etc.) industry, as well as in aerospace industry. Although not expected to bear load, low-density foams still have to exhibit strength and toughness adequate for loading conditions in the intended applications. Various high-stiffness nano- and microfillers such as organically modified clay, carbon nanotubes, and metal oxides [[1]-[4]], as well as carbon microfibers [[5]] have been shown to improve considerably the mechanical response of PUR and PIR foams at relatively low filler loadings. Prediction of strength of foam materials based on micromechanical considerations is complicated due to large variability in foam morphology. However, scaling relations linking foam strength and toughness to density and morphological parameters of the foams and deformability or strength characteristics of the foam struts have been derived and verified experimentally, see e.g. [[6], [7]]. The present study aims at

experimental evaluation of the effect of commercially available fillers on the strength and toughness of RO PIR foams and their relation to the strength of filled solid polymers.

2. Materials

2.1. Polyol synthesis

Polyols on the basis of renewable natural oils, suitable for obtaining PUR and/or PIR, can be obtained by different methods. Most often the esterification or epoxidation of oils is applied. In the present work, for producing of PUR, polyol obtained by amidization of RO with diethanolamine was used. Temperature: 140˚C, catalyst: zinc acetate. The RO / diethanolamine molar ratio was 2.9 / 1.0. RO obtained from the company *Iecavnieks* (Latvia) was used for the synthesis of polyols. Firstly, optimum synthesis conditions of polyols suitable for obtaining PUR were determined. The synthesis process was controlled from the diethanolamine (acid value and NH value) conversion degree. The structure of polyol was characterized from FTIR spectroscopy data.

2.2. Fillers

Four different nanoclays or organically modified montmorillonites (MMT): Cloisite® 15A, Cloisite® 30B, Cloisite® 93A (produced by *Southern Clay Products, Inc.*) and Dellite® 43B (produced by *Laviosa Chimica Mineraria S.p.A.*) were used as fillers of RO PIR foams. The clays are purified natural montmorillonites modified as follows: Cloisite® 15A is modified with a dimethyl dehydrogenated tallow quaternary ammonium having a cation exchange capacity of 125 mequiv/100 g, 30B - modified by methyl tallow bis-2-hydroxyethyl ammonium with a concentration of 90 meq/100 g clay, 93A - modified with a quaternary ammonium salt (methyl, dihydrogenated tallow ammonium) in a concentration of 90 mequiv/100 g of clay, and Dellite® 43B is modified by dimethyl benzylhydrogenated tallow ammonium. Multi-wall carbon nanotubes Nanocyl® NC7000 (produced by *Nanocyl s.a.*) with average diameter of 9.5 nm and average length of 1.5 μm (according to manufacturer's data), as well as zinc oxide nanoparticles Zano® 20 (produced by *Umicore Zinc Chemicals*) with the size of ca. 30 nm were also used for filling the foams.

Carbon-fiber-filled foams were manufactured using Tenax-A milled carbon fibers, with 7 μm diameter, of two types. Type 383 fibers had length within 50-150 μm range with the average length of 100 μm, whereas Type 385 fiber length was in the 40-70 μm range having the average length of 60 μm. The bulk density of the fibers amounted to 350 kg/m^3 and 550 kg/m^3, respectively.

2.3. Foam production

The formulations used in this study were polyols from RO, and a higher functional polyether polyol based on sorbitol Lupranol 3422 (it contains only secondary hydroxyl groups, OH Number 490 mg KOH/g) - from *BASF*. As additives, surfactant NIAX Silicone L6915LV, from *Momentive Performance Materials* and catalyst Polycat 5 from *Air Products* were used. Tris-chloropropyl phosphate (TCPP), used as a flame retardant, was supplied by *Albemarle* and as blowing agent, a

mix of water and cyclo-pentane was used. As an isocyanate, polymeric diphenylmethane diisocyanate - IsoPMDI 92140, supplied by *BASF*, was used.

PIR samples were obtained by mechanically mixing appropriate amounts of IsoPMDI 92140 and the polyol system (polyols, surfactant, catalysts, and blowing agent) for 10-15 s. The unreacted mixture was poured into a plastic mould (20 x 30 x 10 cm) for free foaming. The polymerization reaction took place at room temperature for all the obtained samples and was completed in about 3-5 min. The foam samples were conditioned before tests for at least 24 h.

Nanoclay loadings in the range of 1% to 5% by weight were considered. The exfoliation of MMT nanoclays in RO polyol was performed by MRC Ultrasonic Cell Crusher. The same procedure was applied also for mixing Zano 20 and Nanocyl NC7000 fillers in RO polyol at 1 % wt. When producing microfiber-filled foams, carbon fibers of the selected type were mixed into the polyol system. After stirring, the fiber suspension in polyol was degassed, the foaming agent added, the mixture stirred and foamed. Three different fiber loadings were obtained: 2%, 4% and 6% by weight. Good dispersion was achieved, as suggested by the change in viscosity of the filled polymer for nano- and by optical microscopy for micro-fillers. The content of different fillers in the foams was calculated on the basis of initial weights.

For characterization of the mechanical properties of solid, monolithic unfilled and nanofilled polymers, the mixture prepared as described above was poured in plastic ampoules of ca. 14 mm diameter and 80 mm length. The ampoules were subjected to centrifuging to eliminate bubbles.

3. Characterization of mechanical properties

3.1. Strength

For mechanical testing, specimens were produced from slices of the foam blocks cut along the rise direction of the foams (for illustration of the free foaming , see Fig. 1) . The specimens for tension

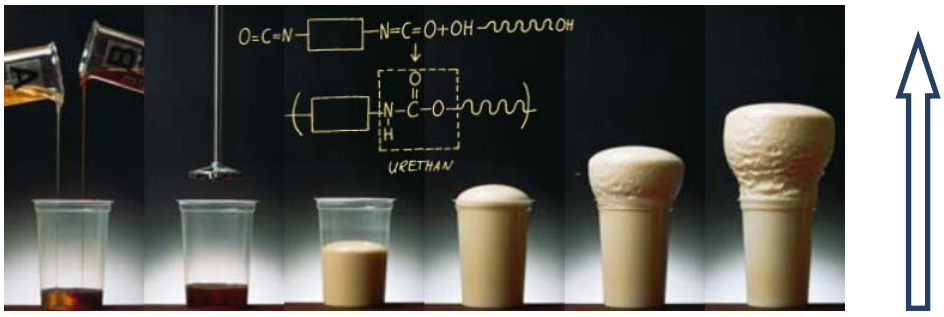

Fig. 1. Illustration of the free foaming process. The arrow shows the foam rise direction.

tests were machined to a dog-bone shape, with a rectangular test section of 85 mm length, 22 mm width, and 20 mm thickness. The specimen orientation was chosen so that the mechanical response in the direction normal to foam rise could be characterized. An extensometer with 50 mm base

length was used for strain measurement in the loading direction. For gripping, metallic plates with hooks were glued to the ends of the specimens. Tensile tests were carried out by stroke control, at a displacement rate of 8 mm/min. For compressive tests, rectangular specimens of dimensions 80 x 30 x 30 mm were cut from the foam slices and loaded at a rate of 10 %/min. Thus comparable specimen gauge length and loading rate was ensured for both, tensile and compressive tests normal to the foam rise direction. Thin Teflon films were put between the top and bottom ends of specimens and the plates of the testing machine to reduce the friction in compression tests.

Apparent density of each of the foam specimens was determined before the tests. The variation of density with filler loading is shown in Figs. 2 and 3 for MMT fillers and in Fig. 4 for carbon fiber fillers (foams with different initial densities in 34 to 50 kg/m^3 range were filled, as seen in Figs. 2-4). Note that the markers in Figs. 2 and 4 have been slightly offset with respect to the correct filler content values for better legibility. The presence of fillers apparently had larger effect on foam density when the initial, neat foam density was lower. Addition of Zano 20 at 1 % wt. increased foam density from ca. 34 for neat foams to 45 kg/m^3, whereas filling by Nanocyl at the same loading produced foams with 55 kg/m^3 density.

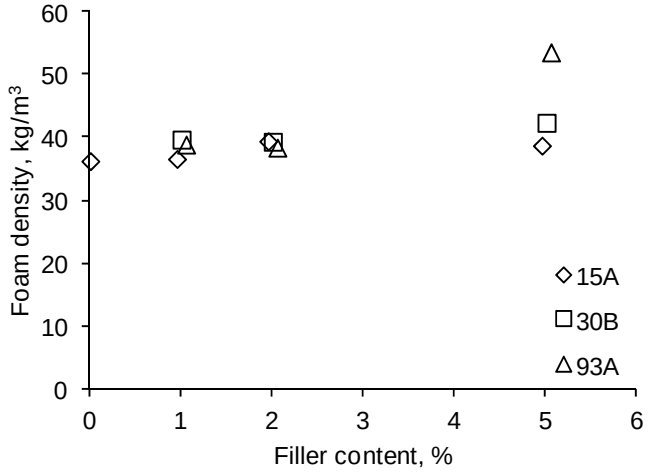

Fig. 2. Foam density vs. Cloisite content

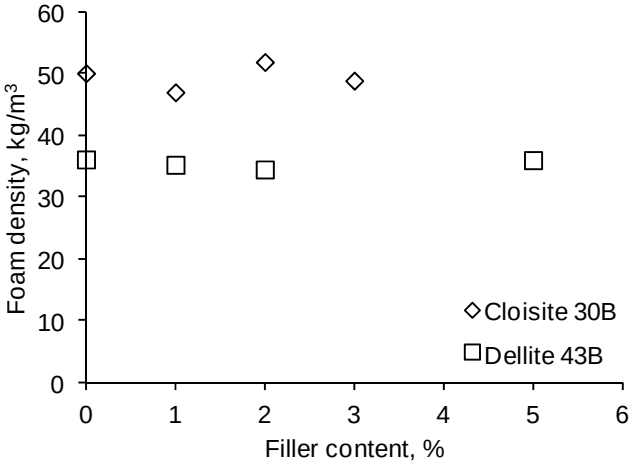

Fig. 3. Foam density vs. MMT content

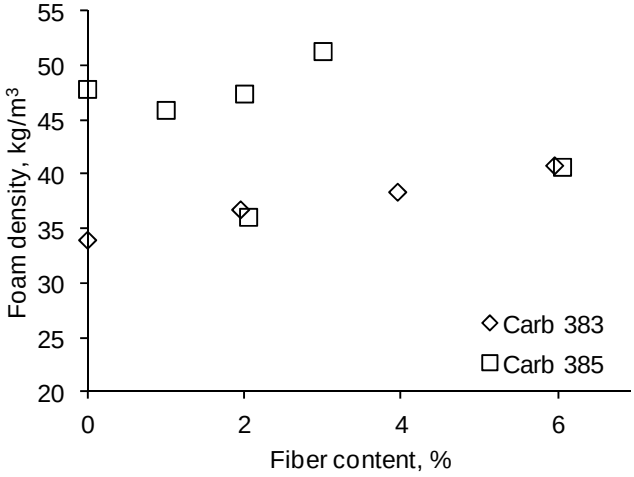

Fig. 4. Foam density vs. carbon fiber content

The solid polymer samples were removed from ampoules upon setting of the polymer, and

cylindrical dog-bone shaped specimens were manufactured by turning. The length of the test section of the specimens amounted to ca. 28 mm and diameter to 5.5 mm. Specimen ends were glued into tubular aluminum tabs. Tensile tests were carried out by stroke control with the displacement rate of 1 mm/min. Young's modulus was determined from the initial, linear part of the stress-strain diagram, while the maximum stress before failure was taken as the tensile strength [[3]].

3.2. Toughness

Fracture toughness of the foams for crack propagation in mode I in the foam rise direction was determined according to ASTM Standard D5045-99. Compact tension specimens with the height and width equal to 65 mm and 20-mm thickness were used. Detailed description of the test procedure and results for neat foams is provided in [[8]].

4. Results and discussion

4.1. Strength of neat polymer foams

By varying the amount of blowing agent, rigid neat RO PIR foams with apparent density in the range from 30 to 60 kg/m^3 were obtained. The dependence of foam strength on density is shown in Fig. 5 for tensile and in Fig. 6 for compressive loading normal to the foam rise direction. It is seen in the graphs that the compressive strength appears to be slightly more affected by foam density than the tensile strength.

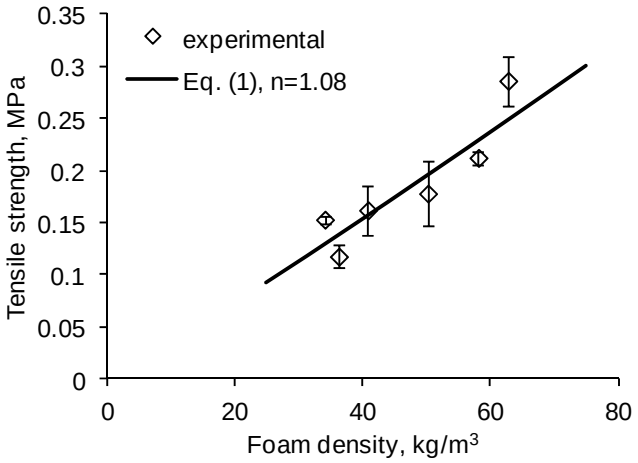

Fig. 5. Tensile strength vs. neat foam density

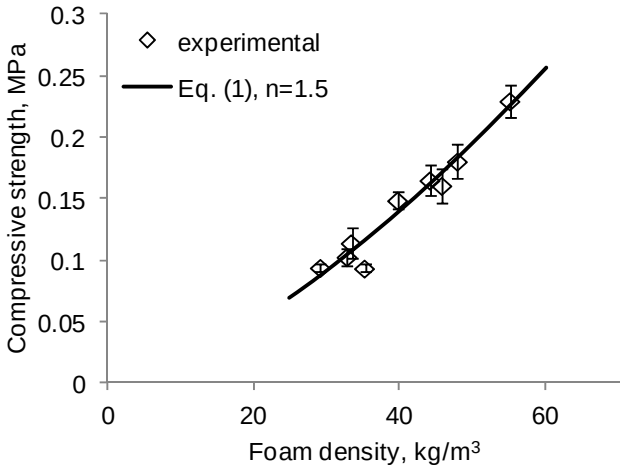

Fig. 6. Compressive strength vs. neat foam density

Assuming a particular geometry of foam cells, a power-low relationship for foam strength σ_f as a function of density ρ_f has been derived in [[6]]

$$\sigma_f = C\rho_f^n \tag{1}$$

where the factor C is related to properties of the cell wall material. For tensile strength of brittle foams, $C = c_8 \sigma_s / \rho_s^n$ where c_8 is a numerical prefactor, σ_s designates tensile strength of the solid cell-wall material and ρ_s - its density. Approximating the respective strength data with Eq.

(1), the value of n = 1.08 was obtained for tensile and n = 1.5 for compressive strength. The agreement of Eq. (1) with the experimental data is reasonably good as seen in Figs. 5 and 6.

4.2. Tensile strength of nanoparticle-filled polymer foams

The presence of nanofiller in a polymer may affect its mechanical characteristics as well as the density and morphology of polymer foams. The scaling relation Eq. (1) should equally apply to filled polymer foams. Hence, the tensile strength of filled polymer foams should scale with solid polymer strength as follows

$$\sigma_f\left(c_{fil}\right) = c_8\left(\frac{\rho_f\left(c_{fil}\right)}{\rho_s\left(c_{fil}\right)}\right)^n \sigma_s\left(c_{fil}\right) \tag{2}$$

where c_{fil} designates filler loading. For low filler concentrations of practical interest, its effect on density of the solid polymer can be neglected, $\rho_s\left(c_{fil}\right) \approx \rho_s(0)$, and polymer strength approximated by a linear function of filler concentration

$$\sigma_s\left(c_{fil}\right) = \sigma_s(0)\left(1 + \mu c_{fil}\right) \tag{3}$$

with μ denoting the reinforcement efficiency factor. It is convenient to introduce the reduced foam strength as follows

$$\sigma_f^*\left(c_{fil}\right) = \sigma_f\left(c_{fil}\right)\left[\rho_f(0)/\rho_f\left(c_{fil}\right)\right]^n \tag{4}$$

(Note that a similar reduction method for foam strength has been introduced in [[9]].) Then, by combining Eqs. (1) – (4), the reduced strength can be expressed via neat foam strength and filler content as follows

$$\sigma_f^*\left(c_{fil}\right) = \sigma_f(0)\left(1 + \mu c_{fil}\right) \tag{5}$$

In order to determine the reinforcement efficiency factor experimentally, the strength of neat and filled foam cell wall material, e.g. struts, should be measured. Such tests are, however, prohibitively complicated even for strut stiffness, due to small dimensions and non-uniform shape of the struts. Macroscopic samples of monolithic polymer are likely to yield only a lower bound for strut strength due to differing flaw structure, with more severe flaws likely to be introduced in polymer samples during manufacture compared to the flaws in microscopic struts arising during rise of the foams. However, μ characterizes the ratio of neat and filled strut strength as seen in Eq. (3) rather than the absolute strength values. Since the flaw distribution in neat and filled polymer samples, prepared following the same procedure, should be comparable, the difference in their strength should reflect variation in intrinsic strength due to the presence of a filler. Hence, as a first approximation, an estimate of μ can be obtained using the ratio of strength of neat and filled polymer samples.

Tensile strength of monolithic neat and filled RO PIR samples is presented in Table 1. Filler content

in the filled solid polymers amounted to 1 % wt. Solving Eq. (3) for μ, expressing c_{fil} in weight percent, and using the average strength data from Table 1, estimates of μ were obtained and presented in Table 1.

Table 1. The effect of filler at 1 wt. % on polymer strength

Filler	no filler	Zano 20	Nanocyl	Cloisite 30B	Dellite 43B
Mean strength, MPa	58.5	65.4	64.9	65.1	60.5
Standard deviation, MPa	6.1	2.7	1.5	2.9	0.7
Number of tests	10	4	4	4	3
μ, 1/%	-	0.119	0.111	0.114	0.034

The reduced tensile strength of foams as a function of nanoclay concentration is shown in Figs. 7 – 9. It is seen that the strength varies almost linearly with filler loading for low concentrations, up to 3 % wt., in qualitative agreement with Eq. (5). At the highest concentration of 5 % wt. considered, the reinforcement efficiency appears to drop, with foam strength being comparable or lower than that at 2 % wt. loading as seen in Figs. 7 and 9.

The strength of low density foams filled with three differently modified Cloisite nanoclays is shown in Fig. 7 as a function of clay loading. It is seen that the strength of all three foams appear to be quite close at the filler concentrations of 1 and 2 % wt., with overlapping scatter bands. The variation of foam strength with filler content, predicted by Eq. (5) using the value of reinforcement efficiency factor μ determined for Cloisite 30B, is in good agreement with test results for the lower fiber loadings. Reasonable agreement of Eq. (5) with strength data is seen also for higher density foams, Fig. 8. However, for low density foams filled with Dellite 43B nanoclay, Eq. (5) using the respective μ value from Table 1 appears to underpredict foam strength shown in Fig. 9.

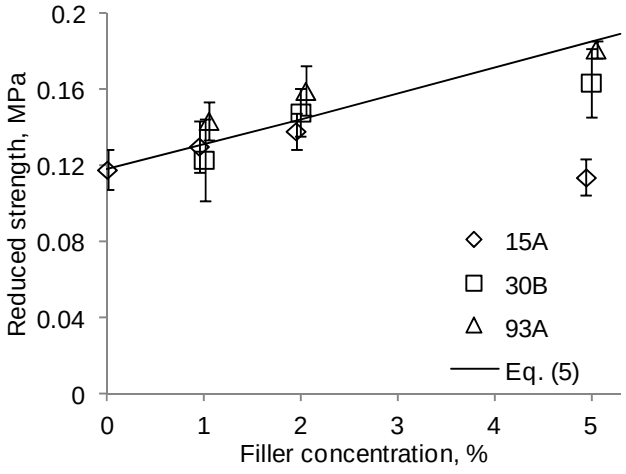

Fig. 7. Reduced tensile strength as a function of nanoclay loading for three Cloisite clays

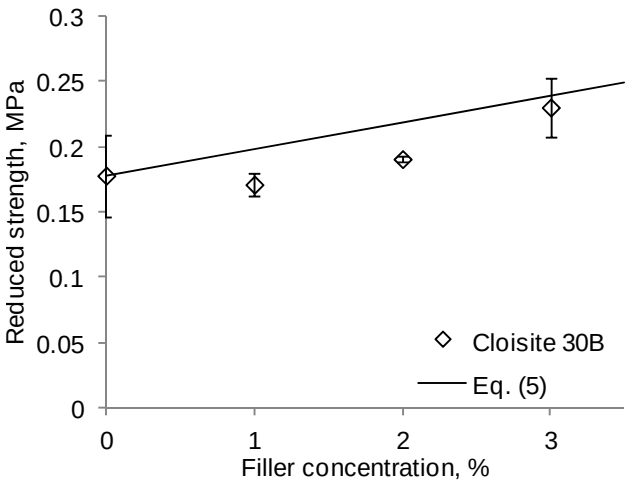

Fig. 8. Reduced tensile strength as a function of Cloisite 30B nanoclay loading

At a given filler loading, the theoretical dependence of tensile strength on foam density can be easily show to have the form

$$\sigma_f\left(c_{fil}\right)=C\rho_f^n\left(1+\mu c_{fil}\right) \tag{6}$$

with the parameter C and n values as determined for neat foams. It is seen in Table 1 that the μ values for ZnO, carbon nanotube, and Cloisite 30B filled polymers are very close, with the average of μ = 0.114. The strength of foams with the fillers mentioned above at 1% wt. is plotted as a function of the filled foam density in Fig. 10. A reasonable agreement with the prediction by Eq. (6) using the average μ value is seen.

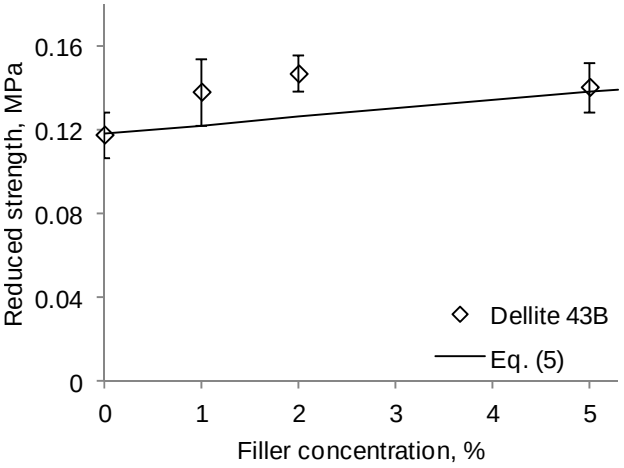

Fig. 9. Reduced tensile strength as a function of Dellite 43B nanoclay loading

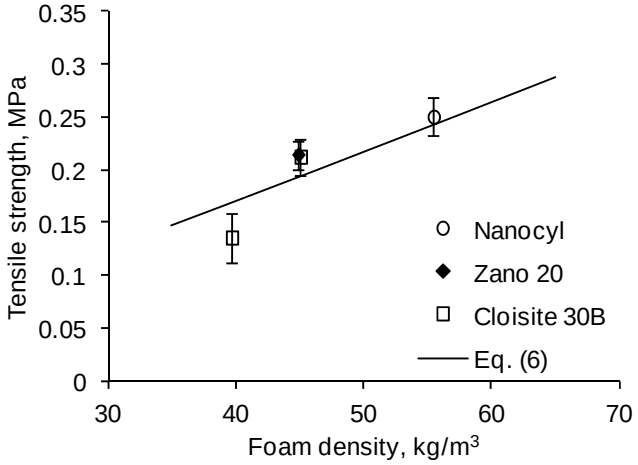

Fig. 10. Tensile strength vs. foam density of filled foams containing 1 % wt. of nanoparticles

4.3. Strength of carbon fiber-filled polymer foams

The reduced tensile strength of foams filled with milled carbon fibers is shown in Fig. 11 as a function of filler content. No apparent effect on the strength is observed for either of the fiber types differing in average length by a factor of ca. 1.7. The reduced compressive strength of foams with two different densities, shown in Fig. 12, was also barely affected by the presence of fiber filler. For ease of comparison, the strength of unfilled foams is indicted by dashed lines in Figs. 11 and 12.

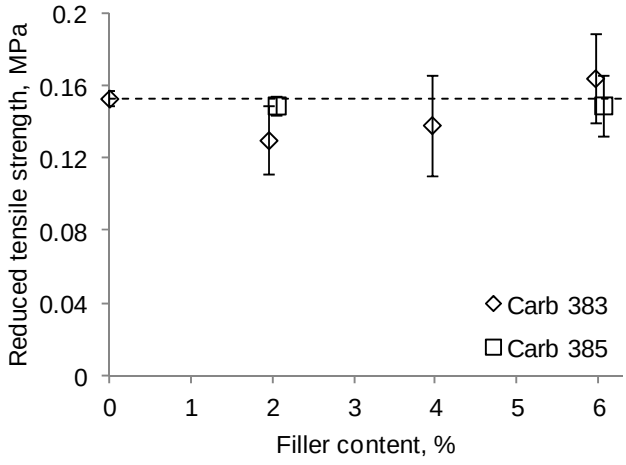

Fig. 11. Reduced tensile strength vs. carbon fiber content

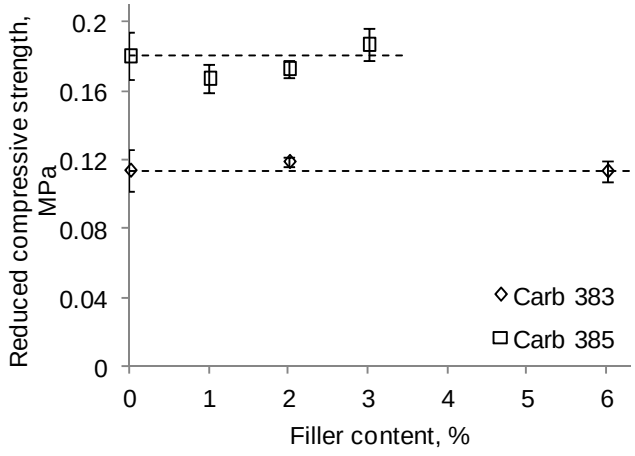

Fig. 12. Reduced compressive strength vs. carbon fiber content

SEM and optical microscopy revealed that the carbon fibers were located within the cell wall

material, in cell struts and nodes, which resulted in appreciable increase in foam stiffness [[5], [10]]. However, polymer struts containing no fibers were also observed even at the highest fiber loading, which might have served as the sites of failure initiation, thus negating any increase in strength of the fiber-reinforced struts.

4.4. Fracture toughness of filled polymer foams

For the range of RO PIR foam density considered, mode I fracture toughness for crack propagation along the foam rise direction was found to vary approximately linearly with foam density [[8]]

$$K_{Icf} = C_k \rho_f \tag{7}$$

Relation Eq. (7) is plotted in Fig. 13 by a solid line together with the experimental toughness values of foams with nano- and microfillers at 1 wt. % loading. It is seen that the presence of carbon microfibers apparently fails to enhance foam resistance to cracking, since the toughness of carbon 385 fiber filled foams agrees within experimental scatter with that of neat foams of comparable density.

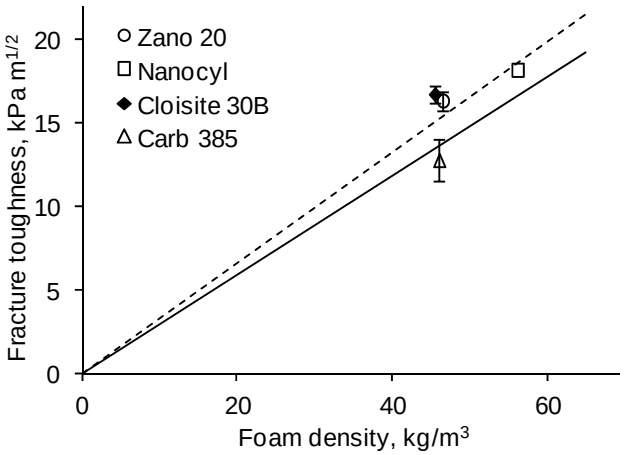

Fig. 13. Fracture toughness of filled foams at 1 wt. % loading. Solid line corresponds to neat foam toughness, dashed line plots prediction by Eq. (9)

Scaling relations derived in [[6], [7]] for foam toughness have the form

$$K_{Icf} = C_k \rho_f^n \tag{8}$$

where $C_k \sim \sigma_s \sqrt{l_s} \big/ \rho_s^n$ with l_s designating strut length and the exponent estimates ranging from n = 1 [[7]] to 1.5 [[6]]. Combining Eqs. (3), (7), and (8) (with n = 1), we obtain for filled foam toughness

$$K_{Icf}\left(c_{fil}\right) = C_k \rho_f \left(1 + \mu c_{fil}\right) \tag{9}$$

with the parameter C_k value as determined for neat foams. The prediction according to Eq. (9) is plotted in Fig. 13 by dashed line, using the average μ value for ZnO, carbon nanotube, and Cloisite 30B filled polymers. It is seen that Eq. (9) reasonably accurately reflects the observed increase of

nanofilled foam toughness with respect to that of neat foams. However, the strut length factor, neglected in Eqs. (7) and (9), should be explicitly incorporated in the toughness relations since the variation of strut length with foam density may differ for neat and filled foams.

5. Conclusions

Production technology of rigid low-density polyisocyanurate foams obtained from renewable resources, with the polyol system comprising up to 80% of rapeseed oil-derived esters, has been developed. The production process is energy-saving and environmental friendly. The effect of nano-scale (organically modified MMTs, carbon nanotubes, ZnO particles) and micro-scale (milled carbon fibers) fillers on the strength and toughness of RO PIR foams has been experimentally evaluated. Taking into account the increase in foam density due to the presence of filler, carbon microfibers yielded negligible effect on the tensile and compressive strength and fracture toughness of foams in the 2 to 6 % wt. loadings studied. By contrast, nanofillers at 1 to 3 % wt. loading increased both strength and toughness of the foams. The reinforcement efficiency of the nanofillers can be roughly estimated by strength tests of filled solid polymers.

Acknowledgements

This work has been funded by ERDF via project 2010/0290/2DP/2.1.1.1.0/10/APIA/VIAA/053.

References

[1] M. Kuranska, A. Prociak, M. Kirpluks, U. Cabulis, Porous polyurethane composites based on bio-components. Compos Sci and Techn 75 (2013) 70–76.

[2] Ł. Piszczyk, M. Strankowski, M. Danowska, J.T. Haponiuk, M. Gazda, Preparation and characterization of rigid polyurethane–polyglycerol nanocomposite foams. Eur Polym J 48 (2012) 1726–1733.

[3] M.C. Saha, Md.E. Kabir, S. Jeelani, Enhancement in thermal and mechanical properties of polyurethane foam infused with nanoparticles. Mater Sci Eng A 479 (2008) 213–222.

[4] M.C. Saha, Md.E. Kabir, S. Jeelani, Effect of nanoparticles on mode-I fracture toughness of polyurethane foams, Polym Compos 30 (2009) 1058-1064.

[5] V. Yakushin, U. Stirna, L. Bel'kova, L. Deme, I. Sevastyanova, Properties of rigid polyurethane foams filled with milled carbon fibers. Mech Compos Mater 46 (2011) 679- 688.

[6] M.F. Ashby, The mechanical properties of cellular solids. Metall Trans A, 14 (1983) 1755-1769.

[7] J.B. Choi, R.S. Lakes, Fracture toughness of re-entrant foam materials with a negative Poisson's ratio: experiment and analysis. Int J Fract 80 (1996) 73-83.

[8] J. Andersons**,** E. Spārniņš**,** U. Cābulis, U. Stirna, Fracture toughness of PIR foams produced from renewable resources. Key Eng Mater 525-526 (2013) 29-32.

[9] M.C. Hawkins, B. O'Toole, D. Jackovich, Cell morphology and mechanical properties of rigid polyurethane foam. J Cell Plast, 41 (2005) 267-285.

[10] J. Andersons, J. Modniks, U. Cābulis, U. Stirna, Modeling the effect of short-fiber filler on the stiffness of polyisocyanurate foams, in: D.T. Tsahalis (Ed.), Proc. of 5th IC-SCCE, Vol. II, 2012, pp. 343- 348.

A Numerical Model to Simulate the Pullout of Carbon Fibre with Radially Grown Carbon Nanotubes

Yuanyuan Jia[1], Zuorong Chen[2], Wenyi Yan[1,*]

[1] Department of Mechanical & Aerospace Engineering, Monash University, Clayton, VIC 3800, Australia
[2]CSIRO Earth Science & Resource Engineering, Clayton North, VIC 3169, Australia
* Corresponding author: wenyi.yan@monash.edu

Abstract A recent development of carbon nanotubes (CNTs) based structural composite materials is to grow CNTs radially on micro-fibres and to use these hybrid fibres to develop superior 3D composites. Due to the extremely high tensile strength and stiffness of CNTs and the increased interfacial areas, it is expected that the fracture toughness of the new composites will be increased substantially. To evaluate the bridging effect of this new hybrid fibre, a finite element model was developed to simulate the pullout of a carbon fibre with radially grown carbon nanotubes. The physical multi-length scale problem is treated at the single macroscopic scale by using equivalent spring elements to simulate the bridging effect from CNTs. The nonlinear properties of the spring elements are obtained from the finite element simulation of a single CNT pullout, where the CNT is simulated by using membrane elements. The bonding and debonding behaviours between the carbon fibre-matrix interface and CNT-matrix interface are described by cohesive laws. The cohesive law for the carbon fibre-matrix interface was calibrated from macroscopic single fibre pullout experimental curves. The cohesive law for the CNT-matrix interface was calibrated from published experimental data on single CNT pullout. The numerical results indicate that the effect of growth CNTs on the carbon fibre is significant. The pullout force of the hybrid fibre has a significant increase at the elastic stage before interfacial debonding, which leads to a higher specific pullout energy.

Keywords carbon nanotube, composite, pullout, cohesive law, finite element

1. Introduction

Carbon fibre, which contains at least 92% carbon [1], has been used in broad fields such as aircraft, marine, energy, biomedical and recreational applications due to its high specific stiffness, specific strength, and low thermal expansion characteristics. Carbon nanotubes (CNTs) are the finest and strongest fibres with tube diameter on the nanoscale and lengths from micro to millimetres (up to 18mm) [2]. They are considered as the new generation of reinforcing phase in fabricating nanocomposite materials. Adding 1wt% of CNTs to matrix material, the stiffness of the composite can increase up to 42% [3]. A recent development of carbon nanotubes (CNTs) based structural composite materials is to grow CNTs radially on micro-fibres and to use these hybrid fibres to develop superior 3D composites, carbon nanotube (CNT)/carbon fibre (CF) hybrid composites, which take the advantages of carbon fibres and carbon nanotubes. The traditional fibres only provide the in-plane (x and y directions in Cartesian coordinates) reinforcement. The delamination always occurs in these traditional laminated composites since there is no reinforcement in the direction of the coordinate z (through-thickness direction) to resist the crack initiation and propagation. Since the CNTs align in multi-directions in the matrix, they can provide the reinforcement to the matrix in different directions as 3D reinforcement.

Due to the extremely high tensile strength and stiffness of CNTs and the increased interface areas, it is expected that the fracture toughness of the new composites will be increased substantially. In recent years, some researchers have grown CNTs on the surfaces of carbon fibres to improve the interfacial strength between the fibres and matrix [4-8]. A single fibre pullout test is one of the most widely used techniques to quantify the interfacial strength. In the past few years, only few researches have been carried out to understand the mechanical performance of CNTs reinforced composites using the single fibre pullout test. For example, Qian, et al. [9] examined the interfacial shear strength of CNT-grafted fibres using both the single fibre pullout and push out test. The

experiment results of the CNT-grafted fibres pullout test showed that the interfacial shear strength have a significant increase (from 75 to 118MPa).

Due to the extremely small size, the role of using this hybrid fibre in composite fracture is still unclear. Thus it is essential to use theoretical and numerical analysis to examine the pullout of this new hybrid fibre from the polymer matrix. Several numerical studies have been carried out on the CNT pullout, but no numerical study on CNT/CF hybrid fibre pullout has been reported. Kulkarni et al. [10] and Nie et al. [11] developed two similar multiscale models to evaluate the effect of interfacial strength on the elastic modulus of CNT/CF fibre reinforced polymer composites. In their simulation, they firstly modelled a nanocomposite formed by a single CNT embedded in the epoxy matrix (CNT/matrix) and numerically predicted the overall mechanical properties of the nanocomposite. The second step is to consider the nanocomposite as an equivalent matrix and use it to form a single carbon fibre nanoreinforced laminated composite.

Cohesive zone modelling is a commonly used technique to investigate the failure governed by crack or debonding propagation. It establishes the traction-separation relation for the interface and bridges the gap between the stress- and energy-based approaches [12]. Many studies have been carried out on the interfacial behaviours of fibre-reinforced polymer (FRP) and concrete under mode II conditions [13, 14] by using cohesive zone modelling. However, very little attention has been paid to use cohesive zone modelling to numerically simulate the CNT/CF hybrid fibre pullout.

The purpose of this paper is to investigate the single CNT/CF hybrid fibre pullout test through coupling the single carbon fibre pullout and CNT pullout. The physical multi-length scale problem is treated at the single macroscopic scale by using equivalent spring elements to simulate the bridging effect from CNTs. The bonding and debonding behaviours between the carbon fibre-matrix interface and between the CNT-matrix interface are described by cohesive laws. In this paper, a finite element model of CNT/CF hybrid fibre pullout is firstly presented. Secondly the single carbon fibre pullout and the single CNT pullout are studied by using cohesive zone modelling. The two different cohesive laws for the carbon fibre-matrix interface and CNT-matrix interface are calibrated from macroscopic single carbon fibre pullout experimental curves and published experimental data on single CNT pullout, respectively. The single CNT/CF hybrid fibre pullout test is investigated by using a cohesive finite element model in which the two pullout processes at different scales are coupled. The effect of CNTs on debonding force and specific pullout energy are investigated.

2. Numerical Model

CNTs can be radially grown on the surface of carbon fibres using chemical vapour deposition (CVD). Fig. 1 shows Scanning Electron Microscope (SEM) image of carbon fibre after CNT growth [15]. These hybrid fibres are then embedded in an epoxy matrix to produce CNT/CF hybrid fibre reinforced composites. The diameter and interfacial area of the fibre are significantly increased by growth CNTs which can improve the fracture toughness of traditional fibre-matrix composites.

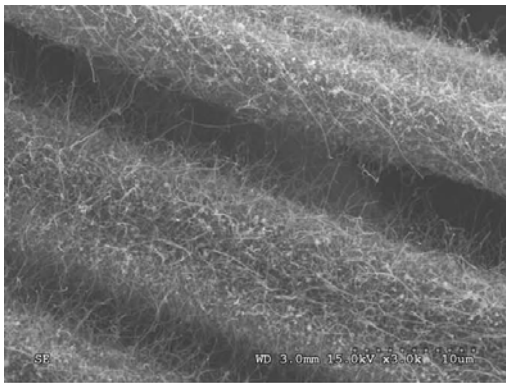

Figure 1. SEM image of a hybrid fiber with CNTs [15]

In a typical single fibre pullout test, there are three stages during the pullout process, including elastic deformation stage before debonding, debonding stage and sliding stage. In the first stage, the fibre and the matrix are well bonded. As the pullout force increases, a crack initiates and propagates along the interface between the fibre and the matrix, leading to a complete debonding, which is the debonding stage. In the last stage, the fibre slides out from the matrix, with friction acting between the two newly formed surfaces. One condition of pullout test is that the length of fibre embedded in the matrix must be less than the critical embedded length for debonding. Otherwise the fibre will break before the debonding occurs.

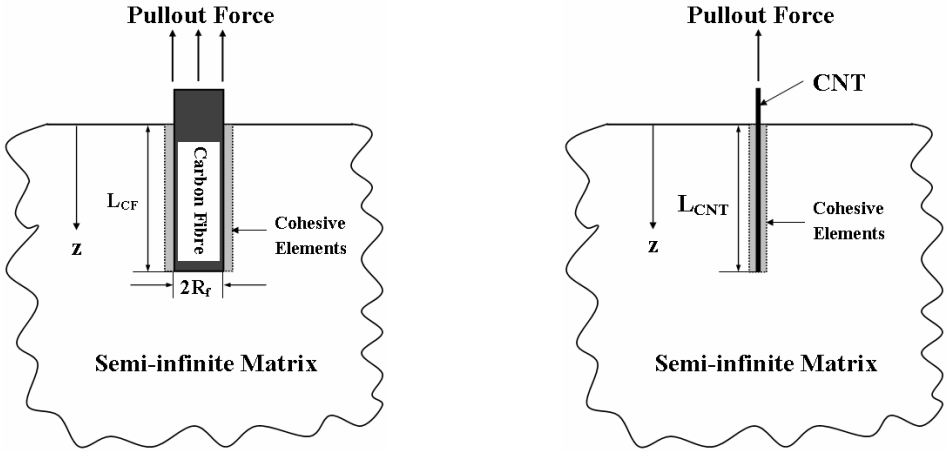

(a) (b)

Figure 2. (a) A schematic diagram of a single carbon fibre pullout model; (b) A schematic diagram of a single CNT pullout model

In this study, the CNT/CF hybrid fibre pullout was simulated through coupling of the single carbon fibre pullout and single CNT pullout. In the single carbon fibre pullout, a pullout displacement was applied uniformly on the top surface of the cylindrical fibre embedded in a semi-infinite matrix in the axial direction as shown in Fig. 2(a). The commercial finite element package Abaqus was used to investigate the carbon fibre pullout problem. A two-dimensional axisymmetric model was constructed with a very fine mesh (element type CAX4 and size 1μm ×1μm) in the area around the interface between the fibre and the matrix to ensure the accuracy of the numerical results. A small number of four-node, axisymmetric cohesive elements (COHAX4) were used to define the cohesive zone [16]. In the single CNT pullout, another two-dimensional axisymmetric model was developed using a single cylindrical CNT embedded in a semi-infinite matrix. A pullout displacement was also applied on the top of the CNT in the axial direction as shown in Fig. 2(b). L_{CNT} is the total embedded CNT length. Due to its extreme small size (in nanoscale), membrane elements (MAX1)

were used to represent the CNT. The membrane element can be used to represent the thin surface which offers strength in the plane of the element without bending stiffness [17]. The axisymmetric cohesive elements (COHAX4) were also used to define the cohesive zone between the interface of CNT and matrix.

The physical problem of the CNT/CF hybrid fibre pullout was treated as a cylindrical carbon fibre attached with spring elements which perform the bridging effect of CNTs embedded in a semi-infinite matrix, as shown in Fig. 3(a). Spring element is defined as a deformable member which is subjected to tensile or compressive loads in the axial direction. In the pullout simulation, the spring elements are elongated and the spring forces resist the fibre to be pulled out [18, 19]. The parameters involved to define the nonlinear spring elements were obtained based on the numerical results from the single CNT pullout. The radius of the fibre is denoted as R_{CF} and L_{CF} is the total embedded fibre length. As the model developed in carbon fibre pullout [16], a pullout displacement will be applied uniformly on the top surface of the fibre in the axial direction. Since the spring elements are used to simulate the force of CNTs applied on the carbon fibre during the pullout, the debonding of CNT-matrix interface will not be explicitly simulated in the hybrid fibre pullout model. Therefore the debonding only occurs between the carbon fibre and matrix interface, which is assumed to initiate at the carbon fibre-matrix interface and propagate longitudinally along the carbon fibre. It is also assumed that the normal stress along the carbon fibre does not exceed its material ultimate strength, so the carbon fibre will not break before it is pulled out. The plastic behaviour is not considered in this paper.

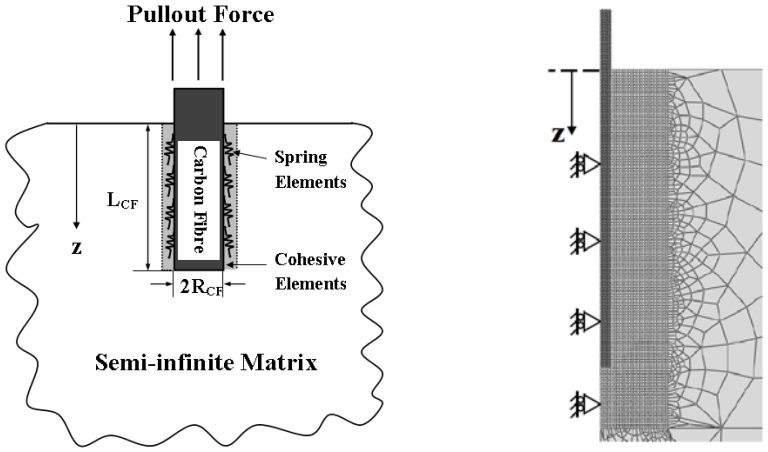

(a) (b)

Figure 3. (a) A schematic diagram of the CNT/CF hybrid fibre pullout model using spring element to perform the CNT; (b) Axisymmetric finite element model for a single CNT/CF hybrid fibre pullout with a fine mesh around the interface

Due to the symmetry of this problem, a two-dimensional axisymmetric model was constructed in this finite element analysis. The radius and depth of the matrix are much larger than the dimensions of the fibre in the numerical models so as to simulate a semi-infinite matrix body. The bottom of the model is constrained in both the radial and axial directions. The vertical side along the axisymmetric axis is constrained only in the radial direction. The model contains a total of 5149 four-node quadrilateral elements. A very fine mesh with the smallest elements (CAX4) of 1μm ×1μm were used in the area around the interface as shown in Fig. 3(b). A small number of four-node, axisymmetric cohesive elements (COHAX4) were used to define the cohesive zone. Nonlinear spring elements (SPRING1) were used to model the bridging effect of CNTs in the CNT/CF hybrid fibre pullout. In reality, the CNTs grown on the carbon fibre surface should be

considered as the CNTs embedded in the matrix at an inclination angle of 90º with respect to pullout direction. For this case, the CNT should be considered as a flexible string passing over a frictional pulley, and a snubbing friction model can be derived to relate the pullout force to the fiber inclination angle [20]. Therefore, a frictional pulley model for pullout force of the single inclined CNT was firstly introduced

$$F_{CNT(\Phi)} = F_{CNT(\Phi=0)} e^{f\Phi} \tag{1}$$

where $F_{CNT(\Phi)}$ is the pullout force of inclined CNT with the pullout direction Φ. f is the snubbing friction coefficient which is assumed as 0.1 in this study. Secondly, the pullout force of the single CNT obtained in FE simulation with pulley effect was applied to define the nonlinear properties of the spring elements.

In addition, two cohesive zones were defined between the carbon fibre-matrix interface and CNT-matrix interface in this study. In the single carbon fibre pullout simulation, a bilinear cohesive law was implemented [16]. In the single CNT pullout simulation, the cohesive zone model was adopted from Tvergaard [21] and Chaboche et al. [22]. The interfacial debonding during a fibre pullout test is a pure mode II fracture problem. Therefore the mode II cohesive law [22] can be simplified as

$$T_t = \left(\frac{27u_t^3}{4\delta_t^3} - \frac{27u_t^2}{2\delta_t^2} + \frac{27u_t}{4\delta_t} \right) \tau_{\max} \tag{2}$$

where u_t is the tangential separation and δ_t is the complete tangential separation. $\tau_{\max}$ is the interfacial crack initiation stress under shear loading condition. Correlating to energy-based fracture mechanics, the fracture energy G_{IIc} is the area under traction-separation curve.

3. Results and Discussion

3.1 Single Carbon Fibre Pullout Simulation

A comparison study between a finite element simulation and an experimental pullout test was first carried out as shown in Fig. 4 [16]. A 7μm diameter HTA-7-6K carbon fibre is embedded in an Epilox epoxy matrix with the embedded length L_{CF} = 100μm, which is consistent with the experiment by Bogoeva-Gaceva et al. [23]. The residual thermal stresses were considered on the assumption of ΔT = -95°C.

From Fig. 4, it can be seen that the simulated pullout curve agrees overall very well with the experimental curve from Bogoeva-Gaceva et al. [23] with these fitted parameters $\tau_{\max(CF)}$ = 45MPa, separation displacement of crack initiation $\delta_{d(CF)}$ = 21.86μm, and the complete separation displacement $\delta_{t(CF)}$ = 25μm. These calibrated parameters of cohesive zone are used to simulate CNT/CF hybrid fibre pullout in the following section.

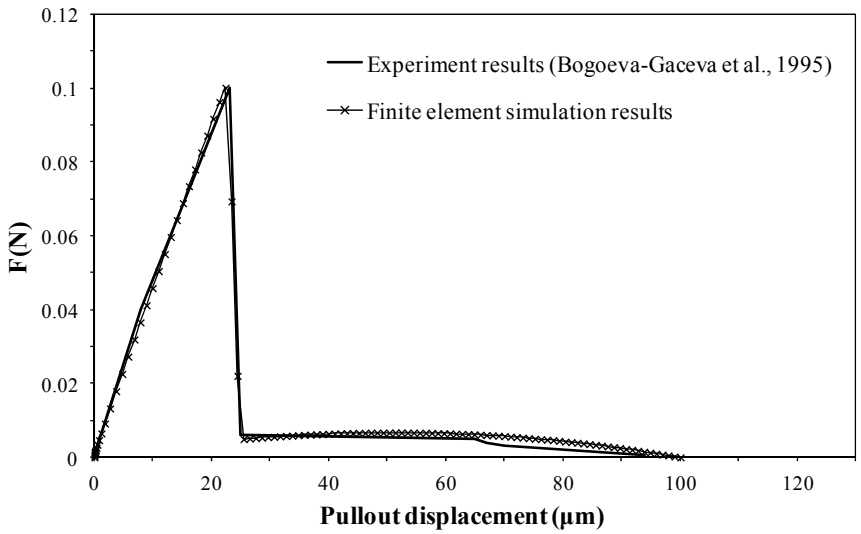

Figure 4. Comparison between experiment and FE simulation for single carbon fibre pullout curve

3.2. Single CNT Pullout Simulation and Validation

Similarly, another comparison study between a finite element simulation and an experimental single CNT pullout test was carried out. In this study, a 24nm diameter multiwalled-carbon nanotube (MWNT) is embedded in an epoxy matrix with the embedded length L_{CNT} = 2.6μm, which is consistent with the experiment by Cooper et al. [24].

Fig. 5 shows the simulated single CNT pullout curve. The numerical results were compared with the experimental results as shown in Table 1. W_{CNT} is the total CNT pullout energy, which is the total area under the pullout force-displacement curve. It can be seen that the numerical results agrees overall very well with the experimental results listed by Cooper et al. [24] with these fitted parameters $\tau_{\max(CNT)}$ = 36MPa, $\delta_{d(CNT)}$ = 140nm, $\delta_{t(CNT)}$ = 410nm which are used to define the nonlinear properties of spring elements in the following section.

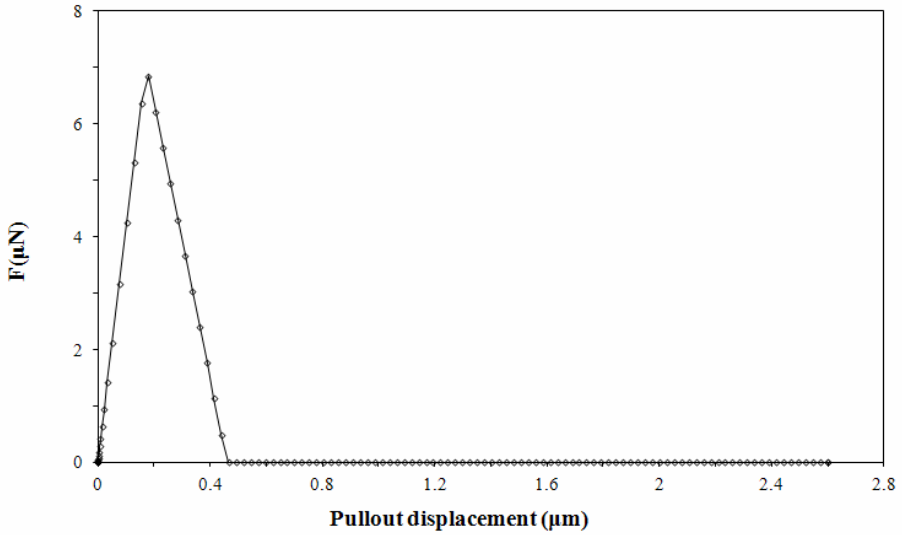

Figure 5. FE simulation for single CNT pullout curve

Table 1. Comparison between experiment and FE simulation for single CNT pullout

	FE simulation	Cooper et al. [24]
Maximum pullout force $F_{\max(CNT)}$ (μN)	6.845	6.8±1.7
Total CNT pullout energy W_{CNT} (J)	1.63×10^{-12}	1.6×10^{-12}

3.3. CNT/CF Hybrid Fibre Pullout

3.3.1. Estimation of length and number of CNT grown carbon fibre

To simulate a single CNT/CF hybrid fibre pullout, the length and number of CNT radially grown on the single carbon fibre should be identified. In this study, the length and number of CNTs were estimated based on the experimental results obtained by Zhang et al. [25]. In their experiment, carbon nanotubes were successully grown on the surface of a 7μm diameter carbon fibre T650 by chemical vapor deposition. The diameter of the CNT/CF hybrid fibre measured was appoximately 20μm. Therefore, the length of CNTs (L_{CNT}) grown on the carbon fibre surface can be estimated as 6.5μm.

The number of CNTs grown on the carbon fibre surface was calculated based on the CNT population density estimated from the experiment. The CNT population density at the carbon fibre surface was estimated as high as 8×10^9 tubes/cm^2 [25]. In this study, it is assumed that CNTs are uniformly grown on the carbon fibre surface. The number of CNTs grown on the carbon fibre surface per unit length can be calculated as 1760 tubes/μm. It is also assumed that there are 100 layers of CNTs uniformly distributed along the carbon fibre-matrix interface (L_{CF} = 100μm with element size 1μm ×1μm). Therefore, the total number of CNTs distributed on each layer was estimated as 1760 tubes. In addition, 99 layers of CNTs were used to joint with the carbon fibre in the hybrid fibre simulation which excluded the bottom layer of CNTs.

3.3.2. CNT/CF hybrid fibre pullout force

The maximum pullout force of hybrid fibre ($F_{\max(H)}$), is one of the most important parameters recorded from a pullout test, which is used to calculate the average interfacial strength. Fig. 6 showed the case of CNTs completely pulled out with the single carbon fibre. It can be seen that the magnitude of the maximum pullout force for CNT/CF hybrid fibre ($F_{\max(H)}$ = 0.39N) is much higher than the carbon fibre pullout ($F_{\max(CF)}$ = 0.1N). The maximum pullout force of the hybrid fibre has a significant increase by 290%. The increased pullout force was observed in the early stage of elastic deformation before the interfacial debonding occurred in carbon fibre. An et al. [26] performed an experiment of the CNT/CF hybrid fiber pullout to confirm that the maximum pullout force of hybrid fibre had a significant increase up to 120%. The difference probably is due to the different number of CNTs and carbon fibre embedded length used in this study.

The interfacial shear strength (IFSS), which is traditionally used to evaluate the interfacial bonding, is normally calculated from the load-displacement curve of a fibre pullout test. It can be defined as [27]

$$\tau_s = \frac{F_{\max}}{2\pi R_{CF} L_{CF}} \tag{3}$$

The IFSS increases from about 45.5MPa to 177MPa. This improvement of the interfacial shear strength is due to the increased interfacial area and roughness, which can provide a stronger interfacial bonding between the CNTs, carbon fibre and the matrix. A significant improvement in the IFSS was also observed in the experiment studies [7, 9, 26, 28]. This study indicates that the effect of growth of CNTs on the carbon fibre surface is significant, which can enhance the adhesion between the fibre-matrix and thus improve the delamination resistance of the composite.

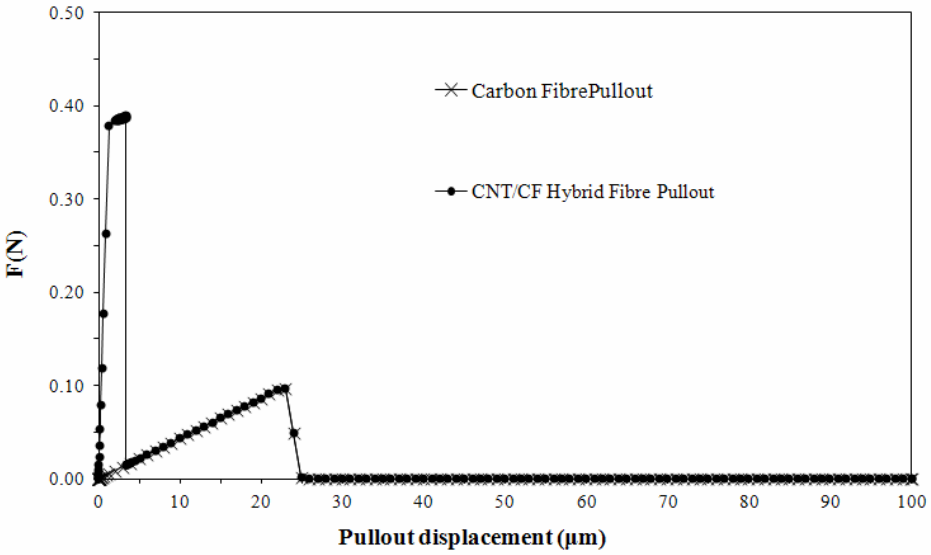

Figure 6. Comparison between the single carbon fibre pullout and the single CNT/CF hybrid fibre completed pullout curve.

3.3.3. Specific pullout energy

The specific pullout energy can be well used to quantify the beneficial effect of growth of CNTs on the bridging resistance of fibres in composites, which is first introduced in this paper. The specific pullout energy ω is defined as

$$\omega = \frac{W}{2\pi R_{CF} L_{CF}} \tag{4}$$

where W is the total fibre pullout energy, which is the total area under the pullout force-displacement curve. Specific pullout energy can be used to quantify the fibre bridging effect in a composite failure analysis. Fibre bridging appears behind a major crack tip in an intralaminar fracture, which enhances the fracture resistance of fibre reinforced composite. According to the calculated results, it can be seen that the influence of growth of CNTs on the specific pullout energy is significant. The magnitude of the specific pullout energy of CNT/CF hybrid fibre (ω_H = 1032J/m^2) is much higher than the carbon fibre (ω_{CF} = 565J/m^2). The specific pullout energy of the CNT/CF hybrid fibre increases by 83%. This is due to the large resistance induced by the carbon nanotubes, which requires more energy to pullout the fibre.

4. Conclusion

A finite element model was developed to simulate the pullout of a carbon fibre with radially grown carbon nanotubes. The bonding and debonding behaviours between the carbon fibre-matrix

interface and CNT-matrix interface were described by cohesive laws. Equivalent nonlinear spring elements were used to simulate the force of CNTs applied on the carbon fibre during the pullout. The numerical results of the CNT/CF hybrid fibre pullout from a case study show that the growth of CNTs on the carbon fibre surface has a significant effect on the maximum pullout force, and they increase the resistance in fibre at the elastic deformation stage before interfacial debonding. There also a signification improvement in the interfacial shear strength, which indicates that growth of CNTs can provide a stronger interfacial bonding between the CNTs, carbon fibre and the matrix. The beneficial effect of growth of CNTs on the bridging resistance of fibres in composites can be well quantified by the specific pullout energy. The increased specific pullout energy of the hybrid fibre indicates that growth of CNTs can enhance the fracture resistance of fibre reinforced composites.

References

[1] E. Fitzer, Carbon fibres filaments and composites, Kluwer Academic, Dordrecht, 1990.

[2] W. Beckman, UC Researchers Shatter World Records with Length of Carbon Nanotube Arrays, 2007 [cited 2012 06-11], Available from: http://www.uc.edu/News/NR.aspx?ID=5700.

[3] D. Qian, E.C. Dickey, R. Andrews, T. Rantell, Load transfer and deformation mechanisms in carbon nanotube-polystyrene composites. Applied Physics Letters, 76(20) (2000) 2868-2870.

[4] E.T. Thostenson, W.Z. Li, D.Z. Wang, Z.F. Ren, T.W. Chou, Carbon nanotube/carbon fiber hybrid multiscale composites. Journal of Applied Physics, 91(9) (2002) 6034-7.

[5] E. Bekyarova, E.T. Thostenson, A. Yu, H. Kim, J. Gao, J. Tang, H.T. Hahn, T.W. Chou, M.E. Itkis, R.C. Haddon, Multiscale carbon nanotube-carbon fiber reinforcement for advanced epoxy composites. Langmuir, 23(7) (2007) 3970-3974.

[6] R.J. Sager, P.J. Klein, D.C. Lagoudas, Q. Zhang, J. Liu, L. Dai, J.W. Baur, Effect of carbon nanotubes on the interfacial shear strength of T650 carbon fiber in an epoxy matrix. Composites Science and Technology, 69(7-8) (2009) 898-904.

[7] F.-H. Zhang, R.-G. Wang, X.-D. He, C. Wang, L.-N. Ren, Interfacial shearing strength and reinforcing mechanisms of an epoxy composite reinforced using a carbon nanotube/carbon fiber hybrid. Journal of Materials Science, 44(13) (2009) 3574-7.

[8] A. Godara, L. Gorbatikh, G. Kalinka, A. Warrier, O. Rochez, L. Mezzo, F. Luizi, A.W. van Vuure, S.V. Lomov, I. Verpoest, Interfacial shear strength of a glass fiber/epoxy bonding in composites modified with carbon nanotubes. Composites Science and Technology, 70(9) (2010) 1346-52.

[9] H. Qian, A. Bismarck, E.S. Greenhalgh, G. Kalinka, M.S.P. Shaffer, Hierarchical composites reinforced with carbon nanotube grafted fibers: The potential assessed at the single fiber level. Chemistry of Materials, 20(5) (2008) 1862-1869.

[10] M. Kulkarni, D. Carnahan, K. Kulkarni, D. Qian, J.L. Abot, Elastic response of a carbon nanotube fiber reinforced polymeric composite: A numerical and experimental study. Composites Part B: Engineering, 41(5) (2010) 414-421.

[11] J. Nie, Y. Jia, P. Qu, Q. Shi, Carbon Nanotube/Carbon Fiber Multiscale Composite: Influence of Interfacial Strength on Mechanical Properties. (2011) 1-4.

[12] N. Chandra, H. Li, C. Shet, H. Ghonem, Some issues in the application of cohesive zone models for metal-ceramic interfaces. International Journal of Solids and Structures, 39(10)

(2002) 2827-2855.

[13] B. Taljsten, Strengthening of concrete prism using the plate-bonding technique. *International Journal of Fracture*, 82(3) (1996) 253-266.

[14] J.G. Teng, H. Yuan, J.F. Chen, FRP-to-concrete interfaces between two adjacent cracks: theoretical model for debonding failure. *International Journal of Solids and Structures*, 43(18-19) (2006) 5750-5778.

[15] K.H. Hung, W.S. Kuo, T.H. Ko, S.S. Tzeng, C.F. Yan, Processing and tensile characterization of composites composed of carbon nanotube-grown carbon fibers. Composites Part A: Applied Science and Manufacturing, 40(8) (2009) 1299-304.

[16] Y. Jia, W. Yan, H.-Y. Liu, Carbon fibre pullout under the influence of residual thermal stresses in polymer matrix composites. Computational Materials Science, 62 (2012) 79-86.

[17] ABAQUS, *ABAQUS 6.11 Documentation*, Dassault Systèmes Simulia Corp., 2012.

[18] W. Yan, H.-Y. Liu, Y.-W. Mai, Numerical study on the mode I delamination toughness of z-pinned laminates. Composites Science and Technology, 63(10) (2003) 1481-93.

[19] W. Yan, H.-Y. Liu, Y.-W. Mai, Mode II delamination toughness of z-pinned laminates. Composites Science and Technology, 64(13-14) (2004) 1937-45.

[20] V.C. Li, Y. Wang, S. Backer, Effect of inclining angle, bundling, and surface treatment on synthetic fibre pull-out from a cement matrix. Composites, 21(2) (1990) 132-140.

[21] V. Tvergaard, Effect of fibre debonding in a whisker-reinforced metal. Materials Science and Engineering A, A125(2) (1990) 203-213.

[22] J.L. Chaboche, R. Girard, P. Levasseur, On the interface debonding models. International Journal of Damage Mechanics, 6(3) (1997) 220-257.

[23] G. Bogoeva-Gaceva, E. Maeder, L. Haeussler, K. Sahre, Parameters affecting the interface properties in carbon fibre/epoxy systems. Composites, 26(2) (1995) 103-107.

[24] C.A. Cooper, S.R. Cohen, A.H. Barber, H.D. Wagner, Detachment of nanotubes from a polymer matrix. Applied Physics Letters, 81(20) (2002) 3873-5.

[25] Q. Zhang, J. Liu, R. Sager, L. Dai, J. Baur, Hierarchical composites of carbon nanotubes on carbon fiber: Influence of growth condition on fiber tensile properties. Composites Science and Technology, 69(5) (2009) 594-601.

[26] F. An, C. Lu, Y. Li, J. Guo, X. Lu, H. Lu, S. He, Y. Yang, Preparation and characterization of carbon nanotube-hybridized carbon fiber to reinforce epoxy composite. Materials and Design, 33(1) (2012) 197-202.

[27] I.M. Daniel, O. Ishai, Engineering Mechanics of Composite Materials. 2 ed, New York, Oxford University Press, 2006.

[28] J.D. Schaefer, A.J. Rodriguez, M.E. Guzman, C.-S. Lim, B. Minaie, Effects of electrophoretically deposited carbon nanofibers on the interface of single carbon fibers embedded in epoxy matrix. Carbon, 49(8) (2011) 2750-2759.

Measurement of Adhesion Energy of Electrospun Polymer Membranes Using a Shaft-loaded Blister Test

Shing-Chung Wong[1,*], Haining Na[1,2], Pei Chen[1]

[1] Department of Mechanical Engineering, University of Akron, Akron, OH 44325, USA
[2] Ningbo Key Laboratory of Polymer Materials, Ningbo Institute of Material Technology and Engineering, Chinese Academy of Sciences, Ningbo, Zhejiang 31520, China
* Corresponding author: swong@uakron.edu

Abstract This study aims to examine the adhesion work of electrospun polymer nano- and micro-fibers. The adhesion energy at the interface of electrospun membrane and a rigid substrate is characterized by a shaft-loaded blister test (SLBT). By controlling the processing parameters, polyvinylidene fluoride (PVDF) fibrous membranes are prepared with fiber diameters ranging from 201 ± 86 nm to 2,724 ± 587 nm. The adhesion energy between electrospun membrane and rigid substrate increases from 8.1 ± 0.7 mJ/m^2 to 258.8 ± 43.5 mJ/m^2 by use of smaller fiber diameters. Adhesion energies between electrospun PVDF membranes and SiC substrates made of different grain sizes are evaluated. Fibrous membrane produces an adhesion energy as high as 420.1 ± 62.9 mJ/m^2 in contact with SiC substrate with a 68 μm grit size. The SLBT methodology is extended to understand the adhesion energy between electrospun membranes. The increase in adhesion work is attributed to an increased area between fiber delaminated surfaces and surface asperities.
Keywords Adhesion energy, Electrospinning, Fiber diameter

1. Introduction

Hierarchical structures are usually evolved by insects and geckos on feet to produce extraordinarily strong adhesion for bodyweight support [1-3]. This phenomenon inspires researchers to use artificial polymer fibrillars in producing film-like adhesives [4-6]. Recently, thin membrane composed by ultrafine fibers is fabricated by electrospinning from polymer melt or solution [7-12] in a very simple process. The obtained electrospun membrane initiates a unique way to produce strong film-like adhesives. It requires a suitable characterization method is produced to evaluate the adhesion property of electrospun membranes.

In our previous an effective Shaft Loaded Blaster Test (SLBT) is reported to measure adhesion energy between electrospun membrane and rigid substrate [13]. As shown in Figure 1, SLBT consists of three main parts including stiff shaft, central holed rigid substrate and electrospun membrane. During SLBT, mechanical load is applied by through the stiff shaft on the center of electrospun membrane to form an axisymmetric conical delamination at membrane-substrate interface. The interrelationship of P-w_0-a between the measureable quantities, is governed by

$$P = \frac{\pi}{4}\left(\frac{Eh}{a^2}\right) w_0^{\,3} \tag{1}$$

Where P is the exterior force; E and h are elastic modulus and thickness of the membrane respectively; a and w_0 respectively refers to debonding radius and central deflection. In SLBT, mechanical equilibrium is exhibited [14-17], that is, the strain energy release rate, G, equals the work of adhesion, W, provided the entire membrane is linear elastic response. The equation is presented as

$$G = W = \frac{1}{4}\left(\frac{P\, w_0}{\pi\ a^2}\right) = \frac{1}{4\pi}\left(\frac{P}{w_0}\right)\cdot\left(\frac{w_0}{a}\right)^2 \tag{2}$$

By understanding of the principle [14-16] and process [13] of SLBT, in this paper we develop a research to discuss the adhesion work of electrospun polymer nano- and micro-fibers. Fiber

diameter is systematically examined to characterize size effect of electrospun fibers on adhesion energy. Surface asperity of rigid substrate is also discussed in detail to show the condition of high adhesion energy between electrospun membrane and rigid substrate.

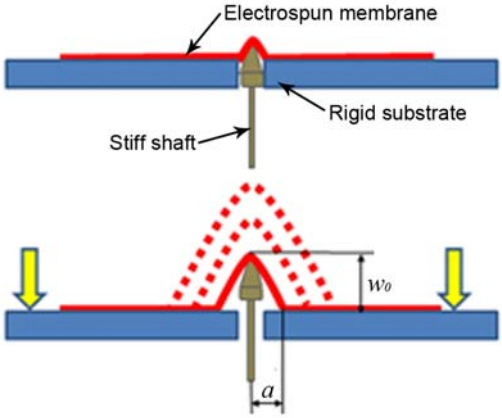

Figure 1. Schematic of shaft loaded blister test

2. Experimental Works

2.1. Materials

PVDF (Kynar 761) is purchased from Arkema Incorporation. N,N-Dimethylformamide (DMF) and acetone are purchase from Fisher Scieare at reagent grade.

2.2. Preparation of electrospun membranes

PVDF membranes for adhesion tests are fabricated by electrospinning. PVDF powder is dissolved in a solvent mixture of DMF and acetone to form PVDF solution. The concentration of PVDF solution is controlled at 0.15-0.20 g/mL. The volume ratio of DMF and acetone is selected as 7:3 and 5:5. Electrospinning is conducted at ambient temperature, solution feed rate 0.3 mL/h under applied voltage at 10 kV. Electrospinning process is proceeded ~10 h to fabricate a 10 μm thick fibrous membrane. Then electrospun PVDF membrane was dried in vacuum oven at 50 ºC for 12 h before used in SLBT.

2.3. Characterization of fiber mophology

Fiber morphology of electrospun membranes is characterized by scanning electron microscopy (JEOL JSM-6510LV). Before imaging, samples are coated with silver by sputter coater (K575x, Emitech) for 1.5 min at 55 mA. Average fiber diameter and fiber density are determined from SEM micrographs by use of the software ImageJ 1.45s. For each sample, five images are used for calculation and total 100 fibers are measured for average diameter calculation. Fiber density is also calculated by measuring the total area occupied by fibers in SEM micrographs.

2.4. Operation of SLBT

PVDF membrane is cut into a square of 30 mm by 30 mm for SLBT. The rigid substrate is prepared from cardboard with inorganic coating (detailed information of the substrate is exhibited in our previous work [13]). The arithmetic average roughness (R_a) of the substrate is approximately 128 nm. In order to make good contact, a lightweight plastic roller (~100 g) was used to roll over the membrane onto the substrate to squeeze air bubbles between membrane and substrate. Figure 1 shows a schematic of SLBT. Electrospun membrane is self-adhered onto the

top surface of rigid substrate. A rigid shaft with spherical cap (R=0.35mm) is used to apply force P to the electrospun membrane. In SLBT, the test speed is consistent at 20 mm/min. Before the test, the shaft is set to just contact with electrospun PVDF membrane, but no debonding between the membrane and substrate happens. During the test, initial vertical displacement leads to a blister debonding of the local area on the membrane close to the shaft end.

In SLBT, P is recorded by a 1 N load cell (Futek Advanced Sensor Tech). The whole test is monitored by 7X-45X Simul-Focal Trinocular Boom Microscope and recorded by a 3M camera (AMscope). Video captures are analyzed by ImageJ 1.45s to obtain in-situ deformation profile. Therefore, the relationship between delamination radius (a) and central deflection (w_0) can be obtained.

Silicon carbide (SiC) substrates with different surface asperities are also used to do the SLBT to evaluate adhesion energy between electrospun membrane and rigid substrate. After the test, adhesion energy is calculated by equation (2).

3. Results and Discussion

3.1. Morphology of Electrospun Membranes

SEM images and fiber diameter of electrospun PVDF membranes are shown in Figure 2. All the electrospun membranes show uniform fibers without bead. Fiber diameter distribution is exhibited

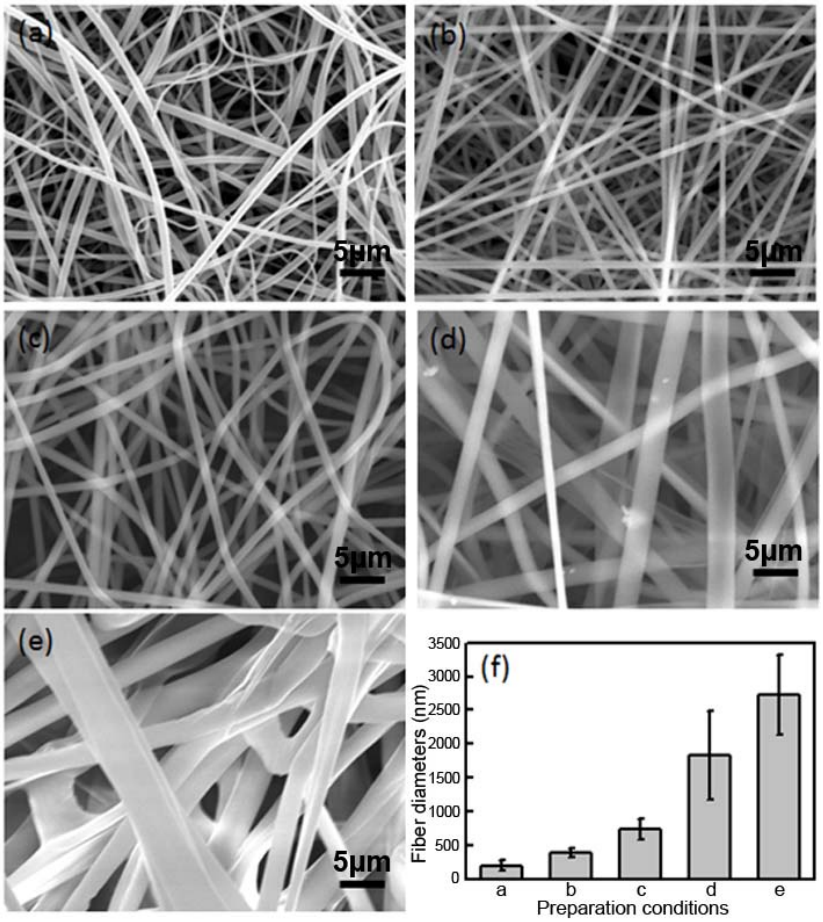

Figure 2. SEM images of electrospun PVDF membrane prepared at conditions of solution concentration and DMF/acetone (a) 0.15 g/mL, 7:3, (b) 0.17 g/mL, 7:3, (c) 0.15 g/mL, 5:5, (d) 0.17 g/mL, 5:5, (e) 0.20 g/mL, 7:3, respectively. Average fiber diameters of (a-e) is summarized at (f).

in Figure 2(f) with a trend of increase from 201 ± 86 nm to 2724 ± 587 nm. The increase of fiber diameter is attributed to high concentration of electrospun PVDF solution and large percentage of high boiling point solvent (DMF). Until today, this phenomenon is clearly recognized as the basically theory of electrospinning supported by a great deal of references [17-22]. Fiber densities of electrospun membranes are summarized in Table 1. Different fiber diameter doesn't result in different fiber density. From Table 1, fiber densities are from 77.81 % to 84.69 % without significant difference.

Table 1 Diameter, fiber density and adhesion energy of electrospun membranes

Preparation conditions	Fiber diameter (nm)	Fiber Density (%)	Adhesion Energy (mJ/m^2)
(a) 0.15 g/mL, 7:3	201 ± 86	84.7 ± 2.3	258.8 ± 43.5
(b) 0.17 g/mL, 7:3	387± 65	77.8 ± 2.8	196.3 ± 23.4
(c) 0.15 g/mL, 5:5	733 ± 154	79.2 ± 1.0	157.0 ± 37.5
(d) 0.17 g/mL, 5:5	1835 ± 653	84.7 ± 5.8	77.0 ± 8.8
(e) 0.20 g/mL, 7:3	2724 ± 587	83.3 ± 6.4	8.1 ± 0.7

3.2. The work of adhesion

The work of adhesion between electrospun membrane and rigid substrate in SLBT is calculated by equation (2) and recorded in Table 1. With the increase of fiber diameter, it shows an obvious decrease in adhesion energy. When the diameter of electrospun PVDF fibers is about 201 ± 86 nm, the adhesion energy is up to 258.8 ± 43.5 mJ/m^2. But, fiber diameter increases to 2724 ± 587 nm leading to 32-fold decrease in adhesion energy to only 8.1 ± 0.7 mJ/m^2. In SLBT, the rigid substrate has an inorganic coating on the surface indicating an arithmetic average roughness (R_a) of ~128 nm. It must form some rough area with several hundred nanometers fluctuant change on height. Because of the nano- and micro-size of electrospun PVDF fibers, they are usually very flexible with the ability to be crushed into the empty space of topographical rough area of the rigid substrate. Thin fiber is easier to produce larger effective contact with the surface of the rigid substrate. It will initiate higher work of adhesion during SLBT. On the contrary, thick fibers with the diameter of 2724 ± 587 nm are too large to be crushed into the small empty space on the topographical rough area at the surface of the rigid substrate. The contact area between electrospun membrane and rigid substrate should be very low. Low adhesion energy can be observed in SLBT.

Adhesion energy between electrospun PVDF membrane and rigid substrate is also enhanced by interlocking effect. Interlocking refers to the multi-point contact between electrospun fibers and rigid substrate. Thin fiber is no doubt flexible and easy to bend to contact many points of rigid substrate surface at the same time. The thinner electrospun PVDF fiber is, the easier the fiber forms effective contact with rigid substrate. In fact, SLBT debonding is a crack propagation process between the electrospun PVDF membrane and the rigid substrate. Formation of interlocking could increase the difficulty of crack propagation resulting in sharp increase of adhesion energy. Stein and co-workers [23] reported the sharp increase in interfacial toughness from 8 J/m^2 to 145 J/m^2 of two immiscible polymer plates by scribing grooves at the interface of plates to induce interlocking effect. By considering the flexibility of electrospun fibers and the principle of interlocking effect, it is concluded that reducing the fiber diameter of electrospun PVDF fibers is one of critical factors for significantly increases in adhesion energy between electrospun membrane and rigid substrate.

3.3. Surface roughness of rigid substrate

In order to understand the relation between adhesion energy and surface roughness of rigid substrate,

a series of SiC substrates with different surface asperities is applied in SLBT to characterize adhesion energy. Figure 3 exhibits the surface morphology and surface profile of SiC substrates. All of the SiC substrates show uniform grit distribution with different grit size [see left side of Figure 3]. The smallest size of grit is 5 μm showing a height fluctuation of ~3 μm on the surface. SiC substrate also exhibits large size of grit at 68 μm with ~30 μm fluctuation on height.

Electrospun PVDF membrane with fiber diameter of 387± 65 nm is used to test the adhesion energy with SiC substrates. By increasing of the grit size on surface of SiC substrates, it shows an increase trend of adhesion energy. When the grit size is lower than 15.3 μm, the adhesion energy is below 150 mJ/m^2. By use of large grit size SiC substrate, the adhesion energy reaches over 400 mJ/m^2. At the grit size of 68 μm, it shows the highest adhesion energy at 420.1 ± 62.9 mJ/m^2.

Large size of grid produces larger empty space between the SiC grids. Electrospun PVDF fibers can

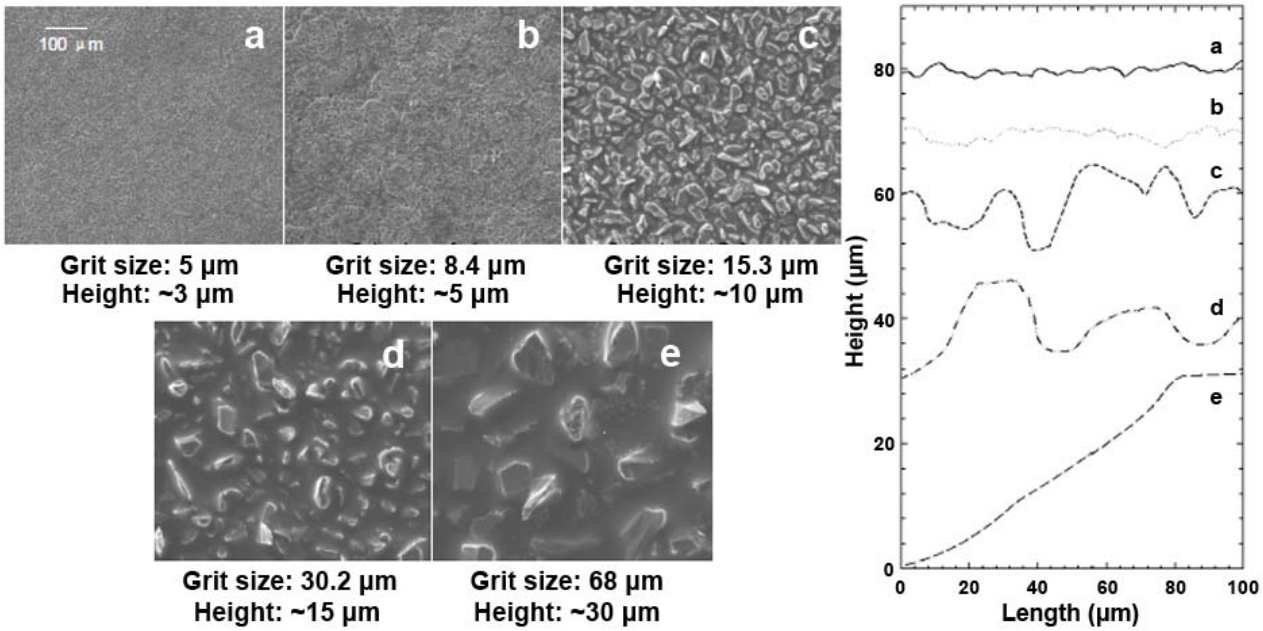

Figure 3. Surface morphology of SiC substrates.SEM images of SiC substrates (a-e) with different grit size are exhibited in left side. Surface scans of the substrate are included in right side.

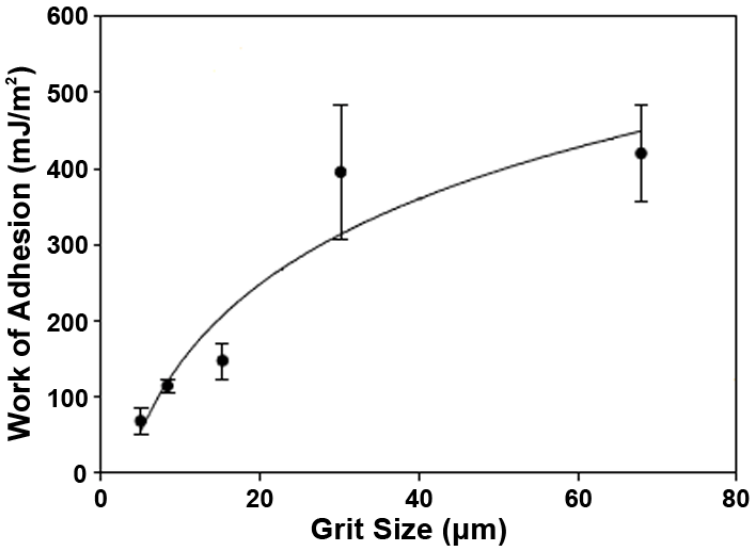

Figure 4. Adhesion energy between electrospun PVDF membrane and SiC substrate.

be easily crushed into the space to produce the high effective contact with substrate surface. When the space is large enough, many fibers can be crushed into the same area. Strong interlocking effect is initiated. As a result, higher work of adhesion can be produced in SLBT. However, when the grid size exceeds a critical value, the space between SiC grids is much larger the diameter of electrospun PVDF fibers. The increase of fiber amount will not produce an obvious increase in surface contact and interlocking effect. In our experiment, there is no large difference shown in adhesion energy between the grid sizes of SiC at 30.2 μm and 68 μm. Only 20 mJ/m^2 difference of adhesion energy is detected by use of the two SiC substrates. The surface asperity also plays an important role to the adhesion energy between electrospun membrane and rigid substrate.

4. Conclusions

SLBT methodology for testing the adhesion energy is conducted to determine the work of adhesion between PVDF membrane and rigid substrate. Electrospun PVDF membranes with increased fibers diameter show an obvious decrease in adhesion energy. The adhesion energy between electrospun membrane and rigid substrate can drop from 258.8 ± 43.5 mJ/m^2 to 8.1 ± 0.7 mJ/m^2 by increasing the fiber diameter from 201 ± 86 nm to 2,724 ± 587 nm. The surface asperity is also a critical factor for adhesion energy. The work of adhesion up to 420.1 ± 62.9 mJ/m^2 is detected between electrospun PVDF membrane and SiC substrate with a 68 μm grit size in SLBT.

Acknowledgements

This work is primarily supported by the National Science Foundation under a CAREER Award to SCW (NSF-CMMI 0746703). One of us (HNN) is partially supported by National Natural Science Foundation of China (Project No. 51102076).

References

[1] K. Autumn, M. Sitti, Y.C.A. Liang, A.M. Peattie, W.R. Hansen, S. Sponberg, T.W. Kenny, R. Fearing, J.N. Israelachvili, R.J. Full, Evidence for van der Waals adhesion in gecko setae. Proc Natl Acad Sci USA, 99 (2002) 12252–12256.

[2] K. Autumn, Y.A. Liang, S.T. Hsieh, W. Zesch, W.P. Chan, T.W. Kenny, R. Fearing, R.J. Full, Adhesive force of a gecko foot-hair. Nature, 405 (2000) 681–685.

[3] H.J. Gao, H.M. Yao, Shape insensitive optimal adhesion of nanoscale fibrillar structures. Proc Natl Acad Sci USA, 101 (2004) 7851–7856.

[4] J. Lee, B. Bush, R. Maboudian, R.S. Fearing, Gecko-inspired combined lamellar and nanofibrillar array for adhesion on nonplanar surface. Langmuir, 25 (2009) 12449–12453.

[5] Q. Shi, K.T. Wan, S.C. Wong, P. Chen, T.A. Blackledge, Do electrospun polymer fiber stick? Langmuir, 26 (2010) 14188–14193.

[6] S. Kim, E. Cheung, M. Sitti, Wet self-cleaning of biologically inspired elastomer mushroom shaped microfibrillar adhesives. Langmuir, 25 (2009) 7196–7199.

[7] H.N. Na, X.W. Liu, J.Q. Li, Y.H. Zhao, C. Zhao, X.Y. Yuan, Formation of core/shell ultrafine fibers of PVDF/PC by electrospinning via introduction of PMMA or BTEAC. Polymer, 50 (2009) 6340–6349.

[8] W.Y. Liu, Y.C. Yeh, J. Lipner, J.W. Xie, H.W. Sung, S. Thomopoulos, Y.N. Xia, Enhancing the stiffness of electrospun nanofiber scaffolds with a controlled surface coating and mineralization. Langmuir, 27 (2011) 9088–9093.

[9] W. Salalha, Y. Dror, R.L. Khalfin, Y. Cohen, A.L. Yarin, E.L. Zussman, Single-walled carbon nanotubes embedded in oriented polymeric nanofibers by electrospinning. Langmuir, 20 (2004) 9852–9855.

[10] H.N. Na, Y.P. Zhao, C.G. Zhao, C. Zhao, X.Y. Yuan, Effect of hot-press on electrospun poly(vinylidene fluoride) membranes. Polym Eng Sci, 48 (2008) 934–940.

[11] A. Baji, Y.W. Mai, Q. Li, S.C. Wong, Y. Liu, Q.W. Yao, One-dimensional multiferroic bismuth ferrite fibers obtained by electrospinning techniques. Nanotechnology, 22 (2011) 235702.

[12] D.H. Reneker, A.L. Yarin, H.K. Fong, S. Koombhongse, Bending instability of electrospinning of nanofibers. J Appl Phys, 87 (2000) 4531–4547.
[13] H.N. Na, P. Chen, K.T. Wan, S.C. Wong, Q. Li, Z.J. Ma, Measurement of adhesion work of electrospun polymer membrane by shaft-loaded blister test. Langmuir, 28 (2012) 6677–6683.
[14] K.T. Wan, Y.W. Mai, Fracture mechanics of a shaft-loaded blister of thin flexible membrane on rigid substrate. Int J Fracture, 74 (1995) 181–197.
[15] K.T. Wan, Fracture mechanics of a shaft-loaded blister test - transition from a bending plate to a stretching membrane. J Adhesion, 70 (1999) 209–219.
[16] K.T. Wan, K. Liao, Measuring mechanical properties of thin flexible films by a shaft-loaded blister test. Thin Solid Films, 352 (1999) 167–172.
[17] S.V. Fridrikh, J.H. Yu, M.P. Brenner, G.C. Rutledge, Controlling the fiber diameter during electrospinning. Phys Rev Lett, 90 (2003) 144502.
[18] M. Chowdhury, G. Stylios, Effect of experimental parameters on the morphology of electrospun Nylon 6 fibres. Inter J Basic Appl Sci, 10 (2010) 116–131.
[19] Z.M. Huang, Y.Z. Zhang, M. Kotaki, S. Ramakrishna, A review on polymer nanofibers by electrospinning and their applications in nanocomposites. Comp Sci Tech, 63 (2003) 2223–2253.
[20] Z.Z. Zhao, J.Q. Li, X.Y. Yuan, X. Li, Y.Y. Zhang, J. Shen, Preparation and properties of electrospun poly(vinylidene fluoride) membranes. J Appl Polym Sci, 97 (2005) 466–467.
[21] J. Shawon, C.M. Sung, Electrospinning of polycarbonate nanofibers with solvent mixtures THF and DMF. J Mater Sci, 39 (2004) 4605–4613.
[22] J.F. Zheng, A.H. He, J.X. Li, C.C. Han, Polymorphism control of poly(vinylidene fluoride) through electrospinning. Macromol Rapid Comm, 28 (2007) 2156-2162.
[23] V. Janarthanan, P.D. Carrett, R. Stein, M. Srinivasarao, Adhesion enhancement in immiscible polymer bi-layer using oriented macroscopic roughness. Polymer, 38 (1997) 105-111.

The tensile and shear failure behavior dependence on chain length and temperature in amorphous polymers

Junhua Zhao*, Timon Rabczuk*
Institute of Structural Mechanics, Bauhaus-University Weimar, 99423 Weimar, Germany
* Corresponding author: junhua.zhao@uni-weimar.de; timon.rabczuk@uni-weimar.de

Abstract
The tensile and shear failure behavior dependence on chain length and temperature in amorphous polymers are scrutinized using molecular dynamics simulations. A wide range chain length of alkane is tested under tension and shear with various temperatures. We find that the broken rate (the broken bond number to all polymer chain number ratios) under tension and shear increases with increasing chain length and temperature. For a given chain length and temperature, the broken rates under shear are always higher than those under tension at a same large strain. For a given chain length, the tensile and shear stresses decrease with increasing temperature. We propose three typical fracture mechanisms to effectively elucidate the ductile fracture response based on the predominance of chain scission process.

Keywords Failure, Chain length, Linear polymers, Molecular dynamics.

1. Introduction

Amorphous polymers are one of the most fundamental polymer molecular shapes that have widely been investigated by many researchers due to the important physical and chemical properties [1,2]. Glass forming polymers ($T<T_g$, T_g is the glass-transition temperature) are of great industrial importance and scientific interest. Their unique mechanical properties arise from the connectivity and random-walk-like structure of the constituent chains [3]. At very small strains, the response is elastic. At slightly larger strains, yielding occurs when intermolecular barriers to segmental rearrangements are overcome. Following yield, the material may exhibit strain softening, a reduction in stress to a level corresponding to plastic flow. At higher strains, the stress increases as the chain molecules orient, in a process known as strain hardening. Strain hardening suppresses strain localization (crazing, necking, shear banding) and is critical in determining material properties such as toughness and wear resistance [4,5]. In the other hand, the yield point of the polymers disappears after $T>T_g$. Recently, we have found that the chain length (CL) and temperature have a large effect on the thermomechanical properties of linear polymers [6-8] based on united-atom (UA) and coarse-grained (CG) molecular dynamics (MD) simulations. Since the UA and CG potentials limitations, the effect of the CL and temperature on the failure behavior is not understood well yet. Especially, the failure behavior under shear has been scarcely reported in previous work. Therefore, understanding the molecular origins of macroscopic fracture behavior such as fracture energy is a fundamental scientific challenge [5,9].

In this paper, the tensile and shear failure behavior dependence on CL and temperature in linear polymers are scrutinized using MD simulations. A wide range chain length of alkane is tested under tension and shear with various temperatures. The fracture mechanism is proposed based on the detailed analysis of the fracture response.

2. Simulations details

The bulk structure of linear polymers can be modeled using the semicrystalline lattice method [10], which utilizes the face-centered cubic (*fcc*) diamond structure as a template to carbon backbones of entangled polymers. The detailed process was detailedly described in our previous work [6]. The total number of beads in the initial structure is kept constant 180000 from CL=9 to CL=1200, in which the number of chains changes accordingly from 20000 (CL=9) to 150 (CL=1200). Since our aim does not simulate a specific polymer, we use a bead-spring polymer model derived from the one suggested by Kremer and Grest [11]. A finitely extendable nonlinear elastic (FENE) backbond potential is applied along the polymer chain

$$U(r) = -\frac{k}{2} R_0^2 \ln\left[1 - \left(\frac{r}{R_0}\right)^2\right], \tag{1}$$

where k=30 and R_0=1.5 to guarantee a certain stiffness of the bonds while avoiding high frequency modes (which would require a rather small time step for the integration) and chain crossing [12]. The beads interact through a truncated Lennard-Jones (LJ) potential of the form

$$\begin{cases} U_{LJ}(r) = 4\in\left[\left(\frac{\sigma}{r}\right)^{12} - \left(\frac{\sigma}{r}\right)^{6} - \left(\frac{\sigma}{r_c}\right)^{12} + \left(\frac{\sigma}{r_c}\right)^{6}\right], r < r_c = 1.5\sigma \\ U_{LJ}(r) = 0, r > r_c \end{cases}, \tag{2}$$

where ε and σ are the characteristic energy and distance parameters that define the shape of the energy distance curve, while r_c is the cutoff distance for the potential. The LJ potential provides a smooth transition to zero values at the cutoff distance. In this work, we adopt the reduced units formalism and all physical quantities are expressed as multiples of m (bead mass), ε, σ and k_b (Boltzmann constant) while these parameters are set equal to one in our computation [13]. The bond is broken as r>1.15σ and the corresponding interaction is shut off, while a non-bonded LJ interaction is introduced between the two beads.

Each generated initial three-dimensional structure is annealed for 1×10^6 steps until the pressure and energy of the system is stable, keeping both the temperature T=1.3ε/k_b and the pressure P=1 (the time step dt=0.002) in the *NPT* ensemble controlled by the Nose-Hoover's thermostat [14]. Then, the system is cooled down to be the given temperature by the same *NPT* ensemble and the density of the system is monitored while cooling step-wise at an effective rate of $1/(1\times10^6$ steps). The system is then kept at the constant temperature (the given temperature) for 1×10^6 steps in the same *NPT* ensemble. The obtained structures are subjected to the uniaxial tension and compression and performed to obtain stress–strain response with different CL and temperature in the non-equilibrium MD simulations [15]. Periodic boundary conditions are applied in all directions. All the MD simulations have been performed using LAMMPS software [16].

3. Results and discussion

3.1 Failure behavior under uniaxial tension

Fig. 1 shows the stress-strain curves with different CL for two different temperature T=0.1 and T=0.3. The typical process (elastic, yielding, softening and hardening) is displayed in Fig. 1, while the hardening process is not evident when CL≤18 and the difference among the nonlinear parts of the stress-strain curves is also not large when CL≤144. The main reason is that the density and entanglement of short CL is lower than those of longer chain, which results in that

the bond number per unit volume in short CL is lower than those in longer CL. So the required external work for the shorter CL is lower than that for the longer CL. That is to say, the stiffness of the shorter CL is lower than that of longer CL. Since the density almost tends to a constant when CL≥140 [6], the effect is not evident in the range of CL≥140. Fig. 2 shows bond broken rate (the number of broken bond / the number of total chains) with different tensile strain for different CL and two temperatures T=0.1 and T=0.3, in which the broke rate increases with increasing CL.

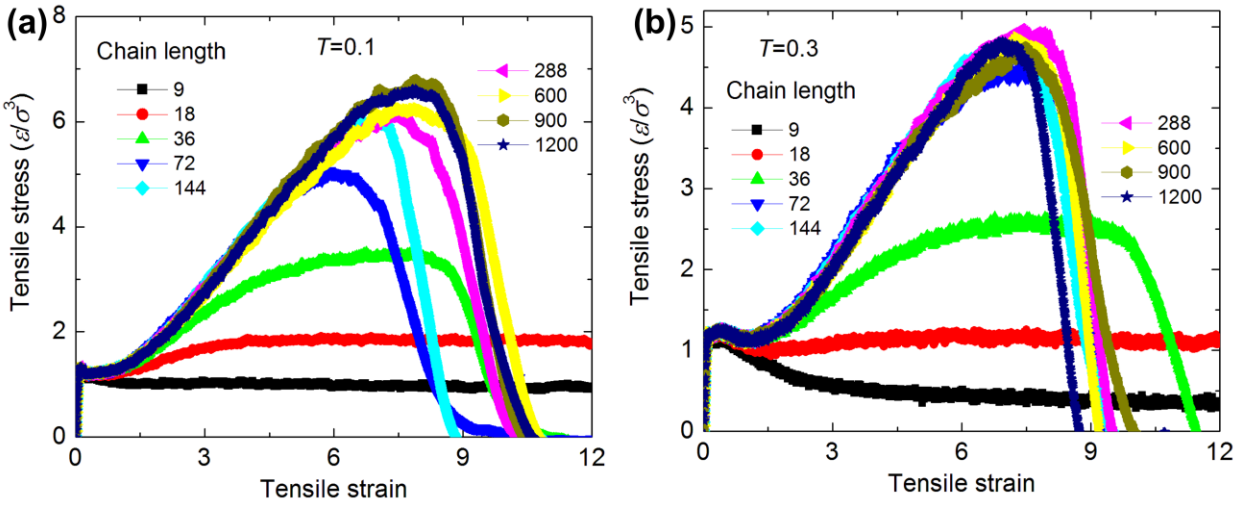

Fig. 1 The tensile stress-strain curves with different chain length for two different temperatures. (a) T=0.1; (b) T=0.3.

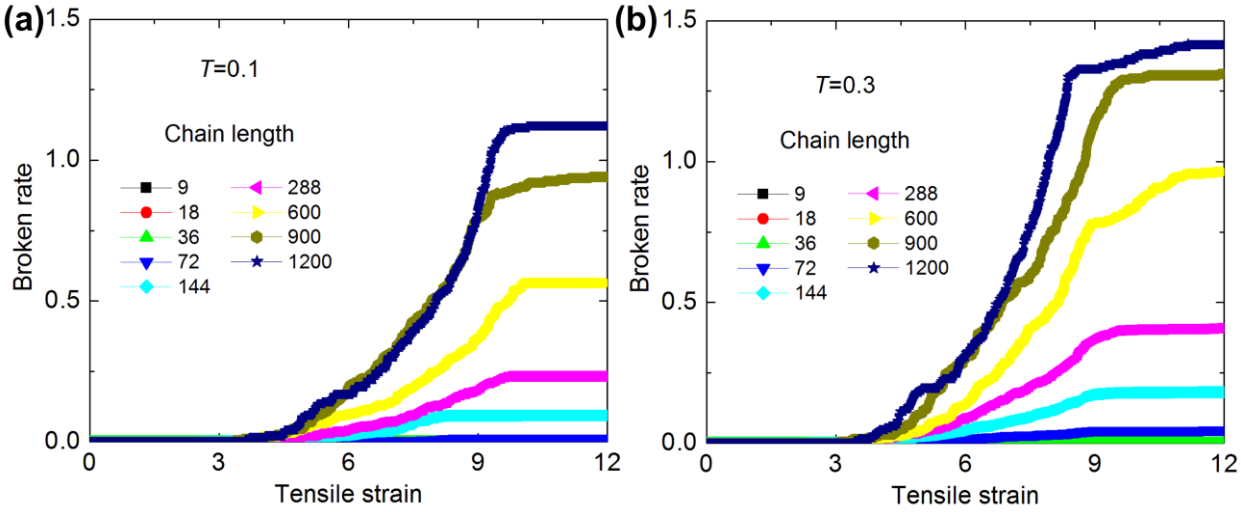

Fig. 2 The broken rate-strain curves with different chain length for two different temperatures. (a) T=0.1; (b) T=0.3.

We also find that the first broken bond is occurred at strain>3 and the stress is still hardening with increasing strain by comparison with Fig. 1 and Fig. 2. After strain>9, the stress decreases and the number of the total broken bonds tends to a constant. Fig. 3 shows the stress-strain curves and broken rate for CL=288 with different temperature. The stress decreases and the

broken rate increases with increasing temperature for same strain. For high temperature (T=0.5 and 0.7), the number of broken bond always increases with increasing strain even if the strain is higher than 12. The possible reason is that the temperature is higher than the glass-transition temperature T_g=0.35 (here) when T=0.5 and 0.7, in which the creep and high-elastic property is more evident in the high temperature and the yield point disappears. To interpret these MD simulations and obtain insight into the difference in fracture behavior of different CL and temperature, we plot the atomic strain distribution in the deformed configuration of the polymer models in Fig. 4 and Fig. 5. The ultimate fracture strain increases with increasing temperature in Fig. 4, which gives a good explanation of the above analysis. In Fig. 5, no void or atomic strain concentration for CL=18 can be found even at strain=12, which validates no broken bond in Fig. 2a. The ultimate fracture strain almost increases with increasing CL when CL≥72, which is also validated from Fig. 2a.

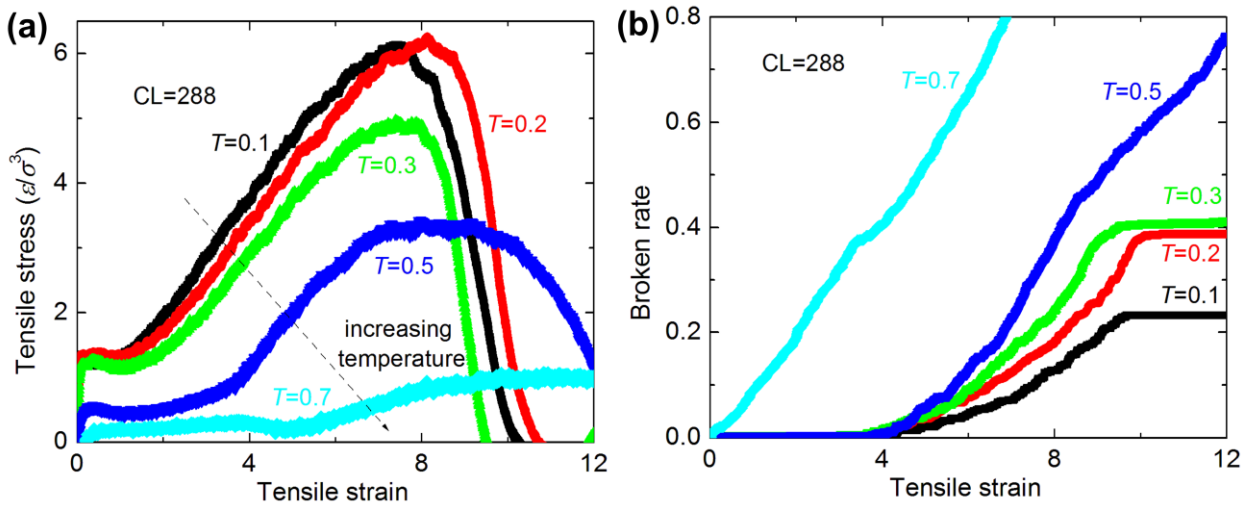

Fig. 3 The tensile stress-strain and broken rate-strain curves with different temperature for CL=288. (a) Stress-strain curves; (b) Broken rate-strain curves.

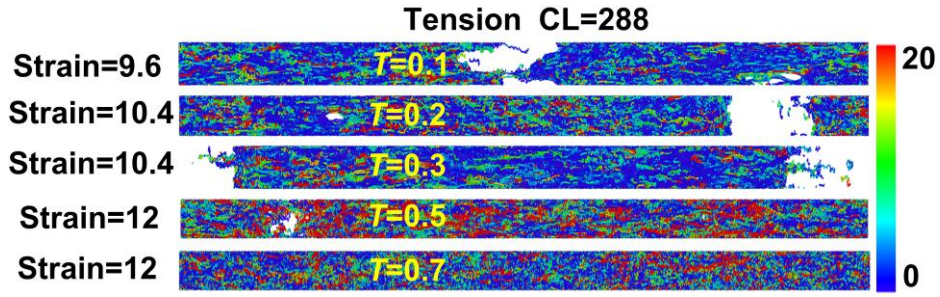

Fig. 4 The atomic strain (along the tensile direction) distribution for CL=288 at different temperature.

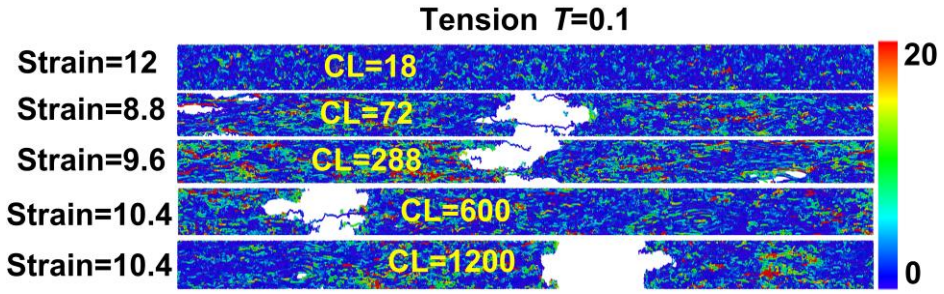

Fig. 5 The atomic strain (along the tensile direction) distribution for different CL at T=0.1.

Three typical mechanisms of the fracture behavior under uniaxial tension are plotted in Fig. 6. Fig. 6a represents the covalent bond broken phenomenon, which requires very high external loading (about 15000 MPa for linear polymers). Fig. 6b represents the polymer chain slipping with each other (about 5000 MPa). Fig. 6c represents the separation between any two polymer chains, which is mainly dominated by van der Waals interactions (about 100 MPa). For short CL, the fracture behavior is mainly determined by the chain slipping and separation. For longer CL, the fracture behavior is dominated by the competition between the chain slipping and bond broken mechanisms, in which the bond broken mechanism increases with increasing CL since the entanglement density increases with increasing CL. For very long CL, the bond broken mechanism mainly dominates the fracture behavior. The three mechanisms provide a good explanation of the MD results from Fig. 1 to Fig. 5.

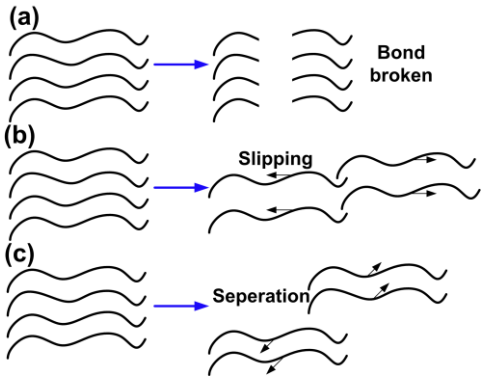

Fig. 6 Three typical mechanisms of microstructural evolution under uniaxial tension in linear polymers.

3.2 Failure behavior under shear

Fig. 7 shows the shear stress-strain curves with different CL for two different temperatures T=0.1 and T=0.3. The typical process (elastic, yielding, softening and hardening) is also displayed in Fig. 7. Unlike tension, the hardening process is also evident even for very short CL. The stress strength (the peak point of the stress) and strain strength (the strain at the stress strength point) both increase with increasing CL when CL≤144. The possible reason is that the polymer chains mainly keep the slipping process even in the hardening stage under shear, while the polymer chains are mainly stretching process after elastic stage under tension.

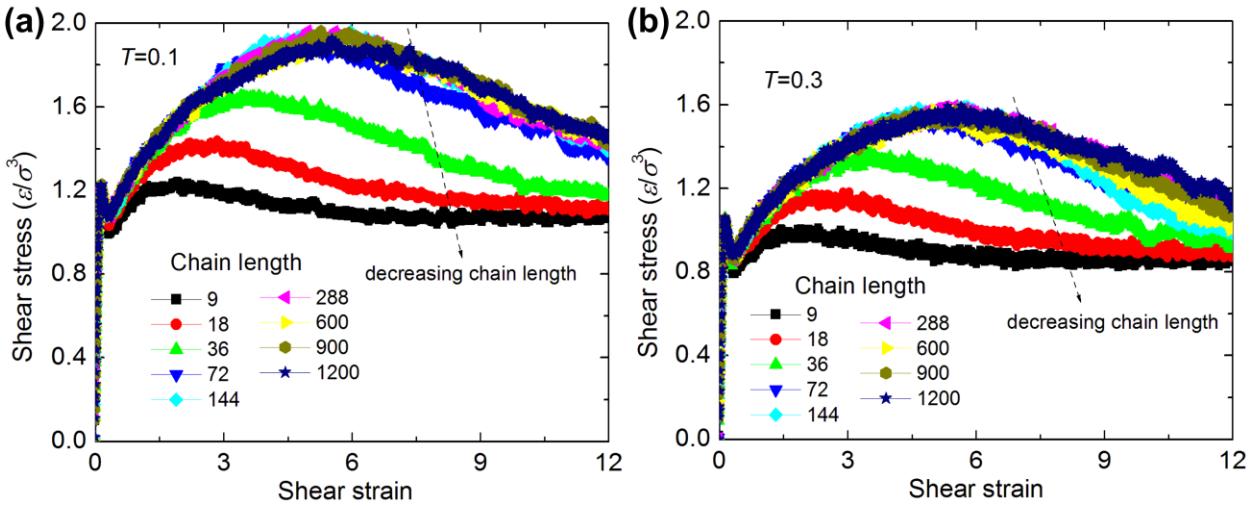

Fig. 7 The shear stress-strain curves with different chain length for two different temperatures. (a) T=0.1; (b) T=0.3.

Fig. 8 shows the corresponding broken rate with different CL for two different temperatures of Fig. 7. Similar to tension, the shear broken rate also increases with increasing CL. Unlike tension, the broke rate always increases with increasing shear strain even strain>12. Fig. 9 shows the ratio of tensile broken rate to shear broken rate with different strain. The ratio is always smaller than 1. In other words, for a given chain length and temperature, the broken rates under shear are always higher than those under tension for a same large strain. The possible reason is that the slipping and separation process mainly dominate the forward stage of the fracture behavior under shear, while the coupling slipping and broken mechanisms determine the fracture behavior under uniaxial tension. The r_c=1.5 of LJ potential is higher than the broken distance of r_{broken}=1.15 (see section 2), which leads to the higher ultimate fracture strain (that is, the structure is broken as two parts) under shear.

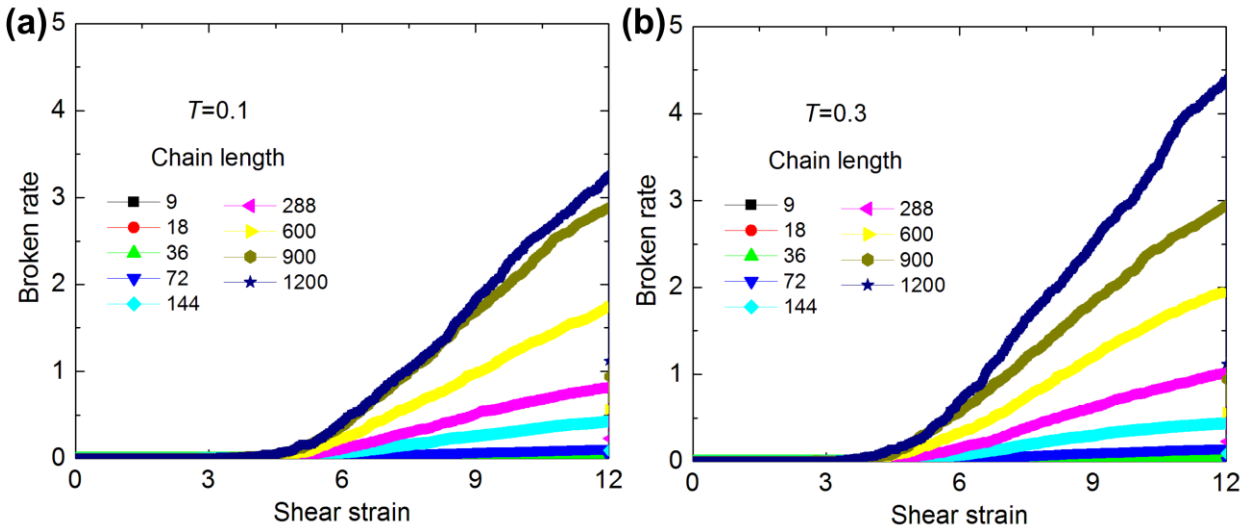

Fig. 8 The shear broken rate-strain curves with different chain length for two different temperature. (a) T=0.1; (b) T=0.3.

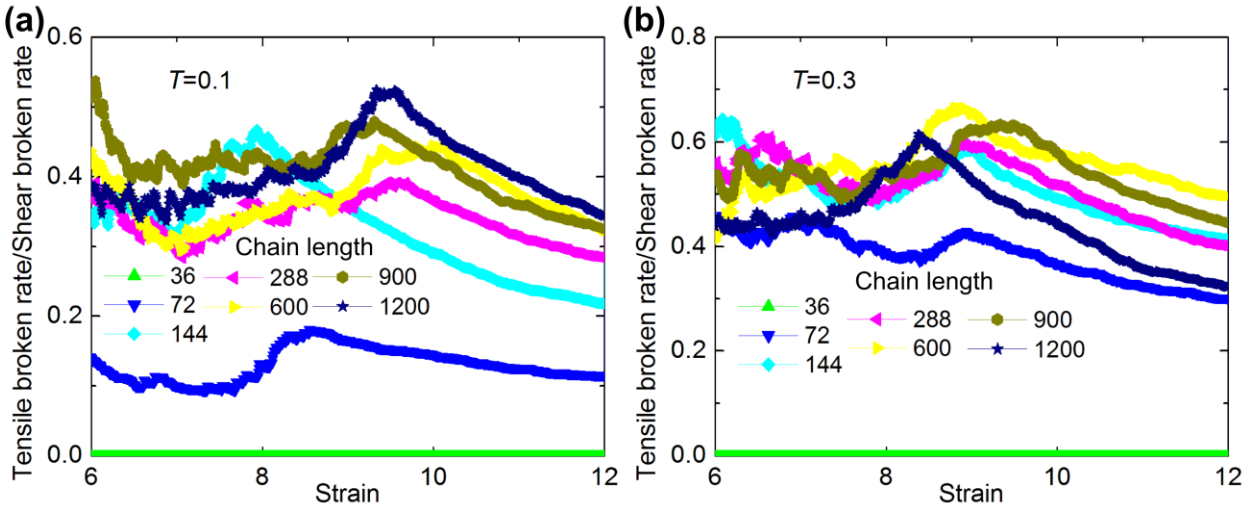

Fig. 9 The tensile broken rate/shear broken rate with different chain length for different temperature. (a) T=0.1; (b) T=0.3.

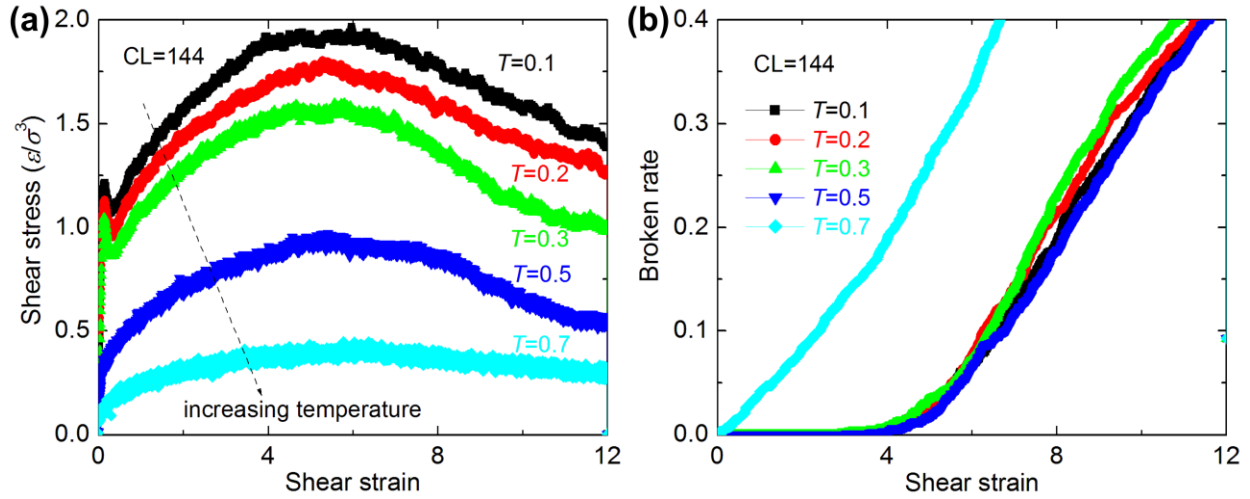

Fig. 10 The shear stress-strain and broken rate-strain curves with different temperature for CL=144. (a) Stress-strain curves; (b) Broken rate-strain curves.

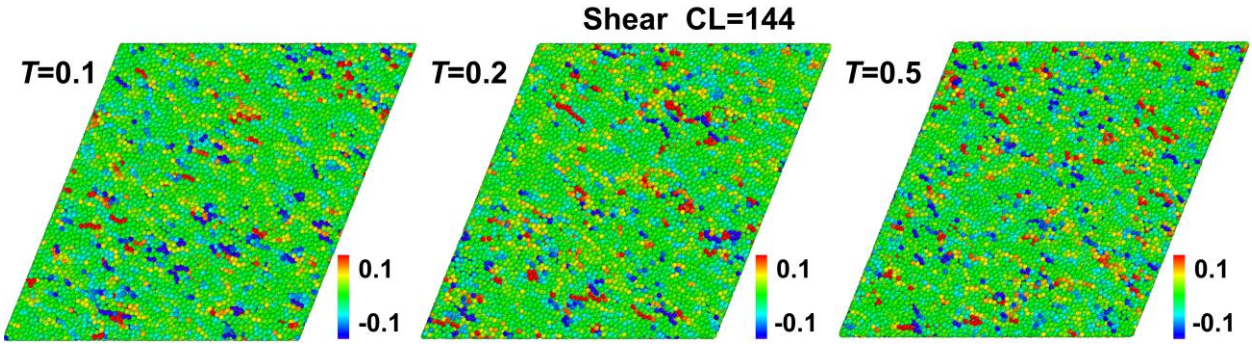

Fig. 11 The atomic strain (along the shear direction) distribution for CL=144 at different temperature under shear strain=58%.

Fig. 10 shows the shear stress-strain curves and broken rate for CL=144 with different temperature. The shear stress decreases with increasing temperature for same strain. For high temperature (T=0.5 and 0.7), no evident yield point can be also seen in Fig. 10a, which is same with tension. The difference of shear broken rate for different temperature is not large as T<0.7. To further understand the response, we plot the atomic strain (along the shear direction) distribution under shear strain (58%) for different temperatures and CL in the deformed configuration of the polymer models in Fig. 11 and Fig. 12. For CL=144 under same shear strain, the difference of the atomic strain distribution with different temperature is not evident in Fig. 11. For T=0.1, the atomic strain concentration increases with increasing CL in Fig. 12. The possible reason is that more entanglements are in large CL, which leads to the atomic stress concentration at these positions.

From above analysis, the ultimate fracture strain increases with increasing temperature under uniaxial tension. Under uniaxial tension, the fracture behavior is mainly determined by the chain slipping and separation for short CL. For longer CL, the fracture behavior is dominated by the competition between the chain slipping and bond broken mechanisms, in which the bond broken mechanism increases with increasing CL since the entanglement density increases with increasing CL. For very long CL, the bond broken mechanism mainly dominates the fracture behavior. Under shear, the atomic strain concentration increases with increasing CL for a given temperature. The shear broken rate is always higher than that under tension for same CL in the same large strain. The possible reason is that the slipping and separation process mainly dominate the forward stage of the fracture behavior under shear, while the coupling slipping and broken mechanisms determine the fracture behavior under uniaxial tension. The r_c=1.5 of LJ potential is higher than the broken distance of r_{broken}=1.15 (see section 2), which leads to the higher ultimate fracture strain (that is, the structure is broken as two parts) under shear.

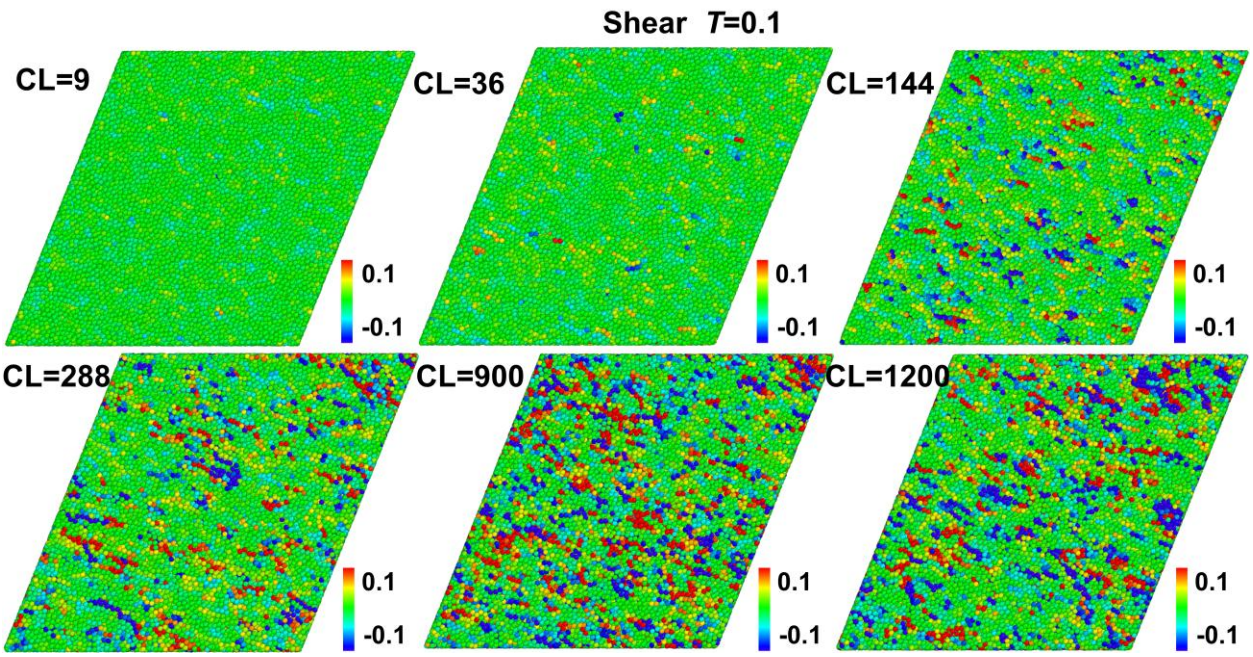

Fig. 12 The atomic strain (along the shear direction) distribution for different CL under shear strain=58% at T=0.1.

4. Concluding remarks

In summary, the tensile and shear failure behavior dependence on chain length and temperature in linear polymers are investigated using molecular dynamics simulations. A wide range chain length of alkane is tested under tension and shear with various temperatures. We find that the broken rate (the broken bond number to all polymer chain number ratios) under tension and shear increases with increasing chain length and temperature. For a given chain length and temperature, the broken rates under shear are always higher than those under tension at a same large strain. For a given chain length, the tensile and shear stresses decrease with increasing temperature. Under uniaxial tension, the fracture behavior is mainly determined by the chain slipping and separation for short CL. For longer CL, the fracture behavior is dominated by the competition between the chain slipping and bond broken mechanisms, in which the bond broken mechanism increases with increasing CL. For very long CL, the bond broken mechanism mainly dominates the fracture behavior. The slipping and separation process mainly dominate the forward stage of the fracture behavior under shear. The r_c=1.5 of LJ potential is higher than r_F=1.15 bond broken, which leads to the higher ultimate fracture strain under shear than that under uniaxial tension.

Acknowledgements

We gratefully acknowledge support by the Germany Science Foundation and and IRSES-MULTIFRAC project.

References

[1] R.H. Boyd, R.H. Gee, Y. Jin, Conformational dynamics in bulk polyethylene: a molecular dynamics simulation study. J Chem Phys, 101 (1994) 788-797.

[2] P.V.K. Pant, J. Han, G.D. Smith, R.H. Boyd, A molecular dynamics simulation of polyethylene. J Chem Phys, 99 (1993) 597-604.

[3] J.E. Shepherd, Multiscale modeling of the deformation of semi-crystalline polymers. Ph. D thesis. Georgia Institute of Technology, USA, 2006.

[4] R.S. Hoy, M.O. Robbins, Strain hardening of polymer glasses: Entanglements, energetics, and plasticity. Phys Rew E, 77(2008) 031801.

[5] R.S. Hoy, M.O. Robbins, Strain hardening in polymer glasses: limitations of network models. Phys. Rev. Lett. 99 (2007) 117801.

[6] J. Zhao, S. Nagao, Z.L. Zhang, Thermo-mechanical properties dependence on chain length in bulk polyethylene: Coarse-grained molecular dynamics simulations, J Mater Res, 25 (2010) 537-544.

[7] J.H. Zhao, S. Nagao, Z.L. Zhang, H. Kristiansen, Coarse-grained molecular dynamics simulations on size effect of glassy polyethylene particles. J Nanosci Nanotech, 10 (2010) 7340–7342.

[8] J. Zhao, J.W. Jiang, N. Wei, Y. Zhang, T. Rabczuk, Thermal conductivity dependence on chain length in amorphous polymers. Appl Phys Lett, under review, 2013.

[9] H.G.H. van Melick, L.E. Govaert, H.E.H. Meijer, On the origin of strain hardening in glassy polymers. Polymer, 44 (2003) 2493-2502.

[10] J.L. Faulon, Stochastic generator of chemical structure. (4) Building polymeric systems with specified properties. J Comput Chem, 22 (2001) 580-590.

[11] K. Kremer, G.S. Grest, Dynamics of entangled linear polymer melts: A molecular - dynamics simulation. J Chem Phys, 92 (1990) 5057-5086.
[12] C. Bennemann, W. Paul, K. Binder, Molecular-dynamics simulations of the thermal glass transition in polymer melts: α-relaxation behavior. Phys Rev E, 57 (1998) 843-851.
[13] M. Panico, S. Narayanan, L.C. Brinson. Simulations of tensile failure in glassy polymers: effect of cross-link density. Modelling Simul Mater Sci Eng, 18 (2010) 055005.
[14] S. Nose, A unified formulation of the constant temperature molecular dynamics methods. J Chem Phys, 81 (1984) 511-519.
[15] F.M. Capaldi, M.C. Boyce, G.C. Rutledge, Molecular response of a glassy polymer to active deformation. Polymer, 45 (2004) 1391-1399.
[16] S. Plimpton, Fast parallel algorithms for short-range molecular dynamics. J Comput Phys, 117 (1995) 1-19.

Assessment of Damage and Long-Term Strength of Polyethylene

P-Y Ben Jar

Department of Mechanical Engineering, University of Alberta, Edmonton, AB, T6G 2G8, Canada
ben.jar@ualberta.ca

Abstract Tensile strength of polyethylene is examined at various crosshead speeds using cylindrical specimens of 20 mm in gauge length. Through monotonic stretch with intermittent halt for load relaxation, the study shows that long-term tensile strength of polyethylene should be around half of the short-term strength determined in the standard test conditions. The study discovers a transition in the localized deformation (commonly known as necking), of which the appearance changes from opaque white to translucent when the crosshead speed is reduced from 0.05 to 0.01 mm/min, possibly due to the suppression of cavitation damage at the low crosshead speed. At a sufficiently high crosshead speed, damage generation can occur at a threshold strain as low as 4% which is way below the yield strain of the material. It is therefore concluded that determining long-term tensile strength of polyethylene needs to consider accumulation of the damage. Since this type of damage is not quantified in any of current standard methods, the study suggests that results from those tests need to be analyzed carefully to ascertain their validity for characterizing long-term performance of polyethylene products.

Keywords Long-term strength, polyethylene, damage, neck

1. Introduction

Polyethylene (PE) is known for its excellent ductility, superb corrosion resistance and strong strain hardening ability [1]. Its reliable performance has expanded the applications to products such as pipes for natural gas transportation that requires service lifetime for more than 50 years. Although standard methods, e.g. ASTM D1598 and D2837, are available to assess serviceability of PE pipes for this purpose, accuracy of the assessment is hindered by uncertainty in the resistance to a fracture behaviour known as slow crack growth (SCG) [2].

SCG development was discovered from early tests on full-sized pipe specimens subjected to internal hydrostatic pressure [3-5]. Results show a transition on the trend line of hoop stress versus time to failure, which yields a much steeper change of stress drop with increase of time to failure after the transition than before, with the former showing crack growth in much more brittle manner than the latter. Therefore, evaluating performance of PE pipes in service requires testing that takes at least one year for each specimen to ensure that the failure behaviour after the transition does not occur in service. In view of the lengthy time required for such tests, many studies have turned to accelerating tests that use small coupon specimens with sharp notches to shorten the time to initiate the crack growth [6, 7]. Although the use of sharp notches prevents the tests from determining the critical stress level for the transition to the SCG development, the results show a trend line that bears some similarity to the transition observed in full-sized pipe tests. As a result, the accelerating test becomes very popular for materials comparison, and is standardized as ASTM F1473.

Fracture generated in the notched specimens is known to be governed by shear deformation, and the transition is due to the change of shear deformation from the macroscopic scale (i.e. in a ductile manner) to the microscopic scale (in a brittle manner) [8, 9]. The latter is also known as craze that contains fibrils in a constrained space in front of the notch tip [10]. Based on results from the accelerating tests, formation of crazes is suggested to be the dominant mechanism for the SCG

development [11]. An extensive testing program has shown that the test method can generate a transition of the trend line for a wide range of PE materials [6].

Results from the above accelerating test are always analyzed as a function of the applied load, in terms of stress without the notch or stress intensity factor [11]. Since the applied load remains constant during the test, it is perceived that loading rate does not play any role on the deformation and fracture behaviour. However, the applied load needs to increase to the targeted level at the beginning of the test, for which the duration is relatively short. At the notch tip, rate of the initial stress increase should be pretty high. If the high loading rate generates damage that leads to different fracture behaviour from that occurs during the SCG development, results from the accelerating test should not be used to evaluate the SCG resistance. To my knowledge, such a scenario has never been seriously considered for the development of the accelerating test.

Work by O'Connell et al. [12] shows a transition from ductile to brittle fracture by testing notched specimens at an extreme combination of low loading rate and high temperature, that is, at a crosshead speed of 0.005 mm/min and temperature of 110^{o}C. The transition is opposite to the effect of loading rate and temperature commonly known for deformation and fracture behaviour of polymers. Fracture surfaces generated in such an extreme condition are featureless and without any indication of whitening. Note that this type of fracture behaviour is different from that shown in the work by Lu et al. [13] using a similar specimen design but subjected to a higher initial loading rate at a lower temperature. The latter always contains a thin but distinct whitening zone adjacent to the fracture surface. Unfortunately, due to the presence of sharp notches, difference of the true loading rates at the notch tips of those specimens cannot be quantified.

Some studies on the accelerating test have adopted notch-free specimens so that the loading rate (in terms of rate of strain increase) and its effect on the deformation behaviour can be quantified. Most of this type of studies applied a strain rate above 10^{-3} s^{-1} [e.g. 14-16], which is equivalent to a test speed about 1.2 mm/min for a gauge length of 20 mm. At the moment when this manuscript is prepared, the lowest strain rate that can be found in the literature is in the order of 10^{-5} s^{-1} [17].

A strain rate of lower than 10^{-5} s^{-1} is used in the work described in this paper to introduce a deformation transition that changes the neck appearance from opaque white to translucent. Based on the observed deformation transition, this paper investigates effects of loading rate on the necking phenomenon of notch-free PE specimens. In addition to the reduction of the crosshead speed, a special loading scheme is used to determine the stress-elongation curve of PE, in order to determine the long-term strength and its change caused by different initial loading rate.

2. Experimental

2.1. Materials

Specimens used for the mechanical testing are prepared from PE plates of 10 mm thick, provided by NOVA Chemicals, of which molecular weight, molecular weight distribution, and density are given in Table 1. The plates were compression-molded from pellets to ensure isotropy of the mechanical properties. Cylindrical specimens with geometry same as those used in ref. [18] were machined from those plates, with dimensions shown in Figure 1. To ensure that necking was always initiated in the middle of the gauge section where an extensometer was placed to monitor the change of cross-sectional dimensions, a small imperfection was introduced there to reduce the diameter by less than 2%. Note that despite the presence of such an imperfection, all specimens could show full neck development in the whole gauge section prior to the final fracture.

Table 1. Material characteristics of PE used in this study [19].

Weight-average molecular weight (M_w) (g/mol)	Number-average molecular weight (M_n) (g/mol)	Branches per 1000 C	Density, ρ (g/cm^{-3})	Crystallinity (%)	Tensile yield strength (MPa)
73,074	30,391	3.4–4.2	0.941	63.6	20.2

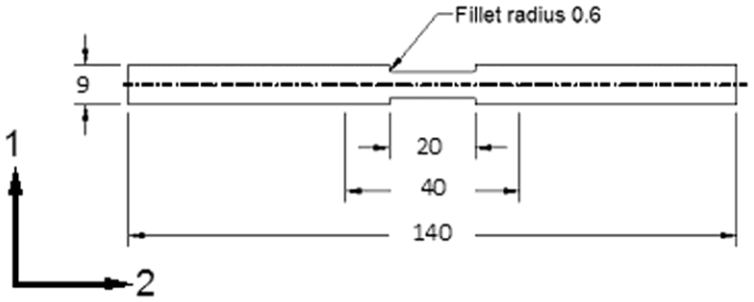

Figure 1. Dimensions of cylindrical specimen used in the study.

2.2. Mechanical Testing

All tests were conducted using a universal testing machine (QUASAR 100) at room temperature. Eight crosshead speeds between 0.001 and 5mm/min were selected for the testing, corresponding to the initial straining rate between $8x10^{-7}$ and $4x10^{-3}$ sec^{-1}. Two types of tensile tests were used. One, named simple tensile test here, applies a constant crosshead speed in the range between 5 and 0.001 mm/min until the stroke reaches a pre-set value. The other, named relaxation test, applies a constant crosshead speed of 1 or 0.001 mm/min, to reach a preset stroke and then, holds the stroke for 100,000 seconds (about 28 hours) while change of the load is recorded. For both types of tests, stress and area strain were calculated. The latter was defined as $ln\ (A_o/A)$ where A_o is the original cross-sectional area and A the cross-sectional area at the moment of measurement.

3. Results and Discussion

3.1. Simple Tensile Test

Figure 1 shows the summary of engineering stress versus stroke from simple tensile tests. As expected, peak stress decreases with the decrease of crosshead speed. In addition, profile around the peak load changes with the crosshead speed. In particular, the curve section around the maximum stress changes from single-peak to double-peak, with the two peaks separating further away with the decrease of the crosshead speed. The post-tested specimens also show a transition with the decrease of the crosshead speed. As shown in Figure 3, by decreasing the crosshead speed, noticeably from 0.05 to 0.01 mm/min, the neck appearance changes from opaque white to translucent. The latter has a similar color of the original specimen.

Figure 4 summaries maximum engineering stress as a function of crosshead speed, in logarithmic scale in Figure 4(a) and linear scale in Figure 4(b). Insert in Figure 4(b) depicts change of the maximum engineering stress at crosshead speeds below 0.01 mm/min. Both figures suggest that

around the lowest crosshead speed used in the study, 0.001 mm/min, the maximum engineering stress does not show any tendency of reaching a plateau value, but prediction from the two figures for the maximum engineering stress at zero crosshead speed is very different. Figure 4(a) suggests that the value could be way below 10 MPa; while Figure 4(b) based on specimens with translucent neck appearance (for crosshead speeds at and below 0.01 mm/min), the value should be about 10.5 MPa.

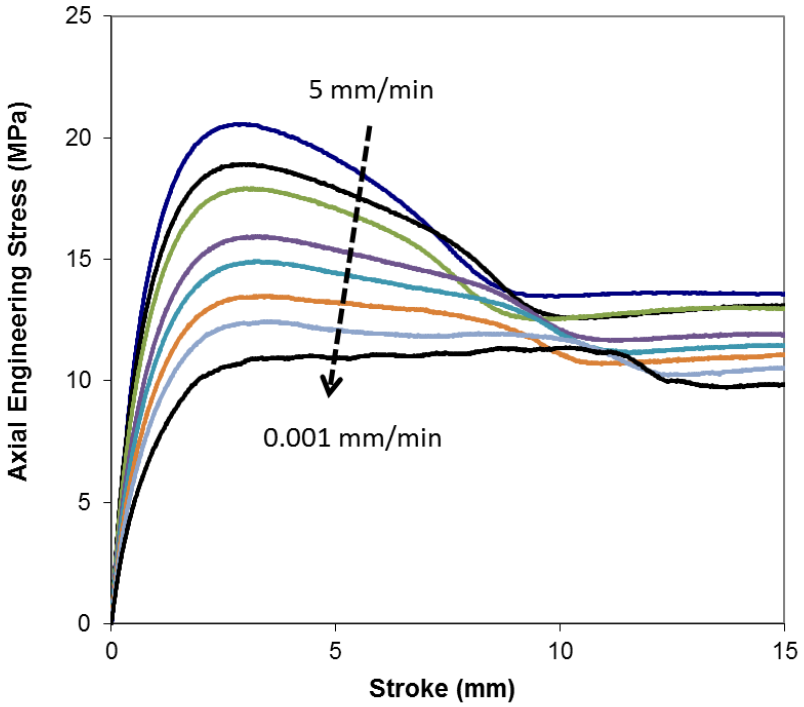

Figure 2. Engineering stress-stroke curves for crosshead speeds from 5 to 0.001 mm/min.

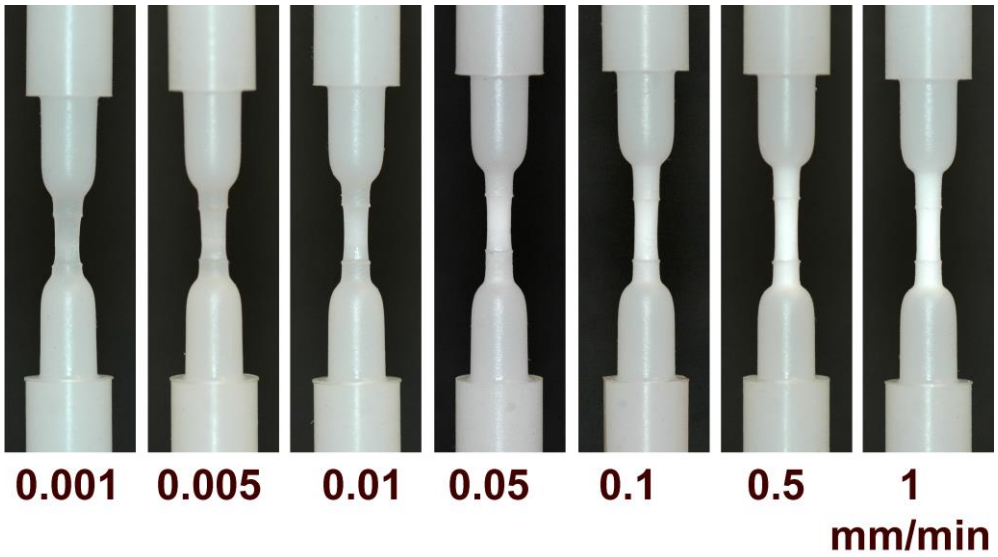

Figure 3. Transition of specimen deformation by changing the crosshead speed from 1 to 0.001 mm/min.

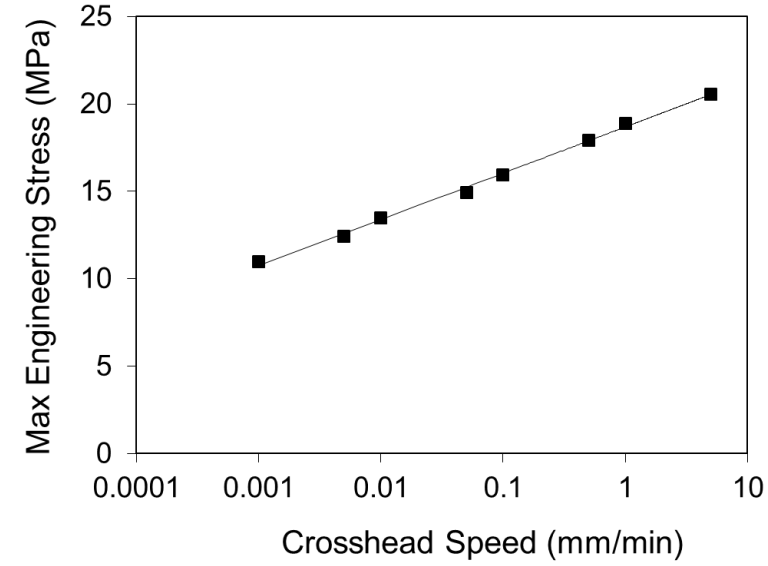

(a)

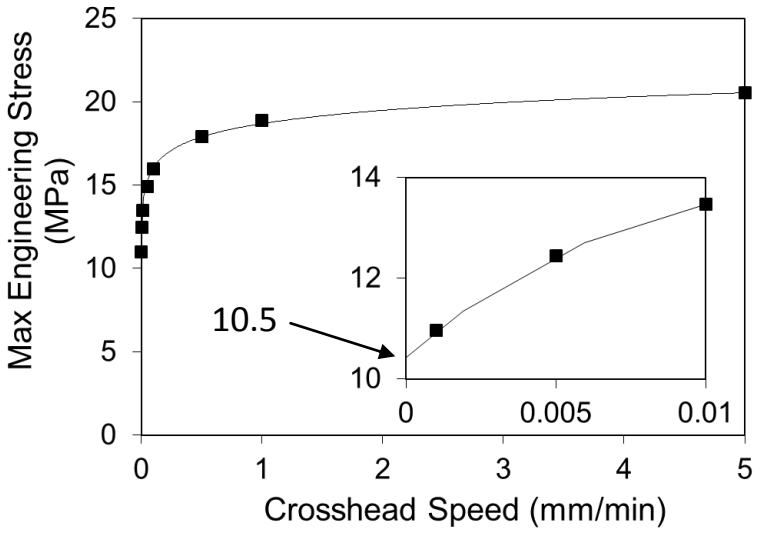

(b)

Figure 4. Maximum engineering stress versus crosshead speed in (a) logarithmic scale and (b) linear scale.

In view of the uncertainty in predicting the strength at zero crosshead speed (regarded as the long-term strength here), another test (named intermittent tensile test) was conducted, at the lowest crosshead speed that is provided by the test machine, 0.001 mm/min. Instead of applying a monotonic increase of stroke, stroke for the intermittent tensile test was programed to reach a pre-set value at 0.001 mm/min and then, the load was allowed to relax for 100,000 seconds. This time period was chosen based on some preliminary tests which suggest that the load maintained at a fairly constant level after 100,000 seconds, after which the further load decrease within the same period is within two times of the load cell resolution (± 0.5N). An example of the engineering stress-stroke curve from the intermittent tensile test is shown in Figure 5, in which the pre-set stroke values range from 0.8 mm to 6 mm. The corresponding long-term stress values at those strokes are then connected to form the long-term stress-stroke curve, also shown in Figure 5. Peak value of the long-term stress-stroke curve is 9.9 MPa, which is very close to that predicted from Figure 4(b), using values from three lowest crosshead speeds, from specimens with translucent neck appearance.

Note that the above pre-set stroke values cannot be applied to intermittent tensile test at a crosshead

speed of 1 mm/min. This is because after the relaxation, the stroke required to resume the tensile loading is much longer than the pre-set increment of the stroke values. As a result, individual relaxation tests, as presented below, are used to compare the long-term stress-stroke curves between two crosshead speeds, 1 and 0.001 mm/min.

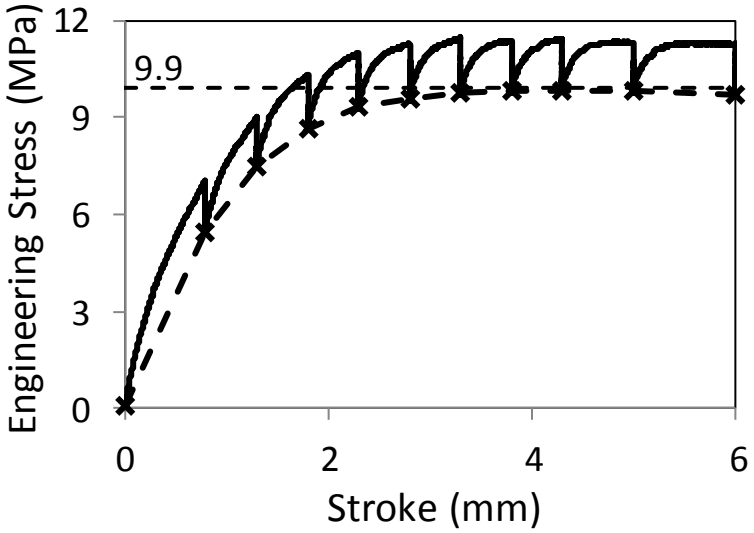

Figure 5. Engineering stress-stroke curves from an intermittent tensile test at crosshead speed of 0.001 mm/min, showing a long-term strength of 9.9 MPa, at a stroke between 3.8 and 4.3 mm.

3.2. Relaxation Test

Relaxation tests for the same period of 100,000 seconds were conducted at pre-selected strokes to establish long-term stress-stroke curves at crosshead speeds of 1 and 0.001 mm/min. Note that for the relaxation tests, each specimen is used only for one pre-set stroke.

Figure 6 summarizes results from the relaxation tests. The overall curve profile at 0.001 mm/min is similar to that shown in Figure 5 with peak stress at 9.9 MPa, and is distinctively above the curve from 1 mm/min. Peak stress for the latter is 8.9 MPa, suggesting that by increasing the crosshead speed from 0.001 to 1 mm/min, the long-term tensile strength of PE is reduced by about 10%. Figure 6 also suggests that with the increase of the stroke, difference of the long-term stress between curves at the two crosshead speeds increases, and the difference exists even at the smallest stroke of 0.8 mm which corresponds to an area strain of 3.6%. The stress decrease by increasing the crosshead speed is an indication of damage introduced by the deformation. Therefore, Figure 6 suggests that damage must have been generated at a very early stage of the deformation process.

Figure 7 depicts the post-test specimens with different strokes at the crosshead speed of 1 mm/min. For strokes below 6 mm, there is no clear neck formation. Therefore, only 1 photograph, taken from a specimen with stroke of 1.3 mm, is shown in the figure. Similar behaviour was found from specimens tested at 0.001 mm/min, except that the neck appears to be translucent, instead of opaque white.

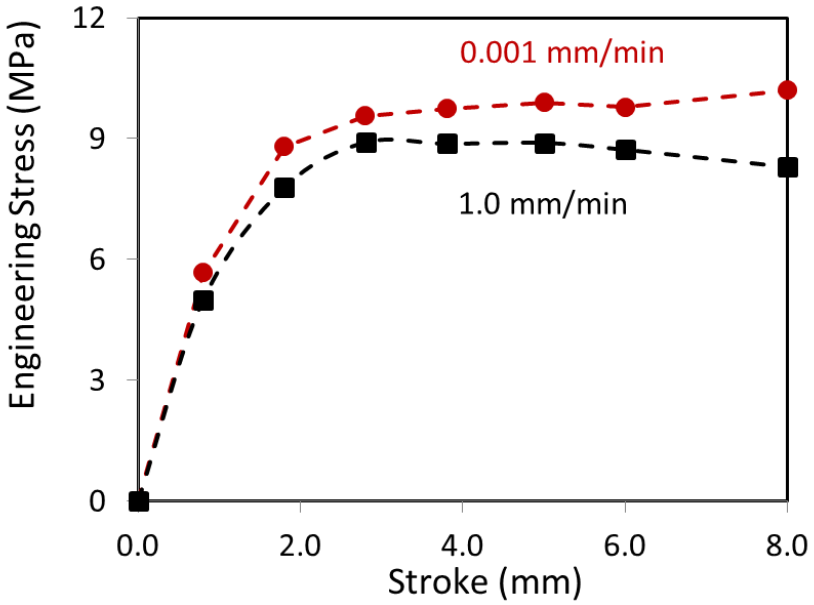

Figure 6. Engineering stress versus stroke from relaxation tests at 2 different crosshead speeds.

Further evidence for the damage generated by a high crosshead speed of 1 mm/min is shown in Figure 8 which contains three engineering stress-stroke curves, all from simple tensile test to a preset stroke of 1.8 mm at a crosshead speed of 0.001 mm/min. The three curves are from a virgin specimen, labeled "As is," and after stretch to 1.8 mm at two crosshead speeds, as labeled by "After 1 mm/min" and "After 0.001 mm/min," respectively. The figure suggests that the prior stretch at 0.001 mm/min does not change much of the stress increase with time, but the prior stretch at 1 mm/min has decreased the stress response. Therefore, even at a crosshead speed of 1 mm/min, corresponding to an initial strain rate of around 8×10^{-4} s^{-1}, damage is introduced way before the yield point. This phenomenon has also been observed by similar tests at other pre-set stroke values of less than 5 mm.

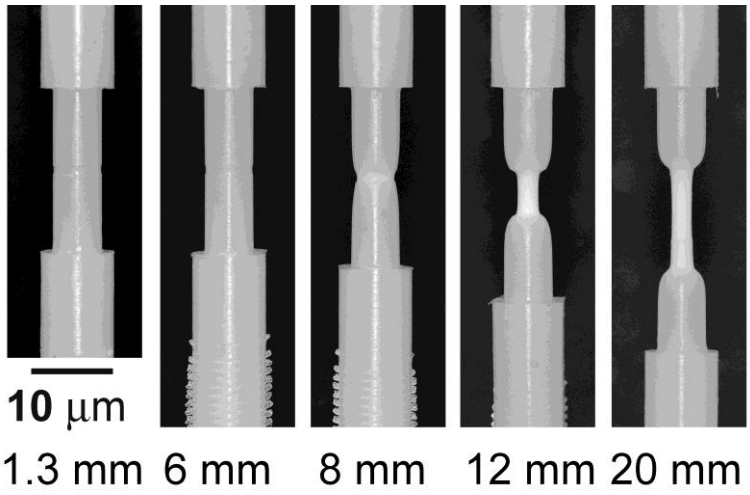

Figure 7. Specimens after being tested at 1 mm/min for different pre-set strokes (given under each photograph). Specimens tested at 0.001 mm/min have similar dimensional changes but do not show any whitening.

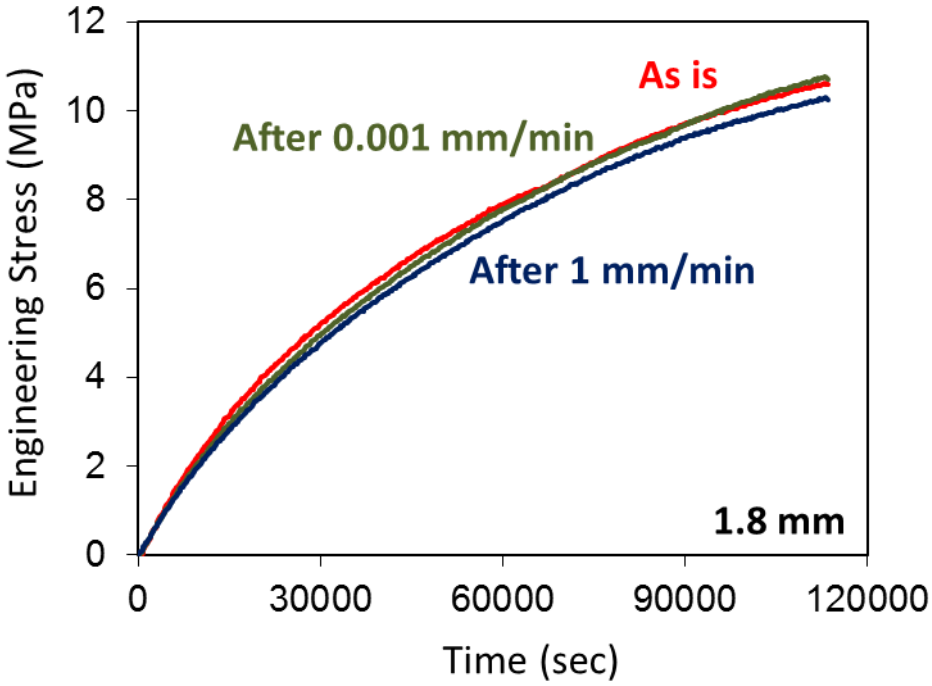

Figure 8. Comparison of engineering stress response with different loading history: as is, after stretch of 1.8 mm at 1 and 0.001 mm/min, respectively.

4. Conclusions

This paper presents an experimental study to assess long-term strength of PE and influence of loading rate on the damage generation. The study is based on a newly discovered "deformation transition" in notch-free specimens which generates translucent neck instead of the common opaque white. The discovery leads to development of a short-term test that uses coupon specimen to quantify the long-term strength of virgin PE. The results suggest that long-term strength of virgin PE is about 50% of its strength determined from the standard test.

The study also shows that long-term strength of virgin PE only represents the upper limit of the strength for PE pipe, as damage generated during the pipe transportation and installation may further reduce the strength. The results indicate that even under a loading rate of 1 mm/min, corresponding to a strain rate around $8x10^{-4}$ s^{-1}, damage can be generated in polyethylene at a strain level less than 4%. Therefore, long-term damage resistance of polyethylene pipes can be very different from the short-term test results that are often determined from virgin material.

The results suggest that assessment of long-term performance of PE pipe should include the damage assessment which may be generated during installation and service. Since such damage assessment is not considered at present, a new methodology is needed to quantify and monitor the damage evolvement in a plastic pipe and to quantify its effect on PE's long-term performance.

Acknowledgements

The work was supported by Natural Sciences and Engineering Research Council of Canada (NSERC). Sincere appreciation is due to Campbell, Waege and Bubenko for specimen preparation and Faulkner for fabrication of the extensometer used in the testing.

References

[1] A. Peterlin, Molecular model of drawing polyethylene and polypropylene, J Mater Sci, 6 (1971) 490-508.
[2] E. N. Allouche, S. T. Ariaratnam, J. S. Lueke, Horizontal directional drilling: profile of an emerging industry, J Construction Eng & Management, 126 (2000) 68-76.
[3] J. Scheirs, L. L. Böhm, J. C. Boot, P. S. Leevers, PE100 resins for pipe applications: continuing development into the 21st century, Trends Polym Sci, 4 (1996) 408-415.
[4] M. Ifwarson, H. Leijström, What controls the lifetime of plastic pipes and how can the lifetime be extrapolated, Studsvik Polymer AB, Sweeden.
[5] M. Ifwarson, Life-time of polyethylene pipes under pressure and exposure to high temperatures, Kunstst Ger Plast, 79 (1989) 20-22.
[6] X. Lu, N. Brown, A test for slow crack growth failure in polyethylene under a constant load, J Polym Testing, 11 (1992), 309–319.
[7] M. Fleissner, Experience with a full notch creep test in determining the stress crack performance of polyethylenes, Polym Eng Sci, 38(2) (1998) 330-340.
[8] X. Lu, N. Brown, The ductile-brittle transition in a polyethylene copolymer, J Mater Sci, 25 (1990) 29-34.
[9] X. Lu, N. Brown, Unification of ductile failure and slow crack growth in an ethylene-octene copolymer, J Mater Sci, 26 (1991) 612-620.
[10] X. Lu, A. McChie, N. Brown, The dependence of slow crack growth in a polyethylene copolymer on test temperature and morphology, J. Polym. Sci.: B: Polym. Phy., 30 (1992) 1207-1214.
[11] N. Brown, X. Lu, A fundamental theory for slow crack growth in polyethylene, Polymer, 36 (1995) 543-548.
[12] P.A. O'Connell, R.A. Duckett, I.M. Ward. Polym. Eng. Sci. 42(7), 2002, 1493-1508.
[13] X Lu, R Qian, N Brown, Discontinuous crack growth in polyethylene under a constant load, J Mater Sci, 26 (199l) 917-924.
[14] C G'Sell, J J Jonas, Yield and transient effects during the plastic deformation of solid polymers, J Mater Sci, 16 (1981) 1956-1974.
[15] R. Hiss, S. Hobeika, C. Lynn, G. Strobl, Network stretching, slip processes, and fragmentation of crystallites during uniaxial drawing of polyethylene and related copolymers. A comparative study, Macromolecules, 32 (1999) 4390-4403.
[16] G. Ayoub, F. Zaïri, M. Naït-Abdelaziz, J. M. Gloaguen, Modelling large deformation behaviour under loading–unloading of semicrystalline polymers: Application to a high density polyethylene, Int J Plasticity, 26 (2010) 329–347.
[17] A. Sedighiamiri, L. E. Govaert, M. J. W. Kanters, J. A. W. van Dommelen, Micromechanics of semicrystalline polymers: Yield kinetics and long-term failure, J Polym Sci B: Polym Phys, 50 (2012) 1664–1679.
[18] P.-Y.B. Jar, S. Muhammad, Cavitation-induced rupture in high-density polyethylene copolymers, Polym Eng Sci, 52(5) (2012) 1005-1014.
[19] Information provided by NOVA Chemicals.

3D Analysis of Amorphous Polymers Deformation under Mode I

Shu Guo[1, 2], Rafael Estevez[2,*], Sabine Weygand[3], Christian Olagnon[1]

[1] MATEIS, INSA Lyon, 69621, France
[2] SIMAP, Université de Grenoble, 38401, France
[3]University of Applied Science, HS Karlsruhe, 76133, Karlsruhe, Germany
* Corresponding author: Rafael.Estevez@simap.grenoble-inp.fr

Abstract Fracture in ductile glassy polymers is usually preceded by noticeable and extensive plastic deformation, as shear yielding takes place in the form of shear bands that are limited by progressive hardening of materials at continuous deformation. In the case of a notched specimen, this induces a noticeable crack blunting before the failure. We use a constitutive law that captures realistically the stress-strain fields of solid glassy polymers. In particular, we account for a rate dependent yield stress followed by intrinsic softening and progressive hardening at continued deformation. We analyzed the 3D crack tip fields around a blunted notch loaded under mode I. With an increasing ratio between thickness versus notch tip radius, the shape of crack tip area evolves from a flame like zone characteristic of plane stress conditions to slip lines when plan strain conditions prevail. For a constitutive law representing the response of polycarbonate, we identified a critical thickness vs notch radius value that indicates the transition between plane stress to plane strain dominant loading conditions. The implication for the geometry necessary to derive material toughness experimentally is pointed out and an examination of the mean stress constraint related to the onset of failure by crazing is reported.

Keywords crack tip plasticity, fracture, glassy polymers, 3D effects

1. Introduction

Fracture in glassy polymer involves the competition between two localized plastic deformation: shear yielding and crazing. Shear yielding is related to the material's mechanical response with the localization of plastic deformation upon yielding followed by progressive hardening that controls the shear bands thickness. Crazing is the mechanism underlying failure that involves also localized plasticity, although at a much smaller scale. In glassy polymers, the crack tip fields around a notch loaded under mode I have been analyzed in a seminal paper by Lai and Van der Giessen [1] for 2D plane strain condition. These authors showed that the specific plastic zone made of a collection of shear bands similar to Hill's slip lines is related to the material's constitutive law with softening trigeering the formation of shear bands of which development is arrested by progressive hardening at continued deformation. This latter feature acts as a shear bands lock that promotes the nucleation of new shear bands to form a specific plastic zone; in the case of thin polymer films, when plane stress conditions prevail, a flame like plastic zone is observed, for instance in tests by the essential work of fracture (EWF) tests [2]. In ductile polymer fracture, when the onset of failure is preceded by noticeable plastic deformation as in polycarbonate, to determine the geometry for which plane strain conditions prevail remains heuristic from an experimental point of view. For instance, Parvin and Williams [3] observed that a ductile to brittle fracture transition takes place in a SENT polycarbonate specimen with increasing the sample's thickness. They ascribed this transition to a critical thickness (t) versus size of the plastic zone (r_p) as t/r_p, with r_p the extent of plastic zone under plane stress condition. By taking K_{c1} the toughness measured for thick samples and K_{c2} that for thin samples, they proposed a empirical relationship that captures the variation on the toughness with the specimen's thickness. More recently, Tvergaard and Needleman [4] investigated the

thickness effects in Izod fracture tests used in polymer samples and pointed out differences in the crack tip fields. For the thicker specimens, the predicted maximum mean stress appears much higher in the midsection than on the free surface. For thin specimens, a similar mean stress constraint is observed across the material's thickness, which indicates that plane stress conditions prevail. For the measure of the material's toughness, one wished to ensure that plane strain conditions prevail and if not, to estimate whether plane stress or a combination between plane stress and plane strain conditions is met. We present an analysis of the crack tip fields along the spirit of Lai and Van der Giessen [1] but within a 3D framework. The results presented here show that the shape of the predicted plastic zone can be used as an indicator of the plane stress/ plane strain condition and a geometrical criterion is proposed for the estimation of the thickness large enough to ensure plane strain conditions.

The paper is organized as follows. We first present the materials constitutive law and report the parameters identified for the polycarbonate under consideration. Then we present the 3D notched configuration and related problem formulation. For identical loading conditions, the influence of the thickness on the predicted crack tip fields in terms of cumulated plastic deformation is reported. The analysis of the variation of the mean stress with thickness, and its comparison with 2D calculations performed for plane stress and plane strain conditions are presented and used for proposing a criterion indicating when plane strain conditions prevail.

2. Material model and parameters identification

2.1. Constitutive Law

The constitutive law used to model the large strain plastic behavior is based on original ideas due to Boyce et al. [5] with some modifications introduced later by Wu and Van der Giessen [6] for the hardening part. In this section, we report the governing equations and materials parameters to be identified to represent the bulk, craze-free, response. The reader is referred to [7] for details on the computational aspects. The 3D constitutive model has been implemented in abaqus [8] within a User Material routine. The mechanics of fully three-dimensional large strain deformation involves the deformation gradient tensor $\boldsymbol{F}$, which maps a material point of the reference configuration into the current configuration. The deformation gradient is multiplicatively decomposed as $\boldsymbol{F} = \boldsymbol{F}^{\mathrm{e}}\boldsymbol{F}^{\mathrm{p}}$, in which $\boldsymbol{F}^{\mathrm{p}}$ describes the deformation from the initial to an intermediate, "relaxed" or "natural" configuration, followed by an elastic transformation $\boldsymbol{F}^{\mathrm{e}}$ up to the final deformation $\boldsymbol{F}$. The velocity gradient in the current configuration is $\boldsymbol{L} = \dot{\boldsymbol{F}}\boldsymbol{F}^{-1} = \dot{\boldsymbol{F}}^{\mathrm{e}}\boldsymbol{F}^{-\mathrm{e}} + \boldsymbol{F}^{\mathrm{e}}\dot{\boldsymbol{F}}^{\mathrm{p}}\boldsymbol{F}^{-\mathrm{p}}\boldsymbol{F}^{-\mathrm{e}}$ of which symmetric and anti-symmetric part correspond to the strain rate and spin tensor, $\boldsymbol{D}$ and $\boldsymbol{W}$ respectively. When the elastic part $\boldsymbol{F}^{\mathrm{e}}$ of the deformation gradient is small compared to the plastic one $\boldsymbol{F}^{\mathrm{p}}$ (i.e. $\boldsymbol{F}^{\mathrm{e}} \approx \mathrm{I}$), the velocity gradient reduces to $\boldsymbol{L} = \boldsymbol{L}^{\mathrm{e}} + \boldsymbol{L}^{\mathrm{p}}$ so that the total strain rate $\boldsymbol{D}$ becomes the sum of the elastic and plastic parts as $\boldsymbol{D} = \boldsymbol{D}^{\mathrm{e}} + \boldsymbol{D}^{\mathrm{p}}$.

Prior to the yield stress, amorphous glassy polymers exhibit a non linear stress strain response due to small viscoelastic effects. These are not considered explicitly but their effect on the mechanical response is accounted for by using a secant Young modulus instead of that derived from ultra-sonic wave velocities. In view of these approximations, the hypo-elastic law is used to express the bulk mechanical response as

$$\overset{\nabla}{\boldsymbol{\sigma}} = \boldsymbol{L}_{\mathrm{e}}\boldsymbol{D}^{\mathrm{e}}, \qquad (1)$$

where $\overset{\nabla}{\boldsymbol{\sigma}}$ is the Jaumann rate of the Cauchy stress, $\boldsymbol{L}_{\mathrm{e}}$ the fourth-order isotropic elastic tensor in terms of secant Young modulus E^{SECANT} and Poisson's ratio ν, which is in Cartesian components $\boldsymbol{L}_{ijkl} = \frac{E}{2(1+\nu)}\left[(\delta_{ik}\delta_{jl} + \delta_{il}\delta_{jk}) + \frac{2\nu}{1-2\nu}\delta_{ij}\delta_{kl}\right]$.

Within the elastic-viscoplastic framework used here, the plastic strain rate is

$$\boldsymbol{D}^{p} = \dot{\gamma}^{p}\frac{\overline{\boldsymbol{\sigma}}'}{\sqrt{2}\tau}, \text{ with } \tau = \sqrt{\frac{1}{2}\overline{\sigma}' \cdot \overline{\sigma}'} \tag{2}$$

being the equivalent shear stress and $\overline{\boldsymbol{\sigma}}$ the deviatoric part of the driving stress. The driving stress itself is defined by $\overline{\boldsymbol{\sigma}} = \boldsymbol{\sigma} - \boldsymbol{b}$. The back stress $\boldsymbol{b}$ responsible for the hardening is due to the entropic back forces generated by the deformation of the polymer chains during the plastic deformation, and will be defined later. The equivalent plastic shear rate $\dot{\gamma}^{p}$ is taken according to Argon's [9] expression

$$\dot{\gamma}^{p} = \dot{\gamma}_{0}^{p} \exp[-\frac{A(s_0 + \alpha p)}{T}(1 - (\frac{\tau}{s_0 + \alpha p})^{5/6})], \tag{3}$$

where $\dot{\gamma}_{0}^{p}$ and A are material parameters and T is the absolute temperature. Following Boyce et al. [5], intrinsic softening is accounted for with the definition of an internal variable s which varies from s_0 to s_{ss} at continued plastic deformation. The internal law

$$\dot{s} = h(1 - s / s_{ss})\dot{\gamma}^{p} \tag{4}$$

governs its variation during deformation, with h a parameter controlling the rate of softening and s_{ss} the value of s in a steady state regime. Furthermore, Equation (3) is modified in order to account for the pressure dependence by using $s + \alpha p$ instead of s_0 in (3), where $-\mathrm{p} = 1/3\mathrm{tr}\sigma$ is the mean (or hydrostatic) stress. The coefficient α represents the pressure sensitivity of the polymer which results in an asymmetric yield stress in tension and compression, for instance.

The description for back stress tensor $\boldsymbol{b}$ is based on ideas borrowed from theories for rubber elasticity with the cross-links of the rubbers considered as "entanglements" in the case of glassy polymers. The deformation of the resulting network is assumed to derive from the cumulated plastic stretch so that the principal back stress components b_α are functions of the principal plastic stretches λ_β as

$$b = \sum_{\alpha} b_{\alpha}\left(e_{\alpha}^{\mathrm{p}} \otimes e_{\alpha}^{\mathrm{p}}\right) , \tag{6}$$

in which $\boldsymbol{e}_{\alpha}^{\mathrm{p}}$ are the principal directions of the plastic stretch. In a description of the fully three-dimensional orientation distribution of non-Gaussian molecular chains in a network, Wu and Van der Giessen [10] showed that $\boldsymbol{b}$ can be estimated accurately with the following combination of the classical three-chain model and the eight-chain description of Arruda and Boyce [11]

$$b = (1-\rho)b^{3-\mathrm{ch}} + \rho b^{8-\mathrm{ch}}, \tag{7}$$

where the fraction $\rho = 0.85\bar{\lambda}/\sqrt{N}$ is based on the maximum plastic stretch $\bar{\lambda} = \max(\lambda_1, \lambda_2, \lambda_3)$ and on N, the number of segments between entanglements. The use of Langevin statistics for calculating b_α

implies a limit stretch of $\sqrt{N}$. The expressions for the principal components of b^{3-ch} and b^{8-ch} contain a second material parameter: the initial shear modulus $C^{R} = nk_{B}T$, in which n is the volume density of entanglements (k_B is the Boltzmann constant).

2.2. Parameters identification

In order to obtain a set of material parameters for the description of the finite strain visco-plastic response of the polycarbonate under consideration, experimental data of the stress-strain response for various strain rates are necessary. In compression, crazing is suppressed and uniaxial experiments are carried out on cylindrical specimens. In order to prevent any buckling, the diameter and the height of the specimen are 10 mm and 6 mm respectively. Low friction along the contact surface between the faces of the cylinder and the plates of the machine is ensured by using a hexagonal boron nitride powder (BN). Therefore, lateral displacement with respect to the direction of compression is allowed so that a uniform stress state prevails along the whole specimen. In order to characterize the rate dependency of the yield stress, a series of strain rates from 1×10^{-5}/s to 1×10^{-1}/s are investigated (see Fig. 1(a)). Following the identification procedure detailed in Saad et al., [12], the parameters are extracted from the uniaxial compression data and are reported in Table 1. The corresponding predictions are presented in Fig. 1(b).

Table 1. Material parameters for Polycarbonate

E^{sec}(MPa)	ν	s_0(MPa)	s_{ss}(MPa)	α	A(K/MPa)	h(MPa)	$\dot{\gamma}_0(s^{-1})$	C^R(MPa)	N
1300	0.39	88	68	0.08	195	450	9.2e09	17	3

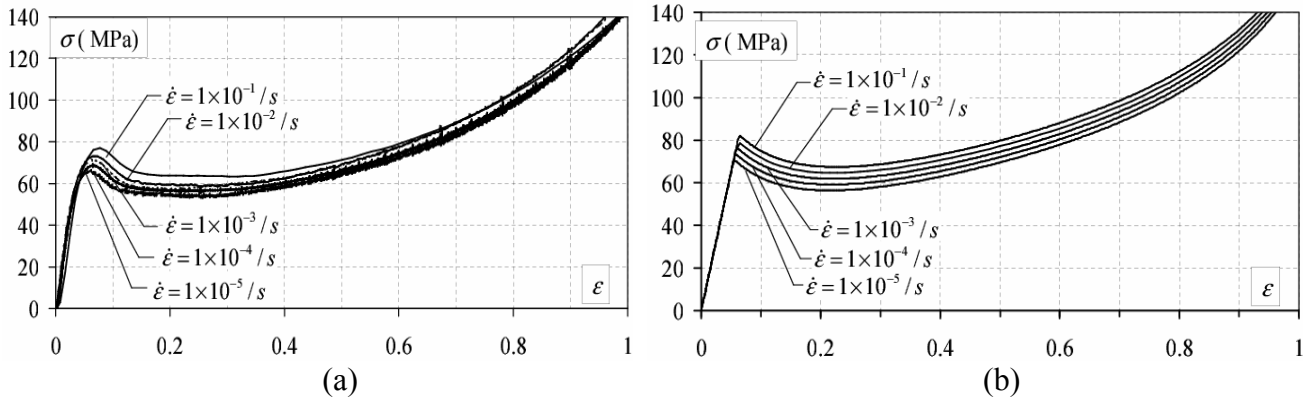

Figure 1.(a)Experimental cylinder compression stress-strain curves at strain rates varying from 1×10^{-5}/s to 1×10^{-1}/s (b) Predicted stress-strain response with the parameters identified in Table 1.

3. Problem formulation

In this section, we present the geometry of the specimen under consideration and the mesh used for the finite element analysis.

3.1. 3D analysis of a notched specimen under tension

The full 3D geometry of standard specimen loaded under mode I has dimension of h= 40 mm, w=20mm and a=10 mm , with a variable thickness B(see Fig. 2, left side). A blunted notch of radii R=0.25mm is considered. We use a blunted notch that would correspond to the blunting of a sharp crack up to this magnitude. It is also motivated by experimental issues in which practically machining a sharp notch is difficult if not impossible experimentally. The preparation of a blunted notch is preferred for the fracture measurements to be reproducible. The constitutive law described in section 2 is implemented in a UMAT subroutine in abaqus 6.10-2 [8] and used.

3.2. Description of the mesh

The geometry and the mesh are presented in Fig. 2. Refined elements are used around the notch to capture the stress-strain fields. In the region remote to the notch area coarser elements are used. The elements consist in C3D20R, which is a 20-node quadratic brick, with reduced integration. The amount of elements across the thickness is increased with the thickness increasing, their dimension remaining identical. For instance with R=0.25 mm and thickness t=1 mm, the mesh comprises of 12 layers of elements through the thickness of the specimen; a total number of 15558 quadratic elements and 70574 nodes are employed. The smallest element has an edge of 0.0027mm. A constant displacement rate $\dot{u}$=5 mm/s is prescribed on the top surface to mimic a Single Edge Notch Tension for all calculations.

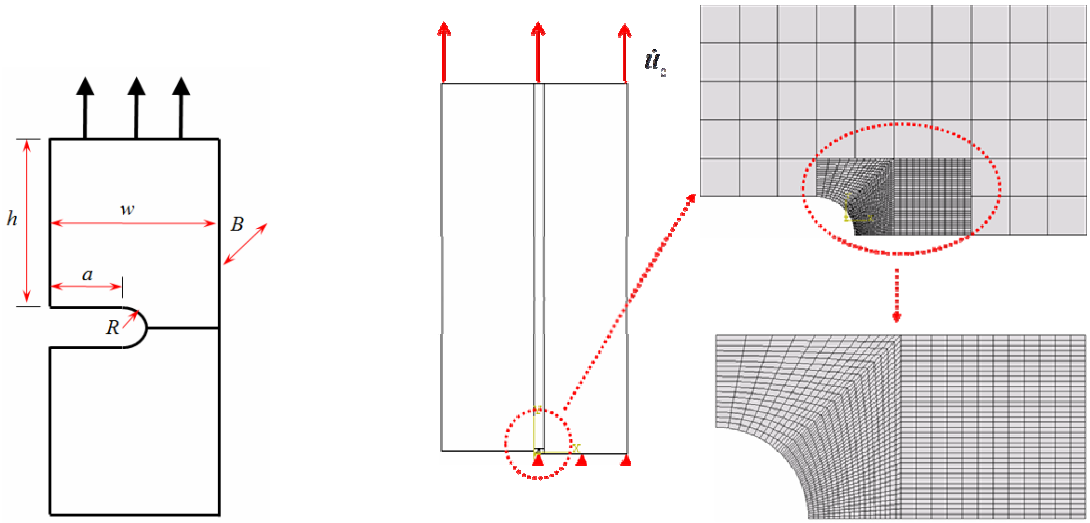

Figure 2. Geometry and mesh description for the Single Edge Notch Tension configuration

4. Results

In this section, we investigate the influence of the thickness on crack tip fields of blunt-notched specimens (see section 4.1.), with notch radius R=0.25mm. During the loading, plasticity initiates at the notch tip and extends on the notch region. The distribution of accumulated plastic shear strain around the notch is reported in Fig. 3. The variation of the maximum mean stress with the loading history represented by the overall axial strain $E_{axial}=u/2h$ is presented next.

4.1. Influence of the thickness on crack tip plasticity

Three sets of plastic shear strain distributions, and related contours, are reported in Fig. 5(a)-(i) at various load levels in terms of axial strain E_{axial} , for specimen thickness t=0.25 mm,1 mm and 4 mm, respectively.

For the thickness t=0.25 mm (t/R=1), we present in Fig. 3(a-c) the plastic shear strain distribution at the onset of plasticity(see Fig. 3(a)) and continued deformation(see Fig. 3(b) and 3(c))on the surface as well as at the center of the specimen. Far from the notch, no plasticity takes place and the response is elastic. Around the notch, we observe that the plastic zone initiates and grows simultaneously at the surface and in the center of the specimen, but the shape of the plastic zone is different. At E_{axial}= 0.75% it is seen that certain amount of plasticity arises around notch tip(see Fig. 3(a)). A homogeneous plastic zone inclined −30° from the equator is observed at the center, whereas a bifurcated plastic zone appears on the surface. With ongoing deformation, plastic zones both inside and outward expand rapidly. In Fig. 3(b), as E_{axial} equals to 0.875%, the plastic zone at the center gets a flame-like profile. At the surface, the plastic zone expands into a flame-like elongated plastic zone as well, which grows nearly parallel to the equator. Finally, as indicated in Fig. 3(c), a larger elongated plastic zone along the equator is observed at the center, whereas a similar elongated plastic zone appears parallel to the equator on the surface. For the configuration with thickness t=1 mm(t/R =4), at E_{axial}= 0.75%, plasticity initiates with very small amount of plasticity on the surface, and in the form of tiny shear bands at the center(see Fig. 3(d)). For E_{axial} about 0.875%, plasticity areas do not proceed much both inside and outward(see Fig. 3(e)), as compared with Fig. 3(b). Finally, instead of forming a flame-like elongated plastic zone as the t/R=1 case, a circular-arc shaped plastic zone concentrated near the crack tip at the center(see Fig. 3(f)). Thus, the plastic zone appears different for t/R=1 and t/R=4 till now. If the thickness of specimen is further increased to t=4 mm(t/R=16), in Fig. 3(g), when plasticity initiates at E_{axial}=0.75% , clear shear bands arise around the notch in the center, whereas on the surface only a tiny area of plasticity is observed. As E_{axial}=0.875%, shear bands continued to widen and diffuse at the mid-thickness, on the other hand, still tiny amount of plasticity exists on the surface (see Fig. 3(h)). With E_{axial} up to 1.125%, plastic deformation on the surface is still confined in a tiny region, whereas shear bands at the center enlarge a lot within a circular-arc, as shown in Fig. 3(i). This observation is similar to the plastic zone reported by Lai and Van der Giessen [1].

For the thinner specimen considered with thickness t=1mm(t/R=1), we observe that the magnitude of plastic zone at the center is comparable to that on the surface, which rationalize the fact that the plane stress conditions prevail. In the case of t/R=4, the plastic zones appear significantly less elongated when compared to the case with t/R=1, both in the middle of the thickness and at the

surface for the same overall deformation. Besides, the plastic strain distribution at the center is no longer comparable to that on the surface as in Fig. 3(a)-(c). This phenomena that plasticity on the surface failed to proceed as much as that at the center(see Fig. 3(d)-(f)) represents a transition from plane stress to plane strain conditions within the material. Finally, for the thick specimen with t/R=16 (thickness of 4mm), the apparent discrepancy in the shape of locally deformed area at the mid-thickness and on the surface indicates that plane strain condition dominates in the specimen.

The shape of the plastic zone corresponding to a flame-like profile under plane stress condition(see Fig. 3(c)), is found to agree well with Hashemi's [2] observations of the plastic zone in thin polymer films tests in EWF method. As the thickness over notch radius ratio $t/R \geqslant 4$, we observe at the center of the specimen the development of shear bands similar to those predicted by Lai and Van der Giessen [1] who performed 2D plane strain calculations, for a mode I load. These observations can be used to estimate the region where plane stress and plane strain prevail. In particular, it can be used as an indicator to assess whether or not plane strain conditions are dominant. Actually, for the case with t/R=16(4mm thickness specimen), plane strain conditions with characteristic shear bands are observed, similarly to those predicted by Lai and Van der Giessen [1] and observed experimentally (Ishikawa et al. [13] for instance). For this series of calculations, plane stress conditions prevail for t/R<4, plane strain effects emerge for t/R=4 and these conditions become dominant when t/R> 4, as shown for the case with t/R=16.

On the other hand, the case corresponding to plane strain conditions exhibits the largest magnitude of the maximum mean stress for a given loading. This case is investigated in detail in Lai and Van der Giessen [1] who evidenced that the location of the maximum mean stress coincides with the intersection of well defined shear bands that enhance its magnitude. The plots of the maximum mean stress with loading of the 3D calculations are bounded by those corresponding to the 2D planes stress and 2D plane strain cases. The calculations with thickness t=1mm (t/R=1) results in a plot of the maximum mean stress with loading close to that of the 2D plane stress case. As the thickness increases, the maximum mean stress-loading curve moves from the 2D plane stress to the 2D plane strain case. The shift is clear when carrying from 1mm to 4 mm in thickness and its variations becomes modest for larger thicknesses. The plots reported in Fig. 4 provide insights on whether plane stress or plan strain condition is dominant, for a given thickness to notch radius ratio. The foregoing observation that plane strain conditions become dominant at about t/R=16 is confirmed by the analysis of the maximum mean stress during loading. This somehow confirms the qualitative analysis based on the shape of the plastic zone presented in the previous section and evidences the influence of the thickness mean stress constraint in the notch region.

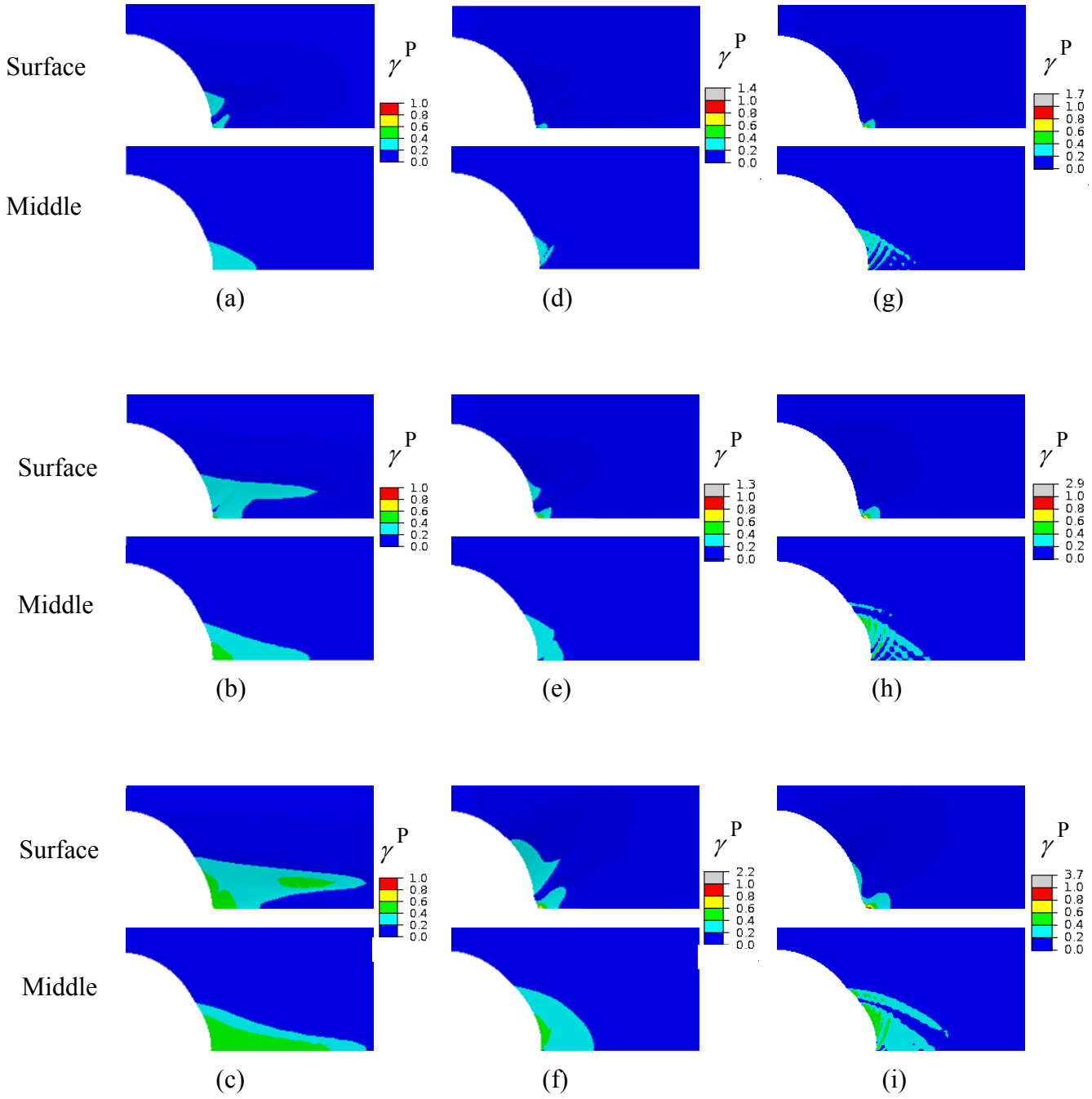

Figure 3. Plastic shear strain distribution at the surface and the mid-thickness, for R=0.25mm, at E_{axial}=0.75%, 0.875% and 1.125%, (a-c) for t=0.25mm; (d-f) for t=1mm; (g-i) for t=4mm.

4. Discussion and conclusion

The calculations performed in present work allow to compare the plastic zone at the center as well as on the surface of specimens. Plastic shear strain distribution of blunt-notched polymer bulks are reported, corresponding to specimens with various thicknesses and an initial blunted notch R=0.25mm.

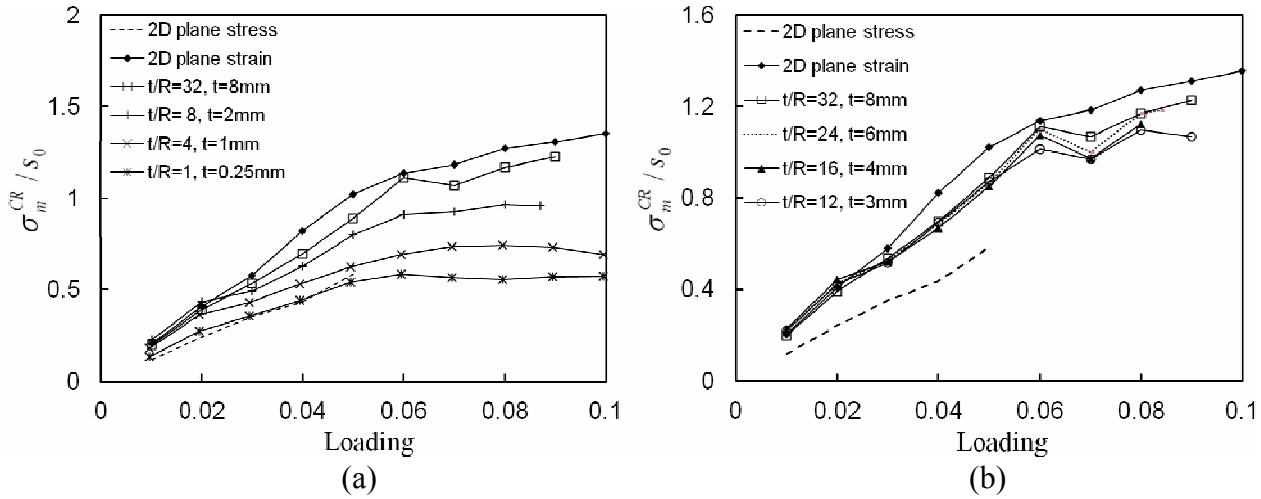

Figure 4. Variation of the maximum mean stress with loading for the 3D specimens of various thicknesses and 2D configurations under plane stress and plane strain conditions (R=0.25mm)

The shape of the plastic zone is shown useful as a marker for identifying if plane stress or plane strain conditions prevail. For the mode I under consideration here, a flame-like plastic contour is observed where plane stress conditions are met, for a small thickness and a ratio $t/R\leq$ □?4(thickness/notch radius). The shape of flame-like elongated plastic zone for the specimen with t/R=1 is in agreement with Hashemi's observations reported in [2]. By increasing the thickness and the ratio t/R, the shape of the plastic zone evolves from the flame-like to a plastic strain distribution. As for specimens with t/R=16, typical shear bands appear at the center of polymer, which are similar to that observed in Hill's slip line field and comparable to that reported by Lai and Van der Giessen[1]. The onset of a transition from plane stress or plane strain condition is observed as soon as the ratio thickness/notch radius t/R= 4. This observation is consistent with that reported by Parvin and Williams [3], if one considers the radius of the blunt crack $R_p\approx$ R is ductile polymer with a blunt notch. Thus, we propose a criterion to distinguish between plane stress and plane strain conditions. Although the criterion $t/R>$ 4 for plane strain conditions to emerge is established to R=0.25mm, we have investigated samples with a smaller (0.1mm) and a larger (0.5mm) notch radius. The variations of the plastic zone shape with the ratios t/R reported in Fig. 3 are also observed for R=0.1mm and R=0.5mm. This observation appears valuable when one considers an initial blunt notch.

For the configuration with an initial sharp crack, the onset of failure is usually taken from a Crack Tip Opening Displacement that is measurable experimentally. The CTOD is the characteristic of the material under consideration and its magnitude could be used as the value of the blunted notch radius and compare to the thickness in order to evaluate the minimum thickness for plane strain conditions. This information is valuable for one concerns with experimental polymer fracture and the issue of the size requirements for the estimation of the material's toughness. The present predictions need to be compared to experimental results. This is currently under progress and some preliminary results can already be reported. We have prepared the samples depicted in Figure 2 and performed some SENT fracture tests. In figure 5, we report the variation of the stress at rupture with the thickness. All samples have the same geometry in terms of crack length versus specimen width and the same height. In Fig. 5, we observe that the stress at rupture decreases with the thickness increasing with a plateau being reached for t/R=16. These first results are consistent with the predictions found here as the lowest stress at fracture is found for a specimen thickness larger than 4mm. A more detailed experimental investigation is under progress and will be addressed in a forthcoming paper.

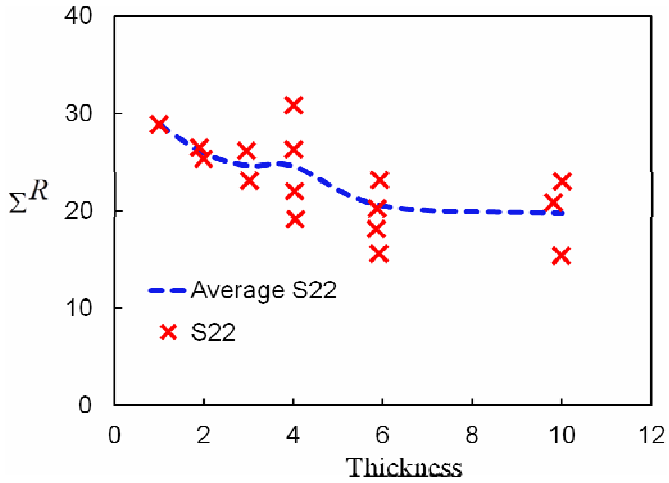

Figure 5. Experimental investigation of the stress at rupture from SENT specimen identical to those depicted in Fig. 2

Acknowledgements

This research program is supported by CSC(China Scholorship Council) in collaboration with INSA Lyon.

References

[1] J.Lai, E. der Giessen, A numerical study of crack-tip plasticity in glassy polymers, Mechanics of Materials, 25 (1997) 183–197.

[2] S. Hashemi, Plane-stress fracture of polycarbonate films, Journal of Materials Science, 28 (1993) 6178–6184.

[3] M. Parvin, J. Williams, Ductile-brittle fracture transitions in polycarbonate, International Journal of Fracture, 11 (1975) 963–972.

[4] V. Tvergaard, A. Needleman, An analysis of thickness effects in the izod test, International Journal of Solids and Structures, 45 (2008) 3951–3966.

[5] M.C. Boyce, D.M. Parks, A.S. Argon, Large inelastic deformation of glassy polymers, part I rate dependent constitutive model, Mechanics of Materials, (1988) 15–33

[6] P. D. Wu, E. der Giessen, On improved network models for rubber elasticity and their applications to orientation hardening in glassy polymers, Journal of the Mechanics and Physics of Solids, 41 (1993) 427–456.

[7] P. D. Wu, E. van der Giessen, Computational aspects of localized deformation in amorphous glassy polymers, European Journal of Mechanics., A/Solids, 15 (1996) 799–823.

[8] Abaqus finite element package, v. 6.10, Simulia, Dassault Systems.

[9] A. S. Argon, A theory for the low-temperature plastic deformation of glassy polymers, Philosophical Magazine, 28 (1973) 839–865.

[10]P. D. Wu, E. der Giessen, On improved network models for rubber elasticity and their applications to orientation hardening in glassy polymers, Journal of the Mechanics and Physics of Solids, 41 (1993) 427–456.

[11] E. M. Arruda, M. C. Boyce, A three-dimensional constitutive model for the large stretch behavior of rubber elastic materials, Journal of Physics and Solids, 41(1993) 389–412.

[12] N.Saad-Gouider, R.Estevez, C.Olagnon, R.Séguéla, Calibration of a viscoplastic cohesive zone for crazing PMMA, Engineering Fracture Mechanics, 73 (2006) 2503–2522.

[13] M. Ishikawa, I. Narisawa, H. Ogawa, Criterion for craze nucleation in polycarbonate, Journal of Polymer Science:Polymer Physics Edition, 15 (1977)17911804.

A Damage Model for Sandwich Plate with Viscoelastic Core in three-Points Bending Fatigue Experiments

Xue QiChao[1], Zou GuangPing, Xiong Hailin

Department of Aerospace and Civil Engineering, Harbin Engineering University, Harbin, 150001, China

Abstract In three-points bending fatigue experiments of sandwich plate with visoelastic core and steel facplates, recovering effects of fatigue life are found for its viscoelastic properties of the core. If the fatigue experiment is interrupted and rest for some time before reloading, there will appear a phenomenon that the deflection doesn't reach the former value immediately but after a specific time or cycles. From defining the damage variable *D* as the ratio between the differences of maximum allowable bending deflection and processing deflection in experiments, the fatigue damage equation are established. To considering the recovering effects, a formula which is similar with deflection of isotropic viscoelatic beam under concentrated load in midspan is introduced in damage equation. The experiments result shows that this damage model considering recovering effects can demonstrate the damage very well for sandwich plate with viscoelastic core. And the existing of viscoelastic core can increase the fatigue life of sandwich beam specimen.

Keywords Sandwich, Viscoelastic Core, Fatigue, Damage Model

1. Introduction

Sandwich plate with viscoelastic core is widely used in civil engineering and shipbuilding fields [1]-[3] for weight reduction, rapid reparation, vibration isolation, noise reduction and resisting impact. It also has better fatigue resistance characteristic than ordinary steel structures. From the fatigue experiment, it is found that the existing of recovering effects by intermittent loading have influences on the fatigue life. Based on damage theory, a fatigue damage model is proposed to elaborate the damage of specimen considering recovering effect. From intermittent test, the recovering effect is affirmed and damage model is verified that it have a certain accuracy.

2.Fatigue experiment phenomenon

In the fatigue experiment process of practical engineering, structural fatigue load applied on structure load is often not continuous, but intermittent. For the exiting of viscoelastic core in sandwich plate, it makes the responses of sandwich beam specimen under three-points bending fatigue load different from ordinary sandwich plate's responses. From the three-points bending fatigue experiment process, the following phenomenon are found:

(1) Under pressure-pressure fatigue load to three-points bending specimen, along with increasing of cycle number, vertical deflection is also increased, for specimens with smaller interlayer cohesive force, the first crack appears in one end and gradually propagates as cycles increasing. When the vertical displacement reaches a certain level, there doesn't appear fracture or crushing phenomenon. But there will be propagation of the crack or tearing of core.

(2) When fatigue loading is intermittent, that is, interrupt fatigue load and unload, after a long time (such as a few hours), fatigue loading is applied once again. Then it is found that the vertical

[1] Xue1736@163.com

displacement cannot directly reach the previous loading position under the same load, but after a certain time or cycles before reaching the former position.

In the entire loading-stop-reloading process, overall fatigue life will increase than under continuous fatigue load. As shown in Figure.1, the curve of ‘a’ is the first load curve. When the loading process reaches a certain positions (at‘d’ or ‘e’), stop and unload for a while, then reload. The cure will follow the curve ‘b’ or curve ‘c’ before reaches the intersection point superimposed with the original curve ‘a’, rather than a direct continuation of load curve ‘a’. In this process, the number of cycles corresponding to the portion shown in the dashed line means the additional growth of fatigue life. The following attempts to establish a fatigue damage model to describe this phenomenon.

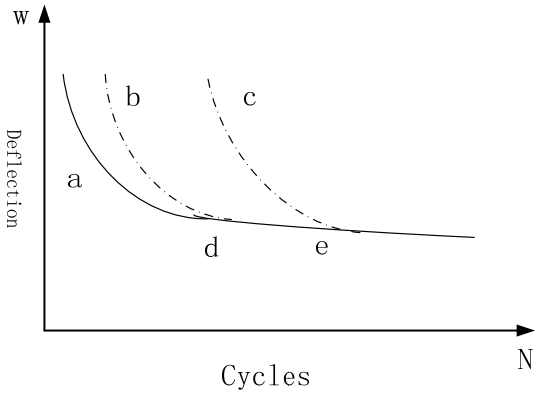

Fig.1 Loading-stop-reloading process

3. The fatigue damage model considering intermittent effects

Substantially the first few cycles of all fatigue tests exist nonlinear characteristic. For the metal material, these cycles does not exceed 100 before reach stable stage, but for the polyurethane elastomer sandwich panel, the presence of viscoelastic core make the initial cyclic loading can last a long time. When the load level is low, the number of cycles can even reach thousands of times. For the whole fatigue life of material, it cannot be ignored. Here according to the classical linear fatigue damage theory [], fatigue damage model will be established to consider the intermittent effect.

In a one-dimensional fatigue damage theory, the damage of the material can be represented by the damage variable *D*, it is usually a function of load cycles:

$$D=f\left(\Delta\sigma,\overline{\sigma},N,\cdots\right) \tag{1}$$

In which $\Delta\sigma$ is the stress amplitude, $\overline{\sigma}$ is stress mean, *N* is the cycles. Then the material damage can be defined by the damage variable:

$$\begin{aligned} D&=0, \quad N=0 \\ D&=1, \quad N=N_{\max} \end{aligned} \tag{2}$$

In order to describe the influences of the recovering effect, here introduce the damage variable D_{eff}, which is defined as the effective damage. When the variable is equal to 1, the material is destructive. It can be obtained by uninterrupted fatigue loading process. It also can be gotten by analysis the curve shown in Fig.1, the solid line corresponds to the effective fatigue life. The dashed parts of the curve can be considered to be invalid damage, but it need to be included in the whole fatigue life.

Suppose it is piecewise loading throughout the cycling loading process, and the loading frequencies are the same. Define the degree of recovery function $N_b\left(t,\Delta\sigma,\overline{\sigma}\right)$, if the stop time is t_{n-1} before the *n-th* loading, after reloading *N* cycles, the damage of reloading can be written as

$$D_{eff,n}=\Delta D_n=\begin{cases}0 & \mathrm{N}_n \le \mathrm{N}_b \\ f((\mathrm{N}-\mathrm{N}_b),\Delta\sigma_n,\overline{\sigma_n}) & \end{cases} \tag{3}$$

In which $D_{eff,n}$ is the damage of *nth* loading, and N_n represents the cycles of *n-th* loading. $f((N-N_b),\Delta\sigma_n,\overline{\sigma_n})$ is the function to calculate cumulated damage. Then whole damage of specimen can be written as:

$$D_{eff,n}=\sum_{n=1}^{n}\Delta D_n \tag{4}$$

Whole loading cycles is:

$$N_{total}=\sum_{n=1}^{n}\mathrm{N}_n \tag{5}$$

Cycles corresponding effective damage is

$$N_{eff}=\sum_{m=1}^{m}N_m\text{-}mN_b \tag{6}$$

In which *m* are times of stop-reload. To identify fatigue damage model considering the effect of recovering, most important thing is to define recover degree of function, it depend on theoretical analysis or experiments.

In order to simplify the analysis, the damage function uses linear cumulative damage model, based on the analysis of the Miner [4], damage parameters is related with the number of cycles, and has nothing to do with the load order. The analysis here supposes the damage is only related with the previous loading:

$$D(n)=\frac{n-n_{if}}{N_f-n_{if}}\quad n\ge n_{if} \tag{7}$$

n_{if} is the threshold of recover degree of function, and *n* is the loading cycles. For constant amplitude fatigue tests, the fatigue damage after load *N* times should be modified as follows:

$$D(N)=\frac{\sum_{m=1}^{m}N_m\text{-}mN_b}{N_{eff}\text{-}N_b}\quad N\ge N_b \tag{8}$$

4. Recover degree function N_b

The Recover degree function is generally determined by the experiment, for the sandwich beam with viscoelastic core it can be roughly determined the by theoretical analysis. For no obvious or small plastic deformation case, the loading loop is stable, and the average displacement can be calculated by followings:

$$w_{2n}^{middle}=\frac{1}{2}(w^{n\to\infty}_{(2n)t_1^+}+w^{n\to\infty}_{(2n)t_1^-})=\frac{Q_1+Q_2}{2}\frac{l^3}{48E_fI_f}+\frac{1}{E_0}\frac{l(1+\mu_c)}{2(A_c)}\frac{1}{1+e^{\frac{E_0}{\eta_0}t_1}}(Q_1+e^{\frac{E_0}{\eta_0}t_1}Q_2)$$
$$w_{2n+1}^{middle}=\frac{1}{2}(w^{n\to\infty}_{(2n)t_1^+}+w^{n\to\infty}_{(2n)t_1^-})=\frac{Q_1+Q_2}{2}\frac{l^3}{48E_fI_f}+\frac{1}{E_0}\frac{l(1+\mu_c)}{2(A_c)}\frac{1}{1+e^{\frac{E_0}{\eta_0}t_1}}(Q_2+e^{\frac{E_0}{\eta_0}t_1}Q_1) \quad (9)$$

In which w_{2n}^{middle} and w_{2n+1}^{middle} are the means of displacements when cycles are equal to *2n* and *2n+1* respectively. E_f is modulus of elasticity, I_f is moment on inertia of specimen; *b* is the width; *l* is the gauge length; A_c is section area of core. E_0, μ_c and η_0 are viscoelastic parameters of core; Q_1 and Q_2 are maximum pressure load and minimum pressure. When the specimen is reloaded after loading a certain cycles, it is equivalent to load a reverse static effect (Q_0) based on former deformation, so the displacement of unload can be obtained by subtracting the two displacements. Here take the mean of deflection of when cycles are equal to *2n*:

$$\begin{aligned}w_{2n}^{unload}&=w_{2n}^{middle}-w(t)\\&=(\frac{(Q_1+Q_2)}{2}-Q_0)\frac{Q_0l^3}{48E_fI_f}+\frac{1}{E_0}\frac{l(1+\mu_c)}{2(A_c)}\frac{1}{1+e^{\frac{E_0}{\eta_0}t_1}}(Q_1+e^{\frac{E_0}{\eta_0}t_1}Q_2)-\frac{Q_0l(1+\mu_c)}{2(A_c)}\frac{1}{E_0}(1-e^{-\frac{E_0t}{\eta_0}})\\&=(\frac{(Q_1+Q_2)}{2}-Q_0)\frac{Q_0l^3}{48E_fI_f}+\frac{1}{E_0}\frac{l(1+\mu_c)}{2(A_c)}\left[\frac{1}{1+e^{\frac{E_0}{\eta_0}t_1}}(Q_1+e^{\frac{E_0}{\eta_0}t_1}Q_2)-Q_0(1-e^{-\frac{E_0t}{\eta_0}})\right]\end{aligned} \quad (10)$$

After stop a certain time t_0, reload the specimen for *k* cycles, Specimen displacement w_{2n}^{reload} can be written as:

$$\begin{aligned}w_{2k}^{reload}&=w_{(2k)t_1^+}+w_{2n}^{unload}\Big|_{t=t_0}\\&=Q_1\frac{l^3}{48E_fI_f}+\frac{1-e^{-\frac{E_0}{\eta_0}2kt_1}}{1+e^{\frac{E_0}{\eta_0}t_1}}\frac{1}{E_0}Q_1\frac{l(1+\mu_c)}{2(A_c)}+\frac{e^{\frac{E_0}{\eta_0}t_1}(1-e^{-\frac{E_0}{\eta_0}(2k+2)t_1})}{1+e^{\frac{E_0}{\eta_0}t_1}}\frac{1}{E_0}Q_2\frac{l(1+\mu_c)}{2(A_c)}\\&+(\frac{(Q_1+Q_2)}{2}-Q_0)\frac{Q_0l^3}{48E_fI_f}+\frac{1}{E_0}\frac{l(1+\mu_c)}{2(A_c)}\left[\frac{1}{1+e^{\frac{E_0}{\eta_0}t_1}}(Q_1+e^{\frac{E_0}{\eta_0}t_1}Q_2)-Q_0(1-e^{-\frac{E_0t_0}{\eta_0}})\right]\end{aligned} \quad (11)$$

Make $w_{2k}^{reload}=w_{2n}^{middle}$, loading times *k* can be approximated solved, which is the extra fatigue life from the reload. When recovering function is determined, we can calculate the extra fatigue life of intermittent fatigue loadings.

5 Intermittent fatigue experiment

In order to verify the proposed fatigue damage model considering intermittent loading, intermittent fatigue experiments are carried out and the theoretical result are also calculated by using of equation (11). Specimens are tested which is shown in Figure. 2 and the loading level is equal to 0.7; ratio of stress is equal to 0.9. The loading frequency is 2Hz, after loading 14000 times, the response of specimen is stable, then unloading and resting for 1 hour, the cycles-deflection curve are shown in fig.2

In the first time loading process, the deflection of specimen is about 10.31mm. Reloading after 1hour, when the deflection reached 10.31mm again, the corresponding cycles is about 2100. If

taking deflection as damage value, it means the extra fatigue life from the rest. The results calculate by using of equation(11) are shown in Fig3, the rising curve of the graph presents the data of w_{2k}^{reload} - w_{2n}^{middle} specimen after resting for 1hour. The straight line presents the coordinate value which is equal to 0. From the Fig3a, the rising curve is infinitely close the straight line, which means in ideal state, the reloading curve is approaching to the straight line of steady state. But in actual experimental conditions, the steady line is an oblique line which declines with cycles increase. So we consider it intersected when the gap between two curves is 0.01mm. In this case, the corresponding cycles of Fig.3a is about 1580. Comparing Fig.2 and Fig.3, a certain error exists which is about 24.7%. One reason is viscoelastic model of polyurethane core is simplified to Kelvin model, another reason is theoretical calculation doesn't consider the plastic deformation of specimen in cyclic loads. According to theoretical analysis, if the rest time is long enough, each rest has same recovering fatigue life. But from the experimental result, the recover fatigue lives are different for multiple reloading. From Fig.2c and Fig.2d, the recover life of third reloading is 1300 cycles, and at the ninth reloading, recover life is 650 cycles. This means in multiple reloading processes, there are damages in the specimen, which cause the decrease of recover fatigue life.

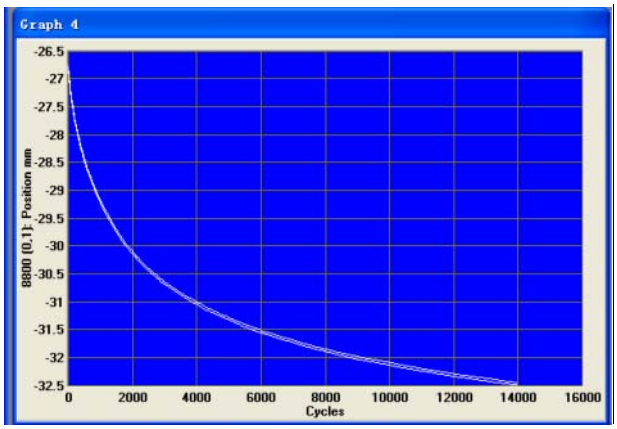

a 1st loading 14000 cycles

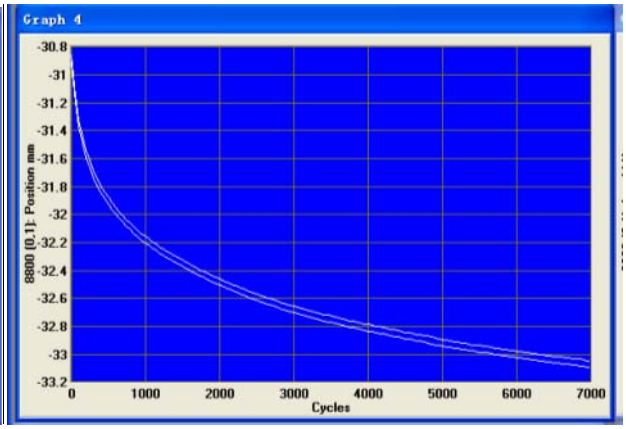

b 2nd loading after resting 1hour

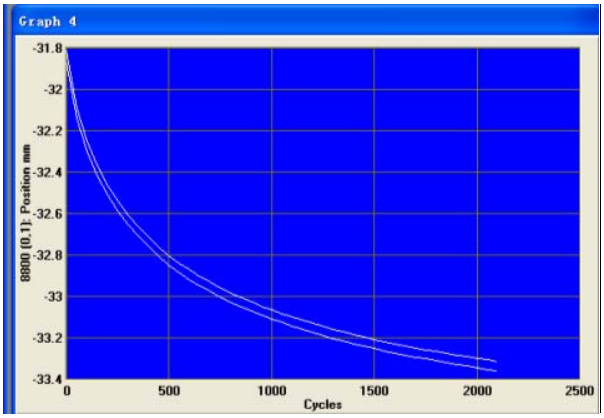

c 3rd loading curve

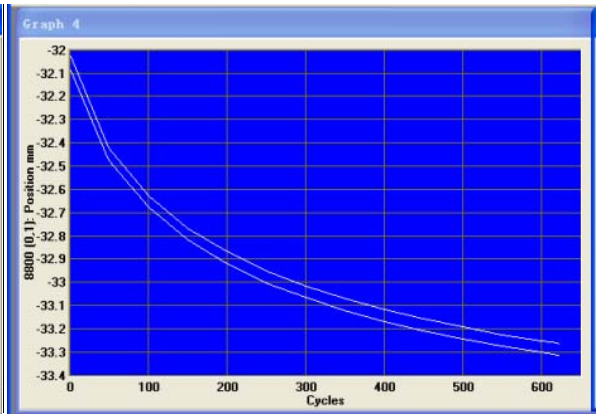

d 9th loading curve

Fig.2 Deflection curve for load-rest-reload process

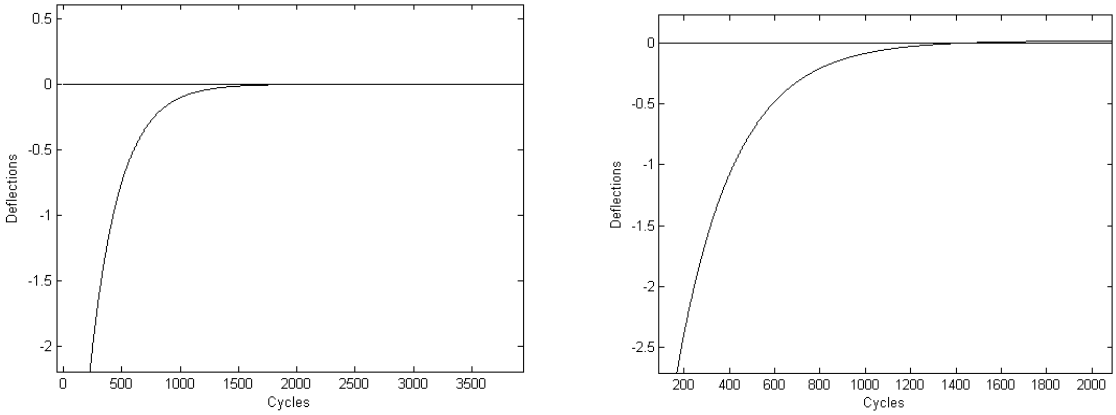

a Rest for 1 hour（60min） b Rest for 6min

Fig.3 Recovering fatigue life curve

Fig.4 is the recover fatigue life calculation results obtained in different rest time by using of formula (11) in ideal state. As can be seen from the graph, the rest time of specimen need is very short. After rest for 750s the specimen can reach a stable state. And the corresponding recover fatigue life is approximately 1580 times, it is same to Fig.2a.

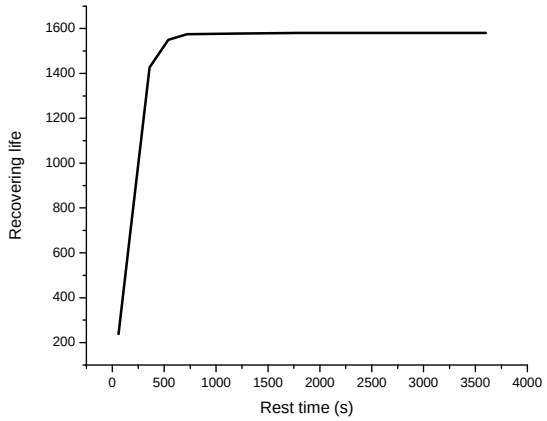

Fig.4 Recovering fatigue life for different rest time

Table.1 Experimental results for single specimen

Rload No.	Rest time（hour）	vertical deflection (mm)	Recover fatigue life	Cycles before rest	Damage
1	1	10.31	2100	14000	0.080
2	1	10.84	2060	7000	0.040
3	2	10.84	1790	2060	0
4	1	10.88	1680	2100	0
5	1	10.88	1360	1680	0
6	16	10.88	1140	1360	0
7	1	10.88	890	1040	0
8	1	10.88	710	890	0
9	1	10.88	600	710	0
10	1	15.03	2230	32700	0.188

11	14	20.1	2140	37300	0.214
12	15	25.3	2210	40700	0.234
13	14	30		41900	0.241
Total				187440	1

Table.1 is intermittent experimental results for single specimen, and it is also found that after multiple times reloading, if the deflection of last reloading is surpass the former loading, the recover fatigue life will increase. This is can be explained by damage viewpoint, that is because the new plastic deflection make the damage-resistance refreshed.

Equivalent damage of each reloading is also calculated by former method and listed in Table.1. Fatigue life result of each experiment is listed too. From Table, the total fatigue life is 187440, in which effective damage cycles is 173600. The recover fatigue life increases about 5.36% than specimen without rest and stop.

6 Conclusion

Recovering effects for sandwich beam with viscoelastic core are found in three-pionts bending fatigue test. A fatigue damage model considering recovering effects and recovering degree function of sandwich beam are proposed here. The intermittent fatigue experiment is carried out and the results show that the recovering fatigue life of specimen should not be ignored in loading-rest-reloading test and the damage model proposed here can describe the fatigue damage considering intermittent effects in certain accuracy.

Acknowledgements

Supported by “the Fundamental Research Funds for the Central Universities”（HEUCFZ1128, HEUCF100211）and “Harbin Municipal Science and Technology Innovation Talents Fund project” (2012RFXXG006)

References

[1] SHAN Chenglin, Research on mechanical properties of orthotropic sandwich bridge deck., China journal of highway and transport. 2012.1

[2] Stephen J. Kennedy. An Innovative "No Hot Work" Approach to Hull Repair on In-Service FPSOs Using Sandwich Plate System Overlay. Offshore Technology Conference. 2003.

[3] Devin K. Harris; Tommy Cousins; Thomas M. Murray; and Elisa D. Sotelino. Field Investigation of a Sandwich Plate System Bridge Deck. JOURNAL OF PERFORMANCE OF CONSTRUCTED FACILITIES © ASCE / SEPTEMBER/OCTOBER 2008 / 305

[4] Miner M A, Cumulative damage infatigue. Journalof Applied Meehanies. 1945, 12(3)，159-164P

Observations and Analysis of Fatigue Crack Growth in Circular Notched Polyethylene Specimens

Byoung-Ho Choi[1,*], Ilhyun Kim[1], Yongjian Zhao[1], Ji Mi Lee[1] and Alexander Chudnovsky[2]

[1] School of Mechanical Engineering, Korea University, Seoul, 136-701, Republic of Korea
[2] Department of Civil and Materials Engineering, University of Illinois at Chicago, Chicago, IL 60607, U.S.A.
* Corresponding author: bhchoi@korea.ac.kr

Abstract Many fundamental as well as technical issues with PENT (ASTM F2136) are identified, for instance the inability of separating crack growth from crack initiation, too long duration of the test for new generation of PE, outdated test conditions unchanged since the original formulation designed for old PE materials, etc. Therefore, there is a quest for a new accelerated test method. Recently, a circular notched specimen (CNS) has been proposed as an accelerated fatigue testing. However, formation of an asymmetric crack in CNS and early transition to a ductile failure limit the applicability of CNS test for studies of SCG. There are several factors responsible for the asymmetry of SCG. Especially, geometric misalignments of CNS are the most common practical weakness of the test. The present paper reports the observation of asymmetric SCG in CNS under fatigue conditions and analysis by finite element method (FEM) of the CNS misalignments effect on the crack growth asymmetry. Root causes of the asymmetric crack growth and its effect on the time to failure (fatigue lifetime) are discussed.

Keywords Fatigue, Polyethylene, Crack path, Crack growth, Circular notched specimen

1. Introduction

Plastic pipes have become popular in the pipe industry owing to their distinct advantages, which include low cost, low weight, good impact resistance, flexibility, and chemical resistance. However, it is known that plastic gas pipes such as polyethylene (PE) pipes do not have enough crack growth resistance to both ductile and brittle fracture as compared to metal gas pipes. To solve these critical problems, the plastic industry has dedicated a lot of effort to improving the crack growth resistance of pipe-grade PE to both ductile and brittle fracture. As a result, PE100/PE125-grade PE gas pipe resin has been developed by several PE resin manufacturers. However, current test standards for characterizing the crack growth resistance of PE are inadequate owing to the unique crack growth characteristics of PE. The American Society for Testing and Materials (ASTM) and the International Organization for Standardization (ISO) have proposed a few standard test methods for quantifying the resistance to slow crack growth of commercial pipe-grade polymeric materials such as PE [1].

However, since current test methods only suggest the recording of the time to failure, it is impossible to observe the response of the deformation and/or the crack growth behavior of the sample during tests. Consequently, most current test standards cannot distinguish between crack initiation and crack growth, which necessitates a new experimental method. The PENT test is suggested in ASTM as a standard test method for evaluating slow crack growth in PE materials [1], but this test lacks the capability to separate the crack propagation and crack initiation characteristics. Moreover, this test is designed only for a single stress level (2.4 MPa) based on old PE material and, therefore, there has been some criticism surrounding this standard. In stage II, it may be important to understand the crack initiation and crack propagation, and these should be addressed separately. In cases of crack propagation determining brittle fracture, there have been many experimental and analytical results, and the crack layer theory [2,3,4] is promising in predicting the complex continuous/discontinuous crack propagation observed in polyethylene. Meanwhile, studies of crack

initiation are relatively scarce due to uncertainty of its mechanism [5]. To solve these problems, some researchers have recently developed a new test that uses a circular notched specimen (CNS) (Fig. 1) to characterize the crack growth resistance and rank PE materials. Numerical investigation of the distribution of the stress intensity factors (SIFs) in CNS has been conducted in [6]. The advantage of the CNS is its moderate processing cost and the ease of fabricating the precrack. The front of the circular notch in the CNS is under triaxial stress conditions, making it possible to generate the highest effective stress, so accelerated tests can therefore be performed under any loading conditions. As a result, research of crack initiation and propagation using CNS is in progress [7,8,9]. However, it is also known that CNS create a problem for characterizing the crack growth behavior of brittle materials, because the crack growth is seldom axisymmetric [10]. In Fig. 2, experimentally observed cases of practically symmetric and typically asymmetric crack growth of PE in CNB specimens are shown [10]. Zhao et al. [10] reported that even initial imperfections in material or specimen geometry may strongly affect final time to failure, and asymmetrical fatigue crack propagation is easily changed in a severely distorted asymmetric manner. This can be critical as once asymmetric crack propagation takes place, recorded time to failure is shorter than that of symmetrical crack growth with all other parameters being the same. Moreover, as described above, the degree of asymmetry increases with crack propagation. As a result, the observed slope of S-N curve for time to failure may not represent the true fatigue behavior of the material, as it depends on specimen geometry imperfections. In other words, the crack growth process is highly sensitive to the variations of specimen geometry. In contrast with that, the crack initiation time is much less sensitive to geometry, except for notch depth variation Therefore it is more reasonable to use CNS testing for ranking materials with respect to the fatigue crack initiation resistance.

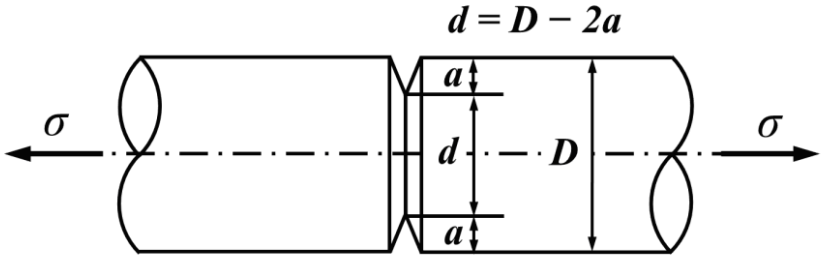

Fig. 1 Geometry of a circular notched specimen (CNS)

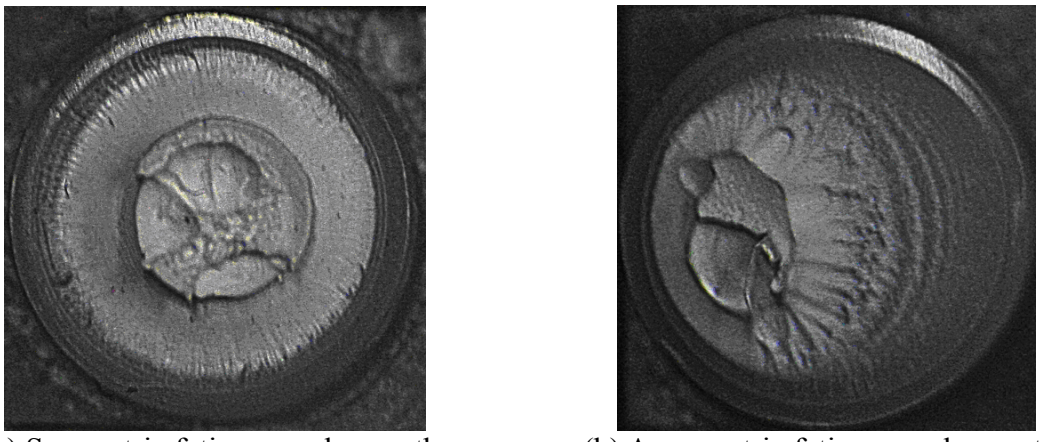

(a) Symmetric fatigue crack growth (b) Asymmetric fatigue crack growth

Fig. 2 Two typical types of fatigue crack growth in CNS

Many technical issues such as the notch sensitivity (brittleness), the anisotropy of the specimen, the initial notch geometry, and the geometric alignment of the centerline of the specimen and the notch should be considered in the interpretation of experimental data for asymmetric crack formation [11].

The effects of two types of noncircular initial notch geometries of a CNB specimen, i.e., the misalignment of the centerlines of the specimen and the notch, and the ellipticity of the notch—on the crack growth behavior have been previously studied by the authors [11]. In addition, the geometric misalignment of the CNB specimen in the experimental setup is also a critical issue. There are two types of geometric misalignment:concentric and angular misalignments as well as a combination of two.— The individual effects of concentric and angular misalignments on the crack growth behavior were considered. The effect of the geometric misalignments of PE on crack growth behavior at the early stage is not very significant, but an asymmetric crack gradually develops as the crack grows.

In this study, the effects of various geometric misalignments of CNB specimens on the fatigue crack growth behavior of pipe-grade PE were investigated by three-dimensional (3D) numerical analyses. Combined misalignments (concentric and angular misalignments) and the effect of the direction of the angular misalignments (0, π/2, π, and 3π/2) of a CNB specimen were considered within the limitations of the practical difficulties created by test conditions. The variation of the SIFs with the progress of a two-dimensional (2D) crack under fatigue loading conditions based on the conventional Paris' equation was studied using 3D finite element analysis (FEA). In addition, the experimental observations of the asymmetric fatigue crack growth were compared with the 3D FEA results. Moreover, the effect of the asymmetric crack growth resulting from combined initial geometric misalignment on the lifetime to failure of the CNB specimen is also discussed.

2. Finite Element Analysis

The combined misalignment of the CNB specimen was studied by 3D FEA. The geometric misalignment,concentric, angular and their combination—were considered. The normalized concentric misalignment (e/R) was varied as 0, 0.004, 0.012, and 0.020, using CNB specimens of radius (R) 5 mm. At the same time, the angular misalignment (e_θ) was varied as 0, 0.1, 0.2, and 0.4. The directions of the angular misalignments were 0, π/2, π, and 3π/2. Combined misalignment is the combination of concentric and angular misalignments. The three types of misalignments—i.e., concentric, angular, and combined—are shown in Fig. 3(a). Fig. 3(b) shows the directions of the angular misalignments (0, π/2, π, and 3π/2). The misalignment conditions of this study are summarized in Table 1.

Table 1 Summary of misalignment conditions

	e/R	e_θ
Concentric misalignment	0.004, 0.012, 0.020	0
Angular misalignment	0	0.1, 0.2, 0.4
Combined misalignment	0.004, 0.012, 0.020	0.1, 0.2, 0.4

A commercial FEA program, ABAQUS, were used for the FEA of a 3D model of the CNB specimens in this study. All the crack tips were remeshed for each calculation of the SIFs by considering their singularities. The element was of type C3D20 (a 20-node quadratic brick), and there were 60,000 elements and 250,000 nodes for each specimen. The physical properties of the material of the FEA are listed in Table 2.

The SIFs were calculated from 16 node points of the circular (notch) crack contour—at 0, π/8, π/4, 3π/8, π/2, 5π/8, 3π/4, 7π/8, π , 9π/8, 10π/8, 11π /8, 3π/2, 13π/8, 7π/4, 15π/8, and 2π. Based on the

calculated SIF at each node, the amount of crack growth for each node was defined using the conventional Paris equation with constants C = 1 x $10^{-11.6}$ and m = 4 [4], as shown in Table 2, with the assumption of a fatigue interval of 10^5 cycles.

The critical SIF (K_c) was 75.7 MPa·$mm^{1/2}$, which was obtained from the experimental results of fractured CNB spec-imens with symmetric crack growths [19]. The lifetime to failure (termination of the crack-growth simulation) was determined when the SIF of any node point of the circular (notch) crack contour reached the critical SIF. The direc-tion of the crack growth was determined as the normal to the tangent to the circular crack (notch) contour based on the maximum tangential stress (MTS) criterion [20], as shown in Fig. 4.

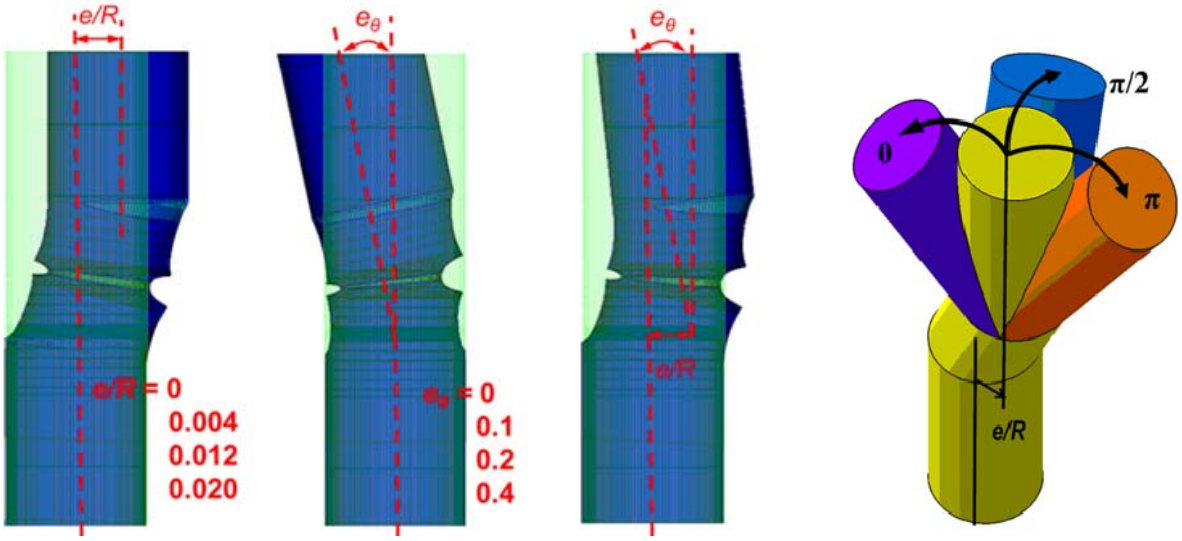

(a) Combined misalignments (Concentric+Angular) (b) Direction of angular misalignment

Fig. 3 Definition of combined misalignments

Table 2 Physical properties of the material

Young's modulus, E (MPa)	Poisson's ratio, ν	Constant for Paris' equation, C	Constant for Paris' equation, m	Remote stress range, $\Delta\sigma$ (MPa)
1250	0.4	$10^{-11.6}$	4	10.8

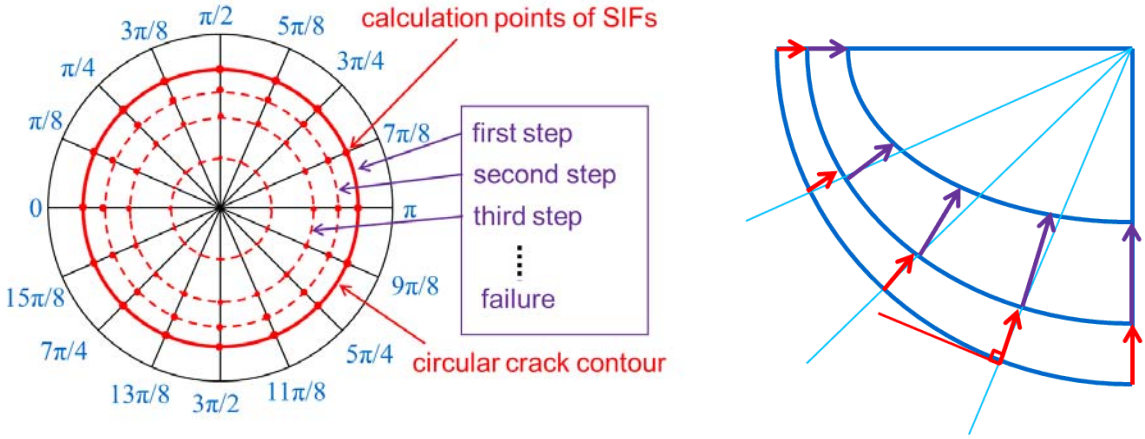

(a) Crack growth steps and crack tip locations (b) Modeling of crack growth

Fig. 4 Modeling of crack growth of CNS in FEA

3. Results and Discussions

The accuracy of the FEA was confirmed by comparing the SIFs calculated using FEA for a symmetric crack with those calculated using an analytical solution. The analytical expression of the SIFs of a CNB specimen was as expressed as below.

$$K = \frac{1}{2}\sigma_{net}\sqrt{\frac{\pi a d}{D}}\left(1+\frac{1}{2}\lambda+\frac{3}{8}\lambda^2-0.363\lambda^3+0.731\lambda^4\right)\cdot\left(1+0.1\sqrt{\frac{2a}{D}}\left(1-\frac{2a}{D}\right)\right), \quad (1)$$

where, σ_{net} is the net section stress, and a and D are respectively the crack length and diameter (d = D - 2a, λ = d/D). It was observed that the SIFs obtained from the FEA and the analytical solution were almost identical.

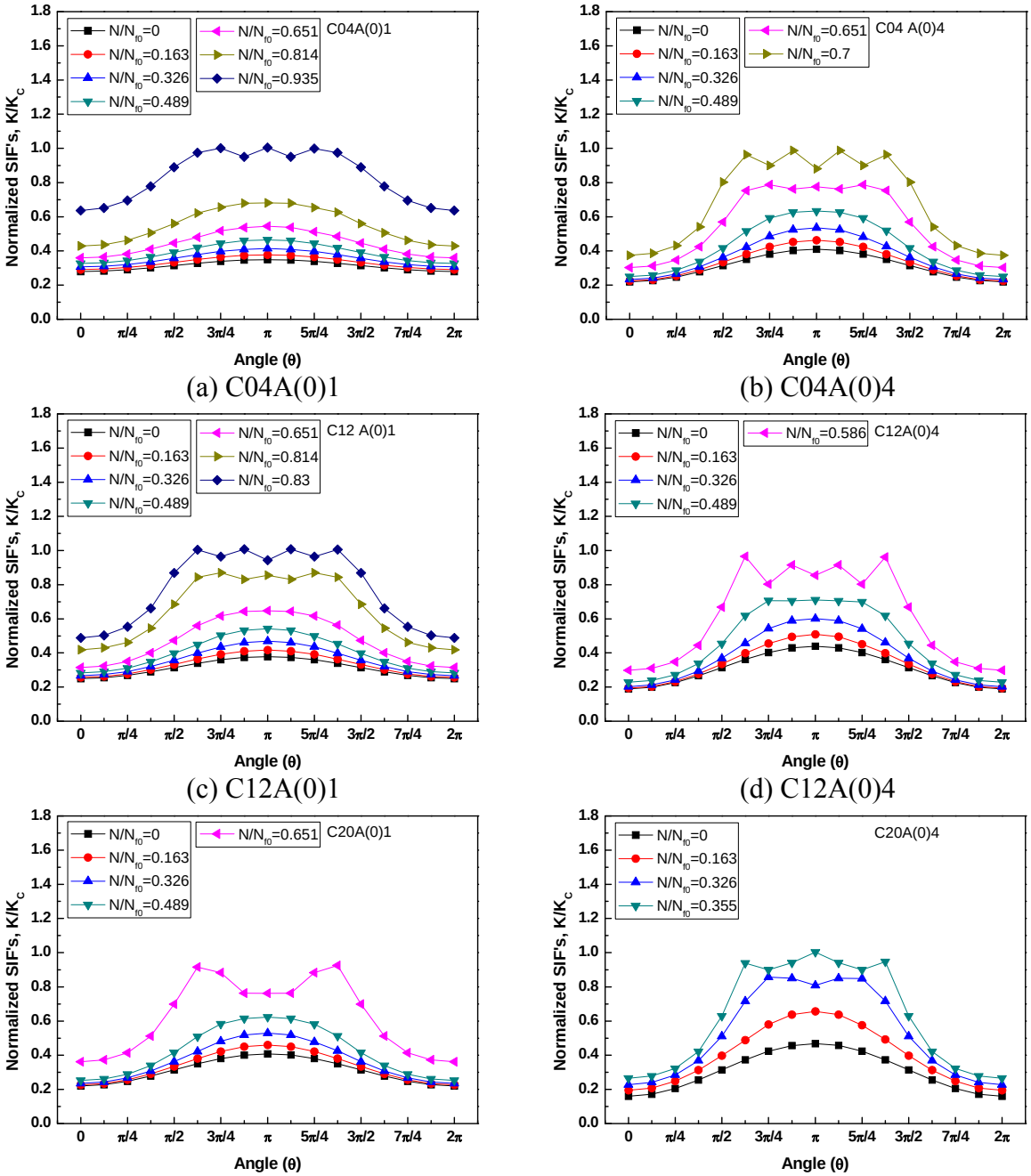

(a) C04A(0)1 (b) C04A(0)4

(c) C12A(0)1 (d) C12A(0)4

(e) C20A(0)1 (f) C20A(0)4

Fig. 5 The variation of normalized SIFs at the circular crack contour for '0' angular direction

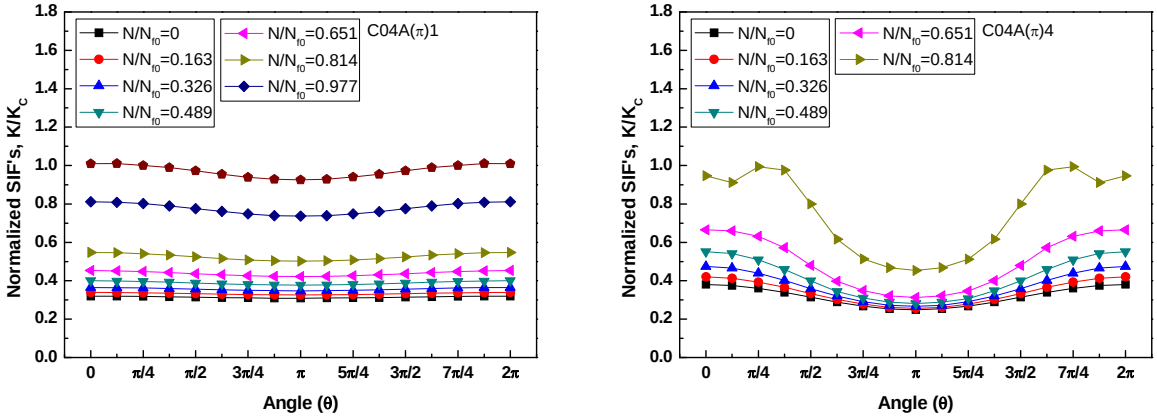

(a) C04A(π)1

(b) C04A(π)4

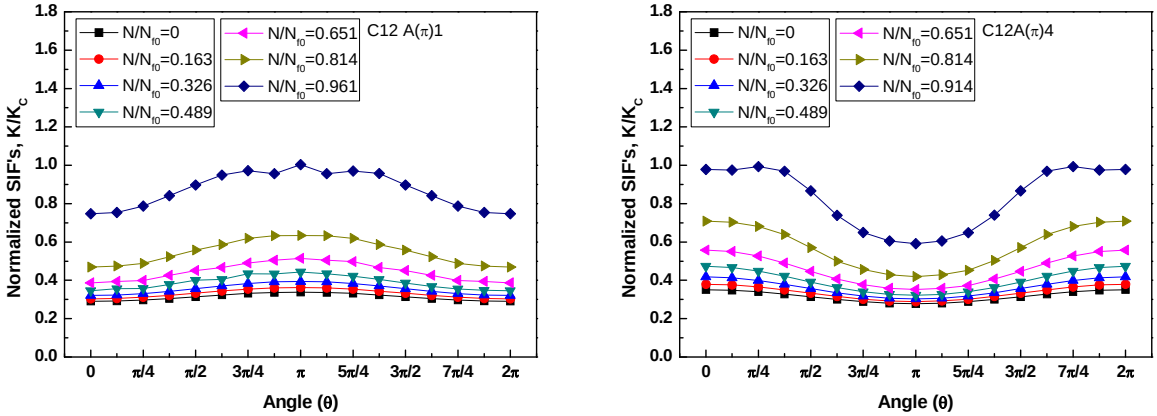

(c) C12A(π)1

(d) C12A(π)4

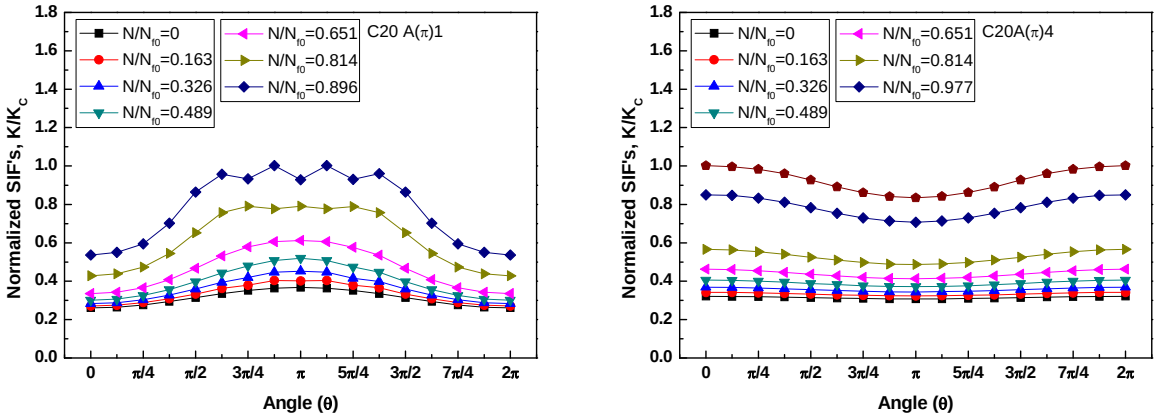

(e) C20A(π)1

(e) C20A(π)4

Fig. 6 The variation of normalized SIFs at the circular crack contour for 'π' angular direction

Combined misalignment (concentric and angular misalignments) and the effect of the directions of the angular mis-alignments (0, π/2, π, and 3π/2) of the CNS specimens were considered within the limitations of the practical difficulties of test conditions.

Fig. 5 shows the FEA results of the variation of the SIFs around the crack contour with a concentric misalignment (e/R) of 0.004-0.020 and angular misalignment (e_θ) of 0.1 and 0.4. For all cases, the direction of the angular misalignment was 0. There were only little differences in the initial SIFs, but the difference between the maximum and minimum SIF values rose as the crack grew. As expected, the maximum SIF was observed at $\theta = \pi$ and the minimum was observed at $\theta = 0$. It was also observed that when the directions of the concentric and angular misalignments were opposite, their effects neutralized each other and the normalized time to failure at high speeds decreased as

the angular misalignment increased. This means that when the direction of the angular misalignment was 0, the directions of the concentric and angular misalignments were actually opposite to each other. However, when the concentric misalignment was small, the two cases of angular misalignments of 0.1 and 0.4 early during the crack propagation had small differences between the maximum and minimum SIF values. However, as the misalignment became noticeable, the difference increased and exceeded those of other cases of the crack propagation. It could be concluded that these large differences at the early stage accelerated the crack propagation and decreased the lifetime.

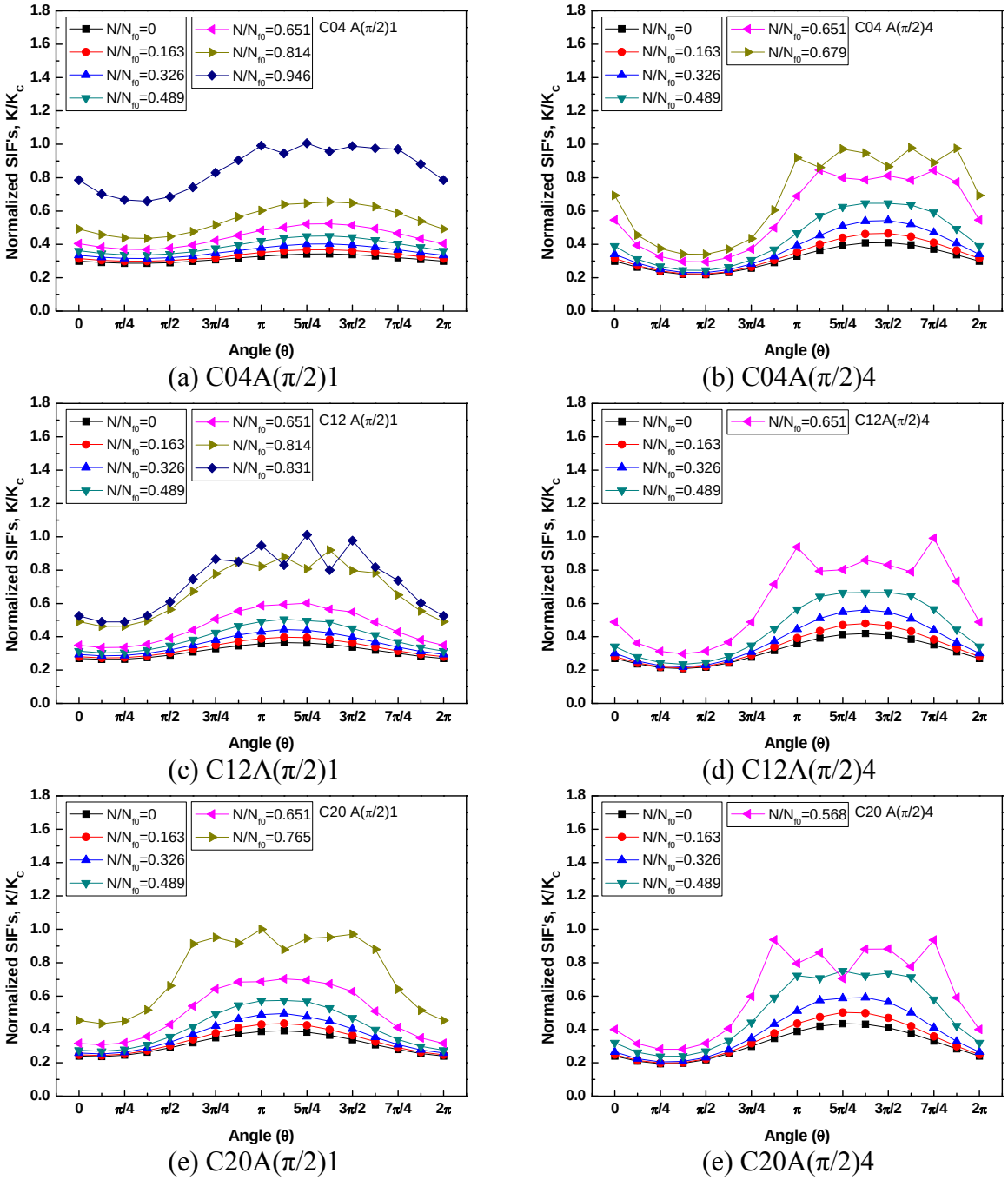

(a) C04A(π/2)1 (b) C04A(π/2)4

(c) C12A(π/2)1 (d) C12A(π/2)4

(e) C20A(π/2)1 (e) C20A(π/2)4

Fig. 7 The variation of normalized SIFs at the circular crack contour for 'π/2' angular direction

Fig. 6 shows the FEA results of the variation of the SIFs around the crack contour for various concentric misalignments (e/R) ranging from 0.004 to 0.200, angular misalignments (e_θ) ranging from 0.1 and 0.4, and angular misalignment direction of π. The angular misalignment direction of π

means that the concentric and angular misalignments were in the same direction. As the concentric misalignment increased, the stress distribution of the angular misalignment showed a different tendency. Although the angular misalignment was 0.1, the difference between the maximum and minimum SIF values was still small. Nevertheless, the asymmetric crack growth developed gradually as the concentric misalignment increased (see Figs. 6(a), 6(c), and 6(e)). It was also observed that as the concentric misalignment increased, the top positions of the maximum and minimum SIFs became upside down. However, when the angular misalignment was 0.4, the difference between the maximum and minimum SIF values was large at the early stage, and then gradually decreased as the concentric misalignment increased (see Figs. 6(b), 6(d), and 6(f)). Moreover, although the concentric misalignment increased, the top positions of the maximum and minimum values were not upside down; only their difference decreased. Based on these results, it can be understood that if the angular misalignment increased beyond 0.4, K/K_c became 1, after which the positions of the maximum and minimum SIF values were reversed and their difference further increased. From this result, it can be deduced that eθ rather than e/R influences the crack growth rate.

Fig. 7 shows the FEA results of the variation of the SIFs around the crack contour for various concentric misalignments (e/R) ranging from 0.004 to 0.020 and angular misalignments (e_θ) ranging from 0.1 and 0.4 when the direction of the angular misalignment was π/2. The angular misalignment direction of π/2 means that the concentric and angular misalignments were perpendicular to each other. It could be observed that the distribution of the SIFs around the crack contour shifted from the previous combination of misalignments. When the angular misalignment was 0.1, the SIFs around the crack contour did not change significantly (see Figs. 7(a), 7(c), and 7(e)). However, the distribution of the SIF around the crack contour varied more significantly. It could thus be deduced that the lifetime to failure varied somewhat as the direction of the angular misalignment changed. The distribution of the SIFs and the lifetime to failure were determined by the two misalignments. In other words, the direction of the misalignments could be critical to the reliability of the test results when using CNB specimens.

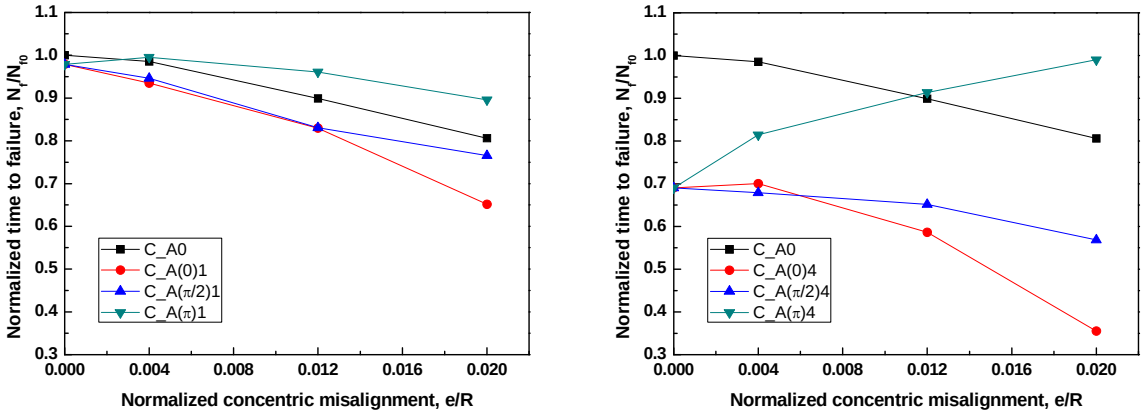

(a) e_θ=0.1 (b) e_θ=0.4

Fig. 8 Variation of the normalized time to failure under combined misalignments

Fig. 8 shows the variation of the normalized time to failure under combined misalignments. When the direction of the angular misalignment was 0, the lifetime to failure decreased regardless of the misalignment conditions. However, when the direction of the angular misalignment was π, the lifetime to failure increased up to a certain level for concentric misalignment. These results were because the concentric and angular misalignments simultaneously determined the distribution of the SIFs of the crack contour. The contributions of the two misalignments can therefore be varied. For example, when the direction of the angular misalignment was π, the shape of the asymmetric crack

growth for the concentric misalignment was opposite to that for the angular misalignment. Several other factors, such as the notch sensitivity (brittleness), anisotropy of the specimen, and notch geometry can also affect the lifetime to failure and the asymmetric crack growth of CNB specimens. However, it is clear that geo-metric misalignments of CNB specimens can significantly affect the crack growth behavior and the lifetime to failure. Therefore, it can be noticed that the installer should be careful to avoid any unintentional misalignment of the CNB specimen in order to produce reliable test results.

3. Conclusions

In this study we investigated the effects of various geometric misalignments of CNB specimens on the fatigue crack growth behavior of pipe-grade PE by means of three-dimensional (3D) numerical analyses. Combined misalignments (concentric and angular misalignments) and the effect of the direction of the angular misalignments (0, $\pi/2$, π, and $3\pi/2$) of a CNB specimen were considered within the limitations of the practical difficulties created by test conditions.

The distribution of the SIF changed with a change in the direction of the misalignments, so the lifetime to failure under combined misalignments could be varied depending on the status of the combined misalignment. For example, the time to failure increases as the angular misalignment in the direction of π increases, for up to 2% concentric misalignment of the radius of the CNB specimen It is not clear. On the contrary, the normalized time to failure for a combination of 2% concentric misalignment and 0.4 angular misalignment decreased by almost 65% compared to that without any misalignment.

Several other factors, such as notch sensitivity (brittleness), anisotropy of the specimen, and notch geometry can also affect the lifetime to failure and asymmetric crack growth in CNB specimens. However, it is clear that geometric misalignments of the specimens significantly affect the crack growth behavior and the lifetime to failure. Such sensitivity of the test results to various misalignments limit the potential of considering this test as a standard.

References

[1] X. Lu, R. Qian, N. Brown, Discontinuous crack growth in polyethylene under a constant load. J Mater Sci, 26 (1991) 917–924.
[2] A. Chudnovsky, Crack layer theory, NASA Report #174634, 1984.
[3] A. Chudnovsky, Y. Shulkin, Application of crack layer theory to modeling of slow crack growth in polyethylene. Int J Fract 97 (1999) 83-102.
[4] B.-H. Choi, W. Balika, A. Chudnovsky, G. Pinter, R.W. Lang, The use of crack layer theory to predict the lifetime of the fatigue crack growth of high density polyethylene, Polym Eng Sci 49 (2009) 1421-1428.
[5] A. Chudnovsky, B. Kunin, A probabilistic model of brittle crack formation. J Appl Phys 62 (1987) 4124-4129.
[6] Y. Lei, B.K. Neale, Non-linear, axi-symmetric finite element analyses of a circumferentially cracked bar specimen. Int J Pressure Vessels Piping 73 (1997) 199–210.
[7] V. Favier, T. Giroud, E. Strijko, J.M. Hiver, C. G'Sell, S. Hellinckx, A. Goldberg, Slow crack propagation in polyethylene under fatigue at controlled stress intensity. Polymer 43 (2002) 1375–1382.
[8] A. Frank, W. Freimann, G. Pinter, R.W. Lang, A fracture mechanics concept for the accelerated characterization of creep crack growth in PE-HD pipe grades. Eng Fract Mech 76 (2009) 2780–2787.
[9] W. Zhou, B.-H. Choi, A. Chudnovsky, Crack initiation in pipe grade polyethylene, in:

Proceddings of SPE/ANTEC 2006. Charlotte, NC, USA: Society of Plastics Engineers, 2006, pp. 2485-2489.

[10] B.-H. Choi, Y. Zhao, Evaluation of the crack initiation characteristics of pipe grade polyethylene under fatigue loads, in: Proceedings of ANTEC 2010. Orlando, FL, USA: Society of Plastics Engineers, 2010. pp. 1644–1648.

[11] Y. Zhao, I. Kim, B.-H. Choi, J.-M. Lee, Variation of the fatigue lifetime with the initial notch geometry of circular notched bar specimens. Int J Fract 167 (2011) 127–134.

The interface debond analysis for sandwich beam with viscoelastic core and steel faceplates

Zou GuangPing, Xue QiChao, Chang ZhongLiang

Department of Aerospace and Civil Engineering, Harbin Engineering University, Harbin, 150001, China

Abstract a interface debond phenomenon appeared between viscoelastic core and steel faceplates when unloading in large deflection 3-point bending experiments for sandwich beam. From analysis of loading and unloading process, a reason of debond is found that it is the large deflection cause the debonding of interface firstly under the effect of shear stress. After unloading, local plastic rotation in the middle of beam lead to residual moment between upper faceplate and bottom faceplate. And the shear stress effect at interfaces is also transformed to tension stress. By double cantilever beam and single cantilever beam experimental results, a calculation method of critical deformation are given to calculate the critical strain energy release rate. then the critical crack length values of different types of the specimen are obtained.

Keywords Sandwich, Viscoelastic Core, Debond , Interfacial crack

1. Introduction

The sandwich plate structure with viscoelastic core is often used as bending components, and more and more applied in practical engineering. Characteristics of crack in viscoelastic plate is widespread concerned[1]-[3]. In this paper, the steel sandwich faceplate specimen with polyurethane viscoelastic elastomer core is tested by using of three-points bending experiments and found that due to the interface material property differences between the faceplate and the core, when the specimen is loaded in large deflection and then unloaded, it leads to delay debond phenomenon of crack for lower interfacial strength specimen. By double cantilever beam and single cantilever beam experimental results, a calculation method of critical deformation are given to evaluate the specimen damage, and determine the critical failure condition of specimen.

2. Three-points bending test

The three-points bending test for polyurethane elastomer steel sandwich plate structure is carried out according with the specification "Sandwich Plate Bending Experiments Norms". Bending strength, shear strength, bending rigidity and shear rigidity of the sandwich structure can be determined through three-points bending test. Thereby the modulus of elasticity and the shear modulus of core can be determined too. The shape of cross-section of specimen is rectangular, the thickness of sandwich core is about 11mm, and the faceplates have a thickness of 2 mm, which is shown in Figure 1.

Four different types of specimen are selected by different preparation methods and hardness of the core, which is numbered as No. 1 to No. 4 respectively. Preparation method of No. 1, 2 and 4 is directly pouring, and No. 3 specimen is the one prepare the elastomer core first, then use a strong glue to paste the faceplate and core together. Fig.2 is deflection-load curve of three-points bending experiments of sandwich plate specimen.

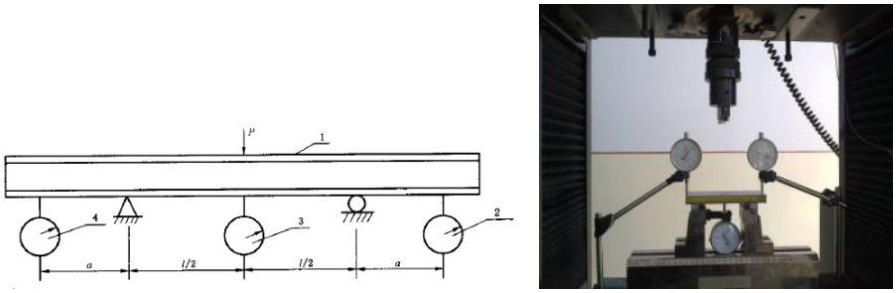

Fig.1 Three-points bending test

Table.1 Parameters and results for three-points bending tests

Specimen No. Item	1	2	3	4
Weight（g）	364.80	385.40	384.50	386.60
Hardness（D）	29	47	51	48
length（mm）	149.84	149.9	150.20	149.90
width（mm）	59.90	59.84	60.60	59.92
Thickness（mm）	13.86	15.64	16.04	14.52
Faceplate thickness（mm）	2. 00	2. 00	2. 00	2. 00
Preparation	Pouring	Pouring	Stick	Pouring
Debonding load（N）	1500	2100	5200	2350
Proportional limit load （N）	1200	1700	2600	1550
Failure load（N）	2600	3400	7000	3600
The maximum load deflection	11.37	12.55	30.02	15.23
Maximum stress (MPa)	26. 27	28. 00	60. 44	36. 90

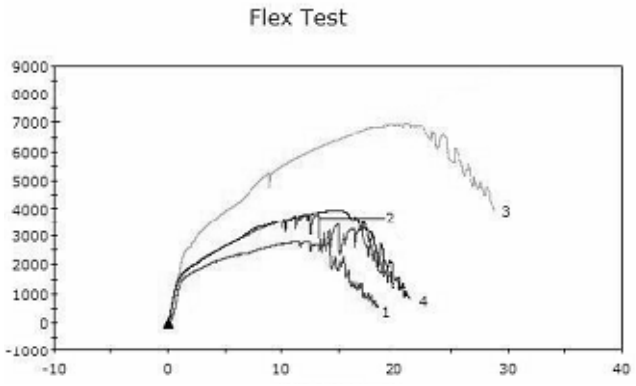

Fig.2 Deflection-load curve for sandwich plate

Observing the whole loading process of three-points bending test of Fig.2, it can be found that the destruction process can be roughly divided into three stages:

1) elastic deformation stage.

In the initial stage of loading, the faceplates and an elastomer core are in the elastic deformation, the internal stress of faceplates distributes uniformly. The faceplates bear the main bending effect, while the core is mainly responsible for shearing effect.

2) Strengthening stage.

When bending stress of faceplates reach the yield limit of the material, plastic hinge appears at the position where the crosshead contact with specimen, and the faceplates rotate around the hinge. In this stage, load-displacement curves rise slowly, on the one hand, this is because the plastic deformation of faceplate, on the other hand, it is because the specimen is constrained by horizontal reaction force at the supports due to deformation increases.

3) Failure stage.

Downward burr will appear on the load-displacement curve when the strengthening phase to a certain extent. As the increasing of load, the more burrs appears. This is because of the phenomenon of debonding between the faceplate and the core. If shear strength between the core and faceplate is smaller, there will be cracked firstly at the corner of the end position. The load curve gradually become horizontal, and great deformation of the faceplates appear along the central plastic hinge zone.

From the breakage of pouring specimen, it can be seen that the failure models of sandwich beam are large bending deformation destruction and shear failure of the interface between the steel faceplate and the polyurethane elastomer core. Such damage often occurs on the upper faceplate, but not obvious when loading. Delayed cracking phenomenon appears when unload. The so-called delayed fracture phenomenon is when the loading displacement reaches a certain limit then unloads, there is no obvious crack propagation at the beginning, but after a while, the crack propagates. For the specimens with weak bonding strength, debonding phenomenon on the upper faceplate will appear; and for the specimens with strong bonding strength, tears of the core occurs at the position of 1/3 length from the edge of the specimen. This is because a large plastic deformation of faceplates causes differences between two faceplates. When unload the specimen, the rebound effect from difference rotate angle between two faceplates make tension stress on the crack surface. When the stress is big enough, and the crack length is reach a certain value, the crack will propagate. For the viscoelasticity of polyurethane core, the crack will not propagate immediately, but for a certain time.

3 strain release rate calculation method of crack when unloading

In three-points bending test, the shearing of the vertical load result in the generation of initial crack in the edge, the bending moment when unloading is the main factors of generate crack propagating. Since the core is viscoelastic material, the crack propagation in the interface of sandwich plate

faceplate having a certain rate, and it sustain for a period of time with energy release in whole process. For isotropic viscoelastic material crack growth studies have been carried out [4], but in most cases of interface viscoelastic crack with different material, corresponding principle is no longer suitable for use. For the complexity from the singularity of the stress field of viscoelastic material interface crack, there is no effective method to solve the problem[5]. The method of this paper is constructed on the simplifications on the followings:

1) Using the critical strain energy release rate of crack to describe the debonding propagation.

2) Type I and II crack critical is obtained in case of not considering the viscoelasticity of the core material. In order to avoid the viscoelastic effect, the experimental process will last a long time. Due to the polyurethane elastomeric material is typical Kelvin solid, so there must be a limit for crack propagation, when the stress or strain energy release rate is less than this limit, the crack does not propagate; when it is greater than this limit, no matter how long the time last, cracks will propagate inevitable.

3) Through observation, crack tip was found that, because the big difference on the elastic modulus between faceplate material and viscoelastic core, when the crack propagate, there is local deformation of interface crack. The crack morphology is shown in Fig. 3a, and we simplify the deformation curve as a straight line shown in Fig. 3b.

4) Because the modulus of elasticity of the core material is low, but the deformation is large, so the stress along the direction of sandwich thickness of core is assumed uniform distribution.

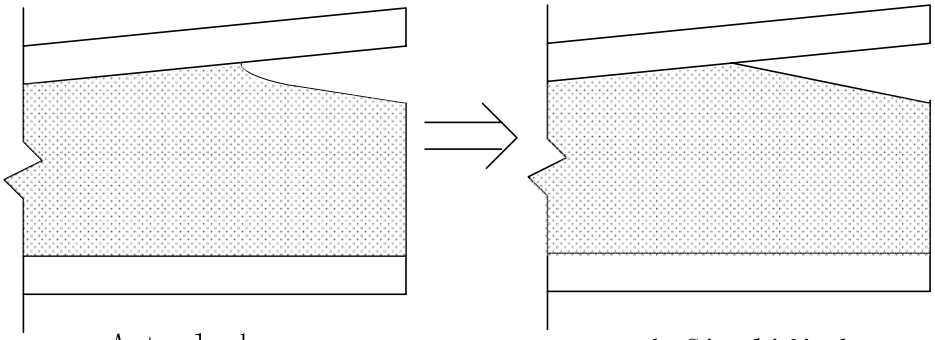

Fig.3 The simplified crack

Crack strain energy release rate can be written as:

$$G = \frac{1}{b}\left(\frac{dU_e}{da} - \frac{dU_s}{da} \right) \tag{1}$$

G is crack strain energy release rate, b is the specimen width, a is the crack length, U_e and U_s are stored strain energy and external forces work done. As shown in Figure 4， the cracking process is assumed that crack opening angle is constant in the interface crack growth, corresponding extended strain energy release rate is the critical strain energy release rate. The classical fracture mechanics

has proven the crack opening displacement and strain energy release rate are equivalent, and here we make this assumption too. Simplification of the crack propagation process is shown in Figure 4:

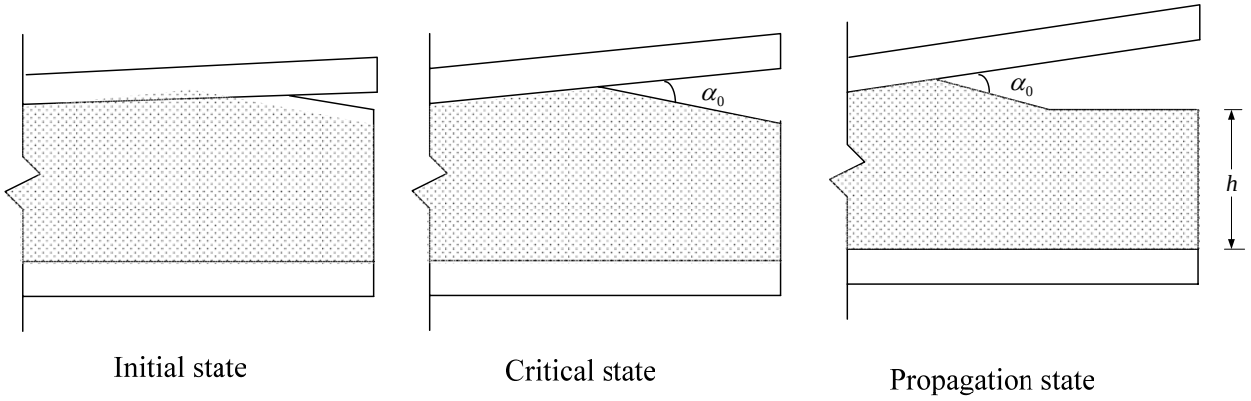

Fig.4 The simplified crack of propagation

For the initial open stage, the crack open angle gradually becomes larger and larger. In the critical state of crack, the core on the right of crack gradually unloaded to the original state, in which the internal stress is 0. In the propagation state of the crack, the crack tip angle unchanged, the right part of crack is not affected by the crack. Only core material of oblique line part is affected. Flat part unloads completely with no stress.

Take the critical state of the cracks to analyze, when crack propagate the length of δa, the corresponding angle of the upper faceplate is β_0, which increase the $\Delta\beta$. Its geometry is shown in Figure 6. When crack extended forward, the flat segment is negligible. Shaded part in Figure 5 is the sandwich viscoelastic core material, the crack extended to point *B2* from point *B1* , crack propagation angle remains unchanged, that is $\angle AB1A1 = \angle AB2A2$,*CA2=B1A1*.

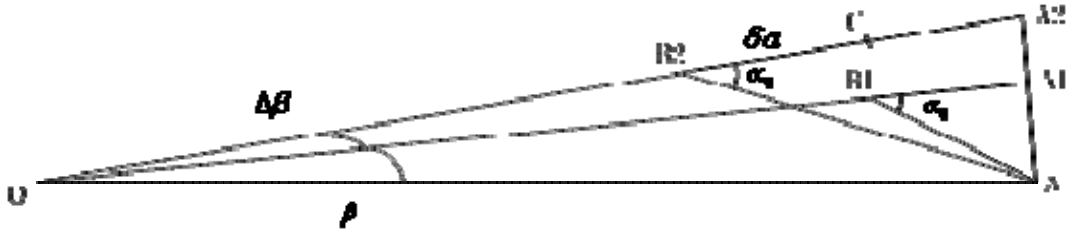

Fig.5 Geometrical relationship of crack propagation

Calculation parameters of the Figure 5, where: the length of *AA2* is $b\sin\left(\frac{\beta+\Delta\beta}{2}\right)$, the length of *AA1* is $b\sin\left(\frac{\beta}{2}\right)$, With the law of sines, we can get length of *B1A1* is $b\sin\frac{\beta}{2}\cos\left(\alpha_0-\frac{\beta}{2}\right)l\sin\alpha_0$, which is also the initial length of the crack:

$$a = l\cdot\sin\frac{\beta}{2}\cos\left(\alpha_0-\frac{\beta}{2}\right)\cdot l\sin\alpha_0 \tag{2}$$

To calculate the variation availables on both sides of the equation, we can get:

$$\delta\beta = \frac{2\sin\alpha_0}{l\cos(\beta - \alpha_0)}\delta a \tag{3}$$

If recover moment can be seen as external forces, external work done is:

$$U_s = M\Delta\beta \tag{4}$$

So the length of *A2B2*:

$$l\sin\frac{\beta}{2}\cos\left(\alpha_0 - \frac{\beta}{2}\right) l\sin\alpha_0 + \delta a \tag{5}$$

Also relationship between crack propagation length and angle changes can also be obtained from the law of sines:

$$\delta a = \frac{l\cos\left(\alpha_0 - \frac{\beta+\Delta\beta}{2}\right)\sin\frac{\beta+\Delta\beta}{2} - b\sin\frac{\beta}{2}\cos\left(\alpha_0 - \frac{\beta}{2}\right)}{\sin\alpha_0} \tag{6}$$

The change of internal energy can be embodied by calculating shaded area differences of bond stress:

$$U_e = \frac{l}{4}b\sigma_{bs}\left[\left(\frac{l}{2} - \delta a - a\right)\sin(\beta+\Delta\beta) - \left(\frac{l}{2} - a\right)\sin\beta\right] \tag{7}$$

Substituting the above formula into the crack strain energy release rate of the formulas (1), critical strain energy release rate can be calculated according to the crack propagation angle:

$$G = \frac{1}{b}\left(\frac{dU_e}{da} - \frac{dU_s}{da}\right) = \frac{1}{b}\left[\frac{1}{4}b\sigma_i\sin\beta - \frac{2M\sin\alpha_0}{l\cos(\beta - \alpha_0)}\right] \tag{8}$$

If internal parameter of formula is known, it can be approximated to the calculated strain energy release rate of the crack.

4 Cracking strain energy release rate calculation example

In order to verify the correctness of the former derivation, we need to determine the strain energy release rate of interface crack between the steel plate and the core. Literature [6] prefabricated interface crack by embedding PVC film before pouring the core. DCB experiment and SLB experiments are carried out to determine the critical strain energy release rate of I type crack for specimens with the soft hard core separately. The measured type I crack strain energy release rates are shown in table 2.

Table 2 Strain energy release rate of sandwich plate

Experiment name	The type of specimen	Energy release rate （N/m^{-1}）

Soft core	G_f	526
Hard core	G_f	1783

Combined with equation (8), at the beginning of propagation, $\beta = 0$, strain energy release rate can be calculate by the following formula:

$$G = \frac{2E_f I_f \theta}{bl\left(\frac{L_0}{2} - a\right)} \tan\alpha_0 \tag{9}$$

In which E_f is modulus of elasticity, I_f is moment on inertia of specimen; b is the width, L_0 is the actual length of specimen after large deflection; l is the gauge length; a is the crack length. When crack propagation angle α_0 and the critical strain energy release rate are determined, we can calculate the critical crack length based on the previous formulas. Since θ is a function of the bending load Q and the plastic rotation angle φ, through the analysis the formula can be obtained as followings:

$$\theta = \frac{Q\sqrt[4]{\frac{1}{4E_f I_f k^3}}}{\frac{l}{\cos\phi} - 2r} \tag{10}$$

In which $k=k_0 b$, k_0 is foundation modulus; r is the radius of supported roll shaft. Bending load Q and the rotation angle φ can be obtained from fitting the experimental load-displacement curve. Based on the former three-points bending experiment, we fit the relationship by bilinear model:

$$\text{Hard core: } Q = 1780 + (\lambda - 1.3)\tan 26.6°$$

$$\text{Soft core: } Q = 1480 + (\lambda - 1.3)\tan 16.0° \tag{11}$$

In the formula, λ is loading displacement. Combined with the crack propagation angle α_0 determined from DCB and SLB experiments, the strain energy release rate corresponding to different crack lengths can be calculated, as shown in Figure 6.

From Figure 6, corresponding to different crack length values, strain energy release rate curve is substantially parallel, and slightly decreased. The larger the crack length is, the higher the strain energy release rates are. If strain energy release rate is larger than critical value, crack propagation occurs. Variation trend (Fig. 6b) of strain energy release rate with loading displacement is similar to Fig. 6a, the error is due to the ideal elastoplastic assumptions for faceplates material. Comparing the results of soft core and hard core, difference of strain energy release rate is not very large. The

critical interface strain energy release rate of soft core and hard core is different, the hard core's critical strain energy release rate is 1.783N/mm, corresponding allowable critical crack length for specimen in this paper is 16mm; the soft core's critical strain energy release rate is 0.525 N/mm, which is less than the value of strain energy release rate at position *a=0*, This means that as long as specimen reach the yield limit, damage will be in the form of inter-layer cracking.

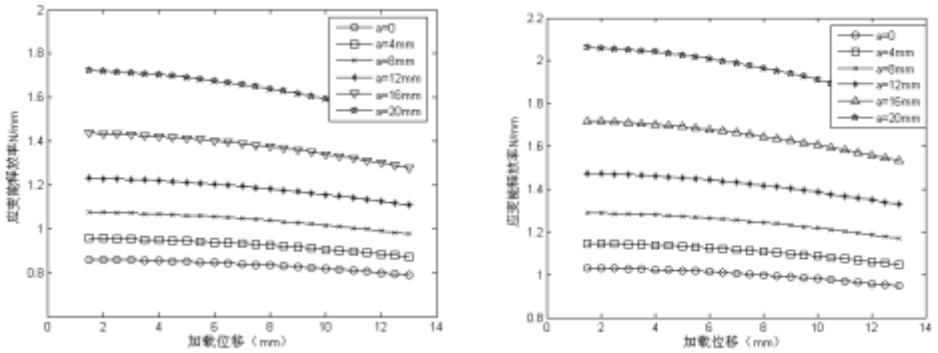

a Soft core specimen b Hard core specimen

Fig.6 Strain energy for different cores of specimen

5 Conclusion

Based on three-point bending experiments for sandwich plate with polyurethane elastomer core, it is found that specimens with different bond strength and core hardness have different failure modes. Here proposed a method of calculating the critical strain energy release rate to obtain the critical crack length values of different types of the specimen. Although there are some errors, but it can be substantially obtained the strain energy release rate and describe the propagation of interfacial crack.

Acknowledgements

Supported by "the Fundamental Research Funds for the Central Universities"（HEUCFZ1128, HEUCF100211）and "Harbin Municipal Science and Technology Innovation Talents Fund project" (2012RFXXG006).

References

[1] R. Frassine,M. Rink,A. Leggio,A. Pavan. Experimental analysis of viscoelastic criteria for crack initiation and growth in polymers[J] ,1996

[2] Schapery R A.A theory of crack initiation and growth in viscoelastic media Ⅰ: Theoretical development. International Journal of Fracture . 1975

[3]LIU Yulan, WANG Biao, WANG Dianfu，on the Calculation of Energy Release Rate for Viscoelastic Cracked Laminates, Applied Mathematics and Mechanics, 2003. 01

[4] Zhang Chunyuan, Zhang Weimin, Elasticity Recovery Correspondence Principle for Solving A Class Of Nonlinear Viscoelastic Problems, Engineering Mechanics, 2002(01)

[5] Xu Jinquan. Interface Mechanics. Science press. 2005.7

[6] Li Jia, An Investigation on buckling behavior and surface/core debonds problem for SPS composite plate, Master degree theies, 2012.3

Fracture of rubbers under biaxial loading: A criterion based upon the intrinsic defect concept

Moussa Naït Abdelaziz[1,*], Fahmi Zaïri[1], Nourredine Aït Hocine[2]

[1] Université Lille 1 Sciences et Technologies, Laboratoire de Mécanique de Lille, F-59655 Villeneuve d'Ascq, France
[2] Université François Rabelais de Tours, Laboratoire de Mécanique et Rhéologie, F-41034 Blois, France
* Corresponding author: moussa.nait-abdelaziz@univ-lille1.fr

Abstract Since the use of rubbers has been widespread in many industrial applications these last decades, the structures integrity including rubber parts requires the mechanical capabilities of such materials to be known and mastered. To prevent failure in the designing process, it is necessary to provide strong criteria taking into account not only their highly extensible capability but also the complex multiaxial loadings to which they could be subjected. In this work, the intrinsic defect concept is introduced and coupled in the fracture mechanics framework with the *J* integral in order to derive a multiaxial fracture criterion. Mechanical tests up to failure on rubber specimens subjected to monotonic biaxial loading paths were achieved on two materials. The fracture criterion requires as an input the critical value of the *J* integral which was also experimentally measured on CCT specimen. A generalized expression of the *J* integral under biaxial loading is proposed on the basis of finite element calculations on a representative volume element containing a small circular defect. The estimated failure elongations were found in very nice agreement with experimental data on the two kinds of rubber materials. Moreover, we have also outlined the predicting capability of this approach when applied to thermoplastic elastomers.

Keywords Rubber, *J* integral, fracture criterion, intrinsic defect.

1. Introduction

The fracture mechanics approach [1, 2], and its extension to rubbers [3-11], has shown its capability when dealing with crack problems. Nevertheless, if the material contains no visible crack or defect, this approach can be adapted assuming that all materials generally contain defects. These defects originated from material process can grow when subjected to mechanical loading and provoke failure of the component. When dealing with rubbers, these defects may be due to the reinforcing particles added to the neat matrix. Even the filler size is generally very small (less than 100 nm) but it can form aggregates, the size of which can have strong effects on the strength [12, 13] or the fatigue life properties [14-16]. In this work, an attempt to predict the fracture of specimen containing no cracks, but assumed to contain intrinsic flaws, by using the fracture mechanics approach is explored. The main assumption which is made is that these intrinsic flaws, as classical cracks, act as potential stress concentrators which are responsible of the fracture. This analysis uses experimental data obtained from mechanical tests under different biaxial loading paths [17, 18].

2. Experimental study

2.1. Materials and experiments

Two materials are used in this study: a Natural Rubber (NR) and a Styrene Butadiene rubber (SBR).

Different loading paths are used: uniaxial tension, pure shear, equal biaxial tension and biaxial tension with three biaxiality ratios. The biaxial loading was obtained by inflating a membrane (elliptical for biaxial loading and circular for equal biaxial loading) up to failure [17, 18]. For each test, the stretches λ_i (defined as the ratio of the actual length over the initial length in the *i* principal direction) in the two loading directions are measured up to complete failure giving the critical values. In the thickness direction λ_3 is estimated by using the incompressibility assumption:

$$\det \mathbf{F} = \lambda_1 \lambda_2 \lambda_3 = 1, \tag{1}$$

where $\mathbf{F}$ is the deformation gradient tensor. The critical *J* integral J_c was measured on center-cracked tension (CCT) specimens [11] for the two hyperelastic materials. The J_c average values were 21 kJ/m² and 13 kJ/m² for SBR and NR, respectively.

2.2. Constitutive laws

Th above mentioned tests were used to identify the parameters of the constitutive laws [17, 18]. For the NR material, it was found the best fitting of the experimental data is given by the Yeoh strain energy density (SED) function [19] while for the NR material a second order Ogden function was preferred [20]. The two SED functions are given by equations (2) and (3) respectively:

$$W = C_{10}\left(I_1 - 3\right) + C_{20}\left(I_1 - 3\right)^2 + C_{30}\left(I_1 - 3\right)^3, \tag{2}$$

$$W = \frac{\mu_1}{\alpha_1}\left(\lambda_1^{\alpha_1} + \lambda_2^{\alpha_1} + \lambda_3^{\alpha_1} - 3\right) + \frac{\mu_2}{\alpha_2}\left(\lambda_1^{\alpha_2} + \lambda_2^{\alpha_2} + \lambda_3^{\alpha_2} - 3\right), \tag{3}$$

where *W* is the SED, I_1 is the first invariant of the right Cauchy-Green strain tensor, λ_i are the principal stretches and C_{ij}, μ_i and α_i are material constants to be determined using a least square method. Table 1 reminds the values of all the material constants.

Table 1. Material constants for the NR and SBR materials.

	C_{10} (MPa)	C_{20} (MPa)	C_{30} (MPa)	
NR	0.298	0.014	0.00016	
	μ_1 (MPa)	α_1	μ_2 (MPa)	α_2
SBR	0.638	3.03	-0.025	-2.35

2.3. Intrinsic flaw size

To determine the intrinsic defect size, the formulation given by Rivlin and Thomas [3] can be used. For plates containing a crack of length *a* and submitted to tensile loading, these authors expressed the tearing energy *T*, equivalent to the *J* integral, as follows:

$$J = T = 2k\left(\lambda\right)Wa, \tag{4}$$

where k is a proportionality factor depending on the stretch ratio, which can be expressed for single edge cracked specimen (SENT) specimens, according to Lindley [21] in the following form:

$$k = \frac{2.95 - 0.08(1-\lambda)}{\sqrt{\lambda}}, \tag{5}$$

For CCT specimens, the expression proposed by Lake [22] is slightly different:

$$k = \frac{\pi}{\sqrt{\lambda}}, \tag{6}$$

Therefore, the intrinsic defect size can be estimated using equation (4). It comes:

$$a_{th} = \frac{J_c}{2k(\lambda_c)W_c}, \tag{7}$$

in which J_c is the critical value of J mentioned earlier in section 2.1, W_c corresponds to the SED at break of a smooth specimen loaded in uniaxial tension which can be computed using equations (2) and (3) and λ_c is the stretch at break under uniaxial tension. Since the intrinsic flaw is supposed embedded in the bulk, the flaw is taken centered in this investigation and equation (6) is used to calculate the k factor. Using equation (7) the size was found equal to 120 μm for NR while for SBR the size is 160 μm.

3. Finite element analyses

3.1. Representative volume element

Assuming a circular defect in order to avoid preferential propagation direction under biaxial loading, a representative volume element (RVE) was introduced to achieve finite element calculations. Since the defect size is estimated from uniaxial tension tests, the size of the square shape RVE was fixed equal to the width of the tensile specimen which is 10 mm as schematically shown in figure 1.

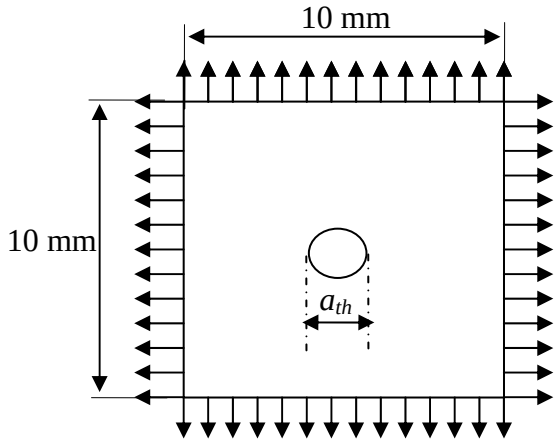

Figure 1. Reference volume element containing a circular defect.

Due to the symmetries of the RVE, only a quarter of the specimen (the shaded part) is modeled in

the finite element program. Such a modeling allows getting uniaxial tension, pure shear and different biaxial loadings by varying the ratio in the assigned displacements respectively in the horizontal and vertical directions.

3.2. *J* integral determination

The numerical analysis is performed under plane stress and finite strain conditions using a total Lagrange framework, the constitutive laws being an input given by SED functions previously introduced in equations (2) and (3). The FE program was Marc MS software.
To calculate *J*, the Begley-Landes method [23] based upon the energy interpretation of *J* was used. which allows to express *J* in the following form:

$$J = -\frac{\partial U}{\partial A}, \tag{8}$$

where U is the stored elastic energy and A is the crack (defect) area. This method requires to estimate the potential energy for varying crack lengths and to plot the energy per unit thickness function of the crack area for a given displacement. The evolution is fitted by straight lines the slope of which gives the *J* value. In this work, for each material, seven defect sizes close to the reference value (i.e. that calculated by using equation (7)) were used to estimate *J*. In order to verify the validity of the Begley-Landes method, preliminary calculations on a RVE containing a sharp crack were achieved. The values obtained were compared to the direct calculation of the *J* integral available on the software. The results, shown in figure 2 for uniaxial tension, highlight the validity of this method, especially for high level of strain.

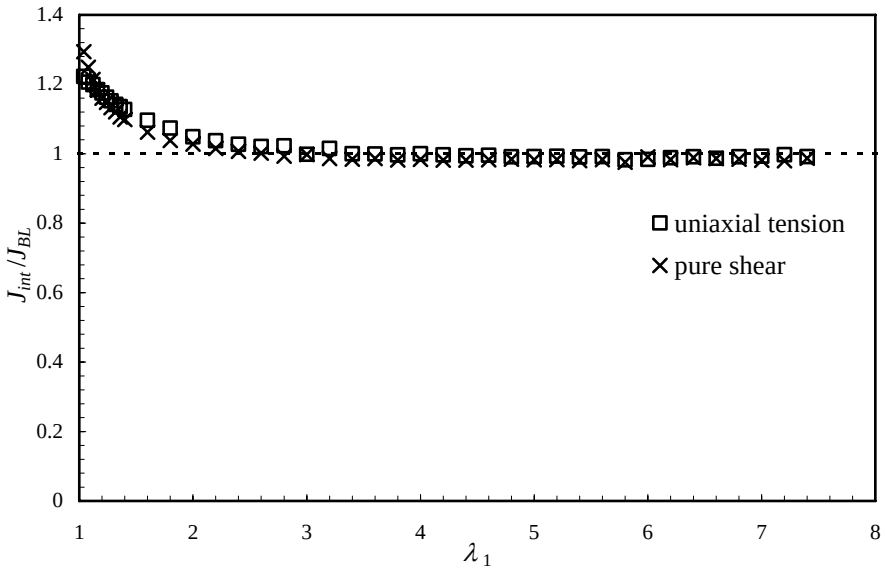

Figure 2. Evolution of the ratio J_{int}/J_{BL} as a function of the principal stretch λ_1 (SBR material).

3.3. *k* factor evolution

Finite element simulations were achieved for uniaxial tension, pure shear and four biaxiality ratios *b* defined as:

$$b = \frac{\lambda_2}{\lambda_1}. \tag{9}$$

The k factor was then computed using equation (4). Figure 3 shows the evolution of this factor as function of the equivalent stretch expressed as follows:

$$\lambda_{eq} = \sqrt{\frac{I_1}{3}}, \tag{10}$$

where I_1 is the first invariant of the right Cauchy-Green strain tensor.
The influence of the loading path is clearly highlighted on this figure. Moreover, we have not found any effect of the kind of material.

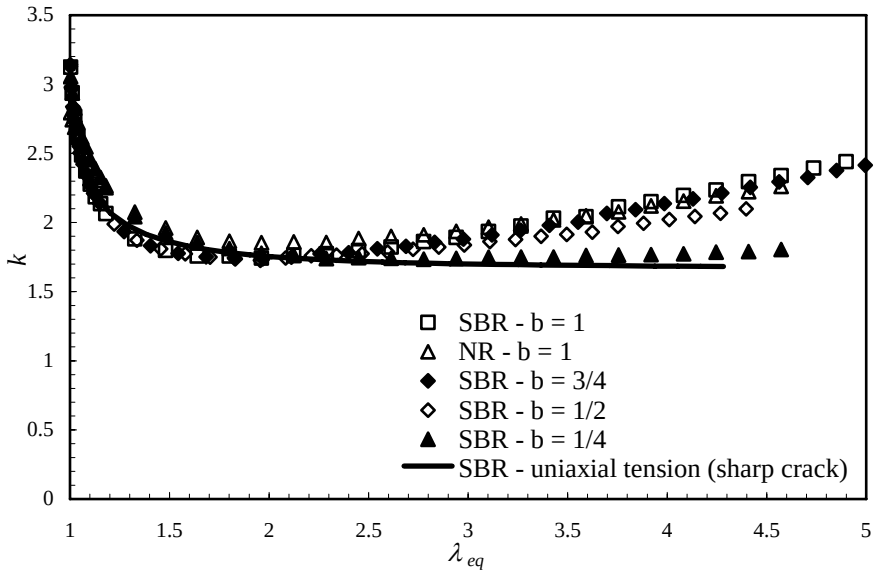

Figure 3. *k* factor as a function of the equivalent stretch λ_{eq} (circular defect, a = 0.06 mm).

4. Results

4.1. A new unified expression of *J*

Since a strong dependence of *k* on the biaxiality ratio is pointed out, the calculation of *J* using equation (4) requires to analytically express the *k* factor for every value of *b*. Another idea is to try to unify these results leading to rewrite *J* in the following form:

$$J = 2 f\left(\lambda_{eq}\right) W a, \tag{11}$$

where *f* is a function of the equivalent stretch which can be expressed in a multiplicative form as follows [24]:

$$f\left(\lambda_{eq}\right) = \left(\lambda_{eq}\right)^{\gamma} g\left(\lambda_{eq}\right), \tag{12}$$

where *g* is another function of the equivalent stretch and γ is an exponent depending on the biaxiality ratio [24] and varying from 1.05 for uniaxial tension to 1.35 for equibiaxial tension. Equation (11) therefore becomes:

$$J = 2\lambda_{eq}^{\gamma} g\left(\lambda_{eq}\right) W a. \tag{13}$$

In this case, as shown in figure 4, all the data can be shifted to get a master curve and the evolution of g can be written in a polynomial form as follows:

$$g\left(\lambda_{eq}\right) = 0.255 + \frac{2.837}{\lambda_{eq}^2} - \frac{2.888}{\lambda_{eq}^4} + \frac{2.507}{\lambda_{eq}^6}, \tag{14}$$

As shown on figure 4 all the data (dots) are well fitted by equation (14) represented by the continuous line.

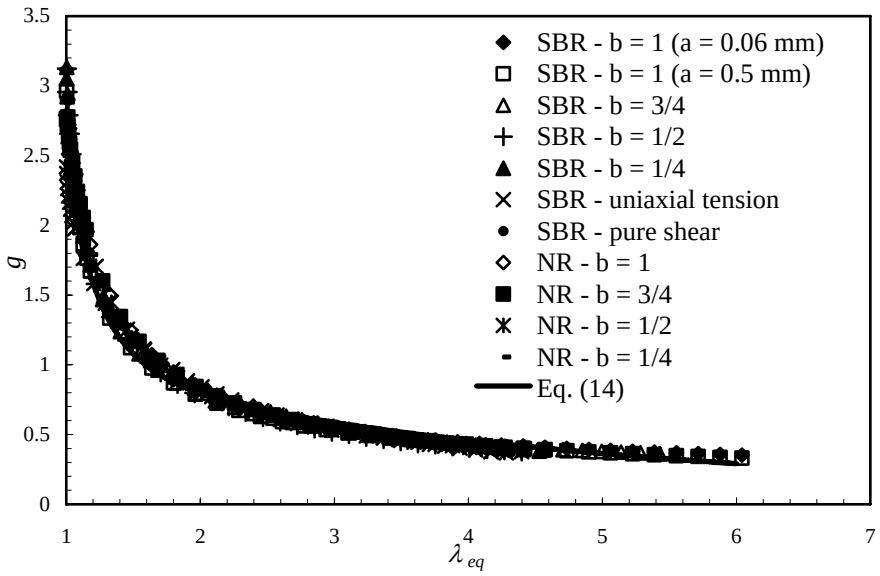

Figure 4. g as a function of the equivalent stretch λ_{eq} (a = 0.06 mm if not reported).

Figure 5 shows the validity of equation (11) to estimate the J integral. Indeed, the values obtained from equation (11) are compared to the data issued from the Begley-Landes method in the case of biaxial loadings.

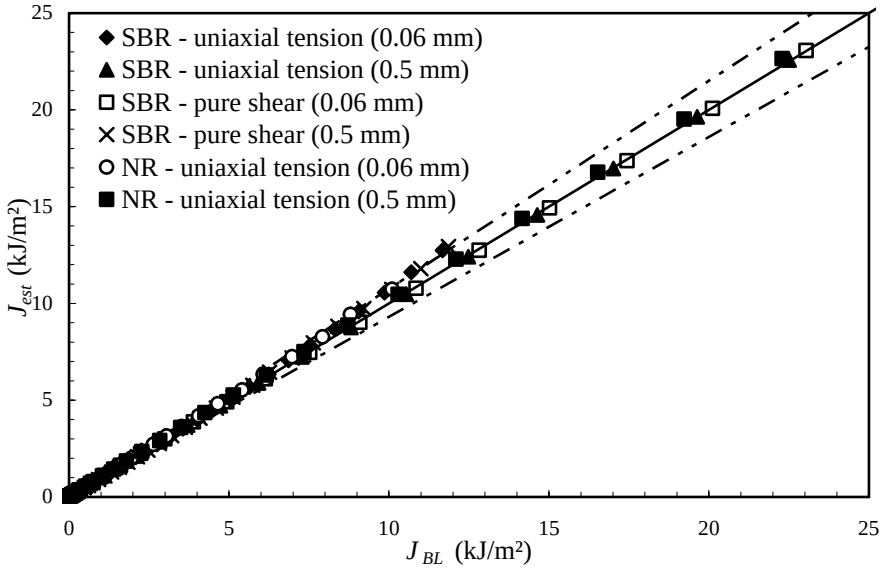

Figure 5. Comparison between J calculated from equation (11) and J_{BL} issued from the Begley-Landes method for biaxial loadings.

The maximum deviation observed is less than 5% (dashed lines). Note, even not reported on the figure, that the accuracy for uniaxial tension and pure shear is improved.

4.2. Fracture criterion

At crack initiation J takes its critical value expressed as follows:

$$J_c = 2\lambda_{eq_c}^{\gamma}\left(0.255+\frac{2.837}{\lambda_{eq}^2}-\frac{2.888}{\lambda_{eq}^4}+\frac{2.507}{\lambda_{eq}^6}\right)W_{0_c}a_c\,, \tag{15}$$

where the subscript c denotes the critical value reached at crack initiation. From equation (15) the critical stretches can be therefore derived for any loading path.

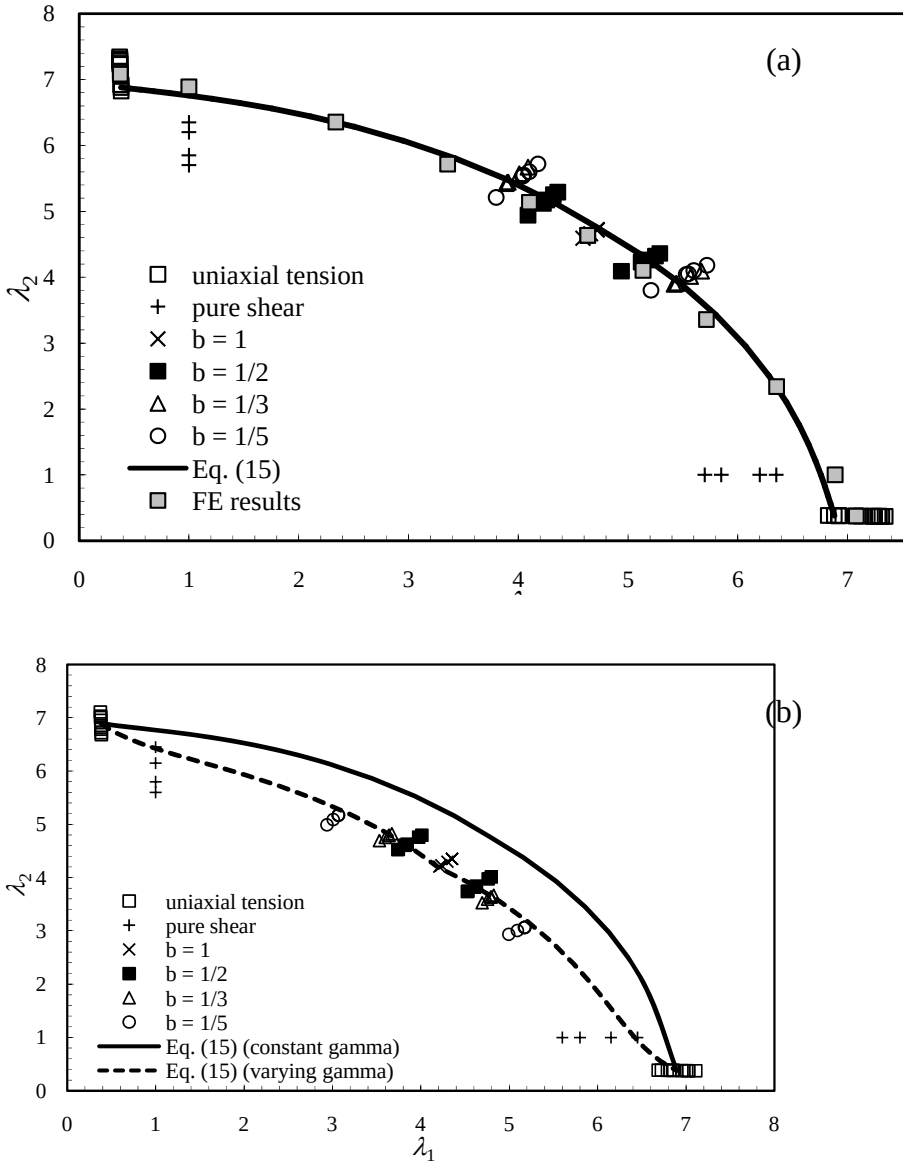

Figure 6. Failure envelopes for (a) NR and (b) SBR.

Figure 6 shows the predictive capability of the proposed approach. The failure envelope in terms of principal stretches is well predicted when using the intrinsic defect concept coupled with fracture mechanics. For NR, the exponent γ can be taken constant while for SBR it is necessary to introduce a slight variation with the biaxiality ratio.

5. Conclusion

A fracture criterion based upon the intrinsic defect concept is an original way to predict the critical stretches at failure when dealing with rubbers. The methodology we have proposed is quite easy to use and only requires two data: the stretch at break under uniaxial tension and the fracture toughness in terms of J_c. The constitutive law of the material is also an input which is necessary. We have also developed a general formulation of J which can be used, whatever the loading path in 2D conditions.

Acknowledgements

This work was supported by the CRITEL project. The authors gratefully acknowledge all the partners associated to the project (ASM, CNAM ITMA, LRCCP, Michelin, SACRED, SNECMA and SNPE). They also gratefully acknowledge the International Campus on Safety and Intermodality in Transportation for its financial support.

References

[1] A.A. Griffith, The phenomenon of rupture and flow in solids. Philosophical Transactions of the Royal Society of London, A221 (1920) 163-198.

[2] J.R. Rice, A path independent integral and the approximate analysis of strain concentration by notches and cracks. Journal of Applied Mechanics, 35 (1968) 379-386.

[3] R.S. Rivlin, A.G. Thomas, Rupture of rubber. Part I: Characteristic energy for tearing. Journal of Polymer Science, 10 (1953) 291-318.

[4] A.G. Thomas, Rupture of rubber. Part II: The strain concentration at an incision. Journal of Polymer Science, 18 (1955) 177-188.

[5] H.W Greensmith, A.G. Thomas, Rupture of rubbers. Part III: Determination of tear properties. Journal of Polymer Science, 18 (1955) 189-200.

[6] H.W. Greensmith, Rupture of rubber. X. The change in stored energy on making a small cut in a test piece held in simple extension. Journal of Applied Polymer Science, 7 (1963) 993-1002.

[7] B.H. Kim, C.R. Joe, Single specimen test method for determining fracture energy (Jc) of highly deformable materials. Engineering Fracture Mechanics, 32 (1989) 155-161.

[8] N. Aït Hocine, M. Naït Abdelaziz, A. Imad, Fracture problems of rubbers: J-integral estimation based upon η factors and an investigation on the strain energy density distribution as a local criterion. International Journal of Fracture, 117 (2002) 1-23.

[9] O.H. Yeoh, Relation between crack surface displacements and strain energy release rate in thin rubber sheets. Mechanics of Materials, 34 (2002) 459-474.

[10] C.W. Extrand, A.N. Gent, Strength under various modes of deformation. International Journal of Fracture, 48 (1991) 281-297.

[11] A. Hamdi, N. Aït Hocine, M. Naït Abdelaziz, N. Benseddiq, Fracture of elastomers under static mixed mode: The strain-energy-density factor. International Journal of Fracture, 144 (2007) 65-75.

[12] C.M. Roland, C.R. Smith, Defect accumulation in rubber. Rubber Chemistry and Technology, 58 (1985) 806-814.

[13] F. Bueche, The tensile strength of elastomers according to current theories. Rubber Chemistry and Technology, 32 (1959) 1269-1285.

[14] M. Braden, A.N. Gent, The attack of ozone on stretched rubber vulcanizates. Part II: Conditions for cut growth. Journal of Applied Polymer Science, 3 (1960) 100-106.

[15] A.N. Gent, P.B. Lindley, A.G. Thomas, Cut growth and fatigue of rubbers. Part I: The relationship between cut growth and fatigue. Journal of Applied Polymer Science, 8 (1964) 455-466.

[16] I.S. Choi, C.M. Roland, Intrinsic defects and the failure properties of cis-1,4-polyisoprenes. Rubber Chemistry and Technology, 69 (1996) 591-599.

[17] A. Hamdi, M. Naït Abdelaziz, N. Aït Hocine, P. Heuillet, N. Benseddiq, A fracture criterion of rubber-like materials under plane stress conditions. Polymer Testing, 25 (2006) 994-1005.

[18] A. Hamdi, M. Naït Abdelaziz, N. Aït Hocine, P. Heuillet, N. Benseddiq, A new generalized fracture criterion of elastomers under quasi-static plane stress loadings. Polymer Testing, 26 (2007) 896-902.

[19] O.H. Yeoh, Characterization of elastic properties of carbon-black-filled rubber vulcanizates. Rubber Chemistry and Technology, 63 (1990) 792-805.

[20] R.W. Ogden, Large deformation isotropic elasticity: On the correlation of theory and experiment for incompressible rubberlike solids. Proceedings of the Royal Society of London, A326 (1972) 565-584.

[21] P.B. Lindley, Energy for crack growth in model rubber components. The Journal of Strain Analysis for Engineering Design, 7 (1972) 132-140.

[22] G.J. Lake, Application of fracture mechanics to failure in rubber articles, with particular reference to groove cracking in tyres. In: Yield, Deformation and Fracture of Polymers, Cambridge, 1970.

[23] J.A. Begley, J.D. Landes, The J integral as a fracture criterion. American Society for Testing and Materials, 514 (1972) 1-20.

[24] M. Naït-Abdelaziz, F. Zaïri, Z. Qu, A. Hamdi, N. Aït-Hocine, J integral as a fracture criterion of rubber-like materials using the intrinsic defect concept, Mechanics of Materials, 53 (2012) 80-90.

Correlation between the dynamic fracture surface energy G_{ID} and the amount of created surface

Jean-Benoît Kopp[1,*], Jean Schmittbuhl[2], Jian Lin[1], Christophe Fond[1]

[1] ICube- 2 rue Boussingault, F67000 Strasbourg
[2] Ecole et Observatoire des Sciences de la Terre, 5 Rue René Descartes, F67000 Strasbourg
* Corresponding author: jbkopp@unistra.fr

Abstract

For rapid crack propagations, two kinds of material behavior have been observed. Typically, most materials show an increase of the fracture energy with the crack tip velocity. However, there do exist a few materials for which the fracture energy tends to decrease with the velocity [1, 2]. They are viscoplastic blend materials like polymers such as rubber toughened polymethylmethacrylate (RT-PMMA). For these materials, crack tips are seen to propagate at the same velocity whatever the loading rate is (or strain energy release rate). This critical velocity has been shown to be the crack branching velocity, at least at a macroscopic scale. Our study shows that the classical approach which considers that the amount of created surface during the propagation can be approximated as the sample thickness multiplied by the crack length is not appropriate. Indeed, this study shows that the exact fracture surface roughness has to be included in the amount of created surface in order to establish an intrinsic material fracture energy G_{ID}. As the fracture surface roughness depends on the scale at which the sample is observed, a self-affine model widely used for fracture surfaces is introduced [3, 4]. This statistical geometrical model of the fracture surface with two parameters, a Hurst exponent and a topothesy is shown to be effective and provides a better estimate of the intrinsic surface fracture energy.

Keywords Dynamic fracture, rapid crack propagation, polymers, energy release rate, self-affine analysis, Hurst exponent.

1. Introduction

Considering rapid crack propagation, two kinds of material behavior have been observed. On the one hand, there are materials for which the fracture energy increases with the crack tip velocity. Fracture velocity changes during the crack propagation when the released energy varies, i.e. the dynamic energy release rate G_{ID}. Practically, a difference of velocity before and after branching is observed and, for instance, the main crack propagates faster than the secondary cracks after branching [5-7]. On the other hand, there are materials for which the fracture energy tends to decrease with velocity. They are viscoplastic blend materials and typically polymers such as rubber toughened polymethylmethacrylate (RT-PMMA) or many semi-crystalline polymers. In these materials, crack tips are seen to propagate at the same macroscopic velocity whatever the macroscopic fracture energy in mode I solicitation [1, 8, 9]. This velocity corresponds to the crack branching velocity, typically $0.6C_r$, where C_r is the Rayleigh wave speed. In the case of rapid crack propagations, as observed in [1], to maintain the propagation at the same macroscopic crack branching speed, the surface roughness evolves as a function of the available energy release rate G_{ID}. Below a minimal value of $G_{ID,}$ cracks stop without any decrease of the crack tip velocity contrarily to the first kinds of materials. Crack arrest phases correspond to relatively smooth fracture surfaces and fracture surface roughness is seen to increase with the value of fracture energy at constant velocity. These observations confirm the aim of this study to explore the roughness of fracture surfaces as a function of the energy release rate G_{ID}. Moreover, classical consideration of the created surface such as the sample thickness times the crack length is not appropriate since several values can be obtained for the fracture energy at constant crack tip velocity. Evaluating the quantity of created surface is not simple since the surface roughness is correlated with the scale at which the sample is observed. Hence, validating the self-affine geometrical model would be of great

interest. The concept of self-affinity [10] of surface roughness has been described for many natural surfaces including fracture surfaces. This concept allows the introduction of the existence of a roughness exponent called the Hurst exponent [11] which is known to be unique and universal between 0.78 and 0.80 for many materials such as rocks [3, 4, 12] wood [13-15], steel [16-18] or polymers [19-21]. This study shows the interest of the self-affine geometrical model of fracture surface, with two parameters being the Hurst exponent and the topothesy.

2. Materials and methods

The general principle of Rubber Toughened (RT) reinforcement is to dissipate energy throughout the material through elastomer particles in contrast to pure amorphous polymers for which the energy dissipation is smaller and only located at the crack tip [22-31]. RT-PMMA consists of a PMMA matrix containing a volume fraction of approximately 20% of spherical elastomer particles of about 200nm in diameter. The elastomer particles are prepared separately and then mixed with PMMA in a fluid state at high temperatures. The glass transition temperature T_g of the matrix is 105°C while that of the elastomer particles is about -30°C. Fig. 1 presents sample characteristics for rapid crack propagation (RCP) tests.

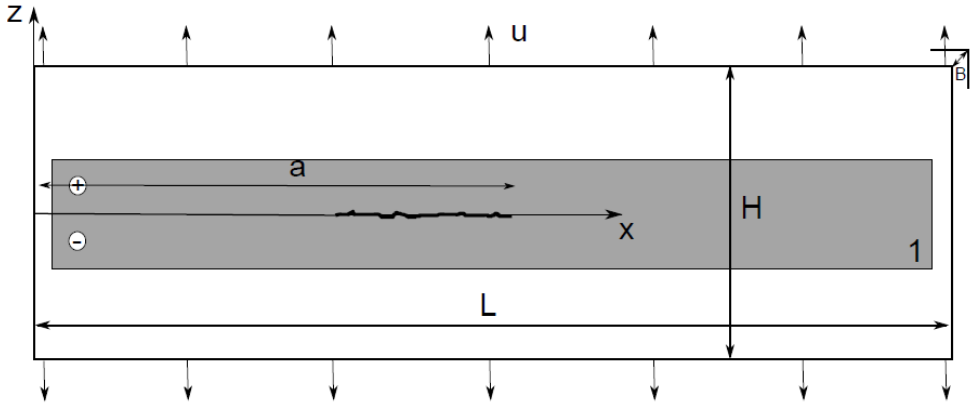

Figure 1. Schematic representation of the strip band geometry (L≈200mm, 25mm<H<45mm, B≈2mm) uniformly loaded with imposed displacements *u* in mode I. A conducting layer (1-an Ag layer of approximately 10 µm is spread on the sample) used to record the crack tip position during propagation.

A conductive layer is sprayed onto the sample and the resistance evolution is recorded during the fracture, with a National Instrument USB-6351 data acquisition which ensures a 1.25 $MS.s^{-1}$ sampling rate. After calibration, fracture tip velocities are measured**.**

The strip band geometry allows a relatively simple mechanical analysis of the structure [32]. Samples are initially preloaded in tension using an Instron tensile testing machine equipped with a 150 kN force cell. A notch $a_0 \approx 5/2.H$ is machined in the sample before loading. Crack propagation is then initiated by an impact of a razor blade at the tip of the notch. The entire test is performed at a quasi-constant temperature of 23°C.

An opto-mechanical stylus profilometer was used to characterize the *post-mortem* fracture surface of the RT-PMMA. A mechanical arm carrying a stylus is moved horizontally at constant speed (about 1 $mm.s^{-1}$) and subjected to a gravity force ensuring that the sapphire tip (φ = 5µm) keeps in contact with the surface. Measurements are discretized along a grid (N_x, N_y) with a mesh (Δ_x, Δ_y). This technique is compatible with surface transparency which prevents the direct use of optical techniques. The present profilometer cumulates optical precision of the height measurement and mechanical description of the air/RT-PMMA interface (no penetration).

First of all, height measurements Z(X,Y) are used to build the topography of fracture surfaces. The chosen mesh grid is: $\Delta_x=\Delta_y=10\mu m$ with a resolution of 2µm. Fracture maps show the surface

roughness during crack propagation, in particular during branching or crack arrest (see Fig. 2-3). Note that for RT-PMMA macroscopic fracture speed is observed to be constant even if the roughness changes [1]. Fig. 2 shows a perspective view of the fracture topography, before a branching zone.

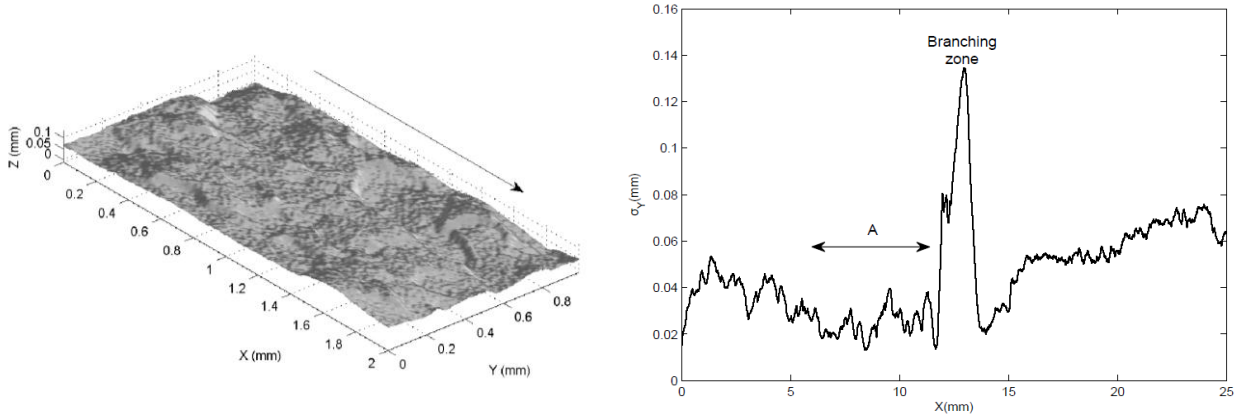

Figure 2. Topography of a fracture surface of RT-PMMA before a branching zone and standard deviation $\sigma_y(x)$ of the height along the Y axis in function of the X axis which defines the stationary state (A) just before a branching zone.

This study also addresses the surface topography decrease just before a crack arrest in a sample of RT-PMMA (Fig. 3) when the fracture energy becomes too low for the crack to continue. A small cut is made to the samples in order to access crack arrests zones. To illustrate the variation of the surface roughness during crack propagation, the standard deviation σ_y (Eq. 1) of the height Z(X,Y) along the Y axis is calculated as a function of the X axis. The amplitude variation of σ_y is used to make the difference between stationary and non-stationary regimes. A stationary regime corresponds to quasi-constant fluctuations of σ_y. Fig. 2 and Fig. 3 show two stationary states before branching (A) and after branching (B):

- Regime A: σ_y amplitudes seem relatively constant just before a branching zone.
- Regime B: σ_y amplitudes seem relatively constant just before a crack arrest.

$$\sigma_y^2 = \frac{1}{N}\sum (h - \bar{h})^2 , \quad (1)$$

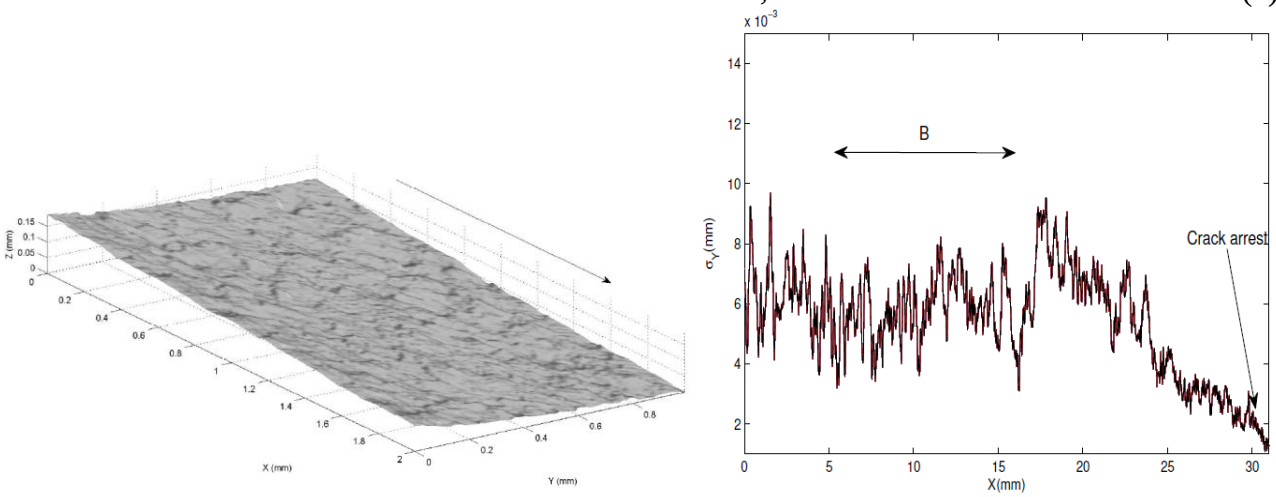

Figure 3. Topography of a fracture surface of RT-PMMA just before a crack arrest and standard deviation $\sigma_y(x)$ of the height along the Y axis in function of the X axis which defines the stationary state (B) just before a crack arrest phase.

In order to estimate fracture surfaces a routine in Fortran was created with two estimating methods. The first method called "spherical convolution" consists to probe the experimental surface with an imaginary profilometer having a variable needle radius R_p. The second method called "sampling" consists in undersampling data, i.e. to keep a point every R_p (Fig. 4). Finally, this program computes the amount of developed fracture surface $\mathcal{A}$ and developed lengths respectively along X and Y axis (l_x, l_y).

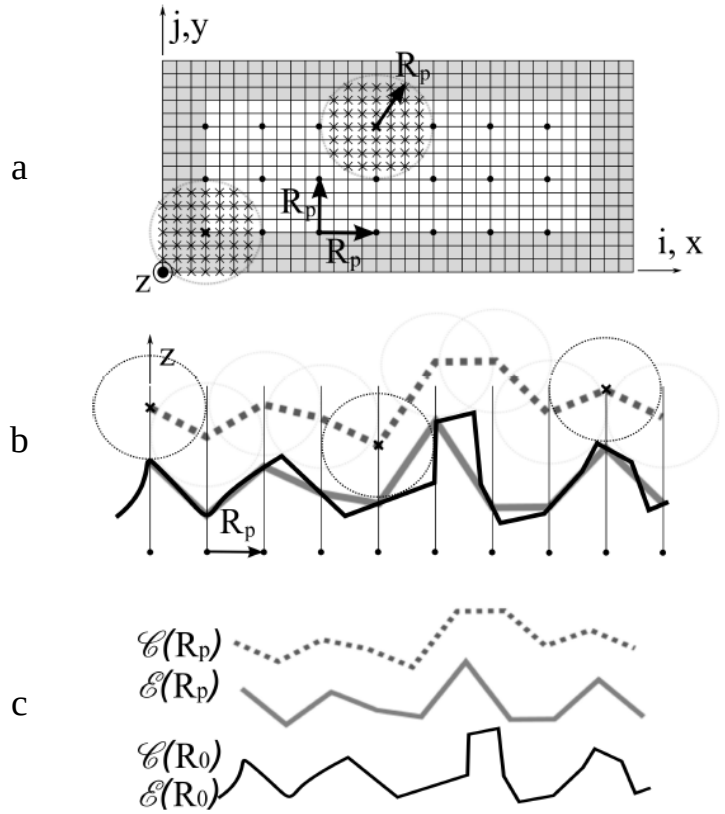

Figure 4. a-Top view of the synthetic profile b- "Spherical convolution" method and "sampling" method c-Profile of fracture surface obtained with the help of "spherical convolution" method or "sampling" method.

Finally, the concept of self-affinity introduced by Mandelbrot [10] is used to describe the roughness of fracture surfaces of RT-PMMA. It applies to surfaces that are statistically invariant under an affine transformation, such as: $X \rightarrow \lambda_x.X$; $Y \rightarrow \lambda_y.Y$; $Z \rightarrow \lambda_z.Z$ with $\lambda_x = \lambda_y$; $\lambda_z = \lambda_x^{\chi}$ with χ, the roughness exponent, or the Hurst exponent ($0<\chi<1$). Today, there are various analytical techniques to analyze stationary and transient self-affinity. Root Mean Square (RMS), Maximum-Minimum (MM), Fourrier Power Spectrum (FPS) and Averaged Wavelet Coefficient (AWC) methods which are used in this study are described in [4, 33-35]. The aim is to determine a self-affine geometrical model of the fracture surface from the estimates of the Hurst exponent and the topothesy l_r or the pre-factor *C*. The topothesy [35-38] which corresponds to the theoretical length scale over which the surface roughness has an average slope of 45° ($\sigma(l_r)=l_r$) is calculated using the RMS method (Eq. 2):

$$\sigma(\Delta x)=C.\Delta x^{\chi} \text{ with } C=l_r^{(1-\chi)}, \quad (2)$$

The energy release rate G_{Id} (Eq. 3) is computed assuming a classical Griffith energy balance accounting for inertial effects such as:

$$G_{Id} = \frac{\Delta W_{ext} - \Delta W_{ela} - \Delta K_{cin} - \Delta W_{dis}}{B\Delta a}, \quad (3)$$

where B is the thickness of the sample, Δa the crack length, W_{ela} the strain elastic energy, K_{cin} the kinetic energy, W_{ext} the work done by external forces and W_{dis} the bulk dissipated energy integrated over the entire structure. It has been largely assessed with optical techniques that Linear Elastic Fracture Mechanics (L.E.F.M.) formalism is valid for the dynamic fracture of amorphous polymers since the process zone is sufficiently confined [39, 40]. When the crack tip position $a(t)$ during propagation and the initial stress state are known, the energy release rate G_{ID} may be calculated between two tip positions a and $a+\Delta a$ by means of a transient dynamic finite element procedure, using the CAST3M software [41]. Dissipated energy, such as damping, does not involve nonlinear behavior in the process zone but only outside the process zone. Indeed, assuming L.E.F.M, the fracture toughness G_{Idc} accounts for non linearities in the process zone by setting $G_{Idc} = G_{Id}$ for crack length increase. Since it has been shown that viscoelasticty is negligible for these experiments, $W_{dis} = 0$ [42].

3. Results

During rapid crack propagation (RCP) tests, the macroscopic crack speed is quasi constant for a given specimen at a given temperature, whether branching occurs or not (Fig. 5). However, for a quasi-constant crack speed, several values of energy released rates have been recorded. The information given in the Table 1 highlights a striking difference of $<G_{ID}>$ for a measured same crack speed.

Table 1. Mean dynamic fracture energy values for cracks which branch ($<G_{ID}>_{max}$) and stop ($<G_{ID}>_{min}$).

$<G_{ID}>_{min}(kJ/m^2)$	$<G_{ID}>_{max}(kJ/m^2)$	$<G_{ID}>_{max}/<G_{ID}>_{min}$
0.58±0.2	1.70±0.2	3.0±0.2

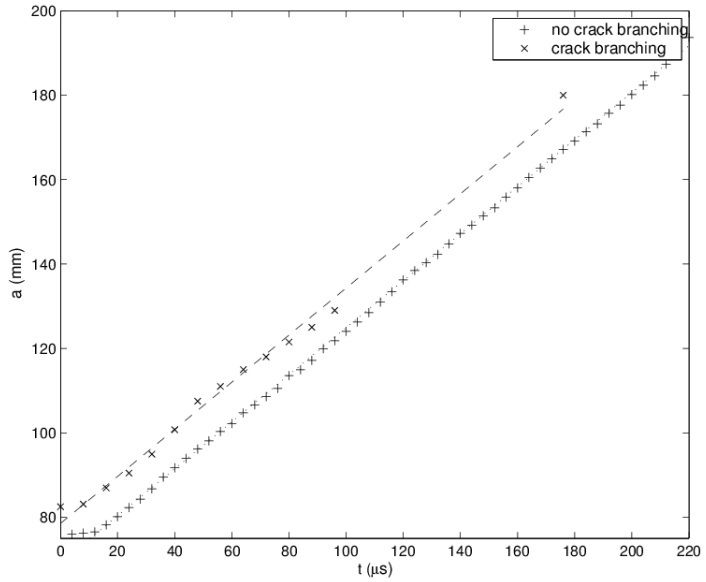

Figure 5. Crack lengths versus time in the case of crack branching and in the case of no macroscopic crack branching.

To quantify the differences of magnitudes of fracture surfaces between stationary states (A) and (B),

pre-factors are compared (Table 2). A significant difference of roughness is highlighted between the roughest and the smoothest surfaces observed on RT-PMMA samples.

Table 2. Pre-factors and topothesy calculated with RMS method before a branching zone (A) and a crack arrest (B).

	Pre-factor C (mm)	Topothesy l_r (mm)	C(A)/C(B)
A	$10^{-1.84}$	1.10^{-4}	2.4±0.2
B	$10^{-2.22}$	9.10^{-6}	

Pre-factors and topothesy are calculated for each regime (A) and (B) for 10 samples of RT-PMMA. The ratio of *C(A)* to *C(B)* is equal to 2.4 ± 0.2. The self-affine geometrical model for stationary states (A) and (B) is defined with two parameters: the Hurst exponent and the topothesy. The results obtained by the two methods (RMS and MM) are shown in Fig. 6.

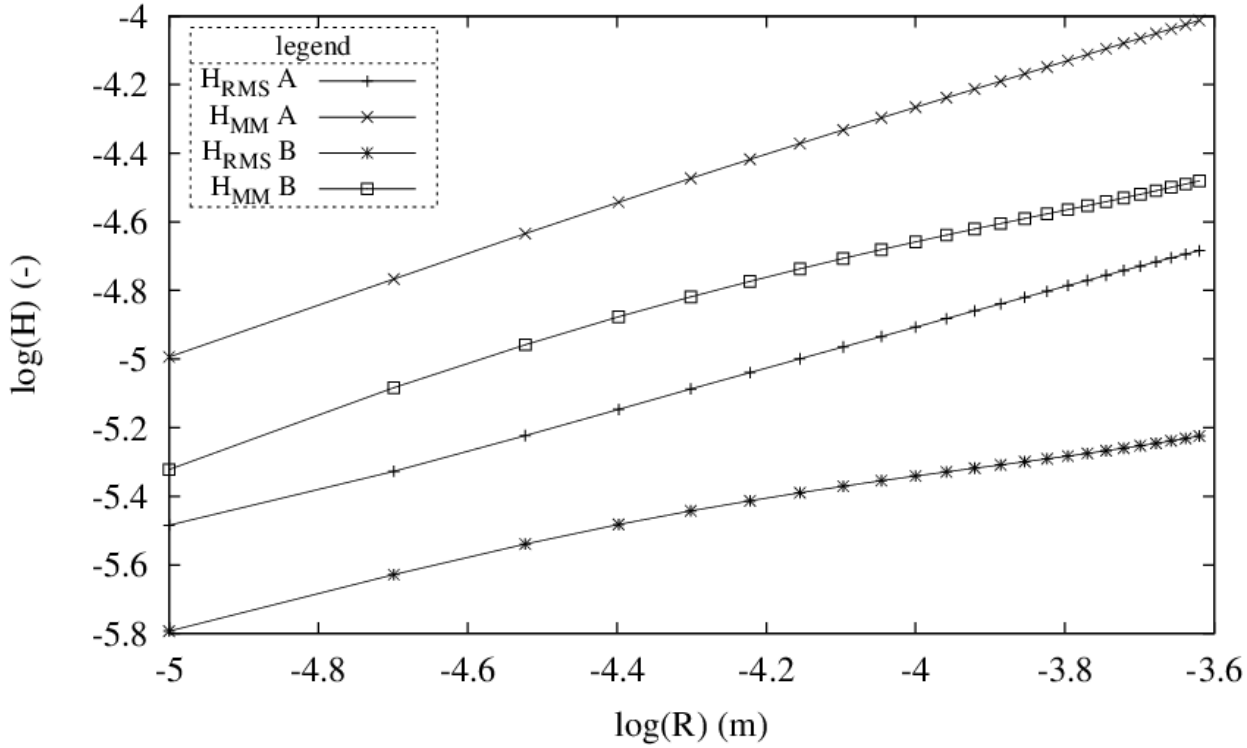

Figure 6. Statistical data analysis (RMS and MM) obtained by the characterization of RT-PMMA fracture surfaces (A and B).

The Hurst exponent is obtained from the average slope β of each curve in a log-log diagram with $\beta=\chi$ for RMS and MM methods. All values of Hurst exponent which have been obtained are summarized in Table 3. The main observation is that the surface roughness of RT-PMMA follows a self-affine model in stationary regimes. In suggested stationary regimes (A and B) the self-affine model stays stable along the crack propagation with$\langle\chi\rangle=0.61 \pm 0.05$. The average value of the Hurst exponent $\langle\chi\rangle$ was calculated using the analysis of 10 profiles.

Table 3. Roughness exponent of RT-PMMA fracture surfaces for stationary states A and B.

Methods	RMS	MM
$\chi(A)$	0.54	0.60
$\chi(B)$	0.56	0.62

Furthermore, a decrease of the prefactor and the topothesy was observed between A and B states (Table 2). This corresponds to a significant decrease of surface roughness. Contrary to the pre-factor and the topothesy, the Hurst exponent stays stable between the two stationary regimes. The interest of analyzing the pre-factor and the topothesy provides an estimate of the difference of fracture surfaces between the two domains. Fig. 7 presents the quantity of developed surface for "spherical convolution" and "sampling" methods for stationary regimes (A) and (B). The amount of developed surface in domain (B) is significantly lower than the amount of developed surface in domain (A).

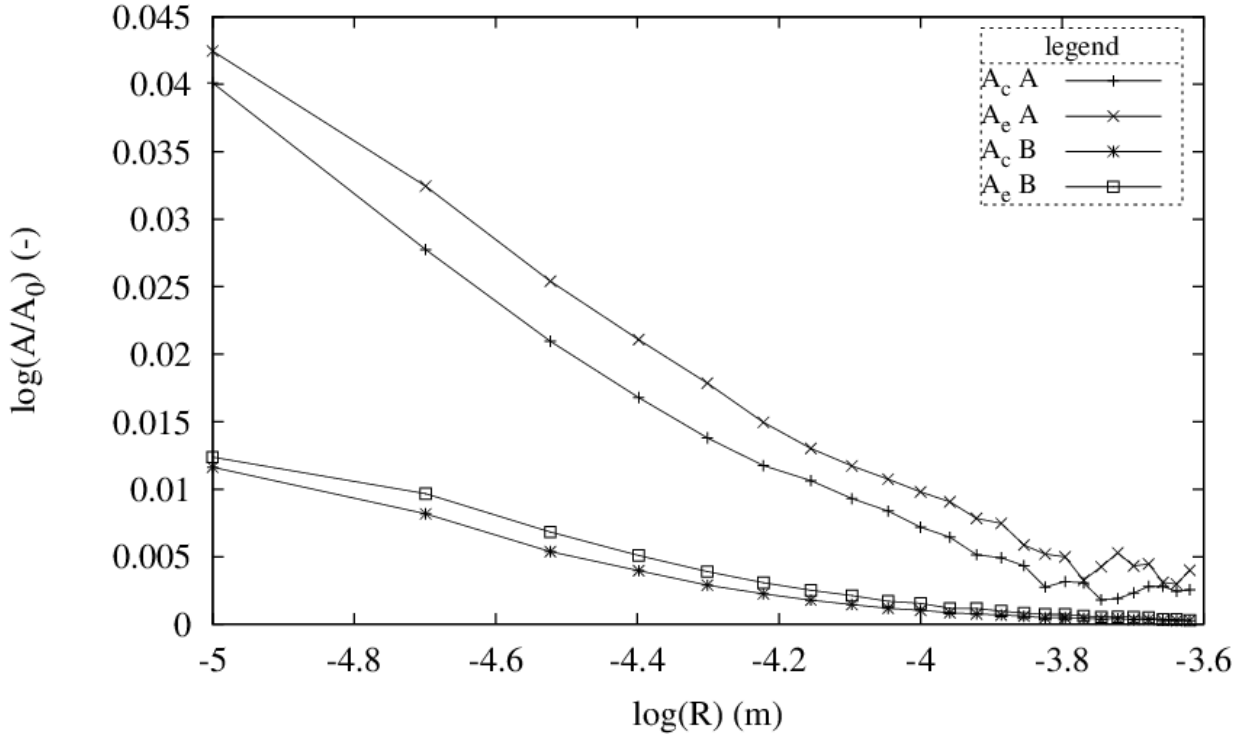

Figure 7. Total fracture surface for "spherical convolution" method ($_c$) or "sampling" method ($_e$) for stationary regimes (A) and (B).

Whatever the method, "spherical convolution" or "sampling", the amount of developed surface which are calculated is relatively similar. The choice of the method thus is indifferent on the result.

4. Discussion and conclusions

Using an dynamic L.E.F.M. approach, RT-PMMA samples have revealed a "loss" of G_{ID} unicity which is related to $B\Delta a$ (Eq. 3) at a crack tip velocity of approximately $0.6C_r$. Indeed, maximum values of fracture energy have been shown to vary up to 3.0 ± 0.2 times the minimum. The results suggest that differences of G_{ID} exist and are associated to the RMS of the fracture surface σ_y. In this article the roughness of fracture surfaces obtained from the analysis of *post-mortem* surfaces, has been quantified with Hurst exponents and pre-factors ratios during stationary regimes (A and B) before and after branching. Surfaces considered as inaccessible, either because of the profilometric technique (5µm sapphire radius tip) or because of local branches (sub-surfaces), are neglected in this study. However it is observed that the amount of fracture of inaccessible surface seems

negligible compared to the accessible surface. It is shown that a crack creates 2.4±0.2 times more surfaces before a branching zone than before a crack arrest. In addition, the self-affine model allows one to say that the surface roughness could be considered as statistically invariant under an affine transformation. Evidently the model could lose its validity below the micrometric scale, i.e. resolution scale. The "loss" of G_{ID} unicity at approximately $0.6C_r$ can therefore be associated with the amount of created fracture surface even if the quantification of $\mathcal{A}$ is practically fastidious. G_{ID} is calculated as a function of the created projected fracture surface ($B\Delta a$) on the average fracture plane. In the case of rubber toughened polymer, and most probably semi-crystallines, experiments thus show that it would be pertinent to correct the real area of the crack surface $\Delta\mathcal{A}/\Delta\mathcal{A}_0$ with $\Delta\mathcal{A}_0 = B\Delta a$ the projected area and $\Delta\mathcal{A}$ the real surface. For these kinds of materials it would be necessary to multiply G_{ID} by $\Delta\mathcal{A}/\Delta\mathcal{A}_0$. Finally, the determination of the Hurst exponent ($\chi=0.61 \pm 0.05$) independently of the fracture domain (A or B) supports the universality of the self-affine scaling of fracture surface for quasi-2D sample geometries. The self-affine geometrical model with two parameters (Hurst exponent and pre-factor or topothesy), shows its effectiveness in this type of study. However, the single Hurst exponent is no longer sufficient, by itself, to describe all the regimes encountered and, more precisely, with these kinds of rubber toughened polymers.

References

[1] C. Fond, R. Schirrer, Dynamic fracture surface energy and branching instabilities during rapid crack propagation in rubber toughened pmma, Notes au C.R.A.S., Series IIb 329 (2001a) 195–200.
[2] C. Fond, R. Schirrer, Influence of crack speed on fracture energy in amorphous and rubber toughened amorphous polymers, Plastics, Rubber and Composites 30 (2001b) 116–124.
[3] J. Schmittbuhl, S. Gentier, S. Roux, Field measurements of the roughness of fault surfaces, Geophysical research letter 20 (1993) 639–641.
[4] J. Schmittbuhl, F. Schmitt, S. C., Scaling invariance of crack surfaces, Journal of geophysical research 100 (1995) 5953–5973.
[5] J. G. Williams, Visco-elastic and thermal effects on crack growth in pmma, International Journal of Fracture 8 (1972) 393–401.
[6] A. Kobayashi, N. Ohtani, M. Munemura, Dynamic stress intensity factors during viscoelastic crack propagation at various strain rates, Journal of Applied Polymer Science 25 (1980) 2789–2793.
[7] W. Döll, Application of an energy balance and an energy method to dynamic crack propagation, International Journal of Fracture 12 (1976) 595–605.
[8] J. Scheibert, C. Guerra, F. Celarie, D. Dalmas, D. Bonamy, Brittle-quasibrittle transition in dynamic fracture: An energetic signature, Phys. Rev. Lett. 104 (2010) 045501–1–045501–4.
[9] E. Sharon, J. Fineberg, Confirming the continuum theory of dynamic brittle fracture for fast cracks, Nature 397 (1999) 333–335.
[10] B. Mandelbrot, The fractal geometry of nature, W.H.Freeman and Company (NewYork) (1982).
[11] K. Maloy, A. Hansen, E. Hinrichsen, S. Roux, Experimental measurements of the roughness of brittle cracks, Phys. Rev. Lett. 68 (1992) 213–215.
[12] J. M. Lopez, J. Schmittbuhl, Anomalous scaling of fracture surfaces, Physical Review E 57 (1998) 6405–6408.
[13] S. Morel, J. Schmittbuhl, J. M. Lopez, G. Valentin, Anomalous roughening of wood fractured surfaces, Phys. Rev. E 58 (1998) 6999–7005.
[14] G. Mourot, S. Morel, G. Valentin, Comportement courbe-r d'un matériau quasi-fragile (le bois): Influence de la forme des specimens d'essai, Colloque MATERIAUX 2002 (2002).
[15] L. Ponson, D. Bonamy, H. Auradou, G. Mourot, S. Morel, E. Bouchaud, C. Guillot, J. Hulin, Anisotropic self-affine properties of experimental fracture surfaces, International Journal of fracture 140 (1992) 27–37.
[16] B. Mandelbrot, D. Passoja, A. J. Paulay, Fractal character of fracture surfaces of metals, Nature 308

(1984) 721–722.
[17] J. P. Bouchaud, E. Bouchaud, G. Lapasset, J. Planès, Models of fractal cracks, Physical review letters 71 (1993a) 2240–2243.
[18] E. Bouchaud, G. Lapasset, J. Planès, S. Naveos, Statistics of branched fracture surfaces, Phys. Rev. B 48 (1993b) 2917–2928.
[19] F. Lapique, P. Meakin, J. Feder, T. Jassang, Self-affine fractal scaling in fracture surfaces generated in ethylene and propylene polymers and copolymers, Journal of Applied Polymer Science 86 (2002) 973–983.
[20] C. Guerrero, E. Reyes, V. Gonzalez, Fracture surface of plastic materials: the roughness exponent, Polymer 43 (2002) 6683–6693.
[21] M. Hinojosa, V. Gonzalez, J. Sanchez, U. Ortiz, Scaling properties of the fracture surfaces of a crystalline polymer, Polymer 45 (2004) 4829–4836.
[22] P. A. Lovell, M. M. Sherratt, R. J. Young, Mechanical Properties and Deformation Micromechanics of Rubber-Toughened Acrylic Polymers, 1996.
[23] C. Fond, Cavitation criterion for rubber materials: A review of void-growth models, Journal of Polymer Science Part B: Polymer Physics 39 (2001) 2081–2096.
[24] C. Fond, R. Schirrer, Renforcement des polymères - mécanismes et modélisations de la cavitation., in: Physique des polymères à l'état solide, volume 17, 2006, pp. 167–208.
[25] O. Julien, P. Béguelin, L. Monnerie, H. H. Kausch, Loading-rate dependence of the fracture behavior of rubber-modified poly(methyl methacrylate), in: Toughened Plastics II, 1996, pp. 233–249.
[26] C. B. Bucknall, R. R. Schmith, Stress-whitening in high-impact polystyrenes, Polymer 6 (1965) 437–446.
[27] H. Keskkula, M. Schwarz, D. R. Paul, Examination of failure in rubber toughened polystyrene, Polymer 27 (1986) 211–216.
[28] G. Dagli, A. Argon, R. Cohen, Particle-size effect in craze plasticity of high-impact polystyrene, Polymer 36 (1995) 2173–2180.
[29] R. Borggreve, R. Gaymans, J. Schuijer, J. Ingen Housz, Brittle-tough transition in nylon-rubber blends: effect of rubber concentration and particle size, Polymer 28 (1987) 1489–1496.
[30] R. Borggreve, R. Gaymans, J. Schuijer, Impact behaviour of nylon-rubber blends: 5. influence of the mechanical properties of the elastomer, Polymer 30 (1989) 71–77.
[31] C. He, A. Donald, Morphology of a deformed rubber toughened poly(methyl methacrylate) film under tensile strain, Journal of Materials Science 32 (1997) 5661–5667.
[32] F. Nilsson, Dynamic stress-intensity factors for finite strip problems, International Journal of Fracture 8 (1972) 403–411.
[33] A.-L. Barabasi, H. E. Stanley, Fractal concepts in surface growth, Cambridge university press edition, 1995.
[34] P. Meakin, Fractals: Scaling and growth far from equilibrium, Cambridge university press edition, 1998.
[35] T. Candela, F. Renard, M. Bouchon, A. Brouste, D. Marsan, J. Schmittbuhl, C. Voisin, Characterization of fault roughness at various scales: Implications of three-dimensional high resolution topography measurements, Pure and Applied Geophysics (2009) 1817–1851.
[36] I. Simonsen, D. Vandembroucq, S. Roux, Wave scattering from self-affine surfaces, Phys. Rev. E 61 (2000) 5914–5917.
[37] J. Schmittbuhl, G. Chambon, A. Hansen, M. Bouchon, Are stress distributions along faults the signature of asperity squeeze, Geophysical Research Letters 33 (2007) L–13307.
[38] J. Schmittbuhl, A. Steyer, L. Jouniaux, R. Toussaint, Fracture morphology and viscous transport, International Journal of Rock Mechanics and Mining Sciences 45 (2008) 422–430.
[39] J. F. Kalthoff, On the measurement of dynamic fracture toughnesses? A review of recent work, International Journal of Fracture 27 (1985) 277–298.
[40] Bohme, W., Kalthoff, J. F., On the quantification of dynamic in impact loading and the practical application for kid-determination, J. Phys. Colloques 46 (1985) C5–213–C5–218.
[41] Castem software: http://www-cast3m.cea.fr/
[42] C. Fond, Endommagement des polymères "choc": modélisations micromécaniques et comportements à la rupture, Habilitation à diriger des recherches en mécanique des solides, Université Louis Pasteur de Strasbourg, 2000.

Influence of crack sharpness on the fracture toughness of epoxy resins

Alicia Salazar[1,*], Yatish Patel[2], J. G. Williams[2,3]

[1] Departamento de Tecnología Mecánica, Universidad Rey Juan Carlos, 28933 Madrid, Spain
[2] Mechanical Engineering Department, Imperial College London, London SW7 2AZ, United Kingdom
[3] Aero, Mechanical and Mechatronics Engineering Department, University of Sydney, Sydney, Australia
* Corresponding author: alicia.salazar@urjc.es

Abstract Notch sharpening of polymeric fracture samples is still an unsolved problem. The existing methodologies for the evaluation of the fracture toughness of polymers recommend the use of contact techniques such as razor sharpening which, in some cases, can induce high scatter in toughness results or even overestimated values.

The present work analyzes the effect of crack sharpness on the fracture toughness of epoxy resins. Three-point bending tests were carried out on specimens with a wide range of tip radii, going from the size of natural cracks, ~ 0.1 μm, to 2 mm. The behavior of the fracture toughness versus the crack tip radius has been modeled using a two criterion elastic model, a length and a stress, to estimate the overestimated toughness values with the crack tip radius and the effect of blunting arising from plastic deformation.

Keywords fracture toughness, crack sharpness, epoxy resins

1. Introduction

The influence of crack sharpness on the fracture toughness values of polymeric materials has recently caught the attention of the scientific community. Several works have appeared in the literature highlighting the role of the notch sharpening technique on the fracture parameters of either semi crystalline heterogeneous polymeric materials such as ethylene-propylene block copolymers [1-3] or amorphous polymers such as polycarbonate [4]. In all these studies, the values of the fracture toughness obtained using different approaches were determined from samples sharpened via two procedures: a non contact technique based on the femtosecond laser ablation and the traditional contact technique using a razor blade. Independently of the material under study, the results always followed the same trend. The fracture toughness determined from the samples sharpened via the femtosecond laser ablation technique showed lower values than those obtained from the specimens sharpened via the traditional razor blade technique. The reason is that the femtosecond pulsed laser ablation is characterized by very rapid creation of vapor and plasma phases, negligible heat conduction and the absence of liquid phase [5-6]. Thus, this technique can remove the material of the notch tip by ablating it with almost no heat dissipation, preventing melting and thermal deformations of the surrounding area. However, the specimens sharpened using the razor blade always showed damage ahead of the crack tip in form of plastic deformation which seems to be the reason of the higher fracture toughness values.

All these discoveries have aroused some questions concerning the well established criteria of the quality of the notch. Both ESIS (European Structural Integrity Society) [7-9] and ASTM (American Society for Testing and Materials) [10-11] indicate that when a natural crack cannot be generated in

polymers by either fatigue cracking, due to hysteretic heating, or by tapping on a new razor blade placed in the notch, the sharpening can be achieved by sliding a new razor blade into the root of the machined notch. The resulting crack tip radius must be lower than 20 μm.

In the light of the previous results, the aim of the present work is to investigate more deeply the effect of the crack tip radius on the fracture parameters of a brittle polymer such as an epoxy resin. Special attention will be paid to the reasons of the overestimated values in the fracture toughness with the crack tip radius and the influence of blunting will be analyzed using an elastic model modified for blunt cracks [12].

2. Theoretical background

Kinloch and Williams [13] showed that in brittle polymers such as epoxy resins, the localized plastic deformation that occurs at the crack tip prior to crack propagation is a controlling factor and thus emphasising the role of crack tip blunting at the instant of fracture. A model based on the elastic solution for the stresses around the tip of an elliptical hole when subjected to a remote tension, σ, normal to the semi-major axis, a, is used to analyze the fracture toughness of specimens with blunt cracks [12]. During loading a specimen with an initial crack tip radius, R_0, the plastic deformation occurring at the crack tip front with length r_C and stress σ_C induces further crack tip blunting resulting in an increase in the crack tip radius, R_C (Figure 1).

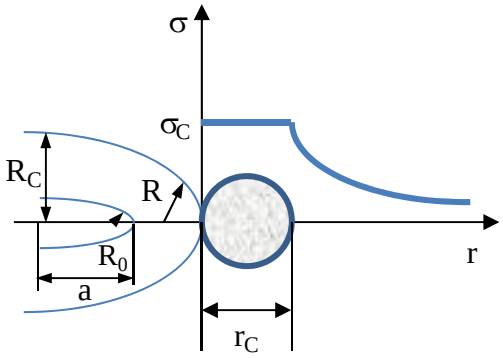

Figure 1. Crack tip front at the instant of fracture of specimens with blunt cracks

The stress σ_C at a distance r_C from the notch tip may be written in terms of the tip radius at the instant of fracture, R, and the remote applied tension σ as [14]:

$$\frac{\sigma_C}{\sigma} = \frac{2\sqrt{a}\left(R + r_C\right)}{\left(R + 2r_C\right)^{3/2}} \tag{1}$$

For a perfectly sharp crack, R=0, we have:

$$\frac{\sigma_C}{\sigma} = \sqrt{\frac{a}{2r_C}} \tag{2}$$

and thus, the fracture toughness of a sharp crack, K_{IC}, can be expressed as a function of either the remote applied tension σ and the crack length a or the near field tension at the crack tip σ_C and length factor at the crack front through:

$$K_{IC} = \sigma\sqrt{\pi a} = \sigma_C\sqrt{2\pi r_C} \tag{3}$$

For blunt cracks, the high level of stress developed at the crack tip implies the use of an apparent fracture toughness, K_b, that is, the fracture toughness of an equivalent sharp crack specimen with a stress distribution at the instant of fracture identical to that of a specimen with a blunt crack. This apparent fracture toughness, K_b, is related to the fracture toughness of the material, K_{IC}, via:

$$\frac{K_b}{K_{IC}} = \frac{\left(1+\frac{R}{2r_C}\right)^{3/2}}{\left(1+\frac{R}{r_C}\right)} \tag{4}$$

Since we are using the elastic field, the contained yielding may be modelled using a line zone with a stress identical to the yield stress, σ_Y, giving a crack opening displacement, δ:

$$\delta = \frac{K_b^2}{E\sigma_Y} \tag{5}$$

For a crack of original radius R_0, the plastic deformation characterized by δ will further blunt the tip and assuming smooth blunting, then:

$$R = R_0 + R_C = R_0 + \frac{\delta}{2} \tag{6}$$

So, the increase in the crack tip radius at the instant of fracture is equal to half the crack opening displacement. On the other hand, the crack tip radius at the instant of fracture, R, can be also expressed as function of the R_0 and R_C through the expression:

$$\sqrt{\frac{R}{r_C}} = \sqrt{\frac{R_0}{r_C}} + \sqrt{\frac{R_C}{r_C}}\left(\frac{K_b}{K_{IC}}\right) \tag{7}$$

Thus, the fracture for blunt cracks is going to be defined in terms of σ_C and r_C, which is also compatible for sharp cracks. For blunt cracks, it is the comparison of R and the length factor r_C which determines the influence of the crack tip radius.

The apparent fracture toughness, K_b, can be obtained from the experimental fracture toughness values, K_I, through the equation:

$$K_b = \frac{2}{\pi}\hat{K}\left[\ln\left(\sec\left(\frac{\pi}{2}\frac{K_I}{\hat{K}}\right)\right)^2\right]^{1/2} \tag{8}$$

where $\hat{K}$ is the plastic fracture toughness, that is, a plastic collapse condition of the uncracked specimen ligament (the width effect [13]) is to be taken into account as the stress level at failure increases with the initial crack tip radius, R_0. $\hat{K}$ has been calculated following the guidelines

given in [12].

Finally, combining equations (4) and (7), we have

$$K_I \approx K_{IC}\left[\frac{1}{2\left(1-\sqrt{\frac{R_C}{8r_C}}\right)}+\frac{\frac{R_0}{8r_C}}{\left(1-\sqrt{\frac{R_C}{8r_C}}\right)^2}\right]^{1/2} \quad (9)$$

For $\frac{R_0}{8r_C}$ too many greater than one, equation (9) reduces to:

$$K_I \to K_{IC}\sqrt{\frac{R_0}{8r_C}} \quad (10)$$

Replacing K_{IC} by the equation (3), equation (10) may be written by

$$K_I \to \sigma_C \frac{\sqrt{\pi}}{2}\sqrt{R_0} \quad (11)$$

From this analysis, it is suggested that K_I will be larger, i.e. ductile behaviour, and the criterion for this condition can be written as

$$\frac{\pi}{8}\frac{\sigma_C^2}{E\sigma_Y}=1 \quad (12)$$

where E is the Young´s modulus of the material.

3. Experimental procedure

The material under study was a commercial diglycidyl ether of bisphenol A (DGEBA) epoxy resin with a Young´s modulus of 2.65 GPa and a yield stress of 85 MPa. The chosen configuration for the fracture toughness tests was the Single Edge Notch Bend specimen (SENB) with overall dimensions of 6x12x54 mm^3. The initial crack length after sharpening to width ratio was 0.5.

All the fracture specimens presented an initial V-machined notch. Different notches were introduced in the materials which can be mainly divided into two groups: samples with sharp cracks and those with blunt notches. The sharp cracks were obtained by two procedures: the traditional contact technique for brittle polymers as tapping and a non-contact technique as the use of a femtosecond pulsed laser ablation or femtolaser. For the contact procedure, a light hammer was used to tap a razor blade placed into the root of the machined notch till a natural crack was attained. The natural crack was inserted with the razor blade at room temperature and frozen at liquid nitrogen temperature. In case of the non-contact technique, the sharpening of the notch was produced through a Femtolaser [5-6], using a commercial Ti:sapphire oscillator (Tsunami, Spectra Physics) plus a regenerative amplifier system (Spitfire, Spectra Physics) based on chirped pulse amplification (CPA) technique. For the epoxy, 120-fs pulses at 395 nm with a repetition rate of 1

kHz were utilized. The scanning speed was 130 μm/s and 4 passes were carried out with pulse energy of 0.008 mJ. The sharp length inserted by the femtolaser was of 500 μm.

For the blunt notched samples, different techniques were used to achieve different crack tip radii which can be divided into three groups depending on the dimensions. To introduce notches with 0.01, 0.02, 0.05, 0.07 and 0.1 mm in diameter, razor blades produced at the Imperial College with different crack tip radii were employed. The razor blade was slid gently across the root of the notch trying to remove the material without pressing.

To introduce notches bigger in size, that is, with diameters of 0.4, 0.6, 0.8, 1, 1.5, 2, 2.5 and 3 mm, a drilling technique was employed using drills with different radii mounted on a high speed drilling machine.

Finally specimens with up to 4 and 7 mm in notch diameters were analyzed and for the insertion of such huge notches a milling machine was used.

Prior to testing, the surfaces of every single specimen were analyzed via optical microscopes and scanning electron microscopy to check the crack tip front and measure the crack tip radius. The samples which presented any type of damage in form of microcracks or areas with different colour or texture were discarded.

The tests were carried out in an electromechanical testing machine (Instron 3365) at room temperature under displacement control at a cross-head rate of 10 mm/min. A three point bending fixture was used with a loading span four times de width. A load cell of ± 1 kN and an extensometer were used to measure the load and load displacement line, respectively. The methodology employed to obtain the fracture toughness and the energy release rate was the ESIS TC4 protocol entitled "K_C and G_C at slow speeds for polymers" [7].

After the tests, the morphology of the fracture surfaces was inspected via optical microscopes.

4. Results and discussion

4.1. Experimental results

Figure 2 shows the experimental fracture toughness values, K_I, as a function of the initial crack tip radius, R_0. As expected, the fracture toughness increases with the notch tip radius. The fracture toughness of the specimens with a natural crack obtained by tapping presented the lowest fracture toughness values, ~0.5 MPa·$m^{1/2}$, and of course the smallest crack tip radii, of 0.2 μm. It is worth mentioning that a small increase in the crack tip radius implies a huge increase in the fracture toughness. For example, even the specimens with sharp cracks sharpened via femtolaser presented values of the fracture toughness almost twice the value obtained from specimens with a natural crack, as the crack tip radius of the former was 0.8 μm, four times bigger.

The rapid increase of the fracture toughness with the crack tip radius is due to blunting as the fractographic analysis reveals. There is a marked change in the morphology of the fracture surfaces as the crack tip radius increases. Figure 3 shows a characteristic fracture surface of a specimen with a sharp crack. As shown, the fracture surface is plain and smooth without any remarkable characteristic.

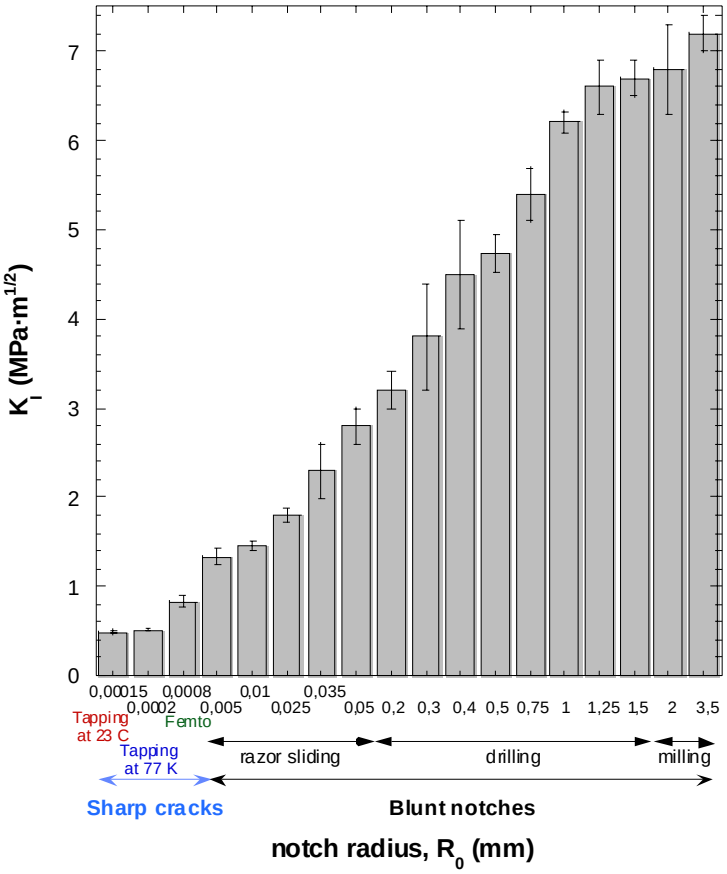

Figure 2. Experimental fracture toughness, K_I, versus the original initial crack tip radius, R_0.

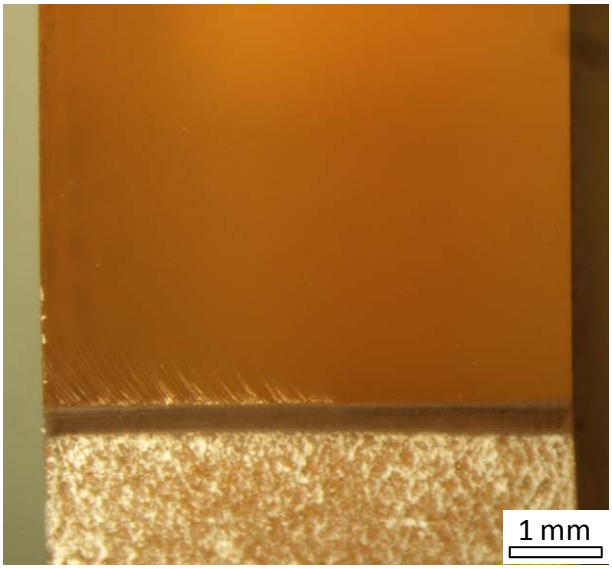

Figure 3. Characteristic fracture surface of a specimen with a sharp crack (specimen sharpened using a femtolaser)

On the other hand, Figure 4 displays the characteristic morphology of the fracture surface of a specimen with a blunt crack introduced via razor sliding. The surface is mainly plain and smooth as in the case of specimens with sharp cracks but some river markings appear close to the notch and become larger and more accentuated as the notch radius is higher.

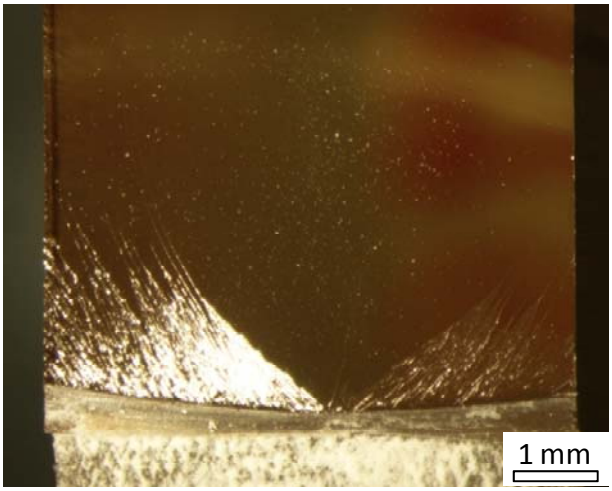

Figure 4. Characteristic fracture surface with a blunt notch introduced via razor sliding (initial crack tip radius of 25 μm)

The morphology of the fracture surfaces of the specimens with blunt notches inserted via drilling or milling changes drastically (Figure 5). The river markings are not longer limited to a tiny area close to the notch but they are spread all over the surface and the roughness is increased with the crack tip radius. Looking more closely to the surface, there is a more or less rounded region from where the unstable crack propagation seems to emerge. This type of morphology is caused by blunting.

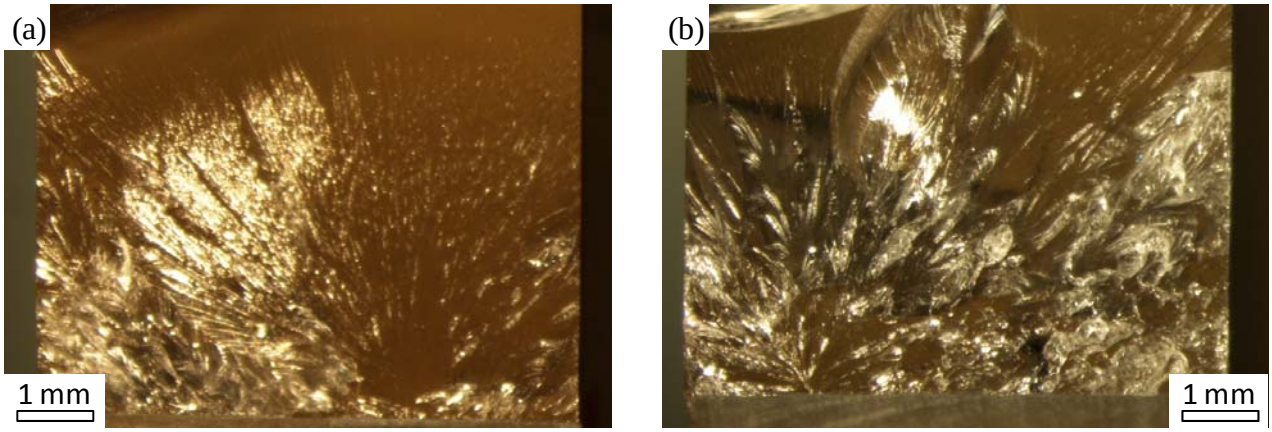

Figure 5. Fracture surfaces of the specimens with blunt notches inserted via (a) drilling (initial crack tip radius of 300 μm) and (b) milling (initial crack tip radius of 1.5 mm)

4.2. Modelling

The model described in the theoretical background was applied to the experimental data presented here to find out the role of blunting on the high values of the fracture values with the increase in the crack tip radius through the parameters σ_C and r_C. Figure 6 shows the apparent fracture toughness, K_b, against the square root of the initial crack tip radius, $\sqrt{R_0}$. Each colour groups the fracture values of specimens with notches introduced via a specific notching technique. In general and independently of the notching procedure, the true fracture toughness increases monotonically with the crack tip radius although some slightly deviations are to be pointed out. First of all, the values obtained from specimens with blunt notches introduced by razor sliding slightly divert from the general trend. These values are higher than expected and the microscopic analysis of the virgin specimens reveals the reason (Figure 7). There is a tiny region ahead of the crack tip with different texture corresponding to some damage caused during the notching process (outlined with a red dotted line). Secondly, from $K_b \approx 7$ MPa·m$^{1/2}$, the increase in the true fracture toughness with the

crack tip radius is not so marked and it seems that from there on the values are tending to a horizontal asymptote.

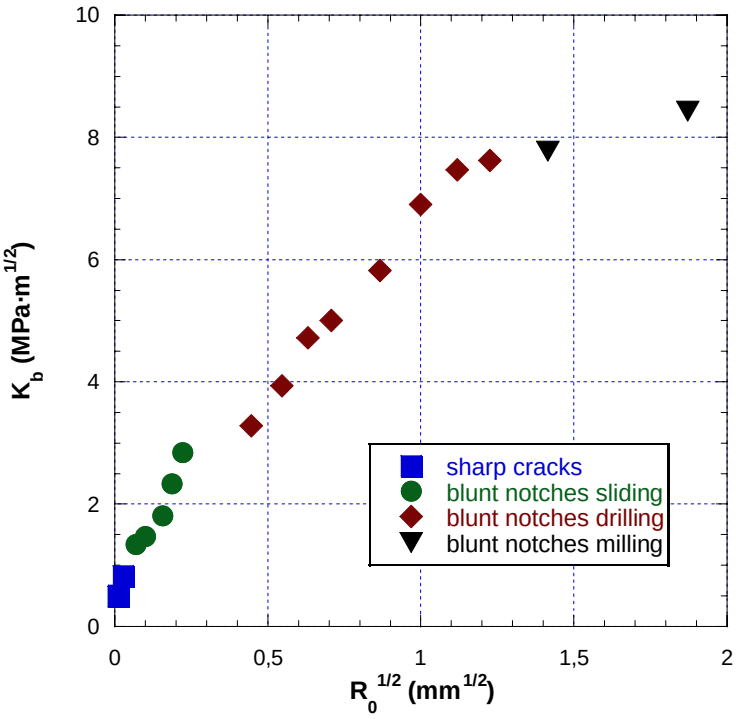

Figure 6. Apparent fracture toughness as a function of the initial crack tip radius

Figure 7. Crack tip front of a specimen with a notch introduced via razor sliding where some damage can be observed ahead of the crack front (initial crack tip radius of 35 µm)

Figure 8 shows K_b vs $R_0^{1/2}$ together with the fitting to equation (9) and table 1 gives the parameters of the model. The fracture toughness resulting from the fitting of the data to equation (9) gives a value of 0.89 MPa·m$^{1/2}$, which is higher than the experimental fracture toughness obtained from specimens with sharp cracks (0.49-0.83) MPa·m$^{1/2}$ but lower than the fracture toughness obtained from samples with blunt notches introduced via razor sliding (1.34-2.80) MPa·m$^{1/2}$ (Figure 2).

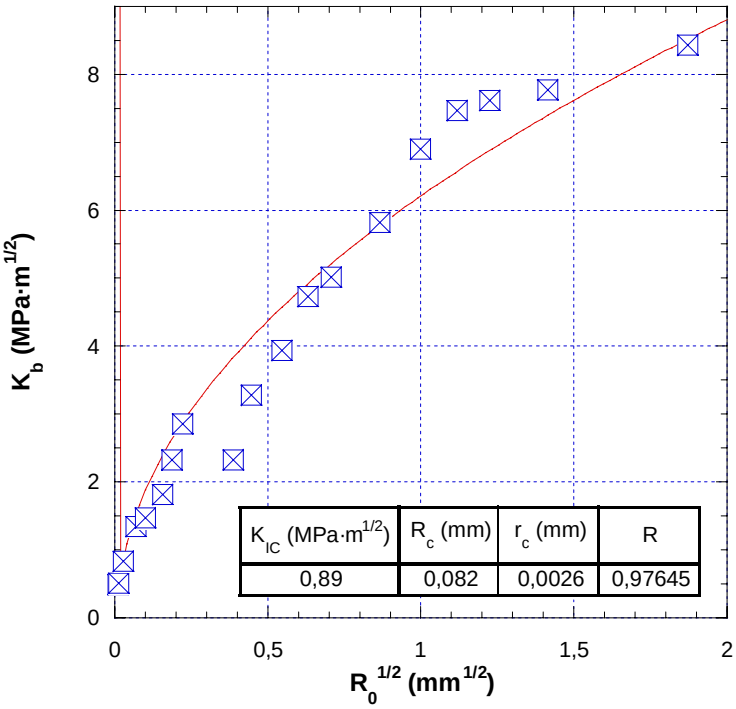

Figure 8. True fracture toughness versus the initial crack tip radius. Line is fitted from equation (9).

Concerning the parameters related to the fracture process, r_C and σ_C describe the critical length and the cohesive stress, respectively. The values of r_C= 2.6 μm and σ_C= 220 MPa are comparable to those found in the literature for similar epoxy resins [13]. It is interesting to note that the value of the plastic condition given by the equation (12) is far away from the unity, so the degree of ductility is relatively small. Finally, the value of the increase in the crack tip radius at the instant of fracture due to blunting, R_C, is 74 μm.

Table 1. Parameters of the model resulting from the data fitting to equation (9)

K_{IC} (MPa·m$^{1/2}$)	R_C (μm)	r_C (μm)	σ_C (MPa)	$\frac{\sigma_C}{\sigma_Y}$	$\frac{\pi}{8}\frac{\sigma_C^2}{E\sigma_Y}$
0.89	82	2.6	220	2.6	0.08

5. Conclusions

This work analyzes the influence of the crack tip radius on the fracture toughness on a brittle polymer such an epoxy resin. Different sharpening techniques were employed to attain different crack tip radii. To introduce sharp cracks, the traditional contact technique such as tapping a razor blade placed into the root of a machined notch and the more sophisticated non-contact procedure as the used of the femtosecond pulsed laser ablation were used. For the blunt notches, the procedures of razor sliding, drilling and milling were utilized to get different crack tip radii. The lowest values of the fracture toughness were obtained for the specimens with sharp cracks, in particular for those with cracks inserted via tapping. The fracture toughness increased rapidly with crack tip radius and the microscopic analysis of the fracture surface indicated that blunting was the reason of the steady increase.

A model based on the line zone model was applied to the experimental data to achieve a useful insight into the crack tip sharpness effects. The parameters obtained from the model denote that the

degree of ductility reached during the fracture process is not large and the plastic length and stresses developed in the crack tip front before the unstable crack propagation are comparable to the critical length and cohesive stress.

Acknowledgements

Authors are indebted to Ministerio de Educación of Spain for their financial support through projects MAT2009-14294 and MAT2012-37762 and to the University Rey Juan Carlos and Fundación Caja Madrid for the research grant of Alicia Salazar.

References

[1] A. Salazar, J. Rodríguez, A. Segovia, A.B. Martínez, Influence of the notch sharpening technique on the fracture toughness of bulk ethylene-propylene block copolymers, Polym Test, 29 (2010) 49-59.

[2] A. Salazar, A. Segovia, A.B. Martínez, J. Rodríguez, The role of notching damage on the fracture parameters of ethylene-propylene block copolymers, Polym Test, 29 (2010) 824-831.

[3] A. Salazar, J. Rodríguez, A. Segovia, A.B. Martínez, Relevance of the femtolaser notch sharpening to the fracture of ethylene-propylene block copolymers. Eur Polym J, 46 (2010) 1896-1907.

[4] A. Salazar, J. Rodríguez, A.B. Martínez, The role of notch sharpening on the J-fracture toughness of thermoplastic polymers. Eng Frac Mech, http://dx.doi.org/10.1016/j.engfracmech.2012.07.006

[5] B.N. Chichkov, C. Momma, S. Nolte, F. von Alvensleben, A. Tünnermann, Femtosecond, picoseconds and nanosecond laser ablation of solids, Appl Phys A–Mater, 63 (1996) 109–115.

[6] P. Moreno, C. Méndez, A. García, I. Arias, L. Roso, Femtosecond laser ablation of carbon reinforced polymers, Appl Surf Sci, 252 (2006) 4110–4119.

[7] J.G. Williams, K_C and G_C at slow speeds for polymes, in: D.R. Moore, A. Pavan, J.G. Williams (Eds.), Fracture Mechanics Testing Methods for Polymers, Adhesives and Composites. Elsevier Science Ltd./ESIS,The Netherlands, 2001, pp. 11-24.

[8] G.E. Hale, F. Ramsteiner, J-fracture toughness of polymers at slow speed, in: D.R. Moore, A. Pavan, J.G. Williams (Eds.), Fracture Mechanics Testing Methods for Polymers, Adhesives and Composites.Elsevier Science Ltd/ESIS, The Netherlands, 2001, pp. 123-157.

[9] E. Clutton, Essential work of fracture, in: D.R. Moore, A. Pavan, J.G.Williams (Eds.), Fracture Mechanics Testing Methods for Polymers, Adhesives and Composites. Elsevier Science Ltd/ESIS, The Netherlands, 2001, pp. 177-195.

[10] ASTM D5045-99, 1999. Standard Test Methods for Plane-Strain Fracture Toughness and Strain Energy Release Rate of Plastic Materials.

[11] ASTM D6068-96, 2002. Standard Test Method for Determining J-R Curves of Plastics.

[12] S. Hashemi, J.G. Williams, Crack sharpness effects in fracture testing of polymers. J Mater Sci, 20 (1985) 922-928.

[13] A.J. Kinloch, J.G. Williams, Crack blunting mechanisms in polymers, J Mater Sci, 15 (1980) 987-996.

[14] S. Hashemi, J.G. Williams, Size and load mode effects in fracture toughness testing of polymers. J Mater Sci, 19 (1984) 3746-3759.

Trouser tear tests of two thin polymer films

Eskil Andreasson[1,2,*], Nasir Mehmood[2], Sharon Kao-Walter[2,3]

[1] Tetra Pak Packaging Solutions, SE 221 86, Lund, Sweden
[2] Dept. of Mech. Eng. School of Eng., Blekinge Institute of Technology, SE 371 79, Karlskrona, Sweden
[3] Faculty of Mech. & El. Eng., Shanghai Second Polytechnic University, 201209, Shanghai, China

* Corresponding author: eskil.andreasson@tetrapak.com

Abstract Trouser tear testing has been concerned in this research work. A polypropylene film and a low density polyethylene film used in the packaging industry are considered. The experimental trouser tear tests showed different results for both materials when they were subjected to load in different material directions. Therefore the hypothesis was verified, that the in-plane material orientation/alignment induced during manufacturing, hence creating anisotropic in-plane mechanical properties, also affects the tearing behavior. A brittle-like failure was shown in the polypropylene film while the low density polyethylene presented a highly ductile behavior. The two polymer films can be classified as one low-extensible and one high-extensible material according to the test method utilized. Material parameters in the principal material directions i.e. manufacturing direction and cross direction were extracted from the experimental tests for further numerical studies. Scanning electron microscope was used for micromechanical and fractographical analysis of the crack tip and crack surfaces created during the tests. The methods discussed will help classify different groups of materials and can be used as a predictive tool for the crack initiation and crack propagation path in packaging material, especially thin polymer films.

Keywords Anisotropic, thin polymer film, crack propagation, fracture mechanics, SEM

1. Introduction

Polymer films are extensively used in food packaging industry due to their beneficial mechanical properties, i.e. the combination of stiffness, strength and ductility. During transportation, handling and usage of packages, polymer films are exerted to different loading conditions. Polymers and rubber-like materials have previously been extensively studied experimentally in various fracture modes [1-3]. For the case of tearing, the experimental and theoretical analysis has been performed in [4-8]. This work will focus and extend the analysis on the experimental trouser tear tests in three different material directions for two types of polymer films used in packaging industry.

Fracture properties related to the specific material parameters such as critical fracture toughness, energy release rate, fracture energy and crack propagation resistance can be determined using a fracture mechanical test method. In brittle material this procedure is well known but for ductile material it is less developed. The two important fracture modes involved in the trouser tear test, mode I – in-plane opening mode and mode III – anti-plane shearing mode together with the mixed mode - trouser tear test are depicted in Fig. 1.

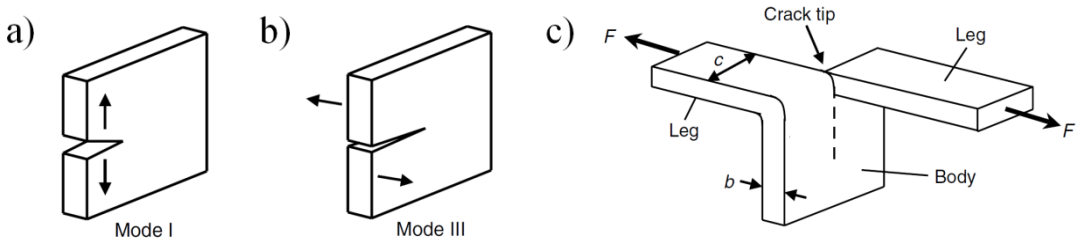

Figure 1. Three loading modes of cracked specimens: a) mode I b) mode III and c) mixed mode trouser tear test [9]

2. Materials

Two types of polymer films with different mechanical behavior were tested and analyzed in this work. One oriented polypropylene (PP) film and one low density polyethylene (LDPE) film were experimentally tested. The mechanical in-plane material properties for these two thin packaging materials have thoroughly been examined in previous works with slightly different scopes and interests [6-7,10-13]. In-plane elastic anisotropic material behavior is shown in the PP film according to (Table 1). To be able to distinguish the principal material directions a naming convention is used i.e. manufacturing direction (MD), cross direction (CD), and 45 degrees to the manufacturing direction (45). These abbreviations are further on used to indicate in which direction the load has been applied. In-plane material properties for the PP and LDPE are presented in (Table 1). In-plane material properties primarily dominate the mechanical behavior in the two polymer films studied. This is due to the thin thickness of the polymer films, hence plane stress assumption is valid. Therefore, out of plane properties are disregarded in this work.

Table 1. In-plane mechanical material properties for thin polymer films [10], [13]

Material	Thickness [μm]	Material orientation [-]	Young's modulus [MPa]	Yield strength [MPa]	Poisson's ratio [–]
PP	18	CD	5100	29	0.43
		MD	2200	28	0.25
		45	2800	28	0.30
LDPE	27	CD	140	5.1	0.4
		MD	140	5.1	0.4
		45	140	5.1	0.4

Manufacturing of polymer films involves several processing steps. During these different steps, polymer chains are aligned or enforced to orient in the manufacturing/rolling direction (MD) or stretching direction (MD or CD). The degree of orientation in the polymer chains vary in different polymer types and mixture of polymers. Temperature, thickness, chemical structure, polymer chain lengths, number of cross-links, entanglements and rate of crystallinity are all parameters affecting the final mechanical properties in the material. Anisotropy, different mechanical behavior in different directions, is therefore most often the case for many polymers. Due to anisotropy, polymer films tend to follow different preferred crack directions and find the lowest resistance path for crack propagation. Initial direction of crack extension depends of loading scheme and type of material. Brittle materials, as PP in this study, usually fracture by mode III defined in Fig. 1. Ductile materials, as LDPE in this study, usually fracture by mode I and mode III defined in Fig. 1 when exerted to a trouser tear test. If a crack is introduced into a specimen, such as in the trouser tear test, the stress distribution is no longer constant and homogenous within the material. The stress will vary and this variation is due to size and shape of crack and geometry of specimen. In fact, the geometry and the type of loading also have a significant influence on the crack propagation behavior. In brittle materials the process zone will be very local and in the vicinity of the crack tip, all the energy dissipates and new crack surfaces are created. On the other hand in a ductile material where a lot of plastic deformation occurs the process zone and active zone is a rather large area surrounding the crack tip. In this case a lot of energy is consumed in the plastic flow and for the trouser tear test in substantial leg deformation.

3. Experimental Procedure

Preparation and cutting of specimens were performed after pre-conditioning of the materials at 23°C and 50% RH for 40 hours prior to test in accordance with the test procedure defined in the standard ASTM D618-08 [16]. Sample cutting of the two types of polymer films were done with a sharp medical knife and it is recommended to frequently change blades. To minimize uncontrolled errors, such as edge effects, the specimens were cut in the same way every time with the same operator. Mounting and handling of the polymer film was carefully done in order to not damage the material and edges. Trouser tear test specimen geometry and dimensions are shown in Fig. 2. When the specimen is mounted in the tensile test equipment it looks like a pair of trousers, which explains the name of the test method. The 'legs' of the trouser specimen are then pulled in opposite directions to create tearing action. One of the grips in the tensile test machine, holding the specimen, is fixed and the other one is moved at a constant rate (10mm/min) during the test. Specimen extension is measured by grip separation. The test method utilized in this work, the American standard ASTM 1938-08 [15], was used for calculation of the tear resistance and is similar to the European standard ISO 6383-1:1983 [17]. These two methods calculate the force necessary to propagate a crack in a trouser tear test in plastic/polymer films with a thickness less than 250 μm. Several experimental tests, minimum five for each material direction, were performed for each test setup to characterize the mechanical behavior of each material and for different material orientations.

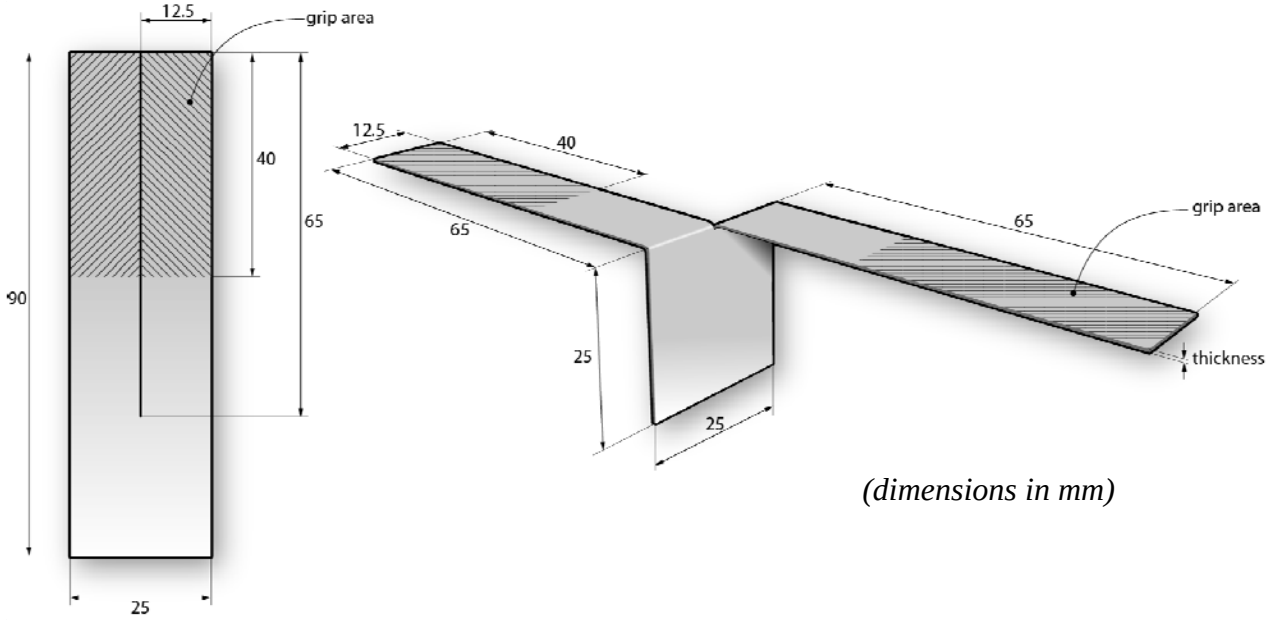

Figure 2. Trouser tear test specimen geometry, illustration by Carl Nordenskjöld

According to Fig. 2 a pre-made crack is introduced in each specimen before mounting in the experimental equipment. During the test, when the legs are separated and thus extended, the pre-made crack will continue to grow. In the figure the grip area is marked (hatched) and the one-color area is the material subjected to load, where the tearing action takes place. PP is brittle and sensitive to stress and to avoid crack initiation prior to the test a small slack (2 mm) was introduced when mounting. The registered forces in the experimental tests are low and therefore it is important that the grippers are rigid and unable to move during the tests. Even a small vibration can cause significant deviation in results and this external noise has to be controlled and minimized. Hence the gripping equipment was adjusted to be ultimately stiff to prohibit any movement of the clamps in the other directions than the stretching direction.

4. Experimental trouser tear testing results

In the test method, ASTM D1938-08, [15] two different types of behavior is classified; in this study PP is a low extensible or non-extensible film and LDPE is a highly extensible film. The generic response graphs from trouser tear tests, for the two different classes of materials are displayed in Fig. 3. Low extensible films, i.e. PP, exhibit a constant load during trouser testing. For highly extensible films, i.e. LDPE, the deformation energy of the specimen legs is significantly higher than the tearing energy. Tearing of highly extensible films is accompanied by significant plastic deformation.

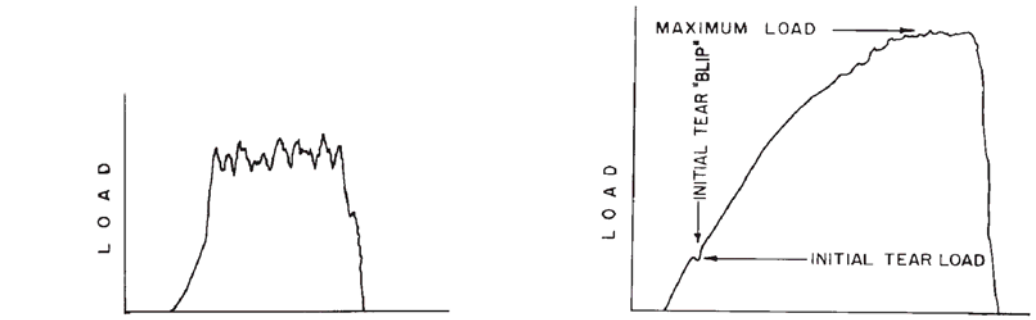

Figure 3. Load vs. time for trouser tear tests in a) low-extensible and b) highly-extensible polymer film, [15]

The force needed to propagate the pre-made crack in a polymer film specimen was experimentally measured in the laboratory at Tetra Pak in Lund. The utilized test method can be used for rating the tear propagation resistance of various plastic/polymer films of comparable thickness. Force and extension were recorded during loading and tearing of the specimens. The results are shown in Fig.4 for PP and in Fig.5 for LDPE. Five different specimens for each direction were studied to get an idea of mechanical behavior and statistical variation in the two types of polymer films. The force registered in the PP-film, as shown in Fig. 4, was low (note the unit mN on the y-axis). There was a significant difference of registered force in all the three material directions.

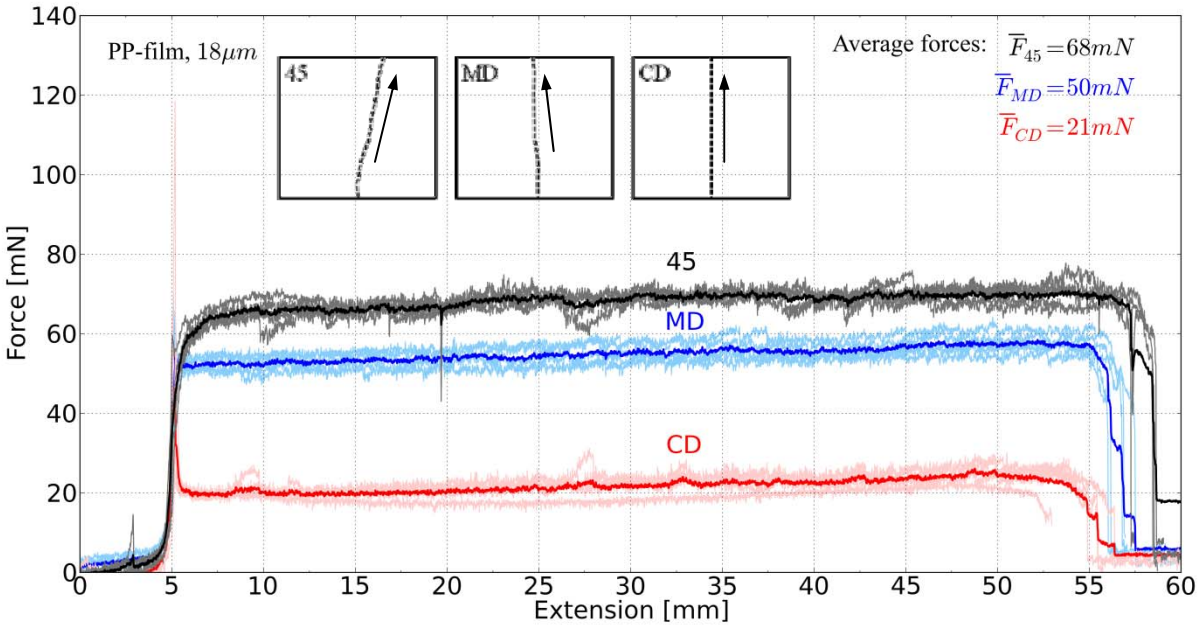

Figure 4. Trouser tear test in material direction 45°, MD and CD for PP-film, force vs. extension. Bold lines represent mean curves for each material direction.

For PP it is possible to clearly distinguish the three different material orientations as shown in Fig. 4. A noticeable high peak is shown in the PP-CD samples which probably indicates the breakage of chemical bonds in-between the polymer chains or the crystallites. The force is significantly higher than the average force for the continuous crack propagation when the material has found the lowest energy crack path direction. Lowest tearing resistance path for PP-45 is along the material alignment in CD, therefore the crack path is not orthogonal to the stretching direction. This means that the highest force is registered in these specimens. The experimental trouser tear test results for PP is depicted in Appendix A at different loading stages. In Appendix A is the three different crack propagation paths noticeable as depicted above in Fig. 4. It is important to note that the small fluctuations in the force values during tearing, present in all PP-graphs in Fig. 4, are not noise from the experimental equipment but rather due to the "stick-slip" behavior observed during fracture in many polymers [8]. The frequency and amplitude of these small fluctuations most probably relates to the morphology and micro mechanism of the polymer material, such as the polymer chain alignment, arrangement of crystallites, and distribution of crystalline and amorphous phases. However, systematic micro structural and fractographical characterization is needed to fully understand the "stick-slip" behavior. The LDPE-specimens don't show these small fluctuations in the force values during tests as shown in Fig. 5. The experimental trouser tear test results for LDPE is depicted in Appendix B at different loading stages.

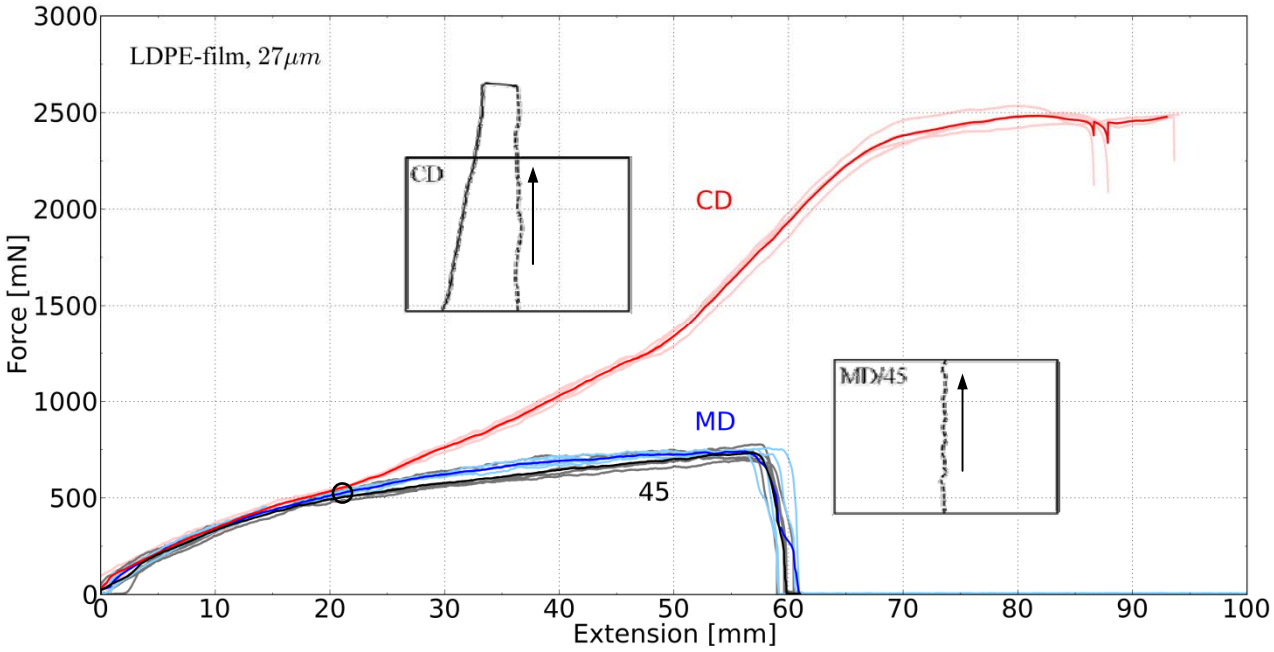

Figure 5. Trouser tear test in material direction CD, MD and 45° for LDPE-film.
Bold lines represent mean curves for each material direction.

For LDPE the total extension of the trouser test is 90 mm in CD and 60 mm in MD and 45. The total extension from tearing is only 50 mm, hence a significant part of the LDPE extension is elongation of the two legs. The un-bundled polymer chains, with the majority oriented in MD, enable a significant stretching in CD. Therefore a lot of energy is dissipated in material rearrangement, plastic work, elongation of the legs and heat generation. However, the initial part, until the circle shown in Fig. 5, similar behavior is presented in all three material directions CD, MD and 45 in LDPE. For low extensible films such as PP on the contrary, there is no deformation of the legs and the total extension is therefore 50 mm, the same length as the minimum possible tearing distance. Test results for highly extensible films, i.e. LDPE is depicted visually in Appendix B, and for low extensible films, i.e. PP in Appendix A.

In addition to the well known fracture mechanical parameters, such as stress intensity factor and J-integral defined in [14], Rivlin and Thomas defined the critical fracture energy from a trouser tear test. This quantity is also known as tearing energy, which is the energy spent per unit thickness per unit increase in crack length. Tearing energy includes surface energy, energy dissipated in plastic flow processes, and energy dissipated irreversibly in viscoelastic processes [1]. The equations described below are derived from the trouser tear test based on theoretical analysis of crack growth behavior [5]. This can simplify the description of the tearing energy from the experimental results. The equation for calculation of tearing energy was derived with experimental test of rubber-like materials and is also applicable for polymers. The tear strength equation to calculate the critical tear energy, T_C, of a propagated crack in LDPE in this study is

$$T_C = \frac{2F\lambda}{t} - wE \tag{1}$$

F is the tear propagation force, w is the initial width of specimen, t is the thickness of specimen, E is the strain energy density. For LDPE the strain energy density can be calculated using the area under stress-strain curve from an ordinary tensile test. It was found that the strain energy for LDPE is, $E_{LDPE} = 2.8\ N/m^2$. λ is the extension ratio of the legs, current length of specimen divided by initial length, which is normally 1 except for some materials which have high extension of legs as LDPE-CD ($\lambda = 1.8$). In case where high stretching of legs is visible, then Eq. 1 will be used to calculate the critical tear energy. Strain energy density, E, becomes zero in materials with no leg extension, in this study for PP, resulting in the general equation used widely for calculation of critical tearing energy in brittle materials,

$$T_C = \frac{2F}{t} \tag{2}$$

The relationship between rate of tearing and strain energy release rate is a material characteristic that is independent of test specimen geometry, when tested low extensible materials [4]. The extension in the specimen legs is negligible and ignored for such cases. It can be confirmed from Eq. 2 that the critical tearing energy is independent of the initial sample geometry and crack length. This assumption is valid only if the specimen undergoes mode III dominated failure. Critical tear energy for the PP & LDPE is calculated using the above equation. Crack propagation for PP is a completely mode III phenomenon so its crack propagation is a complete tearing process, while LDPE has plastic flow and deformation of legs in addition to tearing which is generating a mixed mode I and mode III failure. Tearing or crack propagation force, tearing work, tearing energy & tear extension for PP and LDPE are summarized in (Table 2).

Table 2. Trouser tear test results for two thin polymer films; PP and LDPE

Material	Thickness [μm]	Material orientation [-]	Tearing Force [mN]	Critical Tearing energy [N/m]
PP	18	CD	21	2330
		MD	50	5560
		45	68	7560
LDPE	27	CD	2500	333330
		MD	750	55560
		45	750	55560

The force applied in a trouser tear test for PP and LDPE is plotted versus extension of the clamps in Fig. 6. Both loading and un-loading is presented in the graphs. Arrow 1 indicates the initial extension to start a tear, overcome the threshold value of force needed to start the pre-made crack growing, point F indicates the initial force required to start a crack (crack-initiation), arrow 2 indicates the force needed to propagate the crack which is constant for PP and increasingly non-linear for LDPE. Arrow 3 indicates the final retraction of specimen as applied force is removed. Area below arrow 1 indicates the strain energy stored in specimen before crack growth (energy required to start a crack), area below arrow 2 indicates the energy released during crack extension Arrow 3 indicates the stored energy in the legs at the end of test. The non-linear segments of the curves, prior to tearing and during unloading, correspond to stored strain energy in the legs of the specimen.

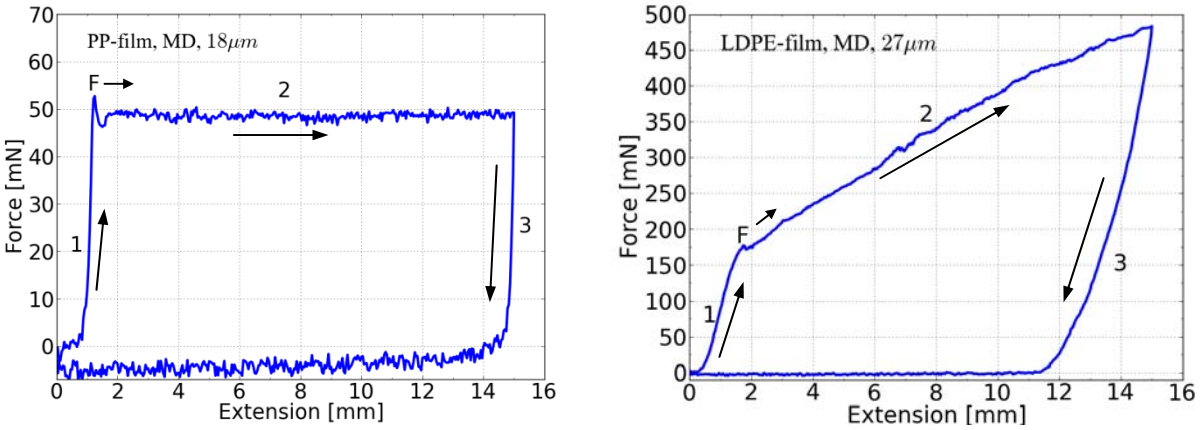

Figure 6. Trouser tear test, loading and unloading for PP and LDPE-film in MD.

From the fracture surfaces shown in Fig. 7 for PP and LDPE it is evident that the fracture mechanical behavior and processes are different in the two materials. Substantial plastic deformation is developed in the LDPE material leading to localized thinning of the cross section. PP material has no plastic deformation in the crack tip for tearing fracture. Fracture edges are presenting a wavy shaped geometry in the LDPE and representing a straight line in PP. This is an area that needs more thorough understanding and knowledge for future studies. The mechanical behavior and also the fracture mechanical behavior are strongly coupled to the manufacturing technology and process settings, what polymers that are used and also the morphology and chemical composition. This subject has to be addressed separately and finding technologies to be able to increase the knowledge and understanding of the micro mechanical behavior is important.

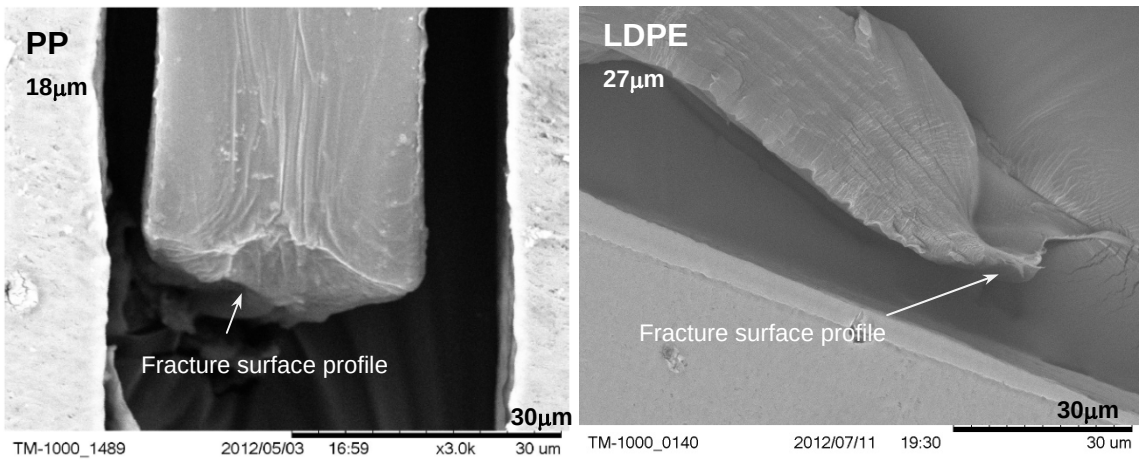

Figure 7. SEM pictures of the fracture surface profile in PP and LDPE.

5. Conclusions and discussion

Experimental trouser tear tests were performed in this research work according to the American standard ASTM 1938-08 [15]. Two polymer films with different fracture mechanisms and micro structural composition were studied, PP and LDPE. Repeatable and reproducible experimental results were obtained after adjustments of the experimental equipment. Non-compliant test equipment was used due to the low forces registered in the tests. For both materials different responses were measured in the three material directions MD, CD and 45.

Trouser tear test results for the highly extensible polymer film, LDPE in this study, show:
- Fracture is governed by a mixed mode material behavior (mode I and mode III).
- The tearing energy is directly proportional to the deformation of the plastic yielded zone at the fracture edge, hence creating increasing deformation zone with increasing force. Thus deformation and strain energy rate is continuously increasing showing higher tearing energy.
- One of the legs elongates when the crack tip exhibit both mode I and mode III failure, which is clearly shown in the case of loading in CD material direction.

Trouser tear test results for the low extensible polymer film, PP in this study, show:
- Fracture is solely governed by mode III material behavior.
- There is no pronounced yielded zone, hence all strain energy is consumed and dissipated into local plastic flow, crack tip growth, polymer chain orientation and heat generation.
- Low covalent bonding forces and voids present in the material gives a knotty or shaky tear graph. Knotty tear is due to that the crack path follows these small voids which result in small variation in forces.

It was found that, the low-extensible PP film requires only a small force to fracture, almost negligible compare to the highly-extensible film, LDPE. If the material fractures in a brittle fashion, PP in this case, the result is independent of the shape of the test specimen and the manner in which the deformation is applied. An almost constant tearing force is needed in brittle materials to propagate the crack in different material directions. In this type of material the local deformation in the surroundings of the crack tip is determining the global response. However, if the material is ductile the behavior is much more complicated. The plastic flow at the crack tip is not directly involved in the fracture process and hence the deformation doesn’t only take place locally in the vicinity of the crack tip. The test specimen size and geometry influence the result and therefore it is hard to find a material parameter governing ductile tearing. To separate the leg extension, the plastic flow and the actual tearing force is therefore challenging. It should be noticed that tearing force is also influenced to a large extent by type of polymer, temperature, material anisotropy and loading rate which has not been tested/discussed in this work. Finally, as seen in the SEM pictures, it is possible to distinguish a low-extensible and a highly extensible material by studying at the fracture surfaces in samples. In the highly extensible material the fractured surface is presenting a wave-shaped geometry. Low-extensible material shows a very sharp crack surface and hence a straight line is created during the trouser tear tests.

Acknowledgements

This research work was carried out at Tetra Pak Packaging Solutions AB in Lund, Sweden with the cooperation of the Department of Mechanical Engineering, Blekinge Institute of Technology, Karlskrona, Sweden.

References

[1] I. M. Ward, J. Sweeney, An introduction to The Mechanical Properties of Solid Polymers, 2nd edition, John Wiley & Sons, Ltd, England, ISBN 0471 49625 1, 2004
[2] Y.W. Mai, B. Cotterell, On the essential work of ductile fracture in polymers, International Journal of Fracture 32:105-125, 1986
[3] D. Gross, T. Seelig, Fracture Mechanics With an Introduction to Micromechanics, Second Edition, Germany, Springer 2011
[4] H.W. Greensmith, A.G. Thomas, Rupture of rubber III, Determination of tear properties, Journal of Polymer Science, 18(88): p. 189–200, 1955
[5] R. S. Rivlin, A. G. Thomas, Rupture of rubber. I. Characteristic energy for tearing, J. Polym. Sci. 10, 291-318, 1953
[6] S. Kao-Walter, M. Walter, A. Leon, Tearing and Delaminating of a Polymer Laminate, Key Engineering Materials, vol. 465, p169-174, 2011
[7] N. Mehmood, T. Mao, G. Bhupati, Tearing Analysis of thin polymer film materials using mode I and mode III - Physical Trouser Tear tests in combination with the virtual tests in ABAQUS, Master Thesis, Department of Mechanical Engineering, Blekinge Institute of Technology, Karlskrona, Sweden, 2012
[8] S. Basu, Determining the Critical Tearing Energy of Thin Polymer Films Using a UTM, Agilent Technologies, http://cp.literature.agilent.com/litweb/pdf/5991-0194EN.pdf, 2012
[9] K. J. Mach, D. V. Nelson, M. W. Denny, Techniques for predicting the lifetimes of wave-swept macroalgae: a primer on fracture mechanics and crack growth, The Journal of Experimental Biology 210, 2213-2230, 2007
[10] A. Jemal, R. R. Katangoori, Fracture Mechanics Applied in Thin Ductile Packaging Materials-Experiments with Simulations, Master Thesis, Department of Mechanical Engineering, Blekinge Institute of Technology, Sweden, 2011
[11] E. Andreasson, A. Jemal, R. R. Katangoori, Is it possible to open beverage packages virtually? Physical tests in combination with virtual tests in Abaqus, Proceedings of the SIMULIA Community Conference, Providence, Rhode Island, USA May, 2012.
[12] K. Majeed, U. Sharif, Fracture Toughness Analysis of Aluminum Foil and its Adhesion with LDPE for Packaging Industry, Master Thesis, Department of Mechanical Engineering, Blekinge Institute of Technology, Karlskrona, Sweden, 2012
[13] A. Dabiri, Y. Tadele, Material Modeling of Thin Isotropic and Anisotropic Polymer Films in ABAQUS, Master Thesis, The Royal Institute of Technology, Department of Mechanical Engineering, Solid Mechanics, Stockholm, Sweden, 2012
[14] T.L. Anderson, Fracture Mechanics: Fundamentals and Applications, 3rd edition, Taylor & Francis Group, CRC Press, 2005
[15] ASTM Standard D1938-08, “Standard Test Method for Tear-Propagation Resistance (Trouser Tear) of Plastic Film and Thin Sheeting by a Single-Tear Method”, ASTM International, West Conshohocken, PA, 2003, DOI: 10.1520/D1938-08, 2008
[16] ASTM Standard D618-08, “Standard Practice for Conditioning Plastics for Testing”, ASTM International, West Conshohocken, PA, 2003, DOI: 10.1520/D0618-08, www.astm.org, 2008
[17] ISO Standard 6383-1:1983, “Plastics -- Film and sheeting -- Determination of tear resistance – Part 1: Trouser tear method”, TC/SC: TC 61/SC 11, ICS: 83.140.10, www.iso.org/, 2009
[18] ASTM Standard D624-00(2012), “Standard Test Method for Tear Strength of Conventional Vulcanized Rubber and Thermoplastic Elastomers”, ASTM International, West Conshohocken, PA, 2003, DOI:10.1520/D0624-00R12, www.astm.org, 2012

Appendix A *– Polypropylene (PP) during trouser tear test,* ASTM D1938-02

a) initial trouser tearing

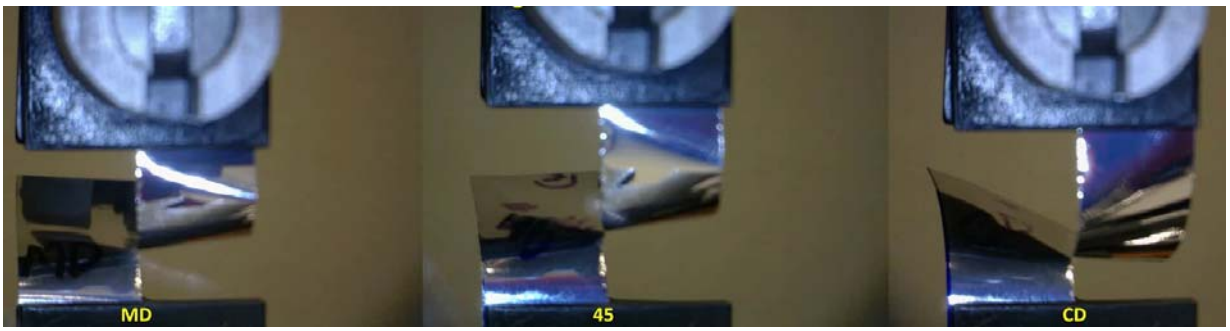

b) continuous trouser tearing

c) final trouser tearing, edge effects may come into consideration

d) finalized trouser tear test

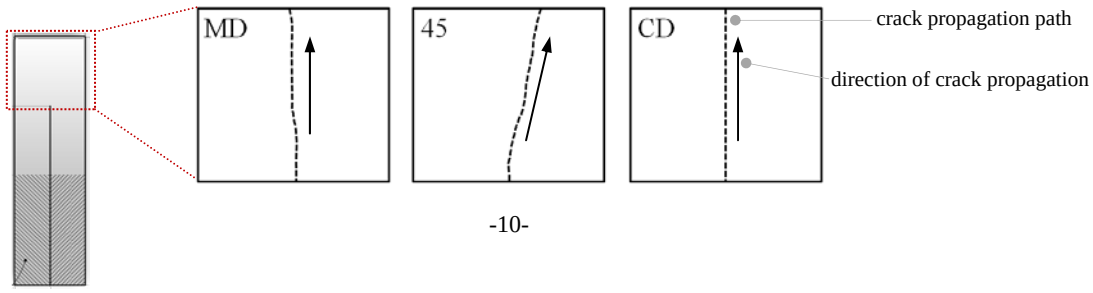

Appendix B *– Low density polyethylene (LDPE) during trouser tear test,* ASTM D1938-08

a) initial trouser tearing

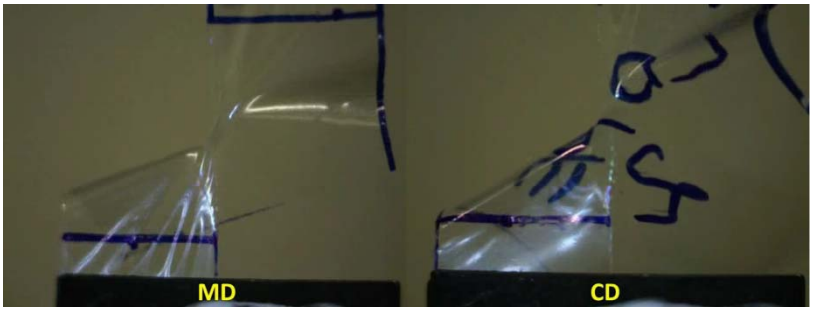

b) continuous trouser tearing

c) final trouser tearing for MD (edge effects), extension of legs in CD

d) finalized trouser tearing for MD, continued extension of legs in CD

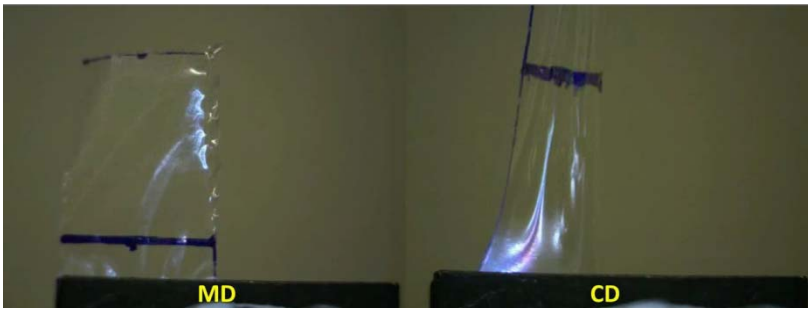

e) finalized trouser tear test for MD, continued extension of legs in CD

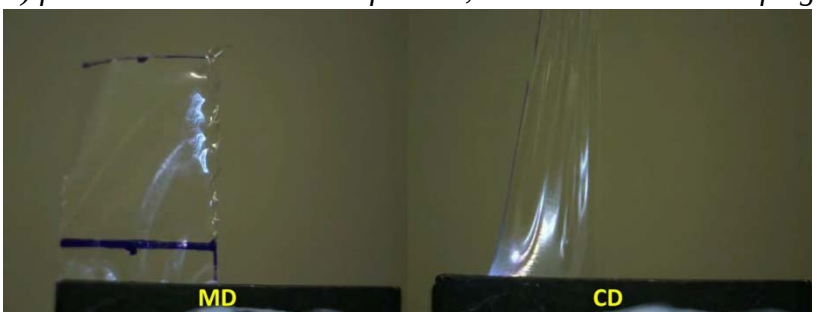

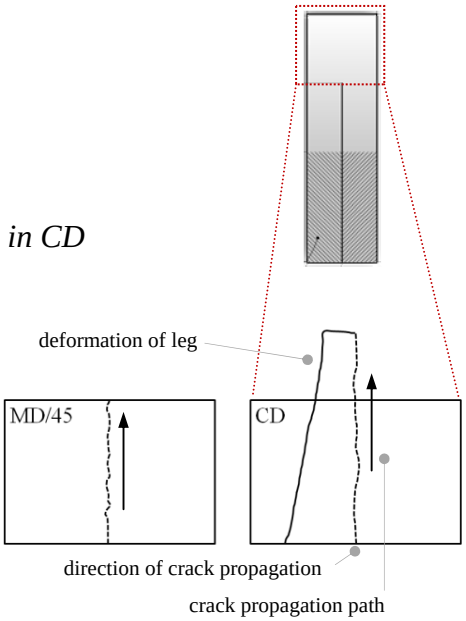

Exploring the contributions of variable network structure on rubber elasticity using model silicone elastomers

Anju R. Babu[1], Namrata Gundiah[1, 2,*]

[1]Centre for Nano Science and Engineering, [2]Department of Mechanical Engineering,

Indian Institute of Science, Bangalore 560 012.

*Corresponding author: namrata@mecheng.iisc.ernet.in

Abstract:

Poly dimethyl siloxane (PDMS) is a highly flexible inorganic polymer currently widely used in soft lithography and microfluidics applications due to its optical transparency, biocompatibility, and gas permeability in addition to the simplicity in fabrication process and ease of controlling the mechanical properties. Recent work has explored phenomenological and structure based entanglement models for a better understanding of entropic mechanisms in elastomers and to address limitations in classical rubber elasticity theory vis-à-vis the topological interaction arising due to chain crossing and their finite extensibility. To quantify the individual effects of physical entanglements and chemical crosslinking on the network structure-property relationships, we prepared two differently crosslinked PDMS elastomers and used swelling of the polymer in xylene to obtain variable microstructures. Highly crosslinked PDMS networks show isotropic swelling in xylene and high values of storage modulus as compared to PDMS obtained using low amounts of crosslinker. Uniaxial tension and biaxial experiments show that an increase in crosslinker leads to a higher modulus of the elastomers. Biaxial mechanical experiments show that the slip link model best fits our experimental data obtained using equibiaxial and nonequibiaxial tests that add constraints to the chain deformations. Dynamic mechanical analysis (DMA) studies show the dynamic variations in the chemical crosslinks and physical entanglements on the properties of the elastomer networks. Such studies relate structure-property relationships in PDMS networks that may be useful in microfluidics, mechanobiology studies to assess effects of substrate stiffness on cellular responses and biosensor applications.

Keywords Polydimethysiloxane, Swelling, Entanglement, Crosslinking

1. Introduction

Poly (dimethylsiloxane) (PDMS) is one of the most flexible known inorganic polymers and is a widely used as adhesives, dampers, and in microelectronics and biomedical devices [1]. PDMS is obtained through differential crosslinking of a base polymer to form tailored networks that can be used to produce dramatic changes the material properties of the crosslinked elastomer. Network properties are dependent on the amount of chemical crosslinking coupled with a high number of physical entanglements produced while keeping all other processing variables constant. Classical rubber elasticity models, obtained using the Gaussian description of the networks, show that the molecular weight of crosslinked polymer networks is directly proportional to the measured shear modulus. Recent investigations have focused on the individual contributions of the chemical

crosslinks and physical entanglements to the mechanical properties of elastomers using phenomenological and microstructure based models for the total strain energy [2, 3]. Of these, the Edward-Vilgis tube model, also referred to as the slip link model [4], and the Arruda-Boyce model [5] are promising models to describe mechanics of crosslinked networks.

Recent investigations in our lab show that the SL model describes the network properties of PDMS networks, crosslinked using differential amounts, to produce PDMS networks with varying network topography of individual chains. The goals of this study are to investigate the effects of varying physical entanglements on the mechanical properties of the PDMS elastomers that are hypothesized to produce a measurable difference in the material properties of the networks. We prepare PDMS elastomers by varying the crosslinking compound to produce two different network compositions and use swelling of the elastomers in xylene to alter the physical entanglements in the structure. Because swelling in solvents may cause removal of the uncrosslinked sol fraction of the polymers comprised of unreacted PDMS and star molecules [6], we use dynamic mechanical analysis (DMA) methods to distinguish between the properties of the prepared elastomers using a linear viscoelasticity framework. Further, to clearly distinguish between the entanglements and crosslinks, we use methods to swell the elastomers and assess changes in network microstructures using DMA measurements. The dynamics of the elastically active networks can be individually tested to quantify the elastic and viscous contributions to the mechanical properties of PDMS and investigate the effects of stoichiometric imbalance caused by differential chemical crosslinking and physical entanglements on the network properties.

2.Materials and Methods

Poly (dimethylsiloxane) was prepared by mixing base silicone elastomer with crosslinker (PDMS, Sylgard®184, Dow Corning) in weight ratios of 10:1 and 40: 1, represented as P10 and P40, in this study. The mixture was degassed to remove air bubbles and cured at 40 ^{0}C for 8 hours to obtain the silicone specimens for the mechanical experiments.

2.1 Swelling behavior

PDMS elastomers were completely immersed in xylene at room temperature for 24 hours and the swollen sample dimensions in the three directions were recorded using a digital camera (n=3). The images were processed to quantify three dimensional changes following swelling. Further, sample weights were obtained to characterize the swelling ratios at various time intervals. Swelling of elastomers in organic solvents is designed to produce alterations to the network conformations whose effects must be quantified using mechanical experiments. Finally, swollen specimens were air dried for 24 hours and tested to delineate differences in chemical crosslinks and physical entanglements on the measured mechanical properties.

2.2 Mechanical characterization

To characterize mechanical properties of PDMS elastomers prepared using differing crosslinking

ratios, monotonic compression and tension experiments were used. Because uniaxial experiments are insufficient to quantify the constitutive properties of elastomers, we also use planar biaxial experiments using variable stretches in two orthogonal directions to produce a wide range of deformations in parameter space. Such data, although scarce in literature, are necessary to quantify the differences in material behaviors and obtain a suitable strain energy function to describe the material. Finally, we use dynamic mechanical analysis (DMA) experiments to quantify changes in specimen microstructure caused due to swelling in xylene.

Uniaxial and biaxial tensile mechanical tests were performed using a custom planar biaxial instrument (Bangalore Integrated System Solutions (P) Ltd, India) details of which are published elsewhere [7]. Dumbbell (ASTM D412–06) shaped samples of P10 and P40 were cut from prepared PDMS sheets using a punching machine with die for uniaxial mechanical experiments. Specimens were clamped between two stretcher arms, preloaded to 20 gram force, and stretched uniaxially under force control (5 gm/sec). Marker points, placed 14 mm apart in the gauge region, were imaged using a video extensometry system, their displacements measured using centroid tracking with a custom MATLAB (v7.8.0.347 (R2009a)) programs which were finally used to quantify strains in the sample. Stretch (λ) at any point of elongation was calculated using a direct method obtained as a ratio of change in length during deformation to the original length. Loads in the specimen during deformation were continuously recorded and converted to engineering stresses using the cross sectional dimensions following prior to the experiment. Young's modulus was calculated using the linear portion of the stress-strain plot which corresponded to about 10% stretch. Biaxial and nonequibiaxial experiments were performed on flat P10 and P40 sample of dimensions 40 mm x 40 mm with thickness ranging from 1-1.6 mm. In this protocol, the elastomer sample was preloaded to 20 grams and stretched in the two orthogonal directions in various load ratios of 4.3:1.7, 3.3:5, 1:2, 2.3:3.3 and 1:1 at a rate of 2 gram/sec.

Monotonic compression test was done using Zwick/RoellZ005 Universal Testing Machine, GmbH Germany. Cylindrical samples (n=3) of PDMS of length 13 mm and diameter 30 mm were prepared and the specimens were compressed at a rate of 0.5 mm/sec, following a preload of 20 gm.

DMA experiments were carried out using P10 and P40 PDMS samples (n=3) of dimensions 40 mm length, 10 mm width and 4-5 mm thickness prepared using the two crosslinking ratios as described earlier. A Bose Electroforce® 3200 instrument (Bose Corp. USA) was used to preload PDMS samples to 0.1 N load followed by sinusoidal cyclic displacement of amplitude 1.5mm over a frequency range from 0.5 to 80 Hz. Discrete Fourier transforms of the analog force and displacement traces were calculated using custom MATLAB programs and the phase difference between these traces, δ, were used to compute the storage (E'), loss moduli (E'') and loss tangent ($\tan\delta$) defined as

$$E' = \mathrm{E}\cos\delta,\ E'' = \mathrm{E}\sin\delta,\ \tan\delta = \frac{E'}{E''} \tag{1}$$

where E is Youngs modulus.

3. Results and discussion

3.1. Effects of swelling on PDMS samples

Weight ratio of swollen PDMS samples, calculated as

$$\%\ Swelling\ Ratio = \frac{W_s - W_u}{W_u} * 100 \quad (2)$$

W_u and W_s in equation (2) are the weights of unswollen and swollen sample respectively. Swelling ratio for P40 and P10 are plotted for various time intervals (Figure 1). These results clearly show that swelling ratio for P40 specimens is significantly higher than that for P10 group at each time interval. Further, specimens from both groups reach equilibrium swelling by 24 hours. Specimens swollen in xylene for 4 and 24 hours were air dried for one day to remove residual xylene and obtain an altered polymer microstructure produced by changes to the physical entanglements in the polymer networks.

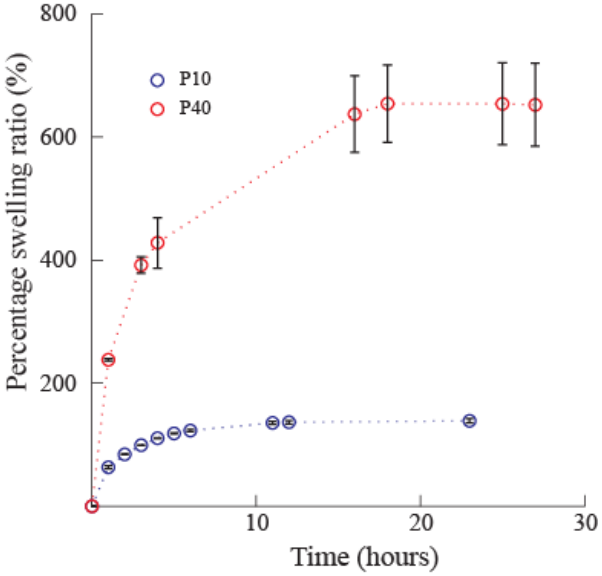

Figure 1. Variations in swelling ratio of P10 and P40 specimens swollen in xylene over a 28 hour period. At each time interval, P40 samples have a higher swelling ratio as compared to P10 specimens.

Table 2 shows corresponding changes in specimen length, width, and thickness following swelling in xylene for 4 hours calculated based on initial sample dimensions before swelling.

	Length (%)	Width (%)	Thickness (%)	
			Before drying	After 24 drying
P10	34.27± 6.02	33.70± 8.88	49.56±12.74	-0.84±0.85
P40	71.62±3.36	63.55±8.61	75.71±2.81	-10.82±3.93

Differences in the swollen weights of P10 and P40 samples correlate with changes in the sample dimensions. All samples swell isotropically in the three dimensions albeit the changes in P40 specimens were significantly higher than P10 samples respectively. We dried the samples in air for 24 hours to investigate possible changes in weight and thickness. Our results show that dried P40

samples have significantly lower weight (-17.03±9.73 %) as compared to control unswollen samples. However, there were no differences in the corresponding dry weights for the P10 specimens (-3.80±0.07%). These differences in specimen weights correlated with a decreased thickness of P40 samples by about -10.82±3.93%. that suggest removal of uncrosslinked PDMS polymer, commonly referred to as sol, from the network structure due to swelling in xylene [5, 8]. Spectroscopic methods, among others, may be useful to investigate such effects and will be used in the future to quantify the effects of xylene treatment on PDMS elastomers. These results are similar to those seen by others to investigate the effects of swelling of different solvents, including xylene, on solubility of PDMS [9].

3.2. Mechanical Characterization

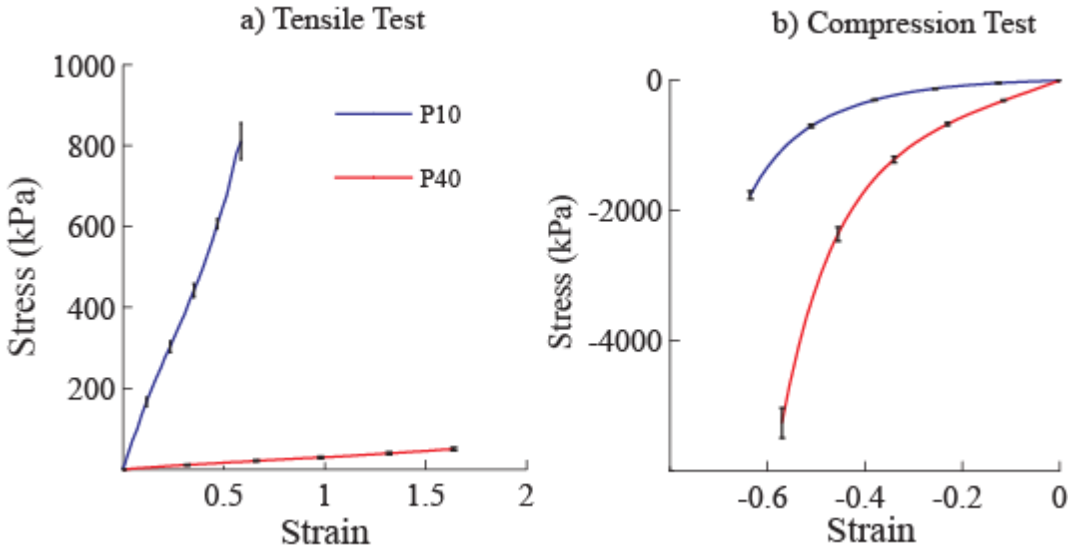

Figure 2. Uniaxial tension (a) and compression (b) results for P10 and P40 samples.

Uniaxial tensile tests in compression and tension were performed on the P10 and P40 specimens (n=2) and the average values of the stress corresponding to each strain value are represented in Figure 2a,b. Tensile moduli were obtained using the slope of stress-strain curves corresponding to strains of about 10%. Results show that P10 samples have a significantly higher modulus ($p<0.05$) of 1400.02±15.84 kPa as compared to P40 specimens (39.46±4.34 kPa). Hence, a decrease in chemical crosslinking amounts causes dramatic differences in the mechanical properties of PDMS. We note a corresponding trend in results from compression experiments with a modulus of 2687±75.65 kPa and 300.48±9.15 kPa for P10 and P40 respectively.

Although uniaxial tests are useful to provide comparisons between the stiffness between groups, they are insufficient to be used to obtain a strain energy function to describe the microstructural properties of elastomers. We must instead rely on comprehensive biaxial tests performed using constraints in two orthogonal directions to obtain a parameter space of deformations. We performed nonequibiaxial and equibiaxial experiments on P10 and P40 samples to explore the contributions caused by strain induced topological adaptations in network structure due to loading in the two orthogonal directions (Figure 3). Equibiaxial experiments confirm that P10 sample has stiffer

response as compared to the P40 specimen.

We use results from biaxial experiments to evaluate phenomenological and microstructural based strain energy models to describe the PDMS networks. These investigations show that the slip link model [10], which considers individual contributions of physical entanglements and chemical crosslinks on microstructural mechanics of elastomer networks, fit the biaxial and uniaxial experimental results better (r^2 =0.958) than Mooney Rivlin model, Arruda-Boyce, and the neo-Hookean models. However comparisons between the model fits to the P40 and P10 samples shows that in highly crosslinked P10 stress-strain behavior have contributions from physical entanglements.

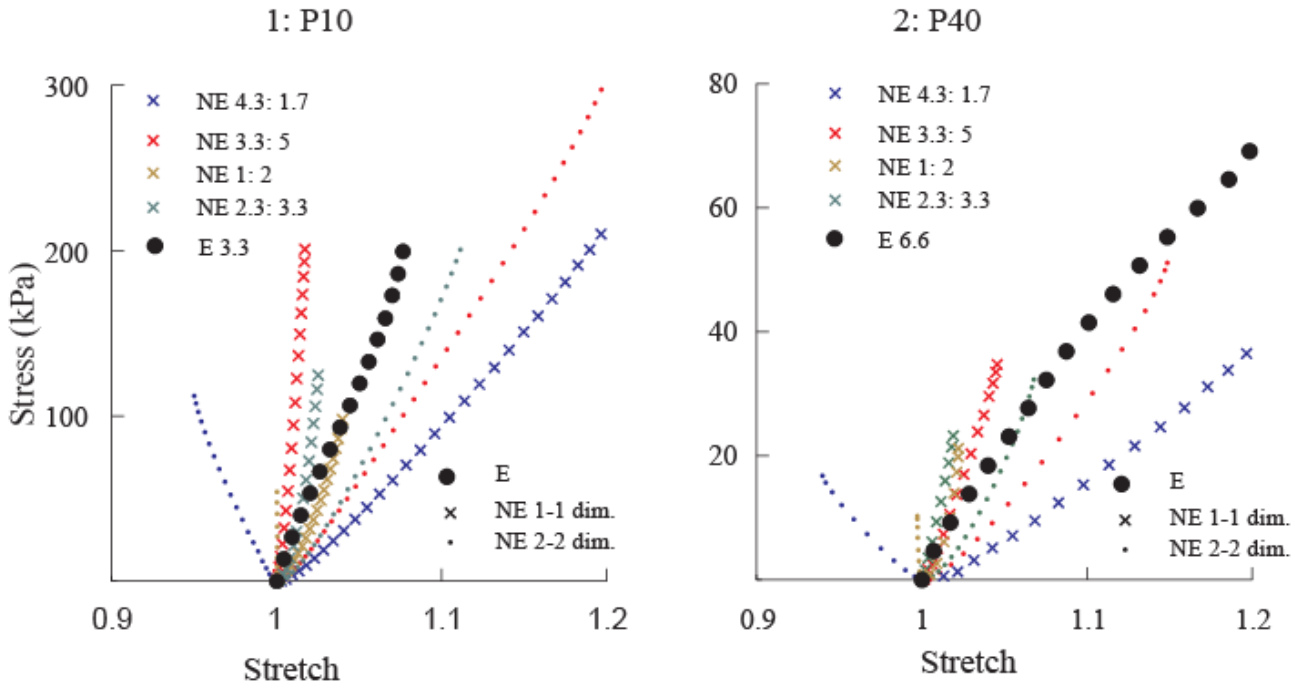

Figure 3. Equibiaxial (E) and nonequibiaxial (NE) stress-stretch results for P10 and P40 samples [10] obtained by differential stretching of samples in two orthogonal directions denoted 1-1 and 2-2 in the figure. The maximum load in the P10 sample was 600 gram whereas that in the P40 was 60 gram. The different ratios in NE experiments were normalized with respect to these maximum loads.

To clearly distinguish between the entanglements and crosslinks, we use methods to swell the elastomers and assess changes in network microstructures using DMA measurements. P10 and P40 samples in the unswollen state and that obtained by swelling and drying the elastomers were subjected to cyclic sinusoidal loading as described earlier (Figure 4).

Higher values of E' as compared to E'' with corresponding low values for tanδ demonstrate the dominance of elastic behavior contributing to the measured viscoelastic property of P10 and P40 samples. In general, E' and E'' for PDMS increases with an increase in frequency. Although entangled chains can slide freely at low frequencies, they are unable to loosen at higher frequencies that result in restriction in the motion of the polymer chains and a corresponding increase in

modulus. The trend of frequency dependent response of storage and loss modulus of swollen P10 is however different as compared to that of unswollen specimen due to the presence of xylene. A similar frequency dependent response for dried samples following swelling and unswollen P10 specimens suggests that the chemical crosslinking of networks was not altered due to swelling. In contrast, there is a large variation in the storage modulus of unswollen and swollen, dried specimen for P40 specimens. Thes differences may arise due to the presence of trapped entanglements in the highly crosslinked P10 samples leading to lower rearrangements in the entanglements during swelling as compared to P40 specimens that also shows loss of sol fraction of uncrosslinked material and a corresponding lower molecular weight. The rate of increase in E' for the P40 specimens with respect to increase in frequency was however high compared to P10 specimens.

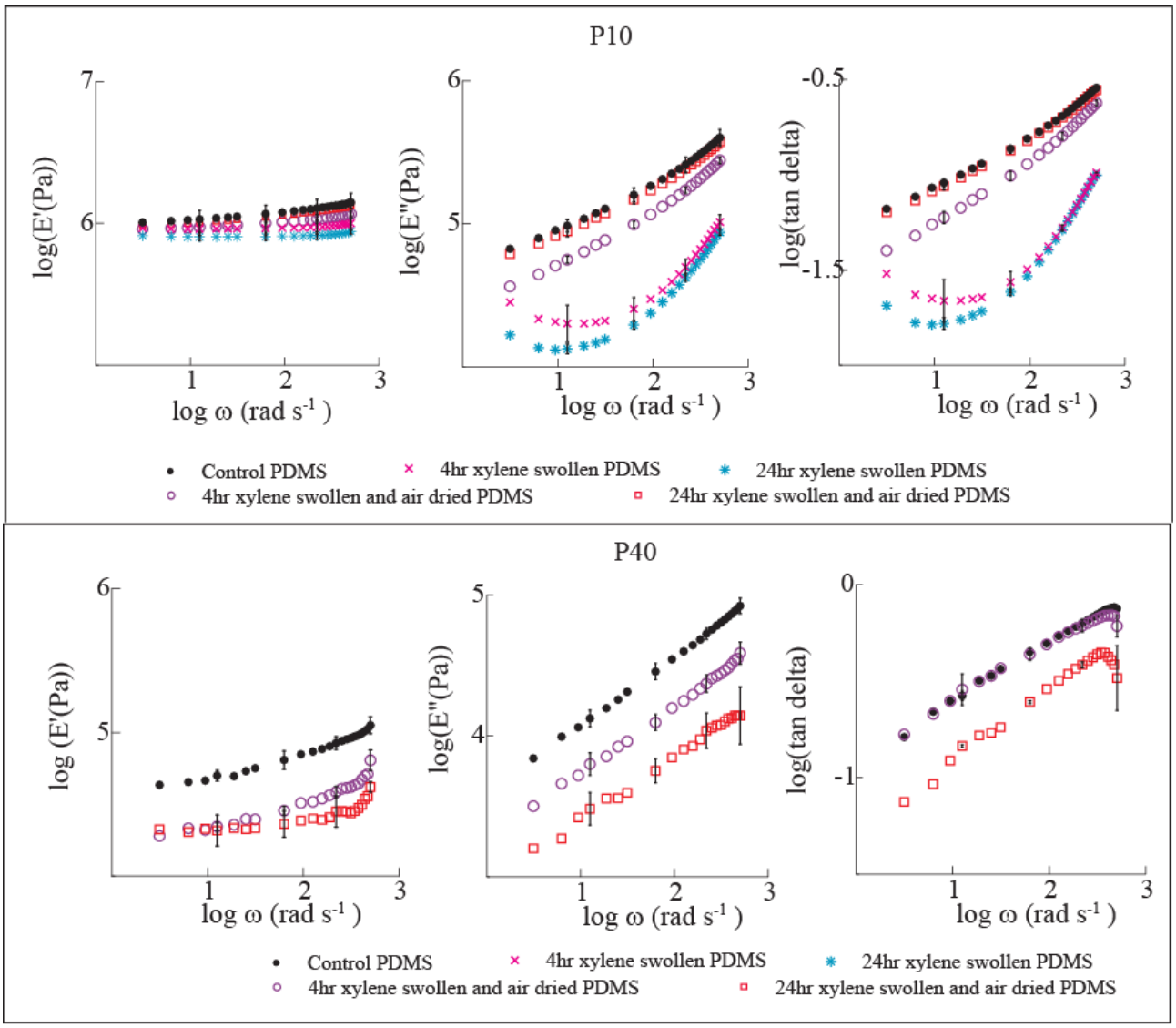

Figure 4. Effect of swelling in xylene on storage modulus (E'), loss modulus (E'') and damping factor (tan δ) for (a) P10 and (b) P40 specimen.

Table 3. Percentage increase E' of P10 and P40 when frequency varies from 1to 80Hz

	Control	Xylene for 4hr, drying	Xylene for 24hr, drying	Xylene for 24hr	Xylene for 4hr
P10	38.09±0.85	28.05±1.39	39.10±1.31	8.15±1.48	7.87±0.01
P40	159.60±10.29	239.35±71.02	103.42±18.62		

4. Conclusions

To study the effect of entanglements and crosslinks in the macroscopic behavior we performed swelling measurements and mechanical characterization of PDMS prepared with different weight ratios of base polymer to crosslinker, denoted as P10 and P40, in this study. Tensile, compression and biaxial mechanical tests show that P10 specimens demonstrate a stiffer response as compared to P40 specimens. Results from biaxial experiments were fit to the Edward-Vilgis slip link model using a nonlinear least squares fit method. Our results show that the mechanical response of elastomers demonstrate individual contributions from chemical crosslinks and physical entanglements. To delineate the effect of crosslinking and entanglements we performed DMA measurements on unswollen control material and those swollen in xylene, and dried in air for the P10 and P40 samples in the study. Our study shows that the P10 specimens have higher values of Young's modulus and storage modulus and a corresponding low swelling ratio due to the higher degree of crosslinking and hence presence of trapped entanglements. In contrast, a low degree of crosslinking in P40 samples demonstrated a higher viscous contribution as compared to the elastic behavior of the P10 elastomers. Our results also show that both P10 and P40 exhibit an increase in rigidity and loss modulus at high frequencies. Dynamic mechanical experiments also show that the elastic and loss moduli decrease due removing of uncrosslinked polymer and locking the chains in different configurations produced by swelling. Ongoing stress relaxation experiments are envisaged to characterize the effects of swelling on the mechanical properties that will lead to a better understanding of the effects of entanglement in the on viscous properties of PDMS.

5. Acknowledgements:

This work is supported by the Department of Science and Technology, India (DST Ramanujan and DSTO1124). We thank. Ankur Goswami (Materials Research Center, Indian Institute of Science) for help with the compression experiments and Achu GB for the analysis software with the DMA experiments.

6. References

1. N. Stafie, D. F. Stamatialis, M. Wessling, Effect of PDMS cross-linking degree on the permeation performance of PAN/PDMS composite nanofiltration membranes. Sep. Purif. Technol, 45 (2005) 220-231.

2. M. C. Boyce, E. M. Aruba, Constitutive models of rubber elasticity: A review. Rubber Chem. and Technol, 73 (2000) 504-523.
3. K. Urayama, T. Kawamura, S.Kohjiya, Structure-mechanical property correlations of model siloxane elastomers with controlled network topology. Polymer, 50 (2009) 347-356.
4. S. F. Edwards, T. Vilgis, The effect of entanglements in rubber elasticity. Polymer, 27 (1986) 483-492.
5. E. M. Arruda and M. C. Boyce, A three-dimensional constitutive model for the large stretch behavior of rubber elastic materials. J. Mech. Phys. Solids. 41 (1993) 389-412.
6. S. Venkatraman, A. Nixon and A. Highe, The deformation behavior of poly(dimethyl siloxane) networks. II. Equilibrium swelling. J. Appl. Polym. Sci., 52 (1994) 1097-4628.
7. V. Agrawal, S. A.Kollimada, A. G. Byju , N.Gundiah, Regional variations in the nonlinearity and anisotropy of bovine aortic elastin. Biomech Model Mechanobiol., doi 10.1007/s10237-013-0474-3 (2013).
8. N. L. Jessamine, C. Park, G. M. Whitsides, Solvent compatibility of Poly(dimethylsiloxane)-based microfluidic. Anal. Chem., 75 (2003) 6544–6554.
9. Ian Macmillan Ward DWH. An introduction to the mechanical properties of solid polymers. J.Wiley & Sons, 1993.
10. A. R. Babu, N.Gundiah, Role of crosslinking and entanglements in the mechanics of silicone networks (under review, Dec 2012).
11. L. Mullins, Determination of degree of crosslinking in natural rubber vulcanizates. Part IV. Stress-strain behavior at large extensions. J. Appl. Polym. Sci. ,2 (1959) 57-263.

Mode-I Fracture Behaviors of a Shear Thickening Fluid as Adhesive Layer under Different Loading Rates

Maisha Tabassum[1], Lin Ye[1,*], Li Chang[1], Klaus Friedrich[2,3]

[1] Center for Advanced Materials Technology, School of Aerospace, Mechanical and Mechatronic Engineering, The University of Sydney, NSW, 2006, Australia
[2] Institute for Composite Materials, University of Kaiserslautern, 67663 Kaiserslautern, Germany
[3] College of Engineering, King Saud University, Riyadh, Saudi Arabia
* Email: lin.ye@sydney.edu.au

Abstract Shear thickening fluids (STFs) classified as Non-Newtonian fluids are fluidic composites of dense suspensions. These fluids display unusual phase transitions between liquid and "solid" phases due to recoverable changes in viscosity at a critical rate of shear. This study characterizes the fracture behavior of a STF with 58 vol.% dispersion of styrene/acrylate particles in ethylene glycol. Double cantilever beam (DCB) specimens with the STF as adhesive layer were utilized to investigate the Mode-I fracture energy of the STF. The fracture behavior of the STF of different thickness was evaluated in detail at different crack opening displacement rates, varying from 1 mm/s to 50 mm/s. The results indicate that the fracture behavior of the STF is very rate-sensitive. However, before the opening displacement rate reaches 5 mm/s, the STF is not showing any "solid" like behavior. The average Mode-I fracture energy of the STF increases with an increase in the opening displacement rate up to 30 mm/s, after that the values are plateaued and almost constant at 240 J/m^2. This is comparable to the fracture toughness of a typical epoxy. The fracture energy of the STF also shows an inverse dependence on the thickness of the STF at low opening displacement rates, but at high rates such dependence was not observed.

Keywords Fracture energy, Shear thickening fluid (STF), Rate effect, Double cantilever beam (DCB), Adhesive thickness

1. Introduction

The ability to divert or dissipate dynamic energy during impact has many engineering challenges in industrial, biomedical and military applications. Shear thickening fluids (STFs) can play a vital role in engineering designs as energy shunting materials. STFs are mostly fluidic composites of dense suspensions that exhibit reversible shear thickening behavior, and STFs are non-Newtonian fluids, which can sometime display intriguing phase transitions between liquid and "solid" phases due to the recoverable changes in viscosity at a critical shear rate [1]. The use of STFs opens up many opportunities in developing new passive, energy-absorbing systems in applications including liquid dampers/brakes, liquid armor, etc.

Over the last few decades, the shear thickening behavior of concentrated dispersions has been a major topic of interest for rheologists owing to their immense importance in industry [1-4]. Shear thickening was initially believed to be a severe problem, because it leads to such issues as failure of mixer motors due to overloading, damage mixer blade and other processing equipment, and induce dramatic changes in suspension microstructure, such as particle aggregation, which results in poor fluid and coating qualities [1]. The early investigations of shear thickening behavior were to mitigate damage on processing equipment caused by the shear thickening transition [5, 6]. Later STFs have become attractive due to their unique property that makes them ideal for energy absorption applications. When subjected to an impact, this shear rate-activated fluid converts from a low viscous to a high viscous state almost instantaneously, and it can absorb some of impact energy while helping to dissipate the remaining energy. Many studies have been done on the energy absorption applications of STFs. For the personal protection with application of STFs as 'liquid armor', it has attracted many efforts in research [1, 7-9], and STFs-treated fabrics showed not only

the enhanced ballistic resistance but also higher flexibility and light weight [10-17] than the untreated ones. STFs have been also used in several other specific applications, especially in ski boot cushioning, liquid couplings, shock absorber fillings, rotary speed limiters, damping and control devices [18, 19].

The previous studies clearly highlight the strong potential of STFs for various industrial applications as new adaptive energy-absorbing materials, owing to their unique mechanism of recoverable liquid-"solid" transitions. The performance of the STF-based systems is greatly dependent on the behavior of STFs near the shear thickening transition as well as their properties after the shear thickening transition in particular. Most existing research has focused on the characterization of STFs using classic rheological methodology. Previous research primarily dealt with examining the response of shear thickening systems, especially in the identification of critical transition which indicates shear thickening occurrence. However, the properties of STFs after the shear thickening transition cannot be captured because of the limitations of conventional rheometers.

In this study the fracture behavior of a STF composed of 58 vol.% dispersion of styrene/acrylate particles in ethylene glycol [20] was investigated to quantitatively evaluate the dilatant ability of STF to shunt energy after shear thickening transition. Virtually for all applications fracture toughness or fracture energy is one of the most important material properties for characterizing energy dissipation capability; and it can be dependent on several factors, such as the type of loading (e.g. tensile and shear), the environmental conditions (e.g. temperature and moisture), the loading rate. Fracture tests were performed using a double cantilever beam (DCB) specimen with STF as adhesive layer to investigate the effect of displacement rate and adhesive layer thickness. A high speed digital (HSD) camera was used to carefully examine the fracture behavior of STF.

2. Experimental

2.1. Material

The STF used in this research work is a water soluble fluid composed of 58 vol.% dispersion of styrene/acrylate particles in ethylene glycol, supplied by BASF AG (Germany). The spatial distribution and the geometry of particles have been examined previously using a Zeiss 902 transmission electron microscope (TEM) and a scanning electron microscope (SEM) [20], and the shape of particles is near-spherical with an average size of about 300 nm; the particles were well dispersed in the ethylene glycol with the existence of micro-sized flocculation.

2.2. Specimen Configuration

There is no standard method to measure the Mode-I fracture energy of STFs. In this work, double cantilever beam (DCB) specimens with the STF as the adhesive layer were adopted in such an approach. The upper and lower beams of DCB specimens were carbon fiber-epoxy (CF/EP) plain woven composite beams, which were selected owing to their high stiffness, lightweight and smooth surface properties. The CF/EP beam was 200 mm long with 30 mm in width and 1.7 mm in thickness. Two aluminium (Al) loading blocks were bonded on the upper and lower surface of CF/EP beams at one end using a high strength adhesive, as shown in Fig. 1.

Before applying the STF, the surfaces of CF/EP beams were cleaned by rinsing with water. After water rinsing and complete drying, STF was uniformly distributed between two beams with a folded Al foil of 0.02 mm in thickness, which replicates a single entity of a start-crack (Fig. 1). The

length of the start-crack amounted to 50 mm. The folded Al foil was chosen to form the start-crack due to its flexibility, thin and smooth surface features. To maintain the uniform thickness of the adhesive layer without voids in it, sufficient STF needs to be applied to allow a continuous spreading of the STF from the center of the specimen to the edges by squeezing flow. Different adhesive layer thicknesses, ranging from 0.2 mm to 2.05 mm, were obtained for the Mode-I fracture experiments.

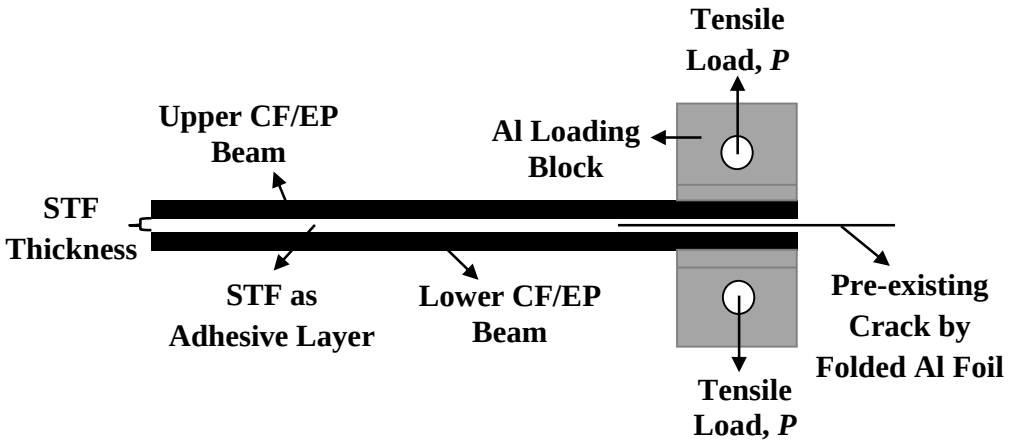

Figure 1. Schematic diagram of a DCB specimen with STF as adhesive layer and Al foil as a pre-existing crack

2.3. Mode-I Fracture Test Procedure

An Instron 8501 servo-hydraulic machine configured with a data acquisition system was utilized to conduct experiments in a displacement-controlled mode. The load experienced throughout the experimental duration with respect to the crack opening displacement was monitored and recorded through the load cell by a digital data acquisition unit at a sampling rate of 1000 Hz. Experiments were performed under various stroke speeds, ranging from 1 to 50 mm/s for the DCB specimens with different STF thickness, while holding all other variables constant. Stroke speeds chosen for experiments were 1, 5, 10, 20, 30, 40, and 50 mm/s, and all tests were undertaken under ambient conditions. Up to 50 experiments were conducted at each displacement rate with different STF thickness.

2.4. High-Speed Photography

Video recording was performed during each experiment using a high speed digital (HSD) camera with a frame rate of 500 frames/sec (fps) at a resolution of 512 ×240 pixels per image, in order to capture the specimen's physical movement. It helped to calibrate the actual displacement, and it also helped to observe the crack opening and crack propagation. With the help of a software program, the fracture behavior of STF in different stages of loading could be evaluated in detail.

2.5. Fracture Energy

The fracture energy of the STF to resist opening separation can be established by accessing the raw data obtained from the experiments. Continuous records of HSD image, load and corresponding opening deflection of CF/EP beams were used for determination of the fracture energy of STF in a DCB specimen. The data reduction scheme to determine the fracture energy for the DCB specimen with an adhesive layer of STF is the 'Modified Beam Theory (MBT) Method' [21] which quantifies the strain energy release rate at the crack initiation and propagation. The fracture energy or the critical energy release of a DCB specimen [22] is expressed as:

$$G_I = \frac{3P_c\delta_c}{2ba} \quad (1)$$

where, P_c = the critical load for crack growth, δ_c = the opening displacement at the critical load P_c, b = the specimen width, and a = the start-crack length.

3. Results and Discussion

3.1. Fracture Load

The response of the STF undergoing DCB fracture test was quantitatively assessed by synchronizing the load experienced by DCB specimen against its opening deflection in conjunction with the records of the HSD camera. Fig. 2 shows the typical load-displacement curve at a displacement rate of 40 mm/s. At point O_1, a local hike in load can be observed, but no crack growth was clearly visible in the specimen, Fig. 3(a). When the load was further increased, reaching its peak, point O_2, a white spot was observed in the STF layer at the tip of the start-crack, Fig. 3(b), showing the initiation of crack growth. After the peak, point O_2, the load started to drop continuously, accompanied by crack propagation in the specimen, Fig. 3(c).

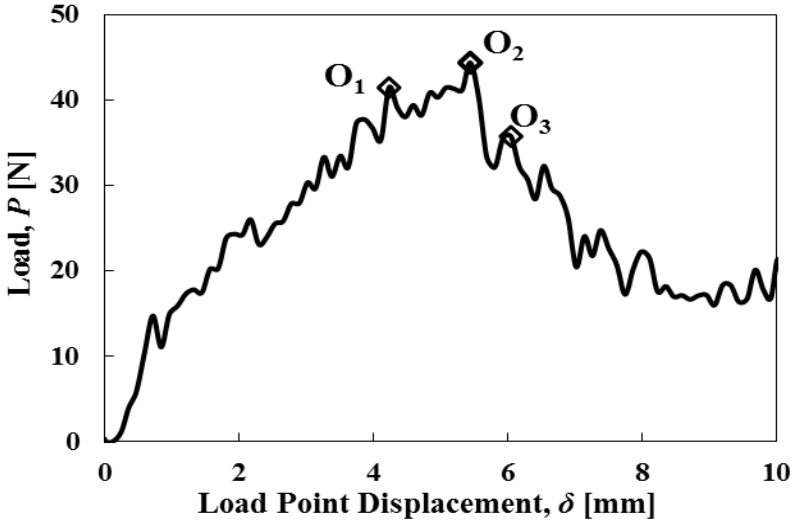

Figure 2. Load-displacement curve of a DCB specimen at a displacement rate of 40 mm/s

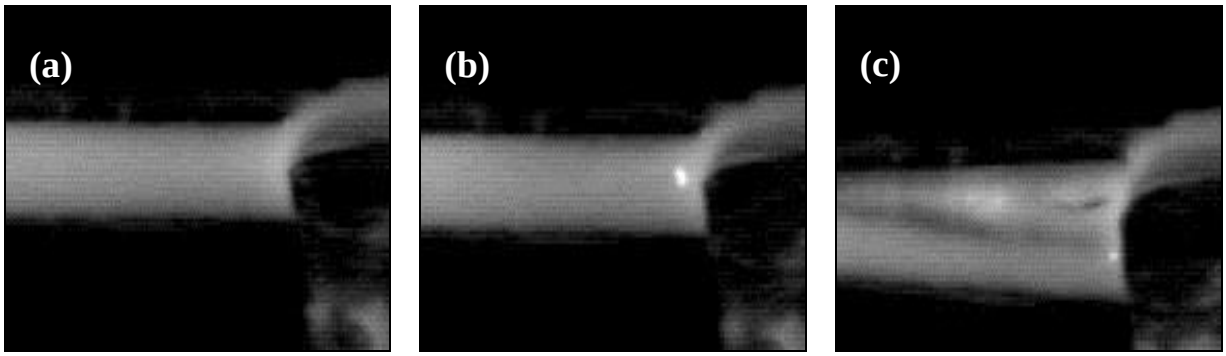

Figure 3. Fracture of STF was observed by HSD camera at dissected points of load-displacement curve in Fig. 2

By comparing the load-displacement curve of each specimen with corresponding video images, the critical load and the corresponding opening displacement for calculating the Mode-I fracture energy of the shear thickening fluid were defined. It was observed that not all DCB specimens showed the fracture behavior as a conventional solid. In particular, specimens tested at low displacement rates or with a thick layer of STF, exhibited an opening during which stretching of the STF with less

bending of the two CF/EP beams occurred. Additional calculation was done to get the effective Young's modulus of the CF/EP beams using the load-displacement curve and following the simple cantilever beam theory. For those DCB specimens, for which the effective Young's modulus of the CF/EP beam was clearly lower than that measured (using the same CF/EP laminate beam under three-point bending and following the procedure of ASTM D7264), the fracture energies calculated using Eq. (1) were excluded from the further discussion.

3.2. Effect of STF Thickness

It was expected that the STF layer thickness is a critical parameter, since the shear thickening phenomenon occurs only in localized regions where the shear rate goes beyond the critical shear rate, which is around 5/s [20]. Therefore the shear thickening effectiveness can disappear with increasing volume of the STF, especially at a reduced shear rate. The relation between the critical load to split the STF and the STF thickness is discerned in Fig. 4, with the STF thickness in a range from 0.2 mm to 2.05 mm. By arranging the maximum forces with respect to the STF thickness, it can be seen that a small STF thickness requires a greater load to split the STF in a DCB specimen, and vice versa. The greater the fluid thickness, the less aggregation or jamming of particles occurs, hence resulting in a lower critical load to split the specimen. However this relation is more obvious for low displacement rates (e.g., Fig. 4(a) for 5 mm/s and Fig. 4(b) for 10 mm/s). With increasing the displacement rate, the effect of the STF thickness on the critical load reduces. For displacement rates from 40 mm/s to 50 mm/s the critical load does not display any significant dependence on the STF thickness, Fig. 4(e) and Fig. 4(f).

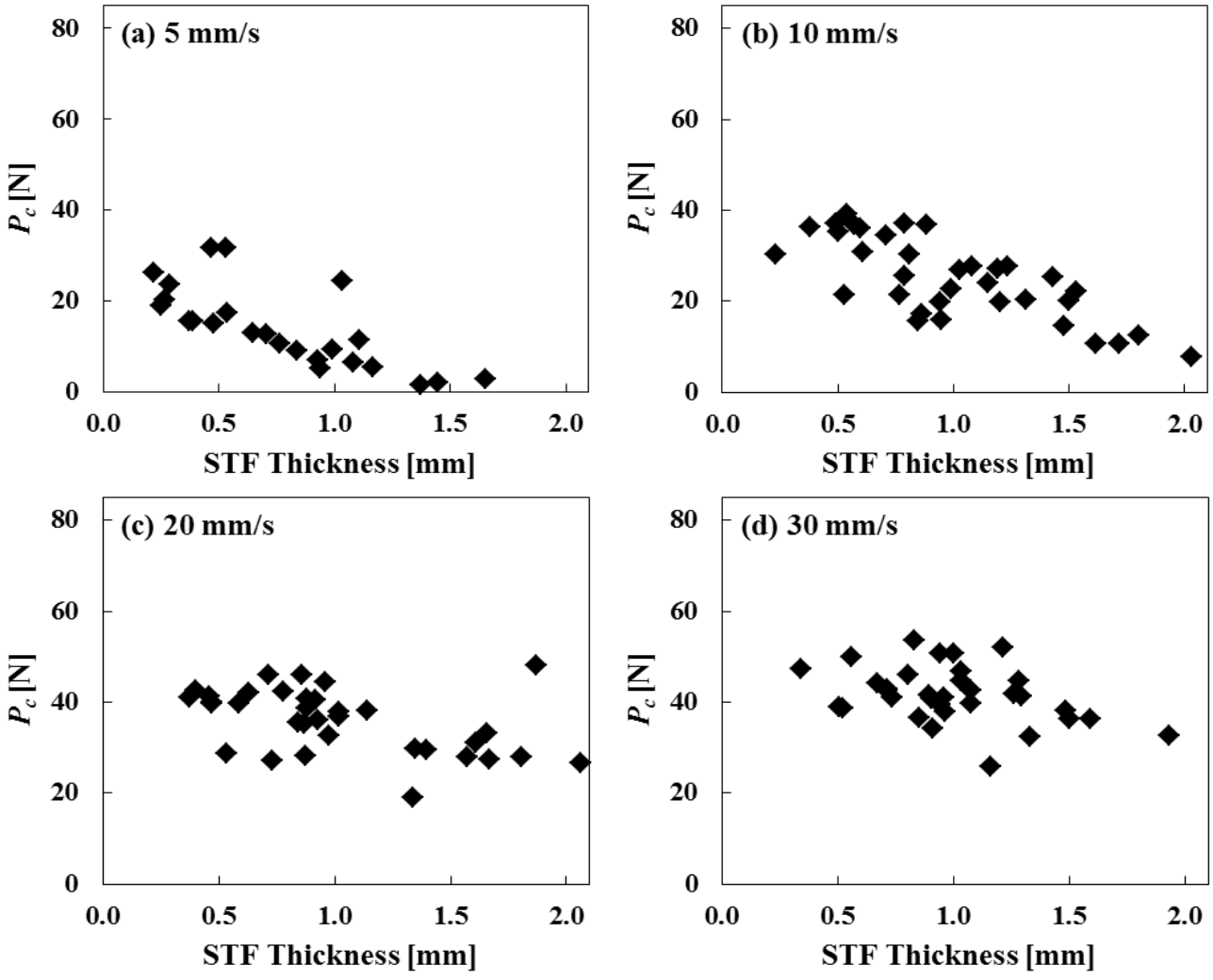

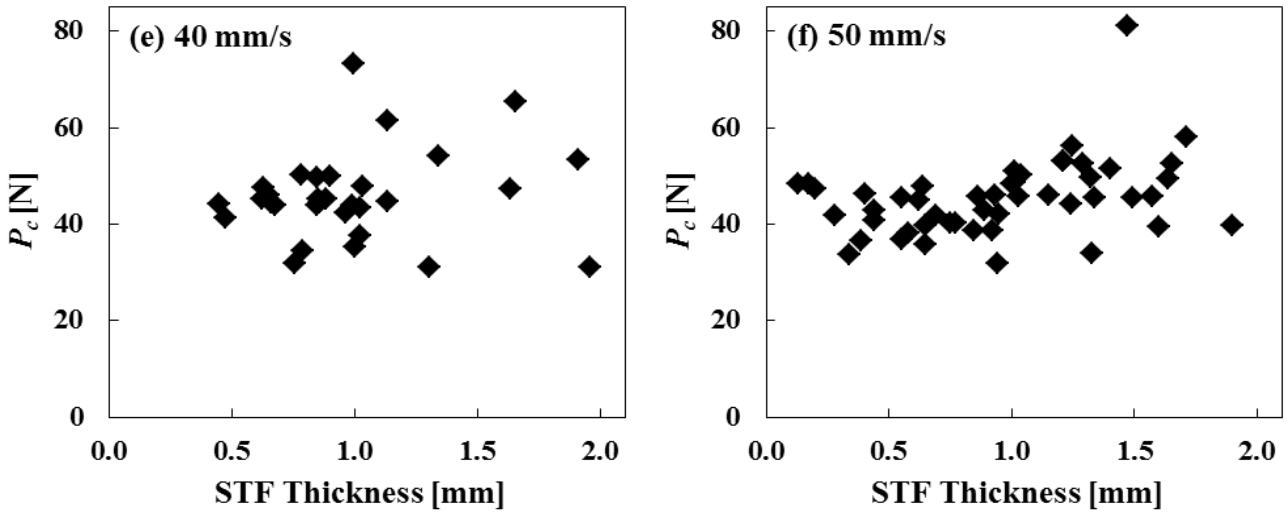

Figure 4. Effect of STF thickness on critical load at different displacement rates

Eq. (1) shows that the Mode-I fracture energy of STF is directly proportional to the critical load, and therefore, it is expected that a similar tread of Mode-I fracture energy in relation to the STF thickness exists. The Mode-I fracture energy versus the STF thickness is plotted for different displacement rates in Fig. 5.

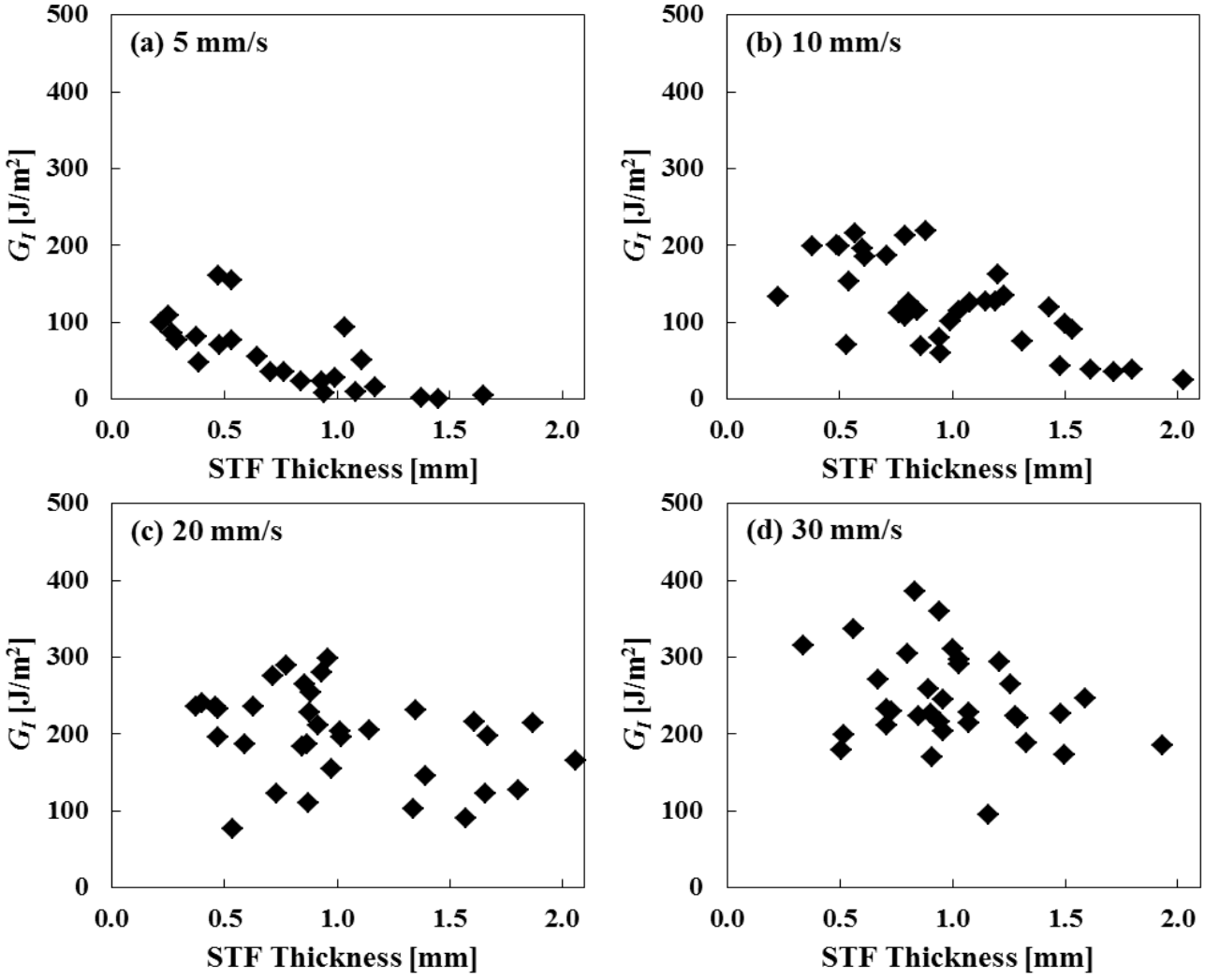

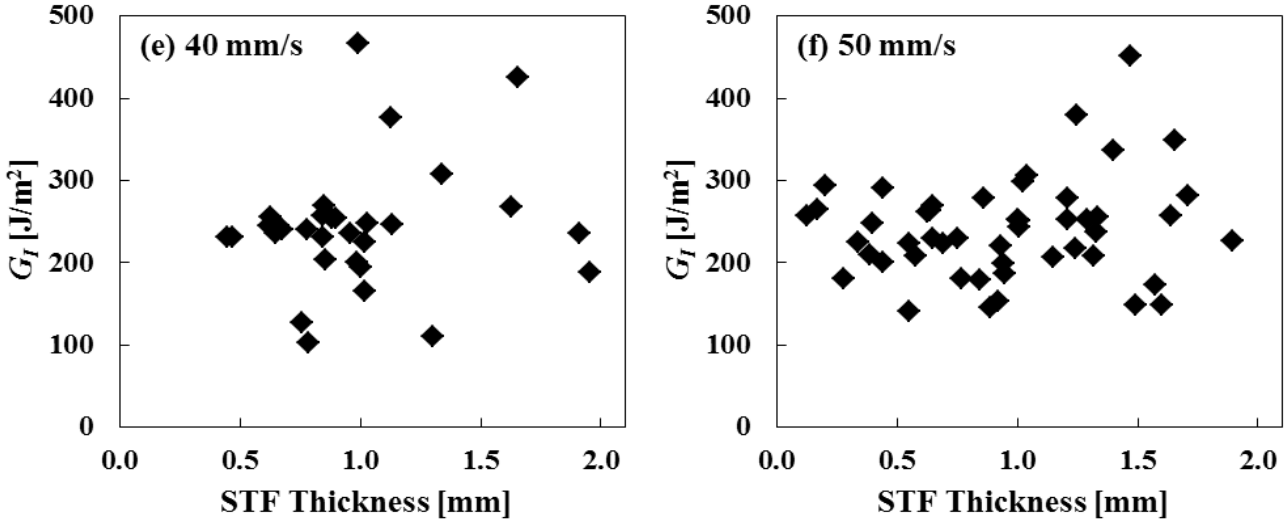

Figure 5. Effect of STF thickness on Mode-I fracture energy at different stroke rates

Up to a displacement rate of 20 mm/s, a reduced fracture energy with increased STF thickness is visible. This means, a larger STF thickness certainly results in a decreasing efficiency of the STF to absorb energy. However, with increasing the displacement rate this inverse relation cannot be observed anymore. For displacement rates from 30 to 50 mm/s, the Mode-I fracture energy does not show any significant relation with the STF thickness, in particular not at 50 mm/s.

3.3. Effect of Loading Rate

The loading or displacement rate is one of the most prominent parameters for examining the fracture behavior of STFs. The rates used here for the DCB fracture experiments were 1, 5, 10, 20, 30, 40, and 50 mm/s. The maximum of 50 mm/s was limited by the capacity of the Instron 8501 testing machine. The actual displacement rate was validated using the synchronized HSD images as well as the calculation from the time and displacement data. It was found that the actual displacement rates were very close to the preset ones in the testing range chosen. Existing differences were small, with a maximum being about ±4% of the preset ones.

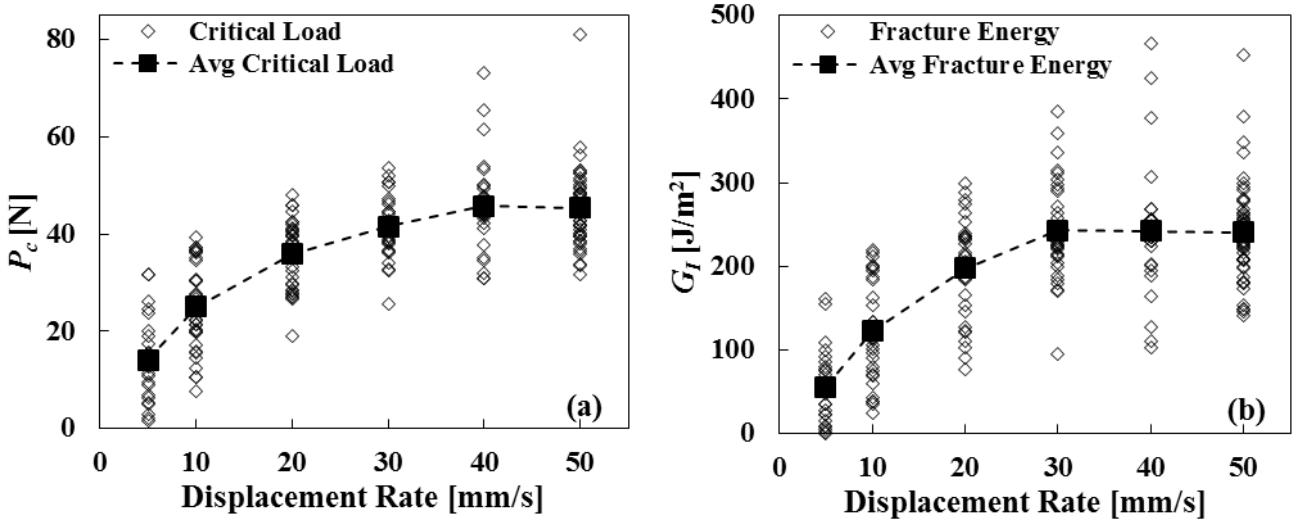

Figure 6. Effect of stroke speed on (a) critical load and (b) fracture energy of STF with different thickness

At a low displacement rate of 1 mm/s, STF is able to flow as an ordinary fluid, and the load cell did not measure any clear load with respect to the opening displacement, indicating such a

displacement rate is not enough for STF to have the transition from liquid to "solid". The HSD camera also shows there is no clear shear thickening effect of STF at this rate. In fact, before the displacement rate reaches 5 mm/s, STF did not show any "solid" like behavior, therefore no "fracture" was visible.

The effects of displacement rate on the critical load and fracture energy of the STF are graphically represented in Fig. 6, showing the results for each individual specimen. Fig. 6(a) presents the critical load with respect to displacement rate from 5 mm/s to 50 mm/s. With increasing deformation rate, the viscosity of the STF at the crack tip sharply increased, thus suppressing flow of the STF; instead it stiffens greatly and is capable of resisting an opening displacement more efficiently, causing a higher load. The increasing trend is supported by studies in the literature, which acknowledge a positive correlation between the STF's viscosity and the rate of deformation. The critical load varies with a substantial scatter for all displacement rates, because of the effect of STF thickness, articulated in the previous section. Other factors may also contribute to the scatter, such as voids or the uneven STF thickness because of leak of STF before the start of a test. However, the mean value of the critical load clearly increases with an increase in displacement rate up to 40 mm/s. A further increase in the displacement rate shows that the average critical load remains almost on a steady value. The mean values as well as the standard deviations of critical loads for different displacement rates are presented in Table 1.

Table 1. Means and standard deviations of critical load and fracture energy at different displacement rates

Displacement Rate [mm/s]	**Critical Load, P_c (Mean ± SD) [N]**	**Fracture Energy, G_I (Mean ± SD) [J/m^2]**
5	14 ± 9	56 ± 46
10	25 ± 9	123 ± 58
20	36 ± 7	198 ± 59
30	42 ± 6	243 ± 60
40	46 ± 9	242 ± 76
50	45 ± 8	240 ± 61

Almost a similar trend is observed for the Mode-I fracture energy of STF for different opening displacement rates in Fig. 6(b). As the critical load values, the fracture energy also shows a clear scatter in the values at each displacement rate, attributed to the effect of STF thickness. Also here, the average values and the standard deviations of fracture energy were calculated and summarized in Table 1. With an increase in the opening displacement rate, a positive relation is found between the fracture energy up to a displacement rate of 30 mm/s. At a low rate of 5 mm/s, the STF is able to absorb a small amount of energy while acting as a viscous "solid", though its actual value may be arguable. After the displacement rate reaches 30 mm/s the average fracture energy of STF is plateaued and remains almost constant with an averaged value about 240 J/m^2. This value indicates that the STF is capable of absorbing a certain amount of fracture energy, being comparable to a low cross-linked epoxy [23]. It seems the average value of Mode-I fracture energy of STF peaks at 30 mm/s, and it tends to reduce slightly after the displacement rate of 30 mm/s. However, such a tendency needs the careful evaluation of further studies, especially with facilities allowing higher displacement rates.

4. Conclusion

In this study, DCB specimens were used to characterize the fracture behavior and Mode-I fracture

energy of a shear thickening fluid (STF), containing 58 vol.% dispersion of styrene/acrylate particles in ethylene glycol. Effects of displacement rate (up to 50 mm/s) and STF thickness in the range of 0.2 to 2.05 mm were evaluated in detail.

The results reveal that as the displacement rate increases, the local shear rate at the crack-tip increases, sharply increasing the viscosity of the STF, thus suppressing the flow of the latter. It stiffens greatly and is capable of resisting an opening displacement efficiently, causing a higher load. Confirmed by the high speed camera images, STF clearly shows a "solid" behavior, fracturing with crack growth, when the opening displacement rate is higher than 20 mm/s. The Mode-I fracture energy of the STF increases with an increase in the displacement rate until 30 mm/s. In addition, the STF thickness was found to have a significant influence on the value of Mode-I fracture energy, attributed to the shear-thickening mechanism.

The most interesting result is that the STF adopted in this study shows almost a constant average value of fracture energy of 240 J/m^2 after the displacement rate is higher than 30 mm/s. This value indicates that the STF is capable of absorbing a certain amount of fracture energy, being comparable to a low cross-linked epoxy.

Future studies will be conducted at higher displacement rates. Such a more comprehensive characterization of the fracture behavior of STFs will certainly aid the development of energy absorbing devices using various STFs.

Acknowledgements

The authors acknowledge BASF AG (Germany) for providing the material. The authors would like to thank Trevor Shearing for his technical assistance and advice to carry out our test program. The project was partly supported by the University of Sydney Bridging Support Grant (Dr. Li Chang). M. Tabassum is grateful to the Australian Postgraduate Award (APA) and the top-up scholarship from the School of AMME, The University of Sydney.

References

[1] H. Barnes, "Shear-thickening ("dilatancy") in suspensions of nonaggregating solid particles dispersed in Newtonian liquids," *Journal of Rheology,* vol. 33, p. 329, 1989.

[2] R. Hoffman, "Discontinuous and dilatant viscosity behavior in concentrated suspensions. I. Observation of a flow instability," *Journal of Rheology,* vol. 16, p. 155, 1972.

[3] R. L. Hoffman, "Discontinuous and dilatant viscosity behavior in concentrated suspensions. II. Theory and experimental tests," *Journal of Colloid and Interface Science,* vol. 46, pp. 491-506, 1974.

[4] W. H. Boersma, J. Laven, and H. N. Stein, "Shear thickening (dilatancy) in concentrated dispersions," *AIChE journal,* vol. 36, pp. 321-332, 1990.

[5] R. L. Hoffman, "Explanations for the cause of shear thickening in concentrated colloidal suspensions," *Journal of Rheology,* vol. 42, p. 111, 1998.

[6] E. E. Bischoff White, M. Chellamuthu, and J. P. Rothstein, "Extensional rheology of a shear-thickening cornstarch and water suspension," *Rheologica acta,* vol. 49, pp. 119-129, 2010.

[7] F. J. Galindo-Rosales, F. J. Rubio-Hernández, and J. F. Velázquez-Navarro, "Shear-thickening behavior of Aerosil® R816 nanoparticles suspensions in polar organic liquids," *Rheologica acta,* vol. 48, pp. 699-708, 2009.

[8] N. J. Wagner and E. D. Wetzel, "Advanced body armor utilizing shear thickening fluids," ed: Google Patents, 2007.

[9] Y. S. Lee and N. J. Wagner, "Dynamic properties of shear thickening colloidal suspensions," *Rheol Acta,* vol. 42, pp. 199-208, 2003.

[10] Y. S. Lee, E. D. Wetzel, and N. J. Wagner, "The ballistic impact characteristics of Kevlar woven fabrics impregnated with a colloidal shear thickening fluid," *Journal of Materials Science,* vol. 38, pp. 2825 – 2833, 2003.

[11] E. D. Wetzel, Y. S. Lee, R. G. Egres, K. M. Kirkwood, J. E. Kirkwood, and N. J. Wagner, "The Effect of Rheological Parameters on the Ballistic Properties of Shear Thickening Fluid (STF)–Kevlar Composites," *NUMIFORM,* pp. 1-6, 2004.

[12] R. G. J. Egres, Y. S. Lee, J. E. Kirkwood, K. M. Kirkwood, E. D. Wetzel, and N. J. Wagner, ""Liquid armor": Protective fabrics utilizing shear thickening fluids," *IFAI 4th Int. Conf. on Safety and Protective Fabrics,* pp. 1-8, 2004.

[13] M. J. Decker, C. J. Halbach, C. H. Nam, N. J. Wagner, and E. D. Wetzel, "Stab resistance of shear thickening fluid (STF)-treated fabrics," *Composites Science and Technology,* vol. 67, pp. 565–578, 2007.

[14] J. M. Houghton, B. A. Schiffman, D. P. Kalman, E. D. Wetzel, and N. J. Wagner, "Hypodermic Needle Puncture of Shear Thickening Fluid (STF)-Treated Fabrics," *Proceedings of SAMPE,* vol. 3, pp. 1-11, 2007.

[15] D. P. Kalman, J. B. Schein, J. M. Houghton, C. H. N. Laufer, E. D. Wetzel, and N. J. Wagner, "Polymer Dispersion Based Shear Thickening Fluid-Fabrics for Protective Applications," *Proceedings of SAMPE,* pp. 1-9, 2007.

[16] B. A. Rosen, C. H. N. Laufer, D. P. Kalman, E. D. Wetzel, and N. J. Wagner, "Multi-Threat Performance of Kaolin-Based Shear Thickening Fluid (STF)-Treated Fabrics," *Proceedings of SAMPE,* pp. 1-11, 2007.

[17] V. A. Grigoryan, I. F. Kobylkin, V. M. Marinin, and I. A. Bespalov, "Ballistic Performance of Textile Armor Treated with Shear Thickening Fluid," *Techniczne Wyroby Włókiennicze,* pp. 12-15, 2009.

[18] H. Laun, R. Bung, and F. Schmidt, "Rheology of extremely shear thickening polymer dispersions (passively viscosity switching fluids)," *Journal of Rheology,* vol. 35, p. 999, 1991.

[19] R. Helber, F. Doncker, and R. Bung, "Vibration attenuation by passive stiffness switching mounts," *Journal of sound and vibration,* vol. 138, pp. 47-57, 1990.

[20] L. Chang, K. Friedrich, A. Schlarb, R. Tanner, and L. Ye, "Shear-thickening behaviour of concentrated polymer dispersions under steady and oscillatory shear," *Journal of Materials Science,* vol. 46, pp. 339-346, 2011.

[21] ASTM, "Standard Test Method for Mode I Interlaminar Fracture Toughness of Unidirectional Fiber-Reinforced Polymer Matrix Composites," in *ASTM Annual Book of ASTM Standard D5528-94a* vol. 15.03, ed, 1999, pp. 283-292.

[22] J. Williams, "The fracture mechanics of delamination tests," *The Journal of strain analysis for engineering design,* vol. 24, pp. 207-214, 1989.

[23] S. Deng, L. Ye, and K. Friedrich, "Fracture behaviours of epoxy nanocomposites with nano-silica at low and elevated temperatures," *Journal of materials science,* vol. 42, pp. 2766-2774, 2007.

Dynamic Growth of Voids under Effects of Thermal and Vapor Pressure in Electronic Packaging

Xiaohu Yao[1,*], Yue Mei[1], Xuejun Fan[2]

[1] School of Civil and Transportation Engineering, South China University of Technology, Guangzhou 510641, China
[2] Department of Mechanical Engineering, Lamar University, TX 77710, U.S.A.
* Corresponding author: yaoxh@scut.edu.cn

Abstract The failure can be caused in polymers by thermal stress and vapor pressure during reflow process. A profound view on dynamic growth of voids during reflow process is provided in this paper. The mechanical model is analyzed at first. Then the dynamic equation is derived via the energy method. Furthermore, we apply the method to numerically solve the dynamic increase of void volume fraction under the linear-elastic model. Also, the increase proceeding under different Young's Modulus is compared. It is interesting that the final void volume fraction remain constant when the Young's Modulus keeps unchanged during the reflow process. At last, the dynamic growth curves on the assumption of super-elastic constitution under different initial void volume fraction are compared. It is notable that the initial void volume fraction is extraordinarily significant for the eventual deformation.

Keywords Polymers, dynamic growth, vapor pressure, electronic packaging

1. Introduction

Polymer materials have wide applications in industry such as being adhesive film in the microelectronic packaging. However, polymers are of high porosity which influences the reliability of electronic packing. Besides, most of polymers are hydrophilic materials which are capable of absorbing a large number of moisture in ambient environment. According to the requirement of electronic packaging, electronic devices would experience a reflow process which is completed within a few minutes. The peak temperature of devices during this process typically ranges from 220℃ and 260℃, consequently moisture stored in polymer materials vaporizes and becomes vapor pressure which also pose serious threat on the reliability of package[1-3]. With regard to instable growth of micro-voids, there are a large number of works related to the field. Ball[4] investigated discontinuous equilibrium solutions of cavitations in the year of 1982. Based upon Ball's theory, Lopez-Pamies et al. [5-6] put forward the defect-growth theory. As to the failure of cavitations caused by vapor pressure, Fan et al. [7] derived a micromechanics based vapor pressure model, Huang et al. [8-9] studied cavitations' instabilities of a central hole in an infinite plate subjected to distributing pressure. And then, Guo et al. [10-12] investigated instabilities of micro-voids subjected pressure on the inner boundary and thermal stress on the outer boundary. Also, there are some literature investigating the cavitation instability in different packaging materials[13-15].However, the former work mainly focuses on the critical load of instable growth of micro-voids. Actually, it is also significant to produce a profound understanding of the dynamic growth process of voids, which will be beneficial to the industrial design. In the industry of electronic packaging, we can control the temperature to optimal processing when electronic devices are manufactured. Therefore, it is of great importance to acquire the responding increase of micro-voids with respect to time.

The outline of the paper is organized as follows: In Section 2, the mechanical model is built up. In Section 3 the energy principle is introduced to derive the transient growth equation of micro-voids to help further the discussion in the next section. In Section3, we utilize the equations in Section 3 to obtain the curve of growth of micro-voids as the time increases under the elastic and super-elastic models, respectively. In the end, the results obtained are compared, and some intriguing phenomena appear through our analysis. This paper will present a good understanding on how the void growth

during reflow process, and will benefit the engineer's design of polymer materials in this industry.

2 Formulation of Mechanical Model

The moisture absorbed by the electronic materials is trapped in numerous pores (or micro-voids). During reflow process, the temperature of the package is raised to about 220℃ or more, which induce the evaporation of moisture in micro-voids. Thus, the micro-voids are subjected to internal vapor pressure p and remote stress σ_r^A, which denotes the thermal stress due to the increased temperature . For the purpose of analysis, it is convenient to consider a spherical volume of material containing a micro-void of spherical shape with initial inner radius R_1 and outer radius R_2. We assume that the matrix material is incompressible. And the micro-void will enlarge when it subjected to the combined effort of vapor pressure p and thermal stress σ_r^A. Therefore, we assume the r_1 and r_2 as the inner and outer radius after deformation. The mechanical model is displayed in Fig. 1.

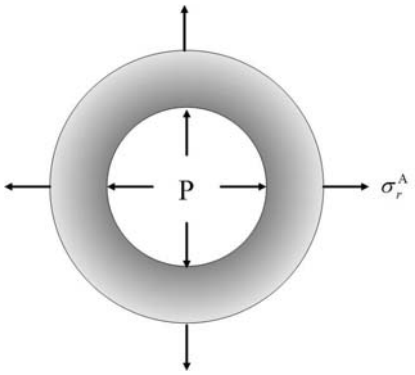

Fig. 1 The mechanical model of micro-voids under the action of vapor pressure and thermal stress

The micro-void is geometrically characterized by the initial and current void volume fractions f_0 and f:

$$f_0 = (\frac{R_1}{R_2})^3 \qquad f = (\frac{r_1}{r_2})^3$$

,

There are numerous vapor pressure models based on various theories. vapor pressure p satisfies the ideal gas law, then the vapor pressure model we use is shown as follows[16]:

$$P = P_0 \frac{T}{T_0} \frac{f_0}{f} \frac{1-f}{1-f_0} \mathrm{e}^{-3\alpha\Delta T} \tag{1}$$

Where p_0 is the initial pressure at room temperature, T represents current temperature, T_0 denotes initial temperature, α represents coefficient of heat expansion, $\Delta T = T - T_0$. During the reflow process in electronic packaging , temperature loading mode will reach the peak temperature more than 220℃, and temperature variation could be represented as the function of time t. Fig.2 displays a kind of temperature loading process with respect to the time.

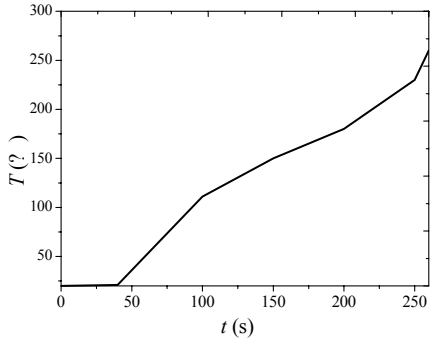

Fig.2 A typical temperature loading

How to utilize the variational principle to derive the growth function of micro-void? Firstly, we describe an arbitrary point(R, Θ, Φ) in the spherical coordinates in the initial configuration, and (r, θ, φ) represents the corresponding coordinates in the deformed micro-voids. It is notable that the deformation is spherically symmetric, therefore

$$\mathrm{r}=r(R),\theta=\Theta,\ \varphi=\Phi \tag{2}$$

Therefore, the domain before deformation is

$$D_0=\{(R,\Theta,\Phi)\,|\,0\le R_1\le R_0<R_2,0<\Theta\le 2\pi,0\le\Phi\le\pi\}$$

According to spherically symmetry, domain after deformation is

$$D=\{(r,\theta,\varphi)\,|\,r=(R)\ge 0,\ \ R_1\le R\le R_2,\Theta=\theta,\Phi=\varphi\}$$

Because of the condition of incompressibility, the volume relation below can be obtained:

$$r^3-r_1^3=R^3-R_1^3 \tag{3}$$

In terms of Eq. (2), the current void volume fraction can be displayed as

$$f=\frac{f_0a^3}{1-f_0+f_0a^3} \tag{4}$$

Where $a=r_1/R_1$ denotes the growth ratio of the micro-void.

3 Derivation of Governing Equation

In the section above, the geometrical configuration has been described. In this section, the fundamental formulation will be discussed in detail. We denote W as the strain energy function of the electronic packages. As to the linearly elastic material, the function is well-known for us[17]. When the ambient temperature is relatively higher or the materials themselves are soft, the super-elastic model should be taken into account. There are a vast amount of super-elastic models. In this paper, the neo-Hookean strain energy function will be introduced when the super-elastic analysis is conducted. The function of neo-Hookean material can be written as

$$W=\frac{\mu}{2}(\lambda_r^2+\lambda_\theta^2+\lambda_\phi^2-3) \tag{5}$$

Where, λ_r, λ_θ, λ_ϕ represent the principal stretches in the respective directions, respectively. Cauchy stress components in spherical coordinate system (r, θ, φ) corresponding to neo-Hookean materials are shown below:

$$\sigma_r=\lambda_r\frac{\partial W}{\partial\lambda_r},\qquad \sigma_\theta=\sigma_\phi=\lambda_\theta\frac{\partial W}{\partial\lambda_\theta} \tag{6}$$

Also, the principal stretches in the respective directions can also be described as:

$$\lambda_r=\frac{dr}{dR}=r'(R),\qquad \lambda_\theta=\lambda_\phi=\frac{r(R)}{R} \tag{7}$$

The total potential energy can be expressed as follows:

$$E=\int_{R_1}^{R_2}4\pi R^2W(\lambda_r,\lambda_\theta,\lambda_\phi)dR-\int_{R_1}^{r_1}4\pi R^2p\left(R\right)dR+\int_{R_2}^{r_2}4\pi R^2\sigma_r^A dR \tag{8}$$

According to the principle of least potential energy, we can obtain the governing equation from the first term in total potential energy after variation. Taking the Eq. (4)-(6) into the newly obtained variatianal equation, the governing function of dynamic growth of micro-void can be formulated.

4 Results and Discuss

In the last section, the derivation of governing function is discussed. In this section, we apply the method discussd above to predict that how void volume fraction f increase with respect to the time.

If we assume the material is linearly elastic, the governing function is shown as follows:

$$\frac{df}{dt}=\frac{9p_0f_0(f_0-f)f(1-f)(1-3\alpha T)\dfrac{dT}{dt}}{4ET_0(1-f_0)f^2e^{3\alpha\Delta T}[\dfrac{f_0}{f}\ln\dfrac{f_0}{f}\dfrac{1-f}{1-f_0}-\ln\dfrac{1-f}{1-f_0}]+9p_0f_0(f_0-f)T} \tag{9}$$

Where E is the Young's modulus of polymer materials applied in electronic devices. Due to the limited influence of thermal loading,thermal stress can be ignored, which means that the vapor pressure plays the major part on the growth of micro-voids on the proceeding of reflow. It is obvious that Eq. (9) is a IVP which can be solved numerically. The initial condition is that when t=0, f= f_0.Another problem is that as the loading temperature increases, the polymer materials will undoubtedly become softer and softer. As a result, the Young's modulus will decrease sharply. Hence, we compare three types of Young's modulus: 1GPa, 0.1GPa and linear decrease from 1GPa to 0.1GPa. The other parameters are selected as follows : f_0=1%, P_0=0.1MPa, T=0.94t+T_0, T_0=25℃， $\alpha=1.5\times10^{-4}$ .The growth of f as the time goes on is demonstrated in Fig. 3.

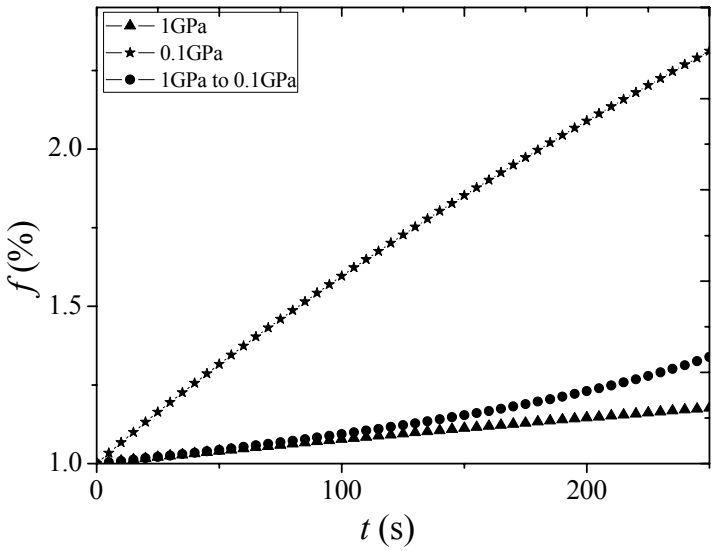

Fig.3 Dynamic growth of micro-void under different Young's Modulus

As it shown in Fig. 3, it is clearly to see the growth of cavitation during reflow process .and it is also notable that the soften the material are , the larger the deformation of micro-void is . In the electronic industry, it is not difficult for us to measure the Young's modulus of polymer materials with regards to different temperature. Thereby, we can accurately simulate the dynamic growth of micro-void regarding to variation of Young's modulus. In addition, the method of temperature loading also influences the transient growth of micro-voids. If the temperature T is non-linearly dependent with time t, the whole increase of void volume fraction will be different from the result in Fig. 3. Fig. 4 depicts the compassion between the linear temperature loading and quadratic temperature loading (T=0.003t^2+0.19t+T_0). We can see that when the temperature loading change, the void will increase in another way. However, it is intriguing to find that the final void volume fraction after the reflow process is the same no matter how matter the temperature is loaded in linear form or quadratic form if the Young's modulus remains unchanged with increasing temperature. However, if Young's modulus of materials varies with temperature, the fascinate

phenomenon will not appear.

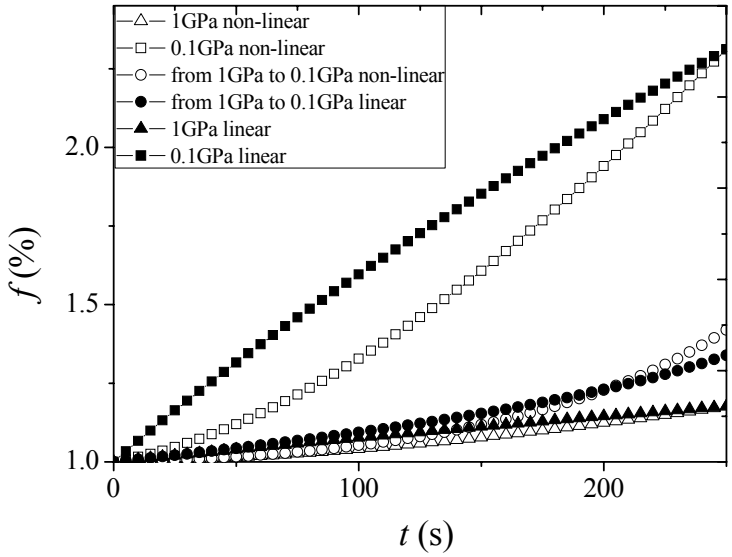

Fig. 4 Comparison between dynamic growth of micro-void under different temperature loadings

In reality, it is impossible for most of polymer materials to maintain the property of linear elasticity. In most of cases, polymers behave as super-elasticity even at the room temperature. The neo-Hookean model is one of the most common models applied in polymer materials. The dynamic growth equation can also be derived via the same method discussed above:

$$\frac{df}{dt}=\frac{P_0 f_0 f(1-f)(1-3\alpha T)\,dT/dt}{2\mu T_0(1-f_0)f^2 e^{3\alpha\Delta T}\{\frac{f_0}{f^2}[(\frac{f_0}{f}\frac{1-f}{1-f_0})^{-\frac{2}{3}}+(\frac{f_0}{f}\frac{1-f}{1-f_0})^{\frac{1}{3}}]-(\frac{1-f}{1-f_0})^{\frac{1}{3}}-(\frac{1-f}{1-f_0})^{-\frac{2}{3}}\}+P_0 f_0 T} \tag{10}$$

The shear modulus μ is set to 333 MPa ,and other variables is of the same value with that in the former discussion. The void growth is shown in Fig. 5. It is notable that the increase of void volume fraction is closely dependent on the value of initial void volume fraction.

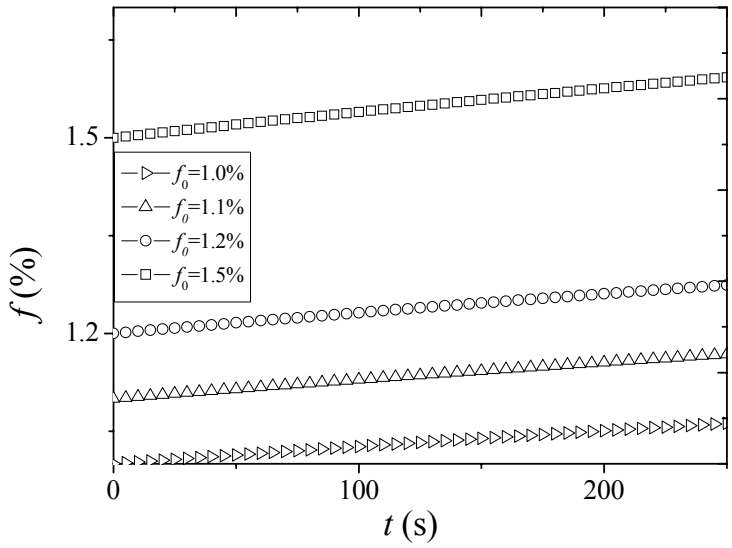

Fig.5 Dynamic growth of super- elastic micro-void under various initial void volume fraction

5 Conclusions

In this paper, theoretical results for dynamic growth of micro-voids are obtained with the context of finite deformation. The numerical method is applied to calculate the deformation of a void under the constitutional model of linear elasticity and super-elasticity. According to results acquired, it is notable that ways of growth are completely different when the temperature loadings are various. Secondly, when the Young's Modulus remains constant, the consequent that the final value of f will never change is fascinating. At last, the increase of void volume fraction is extremely dependent on the initial void volume fraction. Our investigation will provide a good understanding of mechanism of dynamic growth for engineers and researchers.

References

[1] G.Q. Zhang, W.D. van Driel, X.J. Fan,Mechanics of Microelectronics,Springer, 2006.
[2] A.A.O. Tay, T.Y. Lin, Influence of temperature, humidity and defect location on delamination in plastics packages. IEEE Transactions on Components, Packaging and Manufacturing Technologies, Part A, 1999, 22(4), pp. 512-518.
[3] S. Liu, Y. H. Mei, Behavior of delaminated plastic IC packages subjected to encapsulation cooling, moisture absorption, and wave soldering. IEEE Transactions on Components, Packaging, and Manufacturing Technologies, Part A, 1995, 18(3).
[4] Ball, J.M, Discontinuous equilibrium solutions and cavitation in nonlinear elasticity. Philos. Trans. R. Soc. A ,1982,306, pp.557–611.
[5] Oscar Lopez-Pamies, Martin I.Idiart, Toshio Nakamura, Cavitation in elastomeric solids: I—A defect-growth theory. Journal of the Mechanics and Physics of Solids, 2011, 59, pp.1464–1487.
[6] Oscar Lopez-Pamies, Martin I.Idiart, Toshio Nakamura, Cavitation in elastomeric solids: II—Onset-of-cavitation surfaces for Neo-Hookean materials. Journal of the Mechanics and Physics of Solids, 2011, 59, 1488–1505.
[7] X.J. Fan, J. Zhang, G.Q. Zhang, L.J. Ernst, A micromechanics based vapor pressure model in electronic packages. ASME Journal of Electronic Packaging, 2005, 127 (3), pp. 262-267.
[8] Y.Huang, J.W.Hutchinson, V.Tvergaard, Cavitation instabilities in elastic-plastic solid. Journal of the Mechanics and Physics of Solids, 1991, 39(2), pp.223-241.
[9] V.Tvergaard, Y.Huang, J.W.Hutchinson. Cavitation instabilities in a power hardening elastic -plastic solid. Journal of the Mechanics and Physics of Solids, 1992, 11(2), pp.215-231.
[10] T. F. Guo, L. Cheng, Thermal and vapor pressure effects on cavitation and void growth. Journal of Materials Science, 2001, 36, pp.5871 – 5879.
[11] T.F. Guo, L. Cheng, Modeling vapor pressure effects on void rupture and crack growth resistance, Acta Materialia, 2002,50,pp. 3487–3500.
[12] T.F. Guo, J. Faleskog,C.F. Shih, Continuum modeling of a porous solid with pressure - sensitive dilatant matrix. Journal of the Mechanics and Physics of Solids, 2008,56,pp. 2188–2212.
[13] Z.G. Li, X.F. Shu, Cavitation instability in Valanis-Landel hyperelastic IC packaging material[C]. International Conference on Electronic Packaging Technology and High Density Packaging, 2008, pp .4607127.
[14] Z.G. Li, X.Y. Niu, X.F. Shu, Unstable void growth in thermohyperelastic plastic IC packaging material due to thermal load and vapor pressure[C]. Proceedings of the 2007 8th International Conference on Electronic Packaging Technology, ICEPT, 2007, pp.4441453.
[15] Z.G. Li, X.Y. Niu, X.F. Shu. The study of moisture induced vapor pressure and weakened interfacial strength in CSP packages[C]. The 5th International Conference on Nonlinear Mechanics (ICNM-V), 2007, pp.212-215.
[16] X. J. Fan, S. Y. Zhang, Void behaviour due to internal pressure induced by temperature rise. Journal of Materials Science, 1995, 30(13), pp. 3483.
[17] S.P.Timoshenko, J..N.Goodier, Theory of Elasticity, The McGraw-Hill Companies, Inc, 1970.

Fatigue crack growth in the contact wire of railway catenary

Si Hai Mai[1,*], Mac Lan Nguyen-Tajan[1], Arnaud Verrier[1], Josselin Banting[2], Stéphane Avronsart[3]

[1] Innovation &Research, Société Nationale des Chemins de Fer Français (SNCF), 75611 Paris, France
[2] Agence d'Essai Ferroviaire, SNCF, 94407 Vitry Sur Seine, France
[3] Direction de l'Ingénierie, SNCF, 93574 La Plaine Saint Denis, France
* Corresponding author: si-hai.mai@sncf.fr

Abstract

In this paper, we used the eXtended Finite Element Method (XFEM), implemented in the software CAST3M developed by Commissariat à l'Energie Atomique (CEA), to simulate the fatigue crack growth of the contact wire in the railway catenary.

The material characteristics and parameters of the Paris law were identified thanks to experimental tests performed in a laboratory of Société Nationale des Chemins de Fer Français (SNCF). Specimens were cut directly from the contact wire. Two mean-stress levels were considered. The stress intensity factors were calculated by Finite Elements Method.

In order to validate the model and check its robustness, we performed a parametric analysis with different crack geometries. The numerical results showed a good agreement with the experimental observations in terms of the evolution of the crack shape and its growth rate. These results show that this numerical strategy is relevant and efficient to predict the critical size and the residual lifetime of the fatigue cracks detected by maintenance operations (Ultrasonic monitoring).

Keywords: fatigue crack growth, numerical simulation, eXtended Finite Element Method (XFEM), railway catenary.

1. Introduction

The role of the catenary system is to transmit the electrical energy from the energy supply point to trains (Fig. 1). To ensure a good current collection quality during a train passage, the pantograph applies a vertical force on the contact wire. This upward force causes a periodic bending stress. In addition to this periodic bending stress, the contact wire is subjected to a constant mechanical tensile force depending on the maximum speed of the line. The role of this tensile force is to avoid problems of dynamic instabilities in the contact wire. Moreover, the wear due to the pantograph passages reduces the cross section of the contact wire which leads to a higher tensile stress in the wire. These conditions accelerate the risk of fatigue fracture of the contact wire.

To predict the propagation of fatigue crack, different approaches could be considered. The most popular one is Finite Element Method (FEM). However, the conventional FEM using fixed meshes can only deal with this type of problem, either if the crack path travels through mesh nodes, or if we remove mesh elements [1]. This is an extremely important limitation in industrial applications.

In order to overcome the disadvantage of FEM, we used in this paper the eXtended Finite Element

Method (XFEM), implemented in the software CAST3M [4] developed by Commissariat à l'Energie Atomique (CEA), to simulate the fatigue crack growth of the contact wire. The identification of material parameters and the numerical modeling of the contact wire are described in the next sections. The numerical results are shown and discussed in the last section of the paper.

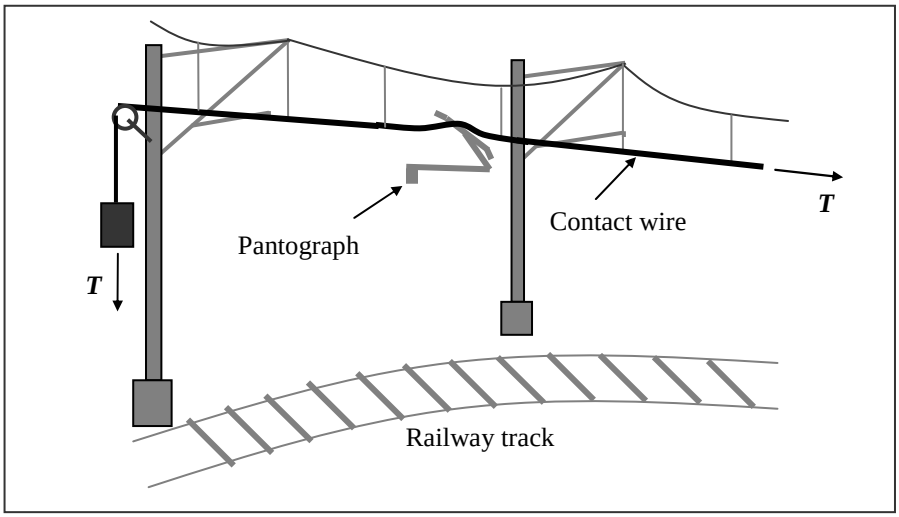

Figure 1. Railway Catenary

2. Fatigue Tests

2.1. Fatigue test specimen

In order to identify the mechanical characteristics and the fatigue crack growth law of copper contact wire, we had carried out fatigue tests with specimens cut directly from the contact wire (Fig. 2). An initial crack of 1mm depth was created on the contact size in the middle of the specimen.

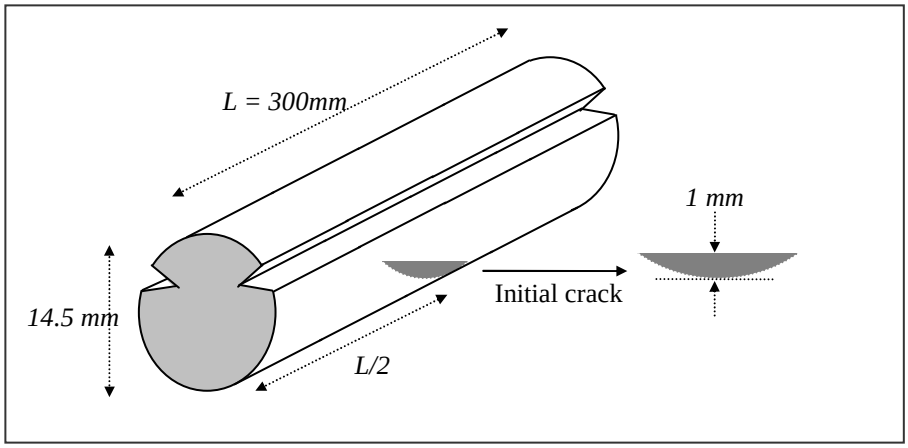

Figure 2. Specimen for fatigue tests (copper contact wire)

2.2. Fatigue crack growth test rig and conditions

The fatigue crack growth test rig is illustrated in Fig. 3. These tests were conducted in air at room temperature on a servo-hydraulic test machine having a load capacity of 50 tons with a frequency of 10 Hz under constant amplitude loading. These tests were conducted at different stress ratio R.

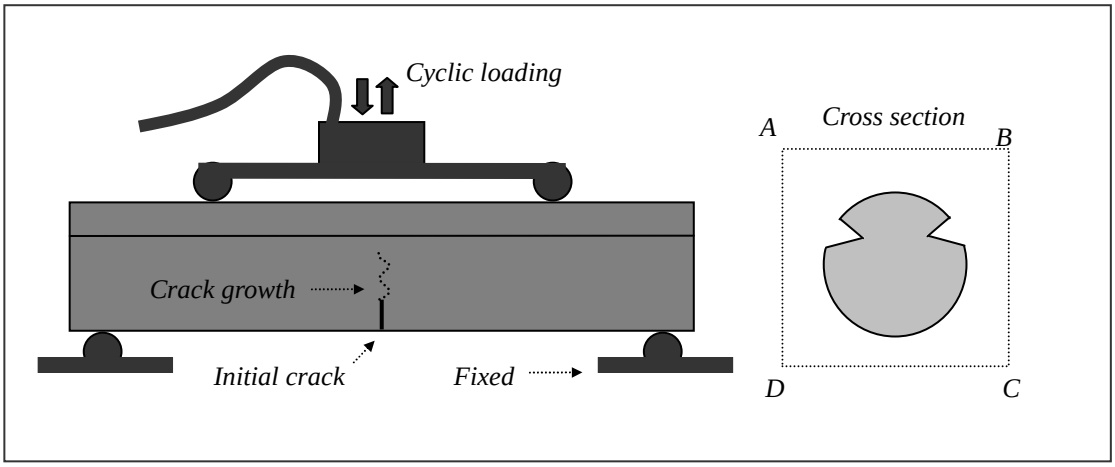

Figure 3. Fatigue crack growth test rig.

2.3. Test results

The test results are shown in the figure 4. Using the test results coupled with numerical calculations (FEM), we identified the parameters of Paris law (m, C) and the toughness (K_{1c}) of the copper material.

Paris law: $$\frac{da}{dN} = C.\Delta K^{m} \quad (1)$$

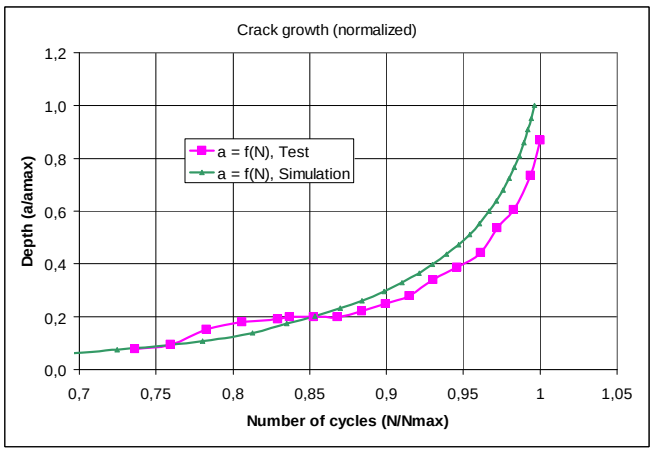

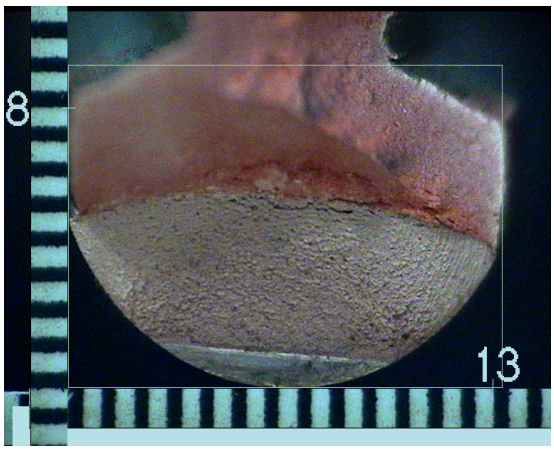

a. Crack growth rate b. Crack geometry

Figure 4. Fatigue crack growth in the contact wire

3. Modeling

3.1. XFEM Model

In this paper, we used the eXtended Finite Element Method for linear elastic fracture mechanics (LEFM), in which an enrichment basis is added to the classical finite element basis approximation. This is done using the partition of unity method developed in Babuska and Melenk [2]. The enriched basis shape functions are associated to new degrees of freedom and the displacement field can be written (see Moes *et al.* [1]):

$$U = \sum_{i \in \mathrm{N}} N_i(x) U_i + \sum_{i \in \mathrm{N}_{cut}} N_i(x) H(x) a_i + \sum_{i \in \mathrm{N}_{branch}} \sum_{\alpha} N_i(x) F_\alpha(x) b_{i,\alpha} \tag{2}$$

N is the set of the standard finite element nodes, N_{cut} the set of nodes which belong to elements completely cut by the crack and N_{branch} the set of nodes containing a crack front. N_i are the standard finite element shape functions, $H(x)$ is a Heaviside function which value is 1 if x is above the crack surface and -1 if x is under the crack surface. $[F_\alpha]$ is derived from the LEFM asymptotic displacement field:

$$[F_\alpha] = \left[\sqrt{r} \sin\left(\frac{\theta}{2}\right), \sqrt{r} \cos\left(\frac{\theta}{2}\right), \sqrt{r} \sin\left(\frac{\theta}{2}\right)\sin(\theta), \sqrt{r} \cos\left(\frac{\theta}{2}\right)\sin(\theta) \right] \tag{3}$$

3.2. Numerical algorithm

The eXtended Finite Element Method (XFEM), implemented in the software CAST3M developed by Commissariat à l'Energie Atomique (CEA), was used in this paper to simulate the fatigue crack growth of the contact wire.

In this XFEM model, the mesh of the structure (three dimensions) without crack is fixed during the crack growth. The position of the crack inside the structure is identified thanks to an independent crack mesh (two dimensions) which needs to be updated after each crack growth step.

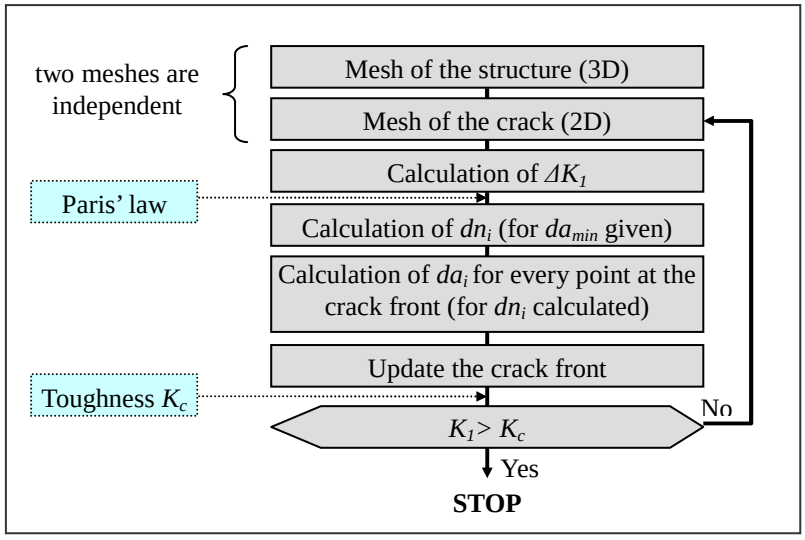

Figure 5: Numerical algorithm for fatigue crack growth simulation.

The numerical algorithm is shown in Fig. 5. The Paris' law and the toughness are material inputs which are identified in the previous section. The calculation of stress intensity factors K_i is done by using the domain integral method (J integral). The crack growth step da_{min} is a numerical input. A convergence study for this numerical input is necessary.

The simulation is stopped if the stress intensity factor K_1 is greater than the toughness K_c of copper material. Otherwise, the crack front is updated and a new crack mesh is constructed.

4. Numerical Results

4.1. Inputs

In this section, we study the fatigue crack growth of a contact wire in flexure using the XFEM presented in previous section.

The meshes of the structure (worn contact wire without crack) and the two initial cracks are shown in Fig. 6. In the cross section of the structure, QUAD elements are used. The final mesh (3D) of the structure is obtained by extrusion of the cross sectional profile. Special 3D XFEM elements are used in the crack zone. Whereas, the elements used to mesh the cracks are classical 2D triangular elements.

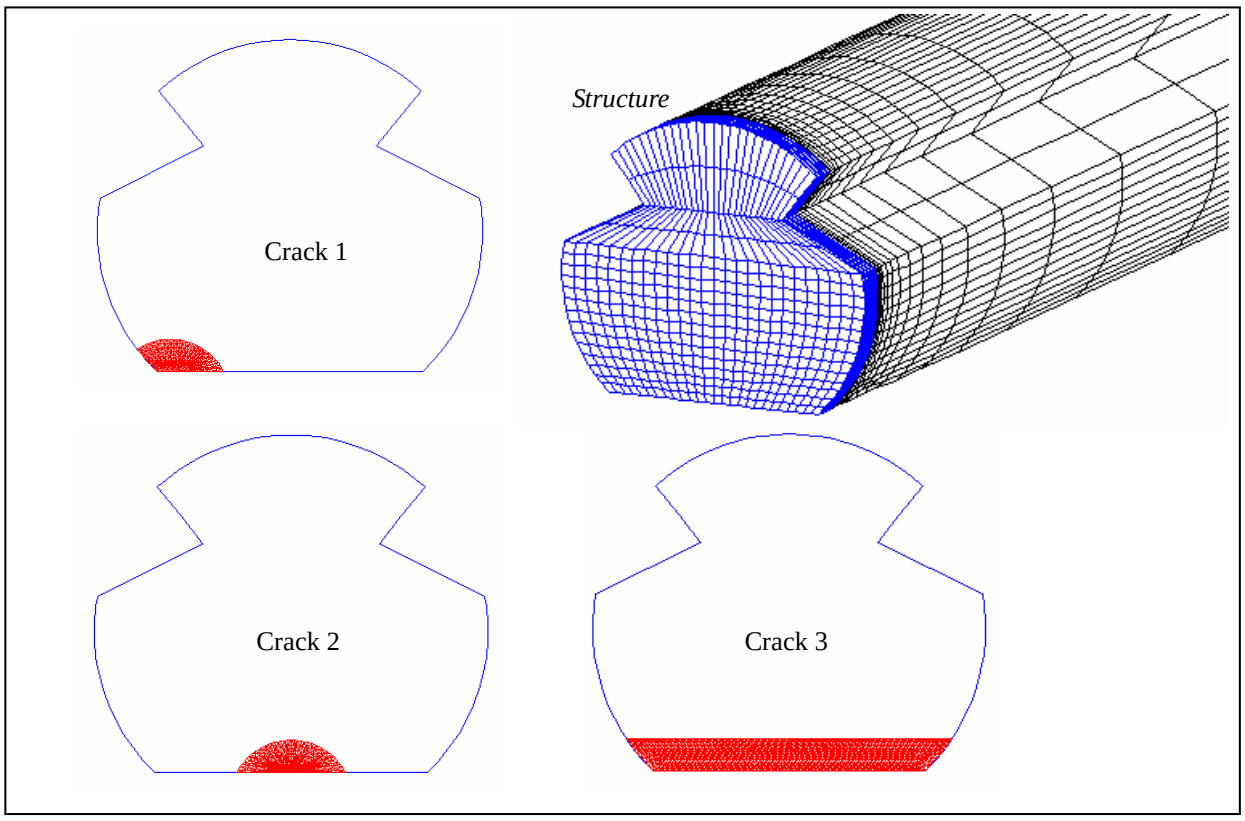

Figure 6: Meshes of the structure and initial cracks

The material parameters (Paris' law and toughness) are identified in the section 2 and the numerical model is presented in the section 3.

4.2. Results

Figure 7 shows the stress intensity factors calculated at the crack front for different types of initial crack. We can see from these results that the mode I is dominant ($K_2 \sim 0$ and $K_3 \sim 0$) in all cases. Thus, the Paris' law is applicable for our model.

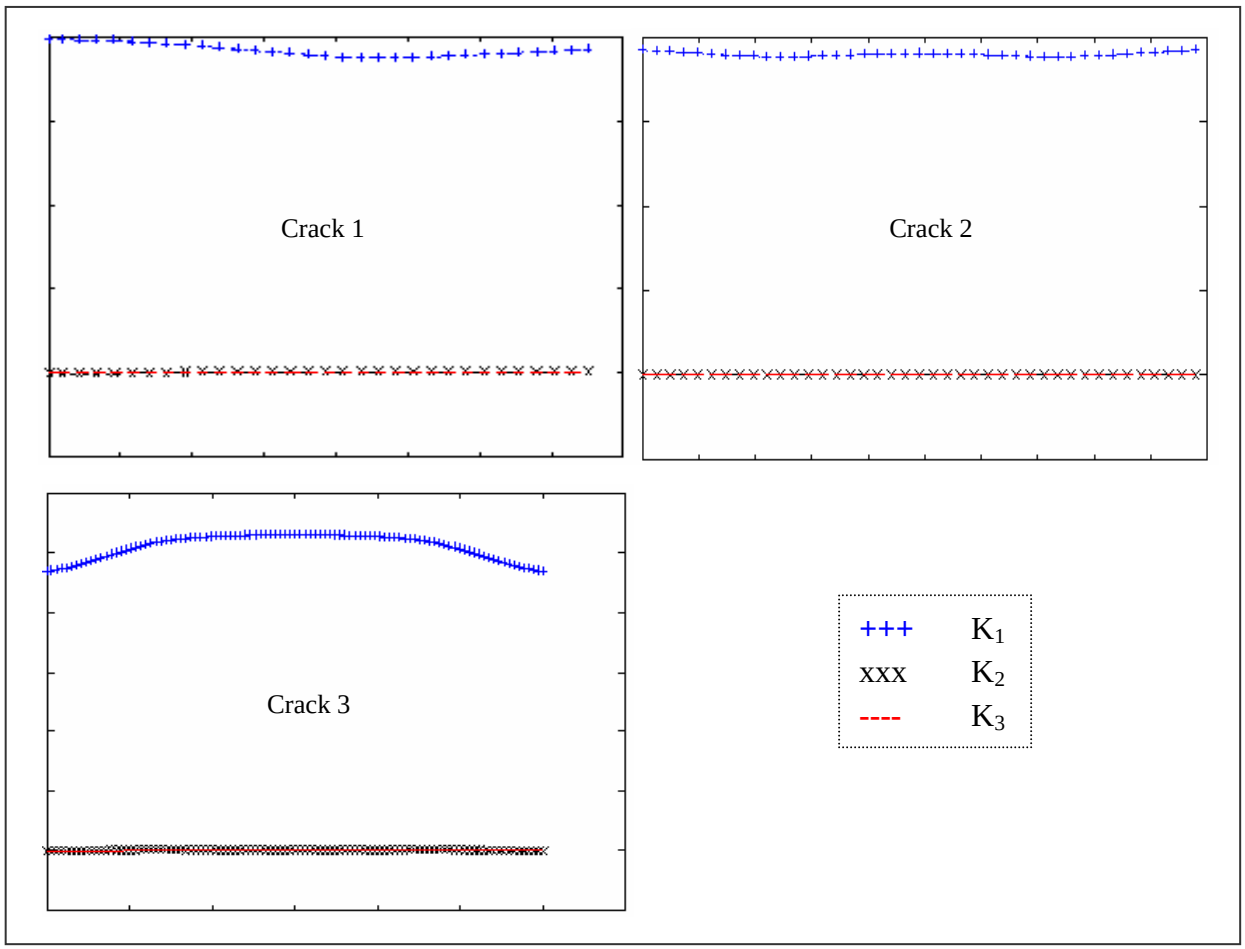

Figure 7: Stress intensity factors for three initial cracks

Using the XFEM model described above, we've performed different crack growth simulations. We can see in the figure 8 a comparison between the numerical simulation and the test result. The numerical results showed a good agreement with the experimental test in terms of the evolution of the crack shape and its growth rate.

In the figure 9, we show the crack growth simulated for three types of initial crack. Figure 10 shows the evolution of the crack depth in function of the loading cycles. This type of curve could be used in combination with the ultrasonic measurements to optimize the maintenance planning of the contact wire. For example, if we detect a crack of contact wire (point A) at the moment *t*, using the numerical curve (Fig. 10) we could estimate the action timescale before reaching the critical crack (point B). To follow the real crack growth, some additional measures could be performed between twos points A and B. If necessary, the critical point B could be modified after each measurement.

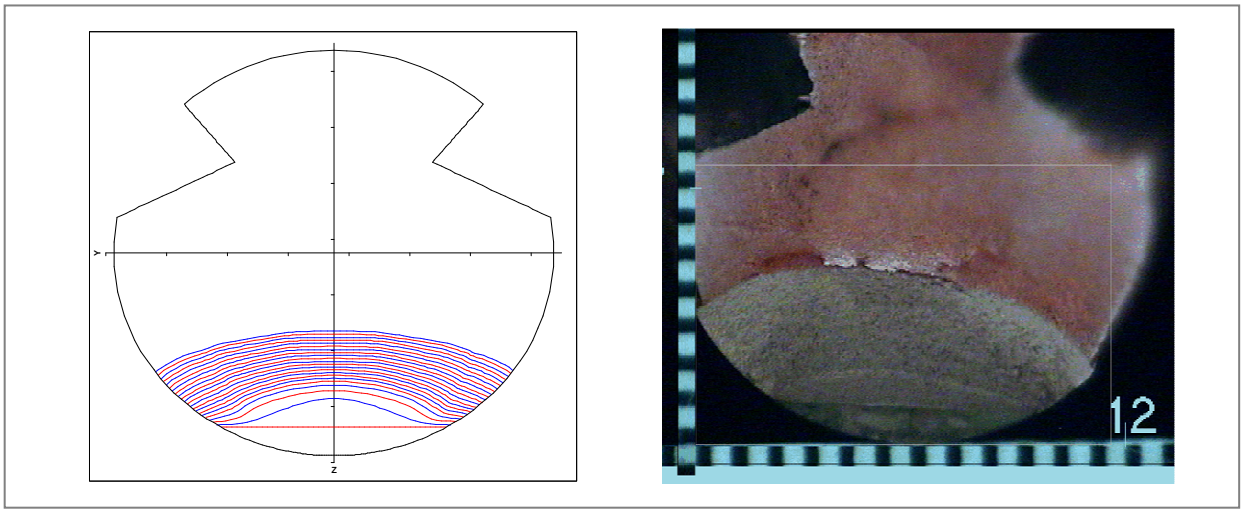

Figure 8: Comparison between the numerical simulation and the test result

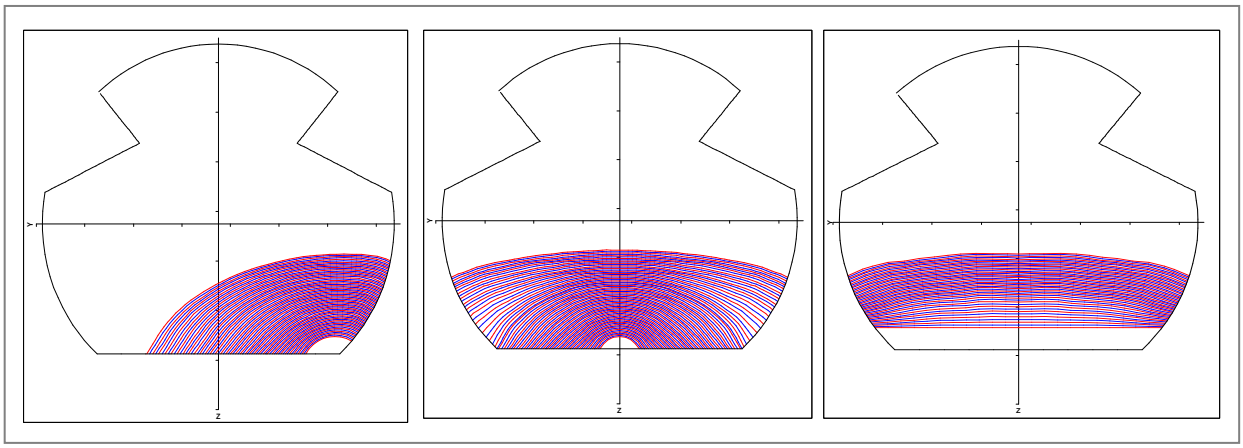

Figure 9: Crack growth for different initial cracks

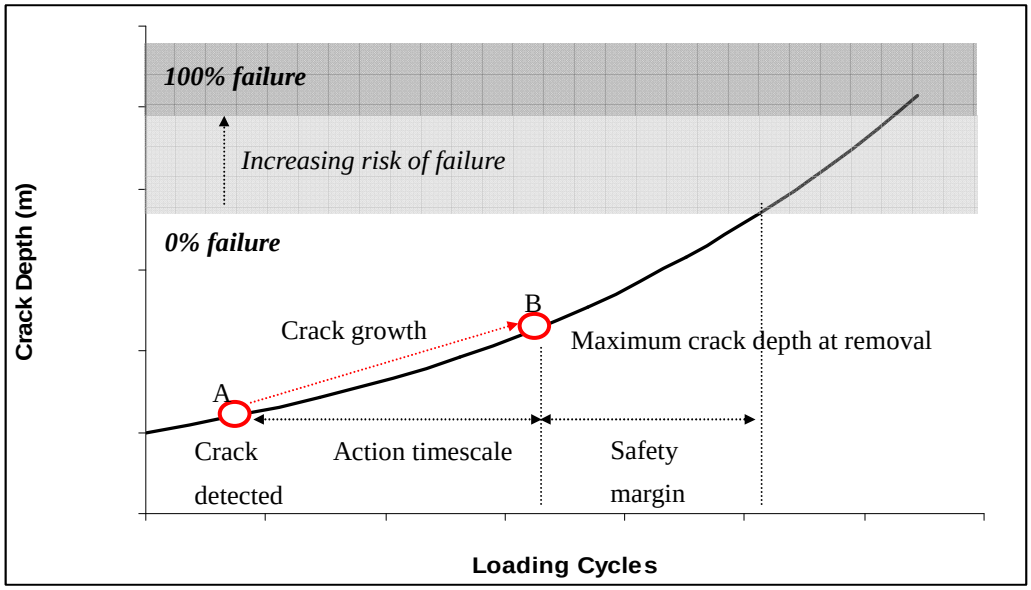

Figure 10: Evolution of the crack depth

5. Conclusion

In this paper, we used the eXtended Finite Element Method (XFEM), implemented in the software CAST3M developed by Commissariat à l'Energie Atomique (CEA), to simulate the fatigue crack growth of the contact wire.

The material characteristics were identified thanks to experimental tests performed in a laboratory of Société Nationale des Chemins de Fer Français (SNCF) with specimens cut directly from the contact wire.

Different geometries of crack were studied. The numerical results showed a good agreement with observation in term of the evolution of the crack shape and its growth rate. Theses preliminary results show that this numerical strategy can be used to predict the critical size and the residual life of fatigue cracks detected by maintenance operations.

A more detailed study on the real cracks detected in the contact wire will be the target of the next step.

Acknowledgements

The authors gratefully acknowledge Jean-Pierre MASSAT from Innovation and Recherche of SNCF for discussions about dynamical behaviour of pantograph-catenary system, engineers from Ingénierie Technologie of SNCF (SNCF-IG-TE-ZC) for discussions about maintenance method of contact wire, Benoit PRABEL from CEA for discussions about XFEM simulation and the Direction SNCF-CSC for the financial support of this project.

References

[1] N. Moes , J. Dolbow, T. Belytschko, A finite element method for crack growth without remeshing, International Journal for Numerical Methods in Engineering ,1999; 46(1):133–150.

[2] I. Babuska, J.M. Melenk , The Partition of unity method, International Journal for Numerical Methods in Engineering 1997; 40:727–758.

[3] S. Pommier , A. Gravouil, A. Combescure, N. Moes, Extended Finite Element Method for Crack Propagation, ISTE Ltd 2011.

[4] Software CAST3M, website http://www-cast3m.cea.fr/.

New Fatigue Life and Durability Evaluating Method of High Speed Train Carbody Structure

BingRong Miao[1,*], WeiHua Zhang[1], Xiang Mei[1],Ying Zhang[1],Wei Li[1]

[1] State Key Laboratory of Traction Power, Southwest Jiaotong University, Chengdu 610031 Sichuan, P.R.China
* Corresponding author: brmiao@home.swjtu.edu.cn

Abstract With the development of new generations of CRH trains in China, one new fatigue integrated analysis method was proposed to evaluate high speed train carbody structure fatigue life and durability. The CRH train's carbody structure was used here as an example for study the interaction relation between vehicle dynamic characteristic and fatigue property running in BEIJING-TIANJIN intercity line. The detail method steps include: Firstly, MBS (Multi Body Simulation) technologies allowed the development of more detailed and accurate vehicle-rail rigid-flexible coupled dynamics model which can be used as input of stress distribution calculation. And The typical carbody structure's fatigue load spectrum and extrapolation were calculated here through quasi-static stress method according to field running condition for different radius curve (400-2500 m), which was random combination of Track irregularity, W/R profile and Cant deficiency. Secondly, Aluminum alloy structure FE (Finite Element) analysis technologies, such as modal analysis, substructure and stress calculation, were used to determine structure critical location and understand carbody structure nature frequencies and mode shapes influence. FM (Fracture Mechanics) assessment analysis for different load condition combination based on the structure stress distribution and stress/strain time histories results. Thirdly, carbody structure fatigue stress distributions in carbody selected dangerous regions were calculated in sub-model. And The analysis results were compared with the field dynamic stress test results. Finally, carbody fatigue life and durability analysis results were estimated based on aluminum material S-N curve with Palmgren-Miner damage cumulative theory. The critical structure fatigue failure influence can be taken into account in stress distribution used as input of FM. This work targets the capabilities of MBS and FEM (Finite Element Method) in the fatigue and durability design early stage and verification phase of the high speed train key structure, such as bogie structure, axle and wheel, etc. The results also illustrate that the proposed numerical simulation method can give an important contribution in terms of high speed train key structure component fatigue and durability evaluation.

Keywords Railway, Carbody, Fatigue life, Multibody Dynamics, FEM

1. Introduction

With the rapid development of high-speed railway in China, the CRH series train's vehicle key structure components fatigue design and analysis method are also facing the serious challenge of many technical difficult problems, such as running safety and ride comfort. Especially for the important structural components fatigue design and durability analysis method, there are many aspects worthy of consideration and study [1-2]. Despite the conventional railway vehicle structure fatigue design method had been applied in some structural components' durability during last years .But with the continuous improvement of vehicle speed, it has been revealed that dynamically loaded structure components' fatigue damage and structure destruction maybe become one of potential technical problems in future. Most of the recent research on the dynamic behaviors of vehicles /rail has been simulated by the need to understand the basically cause of practical service problems arising from the interaction between the vehicle and the track and to develop solutions or treatments for those problems.

With respect to structural fatigue problems, great deals of research have been done these years. During the more recent structure fatigue simulation techniques research, an integrated design methodology had been made use to evaluate structural fatigue (R.K.Luo,et al.1994, Stefan Dietz,1998).These procedures make use of multibody simulation packages (Schielen, 1990;kortum and sharp,1993) to determine the dynamic loads acting through the suspension onto the vehicle structure. Measured track data are generally used as excitation inputs. Using a finite element model of the structural a component on which the dynamic forces are acting, stress concentration locations

are identified and analyzed. Structure dynamic stress histories are determined under simulated loading and the fatigue life is determined using an appropriate fatigue theory. In reference [3], the author had systematically presented one hybrid simulation method to the carbody structure fatigue life assessment based on **MBS** (Multibody Simulation) and **FEM** (finite element method). In this paper, based on some typical literatures' achievements [4-7], one new fatigue life and durability evaluating method of high speed train carbody structure is proposed here to evaluate the carbody structure fatigue property and applied to the structure fatigue design. And one complex railway EMU carbody was used as an example to describe the detail method steps how to use in fatigue design development processes.

2. Structure Fatigue Numerical Calculation Method

There are three main factors, which affect the structure fatigue behavior: The S-N curve of structural components; the load time histories; and structural geometrical features. The carbody structure of railway vehicle is subjected to a very large number of variable amplitude stress cycles during their operational life. Large structural stress and complex load conditions are the main causes which lead to vehicle structural components' fatigue crack initiation and crack growth. And the weld structure manufacturing process of the structural components is one of the main factors which cause the structure destruction. Since this paper focuses on the structural fatigue damage caused by vehicle structural dynamic characteristics, so there will not be to evaluate the structure damage from the perspective of welded structural fatigue. Some weaknesses locations of the carbody structure are studied, such as the location of the secondary suspension, the traction or braking, the corners of the window, and so on.

This method considers the dynamic behavior of the full vehicle. It can greatly reduce the physical prototype test cost and design fault, while it can improve the accuracy of structural durability design and life prediction. Fatigue is one of the primary mechanisms causing deterioration of high speed train vehicle carbody structure during its lifetime. Straight track, tracking/ braking, curve passing, aerodynamics effect and other cyclic or alternating loads easily subject the carbody structure to huge numbers repeated stress over its life time. Cyclic loading causes fatigue cracks initiation, which causes cracks to form in the structure. These cracks grow longer with each stress cycle, degrading the carbody's structural strength and life. A crack initially grows slowly, but the rate accelerates as these cycles accumulate, to the point at which rapid crack growth results in a fracture. Thus, some durability design criteria for carbody are those can endure accumulated fatigue damage during service Life-Cycle to prevent structural failure.

A full vehicle's multibody dynamic model including carbody, bogies, the primary suspension and track are set up using the famous MBS software pack SIMPACK. The vehicle is described as rigid bodies interconnected via several different suspension systems. Several typical load cases, such as tangent line and curve passing, were performed in order to verify the accuracy of the dynamical model in reproducing the full vehicle dynamic behavior simulation. Carbody structure fatigue analysis puts a great demand on accuracy including MBS and FEM model .The quasi-static stress method was performed for carbody to obtain the stress histories. FEM model cannot be too complex since the dynamic analysis and fatigue assessment is time consuming. The finite element analysis method was used in software ANSYS. The load time histories are very important aspects since they are the actual source of fatigue failure prediction. Several complex loading conditions must be determined, either by analytical approaches or by dynamic stress tests. Due to the computational effort involved in dynamic simulations, only selections from the stress history can be used. Decisions as to what loads to apply must therefore be designed and selected analytically. Different types of railway vehicle operational conditions must be considered in additional to some extreme load cases generated from error operation.

A fatigue assessment method describes a sequence of steps to be taken in order to predict fatigue life from a given state of stress and strain. For carbody subjected to variable amplitude stochastic loading, the main steps include:

- Rain flow cycle counting;
- Damage calculation for each cycle;
- Fatigue damage accumulation.

The proposed new method for high speed train carbody structure is shown in Fig.1.

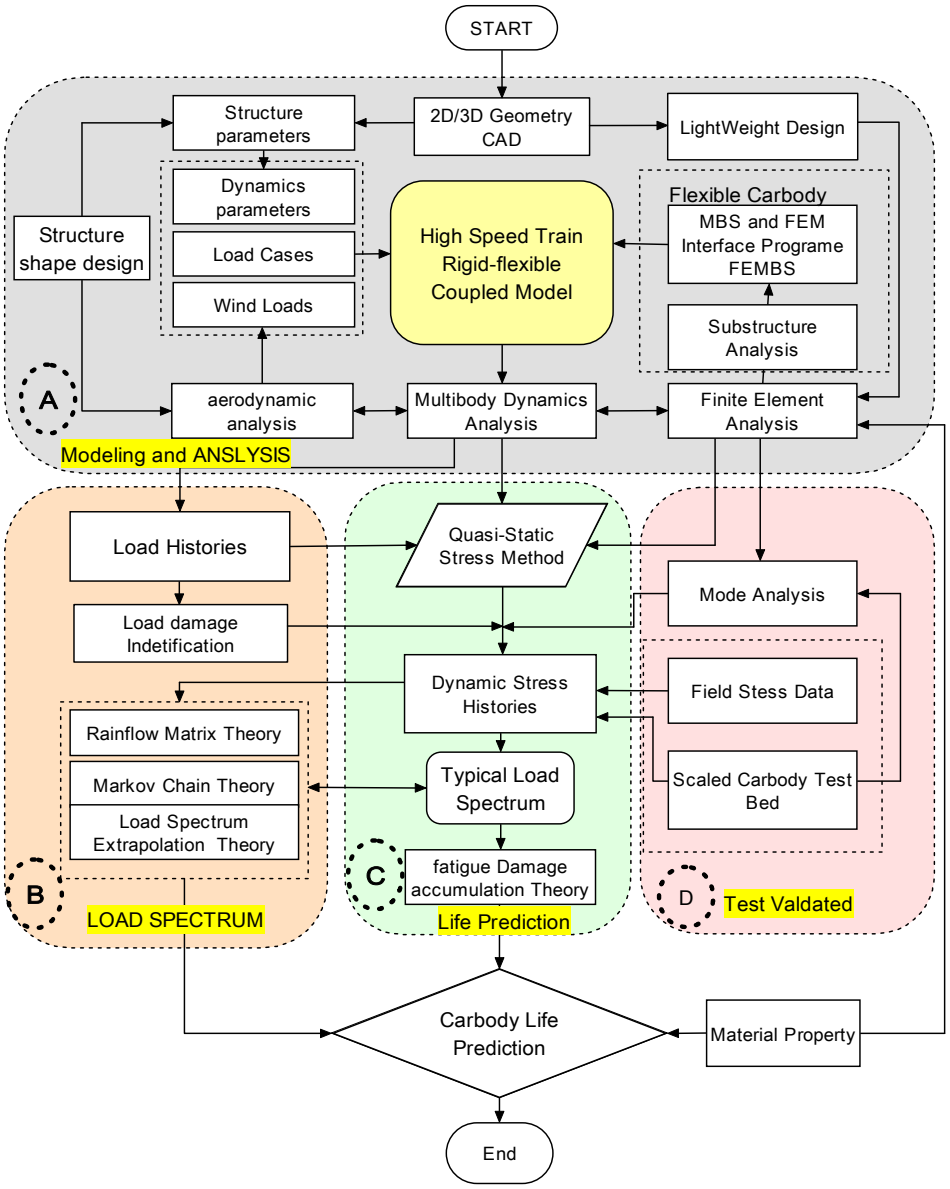

Fig. 1: New carbody structure fatigue life evaluation flowchart

Vehicle Dynamics Simulation with MBS. Dynamics analysis of the full vehicle can be used to obtain the load time histories for the carbody structure in typical running cases, such as the straight and curve lines. The CRH train vehicle was selected for this study to create the detailed multibody dynamics model, which was running between the Beijing-Tianjin intercity lines in China. The model has been substantially altered to accommodate more load cases and used to simulate railway vehicle dynamic behavior. The loads such as inertial loads and external loads derived using multibody dynamics analytical methods are mostly used for fatigue calculation [8].

The vehicle has been modelled with the aid of the MBS software SIMPACK library elements like rigid or flexible bodies, force elements and joints. The carbody was described as rigid body by each other. Several linear spring and damper elements describe the primary and secondary suspension

unites, the bump stops and viscous dampers are represented by nonlinear characteristics. The configuration and suspension characteristics of the system are included in the dynamic model. The full vehicle multibody dynamics model was shown in Fig.2.

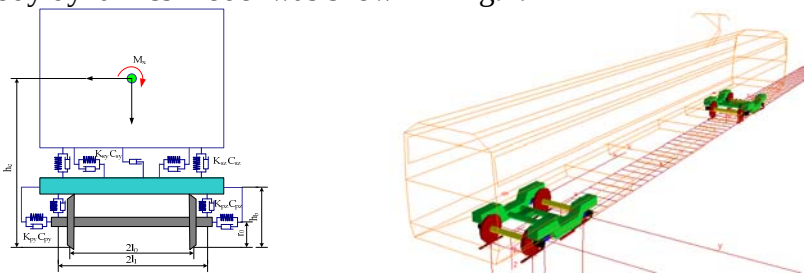

Fig.2: Dynamic model of carbody

The typical running case in operating condition has been designed to perform multibody dynamics simulation, which includes straight running, curve passing and traction/braking etc. The load histories have been calculated in MBS, which include forces, velocities, accelerate and angular velocities etc. And in order to take account of the influence of elastic carbody, the interface program FEMBS between finite element analysis codes and SIMPACK is used here to generate input data for flexible bodies to MBS simulation. The paper adopted the track irregularities is the real track excitation spectrum. They run on a straight railway in speed 200 km/h to 300km/h. Some dynamics simulation results are shown in Fig.3.

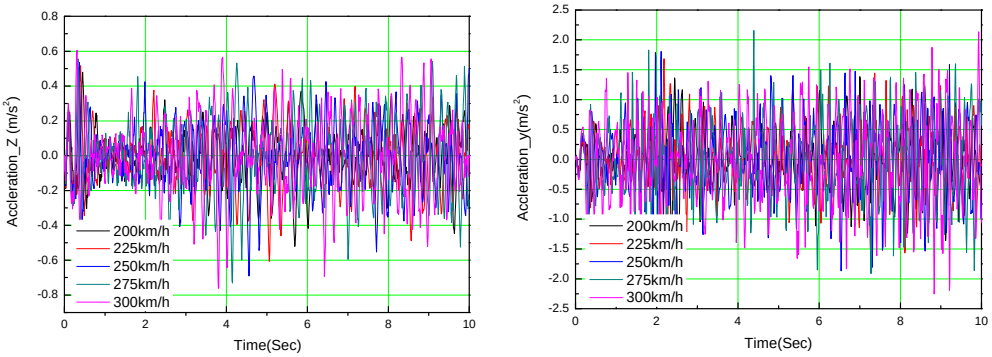

Fig.3: Vertical and lateral acceleration of carbody center

Finite Element Modeling of Carbody. The carbody structure fatigue damage is mainly caused by the vehicle dynamic response, which is usually expressed as stress or strain time history. Stress/Strain calculations for fatigue life estimation can be performed in the time domain or frequency domain. The quasi-static stress method was used to obtain the stress/strain time histories. The detail carbody stress analyses with ANSYS were performed based on MBS and FEM. And mode analysis is also performed here. The finite element model of the carbody is shown in Fig.4. Modal analysis is usually used to determine the natural frequencies and mode shapes of carbody structure. The modal analysis results are shown in Fig.5 and Table1.

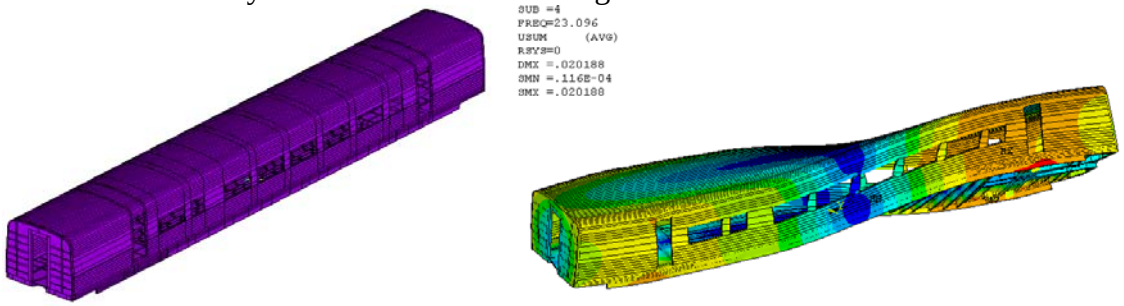

Fig.4: Carbody finite element model Fig.5: The 1st Torsion mode of Carbody structure

Table1.The results of the modal analysis

Mode No.	Frequency(Hz)	Mode shape
1	13.186	1st Lateral bending
2	19.078	1st Vertical bending
3	21.700	2ndLateral bending
4	23.096	1st Torsion
5	23.438	2nd Vertical bending
6	25.627	3rd Lateral bending
7	26.836	3rd Vertical bending
8	30.477	2nd Torsion
9	30.779	4th Vertical bending +Breathing
10	33.762	Breathing

Fatigue Assessment of the Carbody Structure. The carbody structure fatigue life was predicted. and compared with the life calculated from the original test datum. The material used in the carbody was A6N01S-T5.The stress-Life(S-N) curve was created in software *Fe-Fatigue* according to the material fatigue design manual which is used in the fatigue life calculation. Based on the structure *S-N* curve and the Palmgren-Miner rule, the carbody structure fatigue life was evaluated. The results of the rain flow cycle counting are usually presented as a rain flow matrix giving the number of cycles occurring at various combinations of range and mean stress [9, 10]. Then the values of range and mean are rounded off to discrete values to give a matrix of manageable size. The calculation results for test point and node 70770 corresponded to the test points are shown in Fig.6.

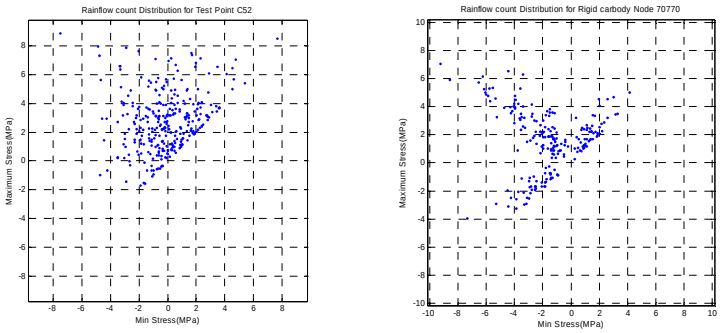

Fig. 6: Rainflow cycle count of C52 and Node 70770

3. Field Lines Dynamic Stress Test

In order to determine the accuracy of strain predicted from the simulation model, the field lines dynamic stress/strain test for carbody was performed to the carbody fatigue estimation. And fatigue life of carbody was calculated from the original field dynamic stress test data. The field dynamic stress/strain test points for the carbody and results for test point C52 are shown in Fig. 7.

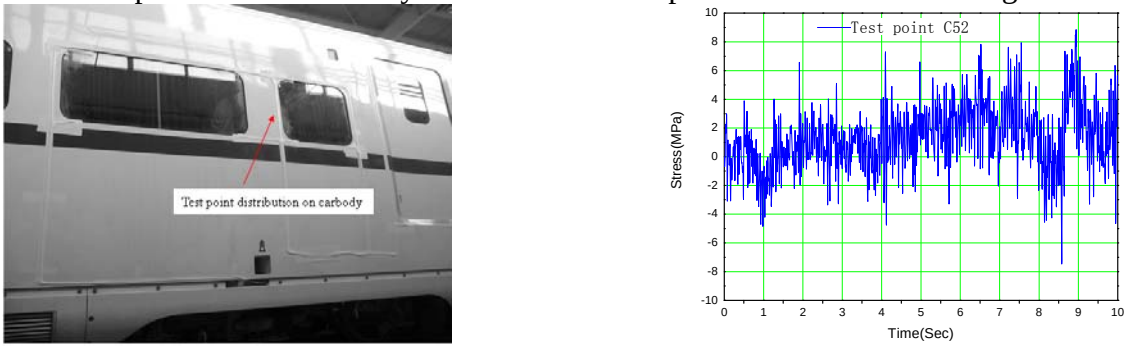

Fig.7 Dynamic stress/strain test and results for carbody

4. Results and Discussion

The primary goal of this paper is shown how to correctly evaluate the railway structure fatigue damage at the critical location of the carbody. It can show the relation mechanism between full vehicle's carbody dynamic characteristic and structure fatigue property. The safety factor analysis based on *S-N* method based stress was used to calculate the carbody damage distribution. Finally, according to rain flow matrix and Markov chain theory, material *S-N* curve, structure dynamic stress, and Palmgren-Miner damage summary theory, carbody structure fatigue life can be evaluated and compared with the field stress test results. Some carbody structure fatigue life calculation results are shown in Table2.And some fatigue analysis results are shown in Fig. 8.

Table 2. Fatigue life estimation comparison

Name	**Mean**(MPa)	**Min** (Mpa)	**Max**(Mpa)	**Range**(Mpa)	**Life repeats**
Test point c52	1.436	-5.814	9.522	15.336	2.694e6
Node 70774	-0.903	-9.253	7.045	16.298	2.278e6

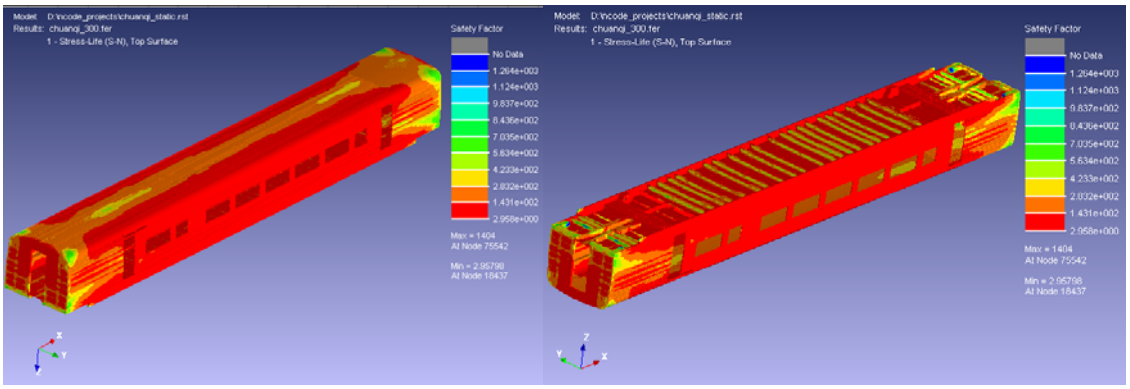

Fig.8: Safety factor analysis results

5. Conclusion

The new fatigue life and durability evaluating method of high speed train carbody structure based on MBS and FEM was proposed to evaluate the CRH vehicle carbody structure fatigue properties. This method can be used in early structure fatigue design in railway carbody structure new product development stage. Some simulation results are also shown and compared with the field dynamic stress test results to validate the method effective. The results also prove that the MBS-FEM simulation method can evaluate the carbody structure correctly. It is also beneficial to understand the influence for dynamic property to structure fatigue life prediction and satisfy with railway key structure component's durability design.

Acknowledgment

This research was supported by National Basic Research Program of Sichuan Province application Base Research Program (2012JY0094), New Teacher Foundation of Education Ministry (20090184120016).

References

[1] R.K.Luo,B.L.Gabbitas,B.V.Brickle.Fatigue life evaluation of a railway vehicle bogie using an integrated dynamic simulation. Part F: Journal of rail and rapid transit, Proc Instn Mech Engrs, 208(1994), 123-132.

[2] S.Dietz, H. Nettlr, D.Sachau.Fatigue life prediction of a railway bogie under dynaic loads through simulation. Vehicle System Dynamics. 29 (1998), 385-402.

[3] H.S.Kim,H.J.Yim,C.B.Kim. Computational durability prediction of body structure in prototype vehicle .International Journal of Automotive Technology. 23 (2000), 129-135.

[4] M.Haiba et al. Review of life assessment techniques applied to dynamically loaded automotive components. Computer and structures .80 (2002), 481-494.
[5] J.A.Ridnour. Methodology for evaluating vehicle fatigue life and durability. The University of Tennessee, Knoxville, 2003.
[6] Masyuki miyamoto.Recent research and development on advanced technologies of high speed trains in Japan. Vehicle system dynamics, 2003(3), 55-99.
[7] Johan Martinsson.Fatigue assessment of complex welded steed structures. Royal institute of technology.Stockholm, 2005.
[8] I.S.Sung, S.P.Choon, K.H.KIM. Fatigue strength evaluation of the aluminum carbody of carbody of urban transit unit by large scale dynamic load test. JSME International Journal.48 (2005) 27-33.
[9] B.R.Miao.Research of locomotive carbody structure fatigue simulation based on MBS and FEM .Southwest Jiaotong University.Chengdu.China. 2006.(In Chinese)
[10].P.Johannesson. Extrapolation of load histories and spectra. Fatigue and fracture for engineering materials and structures. 29(2006), 209-217.
[11]T Morimura,M Seki.The course of achieving 270km/h operational for Tokaido Shinkansen. Proc IMECHE. 219(2005), 21-43.
[12]Jung-Seok Kim,Sang-Jin Lee,Kwang-Bok Shhin. Manufacturing and structural safety evaluation of a composite train carbody carbody.Composite Structures.27 (2007), 468-476.

Safe Life and Damage Tolerance Concepts of Railway Axles

Dietmar Klingbeil*, Uwe Zerbst, Christian Klinger

BAM – Federal Institute for Materials Research and Testing, 12200 Berlin, Germany
* Corresponding author: Dietmar.Klingbeil@bam.de

Abstract

On July 9, 2008 a high speed train derailed in Cologne main station, Germany at a low speed because an axle was broken. Fortunately, the derailment happened at a low speed so that nobody was injured. The reason for the broken axle was investigated and it turned out that most likely large inclusions located shortly underneath the surface in a T-transition were the origin of the final crack. Basing on that result, a systematic investigation on existing safety assessments of railway axles was performed. This results in an analysis of the production process of axles and in a critical review of existing of existing assessments. Improvements and future developments are outlined.

Keywords railway axles, derailment, service loading fatigue, inclusions, safety assessment

1. Introduction

A hollow axle of a German high speed train broke on 9 July 2008. Fortunately, the train derailed at low speed after change of running direction when crossing a Rhein bridge in Cologne. The failure occurred when the axle was in service 3.09 million kilometers which refers to 10^9 loading cycles. A more detailed report on the failure investigation is provided in [1]. Because the fracture surfaces were heavily destroyed no definite answer could be given to the question of the initiation site. However, non-metallic inclusions of unacceptable size were found nearby the crack origin. The investigators assume a similar inclusion to be responsible for fatigue crack initiation. Basing on this event, a critical review of state-of-the-art design is presented and the further development is basically revealed.

2. Safe Life and damage Tolerance Concepts: State-of-the-Art and Necessity of Improvements

2.1. Overview

The design and operation of railway axles are based on a two-stage safety concept comprising “safe life” and “damage tolerance” methods. Figure 1 schematically illustrates the state-of-the-art concept and extends it by further options which are presently under development or offer additional potential in the future. The figure is taken from an extended discussion on axle safe design which the authors of this paper and others presented in [2]. This shall not be repeated here in detail. Instead a number of selected issues shall be briefly discussed which, as the authors think, promise potential for further increasing the safety level of axles. These are:

(a) Limiting the projected lifetime as a consequence of features such as damage accumulation, potential very high cycle (VHCF) effects and corrosion. A specific concept is the “one-million miles axle” based on a worst case scenario including fatigue crack propagation;

(b) Taking into account the most common reasons for fatigue crack initiation, corrosion pits, damage due to flying ballast impacts and non-metallic inclusions in the material by advanced design

rules, and;

(c) Improving the reliability of non-destructive testing (NDT) with respect to its probability of detection (PoD)-crack size characteristics.

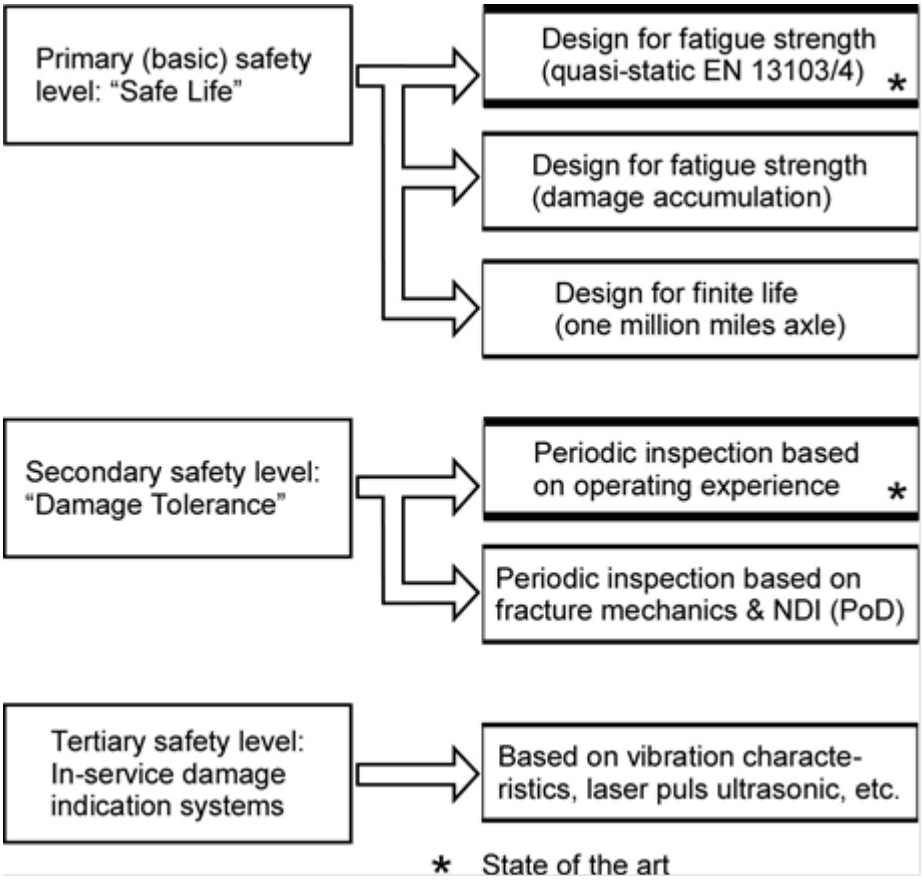

Figure 1: Components of a safety assessment of railway axles. All options not marked with a * refer to present or future development.

2.2 Limiting the Projected Lifetime?

Figure 2 gives a brief overview on the various options of fatigue strength and fatigue life design of railway axles.

Figure 2a: The approach followed by the present standards (in Europe EN 13103 [3] for trailing and EN 13104 [4] for driving axles) implicitly assumes a constant amplitude loading with the stress amplitude being conservatively estimated as superimposed maximum loading, i.e., different to reality all loads are assumed to act simultaneously. Unknowns, e.g., a potential reduction of the admissible stresses below the fatigue limit due to the very high cycle fatigue (VHCF) phenomenon (for a service time of 10^8 and more loading cycles) or other features are covered by ample safety margins. The maximum permissible stress in the axle is given by the fatigue limit of the material under consideration (EA1N carbon steel = C35, normalized and EA4T alloy steel = 25CrMo4, quenched and tempered) but it additionally depends on the type of axle (solid or hollow) and the axle section (away from or beneath the press fits, etc.). If the axle is exposed to corrosion some reduction of the permissible stress is required but no detailed rule is given in the standards cited above. However, EN 13261 ([5], Tab. 11), in such a case, specifies a value of 60% of the maximum

allowable stresses of EN 13103 and EN 13104. For all other cases, where the axles are not exposed to environmental corrosion, it is assumed that no reduction of the fatigue limit due to some kind of damage occurs during service which implicitly means that protection measures have to be taken which exclude such damage or the damage has to be removed soon after it appears in service.

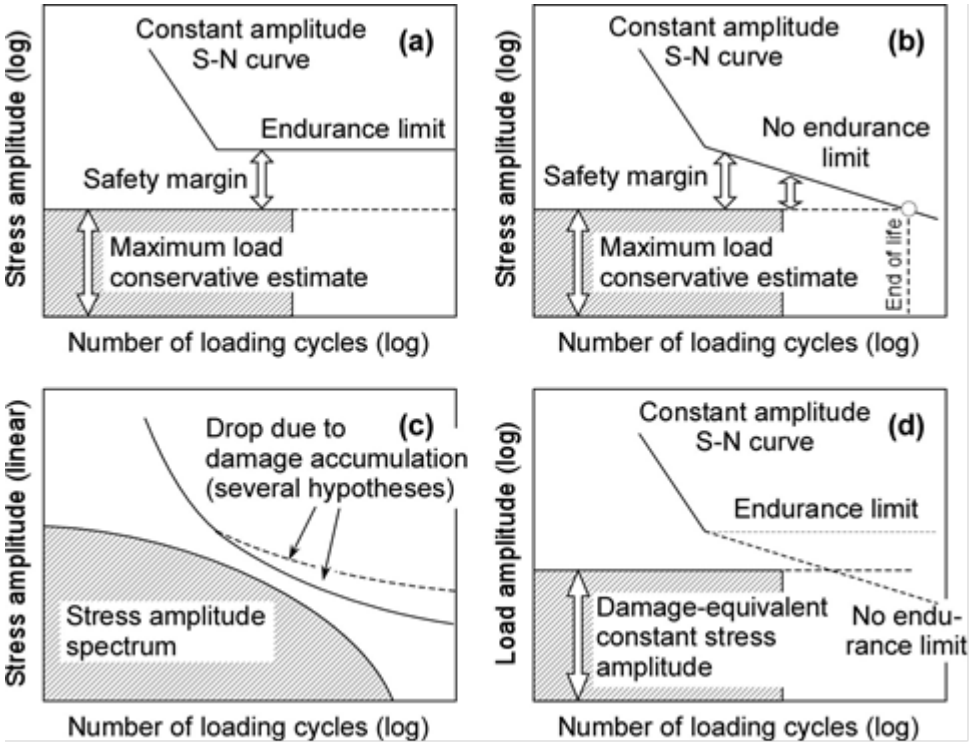

Figure 2: Potential concepts of fatigue strength analysis.

Figure 2b: As an alternative to the standard method, VHCF could be taken into account by replacing the fatigue limit by a sloping curve beyond the knee-point. Sonsino [6], based on the re-analysis of a large body of fatigue data proposes a modified fatigue life diagram with a decrease of 5% per decade loading cycles in logarithmic scales for steels. Note, however, that the author explicitly excludes from this rule cases where environmental or fretting corrosion is present (such as in axle press fits).

Figure 2c: A design stress spectrum, i.e., a histogram of the frequency of occurrence of different stress magnitudes, is compared with an S-N curve corrected for damage accumulation. This is obtained by a modified Palmgren-Miner rule according to one of several proposals. Note that, different to Figure 2b, the drop of the S-N curve beyond the knee-point is not caused by the VHCF effect but by damage accumulation. A special feature of variable amplitude loading is that loading cycles with stress amplitudes below the fatigue limit may contribute to fatigue damage when there is a mixture of stress amplitudes above and below this level. This is the case because the high stress amplitudes (above the fatigue limit), due to their damaging effect, cause subsequent lowering of the fatigue limit. Depending on the applied stress spectrum the drop in the S-N curve can be more pronounced than those caused by the VHCF effect because of which one could think about cases where it “covers” the latter in a conservative way.

Figure 2d: A damage accumulation analysis is used to obtain a damage-equivalent constant stress amplitude. This is then used like the maximum stress amplitude of Figure 2a but it actually describes variable amplitude loading. The fatigue strength analysis is performed as in Figure 2a or b

against the constant amplitude S-N curve.
The approaches according to Figures 2c and 2d have been proposed in some recently finished research projects on the safety of railway axles ([7], see also [8], [9]). Note that they require real stress amplitude spectra, e.g., from test runs. Although a number of those has been determined over the last decade (e.g. [7], [8], [9]) there is still need for generally accepted reference loading spectra for the various kinds of railway transportation (high speed, freight etc.) and different track quality (modern high speed and traditional track, significantly curved track, track with switches and crossovers, e.g., at stations, etc.). As long as generally accepted information of that kind is not available the damage accumulation based analyses are hardly an alternative to the fatigue limit based standards discussed at the beginning of this section. But, although it can be argued that these "cover" the damage accumulation effect by its ample safety margins, damage accumulation based approaches, in the opinion of the authors of this paper, point into the right direction for future development. Note, however, that they have to include further effects such as damage due to corrosion and ballast impacts during service (see Section 2.3).

2.3 In-service effects on Fatigue Life

Corrosion pits and notches due to flying ballast impacts develop during service which means that the fatigue strength is not a material and/or component property established once for all but can reduce during the lifetime of the component. Failures of axles in freight wagons are frequently caused by corrosion pits at the axle shafts. Besides the corrosion effect itself corrosion pits act as stress raisers.

With respect to flying ballast impacts a systematic screening has shown that the latter is a rather typical issue of high-speed traffic [10]. Whereas only on 5% of other axles showed impact notches 30% of the high-speed axles were affected. The reason for flying ballast is aerodynamic effects with respect to the high speed which make impact from debris more likely. On 9 February 2006 a passenger train derailed in New South Wales, Australia after an axle completely fractured at the radius relief area between the gear and wheel seats [11]. Whilst the crack initiation site could not be identified on this specific axle, twelve similar axles were found with fatigue cracks at identical axle sections. Five of these were closer examined. In each case the crack originated from small surface indentations with depths between 0.1 and 0.9 mm which, by means of chemical analyses of crystalline material embedded in the indentations, could be identified as the result of ballast impacts.

The average depth of the detected impact notches was 0.8 mm, i.e., significantly larger than that of typical corrosion pits [10]. The 95% upper bound depth of about 2 mm was close to earlier assumptions in [12]. Of course a ballast-induced notch is not a crack although there is some chance of sharp edges from which small fatigue cracks could easily develop. A systematic investigation on the typical and most dangerous impact notch geometry and its effect on the local stress concentration and small crack initiation and on the residual stress field generated by the impact is due in the future. Note, that impact damage also promotes stress corrosion crack initiation by local damage of the coating and the introduction of complex residual stresses.

2.4 Potential effect of on-metallic inclusions

Non-metallic inclusions originate from the steel manufacturing process such as illustrated in Figure 3. When, e.g., aluminium is added for deoxidisation, oxidic inclusions such as Al_2O_3 are formed, silicon oxides can be introduced form mould powder etc. Besides oxides there may also be sulfides such as MnS or other particles. The size of the inclusions is in the order of ten µm up to mm.

During forging or rolling the inclusions can be crushed, this way forming clusters or inclusion "chains". An example is shown in Figure 4 which belongs to the failure investigation on the German high speed train mentioned in the beginning of Section 1 (for details see [1]).

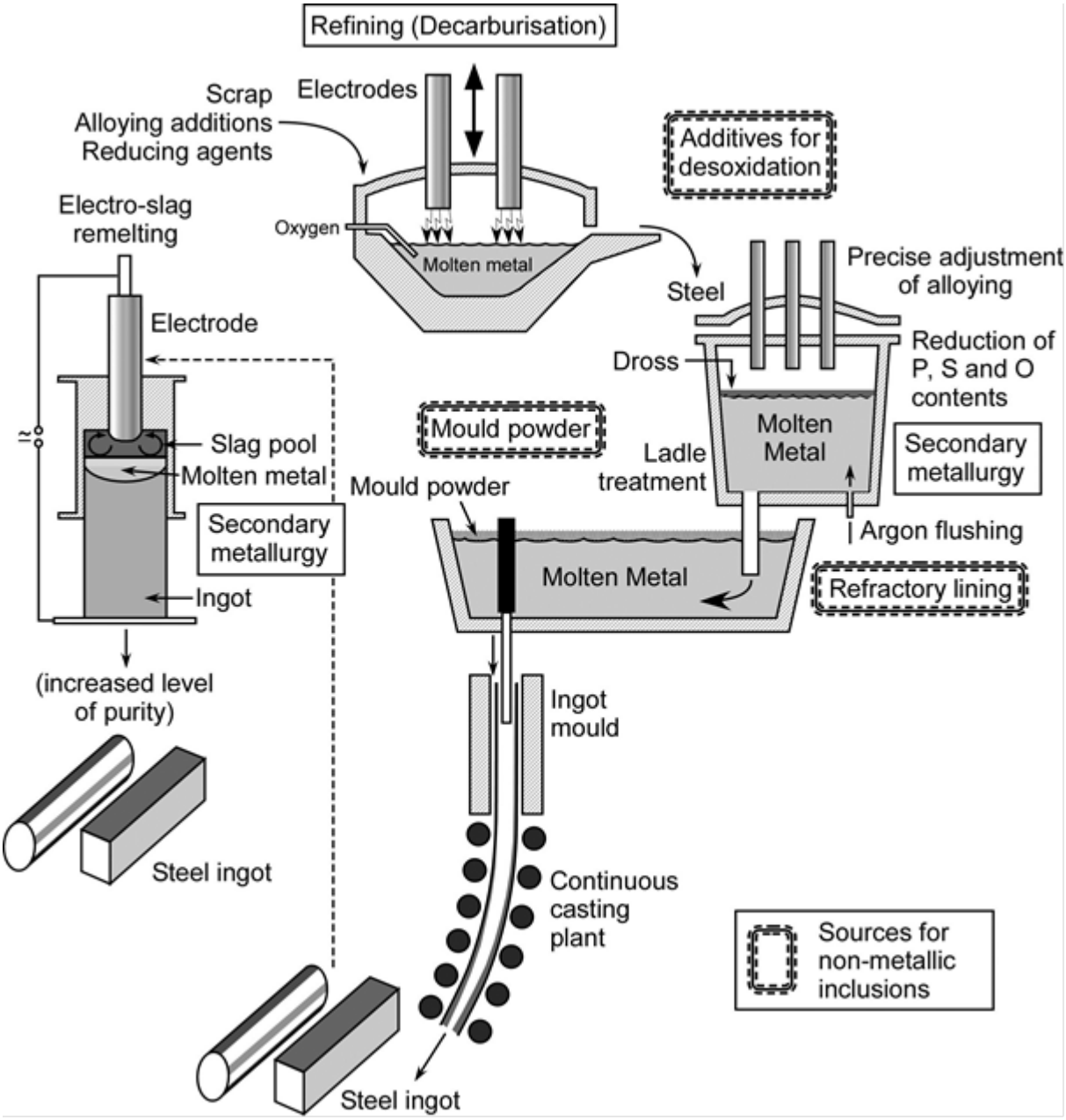

Figure 3: Sources for non-metallic inclusions during steel manufacturing.

In general, the lifetime of a crack consists in the initiation stage, where cracks are formed due to irreversible plastic deformation along slip bands, short crack propagation (up to a size of roughly 0.5 to 1 mm in engineering materials), long crack propagation (beyond that crack size) and final fracture. The effect of the non-metallic inclusions consists in a substantial shortening of the crack initiation stage leaving short crack propagation as the stage which controls lifetime. Inclusions differ from the matrix in several aspects: they have different elastic constants (stiffness mismatch), different strength and hardness properties (strength mismatch) and different thermal contraction coefficients (thermal contraction mismatch). Frequently, they show a square-edged shape which, in

combination with the difference in hardness between particle and matrix causes stress concentrations at the corners and, due to this, local damage in the adjacent matrix material when the component is subjected to applied loading. An example of the effect of inclusions on the lifetime of carbon steel is presented in Figure 5. Note that it is the defect area normal to the loading direction (which, in axles, is much smaller than that in axial direction) that correlates with the fatigue life (and strength).

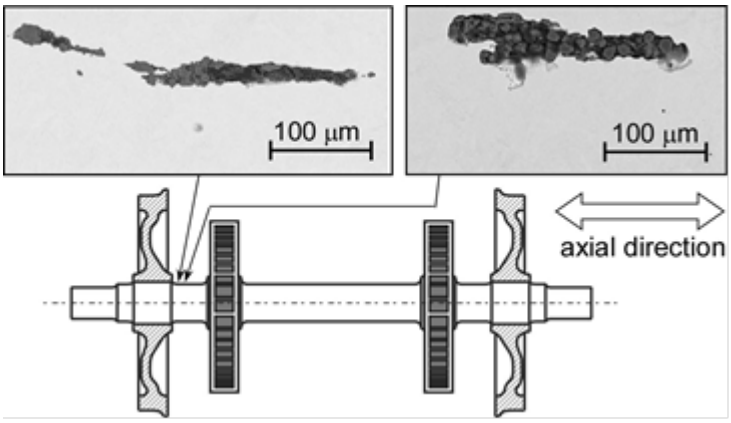

Figure 4: Nearly axially orientated non-metallic inclusions found in sections adjacent to the fracture surface very close to the crack origin in the broken axle of the German high speed train mentioned in Section 1 (according to [1]), axle type shown schematically.

In order to prevent large inclusions EN 13261 refers to the materials standard ISO 4967 which gives rules for maximum tolerable inclusion dimensions between 76 and 436 µm depending on the inclusion type (sulphide, aluminate and silicate globular oxide) and the category of steel quality (1 or 2). The absence of larger particles has to be proven by metallography at a limited (approximately 200 mm2) polished area parallel to the axial direction half-way between surface and centre in solid and between outer and inner surface in hollow axles at the section of the largest diameter (Figure 6). No guidance is given on the number of axles of a batch to be investigated. This is the more problematic as large inclusions at critical positions – which could act as fatigue crack initiation sites – have to be assumed to be very rare in reality; a statement which is obvious at the background of the relative small number of axle failures in reality. It is certainly not consistent to look for seldom events by a very limited sample. In addition, one could ask whether it is meaningful to look for large inclusions in the middle of the wall and not at the potentially critical locations in the axles such as the T notch or other geometric transitions or the press seats.

On one hand microscopic defects in the order of some ten or hundred micrometers which have to be detected by means of metallography based on a very limited sample, on the other hand the exclusion of much larger macroscopic defects in the order of millimetres by NDT screening of the whole component – and in between a gap, at least if one thinks about standard NDT methods.

What could be an alternative to these inconsistent requirements? In [2] the authors proposed to perform a more thorough investigation on a number of carefully chosen axles (e.g. by ultrasonic immersion technique or destructive methods) and to use the result for statistically specifying an upper-bound inclusion size which, by state-of-the-art quality control, will be found with high probability. Smaller defects which could escape its detection have then to be taken as existent even if the NDT record is “negative”. This limit defect size could then be used, in a worst case scenario, for the specification of a general reduction factor for the fatigue strength. The NDT technique has to be developed such that defect sizes larger than the limit are very probably be found by quality control measures which have to be exclusively based on a methodology allowing the complete

screening of the mechanically critical positions of the axles.

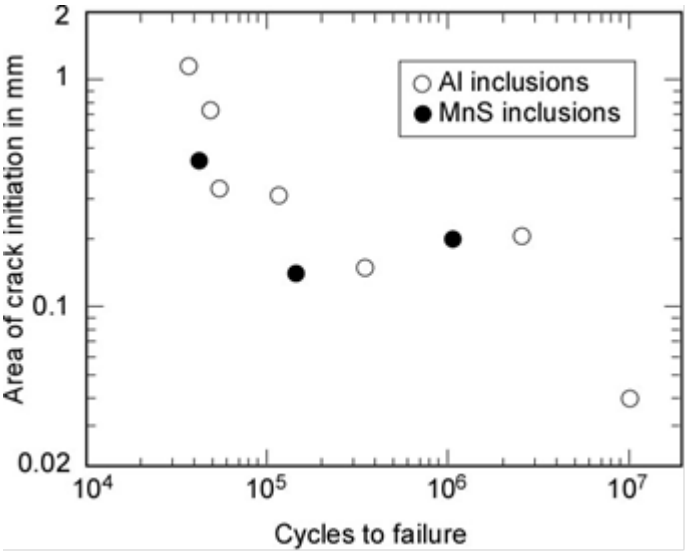

Figure 5: Effect of the defect area normal to the loading direction on the fatigue life of a hot rolled A537 carbon steel at a maximum stress of 260 MPa (according to Ma [13]).

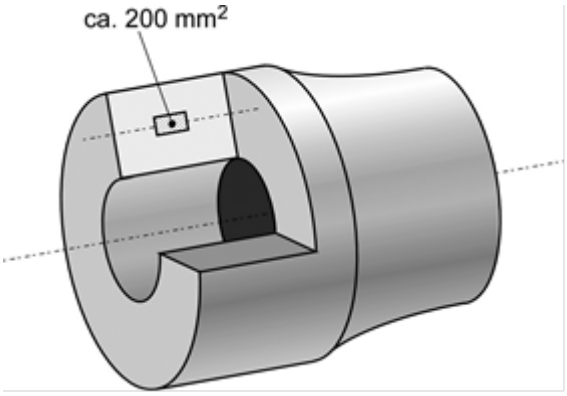

Figure 6: Location for the metallographic proof of the absence of inclusions larger than permissible with respect to ISO 4967 and EN 13261 (not in scale).

2.5 Reliability Issues of Non-destructive Testing (NDT)

A science-based inspection regime consists in two major elements: facture mechanics based residual lifetime and the probability of detecting (PoD) a crack of a certain size. Combining both types of information, the probability to find a potential crack in due time, i.e., before it becomes critical can be determined as a function of the inspection interval. No discussion on the fracture mechanics part shall be provided here, see, however the detailed discussions of the authors in [2].

Non-destructive testing is usually performed by ultrasonic (US) (shorter interval) and magnetic particle inspection (MPI) (larger interval). It seems likely, that MPI is the most cost-effective NDT technique for a bare axle (the wheels, bearings, brake discs etc. are removed) during its overhaul. Note, however, that there might be the risk of scratching during dismantling. Unfortunately fatigue cracks may be initiated and grow to failure in less time than needed to wear out the wheels. Therefore, costly and disruptive axle inspections in between overhauls have to be carried out which are usually based on US as a compromise between a limited intrusiveness, which disrupts train

service, and a lower PoD compared to MPI.

With respect to ultrasonic inspection it has to be distinguished between:

- far end scan (the axle is inspected from the end of the axle to mid-span or further) near end scan (the axle is inspected from the end of the axle to an adjacent seat) and high angle scan (the axle is inspected from the axle body across the seat),
- inspection from the outer surface in solid axles and from the bore in hollow axles,
- manual or automated testing, and
- standard or sophisticated test and analysis methods such as phase array, synthetic aperture focusing technique (SAFT) etc.

PoD-crack size curves for railway axles have first been determined by Benyon and Watson [14] in 2001 (see also the subsequent discussion in [15]). The by now most up-to-date and most systematic study of PoD on railway axles has been performed in the European WIDEM project [16]. In Figure 7 some of these data are shown along with the data of [14]. Note that none of the curves can be generalised because they belong to specific test setups.

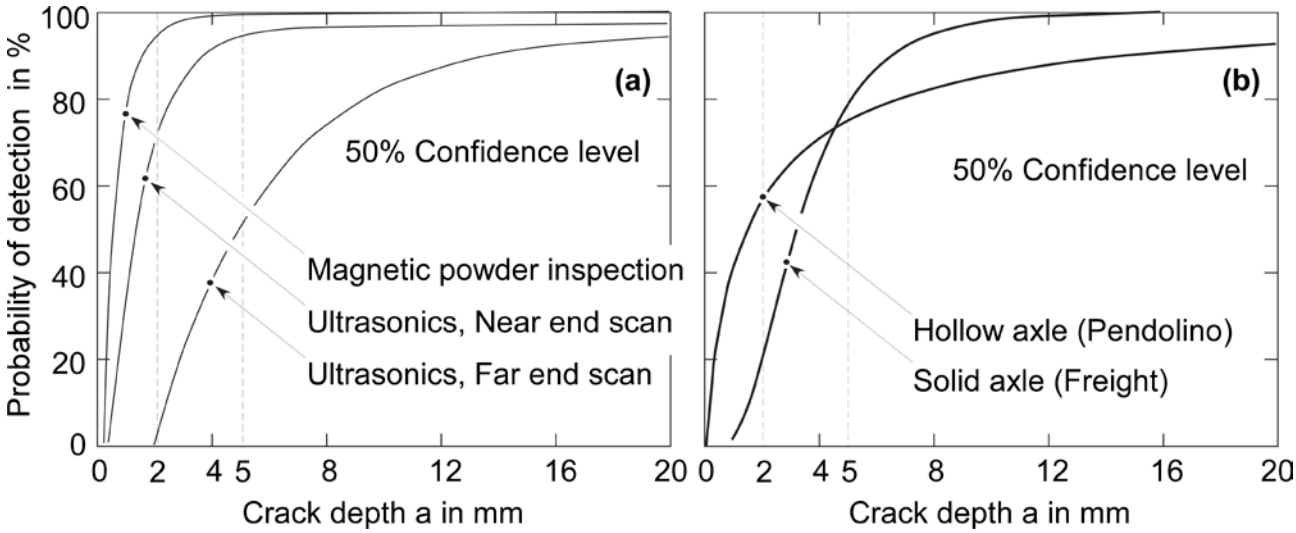

Figure 7: Probability of detection (PoD) of cracks as a function of crack depth. (a) Data obtained by magnetic particle inspection and ultrasonic techniques (according to [14]; 50% confidence level; solid axle); (b) Comparison between ultrasonic near end scan data for solid axles and ultrasonic data obtained from the bore of hollow axles (according to [16]; 50% confidence level).

The overall probability of non-detection (PoND) as the complement to the POD is identical with the probability that an axle with an initial crack of 2 or even more millimeters depth (such as assumed in the fracture mechanics analysis) fails because the crack was not found in due time. This has to be distinguished from the failure probability of an arbitrary axle in the fleet which is smaller by magnitudes since a pre-existing crack of that size is very unlikely.

Besides the fracture mechanics based residual lifetime the steepness of the PoD-crack size curve is the second key parameter for establishing inspection intervals. This is illustrated in Figure 8. The failure probability of the axle, i.e., the probability that the crack will not be found in due time, increases for a larger inspection interval but it significantly reduces for a shorter one, i.e., with any additional inspections before potential failure (Figure right). The PoD of a specific inspection

becomes larger when the crack is more extended and when the PoD-crack size curve is steeper (Figure 8 left). Therefore, measures for improving the PoD-crack size curve [in the figure from (1) to (2)] are of paramount importance for reaching an optimum between safety and cost-efficiency.

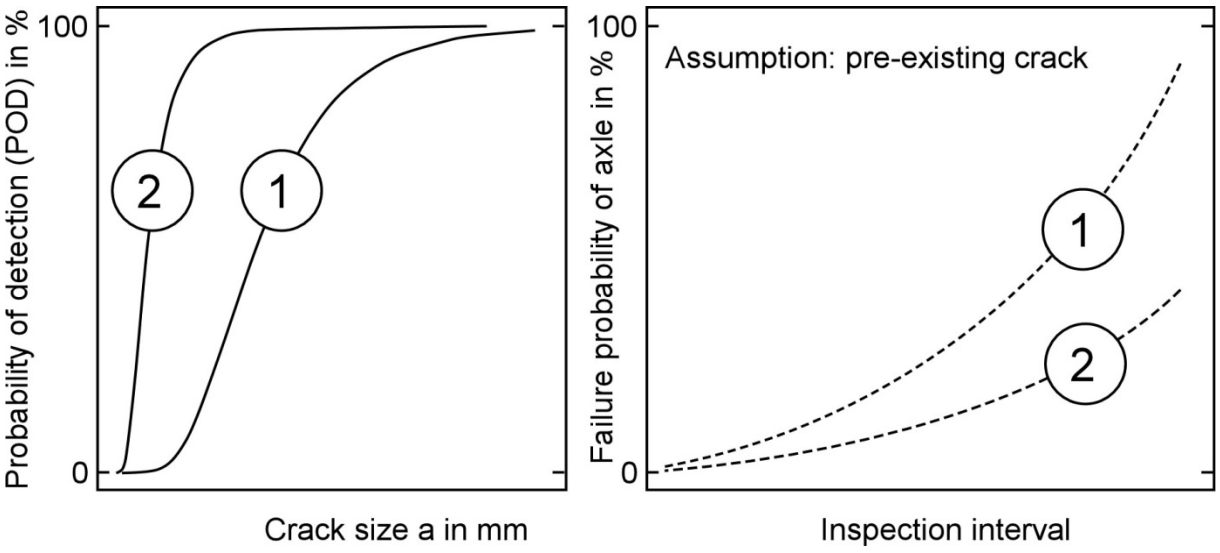

Figure 8: Schematic correlation between the PoD-crack size characteristics of a NDT method, the inspection interval and the failure probability of an axle with a pre-existing crack.

No detailed discussion on options for improving the PoD-crack size characteristics shall be given here because this is a subject of ongoing and future research activity, see however the remarks in [2]. Certainly increasing automation will lead to improvements in NDT quality since, this way, human factors such as the level of training and experience of the inspectors and others which significantly contribute to the variability in manual inspection results are eliminated. Another measure is the application of more sophisticated test and analysis methods, e.g., for US, the application of the phase array or synthetic aperture focusing technique (SAFT). Note, however, that the challenge is not just to have more reliable NDT methods but to optimize these for railway axles with respect to the inspection time needed such that cost-intensive intrusiveness, which disrupts train service, is kept as small as possible.

3. SUMMARY

Starting with an axle failure case and a failure statistics for Europe the paper gives a brief overview on selected issues of existing and potential innovative safe life and damage tolerance methods for railway axles which, as the authors think, promise some potential for further increasing the safety level of axles. The issues addressed comprise questions of limiting the projected lifetime as a consequence of features such as damage accumulation, the potential very high cycle fatigue effect and corrosion including the “one-million miles axle” concept and in-service effects on the fatigue life such as corrosion pits and flying ballast impact notches. Special attention is put on the potential effect of non-metallic inclusions on fatigue strength and lifetime. A gap in the existing quality regulations has been identified. As an alternative it is proposed to carry out a throughout investigation of the as-is state and to correct the design fatigue strength with respect to a limiting defect size which will not be found with acceptable probability in quality control. Defect sizes above this limit have to be found with high reliability by innovative NDT techniques. Finally, the improvement of the PoD-crack size characteristics of NDT has been identified and discussed as a paramount goal for reaching an optimum between safety and cost-efficiency.

REFERENCES

[1] Klinger, C. and Bettge, D.(2013): Axle Fracture of an ICE3 High Speed Train, Engineering Failure Analysis, http://dx.doi.org/10.1016/j.engfailanal.2012.11.008

[2] Zerbst, U., Beretta, S., Köhler, G., Lawton, A., Vormwald, M., Beier, H.Th., Klinger, C., Černý, I., Rudlin, J. Heckel, T. and Klingbeil, D. (2012): Safe life and damage tolerance aspects of railway axles – a review. Submitted to Engng. Fracture Mech.

[3] EN 13103 (2001): Railway Applications – Wheelsets and Bogies – Non Powered Axles – Design Method. European Committee for Standardization (CEN), Brussels, Belgium.

[4] EN 13104 (2001): Railway Applications – Wheelsets and Bogies – Powered Axles – Design Method. European Committee for Standardization (CEN), Brussels, Belgium.

[5] EN 13261 (2009): Railway applications. Wheelsets and bogies. Axles. Product requirements. Annex A. European Committee for Standardization (CEN), Brussels, Belgium.

[6] Sonsino, C.M. (2007): Course of SN-curves especially in the high-cycle fatigue regime with regard to component design and safety. Int. J. Fatigue 29, 2246-2258.

[7] Traupe; M., Meinen, H. and Zenner, H. (2004): Sichere und wirtschaftliche Auslegung von Eisenbahnfahrwerken. Final Report BMBF Project 19 P 0061 A-F; in German.

[8] Beretta, S. and Carboni, M. (2008): Endurance design procedure of wheelsets based on reliable load spectra and reliable Wöhler curves. D5.1.3: Design procedures for axles. European Project "Wheelset Integrated Design and effective Maintenance" (WIDEM), http://www.widem.org/file.php?id=50&save_dialogue=1.

[9] Lütkepohl, K., Esderts, A., Luke, M. and Varfolomeev, I. (2009): Sicherer und wirtschaftlicher Betrieb von Eisenbahnfahrwerken. Final Report BMWi Project 19 P 4021 A-F; in German.

[10] British Railway Safety and Standards Board (RSSB): Project T728: Impact of corrosion upon the high cycle fatigue properties of GB axle Steel.

[11] Australian Transport Safety Bureau (2007): Derailment of XPT passenger train ST22 Harden, New South Wales 9 February 2006; http://www.atsb.gov.au/media/24374/rair2006002_001.pdf

[12] Gravier, N.; Viet, J. J. u. Leluan, A.(1998): Predicting the life of railway vehicle axles. in: Proc. 12th Wheelset Congress, Quigdao, China, 133-146.

[13] Ma, J., Zhang, D., Han, E.-H. and Ke, W. (2010): Effects of inclusion and loading direction on the fatigue behaviour of hot rolled low carbon steel. Int. J. Fatigue, 32, 1116-1125.

[14] Benyon, J. A. and Watson, A. S. (2001): The use of Monte-Carlo analysis to increase axle inspection interval. Proceedings of the 13th Int. Wheelset Congress, Rome, Italy.

[15] Rudlin, J. R. and Shipp, R. (2002): Review of techniques for rail axle inspection. Report for railway safety; also Rudlin, J. R. and Shipp, R. (2003): Review of rail axle inspection methods. Int. Seminar on Fatigue of Axles, Imperial College London, 25-26 Sept. 2003.

[16] Wei, L. (2008): Procedure to define NDT periodicity as function of vehicle service profile; D7.1.8: Results of probabilistic analysis. European Project "Wheelset Integrated Design and effective Maintenance" (WIDEM), http://www.widem.org/file.php?id=54&save_dialogue=1.

Analysis of fatigue crack initiation and propagation in ship structures

Wengang Mao[1,*], Jonas W Ringsberg[1]

[1] Department of Shipping and Marine Technology, Chalmers University of Technology, 412 96 Gothenburg, Sweden
* Corresponding author: Wengang.Mao@chalmers.se

Abstract

Ships structures are subjected to various types of cyclic loads from waves, wind and cargo operations that cause fatigue damages in the structures. There exist rules to regulate the structural design with sufficient fatigue strength to survive their service period. However, fatigue cracks do occur earlier than expected in numerous locations of e.g. ocean-crossing container vessels. The presence of fatigue cracks greatly affects a ship's safety and serviceability. Managing how initiated cracks grow is an important task to ensure a safety and cost-effectiveness ship transportation. The objective of this study is to develop a robust method, which can be used to predict crack growth and crack maintenance in ship structures. A longitudinal stiffener of a 2800TEU container vessel with full-scale measurements of e.g. strain signals and operation conditions are used in the study. Firstly, a spectral *S*-*N* fatigue analysis is adopted to predict when the first crack occurs in the ship's most fatigue-critical region. Then the crack's growth characteristics are modeled by the code FRANC2D. Finally, the time needed for the crack initiation and growth are studied in terms of structural maintenance plan, i.e. crack growth management.

Keywords Fatigue crack, hydrodynamic loads, ship structure, spectral method and wave height.

1. Introduction

The size of ships has increased rapidly during the last decade as a result of the fast growth of the global shipping market and the developments of construction technologies that also makes the high-tensile steels widely used in ships. The increase of dimensions and high-tensile steel usage in ships made the ship structures more flexible when they are operated in waves. The wave (hydrodynamic) loads can cause continuously changing stresses and result in fatigue damages in ship structures, which challenges the ship's structural integrity and thereby its safety. Therefore, ship structures should be designed with sufficient fatigue strength based on the rules [1], where fatigue strength is assessed using stress-based approaches (the high-cycle fatigue analysis). In ship class rules, the stress range distribution is normally provided for the fatigue assessment. But for a novel ship design, the stress range distribution is not available and should be computed by a direct calculation method that demands huge computation powers to consider the ship's specific operation conditions and encountered wave environments. However, large uncertainties cannot be avoided in the above two fatigue design processes [2]. For example, a ship's real encountered wave environments may be different from that used and proposed in the fatigue design rules [3, 4]. The results from the hydrodynamic loads analysis can be large [5]. There are additional factors which are also often disregarded in the fatigue analysis of ship structures, such as analysis of the effects of redistribution of residual stresses from manufacturing, corrosion, weld defects, etc., and these factors contribute to even larger uncertainty in the fatigue assessment. The sum of all these factors may explain why fatigue cracks are found earlier than expected in many vessels. Repairing the entire minor to moderate cracks is expensive and it is seldom an alternative, due to the economic issues related to the maintenance process. Hence, the understanding if "initiated" and visible cracks are critical to the structure's integrity becomes an important issue. Tools and methods for maintenance plan based on

crack growth management should therefore be developed. In the literature, crack propagation under various sailing conditions has been investigated in e.g. [6]. A summary of the progresses of using fracture mechanics in the maritime industry is summarized in [7].

The objective with the current study is to present the derivation of a useful method that can be used to predict the fatigue crack growth in a ship structure. In the development, the special loading characteristics of ship structures are dealt with. It has been formulated to assist maintenance planning with respect to e.g. repair of fatigue cracks. A structural detail with an initiated crack in a 2800TEU container ship is used to demonstrate the approach using fatigue loads from a direct calculation. The results are compared with full-scale measurements made on the vessel. Finally, based on the operation conditions for the current case study vessel and the existing crack, the number of voyages the ship structure can undertake before final rupture is investigated.

2. A spectral method for ship fatigue assessment

For the ship fatigue assessment, the long-term structural stresses are divided into a series of short stationary signals [8]. A stationary process can last for from 20 minutes to several hours. The structural stress under a stationary sea state is caused by the wave loads applied on ships. The waves in a sea state is often described by the significant wave height, H_s, the wave period T_p, and a specific wave spectrum $S(H_s, T_p)$. In order to estimate a ship's fatigue damage under a sea state, its structural stress is often assumed to be Gaussian distributed [9]. Hence, both the hydrodynamic loads and the structural stresses can be computed by linear theories.

2.1. High-cycle fatigue analysis

Ship structures are designed to behave elastically during its design life of around 20 years. The fatigue strength is assessed by stress-based approaches, i.e. high-cycle fatigue design principles. In the analysis, the material behavior is characterized by a *S*-*N* curve, with a log-linear dependence between the number of cycles to failure N, and the stress cycle range S, $\log(N) = \alpha - m\log(S)$. Different *S*-*N* curves exist for different materials, geometries, welds, etc., the parameters a and m are usually categorized based on the properties of structural details in the class rules. The stress ranges, here denoted by S_i, ($i = 1,\ldots,n$), can be obtained by the rainflow counting method for each sea state. Finally, the accumulated damage is calculated using the linear Palmgren-Miner law as:

$$D = \sum_{i=1}^{n} \frac{S_i^m}{\alpha} \tag{1}$$

In order to estimate the fatigue damages accumulated in a sea state, it is necessary to get the total number and distribution of the stress ranges S_i. Since the stress is assumed to be Gaussian, it is sufficient to get the spectrum of structural stresses for the ship fatigue assessment.

2.2. Ship structural stresses in a sea state

The variability of structural stresses, denoted by $X(t)$ here, is mainly caused by the change of the wave loadings applied on ships. Hence, it is essential to get the correct wave (hydrodynamic) loads.

The structural stresses due to the wave loads can be computed by beam theory. To simulate and evaluate realistic ship operation conditions, the computation has to be done for many sea states, at various ship speeds, U, and different heading angles, θ. In general, a frequency domain analysis is used to first compute the Response Amplitude Operators (RAOs) of the hydrodynamic loads using linear potential strip theory [10]. Then, by means of beam theory, the transfer function of structural stresses $H_\sigma(\omega|U, \theta)$ is calculated using the section modulus of the structural detail of interest. Often, a stress concentration factor is added in the transfer function to get the local stresses. Thereafter, the stress spectrum under arbitrary sea states, $S_\sigma(\omega|H_s, T_p)$, can be computed as:

$$S_\sigma(\omega\,|\,U,\theta,H_s,T_p) = |\,H_\sigma(\omega\,|\,U,\theta)\,|^2 \cdot S_e(\omega\,|\,H_s,T_p), \tag{2}$$

where $S_e(\omega|H_s, T_p)$ is the encountered wave spectrum. It is not always explicitly derived for all wave frequencies, but the spectral moments are rather easy to obtain and of great interest in fatigue analysis. The n-th order spectral moments is calculated by:

$$\lambda_n = \int_0^\infty \left|\omega + \omega^2 U\cos\theta / g\right|^n H_\sigma^2(\omega\,|\,U,\theta) S(\omega\,|\,H_s,T_p)\,d\omega. \tag{3}$$

Let R denote the local maxima of the Gaussian stress signal X in a sea state. The distribution of R can be described by Rice's distribution function:

$$F_R(r) = \Phi\left(\frac{r}{\varepsilon\sigma_x}\right) - \sqrt{1-\varepsilon^2}\,\Phi\left(\frac{\sqrt{1-\varepsilon^2}}{\varepsilon}\frac{r}{\sigma_x}\right) e^{-\frac{1}{2}\left(\frac{r}{\sigma_x}\right)^2} \tag{4}$$

where Φ is the standard normal cumulative distribution function, σ_x is the standard deviation of X and $\sigma_x = \sqrt{\lambda_0}$, ε is the spectral width parameter. If $\varepsilon = 0$, Eq. (4) becomes Rayleigh distribution:

$$F_R(r) = 1 - e^{-\frac{r^2}{2\sigma_x^2}}, \text{where } R \geq 0 \tag{5}$$

For the narrow band Gaussian process, the number of local maxima can be computed through the zero-upcrossing frequency of the signal $X(t)$ as $f_z = \frac{1}{2\pi}\sqrt{\frac{\lambda_2}{\lambda_0}}$.

2.3. A spectral fatigue method

Since the waves in a stationary sea state are actually random processes, the stress cycle range S is also a random variable with the probability density function (pdf) denoted by $f_S(s)$. Then, the expected value of S^m is computed by $E[S^m] = \int_0^\infty s^m f_S(s)\,ds$. For a zero mean narrow band Gaussian stress $X(t)$, the stress cycle range S is approximated by two times the stress amplitude R, i.e. $S \approx 2R$. Subsequently, by means of Eq. (5), $E[S^m]$ can be computed by:

$$E[S^m] \approx \int_0^\infty (2r)^m f_R(r)\,dr = \left(2\sqrt{2}\sigma_x\right)^m \Gamma\left(\frac{m}{2}+1\right) \tag{6}$$

where $\Gamma(x)$ is the gamma function. The expected fatigue damage computed by Eq. (1) becomes:

$$E[D]=\frac{N_0}{\alpha}E\left[S^m\right]\approx\frac{N_0}{\alpha}\left(2\sqrt{2}\sigma_x\right)^m\Gamma\left(\frac{m}{2}+1\right) \tag{7}$$

where N_0 is the expected number of stress cycles and computed by $N_0 = T{:}f_z$ for $X(t)$, $t \in [0, T]$. Finally, the expected fatigue damage caused by the narrow band stress $X(t)$ denoted by D_T, is:

$$D_T = E[D]\approx\frac{T}{2\pi\alpha}\sqrt{\frac{\lambda_2}{\lambda_0}}\left(2\sqrt{2\lambda_0}\right)^m\Gamma\left(\frac{m}{2}+1\right) \tag{8}$$

Equation (8) is also known as the narrow band approximation and works quite well even for stress signal with spectral width parameter ε up to 0.5 [10].

3. Crack propagation analysis for ship structures

Ships follow specific inspection and maintenance plans based on rules and regulations. Because of large costs during the repair process [11], ship owners would like to repair ship defects and cracks during the ship's regular hull survey, which should be carried out from every 2 to 5 years depending on the type and age of the vessel. However, it is not practical or possible to repair all the cracks at once. Consequently, it is of great interest to study when fatigue cracks propagate and reach a critical length which requires immediate repairing. In the following, an efficient way for such an analysis is derived and it has been limited to Model I crack propagation according to linear elastic fracture mechanics principles.

3.1. Fatigue crack propagation analysis

The rate of fatigue crack propagation under cyclic loads can be described by the Paris' law [12] as:

$$\frac{da}{dN}=C\cdot\Delta K^k \tag{9}$$

where a is the crack length, N is the number of cycles, da/dN is the crack growth per load cycle, and C and k are material parameters from experiments. The ΔK is the range of the stress intensity factor during a load cycle, i.e. $\Delta K = K_{max}\text{-}K_{min}$, where the stress intensify factor K is defined as $K=\sigma f(a/w)\sqrt{\pi a}$, in which σ is the tensile stress perpendicular to the crack plane, $f(a/w)$ is the dimensionless parameter in terms of the crack geometry. The value of K can be difficult to describe analytically for ship structures due to their geometrical complexity. Alternatively, codes such as FRANC2D [13] can be used to compute K as a function of the crack length. Let $Y = f(a/w)\sqrt{\pi a}$. The stress intensity factor can be written as $K = \sigma Y$. For the computation of Y by Franc2D, the crack growth is treated as a series of stages, i.e. the crack grows from a_j, j = 0,1,..., M, corresponding to the value of Y_j, j = 0,1,..., M. Here, a_0 is the initial crack length and a_M represents the critical crack length defined for crack repair. Finally, the stress intensity factor range becomes $\Delta K = \Delta\sigma Y$.

3.2. Fatigue crack growth under a sea state

Following the reasons in Section 2.3, here the stress signal $X(t)$ is also assumed to be a zero mean narrow band Gaussian process. Further, it is assumed that the compressive stress does not contribute

to the crack propagation. Hence, the stress range $\Delta\sigma$ equals to the local maximum of $X(t)$, $\Delta\sigma = R$. Let T denote a sea state lasting period, say 30 minutes, and assume that Y is constant for a crack from a_j to a_{j+1}, i.e., $Y = Y_j$, which is computed by fracture mechanics codes such as the FRANC2D. The expected number of stress cycle N_0 is known from Section 2.3. Then the expected crack growth in the sea state can be computed by:

$$\Delta a_T = E\left[\sum_{i=1}^{n} C\Delta K_i^n\right] = CN_0 Y_j^k E[\Delta\sigma^k] = \frac{TC}{2\pi}\sqrt{\frac{\lambda_2}{\lambda_0}}\Gamma\left(\frac{k}{2}\right)\left(\sqrt{2\lambda_0}Y_j\right)^k \tag{10}$$

where λ_0 and λ_2 are the spectral moments of $X(t)$ in the sea state as Eq. (3). By means of Eq. (10), it is straightforward to compute how many sea states a ship can sail until the crack of interest reaches to a_M, which is the critical crack length that requires repair, cf. crack growth management.

3.3. Sailing wave environments and ship response

When a ship sails across the ocean, e.g. on the North Atlantic trade, the ship typically encounters one or two storms with high significant wave height H_s, see Fig. 1 (left) for an example. Depending on the weather forecast information, captains can choose different routes for safety and economics reasons. For the prediction of fatigue crack growth, it is of great interest to know the distribution of the wave environment a ship will encounter in a few years. A large amount of data is available, such as wave measurements from satellites, hindcast or buoys, which can be used for this purpose. There also exist statistical models built up based on the data, e.g. [14], which can be used to simulate the mean and covariance of wave environments along various ship routes.

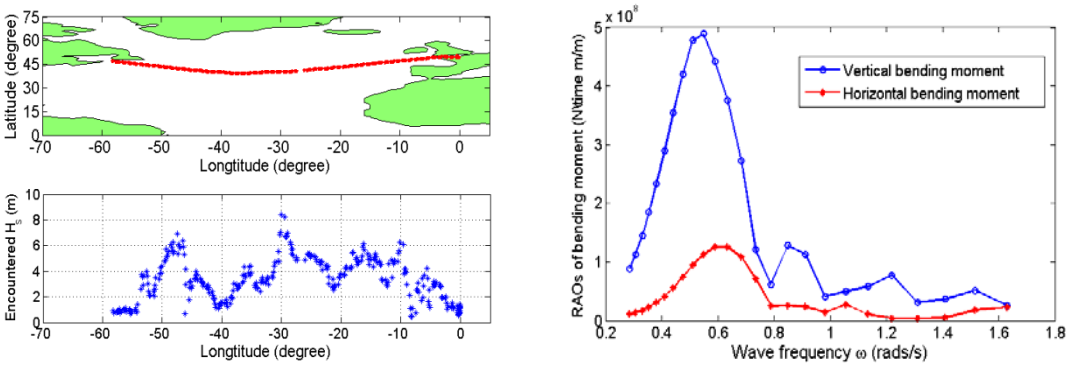

Figure 1. (Left) One voyage from Europe to North America with the significant wave height H_s for all the encountered sea states during the voyage; (Right) response amplitude operators of two bending moments for a ship operating with 10 m/s forward speed and heading angle 20 degrees.

For ship fatigue assessment, the structural response should be computed for all encountered sea states. In the maritime industry, the response is often described by the transfer function, $H_\sigma(\omega|U, \theta)$, which depend on the ship speed and the heading angle. When sailing in the North Atlantic Ocean from Europe to North America, ships usually have to go against waves with a heading angle to the wave encounter direction that varies between 20 to 50 degrees. As a result, the normal stress signal $X(t)$ is composed of stresses from the ship's vertical bending, horizontal bending and Vlasov Torsion. In the right plot of Fig. 2, an example of these two bending moments is depicted.

4. A case study: fatigue analysis of ship structures

A structural detail amidships (see Fig. 2) of a 2800TEU container ship is used to demonstrate the approaches for ship fatigue analysis presented in the previous sections, i.e. fatigue initiation in Section 2 and crack propagation in Section 3. The purpose of the analysis is to explain how the two analysis methods can be implemented to plan the maintenance of ship structures. The structural detail of interest was identified from reports, which stated that fatigue cracks were initiated after less than half of the vessel's fatigue design life. Hence, instruments were installed onboard to measure the time series of strains (stresses), significant wave height, heading angle and ship speed when crossing the North Atlantic. The measurement campaign includes 14 voyages where 7 go from Europe (EU) to North America (NA), while the other 7 go to EU from NA. For the following fatigue analysis, the parameters in the *S-N* curve [9] and the Paris' law [15] are listed in Table 1 .

Table 1. Material parameters in the *S-N* curve and in Paris law for the AH36 steel.

	S-N curve		Paris law	
Parameters	α	m	C	K
Values	$10^{12.76}$	3	1.45×10^{-11}	2.75

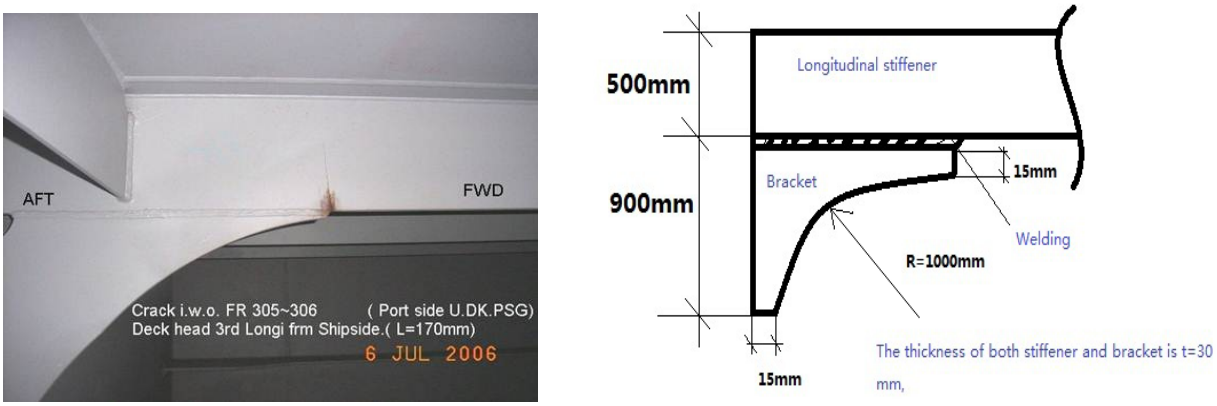

Figure 2. A fatigue crack in the case study vessel and the structural detail in the fracture analysis.

4.1. Fatigue crack initiation analysis

Firstly, by means of the measured stress signals, the fatigue damages accumulated during each individual voyage are computed by the rainflow counting method – they are denoted as the "observed" damages. Secondly, the transfer function of structural stress is computed by means of a 2D strip theory hydrodynamic analysis and the simple beam theory for structure analysis. Then, combining the transfer function with the wave measurements (H_s, T_p) for all encountered sea states, the fatigue damages are computed by the spectral method as Eq. (8). The results from both methods are presented in Fig. 3. It is of interest to focus the study of the fatigue damages during winter season voyages from Europe to North America where the ship were operated in the harshest conditions. For these voyages, the spectral method gives maximum 30% discrepancy from the observed damages, but in the long-term analysis, the spectral method works well in comparison with the rainflow method. The results also confirm the initiation of a fatigue crack observed

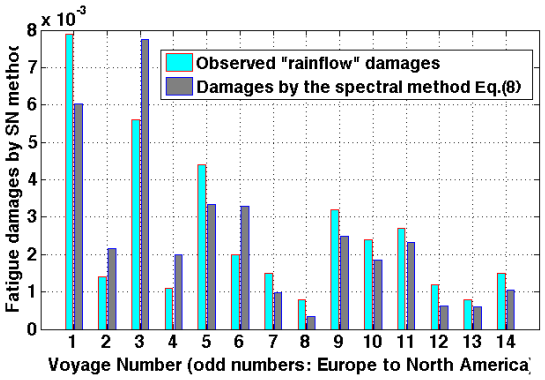

Figure 3. Observed fatigue damages and damages computed by the spectral method introduced in Section 2.3 for all measured voyages. Voyages 1-7 represent winter seasons, 8-14 represent summer seasons.

4.2. Crack propagation analysis and maintenance plan

A ship's structure integrity can be strongly affected by fatigue cracks depending on their locations. Sometimes, the cracks can lead to undesirable consequences, such as oil leakage and compartment flooding, or even structural failure of the entire ship. In principle, the deck plates and longitudinal stiffeners/girders have to undertake the ship's global strength. The cracks around these areas should be repaired well in time before they reach to a critical value. For this purpose, the crack propagation analysis is needed to plan the cracks maintenance. For the example container ship, the critical crack length is assumed to be 200 mm. The crack propagation analysis is performed using the approach presented in Section 3.2. It enables us to estimate how many voyages or sea states the ship can sail before the crack reaches to 200 mm. The initial and interval crack growth length is set to be 5 mm for the linear elastic fracture mechanics analysis. A strong beam is attached on the top of the stiffener to model the deck effect as shown in Fig. 2. A crack is initiated at the connection between the longitudinal stiffener and the associated bracket with high stress concentration. The crack growth path and corresponding stress intensity factors K_I are computed using FRANC2D [13]. For the current boundary and loading conditions, an analysis showed that crack propagation was governed by Mode I. The final stage of the crack propagation and K_I are presented in Fig. 4.

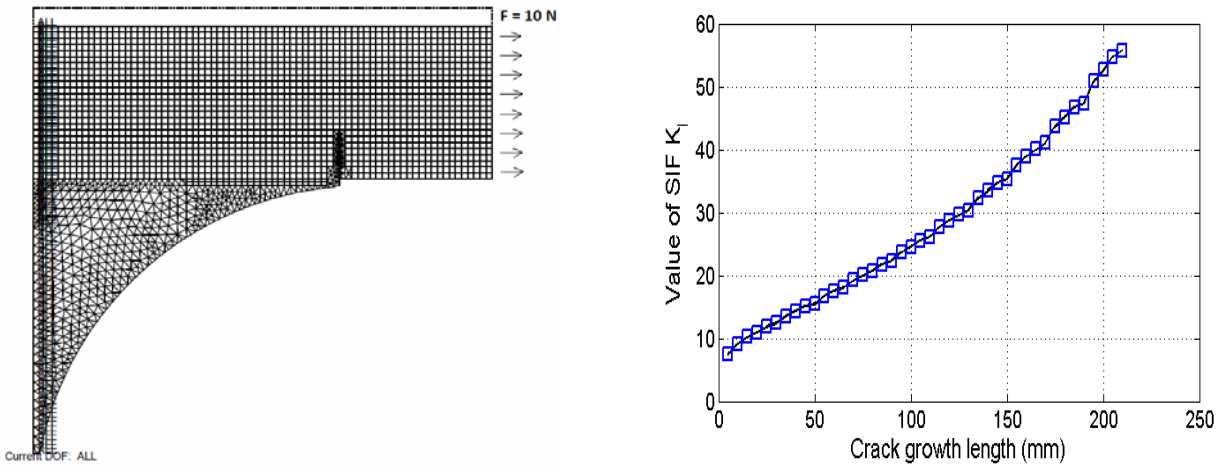

Figure 4. Fatigue crack growth path and stress intensity factors computed by FRANC2D, where the initial crack length is 5mm, the crack is propagated straight upwards, and the element is set to 20 mm.

In order to predict the fatigue crack growth, it is necessary to get the wave environments, which the ship will encounter in the future years' operation. In this study, the ship is assumed to sail along the same routes as the measured 14 voyages. Further, it is assumed that the ship is operated with the same speed and heading angle as the measured ones. The significant wave heights H_s along the measured routes are simulated using a spatio-temporal wave model presented in [14]. It contains the covariance structure of the ocean field in both time and space and enables us to simulate the value of H_s and their correlations for all locations (sea states) along the measured routes. Because of the natural variability of the wave environments, the value of H_s could change as in Fig. 5, together with the observed in one winter voyage. In the study, a stationary sea state is assumed to be 30 minutes and described by the Pierson-Moskowitz (P-M) power spectrum density which is expressed in terms of the significant wave height, H_s, and the wave period, T_p.

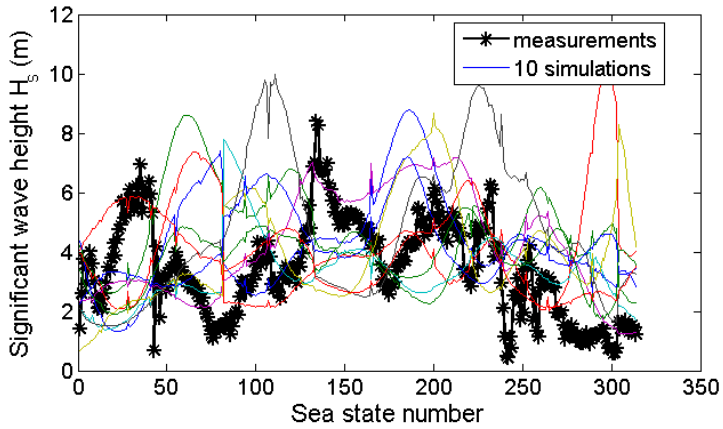

Figure 5. Significant wave heights along the route in Fig. 1 using the spatio-temporal model [14].

The crack propagation analysis is divided into various crack growth stages/intervals. For each stage, the crack increment is computed by Eq. (10) for the ship in a specific condition (H_s, T_p, U and θ). Subsequently, how many sea states the ship can sail for the crack growing from a_i to a_{i+1} can be also calculated. Finally, the repair time, i.e. when the crack reaches to the critical length 200 mm, can be easily predicted. Using the repeated simulations of encountered H_s as in Fig. 5, the mean and variance of the fatigue crack growth under a certain period can be estimated. Therefore, the variation of the total sailing time until the crack propagates to a specific length can be predicted.

Using the wave environments from the wave model simulation [14], the ship can sail for 2.53 years before the crack reaches 200 mm. If the waves are simulated many times from the other approach, the median value of such a period is 2.74 years, while the standard deviation of the period is 0.34 year. Within each interval, the expected number of sea states needed for the crack to grow 5 mm is shown in Fig. 6, as well as the standard deviation of the number. When the crack length is short, more sea states are needed for the crack to propagate 5 mm. It can grow very fast when the crack is close to its critical value. In this case, only a few sea states can cause the crack to propagate 5 mm. It should be noted that the number of sea states for the crack to grow 5 mm does not always decrease as the crack length increase, such as the crack grows to 25 mm, 50 mm etc. This is because the crack can grow slower when the ship meets more calm sea state, e.g. during summer, or/and sails with a better operation condition (speed and heading angles with respect to waves, and less

loadings etc.). These findings can be used in a ship fatigue routing plan, i.e. optimization of ship courses, ship speeds, heading angles and loading conditions. It has to be combined with the shipping schedule, structural ultimate safety, onboard weather forecast information and regular inspection to maximize the ship's serviceability before the regular inspection and maintenance. Further, the large standard deviation in Fig. 6 indicates that the ship has a potential to extend its repair time dramatically if the ship's operation is well planned.

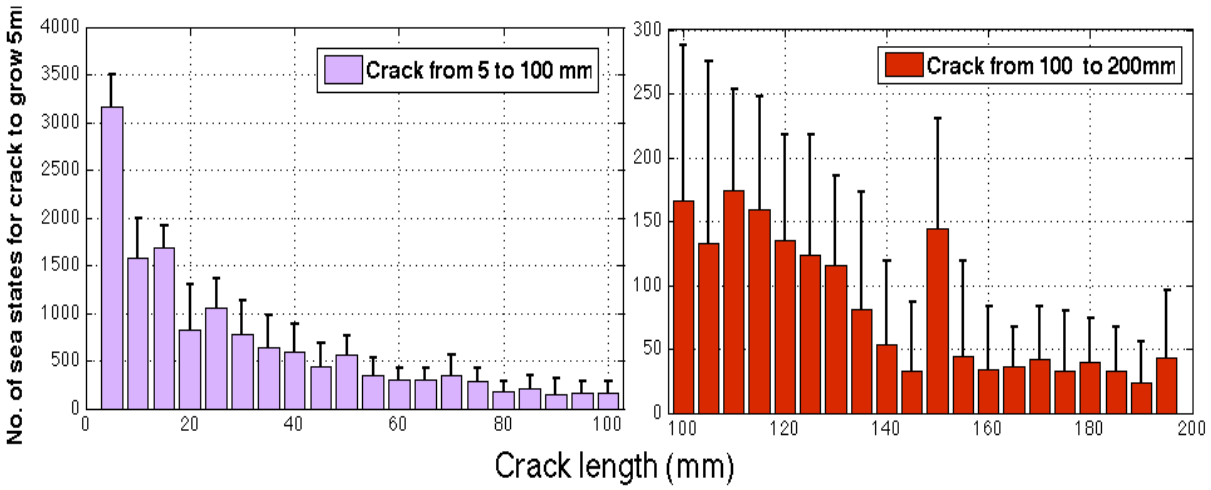

Figure 6. Median and standard deviation of the sailing periods (number of sea states) when the fatigue crack reaches 200 mm. Bars: median values of sea state number; lines: the standard deviation of sea state number needed for the crack to propagate 5 mm.

5. Discussion and conclusions

Conventional fatigue design of ship structures is carried out using high-cycle fatigue approaches, with stress ranges from either empirical data or direct calculations. Because of large uncertainties involved in the ship fatigue design process, such as the variation of encountered wave environments, computation of hydrodynamic fatigue loads and stress concentration factor, etc., fatigue cracks occur much earlier than expected. It is of great interest to study the crack propagation conditions in order to design and plan a maintenance strategy based on crack growth management, which ensures e.g. safety of the vessel. In this study, an efficient method for fatigue crack propagation analysis in ships was derived based on the narrow-band spectral fatigue method. The spectral method was validated by full-scale measurements on a 2800TEU container ship, to give accurate prediction of stress range distributions. In a crack propagation analysis, a case study using an example from reality of a structural detail prone to fatigue was used to demonstrate the application of the proposed method. The results show that depending on the encountered wave environments, the crack is critical and needs to be repaired within 2 to 3 years. During the crack propagation process, many sea states were required for the crack to grow 5 mm, but when the crack reached close to 200 mm, only a few sea states grew the crack 5 mm. It indicates the necessity to repair the crack in time since it can grow so fast that structural integrity and safety may be jeopardized.

References

[1] IACS, Common Structure Rule for Bulk Carriers (Common Structure Rule for Oil Tanker). London, UK, January, 2006.

[2] W. Fricke, W. Cui, H. Kierkegaard, et al., Comparative fatigue strength assessment of a structural detail in a containership using various approaches of classification societies. Marine Structures, 15 (2002) 1-13.

[3] A.S. Olsen, C. Schrøter, J.J. Jensen, Wave Height Distribution Observed by Ships in the North Atlantic. Ships and Offshore Structures, 1 (2005) 1-12.

[4] W. Mao, Fatigue assessment and extreme response prediction of ship structures. Doctoral thesis, Chalmers University of Technology, Gothenburg, Sweden, 2010.

[5] G. Storhaug, J. Vidic-Perunovic, F. Rüdinger, G. Holstmark, J.B. Helmers, X. Gu, Springing/whipping response of a large ocean going vessel - a comparison between numerical simulations and full-scale measurements. In: R.E. Taylor, Editor, Proceedings of hydroelasticity in marine technology, University of Oxford, Oxford, 2003.

[6] Y. Tomita, M. Matoba, H. Kawabe, Fatigue crack growth behavior under random loading model simulating real encountered wave condition. Marine Structures, 8 (1995) 407-422.

[7] ISSC. Technical Committee III.2, Fatigue and fracture. 18th International Ship & Offshore Structures Congress, Rostock, Germany, 2012.

[8] W. Mao, J.W. Ringsberg, I. Rychlik, G. Storhaug, Estimation of Fatigue Damage Accumulation in Ships during Variable Sea State Conditions. Journal of Ship Research, 54 (2010) 281-293.

[9] DNV, Fatigue Assessment of Ship Structures, Classification Note 30.7, Hövik, Norway 2010.

[10] E.V. Lewis, Principles of Naval Architecture: Volume III - Motions in Waves and Controllability, Society of Naval Architects and Marine Engineers, Jersey City, USA, 1989.

[11] N. Hadjiyiannis, Projection of fractures in ships for the evaluation of fatigue resistant design. Master thesis in Naval Architecture and Marine Engineering, Massachusetts Institute of Technology, USA, 2007.

[12] P.C. Paris, M.P. Gomez, W.E. Anderson, A rational analytic theory of fatigue. The Trend in Engineering, 13 (1961) 9-14.

[13] P.A. Wawrzynek, A.R. Ingraffea, Discrete modeling of crack propagation: theoretical aspects and implementation issues in two and three dimensions. Report 91-5, School of Civil and Environmental Engineering, Cornell University, 1991.

[14] A. Baxevani, S. Caires, I. Rychlik, Spatio-temporal statistical modelling of significant wave height. Environmetrics, 20 (2009) 14-31.

[15] Y. Sumi, Fatigue crack propagation and computational remaining life assessment of ship structures. Journal of Marine Science and Technology, 3 (1998) 102-112.

On the Mechanism of Martensite Formation during Short Fatigue Crack Propagation in Austenitic Stainless Steel: Experimental Identification and Modelling Concept

Ulrich Krupp[1,*], Ingmar Roth[2], Hans-Jürgen Christ[2], Martin Kübbeler[2], Claus-Peter Fritzen[2]

[1] Faculty of Engineering and Computer Science, University of Applied Sciences Osnabrück, 49009 Osnabrück, Germany
[2] Faculty IV: Science and Technology, University of Siegen, 57068 Siegen, Germany
* Corresponding author: u.krupp@hs-osnabrueck.de

Abstract During fatigue of metastable austenitic steels, local plasticity is linked with the formation of martensite. It was shown that cubic α´ martensite nucleates at slip band and ε martensite intersection sites ahead of growing fatigue cracks. Since such intersections require the operation of alternate slip systems, martensite formation was found only for shear-controlled single-slip crack propagation (mode II) prevailing during the early propagation phase of microstructurally short fatigue cracks. Surprisingly, cracks were found not to initiate within martensitically transformed grains but by a fraction of 70% along twin boundaries. The extent of martensite formation ahead of a propagating crack increases with increasing crack length and eventually, gives rise to transformation-induced crack-closure effects. The interaction between the crack tip plasticity and the local microstructure was quantitatively analysed by automated electron back-scatter diffraction (EBSD) in the scanning electron microscope (SEM) applied to the electro-polished surfaces of fatigue specimens. Following a geometrical model for martensitic transformation, further analysis of the relevant fatigue mechanism became possible aiming to both mechanism-based life prediction and tailoring fatigue resistant microstructures.

Keywords austenitic steels, martensitic transformation, fatigue crack propagation, short crack model

1. Introduction

Metastable austenitic stainless steels, e.g., AISI 304, may exhibit a transformation from fcc austenite into bcc martensite (α´ martensite) if a certain monotonic or cyclic plastic strain value is exceeded. This so-called TRIP effect (transformation-induced plasticity) is widely technically used, e.g., for work-hardened spring elements. From a thermodynamic point of view, at room temperature the Gibbs free energy difference ΔG between the fcc and the bcc phase is not large enough for spontaneous martensitic transformation to occur. However, this changes when sufficient plastic strain energy ΔG_{mech} is added, as it is schematically represented in Fig. 1a. Generally, the phase relationship between the parent fcc austenite and the martensite can be explained by the Bain relationship as shown in Fig. 1b [1]. From a microstructure point of view, plastic slip along the {111} slip planes of the fcc austenite cause the formation of extended stacking faults (due to the low stacking fault energy of the metastable austenitic steels), i.e., hexagonal ε martensite bands. The cubic α´ martensite nucleates at intersection points of the ε martensite bands (cf. [2,3]). Between the parent austenite and the transformed martensite, the Kurdjumov-Sachs relationship is fulfilled (cf. [4]):

$$\{111\}_{\gamma} \| \{101\}_{\alpha'} \quad \text{and} \quad <110>_{\gamma} \| <111>_{\alpha'} \quad . \tag{1}$$

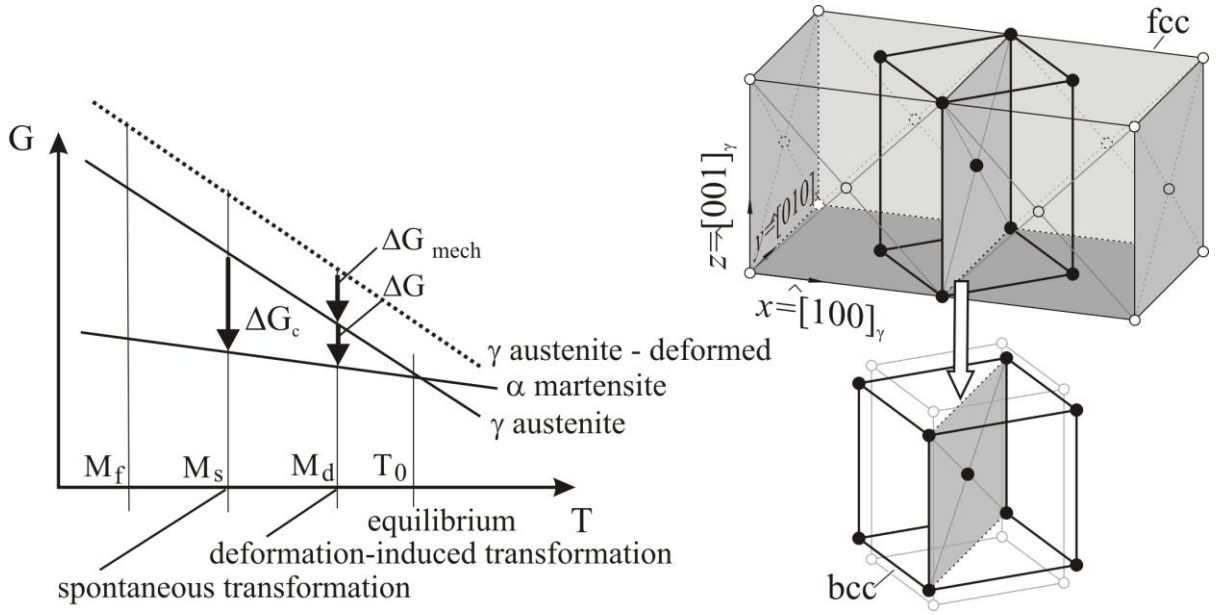

Figure 1. (a) Contribution of the mechanical strain energy ΔG_{mech} to the thermodynamic driving force for austenite-to-martensite transformation and (b) unit cell model of the martensitic transformation, according to Bain [1].

According to Olson and Cohen [3], the α´ martensite volume fraction $f_{\alpha'}$ can be calculated as a function of the plastic strain ε_{pl} by Eq. 2:

$$f_{\alpha'} = 1 - \exp\left(-\beta\left(1 - \exp\left(-\alpha\varepsilon_{pl}\right)\right)^n\right), \tag{2}$$

with n being a material-depending exponent, α a temperature-depending constant, and β accounting for the probability that martensite embryos are formed at shear-band intersections. While under monotonic loading conditions the α´ saturation level is reached at $f_\alpha \approx 0.9$, under cyclic loading conditions the transformation depends on the accumulative plastic strain $\varepsilon_{pl,\,cum}$ and sets in only when a critical threshold of $\Delta\varepsilon_{pl}/2 \approx 0.3$ is exceeded [5]. Under high-cycle fatigue (HCF) loading conditions and correspondingly very small $\Delta\varepsilon_{pl}$, plastic deformation is limited to grains of favorable orientation of the slip systems, with values of the Schmid factor $M_S \approx 0.5$. Smaga et al. [6] use the Olson-Cohen model to define a damage parameter that includes inhomogeneous cyclic hardening due to martensitic transformation. In very-high cycle fatigue (VHCF) Müller-Bollenhagen et al. [7] had shown that the onset of fatigue damage in form of local plasticity is stopped by martensite formation (self healing of defects); they concluded that metastable austenitic stainless steels exhibit a real fatigue limit. However, in the HCF regime short fatigue cracks may initiate without martensitic transformation. The propagation of such cracks cannot be shielded completely by the formation of martensite in the plastic zone ahead of the crack tip [4].

In order to understand and to predict the propagation behavior of microstructurally short fatigue cracks in metastable stainless steels, the geometrical model of Bogers and Burgers [8] was employed. It considers co-operative slip at two austenite slip systems as schematically represented in Fig. 2. Here, bcc α´ martensite nucleation is a product of partial dislocation displacement on every 2nd (T/2) and every 3rd (T/3) {111} slip plane, respectively.

$$\frac{T}{3} = \frac{1}{3}\cdot\frac{1}{6}a\left[211\right]_{fcc} \quad \text{and} \quad \frac{T}{2} = \frac{1}{2}\cdot\frac{1}{6}a\left[21\bar{1}\right]_{fcc} \quad . \tag{3}$$

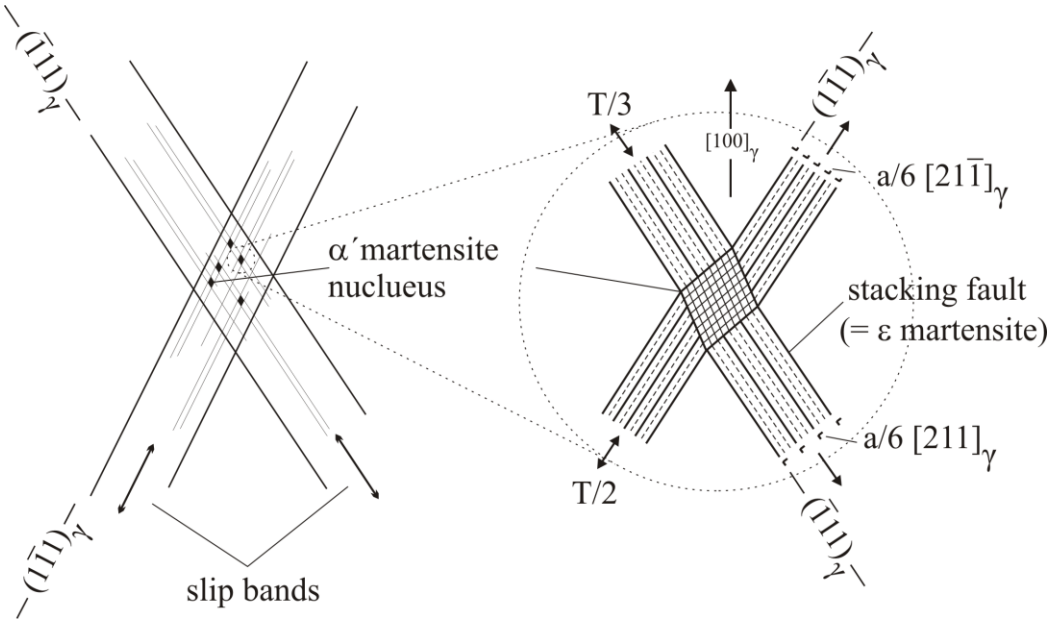

Figure 2. α´martensite nucleation at {111} slip-band intersection points, according to the model of Bogers and Burgers [8].

The Bogers-Burgers model for martensite formation at fcc shear band intersections has been proven experimentally in various studies and is the basis for the modeling concept introduced in section 4.

2. Experimental

The experiments were carried out on cylindrical specimens of the metastable austenitic stainless steel AISI 304L provided by Deutsche Edelstahlwerke Siegen, Germany, with the chemical composition given in Table 1. Prior fatigue testing, the specimen material was solution heat-treated for 1.5h at a temperature of 1050°C in order to homogenize the microstructure resulting in an average austenite grain size of 74µm. To analyze microstructurally short fatigue cracks within a limited area, two shallow notches were machined at 0° and 180° of the gauge length of the specimens (see Fig. 3). To apply electron channeling contrast (ECCI) and electron back-scatter diffraction (EBSD) within the scanning electron microscope (SEM), the surface of the specimens was electrolytically polished at T=-15°C/15V using perchloric acid (8%, cf. [9]).

Table 1. Chemical composition of the metastable austenitic steel used in this study (in wt. %).

alloy	Fe	C	Cr	Ni	Si	Mn	Cu	Mo
AISI 304L	Base	0.03	18.1	8.75	0.62	1.85	0.54	0.37

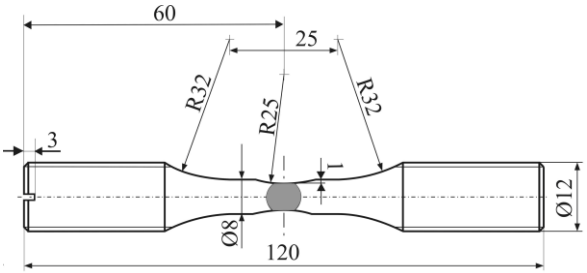

Figure 3. Shallow-notched specimens for microcrack characterization in a servohydraulic testing system.

Fatigue cracks were followed using a MTS810 servohydraulic testing system under load control at a stress ratio of R=-1. Crack length analyses and measurements of the crystallographic orientation/phase distributions were done in the SEM by periodically removing the specimens from the testing machine. The fatigue limit was estimated by rotating bending tests following the staircase approach.

3. Results

The fatigue limit of the AISI 304L test material was found to lie in the range between $\Delta\sigma/2$=230MPa and $\Delta\sigma/2$=240MPa. It is worth mentioning that (i) above a number of cycles of $N\approx5\cdot10^5$ cycles no failure was observed at all and (ii) the fatigue limit is of the same order of magnitude than the 0.2%-offset yield strength of $R_{p0.2}$=237MPa. HCF microcrack propagation studies were carried out at a stress amplitude (fully reversed, R=-1) of $\Delta\sigma/2$=245MPa. After a few thousands of cycles, martensitic transformation occurred in favorable oriented grains of a high Schmid factor close to M_S=0.5. Furthermore, it is believed that the high elastic anisotropy of austenitic steel ($A=2C_{44}/(C_{11}-C_{12})$=3.81, cf. [10]) promotes the local transformation process, but obviously also crack initiation. About 70% of all crack initiation events (48 evaluated cracks) can be correlated with twin boundaries, which exhibit high anisotropy stresses, as it was analyzed in the studies of Heinz and Neumann [11] and Blochwitz and Tirschler [12]. Surprisingly, crack initiation cannot be correlated with martensitic transformation.
Figure 4a shows an example of crack initiation at a twin boundary. Only when the crack path leaves the twin boundary (above and below the twin boundary crack segment) and continues by alternating activation of various {111}<110>-type slip systems, martensite could be identified by means of EBSD phase analysis. Obviously, the slip intersections act as martensite nucleation sites, according to the theory of Olsen and Cohen [3] and Bogers and Burgers [8]. This observation is further supported by Fig. 4b. Again, the crack was initiated at a twin boundary segment. When following the right-hand branch of the crack, one may notice that propagation follows a {110} martensite plane. It is believed that the activation of alternate slip systems in the austenite ahead of the crack tip cause martensite formation. In the following, further crack propagation occurs within the martensite phase. In a more pronounced manner this was observed within the circle area in Fig. 2b. However, as long as fatigue crack propagation is driven by the activation of only one slip system, no martensite formation can be identified.

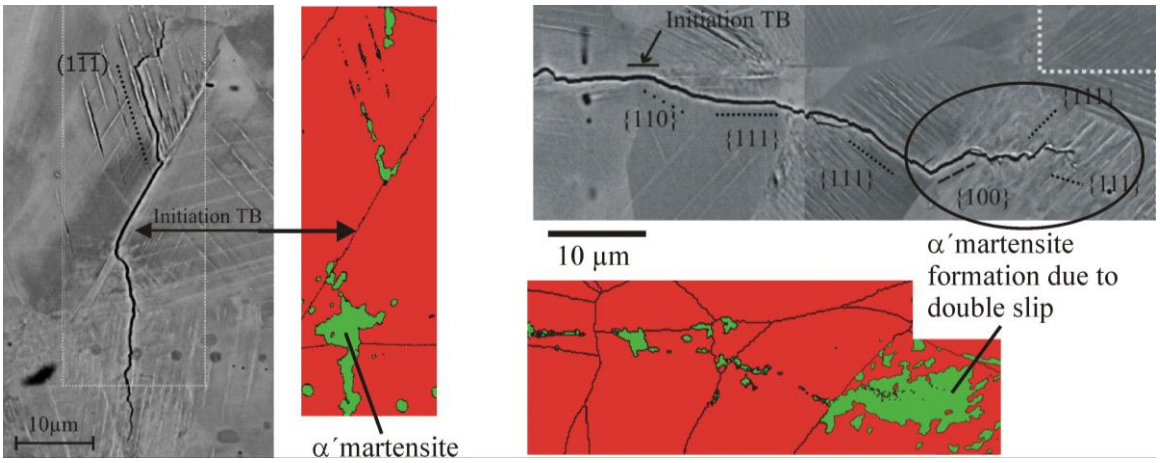

a b

Figure 4. Microstructurally short fatigue cracks: (a) crack initiation at a twin boundary without any martensite formation (see EBSD map beside) and (b) crack propagation operated by alternating slip in combination with massive martensite formation (see EBSD map below).

The Bogers-Burgers mechanism was identified by using transmission electron microscopy (TEM).

Figure 5 shows the intersection of {111} slip bands, which can be interpreted as stacking faults changing the stacking sequence from ABCABC with the fcc austenite to ABAB within the slip band. Such stacking faults correspond to ε martensite bands. Where these bands intersect bcc α´martensite is formed (see Fig. 5a).

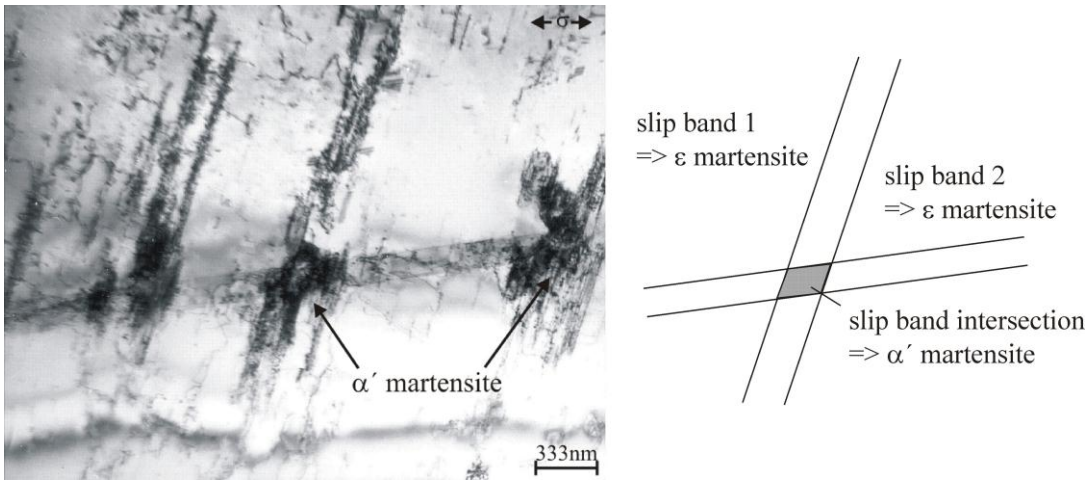

a b

Figure 5. Deformation-induced α´ martensite formation during HCF loading of AISI 304L steel after N=10^5 cycles: (a) TEM micrograph and (b) schematic representation.

Analysis of the crack propagation rate as a function of the local microstructure revealed that the crack propagation rate decreases strongly, when (i) the propagation mode changes from single-slip propagation mode to double slip propagation mode, (ii) the crack propagates into transformation martensite, or when (iii) the crack tip approaches a grain boundary. Generally, the strong interactions between the plastic zone ahead of the crack tip and the local microstructural features give rise to an oscillating crack propagation rate, which was found at lower stress intensity ranges ΔK than the threshold value ΔK_{th}. The comparison of the propagation behavior of several microcracks with the one of a long crack is shown in Fig. 6.

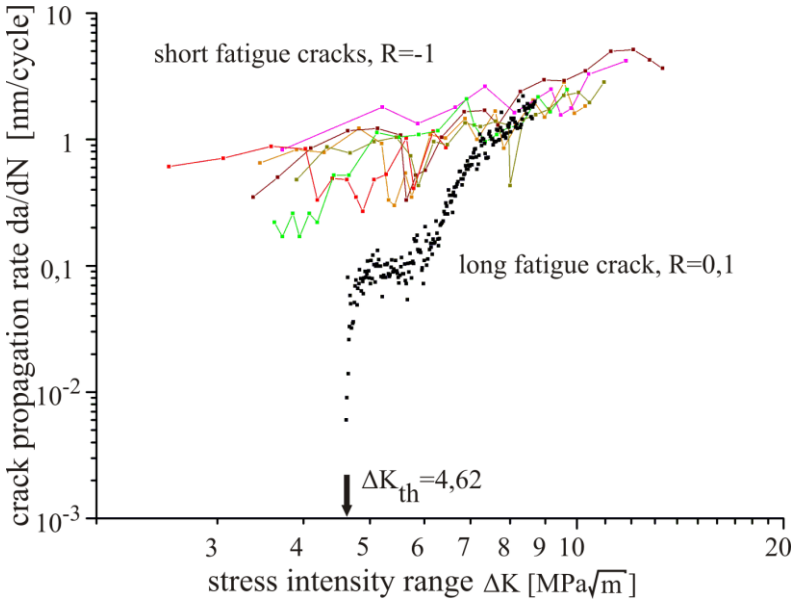

Figure 6. Propagation behavior of short (2a<400µm) and long fatigue cracks in metastable austenitic steel AISI 304L.

4. Modeling Concept and Discussion

It is the aim of the study to predict the complex propagation behavior of microstructurally short fatigue cracks, as presented in section 3. For this purpose a short crack model has been developed where the crack and its plastic zones are meshed by boundary elements (for details see [13,14]). The boundary elements represent shear displacements along individual slip planes and normal and shear displacements within the crack. Accounting for the boundary conditions that (i) within the crack the normal displacements must be positive and no shear stresses are present and (ii) the shear stress values within the slip bands are limited to the friction stress τ_{fr}, the equation system for the displacement distribution along crack and slip bands can be calculated. The crack propagation rate results from the cyclic crack tip slide displacement ΔCTSD as follows

$$\frac{da}{dN} = C \cdot \Delta CTSD\,, \tag{4}$$

where C represents the irreversible part of ΔCTSD that contributes to crack advance.
In order to account for the Bogers-Burgers mechanism of martensitic transformation (see section 1), the model has been extended to alternate slip ahead of the crack tip. Vector addition of the slip displacements b_{t1} and b_{t2} (see Fig. 7) give a resulting displacement b_R. The magnitude of these displacements determines the size of the corresponding martensitic transformation zone. The direction of the resulting displacement does not necessarily correspond to a slip direction of the martensite phase, the displacement b_R is projected onto the current crack propagation direction, eventually resulting in the crack tip displacement b_{RP} corresponding to CTSD within the crack propagation plane.

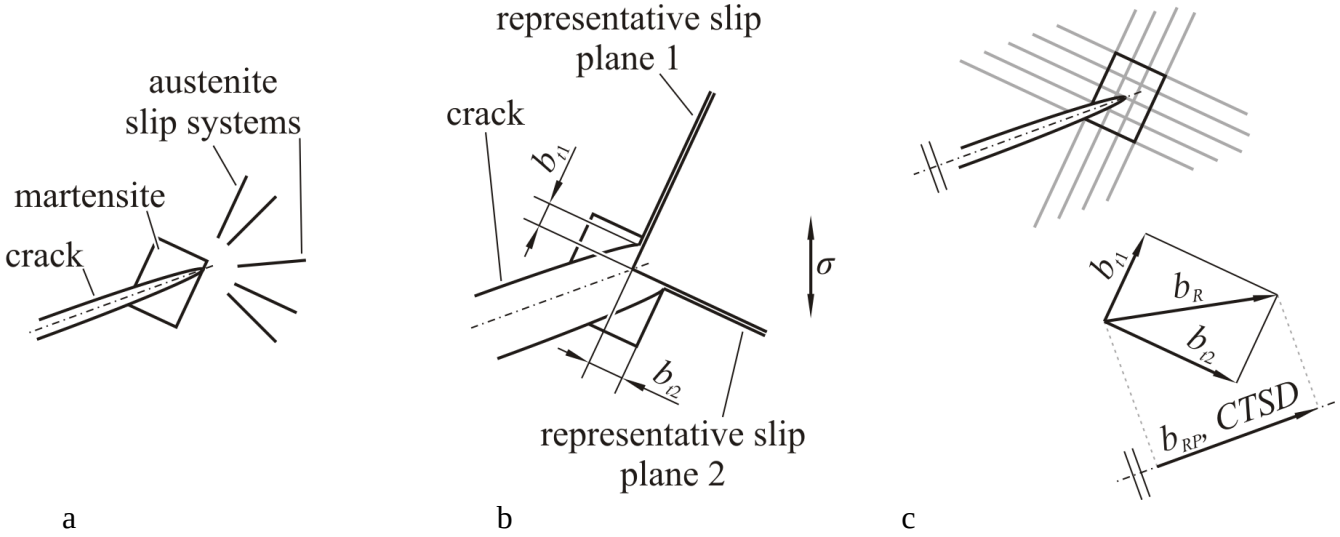

Figure 7. Modeling concept for strain-induced martensite formation ahead of a growing fatigue crack: (a) crack tip with martensite and the various austenite slip systems, (b) displacement at two representative slip planes, and (c) corresponding new martensite zone with the respective crack tip slide displacement.

As mentioned before, the austenite to martensite phase transformation results in a 2.57% volume increase. Therefore, a volume strain ε_m is implemented in the model. As schematically shown in Fig. 8, the martensite phase and the individual grain boundaries are meshed by boundary elements that describe absolute displacements of the boundaries. By superimposing the displacements within the plastic zone ahead of the crack tip (relative displacements) with those of the boundaries (accounting

for the individual elastic properties) and the volume strain within the transformation zone, one can predict crack propagation.

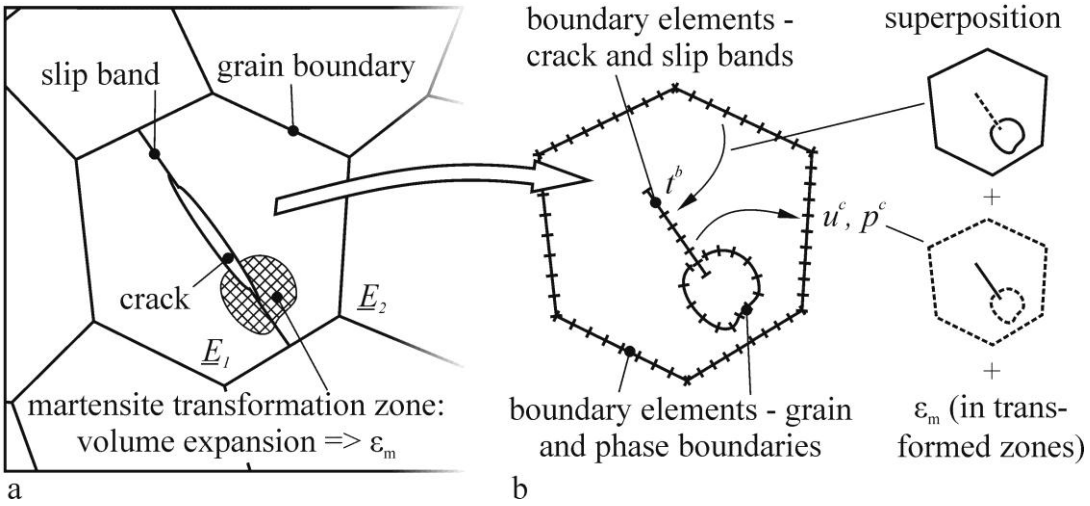

Figure 8: Schematic representation of the boundary element model: (a) crack with adjacent slip bands and martensite transformation zone in an individual grain of stiffness E_1 and (b) superimposition of crack-free grain, crack in an infinite plate and volume expansion strain ε_m.

Figure 9 shows the application of the model to a real microstructurally fatigue crack in AISI 304L. Certainly, the simulation shows a martensite distribution of much higher homogeneity than the experimental evaluation, but the predicted crack propagation rates are in reasonable agreement. Hence, one may conclude that the modeling concept represents the governing mechanisms in the right way, supporting the concept of Bogers and Burgers to be applicable to fatigue crack propagation in combination with martensitic transformation in metastable austenitic steels.

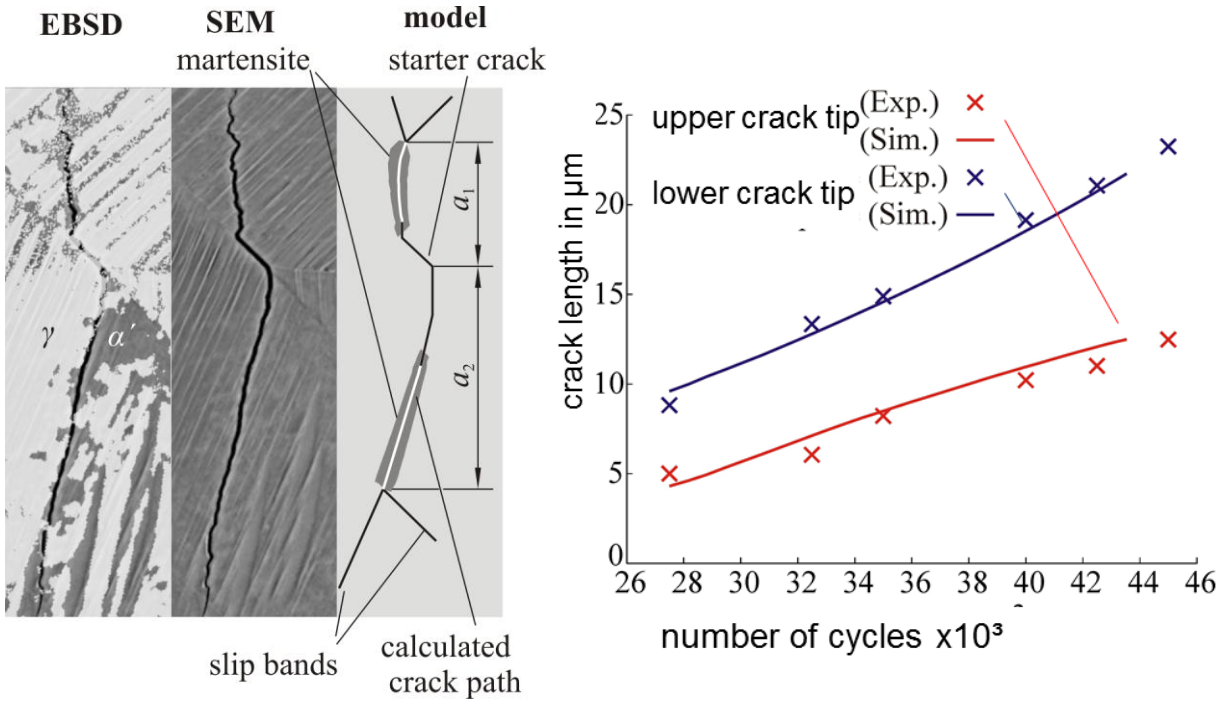

Figure 9. Microstructurally short fatigue crack in AISI 304L: (a) EBSD phase distribution, SEM micrograph and predicted strain induced martensite, (b) corresponding simulated vs. experimental fatigue crack propagation.

5. Conclusions

Crack propagation during high-cycle fatigue loading of metastable austenitic steel AISI 304L is not only governed by interactions with local microstructural features such as the alloy grain boundaries. Moreover, plastic slip ahead of the crack tip causes the formation of strain-induced α´ martensite. According to a geometrical model of Bogers and Burgers, the fcc austenite to bcc martensite phase transformation can be described by co-operative activation of partial dislocations on two intersecting {111} type slip bands. It was proven by scanning and transmission electron microscopy that martensite formation occurs only within areas of multiple slip activation. For crack initiation and propagation along single slip bands no martensite formation was identified. Depending on the local crystallographic orientation of the grains with respect to the remote stress axis and depending an the amount of martensite phase formation, the crack propagation rate is increased or decreased, respectively. This can be qualitatively predicted by computer simulation using a boundary element approach where the crack and the possible slip planes are described by boundary elements allowing for martensitic transformation according to the Bogers-Burgers model.

Acknowledgements

The financial support by Deutsche Forschungsgemeinschaft DFG under grant no. PAK104 - KR1999/11 is gratefully acknowledged.

References

[1] E.C. Bain, The nature of martensite transformation, AIME Steel Division, 70 (1924) 25-46.
[2] H. Schumann, Bildung von α´-Martensit im Schnittbereich von ε-Martensitplatten, Kristall und Technik, 12 (1977) 363-370.
[3] G.B. Olsen, M. Cohen, Kinetics of strain-induced martensitic nucleation, Met. Mat. Trans, 6A (1975) 791-795.
[4] U. Krupp, I. Roth, H.-J. Christ, M. Kübbeler, C.-P. Fritzen: In-Situ SEM Observation and Analysis of Martensitic Transformation during Short Fatigue Crack Propagation in Metastable Austenitic Steel, Adv. Engng Mater., 12 (2010) 255.
[5] M. Bayerlein, H.-J., Christ, H. Mughrabi, Plasticity-induced martensitic transformation during cyclic deformation of AISI304L stainless steel, Mater. Sci. Engng A, 114 (1992) L11.
[6] M. Smaga, P. Starke, D. Eifler, J. Fingerhuth, B. Nieweg, D. Siegele, Bewertung der Ermüdungsfestigkeit metastabiler austenitischer Stähle unter Berücksichtigung zyklischer Ver- und Entfestigungsvorgänge, in: Fortschritte in der Werkstoffprüfung in Forschung und Praxis, M. Borutzki, G. Moninger (Eds.), Verlag Stahleisen, Düsseldorf, 2012, pp. 173-178.
[7] H.-J. Christ, C. Müller-Bollenhagen, M. Zimmermann, Effect of deformation induced martensite on the very high cycle fatigue properties of a metastable austenitic stainless steel, in: Proc. 5th Int. Conf. on Very High Cycle Fatigue (VHCF 5), C. Berger, H.-J. Christ (Eds.), DVM Berlin, 2011, pp. 171-176.
[8] A.J. Bogers, W.G. Burgers, Partial dislocations on the {110} planes in the bcc lattice and the transition of the fcc into the bcc lattice, Acta Metall. 12 (1964) 255-261.
[9] I. Roth, Untersuchungen zum Ausbreitungsverhalten mikrostrukturell kurzer Ermüdungsrisse in metastabilem austenitischen Edelstahl, doctorate thesis, University of Siegen, 2011.
[10] H.M. Ledbetter, Predicted monocrystal elastic constants of 304 type stainless steel, Physica 128B (1985) 1-4.

[11] A. Heinz, P. Neumann, Crack initiation during high-cycle fatigue of an austenitic steel, Acta Met. Mat. 38 (1990) 1933-1940.
[12] C. Blochwitz, W. Tirschler, Twin boundaries as crack nucleation sites, Cryst. Res. Techn. 40 (2005) 32-41.
[13] M. Kübbeler, I. Roth, U. Krupp, C.-P. Fritzen, H.-J. Christ: Simulation of Stage I-Crack Growth Using a Hybrid Boundary Element Technique, Engineering Fracture Mechanics, 78 (2011) 462.
[14] U. Krupp, Fatigue crack propagation in metals and alloys, Wiley VCH, Weinheim 2007.

Suspension Springs – Experimental Proof of Reliability under Complex Loading

Matthias Decker[1,*], Steffen Rödling[1], Manfred Hück[2]

[1] Main Department for Strength, Function, Materials, IABG mbH, Ottobrunn, 85521, Germany
[2] Ing.-Büro Hück, Vaterstetten 85591, Germany
* Corresponding author: decker@iabg.de

Abstract Fatigue strength of suspension springs in service life is subject to numerous influences. Besides the mechanical loading, determined by the kinematics of the suspension system, road conditions and driving maneuvers, fatigue strength of suspension springs is vitally affected by material properties, coating and environmental influences. Typical failure modes of suspension springs and their causes can be divided into several groups like static and cyclic loads, geometry and dimensions, manufacturing influences, mechanical defects of coating or steel surface, corrosion, fretting corrosion and imperfection of steel purity. This paper covers the influence of mechanical loading taking into account the influences of the kinematics of the suspension system, environmental conditions and steel purity. This leads to a comprehensive experimental validation strategy for suspension springs. Also statistical effects are discussed that have to be taken into account for a safe proof out.

Keywords Suspension springs, fatigue, corrosion, steel purity, testing

1. Introduction

Springs are used in many technical applications and play a vital role as elastic elements. In passenger cars, steel coil springs are used widely as suspension springs and as valve springs. Their durability in these cases is vital for the safety and reliability of the vehicle. Therefore, failure of suspension as well as of valve springs must be avoided with a high level of safety. For this, dedicated concepts for design and proof out are necessary.

In this paper, the relevant service loads acting on suspension springs of cars will be shown as well as pictures of typical failure modes. Besides a description of the failure modes leading to a defect of a suspension spring, a concept for proof out of suspension springs will be discussed, taking into account fatigue due to mechanical loading under corrosive media, contact and abrasive wear and damage due to grit impact. Finally, a concept for proof of steel purity is shown.

This paper is focused on coil springs used in passenger car suspensions. However, the methods may be used for evaluation of others springs in other applications with adaptions that take into account the differences in the respective application.

2. Material, Design and Conditions of Installation

Suspension springs of ground vehicles are subject to high static and cyclic loads. In order to realize the wanted stiffness characteristics within a minimum of designed space and mass, high strength steels like 52CrMoV4 or 54SiCr6 with a tensile strength of 1400 up to 2000 MPa are widely used. The local stresses acting in the springs are very high with a high frequency of occurrence. The sensitivity of steels to stress concentrations due to notches increases with increasing tensile strength and yield ratio. Therefore, springs made out of high strength steels will be sensitive to defects on the surface that may be caused by the production process, grit impact, abrasive wear or corrosion.

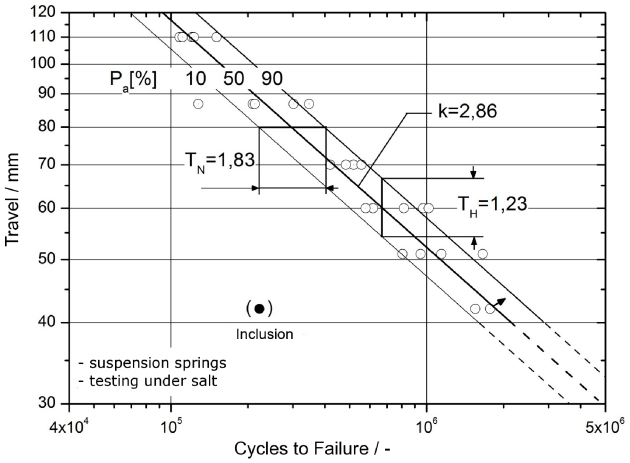

Figure 1. Failure caused by discontinuity of microstructure (inclusion) [2]

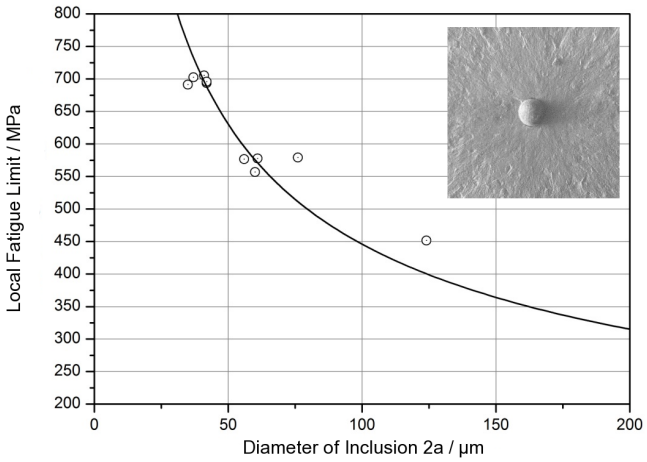

Figure 2. Influence of size of non-metallic inclusions on local fatigue limit [1]

Also, nonmetallic inclusions or other imperfections within the material may cause a failure, especially under high cycle fatigue loading. The combination of high local stresses and defect size may lead to stress concentrations above the threshold value for crack propagation. Hence, a material defect can act as an initial crack, propagating under cyclic loading and leading to a failure of the spring (see Fig. 1). In [1], the influence of nonmetallic inclusions in high strength steels was investigated in a comprehensive way yielding a correlation of the size of inclusion and upper boundary of possible fatigue limit (see Fig. 2). For the design of springs made from high strength steels, this means that the higher the used stress level and therefore the necessary strength level of the material, the more critical steel purity must be taken into consideration in testing for development, qualification and quality assurance. Since nonmetallic inclusions usually follow a different statistical distribution than the cyclic strength values of the base material, these have to be taken into consideration separately. Whether an impurity in the material will be critical for the endurance of a spring, does not only depend only on the size of the impurity but also on its location within the spring, since crack propagation will only occur, if there is a high local stress level at the location of the defect. This fact must be considered with respect to the critically stressed material volume and the statistical size effect. Detailed description on this can be found in [2].

With high strength steels in suspension springs of ground vehicles, special focus must be set on the risk of stress corrosion cracking. This effect may not necessarily depend on a higher tendency for corrosion of the used steel. It may also be caused by the high local stresses in combination with the notch sensitivity of the material. In order to decrease the risk of stress corrosion cracking, nowadays suspension springs are coated with specialized coating systems. Not only do these coatings prevent the spring from corrosion but also from other surface damages like grit impact.

The local stresses acting within a coil spring depend mainly on the geometrical design, the axle kinematics and the load applied. Also the local design, stiffness and surface properties of the spring attachments do influence the local stresses and the risk of abrasive wear and corrosion in the contact area of springs and spring attachments. While in a MacPherson strut, the upper and lower spring attachment will only move in a linear displacement (parallel deflection), in twin lever axle kinematics, also a lateral displacement as well as a rotation between the upper and lower spring attachments usually occur (circular deflection, see Fig. 3). Off course, this will yield different local stresses in the springs. The geometric design as well as the stiffness of the upper and the lower spring attachment as well as the geometric design of the first and last winding of the coil spring can significantly influence the local stresses in this critical area. These effects must be considered both

in the design as well as in the validation process of a spring. The design of the spring attachment does not only influence the local stresses within the spring in the contact area. It also influences the abrasive wear on the spring coating in the contact area, especially in the lower attachment. Especially under corrosive media, the contact area plays a vital role for the fatigue live of a coil spring. Springs that may be deflected up to block experience contact wear at the areas of contact. This also may damage the coating and enable corrosion on the spring.

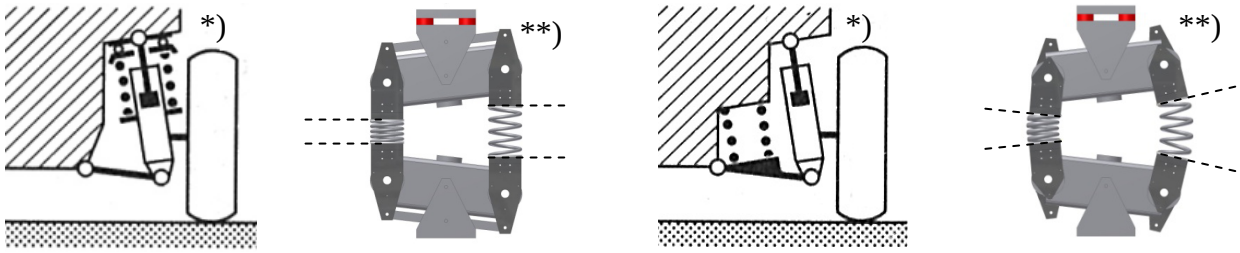

Figure 3. Kinematics of parallel and circular deflection in car suspension and test facility (* [3], ** IABG)

3. Service Loading

Besides geometry, material, production and conditions of installation, the loads and environmental conditions in service determine the service life of springs. The mechanical loads consist of a static preload and superposed cyclic loading. Fig. 4 gives a schematic overview of a typical load history of a suspension spring of its lifetime in a vehicle, beginning with its installation.

Maximum and minimum deflections are determined by the conditions of installation and the axle kinematics. The static preload consists of the preload due to mounting and the preload of the proportional weight of the car. This typically causes car springs to experience cyclic stresses with a high mean-stress. The cyclic loads are caused by driving maneuvers and surface roughness. A typical passenger car will only be moved for about 3% of its service life (counted in days rather than number of cycles). Hence, also effects acting during the 97% of time when the car is parked must be taken into account, since stress corrosion cracking may also act in these periods.

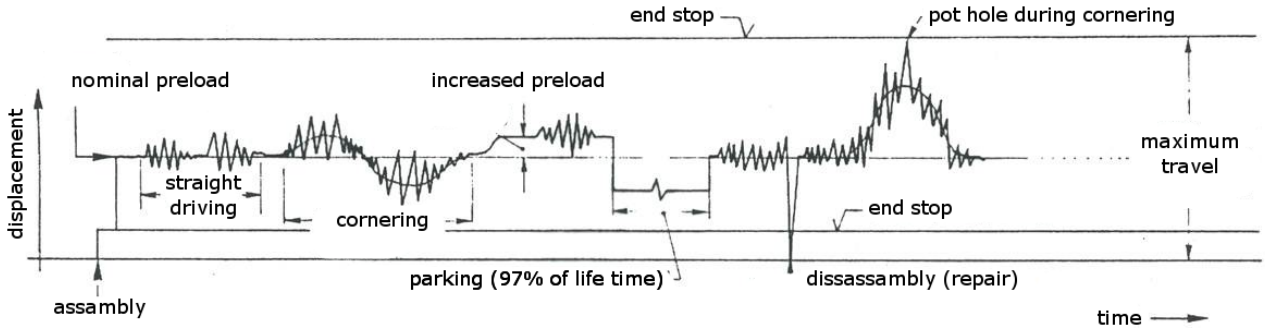

Figure 4. Schematic loading of suspension springs of passenger cars [4]

The cyclic loading of a spring consists of a variety of load cases (see Fig. 4). While cruising on paved roads will cause low to middle load amplitudes, driving on rough roads or off road, dynamic cornering and special incidents like driving through a pothole or over speed bumps will cause much higher loads that also have to be safely taken into account. Also, combinations of different maneuvers must be considered, such as high vertical dynamics due to rough road surface while taking a sharp corner at high speed. Thus, the full possible travel of the spring, from fully extended to fully compressed, usually is covered. For a safe and still economically sensible design and test strategy, both amplitudes as well as number of occurrence of the different load cases must be

investigated by means of extensive road load measurement, road data profiling, multi body simulations, statistical evaluation and extrapolation of the respective results (see also [5]).

Besides mechanical loading, suspension springs in ground vehicles are subject to environmental and service conditions that may influence the service life especially of high strength springs significantly [4]. In many regions, corrosive media are present on the roads at least temporarily. Anything from normal humidity over rain to salt water will be found during driving cars on roads all over the planet. Hence, corrosion can act on the springs if they are not covered by a durable coating. Especially during winter periods, grit that hits the springs may damage this coating making its protection void. Additionally, micro mechanical relative movement in the contact region between spring and spring seat will cause abrasive wear on the coating. This effect may be intensified, if abrasive media like grit or sand are cumulated in the lower spring seat. Due to the permanent static pre load due to assembly and car weight, springs are under a constant pre-stress, thus being subject to the threat of stress corrosion cracking. This threat is significantly higher under the conditions described.

The influences shown on the service life of suspension springs in ground vehicles under cyclic loading are not independent from each other. For example, the influence of corrosive media is much stronger, if the coating of the spring is damaged due to grit impact. Hence, the combination of load influences must be regarded as a complex load scenario in design and testing in order to cover the combined influences.

In commercial vehicles, especially in heavy trucks, leaf springs rather than coil springs usually are used in the suspension. Here, besides the influences described above additional effects may be important. Leaf springs usual front axles of commercial vehicles are subject to additional load cases such as torsional deformation due to vehicle roll and driving over single sided obstacles or S-shaped bending due to breaking moment [11, 12]. These have to be taken into consideration in design and testing.

4. Failure Modes

Coil Springs in passenger car suspensions show a number of typical failure modes, caused by material defects, the production process and complex service loading. Often, failures are caused by a combination of influences. Surface damage due to grit impact and abrasive wear together with corrosion may initiate crack propagation finally yielding a defect of the spring.

The most common failure mode of suspension springs of ground vehicles is the formation of fatigue cracks initiated from surface defects. The high strength steels used for these components are very sensitive to any geometrical or metallurgical discontinuity. In the sense of fracture mechanics, these can be interpreted as cracks. Making use of the potential of the high strength steels used for suspension springs, high local stresses will be allowed in the springs, yielding high stress intensity factors at these cracks. If the threshold value for crack propagation is exceeded, the cracks will propagate under the cyclic loading causing a failure of the component. Fig. 5 shows a typical failure of a suspension spring of a passenger car starting from a surface defect.

Another failure mode is shown in Fig. 6. Here, a fatigue crack started from a non-metallic inclusion below the surface of the spring. Since these internal defects will only lead to a propagating crack, if the threshold value for crack propagation is exceeded, they will only cause a failure, if they are located in a highly stressed volume of the spring. Hence, the frequency of occurrence of this failure

mode is smaller than the one of defects on the surface, where local stresses are naturally high due to the stress distribution over the cross-section under combined torsional and bending loading. Reports about failures due to internal defects can be found e.g. in [6] for coil springs and in [7] for leaf springs. These failures follow a different statistical distribution then failures due to surface defects (see Fig. 1). In component testing, this effect is difficult to cover because of the low probability of occurrence, hence special test methods and statistical evaluation should be used as described in [2].

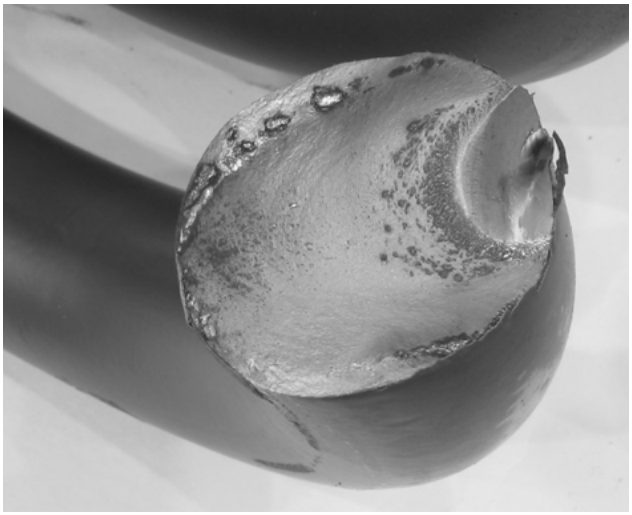

Figure 5: Fatigue fracture of suspension spring initiated at surface [8]

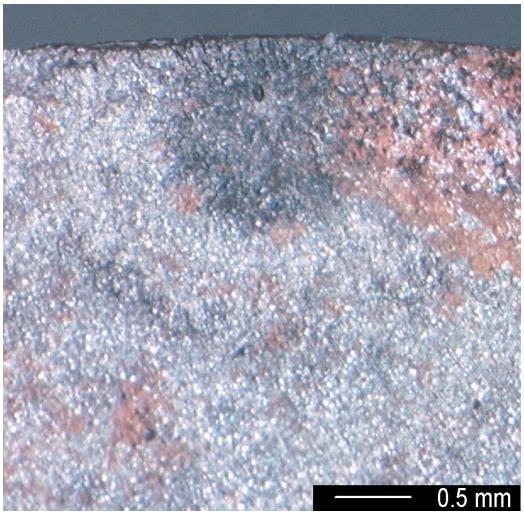

Figure 6. Fatigue fracture of coil spring initiated at non-metallic inclusion [IABG]

Harsh environmental conditions may decrease the cyclic strength of a spring considerably. Grit impact, abrasive wear and corrosive media can form defects acting as starting crack yielding a component failure. Fig. 7 shows a typical fracture surface of a suspension spring. The crack started from a surface defect under corrosion and propagated under cyclic loading. The significant influence of corrosion on the cyclic strength of high strength springs is shown in Fig. 8. Here, numerous springs where tested with constant amplitude cyclic loading in dry air and under a 5% NaCl-solution that was sprayed on the specimens intermittently. The test results were statistically evaluated. For a clearer picture and a better understanding, only the regression lines are shown.

Taking the S-N-curve of the test results under “dry” laboratory conditions as a reference, the influence of corrosion due to salt water can be seen for uncoated springs, coated springs without pre-damage and coated springs with pre-damage due to grit impact. All tests were performed on IABG Corrosion Spring Testing Machines (Fig. 9). The grit impact was generated with an IABG Grit Impact Simulator. The test parameters for grit impact as well as for corrosion were optimized in order to reproduce typical effects as can be seen on springs under service loading for longer periods. It is apparent that corrosion can decrease the cyclic strength of a high strength spring significantly. The effect can be reduced considerably by application of adequate surface coating, but cannot nearly be eliminated. If the surface coating is pre-damaged by grit impact, the better part of the positive effect is lost again. Also note that in all cases, up to $2 \cdot 10^6$ load cycles, no clear endurance limit can be found when testing in corrosive environmental conditions.

Taking into account these results, it is clear that for safe evaluation of the cyclic strength of suspension springs in ground vehicles, a combined test procedure must be defined and obeyed that covers all the effects described. Cyclic testing in dry laboratory conditions still may be very helpful for a first evaluation and optimization of geometry, material and production process. A final qualification test however must also contain grit impact, abrasive wear and corrosive media.

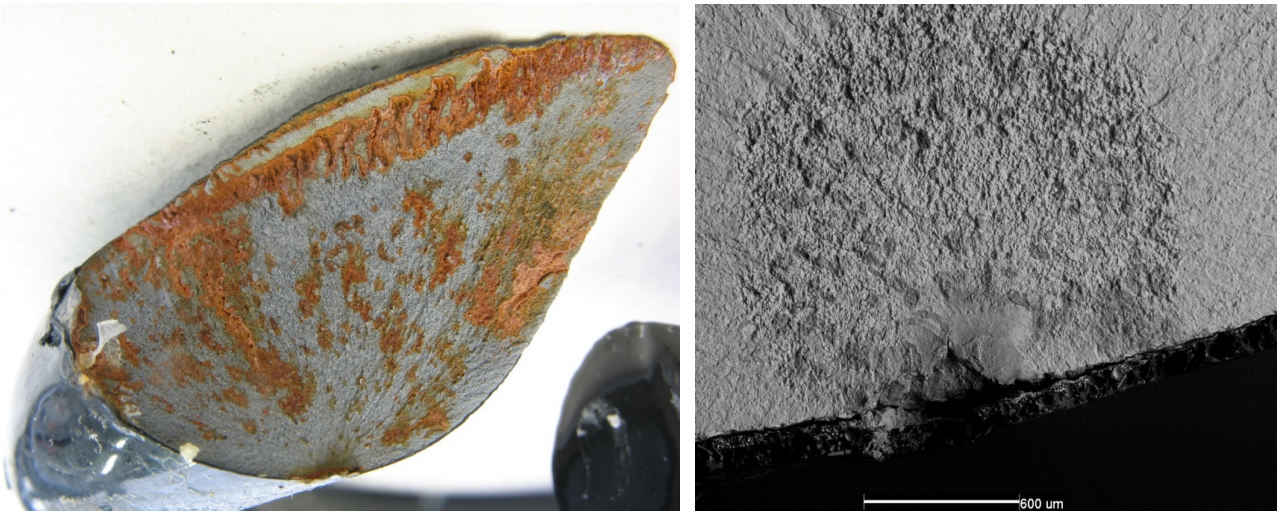

Figure 7. Fatigue fracture initiated by a corrosion pit [8]

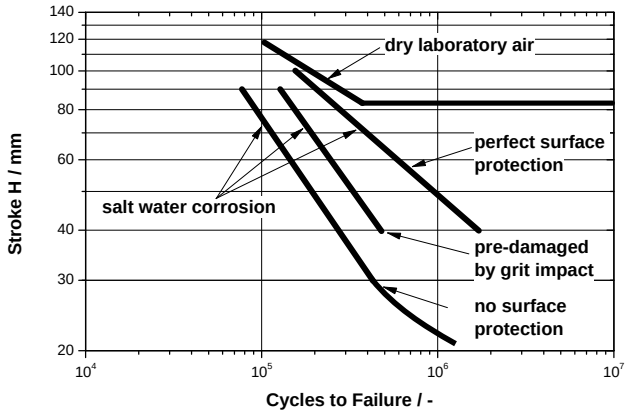

Figure 8. Influence of corrosion and pre-damage on fatigue behavior of suspension springs [9]

Figure 9. Corrosion Spring Testing Machine [IABG]

5. Experimental Proof of Service Strength

A test concept for suspension springs of ground vehicles has to cover all failure modes with the required safety factors in order to limit the probability of failure to an acceptable minimum. Here, a separate definition of development and qualification tests may be reasonable. While development tests may be performed on specimens from the raw material or generic spring geometries in dry laboratory condition, the authors strongly recommend a comprehensive test program with the specific springs from the series production process for a final qualification test.

For evaluation of raw material and semi-manufactured products like the spring wire, the usual tests for static properties like yield strength and ultimate tensile strength etc. should be amended by tests for cyclic properties in order to securely assure the cyclic strength and the steel purity. Fig. 1 shows test results from a large test program where only 1 out of 120 springs failed due to a non-metallic inclusion at very low load amplitude. This is equivalent to a probability of failure of 1 out of 30 cars (usually having 4 springs each), which surely is not acceptable! These inclusions can very hardly be found with component tests. Due to the inhomogeneous stress distribution, only a small portion of the volume of a coil spring is loaded to local stress levels at which a crack will propagate starting from this inclusion. In order to investigate steel purity, special cyclic tests are recommended using

specimens with a high critically stressed volume in order to facilitate the finding of the largest size of inclusion with an affordable effort for testing [2].

To investigate the steel purity in an efficient and safe way, a test machine and test method was developed at IABG using dedicated specimens that cover the critically stressed volume of about 50 springs with only one test. This test does not depend on a specific geometry of a spring and is recommended as development and acceptance test for raw material and semi-manufactured parts like spring-wire. It is much more reliable than the commonly used method for determination of steel purity only based on the analysis of metallographic specimens [2].

To the authors' knowledge and believe, the fatigue strength of a high strength coil spring for use in the suspension of a ground vehicle can only be safely approved, if tests on series production parts are performed in realistic installation conditions (original spring seats and orientation). A simulation of the axle kinematics with special focus on the deviations and deflections of the spring seats in both limits of travel is mandatory. The environmental conditions consisting of corrosive and abrasive media have to be simulated. If the risk of grit impact cannot be eliminated during service life, testing of springs that have undergone a grit impact simulation prior to the fatigue test in corrosive environmental conditions is mandatory. Only with this combined test procedure, realistic results can be obtained that allow for a safe evaluation of the service strength in field use.

A complete simulation of the axle kinematics containing all boundary conditions may be performed in a front or rear axle test facility. However, installation and running costs of these test facilities are very high and a lot of car components are needed for the test that may not be available at the time of testing. Moreover, a specific variation of test parameters in order to investigate the influence of single parameters often is difficult or not possible. Therefore, Resonance Testing Machines are commonly used for testing of coil springs, since they combine extremely low energy consumption, high reliability and a minimum of effort for the single test setup. Using an adjustable axle geometry simulator, the kinematics of the real axle can be reproduced. Corrosive environmental conditions can be generated in a realistic way by a facility for supply and intermittent application of salt water. Abrasive wear can be simulated by application of abrasive media at the lower spring seat where the media would also accumulate in real field use. Hence, all influences that are relevant for the fatigue life of suspension springs under complex loading can be simulated in a precise, effective and cost saving way (see Figure 9).

The number of specimens to be tested as well as the test spectra and the parameters for pre damage, simulation of corrosion and abrasion must be determined in a way that the different types of field use are covered with a high level of certainty, yielding test results correlating well with field experience. To cover statistical effects, the number of tests, the selected test amplitudes and the method for statistical evaluation of the test results must be described precisely.

An example for a description of a qualification program for coil springs was defined by German OEMs in the working group for springs and stabilizer bars [10]. To avoid incidental failures from non-metallic inclusions, the authors additionally recommend a test of the raw material or the half manufactured product for steel purity as described in [2]. A continuous adaption of the test parameters to new information from field use should be performed in order to always keep the test procedure up to the level of technology. A comparison of tested samples with parts from field use can be used to scale and adapt the test parameters in order to generate test results correlating with field use in an optimized way.

Depending on the focus of investigation, research tests may be performed on generic test samples. 360°-sections from cylindrical coil springs have proven a good sample geometry since they can be reproduced with a minimum of manufacturing costs for the samples. With a special Resonance Testing Machine for single coils, specific influences of e.g. material, heat treatment and shot peening can be studied using generic specimens. Compared with tests on designed to specification coil springs, tests on generic test springs can be performed with identical geometry of test sample providing comparable test results over a very long period time. However, the different stress distributions in a single 360°-section and the spires in complete coil spring must be taken into consideration in definition of the tests and in interpretation of the test results.

6. Conclusion and Outlook

It has be shown that for safe qualification of fatigue strength of suspension springs in passenger cars, a test program must be specified and performed consisting of test of series production springs under cyclic loading with simulation of the axle kinematics, environmental conditions and pre-damage. Additional test on specimen for the proof of steel purity are recommended by the authors. This is especially important for springs made out of high strength steels in order to fully make use of the potential of high strength materials with a maximized reliability. For quality assurance, mechanical testing of samples for steel quality as well as testing of springs from series production is recommended.

References

[1] T. Georges: Zur Gewichtsreduzierung von Fahrzeugfedern unter besonderer Beachtung des schwingfestigkeitsmindernden Einflusses bruchauslösender Fehlstellen im Halbzeug Federdraht (Bde. Reihe 5, Nr. 593). VDI Fortschritts-Bericht, 2009
[2] S. Rödling, M. Hück, M. Decker.: Influence of Non-Metallic Inclusions on Acceptable HCF Design Properties, Materials Testing, MP 53 (2001) 7-8, pp. 155-164
[3] Radaufhängungen der Vorderachse, In: Kraftfahrtechnisches Taschenbuch, Hrsg.: Robert Bosch GmbH, Düsseldorf: VDI-Verlag, 1984, p. 480
[4] M. Hück, J. W. Bergmann: Bewertung der Schwingfestigkeit federnder Elemente im Fahrzeugbau, DVM Tag 1994 – Die Feder, Berlin, 1994
[5] H. Schnattinger, A. Beste: Auslegung von Pkw-Schraubenfedern aus der Sicht der Betriebsfestigkeit, DVM Tag 1994 – Die Feder, Berlin, 1994
[6] K.-H. Mayer: Federbrüche und Ihre Beurteilung, TAE Seminar Fahrzeugfedern, Ostfilfdern-Nellingen, 17.-18.03.2009
[7] B. Kaiser: Randschichtzustand und Schwingfestigkeit von Parabelfedern, DVM Tag 1994 – Die Feder, Berlin, 1994
[8] S. Hoffmann: Prüfmethoden für die Entwicklung und Qualitätssicherung von Fahrzeugfedern, VDMA Mitgliedertagung Prüfmaschinen, Ottobrunn, 07.10.2010
[9] M. Hück, M. Decker: Grundsatzuntersuchungen über die Betriebsfestigkeit von Achsfedern, IABG-Bericht B-TA-3903, Ottobrunn, 2003
[10] Federn und Stabilisatoren, Arbeitskreis-Lastenheft AK-LH 07, Index h, Arbeitskreis der Firmen Audi AG, Bayerische Motoren Werke AG, Daimler AG, Porsche AG, Volkswagen AG, 12/2006
[11] M. Decker, G. Savaidis: Measurement and analysis of wheel loads for design and fatigue evaluation of vehicle chassis components, Fatigue and Fracture of Engineering Materials and Structures 25, 2002, pp. 1103-1119
[12] G. Savaidis, L. Riebeck, K. Feitzelmayer: Fatigue life improvement of parabolic leaf springs in the process of simultaneous engineering, Material Testing MP 41 (1999), pp. 234-240

Influence of different microstructures of the welding zone on the fatigue crack growth behaviour of HSLA steels

B. Maier [1,*], Ch. Guster[1], R. Tichy[2] and W. Ecker[2]

[1] Montanuniversität Leoben, Chair of Mechanical Engineering, Franz-Josef-Strasse 18, 8700 Leoben, Austria
[2] Materials Center Leoben Forschung GmbH, Roseggerstrasse 12, 8700 Leoben, Austria
* Corresponding author: bernd.maier@unileoben.ac.at

Abstract To meet the cost and weight reduction requirements in welded structures, high-strength low-alloy (HSLA) steels are increasingly used in all fields of mechanical engineering. However, in comparison to low-strength steels these materials are more susceptible to notches or initial cracks. Therefore, an extensive investigation of fatigue crack growth behaviour in the different microstructural zones of the heat-affected zone (HAZ) of the weld is necessary for an appropriate lifetime evaluation of welded joints.
For this purpose, fracture mechanics parameters like thresholds and crack growth rates in the different microstructural zones of the HAZ as well as in the base material are characterized by single edge notched bending (SENB) specimens. The different microstructures are reproduced with a Gleeble thermal simulator system using the same heating curves as measured previously during the welding process of a representative joint. The specimens feature the three characteristic microstructural zones of the HAZ (intercritical, fine-grained and coarse-grained zone). The effect of varying stress ratio R on the crack growth threshold and the crack growth curves is also assessed.

Keywords fatigue crack growth, HAZ, microstructures, HSLA

1. Introduction

For cost reduction reasons in mechanical engineering, especially in the field of welded constructions, the use of high-strength steels increases. Low-strength steels are uncomplicated in construction and usage due to notch insensitivity and good-natured crack propagation behaviour, whereas high-strength steels are much more challenging in construction and processing. With rising strength these steels are more susceptible to notches, pores or initial cracks, so the adequate dimensioning of welds made of such steels requires a high degree of knowledge of material-specific values. Although post-welding conditioning like high-impact treatment is common for such welds, the effects of these treatments have been investigated only phenomenologically so far. Especially the shift of the mean stress and its influence on the fatigue behaviour of the different microstructural zones in the heat affected zone of the weld has to be investigated. Whereas the effects of the weld toe can be described with classical stress-based approaches, the effects of pores or initial cracks require a more sophisticated fracture mechanic approach. In corresponding guidelines like the IIW recommendations [1] thresholds of only 2 MPa$\sqrt{m}$ are used, which lies below the effective threshold $\Delta K_{theff.}$. This leads to a high safety factor on one hand, but is in conflict with the principle of lightweight design on the other hand. Furthermore, only the crack propagation behaviour of the base material is well known, while the other microstructural zones of the weld are ignored. So the aim of this work is the investigation of the fatigue crack propagation behaviour in the different characteristic microstructural zones of the HAZ of a welded joint at different stress ratios.

2. Manufacturing of the different microstructural zones

The HAZ of a welded joint can be subdivided into three different zones, where the microstructure differs significantly from that of the base material (Fig. 1). The base material (BM) is a

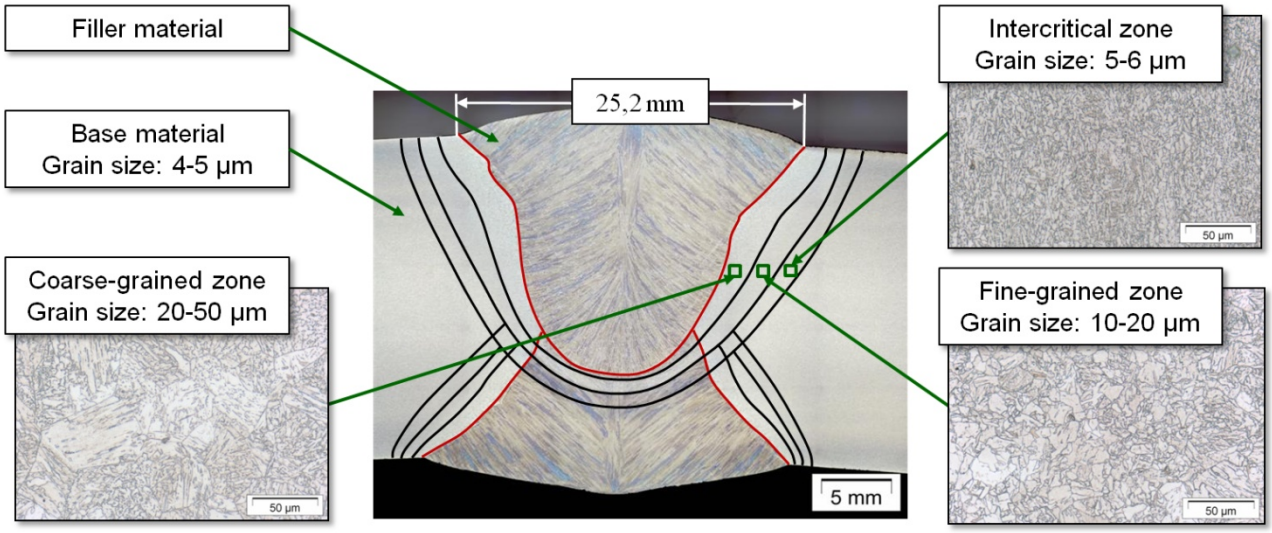

Figure 1. Characteristic microstructural zones of the HAZ of a double-submerged arc-welded joint [3]

thermomechanically rolled high-strength steel with an average grain size of 4-5 µm. The so-called intercritical zone (IZ) has a fine microstructure with an average grain size of about 5 to 6 µm, while in the fined-grained zone (FZ) an average grain size of about 10 to 20 µm was determined. The coarse-grained zone (CZ) shows an average grain size of up to 50 µm. The chemical composition of the base material is shown in Tab.1.

Before reproducing the microstructures it is necessary to get information about the local "heat treatment" due to the welding process for the formation of the characteristic zones of the HAZ. For this purpose metal sheets with a thickness of 20 mm are double-submerged arc-welded to represent the real welding process. For the appropriate measurement of the temperatures sensors are pinned onto the blank sheets in defined distances to the weld (Fig. 2, left). The gathered temperature curves (intercritical zone IZ, fine-grained zone FZ) are shown in Fig. 2 (right).

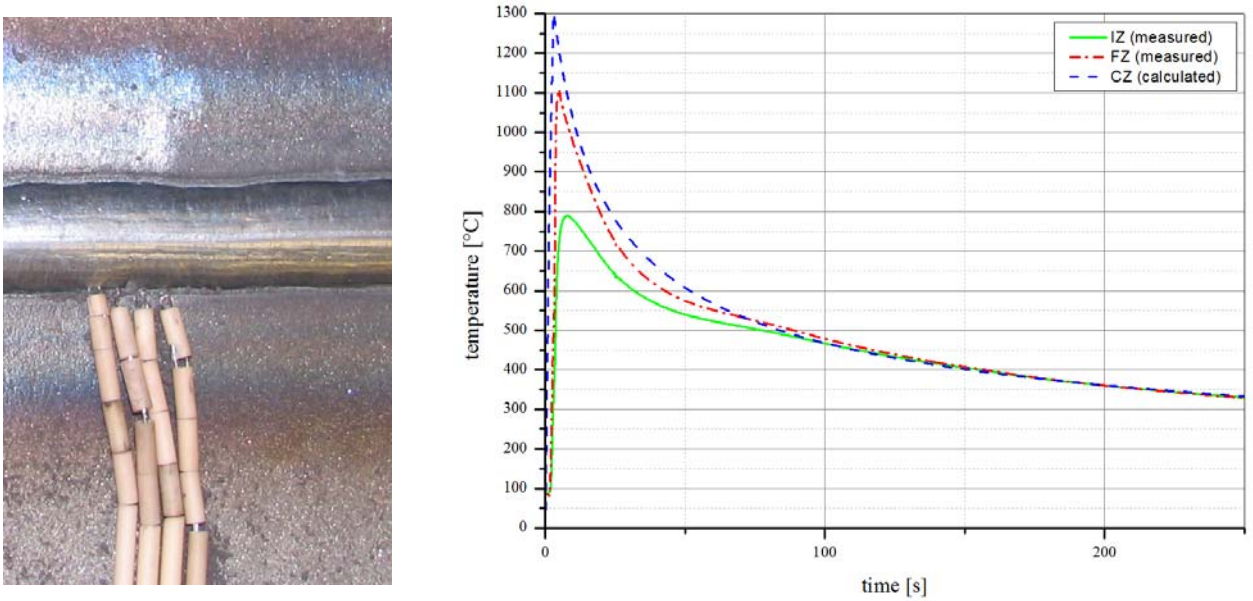

Figure 2. Positioning of the temperature sensors (left) and temperature curves for the heat treatment (right) [3]

Table 1. Chemical composition of the base material [%]

C	Si	Mn	P	S	Al	Cr	Ni	Mo	Cu	V	Nb	Ti
0.05	0.3	1.8	0.009	0.001	0.04	0.2	0.0	0.1	0.0	0.00	0.04	0.01

The temperature curve of the coarse-grained zone (CZ) was calculated according to SEW 088 [2] based on the other measured temperature curves. These heating curves, especially the cooling rates and peak temperatures, are the input for the heat treatment of metal blanks in a Gleeble thermal simulator. With this procedure, blanks with similar microstructures as found in the IZ, FZ and CZ are produced.

After producing these so-called Gleeble blanks, the homogeneity of the resulting microstructures has to be verified. After grinding, polishing and etching of the microsections of the three distinctive zones, they were investigated at different positions across the specimen cross section with optical microscopy and EBSD[1] captures. The results were compared with the results of the investigations of the HAZ of the laboratory weld. As a preliminary result, the microsections differ marginally in grain size, but show a good correlation along the width of the specimen. Additional information from hardness measurements with the Vickers method confirms the overall picture, that the Gleeble blanks exhibit a homogeneous microstructure in the areas of interest and no deviation of crack propagation and fatigue endurance limit due to differing microstructures should occur.

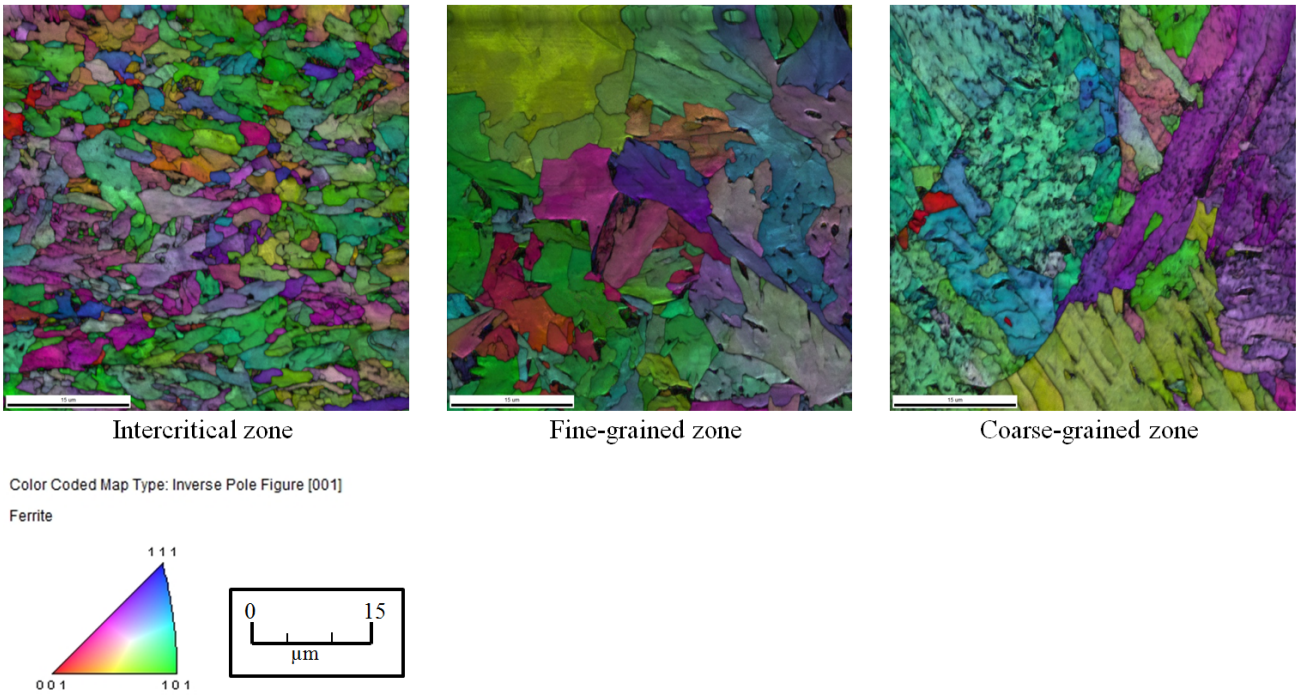

Figure 3. EBSD captures of the different zones

It was also found that due to thermomechanical rolling a distinctive texture orientation is established in the microstructure of the base material. This orientation can also be found in the intercritical zone. Because of the lower temperatures, no microstructural changes occur in this zone. Due to higher temperatures in the FZ and CZ a phase change takes place and the original orientation of the base material is eliminated; the evolution of orientation and average grain size can be seen from Fig. 3.

[1] Electron backscatter diffraction

3. Fatigue crack growth

For the investigation of the crack propagation behaviour, single-edge notched bending (SENB) specimens are used. The tests are performed on a RUMUL Cracktronic resonance testing rig. For crack length measurements a direct-current potential-drop (DCPD) measurement system developed in-house is used. For minimizing the effect of the plastic zone, the so called CPCA testing method is used. This method and its differences to the method according to ASTM [4] are well described in the literature [5]; for the sake of completeness, the general procedure will be described here. The specimens are initially compression pre-cracked for gathering a small plastic zone around the initial crack tip. After this, the specimen is loaded with an initial bending moment resulting in a stress intensity factor higher than the effective threshold ΔK_{theff} but lower than the long-crack threshold ΔK_{th}. The crack will start to grow and will stop after a certain distance due to crack closure effects. Now the bending moment is increased, the same procedure as described before will occur. This procedure is repeated until the stress intensity reaches the long-crack threshold. There the crack will not stop, and the fatigue crack growth curve (FCG) is obtained. For region I of the FCG curve a modified Klesnil-Lukas approach (Eq. 1) and for region II the classic Paris-Erdogan law (Eq. 2) is used. The findings of the different microstructures can be found in Tab. 2 (base material), Tab. 3 (intercritical zone), Tab. 4 (fine-grained zone) and Tab. 5 (coarse-grained zone). Due to missing K_{Ic}-Values fitting of region III has to be skipped. In the following figures the crack propagation curves are only extended without consideration of K_{Ic} until a stress intensity of 50 MPa√m is reached, and then truncated.

$$\frac{da}{dN} = C \cdot \Delta K^{m-p} \cdot \left(\Delta K^{p} - \Delta K_{th}^{p}\right), \tag{1}$$

$$\frac{da}{dN} = C \cdot \Delta K^{m}, \tag{2}$$

Table 2: Crack propagation behaviour of the base material

Specimen	R	ΔK_{th}	C	m
BM-A	0,5	2,92	1,95E-08	2,60
BM-B	0,5	2,90	2,57E-08	2,56
BM-C	0,1	4,40	6,05E-09	2,93
BM-D	0,1	3,56	3,88E-09	3,01
BM-E	-1	13,35	5,85E-10	2,90
BM-F	-1	9,05	2,61E-10	2,98

Table 3: Crack propagation behaviour of the intercritical zone

Specimen	R	ΔK_{th}	C	m
IZ-A	0,5	7,70	5,48E-09	2,87
IZ-B	0,5	7,20	5,40E-09	2,95
IZ-C	0,1	11,90	3,97E-10	3,39
IZ-D	0,1	12,55	3,95E-11	4,25
IZ-E	-1	28,50	3,82E-10	2,59
IZ-F	-1	29,65	3,48E-13	4,28

Table 4: Crack propagation behaviour of the fine-grained zone

Specimen	R	ΔK_{th}	C	m
FZ-A	0,5	4,80	1,86E-09	3,37
FZ-B	0,5	5,30	1,47E-09	3,45
FZ-C	0,1	6,50	3,27E-11	4,41
FZ-D	0,1	6,80	4,19E-12	4,99
FZ-E	-1	19,98	2,44E-13	4,66
FZ-F	-1	17,50	1,10E-13	4,88

Table 5: Crack propagation behaviour of the coarse-grained zone

Specimen	R	ΔK_{th}	C	m
CZ-A	0,5	4,90	1,99E-09	3,29
CZ-B	0,5	4,60	6,37E-09	2,97
CZ-C	0,1	7,05	3,68E-10	3,58
CZ-D	0,1	8,60	2,40E-10	3,73
CZ-E	-1	18,84	1,59E-12	4,33
CZ-F	-1	18,00	3,00E-13	4,76

4. Comparison of the fatigue crack behaviour of the different microstructures

The tabular data of the different microstructures can be found in Tables 2-5; in the following discussion this data will be graphically formatted to demonstrate the differences. As expected the diagrams show a shift from lower thresholds at R=0.5 (Fig. 4) to higher ones at R=0.1 (Fig. 5) and R=-1 (Fig. 6). In general the following trend correlates through all stress ratios: the base material shows the lowest thresholds, followed by the coarse-grained and the fine-grained zone.

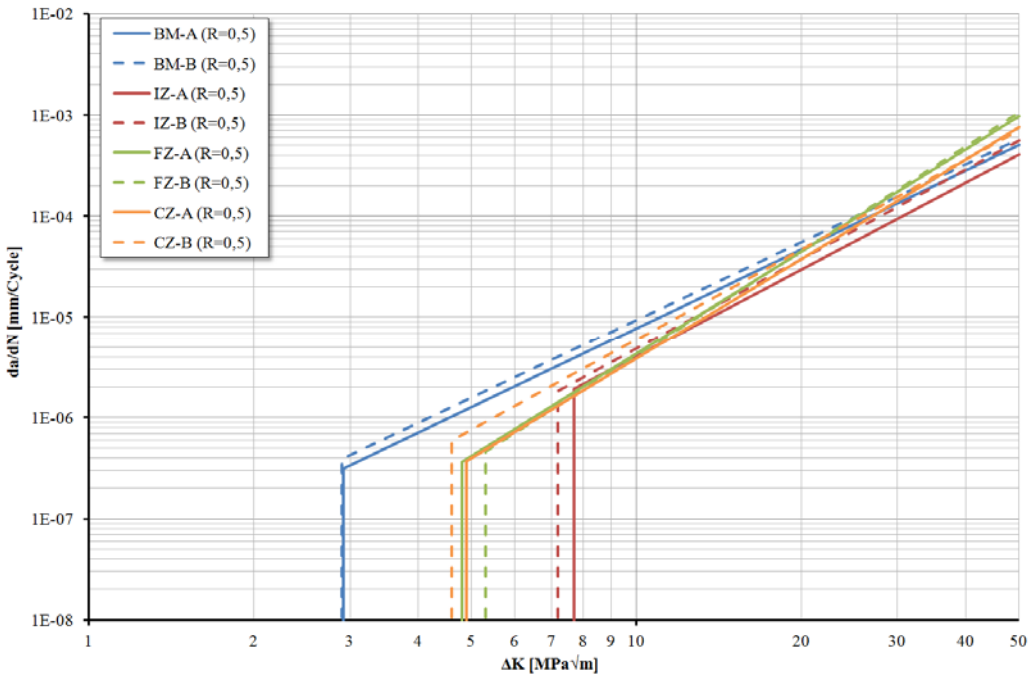

Figure 4. Comparison of the FCG behaviour of the different zones at R=0.5

The intercritical zone shows disproportionately high thresholds in comparison to the other zones, which is due to the long $t_{8/5}$-time of nearly 70 seconds resulting in a soft-annealing of the microstructure and leading to an increase in ductility. The slopes of the Paris-Erdogan regime show values between 2.56 and 4.88. Because of the setup of the crack measurement system (measurement of the potential drop by spring probes) especially the experiments with a stress ratio of R=-1 are hard to execute. The spring probes are losing the contact to the surface of the specimen, in particular at higher amplitudes. Therefore the scatter of the measured voltages increases, leading to a higher scatter of the thresholds and the crack propagation rates.

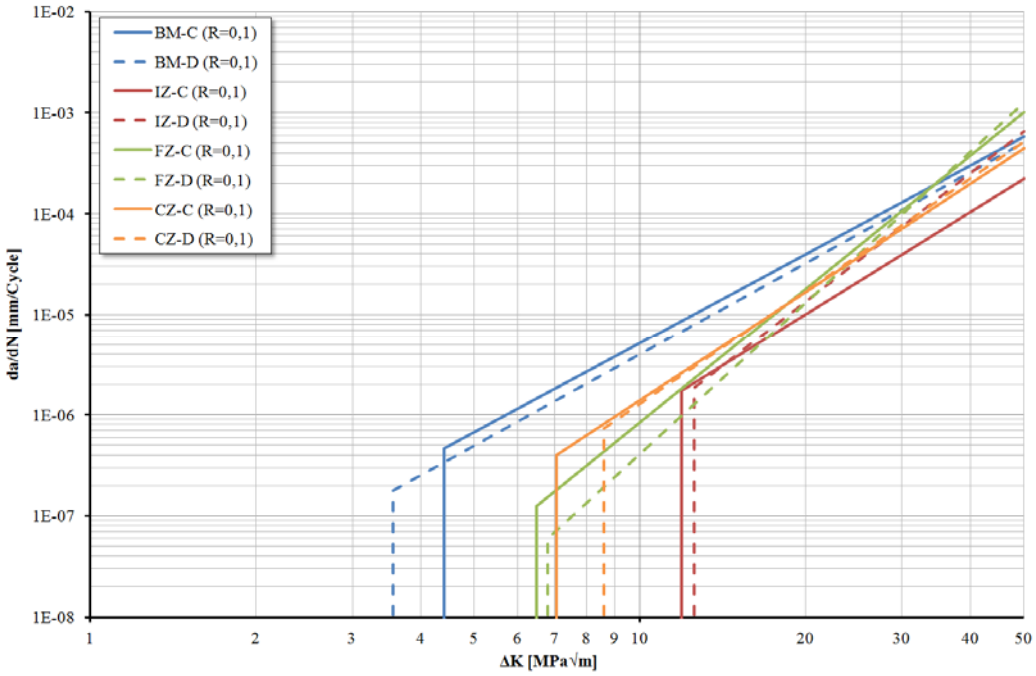

Figure 5. Comparison of the FCG behaviour of the different zones at R=0.1

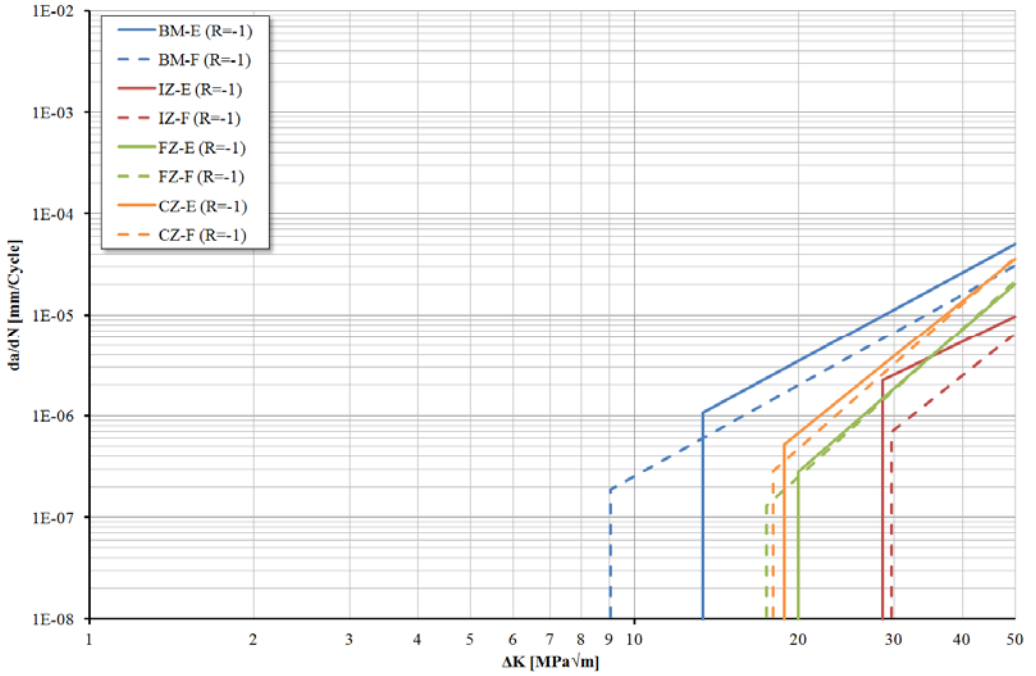

Figure 6. Comparison of the FCG behaviour of the different zones at R=-1

5. Conclusion

The results show that surprisingly, the base material has the lowest thresholds among all microstructures of the HAZ of the representative weld. This could presumably be due to the distinctive texture or the residual stresses in the metal blanks stemming from the rolling process. If no post-weld treatments like machining of the weld or impact treatments are performed, the geometric notch at the weld toe is the crack initiation point. Under cyclic loading, the conservative approach of the low thresholds of 2 MPa√m as a base of a fracture mechanics design approach in the studied case (double-submerged arc-welded with high $t_{8/5}$ times) only makes sense if the geometric notch has a low influence and crack initiation occurs in the base material. With these results it also can be shown how a shift of the stress ratio R influences the crack propagation thresholds within the HAZ. Further investigations concerning the residual stress state in the metal sheet blanks are necessary, however. This work represents an important preliminary contribution to a better understanding and interpretation of different effects due to manufacturing, machining and post-welding processes in the different regions of the HAZ and their influence on the fatigue crack propagation behaviour.

Acknowledgements

Financial support by the Austrian Federal Government and the Styrian Provincial Government, represented by Österreichische Forschungsförderungsgesellschaft mbH and Steirische Wirtschaftsförderungsgesellschaft mbH, within the research activities of the K2 Competence Centre on “Integrated Research in Materials, Processing and Product Engineering”, operated by the Materials Center Leoben Forschung GmbH under the frame of the Austrian COMET Competence Centre Programme, is gratefully acknowledged.

References

[1] A. Hobbacher: Recommendations for fatigue design of welded joints and components, IIW Document IIW-1823-07, December 2008

[2] Technical document SEW 088, Beiblatt 2, 4.Ausgabe, 1993

[3] B. Maier, B. Oberwinkler B., R. Tichy, W. Ecker, Development of a FE-based fracture mechanical method for fatigue life assessment of double-submerged welded pipelines considering residual stresses and local microstructures, Proceedings of the 19th European Conference on Fracture, Kazan, 2012

[4] ASTM E647, Standard Test Method for Measurement of Fatigue Crack Growth Rates, Standards of ASTM International, West Conshohocken, PA

[5] R. Pippan, H.P. Stüwe, K. Golos, A Comparison of Different Methods to Determine the Threshold of Fatigue Crack Propagation, Int. Journal of Fatigue, Vol. 16, 579–582, 1994

[6] J. Kohout, A new function describing fatigue crack growth curves, Int. Journal of Fatigue, Volume 21, 813-821, 1999

Pit-To-Crack Transition and Corrosion Fatigue of 12% Cr Steam Turbine Blade Steel

Bernd M. Schönbauer[1,*], Andrea Perlega[1], Stefanie E. Stanzl-Tschegg[1]

[1] Institute of Physics and Material Sciences, University of Natural Resources and Life Sciences, BOKU, Peter-Jordan-Str. 82, 1190 Vienna, Austria
* Corresponding author: bernd.schoenbauer@boku.ac.at

Abstract Several cases of undefined conditions during operation of steam turbines, such as shut down of the turbine or leaking of the condenser, can lead to a corrosive environment. If the concentration of oxygen and chloride exceeds a critical level, pitting corrosion can occur. Since corrosion pits increase the local stress field, the initiation of fatigue cracks is facilitated and – under adverse conditions – these cracks can lead to final failure.
In this work, the results of fatigue tests on 12% Cr martensitic stainless steel, which is a standard blade material in the low pressure part of a steam turbine, are presented. The influence of corrosion pits and environment on the fatigue limit is investigated. Pit-to-crack transition is studied by optical observation and fractographic examination. The test environments were air at 90 °C and an aqueous solution with defined content of chloride and oxygen. To simulate an aggressive environment in which corrosion pits can form, fatigue tests in aerated 6 ppm Cl^- solution at 90 °C are performed.

Keywords Corrosion Fatigue, Pitting Corrosion, Very High Cycle Fatigue, Kitagawa Diagram, 12% Cr Steel

1. Introduction

Failure of steam turbines often takes place at the last stage of the low pressure blades where early condensate occurs. Although steam turbines were designed for a maximum operational time of 20 years, several turbines are in service since more than four decades. The turbine blades are loaded by different kinds of stresses. High mean stresses due to centrifugal forces and superimposed cyclic loading with low stress amplitudes induced by inhomogeneous steam flow with load frequencies of ca. 2 kHz are acting. Therefore, fatigue life data for high stress ratios in the very high cycle fatigue (VHCF) regime are important to predict fatigue life. Fatigue cracks were frequently observed to initiate at corrosion pits. During standard operational conditions the absence of impurities – such as chlorides – and oxygen prevents the material from corrosion. But shut down of the turbine or leaking of the condenser leads to undefined conditions where corrosion pitting may occur. Martensitic 12% Cr steel is a standard material for blades in the low pressure part of steam turbines. Extensive research was started already in the 1980s to simulate and understand the phenomenon of corrosion assisted fatigue of blading materials [1,2]. A project with the aim to develop a methodology for the prediction of corrosion fatigue life in steam turbine blades is still in progress [3] and several results were already presented [4-7].
In the present work, fatigue life test results are presented for smooth and pre-pitted specimens. The influence of stress range R and pit dimension is discussed for different environments. Fatigue tests were performed at 90 °C in air and aqueous solution. De-aerated 300 ppb Cl^- solution is often used to simulate service conditions in the low pressure part of steam turbines where early condensate occurs [8]. Since fatigue life tests in de-aerated solution and air lead to similar results [5], only the data determined in air are discussed in this work. To simulate a more aggressive environment in which corrosion pits may form, additional tests in aerated 6 ppm Cl^- solution at 90 °C were carried out. Crack initiation at corrosion pits was investigated by optical observation during fatigue loading. The fatigue crack growth rates (FCGRs) were determined and compared to measurements of long crack growth [7]. Fractographic examinations with scanning electron microscope (SEM) were performed in order to investigate crack initiation mechanisms.

2. Materials and experimental procedure

2.1. Material

The investigated material is a dual certified 403/410 martensitic 12% Cr steel. The material was hardened at 913 °C and tempered. The chemical compositions and the mechanical properties (provided by the supplier) are listed in Table 1 and 2. The mean grain size was 6 μm.

Table 1. Chemical composition of 403/410 SS (in weight %)

C	Cr	Mn	Si	Ni	Mo	Cu	S	P
0.13-0.14	11.79-11.8	0.41-0.49	0.18-0.26	0.28-0.33	0.13-0.18	0.07-0.10	<0.002	<0.020

Table 2. Mechanical Properties of 403/410 SS at room temperature

Tensile Strength (MPa)	Yield Strength (MPa)	Elongation (%)	Reduction of Area (%)
767	596	23	68

2.1. Test specimens

The shape of the test specimen for fatigue life tests is shown in Figure 1a. The specimens were machined, ground and polished with abrasive paper (up to grade #4000). The obtained mirror-like finish enabled observation of fatigue cracks that initiated at corrosion pits. To eliminate residual stresses, the specimens were stress-relief annealed in high vacuum (10^{-6} Pa). The stress relief procedure was: Heating from room temperature to 600 °C 1 h, holding for 2 h, cooling from 600 °C to 400 °C in 2 h and to room temperature in approx. 12 h. Additional specimens were produced with corrosion pits located in the gauge length of the specimen. A typical corrosion pit on the surface of a test specimen is shown in Figure 1b. The pre-pitting procedure was developed and arranged at the National Physical Laboratory and is described in more detail in [9]. Corrosion pits with depths of ca. 50, 100 and 250 μm were used. The actual depths were ±10% of the targeted value.

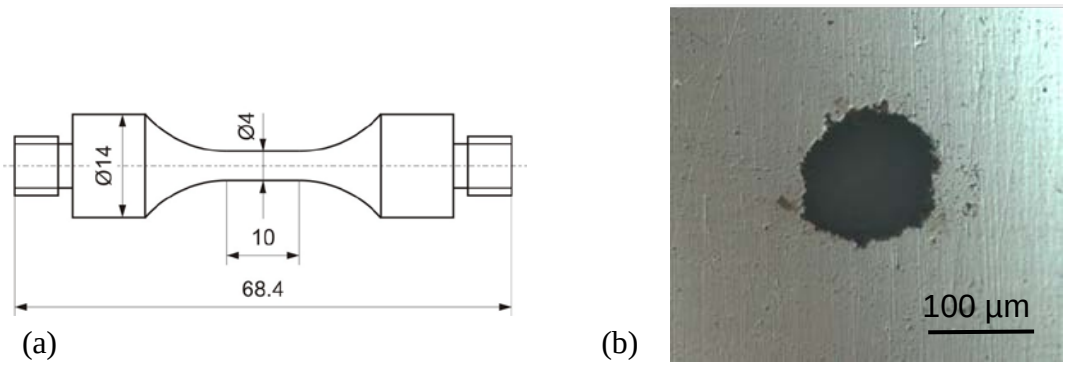

(a) (b)

Figure 1. Specimen shape for fatigue life tests (a) and corrosion pit in the gauge lengths of the specimen (b)

2.2. Fatigue testing method

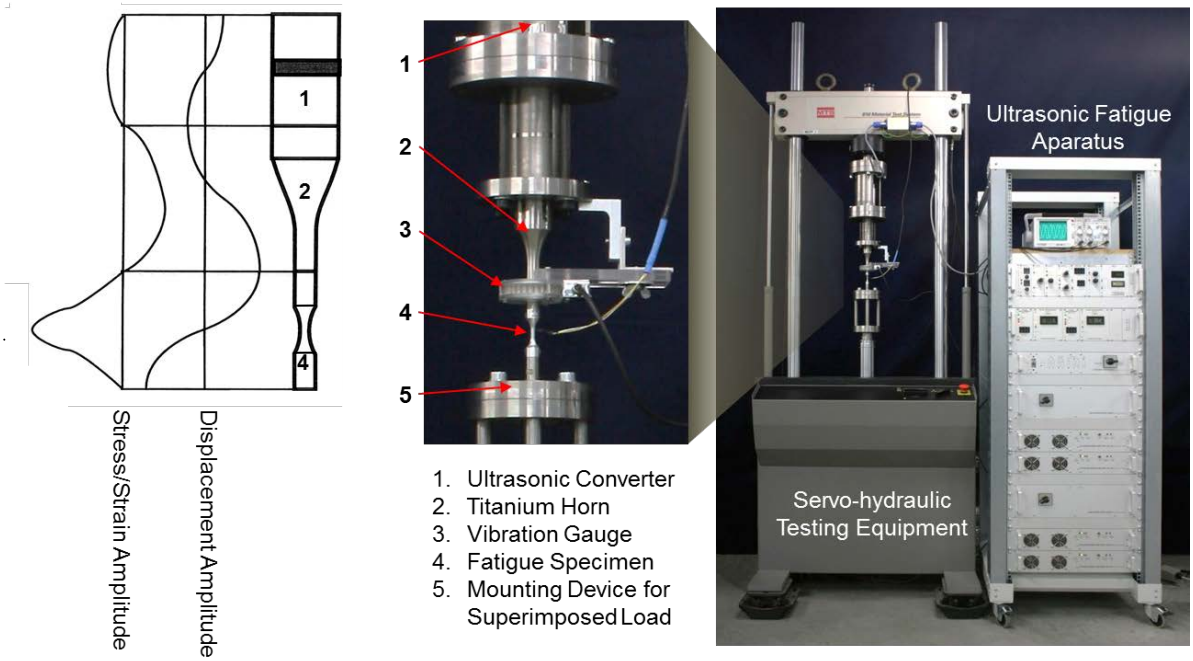

Figure 2. Ultrasonic fatigue test setup

The fatigue tests were conducted with an ultrasonic fatigue testing equipment. The ultrasonic converter is attached to a servo-hydraulic testing equipment which allows testing at higher stress ratios by superimposing static loads. The ultrasonic fatigue technique works by stimulating specimens to resonance vibration. The geometry of the resonance system – including the test specimen – is adjusted to achieve a resonance frequency of approximately 20 kHz. The failure location (region with maximum stress/strain amplitude) is stationary and therefore can be observed optically during fatigue testing. This is due to the absence of a vibration amplitude at the node of the standing wave during oscillation. An optical system with 250x magnification was used to detect crack elongations of less than 10 µm.

2.3. Aqueous solution circulation system

A water circulation loop with a 35-l-reservoir was used for measurements in aqueous environments. The set-up is shown schematically in Figure 3 and described in more detail in [7]. It allows testing in solutions with defined content of chloride and oxygen at constant temperature. Aeration was achieved by passing laboratory air with a diaphragm pump into the solution. Conductivity and oxygen level were detected during measurement. The flow rate of the liquid was 3 l/hour. The corrosion potential was measured using an Ag/AgCl reference electrode but the potentials quoted are referred to the saturated calomel electrode (SCE) at 25 °C. The corrosion potential during fatigue testing in aerated 6 ppm Cl^- solution was between -0.18 V(SCE) and 0.01 V(SCE).
Ultrapure water (initial conductivity of 0.06 µS/cm and AR grade NaCl) was used to prepare the solution. A new solution was used whenever the conductivity of the water increased by 10% of the initial value.

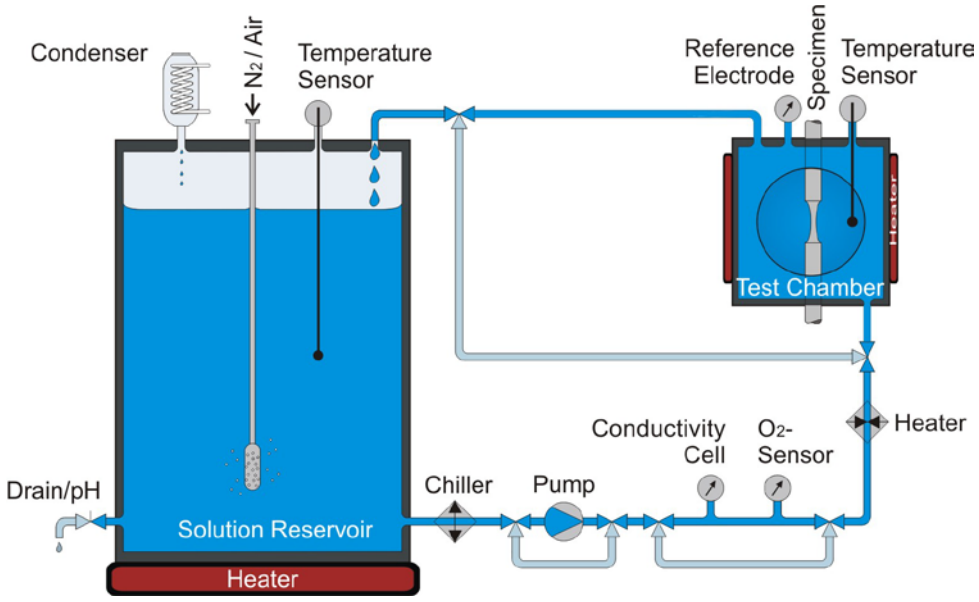

Figure 3. Schematic of the aqueous solution circulation system

3. Results

S-N tests were performed on smooth and pre-pitted specimens with pit depths of 50, 100 and 250 µm. The fatigue limit $\Delta\sigma_0$ was defined as the cyclic stress range where at least two specimens survived a minimum of 1×10^9 cycles. Specimens that did not fail – so called run-outs – are marked with arrows in the *S-N* plots. The fracture surfaces were observed by scanning electron microscopy (SEM).
The dimensions of the pits were determined from the fracture surface. The maximum variability in pit depth was defined to be ±10% of the proposed size. 55 pre-pitted specimens met that requirement and are plotted in *S-N* diagrams. To enable measurement of the run-out specimens with corrosion pits, they were loaded at higher stress ranges until failure occurred.

3.1. Fatigue lives in air at 90 °C

Results of the *S-N* tests in air at 90 °C are shown in Figure 4a. A significant decrease of the fatigue limit $\Delta\sigma_0$ with increasing stress ratio and pit size is obvious.
The determined fatigue limits $\Delta\sigma_0$ are plotted in a Haigh diagram where the stress amplitude $\Delta\sigma/2$ is plotted versus the mean stress σ_m, see Figure 4b. For both, smooth and pre-pitted specimens, the results can be fitted by Gerber parabolas:

$$\Delta\sigma_0 = \Delta\sigma_{0,R=-1} \cdot (1 - \sigma_m/\sigma_u)^2). \quad (1)$$

Since the fatigue limits at fully reversed loading ($R = -1$) $\Delta\sigma_{0,R=-1}$ (which is equivalent to the values at the ordinate in the Haigh diagram) were not determined, the values were obtained by extrapolation of the curves. Both the determined fatigue limits and the assumed values for $R = -1$ are summarised in Table 3.

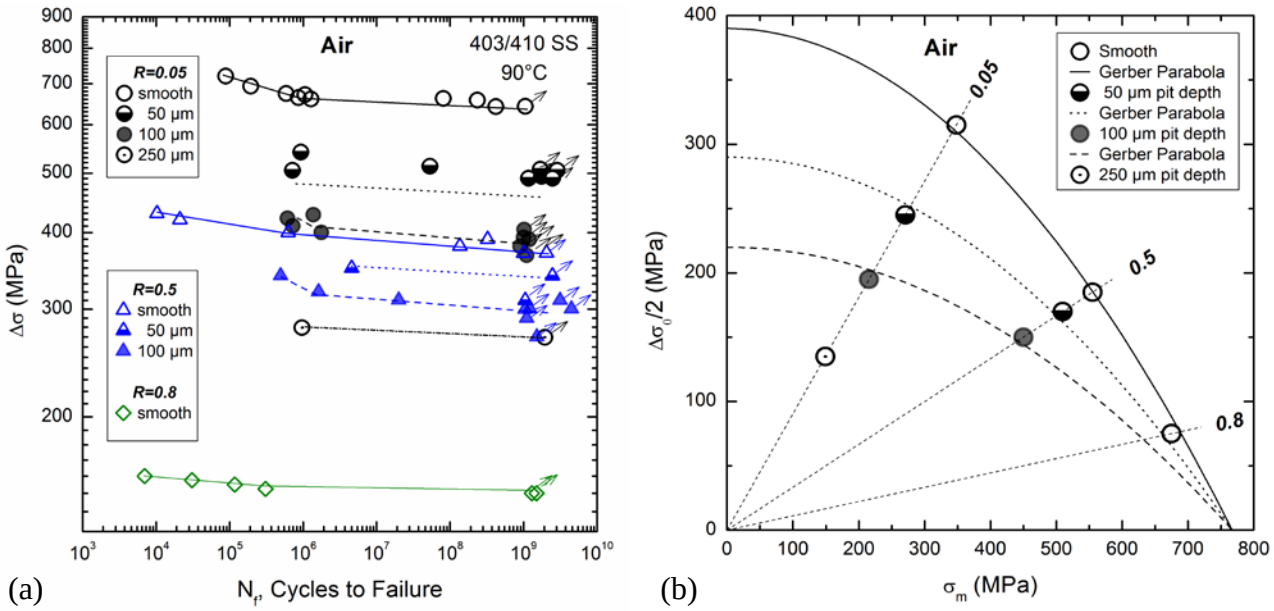

Figure 4. *S-N* plot (a) and Haigh diagram (b) for smooth and pre-pitted specimens in air at 90 °C

Table 3. Fatigue limits determined in air at 90 °C (in MPa)

Pit size	R = 0.05	R = 0.5	R = 0.8	R = −1*
Smooth	630	370	150	780
50 µm	490	~340	-	580
100 µm	390	300	-	580
250 µm	~270	-	-	-

* stress ranges for R = −1 obtained by extrapolation

3.2. Fatigue lives in aerated 6 ppm Cl^- solution at 90 °C

Results of the *S-N* tests in aerated 6 ppm Cl^- solution at 90 °C are shown in Figure 5a. The fatigue limits are again plotted in a Haigh diagram (Figure 5b) and summarised in Table 4. The Gerber parabola according to Eq. 1 fits well for smooth specimens. But for pre-pitted specimens, the deviation from the parabola is higher.

Table 4. Fatigue limits determined in aerated 6 ppm Cl^- solution at 90 °C (in MPa)

Pit size	R = 0.05	R = 0.5	R = 0.8	R = −1*
Smooth	530	330	145	600
100 µm	350	220	~130	320
250 µm	-	-	105	

* stress ranges for R = −1 obtained by extrapolation

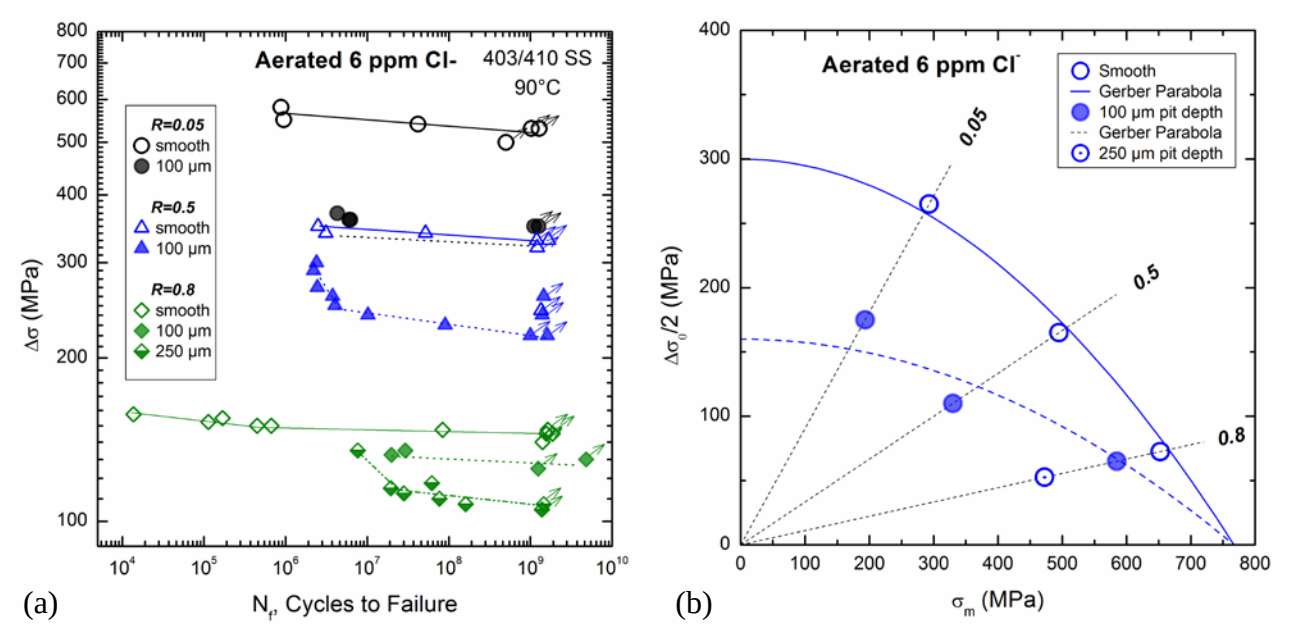

Figure 5. *S-N* plot (a) and Haigh diagram (b) for tests in 6 ppm Cl^- solution at 90 °C

3.3. Pit-to-crack transition

Pit-to-crack transition was observed by optical observation of the pit during fatigue loading. FCGRs were determined by measuring the crack extension during fatigue loading. The applied stress range was kept constant during testing which consequently increased the stress intensity factor range with crack elongation. Cracks were observed at stress ranges below the fatigue limit of pre-pitted specimens that initiated during fatigue loading but became non-propagating. The stress intensity factor range was calculated assuming a semi-circular crack shape. Figure 6a shows the FCGR curves for cracks emanating from pits with depths of 50 µm and 100 µm. For each pit size, the growth rates of a crack that caused final failure and one that became non-propagating are shown.

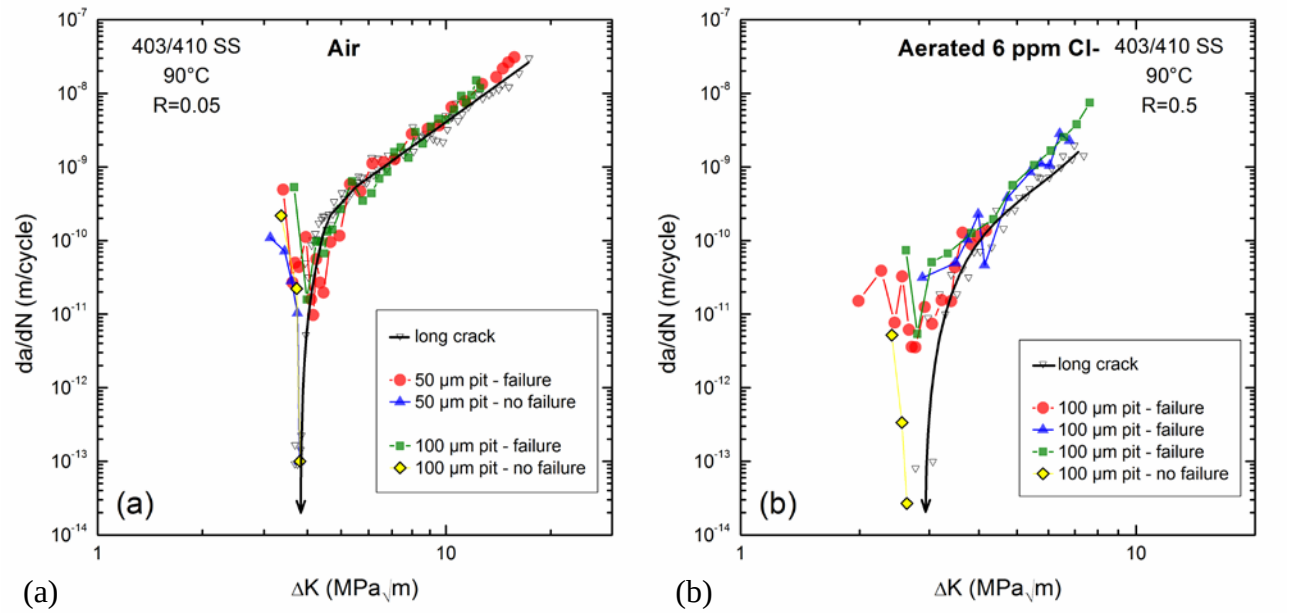

Figure 6.d*a*/d*N* vs. Δ*K* for cracks emanating from corrosion pits in: air (a) and aerated 6 ppm Cl^- solution (b)

The same is shown in Figure 6b for measurements in 6 ppm Cl^- solution. The FCGR curves are compared with long crack growth rate curves of the same material [3,7]. The cracks that initiated at the pits show the typical short-crack behaviour of crack elongation at stress intensities below the threshold. These cracks either arrest at microstructural barriers or progress and become long cracks. This behaviour was found for both environments as can be seen in Figure 6 although the calculated stress intensities for cracks that initiated at pits are only a rough estimation.

3.4. Fractography

3.4.1. Fatigue tests in air at 90 °C

Observation of the fracture surfaces with SEM and optical microscope gave information about crack initiation site and mechanisms. At $R = 0.05$, the smooth specimens failed from surface inclusions as shown in Figure 7a. Analysis with EDX identified these non-metallic inclusions with diameters of approx. 10 µm as Al_2O_3. Two specimens that failed during testing in air after 10^8 cycles failed from the interior. A so called fish-eye fracture was found. Crack initiation was in the matrix, and no inclusion could be detected.

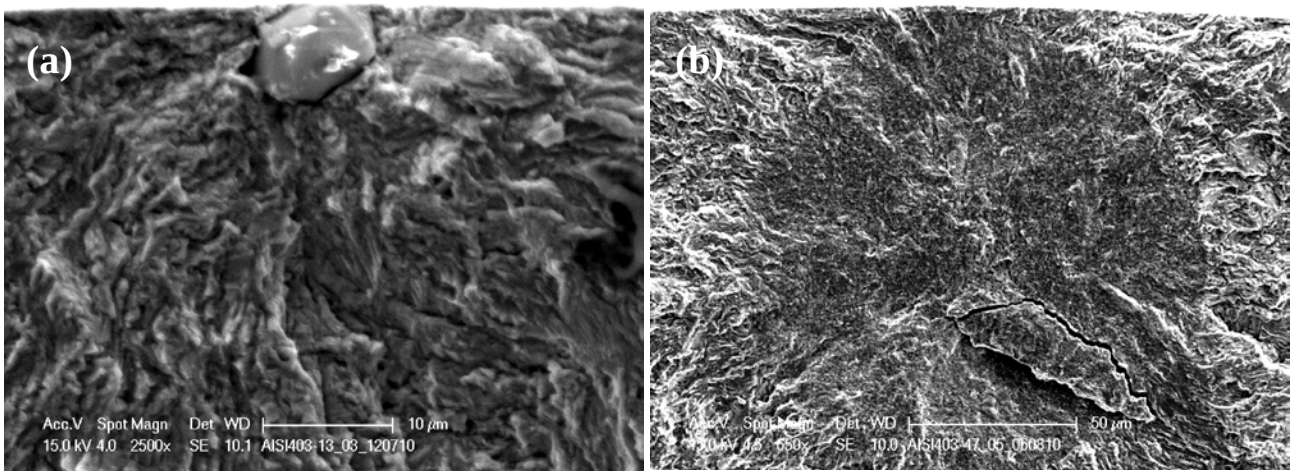

Figure 7. Fracture surfaces of smooth specimens tested at $R = 0.05$ in air at:
$\Delta\sigma = 672$ MPa ($N_f = 1.06 \times 10^6$) (a) and $\Delta\sigma = 642$ MPa ($N_f = 4.20 \times 10^8$) (b)

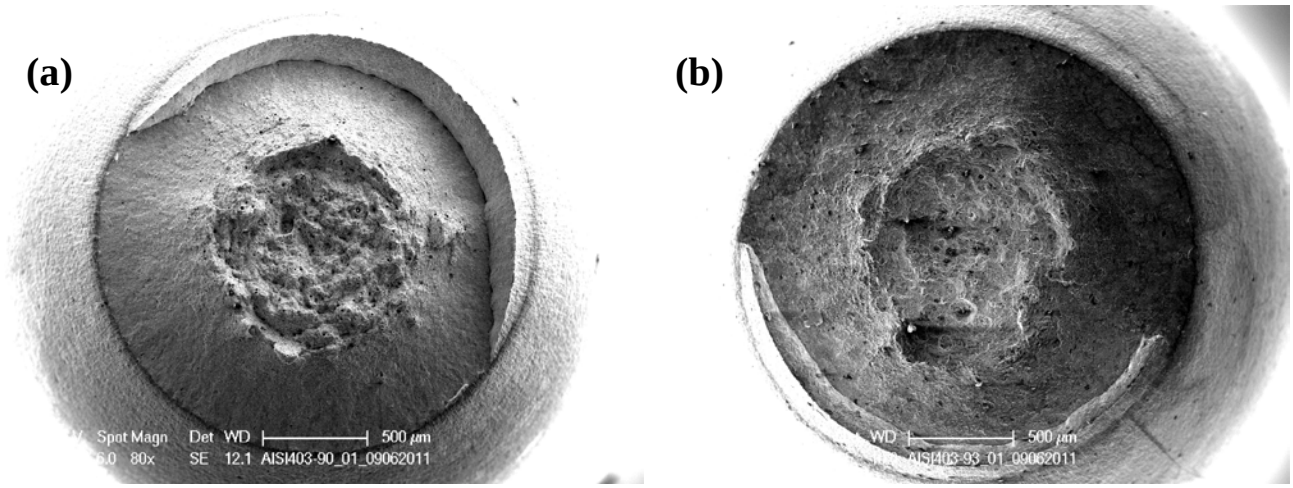

Figure 8. Fracture surfaces of smooth specimens tested at $R = 0.5$ in air at:
$\Delta\sigma = 380$ MPa ($N_f = 1.36 \times 10^8$) (a) and $\Delta\sigma = 400$ MPa ($N_f = 6.25 \times 10^5$) (b)

At $R = 0.5$ and $R = 0.8$, the crack initiation site for smooth specimens is not detectable since very high deformation at the fractured surface was observed. The cup-and-cone fracture as shown in Figure 8a and b was found for all smooth specimens. This kind of fracture surface is usually observed after tensile testing and suggests the dominance of cyclic creep due to the high maximum stress. Cyclic softening of the material during testing is supposed as reported by Kovacs et al. [10] for 12% Cr steel martensitic steel (X10CrNiMoV12-2-2). Nevertheless, failure occurred above 10^8 cycles.

For pre-pitted specimens tested at $R = 0.05$, crack initiation was always found at the pit. Figure 9 shows corrosion pits of different depths at the crack initiation sites. But at higher stress ratios, corrosion pits need not necessarily cause final failure. At $R = 0.5$, one of three pre-pitted specimens with a pit depth of ca. 50 µm showed high plastic deformation and a short crack after fatigue failure (Figure 10a). The corrosion pit was found some millimetres away from the fractured surface and the fracture was cup-and-cone like (Figure 10b). Similarly, short cracks were found at 100 µm deep pits when they were tested at $R = 0.8$ but none of these caused final failure. This means that there is a critical pit size depending on the stress ratio which may cause final failure. A greater pit size leads to a lower fatigue limit. Consequently, cyclic creep becomes an opposing mechanism when the maximum stress – i.e. the stress ratio – is higher. If the pit is rather small, high stresses are necessary to initiate a fatigue crack, and the material shows cyclic softening.

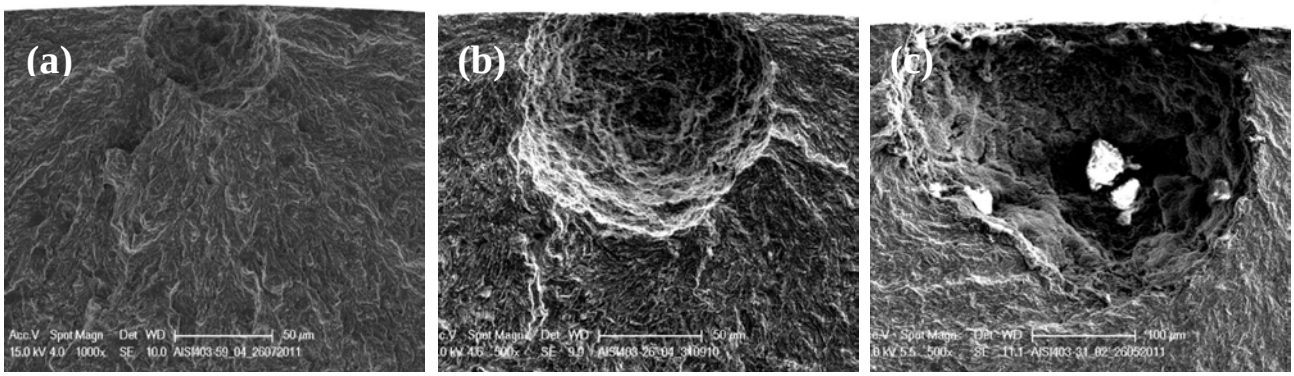

Figure 9. Fracture surfaces of pre-pitted specimens tested at $R = 0.05$ in air with a pit depth of: 50 µm ($\Delta\sigma = 507$ MPa, $N = 1.69 \times 10^9$) (a), 108 µm ($\Delta\sigma = 422$ MPa, $N_f = 6.11 \times 10^5$) (b) and 277 µm ($\Delta\sigma = 280$ MPa, $N_f = 9.65 \times 10^5$) (c)

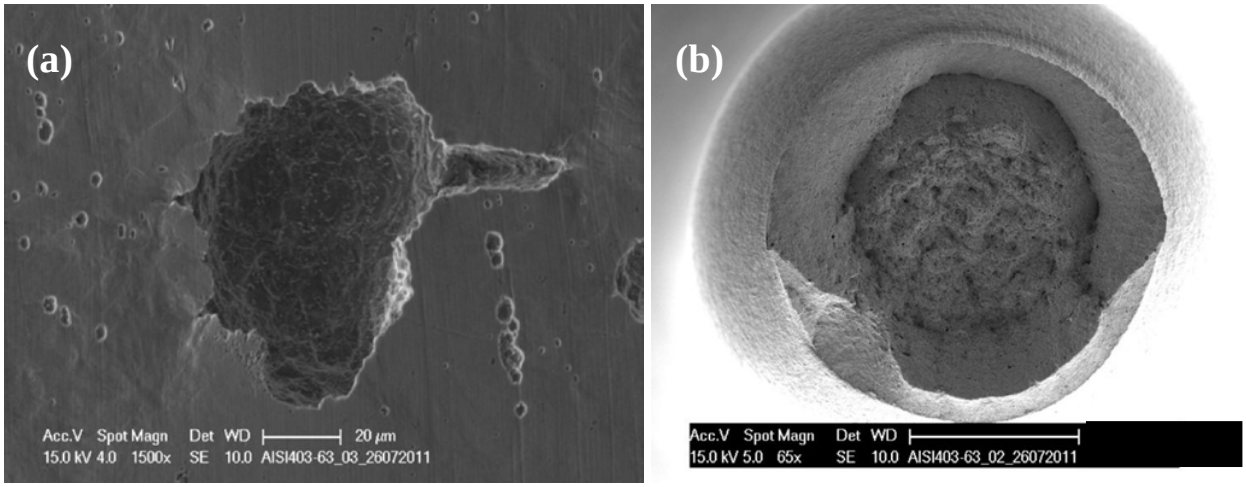

Figure 10. Corrosion pit with a depth of 48 µm (a) and fracture surface (b) of a specimen tested at $R = 0.5$ at $\Delta\sigma = 651$ MPa ($N_f = 2.38 \times 10^8$)

2.4.2. Fatigue tests in aerated 6 ppm C^- solution at 90 °C

S-N tests with smooth specimens showed a similar crack initiation behaviour like tests in air. Al_2O_3 inclusions were found again at the crack initiation site. Due to the decrease of the fatigue limit in the corrosive liquid, the cup-and-cone like fracture caused by cyclic creep was found only for tests at $R = 0.8$. Figure 11a shows a smooth specimen that was fatigue loaded at $R = 0.5$. An Al_2O_3 inclusion is located at the crack initiation site. Also the critical pit size for causing final failure at higher stress ratios is reduced. All pre-pitted specimens that were tested in the solution showed failure emanating from the pit. A corrosion pit with a depth of 100 µm is shown on the fracture surface of a specimen tested at $R = 0.8$ in Figure 11b.

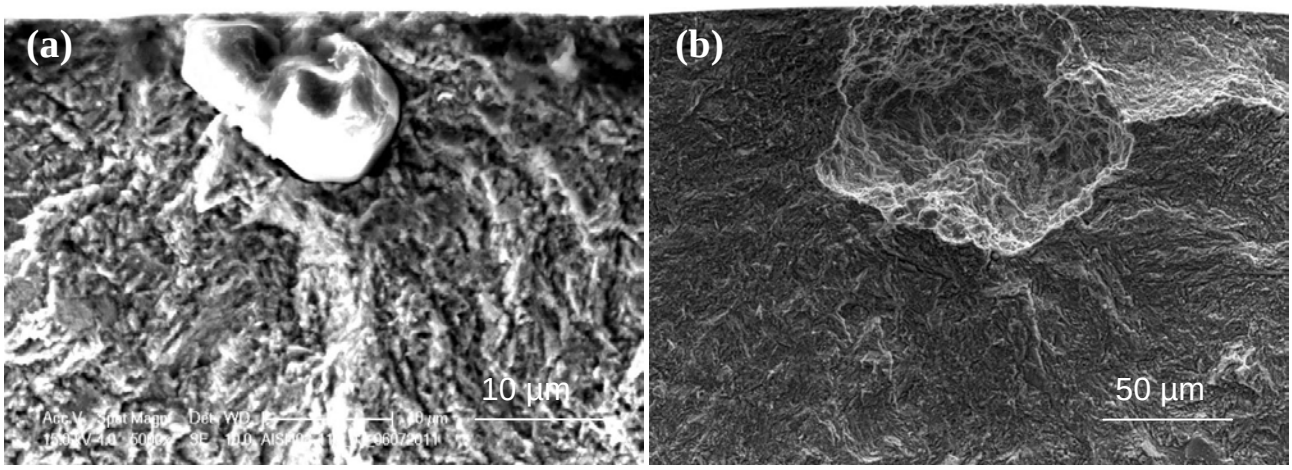

Figure 11. Fracture surfaces after testing in aerated 6 ppm Cl^- solution: smooth specimen at $R = 0.5$ ($\Delta\sigma = 340$ MPa. $N_f = 3.11 \times 10^6$) (a) and 101 µm deep pit at $R = 0.8$ ($\Delta\sigma = 135$ MPa, $N_f = 2.93 \times 10^7$) (b)

Acknowledgements

The presented results were achieved during a program to develop a methodology for the prediction of corrosion fatigue life in steam turbine blades, being conducted by the Electric Power Research Institute (EPRI) of Charlotte NC.

References

[1] EPRI. Proceedings of *Corrosion Fatigue of Steam Turbine Blade Materials*, R.I. Jaffe (Ed.), 21-24 Sept. 1981, Palo Alto, Ca, Pergamon Press, New York Oxford Toronto Sydney Frankfurt Paris, (1983).

[2] *Corrosion Fatigue of Steam Turbine-Blading Alloys in Operational Environments*. EPRI, Final Report CS-2932: 1984.

[3] *Program on Technology Innovation: Development of a Corrosion-Fatigue Prediction Methodology for Steam Turbines, Test Results of 12% Cr Blade Steel (403/410SS).* EPRI, Final Report 1023196: 2012.

[4] B. Schönbauer, S. Stanzl-Tschegg, N. Rieger, R. Salzman, A. Turnbull, S. Zhou and D. Gandy, *Crack Initiation and Propagation in 12% Cr Steam Turbine Blade Steel*. Proceedings of *VHCF5*, 28-30 June 2011, Berlin, (2011) pp. 545-550.

[5] B. Schönbauer, A. Perlega, S. Tschegg, N. Rieger, R. Salzman and D. Gandy, *Influence of*

Corrosion Pits and Environment on the Fatigue Life of 12% Cr Steam Turbine Blade Steel. Proceedings of *ICMFM-XVI*, 24-26 Sept. 2012, Brno, (2012) pp. 25-32.

[6] B. Schönbauer, S. Stanzl-Tschegg, N. Rieger, R. Salzman and D. Gandy, *Influence of Corrosion Pits on the Fatigue Limit of 12% Cr Steam Turbine Blade Steel*. Proceedings of *ECF 19*, 26-31 Aug. 2012, Kazan, (2012).

[7] B.M. Schönbauer and S.E. Stanzl-Tschegg, *Influence of Environment on the Fatigue Crack Growth Behaviour of 12% Cr Steel.* Ultrasonics (Ultrasonic Fatigue of Advanced Materials) (2013).

[8] S. Zhou and A. Turnbull, *Steam Turbine Operating Conditions, Chemistry of Condensates and Environment Assisted Cracking - An Overview*. NPL, Report MATC (A) 45: 2002.

[9] *Corrosion-Fatigue Prediction Methodology*. EPRI, Report EP-P31022/C14387: 2009.

[10] S. Kovacs, T. Beck and L. Singheiser, *Influence of mean stresses on fatigue life and damage of a turbine blade steel in the VHCF-regime.* Int J Fatigue 49 (2013) 90-99.

Influence of micro-shrinkage on the fatigue behavior of ductile iron

Paul Kainzinger[1,*], Christoph Guster[1], Martin Severing[2], Anton Wolf[3]

[1] Chair of Mechanical Engineering, Montanuniversitaet Leoben, Leoben, Austria
[2] SHW Casting Technologies, Aalen-Wasseralfingen, Germany
[3] AMSC Austria, Klagenfurt, Austria
* Corresponding author: paul.kainzinger@unileoben.ac.at

Abstract Fatigue crack growth and conventional fatigue tests have been carried out from different sampling locations within a wind turbine hub. S/N curves as well as fatigue crack propagation properties have been determined in dependency of the local microstructure. Subsequent fractographic analysis of the conventional fatigue tests showed micro-shrinkage to be the dominant reason for crack initiation. Statistical analysis of these micro-shrinkages showed a relationship between their size and the local solidification conditions. A model is proposed, linking the size of the shrinkages and the fatigue strength of nodular cast iron. Using this model, it is possible to describe the fatigue strength of nodular cast iron in dependence of the local solidification conditions or local microstructure, respectively.

Keywords Ductile Iron, fatigue, defects, micro-shrinkage

1. Introduction

Nodular cast iron is widely used for structural components of wind turbines due to its very good castability. Guidelines and codes dominate the design process of such components, which are rather conservative regarding the tolerable stresses [1,2]. Although these components can easily weigh up to several ten tons, their material properties are far from homogeneous. Large wall thicknesses and added chill irons result in different solidification conditions leading to different microstructures. Different material properties arise, depending on the local microstructure. Casting simulation tools are able to estimate local solidification conditions and the resulting local static material properties [3]. If the materials full potential should be used, the estimation of the dynamic material properties using empirical relationships between static and dynamic properties, which is common for guidelines, is not sufficiently accurate. In this paper, the Kitagawa Takahashi diagram [4] modified by El-Haddad [5] is used to describe the local cyclic material properties of nodular cast iron based on metallographic parameters. Therefore, fatigue crack growth experiments as well as conventional fatigue tests have been carried out using specimen with different characteristic microstructures. The Woehler experiments used for these investigations have already been published in [6]. The results of further investigations of the fractured specimen's surfaces, as well as the results of crack growth experiments are presented in this paper.

2. Experimental Procedure

A wind turbine hub made of EN-GJS-400-18U-LT standardized in [7] was used as base material for these investigations. The material has been taken from different sampling locations within the wind turbine hub in order to retrieve material with various solidification conditions and microstructures resulting in different material properties. The reader is referred to [6] for a detailed description of the sampling locations.
Fatigue crack growth experiments have been carried out according to [8] at room temperature and ambient air using the direct current potential drop method. The specimens have been subjected to four-point bending loads. For further information on the testing equipment refer to [9].

Single edge notched specimens have been used, their geometry is illustrated in Figure 1. To ensure a sound specimen surface, all the specimens have been grinded using a P320 sandpaper. The notch of the specimens has been pre-scratched.
Crack growth tests have been carried out using R-ratios of R=-1, R=0 und R=0.3. Only the threshold of the stress intensity factor K_{th} has been evaluated.

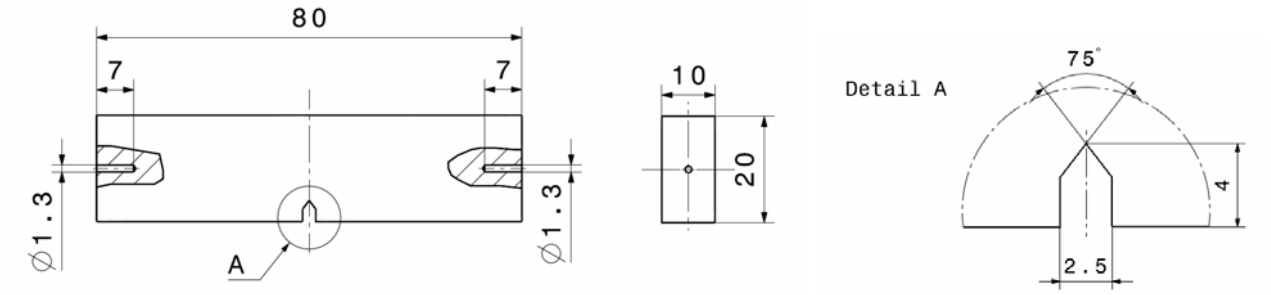

Figure 1: Geometry of the crack growth specimen

Constant amplitude Woehler experiments have been carried out at room temperature and ambient air. A resonance test rig Sincotec Exciting MAG was used to test the specimens up to 10^7 load cycles with a frequency of about 120Hz. All specimens have been tested under fully reversed loading (R=-1).
The finite life region was evaluated according to ASTM E739 [10]. The existence of a distinct fatigue limit is assumed according to [11], because the investigated material was fully ferritic and no retained austenite was found. The evaluation of the fatigue limit was carried out using the arcsin $\sqrt{p}$ transformation [12] with the estimator according to [13, 14].
Fractographic analysis of the fractured specimen surface has been carried out using a scanning electron microscope (Zeiss EVO MA15). Micro-shrinkages found in the fractured surfaces have been manually traced and two parameters (square root of particle area and maximum dimension) have been evaluated.

3. Crack Growth Experiments

At first, the specimens have been categorized using a qualitative measurement of the solidification rate depending on their sampling location (fast, medium, normal, slow). The number of tested specimen is available in Table 1.

Table 1: Test plan for the crack growth tests

Solidification speed	fast	medium	normal	slow	medium	slow	fast	medium	Slow
Stress-ratio R	0	0	0	0	0.3	0.3	-1	-1	-1
Number of samples	2	1	2	4	2	2	2	2	2

The results of the fatigue crack growth experiments are summarized in Figure 2. It is clearly visible, that the threshold K_{th} is decreasing with increasing stress ratio. Furthermore, the dependence of the microstructure becomes obvious, faster solidification (fine microstructure) leads to a lower threshold then slow solidification (coarse microstructure). The same trend has also been observed by Huebner et al. in [15] as well as Komber in [16] who also observed this trend for lamellar cast iron. She proposed a model to describe the threshold for crack initiation in dependence of microstructural parameters, namely the shape factor of the graphite nodules f and the mean distance between the graphite particles λ. This trend is contributed to the fact that the graphite particles act as crack stoppers. Huebner also observed lower crack growth rates in region II and a delayed transition to the region III for slower solidification rates in [15].

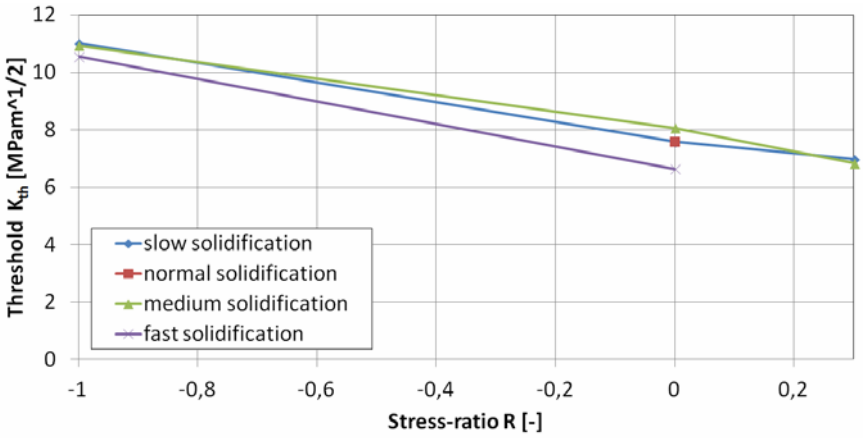

Figure 2: Threshold for crack propagation K_{th} in dependence of stress ratio and microstructure

To further quantify the solidification speed and to compare the results with those found in the literature, several metallographic parameters have been evaluated for each tested specimen. Therefore, the following parameters of the graphite particles from metallographic grindings made from each tested specimen have been evaluated:

- mean distance between the particles λ
- particle diameter d
- shape factor of the particle f
- number of particles per square millimeter n

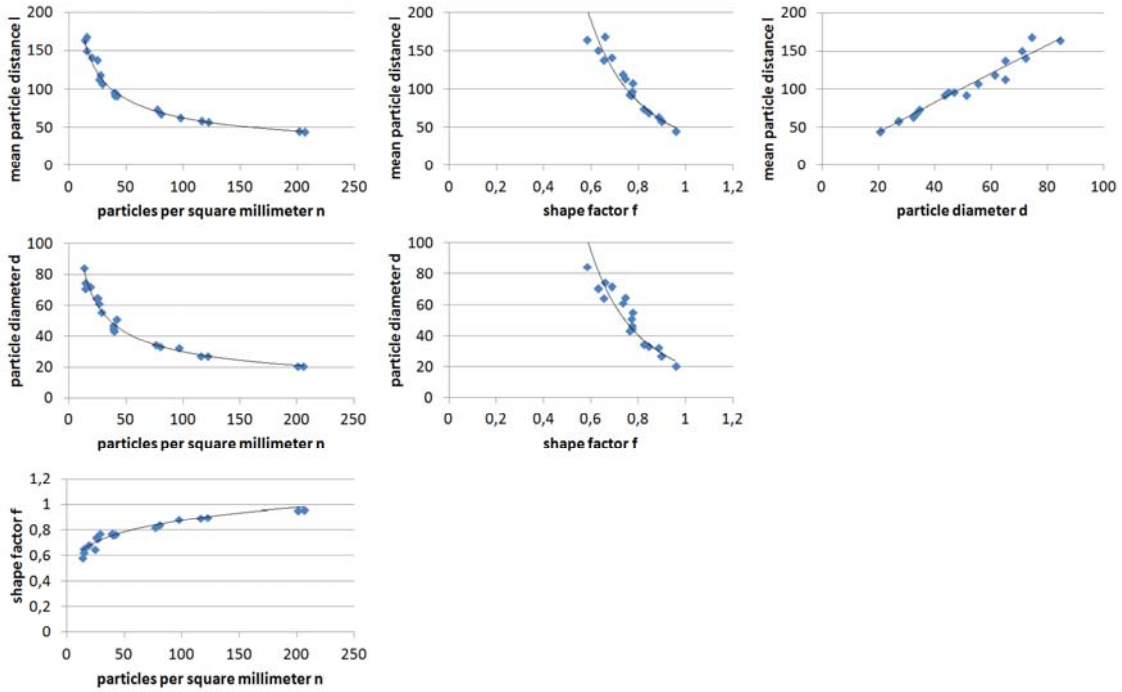

Figure 3: Comparison of the evaluated metallographic parameters (λ, d, f, n)

These four parameters have been plotted against each other in Figure 3. One can observe that all parameters are depending on each other. Slower solidification leads to larger mean distances λ, larger particle diameters d, smaller shape factors f (more degenerated graphite particles), a smaller number of particles n and vice verca. No distinct effect of the shape of the graphite nodules could be isolated. Therefore, describing the threshold K_{th} by more than one parameter, as Komber did in

[16] for different types of cast iron, is not necessary for nodular cast iron. The coefficient of determination illustrated in Figure 4 shows only a slight improvement compared to the fit using only the number of nodules per square millimeter. One can also see that the scatter of both empirical fits is very high, resulting in a quite low coefficient of determination. The fit parameters are summarized in Table 2.

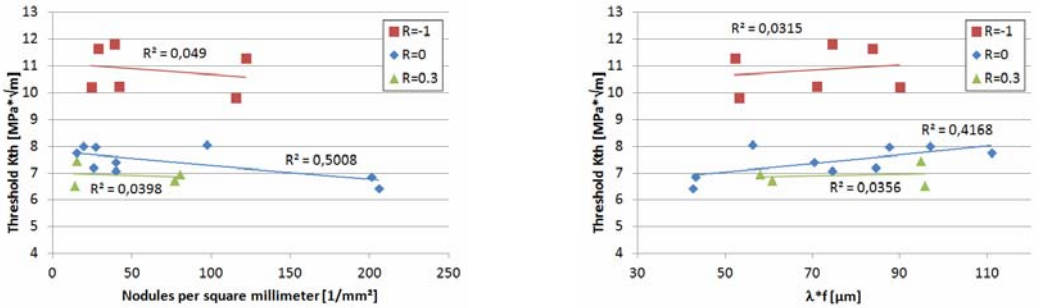

Figure 4: Threshold Kth in dependence of the number of particles per square millimeter (left) and the formalism used in [12,13] (right)

Table 2: Parameters of the empirical fit of the threshold K_{th}.

	Nodules/mm² [1/mm²]			λ*f [µm]		
	R=-1	**R=0**	**R=0.3**	**R=-1**	**R=0**	**R=0.3**
Slope	-0,0042	-0,0052	-0,0022	0,0097	0,0157	0,0037
y-intercept	11,11	7,82	7,01	10,16	6,27	6,63

Figure 5 shows a comparison of thresholds found in the literature [15,16,17]. As Zambrano already pointed out in [17], considerable differences are found in the resulting thresholds. The data presented in this paper shows good agreement with [15,16] for R=0 and R=0.3. Significant differences for the R=-1 tests have been found compared to [17]. It should be pointed out, that [15,16] used three-point bending specimen, [17] used edge cracked tension specimen and four point bending specimen have been used in the present investigations.

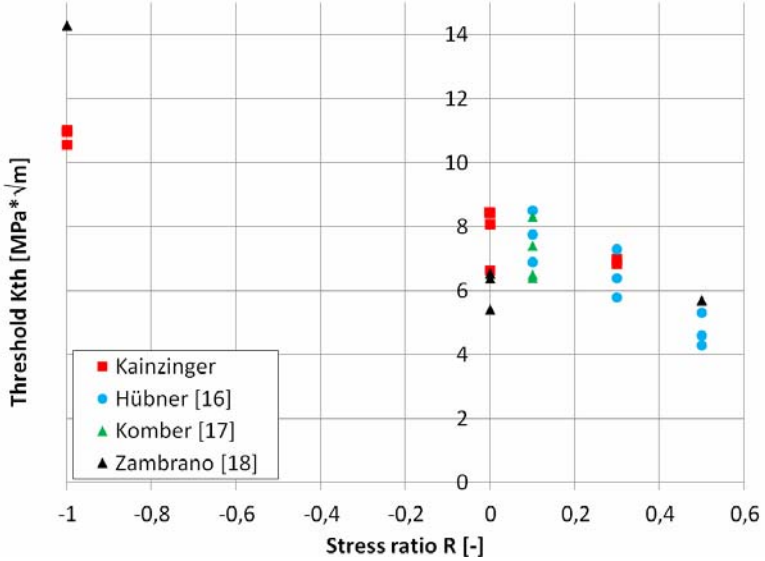

Figure 5: Comparison of thresholds found in the literature

4. Woehler Experiments

The Woehler experiments used for this paper have already been published in [6]. To improve the readability the results will be summarized shortly. For detailed information the reader is referred to the original paper.
Specimens have been taken from different sampling locations within the aforementioned wind turbine hub to cover a variety of different solidification conditions ranging from very slow solidification (coarse microstructure) in the center of a 100mm thick wall (position 1) to very fast solidification (fine microstructure) beneath chill irons (position 4). The results of these S/N curves are summarized in Figure 6. The fatigue strength increases with decreasing solidification time. In [6] an empirical model was proposed linking the parameters of the S/N curve with the local number of nodules per square millimeter. Good correlation was achieved between the model and the experiments. In the following part of this paper, a more physically based approach is proposed using the Kitagawa Takahashi diagram [4] modified by El Haddad [5].

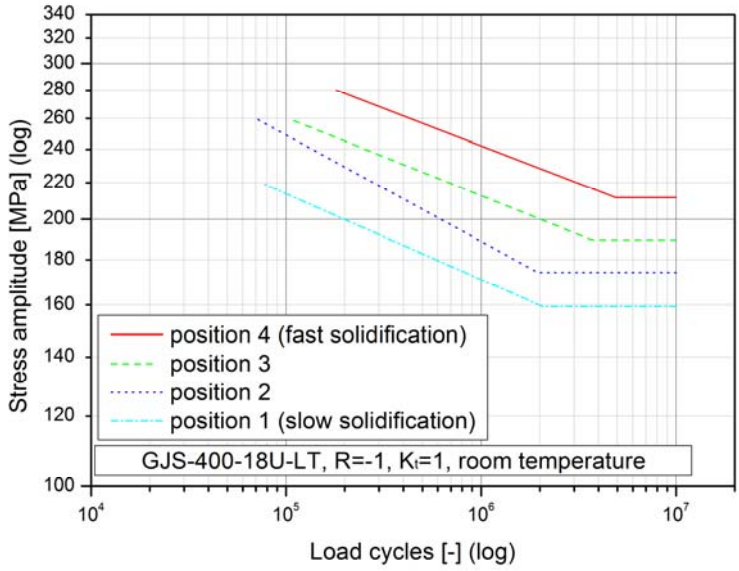

Figure 6: Results of the S/N curves from different sampling positions [8]

5. Fractographic Analysis

The fractured specimen surface has been analyzed using a scanning electron microscope. Micro-shrinkages have been found to be the dominant site of crack initiation (cf. Figure 7). This has also been confirmed by other authors, e.g. [18,19].

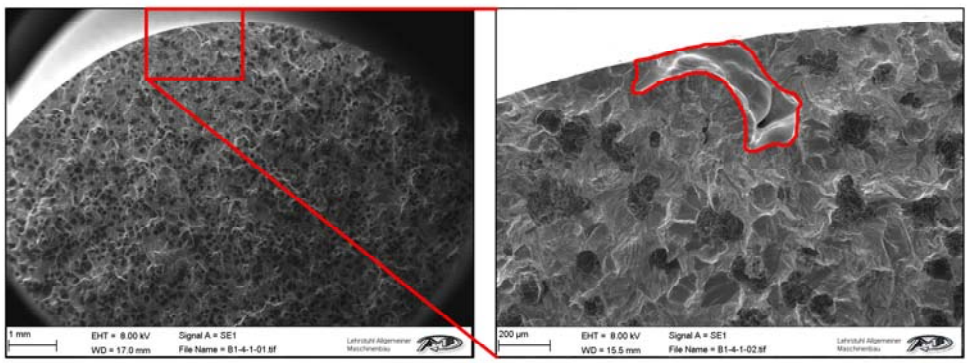

Figure 7: Micro-shinkages of different sizes found in the fractured specimen surface.

All micro-shrinkages were located at the specimen surface. Subsequent measurement of these micro-shrinkages has been carried out. The square root of the area [20] and the maximum dimension of the defects have been measured for all tested specimen. Some fracture surfaces revealed more than one micro-shrinkage, these specimens have not been evaluated due to the interaction effects of the micro-shrinkages.

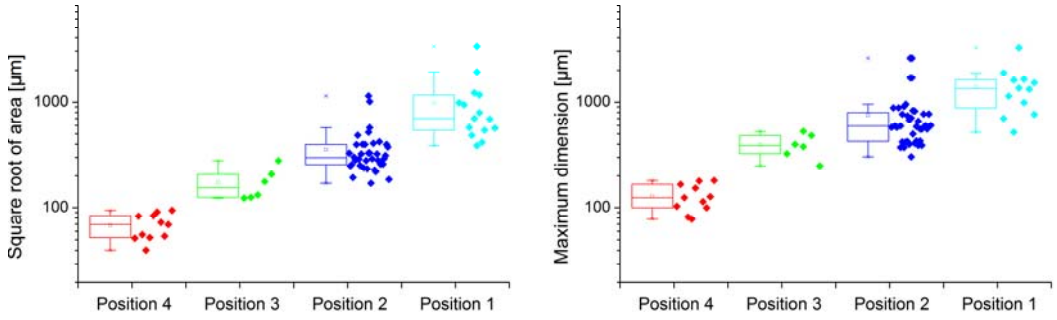

Figure 8: Box-plot of the size of the microshrinkages found in the fractured specimen surface. The square root of the area is displayed on the right side, the maximum dimenson on the left.

It has been observed that the size of the micro-shrinkages significantly decreases with decreasing solidification time (fine microstructure), which is illustrated by means of a box-plot in Figure 8. This trend is visible for both, the square root of the area as well as the maximum dimension.

6. Discussion

When considering both experimental results on their own, the observed trend is contradictory. The crack growth experiments indicate higher thresholds and lower crack growth rates (cf. [15]) for a coarse microstructure (slow solidification, respectively). This should result in better fatigue properties but the results of the fatigue tests show the exact opposite, a coarse microstructure leads to worse fatigue properties. The missing links are the micro-shrinkages of different sizes. Figure 8 shows the size of the shrinkages in dependence of the microstructure. Their mean values of the square root of their area ranges from 68µm for the fine microstructure up to 688µm for the coarse microstructure. This compensates the effect of the better crack growth properties of the coarse microstructure. The fatigue properties get worse, due to the disproportionally big size of the micro-shrinkages.

7. Local Fatigue Model

The Kitagawa Takahashi diagram modified by El Haddad, compensating the effects of short crack growth, will be used to describe the effect of micro-shrinkages on the fatigue behavior of ductile iron. The used equation is the following:

$$\sigma_a = \frac{\Delta K_{th}}{Y \cdot 2 \cdot \sqrt{\pi \cdot (a + a_0)}} \tag{1}$$

The threshold for crack propagation K_{th} is not constant throughout the material, it increases in case of a more coarse microstructure. For a better illustration of all sampling positions in a single diagram Eq. (1) has been normalized by being devided by the threshold:

$$\frac{\sigma_a \cdot 2}{\Delta K_{th}} = \frac{1}{Y \cdot \sqrt{\pi \cdot (a + a_0)}} \tag{2}$$

The corresponding threshold for the S/N curves from positions 1-4 have been calculated using the empirical fit using only the number of graphite nodules per square millimeter in Figure 4. A constant geometry factor of Y=0.65 has been used.
The El Haddad approach requires a fatigue limit of a defect free material to calculate the intrinsic crack length a_0. Since no defect free material was available for this research, the parameter a_0 was fitted to yield the best correlation between the estimated and the tested fatigue limits. A value of a_0=425µm led to the best results. This value of a_0 results in a theoretical fatigue limit of the defect free material of 212 to 231MPa, depending on the used threshold (10.1 and 11MPam^1/2, respectively). This defect free fatigue limit shows very good correlation with the empirical model proposed in [8].

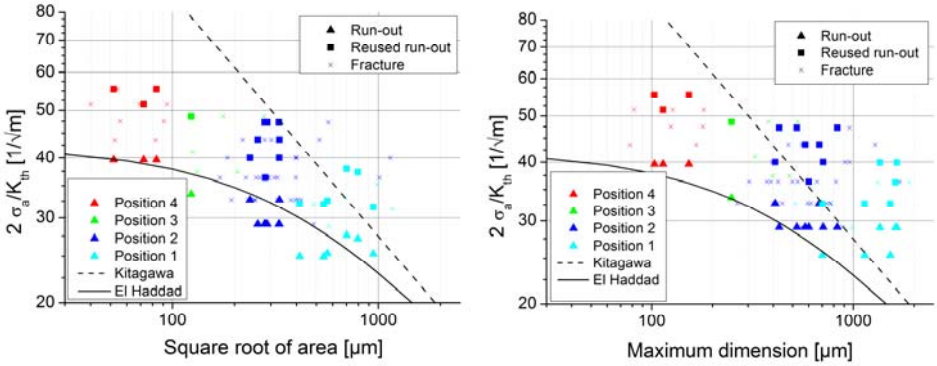

Figure 9: Normalized Kitagawa Takahashi diagram for all four sampling positions using the square root of the area (left) and the maximum dimension (right).

The Kitagawa Takahashi diagram using the square root of the area and the maximum dimension of the micro-shrinkage is illustrated in Figure 9. Using the square root of the area results in an overall good correlation, the use of the maximum dimension always led in conservative estimations of the fatigue limit. This is also emphasized in Figure 10, where the estimated fatigue limit is plotted against the experimental result. Therefore, the mean defect size (square root of area or maximum dimension, respectively) has been used to calculate the corresponding estimation using Eq. (1).

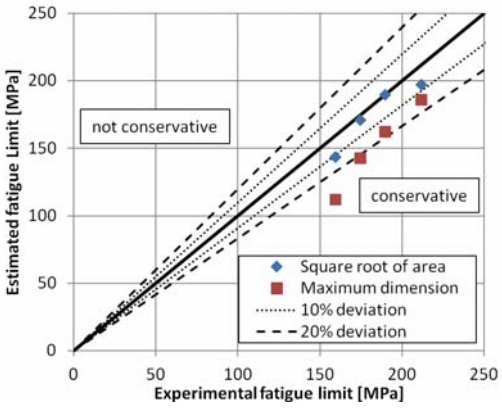

Figure 10: Comparison of the experimental and estimated fatigue limits.

8. Summary

- Fatigue crack growth as well as conventional fatigue tests have been carried out on specimens from different locations within a wind turbine hub. The sampling locations represent different solidification conditions which result in different microstructures.
- It has been found, that the fatigue crack propagation properties as well as the parameters of the S/N curve significantly depend on the local microstructure. The threshold for crack propagation K_{th} decreases with decreasing solidification time (fine microstructure), the fatigue properties increase with decreasing solidification time (resulting in a large number of particles per square millimeter).
- A contradictory trend has been found comparing the crack growth and conventional fatigue tests with different microstructures. Crack growth experiments show better fatigue properties for coarse microstructures, whereas conventional fatigue tests showed worse properties.
- Micro-shrinkages have been found to be the dominant site for crack initiation. The size of these micro-shrinkages compensates for the contradictory trend mentioned above.
- Subsequently, the local fatigue crack properties and the size of the micro-shrinkages are combined in the Kitagawa Takahashi diagram modified by El Haddad. Using the square root of the defect area leads to very good results. The maximum dimension always leads to conservative results.

Acknowledgements

Financial support by the Austrian Federal Government (in particular from the Bundesministerium fuer Verkehr, Innovation und Technologie and the Bundesministerium fuer Wirtschaft und Arbeit) and the Styrian Provincial Government, represented by Oesterreichische Forschungsfoerderungsgesellschaft mbH and by Steirische Wirtschaftsfoerderungsgesellschaft mbH, within the research activities of the K2 Competence Centre on ‘Integrated Research in Materials, Processing and Product Engineering’, operated by the Materials Center Leoben Forschung GmbH in the framework of the Austrian COMET Competence Centre Programme, is gratefully acknowledged. Furthermore, the authors would like to thank their project partners SHW Casting Technologies GmbH and AMSC Austria GmbH for their support.

References

[1] Rechnerischer Festigkeitsnachweis furr Maschinenbauteile, FKM Richtlinie, 4. Ausgabe, 2002.
[2] Guideline for the Certification of Wind Turbines, Germanischer Lloyd, Edition 2003 with Supplement 2004.
[3] J. Strum: Cast iron - a predictable material, World Foundry Congress, 2010.
[4] H. Kitagawa, S. Takahashi: Applicability of fracture mechanics to very small or cracks in the early stage, Proc. Of the second int. Conference on mech. behaviour of materials, ASM, 1976; 627-631.
[5] M.H. El Haddad, K.N. Smith, T.H. Topper: "Fatigue crack propagation of short cracks", ASME transactions, vol. 101, 1979.
[6] P. Kainzinger, C. Guster, M. Severing, A. Wolf: Abschaetzung der lokalen Woehlerlinie von Gusseisen mit Kugelgraphit aus der Giesssimulation, DVM-Bericht 139, 2012
[7] DIN EN 1563, Giessereiwesen - Gusseisen mit Kugelgraphit, 2011
[8] ASTM E647, Standard Test Method for Measurement of Fatigue Crack Growth Rates, 2010
[9] A. Leitgeb, Bruchmechanik und schadenstolerante Konstruktion im Automobilbau, PhD thesis, Montanuniversitaet Leoben, 2010.

[10] Standard Practice for Statistical Analysis of Linear or Linearized Stress-Life (S-N) and Strain-Life (e-N) Fatigue Data, ASTM E 739-91, 1998.
[11] E. Haibach, A Likely Explanation of Very High Cycle Fatigue in Steel, FEMFAT User Meeting, 2011.
[12] D. Degnel, Die arcsin $\sqrt{p}$ -Transformation - ein einfaches Verfahren zur grafischen und rechnerischen Auswertung geplanter Woehlerversuche, Journal of Materials Technology, 1975, Issue 8, P. 253-288.
[13] W. Weibull, Fatigue Testing and Analysis of Results, 1961.
[14] G. Blom, On linear estimates with nearly minimum variance, Ark. Mat. 3, P. 365-369, 1956.
[15] P. Huebner, H. Schlosser, G. Pusch, H. Biermann, Load history effects in ductile cast iron for wind turbine components, International Journal of Fatigue, 2007
[16] B. Komber Bruchmechanische Bewertung des Rissausbreitungsverhaltens ferritischer Gusseisenwerkstoffe bei zyklischer Beanspruchung, PhD thesis, TU Bergakademie Freiberg, 1995.
[17] H. R. Zambrano: Fracture toughness and growth of short and long fatigue cracks in ductile cast iron EN-GJS-400-18-LT, 2011
[18] M. Wohlfahrt: Einfluesse auf die Schwingfestigkeit von Gusseisen und deren Einbindung in die Berechnung der Bauteillebensdauer, VDI Report Nr. 2122, 2011.
[19] B. Pyttel, I. Brunner, D. Schwerdt, C. Berger: Influence of defects on fatigue strength and failure mechanisms in the VHCF-region for quenched and tempered steel and nodular cast iron, International Journal of Fatigue, 2012
[20] Y. Murakami: Metal fatigue: Effects of small defects and nonmetallic inclusions. Elesevier, 2002

Reliability-based Fatigue Life Prediction Method for Compressor Wheel Rub of Turbocharger for Vehicle Application

WANG Zheng[1, *], WANG Zeng-quan[1], XING Weidong[1], WANG A-na[2]

[1] National Key Laboratory of Diesel Engine Turbocharging Technology, China North Engine Research Institute, Tianjin 022, China

[2] Center of Engine Test and Measurement, China North Engine Research Institute, Tianjin 022, China

* Corresponding author: wzneu@126.com

Abstract The fatigue failure of compressor wheel rub is one of important failure modes of turbocharger for vehicle application. Because the operating state of turbocharger in the life cycle changes as the work condition of diesel engine changes, the compressor wheel rub of turbocharger is applied by the variable stress which can causes the fatigue failure. In this paper, the effect of centrifugal load, thermal load and aerodynamic load on the stress of compressor wheel rub is studied, and then the fatigue stress spectrum of compressor wheel rub is developed based on the endurance test profile of vehicle engine. In order to research the fatigue strength of compressor wheel rub, the fatigue specimen is designed and the relationship between the stress and fatigue life of compressor wheel rub is built. Then, utilizing the linear Miner cumulative damage rule and the first-order reliability method, the reliability model of compressor wheel rub with fatigue failure mode is derived, and the rule that the reliability of compressor wheel rub changes with life is studied. Based on the reliability model of compressor wheel rub with fatigue failure mode developed, the method for determining the reliable fatigue life of compressor rub of turbocharger is proposed. The result shows that with the method developed in this paper the fatigue life of compressor wheel rub for the given reliability can be predicted reasonably, and the reliability of compressor wheel rub can also be calculated for the given fatigue life.

Keywords Fatigue, Life prediction, Turbocharger, Compressor wheel, Reliability, Reliable life

1. Introduction

Turbocharger has been applied into all kinds of vehicle engines to improve the performance and reduce the emission in recent years [1-3]. The compressor wheel is one of the most key components of turbocharger, which can transform the mechanical energy recovered by the turbine to the energy of air and improve the intensity of inlet air of engine. For the turbochargers for vehicle application, because of the complex and variable operating section of vehicle engine, the running status of compressor wheel of turbocharger changes continuously and the compressor wheel is applied by the variable loading process, which can cause the fatigue failure of compressor wheel rub [4-5]. Once the fatigue failure happens in the compressor wheel, the turbocharger can not work normally. Thus, it is very important that analyze the reliability of compressor wheel rub with fatigue failure mode and predict its fatigue life scientifically.

Because the fatigue reliability and life of compressor wheel rub is related with the real operating profile of engine equipped with the turbocharger, it is very important that obtain the exact operating profile of engine in the process of analyzing the reliability and life of compressor wheel of turbocharger. However, in the development stage of turbocharger, it is hard to obtain the exact operating profile of engine or the turbocharger, especially for the engines for vehicle application, and in most cases it is very difficult to analyze the fatigue life and reliability of turbocharger compressor wheel.

In this paper, a new method for analyzing the fatigue reliability and predicting the life of compressor wheel rub of turbocharger is developed based on the endurance test profile of engine for vehicle application. The reliability model of compressor wheel rub with fatigue failure mode is derived, and the method for predicting the fatigue life of compressor wheel rub corresponding to the

different given reliability is proposed.

2. Stress Analysis of Compressor Wheel Rub with Fatigue Failure Mode

The sketch of compressor wheel of turbocharger and its critical locations of fatigue failure (namely, the maximal stress appearing areas) are shown as Figure 1, and it can be seen that the maximal stress of compress wheel generally appears in the rub for the normal operating cases of turbocharger.

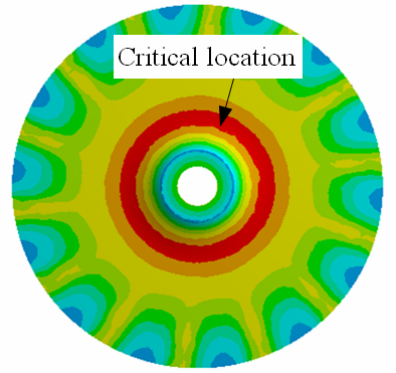

Figure 1. Critical locations of compressor wheel with fatigue failure mode

In the work process of turbocharger, the compressor wheel is applied by the centrifugal load, thermal load and aero dynamical load, simultaneously, and the stress value of compressor wheel rub is dependent on the running status parameters of compressor wheel of turbocharger, including the rotational speed, inlet and outlet temperature, inlet and outlet pressure, and so on.
Because in the development stage of turbocharger it is very hard to obtain the exact running status parameters of compressor wheel and the real operating profile of engine for vehicle application, in the following based on the endurance test profile of engine, the operating modes of engine which is composed of four main operating modes, is determined, and corresponding to different operating modes of engine the running status parameters of compressor wheel of turbocharger is studied. Further, according to the running status parameters of compressor wheel in different operating mode of engine, the stress of compressor wheel rub is calculated, shown as Table 1.

Table 1. Stress of compressor wheel rub corresponding to the operating modes of the endurance test profile of engine

Operating mode of engine	The running status parameters of compressor wheel of turbocharger						Stress of compressor wheel rub (MPa)
	Rotating Speed(r/min)	Inlet Temperature (K)	Outlet Temperature (K)	Inlet Pressure (Bar)	Outlet Pressure (Bar)	Flow (kg/s)	
1	104019	297	483	0.896	3.340	0.569	267
2	98735	297	479	0.894	3.216	0.548	223
3	95420	297	471	0.892	3.025	0.503	209
4	91984	297	468	0.891	2.873	0.476	195

According to the endurance test profile of engine and the stress of compressor wheel rub shown as Table. 1, the fatigue stress history of compressor wheel rub is built, shown as Figure 2.

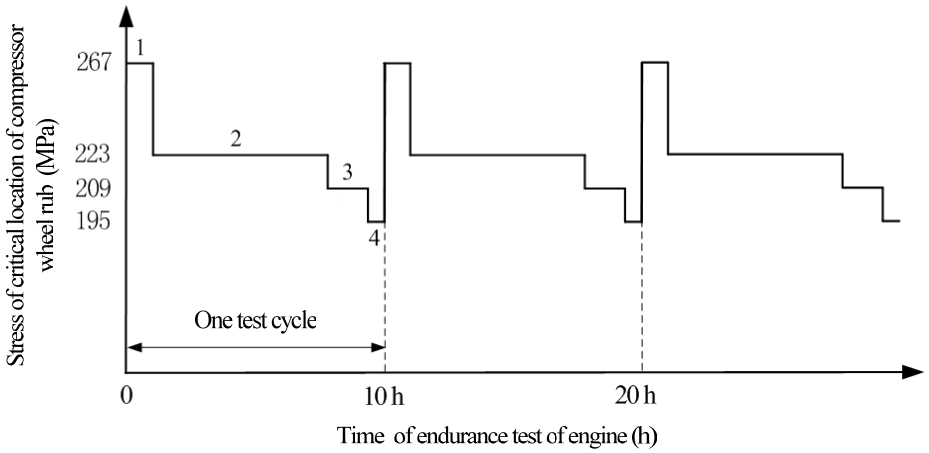

Figure 2. Fatigue stress history of compressor wheel rub corresponding to the endurance test profile of engine

3. Study on the strength of Compressor Wheel Rub with Fatigue Failure Mode

In order to study the fatigue strength of compressor wheel rub of turbocharger, the test specimen which can reflect the effect of structural characteristics and manufacturing process on the fatigue strength, is designed as Figure 3. Forty-five specimens of compressor wheel rub are manufactured and the fatigue test of these specimens is done at the fatigue-testing machine.

According to the results of fatigue test of compressor wheel rub specimen, the relationship between the fatigue life of compressor wheel rub and stress is subjected to the form of exponential function, namely,

$$Ne^{\alpha s} = C \tag{1}$$

And the relationship between the logarithm mean value $\mu_{\lg N}$ of fatigue life N of compressor wheel rub and stress s can be expressed as

$$\mu_{\lg N} + 0.02498\, s = 16.7535 \tag{2}$$

The relationship between the logarithm standard deviation value $\sigma_{\lg N}$ of fatigue life N of compressor wheel rub and stress s can be expressed as

$$\sigma_{\lg N} + 0.02522\, s = 13.5866 \tag{3}$$

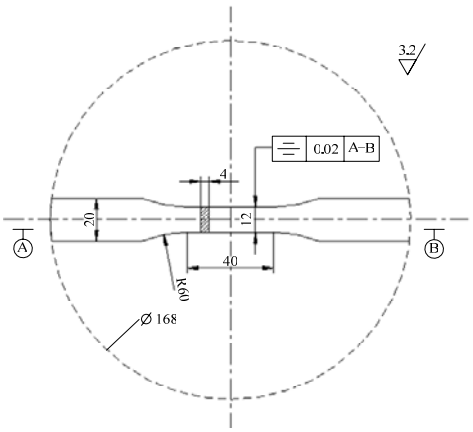

Figure 3. Fatigue test specimen of compressor wheel rub

4. Fatigue Reliability Modeling and Reliable Life Prediction of Compressor Wheel Rub

According to the linear Miner cumulative damage rule, the fatigue cumulative damage ΔD of compressor wheel rub corresponding to one cycle of endurance test of engine, can be expressed as

$$\Delta D = \frac{1}{N_1} + \frac{1}{N_2} + \frac{1}{N_3} + \frac{1}{N_4} = \sum_{i=1}^{4} \frac{1}{N_i} \tag{4}$$

Where, N_i is the fatigue life of compressor wheel rub corresponding to the stress s_i.

And the number of test cycles of engine endurance test to which the fatigue failure happened in the compressor wheel rub of turbocharger, can be derived as

$$n = \frac{1}{\Delta D} = \frac{1}{\sum_{i=1}^{4} \frac{1}{N_i}} \tag{5}$$

And the limit state function of compressor wheel rub with fatigue failure mode can be expressed as

$$Z = n\Delta D - 1 = n\sum_{i=1}^{4} \frac{1}{N_i} - 1 \tag{6}$$

When the fatigue life of compressor wheel rub is measured with the number of test cycles of endurance test of engine, the relationship between the fatigue reliability of compressor wheel rub of turbocharger and its life parameter can be developed as

$$R(n) = P\left(n\sum_{i=1}^{4} \frac{1}{N_i} - 1 < 0 \right) \tag{7}$$

Let $x_i = \log N_i$, and using the second moment method, the limit state function of compressor wheel rub with fatigue failure mode can be expressed as

$$\begin{aligned} Z &= n\sum_{i=1}^{4} 10^{-x_i} - 1 \\ &= n\sum_{i=1}^{4} 10^{-\mu_{x_i}} - 1 - n\ln 10 \sum_{i=1}^{4} 10^{-\mu_{x_i}} (x_i - \mu_{x_i}) \end{aligned} \tag{8}$$

And the mean value and standard deviation value of the limit state function of compressor wheel rub with fatigue failure mode can be expressed as

$$\mu_Z = n\sum_{i=1}^{4} 10^{-\mu_{x_i}} - 1 \tag{9}$$

$$\sigma_Z = n\ln 10 \sqrt{\sum_{i=1}^{4} \left(10^{-\mu_{x_i}} \sigma_{x_i} \right)^2} \tag{10}$$

With Eq. (2) and Eq. (3), the logarithm mean value and the logarithm standard deviation value of fatigue life of compressor wheel rub corresponding to the different stress shown as Tab. 1, can be calculated. and the result is substituted into Eq. (9) and Eq. (10), we have

$$\mu_Z = 9.0325 \times 10^{-11} n - 1 \tag{11}$$

$$\sigma_Z = 0.002772n \tag{12}$$

Further, according to Eq. (7), the reliability model of compressor wheel rub with fatigue failure mode can be developed as

$$R(n) = \Phi\left(-\frac{\mu_Z}{\sigma_Z} \right) = \Phi\left(\frac{1 - 9.0325 \times 10^{-11} n}{0.002772n} \right) \tag{13}$$

where, $\Phi(\cdot)$ denotes the cumulative distribution function of standard normal distribution.

The rule that the reliability of compressor wheel rub with fatigue failure mode changes as the number of test cycles of endurance test of engine can be obtained with Eq.(9), and it is shown as Figure 4.

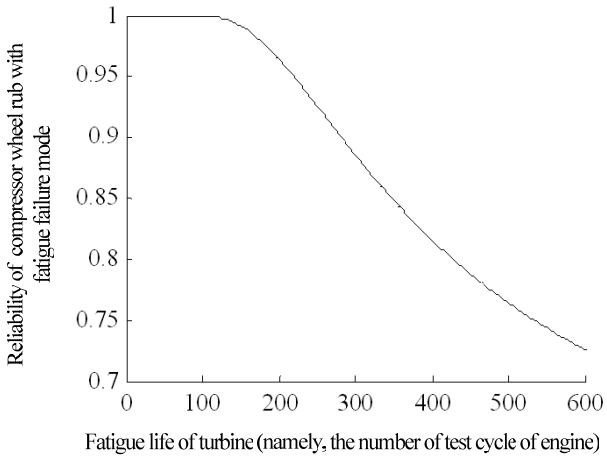

Figure 4. Reliability curve of compressor wheel rub with fatigue failure mode

From Figure 4, it can be concluded that the reliability of compressor wheel rub with fatigue failure mode decreases as the life parameter increases.

According to the relationship between the reliability of compressor wheel rub with fatigue failure mode and its life parameter, the reliable fatigue life of compressor wheel rub can be determined rationally. As shown in Fig. 5, when the reliability of compressor wheel rub with fatigue failure mode is 0.95, the reliable life $w_{0.95}$ is 220 cycles of endurance test of engine, and when the reliability is 0.9, the reliable life $w_{0.9}$ is 281 cycles of endurance test of engine.

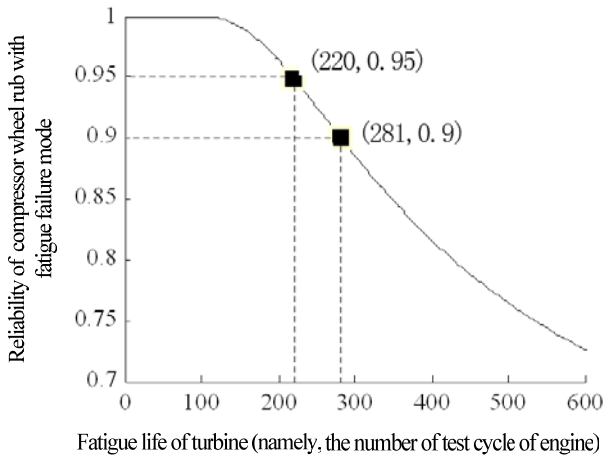

Figure 5. Reliable life of compressor wheel rub with fatigue failure mode corresponding to different reliability

5. Conclusions

The reliability and life of turbocharger compressor wheel rub with fatigue failure mode is studied in this paper. Based on the endurance test profile of vehicle engine, the running status of compressor wheel of turbocharger is analyzed when engine works in different operating modes, and the fatigue stress process of compressor wheel rub corresponding to the endurance test profile of engine is built. And the relationship between the fatigue life of compressor wheel rub and stress is developed

through the fatigue test of fatigue specimen. The reliability model of compressor wheel rub with fatigue failure mode is derived, and then the method for determining the reliable fatigue life of compressor wheel rub is proposed. The result shows that as the life parameter increases, the reliability of compressor wheel rub with fatigue failure mode decreases. When the reliability is given, the reliable fatigue life of compressor wheel rub can be predicted with the method proposed rationally.

Acknowledgements

This work was financially supported by the National Natural Science Foundation of China with the grant No.50905007, and the Open Research Fund Program of the National Key Laboratory of Diesel Engine Turbocharging Technology.

References

[1] Zhu Daxin, Turbocharging and Turbocharger, China Machine Press, Beijing, 1992.
[2] Zhang Hong and Ma Chaochen, Structure computation and analysis of vehicle turbocharger compressor impeller, Chinese Internal Combustion Engine Engineering, 2007, 28, pp. 62-66, 20.
[3] Chen Xiaowei, Zhu Meilin, Xu Kai, etc. A new approach to calculate safety index of the ICE components. Journal of Huazhong University of Science & Technology, 1999, 27, pp. 51-52.
[4] WANG Zheng, WANG A-na, GUO Kai, et al, Reliability evaluation method for turbocharger turbine with overspeed failure mode, Proceedings of International Conference on Reliability, Maintenance and Safety, Guiyang, China, 2011, pp. 992-996.
[5] Wang Zheng, Wang Zengquan, Guo kai, et al, Dynamic reliability model of turbine impeller of turbocharger under ultimate load, Transactions of the Chinese Society for Agricultural Machinery, 2011, 42: pp. 32-35.

A Software Tool for the Fatigue Growth Analysis of Multiple 3D Cracks from Fastener Holes

Yixiu Shu[1], Yazhi Li[1], Zhenxing Fan[1]
[1]School of Aeronautics, Northwestern Polytechnical University, Xi'an, 710072
* Corresponding author: shuyixiu@126.com

Abstract A software tool is developed to carry on automatic fatigue crack propagation analysis for the multiple three-dimensional (3D) cracks initiated from fastener holes. It is a computer code package being capable of handling the cases of multiple 3D cracks with quadratic curve fronts. The object-oriented programming language is used to develop user interfaces for the input of the initial data and output of the simulation results. To achieve life-span numerical simulation for the multiple 3D crack growth, ANSYS Parametric Design Language is used to create finite element model, conduct the stress analysis and regenerate finite element mesh for new crack configurations. Stress intensity factors of the cracks are determined using the crack opening displacements and incorporated into crack propagation laws to estimate the crack extension. An algorithm for the fast integration of crack growth equations is adopted to predict the fatigue crack growth life. As examples, two scenarios of corner cracks initiated from countersunk fastener hole in 2324-T39 alloy sheets are analyzed throughout their fatigue growth lives. The simulation results correlate well with the experimental ones.

Keywords Fastener hole, multiple 3D cracks, fatigue crack growth, numerical simulation, software tool

1. Introduction

Widespread fatigue damage (WFD) is one of the major concerns for the fleet of aging airplanes and significantly decreases the residual strength and residual fatigue life of the aircraft structures. The multiple site damage (MSD) is a kind of WFD happened in similar places of a single structure element and often appears as the multiple cracks initiated from the fastener holes of the aircraft panel structures. The link-up of these cracks is one of the critical conditions and probably leads to the final structure failure. Although most of the available studies are referring to the two-dimensional cracks [4-8], cracks in the panel structures usually initiate as three dimensional (3D), especially the corner cracks from fastener holes of thick panels. A cracks initiated from fastener hole side can be spotted from panel surface only if it has grown out of the area covered by fastener head, washer or nut, or penetrated the panel thickness. The period of the crack growth from initiation to visible takes a large proportion of its total life. Therefore, it is significant to study the behavior of multiple 3D crack growth from very beginning to final failure and achieve an adequate estimation of the crack growth life.

This paper deals with the fatigue growth analysis of multiple 3D cracks initiated from an array of countersunk holes, the scenario that is even more complicated than the kind of cracks from the regular through holes. There are two essentials to conduct such analysis. The first is to attain the stress intensity factors (SIFs) along the front curves of each crack. Because of the varying and complexity of the crack geometry, there is no closed form solution or data available for the SIF. The solution of the SIFs must be determined numerically, mainly by the finite element analysis, such as the calculations of Shen[9], Fawaz[10] and Park[11]. For the simulation of the scenario throughout the whole crack growth history, it is essential to develop a robust technique to take on the task of finite element modeling for given crack pattern and do remeshing over and over again for the various crack sizes and shapes relative to structure geometry during the crack growth. The second requirement is to apply an approach being able to make fast integration of crack growth equation and achieve consistent growth of the multiple cracks with error control, so as to attain adequate crack growth life prediction efficiently. The applicable approaches include the trial and error

method [15], variable optimization method [16] and load cycle segmentation method [11-13], etc., which have been used mainly for multiple 2D cracks. The reason of the more complexity of the present scenario over the multiple 2D crack issue is that the growth of every single 3D crack can be taken as that of several 2D cracks.

This paper describes the development of a computer tool based on commercial finite element software package, aiming to accomplish efficient and automatic simulation for the multiple 3D crack growth and life prediction. Design philosophy, analysis procedure and finite element modeling technique are described in detail. Examples are given to demonstrate the capability of the tool. Comparison is made between simulation results and the experimental ones.

2. Principal of multiple 3D crack growth analysis

2.1 Brief introduction of the tool

Although most of the present commercial finite element packages already have the function module to analyze fracture parameters, difficulty still remain in creating and updating finite element meshes for different crack patterns during crack growth, particularly for the situation of multiple site 3D cracks. So we decided to develop a tool to handle the analysis process of multiple 3D cracks over the whole fatigue growth life, without artificial intervention. The basic steps and module of performing such an analysis are shown in Fig. 1. The commercial software ANSYS are adopted as the computational engine, since the ANSYS Parametric Design Language (APDL) is easily edited and compiled to perform pre- and post- data processing, damage accumulation and result visualization during the analysis. The object-oriented language Visual Basic (VB) is used to develop user interfaces to facilitate operation and result representation.

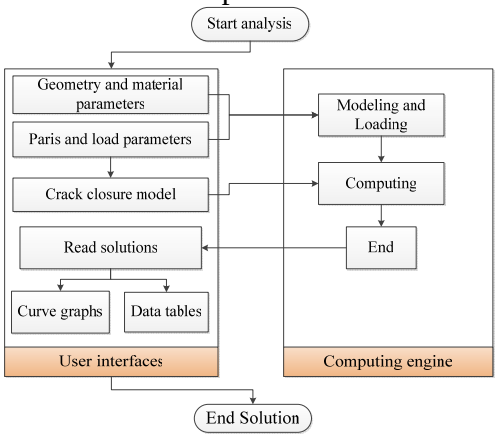

Figure 1. Flow chart of the tool

The tool has been tested under Windows XP and Windows 7 operation systems. It focuses on the sheet specimens with coplanar fastener holes (both countersunk and simple circular through ones) and multiple 3D cracks alongside them. The specimens are subject to constant amplitude loading and cracks may initiate from both sides of each fastener hole. Whole process of multiple crack growth can be simulated. Finite element modeling is parameterized, so as to adapt different geometries of structure and cracks. The parameters of geometry, material properties, loads and constraints are written to the file according to the APDL convention to parameter definition and passed to ANSYS. The analysis process is then running in background.

2.2 Philosophy of crack growth analysis

2.2.1 The fatigue crack growth model

3D cracks are supposed to propagate along the direction normal to their fronts. The Paris-form of crack growth rate equation is used [1]:

$$\frac{da}{dN} = C(\Delta K)^n \tag{1}$$

where ΔK is the stress intensity factor range.
Elber [2] discovered the phenomenon of fatigue crack closure and ΔK was replaced by its effective value

$$\Delta K_{eff} = K_{\max} - K_{open} = U\Delta K \tag{2}$$

where K_{open} is the value of stress intensity factor that causes crack opening during load cycling. U is crack closure function defined as the ratio of ΔK_{eff} to ΔK.

Elber carried out experiments on the Al-alloy 2024-T3 and found that for the stress ratio $R = -0.1$ to 0.7, U can be described as:

$$U = 0.5 + 0.4R \tag{3}$$

An improved function with a more realistic behavior for negative R-values was proposed by Schijve [3]:

$$U = 0.55 + 0.33R + 0.12R^2 \tag{4}$$

The crack growth life prediction program AFGROW [17, 18], developed by J. A. Harter uses a crack closure model in which a closure factor C_f is introduced.

$$K_{open} = C_f K_{\max} \quad ; \quad C_f = 1 - \left[\left(1 - C_{f0}\right)\left(1 + 0.6R\right)\left(1 - R\right)\right] \tag{5}$$

where C_{f0} is the value of C_f for $R = 0$. thus

$$\begin{aligned} \Delta K_{eff} &= K_{\max} - K_{open} = \frac{1 - C_f}{1 - R}\Delta K \quad \text{if } K_{open} \geq K_{\min} \\ \Delta K_{eff} &= K_{\max} - K_{\min} = \Delta K \quad \text{if } K_{open} < K_{\min} \end{aligned} \tag{6}$$

The Schijve model and the AFGROW model are implemented in our tool using APDL code.

2.2.2 Stress intensity determination

Stress intensity factors are determined by the finite element analysis of cracked structure as well as the crack tip opening displacement (CTOD) approach. As shown in Figure 8, for 2D crack case, K value at point *P* located on crack surface and close to crack tip can be calculated :

$$K_{IP} = \frac{2G}{1 + \kappa} \cdot \sqrt{\frac{2\pi}{r_P}} \cdot \left| v\left(r_P\right) \right| \quad \left(P = J, K\right) \tag{7}$$

where: $\kappa = \begin{cases} 3 - 4\upsilon & \text{plane strain} \\ \dfrac{3 - \upsilon}{1 + \upsilon} & \text{plane stress} \end{cases}$.

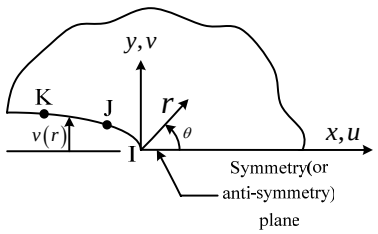

Figure 2. Normal section of a crack

Then the stress intensity factor at crack tip can be determined by displacement extrapolation techniques:

$$K_{\mathrm{I}} = \frac{c}{c-1} K_{\mathrm{I}J} - \frac{1}{c-1} K_{\mathrm{I}K} \tag{8}$$

where: $c = L_{\mathrm{K}} / L_J$, L_K and L_J are distances from the point *K*/*J* to the crack front respectively.

2.2.3 Denotation of different crack configurations

For the present 3D cracks, SIF at any point of a crack front curve is determined by taking Figure 2 as the plane passing that point and normal to the tangent of the curve. The crack front of a corner crack is assumed as a quadratic curve, as is shown in Figure 3. The crack growth is simulated stepwise using remeshing technique combining with fatigue crack growth model. In each analysis step, three sampling points are chosen on every crack front, one in the middle of the curve and two others are close to both ends of the curve. The increments of crack growth on these points are assumed along the directions normal to the crack front curve. We are not choosing both ends of the curve as the sampling points, since the curve may not be perpendicular to the free boundaries on its ends and this will bring error to the stress intensity determination. The crack front curve at the end of present step is updated as a new quadratic curve according to the new positions of the sampling points.

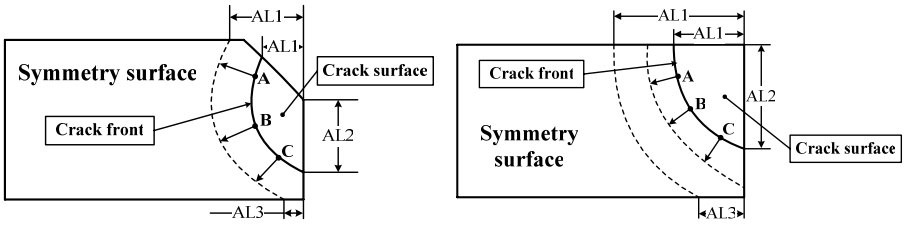

Figure 3. Crack shape and location of sampling points.

2.2.4 Criterion for the multiple crack growth

Fatigue cracks are growing cycle by cycle by their nature, but we cannot afford doing in this way in our simulation. It is possible to boost the calculation by splitting total number of load cycles into several steps. The number of cycles in each step is determined with error control. By this way the crack size increments are calculated stepwise. A criterion proposed by Zhang [11, 12] for multiple 2D crack case is adopted for the present multiple 3D cracks. All the sampling points on every crack front curve should meet the following criterion for crack size increment:

$$\Delta a_{ij} \le 2a_{ij}\left[\left(1-et\right)^{-\frac{1}{2n}} - 1\right] \tag{9}$$

where a_{ij} is the crack size at point *j* in computing step *i*, Δa_{ij} is the corresponding crack size increment, *n* is the exponent parameter in equation (1) and *et* is the error limit (normally as 0.01~0.1). Substituting equation (1) into equation (9), we obtain the upper bound of the number of load cycles:

$$\left(\Delta N\right)_{ij} = \frac{\Delta a_{ij}}{C \cdot \left(\Delta K_{ij,eff}\right)^n} \le \frac{2a_{ij}\left[\left(1-et\right)^{-\frac{1}{2n}} - 1\right]}{C \cdot \left(\Delta K_{ij,eff}\right)^n} \tag{10}$$

2.2.5 Failure criterion

The specimen is considered failing if any one of the following conditions is met: all cracks have separated its ligament (crack front approaches plate edge or the opposite hole edge or the distance between two approaching crack fronts is less than a small amount, such as 0.3mm (crack linking up)); or the average level of net section tensile stress has reached the yield strength of the material.

3. Finite element modeling technique.

3.1 FE model of fatigue crack growth

As the example to demonstrate the modeling technique of our software, consider a rectangular plate containing a central countersunk hole with both side corner cracks. As shown in Fig. 4, half-length model is used because of the symmetry of the specimen. The solid model is divided into three parts by two parallel cross sectional planes. The part including the hole is part 1 and the one next is part 2. Part 1 is re-divided into two blocks so that each crack belongs to a single block. Crack front curves are assumed quadratic. Two narrow volumes with rectangular cross section are created along each crack front (Fig. 5). A narrow volume is the crack front body used to build the mesh locally to the crack front.

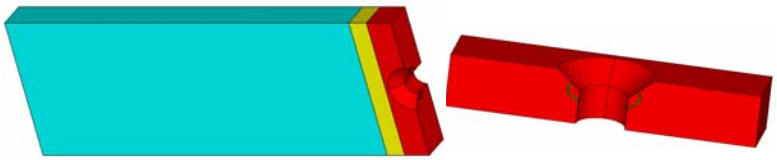

Figure 4. Model divisions

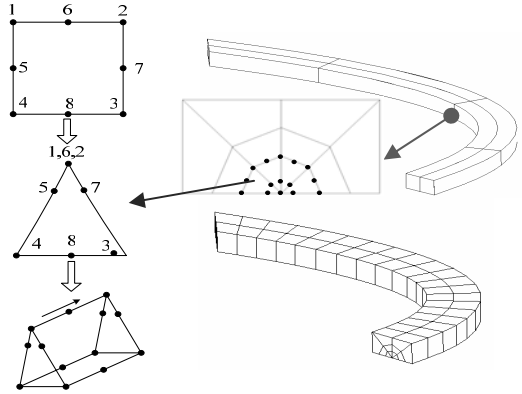

Figure 5. Finite element mesh for crack tip volumes

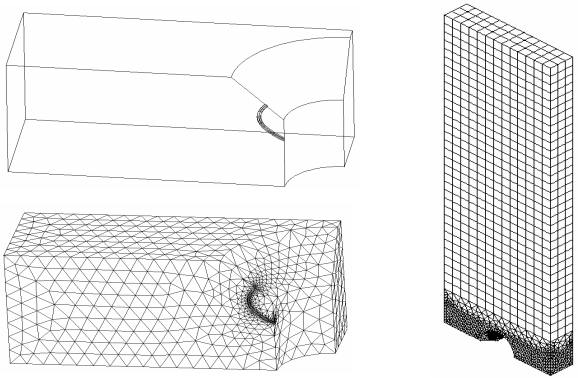

Figure 6. Finite element mesh

Cut each crack front body with three planes normal to the crack front curve, one in the middle and two others close to both ends of the body. We first mesh the cross sectional area created by the middle plane with eight-node isotropic 2D elements in which the four elements around crack tip are converted to the 8-node triangular elements by collapsing the three nodes on one of the four edges of each element to crack tip, and the mid nodes on the edges adjoining to crack tip have been moved toward crack tip to the quarter length position to produce crack tip singularity. We then sweep the area mesh both ways along the crack front to create the 3D mesh of the crack front body. The rest volume of part 1 is modeled by tetrahedron 3D elements. Part 3 is built with twenty nodes 3D elements. Part 2 is the transitional volume between part1 and part 3 and is modeled by tetrahedron 3D elements. Meshing details are shown in figure 5 and figure 6.

3.2 Considerations for the crack geometry change during remeshing

With the use of APDL language and the technique described in section 3.1, it is easy to accomplish

remeshing for the crack configuration shown in Figure 3. Nevertheless, the remeshing will fail when one of the crack front curve ends is moving across a vertex of the cross sectional area, because of the element distortion. So, “transitional zones” are specified around those vertexes for different crack scenarios, as shown in Figure 7. The radius of a transit zone is about 5~6 times of the crack tip element size (fixed as 0.2mm in our tool). If one of the crack front ends has just entered the transit zone, user defined crack front will be instead.

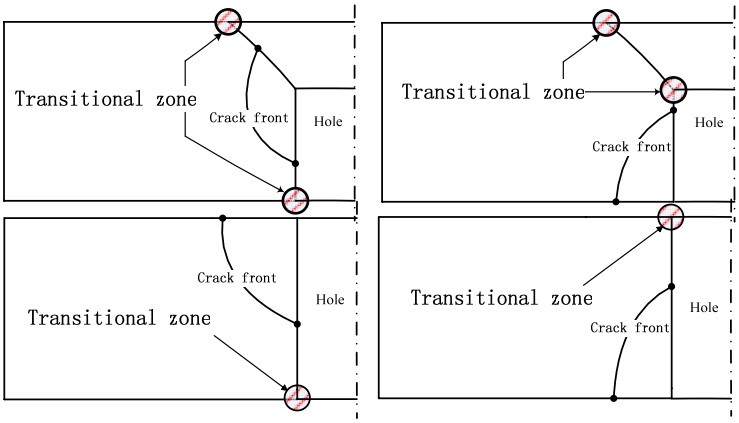

Figure 7. The transitional zones for different corner cracks from hole side

As example, corner cracks have initiated from a countersunk hole (Figure 8). There are two conditions for a crack front curve end moving across the vertex: before and after crossing. If a crack front curve end has moved in the transitional zone and has not cross the vertex, we bring the end back to the intersection point of the model boundary and the transitional zone. But the increment calculated in this step is stored and added to next step of calculation until the crack cross the vertex. In another condition that the end has passed the vertex but is still within the transitional zone, we move the end forward to the intersection point of the model boundary and the transitional zone. The two procedures make it possible to avoid element distortion and program crushing down. Simulation results shown in Figure 9 reveal that the procedures have only disturbed the form of a-n curve a little locally and not fundamentally affected the curve.

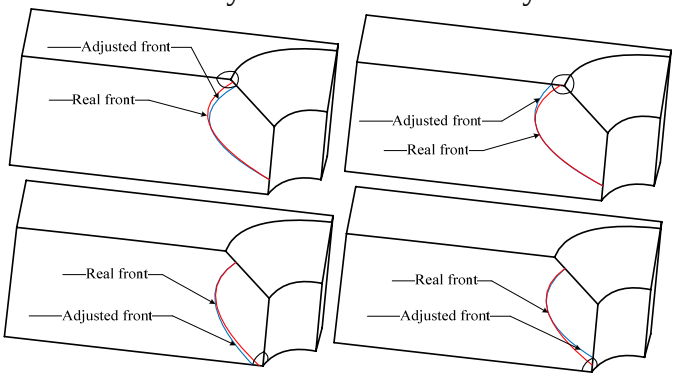

Figure 8. Crack adjustment when crossing a vertex.

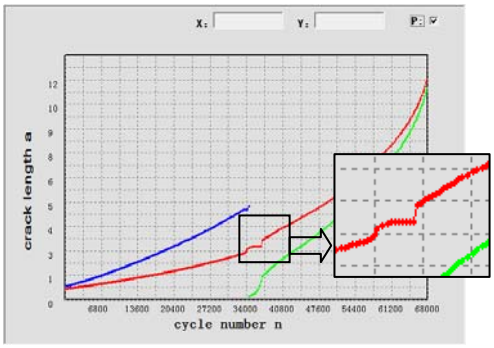

Figure 9. The effect of transitional zone treatment on a-n curves

4 User interfaces of the software.

4.1 Data preparation for the crack growth simulation.

Figure 10 shows the main interface of our software. There are two areas on the interface: the menu tree (area ①) and the operation area (area ②). Buttons for selecting models are listed on the menu tree on the left side of the interface and submenu belonging to each model can be unfolded by click on the corresponding button. The corresponding functions are then displayed on the operation area.

Parameters list on the operation area need to be input correctly. Explanations to the parameters are illstrated on the schematic diagrams at right hand side of the area.

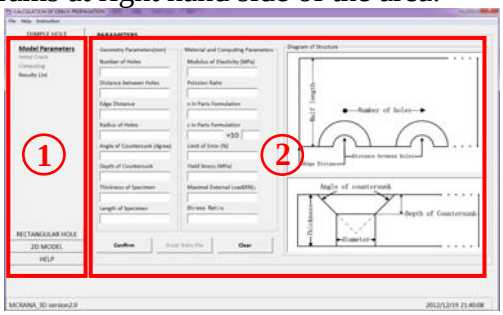

Figure 10. Main interface

Initial cracks are defined by inputing the parameterized sizes for each crack, as shown in Fig. 11. Two possible sites of crack initialization are indicated and each crack is quantified by three crack size parameters. For countersunk holes, crack located at countersink edge when the value of AL3(AR3) is zero and at the right angle edge when the value of AL1(AR1) is zero. Similarly, upper edge and bottom edge respectively for round through holes. All the three parameters for a crack are set to zero if it does not exist. Up to ten cracks are allowed in the software. A couple of crack growth equations are available. During execution, the real-time display of crack pattern can be observed on the computing window shown in Fig. 12.

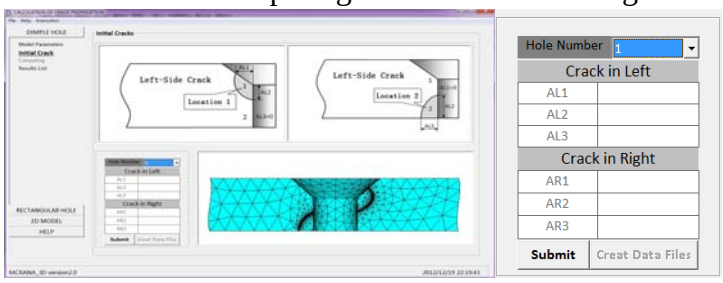

Figure 11. Interface for setting initial cracks.

Figure 12. Computing interface

4.2 Result Lists

Results are displayed in the form of data tables and curve graphs: data of parameterized crack sizes, stress intensity factors at sampling points, curves of crack sizes vs. load cycles and curves of stress intensity factors vs. crack sizes. All the data and curves can be saved as data files or image files. Figure 13 shows the examples of result display.

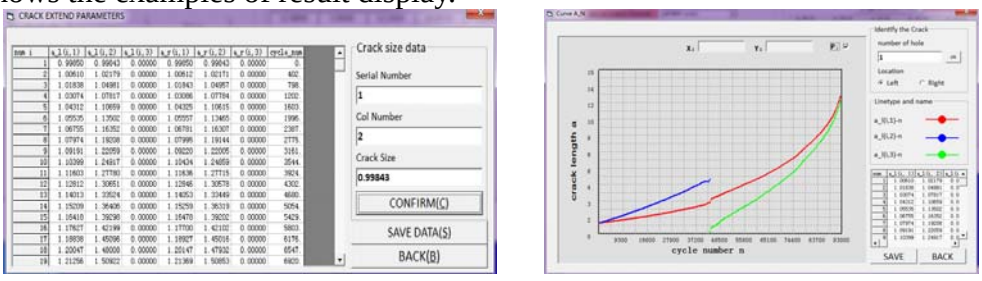

Figure 13. Two of the four interfaces of results representation

5. Simulation examples

5.1 Specimens.

Test has been carried out for the specimen with central countersunk hole, as shown in Fig. 14.

Material of the specimen is 2324-T39. The tensile strength is 8.6Mpa and the yield stress is 448MPa. The Paris law constants for 2324-T39 are $C = 2.74284\times10^{-7}$ and n=2.5269, with the units of ΔK in $\mathrm{MPa}\sqrt{\mathrm{mm}}$ and da/dN in mm/cycle.

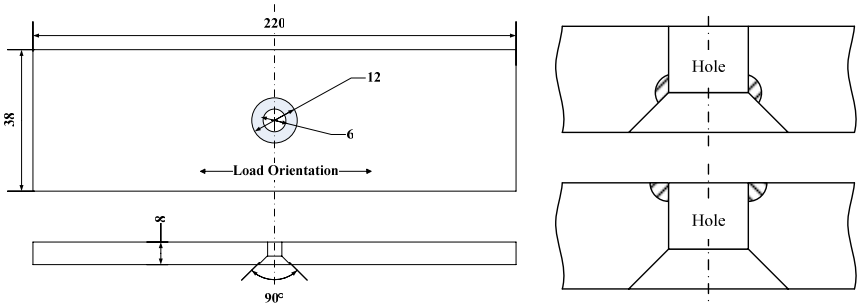

Figure 14. Specimen with a central hole and location of initial cracks.

There are two scenarios of initial cracks. Scenario 1 is double side sector-shape corner cracks from the edge of the countersunk and round through hole. Scenario 2 is the double side quarter disk corner cracks from the edge of the through-hole and back surface. The sizes of the initial cracks are listed in Table.1. The sizes of both side initial cracks are unequal for both scenarios.

Table.1 Sizes of initial cracks

Crack sizes	AL1	AL2	AL3	AR1	AR2	AR3
Model1	0.809	1.05	0	0．85	0.90	0
Model2	0	0.75	0.567	0	0.66	0.614

Constant amplitude tensile cyclic load was applied. The peak load is 26KN and the stress ratio is 0.06.

5.2 Simulation results.

Two crack growth models were used in simulation: Paris law and AFGROW model with $C_{f0} = 0.2$. Analysis was made throughout the total life of crack propagation: corner cracks - partially through the thickness cracks - fully through cracks - final failure. Figure 15 gives the testing and predicted crack growth curves for scenario 1. Figure 16 shows the images of crack growth for the scenario during the simulation. Similar results for the scenario 2 are given in Figures 17 and 18. Table 2 gives the test results and predictions for the fatigue crack growth lives. The results indicate that the software tool works well and the simulation of the Paris law is quite conservative, while the AFGROW model gives more satisfactory estimation.

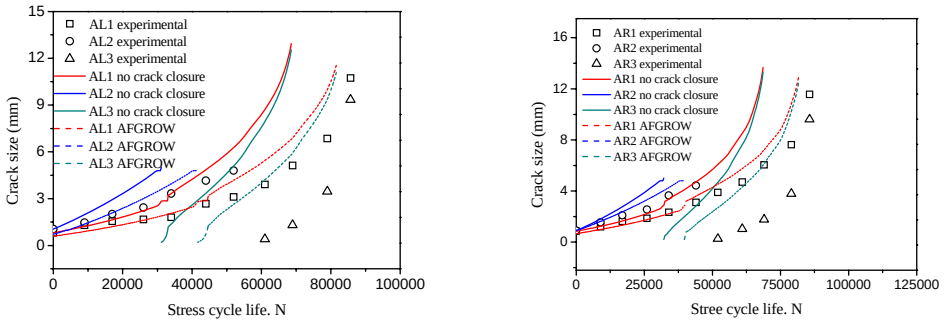

(a) (b)

Figure 15. Crack growth curves of scenario 1
(a). Left crack (b). Right crack

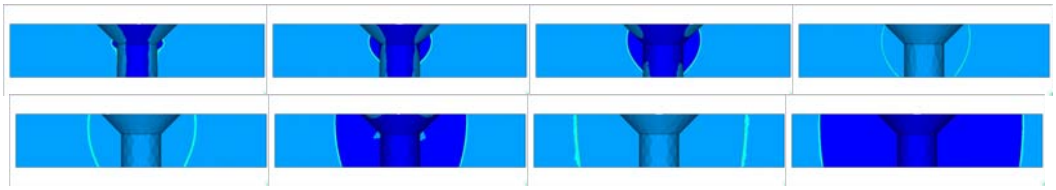

Figure 16. Images of crack growth of scenario 1

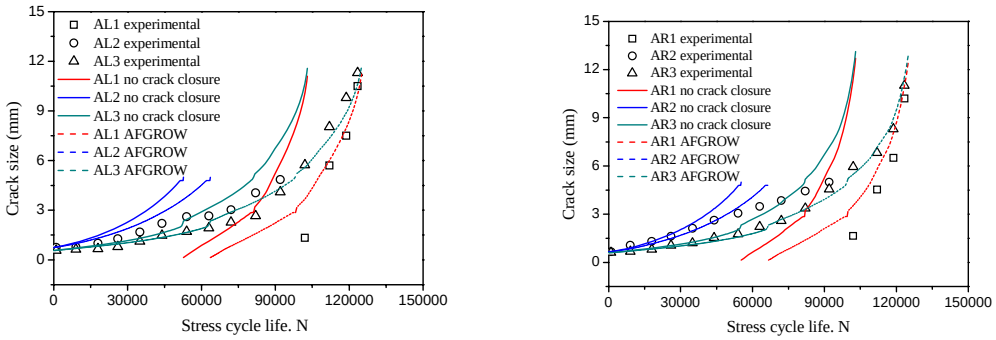

(b) (b)

Figure 17. Crack growth curves of scenario 2
(a). Left crack (b). Right crack

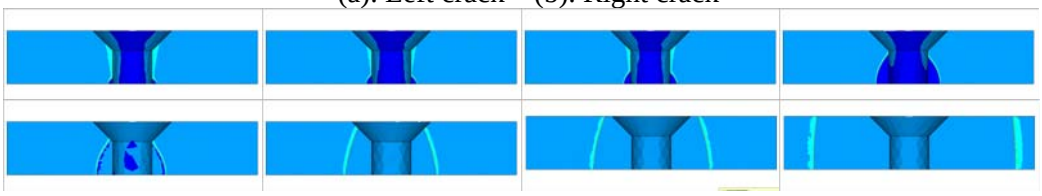

Figure 18. Images of crack growth of scenario 2

Table.2 Test and simulated results

	Crack location	Test life	No crack closure	AFGROW model
Scenario 1	countersunk side	85688	68587	81733
Scenario 2	rear side	123397	103027	125054

Further development of the tool involves extending the model type to the mechanically fastened joints through the consideration of fastener-hole contact.

6. Conclusions

A software tool has been developed using the ANSYS APDL and Visual Basic programming languages to simulate the multiple crack growth. This tool is capable of modeling metallic plate with coplanar countersunk holes or round through holes with different scenarios of multiple 3D cracks. 2D modeling function for through cracks is also available in our tool. Parameterized modeling is used to facilitate the pre-processing procedure. The Paris-form crack growth law and two crack closure models are included in the software. As the output of the execution, the lists of stress intensity factors and the curves of crack sizes vs. load cycles can be obtained. A useful function of our tool is the real-time visualization of the crack geometries during crack growth simulation. The results of example calculations indicate that the simulated crack growth behavior and fatigue growth lives agree well with the experimental results.

Acknowledgement

The research of this paper is a part of the project funded by Shanghai Aircraft Design and Research

Institute of COMAC.

References

[1] P. C. Paris, F. Erdogan. A critical analysis of crack propagation laws. J Basic Engng 1960, 85:528-34.
[2] Elber W. The significance of fatigue crack closure. Damage tolerance in aircraft structures. ASTM STP 1971, 486:230–42.
[3] Schijve J. Fatigue of structures and materials. Kluwer Academic Publishers, 2001.
[4] D. S. Dawicke and J. C. Newman, Jr. Analysis and prediction of multiple-site damage (MSD) fatigue crack growth, 1992, NASA-TP-3231.
[5] S. Pitt, R. Jones. Multiple-site and widespread fatigue damage in aging aircraft, Engineering Failure Analysis, 1997, 4(4): 237-257.
[6] R. M. V. Pidaparti, M. J. Palakal, Z.A. Rahman. Simulation of structural integrity predictions for panels with multiple site damage, Advances in Engineering Software, 2000, 31: 127-135.
[7] D. A. Cope, T. E. Lacy. Stress intensity determination in lap joints with mechanical fasteners, The 41th AIAA/ASME/ASCE/AHS/ASC Structures, Structural Dynamics and Materials Conference and Exhibit, 2000.
[8] F. S. Lucas, J. P. M. Goncalves, F. M. F. Oliveira. Multiple-site damage in riveted lap-joints: experimental simulation and finite element prediction [J]. International Journal of Fatigue, 2000, 22: 319-338.
[9] H. J. Shen, W. L. Guo. 3D finite element analysis of SIF of the structure with dimple hole [J]. Acta Aeronautica et Astronautica Sinica, 2002, 23(2): 106-110 (In Chinese)
[10] S. A. Fawaz, B. Andersson. Accurate stress intensity factor solutions for corner cracks at a hole, Engineering Fracture Mechanics, 2004, 71: 1235-1254
[11] C. S. Wang. A study on prediction of MSD occurrence probability and residual strength/crack growth for typical structures. Dissertation of Beijing Beihang University, 2006: 69-71 (In Chinese)
[12] J. Y. Zhang, et al. Crack growth life estimating for MSD panel. Advanced Materials Research, 2008, 33(37): 175-180.
[13] X. Wang, M. Modarres, P. Hoffman. Analysis of crack interactions at adjacent holes and onset of multi-site fatigue damage in aging airframes, Int J Fract, 2009, 156: 155-163
[14] C. Y. Park, A.F. Grandt Jr., J. J. Suh. Stress intensity factors for surface cracks at countersunk holes, Engineering Fracture Mechanics, 2006, 73: 1878-1898
[15] M. F. Zhang. Durability and damage tolerance design manual of commercial aircraft structures: Damage tolerance design and analysis. Beijing: Aviation Industry Press, 2003. (In Chinese)
[16] Y. Q. Zhou, S. N. Wang. A variable optimization method-A new technique for multiple crack growth analysis in structure details. Acta Aeronautica et Astronautica Sinica. 1995, 16(2): 178-181 (In Chinese)
[17] AFGROW manual, Air Vehicles Directorate, US Air Force, 2006.
[18] J. A. Harter. Comparison of contemporary FCG life prediction tools. Int J Fatigue 1999; 21: 181-5.

Residual Stresses Induced by Surface Enhancement Processes

Yukui Gao*, Zheng Zhong
College of Aerospace Engineering and Applied Mechanics, Tongji University, Shanghai 200092, China
* Corresponding author: yukuigao@tongji.edu.cn

Abstract The residual stress field caused by shot peening, hole cold expansion, laser shock peening and ultrosonic peening were presented and the influence of residual stresses on fatigue properties were investigated. The results show that shot peening can enhance the fatigue property, especially for high strength alloys. Moreover, hole cold expansion can increase the fatigue strength more than shot peening due to deeper residual compressive stress fields in surface strained layer and smoother surface. Laser shock peening and ultrasonic peening are the high intensity peening processes and can induce both the deeper residual compressive stress layer and the fine microstructure in surface strained layer, therefore they should have more important engineering applications in future.

Keywords residual stress, shot peening, hole cold expansion, laser shock peening, X-ray diffraction

1. Introduction

The weight objectives and aggressive performance are driving components made of advanced high strength materials and manufactured by some special surface enhancement processes to induce compressive residual stress. There are many surface enhancement processes that can introduce beneficial residual stress and improve fatigue property in localized, but critical areas. Shot peening is used on components of almost any shape due to its flexibility. Hole cold expansion is mainly employed to increase the fatigue strength and prolong fatigue life of parts with holes. Laser shock peening (also called as laser peening or shot peening) was originally developed in aeronautical industry to increase the resistance of foreign object damage (FOD) of blades, and then was employed to improve fatigue property of components with or without FOD and corrosion resistance of engine key parts (for example blisks and obturating ring). Ultrasonic peening was used to induce compressive residual stress and get fine microstructure in welded components.

Residual stress is stress present in a structure or component without any external load or any external moment and keeps itself balance. Residual compressive stress always occurs with residual tensile stress. The significance of residual stresses for fatigue is important in various practical problems. Unintentional tensile residual stress can have an adverse effect on fatigue performance, while beneficial compressive residual stress can significantly improve fatigue resistance.

Fatigue cracks generally starts at the free surfaces of components. As a consequence, the surface conditions are most significant for the fatigue behavior of a structure [1-4]. Surface enhancement to improve the fatigue resistance was developed a long time ago and now is still developing toward the high energy, deep surface layer, and complex treatments. Surface integrity is defined as surface conditions and functions for perfect or enhanced component surface and residual stress is the main aspect of surface integrity. Surface enhancement processes improve the fatigue property, stress corrosion cracking resistance and wear mainly by modifying surface integrity. Residual stress plays the important role in increase the resistance of fatigue and stress corrosion cracking.

There are many investigations on measurements and simulations of residual stresses and the role of residual stresses on fatigue crack initiation and propagation behaviors, while there are few quantitative studies on residual stress effects on fatigue strength/limits or fatigue life. Many scientific questions are not well answered and some phenomena cannot be reasonably explained. It is well known that fatigue crack usually starts subsurface where maximum tensile residual stress is for the surface enhanced specimens and fatigue strength is increased, then why can residual tensile stress improve fatigue resistance? Therefore, we should consider the influence of residual stresses on fatigue property in the view of both mechanics and materials science or other theories.

This paper focus on residual stress fields induced by surface enhancement processes and gives a brief review on the role of residual stress in the fatigue crack initiation and propagation behavior based on our many investigations.

2. Residual stress field characteristics and its effects on fatigue property for surface enhanced specimens

2.1. Residual stress field features induced by surface enhancement processes

It is important to obtain the residual stress field features before analyzing the effects of residual stress on fatigue performance. Many surface enhancement processes induce compressive residual stress in surface layer by elastic-plastic deformation, so the residual stress distribution in a material is often as a result of the retained strain of inhomogeneous plastic deformation. It should be pointed out residual stresses discussed here occur just on the macroscale. On a much smaller scale, another kind of residual stress can be present. It is well known that plastic deformation on a microscale is not a homogenous process and mainly induced by dislocation slips or twins or kinks which depend on deformation strain and strain rate as well as the tested material. Therefore, it is different from grain to grain, and even inside a single grain, the plastic deformation may be just concentrated into a few slip bands. The microresidual stresses are significant for explaining fatigue mechanism although it is not easy to obtain the precise and accurate values unless the deformation mechanism is clear. The characteristics of residual stress field induced by surface enhancement processes were briefly described as follows.

(1) Shot peening

Shot peening is a well-known process to introduce favorable residual stresses at the material surface of a component. This process plastically stretches the surface layer of a material and the elastic substrate material restrains this plastic deformed surface layer, therefore, residual stresses are induced. A typical residual stress field caused by shot peening is illustrated in Figure 1 and some parameters were proposed to analyze the characteristics of residual stress field by shot peening.

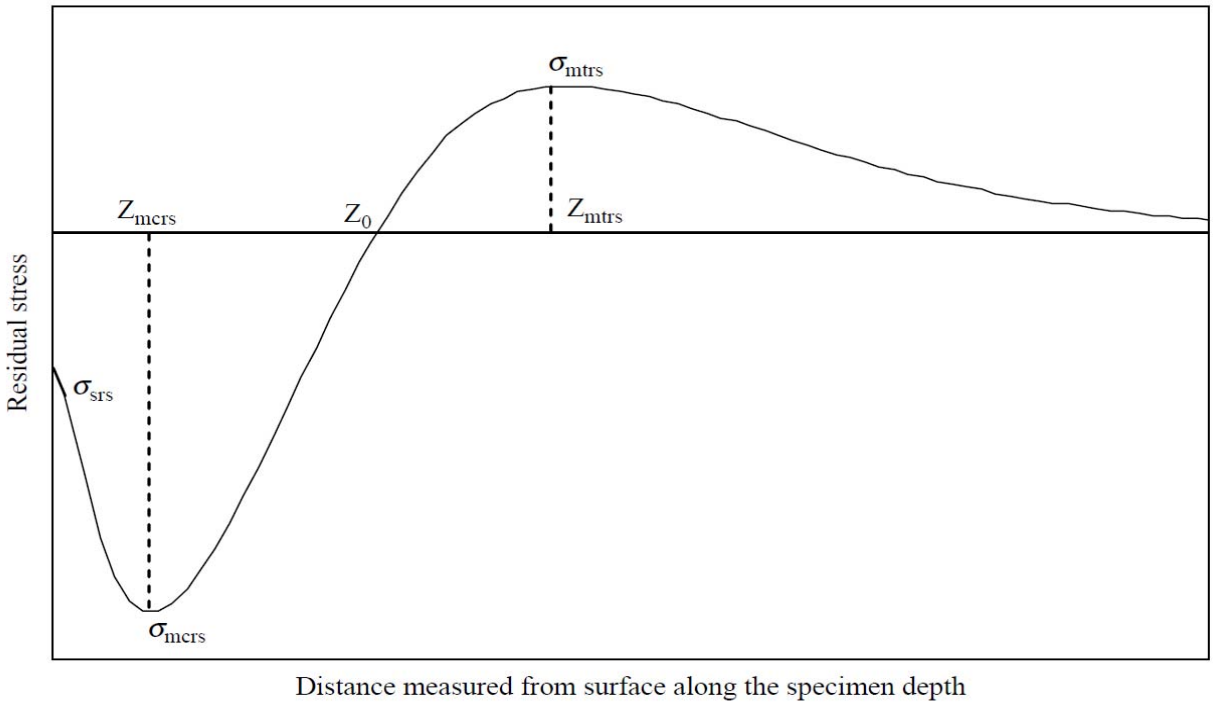

Fig. 1 Schematic residual stress field caused by shot peening

There are six parameters to show the residual stress distribution shown as in the Figure 1. σ_{srs} is the residual stress at the surface or call it as surface residual stress. σ_{mcrs} is the maximum compressive residual stress and its value is often more than half yield strength even in some cases near the yield strength for fcc crystalline metals but it is usually near the surface in the most cases. σ_{mtrs} is the maximum tensile residual stress its value is the order of tenth to half of the value of σ_{mcrs}, this

depends on the thickness of specimens. Z_{mcrs} is the distance from surface where compressive residual stress is the maximum. Z_0 is the depth where residual stress becomes zero and beneath where residual stress will change from compressive to tensile. Z_{mtrs} is the distance from surface where tensile stress is the maximum one. The values of these parameters are related to shot peening process parameters (such as shot peening intensity, surface coverage, shot's size and hardness etc.) and the peened material. The relationship of the values of these parameters to process parameters and material's property is given in the references [5, 6].

(2) Hole cold expansion

Hole cold expansion has been developed to increase fatigue resistance of components with holes. The hole is firstly drilled to a slightly undersized one which is a few percent smaller than the design size. Then a tapered pin or a split sleeve over a mandrel pulled through the hole to expand material around hole. As a result, plastic deformation occurs and the plastic zone has been stretched tangentially because it pushed outwards in the radial direction. The plastic zone has a larger diameter than before and the elastically strained material around this plastic zone will exert a pressure on the plastic zone, therefore tangential compressive stresses around the hole are introduced. The values of residual stress depend on the interference of hole to the tapered pin or the thickness of split sleeve over mandrel as well as the cold expanded material. A typical residual stress distribution along the cold expanded hole is given in Figure 2 [7].

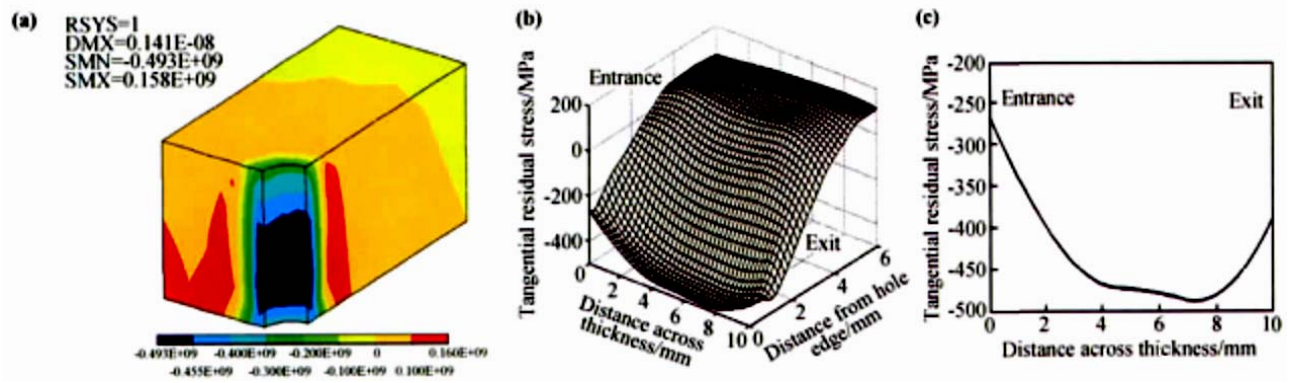

Fig.2 Tangential residual stress distribution of hole cold expanded 7050-T7451 aluminum alloy in (a) the whole component, (b) smallest cross-section plane and (c) hole edge along thickness [7]

The maximum compressive residual stress is not at the upper entrance surface or lower exit surface but the middle surface near exit surface. Moreover, the residual stress at entrance surface is less than one at the exit surface. Therefore, the 2-D residual stress could result in significantly under or overestimating fatigue life.

(3) Laser shock peening

Laser shock peening exposes the surface of a workpiece to laser pulses with pulse duration in the nanosecond range and obtains a modified surface layer on the order of millimeters. A typical residual stress distribution caused by laser shock peening is shown in Figure 3. The values of residual stresses depend on process parameters and peened material. The main parameters are pulsed energy, pulsed times and pulse duration. The mechanisms of deformation which occur in plastic shock wave deformation are highly dependent on the strain rate. It is well known that twin formation becomes particularly relevant as strain rate grows. Deformation is strongly determined by stacking fault energy, which constitutes a measure of the probability of cross slip of screw dislocations. Moreover, it is should be noted that any kind of thermal manipulation must be avoided; otherwise it will induce tensile residual stress. Consequently, the absorption layer must be thick enough to prevent thermal effects on the workpiece itself, and particularly in cases of overlapping irradiation, the absorbing layer should not have sustained damage that may result in thermal effects on the workpiece during the final irradiation. There are some differences in the values of residual stresses for different pulse times for easy plastic-deformation alloy as shown in Figure 3.

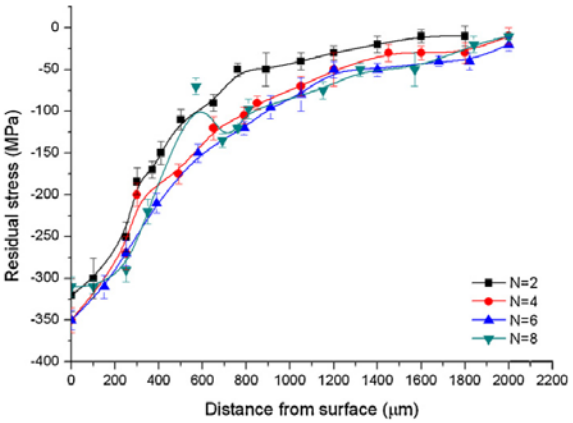

Fig.3 Residual stresses caused by laser shock peening in 7050-T7451 aluminum alloy [8]

(4) Ultrasonic peening

Ultrasonic peening induces deeper residual stress surface layer than conventional shot peening [9], as illustrated in Figure 4. Compared with shot peening, the value of surface residual stress for ultrasonic peened specimens is almost same as shot-peened one, while the maximum residual stresses of compressive and tensile are larger than shot-peened ones.

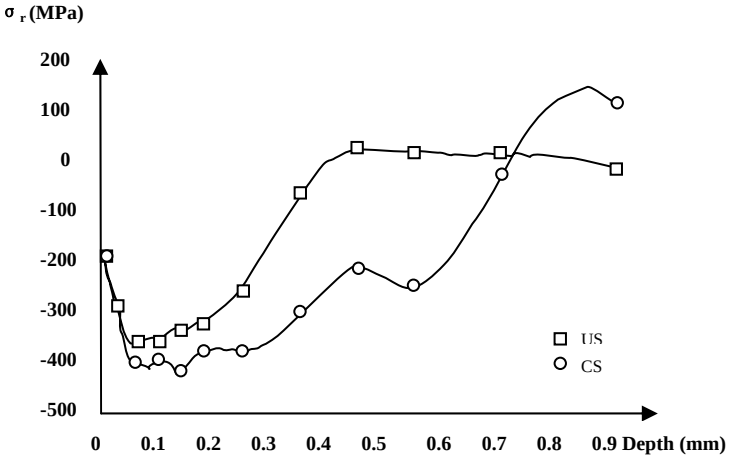

Fig.4 In-depth profile of residual stress in 2014-T6 aluminum alloy produced by conventional shot peening (CS) and ultrasonic peening (US) [9]

2.2. Effects of residual stress on fatigue crack initiation behavior

There are many investigations on residual stress on fatigue performance, and now we just provide some results of our studies. The rotating bending fatigue tests (stress ratio R=-1) were conducted for some aeronautical metallic materials including high strength steels, aluminum alloys, and titanium alloys. A total of 20 specimens were tested as a group to determine the fatigue strengths/limits for each alloy at 1×10^7 cycles by staircase method [10]. The experimental results are shown in Table 1. The apparent or nominal fatigue strength or limit, σ_{app}, is determined by the applied stress range, σ_a, for rotating bending fatigue tests. The local strength or limit, σ_{loc}, is calculated as the critical stress for fatigue crack initiation by combing the local applied stress, σ_{locapp}, with the local residual stress, σ_{locrs}, that is $\sigma_{loc} = \sigma_{locapp} + \sigma_{locrs}$. Moreover, the effect of surface enhancement is illustrated in the fatigue strengthens/limits increase of surface-enhanced specimens compared with unenhanced ones by as given in Table 1. The fatigue crack sources were determined by scanning electron microscope (SEM) and the locations of fatigue crack sources were determined by the distance from surface [11]. Some typical fatigue crack sources are shown in Figure 5. The fatigue crack sources always locate at the surface for unenhanced specimens, whereas for those surface-enhanced ones,

they are located beneath the surface-enhanced layer where residual stress is tensile.

Table 1 Rotating bending fatigue strengths/limits of high strength aeronautical structural materials

Material	Surface condition	σ_{app}/MPa	σ_{loc}/MPa	σ_{sur}/MPa	σ_{int}/MPa	$\sigma_{int}/\sigma_{sur}$
40CrNi2SiMoVA steel	Machining	718	750	750	1065	1.42
	Shot peening	1040	1065			
16Co14Ni10Cr2Mo steel	Machining	720	720	720	966	1.34
	Shot peening	835	966			
0Cr13Ni8Mo2Al steel	Machining	763	738	738	997	1.35
	Shot peening	887	997			
2121-T851 aluminum alloy	Machining	160	160	160	224	1.40
	Shot peening	206	224			
7050-T7451 aluminum alloy	Machining	185	185	185	261	1.41
	Shot peening	223	252			
	Laser peening	263	261			
7475-T7351 aluminum alloy	Machining	170	150	150	206	1.37
	Shot peening	202	206			
TC21 titanium alloy	Machining	420	400	400	560	1.40
	Shot peening	550	560			
Ti60 titanium alloy	Machining	416	430	430	594	1.38
	Shot peening	580	594			

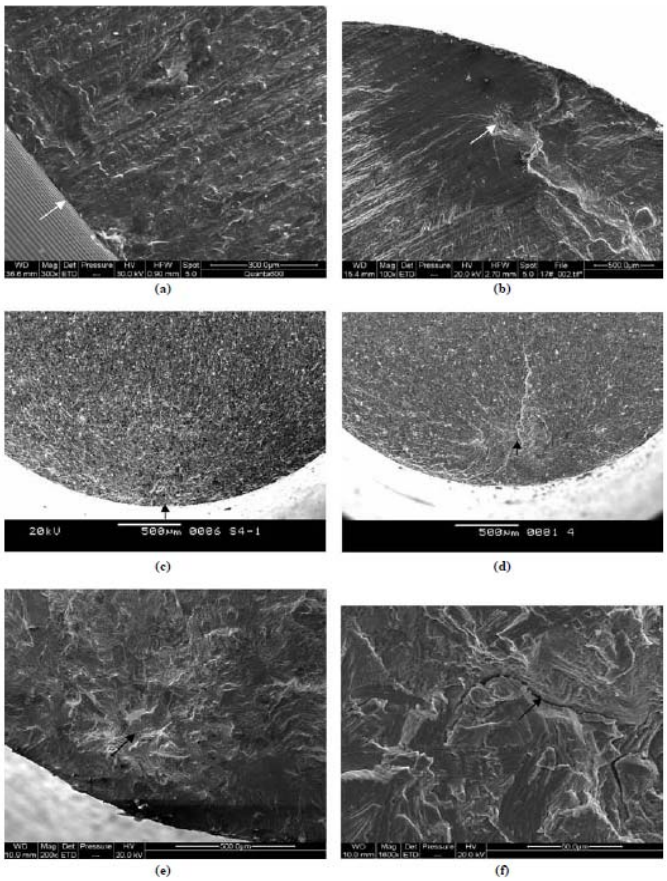

Fig.5 Typical fatigue crack sources (a) Machined specimens of 7050-T7451 aluminum alloy, (b) shot-peened specimens of 7050-T7451 aluminum alloy, (c) machined specimens of Ti60 titanium alloy, (d) shot-peened specimens of Ti60 titanium alloy, (e) shot-peened specimens of TC21 titanium alloy, (f) fatigue cracks in the fatigue crack sources of shot-peened specimens of TC21 titanium alloy

2.3. Influence of residual stress on fatigue crack propagation performance

The effect of shot peening on small crack growth was investigated in a 7475-T7351 aluminum alloy [12]. A single edge notch tensile specimen was employed and the notches were shot peened. Small crack growth fatigue testing was performed in an MTS fatigue tester using constant amplitude loading (stress ratio R=0.06 and maximum stress σ_{max} =160MPa) in a frequency of 10Hz at room temperature under laboratory air conditions. The plastic replica method was used to record small crack data at the notch root. To acquire accurate small crack lengths, acetyl cellulose plastic replicas (often called AC paper) were employed to monitor the small crack length as a function of the number of load cycles. Stress intensity factors for small cracks subjected both to external loads and to shot peening induced residual stresses were determined using weight function methods [12, 13]. The fatigue small crack growth rate was analyzed by FASTRAN software [14] and the crack propagation behavior of unpeened and shot-peened specimens is shown in Figure 6 and Figure 7, respectively.

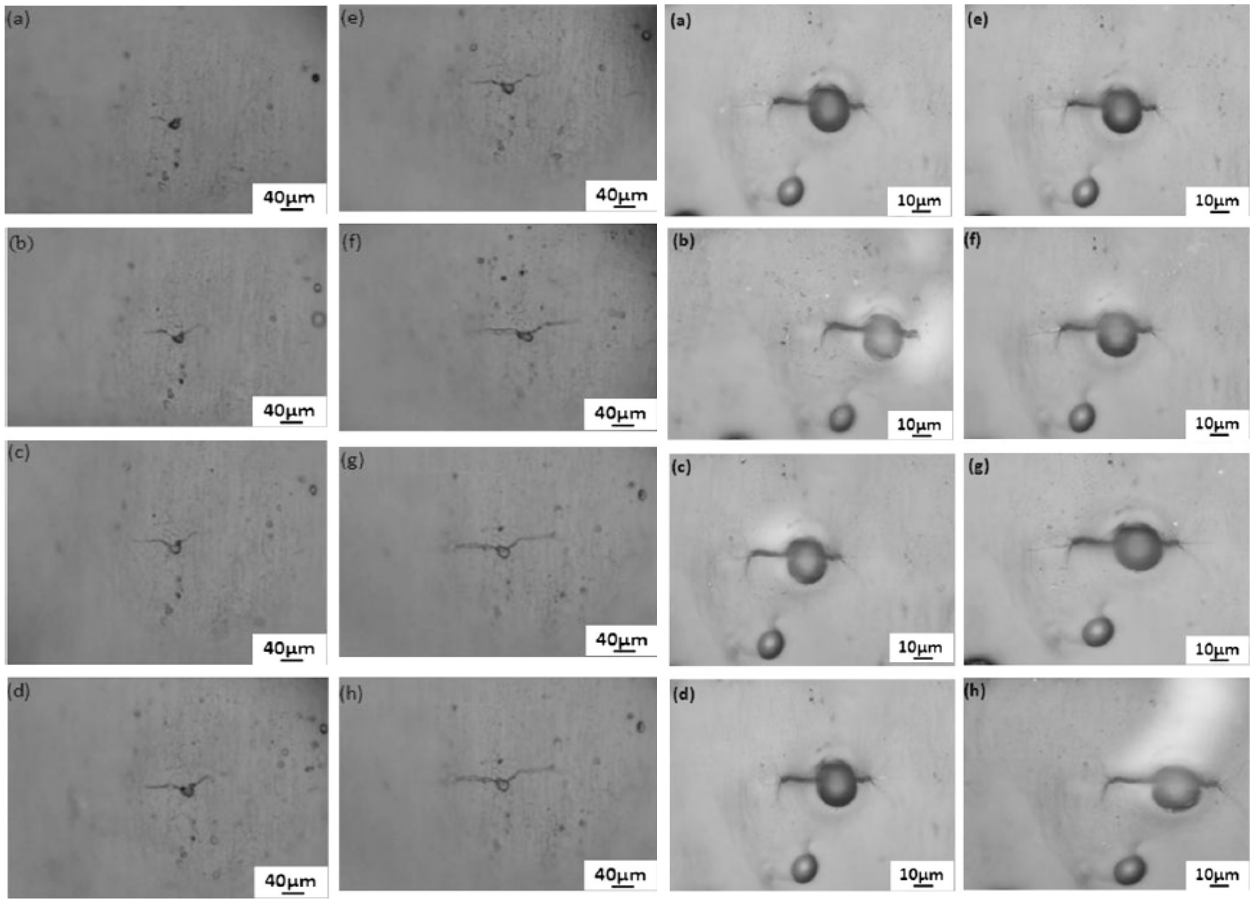

Fig.6 Replica SEM images showing small crack growth in an unpeened specimen of 7475-T7351 aluminum alloy for N cyles: (a) N=3000, (b)N= 6000, (c) N=9000, (d) N=10000, (e) N=11000, (f)N=13000, (g) N=15000, (h) N=18000. Finial failure occurred at 28000 cycles.

Fig.7 Replica SEM images showing small crack growth in an peened specimen of 7475-T7351 aluminum alloy for N cyles: (a) N=6000, (b)N= 7000, (c) N=8000, (d) N=10000, (e)N=12000,(f) N=14000, (g) N=16000, (h) N=19000. Finial failure occurred at 84000 cycles.

Compared with unpeened specimens, the small crack growth rates are very much lower for shot peened specimens. It is obvious that the small crack growth will show lower curves rate than large one if the residual stress effect is not considered, while it is normal rate if the effect of residual stress is considered, as shown in Figure 8. Therefore, the influence of residual stress on fatigue crack propagation behaviors or growth rates should be considered.

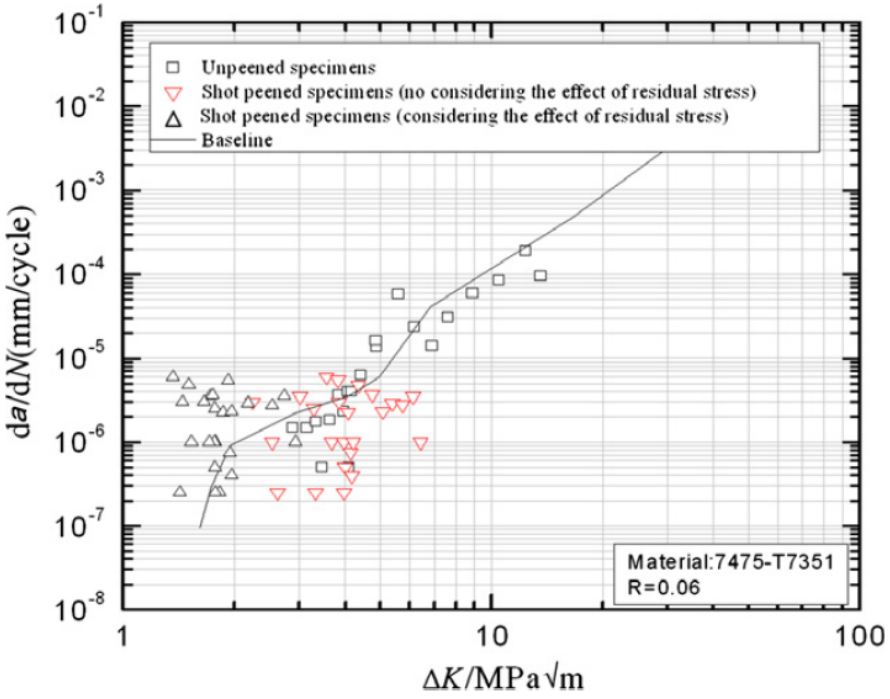

Fig.8 da/dN-△K curves for 7475-T7351 aluminum alloy

3. Conclusions and Recommendations

Residual stress has a significant effect on fatigue, stress corrosion cracking and other fracture performances. The residual stress distribution should be investigated quantitatively by experimental measurements or simulations and obtain the three dimensional characteristics.

(1) Surface enhancement processes introduce compressive residual stresses in surface layer and there are some parameters to describe the features of residual stress fields caused by surface enhancement treatments.

(2) Compressive residual stress can be measured by X-ray diffraction or neutron scatting and simulated by finite element methods or boundary element methods, therefore its effects on fatigue and fracture can be analyzed quantitatively.

(3) The fatigue crack can be initiated beneath compressive residual stress filed for surface enhanced specimens and the effect of residual stress should be considered both in the view of mechanics and materials science. Fatigue strengths/limits are increased by compressive residual stresses and surface cold worked layer for surface enhanced specimens.

(4) Fatigue crack growth rate is lower in the compressive residual stress filed for surface enhanced specimens compared to unenhanced ones; the effect of residual stress can be quantitatively analyzed by weight function methods and FASTRAN software.

References

[1] Dale L. Ball, The influence of residual stress on the design of aircraft primary structure, Journal of ASTM International, 5(2008):1-17.

[2] Volker Schulze, Modern Mechanical Surface Treatment, Wiley-VCH, Weinheim, 2006.

[3] Pietro Paolo Milella, Fatigue and Corrosion in Metals, Springer, 2013.

[4] Jeffrey O. Bunch, M. R. Mitchell, Residual stress effects on fatigue and fracture testing and incorporation of results into design, ASTM International, PA, USA, 2007.

[5] Yu-kui Gao, Bending fatigue strengths/limits of smooth specimens with and without surface-enhanced layer of aeronautical metallic alloys, International Journal of Structural Integrity,

2(2011):357-365.
[6] Yu-kui Gao, Mei Yao, Jin-kui Li, An analysis of residual stress fields caused by shot peening, Metallurgical and Materials Transactions A, 33A(2002): 1775-1778.
[7] Liu Xiao-long, Gao Yu-kui, Liu Yun-tao, Chen Dong-feng, 3D finite element simulation and experimental test on residual stress field by hole cold expansion, Journal of Aeronautical Materials, 31(2011):24-27.
[8] Y.K. Gao, Improvement of fatigue property in 7050-T7451 aluminum alloy by laser peening and shot peening, Materials Science and Engineering A, 528(2011):3823-3828.
[9] J. Lu, P. Peyre, C. Oman Nonga, A. Benamar, J. Flavenot, Residual stress and mechanical surface treatment, current trends and future prospects, Proceedings of the 4th International Congress on Residual Stresses (ICRS), Maryland, USA, 1994:1154-1163.
[10] S.K. Lin, Y.L. Lee, M.W. Lu, Evaluation of the staircase and the accelerated test methods for fatigue limit distributions, International Journal of Fatigue, 23(2001):75-83.
[11] Yu-kui Gao, Xiang-bin Li, Qing-xiang Yang, Mei Yao, Influence of surface integrity on fatigue strength of 40CrNi2Si2MoVA steel, Materials Letters, 61(2007):466-469.
[12] Y.K. Gao, X.R. Wu, Experimental investigation and fatigue life prediction for 7475-T7351 aluminum alloy with and without shot peeing-induced residual stresses, Acta Msterialia, 59(2011):3737-3747.
[13] X.R.Wu, A.J. Carlsson, Weight functions and stress intensity factor solutions. Pergamon Press, Oxford, 1991.
[14] Newman JC, FASTRAN-2: a fatigue crack growth structural analysis program, Technical memorandum 104159, NASA, Langley Research Center, Virginia, USA, 1992.

3D FE analysis of shot peening of strain-rate sensitive materials Accounting for Multiple and Repeated Impingement

Shaker A. Meguid[1,*], Fan Yang[1], Chen Zhuo[1], Mario Guagliano[2]

[1]Mechanical and Aerospace Design Laboratory, University of Toronto, Toronto ON M4Y 1R5, Canada
[*]Corresponding author: meguid@mie.utoronto.ca
[2]Dipartimento di Meccanica_Politecnico di Milano, Via La Masa, 1, 20156 Milano, Italy

Abstract This paper is devoted to the investigation of the shot-peening process using 3D finite element (FE) model of multiple impingement. In this analysis, we implement a novel ‘‘symmetry cell’’ approach to examine the impact effect of a large number of rigid and deformable shots on a high-strength steel target made from AISI 4340. Dynamic elasto-plastic simulations were conducted using a rate sensitive material model. A number of convergence tests, which account for element size and stiffness of contact elements, were carried out. In addition, efforts were devoted to determine the appropriate material damping parameters needed to dampen unwanted numerical oscillations associated with the explicit solver of LS-DYNA for this class of problems. The model was used to predict the effect of peening coverage upon the mechanically induced residual stress field for rate sensitive materials under multiple and repeated impacts.

Keywords Shot-peening, Multiple impacts, Residual stress, Finite elements, Rate sensitive

1. Introduction

Shot-peening is a cold-working process accomplished by bombarding the surface of the component with small spherical shots made of hardened cast-steel, conditioned cut-wire, glass or ceramic beads at a relatively high impingement velocity (40–70 m/s). It is used mainly to improve the fatigue life of metallic components [1]. During impingement, a plastic indentation surrounded by an elastic zone is formed. After contact between the shot and the target has ceased, the elastically stressed region tends to recover to the fully unloaded state, while the plastically deformed region sustains some permanent deformation. This inhomogeneous elasto-plastic deformation results in the development of a compressive residual stress field in the exposed upper most layers. To maintain equilibrium in the peened component, a tensile residual stress field is developed in the depth of the component. The mechanically induced surface compressive residual stresses have been found to be highly effective in enhancing the fatigue resistance of critical load bearing components.

The effectiveness of the peening treatment depends, to a large measure, on the peening intensity and the peening coverage. Peening intensity is a measure of the consistency of the treatment and of the plastic dissipation of the impinging shots. Peening coverage, on the other hand, is a measure of the obliteration of the original surface texture and can be defined as the ratio of the area covered by peening indentations to the total exposed surface area. Intensity and coverage depend on numerous variables, including work-piece characteristics, shot characteristics, flow conditions, stand-off distance and exposure time.

Direct residual stress measurements inside the compressed layer are expensive, time consuming, and requires the use of semi-destructive methods. Therefore, the modelling of the shot-peening process has received increasing attention from the scientific community. Several issues have emerged and received extensive investigations about modelling and simulations of multiple impact collisions. The first is concerned with the use of static or dynamic analysis to treat the peening process. Several contributions were made using quasi-static analysis [2-5]. However, some investigations [6-8] have shown that the indentation shape and residual stress distribution caused by static compression are different from those caused by dynamic impact. For example, according to

Kobayashi et al. [8], tensile residual stresses were developed at the centre of the indentation as a result of dynamic impact, while the residual stress caused by static compression is approximately zero at the centre of indentation. Therefore, more realistic approach must be considered to analyze the impact-related phenomena caused by shot-peening. The dynamic modelling of a single shot was initially conducted by Johnson [9] using a pseudodynamic approach, in which only the inertial properties of the shot was taken into account. More work used explicit solvers to model the dynamic process. This includes the contributions made by Klemenz et al. [10], Gariépy et al. [11] etc.

The second issue of simulation is how to model the shot-peening process that involves a large number of impact events. Some authors investigated single or twin shot impacts. For example, Edberg et al. [12] carried out dynamic FE analysis of a single shot on both viscoplastic and isotropic elasto-plastic targets. More and Kulkarni [13], Hong et al. [14] investigated the residual stress patterns from a single shot simulation. Meguid et al. [15,16] examined the effects of shot and target parameters upon the plastic zone development and induced residual stresses from both single and twin shot impacts. Despite the importance of the analysis of single and twin shot impacts to the understanding of the phenomena involved, modelling of the entire peening process should lead to more accurate results. Schiffner and Helling [17] used a simplified approach to model quasi-static target behaviour using time-dependent load functions obtained from the dynamic axisymmetric FE analysis of the impact of a single spherical shot. Their results showed that the influence of adjacent shots cannot be ignored. Meguid et al. [18] developed an enhanced symmetry cell to describe the high-density multiple impacts, and compared the predicted average residual stresses inside the target to experimental measurements using the holedrilling technique. Recently, Mylonas and Labeas [19], Sheng et al. [20] carried out 3D analysis implementing a large number of random shots. Kim et al. [21] investigated the residual stress for multiple shots at oblique impinging angles.

Another issue is to model the effect of the highly localized strain rates involved in the shot-peening process during impingement and rebounding of the jet stream. Some work modeled the target as rate insensitive materials [12,14,16]. However, for many real materials, dynamic analysis accounting for both inertia and rate effects would be essential. Meguid et al. [18] showed that using rate insensitive and rate sensitive material models would lead to different residual stress and plastic strain distributions. Strain rate dependent material was then used to model the target in the work by Kim el al. [21]. In this paper, we provide a 3D FE analysis of shot-peening process using a multiple impingement model for strain-rate sensitive targets and rigid shots. The residual stress distribution was analyzed and the effect of the peening coverage was investigated.

2. Finite element modelling

2.1. Configuration and boundary condition

The investigated situation is that a large number of identical shots impinge a metallic target at normal incidence. In this case, the effect of the boundary of the target can be considered negligible at the centre of the area examined. This has led us to the use of a symmetry cell, which would reduce the modelling considerably. The dimensions of the proposed symmetry cell are $C \times C \times H$, where C is the distance between adjacent shots in one row and H is the cell height, as outlined in Figure 1. The selected cell depth should be large enough to prevent interference from the boundary, while be small enough to maintain reasonable computational time. The single and twin shot impact

results published earlier in Refs. [14,16] indicate that a height no smaller than 4*R* is suitable for the different shot velocities examined in these papers. Here *R* is the shot radius taken as 1.0 mm. For the current multiple-indentation problem $H = 4R$. The distance *C* can be changed to get different peening intensity.

Symmetry boundary conditions were used at the four side faces of the cell. In addition, all displacements of the cell bottom were restrained. To provide a greater degree of accuracy, full eight-node integration was used. The mesh near the impinging locations was refined. All shots were identically modelled as rigid body discretized using eight-node brick elements with a coarser mesh density. Convergence tests were conducted using different meshes. The convergence test results indicated that the mesh depicted in Figure 1(b) was capable of representing the peening process in a cost-effective manner, as measured by the marginal difference in the maximum residual stress results. Accordingly, this mesh was used for the remainder of the study.

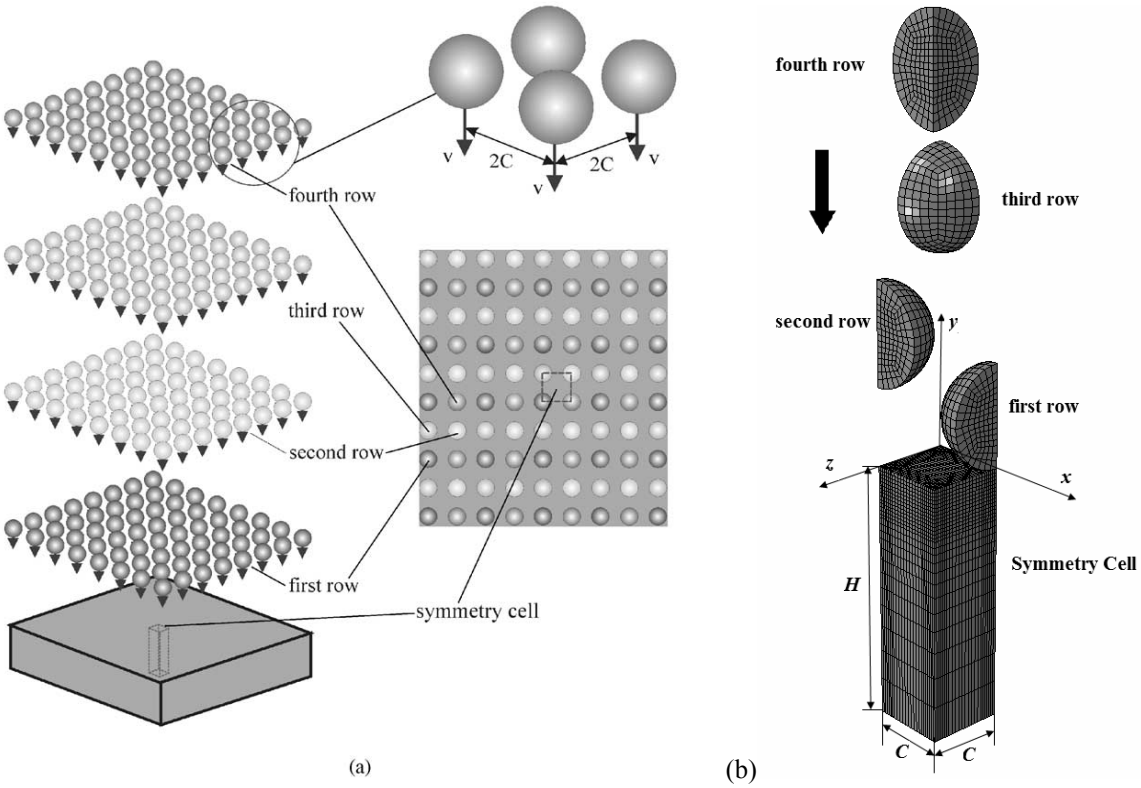

Figure 1. FE multiple impingement model: (a) full model, and (b) discretised symmetry cell.

2.2. Material models

The material of the target was high-strength steel AISI 4340 with density of 7850 kg/m3, which is widely used for shot-peening applications [14,16,18]. A bilinear isotropic hardening elasto-plastic constitutive law was used to model AISI 4340 with Young's modulus of 205 GPa and Poisson's ratio of 0.25 [22]. The strain-rate sensitivity was accounted for by using the data developed by Premack and Douglas [22], since they appear to be more reliable and cover a wider range of strain-rate values which are comparable to those observed in shot-peening (up to 10^5 1/s). These data are incorporated in the FE model by scaling the quasi-static stress–strain curve for different strain rates according to [22]. The shots were made of high carbon steel with the density assumed as being 7850 kg/m3.

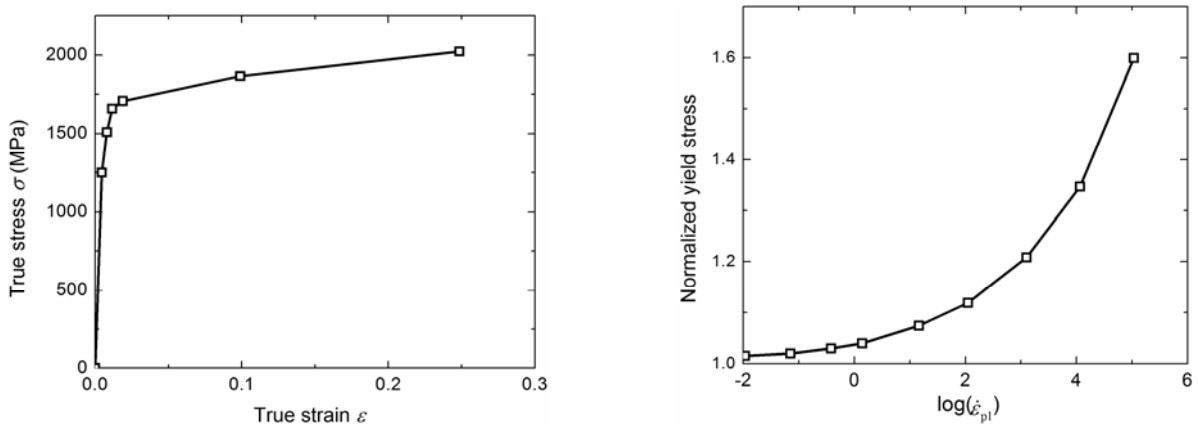

(a) (b)

Figure 2. Stress–strain relationship for AISI 4340 steel [22]: (a) quasi-static uniaxial stress–strain curve, and (b) the normalised effective yield stress accounting for strain-rate sensitivity.

2.3. Simulation procedure

The peening treatment of the cell was simulated by the impingement of rows of identical shots with a symmetric layout inside each row. These rows are further combined in series of four rows each. To achieve higher peening coverage, each subsequent row in the series is shifted laterally so that the shots in this row impinge different areas of the target symmetry cell as shown in Figure 1. To achieve higher peening intensity, several series of shot rows were used to impact the cell. A total of four series was used, which brings the total number of shot rows to 16.

The 16 shots were impinging to the target surface of the symmetry cell one by one as shown in Figure 1(b). The impinging velocity was unanimously chosen as 75 m/s in this study. A time interval of 10 ms was chosen between subsequent impacts. It is necessary to introduce material damping in order to prevent unnecessary long post-impact residual oscillations. If these oscillations are not reduced significantly prior to the following impingement taking place, they could accumulate leading to numerical instability. However, care must be taken so that the introduction of this damping should not disturb the solution. The material damping was introduced as being Eq. (1).

$$D = \alpha M + \beta K \,, \tag{1}$$

Where D, M and K are the damping, mass and stiffness matrices, respectively. As a result of a number of trial runs, it was determined that effective damping can be achieved using a stiffness proportional damping coefficient β = 2 x 10^{-9} s. To obtain reliable values of mass proportional damping α the following approach was adopted. For the given symmetry cell, the minimal modal frequency ω_0 could be estimated as in Eq. (2).

$$\omega_0 = \frac{1}{H}\sqrt{\frac{2E}{\rho}} \,, \tag{2}$$

Where E is the target Young's modulus, ρ is its density and H is the height of the symmetry cell. The mass proportional damping is then determined as in Eq. (3).

$$\alpha = 2\omega_0 \xi \,, \tag{3}$$

Where ξ is the corresponding modal damping parameter. In this study, ξ was selected as 0 during the impact stage and changed to 0.5 between subsequent shot impacts to decay the unwanted low-frequency oscillations.

3. Results

The FE model was developed using the explicit commercial finite element code ANSYS/LS-DYNA version 13. In contrast to the single shot impact, the current model is capable of modelling the effect of peening coverage. This was achieved by varying the separation distance C between adjacent shots. Figure 3 shows the residual stress distribution along the target depth direction. The residual stress σ_{xx} is plotted versus the target depth at three locations A–A, B–B and C–C as indicated in Figure 3(a). Three normalized separation distances were investigated as shown in Figures 3(a)–(c), respectively for C/R=1, 1.5 and 2. The corresponding stress distribution beneath the centre-line after repeated impact of four subsequent shots that hit the target in the same place is also provided for comparison. The results show that multiple shot impacts lead to interaction between the unloading residual stress fields resulting from individual impacts. This interaction effects lead to a much more uniform distribution of residual stresses along the target surface and subsurface regions than the results of single and twin shot impact models. As expected, the decrease in the separation distance leads to a more uniform residual stress distribution across the target as can be seen from the smaller distinction between the three curves of different locations. This is attributed to stronger interaction between individual shot impacts. The average depth of the compressed layer increases with the decrease in the normalized separation distance. However, the maximum values of the compressive residual stress are comparable for all the three cases examined. For separation distance $C/R \geq 2$, the residual stress distributions beneath the shot corresponding to the multiple impingement model are very close to those of the repeated impact sequence of four coincident shots.

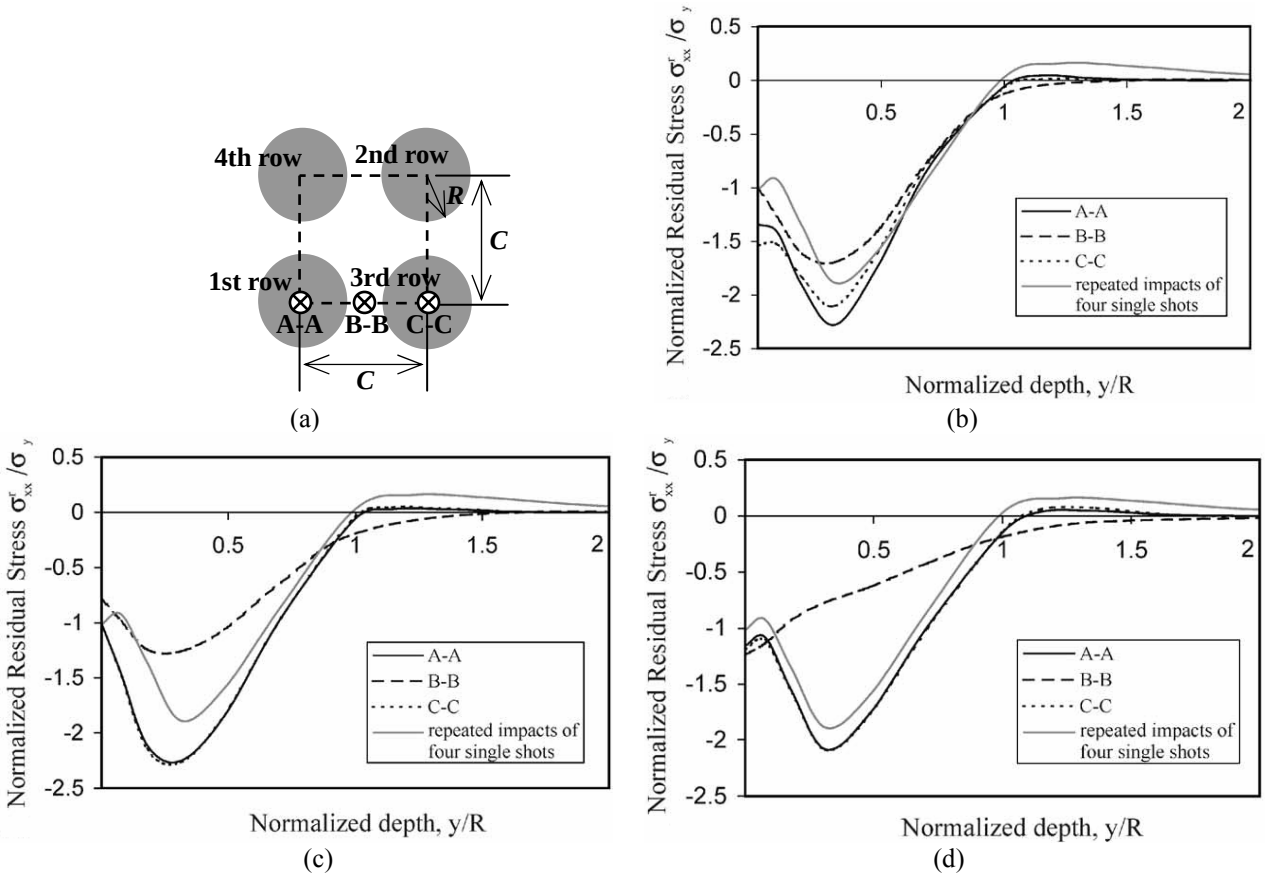

Figure 3. Effect of separation distance C/R upon residual stress distributions along target depth direction at three locations as indicated in (a) after rebound of fourth series (16 row) of shots: (b) C/R=1, (c) C/R=1.5, and (d) C/R=2. Also compared is the distribution along the center line for the case of four subsequent shots hitting the target at the same place.

4. Conclusions

A comprehensive 3D dynamic elasto-plastic finite element analysis was conducted to simulate the shot-peening process using rate sensitive targets, multiple and repeated impingements. The mechanically induced residual stress distributions were examined using a representative symmetry cell. It indicated that multiple shot impacts resulted in a more uniform residual stress at and immediately beneath the exposed surface layers compared to single and twin shot impacts. The separation distance between shots influences the residual stress field significantly. The decrease in separation distance leads to a more uniform residual stress distribution in the treated target. The average depth of the compressed layer increases with a decrease in the normalized separation distance C/R from 2 to 1. However, the maximum value of the compressive residual stress and plastic strain fields are comparable for all the three cases examined. For separation distances $C/R \geq 2$, the interaction between different shot impacts along the target surface are negligible.

Acknowledgements

We acknowledge the financial support of Natural Sciences and Engineering Research Council of Canada (NSERC).

References

[1] S.A. Meguid, Impact surface treatment. Amsterdam, Elsevier Applied Science; 1986.
[2] S.A. Meguid, M.S. Klair, An examination of the relevance of co-indentation studies to incomplete coverage in shotpeening using the finite-element method. J Mech Working Technol, 11 (1985) 87–104.
[3] S.A. Meguid, M.S. Klair, Elasto-plastic co-indentation analysis of a bounded solid using finite element method. Int J Mech, 27 (1985) 157–68.
[4] A.K. Li, M. Yao, D. Wang, R. Wang, Mechanical approach to the residual stress field induced by shot-peening. Mater Sci Eng, A147 (1991) 167–73.
[5] M. Frija, T. Hassine, R. Fathallah, C. Bouraoui, A. Dogui, Finite element modelling of shot peening process: prediction of the compressive residual stresses, the plastic deformations and the surface integrity. Mat Sci Eng A, 426 (2006) 173–180.
[6] N. Hasegawa, Y. Watanabe, K. Fukuyama, Creation of residual stress by high speed collision of a steel ball, in: Symposium on Resent Research of Shot Peening, JSSP, Society of Shot Peening Technology of Japan, 1996, pp. 1–7.
[7] Y. Watanabe, N. Hasegawa, Y. Matsumura, Simulation of residual stress distribution in shot peening. J Soc Mat Sci Jpn, 44 (1995) 110–5.
[8] M. Kobayashi, T. Matsui, Y. Murakami, Mechanism of creation of compressive residual stress by shot peening. Int J Fatigue, 20 (1998) 351–7.
[9] W. Johnson, Impact strength of materials, Arnold, London, 1972.
[10] M. Klemenz, V. Schulze, I. Rohr, D. Lohe, Application of the FEM for the prediction of the surface layer characteristics after shot peening. J Mater Process Tech, 209 (2009) 4093–4102.
[11] A. Gariépy, S. Larose, C. Perron, M. Lévesque, Shot peening and peen forming finite element modelling – Towards a quantitative method, Int J Solids Struct, 48 (2011) 2859–2877.
[12] J. Edberg, L. Lindgren, K. Mori, Shot peening simulated by two different finite element formulations, in: Shen & Dawson (Eds.), Simulation of materials processing: theory, methods and applications, Rotterdam, Balkema, 1995, pp. 425–30.
[13] S.P. More, V. V. Kulkarni, Finite element modelling for prediction of residual stress pattern from single shot impacting on aluminium (LM 13). Int J Eng Res Tech, 1 (2012) 1–6.
[14] T. Hong, J.Y. Ooi, B.A. Shaw, A numerical study of the residual stress pattern from single shot impacting on a metallic component. Adv Eng Softw, 39 (2008) 743–756.
[15] S.A. Meguid, G. Shagal, J.C. Stranart, J. Daly, Three-dimensional dynamic finite element analysis of shot-peening induced residual stresses. Finite Elements Anal Des, 31 (1999), 179–91.
[16] S.A. Meguid, G. Shagal, J.C. Stranart, Finite element modelling of shot-peening residual stresses. Mater Proces Tech, 92-93 (1999) 401–404.
[17] K. Schiffner, C. Droste gen. Helling, Simulation of residual stresses by shot peening. Comput Struct, 72 (1999) 329–40.
[18] S.A. Meguid, G. Shagal, J.C. Stranart, Development and validation of novel fe models for 3d analysis of peening of strain-rate sensitive materials. J Eng Mater Tech, 129 (2007) 271–283.
[19] G.I. Mylonas, G. Labeas, Numerical modelling of shot peening process and corresponding products: residual stress, surface roughness and cold work prediction. Surf Coat Tech, 205 (2011) 4480–4494.
[20] X. Sheng, Q. Xia, X. Cheng, L. Lin, Residual stress field induced by shot peening based on random-shots for 7075 aluminum alloy, Trans Nonferrous Met Soc China, 22 (2012) 261−267.

[21] T. Kim, H. Lee, H. Hyun, S. Jung, Effects of Rayleigh damping, friction and rate-dependency on 3D residual stress simulation of angled shot peening. Mater Design, 46 (2013) 26–37.
[22] T. Premack, A.S. Douglas, Three-dimensional analysis of the impact fracture of 4340 steel. Int J Solid Struct, 32 (1995) 2793–812.

Determination of Residual Stresses in Structural Elements Using Electron Speckle Interferometry Method

Leonid Lobanov*, Vyacheslav Pivtorak, Viktor Savitsky, Galina Tkachuk

E.O.Paton Electric Welding Institute, Kyiv, Ukraine
* Corresponding author: holo@paton.kiev.ua

Abstract Electron speckle-interferometry can be used in combination with hole drilling for an accurate determination of residual stresses (ESPI-HD method). Technology and compact equipment for efficient measurement of residual stresses based on ESPI-HD method have been described.

The computation method for calculation the values of stress tensor components based on surface displacements data has been suggested. Use of the ESPI-HD method allows increasing the accuracy of residual stress determination. High sensitivity of the instrumentation allows conducting investigations of the stressed state on a small base (0.5 mm) without loss of the experiment accuracy.

A special new approach to the conventional method of speckle-interferometry in order to investigate stress gradients over the surface of the test object has been added. The efficiency of application of the offered procedure for evaluation of the gradient of stresses is shown for investigation of residual stresses in welded structures.

Keywords residual stresses, electron speckle-inteferometry, hole-drilling method, welding

1. Introduction

In the production of the welded structures the high-strength steels and cast alloys find the more wide application. However, the serviceability and reliability of these materials depend greatly on the effect of residual stresses, the high level and the local gradient of which can lead to the initiation of cracks, reduction in corrosion resistance, etc. Therefore, the development of the reliable and informative methods of investigation of a stressed state in structures is important.

One of the most widely used methods for determination of residual stresses is the hole-drilling strain-gage method, in which a through-thickness or blind hole is made in the inspected point of the surface, and the strains, caused by unloading of the material volume during the residual stresses release, are measured in the vicinity of the hole. The values of these strains are subsequently used to calculate the main directions and appropriate values of the residual stresses.

The contactless methods, based on the laser interferometry for measuring the surface displacements, can overcome the difficulties, related to the bonding of the strain gauge arrays in the vicinity of the holes, and can also provide more information about the residual stress state of the object [1-3].

2. Determination of residual stresses by means of the ESPI-HD method

The electron speckle-interferometry (ESPI) in the combination with the hole-drilling can be used for fast and accurate determination of residual stresses [4, 5]. The speckle-interferometry method for determination of residual stresses is based on the application of the optical scheme of the interferometer in which the investigated section of the object is illuminated under the same angle

symmetrically from two directions, so that it is possible to determine the in-plane components of the displacement vector, which characterize the deformation of the object.

The displacements, caused by relaxation of residual stresses in the bulk material due to drilling of the blind holes, are measured using the ESPI method. The measurements are made in the following sequence [4]: the device is placed on the surface of the object. The reflected speckle-pattern, characterizing the initial condition before hole-drilling in the controlled section, is stored in the computer memory using a CCD-camera.

After unloading of the stresses due to drilling of a blind hole with the diameter and depth of approximately 0.4-1.0 mm, the reflected second speckle-pattern is also stored in the computer. After the computer processing of these two speckle-patterns, the monitor shows the interference fringes in the vicinity of the hole that contains the information about the displacements (Fig. 1).

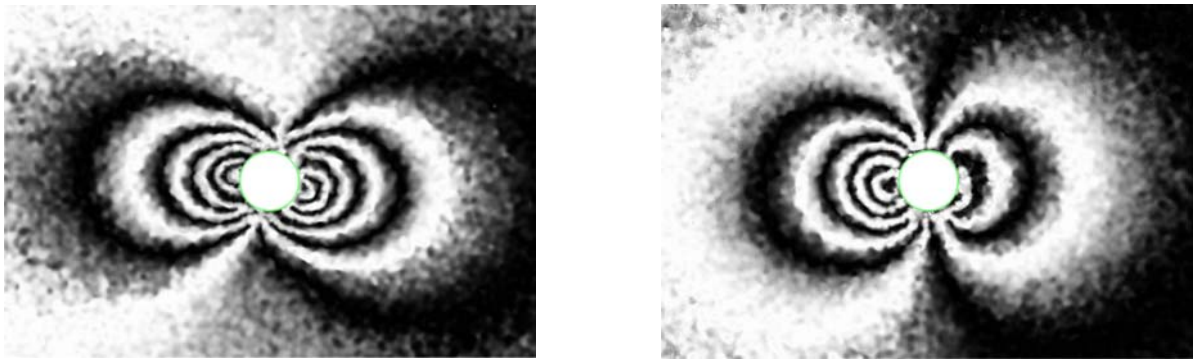

a) b)

Figure 1. Typical fringe patterns in the vicinity of a drilled blind hole in a stressed material: a) symmetrical fringe pattern. The gradient of residual stresses over the surface on the base of the measurements is absent; b) non-symmetrical fringe pattern. The gradient of residual stresses over the surface is present

Based on the computer processing of the fringe patterns, the displacements in the irradiated area can be evaluated, as well as the residual stresses can be calculated.

The developed procedure provides the measurement with the help of the speckle-interferometry of a displacement component u_x at a constant distance from the hole center (for instance, $r = 2{,}5r_0$). In this case the dependence of the measured displacements u_x, resulting from relaxation of stresses σ_{xx}, σ_{yy} and τ_{xy} is expressed by the formula [3]:

$$u_x(\theta)=F(\theta)\,\sigma_{xx}+G(\theta)\,\sigma_{yy}+H(\theta)\,\tau_{xy} \qquad (1)$$

where $F(\theta)$, $G(\theta)$ and $H(\theta)$ are the functions, which depend on the mechanical properties of the material, the distance from the hole center and its diameter, angle θ determines the coordinates ($x = 2{,}5r_0\cos(\theta)$; $y = 2{,}5r_0\sin(\theta)$) of the point, where the displacement is measured.

Determination of residual stresses, using the offered procedure, is realized in the following stages:

- points at distance of $2.5r_0$ from the center of the drilled hole of the radius r_0 at the different angles θ relative to the axis of illumination are selected;
- displacements $u_x(\theta)$ at the chosen points are measured, using a speckle-interferometer;
- components σ_{xx}, σ_{yy} and τ_{xy} are calculated from Eq. 1, using the least squares method;
- values of principal stresses σ_1, σ_2 and principal angle are determined.

A small device, positioned directly on the surface of the investigated object (Fig. 2) has been designed for determination of residual stresses in the elements and sections of the structures. Software 'Fringe Editor' for automatic image processing has been developed (Fig. 3).

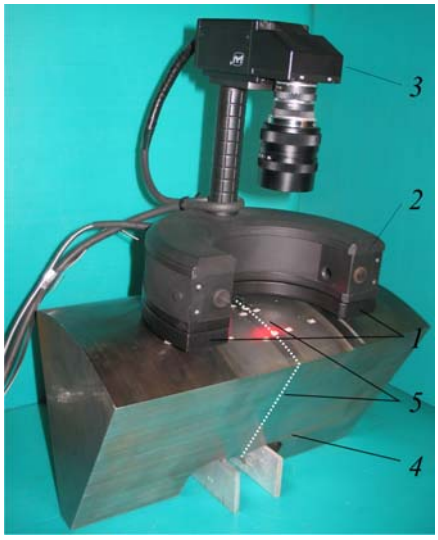

Figure 2. General view of the optical device, including: 1 – basement; 2 – removable module of speckle-interferometer; 3 – CCD-camera; 4 – sample of a welded joint; 5 – a weld seam

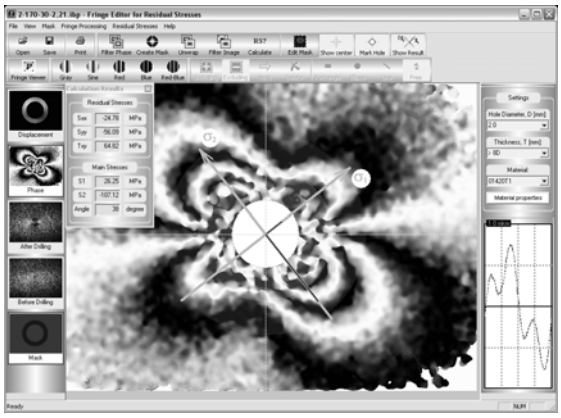

Figure 3. General view of the software user interface

The unit for determination of residual stresses, using the ESPI-HD method, includes a system of illumination and observation, which makes it possible to measure the displacements in the plane of the object examined. The unit consists of two parts: a basement 1 and a removable module 2, in which the optical system of the interferometer is assembled (Fig. 2). The basement is mounted on the sample examined and remains fixed while the measurements are being carried out for the point selected.

The solution of the well-known problem about the bending of a console beam with a fixed end by a force applied to a free end was used to evaluate the accuracy of the displacement measurements, using the developed small-sized speckle-interferometer and automated computer processing of speckle-patterns. The experiments have shown that the deviation of the values of stresses, which were determined by the ESPI-HD method, from the analytically estimated values, does not exceed 6 % of yield strength of the material tested [5].

3. Stress gradient over a surface

Determination of residual stresses on the basis of the hole-drilling methods assumes that stresses in the directions *x* and *y* are not changed. However, there is a non-homogeneous stressed state in the weld and HAZ, i.e. a gradient of residual stresses is present in those areas. (Fig. 4, 5). In this connection, it is suggested to use the drilling of the small-diameter holes at these areas to increase the accuracy of stress determination. It should be noted here, that the decrease of the holes' diameter leads to the reduction of the displacement measuring sensitivity and to the complication of the the process of drilling the holes in the high-strength metals and alloys.

It is known that the application of electron speckle-interferometry for determination of residual stresses makes it possible to gather more information about the residual stress state of the object compared with the data from the resistance strain gauges, that is achieved by calculating a significantly larger amount of values of the displacements caused by the hole-drilling.

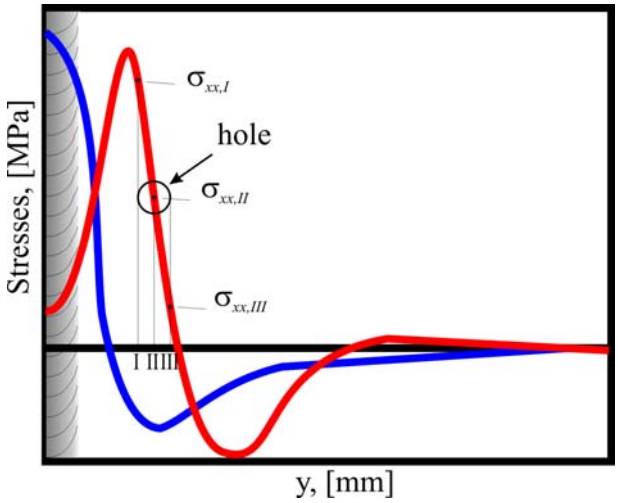

Figure 4. Typical distributions of longitudinal residual stresses versus distance from the weld center line

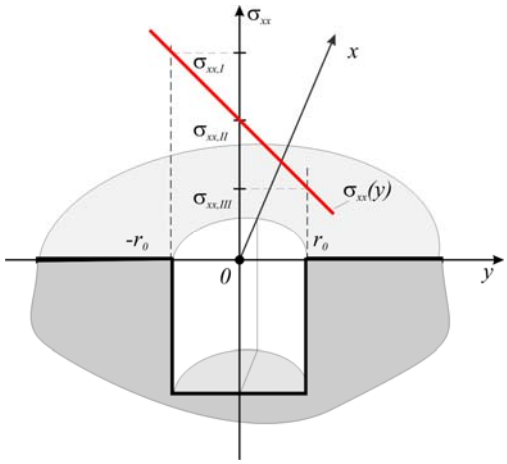

Figure 5. Local distribution of residual stresses across the hole

The ESPI-HD method for determination of residual stresses has been improved with a new approach for investigation of the stress gradient over the surface of the objects being examined. The principle of the approach will be briefly described below.

The area around the hole is divided into sectors. The displacements and their values, which are used for computing the stresses, are measured in those sectors (Fig. 6). The displacements data in the first and fourth circumference quadrants are used to determine the residual stresses for sector C_1, in the second and third quadrants – for sector C_2, the whole data about the displacement values along the circumference are used for determination of residual stresses corresponding to sector C_0 (Fig. 6).

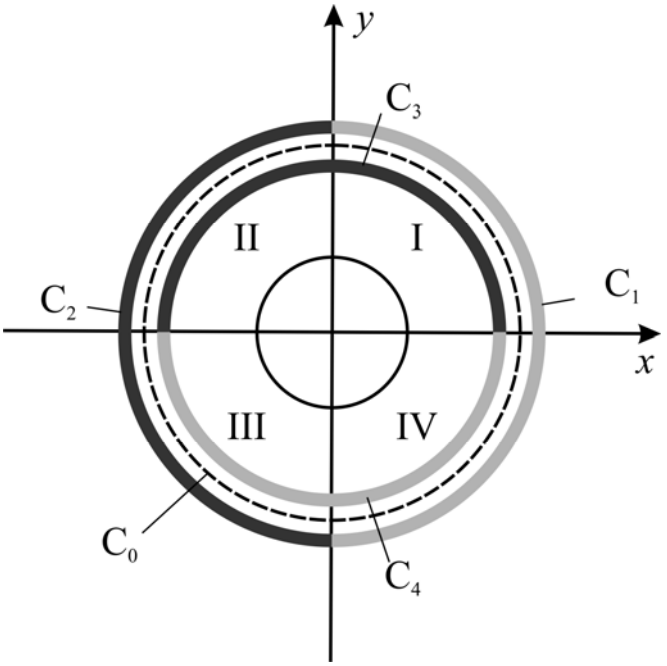

Figure 6: Scheme of an area division into sectors for investigation of the stresses' gradient in the hole zone

In order to assess the stress gradient it is necessary to determine stresses, using the data about displacements in the points both along the entire circumference around the drilled hole (Fig. 5) and in the points, located in the separated sectors around the drilled hole (compare Fig. 5). The computations, made with FEM, have shown that stresses, calculated from the data about displacements in all the points of the circumference (C_0), will have averaged values ($\sigma_{xx,avr}$) as compared with stresses from the measurements in the separated sectors (C_1 and C_2). The higher the stress gradient in the hole zone is, the larger the difference between the results of the stresses' calculation from displacements data in sectors C_1 and C_2. This gives the possibility to determine the direction of the stress gradient around the hole contour that allows to find the extreme values of residual stresses at a high accuracy.

To evaluate the gradient of stresses we have to plot the stress diagram. The data of the displacements, measured in the points along the circumference *2* (Fig. 7), located at a certain distance ($2.5r_0$) from the drilled hole center *1* (radius r_0), are used for determination of averaged residual stresses. If the stresses $\sigma_{xx,}$ calculated from the data from the different sections, are not equal, then the gradient of stresses over the object surface is present. In that case there is a dependence of stresses, being calculated on angle α (angle between radius-vector *b* and axis *OX*, Fig. 7). To assess the gradient of stresses in the hole vicinity, the diagram of the changes of stresses along the circumference is plotted on the base of the displacements data in the points of the sector 3 from angle α (the points of the sector 3 have polar coordinates within the range from $\alpha - \pi/2$ up to $\alpha + \pi/2$).

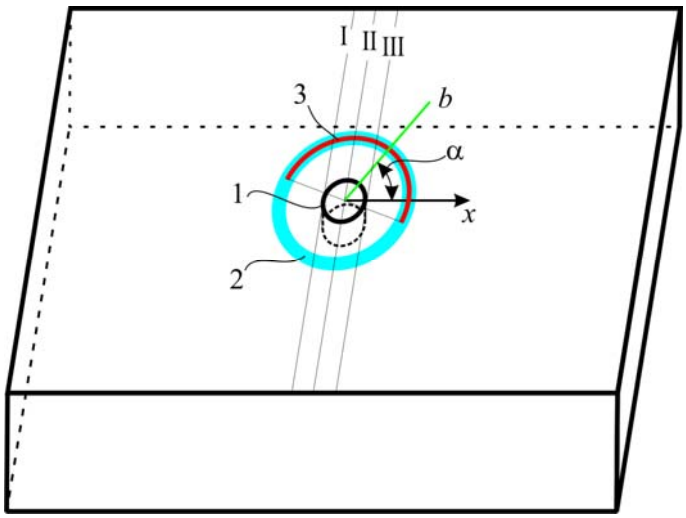

Figure 7. Scheme of the location of the points, in which the stresses are determined from the displacements data, where: 1 – hole; 2 – circumference, along which the displacements have been measured, used for calculation of stresses; 3 – circumference sector, in which the displacements are measured, used for determination of the stressed state when analyzing the stress gradient over the surface

An example of the calculated stress diagram is shown in Fig. 8. A conclusion about the presence of the residual stresses gradient can be drawn based on deviation of a curve of stresses from the circle with the radius, which is equal to the averaged value of stresses.

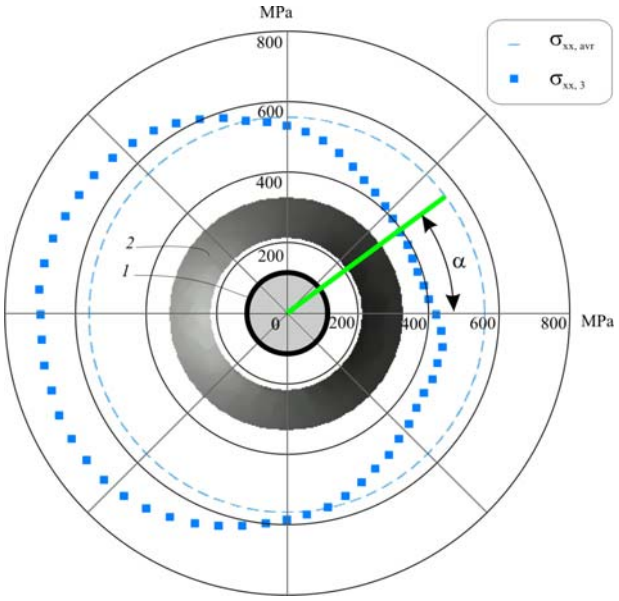

Figure 8. Graphical presentation of stresses σ_{xx} (square dots), with the use of the data about the displacements in the sector 3 (Fig. 7), illustrating deviations from the averaged values $\sigma_{xx,avr}$ and indicating the gradient of residual stresses over the surface. 1 – hole; 2 – measured displacements are presented in the form of a grayscale values

4. Application

The procedure of determination of residual stresses and the equipment, designed for this purpose, have been used for study of the stressed state in 1020 mm diameter welded gas and oil pipelines (Fig. 9). The ESPI-HD method has made it possible to determine residual stresses in the different areas of the welds. This technique does not require strong surface preparation. Drilling of holes with diameters and depths from 0.5 up to 1.0 mm provided high accuracy and relatively small damage.

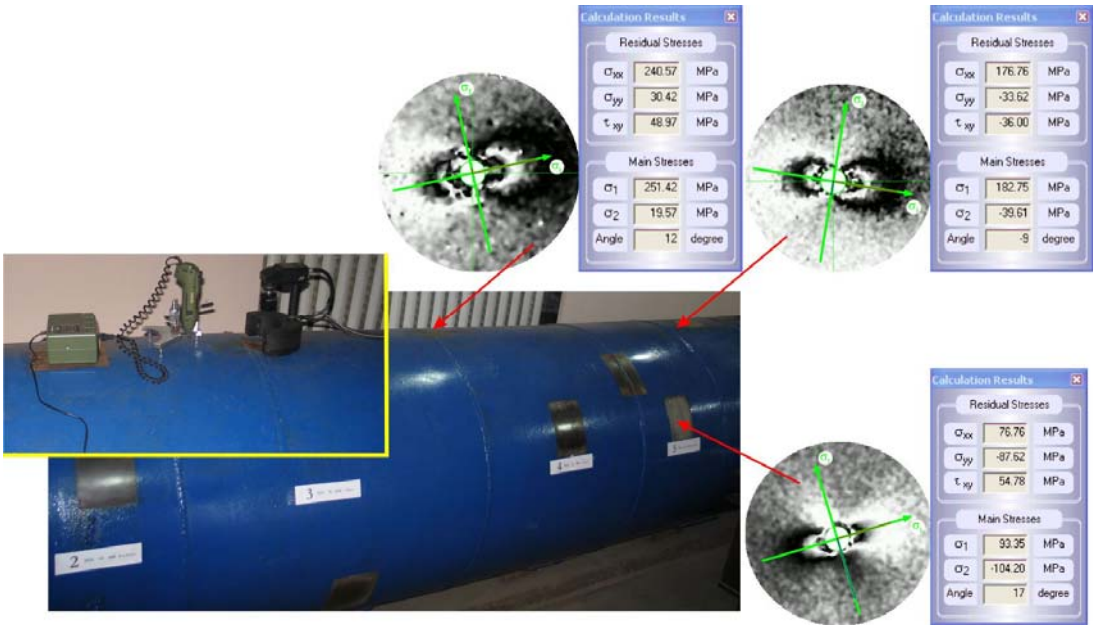

Figure 9. Determination of residual stresses in welded joints of gas and oil pipelines.

Another important advantage of the ESPI-HD method in comparison with the strain-gage hole-drilling method is that it does not require the removal of the weld reinforcement, which can lead to a redistribution of residual stresses.

Residual stresses have been determined in the Cr-Mo-V turbine element (Fig. 2). Typical distribution of circumferential residual stresses in the surface welded turbine rotor is presented at Fig. 10a, where compressive residual stresses are obtained due to phase transformation. However, the use of the proposed methodology for evaluating the stress gradient over the surface revealed two sharp peaks in HAZ, which have resulted from the martensitic transformations in the narrow zones of the width up to 2 mm (Fig. 10b). Thus, the use of the proposed techniques for the stress gradient analyses enabled to clarify the data about distribution of residual stresses and to identify a number of the important features.

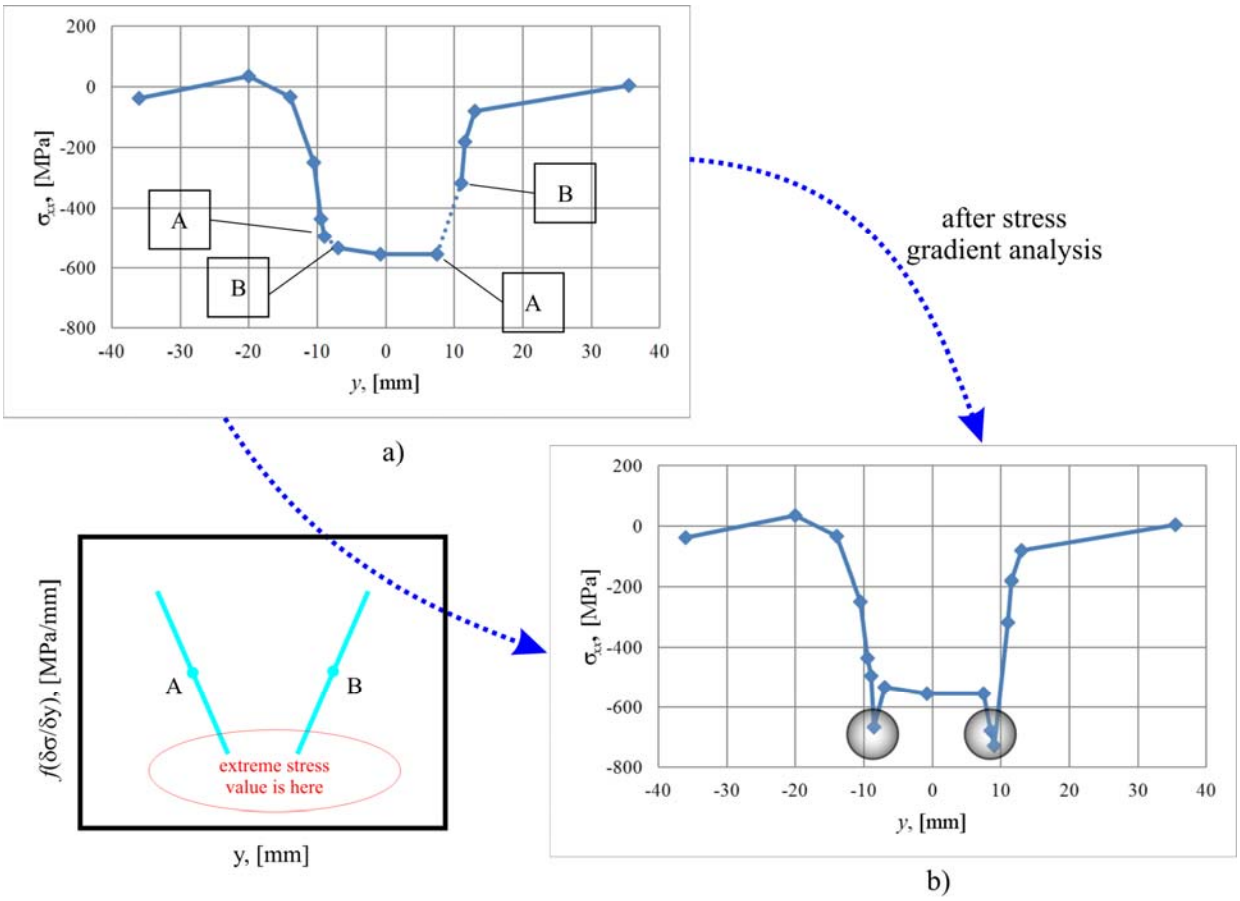

Figure 10. Distribution of circumferential residual stresses in the surface welded rotor obtained by: a) – conventional method of determination of residual stresses; b) – ESPI-HD – method with the technology of evaluating the stress gradient over the surface

5. Summary

Thus, the use of the ESPI-HD method makes it possible to increase the accuracy of residual stress determination and also gives an additional opportunity of the stress gradient assessment on the basis of the drilled out hole. The high sensitivity of the device enables to conduct the investigations of the stressed state on a small base (from 0.5 mm) without any loss of the experiment accuracy. The developed procedure of residual stress determination, compactness of the equipment and efficiency of the computer processing of the optical information open the new possibilities for examining the structures under the laboratory and industrial conditions.

The efficiency of the application of the offered procedure for evaluation of the stress gradient over the surface in order to investigate residual stresses in the welded structures has been shown.

References

[1] L.M.Lobanov, B.S.Kasatkin, V.A.Pivtorak, S.G.Andrushchenko Procedure for investigation of residual stresses by the interference holography method. Avtomat.svarka. 3, pp. 1-6, 1983.

[2] Makino A., Nelson D., "Residual stresses determination by single-axis holographic interferometry and hole-drilling. Part I. Theory Exp. Mech., 34, pp. 66-78, 1994.

[3] L.M.Lobanov, V.A.Pivtorak., Development of holographic interferometry for study of the stress-strain state and quality control of welded structures. In: Advanced materials science of the 21st century. Kiev: Naukova Dumka, 1998.

[4] L.M.Lobanov, V.A.Pivtorak, I.V.Kyjanets, V.V. Savitsky, G.I.Tkachuk: Express control of quality and stressed state of welded structures using method of electron shearography and speckle-interferometry. The Paton Welding Journal, August, 2005, pp.35-40.

[5] L. M. Lobanov, V. A. Pivtorak, V.V. Savitsky, G. I. Tkachuk: Procedure for Determination of Residual Stresses in Welded Joints and Structural Elements using Electron Speckle-Interferometry. The Paton Welding Journal. 1/2006, pp.24-29.

Surface Integrity and the Influence of Tool Wear in High Speed Machining of Inconel 718

**Ru Lin Peng[1,*], Jinming Zhou[2], Sten Johansson[1], Annethe Billenius[1]
Volodymr Bushlya[2], Jan-Eric Stahl[2]**

[1] Department of Management and Engineering, Linköping University, 58183 Linköping, Sweden
[2] Department of Mechanical Engineering, Lund University, 22100 Lund, Sweden
* Corresponding author: ru.peng@liu.se

Abstract The influence of high speed turning and tool wear on the microstructure and residual stresses of Inconel 718 was investigated. The turning was performed using whisker reinforced alumina ceramic inserts and a cutting fluid. By electron channelling contrast imaging in SEM, significant microstructural changes, including grain-refinement in a thin surface layer and heavily deformed microstructure to a certain depth, were observed in turning using a new tool. X-ray diffraction measurements also revealed a characteristic residual stress field with surface tensile stresses and subsurface compressive stresses. With the development of wear in the tool flank, mechanical forces and heat involved in the cutting operation increased, leading to a much larger cutting affected zone and more drastic changes in the surface integrity. High surface tensile residual stresses, up to 1500 MPa, and dissolution of reinforcing precipitates and recrystallization of the surface layer were induced by severe tool wear, both of which can significantly affect the fatigue strength of the machined part.

Keywords High speed machining, Surface integrity, Residual stress, Tool wear, Inconel 718

1. Introduction

Various machining operations such as turning, milling and drilling are widely employed to create designed shapes and dimensions of engineering parts with the help of cutting tools. During such a manufacturing process, material is removed from the surface of a part with the help of a cutting tool, causing severe localized plastic deformation and shearing. Because of the mechanical work done and friction between the cutting tool and both the newly formed workpiece surface and the chip, the temperature in the cutting zone is unavoidably raised. The nature of such a process involving localized plastic deformation and heating means structural development and thereby property changes in the surface as well as subsurface of the machined part. Plastic deformation, heat induced microstructural changes, hardness variations and residual stresses are frequently observed in the cutting affected zone [1-4]. Such changes may have a direct impact on the performance and reliability of machined parts and therefore are constantly a subject of interest in research.

The current project investigates the influence of high speed turning on the surface integrity of nickel based superalloy Inconel 718. Nickel based superalloys have good strength as well as excellent oxidation and corrosion resistance at elevated temperatures. They constitute a very important group of structural materials suitable for high temperature applications in the aerospace and energy conversion industries. However, the alloys are also known as hard-to-cut materials due to their high strain hardening rate, poor heat conductivity and high-temperature strength. The poor machinability not only contributes to a low material removal rate but also induces rapid tool wear [5] which changes the cutting geometry of the tool. For wear in the tool flank, the increased tool-workpiece contact area and vanished clearance angle lead to increased mechanical forces and heat generation during cutting [5]. As a result, machining influence on the surface integrity of the workpiece is enhanced [4]. Microstructure alterations and residual stresses in turning of Inconel 718 by worn tools were studied in a few publications. Sharman et al. through optical microscopy and microhardness testing revealed that tool wear during turning of Inconel 718 increased the plastic

deformation depth, and at the higher speed end of the studied range of 40–120 m/min it also enhanced strain hardening of the subsurface [5]. Analysis by high resolution imaging of electron channeling contrast (ECC) in backscatter detectors and electron backscatter diffraction (EBSD) revealed that recrystallization and partial recrystallization also occurred in an immediate subsurface layer of 200–300 nm at a cutting speed of 300 m/min [6]. In [7], tool wear was reported to promote the formation of a so called white layer, independent of the application of coolant. Cutting using a worn tool is often found to increase the surface tensile residual stresses. In turning of Inconel 718 at low cutting speed (40 m/min), high surface tensile residual stresses up to 1043 MPa were reported in a surface prepared using a worn tool and the surface tensile stresses was found to decrease with increasing cutting speed [8]. For face finishing turning of RR1000 alloy, residual stress profile measurements revealed that tool flank wear not only increased the surface tensile residual stresses but also extended the compressive peak stresses to a larger depth [9].

This paper presents results from studies on the evolution of microstructural changes and residual stresses with the development of tool wear for high speed turning of Inconel 718 at 200 m/min with a cutting fluid. The influence of tool wear on residual stresses for cutting using the same tooling conditions but without the application of cutting fluid can be found in [10]. In [6], research work on subsurface deformation and their correlation to tool wear for turning at higher speed was reported.

2. Experimental Details

2.1. Material and machining operations

The Inconel 718 used in the current investigation has a nominal composition of: 53.8% Ni, 18.1% Cr, 5.5% Nb, 2.9% Mo, 1% Ti, 0.55% Al, 0.25% C, 0.04% Si and balance Fe (in weight). Round bars of 70 mm diameter and 200 mm length were received in solution annealed and aged condition with a nominal bulk hardness of 45±1 HRC. The backscatter electron images in Fig. 1 reveals a microstructure of equiaxed γ grains of nickel solid solution strengthened by very fine intermetallic γ" (coherent body centered tetragonal Ni_3Nb) particles visible at higher magnification. Elongated δ (an incoherent orthorhombic Ni_3Nb) particles are observed at grain-boundaries with some of them penetrating deep into the grains.

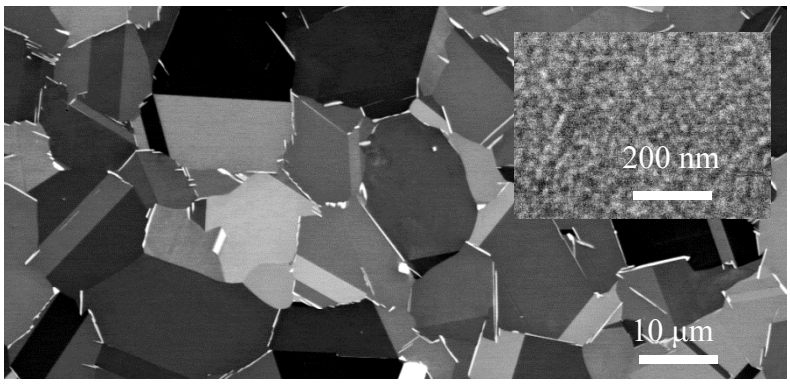

Fig. 1 Backscatter electron image of the as received alloy with a nickel base solid solution γ and reinforcing γ" precipitates (the inset). The elongated bright particles often located at grain boundaries are δ precipitates.

The as-received bars were machined down to 40 mm before further turning using whisker reinforced alumina ceramic (Al_2O_3+SiC_w) tools to prepare samples for the investigation. The cutting tool had a honed cutting edge and negative rake chamfer ($0.1x20^o$). The insert was mounted in a CDJNL3025P11 (ISO) type tool holder with a tool geometry of -6^o rake angle, 6^o clearance angle,

93^o edge major tool cutting and -6^o cutting edge inclination angle. To investigate the influence of tool wear on the machined surface quality, samples were also prepared with used tools of two degrees of flank wear, namely semi-worn tools (VB_{max} = 0.15 mm) and worn tools (VB_{max} = 0.3 mm). The cutting speed, feed rate, and cutting depth were 200 m/min, 0.2 mm/revolution, and 0.3 mm, respectively. All machining trials were conducted on a SMT500 CNC turning machine with a spindle speed up to 4000 rpm and a drive motor rated up 70kW. The cutting fluid was Sitala D 201-03 (Shell) containing 5% of semi-synthetic emulsion in solution and provided with 5 MPa at 40 l/min through an orifice 5 mm in diameter.

2.1. Surface integrity characterization

X-ray diffraction stress analysis is based on evaluating changes in the interplanar spacings of certain (hkl)-planes, namely the elastic strains, from which the residual stresses responsible for causing the changes are derived. Measurements in the current study were carried out in ψ-mode [11] on a Seifert X-ray diffractometer. With ψ being the angle of sample tilt around an axis passing through the goniometer center in the diffractometer plane, the commonly used $\sin^2\psi$-method [11] was employed to calculate residual stresses from the interplanar spacing measurements made in multiple ψ angles. To obtain a stress value, thirteen ψ-angles spreading in equal $\sin^2\psi$ interval between ($\psi = -50^o$) and ($\psi = 50^o$) were used. Diffraction peaks from the nickel γ-220 reflection were obtained using the Cr-K_α radiation and a pinhole collimator of 2 mm diameter. The peak positions and widths were determined by curve fitting with two pseudo-Voigt functions for $K_{\alpha1}$ and $K_{\alpha2}$, respectively. The X-ray diffraction elastic constant for nickel γ-(220) plane, needed for the stress calculation, is 4.65×10^{-6} MPa^{-1} [12]. To obtain depth profiles of residual stresses, stepwise electrolytic polishing was employed to expose the underlying material for diffraction measurements. The stress profiles presented in this paper are as measured results without any correction for possible stress relaxation due to the electrolytic polishing.

Small samples were cut from the machined bars. A surface encompassing both the cut and feed directions was then mechanically ground and polished following a procedure for preparing samples for electron backscatter diffraction (EBSD) analysis. The microstructural characterization was carried out in a Hitachi SU-70 FESEM scanning electron microscope. Annular solid state backscatter detectors from Hitachi were used to obtain images of electron channeling contrast (ECC) from the polished surface. The plastic deformation depth was also characterized by measuring the density of low angle grain boundary (LAGB) in EBSD using a Nordlys detector from Oxford Instruments. Scans with a step size of 0.5 μm were then performed along lines perpendicular to the cutting surface. The LAGB was defined as a misorientation of 1 to 10 degrees between two contiguous measurement positions along a scanned line. Its density at a particular sample depth was then calculated by averaging the number of lines containing a LAGB at the depth over the total number of scanned lines.

3. Results and Discussions

3.1 Microstructure of machining affected zone

As a reference state to illustrate the effect of dry cut, microstructure in the sample prepared using a new tool was briefly described in [10]. A more detailed analysis with regards to the cutting induced plastic deformation and temperature rise is given here. Fig. 2(a) presents an overview of microstructural alterations in the cutting affected zone. A plastic deformation gradient varying from surface towards depth is revealed by the ECC. Lattice distortions visible as contrast variations are seen at a depth up to about 60 μm. This zone, corresponding to the deformation depth indicated by

the LAGB density profile from EBSD line scans (Fig. 3(a)), is hereafter termed heavy deformation zone. Although slip bands related to cutting induced plastic deformation can be found in grains at a larger depth, the analysis here is limited to the zone of heavy deformation. Different microstructural features identified along the depth near the machined surface are shown in Fig. 2(b). In the outmost surface, Fig.2(c) discloses a discontinuous layer of less than 1 μm thick, distinguished from the material beneath by its very fine structure consisting of elongated grains lying in the cutting direction and some equiaxed grains. Such a layer with ultrafine or nano-sized grains has been reported in surfaces machined under certain cutting conditions [13,14] and is often attributed to severe plastic deformation with possible influence of a high temperature. In the current sample, deformation bands extended from the layer beneath are still recognizable and fragmented δ-particles are visible (Fig. 3(c)). These observations imply that severe plastic deformation is the main cause of the grain-refinement but the cutting heat may cause recovery and even partial recrystallization, producing the sharp boundary to the layer beneath.

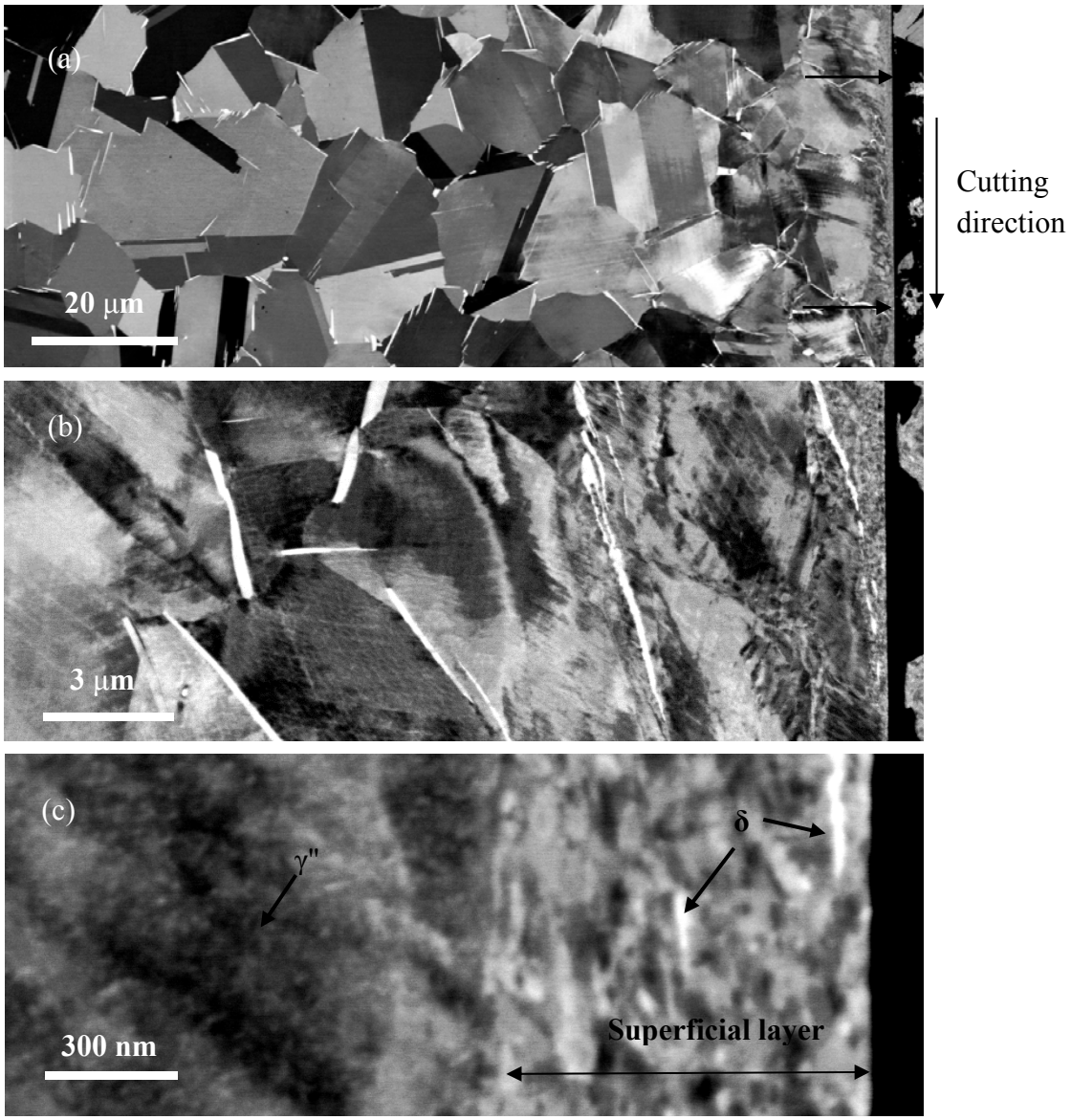

Fig. 2 Backscatter images showing microstructural alternations in machining affected zone of the sample prepared using a new tool. The machined surface is indicated by the arrows.

The next layer which extends to a depth of 10 to 25 μm contains severely deformed grains (Fig. 2(b)). In the literature, distorted grain boundaries and deformation bands are frequently reported from optical microscopic study on etched surfaces, see for example [7]. In comparison, the backscatter image in Fig. 2(b) reveals finer microstructural features such as fine slip bands and concentrated plastic strains in the vicinity of grain boundaries. As can be seen in the region close to the superficial layer, elongated grains inclining towards the cutting direction prevail. Stretching and rotation of the grains are accomplished by shear, leaving dense deformation bands extending over the grains. In many grains, the deformation bands tend to bend towards the cutting direction with rather abrupt change of the bands orientation. Fine slip bands are also observed in the regions between the deformation bands. In other grains which are less distorted, dislocation slip on multiple slip systems results in cell-like features. The δ-precipitates in this zone either deform following the grain boundaries and/or are sheared together with the deformation bands. It can be concluded from the above observations that heat from the cutting process has little effect on the already deformed structure; the forced cooling by cutting fluid and the poor thermal conductivity of the superalloy prevent a large amount of the cutting heat from penetrating into the depth. The retained strain hardening effect is expected to locally increase the hardness but at a cost of the ductility. Deeper in the sample, plastic deformation is less significant. The grains are characterized by cross-slip bands but the grain boundaries remain essentially undistorted (Fig. 2(a)).

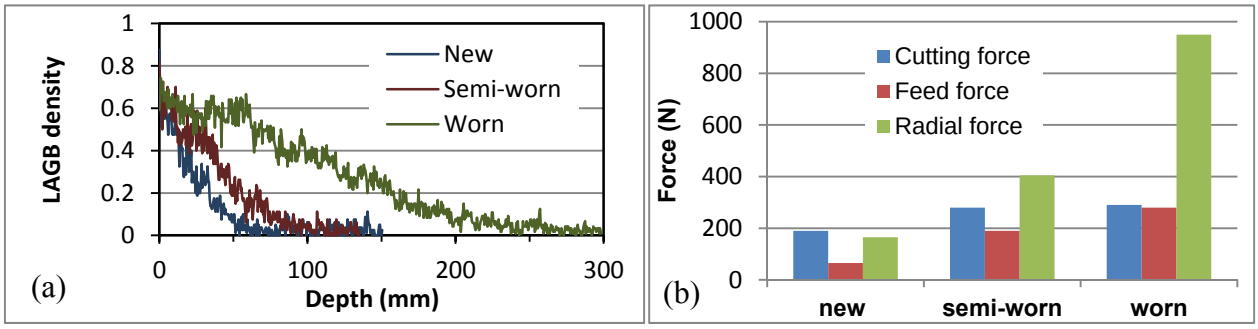

Fig. 3 Depth distribution of low angle grain boundary (a) and mechanical force components (b) for cutting under different tool conditions.

Cutting by a semi-worn tool with flank wear of VB_{max} = 0.15 mm leads to a larger cutting affected depth, as disclosed in Figs. 3(a) and 4(a). The depth of heavy plastic deformation shown in Fig. 4(a) is now slightly over 100 μm (Fig. 3(a)) and the severely deformed zone with distorted grains and grain boundaries extends to about 30 μm. The increased plastic deformation in association with tool wear is related to a higher cutting temperature and larger mechanical forces [5]. Wear in the tool flank results in a larger contact area between the tool and the sample surface as well as vanishing of the clearance angle. Subsequently, larger mechanical forces are required for material removal, as revealed by Fig. 3(b), leading to a larger deformation depth. Because of both the increased mechanical energy input and friction between the sample and tool, the cutting heat also increases which not only enhances plastic deformation by reducing the strength of the affected surface layer but also causes more significant microstructural changes. As can be seen in Fig 4(b), almost complete recrystallization occurs in the surface layer and partial recrystallization in some grain boundary regions beneath.

As a result of further increase in the mechanical forces (Fig. 3(b)) and heat, a much larger mechanical and temperature influence is found for cutting using a worn tool (VB_{max} = 0.3 mm). The heavy deformation depth reaches over 250 μm (Fig. 3(a)) with the severely deformed layer extending to about 60 μm below the surface (Fig. 5(a)). The fully recrystallized surface layer

containing equiaxed grains of over 100 nm in size and annealing twins becomes as thick as 3 μm (Figs. 5(b) and (c)). The strengthening γ'' particles completely disappeared from the layer, which may facilitate recrystallization of the layer. In some places, a very thin but extremely fine featured layer can be observed on top of the recrystallized zone, as can be seen in Fig. 5(c). This layer may form because of remelting by a high surface temperature [6] and quenching by the cutting fluid. Such changes in the microstructure greatly improves the surface ductility but at the cost of strength. In the depth between 2 to 10 μm, bands containing ultrafine, elongated or equiaxed grains or cell-structures associated with grain boundaries lie in a low angle to the cutting surface (Fig. 5(b)). It seems that as more cutting heat penetrates deeper into the material, the extremely distorted grain boundary regions may partly recrystallize. Between the heat affected grain boundaries are parallel short deformation bands and coarser cells formed by crossed slip bands. The rest of the heavy deformation zone shows similar microstructural feature to those in the samples prepared by the new tool and semi-worn tool.

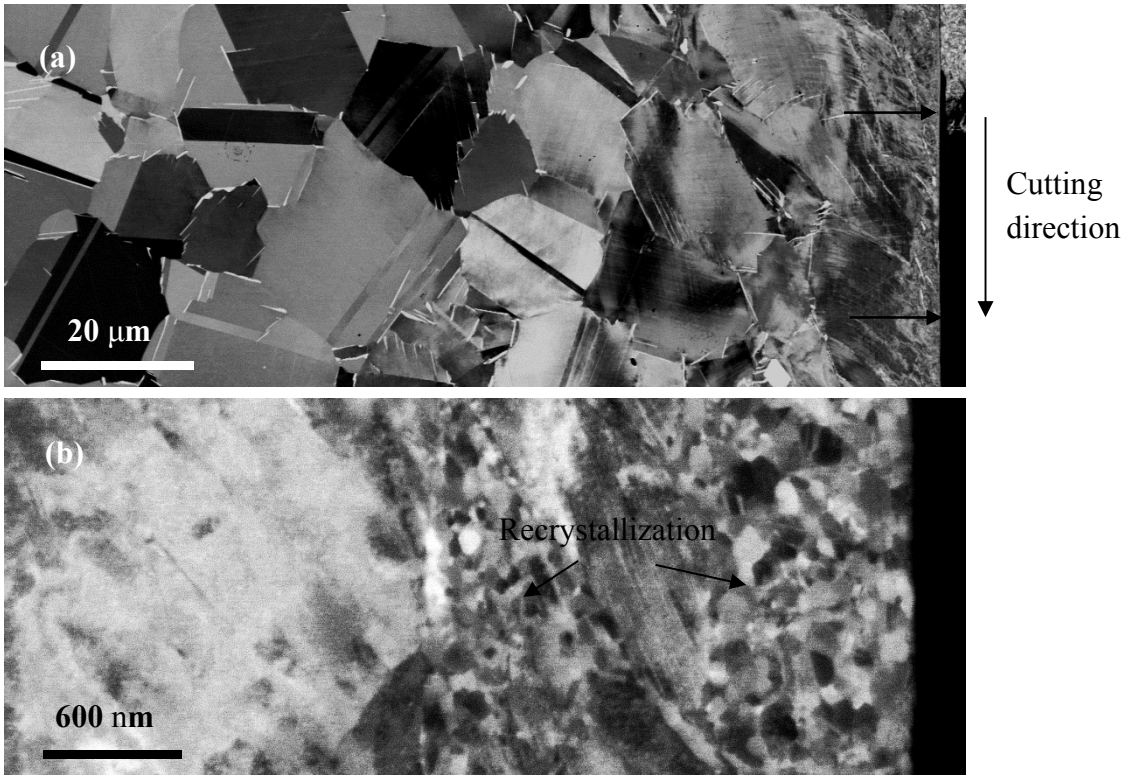

Fig. 4 Machining affected depth of the sample prepared by turning using a semi-worn tool.

3.2 Residual stresses

Residual stress profiles are presented in Fig. 6. As can be seen, tensile residual stresses are found in a thin surface layer and compressive stresses in the subsurface zone. The cutting tool condition affected both the extent of the tension and compression zones and the peak stress values. The diffraction peak width, given as full width at half maximum intensity (FWHM) in Fig. 6, is related to lattice distortion and grain size. Except for the surface layer containing ultrafine grains, the observed peak broadening can be attributed mainly to cutting induced plastic strains. The cutting affected depths indicated by the FWHM profiles are somewhat larger than that observed in Section 3.1 (Fig. 3(a)), indicating that X-ray diffraction is more sensitive for small plastic strains.

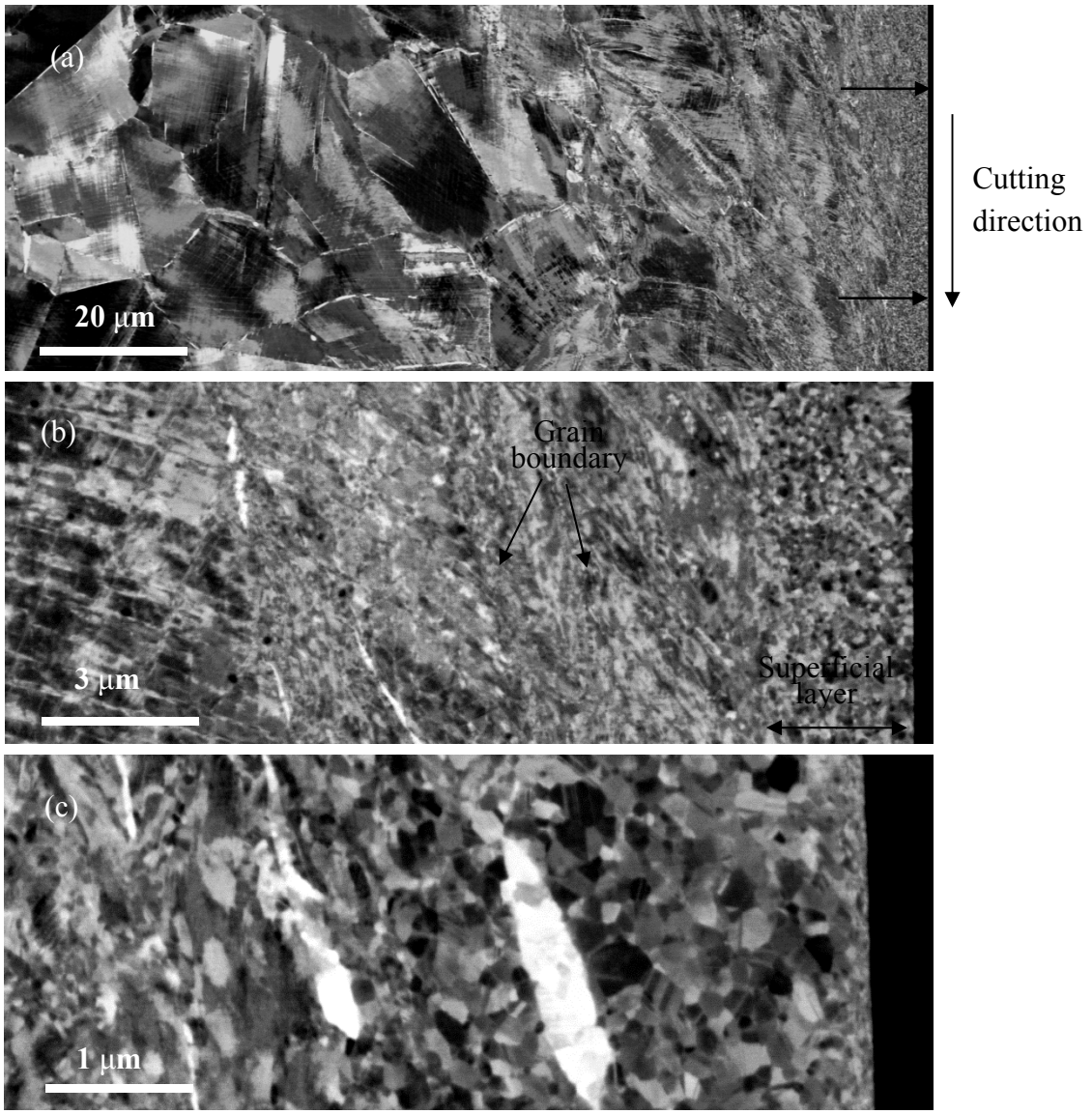

Fig. 5 Microstructure of the cutting affected depth prepared by a worn tool.

A 10 μm thick tensile zone with relatively low peak stresses is induced by cutting using the new tool, see Fig. 6(a). The residual stress field is slightly anisotropic, with a more rapidly decreasing stress in the feed direction. After reaching maximum compressive stresses at about 50 μm, both the stress components decrease, approaching zero at a depth of about 150 μm. The depth affected by plastic deformation reaches about 100 μm. A similar residual stress field with surface tensile stresses and subsurface compressive stresses has been reported for nickel-based alloys machined under different cutting conditions, for example, in the cutting speed range between 40 m/min and 120 m/min [8,15,16] and over 400 m/min [9,13,17]. Surface tensile stresses are often attributed to a dominant thermal effect from the cutting process [13,18]. When the contraction of a surface layer on cooling is hindered by the subsurface material of lower temperature, the surface layer will be put in tension and the subsurface layer in compression. On the other hand, plastic deformation involved in the cutting process which is mostly in-plane expansion has the opposite effect and will introduce compressive stresses in the surface layer [18]. Analogously, microstructural changes leading to a volume expansion of the surface layer will result in surface compression and subsurface tension. As analyzed in [10] for turning under the same cutting conditions but without the application of a cutting fluid, the observed stress field in Fig. 6(a) can be attributed to superposed mechanical and thermal effects: a somewhat anisotropic residual stress field with surface compression is induced by

surface plastic deformation and thermal stresses from cooling of a heated surface layer reverse the surface compression to tension.

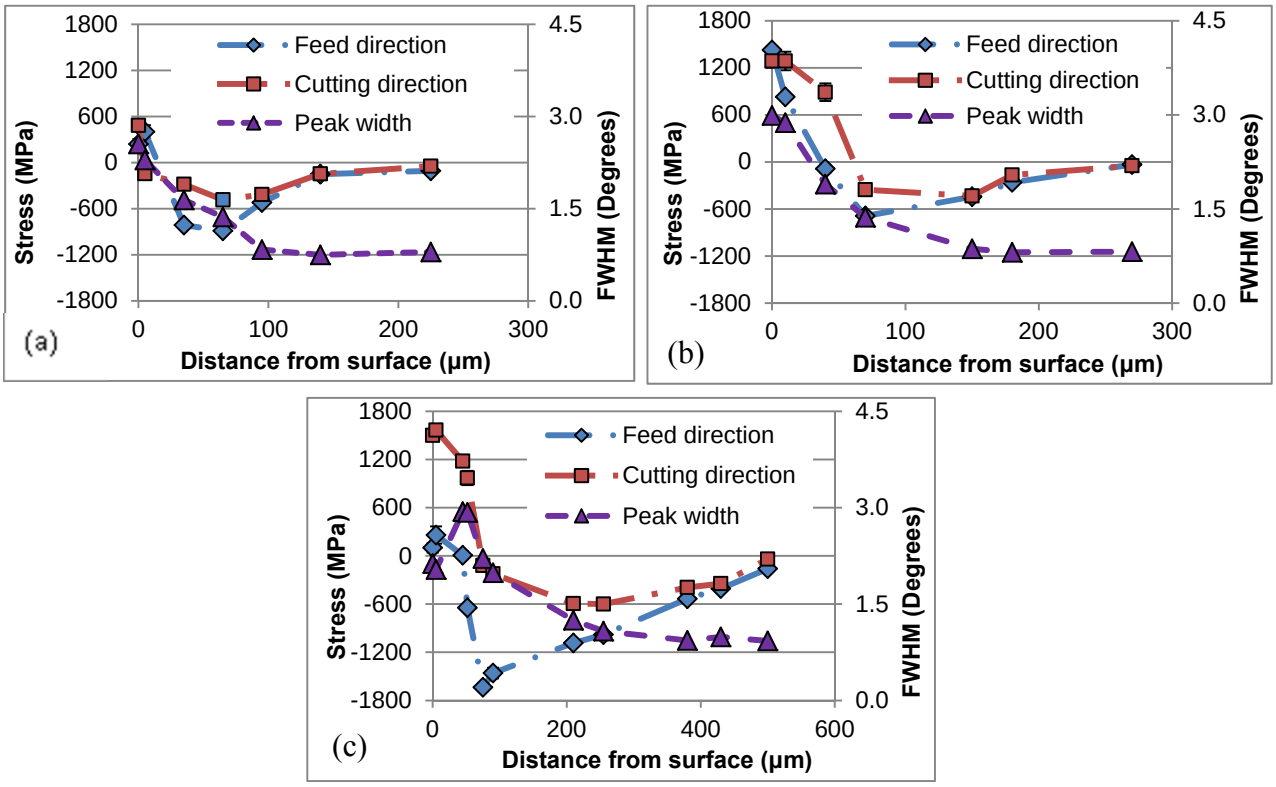

Fig. 6 Residual stresses and FWHM in the machining affected depth prepared using new tool (a), semi-worn tool (b) and worn-tool (c).

The higher cutting heat generated when using the semi-worn tool has a large influence on the surface tensile zone. The size of the zone is increased and the surface stresses are raised from about 240 MPa to 1400 MPa in the feed direction and 480 to 1300 MPa in the cutting direction (Fig. 6(b)). The higher mechanical forces (Fig. 3(b)) have little effect on the peak compressive stresses but enhance strain hardening in the near surface region, as revealed by the higher FWHM values, as well as expand the compression zone to a larger depth of 270 μm.

For the turning by the worn tool (VB_{max} = 0.3 mm), Fig. 6(c) reveals a surface tensile stress of 1500 MPa and a subsurface compressive peak of 600 MPa in the cutting direction. On the other hand, the surface tensile stress in the feed direction is reduced to 100 MPa, and at the same time the compressive stress peak is increased to about 1100 MPa. While the plastic deformation depth is further increased, to about 400 μm, recrystallization in the surface layer and partial recrystallization in the subsurface layer (Fig. 5) fully or partly removes the strain hardening effect, leading to low peak widths in the region (Fig. 6(c)). In spite of a stronger temperature effect on the microstructure, the observed residual stress anisotropy and the larger hardening depth suggest a more significant mechanical effect on the residual stress profiles in comparison with cutting using the semi-worn tool. The severe flank tool wear increases the feed and radial force components but has little effect on the cutting force component (Fig. 3(b)), which may result in a large difference between the two residual stress components. The recrystallization of the outer layer then relaxes the surface compressive stresses and residual stresses of tensile nature are generated later during cooling. It is interesting to compare the influence of tool wear with that of cutting speed for which increasing cutting speed also leads to a higher cutting temperature but lower mechanical forces [19] in contrast

to tool wear. Inspection of the results from face grooving of Inconel 718 published by Schlauer et al. [17] reveals that the increased thermal effect accompanying an increase in cutting speed from 410 m/min to 810 m/min enhances mainly surface tension and subsurface compression but has little influence on the stress anisotropy.

4. Conclusions

Electron channeling contrast imaging and X-ray diffraction were used to study machining induced microstructural changes and residual stresses, respectively, in Inconel 718 samples prepared by high speed turning under different cutting conditions. The following conclusions can be drawn from the investigation:

Mechanical forces and heat generated in the cutting process induced significant microstructural changes in the cutting affected zone. For cutting using a new tool, a surface layer of ultrafine grains formed because of local severe plastic deformation and high cutting heat. The layer beneath was heavily deformed, showing distorted grains and grain boundaries, deformation bands, and crossed slip bands; however, little influence of cutting temperature on the deformed microstructure was observed.

With the development of wear in the tool flank, the thicknesses of the fine-structured layer and the heavily deformed zone were increased as a result of increased mechanical forces and cutting heat. The temperature influence on the deformed microstructure was also enhanced. For turning using a worn tool, full recrystallization and dissolution of the strengthening γ" were observed in a surface layer up to several micrometer thick.

All the investigated samples showed a characteristic residual stress field with surface tensile stresses and subsurface compressive stresses, generated due to the localized plastic deformation and heating.

The increased cutting heat input and mechanical forces because of tool wear expanded both the tension and compression zones and resulted in much higher surface tensile stresses, up to 1500 MPa. When severe tool wear occurred, the residual stress field became strongly anisotropic, which could probably be ascribed to the different dependence of cutting force components on tool wear.

It has been shown that as tool wear progressed, surface damage in the form of microstructural alterations and tensile residual stresses increased. The level of tool wear is therefore crucial to the surface and subsurface quality of the machined part and severe tool wear may significantly affect its fatigue strength.

References

[1] R. M'Saoubi, J.C. Outeiro, H. Chandrasekaran, O.W. Dillon J., I.S. Jawahir, A review of surface integrity in machining and its impact on functional performance and life of machined products, International Journal of Sustainable Manufacturing. 1 (2008) 203-36.

[2] Y.B. Guo, W. Li, I.S. Jawahir, Surface integrity characterization and prediction in machining of hardened and difficult-to-machine alloys: a state-of-art research review and analysis, Mach. Sci. Technol. 13 (2009) 437-70.

[3] A. Devillez, G. Le Coz, S. Dominiak, D. Dudzinski, Dry machining of Inconel 718, workpiece surface integrity, J. Mater. Process. Technol. 211 (2011) 1590-1598.

[4] D. Ulutan, T. Ozel, Machining induced surface integrity in titanium and nickel alloys: A review, International Journal of Machine Tools & Manufacture. 51 (2011) 250-80.
[5] A.R.C. Sharman, J.I. Hughes, K. Ridgway, Workpiece surface integrity and tool life issues when turning Inconel 718 nickel based superalloy, Mach. Sci. Technol. 8 (2004) 399-414.
[6] J.M. Zhou, V. Bushlya, R.L. Peng, S. Johansson, P. Avdovic, J.-. Stahl, Effects of tool wear on subsurface deformation of nickelbased superalloy, Procedia Engineering 19 (2011) 407-413.
[7] V. Bushlya, J.M. Zhou, F. Lenrick, P. Avdovic, J. Stahlan, Characterization of white layer generated when turning aged inconel 718, 19 (2011) 60-66.
[8] A.R.C. Sharman, J.I. Hughes, K. Ridgway, An analysis of the residual stresses generated in Inconel 718 when turning, J. Mater. Process. Technol. 173 (2006) 359-67.
[9] W. Li, P.J. Withers, D. Axinte, M. Preuss, P. Andrews, Residual stresses in face finish turning of high strength nickel-based superalloy, J. Mater. Process. Technol. 209 (2009) 4896-902.
[10] R. Lin Peng, J.M. Zhou, J.M. S. Johansson, A. Billenius, V. Bushlya, J.-E. Stahl, Influence of dry cut and tool wear on residual stresses in high speed machining of nickel-based superalloy, To appear in Materials Science Forum. (2013).
[11] I.C. Noyan, J.B. Cohen, Residual Stress Measurement by Diffraction and Interpretation, (1987).
[12] P.S. Prevey, A method of determining the elastic properties of alloys in selected crystallographic directions for X-ray diffraction residual stress measurement, (1977) 345-54.
[13] C. Schlauer, M. Oden, Residual stress evolution and near-surface microstructure after turning of the nickel-based superalloy Inconel 718, Zeitschrift fur Metallkunde. 96 (2005) 385-92.
[14] R. Calistes, S. Swaminathan, T.G. Murthy, C. Huang, C. Saldana, M.R. Shankar, S. Chandrasekar, Controlling gradation of surface strains and nanostructuring by large-strain machining, Scr. Mater. 60 (2009) 17-20.
[15] J. Kenda, F. Pusavec, J. Kopac, Analysis of residual stresses in sustainable cryogenic machining of nickel based alloy - Inconel 718, J. Manuf. Sci. Eng. Trans. ASME. 133 (2011).
[16] D. Ulutan, M. Sima, T. Ozel, Prediction of machining induced surface integrity using elastic-viscoplastic simulations and temperature-dependent flow softening material models in titanium and nickel-based alloys, 223 (2011) 401-410.
[17] C. Schlauer, R.L. Peng, M. Oden, Residual stresses in a nickel-based superalloy introduced by turning, Mater. Sci. Forum. 404-407 (2002) 173-8.
[18] D.A. Axinte, R.C. Dewes, Surface integrity of hot work tool steel after high speed milling-experimental data and empirical models, J. Mater. Process. Technol. 127 (2002) 325-335.
[19] D. Dudzinski, A. Devillez, A. Moufki, D. Larrouquere, V. Zerrouki, J. Vigneau, A review of developments towards dry and high speed machining of Inconel 718 alloy, International Journal of Machine Tools & Manufacture. 44 (2004) 439-56.

Isolation of Contributions of Residual Stress and Weld Microstructure to Fatigue Crack Growth Rates in Welds

Rui Bao[1,*], Ning Tang[1], Xiang Zhang[2]

[1] Institute of Solid Mechanics, School of Aeronautic Science and Engineering, Beihang University, Beijing, 100191, P.R. China
[2] Department of Aerospace Engineering, School of Engineering, Cranfield University, Bedford, MK43 0AL, U.K.
* Corresponding author: rbao@buaa.edu.cn

Abstract Weld residual stresses and microstructural changes show coupled effects on fatigue crack growth rates resulting in more difficulties and complexity in crack growth life analysis for weld joints. Uncoupling these effects is a desirable option for understanding the influence of each factor and establishing more accurate crack growth prediction methods. A method for isolating the contributions of residual stress and weld microstructure change to fatigue crack growth rates in welds is presented in this paper. The proposed method is based on the superposition rule in fracture mechanics. Example of fusion weld specimens of different configurations and subjected to different loading conditions are presented to demonstrate the procedure of the method. Factors that will influence the solution, such as the applied and residual stress intensity factors, effective stress intensity factor ratio, choice of crack growth laws etc. are assessed and discussed in details.

Keywords Fatigue crack growth rate, Weld, Residual stress, Microstructural change, Isolation

1. Introduction

The application of advanced welding technologies to fabricate aircraft structural components is recognized as one of the most promising methods to achieve further structure weight reduction and manufacture cost saving, which requires a step change in the structural integrity assessment and, consequently, sets new challenges to the damage tolerance evaluation for welded joints. Crack growth life estimation is one of the key tasks in damage tolerance assessment. Welding procedure will introduce micro-structural changes as well as weld residual stress (RS), both of which have shown significant effects on fatigue crack growth (FCG) rates. Significant amount of research has been conducted in the past 20 years to understand the crack growth behaviors in aerospace aluminum alloys joined by different advanced welding technologies, e.g. fusion, laser and friction stir welding (FSW), which have different characteristics in RS levels and microscopic texture [1-9].

Effects of microstructure and residual stress on FCG depend on the relative positions of the crack to the weld zone. Tests on specimens with crack parallel to the weld line indicate that the growth rate in the regime with low hardness is much slower and of higher threshold [10, 11], while it is not always the same for longitudinal welded specimen (crack propagates perpendicular to the weld line). Fratini et al. [4] presented similar results in the study on longitudinal welded 2024-T351 aluminum alloy showing changes in microstructure and hardness play a major role in the fusion zone (FZ) and residual stresses take the first place outside the FZ. Pouget et al. [9] predicted crack growth rate in longitudinal FSW 2050 aluminum alloy by finite element simulation showing that the material parameters in FZ could have significant effects on predicting results. Therefore, it is a common practice that only the primary influential factor is considered in crack growth analysis of welds. For example, studies [7, 12-14] have concluded that RS plays a major role on the FCG rates for crack propagation perpendicular to a weld, consequently, superposition rule is adopted in this case to account for the combined effects of residual and applied stresses on crack growth, microstructural changes effect, although present obviously in weld nugget, is ignored. For crack propagation within

and parallel to a weld, crack growth rates have been found to be considerably lower than that in the base material (BM) [11]; effect of microstructural and hardness changes on FCG rate is most important and hence must be considered in this circumstance. However, in most cases, both microstructural change and residual stresses contribute to the change in crack growth rate in welds compared with that in the BM, and the two contributions couple each other [4,9,10,15]; neglecting any of the two (to simplify the crack growth analysis procedure) will result in inaccurate analysis.

On the other hand, it is well-known that RS magnitude and distribution are different for different dimensions, but the weld metal (WM) microstructural change should be the same for the same welding process parameters even though the dimensions of the test coupon and component are different. If the coupled effects on FCG rate can be isolated, it will provide a more accurate analysis tool for predicting crack growth life, and have wider applicability.

A method for isolating the contributions of RS and weld micro-structure change to fatigue crack growth in welds is presented in this paper, which is based on the superposition rule in fracture mechanics. An example of VPPA (Variable Polarity Plasma Arc) welded specimens is presented to demonstrate the isolation procedure. The characteristic parameter, i.e. stress intensity factors due to residual and applied stresses, is calculated by finite element method. Factors which will influence the results, such as applied and residual stress intensity factors, effective stress intensity factor ratio, choice of crack growth laws, etc. are assessed and discussed in details.

2. Methodology for Isolating the Contributing Factors

2.1. Basic idea

The difference in the crack growth rate between the WM and the BM is:

$$\Delta = \left(da/dN\right)_w - \left(da/dN\right)_b \qquad \text{* MERGEFORMAT (1)}$$

where $\left(da/dN\right)_w$ and $\left(da/dN\right)_b$ are the crack growth rates in the WM and BM respectively.

The difference Δ is the summation of the two contributing parts; one arises from weld residual stresses, labeled as Δ_1, and the other is due to the microstructural change introduced by the welding process, marked as Δ_2. Fig. 1 shows schematically the changes in crack growth rate consisting of Δ_1 and Δ_2. These increments, Δ, Δ_1 and Δ_2, can be either positive or negative and may not be kept the same with the increase of the stress intensity factor range ΔK.

As mentioned, Δ_1, arising from the residual stress, is associated with the configuration of the weld component, and Δ_2 depends only on the weld process parameters. If Δ_1 and Δ_2 can be obtained respectively, the contributions of residual stress and microstructural change on crack growth can be isolated.

2.2. Method for determining Δ_1

Since Δ_1 arises from RS, it is reasonable to assume that a weld procedure introduces residual stress only without changing the microstructure. The crack growth rate in this case is:

$$\left(da/dN\right)_R = \left(da/dN\right)_b + \Delta_1 \qquad (2)$$

where $(da/dN)_b$ is the crack growth rate in the BM subjected to externally applied load, and can be correlated by stress intensity factor range ΔK, stress ratio R, and material property constants A_1, A_2, …, A_n. Commonly used correlation equations are the Paris, Walker, Forman, and NASGRO equations etc. [16]. A general form of these laws can be expressed by Eq. (3), where $(da/dN)_R$ is the crack growth rate due to the combined applied stress and RS. Because there is no material property change, the superposition rule [17] can be used reasonably, and $(da/dN)_R$ can be found by Eq. (4).

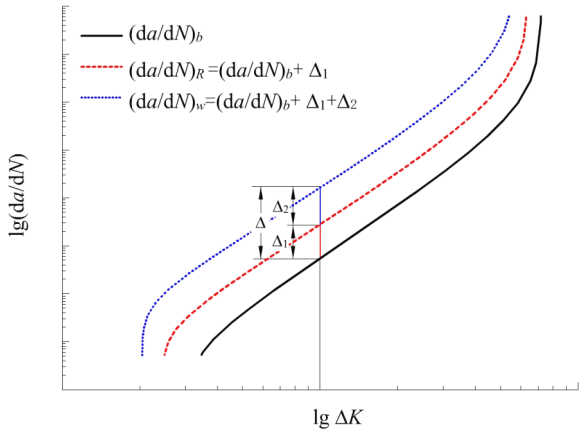

Fig. 1. Schematic of contribution of weld RS and material property change to FCG rate in WM

$$\left(da/dN\right)_b = f\left(\Delta K_{app}, R_{app}, A_1, \cdots, A_n\right) \tag{3}$$

$$\left(da/dN\right)_R = f\left(\Delta K_{tot}, R_{eff}, A_1, \cdots, A_n\right) \tag{4}$$

where ΔK_{app} and ΔK_{tot} are the stress intensity factor range due to the applied and total (applied + residual) stresses, respectively. R_{app} and R_{eff} are the stress intensity factor ratios due to the applied and total stress, respectively.

$$\Delta K_{tot} = K_{tot\max} - K_{tot\min} = \left(K_{app\max} + K_{res}\right) - \left(K_{app\min} + K_{res}\right) = \Delta K_{app} \tag{5}$$

$$R_{eff} = \frac{K_{app\min} + K_{res}}{K_{app\max} + K_{res}} \tag{6}$$

K_{res} is the stress intensity factor due to the RS, which can be calculated by either the finite element or weight function method [18]. Therefore, if the distribution of RS is available, both $(da/dN)_b$ and $(da/dN)_R$ can be calculated. Hence, Δ_1 could be obtained by:

$$\Delta_1 = \left(da/dN\right)_R - \left(da/dN\right)_b \tag{7}$$

2.3. Method for determining Δ_2

It may be imagined that if a weld procedure introduces no RS, then the only difference in crack growth rates between BM and WM is due to the change in material prosperities. In this case, the crack growth rate should be the intrinsic one which does not related to RS (in consequence to the specimen configuration):

$$\left(da/dN\right)_{Int} = \left(da/dN\right)_b + \Delta_2 \tag{8}$$

Since the change in crack growth rate is due to microstructural changes, $(da/dN)_{int}$ cannot be estimated by the theory of macroscopic fracture mechanics. It cannot be measured either because no weld procedure will introduce zero RS. However, it is possible to estimate Δ_2 by Eq. (9) after Δ_1 is

determined.

$$\Delta_2 = \Delta - \Delta_1 = \left[\left(da/dN\right)_w - \left(da/dN\right)_b\right] - \left[\left(da/dN\right)_R - \left(da/dN\right)_b\right] = \left(da/dN\right)_w - \left(da/dN\right)_R \quad (9)$$

where $(\mathrm{d}a/\mathrm{d}N)_w$ can be obtain by crack growth tests of WM specimens, quantity $(\mathrm{d}a/\mathrm{d}N)_R$ could be determined by Eq. (4).

3. Demonstration Example of the Isolating Method

3.1. Introduction of the Example

Due to the availability of RS and FCG rate test data, 2024-T3 VPPA weld specimens are used as a demonstration example. The VPPA welding process was firstly investigated in 1940s and developed extensively in 1980s by the NASA for achieving high quality welds in aluminium alloys [19]. During the welding process, the molten pool and the heat input produce significant metallurgical changes compared with the BM. Both middle crack tension (MT) and compact tension (CT) specimens are used in this example. The specimen geometries are shown in Fig. 2. Measured RS distributions in the MT and CT specimens are given in Fig. 3 [7, 13]. For the configurations with longitudinal weld, crack grows across the fusion zone (FZ), heat affected zone (HAZ) and BM. The hardness in the FZ, where the molten material is solidified, is the lowest as this area contains a fairly coarse dendritic structure with little precipitation hardening [20]. Material in the HAZ has been thermally treated by the heat input during welding. These microstructure changes result in different crack growth rates comparing with that of the BM. FCG tests data are reported in [7, 21] and shown here in Fig. 4. Two applied loading conditions are considered, i.e. constant amplitude (CA) and constant ΔK (CK), of which $R = 0.1$ and 0.6 for the CA condition and $\Delta K = 6$, 11, and 15 MPa$\sqrt{\text{m}}$ for the CK condition.

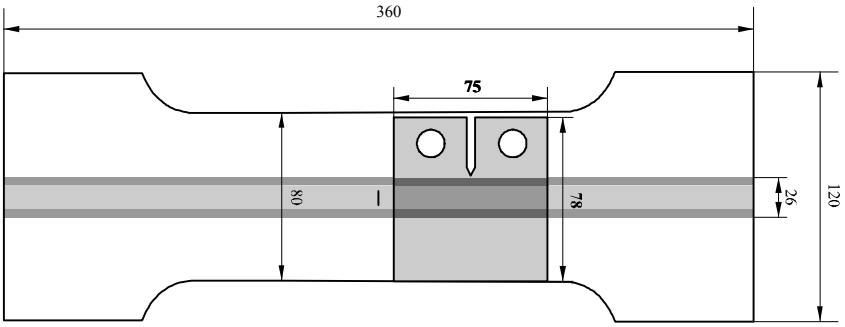

Fig. 2. MT and CT specimen configurations; CT is cut form an MT specimen [21]; unit: mm

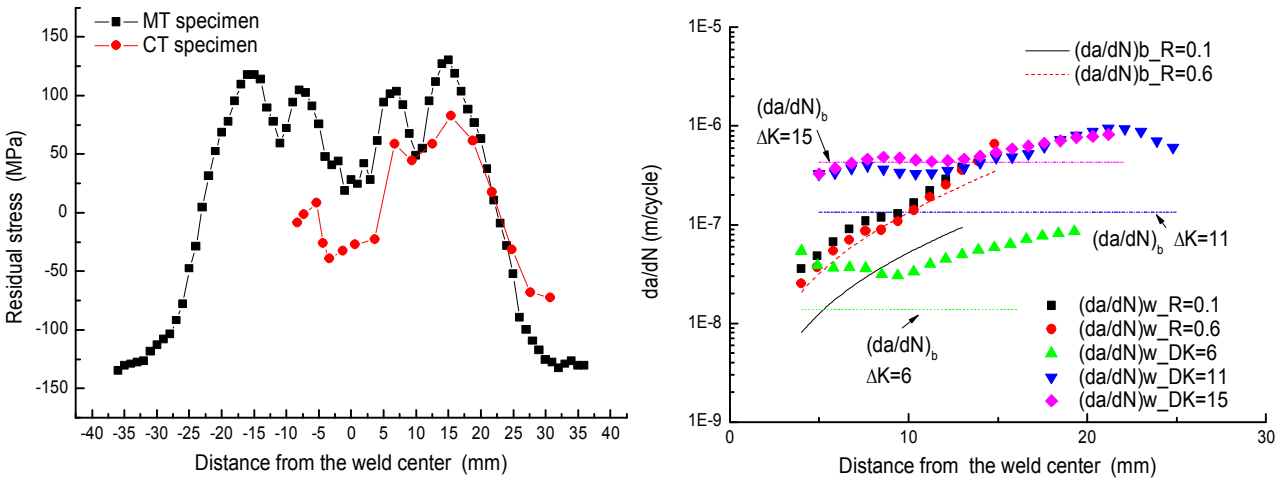

Fig 3. Longitudinal RS distribution

Fig. 4. Measured crack growth rates in BM & WM

3.2. Estimation of Δ_1

Δ_1 can be evaluated by Eq. (7), in which, both $(da/dN)_b$ and $(da/dN)_R$ are calculated by the NASGRO equation [16] expressed in Eq. (10)-(12). For $(da/dN)_b$, ΔK and R corresponding to the externally applied load, whereas, for the calculation of $(da/dN)_R$, ΔK and R in the following equations should be replaced by ΔK_{tot} and R_{eff} as given in Eq. (5) and (6). While, the material constants used in the equations are kept unchanged of the BM according to the presented method, which are available in the data base of the software AFGROW.

$$\frac{da}{dN} = C\left[\left(\frac{1-f}{1-R}\right)\Delta K\right]^n \frac{\left(1-\frac{\Delta K_{th}}{\Delta K}\right)^p}{\left(1-\frac{K_{\max}}{K_{crit}}\right)^q}, \tag{10}$$

$$f = \frac{K_{op}}{K_{\max}} = \begin{cases} \max(R, A_0 + A_1 R + A_2 R^2 + A_3 R^3) & R \geq 0 \\ A_0 + A_1 R & -2 \leq R \leq 0 \\ a_0 - 2A_1 & R \leq -2 \end{cases}. \tag{11}$$

$$\Delta K_{th} = \Delta K_0 \frac{\left(\frac{a}{a+a0}\right)^{\frac{1}{2}}}{\left(\frac{1-f}{(1-A_0)(1-R)}\right)^{1+C_{th}R}}. \tag{12}$$

where C, n, p, q, f are empirical material constants. Coefficients A_0, A_1, A_2 and A_3 are parameters associated with the stress state (sample thickness). The thickness effect is also considered by the apparent fracture toughness K_{crit}. Intrinsic crack length a_0 is set as 0.0015 in (0.0381 mm).

In the procedure of evaluating $(da/dN)_R$, one of the most important work is to calculate K_{res}. Both the Finite Element Method (FEM) and Weight Function Method (WFM) can be used [18]. It is worth mentioning that the RS will redistribute during the cutting of the specimens or during the self-balance procedure in the FE analysis. Therefore, it is of great importance to make sure that the distribution of RS in the FE model agrees reasonably with that in the specimen. The input and output RS in the example are given in Fig. 5. It can be seen that there is a difference in the input and output RS in the CT specimen. The input one is the same as that in MT specimen since CT specimen is cut from the MT specimen. The output RS is the redistributed result after making a slot in FE model, which is consistent with that in the actual CT specimen [7]. If the measured RS in CT specimen was input into the FE model, then the output RS would be much smaller than that in the actual specimen, which will lead to underestimation of K_{res}. K_{res} is subsequently calculated using soft package ANSYS. Calculated K_{res} distributions are also shown in Fig. 5 and compared with the WFM solution from [22]. Calculated Δ_1 values are illustrated in Fig. 6.

It can be seen from Fig. 5(a) that estimated Δ_1 varies with the specimen configuration and externally applied load. Fig. 5(b) indicates that for the MT specimens the ratio $\Delta_1/(da/dN)_b$ shows similar characteristic shape as the K_{res} distribution except for the case of $R = 0.6$. The influence of applied stress on Δ_1 will be discussed in Section 4. Evaluated Δ_1 for the CT specimen is negative indicating that crack growth rate in CT specimen is reduced remarkably due to the presence of residual stress.

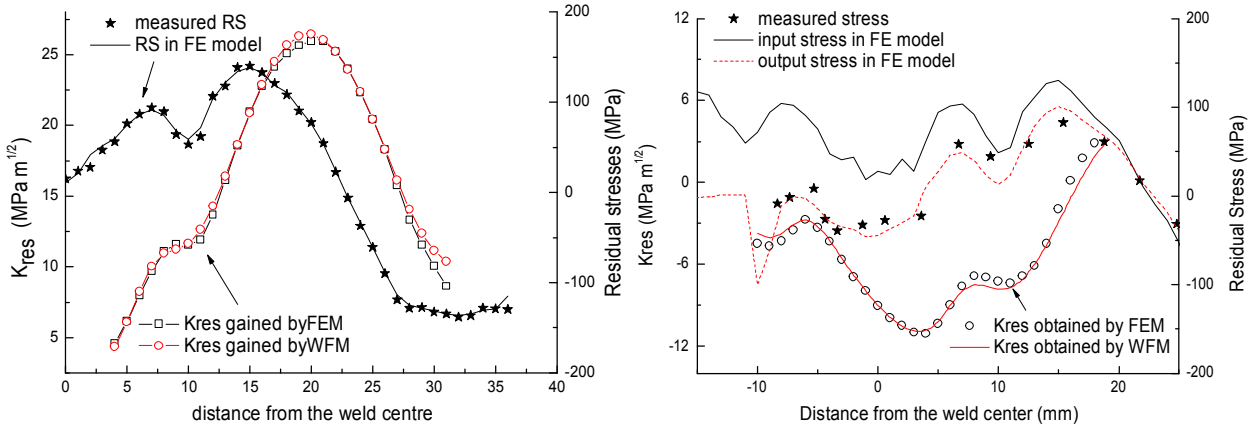

(a) (b)

Figure 5. Input, output RS and calculated K_{res} in (a) MT and (b) CT specimens

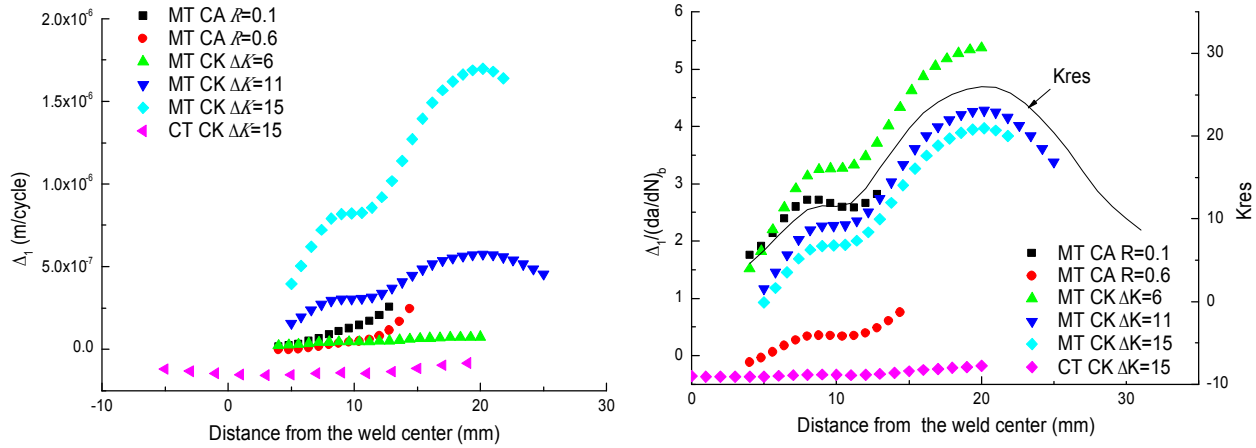

(a) (b)

Figure 6. (a) Estimated Δ_1 and (b) ratio $\Delta_1/(\mathrm{d}a/\mathrm{d}N)_b$

3.2. Evaluation of Δ_2

Since $(\mathrm{d}a/\mathrm{d}N)_w$ is obtained by tests, $(\mathrm{d}a/\mathrm{d}N)_R$ is calculated in section 3.1, Δ_2 can be evaluated by Eq. (9). The calculated results are given in Fig. 7. It can be seen from Fig. 7 that: (1) for the MT specimen with longitudinal weld (weld line parallel to the external stress), evaluated Δ_2 is lower than Δ_1 except the case ΔK=15MPa√m, which will be discussed in Section 4; (2) the ratio $\Delta_2/(\mathrm{d}a/\mathrm{d}N)_b$ shows similar characteristic shape as the hardness variation.

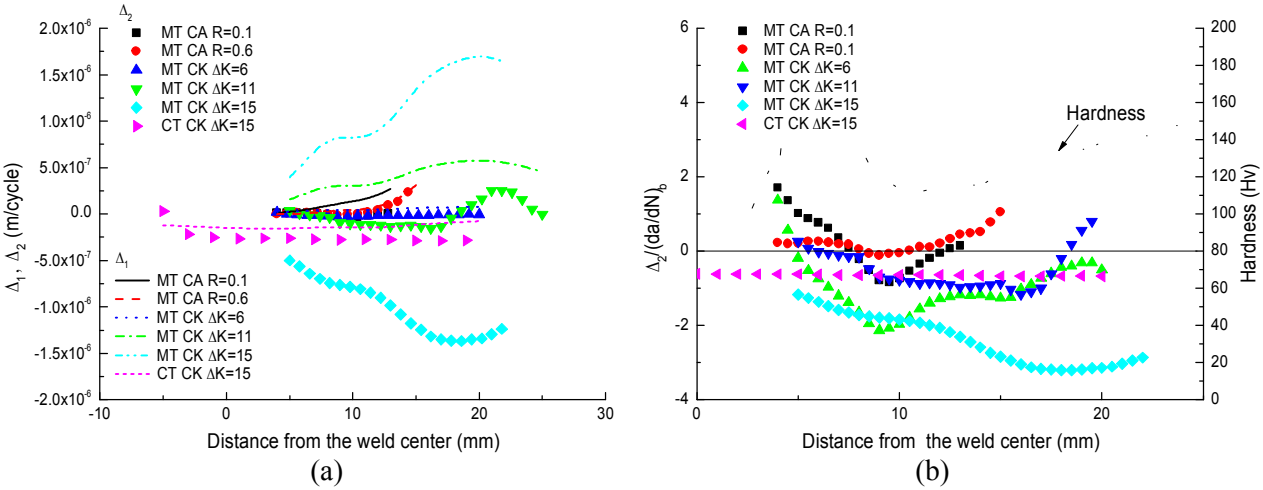

(a) (b)

Figure 7. (a) Estimated Δ_2 and (b) ratio $\Delta_2/(da/dN)_b$

4. Discussion on the Isolation Method

According to the results in Fig. 6 and 7, MT geometry is a better choice than the CT for isolating Δ_1 and Δ_2 in longitudinal weld specimen. Therefore, the following discussion is based on the MT configuration only.

4.1. Influence of applied stress level on isolation results

Evaluated Δ_1 and Δ_2 are functions of the externally applied stress, as shown in Fig. 6(a) and 7(a). Effect of applied stress on crack growth rate could be correlated by R_{app} and ΔK_{app}. Since $\Delta_1 = (da/dN)_R - (da/dN)_b$ and $\Delta_2 = (da/dN)_w - (da/dN)_R$, in which $(da/dN)_w$ is test data, evaluated Δ_1 and Δ_2 depend on the calculation of $(da/dN)_R$. Sensitivity analysis on the effects of R_{app} and ΔK_{app} on $(da/dN)_R$ is carried out. For the discussion of the effect of R_{app}, constant ΔK loading condition is considered with the applied ΔK = 6, 11, and 15 MPa√m, respectively. For the sensitivity of ΔK_{app}, three stress ratios are selected, i.e. R = 0.1, 0.3, 0.6. Sensitivity factors are obtained by taking the partial derivative of the output $(da/dN)_R$ with respect to an input factor R_{app} or ΔK_{app}. The results are given in Fig. 8.

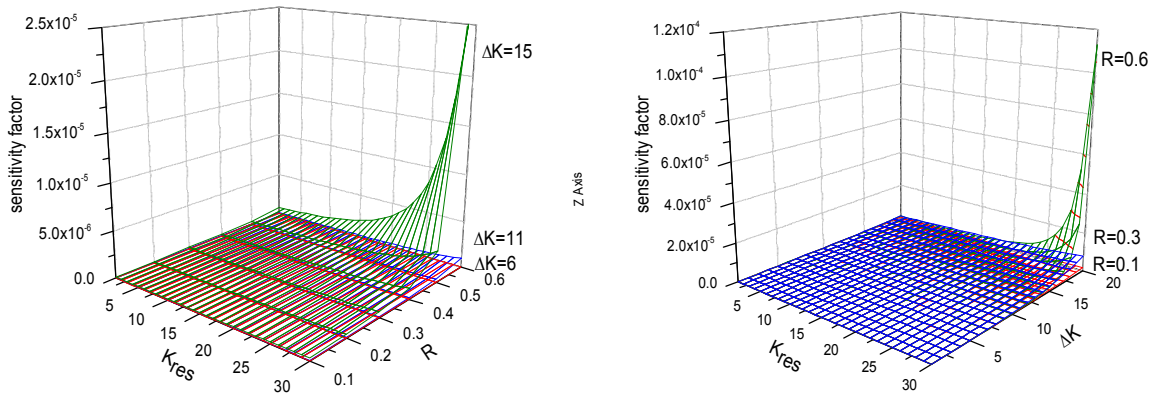

(a) (b)

Figure 8. Sensitivity analysis on (a) R_{app} and (b) ΔK_{app}

Fig. 8(a) indicates that if the applied ΔK level is low, e.g. 6 MPa√m, then calculated $(da/dN)_R$ is not very sensitive to the stress ratio; if the applied ΔK level is high, e.g. 15 MPa√m, the sensitivity factor increases significantly with the increase of R_{app} and K_{res}. Fig. 8(b) tells that if R_{app} levels are keep low, e.g. below 0.3, $(da/dN)_R$ is not very sensitive to ΔK_{app} level. Since $(da/dN)_R$ represents the effect of RS on crack growth rate, it is expected that $(da/dN)_R$ is sensitive to RS rather than applied stress. Therefore, high R ratios and high ΔK levels are not suitable for isolating Δ_1 and Δ_2.

4.2. Sensitivity analysis on K_{res}

Since K_{res} is calculated from measured RS distribution and scatter in RS data is unavoidable, it is unexpected that dispersion in RS data will introduce significant variation in the evaluated Δ_1 and Δ_2. Since K_{res} is calculated directly from RS, which keeps the error in RS, sensitivity analysis on the effects of K_{res} on $(da/dN)_R$ is performed using the same method as in Section 4.1. Two kinds of externally applied stress are used, one is the CA condition of $\Delta\sigma$ = 35 MPa and R_{app} = 0.1, 0.3 or 0.5,

the result is given in Fig. 9(a); the other is the CK condition with ΔK levels of 6, 11, and 15 MPa$\sqrt{m}$, corresponding results are shown in Fig. 9(b).

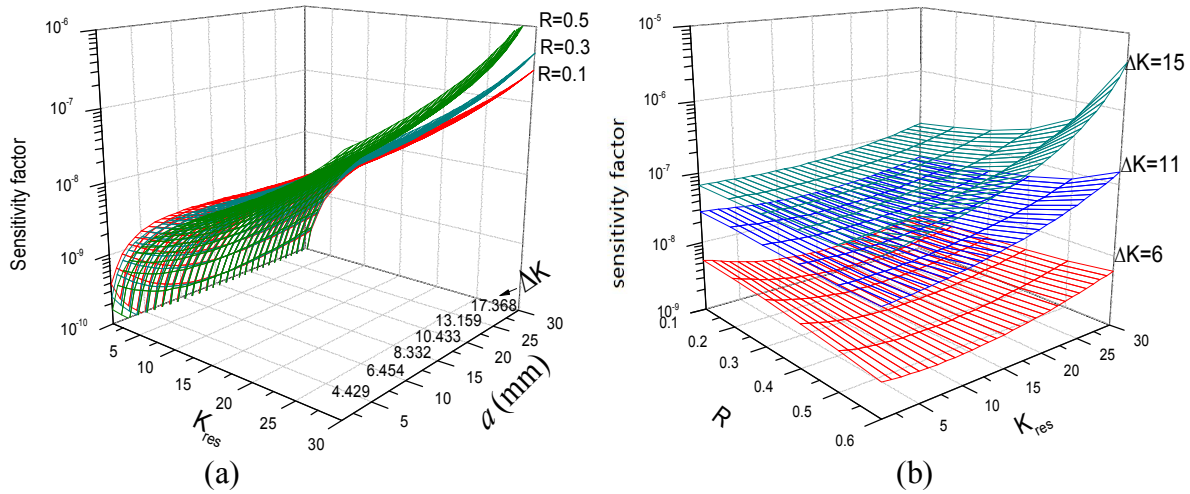

Figure 9. Sensitivity analysis on K_{res}

Fig. 9 indicates that the sensitivity factor of $(\mathrm{d}a/\mathrm{d}N)_R$ with respect to K_{res} depends on the ΔK level significantly, while, R_{app} shows little effect on it. It is expected that $(\mathrm{d}a/\mathrm{d}N)_R$ has certain sensitivity on K_{res} to reflect the effect of RS on crack growth rate, but sensitivity factor could better be kept in an acceptable level, otherwise, the error in measure RS data will show remarkable influence on the isolation results.

4.3. Influence of Crack Growth Laws on Isolation Results

The above discussions on the isolation method are all based on the NASGRO equation as shown in Eq. (10-12). Many other forms of crack growth rate correlation are available. Any crack growth law can be used in the isolation procedure if the parameters of R_{eff} and ΔK_{tot} are included in the equation. A popular and simple one is the Walker Equation [22] shown in Eq. (13).

$$\frac{\mathrm{d}a}{\mathrm{d}N} = C(\Delta K(1-R)^{(m-1)})^n . \tag{13}$$

Let the crack growth rate in BM be described by the Walker equation in accordance with that in the NASGRO equation, parameters in the Walker equation are set as $C = 4.8\times 10^{-11}$, n=3.2, m=0.6937, in unit of m and MPa. The loading case studied is the CA condition of R = 0.1, $\Delta\sigma_{\text{app}}$ = 35 MPa. Comparison of $(\mathrm{d}a/\mathrm{d}N)_b$ and $(\mathrm{d}a/\mathrm{d}N)_R$ obtained by these two equations is shown in Fig. 10(a) and evaluated Δ_1 and Δ_2 are in Fig. 10(b). It is can be seen that: (1) $(\mathrm{d}a/\mathrm{d}N)_R$ calculated by the two equations are slightly different, although $(\mathrm{d}a/\mathrm{d}N)_b$ correlated by the two equations are almost the same; (2) $(\mathrm{d}a/\mathrm{d}N)_R$ calculated by the Nasgro equation is a little higher than that by the Walker equation. This is because the effect of fracture toughness K_C is considered only in the Nasgro equation, and when $K_{\max} + K_{\text{res}}$ is close to K_C, the Nasgro equation will give better prediction; (3) the evaluated Δ_1 and Δ_2 by these two equations are the same in trends and show slightly difference in value, this difference could be covered by the scatter in crack growth rate; (4) the Walker equation is simple in format and easy for assessing the influence of applied and residual stresses, which is a good choice when the applied and residual stresses are in a acceptable level.

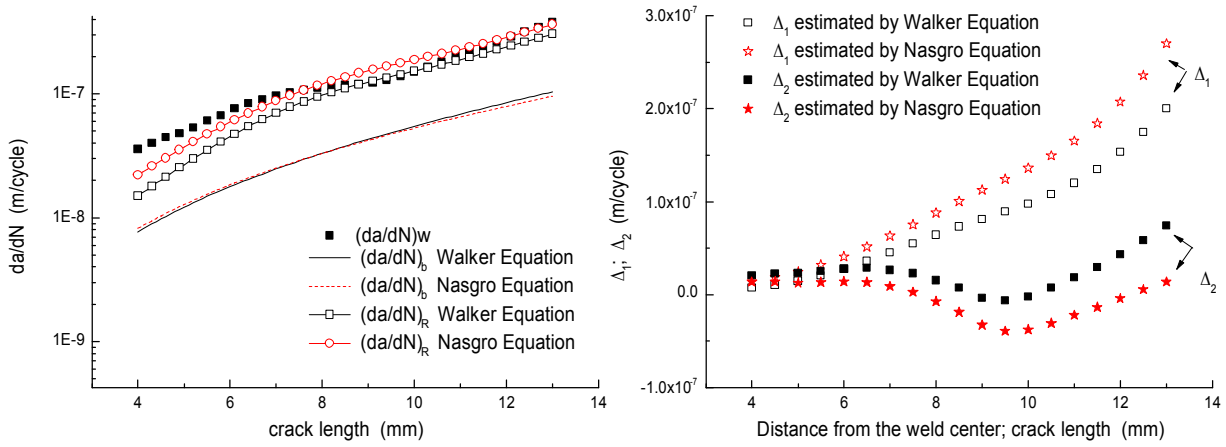

Figure 10. Comparison of the isolation results obtained by the Walker and Nasgro Equations

5. Conclusion

An isolation method for the contributions of residual stress and microstructural change in weld on fatigue crack growth rate is presented, and the factors affecting the isolation results are identified. It can be concluded that: (1) the presented method is applicable; (2) for specimens containing longitudinal weld, MT configuration is better than CT in the application of the isolation method; (3) the isolation results are found to be influenced by the test loading condition. High R_{app} or high ΔK_{app} are not good choice for studying the influential factors, but too low in R_{app} or ΔK_{app} can introduce crack closure in negative RS region, which is not good choice either; (4) if the applied stress is kept in a suitable level, a simpler crack growth law that include the effect of R and ΔK can be used in the presented method.

Acknowledgements

The National Natural Science Foundation of China is acknowledged for supporting the project (11272029).

References

[1] C.Dalle Donne, G.Biallas, T.Ghidini, G.Raimbeaux. Effect of weld imperfection and residual stress on the fatigue crack propagation in friction stir welded joints.In:Proceedings of the second international symposium on friction stir welding, Gothenberg, Sweden,June 2000.

[2] R.John, K.V.Jata, K.Sadananda, Residual stress effects on near threshold fatigue crack growth in friction stir welds in aerospace alloys. Int J Fatigue, 25 (2003) 939-948.

[3] Y.C.Lam, K.S. Lian, The effect of residual stress and its redistribution on fatigue crackgrowth.Theor Appl Fract Mech, 12 (1989) 59-66.

[4] L.Fratini, S.Pasta, A.P.Reynolds, Fatigue crack growth in 2024-T351 friction stir welded joints: Longitudinal residual stress and microstructural effects. Int J Fatigue, 31 (2009) 495-500.

[5] R.Galatolo, A.Lanciotti, Fatigue crack propagation in residual stress fields of welded plates. Int J Fatigue, 19 (1997) 43-49.

[6] T.Ghidini, C.D.Donne, Fatigue crack propagation assessment based on residual stresses obtained through cut-compliance technique. Fatigue Fract Eng Master Struct, 30 (2007) 214-222.

[7] C.D.M.Liljedahl, J.Brouard,et al, Weld residual stress effects on fatigue crack growth behavior of aluminium alloy 2024-T351.Int J Fatigue, 31 (2009) 1081-1088.

[8] J.Christopher. Lammi, A.Diana. Lados, Effects of residual stress on fatigue crack growth behavior of structural materials:Analytical corrections. Int J Fatigue, 33 (2011) 858-867.

[9] G.Pouget, A.P.Reynolds, Residual stress and microstructure effects on fatigue crack growth in AA2050 friction stir welds. Int J Fatigue, 30 (2008) 463-472.
[10] G..Bussu, P.E.Irving, The role of residual stress and heat affected zone properties on fatigue crack propagation in friction stir welded 2024-T351 aluminium joints. Int J Fatigue 25 (2003) 77-88.
[11] K.V.Jata, K.K.Sankaran, J.J.Ruschau, Friction-stir welding effects on microstructure and fatigue of aluminium alloy 7050-T7451. Metallurgical and Material Transactions, 31A (2000) 2181-2192.
[12] Y.E.Ma, P.Staron., T.Fischer, P.E.Irving, Size effects on residual stress and fatigue crack growth in friction stir welded 2195-T8 aluminium-Part: Modelling. Int J Fatigue, 33 (2011) 1426-1434.
[13] C.D.M.Liljedahl, O.Zanellato, M.E.Fitzpatrick, J.Lin, L.Edwards, The effect of weld residual stresses and their re-distribution with crack growth during fatigue under constant amplitude loading. Int J Fatigue, 32 (2010) 735-743.
[14] G.Servetti, X.Zhang, Predicting fatigue crack growth rate in a welded butt joint: The role of effective R ratio in accounting for residual stress effect, 76 (2009) 1589-1602.
[15] M. A.Sutton, A.P.Reynolds, BC. Yang, R. Taylor, Mode Ⅰ fracture for 2024-T3 friction stir welds. Materials Science and Engineering A, 354 (2003) 6-16.
[16] J.A.Harter, AFGROW user guide and technical manual. AFRL-VA-WPTR-2008, XXXX,AFGROW for Windows XP /VISTA,Version 4.0012.15, July 2008.
[17] D.V.Nelson, Effects of residual stress on fatigue crack propagation. in: ASTM STP 776 American Society for Testing and Materials, Philadelphia, 1982, pp.172-194.
[18] R. Bao, X. Zhang, N. A. Yahaya, Evaluating stress intensity factor s due to weld residual stress by the weight function and finite element methods. Eng Frac Mechanics, 77 (2010) 3143-3156.
[19] R.Hou, D.M.Evans, J.C.McClure, A.C.Nunes, G.Garcia, Shielding gas and heat transfer efficiency in plasma arc welding. Weld J.75 (1996) 305-310.
[20] F.Lefebvre, Micromechanical assessment of fatigue in airframe fusion welds. PhD Thesis. University of Southampton, UK,2003.
[21] J.Brouard, J.Lin,P.E.Irving, Effects of residual stress and fatigue crack closure during fatigue crack growth in welded 2024 aluminium. In: Proceedings of fatigue, Atlanta, USA,June 2006.
[22] K.Walker, The effect of the stress ratio during crack propagation and fatigue for 2024-T3 and 7075-T6 aluminium.in: ASTM STP 462,Amrican Society for Testing and Materials, Philadelphia,1976,pp.1-14.

Polymeric Fiber Arrays for Adhesion

Shing-Chung Wong*, Johnny F. Najem, Guang Ji, Shuwen Chen

Department of Mechanical Engineering, The University of Akron, Akron, OH 44325-3903
* Corresponding author: swong@uakron.edu

Abstract The ability of geckos to adhere to vertical solid surfaces comes from their remarkable feet with millions of projections terminating in nanometer spatulae. In this paper, we present a simple yet robust method for fabricating directionally sensitive dry adhesives. By using electrospun nylon 6 nanofiber arrays, we create gecko-inspired dry adhesives, that are electrically insulating, and that show shear adhesion strength of 27 N/cm^2 on a glass slide. This measured value is 270% that reported of gecko feet and 97-fold above normal adhesion strength of the same arrays. The data indicate a strong shear binding-on and easy normal lifting-off. Size and surface boundary of fibers both affect on the shear adhesion. This anisotropic strength distribution is attributed to enhanced shear adhesion strength with decreasing fiber diameter and an optimum performance of nanofiber arrays in the shear direction over a specific range of thicknesses.

Keywords dry adhesion, high aspect ratio structure, electrospun nylon 6 nanofibers

1. Introduction

Geckos are exceptional in their ability to climb on smooth and rough surfaces. The feet of a gecko possess the most versatile adhesive known in nature which produces a clinging capability of 10 N/cm^2 [1]. With growing interest in detachable adhesives, new materials are explored such as the types that employ elastomers, thermoplastics, and pressure-sensitive polymers [2]. Generally, these adhesives produce substantial shear adhesion strengths but are considerably difficult to detach from surfaces. Commercial high strength adhesives make use of chemical interactions such as glues and permanently attach two surfaces. Subsequently, fabrication of dry adhesives with anisotropic force distributions has the potential in several applications such as tapes, fasteners, treads of wall-climbing robots, spiderman's suits, microelectronics, medical and space applications.

There are obvious size effects when the scaling decreases to nanoscale. High aspect ratio (AR) structures exhibit significant shear adhesion strength compared to ones with low AR(s) [3,4]. Electrospinning presents a versatile technique for fabricating nanofibers with significant AR [5,6]. Little has been done for fabricating dry adhesives, which are electrically insulating, and which possess significant shear adhesion strength with easy normal detachment.

With use of electrospun nylon 6 nanofiber membrane, we report herein the fabrication of electrically insulating dry adhesives with high shear adhesion strength for strong shear binding-on but with substantial normal detachment strength (V) for easy normal lifting-off. With the aid of microscopy and microanalyses, we investigate the effects of the fiber diameter, fiber surface roughness, and thickness of membrane on their corresponding adhesion strengths. Our research group first measured the adhesion work of electrospun polymer fibers [7-9] and, in this paper, we will focus on the bending stiffness and dimensional characteristics of these fiber fabrics. In our

study, we found that the stiffness of fiber fabrics and dimensional characteristics play a critical role in optimizing the van der Waals (vdW) interactions and thus the shear adhesion strength between electrospun nylon 6 and surface asperities.

2. Experimental

2.1. Collection of aligned electrospun fibers

Nylon 6 pellets (Sigma Aldrich, CAS 25038-54-4) are dissolved in formic acid (EMD Corporation, CAS 64-18-6) and magnetically stirred overnight. A syringe pump is employed for maintaining a solution drop on the tip of a stainless steel needle (Gauge 24). The latter needle is attached to a 5 mL capacity syringe filled with the solution. The needle is charged with a high voltage of 25 kV. The gap distance between the tip of the needle and the top of rotating disc collector is set to be 150 mm. Collector has a diameter of 150 mm and electrospun fibers are collected at take-up velocity of 20 m/s.

2.2. Fabrication of high AR nanofiber membrane

After collecting electrospun fibers for 10 minutes, a portion of the membrane is discarded to prepare the surface of the collector for peeling. A small part of the membrane is then placed on a glass slide using the tapered tip of a needle. The glass slide is thereafter rotated in the plane where membranes overlap one another. Subsequently, membranes with substantial thickness are obtained. These membranes are then installed in a holder.

2.3. Atomic Force Microscopy (AFM)

Contact-mode AFM is performed for investigating the elastic modulus of fiber E. A contact-mode probe (Veeco Inc.), with a tip radius of 12 nm and a cantilever spring constant of 0.125 N/m, is employed. The diameter and surface roughness of fibers are determined using tapping-mode AFM. A tapping-mode probe (MikroMasch Inc.), with a tip radius of 10 nm and a cantilever spring constant of 40 N/m, is employed. Scanning is done at a frequency of 0.5 Hz and data are analyzed by employing SPI3800N probe station software (Seiko, Inc.). Surface roughness of the nanofiber is obtained by tracing a line along the fiber axis. An average roughness of the fiber surface is determined.

2.4. Macroscopic adhesion testing

Nanofiber membrane is finger-pressed on a glass slide and then the weight is added to the end of the line. The weight consists of a beaker which is incrementally filled with water until membranes get separated from the glass slide. The contact area between membrane and a glass slide has a width and a length of 3 mm and 2 mm, respectively. The only two parameters which vary are membrane thickness and nanofiber diameter. No external normal load is applied to the membrane while being tested.

3. Results and discussion

3.1. Effects of membrane thickness (*T*) on shear adhesion

As shown in Figure 1A, nanofiber membrane displays low shear adhesion strengths for T less than 12 µm. However, for T ranging between 15 µm and 40 µm, the shear adhesion strength of nanofiber arrays substantially increases with rising T and reaches peak values. For T greater than 40 µm, the shear adhesion strength of membrane is significantly reduced with increasing T and reaches considerably low values above T of 80 µm. Shear adhesion testing is performed at an angle θ of 0° with the glass slide. The highest shear adhesion strength of 27 N/cm^2 is reached for membranes having fibers with d of 50 nm and T of 30 - 40 µm. A glass beaker is filled with water (total weight of 170 g, shear adhesion strength of 28.3 N/cm2) and carried by a small piece of membrane (3 mm by 2 mm). This shear adhesion strength is 415% greater than the one reported for PC nanofiber-based dry adhesives [10]. As shown in Figure 1B, nanofibrous membranes may be considerably flexible with a weak tensile strength for *T* less than 12 µm. Subsequently, these membranes are expected to retain a minimal real contact area with a substrate. Thus, the latter membranes have limited vdW interactions and hence could not carry a heavy load. Nevertheless, as presented in Figure 1C, it is suggested that the flexibility and tensile strength of membranes reach optimum performances for T between 30 and 40 µm. Thus, membranes retain a significant real contact area with the glass substrate during loading, which leads to a substantial shear adhesion strength. However, as shown in Figure 1D, it is proposed that nanofibrous membranes start losing their flexibility for *T* greater than 40 µm. This phenomenon causes an extensive decrease in the real contact area between the fibers and the glass slide leading to deteriorating shear adhesion strength.

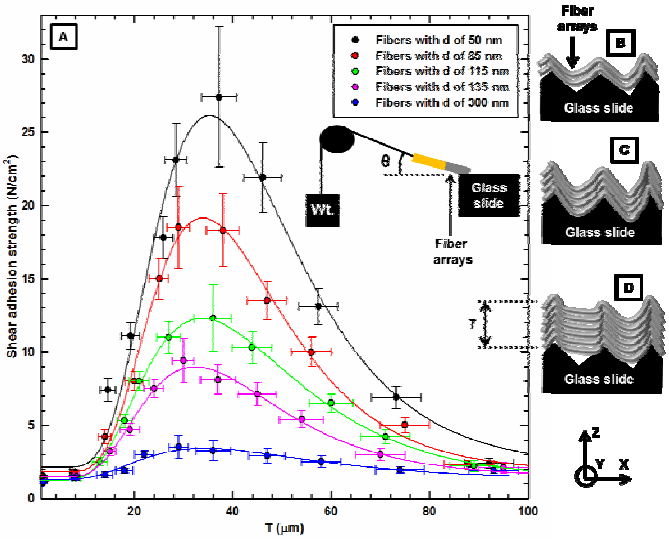

Figure 1. Shear adhesion strength as a function of *T* for aligned fiber membranes attached onto a glass slide with a preloading of 2kg

3.2. Effects of fiber packing density, nanofiber diameter (*d*) and fiber surface roughness on adhesion

As shown in Figure 2A-E, the packing density and aspect ratio of fibers are both noticeably enhanced with decreasing d. This enhancement is suggested to augment vdW interactions between

the fibers and the substrate leading to an upsurge in shear adhesion strength. As shown in Figure 2F, *d* extensively diminishes with decreasing concentration of polymer solution (*R*). The fiber packing density is characterized via SEM (FEI Quanta 200). Theoretical studies have shown that significant adhesion could be obtained by size reduction. Furthermore, the side contact of fibers with a substrate over a large contact area causes significant adhesion.

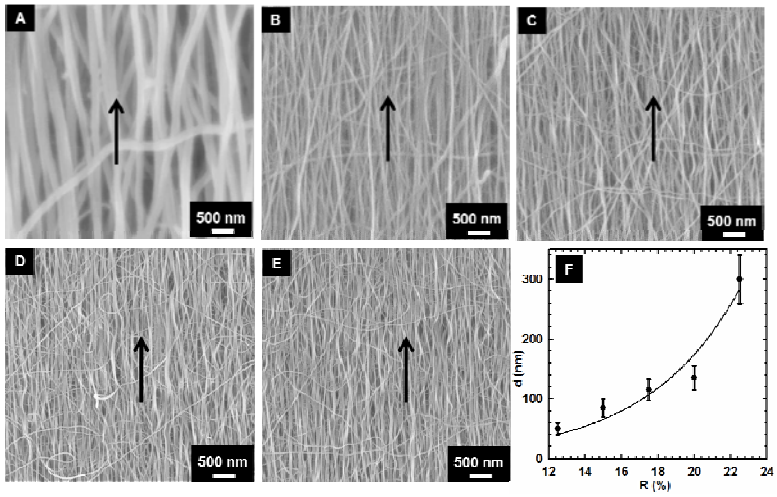

Figure 2. (A-E) Scanning electron microscopy (SEM) images of electrospun nylon 6 fibers with different *d*(s): 300 nm, 135 nm, 115 nm, 85 nm, and 50 nm, respectively; (F) *d* as a function of *R*

Surface boundary of fibers also makes contribution to the shear adhesion. For side wall contacts of fibers, the attractive force per unit length between the nanofiber and substrate is:

$$F_v = A\sqrt{d}\,/\left(16D^{2.5}\right) \tag{1}$$

Where A is the Hamaker constant, and D the gap distance between the surface of the nanofiber and the substrate [11,12]. There exists a cut-off gap distance $D=D_0$ which represents the effective separation between the nanofiber and substrate and at which the maximum F_v (F_{vM}) is estimated. The total F_{vM} is:

$$F_{vMK} = NLA\sqrt{d}\,/\left(16D_0^{2.5}\right) \tag{2}$$

Where N represents the total number of fibers along the contact width between the nanofiber arrays and the substrate (W) and is $N = W/d$. Replacing the value of N in the previous equation, we obtain:

$$F_{vMK} = LWA/\left(16D_0^{2.5}\sqrt{d}\right) \tag{3}$$

For constant values of *W* and the contact length between the nanofiber arrays and the substrate (*L*), F_{vMK} radically increases with decreasing *d*. These results suggest a substantial increase in the shear adhesion strength with diminishing *d*.

As shown in Figure 3, the surface roughness of fibers considerably diminishes with decreasing *d*. The latter decrease leads to a significant enhancement in shear adhesion strength between membrane and a substrate due to a considerable proliferation in the effective contact area.

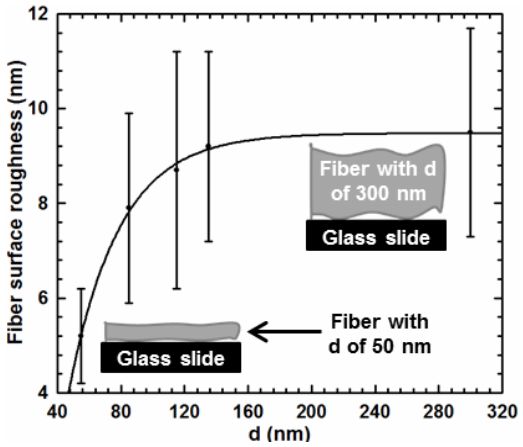

Figure 3. The surface roughness of a nanofiber as a function of *d*

3.3. Normal adhesion force

Membranes are easily peeled off a glass slide for $\theta = 90°$. For a contact area of (3x2) mm^2 with a glass slide, the normal adhesion force of the membranes is roughly 0.015 N, regardless of d and *T*. Meanwhile, the maximum shear adhesion force for nanofiber arrays is 1.6 N (Fibers with d of 50 nm) which leads to a $V = 100$. Thus, these nylon 6 fiber membranes are 10 times easier to detach from a glass slide in the normal direction dry adhesives. This significant *V* value is suggested to be due to the high AR of the nanofibers in this work. Thus, a significant decrease in the effective contact area between the nanofibers and the substrate arises during vertical detachment, which leads to an easy normal lifting-off.

3.4. Effect of Nanofiber Bending Stiffness on Adhesion

The bending stiffness of a nanofiber is $b = EI$ where *I* is the moment of inertia of the cross section of a nanofiber [13]. The indentation of a cantilever tip into the nanofiber is directly proportional to lateral deflection of the cantilever (ΔX) [2]. According to the Hertz model, ΔX is defined as:

$$h = \left[2\left(1-\nu^2\right)f/4a^{0.5}E\right]^{2/3} \tag{4}$$

Where *a* is the AFM probe tip radius, *v* the Poisson's ratio of the tested material, and f the applied normal load on a fiber. *f* is directly proportional to a sinusoidal drive signal (λ). As shown in Figure 4, ΔX continuously rises with increasing λ. Fibers with d of 300 nm display the largest slope (*P*). Fibers with d of 50 nm possess the smallest *P* where the latter is directly proportional to *E*. *P* of fibers with d of 300 nm (P_o) is taken as a reference value for determining the relative modulus of a fiber:

$$E_r = P/P_0 \tag{5}$$

As shown in Figure 5A, E_r for fibers with d of 50 nm is 6-fold above the one for fibers with *d* of 300 nm. This upsurge is mainly caused by the increase in molecular orientation during

electrospinning and nanofiber collection when d diminishes. Thus, it becomes more difficult for the tip of an AFM probe to penetrate deeper in the polymer chains of a fiber leading to a smaller ΔX value for a specific λ value [2]. Assuming that a nanofiber has a circular cross section [13],

$$I = \pi d^4/64 \tag{6}$$

The relative moment of inertia is:

$$I_r = I/I_0 = (d/d_o)^4 \tag{7}$$

Where d_0 is 300 nm and I_0 is I for d_0. The relative bending stiffness is:

$$b_r = E_r I_r \tag{8}$$

And thus:

$$b_r = E_r (d/d_0)^4 \tag{9}$$

As shown in Figure 5B, $1/b_r$ significantly rises with decreasing d for fibers with d less than 120 nm. Fibers with d of 50 nm are 150 times more flexible than the ones with d of 300 nm. As shown in insets of Figure 5B, this noteworthy flexibility is suggested to cause a substantial enhancement in the real contact area between a nanofiber and a glass slide. This enhancement could play a critical role to significantly increase the shear adhesion strength between a nanofiber and a glass slide.

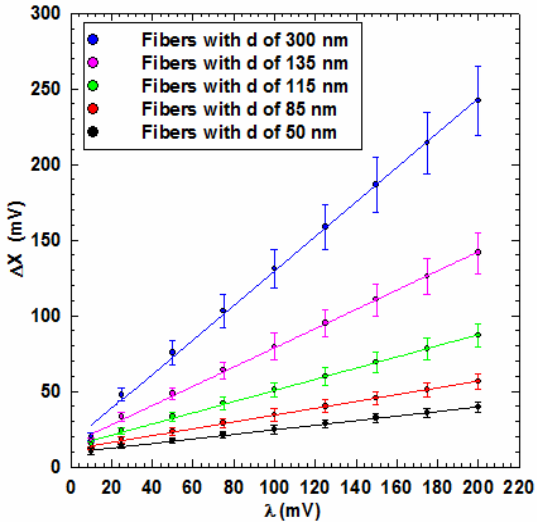

Figure 4. ΔX as a function of λ for fibers with varying d

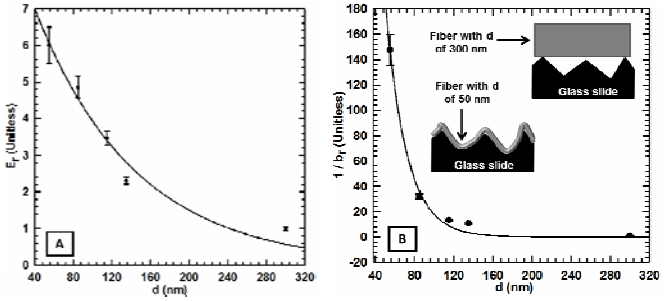

Figure 5. (A) E_r as a function of d. (B) $1/b_r$ as a function of d

4. Conclusions

We presented a technique for fabricating electrically insulating dry adhesives from electrospun nylon 6 nanofibers. These adhesives possess shear adhesion strength as high as 27 N/cm^2 on a glass slide. This measured value is 97-fold above normal adhesion strength of the same adhesive. For a definite d, the shear adhesion strength of membranes reaches optimum values for a specific range of arrays thicknesses while deteriorating otherwise. These optimum values suggest that these arrays could retain a significant real contact area with the substrate during loading. Fiber bending stiffness and fiber packing density are significantly increased with decreasing d while fiber surface roughness is noticeably reduced. These enhancements are proposed to considerably increase the shear adhesion strength between a nanofibrous membrane and a glass slide. The drastic increase is mainly attributed to a sizeable proliferation in vdW forces with enhanced contact area. This finding enables us to create electrically insulating dry adhesives with a strong shear adhesion and relatively weak normal adhesion for easy detachment.

Acknowledgements

This work is supported by National Science Foundation awards to SCW under CMMI 0746703 and IIP 1246773.

References

[1] Autumn, K.; Dittmore, A.; Santos, D.; Spenko, M.; Cutkosky, M. Frictional, the Journal of Experimental Biology. 209 (2006), pp. 3569-3579.
[2] Y Ji, C Li, G Wang, J Koo, S Ge, B Li, J Jiang, B Herzberg, T Klein, S Chen, J Sokolov, M Rafailovich, Euro Physics Letters (EPL), 84 (2008), pp.1-5.
[3] C Greiner, A DelCampo, E Arzt, Langmuir, 23 (2007), pp. 3495-3502.
[4] B Aksak, M Murphy, M Sitti, Langmuir, 23 (2007), pp. 3322-3332.
[5] M Jose, B Steinert, V Thomas, D Dean, M Abdalla, G Price, G Janowski, Polymer, 48 (2007), pp. 1096-1104.
[6] S-C Wong, A Baji, S Leng, Polymer, 49 (2008), pp. 4713-4722.
[7] Q. Shi, K.-T. Wan, S.-C. Wong, P. Chen, T.A. Blackledge, Langmuir, 26 (2010), pp. 14188–14193.
[8] H. Na, P. Chen, K.T. Wan, S.-C. Wong, Q. Li, Z. Ma, Langmuir 28 (2012) pp. 6677-6683 DOI: 10.1021/la300877r.
[9] Q. Shi, S.-C. Wong, W. Ye, J. Hou, J. Zhao, J. Yin, Langmuir 28 (2012) pp. 4663-4671.
[10] Ho A Yee, L Yeo, Y Lam, I Rodriguez, ACS Nano, 5 (2011), pp. 1897-1906.
[11] Qu L., Dai L., Stone M., Xia Z., Wang Z., Science, 322 (2008), pp. 238-242.
[12] Leckband, D.; Israelachvili, J. Quarterly Reviews of Biophysics, 34 (2001), pp. 105-267.
[13] B Chen, P.D. Wu, H Gao, R.Soc. Proceeding of the Royal Society, Series A, 464 (2008), pp. 1639-1652.

Influence of Surface Effects and Flexoelectricity on Vibration of Piezoelectric Nanobeams

Zhi Yan, Liying Jiang*

Department of Mechanical & Materials Engineering, Western University, London N6A 5B9, Canada
* Corresponding author: lyjiang@eng.uwo.ca

Abstract Nanostructured piezoelectric materials hold a promise for the development of novel nanodevices in nanoelectromechanical systems (NEMS) due to their efficient electromechanical coupling. To fulfill their potential applications, it is essential to quantitatively predict their fundamental physical and mechanical properties. In this work, the unique size-dependent properties of piezoelectric nanomaterials, which are believed to attribute to surface effects and flexoelectricity, are investigated through a modified Euler beam model. The surface effects are accounted in a modified beam theory through the surface piezoelectricity model and the generalized Young-Laplace equations, while the flexoelectricity is considered by using the higher-order theory of piezoelectricity. Simulation results on the vibration analysis of piezoelectric nanobeams reveal that the influence of surface effects and flexoelectricity varies with beam thickness and aspect ratio, in particular, such influence becomes more pronounced with the decrease of beam thickness. Vibration analysis also identifies possible frequency tuning of piezoelectric nanobeams by electrical load. In addition, the effect of axial boundary constraints in modeling has been studied, which provides a clear interpretation on the relaxation phenomenon of nanobeams under certain boundary constraints. This study is expected to provide a quantitative understanding on the fundamental physics of piezoelectric materials, thus leading to a better design for piezoelectric nanobeam-based devices.

Keywords Surface effects, Flexoelectricity, Size-dependent properties, Piezoelectric nanobeam

1. Introduction

One-dimensional piezoelectric nanostructures, such as piezoelectric nanowires, nanobelts and nanorods have been extensively used in nanoelectromechanical systems (NEMS) as nanosensors [1], nanoresonators [2] and nanogenerators [3, 4]. The superior performances exhibited by these devices can be attributed to the novel electromechanical coupling properties of piezoelectric materials at nanoscale. Therefore, to reveal the underlying physical mechanisms of piezoelectric nanomaterials and to achieve the unprecedented improvements of these nanosized devices, it is essential to conduct a quantitative study on the physical and mechanical properties of nanostructured piezoelectric materials.

"Small is different", it is expected that the physical properties of piezoelectric nanomaterials differ from their bulk counterparts. Efforts have been devoted to investigating the physical properties of piezoelectric nanostructures. For example, it was experimentally observed that the elastic and fracture properties of piezoelectric nanowires demonstrated a size-dependent behavior unlike the bulk piezoelectric wires [5, 6]. The size-dependent mechanical properties of piezoelectric nanomaterials have also been confirmed by conducting atomistic modeling and simulations [7]. Based on a molecular dynamics study, the size effects were found to have a prominent influence on the polarization distribution, piezoelectric coefficient and hysteresis behaviors of $BaTiO_3$ nanowires [8]. All the aforementioned studies indicated the size effects played a significant role in predicting the mechanical and physical properties of piezoelectric nanostructures. In parallel to experimental work and atomistic studies, continuum mechanics modeling, as an alternative and efficient tool, has

been naturally resorted to investigate the mechanical properties of nanostructured materials. However, classical continuum approaches, which ignore the variation of interatomic quantities, fail to capture the size effects of materials at nanoscale. Therefore, non-classical continuum models with the consideration of size effects are necessary to conduct the mechanical and physical analysis of nanoscale structures.

Due to the large surface area to volume ratio of typical nanostructures, surface effects are believed to attribute to the size-dependent properties of these structures. By taking into account of surface effects, Gurtin and Murdoch proposed a surface elasticity model for elastic materials [9], in which a surface is modeled as a thin layer with negligible thickness adhered to the bulk without slipping, and the constitutive and equilibrium equations for the surface layer are different from those in the bulk of the solid. Using this model, the size-dependent properties of elastic nanomaterials have been successfully predicted [10-12]. However, the surface elasticity model is not sufficient to investigate the mechanical behaviors of piezoelectric nanostructures with electromechanical coupling properties. In order to solve this problem, modified continuum model with electric field dependent surface effects has been developed for piezoelectric nanostructures [13]. In this surface piezoelectricity model, the surface stresses depend on surface piezoelectricity in addition to surface elasticity and residual surface stress incorporated in the surface elasticity theory. Based on this novel surface piezoelectricity model, the static and dynamic behaviors of various piezoelectric nanostructures have been investigated [13-16]. Simulation results indicated that the surface effects had a significant influence on the static bending, vibration and mechanical buckling properties of these piezoelectric nanostructures.

In literature, flexoelectricity was also believed to be responsible for the size-dependent properties of piezoelectric nanomaterials, which refers to a spontaneous polarization of dielectric materials due to a strain gradient or a non-uniform strain field. Maranganti *et al.* proposed a theoretical framework for dielectrics with the consideration of flexoelectricity, elucidating the mechanism for size-dependent electromechanical coupling due to strain or polarization gradients [17]. The strong size-dependent enhancement of the effective piezoelectric coefficients of piezoelectric nanomaterials was demonstrated by Majdoub *et al.* [18] with the incorporation of flexoelectricity into piezoelectricity theory. Eliseev *et al.* investigated the renomalization in properties of nanoferroics due to spontaneous flexoelectric effect [19]. Recently, Liu *et al.* studied the effect of flexoelectricity on electrostatic potential in a piezoelectric nanowire [20]. These existing studies indicated the necessity of considering flexoelectric effect in characterizing the properties of nanostructured piezoelectric materials.

The objective of this work is to conduct the vibration analysis of a piezoelectric nanobeam with the consideration of surface effects and flexoelectricity. The surface effects are accounted in a modified beam theory through the surface piezoelectricity model and the generalized Young-Laplace equations. It should be mentioned that in the current study, the surface effects on the vibration of the piezoelectric nanobeam will be investigated with the consideration of axial boundary constrains, which have been ignored in existing studies. In addition, the flexoelectric effect on the vibration behavior of a piezoelectric nanobeam will be studied using the higher order theory of

piezoelectricity.

2. Surface Effects on the Vibration of Piezoelectric Nanobeams

In this work, the vibration of a piezoelectric nanobeam with length L, thickness h and width b is studied with surface effects. As seen from Fig. 1(a), the beam is modeled as a bulk core surrounded by surface layers with negligible thickness. A Cartesian coordinate (x, y, z) is used to describe the piezoelectric beam, which is poled in z direction. An electric potential V is applied between the upper and lower surfaces of the beam with the electric boundary conditions $\Phi\left(h/2\right)=V$ and $\Phi\left(-h/2\right)=0$. The electric field is assumed to exist only in the beam thickness direction and can be determined from the electric potential Φ as $E_z=-\partial\Phi/\partial z$. To account for the surface effects, a surface piezoelectricity model is adopted here [13, 14]. According to this model, the constitutive equations for the surface and bulk of the one-dimensional beam can be expressed as follows:

$$\sigma_x^{\mathrm{s}}=\sigma_x^0+c_{11}^{\mathrm{s}}\varepsilon_x-e_{31}^{\mathrm{s}}E_z,\ D_x^{\mathrm{s}}=D_x^0, \tag{1}$$

$$\sigma_x=c_{11}\varepsilon_x-e_{31}E_z,\ D_z=e_{31}\varepsilon_x+\kappa_{33}E_z, \tag{2}$$

where σ_x^{s} and D_x^{s} are surface stress and surface electric displacement; σ_x^0 and D_x^0 are residual surface stress and surface electric displacement; c_{11}^{s} and e_{31}^{s} are surface elastic and piezoelectric constants; σ_x and D_z are bulk stress and bulk electric displacement; c_{11}, e_{31} and κ_{33} are bulk elastic, piezoelectric and dielectric constants; ε_x and E_z are the strain and electric field.

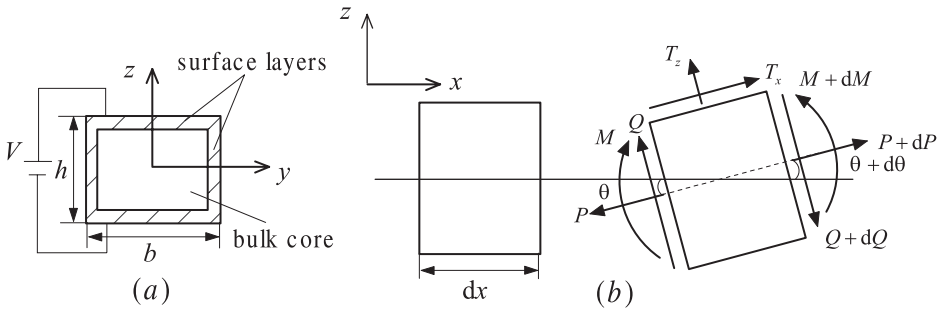

Figure 1. (*a*) Cross sectional view of a piezoelectric nanobeam with surface layers and bulk core. (b) An incremental element of the beam

The existence of surface stress induces traction jumps exerting on the bulk of the beam, as shown in Fig. 1(b). It should be mentioned that these traction jumps exist on the circumferential surfaces of the beam. According to the generalized Young-Laplace equations [21], traction jumps T_x and T_z can be written as:

$$T_x=\frac{\partial\sigma_x^{\mathrm{s}}}{\partial x},\ T_z=\frac{\sigma_x^{\mathrm{s}}}{R}, \tag{3}$$

with R being the radius of curvature defined positively when the normal of surface is pointed towards the center of curvature. Based on the free-body diagram of an incremental element of the beam, as shown in Fig. 1(b), the governing equations of the piezoelectric nanobeam are derived as follows:

$$\frac{\partial P}{\partial x}+\int_c T_x \mathrm{d}c=\rho bh\frac{\partial^2 u_0(x,t)}{\partial t^2}, \tag{4}$$

$$\frac{\partial^2 M}{\partial x^2}-P\frac{\partial^2 w(x,t)}{\partial x^2}-\int_c T_z \mathrm{d}c-\frac{\partial\int_c T_x z\mathrm{d}c}{\partial x}=-\rho bh\frac{\partial^2 w(x,t)}{\partial t^2}, \tag{5}$$

where c is the perimeter of the beam cross-section; ρ is the mass density; $P=\int\sigma_x \mathrm{d}y\mathrm{d}z$ and $M=-\int\sigma_x z\mathrm{d}y\mathrm{d}z$ are the axial force and bending moment; $u_0(x, t)$ and $w(x, t)$ are the axial displacement at z=0 and the transverse displacement.

Assuming that the beam thickness is much smaller than the radius of curvature induced by the applied loads and the beam cross section is constant along its length, thus, the Euler-Bernoulli beam theory can be adopted for modeling the piezoelectric nanobeam and the axial strain is expressed as:

$$\varepsilon_x=\frac{\partial u_0(x,t)}{\partial x}-z\frac{\partial^2 w(x,t)}{\partial x^2}. \tag{6}$$

It is worth noting that in existing studies of both elastic and piezoelectric nanobeams, $u_0(x, t)$ was assumed as zero based on the conventional Euler-Bernoulli model, therefore, the first term of Eq. (6) was ignored accordingly [10-12, 14, 15]. However, this assumption may not be accurate since $u_0(x, t)$ is not necessary zero for the nanobeam with surface effects. For example, the existence of surface stress induces an axial relaxation displacement as discussed in literature [22]. In addition, for piezoelectric nanobeams, the applied electrical load may also induce an axial displacement due to the inherent electromechanical coupling of piezoelectric materials. In fact, the beam can be either constrained without axial movement or allowed to have free movement with traction free boundary conditions. Therefore, the axial boundary conditions may influence the surface effects on the vibration behavior of piezoelectric nanobeams, which will be discussed later in this section.

In the absence of free electric charges, the electric displacement satisfies Gauss's law $\partial D_x/\partial x+\partial D_y/\partial y+\partial D_z/\partial z=0$, which gives an explicit expression of the electric field. Assuming $u_0(x,t)$ is independent of time t and substituting Eqs. (1)-(3) and (6) into Eqs. (4) and (5), the following governing equations can be obtained as:

$$\left[c_{11}bh+(2b+2h)c_{11}^{\mathrm{s}}\right]\frac{\partial^2 u_0(x)}{\partial x^2}=0, \tag{7}$$

$$(EI)^*\frac{\partial^4 w(x,t)}{\partial x^4}-N^*\frac{\partial^2 w(x,t)}{\partial x^2}=-\rho bh\frac{\partial^2 w(x,t)}{\partial t^2}, \tag{8}$$

in which $(EI)^*=\left(c_{11}+e_{31}^2/\kappa_{33}\right)bh^3/12+\left(c_{11}^{\mathrm{s}}+e_{31}^{\mathrm{s}}e_{31}/\kappa_{33}\right)\left(h^3/6+bh^2/2\right)$ is the effective bending rigidity of the beam and $N^*=\left[c_{11}\partial u_0/\partial x+e_{31}V/h\right]bh+2\left[\sigma_x^0+c_{11}^{\mathrm{s}}\partial u_0/\partial x+e_{31}^{\mathrm{s}}V/h\right]b$.

In this work, the vibration analysis will be conducted for cantilever (C-F), simply-supported (S-S)

and clamped-clamped (C-C) piezoelectric nanobeams, respectively. The boundary conditions are prescribed as:

$$u_0 = w = \frac{\partial w}{\partial x} = 0 \text{ at } x = 0,\ P^* = M^* = Q^* = 0 \text{ at } x = L \quad \text{(C-F)}, \tag{9}$$

$$\begin{cases} u_0 = w = M^* = 0 \text{ at } x = 0 \text{ and } x = L \text{ (Case 1)} \\ P^* = w = M^* = 0 \text{ at } x = 0 \text{ and } x = L \text{ (Case 2)} \end{cases} \text{(S-S)}, \tag{10}$$

$$u_0 = w = \frac{\partial w}{\partial x} = 0 \text{ at } x = 0 \text{ and } x = L \quad \text{(C-C)}, \tag{11}$$

where $P^* = \int \sigma_x \mathrm{d}y\mathrm{d}z + \int_c \sigma_x^{\mathrm{s}} \mathrm{d}c = \left[c_{11}\partial u_0/\partial x + e_{31}V/h\right]bh + 2\left[\sigma_x^0 + c_{11}^{\mathrm{s}}\partial u_0/\partial x + e_{31}^{\mathrm{s}}V/h\right](b+h)$ is the effective axial force; $M^* = (EI)^* \partial^2 w/\partial x^2$ is the effective moment; and $Q^* = (EI)^* \partial^3 w/\partial x^3 - N^* \partial w/\partial x$ is the effective shear force. It should be mentioned that two different axial boundary conditions may apply for simply-supported piezoelectric beam, as shown from Eq. (10). The beam is constrained without axial moving under the Case 1 boundary condition while traction free is adopted under the Case 2 boundary condition. The traction free boundary condition is also adopted for the cantilever beam as indicated in Eq. (9). Under this condition, an uniform strain $\varepsilon = \partial u_0/\partial x = -\left[e_{31}Vb + 2\sigma_x^0(b+h) + 2e_{31}^{\mathrm{s}}V(b+h)/h\right] / \left[c_{11}bh + 2c_{11}^{\mathrm{s}}(b+h)\right]$ is induced by the applied electrical load and surface effects, which will influence the vibration behavior of piezoelectric nanobeams. After applying these boundary conditions, the resonant frequencies of the piezoelectric nanobeams can be determined. For conciseness, the derivation procedures are omitted here.

To show the surface effects on the vibration behavior of a piezoelectric nanobeam quantitatively, PZT-5H is taken as an example material with the bulk material properties being c_{11}=126 GPa, e_{31}=-6.5 C/m^2 and κ_{33}=1.3×10^{-8} C/V·m. In addition, the surface properties are taken as $c_{11}^{\mathrm{s}} = 7.56$ N/m, $e_{31}^{\mathrm{s}} = -3\times10^{-8}$ C/m and $\sigma_x^0 = 1.0$ N/m. In the current work, only the first mode resonant frequency of the piezoelectric nanobeam is studied. Firstly, the variation of the normalized resonant frequency $\omega^{\mathrm{s}}/\omega^0$ of a simply-supported piezoelectric nanobeam with beam thickness h under both Case 1 and Case 2 axial boundary conditions is plotted in Fig. 2. ω^0 is the resonant frequency calculated without the consideration of surface effects and the applied electrical load. The beam geometry is set as b=h and L=10h. It is clearly seen from this figure that the axial boundary constraint has a significant influence on the vibration of the piezoelectric nanobeam, as evidenced by the dissimilar variation trends. For example, when the axial boundary constraint is set as described in Case 1, the combined effects of surfaces and electrical load increase the resonant frequency of the piezoelectric nanobeams. When V=-0.1 V, the influence is the largest ($\omega^{\mathrm{s}}/\omega^0$ is about 1.2 at h=10 nm). However, under Case 2 boundary constraint, the resonant frequency can be either enhanced or reduced by the surface effects and the applied electrical load ($\omega^{\mathrm{s}}/\omega^0$ is about 1.01 and 0.95 when V=0.1 V and -0.1 V, respectively at h=10 nm). It is noted that the variation of resonant frequency with the applied electric potential in this figure indicates a possible avenue for frequency tuning of piezoelectric nanobeams. It is also observed that the surface effects have more prominent influence on the resonant frequency of a beam with smaller thickness. While such surface effects decrease with the increase of beam thickness h. Fig. 3 shows the variation of the normalized resonant frequency of a piezoelectric nanobeam against the beam thickness. The beam has the same geometric parameters as the one in Fig. 2 without any applied electrical load. It

demonstrates that the surface effects on the resonant frequencies of piezoelectric nanobeams are significantly influenced by the beam boundary conditions. For the S-S beam with Case 1 boundary constraint and the C-C beam, surface effects increase the resonant frequencies, while the trend is opposite for the S-S beam with Case 2 boundary constraint and the C-F beam. Again, surface effects are more significant for the beam with smaller thickness h and reduce with the increase of h. From these two figures, it is conduced that the axial boundary condition plays a substantial role in the transverse vibration of piezoelectric nanobeams with surface effects. Therefore, it is essential to consider the axial boundary constraints in predicting the vibration behavior of piezoelectric nanobeams.

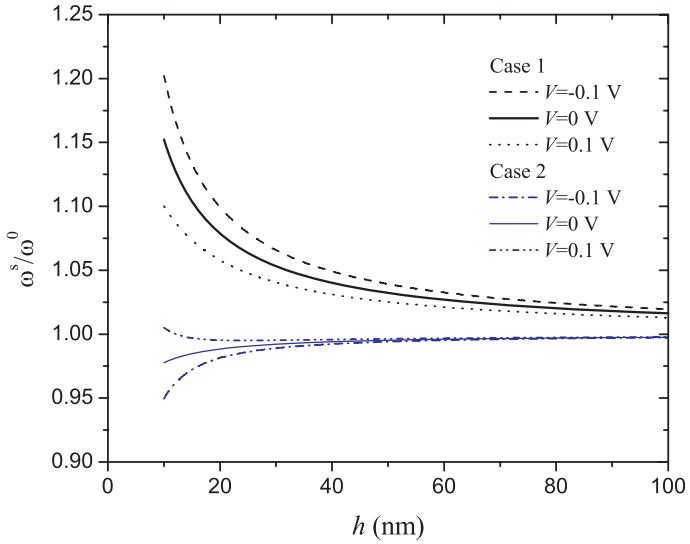

Figure 2. The normalized resonant frequency ω^s / ω^0 versus beam thickness h for a simply-supported piezoelectric nanobeam with surface effects under different axial boundary conditions

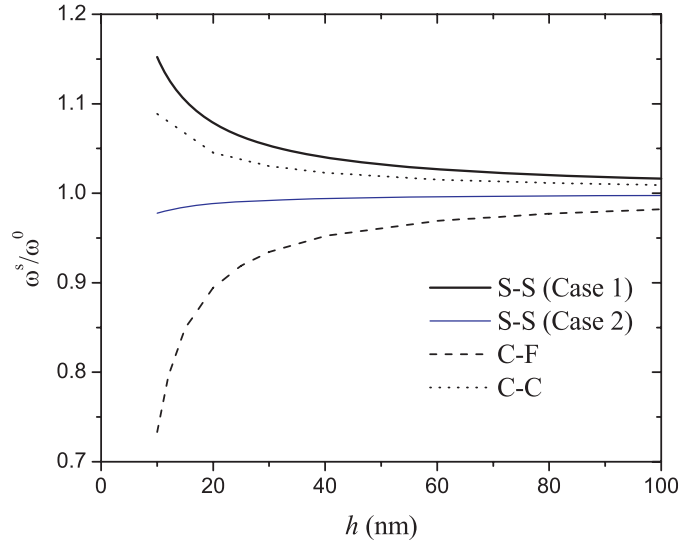

Figure 3. The normalized resonant frequency ω^s / ω^0 versus beam thickness h for a piezoelectric nanobeam with surface effects under different boundary conditions

As mentioned before, the applied electrical load and surface effects will induce an axial strain when the axial traction free condition is prescribed for the beam. As shown in Fig. 4, without the consideration of the surface effects, the product of this axial strain with the beam thickness is a

constant, i.e., $\varepsilon h = -e_{31}V / c_{11}$. When V=0 V, no axial strain is induced for the beam without considering the surface effects. However, the existence of the residual surface stress will still induce a relaxation strain as shown by the curve V=0 V with surface effects in Fig. 4. This relaxation phenomenon has been well discussed in [22] based on atomistic simulations. It is also observed in this figure that the surface effects lead to the size-dependency of this axial strain.

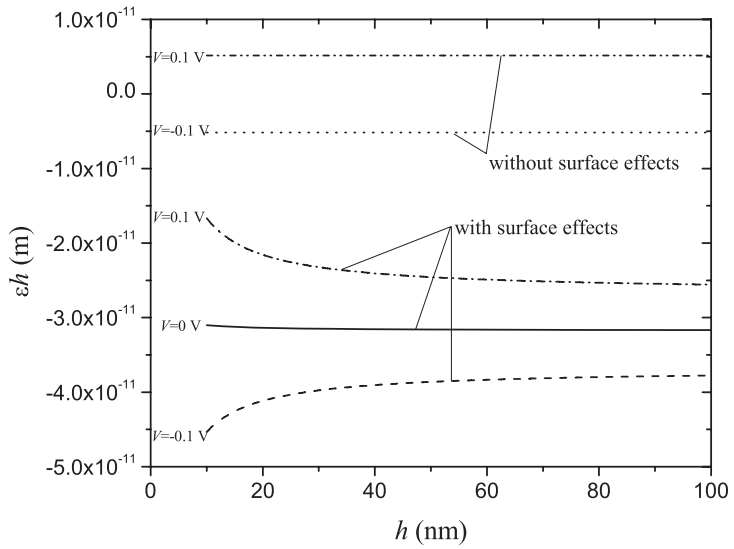

Figure 4. Axial strain εh versus beam thickness h for a piezoelectric nanobeam under different applied electrical load

3. Flexoelectricity on the Vibration of Piezoelectric Nanobeams

Flexoelectricity is induced by non-uniform deformation or strain gradient, which becomes significant as the structural size scales down to nanometers. To account for this effect, the higher order theory of piezoelectricity incorporating the strain gradient term will be adopted in the current work for a C-C beam. The same Cartesian coordinate system as shown in Fig. 1 is used to describe a piezoelectric nanobeam with flexoelectricity. The geometry, poling direction and electric boundary conditions of the beam are the same as those stated in Section 2. Under Euler-Bernoulli assumption, the axial strain can be defined as $\varepsilon_x = -z\partial^2 w / \partial x^2$. In the current study, we only consider the strain gradient $\varepsilon_{x,z}$, while $\varepsilon_{x,x}$ is ignored due to the large length scale along the beam axis direction. The relevant stress and electric field are σ_x and E_z, which can be expressed as [18]:

$$\sigma_x = c_{11}\varepsilon_x + d_{31}P_z,\ E_z = a_{33}P_z + d_{31}\varepsilon_x + f_{13}\varepsilon_{x,z}, \tag{12}$$

where P_z is polarization; a_{33} is dielectric susceptibility; and f_{13} is the flexoelectric coefficient. In addition, a higher order stress $\sigma_{xxz} = f_{13}P_z$ is introduced in the piezoelectricity theory. In the absence of free surface charges, the Gauss's law can be written as:

$$-\varepsilon_0 \frac{\partial^2 \Phi}{\partial z^2} + \frac{\partial P_z}{\partial z} = 0, \tag{13}$$

where $\varepsilon_0 = 8.85\times10^{-12}$ F/m is the dielectric permittivity of a vacuum. From Eqs. (12) and (13) with the consideration of electric boundary conditions of the beam, the polarization in the piezoelectric beam can be determined as:

$$P_z = \frac{\varepsilon_0 d_{31}}{\varepsilon_0 a_{33}+1} z \frac{\partial^2 w(x,t)}{\partial x^2} + \frac{f_{13}}{a_{33}} \frac{\partial^2 w(x,t)}{\partial x^2} - \frac{V}{a_{33} h}. \tag{14}$$

It is clearly seen from this equation that polarization can be induced by flexoelectricity. The governing equation of the flexoelectric nanobeam is formulated from Hamilton's principle [18]:

$$\delta U - \delta T - \delta W = 0, \tag{15}$$

where $U = \frac{1}{2}\int_{t_1}^{t_2}\int_{\Pi}\left(\sigma_x \varepsilon_x + \sigma_{xxz}\varepsilon_{x,z}\right)\mathrm{d}\Pi \mathrm{d}t$ (t is the time and Π is the entire domain of the structure) is the strain energy, and $T = \frac{1}{2}\int_{t_1}^{t_2}\int_{\Pi}\rho\left(\frac{\partial w}{\partial t}\right)^2 \mathrm{d}\Pi \mathrm{d}t$ is the kinetic energy. The resultant axial force is defined as $P_x = b\int_{-h/2}^{h/2}\left(\sigma_x - \sigma_{xxz,z}\right)\mathrm{d}z$, with the consideration of applied shear force Q_0, Q_L and moment M_0, M_L, the work is defined as $W = -\frac{1}{2}\int_{t_1}^{t_2}\left[\int_0^L P_x\left(\frac{\partial w}{\partial x}\right)^2 \mathrm{d}x + M_L \left.\frac{\partial w}{\partial x}\right|_L - M_0 \left.\frac{\partial w}{\partial x}\right|_0 - Q_L w_L + Q_0 w_0\right]\mathrm{d}t_0$. With these defined quantities, the governing equation is derived from Eq. (15) as:

$$A^* \frac{\partial^4 w(x,t)}{\partial x^4} + \frac{d_{31}}{a_{33}} Vb \frac{\partial^2 w(x,t)}{\partial x^2} = -\rho bh \frac{\partial^2 w(x,t)}{\partial t^2}, \tag{16}$$

with $A^* = \left[c_{11} - \varepsilon_0 d_{31}^2 / \left(\varepsilon_0 a_{33}+1\right)\right] bh^3/12 - f_{13}^2 / a_{33} bh$.

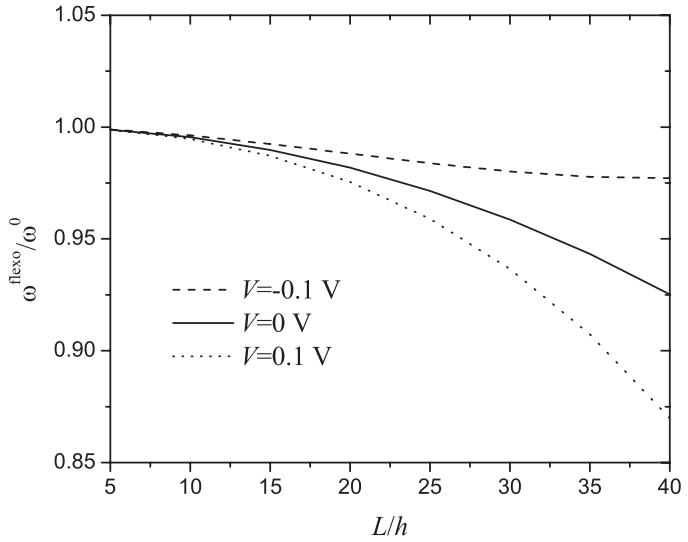

Figure 5. The normalized resonant frequency $\omega^{\text{flexo}} / \omega^0$ versus beam length to thickness ratio L/h for a piezoelectric nanobeam with flexoelectricity

For case study, the vibration of a clamped-clamped (C-C) piezoelectric nanobeam is investigated with the consideration of flexoelectricity. $BaTiO_3$ is taken as the example material with material properties being $c_{11} = 167.5$ GPa, $d_{31} = 3.5\times10^8$ V/m and $a_{33} = 0.8\times10^8$ V·m/C. The flexoelectric coefficients of $BaTiO_3$ can be determined from experiments or atomistic simulations. Following Ref. [19], in which the typical value of the flexoelectric coefficient is 1−10 V, we take $f_{13} = 5$ V. The variation of the normalized resonant frequency $\omega^{\text{flexo}} / \omega^0$ of the piezoelectric nanobeam against the beam length to thickness ratio L/h is plotted in Fig. 5, in which ω^0 is the resonant frequency calculated without the consideration of flexoelectricity and applied electrical load. The beam length is L=500 nm and b/h=1. When the applied electric potential is V=0 V, it is seen that flexoelectricity

decreases the resonant frequency of the clamped-clamped beam and this influence increases with the increase of L/h. The size-dependency of flexoelectricity is clearly demonstrated in this figure and such effect becomes negligible when the beam thickness becomes large, for example, the results with the consideration of the flexoelectricity approach to those from the classical theory when L/h=5. It is also observed that the influence of flexoelectricity on the normalized resonant frequency of the piezoelectric nanobeam depends on applied electrical load, as evidenced by the discrepancies among the results under different applied electrical load, which again indicate the possible frequency tuning of piezoelectric nanobeam by applying electrical load. However, such frequency tuning of piezoelectric nanobeams must incorporate the influence of flexoelectricity.

4. Conclusions

The influence of surface effects and flexoelectricity on the vibration behavior of piezoelectric nanobeams is investigated in the current work. Surface effects are incorporated into the modeling through the surface piezoelectricity model and the generalized Young-Laplace equations. In addition to the transverse boundary conditions, the axial boundary constraints are also considered for the beam with surface effects. Simulation results indicate both axial and transverse boundary constraints significantly influence the surface effects on the resonant frequencies of piezoelectric nanobeams. An axial strain relaxation is also observed under axial traction free boundary condition. Both applied electrical load and surface effects will affect such a relaxation phenomenon. Flexoelectricity is considered by adopting higher order theory of piezoelectricity. It is found that flexoelectric effect also has a substantial effect on the vibration of piezoelectric nanobeams. Both surface effects and the effect of flexoelectricity are more prominent for piezoelectric nanobeams with smaller thickness, which are attributed to the size-dependent properties of piezoelectric nanobeams. It is also observed that the resonant frequencies can be tuned by adjusting the applied electrical load. This work is expected to provide a better physical understanding of piezoelectric nanobeams and a guideline for the design of piezoelectric nanobeam-based devices.

Acknowledgements

This work was supported by the Natural Sciences and Engineering Research Council of Canada (NSERC).

References

[1] C.S. Lao, Q. Kuang, Z.L. Wang, M.C. Park, Y.L. Deng, Polymer functionalized piezoelectric-FET as humidity/chemical nanosensors. Appl Phys Lett, 90 (2007) 262107.
[2] S.M. Tanner, J.M. Gray, C.T. Rogers, K.A. Bertness, N.A. Sanford, High-Q GaN nanowire resonators and oscillators. Appl Phys Lett, 91 (2007) 203117.
[3] Z.L. Wang, J.H. Song, Piezoelectric nanogenerators based on zinc oxide nanowire arrays. Science, 312 (2006) 242–246.
[4] W.S. Su, Y.F. Chen, C.L. Hsiao, L.W. Tu, Generation of electricity in GaN nanorods induced by piezoelectric effect. Appl Phys Lett, 90 (2007) 063110.
[5] A.V. Desai, M.A. Haque, Mechanical properties of ZnO nanowires. Sens Actuators A: Phys, 134 (2007) 169–176.
[6] R. Agrawal, B. Peng, E.E. Gdoutos, H.D. Espinosa, Elasticity size effects in ZnO nanowires-A combined experimental-computational approach. Nano Lett, 8 (2008) 3668–3674.
[7] R. Agrawal, B. Peng, H.D. Espinosa, Experimental-computational investigation of ZnO nanowires strength and fracture. Nano Lett, 9 (2009) 4177–4183.

[8] Y.H. Zhang, J.W. Hong, B. Liu, D.N. Fang, Strain effect on ferroelectric behaviors of BaTiO3 nanowires: a molecular dynamics study. Nanotechnology, 21 (2010) 015701.
[9] M.E. Gurtin, A.I. Murdoch, A continuum theory of elastic material surfaces. Arch Ration Mech Anal, 57 (1975) 291–323.
[10] J. He, C.M. Lilley, Surface effect on the elastic behavior of static bending nanowires. Nano Lett, 8 (2008) 1798–1802.
[11] G.F. Wang, X.Q. Feng, Timoshenko beam model for buckling and vibration of nanowires with surface effects. J Phys D: Appl Phys, 42 (2009) 155411.
[12] C. Liu, R.K.N.D Rajapakse, Continuum models incorporating surface energy for static and dynamic response of nanoscale beams. IEEE Trans Nanotechnol, 9 (2010) 422–431.
[13] G.Y. Huang, S.W. Yu, Effect of surface piezoelectricity on the electromechanical behaviour of a piezoelectric ring. Phys Status Solidi B-Basic, 243 (2006) R22–R24.
[14] Z. Yan, L.Y. Jiang, Surface effects on the electromechanical coupling and bending behaviours of piezoelectric nanowires. J Phys D-Appl Phys, 44 (2011) 075404.
[15] Z. Yan, L.Y. Jiang, The vibrational and buckling behaviors of piezoelectric nanobeams with surface effects. Nanotechnology, 22 (2011) 245703.
[16] Y.H. Li, B. Fang, J.H. Zhang, J.Z. Song, Surface effects on the wrinkling of piezoelectric films on compliant substrates. J Appl Phys, 110 (2011) 114303.
[17] R. Maranganti, N.D. Sharma, P. Sharma, Electromechanical coupling in nonpiezoelectric materials due to nanoscale size effects: Green's function solutions and embedded inclusions. Phys Rev B, 74 (2006) 014110.
[18] M.S. Majdoub, P. Sharma, T. Cagin, Dramatic enhancement in energy harvesting for a narrow range of dimensions in piezoelectric nanostructures. Phys Rev B, 78 (2008) 121407.
[19] E.A. Eliseev, A.N. Morozovska, M.D. Glinchuk, R. Blinc, Spontaneous flexoelectric/flexomagnetic effect in nanoferroics. Phys Rev B, 79 (2009) 165433.
[20] C.C. Liu, S.L. Hu, S.P. Shen, Effect of flexoelectricity on electrostatic potential in a bent piezoelectric nanowire. Smart Mater Struct, 21 (2012) 115024.
[21] T.Y. Chen, M.S. Chiu, C.N. Weng, Derivation of the generalized Young-Laplace equation of curved interfaces in nanoscaled solids. J Appl Phys, 100 (2006) 074308.
[22] H.S. Park, P.A. Klein, Surface Cauchy-Born analysis of surface stress effects on metallic nanowires. Phys Rev B, 75 (2007) 085408.

Revisit on the fractal dimension in damage and fracture

Chunsheng Lu[1,*]

[1] Department of Mechanical Engineering, Curtin University, Perth, WA 6845 Australia
* Corresponding author: c.lu@curtin.edu.au

Abstract The catastrophic failure of materials is a complicated process, involving the nucleation, growth and coalescence of numerous cracks with a wide range of time and length scales. In this paper, the variation of fractal dimension and entropy during a damage evolution process, especially in the vicinity of a critical failure, is revisited. The results show that, as damage evolves, both the fractal dimension and entropy of the spatial distribution of microcracks decrease. A sudden drop of fractal dimension or entropy can be viewed as a likely precursor of fracture and its implications for the prediction of natural disasters such as mining-induced rock bursts and earthquakes are discussed.

Keywords Damage evolution, Fracture, Fractal dimension, Entropy

1. Introduction

The catastrophic failure of materials is a complicated natural process, which is usually induced by the nucleation, growth and coalescence of numerous cracks and/or voids with a wide range of time and length scales from micro- to macro-levels [1,2]. Although great efforts have been made on the study of the damage evolution and fracture process, it is still a big challenge of how to identify a physical parameter that can be used as a potential precursor of an impending failure. Fractal, known as the geometry of nature, has been widely applied to describe a variety of irregular, rough and fragmented structures that bear a special scaling relationship [3−9]. The study on fractal fracture has been attracting much interest from scientists in materials science and solid mechanics, and about half a hundred papers have been published each year over the last decade [10].

Experimental and simulation results have indicated that the fractal character of fracture surfaces of materials, either natural or artificial, is ubiquitous [4−10]. This finding provides both a novel method for fractography and a useful theory for building a linkage between the micro and macro-mechanics. The concept of fractal can provide insights into understanding several important issues in a damage evolution and fracture process, such as the fracture precursor and the influence of disorder on macroscopic mechanical properties.

2. Fractal dimension and entropy

Fractal refers to a geometric object or a natural phenomenon, possessing the properties of self-similarity, which can be described by a power law with the exponent defined as fractal dimension [3,5]. Let us assume that a damaged solid is divided into a number of small elements and the number of damaged elements n yields

$$n = r^{-d_f}, \tag{1}$$

where r is a dimensionless scale (e.g., the ratio of the characteristic size of microstructures and the length of a specimen) and d_f is the fractal dimension.

In continuum damage mechanics, a simple damage variable can be defined as, $D = n/N$, where N is the total number of (damaged and undamaged) elements, and $N = r^{-d}$ (d is the Euclidean dimension and here, $d = 3$). If the distribution of microcracks in a material is fractal, it is necessary to introduce fractal dimension in the definition of a damage variable [11]. According to Eq. (1), the

damage variable D can be expressed as

$$D = D_0 r^{d-d_f}, \tag{2}$$

where D_0 is the traditional damage parameter in the case of $d_f = d$. It is obvious that, therefore, $D_0 = 0$ and $D_0 = 1$ indicate the undamaged and fracture states, respectively.

Another simple method to measure the degree of disorder is to calculate the entropy of the spatial distribution of microcracks [12]. Entropy quantifies the diversity, uncertainty, or randomness of a system. Here, let us still assume that a solid consists of a total of N elements, and the number of microcracks in each element is evaluated just as in a box-counting method for calculating fractal dimension [3,5]. Then, the entropy S can be calculated by

$$S = -\sum_{i=1}^{N} \frac{n_i}{N} \ln \frac{n_i}{N}, \tag{3}$$

where n_i be the number of microcracks in the i-th element. The normalised entropy can be represented as S/S_0, where S_0 is the equipartition entropy, provided that microcracks are uniformly distributed in a sample [12]. Thus, we have $0 < S/S_0 \le 1$, and S_0 corresponds to the case with the maximum entropy. That is, as disorder of the spatial distribution of microcracks increases, entropy decreases.

3. A likely precursor of fracture

Based on the assumption of strain equivalence, the relationship between stress σ and strain ε in a damaged material can be written as, $\sigma = E(1-D)\varepsilon$, with E being the Young's modulus [13]. In consideration of the fractal distribution of microcracks, the constitutive relationship between stress and strain can be rewritten as

$$\sigma = E(1 - D_0 r^{d-d_f})\varepsilon, \tag{4}$$

where the fractal dimension d_f is a function of time t in a damage evolution and fracture process.

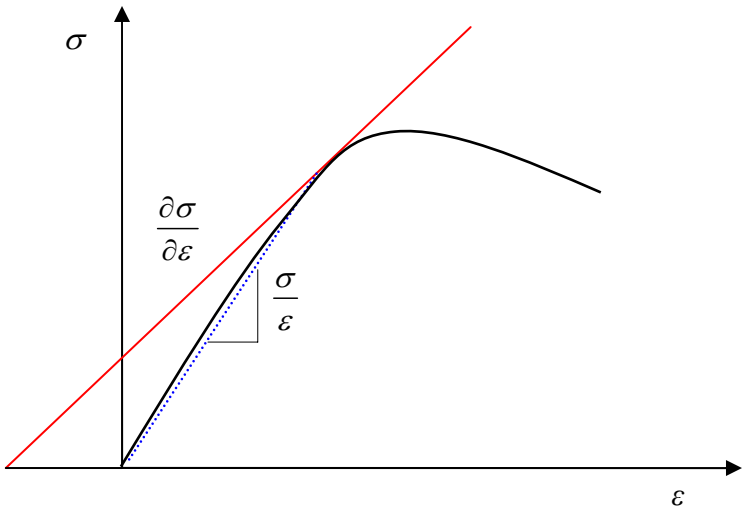

Figure 1. Illustration of a stress-strain curve during a damage evolution and fracture process, where $\partial\sigma/\partial\varepsilon$ and σ/ε are the tangent and secant slopes, respectively (adapted from [11]).

Differentiating both sides of Eq. (4), we have

$$\frac{\partial\sigma}{\partial\varepsilon} - \frac{\sigma}{\varepsilon} = -ED_0 A \frac{\varepsilon}{\dot{\varepsilon}} \frac{\partial d_f}{\partial t}, \tag{5}$$

where $\dot{\varepsilon} = \partial\varepsilon/\partial t$, $\partial\sigma/\partial\varepsilon$ and σ/ε are the slopes of tangent and secant lines of a stress-strain

curve, respectively, and $A = r^{d-d_f} \ln r < 0$ due to $0 < r < 1$ [11]. As illustrated in Fig. 1, it is seen that the following condition

$$\frac{\partial d_f}{\partial t} < 0, \tag{6}$$

is valid because of $\partial\sigma / \partial\varepsilon < \sigma/\varepsilon$, which means that, as damage evolves, fractal dimension of the spatial distribution of microcracks decreases.

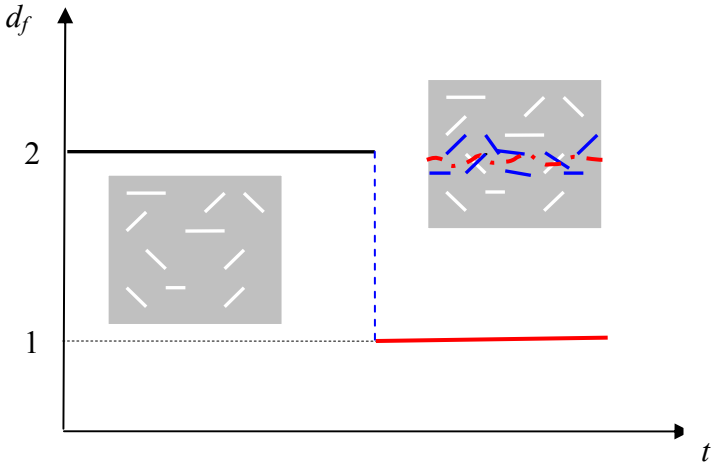

Figure 2. Schematic of fractal dimension versus time during a two-dimensional damage evolution process, where insets are two typical patterns at the initial and final damage stages (adapted from [11]).

As schematically shown in Fig. 2, in the initial damage stage, microcracks are uniformly nucleated in a specimen, but in the final stage and especially near the critical failure, cracks are localized on a surface, which will be the preferential site of fracture. As for the variation of fractal dimension, this corresponds to a roughly one-dimensional fracture profile (or a two-dimensional surface) in a two-dimensional (or three-dimensional) material. As we know, large stress or strain fluctuations in a damage evolution process indicate the divergence to failure, which is usually viewed as a critical phenomenon. As the damage localization approaches a critical point, a sudden drop of fractal dimension occurs.

4. Mining-induced rock bursts: a case study and its implications

As a case study, let us examine the data of a rock-burst-prone pillar in a galena mine, monitored by acoustic emission techniques [14]. The distribution of rock noise locations for 5 days prior to a major rock burst was collected. Based on Eqs. (1) and (3), fractal dimension and entropy of the spatial distribution of daily rock bursts can be calculated [6,11]. Fig. 3 shows the variation of fractal dimension and normalised entropy, and it is seen that both the fractal dimension and entropy decrease as the increase of time. The increase of the clustering degree of microcracks can be intuitively observed from the spatial distribution of rock bursts [14]. Prior to the major rock burst on 24 May, a sudden drop of fractal dimension or entropy occurs. This is in good agreement with our theoretical analysis. Thus, the reduction and sudden-drop of fractal dimension or entropy can be considered as a precursor of a catastrophic failure. However, the prediction of an exact occurrence time is still very difficult since there are small fluctuations of fractal dimension or entropy with time caused by floor de-stressing, and even there is a quiescent period before the main rock burst [11].

An earthquake is rock failure at a large scale. The well-know frequency-magnitude relationship (or the Gutenberg-Richter law) is equivalent to a fractal (power-law) distribution between the number

of earthquakes and the characteristic size of faults, and the value of fractal dimension of regional or world-wide seismicity is twice the famous *b*-value in seismology, that is, $d_f = 2b$ [15−17]. Therefore, a sudden drop of fractal dimension corresponds to the reduction of *b*-value, which is also considered as a possible precursor of earthquakes [18].

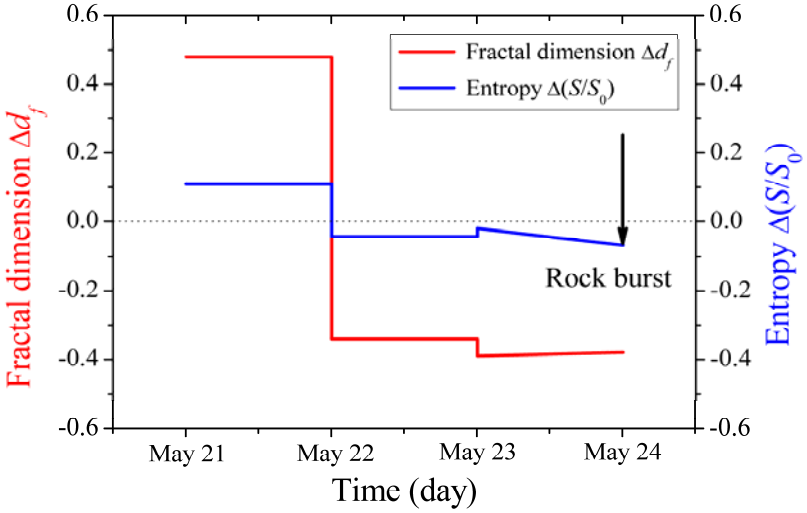

Figure 3. The variation of fractal dimension and normalized entropy versus time in a galena mine, where a major rock burst occurred on 24 May 1979 (data from [14]).

It is worth noting that, however, as the *b*-value or fractal dimension is a highly concentrated parameter, more physical details on the reduction of fractal dimension or *b*-value, especially at critical failure, are needed for reliable prediction. This can be resorted to the variation of high-order or multifractal dimensions.

5. Conclusions

In summary, the definition of a damage parameter can be extended to consider the fractal character of the spatial distribution of microcracks. It is shown that there is a universal character in a damage evolution and fracture process: the decrease of fractal dimension or entropy and the ordering of the spatial distribution of microcracks. A sudden drop of fractal dimension or entropy provides a quantitative indicator of the damage localization, which can be viewed as a likely precursor prior to catastrophic failure. Similarly, the decrease of *b*-value in seismology can be considered as a precursor for a large earthquake. These results imply that the strong fluctuations of physical parameters near the critical point such as the concentration of microcracks (mining-induced rock bursts or seismicity) could provide useful clues for the prediction of fracture and earthquakes.

Acknowledgements

This work was supported by the Australian Research Council and the Opening Fund of State Key Laboratory of Nonlinear Mechanics in China.

References

[1] Y.L. Bai, C. Lu, F.J. Ke, M.F. Xia, Evolution induced catastrophe. Phys Lett A, 185 (1994), 196–200.

[2] C. Lu, D. Vere-Jones, H. Takayasu, Avalanche behaviour and statistical properties in a micro-crack coalescence process. Phys Rev Lett, 82 (1999), 347−350.

[3] B.B. Mandelbrot, The Fractal Geometry of Nature, Freeman, San Francisco, 1982.
[4] B.B. Mandelbrot, D.E. Passoja, A.J. Paullay, Fractal character of fracture surfaces of metals. Nature, 308 (1984), 721–722.
[5] H. Takayasu, Fractals in the Physical Sciences, Manchester University Press, Manchester, 1990.
[6] H. Xie, Fractals in Rock Mechanics, A. A. Balkema, Rotterdam, 1993.
[7] A. Carpinteri, Scaling laws and renormalization groups for strength and toughness of disordered materials. Int J Solids Struct, 31 (1994), 291–302.
[8] C. Lu, Y.-W. Mai, Y. Bai, Fractals and scaling in fracture induced by microcrack coalescence. Philos Mag Lett, 85 (2005), 67−75.
[9] A. Carpinteri, N. Pugno, Are the scaling laws on strength of solids related to mechanics or to geometry?. Nat Mater, 4 (2005), 421–423.
[10] C. Lu, Some notes on the study of fractals in fracture, in: Proceedings of the 5th Australasian Congress on Applied Mechanics, Brisbane, 2007, pp. 234–239.
[11] C. Lu, Y.-W. Mai, H. Xie, A sudden drop of fractal dimension: a likely precursor of catastrophic failure in disordered media. Philos Mag Lett, 85 (2005), 33−40.
[12] A. Guarino, A. Garcimartin, S. Ciliberto, An experimental test of the critical behaviour of fracture precursors. Eur Phys J B, 6 (1998), 13–24.
[13] D. Krajcinovic, Damage Mechanics, North-Holland, Amsterdam, 1996.
[14] F. Leighton, A Case History of a Major Rock Burst, Report RI8701, U.S. Bureau of Mines, 1982.
[15] C. Lu, H. Xie, A physical limit of Weibull modulus in rock fracture. Int J Fracture, 69 (1995), R55–R58.
[16] I. Main, Statistical physics, seismogenesis, and seismic hazard, Rev Geophys, 34 (1996), 433–462.
[17] D.L. Turcotte, Fractals and Chaos in Geology and Geophysics, Cambridge University Press, Cambridge, 1997.
[18] S.M. Potirakis, G. Minadakis, K. Eftaxias, Sudden drop of fractal dimension of electromagnetic emissions recorded prior to significant earthquake. Nat Hazards, 64 (2012), 641–650.

Scaling Behavior in Quasi Static and Impact Fragmentation of Brittle Materials

Marina Davydova[1,*], Sergey Uvarov[1]

[1] Institute of Continuous Media Mechanics, Ural Branch of Russian Academy of Sciences, Perm 614013, Russia
* Corresponding author: davydova@icmm.ru

Abstract An investigation was conducted to examine experimentally the process of fragmentation of brittle materials (glass plates and quartz rods) under quasi-static and dynamic loading conditions. In the quasi-static tests of glass plates, two types of scaling laws were considered. Of these, one was based on the fractal relation similar to the Dielectric Breakdown Model or the Diffusion-limited Aggregation Model, and the other involved the definition of the fragment size distribution. The results of investigation indicate that fragment size distributions mainly follow power-law distributions. Variations in the fragmentation mechanism correlate with quantitative changes in the fractal dimension observed in different regions of the fragmented specimen. The dynamic fragmentation statistics was studied in the recovery experiments with quartz cylindrical rods. The mechanoluminescence-based method was used to measure the distribution of time quantities. Impact loading applied to specimens leads to the formation of fracture surfaces, which produces intensive light emission registered then by Photo Multiplayer Tubes. The data recovery technique allows us to save the fragments and to determine the size distribution of fragments. Both the fragment size distribution and the time interval distribution show evidence of obeying scaling laws.

Keywords: Fractal, Brittle fragmentation, Scaling law, Self-organized criticality

1. Introduction

Results of fragmentation processes (the breakup of matter into smaller pieces) are visible everywhere. In nature these may be rock fragments of sizes varying from stones to sand and dust, or arctic sea ice fragments. Almost all kinds of explosions and collisions result in fragmentation. Common to brittle fragmentation processes is that the fragment-size distribution is given by a power law [1-8]. The origin of this power law has attracted much attention lately. The assumption that the exponential distribution is typical of the fragmentation of ductile materials and the power-law distribution characterizes brittle fragmentation has been discussed by Grady [9]. However, in some experiments with brittle materials the exponential or log-normal laws were observed [10-13]. Donald Turcotte [14] has pursued the fragmentation of brittle materials as a fractal process resulting in the power law distribution function $N \sim x^{-D}$, where N is the number of fragments, x is the linear dimension of fragments, and D is the fractal dimension. The fractal character of the distribution function in a wide range of fragment sizes allows Oddershede et al. [7] to suppose that the fragmentation exhibits self-organized criticality (SOC) [15].

2. Glass fragmentation

Fragmentation processes are complex and involve propagation of many cracks and their interaction. Therefore, it is of interest to study the overall statistical aspects. Quasi-static testing was performed in the experiments with glass plates loaded in a “sandwich” to save the glass fragmentation pictures (Fig. 1a). Using the original software, the images were transformed into the schematic pictures corresponding to the fragmentation patterns (Fig. 1b).

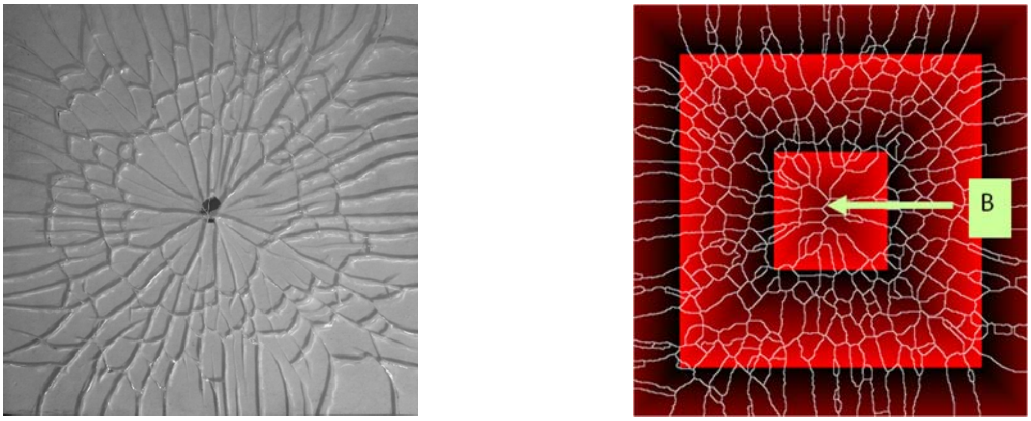

a) b)

Figure 1. a) Photographs of typical fragmentation patterns. b) Schematic pictures of fragmentation patterns to determine the size and number of fragments and the total length of cracks.

This made it possible to determine the size and number of fragments and the total length of cracks. We consider two types of scaling. The first type is based on the relation

$$L(r) \sim r^{D}, \tag{1}$$

where $L(r)$ is the total crack length in the boxes of a size $r \times r$ centred at the point B (Fig. 1b), and D is the fractal dimension. The second type is the traditional definition of the cumulative distribution of fragment sizes, that is, the calculation of the number of fragments N with a size larger than S.

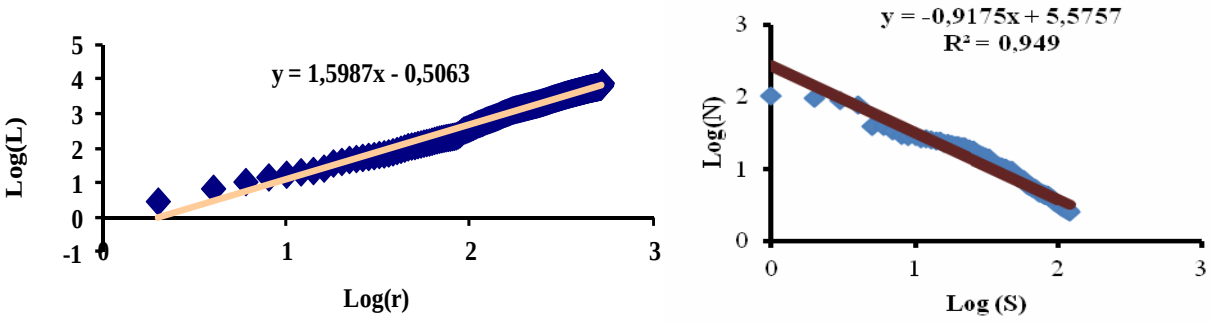

a) b)

Figure 2. a) Scaling law obtained using the relation for crack length (1). b) Cumulative log-log plots of the fragments size distributions.

The use of Eq. (1) was discussed by Sornette et al. [16]. However, it should be noted that the fracture pattern [16] does not have a distinct central point. At the same time, the examined fragmentation patterns have a central point, and their configuration is similar to that created with the

model of diffusion-limited aggregation (DLA) [17] or the model of dielectric breakdown (DB) [18]. Relation (Eq.1) can be used to define the fractal dimension for both these models. In the case of the DB model, $L(r)$ is the total length of the discharge branches within the circle of radius r For the DLA model, $L(r)$ is the number of particles. By analogy with the DLA and DB models, to determine the fractal dimension of the fragmentation patterns, we use Eq.(1), where $L(r)$ is the total length of cracks in the boxes of a size $r \times r$ centred at the point B (Fig. 1b). The minimal number of the boxes used for calculation of the fractal dimension is 200. The scaling law obtained using the relation for crack length (Eq.1) is presented in Fig. 2a. The processing of the fragment sizes shows that the relation between the fragment area and the number is also fitted by a power law (Fig. 2b and Fig. 6).

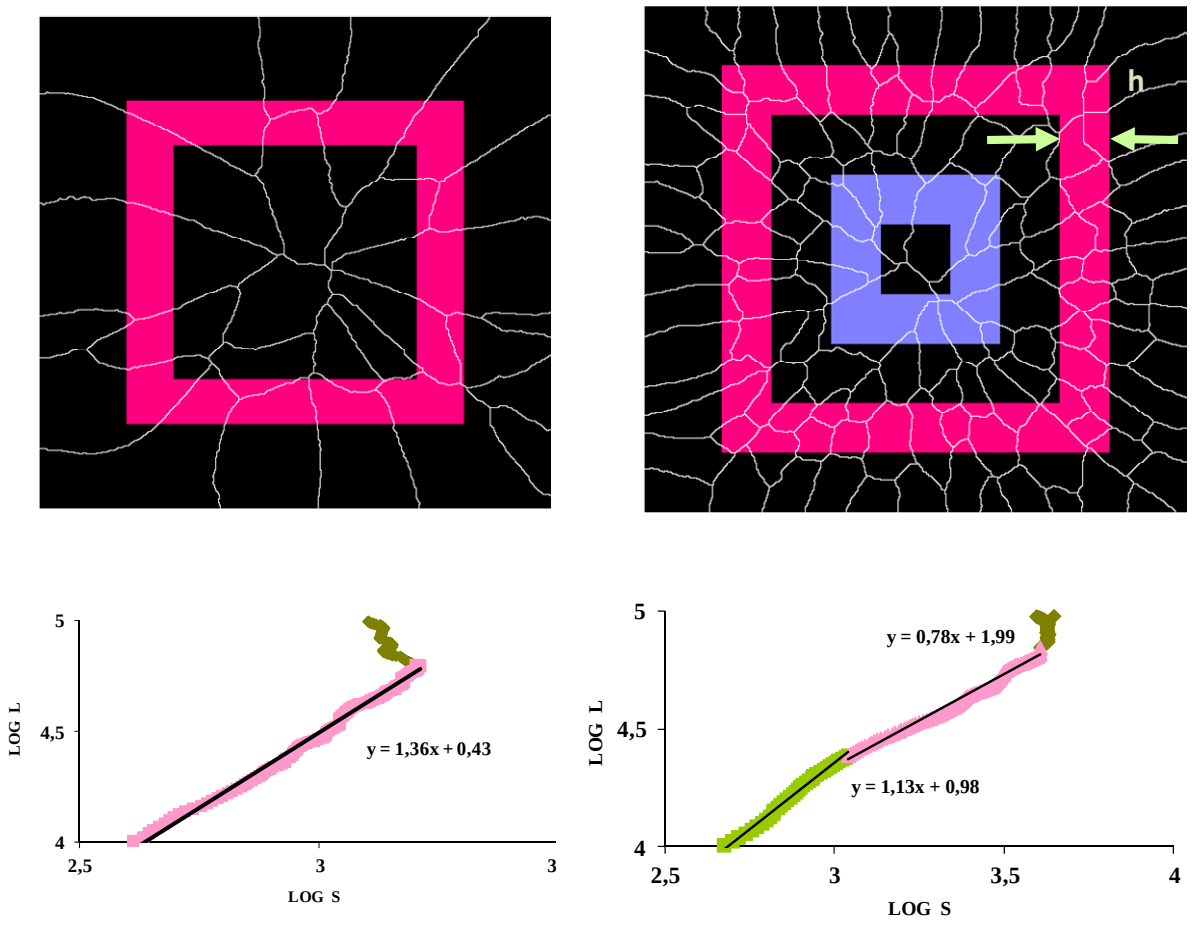

a) b)

Figure 3. a) Fragmentation pattern and fractal dimension definition for the fracture accompanied by radial crack formation. b) Fragmentation pattern and fractal dimension definition for the fracture accompanied by a change in the fracture mechanism.

There are two types of energy-dependent fragmentation patterns leading to a breakup (Fig. 3). Fig.3a presents a fragmentation pattern that illustrates the fracture accompanied by radial crack formation. The right fragmentation pattern (Fig. 3b) has two zones corresponding to two different fracture mechanisms. The central zone has a radial crack only. In the second zone, the crack

branching process is observed. Assuming that different fracture mechanisms characterize different fractal dimensions, we have

$$L(S) \sim S^D, \tag{2}$$

where $L(S)$ is the total crack length inside the square frame with a thickness h (Fig. 3b), S is the frame area, and D is the fractal dimension. Calculation the fractal dimension using expression (Eq.2) shows that, for the left fragmentation pattern (Fig. 3a), the data is fitted by a single line. For the right pattern, the log-log representation of $L(S)$ changes its slope, and the power-law exponent D decreases. A change in the fracture mechanism (from radial crack formation to crack branching) correlates with the qualitative changes in the fractal dimension.

3. Quartz fragmentation

3.1. Loading condition.

The first stage of the experiment was to evaluate the effect of loading conditions and the shape and size of the sample on the fragment size distribution function. Three types of loading conditions (I, II, III) were realized using a ballistic set-up:

- fragmentation as a result of interaction of direct and reflected compression waves (I) (Fig.4a);
- fragmentation under the action of a compression wave (II) (Fig.4b);
- fragmentation induced by a direct compression wave and its reverberation in rod (III) (Fig.4c).

Loading Condition I. The ballistic set-up consists of a gas gun with a bore of 19.3 mm diameter, a velocity registration system, and a base where the sample is mounted (Fig. 4a). The sectional glass rod is composed of a buffer and the main part covered by an elastic shell. The buffer was used for realization of uniaxial loading produced by a cylindrical projectile of mass 13.9 g accelerated up to the velocities of 6-22 m/s.

Loading Condition II. To avoid the possible influence of the reflected wave on the fragmentation scenario, the ballistic set-up was modified. The sample was placed into a steel cylinder filled with plastic foam (Fig. 4b). The sectional glass rod was composed of a buffer, main part and outer parts. The presence of the last part made it possible to catch the reflected wave.

Loading Condition III. The scheme given in Fig. 4c illustrates the experimental technique used to measure the distribution of time quantities. Impact leads to the formation of fracture surfaces, which produce intensive light emission (mechanoluminescence or fractoluminescence).The intensity of the light is registered by the Photo Multiplayer Tube connected with the oscilloscope (oscilloscope sample rate is 1 GHz).

3.2. Fragment mass distribution.

The mass of the fragments passing through the sieves was obtained by weighing the fragments using an electronic balance HR-202i (accuracy 10^{-4} g). The mass of the fragments corresponding to the maximum of the probability density function varied in the range from $2*10^{-4}$g to $6*10^{-4}$ g

(Fig.5a). At low energy, a more considerable scattering was found for this value (Fig.5b). This actually means that for low energy we have two or three sieves with a comparable number of fragments, and for high energy - only one sieve with a predominant number of fragments.

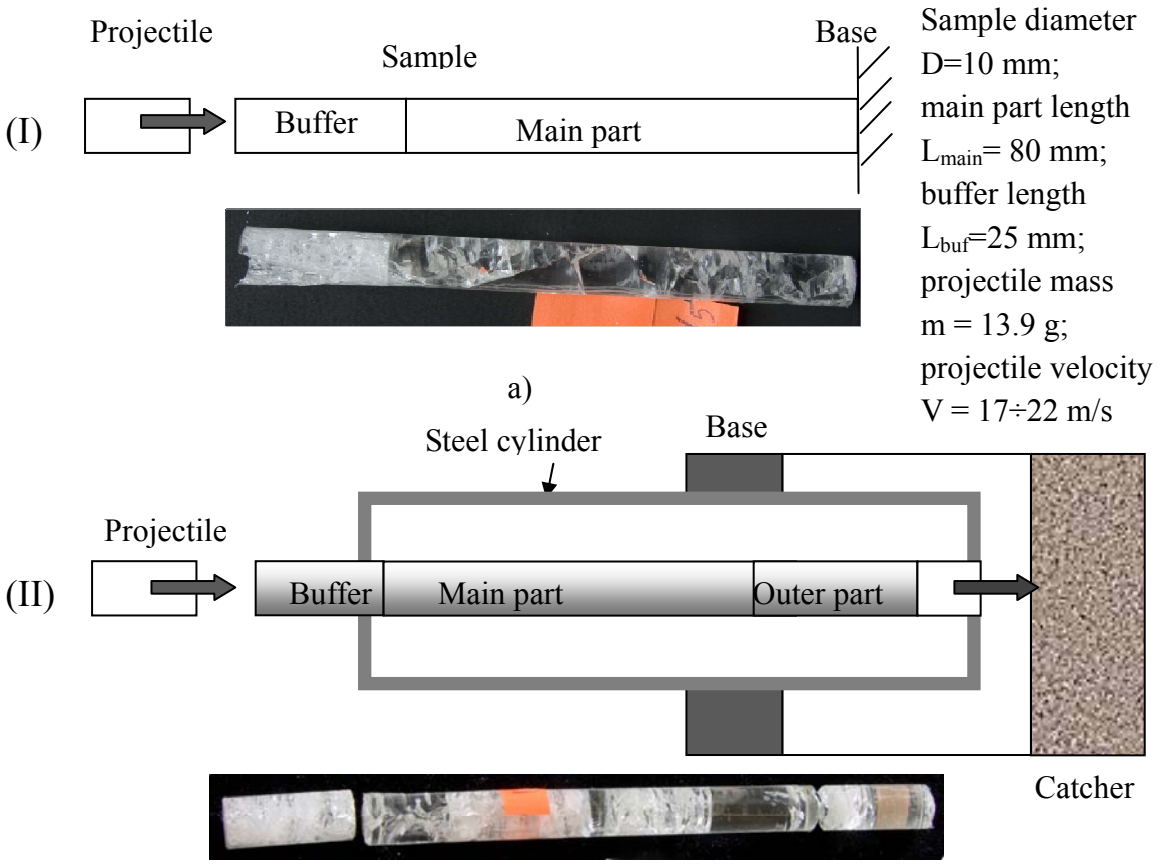

Sample diameter D=12 mm; main part length L_{main} = 120 mm; buffer length L_{buf} =25 mm; outer part length L_{out}= 30 мм; projectile mass m = 6.3 g; V = 40÷50 m/s

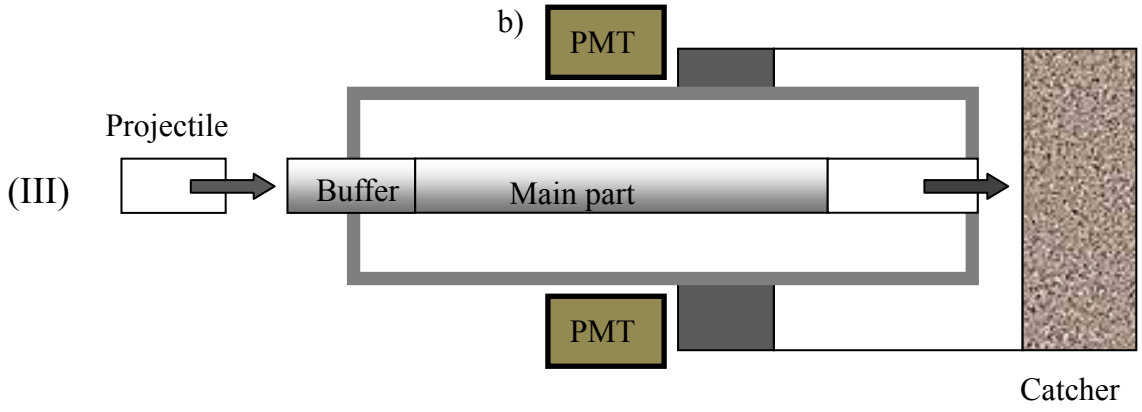

Sample diameter D=12 mm; main part length L_{main} = 120 mm; buffer length L_{buf} =25 мм;

c)

Figure 4. Schemes of loading: a) condition I; b) condition II; c) condition III.

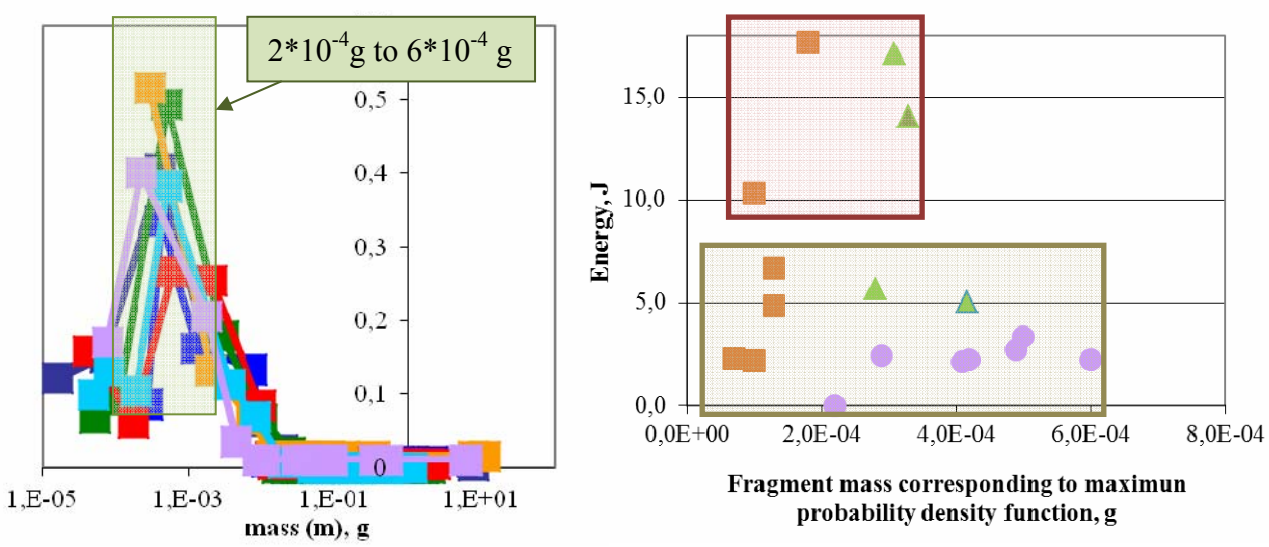

a) b)

Figure 5. a) Probability density function. b) Dependence of the fragment mass corresponding to maximum probability density function on the projectile energy. The markers indicate the loading type: I-circles; II-triangles; III-boxes.

The fragmentation statistics was analyzed by varying the sample size and load intensity (projectile velocity). The results of experiments have indicated that the variation in the sample size and loading conditions does not lead to the change in the type of the probability density function.

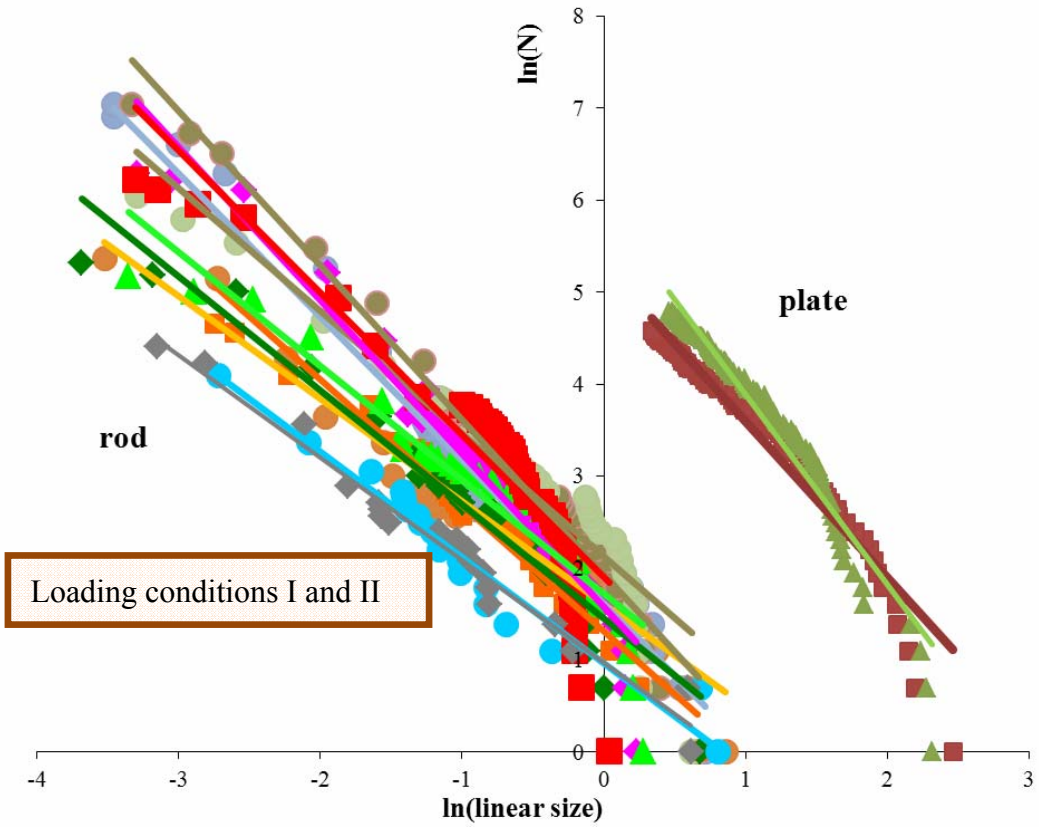

Figure 6. Double logarithmic plot of the cumulative distribution function for plate and rod.

Thus, the cumulative distributions illustrating the relation between the numbers of fragments and their linear dimension are represented as a log-log plot (Fig. 6). The linear dimension is defined as a cube root of mass or a square root of area. The distribution is fractal by nature with a power law in the form $N(>r) = Cr^{-D}$, where N is the number of fragments with a characteristic linear dimension greater than r. The fractal dimension D varies from 1.6 to 2.0 for the plate and from 1.1 to 1.7 for the rod (Loading Conditions I and II).

3.3 Distribution of time interval between the impulses of intensive light emission

To measure the scaling of spatial and time quantities corresponding to the same sample, we have developed the experimental scheme presented in Fig.4c (Loading Condition III). Fracture surfaces formed under impact loading produced intensive light emission (mechanoluminescence or fractoluminescence). The mechanoluminescence impulses were registered by two PMT connected with the oscilloscope (Fig.7). The second PMT was used to provide the reliability of measurements.

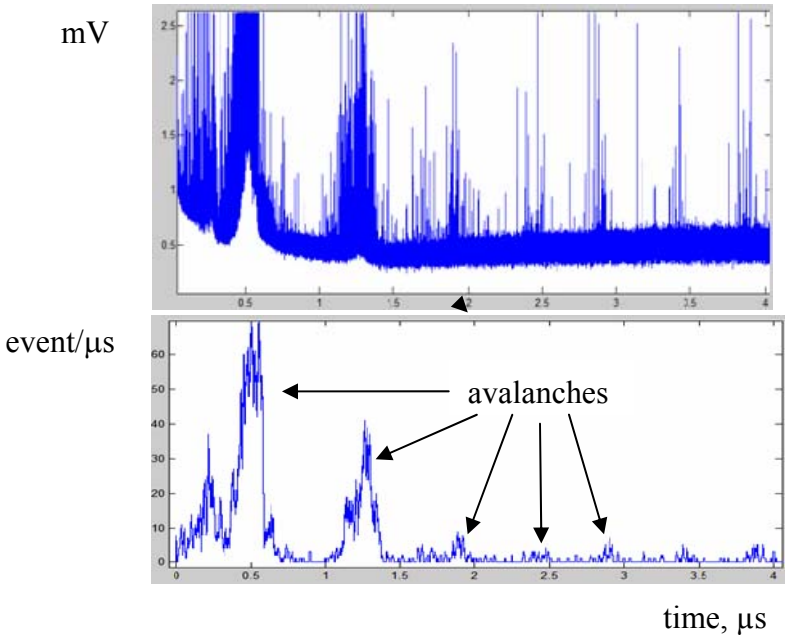

Figure. 7. Signal of the oscilloscope and the frequency of impulse appearance.

The process of light reflection looks like the process of avalanche spreading (Fig. 7). The lower plot represents the event frequency. The events are distributed in blocks.

The cumulative distribution function of the time interval (registered by two PMT) in the double logarithmic plot (Fig.8b) is fitted by the straight line (90% of the total number points). At small sizes (8% of the total number of points), the curve deviates from the straight line because the size of time interval is comparable with the oscilloscope sample rate (1 GHz). The falloff at the largest interval sizes (2% of the total number of points) is due to finite-size effects. In this case, the time interval is comparable with the process time. The central part is the line covering 90% of the total number of points. It has been found that the fragment size distributions (Fig.8a) and the time interval

distributions (Fig.8b) obey scaling laws, which suggests the possibility of self-organized criticality in fragmentation.

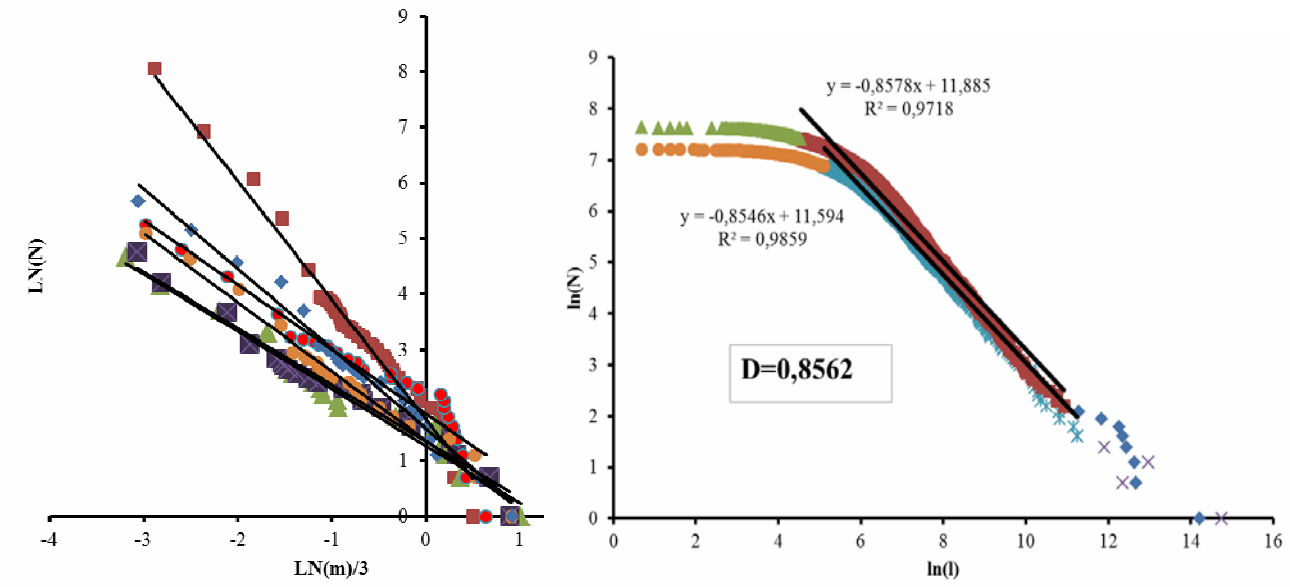

a) b)

Figure 8. a) Fragment size distribution (spatial scaling) for loading condition III. b) Distribution of time interval separating the fractoluminescence impulses (for one sample). *D* is the average exponent for the signals corresponding to two PMT placed near the opposite side of the sample.

The fractal dimension D varies from 1.02 to 2.14 for the spatial variable (Fig.8) and from 0.28 to 0.85 for the time variable (Fig.9).

4. Conclusion

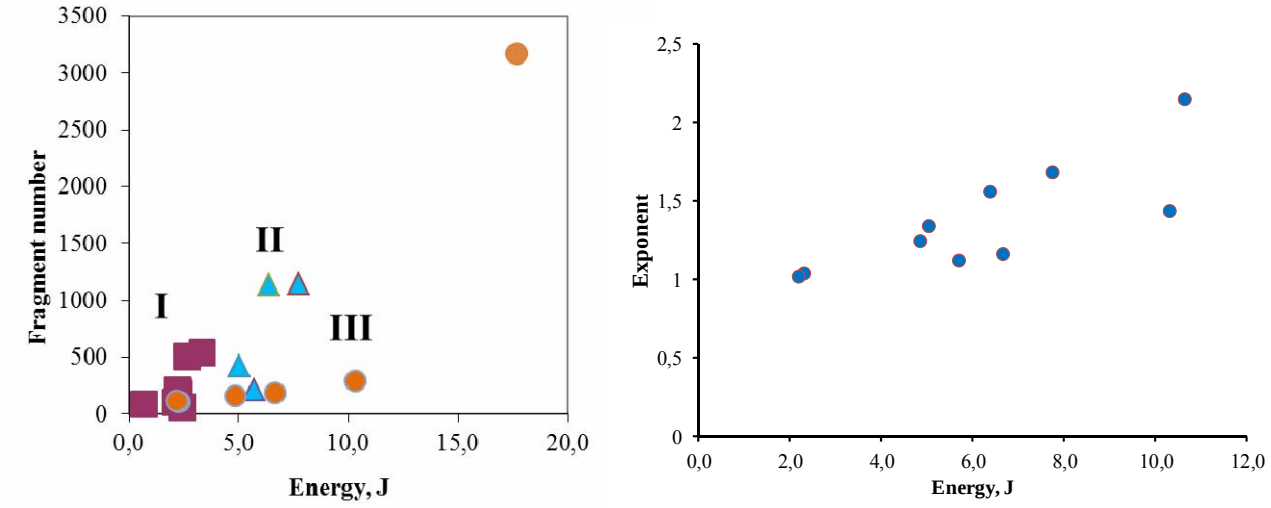

a) b)

Figure 9. a) Fragment number versus projectile energy. I, II, III indicate loading conditions. b) Power law exponent for different levels of projectile energy.

Experimental investigations were carried out to examine the fragmentation of brittle materials under quasi-static and dynamic loading conditions. Based on the obtained results, the following conclusions can be derived:

- fragmentation patterns of glass plates are fractal;
- variation in the fracture mechanism of plates correlates with the changes in the fractal dimension;
- number of fragments occurred during the fragmentation of quartz rods (Fig. 9a) depends on loading conditions;
- power law exponent for fragment size distributions of quartz (Fig. 9b) increases with growth of projectile energy;
- fragment size distribution for the observed type of fragmentation (glass plates and quartz rods) is fractal and satisfies the relation $N(>r) = Cr^{-D}$;
- fragment size distributions and time interval distributions are governed by scaling laws, which is indicative of the self-organized critical behavior during the fragmentation process.

Acknowledgements

The author would like to acknowledge the Russian Foundation for Basic Research (grant RFBR 11-01-96010, grant RFBR 11-01-00712)

References

[1] R.Ye. Brodskii, P.V. Konevskiy, R.I. Safronov, Size distribution of sapphire fragments in shock fragmentation. Functional Materials, 18, N2 (2011) 200-205.

[2] E.S.C. Ching, S.L. Lui, Ke-Qing Xia, Energy dependence of impact fragmentation of long glass rods. Physica A, 287 (2000) 83 – 90.

[3] T. Kadono, Fragment mass distribution of plate like objects. Physical Review Letters, 78, N 8, (1997) 1444-1447.

[4] T. Kadono, M. Arakawa, Crack propagation in thin glass plates caused by high velocity impact. Physical Review E, 65, (2002) 035107(R)

[5] H. Katsuragi, D. Sugino, H. Honjo, Scaling of impact fragmentation near the critical point. Physical Review E 68, (2003) 046105

[6] A. Meibom, I. Balslev, Composite Power Laws in Shock Fragmentation. Physical Review Letters, 76, N14 (1996) 2492-2494.

[7] L. Oddershede, P. Dimon, J. Bohr, Self-organized criticality in fragmenting. Physical Review Letters, 71, N 19 (1993) 3107-3110.

[8] F. P. M. dos Santos, V. C. Barbosa, R. Donangelo, S. R. Souza, Experimental analysis of lateral impact on planar brittle material. Physical Review E 81, (2010) 046108

[9] D.E. Grady, Length scales and size distributions in dynamic fragmentation. International Journal of Fracture, 153, N 1-2 (2010), 85-99.

[10] J. A. Astrom, R. P. Linna, J. Timonen, P. F. Moller, L. Oddershede, Exponential and power-law mass distributions in brittle fragmentation. Physical Review E 70, (2004) 026104

[11] H. Katsuragi, S. Ihara, H. Honjo, Explosive fragmentation of a thin ceramic tube using pulsed power. Physical Review Letters, 95, (2005) 095503

[12] H. Katsuragi, D. Sugino, H. Honjo, Crossover of weighted mean fragment mass scaling in two-dimensional brittle fragmentation. Physical Review E 70, (2004) 065103(R)

[13] V.V. Sil'vestrov, Application of the gilvarry distribution to the statistical description of fragmentation of solids under dynamic loading. Combustion, Explosion, and Shock Waves, 40, N 2, (2004) 225–237.

[14] D. L.Turcotte, Fractals and chaos in geology and geophysics, Cambridge University Press, UK, 1997.

[15] P.Bak, C.Tang, K.Wiesenfeld, Self-organized criticality: an explanation of 1/f noise. Physical Review Letters, 59, N4 (1987) 381-384.

[16] A.Sornette, P. Davy, D.Sornette, Growth of fractal fault patterns. Physical Review Letters, 65, N18 (1990) 2266-2269.

[17] L.Niemeyer, L.Pietronero, and H.J.Wiesmann, Fractal Dimension of Dielectric Breakdown. Vol. Physical Review Letters, 52, N12, (1984) 1033-1036.

[18] T.A.Witten, L.M.Sander, Diffusion-limited aggregation, a kinetic critical phenomenon. Physical Review Letters 47, N19 (1981) 1400-1403.

Structural Hierarchy and Dynamic Size Effect of Rock Strength

Chengzhi Qi[1,*], Qihu Qian[2] , Qingming Li[3], Mingyang Wang[2] ,

[1]Beijing Higher Institution Research Center of Engineering Structures and New Materials, Beijing University of Civil Engineering and Architecture, Beijing 100044, China;
[2]Civil Engineering Institute, PLA University of Science and Technology, Nanjing 210007, China
[3]School of Mechanical, Aerospace and Civil Engineering, The University of Manchester, PO Box 88, Manchester M60 1QD , UK
* Corresponding author: qczbicea@yahoo.com.cn

Abstract The mechanism of dynamic size effect of strength of rock is studied from the viewpoint of structural hierarchy. Relaxation model of Maxwell type for rock is used to obtain the relationship between strength, sample size and strain rate. It is shown that because of the finiteness of crack propagation velocity, when the strain rate is well above certain characteristic strain rate, dynamic loading process takes predominant role, the stresses in sample have not enough time to relax, the larger the sample size is, the more time is needed for cracks in sample to go through the sample, the ultimate applied stresses before macrofracture are greater and the strength is higher. From other hand because of the size effect the higher dynamically applied stresses will activate the cracking at smaller scale levels of rock sample, and the fragment size is smaller. Based on the presented model the characteristic strain rate separating the predominant diapasons for static and dynamic size effect is determined, and the fragment size is predicted satisfactorily.

Keywords rock, structural hierarchy, dynamic size effect, static size effect

1. Introduction

The strength of rock-like materials has size effect, i.e. it depends on the size of the samples. The general law of the size dependence of strength is that it decreases with the increase of the sample size.

Static size effect of strength has been studied by many scientists. According to Bazant size effect of strength can be separated into two kinds [1]：(1) statistical, described by the Weibull [2, 3, 4] theory of random local material strength, and (2) energetic (deterministic). The latter includes type I size effect[5-10], occurring in materials that fail at crack initiation from a smooth sample surface, and type II size effect[5, 11-14], occurring in materials with a deep notch or deep stress-free crack formed stably before reaching the maximum load. Another approach to size effect is based on the concept of fractality. The self-similarity (fractality) in concrete deformation and fracture has been studied by Z. Bazant Z.[7], Carpinteri A., Pussi. S., Pugno N.M. et al [15, 16]. And the mechanics of hierarchical materials has been also developed [17].

As to size effect of dynamic strength of rocks, the research is relatively rare and the reached conclusions are controversial [18, 19, 20, 21]. For clarification of the size effect of rock strength under dynamic loading condition, recently Hong Liang, Li Xibing et al. have performed refined research on size effect of rock dynamic strength and strain rate sensitivity[22]. The reached conclusions are interesting. The test results show that the rock dynamic strength increases with strain rate in power law which agrees with the research results of many other scientists. The interesting result is that the larger the specimen size is, the more notable the strain rate sensitivity of dynamic strength of rock is; the rock dynamic strength increases with the increase of specimen size

under the same strain rate which is opposite to the size effect under static loading condition (see Fig.1 and 2 for granite). The size effect of dynamic strength becomes weaker with the decrease of strain rate and there exist a critical strain rate below which static size effect takes dominant position. In addition, experiments show that the fragment size decreases significantly with the increase of sample size (see Fig.3). The less the sample size is, the more is the dispersion of the experimental results.

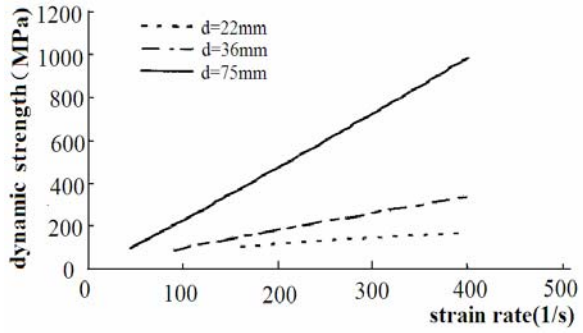

Fig. 1 Strain rate effect of strength of granite under different strain specimens diameters

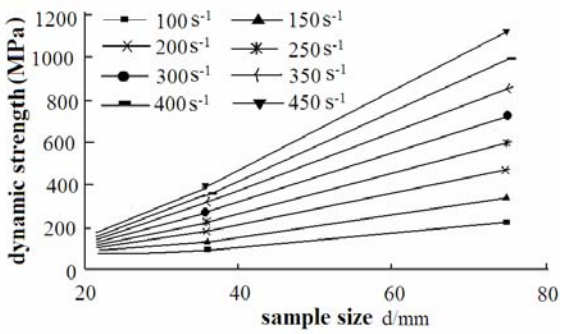

Fig. 2 Size effect of strength of granite under different strain rates

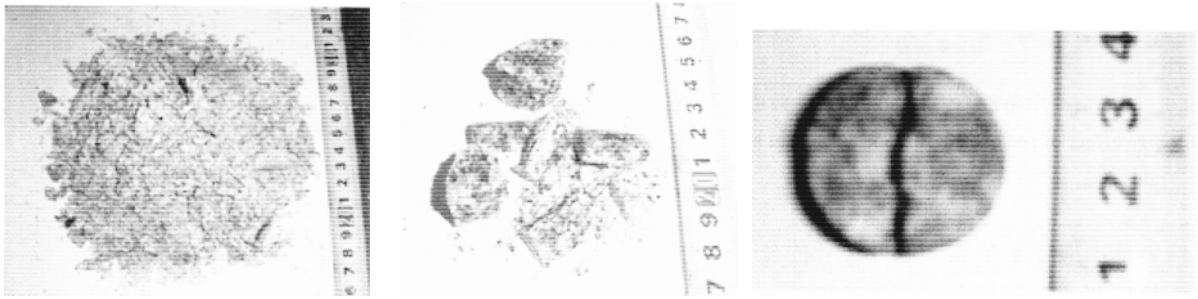

(a) d=75mm, $\dot{\varepsilon} = 98.23s^{-1}$ (b) d=36mm, $\dot{\varepsilon} = 99.75s^{-1}$ (c) d=22mm, $\dot{\varepsilon} = 164.38s^{-1}$

Fig.3 Fragmentation of granite specimens with different sizes

Until now the underlying mechanism of dynamic size effete of rocks has not been intepretated. Therefore in the present paper we will make a trial to perform some theoretical study aiming at clarifying the underlying mechanism of dynamic size effect of rock.

2. Mechanism underlying dynamic size effect of rock strength

As natural materials rock-like materials have complex internal structure, the scales of which span a huge scale range. For rock mass an important peculiarity is the similarity of the internal structure in a wide range of sizes. Investigations [23]showed that, a fundamental canonical series for the sizes Δ_i of geo-blocks exists：

$$\Delta_i = \left(\sqrt{2}\right)^{-i} \Delta_0 \tag{1}$$

where $\Delta_0 = 2.5 \times 10^6$ m is the radius of Earth's core; i is positive integers. As demonstrated in [24], the atomic-ionic radii of different valent orbits of 98 elements in the table of Medeleev also obey canonical series of Eq.(1). Therefore canonical series of Eq.(1) is valid for huge range of scale sizes from continental level to atomic-ionic level.

Some relation between the thickness of the weakened structural surfaces (or the opening of cracks) separating structural elements and the characteristic size of the elements at the given scale level exists. According to investigation in [25], the ratio of the openings of cracks δ_i to the characteristic linear size of the blocks Δ_i separated by the weakened structural surfaces (or cracks) at *i*-th scale level is stable, and can be described by the following relation which has a normal statistical distribution:

$$\mu_\Delta(\delta) = \frac{\delta_i}{\Delta_i} = \Theta \cdot 10^{-2} \tag{2}$$

where Θ is a coefficient changing in the interval 1/2—2, and parameter μ_Δ is termed as "geo-mechanical invariant" in [25].

In-situ observations of destruction of earth's crust[26] and theoretical and experimental studies on smaller scale rock samples [27] revealed that the deformation and fracture of rock-like materials are governed by laws of Maxwell bodies. This conclusion allows us to describe the deformation and fracture of rock-like materials by Maxwell model.

The internal structure of rocks has decisive impact on mechanical behavior of rocks. If the strength of crystals with ideal regular lattices is their theoretical strength, then the strength of real materials is about 2-3 orders lower than the theoretical strength for ideal crystals. Obviously, the complex hierarchic internal structure of real materials will causes the stress concentration and strain localization which are responsible for lowering of real material strength.

As a reference medium we take ideal crystal with ideal regular lattices. Image that such ideal crystal is subjected to intensive external loading, the intensity of which is high enough, but the induced stress state is well below the strength limit. In this case in crystal no damage and fracture occur and no stress relaxation takes place. But if the ideal crystal is replaced by real rock mass with complex internal structure, then under the action of such intensive external loading stress concentration and successively damage and fracture will occur. Consequently part of the stresses in rock mass will relax. Therefore we can think that in such solid stresses are consisted of two components: elastic stresses caused by the reversible volume and shear deformations, and the local inelastic stresses in heterogeneities which are responsible for the irreversible deformations. The elastic stresses are related to the reversible deformations linearly. As to the residual stresses (inelastic stresses), they arise at definite strain rate, and relax with time. The evolution equation for the residual stress deviator Δs_{ij}^l in heterogeneities may be described by Maxwell model

$$\frac{d\Delta s_{ij}^{l}}{dt} = 2\rho c_s^2 \dot{\varepsilon}_{ij} - \nu \frac{\Delta s_{ij}^{l}}{l} \qquad (3)$$

where Δs_{ij}^{l} is the residual stress deviator components in heterogeneities with characteristic scale l; $\dot{\varepsilon}_{ij}$ is the residual strain rate deviator components; ρ is the density of the medium; ν is the relaxation velocity, which may be looked at as the effective propagation velocity of single or multiple cracks depending on the loading conditions; c_s is the propagation velocity of the elastic shear wave. Here we suppose that all residual stress components relax with the same relaxation time. Essentially l/ν may be considered as relaxation time $\tau = l/\nu$.

The main feature of this model is that, the relaxation rate of the residual stresses in heterogeneities is proportional to the magnitude of the residual stresses, and inversely proportional to the size of the heterogeneities. The growth of residual stresses is controlled by two contradicting factors in the right hand side of Eq.(1): the residual stress growth rate $2\rho c_s^2 \dot{\varepsilon}_{ij}$ and the relaxation rate of residual stresses $\nu \Delta s_{ij}^{l} / l$. It is necessary to note that this model is applicable not only to different rock-like materials with great variation range of relaxation times, but also applicable to highly viscous fluids for which the relaxation time is relatively short [28].

The solution of Eq. (4) has the following form:

$$\Delta s_{ij}^{l} = 2\rho c_s^2 \dot{\varepsilon}_{ij} \frac{l}{\nu}\left[1 - e^{-\nu t/l}\right] = 2\rho c_s^2 \dot{\varepsilon}_{ij} \tau \left[1 - e^{-t/\tau}\right] \qquad (4)$$

For short loading time $t << \tau$, relaxation process has not enough time to develop, and the loading process is the predominant factor, in this case Eq.(4) gives

$$\Delta s_{ij}^{l} \approx 2\rho c_s^2 \dot{\varepsilon}_{ij} t = 2\rho c_s^2 e_{ij} \qquad (5)$$

i.e. the residual stresses will increase almost linearly.

For long loading time $t >> \tau$, relaxation process has enough time to develop, loading process is limited by the relaxation time, in this case Eq.(4) gives

$$\Delta s_{ij}^{l} \approx 2\rho c_s^2 \dot{\varepsilon}_{ij} \tau = 2\rho c_s^2 \dot{\varepsilon}_{ij} \frac{l}{\nu} \qquad (6)$$

For the occurrence of macrofracture, it is necessary that the loading time is greater than relaxation time $t > \tau$, therefore Eq.(6) is appropriate for study of macrofracture of the samples.

Substituting Eq.(6) into the expression $\Delta\sigma_I = \sqrt{3\Delta s_{ij}^{l} \Delta s_{ij}^{l} / 2}$ for intensity of residual stress deviator, we obtain

$$\Delta\sigma_I = 3\rho c_s^2 \dot{\varepsilon}_I \frac{l}{\nu} \qquad (7)$$

where $\dot{\varepsilon}_I = \sqrt{2\dot{\varepsilon}_{ij}\dot{\varepsilon}_{ij}/3}$ is the residual strain rate intensity.

It can be seen from Eq. (7) that if we fix the applied strain rate, then the greater the size of the heterogeneities is, the greater the residual stresses are. If the size of the body is infinite, then we can

always find large enough heterogeneities that their residual stresses are large enough to cause the fracture of the body. In this way, at constant strain rate among the parameters of solid a parameter with dimension of length arises. Stress concentration causing residual stress in heterogeneous media is the main cause for material fracture, the limit residual stress causing fracture of the body σ^* may be looked at as the strength σ_Y of the sample with size D. Therefore Eq.(7) may be rewritten as

$$\sigma_Y = 3\rho c_s^2 \&_Y \frac{D}{v} \tag{8}$$

Eq.(8) explicitly shows that dynamic strength is proportional to the size of sample, and inversely proportional to the the relaxation velocity. The physical mechanism is as follows. Experiments show that the maximum crack growth velocity is limited and is below the Rayleigh wave speed C_R [29] (Fineberg, Marder, 1999). Therefore the relaxation velocity is also limited. The larger the sample size is, the more is the time needed for the occurrence of macrofracture, and the higher is the reached ultimate amplitude of loading.

Now let us use the obtained fequation (8) to model the dynamic size effect.

For granite we take the Young's elastic modulus as $E = 5.5\times10^{10} Pa$, Poisson's ratio as $\mu = 0.29$, then the shear modulus is $G = 2.13\times10^{10} Pa$. Now let us with the help of Eq.(8) to fit the experimental data.

For sample with size $D = 22mm = 0.022m$, we obtain that the effective relaxation velocity is $v = 3515m/s$.

For sample with size $D = 36mm = 0.036m$, we obtain that the effective relaxation velocity is $v = 2465m/s$.

For sample with size $D = 75mm = 0.075m$, we obtain that the effective relaxation velocity is $v = 1867m/s$.

It is clear that the effective relaxation velocity is dependent of the specimen size and decreases with the increase of sample size. The dependence of effective relaxation velocity on sample size is shown in Fig.4.

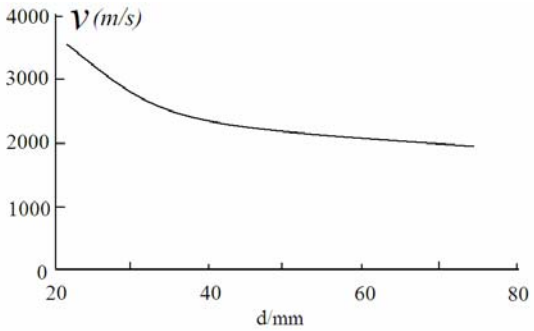

Fig.4 The dependence of velocity of crack propagagtion on specimen size

In the diapason of the sample sizes tested we will use the following equation to interpolate the

dependence of crack propagation velocity on the sample size

$$v(D)=112.59D^2-1403D+6056.6 \tag{9}$$

where the unit of d is cm.

Therefore we now should use the following equation for determination of the dynamic strength of material.

$$\sigma_Y = 3\rho c_s^2 \dot{\varepsilon} \frac{D}{v(D)} \tag{10}$$

Using Eq. (10) we can accurately fit the experimental data shown in Fig.(2) and (3).

Now let's analyze the size effect on dynamic fragmentation.

3. The determination of fragment size of rock

The static size effect and dynamic size effect are depicted in Fig.5.

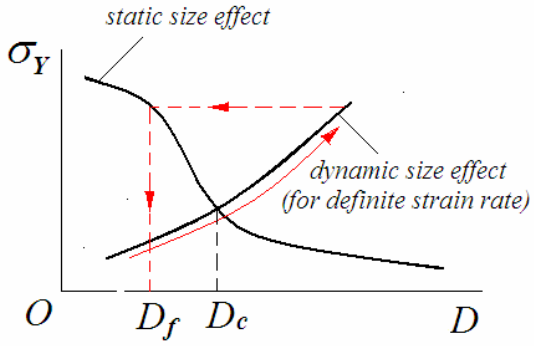

Fig.5 The mechanism of dynamic fragmentation

The static strength of rock mass depends on the sample size. Generally, the compressive strength of materials σ_D can be expressed as a function of the sample size D as follows [5]:

$$\sigma_D = \sigma_0(1+D/D_0)^{-1/2} \tag{11}$$

where σ_0 and D_0 are constants. Eq.(11) can be rewritten as

$$D = D_0\left[(\sigma_0/\sigma)^2-1\right] \tag{12}$$

where parameter σ_D is replaced by σ representing the applied loading.

For fast dynamic loading process, because of the finiteness of relaxation velocity, failure will be delayed, and overloading will take place. Therefore for large enough rock sample dynamic strength will be higher than static one. The higher loading will activate the deformation and fracture process in rock at smaller scale element levels, and the rock will fracture according to the static size effect law of rock as shown in Fig.5.

Replacing σ in Eq. (12) by σ_Y in Eq. (11), we obtain the following formula for determining the fragment size of fractured rock mass D_f :

$$D_f = D_0\left[\left(\frac{\sigma_0}{\sigma_Y}\right)^2 - 1\right] = D_0\left[\left(\frac{\sigma_0 v(D)}{3\rho c_s^2 \dot{\varepsilon} D}\right)^2 - 1\right] \tag{13}$$

For determing σ_0 and D_0, we use the data in Fig.3(a) and (b):

For $d = 75mm, \dot{\varepsilon} = 98.23s^{-1}$, the dynamic strength is $\sigma_Y = 220MPa$, and the fragment size is approximately $D_f = 0.2cm$

For $d = 36mm, \dot{\varepsilon} = 99.75s^{-1}$, the dynamic strength is $\sigma_Y = 105MPa$, and the fragment size is approximately $D_f = 1.47cm$.

From these data we obtain $D_0 = 1.75mm$, $\sigma_0 = 3.22\times10^8 Pa$.

Hence we have

$$D_f = D_0\left[(\sigma_0/\sigma)^2 - 1\right] = 1.75\times10^{-3}\left[\left(3.22\times10^8/\sigma_Y\right)^2 - 1\right] \tag{14}$$

Now let us use Eq.(14) to predict the experimental result shown in Fig.3(c). For the case shown in Fig.3(c), $d = 22mm$. We know from Fig.1 (a) that for $\dot{\varepsilon} = 164.38s^{-1}, \sigma_Y \approx 100MPa$. Substituting $\sigma_Y \approx 100MPa$ into Eq.(14) we have $D_f = 16.4mm$, which is very close to the fragment size in Fig.3 (c): $D_f \approx 22/\sqrt{2} = 15.6mm$. Therefore the model is sufficiently good for the description of the dynamic effects on strength and on dynamic fragmentation.

4. The determination of characteristic size and characteristic strain rate for rock

Now let us discuss the characteristic size and characteristic strain rate for rock samples.

For fixed strain rate $\dot{\varepsilon}$, from the following equation

$$\sigma_D = \sigma_0\left(1 + D_c/D_0\right)^{-1/2} = \sigma_Y = 3\rho c_s^2 \dot{\varepsilon} \frac{D_c}{v(D_c)}$$

we can determine the characteristic size D_C for rock, above which dynamic size effect of rock strength will predominate.

From other hand for fixed rock sample size D from equation

$$\sigma_D = \sigma_0\left(1 + D/D_0\right)^{-1/2} = \sigma_Y = 3\rho c_s^2 \dot{\varepsilon}_c \frac{D}{v(D)}$$

we obtain the characteristic strain rate

$$\dot{\varepsilon}_c = \frac{\sigma_0 v(D)}{3\rho c_s^2 D\left(1 + D/D_0\right)^{1/2}} = \frac{\sigma_0 v(D)}{3GD\left(1 + D/D_0\right)^{1/2}} \tag{15}$$

From Eq. (15) it is clear that under fixed rock sample size D, when strain rate $\dot{\varepsilon} > \dot{\varepsilon}_c$, dynamic

size effect takes dominant position, and when $\dot{\varepsilon} \ll \dot{\varepsilon}_{Ic}$ static size effect predominates. From other hand, under fixed strain rate $\dot{\varepsilon}_{Ic}$, when strain rate $D > D_c$, dynamic size effect takes dominant position, and when $D < D_c$ static size effect predominates.

Now let's evaluate the order of the predicted characteristic strain rates.

For $d = 75mm$, $v = 1867m/s$, $G = 2.13\times10^{10}\,Pa$, $D_0 = 1.75mm$, $\sigma_0 = 3.22\times10^{8}\,Pa$, the predicted characteristic strain rate is

$$\dot{\varepsilon}_{Ic} = \frac{\sigma_0 v(D)}{3GD(1+D/D_0)^{1/2}} = \frac{3.22\times10^{8}\times1.867\times10^{3}}{3\times2.13\times10^{10}\times7.5\times10^{-2}\times(1+75/1.75)^{1/2}} = 18.9/s$$

For $d = 36mm$, $v = 2645m/s$, $G = 2.13\times10^{10}\,Pa$, $D_0 = 1.75mm$, $\sigma_0 = 3.22\times10^{8}\,Pa$, the predicted characteristic strain rate is

$$\dot{\varepsilon}_{Ic} = \frac{\sigma_0 v(D)}{3GD(1+D/D_0)^{1/2}} = \frac{3.22\times10^{8}\times2.465\times10^{3}}{3\times2.13\times10^{10}\times3.6\times10^{-2}\times(1+36/1.75)^{1/2}} = 74/s$$

For $d = 22mm$, $v = 3515m/s$, $G = 2.13\times10^{10}\,Pa$, $D_0 = 1.75mm$, $\sigma_0 = 3.22\times10^{8}\,Pa$, the predicted characteristic strain rate is

$$\dot{\varepsilon}_{Ic} = \frac{\sigma_0 v(D)}{3GD(1+D/D_0)^{1/2}} = \frac{3.22\times10^{8}\times3.515\times10^{3}}{3\times2.13\times10^{10}\times2.2\times10^{-2}\times(1+22/1.75)^{1/2}} = 227/s$$

Comparing with Fig.1 we can see that if the static strength of granite is 70 Mpa, the predictions are good enough.

5. Conclusion

Rock-like materials have complex internal structure, the scales of such complex structure span a huge scale range. At the same time deformation and fracture of rocks proceed in real time, and their temporal scales are related to the internal structure and physical-mechanical properties of rocks. To understand the nature of dynamic size effect of strength of rocks it is necessary to consider the structural hierarchy and the temporal properties of deformation and fracture process of rocks. In the present paper relaxation model of Maxwell type for rock is used to obtain the relationship between strength, sample size and strain rate. It is shown that when the strain rate is well above certain characteristic strain rate dynamic loading process takes predominant role. Because of the finiteness of crack propagation velocity, the larger the sample size is, the more time is needed for cracks in sample to go through the sample, and the ultimate applied stresses before macrofracture are more and the strength is higher. Factually the dynamic strength is induced by overloading. From other hand because of the size effect of rock strength, the overloading will activate the cracking at smaller scale levels of rock sample, and the fragment size is smaller. From the present model the characteristic strain rate separating the predominant diapasons for static and dynamic size effect is determined, the dynamic fragmentation size is predicted well.

Acknowledgements

The study was conducted with financial support of the Natural Science Foundation of China

(NSFC grants No. 51174012), the “973” Key State Research Program No. 010CB732003, Science Fund for Creative Research Groups of the National Natural Science Foundation of China（No. 51021001）, Fund of Scientific School of Modeling and Analysis of Nonlinear Systems (grant No PHR201107123).

References

[1] Z.P.Bazant, Q.Yu, Universal size effect law and effect of crack depth on quasi-brittle structure strength. J Eng Mech, 135(2) (2009) 78-84.
[2] W. Weibull, The phenomenon of rupture in solids. Proc., Royal Swedish Institute of Engineering Research (Ingenioersvetenskaps Akad. Handl.), 153, (1939) 1-55.
[3] W.Weibull, A statistical theory of the strength of materials. Proc., Royal Swedish Academy of Engineering Science, 151, (1939)1-45.
[4] W.Weibull, A statistical distribution function of wide applicability. J Appl Mech1. 8(3) (1951) 293-297.
[5] Z.P.Bazant, Size effect in blunt fracture: Concrete, rock, cracks. J Eng Mech, 110 (4) (1984) 518-535.
[6] Z.P Bazant, Y.Xi, Statistical size effect in quasi-brittle structure: II. Nonlocal theory. J Eng Mech, 117(11) 19912623-2640.
[7] Z.P Bazant, Scaling of quasi-brittle fracture: asymptotic analysis. Int. J Fract, 83(1) (1997) 19-40.
[8] Z.P Bazant and D. Novak, Probabilistic nonlocal theory for quasibrittle fracture initiation and size effect. I: Theory. J Eng Mech, 126(2) (2000)166-174.
[9] Z.P Bazant and S.D.Pang, Activation energy based on extreme value statistics and size effect in brittle and quasi-brittle fracture. J Mech Phys Solids, 55(1) (2007) 91-134.
[10] Z.P Bazant, M.Vorenchovsky, D.Novak, Asymptotic prediction of energetic-statistical size effect from deterministic finite-element solution. J Eng Mech, 133(2) (2007) 153-162.
[11] Z.P Bazant, M.T.Kazemi, Determination of fracture energy, process zone length and brittleness number from size effect, with application to rock and concrete. Int. J Fract, 44(1) (1990) 111-131.
[12] Z.P. Bazant and J. Planas, Fracture and size effect in concrete and other quasi-brittle materials, CRC Press, Roca Raton, Fla., Chap.12, 1998.
[13] X.Z.Hu, K.Duan, Size effect and quasibrittle fracture: the role of FPZ. Int J Fract, 154 (1-2) (2008) 3-14.
[14] S.Morel, Size effect in quasibrittle fracture: derivation of the energetic size effect law from equivalent LEFM and asymptotic analysis. Int. J Fract, 154 (1-2) (2008)15-26.
[15] A.Carpinteri, Scaling law and renormalization group for strength and toughness of disordered materials. Int J Solida& Structures, 31(1994) 291-302.
[16] A.Carpinteri, S.Puzzi, Self-somilarity in concrete fracture: size-scale effecte and transition between different collapse mechanisms. Int J Fracture, 154(1-2) (2008) 167-175.
[17] A.Carpinteri, N.M.Pugno, Mechanics of hierarchical materials. International Journal of Fracture, 150 (1-2) (2008) 221-226.
[18] X. Li, A study on the dynamic properties and energy absorption of rocks, M.S. thesis, Central South University of Technology, Changsha, P R China, 1986. (In Chinese)
[19]. I.Maekawa, Hida J. Damage induced by pulsating impact load [J]. J. of the Society of Material Science, Japan, 29(320) (1980) 461-481.
[20] T.Krauthemerat, M.M.Elfahala, J.Lim et al, Size effect for high strength concrete cylinders subjected to axial impact. Int J Impact Engineering, 28(9) (2003)1001-1016.
[21] M.M.Elfahala, T.Krauthemerat, T.Ohnob et al, Size effect for normal strength concrete cylinders subjected to axial impact. Int J Impact Engineering, 31(4) (2005)461-481.
[22] L.Hong, X.Li, C.Ma et al, Study on size effect of rock dynamic strength and strain rate sensitivity. Chinese Journal of Rock Mechanics and Engineering, 27(3) (2008)526－533.
[23] V.N.Oparin, J V.F.ushkin, A.A.Akinin, E.G.Balmashnov, On new scale of structural hierarchy presentation as basic characteristic of geological objects [J]. Journal of Mining Science, 34(5)

(1998) 16-33.

[24] M.V.Kurlenia, V.N.Oparin, About scale factor in the phenomenon of zonal disintegration of rocks and canonical serials of atomic-ionic radii. Journal of Mining Science, 30(2) (1996) 3-14.

[25] M.V.Kurlenia, V.N.Oparin, A.A.Eremenko, On relation between linear sizes of rock blocks and opening of cracks in structural hierarchy of rock mass. J Mining Sci, 27(3) (1993)3-10.

[26] S.I.Sherman, K.Z.Seminsky, A.N.Adamovich et al, Fault formation in lithosphere, zone of tension. Edited by Logachev N.A. Nauka, Novosibirsk, 1992.

[27] V.N.Radionov, I.A.Sizov, V.M.Tsvetkov, Fundamental of geo-mechanics. Nedra, Moscow, 1986.

[28] L.D.Landau, E.M.Lifshitz, Course of theoretical physics, vol.7, Theory of elasticity, Beijing World Publishing Cooperation, Beijing, P.R.China, 1999.

[29] J.Fineberg, M.Marder, Instability in dynamic fracture, Phys. Rep. 313(1999) 101-108.

[30] E.Bouchbinder, A.Livne, J.Fineberg. Weakly nonlinear fracture mechanics: experiments and theory. Int J Fract. 162(2012)3-20.

Effect of Stress Singularities on Scaling of Quasibrittle Fracture

Jia-Liang Le[1,*], Mathieu Piechout[1], Roberto Ballarini[1]

[1] Department of Civil Engineering, University of Minnesota, Minneapolis, 55455, United States
* Corresponding author: jle@umn.edu

Abstract Modern engineering structures are often made of quasibrittle materials, which are brittle and heterogeneous. Typical examples include concrete, fiber composites, woven composites, tough ceramics, and nano-composites. The salient feature of quasibrittle structures is that the size of the fracture process zone is not negligible compared to the structure size, which leads to an intricate size effect on the structural strength. The current understanding of scaling of quasibrittle fracture is limited to structures with either strong stress singularities or zero stress singularities. Nevertheless, many engineering structures are designed to have complex geometries, which could cause weak stress singularities. This paper investigates the effect of stress singularities on the scaling of quasibrittle fracture both analytically and numerically. The theoretical analysis is derived from a generalized weakest link model where the energetic scaling of quasibrittle fracture is incorporated into the classical finite weakest link model. The proposed model yields a general scaling equation, which captures the transition from the energetic scaling to statistical scaling as the stress singularity gets weaker. The proposed analytical model is then verified by a numerical study on the fracture of concrete beams with a V-notch under three-point bending, where a wide range of notch angles representing different orders of stress singularities is considered.

Keywords Size Effect, Deterministic Analysis, Finite Weakest Link Model, Quasibrittle Materials.

1. Introduction

Many large-scale engineering structures, such as bridges, dams, aircraft and ships, are usually designed by extrapolating the results of small-scale laboratory experiments. In order to correctly perform this design extrapolation, it is of paramount importance to understand the scale effect on the structural strength. This study focuses on structures that are made of brittle heterogeneous (quasibrittle) materials, which include concrete, fiber composites, tough ceramics, rocks, sea ice, etc. For two-dimensional problems, the nominal structural strength is usually defined as $\sigma_N = cP_{\max}/bD$, where $P_{\max}$ = load capacity of structure, D = characteristic structural size to be scaled, b = width of the structure in the transverse direction, and c = constant which could be chosen such that σ_N represents some familiar parameter such as the maximum stress in the structure in the absence of the stress concentration. It has been demonstrated that the nominal strength of quasibrittle structures is subjected to an intricate size effect. The underlying reason is that for quasibrittle structures the size of the material inhomogenieties is not negligible compared to the structure size, which directly leads to a size-dependent failure behavior [1, 2]. So far, two independent mechanisms have been identified to explain the scaling of strength of quasibrittle structures:

1) *Type-1 size effect*: the maximum load of the structure is attained after the stable formation of a large fracture process zone (FPZ) with distributed cracking, which typically occurs in structures with a smooth boundary. The Type-1 size effect for small and medium-size structures is energetic,

which can be derived based on the Taylor expansion of the energy release rate function at zero crack length [1, 2]. The large size asymptote of this type of size effect is governed by the Weibull statistics of material strength. The statistical size effect can be amalgamated with the energetic size effect to form the complete *energetic-statistical* Type-1 size effect [3]. Recent studies also showed that this size effect can be alternatively derived from a finite weakest link model where the structure is statistically represented by a finite chain of representative volume elements (RVEs) and the probability distribution of RVE strength is derived from fracture mechanics of nanocracks propagating by small, activation-energy-controlled, random jumps through a nano-structure [4-7].

2) *Type-2 size effect*: the maximum load of the structure is reached once a single large crack is formed. The Type-2 size effect typically applied to quasibrittle structures containing a large notch or a large stress-free (fatigued) crack formed prior to maximum load. This size effect is purely *energetic* because the fracture must happen at the pre-existing crack tip. The Type-2 size effect can be derived by using the asymptotic approximation of the energy release function for the propagating crack or the J-integral [1,2,8].

It is clear that the Type-1 and Type-2 size effects can be considered as two limiting cases in terms of the order of stress singularity of the structure. The Type-1 size effect law represents the case of zero stress singularity whereas the Type-2 size effect law represents the case of the strongest stress singularity (i.e. "−1/2" stress singularity). Nevertheless, many modern engineering structures are designed with geometric discontinuities, which produce weak stress singularities. There is still a lack of understanding on the transition between these two size effects as a function of the magnitude of the stress singularities. This study aims to formulate a universal size effect equation for quasibrittle structures through both theoretical and numerical investigations on the fracture of structures with a V-notch under mode-I loading.

2. Review of energetic and statistical size effects

Consider a structure of positive geometry containing a V-notch and subjected to mode-I loading (Fig. 1), where the notch angle is denoted by γ. Positive geometry is defined such that the peak load is reached once the fracture process zone (FPZ) is fully developed. Here we further assume that the notch is sufficiently deep, i.e. $\alpha = a/D > 0.1$, where a = notch depth and D = depth of the structure (Fig. 1). In general, the stress concentration at the V-notch tip is governed by two distinct stress singularities, which represent the symmetrical and anti-symmetrical deformation modes [9-11]. For mode-I fracture, only one stress singularity λ prevails, which corresponds to the symmetrical mode. This section briefly reviews the two existing scaling theories, namely energetic and statistical scaling.

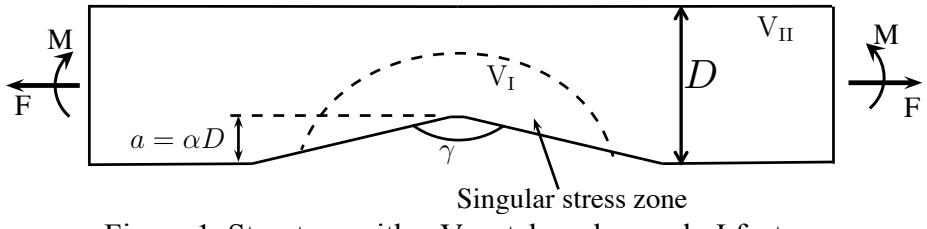

Figure 1. Structure with a V-notch under mode-I facture

2.1. Energetic scaling

Consider the case where the stress singularity is sufficiently strong. It is clear that due to the significant stress concentration the FPZ must form at the notch tip. Therefore, the corresponding scaling mechanism is deterministic. Based on the Williams solution [9], the stress field near the notch tip under mode-I loading can be written as:

$$\sigma_{ij} = Hr^{\lambda} f_{ij}(\theta,\gamma) \tag{1}$$

where r = radial distance from the notch tip, f_{ij} = dimensionless function describing the angular dependence of the stress, and H = stress intensity factor. Based on dimensional analysis, H can be further written as:

$$H = \sigma D^{-\lambda} h(\gamma) \tag{2}$$

where σ = nominal stress = cP/bD, P = applied load, and $h(\gamma)$ is the dimensionless stress intensity factor, which is determined by the structural geometry. One commonly used mode-I fracture criterion for structures with a V-notch is that the peak load is attained when the stress at the distance c_f from the notch tip reaches the material tensile strength f_t [12]. Therefore, we obtain the nominal strength of the structure:

$$\sigma_N = f_t \varphi(\gamma)(D/c_f)^{\lambda} \tag{3}$$

where $\varphi(\gamma) = h^{-1}(\gamma) f_{\theta\theta}^{-1}(0,\gamma)$, which can easily calculated by an elastic analysis.

Since Eq. 3 is derived based on the linear elastic fracture mechanics, it represents the large-size asymptote of the energetic size effect law. The small-size asymptote is very easy to construct. For small-size structures, the FPZ occupies the entire notch ligament and consequently the ligament must behave like a crack filled with plastic glue. At this plastic limit, the size effect must vanish. An approximate equation that bridges the small- and large-size asymptotes has been proposed:

$$\sigma_N = \sigma_s \left[1 + (D/D_{0\gamma})^{1/\beta_\gamma}\right]^{\lambda\beta_\gamma} \tag{4}$$

where σ_s = nominal strength at the small-size limit, β_γ = model parameter, and $D_{0\gamma}$ = transitional size $= D_0\varphi(\gamma)/\varphi(0)$ ($D_0 = D_{0\gamma}$ at $\gamma = 0$). When $\lambda = -1/2$ and $\beta_\gamma = 1$, Eq. 4 converges to the classical Type-2 size effect proposed by Bažant [1, 2], which applies to structures with a large pre-existing crack.

2.2. Statistical size effect

The statistical size effect usually applies to structures without stress singularities, e.g. unnotched beams. A salient feature of the failure of these structures is that the location of damage initiation and localization is uncertain, which is often governed by the randomness of local material strength. Furthermore, these structures reach the peak load once any one of the representative volume elements (RVEs) is damaged and thus the RVE is here defined as the smallest material volume whose failure triggers that failure of the entire structure. The size of RVE l_0 is approximately 2-3 times the size of material inhomogeneities [5]. Statistically speaking, the structure can then be represented by a chain of RVEs. Since the RVE size is about the same as the autocorrelation length of the random material strength field [7], the RVE strength can be treated as an independent random variable and the failure probability of the entire structure can be written as:

$$P_f(\sigma_N) = 1 - \prod_{i=1}^{N} \left[1 - P_1(\sigma_N s(x_i))\right] \tag{5}$$

where P_1 = cumulative distribution function (cdf) of strength of one RVE, N = number of RVEs in the structure, and $s(x_i)$ = dimensionless stress field such that $\sigma_N s(x_i)$ = maximum elastic principal stress at the center of the ith RVE located at x_i. Recent studies have shown that, based on atomistic fracture mechanics and a multiscale transition model for strength statistics, the cdf of RVE strength can be approximated by a Gaussian distribution onto which a Weibull tail is grafted at a probability about 10^{-4} — 10^{-2} [6-7].

The mean strength of the structure can then be calculated as:

$$\bar{\sigma}_N = \int_0^1 \sigma_N \, \mathrm{d}P_f = \int_0^\infty \left[1 - P_f(\sigma_N)\right] \mathrm{d}\sigma_N \tag{6}$$

By considering geometrically similar structures with different sizes, we can obtain the size effect on mean structural strength. Though a closed-form expression seems not possible, an approximate form has been proposed:

$$\bar{\sigma}_N = \left[N_a / D + \left(N_b / D \right)^{rn/m} \right]^{1/r} \tag{7}$$

where n = dimension of scaling and N_a, N_b, and r are constants, which can be determined by the statistical parameters of the cdf of RVE strength. It should be pointed out that Eq. 7 shall not be applied to structures as D approaches 0. A recent study [13] has shown that for small and intermediate-size structures the size effect derived from this finite weakest link model with the use of elastic stresses agrees well with the prediction from the nonlinear deterministic calculation. This is because the mean size effect behavior for small-size and intermediate-size structures is mainly caused by the operative stress redistribution mechanism, which can be well predicted by the nonlinear deterministic calculation. At the same time, this mechanism can also be captured by the finite weakest link model, where the statistical multiscale transition model used for the formulation of the cdf of RVE strength consists of statistical bundles and chains that represent the damage localization and load redistribution mechanisms at different scales (albeit only the elastic stresses are used) [5-7]. For large-size structures, the zone of stress redistribution is negligible compared to structure size and the size effect is mainly caused by randomness of material strength, which cannot be captured by the deterministic calculation. Therefore, the size effect curve for the case of zero stress singularity can be completely explained by the finite weakest link model [4-7].

3. Generalized weakest link model

For structures with a wide V-notch and therefore a weak stress singularity, there is no guarantee that the FPZ would form at the tip of the V-notch. This means that the failure of the structure can be statistically represented by the weakest link model. On the other hand, there exists a singular stress field at the V-notch tip even though the degree of stress concentration is not significant. Furthermore, the fracture of the V-notch itself is associated with an energetic scaling law shown as Eq. 4, which cannot be represented by the existing finite weakest link model. This prompts us to derive a new scaling model by generalizing the classical finite weakest link model to include the energetic scaling of fracture of the V-notch.

In the proposed generalized weakest link model, we isolate the singular stress zone from the remaining part of the structure (Fig. 1), where the singular stress zone can be determined by comparing Eq. 1 to the numerically simulated elastic stress field. Since the singular stress zone is influenced by the presence of the V-notch, whose fracture exhibits an energetic scaling (i.e. Eq. 4), we propose to include this energetic scaling for the calculation of the failure probability of the

singular stress zone:

$$P_{f,V_I}(\sigma_N) = 1 - \prod_{i=1}^{N_1} \left\{ 1 - P_1 \left[\mu(D) \sigma_N s(x_i) \right] \right\} \tag{8}$$

where $\mu(D) = \left[1 + (D / D_{0\gamma})^{1/\beta_\gamma} \right]^{-\lambda\beta_\gamma}$, and N_I = number of RVEs in the singular stress zone. The failure probability of the remaining part of the structure can be calculated by the usual weakest link model with the elastic principal stresses:

$$P_{f,V_{II}}(\sigma_N) = 1 - \prod_{i=1}^{N_2} \left\{ 1 - P_1 \left[\sigma_N s(x_i) \right] \right\} \tag{9}$$

where N_2 = number of RVEs in the region outside the singular stress zone. The failure probability of the entire structure can then be written as:

$$P_f(\sigma_N) = 1 - \left[1 - P_{f,V_I}(\sigma_N) \right] \left[1 - P_{f,V_{II}}(\sigma_N) \right] \tag{10}$$

from which we can calculate the mean size effect. Similar to the case of statistical scaling, a closed form expression is impossible. Since the entire framework still relies on the finite weakest link model, we can use the same asymptotic matching technique as that for the statistical scaling to obtain an approximate scaling law:

$$\bar{\sigma}_N = \sigma_0 \left\{ C_1 \left[\mu^m(D) \psi_1 + \psi_2 \right]^{-r/m} \left(\frac{D + l_s}{l_0} \right)^{-2/m} \exp[-(\lambda / \lambda_1)^2] + \frac{\mu^{-r}(D) D_b}{\exp[-(\lambda / \lambda_2)^2] D + l_p} \right\}^{1/r} \tag{11}$$

where σ_0 = reference stress, C_1, r, λ_1, λ_2, l_s, l_p, D_b = constants, m = Weibull modulus, $\psi_1 = \int_{V_I} \left\langle s(x) \right\rangle^m \mathrm{d}V(x)$, and $\psi_2 = \int_{V_{II}} \left\langle s(x) \right\rangle^m \mathrm{d}V(x)$. Note that here we introduced l_s and l_p to regularize the functional behavior as D approaches 0. Furthermore, it is easy to show that the large- and small-size asymptotes of the mean strength requires:

$$\sigma_0 C_1^{1/r} = s_0^{1/r} \Gamma(1 + 1/m) \tag{12}$$

$$\sigma_s = \sigma_0 \left\{ D_b / l_p + C_1 (\psi_1 + \psi_2)^{1/m} (l_s / l_0)^{-2/m} \exp[-(\lambda / \lambda_1)^2] \right\}^{1/r} \tag{13}$$

where s_0 = Weibull scaling parameter. The small-size strength limit σ_s can usually be obtained by simple plastic analysis by treating the ligament as a crack filled by the plastic glue.

It is clear that Eq. 11 converges to Eqs. 4 and 7 in the two limiting cases. For the transition between these two limits, the size effect consists of both energetic and statistical components. At the small-size limit, the size effect is mainly governed by the statistical scaling component since the energetic scaling term predicts a weak size effect. At the large-size limit, the scaling is governed by the Weibull statistics modified by an energetic scaling term, which leads to a compound energetic-Weibull statistical scaling. Though the focus of this study is on mode-I fracture, the present framework has been extended to general mixed-mode fracture, which is applicable to bimaterial structures. When dealing with mixed-mode fracture, the energetic scaling term would generally contain two distinct stress singularities [14].

4. Numerical simulation

To verify the proposed analytical model, we investigate the size effect on strength of concrete beams with a V-notch under three-point bending (Fig. 2). The beam has a 1:6 depth-to-span ratio and notch depth is 20% of the beam depth. In the simulation, we consider different notch angles, i.e. $\gamma = 0°$, 90°, 120°, 135°, and 170°. For each notch angle, a series of geometrically similar specimens with a size range 1: 2: 4: 8: 16: 64: 128 (the depths of the smallest and largest beams are 37.5 mm and 4.8 m, respectively) is simulated. Based on the Williams solution, these notch angles correspond to the following orders of mode-I singularity: $\lambda = -0.5,\ -0.455,\ -0.3843,\ -0.3264,\ -0.0916$.

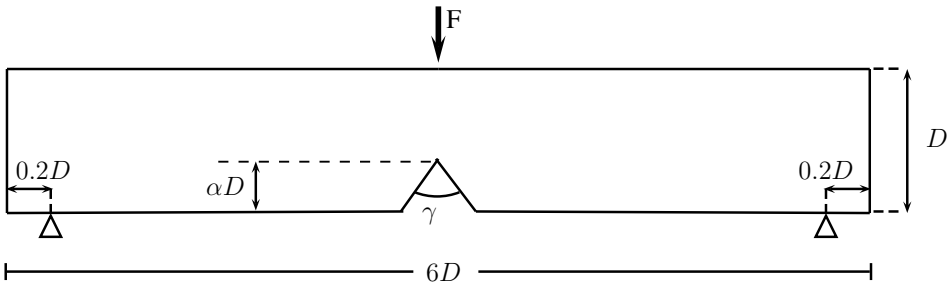

Figure 2. Numerical simulation of three-point bend beam

It is well known that concrete exhibits a complex constitutive behavior. Extensive efforts have been devoted to numerical modeling of fracture of concrete, e.g. [15-18]. Since we are interested in static mode-I fracture, we adopt the default plastic-damage model in ABAQUS because it is sufficient for the purpose of the present study; a detailed description of this constitutive model can be recovered from [19]. The material properties are chosen as follows: Young's modulus E = 30 GPa, Poisson ratio ν = 0.2, tensile strength f_t = 3 MPa, compressive strength f_c = 30 MPa, and Mode-I fracture toughness G_f = 100 N/m. Though we specify the compressive strength, the compressive region of the beam is expected to remain elastic. Therefore, the nonlinear part of the compressive behavior is not of particular interest for the present study. All the specimens undergo displacement-controlled loading. In this study, the numerical simulation is performed within a deterministic framework. Previous studies have shown that the deterministic simulation with a strain-softening constitutive model can successfully capture the entire size effect for the case of strong stress singularity and the size effect for the small- and intermediate structure sizes for the case of zero stress singularity [1-2]. Therefore, we expect that for the case of weak stress singularity the deterministic numerical model is sufficient for simulating the size effect for the small-and intermediate structure sizes. For the large-size asymptote, the deterministic simulation cannot yield the statistical scaling components. In this study, we mainly focus on the small- and intermediate size range, which is applicable to most engineering designs. Therefore, only deterministic simulation is necessary. As will be shown later, the influence of the statistical scaling component only prevails in structures of very large size.

For the finite element modeling, the notch tip is considered to have a very small width, i.e. 5 mm, which is a constant for all the geometries and sizes. For the deterministic simulation, the damage occurs near the mid-span of the beam. Therefore, to reduce computational efforts, we model the middle portion of the beam with a refined mesh (i.e. 5 mm) and the damage plasticity model whereas the rest part of the beam is modeled by a coarse mesh with a purely elastic model. For each

specimen, the assumed region, where the nonlinear material model is used, is further checked as part of the simulation. As the notch angle increases, this nonlinear region becomes larger. It should be pointed out that the present modeling is not as efficient as the crack band model and the nonlocal model, where larger element sizes can be used. However, the use of the crack band and nonlocal models requires extensive modeling efforts with special cautions such as the choice of crack band width [20] and treatment of the nonlocal weighting function along the structural boundary.

Fig. 3 presents the simulated nominal stress-relative deflection curves for specimens of all sizes and all different notch angles, where the nominal stress is defined as = P/bD and the relative displacement is defined as $\delta = \Delta/D$ (Δ = load-point displacement). It is observed that as the structure size increases the post-peak softening portion of the load-deflection curve becomes steeper, which implies a more brittle failure behavior. It should be noted that for large specimens (i.e. D = 1.2, 2.4, and 4.8m) the post-peak behavior is not captured, which indicates that a snap-back instability may have occurred. The snap-back behavior could be captured by loading the specimens by the crack mouth opening displacement. This is not done because we are interested only in the peak load.

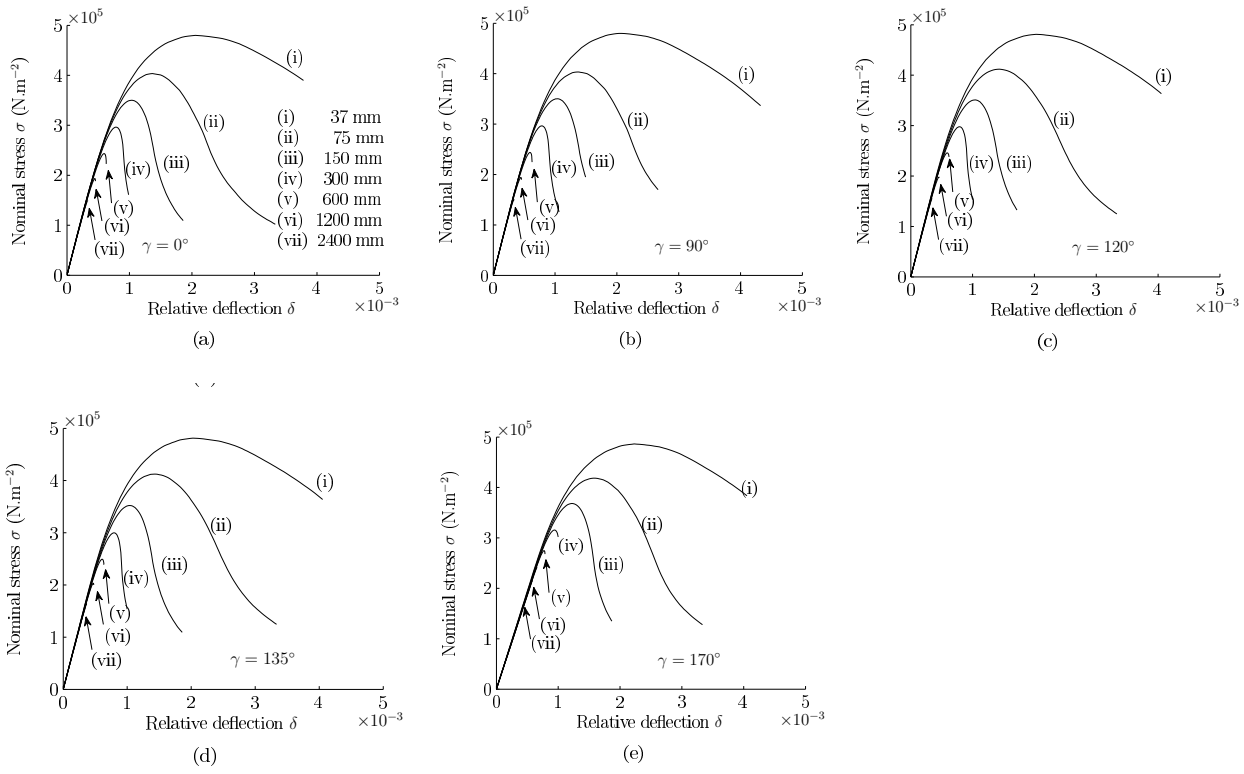

Figure 3. Simulated nominal stress-relative displacement curves

For the 2D specimens, we can simply define the nominal strength of the beam as $\sigma_N = P_{\max}/bD$, where b = 1. Fig. 4 shows the simulated size effects on the nominal strength for different notch angles and the optimum fitting by Eq. 11. As mentioned previously, the small-size strength limit σ_s can easily be calculated by plastic analysis, and the Weibull modulus for concrete is known to be 24. From the fitting, we obtain l_p = 40 mm, l_s = 150 mm, r = 0.88, s_0 = 0.488 MPa, D_0 = 90 mm, λ_1 =

0.301, $\lambda_2 = 0.208$, and β_γ =1, 1, 1.5, 2, 1.1 for γ = 0°, 90°, 120°, 135°, and 170°. It is clear from Fig. 4 that the Eq. 11 agrees well with the simulation results. It should be noted that the simulated size effect curve does not match well with Eq. 11 at the large-size limit for beams with a 170° V-notch. This is due to the fact that we used deterministic simulation, which cannot capture the associated large-size asymptote of the classical Weibull scaling relation. Furthermore, it is observed that such a difference occurs for very large beam size (i.e. D > 1.2m), which indicates that deterministic calculation is sufficient for most normal-size concrete beams.

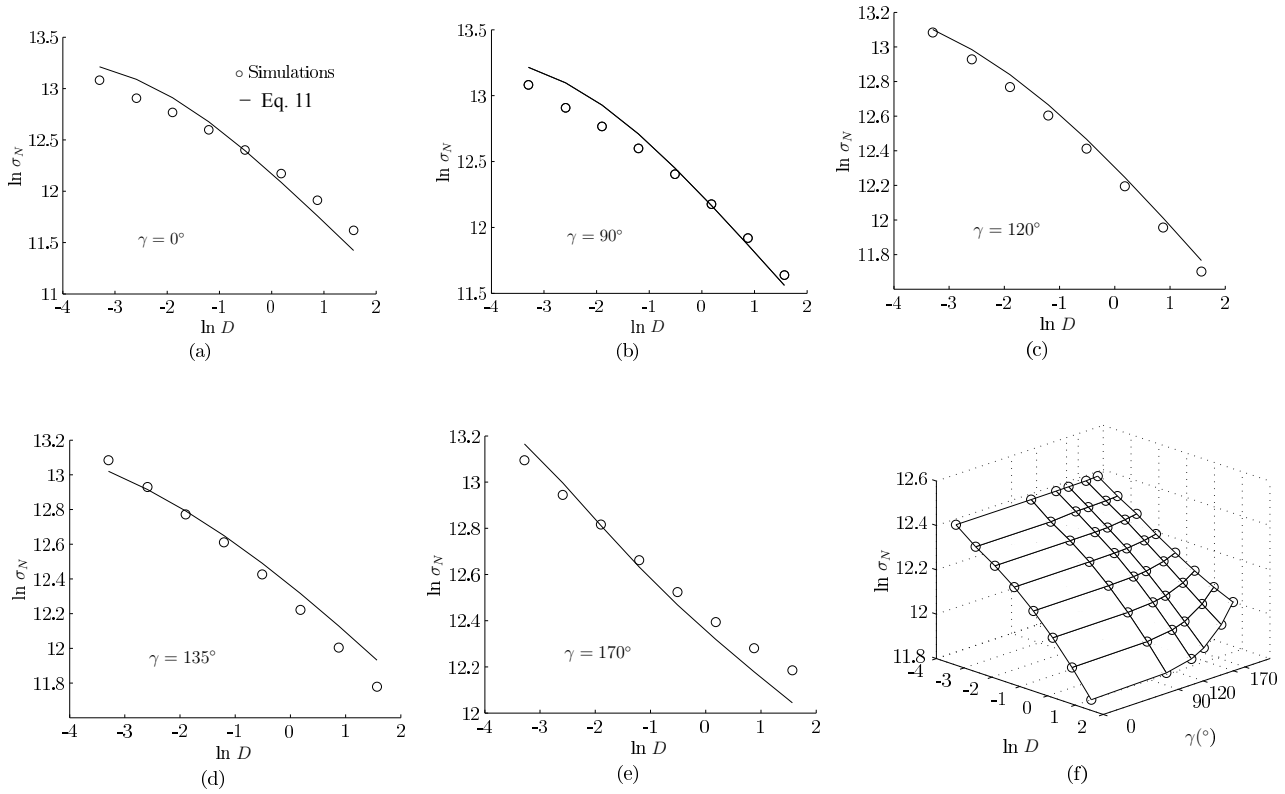

Figure 4. Size effect curves for notched beams: a)-e) Simulated size effect curves fitted by Eq. 11 and f) 3D plot of simulated effects of structural size and notch angle on nominal strength

5. Conclusions

This paper shows that the scaling of strength of quasibrittle structures is strongly dependent on the magnitude of the stress singularities. Such dependence can be derived from a generalized weakest link model, where the classical energetic scaling law is combined with the finite weakest link model. For the case of strong stress singularities, the scaling of fracture is purely energetic, which can be derived from fracture mechanics. For the case of zero stress singularity, the size effect can be explained by random material strength through the finite weakest link model. For the case of weak stress singularities, the scaling is governed by both energetic and statistical mechanisms.

References

[1] Z. P. Bažant, Scaling theory of quasibrittle structural failure. Proc. Nat'l Acad. Sci. USA, 101(37) (2004) 13397–13399.
[2] Z. P. Bažant, Scaling of Structural Strength, 2nd Ed. Elsevier, London, 2005.

[3] Z. P. Bažant, and D., Novák, Energetic-statistical size effect in quasibrittle fracture at crack initiation. ACI Mater. J. 97(3), (2000), 381-392.

[4] Z. P. Bažant, and S.D. Pang, Mechanics-based statistics of failure risk of quasibrittle structures and size effect on safety factors. Proc. Nat'l Acad. Sci. USA, 103(25) (2006) 9434–9439.

[5] Z. P. Bažant, and S.D. Pang, Activation energy based extreme value statistics and size effect in brittle and quasibrittle fracture. J. Mech. Phys. Solids 55, (2007) 91–134.

[6] Z. P. Bažant, J.-L. Le, and M. Z. Bazant, Scaling of strength and lifetime of quasibrittle structures based on atomistic fracture mechanics. Proc. Nat'l Acad. Sci. USA, 106(28) (2009) 11484–11489.

[7] J.-L. Le, and Z. P. Bažant, Unified Nano-Mechanics Based Probabilistic Theory of Quasibrittle and Brittle Structures: I. Strength, Crack Growth, Lifetime and Scaling. J. Mech. Phys. Solids, 59 (2011), 1291-1321.

[8] Z. P. Bažant, and K. T. Kazemi, Determination of fracture energy, process zone length and brittle number from size effect, with application to rock and concrete. Int. J. Frac. 44, (1990), 111-131.

[9] M. L. Williams Stress singularities resulting from various boundary conditions in angular corners of plates in extension. J. Appl. Mech. 74 (1952), 526-528.

[10] W. C. Carpenter, Mode I and mode II stress intensities for plates with cracks of finite opening. Int. J. Frac., 26, (1984). 201-214.

[11] X. H. Liu, Z Suo, and Q, Ma, Split singularities: Stress field near the edge of silicon die on polymer substrate. Acta Mater., 47, (1999) 67-76.

[12] Z. P. Bažant, and Q. Yu, Size effect on strength of quasibrittle structures with reentrant corners symmetrically loaded in tension. J. Engrg. Mech. 129(11) (2006), 1168-1176

[13] J.-L. Le, J. Elias and Z. P. Bažant, Computation of probability distribution of strength of quasibrittle structures failing at macro-crack initiation. J. Engrg. Mech., ASCE 138(7), (2012) 888–899.

[14] J.-L. Le, General size effect on strength of bi-material quasibrittle structures. Int. J. Frac. 172 (2011), 151-160.

[15] Z. P. Bažant, F. C. Caner, I. Carol, M.D. Adley, and S.A. Akers. Microplane model M4 for concrete: I. Formulation with work conjugate deviatoric stress. J. Engrg. Mech., ASCE 126(9), (2000), 944-953.

[16] J. Lee, and G.L. Fenves. Plastic-damage model for cyclic loading of concrete structures. J. Struct. Engrg. ASCE, 124(8), (1998), 892-900.

[17] J. Lubliner, J. Oliver, S. Oller, and E. Onate. A plastic-damage model for concrete. Int. J. Solids Structures, 25(3) (1989), 299-326.

[18] M. Jiŕasek and Th., Zimmermann Rotating crack model transition to scalar damage. J. Engrg. Mech., ASCE. 124, (1998), 277-284.

[19] ABAQUS 6.11 documentation SIMULIA, Providence, RI.

[20] M. Jiŕasek and M. Bauer Numerical aspect of the crack band approach. Comp. Struct. Vol.110-111, (2012), 60-78.

Experimental Validation of the Relationship between Parameters of 3P-Weibull Distributions Based in J_C or K_{JC}

Juan E. Perez Ipiña[1,*], Carlos Berejnoi[2]

[1] Grupo Mecánica de Fractura, Universidad Nacional del Comahue / CONICET, 8300 Neuquén, Argentina
[2] Facultad de Ingeniería, Universidad Nacional de Salta, 4400 Salta, Argentina
* Corresponding author: juan.perezipina@fain.uncoma.edu.ar

Abstract The characterization of fracture resistance of ferritic steels in the ductile to brittle transition zone is problematic due to the great scatter of test results. The statistical treatment in the literature is mainly based on the Weibull distribution, but some authors based their analysis on such a distribution with two parameters (2P-W), while others use a three parameters Weibull distribution (3P-W). Besides this, it is not homogeneous the use of these distributions in terms of J or K, and in general is acceptable that the Weibull slope for a K based distribution is twice the corresponding slope for the distribution based on J values. In previous works, the authors have shown that this relationship between slopes is not valid, except for the case of a 2P-W distribution, and have proposed a new factor (ξ) different from two that is calculated once the three parameters of the 3P-W distribution are estimated. In this paper it is demonstrated, using datasets with 100% cleavage from the Euro Round Robin in order to analyze cases where the weakest link model is valid, that this new factor works quite well, and that even when 3P-W distributions based on J and K values are not equivalent, both could be used to describe the results of fracture mechanics toughness tests.

Keywords Fracture toughness, Ductile-to-brittle transition, Scatter, Weibull distribution

1. Introduction

The experimental determination of fracture toughness in ferritic steels in the brittle-to-ductile transition region is generally based on J_C tests because K_{IC} valid values require too large specimens to meet small scale yielding conditions. Additionally, this characterization is problematic because of the scatter in results that need to be adjusted with the aid of a statistical distribution, being the Weibull distribution the most employed in literature.

This distribution has been used with two (2P-W) or three parameter (3P-W), and in both cases, adjusting data from J_C tests, or data expressed in terms of K converted from J_C (K_{JC}). For instance, Landes and Shaffer [1], Iwadate *et al.* [2], Anderson *et al.* [3], Landes *et al.* [4], and Heerens *et al.* [5] made use of a 2P-W distribution based on J_C values, while Landes and McCabe [6], Neville and Knott [7], and Perez Ipiña *et al.* [8] based their analysis on the 3P-W distribution using J_C data. The use of such distributions based on K values was promoted by Wallin, with a 2P-W distribution [9], and later with a 3P-W distribution [10].

The parameters to be determined in the 2P-W distribution are the shape parameter (also known as Weibull slope), and the scale parameter. For a 3P-W distribution, the threshold parameter is added. Besides the possibility of working with two or three parameters, and also with J or K data, some authors have proposed a fixed shape parameter with a given value: 2 when working with J_C [3, 4, 5, 11] and 4 when working with K_{JC} [10, 12, 13].

The advantage of using a 3P-W distribution with a fixed shape parameter is that an adjusted to experimental data distribution would be obtained with a smaller number of tests.

According to the theoretical deduction performed by Wallin [10], the value of the shape parameter is four when adjusting K values, and by the well-known relationship between K and J for small

scale yielding, this value would be two when working with J values.

As was shown by Larrainzar *et al.* [14], this relationship is only valid for 2P-W distributions. For 3P-W distributions there is no exact equivalence between that expressed in terms of J and the one in terms of K.
Equations (1) and (2) present 3P-W distributions expressed in terms of J or K, respectively.

$$P = 1 - e^{-\left(\frac{J - J_{\min}}{J_0 - J_{\min}}\right)^{b_J}} \quad (1)$$

$$P = 1 - e^{-\left(\frac{K - K_{\min}}{K_0 - K_{\min}}\right)^{b_K}} \quad (2)$$

The scale parameter values are J_0 and K_0, while J_{min} and K_{min} are the threshold parameter values, and b_J and b_K are the shape parameter values of the distributions given by Eq. (1) and (2). All these parameters can be estimated by linear regression, using experimental data in J or these data converted to K.
As was already established, there is no exact equivalence between distributions expressed by Eqs. (1) and (2). The relationship between b_K and b_J given by Eq. (3) is not valid for a general case, instead that given by Eq. (4) has been proposed as a good approximation.

$$b_K = 2b_J \quad (3)$$

$$b_K = \xi . b_J \quad (4)$$

Where ξ is given by Eq. (5), and its value ranges between 1 and 2.

$$\xi = \frac{2K_0}{K_0 + K_{\min}} \quad (5)$$

There is an exact relationship between the threshold and scale parameters (Eq. 6 and Eq. 7).

$$K_0 = \sqrt{\frac{EJ_0}{\left(1 - \nu^2\right)}} \quad (6)$$

$$K_{\min} = \sqrt{\frac{EJ_{\min}}{\left(1 - \nu^2\right)}} \quad (7)$$

Where E is the material Young modulus, and < is the material Poisson coefficient.
In this work the relationship between shape parameters in 3P-W distributions, based in K, and J and given by Eq. (4), is validated with experimental data obtained from the Euro Fracture Toughness Dataset. For such a purpose, the parameters of both 3P-W distributions based in J and in K were estimated. Then it was performed a comparison between the parameters of the last one with those converted from 3P-W based in J (by means of Eqs. 4, 6 and 7).

2. Material and Method

Data taken from the Euro Fracture Toughness Dataset [15] were used in the present work. They

correspond to the Round Robin organized by the European Structural Integrity Society (ESIS) and all the information is available in ftp://ftp.gkss.de/pub/eurodataset.
The material tested in the project was a ferritic steel DIN 22NiMoCr37 forged, quenched and tempered.
Figure 1 shows the test matrix performed in the ESIS Round Robin. As the figure shows, tests were performed at different temperatures (-154°C, -110°C, -91°C, -60°C, -40°C, -20°C, 0°C and 20°C) and with different specimen thicknesses C(T) (½", 1", 2" and 4"), with a thickness to width ratio B/W=0.5. Specimens were fatigue pre-cracked to be inside the range 0.52 < a0/W < 0.6. Side grooving was performed after pre-cracking in a few specimens. Tests were carried out in order to obtain the fracture toughness at the point of fracture J_C.

From the tested sets, only those in which all the specimens presented cleavage were considered in the present work. They corresponded generally to the lowest temperatures and largest sizes and are color marked out in squares in Fig. 1. Figure 2 shows the results for all the analyzed sets. This selection was decided in order to avoid sets where two different failure modes coexist, implying that a 3P-W function could not adequately describe the scatter. It is important to note that some datasets included values greater than the allowed J_{max} for the corresponding thickness (½ T at -60°C, 1T at -40°C, 1T at -20°C and 2T at 0°C). Each J_C value was converted to its K_{JC} equivalent, by means of Eq. (8), considering E=210 GPa and <=0.3.

$$K_{J_C} = \sqrt{\frac{EJ_C}{\left(1-\nu^2\right)}} \qquad (8)$$

The parameters of both 3P-W distributions in terms of J and K were estimated for all the analyzed sets. In this way the slopes (b_J and b_K), the thresholds (J_{min} and K_{min}), and the scale (J_0 and K_0) parameters were obtained. Following, the parameters of another 3P-W distribution in terms of K ($K_0(J)$, $K_{min}(J)$ and $b_{K\xi}$), were calculated from the estimations of J_0, J_{min} and b_J already obtained, using Eqs. (6), (7) and (4) respectively.

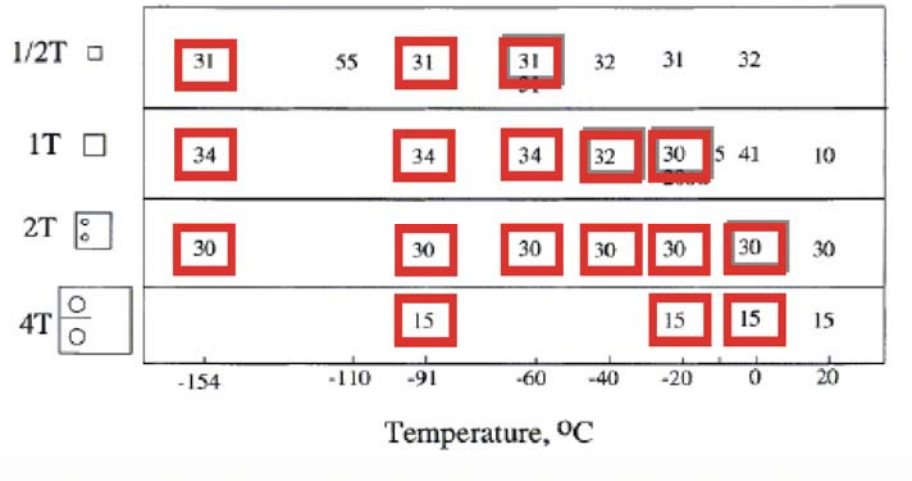

Figure1. Test matrix performed in the ESIS Round Robin. The sets marked out in squares presented only cleavage results and were analyzed in this work. Those shadowed correspond to data sets where some results exceeded J_{max}

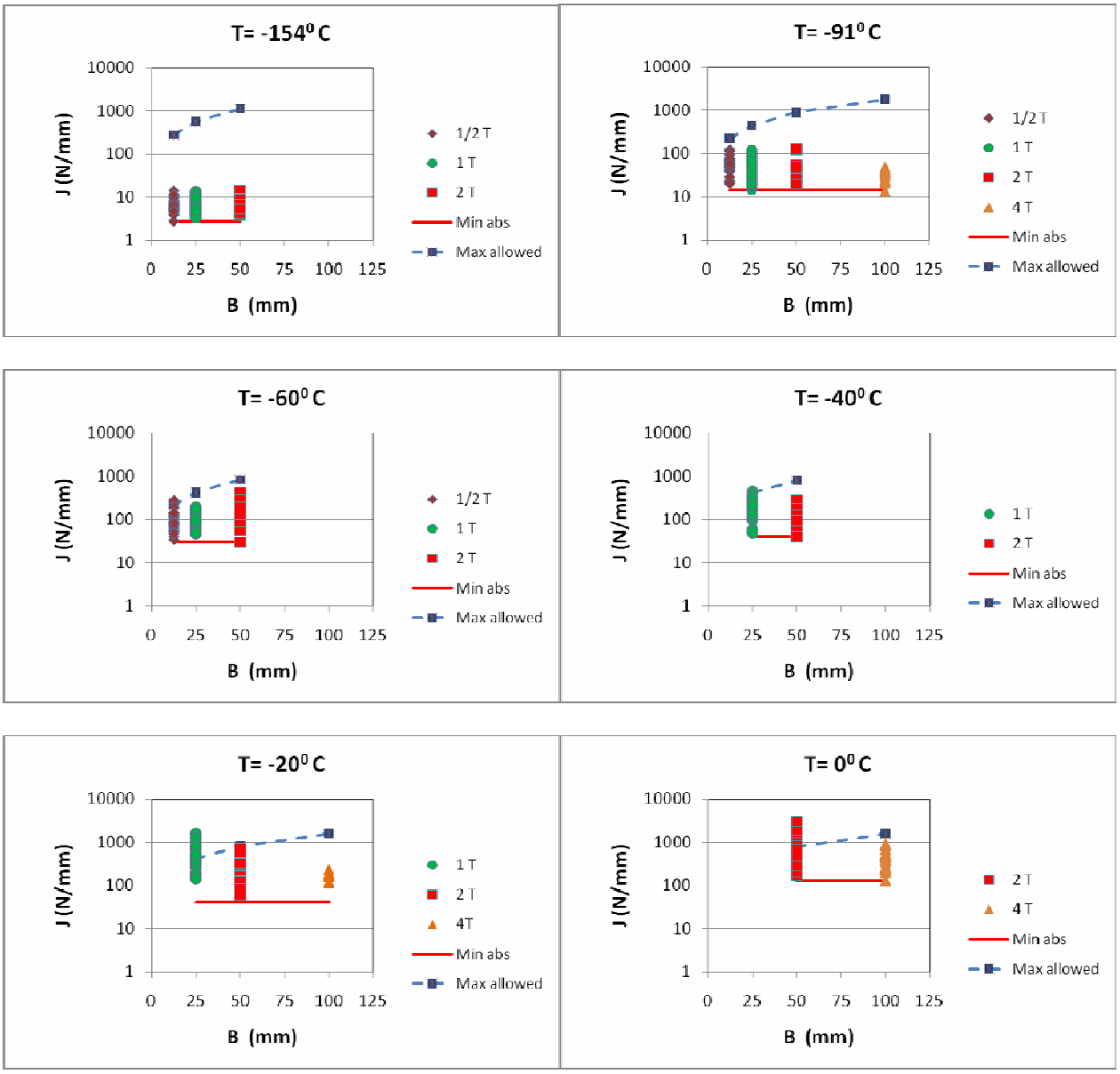

Figure 2. Experimental results for all the analyzed temperatures

3. Results, analysis and discussion

Table 1 shows the 3P-W parameters estimated for all the analyzed sets: the slopes (b_J and b_K), the thresholds (J_{min} and K_{min}), and the scale (J_0 y K_0) parameters. The parameters of the distribution in terms of K(J), calculated from the estimations of J_0, J_{min} and b_J already obtained, as well as the values of ξ , and the b_K/b_J ratio are also shown in the table.

Nearly all the sets produced "acceptable" values of Weibull parameters, especially K_{min}. The set corresponding to B=25mm and T=-40°C was the exception in which physically impossible values of J_{min} and K_{min} were obtained, so the threshold value was considered as zero. In this set, only one of the 32 results was larger than the J_{max} corresponding to this thickness, although there were more than one non-valid results in other sets and the Weibull parameters were physically "acceptable".

Table 1. 3P-W parameters in terms of **J** [kJ/m^2] and **K** [MPa/m$^{1/2}$], all temperatures and sizes

		Estimated from experimental data			Estimated from converted experimental data K_{JC}				Converted from estimated J parameters			
T (ºC)	Size	J_0	J_{min}	b_J	K_0	K_{min}	b_K	b_K/b_J	$K_0(J)$	$K_{min}(J)$	$b_{K\xi}$	ξ
-154	1/2T	7.92	1.80	2.22	42.67	18.54	3.23	1.45	42.76	20.41	3.01	1.35
	1T	7,28	3,06	1,57	40,86	26,05	1,95	1,24	41	26,57	1,90	1,21
	2T	6,31	3,67	1,31	38,02	28,94	1,50	1,15	38,16	29,10	1,49	1,13
-91	1/2T	65.66	9.95	1.85	123.08	34.38	3.21	1.73	123.09	47.93	2.67	1.44
	1T	55,68	11,84	1,44	112,91	47,93	2,08	1,44	113,35	52,27	1,97	1,37
	2T	41,21	17,37	1,44	97,15	61,39	1,87	1,3	97,52	63,31	1,75	1,21
	4T	35.52	4.07	2.68	90.49	22.43	4.54	1.69	90.54	30.65	4.00	1.49
-60	1/2T	115.91	28.72	1.39	162.52	77.28	1.92	1.38	163.55	81.41	1.86	1.36
	1T	107,13	41,19	1,41	156,74	94,08	1,84	1,30	157,23	97,50	1,74	1,23
	2T	157,71	16,12	1,75	190,06	50,64	2,83	1,62	190,77	60,99	2,65	1,52
-40	1T	236,76	0	2,11	233,75	0	4,22	2	233,75	0	4,22	2
	2T	144,49	22,55	2,07	182,12	62,58	3,20	1,55	182,60	72,14	2,97	1,43
-20	1T	564,71	125,55	1,08	357,50	162,19	1,50	1,39	361	170,21	1,47	1,36
	2T	277,41	37,70	1,52	252,25	77,60	2,43	1,60	253,02	93,27	2,22	1,46
	4T	190.96	58.45	2.97	209.89	101.59	4.44	1.49	209.92	116.14	3.83	1.29
0	2T	953.58	166.33	0.83	458.32	191.46	1.13	1.36	469.10	195.92	1.18	1.41
	4T	458.66	81.30	1.31	324.15	118.66	2.02	1.54	325.34	136.97	1.85	1.41

Table 1 shows that the parameters estimated by linear regression from K values converted from J (shown in column "Estimated from converted experimental data K_{JC}" in Table 1) and also using the parameters obtained by means of Eqs. (4), (6) and (7) (shown in column "Converted from J parameters" in Table 1) are very close. Figure 3 shows some Weibull cumulative distribution functions with parameters obtained by the two ways, together with the experimental points and the agreement is confirmed.

Table 2 and Fig. 4 show the comparison between ξ, obtained using Eq. (5), and the ratio b_K/b_J, where b_K and b_J are the shape parameters estimated for J experimental values and K_J. These values are quite similar, although b_K/b_J resulted always larger than ξ, except in one case. The horizontal line in the figure corresponds to the hypothetical case given by Eq. (3) ($b_K=2b_J$), which is not satisfied except when $J_{min}=0$, as already justified.

Figures 5 to 7 compare the three Weibull parameters in K: those obtained from the K_{JC} values and those obtained from J_C values (3P-W(J)) and transformed to K by using Eqs. (4), (6) and (7).

Figure 8 shows the predicted thresholds against the minimum experimental values. It can be

observed from this figure and also from Fig. 5 and Table 1 that $K_{min}(J)$ values, those obtained using ξ, resulted less conservative than the K_{min} ones, although their values were always lower than the corresponding experimental minimum.

As it is seen from Fig. 3, it resulted clear that the methodology proposed (that uses Eqs. 4, 6 and 7) adjusts the experimental data very well.

Table 2. Difference $b_K/b_J - \xi$ relative to ξ

T (ºC)	W=25 mm	W=50 mm	W= 100 mm	W= 200 mm
-154	7.41%	2,48 %	1,77 %	-
-91	20.14%	5,11 %	7,44 %	13.10%
-60	1.47%	5,69 %	6,59 %	-
-40		0 %	8,39 %	-
-20		2,21 %	9,59 %	15.50%
0			-3.55%	9.22%

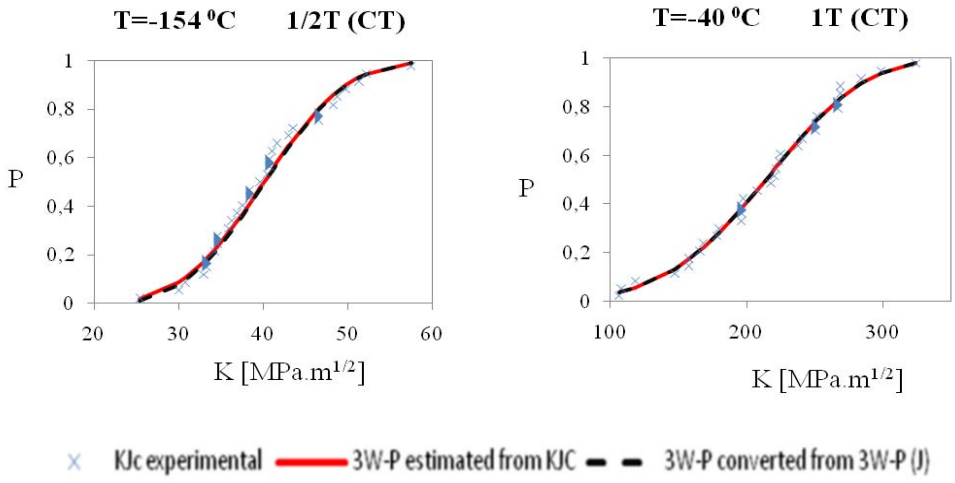

Figure 3. 3P-W distributions comparison with parameters obtained by linear regression and by J_0, J_{min} and b_J. conversion, for two datasets

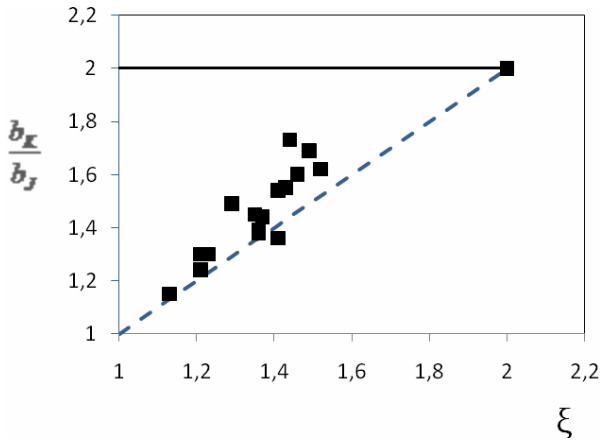

Figure 4. Comparison between b_K/b_J and ξ (R^2 for the linear regression equal to 0.83254927)

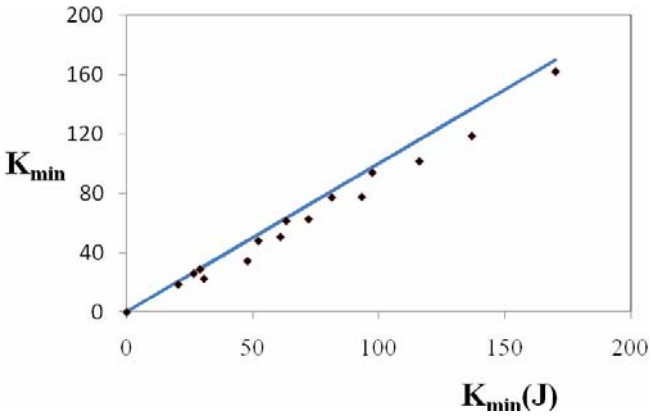

Figure 5. Comparison between $K_{min}(J)$ and K_{min} (R^2 for the linear regression equal to 0.9870869)

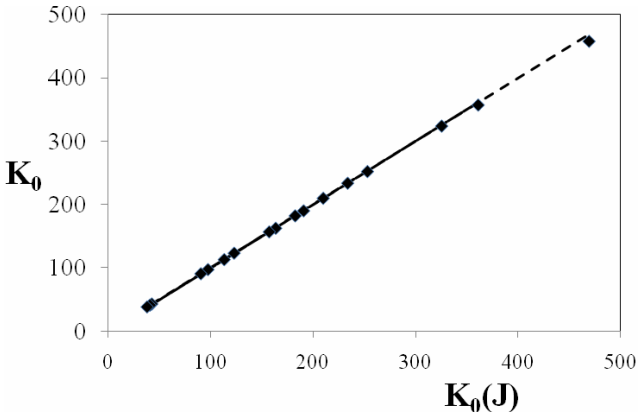

Figure 6. Comparison between $K_0(J)$ and K_0 (R^2 for the linear regression equal to 0.99979445)

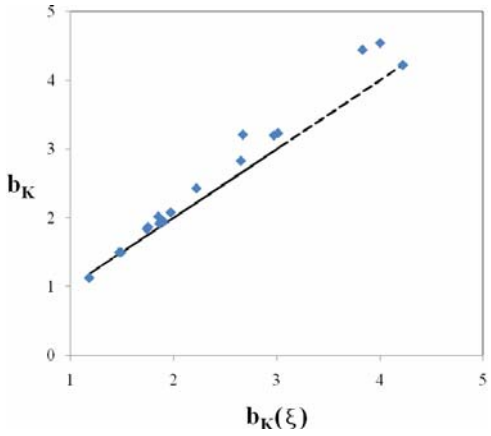

Figure 7. Comparison between $b_K(\xi)$ and b_K (R^2 for the linear regression equal to 0.97867302)

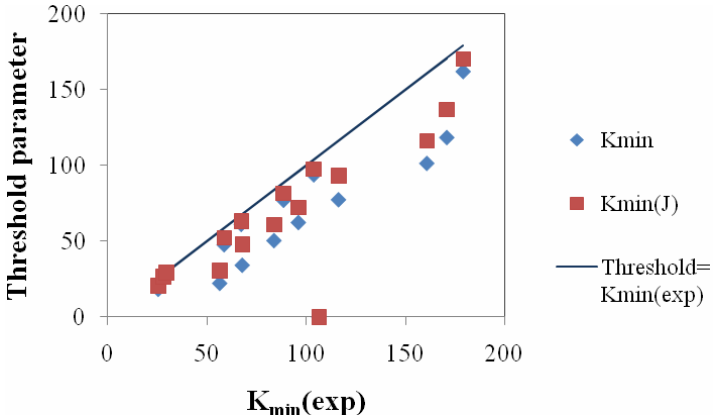

Figure 8. Comparison between $K_{min}(J)$, K_{min} and $K_{min}(exp)$

Table 3. Percentual differences between K_{min} and experimental K_{min}

	T (^{0}C)	$\frac{K_{min} - K_{min}(exp)}{K_{min}(exp)}(\%)$	$\frac{K_{min}(J) - K_{min}(exp)}{K_{min}(exp)}(\%)$
1/2T	-154	-27.06	-19.71
	-91	-49.27	-29.27
	-60	-12.76	-8.09
1T	-154	-7.00	-5.14
	-91	-18.26	-10.86
	-60	-9.37	-6.08
	-40 *	-100.00	-100.00
	-20	-9.44	-4.96
2T	-154	-2.27	-1.73
	-91	-8.72	-5.86
	-60	-39.54	-27.18

	-40	-34.86	-24.91
	-20	-33.27	-19.79
	0	-4.54	-2.31
4T	-91	-60.25	-45.69
	-20	-36.81	-27.76
	0	-30.55	-19.83

*: In this case, threshold parameter was forced to zero because a negative value was obtained from the estimation, resulting a difference of 100% between K_{min} and experimental K_{min}

There is no clear evidence that the 3P-W distribution based in J is better than the corresponding to that based in K values. Both fitted well the experimental results and predicted good threshold parameters.

4. Conclusions

- The theoretical relationship between b_J and b_K given by eq. (5) is consistent with the obtained from experimental data from the ESIS Round Robin.
- The Weibull slope in terms of K is not consistent with a fixed value equal to 4, instead it appears to calculate it from b_J by using Eq. (3), or estimating it from experimental data converted toK.
- The 3P-W parameters in terms of K, that can be estimated from experimental Jc converted to K_{Jc}, result more consistent with reality when they are calculated converting the corresponding estimated in terms of J.

Acknowledgements

To Consejo Nacional de Investigaciones Científicas y Tecnológicas (CONICET) by the support to this work.

References

[1] Landes, J. D. and Shaffer, D. H. (1980) Statistical Characterization of Fracture in the Transition Region. ASTM STP 700, 368-382.

[2] Iwadate, T., Tanaka,Y., Ono, S. and Watanabe, J. (1983) An Analysis of Elastic-Plastic Fracture Toughness Behavior for JIC Measurement in the Transition Region. ASTM STP 803, 531-561.

[3] Anderson, T. L., Stienstra, D. and Dodds, R. H. (1994) A Theoretical Framework for Addressing Fracture in the Ductile-Brittle Transition Region. ASTM STP 1207, 186-214.

[4] Landes, J.D., Zerbst, U., Heerens, J., Petrovski, B. and K.H. Schwalbe (1994) Single-Specimen Test Analysis to Determine Lower-Bound Toughness in the Transition. ASTM STP 1207, 171-185.

[5] Heerens, J., Zerbst, U. and Schwalbe, K.H. (1993) Strategy for Characterizing Fracture Toughness in the Ductile to Brittle Transition Regime. Fatigue Fracture Eng. Mater. Struct., 16 (11), 1213-1230.

[6] Landes, J.D. and McCabe, D.E. (1982) Effect of Section Size on Transition Behavior of Structural Steels. Scientific Paper 81-1D7-Metal-P2, Westinghouse R&D Centre.

[7] Neville, D. and Knott, J. (1986) Statistical Distributions of Toughness and Fracture Stress for Homogeneous and Inhomogeneous Materials. J. Mech. Phys. Solids, 34(3), 243-291.

[8] Perez Ipiña, J.E., Centurion, S.M.C. and Asta, E.P. (1994) Minimum number of specimens to characterize fracture toughness in the ductile-to-brittle transition region. Engng. Fracture Mech., 47 (3), 457-463.

[9] Wallin, K. (1984) The Scatter in K_{IC} – Results. Engng. Fracture Mech., 19(6), 1085-1093.

[10] Wallin, K. (1993) Statistical Aspects of Constraint with Emphasis on Testing and Analysis of Laboratory Specimens in the Transition Region. ASTM STP 1171, 264-288.
[11] McCabe, D. E. (1993) A Comparison of Weibull and ßIC Analyses of Transition Range Data. ASTM STP 1189, 80-94.
[12] Miglin, M., Oberjohn, L. and Van Der Sluys, W. (1994) Analysis of Results from the MPC/JSPS Round Robin Testing Program in the Ductile-to-Brittle Transition Region. ASTM STP 1207, 342-354.
[13] ASTM E 1921 (2002) Standard Test Method for Determination of Reference Temperature, T0, for Ferritic Steels in the Transition Range. In: Annual Book of ASTM Standards 2002, Vol. 03.01.
[14] Larrainzar, C., C. Berejnoi, C. & J.E. Perez Ipiña, Transformaciones de valores Jc en Kjc usando la función de Weibull, Jornadas Regionales de Ciencia y Tecnología de las Facultades de Ingeniería del NOA, Catamarca, 2006.
[15] Heerens J. & D. Hellmann, Development of the fracture toughness Dataset, Engineering Fracture Mechanics, 69, 421-449, 2002.

Scale Effect of the Tensile Strength of Aligned-Flax-Fiber Reinforced Composite

Jānis Andersons[1,*], Edgars Spārniņš[1], Jānis Modniks[1]

[1] Institute of Polymer Mechanics, University of Latvia, Riga LV-1006, Latvia
* Corresponding author: janis.andersons@pmi.lv

Abstract Application of plant-derived natural fibers as the reinforcement of polymer-matrix composites is driven by economic and environmental reasons. In order to fully exploit the reinforcing effect of the fibers, they have to be aligned in the composite material. When using such UD composites in load-bearing applications, the dependence of strength on the material volume subjected to loading, i.e. the scale effect of strength, should be taken into account in design. UD-reinforced flax fiber/epoxy matrix composites, produced from prepregs, were tested in tension in fiber direction in order to elucidate the scale effect of the tensile strength. The strength distribution at a fixed specimen size and the dependence of the mean strength on the size were shown to agree reasonably well with the Weibull strength statistics, corroborating the previous results for flax-fabric-reinforced composites. A probabilistic model of the strength in tension along the reinforcement direction, using fiber strength distribution, interfacial shear strength and morphology parameters, was applied to theoretically evaluate the magnitude of scale effect.

Keywords flax fibers, polymer composites, strength, Weibull distribution

1. Introduction

Application of plant-derived natural fibers as the reinforcement of polymer-matrix composites is driven by economic and environmental reasons. In order to fully exploit the reinforcing effect of the fibers, they have to be aligned in the composite material. For bast fibers, this is achieved either by using traditional textile technologies to produce aligned fiber yarns (with a twist level optimized for processing) or by manufacturing prepregs with unidirectional (UD) bast fiber orientation. When using such UD composites in load-bearing applications, the dependence of strength on the material volume subjected to loading, i.e. the scale effect of strength, should be taken into account in design. For brittle composites, the scale effect closely follows the weakest-link statistics [1] reflected by the Weibull strength distribution:

$$P(\sigma)=1-\exp\left[-\frac{V}{V_0}\left(\frac{\sigma}{\beta}\right)^{\alpha}\right] \tag{1}$$

where V is the specimen volume subjected to stress σ and α and β denote Weibull shape and scale parameters, respectively. Aligned flax fiber composites with textile reinforcement have been shown to exhibit scale effect of tensile strength consistent with Eq. (1) when subjected to tensile loading along the fibers [2].

Probabilistic models of fracture of UD continuous-fiber reinforced composites provide expressions of Eq. (1) parameters in terms of fiber, interface and matrix properties, see e.g. [3-5]. Flax fibers, although being relatively long, are discontinuous; moreover, typical reinforcement of a UD composite contains both elementary and technical fibers, defects in the latter triggering fracture of the composite [6]. Therefore, direct application of the probabilistic strength models derived for

uniform continuous fiber composites to bast fiber composites is likely to yield an upper estimate of their strength [7]. The current study concerns experimental evaluation of the scale effect of tensile strength of UD flax-fiber composites made of commercially available prepregs. Probabilistic strength model [4] is applied for approximate evaluation of strength.

2. Experimental

2.1. Material

A composite plate was produced from LINEO flax/epoxy prepreg FLAXPLY©. Six UD prepreg plies of the areal density of 150 g/m^2 were aligned, stacked and cured in a thermopress for one hour at ~1 atm pressure and 130 ˚C temperature. Four groups of specimens, with widths w = 10, 20, 40, and 70 mm, were cut out of the plate along the fiber direction so that the gauge length to width ratio for all specimens amounted to 5.

2.2. Tests

Fiberglass tabs were glued onto the specimen ends. The specimens were tested for strength by applying a stroke-controlled tensile loading in the fiber direction. The loading rate was varied according to specimen gauge length so that the nominal strain rate for all the specimens tested amounted to 0.75 %/min. The strength was evaluated from the failure load employing the average width of a specimen and the average thickness of the plate

3. Model

3.1. Weibull scale effect

For the rectangular geometry considered, the specimen volume subjected to load is a product of its width, gauge length, and thickness $V = wLt$ (resp. unit volume $V_0 = w_0 L_0 t_0$). Due to uniform thickness of the specimens, we select $t_0 = t$, hence Eq. (1) takes the form:

$$P(\sigma) = 1 - \exp\left[-\frac{wL}{w_0 L_0} \left(\frac{\sigma}{\beta} \right)^{\alpha} \right] \tag{2}$$

It follows from Eq. (2) that the mean strength $\langle \sigma \rangle$ depends on specimen dimensions as follows:

$$\langle \sigma \rangle = \beta \left(\frac{wL}{w_0 L_0} \right)^{-\frac{1}{\alpha}} \Gamma\left(1 + \frac{1}{\alpha} \right) \tag{3}$$

Hence, having determined the strength distribution Eq. (2) parameters from test results at one gauge length, the dependence of mean strength on specimen size can be evaluated according to Eq. (3) if the Weibull scale effect of brittle fracture applies.

3.2. Strength model

A probabilistic model of the tensile strength of UD continuous fiber reinforced composites has been elaborated in [4] for fibers with the Weibull two-parameter strength distribution

$$P(\sigma)=1-\exp\left[-\frac{l}{l_0}\left(\frac{\sigma}{\beta_f}\right)^{\alpha_f}\right] \tag{4}$$

where l stands for fiber length, l_0 is a unit length, and the distribution shape and scale parameters are designated as α_f and β_f, respectively.

In the following we briefly recapitulate the principal relations of the model [4]. Distribution of the average (over cross-section of the composite normal to the fibers) stress taken by the fibers at the failure of a UD composite is given by

$$P(\sigma_f)=1-\exp\left[-\left(\frac{\sigma_f}{\widetilde{\sigma}}\right)^{\widetilde{\rho}}\right] \tag{5}$$

The scale, $\widetilde{\sigma}$, and shape, $\widetilde{\rho}$, parameters of the Weibull distribution Eq. (5) are evaluated as follows

$$\widetilde{\sigma}=\sigma_c b_{m,n} \tag{6}$$

and

$$\widetilde{\rho}=b_{m,n}/a_{m,n} \tag{7}$$

where $a_{m,n}$ and $b_{m,n}$ are expressed by following relations

$$a_{m,n}=\frac{\gamma^{**}_{n_l}}{\sqrt{2\ln(m\cdot n)}} \tag{8}$$

and

$$b_{m,n}=\mu^{*}_{n_l}+\gamma^{**}_{n_l}\left(\frac{\ln(\ln(m\cdot n))+\ln(4\pi)}{\sqrt{8\ln(m\cdot n)}}-\sqrt{2\ln(m\cdot n)}\right) \tag{9}$$

The characteristic stress entering Eq. (6) is given by

$$\sigma_c=\left(\frac{\beta_f^{\alpha_f}\tau\, l_0}{r}\right)^{\frac{1}{1+\alpha_f}} \tag{10}$$

where r is fiber radius and τ designates the interfacial shear strength (IFSS) between fibers and matrix. In Eqs. (8) and (9), $\mu_{n_l}^{*}$ and $\gamma_{n_l}^{**}$ are theoretical mean and standard deviation of strength of a bundle of n_l fibers with n_l - the number of fibers in a critical element. The latter is given by

$$n_l = 403\alpha_f^{-1.28} \tag{11}$$

for $2 \le \alpha_f \le 10$. Length of the critical element δ_l is

$$\delta_l = 0.4\,\delta_c \tag{12}$$

where δ_c is the characteristic length given by

$$\delta_c = \frac{r\sigma_c}{\tau} \tag{13}$$

In Eqs. (8) and (9), $m = L/\delta_l$ and $n = n_f / n_l$, where L is the length of composite subjected to load and n_f - number of reinforcing fibers the composite contains.

4. Results and discussion

The parameters of the strength distribution were determined from the strength data of 50-mm-gage-length specimens, shown in Fig. 1, by the maximum likelihood method, as α = 22.8 and β = 404 MPa (at $w_0 = L_0 = 1$ mm). The empirical fiber fracture probabilities, P, have been evaluated via the median rank of the measured strength values using the approximation $P = (i - 0.3)/(n + 0.4)$, where i is the i-th number in ascendingly ordered strength data of the sample and n is the number of specimens.

Flax reinforcement is inherently heterogeneous since it contains not only elementary flax fibers but also technical fibers (i.e. naturally adhering elementary fiber bundles) of various sizes; an additional characteristic length is introduced by the presence of transverse stitching fibers in a prepreg. For heterogeneous quasi-brittle materials, strength distribution has been shown to change gradually from normal to Weibull with increasing size and brittleness of the specimen or structure [8]. At intermediate sizes, the strength distribution possesses a Weibull left tail switching to normal distribution for high strengths. A kink can be discerned in Fig. 1 suggesting the presence of such a transition. It appears of interest to establish the size of a representative volume element for strength in flax-fiber composites and its relation to reinforcement structure, thus potentially enabling a more accurate modeling of the scale effect of strength.

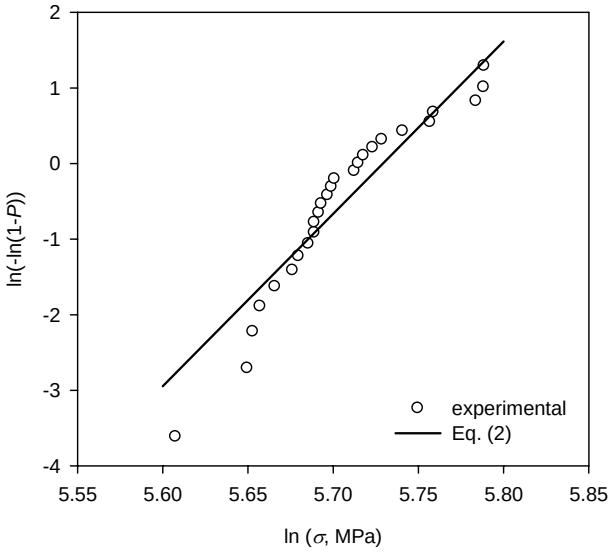

Fig. 1. Tensile strength distribution of specimens with width w = 10 mm in Weibull co-ordinates.

Comparison of the experimental dependence of the mean strength on specimen size and the prediction by Eq. (3) is shown in Fig. 2. It is seen that both, strength scatter at a fixed specimen size, Fig. 1, and strength-size scaling, Fig. 2, agree reasonably well with the Weibull statistics. Note that the sale effect of strength for a UD flax-fabric-reinforced composite has also been shown to follow the scaling of Eq. (2), although with a somewhat smaller Weibull shape parameter α of ca. 18 [2]. The higher scatter of strength in the case of textile UD reinforcement is likely to result from the additional geometrical variability associated with yarn alignment in the composite.

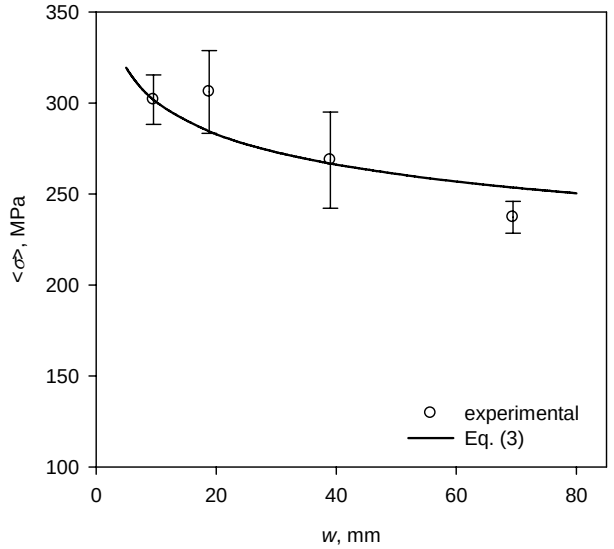

Fig. 2. Dependence of the mean tensile strength $<\sigma>$ on specimen width w

Application of the probabilistic strength models is hampered in this case by lack of information regarding flax fibers used in prepreg manufacture and their adhesion to the epoxy matrix. Nevertheless, for the purposes of qualitative comparison, strength distribution Eq. (5) parameters were estimated for several types of flax fibers assuming a plausible IFSS value. IFSS of bast fibers and epoxy matrix is reported to range from ca. 10 to 33 MPa [9-11]. For a conservative estimate,

IFSS of 10 MPa was assumed. Strength distribution Eq. (4) parameters, evaluated from test results of elementary flax fibers at 10 mm gauge length, are presented in Table 1 (at l_0 = 1 mm). Fiber diameter 16 μm was used in calculations.

Table 1. Strength distribution Eq. (4) parameters of elementary flax fibers

Reference	Shape parameter α_f	Scale parameter β_f, MPa
[12]	3	2080
[13]	1.8	2033
[错误!未找到引用源。]	2.7	1913

The parameters of composite strength distribution, Eq. (5), were evaluated for composite specimens with 50 mm gauge length and 10 mm width by Eqs. (6) and (7) using the fiber and interface parameters listed above. The results are presented in Table 2. Note that the product of fiber volume fraction and the predicted scale parameter is given in Table 2 for ease of comparison with the experimental scale parameter.

Table 2. Strength distribution Eq. (5) parameters of UD composite with 50 mm length

Fiber strength from reference	Shape parameter $\tilde{\rho}$	Reduced scale parameter $v_f\tilde{\sigma}$, MPa
[12]	107	502
[13]	117	508
[错误!未找到引用源。]	110	511

It is seen that the predicted shape parameter, characterizing strength scatter, is about 5 times higher than the experimentally determined value. This is likely to stem from such factors as fiber misalignment, heterogeneity, and clustering not allowed for in the theoretical model and increasing the variability of strength. Note also that the predicted scale parameter values exceed the experimental one, i.e. the model provides an upper limit of the tensile strength of flax fiber reinforced composite.

5. Conclusions

Scale effect of the tensile strength of UD flax/epoxy composite has been characterized experimentally and shown to comply with strength-specimen size scaling implied by the Weibull two-parameter distribution of strength. Hence strength distribution parameters, determined using only specimens of a fixed size, can be used to predict the variation of strength with volume of the composite subjected to load. A probabilistic model of composite strength has been shown to underestimate the scatter in strength and overestimate mean strength. This is likely to be related to the heterogeneity inherent in natural fiber composites and not reflected in the models derived for synthetic continuous fiber composites.

References

1. M.R. Wisnom, Size effects in the testing of fibre-composite materials, Compos Sci Technol 59 (1999) 1937-1957.
2. J. Andersons, E. Spārniņš, B. Nyström, R. Joffe, Scale effect of the tensile strength of

flax-fabric-reinforced polymer composites. J Reinf Plast Compos 30 (2011) 1969–1974.
3. S.L. Phoenix, I.J. Beyerlein, Statistical strength theory for fibrous composite materials, in: A. Kelly, C. Zweben (Eds.), Comprehensive composite materials, vol. 1; 2000, pp. 559–639.
4. M. Ibnabdeljalil, W.A. Curtin, Strength and reliability of fiber reinforced composites: localized load-sharing and associated size effects. Int J Solids Struct 34 (1997) 2649-2668.
5. W.A. Curtin, Tensile strength of fiber-reinforced composites: III. Beyond the traditional Weibull model for fiber strengths. J Compos Mater 34 (2000) 1301-1332.
6. M. Rask, Bo Madsen, B.F. Sørensen, J.L. Fife, K. Martyniuk, E.M. Lauridsen, In situ observations of microscale damage evolution in unidirectional natural fibre composites. Compos A 43 (2012) 1639–1649.
7. J. Andersons, R. Joffe, Estimation of the tensile strength of an oriented flax fiber-reinforced polymer composite. Compos A 42 (2011) 1229–1235.
8. Z.P. Bažant, S.-D. Pang, Activation energy based extreme value statistics and size effect in brittle and quasibrittle fracture. J Mech Phys Solids 55 (2007) 91–131.
9. J.-M. Park, T.Q. Son, J.-G. Jung, B.-S. Hwang, Interfacial evaluation of single Ramie and Kenaf fiber/epoxy resin composites using micromechanical test and nondestructive acoustic emission. Compos Interf 13 (2006)105–129.
10. R. Joffe, J. Andersons, L. Wallström, Interfacial shear strength of flax fiber/thermoset polymers estimated by fiber fragmentation tests. J Mater Sci 40 (2005) 2721-2722.
11. C. Guillebaud-Bonnafous, D. Vasconcellos, F. Touchard, L. Chocinski-Arnault, Experimental and numerical investigation of the interface between epoxy matrix and hemp yarn. Compos A 43 (2012) 2046–2058.
12. J. Andersons, E. Spārniņš, R. Joffe, L. Wallström, Strength distribution of elementary flax fibres. Compos Sci Technol 65 (2005) 693–702.
13. J. Andersons, E. Spārniņš, E. Poriķe, Strength and damage of elementary flax fibers extracted from tow and long line flax. J Compos Mater 43 (2009) 2653-2664.
14. J. Andersons, E. Poriķe, E. Spārniņš, Limit strain and deformability of elementary flax fibers. J Strain Anal Eng Design 46 (2011) 428-435.

Electroelastic analysis of four mode-III cracks originating from a circular hole in piezoelectric materials

JunHong Guo[1,*], ZiXing Lu[2], Jing Yu[1]

[1] College of Science, Inner Mongolia University of Technology, Hohhot 010051, China
[2] Institute of Solid mechanics, Beihang University, Beijing 100191, China
* Corresponding author: jhguo@imut.edu.cn

Abstract The fracture behavior of four non-symmetric radial cracks originating from a circular hole in piezoelectric materials subjected to remotely uniform in-plane electric loading and anti-plane mechanical loading is studied in this paper. The problem is transformed using the complex variable method and the technique of conformal mapping into Cauchy integral equations. To solve the Cauchy integral equations, the analytical solutions of the stress and the electric displacement intensity factors, energy release rate and mechanical strain energy release rate are obtained under the electrically impermeable and electrically permeable assumptions, respectively. Several known results are the special cases of the present results and new models used for simulating more practical defects in piezoelectric materials are derived as well, such as three radial cracks originating from a circular hole, semi-circular hole with an edge crack originating from a semi-infinite plane and a semi-infinite plane with an edge crack. Numerical examples are provided graphically to show the effects of the geometrical parameters on the energy release rate and the mechanical strain energy release rate.

Keywords Piezoelectric materials, Circular hole, Edge cracks, mapping function, Analytical solution

1. Introduction

Due to their intrinsic electromechanical coupling phenomenon, piezoelectric materials have been widely used as transducer and sensor in smart structures and devices. However, one inherent weakness of piezoelectric ceramics is the brittleness in mechanical behavior. When subjected to mechanical and electric loading in service, the stress concentrations can induce crack initiation and propagation, which will lead to the failure of these piezoelectric materials. Therefore, it is of great importance to analyze the fracture behavior of piezoelectric materials, especially when cracks emanating from holes are involved.

In recent years, the crack problems of piezoelectric materials have received considerable attention under anti-plane shear loading due to the practical importance [1-6]. In fact, there exist many kinds of complicated configurations during manufacture and service of the holed structures, e.g., cracks originating from circular hole, semi-circular hole with an edge crack originating from a semi-infinite solid, T-shaped crack, cross-shaped crack, etc. Recently, Wang and Gao [7] solved the two symmetrical cracks and a single crack originating from the edge of a circular hole in a piezoelectric solid by introducing mapping fucntion, and presented the exact solutions of the field intensity factors and the energy release rate. By developing new mapping functions, Guo et al. [8,9] investigated the two asymmetrical edge cracks emanating from an elliptical hole in a piezoelectric material under the electrically impermeable and the electrically permeable boundary conditions, respectively, and obtained the exact solutions of the field intensity factors and the energy release rate. To ours' knowledge, the existing research is focused on the collinear cracks parallel to the x-axis originating from holes. For an occurrence of the cracks parallel to y-axis direction originating from holes, however, the corresponding research is very lacking in a piezoelectric solid, which may have the surprise results. Thus, it is practical and necessary to study the fracture behavior of four

non-symmetrical radial cracks at the edge of a circular hole. Furthermore, it is very challenging and meaningful to present the analytical solutions for the complicated crack problems, since these solutions can provide the theoretical analysis for fracture problems in piezoelectric materials, and can also serve as a benchmark for the purpose of judging the accuracy and efficiency of various numerical and approximate methods.

In this paper, we study the anti-plane problem of four non-symmetrical radial cracks at the edge of a circular hole in a transversely isotropic piezoelectric solid based on two kinds of electric boundary conditions, i.e., the electrically impermeable and the electrically permeable. A new conformal mapping is developed to reduce the problem to the solution of Cauchy integral equation. In addition, the analytical solutions of the field intensity factors, the energy release rate (ERR) and the mechanical strain energy release rate (MSERE) are derived. It is seen that the stress intensity factors of some special cases derived from the present results agree well with the corresponding results of the pure elastic materials.

2. Basic formulation

In a rectangular coordinate system $x_i (i = 1, 2, 3)$, consider a transversely isotropic piezoelectric solid with the poling direction along the positive x_3 axis and the isotropic plane in the $x_1 - x_2$ plane. The constitutive equation for a linear piezoelectric media can be given as

$$[s_{3i}, D_i]^{\mathrm{T}} = \mathbf{B}_0 [g_{3i}, -E_i]^{\mathrm{T}} \tag{1}$$

where i=1, 2, T denotes a transpose of a matrix, and

$$\mathbf{B}_0 = \begin{matrix} 矫 \\ 压 \\ 猫 \\ 膜 \end{matrix} \begin{matrix} c_{44} & e_{15} \\ e_{15} & -\varepsilon_{11} \end{matrix} \tag{2}$$

where c_{44}, e_{15} and ε_{11} are the elastic constant, the piezoelectric constant and the dielectric permittivity, respectively.

The generalized strain-displacement relations have the form

$$g_{3i} = w_{,i}, \quad E_i = -\varphi_{,i} \tag{3}$$

where a comma in the subscripts stands for a partial differentiation.

The equilibrium equation and the charge conservation equation, in the absence of the body force and electric charge densities, can be written as

$$s_{3i,i} = 0, \quad D_{i,i} = 0 \tag{4}$$

Substituting Eqs. (1) and (2) into Eq. (4), we have

$$\nabla^2 w = 0, \quad \nabla^2 \varphi = 0 \tag{5}$$

The general solution of Eq. (5) can be expressed by the analytical function $\mathbf{f}(z)$ [4]

$$\mathbf{u} = \mathbf{A}\mathbf{f}(z) + \overline{\mathbf{A}\mathbf{f}(z)}, \quad \mathbf{u} = (w, \varphi)^{\mathrm{T}} \tag{6}$$

where $z = x_1 + \mathrm{i}x_2$. Thus, the stress and electric displacement can be expressed as

$$[s_{31} - \mathrm{i}s_{31}, D_1 - \mathrm{i}D_2]^{\mathrm{T}} = \mathbf{B}_0[g_{31} - \mathrm{i}g_{32}, -E_1 + \mathrm{i}E_2]^{\mathrm{T}} = \mathbf{B}_0\mathbf{f}'(z) \tag{7}$$

Let we introduce a potential function ϕ, such that

$$[s_{31}, D_1]^{\mathrm{T}} = -\mathbf{f}_{,2}, \quad [s_{32}, D_2]^{\mathrm{T}} = \mathbf{f}_{,1} \tag{8}$$

From Eqs. (7) and (8), one finds

$$\mathbf{f}'(z) = \mathbf{B}\mathbf{f}(z) \tag{9}$$

where $\mathbf{A}$ and $\mathbf{B}$ stand for the material constant matrices defined as

$$\mathbf{A} = \mathbf{I}, \quad \mathbf{B} = \mathrm{i}\mathbf{B}_0 \tag{10}$$

where $\mathbf{I}$ is a 2×2 unit matrix.

The boundary conditions along the surfaces of crack and circular hole can be written as

$$\int_s [t_3, D_n]^{\mathrm{T}}\,\mathrm{d}s = -\int_s [s_{32}\mathrm{d}x_1 - s_{31}\mathrm{d}x_2, D_2\mathrm{d}x_1 - D_1\mathrm{d}x_2]^{\mathrm{T}}\,\mathrm{d}s = -\,\mathrm{Re}\int_s \mathrm{d}\mathbf{f} = \mathrm{Re}[\mathbf{B}\mathbf{f}(z)] \tag{11}$$

where t_3 and D_n represent the anti-plane shear traction and the normal component of electric displacement along the boundary.

3. Mapping function and field intensity factors

Consider four non-symmetrical radial cracks at the edge of a circular hole in an infinite piezoelectric solid, as shown in Fig. 1. Using the technique of conformal mapping and complex variable method, we study the complex potentials, the field intensity factors, ERR and MSERR under two different electric boundary conditions as follows.

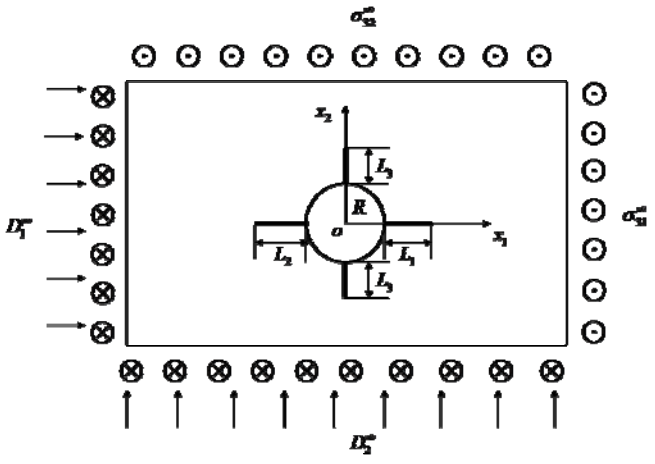

Fig. 1. Four non-symmetrical radial cracks at the edge of a circular hole in an infinite piezoelectric solid

In this case, the potential vector has the form (Zhang and Gao [6])

$$\mathbf{f}(z) = \mathbf{c}^{\infty} z + \mathbf{f}_0(z) \tag{12}$$

where $\mathbf{c}^{\infty}$ is a complex constant related to the remote loading conditions, and $\mathbf{f}_0(z)$ is an

unknown complex function that nulls at infinity, i.e., $\mathbf{f}_0(\infty)=\mathbf{0}$.

When the piezoelectric solid is subjected to uniform remote out-plane shear and in-plane electric field loadings, i.e., $\boldsymbol{\Sigma}_{2\infty}=[\sigma_{32}^{\infty},D_2^{\infty}]^{\mathrm{T}}$ and $\boldsymbol{\Sigma}_{1\infty}=[\sigma_{31}^{\infty},D_1^{\infty}]^{\mathrm{T}}$, the complex constant vector $\mathbf{c}^{¥}$ in Eq. (12) can be determined as

$$\mathbf{c}^{?}=\mathbf{B}^{1}[s_{31}^{\prime\prime}-\mathrm{i}s_{32},D_1^{\prime\prime}-\mathrm{i}D_2]^{\mathrm{T}} \tag{13}$$

In this study, two kinds of electric crack surface conditions are examined, i.e., electrically impermeable and permeable. For simplicity, they are identically expressed as

$$[s_{32},D_2]^{\mathrm{T}}=\text{矯}D_2^0]^{\mathrm{T}} \tag{14}$$

For the electrically impermeable case, $D_2^0=0$, whereas for the electrically permeable case, D_2^0 is unknown to be determined from the potential function continuity conditions along the surfaces of cracks and hole

$$\boldsymbol{\phi}^{+}=\boldsymbol{\phi}^{-},\ \varphi^{+}=\varphi^{-} \tag{15}$$

where superscript + and – denote the potential functions inside and outside the cracks and hole, respectively.

3.1. Electrically impermeable case

If the crack length is shorter than the hole-size, and the electric field inside the hole is smaller, the assumption of impermeable electric boundary condition is more reasonable. Thus, noting Eq. (13), Eq. (12) can be reduced to

$$\mathbf{B}\mathbf{f}_0(z)+\overline{\mathbf{B}\mathbf{f}_0(z)}=-(\mathbf{B}\mathbf{c}^{\infty}z+\overline{\mathbf{B}\mathbf{c}^{\infty}z}) \tag{16}$$

We develop a new mapping function as follows

$$z=\omega(\zeta)=\frac{R}{4\zeta}\left\{\sqrt{\left[f(\zeta+1)^2+g(\zeta-1)^2\right]^2-16a^2\zeta^2}+\sqrt{\left[f(\zeta+1)^2+g(\zeta-1)^2\right]^2-16(a^2+1)\zeta^2}\right\} \tag{17}$$

where

$$\begin{aligned}&f=\sqrt{a^2+c^2},\quad g=\sqrt{a^2+b^2}\\&a=\frac{1}{2}\left(\frac{R+L_3}{R}-\frac{R}{R+L_3}\right),\quad b=\frac{1}{2}\left(\frac{R+L_2}{R}+\frac{R}{R+L_2}\right),\quad c=\frac{1}{2}\left(\frac{R+L_1}{R}+\frac{R}{R+L_1}\right)\end{aligned} \tag{18}$$

It can be shown that Eq. (17) provides a mapping function from the outside region of the circular hole and cracks to the interior of a unit circle in the ζ-plane, and $z=R+L_1=\omega(1)$.

In the ζ-plane, Eq. (16) can be transformed into

$$\mathbf{B}\mathbf{f}_0(\sigma)+\overline{\mathbf{B}\mathbf{f}_0(\sigma)}=-\left[\mathbf{B}\mathbf{c}^{\infty}\omega(\sigma)+\overline{\mathbf{B}\mathbf{c}^{\infty}}\,\overline{\omega(\sigma)}\right] \tag{19}$$

where σ is the point on the unit circle, and $\mathbf{f}_0(\sigma)=\mathbf{f}_0(\omega(\sigma))$ is defined.

Taking Cauchy integrals $\frac{1}{2\pi \mathrm{i}}\int_\gamma \frac{d\sigma}{\sigma-\zeta}$ at the two sides of Eq. (19), we obtain

$$\mathbf{B}\mathbf{F}_0(\zeta)=-\boldsymbol{\phi}_{,1}^{\infty}\left[\omega'(\zeta)+\frac{R(f+g)}{2\zeta^2}\right] \tag{20}$$

The vector of field intensity factors can be expressed in the ζ-plane, as [8]

$$\boldsymbol{k}=(k_\sigma,k_D)^{\mathrm{T}}=2\sqrt{\pi}\lim_{\zeta\to 1}\frac{\mathbf{B}\mathbf{F}_0(\zeta)}{\sqrt{\omega''(\zeta)}} \tag{21}$$

Substituting Eqs. (17) and (20) into Eq. (21), one finally has

$$\boldsymbol{k}_{\mathrm{imp}}=\sqrt{\pi L_1}\begin{pmatrix}\sigma_{32}^{\infty}\\ D_2^{\infty}\end{pmatrix}K \tag{22}$$

where K called the dimensionless intensity factor is defined as

$$K=\sqrt{\frac{2Rc(f+g)\sqrt{c^2-1}}{L_1 f\left(c+\sqrt{c^2-1}\right)}} \tag{23}$$

3.2. Electrically permeable case

According to the method of Guo et al. [9], the potential functions inside the cracks and hole can be expressed as

$$\boldsymbol{\phi}^{+}=(D_2^0x_1-D_1^0x_2)\mathbf{i}_2, \tag{24}$$

$$\varphi^{+}=-E_1^0x_1-E_2^0x_2, \tag{25}$$

where $\mathbf{i}_2=[0,1]^{\mathrm{T}}$, and D_k^0 and E_k^0 are the components of the electric displacement and electric field inside the elliptical hole and the cracks, respectively, which are constant and to be determined by the loading condition.

The potential functions outside the cracks and hole can be expressed as

$$\boldsymbol{\phi}^{-}=\boldsymbol{\Sigma}_{2\infty}x_1-\boldsymbol{\Sigma}_{1\infty}x_2+2\mathrm{Re}[\mathbf{k}_0(z)], \tag{26}$$

$$\varphi^{-}=-E_1^{\infty}x_1-E_2^{\infty}x_2+2\mathrm{Im}[\mathbf{Y}\mathbf{k}_0(z)]_2, \tag{27}$$

where $\mathbf{k}_0(z)=\mathbf{B}\mathbf{f}_0(z)$, $\mathbf{Y}=\mathrm{i}\mathbf{A}\mathbf{B}^{-1}$.

Substituting Eqs. (24)-(27) into Eq. (15), we get

$$\mathbf{BF}_0(\zeta)=\frac{(a+b)(\varepsilon_1+\varepsilon_2)}{4\zeta^2}\boldsymbol{\Sigma}^{2\infty}, \tag{28}$$

$$D_2^0=D_2^\infty-\frac{e_{15}}{c_{44}}\sigma_{32}^\infty. \tag{29}$$

where $\boldsymbol{\Sigma}^{2\infty}=[\sigma_{32}^\infty, D_2^\infty-D_2^0]^{\mathrm{T}}$.

Substituting Eqs. (28) and (29) into Eq. (21), one finally has

$$\boldsymbol{k}_{\mathrm{per}}=\sqrt{\pi L_1}\begin{pmatrix}\sigma_{32}^\infty\\ D_2^\infty-D_2^0\end{pmatrix}K \tag{30}$$

The dimensionless intensity factor K can be used to determine the field intensity factors and the ERR of four non-symmetrical radial cracks at the edge of a circular hole. In some limiting special cases, the known results [7-12] are the special cases of the present solutions. Furthermore, new configurations such as three radial cracks originating from a circular hole, semi-circular hole with an edge crack originating from a semi-infinite plane and a semi-infinite plane with an edge crack can be simulated from the present results.

4. Energy release rate

As mentioned above, the stress intensity factors (SIFs) and the electric displacement intensity factors (EDIFs) are independent and they are only related to the corresponding mechanical and electrical loading for the electrically impermeable boundary condition. For the electrically permeable case, both the SIFs and the EDIFs are independent on the electrical loading at infinity. So the SIFs and EDIFs can not perfectly describe the fracture characteristics of piezoelectric materials. In this study, the ERR and the MSERR are chosen as the fracture criterion to analyze the fracture behavior of four cracks emanating from a circular hole in piezoelectric materials.

The computational expressions of the ERR and the MSERR can be written as the following forms, respectively

$$G=\frac{1}{2}\boldsymbol{k}^{\mathrm{T}}\mathbf{B}_0^{-1}\boldsymbol{k} \tag{31}$$

$$G^M=\frac{1}{2}k_\sigma k_\gamma, \tag{32}$$

where

$$k_\gamma=\frac{e_{15}k_D+\varepsilon_{11}k_\sigma}{e_{15}^2+\varepsilon_{11}c_{44}}. \tag{33}$$

Substituting Eqs. (2), (22) and (30) into Eq. (31), the ERR for the electrically impermeable and the electrically permeable cases are obtained, respectively

$$G_{\mathrm{imp}}=\frac{\pi L_1K^2}{2(e_{15}^2+\varepsilon_{11}c_{44})}\left(\varepsilon_{11}\sigma_{32}^{\infty 2}+2e_{15}\sigma_{32}^\infty D_2^\infty-c_{44}D_2^{\infty 2}\right) \tag{34}$$

$$G_{\text{per}} = \frac{\pi L_1 K^2}{2c_{44}} (\sigma_{32}^{\infty})^2 \tag{35}$$

It is seen that the ERR for the electrically impermeable case is dependent on the applied mechanical and electrical loadings at infinity, while it is only dependent on the applied mechanical loading at infinity for the electrically permeable one.

Substituting Eqs. (22), (30) and (33) into Eq. (32), the MSERR for the electrically impermeable and the electrically permeable cases are obtained, respectively

$$G_{\text{imp}}^{M} = \frac{\pi L_1 K^2}{2(e_{15}^2 + \varepsilon_{11} c_{44})} \left(\varepsilon_{11} \sigma_{32}^{\infty 2} + e_{15} \sigma_{32}^{\infty} D_2^{\infty} \right) \tag{36}$$

$$G_{\text{per}}^{M} = \frac{\pi L_1 K^2}{2c_{44}} (\sigma_{32}^{\infty})^2 \tag{37}$$

It is found that from Eq. (35) and (37), the MSERR is equal to the ERR for the electrically permeable boundary condition.

5. Numerical results

To illustrate the singular electro-elastic fields at the tip of crack, numerical examples for a cracked PZT-5H piezoelectric ceramic are given, material properties of which are [1] $c_{44} = 3.53 \times 10^{10}\ \text{N/m}^2$, $e_{15} = 17.0\,\text{C/m}^2$, $\varepsilon_{11} = 151 \times 10^{-10}\,\text{C/Vm}$ and $G_{\text{cr}} = 5.0\,\text{N/m}$, where G_{cr} is the critical energy release rate.

Figs. 2-4 show the variation of the normalized ERR with geometrical parameters for a fixed-size hole of $R = 0.01\text{m}$ under combined mechanical loading $\sigma_{32}^{\infty} = 6\,\text{MPa}$ and electric loading $D_2^{\infty} = 2\text{e}-3\,\text{C/m}^2$. It will be noted that the electrically permeable case gives the highest value of G/G_{cr}, while the electrically impermeable case yields the lowest value of G/G_{cr}. It is easily seen from Figs. 2 and 3 that an increase of the right and the left cracks length always enhances the crack growth. The same conclusion has been drawn in Refs. [7-9]. Fig. 4 shows the variation of G/G_{cr} with the perpendicular crack length L_3 for given the right crack length $L_1 = 0.005\,\text{m}$ and different values of the left crack length L_2. It is interesting to note that when the ratio of L_2/R equals to 0.5, i.e., $L_2 = L_1$, the normalized ERR at the tip of the right crack is not affected by the change of the perpendicular crack length. This conclusion is derived from the geometrical symmetry for the present model under the symmetrical loading conditions. For the other values of

L_2/R, there are following two trends: When the value of L_2/R is larger than 0.5, i.e., $L_2 > L_1$, the normalized ERR decreases with the ratio of L_3/R increasing. On the other hand, when the value of L_2/R is smaller than 0.5, i.e., $L_2 < L_1$, the normalized ERR increases as the ratio of L_3/R becomes large. The results show that if the length of left crack is larger than that of right crack, an increase of length of the perpendicular cracks can retard the crack growth. In contrast to that, if the length of left crack is smaller than that of right one, the increase of the length of the perpendicular cracks can enhance the crack propagation. These useful conclusions will provide the theoretical instruction on fracture analysis and structural design in engineering. In addition, the normalized ERR is close to constants as L_3/R tends to infinite, which corresponds to the case of semi-circular hole with an edge crack at the edge of semi-infinite solid.

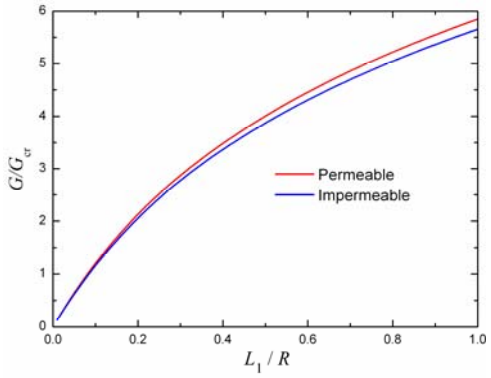

Fig. 2 Variation of G/G_{cr} with a ratio of L_1/R

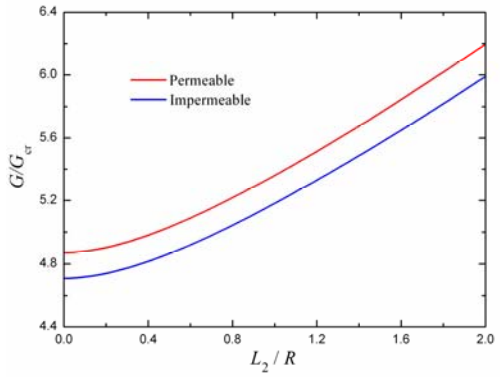

Fig. 3 Variation of G/G_{cr} with a ratio of L_2/R

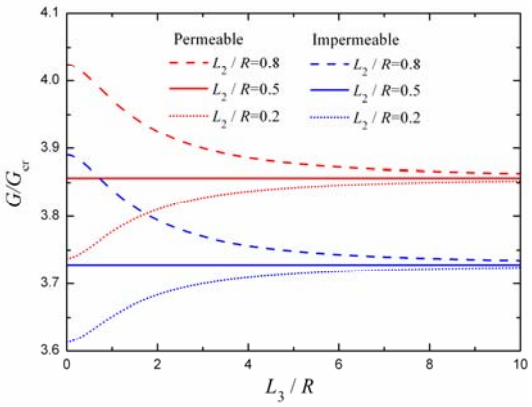

Fig. 4 Variation of G/G_{cr} with a ratio of L_3/R

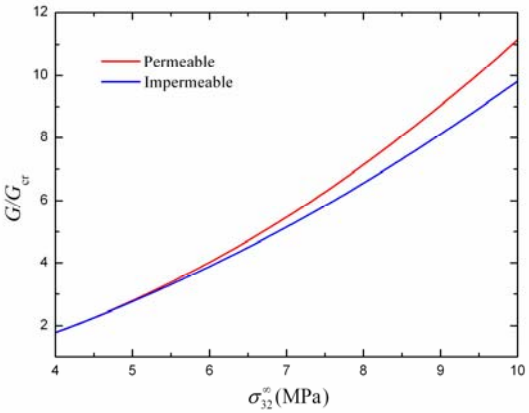

Fig. 5 Effect of applied mechanical loading on the normalized ERR

In what follows, to consider the effects of applied mechanical and electric loadings on the normalized ERR, we suppose a fixed-size hole of $R = 0.01\,\mathrm{m}$ and the cracks lengths $L_1 = 0.005\,\mathrm{m}$,

$L_2 = 0.008\,\mathrm{m}$ and $L_3 = 0.003\,\mathrm{m}$. Fig. 5 shows the influence of the applied mechanical loading on the normalized ERR under given electric load $D_2^{\infty} = 2\mathrm{e}-3\,\mathrm{C/m}^2$. As seen in the figure, the applied mechanical loading always promotes the crack growth, which is expectable. The effects of the applied electric load on the normalized ERR and the normalized MSERR are depicted under given mechanical loading $\sigma_{32}^{\infty} = 6\,\mathrm{MPa}$ in Figs. 6 and 7, respectively, where G_0^M denotes the value of the MSERR in the absence of remote electric load. It is seen from Figs. 6 and 7 that for the electrically permeable boundary condition, the normalized ERR and the MSERR are independent on the electric load, but dependent only on the mechanical loading. In other words, an applied electric field has no effect on the propagation of an electrically permeable case, which is in accordance with the results in Zhang and Gao [6]. As shown in Fig. 6, for the electrically impermeable case if a mechanical loading is applied, a negative electric load always decreases the normalized ERR, but a positive electric load either increases or decreases the normalized ERR. The result implies that a negative electric load is prone to retard the crack growth than a positive one. In contrast to Fig. 6, the positive electric field always increases the normalized MSERR, while the negative electric field always decreases the normalized MSERR in Fig. 7.

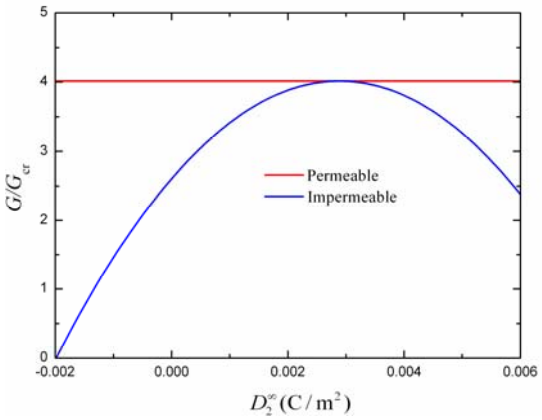

Fig. 6 Effect of applied electric loading on the normalized ERR

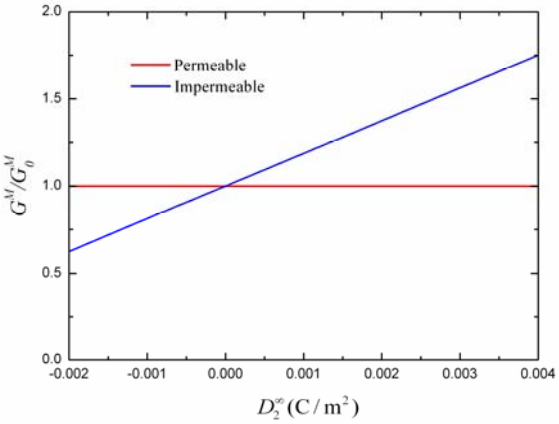

Fig. 7 Effect of applied electric loading on the normalized MSERR

6. Conclusions

The anti-plane problem of four non-symmetrical radial cracks at the edge of a circular hole in an infinite piezoelectric solid is investigated using the complex variable method and a new mapping function. This work is focused on the study of explicit and exact solutions in closed-form of the field intensity factors, ERR and MSERR. Several known results can be derived as special cases from the present solutions. Numerical results are provided to show the effects of geometrical parameters, applied mechanical and electric loads on ERR and MSERR. The results show that:

(a) The increase of the left crack length L_2 or right crack length L_1 always promotes the failure of piezoelectric materials for the case of four non-symmetric radial cracks at the edge of a circular hole.There are following three different results for the effects of the perpendicular crack on the

propagation of the horizontal crack. If the lengths of the left crack and the right crack originating from a circular hole are equal, an occurrence of the perpendicular cracks has no effect on the crack growth. If the length of left crack is larger than that of right crack, an increase of lengths of the perpendicular cracks can retard the crack growth. If the length of left crack is smaller than that of right crack, an increase of the length of the perpendicular cracks can promote the crack propagation.
(b) The electrically permeable boundary condition gives the highest value of ERR or MSERR, while the electrically impermeable case yields the lowest value of ERR or MSERR.
(c) The applied mechanical loading always promotes the crack growth, but the effects of applied electric fields on the crack growth depend on the different fracture parameters.

Acknowledgements

The authors thank the support from the National Natural Science Foundation of China (Nos.11262012 and 11262017), the Scientific Research Key Program of Inner Mongolia University of Technology (Grant No. ZD201219).

References

[1] Y.E. Pak, Crack extension force in a piezoelectric material, J Appl Mech, 57 (1990) 647– 653.
[2] Z. Suo, C. M. Kuo, D. M. Barnett, et al., Fracture Mechanics for Piezoelectric Ceramics, J Mech Phy Solids, 40 (1992) 739-765.
[3] H. Sosa, On the Fracture Mechanics of Piezoelectric Solids, Int J Solids Struct, 29 (1992) 2613-2622.
[4] W.T. Ang, L. Athanasius, A boundary integral approach for plane analysis of electrically semi-permeable planar cracks in a piezoelectric solid, Eng Analy Bound Elemen, 35 (2011) 647-656.
[5] C.Y. Fan, Y.F. Zhao, M.H. Zhao, E. Pan, Analytical solution of a semi-permeable crack in a 2D piezoelectric medium based on the PS model, Mech Res Commun, 40 (2012) 34-40.
[6] T.Y. Zhang, C.F. Gao, Fracture behaviors of piezoelectric materials, Theo Appl Fract Mech, 41 (2004) 339-379.
[7] Y.J. Wang, C.F. Gao, The mode III cracks originating from the edge of a circular hole in a piezoelectric solid, Int J Solids Struct, 45 (2008) 4590-4599.
[8] J.H. Guo, Z.X. Lu, H.T. Han, Z. Yang, Exact solutions for anti-plane problem of two asymmetrical edge cracks emanating from an elliptical hole in a piezoelectric material. Int J Solids Struct 46 (2009) 3799-3809.
[9] J.H. Guo, Z.X. Lu, H.T Han, Z. Yang, The behavior of two non-symmetrical permeable cracks emanating from an elliptical hole in a piezoelectric solid, Euro J Mech A/Solids, 29 (2010) 654-663.
[10] G.C. Sih, Stress distribution near internal crack tips for longitudinal shear problems, J Appl Mech, 32 (1965) 51.
[11] H. Tada, P.C. Paris, G.R. Irwin, The stress analysis of cracks handbook, Hellertown, PA: Del Research Corporation, 1973.
[12] T. Yokobori, M. Ichikawa, S. Konosu, R. Takahashi, A criterion for brittle fracture of notched solid, Japanese Society for strength and Fracture of Materials, 6 (1971) 58-67.

Dynamic response of an interface crack between magnetoelectroelastic and functionally graded elastic layers

Keqiang Hu[1,*], Zengtao Chen[1], Jiawei Fu[1,2]

[1] Department of Mechanical Engineering, University of New Brunswick, Fredericton, NB, E3B 5A3, Canada
[2] Department of Mechanical Engineering, Nanjing University of Science and Technology, Nanjing 210094 China
* Corresponding author: keqianghu@163.com

Abstract The dynamic response of an interface crack between magnetoelectroelastic and functionally graded elastic layers under anti-plane shear and in-plane electric and magnetic impacts is investigated by the integral transform method. The mixed boundary value problem of the interface crack is reduced to dual integral equations, which can be further expressed in terms of a Fredholm integral equation of the second kind. The singular stress fields near the crack tip are obtained asymptotically, and the stress intensity factor (SIF) is defined. Based on the criterion of maximum hoop stress, the crack will propagate along the original crack plane and won't kink. Numerical results show that the dynamic SIF is influenced by the material properties and geometric size ratios.

Keywords Dynamic response, Interface crack, Magnetoelctroelastic layer, Functionally graded elastic layer, Stress intensity factor

1. Introduction

Composites made of piezoelectric/piezomagnetic materials exhibit magnetoelectric effect that is not present in single-phase piezoelectric or piezomagnetic materials. Studies on the properties of piezoelectric/piezomagnetic composites have been carried out by numerous researchers [1, 2]. In particular, there is a growing interest among researchers in solving fracture mechanic problems in media possessing coupled piezoelectric, piezomagnetic and magnetoelectric effects, that is, magnetoelectroelastic effects. The crack initiation behavior in magnetoelectroelastic composite under in-plane deformation was investigated by Song and Sih [3]. Gao et al. [4] presented some exact treatments on the crack problems in magnetoelectroelastic solids. Wang and Mai [5] considered the mode III crack problems in an infinite piezoelectromagnetic medium using complex variable technique. Qin [6] obtained two dimensional (2D) Green's functions of defective magnetoelectroelastic solids under thermal loading, which can be used to establish boundary formulation and to analyze relevant fracture problems. Li [7] made the transient analysis of a cracked magnetoelectroelastic medium under antiplane mechanical and inplane electric and magnetic impacts. Hu and Li [8] studied the crack in a magnetoelectroelastic strip under longitudinal shear. A moving crack problem in magnetoelectroelastic materials has been solved by Hu and Li [9]. Interface crack moving along dissimilar magnetoelectroelastic materials has been studied by Hu et al. [10], and Zhong and Li [11], respectively. The dynamic response of a penny-shaped crack in a magnetoelectroelastic layer was studied by Feng et al., [12]. Boundary element method was developed by Rojas-Díaz et al., [13] to study crack problems in linear magnetoelectroelastic materials under static loading conditions. The transient anti-plane problem of a magnetoelectroelastic strip containing a crack is considered by Yong and Zhou [14]. An anti-plane shear crack in a magnetoelectroelastic layer sandwiched between dissimilar half spaces has been investigated by Hu et al. [15]. Zhou and Chen [16] analyzed a partially conducting mode I crack in a piezoelectromagnetic material. Wang and Han [17] studied the effect of interfacial cracks on the

magnetoelectric coupling properties of a magneto-electro-elastic composite laminate. Recently, Hu and Chen [18] conducted the pre-curving analysis of a crack in a magnetoelctroelastic strip under in-plane dynamic loading and the same authors [19] also studied the anti-plane problem of a magnetoelectroelastic strip sandwiched between elastic layers. Wan et al. [20] investigated a mode III crack crossing the magnetoelectroelastic bimaterial interface under concentrated magnetoelectromechanical loads.

The objective of this paper is to study an interface crack between magnetoelectroelastic and functionally graded elastic layers under anti-plane shear and in-plane electric and magnetic impact loading. Fourier and Laplace transforms are applied to reduce the mixed-boundary-value problem to dual integral equations, which can be further expressed in terms of a Fredholm integral equation. The stress intensity factors are obtained and the effect of geometric size and material properties are analyzed.

2. Basic equations

Consider a transversely isotropic, linear magnetoelectroelastic material. Suppose the Cartesian coordinates x, y, z are the principal axes of the material symmetry, and the poling direction is oriented in the z–axis. Consider only the out-of-plane displacement, the in-plane electric field and in-plane magnetic field, i.e.,

$$u_x = u_y = 0, \quad u_z = u_z(x, y, t) \tag{1}$$

$$E_x = E_x(x, y, t), \quad E_y = E_y(x, y, t), \quad E_z = 0 \tag{2}$$

$$M_x = M_x(x, y, t), \quad M_y = M_y(x, y, t), \quad M_z = 0 \tag{3}$$

$$u_x^e = u_y^e = 0, \quad u_z^e = u_z^e(x, y, t) \tag{4}$$

where u_i, E_i and M_i $(i = x, y, z)$ are components of displacement, electrical field and magnetic field, respectively; the superscript "e" denotes the quantities of the elastic layers.

The constitutive equations for magnetoelectroelastic materials and elastic materials under anti-plane shear take the forms as:

$$\begin{pmatrix} \sigma_{zy} \\ D_y \\ B_y \end{pmatrix} = \begin{pmatrix} c_{44} & e_{15} & h_{15} \\ e_{15} & -\lambda_{11} & -\beta_{11} \\ h_{15} & -\beta_{11} & -\gamma_{11} \end{pmatrix} \begin{pmatrix} \dfrac{\partial u_z}{\partial y} \\ \dfrac{\partial \phi}{\partial y} \\ \dfrac{\partial \varphi}{\partial y} \end{pmatrix}, \quad \begin{pmatrix} \sigma_{zx} \\ D_x \\ B_x \end{pmatrix} = \begin{pmatrix} c_{44} & e_{15} & h_{15} \\ e_{15} & -\lambda_{11} & -\beta_{11} \\ h_{15} & -\beta_{11} & -\gamma_{11} \end{pmatrix} \begin{pmatrix} \dfrac{\partial u_z}{\partial x} \\ \dfrac{\partial \phi}{\partial x} \\ \dfrac{\partial \varphi}{\partial x} \end{pmatrix} \tag{5}$$

$$\sigma_{zy}^e = c_{44}^e \frac{\partial u_z^e}{\partial y}, \quad \sigma_{zx}^e = c_{44}^e \frac{\partial u_z^e}{\partial x} \tag{6}$$

where σ_{zj}, D_j and B_j ($j = x, y$) are components of stress, electrical displacement and magnetic induction; c_{44}, e_{15}, h_{15} and β_{11} are elastic, piezoelectric, piezomagnetic and electromagnetic constants; λ_{11} and γ_{11} are dielectric permitivity and magnetic permeability; ϕ and φ are electric potential and magnetic potential, respectively.

By introducing two new functions Φ and Ψ as [9]

$$\Phi = \phi + mu_z = \phi + \frac{\beta_{11}h_{15} - \gamma_{11}e_{15}}{\lambda_{11}\gamma_{11} - \beta_{11}^2}u_z, \quad \Psi = \varphi + nu_z = \varphi + \frac{\beta_{11}e_{15} - \lambda_{11}h_{15}}{\lambda_{11}\gamma_{11} - \beta_{11}^2}u_z \tag{7}$$

The dynamic equilibrium equations can be obtained as

$$\nabla^2 u_z = \left(\partial^2 u_z / \partial t^2\right) / V^2, \quad \nabla^2\Phi = 0, \quad \nabla^2\Psi = 0 \tag{8}$$

$$V = \sqrt{\mu/\rho}, \quad \mu = c_{44} + \left(\gamma_{11}e_{15}^2 + \lambda_{11}h_{15}^2 - 2\beta_{11}e_{15}h_{15}\right) / \left(\lambda_{11}\gamma_{11} - \beta_{11}^2\right) \tag{9}$$

where $\nabla^2 = \partial^2/\partial x^2 + \partial^2/\partial y^2$ is the two-dimensional Laplacian operator and V, μ, and ρ are the speed of the magnetoelectroelastic shear wave, the magnetoelectroelastic stiffened elastic constant, and the mass density of the magnetoelectroelastic material, respectively.

3. Problem formulation

Now let us consider an interface crack of length $2c$ between a magnetoelectroelastic layer **(M)** and a functionally graded elastic layer **(F)**, as shown in Fig. 1. The composite structure is under anti-plane shear and in-plane electric and magnetic impacts, and the thickness of the magnetoelectroelastic and functionally graded elastic layer are h_1 and h_2, respectively. Due to symmetry in geometry and loading conditions, it is sufficient to consider the problem for $0 \le x < \infty$, $-h_2 \le y \le h_1$ only.

The material properties of the functionally graded elastic layer vary continuously along the y-direction in the form as

$$c_{44}^e = c_{44}^{e0} \cdot \exp(\beta y), \quad \rho^e = \rho^{e0} \cdot \exp(\beta y) \qquad (0 \le y \le h_1) \tag{10}$$

where β is a constant and the superscript "0" denotes the material properties of the functionally graded elastic layer at the plane $y = 0$, i.e., c_{44}^{e0} and ρ^{e0} are the elastic constant and the material density of the functionally graded elastic layer at the plane $y = 0$, respectively.

The governing equation for the functionally graded elastic layer under anti-plane deformation can be obtained as:

$$\nabla^2 u_z^e + \beta\frac{\partial u_z^e}{\partial y} = \frac{1}{V_0^2}\frac{\partial^2 u_z^e}{\partial t^2} \tag{11}$$

where $V_0 = \sqrt{c_{44}^{e0}/\rho^{e0}}$ is the speed of the elastic shear wave induced by the functionally graded

elastic layer.

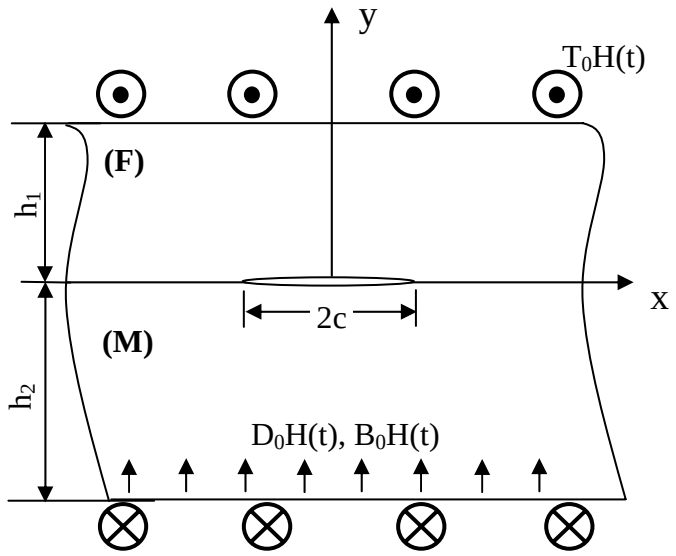

Figure 1. An interface crack between magnetoelectroelastic and functionally graded elastic layers

The electrical and magnetic boundary conditions on the edges of the magnetoelectroelastic layer are considered as follows:

$$D_y(x,0,t) = D_y(x,-h_2,t) = D_0 H(t), \quad B_y(x,0,t) = B_y(x,-h_2,t) = B_0 H(t) \tag{12}$$

where D_0 and B_0 are uniform electric displacement and magnetic induction applied on the magnetoelectroelastic layer, $H(t)$ is the Heaviside step function, $H(t) = 0$ for $t < 0$, and $H(t) = 1$ for $t \geq 0$.

The mechanical boundary conditions are:

$$\sigma_{zy}(x,0,t) = \sigma_{zy}^{e}(x,0,t) = 0, \qquad (0 \leq x < c) \tag{13}$$

$$u_z(x,0,t) = u_z^{e}(x,0,t), \qquad (x \geq c) \tag{14}$$

$$\sigma_{zy}^{e}(x,h_1,t) = \sigma_{zy}(x,-h_2,t) = T_0 H(t) \qquad (x \geq 0) \tag{15}$$

$$\sigma_{zy}(x,0,t) = \sigma_{zy}^{e}(x,0,t), \qquad (x \geq c) \tag{16}$$

where T_0 is the uniform shear stress.

4. Derivation of the integral equations

Appropriate solutions of Eq. (8) and Eq. (11) in the Laplace transform domain may be expressed as

$$u_z^{e*}(x,y,p)=\frac{2}{\pi}\int_0^\infty [A_1(s,p)\exp(k_1 y)+A_2(s,p)\exp(k_2 y)]\cos(sx)ds + a_0\,[\exp(-\beta y)-1]/p \tag{17}$$

$$u_z^{*}(x,y,p)=\frac{2}{\pi}\int_0^\infty [B_1(s,p)\exp(ky)+B_2(s,p)\exp(-ky)]\cos(sx)ds + b_0\frac{y}{p} \tag{18}$$

$$\phi^{*}(x,y,p)=\frac{2}{\pi}\int_0^\infty [C_1(s,p)\exp(sy)+C_2(s,p)\exp(-sy)]\cos(sx)ds + c_0\frac{y}{p} - \frac{2}{\pi}m\int_0^\infty [B_1(s,p)\exp(ky)+B_2(s,p)\exp(-ky)]\cos(sx)ds - mb_0\frac{y}{p} \tag{19}$$

$$\varphi^{*}(x,y,p)=\frac{2}{\pi}\int_0^\infty [D_1(s,p)\exp(sy)+D_2(s,p)\exp(-sy)]\cos(sx)ds + d_0\frac{y}{p} - \frac{2}{\pi}n\int_0^\infty [B_1(s,p)\exp(ky)+B_2(s,p)\exp(-ky)]\cos(sx)ds - nb_0\frac{y}{p} \tag{20}$$

where p is the Laplace transform parameter, $A_j(s,p)$, $B_j(s,p)$, $C_j(s,p)$ and $D_j(s,p)$ ($j=1,\ 2$) are the unknown functions to be solved and a_0, b_0, c_0 and d_0 are real constants determined by considering the boundary and interface conditions as

$$a_0=-T_0/(c_{44}^{e0}\beta)$$
$$\begin{pmatrix} b_0 \\ c_0 \\ d_0 \end{pmatrix}=\begin{pmatrix} \mu & e_{15} & h_{15} \\ 0 & \lambda_{11} & \beta_{11} \\ 0 & \beta_{11} & \gamma_{11} \end{pmatrix}^{-1}\begin{pmatrix} T_0 \\ -D_0 \\ -B_0 \end{pmatrix} \tag{21}$$

and the parameters k and k_1, k_2 are defined as

$$k=\sqrt{s^2+p^2/V^2},\quad k_{1,2}=\left[-\beta\pm\sqrt{\beta^2+4(s^2+p^2/V_0^2)}\right]/2 \tag{22}$$

A simple calculation leads to the expressions for the stresses as

$$\sigma_{zy}^{e*}=T_0/p+\frac{2}{\pi}c_{44}^{e}\int_0^\infty [k_1A_1(s,p)\exp(k_1y)+k_2A_2(s,p)\exp(k_2y)]\cos(sx)ds \tag{23}$$

$$\sigma_{zy}^{*}=T_0/p+\frac{2}{\pi}\int_0^\infty k\mu[B_1(s,p)\exp(ky)-B_2(s,p)\exp(-ky)]\cos(sx)ds + \frac{2}{\pi}\int_0^\infty e_{15}s[C_1(s,p)\exp(sy)-C_2(s,p)\exp(-sy)]\cos(sx)ds + \frac{2}{\pi}h_{15}\int_0^\infty h_{15}s[D_1(s,p)\exp(sy)-D_2(s,p)\exp(-sy)]\cos(sx)ds \tag{24}$$

From the boundary conditions (12), (15) and (16), there is only one independent unknown function (say $B_1(s,p)$). The following dual integral equations can be obtained from the mixed

boundary conditions in Eqs. (13, 14) as

$$\int_0^\infty k\mu[1-\exp(-2kh_2)]B_1(s,p)\cos(sx)ds = -\frac{\pi T_0}{2p}, \quad (0 \le x < c) \tag{25}$$

$$\int_0^\infty F(s,p)B_1(s)\cos(sx)ds = 0, \qquad (x \ge c) \tag{26}$$

where function $F(s,p)$ is defined as

$$F(s,p) = 1+\exp(-2kh_2) + \frac{k\mu[1-\exp(-2kh_2)]\{k_2\exp[(k_2-k_1)h_1]-k_1\}}{c_{44}^{e0}k_1k_2\{1-\exp[(k_2-k_1)h_1]\}} \tag{27}$$

The dual integral equations can be solved by introducing auxiliary functions $\Phi(x,p)$ as

$$B_1(s,p) = -\frac{\pi(\mu+c_{44}^{e0})T_0}{2c_{44}^{e0}\mu pF(s,p)}c^2\int_0^1 x\Phi(x,p)J_0(scx)dx \tag{28}$$

where $J_0(\ \ )$ is the zero-order Bessel function of the first kind, and the function $\Phi(x,p)$ satisfies the Fredholm integral equations of the second kind

$$\Phi(x,p) + \int_0^1 \Phi(\eta,p)Q(\eta,x,p)d\eta = 1 \tag{29}$$

where the kernel functions $Q(\eta,x,p)$ is defined as

$$Q(\eta,x,p) = \eta\int_0^\infty s[R(s/c,p)-1]J_0(sx)J_0(s\eta)ds \tag{30}$$

where

$$R(s,p) = \frac{k(c_{44}^{e0}+\mu)[1-\exp(-2kh_2)]}{c_{44}^{e0}sF(s,p)} \tag{31}$$

5. Field intensities

Once functions $\Phi(x,p)$ is obtained by solving the Fredholm integral equations of the second kind Eq. (30), the singular stress fields near the crack tip in the Laplace domain can be obtained asymptotically as

$$\sigma_{zy}^*(r,\theta,p) + i\sigma_{zx}^*(r,\theta,p) = \exp(-i\theta/2)K^{T*}(p)/\sqrt{2\pi r} \tag{32}$$

where r and θ are defined as

$$r = \sqrt{(x-c)^2+y^2}, \quad \theta = \tan^{-1}[y/(x-c)] \tag{33}$$

the stress intensity factor (SIF) K^{T*} is defined as

$$K^{T*}(p) = \lim_{r\to 0^+}\sqrt{2\pi r}\,\sigma_{zy}^*(r,0,p) = T_0\Phi(1,p)\sqrt{\pi c}/p \tag{34}$$

The stress intensity factor in the time domain can be expressed as

$$K^T(t) = T_0\sqrt{\pi c}\,/2\pi i\int_{Br}\exp(pt)\Phi(1,p)/p\,dp \tag{35}$$

where "*Br*" stands for the Bromwich path of integration. It should be noted that the stress intensity factor is only dependent on the mechanical loading, as seen from Eqs. (34), (35) and (27)-(31).

The dynamic hoop stress around the crack tip can be obtained as

$$\sigma_{z\theta}(r,\theta,t) = K^T(t)/\sqrt{2\pi r}\cos(\theta/2) \qquad (-\pi \le \theta \le \pi) \tag{36}$$

It is clear that the maximum hoop stress always appears at the direction $\theta = 0^{\circ}$, which means that if the fracture toughness of the material is same in all directions, the crack will propagate along the original crack plane and no crack kinking should appear.

6. Numerical results and discussions

The material properties of the magnetoelectroelastic layer are taken as [21]

$$\begin{aligned} &c_{44} = 5.0\times10^{10}\ (\mathrm{N/m^2}), \quad e_{15} = 0.2\ (\mathrm{C/m^2}), \quad h_{15} = 180\ (\mathrm{N/Am}) \\ &\lambda_{11} = 2.5\times10^{-10}\ (\mathrm{C^2/Nm^2}), \quad \gamma_{11} = -2.0\times10^{-6}\ (\mathrm{Ns^2/C^2}) \\ &\beta_{11} = 5.3\times10^{-9}\ (\mathrm{Ns/VC}), \quad \rho = 5.7\times10^{3}\ (\mathrm{Kg/m^3}) \end{aligned} \tag{37}$$

Fig. 2 shows the variation of the normalized dynamic SIFs K_T versus normalized time for different values of functionally graded material parameter β when $V = V_e$ and $h_1/c = h_2/c \to \infty$. The SIFs increase as the dimensionless time increases and reach the peak points at about $tV/c = 2.1$ and oscillate about their static values. As $tV/c \to \infty$, the dynamic SIFs appoach their static values. The magnitudes of the SIFs decrease as the functionally graded material parameter β increases from negative to positive value. Fig. 3 displays the normalized dynamic SIFs K_T vs normalized time for different values of geometric size ratio $h_1/c = h_2/c$ when $\beta = +1$ and $V = V_e$. It needs more time for the cracked composite with smaller size ratio $h_1/c = h_2/c$ to reach the stabilized values of K_T. The second peak value of the dynamic SIF seems to increase and appear earlier when the geometric size ratio $h_1/c = h_2/c$ decreases. Fig. 4 shows the normalized dynamic SIFs K_T vs normalized time for different material property

$R = c_{44}^{e0}/\mu$ when $\beta = +1$, $\rho = \rho^{e0}$ and $h_1/c = h_2/c \to \infty$. The increase of the ratio $R = c_{44}^{e0}/\mu$ will lead to the larger peak values of the dynamic SIFs as well as larger corresponding static values.

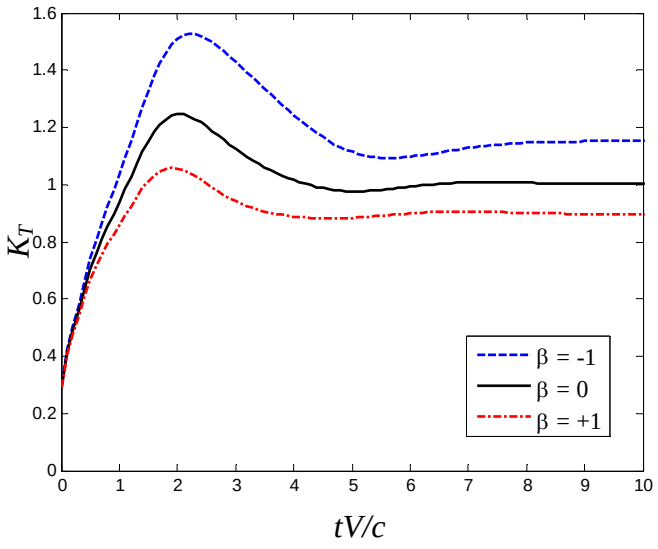

Figure 2. Normalized dynamic SIFs K_T vs normalized time for different functionally graded material parameter β when $V = V_e$

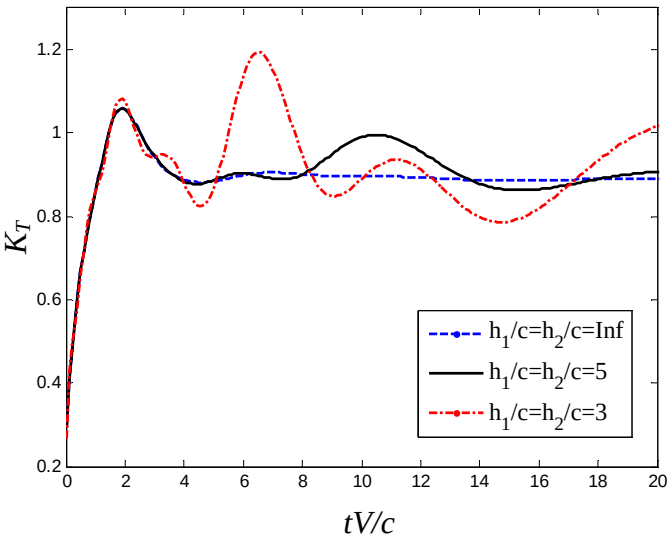

Figure 3. Normalized dynamic SIFs K_T vs normalized time for different geometric size $h_1/c = h_2/c$ when $\beta = +1,\ V = V_e$

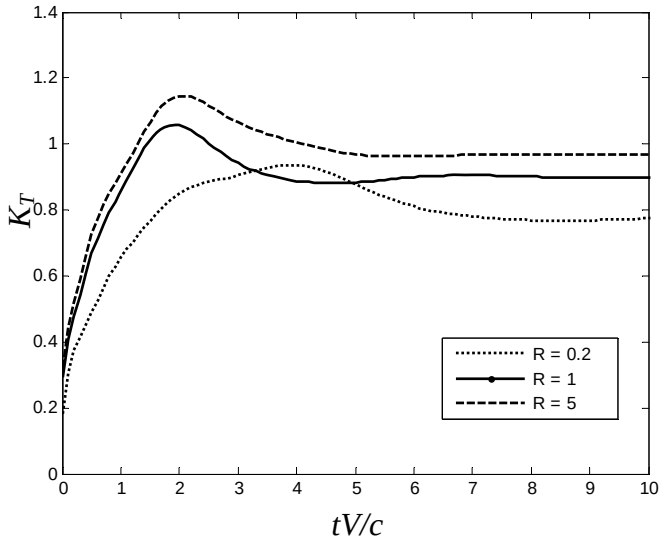

Figure 4. Normalized dynamic SIFs K_T vs normalized time for different material property $R = c_{44}^{e0} / \mu$ when $\beta = +1$

7. Conclusions

The dynamic fracture analysis of an interface crack between magnetoelectroelastic and functionally graded elastic layers under anti-plane shear and in-plane electric and magnetic impacts is performed using the integral transform method. The mixed-boundary-value problem of the interface crack is reduced to solving dual integral equations, which are further expressed in terms of Fredholm integral equations of the second kind. The asymptotic stress fields near the crack tip are obtained and the stress intensity factor is calculated. Crack propagation direction is predicted based on the maximum hoop stress intensity factor criterion, which shows that the crack will propagate along the extension of the original plane. Numerical results show that the SIFs are influenced by the geometric size ratios and the material properties of the magnetoelectroelastic composite. The obtained results are very useful for the safety and reliability design of the magnetoelectroelastic composite.

References

[1] C.W. Nan, Magnetoelectric effect in composites of piezoelectric and piezomagnetic phases. Phys Rev B, B50 (1994) 6082-6088.

[2] X. Wang, Z. Zhong, A circular tube or bar of cylindrically anisotropic magnetoelectroelastic material under pressuring loading. Int J Eng Sci, 41 (2003) 2143-2159.

[3] Z.F. Song, G.C. Sih, Crack initiation behavior in a magnetoelectroelastic composite under in-plane deformation. Theor Appl Fract Mech, 39 (2003) 189-207.

[4] C.F. Gao, K. Hannes, B. Herbert, Crack problems in magnetoelectroelastic solids. Part I: exact solution of a crack. Int J Eng Sci, 41 (2003) 969-981.
[5] B.L. Wang, Y.W. Mai, Fracture of piezoelectromagnetic materials. Mech Re Commu, 31 (2004) 65-73.
[6] Q.H. Qin, 2D Green's functions of defective magnetoelectroelastic solids under thermal loading. Eng Anal Bound Elem, 29 (2005) 577-585.
[7] X.F. Li, Dynamic analysis of a cracked magnetoelectroelastic medium under antiplane mechanical and inplane electric and magnetic impacts. Int J Solids Struct, 42 (2005) 3185-3205.
[8] K.Q. Hu, G.Q. Li, Electro-magneto-elastic analysis of a piezoelectromagnetic strip with a finite crack under longitudinal shear. Mech Mater, 37 (2005) 925-934.
[9] K.Q. Hu, G.Q. Li, Constant moving crack in a magnetoelectroelastic material under anti-plane shear loading. Int J Solids Struct, 42 (2005) 2823-2835.
[10] K.Q. Hu, Y.L. Kang, G.Q. Li, Moving crack at the interface between two dissimilar magnetoelectroelastic materials. Acta Mech, 182 (2006) 1-16.
[11] X.C. Zhong, X.F. Li, A finite length crack moving along the interface of two dissimilar magnetoelectroelastic materials. Int J Eng Sci, 44 (2006) 1394-1407.
[12] W.J. Feng, E. Pan, X. Wang, Dynamic fracture analysis of a penny-shaped crack in a magnetoelectroelastic layer. Int J Solids Struct, 44 (2007) 7955-7974.
[13] R. Rojas-Diaz, F. Garcia-Sanchez, A. Saez, C. Zhang, Fracture analysis of magnetoelectroelastic composite materials. Key Eng Mat, Advances in Fracture and Damage Mechanics VI, 348-349 (2007) 69-72.
[14] H.D. Yong, Y.H. Zhou, Transient response of a cracked magnetoelectroelastic strip under anti-plane impact. Int J Solids Struct, 44 (2007) 705-717.
[15] K.Q. Hu, Q.H. Qin, Y.L. Kang, Anti-plane shear crack in a magnetoelectroelastic layer sandwiched between dissimilar half spaces. Eng Fract Mech, 74 (2007) 1139-1147.
[16] Z.G. Zhou, Z.T. Chen, Fracture mechanics analysis of a partially conducting mode I crack in piezoelectromagnetic materials. Eur J Mech-A Solid, 27 (2008) 824-846.
[17] B.L. Wang, J.C. Han, Effect of Finite Cracking on the Magneto-electric Coupling Properties of Magneto-electro-elastic Composite Laminates. J Intel Mat Syst Str, 21 (2010) 1669-1679.
[18] K.Q. Hu, Z.T. Chen, Pre-curving analysis of an opening crack in a magnetoelectroelastic strip under in-plane impact loadings. J Appl Phys, (2012) In Press.
[19] K.Q. Hu, Z.T. Chen, Dynamic response of a cracked magnetoelectroelastic layer sandwiched between two elastic layers. ZAMM Z Angew Math Mech, DOI 10.1002/zamm.201200105.
[20] Y.P. Wan, Y.P. Yue, Z. Zhong, Z., The mode III crack crossing the magnetoelectroelastic bimaterial interface under concentrated magnetoelectromechanical loads. Int J Solids Struct, 49 (2012) 3008-3021.
[21] G.R. Buchanan, Layered versus multiphase magneto-electro-elastic composites. Compos Part B, 35 (2004) 413-420.

Parameter identification of a modified dynamical hysteresis model with immune clone algorithm

Yong Fei Zhang [1], You-He Zhou [1,*]

[1] Key Laboratory of Mechanics on Disaster and Environment in Western China attached to the Ministry of Education of China, Lanzhou University, Lanzhou, Gansu 730000, PR China
[1] Department of Mechanics and Engineering Sciences, College of Civil Engineering and Mechanics, Lanzhou University, Lanzhou, Gansu 730000, PR China
* Corresponding author: zhouyh@lzu.edu.cn

Abstract This paper focuses on application of immune clone algorithm to identify parameters of a modified dynamical hysteresis model for giant magnetostrictive materials (GMM). The domain flexing function proposed by Damijan Miljavec et al, is added into this model, which resulted in one extra parameter, to overcome the unphysical negative susceptibility problem. Thus, the immune clone algorithm is applied to identify the parameters in this revised model. The efficiency of the parameter identification with immune clone algorithm is verified by comparing the model generated curves between the identified parameters and the selected parameters. Moreover, it can be seen the unphysical behavior of minor hysteresis loop is suppressed by comparing the identified model curve with the original model curve and a set of representative experimental data.

Keywords Parameter identification, Immune clone method, Hysteresis, Minor loop

1. Introduction

Some magnetic materials when located in an applied magnetic field can elongate or contract in magnetization direction due to an induced magnetic field in these materials. The generated strains are attributed to the realignment of a large amount of magnetic domains caused by spontaneous magnetization. This phenomenon is called magnetostriction. Giant magnetostrictive materials (GMM) have some distinctive advantages over other smart materials, for example, the ability to generate large forces at a lower voltage than piezoelectric ceramic material (PZT), to react more rapidly than shape memory alloy (SMA), to keep their properties even been grinded into particles. Such distinctive advantages motivate many researchers to investigate the applications of GMM in many aspects such as high power ultrasonic transducers, linear motors, micro pumps, micro valves, micro positioners and active vibration absorbers[1-2].

To utilize the full potential of GMM in practical applications, the intrinsic nonlinear magnetic-elastic-thermal coupling properties and hysteresis behavior of GMM need be described clearly. Thus, different models, including physical-based and nonphysical ones [3-5], have been proposed to describe the unique characteristics of GMM. Extended from the most typical physical-based J-A model, Zheng and her co-workers proposed a new model [6] in which nonlinear magnetic-elastic-thermal coupling properties and hysteresis behavior are displayed clearly. However, like the J-A model, this new model encountered the same parameter problem in choosing optimal parameters. Thus, a general method to obtain the optimal parameters is needed for this constitutive relation of GMM.

Generally speaking, two kind methods to overcome the parameter problem of J-A model have been proposed. First, a step-by-step methodologies based on the physical meaning of the determinable parameters are available [7]. But this classic procedure sensitive to initial values of parameters and the order of evaluation of the equations, may pose convergence problem as noticed in [8]. Second, a mathematical approach of the parameter identification disregarding the physical background works in the parameters state-space and tries to find the optimal combination of the parameters [9-12]. The main idea of using immune clone method to optimization problem is heuristic searching in the

trusted solution space and recording the optimal solution in each iteration step until no better solution can be found [13-14]. Thus, adopt the immune clone method to do parameter identification is feasible.

The aim of the present paper is to provide an alternative estimation procedure of parameters based on immune clone algorithm for the modified dynamical hysteresis model of GMM. In section 2 the dynamical magnetic-elastic-thermal coupled hysteresis model is modified by introducing the domain flexing function. Then the immune clone algorithm is adopted to identify the parameters in this devised model in section 3. The immune clone algorithm is verified by comparing the identified model curve with the reduced static model generated curve. In section 4, by comparing the identified model curve with a set of representative experimental data the unphysical behavior of minor hysteresis loops are suppressed.

2. Dynamic hysteresis model and the domain flexing function

The following form of dynamic hysteresis model is considered [6]:

$$\begin{aligned}&\frac{\mu_0 d^2}{2\rho\tilde{\beta}}\left(\frac{dH}{dt}\right)\left(\frac{dM}{dH}\right)^2+\left(\frac{GSV_0\mu_0}{\rho}\right)^{1/2}\left(\frac{dH}{dt}\right)^{1/2}\left(\frac{dM}{dH}\right)^{3/2}\\&+\left(\varsigma K-\overline{\eta}\left(M_{an}-M+\varsigma Kc\frac{dM_{an}}{dH_e}\right)\right)\left(\frac{dM}{dH}\right)\\&-\left(M_{an}-M+\varsigma Kc\frac{dM_{an}}{dH_e}\right)=0\end{aligned}\tag{1}$$

$$\lambda=-\frac{\tilde{B}\Delta TM^2}{M_s^2}+\begin{cases}\dfrac{[1-\tanh(\sigma/\sigma_s)]\lambda_s}{M_s{}^2}M^2 & \sigma/\sigma_s\geq 0\\ \dfrac{[2-\tanh(2\sigma/\sigma_s)]\lambda_s}{2M_s{}^2}M^2 & \sigma/\sigma_s<0\end{cases}\tag{2}$$

In which:

$$\overline{\eta}=\eta-\frac{2\tilde{B}\Delta T\sigma}{\mu_0 M_s{}^2}+\begin{cases}\dfrac{2\sigma-2\sigma_s\ln[\cosh(\sigma/\sigma_s)]}{\mu_0 M_s{}^2}\lambda_s, & \sigma/\sigma_s\geq 0\\ \dfrac{4\sigma-\sigma_s\ln[\cosh(2\sigma/\sigma_s)]}{2\mu_0 M_s{}^2}\lambda_s, & \sigma/\sigma_s<0\end{cases}\tag{3}$$

$$M_{an}=M_s\frac{\left(1-\dfrac{\Delta T+T_r+273}{T_c+273}\right)^x}{\left(1-\dfrac{T_r+273}{T_c+273}\right)^x}\left(\coth\left(\frac{3\chi_m\left(1-\dfrac{T_r+273}{T_c+273}\right)^x}{M_s\left(1-\dfrac{\Delta T+T_r+273}{T_c+273}\right)^x}H_e\right)-\frac{M_s\left(1-\dfrac{\Delta T+T_r+273}{T_c+273}\right)^x}{3\chi_m H_e\left(1-\dfrac{T_r+273}{T_c+273}\right)^x}\right)\tag{4}$$

$$H_e=H+\eta M-\frac{2\tilde{B}\Delta T\sigma M}{\mu_0 M_s{}^2}+\begin{cases}\dfrac{2\sigma-2\sigma_s\ln[\cosh(\sigma/\sigma_s)]}{\mu_0 M_s{}^2}\lambda_s M, & \sigma/\sigma_s\geq 0\\ \dfrac{4\sigma-\sigma_s\ln[\cosh(2\sigma/\sigma_s)]}{2\mu_0 M_s{}^2}\lambda_s M, & \sigma/\sigma_s<0\end{cases}\tag{5}$$

And $\mu_0=4\pi\times 10^{-7}H/m$ is the vacuum permeability, d is diameter for Terfenol-D rod, ρ is the resistivity, $\tilde{\beta}=16$ and G = 0.1356 are a geometrical factor for cylinders and a dimensionless constant respectively, S is the cross-sectional area and V_0 is a parameter representing the internal

potential experienced by domain walls, the parameter ς is taken +1 and −1 respectively when the intensity of the applied AC field increases and decreases, K is the pinning constant, c is the ratio of the initial normal magnetic susceptibility to the initial anhysteretic susceptibility. η is the Weiss molecular field coefficient, $\tilde{B}$ is equal to the slope of magnetostrictive strain versus increment temperature at the saturation magnetization, $\Delta T = T - T_r$ (where T is temperature and T_r is the spin reorientation temperature, T_c stands for the Curie temperature), χ_m is the magnetic susceptibility at the initial linear segments of magnetic curves. M_s, σ_s and λ_s are reference magnetization, stress and strain，respectively.

The domain flexing function is introduced as follows [16]:

$$c(H) = c_0 + e^{(|H|/H_{\max})-(1+\beta)} \tag{6}$$

In which, constant parameter c_0 is physically identical to the original parameter c. It describes the amount of the domain wall translation and bending with regard to the difference between the anhysteretic and irreversible magnetization. The exponential part with parameter β characterizes the amount of reversible relaxation of the domain wall bulged. The parameter β also depends on the maximum induction level. H represents a temporary value of the excitation magnetic field and $H_{\max}$ is its maximum value.

Now substituting (3)–(6) into (1) and then substituting the solved M into (2), the calculated magnetostriction λ can be obtained.

In order to identify the parameters, the follow optimization problem is constructed:

$$\begin{aligned} \min \quad & E(\boldsymbol{\theta}) = \sum_{k=1}^{Q} \left(\lambda(k) - \tilde{\lambda}(k)\right)^2 = \sum_{k=1}^{Q} e^2(k, \boldsymbol{\theta}) \\ \text{s.t.} \quad & d_r \le \theta_r \le b_r \qquad r = 1, 2, \ldots \end{aligned} \tag{7}$$

In which k is the *kth* sample time, Q is the number of all samples, $\tilde{\lambda}(k)$ is the experimental magnetostriction, $\lambda(k)$ is the calculated magnetostriction, $e(k, \boldsymbol{\theta}) = \lambda(k) - \tilde{\lambda}(k)$ is the magnetostriction error, θ_r is the *rth* element of the parameter $\boldsymbol{\theta}$, d_r and b_r are the lower and upper bounds on θ_r. Let $e(\boldsymbol{\theta}) = \left[e(1, \boldsymbol{\theta}) \quad e(2, \boldsymbol{\theta}) \quad \ldots \quad e(Q, \boldsymbol{\theta}) \right]$ be the magnetostriction error vector, the minimization problem (7) can be solved using the following immune clone algorithm.

3. Implementation of immune clone algorithm

As detailed in [13-14], immune clone algorithm can be used in optimization problem effectively. So here the minimization problem (7) is solved with it. The pseudocode is as follows:

Repeat:

a. Select a representative experimental magnetostriction $\tilde{\lambda}(k)$ (an antigen A) from a set of experimental data (population of antigens PA).
b. Take randomly R parameter vectors $\boldsymbol{\theta}$ (antibodies) from parameter space $\mathbf{d} \le \boldsymbol{\theta} \le \mathbf{b}$ (population of antibodies PS).
c. Substitute each parameter vector $\boldsymbol{\theta}$ (antibody) into the modified dynamical hysteresis model, then obtain the calculated magnetostriction $\lambda(k)$, match it against the selected experimental data $\tilde{\lambda}(k)$ (antigen A).
d. Find the parameter vector $\boldsymbol{\theta}$ (antibody) with the highest match score.
e. Add match score of winning parameter vector $\boldsymbol{\theta}$ (antibody) to its fitness.

Until the max number of cycles reached.

4. Identification results and discussions

First, in order to check the parameter identification program the dynamical magnetic-elastic-thermal coupled hysteresis model is reduced to a static form as follows [6]:

$$\left(\frac{dM}{dH}\right)=\frac{\left(M_{an}-M+\varsigma Kc\frac{dM_{an}}{dH_e}\right)}{\left(\varsigma K-\bar{\eta}\left(M_{an}-M+\varsigma Kc\frac{dM_{an}}{dH_e}\right)\right)} \tag{8}$$

$$\lambda=-\frac{\tilde{B}\Delta TM^2}{M_s^2}+\begin{cases}\dfrac{[1-\tanh(\sigma/\sigma_s)]\lambda_s}{M_s^{\,2}}M^2\\ \dfrac{[2-\tanh(2\sigma/\sigma_s)]\lambda_s}{2M_s^{\,2}}M^2\end{cases} \tag{9}$$

A hysteresis curve has been generated by the above form itself to check the agreement between the original and the fitted curve. The generated curve is considered to be the experimental curve and then the identification program is used to fit curve while the identified parameters is also obtained in the same procedure. Figure 1 shows the fitted results matched perfectly with the generated one. From table 1, one can see that the discrepancies between the original parameters and the estimated parameters are less than 5%. Figure 2 displays the convergence procedure of parameter identification. These results confirm us that the identification program proposed above is effective and successful.

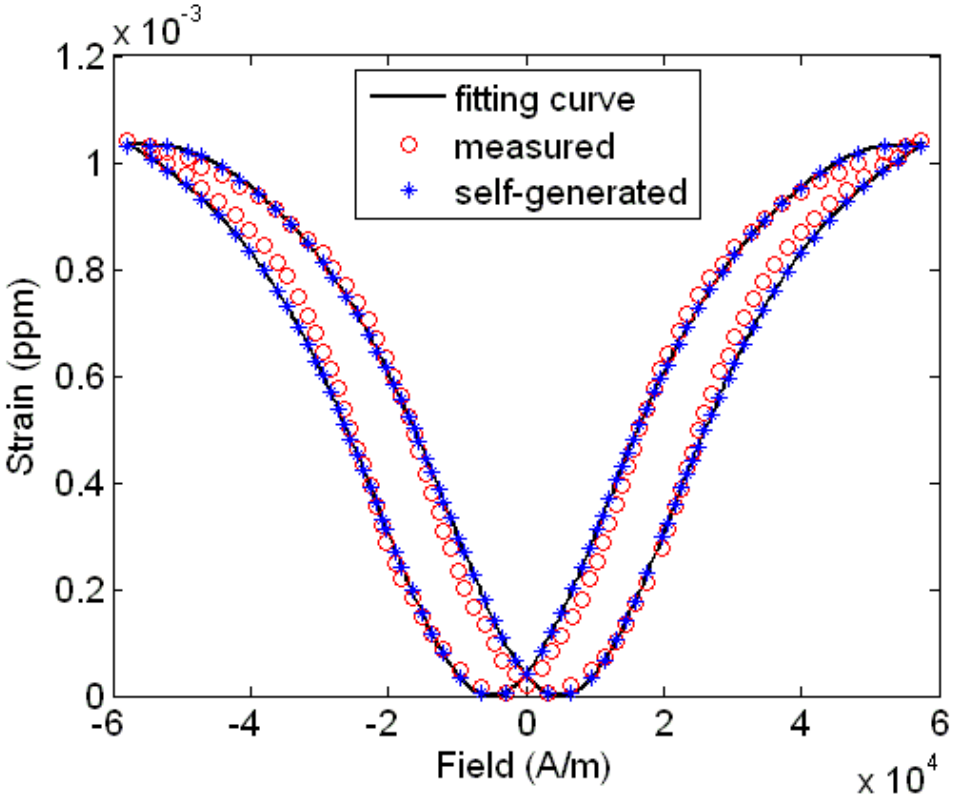

Figure 1 Fitting to the self-generated hysteresis loop of magnetic field versus strain relation.

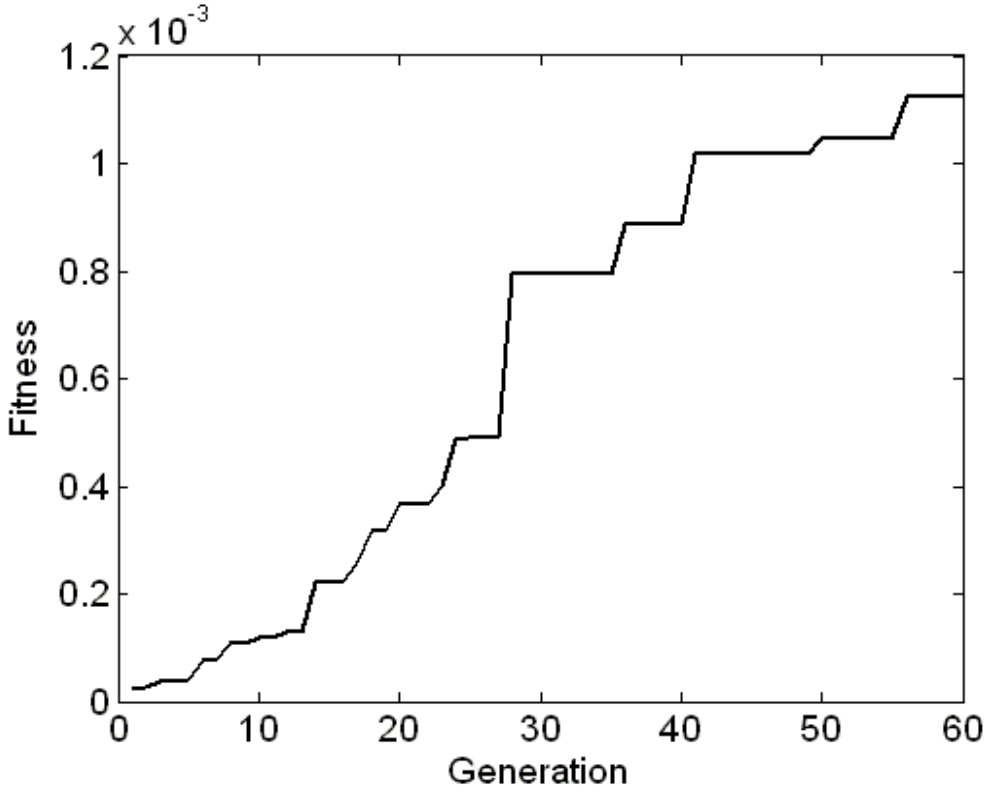

Figure 2 Fitness in the iteration procedure.

Table 1: The bounds for parameters, the parameters for self-generated curve, the estimation results and the estimation errors for parameters ($\mu_0 = 4\pi \times 10^{-7} H/m$)

Parameter	Parameter range	Original Parameter	Estimated parameter	Error (%)
K	$[3000.0\times\mu_0 ; 6000.0\times\mu_0]$	$5000.0\times\mu_0$	$4964.8\times\mu_0$	0.70
c	$[0.0000 ; 0.3000]$	0.1000	0.0956	4.40
M_s	$[0.6000/\mu_0 ; 1.5000/\mu_0]$	$0.9500/\mu_0$	$0.9493/\mu_0$	0.08
σ_s	$[150.00\times10^6 ; 250.00\times10^6]$	200.00×10^6	200.44×10^6	0.22
η	$[0.0100 ; 0.0300]$	0.02000	0.01995	0.25
χ_m	$[10.000 ; 50.000]$	35.000	35.103	0.29

Next, to overcome the unphysical phenomena of the minor loops encountered in previous models, the modified model and parameter identification program proposed in this paper are adopted. Figure 3 demonstrates the fitted results when the exciting frequency is 100Hz. It is clear to see that the unphysical tip of the minor loop is suppressed effectively. That means an optimal parameter vector for 100Hz is identified. Then the proposed parameter identification algorithm is adopted to predict the curve when exciting frequency is 500Hz. Figure 4 shows that the modified model does not give us the expected results when exciting frequency is 500Hz due to dynamical effect of the transducer under higher exciting frequency [12, 17-19].

Now the domain flexing function is considered more specifically. One can see clearly that an extra parameter β in the domain flexing function is introduced but do not give any explicit meaning of it. According to the above numerical results, perhaps the extra parameter is a function of the exciting frequency. A further step investigation of the extra parameter is lost in this paper, because of the limited experiment data.

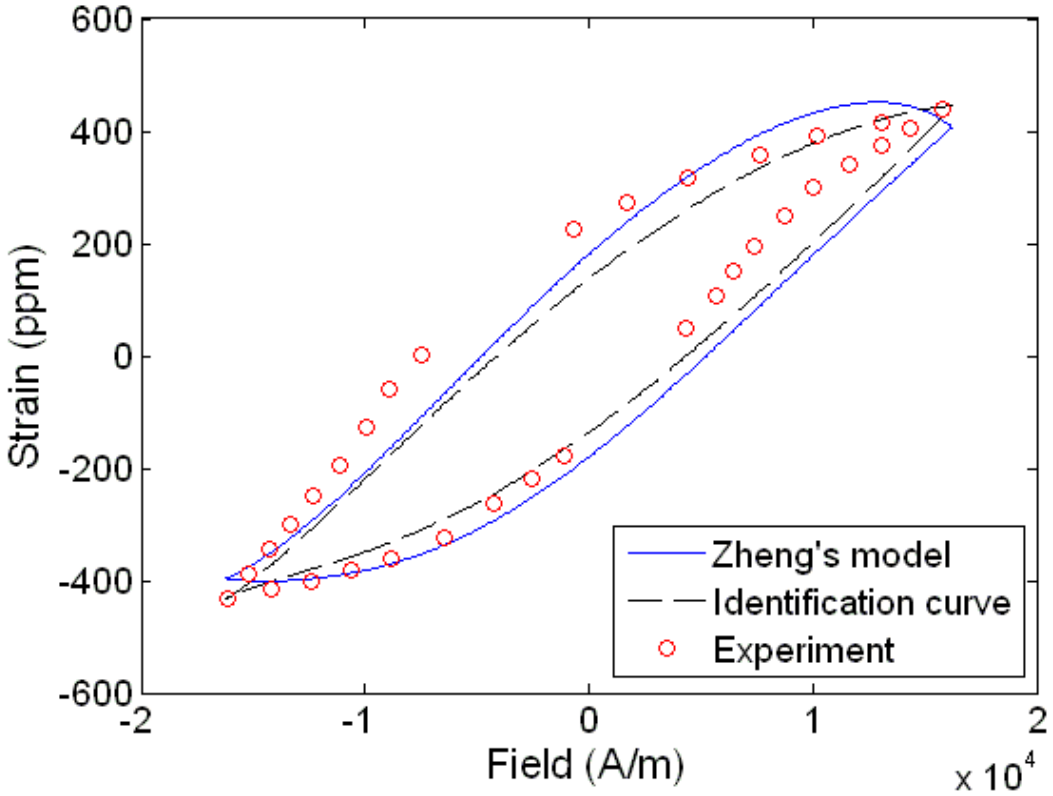

Figure.3. Fitted curve when exciting frequency is 100Hz.

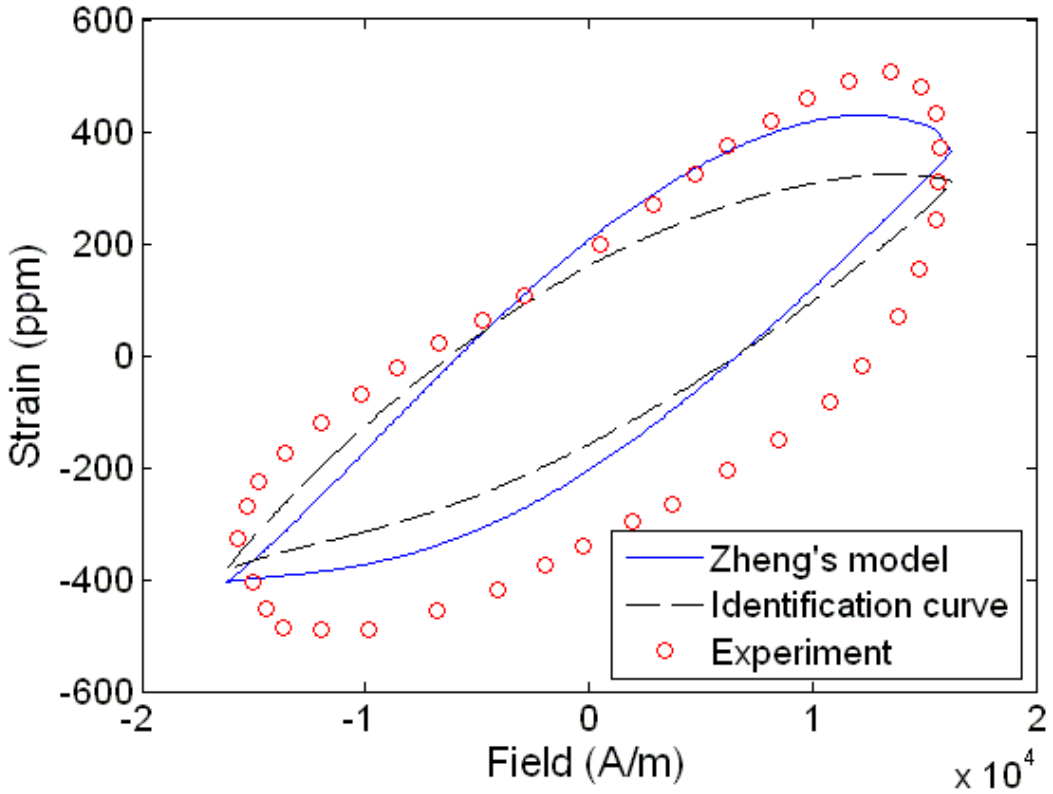

Figure.4. Fitted curve when exciting frequency is 500Hz.

5. Conclusions

The domain flexing function is introduced to the dynamical magnetic-elastic-thermal coupled hysteresis model to overcome the unphysical minor loop tip encountered in previous models. After doing so an immune clone algorithm is adopted to identify the model parameters. The results show that the modified model has effectively suppressed the unphysical phenomena appeared on the tips of minor loops when frequency of the exciting magnetic field is 100 Hz. But the extra parameter in domain flexing function has a great influence on the predicting results. A further investigation of this extra parameter will be included in the future investigation.

The parameter identification procedure based on the immune clone algorithm is performed successfully in above cases. The effectiveness of this procedure is proofed in Figure1 and Table1. Discrepancies between the identified parameters and the original chosen parameters are less than 5%.

Acknowledgements

This research was supported by the Fund of Natural Science Foundation of China (Nos. 10972094, 11032006, 11121202 and 11202087) and the Fundamental Research Funds for the Central Universities (lzujbky-2011-6) and Specialized Research Fund for the Doctoral Program of Higher Education under Grant 20110211120027. The authors gratefully acknowledge the support.

References

[1] C.F. Ralph, R.D. James, A.B. Dariusz, G. Vijay, D.H. Norman, Terfenol-D driven flaps for helicopter vibration reduction. Smart Materials and Structures, 5 (1996) 49-57.

[2] N. Yoshiya, N. Masanao, M. Keiji, T. Kiyoshhi, Y. Masashi and F. Takafumi, Development of active six-degrees-of-freedom microvibration control system using giant magnetostrictive actuators. Smart Materials and Structures, 9 (2000) 175-185.

[3] D.C. Jiles, D.L. Atherton, Theory of ferromagnetics hysteresis. Journal of Magnetism and Magnetic Materials, 61 (1986) 48-60.

[4] X. Feng, Studies on the Constitutive Theory and Experiment of Ferromagnetic Materials. Doctor thesis (2002) Tsinghua University.

[5] R.C. Smith, Hysteresis modeling in magnetostrictive materials via Preisach operators. Journal of Mathematical Systems, Estimation and Control, 8 (1998) 1-23.

[6] X.J. Zheng, L. Su, K. Jin, A dynamical hysteresis constitutive relation for giant magnetostrictive materials. Mechanics of Advanced Materials and Structures, 16 (2009) 516-521.

[7] D.C. Jiles, J.B. Thoelke, M.K. Devine, Numerical determination of hysteresis parameters for the modeling of magnetic properties using the theory of ferromagnetic hysteresis. IEEE Transaction on Magnetics, 28 (1992) 27-35.

[8] L. Dieter, I. Hajime, K. Arnulf, H. Toshihisa，On the Parameter Identification and Application of the Jiles-Atherton Hysteresis Model for Numerical Modelling of Measured Characteristics. IEEE Transaction on Magnetics, 35 (1999) 1211-1214.

[9] K. Chwastek, J. Szczyglowski, Identification of a hysteresis model parameters with genetic algorithms. Mathematics and Computers in Simulation, 71 (2006) 206-211.

[10] P. Kis, A. Ivanyi, Parameter identification of Jiles-Atherton model with nonlinear least-square method. Physica B, 343 (2004) 59-64.

[11] K. Chwastek, J. Szczyglowski, An alternative method to estimate the parameters of Jiles-Atherton model. Journal of Magnetism and Magnetic Materials, 314 (2007) 47-51.

[12] J. Zheng, S. Cao, H. Wang, Huang W., Hybrid genetic algorithms for parameter identification of a hysteresis model of magnetostrictive actuators. Neurocomputing, 70 (2007) 749-761.

[13] L.N. Castro, and F. J. VonZuben, The Clonal selection algorithm with engineering applications. Workshop on Artificial Immune Systems and Their Applications, Las Vegas, USA, July 2000.

[14] C.A. Coello, N.C. Cortes, Solving multiobjective optimization problems using an artificial immune system. Genetic Programming and Evolvable Machines, 6 (2005) 163-190.
[15] K.Chwastek, Modelling offset minor hysteresis loops with the modified Jiles-Atherton description. Journal of Physics D: Applied Physics, 42 (2009) 165002.
[16] D. Miljavec, B. Zidaric, Introduction a domain flexing function in the Jiles-Atherton hysteresis model. Journal of Magnetism and Magnetic Materials, 320 (2008) 763-768.
[17] M.J. Dapino, R.C. Smith, A.B. Flatau, Structural magnetic strain model for magnetostrictive transducers. IEEE Transactions on Mangetics, 36 (2000) 545-556.
[18] K. Jin, Y. Kou, Y.R. Liang, X.J. Zheng, Effects of hysteresis losses on dynamic behavior of magnetostrictive actuators. Journal of Applied Physics, 110 (2011) 093908.
[19] T.Z. Wang, Y.H. Zhou, Nonlinear transient dynamic model with multi-fields coupling effects for giant magnetostrictive transducers. Journal of Applied Physics (under review).

An opening crack model for thermo-magneto-electro-elastic solids

Xian-Ci Zhong[1,2,*]

[1] Department of Mathematics and Information Science, Guangxi University,
Nanning Guangxi, 530004, China
[2] Key Laboratory of Disaster Prevention and Structural Safety, Guangxi University,
Nanning Guangxi, 530004, China
* xczhong@gxu.edu.cn, zhongxianci@163.com

Abstract In previous studies of fracture analysis for a thermo-magneto-electro-elastic solid, the crack-face thermal boundary condition is always assumed to be fully insulated or conductive. In the present paper, an opening crack model is proposed by considering the various physical properties of crack interior. The thermal flux, electric displacement and magnetic induction at the crack surfaces are assumed to be dependent on the crack opening displacement. The effects of applied magneto-electro-mechanical loadings and the thermal conductivity inside a crack on the thermal stress intensity factor are investigated. The obtained results reveal that the thermal stress intensity factor depends not only on applied thermal loadings but also on applied magneto-electro-mechanical loadings and various physical properties of crack interior.

Keywords Thermo-magneto-electro-elastic solid, Opening crack model, Thermal stress intensity factor

1. Introduction

Due to the giant magnetoelectric coupling effects, magnetoelectroelastic materials own significant technological promise in manufacturing the novel multifunctional devices [1]. Moreover, since the temperature change will affect the overall performance of the smart devices, it is important to investigate the responses of magnetoelectroelastic materials under a thermal loading [2-4]. It is noted that the fracture analysis of a cracked thermo-magneto-electro-elastic solid has attracted much attention [5-9]. One can see that the thermal boundary condition on the crack surfaces is always assumed to be thermally insulated, and the effects of the thermal properties inside the crack on the crack-tip fields are not considered. Recently, in order to investigate the effects of the medium inside a crack on the thermal stress intensity factor, the thermal-medium crack model has been proposed [10]. The obtained results have also revealed that applied mechanical loadings have great influences on the thermal stress intensity factor. On the other hand, some known observations show that the electric permittivity and magnetic permeability of crack interior cannot be disregarded for the fracture analysis of a cracked magnetoelectroelastic solid [11]. It is also seen that the semi-permeable crack-face magnetoelectric boundary conditions have been proposed [12]. Consequently, to address the effects of various physical properties of medium inside a crack, we propose the following crack-face boundary conditions for a cracked thermo-magneto-electro-elastic solid:

$$D^c = -\varepsilon^c \frac{\Delta\phi}{\Delta u_z}, \qquad B^c = -\mu^c \frac{\Delta\varphi}{\Delta u_z}, \qquad q^c = -\lambda^c \frac{\Delta\theta}{\Delta u_z} \tag{1}$$

where the constants ε^c, μ^c and λ^c denote the dielectric permittivity, magnetic permeability and thermal conductivity of crack interior and they are given as $\varepsilon^c = \varepsilon_r\varepsilon_0 (\varepsilon_0 = 8.85\times10^{-12} F/m)$, $\mu^c = \mu_r\mu_0 (\mu_0 = 1.26\times10^{-6} Ns^2/C^2)$ and $\lambda^c = \lambda_r\lambda_0 (\lambda_0 = 0.024 W/Km)$ respectively. D^c, B^c and q^c are the electric displacement, magnetic induction and heat flux at the crack faces respectively. $\Delta\phi, \Delta\varphi$ and $\Delta\theta$ are the jumps of electric potential, magnetic potential and temperature change across the crack, respectively. One can find that eight ideal crack models associated with a

combination of permeable and impermeable thermal-magnetic-electric boundary conditions can be obtained by considering the limiting cases of Eq. (1).

The objective of the present paper is to investigate the dependence of the thermal stress intensity factor on applied magneto-electro-mechanical loadings and various physical properties of crack interior. Applying the boundary conditions in Eq. (1), the stationary behavior of a cracked thermo-magneto-electro-elastic solid is considered under a combination of applied magneto-electro-mechanical loadings and a uniform heat flux. The closed-form solution of the thermal stress intensity factor is obtained. Numerical results are carried out to show the variations of the thermal stress intensity factor on applied magneto-electro-mechanical loadings and various physical properties of crack interior.

2. Basic equations and boundary conditions

Consider that a Griffith crack is embedded in a transversely isotropic magnetoelectroelastic solid with the thermal effect. As shown in Fig. 1, we use Cartesian coordinates system *xoz* and assume that the crack is located at $-a < x < a$. Applied thermo-magneto-electro-mechanical loadings σ_0, D_0, B_0, q_0 are acting on the crack surfaces. Using the boundary conditions in Eq. (1), we have

$$\sigma_{zz}(x,0) = -\sigma_0, \qquad D_z(x,0) = -(D_0 - D^c), \qquad -a < x < a \tag{2}$$

$$B_z(x,0) = -(B_0 - B^c), \qquad q_z(x,0) = -(q_0 - q^c), \qquad -a < x < a \tag{3}$$

Hereafter $\sigma_{ij}, D_i, B_i, q_i$ stand for the components of stress, electric displacement, magnetic induction and heat flux.

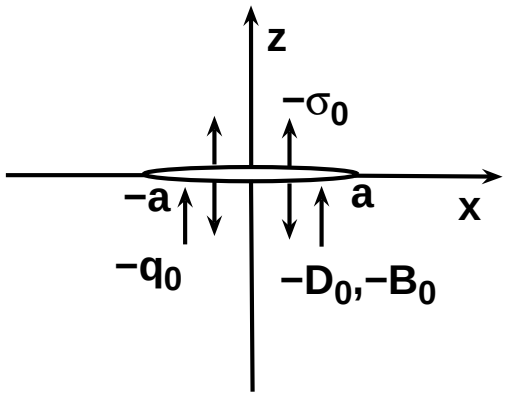

Figure 1. An opening crack in a thermo-magneto-electro-elastic solid

Under the assumption of plane deformation and linear thermo-magneto-electro-elasticity, the constitute equations can be written as

$$\sigma_{xx} = c_{11}\frac{\partial u_x}{\partial x} + c_{13}\frac{\partial u_z}{\partial z} + e_{31}\frac{\partial \phi}{\partial z} + h_{31}\frac{\partial \varphi}{\partial z} - \beta_x \theta \tag{4}$$

$$\sigma_{zz} = c_{13}\frac{\partial u_x}{\partial x} + c_{33}\frac{\partial u_z}{\partial z} + e_{33}\frac{\partial \phi}{\partial z} + h_{33}\frac{\partial \varphi}{\partial z} - \beta_z \theta \tag{5}$$

$$\sigma_{xz} = c_{44}\left(\frac{\partial u_x}{\partial z} + \frac{\partial u_z}{\partial x}\right) + e_{15}\frac{\partial \phi}{\partial x} + h_{15}\frac{\partial \varphi}{\partial x} \tag{6}$$

$$D_x = e_{15}\left(\frac{\partial u_x}{\partial z} + \frac{\partial u_z}{\partial x}\right) - \varepsilon_{11}\frac{\partial \phi}{\partial x} - d_{11}\frac{\partial \varphi}{\partial x} \tag{7}$$

$$D_z = e_{31}\frac{\partial u_x}{\partial x} + e_{33}\frac{\partial u_z}{\partial z} - \varepsilon_{33}\frac{\partial \phi}{\partial z} - d_{33}\frac{\partial \varphi}{\partial z} + p_z\theta \tag{8}$$

$$B_x = h_{15}\left(\frac{\partial u_x}{\partial z} + \frac{\partial u_z}{\partial x}\right) - d_{11}\frac{\partial \phi}{\partial x} - \mu_{11}\frac{\partial \varphi}{\partial x} \tag{9}$$

$$B_z = h_{31}\frac{\partial u_x}{\partial x} + h_{33}\frac{\partial u_z}{\partial z} - d_{33}\frac{\partial \phi}{\partial z} - \mu_{33}\frac{\partial \varphi}{\partial z} + m_z\theta \tag{10}$$

where u_i, ϕ, φ and θ are the components of elastic displacement, electric potential, magnetic potential and temperature change. $c_{ij}, e_{ij}, h_{ij}, \varepsilon_{ij}, d_{ij}, \mu_{ij}, p_z$ and m_z are the elastic, piezoelectric, piezomagnetic, dielectric permittivity, magnetoelectric, magnetic permeability, pyroelectric and pryomagnetic constants, respectively. β_x and β_z are the stress-temperature coefficient. Application of the equilibrium equation leads to the following partial differential equations

$$c_{11}u_{x,xx} + c_{44}u_{x,zz} + (c_{13}+c_{44})u_{z,xz} + (e_{31}+e_{15})\phi_{,xz} + (h_{31}+h_{15})\varphi_{,xz} = \beta_x\theta_{,x} \tag{11}$$

$$c_{44}u_{z,xx} + c_{33}u_{z,zz} + (c_{13}+c_{44})u_{x,xz} + e_{15}\phi_{,xx} + e_{33}\phi_{,zz} + h_{15}\varphi_{,xx} + h_{33}\varphi_{,zz} = \beta_x\theta_{,z} \tag{12}$$

$$e_{15}u_{z,xx} + e_{33}u_{z,zz} + (e_{31}+e_{15})u_{x,xz} - \varepsilon_{11}\phi_{,xx} - \varepsilon_{33}\phi_{,zz} - d_{11}\varphi_{,xx} - d_{33}\varphi_{,zz} = -p_z\theta_{,z} \tag{13}$$

$$h_{15}u_{z,xx} + h_{33}u_{z,zz} + (h_{31}+h_{15})u_{x,xz} - d_{11}\phi_{,xx} - d_{33}\phi_{,zz} - \mu_{11}\varphi_{,xx} - \mu_{33}\varphi_{,zz} = -m_z\theta_{,z} \tag{14}$$

On the other hand, from the theory of the Fourier heat conduction, one has the following constitute and equilibrium equations

$$q_x = -\lambda_x\frac{\partial \theta}{\partial x}, \qquad q_z = -\lambda_z\frac{\partial \theta}{\partial z}, \qquad \frac{\partial q_x}{\partial x} + \frac{\partial q_z}{\partial z} = 0 \tag{15}$$

Then it follows that

$$\lambda^2\frac{\partial^2\theta}{\partial x^2} + \frac{\partial^2\theta}{\partial z^2} = 0, \qquad \lambda = \sqrt{\frac{\lambda_x}{\lambda_z}}\,. \tag{16}$$

3. Thermal stress intensity factor

Since the considered problem is linear and only related to the stationary behavior of a cracked thermo-magneto-electro-elastic solid, the magnetoelectroelastic field can be obtained by considering the superposition of that induced by applied magneto-electro-mechanical loadings and that induced by applied uniform heat flux. For the temperature field, similar to those given in [13], one can easily obtain the jump of temperature change across the crack as

$$\theta(x,0) = -\frac{q_0 - q^c}{\lambda\lambda_z}\sqrt{a^2 - x^2}\,, \qquad -a < x < a\,. \tag{17}$$

Moreover, using the known results in [12], we give the jump of elastic displacement across the crack, namely

$$u_z(x,0) = \frac{\sigma_0}{\sum_{j=1}^{4}\beta_{1j}a_j}\sum_{j=1}^{4}\eta_{3j}\alpha_j a_j\sqrt{a^2 - x^2}\,, \qquad -a < x < a \tag{18}$$

where the constants $\beta_{kj}, \alpha_j, a_j$ and η_{3j} are defined as those given in [12]. From the third relation in Eq. (1) , Eqs. (17) and (18), the heat flux q^c can be calculated as

$$q^c = \frac{\lambda^c q_0 \sum_{j=1}^{4}\beta_{1j}a_j}{\lambda^c\sum_{j=1}^{4}\beta_{1j}a_j + \lambda\lambda_z\sigma_0\sum_{j=1}^{4}\eta_{3j}\alpha_j a_j} \quad \text{for } \sigma_0 \neq 0\,, \tag{19}$$

$$q^c = \frac{\lambda^c q_0 \sum_{j=1}^{4} \beta_{4j} a_j}{\lambda^c \sum_{j=1}^{4} \beta_{4j} a_j + \lambda\lambda_z (D_0 - D^c) \sum_{j=1}^{4} \eta_{3j} \alpha_j a_j} \quad \text{for} \quad \sigma_0 = 0, D_0 \neq 0, \qquad (20)$$

$$q^c = \frac{\lambda^c q_0 \sum_{j=1}^{4} \beta_{6j} a_j}{\lambda^c \sum_{j=1}^{4} \beta_{6j} a_j + \lambda\lambda_z (B_0 - B^c) \sum_{j=1}^{4} \eta_{3j} \alpha_j a_j} \quad \text{for} \quad \sigma_0 = 0, B_0 \neq 0. \qquad (21)$$

As observed in [10], the heat flux q^c is dependent on the material properties, applied mechanical loading and thermal conductivity of crack interior. In addition, applied magnetoelectric loadings, electric permittivity and magnetic permeability of crack interior also have influences on the heat flux q^c since they may affect crack opening displacement. Moreover, when $\lambda^c = 0$, one has $q^c = 0$ and the crack is thermally insulated. When $\lambda^c \to \infty$, we get $q^c = q_0$ and the crack is fully conductive.

On the other hand, we can give the explicit solution of the stress field near the crack tip induced by applied uniform heat flux. For saving spaces, we neglect the detail solution procedure and give the thermal stress intensity factor as

$$K_{II} = -\frac{\kappa(q_0 - q^c)a}{2\lambda\lambda_z} \sqrt{\pi a} \sum_{j=1}^{4} \beta_{2j} b_{j1}, \qquad (22)$$

where

$$[b_{kj}]_{4\times 4} = \begin{bmatrix} 1 & 1 & 1 & 1 \\ \beta_{11} & \beta_{12} & \beta_{13} & \beta_{14} \\ \beta_{41} & \beta_{42} & \beta_{43} & \beta_{44} \\ \beta_{61} & \beta_{62} & \beta_{63} & \beta_{64} \end{bmatrix}^{-1}. \qquad (23)$$

The constant κ is only related to the material properties and it can be calculated as

$$\kappa = \frac{M_1 \sum_{j=1}^{4} \beta_{2j} b_{j1} - \kappa_1 \sum_{j=1}^{4} \beta_{2j} b_{j2} - \kappa_2 \sum_{j=1}^{4} \beta_{2j} b_{j3} - \kappa_3 \sum_{j=1}^{4} \beta_{2j} b_{j4}}{\sum_{j=1}^{4} \beta_{2j} b_{j1}}, \qquad (24)$$

with

$$\begin{bmatrix} M_1 \\ M_2 \\ M_3 \\ M_4 \end{bmatrix} = \begin{bmatrix} c_{11} - \lambda^2 c_{44} & -(c_{13} + c_{44})\lambda & -(e_{31} + e_{15})\lambda & -(h_{31} + h_{15})\lambda \\ (c_{13} + c_{44})\lambda & c_{44} - c_{33}\lambda^2 & e_{15} - e_{33}\lambda^2 & h_{15} - h_{33}\lambda^2 \\ -(e_{31} + e_{15})\lambda & e_{33}\lambda^2 - e_{15} & \varepsilon_{11} - \varepsilon_{33}\lambda^2 & d_{11} - d_{33}\lambda^2 \\ -(h_{31} + h_{15})\lambda & h_{33}\lambda^2 - h_{15} & d_{11} - d_{33}\lambda^2 & \mu_{11} - \mu_{33}\lambda^2 \end{bmatrix} \begin{bmatrix} \beta_x \\ \beta_z \lambda \\ p_z \lambda \\ m_z \lambda \end{bmatrix}, \qquad (25)$$

$$\kappa_1 = c_{13} M_1 - c_{33} M_2 \lambda - e_{33} M_3 \lambda - h_{33} M_4 \lambda - \beta_z, \qquad (26)$$

$$\kappa_2 = e_{31} M_1 - e_{33} M_2 \lambda + \varepsilon_{33} M_3 \lambda + d_{33} M_4 \lambda + p_z, \qquad (27)$$

$$\kappa_3 = h_{31} M_1 - h_{33} M_2 \lambda + d_{33} M_3 \lambda + \mu_{33} M_4 \lambda + m_z. \qquad (28)$$

It is seen that the thermal stress intensity factor K_{II} is dependent on the heat flux at the crack faces q^c. When $q^c = 0$, corresponding to a thermally insulated crack, the thermal stress intensity factor is only dependent on applied thermal loading, material properties and the crack length. When $q^c = q_0$, corresponding to a fully conductive crack, the thermal stress intensity factor is zero. When a crack is full of a medium, the thermal stress intensity factor is dependent on applied thermo-magneto-electro-mechanical loadings and various physical properties of the medium inside the crack. For convenience, the thermal stress intensity factor for $q^c = 0$ is rewritten as K_m and

one get

$$\frac{K_{II}}{K_m}=1-\frac{q_c}{q_0}. \tag{29}$$

That is, application of (19)-(21) yields

$$\frac{K_{II}}{K_m}=\frac{\lambda\lambda_z\sigma_0\sum_{j=1}^{4}\eta_{3j}\alpha_j a_j}{\lambda^c\sum_{j=1}^{4}\beta_{1j}a_j+\lambda\lambda_z\sigma_0\sum_{j=1}^{4}\eta_{3j}\alpha_j a_j}\quad \text{for}\ \ \sigma_0\neq 0, \tag{30}$$

$$\frac{K_{II}}{K_m}=\frac{\lambda\lambda_z(D_0-D^c)\sum_{j=1}^{4}\eta_{3j}\alpha_j a_j}{\lambda^c\sum_{j=1}^{4}\beta_{4j}a_j+\lambda\lambda_z(D_0-D^c)\sum_{j=1}^{4}\eta_{3j}\alpha_j a_j}\quad \text{for}\ \ \sigma_0=0, D_0\neq 0, \tag{31}$$

$$\frac{K_{II}}{K_m}=\frac{\lambda\lambda_z(B_0-B^c)\sum_{j=1}^{4}\eta_{3j}\alpha_j a_j}{\lambda^c\sum_{j=1}^{4}\beta_{6j}a_j+\lambda\lambda_z(B_0-B^c)\sum_{j=1}^{4}\eta_{3j}\alpha_j a_j}\quad \text{for}\ \ \sigma_0=0, B_0\neq 0. \tag{32}$$

4. Numerical results and discussions

In order to investigate the effects of applied magneto-electro-mechanical loadings and the physical properties of crack interior on the thermal stress intensity factor, we choose a special thermo-magneto-electro-elastic solid for numerical computations and the material properties are given in Table 1 [3]. For the sake of simplicity, we further suppose that $\varepsilon_r=\mu_r=\lambda_r=\omega$. When $\omega=0$, the crack is fully thermo-magneto-electric impermeable. When $\omega\to\infty$, the crack is fully thermo-magneto-electric permeable. When $\omega=1$, the crack is full of air.

Table 1. The material properties

Elastic constants ($\times10^{10}$ N/m^2)				Piezoelectric constants (C/m^2)			Dielectric permittivity ($\times10^{-11}$C^2/Nm^2)	
c_{11}	c_{13}	c_{33}	c_{44}	e_{31}	e_{33}	e_{15}	ε_{11}	ε_{33}
7.41	3.93	8.36	1.32	-0.16	0.347	-0.138	8.26	9.03

Magnetic permeability ($\times10^{-6}$Ns^2/C^2)		Electromagnetic constants ($\times10^{-11}$Ns/VC)		Piezomagnetic constants (N/Am)		
μ_{11}	μ_{33}	d_{11}	d_{33}	h_{31}	h_{33}	h_{15}
5	10	-3612.68	-2.4735	580.3	699.7	550

Thermal moduli ($\times10^5$N/Km^2)		Pyroelectric constant ($\times10^{-6}$C/N)	Pyromagnetic constant ($\times10^{-6}$N/AKm)	Heat conduction coefficients (W/Km)	
β_x	β_z	p_z	m_z	λ_x	λ_z
6.21	5.51	-2.94	5.187	9	9

Fig. 2 is depicted to show the variation of the normalized thermal stress intensity factor K_{II}/K_m versus ω under the loadings of $\sigma_0=10MPa$, $D_0=1\times10^{-4}C/m^2$ and $B_0=0.01N/Am$. It is seen from Fig. 2 that with the increasing of ω, the normalized thermal stress intensity factor K_{II}/K_m is decreasing rapidly. The phenomenon is in accordance with that given in [10] for an opening crack in a purely elastic material. For $\omega=0$, one has $K_{II}/K_m=1$. For $\omega\to\infty$, $K_{II}/K_m=0$. For a crack full of a medium, the thermal stress intensity factor is located between

that for a fully permeable crack and that for a fully impermeable one. One can see that the thermal stress intensity factor is always overestimated for a thermally insulated crack.

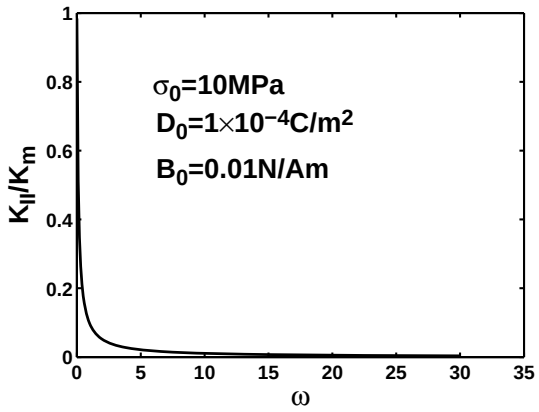

Figure 2. The variations of the normalized thermal stress intensity factor K_{II}/K_m versus ω under the loadings of $\sigma_0 = 10MPa$, $D_0 = 1\times10^{-4} C/m^2$ and $B_0 = 0.01N/Am$.

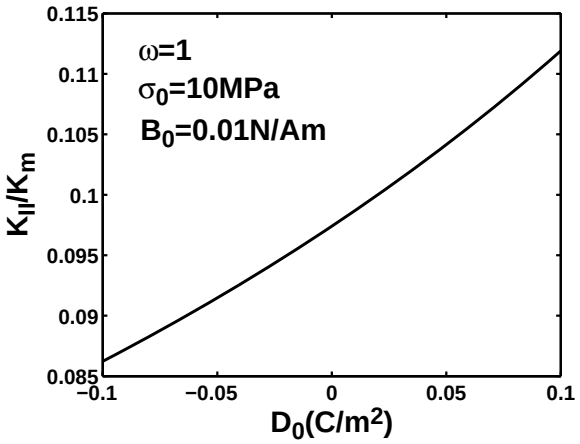

Figure 3. The variations of the normalized thermal stress intensity factor K_{II}/K_m versus D_0 under the loadings of $\sigma_0 = 10MPa$ and $B_0 = 0.01N/Am$ for an air crack.

Moreover, for an air crack, it is very interesting to investigate the effects of applied magneto-electro-mechanical loadings on the thermal stress intensity factor, since the important issue is little to be considered in the open literatures [5-9]. Fig. 3 presents the variations of the normalized thermal stress intensity factor K_{II}/K_m versus the electric loading D_0 for $\sigma_0 = 10MPa$ and $B_0 = 0.01N/Am$. One can find from Fig. 3 that a positive electric loading enhances the normalized stress intensity factor, and a negative one impedes the normalized stress intensity factor. It is attributed to the fact that for an air crack, a positive electric loading aids the crack opening displacement and a negative one decreases the crack opening displacement [12]. Similarly, it is seen from Fig. 4 that the effects of applied magnetic loadings on the normalized thermal stress intensity factor are in agreement with those of applied electric loadings. On the other hand, Fig. 5 is drawn to show the dependence of the normalized thermal stress intensity factor on applied mechanical loadings. It is found that an increase of applied mechanical loading σ_0 enhances the normalized thermal stress intensity factor, which is similar to the observation in [10]. For a practical situation, always a combination of applied thermo-magneto-electro-mechanical loadings is acting on the smart devices. One can observe from the above phenomena that to address the thermal stresses near the crack tips, the effects of applied magneto-electro-mechanical loadings and the physical properties of crack interior should be considered comprehensively.

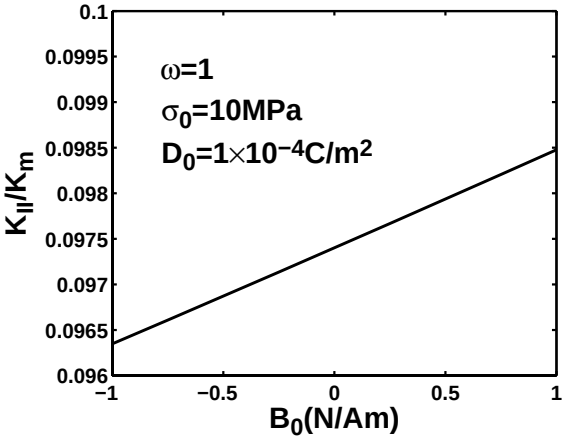

Figure 4. The variations of the normalized thermal stress intensity factor K_{II} / K_m versus B_0 under the loadings of $\sigma_0 = 10MPa$ and $D_0 = 1\times10^{-4} C / m^2$ for an air crack.

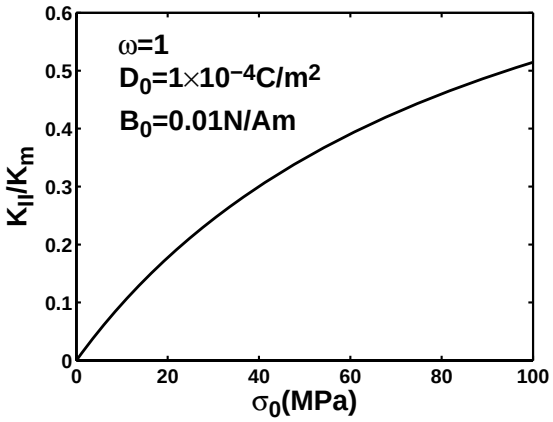

Figure 5. The variations of the normalized thermal stress intensity factor K_{II} / K_m versus σ_0 under the loadings of $D_0 = 1\times10^{-4} C / m^2$ and $B_0 = 0.01N / Am$ for an air crack.

4. Conclusions

To address the effects of various physical properties of crack interior on the thermal stress intensity factor, an opening crack model is proposed in the paper. Eight ideal crack models are the limiting cases of the proposed one. The problem of an opening crack embedded in an infinite thermo-magneto-electro-elastic solid is investigated. The closed-form solution of the thermal stress intensity factor is given. Numerical results are carried to show the influences of applied magneto-electro-mechanical loadings and various physical properties of crack interior on the thermal stress intensity factor. The results reveal that for an opening crack full of a medium, the effects of applied magneto-electro-mechanical loadings and various physical properties of crack interior on the thermal stress intensity factor should be considered. Under the assumption of thermally insulated crack model, the thermal stress intensity factor is always overestimated.

Acknowledgements

The work was supported by the Guangxi Natural Science Foundation (No: 2011GXNFA018132) and the Scientific Research Foundation of Guangxi University (XBZ111497).

References

[1] C.W. Nan, M.I. Bichurin, S. Dong, D. Viehland, G. Srinivasan, Multiferroic magnetoelectric composites: Historical perspective, status, and future directions. J Appl Phys, 103 (2008) 031101.

[2] M. Aouadi, Some theorems in the generalized theory of thermo-magnetoelectroelasticity under Green–Lindsay's model, Acta Mech, 200 (2008) 25-43.

[3] P. F. Hou , G. H. Teng, H. R. Chen, Three-dimensional Green's function for a point heat source in two-phase transversely isotropic magneto-electro-thermo-elastic material, Mech Mater, 41 (2009) 329-338.

[4] M. I. A. Othman, Generalized electro-magneto thermoelasticity in Case of thermal shock plane waves for a finite conducting half space with two relaxation times. Mech Mech Engng, 14 (2010) 5-30.

[5] C. F. Gao, H. Kessler, H. Balke, Fracture analysis of electromagnetic thermoelastic solids. Eur J Mech A/Solids, 22 (2003) 433-442.

[6] W. Q. Chen, K. Y. Lee, H. J. Ding, General solution for transversely isotropic magneto-electro-thermo-elasticity and the potential theory method. Int J Solids Struct, 42 (2004) 1361-1379.

[7] B. L. Wang, O. P. Niraula, Transient thermal fracture analysis of transversely isotropic magneto- electro-elastic materials. J Thermal Stresses, 30 (2007) 297–317.

[8] J. Sladek, V. Sladek, P. Solek , Ch. Zhang, Fracture analysis in continuously nonhomogeneous magneto-electro-elastic solids under a thermal load by the MLPG. Int J Solids Struct, 47 (2010) 1381-1391.

[9] W. J. Feng, P. Ma, R.K.L. Su, An electrically impermeable and magnetically permeable interface crack with a contact zone in magnetoelectroelastic bimaterials under a thermal flux and magnetoelectromechanical loads. Int J Solids Struct, 49 (2012) 3472-3483.

[10] X. C. Zhong, K. Y. Lee, A thermal-medium crack model. Mech Mater, 51 (2012) 110-117.

[11] B. L., Wang, Y.W Mai, Applicability of the crack-face electromagnetic boundary conditions for fracture of magnetoelectroelastic materials. Int J Solids Struct 44 (2007) 387–398.

[12] X. C. Zhong, X. F. Li, Magnetoelectroelastic analysis for an opening crack in a piezoelectromagnetic solid, Eur J Mech A/Solids, 26 (2007) 405-417.

[13] Y. M. Tsai, Orthotropic thermoelastic problem of uniform heat flow disturbed by a central crack. J Compos Mater, 18 (1984) 122–131.

Physical mechanisms of magnetostriction or electrostriction induced interfacial fracture in a bi-layered multiferroic smart composite

Hao Zhao[1], Tao Xiong[1], Yong-Dong Li[1,*], Kang Yong Lee[2]

[1] Department of Mechanical Engineering, Academy of Armored Force Engineering, Beijing 100072, China
[2] State Key Laboratory of Strutural Analysis for Industrial Equipment, Department of Engineering Mechanics, Dalian University of Technology, Dalian 116024, China
* Corresponding author: lydbeijing@163.com;

Abstract The physical mechanisms of interfacial fracture in a multiferroic bimaterial under magnetostriction or electrostriction have been investigated by the methods of distributed dislocations and Green's function. The numerical results of the stress intensity factor are discussed and the physical mechanisms are then explained.

Keywords Magnetostriction, Electrostriction, Piezomagnetic stiffening, Piezoelectric stiffening, Interfacial fracture

1. Introduction

In layered multiferroic composites composed of alternate piezoelectric and piezomagnetic layers [1], interfaces are key regions to realize the magneto-electric coupling performance [2]. However, when these composites are in service, their interfaces might be damaged by magnetostriction or electrostriction. Therefore, it is significant to investigate the interfacial fracture behavior of layered multiferroic composites. In preceding work [2-3], we analyzed the idealized problems of a single interfacial crack. For practical composites, multiple cracks may simultaneously exist on their interfaces, which would affect the magneto-electric coupling behavior more seriously and also give more difficulties to fracture analysis. The present paper continues to study the more general problem of multiple interfacial cracks in a bi-layered multiferroic composite, and try to give theoretical explanation on the underlying physical mechanisms of magnetostrictive or electrostrictive interfacial fracture.

2. Problem formulatiuon and fracture analysis

Consider a bi-layered multiferroic composite with multiple interfacial cracks shown in Fig. 1. The two layers are poled along the z direction and isotropic in the xoy plane. Assume that it is loaded by in-plane magnetic field H_0 or electric field E_0 normal to the interface and surfaces, and the upper and lower surfaces are constrained mechanically. Then, only the anti-plane deformation is coupled with the in-plane magnetic/electric field, and the basic equations reduce to

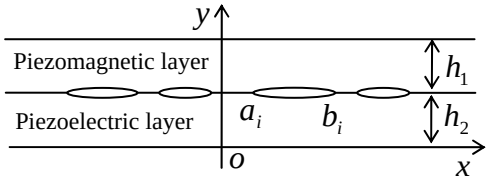

Fig. 1 Interfacial cracks in a multiferroic composite

$$\left.\begin{aligned} \tau_{kz}^{(1)} &= c_{44}^{(1)}\frac{\partial w_1}{\partial k}+h_{15}\frac{\partial \varphi}{\partial k};\quad B_k = h_{15}\frac{\partial w_1}{\partial k}-\mu_{11}\frac{\partial \varphi}{\partial k} \\ \tau_{kz}^{(2)} &= c_{44}^{(2)}\frac{\partial w_2}{\partial k}+e_{15}\frac{\partial \phi}{\partial k};\quad D_k = e_{15}\frac{\partial w_2}{\partial k}-\varepsilon_{11}\frac{\partial \phi}{\partial k} \end{aligned}\right\},\ k=x,y \tag{1}$$

The governing equations are [2]

$$\nabla^2 w_j = 0\,,\ (\,j=1,2\,),\ \ \nabla^2\varphi = 0\,,\ \ \nabla^2\phi = 0\,. \tag{2}$$

For the magnetostriction (MS) case, the boundary and continuity conditions are

$$\tau_{yz}^{(1)}(x,h_1+h_2) = \tau_{yz}^{(2)}(x,0) = \tau_0\,,\ \ \tau_{yz}^{(1)}(x,h_2) = \tau_{yz}^{(2)}(x,h_2) \tag{3}$$

$$B_y(x,h_1+h_2) = B_y(x,h_2) = H_0\,,\ \ D_y(x,h_2) = D_y(x,0) = 0 \tag{4}$$

$$w_1(x,h_2) = w_2(x,h_2)\,,\ \ x\notin(a_j,b_j)\,,\ \ j=1,2,\Lambda\,,n \tag{5}$$

$$\tau_{yz}(x,h_2) = 0\,,\ \ x\in(a_j,b_j)\,,\ \ j=1,2,\Lambda\,,n \tag{6}$$

where τ_0 is the mechanical constraining traction that can be determined by magnetoelectroelastic analysis [2]. For the electrostriction (ES) case, Eq. (4) should be replaced by

$$B_y(x,h_1+h_2) = B_y(x,h_2) = 0\,,\ \ D_y(x,h_2) = D_y(x,0) = D_0 \tag{7}$$

The methods of distributed interfacial dislocations, Green's function and Cauchy singular integral equation are employed to perform the fracture analysis [4]. For simplicity, the details of the theoretical derivation and numerical computation are omitted here.

3. Numerical results and conclusion

Assume that the piezomagnetic and piezoelectric layers are CoFe2O4 and BaTiO3, respectively, and their material constants are perturbed to reveal their effects on the stress intensity factor (SIF), respectively. Based on the numerical results of SIF shown in Fig. 2, the magnetostrictive or electrostrictive interfacial fracture behavior is explained through the following physical mechanisms of "initiative/passive deformation", "magneto/electro-mechanical coupling" and "piezomagnetic/piezoelectric stiffening".

(a) The shear modulus (i.e. material stiffness) affects the SIF via the mechanism of initiative and passive deformation.

(b) The piezoelectric and dielectric coefficients affect the SIF in the ES case via the mechanism of electromechanical coupling, but they affect the SIF in the MS case through the mechanism of piezoelectric stiffening.

(c) The piezomagnetic coefficient and magnetic permeability affect the SIF in the MS case through the mechanism of magnetomechanical coupling, but they take effect in the ES case through the mechanism of piezomagnetic stiffening.

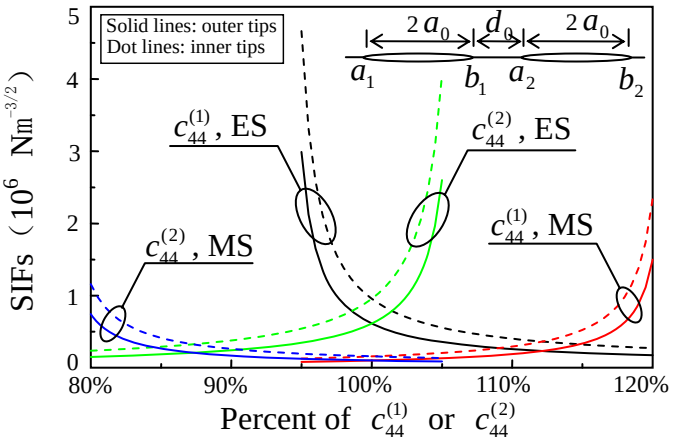

(a) Perturbation of shear modulus

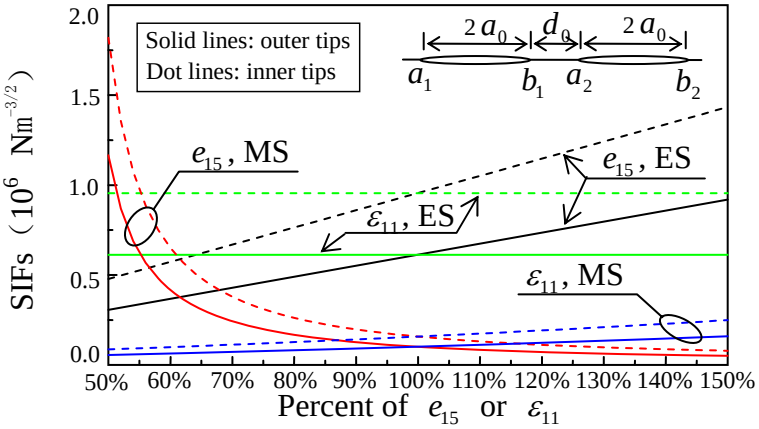

(b) Perturbation of piezoelectric coefficient and dielectric coefficient

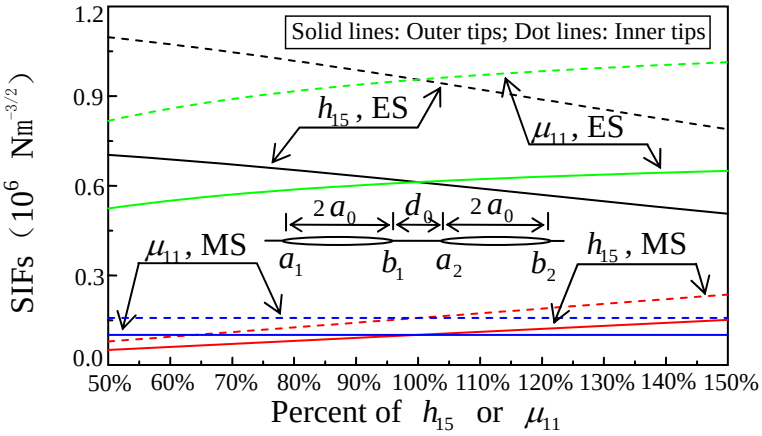

(c) Perturbation of piezomagnetic coefficient or magnetic permeability

Fig. 2 Effects of material parameters on the SIF

($h_1 = h_2 = 10$mm; $d_0 = 0.1$mm; $a_0 = 1$mm)

References

[1] W. Eerenstein, N.D. Mathur, J.F. Scott, Multiferroic and magnetoelectric materials. Nature 2006, 442(7104): 759–765.
[2] Y.D. Li, K.Y. Lee, Effects of magneto-electric loadings and piezomagnetic/piezoelectric stiffening on multiferroic interface fracture. Engineering Fracture Mechanics 2010, 77(5): 856–866.
[3] Y.D. Li, K.Y. Lee, Magnetostrictive fracture of a cylindrical multiferroic composite. International Journal of Engineering Science 2010, 48(2): 199–208.
[4] Y.D. Li, F.X. Feng, H. Zhao, Multiple interfacial cracks in a bi-layered multiferroic composite under magnetostriction or electrostriction. Engineering Fracture Mechanics 2012, 90(1): 65–75.

On the Dynamic Behaviour of Surface-Bonded Piezoelectric Sensors/Actuators with Partially Debonded Adhesive Layers

Congrui Jin, Lu Han, Guoliang Huang, Xiaodong Wang*

Department of Mechanical Engineering
University of Alberta, Edmonton, Canada T6G 2G8
* Corresponding author: xiaodong.wang@ualberta.ca

Abstract The current work presents the analytical study of the effect of the mechanical and geometrical properties of the adhesive layer on the coupled dynamic electromechanical behaviour of thin piezoceramic sensors/actuators bonded to elastic media. A sensor/actuator model with an imperfect adhesive bonding layer is proposed to simulate the two dimensional electromechanical behaviour of the integrated system. The analytical solution of the problem is provided to study the effect of the bonding layer upon the dynamic behaviour of the sensors/actuators under different loading frequencies. The interfacial debonding and its effect on the interlaminar strain and stress transfer mechanisms are discussed in detail. Numerical results obtained show that even for perfectly bonding cases the dynamic coupling between the sensors/actuators and the host structure is significantly affected by the material and geometric properties of the bonding layer. For imperfect bonding layers, debonding and loading frequency interact strongly to each other at certain frequencies, showing a significant coupling effect.

Keywords Piezoelectric, Electromechanical, Debonding, Sensor, Actuator

1. Introduction

Using piezoelectric sensors/actuators in smart structures for position control, vibration control, and damage detection has attracted significant attention from the research community [1-4]. Piezoelectric patches could be permanently bonded to host structures using proper adhesives. The adhesive layer transfers the load between the sensor/actuator elements and the host structure and significantly influences the efficiency of the sensing/actuating process. It is, therefore, an important issue to study the effect of the adhesive layer in such smart structures.

Beam, plate and shell elements have been extensively used [5-7] to study the global electromechanical behaviour of piezoelectric structures. To understand the load transfer through bonding layers in these structures, detailed local deformation near actuators/sensors must be studied. A one-dimensional actuator model has been developed to study the static local stress field near a thin-sheet piezoelectric element attached to an infinite elastic medium [8]. A similar analysis was also conducted based on a more general model which included both interfacial and normal stresses [9, 10]. The development of techniques of generating and collecting diagnostic elastic waves using piezoelectric actuators/sensors has showed the great potential of continuous monitoring of composite structures using distributed piezoelectric actuators/sensors [11]. The study showed very promising results for using integrated piezoelectric actuator/sensor systems in structural health monitoring. A special application of piezoelectric actuators/sensors is in the electromechanical impedance method, which was developed for identifying damage by monitoring the changes in the impedance of the structure [12-15]. Piezoelectric actuators/sensors are also used to generate wave propagation in smart structures for the health monitoring of the structures. To study the high-frequency dynamic behaviour of a piezoelectric thin-sheet actuator, a one-dimensional model was developed and used to evaluate the effect of geometric and loading parameters upon the load transfer between the actuators and the host structure [16, 17]. This actuator model is further modified to study problems with varying electric field distribution along the actuators [18]. Newly developed piezoelectric actuators can sustain a very high electric field without electric breakdown, and, therefore, can generate relatively high strain in the adhesive along the edge of the actuator, and

may finally result in debonding [19, 20]. Existing studies on the electromechanical behaviour of piezoelectric actuators with imperfect bonding have been mainly confined to the global response of piezoelectric structures [21-23].

The current work reviews and presents the analytical study of the effect of the mechanical and geometrical properties of adhesive layers on the coupled dynamic electromechanical behaviour of thin piezoceramic sensors/actuators bonded to elastic media. A sensor/actuator model with an imperfect adhesive bonding layer is used to simulate the two dimensional electromechanical behaviour of the integrated system. The analytical solution of the problem is provided to study the effect of the bonding layer upon the dynamic behaviour of the sensors/actuators under different loading frequencies. The interfacial debonding and its effect on the interlaminar strain and stress transfer mechanisms are discussed. Numerical results obtained show that even for perfectly bonding cases the dynamic coupling between the sensors/actuators and the host structure is significantly affected by the material and geometric properties of the bonding layer. For imperfect bonding layers, debonding and loading frequency interact strongly to each other at certain frequencies, showing a significant coupling effect.

2. Formulation of the Problem

For surface-bonded piezoelectric thin sheets with the poling direction along the thickness, as either actuators or sensors, the axial deformation will play a dominant role. Since the thickness of the host medium is usually much larger than that of the piezoelectric elements, the host medium can be modelled as a semi-infinite medium. Accordingly, consider the plane strain problem of a thin piezoceramic sheet bonded to a homogeneous and isotropic elastic half plane through a thin bonding layer, as illustrated in Fig. 1. In the figure *a* represents the half length of the actuator/sensor, and the thicknesses of the actuator and the bonding layer are assumed to be *h* and *h'*, respectively. Debonding at the bonding layer forms an interfacial crack, with the half length being *d*.

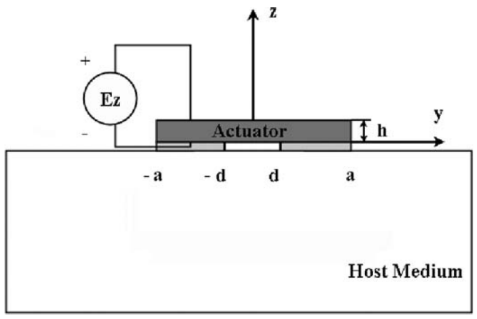

Figure 1. A surface piezoelectric element with debonding

For an actuator, a voltage is applied between the upper and lower electrodes of the piezoelectric element, which results in an electric field $E_z\, exp(-i\omega t)$ along the thickness of the actuator, where *Ez* is the magnitude of the electric field intensity, and ω is the angular frequency. For steady state problems, all field quantities contain the same temporal factor $\exp(-i\omega t)$, which is hereafter omitted for brevity.

2.1 Modelling of the piezoelectric elements

For a thin-sheet actuator/sensor, the axial stress and strain can be assumed to be uniform across the thickness. The normal stress between the actuator and the host medium is ignored because the upper surface of the thin actuator/sensor is traction free. The piezoelectric element can then be modelled

as a one-dimensional element subjected to interfacial shear stress and electric field with the governing equation being

$$\frac{\mathrm{d}\sigma_y^a(y)}{\mathrm{d}y} + \frac{\tau(y)}{h} + \rho^a \omega^2 u_y^a = 0 \tag{1}$$

where $\sigma^a{}_y$, ρ^a, and $u^a{}_y$ are the axial stress, the mass density, and the axial displacement of the actuator, respectively. The axial stress of the actuator is related to the axial strain $\epsilon^a{}_y$ and the electric field E_z by the following general constitutive relation

$$\sigma_y^a(y) = E^a \epsilon_y^a(y) - e^a E_z \tag{2}$$

where E^a and e^a are the effective stiffness and piezoelectric constants [].

Based on this simplified model, axial the strsin and displacement in the piezoelectric element can be determined in terms of the interfacial shear stress (τ) and the applied electric field intensity (E_z) as

$$\begin{aligned}
\epsilon_y^a(y) = {} & \frac{e^a E_z}{E^a}\frac{\cos k^a y}{\cos k^a a} + \frac{\sin[k^a(a+y)]}{E^a h \sin 2k^a a}\int_{-a}^{a}\cos[k^a(\xi-a)]\tau(\xi)\mathrm{d}\xi \\
& -\frac{1}{E^a h}\int_{-a}^{y}\cos[k^a(y-\xi)]\tau(\xi)\mathrm{d}\xi, \quad |y|<a, \\
u_y^a(y) = {} & \frac{e^a E_z}{E^a}\frac{\sin k^a y}{k^a \cos k^a a} - \frac{\cos[k^a(a+y)]}{k^a E^a h \sin 2k^a a}\int_{-a}^{a}\cos[k^a(\xi-a)]\tau(\xi)\mathrm{d}\xi \\
& -\frac{1}{k^a E^a h}\int_{-a}^{y}\sin[k^a(y-\xi)]\tau(\xi)\mathrm{d}\xi, \quad |y|<a,
\end{aligned} \tag{3}$$

which represents the deformation of the piezoelectric element caused by the interfacial shear stress and the applied electric field.

2.2 The bonding layer

The bonding layer connects the piezoelectric element and the host medium by transferring shear stress. The shear stress in the bonding layer is given by its constitutive relation as

$$-\tau(y) = \frac{\mu^b - i\omega\gamma^b}{h'}[u^+(y) - u^-(y)] \tag{4}$$

where μ^b and γ^b are the shear modulus and the coefficient of viscosity of the bonding layer, respectively, and $u+$ and $u-$ are the longitudinal displacements of the upper and lower surfaces of the bonding layer, respectively.

2.3 The governing equations for debonded piezoelectric elements

When debonding occurs, the shear stress in the debonded part of the piezoelectric element will be zero. By solving the governing equations for the piezoelectric element and that for the elastic host medium, and satisfying the continuity conditions at all interfaces, the following governing equation for the entire system with interfacial debonding can be obtained,

$$\frac{e^a E_z}{E^a}\frac{\cos k^a y}{\cos k^a a} = -\frac{1}{\pi\mu^h}\int_0^\infty \left[\frac{\beta k^2 s}{(2s^2-k^2)^2-4s^2\alpha\beta}+\frac{\lambda_0}{2}\right]\left\{\int_{-a}^{-d}\tau(\xi)\sin[s(y-\xi)]\mathrm{d}\xi + \int_d^a \tau(\xi)\sin[s(y-\xi)]\mathrm{d}\xi\right\}\mathrm{d}s + \frac{\lambda_0}{2\pi\mu^h}\left[\int_{-a}^{-d}\frac{\tau(\xi)}{y-\xi}\mathrm{d}\xi + \int_d^a \frac{\tau(\xi)}{y-\xi}\mathrm{d}\xi\right] - \frac{h'}{\mu^b - i\omega\gamma^b}\frac{\mathrm{d}\tau(y)}{\mathrm{d}y},$$
$$-\frac{\sin[k^a(y+a)]}{E^a h\sin 2ak^a}\left\{\int_{-a}^{-d}\cos[k^a(\xi-a)]\tau(\xi)\mathrm{d}\xi + \int_d^a \cos[k^a(\xi-a)]\tau(\xi)\mathrm{d}\xi\right\}$$
$$+\frac{1}{E^a h}\left\{\int_{-a}^{-d}\cos[k^a(y-\xi)]\tau(\xi)\mathrm{d}\xi + \int_d^y \cos[k^a(y-\xi)]\tau(\xi)\mathrm{d}\xi\right\}, \quad d<y<a, \tag{5}$$

which represents the continuity condition across the adhesive layer. In addition, in the debonded part of the adhesive layer following continuity condition should be satisfied,

$$-\frac{1}{\pi\mu^h}\int_0^\infty \left[\frac{\beta k^2 s}{(2s^2-k^2)^2-4s^2\alpha\beta}+\frac{\lambda_0}{2}\right]\int_{-d}^{d}\left\{\int_{-a}^{-d}\tau(\xi)\sin[s(y-\xi)]\mathrm{d}\xi + \int_d^a \tau(\xi)\sin[s(y-\xi)]\mathrm{d}\xi\right\}\mathrm{d}y\mathrm{d}s + \frac{\lambda_0}{2\pi\mu^h}\int_{-d}^{d}\left[\int_{-a}^{-d}\frac{\tau(\xi)}{y-\xi}\mathrm{d}\xi + \int_d^a \frac{\tau(\xi)}{y-\xi}\mathrm{d}\xi\right]\mathrm{d}y$$
$$+\frac{h'}{\mu^b - i\omega\gamma^b}[\tau(-d)-\tau(d)] = \frac{2(\sigma_d + e^a E_z)\tan k^a d}{E^a k^a}. \tag{6}$$

from which the interfacial shear stress can be determined. In this equation, $\lambda_0=2(1-\nu^h)$, and

$$\alpha = \begin{cases} \sqrt{s^2-K^2} & |s|>K, \\ -i\sqrt{K^2-s^2} & |s|<K, \end{cases} \qquad \beta = \begin{cases} \sqrt{s^2-k^2} & |s|>k, \\ -i\sqrt{k^2-s^2} & |s|<k, \end{cases}$$

which are determined from the elastodynamic solution of the host medium. $K=\omega/c_L$, $k=\omega/c_T$ are two wave numbers with c_L and c_T being the longitudinal and transverse shear wave speed of the host medium.

2.4 The singular behaviour of the debonded piezoelectric elements

Interficial debonding forms interfacial cracks. In general, oscillating singularity will occur at the tips of the debonding. For the current piezoelectric element with a partially debonded layer, however, the well-known oscillating singularity disappears based on the model used and the corresponding governing equations, because the oscillating singularity occurs only at perfectly bonded interfaces.

3. Results and Discussion

The existence of adhesive layers could significantly affect the behaviour of the piezoelectric actuator/sensor [24-27]. The response of the piezoelectric element to an applied electric field

(actuator) or an incident wave (sensor) has been studied under different geometric and loading conditions to evaluate the effect of the bonding layer upon the load transfer between the actuator/sensor and the host medium. In the following discussion, only the magnitude of the physical stress is presented. The numerical calculation is conducted by solving the governing equations using Chebyshev polynomials expansion of the shear stress τ. The convergence of the solution has been carefully evaluated.

The piezoelectric material considered is piezoceramics with its material property being given in Table 1 [28]. The properties of the bonding layer [3] and the host medium [29] are given in Table 2. The mass densities of the actuator and the host medium are assumed to be 2,700 kg/m^3 [28].

Table 1. Piezoelectric properties

Elastic	c_{11}	c_{12}	c_{13}	c_{33}	c_{44}
(Pa)	13.9×10^{10}	6.78×10^{10}	7.43×10^{10}	11.5×10^{10}	2.56×10^{10}
Piezoelectric	e_{31}	e_{33}	e_{15}		
(C/m^2)	-5.2	15.1	12.7		
Dielectric	λ_{11}	λ_{33}			
(C/Vm)	6.45×10^{-9}	5.62×10^{-9}			

Table 2. Properties of the host and the bonding layer

Host medium	
Young's modulus E^h (Pa)	2.74×10^{10}
Poisson's ratio ν^h	0.3
Bonding layer	
Shear modulus μ^b (Pa)	1.0×10^9

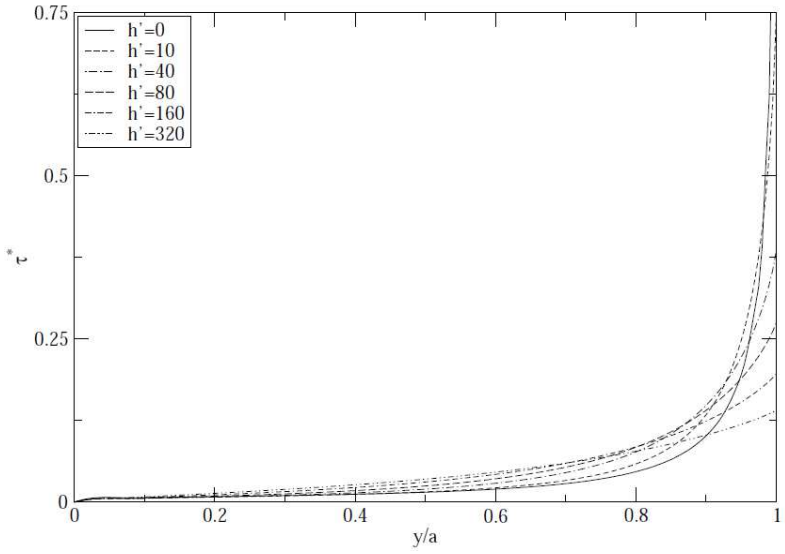

Figure 2 Shear stress distribution along the adhesive layer of an actuator

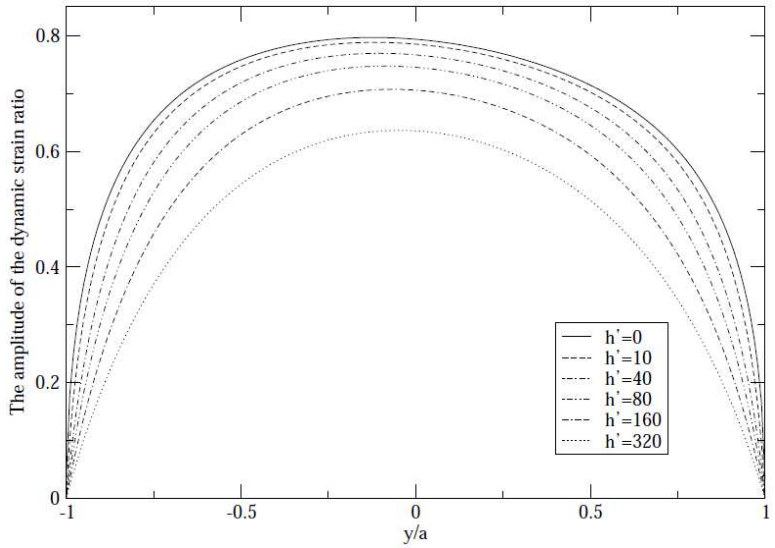

Figure 3 Axial strain distribution along a sensor

One major effect of the adhesive layer is that it reduces stress concentration at the end of an actuator. Figure 2 shows the shear stress distribution ($\tau=qE^aE_z$, $q=\pi E^h/(1-\nu^{h2})/E^a$) along an actuator with $a=1cm$ and $h=0.5mm$, for the case where the loading frequency is $ka=1.0$ and $\gamma_b = 0.0$ for different thicknesses of the bonding layer. Evaluating the six curves in this figure shows that, as the h' value increases from 0 to $320\mu m$, the stress concentration at the tip of the actuator, $y/a = 1.0$, decreases significantly. The adhesive layer also has a significant effect on the response of the piezoelectric element as a sensor. Figures 3 shows the amplitude of the normalized strain along the sensor caused by a normal incident wave for the case where $ka=1.0$ for different bonding layer thickness $0, 10, 40, 80, 160$ and $320\ \mu m$. Significant decrease of the strain with increasing bonding layer thickness is observed.

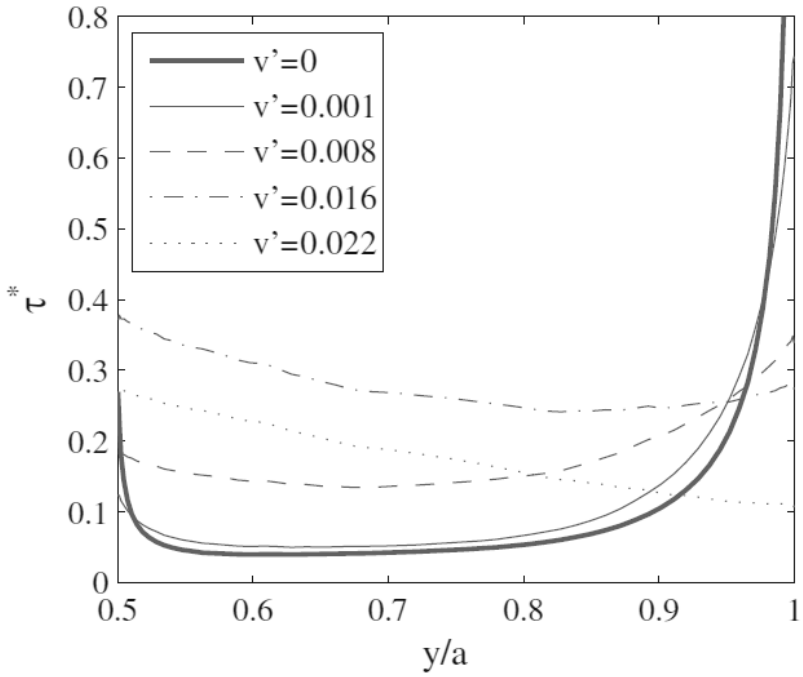

Figure 4 Shear stress distribution along a partially debonded adhesive layer of an actuator

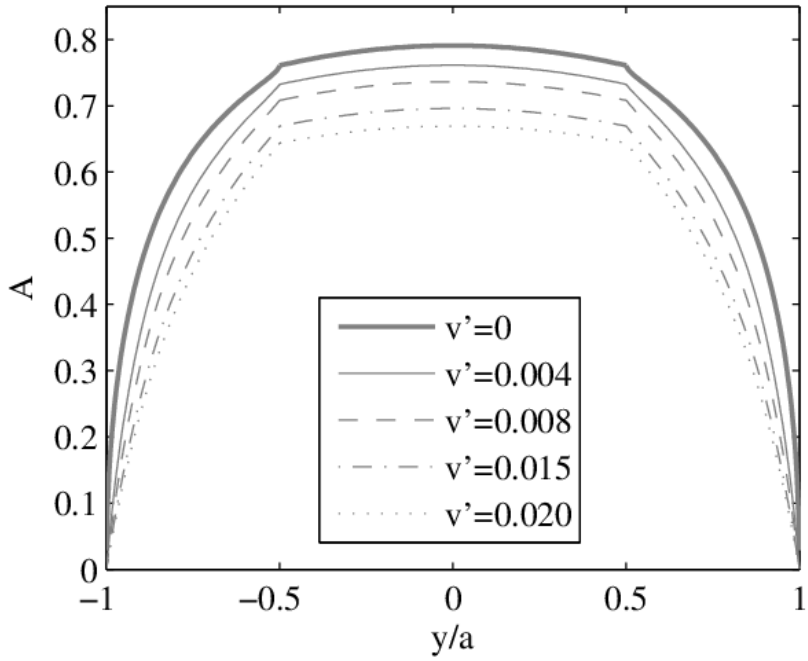

Figure 5 Axial strain distribution along a partially debonded sensor

When debonding occurs at the adhesive layer, the shear stress in the debonded region will disappear and the shear stress will be redistributed in the bonded region. Figure 4 shows the shear stress distribution in the bonded region of the adhesive layer for an actuator under the same geometric and loading conditions as that discussed in Figure 2, for the case where the debonding region is *-0.5a<y<0.5a,* for different thicknesses of the bonding layer (*v'=h'⁄a*). For very small layer thickness the shear stress shows square-root singularity at both the end of the actuator and the tip of the debonding. The existence of the adhesive layer will remove this singularity and generate stress concentration, which reduces with the increase of the layer thickness. Figure 5 shows the corresponding normalized axial strain distribution of a sensor in response to a normal incident wave. Significant decrease of the strain with increasing bonding layer thickness is observed. The adhesive layer also has a significant effect on the response of the piezoelectric element as a sensor. Figures 5 shows the amplitude of the normalized strain along the sensor caused by a normal incident wave for the case where *ka = 1.0* for different bonding layer thickness *0, 10, 40, 80, 160* and *320* μ*m*. It is observed that debonding (*-0.5a<y<0.5a*) significant decreases the strain level in the sensor bot only in the debonded region but also in the bonded parts of the sensor.

Acknowledgements

This research is supported by the Natural Sciences and Engineering Research Council of Canada.

References

[1] Gandhi, M.V., Thompson, B.S., Smart Materials and Structures. Chapman Hall, London, 1992.
[2] Boller, C., Next generation structural health monitoring and its integration into aircraft design. Int. J. Syst. Sci. **31** (2000), 1333–1349.
[3] Park, J.M., Kim, D.S., Han, S.B., Properties of interfacial adhesion for vibration controllability of composite materials as smart structures. Comput. Sci. Tech. **60** (2000), 1953–1963.
[4] Rabinovitch, O., Vinson, J.R., Adhesive layer effects in surface-mounted piezoelectric actuators. J. Intell. Mater. Syst. Struct. **13** (2000), 689–704.
[5] Lin, M.W., Rogers, C.A., Actuation response of a beam structure with induced strain actuators. Adapt. Struct. Mater. Syst. AD **35** (1993), 129–139.

[6] Wang, B.-T., Rogers,C.A., Laminate plate theory for spatially distributed induced strain actuators. J.Comput.Mater. **25**(1991), 433–452.
[7] Wang, J., Yang, J., Higher-order theories of piezoelectric plates and applications. Appl. Mech. Rev. **53**, (2000), 87–99.
[8] Wang, X.D., Meguid, S.A., On the electroelastic behaviour of a thin piezoelectric actuator attached to an infinite host structure, Int. J. Solids Struct. **37** (2000), 3231–3252.
[9] Zhang, J.Q., Zhang, B.N., Fan, J.H. A coupled electromechanical analysis of a piezoelectric layer bonded to an elastic substrate: Part I. Development of governing equations. Int. J. Solids Struct. **40** (2003), 6781–6797.
[10] Zhang, B.N., Zhang, J.Q., Fan, J.H., A coupled electromechanical analysis of a piezoelectric layer bonded to an elastic substrate: Part II. Numerical solution and applications. Int. J. Solids Struct. **40** (2003), 6612–6799.
[11]Choi, K.Y., Chang, F.K., Identification of foreign object impact in structures using distributed sensors. J. Intell. Mater. Syst. Struct. **5** (1994), 864–869.
[12] Giurgiutiu, V., Rogers, C.A., Modeling of the electro-mechanical (E/M) impedance response of a damaged composite beam. Adapt. Struct. Mater. Syst. **59** (1999), 39–46.
[13] Quinn, P., Palacios, L., Carman, G., Speyer, J., Health monitoring of structures using directional piezoelectrics. 1999 ASME Mechanics and Materials Conference, Blacksburg, VA, June 27–30, 1999.
[14] Lopes V. Jr., Park, G., Cudney, H., Inman, D., Smart structures health monitoring using artificial neural network. 2nd International Workshop of Structural Health Monitoring, Stanford University, 8–10 September, 1999.
[15] Giurgiutiu, V., Zagrai, A., Bao, J., Embedded active sensors for in-situ structural health monitoring of thin-wall structures. ASME J. Press. Vess. Technol. **124** (2002), 134–145.
[16] Wang, X.D., Coupled electromechanical behavior of piezoelectric actuators in smart structures. J. Intell. Mater. Syst. Struct. **10** (1999), 232–241.
[17] Wang, X.D., Huang, G.L., Wave propagation in electromechanical structures: induced by surface bonded piezoelectric actuators. J. Intell. Mater. Syst. Struct. **12** (2001), 105–115.
[18] Wang, X.D., Huang, G.L., Wave propagation generated by piezoelectric actuators attached to elastic substrates. Acta Mech. **183** (2006), 155–176.
[19] Sun, D.C., Tong, L., Atluri, S.N., Effects of piezoelectric sensor/sensor debonding on vibration control of smart beams. Int. J. Solids Struct. **38** (2001), 9033–9051.
[20] Tong, L., Sun, D.C., Atluri, S.N., Sensing and actuating behaviors of piezoelectric layers with debonding in smart beams. Smart Mater. Struct. **10** (2001), 713–723.
[21] Seeley, C.E., Chattopadhyay, A., Modeling delaminations in smart composite laminates. In: Proceedings of the 37th AIAA/ASME/ASCE/AHS/ASC Structures, Structural Dynamics and Materials Conference, Salt Lake City, UT, 18–19 April, 1996, 109–119.
[22] Kim, S.J., Jones, J.D., Effects of piezo-actuator delamination on the performance of active noise and vibration control system. J. Intell. Mater. Syst. Struct. **7** (1996), 668–676.
[23] Tylikowski, A., Effects of piezoactuator delamination on the transfer functions of vibration control systems. Int. J. Solids Struct. **38** (2001), 2189–2202.
[24] Han, L.,Wang, X.D., Zuo, M., The dynamic behavior of a surface-bonded piezoelectric actuator with a bonding layer. Acta Mech. (2008).
[25] Han, L., Wang, X.D., Sun, Y., The effect of bonding layer properties on the dynamic behaviour of surface-bonded piezoelectric sensors. Int. J. Solids Struct. **45** (2008), 5599-5612.
[26] Jin, C., Wang, X.D., The effect of adhesive layers on the dynamic behavior of surface-bonded piezoelectric sensors with debonding, J. Intell. Mater. Syst. Struct. **22** (2011), 655-670.
[27] Jin, C., Wang, X.D., Zuo, M.J., The dynamic behaviour of surface-bonded piezoelectric actuators with debonded adhesive layers. Acta Mech. **211** (2010), 215–235.
[28] Park, Y.E., Crack extension force in a piezoelectric material. ASME J. Appl. Mech. **57** (1990), 647–653.
[29] Wang, X.D., Huang, G.L., The coupled dynamic behaviour of piezoelectric sensors bonded to elastic media. J. Intell. Mater. Syst. Struct. **17** (2006), 883–894.

Modeling of isothermal stress cycling degradation of shape memory alloys using non-constant material parameters

Xiaoyong ZHANG[1,*], Xiaojun YAN[2], Huimin XIE[1]

[1] AML, School of Aerospace, Tsinghua University, Beijing, 100084, China.
[2] School of Energy and Power Engineering, Beihang University, Beijing 100191, China.
* Corresponding author: zhangyong9119@163.com

Abstract Experimental investigations on superelastic shape memory alloy (SMA) wires subjected to isothermal stress cycling show significant performance degradations, including the accumulation of the plastic strain, the reduction of the maximum transformation strain and the evolution of the transformation temperatures. The cyclic degradation of SMAs must be carefully studied and understood when the alloys are used in the SMA based actuators and vibration isolators. Motivated by these issues, the present work aims to develop a comprehensive approach for the cyclic behavior of SMAs taking into account degradations caused by isothermal stress cycling in the superelastic regime. The new cyclic constitutive model is constructed based on the thermodynamic frame proposed by Boyd and Lagoudas, and evolution laws for the plastic strain as well as non-constant material parameters including the maximum transformation strain and four transformation temperatures are also constructed. Finally, numerical simulations based on the proposed constitutive model are also performed in our work, and good correlations are observed.

Keywords Shape Memory Alloys, Cyclic Degradation, Constitutive Model, Non-constant Material Parameters

1. Introduction

Shape memory alloys (SMAs) exhibit many special properties due to their thermo-elastic martensite transformation, such as shape memory effect, superelasticity (or pseudoelasticity) and damping [1]. Among these thermal-mechanical behaviors, superelasticity is particularly interesting. Superelastic behavior is revealed when the SMA material is mechanically loading under a surrounding temperature higher than the austenite finish temperature. After unloading, SMA material can recover its initial shape and the stress–strain response shows a typical hysteretic loop. This unique superelasticity promotes SMAs to be used in medical applications, such as arterial stents, medical guidewires and catheters [2]. Also, the typical hysteretic loop in the stress–strain space reveals that SMA is a kind of energy dissipation material. Taken the advantage of this property, SMAs are also used in vibration isolation applications, such as seismic isolation and mechanical vibration isolation.

Motivated by these applications, many constitutive models were developed to simulate the thermal-mechanical behavior of SMAs in the superelastic regime over the last thirty years [3-10]. However, among these investigations, very few studies consider the performance degradation of SMAs under isothermal stress cycling, which is more pertinent when SMAs are used in vibration isolation applications [11-15]. Until recently, Kan and Kang introduced the cumulated martensite volume fraction as an internal variable to account for the evolution of residual induced martensite and transformation induced plastic strain during stress-controlled cyclic loading [16]. Zaki and Moumni used internal stress, residual strain and cumulated martensite volume fraction as internal variables to simulate the behavior of SMA in the case of cyclic superelasticity [17]. Saint-Sulpice et al. introduced the residual martensite volume fraction to account for the evolution of residual strain and transformation surface during isothermal stress cyclic loading [18].

The aforementioned models usually consider the plastic strain accumulation and/or the transformation surface evolution (which is associated with the evolution of maximum

transformation strain). However, the transformation temperatures of the alloy were demonstrated to change as a function of the thermal/stress cycling number [19-21]. Moreover, the evolution of transformation temperatures can significantly affect the critical stresses for the onset and finish of phase transformations and the area of the stress–strain hysteretic loop.

Therefore, this paper aims to develop a constitutive model for SMAs taking into account the isothermal stress cycling degradation, including the accumulation of plastic strain, the evolution of the maximum transformation strain and four transformation temperatures. The new constitutive model is constructed based on the thermodynamic frame proposed by Boyd and Lagoudas [22, 23]. The organization of the paper is as follows: Section 2 presents the observation of cyclic degradation in SMAs through the isothermal stress cycling experiment. The 1-D constitutive model considering the cyclic evolution of the plastic strain, the maximum transformation strain and transformation temperatures is presented in Section 3, while in Section 4, numerical examples are presented and discussed. The conclusions and future work are summarized in the final section.

To simplify the presentation, we denote the two phases related with superelasticity by A and M^d for austenite and detwinned martensite, respectively. The forward and reverse phase transformations are denoted by $A \rightarrow M^d$ and $M^d \rightarrow A$ for austenite to detwinned martensite and detwinned martensite to austenite, respectively.

2. Observation of cyclic degradation

We performed an isothermal stress cycling experiment to a NiTi wire, the wire was repeatedly stressed up to 900 MPa under 28 ^oC. The stress–strain response of the wire is shown in Fig. 1, a simplified diagram which features the evolution of plastic strain, maximum transformation strain and transformation temperatures is shown in Fig. 3, and typical features of cyclic degradation are outlined as follows:

1) The isothermal stress cycling of the NiTi alloy presents an apparent cyclic accumulation of the plastic strain. As shown in Fig. 3(a), after the first cycle, the NiTi wire cannot recover to its original length, and a plastic strain, donated as ε^{p1}, is produced. Similarly, after the second cycle, the total cumulated plastic strain is ε^{p2}, and after the *n*th cycle, the accumulation of the plastic strain becomes ε^{pn}. Furthermore, the plastic strain evolves as an exponential function of cycle number before stabilizing, as shown in Fig. 1 and Fig. 2.

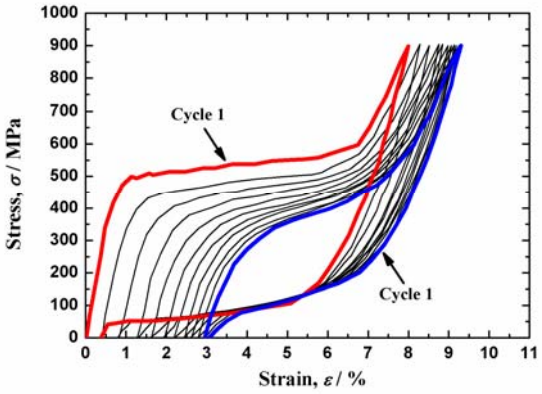

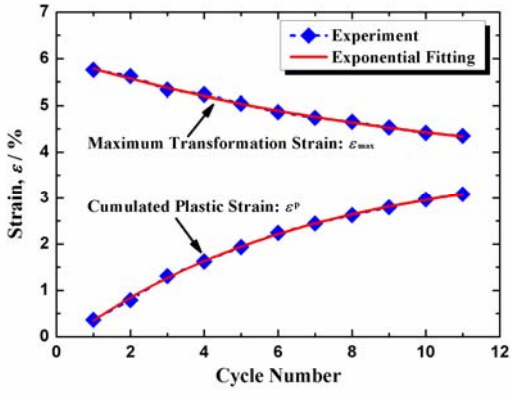

Figure 1. Experimental results of isothermal stress cyclic loading on NiTi wire
Figure 2. Evolution of the maximum transformation strain ε_{max} and plastic strain ε^p during cyclic loading, the experimental results are compared with the exponential fitting results

2) The maximum transformation strain (also referred to as the saturation recovery strain) changes from cycle to cycle. As shown in Fig. 3(a), the maximum transformation strain for cycle 1 is ε_{max1}, while for cycle 2, it reduces to ε_{max2}. Similarly, after the nth cycle, the maximum transformation strain will reduce to ε_{maxn}. Also, as shown in Fig. 2, ε_{max} is found to increase exponentially with respect to the cycle number up to an asymptotic value.

3) The four transformation temperatures change as a function of the cycle number. As shown in Fig. 3 (b), during the first cycle, the four transformation temperatures are M_{s1}, M_{f1}, A_{s1} and A_{f1}, respectively. While in the second cycle, the four temperatures change to M_{s2}, M_{f2}, A_{s2} and A_{f2}. So we can deduce that the four temperatures will change as the cycle number increases. The same phenomenon was reported in literatures [19-21].

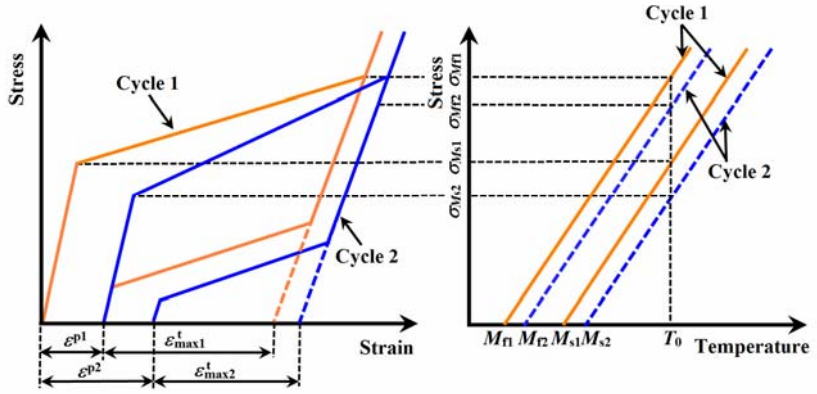

(a) strain evolution (b) transformation temperatures evolution

Figure 3. The evolution of (a): plastic strain, maximum transformation strain in the stress–strain space and (b): transformation temperatures in the stress–temperature space under isothermal stress cycling. For clarity, the evolution of austenite start and finish transformation temperatures is not shown in the stress–temperature space

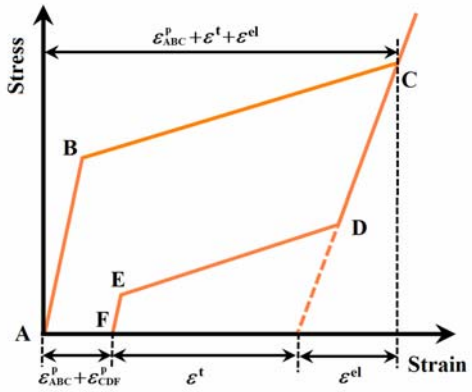

Figure 4. Schematic explanation for the evolution of plastic strain

In order to investigate when the evolution of plastic strain occurs during the whole transformation process, the stress vs. strain response of a typical cycle is presented in Fig. 4. We assume that the plastic and transformation strains produced in A→M^{d} (corresponding loading path is ABC) are separately ε^{p}_{ABC} and ε^{t}, and the elastic strain of point C is ε^{el}. Following these assumptions, the total strain of point C (shown in Fig. 4) becomes:

$$\varepsilon_{C} = \varepsilon^{el} + \varepsilon^{p}_{ABC} + \varepsilon^{t} \tag{1}$$

Assume that the plastic strain for M^{d}→A (corresponding loading path is CDEF) is ε^{p}_{CDF}. Therefore the plastic strain cumulated during the forward and reverse transformations (corresponding loading

path is ACF) is $\varepsilon^{p}_{ABC}+\varepsilon^{p}_{CDF}$. Since the transformation strain can be fully recovered after the $M^{d}\rightarrow A$ transformation, the reduction of the transformation strain during $M^{d}\rightarrow A$ is ε^{t} (corresponding loading path is CDEF, as shown in Fig. 4). Consequently, the total strain of point C can be expressed as:

$$\varepsilon_{D} = \varepsilon^{el} + \varepsilon^{p}_{ABC} + \varepsilon^{p}_{CDF} + \varepsilon^{t} \tag{2}$$

From Eqs. (1) and (2), we can deduce that $\varepsilon^{p}_{CDF}=0$. Following the derivation above, we can assume that the accumulation of plastic strain ε^{p} only occurs during $A\rightarrow M^{d}$.

Consequently, to model the cyclic degradation of shape memory alloys under isothermal stress cycling, the evolution of the plastic strain and maximum transformation strain in $A\rightarrow M^{d}$ and the evolution of transformation temperatures in both forward and reverse transformations must be considered, also related evolution laws should be established.

3. Constitutive model

A constitutive model taking into account the cyclic degradation due to isothermal stress cycling is proposed. It is constructed in the generalized plasticity framework which was employed by Boyd and Lagoudas [22, 23] to simulate the thermo-mechanical behavior of SMA. The construction of the constitutive model is stated in details as follows.

3.1. Strain decomposing and internal variables

3.1.1. Strain decomposing

With the infinitesimal strain assumption, the total strain ε is decomposed into an elastic strain ε^{el} and an inelastic strain ε^{in}:

$$\varepsilon = \varepsilon^{e} + \varepsilon^{in} \tag{3}$$

In which, the inelastic strain ε^{in} can be further decomposed into a thermal expansion strain ε^{th}, a transformation strain ε^{t}, and a plastic strain ε^{p}:

$$\varepsilon^{in} = \varepsilon^{th} + \varepsilon^{t} + \varepsilon^{p} \tag{4}$$

The thermal expansion strain ε^{th} is neglected because the value is much smaller than the others, so the following expression can be got:

$$\varepsilon = \varepsilon^{el} + \varepsilon^{t} + \varepsilon^{p} \tag{5}$$

3.1.2. Internal variables definition

As shown in Eq. (5), two internal variables are needed to account for the evolution of the transformation strain ε^{t} and the plastic strain ε^{p}. Generally, the martensite volume fraction ξ is used as an internal variable to related with ε^{t} [24]:

$$\varepsilon^{t} = \varepsilon_{max}\xi \tag{6}$$

Where ε_{max} is the maximum transformation strain. Following the observation of cyclic degradation stated in Section 2, the plastic strain ε^{p} and the maximum transformation strain ε_{max} change as a function of the cycle number. In order to account for these evolution processes, the cumulated martensite volume fraction ξ^{c} is defined:

$$\xi^{c} = \xi^{ac} + \xi^{mc} \tag{7}$$

Where ξ^{ac} and ξ^{mc} represent the cumulated martensite volume fractions in A→M^{d} and M^{d}→A, respectively. Following these definitions, ξ^{ac} and ξ^{mc} can be expressed as follows:

$$\xi^{ac} = \int \left| \dot{\xi}^{A\to M^{d}} \right| dt,\ \xi^{mc} = \int \left| \dot{\xi}^{M^{d}\to A} \right| dt \tag{8}$$

In which, t is a kinematic time. $\dot{\xi}^{A\to M^{d}}$ and $\dot{\xi}^{M^{d}\to A}$ denote the martensite production rate during A→M^{d} and M^{d}→A.

3.2. Free energy and transformation hardening function

The total Helmoltz free energy ψ for polycrystalline SMAs is given based on Boyd and Lagoudas's work:

$$\psi = E\left(\varepsilon - \varepsilon^{t} - \varepsilon^{p}\right)^{2} \Big/ 2\rho + c\left[\left(T - T_{0}\right) - T\ln\left(T/T_{0}\right)\right] + u_{0} - \eta_{0}T + f(\xi, \dot{\xi}) \tag{9}$$

Where E, c, ρ, η_0 and u_0 are the Young modulus, effective specific heat, mass density, effective specific entropy, and effective specific internal energy at the reference state, respectively. The symbols T and T_0 denote the temperature and reference temperature, respectively. The terms $E(\varepsilon-\varepsilon^{t}-\varepsilon^{p})^{2}/2\rho$, $c[(T-T_0)-T\ln(T/T_0)]$ and $u_0-\eta_0 T+ f(\xi,\dot{\xi})$ represent the elastic strain energy, thermal energy, and the energy related to transformations, respectively.

The effective specific heat c hardly varies during phase transformations, so it is assumed to be constant. However, other material properties in Eq. (9) are assumed to vary with the martensite volume fraction as:

$$E\left(\xi\right) = E^{A} + \xi\left(E^{M} - E^{A}\right) = E^{A} + \xi\Delta E \tag{10}$$

$$\eta_{0}\left(\xi\right) = \eta_{0}{}^{A} + \xi\left(\eta_{0}{}^{M} - \eta_{0}{}^{A}\right) = \eta_{0}{}^{A} + \xi\Delta\eta_{0} \tag{11}$$

$$u_{0}\left(\xi\right) = u_{0}{}^{A} + \xi\left(u_{0}{}^{M} - u_{0}{}^{A}\right) = u_{0}{}^{A} + \xi\Delta u_{0} \tag{12}$$

Where the superscripts A and M represent the austenite and martensite phases, respectively. The symbol Δ denotes the difference of the corresponding material parameter between the martensite and austenite phases.

In particular, the term $f(\xi,\dot{\xi})$ is the transformation hardening function which is used to account for the interactions between the austenite phase and the martensite phase. In this work, a nonlinear transformation hardening model is established:

$$f(\xi,\dot{\xi}) = \left\{a\left[1-\mathrm{sgn}\left(\dot{\xi}\right)\right] + b\left[1+\mathrm{sgn}\left(\dot{\xi}\right)\right]\right\}\left[\left(\frac{\xi}{2}\right)^{2} + \frac{\left(\xi - 1/2\right)^{4}}{2} + \frac{\xi}{4}\right] \tag{13}$$

Where a and b are constitutive model parameters for transformation hardening and they are related to material constants. The function sgn(·) is a signum function of a real number m, it is defined as follow:

$$\mathrm{sgn}(m) = \begin{cases} 1 & \text{if } m > 0 \\ 0 & \text{if } m = 0 \\ -1 & \text{if } m < 0 \end{cases} \tag{14}$$

3.3. Thermodynamic force and constitutive relation

Following the formalism of Truesdell and Noll [25], the Helmoltz free energy ψ and the internal energy u are substituted into the first and second law of thermodynamics to derive thermodynamic constraints on the state of the system resulting in the following constitutive relation:

$$\sigma = \rho \frac{\partial \psi}{\partial \varepsilon} = E\left(\varepsilon - \varepsilon^{\mathrm{t}} - \varepsilon^{\mathrm{p}}\right) \tag{15}$$

Similarly, thermodynamic force X, which is conjugate to the martensite volume fraction ξ, is given:

$$X = -\rho \frac{\partial \psi}{\partial \xi} = -\left[\frac{1}{2}\Delta E\left(\varepsilon - \varepsilon^{\mathrm{t}} - \varepsilon^{\mathrm{p}}\right)^2 - \sigma \frac{d\varepsilon^{\mathrm{t}}}{d\xi} + \rho\left(\Delta u_0 - \Delta \eta_0 T\right) + \frac{df}{d\xi}\right] \tag{16}$$

As assumed in Section 2, the accumulation of plastic strain ε^{p} and the reduction of maximum transformation strain $\varepsilon^{\mathrm{t}}_{\max}$ only occur during A→M$^{\mathrm{d}}$. Therefore, the thermodynamic force Q, which accounts for the evolution of ε^{p} and $\varepsilon^{\mathrm{t}}_{\max}$, is conjugate to the cumulated martensite volume fraction ξ^{ac}. Similar to thermodynamic force X, it can be expressed as:

$$Q = -\rho \frac{\partial \psi}{\partial \xi^{\mathrm{ac}}} = \rho\left(\frac{d\varepsilon^{\mathrm{p}}}{d\xi^{\mathrm{ac}}} + \frac{d\varepsilon^{\mathrm{t}}}{d\xi^{\mathrm{ac}}}\right) \tag{17}$$

3.4. Transformation functions and Kuhn-Tucker inequalities

Borrowed from yield functions in the classical theory of plasticity, transformation functions associated with A→M$^{\mathrm{d}}$ and M$^{\mathrm{d}}$→A are defined as:

$$F^{+} = X + Q - R^{+} \quad \text{when } \dot{\xi} > 0 \quad \text{For the phase transformation: A}\rightarrow\text{M}^{\mathrm{d}} \tag{18}$$

$$F^{-} = -X + Q - R^{-} \quad \text{when } \dot{\xi} < 0 \quad \text{For the phase transformation: M}^{\mathrm{d}}\rightarrow\text{A} \tag{19}$$

Where the constitutive model parameters R^{+} and R^{-} are the radius of the respective transformation domains.

Constraints on the evolution of the martensite volume fraction for the forward and reverse phase transformations are expressed in terms of the Kuhn-Tucker inequalities:

$$\begin{cases} \dot{\xi} \geq 0 \quad F^{+} \leq 0 \quad \dot{\xi} F^{+} = 0 & \text{For the phase transformation: A} \rightarrow \text{M}^{\mathrm{d}} \\ \dot{\xi} \geq 0 \quad F^{-} \leq 0 \quad \dot{\xi} F^{-} = 0 & \text{For the phase transformation: M}^{\mathrm{d}} \rightarrow \text{A} \end{cases} \tag{20}$$

3.5. Evolution laws

Following Eq. (6), the evolution law for the transformation strain ε^{t} can be got:

$$\dot{\varepsilon} = \varepsilon_{\max} \dot{\xi} \tag{21}$$

It is concluded from the experimental results that the material parameter: maximum transformation strain $\varepsilon_{\max}$, varies as an exponential function of the cycle number, as shown in Fig. 2. Furthermore, as explained in Section 3.1.2, $\varepsilon_{\max}$ is assumed to vary only in A→M$^{\mathrm{d}}$, which implies that $\varepsilon_{\max}$ changes as an exponential function of ξ^{ac}. Therefore, from a theoretical point of view, a non-constant material parameter $\varepsilon_{\max}$ can be defined using the evolution law:

$$\dot{\varepsilon}_{\max} = m6\varepsilon^{t}_{\max} e^{-\xi^{ac} m6} \dot{\xi}^{c} \tag{22}$$

Analogous to $\varepsilon_{\max}$, evolution laws of $\varepsilon^{p}_{\max}$ and four material parameters: M_s, M_f, A_s and A_f are given:

$$\dot{\varepsilon}^{p}_{\max} = m5\varepsilon^{p}_{\max} e^{-\xi^{ac} m5} \dot{\xi}^{c} \tag{23}$$

$$M_s = M_{s0} - M_{s\max}\left(1 - e^{-\xi^{c} m1}\right) \tag{24}$$

$$M_f = M_{f0} - M_{f\max}\left(1 - e^{-\xi^{c} m2}\right) \tag{25}$$

$$A_s = A_{s0} - A_{s\max}\left(1 - e^{-\xi^{c} m3}\right) \tag{26}$$

$$A_f = A_{f0} - A_{f\max}\left(1 - e^{-\xi^{c} m4}\right) \tag{27}$$

Where $\varepsilon^{t}_{\max}$, $\varepsilon^{p}_{\max}$, M_{fmax}, M_{smax}, A_{fmax} and A_{smax} denote saturation values of $\varepsilon_{\max}$, ε_p, M_f, M_s, A_f and A_s due to cyclic loading, which can be got through isothermal stress cycling experiments. The variables $m1$~$m6$ can be obtained from the experimental curves by nonlinear fitting method.

So far, the constitutive model of SMAs taking into account the function degradation caused by isothermal stress cyclic loading has been fully established. In the following section, numerical simulations will be performed to verify the proposed model.

4. Simulated results and discussions

To show the model's capability of simulating the macroscopic behaviour of SMA material under isothermal stress cycling, we performed a cyclic tensile test at 5.5% strain amplitude under 27.5 ^{o}C for a SMA wire. Fig. 5 illustrates cyclic stress vs. strain response of the SMA wire for 10 cycles. Numerical simulations are obtained using the constitutive model proposed in this work, and the related material parameters are shown in Table 1. The simulated cyclic stress vs. strain response is shown in Fig. 6. From Fig. 5 and Fig. 6, it may be noticed that the model is able to simulate correctly the main characteristics of the isothermal stress cyclic response of a SMA wire. In particular, the stress vs. strain curves for the 1st, 4th and 10th cycles are shown in Fig. 7 and good agreements between experimental and simulated results are observed.

Table 1. Material parameters used in the constitutive model.

General material parameters	Values	Cyclic material parameters	Values
E^{A}	42200 MPa	M_{smax}	21 K
E^{M}	23500 MPa	M_{fmax}	1.5 K
$\Delta\eta_0$	– 17.77 J /(kg·K)	A_{smax}	0 K
Δu_0	– 20 J /kg	A_{fmax}	0 K
c	4×10^{6} J /(kg·K)	$\varepsilon^{t}_{\max}$	0.0121
ρ	6.5×10^{-9} kg/m^3	$\varepsilon^{p}_{\max}$	0.0141
$A_s(0)$	274K	$m1$	0.14
$A_f(0)$	300 K	$m2$	0.98
$M_s(0)$	270 K	$m3$	0.081
$M_f(0)$	232 K	$m4$	0.05
C_A	9.4 MPa/K	$m5$	0.271
C_M	6.7 MPa/K	$m6$	0.23
$\varepsilon_{\max}(0)$	0.0348		

In order to further investigate the ability of the model to predict the evolution of $\varepsilon_{\max}$, ε^{p} and four

transformation temperatures, the corresponding experimental results are compared with simulated results, as shown in Figs. 8 and 9. It can be seen from these figures that for the evolution of ε_{max}, ε^{p}, M_s, M_f and A_f, the experimental and simulated results are close to each other. However, for the evolution of A_s, a certain disagreement occurs, which can perhaps be explained that A_s indeed does not evolve exponentially with respect to the cycle number.

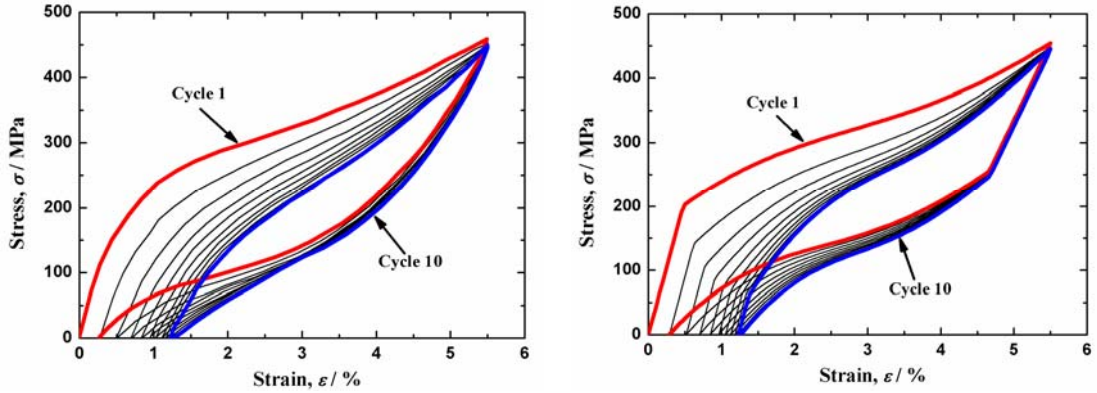

Figure 5. Experimental results of the SMA wire. Isothermal stress cycling at 5.5% strain amplitude under 27.5 °C for 10 cycles.

Figure 6. Simulated cyclic stress vs. strain curves for 10 cycles using the proposed constitutive model.

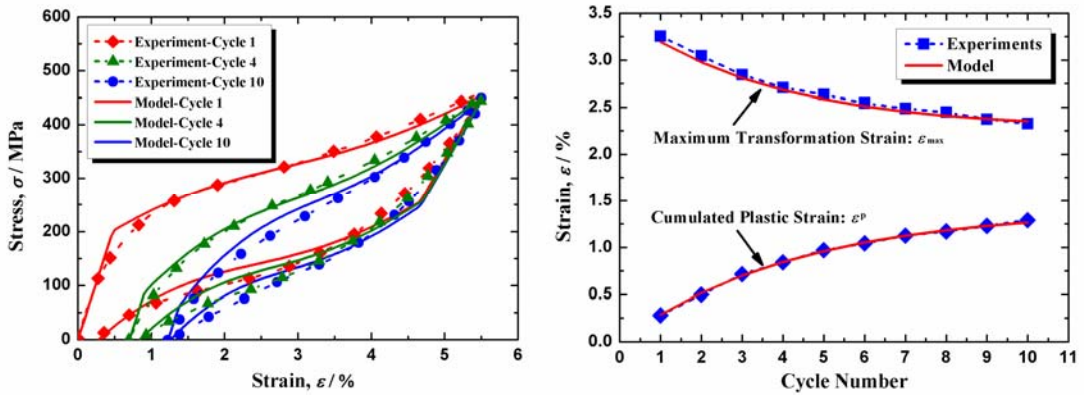

Figure 7. Simulation vs. isothermal stress cyclic loading experimental results for cycle 1, cycle 4 and cycle 10.

Figure8. A comparison of the evolution of plastic strain (ε^{p}) and maximum transformation strain (ε_{max}) between experimental results and model simulations.

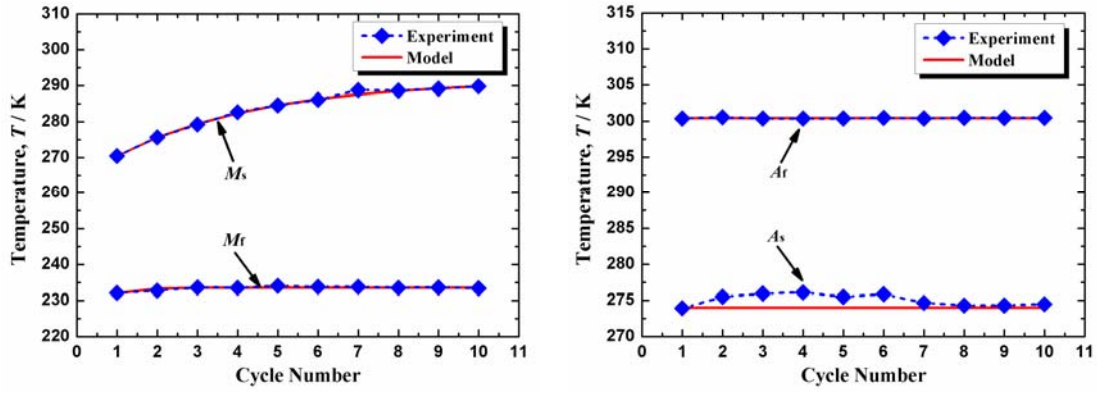

(a) (b)

Figure 9. A comparison of evolution of four transformation temperatures between experimental results and model simulations: (a) M_s and M_f and (b) A_s and A_f.

5. Conclusions and future work

A new 1-D phenomenological model of SMA taking into account the evolution of the plastic strain, maximum transformation strain and transformation temperatures during isothermal stress cycling was introduced in this paper. Since different phase transformation has different influence in the cyclic behaviour, the cumulated martensite volume fraction ξ^{c} was decomposed into ξ^{ac} and ξ^{mc} to account for cyclic effects during corresponding transformation processes. Non-constant material parameters including maximum transformation strain and four transformation temperatures are used. Evolution laws for the non-constant material parameters and plastic strain were established to depict the evolution of maximum transformation strain, transformation temperatures and plastic strain under cyclic loading. Experimental verifications were given and the results showed that the model was able to quantitatively capture the effect of isothermal stress cyclic loading. However, the model cannot simulate the evolution of A_s correctly, which maybe attribute to that A_s actually evolves with a non-experimental function. As a result, future work will introduce a new evolution law for A_s based on experimental studies.

Acknowledgements

The authors are grateful to the financial supported by the National Basic Research Program of China ("973" Project) (Grant No.2010CB631005, 2011CB606105), the National Natural Science Foundation of China (Grant Nos. 90916010, 11172151, 11232008, 11272025) Specialized Research Fund for the Doctoral Program of Higher Education (Grant No.20090002110048), Tsinghua University Initiative Scientific Research Program.

References

[1] K. Otsuka, C.M. Wayman, Shape memory materials, Cambridge Univ Pr, 1999.
[2] N.B. Morgan, Medical shape memory alloy applications - The market and its products. Mater. Sci. Eng. A, 378 (2004) 16-23.
[3] F. Falk, Model free energy, mechanics and thermodynamics of shape memory alloys. Acta Metall., 28 (1980) 1773-1780.
[4] K. Tanaka, Thermomechanical sketch of shape memory effect: one-dimensional tensile behavior. Res. Mech., 18 (1986) 251-263.
[5] Q.P. Sun, K.C. Hwang, Micromechanics modelling for the constitutive behavior of polycrystalline shape memory alloys. II. Study of the individual phenomena. J. Mech. Phys. Solids, 41 (1993) 19-33.
[6] Q.P. Sun, K.C. Hwang, Micromechanics modelling for the constitutive behavior of polycrystalline shape memory alloys. I. Derivation of general relations. J. Mech. Phys. Solids, 41 (1993) 1-17.
[7] D.C. Lagoudas, Z. Bo, M.A. Qidwai, Unified thermodynamic constitutive model for SMA and finite element analysis of active metal matrix composites. Mech. Compos. Mate.r Struct., 3 (1996) 153-179.
[8] F. Auricchio, R.L. Taylor, Shape-memory alloys: Modelling and numerical simulations of the finite-strain superelastic behavior. Comput. Methods Appl. Mech. Eng., 143 (1997) 175-194.
[9] X.W. Du, G. Sun, S.S. Sun, Piecewise linear constitutive relation for pseudo-elasticity of shape memory alloy (SMA). Mater. Sci. Eng. A, 393 (2005) 332-337.
[10] S. Reese, D. Christ, Finite deformation pseudo-elasticity of shape memory alloys -

Constitutive modelling and finite element implementation. Int. J. Plast., 24 (2008) 455-482.

[11] C. Lexcellent, G. Bourbon, Thermodynamical model of cyclic behaviour of Ti-Ni and Cu-Zn-Al shape memory alloys under isothermal undulated tensile tests. Mech. Mater., 24 (1996) 59-73.

[12] R. Abeyaratne, S.J. Kim, Cyclic effects in shape-memory alloys: A one-dimensional continuum model. Int. J. Solids Struct., 34 (1997) 3273-3289.

[13] F. Auricchio, E. Sacco, Thermo-mechanical modelling of a superelastic shape-memory wire under cyclic stretching-bending loadings. Int. J. Solids Struct., 38 (2001) 6123-6145.

[14] K. Tanaka, F. Nishimura, T. Hayashi, H. Tobushi, C. Lexcellent, Phenomenological analysis on subloops and cyclic behavior in shape memory alloys under mechanical and/or thermal loads. Mech. Mater., 19 (1995) 281-292.

[15]X. Feng, Q. Sun, Shakedown analysis of shape memory alloy structures. Int. J. Plast., 23 (2007) 183-206.

[16] Q. Kan, G. Kang, Constitutive model for uniaxial transformation ratchetting of super-elastic NiTi shape memory alloy at room temperature. Int. J. Plast., 26 (2010) 441-465.

[17] W. Zaki, Z. Moumni, A 3D model of the cyclic thermomechanical behavior of shape memory alloys. J. Mech. Phys. Solids, 55 (2007) 2427-2454.

[18] L. Saint-Sulpice, S. Arbab-Chirani, S. Calloch, Thermomechanical cyclic behavior modeling of Cu-Al-Be SMA materials and structures. Int. J. Solids Struct., 49 (2012) 1088-1102.

[19] M.F.X. Wagner, S.R. Dey, H. Gugel, J. Frenzel, C. Somsen, G. Eggeler, Effect of low-temperature precipitation on the transformation characteristics of Ni-rich NiTi shape memory alloys during thermal cycling. Intermet., 18 (2010) 1172-1179.

[20] Q. Hu, W. Jin, X.P. Liu, M.Z. Cao, S.X. Li, The transformation behavior and the shape memory effect due to cyclic stress/strain for Ti-49.6Ni alloy. Mater. Lett., 54 (2002) 114-119.

[21] D.A. Hebda, S.R. White, Effect of training conditions and extended thermal cycling on nitinol two-way shape memory behavior. Smart Mater. Struct., 4 (1995) 298-304.

[22] J. Boyd, A thermodynamical constitutive model for shape memory materials. Part I. The monolithic shape memory alloy. Int. J. Plast., 12 (1996) 805-842.

[23] J. Boyd, A thermodynamical constitutive model for shape memory materials. Part II. The SMA composite material. Int. J. Plast., 12 (1996) 843-873.

[24] P. Vacher, C. Lexcellent, Study of pseudoelastic behaviour of polycrystalline shape memory alloys by resistivity measurements and acoustic emission. Proceedings of the 6th International Conference on Mechanical Behaviour of Materials, 07/29 - 08/ - 2/91 (Kyoto, Jpn, 1992).

[25] C. Truesdell, W. Noll, S.S. Antman, The non-linear field theories of mechanics, Springer Verlag, 2004.

Pre-fracture zone model on magnetoelectrically permeable interface crack between two dissimilar magnetoelectroelastic materials

Peng MA[1], Wenjie Feng[2,*], Ray Kai Leung Su[1]

[1] Department of Civil Engineering, The University of Hong Kong, PR China
[2] Department of Engineering Mechanics, Shijiazhuang Tiedao University, Shijiazhuang 050043, PR China
* Corresponding author: wjfeng9999@yahoo.com (W.J. Feng)

Abstract A plane strain problem for two magnetoelectroelastic (MEE) half-planes adhered by a thin isotropic interlayer is considered. A novel crack model, i.e., a magnetoelectrically permeable interface crack with pre-fracture zones is introduced for MEE bimaterial system. The stresses in pre-fracture zones and the lengths of pre-fracture zones are unknown, which are determined by solving the corresponding Hilbert problem and solving nonlinear equations introduced by yielding condition on the pre-fracture zones. Some particular cases are further analyzed and numerically discussed. In the suggested model, any singularities connected with the crack are eliminated, and the results presented in this paper should have potential applications to the design of multilayered MEE structures and devices.

Keywords Pre-fracture zone, Interface crack, Magnetoelectrically permeable, Magnetoelectroelastic plane

1. Introduction

Magnetoelectroelastic (MEE) materials have been widely used in electronics industry. In the design of MEE structures, it is important to take into account the defects/imperfections, such as cracks, which are often pre-existing or are generated by external loads during the service life. Therefore, in recent years, research on fracture mechanics of MEE materials has drawn a lot of interest, and lots of achievements have been made for two-dimensional (2-D) internal crack problems [1-5] and 2-D interface crack problems [6-8]. It is noted that in the works of [7] and [8], the contact zone model is firstly extended to interface crack problems of MEE materials.

However, all the above-mentioned works related to interface crack problems, the singularity behavior on the crack tips always exists. On the other hand, two kinds of MEE materials, as well known, generally cannot be connected directly. Thus, in this study, a novel interface crack model for MEE bimaterial, i.e., the model of interface crack with pre-fracture zones is put forward. For simplicity, the interface is assumed to be magnetoelectrically permeable. The problem is reduced to solve a Hilbert problem and two nonlinear equations introduced by Mises yielding condition. The particular cases of symmetric loads and identical MEE material are further analyzed, and some numerical results are presented. These obtained results and/or conclusions could be of interest to the analysis and design of smart sensors/actuators constructed from MEE composite laminates.

2. Statement of the problem

Referring to Ref. [9], it is assumed that the MEE half-spaces are adhered by means of an isotropic interlayer with shear modulus μ, Poison's ratio ν and yield limit σ_{Y}. Furthermore, the half-spaces are assumed to be loaded at infinity with uniform stresses $\sigma_{33}^{(m)}=\sigma_0$, $\sigma_{31}^{(m)}=\tau_0$, uniform electrical displacement $D_3^{(m)}=d_0$ and magnetic induction $B_3^{(m)}=b_0$ (m=1 stands for the upper domain, and m=2 for the lower one). In this paper, although the interlayer thickness will not be taken into account as usual, the properties of the interlayer and its influence upon the fracture process will be considered by means of introduction of pre-fracture zones with cohesive stresses. As shown in Fig. 1, the pre-fracture zones are, respectively, denoted by $[a_1, a]$ and $[b, b_1]$, and the

open part of the crack is denoted by $[a, b]$.

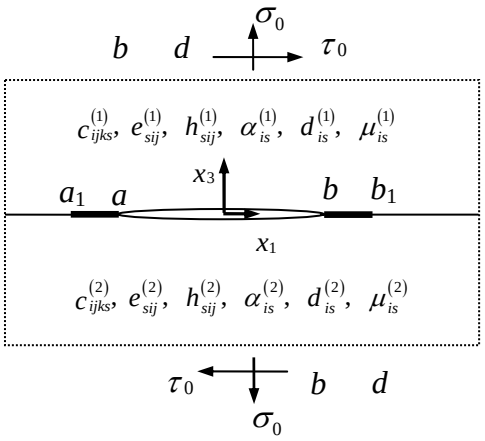

Figure 1. An interface crack with pre-fracture zones between two semi-infinite MEE planes

Assume that the MEE materials are poled in the x_3-direction. As pointed out before [8], the displacement u_2 decouples in the $(x_1, x_3)-$plane from the displacement components u_1, u_3, electrical potential φ and magnetic potential ϕ. And in present study, our attention will be focused only on the generalized plane strain problem for the components u_1, u_3, φ and ϕ. Thus, for the considered magnetoelectrically permeable interface crack, the continuity and boundary conditions at the interface can be written in the form

$$\left[[u_1],\ [u_3],\ [\varphi],\ [\phi]\right]^{\mathrm{T}} = \mathbf{0},\ \left[[\sigma_{31}],\ [\sigma_{33}],\ [D_3],\ [B_3]\right]^{\mathrm{T}} = \mathbf{0},\ x_1 \notin (a,b), \tag{1}$$

$$[\varphi] = 0,\ [D_3] = 0,\ [\phi] = 0,\ [B_3] = 0,\ x_1 \in (a,b), \tag{2}$$

$$\sigma_{33}^{(m)}(x_1,0) \equiv p_1(x_1) = \begin{cases} \sigma' & x_1 \in [a_1, a], \\ \sigma, & x_1 \in [b, b_1], \\ 0, & x_1 \in [a, b], \end{cases} \quad \sigma_{31}^{(m)}(x_1,0) \equiv p_2(x_1) = \begin{cases} \tau' & x_1 \in [a_1, a], \\ \tau, & x_1 \in [b, b_1], \\ 0, & x_1 \in [a, b], \end{cases} \tag{3}$$

where T denotes transposition, $[\Pi] = \Pi(x_1 + \mathrm{i}0) - \Pi(x_1 - \mathrm{i}0)\ (\Pi = u_1, u_3, \text{etc.})$, and the values σ, τ, σ' and τ' are unknown to be determined.

In addition, as pointed out in Ref. [9], because the interlayer is usually much softer than the MEE materials, the interlayer yielding or damage will appear firstly. Thus, some law of interlayer material yielding or damage, for example, $f(\sigma, \tau, \sigma_1) = 0$ for the right pre-fracture zone and $f(\sigma', \tau', \sigma_1') = 0$ for the left pre-fracture zone, respectively, should be satisfied. For simplicity, $\sigma_1 = \sigma_1' = 2\sigma_{\mathrm{Y}}$ are assumed in present study [9].

Up till now, boundary conditions (i.e., Eqs. (1-3)) together with the known governing equations (see Ref. [8]) have formulated a plane strain problem of linear fracture mechanics for a crack $[a_1, b_1]$ between two half-planes, where the components σ, τ, σ' and τ' at the crack faces and the positions of point a_1 and b_1 are all unknown to be determined.

3. The magnetoelectroelastic solution

From the early work [8], it is known that for the case of plane strain, the following expressions at

the interface hold true:

$$\mathbf{V}'(x_1)=\left[V_1',\ \ V_3',\ \ V_4',\ \ V_5'\right]^{\mathrm{T}}=\left[u_1'(x_1),u_3'(x_1),\varphi'(x_1),\phi'(x_1)\right]^{\mathrm{T}}=\mathbf{W}^{+}(x_1)-\mathbf{W}^{-}(x_1),$$

$$\mathbf{t}^{(1)}(x_1,0)=\left[\sigma_{31}^{(1)},\ \ \sigma_{33}^{(1)},\ \ D_3^{(1)},\ \ B_3^{(1)}\right]^{\mathrm{T}}=\mathbf{G}\mathbf{W}^{+}(x_1)-\bar{\mathbf{G}}\mathbf{W}^{-}(x_1),$$

where $\mathbf{W}(z)=\left[W_1(z),\ \ W_3(z),\ \ W_4(z),\ \ W_5(z)\right]^{\mathrm{T}}$ is an introduced unknown vector function, and $\mathbf{W}^{+}(x_1)=\mathbf{W}(x_1+\mathrm{i}0)$, $\mathbf{W}^{-}(x_1)=\mathbf{W}(x_1-\mathrm{i}0)$; the matrix $\mathbf{G}$ has been given in Ref. [8].

Considering that the crack is magnetoelectrically permeable, and that $\mathbf{t}^{\infty}=\mathbf{t}^{(1)}(x_1,0)\big|_{x_1\to\infty}=\left(\mathbf{G}-\bar{\mathbf{G}}\right)\mathbf{W}(z)\big|_{z=x_1+\mathrm{i}x_3\to\infty}$ with $\mathbf{t}^{\infty}=\left\{\tau_0,\ \ \sigma_0,\ \ d_0,\ \ b_0\right\}^{\mathrm{T}}$, we easily get

$$W_4=\left\{\left(\mathbf{G}-\bar{\mathbf{G}}\right)^{-1}\mathbf{t}^{\infty}\right\}_3,\ \ W_5=\left\{\left(\mathbf{G}-\bar{\mathbf{G}}\right)^{-1}\mathbf{t}^{\infty}\right\}_4.$$

Taking into account that $W_4(z)=\mathrm{const}$ and $W_5(z)=\mathrm{const}$ and noting the structure of **G**, we can further obtain

$$\sigma_{33}^{(1)}(x_1,0)+\mathrm{i}\,m_j\sigma_{31}^{(1)}(x_1,0)=t_j\left[\Phi_j^{+}(x_1)+\gamma_j\Phi_j^{-}(x_1)\right],\tag{4}$$

$$\left[u_1'(x_1)\right]+\mathrm{i}s_j\left[u_3'(x_1)\right]=\Phi_j^{+}(x_1)-\Phi_j^{-}(x_1).\tag{5}$$

where

$$\Phi_j(z)=\Omega_j(z)+\Phi_j^0,\ \ \Phi_j^0=\frac{2\mathrm{i}\left(g_{34}W_4+g_{35}W_5\right)}{t_j\left(1+\gamma_j\right)},\quad j=1,3,$$

$$\Omega_j(z)=W_1(z)+\mathrm{i}\,s_jW_3(z),\quad \gamma_j=-\frac{g_{31}+m_jg_{11}}{t_j},\ \ t_j=g_{31}-m_jg_{11},\quad j=1,3,$$

$$\left[u_1'\right]=W_1^{+}-W_1^{-},\ \ m_{1,3}=\mathrm{m}\sqrt{-\frac{g_{31}g_{33}}{g_{11}g_{13}}},\ s_{1,3}=-m_{1,3},$$

and g_{ij} are the elements of **G**.

Considering that $\Phi_j^{+}(x_1)=\Phi_j^{-}(x_1)=\Phi_j(x_1)$ for $x_1\notin(a_1,b_1)$, it follows from Eq. (4) that

$$\Phi_j(z)\big|_{z\to\infty}=\left(\sigma_0+\mathrm{i}\,m_j\tau_0\right)\big/t_j\left(1+\gamma_j\right).\tag{6}$$

Using Eq. (4) for $j=1$ and the corresponding interface conditions (3) yields the following Hilbert problem

$$\Phi_1^{+}(x_1)+\gamma_1\Phi_1^{-}(x_1)=P(x_1)/t_1,\quad x_1\in(a_1,b_1),\tag{7}$$

where

$$P(x_1)=p_1(x_1)+\mathrm{i}m_1p_2(x_1).$$

The solution of Eq. (7) satisfying Eq. (6) can be expressed as

$$\Phi_1(z)=\frac{1}{2\pi\,\mathrm{i}\,X(z)}\left[C_0+C_1z+\frac{1}{t_1}\int_{a_1}^{b_1}\frac{P(t)X^{+}(t)}{t-z}\mathrm{d}t\right],\tag{8}$$

where

$$X(z)=(z-a_1)^{0.5-\mathrm{i}\varepsilon}(z-b_1)^{0.5+\mathrm{i}\varepsilon},$$

$$C_0=-2\pi\mathrm{i}\frac{\sigma_0+\mathrm{i}m_1\tau_0}{t_1\left(1+\gamma_1\right)}\left(\frac{a_1+b_1}{2}+\mathrm{i}\varepsilon l_1\right),\ \ C_1=2\pi\mathrm{i}\frac{\sigma_0+\mathrm{i}m_1\tau_0}{t_1\left(1+\gamma_1\right)},\varepsilon=\ln\gamma_1/2\pi,\ \ l_1=b_1-a_1.$$

Substituting Eq. (8) into Eq. (4) and noting that $\Phi_j^{+}(x_1)=\Phi_j^{-}(x_1)=\Phi_j(x_1)$ for $x_1\notin(a_1,b_1)$, the following relation at the interface can be derived

$$\sigma_{33}^{(1)}\left(x_1,0\right)+\mathrm{i}\,m_1\sigma_{31}^{(1)}\left(x_1,0\right)=\frac{1}{2\pi\,\mathrm{i}\,X\left(x_1\right)}\left\{2\pi\,\mathrm{i}\left(x_1-\frac{a_1+b_1}{2}-\mathrm{i}\,\varepsilon l_1\right)\left(\sigma_0+\mathrm{i}m_1\tau_0\right)+\right.$$
$$\left.\left(1+\gamma_1\right)\left[\left(\sigma'+\mathrm{i}\,m_1\tau'\right)\int_{a_1}^{a}\frac{X^{+}\left(t\right)}{t-x_1}\mathrm{d}\,t+\left(\sigma+\mathrm{i}m_1\tau\right)\int_{b}^{b_1}\frac{X^{+}\left(t\right)}{t-x_1}\mathrm{d}\,t\right]\right\}. \tag{9}$$

Noting the finiteness of the stresses at the point a_1 and b_1, we can further obtain the following system of linear algebraic equations

$$\begin{Bmatrix}\sigma'+\mathrm{i}m_1\tau'\\ \sigma+\mathrm{i}m_1\tau\end{Bmatrix}=\frac{\pi\,\mathrm{i}\,l_1}{1+\gamma_1}\left(\sigma_0+\mathrm{i}m_1\tau_0\right)\left[\mathbf{N}\right]^{-1}\begin{Bmatrix}1+2\,\mathrm{i}\,\varepsilon\\ -\left(1-2\,\mathrm{i}\,\varepsilon\right)\end{Bmatrix}, \tag{10}$$

where the components of matrix $\mathbf{N}=\left[N_{ij}\right]\left(i,j=1,2\right)$ have the following form

$$N_{11}=\int_{a_1}^{a}\left[\left(t-b_1\right)/\left(t-a_1\right)\right]^{0.5+\mathrm{i}\varepsilon}\mathrm{d}\,t,\quad N_{12}=\int_{b}^{b_1}\left[\left(t-b_1\right)/\left(t-a_1\right)\right]^{0.5+\mathrm{i}\varepsilon}\mathrm{d}\,t, \tag{11a}$$

$$N_{21}=\int_{a_1}^{a}\left[\left(t-a_1\right)/\left(t-b_1\right)\right]^{0.5-\mathrm{i}\varepsilon}\mathrm{d}\,t,\quad N_{22}=\int_{b}^{b_1}\left[\left(t-a_1\right)/\left(t-b_1\right)\right]^{0.5-\mathrm{i}\varepsilon}\mathrm{d}\,t. \tag{11b}$$

For the sake of simplicity to calculate, Eq. (11) can be further approximated (see Ref. [9]).

After substituting Eq. (10) into yielding conditions, a system of nonlinear equations is then derived as

$$\Psi_i\left(\Delta_a,\Delta_b,\sigma_0,\tau_0\right)=0\quad i=1,2, \tag{12}$$

where $\Delta_a=a-a_1$ and $\Delta_b=b_1-b$ are the pre-fracture zone lengths.

Using Eq. (5), (7) and using (8), one arrives at the following equation on displacement jumps

$$\left[u_1\left(x_1\right)\right]+\mathrm{i}s_1\left[u_3\left(x_1\right)\right]=\frac{1}{2\pi\,\mathrm{i}\,\gamma_1 t_1}\left\{2\pi\,\mathrm{i}\left(\sigma_0+\mathrm{i}m_1\tau_0\right)\left(x_1-a_1\right)^{0.5-\mathrm{i}\varepsilon}\left(x_1-b_1\right)^{0.5+\mathrm{i}\varepsilon}+\right.$$
$$\left.\left(1+\gamma_1\right)\left[\left(\sigma'+\mathrm{i}m_1\tau'\right)J_1\left(x_1\right)+\left(\sigma+\mathrm{i}m_1\tau\right)J_2\left(x_1\right)\right]\right\}-\frac{1-\gamma_1}{2\gamma_1 t_1}h\left(x_1\right), \tag{13}$$

where

$$J_1\left(x_1\right)=\int_{a_1}^{x_1}\frac{1}{X\left(v\right)}\int_{a_1}^{a}\frac{X^{+}\left(t\right)}{t-v}\mathrm{d}\,t\,\mathrm{d}\,v,\ J_2\left(x_1\right)=\int_{a_1}^{x_1}\frac{1}{X\ \left(v\right)}\int_{b}^{b_1}\frac{X^{+}\left(t\right)}{t-v}\mathrm{d}\,t\,\mathrm{d}\,v,h\left(x_1\right)=\int_{a_1}^{x_1}P\left(t\right)\mathrm{d}\,t.$$

The integral for $h_1\left(x_1\right)$ can be calculated analytically, and the integrals for $J_1\left(x_1\right)$ and $J_2\left(x_1\right)$ can be presented via hyper-geometric functions. As well known, for a real MEE bimaterial, ε is very small [6] and the influence of the oscillation on the value of $J_1\left(x_1\right)$ and $J_2\left(x_1\right)$ is negligibly small. Therefore by assuming $\varepsilon=0$ in evaluating $J_1\left(x_1\right)$ and $J_2\left(x_1\right)$, one gets [9]

$$J_1\left(x_1\right)\approx J_{10}\left(x\right)=\cos^{-1}\left(\alpha_1\right)\sqrt{\left(x-a_1\right)\left(b_1-x\right)}+\frac{x-a}{2}H\left(a_1,b_1,x,a\right),$$

$$J_2\left(x_1\right)\approx J_{20}\left(x\right)=\cos^{-1}\left(\alpha_1\right)\sqrt{\left(x-a_1\right)\left(b_1-x\right)}-\frac{x-b}{2}H\left(a_1,b_1,x,b\right),$$

where $\alpha_1=\left(b_1+a_1-2a\right)/l_1$, and $H\left(a,b,x,\xi\right)$ is a known function given in [9].

Thus, Eq. (13) can be rewritten as

$$\left[u_1\left(x_1\right)\right]+\mathrm{i}s_1\left[u_3\left(x_1\right)\right]=\left(\sigma_0+\mathrm{i}\,m_1\tau_0\right)\left(x_1-a_1\right)^{0.5-\mathrm{i}\varepsilon}\left(x_1-b_1\right)^{0.5+\mathrm{i}\varepsilon}/\gamma_1 t_1+$$
$$\left(1+\gamma_1\right)\left[\left(\sigma'+\mathrm{i}\,m_1\tau'\right)J_{10}\left(x_1\right)+\left(\sigma+\mathrm{i}\,m_1\tau\right)J_{20}\left(x_1\right)\right]/2\pi\,\mathrm{i}\,\gamma_1 t_1-h\left(x_1\right)\left(1-\gamma_1\right)/2\gamma_1 t_1. \tag{14}$$

Crack opening displacements (COD) at the initial crack tips are defined as follows

$$\delta_1^a=\left[u_1\left(a\right)\right],\quad \delta_3^a=\left[u_3\left(a\right)\right],\quad \delta_1^b=\left[u_1\left(b\right)\right],\quad \delta_3^b=\left[u_3\left(b\right)\right]. \tag{15}$$

After substituting $x_1 = a, b$, respectively, into the expressions of $\left[u_1(x_1)\right]$, $\left[u_3(x_1)\right]$ and the COD in Eq. (15) will be then acquired as well. In addition, carrying out a similar derivation to the one given in [9], the expressions for the electrical displacement and magnetic induction at different segments of the interface can be easily obtained (omitted here).

It is remarked that both the electrical displacement $D_3^{(1)}(x_1, 0)$ and magnetic induction $B_3^{(1)}(x_1, 0)$ are not singular as well at either the initial crack tips or the points a_1 and b_1. Thus, the proposed model removes singularities in all components of the magnetoelectromechanical field. On the other hand, it should be pointed out that both the electrical displacement and magnetic induction in the pre-fracture zone are not only directly related to the material parameters of MEE bimaterial and the applied tension load, but also related to $\left[u_1'(x_1)\right]$ and the normal stress in the pre-fracture zone, and that the electrical displacement in the pre-fracture zone depends on the applied electrical load, and magnetic induction on magnetic load. However, both the normal and shear stresses in the pre-fracture zone are independent of the applied magnetoelectrical load.

4. Simplified case of symmetrical loads

For the case of symmetrical loads, i.e., $\tau_0 \equiv 0$, placing the apex of the coordinate system in the middle point of the crack, one has $a = -b$, $a_1 = -b_1$, $\tau' = -\tau$, $\sigma' = \sigma$. In Eq. (10), only one of the equations is necessary, which can be expressed as

$$\left(\sigma - \mathrm{i}\, m_1 \tau\right) N_{21}^{sym} + \left(\sigma + \mathrm{i}\, m_1 \tau\right) N_{22}^{sym} = -\frac{2\pi \mathrm{i}\, b_1}{1+\gamma_1} \sigma_0 \left(1 - 2\mathrm{i}\,\varepsilon\right). \tag{16}$$

where

$$N_{21}^{sym} = \frac{1}{1.5 - \mathrm{i}\,\varepsilon}\left(-2b_1\right)^{-0.5+\mathrm{i}\varepsilon}\left(b_1 - b\right)^{1.5-\mathrm{i}\varepsilon}, \quad N_{22}^{sym} = -\frac{1}{0.5 + \mathrm{i}\,\varepsilon}\left(2b_1\right)^{0.5-\mathrm{i}\varepsilon}\left(b - b_1\right)^{0.5+\mathrm{i}\varepsilon}.$$

Extracting the real and imaginary parts of Eq. (16), we arrive at the system of linear algebraic equations with respect to σ and τ. The solution of the obtained system can be expressed as

$$\sigma = r m_1 \sigma_0 \left(2\varepsilon a_{22} - a_{12}\right), \quad \tau = r \sigma_0 \left(2\varepsilon a_{21} + a_{11}\right), \tag{17}$$

where the expressions for r and $a_{ij}(i, j = 1, 2)$ are the same as those given in [9]. It is worth noting that the values of r, a_{ij} and consequently σ and τ all depend on the pre-fracture zone length $g = b/b_1$.

Substituting Eq. (17) into the second equation of Eq. (12) and taking into account that $\Delta_a = \Delta_b$ in the considered case, one arrives at a transcendental equation with respect to g as follows

$$\left[m_1\left(2\varepsilon a_{22} - a_{12}\right) - \frac{\sigma_1}{r\sigma_0}\right]^2 + 4\left(2\varepsilon a_{21} + a_{11}\right)^2 = \frac{4}{3r^2}\left(\frac{\sigma_Y}{\sigma_0}\right)^2,$$

where the Mises yielding condition $f(\sigma, \tau, \sigma_1) \equiv \left(\sigma - \sigma_1\right)^2 + 4\tau^2 - \frac{4}{3}\sigma_Y^2 = 0$ and $\sigma_1 = 2\sigma_Y$ are used [9].

From Eq. (14), the displacement jumps for $x_1 \in \left(-b_1, b_1\right)$ can be then obtained as

$$\begin{aligned}\left[u_1(x_1, 0)\right] + \mathrm{i}\, s_1 \left[u_3(x_1, 0)\right] \approx{}& \sigma_0 \left(x_1 + b_1\right)^{0.5-\mathrm{i}\varepsilon}\left(x_1 - b_1\right)^{0.5+\mathrm{i}\varepsilon} \Big/ \gamma_1 t_1 \\ &+ \left(1+\gamma_1\right)\left[\left(\sigma - \mathrm{i}\, m_1 \tau\right) J_{10}^{sym}(x_1) + \left(\sigma + \mathrm{i}\, m_1 \tau\right) J_{20}^{sym}(x_1)\right] \Big/ 2\pi \mathrm{i}\, \gamma_1 t_1 - h(x_1)\left(1 - \gamma_1\right)/2\gamma_1 t_1,\end{aligned}$$

where $J_{i0}^{sym}(x_1) = J_{i0}(x_1)(i = 1, 2)$ with $a = -b$, $a_1 = -b_1$. And the electrical displacement and magnetic induction can be expressed as

$$D_3^{(1)}(x_1,0)=-\gamma_{43}\gamma_{33}^{-1}\sigma_0+d_0+\begin{cases}\eta_1\left[u_1'(x_1)\right]+\gamma_{43}\gamma_{33}^{-1}\sigma, & x_1\in(a_1,a)\cup(b,b_1),\\ \eta_1\left[u_1'(x_1)\right], & x_1\in(a,b),\\ \gamma_{43}\gamma_{33}^{-1}\sigma_{33}^{(1)}(x_1,0), & x_1\notin(a_1,b_1),\end{cases}$$

$$B_3^{(1)}(x_1,0)=-\gamma_{53}\gamma_{33}^{-1}\sigma_0+b_0+\begin{cases}\eta_2\left[u_1'(x_1)\right]+\gamma_{53}\gamma_{33}^{-1}\sigma, & x_1\in(a_1,a)\cup(b,b_1),\\ \eta_2\left[u_1'(x_1)\right], & x_1\in(a,b),\\ \gamma_{53}\gamma_{33}^{-1}\sigma_{33}^{(1)}(x_1,0), & x_1\notin(a_1,b_1),\end{cases}$$

where $\eta_1=\gamma_{41}-\gamma_{43}\gamma_{31}/\gamma_{33}$, $\eta_2=\gamma_{51}-\gamma_{53}\gamma_{31}/\gamma_{33}$.

5. Case of equivalent properties of the upper and lower bimaterial components

In this case, $\gamma_1=1$, $\varepsilon=0$ hold true and Eq. (9) takes the form

$$\begin{aligned}\sigma_{33}^{(1)}(x_1,0)+\mathrm{i}m_1\sigma_{31}^{(1)}(x_1,0)=&\frac{\sigma_0+\mathrm{i}m_1\tau_0}{X_0(x_1)}\left(x_1-\frac{a_1+b_1}{2}\right)+\\&+\frac{1}{\pi\mathrm{i}\,X_0(x_1)}\left[(\sigma'+\mathrm{i}m_1\tau')\int_{a_1}^{a}\frac{X_0^+(t)}{t-x_1}\mathrm{d}t+(\sigma+\mathrm{i}m_1\tau)\int_{b}^{b_1}\frac{X_0^+(t)}{t-x_1}\mathrm{d}t\right],\quad x_1\notin(a_1,b_1),\end{aligned}\tag{18}$$

where $X_0(z)=\sqrt{(z-a_1)(z-b_1)}$.

Using Eq. (10), the pre-fracture zone stresses can be calculated by the following formula

$$\begin{Bmatrix}\sigma'+\mathrm{i}m_1\tau'\\ \sigma+\mathrm{i}m_1\tau\end{Bmatrix}=\frac{\pi\mathrm{i}l_1}{2}(\sigma_0+\mathrm{i}m_1\tau_0)\mathbf{N}^{-1}\begin{Bmatrix}1\\-1\end{Bmatrix}.$$

Components of the matrix **N** can be written exactly as

$$N_{11}=\mathrm{i}\frac{l_1}{2}\left[\sqrt{1-\alpha_1^2}+\cos^{-1}(\alpha_1)\right],\qquad N_{12}=\mathrm{i}\frac{l_1}{2}\left[\cos^{-1}(\alpha_2)-\sqrt{1-\alpha_2^2}\right],$$

$$N_{21}=\mathrm{i}\frac{l_1}{2}\left[\sqrt{1-\alpha_1^2}-\cos^{-1}(\alpha_1)\right],\qquad N_{22}=-\mathrm{i}\frac{l_1}{2}\left[\cos^{-1}(\alpha_2)+\sqrt{1-\alpha_2^2}\right],$$

where $\alpha_2=(2b-b_1-a_1)/l_1$.

For this case, the expression for the displacement jump has the following form

$$\begin{aligned}\left[u_1(x_1,0)\right]+\mathrm{i}s_1\left[u_3(x_1,0)\right]=&(\sigma_0+\mathrm{i}m_1\tau_0)\sqrt{(x_1-a_1)(x_1-b_1)}/t_1\\&+\left[(\sigma'+\mathrm{i}m_1\tau')J_{10}(x_1)+(\sigma+\mathrm{i}m_1\tau)J_{20}(x_1)\right]/\pi\mathrm{i}t_1,\quad x_1\in(a_1,b_1).\end{aligned}\tag{19}$$

And δ_1^a, δ_3^a, δ_1^b and δ_3^b can then be obtained easily.

In this case of homogeneous material with symmetrical loading, one has $\tau=\tau'=0$ and $\sigma'=\sigma$. In the coordinate system with apex in the middle of the crack, $\sigma_{31}^{(1)}(x_1,0)=0$, $a=-b$, $a_1=-b_1$ hold true. And only one equation of Dugdale –type $\sigma=\sigma_c$ [10] can be considered. In addition, according to the von Mises yielding condition given before, σ_c is related to the material parameters of interlayer, which can be taken as $2\left(1+1/\sqrt{3}\right)\sigma_{\mathrm{Y}}$. Furthermore, for this case $\alpha_2=\alpha_1=b/b_1$ and Eq. (18) can be reduced as

$$\sigma_{33}^{(1)}(x_1,0)=\frac{1}{\sqrt{x_1^2-b_1^2}}\left\{\sigma_0x_1+\frac{\sigma_c}{\pi\mathrm{i}}\left(\int_{-b_1}^{-b}+\int_{b}^{b_1}\right)\frac{\sqrt{t^2-b_1^2}}{t-x_1}\mathrm{d}t\right\},\quad x_1\notin(a_1,b_1).\tag{20}$$

By setting the expression in the brackets to zero, one gets the following equation

$$\frac{b}{b_1}=\cos\frac{\pi\sigma_0}{2\sigma_c}. \tag{21}$$

Thus, the pre-fracture zone length can easily be determined from Eq. (21). By the way, it is easily known that for internal crack problem of identical MEE material, although the length of pre-fracture zone depends on σ_0, σ in the pre-fracture zone is independent of it.

It is worth noting that after evaluating the integrals in Eq. (20) and using (21), one gets [9]

$$\sigma_{33}^{(1)}\left(x_1,0\right)=\sigma_c+\frac{\sigma_c}{\pi}\left[\sin^{-1}\frac{b_1^2-x_1b}{b_1\left(x_1-b\right)}-\sin^{-1}\frac{b_1^2+x_1b}{b_1\left(x_1+b\right)}\right],\quad x_1\notin\left(a_1,b_1\right).$$

Considering only imaginary part of Eq. (19) and noting $\left[u_1\left(x_1\right)\right]=0$ and Eq. (21), we have

$$\left[u_3\left(x_1\right)\right]=\frac{\sigma_c}{2\pi t_1s_1}\left[\left(x_1-b\right)H\left(-b_1,b_1,x_1,b\right)-\left(x_1+b\right)H\left(-b_1,b_1,x_1,-b\right)\right]. \tag{22}$$

The COD at the initial crack tip can be obtained for $x_1=b$ and can be written in the form

$$\delta_3^b=-\frac{2b\sigma_c}{\pi t_1s_1}\ln\left(\cos\frac{\pi\sigma_0}{2\sigma_c}\right). \tag{23}$$

It is important to note that for the case of isotropic upper and lower bimaterial components with $t_1=2\mu/\left(1+\kappa\right)$, $s_1=1$ [11], Eqs. (22) and (23) formally coincide with the associated equation of Panasyuk [12], and that the expressions for the electrical displacement and magnetic induction at the interface can be expressed in a simple form (omitted here).

6. Numerical results and discussion

In this section, for simplicity, numerical calculations only for the case of symmetric loads are carried out. As an example, material combination A/B of material A (upper material) and B (lower one) is mainly investigated. The material constants of them for material A with volume fraction v_f=0.3 and for material B with volume fraction v_f=0.5 are given by Sih and Song [13]. The interface layer was assumed to be elastic-perfectly plastic material with yield stress $\sigma_{\mathrm{Y}}=220\mathrm{MPa}$ [9]. In addition, loading combination parameters $\lambda_D=d_0\,e_{33}^{(1)}/\left(\sigma_{\mathrm{Y}}\alpha_{33}^{(1)}\right)$ and $\lambda_B=b_0\,h_{33}^{(1)}/\left(\sigma_{\mathrm{Y}}\mu_{33}^{(1)}\right)$ are introduced to reflect the applied electrical and magnetic loads, respectively.

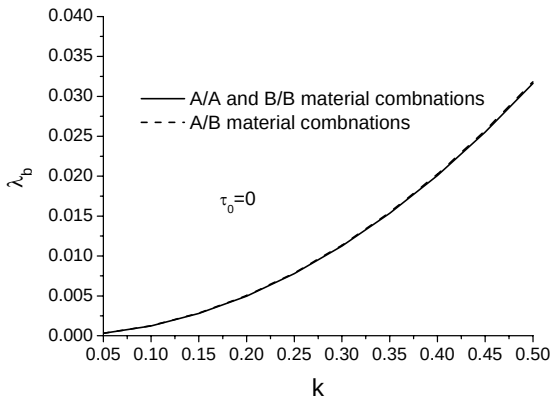

Figure 2. Relative pre-fracture zone lengths versus the applied tension load

The numerical results for the relative pre-fracture zone lengths, stresses in pre-fracture zones and

the CODs at the initial crack tips with respect to the normalized applied normal load for different material combinations are presented in Figures 2-6, where $k=\sigma_0/\sigma_Y$, $l=(b-a)/2$, $\lambda_b=\Delta_b/l$ and $\lambda_D=\lambda_B=0$. And if no special explanation is given, all the curves in these figures consider only A/B combination. It is remarked that because of the symmetry, only the corresponding numerical results for the right pre-fracture zone are plotted.

Figure 2 shows that the pre-fracture zone length of all current material combinations increases with the increasing of applied tension load and it is interesting to note that the pre-fracture zone length of A/B material combination is only slightly larger than that of A/A or B/B material combinations. Besides, the values of pre-fracture zone length are much smaller than the crack length, even for a relatively large external load. Figure 2 also indicates that for the internal crack problem of identical MEE material, the pre-fracture zone length is independent of the material properties of MEE material.

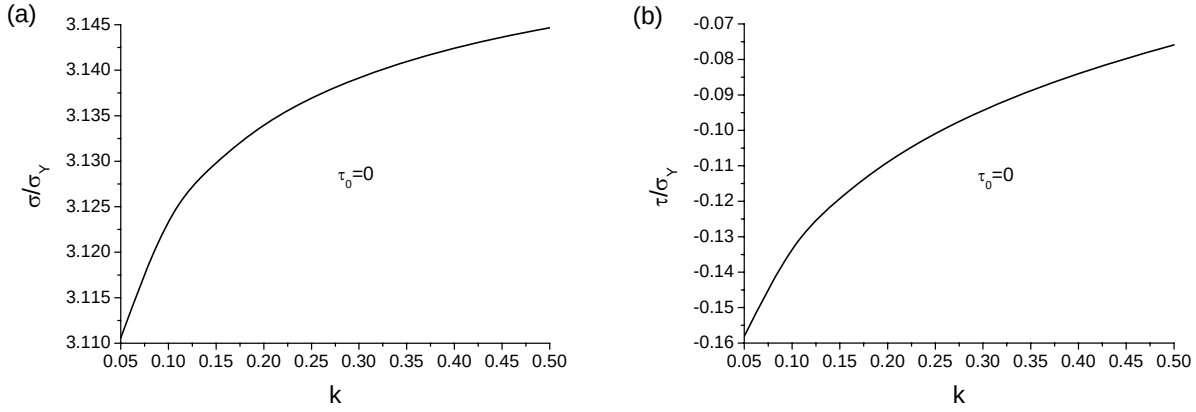

Figure 3. Normalized (a) normal stress and (b) shear stress in the pre-fracture zone versus the applied tension load

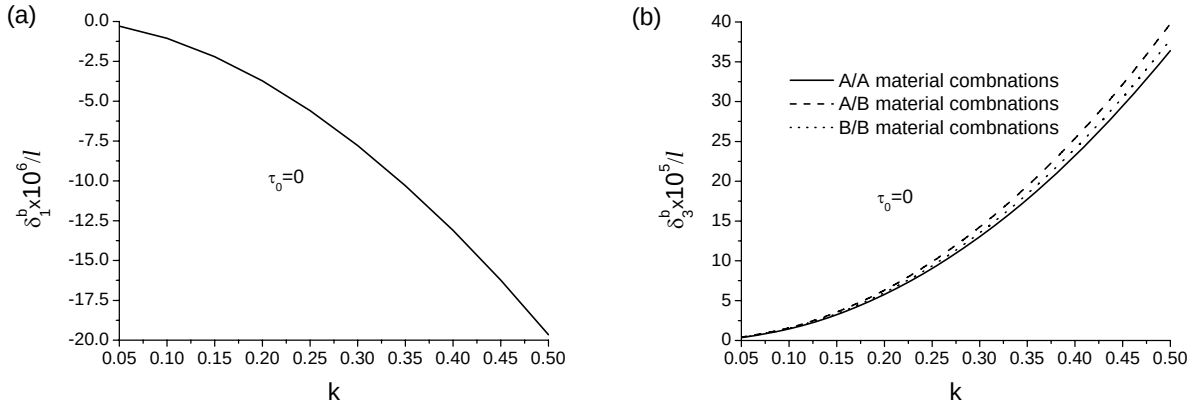

Figure 4. Normalized CODs at the initial crack tip versus the applied tension load

From Figure 3, it can be seen that for A/B material combination, the normal stress in the pre-fracture zones increases with the increasing of normalized normal load k, while the magnitude of shear stress decreases with the increasing of normalized tension load. The similar phenomena have been observed by Loboda et al. [9] for interface crack problem of piezoelectric bimaterial.

As shown in Figure 4, with the increasing of normalized normal load, although δ_1^b is negative, the

magnitude of δ_1^b at initial crack tips increases for A/B combination, and δ_3^b increases for A/B, A/A and B/B combinations. It should be pointed out that, as expected, for the considered loading cases, δ_3^b is much larger than δ_1^b. In addition, it is interesting to note from Figure 4b that for A/B combination, δ_3^b is slightly larger than that of both A/A and B/B combinations, which is a novel phenomenon different to the one observed in [9] for piezoelectric bimaterial problem.

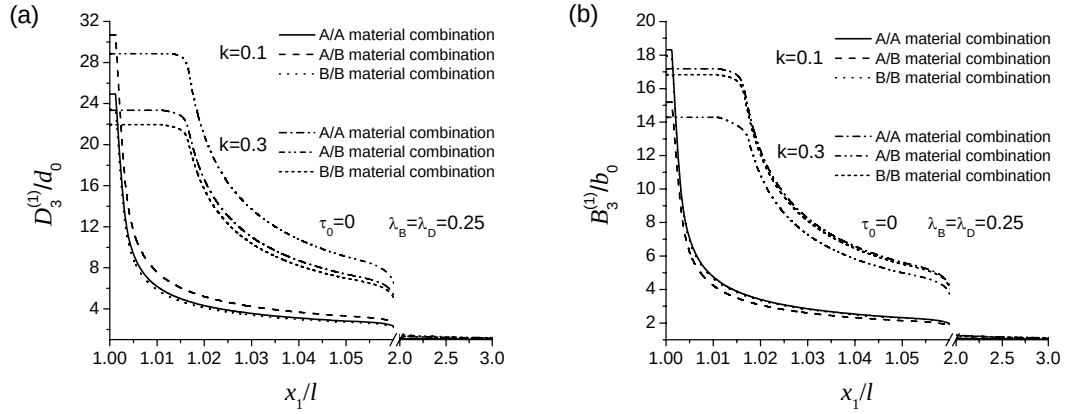

Figure 5. Normalized (a) electrical displacement and (b) magnetic induction along the interface under different tension loads

In Figure 5, the distributions of normalized electrical displacement $D_3^{(1)}\left(x_1,0\right)/d_0$ and normalized magnetic induction $B_3^{(1)}\left(x_1,0\right)/b_0$ along the crack face are presented, where $\lambda_D=\lambda_B=0.25$. For $k=\sigma_0/\sigma_Y=0.1$ and 0.3, the pre-fracture zone lengths can be easily determined by Eq. (21). They are, respectively, $\lambda_a=\lambda_b=0.00124$ and 0.01124, which, in fact, are the same as those given by Loboda et.al [9] for piezoelectric crack problem with pre-fracture zone. As shown in Figure 5, on one hand, the applied tension loads have significant effects on both the electrical displacement and magnetic induction in the pre-fracture zone. On the other hand, for a definite tension load, both the electrical displacement and magnetic induction in the pre-fracture zone are almost unchanged. In addition, with the increasing of x_1/l, both the electrical displacement and magnetic induction decrease rapidly, and as expected, the values of $D_3^{(1)}\left(x_1,0\right)/d_0$ and $B_3^{(1)}\left(x_1,0\right)/b_0$ finally approach to 1.

6. Conclusion

A plane strain problem for two MEE half-planes adhered by means of a very thin isotropic interlayer has been considered. A novel interface crack model, i.e., an interface crack with both open part and pre-fracture zone is put forward. The crack surfaces are assumed to be magnetoelectrically permeable. The problem is firstly reduced to a Hilbert problem on the unknown normal stress and shear stress in the pre-fracture zones, which can be solved exactly. By introducing Mises yielding conditions on interface layer, a system of nonlinear equations is established to determine pre-fracture zone lengths. Finally, the corresponding results for both cases of symmetric load and equivalent properties of the upper and lower bimaterial components are further obtained. From the theoretical and numerical results, the following conclusions can be drawn:

• For the suggested model, all mechanical, electrical and magnetic characteristics are limited in the near-crack tip region, i.e., all singularities connected with the model are eliminated.

• For the magnetoelectrically permeable interface crack with pre-fracture zones, δ_3^b plays a very important role in the fracture analysis of the interface crack because it is much larger than δ_1^b. And in general, increasing tension loads will cause crack growth and propagation.
• For the internal crack problem of identical MEE material under symmetrical load, the pre-fracture zone lengths are independent of material properties, and the normal stress in the pre-fracture zone is independent of applied tension load.

Acknowledgement

The supports from the National Natural Science Foundation of China (Grant Nos. 10772123 and 11072160) are acknowledged.

References

[1] C.F. Gao, H. Kessler, H. Balke, Crack problems in magnetoelectroelastic solids. Part I: Exact solution of a crack. Int J Eng Sci 41(2003) 969-981.
[2] G.C. Sih, R. Jones, Z.F. Song, Piezomagnetic and piezoelectric poling effects on mode I and II crack initiation behavior of magnetoelectroelastic materials. Theor Appl Fract Mech 40(2003) 161-186.
[3] W.Y. Tian, U. Gabbert, Macrocrack-microcrack interaction problem in magnetoelectroelastic solids. Mech Mater 37(2005) 565-592.
[4] X.H. Chen, Energy release rate and path-independent integral in dynamic fracture of magneto-electro-thermo-elastic solids. Int J Solids Struct 46(2009) 2706-2711.
[5] X.C. Zhong, F. Liu, X.F. Li, Transient response of a magnetoelectroelastic solid with two collinear dielectric cracks under impacts. Int J Solids Struct 46(2009) 2950-2958.
[6] R. Li, G.A. Kardomateas, The mixed mode I and II interface crack in piezoelectromagneto-elastic anisotropic bimaterials. ASME J Appl Mech 74(2007) 614-627.
[7] K.P. Herrmann, V.V. Loboda, T.V. Khodanen, An interface crack with contact zones in a piezoelectric/piezomagnetic biomaterial. Arch Appl Mech 80(2010) 651-670.
[8] W.J. Feng, P. Ma, E. Pan, J.X. Liu, A magnetically impermeable and electrically permeable interface crack with a contact zone in a magnetoelectroelastic bimaterial under concentrated magnetoelectromechanical loads on the crack faces. Sci China: Physics, Mechanics and Astronomy 54(2011) 1666-1679.
[9] V. Loboda, Y. Lapusta, A. Sheveleva, Electro-mechanical pre-fracture zones for an electrically permeable interface crack in a piezoelectric bimaterial. Int J Solids Struct 44(2007) 5538-5553.
[10] D.S. Dugdale, Yielding of steel sheets containing slits. J Mech Phys Solids 8(1960) 100–108.
[11] K.P. Herrmann, V.V. Loboda, I.V. Kharun, Interface crack with a contact zone in an isotropic bimaterial under thermomechanical loading. Theor Appl Fract Mech 42(2004) 335–348.
[12] V.V. Panasyuk, Limiting equilibrium of brittle solids with fracture [in Russian], Naukova, 1968, Dumka Publishers, Kiev, translation in English: Detroit. Michigan Inform. Serv, 197, pp 284.
[13] G.C. Sih, Z.F. Song, Magnetic and electric poling effects associated with crack growth in $BaTiO_3$–$CoFe_2O_4$ composite. Theor Appl Fract Mech 39(2003) 209–227.

Ideal strength of twinned and perfect NiTi martensite crystal

Petr Sestak[1,*], Miroslav Cerny[1,2], Jaroslav Pokluda[1,2]

[1] Faculty of Mechanical Engineering, Brno University of Technology, Brno CZ-61600, Czech Republic
[2] Central European Institute of Technology – CEITEC VUT, Brno CZ-61600, Czech Republic
* Corresponding author: sestak@fme.vutbr.cz

Abstract This paper is focused on the determination of the ideal (theoretical) tensile strength of the NiTi martensite crystal with B19' and BCO structures which contain (100) compound twins. For comparison, the strength of a perfect austenitic B2 structure is also studied. The model of the twinned martensite is represented by a supercell containing 40 atoms (20Ni:20Ti) arranged in two variants of the martensite. The results show that the presence of twins slightly decreases the ideal strength of NiTi martensite. The ideal strength of the B2 structure is three-times higher than that of the BCO one.

Keywords NiTi SMA, twinning, theoretical strength, ab initio

1. Introduction

The shape memory alloys (SMA) represent advanced materials usable in many industrial as well as medical applications owing to their shape memory effect which is based on transformations between austenitic and martensitic phases. The most frequently used SMA is a binary alloy with a nearly equiatomic proportion of nickel and titanium (NiTi). The NiTi alloy crystallizes either into a high temperature B2 (austenite) or a low temperature B19' (martensite) structure. An extensive overview regarding the NiTi SMA can be found in the paper of Otsuka [1].
There is, however a disagreement between experiment and theory since ab initio simulations predict, as a structure with the lowest total energy E_{tot} the base centered orthorhombic structure (BCO) instead of the experimentally observed monoclinic B19' one [2]. This disagreement raises a question why the theoretical simulations do not predict and confirm the experimentally observed martensitic structure. One of possible explanations is that the experimental results were measured on a polycrystal while the theoretical models consider a perfect crystal that does not contain the planar crystallographic defects, like twins or dislocations. Indeed, the real NiTi martensite always contains twins and, therefore, it is necessary to include these defects into the theoretical model. In our previous ab initio study we considered a sample of the (100) compound twins in NiTi martensite. Received results revealed that presence of the selected twins can significantly contribute to stabilization of the B19’ structure against the BCO one. Hence, the knowledge of the twinning in NiTi SMA at atomistic level is important for deeper understanding the ongoing processes (detwinning, martensitic transformation, etc.) in this unique material.
In this theoretical study we present the ab initio simulations of the (100) twinned NiTi martensite subjected to a uniaxial tensile loading that is oriented perpendicular to the twinning planes.

2. Theoretical model of the twinned NiTi martensite

2.1. NiTi twinned martensite

The studied theoretical model of the (100) compound twins in the NiTi martensite is represented by a supercell containing 40 atoms (20Ni:20Ti) arranged in two variants of the martensite. From now on, this basis will be referred to as TSC – twinned supercell. This TSC is identical to that already published in our previous research paper [3] that also contains a detailed description the TSC construction. The sample of the (100) twinned structure is depicted in Fig. 1.

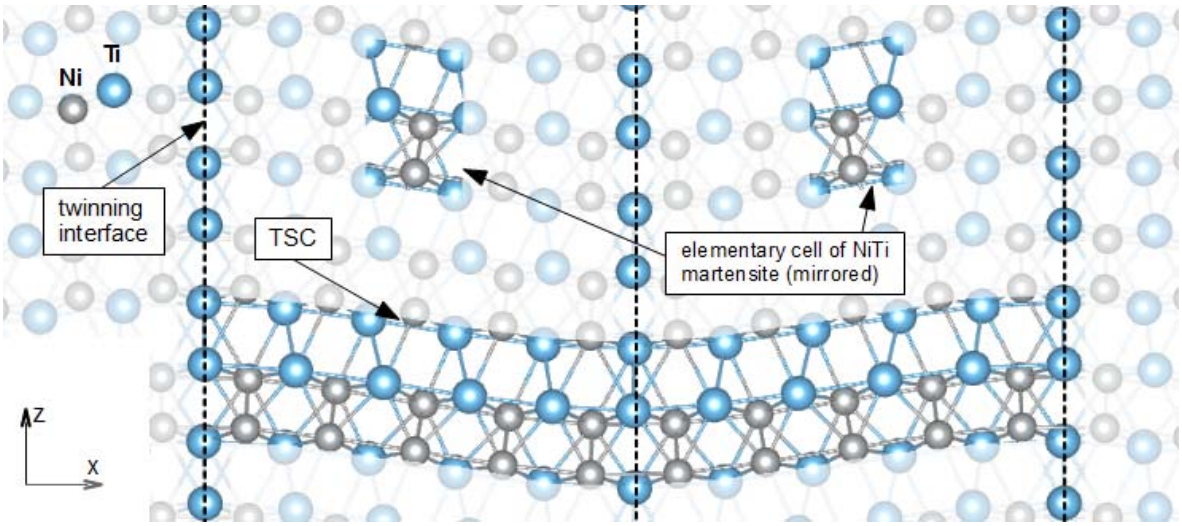

Figure 1. The sample of (100) twinned NiTi martensite with marked twinned supercell (TSC), both martensite variants and twinning interfaces. The tensile loading was applied parallel to the z axis.

2.2. Theoretical simulations

The ab initio simulations were performed within the density functional theory (DFT) developed by Kohm and Sham [4]. We used the VASP code (Vienna Ab initio Simulation Package) [5, 6] as a particular implementation of DFT to determine the total energy (E_{tot}) of the studied system, the stress tensor (σ_i in Voigt notation) and the forces (F) acting on individual atoms. The VASP uses the pseudopotential approach that represents a very efficient way how to reliably describe the valence electrons.

In the present study we utilized the PAW (Projector Augmented Waves) [7] pseudopotential treating p-electrons of Ti as valence and the exchange correlation energy by mean of the GGA (Generalized Gradient Approximation) with parametrization of Perdew Wang [8]. The cut-off energy restricting the number of plane waves in the basis set was 500 eV and the solution is considered to be self consistent when the difference of two subsequent total energies is lower than 1.0×10^{-8} eV. Meshes containing 1×13×13 (for TSC), 19×13×13 (for BCO) and 19×19×19 (for B2) of equidistantly spaced k-points were constructed for integration over the Brillouin zone.

The modeled deformation of a crystal lattice is represented by a uniaxial distortion of TSC in the selected direction that is perpendicular to the twinning interfaces. The relaxation procedure was applied during the entire deformation process to achieve the Poisson contraction (relaxation of the lateral stress tensor components). This relaxation means alternating the optimization of the translation vectors with optimization of the atomic positions until the relaxed stress tensor components reached values below 200 MPa and forces between individual atoms were lowered to 1×10^{-2} eV/ Å.

3. Results

3.1. Structure optimization

The uniaxial deformation begins from the equilibrium state and therefore it was necessary to determine lattice parameters for all studied structures. The lattice parameters of TSC were taken from our previous ab initio study [3] whereas the lattice parameters of the BCO and the B2

structures were obtained by a full optimization of those experimentally measured. These parameters are listed in Table 1 along with the experimental data [1, 9]. Comparing the presented ab initio data with those published in literature one can note a good agreement. This proves that the selected VASP settings are sufficient for reliable ab initio simulations.

Table 1. The computed equilibrium lattice parameters of the NiTi SMA. The table also contains the experimental and the theoretical data that are available in literature.

Structure	a_0 / Å	b_0 / Å	c_0 / Å	β / [°]
TSC [3]	28.7	4.11	4.65	90.0
BCO present *	2.94	4.00	4.93	107.3
BCO [2]	2.85	3.92	4.82	107.2
B19' experiment [9]	2.90	4.11	4.65	97.8
B2 present	3.00	3.00	3.00	90.0
B2 experiment [1]	3.02	3.02	3.02	90.0

3.2. Theoretical tensile strength

The investigated structures were subjected to a uniaxial loading in the ⟨100⟩ direction. The deformation path started with the equilibrium lattice parameters and continued until the tensile stress exceeded its maximal value. The tensile stress σ_1 is plotted in Fig. 2 as a function of the strain ε_1 for all studied structures. The theoretical strengths of the TSC and the perfect martensite are identified with the maxima in the stress-strain dependences (see Fig. 2a) since behind these maxima, the structures transform into different ones. Fig. 2b contains the stress-strain dependence for the austenite where two maxima can be found. Since, there is no structure change during the deformation we consider the global maximum as the ideal strength of the austenite.

The highest theoretical strength σ_1 = 34.5 GPa corresponds to the B2 austenite whereas the lowest value of 7.6 GPa to the TSC structure. The value of 8.8 GPa for the BCO structure is rather close to that computed for the TSC but, indeed, the presence of selected twins slightly reduce the strength of the NiTi martensite. The results also revealed that the computed theoretical strengths for both the

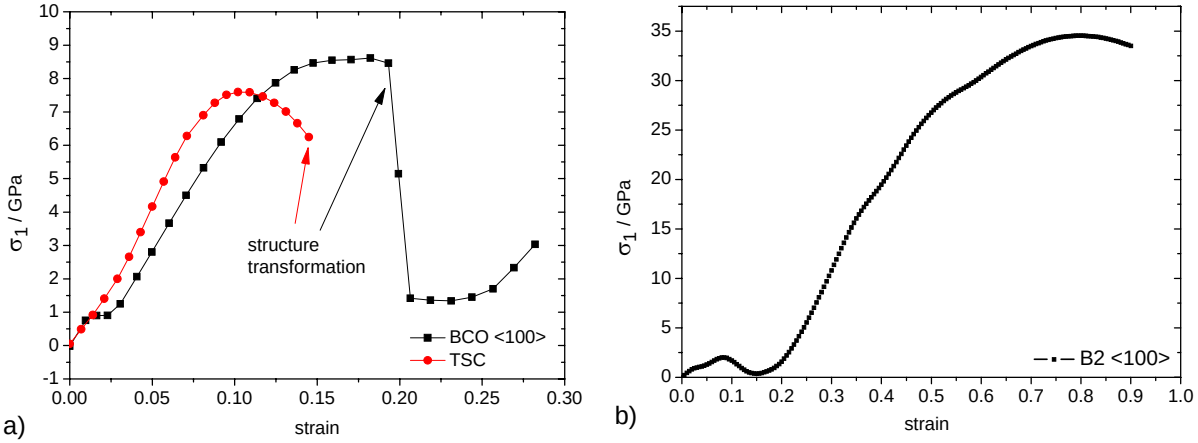

Figure 2. The dependence of the tensile stress σ_1 on the axial strain ε_1 for the twinned structure (TSC) and the perfect structures (B2 and BCO) of NiTi. The direction of deformation is perpendicular to the twinning interfaces.

TSC and the BCO lattice are significantly different from that for the austenite which is three times higher. A similar difference can be found when comparing the critical strain values. All the computed theoretical data are summarized in Table 2.

Table 2. The theoretical tensile strengths σ_{max} of the studied structures along with strain values.

Structure	σ_{max} / GPa	ε
TSC	7.6	0.106
BCO	8.8	0.219
B2	34.5	0.795

4. Conclusion

The theoretical tensile strength of the twinned NiTi martensite in the ⟨100⟩ direction was computed using the ab initio simulations and compared with those of perfect martensite and austenite structures. The results revealed that the presence of twins in the NiTi martensite only slightly reduces its theoretical strength. The results also show that the strength of the austenitic crystal is three times higher than that of the martensitic one.

Acknowledgements

Authors acknowledge the financial support of the project P108/10/P412 (Czech Science Foundation) and the project CZ.1.05/1.1.00/02.0068 (European Regional Development Fund).

References

[1] K. Otsuka, X. Ren, Physical metallurgy of Ti–Ni-based shape memory alloys. Prog. in Mater. Sci., 50 (2005) 511–678.
[2] X. Huang, G. Ackland, K. M. Rabe, Crystal structures and shape-memory behaviour of NiTi, Nat. Mater, 2 (2003) 307–311.
[3] P. Sestak, M. Cerny, J. Pokluda, Can twinning stabilize B19' structure in NiTi martensite?, Intermetallics, 19 (2011) 1567–1572.
[4] W. Kohn, L. J. Sham, Self-Consistent equations including exchange and correlation effects, Phys. Rev. A, 140 (1965) A1133–A1138.
[5] G. Kresse, J. Hafner, Norm-conserving and ultrasoft pseudopotentials for first-row and transition elements, J. Phys.: Condens. Matter, 6 (1994) 8245–8257.
[6] G. Kresse, J. Furthmuller, Efficient iterative schemes for ab initio total-energy calculations using a plane-wave basis set, Phys. Rev. B, 54 (1996) 11169–11186.
[7] D. Vanderbilt, Soft self-consistent pseudopotentials in a generalized eigenvalue formalism, Phys. Rev. B, 41 (1990) 7892–7895.
[8] J. P. Perdew, Y. Wang, Accurate and simple analytic representation of the electron-gas correlation energy., Phys. Rev. B, 45 (1992) 13244–13249.
[9] Y. Kudoh, M. Tokonami, S. Miyazaki, K. Otsuka, Crystal structure of the martensite in Ti-49.2 at.%Ni alloy analyzed by the single crystal X-ray diffraction method., Acta. Metal, 33 (1985) 2049–2056.

Machining effects on damage evolution in sinter powder metals

S. Ma, H. Yuan*

Department of Mech. Engineering, University of Wuppertal, Wuppertal 42119, Germany
* Corresponding author: h.yuan@uni-wuppertal.de

Abstract The sinter powder metals have found extensive engineering applications in industry. The mechanical property of sinter metals is characterized by high porosity and micro-cracks. Inelastic behavior of the materials is coupled with micro-crack propagation and coalescence of open voids. The machining of sinter metals has significant influence on material behavior. In the present paper the machining effect on damage evolution of sinter iron is investigated under tension and torsion loading conditions experimentally and computationally. The tests indicated that damage of the sinter iron initiated already at a stress level much lower than the macroscopic yield stress. Based on the uniaxial tensile test an elastic-plastic continuum damage model was developed which predicts influence of machining on the damage evolution in the sinter iron under tension and torsion loading conditions. The proposed damage model can reasonably predict the damage evolution under tension loading for sintered iron. Deviation to the torsion damage is significant which implies anisotropic damage evolution.

Keywords Sintered metal, continuum damage model, damage evolution, machining effects

1. Introduction

Powder metallurgy (PM) technology has many advantages in comparison with melting metallurgy technology, e.g. low manufacturing cost, high production efficiency, high precision geometry and flexible composition of metal elements. With development of powder metallurgy technology many high performance components working under high and complex loading conditions are made of PM steel in recent years. Microstructure of sintered metals is characterized by high porosity and micro-cracks. Inelastic behavior of the material is coupled with inelastic deformations of powder particles, micro-crack propagation and coalescence of voids [6]. Interconnected porosity may cause higher stress concentrations near the particle connecting necks, while isolated porosity results in more homogeneous deformations [13]. Microscopic damage mechanism of sintered metals is investigated in monotonic in-situ tensile tests [3]. It is found that micro-cracks always initiate at pores of which the long axis is perpendicular to the tensile axis. These micro-cracks open and/or propagate under the mode I crack direction. Additional effects on material property are related to machining of sinter materials [13]. Experimental observations confirm that both mass density and elasticity modulus are significantly changed due to turning manufacture. A dramatic drop is determined in the fracture strain, which decreases from 14% to 3-4%, as reported in [13]. It is of importance to quantify effects of machining in mechanical property of sinter metal parts.

In the present work, damage from machining is studied experimentally and computationally. The damage evolution in specimens fabricated in two different machining processes is investigated under tension and torsion loading conditions. The damage variable is defined within the framework of thermodynamics and experimentally determined by monitoring changes of Young's modulus or shear modulus. It is found that damage in the sintered iron nucleates at a load level much lower than yield stress and fractured in the semi-brittle manner in spite of large plastic deformations. The machining effects on the mechanical properties were experimentally quantified and represented as state variable in the proposed continuum damage model. The continuum damage model should be able to predict the damage evolution in the sintered iron and verified based on detailed experiments. The influence of machining on the damage evolution was predicted with the proposed damage model, where the initial damage duo to machining is considered.

2. Materials and Specimen fabrication

To investigate mechanical behavior of sinter metals, the pure iron powder (atomized Hoeganaes ASC.100.29) from Hoeganaes Corporation was used to produce specimens. The organic binder (0.6% HDL-wax) is added into iron powder to improve lubricity during compaction of the green material. The green material is sintered at 1120°C for 60 min in the 95% N_2 and 5% H_2 atmosphere. The binder was burned out in the first stage of sintering. The average density of material after sintering is 7.2g/cm3, that is, the material contains ca. 8% air, i.e. porosity. The tensile bars specimens (Fig. 1) are fabricated directly by compacting and sintering, which is considered as reference material to determine machining effect on mechanical properties of material. The tubular specimens (Fig. 2), however, cannot be sintered directly and have to be machined from large piece of sinter materials. In the present work, the tubular parts are taken from cylindrical blanks with a diameter of 200mm. Generally speaking, the material property of the sinter iron is very sensitive to machining process.

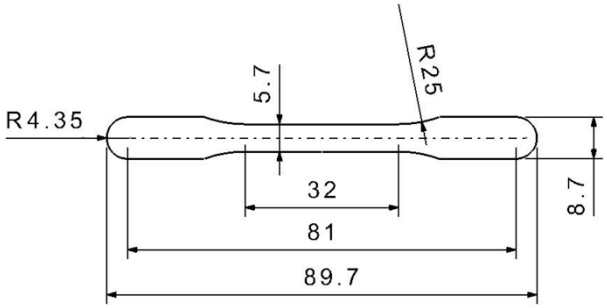

Figure 1. MPA specimen without machining

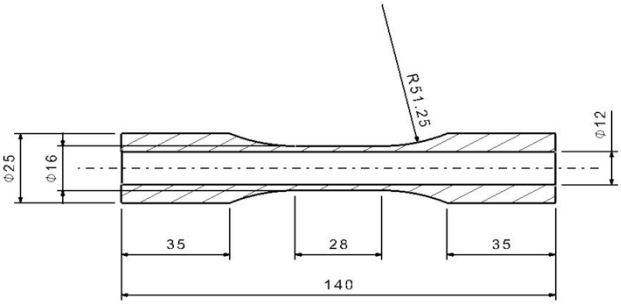

Figure 2. Thin-walled tube specimen by machining

The tubular specimens were machined with two different fabrication procedures in order to investigate the influence of machining procedure. The first procedure is followed by a conventional mechanical machining procedure of tubular specimen: Drilling-boring-turning (TBD). In this machining procedure the machining speed was well controlled. With the second machining method, the hole of the tubular specimen was mainly fabricated with the wire cut electrical discharge machining (WEDM) technology. After wire cutting, the remained thin oxide layer was removed by grinding. In compare with conventional machining procedures, the second fabrication procedure is more time-consuming.

3. Experimental results

3.1. Machining effect on the stress-strain curve

For investigating the effect of machining on mechanical properties of sintered iron, tensile tests were carried out with both tensile bar specimens und tubular specimens fabricated by different machining procedures. The tensile bar specimen is as-sintered without additional machining, which is the reference specimen for tension test of sintered steel according to DIN EN ISO 2740. In Fig. 3, it is shown that the tensile bar specimen shows a distinct Lüder's band, whereas it was not observed in the tubular specimen fabricated by TBD. The machining induces severe plastic deformations into specimen and the material seems strong to be hardened due to cold-working. The Lüder's band disappear in the TBD tubular specimen. With WEDM the tubular specimen seems not much different and its stress-strain curve nearly coincides with that of the tensile bar specimen (Fig 3). The most dramatic change due to machining is observed in the fracture strain, whereas the tensile bar specimen was broken at 12-14% of elongation, the TBD specimen shows 3.8% as fracture strain. More mechanical properties of both as-sintered and machined specimens are summarized in Table 1. Whereas WEDM does not distort sinter material, TBD generates significant damage to the specimen. Damage from conventional machining can affect sinter metal property substantially.

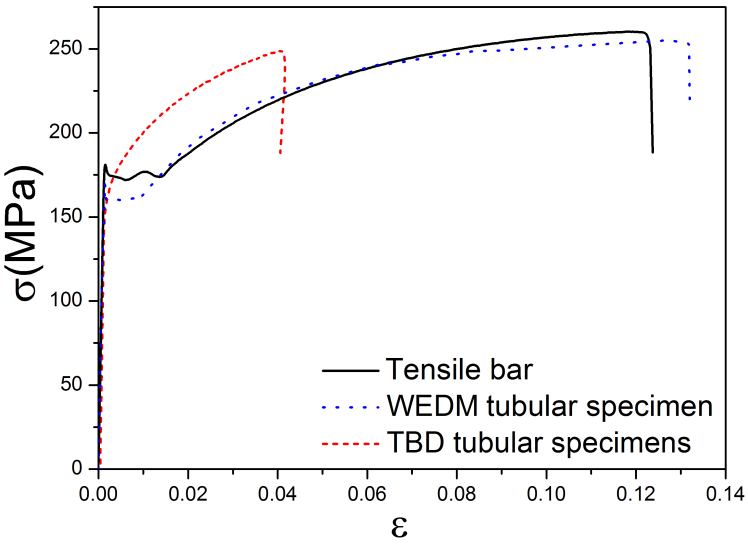

Figure 3. Stress-strain curves from differently fabricated specimens.

The porosity of specimens was measured before and after conventional machining by image analysis technique and Archimedes method, respectively. Optical micrographs revealed a significant increase of porosity after TBD machining. The average density of specimens after machining was increased from 7.2g/cm^3 to 7.4g/cm3, which is higher than the density before machining. In other words, the porosity of specimen before machining was reduced from 8.5% to 6% after machining procedure (TBD). The material of specimen was densified during machining.

Table 1. Mechanical properties of tensile specimen and tubular specimens.

Specimen Type	E [GPa]	σ_y [MPa]	σ_u [MPa]	ε_f [%]
Tensile bar without machining	164	135	255	12.3
Tubular specimen (TBD)	163	130	248	3.8
Tubular specimen (WEDM)	162	134	254	12.7

For sintered metal, Young's modulus can be expressed as a function of the porosity of material

$$\frac{E}{E_{ful}} = (\frac{\rho}{\rho_{ful}})^{\omega}, \tag{1}$$

where ρ is the porosity of material, ρ_{ful} is density of fully dense material (ρ_{ful}=7.86g/cm^3 for iron), and E_{ful} is the Young's modulus of fully dense material (according to literature the Young's modulus of fully dense iron is 201GPa) [3]. With the elastic modulus of specimen for density 7.2 g/cm^3, one obtains that ω=2.46. For the material of density 7.4 g/cm^3 the theoretical elastic modulus should be 176GPa. Compared with elastic modulus determined in the experiment, it implies that the specimen contains initial damage after conventional machining, which reduces the elastic modulus.

Summarizing observations above, one may conclude that the conventional machining procedure will harden and embrittle the sintered iron significantly. Furthermore, the material is densified and damaged during machining. With the WEDM machining, the machining effect is insignificant. The material properties of as-sintered material can be approximated by the WEDM

tubular specimen.

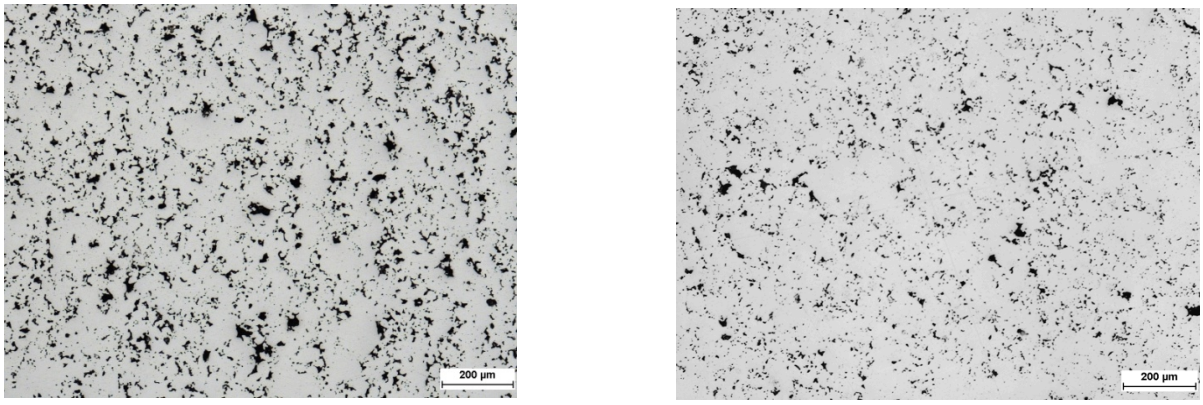

(a) (b)

Figure 5. Microstructures of the sintered iron ASC.100.29 with density 7.2g/cm^3. (a) Before machining. (b) After conventional machining (TBD) the material is densified to 7.4g/cm^3.

3.2. Damage evolution in different specimens

The loading and unloading cycles were designed to accomplish in different loading stage in order to investigate the damage evolution in the whole loading range. All tests were performed at a strain rate about 10^{-4}/s and at room temperature in MTS 809 axial/torsion testing machine. Axial/torsional extensometer of MTS Corp. was used to measure axial and torsional strains during tests. The gauge length of the extensometer used was 25mm.

Material damage can be expressed by diminishing of the elastic modulus [10],

$$D = 1 - \frac{E(\epsilon)}{E_0} \tag{2}$$

where E_0 denotes the initial elasticity modulus of the sintered metal without damage and E depending on deformations stands for actual elasticity modulus. With developing material damage, the material stiffness, i.e. E-modulus, decreases. In experiments E is determined from unloading controlled by stress to avoid compression according to the suggestion of Lemaitre [10], as shown in Fig. 6(a). Since unloading is limited within a small range, damage due to unloading is negligible.

The damage evolution in the uniaxial tension test is plotted in Fig. 6(b). In the figure the damage evolutions of tensile bar and WEDM tubular specimen are nearly identical. That is, the WEDM machining has negligible influence on the damage evolution. On the other side, the material stiffness loses dramatically in very small strain and then diminishes almost linearly. This result implies that material damage nucleates even under elastic loading condition and develops with further inelastic strains. The relation between damage and stress/strain can be approximated by the known Ramberg-Osgood model, as

$$D = A\sigma + B\epsilon^m \tag{3}$$

with A, B and m>1 as fitting parameters. The damage relation in Eq. (3) is shown in Fig. 6(b) and its development is dominated by the linear term in small loading region. Damage is nucleated under elastic material state and mainly linear proportional to applied stress, since the nonlinear term is vanishingly small for small strain. If the material becomes plastic, the strain will grow over-proportionally, so that the influence of the linear term disappears. The exponent m is larger than 1, so that the damage curve for the sintered metals is convex. From dense ductile materials it is known that damage nucleates at large plastic strain and grows very gradually, the damage evolution curve is concave [10]. The convex development implies a very different damage mechanism in the

sintered metal.

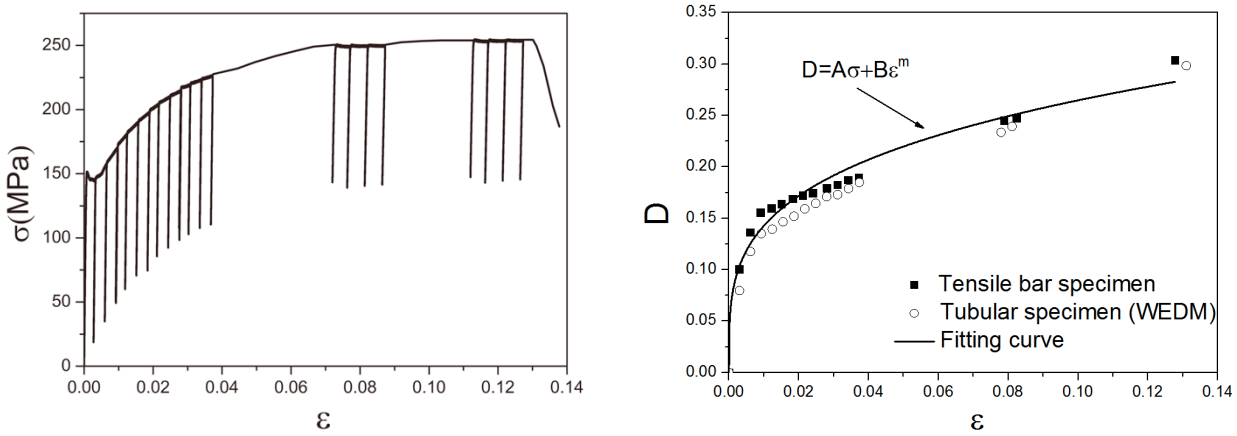

Figure 6. Uniaxial tensile tests. (a) Loading-unloading cycle to determine elastic modulus. (b) Damage as a function of strain.

Damage evolution in torsion can be determined in the same way as that in tension. The influence of machining on damage evolution is shown in Fig. 7 for both tension and torsion loadings, where damage is expressed as a function of the equivalent strain, $\varepsilon_{eq} = \sqrt{\varepsilon^2 + \gamma^2/3}$. The experiments reveal that the damage evolution under shearing is similar to that under tension. But the fracture strain of torsion is dramatically larger than that from tension, which implies effects of the stress triaxiality. As expected, damage in the TBD specimens develops more quickly than that in the WEDM specimens and the TBD specimens fail at smaller strains for both tension and torsion loadings. But the influence of machining on the damage evolution under torsion loading is smaller than under tension.

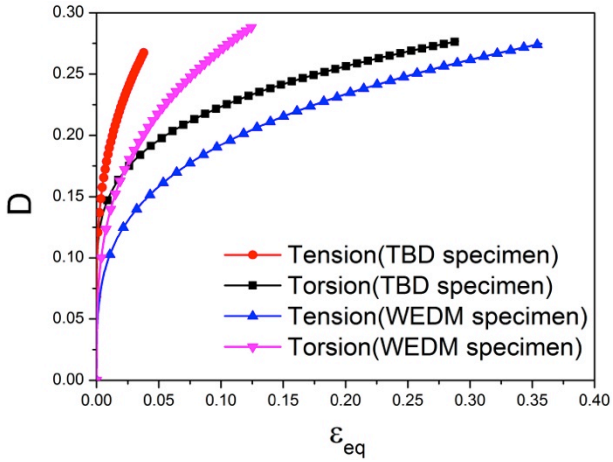

Figure 7. Evolutions of damage in different specimens.

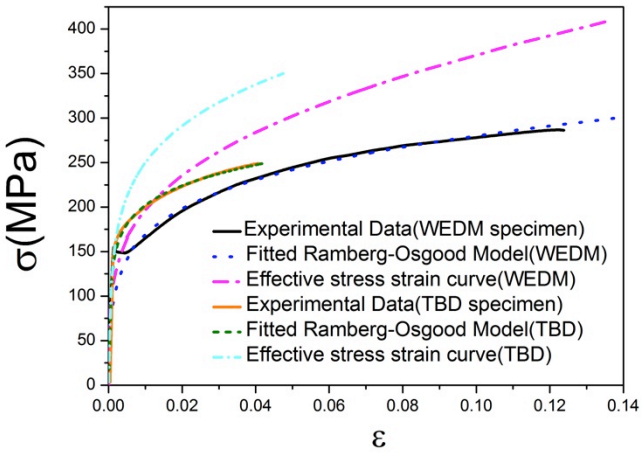

Figure 8. Effective stress-strain curves

4. Continuum damage model

In the framework of infinitesimal deformation, the strain rate tensor is decomposed into elastic and plastic part as

$$\dot{\epsilon}_{ij} = \dot{\epsilon}^e_{ij} + \dot{\epsilon}^p_{ij}. \tag{4}$$

In the present work, the scalar damage variable as defined in (1) is introduced to describe degradation of the sintered metal in the framework of continuum damage mechanics. Based on the strain equivalence hypothesis, the effective stress in the undamaged configuration is defined as [1,2,10]

$$\tilde{\sigma}_{ij} = \frac{\sigma_{ij}}{(1-D)}. \tag{5}$$

The effective stress-strain curves for both types of specimens are plotted in Fig. 8. Then, the thermodynamic driving force associated with damage variable D is given based on the thermodynamic framework for continuum damage model proposed by Lemaitre [8,10] as

$$Y = \frac{\sigma_e^2}{2E_0(1-D)^2} f(\eta), \tag{6}$$

with

$$f(\eta) = \frac{2}{3}(1+\nu) + 3(1-2\nu)\eta^2. \tag{7}$$

Above $f(\eta)$ represents dependence on the stress triaxiality, $\eta = \sigma_H / \sigma_{eq}$, where σ_H is the hydrostatic stress and σ_{eq} is Mises stress.

4.1. The damage evolution law with initial damage

Experimental observations for the sintered metals reported in the previous section reveal that material damage occurs under very low stress amplitude, i.e. damage is induced by elastic deformations before the material is plastic. Thus, the damage variable can be decomposed into elastic damage and plastic damage, as

$$D = D^e + D^p. \tag{8}$$

Obviously, the decomposition is consistent to experimental data for the uniaxial state, Eq. (3).

4.1.1. Elastic damage evolution

The elastic damage was known in brittle materials, such as concrete, rocks etc. Various elastic CDM models have been developed for modeling elastic damage accumulation in the brittle materials [7，9], which can be extended to characterize the elastic damage in the sintered metal. The potential function for the elastic damage is defined as

$$F_e^D = Y - Z(D_e), \tag{9}$$

where Z is the material resistance against material damage. Following the material resistance can be expressed in the exponential form

$$Z = Y_0 + \frac{1}{b}\ln\left(\frac{D_e^{sa} - D_e^0}{D_e^{sa} - D_e}\right), \tag{10}$$

where Y_0 is the initial resistance against material damage and b is a model parameter. D_e^{sa} represents the saturation of the elastic damage since in elastic-plastic materials the elastic damage will not finally destroy the structure but accelerate the final failure. D_e^0 denotes initial elastic damage, which can be induced by manufacturing process or previous loading history. From the maximum dissipation principle, the damage evolution law is expressed in the rate-form as

$$\dot{D}_e = \dot{\lambda}_b \frac{\partial F_e^D}{\partial Y} = \dot{\lambda}_b. \tag{11}$$

In case with damaging, the damage multiplier $\dot{\lambda}_b$ is determined by the damage consistency condition,

$$dF_e^D = \frac{\partial F_e^D}{\partial Y}\dot{Y} - \frac{\partial Z}{\partial D_e}\dot{\lambda}_b = 0. \tag{12}$$

The evolution equation of the elastic damage is expressed as

$$\dot{D}_e = (D_e^{sa} - D_e^0)\, b \exp\left[-b\left\langle Y - Y_0 \right\rangle\right]\dot{Y}, \tag{13}$$

or

$$D_e = D_e^0 + (D_e^{sa} - D_e^0)\left\{1 - \exp\left[-b\left\langle Y - Y_0 \right\rangle\right]\right\}. \tag{14}$$

where $\left\langle \cdot \right\rangle$ is the Macauley bracket, i.e. $\left\langle x \right\rangle = \left(|x| + x\right)/2$.

4.1.2 Plastic damage evolution

In ductile materials the damage is mainly accumulated due to plastic deformations. Following the concept by Bonora et al. [1, 2] interactions between plastic dissipation and damage dissipation can be neglected. The plastic damage dissipation potential F exists and can be expressed as sum of plastic damage potential, F_p^D, and plastic deformation potential, Ψ_p, as

$$F = F_p^D + \psi_p. \tag{15}$$

Based on the hypothesis of the strain equivalence and the effective stress concept, the plastic dissipation potential for the material can take the form of the J_2 plasticity theory,

$$\psi_p = \tilde{\sigma}_e - \tilde{\sigma}_{y0} - R(r), \tag{16}$$

where the effective Mises stress is defined as

$$\tilde{\sigma}_e = \sqrt{\frac{3}{2}\left(\frac{s_{ij}}{1-D}\right)\left(\frac{s_{ij}}{1-D}\right)} \tag{17}$$

with s_{ij} as the deviatoric stress tensor. The damage dissipation potential proposed after Bonora et al. [1, 2] for the plastic damage model is written as

$$F_p^D = \left[\frac{1}{2}\frac{Y^2}{S_0}\frac{1}{1-D}\right]\frac{(D_{cr}^p - D_p)^{(\alpha-1)/\alpha}}{p^{(2+n)/n}}, \tag{18}$$

where S_0 is damage material parameter, n is the plastic hardening exponent in the Ramberg-Osgood model, α is the damage exponent that determines the shape of the damage evolution law and p is the accumulated plastic strain. D_p^{cr} is critical plastic damage value.

Based on the maximum dissipation principle, the evolution of internal variables can be obtained via the normality rule as

$$\dot{\epsilon}_{ij}^p = \dot{\lambda}_p \frac{\partial F}{\partial \sigma_{ij}} = \dot{\lambda}_p \frac{\partial \psi_p}{\partial \sigma_{ij}}, \dot{D}_p = \dot{\lambda}_p \frac{\partial F}{\partial Y} = \dot{\lambda}_p \frac{\partial F_p^D}{\partial Y}, \dot{\lambda}_p = \dot{p}(1-D). \tag{19}$$

The effective stress can be formulated as a function of the plastic strain in the Ramberg-Osgood law,

$$\tilde{\sigma}_{eq} = \frac{\sigma_{eq}}{1-D} = Kp^{1/n}. \tag{20}$$

Recalling Eqs. (18) - (20) and Eq. (6), the plastic damage evolution law is derived as

$$\dot{D}_p = \begin{cases} 0 & \text{if } p < \epsilon_{th} \text{ or } \sigma_H \le 0), \\ \dfrac{K^2}{2E_0 S_0} f(\eta) \left(\dfrac{(D_p^{cr} - D_p)^{(\alpha-1)/\alpha}}{p} \right) \dot{p} & \text{if } p \ge \epsilon_{th} \text{and } \sigma_H \ge 0). \end{cases} \tag{21}$$

It is assumed that the plastic damage will not grow in the compression stress state [2]. The plastic damage process remains inactive until the effective accumulated plastic strain p reaches the threshold strain ϵ_{th} for the positive hydrostatic stress.

With $D_p = D_p^{cr}$ at $p = p_{cr}$ as the final critical damage to fracture, integrating the equation above over $[D_p^0, D_p^{cr}]$ for D and $[\epsilon_{th}, p_{cr}]$ for p under proportional loading condition, where D_p^0 is initial plastic damage, one gets

$$[D_p^{cr} - D_p^0]^{1/\alpha} = \frac{1}{\alpha} \frac{K^2}{2E_0 S_0} f(\eta) \ln\left(\frac{p_{cr}}{\epsilon_{th}} \right). \tag{22}$$

Integrating the equation above over $[D, D_p^{cr}]$ for D and $[p, \epsilon_{cr}]$ for p, one gets

$$[D_p^{cr} - D^p]^{1/\alpha} = \frac{1}{\alpha} \frac{K^2}{2E_0 S_0} f(\eta) \ln\left(\frac{p_{cr}}{p} \right). \tag{23}$$

For uniaxial tension $f(\eta) = 1, p_{cr} = \varepsilon_{cr}$, Eq. (23) can be re-written into

$$[D_p^{cr} - D_p^0]^{1/\alpha} = \frac{1}{\alpha} \frac{K^2}{2E_0 S_0} \ln\left(\frac{\varepsilon_{cr}}{\epsilon_{th}} \right). \tag{24}$$

Dividing Eq. (24) with Eq. (23), one obtains the explicit expression for plastic damage as a function of the equivalent plastic strain for proportional loading cases

$$D_p = D_p^0 + (D_p^{cr} - D_p^0) \left\{ 1 - \left[1 - \frac{\ln(p/\epsilon_{th})}{\ln(\epsilon_{cr}/\epsilon_{th})} f(\eta) \right]^{\alpha} \right\}. \tag{25}$$

Dividing Eq. (23) by Eq. (25), the fracture strain under proportional loading can be expressed as

$$p_{cr} = \epsilon_{th} \cdot \left(\frac{\varepsilon_{cr}}{\epsilon_{th}} \right)^{1/[f(\eta)]} \tag{26}$$

4.2. Identification of model parameters

Identification of the damage model parameters is accomplished with uniaxial tests using the WEDM tubular specimens, i.e. tensile and compressive tests. For verification, the fracture strain in multi-axial experiments and influence of machining on the damage evolution of specimen should be predicted by the CDM [11].

In Fig. 8, the material parameters for Ramberg-Osgood power law can be obtained by fitting for both machining procedures. According to the experimental results, the average density of material is increased after machining. On the other words, the material is compressed during machining. It is well known that ductile damage grows more slowly in compression stress state. The initial plastic damage is negligible. The initial damage is considered as elastic damage. And the initial plastic damage is not activated during machining, $D_p^0 = 0$. The initial elastic damage is calculated by $D_e^0 = 0.074$, E_0 is 176GPa for material with density 7.4g/cm^3.

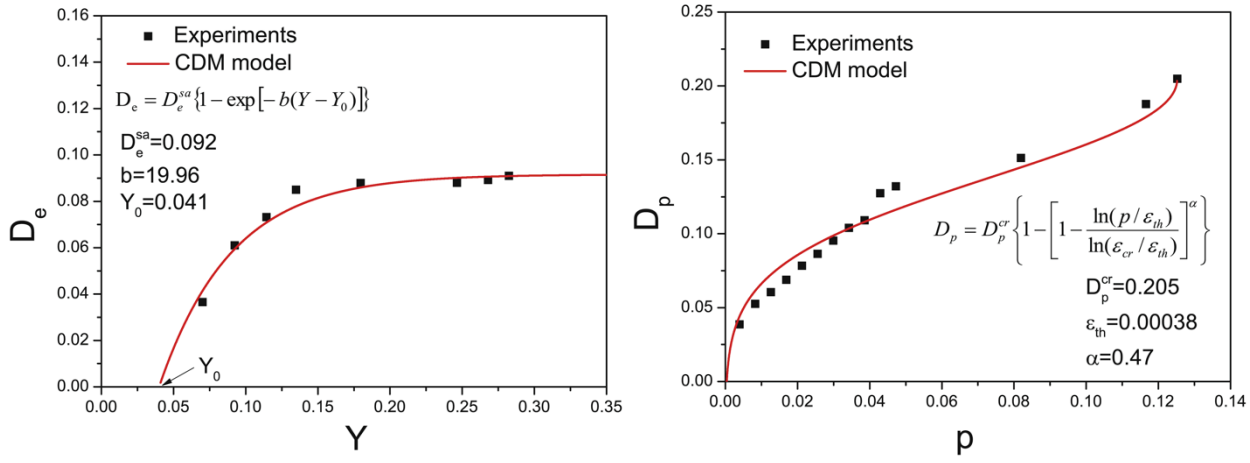

(a) (b)

Figure 9. Development of the damage as a function of applied load. Symbols denote experimental data and curves are results from the CDM model. (a) Evolution of the elastic damage with energy release rate. (b) Plastic damage evolution with the plastic strain.

Since it is assumed that plastic damage will not accumulate in the compressive stress state, the compression test is used to identify the model parameters of the elastic damage evolution for the isotropic elastic damage. The elastic damage becomes almost stationary for higher loading. The model parameters D_e^{sa}, b and Y_0 are identified by fitting the experimental curve as shown in Fig 9(a).

The plastic damage evolution should be obtained from the elastic-plastic tensile tests. From the uniaxial tensile tests the critical ductile damage can be approximated by $D_p^{cr} = D_{cr} - D_e^{sa}$. The result of Eq. (25) is plotted in Fig. 9(b), in which the ductile damage is expressed as a function of the plastic strain. The material parameters of the elastic-ductile damage model for sintered iron are summarized in Table 2.

Table 2. Summary of the material model parameters for the sintered iron

Elasto-plastic material properties:
Tubular specimen(Conventional machining)
E_0 = 176000MPa; ν = 0.27; σ_{y0} = 135MPa; n = 4.955; K = 608MPa
Tubular specimen(WEDM)
E_0 = 162000MPa; ν = 0.27; σ_{y0} = 135MPa; n = 4.714; K = 549MPa
Elastic damage evolution law:
D_b^{sa} = 0.091; b = 19.961; Y_0 = 0.04MPa,
Plastic Bonora damage evolution law:
ϵ_{th} = 0.00038; α = 0.47; S_0 = 27.85MPa; ϵ_{cr} = 0.12522; D_p^{cr} = 0.205; D^{cr} = 0.296

4.3. Failure Prediction of the CDM model

Using the material parameters identified in the previous section, damage evolution of sintered iron is predicted for both tension and torsion loading condition according to Eq. (25). Furthermore, the equivalent fracture strain is also predicted for combined tension-torsion condition with Eq. (26).

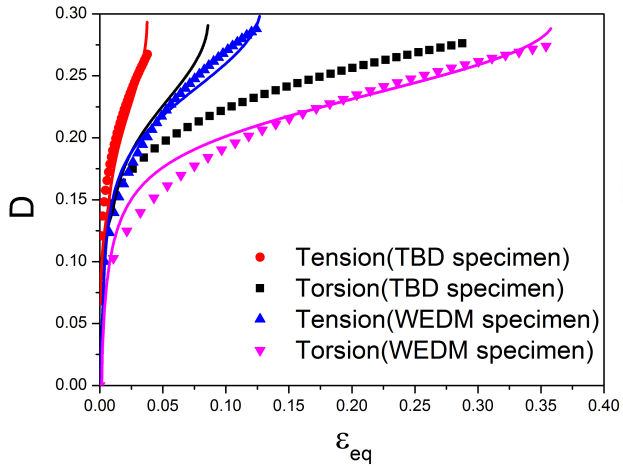

Figure 10. Comparison between experiments and computational predictions

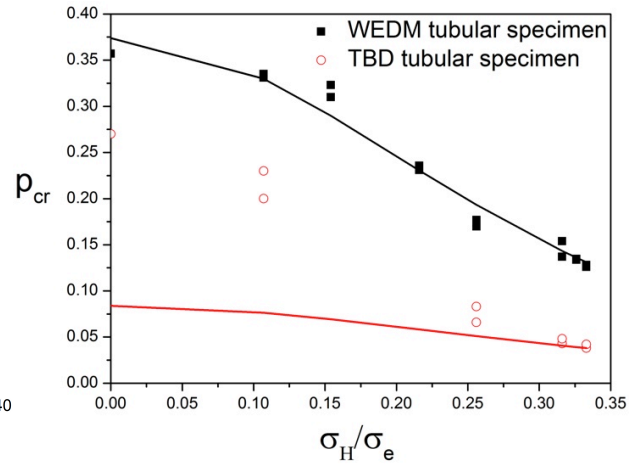

Figure 11. Variations of final fracture strain in tension-torsion specimens.

Experimental observations of different sinter metal specimens are plotted in Figs. 10 and 11 in which symbols denote experimental data. With increasing stress triaxiality, the material behaves more brittle, that is, the fracture strain decreases rapidly. Obviously, the prediction from the CDM model is accurate for the WEDM specimens in comparison with the tension and torsion tests.

For the TBD specimen, it is seen that the proposed model is not able to accurately predict the machining effect on the damage evolution under torsion loading. The deviation becomes more significant with decreasing stress triaxiality in the range of $\eta < 0.25$. That means that the machining influence on the damage evolution is strongly depending on loading mode. In the machining process, the initial damage induced by mainly shearing in specimen. Under this situation the damage in the form of micro-cracks would be perpendicular to the specimen axis, which is very sensitive to axial tension, not to the torsion. That is, the damage is strongly anisotropic. Additionally, the initial damage is not constant in the tubular specimen. It will lead to stress gradient in the subsurface of specimen. For this reason, the initial damage gradient has to be considered in investigation of machining effect in order to reasonably predict the damage evolution of material contains machining effect.

5. Conclusions

In the present work damage evolution in a sinter iron is studied experimentally and computationally. Based on both analytical and computational discussions following conclusions can be drawn:

- Experiments on both tension and torsion tests confirm that the sinter material stiffness decreases rapidly with applied load. The degradation of material occurs at much lower load level than yield stress.
- The damage variable in the continuum damage model is decomposed into elastic damage and plastic damage, where the elastic damage is characterized by the stress and the plastic damage is mainly controlled by the plastic strain. The evolution equations for both damage variables have been developed within the framework of thermodynamics. The initial damage is considered in the damage evolution law. Explicit expressions for both damage evolutions have been obtained.
- Conventional machining (TBD) has significant influence on the mechanical properties of the

sintered iron. The sinter metal is densified，hardened and damaged. Fracture strain decreases dramatically. The machining changes the dependence of damage evolution on loading mode. The results show that the proposed damage model is able to predict machining influence on damage evolution under tension loading, but not under torsion.

References

[1] N. Bonora. A nonlinear CDM model for ductile failure. Engineering Fracture Mechanics 58 (1) (1997) 11–28.
[2] N. Bonora, D. Gentile, a. Pirondi, G. Newaz. Ductile damage evolution under triaxial state of stress: theory and experiments. International Journal of Plasticity 21 (5) (2005) 981–1007.
[3] S. Carabajar, C. Verdu, R. Fougeres. Damage mechanisms of a nickel alloyed sintered steel during tensile tests. Materials Science and Engineering: A 232 (1-2) (1997) 80–87.
[4] J. L. Chaboche, M. Boudifa, K. Saanouni. A CDM approach of ductile damage with plastic compressibility. International Journal of Fracture 137 (1-4) (2006) 51–75.
[5] N. Chawla, B. Jester, D. Vonk. Bauschinger effect in porous sintered steels. Materials Science and Engineering: A 346 (1-2) (2003) 266–272.
[6] J. Chen, H. Yuan, M. Schneider. Investigation of micromechanical deformation mechanisms in sinter powder metals. Advanced Material Research, in print.
[7] U. Cicekli, G. Z. Voyiadjis, and R. K. Abu Al-Rub. A plasticity and anisotropic damage model for plain concrete, International Journal of Plasticity 23 (10-1) (2007) 1874–1900.
[8] R. Desmorat, S. Cantournet. Modeling microdefects closure effect with isotropic/anisotropic damage. International Journal of Damage Mechanics 17 (1) (2007) 65–96.
[9] O. Kintzel, S. Khan, J. Mosler. A novel isotropic quasi-brittle damage model applied to LCF analyses of Al2024. International Journal of Fatigue 32 (12) (2010) 1948–1959.
[10] J. Lemaitre, R. Desmorat. Engineering damage mechanics: Ductile, creep, fatigue and brittle failures, Springer-Verlag, 2005.
[11] S. Ma, H. Yuan. Damage evolution and modeling of sinter metals under multi-axial loading conditions. Computational Materials Science, submitted for publication.
[12] X. Pan, H. Yuan. Computational algorithms and applications of element-free Galerkin methods for nonlocal damage models. Engineering Fracture Mechanics 77 (2010), 2640-2653
[13] M. Schneider, H. Yuan. Experimental and computational investigation of cyclic mechanical behavior of sintered iron. Computational Materials Science 57 (2012) 48 – 58.
[14] C. M. Sonsino. Zukunftsperspektiven für die Pulvermetallurgie durch die Betriebsfestigkeit. Materialwissenschaft und Werkstofftechnik 37 (3) (2006) 240–248.
[15] H. Yuan, J. Chen, K. Krompholz, F.H. Wittmann. Investigations of size effects in tensile tests based on a nonlocal micromechanical damage model. Computational Materials Science 26 (2003) 230-243

Mechanical and Fracture Behavior of Gelatin Gels

M. Czerner, J. Martucci, L. A. Fasce, R. Ruseckaite and P. M. Frontini[1,*]

[1] INTEMA, Universidad Nacional de Mar del Plata, B7608FDQ, Argentina
* Corresponding author: pmfronti@fi.mdp.edu.ar

Abstract
Hydrogels were prepared from bovine and porcine gelatin powders of different Bloom values. Gelatin concentration and pH were selected to obtain self-supporting gels with stiffness in the range of those employed in structural applications in foodstuff, ballistic and pharmacy. Glycerol and sorbitol were also added in gel formulations. Deformation and fracture behaviors were assessed by means of gel strength measurements, uniaxial compression tests and wire cutting experiments. All gels showed non-linear elastic deformation with strain hardening and brittle fracture. Large deformation was described with a first order Ogden constitutive model. Strain hardening was attributed to protein chains renaturation capability under stress. It was found that neat porcine gelatin gels displayed higher gel strength, shear modulus, failure strain and stress, fracture toughness and water retention than bovine gelatin gels. The addition of sorbitol and glycerol caused an increase in water retention capability and a marked enhancement in gels´ fracture toughness. The major content of hydrophilic amino acids in the gelatin, the stronger the effect of glycerol and sorbitol on gelatin network morphology. The correlation between large deformation and fracture toughness parameters with the technological gel strength values was also investigated.

Keywords: hydrogels, gelatin, fracture toughness, depth sensing indentation

1. Introduction

Hydrogels consist of three-dimensional hydrophilic polymer network with the ability of swelling and retain large volumes of water without dissolution [1]. Hydrogels can be obtained from synthetic polymers, but those derived from biopolymers such as proteins and polysaccharides are being preferred due to their renewable nature, low toxicity, biodegradability and biocompatibility [2]. Among natural polymers gelatin is an attractive candidate as raw material for preparing hydrogels because its gelling ability. It is unique among hydrocolloids in forming thermo-reversible physical gels with a melting point close to body temperature [1].

The main gelatin hydrogels applications include their use as: *i)* ingredients to improve elasticity, consistency and stability of foods [3]; *ii)* human tissue simulants in ballistic studies [4]; *iii*) carriers for drug delivery systems [5]; iv) scaffolds for cell growth in tissue engineering [6]. Mechanical requirements for hydrogels in the aforementioned applications are large deformation capability together with proper toughness and stiffness level. Independent tuning of elastic modulus, deformation capability and fracture toughness becomes highly desirable to the development of hydrogels with tailored properties. So that, the assessment of mechanical properties and the knowledge of whether they are influenced by gelatin source and additives are of fundamental importance and constitute the aim of this research.

Determining reliable mechanical properties of soft materials like hydrogels is a challenged task due to its low modulus (of the order of kPa) and complex mechanical behavior. Hydrogels are soft but exhibit brittle failure and show dependence with strain rate, as polymers does (see for example in [7]).

The gel strength is the most popular property used to mechanically characterize gelatin gels [8]. It is determined using the so-called Bloom test, which consists on performing an indentation test under

specifically defined conditions -gelatin concentration (6.67 %), temperature (10 ºC), maturation time (17 h), indentation depth (4 mm), cylindrical plunger (12.5 mm diameter)- thus allowing gel strength to be expressed in the normalized Bloom value. It has been shown that the Bloom value is linked to the stiffness of the gel network [9].
In this work, deformation behavior and fracture toughness of gels based on two commercial mammalian gelatins differing in collagen source (*ie.* with different amino acid composition [10]) and Bloom value are assessed. Large deformation behavior is evaluated by uniaxial compression experiments and for fracture toughness, the Gc parameter is determined by the wire cutting technique [7]. The effect of adding sorbitol and glycerol, two common additives in gels formulations, on mechanical performance is also analyzed and discussed. The relationship between gel strength and shear modulus, fracture toughness and ultimate deformation properties is also investigated.

2. Experimental

2.1. Gelatin Gels preparation

Bovine hide gelatin type B, Bloom 200, isoionic point (Ip) 4.7-5.4 and porkskin gelatin type A, Bloom 250, Ip 7-9 were kindly supplied by Rousselot (Argentina). Glycerol analytical grade were purchased from DEM Chemicals (Mar del Plata, Argentina). D-Sorbitol monhydrate (S) and buffer solution pH 7 and pH 10 were purchased from Anedra (Buenos Aires, Argentina).
Gelatin solutions were prepared by dissolving the gelatin powder (20wt%) in a buffer solution with continuous stirring at 50ºC. The buffer was selected over the gelatins' isoionic points (pH=7 for bovine and pH=10 for porcine gelatins). In addition, glycerol and sorbitol were incorporated at a concentration of 25wt% (based on dry gelatin powder). Glycerol and Sorbitol are non-solvents for gelatins so that the initial gelatin concentration in water was kept constant in each formulation. The designation of prepared gels is *B0*, *B1* and *B2* for bovine based gels containing neat gelatin, glycerol and sorbitol, respectively. Analogous, porcine gelatin gels are designated as *P0*, *P1* and *P2*.
The resulting homogeneous solutions were poured into specially design Delrin® molds and kept at room temperature during 15min to form the gels. Specimens were then wrapped in film in order to minimize drying out and stored at 4 ºC during 48 h. Before testing samples were conditioned at 21 ºC during 2 h.

2.2. Physical and mechanical characterization

2.2.1 Water Retention: For each formulation, three gel specimens were dried in an air circulating oven at 105ºC until constant mass. Samples were weighted with an accuracy of 0.0001g before and after drying to determine the initial mass (m_i) and the gelatin dry matter (m_0), which was normalized by the glycerol and sorbitol content. Gel water retention (WR) was then calculated as:

$$WR(\%) = \frac{m_i - m_0}{m_0}.100 \quad (1)$$

2.2.2 Transmission optical microscopy (TOM): Inspection was performed on gels samples employing a Leica DMLB microscope provided with a video camera Leica DC 100.
2.2.3 Scanning Electron Microscopy (SEM): Inspection was performed in a JEOL JSM-6460LV microscope in order to analyze the ultra-structure of gelatin gels. The prepared samples were frozen, lyophilized, cryofractured and coated with a thin film of Au/Pd before inspection.
2.2.4 Gel Strength: Measurements were carried out on prepared gels using an INSTRON 3369 universal testing machine. Samples were cylindrical blocks having 25 mm of diameter and height. Gel strength was determined as the maximum load measured after a steel cylindrical plunger penetrated 4mm into the sample surface [11]. The plunger was flat-faced and had a diameter of 10 mm. A Load cell of 0.1 kN was used and the penetration speed was 25mm/min. The gel strength was taken as the average value of four measurements performed on different samples.
2.2.5 Uniaxial compression: Tests were performed on cylindrical samples with a diameter and height of 25mm in an INSTRON 4469 universal testing machine. Experiments were conducted at two loading rates (5 and 25 mm/min). A 0.5 kN load cell was used. A Teflon spray was applied at the interface between sample and compression platens in order to diminish friction. At least five replicates were tested at each loading rate. Samples were loaded up to fracture. The obtained load (P)- displacement (v) data were converted to true stress (σ) vs. true strain (ε) curves assuming that the material was incompressible. Data were also expressed in terms of and true stress (σ) – stretch ratio ($\lambda = e^{\varepsilon}$).
2.2.6 Wire Cutting tests: Experiments were carried out in an INSTRON 4469 universal testing machine equipped with a specially designed grip and a 0.5 kN load cell. The grip allows the wire to be tight and perfectly aligned with the sample surface. Seven steel wires of different diameters (d) ranging from 0.2 to 0.8 mm were used and the cutting rate was 25 mm/min. The samples were rectangular blocks of length 30 mm, width 20 mm and height 20 mm. For each wire diameter at least five cuts were performed. The steady-state cutting energy was obtained by dividing the cutting force, F_c, by the specimen width, b. A linear relationship between the normalized cutting force F_c/b and wire diameter d is postulated [12]:

$$\frac{F_c}{b} = G_c + \sigma_y \left(1 + \mu_k\right) d \tag{2}$$

where σ_y is a characteristic stress and μ_k is the kinetic friction coefficient. By extrapolating the steady state cutting energy to zero wire diameter, G_c is obtained (Eq. 2) since the work input is consumed solely by the propagating crack.
2.2.7 Statistical Analysis: Analysis of variance (ANOVA) was carried out to find differences in the measured properties of gelatin gels due to the addition of glycerol and sorbitol. The bovine gelatin gel series (*B0, B1* and *B2*) and the porcine gelatin gel series (*P0, P1, P2*) were analysed by an independent ANOVA. Differences between means were analysed using the Tukey´s test for post hoc comparison ($p < 0.01$). Analysis was performed using STATISTICA 6.0 (Statsoft, Inc., Tulsa, USA).

3. Results and Discussion

Gelatin powder concentration, pH and temperature values used in gels formulation were selected to obtain self-supporting gels with stiffness in the middle range of those employed in structural applications in foodstuff, ballistic and pharmacy (E = 1 to 10^3 kPa) [13,14]. Gelatin concentration

was kept constant in all materials, but owing to the different amino acid composition [10] and molecular weight of both types of gelatins and due to the presence of additives, different gel mechanical properties are expected.
All prepared gelatin gels show optically clear appearance and transparency. The incorporation of additives- glycerol and sorbitol- seems to not alter their physical integrity or optical appearance.

3.1 Water Retention Capability

As can be seen in Table 1, *P0* gel shows higher water retention capability than *B0*. The incorporation of glycerol and sorbitol increases the amount of retained water in both types of gels. In comparison, the increase in water retention capability is larger in gels containing glycerol than in those with sorbitol because glycerol molecules are more hygroscopic than sorbitol ones due to its smaller size.

3.2 Gel Strength

Gel strength values of gelatin gels are also given in Table 1. Gel strength of *P0* is higher than *B0* in agreement with the larger Bloom value of porcine gelatin. As well, all porcine gelatin based gels are stronger than bovine based ones, being *P2* the strongest gel of the series.
Gel strength values do not decrease with increasing water content in modified gels, indicating a strong impact of glycerol and sorbitol on gelatin gels network structure. The increase in gel strength is consistent with the explanation that the addition of polyhydric alcohols may create a shorter mean distance between junction zones by increasing the number of crosslinking points [15] and that co-solvent do not participate in the interlinking of protein molecules but they reduce the available water by preferential hydrogen bonding with water molecules [16].

Table 1. Water retention and gel strength of prepared gelatin gels.

Gel	Water Retention (%)	Gel Strength (N)
B0	355.6 ± 1.5^{a}	4.09 ± 0.12^{a}
B1	447.7 ± 1.9^{b}	3.61 ± 0.24^{b}
B2	365.7 ± 3.1^{c}	3.88 ± 0.14^{ab}
P0	429.3 ± 6.4^{A}	4.40 ± 0.08^{A}
P1	448.3 ± 2.9^{B}	4.12 ± 0.01^{B}
P2	437.4 ± 1.8^{B}	4.71 ± 0.10^{C}

Different letters in the same column indicate significant differences between means ($p<0.05$).

3.2 Large Deformation Properties

Previous investigations [17, 18] demonstrated that the uniaxial compression response of the studied

gelatin gels is independent of strain rate within a range from 0.1 to 10min^{-1} and that it is completely reversible.

Figure 1 shows the stress-strain curves obtained for bovine (Fig. 1-a) and porcine (Fig. 1-b) based gelatin gels in uniaxial compression experiments at a strain rate of 1/min. The compression response of all gels is non-linear elastic with strain hardening up to catastrophic fracture. The scattering in uniaxial compression curves is wider in porcine gels than in bovine gels. This maybe related to the higher content of trapped air microbubbles in the porcine gels as thrown by TOM inspection of gel samples.

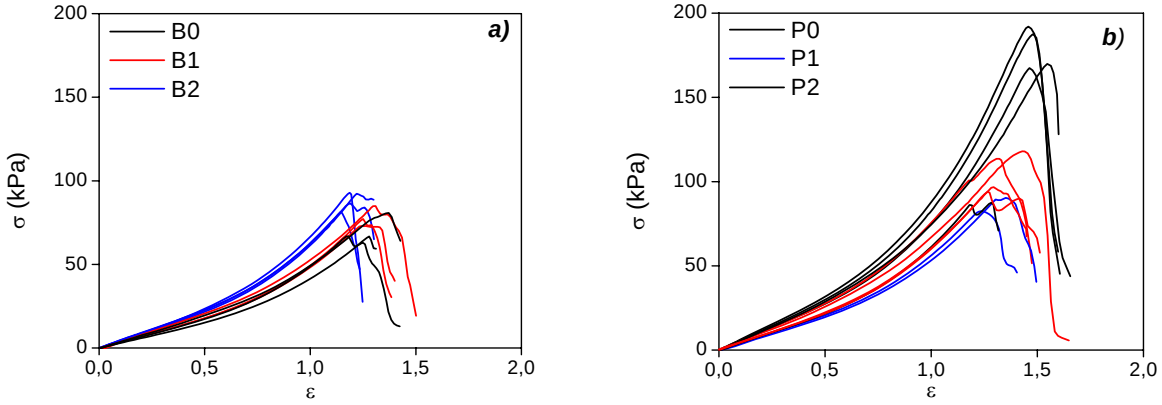

Figure 1. Stress-strain curves obtained in uniaxial compression tests for a) bovine and b) porcine based gelatin gels.

The simplest law used to model materials that behave elastically and show strain hardening when subjected to large strains is the first order Ogden constitutive equation. It can be expressed in terms of true stress σ and stretch ratio λ, as:

$$\sigma = \frac{2\mu}{\alpha}\left(\lambda^{\alpha} - \lambda^{-\alpha/2}\right) \tag{3}$$

where μ is equal to the material shear modulus and α is a parameter related with strain hardening capability [19]. More negative α values indicate large strain hardening, while less negative ones stands for more linear elastic behavior.

For each experimental set of curves, a least square fit was performed taking all stress-stretch ratio data up to λ=0.35. The obtained model parameters are given in Table 2. This simple model (Eq. 3) is able to well describe the behavior of gelatin gels as judged by the values of the regression coefficients (R^2) and the errors in the model parameters. The source of strain hardening capability of gelatin gels may rely on the ability of the protein molecules to recover the native collagen triple helix configuration under stress. This behavior has already been suggested to explain improvements in mechanical properties of gelatin films [20]. As protein renaturation is a completely reversible process, gelatin gels are capable to recover its original configuration after load removal, displaying non-linear elastic behavior. *P0* is more able to strain harden than *B0* (see the more negative α value in Table 2).

The shear modulus of *P0* gel is larger than the one determined for *B0* gel (Table 2), consistently with its higher Bloom value. The addition of sorbitol and glycerol slightly modifies the Ogden constitutive parameters except for the *P2* gel in which α becomes less negative and μ decreases. The change in α is consistent with a larger amount of physical crosslinking points in the gelatin network, which

constrains renaturation of protein molecules under stress. The decrease in μ maybe related to the higher water content in the gel.

Table 2. Mechanical parameters obtained from uniaxial compression tests.

Gel sample	μ (kPa)	α	R^2	Fracture stress (kPa)	Fracture strain
B0	9.29 ± 0.09^{a}	-1.40 ± 0.02^{a}	0.9826	69.2 ± 8.1^{a}	1.23±0.12
B1	12.07 ± 0.06^{b}	-1.44 ± 0.01^{b}	0.9954	90.6 ± 3.5^{b}	1.20±0.02
B2	9.57 ± 0.04^{c}	-1.37 ± 0.01^{c}	0.9983	79.1 ± 5.1^{ab}	1.23±0.06
P0	14.59 ± 0.15^{A}	-1.53 ± 0.01^{A}	0.9747	176.6 ± 35.4^{A}	1.42±0.14
P1	13.52 ± 0.19^{B}	-1.38 ± 0.04^{B}	0.9599	102.8 ± 32.9^{B}	1.31±0.04
P2	10.88 ± 0.19^{C}	-1.14 ± 0.05^{C}	0.9507	83.1 ± 7.4^{B}	1.37±0.10

Different letters in the same column indicate significant differences between means. Differences in fracture strain were not significative for both B and P series ($p<0.05$)

The ultimate properties obtained from the failure point in the stress-strain curves are also reported in Table 2. Fracture stress and strain are related to crosslinking density and network strength but also depend on microstructural defects. *B0* gel displays lower ultimate properties than *P0* gels despite the presence of microbubbles. In brief, porcine gelatin gels structure is more resistant and has a larger deformation capability than bovine gelatin one. Surprisingly, the addition of sorbitol and glycerol has a marked impact in the ultimate properties of porcine based gels but slightly influences the bovine ones. The detriment in fracture strain can be explained by an increase in protein-protein interactions, which leads to a more physically crosslinked network.

The ultra-structures of *P0*, *P2*, *B0* and *B2* gels were analyzed by SEM. The images of the morphologies are shown in Figure 2. All gels exhibit a network structure, but the addition of sorbitol in gel formulations appears to promote a large number of bridging sites in the gel main network (Fig. 2 *b* and *d*). This effect is more pronounced in P2 gel (Fig. 2 *b*), consistently with the major change in ultimate stress and strain hardening capability. It can also be observed that the network is more opened in *P2* gel even it is more interconnected. These features can explain the decrease in gel stiffness and are in agreement with the higher water retention capability of *P2* gel.

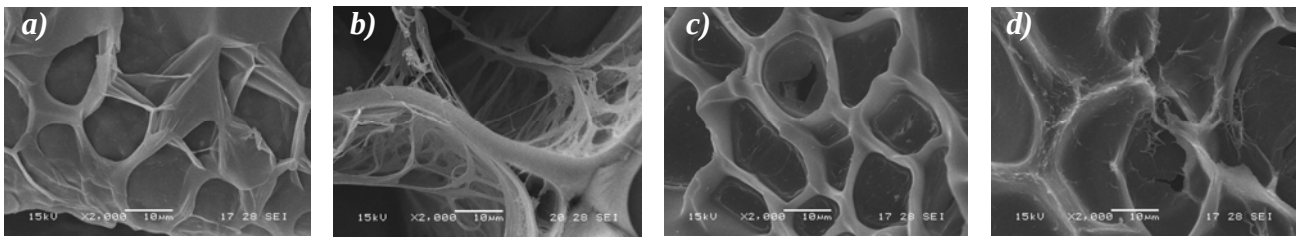

Figure 2. SEM images of gelatin gels revealing the detailed morphology of gelatin network ultra-structure a) P0, b) P2, c) B0 and d) B2.

3.3 Fracture Toughness

For all samples, wire cutting curves show two phases: an indentation phase and a steady- state cutting phase. First, the wire indented into the gel up to a given point at which the material starts to fracture. From such point, the load decreased suddenly reaching an almost constant force that corresponds to the steady-state cutting phase, F_c. In every case, the cutting force increases with increasing wire diameter. Figure 3 shows typical force-displacement curves obtained at different wire diameters for one of the tested gels (*B0*). The same wire cutting behavior was described for other soft materials [see for example in [7, 12, 21].

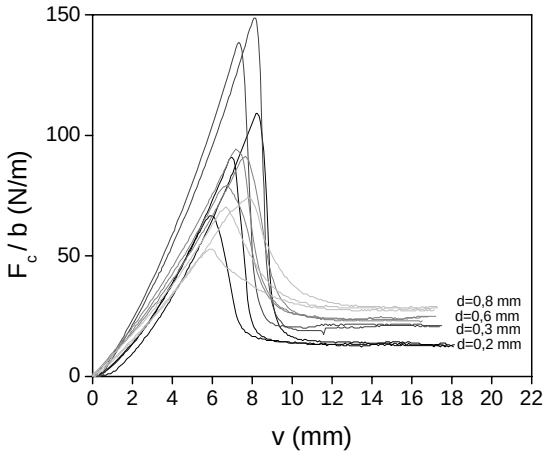

Figure 3. *Typical normalized load-displacement data measured in wire cutting tests of B0 gel using different wire diameters.*

The cutting energy versus wire diameter plots are shown in Figure 4. All data obtained for each wire diameter were averaged and plotted with its error. Data were linearly fitted according to Eq. 2 using Least Squares. Data lying outside the 95% confidence limits from the first best fit line were eliminated from the analysis. The arisen fitted parameters are listed in Table 3.

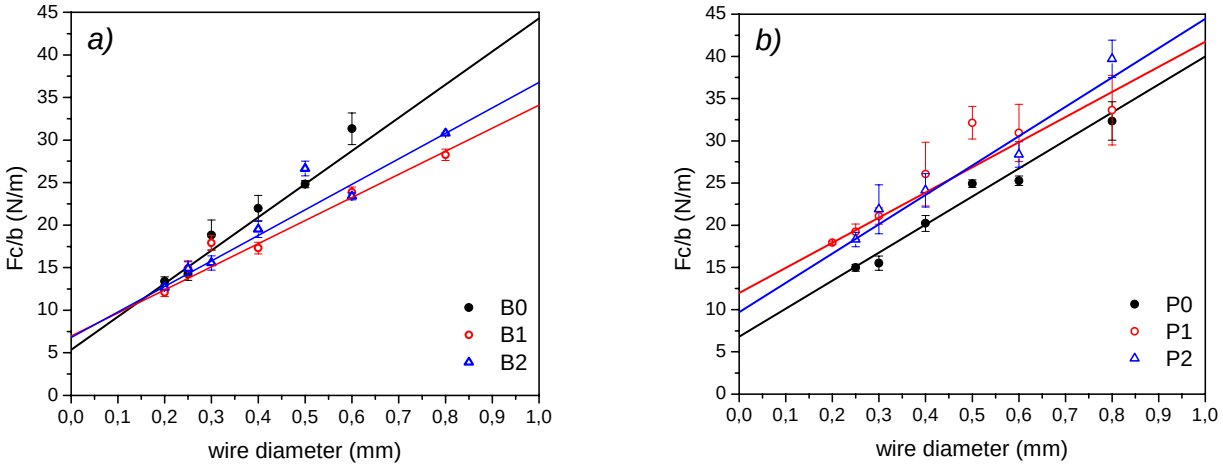

Figure 4. *Wire cutting data measured for a) bovine and b) porcine gelatin gels.*

The resulting experimental trend agreed with the wire cutting method proposal (Eq. 3) as judged by the obtained R^2 values greater than 0.93. Better regression coefficients values yield from bovine gelatin gels than for porcine gelatin gels. This can be attributed to the larger content of

microbubbles in the porcine gels.

The fracture toughness values are in the range of those required in pharmacy and tissue engineering applications (1 to 10 N/m) [13]. *P0* gels exhibit higher fracture toughness than *B0* gels, despite its larger amount of retained water. This is also true for the whole bovine and porcine series. Moreover, the addition of sorbitol and glycerol in gel formulation has a beneficial effect on the fracture toughness of both bovine and porcine gelatin gels. The enhancement in fracture toughness is more pronounced in porcine gels according to the development of a more interconnected network (Figure 2).

Table 4. *Fracture toughness of gelatin gels, G_c*

Gel sample	Gc (N/m)	$\sigma_0(1+\mu)$ (kPa)	R^2
B0	5.35± 0.78	38.95± 1.98	0.99222
B1	6.96± 0.71	27.15± 1.44	0.98887
B2	6.81± 0.25	29.96± 0.33	0.99951
P0	6.81± 1.66^{A}	33.16± 3.81	0.93736
P1	11.98± 0.42^{B}	29.75± 1.99	0.97802
P2	9.70± 1.58^{B}	34.44± 3.76	0.95393

Different letters in the same column indicate significant differences between means. Differences in Gc were not significative in B serie ($p<0.05$).

4. CONCLUSIONS

Gelatin hydrogels with stiffness values in the range required for applications in ballistic, food, pharmaceutical and tissue engineering were prepared from commercial powders and their large deformation and fracture behaviors were investigated. The main findings of this research are summarized as follows:

- Under uniaxial compression, bovine and porcine gelatin gels behave as non-linear elastic materials with strain hardening, which can be attributed to partial protein renaturation under stress. Gelatin gels were able to support deformation levels over 120% before failure.
- Gelatin gels show brittle fracture behavior with fracture toughness values in the range of those required in pharmacy and tissue engineering.
- Neat porcine gelatin gels exhibit higher gel strength, shear modulus, failure strain and stress, fracture toughness and water retention capability than bovine gels.
- The addition of sorbitol and glycerol causes an increase in water retention capability of both types of gelatin gels as well as a marked enhancement in fracture toughness.
- The ultra-structure of modified gelatin gels presents a more opened network but contains a higher amount of interconnection sites than the neat gelatin gels.
- The effect of additives on elastic modulus and ultimate properties is detrimental in porcine gelatin gels and negligible in bovine gelatin gels.
- A correlation between the technological gel strength measurement with fracture and mechanical parameters was not found for gelatin gels containing additives.

5. REFERENCES

1. D.Achet, X.W. He, Determination of renaturation level in gelatin films. *Polymer* **36**(4): 787-791 (1995).

2. S.Young, M. Wong, Y. Tabata, A.G. Mikos, Review: Gelatin as a delivery vehicle for the controlled release of bioactive molecules, *J. Controlled Release* **109**: 256– 274 (2005).

3. L.M.Barrangou, M.A. Drake, C. Daubert, E.A. Foegeding, Sensory texture related to large-strain rheological properties of agar/glycerol gels as a model food, *J. Texture Stud.* **37**: 241–262 (2006).

4. J. Kwon, G. Subhash, Compressive strain rate sensitivity of ballistic gelatin, *J. Biomech.* **43**: 420-425 (2010).

5. H. Saito, T. Taguchi, H. Kobayashi, K. Kataoka, J. Tanaka, S. Murabayashi, Y. Mitamura, Physicochemical properties of gelatin gels prepared using citric acid derivative, *Mater. Sci. Eng., C* **24**: 781-785 (2004).

6. W. Thein-Han, J. Saikhun, C. Pholpramoo, R.D.K. Misra, Y. Kitiyanant, Chitosan–gelatin scaffolds for tissue engineering: Physico-chemical properties and biological response of buffalo embryonic stem cells and transfectant of GFP–buffalo embryonic stem cells, *Acta Biomater.* **5**: 3453-3466 (2009).

7. C. Gamonpilas, M.N.Charalambides, J.G.Williams, Determination of large deformation and fracture behaviour of starch gels from conventional and wire cutting experiments, *J. Mater. Sci.* **44**: 4976-4986 (2009).

8. F. W. Wainewright, Physical tests for gelatin and gelatin products. In: A.G. Ward, A. Couts (Eds.), The Science And Technology of Gelatin. New York: Academic Press (1977), pp. 507-534.

9. J. Eysturskarð, I.J. Haug, A.-S. Ulset, K.I. Draget, Mechanical properties of mammalian and fish gelatins based on their weight average molecular weight and molecular weight distribution, *Food Hydrocolloids* **23**: 2315-2321 (2009).

10. R.N. Raja Mohd Hafidz, C.M. Yaakob, I. Amin, A. Noorfaizan, Chemical and functional properties of bovine and porcine skin gelatin, *Int. Food Res. J.* **18**: 813-817 (2011).

11. B. Chiou, R.J. Avena-Bustillos, J. Shey, E. Yee, P.J. Bechtel, S.H.Imam, G.M. Glenn, W.J. Orts, Rheological and mechanical properties of cross-linked fish gelatins, *Polymer* **47**: 6379-6386 (2006).

12. S.M. Goh, M.N Charalambides, J.G.Williams, On the mechanics of wire cutting of cheese, *Eng. Fract. Mech.* **72**: 931–946 (2005).

13. A. Sina Naficy, R. Hugh, A.B. Brown, M. Joselito, A. Razal, M. Geoffrey, A.B. Spinks, G. Philip, A.C. Whitten, Progress Toward Robust Polymer Hydrogels, *Aust. J. Chem.* **64**: 1007–1025 (2011).

14. R. Myhan, I. Białobrzewski, M. Markowski, An approach to modeling the rheological properties of food materials, *J. Food Engn*. **111:** 351-359 (2012).

15. M. Watase, K. Nishinari, Dynamic viscoelasticity and anomalous thermal behaviour of concentrated agarose gels, *Die Makromolekulare Chemie* **188**: 1177–1186 (1987).

16. S. Sanwlani, P. Kumar, H.B. Bohidar, Hydration off gelatin molecules in glycerol-water solvent and phase diagram of gelatin organogels, *J. Phys. Chem. B* **115**: 7332-7340 (2011).

17. M.Czerner, L. Fasce, J.Martucci, R. Ruseckaite, P. Frontini, Compresión uniaxial de hidrogeles de proteína bovina y porcina, 11º Congreso Binacional de Metalurgia y Materiales- SAM/CONAMET 2011, Rosario, Argentina, #971 (2011).

18. M. Czerner, L.Fasce, P. Frontini, Deformation and fracture of mammalian protein based gels. Polymers Moulds Innovations Conference Proceedings. Ghent, Belgion, pp.230-237 (2012).

19. C. Gamonpilas, M. N. Charalambides, J.G. Williams, Predicting the mechanical behaviour of starch gels through inverse analysis of indentation data, *Applied Rheology* **20**: 33283 1-9 (2010).

20. A. Bigi, B. Bracci, G. Cojazzi, S. Panzavolta, N. Roveri, Drawn gelatin films with improved mechanical properties, *Biomaterials* **19**: 2335–2340 (1998).
21. F. Baldi, F. Bignotti, I. Peroni, S.Agnelli, T.Riccò, On the measurement of the fracture resistance of polyacrylamide hydrogels by wire cutting tests, *Polym. Test.* **31**: 455-465 (2012).

Electromechanical stability of cone dielectric elastomer actuator

Xiaohong Wu, Wenjie Sun, Meier Li, Jinxiong Zhou*

State Key Laboratory for Strength and Vibration of Mechanical Structures and School of Aerospace, Xi'an Jiaotong University, Xi'an 710049, China
* Corresponding author: jxzhouxx@mail.xjtu.edu.cn

Abstract Dielectric elastomer actuators are susceptible to electromechanical instability, limiting operational voltages and attainable deformations. In this work, electromechanical stability is investigated at the example of a cone dielectric elastomer actuator. Under the preload and applied voltage, deformation of cone actuator is inhomogeneous. The electromechanical instability occurs when the Hessian of free-energy function of anyone particle in the membrane ceases to be positive definite. Critical voltage of the membrane decreases as the preload increases. The critical actuation stretches are proportional to the critical voltages. As the prestretch increases, the critical voltage decreases while the critical true electric field increases. These results can be used to guide the design of cone actuator.

Keywords dielectric elastomer actuator, electromechanical instability, inhomogeneous deformation

1. Introduction

Dielectric elastomer (DE) is a particularly promising class of EAP (Electroactive polymers) which can overcome many limitations of traditional smart material and transducer technologies. DE based actuators usually consist of elastomer membranes coated with compliant electrodes on both sides. Giant deformation of area expansion rates over 100% can be achieved by applying a voltage.[1] This kind of actuators have been rising as a potential candidate in diverse applications including medical device, soft robotics, energy harvesters and optics etc.[2-4]

Despite good laboratory performance, DEAs are susceptible to various modes of failure[5-6] which prevent their practical application. One of important failure modes is the electromechanical instability, limiting operational voltages and attainable deformations. The study on the failure and nonlinear electromechaniacl stability of DEAs has attracted intensive research [7-9]. Zhao and Suo[7] proposed a general method based on the nonlinear field theory of deformable dielectrics to study the stability. Along this line a series of works have been completed. Xu *et al.*[9] presented an explicit expression for critial stability electric fields by the concept of total stress. In these works, EMI is investigated at the example of parallelepiped actuators.

Cone actuators have a potential application as artifical muscles and were studied by Artificial Muscle Inc.(AMI) and MIT. The understanding of the electromechanical stability for cone actuators is important for their design. In this paper, we consider the definite positiveness of the Hessian matrix representing the electromechanical stability criteria. The critical voltages under different preload of the cone actuator are obtained. The actuation stretches of the actuator are related to the critical voltages. The effect of prestretch on the the critical voltage and the critical true electric field is also investigated.

2. State equations of cone actuators

Figure 1 gives a schematic illustration of cone actuator. A circular dielectric membrane in the undeformed state with thickness H and radius B is coated by two compliant electrodes on both sides [Fig.1(a)]. A general particle of the membrane is at a distance R from the center. Cone actuator is finished by sticking the membrane with a rigid inner frame of radius a and a rigid outer ring of radius b. When a preload F is applied to the inner frame and a voltage ϕ is applied between the two electrodes, the elastomer deforms into an out-of-plane axisymmetric shape with stretches

λ_1, λ_2 and λ_3 as well as gains a distance *u* of the inner frame relative to the ring and an amount of charge Q on either electrodes, and the particle *R* moves to a place with coordinate *r*(*R*) and *z*(*R*) [Fig.1(b)]. Where the longitudinal stretch λ_1 is defined by the distance between the two particles in the deformed state divided by that in the undeformed state, $\lambda_1 = dl/dR$ and the latitudinal stretch is $\lambda_2 = r/R$. Suppose the membrane is incompressible, the free energy density is a function of the three kinematic variables as

(*a*)

(*b*)

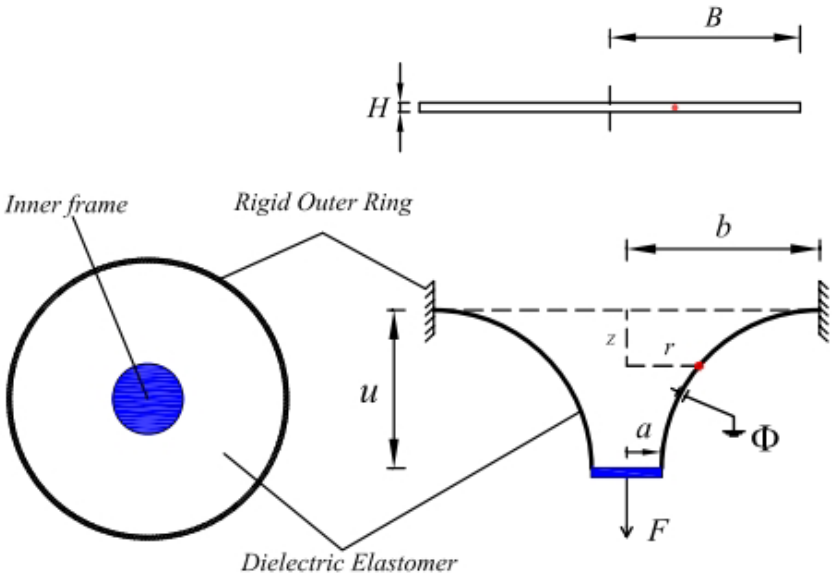

Figure 1. schematic illustration of a cone actuator

$W(\lambda_1, \lambda_2, \tilde{D})$, where $\tilde{D}$ is the nominal electric displacement defined as charge divided by the undeformed area of the membrane. Nominal stresses s and nominal electric field $\tilde{E} = \phi/H$ (the electric field in the undeformed state) can then be expressed as

$$s_1 = \frac{\partial W(\lambda_1, \lambda_2, \tilde{D})}{\partial \lambda_1}, \qquad s_2 = \frac{\partial W(\lambda_1, \lambda_2, \tilde{D})}{\partial \lambda_2}, \quad \tilde{E} = \frac{\partial W(\lambda_1, \lambda_2, \tilde{D})}{\partial \tilde{D}} \tag{1}$$

The true stresses σ_1 and σ_2 relate to the nominal stress as $\sigma_1 = \lambda_1 s_1$ and $\sigma_2 = \lambda_2 s_2$. Adopting the Neo-Hookean strain energy model and the linear electrostatic energy function, the free energy function take the form[10]

$$W(\lambda_1, \lambda_2, \tilde{D}) = \frac{\mu}{2}(\lambda_1^2 + \lambda_2^2 + \lambda_1^{-2}\lambda_2^{-2} - 3) + \frac{\tilde{D}^2}{2\varepsilon}\lambda_1^{-2}\lambda_2^{-2} \tag{2}$$

where μ is the shear modulus, ε is the permittivity.

Inserting Eq.(2) into Eq.(1), we get

$$s_1 = \mu(\lambda_1 - \lambda_1^{-3}\lambda_2^{-2}) - \frac{\tilde{D}^2}{\varepsilon}\lambda_1^{-3}\lambda_2^{-2}, \quad s_2 = \mu(\lambda_2 - \lambda_2^{-3}\lambda_1^{-2}) - \frac{\tilde{D}^2}{\varepsilon}\lambda_2^{-3}\lambda_1^{-2} \tag{3}$$

$$\tilde{E} = \frac{\tilde{D}}{\varepsilon}\lambda_1^{-2}\lambda_2^{-2} \tag{4}$$

Equations of equilibrium can be obtained by balancing forces in the directions of *z* and *r* as

$$\frac{F}{2\pi HR\sin\theta} = s_1 \ , \qquad \frac{d(Rs_1\cos\theta)}{dR} = s_2 \tag{5}$$

For the actuator system, the thermodynamic stability requires that the following Hessian matrix

$$H=\begin{bmatrix} \mu(1+3\lambda_1^{-4}\lambda_2^{-2})+\dfrac{3\tilde{D}^2}{\varepsilon}\lambda_1^{-4}\lambda_2^{-2} & 2\mu\lambda_1^{-3}\lambda_2^{-3}+\dfrac{2\tilde{D}^2}{\varepsilon}\lambda_1^{-3}\lambda_2^{-3} & -\dfrac{2\tilde{D}}{\varepsilon}\lambda_1^{-3}\lambda_2^{-2} \\ 2\mu\lambda_1^{-3}\lambda_2^{-3}+\dfrac{2\tilde{D}^2}{\varepsilon}\lambda_1^{-3}\lambda_2^{-3} & \mu(1+3\lambda_2^{-4}\lambda_1^{-2})+\dfrac{3\tilde{D}^2}{\varepsilon}\lambda_2^{-4}\lambda_1^{-2} & -\dfrac{2\tilde{D}}{\varepsilon}\lambda_2^{-3}\lambda_1^{-2} \\ -\dfrac{2\tilde{D}}{\varepsilon}\lambda_1^{-3}\lambda_2^{-2} & -\dfrac{2\tilde{D}}{\varepsilon}\lambda_2^{-3}\lambda_1^{-2} & \dfrac{1}{\varepsilon}\lambda_1^{-2}\lambda_2^{-2} \end{bmatrix} \tag{6}$$

must be definite positive at the equilibrium state. Eqs.(3～5) can determine the equilibrium values of the generalized coordinates $\lambda_1, \lambda_2, \tilde{D}$. It is noticeable that the deformation is inhomogeneous, so the λ_1 and λ_2 are different along coordinate r in the membrane. For a given dead mechanical preload F, we vary the voltage ϕ. When the voltage is small, the Hessians of all particles are positive definite. Once the Hessian of anyone particle ceases to be positive definite, the voltage reaches a critical value ϕ_c. The critical condition of EMI is set by $\det \mathrm{H}=0$. The condition $\det \mathrm{H}=0$, along with the equilibrium equations [Eqs.(3～5)], determine the critical values $\tilde{E}_c$, $\tilde{D}_c$ and the distrubtion of λ_1^c, λ_2^c in the membrane for any given dead preload F.

3. Electromechanical instability analysis and discussions

The stability criteria can be expressed as the positive sign for the Hessian matrix containing the second–order variations of the energy function as it has been formulated above, which we solve numerically. In presenting the results, we normalize the four variables into dimensionless forms: $\dfrac{F}{2\pi\mu Ha}$, $\dfrac{Q}{2\pi\sqrt{\varepsilon\mu}a^2}$, $\dfrac{\Phi}{H\sqrt{\mu/\varepsilon}}$, $\dfrac{D}{\sqrt{\varepsilon\mu}}$. We first fix the geometrical dimensionless parameters to special values, $b/B=1$, $b/a=4$. This condition means there is no prestress in the membrane.

Fig.2 shows the effect of the dead preload on the critical voltage ϕ_c. As the preload increases, the critical voltage of the membrane decreases. The result reveals a drop of the withstanding voltage ϕ_c of the membrane is part due to the decrease in the thinkness with increasing deformation of preload. Recall that the membrane deformation is inhomogeneous while the applied critical voltage ϕ_c is homogeneous in the membrane. the distribution of the critical true electric field E_c in the membrane is ploted in Fig.3. This figure shows that the distribution is more uneven and lower as the preload is bigger, but the maxima at the inner frame boundary are very close.

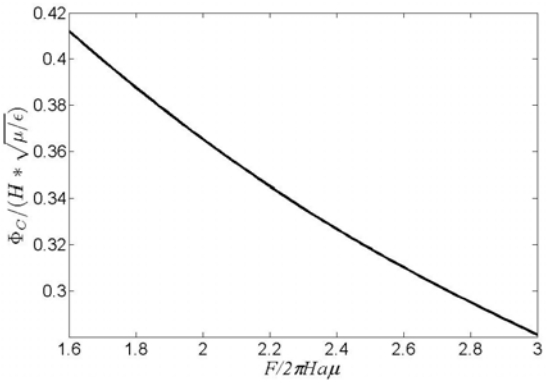

Figure 2. The effect of the dead preload on the critical voltage

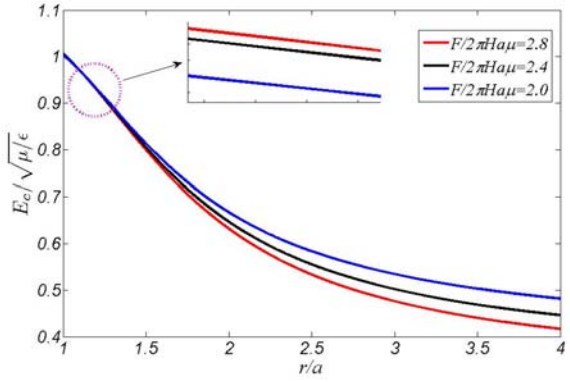

Figure 3. The distribution of the critical true electric field in the membrane

The longitudinal true stress σ_1 is always tensile in order to balance the preload. However, the latitudinal true stress σ_2 can become compressive when the applied voltage is large. The loss of

tension may cause the membrane to buckle. Figure 4 shows the possible failure modes of the actuator. It is indicated that the loss of tension is expected to occur first and EMI comes next. EMI may finally result in electrical breakdown. Rupture will not occurr. This trend coincides with the experimental report.

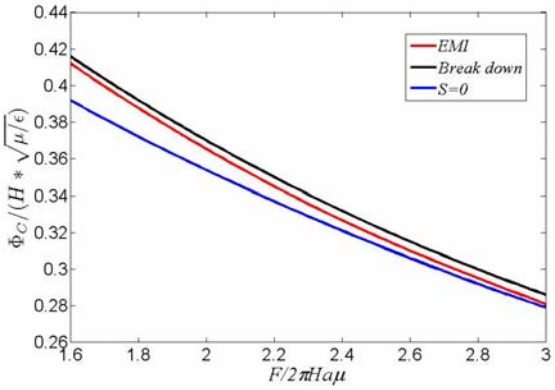

Figure 4. The possible failure modes of the actuator

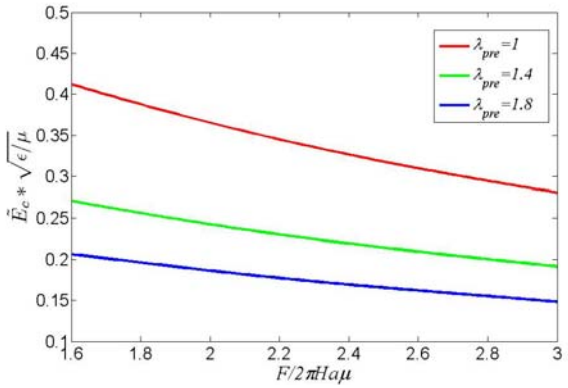

Figure 5. The effect of equal biaxial prestretch on the critical voltage

Figure 5 and Figure 6 show the effect of equal biaxial prestretch on the critical voltage and critical true electric field, respectively. As the prestretch increases, the critical voltage decreases while the critical true electric field increases. It is desirable for the cone actuator to work under a low voltage and a low true electric field, but generate large displacement output. Displacement output is an important performance of actuator and will also influence the force output. The displacement output vs preload is ploted in figure 7. The displacement output is decreases as the preload increases and

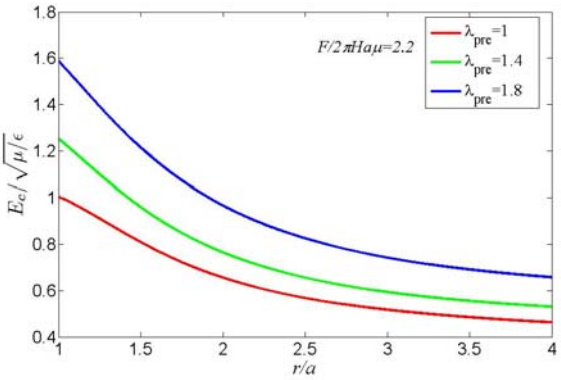

Figure 6. The effect of equal biaxial prestretch on the critical true electric field

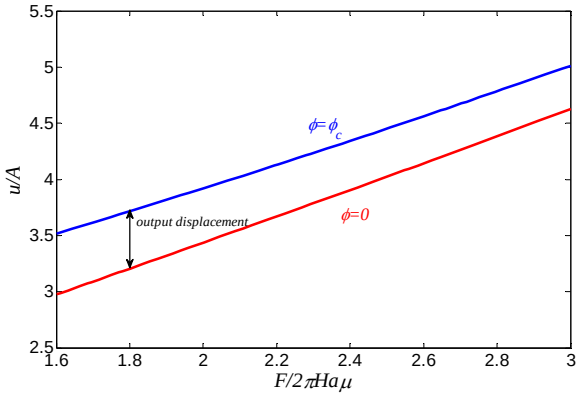

Figure 7. The dead preload vs the output displacement

critical voltage decreases. According to the presented theoretical model, when the actuator is applied by low preload and prestressed, the critical voltage is high, and the actuation stretch and displacement output is large. As a summary, The electromechanical instability occurs when the Hessian of free-energy function of anyone particle in the membrane ceases to be positive definite. The dead preload has significant influence on the electromechanical stability of cone actuator. As the preload increases, the critical voltage of the membrane decreases. Prestress can markedly increase the critical voltage and decrease the critical true electric field.

Acknowledgements

This research is supported by Natural Science Foundation of China through grant Nos. 11102149, 10872157, 11072185 and 10972174.

References

[1] R. Pelrine, R. Kornbluh, Q. B. Pei, J. Joseph, High-speed electrically actuated elastomers with strain greater than 100%. Science, 287 (2000)836–839.
[2] A. O'Halloran, F. O'Malley, P. McHugh, A review on dielectric elastomer actuators, technology, applications, and challenges. J. Appl. Phys., 104 (2008)071101.
[3] X. H. Zhao, Z.G. Suo, Theory of dielectric elastomers capable of giant deformation of actuation. Phys. Rev. Lett., 104 (2010)178302.
[4] R. Heydt, R. Pelrine, J. Joseph, J. Eckerle, R. Kornbluh, Acoustical performance of an electrostrictive polymer film loudspeaker. J. Acoust. Soc. Am., 107 (2000)833–839.
[5] J.S. Plante, S. Dubowsky, Large-scale failure modes of dielectric elastomer actuators. Int. J. Solids Struct., 43 (2006)7727-7751.
[6] J. Zhu, H. Stoyanov, G. Kofod, Z.G. Suo, Large deformation and electromechanical instability of a dielectric elastomer tube actuator. J. Appl. Phys., 108 (2010)074113.
[7] X.H. Zhao, Z.G. Suo, Method to analyze electromechanical stability of dielectric elastomers. Appl. Phys. Lett., 91 (2007)061921.
[8] L.W. Liu, Y.J. Liu, B. Li, K. Yang, T.F, Li, J.S. Leng, Thermo-electro-mechanical instability of dielectric elastomers. Smart Mater. Struct., 20 (2011) 075004.
[9] B.X. Xu, R. Mueller, M. Klassen, D. Gross, On electromechanical stability of dielectric elastomer actuators. Appl. Phys. Lett., 97 (2010)162908.
[10] X.H. Zhao, W. Hong, Z.G. Suo, Electromechanical coexistent states and hysteresis in dielectric elastomers. Physical Review B, 76 (2007)134113.

Mechanics of Gelatin and Elastin based hydrogels as Tissue Engineered Constructs

Achu G. Byju[1], Ankur Kulkarni[2], Namrata Gundiah[1],*

[1] Department of Mechanical Engineering, Indian Institute of Science, Bangalore 560012, India
[2] Biological Sciences Division, Indian Institute of Science, Bangalore 560012, India
* Corresponding author: namrata@mecheng.iisc.ernet.in

Abstract

Engineered soft hydrogels have recently garnered attention for their application as scaffolds for tissue engineering, drug delivery, and as model extracellular matrices such as arteries and cartilage that experience dynamic loading. Hydrogels exhibit nonlinear, composite, viscoelastic, and anisotropic behaviors and hence, mechanical models used to describe such materials are challenging. In this study, we synthesized three dimensional gelatin and elastin hydrogels of varying compositions and crosslinking degrees and characterized their structure-property relationships. Mechanical properties were measured using monotonic compression, dynamic mechanical analysis (DMA), and quasi-static stress relaxation tests. Compressive moduli for the gels range from 1.5 to 15 kPa and these measurements correlate with the values of storage modulus obtained from DMA studies ($p<0.05$). Ongoing studies are aimed at using stress relaxation data to create mechanical spring-dashpot models to describe the viscoelastic behavior of these materials. Scanning electron microscopy was used to assess the gel microstructure. Our results demonstrate that varying the gelatin and crosslinker concentrations leads to significant ($p<0.05$) changes in pore sizes with the lowest stiffness group exhibiting considerably larger porosity. Incorporation of elastin resulted in increased stiffness, change in hydrogel microstructure and swelling properties of the hydrogels.

Keywords: hydrogels, viscoelasticity, gelatin, elastin, tissue engineered scaffolds

1. Introduction

Tissue engineering scaffolds aim to synthesize living tissues *in vitro* by creating suitable mechanical and chemical environments for tissue growth. These scaffolds typically have compositions and mechanical properties similar to that of the native tissues which predominantly contain structural proteins collagen and elastin [1]. Collagen, of which gelatin is a denatured form, is a ubiquitous protein that gives tissues stiffness and mechanical strength. In contrast, elastin is a fatigue resistant rubber-like protein present in dynamic structures, such as arteries and ligaments, which undergo repeated cyclic deformation. Collagen and elastin composite hydrogels present multiple challenges towards our understanding of the material responses due to their non linear and viscoelastic nature while being fracture resistant and able to sustain cyclic loads to serve as biological replacements. Earlier studies characterizing the mechanical properties of biocompatible hydrogels have employed various mechanical testing methods from monotonic compression and tension [2, 3], to viscoelasticity studies through dynamic mechanical analysis and stress relaxation [4–7]. These tests provide insights into the material response of soft materials for a better tuning of the tissue properties. Few studies have however focused on characterizing the mechanics of elastin and collagen based composite hydrogels aimed toward better design of scaffolds that replicate the *in vivo* cellular environments.

The aims of this study are threefold: first, to fabricate gelatin and elastin based crosslinked hydrogels of varying material stiffness to emulate native tissue environments. Crosslinking of hydrogels is necessary to maintain the integrity and long term viability of the hydrogels. Second, to study the microstructure and water uptake behavior of the hydrogels using scanning electron microscopy and swelling experiments. Third, to quantify mechanical properties through monotonic compression tests, dynamic mechanical analysis and stress relaxation experiments. Ongoing studies in our lab are also aimed at characterizing the fracture properties of hydrogels. Because the growth

and behavior of biological tissues are exquisitely sensitive to the mechanical properties of their environment, we hope such studies will help in the design of engineered hydrogels to better emulate native tissue environments [8].

2. Materials and Methods

2.1 Isolation of elastin from bovine aorta

Native aortic tissues typically contain elastin, collagen and proteoglycans. Protocols for elastin isolation from native tissues rely on its chemical inertness and insolubility in various reagents at elevated temperatures. We used the hot alkali treatment to extract elastin from bovine thoracic aorta in this study to obtain a relatively pure and insoluble elastin protein [9]. In this method, artery samples were thoroughly washed with distilled water to clean tissues, minced using a grinder and kept in a solution of 0.1 M NaCl overnight. Treated tissues were washed thrice with distilled water to remove the salt and boiled for 45 minutes in 0.1 M NaOH solution at 95°C to remove contaminant proteins, such as collagen and proteoglycans, from aorta samples. Tissues were washed twice with distilled water and dried at 60°C to obtain purified and insoluble elastin. Finally, the dried material was powdered, sieved (150 µm pore size) and stored at 4°C until use.

2.2 Preparation of crosslinked gelatin and elastin hydrogels

Porcine gelatin Type-B powder (Sigma Aldrich, India) was dissolved in double distilled water at 50° C to obtain a clear solution. Because gelatin is soluble in water, it is necessary to crosslink the material to preserve the hydrogel structure. Collagenous materials, such as gelatin, are generally crosslinked using methods which exploit the large number of functional side groups. We used glutaraldehyde (Sigma Aldrich, India, 25% stock) as a crosslinking agent by combining it with dissolved gelatin solution in this study [10]. A cylindrical mold, containing 9 wells of dimensions 16 mm diameter and 20 mm height each, was fabricated using polydimethylsiloxane (PDMS, Sylgard ®184, Dow Corning). The inner surface of each individual well of the mold was coated with petroleum jelly to prevent adhesion to the hydrogel. Two different concentrations of gelatin and one composite gelatin-elastin hydrogel were prepared in this study. Gels were poured in each well and cured at 4° C for 6 hours. To reduce dehydration of the hydrogels during crosslinking, the mold was wrapped in plastic film. Finally, the gels were soaked in 0.1 M glycine solution to block additional glutaraldehyde action and stored in distilled water overnight prior to mechanical testing [11]. Gelatin-elastin hydrogels were prepared by suspending the insoluble elastin in gelatin solution and vortexing the mixture before adding glutaraldehyde to crosslink the gels.

Table 1 Composition of hydrogels used in the study

Group	Gelatin (gm/ml)	Elastin (gm/ml)	Glutaraldehyde (%v/v)
3G	0.03	0	0.5
5G	0.05	0	1
5GE	0.05	0.05	1

2.3 Swelling characteristics of hydrogels

Hydrogel samples were lyophilized for 24 hrs and their dry weight measured. Samples were immersed in 5 ml of distilled water at room temperature and the wet weight was measured at

regular time intervals. Before weighing, the samples were gently patted dry using tissue paper and the swelling ratios calculated at each time point as

$$Swelling\ Ratio\ (\%) = \frac{W_s - W_d}{W_d} \times 100 \quad (1)$$

w_s is the weight of the swollen sample at each time period. To determine the fluid content of the hydrogels in their maximum swollen state, Equilibrium Water Content (EWC) was calculated using

$$EWC(\%) = \frac{W_e - W_d}{W_e} \times 100 \quad (2)$$

w_e is the equilibrated sample weight and w_d is the sample weight in its dry state in equation (2).

2.4 Mechanical Tests

2.4.1 Determination of modulus of the hydrogels

Monotonic compression tests were performed on a Bose Electroforce® 3200 (Bose Corp., USA) Dynamic Mechanical Analysis (DMA) instrument equipped with two parallel compression platens. Displacements were measured using a LVDT and the forces obtained using a transducer (Bose Corp., ±22.5N). The height and diameter of gels were measured from a photograph of the gels (Nikon D7000 camera) using ImageJ software [12]. Hydrogel specimens were preloaded in the DMA instrument to 5 grams and preconditioned for 30 cycles of 10% compressive strain at 0.05Hz to obtain a repeatable material response [6, 13]. Following preconditioning, samples were compressed at a rate of $0.01s^{-1}$ until either the maximum displacement limit of the instrument was reached or the gels failed. Custom written programs in MATLAB (v7.8.0.347 (R2009a)) were used to analyze the data. Compressive moduli were calculated using the stress-strain data upto 4% strain. In all, 4 samples were tested in each of the 3G, 5G and 5GE groups and an average modulus was calculated for each group.

2.4.2 Dynamic Mechanical Testing

To obtain viscoelastic properties of the hydrogels in each of the three groups, we used fresh compression samples by preloading the hydrogel to 5 gram force and subjecting them to cyclic sinusoidal loading between 0 and 10% compressive strain over a frequency range of 0.05 to 130 Hz. 4 samples were tested in each hydrogel group. Data were acquired at least 30 times the loading frequency and the traces (Figure 1) were analyzed using custom software. In this method, a discrete Fourier transform was performed on the stress and strain data for each acquired frequency block. The phase and amplitude of the relevant portion of the resulting spectra of the stress and strain were used to compute the storage modulus (E′), loss modulus (E″) and phase angle (δ) for the hydrogel [14].

Variation in the strain with angular frequency (ω) is given as

$$\varepsilon(t) = \varepsilon_o \ \sin(\omega t) \quad (3)$$

Stress corresponding to the strain loading is represented by

$$\sigma(t) = \sigma_o \ \sin(\omega t + \delta) \quad (4)$$

σ_o and ε_o are the amplitudes of the sinusoidal stress and strain curves respectively.

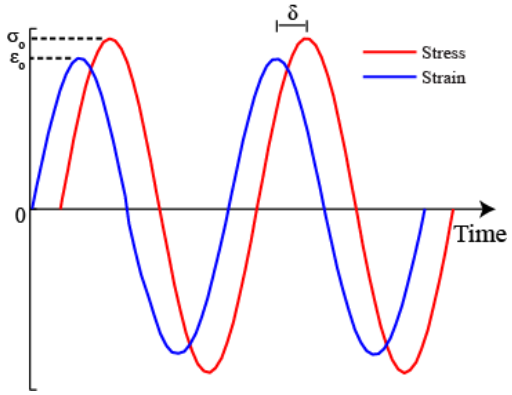

Figure 1. Schematic representation of stress-strain traces from DMA experiments used to compute the various parameters as described below.

The complex modulus, given as $E^* = E' + iE''$, has components

$$E' = \frac{\sigma_o}{\varepsilon_o}\cos(\delta) \text{ and } E'' = \frac{\sigma_o}{\varepsilon_o}\sin(\delta) \quad (5)$$

2.4.3 Stress Relaxation Experiments

We also performed quasi-static stress relaxation experiments by subjecting the hydrogels to a step displacement loading of 10% and a hold time of 15 minutes. Prior to this, each hydrogel was preloaded to 5 gram force as described earlier. Strains in the hydrogels were next increased to a total of 30% in two discrete steps with a hold time of 15 minutes (Figure 2). Data were acquired at 30 Hz for the first five minutes after each strain increment followed by 3Hz for the next five minutes. The remaining data were acquired at 1Hz to capture the total decay in forces during the hold period. Such experiments are useful to arrive at suitable viscoelastic models, obtained using a combination of springs and dashpots, to describe the mechanics of hydrogels.

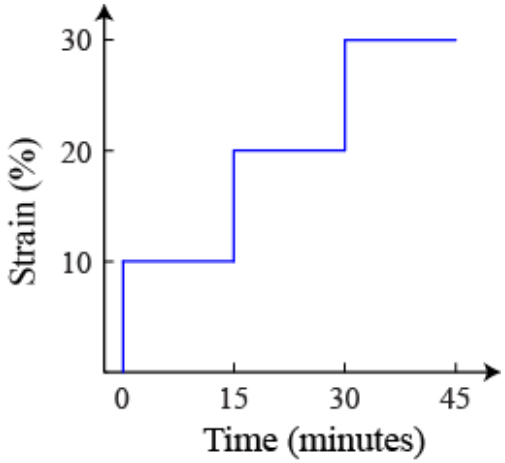

Figure 2. Schematic plot of a stress relaxation experiment obtained by imposing a constant step strain to the sample for a finite period

2.5 Microstructure of the hydrogels

Transverse sections of hydrogel samples were lyophilized for 20 hours and observed using an environmental scanning electron microscope (ESEM, Quanta 200). Image J was used to calculate the pore sizes of the hydrogels [12].

3. Results and Discussion

3.1 Morphology of hydrogels

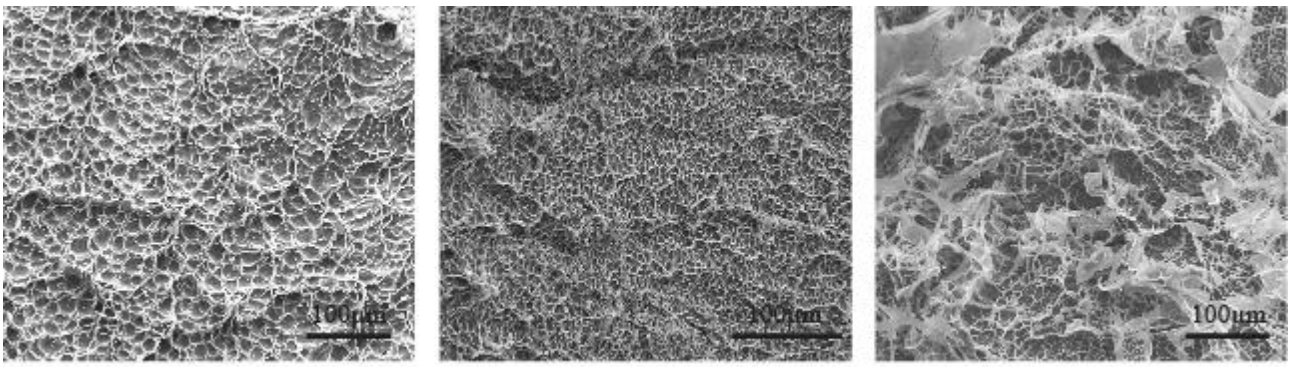

Figure 3. ESEM of gelatin and gelatin-elastin hydrogels show differing microstructures

When imaged using ESEM, hydrogels display a highly porous microstructure (Fig 3.) with variations in the degree of porosity and heterogeneity between the different groups considered in the study. The 3G and 5G hydrogels are predominantly homogeneous with differing porosities. In contrast, regions of heterogeneity exist in the 5GE gels with insoluble elastin forming sheet-like fibrous islands shown as white regions in the micrograph. To quantify the areal porosity of hydrogels, we used image processing tools in ImageJ. These results show that there are no significant differences ($p<0.05$) in the average pore size for the 5G (6.2±1.4 μm) and 5GE (6.5±1.5μm) samples. However, we note a significant difference in average pore size in comparisons of the 3G (15.8±3.4 μm) gel with the other groups respectively ($p<0.05$). Differences in the hydrogel porosity are attributed to variations in the polymer and crosslinker concentrations used in the fabrication of the 3G and 5G hydrogels. An increase in polymer concentration, while keeping other processing variables constant, may lead to a tighter packing of individual biopolymer chains and consequently a smaller pore size. Further, the amount of glutaraldehyde was doubled in the 5G gels as compared to the 3G hydrogels which may lead to a higher crosslink density and a possible reduction in the pore size. Similar results on decrease in pore size with an increase in the base polymer concentration is observed in non crosslinked gelatin hydrogels [15]. Because gel porosities affect diffusion of nutrients in the hydrogels, control of these pore dimensions will ultimately be dictated by requirements posed by different cells cultured in the hydrogels to serve as viable tissue engineered scaffolds.

3.2 Variation in the swelling characteristics of the hydrogels

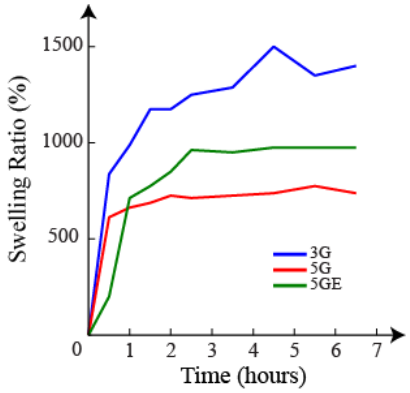

Figure 4. Swelling ratios of 5G 5GE and 3G hydrogels calculated as a function of time

Data from swelling studies (Figure 4) suggest that an increase in polymer and crosslinker concentrations leads to decrease in the swelling ratio that are in agreement with earlier work [16]. The EWC for the hydrogels also decreases with increasing polymer and crosslinker concentration with the 3G gels having the highest EWC and the 5GE gels showing the lowest EWC (Table 2). Increasing the monomer concentration leads to the formation of a higher number of network chains that reduces the diffusion of solvent through the sample and hence a corresponding decrease in hydrogel swelling behavior. Further, an increase in the crosslinker concentration causes the formation of a higher density of crosslinked chains that may consequently reduce the swelling of the hydrogels [17]. The decrease in pore size due to increasing polymer and crosslinker concentration hence results in the lowering of the EWC of the hydrogels because of reduced water absorption and retention in the hydrogel. The presence of sheet-like fibrous islands of elastin in the 5GE gels may further lead to blocking of pores in the gel that prevent water uptake and hence results in the low EWC noted in this study. However, additional samples are required to show statistically significant results.

Table 2. Equilibrium water content (EWC) for a hydrogel sample in each group

Group	EWC (%)
5G	**88.05**
5GE	**76.74**
3G	**93.33**

3.2 Mechanical Characterization

3.2.1 Variation in the moduli of the hydrogels

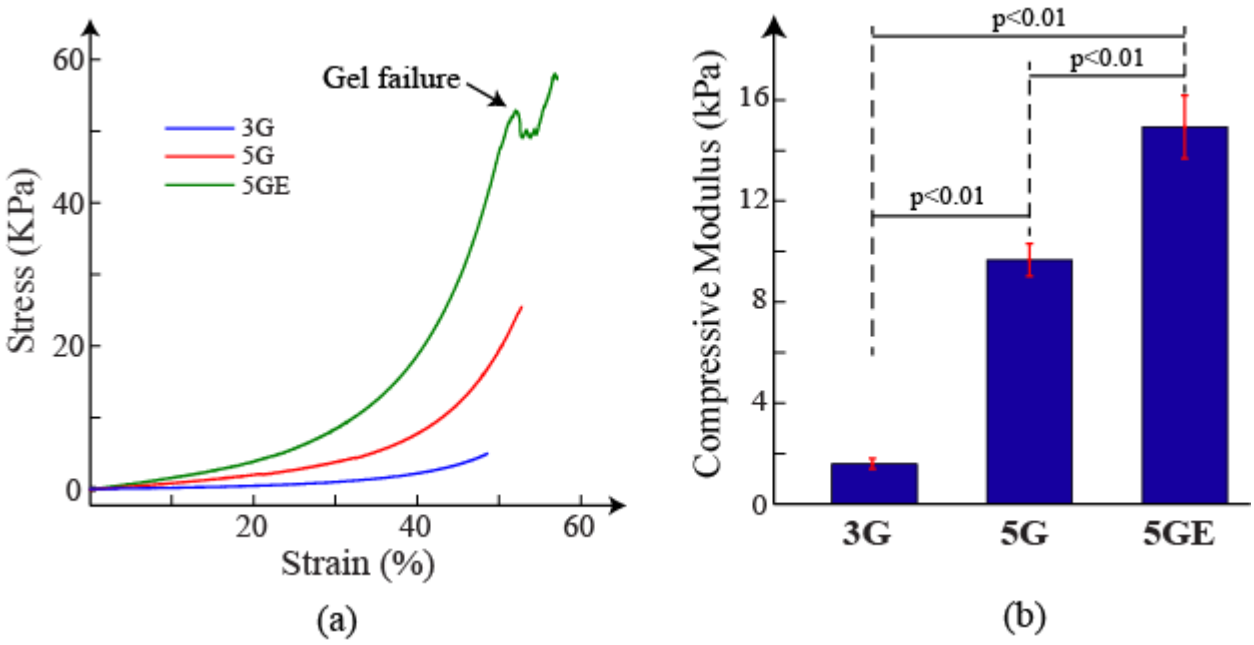

Figure 5. (a) Representative traces from monotonic compression tests on Gelatin and Gelatin - Elastin hydrogels (b) Compressive modulus for Gelatin and Gelatin - Elastin hydrogels at 4% strain

Preconditioning of gels, though not reported in most studies [2, 18], seems crucial and is an established method for reporting the stress-strain results for soft tissue materials [13]. Our results show a clear variation in the peak amplitude of load from the first to the last reported cycle during preconditioning with maximum differences visible between the first and second cycles of loading.

In contrast, data from the last five cycles show repeatable stress-strain response for all hydrogel groups in this study. Representative traces of stress-strain responses (Figure 5a) corresponding to the three hydrogel groups show that an increase in gelatin content or addition of elastin leads to an increased nonlinear material response in the observed strain range. The 5G and 5GE groups demonstrate a response similar to that observed for native tissues such as arteries and cartilage whereas the 3G gels have a highly compliant response [2, 13, 18]. Compressive moduli were calculated for all samples and are reported in Figure 5b. The higher moduli in the 5EG group (14.938±1.253 kPa) and 5G samples (9.669±0.644 kPa) correlate with an increase in the amount of material and glutaraldehyde concentrations as compared to the 3G group (1.591±0.210 kPa). However, our studies show that elastin containing hydrogels fractured at strains of about 0.54±0.02 whereas the gelatin gels showed no signs of damage at these strains.

3.2.2 Viscoelastic characterization of hydrogels

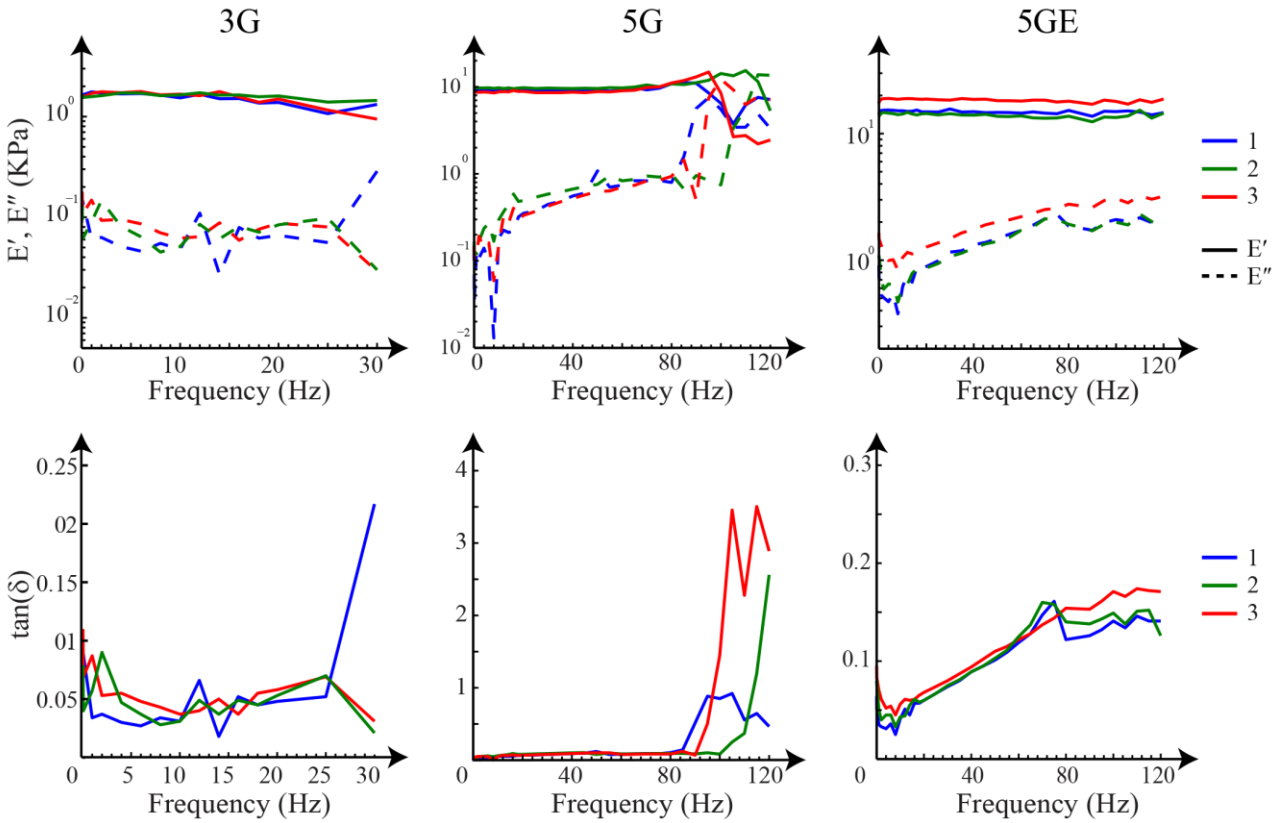

Figure 6. Variation in E′, E″ and tan δ with frequency for each of the hydrogels

Table 3 Mean values of tan δ, E′ and E″ for 3G gels upto 25Hz, 5G gels upto 80Hz and 5GE gels upto 6Hz (n=3)

	3G Group	5G Group	5GE Group
Compressive Modulus (kPa)	1.591±0.210	9.669±0.644	14.938±1.253
Storage Modulus (kPa)	1.594±0.032	9.341±0.428	15.872±2.214
Loss Modulus (kPa)	0.082±0.011	0.456±0.067	-
tan δ	0.051±0.006	0.048±0.005	-

Gelatin gels show a mostly flat response in E′ and E″ with variation in the frequency (Figure 6). However, we note unusual behavior in the 3G gels above a frequency of about 30 Hz that lead to negative values in tan δ. We do not hence report results for 3G samples above this frequency.

Further, we note a high increase in the tan δ in the 5G group above 80 Hz. These effects may be due to possible resonance and cavitation occurring in the hydrogels that results in micro-damage to the samples [19]. Results from our study show that the storage moduli for the gelatin-elastin hydrogels have the highest values. The gelatin gels had lower storage moduli with 5G gels having greater values than the 3G gels. These storage moduli results also showed good correlation with the moduli obtained from monotonic compression experiments ($p<0.05$) (Table 3). However, DMA tests showed no significant difference in the tan δ values between the tested groups. Since 5GE gels show increase in the tan δ and E″ and a decrease in E′ with frequency, we calculated an average E′ over a small range of frequencies for these gels. There is a drop in the tan δ and loss modulus at 85 Hz for these gels, which might also be due to the resonance effects described above.

We hypothesized that the addition of elastin would result in a more elastic behavior. However data suggests that there is no significant difference in the response. This is likely due to the use of insoluble elastin which does not form a homogenous hydrogel. These are, to the best of our knowledge, the only available results from DMA experiments on crosslinked gelatin and gelatin-elastin hydrogels. Future experiments aim to use soluble elastin to delineate the mechanical properties and assess differences in the fracture properties of hydrogels using single edge notch samples. Biopolymers like elastin are present in animals that have a closed circulatory system and see minor variations in temperature. Because elastin and collagen containing tissues such as arteries and cartilage undergo variation in their loading frequencies and rates, we performed a frequency sweep instead of a temperature sweep in this study to obtain physiologically relevant results.

3.1.3 Stress Relaxation of the hydrogels

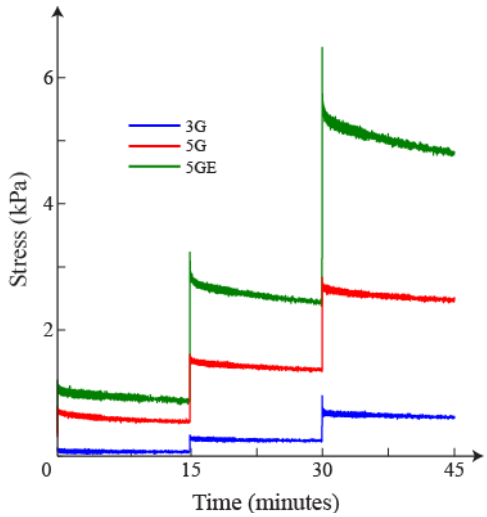

Figure 7. Representative traces from stress relaxation tests on gelatin and gelatin - elastin hydrogels

Stress relaxation data (Figure 7) indicate no significant difference in the amount of relaxation for each of the tested groups ($p<0.05$). This is in agreement with the results from DMA analysis which show no significant difference in the viscoelasticity between the gel groups. The hydrogel samples are covalently cross linked and hence the stress relaxation occurs mainly through migration of water through the gel [4]. It is possible that choosing a wider range of gel compositions may result in significant differences in the stress relaxation properties owing to larger differences in fluid migration through the gel. Although we hypothesized the addition of elastin would result in less relaxation of the gels, our data indicate otherwise that may likely be attributed to the presence of heterogeneous distribution of insoluble elastin through the sample. Future studies are aimed at using soluble elastin which has been shown to interact better with gelatin [18] and hence might show a

larger difference in the stress relaxation behavior due to formation of a homogenous network. The shape of the observed stress relaxation curves show similarity to those reported in other studies [5, 6] though variations have been observed among other studies [4–6]. Ongoing studies are aimed at modeling this response of the hydrogels and quantifying the relaxation times.

4. Conclusions

Our data on gelatin and elastin-gelatin composite hydrogels show that a variation in the monomer and crosslinker concentrations allow for tuning of the hydrogel stiffness which is essential in the fabrication of tissue engineered constructs. Microstructural analysis reveals differences in porosities of hydrogels which affects the permeability and mass transport properties through the gels. This is important in the case of nutrient transport through hydrogels when used for cell culture. The water uptake of hydrogels is also dependent upon monomer and crosslinker concentration. Addition of elastin leads to a decrease in the water content as well as the swelling ratios of the hydrogels. DMA and stress relaxation studies show no significant differences in viscoelastic nature of the gelatin hydrogels. Because incorporation of insoluble elastin did not have a significant effect on the viscoelastic properties of gels, we hope to use soluble elastin in future studies. We hope that such studies on soft materials will be useful in fabrication of tissue engineered constructs capable of closely mimicking the *in vivo* mechanical environment of the tissue.

Acknowledgment

This work was supported by Department of Biotechnology (DBTO326), Department of Science and technology (DSTO983) for fellowship and grant to NG and through intramural Institute grants. We thank Mr. Kundanati Lakshminath for help with SEM and Mr. Arka Bakshi for help with the lyophilisation experiments.

References

[1] L. Buttafoco, First steps towards tissue engineering of small-diameter blood vessels: preparation of flat scaffolds of collagen and elastin by means of freeze drying, J. Biomed. Mater. Res., Part B, 77, (2006), 357–68.

[2] H. A. Awad, M. Q. Wickham, H. A. Leddy, J. M. Gimble, and F. Guilak, Chondrogenic differentiation of adipose-derived adult stem cells in agarose, alginate, and gelatin scaffolds, Biomaterials, 25, (2004), 3211–22.

[3] S. Cram, H. Brown, G. G. M. Spinks, D. Hourdet, and C. Creton, Hydrophobically modified acrylamide-based hydrogels, Proc. SPIE, 5648, (2004), 153–162.

[4] X. Zhao, N. Huebsch, D. J. Mooney, and Z. Suo, Stress-relaxation behavior in gels with ionic and covalent crosslinks., J. Appl. Phys., 107, (2010), 63509.

[5] S. Bryant, T. Chowdhury, and D. Lee, Crosslinking density influences chondrocyte metabolism in dynamically loaded photocrosslinked poly (ethylene glycol) hydrogels, Ann. of Biomed. Eng., 32, (2004), 407–17.

[6] S. Kalyanam, R. Yapp, and M. Insana, Poro-viscoelastic behavior of gelatin hydrogels under compression-implications for bioelasticity imaging, J. Biomech. Eng., 131, (2009), 081005 – 1–13.

[7] M. G. Cascone, Dynamic-Mechanical Properties of Bioartificial Polymeric Materials, Polym. Int., 43, (1997), 55–69.

[8] D. E. Discher, P. Janmey, and Y. Wang, Tissue Cells Feel and Respond to the Stiffness of Their Substrate, Science, 310, (2005), 1139–1143.

[9] A. I. Lansing, T. B. Rosenthal, M. Alex, and E. W. Dempsey, The structure and chemical characterization of elastic fibers as revealed by elastase and by electron microscopy, Anat. Rec., 114, (1952), 555–75.
[10] A. Bigi, G. Cojazzi, S. Panzavolta, K. Rubini, and N. Roveri, Mechanical and thermal properties of gelatin films at different degrees of glutaraldehyde crosslinking, Biomaterials, 22, (2001), 763–8.
[11] H. W. Kang, Y. Tabata, and Y. Ikada, Fabrication of porous gelatin scaffolds for tissue engineering, Biomaterials, 20, (1999), 1339–44.
[12] M. D. Abràmoff, P. J. Magalhães, and S. J. Ram, Image processing with ImageJ, Biophotonics international, 11, (2004), 36–42.
[13] Y. C. Fung, Biomechanics: Mechanical Properties of Living Tissues. Springer, 1993.
[14] I. M. Ward and J. Sweeney, An Introduction to the Mechanical Properties of Solid Polymers. John Wiley & Sons, 2004.
[15] S. Van Vlierberghe, V. Cnudde, P. Dubruel, B. Masschaele, A. Cosijns, I. De Paepe, P. J. S. Jacobs, L. Van Hoorebeke, J. P. Remon, and E. Schacht, Porous gelatin hydrogels: 1. Cryogenic formation and structure analysis, Biomacromolecules, 8, (2007), 331–337.
[16] J. P. Baker, L. H. Hong, H. W. Blanch, and J. M. Prausnitz, Effect of Initial Total Monomer Concentration on the Swelling Behavior of Cationic Acrylamide-Based Hydrogels, Macromolecules, 27, (1994), 1446–1454.
[17] A. K. Bajpai and A. Giri, Water sorption behaviour of highly swelling (carboxy methylcellulose-g-polyacrylamide) hydrogels and release of potassium nitrate as agrochemical, Carbohyd. Polym., 53, (2003), 271–279.
[18] C. N. Grover, R. E. Cameron, and S. M. Best, Investigating the morphological, mechanical and degradation properties of scaffolds comprising collagen, gelatin and elastin for use in soft tissue engineering, J. Mech. Behav. Biomed. Mater., 10, (2012), 62–74.
[19] V. Placet and E. Foltête, Is Dynamic Mechanical Analysis (DMA) a non-resonance technique?, EPJ Web Conf., 6, (2010), 41004.

Fractional-order Modeling of Linear Viscoelastic Creep in Hami Melon

Zheng Xu[1,2], Wen Chen[1,*]

1.Institute of Soft Matter Mechanics, Department of Engineering Mechanics, Hohai University, Nanjing, Jiangsu 210098, China

2.College of Water Conservancy & Architectural Engineering，Shihezi University，Shihezi，Xinjiang 832003，China

* Corresponding author: chenwen@hhu.edu.cn

Abstract: This paper describes our experimental testing of linear viscoelastic creep behaviors in Hami Melon. Experimental data shows that Hami Melon has complex viscoelastic property which can not be well described by the standard model. Consequently, this study develops a fractional derivative model to describe such complex viscoelastic creep behaviors of Hami Melon. The analytical creep function of the proposed fractional linear viscoelastic models is derived via the Boltzmann superposition principle and discrete inverse Laplace transform. And then such analytical solutions are used to fit the experimental data of viscoelastic Hami Melon. Our study shows that the present fractional linear viscoelastic model with merely three parameters is more efficient and accurate than the generalized Kelvin viscoelastic model of six parameters to describe the stress—strain constitutive relations of Hami Melon. It is noted that the present fractional model with adjustable parameters can also be used to describe creep damage.

Keywords: Hami Melon; experiment; viscoelasticity; fractional derivative; creep

1. Introduction

Hami Melon is famous for its delicious taste and aroma, and has become one of the most characteristic fruits in Xinjiang, China. However, a large amount of Hami Melon is often destroyed due to decay in storage and transport, which may be attributed to its high water content and maturates in hot summer. It has been recognized that biomaterials exhibit unique viscoelastic behaviours [1]. Such viscoelasticity has been investigated to minimize physical damage and improve textural quality of fruits. However, it is noted that the transient and dynamic measurements in most existing methods are restricted to small deformations within the linear viscoelastic range of specimens [4,5].These traditional linear models can not accurately describe complex viscoleastic behaviors of Hami Melon.

On the other hand, the characterisation of non-linear behaviour of apple flesh under stress relaxation and the basic homogeneous assumption have been studied by Lu and Puri [1]. The measured vibrations can be visualised with experimental modal analysis, used in the past with pineapples and melons [6]. However, the classical nonlinear models are mathematically complex and require some obscure parameters which are not easy to obtain from measurement data.

In recent decade, fractional derivative model has attracted great attention in the description of memory-dependent mechanics behaviours, such as dynamical behaviours of complex viscoelastic materials [7]. Fractional derivative viscoelastic models are presented by some researchers [7-14] and have been applied to a wide range of problems in bioengineering [15-19]. But little has so far been done on melon [6,15].

In this study, we employ the fractional-order Maxwell viscoelastic model to characterize the viscoelasticity of Hami Melon. Compared with the classical viscoelasitc model, our results show

that the present fractional derivative model can characterize creep behaviour of Hami Melon with better accuracy and fewer parameters.
Among the objectives of this study are:
(1) to describe experiments for measuring the anisotropic creep properties of Hami Melon;
(2) to present a fractional linear viscoelastic model and determine its creep function;
(3) to make a comparison between the fractional and classical models in terms of our experimental data.

2. Experimental materials and methodology

2.1. Preparation of Hami Melon specimens

Fresh Hami Melons for experiments were hand-harvested on 25 August 2010 from the same orchard in Hami city, Xinjiang, China and were selected in terms of uniformity and placed in cold storage (6°C to 7°C and 70–80%RH). Four hours before testing, melons were taken to equilibrate at room temperature (20°C). Each specimen was peeled and cut in half longitudinally. After having removed the central and near the hull (approximately 1.5cm of each side) parts, cylindrical axial and radial specimens (50mm diameter by 10mm height) were put into a sealed container for experimental measurements.
Anisotropic creep properties of melons were evaluated using cylindrical specimens taken in orthogonal radial and axial orientations, as shown in Fig. 1.

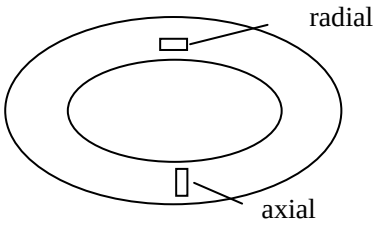

Figure 1. Location of specimens

2.2. Creep testing

Creep tests, in which a shear stress is instantaneously applied to the specimen and then maintained constant, allow us to observe elastic, viscoelastic, and viscous flow behaviours, separately. Deformation and compliance increase with time. In the initial state of creep, the sample material behaves like a solid and subsequently like a fluid. Viscoelastic properties were characterized at 20°C in a TA.XT plus Texture Analyser made by Stable Micro Systems Ltd, UK. 0.06% strain value was selected for experiments to ensure linearity for all specimens.
Creep tests of melons were conducted by enforcing a constant shear stress 20Pa for duration of 60 seconds. An often-encountered problem in measuring the physical properties of fresh or minimally processed tissues is that they are usually alive and respiring, and can be dehydrated by high strain rate during measurements. Thus, the interpretation of creep behaviour in this paper ascribes considerable importance to the time scale over which creep occurs.

2.3. Analysis of data

In this section, compliance data from creep experiments were fitted by a mechanical model consisting of one Maxwell model connected in series with two Kelvin models. It is noted that each Kelvin model has a spring and a dashpot in parallel as shown in Fig.2, which is described by the generalized Kelvin six parameters model [5],

$$J(t,\sigma_c)=(J_0)+\sum_{i=1}^{2}(J_i)(1-e^{-t/\lambda_i})+t/\eta_0\ , \tag{1}$$

where $J(t,\sigma_c)=\varepsilon(t)/\sigma_c$ denotes the creep compliance, $\varepsilon(t)$ is the strain at instant *t*, and σ_c is the constant stress; $J_0=1/E_0$ stands for the instantaneous compliance at *t*=0; $J_i=1/E_i$ (i=1,2) means the retarded compliances; $\lambda_i=\eta_i\times J_i$ (i=1,2) represents the retardation times, and η_i (i=1,2) is the coefficients of viscosity associated with the Voigt elements; η_0 denotes the coefficient of viscosity associated with Newtonian flow, and its inverse is the steady-state fluidity of the material. The parameters are optimally chosen by an exhaustive algorithm which results in the minimum errors between the fitting curve and the observed data.

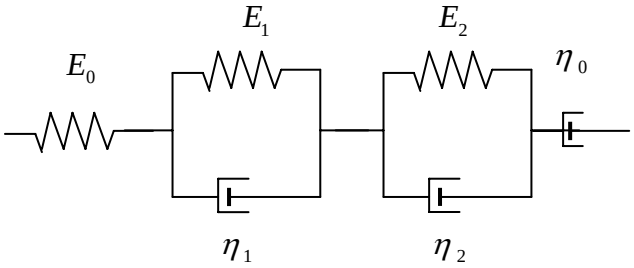

Figure 2**.** Generalized Kelvin model describing creep behaviours of

2.4. Fractional Maxwell modelling of creep

The configuration of a fractional Maxwell model is shown in Fig.3 and consists of a spring and an Abel dashpot connected in series, which is characterized by replacing a Newtonian dashpot in the classical model with the fractional derivative Abel dashpot.

$$\sigma_E=E\varepsilon_E\ ,\quad \sigma_V=\eta d^{\alpha}\varepsilon_V/dt^{\alpha}\quad (0\le\alpha\le 1), \tag{2}$$

$$\varepsilon=\varepsilon_E+\varepsilon_V\ ,\quad \sigma=\sigma_E=\sigma_V\quad , \tag{3}$$

where σ and ε denotes the stress and strain, respectively; *E* represents elastic coefficients of the spring; η is the viscous coefficient of the Abel dashpot; subscript *E* means the spring, and subscript *V* devotes the dashpot.

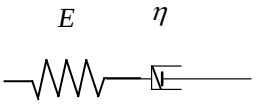

Figure 3**.** Fractional Maxwell

Fractional Maxwell model of constitutive equation is as follows

$$\frac{d^{\alpha}\sigma}{dt^{\alpha}}+\frac{1}{\tau}\sigma=E\frac{d^{\alpha}\varepsilon}{dt^{\alpha}}\ ,\quad \tau=\frac{\eta}{E}\ , \tag{4}$$

where τ is the retard time. The fractional integral is defined by, see Ref. [9,20],

$${}^{R}I^{\alpha}f(t)=\frac{1}{\Gamma(\alpha)}\int_a^t(t-\tau)^{\alpha-1}f(\tau)d\tau(0<\alpha<1). \tag{5}$$

Applying the Laplace transformation to Eq. (4) yields

$$s^{\alpha}\bar{\varepsilon}=\frac{1}{E}s^{\alpha}\bar{\sigma}+\frac{1}{\eta}\bar{\sigma}\ . \tag{6}$$

Consequently, we have

$$J(s)=\eta^{-1}\sum_{k=0}^{\infty}(-1)^k(\frac{\eta}{E})^k s^{-\alpha k-\alpha-1}\ . \tag{7}$$

Applying the discrete inverse Laplace transformation, we obtain

$$J(t)=\frac{1}{E}+\frac{1}{\eta}\frac{t^{\alpha}}{\Gamma(1+\alpha)}\ \ , \tag{8}$$

where $\Gamma(g)$ denotes the Gamma function,

$$\Gamma(z)=\int_0^{\infty}e^{-t}t^{z-1}dt\ . \tag{9}$$

In particular, when α is equal to 1, Eq. (8) is reduced to the standard Maxwell model for creep compliance,

$$J(t)=\frac{1}{E}+\frac{1}{\eta}\frac{t}{\Gamma(1)}=\frac{1}{E}+\frac{t}{\eta}\ , \tag{10}$$

namely, Eq.(10) is the standard integer-order model [7].

3. Results and discussions

3.1. Classical viscoelastic model

Creep compliance curves of Hami Melon specimens are illustrated in Fig. 4. Deformation of all samples is finite after 60s creep. Figs. 4(a) and 4(b) display the curves of radial and axial specimens, respectively. For the time scale of the experiments, the behaviours were described via the six parameters in the creep model Eq. (1). Table 1 provides the mechanical parameters that define creep behaviour of Hami Melon tissues. According to the interpretation in Mittal [21], J_0 represents those bonds of structural units that are stretched elastically when the stress is applied and characterizes instantaneous and complete recoveries when the stress is removed. The linear region of Newtonian compliance t/η_0 reflects those bonds that are ruptured during the shear creep, and its time required to deform is longer than the creep-recovery period.

As seen from Fig. 4, the viscoelastic creep compliances are significantly different between axial and radial specimens. The axial specimen has larger creep compliance than the radial one.

Table 1 displays the relatively larger standard deviations observed in the creep experiments for measured viscoelastic properties of melon tissues. Much of this variability can be attributed to physiological factors, i.e., anisotropism and non-homogeneity, which change their mechanical properties with age, moisture content, and locations around the melon and depth from which the specimen is taken [21,22].

Table 1 Creep compliance parameters of fresh Hami melon tissues in Eq. (1)

specimen	J_0 (1/Pa)×10^{-5}	J_1 (1/Pa)×10^{-5}	J_2 (1/Pa)×10^{-5}	λ_1(s)	λ_2(s)	η_0 (Pa·s)×10^{7}
radial	0.5	0.41	0.21	18	3.1	5
axial	0.65	0.72	0.51	18.1	5.1	7

3.2. Fractional Maxwell model

It is worth stressing that the curves displayed in Fig. 4 match quite well with the experimental creep data. This highlights the validity of the present fractional constitutive expression of Hami Melon

viscoelasticity, which captures experimental data of creep tests by using merely the three parameters as shown in Table 2. The next experiment will examine if the fractional order constitutive model can depict the nonlinear gradual process of strain in creep.

Table 2. Creep compliance parameters for fresh Hami Melon tissues in Eq.(8)

Sample	E(MPa)	η(MPa.s)	α
radial	0.2	0.56	0.3
axial	0.14	0.49	0.38

3.3. Comparisons

We can see from Fig. 4(a) that compared with the classical viscoelasitc models, the fractional Maxwell model has the same level of accuracy in the fitting of experimental data but requires significantly fewer adjustable parameters. Fig. 4(b) shows that the classical model only fits well the elastic variation, initial small value of *J*, and then has a large departure from experimental data when viscosity comes into play. In stark contrast, the fractional model agrees pretty well with the experimental data for the whole viscoelastic duration with three parameters. In general, our results show that the present fractional derivative model can characterize creep behaviour of Hami Melon with better accuracy and fewer parameters.

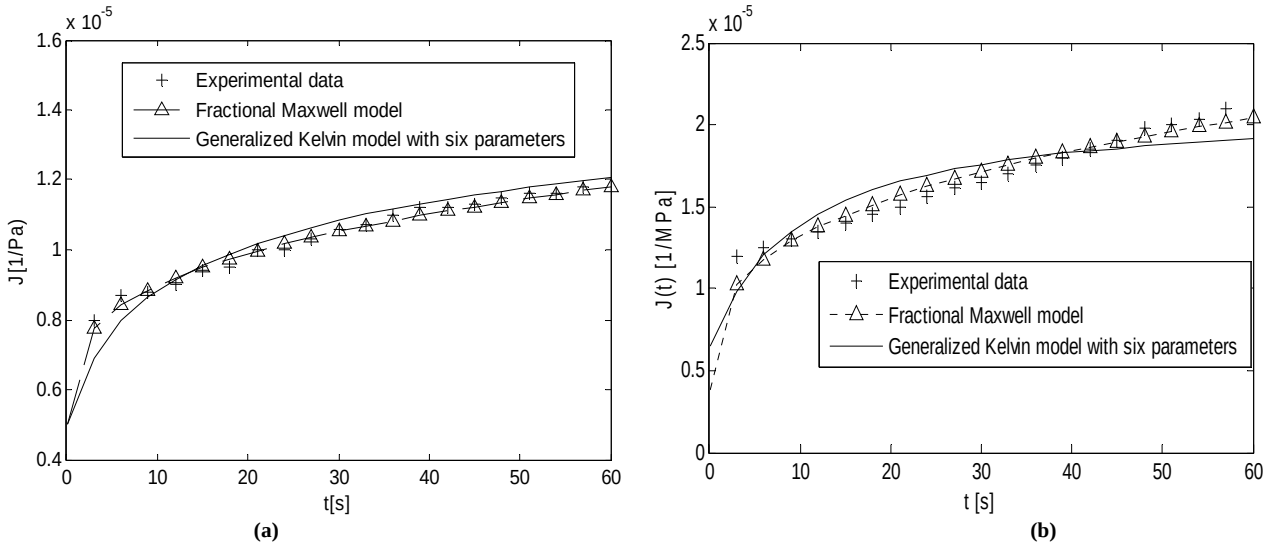

Figure 4. Creep compliance curve; a)radial; b)axial

4. Conclusions

This work shows the experimental results of creep tests of Hami Melon. All tests have been conducted in a range of small deformation, so that such creep can be reasonably treated as linear viscoelasticity. The standard linear and the present fractional derivative creep models have been investigated for comparisons in fitting our experimental data. The fractional derivative model not only reduces the computational effort in identification of coefficients, but also appears more promising in modeling of different loading conditions, with fewer parameters.

The creep tests for the specimens in different locations of Hami Melon has illustrated that the creep modulus is significantly influenced by the location and orientation of the specimens. The proposed fractional derivative model can accurately simulate the creep characteristics of different specimens, and the creep damage of Hami Melon in the transport and storage can be predicted. This study is very encouraging and more work is under way to apply the fractional model to damage behaviours of fruits, which will be reported in a subsequent paper.

Acknowledgements

The work described in this paper was supported by the National Basic Research Program of China (973 Project No. 2010CB832702), the National Science Funds for Distinguished Young Scholars of China (11125208), the National Science Funds of China (11162016), the R&D Special Fund for Public Welfare Industry (Hydrodynamics, Project No. 201101014), and the 111 project under grant B12032.

References

[1] R Lu, V.M. Puri. Characterization of nonlinear behaviour of apple flesh under stress relaxation. Journal of Rheology 36(1992) 303–318.

[2] R.E. Pitt, H.L.Chen. Time-dependent aspects of the strength and rheology of vegetative tissue. Transactions of the American Society of Agricultural Engineers 26 (1983) 1275–1280

[3] Sadato, K. Takayuki. Studies on mechanical properties of agricultural products (Part 2). Journal of Japan Society of Acupuncture and Moxibustion 32 (1970) 59–64.

[4] R.S. Lakes. Viscoelastic measurement techniques.Review of Scientific Instruments 75(2004) 797–810.

[5] S.M. Alzamora, P. E. Viollaz, V. Y. Martínez, A. B. Nieto and D. Salvatori. Exploring the Linear Viscoelastic Properties Structure Relationship in Processed Fruit Tissues. Food Engineering Series, Food Engineering: Integrated Approaches 50(2008)155-181.

[6] H. Chen, De Baerdemaeker J G. Modal analysis of the dynamic behavior of pineapples and its relation to fruit firmness. Transactions of the American Society of Agricultural Engineers 36(1993) 1439–1444.

[7] F. Mainardi. Fractional Calculus And Waves In Linear Viscoelasticity: An Introduction to Mathematical Models.World Scientific.2010.

[8] H. Schiessel, R. Metzler, A. Blumen, T. F. Nonnenmacher. Generalized viscoelastic models: their fractional equations with solutions. Journal of Physics A-Mathematical and General 28(1995) 6567-6584.

[9] W. Chen, H. G. Sun and X. C. Li. Fractional derivative modeling in mechanics and engineering. Science Press. 2010.

[10] D.Baleanu, K.Diethelm, E.Scalas, J. J.Trujillo. Fractional Calculus Models and Numerical Methods (Series on Complexity, Nonlinearity and Chaos), World Scientific.2012.

[11] S.W. J. Welch, R.A.L. Rorrer and R. G. Jr. Duren. Application of time-based fractional calculus methods to viscoelastic creep and stress relaxation of materials. Mechanics of Time-Dependent Materials 13(1999) 279-303.

[12] R.L.Bagley, P. J. Torvik. A theoretical basis for the application of fractional calculus to viscoelasticity. Journal of Rheology 27(1983) 201-210.

[13] M. Di Paola, A. Pirrotta and A. Valenza. Visco-elastic behavior through fractional calculus: An easier method for best fitting experimental results. Mechanics of Materials 43 (2011) 799–806.

[14] F.C. Meral, T.J. Royston and R. Magin. Fractional calculus in viscoelasticity: An experimental study.Commun Nonlinear Sci Numer Simulat 15 (2010) 939-945.

[15] R.L. Magin. Critical reviews in biomedical engineering. Critical reviews in biomedical engineering 32(2004) 1-104.

[16] R.L. Magin. Fractional calculus models of complex dynamics in biological tissues. Computers and Mathematics with Applications 59(2010) 1586-1593.

[17] D. Craiem, R.L. Armentano. A fractional derivative model to describe arterial viscoelasticity. Biorheology 44(2007) 251-263.

[18] D. Craiem, F.J. Rojo, J.M. Atienza, R.L. Armentano and G.V. Guinea. Fractional-order viscoelasticity applied to describe uniaxial stress relaxation of human arteries. Physics in Medicine and Biology 53 (2008) 4543-4554.

[19] N. Heymans, Dynamic measurements in long-memory materials: Fractional calculus evaluation of approach to steady state. Journal of Vibration and Control 14 (2008) 1587-1596.

[20] D.Baleanu, S.I.Muslih. Lagrangian formulation of classical fields within Riemann-Liouville fractional derivatives. Physica Scripta 72(2005) 119-121.
[21] J. P. Mittal, N.N.Mohsenin. Rheological characterization of apple cortex. Journal of Testing and Evaluation 18(1987) 65-93.
[22] Gustavo F. Gutiérrez-Lopez, Jorge Welti-Chanes and Efrén Parada-Arias. Food Engineering: Integrated Approaches. Springer, New York. 2008.

Large Deformation Study of Temperature-Sensitive Hydrogel

Jianying Hu[1], Zhiwei Ding[2], Zishun Liu[1,*]

[1] Int. Center for Applied Mechanics; State Key Laboratory for Strength and Vibration of Mechanical Structures, Xi'an Jiaotong University, Xi'an, 710049, China
[2] Engineering Science Programme, National University of Singapore, Singapore, 117576
* Corresponding author: zishunliu@mail.xjtu.edu.cn

Abstract When the elastomer submerged in aqueous solution, temperature-sensitive hydrogels undergo a phase transition at a particular temperature, i.e. the volume of hydrogels changes with temperature discontinuously. In this paper, the inhomogeneous large deformation of temperature-sensitive hydrogels has been studied. Based on the monophasic gel inhomogeneous field theory, the governing equations and conditions of equilibrium for temperature-sensitive hydrogel have been derived. Furthermore, the free-energy function and derived constitutive equations for temperature-sensitive hydrogel are implemented using Finite Element Method. As an example, a uniaxially constrained-swelling hydrogels with cubic initial shape is studied. The simulating results are in reasonable agreement with available experimental data and analytical solutions. By analyzing the factors affecting the phase transition temperature of hydrogel, we suggest one possible chemical mechanism for the swelling behavior of temperature-sensitive gel during the phase transition process. Also we demonstrate the application of the proposed approach in the analysis of the complex phenomenon, such as to explain the deformation of implant in skin reconstruction. We hope this approach can explain various complex phenomena and provide a useful tool for further theoretical and experimental studies.

Keywords FEM, Inhomogeneous deformation, Phase transition temperature, Swelling behavior, Temperature-sensitive hydrogel,

1. Introduction

Long and flexible polymers chains can chemically crosslink to a three-dimensional network by covalent bonds. When the rubber-like material is submerged into an aqueous solvent, the network imbibes the solvent and swells, resulting in an elastomer gel. Great attention has been drawn to these polymeric gels due to their large and reversible deformation variation to many stimuli, including pH values[1, 2], forces[3], ionic concentration[4], temperature[5], electrical field[6, 7], and magnetic field, etc. For example, a temperature-sensitive hydrogel PNIPAM based on poly-(N-isopropyl-acrylamide) which exhibits the volume phase transition, has been investigated in the past years and the temperature-sensitive hydrogel has been developed for numerous applications[8-11], such as actuator[12], sensor[13, 14], switching device[15]. Furthermore, the temperature sensitive gels can be developed as drug delivery systems in the human body, where the gel releases a drug at a particular location in the body in response to the change of temperature.

The stimuli responsive behaviors of hydrogel have also motivated a large number of theoretical and numerical studies. Based on the statistical-mechanical hydrogel model developed by Flory and Rehner, Suo group proposed a gel theory coupling the two phase's deformation into a single phase[16]. Following this approach, Hong et al. implemented the finite element method (FEM) on polymeric gel theory by coding a UHYPER subroutine in the commercial software ABAQUS[17]. Meanwhile Marcombe et al. and Cai and Suo developed FEM for pH-sensitive gel[2] and temperature-sensitive gel[5], respectively. To perform the transient analysis of large deformation, Zhang et al. formulated FEM of mass transport in gel microfluidic valves, using fluid-structure

interaction (FSI)[18]. Liu et al. studied the buckling phenomena of gels[19, 20]. Toh et al. developed a dynamic FEM for inhomogeneous deformation[21, 22].

In this paper, we adopt Suo's monophasic model for temperature-sensitive hydrogel[5], which regard the interaction parameter as a function of temperature and concentration, and then a specific material model is employed in the finite element implementation by providing a user subroutine to analyze the deformation of the PNIPAM hydrogel. This implementation enables us to analyze diverse phenomena of temperature-sensitive gel including large deformation, contact, bifurcation, buckling of hydrogel, etc.

2. Gel theory for temperature-sensitive gel

When a dry polymer network is immersed in a solvent, e.g. water, the solvent molecules enter the polymer network and result in swelling. We define the initial state as the reference state X_K and the deformed state as the current state x_i. The state of deformation is characterized by the deformation gradient F_{iK}, defined by the mapping from the reference coordinates to the current coordinates,

$$F_{iK} = \frac{\partial x_i(X)}{\partial X_K}, \tag{1}$$

Using statistical theories and simplified network models, a free energy expression can be formulated. A free energy expression for the temperature-sensitive gel includes two parts (i) the stretching of the network W_s and (ii) the mixing energy of the polymer and the solvent W_m.

$$W = W_s + W_m = \frac{1}{2}NkT[F_{ik}F_{ik} - 3 - 2\log(det\mathbf{F}) + kT[Clog\frac{\upsilon C}{1+\upsilon C} + \frac{\chi C}{1+\upsilon C}] \tag{2}$$

where N is the number of polymer chains per unit dry volume, kT is the temperature in terms of energy, ν is the volume per water molecule, $\mathbf{F}$ is the deformation gradient relative to the dry network, C is the nominal concentration of solvent water molecule and χ is a dimensionless measure of the strength of pairwise interactions between species. This parameter χ is used to fit experimental data in the following form:

$$\chi(T, \phi) = \chi_0 + \chi_1\phi \tag{3}$$

$$\chi_0 = A_0 + B_0T, \chi_1 = A_1 + B_1T \tag{4}$$

Hong et al. assume that these individual long polymers and solvent molecules are incompressible[17]. The condition of molecular incompressibility can be expressed as following:

$$\phi = \frac{1}{1+\upsilon C} = \frac{1}{det(\boldsymbol{F})} \tag{5}$$

ϕ is the volume fraction of the polymer in the hydrogel. The values of A_0, B_0, A_1 and B_1 will be different for different types of temperature-sensitive hydrogel. Afroze et al. [23] provided the values of these parameters for a particular polymer: poly(N-isopropylacrylamide) (PNIPAM) as:

$$A_0 = -12.947, B_0 = 0.04496, A_1 = 17.92, B_1 = -0.0569 \tag{6}$$

To fully define the material in the subroutine, we adopt the above properties of PNIPAM gels in the examples presented herein.

The free energy is written in the form of $W = W(\mathbf{F}, T, C)$. Since the chemical potential must be a constant at the equilibrium state, we introduce another free-energy function $\widehat{W}$ with $\mathbf{F}$, μ and T as independent parameters via Legendre transform.

$$\widehat{W}(\mathbf{F}, T, \mu) = W - \mu C \tag{7}$$

$$\widehat{W}(\boldsymbol{F},T,\mu)=\frac{1}{2}NkT\left[J^{\frac{2}{3}}\bar{I}_1-3-2\,log(J)\right]+\frac{KT}{v}\left[(J-1)\log\left(\frac{J-1}{J}\right)+(J-1)*\left(\frac{\chi_0}{J}+\frac{\chi_1}{J^2}\right)\right]-\frac{\mu}{v}(J-1) \quad (8)$$

Define the nominal stress as,

$$s_{iK}=\frac{\partial\widetilde{W}}{\partial F_{iK}}=NkT(F_{ik}-H_{ik})+J\left[log\left(\frac{J-1}{J}\right)+\frac{1}{J}+\frac{\chi_0-\chi_1}{J^2}+\frac{2\chi_1}{J^3}\right]H_{ik}-\frac{\mu}{v}JH_{ik} \quad (9)$$

where **H** is the transpose of the inverse of the deformation gradient **F**. This equation of state relates the nominal stress to the deformation gradient when the gel is hold at a constant chemical potential and constant temperature. The finite element modeling of large deformation process of temperature-sensitive gel is possible by utilizing currently gel monophasic theory and properties of PNIPAM.

3. Phase transition

Phase transition phenomena have been observed and studied by many researchers. The phase transition temperature is referred to as the temperature of the coexistent state, at which a sharp volume transition can be observed. Since gel's swelling process can be referred as a hydrated reaction, we assume that the gel may have two different phases before and after phase transition temperature, which imply two different hydrated quantities of hydrogel. In our previous work[24], we inferred variation of temperature leads to different hydrated quantities of hydrogel and thus the volume of gel changes significantly. When gel reaches the phase transition temperature, the free energy density function $W(\mathbf{F},\mu,T)$ has two local minima of equal value. Specifically, if the chemical potential is kept at a certain constant value μ_0, at a particular temperature T^*-the so called phase transition temperature, the two local minima of the free energy density function $W(\mathbf{F},\mu,T)$ would occur at two different deformation gradients $\mathbf{F_1}$ and $\mathbf{F_2}$, i.e.,

$$W(\mathbf{F_1},\mu_0,T^*)=W(\mathbf{F_2},\mu_0,T^*) \quad (10)$$

4. Numerical examples and discussions

4.1. Uniaxially constrained-swelling hydrogels

In our previous work[24], we investigated a PNIPAM hydrogel cube, which immersed in water ($\mu=0$) at certain temperature and allowed to frees welling. Now we adopt 8-node brick elements to model the uniaxial constrained swelling hydrogel. In the modeling, a hydrogel bar is first submerged in water and reaches an isotropic swelling stretch λ_0, and then the gel bar is stretched in longitudinal directions with fixed length. The stress in the transverse directions vanish, so that (9) gives

$$\frac{Nv}{{\lambda_2}^2\lambda_1}(\lambda_2^2-1)+\ln\left(1-\frac{1}{{\lambda_2}^2\lambda_1}\right)+\frac{1}{{\lambda_2}^2\lambda_1}+\left(\frac{\chi_0-\chi_1}{\lambda_2^4\lambda_1^2}+\frac{2\chi_1}{\lambda_2^6\lambda_1^3}\right)-\frac{\mu_0}{kT}=0 \quad (11)$$

$J=\frac{V}{V_0}={\lambda_2}^2\lambda_1$; for water $\mu_0=0$. Using the material model, we can also obtain the volume-temperature curve numerically by FEM. Since the value for Nv was not given in the report Suzuki et al. [25], we have to vary the value of the parameter Nv to fit the experiment data. The symbol k is the Boltzmann constant, and T_0 = 300K, $kT_0\approx 4.14\times10^{-21}J$. It's clearly shown in Figure 1 that when the level of longitudinal stress is different, volume changes sharply but the phase transition temperature alters just mildly.

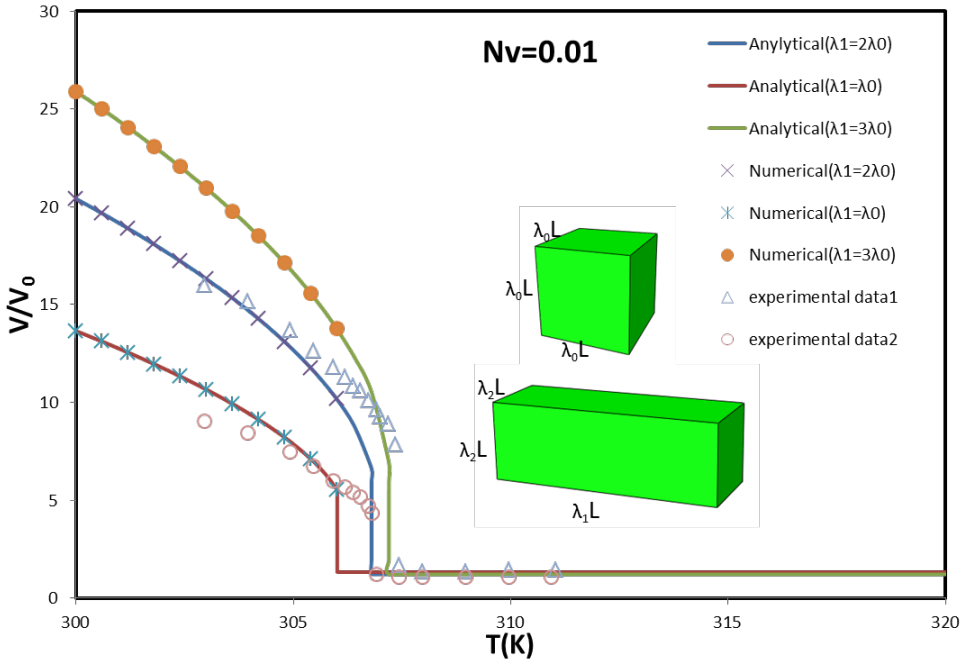

Figure 1. The volumes of uniaxially constrained-swelling hydrogels as functions of temperature. The solid curves are calculated for hydrogels of three levels of longitudinal stretches. The solid curves are obtained analytically for the free swelling of hydrogel at the three values of crosslink density. The marks on the curves are the corresponding numerical predictions. The triangle and circle symbols are experimental data for the corresponding longitudinal stretches taken from Suzuki et al[25].

4.2. Simulation of the reconstructed skin

When aged or damaged, the skins of human beings can easily result in winkles or scars. Hillel et al. developed a biosynthetic soft gel replacement that can be injected and swelling in situ with stimuli[26], whereby the swelling of soft fillers of skin reduces or eliminates the skin wrinkles. In this study, we try to model the skin reconstruction procedure and explain how the soft fillers works in skin repair by using temperature-sensitive hydrogel deformation. It is assumed that the skin implant could be modeled as a temperature-sensitive gel material, in which temperature-sensitive hydrogel is injected into the dermis layer. Furthermore, by modulating the parameters of temperature-sensitive hydrogel, we can control the repair process.

As the temperature changes, the injected temperature-sensitive gel will swell. This corresponds to the deformation of soft fillers in the skin repair process. Fig. 2 (a) shows the initial stage which injected implant gel has not been deformed. The deformation pattern of the skin under reconstruction at deformed stage is illustrated in Fig. 2 (b). From Fig. 2 (b), it can be observed that the skin wrinkles can be eliminated. To better understand the skin repair process, the schematic diagrams of reconstructed skin procedure which is taken from Hillel et al.[26] are also shown in the Fig. 2 (c) and (d).

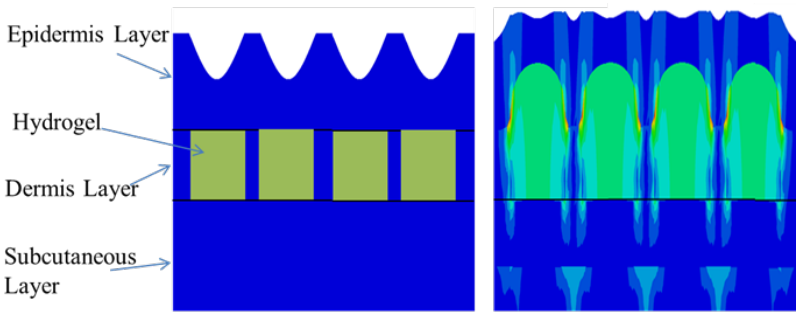

(a) (b)

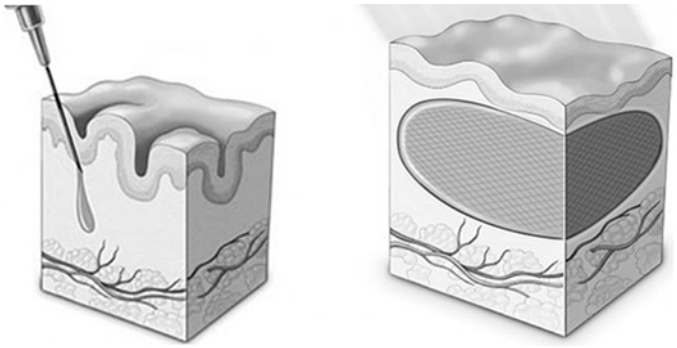

(c) (d)

Figure 2. After the temperature-sensitive gel is injected into beneath of skin, the wrinkled skin can be eliminated. (a) The pattern of the repaired skin at initial stage; (b) the pattern of the repaired skin at deformed stage. (c) and (d) the schematic of the reconstructed skin taken from Hillel et al[26].

Conclusion

This paper focuses on large deformation of temperature-sensitive hydrogels in equilibrium with a solvent and mechanical load at varying temperature. Adopting a specific free energy density function and obtained constitutive equation, we have developed a finite element method for equilibrium analysis of temperature-sensitive hydrogels and implemented the theory via a user-defined subroutine in ABAQUS. From the simulated results, we demonstrate the potential applications of the proposed approach in the analysis of the complex phenomenon, such as how to explain the deformation of implant in skin reconstruction. We hope that this work can explain various complex phenomena in nature and can provide a useful tool for the future theoretical and experimental studies on temperature-sensitive hydrogel.

ACKNOWLEDGMENTS

The authors are grateful for the support from the National Natural Science Foundation of China through grant number 11242011 and number 11021202.

References

[1] A.W. Chan, R.J. Neufeld. Modeling the controllable pH-responsive swelling and pore size of networked alginate based biomaterials. Biomaterials, 30 (2009) 6119-6129.

[2] R. Marcombe, S. Cai, W. Hong, X. Zhao, Y. Lapusta, Z. Suo. A theory of constrained swelling of a pH-sensitive hydrogel. Soft Matter, 6 (2010) 10.

[3] M. Doi. Gel Dynamics. Journal of the Physical Society of Japan, 78 (2009).

[4] T. Tanaka, D. Fillmore, S.-T. Sun, I. Nishio, G. Swislow, A. Shah. Phase Transitions in Ionic Gels. Physical Review Letters, 45 (1980) 1636-1639.

[5] S.Q. Cai, Z.G. Suo. Mechanics and chemical thermodynamics of phase transition in temperature-sensitive hydrogels. Journal of the Mechanics and Physics of Solids, 59 (2011) 20.

[6] Y. Osada, J. Gong. Soft and wet material: polymer gels. Advanced Materials, 10 (1998) 11.

[7] T. Shiga. Deformation and Viscoelastic Behavior of Polymer Gels in Electric Fields. Advances

in Polymer Science, 134 (1997) 33.
[8] I. Berndt, W. Richtering. Doubly Temperature Sensitive Core-Shell Microgels. Macromoleculs, 36 (2003) 6.
[9] R.O.R. Costaa, R.F.S. Freitasb. Phase behavior of poly(N-isopropylacrylamide) in binary aqueous solutions. Polymer, 43 (2002) 7.
[10] A.V. Gorelov, A.D. Chesne, K.A. Dawson. Phase separation in dilute solutions of poly (N-isopropylacrylamide). (1997) 10.
[11] R.M.K. Ramanan, P. Chellamuthu, L. Tang, K.T. Nguyen. Development of a Temperature-Sensitive Composite Hydrogel for Drug Delivery Applications. Biotechnol. Prog, 22 (2006) 8.
[12] F. Carpi, C. Menon, D. De Rossi. Bio-Inspired Distributed Electroactive Polymer Actuators for Possible Space Applications: Concept Design. Artificial Muscle Actuators Using Electroactive Polymers, 61 (2009) 180-185.
[13] D.J. Beebe, J.S. Moore, J.M. Bauer, Q. Yu, R.H. Liu, C. Devadoss, B.H. Jo. Functional hydrogel structures for autonomous flow control inside microfluidic channels. Nature, 404 (2000) 588-+.
[14] K.K. Westbrook, H.J. Qi. Actuator designs using environmentally responsive hydrogels. Journal of Intelligent Material Systems and Structures, 19 (2008) 597-607.
[15] A. Richter, S. Howitz, D. Kuckling, K.F. Arndt. Influence of volume phase transition phenomena on the behavior of hydrogel-based valves. Sensors and Actuators B-Chemical, 99 (2004) 451-458.
[16] W. Hong, X.H. Zhao, J.X. Zhou, Z.G. Suo. A theory of coupled diffusion and large deformation in polymeric gels. Journal of the Mechanics and Physics of Solids, 56 (2008) 1779-1793.
[17] W. Hong, Z.S. Liu, Z.G. Suo. Inhomogeneous swelling of a gel in equilibrium with a solvent and mechanical load. International Journal of Solids and Structures, 46 (2009) 3282-3289.
[18] Y. Zhang, Z.S. Liu, S. Swaddiwudhipong, H.Y. Miao, Z.W. Ding, Z.Z. Yang. pH-Sensitive Hydrogel for Micro-Fluidic Valve. Journal of Functional Biomaterials, 3 (2012) 16.
[19] Z.S. Liu, S. Swaddiwudhipong, W. Hong. Pattern formation in plants via instability theory of hydrogels Soft Matter, 9 (2013) 11.
[20] Z.S. Liu, S. Swaddiwudhipong, F.S. Cui, W. Hong, Z.G. Suo, Y.W. Zhang. Analytical Solutions of Polymeric Gel Structures under Buckling and Wrinkle. International Journal of Applied Mechanics, 03 (2011) 235-257.
[21] W. Toh, T.Y. Ng, Z.S. Liu. Non-Linear Large Deformation Kinetics of Polymeric Gel. Key Engineering Materials, 535-536 (2013) 338-341.
[22] W. Toh, Z.S. Liu, T.Y. Ng, W. Hong. Inhomogeneous Large Deformation Kinetics of Polymeric Gels. Inter Journal of Applied Mechanics, 5 (2013).
[23] F. Afroze, E. Nies, H. Berghmans. Phase transitions in the system poly(N-isopropylacrylamide)/water and swelling behaviour of the corresponding networks. Journal of Molecular Structure, 554 (2000) 55-68.
[24] Z.W. Ding, Z.S. Liu, J.Y. Hu, S. Swaddiwudhipong, Z.Z. Yang. Inhomogeneous Large Deformation Study of Temperature-Sensitive Hydrogel, submitted for publication.
[25] A. Suzuki, T. Ishii. Phase coexistence of neutral polymer gels under mechanical constraint. Journal of Chemical Physics, 110 (1999) 2289-2296.

[26] A.T. Hillel, S. Unterman, Z. Nahas, B. Reid, J.M. Coburn, J. Axelman, J.J. Chae, Q. Guo, R. Trow, A. Thomas, Z. Hou, S. Lichtsteiner, D. Sutton, C. Matheson, P. Walker, N. David, S. Mori, J.M. Taube, J.H. Elisseeff. Photoactivated Composite Biomaterial for Soft Tissue Restoration in Rodents and in Humans Science Translational Medicine, 3 (2011).

A strategy to evaluate the properties of circular ring dielectric actuators

Yin Wang, Jinxiong Zhou*, Xiaohong Wu and Ling Zhang

State Key Laboratory for Strength and Vibration of Mechanical Structures and School of Aerospace, Xi'an Jiaotong University, Xi'an 710049, China
* Corresponding author: jxzhouxx@mail.xjtu.edu.cn

Abstract Dielectric elastomer actuator can be used to adjust the properties of many optical elements. For example, place a diffractive transmission grating on the center of a circular ring actuator. The deformation of the actuator under voltage can change the grating period. The circular ring actuator is an annular dielectric elastormer coated with soft electrodes sandwiched between an elastic circle and an elastic annulus. When subject to a voltage, the active dielectric region will expand and compress the central elastic circle as well as the outer elastic annulus. The compressive deformation of the central elastic circle changes the grating period. We study the properties of circular ring actuators based on the ideal dielectric model combined with the Arruda-Boyce hyperelastic constitutive law and obtain the relationship between the applied voltage and the grating period. The strategy presented here is generic and the results may contribute to the use of dielectric actuators in optical devices.

Keywords Dielectric elastomer actuator; Tunable grating; Ideal dielectric

1. Introduction

Adaptive optical elements are of great importance in a wide range of scientific applications [1]. For the active dynamic tuning of the optical elements, a variety of methods has been proposed, ranging from change the refractive index of a material [2] to rely on the acousto-optic effect[3]. But so far, these methods are not so successful in the tuning of optical elements.

Now the tunable diffraction grating is based on relatively stiff materials and can only achieve a limited spatial tuning grating. A promising approach for combining rapid response time, good optical quality and large actuation amplitude is the use of dielectric actuators [4-6], which is known as "artificial muscles". When a DE is used as an actuator, it can achieve a large voltage-induces strain and can be driven at acoustic frequencies [7].

Here, we investigate a pre-stretched polymer film of VHB4910 which is fixed by a rigid frame and partially covered with high conductive carbon grease as electrodes. Then a polymeric diffractive structure is bonded onto the actuator, similar to the previous work[8-10]. our work is investigate the previous structure with new theory analysis method. The results can be used in the calculation of the tunable transmission grating.

2. Circular ring actuator analysis

The schematic arrangement of a circular ring dielectric actuator is shown in Fig. 1. A circular ring actuator is made from pre-stretched elastomer with a soft electrode annulus which is sandwiched by two electrode-less regions. When subject to a voltage, the active dielectric region will expand and compress the central elastic circle as well as the outer elastic annulus. The inner passive region deforms from its reference configuration with initial radius A, to its current configuration with radius a. The active region evolve from its reference configuration with inner radius A and outer radius B to its current configuration with inner radius and outer radius b, respectively. The outer passive region evolves from its reference configuration with inner radius B and outer radius C to its current configuration with inner radius b and outer radius fixed, respectively. All kinetic variables are

expressed in the reference polar coordinates R, Θ, Z systems, which are denoted by the subscript 1, 2 and 3.The inner passive region, middle active region and outer passive region, are denoted by superscript 1, 2 and 3, respectively.

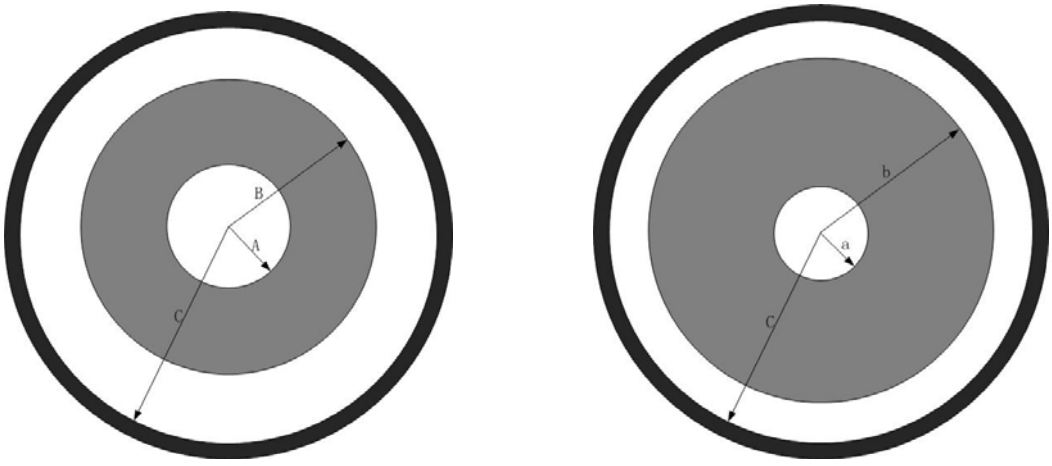

Voltage off Voltage on

Figure 1. The schematic of a typical experimental arrangement of a circular ring dielectric actuator. The central gray area is the dielectric actuator, and outer black area is the rigid frame to apply pre-stretch.

Here the strain energy of an ideal dielectric material is rewritten in terms of stretches and nominal electric field, i.e.,

$$W(\lambda_1, \lambda_2, \tilde{E}) = W_0(\lambda_1, \lambda_2) + W_{ele}(\lambda_1, \lambda_2, \tilde{E}), \tag{1}$$

For the two passive regions, the material laws are only given the first term of the Eq. (1). Based on the elastic theory, the geometric relationship can be obtained readily as

$$\lambda_1 = \frac{\partial r}{\partial R}, \quad \lambda_2 = \frac{r}{R} \tag{2}$$

where λ_1 and λ_2 are radial and hoop stretches, respectively. The equilibrium equation is

$$\frac{\partial s_1}{\partial R} + \frac{s_1 - s_2}{R} = 0 \tag{3}$$

We use the Arruda-Boyce material to express the hyper-elastic part $W_0(\lambda_1, \lambda_2)$, and it gives

$$W_0(I) = \mu\left[\frac{1}{2}(I-3) + \frac{1}{20N}(I^2-9) + \frac{11}{1050N^2}(I^3-27) + \ldots\right] \tag{4}$$

where $I = \lambda_1^2 + \lambda_2^2 + \lambda_1^{-2}\lambda_2^{-2}$ is the first principle invariant. We use nominal stress and nominal electric field as well as electric displacement as mechanical and electrostatic measures. The nominal stresses of the material are given by the following material laws

$$s_1 = \frac{\partial W}{\partial \lambda_1} = \frac{\partial W_0}{\partial I}\frac{\partial I}{\partial \lambda_1} + \frac{\partial W_{ele}}{\partial \lambda_1} \tag{5}$$

$$s_2 = \frac{\partial W}{\partial \lambda_2} = \frac{\partial W_0}{\partial I}\frac{\partial I}{\partial \lambda_2} + \frac{\partial W_{ele}}{\partial \lambda_2} \tag{6}$$

Taking derivative of Eq. (5) with respect to R and substituting Eq. (5) and (6) into Eq. (2) gives the

following ODE

$$\frac{\partial \lambda_1}{\partial R} = \frac{1}{R} g_1(\lambda_1, \lambda_2)(\lambda_2 - \lambda_1) + \frac{1}{R} g_2(\lambda_1, \lambda_2) \tag{7}$$

Another equation can be deduced by invoking Eq. (2) and gives

$$\frac{\partial \lambda_2}{\partial R} = \frac{1}{R}(\lambda_1 - \lambda_2) \tag{8}$$

The $g_1(\lambda_1, \lambda_2)$ and $g_2(\lambda_1, \lambda_2)$ functions in Eq. (7) are expressed as

$$g_1(\lambda_1, \lambda_2) = \frac{\dfrac{\partial^2 W_0(I)}{\partial I^2}\dfrac{\partial I}{\partial \lambda_1}\dfrac{\partial I}{\partial \lambda_2} + \dfrac{\partial W_0(I)}{\partial I}\dfrac{\partial^2 I}{\partial \lambda_1 \partial \lambda_2} + \dfrac{\partial^2 W_{ele}}{\partial \lambda_1 \partial \lambda_2}}{\dfrac{\partial^2 W_0(I)}{\partial I^2}\left(\dfrac{\partial I}{\partial \lambda_1}\right)^2 + \dfrac{\partial W_0(I)}{\partial I}\dfrac{\partial^2 I}{\partial \lambda_1^2} + \dfrac{\partial^2 W_{ele}}{\partial \lambda_1^2}} \tag{9}$$

$$g_2(\lambda_1, \lambda_2) = \frac{\dfrac{\partial W_0(I)}{\partial I}\left(\dfrac{\partial I}{\partial \lambda_2} - \dfrac{\partial I}{\partial \lambda_1}\right) + \left(\dfrac{\partial W_{ele}}{\partial \lambda_2} - \dfrac{\partial W_{ele}}{\partial \lambda_1}\right)}{\dfrac{\partial^2 W_0(I)}{\partial I^2}\left(\dfrac{\partial I}{\partial \lambda_1}\right)^2 + \dfrac{\partial W_0(I)}{\partial I}\dfrac{\partial^2 I}{\partial \lambda_1^2} + \dfrac{\partial^2 W_{ele}}{\partial \lambda_1^2}} \tag{10}$$

For the passive region, the inner region's deformation are equal biaxial and $\lambda_1 = \lambda_2 = \lambda$ and $s_1 = s_2 = s$. The nominal stress $s_{1,2}$ is given by

$$s_{1,2}^1 = \frac{\partial W_0(I)}{\partial I} 2\left(\lambda - \lambda^{-5}\right) \tag{11}$$

For the active region, the stresses are given by Eq. (5) and Eq. (6):

$$s_1^2 = \frac{\partial W_0}{\partial I}\left(2\lambda_1 - 2\lambda_1^{-3}\lambda_2^{-2}\right) - \varepsilon E^{\theta/\theta_0}\lambda_1\lambda_2^2 \tag{12}$$

$$s_2^2 = \frac{\partial W_0}{\partial I}\left(2\lambda_2 - 2\lambda_1^{-2}\lambda_2^{-3}\right) - \varepsilon E^{\theta/\theta_0}\lambda_1^2\lambda_2 \tag{13}$$

And the outer passive region' stresses can be obtained in the same way:

$$s_1^3 = \frac{\partial W_0(I)}{\partial I}\left(2\lambda_1 - 2\lambda_1^{-3}\lambda_2^{-2}\right) \tag{14}$$

$$s_2^3 = \frac{\partial W_0(I)}{\partial I}\left(2\lambda_2 - 2\lambda_1^{-2}\lambda_2^{-3}\right) \tag{15}$$

The stresses given by Eq. (11) ~ (15) should satisfy the following force balance requirement

$$s_1^1(R = A) = s_1^2(R = A) \tag{16}$$

$$s_1^2(R = B) = s_1^3(R = B) \tag{17}$$

The stretches across the interface should also fulfill the following boundary conditions

$$\lambda_2^1(R = A) = \lambda_2^2(R = A) \tag{18}$$

$$\lambda_2^2(R = B) = \lambda_2^3(R = B) \tag{19}$$

Eq. (7) and (8) together with the boundary conditions (16) ~ (19) constitute the nonlinear ODEs that

should be calculated numerically. We use a shooting technique to solve these ODEs by iterating a assumed radial stretch until the computed hoop stretch on the outer boundary equals to the prescribed pre-stretch, and the computed stress on the inner boundary fulfill the force balance equation, Eq. (16) and (17).

Based on the above-mentioned procedure, the properties of the circular ring dielectric actuator can be evaluated. In a simulation example, we fixed A=4mm, B=9mm, C=10.5mm, λ_p =1.2 and $\bar{E}=E\sqrt{\mu/\varepsilon}$=0.5 .Fig. 2 shows the deformation of the circular ring actuator under a pre-stretch and a dimensionless nominal electric field. It is noted that the middle active region's deformation is unhomogeneous and the inner radius deforms greater than the others which results the inner passive region is compressed more obvious. Also the radical's deformation is incontinuous along the radius which is unknown before the calculation. Fig. 3 shows the dimensionless nominal stress versus radius R. From this figure, we know the distribution of the nonimal stress along the radius and the radius R=A and R=B are likely to suffer loss of tension when the voltage is increasing.

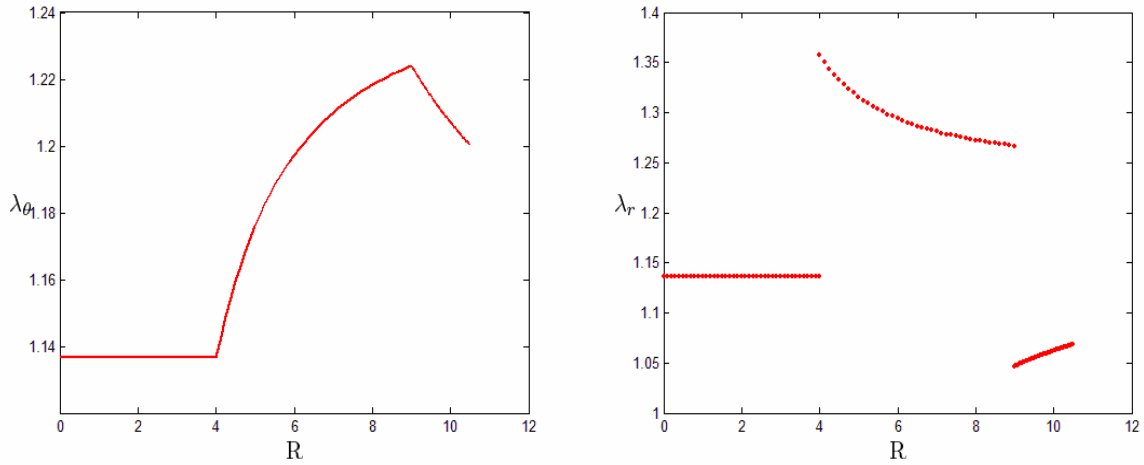

Figure 2. The radius R versus hoop and radial stretches

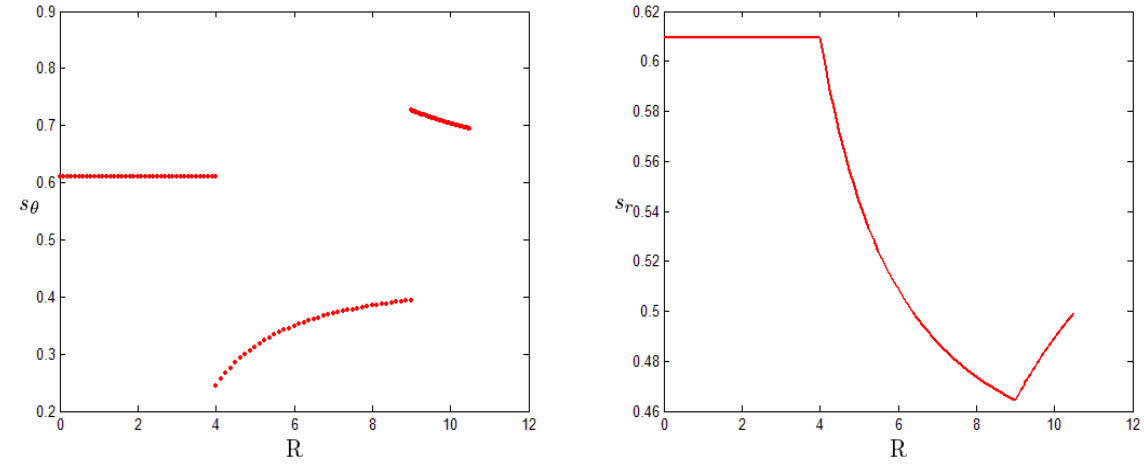

Figure 3. The radius R versus hoop and radial dimensionless nominal stress

3. Applications in tunable transmission grating

Tunable transmission grating is bonded onto circular ring actuator, as showed in Fig. 4. When the voltage is applied, the middle active region enables a compact implementation and results in a change of the grating period,

$$d = (1 - s_{center})d_0 \tag{20}$$

where d_0 is the grating period at $V = 0$, and s_{center} is the planar strain in the inner passive region. In the above simulation example, the grating period changes from $2\mu m$ to $1.9\mu m$

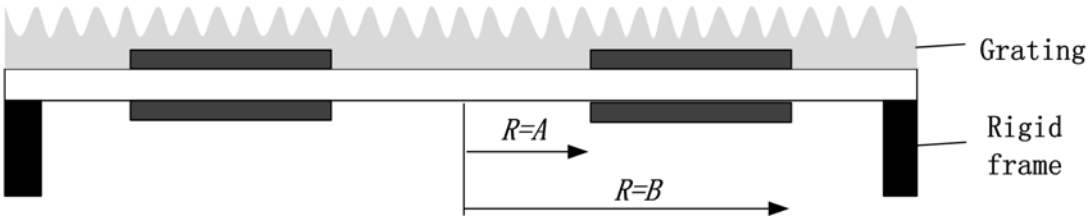

Figure 4. The tunable transmission grating based on circular ring dielectric actuators

Once the stretch in the inner passive region under a certain voltage is calculated, the grating period is also determined by Eq. (20).

Acknowledgements

This work was supported by NSF China (Grant NO. 10972174, 10872157 and 11072185).

References

[1] U. Wittrock, Adaptive optics for industry and medicine, Springer, Berlin, 2005.

[2] R. Lucas and P. Biquard, Optical properties of solid and liquid Medias subjected to high-frequency elastic vibrations. J. Phys. Radium, 71 (1932) 464–477.

[3] D. Ciplys, R. Rimeika, M.S. Shur, R. Gaska, J. Deng, J.W. Yang, M.A. Khan, Acousto-optic diffraction of blue and red light in GaN. Appl. Phys. Lett, 80(10) (2002) 1701-1703.

[4] R. Pelrine, R. Kornbluh, Q. B. Pei, J. Joseph, High-speed electrically actuated elastomers with strain greater than 100%. Science, 287 (2000) 836–839.

[5] F. Carpi, P. Chiarelli, A. Mazzoldi, D. De Rossi, Electro-mechanical characterisation of dielectric elastomer planar actuators: comparative evaluation of different electrode materials and different counter loads. Sens. Actuators A Phys, 107 (2003) 85–95.

[6] A. O'Halloran, F. O'Malley, P. McHugh, A review on dielectric elastomer actuators, technology, applications, and challenges. J. Appl. Phys, 104 (2008) 071101.

[7] R. Heydt, R. Pelrine, J. Joseph, J. Eckerle, R. Kornbluh, Acoustical performance of an electrostrictive polymer film loudspeaker. J. Acoust. Soc. Am, 107 (2000) 833–839.

[8] M. Aschwanden, M. Beck, A. Stemmer, Diffractive transmission grating tuned by dielectric elastomer actuator. Ieee Photonic Tech L, 19(13-16) (2007) 1090-1092.

[9] S. Koh, T.F. Li, J.X. Zhou, X.H. Zhao, W. Hong, J.A. Zhu, Z.G. Suo. Mechanisms of Large Actuation Strain in Dielectric Elastomers. J Polym Sci Pol Phys, 49(7) (2011) 504-515.

[10] Z.H. Fang, C. Punckt, E.Y. Leung, H.C. Schniepp, I.A. Aksay, Tuning of structural color using a dielectric actuator and multifunctional compliant electrodes. Appl Optics, 49(35) (2010) 6689-6696.

Analytical solution of swell-induced surface instability for graded hydrogel layers

Zhigen Wu[1,*], Rui Huang[2], Yihua Liu[1], Hao Li[1]

[1] School of Civil Engineering, Hefei University of Technology, Hefei, Anhui 230009, China
[2] Department of Aerospace Engineering and Engineering Mechanics, University of Texas, Austin, TX 78712, USA
* Corresponding author: zhigenwu@hfut.edu.cn

Abstract To obtain a theoretical solution for the critical condition of swell-induced surface instability, a graded hydrogel layer on a rigid substrate is divided into *n* fictitious sub-layers. By considering the boundary condition and interface continuity, a governing equation for surface instability is established. Hydrogel layers with the crosslink density varying in the thickness direction are examined in details. The results show that both the critical condition and the instability mode relate to the variation of the material properties. For a soft-on-hard graded layer, the onset of surface instability is determined by a short-wave mode with a limiting short wavelength. In contrast, for a hard-on-soft graded layer, a long-wave mode with a finite wavelength emerges as the critical mode at the onset of surface instability. The critical swelling ratio of the long-wave mode for hard-on-soft graded layers is considerably lower than that of the short-wave limit for soft-on-hard ones with the same shape factor. In addition, we found that both the critical swelling ratio and the characteristic wavelength depend on the gradient profile of material properties.

Keywords Hydrogel, Surface instability, Graded layer

1. Introduction

A hydrogel swells significantly when imbibing a large amount of solvent. Swell-induced surface instability of hydrogels has been observed by many researchers[1-6], and a lot of theoretical and numerical studies have also been reported[7-12]. Most of the theoretical studies to date have assumed the hydrogel to be homogeneous before swelling. Recently, a series of experiments by Guvendiren et al.[7,13,14] have observed a rich variety of surface patterns (including creases and wrinkles) by using hydrogels with depth-wise crosslink gradients. It was found that both the critical condition and the characteristic length scale of the surface patterns depended on the crosslink gradient. Motivated by these experiments, we present a theoretical analysis on swell-induced surface instability of graded hydrogel layers, i.e., the layer with material properties varying in the thickness direction.

The critical condition for the onset of swell-induced surface instability in hydrogels has become an interesting subject of theoretical studies recently. By an energetic consideration, Hong et al.[7] predicted a critical strain for surface creasing of an elastomer. More recently, Cao and Hutchinson[12] found that surface wrinkling in an elastomer is highly unstable and extremely sensitive to imperfections that could significantly reduce the critical strain. For a hydrogel layer on a rigid substrate, the critical condition for swell-induced surface instability is similar to the elastomers under compression, but with subtle differences due to the interaction between solvent and the polymer network. Following a procedure similar to Biot's linear perturbation analysis, Kang and Huang[9] predicted that the critical swelling ratio for wrinkling instability of a hydrogel layer varies over a wide range, depending on the material parameters.

The theoretical studies predict no characteristic length scale for the surface instability in homogeneous elastomers and hydrogels. By considering the effect of surface tension, Kang and Huang[10] predicted a characteristic wrinkle wavelength that scales almost linearly with the

thickness of the hydrogel layer. Alternatively, a characteristic length scale may be introduced by assuming a thin skin layer at the surface of the hydrogel[15] or more generally, by assuming a gradient of the material properties in the thickness direction. In this paper, by dividing a layer into fictitious sub-layers, we present theoretical results for the stability analysis for swelling of graded hydrogel layers. The results suggest that both the critical condition and the characteristic wavelength depend sensitively on the depth-wise variation of the material properties in the hydrogel layer.

2. Theory of confined homogeneous hydrogel layers

In this section we briefly review the homogeneously swelling and a linear perturbation analysis for confined hydrogel layers[9,16,17].

2.1. Constrained swelling

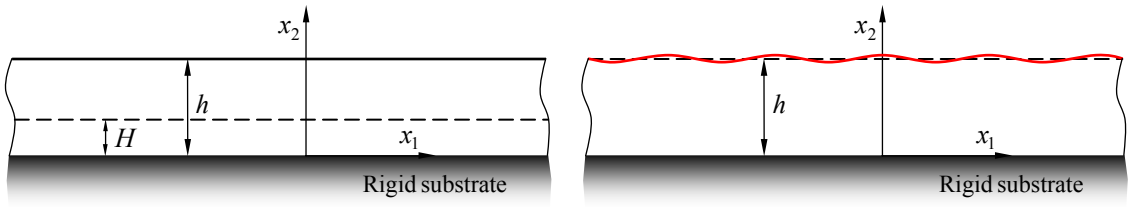

(a) (b)

Fig. 1. Schematic of a hydrogel layer on a substrate: (a) a homogeneous swollen state; (b) a perturbation to the swollen state.

A homogeneous hydrogel layer is attached to a rigid substrate as shown in Fig. 1a. Since confined to the substrate, the hydrogel will swell only in the thickness direction with the thickness varying from H (at dry state) to h (at the swollen state). In the equilibrium state, the swelling ratio $\lambda_h = h/H$ can be obtained as a function of the chemical potential ($\hat{\mu}$) of external solvent in the following form[9]:

$$\log\left(1-\frac{1}{\lambda_h}\right)+\frac{1}{\lambda_h}+\frac{\chi}{\lambda_h^2}+N\Omega\left(\lambda_h-\frac{1}{\lambda_h}\right)=\frac{\hat{\mu}-p\Omega}{kT} \tag{1}$$

where $N\Omega$ and χ are two dimensionless parameters for material properties of the hydrogel, N represents the effective number of polymer chains per unit volume of the polymer network at the dry state, Ω is the volume per solvent molecule, χ reflects the interaction between the solvent molecules and the polymer, $\hat{\mu}$ is commonly a function of the temperature (T) and pressure (p), k the Boltzmann constant. Assuming an ideal gas phase ($p < p_0$) and an incompressible liquid phase ($p > p_0$), the external chemical potential is given by

$$\hat{\mu}(p,T)=\begin{cases}(p-p_0)\Omega, & \text{if } p>p_0,\\ kT\log(p/p_0), & \text{if } p<p_0,\end{cases} \tag{2}$$

where p_0 is the equilibrium vapor pressure of the solvent.

2.2. Linear perturbation fields

For a linear stability analysis, a two dimensional perturbation is assumed as small displacements added to the swollen state of the confined hydrogel layer (Fig. 1b), namely

$$u_1 = u_1(x_1,x_2) \quad \text{and} \quad u_2 = u_2(x_1,x_2). \tag{3}$$

The nominal stresses are obtained by the partial differentiation of the free energy with respect to the deformation gradient components as

$$s_{iJ} \approx NkT[\widetilde{F}_{iJ} - (\lambda_h - \xi_h \varepsilon) H_{iJ}] - pH_{iJ} \tag{4}$$

where $\xi_h = \frac{1}{\lambda_h} + \frac{1}{N\Omega}\left(\frac{1}{\lambda_h - 1} - \frac{1}{\lambda_h} - \frac{2\chi}{\lambda_h^2}\right)$, $\varepsilon = \frac{\partial u_1}{\partial x_1} + \frac{\partial u_2}{\partial x_2}$, and $H_{iJ} = \frac{1}{2} e_{ijk} e_{JKL} F_{jK} F_{kL}$.

Assume the perturbation displacements to be periodic in the x_1 direction, taking the form:

$$u_1 = U_1(x_2)\sin \omega x_1 \quad \text{and} \quad u_2 = U_2(x_2)\cos \omega x_1, \tag{5}$$

where ω is the wave number. Applying Eq. (5) to Eq. (4) and then inserting it to the mechanical equilibrium equation

$$\frac{\partial s_{iJ}}{\partial X_J} = 0, \tag{6}$$

the equilibrium equation is finally derived as follows:

$$\lambda_h^2 U_1'' - \omega^2 (1 + \lambda_h \xi_h) U_1 - \omega \lambda_h \xi_h U_2' = 0, \tag{7}$$

$$\omega \lambda_h \xi_h U_1' + \lambda_h (\xi_h + \lambda_h) U_2'' - \omega^2 U_2 = 0. \tag{8}$$

And the perturbation displacement field can be solved from Eqs. (7) and (8) as

$$U_1(x_2) = A_1 e^{\omega x_2 / \lambda_h} + A_2 e^{-\omega x_2 / \lambda_h} + A_3 e^{\beta \omega x_2} + A_4 e^{-\beta \omega x_2}, \tag{9}$$

$$U_2(x_2) = -A_1 \lambda_h e^{\omega x_2 / \lambda_h} + A_2 \lambda_h e^{-\omega x_2 / \lambda_h} - A_3 \beta e^{\beta \omega x_2} + A_4 \beta e^{-\beta \omega x_2}, \tag{10}$$

where $\beta = \sqrt{(1 + \lambda_h \xi_h)/(\lambda_h^2 + \lambda_h \xi_h)}$.

3. A model of graded hydrogel layers

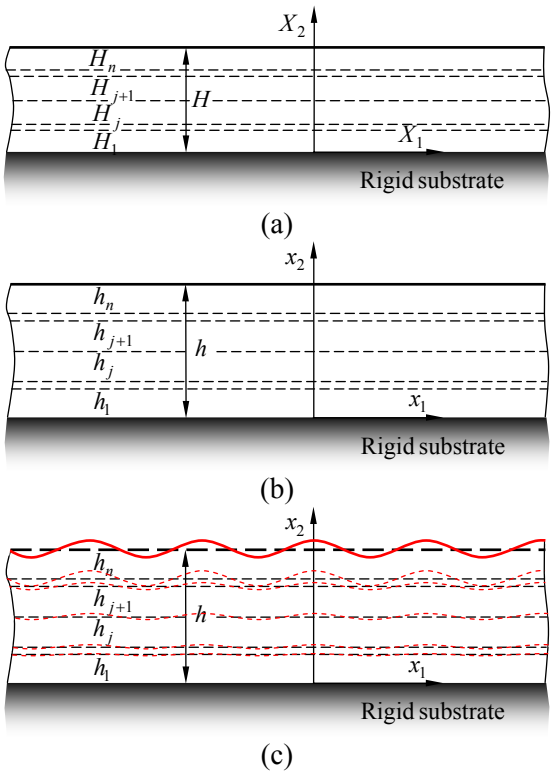

Fig. 2. Schematic of a graded hydrogel layer: (a) the dry state; (b) a transversely homogeneous swollen state; (c) a perturbation to the swollen state.

Consider a confined graded hydrogel layer as shown in Fig. 2. Set a Cartesian coordinate system in the dry state so that X_1 and X_3 are along the interface and X_2 in the thickness direction (Fig. 2a). Now we divide the layer into n fictitious sub-layers, each of which may have different thickness and different material properties. When n approaches infinity, the thicknesses of the sub-layers approach zero uniformly and also the laminated layers approach graded layer.

For the ith sub-layer considered as a homogeneous layer, the perturbation displacements (Fig. 2c) are in the form as Eqs. (9) and (10), i.e.,

$$U_1^{(i)} = A_1^{(i)} e^{\omega x_2/\lambda_{hi}} + A_2^{(i)} e^{-\omega x_2/\lambda_{hi}} + A_3^{(i)} e^{\beta_i \omega x_2} + A_4^{(i)} e^{-\beta_i \omega x_2}, \tag{11}$$

$$U_2^{(i)} = -A_1^{(i)} \lambda_{hi} e^{\omega x_2/\lambda_{hi}} + A_2^{(i)} \lambda_{hi} e^{-\omega x_2/\lambda_{hi}} - A_3^{(i)} \beta_i e^{\beta_i \omega x_2} + A_4^{(i)} \beta_i e^{-\beta_i \omega x_2}, \tag{12}$$

where $\beta_i = \sqrt{(1+\lambda_{hi}\xi_{hi})/(\lambda_{hi}^2 + \lambda_{hi}\xi_{hi})}$.

For the laminated layers, in addition to the boundary conditions, namely

$$U_1^{(1)} = U_2^{(1)} = 0, \qquad \text{at } x_2 = 0, \tag{13}$$

$$(\xi_{hn} - \lambda_{hn})\omega U_1^{(n)} + (\xi_{hn} + \lambda_{hn})\frac{\mathrm{d}U_2^{(n)}}{\mathrm{d}x_2} = 0 \quad \text{and} \quad \frac{\mathrm{d}U_1^{(n)}}{\mathrm{d}x_2} - \omega U_2^{(n)} = 0, \quad \text{at } x_2 = h, \tag{14}$$

the perturbation displacements and the associated tractions must be continuous along the interface of any two adjacent sub-layers, namely

$$U_1^{(j)}(x_{hj}) = U_1^{(j+1)}(x_{hj}) \quad \text{and} \quad U_2^{(j)}(x_{hj}) = U_2^{(j+1)}(x_{hj}), \tag{15}$$

$$s_{12}^{(j)}(x_{hj}) = s_{12}^{(j+1)}(x_{hj}) \quad \text{and} \quad s_{22}^{(j)}(x_{hj}) = s_{22}^{(j+1)}(x_{hj}), \tag{16}$$

where $x_{hj} = h_1 + h_2 + \mathrm{K} + h_j$ (j = 1, 2, …, n–1). Substituting Eqs. (11) and (12) into Eqs. (13)-(16) yields 4n linear homogeneous equations with respect to the coefficients $A_m^{(i)}$ ($m = 1 \sim 4$, $i = 1 \sim n$), which can be written in a matrix form:

$$\mathbf{DA} = \mathbf{0}, \tag{17}$$

where $\mathbf{D}$ is a $4n \times 4n$ matrix.

The critical condition for onset of the surface instability in the graded hydrogel layer is then obtained by setting the determinant of the matrix $\mathbf{D}$ equal to zero, namely

$$\det(\mathbf{D}) = f(\omega H, \mu; N_i\Omega, \chi_i, k_i) = 0. \tag{18}$$

For each normalized wave number (ωH), we solve Eq. (18) to find the critical chemical potential μ_c, which depends on the material properties of sub-layer ($N_i\Omega$, χ_i) as well as its volume fraction $k_i = H_i / H$. The swelling ratio of each sub-layer at the critical chemical potential, $\lambda_{hi}(\mu_\mathrm{c})$, is then calculated from Eq. (1). Subsequently, the general critical swelling ratio for the graded layer can be calculated from

$$\lambda_\mathrm{c} = h/H = \sum_{i=1}^{n} k_i \lambda_{hi}. \tag{19}$$

4. Results and discussion

In this section, we apply the approach developed in the previous section to present the analytical results for the critical condition of surface instability for both hydrogel bilayers and graded hydrogel layers, and the effects of material properties are discussed as well.

4.1. Hydrogel bilayer instability

Fig. 3a plots the critical chemical potential as a function of the perturbation wave number for two bilayers (A and B), in comparison with a homogeneous layer. The corresponding critical swelling ratios are plotted in Fig. 3b. For the bilayers, the critical chemical potential varies with the perturbation wave number non-monotonically. If the top layer is softer than the underlayer ($N_2 < N_1$), the critical chemical potential has a local minimum μ_c^*, corresponding to a long-wave mode ($\omega = \omega^*$). The local minimum μ_c^* however is greater than the critical chemical potential at the short-wave limit ($\omega \to \infty$), i.e., $\mu_c^* > \mu_c^\infty$. Therefore, the onset of surface instability for such a bilayer (*soft-on-hard*) is expected to be determined by the short-wave limit. On the other hand, if the top layer is stiffer than the underlayer ($N_2 > N_1$), the minimum critical chemical potential occurs at a long-wave mode and is lower than the short-wave limit, i.e., $\mu_c^* < \mu_c^\infty$. Consequently, the critical condition for onset of surface instability for such a bilayer (*hard-on-soft*) is determined by a critical long-wave mode, with a characteristic length ($L^* = 2\pi/\omega^*$). In this case, the critical chemical potential for long-wave mode and the corresponding critical swelling ratio are considerably lower than that for a homogeneous layer.

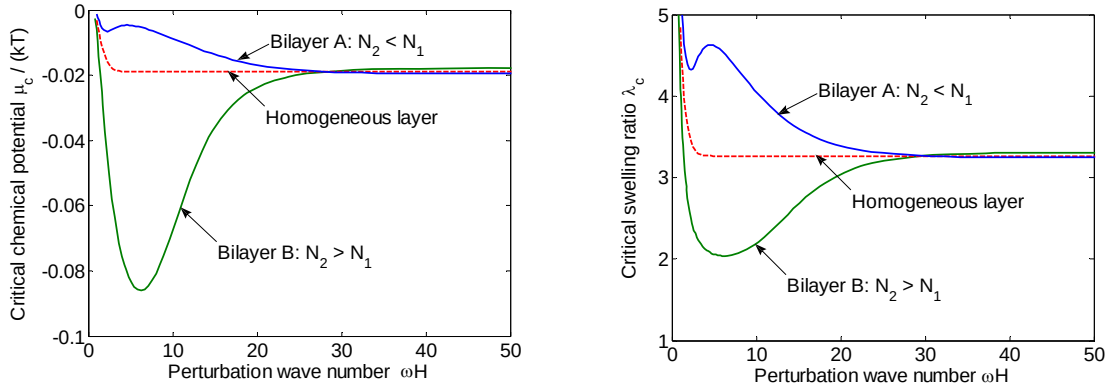

(a) (b)

Fig. 3. (a) Critical chemical potential and (b) the corresponding swelling ratio versus the perturbation wave number for two hydrogel bilayers (A: $N_2\Omega = 4\times10^{-4}$; B: $N_2\Omega = 2\times10^{-3}$), both with $N_1\Omega = 10^{-3}$ and $k_1 = 0.9$, in comparison with a homogeneous hydrogel layer ($N\Omega = 10^{-3}$).

To highlight the distinct surface instability behaviors for the soft-on-hard and hard-on-soft hydrogel bilayers, a nonlinear finite element method developed previously[8] is used to simulate swell-induced deformation and evolution of surface instability of the hydrogel bilayers, as shown in Fig. 4. The two models are identical in geometry, mesh, initial surface perturbation, boundary conditions, and volume fraction $k_1 = 0.9$. The common material properties are: $N_1\Omega = 10^{-3}$ and $\chi_1 = \chi_2 = 0.4$. The soft-on-hard bilayer, with $N_2\Omega = 4\times10^{-4}$, develops multiple surface creases without appreciable wrinkling (Fig. 4a and 4b), similar to that of a homogeneous layer[9]. For the hard-on-soft bilayer, with $N_2\Omega = 10^{-2}$, the behavior is drastically different: the wrinkles grow significantly before creases form (Fig. 4c and 4d). The critical chemical potential or the critical swelling ratio for the onset of surface wrinkling in the hard-on-soft bilayer is considerably lower than that for surface creasing in the soft-on-hard bilayer.

Therefore, the two types of hydrogel bilayers (soft-on-hard vs hard-on-soft) exhibit distinct behavior at the onset of surface instability: for the soft-on-hard bilayer, with no characteristic length, surface wrinkling is highly unstable and is likely to collapse into creases; for the hard-on-soft

bilayer, surface wrinkling is stable with a finite wavelength.

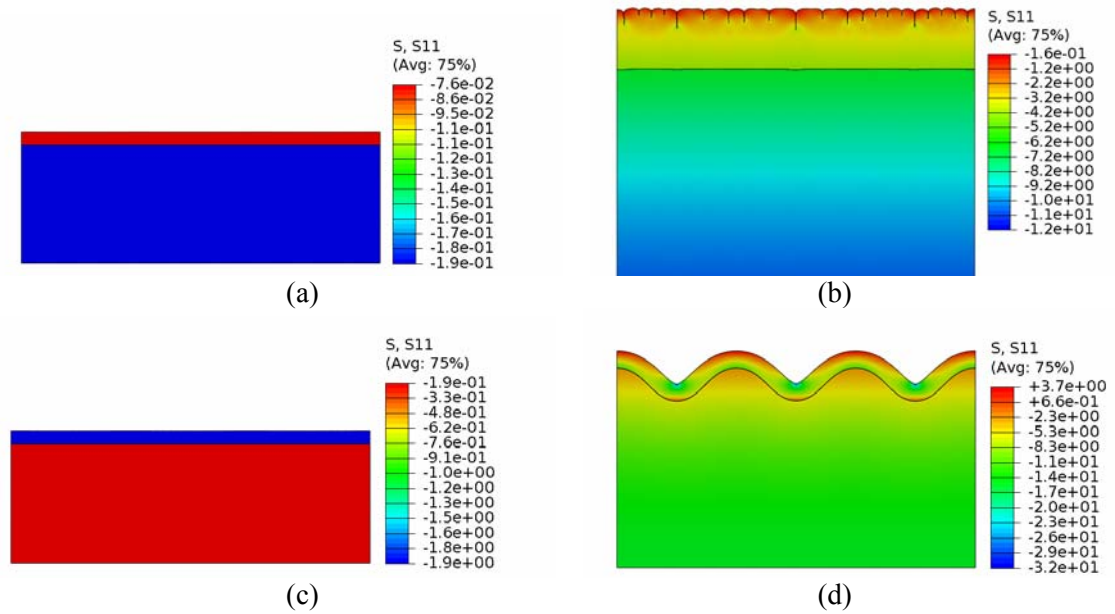

Fig. 4. Numerical simulations of swell-induced surface instability. (a) and (b): μ/kT =-1.158 and -0.004 for a soft-on-hard bilayer ($N_1\Omega$ = 10^{-3} and $N_2\Omega$ = 4×10^{-4}); (c) and (d): μ/kT =-1.158 and -0.1513 for a hard-on-soft bilayer ($N_1\Omega$ = 10^{-3} and $N_2\Omega$ = 10^{-2}).

4.2. Graded hydrogel layer instability

To illustrate the effect of material parameters varying in the thickness direction on surface stability, we consider a graded hydrogel layer with linearly or exponential graded crosslink density. Since the effective number of polymer chains per unit volume is proportional to the crosslink density, we have

$$N(X_2) = N_{\text{bot}} + (N_{\text{sur}} - N_{\text{bot}})\frac{X_2}{H}, \tag{20}$$

or

$$N(X_2) = N_{\text{bot}} + (N_{\text{sur}} - N_{\text{bot}})\frac{\exp(\eta X_2/H)-1}{\exp(\eta)-1}, \tag{21}$$

so that $N = N_{\text{bot}}$ at the bottom face of the hydrogel layer ($X_2 = 0$) and $N = N_{\text{sur}}$ at the surface ($X_2 = H$). The other material parameter, χ, is assumed to be a constant.

Fig. 5 shows the critical chemical potential and the critical swelling ratio as functions of the perturbation wave number for the graded hydrogel layer with $N_{\text{sur}}\Omega$ = 0.01, $N_{\text{bot}}\Omega$ = 0.001, χ = 0.4, and the shape factor η = 0. The three curves in each figure represent the results for the graded layer divided into 5, 10, and 20 sub-layers, respectively. Similar to the hard-on-soft hydrogel bi-layer in Fig. 3, there exist the minimum critical chemical potential μ_c^* at a long-wave mode ω^*. It can also be observed that the results converge very fast, especially μ_c^*, ω^*, and the according critical swelling ratio λ_c^* coincide very well. Therefore, the enough accurate results may be obtained by using 20 sub-layers.

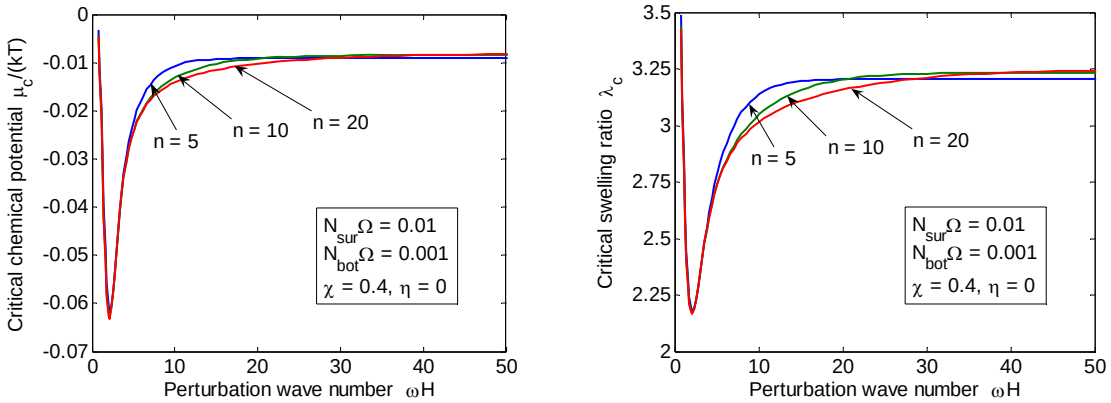

(a) (b)

Fig. 5. (a) Critical chemical potential and (b) the corresponding swelling ratio versus the perturbation wave number for the graded hydrogel layer divided into 5, 10, 20 sub-layers, respectively.

The critical swelling ratios for different gradient profile with η = -5, 0, 5 are plotted in Fig. 6. It is interesting that critical swelling ratios relate to the shape factor η. For soft-on-hard graded layers (N_{sur}<N_{bot}), the critical swelling ratio decreases monotonically with increasing wave number, which is similar to the case of soft-on-hard bi-layers, but without a local minimum λ_c^*. The onset of surface instability is determined by short-wave limit and the according swelling ratio λ_c^∞ decreases as the shape factor increases (Fig. 6a). For hard-on-soft graded layers (N_{sur}>N_{bot}), the critical swelling ratio for the long-wave mode (λ_c^*) and the according wavelength (L^*) depend on gradient profile as shown in Fig. 6b, and apparently λ_c^* is considerably lower than λ_c^∞ for the soft-on-hard graded layer with the same shape factor. The critical swelling ratio for the long-wave mode (λ_c^*) varies with the shape factor η monotonically as shown in Fig. 7a. The swelling ratio decreases as the shape factor increases. However, the wavelength of the critical long-wave mode ($L^* = 2\pi/\omega^*$), normalized by the layer thickness H, first increases and then decreases with the increasing shape factor η as plotted in Fig. 7b.

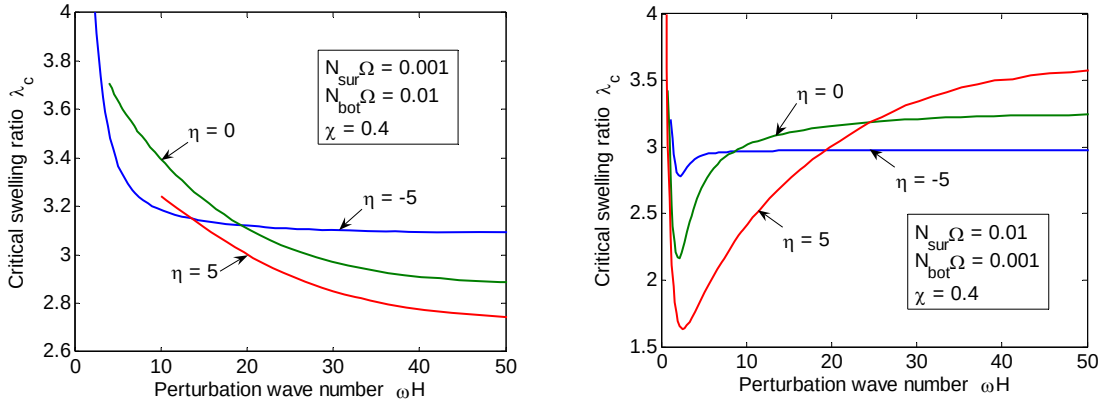

(a) (b)

Fig. 6. Critical swelling ratio obtained by 20 sub-layers versus the perturbation wave number for: (a) soft-on-hard and (b) hard-on-soft graded hydrogel layers with different shape factors.

From the results for graded hydrogel layers, we can predict that the behavior at the onset of surface instability for graded hydrogel layers is similar to that of hydrogel bilayers, i.e., the soft-on-hard graded layer with no characteristic length and the hard-on-soft graded layer with a finite wavelength. Furthermore, both the critical swelling ratio and the wavelength depend on the gradient profile.

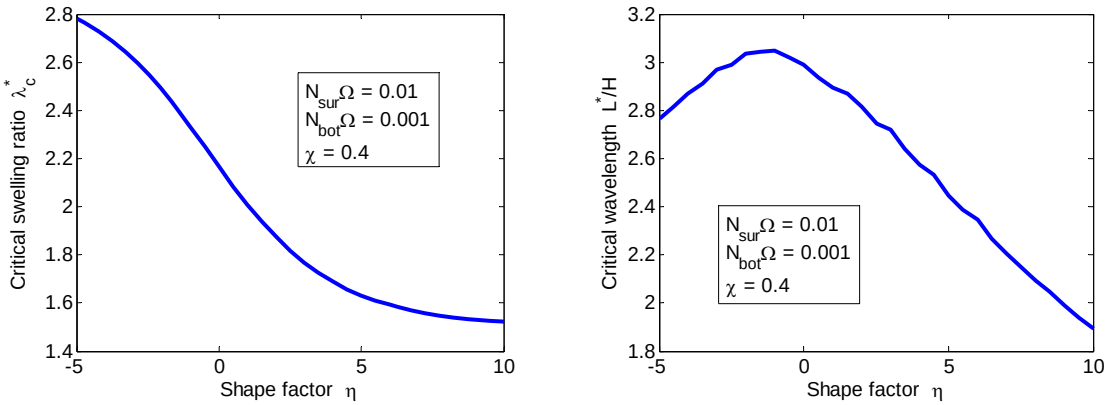

(a) (b)

Fig. 7. (a) The critical swelling ratio for the long-wave mode and (b) the corresponding wavelength with shape factor η ranging from -5 to 10.

5. Conclusions

Based on the theory for homogeneous hydrogel layers, we presented a theoretical solution for the critical condition of swell-induced surface instability for a graded hydrogel layer on a rigid substrate. Graded hydrogel layers with the crosslink density varying in the thickness direction as well as hydrogel bilayers were examined as examples. The results show that both the critical condition and the instability mode depend on the variation of the material properties. For a soft-on-hard graded layer, the onset of surface instability is determined by a short-wave mode with a limiting short wavelength. In contrast, for a hard-on-soft graded layer, a long-wave mode with a finite wavelength emerges as the critical mode at the onset of surface instability. The critical swelling ratio of the long-wave mode for hard-on-soft graded layers is considerably lower than that of the short-wave limit for soft-on-hard ones with the same shape factor. In addition, we found that both the critical swelling ratio and the characteristic wavelength depend on the gradient profile of material properties.

Acknowledgements

The corresponding author gratefully acknowledges the financial support by Hefei University of Technology for his visiting as a scholar at The University of Texas at Austin.

References

[1] E. Southern, A.G. Thomas, Effect of constraints on the equilibrium swelling of rubber vulcanizates. J Polym Sci, A3 (1965) 641–646.
[2] T. Tanaka, S.-T. Sun, Y. Hirokawa, S. Katayama, J. Kucera, Y. Hirose, T. Amiya, Mechanical instability of gels at the phase transition. Nature, 325 (1987) 796–798.
[3] V. Trujillo, J. Kim, R.C. Hayward, Creasing instability of surface-attached hydrogels. Soft Matter, 4 (2008) 564–569.
[4] M. Guvendiren, S. Yang, J.A. Burdick, Swelling-induced surface patterns in hydrogels with gradient crosslinking density. Adv Funct Mater, 19 (2009) 3038–3045.
[5] J. Dervaux, Y. Couder, M.-A. Guedeau-Boudeville, M. Ben Amar, Shape transition in artificial tumors: from smooth buckles to singular creases. Phys Rev Lett, 107 (2011) 018103.
[6] S.S. Velankar, V. Lai, R.A. Vaia, Swelling-induced delamination causes folding of surface-tethered polymer gels. ACS Appl Mater Interf, 4 (2012) 24–29.

[7] W. Hong, X. Zhao, Z. Suo, Formation of creases on the surfaces of elastomers and gels. Appl Phys Lett, 95 (2009) 111901.
[8] M.K. Kang, R. Huang, A variational approach and finite element implementation for swelling of polymeric hydrogels under geometric constraints. J Appl Mech, 77 (2010) 061004.
[9] M.K. Kang, R. Huang, Swell-induced surface instability of confined hydrogel layers on substrates. J Mech Phys Solids, 58 (2010) 1582–1598.
[10] M.K. Kang, R. Huang, Effect of surface tension on swell-induced surface instability of substrate-confined hydrogel layers. Soft Matter, 6 (2010) 5736–5742.
[11] J. Dervaux, M. Ben Amar, Buckling condensation in constrained growth. J Mech Phys Solids, 59 (2011) 538–560.
[12] Y. Cao, J.W. Hutchinson, From wrinkles to creases in elastomers: the instability and imperfection-sensitivity of wrinkling. Proc Royal Soc, A468 (2012) 94–115.
[13] M. Guvendiren, J.A. Burdick, S. Yang, Kinetic study of swelling-induced surface pattern formation and ordering in hydrogel films with depth-wise crosslinking gradients. Soft Matter, 6 (2010) 2044–2049.
[14] M. Guvendiren, J.A. Burdick, S. Yang, Solvent induced transition from wrinkles to creases in thin film gels with depth-wise crosslinking gradients. Soft Matter, 6 (2010) 5795–5801.
[15] E. Hohlfeld, L. Mahadevan, Unfolding the Sulcus. Phys Rev Lett, 106 (2011) 105702.
[16] W. Hong, Z. Liu, Z. Suo, Inhomogeneous swelling of a gel in equilibrium with a solvent and mechanical load. Int J Solids Struct, 46 (2009) 3282–3289.
[17] Z. Wu, N. Bouklas, R. Huang, Swell-induced surface instability of hydrogel layers with material properties varying in thickness direction. Int J Solids Struct, 50 (2013) 578–587.

ECM-Based Statistical Simulation of Progressive Failure in Symmetric Laminates Damaged by Transverse Ply Cracking

Fang Wang[1,*], Junqian Zhang[2], Lu Li[1], Zhiqian Chen[1]

[1] School of Materials Science and Engineering, Southwest University, 400715, China
[2] Department of Mechanics and Shanghai Key Laboratory of Mechanics in Energy and Environment Engineering, Shanghai University, 200444, China
* Corresponding author: wangfang_cq1978@163.com

Abstract The purpose of the present paper is to propose an analytical model that enables the evolution of transverse ply cracking to be investigated in fiber reinforced laminated composites subjected to in-plane tensile loading and thermal residual stress. The strain energy release rate associated with matrix cracking in transverse layer is derived using a 2-D shear-lag stress analysis and the equivalent constraint model (ECM). An energy criterion, based upon the fracture mechanics approach, is proposed to describe the initiation and propagation of the transverse ply cracking. This work is also concerned with statistical distributions of the defects with due consideration given to the scale size effect. Monte-Carlo simulation technique is implemented to predict mechanical behaviors of composite structures by taking into account the statistic of critical fracture toughness G_c of the transverse ply. The results deduced from the numerical procedure are in good agreement with the experimental results obtained for laminated composites formed by unidirectional fiber reinforced laminae with different orientations.

Keywords Laminated composites, Transverse cracking, Fracture mechanics, Statistical analysis, Modelling

1. Introduction

Composite laminates have gained widespread acceptance in many structural applications on account of their high specific strength and stiffness. There is a strong need of comprehensively understanding damage mechanisms to ensure the structural integrity of composite materials.

Performance in service of a composite structure is influenced by the progressive occurrence and interaction of some or all of the many multi-mechanisms of damage such as matrix cracking, delamination, fiber fracture and fiber/matrix debonding under loading and environment conditions. The early stage of damage is dominated is matrix cracking parallel to the fibers in the off-axis piles. These matrix cracks develop in the fiber direction and extend across the laminates from the free edges of test specimens. The number of cracks increases with increasing the load until a saturation crack density. Matrix cracking is usually referred as transverse cracking because the crack plane is commonly transverse to the laminate middle-plane. It can result in significant deterioration of the residual stiffness and loading-bearing capacity of laminates and triggers development of other more harmful damage mechanisms [1].

The detailed mechanisms of transverse ply cracking in laminates have been a subject of active research effort. A large variety of analyses have been conducted to investigate the damage phenomena of composite laminates: different modifications of the shear-lag model [2], variational approach based on minimization of complementary energy [3], continuum damage mechanics approach [4] and numerical methods, for example, based on finite element analysis [5]. The overwhelming majority of studies investigating behavior and properties of composite laminates with matrix cracks assume that cracks are equally spaced [6]. Such a deterministic approach, which ignores the fact that transverse cracking is a progressive damage mode, predicts the appearance of many transverse cracks simultaneously when the first transverse cracking strain is reached [7]. In fact, the transverse matrix cracking is an inherently stochastic process due to the random variations of local material properties of the plies caused by inner original defects [8]. The random distribution

of these defects is the major factor that affects both crack initiation and propagation. Prediction on the durability of these materials tends to be probabilistic in character. Modelling of transverse cracking in laminated composites should, therefore, consider the details of its construction and the use of statistical analysis.

In the present study we derive an analytical model which has the capacity of representing and predicting the fracture of laminated composite structures damaged by transverse cracking, appropriate for the mechanical analysis of fiber reinforced composite laminates. The energy release rate associated with matrix cracking in the transverse layer of general symmetric composite laminates is presented using a 2-D shear lag stress analysis and the equivalent constraint model (ECM) [9,10]. An energy criterion, based on fracture mechanics approach, is proposed to predict and describe the ignition and propagation in symmetrical composite laminates subjected to in-plane loading. This work is also concerned with a stochastic description of the inner defects with due consideration given to the scale size effect. The random properties are introduced with the use of Weibull two-parameter probability density function. A numerical procedure is developed to investigate the multiplication of transverse cracking and predict the statistical failure strengths of composite structures by taking into account the statistic of critical fracture toughness. The results are also compared with those obtained from experiments and other existing models.

2. Formulation and algorithm

2.1. Analytical model

Micro-cracking has been a mechanism of failure extensively studied in many investigations. This mechanism occurs under transverse tensile or longitudinal shear loading conditions. A known analytical modeling of mechanical properties due to transverse cracking was performed by using the suggested “equivalent constraint model” (ECM) to determine the in-plane stress distributions in the damaged layers [11, 12]. The reduction in stiffness properties due to transverse ply crack was described by two in-situ damage effective functions introduced in Refs. [9, 11, 12]. It was shown that a crack lamina behaves within a laminate in a different manner compared to an infinite effective medium containing many cracks [13].

Our simulation reproduces the initial crack and its propagation in the thickness direction using the energy criterion. Indeed, the potential energy method has been presented by Zhang et al.[12, 14] for the evaluation of the energy release rate for damage initiation and propagation due to transverse ply cracking. The required energy release rate, G, for damage growth can be calculated using energy approach and then predicting that damage will grow when G exceed the critical energy release rate, G_c , or toughness of the material.

Energy release rate G associated to the appearance of a crack for a given stress state according to fracture mechanics is defined by the following expression,

$$G = \frac{\partial}{\partial A}\Pi(\sigma, A). \tag{1}$$

where Π is the strain energy of the whole laminate. A is crack surface area. σ is the applied laminate stress.

An opening displacement of transverse crack (COD) solution for a crack is introduced to obtain the strain energy release rate due to matrix cracking, such that

$$G_n(\sigma, D_n) = g_n(L, D_n)\left(\frac{\sigma_x^{0(2)}}{Q_{22}^0}\right)^2. \tag{2}$$

where $\sigma_x^{0(2)}$ is the x-axis normal stress in the xy-plane and superscript 0 is used to indicate the quantities that belongs to the undamaged state. Q_{ij}^0 are the in-plane stiffness components of an undamaged lamina, and $g_n(L, D_n)$ is the normalized energy release rate, which is independent of the applied load. A complete description of the strain energy based model was presented by Zhang [10, 15].

A damage criterion is proposed to predict the evolution of matrix cracking. Estimated quantity is compared with the associated critical value of the stain energy release rate

$$G(\sigma, D_n) = G_c. \tag{3}$$

where G_c denotes the fracture toughness of the composite materials.

2.2. Modelling of progressive cracking

The origins of transverse cracking are the inherent material defects such as the microcracks, voids, debonded fibers, areas of high fiber volume fraction, etc [8]. This causes the transverse layer to have a statistical nature of the fracture toughness along its length. Thus the transverse cracking propagation can be investigated by assigning a random distribution of the fracture toughness along the transverse layers.

In the present paper, the crack multiplication can be simulated by dividing the initial gage length into equal elements along the direction of the length $2L$ and randomly assigning fracture toughness G_c to each of them in accordance with two-parameter Weibull distribution.

Based on the Weibull statistics, the fracture toughness is given as

$$G_c = G_0 \cdot \left[\ln\left(\frac{1}{1-F}\right)\right]^{\frac{1}{m}}. \tag{4}$$

where G_0 represents the scale parameter, or characteristic quantity of the material. The Weibull modulus or shape parameter m controls the degree of disorder in the distribution, experimentally found to describe a variety of materials. $F \in [0,1]$ is a random number. The parameters m and G_0 can be calculated by statistical method

$$\overline{G}_c = E(G_c) = G_0 \Gamma\left(1 + \frac{1}{m}\right), \tag{5}$$

$$D(G_c) = G_0^2 \left\{\Gamma\left(1 + \frac{2}{m}\right) - \left[\Gamma\left(1 + \frac{1}{m}\right)\right]^2\right\}. \tag{6}$$

Where $E(G_c)$ and $D(G_c)$ are the mean and variance of random variable, respectively. In the approach we use here, transverse cracking at some location takes place when the energy released by a cracking event becomes equal to the critical strain energy release rate, G_c , at this position.

In fiber-reinforced composites, the largest portion of the loads is resisted by the fibers. When matrix

crackings occur, the internal loads must redistribute to other areas of the structures, and may cause a structural collapse [16]. For every state of stress, a simple criterion such as Hoffman criterion is expressed mathematically in the following fashion,

$$\frac{\sigma_1^2 - \sigma_1\sigma_2}{X_t X_c} + \frac{\sigma_2^2}{Y_t Y_c} + \frac{X_c - X_t}{X_t X_c}\sigma_1 + \frac{Y_c - Y_t}{Y_t Y_c}\sigma_2 + \frac{\tau_{12}^2}{S^2} = 1. \quad (7)$$

in which σ_1, σ_2 and τ_{12} are longitudinal stress, transverse stress and shear stress, respectively. X_t, X_c are the tensile strength and compressive strength of the unidirectional layer parallel to the fiber direction; Y_t, Y_c are the tensile strength and compressive strength one of the unidirectional layer transverse to the fiber direction; S is the shear strength of the unidirectional layer transverse and parallel to the fiber direction, respectively.

It should be mentioned that in the present study the ultimate failure of materials takes place when the stress state of the primary load-bearing lamina satisfies the condition mentioned [17].

2.3. Numerical algorithm

The simulation was conducted by controlling the stress loading of the model. Fig. 1 shows the progressive failure analysis algorithm for estimating damage growth:

Step 1. Ply material and ply orientation are selected to form a laminate. The critical strain energy release rate, G_c , is assigned to of each element. A virtual crack was introduced in all positions as possible sites for failure and the work performed to close the crack surfaces [18] was calculated. New transverse cracking happens in any location once the energy released by a cracking event is equal to the critical value. The virtual cracking procedure was repeated unceasingly until cracking is terminated under the same applied stress.

Step 2. The equivalent constraint model is employed to analyzing the damaged lamina. In the ECM, all the laminae below and above the damaged lamina under consideration are replaced with homogeneous layers [9]. The reduced stiffness properties of the damaged layer can be calculated by applying the laminated plate theory to the ECM. Thus, the in-plane microstresses of the primary loading-bearing lamina can be obtained by the constitutive relationship.

Step 3. With the stresses calculated, they are substituted in the failure criteria Eq. (7) to check for failure. When the loads are increased monotonically, the matching strains are computed and the resulting stresses are substituted in the failure criteria until they are satisfied. The ultimate load of the laminate is thus determined.

4. Results and discussion

A detailed analysis is conducted to assess the predictive capabilities of the present methodology. The mechanical properties of each type of unidirectional laminate used in this work are given in Ref [17]. Each set of Monte-Carlo simulation consists of 200 data points. The element length of 2.5×10^{-2} mm is chosen for the sake of efficiency [7].

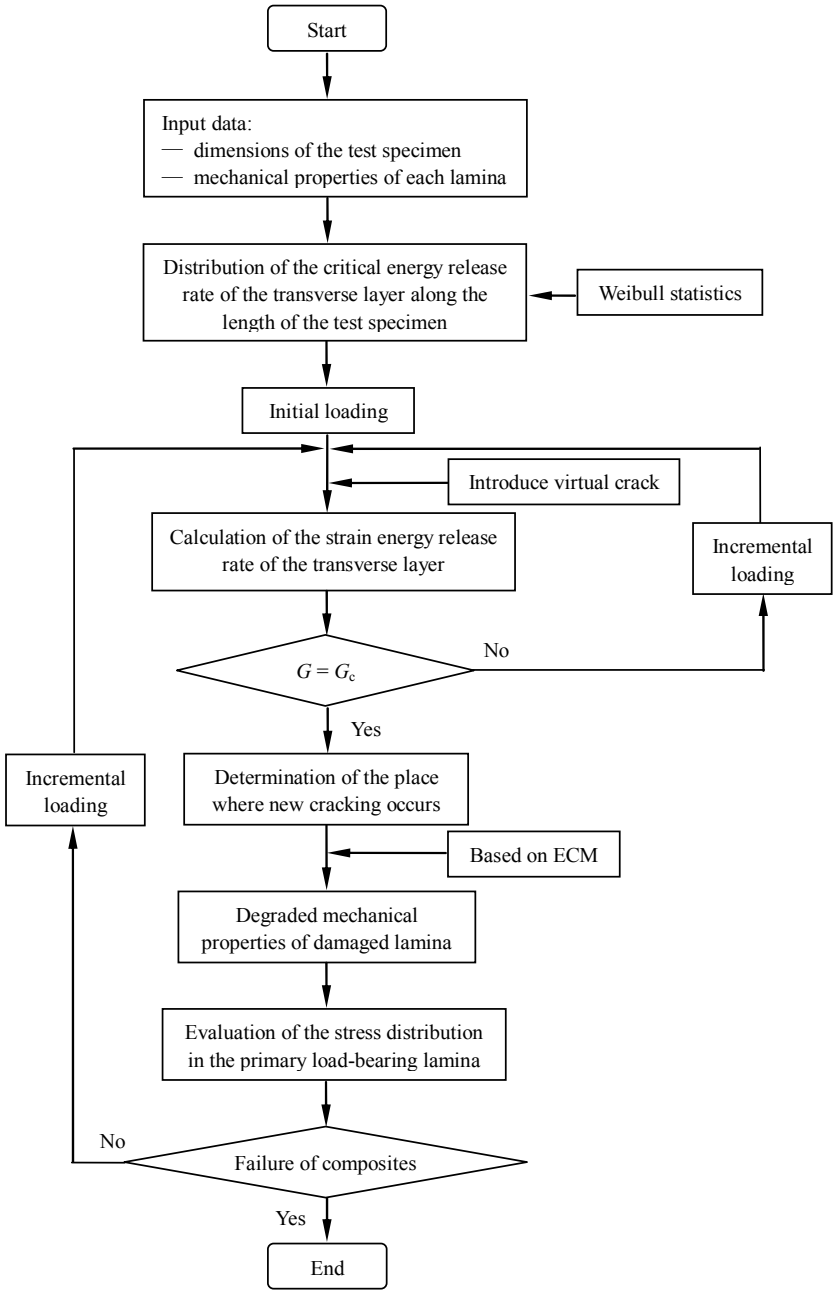

Figure 1. Schematic diagram of the procedure implemented for the analysis of the progression of transverse cracking

4.1. Prediction of stiffness reduction

It is well understood that transverse matrix cracking may occur long before final failure. Matrix cracking causes stiffness degradation and induces other failure modes. Figs. 2 and 3 shows the evolution of the longitudinal Young's modulus and Poisson's ratio for $[0_2/90_4]_s$ glass-fibre/epoxy laminate as a function of matrix crack density. It must be pointed out that the numerical result of each case is the average value of 200 data. The figures exhibit the comparison between the predictions provided by the analytical approach and experimental values. It is shown that the degradations in Poisson's ratio are much higher than the ones observed for the longitudinal Young's modulus. This can be explained by the fact that the Poisson's ratio is a transverse property as compared to the longitudinal nature of the Young's modulus.

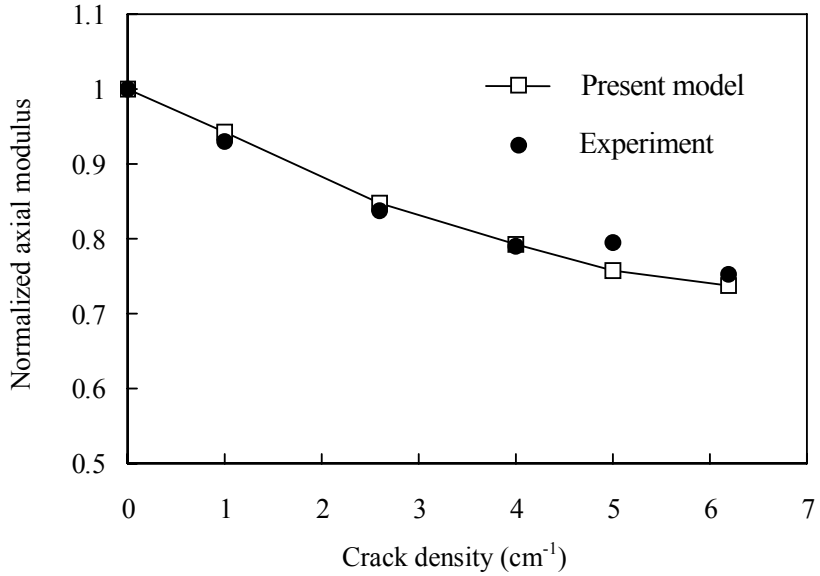

Figure 2. Change of normalized axial modulus as a function of crack density for $[0_2/90_4]_s$ laminate

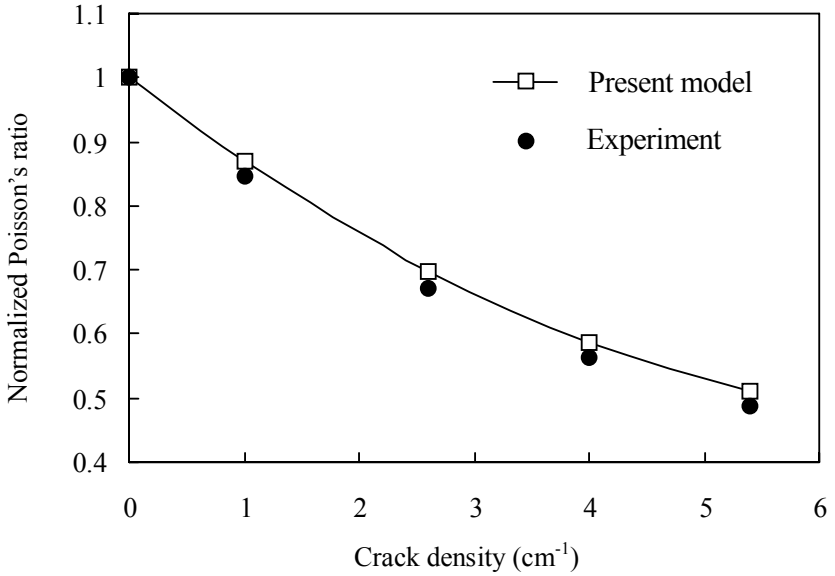

Figure 3. Change of normalized Poisson's ratio as a function of crack density for $[0_2/90_4]_s$ laminate

4.2. Analysis of progressive cracking

Transverse cracking is a progressive damage mode which evolves with increasing in the applied load and a measure of accumulated damage is the crack density. $G_0 = 750\ J/m^2$ and $\beta = 10$ are used as the scale parameters in the Weibull distribution for the glass-epoxy laminates with a stacking sequence of $[\pm 15/90_4]_s$. The simulation results are shown in Fig. 4 compared with experimental values. Since the fracture toughness in transverse layer follows Weibull distribution, the transverse cracking procedure is related to statistical aspect instead of deterministic one. Indeed, the distribution of cracking space is determined by load level and transverse fracture toughness distribution. It is found that the energy criterion can predict and describe the initiation and propagation of matrix cracking.

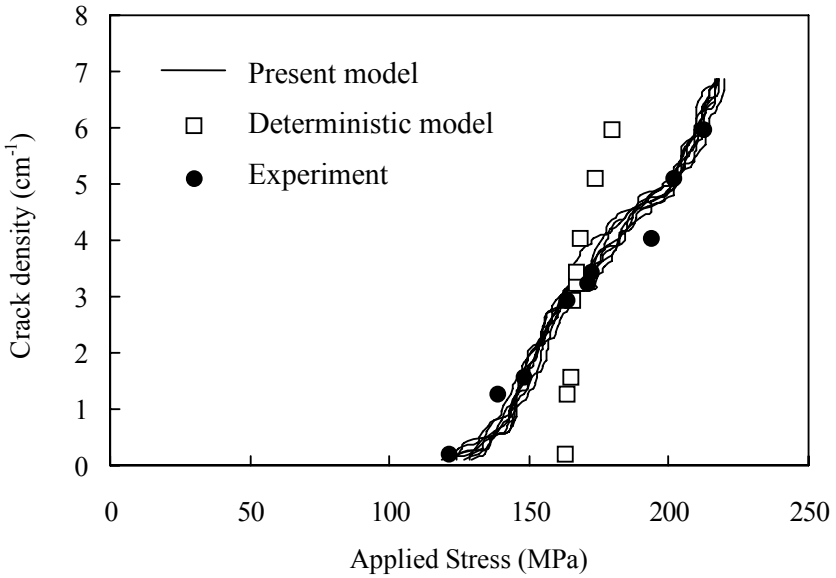

Figure 4. The crack density as a function of the stress applied to $[\pm 15/90_4]_s$ glass-fibre/epoxy laminates

4.3. Estimation of ultimate strength

In Fig. 5, the uniaxial strengths predicted by the current analysis are compared with experimental measurements for the CFRP $[0_2/90_m]_s$ laminates. The prediction is in good agreement with experimental data. The observed offset of ultimate strength is due to the lack of the micro-delamination mechanism in this approach. Especially for thicker layers, delamination at the interface is the dominant damage mode. One feature worthy of note, which is demonstrated by the deterministic model predictions [17], is that the current theory correctly takes account of the effects of the variability in fracture toughness due to microflaws distributed randomly along the length.

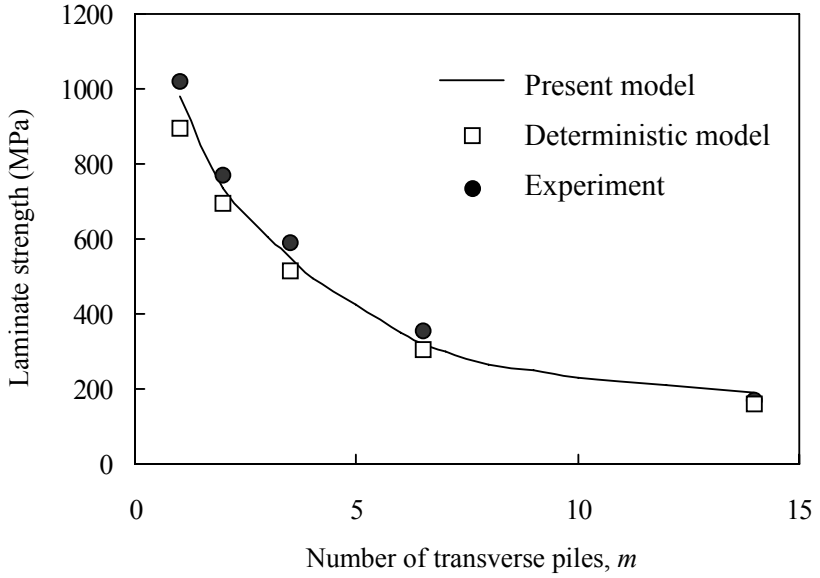

Figure 5. Influence of the 90° lamina thickness on the ultimate strength of the $[0_2/90_m]_s$ CFRP laminates

4.4. Investigation of faliure envelopes

Fig. 6 is biaxial failure envelopes predicted for a $[90/\pm45/0]_s$ AS4/3501-6 epoxy laminate under combined σ_x and σ_y stresses. It is clearly seen that numerical predictions exhibit good agreement with the experimental results present by Soden et al. [19]. It is interesting to note that locating the 90° ply adjacent to the laminate mid-plane will lower the laminate strength. This is because in such case the length of ply cracks in the through-thickness direction is double that for the other laminates, leading to a larger stress concentration in the 0° plies and to fiber failures at lower stresses [20].

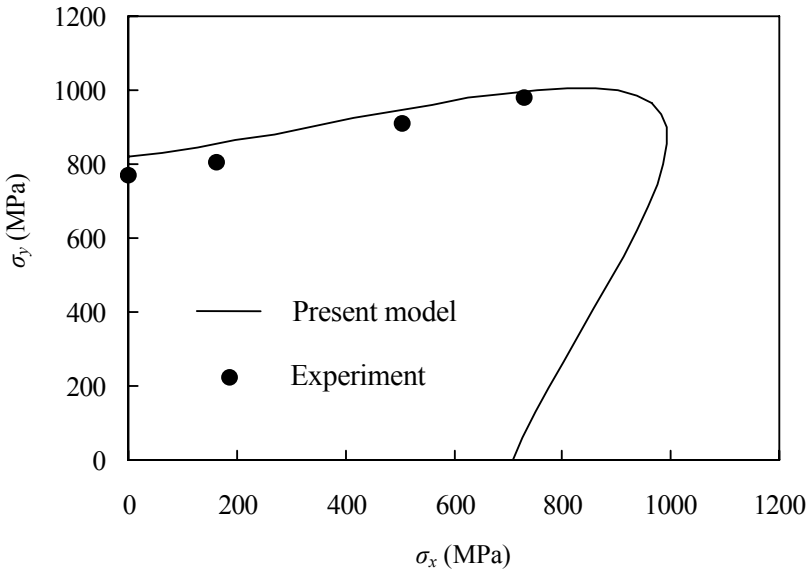

Figure 6. Biaxial failure envelope for $[90/\pm45/0]_s$ laminate made of AS4-3501/6 under combined loading

5. Conclusions

The objective of this exercise is to approach the modelling of progressive damage and failure in composite laminates. A statistical model based on the computation of the strain energy release rate associated with matrix cracking is proposed to study the stiffness reduction and predict ultimate strength of in symmetric laminated composite. The statistical distribution of the critical energy release rate, G_c, in the transverse layer is described by a two-parameter Weibull function in this article. Several sets of application examples and comparison with experimental results show that the present numerical model is able to reproduce the mechanical behavior of laminated composite formed by unidirectional fiber reinforced laminae with different orientations.

Acknowledgements

This work was partially funded by the National Science Foundation of China under Grant No. 11102169, and the Natural Science Foundation Project of CQ CSTC 2012 JJA70002.

References

[1] T. Okabe, M. Nishikawa, N. Takeda, Numerical modeling of progressive damage in fiber reinforced plastic cross-ply laminates. Compos Sci Technol, 68 (2008) 2282–2289.
[2] M. Kashtalyan, C. Soutis, The effect of delaminations induced by transverse cracks and splits on stiffness properties of composite laminates. Compos Part A, 31 (2000) 107–119.
[3] Z. Hashin, Analysis of cracked laminates: a variational approach. Mech Mater, 4 (1985) 121–136.
[4] K.W. Kang, D.M. Lim, J.K. Kim, Probabilistic analysis for the fatigue life of carbon/epoxy

laminates. Compos Struct, 85 (2008) 258–264.
[5] M.V.C. Alfaro, A.S.J. Suiker, R.D. Borst, J.J.C. Remmers, Analysis of fracture and delamination in laminates using 3D numerical modelling. Eng Fract Mech, 76 (2009) 761–780.
[6] J.W. Lee, I.M. Daniel, Progressive transverse cracking of cross ply composite laminates. J Compos Mater, 24 (1990) 1225–1243.
[7] R. Joffe, A. Krasnikovs, J. Varna, COD-based simulation of transverse cracking and stiffness reduction in $[S/90_n]_s$ laminates. Compos Sci Technol, 61 (2001) 637–656.
[8] J.M. Berthelot, J.F. Le Corre, Statistical analysis of the progression of transverse cracking and delamination in cross-ply laminates. Compos Sci Technol, 60 (2000) 2659–2669.
[9] J.Q. Zhang, K.P. Herrmann, Stiffness degradation induced by multiplayer intralaminar cracking in composite laminates. Compos Part A, 30 (1999) 683–706.
[10] J.Q. Zhang, K.P. Herrmann, J.H. Fan, A theoretical model of matrix cracking in composite laminates under thermomechanical loading. Acta Mech Solida Sinica, 14 (2001) 299–305.
[11] J.Q. Zhang, J.H. Fan, C. Soutis, Analysis of multiple cracking in $[\pm\theta_m/90_n]_s$ composite laminates. Part I: In-plane stiffness properties. Composites, 23 (1992) 291–298.
[12] J.Q. Zhang, J.H. Fan, C. Soutis, Analysis of multiple cracking in $[\pm\theta_m/90_n]_s$ composite laminates. Part II: Development of transverse ply crack. Composites, 23 (1992) 299–304.
[13] M. Kashtalyan, C. Soutis, Stiffness degradation in cross-ply laminates damaged by transverse cracking and splitting. Compos Part A, 31 (2000) 335–351.
[14] J.Q. Zhang, C. Soutis, J.H. Fan, Effects of matrix cracking and hygrothermal stresses on the strain energy release rate for edge delamination in composite laminates. Composites, 25 (1994) 27–35.
[15] K.P. Herrmann, J.Q. Zhang, J.H. Fan, An energy-based statistical model for multiple fractures in composite laminates. Int J Multi-scale Comp Eng, 1 (2003) 1–21.
[16] K.L. Reifsnider, W.W. Stinchcomb, A critical-element model of the residual strength and life of fatigue-loaded composite coupons, in: H.T. Hahn (Eds.), Composite Materials: Fatigue and Fracture, ASTM STP 907, Philadephia PA, 1986, pp. 298–313.
[17] F. Wang, X.G. Zeng, J.Q. Zhang, Predictive approach to the failure of composite laminates with equivalent constraint model. Acta Mech Solida Sinica, 23 (2010) 230–247.
[18] G.R. Irwin, Fracture, in: S. Flugge (Eds.), Handbuch der Physik VI, Springer-Verlag, Berlin, 1958, pp. 551–590.
[19] P.D. Soden, M.J. Hinton, A.S. Kaddour, Biaxial test results for strength and deformation of a range of E-glass and carbon fiber reinforced composite laminates: failure exercise benchmark data. Compos Sci Technol, 62 (2002) 1489–1514.
[20] L.N. McCartney, Energy-based prediction of progressive ply cracking and strength of general symmetric laminates using an homogenization method. Compos Part A, 36 (2005) 119–128.

Intermittency in brittle cracks: Model experiment in artificial rocks

Jonathan Barés[1]*, Lamine Hattali[1], Davy Dalmas[2], Daniel Bonamy[1]

[1] CEA IRAMIS SPCSI, Saclay France 91191
[2] UMR CNRS Saint-Gobain, Aubervillier France 93300
* Corresponding author: jonathan.bares@cea.fr

Abstract

Stress enhancement in the vicinity of brittle cracks makes the macroscale failure properties extremely sensitive to the microscale material disorder. As a result, crack propagation is sometimes observed to display a jerky dynamics with seemingly random sudden jumps spanning a broad range of scales, reminiscent of earthquakes. This so-called crackling dynamics cannot be captured via standard continuum fracture theory. The understandings of the key processes that drive such a dynamics then represent a crucial step toward predictive statistical models for heterogeneous brittle failure.

In this context, we designed an experimental setup which permits to drive brittle cracks in opening mode at adjustable velocity throughout model materials of adjustable microstructure. During the fracture, both the mechanical behavior and the acoustic emission are recorded in real time, and *post-mortem*, the morphology of the fracture surface is obtained by profilometry. Accurate statistical analysis of these experimental data and their interplay is believed to provide a deeper understanding of the key mechanisms responsible for crackling in heterogeneous brittle fracture.

Keywords

Brittle crack, Experiment, Crackling dynamics, Model rock, Acoustic

1. Introduction

The effect of materials heterogeneities onto their failure properties remains far from being understood (see [1,2] for reviews of recent progresses in this field). In particular, in heterogeneous materials under slow external loading, cracks growth sometimes displays a jerky dynamics, with sudden jumps spanning a broad range of lengthscales. Such a complex dynamics, also referred to as crackling noise [3] was directly imaged in interfacial crack experiments [4]. It was also suggested from the acoustic emission accompanying paper peeling experiments [5], from the anomalous activity recorded in some calorimeters for high energy physics experiments [6], and - at much larger scale - from the seismic activity associated to earthquakes [7,8]. The salient features of such a crackling dynamics is to exhibit universal scale free statistical features reminiscent of self-organized-criticality [3].

Standard continuum approaches fails to describe such a crackling dynamics. Conversely, recent theoretical and numerical works suggested that some of the approaches developed in statistical and non-linear physics may be relevant. In this context, it has been proposed to identify the crack front with a long-range elastic line [9,10] and to map crack destabilization with a critical depinning transition [11,12]. By subsequently extending this formalism to stable crack growth, it then becomes possible to reproduce a crackling dynamics [13], and to precise the conditions required to

observe it [14]. Still, these models are derived by invoking very restrictive assumptions (1D line moving within a 2D random potential) and lack for quantitative comparisons with real fracture experiments (i.e. breaking of bulk 3D solids). One need also to further understand how the crackling statistics predicted theoretically translates into the acoustic emission and seismograph signals analyzed in fracture and earthquake problems.

The goal of the experiments described thereafter is to fill this lack.

2. Experimental setup

Slow stable cracks are driven via the wedge-splitting geometry [15] sketched in Fig. 1. Specimens were prepared from rectangular plates of size 12x14cm² and thickness 1.5cm. A notch is machined in each of the specimens i) by cutting out a 2.5x2.5cm² square from one side; ii) by subsequently adding a 8mm long thick groove with a diamond saw; and iii) by finally introducing a seed crack (~2mm-long) with a razor blade. The resulting specimens are loaded by placing two steel jaws equipped with roller bearing (to avoid friction) on both sides of the cutout and by pushing a steel wedge (semi-angle of 15°) in between. The opposite side is also made laid on a pivot to avoid friction when breaking. This geometry permits a stable propagation of the crack tip splitting the sample in two symmetric halves.

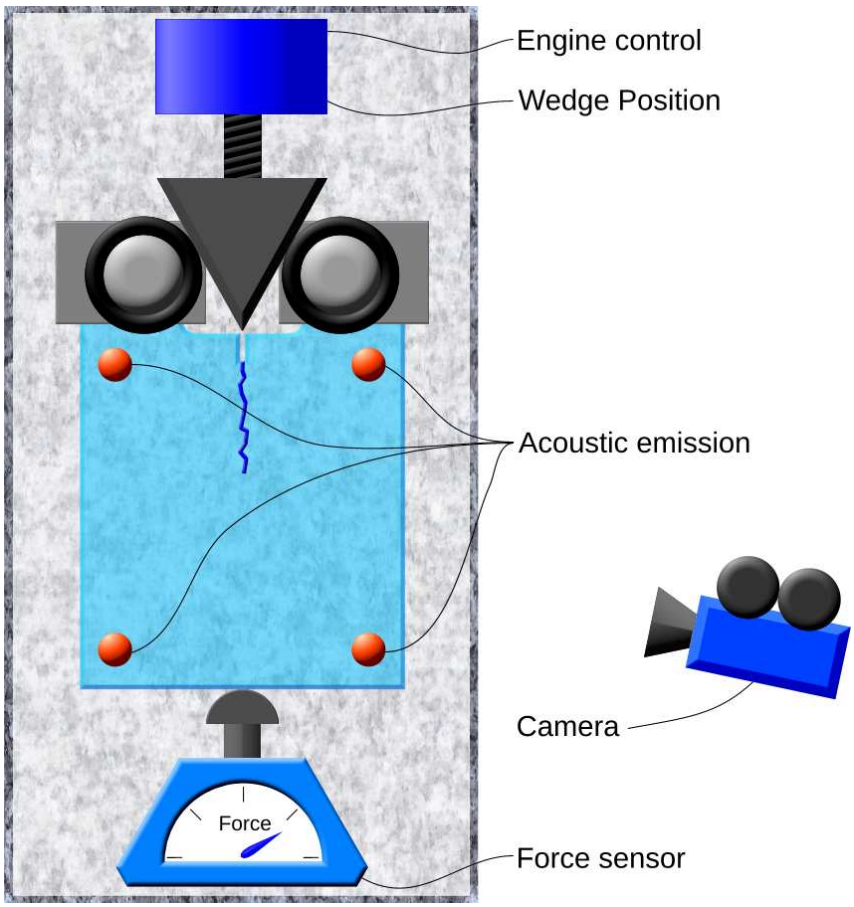

Figure 1. Experimental wedge-splitting device

Fracture experiments are performed on artificial rocks made from sintered polymer beads (Fig. 2D): Plexiglas or polystyrene monodisperse beads of an adjustable diameter (Fig. 2A) are heated up to a temperature slightly below glass transition (110° C), and then compressed in a rigid mold at a fixed pressure during 45min (Fig. 2B). An annealing process just above the glassy temperature during 1h is then applied to limit residual stress, and the so-obtained specimen is slowly cooled down (Fig. 2C).

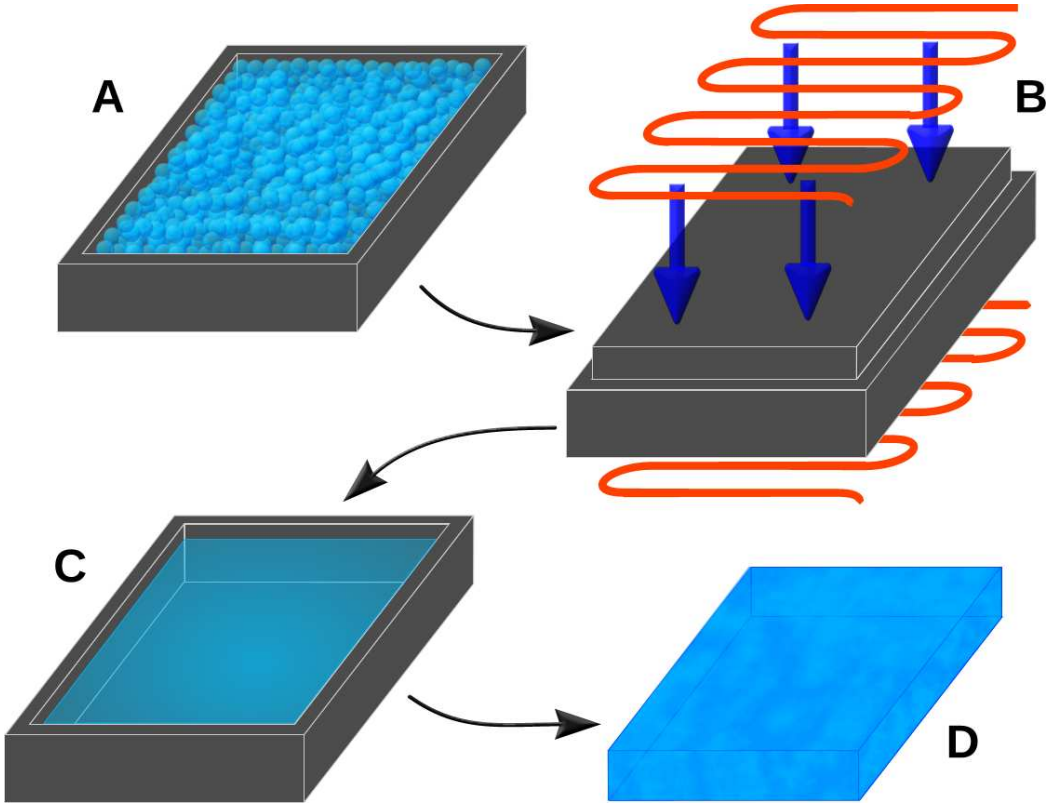

Figure 2. Protocol to synthesize artificial rock of adjustable microstructure

Bead diameters and sintering pressure have been varied, from 20 to 500µm and from 10 to 800kPa respectively, to modulate the microstructure length-scale and the porosity. Wedge speed was varied from 1.6 to 1600 nm/s to study the effect of driving rate. During the tests, a force sensor connected to the bottom of the sample (see Fig. 1) records in real-time the force f applyed on the specimen (acquisition rate of 50kHz with an accuracy of 1N). Similarly the wedge position u is recorded at each time step (acquisition rate of 1Hz) with nanometer precision. Crack propagation is imaged at the specimen surface (30 frames per second with a pixel size of 130µm) and 8 acoustic sensors (4 on both side of the sample) permit a record of the acoustic emission (and its further localization) with MHz acquisition rate and aJ precision.

3. Experimental results

Measurement of the wedge position u and of the applied force f gives full access to the exact mechanical energy stored in the system at each time step (see Fig. 3A). It also provides the time variation of the specimen stiffness (f / u). This signal is plotted as a function of the crack length c

measured from the direct imaging of the surface (Fig. 3B). This curve is noisy, but since noise has no physical meaning in this case, the curve is smoothed and an accurate one-to-one measure of the crack length as a function of the stiffness and of the time is get (black arrows in Fig. 3B). The failure speed can then be directly deduced, with a fairly high signal to noise ratio, by differentiating these data (see Fig. 3C). By limiting friction and plastic dissipation in our experiments, we ensured that the fracture process zone at the tip of the propagating crack is the sole source of mechanical energy dissipation in the system. Hence, from the knowledge of the time evolution for stored elastic energy and crack length, one can compute the energy release rate *G* (see Fig. 3D). Acoustic sensors give access to the energy (see Fig. 3E) of the acoustic events and time delays permit to localize each acoustic source (see Fig. 3F). Finally, the fracture surface is analyzed post-mortem via profilometer (see Fig. 3G).

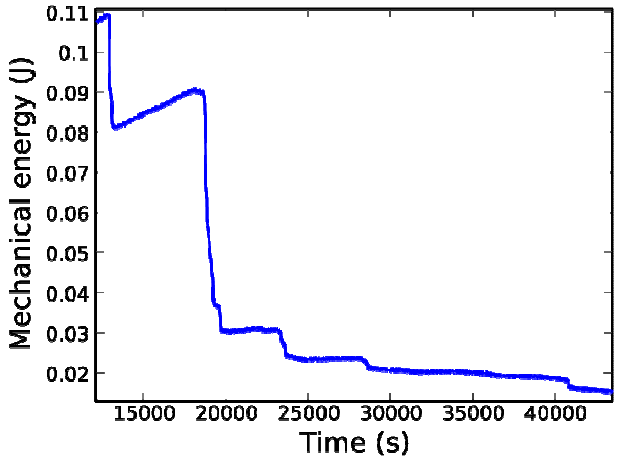

A

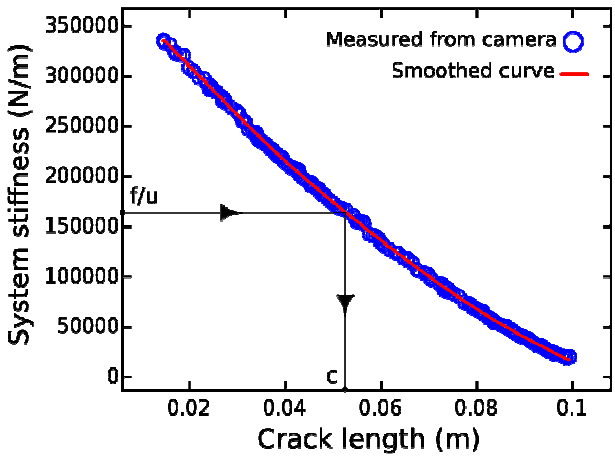

B

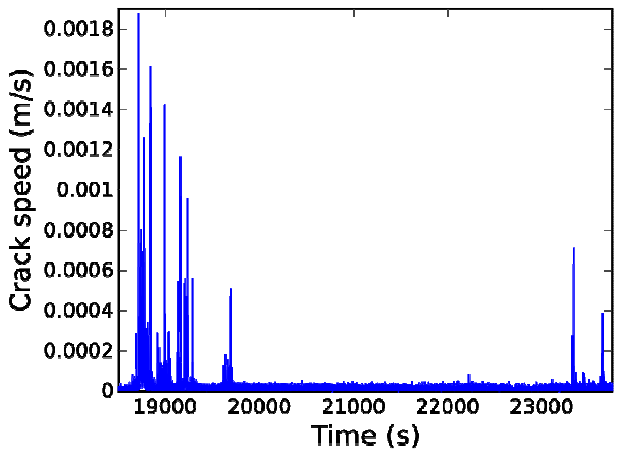

C

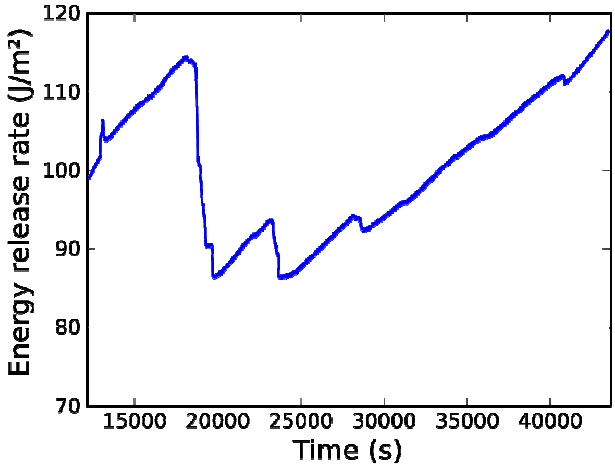

D

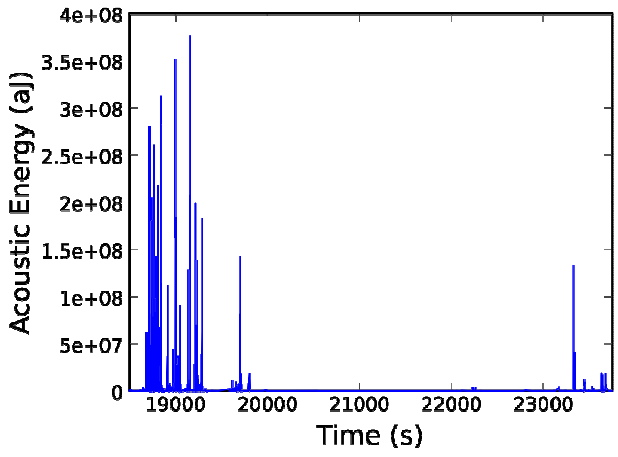

E

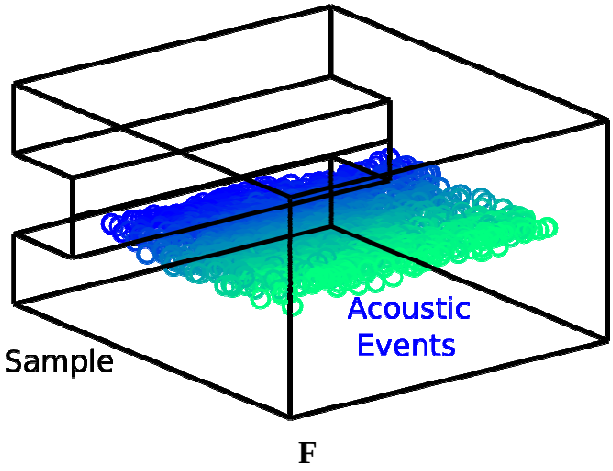

F

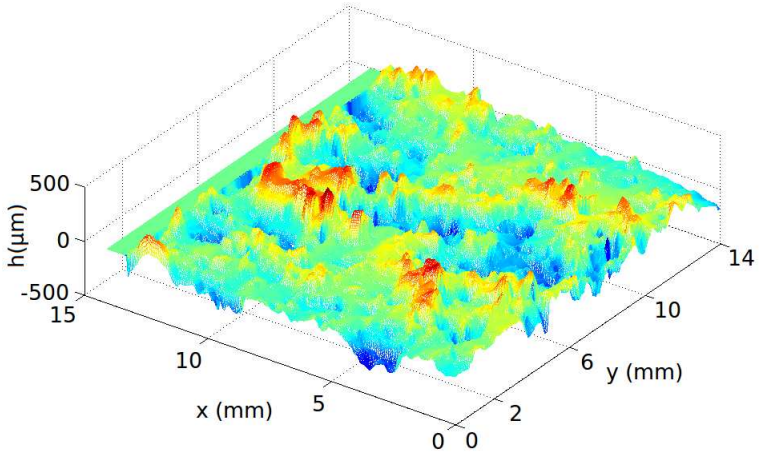

G

Figure 3. Graph of experimental results. A: Elastic energy stored in the whole system as function of time ; B: Crude and smoothed curve of the stiffness system as a function of the crack length measured by camera ; C: Speed of the crack front as a function of time ; D: Energy release rate as a function of time ; E: Acoustic energy of the fracture events ; F: Acoustic location of the fracture events in the sample geometry (colors correspond with time of occurrence) ; G: Post-mortem fracture surface of a piece of sample

As seen in Fig. 3, a crackling signal is observed in our experiments. The statistical analysis of the various signals and their interplay are currently underway and will be presented at ICF13.

4. Concluding discussion

The experimental setup presented here is the first one which permits to observe a crackling dynamics for the steady bulk crack propagation within a 3D brittle solid. A precise sintering protocol has been set up to build this material from mono-disperse polymer beads. Hence, all material parameters (microstructural texture, porosity, toughness) are tunable. The wedge-splitting experimental device set up to fracture this material controlling the loading permits to have access to an accurate measurement of the acoustic and mechanical parameters evolution.

The statistical analysis of these quantities and their interplay is currently in progress. It will allow qualifying the depinning approaches developed in statistical physics [8] to address the problem of brittle heterogeneous fracture.

References

[1] M. J. Alava, P. K. V. V. Nukala, S. Zapperi, Statistical models of fracture. Advances in Physics, 55 (2006) 349-476.
[2] D. Bonamy, E. Bouchaud, Failure of heterogeneous materials: A dynamic phase transition ? Physics Reports, 498 (2011) 1-44.
[3] J. P. Sethna, K. Dahmen, C. Myers, Crackling noise. Nature, 410 (2001) 242-250
[4] K. J. Måløy, S. Santucci, J. Schmittbuhl, R. Toussaint, Local waiting time fluctuations along a randomly pinned crack front. Phys. Rev. Lett., 96 (2006) 045501
[5] J. Koivisto, J. Rosti, M. J. Alava, Creep of a fracture line in paper peeling. Phys. Rev. Lett., 99 (2007) 145504
[6] J. Åström et al, Fracture process observed with a cryogenic detector. Phys. Lett. A, 356 (2006) 262-266
[7] M. Grob, J. Schmittbuhl, R. Toussaint, L. Rivera, S. Santucci, K. J. Måløy, Quake catalogs from an optical monitoring of an interfacial crack propagation. Pure Appl. Geophys., 166 (2009) 777-799
[8] D. Bonamy, Intermittency and roughening in the failure of brittle heterogeneous materials. J. Phys. D: Appl. Phys., 42 (2009) 214014
[9] H. Gao, J. R. Rice, A first order perturbation analysis on crack trapping by arrays of obstacles. J. Appl. Mech., 56 (1989) 828
[10] J. Schmittbuhl, S. Roux, J. P. Vilotte, K. J. Måløy, Interfacial crack pinning: effect of nonlocal interactions. Phys. Rev. Lett., 74 (1995) 1787-1790
[11] S. Roux, D. Vandembroucq, F. Hild, Euro. J. Mech. A/Solids, Effective toughness of heterogeneous brittle materials. 22 (2003) 743-749
[12] L. Ponson, Depinning transitioin in the failure of inhomogeneous brittle materials. Phys. Rev. Lett., 103 (2009) 055501
[13] D. Bonamy, S. Santucci, L. Ponson, Crackling dynamics in material failure as the signature of a self-organized dynamics phase transition. Phys. Rev. Lett., 101 (2008) 045501
[14] J. Barés, L. Barbier, D. Bonamy, Crackling vs. continuum-like dynamics in brittle failure. Submitted
[15] E. Brühwiler, F. H. Wittmann, The wedge splitting test, a new method of performing stable fracture mechanics tests, Eng. Fract. Mech., 35 (1990) 117-125

Non-Gaussian statistics and extreme events on experimental facture surfaces

Yuanyuan Cao[1], Stéphane Vernède[2,3] and Laurent Ponson[1,*]

[1] *Institut Jean Le Rond d'Alembert (UMR 7190), CNRS - UPMC Université Paris 06, 75005 Paris, France.*
[2] *EO Technology, Fengrun Building 606, 280 Heping North Road, 213000 Changzhou, China.*
[3] *Baseline Consulting Services (Shanghai) Co., A-401, 125 Jiangsu North Road, 200042 Shanghai, China;*
[*] *Corresponding author : laurent.ponson@upmc.fr*

Abstract: Experimental studies show that fracture surfaces exhibit rather remarkable scaling properties characterized by universal roughness exponents, close to $\zeta = 0.4$ in brittle materials and close to $\zeta = 0.8$ in quasi-brittle and ductile materials. In this work, we go beyond the value of the roughness exponent, and focus on the distribution of height fluctuations on the fracture surface of a large range of materials, from brittle to ductile and quasi-brittle solids. At first, we show how damage accompanying crack propagation results on average into deviations to the Gaussian statistics observed on brittle fracture surfaces. Then, we identify on the fracture surface the location of the largest jumps responsible for the fat tails observed on these distributions, and show that these extreme events are actually organized in a network of clusters made of connected events. The statistical analysis of these clusters show many interesting features, including a characteristic sizes reminiscent of the typical size of the damage processes in the material studied, a power law distribution of cluster size for ductile and quasi-brittle fracture surface, while their probability distribution decay exponentially in brittle fracture surface. This new approach in the analysis of the morphology of fracture surface is a first step into a better understanding of the damage processes occurring within the process zone during crack propagation, and open promising perspectives into the description of damage mechanisms in a large range of materials by an unified theory.
Keywords: Fracture surface, roughness statistics, scaling behavior.

1 Introduction

Understanding the failure properties of a solid is a constant goal in material science. A fine description of these properties can have important applications for the design of new materials and the expertise of failures. Experimental studies show that fracture surfaces exhibit rather remarkable scaling properties characterized by universal roughness exponents, close to $\zeta = 0.4$ in brittle materials and close to $\zeta = 0.8$ in quasi-brittle and ductile materials. However, much more information about the failure process remains encoded in the fracture surface as the crack roughness reveals the interaction between the crack fronts and the material microstructure. Therefore a fine description of the statistics of fracture surface shall guide the development of more accurate models of fracture propagation and therefore allows a finer understanding of the failure process.

2 Material and methods

Aluminum alloy and mortar are chosen as the archetypes of ductile and quasi-brittle materials, respectively. The alloy specimens are aluminum 4 wt$\%$ copper with an as-casted microstructure. They are broken under uniaxial mode I tension with constant traction velocity (strain rate of approximately $1.6 \times 10^{-2}\mathrm{s}^{-1}$)[1]. Their fracture surfaces are observed with a scanning electron microscope at two tilt angles. A high resolution elevation map is produced from the stereo pair using the cross-correlation based surface reconstruction technique. The reconstructed image of the topography represents a rectangular field of 3.7×2.7 mm (1250×950 pixels). The in-plane and out-of-plane resolutions are of the order of $3\ \mu$m. We present results for sample broken at different temperatures, i.e. $480°$ for the sample #1 and $620°\mathrm{C}$ for the sample #2. A part of the fracture surface of aluminum #2 (2.7×2.7 mm) is represented on Fig. 1(a). Mortar fracture surfaces are obtained by applying four points bending under controlled displacement conditions to a notched beam. The length of the beam is $1400\,\mathrm{mm}$ and its height and thickness are both equal to $140\,\mathrm{mm}$. The topography of the fracture surfaces is recorded using an optical profilometer. The maps include 400 profiles of 4096 points each. We make sure that the analyzed profiles are located far enough from the initition region, so that the roughness properties are statistically stationnary. The sampling step along profiles is $20\,\mu$m. Two successive profiles are separated by $50\ \mu$m along the direction of crack propagation. The lateral and vertical accuracy are of the order of $5\,\mu$m (see [2] for more experimental details). A part of the fracture surface #2 (20×20 mm) is represented on Fig. 1(b). In situ observations and acoustic emissions analysis show that failure occurs by multicracking processes present in an extended zone ahead of the notch. To compare our findings with a reference material that does not involve damage mechanisms, fracture surfaces of brittle ceramics made of sintered glass beads are also analyzed. For this material, the process zone was shown to be much smaller than the diameter $d \simeq 100\,\mu$m of the grains [12]. Tapered Double Cantilever Beam with width and length equal to $20\,\mathrm{mm}$ (perpendicular to the crack propagation) and $60\,\mathrm{mm}$ (parallel to it) respectively, are broken at constant opening rate. The tapered shape of these specimens allows us to obtain a stable quasi-static mode I crack growth. The roughness of the fractured specimens is measured using a mechanical stylus profilometer (™Talysurf Intra) with a $10\,\mathrm{nm}$ vertical and a $2\,\mu$m lateral resolutions. The obtained fracture surface (8×8 mm) is shown on Fig. 1(c).

3 Non-Gaussian statistics of fracture surface roughness

We first study the distribution of height fluctuation on the fracture surfaces. For a given increment $\delta\vec{x}$ of the coordinates in the average fracture plane, we note $p(\delta h|\delta\vec{x})$ the probability distribution of an height increment $\delta h = h(\vec{x}) - h(\vec{x} + \delta\vec{x})$ where the sampling of the distribution is done on all admissible coordinates $\vec{x}$. We also note $p(\delta h|\delta r)$ the distribution of δh where the sampling is done on all admissible $\vec{x}$ and $\delta\vec{x}$ such as $|\delta\vec{x}| = \delta r$. The distribution $p(\delta h|\delta r)$ at different δr is shows in a semi-logarithmic scale on Fig. 2 for (a) aluminum alloy sample $\#2$, (b) For the aluminum and mortar samples (Fig. 2(a)(b)), the distribution of height fluctuations shows a strong non-Gaussian behavior at small scale δr with prononced fat tail. As the scale δr is increased, the tails of the distribution become less pronounced. At a sufficiently large scale, the distribution can barely be distinguished from a Gaussian distribution , taking a parabolic shape in this semi-logarithmic representation. For

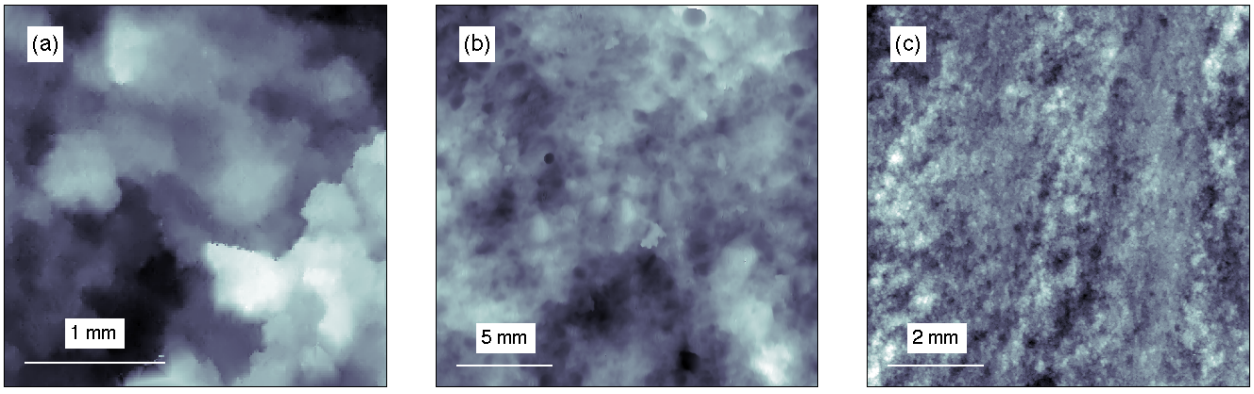

Figure 1: Fracture surfaces of (a) aluminum #2 (2.7×2.7 mm), (b) mortar (20×20 mm) and (c) a brittle ceramics (8×8 mm): the height of the surface is encoded using grey shades, with white representing the highest points while black corresponding to the lowest ones. The typical height denivelation on this surface is (a) $1.3\,\mathrm{mm}$, (b) $2.3\,\mathrm{mm}$ and (c) $250\,\mu\mathrm{m}$, respectively.

the brittle ceramic sample (Fig. 2(c)), the distribution of height fluctuations shows an essentially Gaussian behavior at all scales. As the scale δr is increased, the standard deviation of the distribution is increased but the shape of the distribution remains essentially the same. The evolution of these distributions can be described by a familly of Student t distributions (Fig. 2). The detailed analysis of this behavior will be presented elsewhere [4].

4 Spatial organization of large fluctuations on fracture surfaces

The distributions of height fluctuations in the materials investigated do not follow a Gaussian behavior because of the fat tails. In this part, we proceed to a detailed analysis of these extreme events or largest height variations that are present in an abnormally high proportion on fracture surfaces and that are directly responsible for these tails. Our analysis will reveal a fundamental difference between the morphology of fracture surfaces obtained by brittle failure, and the one obtained by damage mechanisms. It will also provide interesting clues on the origin of this deviation from the Gaussian behavior.

4.1 Revealing the spatial organization of the extreme events on fracture surfaces

The maps of extreme events with clusters are extracted from the fracture surface using the following procedure. We define the operator

$$\overline{\delta h}(\delta r, \vec{x}) = \langle [h(\vec{x} + \delta\vec{x}) - h(\vec{x})]^2 \rangle^{\frac{1}{2}}_{|\delta\vec{x}|=\delta r} \tag{1}$$

where the average $\langle . \rangle$ is done on a circle of radius δr, i.e. for all admissible $\delta\vec{x}$ such as $|\delta\vec{x}| = \delta r$. This operator has several interesting properties. First, at a given scale δr, the operator is uniquely

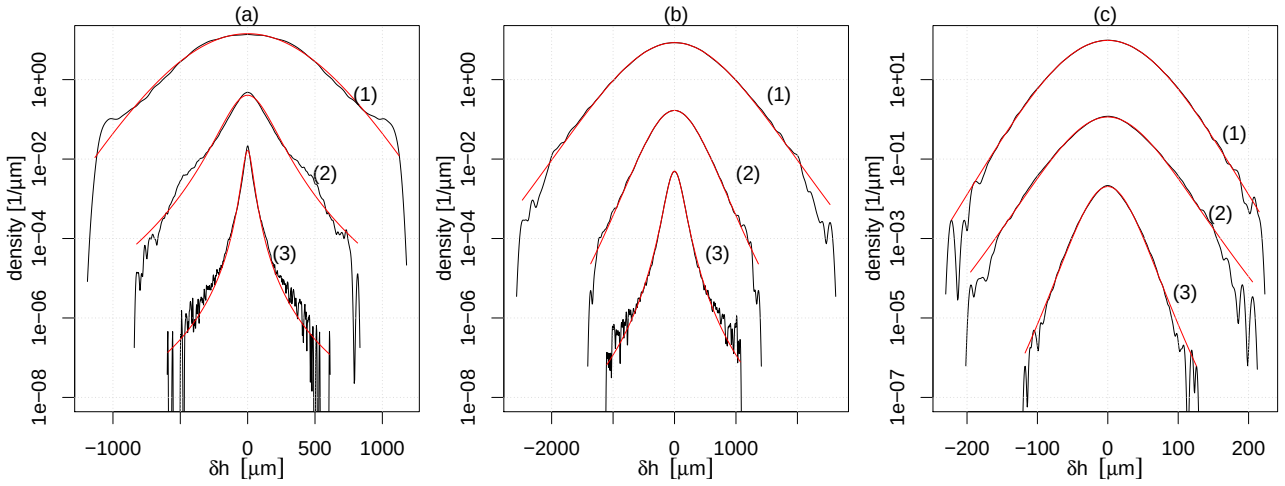

Figure 2: Distribution of height fluctuations $p(\delta h|\delta r)$ at various scales δr.(a) Aluminum alloy $\#2$ with δr = (1) 25 μm, (2) 115 μm, (3) 550 μm; (b) Mortar sample with δr = (1) 225 μm, (2) 915 μm, (3) 3.8mm; (c) Brittle ceramic sample with δr = (1) 60 μm, (2) 310 μm, (3) 1.5mm. The experimental distributions are represented in black, and the corresponding fit with a Student t distribution are representend in red/grey. For readability the distributions have been multiplied by 10^4 for (1) and by 10^2 for (2)

defined for each point of the experimental map and defines a transformation of the original map. Second, it is perfectly isotropic. Third, the average procedure makes it robust to measurement artifact. Qualitatively, this operator describes the local intensity of the height variation at a scale δr. The fields $\overline{\delta h}(\delta r, \vec{x})$ obtained from (a) the aluminum #2, (b) the mortar and (c) the ceramics fracture surfaces are represented on Fig. 3 at scale $\delta r = 6\,\mu$m, $\delta r = 100\,\mu$m and $\delta r = 15\,\mu$m, respectively. Here, the largest height variations are presented in white while the smallest ones are in black. Strikingly, the extreme events are spatially correlated and form a network of rough lines for the alloy [Fig. 3(b)] and the mortar [Fig. 3(c)], while they are rather uniformly distributed for the ceramic fracture surface [Fig. 3(a)]. At first sight, the differences between these maps are obvious. But to proceed to a quantitative analysis and describe their differences, we need to threshold these maps. As we are interested by the fat tails only, we define maps that contain the largest height variations only. As a result, we introduce a threshold $\delta h_{\rm th}$ so that for value of $\overline{\delta h}(\delta r, \vec{x})$ higher than h_c, we assign a value unity to the point $\vec{x}$ (in white on Fig. 4), while a value zero is attributed to the points $\vec{x}$ for which $\overline{\delta h}(\delta r, \vec{x}) < \delta h_{\rm th}$ (in black on Fig. 4). Two parameters need to be chosen in order to obtain the maps of extreme events represented on Fig. 4: the value of δr that sets the scale at which the height variations $\overline{\delta h}(\delta r, \vec{x})$ are computed and the value of the threshold that distinguish the extreme events from the regular ones. In the following, instead of $\delta h_{\rm c}$, we will use the quantity $p_{\rm th}$ that indicates the proportion of points $\vec{x}$ with value $\overline{\delta h}(\delta r, \vec{x}) > \delta h_{\rm c}$ defined as extreme events. Since we investigate the tail of the roughness distribution, typical values of $p_{\rm th}$ will be in the range $5\% - 25\%$. In the following, we will see that the actual value of $p_{\rm th}$ as well as the value of δr have actually a limited influence on the statistical properties of the extreme events.

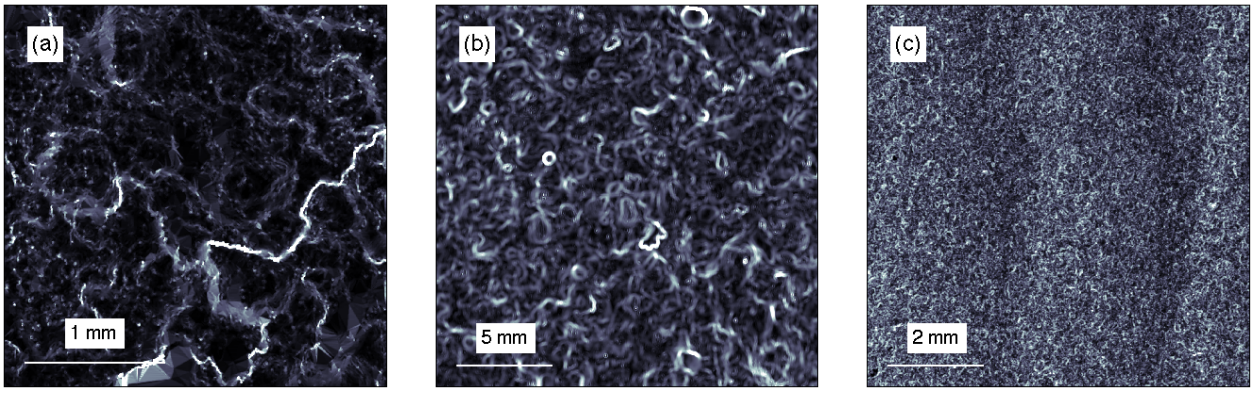

Figure 3: Maps of height variations $\overline{\delta h}$ computed on the fracture surfaces of (a) the aluminum alloy #2 for $\delta r = 6\mu\mathrm{m}$, (b) the mortar and (c) the brittle ceramics shown on Fig. 1.

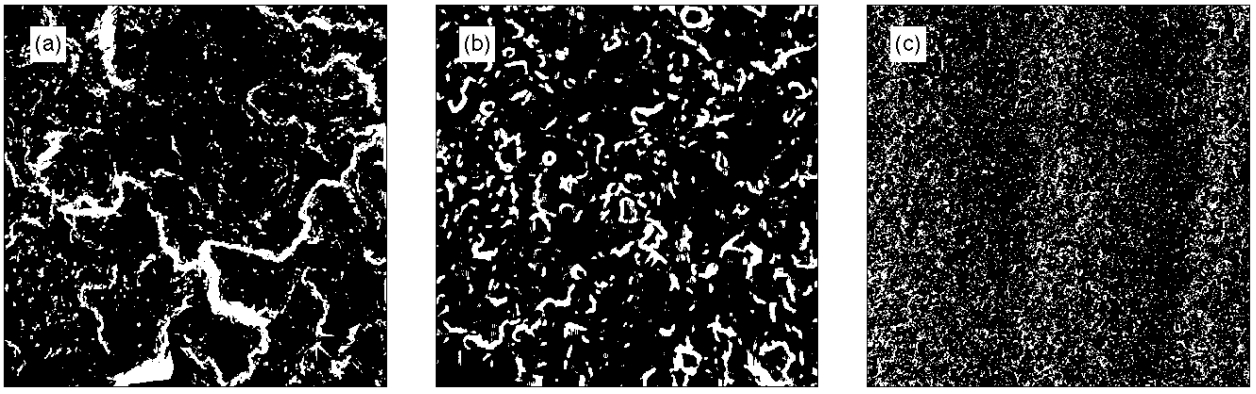

Figure 4: Threshold maps of the height variations $\overline{\delta h}$ shown on Fig. 3 computed on the fracture surfaces of (a) the aluminum alloy #2, (b) mortar and (c) brittle ceramics. Here, only the largest events that represents $p\mathrm{th} = 15\%$ of all the points on surfaces have been kept.

4.2 Statistical properties of clusters of extreme events

A rapid look at the spatial distribution of the extreme events shown on Fig. 4 shows that they organize in clusters of connected points. In this part, we investigate the properties of these clusters, such as their fractal dimension and their size distribution. For analyzing the cluster statistics, we define for each cluster isolated from the other ones three quantities that characterize their size, namely ℓ_x, ℓ_z and R_g, as well as one quantity S characterizing their area. ℓ_x is the maximum extent of the cluser along the x direction while ℓ_z is the maximum extent of the cluster along the z direction - let us note that x and z corresponds to the direction of the propagation, and the perpendicular one, respectively. R_g is the radius of gyration of the cluster. It is obtained by defining the center of gravity C of each cluster, and then compute the average distance between C and the points $\{M_k\}_{1\leq k\leq N}$ belonging to the cluster, i.e. $R_g = \sqrt{\sum_{k=1}^{N} |C\vec{M}_k|^2}$ with $\sum_{k=1}^{k} C\vec{M}_k = 0$. For each cluster, we have so three variables characterizing its length while S defined as the total number N of of points of pixels that belongs to

the cluster times the area of one pixel represents its area. As shown on the Figs. 5 that shows the relation between length and area for each cluster for the , the three quantities ℓ_x, ℓ_z and R_g are found to follow the same scaling $S \sim \ell^D$ with the cluser area S. This indicates a fractal geometry of these objects with dimension $D \simeq 1.70$ that depends very weakly of the considered material (see Table 1 for the values of D of each material). This result indicates that any of the three quantities ℓ_x, ℓ_z and R_g can be used to investigate the cluster size distribution. In the following, we choose the radius of gyration. The probability distribution of the cluster sizes is shown on Fig. 6 for (a) aluminum alloy #1

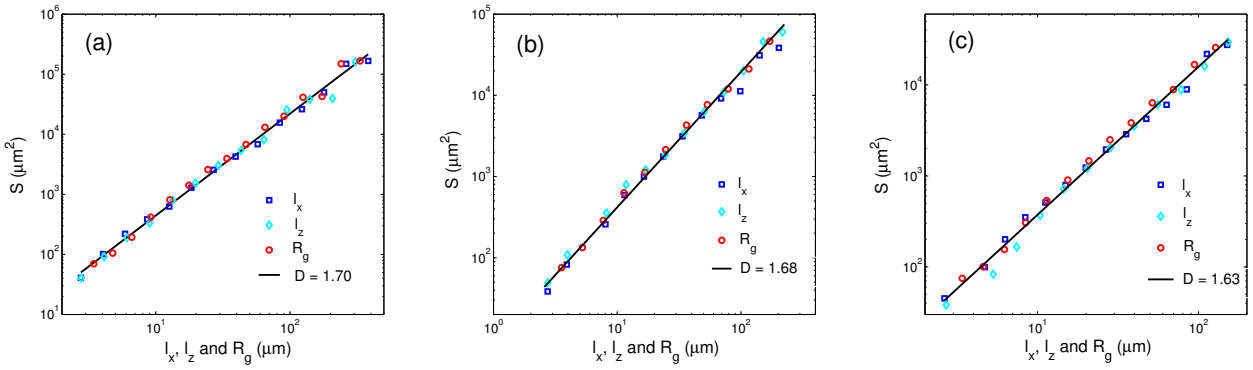

Figure 5: Relationship between length and area of the clusters of extreme events for (a) the aluminum #1, (b) the mortar and (c) the brittle ceramics. The scaling of the cluster rarea with its radius of gyration indicates a fractal dimension $D \simeq 1.70$, irrespective of the material considered.

and (b) mortar for different values of $p_{\rm th}$ for $\delta r = 6\,\mu$m and $\delta r = 100\,\mu$m, respectively. Irrespective of the actual value of the threshold probability $p_{\rm th}$, the distribution for mortar and aluminum fracture surfaces follow a power law $P(R_g) \sim R_g^{-\alpha}$ with exponent $\alpha \simeq 2.2$. The picture is rather different

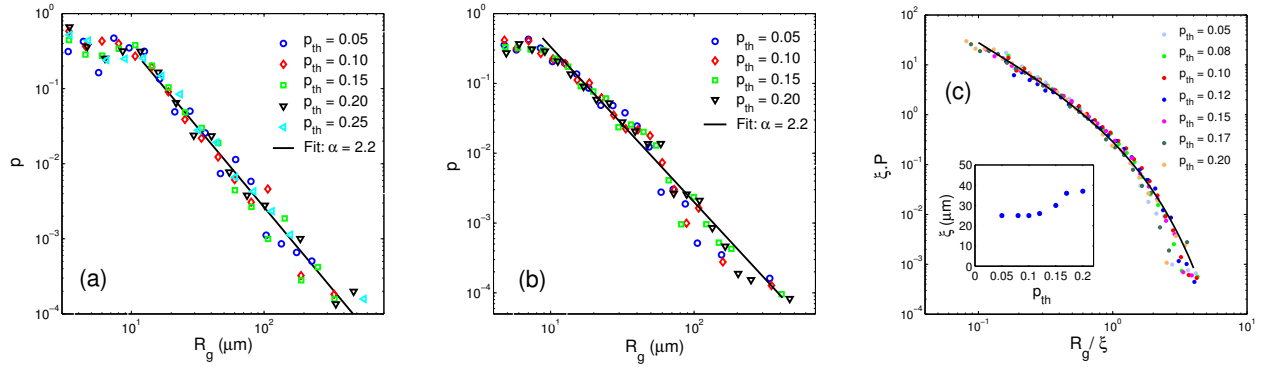

Figure 6: Distribution of cluster sizes R_g for (a) the aluminum alloy #1, (b) the mortar and (c) the brittle ceramics fracture surfaces.

for brittle fracture surfaces: as shown on Fig. 6(c) for $\delta r = 16\,\mu$m, the distribution of cluster sizes follows an exponential law $P(R_g) \sim e^{-R_b/\xi}$ characterized by the length scale $\xi \simeq 25\,\mu$m, the value of which depends very weakly of the threshold $p_{\rm th}$, as shown in the inset of Fig. 6(c). This exponential

behavior confirms the visual observations made on Fig. 4: for ceramics fracture surfaces, the largest height variations do not form any large scale structures, contrary to mortar and aluminum. As a result, clusters of size larger than $\xi = 25\,\mu$m are exponentially rare. These results are confirmed on another brittle material, a natural sandstone. For its fracture surface also, the density probability of cluster size decreases exponentially, with a characteristic length scale $\xi \simeq 50\,\mu$m (see Table 1). This length might be directly related to the material microstructure since the grain size d in the ceramics and the sandstone are of the same order than this cut-off length, i.e. $d = 100\,\mu$m and $d = 200\,\mu$m, respectively [5, 6]. We investigate now the effect of the length scale δr chosen to compute the field of height variations $\overline{h}(\delta r, \vec{x})$ on these properties. Figure 7 shows such maps obtained on the aluminum #1 fracture surface calculated at different scales, i.e. for (a) $\delta r = 6\mu$m, (b) $\delta r = 12\mu$m and (c) $\delta r = 18\mu$m. We see that changing this scale mainly affects the thickness of the lines constituting the network of extreme events, but does not really affect their geometry. This impression is confirmed on Fig. 8 where the statistical properties of the clusters obtained from these different maps are compared. The scale δr has a weak effect on both (a) the relation between the area and the radius of gyration of each cluster and (b) their size distribution. In other words, changing the scale δr in the range investigated does not affects significantly the value of the exponents $D \simeq 1.70$ and $\alpha \simeq 2.2$.

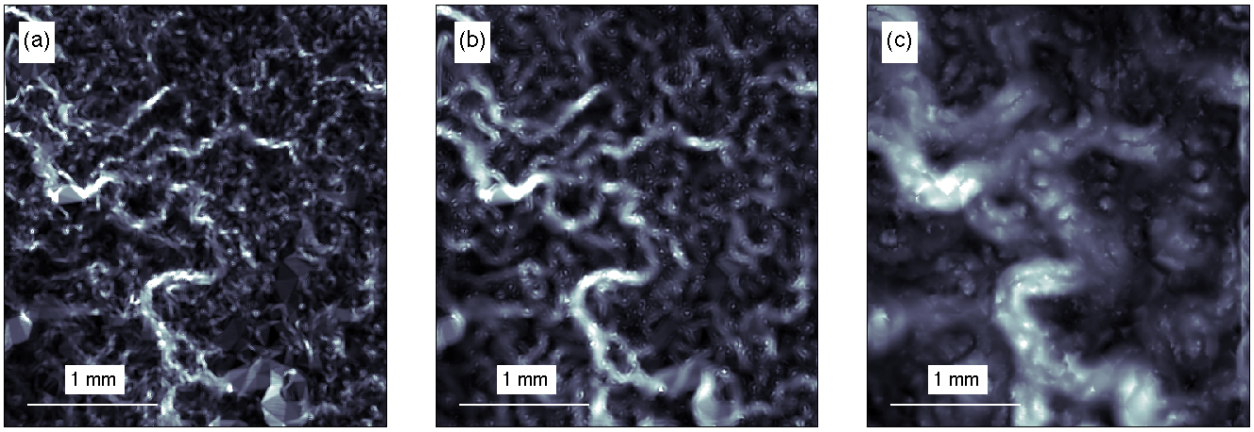

Figure 7: Map $\overline{\delta h}(\delta r, \vec{x})$ of height vatiations computed at different length scales (a) $\delta r = 6\,\mu$m, (b) $\delta r = 12\,\mu$m and (c) $\delta r = 18\,\mu$m for the aluminum #1.

5 Discussion

We would like now to connect the statistical properties of the roughness showing deviations to the Gaussian behavior with the complex spatial distribution of extreme events observed on the height variations maps $\overline{\delta h}(\delta r, \vec{x})$. To bridge these both properties, it is relevant to consider the decomposition $\delta h(\vec{x}, \delta\vec{x}) = h(\vec{x}, \delta\vec{x}) - h(\vec{x}) = \sum_{k=1}^{n} h(\vec{x} + \frac{k}{n}\delta\vec{x}) - h(\vec{x} + \frac{k-1}{n}\delta\vec{x}) = \Sigma_{k=1}^{n}\delta h(\vec{x} + \frac{k-1}{n}, \delta\vec{x}/n)$ that expresses a height variation calculated at the scale $\delta r = |\vec{\delta x}|$ in position $\vec{x}$ as the sum of n height variations calculated at a smaller scale $\delta r/n$ near $\vec{x}$. For an uncorrelated map of height variations, the central limit theorem predicts then that the statistics of height variations - that writes as the sum

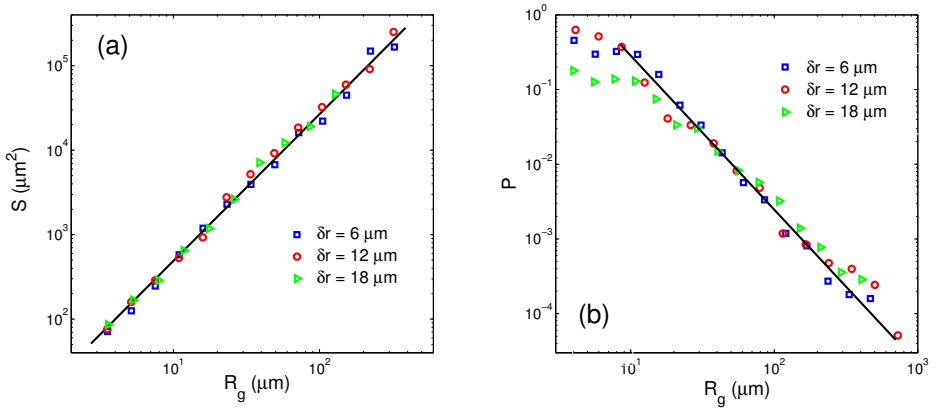

Figure 8: Effect of the length scale δr on the statistics of clusters of extreme events: (a) Relationship between area and length of clusters showing $D \simeq 1.70$ for the fracture surface of aluminum #1. (b) Distribution of cluster sizes R_g showing $\alpha \simeq 2.1$ on aluminum #1 fracture surface.

of uncorrelated variables - belongs to one of the three stable distributions, i.e. Gumble, Weibull or Gaussian distributions. Here, we expect the statistics of our fracture surfaces to follow a Gaussian distribution. This agrees with our observations made on brittle fracture surfaces that exhibit both Gaussian statistics and uncorrelated maps of height variations. On the contrary, quasi-brittle and ductile failure mechanisms that produce correlated height variations maps [Fig. 4 (a) and (b)] also display strong deviations to the Gaussian behavior. But once investigated at scales much larger than the typical size of those patterns, the height variations becomes uncorrelated, and so a Gaussian statistics might be expected: this explains the transition from fat tail distribution at small scale to a Gaussian statistics at large scales, as shown on Fig. 2. An analysis of the distribution $p(\delta h|\delta r)$ of height variations at different scales δr allows for an estimation of the crossover length $\delta r = \xi$ corresponding to the transition from fat tails to Gaussian statistics. Its value measured on mortar and the various aluminum alloys fracture surfaces is given in Table 1 . In this case, a typical value of the cluster size could not be extracted from their distribution as for brittle failure, due to the limited dimension of the fracture surfaces investigated. However, the previous connection between the roughness statistics and the patterns of extreme events suggests that the roughness recovers a Gaussian behavior once δr is much larger than the typical cluster size. This means that the length scale extracted from the cluster size distribution might be quite close to the crossover length between power law tail and Gaussian statistics. For this reason, we have used the same notation ξ whenever this length was extracted from the roughness statistics or the cluster size distribution. Our results show that that when fracture surfaces investigated at scales $\delta r \ll \xi$ display spatially correlated roughness characterized by a power law tail statistics, while investigated at scale $\delta r \gg \xi$, they follow a Gaussian behavior without exhibiting any spatial correlation on the height variations map. Interestingly, the deviations to the Gaussian behavior that are characterized by a change in the shape of the roughness distribution $p(\delta h|\delta r)$ with the scale δr results in a multi-affine behavior, that means that the various moments of this distribution scale with different exponents, contrary to mono-affine brittle surfaces for which one roughness exponent ζ is sufficient to fully describe the roughness statistics and the scaling of the different moments. Multi-scaling is classically associated with the presence of spatially correlated fluctuations. This in-

	ζ	D	α	ξ
Aluminum #1	0.74	1.70	2.2	$450\,\mu$m
Aluminum #2	0.73	1.70	2.3	$550\,\mu$m
Mortar	0.73	1.61	2.2	$1.3\,$mm
Sandstone	0.45	$\times$	$\times$	$25\,\mu$m
Ceramics	0.43	$\times$	$\times$	$25\,\mu$m

Table 1: Scaling exponents extracted from the fracture surfaces resulting from ductile and quasi-brittle (upper part of the table) and brittle failure (lower part): the roughness exponent ζ characterizes the scaling behavior of the roughness correlation, the exponents D and α describe the patterns made by the largest height variations on the fracture surfaces presented on Fig. 4. The length ξ provides the crossover length between fat tail and Gaussian statistics for damage accompanied failure (alloy and mortar) while it gives the characteristic length of the exponential decay of the cluster size distribution for brittle failure.

terpretation is then fairly consistent with our observations. Let us note that this might also be the case in various other materials where multi-scaling were reported at small scale, before a transition towards a Gaussian behavior [7, 8]. We would like now to propose a physical interpretation of the length ξ and the origin of the complex features observed on the height variations maps. Various findings presented here suggest that the deviations to Gaussian statistics and the associated patterns of extreme events find their origin in the microcracking processes accompanying failure of mortar and aluminum alloys. This is supported by the following observations:

(i) For mortar and aluminum fracture surfaces, abnormally large height fluctuations producing fat tail statistics of crack roughness organizes into a network of rough lines. This features are not present on brittle fracture surfaces for which damage mechanisms does not come into play, suggesting a direct link between clusters of extreme events and damage processes.

(ii) The size of the clusters observed on the height variation maps is power law distributed, up to a cut-off length scale ξ that coincides well with the typical size associated with the damage processes in these materials: a few grain or a few hundreds of micrometers in aluminum alloy and a few millimeters in mortar. In addition, direct observations of the failure processes within the damage zone ahead of cracks in some quasi-brittle rocks show the presence of a forest of microcracks with power law distributed sizes. Direct observations have not been reported in mortar nor in aluminum alloys, but the acoustic emission following power law statistics in these materials suggest a similar behavior.

(iii) In a recent study, networks of lines observed on PMMA fracture surfaces were shown to result from microcracking processes [9]. The mechanisms into play can be described by considering the coalescence of two interacting microcracks that start to avoid before attracting each to let a bump on the fracture surface [10]. Contrary to mortar or aluminum alloys, the PMMA is rather homogeneous at the scale where these lines where observed, allowing a straightforward observation, and even a quantitative interpretation of these features in terms of microcracking

history in the material [11]. In mortar and aluminum alloy, the network made by these lines is hidden by the surrounding roughness generated by the material heterogeneities. In addition, the microcrack density might be much larger in these materials, so that such an interpretation of the clusters observed for these materials is much more complex. However, they might be signature of microcracking and their size distribution might be closely connected with the size distribution of microcracks.

6 conclusion

The fracture surface investigated in this study revealed a much more complex roughness than their classical description based on the measurement of the roughness exponents. Neglecting for this study the anisotropy of fracture surfaces [12], we showed that one roughness exponent $\zeta \simeq 0.4$ remains sufficient to fully describe the roughness statistics. However, in quasi-brittle and ductile materials where the roughness exponent is found to be larger with $\zeta \simeq 0.75$, the full distribution of height variations is found to be highly non-Gaussian with the presence of fat tails. However, these deviations disappear as the investigation scale increases, leading to a Gaussian statistics at a sufficiently large scale. This behavior can be described with a family of Student's t distributions.
We proceeded then to the analysis of the largest height jumps on the surface, responsible for the fat tails observed in the roughness distribution. For this purpose, we defined maps of extreme events that displayed connected clusters of large fluctuations. These clusters of spatially correlated large fluctuations are shown to follow power law statistics: they have a fractal geometry with dimension $D \simeq 1.7$ with a power law distributed size with exponent $\alpha \simeq 2.2$. In brittle materials like sandstone and ceramics, the size distribution of these cluster follows a power law distribution characterized by the length scale ξ. In other words, we have a very small probability to find big clusters in brittle material that was shown to be in agreement with a Gaussian statistics.
The length scale ξ that we defined alternatively on quasi-brittle and ductile fracture surfaces from the crossover length from fat tail statistics at small scale to Gaussian statistics at large scale reveals the microscale failure mechanisms of materials. Our observations suggest that this length is connected with the typical length of micro cracks in materials. A possible interpretation is that the coalesence between micro cracks leads a signature on the fracture surface that we identified as abnormally large height fluctuations. According to this scenario, the length ξ extracted from the fracture surfaces might be connected to the typical damage zone size ahead of the crack during failure.

References

[1] S. Vernède. A granular model of solidification as applied to hot tearing. *Ph.D. thesis*, 3795, EPFL, 2007.

[2] S. Morel and D. Bonamy and L. Ponsons and E. Bouchaud. Transient damage spreading and anomalous scaling in mortar crack surfaces. *Phys. Rev. E*, 78:016112; 2008.

[3] L. Ponson and H. Auradou and P. Vié and J.-P. Hulin. Low self-affine exponents of fracture glass ceramics surfaces. *Physical Review Letters*, 87:105502, 2001.

[4] S. Vernède, Y. Cao, L. Ponson. Non-Gaussian statistics and spatially-organized extreme events on experimental fracture surfaces. In preparation

[5] L. Ponson, H. Auradou, M. Pessel, V. Lazarus and J.-P. Hulin. Failure mechanisms and surface roughness statistics of fractured Fontainebleau sandstone. *Phys. Rev. E*, 76:036108 , 2007.

[6] L. Ponson, H. Auradou, P. Vié and J. P. Hulin. Low self-affine exponents of fractured glass ceramics surfaces. *Phys. Rev. Lett.*, 97:125501, 2006.

[7] S. Santucci, K. J. Måløy, A. Delaplace, J. Mathiesen, A. Hansen, J. Bakke, J. Schmittbuhl, L. Vanel and P. Ray. Statistics of fracture surfaces. *Phys. Rev. E*, 75:016104, 2007.

[8] E. Bouchbinder, I. Procaccia, S. Santucci and L. Vanel. Fracture surfaces as multiscaling graphs. *Phys. Rev. Lett.*, 96:055509, 2006.

[9] J. Scheibert, C. Guerra, F. Célarié, D. Dalmas and D. Bonamy, Brittle-qausibrittle transition in dynamic fracture: An energetic signature. *Phys. Rev. Lett.*, 104:045501, 2010.

[10] M. L. Fender, F. Lechelault and K. E. Daniels. Universal shapes formed by two interacting cracks. *Phys. Rev. Lett.*, 105:125505, 2010.

[11] C. Guerra, J. Scheibert, D. Bonamy and D. Dalmas. Understanding fast macroscale fracture from microcrack post mortem patterns. *Proc. Nat. Acad. Sci.*, 109:390-394, 2012.

[12] L. Ponson, D. Bonamy and E. Bouchaud. Two-dimensional scaling properties of experimental fracture surfaces. *Phys. Rev. Lett.*, 97:125501, 2006.

Modeling of Mechanical Response and Progressive Failure of Tri-axially Woven SiC_f-SiC Composites

S. G. Kulkarni[1], X.-L. Gao[2,*]

[1] Department of Mechanical Engineering, Texas A&M University, College Station, TX 77843

[2] Department of Mechanical Engineering, University of Texas at Dallas, Richardson, TX 75080-3021

* Corresponding author: Xin-Lin.Gao@utdallas.edu

Abstract Effective properties and progressive failure of SiC matrix composites reinforced by tri-axially woven SiC fibers (SiC_f) (as a fabric) are predicted. Three different orientations of the woven fabric are considered in geometrical modeling, including –60°-0°-60°, –55°-0°-55° and –45°-0°-45°. Three-dimensional unit cells with the matrix reinforced by the fabrics in such orientations are constructed and used. Homogenization analyses are carried out using the finite element method (FEM). It is found that the –60°-0°-60° fabric orientation provides the highest values for the effective elastic moduli, while the –45°-0°-45° orientation gives the lowest values. The effective properties obtained are then used to conduct a progressive failure analysis of the SiC_f-SiC composite subjected to uni-axial tensile loading. The progressive failure analysis incorporates both geometrical and material non-linearities, and describes the progressive damage induced by crack initiation and propagation through a material degradation model. The Tsai-Wu failure criterion is used, and a two-parameter Weibull distribution is employed to account for the changes in strength with increasing specimen volume. Based on this progressive failure analysis, stress-strain curves for the SiC_f-SiC composites are plotted, and the –60°-0°-60° orientation is found to have the smallest deformations at given loads.

Key words Woven composite, Effective property, Homogenization, Progressive failure analysis, SiC_f-SiC

1. Introduction

SiC fabric reinforced SiC matrix composites have emerged as a class of strong, radiation-resistant, high-temperature structural materials that are suitable and ready for nuclear fusion applications [1]. SiC has been used as a nuclear fuel cladding material since it offers greater strength at high temperatures than conventional zirconium alloys. SiC has excellent irradiation tolerance, low chemical reactivity, and low tritium permeability [2].

Textile composites represent a class of advanced materials that are reinforced by fabric preforms. The smallest constituent of a textile composite is a fiber. A yarn is an assembly of fibers. Yarns are generally used as unit elements to form fabrics. A tri-axially woven fabric has three sets of yarns forming equilateral triangles at the intersections. Tri-axially woven fabrics have no weak dimension or bias and offer high resistance to shear or tear. They also have the ability to accommodate compound curvatures and are therefore suitable for molded manufacturing. These features make tri-axially woven fabric composites ideal for cladding tube applications, where high temperatures can cause considerable normal and shear stresses in cladding tubes.

Effective properties and progressive failure of tri-axially woven SiC_f-SiC ceramic matrix composites are studied in the current paper using micromechanics and the finite element method. Representative volume elements are identified for three different fabric configurations. The matrix material is regarded as isotropic, while the fabric yarns are treated as transversely orthotropic. Homogenization analyses are performed to determine effective properties, and progressive failure studies are then conducted to obtain stress-strain curves for the SiC_f-SiC composites.

2. Unit Cells

Most fabrics are woven with two sets of orthogonal yarns called the warp and weft yarns [3]. This is known as bi-axial weaving. The most common tri-axially woven fabrics are the ones where the fiber yarns are arranged in the +45°, 0°, and –45° orientation. However, tri-axially woven fabrics can be made with any orientation ranging from ±20° and ±70°. In the current study, three different orientations are considered to evaluate effective properties of tri-axially woven SiC_f-SiC ceramic matrix composites. The three orientations considered are –60°, 0°, +60°; –55°, 0°, +55°; and –45°, 0°, +45°. For each of these three configurations, a repetitive structure can be taken as a unit cell. The cross section of each yarn is assumed to be lenticular, as was done by others. Figure 1 shows a unit cell of the composite reinforced by the –60°- 0°-60° fabric.

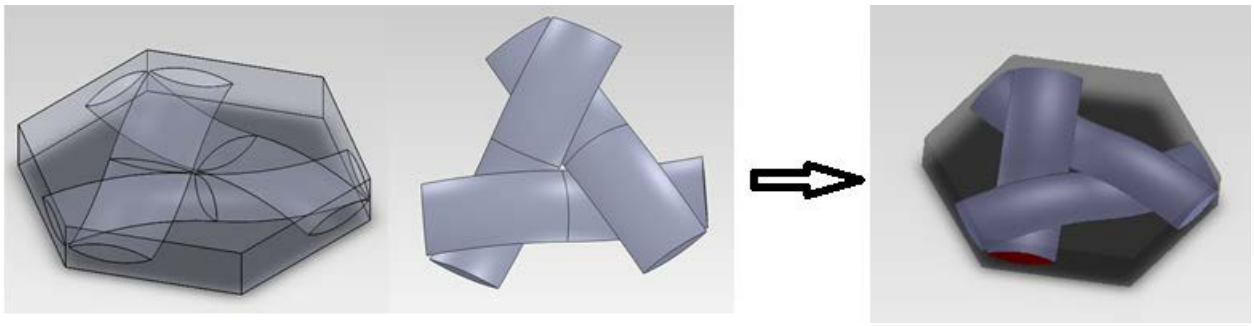

Figure 1. Unit cell of a tri-axially woven fabric reinforced composite

The tri-axially woven fabric of SiC fibers will serve as the reinforcement of the ceramic matrix composite. It can be seen from Figs. 1 and 2 that the tri-axially woven yarns form equilateral triangles and hexagonal holes, which change in size with the yarn orientation, as shown in Fig. 3. For SiC_f-SiC composites, the matrix and fibers are made from the same material. Therefore, the matrix adds considerable stiffness to the composite and the matrix material in the holes and triangles may not be neglected in a homogenization analysis. In constructing the models, the matrix pocket and woven fabric are first generated separately. The fabric and matrix pocket are then assembled to yield the composite unit cell, as shown in Fig. 1. Bonded contact between the matrix and the fabric is assumed to represent perfect bonding.

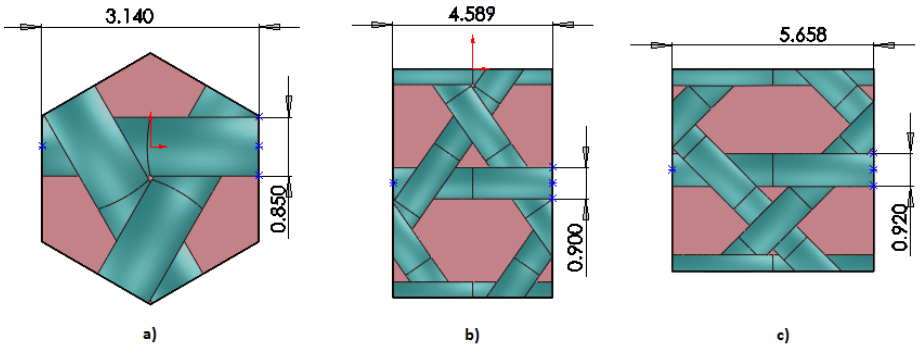

Figure 2. a) Hexagonal unit cell for the –60°-0°-60° fabric configuration; b) rectangular unit cell for the –55°-0°-55° configuration; and c) rectangular unit cell for the –45°-0°-45° configuration

In the homogenization analysis, the matrix material is considered as isotropic, and the fiber yarn is regarded as a transversely isotropic material that has five independent elastic constants.

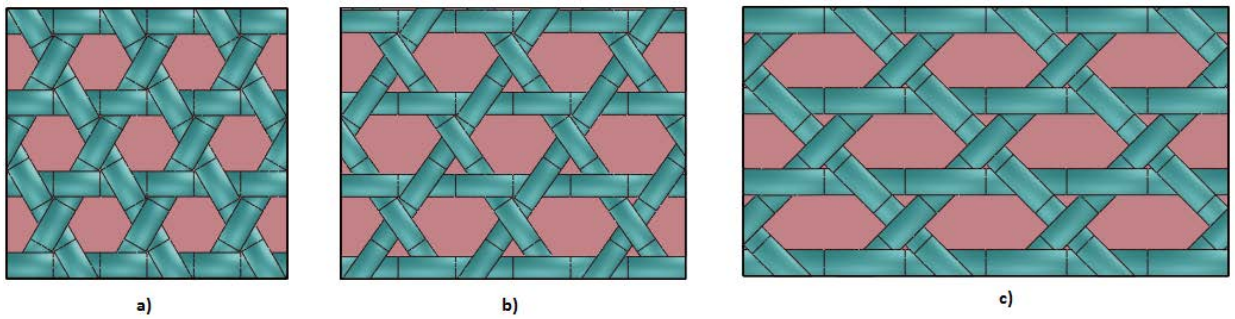

Figure 3. Composite specimens: a) –60°-0°-60°, b) –55°-0°-55°, and c) –45°-45°-45°

3. Finite Element Analysis

A finite element analysis is performed on each of the three unit cells identified in Fig. 2 to obtain effective properties of the SiC_f-SiC ceramic matrix composites using the commercial software package ANSYS. The material properties used are listed in Table 1, which are taken from [4]. The unit cell is meshed using three-dimensional, 10-node solid elements, as shown in Fig. 4. These elements are well suited to model irregular geometries. Each of these solid elements has three degrees of freedom at every node: translations in the X, Y and Z nodal directions.

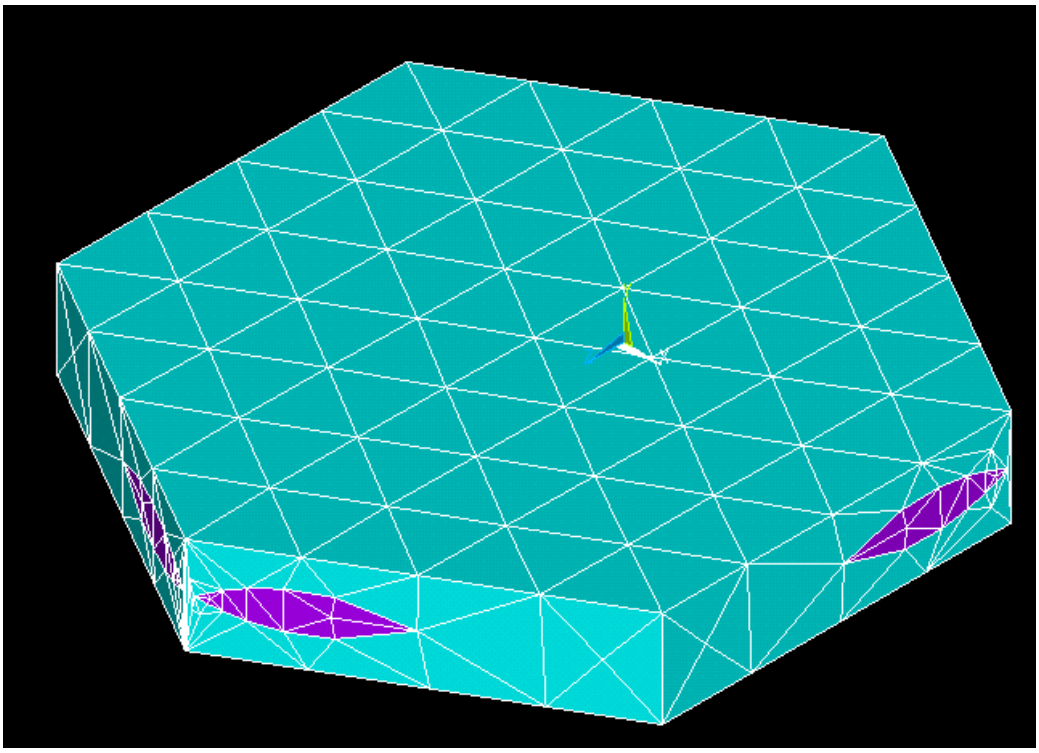

Figure 4. Finite element mesh for the unit cell shown in Fig. 2a)

Table 1. Properties of the matrix and yarn [4]

Material Properties	**Matrix**	**Yarn**
E_{11}	251 GPa	221 GPa
E_{22}	251 GPa	219.8 GPa
E_{33}	251 GPa	219.8 GPa
v_{12}	0.16	0.214
v_{23}	0.16	0.193
v_{13}	0.16	0.193
G_{12}	108 GPa	108 GPa
G_{23}	108 GPa	90.4 GPa
G_{31}	108 GPa	90.4 GPa
α_1	4×10^{-6} K^{-1}	3.43×10^{-6} K^{-1}
α_2	4×10^{-6} K^{-1}	3.38×10^{-6} K^{-1}
α_3	4×10^{-6} K^{-1}	3.38×10^{-6} K^{-1}

3.1 Periodic Boundary Conditions

In modeling uniaxial and biaxial tensile tests, displacement boundary conditions are frequently used. Since a representative volume element (RVE) is cut out of an infinite composite, spatially periodic

boundary conditions should be applied to ensure that the predicted properties of the RVE represent those of the composite [5-7].

The periodic boundary conditions are implemented using the CE option available in ANSYS. Deformations of two unit cells subject to periodic boundary conditions are shown in Fig. 5.

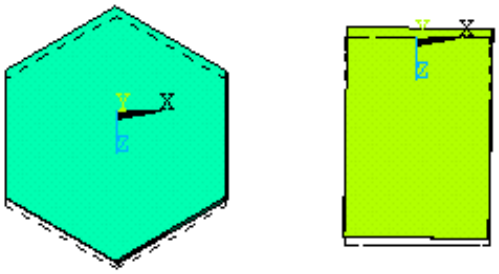

Figure 5. Deformations of hexagonal and rectangular unit cells under periodic boundary conditions

3.2 Model Validation

The model validation is carried out by comparing the simulation results with the experimental data obtained in Fujita et al. [8] for a tri-axially woven carbon fiber reinforced epoxy matrix composite. As shown in Fig. 6, the effective tensile modulus predicted by the current unit-cell based model using periodic boundary conditions agrees well with the experimental value of Fujita et al. [8], thereby supporting the model.

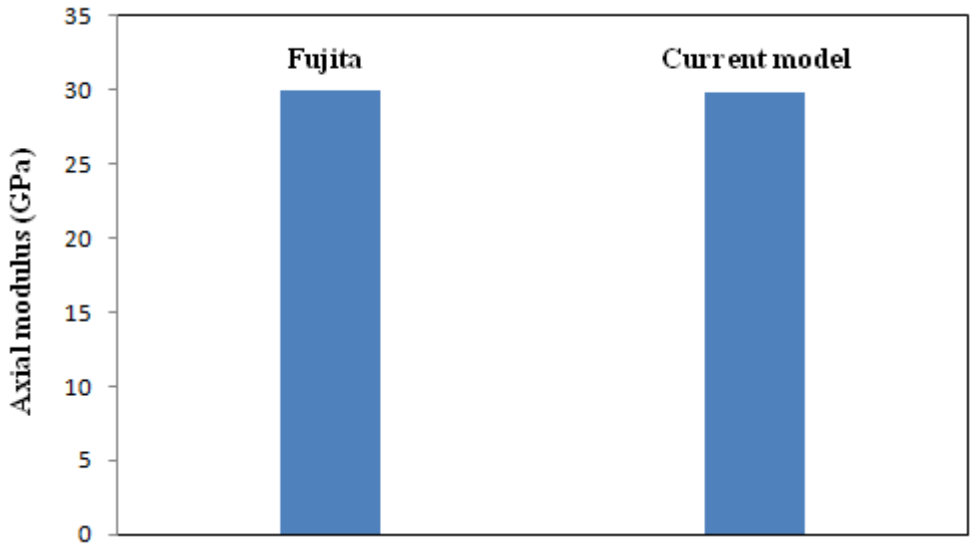

Figure 6. Comparison with the experimental result of Fujita et al. [8]

3.3 Effective Properties

With the unit-cell based FE model validated, simulations are performed using the three unit cell configurations shown in Fig. 2 and the constituent properties listed in Table 1. The in-plane effective properties obtained in the simulations are given in Table 2.

Table 2**.** Effective properties for different fabric orientations

Boundary Conditions	**Effective Properties**	**60° Orientation**	**55° Orientation**	**45° Orientation**
Periodic Boundary Conditions	E_{11} (GPa)	285.857	244.333	239.8992
	E_{22} (GPa)	252.587	242.992	226.224
	E_{33} (GPa)	252.587	242.992	226.224
	ν_{12}	0.1713	0.15266	0.15814
	G_{12} (GPa)	105.26	98.644	98.111

The fiber volume fraction for all the three unit cells is kept equal (within ±2%). It can be seen from Table 2 that the –60°-0°-60° orientation has the highest values of the elastic moduli, while the –45°-0°-45° orientation has the lowest values.

4. Progressive Failure Analysis

Catastrophic failure of a composite structure does not occur at the material failure strength. Composite structures typically fail after propagation or accumulation of localized damages such as matrix cracking, fiber breakage, and fiber-matrix debonding. These mechanisms ultimately lead to the loss of load-carrying ability of the composite structure. Hence, progressive failure analysis is needed to simulate damage propagation and ultimately failure of a composite structure. In the current work, a progressive failure analysis is carried out for uniaxial tension tests. Stress-strain curves are determined for all three fabric reinforcement configurations.

The procedure for the progressive failure analysis is as follows:

a. Each composite specimen (see Fig. 3) is subjected to uniaxial tension. Before the initiation of the first failure, only geometrical nonlinearities (large deformations) are accounted for.
b. After each load increment, stresses at each node are evaluated against a failure criterion.
c. If there is no failure initiation, load is further increased.
d. Upon failure initiation at a node, the elastic modulus in the loading direction is degraded for all elements connected to that node using a material degradation model.
e. The load is then increased.

This procedure is repeated until the specimen loses its load-carrying capability or up to a certain strain level.

5. Failure Criterion and Material Degradation Model

The Tsai-Wu failure model [9,10] is used as the failure criterion. Failure analysis by comparing with a failure criterion is deterministic in nature [11]. In such an analysis, the risk of fracture remains unknown. Therefore, probabilistic fracture analysis is required for better predictions. For a brittle material like SiC, its properties display strong scattering. Brittle materials also show a pronounced

decrease in strength with increasing specimen volume owing to defect distributions. As the material volume increases, the occurrence probability of critical defects increases. Probabilistic analysis takes into account uncertainties in material properties, loading conditions, and defect distributions. In the current work, these uncertainties are accounted for by using the following two-parameter Weibull distribution [4,11]:

$$P_f = 1 - \exp\left[-\frac{V}{V_0} \left(\frac{\sigma - \sigma_u}{\sigma_0} \right)^m \right], \tag{1}$$

where P_f is the fracture probability, V is the specimen volume under consideration, σ is the stress induced in the specimen, V_0 and σ_0 are normalization parameters, m is the Weibull shape parameter, and σ_u is the threshold stress below which the fracture probability is zero. For SiC, m can be taken as 7.6, σ_0 as 270 MPa, V_0 as 65.49 mm^3, and σ_u as zero [1]. P_f gives the failure probability for the specimen volume V under stress σ. For every load increment, P_f is evaluated for each individual element. Failure occurs if P_f = 0.99.

When failure is detected at any node in the composite, the elastic properties are reduced for all the surrounding elements containing that node using a material degradation model. The crack band theory developed for concrete [12] is adopted as the material degradation model. According to the crack band theory, the post failure relation between the normal stresses σ_x, σ_y, σ_z and the normal strains ε_x, ε_y, ε_z can be written as

$$\begin{Bmatrix} \varepsilon_x \\ \varepsilon_y \\ \varepsilon_z \end{Bmatrix} = \begin{bmatrix} C_{11}\mu^{-1} & C_{12} & C_{13} \\ & C_{22} & C_{23} \\ symmetric & & C_{33} \end{bmatrix} \begin{Bmatrix} \sigma_x \\ \sigma_y \\ \sigma_z \end{Bmatrix}, \tag{2}$$

where μ is a cracking parameter, and C_{ij} are compliance constants. The cracking parameter μ depends on the material properties and strain level and is given by

$$\frac{1}{\mu} = \frac{E}{-E_t} \frac{\varepsilon_x}{\varepsilon_0 - \varepsilon_x}, \tag{3}$$

where ε_x is the strain in the loading direction, E is Young's modulus, E_t is the tangent (softening) modulus, and ε_0 is a constant. Note that μ = 1 in an un-cracked material and μ = 0 is a continuously cracked material. After failure is detected, Young's modulus in the loading direction is degraded by a factor μ, while the other properties remain the same. When a crack is introduced in the composite, no normal stress can be transferred across the crack surfaces. However, after the load is increased, the stresses in the surrounding region still increase because of the load transfer from undamaged parts of the composite. Therefore, multiple cracks can occur in one element. This simulation is continued until the composite loses its ability to carry any more load.

6. Stress-Strain Curves

The properties obtained in the progressive failure analysis are used to plot stress-strain curves for all

three configurations, as shown in Figs. 7 and 8. These are based on the uniaxial tension tests of the composite specimens displayed in Fig. 3.

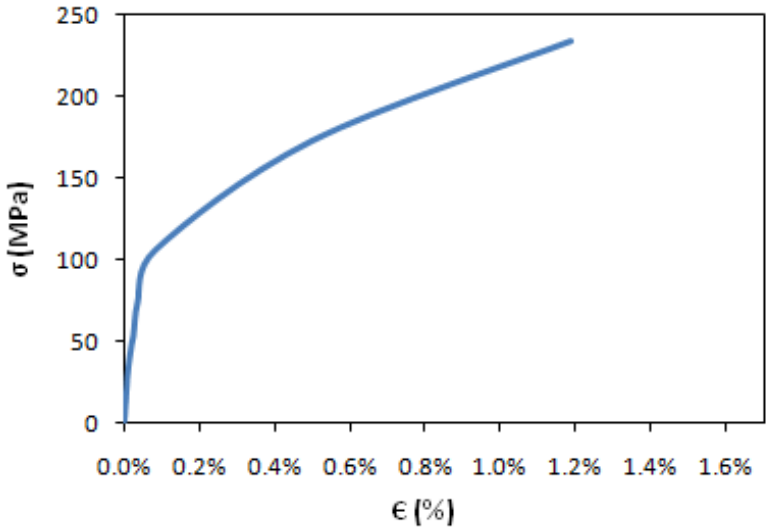

Figure 7. Stress-strain curve from the –60°-0°-60° specimen

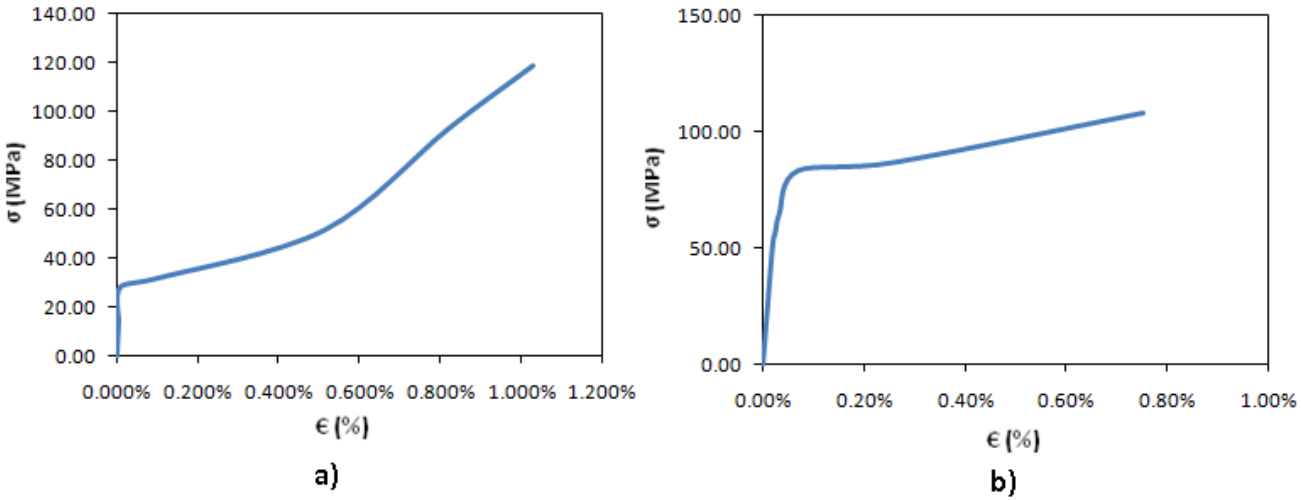

Figure 8. a) Stress-strain curves from a) the –55°-0°-55° specimen and b) the –45°-0°-45° specimen

The progressive failure analysis has revealed that crack initiation occurs first in the transverse direction and at the fabric-matrix interfaces. The linear material behavior ends with the initiation of cracks. The material degradation model discussed in Section 5 is then applied to introduce Mode I cracks in the mesh. After the cracks have been introduced, stresses in the composite specimen may increase or decrease in the next immediate load increment, since no normal stress can be transferred across the crack surfaces. However, as the load is further increased, the stresses begin to increase because of the stress transfer from the surrounding undamaged parts of the composite.

It can be seen from Figs. 7 and 8 that the –60°-0°-60° configuration has the smallest deformations at given loads.

Acknowledgements

The work reported here was funded by a contract from the U.S. Department of Energy. This support is gratefully acknowledged.

References

[1] L.L. Snead, T. Nozawa, Y. Katoh, T.S. Byun, S. Kondo, D.A. Petti, Handbook of SiC properties for fuel performance modelling. J. Nuclear Mater., 371(2007) 329–377.
[2] Y. Katoh, L.L. Snead, C.H. Henager Jr., A. Hasegawa, A. Kohyama, B. Riccardi, H. Hegeman, Current status and critical issues for development of SiC composites for fusion applications. J. Nuclear Mater., 367-370 (2007) 659–671.
[3] X.-L. Gao, S. Mall, A two-dimensional rule-of-mixtures micromechanics model for woven fabric composites. ASTM J. Compos. Tech. Res., 22 (2000), 60–70.
[4] H. Ismar, F. Schroter, F. Streicher, Modeling and numerical simulation of the mechanical behavior of woven SiC/SiC regarding a three dimensional unit cell. Comput. Mater. Sci., 19 (2000) 320–328.
[5] K. Li, X.-L. Gao, G. Subhash, Effects of cell shape and cell wall thickness variations on the elastic properties of two-dimensional cellular solids. Int. J. Solids Struct., 42 (2005) 1777–1795.
[6] K. Li, X.-L. Gao, G. Subhash, Effects of cell shape and strut cross-sectional area variations on the elastic properties of three-dimensional open-cell foams. J. Mech. Phys. Solids, 54 (2006) 783–806.
[7] Z. Xia, Y. Zhang, F. Ellyin, A unified periodical boundary conditions for representative volume elements of composites and applications. Int. J. Solids Struct., 40 (2003) 1907–1921.
[8] A. Fujita, H. Hamada, Z. Maekawa, Tensile properties of carbon fiber triaxial woven fabric composites. J. Compos. Mater., 27 (1993) 1428–1441.
[9] S.W. Tsai, E.M. Wu, A general theory of strength for anisotropic materials. J. Compos. Mater., 5(1971) 58–80.
[10] S.S. Zhou, X.-L. Gao, G.W. Griffith, Analysis and structural optimization of a three-layer composite cladding tube under thermo-mechanical loads. ASME J. Eng. Mater. Tech., 134 (2012) 031001-1–12.
[11] D. Gross, T. Seelig, Fracture Mechanics: with an Introduction to Micromechanics, Springer-Verlag, Berlin, Germany, 2006.
[12] Z.P. Bazant, B.H. Oh, Crack band theory for fracture of concrete. Mater. Struct., 16 (1983) 155–177.

Evaluation of Strength Statistics of Quasibrittle Structures Based on Mean Size Effect Analysis

Jia-Liang Le[1,*], Augusto Cannone Falchetto[1], Mihai O. Marasteanu[1]

[1] Department of Civil Engineering, University of Minnesota, Minneapolis 55455, United States
* Corresponding author: jle@umn.edu

Abstract This paper presents a new method to indirectly determine the probability distribution function of strength of quasibrittle structures. Based on the finite weakest link model, which relates the probability distribution of the structural strength to the size dependence of mean strength, it is shown that that the cumulative distribution function of structural strength can be directly determined from the parameters of the mean size effect curve. A comprehensive experimental set of tests, which includes both strength histograms and mean size effect tests on specimens of asphalt mixture at low temperature, is used to verify the proposed method. The predicted strength histograms obtained with this method are found to be in very good agreement with the experimental histograms of asphalt mixture specimens of different sizes, confirming the validity of the newly proposed formulation.

Keywords Strength Statistics, Histogram Testing, Scaling, Weakest Link Model

1. Introduction

Most engineering structures, such as buildings, bridges, are designed for a very low failure probability (less than 10^{-6}) [1]. Determining the design strength corresponding to such low failure probability directly from histogram testing is prohibitive and, therefore, we need to rely on probabilistic models for indirectly determining the statistics of structural strength.

Simple statistical models can be used for describing the strength distribution in the case of perfectly ductile and brittle structures. For ductile structures, the peak load is equal to the weighted sum of random strengths of material elements along the failure surface. Therefore, according to the Central Limit Theorem, the cumulative distribution function (cdf) of strength of ductile structures follows the Gaussian distribution. On the other hand, the failure of brittle structures is triggered by the failure of one material element whose size is negligible compared to the structure size. Based on the infinite weakest link model (WLM), the strength cdf of brittle structures follows the Weibull distribution [2, 3]. Both Guassian and Weibull distribution are two-parameter probability distribution functions for which the statistical parameters can be easily obtained by histogram testing involving a limited number of specimens.

This is not true for structure made of quasibritte materials, which are brittle heterogenous materials such as concrete and asphalt mixture (at low temperature). For this type of structures the size of inhomogenieties is not negligible compared to the structure size. By limiting our focus to quasibrittle structures for which the peak load is reached as a macro-crack initiates from one representative volume element (RVE) [2-4], it is possible to statistically model this class of structures as a finite chain of RVEs [2-4]. Therefore, the cdf of strength of each RVE must be known for calculating the strength cdf of the entire structure. Recent studies [3, 4] showed that the strength cdf of one RVE can be described by a Weibull distribution grafted on the left tail of a Gaussian cdf. At structural level, the finite WLM shows that the strength cdf consists of an upper part, which can be calculated as a finite chain of Gaussian elements, and a lower segment that follows the Weibull distribution [2-4] resulting into an intricate size effect on the mean structural strength. Determining such a type of strength distribution through histogram testing requires a large number of specimens, which could be very costly and time consuming, due to material and labor.

This paper presents an alternative method to determine the strength cdf of quasibrittle structures, which is anchored at the analysis of the mean size effect curve. The proposed method is experimentally verified by a comprehensive set of tests on the asphalt mixture at a low temperature.

2. Theoretical background

The weakest link model schematizes a structure as finite chain of RVEs. Based on the joint probability theorem, which provides a mathematical expression of the WLM, the failure probability of the entire structure, P_f, made of N RVEs can be obtained according to Eq. 1:

$$P_f(\sigma_N) = 1 - \prod_{i=1}^{N}\left[1 - P_1(s_i\sigma_N)\right] \tag{1}$$

where P_1 is the cdf of strength of one RVE having characteristic size l_0, $\sigma_N = cP_{max}/bD$ is the nominal strength of the structure, P_{max} is the maximum load that the structure can sustain, D is the structure characteristic size, b is the width of the structure, c is a constant such that σ_N represents the maximum elastic principal stress in the structure and s_i dimensionless stress field such that $\sigma_N s_i$ corresponds to the maximum elastic principal stress at the center of i^{th} RVE. Based on atomistic fracture mechanics and a statistical multi-scale transition model [3,4] it was recently demonstrated that the failure cdf of one RVE can be approximated by a Weibull cdf grafted on the left tail of a Gaussian cdf (core) at a point with a probability of about 10^{-4}—10^{-2}. The grafted cdf of strength of one RVE can be expressed as [2-4]:

$$P_1(\sigma) = 1 - \exp[-(\sigma / s_0)^m] \approx \langle \sigma / s_0 \rangle^m \qquad (\sigma_N \le \sigma_{gr}) \tag{2a}$$

$$P_1(\sigma) = P_{gr} + \frac{r_f}{\delta_G\sqrt{2\pi}}\int_{\sigma_{gr}}^{\sigma_N}\exp\left\{-\left[\frac{(\sigma' - \mu_G)^2}{2\delta_G^2}\right]\right\}d\sigma' \qquad (\sigma_N > \sigma_{gr}) \tag{2b}$$

where σ is the maximum elastic principal stress at the center of the RVE, m is the Weibull modulus, s_0 is scale parameter of the Weibull tail, $\langle x \rangle = \max(x, 0)$, μ_G and δ_G are the mean and the standard deviation of the Gaussian core. P_{gr} is the grafting probability between the Gaussian and the Weibull parts of the distribution, σ_{gr} is the grafting stress and r_f is a scaling factor ensuring that Weibull-Gaussian grafted cdf is normalized: $P_1(\sigma \to \infty) = 1$. Six statistical parameters, μ_G, δ_G m, s_0, r_f and σ_{gr} are used to describe the failure distribution of one material RVE; however, due to normalization and continuity conditions, only four of these parameters are independent, and suffice to define $P_1(\sigma)$.

The strength distribution of the entire structure can be calculated by mean of the WLM together with Eqs. (2a) and (2b). The mean structural strength for structures of different sizes can be obtained according Eq. 3:

$$\bar{\sigma}_N = \int_0^1 \sigma_N \mathrm{d}P_f = \int_0^\infty [1\text{-}P_f(\sigma_N)]\mathrm{d}\sigma_N \tag{3}$$

However, a closed form does not exist for Eq. 3, and, therefore, a numerical solution is needed to determine the effect of structure size, D, on the mean strength for geometrically similar specimens. Based on asymptotic matching, Bažant and co-workers [2, 5] proposed an approximate expression for the size dependence of the mean strength:

$$\bar{\sigma}_N = \left[C_1 / D + \left(C_2 / D\right)^{rn/m}\right]^{1/r} \tag{4}$$

where m is the Weibull modulus, n is the number of dimensions to be scaled (n = 1, 2 and 3). C_1, C_2, and r can be determined using the following asymptotic conditions for small and large-size limits: $[\bar{\sigma}_N]_{D\to l_m}$, $[d\bar{\sigma}_N / dD]_{D\to l_m}$ and $[\bar{\sigma}_N / D^{n/m}]_{D\to\infty}$, where l_m represents the small size limit of the structure.

3. Relation between mean size effect curve and strength distribution of one RVE

In this section a method to relate the statistical parameters, μ_G, δ_G m, s_0, of $P_1(\sigma)$ to the properties of the size effect curve of mean structural strength is proposed as an alternative to calibration through histogram testing. The mean size effect (Eq. 4) is determined by five parameters: n, m, r, C_1 and C_2. The scaling dimension, n, is known a priori, while m is the Weibull modulus, which is also one of the four statistical parameters of $P_1(\sigma)$. Therefore, the remaining three parameters μ_G, δ_G and s_0, must be determined from the three statistical parameters r, C_1 and C_2.

Since $rn/m << 1$, the large-size limit of Eq. 4 can be rewritten as $\bar{\sigma}_N = (C_2 / D)^{n/m}$. In such a case the RVE size becomes negligible compared to the structure size. Therefore, the classical extreme value statistics can be applied. Since the strength cdf has a power-law tail, the resulting strength cdf of the entire structure must follow the Weibull distribution [2, 3, 6, 7]. Therefore, the mean strength of very large structures can be calculated as [2-4, 8]:

$$\bar{\sigma}_N = s_0 \Gamma\left(1+1/m\right)\left(D_0 / D\right)^{n/m} \tag{5}$$

where $D_0 = l_0 \left[\int_V \left\langle s(\xi)\right\rangle^m \mathrm{d}V(\xi)\right]^{-1/m}$, $\xi = \mathbf{x}/D$ is the normalized coordinate, and $\Gamma(x)$ is the Eulerian gamma function. By equating Eq. 5 with the large size expression of Eq. 4, it is possibile obtaining the Weibull scaling parameter s_0 in terms of the parameter C_2:

$$s_0 = \left(C_2 / D_0\right)^{n/m} \Gamma^{-1}\left(1+1/m\right) \tag{6}$$

In order to use Eq. 6, the RVE size l_0 must be known a priori. Based on a recent study [2] the RVE size can be estimated as 2 times of size of the material inhomogeneities, which can be determined through digital image analysis [9] or from the aggregates gradation curve as was done in this study. At the small size limit two asymptotic conditions can be written for relating μ_G and δ_G to r and C_1:

$$\bar{\sigma}_N\big|_{D\to l_m} = \int_0^\infty \prod_{i=1}^{N_m} [1 - P_1(s_i\sigma_N)]\mathrm{d}\sigma_N = \left[\frac{C_1}{l_m} + \left(\frac{C_2}{l_m}\right)^{rn/m}\right] \tag{7}$$

$$\left.\frac{\mathrm{d}\bar{\sigma}_N}{\mathrm{d}D}\right|_{D\to l_m} = -\int_0^\infty \frac{\mathrm{d}P_f}{\mathrm{d}D}\mathrm{d}\sigma_N = -\frac{1}{r}\left[\frac{C_1}{l_m^2} + \frac{nr}{ml_m}\left(\frac{C_2}{l_m}\right)^{rn/m}\right]\left[\frac{C_1}{l_m} + \left(\frac{C_2}{l_m}\right)^{rn/m}\right]^{1/r-1} \tag{8}$$

where N_m is the number of RVEs in the structure at the small-size limit and l_m is the smallest specimen size which makes physical sense. Recent studies showed that for beams under three-point bending, which is commonly used in the laboratory testing, the minimum depth of the beam for the WLM to be valid is about 4 RVEs [10]. By using the logarithm of the WLM (Eq. 1) and integrating over the entire structure, the left hand side of Eq 8 can be rewritten as:

$$-\int_0^\infty \frac{\mathrm{d}P_f}{\mathrm{d}D}\mathrm{d}\sigma_N = \frac{n}{D}\int_0^\infty \prod_{i=1}^{N_m}[1 - P_1(s_i\sigma_N)] \sum_{i=1}^{N_m} \ln[1 - P_1(s_i\sigma_N)]\mathrm{d}\sigma_N \tag{9}$$

At the small size limit, N_m is usually small (i.e. 4 RVEs) and, therefore, it is expected that the Weibull tail of the strength cdf is very short. Hence, the cdf of strength can be entirely approximated by the Gaussian core; $P_1(\sigma)$ can be replaced by a Gaussian distribution, which has a mean μ_G and standard deviation δ_G. Eqs. 7 and 8 can then be reformulated as:

$$\int_0^\infty \prod_{i=1}^{N} [1 - \Phi_G(s_i\sigma_N, \mu_G, \delta_G)]\mathrm{d}\sigma_N = \left[\frac{C_1}{l_m} + \left(\frac{C_2}{l_m}\right)^{rn/m}\right]^{1/r} \tag{10}$$

$$\frac{n}{l_m}\int_0^{\infty}\prod_{i=1}^{N_m}[1-\Phi_G(s_i\sigma_N,\mu_G,\delta_G)]\sum_{i=1}^{N_m}\ln[1-\Phi_G(s_i\sigma_N,\mu_G,\delta_G)]\mathrm{d}\sigma_N = \\ =-\frac{1}{r}\left[\frac{C_1}{l_m^2}+\frac{nr}{ml_m}\left(\frac{C_2}{l_m}\right)^{rn/m}\right]\left[\frac{C_1}{l_m}+\left(\frac{C_2}{l_m}\right)^{rn/m}\right]^{1/r-1} \tag{11}$$

where $\Phi_G(s_i\sigma_N,\mu_G,\delta_G)=(2\pi)^{-1/2}\int_{-\infty}^{s_i\sigma_N}\exp[-(x-\mu_G)^2/2\delta_G^2]\mathrm{d}x$.

By solving the system of Eqs. 10 and 11, together with Eq. 6 and the Weibull modulus m, it is possible to determine the four parameters of the strength cdf of one RVE (μ_G, δ_G m, s_0) from the mean size effect curve. This permits us to calculate the strength distribution of structures of any size and geometry through the WLM.

4. Material and testing

A comprehensive set of experiments, including both mean strength tests on asphalt mixture specimens of different sizes and strength histogram testing at a low temperature, was used to verify the proposed method for indirectly determining the strength distribution from the mean strength curve. The asphalt mixture used for the experimental phase was prepared with a blend of aggregates, consisting of taconite aggregates (55% of MIN TAC tailings and 10% of ISPAT tailings) and pit sand (35%), and a PG 64-34 asphalt binder (7.4% by weight) [11]. The nominal maximum aggregate size was 4.75mm. Based on the sieve size analysis, the dimension of the asphalt mixture RVE was estimated to be twice the size of the material inhomogeneities, which for asphalt mixture corresponds to the average aggregate size. For the particular asphalt mixture considered in this study, we estimated an average aggregate size to be 1.22 mm and an RVE volume V_0 to be 14.4 mm^3.

Since the objective of this study is to derive the strength distribution from the mean size effect curve, a large size range is needed. Therefore, size effect tests were performed by using three-point bend (3PB) beams (Fig. 1).

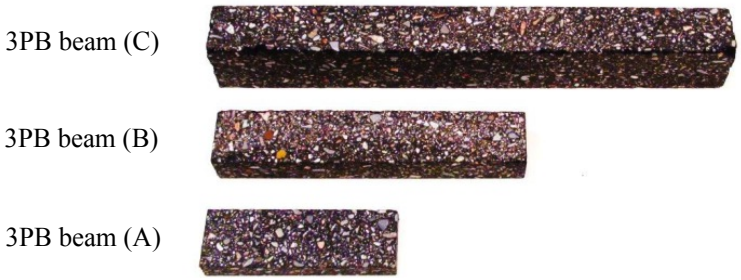

Figure 1. Beam specimens

Nevertheless, the sizes of the climatic chamber and of the testing machine limited the size of the beam specimens. Therefore, an alternative type of test was required to achieve a sufficiently large range of sizes to fully verify the ductile-to-brittle transition of material behavior as structure size increases. For this reason, mean strength tests were also conducted on prismatic specimens in direct tension (DT) configuration. Such an approach was selected because by varying test type and geometry both stress field and failure probability change. Therefore, given the same mean strength, it is possible to convert the dimensions of a structure for a specific stress field and geometry into a different structure with different stress field and geometry [2]. Since Weibull distribution governs the cdf of very large structures, the size of the DT specimen was set as the largest possible. This

ensures that the DT specimen consists of a large number of RVEs and thus the classical Weibull statistics can directly be used to calculate the size of the equivalent three-point bend beam.

Specimens were obtained from twenty-six slabs of asphalt mixture (size 380mm by 200mm) compacted at target air voids of 7% by mean of a Linear Kneading Compactor (LKC). Asphalt mixture beams for 3PB tests present thickness to span ratio equal to 1 : 6 and size ratio $1:\sqrt{3}:3$; since 2D scaling was used for beams, a constant width b = 40 mm was selected. The forth specimen type used for DT tests was prepared by cutting one-size asphalt mixture prisms. Table 1 presents detailed information on the specimens used. The thickness of the beams, D, and the width of the prism were assumed as characteristic dimensions for the three-point bend and DT specimens, respectively (Figure 2a and 2b). The dimensions of the specimens were chosen based on the dimensions of the compacted slabs and on the limitation imposed by the climatic chamber and loading frame.

Table 1. Specimen details and mean strength results

Specimen ID	Replicates #	Dimensions (L x D x b)	Test Type	Mean/Histogram	Mean Strength $\overline{\sigma}_N$(MPa)
A	12	100 x 16.7x 40 mm	3PB	Mean	14.3
B	28	173 x 28.9 x 40 mm	3PB	Histogram	12.4
C	30	300 x 50 x 40 mm	3PB	Histogram	11.4
D	7	255 x 55 x 55 mm	DT	Mean	8.2

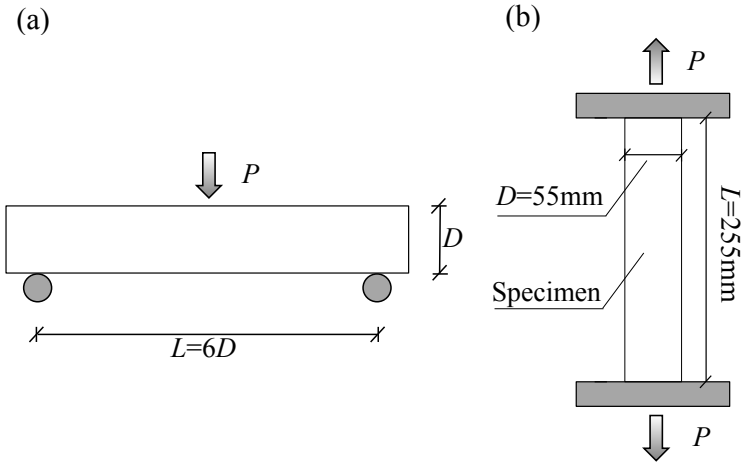

Figure 2. Schematics of (a) three-point bend test and (b) direct-tension test

Testing temperature was set to T=-24°C (low PG+10°C), which is close to the glass transition temperature of the asphalt mixture used. Together with very short tests duration this reduces the viscoelastic effect of the binder component. The desired testing temperature was achieved through a controlled flow of nitrogen inside the climatic chamber of the MTS device used for testing; a conditioning time of three hours was imposed to all the type of specimens before testing.

DT tests were performed by gluing the specimens to a set of plates with an epoxy compound, and then attached to loading frame through a set of screws. Since only the peak load is of interest for this study, both 3PB and DT tests were conducted in load-control mode. In order to minimize the loading rate effect and achieve a similar loading rate of the fracture process zone (FPZ), a time to failure of about 5 minutes was set for all the specimens. Consequently, different loading rates were set for each specimen type; for this reason, a rate calibration was initially performed by testing four

to six additional specimens at each testing condition.

5. Size effect analysis

The nominal strength of three-point bend σ_N^B and direct tension σ_N^T were calculated as $\sigma_N^B = (3P_{\max}L)/2bD^2$ and $\sigma_N^T = P_{\max}/bD$, where P_{max} is the peak load, L is the length of the beam, D is the scaling dimension (the thickness of the beam or the width of the DT prism) and b is the depth of the beam for three-point bend (40mm) or the depth of the prism (55mm) for DT specimens. Table 1 presents the mean nominal strength for all the specimens and the number of replicates used. In order to calculate the probability distribution of nominal strength of beam series B and C (Table 1), the strength values were ranked in an ascending order, i = 1, ...,N, where i is the rank and N is the total number of test specimens, and the strength cdf was next calculated according to the midpoint position method [12] as $P_f(\sigma_N^B) = (1-0.5)/N$. The resulting strength histogram is shown in Fig. 3 on the Weibull scale.

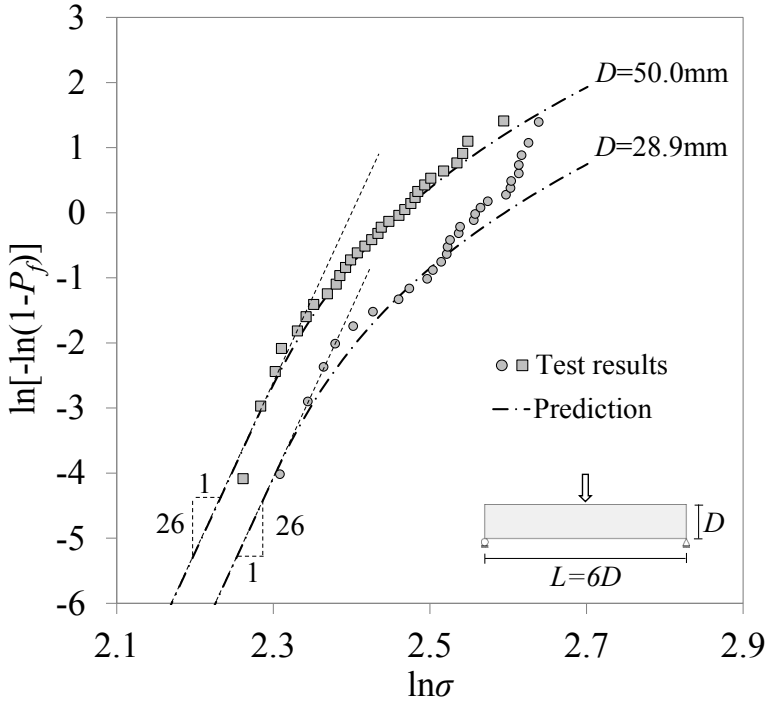

Figure 3. Experimental strength histograms and WLM predictions

The experimental strength histogram presents a trend which is common to many other quasibrittle materials such as concrete and engineering ceramics [13, 14], and is composed of two segments separated by a kink point: the lower segment follows a straight line (i.e. a Weibull distribution) while the upper portion is curved, according to the finite WLM. The experimental histograms indicate that the strength distribution strongly depends on the structure size: as the size increases, the Weibull portion becomes more and more dominant. The Weibull modulus, m, of the lower part of the two histograms can be obtained by fitting; this value is identical and equal to 26, which implies that the Weibull modulus does not vary with the structure size.

The mean strength of DT specimens needs to be converted into the corresponding equivalent 3PB beam to be next used for plotting the mean strength size effect curve. The DT specimen used in this investigation has a volume of 756,000 mm^3 (Table 1), which consists of almost $5.25 \cdot 10^4$ RVEs (V_0=14.4 mm^3). Such a large number of RVEs ensures that the failure cdf of DT specimens is fully

governed by the Weibull distribution, and, therefore, by the two parameters m and s_0. The mean strength of DT specimens, σ_N^T, and the mean strength of the equivalent 3PB beams, σ_N^B, can be written as:

$$\bar{\sigma}_N^T = N_T^{-1/m} s_0 \Gamma\left(1+1/m\right) \quad \text{and} \quad \bar{\sigma}_N^B = N_{eq,B}^{-1/m} s_0 \Gamma\left(1+1/m\right) \tag{12}$$

where N_T is the number of RVEs in the direct tension specimen and the equivalent number of RVEs in the 3PB beam is obtained as: $N_{eq,B} = \frac{b}{l_0^3}\int_V [(\sigma(\mathbf{x})/\sigma_N^B)]^m \, \mathrm{d}V(\mathbf{x})$, where V is the volume of the beam.

The equivalent characteristic size, D_{eq} (thickness), of the three-point bend beam, which has a nominal strength equal to $\bar{\sigma}_N^T$, is obtained by equating Eqs. 12:

$$D_{eq} = \sqrt{[(m+1)^2 N_T V_0]/(3b)} = 2143 \text{ mm} \tag{13}$$

Therefore, by simply selecting a different loading mode it is possible to achieve significantly different equivalent structure sizes, which allows obtaining size effect curve for a much wider size range. At the same time, based on the measured mean strength of DT specimens, and by using Eq. 12 for DT, we can directly estimate the value of the Weibull scaling parameter s_0 = 12.68 MPa. For beam specimens with 2D scaling (i.e. n = 2), we can consider that the damage is throughout the entire beam thickness. Therefore, the effective size of the RVE can be obtained as $l_0 = \sqrt{V_0/b} = 0.6$ mm; based on this condition and on Eq. 6, the following value of C_2 can be calculated: $C_2 = (m+1)/\sqrt{3} \cdot l_0 s_0^{m/2} \left[\Gamma\left(1+1/m\right)\right]^{m/2} = 1.55 \cdot 10^{15}$.

Fig. 4 shows the mean size effect curve of structural strength for 3PB beams and DT specimens (with their equivalent 3PB size). The experimental mean strength curve presents a pattern that is typical to that observed in other quasibrittle structures such as concrete beams [5, 15].

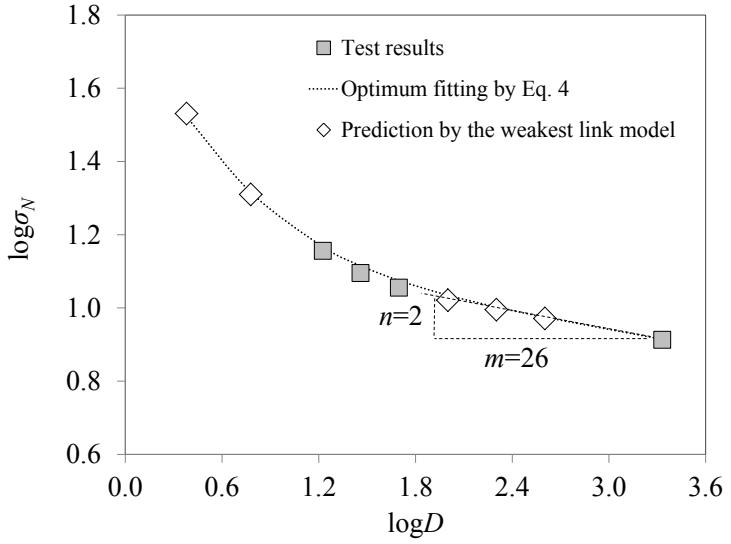

Figure 4. Mean strength curve

However, it is clear that the four mean strength data points obtained experimentally are not sufficient to determine the large-size asymptote of the size effect curve. For this reason, the Weibull modulus, m, was determined from the lower portion of the strength histogram as shown earlier in this paper. Therefore, *C2* was calculated from the DT specimen Weibullian mean. If we tested DT specimens of two different sizes, m could be calculated easily by fitting the linear portion of the mean strength curve at the large size limit and, hence, obtain s_0 directly from Eq. 6.

Parameters C_1 and r in Eq. 4 can be finally determined by non-linear fitting of the experimental mean strength data: the following values were obtained: C_1 = 49.49 and r = 1.01 which agrees well with the analytically derived size effect on the modulus of rupture of three-point bend beams [16]. By knowing C_1 and r, and solving Eqs. 10 and 11, it is possible to obtain the remaining two parameters of the Gaussian core, μ_G, δ_G, of the of the RVE strength cdf. Since for this computation we are interested to the small size limit, the smallest beam size which can be used has a characteristic size $D = 4l_0$ (Fig. 5). According to the elastic stress field two layer of RVE are subjected to tensile stress. The stress at the center of the RVEs upper-layer is half of the stress at the center of the RVEs bottom-layer. Moreover, along the beam span there is a significant decay of stress moving away from the two central RVEs, "C", of 9.5% and 26% for RVEs "L" and "A", respectively. Given the large value of the Weibull modulus, it is reasonable to only include the bottom-layer RVEs "C" and "L" for the calculation of μ_G, δ_G.

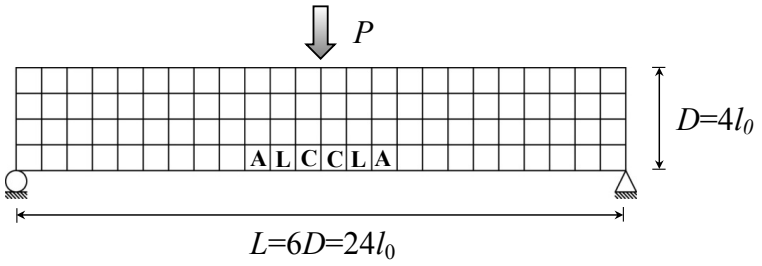

Figure 5. Small size limit beam

Therefore, Eqs. 10 and 11 can be rewritten as:

$$\int_0^\infty \prod_{i=1}^{2} [1-\Phi_G(s_i\sigma_N,\mu_G,\delta_G)]^2 \mathrm{d}\sigma_N = \left[\frac{C_1}{4l_0}+\left(\frac{C_2}{4l_0}\right)^{2r/m}\right]^{1/r} \tag{14}$$

$$\frac{1}{l_0}\int_0^\infty \left\{\prod_{i=1}^{2}[1-\Phi_G(s_i\sigma_N,\mu_G,\delta_G)]^2 \sum_{i=1}^{2}\ln[1-\Phi_G(s_i\sigma_N,\mu_G,\delta_G)]\right\}\mathrm{d}\sigma_N = \\ = -\frac{1}{r}\left[\frac{C_1}{16l_m^2}+\frac{2r}{4l_0 m}\left(\frac{C_2}{4l_0}\right)^{2r/m}\right]\left[\frac{C_1}{4l_0}+\left(\frac{C_2}{4l_0}\right)^{2r/m}\right]^{1/r-1} \tag{15}$$

where s_1 = 0.718, and s_2 = 0.656. The system of Eqs. 14 and 15 can be numerically solved, yielding μ_G = 45.24 MPa and δ_G = 14.82 MPa, which, can be easily demonstrated, are the only couple of values satisfying Eqs. 14 and 15.

With knowing μ_G, δ_G m and s_0 the strength distribution of one RVE (Eqs. 2a and 2b) can be evaluated. With the finite WLM (Eq. 1), it is possible predicting the strength cdf of beams series B and C. Fig. 3 shows that the predicted strength cdf matches very well the measured strength histograms for both beam sizes. This indicates the statistical parameters of strength cdf can be calibrated from the mean size effect curve. By using the WLM we can further calculate the strength distribution and the mean strength of beams with other different sizes; Fig. 4 indicates that the mean structural strength predicted from the WLM lies on the size effect curve represented by Eq. 4, supporting the validity of this expression in providing a good approximation of the exact size effect curve calculated from the finite WLM.

In previous studies [2-4] it was shown that the finite WLM could correctly describe the deviation of the strength histogram of quasibrittle structures of a single size from the two-parameter Weibull distribution. Based on the strength histograms of structures of two sizes, this study provides a

further validation of the finite WLM; by properly selecting specimen sizes and number of replicates the size effect on the grafted strength distribution was clearly demonstrated (Fig. 3). The good agreement between the predicted and measured strength distributions of beams of two sizes indicates that the recently proposed finite WLM can well capture the size effect on the strength cdf of quasibrittle structures.

6. Conclusions

In this paper an analytical and experimental demonstration on the possibility of indirectly determining the strength cdf of quasibrittle from the mean size effect curve was presented. This method provides a valid alternative to the conventional histogram testing, it requires a smaller number of specimens, and it is less prone to experimental errors. The size effect tests on the strength histogram of asphalt mixture indicates that the probability distribution of structural strength strongly depends on the structure size, and such dependence can be well explained by the finite weakest link model.

Acknowledgements

The support provided by NCHRP-IDEA 151 is gratefully acknowledged. The results and opinions presented do not necessarily reflect those of the sponsoring agency.

References

[1] K. Duckett, Risk analysis and the acceptable probability of failure. Struct Eng 83(15) (2005) 25–26.
[2] Z. P. Bažant, S.-D. Pang, Activation energy based extreme value statistics and size effect in brittle and quasibrittle fracture. J Mech Phys Solids 55 (2007) 91–134.
[3] J.-L. Le, Z. P. Bažant, M. Z. Bažant, Unified nano-mechanics based probabilistic theory of quasibrittle and brittle structures: I. Strength, static crack growth, lifetime and scaling. J Mech Phys Solids 59 (2011) 1291-1321.
[4] Z. P. Bažant, J.-L. Le, M. Z. Bažant, Scaling of strength and lifetime distributions of quasibrittle structures based on atomistic fracture mechanics. Proc Natl Acad Sci USA (2009) 11484-11489.
[5] Z. P. Bažant, D. Novák , Energetic-statistical size effect in quasibrittle failure at crack initiation. ACI Mater J 97(3) (2000) 381–392.
[6] R. A. Fisher, L. H. C. Tippett, Limiting forms of the frequency distribution of the largest and smallest member of a sample. Proc Camb Philos Soc 24 (1928) 180–190.
[7] E. J. Gumbel, Statistics of extremes, Columbia University Press, New York, 1958.
[8] Z. P. Bažant, J. Planas, Fracture and size effect in concrete and other quasibrittle materials, CRC Press, London, (1998).
[9] Cannone Falchetto, A. Montepara, G. Tebaldi, M. O. Marasteanu, Microstructural characterization of asphalt mixtures containing recycled asphalt materials. J Mater Civ Eng ASCE doi: 10.1061/(ASCE)MT.1943-5533.0000544 (in press).
[10] J.-L. Le, J. Eliáš, Z. P. Bažant, Computation of probability distribution of strength of quasibrittle structures failing at macro-crack initiation." J Eng Mech ASCE 138(7) (2012) 888-899.
[11] AASHTO M320-10-UL, Standard method of test for performance graded asphalt binder. Am Assoc State Highw Transp Off (2010).
[12] H. Rinne, The Weibull distribution. A Handbook, CRC Press, London, (2009).
[13] B. Gross, Least squares best fit method for the three parameter Weibull distribution: analysis of tensile and bend specimens with volume or surface flaw failure. NASA TM-4721 (1996) 1-21.

[14] U. Lohbauer, A. Petchelt, P. Greil, Lifetime prediction of CAD/CAM dental ceramics. J Biomed Mater Res 63(6) (2002) 780–785.
[15] Z. P. Bažant, Scaling of structural strength. 2nd Ed, Elsevier, London (2005).
[16] Z. P. Bažant, Z. Li, Modulus of rupture: size effect due to fracture initiation in boundary layer. J Struct Eng ASCE, 121(4) (2005) 739–746.

Study of Ductile-Brittle transition in Fiber Bundle Model Under Mean-Field Approximation

Subhadeep Roy[1*], Purusattam Ray[1]

[1] The Institute of Mathematical Sciences, Taramani, CIT Campus, Chennai 600113, Tamil Nadu, India
* Corresponding author : sroy@imsc.res.in

Abstract Defects play crucial role in the process of nucleation and propagation of fracture. We study fracture as a non-equilibrium statistical mechanical system with a threshold activated extremal dynamics. The dispersion δ in the breaking thresholds shows a transition at $\delta = \delta_c$. For $\delta < \delta_c$, the fracture or failure takes place sharply at a certain applied stress or voltage. For $\delta > \delta_c$, the fracture or failure takes place gradually with increasing stress or voltage, leading to a non-linear region in the stress-strain or current-voltage curve prior to failure. We discuss the transition point For δ_c from the point of view of ductile-brittle transition. We present analytical results on fiber bundle model and numerical results on two dimensional random resistor network model.

Keywords Ductile-brittle transition, Threshold activated dynamics, Fiber bundle model, Random resistor network model.

1. Introduction

In material science and engineering ductile and brittle behaviors have received lots of attention over the past years. It is widely known that most ductile materials become brittle when the temperature or pressure is lowered or by radiation bombardment and atmospheric reaction. This phenomenon, known as ductile-brittle transition, has been extensively studied by engineers, material scientists and physicists. Disorder is known to play a crucial role in fracture. It is now known that topological disorders like dislocations and their cooperative motion give rise to ductile fracture. Brittle fracture on the other hand originates from a single micro-crack, the most vulnerable one. Thus ductile fracture can be thought of as a co-operative process of defects whereas brittle fracture is determined by extreme events [1]. Though several aspects of fracture are now understood, the mechanism and the nature of ductile-brittle transition is not clear yet. In this paper, we study the effect of dispersion (δ) in the local strengths in a material on the nucleation and propagation of fracture. We show for low δ the system behaves like a brittle material where failure happens sharply at a certain value of applied stress or voltage and the response of the system remains linear up to the failure point. For high δ the breakdown of the system happens gradually through local failures till the entire system breaks. The stress-strain curve in the elastic system or the voltage-current characteristics in electrical system shows non-linear region prior to failure. We argue for a transition point δ_c separating the low and high δ regions.

We have studied two models: fiber bundle model and random resistor network model. The fiber bundle model is solved analytically under mean field approximation. We have provided the numerical results for both the models. The models perceive fracture as a threshold activated extremal dynamical system. The disorder in these models is introduced in terms of random threshold stress of individual fibers or current in resistors.

We have found a transition point of threshold distribution ($\delta = \delta_c$) which clearly separates two different regions in the model. For $\delta < \delta_c$, the fracture phenomena is very sharp and similar to that of brittle fracture. The sharpness of this failure is expressed by the sudden jump of the fraction of unbroken bonds in fiber bundle model and conductance in random resistor network model, at the fracture point. Where for $\delta > \delta_c$, the bonds or resistors break in a correlated manner producing avalanches of all sizes and the model shows the features of ductility. We have also studied the

mechanical and electrical response of the model. For δ less then δ_c the response curve shows a perfectly linear brittle like nature where as for δ greater than δ_c, the response curve contains a ductile like non-linear or plastic region.

2. Fiber Bundle Model

The review of modern physics written by S. Pradhan, A.Hansen and B.K.Chakrabarti has a very good overview on fiber bundle model [2]. The model consist of two parallel bars between which rigid fibers are attached (Fig 1a). One of the two bars is fixed and an amount of force F is applied on the other one. If there are N number of fibers then force per fiber i.e stress applied on the system is, f_0 =F/N.

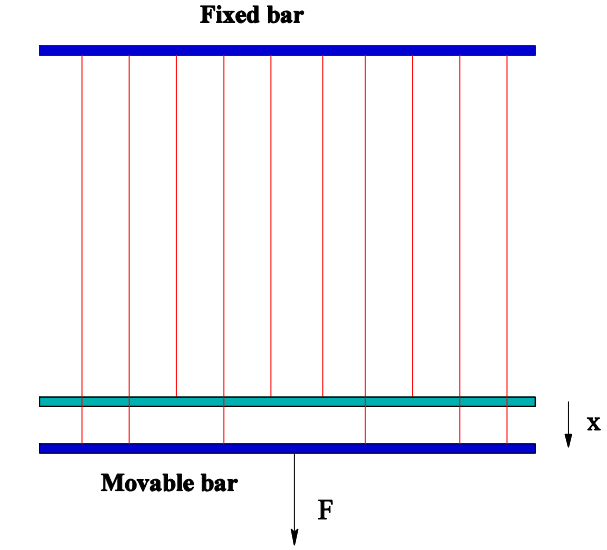

Figure 1a: Fiber Bundle Model

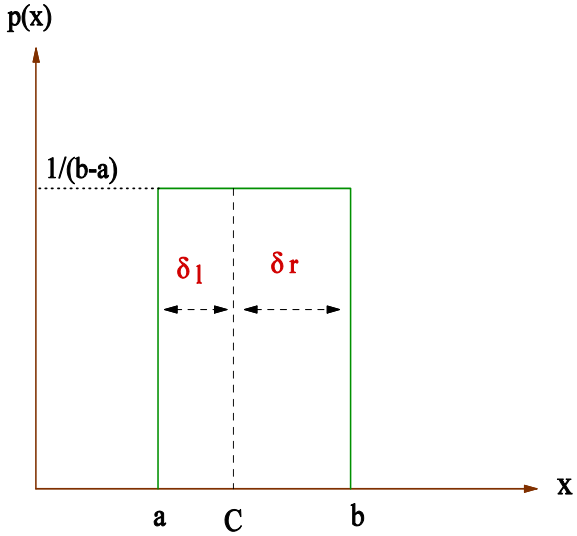

Figure 1b: Threshold Distribution

Every fiber has some threshold stress value and when the external stress exceeds this value it breaks. After breaking of one fiber the stress is re-distributed among all other fibers according to global stress re-distribution scheme; which would increase the stress and may cause further breaking of fibers. For example, at a constant applied force F, the re-distributed stress will be F/(N-1) after breaking of one

fiber, F/(N-2) after breaking of two fibers and so on. This process will continue until either all the fibers break or the redistributed stress is less than the next threshold value. At this stage the model comes to equilibrium. The number of remaining fibers at each equilibrium is denoted by N_{eq}. Then the fraction of fibers remained at equilibrium point is $n_{eq} = N_{eq}/N$. Next we increase the external stress ($F \rightarrow F+\Delta F$); which leads to further breaking, re-distribution and equilibration. This process goes on until all the fibers break. The threshold stress is given to the fibers in a random way, picking random numbers between 0 to 1 from an uniform distribution around any mean value C and width δ_r and δ_l respectively on right and left side of the mean value (Fig 1b). We are considering the vulnerability of the defect in the form of a breaking threshold of a fiber. The threshold distribution represents the fluctuations of these vulnerabilities in mean field limit (where the stress fluctuation on the bonds are neglected). The fiber bundle model gives us an idea of the correlations in the breaking processes in fibers. The fluctuations in the breaking threshold gives rise to the cooperative nature in the breaking processes in fibers which is the essence of ductile fracture.

2.1 Analytical Calculations

In this paper we provide the analytical calculations for the static and dynamic behavior of the model. We have compared our results with some previously calculated values depending on some specific choices of the mean and width of threshold distribution. At first we will study the distribution for giving threshold to the fibers. From figure 1b we can see that the mean is at C which is in between 0 and 1. Then the point 'a' and 'b' is at ($C- \delta_l$) and ($C+ \delta_r$) respectively. Now we can take $\delta_r=\delta$ and relate this with δ_l by the relation : $\delta_l=\alpha\delta_r=\alpha\delta$. For the analytical calculations we will take $\alpha=1$. This will give us a distribution of width 2δ ranging from a to b. Then the fraction of broken bond at every equilibrium will be given by

$$1 - n_{eq} = \int_0^{f_0/n_{eq}} P(\sigma)d\sigma \qquad \ldots\ldots\ldots\ldots 1$$

We are interested in the region $a \leq f_0/n_{eq} \leq b$ as the other regions are quite trivial. For $f_0/n_{eq} > b$, all fibers are broken while for $f_0/n_{eq} < a$, all fibers are intact.

2.1.1 Determination of fraction of unbroken bonds at equilibrium points

Within the region $a \leq f_0/n_{eq} \leq b$ we can express the fraction of unbroken bonds as

$$1 - n_{eq} = \int_a^{f_0/n_{eq}} \frac{1}{2\delta} d\sigma$$

$$= (1/2\delta)(f_0/n_{eq} - a) \qquad \ldots\ldots\ldots\ldots 2$$

This will give us a quadratic equation of n_{eq} :

$$n_{eq}{}^2 - \left(1 + \frac{a}{2\delta}\right) n_{eq} + \frac{f_0}{2\delta} = 0 \qquad \ldots\ldots\ldots\ldots 3$$

The solution of the above equation will give us the fraction of unbroken bonds :

$$n_{eq} = \frac{1}{2}\left(1 + \frac{a}{2\delta}\right) \pm \frac{1}{2}\sqrt{\left(1 + \frac{a}{2\delta}\right)^2 - \frac{2f_0}{\delta}} \qquad \ldots\ldots\ldots\ldots 4$$

2.1.2 Determination of critical stress of the model

At critical point all the bonds break on application of an external stress, f_c, known as critical stress. The number of fractional bonds remaining just before the breakdown is nc. Thus at $f_0=f_c$, n_{eq} has only one value. This implies that the term in the square root in Eq.(4) should be zero; which in turn gives us,

$$\frac{2f_c}{\delta} = \left(1+\frac{a}{2\delta}\right)^2$$

Or, $f_c = \frac{\delta}{2}(1 + a/2\delta)^2$ ……..5

2.1.3 Fraction of unbroken bonds at critical stress

We can get the fraction of unbroken bond at critical stress by inserting the value of f_c from Eq.(5) in Eq.(4). Then we will get

$$n_c = n_{eq}|_{f_0=f_c}$$

Or, $n_c = \frac{1}{2}(1 + a/2\delta)$ ……..6

We find from Eq.(6), n_c starts increasing from a value 0.5 at $\delta = 0.5$ and reaches a value 1 at $\delta = \delta_c$. For $\delta < \delta_c$, n_c remains at 1 since it is at its maximum point and can't attain a higher value.

2.1.4 Study of Ductile-Brittle transition point

We have the expression of the critical stress given by Eq.(5). Now for $f_0/n_{eq} < a$, all bonds are intact and at the critical limit we can write

$$\frac{f_0}{n_{eq}}|_{f_0=f_c, n_{eq}=n_c=1} = a \qquad \ldots\ldots\ldots 7$$

Replacing the value of f_c from Eq.(5) in Eq.(7) we get the critical value of $\delta(\approx \delta_c)$ as :

$$\frac{\delta}{2}\left(1+\frac{a}{2\delta}\right)^2|_{\delta=\delta_c} = a$$

Or, $\delta_c = a/2$ ……8

2.2 Numerical Results

For numerical results we will set C=0.5 and α=1. This gives a threshold distribution with a mean at 0.5 and width δ on both side of the mean. The system size is taken to be 10^6. All simulated results are over 100 configuration averages.

2.2.1 Variation of fraction of unbroken bonds (n_{eq}) with applied stress (f_0)

We have plotted the fraction of unbroken bonds at each equilibrium (n_{eq}) with applied stress (f_0) for a series of δ's between 0.1 and 0.5. The results are given by figure 2. As δ increases the critical applied stress(f_c) at which the total model breaks decreases from 0.5 and reaches 0.25 at δ=0.5.

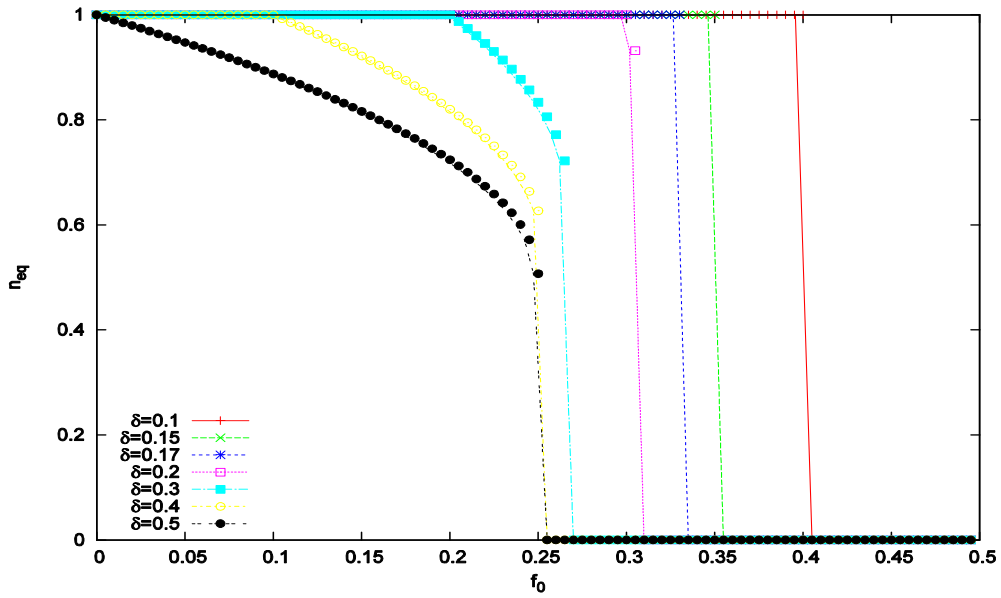

Figure 2: Fraction of unbroken bonds(n_{eq}) with applied stress(f_0)

Moreover up to a certain value δ≈0.17, the fraction of unbroken bonds at critical point (n_c) remains 1. Beyond this value, n_c starts decreasing and comes to a value 0.5 at δ=0.5. The point δ≈0.17 is like a critical point. This is quite consistent with the value we obtained analytically. At one side of the this point the model behaves like ductile materials showing a fracture through a number of equilibrium configurations at a low critical stress; where on the other side it behaves like brittle materials showing an abrupt fracture at a higher critical stress. We have studied this critical point in detail in our other simulated results.

2.2.2 Variation of redistributed stress ($f=f_0/n_{eq}$) with applied stress (f_0) for different δ's

Since the fibers are totally rigid, there is no strain in the model in true sense. We will treat the re-distributed stress as strain since the non-linearity is introduced in the model through this re-distributed stress.

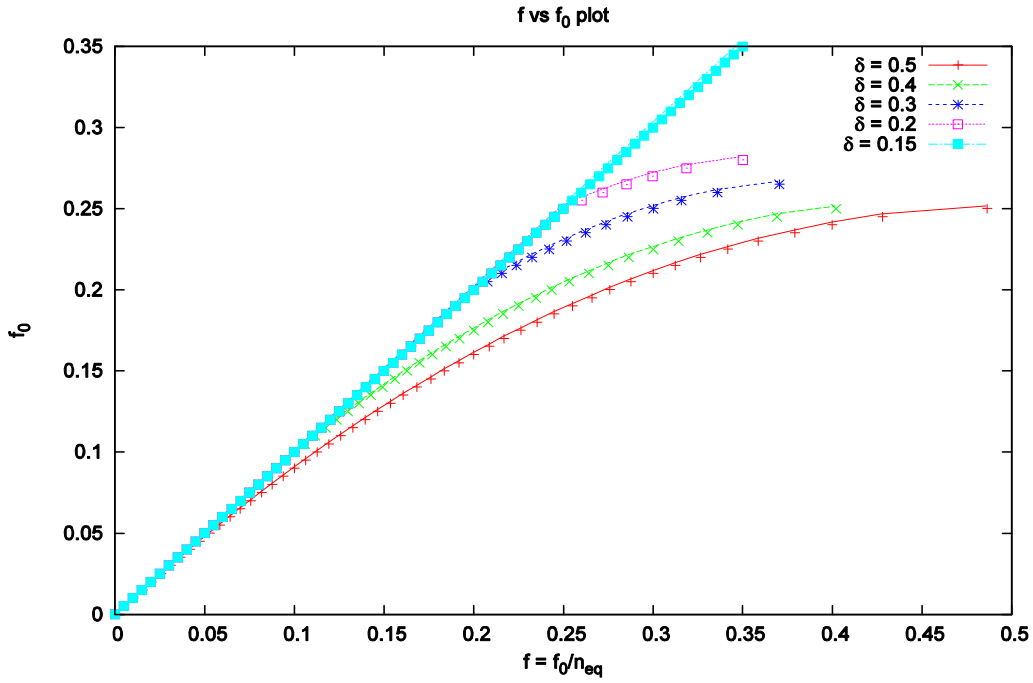

Figure 3: Stress-strain curve (f_0 vs f_0/n_{eq}) for the model

This is very similar to the response curve of mechanical systems. We have plotted f_0 with f_0/n_{eq} for different δ's with in 0.1 and 0.5. Figure 3 shows that for $\delta \leq 0.15$, the model behaves like brittle materials while for $\delta \geq 0.2$ the model shows ductility. There must be a critical value of threshold distribution width (δ_c) within the range $0.15 < \delta_c < 0.2$, where this ductile-brittle like transition occurs.

2.2.3 Variation of critical stress (f_c) with threshold distribution width (δ)

We have already shown that the critical stress to create fracture in the model increases with decreasing δ values. Figure 4 gives us an idea how this critical stress decreases with a continuous increase in threshold distribution width. Figure 4 shows that, the critical stress (f_c) decreases with increasing δ and falls from 0.4 to 0.25 within the range between 0.1 and 0.25 in δ value. Though the transition point is not quite evident from the plot, we can estimate it as the average of the above mentioned δ region. So, from above study we get $\delta_c \approx 0.17$. This agrees with the value we obtained analytically and other simulated results. The variation of critical stress (f_c) with δ and the nature of response curve is obtained before in two dimensional fiber bundle model which consists of two square plates in which fibers are intact [3]. We have reproduced the same result in a relatively easier model.

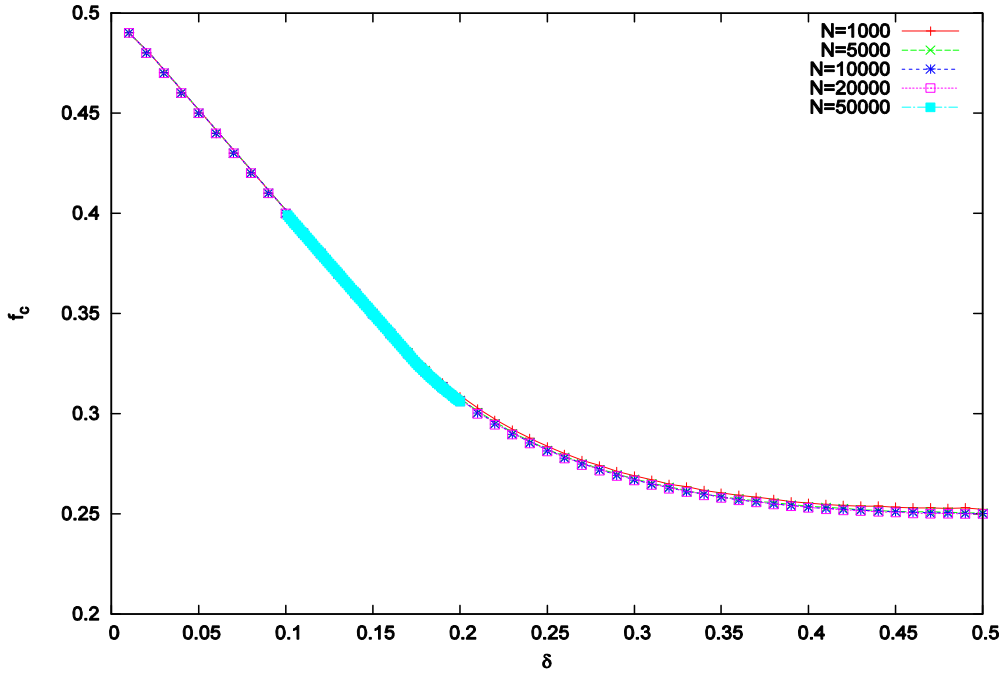

Figure 4: Variation of critical stress (f_c) with δ

2.2.4 Fraction of unbroken bonds (n_c) at critical stress with threshold distribution width (δ)

Above study of critical stress is unable to give us a clear distinction between ductile and brittle region in the model. This distinction can be drawn from the study of fraction of unbroken bonds at critical point (n_c) with varying δ value.

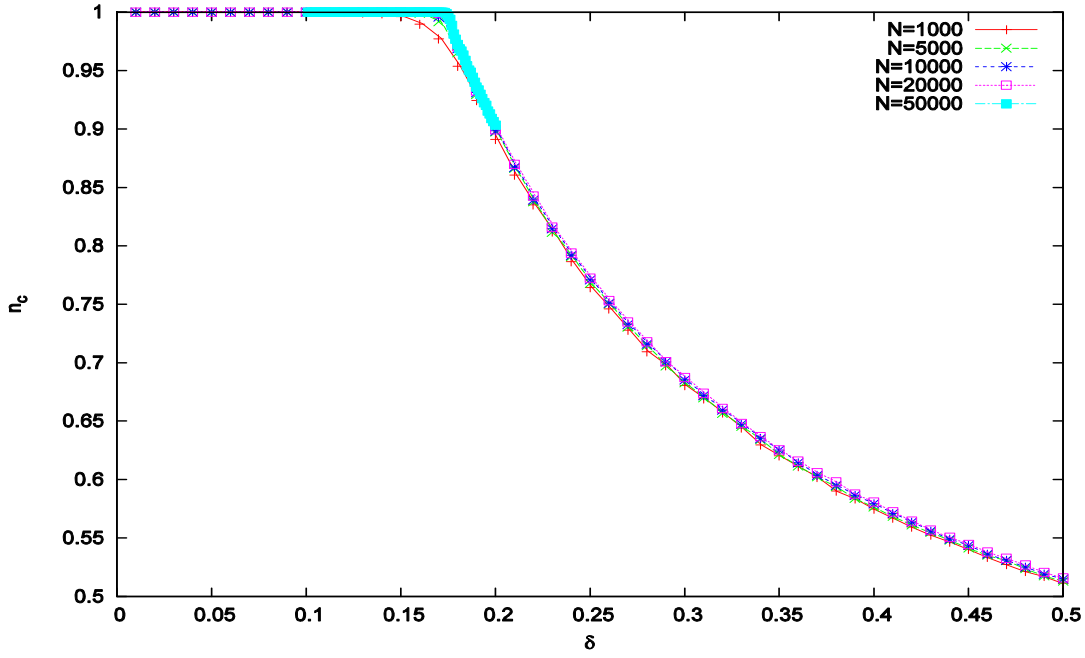

Figure 5: Variation of n_c with δ

One of the strong points that helps us to denote low δ region as brittle is, the value n_c remains 1 up to a certain low value of δ characterizing a abrupt fracture in the model. Figure 5 reflects the same

fact. Up to a value $\delta_c \approx 0.17$, n_c remains 1. This is the brittle region for the model. If we increase δ beyond this n_c starts to fall and goes to 0.5 at $\delta=0.5$. This is the ductile region. The above critical point ($\delta_c \approx 0.17$) separates these two regions very clearly.

2.2.5 Variation of (f_c/n_c) with threshold distribution width (δ)

A plot of f_0/n_{eq} with δ gives us a clear idea about the point at which the ductile to brittle like transition occurs. The point with coordinate ($f_0/n_{eq}=0.32$, $\delta_c \approx 0.17$) in the plot denotes the transition point from brittle to ductile region and vice verse.

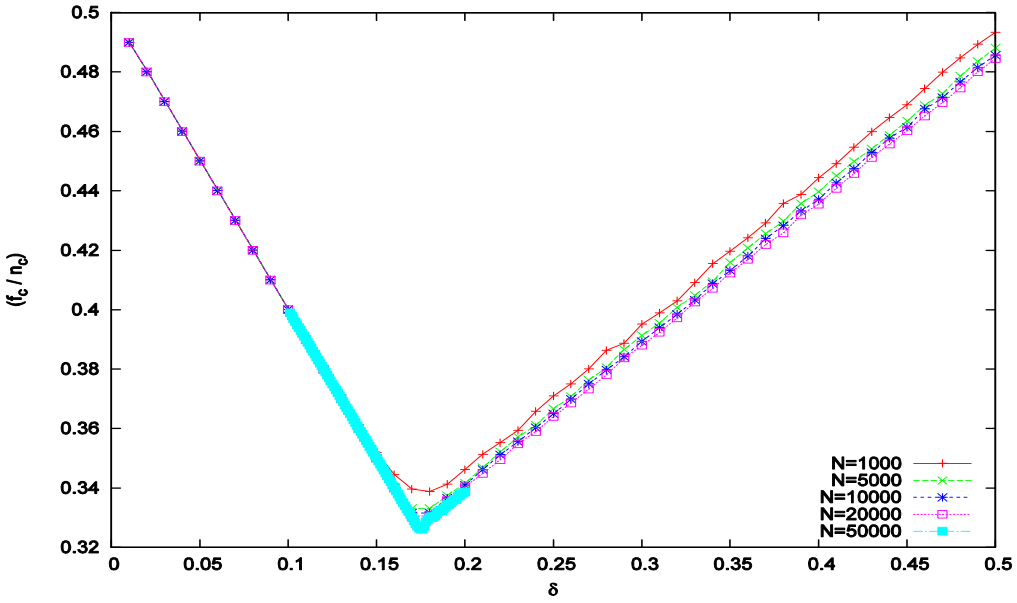

Figure 6: Variation of f_c/n_c with δ

The obtained value of δ at which the transition occurs is $\delta_c \approx 0.17$; which is very similar to the values obtained from other numerical studies and analytical calculation.

2.2.7 Phase diagram for the model

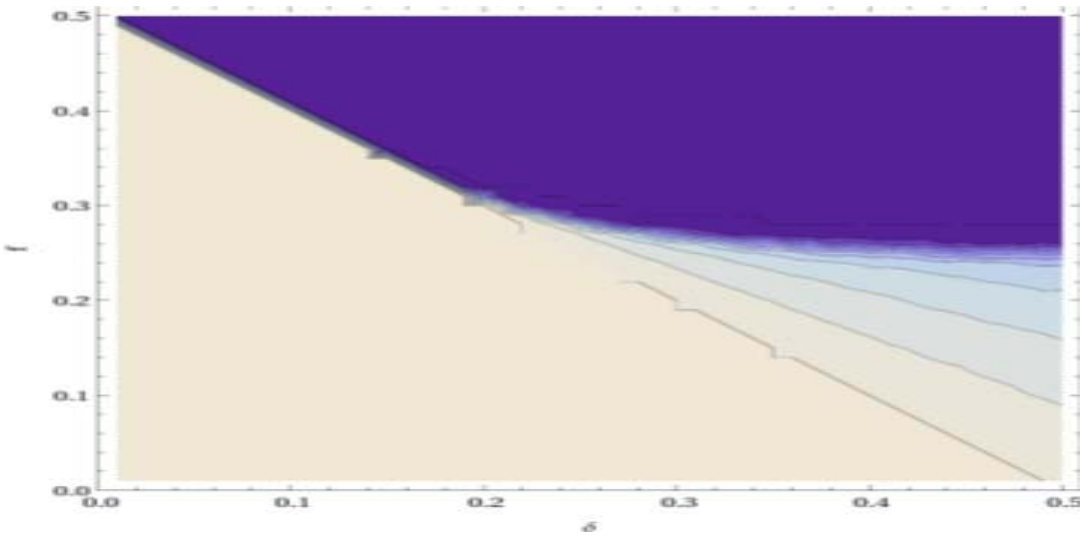

Figure 7: Phase diagram for fiber bundle model

We have constructed a phase diagram for the model and given by figure 7. The darkest color corresponds to n_{eq}=0 and the lightest color for n_{eq}=1. A very important observation is related to this diagram. For δ<0.166, n_{eq} fall to zero abruptly. When we cross this particular point the behaviour of n_{eq} changes. For δ>0.166, n_{eq} falls to zero after crossing a number of equilibrium points. This is the point where the transition occurs. On one side of this point the material shows ductile like fracture and on the other side the fracture resembles abrupt brittle fracture.

3. RANDOM RESISTOR NETWORK MODEL

We have constructed a tilted square lattice whose each bond is a resistor with a resistance 1. A potential difference of V volts is applied to two opposite ends of the lattice. On the other two ends periodic boundary condition is applied (Fig 8a). All resistors are given a random threshold taken from the same uniform distribution same as the case of fiber bundle model.

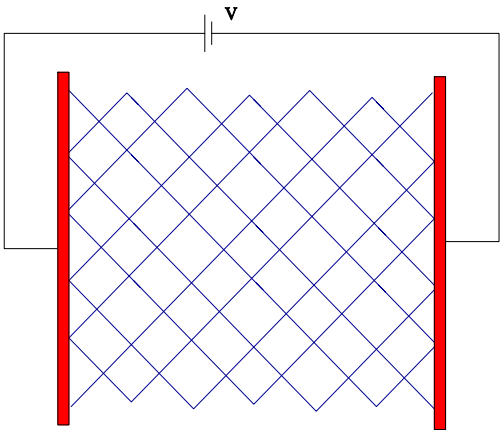

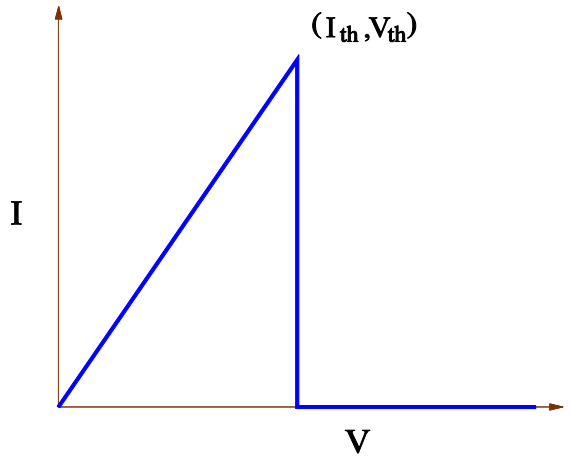

Figure 8a: Random resistor network model

Figure 8b: Response of individual resistors

The potential at each lattice point is calculated by solving 'Kirchoff's law' with a series of iterations. Whenever the potential drop between two lattice points becomes less than the threshold value given to the resistor joining these two points, the resistor breaks irreversibly (Fig 8b). Then we apply 'Kirchoff's law' again to calculate the new potentials due to the breaking of the fiber. When no more fiber breaks, we increase the applied potential and do the same thing. This process goes on until the conductance of the system becomes zero. This is the critical point for the model.

3.1 Numerical Results

For numerical simulations we have taken the same specifications like fiber bundle model. The lattice size is taken to be 16×16.

3.1.2. Variation of conductance (G) with applied voltage

Conductance is the parameter which denotes the fracture point for the model. The rate at which the conductance drops to zero is the abruptness of the fracture. We have plotted conductance with applied voltage and observed its behavior at various values of δ.

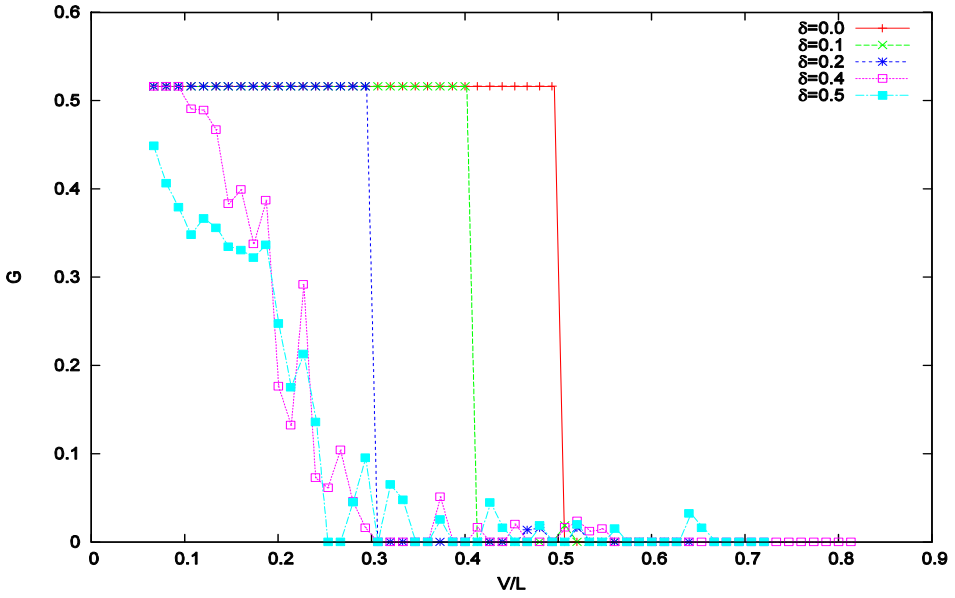

Figure 9: Variation of conductance with applied voltage

Up to δ=0.2 the conductance falls very sharply causing an abrupt fracture in the model. This behavior is analogous to sharp brittle fracture. With increasing δ this sharpness decreases. For δ ≥0.3 the fracture occurs in a co-operative manner like ductile materials. Moreover the constant initial value of conductance corresponds to a linear region in current voltage characteristic curve prior to fracture. This behavior is like brittle materials. As δ increases the conductance start decreasing from this constant value after a certain value δ= δ_c. Above this δ value current-voltage charecteristics curve stars showing non-linearity and behaves like a ductile material.

4. DISCUSSION AND CONCLUSIONS

As an outcome of this paper we can point out some important results :
1. Variation of conductance in random resistor network and fraction of unbroken bond at critical point (n_c) in fiber bundle model with δ shows that the behavior of the model in low δ is brittle like and that for high δ is ductile like.
2. The mechanical and electrical response shows a pure linear or a linear behavior with small non-linear part before some critical value of δ. Beyond that the model behaves non-linearly like ductile materials. For fiber bundle model this critical value is, $\delta_c \approx 0.16667$. For random resistor network model this critical value δ_c remains within δ value 0.2 and 0.3. More studies are required to locate the exact transition point for random resistor network model.
3. The critical stress to create fracture in the fiber bundle model decreases to lower values with increasing δ's. This signifies a decrease in hardness of the model when δ is increased.
At this stage it is difficult to draw some analogy between any exact material property that causes ductile-brittle transition and the parameter δ in our model. Still we can suggest a possible parameter similar to δ. Early studies in material science prove that ductility in materials is a consequence of cooperative motion of defects (mainly dislocation) within it [1]. The material becomes brittle if the defects within it are immobile. There are also some external parameter like temperature or pressure [4] that control this mobility of defects. Because of this characteristic, materials show ductile-brittle transition with respect to these parameters. If we can define any quantity that deals with the cooperative motion of the defects in the materials and increases with increasing mobility of defects, then that quantity will be analogous to the δ parameter. If it is possible to find some critical value of this quantity, depending on the change of external parameters (temperature, pressure or any other

parameters), which distinguishes between ductile and brittle region in the materials; then it will be similar to δ_c, the ductile-brittle transition point.

Acknowledgements

I acknowledge Soumyadeep Bhattacharya for his guidance and suggestions from time to time. I also thank my parents, grandmother and specially my brother for their support and encouragement.

References

[1] George E.Dieter, Mechanical Metallurgy, McGraw-Hill Book Company, 1928.
[2] S. Pradhan, A.Hansen and B.K.Chakrabarti, Failure processes in elastic fiber bundles, Reviews of Modern Physics 82 (2010) 499-555.
[3] Frank Raischel, Ferenc Kun and Hans J. Herrmann, Local load sharing fiber bundles with a lower cutoff of strength disorder. Physical Review E-Statistical, Nonlinear and Soft Matter Physics, 74 (2006), 035104(R).

[4] R. D. Isaac and A. V. Granato , Rate theory of dislocation motion: Thermal activation and inertial effects. Phys. Rev. B 37, 92789285 (1988).

[5] B. Kahng, G. G. Batrouni, S. Redner, Electrical breakdown in a fuse network with random distributed breaking strengths. Physical Review B, Volume 37, Number 13, 1988.

Propagation of tensile planar cracks in highly heterogeneous media: A numerical study

M. Vasoya[1,2,*], V. Lazarus[1], and L. Ponson[2]

[1] *UPMC Univ Paris 6, Univ Paris-Sud, CNRS, UMR 7608, Lab FAST, Bat 502, Campus Univ, F-91405, Orsay, France;*
[2] *UPMC Univ Paris 6, CNRS, UMR 7190, Institut Jean Le Rond d'Alembert, Boite courrier 161-2, 4 Place Jussieu, F-75005, Paris, France;*
[*] *Corresponding author : vasoya@dalembert.upmc.fr*

Abstract: Effect of highly heterogeneous fracture properties on tensile penny-shape planar crack propagation governed by Irwin's criterion is investigated numerically by taking into account the large crack front deformations induced by the high toughness contrasts. To compute the variations of stress intensity factor (SIF) along the crack front arising from its progressive deformation, perturbation approach based on Bueckner-Rice weight function theory is used iteratively. Effective fracture toughness is obtained from the local toughness map for a few examples. It is shown that when Irwin's criterion is satisfied all along the crack front, the effective toughness is equal to the mean value of the local ones along the crack front. This value depends on the shape of the front, and so is different from the total mean value of the toughness in the plane. In the examples studied here, the weak toughness zones are favored by the crack front deformations, so that the effective toughness is lower than its spatial average.
Keywords: Tensile planar crack; Heterogeneous medium; Effective failure properties; Perturbation method; Linear elastic fracture mechanics.

Quantifying the effective fracture properties of a planar crack propagating in a heterogeneous material is a key issue in material science. Since the crack propagation results from the interplay of local material properties with long range elastic interactions, the problem is not trivial and can not, in general, be reduced to take the spatial mean value of the fracture properties. Two regimes shall be distinguished [1]: For slightly fluctuating maps of local toughness, the elasticity of the crack front dominates over the destabilizing effects of heterogeneities, and the motion of the front is smooth (weak pinning). For materials with stronger heterogeneities with larger gradient of toughness, the crack front can jump abruptly from one equilibrium position to the other (strong pinning) [3]. In the weak pinning regime, it has been shown in the limit of a first order approach that the effective macroscopic toughness can be obtained by averaging the local toughnesses, contrary to the strong pinning case where the effective macroscopic toughness is *larger* than the average local toughness [1].

Here, we address these questions in the context of highly heterogeneous local fields of toughness for which the first order approach can not be used. In particular, we take into account the effect of large crack front deformations induced by high toughness contrasts, and investigate the relationship between local toughness map and macroscopic effective toughness. In this paper, we will limit our

study to the weak pinning quasistatic regime. We consider the case of a circular embedded crack propagating under remote mode I loading in an axisymmetric toughness map (see § 1). We solve the problem by using an incremental method [4, 5], based on Rice's perturbation approach [6, 7]. This method is presented in § 2 and then applied in § 3 to the resolution of our problem.

1 Problem definition

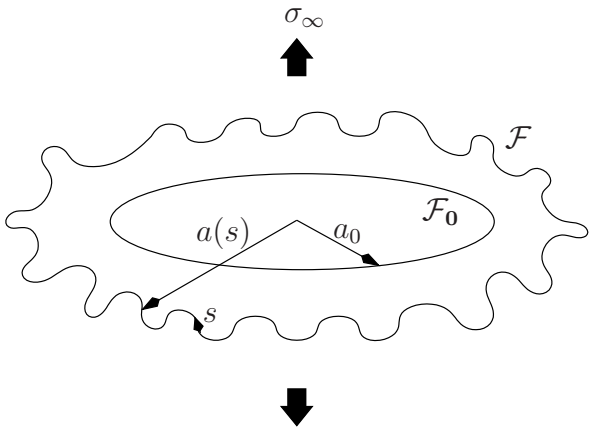

Figure 1: A tensile planar crack in an infinite body under uniform stress σ_∞

Consider a planar penny shape crack $\mathcal{F}$ of initial radius a_0, embedded in an infinite isotropic elastic medium with heterogeneous fracture toughness properties and loaded in pure mode I through some uniform remote stress applied at infinity σ_∞ (see Fig. 1). We assume a quasistatic propagation of the crack front, so that the crack advance at a point M of the front is governed by Irwin's criterion:

$$\begin{cases} K(M) < K_c(M) & : \quad \text{no crack advance} \\ K(M) = K_c(M) & : \quad \text{possible crack advance,} \end{cases} \tag{1}$$

where $K(M)$ is the SIF and $K_c(M)$ the toughness at point M. Let us denote $\overline{K_c}$ the average material toughness, $\kappa_c (= \Delta K_c / \overline{K_c})$ its relative contrast and $\eta(M)$ the toughness fluctuations. With these notations, we have:

$$K_c(M) = \overline{K_c}\,[1 + \kappa_c \eta(M)] \tag{2}$$

We suppose that the remote loading σ_∞ adapts in order to stay in the quasistatic regime and to ensure crack propagation at least, on some part of the front. This implies that at each moment:

$$\max_{M \in \mathcal{F}} \frac{K(M)}{K_c(M)} = 1 \tag{3}$$

Under the assumption of quasistatic propagation, the problem is to find, for a given toughness map $K_c(M)$, the successive positions of the crack front and the corresponding loading σ_∞. From them, one can obtain the SIF along the crack front and consequently its mean value. In the homogeneous

case ($\kappa_c = 0$), the problem can be solved analytically. One has at each moment $K = \overline{K_c}$ all along the front, the successive positions of the crack front are circles of radius a and the corresponding loading follows $\sigma_\infty = \frac{\overline{K_c}}{2}\sqrt{\frac{\pi}{a}}$. In the heterogeneous case, the crack front deforms. In an homogenization process, we shall replace it by an equivalent circular crack of

- radius a_m given by the mean value of the crack extension a:

$$a_m = \frac{1}{L}\int_{\mathcal{F}} a(M(s))\mathrm{d}s \tag{4}$$

- SIF K_m given by the mean value of K:

$$K_m = \frac{1}{L}\int_{\mathcal{F}} K(M(s))ds \tag{5}$$

where s is the curvilinear abscissa and L is total length of the crack front.
We will see in the following that in the cases investigated here, K_m tends to a constant stationary value after some transient propagation regime. As a result, this stationary value will be used to define the macroscopic effective toughness K_c^{eq} of the heterogeneous media studied here. Alternatives would have been to define K_c^{eq} as the maximum value of K_m during crack propagation or its mean value during propagation. However, we would like to define an effective toughness as a quantity that does not depend of the initial geometrical configuration of the crack, so the value of K_m in the stationary regime seems the most appropriate definition.
The aim of the paper is to discuss the influence of the toughness map $K_c(M)$ on this effective toughness. In this paper, we consider it periodical and axisymmetric given by:

$$K_c(M) = \overline{K_c}\,[1 + \kappa_c \cos(k\theta(M))] \text{ where } \theta(M) \text{ denotes the polar angle of } M, \tag{6}$$

and discuss the influence of toughness contrast κ_c and spatial wavenumber k on K_m, hence on K_c^{eq}. This choice of K_c allows to obtain a weak pinning regime and to focus, as wanted, on the influence of the large deformations of the crack front on the effective toughness.

2 Numerical Procedure

A characteristic feature of this problem is that the shape of crack is determined by the variation of SIF and material properties. In general, neither the distribution of SIF, nor the geometry of the crack are known a priori and must be determined as part of the solution. An appealing perturbative technique for solving such problems is provided by the studies of Rice [6], who has developed a linear scheme for calculating the variation in SIF due to small changes in the crack geometry. For large deformations of the front, Bower and Ortiz [4] followed by Lazarus [5], developed a powerful method based on the iteration of the linear scheme. The efficiency of this method arises from the need for the sole 1D meshing of the crack front. In the sequel, we extend the numerical notations and procedures developed by Lazarus [5]. For dimensional reasons, we can introduce the dimensionless SIF $\widehat{K}$ by writing:

$$K = \sigma_\infty \sqrt{a_0}\,\widehat{K} \tag{7}$$

This quantity depends only on the crack shape.
We start from the initial situation of a crack of radius a_0 for which $\widehat{K} = \frac{2}{\sqrt{\pi}}$. We then use a regularization of Irwin's criterion to obtain the crack front displacement $\delta a(s)$ by a Paris' type law [5]:

$$\delta a(s) = \delta a_{max} \left(\frac{\widehat{K}(M(s))/K_c(M(s))}{\max_{M\in\mathcal{F}} \widehat{K}(M(s))/K_c(M(s))} \right)^{\beta} \text{ with } \beta \gg 1. \tag{8}$$

where δa_{max} corresponds to the maximum crack advance during a numerical step. The corresponding loading is obtained by introducing the definition 7 of $\widehat{K}$ in equation 3:

$$\frac{\sigma_\infty \sqrt{a_0}}{\overline{K}_c} = \left[\max_{M\in\mathcal{F}} \frac{\widehat{K}(M)}{1+\kappa_c \eta(M)} \right]^{-1} \tag{9}$$

Subsequently, Rice's formulae (see Refs. [6, 5]) are used for updating the dimensionless SIF $\widehat{K}$ corresponding to the advance $\delta a(s)$ and the whole step (determination of δa, updating of $\widehat{K}$) is reitirated as long as necessary.

3 Results

The previous procedure is applied to the toughness map given by Eq. (6). In § 3.1, the propagation in the case of a given value of k and κ_c is studied. In §3.2, the influence of those parameters on the mean quantities K_m and a_m is considered.

3.1 Propagation for a given toughness map

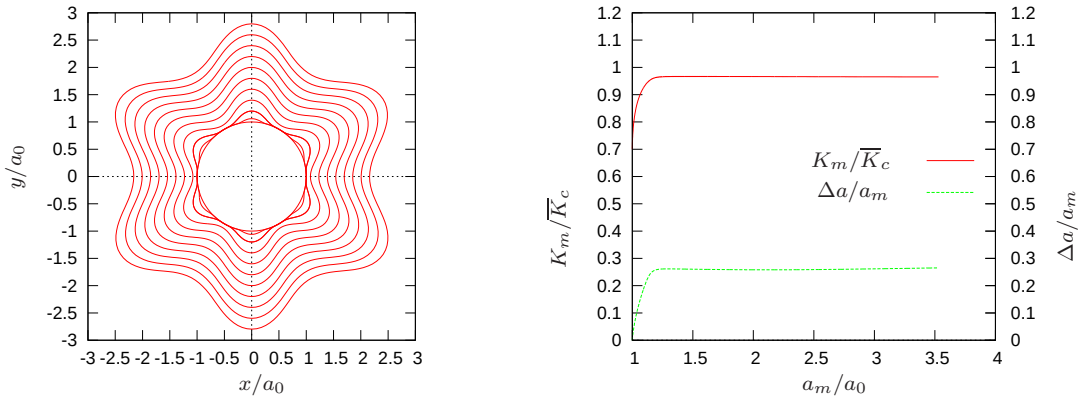

(a) Successive crack front positions

(b) Evolution of key quantities during propagation

Figure 2: Case $k = 6$ and $\kappa_c = 0.3$

As a typical example, the results for $k = 6$ and $\kappa_c = 0.3$ are shown in Fig. 2. On Fig. 2(a), successive equilibrium positions of the crack fronts are plotted. The propagation is continuous without jumps,

showing that the pinning is weak. One can notice that first the crack front deforms from a circular crack to a k-petals flower shape, which then remains the same. The process is as follows. In the initial stage, the crack is circular, so that only the points where K_c is minimum propagate. Then, more and more points reach the threshold and propagate at the same time. Finally, the crack front attains and stays in a shape for which all of its points satisfy $K = K_c$ (stationary regime) so that K_m is equal to the mean value of K_c along the crack front:

$$K_m = \frac{1}{L}\int_{\mathcal{F}} K_c(M(s))\mathrm{d}s \tag{10}$$

To quantify the moment where the crack shape becomes stationary, we introduce the amplitude Δa of $a(s)$, the value of $\Delta a/a_m$ remaining constant for a given shape. The evolutions of $\Delta a/a_m$ and of the normalized mean SIF $K_m/\overline{K}_c$ as a function of the mean radius a_m are plotted on Fig. 2(b). It can been seen that both quantities increase until a plateau is reached. The plateau corresponds to the stationary regime. Once in this stationary regime, the effective toughness K_c^{eq}, whether it is defined as the maximum or mean value of K_m, corresponds to the value of this plateau, hence to the mean value of K_c along the crack front. It shall be noticed that $K_c^{\mathrm{eq}} < \overline{K}_c$. Physically, it is due to the fact that the length of the crack front which is in the weaker zone is higher than in the stronger one, so that the mean value of K_c along the crack front is lower than the mean value $\overline{K}_c$ of K_c in the whole plane. This result is specific to the circular geometry, and it is linked to the dependance of the SIF on the crack size. In next section, we discuss the influence of k and κ_c on the value of K_c^{eq}.

3.2 Influence of the geometrical parameters of the toughness field

Figure 3 shows the effect of the toughness contrast κ_c and toughness spatial repartition k on the normalized effective toughness $K_c^{\mathrm{eq}}/\overline{K}_c$ and on the crack front deformation $\Delta a/a_m$.

For a given values of k, $K_c^{\mathrm{eq}}/\overline{K}_c = 1$ for $\kappa_c \ll 1$ and decreases, whereas $\Delta a/a_m$ increases, with κ_c. Physically, it looks obvious, that in case of higher contrast, the crack front deforms more, hence propagates more in weaker regions and therefore, the mean toughness along the front is decreasing as the contrast increases. For small $\kappa_c \ll 1$, it remains equal to one, as linear theory predicts [1, 8].

Now for a given value of κ_c, $K_c^{\mathrm{eq}}/\overline{K}_c$ increases, whereas $\Delta a/a_m$ decreases with the heterogeneity wavenumber k, that is when the number of defects increases along the crack front. Physically, it is due to the fact that when k increases, the amplitude of the deformation has less space to develop, and so the front becomes more straight.

4 Conclusion

In this paper, we defined the effective toughness K_c^{eq} of a heterogeneous field of toughness as the stationary mean value of the SIF along the crack front. In order to focus on the effect of the large crack front deformations on this effective toughness, we studied numerically the case of a circular crack propagating in an axisymmetric infinite toughness map. This allows us to reach a stationary crack front shape regime in which Irwin's threshold is reached at each point of the front. In this

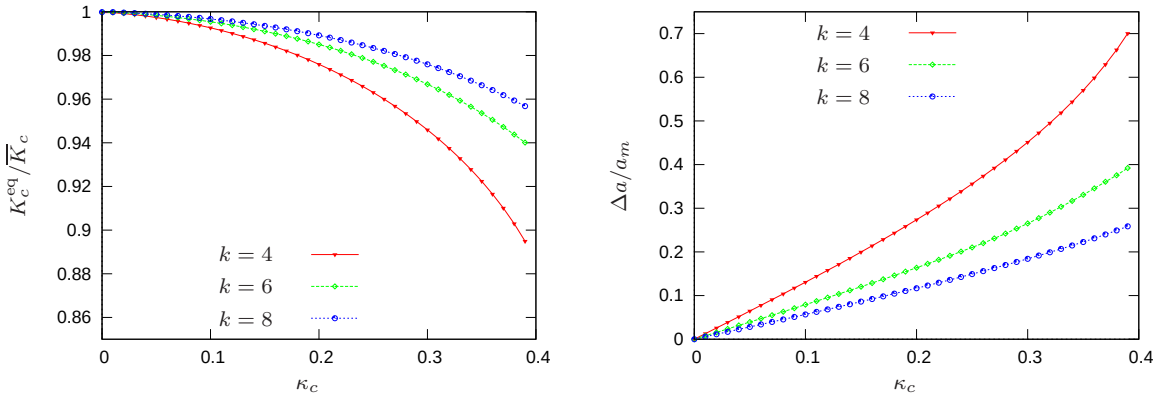

(a) Normalized mean toughness versus κ_c

(b) $\frac{\Delta a}{a_m}$ versus κ_c

Figure 3: Influence of mapping parameter on the stationary regime

regime, we find that the SIF K_m averaged along the front reaches a plateau that is equal to the mean value of K_c along the crack front. Since the crack front deforms due the heterogeneities, this mean value is different from the mean value $\overline{K}_c$ of K_c in the whole plane. It depends on the crack front deformations, which themselves depend on the local toughness values. In the case studied here, the deformations are more important in the weak part of the toughness map so that K_c^{eq} is lower than $\overline{K}_c$, the ratio $K_c^{\text{eq}}/\overline{K}_c$ decreasing with increasing toughness heterogeneity or with decreasing the number of obstacles. The next step is to extend this study to the case of strong pinning with large crack front deformations. Defining the equivalent toughness from the macroscopic loading required to make the crack propagate, and not only from the local values of SIF along the front might then become crucial.

References

[1] S. Roux, D. Vandembroucq, and F. Hild. Effective toughness of heterogeneous brittle materials. *European Journal of Mechanics - A/Solids*, 22(5):743–749, 2003.

[2] S. Patinet and L. Alzate and E. Barthel and D. Dalmas and D. Vandembroucq and V. Lazarus. Finite size effects on crack front pinning at heterogeneous planar interfaces: Experimental, finite elements and perturbation approaches. *Journal of the Mechanics and Physics of Solids*, 61:311–324, 2013.

[3] K. J. Måløy and J. Schmittbuhl. Dynamical event during slow crack propagations. *Physical Review Letters*, 87:105502, 2001.

[4] A. F. Bower and M. Ortiz. Solution of three-dimensional crack problems by a finite perturbation method. *Journal of the Mechanics and Physics of Solids*, 38(4):443–480, 1990.

[5] V. Lazarus. Brittle fracture and fatigue propagation paths of 3D plane cracks under uniform remote tensile loading. *International Journal of Fracture*, 122(1-2):23–46, 2003.

[6] J. R. Rice. Weight function theory for three-dimensional elastic crack analysis. In R. P. Wei and R. P. Gangloff, editors, *Fracture Mechanics : Perspectives and Directions (Twentieth Symposium)*, pages 29–57, Philadelphia, USA, 1989. American Society for Testing and Materials STP 1020.

[7] V. Lazarus. Perturbation approaches of a planar crack in linear elastic fracture mechanics: a review. *Journal of the Mechanics and Physics of Solids*, 59(2):121–144, 2011.

[8] H. Gao and J. R. Rice. Somewhat circular crack. *International Journal of Fracture*, 33:155–174, 1987.

Size effects on compressive strength from a statistical physics perspective

Jérôme Weiss[1,*], Lucas Girard[2], David Amitrano[3]

[1] LGGE, CNRS/University of Grenoble, 38402 St Martin d'Hères, France
[2] Department of Geography, University of Zürich, CH-8051, Switzerland
[3] IsTerre, CNRS/University of Grenoble, 38041 Grenoble, France
* Corresponding author: jerome.weiss@ujf-grenoble.fr

Abstract Compression is a loading mode that stabilizes microcrack propagation. Consequently, the weakest-link approach becomes inappropriate to account for size effects on compressive strength of brittle materials such as rocks, ice, or concrete. Instead, compressive failure is characterized by an apparent power law decay of the mean strength at small sizes but a non-vanishing strength towards large sizes, associated to an increasing variability towards small sizes. Here we show from a progressive damage model that compressive failure can be considered as a critical phase transition, with a correlation length diverging at failure. Specific scaling laws for the mean as well as the standard deviation of the strength ensue, which are in full agreement with the experimental observations.

Keywords compressive strength, size effect, critical transition, rocks

1. Introduction

The size effect on strength of materials is an old problem, already discussed by Leonardo da Vinci [1] and Edmé Mariotte [2] several centuries ago. The experimental tensile strength is generally orders of magnitude lower than expected from atomic scale calculations, decreases with increasing scale and is associated to a large scatter that also decreases with increasing scale. A statistical approach based on the presence of internal defects and on the weakest-link concept has been developed for structural materials a long time ago [3,4]. This weakest-link approach is based on the following assumptions: (i) defects do not interact with one another, (ii) failure of the whole system is dictated by the activation of the largest pre-existing flaw, and (iii) the material strength can be linked directly to the critical defect size. Assuming a power law distribution of defect size s, $P(s) \sim s^{-\alpha}$ (with generally $\alpha >> 3$), and following linear elastic fracture mechanics (LEFM) principles for which the activation of a flaw of size s occurs at a stress $\sigma_c \sim s^{-1/2}$, one gets extremal Weibull statistics for the strength σ_f, and the following scalings for the mean strength $\langle \sigma_f \rangle$ and the associated standard deviation $std(\sigma_f)$:

$$\langle \sigma_f \rangle(L) \sim std(\sigma_f)(L) \sim L^{-d/m} \quad (1)$$

where $m=2(\alpha-1)$ is Weibull's modulus and d the topological dimension [5]. Although based on strong assumptions, this approach has been successfully applied to the statistics of failure strength of structural materials under tension (e.g.[4,6]), with m in the range 6 to 25. Relation (1) implies a continuously decreasing average strength towards large scales, i.e. a vanishing strength for $L \to +\infty$, although this decrease can be rather shallow, owing to the large values of m often reported.

These assumptions are reasonable for materials with relatively weak disorder loaded under tension, but do not hold for heterogeneous materials with a broad distribution of initial disorder, or

for loading conditions that stabilizes crack propagation, such as compression. Nevertheless, it has been shown recently that the weakest link hypothesis remains essentially valid even in the presence of long-range elastic interactions in heterogeneous media [7]. We consider here a different problem, the case of compressive failure of brittle materials such as rocks, concrete, or ice; a loading mode that stabilizes microcrack propagation, making the assumptions of the weakest-link approach inappropriate.

2. Brittle compressive failure and associated size effects

Brittle compressive failure is a complex process, as the local tensile stresses at crack tips are counteracted by the far-field compressive stresses. Consequently, Griffith-like energy balance arguments, or related LEFM tools such as fracture toughness, cannot be developed in this case to describe the instability leading to terminal failure, thus making the weakest-link approach inoperative. Instead, compressive failure involves an initiation phase, elastic interactions and stress redistributions, as well as frictional sliding along rough surfaces. During the initiation phase, secondary cracks nucleate from the local tensile stresses generated by the frictional sliding along pre-existing defects such as grain boundaries, small joints, or microcracks [8,9]. The propagation of these mode I secondary cracks is however rapidly stopped by the far-field compression. Instead, such nucleation events locally soften the material and thus cause a redistribution of elastic stresses, which in turn can trigger other microcracking events. Then, in the course towards the failure, the linking of en echelon arrays of secondary cracks is considered to be at the onset of shear fault formation, from which the macroscopic instability is thought to result [9]. This process is characterized by a progressive localization of microfracturing and deformation along a fault [10]. From this qualitative description, one sees that all the assumptions of the weakest-link theory listed above are inappropriate.

When the compressive strength of brittle materials is measured from laboratory tests over a limited scale range (generally between ~ 10^{-2} m and ~ 10^{-1} m), either non-significant [11,12] or limited (e.g. [13]) size effects are reported on $\langle\sigma_f\rangle$, whereas, when reported, the associated variance is relatively large and increases towards small scales [11]. Consequently, empirical or theoretical size effect formulations are hardly constrained by these results. Some studies were performed several decades ago over a much larger scale range (~ 10^{-2} m to few m), combining laboratory experiments and in-situ tests [14,15,16]. All of them reported a significant decrease of $\langle\sigma_f\rangle$ at small scales, which can be tentatively and empirically fitted as a power law decrease $\langle\sigma_f\rangle(L)\sim L^{-\beta}$ [16], but also a saturation of this decay towards large scales which is not explained by the weakest link approach. Note that these results were obtained for natural rock samples that did not contain a pre-existing fault or joint coming through the entire sample. Indeed, in this latter case, one may expect that the flaw size dependency on sample size and the reactivation of this flaw would lead to a power law decrease of $\langle\sigma_f\rangle$ with L, with $\beta\approx1/2$ and without saturation at large sizes [17].

So far, there is no clear explanation for this non-vanishing compressive strength at large sizes in the literature. Instead, empirical [16,18] or more theoretical formulations (based on stored strain energy caused by buckling [5]) of size effects on compressive strength of brittle materials generally

ignore such asymptotic behaviour. Following observations at small sizes, all these formulations share a common power law scaling $\langle\sigma_f\rangle(L)\sim L^{-\beta}$, with β varying from very small values [13] (i.e. almost no size effect), to values between 1/2 and 1. The weakest-link concept has been sometimes put forth to explain this scaling for small β values [13], although it is clear from above that this approach is irrelevant in case of compressive failure.

In what follows, we propose an entirely different approach, based on the mapping of brittle compressive failure on a critical phase transition. Using a numerical progressive damage model, we demonstrate the relevance of this mapping, and show that it implies a formulation of size effects on strength which explains (i) the power law-like decay of the mean strength at small sizes, (ii) a non-vanishing strength for $L\rightarrow+\infty$, and (iii) an increasing variability towards small sizes.

3. A model of progressive damage

The model, described in more details elsewhere [19,20], considers a continuous 2D elastic material (Hooke's law) under plane stress, with progressive local damage. Damage is represented by a reduction of the isotropic elastic modulus Y_i of the element i, $Y_i(n+1)=Y_i(n)d_0$, with d_0= 0.9, each time the stress state on that element exceeds a given threshold. This elastic softening simulates an increase in microcrack density at the element scale [21] as supported by experiments [22]. The stress field is recalculated each time a damage event occurs by solving the equation of static equilibrium using a finite element scheme. As the result of elastic interactions, the stress redistribution following a damage event can trigger an avalanche of damage, which stops when the damage threshold is no longer fulfilled by any element.

The Coulomb criterion, $\tau=\mu\sigma_N+C$, of wide applicability for brittle materials under compressive stress states [23], defines the damage threshold. τ and σ_N are respectively the shear and normal stress on the element (sign convention positive in compression), μ is an internal friction coefficient identical for all elements, whereas quenched disorder is introduced through the cohesion C randomly drawn from a uniform distribution ($0.2\times10^{-3}Y_0\leq C\leq 10^{-3}Y_0$). We use μ = 0.7, a common value for most geomaterials [23]. This envelope is completed by a truncation in tension in the Mohr's plane, i.e. the element is damaged if σ_N= $-2.10^{-3}\times Y_0$. The simulations start with undamaged material ($Y_i = Y_0$ = const) and are performed on rectangular meshes of randomly oriented triangular elements. Uniaxial compression is applied by increasing the vertical displacement of the upper boundary (strain-driven loading), while left and right boundaries can deform freely.

Series of simulations with meshes of linear size L varying from 8 to 128, composed of N=4L(L-1) triangular elements, were performed with the following number of independent simulations: 5×10^4 for L=8, 3×10^4 for L=16, 5×10^3 for L=32, 10^3 for L=64, and 100 for L=128.

It was shown previously that this model remarkably well reproduces both the macroscopic (strain softening before failure, large stress drop at failure) and microscopic (progressive localization of damage towards the failure along an inclined shear fault, increasing rate of damage avalanches,..) features of compressive failure [19,20]. In a recent work [20,24], we have shown from this modeling framework that brittle compressive failure can be considered as a critical phase

transition: (i) the size of the largest damage cluster as well as of the largest damage avalanche diverge at peak load, which just precedes failure, and (ii) the divergence of a correlation length ξ at failure can be identified either from a spatial correlation analysis of damage events, or from a coarse-graining analysis of the strain-rate field. This divergence takes the form $\xi \sim \Delta^{-1/\nu}$, where $\Delta = \frac{\epsilon_{mf} - \epsilon_m}{\epsilon_{mf}}$ is the control parameter, ϵ_m the macroscopic (applied) strain, ϵ_{mf} the corresponding value at peak load (failure), and ν=1.0±0.1 a critical exponent.

If this interpretation is correct, ν is a finite-size exponent and one may expect and the following size effect on strength, from a mapping of this critical transition to the depinning transition of an elastic manifold [25,26]:

$$std(\sigma_f)(L) \sim L^{-\frac{1}{\nu}} \tag{2a}$$

$$\langle \sigma_f \rangle (L) = A\, L^{-\frac{1}{\nu}} + \sigma_\infty \tag{2b}$$

where A is a constant and σ_∞ a non-vanishing asymptotic value of the strength for $L \to +\infty$.

4. Results and conclusion

Figure 1 shows the standard deviation of the compressive strength in the model, defined as the maximal macroscopic stress in the direction of loading, as a function of system size. The power law scaling is in full agreement with equation (2a), however with a corresponding finite-size scaling exponent ν=1.47 larger than the value expected from the divergence of the correlation length at failure.

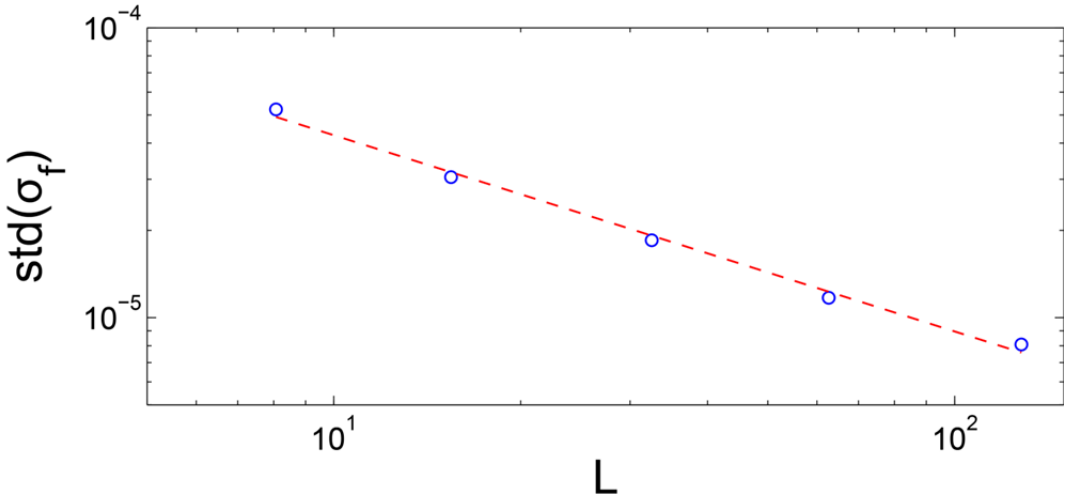

Figure 1. Progressive damage model: Evolution of the standard deviation of the compressive strength, $std(\sigma_f)$, in units of Y_0, as a function of system size L. The red dashed line shows a power law scaling with a exponent of -0.68, corresponding to a finite-size exponent of ν=1.47, in agreement with relation (2a).

This value of ν can be used to test the relevance of equation (2b) to describe the scale dependence of the mean strength. Figure 2 demonstrates the validity of this scaling and the existence of a

non-vanishing strength for $L \to +\infty$.

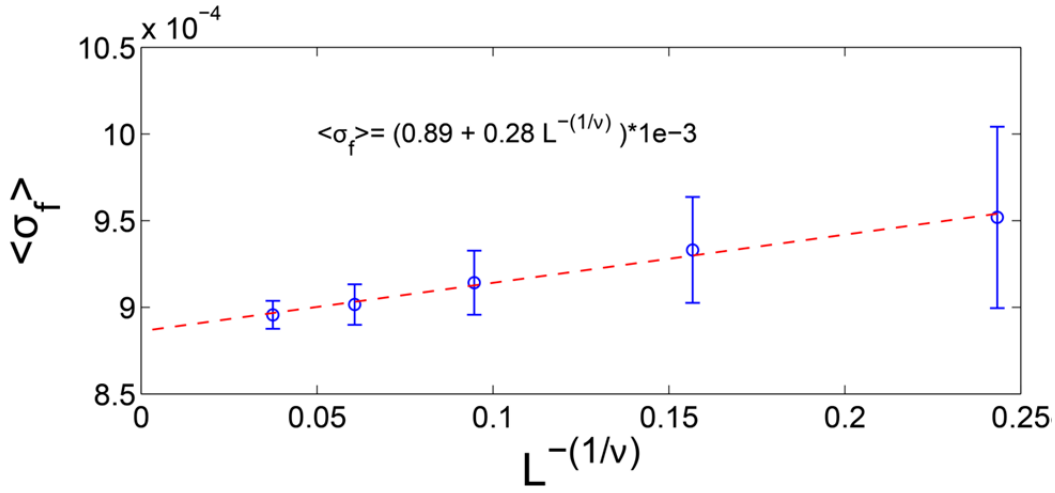

Figure 2. Progressive damage model: Mean compressive strength $\langle \sigma_f \rangle$ as a function of $L^{-\frac{1}{\nu}}$, where L is the system size and ν=1.47 is obtained from Figure 1. The red dashed line corresponds to equation (2b) with an asymptotic strength σ_∞=8.9 $10^{-4}\times$ Y_0.

Figure 3 shows the distributions of compressive strength at various scales in a normal probability plot. The collapse along a straight line (i) demonstrates that compressive strengths are distributed according to a Gaussian PDF, and (ii) confirms the power law scaling of the standard deviation (equation (2a)). Compressive strengths are therefore clearly not distributed according to a Weibull distribution (the same data are not aligned and do not collapse in a Weibull probability plot). This is a further confirmation of the irrelevance of the weakest-link concept in compressive failure.

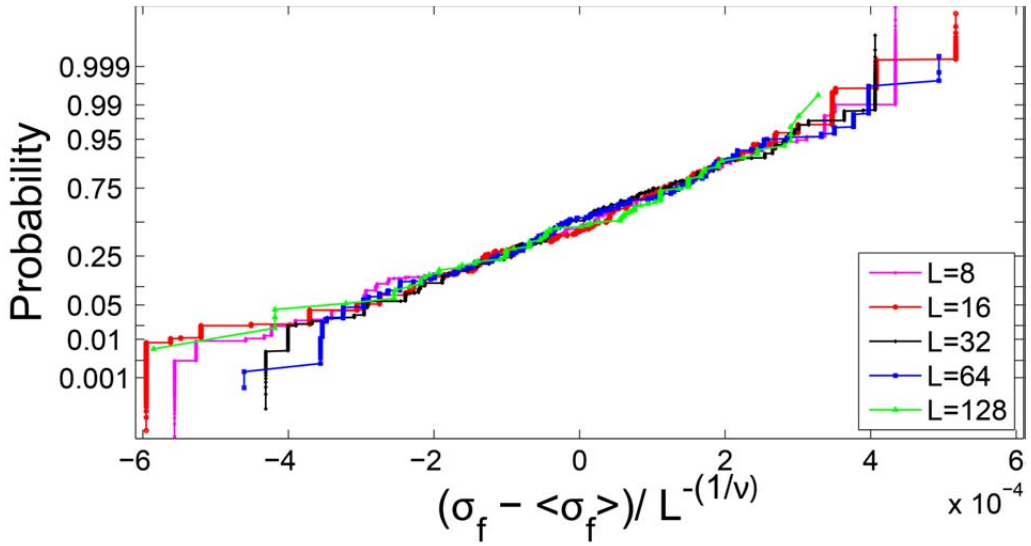

Figure 2. Normal probability plot of the distributions of strength at various scales. Albeit minute deviations, the plot shows a collapsed straight line, as expected for a Gaussian distribution. The collapse also confirms the power law scaling of the standard deviation (equation (2a)).

In conclusion, we have shown that the weakest-link concept is irrelevant for brittle failure under compressive stress states. Instead, compressive failure is a complex process characterized by the divergence of a correlation length at peak (failure) load. This argues for an interpretation of

compressive failure as a critical phase transition. From this interpretation, and mapping this transition to the well-described depinning transition, we propose specific scaling laws for the mean compressive strength as well as the associated variability (equation (2)). This scaling implies (i) an apparent power law decay of the mean strength at small sizes, (ii) a non-vanishing strength for $L \to +\infty$, and (iii) an increasing variability towards small sizes; these three aspects being in full agreement with experimental data (see section 2). In addition, modelling results show that compressive strengths are normally distributed.

This has important consequences including the fact that brittle compressive strengths are expected to be less scattered (normally distributed) than tensile strengths (extremal Weibull statistics), and a reasonable estimate of large scale compressive strength can be obtained from laboratory tests if the obtained experimental size effect is limited.

Acknowledgements

S. Zapperi and D. Vandembroucq are acknowledged for interesting discussions and suggestions. J.W. acknowledges the hospitality of the Aspen Center for Physics, which is supported by the National Science Foundation Grant No. PHY-1066293, as the seminal ideas of this work came up during his stay at the Center.

References

[1] da Vinci, L., I libri di Meccanica, Hoepli U. ed., Milano, 1942

[2] E. Mariotte, Traité du mouvement des eaux et des autres corps fluides, Paris, 1686.

[3] W. Weibull, A statistical theory of the strength of materials, Proc. Royal Swedish Academy of Eng. Sci. 151(1939) 1-45.

[4] F.M. Beremin, A local criterion for cleavage fracture of a nuclear pressure vessel steel, Metallurgical Transactions A 14A(1983) 2277-2287.

[5] Bazant, Z.P., and J. Planas, Fracture and size effect in concrete and other quasibrittle materials, CRC Press, Boca Raton, 1998.

[6] Miannay, D., Fracture Mechanics, Springer, Berlin, 1998.

[7] Manzato, C., Shekhawat, A., Nukala, P.K.V.V., Alava, M.J., Sethna, J.P., and Zapperi, S., Fracture strength of disordered media: Universality, interactions, and tail asymptotics, Phys. Rev. Lett., 108(2012) 065504

[8] Nemat-Nasser, S. and Horii, H., Compression-induced nonplanar crack extension with application to splitting, exfoliation, and rockburst, J. Geophys. Res., 87(1982), 6805-6821

[9] Schulson, E.M., Iliescu, D. and Renshaw, C.E., On the initiation of shear faults during brittle compressive failure: A new mechanism, J. Geophys. Res., 104(1999), 695-705

[10] Lockner, D., Int. J. Rock Mech. Min. Sci. & Geomech. Abstr., 30(1993), 883-899

[11] Kuehn, G.A., Schulson, E.M., Jones, D.E., and Zhang, J., The compressive strength of ice cubes of different sizes, Proc. OMAE Conf., Vol. IV, ASME, 1992, pp 349-356

[12] van Mier, J.G.M., Multiaxial strain-softening of concrete, Part I: Fracture, Materials and Structures, 19(1986), 179-190

[13] Mogi, K., The influence of the dimensions of specimens on the fracture strength of rocks, Bull. Earthquake Res. Inst., 40(1962), 175-185

[14] Pratt, H.R., A.D. Black, W.S. Brown, and W.F. Brace, The effect of specimen size on the mechanical properties of unjointed diorite, Int. J. Rock Mech. Min. Sci., 9(1972), 513-529
[15] Bieniaswski, Z.T., The effect of specimen size on compressive strength of coal, Int. J. Rock Mech. Min. Sci., 5(1968), 325-335
[16] Hustrulid, W.A., A review of coal pillar strength formulas, Rock Mechanics, 8(1976), 115-145
[17] Scholz, The mechanics of earthquakes, Cambridge University Press, Cambridge, 2002
[18] Heuze, F.E., Scale effects in the determination of rock mass strength and deformability, Rock Mechanics, 12(1980) 167-192
[19] Amitrano, D., From diffuse to localised damage through elastic interaction, Geophys. Res. Lett., 26(1999), 2109-2112
[20] Girard, L., Amitrano, D. and Weiss, J., Failure as a critical phenomenon in a progressive damage model, JSTAT, (2010), P01013
[21] Kachanov, M., Elastic solids with many cracks and related problems, Adv. Appl. Mech., 30(1994), 259-445
[22] Cox, S.J.D. and Meredith, P.G., Microcrack formation and material softening in rock measured by monitoring acoustic emission, Int. J. Rock Mech. Min. Sci. & Geomech. Abstr., 30(1993),
[23] Weiss, J. and Schulson, E.M., Coulombic Faulting from the grain scale to the geophysical scale: lessons from ice, J. Phys. D: Appl. Phys., 42(2009), 214017
[24] Girard, L., Weiss, J., and Amitrano, D., Damage-cluster distributions and size effect on strength in compressive failure, Phys. Rev. Lett., 108(2012), 225502
[25] Narayan, O. and Fisher, D.S., Threshold critical dynamics of driven interfaces in random media, Phys. Rev. B, 48(1993), 7030-7042
[26] Zapperi, S., Current challenges for statistical physics in fracture and plasticity, Eur. Phys. J. B, 85(2012), 329

Thermally induced creep rupture of fiber bundles

Naoki Yoshioka[1,*], Ferenc Kun[2], Nobuyasu Ito[3]

[1] Yukawa Institute for Theoretical Physics, Kyoto University, Kitashirakawa Oiwake-cho, 606-8502 Kyoto, Japan
[2] Department of Theoretical Physics, University of Debrecen, H-4010 Debrecen, P.O. Box 5, Hungary, EU
[3] Department of Applied Physics, Graduate School of Engineering, The University of Tokyo, 7-3-1, Hongo, Bunkyo-ku, 113-8656 Tokyo, Japan
* Corresponding author: naoki@yukawa.kyoto-u.ac.jp

Abstract Subcritical fracture driven by thermally activated crack nucleation is studied in the framework of a fiber bundle model. Based on analytic calculations and computer simulations, we show that, in the presence of stress inhomogeneity thermally activated cracking results in an anomalous size effect, i.e., the average lifetime of the system decreases as a power-law of the system size. We propose a modified Arrhenius law which provides a comprehensive description of the load, temperature, and size dependence of the lifetime of the system. On the microscopic level, thermal fluctuations trigger bursts of breaking events which proved to have a power-law size distribution. The waiting times between consecutive bursts are also power-law distributed with an exponent switching between 1 and 2 as the load and temperature are varied. Analyzing the structural entropy and the location of consecutive bursts, we show that, in the presence of stress concentration, the acceleration of the rupture process close to failure is the consequence of damage localization.

Keywords Subcritical fracture, Fiber bundle model

1. Introduction

Sub-critical rupture, occurring under a constant load below the fracture strength of materials, is of fundamental importance in a wide range of physical, biological, and geological systems. Depending on the type of materials, creep rupture can have a wide variety of microscopic origins from the existence of frictional interfaces through the viscoelasticity of the constituents, to thermally activated aging processes. Recent experimental and theoretical investigations revealed the high importance of thermally activated micro-crack nucleation in creep phenomena with consequences reaching even to geological scales [1–7]. Under creep loading failure often occurs as a sudden unexpected event following a short acceleration period which addresses safety problems for e.g. components of engineering constructions. Additionally, creep rupture underlies natural catastrophes such as landslides, stone and snow avalanches and it is also involved in the emergence of earthquakes.

On the macroscopic scale the rupture process is characterized by the strain-time diagram and by the lifetime of the system, which both have a complex dependence on the external load and on the temperature. In spite of the smooth macroscopic evolution, thermally activated breakdown proceeds in bursts on the microscopic scale. They may be exploited to gain information about the approach of the system to failure. In the present paper we investigate this problem in the framework of a fiber bundle model of thermally activated breakdown. In order to reveal the effect of the range of load redistribution we carry out computer simulations considering strongly localized stress redistribution after failure events and compare the outcomes to the analytic results obtained in the mean field limit [10–12].

2. Model

Our approach is based on the fiber bundle model (FBM), which has proven very successful during

the past decades for the investigation of fracture phenomena [1–15]. In the model we consider N parallel fibers having a brittle response with identical Young modulus E. The bundle is subject to a constant external stress σ parallel to the fibers' direction. During the past decades several ways have been proposed to introduce time dependent rupture in stochastic fracture models. Following the pioneering works of Coleman on time dependent FBM [5], the models were further extended to a broad class of time dependent damage accumulation laws and fiber strength by Phoenix and Curtin [6–8]. In our work we apply the approach of Guarino et al. [1–4], i.e. we assume that the local load σ_i of fibers has time-dependent fluctuations $\xi_i(t)$ due to the presence of thermal noise so that the actual load of fiber i at time t reads as

$$\sigma_i(t) = \sigma_i^0(t) + \xi_i(t) . \tag{1}$$

Here $\sigma_i^0(t)$ denotes the deterministic part of the stress, i.e., the local stress arising due to the external load and to load transfer following breaking events. The fibers have a finite strength characterized by a failure threshold σ_{th}^i, which is, in general, a random variable. A fiber fails during the time evolution of the bundle when the total load on it $\sigma_i(t)$ exceeds the respective threshold value σ_{th}^i. For simplicity, we assume that the system consists of homogeneous fibers, i.e. all the breaking thresholds are the same $\sigma_{th}^i = \sigma_{th}$, $i = 1,\mathrm{K}\,,N$, where $\sigma_{th} = 1$ is set. The assumption of homogeneity implies that there is no quenched disorder in the system. Thermally induced stress fluctuations $\xi(t)$ have a Gaussian distribution with zero mean and a variance controlled by the temperature T of the system

$$p(\xi) = \frac{1}{\sqrt{2\pi T}} \exp\left(-\frac{\xi^2}{2T} \right), \tag{2}$$

from which the complementary cumulative distribution follows as $P(\xi) = \int_{\xi}^{+\infty} p(x)dx$. The strength of thermal fluctuations is controlled by the value of T which can be scaled to the absolute temperature of the system. After fiber breakings, the load of broken fibers has to be redistributed over the remaining intact ones. In order to understand the effect of the range of load transfer on the process of thermally enhanced creep, we consider two limiting cases for the load redistribution: in the case of equal load sharing (ELS) all surviving fibers overtake equal fraction of the load. ELS ensures that the stress distribution remains homogenous in the bundle until the end of time evolution which also facilitates to perform analytical calculations. To study the effect of stress inhomogeneity on thermally activated breakdown, in our model the fibers are organized on a square lattice of size $L \times L$ and localized load sharing (LLS) is considered: the load of broken fibers is redistributed over their nearest intact neighbors, giving rise to high stress concentration around failed regions. Since the LLS case cannot be investigated by analytical means, computer simulations were carried out varying the load σ, temperature T, and the lattice size L in broad ranges.

3. Results and Discussions

Subjecting the bundle to a constant external load σ, two competing physical mechanisms contribute to the failure of fibers: When the load is small enough even a single fiber can sustain the entire load and the load increments arising in the vicinity of failed fibers are not sufficient to trigger further breakings. Hence, in this load regime, the failure process is dominated by the thermal fluctuations and there is practically no difference between ELS and LLS calculations since the range of interaction is irrelevant. However, at high load values $\sigma \to \sigma_{th}$, the load redistributions give rise to considerable increments of the local load on intact fibers leading to additional breakings. In the initial state of the system all the fibers have the same load $\sigma_i^0 = \sigma$, $i = 1,\mathrm{K}\,,N$. When a fiber breaks

due to thermal noise $\sigma_i^0 + \xi_i \geq \sigma_{th}$, the deterministic part of the load σ_i^0 is transferred to its four intact neighbors resulting in the increment $\Delta\sigma^0 = \sigma/4$. If the updated load exceeds the breaking threshold $5\sigma/4 > \sigma_{th}$ the fibers break again transferring the load further to their intact neighbors. Once this breaking sequence starts, removing all four neighbors of the initial one, it does not stop until all fibers break leading to macroscopic fracture. It follows that due to the localized stress transfer, the system has a critical load $\sigma_c = 4\sigma_{th}/5$ above which even a single fiber breaking triggers the immediate collapse [10–12].

3.1. Scaling behavior of lifetime

The most important macroscopic characteristic quantity of the system is the average lifetime $\langle t_f \rangle$ which has a finite value even at zero external stress $\sigma = 0$ in the model if the temperature is finite $T > 0$. Under the assumption of equal load sharing it has been shown analytically in FBMs with a fixed breaking threshold σ_{th} that $\langle t_f \rangle$ follows the Arrhenius law $\langle t_f \rangle \propto \left(\sqrt{2\pi T}/\sigma\right)\exp\left((\sigma_{th}-\sigma)^2/2T\right)$ without any dependence on the system size N [1,2].

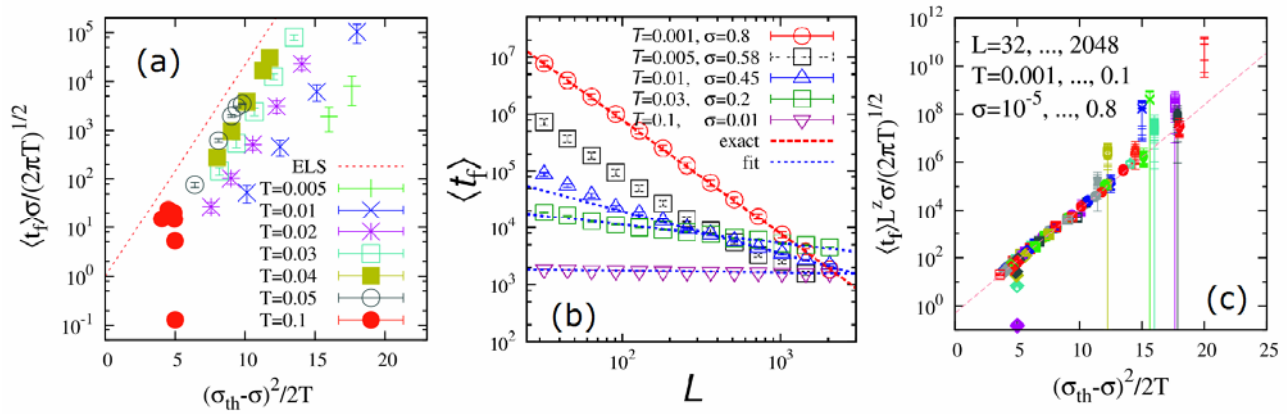

Figure 1. (a) Scaling plot of lifetime $\langle t_f \rangle$ obtained at different load σ and temperature T values by LLS simulations on a square lattice of size $L = 1024$. No data collapse is obtained. The simple Arrhenius law is indicated by the straight line of ELS. (b) Size scaling of lifetime. When stress concentration is dominated, power-law dependence is obtained with a high precision. Note that $\sigma_c = 0.8$ in the model. (c) Correcting the Arrhenius scaling form with the size dependence of lifetime a high quality data collapse is obtained.

Figure 1(a) presents the scaling plot of lifetime obtained by our computer simulations with the LLS FBM at the system size $L = 1024$ varying the load σ and the temperature T. No data collapse is obtained in the figure, which implies that the simple Arrhenius law does not hold when stress concentrations are present [10]. Our analytical and numerical calculations revealed that the interplay of stress concentrations and annealed disorder results in an anomalous size effect of the lifetime of the system, which is responsible for the discrepancy observed above [10]. In order to clarify the size scaling of the lifetime we carried out computer simulations varying the system size in a broad range $L = 32 - 2048$. These simulations showed that at any finite load value σ the average lifetime of the system decreases as a power law of the lattice size $\langle t_f \rangle \propto L^{-z(T,\sigma)}$. See Fig. 1(b). For the limiting cases of low ($\sigma \to 0$) and high ($\sigma \to \sigma_c$) loads the exponent z can be obtained analytically to be 0 and 2, respectively. Numerical calculations showed that varying the temperature

and external load the scaling exponent z takes values between the two limits $0 \le z(T,\sigma) \le 2$ [10]. We propose a modified form of the Arrhenius law which takes into account the size scaling of lifetime

$$\langle t_f \rangle \cong \frac{L^{-z(T,\sigma)}}{2} \frac{\sqrt{2\pi T}}{\sigma} \exp\left(\frac{(\sigma_{th} - \sigma)^2}{2T} \right). \tag{3}$$

Figure 1(c) demonstrates that the modified Arrhenius law provides an excellent scaling of the numerical data obtained by computer simulations of LLS FBM varying the system size L, the temperature T, and the external load σ in the ranges $L = 32 - 2048$, $T = 0.001 - 0.1$, and $\sigma = 10^{-5} - 0.8$, respectively.

3.2. Microscopic time evolution

On the microscopic level, the fibers primarily break due to thermal fluctuations when their actual load exceeds the fixed breaking threshold $\sigma_i(t) > \sigma_{th}$. Of course, depending on the temperature in a given time step more than one fiber can break at the same time. The load of broken fibers is then redistributed over the intact ones according to the selected load sharing rule. The load increments on intact fibers can trigger additional breakings and eventually generate an entire breaking burst. Hence, irrespective of the range of load sharing, the failure of the bundle proceeds in bursts which are separated by silent periods with no breakings. The size of the burst Δ is simply the number of fibers breaking in a correlated trail of failure events, while the waiting time t_w is defined as the number of iteration steps without breaking events between two consecutive avalanches.

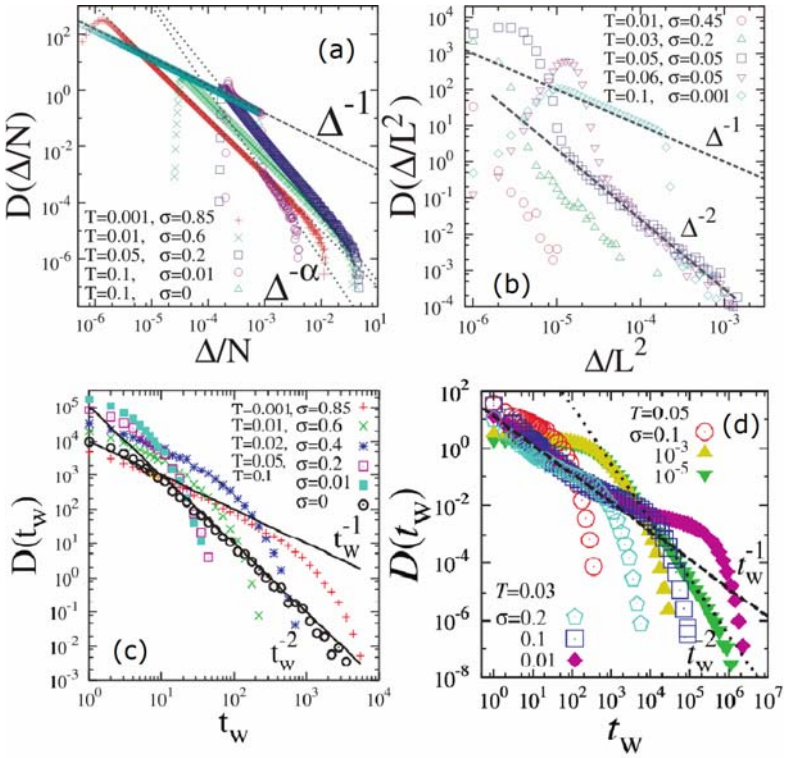

Figure 2. Size distribution of bursts for ELS (a) and LLS (b), and that of waiting time for ELS (c) and LLS (d). Power law functional forms are obtained followed by an exponential cutoff.

Bursts of breaking events generate acoustic waves so that they are responsible for the crackling noise accompanying the process of creep rupture [3]. In order to characterize the statistics of crackling events of our model, we analyzed the probability distribution of burst sizes $P(\Delta)$ and

waiting times $P(t_w)$. For the ELS case the burst size distribution $P(\Delta)$ proved to have a power law functional form $P(\Delta) \propto \Delta^{-\alpha}$ with an exponential cutoff. See Fig. 2(a). The value of the exponent has a complex dependence on the load and temperature [10]. For localized load sharing computer simulations revealed that $P(\Delta)$ has a Gaussian form for small bursts followed by a power law regime over a broad range. See Fig. 2(b). It is important to emphasize that the power law exponent α of the LLS case does not vary continuously with the model parameters. Instead, it suddenly switches from $\alpha = 1$ to $\alpha = 2$ when the external load approaches the critical value $\sigma \to \sigma_c$, which is accompanied by the shrinking of the Gaussian regime. In the vicinity of σ_c, the system becomes very sensitive to the thermal fluctuations and cannot tolerate large bursts, which is expressed by the higher value of the exponent α (Figs. 2(a) and (b)). This is an important unique feature of thermally driven creep rupture; when quenched disorder dominates the rupture process the opposite effect occurs, i.e. the burst exponent decreases when approaching catastrophic failure [13–15]. The probability distribution of waiting times $P(t_w)$ shows the same qualitative behavior as the distribution of burst sizes, i.e. $P(t_w)$ has a power law functional form $P(t_w) \propto t_w^{-\beta}$ with an exponential cutoff, where the value of the exponent β depends both on the load and on the temperature [12]. See Figs. (c) and (d)

3.2. Acceleration due to localization

The overall time evolution of the rupture process can be characterized by studying the average waiting time $\langle t_w \rangle$ between consecutive bursts as a function of the fraction of broken fibers ϕ, where $0 \le \phi \le 1$ holds. For ELS $\langle t_w \rangle(\phi)$ can be cast into a closed analytical form, while for LLS we determined it numerically [12]. Calculations showed that at zero load the breaking process continuously slows down in such a way that the average waiting time has a power law divergence $\langle t_w \rangle \propto (1-\phi)^{-1}$ when approaching macroscopic failure $\phi \to 1$. It can be observed in Fig. 3(a) that for finite load values $\sigma > 0$ the slow-down is followed by acceleration such that the accelerating regime starts earlier when the load increases. It is interesting to note that when the load is high enough, acceleration is obtained right from the beginning of the process, i.e. in this parameter regime the rupture process continuously accelerates towards failure [12]. The most remarkable feature of the results is that in the case localized load sharing the qualitative behavior remains the same, however, the acceleration sets on earlier (see Fig. 3(a)).

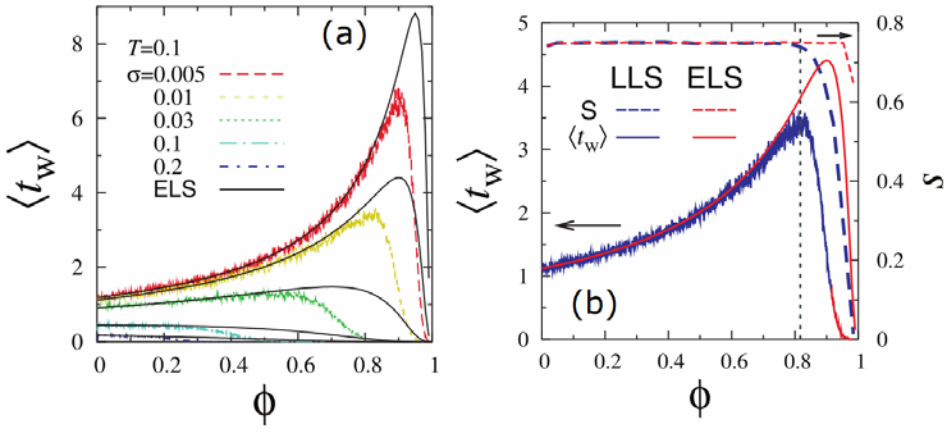

Figure 3. (a) Average waiting time for ELS and LLS as function of the fraction of broken fibers ϕ. (b) Comparison of the curves of average waiting time and entropy as a function of ϕ. For LLS the

entropy starts to decrease when the acceleration sets on.

In order to understand the background of early acceleration for LLS systems, Figs. 4(a)–(d) presents snapshots of the time evolution of an LLS bundle. Two regimes can easily be distinguished: at the beginning of the process cracks occur randomly all over the bundle (Fig. 4(a)). As time elapses more cracks nucleate and some of the previous cracks extend their size (Fig. 4(b)). Along the perimeter of growing cracks large stress is concentrated on the intact fibers, which increases the probability of further crack growth. As a consequence, one of the cracks gets selected and starts to grow rapidly, i.e. all bursts get localized along the front of a growing crack which then accelerates the process and leads to global failure (Figs. 4(c) and (d)) [12]. To quantify the degree of localization we introduced a so-called structural entropy S, which measures how scattered the new breaking events are in the bundle [12]. Large value of the entropy $S \to 1$ implies random cracking, while the small one $S \to 0$ marks the onset of localization. It can be observed in Fig. 3(b) that in the ELS case where there is no stress concentration and spatial correlation in the system the entropy is always high $S \approx 0.8$, even during the acceleration phase.

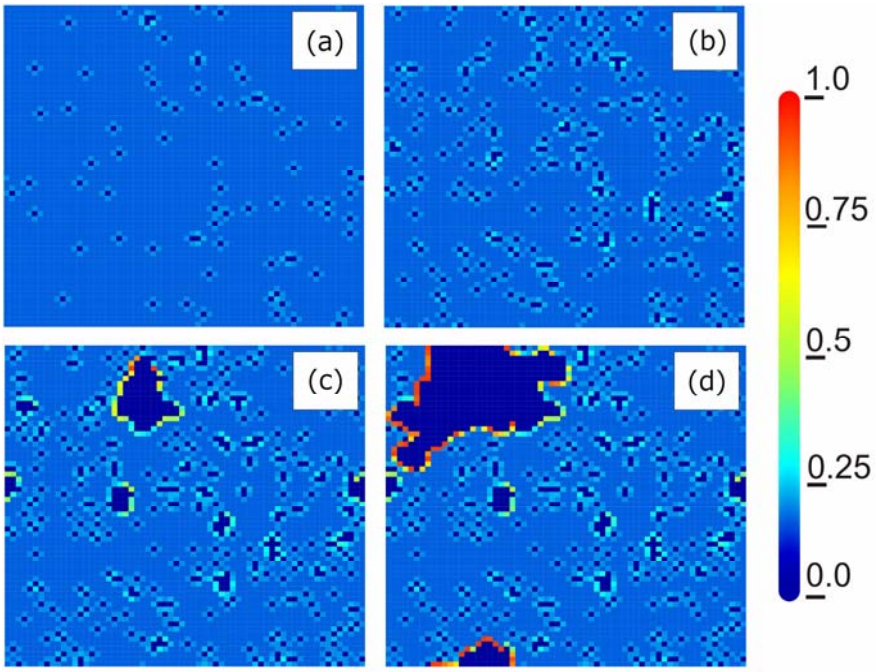

Figure 4. Snapshots of an evolving system, where fibers are colored according to their load. Deep blue represents zero load hence indicating cracks in the system.

On the contrary, in the presence of stress concentration, the entropy is high during the slow-down phase, however, it rapidly decreases to zero as soon as acceleration sets on (see Fig. 3(b)). Our results give a quantitative proof that the acceleration towards failure occurs due to the spatial localization of breaking events to the front of a growing crack [12].

4. Conclusions

Based on a fiber bundle model we showed that stress inhomogeneity play a crucial role in the process of thermally activated subcritical rupture giving rise to a broad spectrum of novel behaviors. Stress concentrations, arising in the vicinity of failed regions of the material, make the system more sensitive to thermal fluctuations. As a consequence, an astonishing size effect emerges where the average time-to-failure of the model system decreases as a power law of the system size. The size scaling exponent depends both on the temperature and on the external load. We proposed a

modified form of the Arrhenius law of lifetime which provides a comprehensive description of thermally activated breakdown phenomena [10–12].

On the micro-level, thermally driven breakdown proceeds in bursts of breakings which are separated by waiting times. The size distribution of bursts and the distribution of waiting times between consecutive events proved to have power law functional forms followed by an exponential cutoff. The power law exponents have a complex dependence on the load and temperature of the system [10,12]. To characterize the overall time evolution of the system, we analyzed the average waiting time between bursts as a function of the fraction of broken fibers. Calculations showed that the thermally induced creep process has two phases: at low loads and high temperatures the process slows down after the load is set, which is then followed by an accelerating period. However, when the load is high enough the system continuously accelerates towards failure. We demonstrated that in the case of localized load sharing, the stress concentration around cracks leads to spatial correlation of breaking events and to an enhanced breaking probability which in turn is responsible for the early acceleration [10–12].

In order to quantify the effect of spatial correlation on the time evolution of the creep rupture process, we evaluated the structural entropy of avalanches and their consecutive positioning. As a very important outcome, our calculations revealed that the decreasing extension and the spatial localization of avalanches to a bounded region of the specimen are responsible for the acceleration towards macroscopic failure. Final failure is driven by a single growing crack which becomes unstable as the avalanches localize to its perimeter [12].

Acknowledgements

The work is supported by TAMOP-4.2.2.A-11/1/KONV-2012-0036 and TAMOP-4.2.2/B-10/1-2010-0024 projects. The projects are implemented through the New Hungary Development Plan, co-financed by the European Social Fund and the European Regional Development Fund. F. Kun acknowledges the support of OTKA K84157. This work was also supported by the European Commission by the Complexity-NET pilot project LOCAT, by the MTA-JSPS project JP-24/2009 and by the Grant-in-Aid for JSPS Fellows.

References

[1] A. Guarino, A. Garcimartin, S. Ciliberto, Failure time and microcrack nucleation. Europhys Lett, 47 (1999) 456–461.
[2] R. Scorretti, S. Ciliberto, A. Guarino, Disorder enhances the effects of thermal noise in the fiber bundle model. Europhys Lett, 55 (2001) 626–632.
[3] A. Saichev, D. Sornette, Andrade, Omori, and time-to-failure laws from thermal noise in material rupture. Phys Rev E, 71 (2005) 016608-1–5.
[4] S. Roux, Thermally activated breakdown in the fiber-bundle model. Phys Rev E, 62 (2000) 6164–6169.
[5] B. D. Coleman, The Dependence of Mechanical Breakdown Phenomena. J Appl Phys, 29 (1956) 862–866.
[6] S. L. Phoenix, L. J. Tierney, A statistical model for the time dependent failure of unidirectional composite materials under local elastic load-sharing among fibers. Eng Fract Mech, 18 (1983) 193–215.
[7] W. I. Newman, S. L. Phoenix, Time-dependent fiber bundles with local load sharing. Phys Rev E, 63 (2001) 021507-1–20.
[8] W. A. Curtin, H. Scher, Time-dependent damage evolution and failure in materials. I. Theory. Phys Rev B, 55 (1997) 12038–12050.
[9] R. C. Hidalgo, Y. Moreno, F. Kun, H. J. Herrmann, Fracture model with variable range of

interaction. Phys Rev E, 65 (2002) 046148-1–8.
[10] N. Yoshioka, F. Kun, N. Ito, Size Scaling and Bursting Activity in Thermally Activated Breakdown of Fiber Bundles. Phys Rev Lett, 101 (2008) 145502-1–4.
[11] N. Yoshioka, F. Kun, N. Ito, Kertész line of thermally actiated breakdown phenomena. Phys Rev E, 82 (2010) 055102(R)-1–4.
[12] N. Yoshioka, F. Kun, N. Ito, Time evolution of damage in thermally induced creep rupture. Europhys Lett, 97 (2012) 26006-p1–p6.
[13] F. Kun, H. A. Carmona, J. S. Andrade, Jr., H. J. Herrmann, Universality behind Basquin's Law of Fatigue. Phys Rev Lett, 100 (2008) 094301-1–4.
[14] M. Kloster, A. Hansen, P. C. Hemmer, Burst avalaches in solvable models of fibrous materials. Phys Rev E, 56 (1997) 2615–2625.
[15] K. Kovacs, S. Nagy, R. C. Hidalgo, F. Kun, H. J. Herrmann, I. Pagonabarraga, Critical ruptures in a bundle of slowly relaxing fibers. Phys Rev E, 77 (2008) 036102-1–8.

Acoustic Emissions in Fracturing Paper

Menka Stojanova[1], Stéphane Santucci[2], Loïc Vanel[1], Osvanny Ramos[1,*]

[1] Institut Lumière Matière, UMR5306 Université Lyon 1-CNRS, Université de Lyon 69622 Villeurbanne cedex, France
[2] Laboratoire de Physique, CNRS UMR 5672, Ecole Normale Supérieure de Lyon, Université de Lyon 46 allée d'Italie, 69364 Lyon Cedex 07, France
* Corresponding author: osvanny.ramos@univ-lyon1.fr

Abstract The fracture dynamics of heterogeneous materials is a rich subject with obvious practical interests, especially the subcritical fracture, where a material breaks through a series of successive, non-correlated and localized fracture events until the arriving to a critical situation where the whole material fails. Paper has been a common model material to study this phenomenon, and high-resolution and high-speed visualization are the usual ways to follow the dynamics of the process. However, visualization presents many limitations, especially for long experiences. That is one of the reasons why we are coupling acoustics to the measurements in an attempt to establish it as the main source of information. Acoustics presents a much better temporal resolution and captures a higher number of events than visualization. By thresholding the amplitude of the acoustic signal, it is possible to get similar activities in both measurements. The waiting times between events and the energy of the events are both distributed in power laws with exponents which are similar for the two different kind of measurements (visualization and acoustics), corroborating that the recorded acoustic data corresponds indeed to the fracture process.

Keywords Subcritical fracture, Acoustic emissions, crack propagation, scale invariance.

1. Introduction

Industrial designs evolve continuously toward thinner and lighter, however stronger structures, many of them submitted to a permanent stress. It is known that stresses intensify around a flaw in the material [1]; and even if the system resists at a particular instant, a micro-crack can start growing, in an intermittent manner (the case of heterogeneous materials), until reaching a critical length where the whole system fails. This process, denominated *subcritical fracture*, has captured the attention of scientist and engineers for more than half a century, and the progresses in experimental results are quite related to the technological advances in the period. Already in the sixties, some models based on thermally activated rupture were proposed [2, 3], supported by measurements of the lifetime of the sample as a function of the global stress and the temperature [2, 3]. In the nineties, during the early stages of the digital era, acoustics allowed the statistical analysis of the burst-like fracture events provoked by the intermittent growing of a crack [4, 5]. Power law distributions of amplitude and waiting time between fracture events were often interpreted as a signature of a "self-organized critical" process [6, 7]. In the latest years, high-speed and high-resolution video acquisition have played a major role in the study of the subcritical fracture of diverse materials [8-10]. Paper presents several good properties that have set it as a common model material: two-dimensionality, high degree of heterogeneity and variability, quasi-brittle character and a very low cost. Many different results have been obtained with direct observations in paper [8, 11, 12]. However, several issues seem favoring the implementation of acoustics measurements. Beyond lab limits, most objects are three-dimensional and non-transparent, thus analyzing their interior belongs mainly to the acoustics' domain. The earth's interior is one of their most relevant examples, and the statistical similitude between earthquakes and subcritical fracture [13] is an invitation to use the same source of information, i.e., acoustics. Also, in high-speed cameras there is a compromise between spatial resolution and frame rate, as well as size of the image vs. number of images. Having two characteristic frequencies in our study: one low, where a priori there is not much activity, and another very high, taking place during a local fracture event, direct observation may result in a lost of information. We are coupling acoustic to the measurements in an attempt to

establish it as the main source of information. The main aim of this paper is to verify the agreement between acoustics and direct observation. By thresholding the amplitude of the acoustic signal, we get a very similar temporal activity in both measurements. The waiting times between events and the energy of the events are both distributed in power laws with exponents which are similar for the two different kind of measurements (direct observation and acoustics), corroborating that the recorded acoustic data corresponds indeed to the fracture process. Earlier studies have used acoustic as the main source of information to analyse a fracture process in paper [14-15]; however, as far as we know, this is the first report validating the results of the acoustic measurements through simultaneous direct observations.

We also discuss the advantages and challenges of the use of acoustics in our experiment. Some experiments have been done to study the acoustic emission of fracturing paper [14-15], but as far as we know this is the first time that acoustics are compared to another observation method-direct visualization of fracture propagation.

2. Experimental procedure

We use fax paper samples from *Alrey* having a thickness of 50 μm and effective dimensions 21 cm × 4 cm, being fixed along the longer sides and free in the perpendicular direction. An initial crack of length l_0 is prepared at one free side of the sample, both in a parallel direction and equidistant from the fixed borders. Experiments are performed by applying a constant force F perpendicularly to the direction of the initial crack. By adjusting l_0 = 4.75 cm and F = 200 N, the crack grows reaching a critical length, l_c ~ 8 cm, approximately between 10 minutes and 30 minutes after the application of the force. The critical length l_c separates the slow dynamics from the quasi-instantaneous rupture. Two piezoelectric transducers of diameter 2.3 mm (*Valpey Fisher VP-1.5*) are placed in contact with the paper at 5 cm and 9 cm from the free side containing the initial crack and at 1 cm from the fixed border (which also corresponds to a 1 cm distance to the direction of the initial crack). An ultrasonic gel guarantees a good contact between the sensor and the sheet of paper. The acoustic signals are amplified 64 db and recorded continuously during the whole experience by a *NI USB-6366* card at 2 MHz. A high-speed camera (*Photron FASTCAM SA4*) takes images in a rectangular area containing the advancing crack at a frequency of 10 Hz and a spatial resolution of 100 μm / pixel. All experiences have been performed under the same conditions. The temperature and relative humidity were 26.5 ± 1 °C and 45 ± 2% respectively. A scheme of the experimental setup with the crack and the position of the sensors is represented on figure 1.

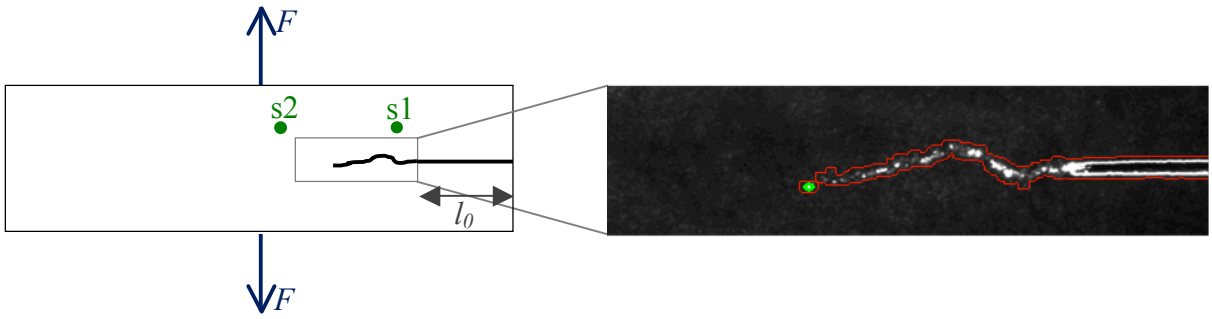

Figure 1. On the left, scheme of the experimental setup. l_0: initial crack length, s_l: projection of the crack length on the initial crack direction, F: applied force, s1 and s2: positions of the piezoelectric transducers. On the right, experimentally obtained image of the crack with the extracted crack contour (red line) and crack tip (green).

The amplitude of the acoustic signal depends on the contact between the transducer and the sheet of paper, which varies between different realizations. In order to compare events from different experiences, a calibration was performed. It consisted of the averaged response of each sensor to six localized rupture events produced on every sample (by piercing it with a computer controlled thin needle of 250 μm of diameter) before complete loading. Additional series of experiments were performed in order to study the attenuation of the acoustic waves in paper. 10 to 20 localized rupture events were induced on a sheet of paper submitted to a force of 200 N, but with no initial crack so to be sure that no uncontrolled rupture would occur. The events were made on a line parallel to the longer sides of the paper, in the same direction as the fracture in previous experiments. The acoustic signal was recorded by two sensors placed at 4 cm from each other.

2.1. Data Analysis

Images: crack contours are extracted using a digital image analysis routine. For each image the position of the crack tip is found (figure 1). Three variables are defined: s, the real length of the interface of the fracture created between two consecutive images; the size of the jump s_s, defined as the distance between the crack tip of two successive images, and s_l, defined as the projection of s on the initial direction of the crack.

Acoustics: The detection of acoustic events is made through the *spectral distance* calculation, which corresponds to the spectral distance between the recorded signal and the noise (the noise sample is recorded during the calibration, before the complete loading of the paper, so no cracks have occurred during it) over a temporal window of length w=100 μs. Spectral distances are usually calculated using the logarithms of the power spectra [16, 17], but we prefer using the power spectra directly so to obtain a distance that is directly proportional to the acoustic energy:

$$D(t) = \frac{1}{w}\int_{t-\frac{w}{2}}^{t+\frac{w}{2}} \langle S(t')\rangle - \langle \overline{N}\rangle \, dt' \qquad (1)$$

where $\langle S(t)\rangle$ is the mean value of the signal's power spectrum averaged over all the frequencies and $\langle \overline{N}\rangle$ the mean value of the noise's power spectrum averaged over time and frequency. Detecting acoustic events and determining their duration is done by thresholding the spectral distance. The energy of an event is calculated as the integral of the spectral distance over its duration. Thanks to the spectral distance the number of detected events is almost four times greater than by thresholding the raw data and we are able to detect events with slightly smaller energy.

3. Results

As the applied force is subcritical and the material heterogeneous, the initial crack propagates in an intermittent manner [8]: images show that the length of the fracture is constant for most of the time and increases by making fast discrete crack steps, denominated *jumps* or avalanches. The acoustic data shows discrete *bursts* with a finite duration. Each burst constitutes an acoustic event. First, we compared the number and occurrence times of jumps and acoustic events, without considering their energy value. For each experiment the number of acoustic events was significantly larger than the number of jumps, even when adjusting the acoustic time resolution to the images' frame rate. This is a clear indication that the acoustics is much more sensitive to crack propagation than the image analysis. Nevertheless, if we only consider acoustic events having an energy larger than a threshold value their number will decrease. By setting the threshold energy to an optimal value we can get the

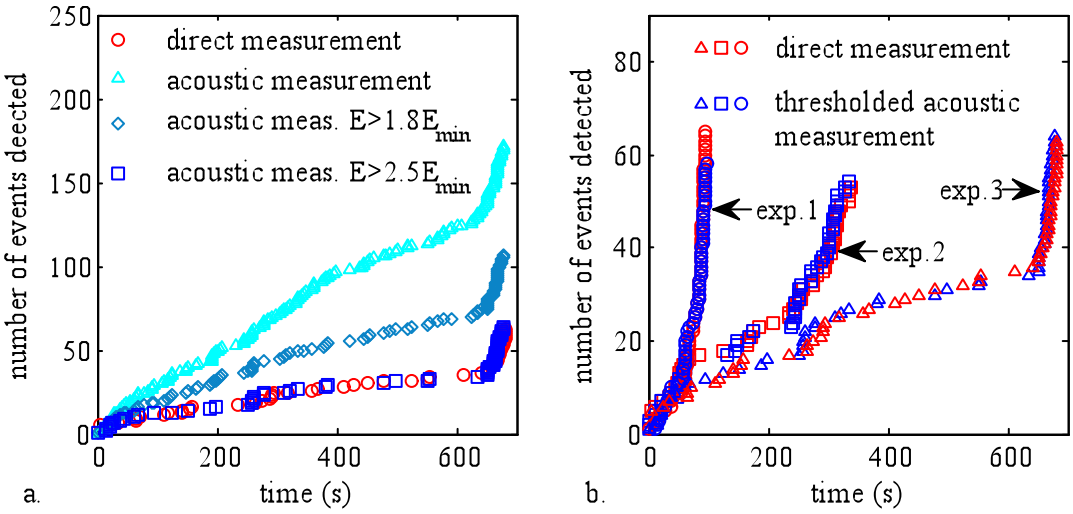

Figure 2. a. Activities obtained by direct observation (jumps) and acoustic monitoring for one experiment: acoustic monitoring results in much more events than direct observation. By considering only acoustic events with energy superior to a threshold value we get very similar activities for both methods. b. Comparison of activities obtained by direct observations and acoustic monitoring for three experiments.

same number of events for both methods. In this situation, time intervals with many acoustic events correspond to the ones with many jumps (figure 2). This global similarity between the two activities confirms the relationship between the propagation of the crack (jumps) and acoustic events. However, when considering the events' energy, the relationship between jumps and acoustics events is not as obvious as previously. Large jumps are not always associated to high acoustic energy and the temporal correlation between the two signals is very poor. The temporal correlation between the two signals is also very poor in the case of not considering the energy values. This can be a consequence of the combination of two facts: the low acquisition rate of the images (10 Hz) and the fact that there is a temporal shift between the rupture of the material (acoustic event) and the macroscopic opening of the fracture (jump). This lack of correlation makes it impossible to match jumps and acoustic events individually, but our data is suitable for statistical analysis: each experiment results in approximately 50 jumps and few hundreds to few thousands of acoustic events, providing enough data for such approach. Here we will study and compare the probability distributions of two different variables characterizing subcritical fracture: waiting times and energies.

Waiting Times: For subcritical fractures the time between two discrete events, referred to as the waiting time, follows power-law distributions [18-20]. Figure 3 shows the probability distributions of waiting times between the events for the jumps and the acoustic data. Both waiting times are power law distributed (with a slight cutoff for long waiting times). The distributions were fitted as power laws within the domains delimited by the vertical lines on the figures, and the exponent obtained are very similar: 1.1 and 1.0 for the jumps and acoustic waiting times respectively.

The distributions are represented on the same plot in figure 4. Since acoustic data acquisition has a much better time resolution, acoustic waiting times spread on a larger set of values. To compare the two distributions we can adjust the distributions' normalization coefficients. Figure 4.a shows that with well-chosen coefficients the distributions collapse. Another solution is ignoring acoustic waiting times smaller than the image frame rate (0.1 s). In this case the two distributions also match (figure 4.b). The similitude between the two probability distributions indicates that the acoustic activity and the detected propagation of the fracture are indeed issued from the same mechanism.

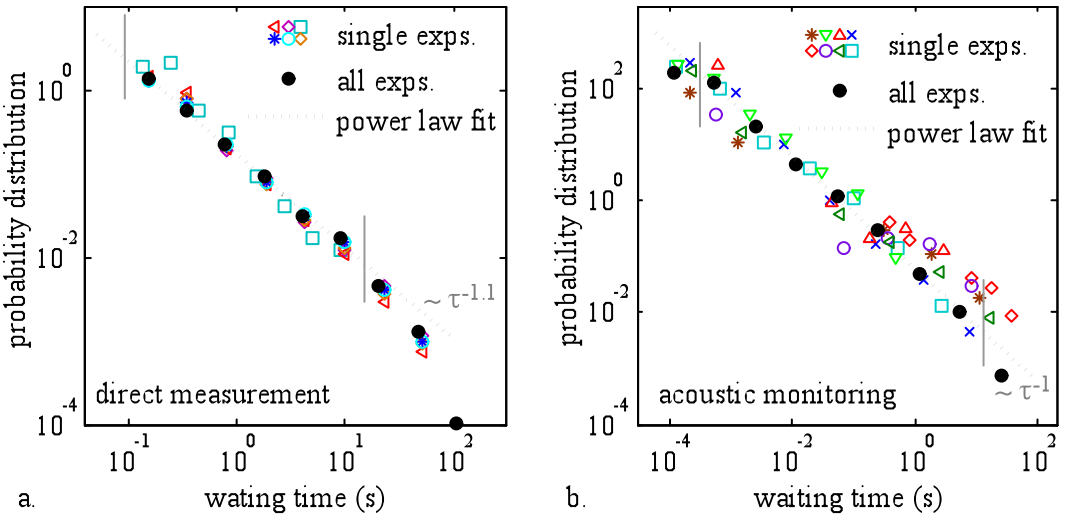

Figure 3. a. Distribution of waiting times determined by the direct observations (jumps). b. Distribution of waiting times determined by acoustic monitoring. Open symbols: waiting times of each experiment separately, solid symbols: waiting times of all the experiments, dotted line: a power law fit of the distribution of the waiting times of all experiments in a range limited by vertical lines.

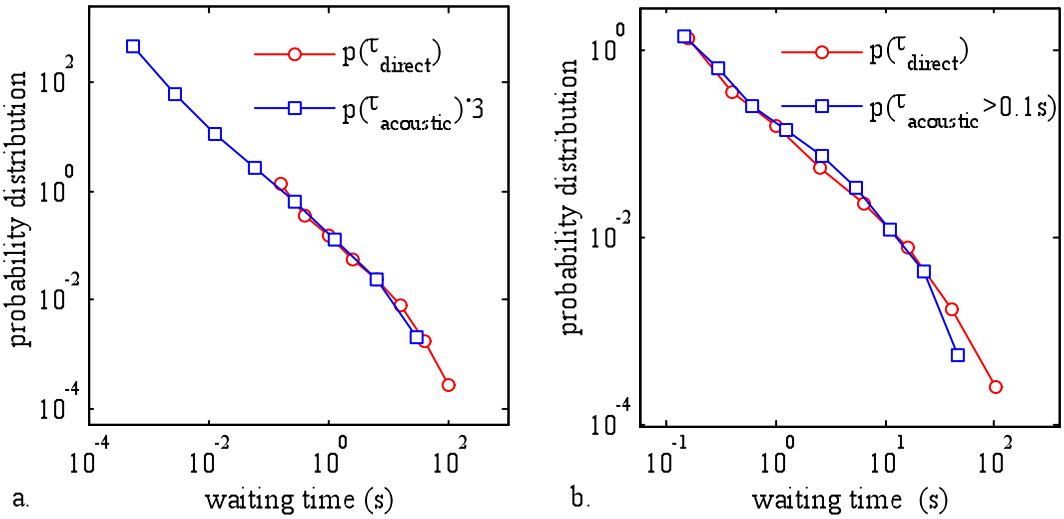

Figure 4. a. Distribution of waiting times of the jumps, obtained by direct observations (red circles) and distribution of waiting times obtained by acoustic monitoring multiplied by 3 (blue squares). b. Distribution of waiting times obtained by direct observations (red circles) and distribution of waiting times greater than the image frame fate (0.1 s) obtained by acoustic monitoring (blue squares).

Furthermore, some test showed that the acoustic waiting time distribution is not affected by thresholding the event's energy; and considering all the detected acoustic events, the same power law distribution is found. This result indicates that all the acoustic bursts correspond to fracture events.

Energies: in this two-dimensional system fracture energy scales as the fracture's length. Therefore, the normalized distribution of jump sizes is equal to the normalized distribution of jump energies. The probability distribution of s (the real crack length), s_s (the distance between crack tips on two successive images) and s_l (the projection of s on the initial direction of the crack), are represented in

figure 5.a. The three distributions follow a power law over approximately a decade followed by a cutoff. We extracted power laws with exponent 1.2 for s_s and s_l and 1.0 for s. Because of the relatively small number of jumps and the limited span of the power law we must consider these results with precaution and will not discuss the differences between the probability distributions. We will rely on results from previous experiments: an exponent of 1.23 has been found previously for the power law distribution of s_l [8, 21], which matches our observations.
The energy of acoustic events is defined as the integral of the spectral distance (equation 1) over an event's duration. The event is the part of the spectral distance overcoming a chosen threshold. We prefer this definition to the maximal amplitude of the signal (or of the spectral distance) because acoustic events are not single punctual bursts: they sometimes have irregular shapes in time, presenting few local maxima as consequence of the fact that few fibers can break consecutively in a very small lapse of time, appearing as one single event. Taking into account only one of these maxima would result in neglecting a considerable proportion of the acoustic energy. Integrating the spectral distance rather than the square of the signal itself decreases the influence of the noise. This definition provides an estimation of the acoustic energy detected by the sensors, which does not exactly correspond to the energy at the event's source. This energy needs to be corrected by taking into account the attenuation of the acoustic waves, which can be scattered or absorbed by paper fibers. The experiments on crack-free paper provided data on the position and energy of about hundred events relative to the two different sensors. By comparing the energy ratio of signals detected by the two sensors, to the distance separating each event from the sensors, we obtained that the energy is attenuated exponentially with a characteristic length of 3.2 cm. To determine the position of the source of an acoustic event we use the images and suppose that it occurred at the position of the crack tip at the corresponding time. By knowing the distance between the source and the sensor, we can compute the attenuation of the energy. Figure 5.b shows the distribution of the estimated acoustic energy at the events' source. Energies follow a power law over more than three decades with an exponent of 1.3, very close to the one found for the distributions of jump sizes. Once again, the similarity between the power laws of jumps and acoustic energy indicates that acoustic emissions are a consequence of the paper's fracture.

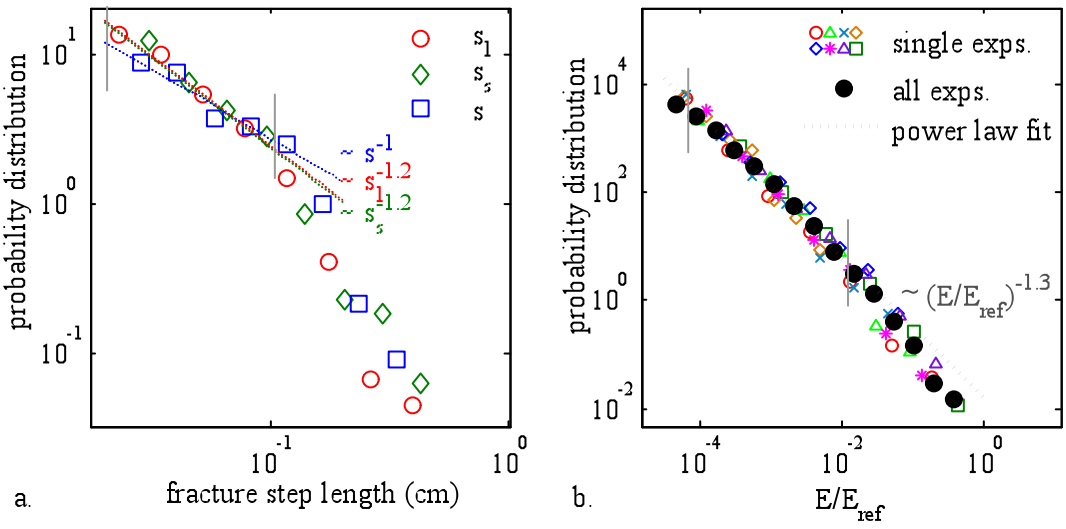

Figure 5. a. Probability distribution of fracture jumps (s, s_l and s_s) with power law fits in a range limited by vertical lines. b. Distribution of the energies of the acoustic events. Open symbols: energies of each experiment separately. Solid symbols: energies of all the experiments, dotted line: a power law fit of the distribution of the energies of all experiments in the signalized range.

4. Conclusion

We studied the subcritical crack growth of a single crack in a sheet of paper submitted to constant force. The system was observed directly by image analysis and indirectly by recording the acoustic emissions. Both methods show similar activities over time. Two variables, the waiting times between the events and the energy released at each event, were statistically analyzed. They both present power law distributions that are very similar for the two different measurements (direct or acoustic emissions), corroborating that the recorded acoustic data corresponds indeed to the fracture process. Having better time resolution and sensibility than image analysis, acoustic monitoring seems more promising for the future development of subcritical fracture in heterogeneous materials.

Acknowledgements

We acknowledge financial support from the "A. M. Ampère" Physics Federation of Lyon.

References

[1] A. A. Griffith, The phenomena of rupture and flow in solids. Philos. Trans. R. Soc. London, Ser. A. 221 (1920) 163-198.
[2] S. S. Brenner, Mechanical behavior of sapphire whiskers at elevated temperatures. J. Appl. Phys. 33 (1962) 33-39.
[3] S. N. Zhurkov, Kinetic concept of the strength of solids. Int. J. Fract. Mech. 1 (1965) 311-322.
[4] A. Petri, G. Papro, A. Vespignani, A. Alippi, and M. Constantini, Experimental Evidence for Critical Dynamics in Microfracturing Processes. Phys. Rev. Lett. 73 (1994) 3423-3426.
[5] A. Garcimartin, A. Guarino, L. Bellon, and S. Ciliberto, Statistical Properties of Fracture Precursors. Phys. Rev. Lett. 79 (1997) 3202-3205.
[6] P. Bak, C. Tang, K. Wiesenfeld, Self-organized criticality: An explanation of the 1/*f* noise**.** Phys. Rev. Lett. 59 (1987) 381-384.
[7] H. J. Jensen, Self-organized Criticality, Emergent Complex Behavior in Physical and Biological Systems (Cambridge Univ. Press, 1998).
[8] S. Santucci, L. Vanel, S. Ciliberto, Subcritical Statistics in Rupture of Fibrous Materials: Experiments and Model. Phys. Rev. Lett. 93 (2004) 095505.
[9] P.-P. Cortet, S. Santucci, L. Vanel, and S. Ciliberto, Slow crack growth in polycarbonate films. Europhys. Lett. 71 (2005) 242.
[10] K. J. Maloy, S. Santucci, J. Schmittbuhl, R. Toussaint, Local Waiting Time Fluctuations along a Randomly Pinned Crack Front. Phys. Rev. Lett. 96 (2006) 045501.
[11] S. Santucci, P.-P. Cortet, S. Deschanel, L. Vanel, S. Ciliberto, Subcritical crack growth in fibrous materials. Europhys. Lett. 74 (2006) 595.
[12] L. Vanel, S. Ciliberto, P.-P. Cortet, S. Santucci, Time-dependent rupture and slow crack growth: elastic and viscoplastic dynamics. P Journal of Physics D: Applied Physics, 42 (2009) 214007.
[13] B. Gutenberg and C. F. Richter Magnitude and energy of earthquakes. Ann. Geophysics 9 (1956) 1.
[14] J. Rosti, J. Koivisto, M.J. Alava, Statistics of acoustic emission in paper fracture: precursors and criticality. J. Stat. Mech. (2010) P02016.

[15] L. I. Salminen, A. I. Tolvanen, M. J. Alava, Acoustic Emission from Paper Fracture. Phys. Rev. Lett. 89 (2002) 185503.

[16] M. Basseville, Distance measures for signal processing and pattern recognition. Signal Processing 18 (1989) 349-369.

[17] N. Mallick, Examples of scale invariance in the fracture of brittle disordered materials. PhD thesis, Université de Lyon (2010).

[18] S. Deschanel, L. Vanel, N. Godin, G. Vigier and S. Ciliberto, Experimental study of crackling noise: conditions on power law scaling correlated with fracture precursors. J. Stat. Mech. (2009) 01018.

[19] F. Kun, Z. Halász, J. S. Andrade Jr, H. J. Herrmann , Crackling noise in sub-critical fracture of heterogeneous materials. J. Stat. Mech. (2009) 01021.

[20] S. Santucci, L. Vanel, S. Ciliberto, Slow crack growth: Models and experiments. Eur. Phys. J. Special Topics 146 (2007) 341-356.

[21] S. Santucci, P-P. Cortet, L. Vanel, and S. Ciliberto, Physics of sub-critical crack growth in a fibrous material: Experiments and model. 11th International Conference on fracture (2005).

Acoustic Emission multiplets during fatigue of aluminum.

Wafa Ben Rhouma[1,2], Stéphanie Deschanel[1,*], Jérôme Weiss[2]

[1] Université de Lyon, INSA-Lyon, MATEIS, CNRS UMR 5510, F-69621 Villeurbanne, France
[2] LGGE, CNRS, UJF-Grenoble , 38402 St Martin d'Hérès, France
* Corresponding author: stephanie.deschanel@insa-lyon.fr

Abstract A series of uniaxial low cycle fatigue tests on pure Aluminum is investigated via the analysis of acoustic emission (AE). The different stages of macroscopic fatigue behavior are clearly differentiated in terms of AE. We define five different stages: initial hardening, initial softening, secondary hardening during shakedown stage, onset of secondary softening and failure. When most of the acoustic activity recorded in the two/three first stages is related to dislocation dynamics, the acoustic activity in the last stages is mostly due to the fracture phenomenon. Now, a detailed analysis of the discrete AE allowed to highlight the appearance, in the last third of the test, of acoustic signals occurring almost every cycle at a same given stress and having a quasi identical acoustic signature. We hypothesize that such multiplets, shown for the first time in acoustic emission, are the signature of the propagation, cycle after cycle, of a fatigue crack whose trace may be seen post-mortem with the fatigue striations on a fracture surface. This way, these signals could be considered as fracture precursors about several hundred cycles before the final failure of the material.

Keywords Acoustic Emission, Fatigue, Fracturing process, AE multiplet, Cracks

1. Introduction

Fatigue is perhaps the most dangerous and simultaneously less well understood mechanism of mechanical failure encountered in a variety of modern structures ranging from nuclear reactors to micro-electronic connections in cell-phones. Failure in cyclic loading appears unexpectedly when the structure is operating in a safe and apparently steady state regime. Despite a long history of theoretical and experimental studies, modern technology still lacks reliable tools capable of predicting the catastrophic failure in cyclic loading. The situation is particularly troublesome with early precursors of fatigue and thus it would be important to find new ways to follow fundamental changes in the development of fatigue at a microstructural scale in order to identify early precursors to fracture.

An appropriate tool to analyze dynamic instabilities involving such topological defects as dislocations, twin/martensitic boundaries and micro-cracks is certainly the monitoring of the Acoustic Emission (AE). To simplify the analysis of the signal, it seems appropriate to reduce the different possible sources of AE events. Therefore, for an easier understanding, we have chosen to work on pure Aluminum for which the expected AE sources are associated with dislocation dynamics and microcraking only.

AE monitoring has been developed as an effective non-destructive technique for the detection, location and monitoring of fatigue cracks. Several studies showed a correlation between AE count rates and crack propagation rates [1-3] or a relationship for acoustic emissions and the applied range of stress intensity [4]. We focus here on discrete AE (signals above a threshold) to study the dynamics of dislocations and cracks during low cyclic fatigue tests and we explore AE waveforms to extract promising information about the signature of crack propagation. In particular, we reveal the existence of multiplets, i.e. almost identical waveforms reoccurring at each fatigue cycle during the final part of the fatigue life, and which likely signatures of fatigue crack growth.

2. Experimental details

2.1. Material and experiments

We chose to study 99.95% pure aluminum in order to restrict the potential sources of AE to collective dislocation motions and microfracturing process. Indeed, impurities and phase transformations [5] in a material are possible AE sources but do not exist for pure aluminum. The base material was not pretreated, its polycrystalline structure consisting of large elongated grains, ~10 mm for the major axis and ~3 mm for the minor axis. This large grain size implies a lower impact of grain boundaries on the acoustic activity generated in the material [6].
Uniaxial tension-compression ($\varepsilon_{min}/\varepsilon_{max}$=-1) low cycle fatigue tests are performed at room temperature using an hydraulic machine designed and realized at MATEIS Lab [7, 8]. The cyclic total strain was imposed with an amplitude $\Delta\varepsilon$ varying from 0.5% to 1.8% and a loading frequency from 0.1 to 1 Hz. The specimens are cylindrical with 18mm gauge length and 9mm diameter. Stress and strain are recorded up to the macroscopic fracture.

2.1. Acoustic Emission

Acoustic emission is continuously monitored during the tests using a PCI2 Mistras data acquisition system of European Physical Acoustic (EPA) with a 8MHz sample rate and a 60 dB pre-amplification, the bandwidth being 50 kHz–1.2MHz. Our measurements are achieved with two resonant Nano30 EPA piezoelectric sensors (peak of resonance at 140 kHz) coupled to the material with silicon grease. The sensors are placed on the heads of the specimens. Three kind of measurements are performed: (i) the continuous AE measuring the mean acoustic power, sampled at 10Hz all along the test, (ii) the discrete AE which is an automatic detection of transient elastic waves distinguished from the background noise, above a given threshold (34dB) and (iii) a complete recording of the acoustic signal, sampled at 5 MHz: "datastreaming" for a few selected loading cycles.
In this paper, we focus on the discrete AE only. We distinguish AE hits from events: hits are AE signals detected by a single sensor whereas events are signals whose intensity is big enough to reach both sensors and that can be located along the specimen length. In general the form of the primitive wave changes during propagation through the medium, and the amplified signal from a resonant piezoelectric sensor bears little resemblance to the original pulse. Nevertheless, this coloration does not erase the differences or similarities in the sources and we assume that if the signals are similar at the source then the signals received by the sensors are similar.

3. Results and discussion

3.1. Macroscopic cyclic response and discrete AE

Let us take the example of a 1 Hz cyclic fatigue test at imposed total strain $\Delta\varepsilon$=0.96% that failed after 3383 cycles. The macroscopic response (maximum stress reached at each cycle) is represented in Figure 1 together with the evolution of the discrete AE activity (cumulative number of hits (Figure 1a) and acoustic energy of hits (Figure 1b)). The different stages of fatigue are clearly differentiated in terms of AE. We define five different stages, each of them being associated to a color: (1, black) initial hardening during the first cycles, (2, red) initial softening at the beginning of a shakedown stage corresponding to a saturation of the stress, (3, green) secondary hardening during shakedown stage, (4, green) onset of secondary softening stage associated to increasing damage before (5, pink) the final failure of the material.

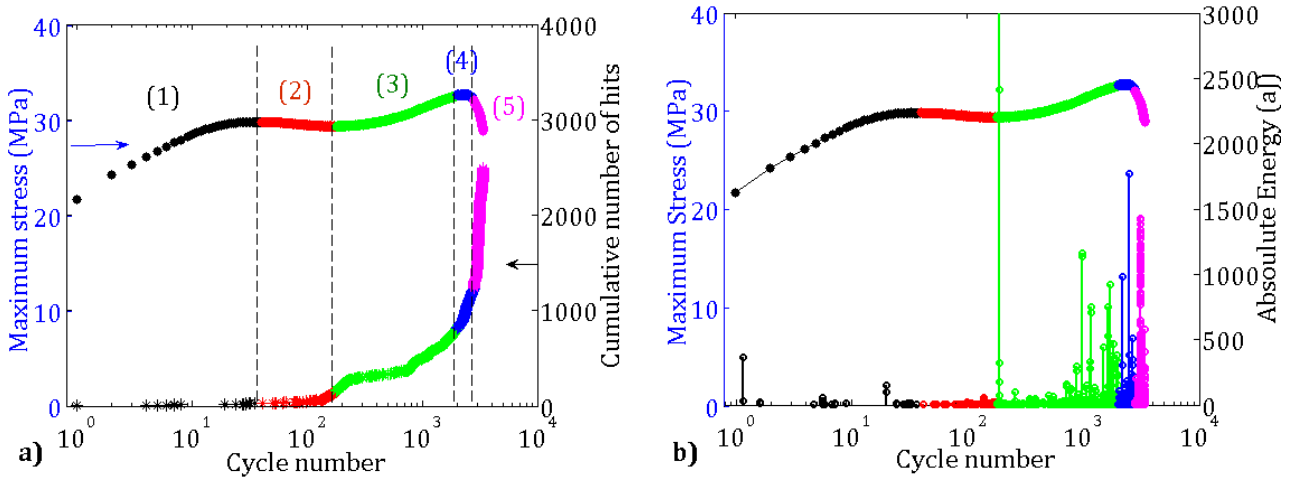

Figure 1 Evolution of the maximum stress during a fatigue test at Δε=0.95% on aluminum (99.95%) along the five different stages, together with a) the cumulative number of hits and b) the acoustic energy of the hits.

The acoustic activity is also represented in Figure 2 with the stress as a function of time along the cycles; Figure 2a shows the occurrence of hits and events and Figure 2b represents the evolution of the discrete AE (normalized number of hits) during selected loading stages of the fatigue test.

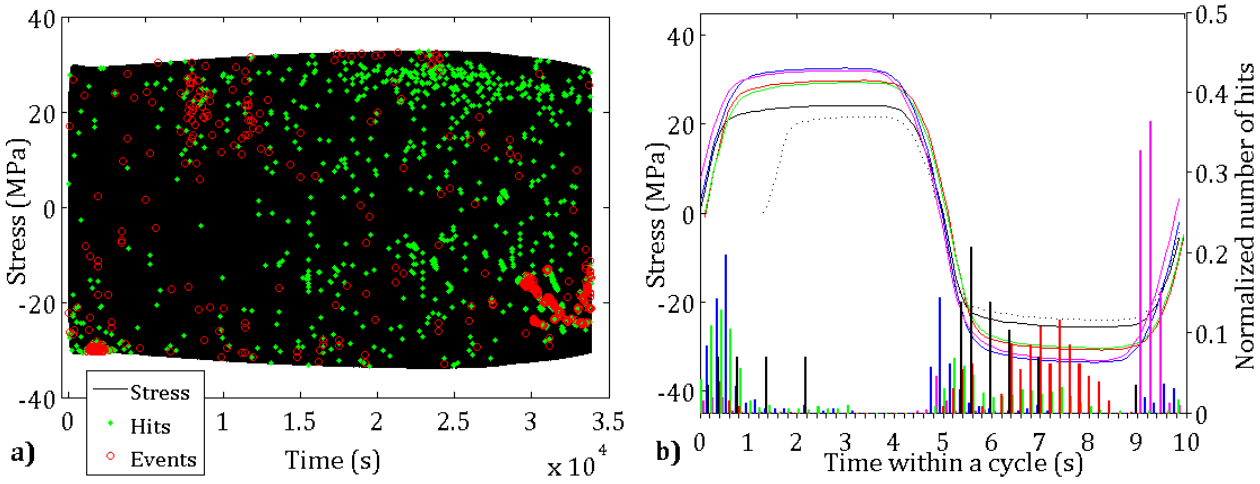

Figure 2 a) Acoustic activity during a fatigue test at Δε=0.95% on aluminum at 1Hz b) Normalized number of hits for each fatigue stage: time of occurrence within a cycle (10s) in correspondence to the stress. Black, red, green, blue, pink colors correspond to the five different stages respectively.

During the first stage, formation of dislocation structures such as cells and walls result in a strong strain hardening of the loaded material [9, 10]. AE hits, recorded during the elastic-plastic transition (Figure 2b), may be due to collective dislocation avalanches. The initial softening exhibits a lower and less energetic discrete AE activity that may be due to the formed microstructures which restrains the spreading of dislocation avalanches. Stronger hits are recorded at the secondary hardening during shakedown stage associated with sudden dislocation cell rearrangements. This stage is characterized by AE hits of various sizes in both tension and compression (Figure 2b). The hits recorded in the last part of this third stage could already be the onset of microcracking and damage. The secondary softening is associated with a strong increase of discrete AE activity that could be a signature of the cell structure destabilization. During the last stage, the acoustic activity rises even more as the result of microcracking leading to the collapse of the macroscopic properties of the material. This activity, mainly due to the fracture phenomenon, is strongly asymmetrical (tension vs compression): most of the hits occur when the material is loaded only, at the onset of

stretching but still under compression (Figure 2b). These AE signals could then be an indicator of the friction between the surfaces of the cracks and their growth.

3.2. AE multiplets

On the last third of the studied cyclic fatigue tests carried out on pure aluminum, we have observed the appearance of acoustic signals occurring almost every cycle at a given stress level during a certain number of cycles. Figure 3 shows these lines of hits or events arising at a quasi-identical level of stress (plotted as a function of time) in the end of a fatigue test at $\Delta\varepsilon$=0.95%. We notice several lines at negative stresses but Figure 3b evidences that the AE signals appear at positive stress rate.

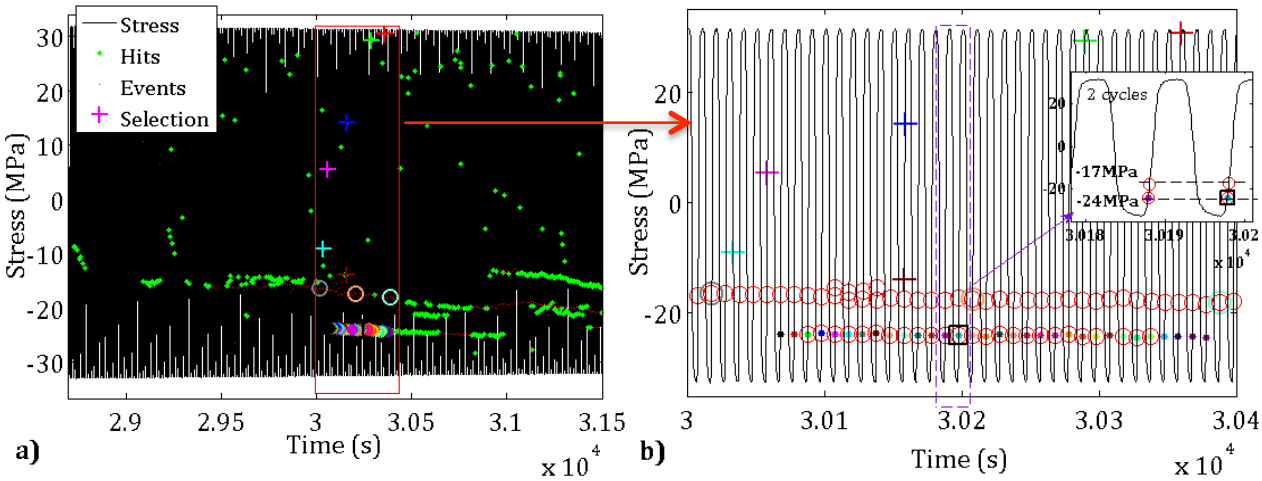

Figure 3 a) Hits or events occurring at specific values of stress, cycle after cycle, in the last stage of a fatigue test at $\Delta\varepsilon$=0.95%. b) Zoom corresponding to the red rectangle. Colored dots correspond to AE signals occurring almost every cycle at a same given stress (~ -24 MPa). Red circles are events. Crosses correspond to random hits occurring at random stress. Inset: 2 cycles.

In order to compare their waveforms, we select several AE signals (colored dots of Figure 3) arising at about -24MPa (when the material is loaded again), cycle after cycle, in a 310s time window (30068s-30378s, 32 waveforms in 32 cycles). We notice in Figure 4a that their waveforms are almost identical. We therefore name these acoustic signals occurring at a same stress level "AE mutliplets". Multiplets have been studied in seismology [11-13]: multiplet is a group of microseismic events with very similar waveforms and is likely the expression of stress release on the same structure. Here they are AE multiplets and we notice in the cyclic fatigue tests we have studied on pure Aluminum that they appear several hundred cycles before the final failure.
In addition, Figure 4a shows a slight tendency for the values of the waveform maximum amplitude to increase with the stress at which they occurred -the amplitude increases roughly of 0.06V (or about 3dB) per Mpa-.
In Figure 4b we compare waveforms taken randomly in the same time window: the colored crosses, the grey orange green circles and the black square of Figure 3. We notice this time that they do not match, thus confirming the special nature of the aforementioned multiplets.

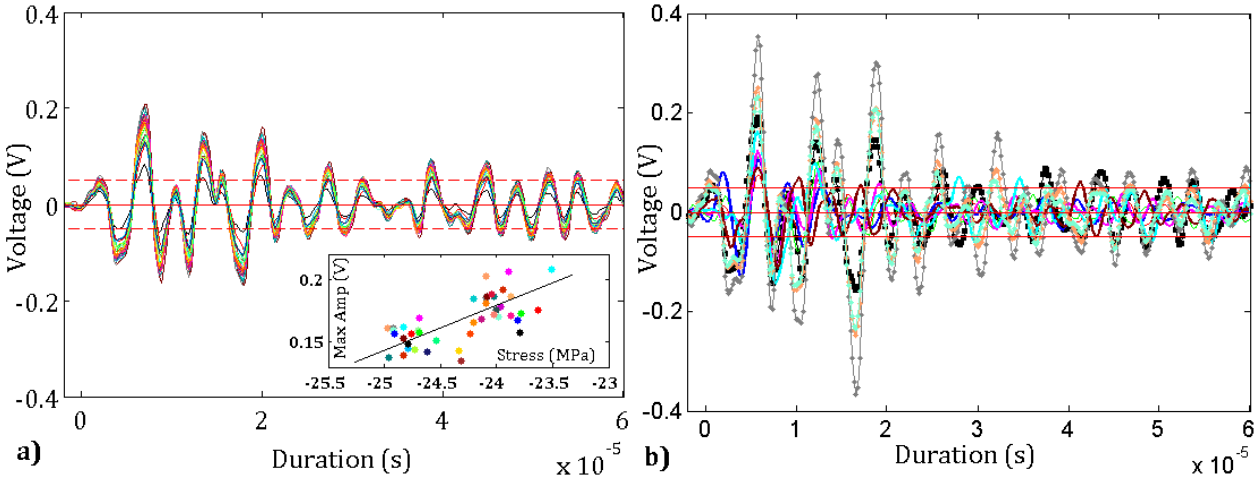

Figure 4 a) Waveforms corresponding to the colored dots of figure 3 (AE signals occurring every cycle at ~ -24 MPa during more than 30 cycles). Inset: maximum of amplitude as a function of the stress where the AE signal occured. b) Ten waveforms corresponding to the selection of AE signals of figure 3 (colored crosses at random stresses, grey orange green circles at ~ -17 MPa and the black square at ~ -24 MPa). Colors of waveforms correspond to colors of markers.

Figure 5a exhibits two other groups of AE events occurring at a given level of stress in the last stage of the test: colored crosses around -17 MPa and colored stars around -15 MPa. Figure 5b shows the location along the gauge length of the specimen and the waveforms of those AE events. We notice that the AE signals appearing at the same stress level are located at about the same site on the specimen and have a same type of waveform (Figure 5b).

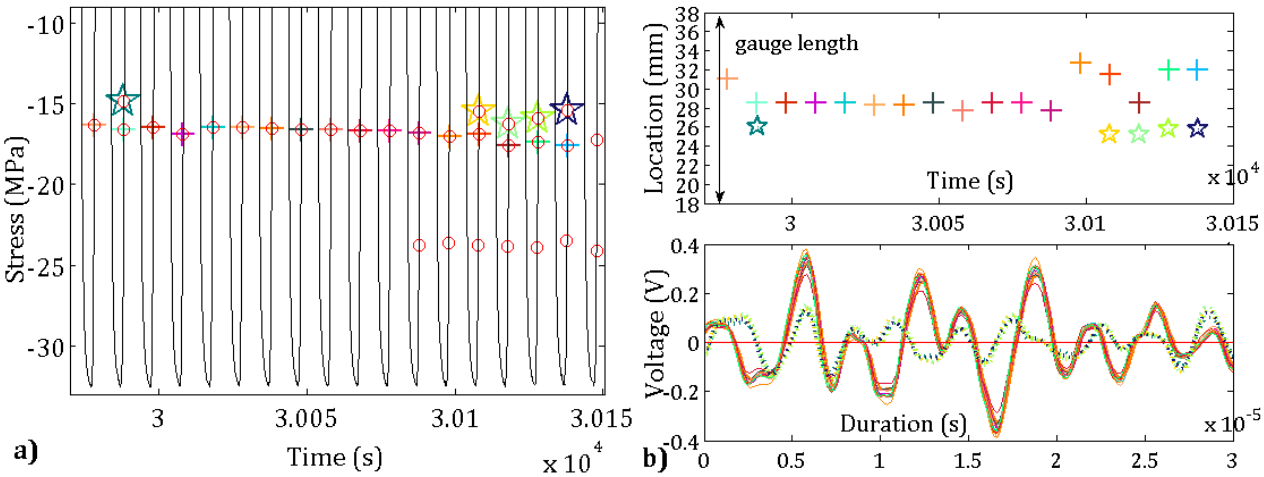

Figure 5 a) Groups of AE events occurring at a same level of stress in the last stage of a fatigue test on aluminum ($\Delta\varepsilon$=0.95%). b) Linear location of AE events along the gauge length of the specimen and corresponding waveforms, continuous lines for the crosses and dashed lines for stars.

Each line of AE signals would come from the same source, being activated again when approximately the same level of stress is reached. Therefore, we hypothesize that such multiplets, shown for the first time in acoustic emission, are the signature of the propagation, cycle after cycle, of a fatigue crack whose trace may be seen post-mortem with the fatigue striations on a fracture surface (Figure 6).

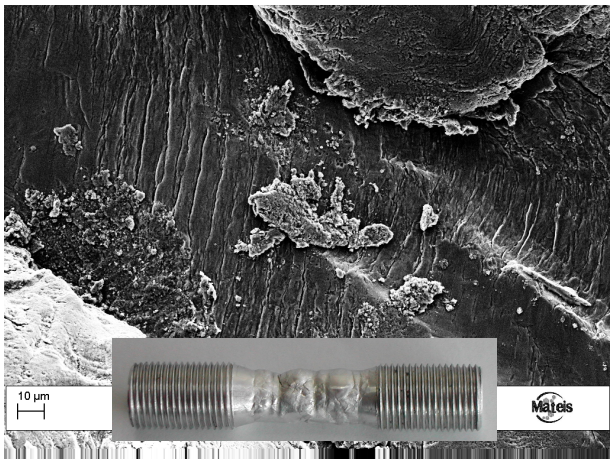

Figure 6 SEM observation of fatigue striations on a fracture surface of pure aluminum after 3024 cycles of a fatigue test at $\Delta\varepsilon$=0.95%. Inset: picture of a specimen just before final failure.

3. Conclusion

Although preliminary, these results give insights into the presence of multiplets in acoustic emission being the signature of the propagation, cycle after cycle, of a fatigue crack. These acoustic signals, with identical waveforms, could therefore be considered as fracture precursors as they appear several hundred cycles before the final failure of the material.

Acknowledgements

This work has been supported by the French ANR-2008 grant EVOCRIT. We thank A. Constantinescu, L. Truskinovski and Z. Moumni for interesting scientific discussions.

References

[1] A. Berkovits, D. Fang, Study of fatigue crack characteristics by acoustic emission. Engineering Fracture Mechanics, 51 (1995) 401-416.

[2] T. Roberts, M. Talebzadeh, Fatigue life prediction based on crack propagation and acoustic emission count rates. Journal of constructional steel research, 59 (2003) 679-694.

[3] T.M. Roberts, M. Talebzadeh, Acoustic emission monitoring of fatigue crack propagation. Journal of Constructional Steel Research, 59 (2003) 695-712.

[4] T.M. Morton, R.M. Harrington, J.G. Bjeletich, Acoustic emissions of fatigue crack growth. Engineering Fracture Mechanics, 5 (1973) 691-697.

[5] M. Shaira, N. Godin, P. Guy, L. Vanel, J. Courbon, Evaluation of the strain-induced martensitic transformation by acoustic emission monitoring in 304L austenitic stainless steel: Identification of the AE signature of the martensitic transformation and power-law statistics. Mater. Sci. Eng., A, 492 (2008) 392-399.

[6] T. Richeton, J. Weiss, F. Louchet, Dislocation avalanches : Role of temperature, grain size and strain hardening. Acta Mater., 53 (2005) 4463-4471.

[7] J. Chicois, R. Fougeres, G. Guichon, A. Hamel, A. Vincent, Mobilite des dislocations lors de la sollicitation cyclique de l'aluminium polycristallin. Acta Metallurgica, 34 (1986) 2157-2170.

[8] A. Slimani, P. Fleischmann, R. Fougères, Etude par émission acoustique de la dynamique

des dislocations pendant la déformation cyclique de polycristaux d'aluminium. J. Phys. III France, 2 (1992) 933-945.

[9] M. Videm, N. Ryum, Cyclic deformation and fracture of pure aluminium polycrystals. Materials Science and Engineering: A, 219 (1996) 11-20.

[10] M. Videm, N. Ryum, Cyclic deformation of [001] aluminium single crystals. Materials Science and Engineering: A, 219 (1996) 1-10.

[11] O. Lengliné, D. Marsan, Inferring the coseismic and postseismic stress changes caused by the 2004 Mw = 6 Parkfield earthquake from variations of recurrence times of microearthquakes. Journal of Geophysical Research: Solid Earth, 114 (2009) B10303.

[12] H. Moriya, H. Niitsuma, R. Baria, Multiplet-Clustering Analysis Reveals Structural Details within the Seismic Cloud at the Soultz Geothermal Field, France. Bulletin of the Seismological Society of America, 93 (2003) 1606-1620.

[13] A.M. Rubin, D. Gillard, J.-L. Got, Streaks of microearthquakes along creeping faults. Nature, 400 (1999) 635- 641.

Understanding the evolution of mechanical properties under irradiation in nuclear glasses via experiments

Marina Barlet[1,*], J-M. Delaye[2], D. Bonamy[1], C. Rountree[1]

[1] CEA/IRAMIS/SPCSI, Groupe Complex Systems & Fracture
F91191 Gif-sur-Yvette, France;
[2] CEA Valrhô-Marcoule DEN/DTCD/SECM/LMPA
* Corresponding author: marina.barlet@cea.fr

Abstract: More than 80% of France's electricity needs are met via nuclear power plants. Due to France's nuclear power program it maintains a high level of energy independence and one of the lowest costs of electricity in the world. Furthermore, with today's worry about global warming, it also lays claim to an extremely low level of CO_2 emissions per capita. However a big disadvantage to nuclear energy is the long term storage of the nuclear waste. The high-level wastes are stored in a complex borosilicate glass matrix to protect the environment from radioactivity for hundreds to thousands of years. But glass is a brittle material which the life time can be limited by micro cracks generated during the fabrication. This glass must also resist to leaching by groundwater. It's why it is important to understand the mechanisms of crack propagation in a corrosive environment. The aim of this study is the comprehension of how the toughness is affected by the structural changes on simplified borosilicate glasses under irradiation and variation of the chemical composition of the glasses.

Simplified borosilicate glasses are irradiated to simulate alpha and beta decays using He^{2+} ions and electrons. The subcritical stress corrosion fracture properties of glasses are studied using DCDC samples which permit fracture growth in this regime. The experimental measurements of the crack propagation velocities as a function of the applied stress intensity factor is presented as a $v=f(K_I)$ curves. To understand how structural modifications are linked to failure mechanisms RAMAN, NMR and EPR spectra are investigated.

Keywords: Fracture, stress corrosion, irradiation

1. Introduction

Originally spent fuel was supposed to remain in spent fuel pools for 10-15 years. However many countries have left the fuel in for more than 20 years, and there is no end in sight. Spent fuel contains Uranium (~95%), Plutonium (~1%), Minor Actinides (~0.1%; Neptunium, Americium, and Curium), and Fission Products (~4%), and it poses a significant security risk as seen during Fukushima. France has chosen to close the fuel cycle by reprocessing spent fuel. Uranium (~95%), Plutonium (~1%) are reprocessed into MOX fuel, and the minor actinides and fission products are imbedded into nuclear glass packages (NGP, a complex Borosilicate Glass matrix frequently called R7T7 in France). These systems are subject to self-irradiation stresses which arise due to α disintegrations and β/γ decay processes of minor actinides (^{237}Np, ^{241}Am, and ^{244}Cm to name a few) and fission products in NGP. Piecewise studies concerning the structural modifications and how they affect the material properties have been conducted; however the origin and the extent to which these modifications affect the glass are not fully understood [1, 3, 5, 8, 9, 13, 16, 18, 19].

Numerous studies carried out investigate the impact of alpha and beta irradiation at macroscopic and microscopic scales[6, 15, 17, 18]. Variations in mechanical properties include: (1) up to 30% decrease of the hardness depending on irradiation doses and (2) about 60% increase in the toughness before stabilization.

Some authors concluded these evolutions are due to variations of the glassy molecular structure.

Over the past century multiple methods have been discovered and implemented and moreover today are widely used to study structural variations. Two techniques which will be implemented herein are Electron Paramagnetic Resonance (EPR) which is a very sensitive tool for the analysis of paramagnetic defects in glasses and Raman spectra usually employed in the examination of vibrational, rotational and other low frequency modes in complex sodium borosilicate glasses. From these spectra, scientists are able to extract information on the electronic defects, and some structural characteristics about local entities, local angles, local coordinations [7][5]…. Moreover after heavy ions irradiation scientists have evidenced[9][8][14, 17]: (1) decreasing of Si-O-Si angle; (2) depolimerization of the borate network; (3) change in sodium's role (network compensator/modificator)…. These structural evolutions are proposed to explain the modifications of the macroscopic properties. These recent conclusions contradict some older experiments that suggest these variations are due to electronic process[1].

To better understand the source of the changes in the macroscopic properties, and in particular the hardness of nuclear glasses, simplified borosilicate glasses are subject to a controlled external irradiation. Herein we will report results on samples which undergo electron irradiation. Hardness results are acquired via Vickers indentation tests. An investigation is also underway concerning how the fracture behavior at macroscopic scale and the structure modification at microscopic scale are linked.

2. Experimental methodology

2.1) Glass samples:

Nuclear glass packages are complex systems which contain more than 30 different oxides and undergo self-irradiation. In order to understand the role of each oxide the composition has to be simplified. A reasonable simplification of the NGP is sodium borosilicate glasses (SiO_2-B_2O_3-Na_2O), or SBN glasses, as these are the three main components of the NGP system. Herein we will concentrate on three compositions: SBN14, SBN35 and SBN55 (see table 1) which are defined by R_{OG} ($[Na_2O]/[B_2O_3]$) and K_{OG} ($[SiO_2]/[B_2O_3]$). It should be noted that due to the crucibles used in the glass fusion processes, a minimal amount of iron was found in all samples. Secondly as crucibles are recycled SBN35 and SBN55 also have a minimal amount of zirconium. The amount of iron and zirconium has been quantified and it is less that .1% molar mass.

To simulate electronic damage due to self-irradiations, the glasses are externally irradiated via electrons. Electron irradiations were conducted at LSI Sirius. Sirius is a 2.5 MeV Van de Graaff accelerator. At 2.5MeV electrons can penetrate the full our sample thickness (0.8mm thick). Thus our samples are considered homogeneous irradiation. An integrated dose of 0.5, 1, 1.5 or 2 GGy irradiation dose was reached on each sample with a 12 µA beam. During irradiation the sample temperature was maintained at less than 40°C.

OG name	SiO_2	Na_2O	B_2O_3	R_{OG}	K_{OG}
SBN14	67.73	14.23	18.04	0.79	3.76
SBN 55	55.3	29.99	14.71	2.04	3.76
SBN 35	43.95	35.42	20.63	1.72	2.12

Table 1: Composition of glasses (% of molecular oxides)

2.2) Marco-hardness tests:

Microscopic indentation tests were conducted using an Anton Paar MHT-10 Microhardness Tester. These tests were performed on glass specimens irradiated with electrons, and the load mass varied from 10g to 100g. The duration of each load was 15 seconds. The hardness values are determined as follows:

$$H_v = \frac{2*F*\sin(\frac{\theta}{2})}{d^2} \qquad (1)$$

where F is the applied force in Newtons, θ corresponds to the angle of the indenter (136° herein), and d is the averaged diagonal length of the residual print in mm (figure1). Hardness values presented herein are the average of 10 tests with a load of 50g.

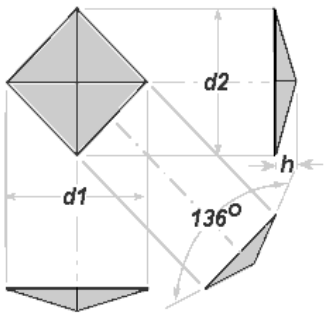

Figure 1 : Sketch of the Vickers diamond pyramid indenter

2.3) Structural measurements

Structural quantifications have been conducted via two techniques herein: RAMAN and EPR measurements. These measurements provide us with some insight on local variations and defects creation.

RAMAN measurements:

Raman spectroscopy measures the vibration modes of a system; moreover, it depends on Raman (inelastic) scattering of visible light. The incident photon interacts with the electron cloud; the return to a lower level emits a photon shift if the final state is different from the initial state. The frequency shift is called the Stokes shift. To improve the weak Raman intensity why several techniques are invoked (filters, high power...). Herein a Jobin Yvon HR 800 spectrometer was used to acquire RAMAN spectra. The wavelength of the laser on the instrument was 532 nm. Also the laser power was maintained at a low level to avoid heating of the sample.

EPR measurement:

Electron Paramagnetic Resonance (EPR) techniques permit a detailed identification of paramagnetic defects on the atomic scale in solids. Within the literature, there are several common defects which EPR spectroscopy can detect: oxygen hole center, E' centers, hole centers associated with boron atoms, hole centers near alkaline ions, etc**[4, 12]**Hence, the aim of this work is to inspect the paramagnetic defects as a function of the irradiation dose, and secondly how the paramagnetic defects vary as a function of the chemical composition in SBN samples. Electron Paramagnetic Resonance (EPR) spectra were obtained to

evaluate the paramagnetic defects due to electron irradiation. EPR spectra are obtained using an X band (v~10GHz) ESP300 Bruker spectrometer. Multiple spectra were run at different powers (1µW, 1mW and 10mW) to enhance or subdue defects.

2.4) Stress corrosion cracking

In moist environments, subcritical crack propagation, or stress-corrosion fracture, is feasible, i.e. $K << K_c$, due to the stress enhanced corrosive action of water molecules on the stretched molecules within the PZ[10]. The stress-corrosion cracking regime is of primary importance in the storage of nuclear waste since it can modify the storage quality over the long term. In this regime, the crack velocity can be very small, down to a few picometers per second. The global form of the curve $v(K,T,H)$ in OG (where K, T, and H refer to stress intensity factor, temperature and humidity, respectively) has partially rationalized over these last 4 decades[20][11] for a recent review]. It was shown to exhibits three regions:

- Region I where the crack velocity is set by the rate of the stress enhanced chemical reaction between water molecules and stretched chemical bonds in the OGs.
- Regime II where the crack velocity is limited by the transport of water molecules to the crack tip.
- Regime III where the velocity raises sharply with K.

The experimental set up which will be employed herein has been tested frequently over the past 10 year within the Complex systems and Fracture Group. These experiments are performed on DCDC (Double Cleavage Drilled Compression) specimens. Samples will be placed between the jaws of a compressive Deben machine (Figure 2). The force will then be gradually increased up to the initiation of two cracks that propagate symmetrically on both sides of the hole. During the propagation of cracks, a CDC camera will be used to gather information on the velocity of the crack front. Thus with this information we can plot the velocity versus the stress intensity factor (K_I).

Figure 2 : Experimental setup used to fracture glass sample at low velocity in stress corrosion.

3. Experimental results

In SBN samples presented herein electrons should uniformly irradiate the system; hence leaving homogenous samples to be examined. This is contrary to light and heavy ion irradiation (not presented herein) which only penetrate the samples by a few μm. SBN55 and SBN35 irradiated from until 0 to 2GGy were found to have little to no variation on the hardness. On the contrary the SBN14 composition presents another behavior: the hardness decreases by about 20 % at 1 GGy (figure 3).

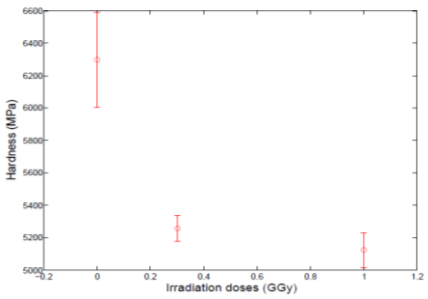

Figure 3 : Hardness variation (MPa) versus electronic irradiations doses for SBN 14 glass

In order to quantify and qualify some of the smallest variations, i.e. variations in the paramagnetic defects of the glasses, we will study the EPR spectra. In all cases non-irradiated glasses revealed defects due to contamination during elaboration (Zr^{3+} and Fe^{3+})[2]. SBN14 irradiated glasses (figure 4a)) did expose E' centers, Oxygen hole centers, hole centers near alkaline ions [4]…. A dependence on the irradiation dose is revealed. Moreover we find an evolution in paramagnetic defects versus the chemical composition (figure 4a et 4b) right).

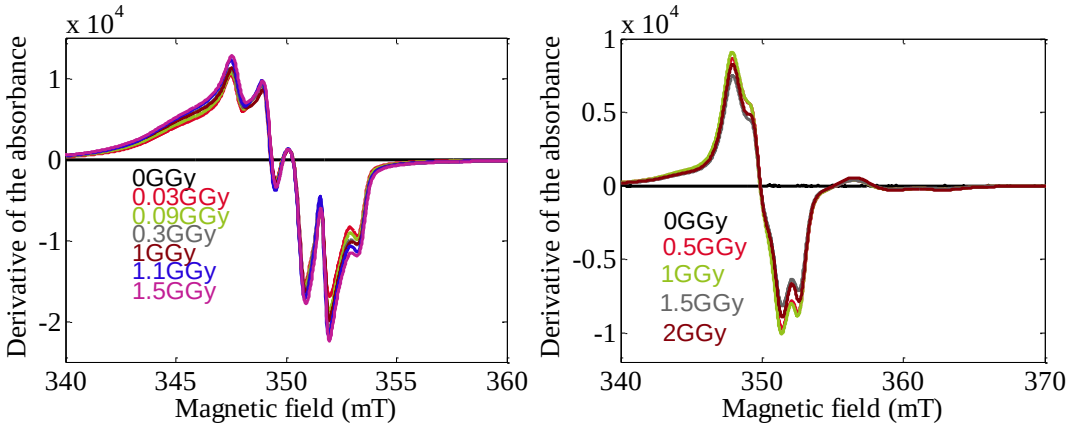

Figure 4 : EPR spectra for a) SBN 14 and b) SBN 35 at 1μW.

Figure 6 depicts the RAMAN spectra for SBN35 at irradiation doses 0, 0.5, 1, 1.5 and 2GGy,. Herein minute dependencies are found on the dose for SBN35 samples.

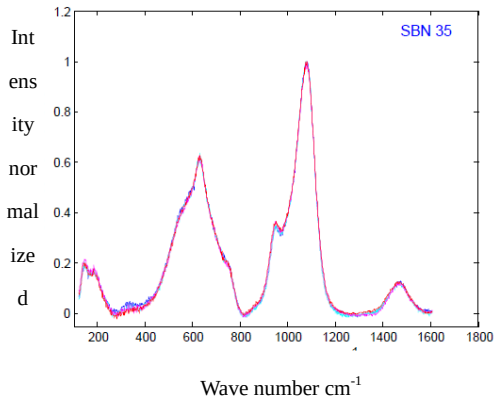

Figure 5 : RAMAN spectra for SBN 35 at different doses: 0, 0.5, 1.5 and 2GGy

4. Discussion and conclusion

Electronic damages induced in glass vary with composition. No influence until 2 GGy have been observed for two borosilicate glasses SBN35 and SBN55. The SBN 14 presents a marked behavior.

The variations affect the macroscopic scale with a decrease of the hardness value and an increase of the toughness which can be explained by the variation at microscopic scale. To understand the relation between electronic damages and glass compositions other studied are needed. Finally let us add that stress corrosion fracture studies are still underway and will be presented at the conference.

5. Acknowledgements

Electron irradiation were conducted at LSI (Laboratoire des Solides Irradiés), Palaiseau, France and supported by the French Network EMIR. The electron irradiation facility at LSI was supported by grants from Région Ile-de-France. Atomic Force Microscopy results were conducted at SPCSI (Service de Physique et Chimie des Surfaces et Interfaces), CEA-Saclay, Gif-Sur-Yvette, France and supported by grants from Région Ile-de-France and Triangle de la Physics (RTRA).

Bibliography

[1] Arnold, G.W. 1988. ION-IMPLANTATION-INDUCED STRESS IN GLASSES - VARIATION OF DAMAGE MODE EFFICIENCY WITH CHANGES IN GLASS STRUCTURE. *NUCLEAR INSTRUMENTS & METHODS IN PHYSICS RESEARCH SECTION B-BEAM INTERACTIONS WITH MATERIALS AND ATOMS*. 32, 1-4 (1988).

[2] Boizot, B. et al. 2001. Dose, dose rate and irradiation temperature effects in beta-irradiated simplfied nuclear waste glasses by EPR spectroscopy. *Journal of Non-Crystalline Solids*. 283, (2001), 179–185.

[3] Boizot, B. et al. 2000. Migration and segregation of sodium under beta-irradiation in nuclear glasses. *NUCLEAR INSTRUMENTS & METHODS IN PHYSICS RESEARCH SECTION B-BEAM INTERACTIONS WITH MATERIALS AND ATOMS*. 166, (2000), 500–504.

[4] Boizot, B. et al. 1998. Radiation induced paramagnetic centres in nuclear glasses by EPR spectroscopy.

Nuclear Instruments and Methods in Physics Research B. 141, (1998), 580–584.

[5] Boizot, B. et al. 1999. Raman study of b-irradiated glasses. *Journal of Non-Crystalline Solids*. 243, 2-3 (1999), 268–272.

[6] De Bonfils, J. et al. 2007. Behaviour of simplified nuclear waste glasses under gold ions implantation: A microluminescence study. *JOURNAL OF NUCLEAR MATERIALS*. 362, 2-3 (2007), 480–484.

[7] De Bonfils, J. et al. 2010. Effect of chemical composition on borosilicate glass behavior under irradiation. *JOURNAL OF NON-CRYSTALLINE SOLIDS*. 356, 6-8 (2010), 388–393.

[8] De Bonfils, J. 2007. *Effets d'irradiation sur la structure de verres borosilicates -Comportement à long terme des matrices vitreuses de stockage des déchets nucléaires*. Université Lyon 1.

[9] Bureau, G. 2008. *Compréhension struturale des effets d'auto-irradiation alpha dans les verres : couplage entre études spectroscopiques et modélisation atomistique*. Université Paris VI.

[10] Charles, R.J. and Hillig, W.B. 1962. Symposium on Mechanical Strength of Glass and Ways of Improving It. *Union Scientifique Continentale du Verre* (1962).

[11] Ciccotti, M. 2009. Stress-corrosion mechanisms in silicate glasses. *Journal of physics d-applied physics*. 42, 21 (2009).

[12] Devine, R. 1994. The structure of SiO2, its defects and radiation hardness. *IEEE transaction on nuclear science*. 41, 3 (1994), 452–459.

[13] Ewing, R.C. et al. 1995. Radiation effects in nuclear waste forms for high-level radioactive waste.

[14] Inagaki, Y. et al. 1992. MICROSTRUCTURE OF SIMULATED HIGH-LEVEL WASTE GLASS DOPED WITH SHORT-LIVED ACTINIDES, 238PU AND 244CM. *SCIENTIFIC BASIS FOR NUCLEAR WASTE MANAGEMENT XV*. 257, (1992), 199–206.

[15] Le-Hai, K. 2011. *Compréhension de l'origine de l'évolution sous irradiation de la ténacité des verres nucléaires*. Ecole Polytechnique.

[16] Peuget, S. et al. 2006. Effects of deposited nuclear and electronic energy on the hardness of R7T7-type containment glass. *Nuclear Instruments and Methods in Physics Research B*.

[17] Peuget, S. et al. 2006. Irradiation stability of R7T7-type borosilicate glass. *Journal of Nuclear Materials*.

[18] Peuget, S. et al. 2005. *Note technique DTCD/SECL/2005/15*.

[19] Weber, W.J. et al. 1997. Radiation effects in glasses used for immobilization oh highlevel waste and plutonium disposition.

[20] Wiederhorn, S.M. and Bolz, L.H. 1970. Stress corrosion and static fatigue of glass. *JOURNAL OF THE AMERICAN CERAMIC SOCIETY*. 53, 10 (1970), 543.

Thickness-dependent lower bounds of fracture toughness of ferritic steels in the ductile-to-brittle transition regime

Hans-Jakob Schindler [1*] **and Dietmar Kalkhof** [2]

[1] Mat-Tec AG, Unterer Graben 27, CH-8401 Winterthur, Switzerland

[2] Swiss Federal Nuclear Safety Inspectorate, CH-5200 Brugg, Switzerland

* schindler@mat-tec.ch

Abstract. The inherent scatter of fracture toughness of ferritic steels in the brittle-to-ductile transition regime require statistical methods to be applied for testing and evaluation. However, for engineering purposes lower bounds of K_{Ic} such as the ASME-reference curve are often preferred since they allow deterministic worst-case predictions to be made. So the question is how to derive lower bounds of a quantity that is governed by weakest-link-statistics. Actually, neither the MC-approach nor the empirical ASME-reference curve deliver well-founded lower bounds for components of relatively small thicknesses. A theoretical model is suggested to fill this gap. The key element of the approach is the hypothesis that the weakest-link-effect is saturated at a certain thickness. The corresponding upper limit of size-dependence turned out to be close to the minimum thickness required for plane-strain conditions at the crack-front. The derived mathematical relations enables K_{Ic} to be calculated from K_{Jc} as measured on a smaller specimen. In reverse, from a lower-bound K_{Ic} as provided by the ASME-code a thickness-dependent lower bound of K_{Jc} can be obtained. The proposed model is shown to yield predictions that are consistent with experimental data as well as with the ASME-lower bound.

Keywords Ductile to brittle transition, reference temperature, ferritic steel, lower bound, fracture toughness, plane strain.

1. Introduction

For physical reasons fracture toughness of ferritic steels in the brittle-to-ductile transition regime is affected by a pronounced scatter, which requires statistical methods to evaluate test data as well as to predict the load-bearing capacity of a structural component that contains a crack. Since initiation of cleavage is governed by weakest-link-statistics, fracture toughness is associated with a certain probability of failure and dependent on the size of the tests specimen or structural component. According to the Mastercurve- (MC-) approach [1, 2] fracture toughness K_{Jc} of ferritic steel exhibited by a 1T-specimen (i.e. thickness of B_{1T}=1inch=25.4 mm) can be expressed in terms of the cumulative probability of failure (p_f) as

$$K_{Jc}(B_T = 0.0254m, p_f) = K_{\min} + \left[\ln\left(\frac{1}{1-p_f}\right)\right]^{1/4} \{11 + 77\exp[0.019\cdot(T - T_0)]\} \qquad (1)$$

where K_{min}=20 MPa·m$^{0.5}$. The reference-temperature T_0 is a characteristic material property that has to be determined experimentally as prescribed in [2]. If the thickness B deviates from B_{1T}=0.0254 m, then K_{Jc} shall be size-adjusted by

$$K_{Jc}(B, p_f) = K_{\min} + \left[K_{Jc}(B_T, p_f) - K_{\min}\right] \cdot \left(\frac{B_T}{B}\right)^{0.25} \quad (2)$$

where B is the arbitrary thickness of a component and B_T is the thickness of the test specimen, for example B_T =0.0254 m for standard 1T-specimens [2].

In an engineering safety analysis usually fracture toughness corresponding to very low values of p_f and relatively large thicknesses are required. It is plain to see that (1) and (2) do not exhibit the correct asymptotical behaviour of K_{Jc} for $p_f \rightarrow 0$ and for $B \rightarrow \infty$, since both of them predict K_{Jc} to approach K_{min}=20 MPa·m$^{0.5}$, which is a auxiliary number that serves well to evaluate test-data, but not to predict fracture toughness values for low p_f and high B. Instead, for physical reasons a lower-bound of fracture toughness that depends on temperature and yield strength is expected to exist [3, 4, 5]. In fact, there is strong experimental evidence that K_{Jc}(B) does not follow (2) for about $p_f < 0.025$ but approaches for $p_f \rightarrow 0$ a well-defined lower bound value $K_{Jc(LB)}$ [6].

Concerning the effect of thickness on fracture toughness, the classical concept of linear-elastic fracture mechanics presumes that fracture toughness reaches a minimum denoted as K_{Ic} if plane-strain-conditions prevail in the plastic zone. According to current K_{Ic}-testing standards [7, 8, 9] this is guaranteed if the specimen thickness B_T fulfills the condition

$$B_T \geq B_{p\varepsilon} = \alpha \cdot \left(\frac{K_{Jc}}{R_p}\right)^2 \quad (3)$$

with α=2.5 and R_p denoting the yield stress. However, like K_{Jc}, K_{Ic} in the ductile-to-brittle transition regime of ferritic steels is affected by an inherent scatter. For this reason in engineering safety analysis it is common to use lower bound fracture toughness values. For reactor pressure vessel (RPV-) steels, the ASME-code [10] provides the following lower bound of K_{Ic}:

$$K_{Ic(ASME)}(T) = 36.5 + 22.8 \cdot \exp\left[0.036 \cdot (T - RT_{NDT})\right] \quad (4)$$

RT_{NDT} is the so-called nil-ductility temperature that originally had to be determined by Charpy- and drop- weight-tear-tests [10]. Both eqs. (1) and (4) contain just one material parameter, i.e. T_0 and RT_{NDT}, respectively, so a relation between them is expected to exist. In fact, experimental data of RPV-steels revealed the following empirical correlation [11, 12]:

$$RT_{NDT} = T_0 + 19.4K \quad (5)$$

Despite of this relationship, concerning the thickness-effect there is a fundamental inconsistency between the MC-approach and the classical concept of linear-elastic fracture mechanics, where plane strain fracture toughness is regarded as the asymptotical minimum value of K_{Jc}. In the framework of the ASTM-standards this conflict is resolved simply by excluding ferritic steels from K_{Ic}-testing according to E399 [7], which is not quite satisfying from a scientific point of view. Inspired by a similar task by Merkle et al. in [13], in the present paper an attempt is made to bridge the gap between the above mentioned approaches by imposing an upper limit on the range of validity of Weibull-statistics as far as the thickness is concerned, and by introducing a temperature- and size-dependent lower bound of the corresponding fracture toughness as far as the failure probability is concerned. In reverse, the present approach leads in a straightforward way to an

effective thickness-dependent lower bound of fracture toughness for structural components that are too thin to fulfill criterion (3) for plane strain. These are cases where eq. (4) tends to predict too low fracture toughness values, which can lead to an over-conservative assessment of the safety of the corresponding structure.

2. Saturation of statistical thickness-effect

According to Weibull-statistics, the cumulative probability of failure, p_f, is a function of the fracture-controlling volume V_c next to the crack-front, where the stresses are high enough for cleavage to be initiated. Whether or not an unstable crack extension is triggered depends on the presence of a weak spot such as a local defect or a brittle particle. The in-plane dimensions of V_c are known to be in the order of the crack-tip opening displacement (CTOD) [3], which is proportional to K_I^2, so V_c is proportional to $K_{Jc}^4(B)\cdot B$ for a component of thickness B. For a 2-parameter Weibull-distribution this leads to the following dependence of K_{Jc} on the component thickness B:

$$K_{Jc}(B, p_f) = K_{Jc}(B_T, p_f)\cdot\left(\frac{B_T}{B}\right)^{0.25} \tag{6}$$

Obviously, the asymptotical behaviour of (6) for $B\rightarrow\infty$ is not correct. However, instead of using a 3-papameter approach with a threshold K_{min} as in eq. (2), we postulate that the validity of (6) is restricted to the range $B_{p\sigma}<B<B_{sat}$. Its lower limit, $B_{p\sigma}$, is imposed by the transition to plane stress conditions, which can be considered as a cut-off at upper-shelf toughness $K_{J(US)}$. The upper limit, B_{sat}, reflects the hypothetical assumption that the thickness-effect (6) saturates at a certain thickness B_{sat}, so K_{Jc} for $B>B_{sat}$ is no longer decreasing, but remains constant at the level K_{sat}, as sketched in Fig. 1.

The postulated saturation of the thickness effect for $B>B_{sat}$ is attributed to the extreme slenderness of the fracture-controlling volume V_c along the crack front. V_c has a width of B and in-plane dimensions in the order of magnitude of CTOD, which is in the order of $K_{Jc}^2/(E\cdot R_p)$, thus two or three orders of magnitude smaller than B. Physically, the postulated saturation can be explained by the unlikeliness that under a given load a cleavage fracture can be obtained by a further increase of B, if the latter is already two or three orders of magnitudes larger than the in-plane dimensions of V_c. Unstable crack extension is much more likely to be obtained, if CTOD is increased, since in this case not only V_c but also the global energy release rate are increased. Thus, the saturation is likely to occur if the ratio B/CTOD reaches a certain value. Therefore the parameter

$$\beta = \frac{B\cdot E\cdot R_p}{K_{Jc}^2} \tag{7}$$

is introduced to quantify the slenderness of V_c. The postulated saturation of the thickness effect is assumed to be reached for

$$\beta \geq \beta_{sat} = \frac{B_{sat}\cdot E\cdot R_p}{K_{Jc}^2} \tag{8}$$

The corresponding curve $K_{Jc}(B, p_f)$ shown in Fig. 1 can be written as

$$K_{Jc}(B, p_f) = \begin{cases} K_{Jc}(B_T, p_f) \cdot \left(\frac{B_T}{B}\right)^{0.25} & for\ B_{p\sigma} < B < B_{sat} \\ K_{sat}(p_f) & for\ B > B_{sat} \end{cases} \quad (9)$$

B_{sat} is obtained as the intersection of (6) with

$$K_{Jc} = \sqrt{\frac{B \cdot E \cdot R_p}{\beta_{sat}}} \quad (10)$$

that follows from (8). Equalizing (10) and (6) delivers

$$B_{sat} = \left(\frac{\beta_{sat}}{R_p \cdot E}\right)^{2/3} \cdot B_T^{1/3} \cdot K_{Jc}^{4/3}(B_T) \quad (11)$$

By inserting (11) in (10) one obtains

$$K_{sat} = \left(\frac{B_T \cdot E \cdot R_p}{\beta_{sat}}\right)^{1/6} \cdot K_{Jc}^{2/3}(B_T) \qquad \text{for } B_T < B_{sat} \quad (12)$$

Eq. (12) enables K_{sat} to be predicted from K_{Jc} measured by a specimen with relatively small thickness B_T, provided β_{sat} is known. The latter is determined in Section 4.

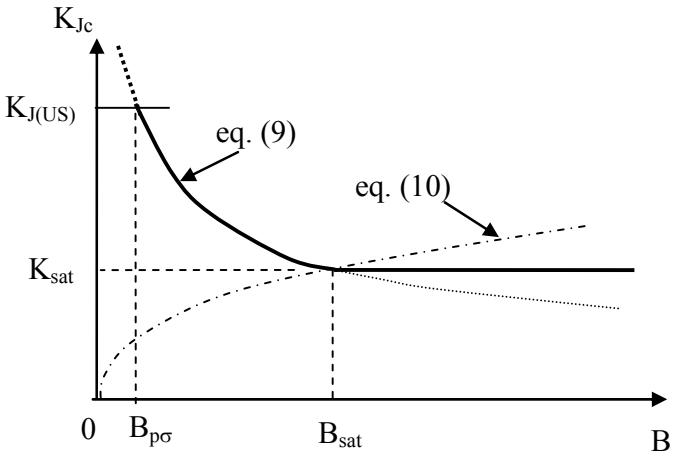

Fig. 1: Dependence of $K_{Jc}(p_f)$ on the thickness B according to the proposed model

3. Lower bound $K_{Jc}(B)$

K_{sat} as given in eq. (12) represents a lower limit of K_{Jc} only with respect to the effect of thickness, but not with respect to p_f. However, as discussed in the introduction, a certain minimum K_I is required for unstable cleavage to occur for energetic reasons. Thus, there must be a lower bound of the scatter band of K_{sat}. It is likely that $K_{Ic(ASME)}(T)$ according to eq.(4), which was determined

empirically as the lower envelope to a large number of valid K_{Ic}-data, represents a good approximation of the physical lower bound of K_{sat}. This means formally

$$K_{sat}(T, p_f = 0) = K_{Ic(ASME)}(T) \tag{13}$$

Since eq. (12) holds for any value of p_f, it also does for the hypothetical case "p_f=0" that represents a lower bound. Correspondingly, as shown graphically in Fig. 2, $K_{Ic}(T, p_f=0)$ is associated with a lower bound curve $K_{Jc(LB)}$ for $B<B_{sat}$. This curve is obtained by equalizing K_{sat} given in (12) with $K_{Ic(ASME)}$ given in (4), which results in

$$K_{Jc(LB)}(B) = \left(\frac{\beta_{sat}}{R_p \cdot E \cdot B}\right)^{1/4} \cdot \left\{36.5 + 22.8 \cdot \exp\left[0.036 \cdot (T - T_0 - 19.4K)\right]\right\}^{3/2} \quad \text{for } B<B_{sat(LB)} \tag{14a}$$

and

$$K_{Jc(LB)} = 36.5 + 22.8 \cdot \exp\left[0.036 \cdot (T - T_0 - 19.4K)\right] \quad \text{for } B>B_{sat(LB)} \tag{14b}$$

where

$$B_{sat(LB)} = \frac{\beta_{sat} \cdot K^2_{Ic(ASME)}}{R_p \cdot E} \tag{14c}$$

As shown in the next section, an appropriate value of β_{sat} turned out to be 1150.

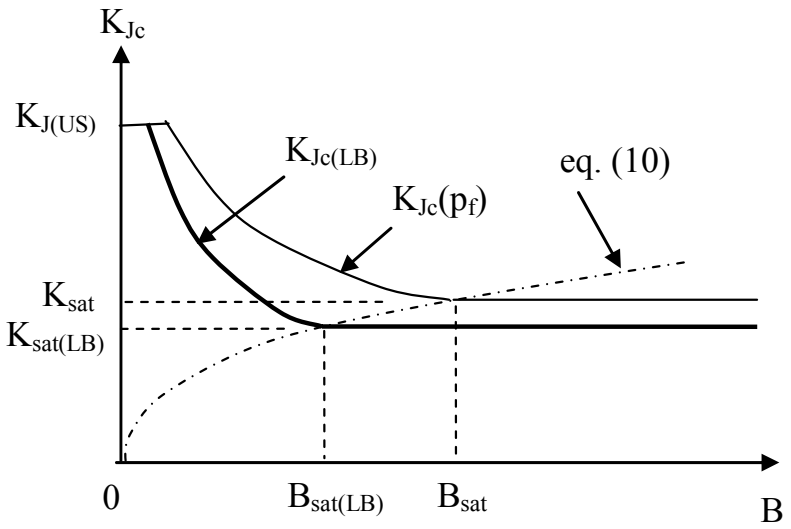

Fig. 2: Dependence of the lower bound of K_{Jc} on the thickness B according to the proposed model

Table 1: T_0-values according to [2] determined from the data shown in Fig. 3 for the individual specimen sizes.

	1T-CT	3.2T-SEB	1.6T-SEB	0.8T-SEB	0.4T-SEB
Thickness B[mm]	25.4	80	40	20	10
T_0 [°C]	-71	(*)	-75.2	-85.8	-86.1

(*) not enough specimens available to determine a valid T_0 according to [2]

4. Experimental Confirmation

Eqs. (14) represent a lower bound of $K_{Jc}(B)$ analogously to $K_{Ic(ASME)}$ as given in eq. (4), but for thicknesses $B<B_{sat(LB)}$. In the following, the predicted lower bound is compared with experimental data. Since (14a, c) contain the open parameter β_{sat}, this comparison offers the possibility to determine β_{sat} experimentally. As a representative test material RPV-steel 22NiMoCr 3-7 was chosen, which is similar to steel A508. Standard 1T-CT-specimens (B=25.4 mm) and 3-point bending specimens (SEB) of square cross sections and different sizes were used (from B=W=10 mm (denoted as 0.4T) up to B=W=80 mm (3.2T)). The multi-temperature option of [2] was applied to evaluate T_0 for each specimen type and size. The test procedure and the results are documented in detail in [14]. The obtained T_0 are given in Table 1. Note that T_0 from the 0.4T-SEB-specimens are significantly lower than T_0 from CT-specimens, which corresponds to a well-known bias of T_0 [15]. In the following comparisons, T_0 corresponding to 1T-CT-specimens (i.e. T_0 =-71°C) is taken as the reference value.

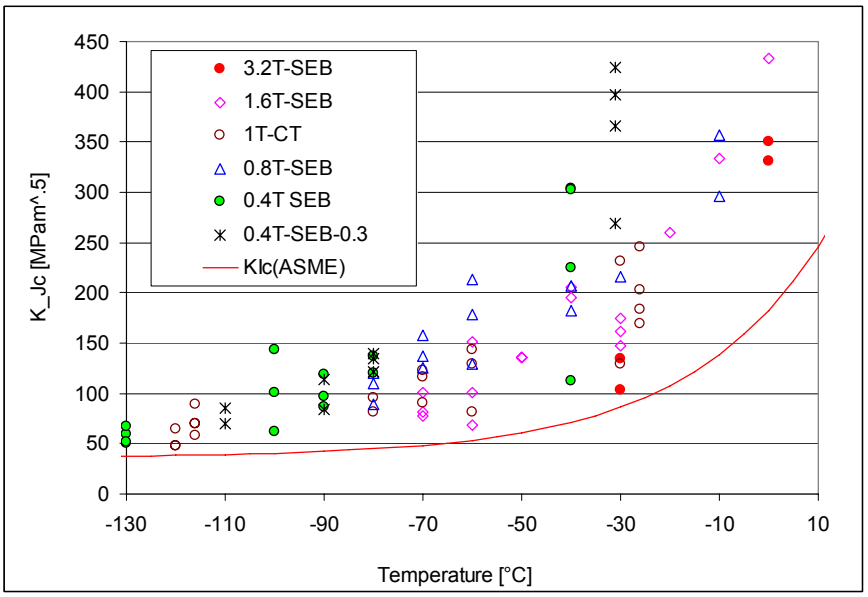

Fig. 3: K_{Jc}-data of different specimens in comparison with the lower bound $K_{Ic(ASME)}(T)$

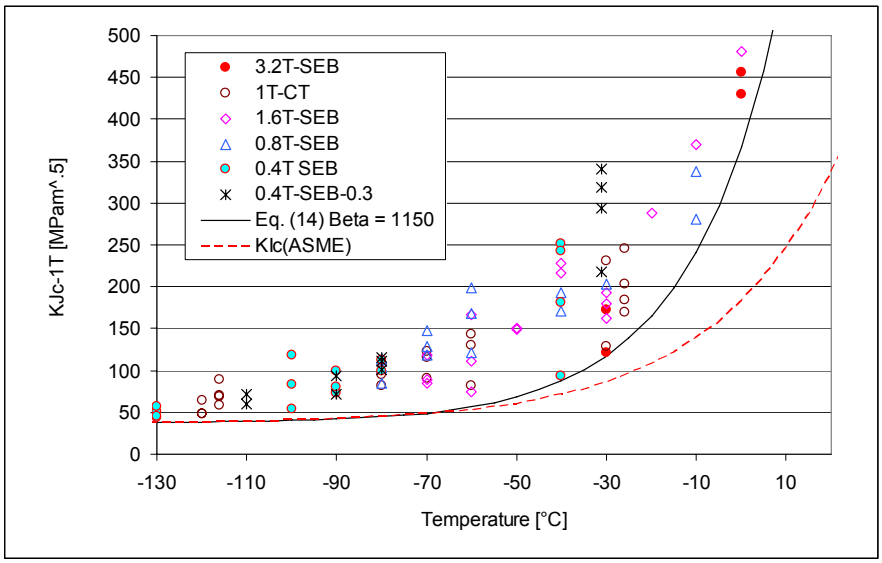

Fig. 4: Experimental data normalized to B_T=0.254m in comparison with eq. 14 with β_{sat}=1150

Fig. 3 shows the experimental K_{Jc}-data, in comparison with the lower bound eqs. (4)/(5). Obviously, the latter envelopes the experimental data with a rather large margin of safety, particularly in the upper transition range. In order to compare the experimental data with the lower bound predicted by eqs. (14) the K_{Jc}-values shown in Fig. 3 are normalized in Fig. 4 to the thickness of standard 1T-specimens (i.e. B=0.0254 m) by means of eq. (2). The parameter β_{sat} was chosen such that eqs. (14) forms the close lower envelope shown in Fig. 4, which is the case for

$$\beta_{sat}=1150 \qquad (14d)$$

In Fig. 5 the experimental data of the individual specimen sizes are compared with the lower bounds predicted by eqs. (14) with β_{sat} according to eq. (14d). Note that the predicted size-dependent lower bounds envelope not only the valid data, but also those beyond the validity limit of E1921. Actually, eqs. (14) seem to hold approximately up to the transition to upper-shelf behaviour, which takes place at about K_I=350MPa for the present steel. As expected and also shown in Fig. 5, $K_{Ic(ASME)}(T)$ is significantly too low if applied to relatively small specimens or components. In all cases eqs. (14) represents more realistic lower bounds. Furthermore, as shown by the example of p_f=2.5% in Fig. 5, one can see that tolerance bounds based on the MC-approach (eqs. (1) and (2)) match even worse with the experimental data, particularly for the larger specimens.

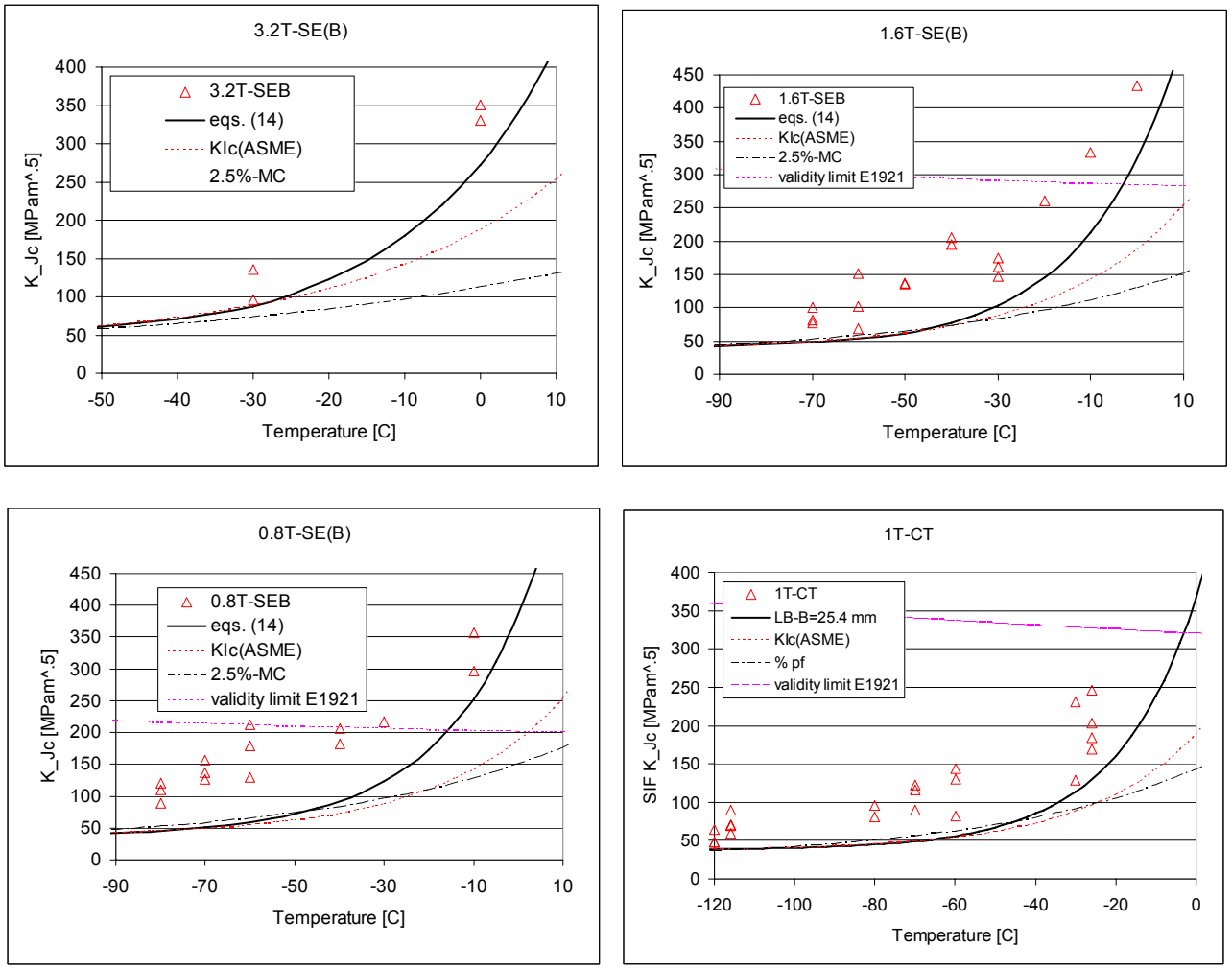

Fig. 5: K_{Jc}-data obtained from SEB-specimens of different sizes and 1T-CT-specimens, in comparison with possible lower bounds as discussed in the text.

5. Discussion

The lower-bound of K_{Ic} reflects a threshold that is imposed by physical requirements for unstable cleavage [4]. $K_{Jc(LB)}$ as given by eqs. (14) is different. It has to be regarded as an "effective" lower-bound, which is caused mainly by effects of weakest-link-statistics. However, as shown by comparison with experimental data, it still represents a reliable lower bound of K_{Ic}. It can serve as a basis for failure assessment of relatively small components, where the ASME-lower-bound tends to over-conservative predictions. Since it is governed by weakest-link statistics, it also is applicable to surface cracks, where B has to be replaced by the length of the crack-front.

In the derivation of the size-dependent lower bound use is made of the lower-bound of K_{Ic} according to ASME [10]. Thus, formally, eqs. (14) underlie the same restrictions as eqs. (4) and (5) as far as the material is concerned. However, according to the MC-concept, fracture toughness of all ferritic or bainitic steels with yield strengths lower than 800 MPa is characterized just by T_0. Correspondingly, lower bounds are expected to depend on just one parameter as well. This means that the applicability of eqs. (14) corresponds to the one of [2], thus to ferritic or bainitic steels with $R_p < 800$ MPa. Since R_p appears in eq. (14) only in the power of ¼, a rough estimation of $R_p(T)$ at the actual temperature is sufficient. Detailed knowledge of $R_p(T)$ is not required.

The presented model is similar as the one proposed by Merkle et al. in [13]. However, besides some minor differences in the mathematical derivations, there is a fundamental difference in the assumptions concerning the saturation of the thickness-effect: Based mainly on intuition, in [13] saturation was assumed to occur at $B=B_{p\varepsilon}$, which means that α as defined in eq. (3) was chosen to be 2.5, whereas in the present model this effect is attributed for physical reasons to the slenderness of the fracture controlling volume in the vicinity of the crack front. The corresponding thickness of saturation was considered as unknown by introducing an open constant β_{sat} that was determined by comparison with experimental data. A comparison of (3) and (7) reveals that β_{sat} is related to α by

$$\beta_{sat} = \frac{\alpha \cdot E}{R_p} \tag{15}$$

From eq. (15) one can see that $\beta_{sat}=1150$ as found above (eq. (14d)) is nearly equivalent wit $\alpha=2.5$ for medium strength steel (with R_p being about 450 MPa). This confirms the assumption in [13] and means that K_{sat} evaluated by eq. (12) represents a "valid" plane strain fracture toughness value K_{Ic}. Inserting (15) with $\alpha=2.5$ in eq. (12) leads to the simple equation

$$K_{Ic}(p_f) = 0.858 \cdot R_p^{1/3} \cdot B_T^{1/6} \cdot K_{Jc}^{2/3}(B_T, p_f) \qquad \text{for } B_T < B_{p\varepsilon} \tag{16}$$

which enables "valid" K_{Ic} to be estimated from a K_{Jc}–value measured on a smaller specimen of thickness B_T. Quantitatively, the resulting K_{Ic} is nearly the same as the one from the mathematically more complex relation provided in [13]. Note that the obtained K_{Ic} is associated with the same probability of failure p_f as the original K_{Jc}-value. If applied to an empirical lower envelope to experimental date, such as the curve shown in Fig. 4, eq. (16) enables a lower-bound curve for K_{Ic} to be predicted. In this way, one could have obtained from the presented experimental data a lower bound that is in very good agreement with the ASME lower bound, eqs. (4) and (5), confirming these empirical relations semi-analytically.

Using (15) with α=2.5 leads to the following approximation of eq. (14a) and (14(c):

$$K_{LB(B)}(T) = \frac{1.257}{B^{0.25} \cdot \sqrt{R_p}} \cdot \left\{36.5 + 22.8 \cdot \exp\left[0.036 \cdot (T - T_0 - 19.4°)\right]\right\}^{3/2} \quad \text{for } B < 2.5 \cdot \left(\frac{K_{LB(B)}}{R_p}\right)^2 \quad (17)$$

6. Conclusions

An engineering model is presented by which the fundamental conflict between the weakest-link statistics and the classical concept of lower-bound plane strain fracture toughness can be resolved. It is based on the hypothesis that the statistical thickness-effect saturates at a certain thickness. The latter turned out to be roughly the same as the one required for plane strain fracture toughness testing, confirming a similar hypothesis made by Merkle et al. in [13]. The model enables "valid" K_{Ic}-values to be calculated from K_{Jc} measured on relatively small specimens and – in reverse – lower bounds of K_{Jc} for relatively small components (or crack-front lengths, respectively) to be predicted from lower-bound K_{Ic}–values. These lower bound curves are less conservative than the ASME lower bound for smaller thicknesses. They are shown to be much closer to the experimental data than the original ASME-lower bound curve, which means that a safety assessment based them results in less conservative – i.e. more realistic - predictions.

The present investigation confirms independently the model of Merkle et al. [13] and its underlying assumptions. Furthermore, the ASME lower bound, which was determined empirically as the lower envelope of a large number of valid K_{Ic}-tests, could be obtained semi-empirically from relatively few K_{Jc}-data. This good agreement confirms mutually the presented theory as well as the empirical ASME-curve. Note that for eq. (5) to be valid T_0 as obtained from 1T-CT-specimens should be used; T_0 from 0.4T-SEB-specimens can lead to non-conservative predictions.

Tolerance bounds based on the statistical MC-relations are shown to be less suitable as lower bounds, particularly if applied to relatively large components. Therefore and because of their formal restriction to $T<T_0+50K$, it is recommended that the MC-approach is used just for the evaluation of T_0 from test data, but not to predict K_{Jc} for larger components at the low failure probabilities required in an engineering failure analysis.

Acknowledgements

The authors wishe to thank the Swiss Federal Nuclear Safety Inspectorate (ENSI) for sponsoring this investigation.

References

[1] Wallin, K, "Recommendation for Application of Fracture Toughness Data for Structural Integrity Analysis," Proc. CSNI/IAEA Specialists' Meeting, Oak Ridge, TN, 1992
[2] American Soc. For Testing and Materials, ASTM-Standard E 1921-11
[3] Anderson T.L., Rose1 B.D., A Modified Weibull Stress Model for Cleavage Fracture that Incorporates Threshold Toughness, Proceedings of 12th Int. Conf on Fracture, Ottawa, 2010
[4] Schindler, H.J., Kalkhof, D., Tipping, Ph., Determination of Transferable Lower-Bound Fracture Toughness from Small Specimens, J. ASTM International, Vol. 5, No. 8
[5] Schindler, H.J., and Kalkhof, D. (2010), Lower-bound fracture toughness in the transition regime from small specimen data, DVM Bericht 242, S. 217-226 (in german)

[6] Heerens J., Pfuff M., Hellmann D., Zerbst U., The lower bound toughness procedure applied to the Euro fracture toughness dataset, Engineering Fracture Mechanics 69 (2002) 483–495
[7] American Soc. For Testing and Materials, ASTM-Standard E399-09
[8] American Soc. For Testing and Materials, ASTM-Standard E1820-08a
[9] International Standard Organization, Standard ISO 12135, 2002
[10] ASME Boiler and Pressure Vessel Code, Section XI, Division 1, NB 2331, American Society of Mechanical Engineers, New York, 2004
[11] Rosinski, S.T., Server W.L., Application of Master Curve in the ASME Code, Int. J. Pressure Vessels and Piping, 77, 2000, 591-598
[12] ASME Boiler and Pressure Vessel Code, Code Case N-629, Section XI, Division 1, American Society of Mechanical Engineers, New York, 1999
[13] Merkle, J.G., Sokolov, M.A., Nanstad, R.K., Mc Cabe, D.E., Statistical representation of valid KIc Data for irradiated RPV-Steels, ORNL/NRC/LTR-01/08, Oak Ridge National Laboratory, August 2002
[14] Viehrig H.W., Schindler H.J., Kalkhof, D., Effects of Test Parameters on the Master Curve Reference Temperature, 18th Europ. Conf. on Fracture (ECF 18), Dresden, 2010
[15] Kalkhof, D., Schindler, H.J., Uncertainties in T_0 and Required Safety Margins in Lower Bounds of KIc in the Ductile-to-Brittle Transition Regime of Ferritic Steels, Proc. 19th European Conference on Fracture (ECF19), Paper ID 257, Kazan, RU, 2012

Experimental verification of optimal strain gage locations for the accurate determination of stress intensity factors

H. Sarangi[1], K.S.R.K. Murthy[2*], D. Chakraborty[2]

[1] Research Scholar, Department of Mechanical Engineering, IIT Guwahati, Guwahati 781039, India
[2] Faculty of Department of Mechanical Engineering, IIT Guwahati, Guwahati 781039, India
* Corresponding author: ksrkm@iitg.ernet.in

Abstract In the present investigation experimental verification of optimal strain gage locations and their importance in accurate determination of mode I stress intensity factors (SIFs) using Dally and Sanford's single strain gage technique (DS technique) has been carried out. The results of the present experimental study are also used to substantiate the efficacy of the methodology for determination of maximum permissible strain gage radial location proposed earlier by the same authors for locating the optimal strain gage locations. Experiments have been conducted using an edge cracked plate made of Polymethylmethacrylate. Results clearly demonstrate that very accurate values of mode I SIFs can be determined if the strain gages are placed at the optimal locations. On the other hand, the experimental results also show that the mode I SIFs obtained using strain gages placed at non-optimal locations contain significant and unacceptable errors. The results of the present investigation clearly confirm the importance of knowing the maximum permissible strain gage radial location corresponding to an experimental specimen before conducting experiment for determination of mode I SIF using the DS strain gage technique.

Keywords Stress intensity factor, Strain gage, Gage location, Optimal

1. Introduction

Stress intensity factor is an important parameter in linear elastic fracture mechanics. Strain gage based experimental techniques for the determination of stress intensity factors (SIFs) are equally powerful in experimental fracture mechanics as other methods such as photoelasticity, caustics and moiré interferometry etc. [1]. For many years, local yielding, high strain gradients, strain gradient effects due to finite size of gages and three dimensional effects near the crack tip were the major problems associated with the application of strain gage techniques for accurate determination of SIFs.

Dally and Sanford [2] was the first to propose a practically feasible single strain gage technique to overcome most of the above mentioned difficulties. Their technique (DS technique) is theoretically well supported and is proposed for determination of mode I SIF, K_I of two dimensional single ended cracked configurations made of isotropic materials. Many different strain gage techniques for determination of SIFs under different situations have been proposed subsequently by various researchers [3-6]. Among the available strain gage techniques for the determination of K_I, DS technique [2] has been more widely employed [7-11] in different contexts.

Referring to Fig. 1, it is evident that in order to obtain accurate values of the SIFs, it is very important to decide strain gage angular location and orientation (defined by θ and α) with

respect to the crack axis and radial location (r) from the crack tip to the center of the gage. The most difficult and challenging problem is in deciding the appropriate radial distance (r) for each of the selected number of strain gages for the measurement of K_I. The radial location of strain gages r is restricted by plasticity effects, three dimensional (3D) effects, strain gradients and the analytical strain series used. To avoid plasticity, strain gradient and 3D effects strain gages should not be placed very close to the crack-tip [2, 6]. On the other hand, strain gages placed at a large distance from the crack-tip may not be represented by the selected strain series. Thus, the radial location of a strain gage from the crack-tip is one of the most important parameters required to be known apriori for accurate determination of the SIFs using strain gage techniques.

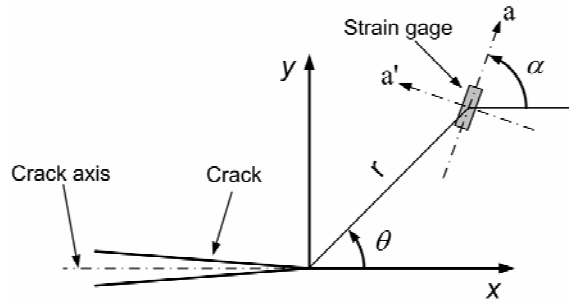

Figure 1. Location of a strain gage from the crack tip

Literature review on strain gage techniques [2-11] show that until recently, no recommendation, or no methodology, or no solution in any form is available for selection of appropriate radial locations (r) for the strain gage in the DS technique despite its popularity. As a consequence, the issue of valid strain gage locations for determination of SIFs using the DS technique remained as an open problem for long time [1].

Recently, Sarangi et al. [12, 13] proposed an approach for determination of optimal or valid radial locations for single strain gage in the DS technique. A methodology based on the finite element analysis (FEA) supported by theoretical foundations has been presented by them [12, 13] for the first time for obtaining the optimal radial gage locations. They defined a parameter $r_{\max}$ which is the upper bound on the radial location for the strain gage which in turn can be used for locating the optimal or valid radial locations for strain gages. Further details on $r_{\max}$ can be found in Refs. [12, 13].

No experimental investigation is reported till date to demonstrate the existence of optimal radial locations for strain gages and their usefulness in accurate determination of mode I SIFs using the DS technique. Thus, the objectives of the present investigation are (a) experimental verification of the optimal strain gage locations obtained using the approach proposed by Sarangi et al. [12, 13], (b) to show the usefulness of these locations in obtaining accurate mode I SIFs of cracked configurations using the DS technique and (c) to substantiate the usefulness of methodology for

determination of maximum permissible strain gage radial location $r_{\max}$ proposed by Sarangi et al. [12, 13] for locating the optimal strain gage locations.

2. Theoretical Background

A very brief theoretical background on the DS technique [2] and determination of optimal strain gage locations for this technique proposed by Sarangi et al. [12, 13] is presented in this section. It can be shown that the strain ε_{aa} (Fig. 1) at a point *P* (defined by r and θ) in the direction of an arbitrary angle α (with respect to the crack axis) for plane stress conditions is given by [2, 12, 13]

$$\begin{aligned} 2G\varepsilon_{aa} = A_0 r^{-1/2}\left[\kappa\cos\frac{\theta}{2} - \frac{1}{2}\sin\theta\sin\frac{3\theta}{2}\cos 2\alpha + \frac{1}{2}\sin\theta\cos\frac{3\theta}{2}\sin 2\alpha\right] \\ + A_1 r^{1/2}\cos\frac{\theta}{2}\left[\kappa + \sin^2\frac{\theta}{2}\cos 2\alpha - \frac{1}{2}\sin\theta\sin 2\alpha\right] + B_0\left(\kappa + \cos 2\alpha\right) \end{aligned} \tag{1}$$

where $\kappa = (1-\nu)/(1+\nu)$ and A_0, A_1 and B_0 are unknown coefficients. Eq. (1) is obtained using the three parameter representation of the strain field (in terms of coefficients A_0, A_1 and B_0) around the crack tip. Using the definition of K_I it can be shown that the singular coefficient A_0 is related to the mode I SIF K_I as

$$K_I = \sqrt{2\pi}\, A_0 \tag{2}$$

The coefficient of B_0 term in Eq. (1) can also be eliminated by selecting the angle α such that

$$\cos 2\alpha = -\kappa \quad = -\frac{1-\nu}{1+\nu} \tag{3}$$

Similarly coefficient of A_1 can also be made zero if the angle θ is selected as

$$\tan\frac{\theta}{2} = -\cot 2\alpha \tag{4}$$

With α and θ as defined by Eqs. (3) and (4), the simplified form of Eq. (1) is given by

$$2G\varepsilon_{aa} = \frac{K_I}{\sqrt{2\pi r}}\left[\kappa\cos\frac{\theta}{2} - \frac{1}{2}\sin\theta\sin\frac{3\theta}{2}\cos 2\alpha + \frac{1}{2}\sin\theta\cos\frac{3\theta}{2}\sin 2\alpha\right] \tag{5}$$

Thus, by placing a single strain gage (Fig. 1) with α and θ as defined by Eqs. (3) and (4) the strain ε_{aa} can be measured and K_I can be determined using Eq. (5).

Using numerical and experimental studies [14, 15] it has been established that the 3D effects prevail up to a radial distance equal to half the thickness of the plate from the crack tip. Therefore, the minimum radial distance $r_{\min}$ for strain measurements on the free surface should be greater than half the thickness of the plate [2]. As a consequence, the optimal or valid radial location r for a strain gage in DS technique can now be given as

$$r_{\min} \quad (= \frac{\text{thickness of plate}}{2}) \leq r \leq r_{\max} \tag{6}$$

where the unknown parameter $r_{\max}$ is defined as the maximum permissible radial distance for the strain gage or the extent of validity of Eq. (5) from the crack tip. It is clear that Eq. (5) can accurately describe the strain field in the given direction θ only up to a radial distance $r_{\max}$ from the crack tip and beyond this radial distance more number of coefficients other than A_0, A_1 and B_0 are needed to represent the strain field. Clearly, with this definition of $r_{\max}$, any radial distance of strain gage satisfying the Eq. (6) is an optimal radial location. According to Sarangi et al. [12, 13], for a given configuration, applied load, Young's modulus E and Poisson's ratio ν Eq. (5) can be simplified as,

$$\varepsilon_{aa} = \frac{C}{\sqrt{r}} \tag{7}$$

where C is a constant. Taking logarithm on both sides of Eq. (7)

$$\ln(\varepsilon_{aa}) = -\frac{1}{2}\ln(r) + \ln(C) \tag{8}$$

Clearly Eq. (8) is valid along the line given by Eq. (4) for $r \leq r_{\max}$. Thus a plot of Eq. (7) on log-log axes ($\ln(\varepsilon_{aa})$ versus $\ln(r)$) depicts a straight line of slope equals to – 0.5, with an intercept of $\ln(C)$. Theoretically, the straight line property will break beyond $r > r_{\max}$ as more than three parameters are needed in Eq. (1) to estimate the ε_{aa}. Using the straight line property exhibited by Eq. (8), the value of $r_{\max}$ can be accurately estimated from the log-log plots of ε_{aa} and r. Other details on computation of $r_{\max}$ can be found in Refs.[12, 13].

3. Experimental Verification

Present section describes experimental verification of optimal radial locations of strain gages obtained using the approach described in the previous section and their use in determination of accurate mode I SIFs. The following equations are employed for determination of normalized SIF K_I

$$F_I = \frac{K_I}{\sigma\sqrt{\pi a}} \tag{9}$$

where σ is the nominal stress and a is the crack length and the % relative error in F_I is calculated as

$$\%\,\text{Relative error} = \left(\frac{F_I^{\textit{reference solution}} - F_I^{\textit{experimental}}}{F_I^{\textit{reference solution}}} \right) \times 100 \tag{10}$$

3.1 Details of experimental specimen

In the present experimental investigation, commercially available Polymethylmethacrylate (PMMA) has been used as the material for the test specimen. It is well known that PMMA is a homogeneous, isotropic and brittle material at room temperature [16]. The test specimen considered in the present investigation is straight edge cracked plate subjected to tensile loading as shown schematically in Fig. 2(a). The details of geometry and that of pre-crack are also shown in Fig. 2(a). Experiments have been conducted using an edge cracked plate having a/b ratio 0.493. The geometric and other details of the experimental specimen have been presented in Table 1. Fig. 2(b) shows actual specimen with strain gages mounted on the surface. Dimensions and loading conditions in the test specimen have been chosen so as to ensure plane stress conditions during the experiments. The elastic properties of PMMA sheet obtained from tensile tests have also been presented in Table 1.

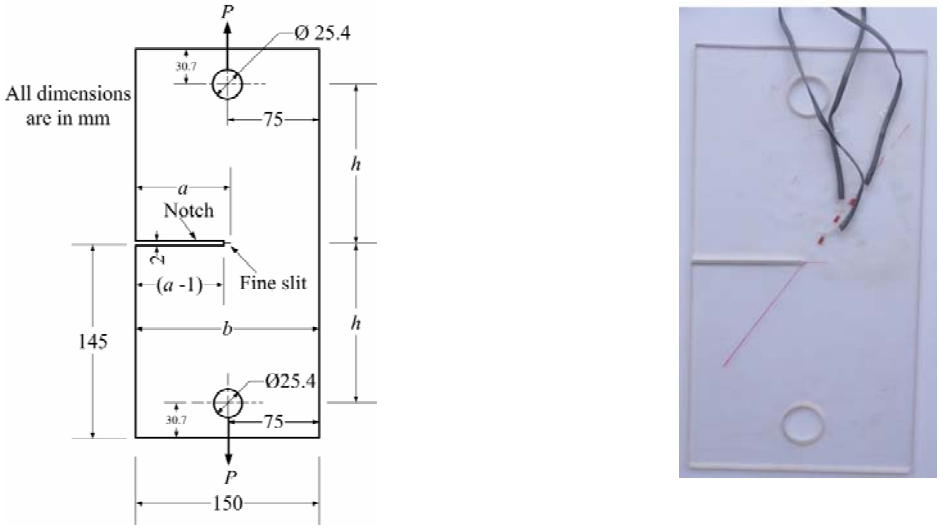

(a) (b)

Figure 2. (a) schematic of edge cracked specimen (b) actual specimen

3.2 Determination of $r_{\max}$ and normalized mode I SIF of the experimental specimen

Material properties from the tensile tests (Table 1) for the PMMA have been used to evaluate the $r_{\max}$ values for the selected mode I edge cracked experimental specimen (Table 1 and Fig. 2).

Following the numerical approach proposed by Sarangi et al. [12, 13] the r_{max} of the experimental edge cracked specimen is found to be 37.0 mm which is indicated in Table 1. Further, using the same FE meshes (that are used for determination of r_{max}) mode I SIF K_I has been computed. Result of computed normalized SIF, F_I (Eq. 9) for the selected experimental specimen is also presented in Table 1. All these finite element analyses have been carried using commercial software ANSYS^{TM}.

Table 1 Details of different parameters of the edge cracked experimental specimen

Parameters	Values
a/b	0.493
Crack length a	74 mm
Width b	150 mm
Height h	114.3 mm
Thickness t	5.6 mm
Young's modulus E	2916.91 MPa
Poisson's ratio ν	0.382
r_{max}	37 mm
Normalized mode I SIF F_I	2.777738

3.3 Details of experiment

The selected edge cracked specimen has been loaded in a closed loop servo hydraulic INSTRON 8801 machine with 100 kN capacity under displacement control with an actuator speed 0.1 mm/min. Clevis grips have been used for transferring the tensile load from the machine to the specimen. Strain measurements on the loaded specimens have been carried out using the electrical resistance strain gages of type FLA-1-11-3LT (gage length of 1 mm) and make: TML Japan. The measured strains have been acquired, digitized and processed using NI data acquisition system comprising of cDAQ9178 chassis. Strain measurements have been carried out using NI 9237 (4 channels 24 Bit, half-full bridge analog input module). Experiments have been repeated three times to ensure the repeatability of the results.

4. Results and Discussion

Here mode I SIFs have been determined using the DS technique (single strain gage technique) in

order to verify the optimal strain gage locations in mode I specimen and validation of methodology for determination of r_{max} (which is useful in deciding optimal locations) proposed by Sarangi et al. [12, 13]. Fig. 2(b) shows the photograph of the edge cracked specimen with $a/b = 0.493$ and made of PMMA which has been used in the present experiments. Corresponding to Poisson's ratio ν = 0.382 of the specimen material (Table 1), the orientation of the gage line θ is 53.13^0 (Eq. 4) and the orientation of the gage α is 58.28^0. (Eq. 3).

According to Sarangi et al. [12, 13], the optimal locations for the strain gages should be in the range $t/2 \le r \le r_{max}$ in order to obtain the accurate value of SIF. Strain gages located beyond the r_{max} will result in inaccurate values of SIF K_I and thus are non-optimal locations. Based on these observations, strain gage locations have been decided in the present experiments as shown in Table 2.

Table 2 Selected radial locations for strain gages

r_{max} (mm)	Radial locations		
	r_1 (mm) (Optimal)	r_2 (mm) (Optimal)	r_3 (mm) (Non-optimal)
37.0	17.5	35	50

Fig. 3 show the raw data of measured strain ε_{aa} (circled data points) by the strain gages at r_1 = 17.5 mm, r_2 = 35 mm and at r_3 = 50 mm, respectively in a typical test versus the applied load. Fig. 3 also shows best-fit straight lines (solid lines) to the raw data with the corresponding slopes and the correlation coefficients R^2. As anticipated, at all the strain gage locations, the measured strains are linearly proportional to the applied load as shown by very good values of R^2. Similar trends with identical values of slopes of best-fit lines and correlation coefficients R^2 have been obtained at all the locations of strain gages in all the three repeated tests.

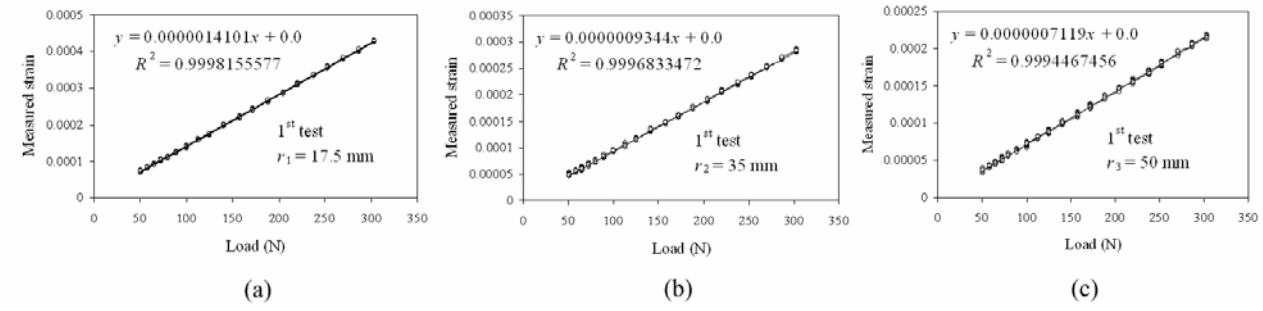

Figure 3. Measured strain versus load (a) at r_1 = 17.5 mm (b) at r_2 = 35 mm and (c) at r_3 = 50 mm

Table 3 shows the experimental values of F_I obtained at all three gage locations r_1, r_2 and r_3 for each of the three repeated experiments for a/b = 0.493 and their average values. It could be observed that in all the three tests at a given location F_I values are very close to each other showing the good repeatability of the results.

Table 4 Experimental values of F_I obtained in all three repeated tests

Test	F_I		
	$r_1 = 17.5$ mm	$r_2 = 30$ mm	$r_3 = 50$ mm
1	2.68641731	2.51751109	2.29249573
2	2.81463225	2.60103297	2.38073057
3	2.84759092	2.66946702	2.53659065
Average	2.78288016	2.59600369	2.40327232

Table 5 shows the comparison of experimentally determined averaged F_I values (Table 4) obtained at the optimal and non-optimal locations of strain gages (r_1, r_2 and r_3) with the reference solution obtained using ANSYS (Table 1) in terms of the % relative error. The percent relative error in F_I is determined using Eq. (10).

Table 5 Experimental values of F_I at different gage locations ($r_{max} = 37$ mm)

Location	F_I		% Relative error
	Reference solution (Table 1)	Experimental value	
Optimal ($r_1 = 17.5\,\text{mm} < r_{max}$)	2.777738	2.78288016	0.19
Optimal ($r_2 = 35\,\text{mm} < r_{max}$)		2.59600369	6.54
Non optimal ($r_3 = 50\,\text{mm} > r_{max}$)		2.40327232	13.48

It is interesting to observe from Table 5 that the % relative error in F_I is only 0.19% for the strain gage located at the optimal location i.e., at $r_1 = 17.5\,\text{mm}$ $(< r_{\max})$ while F_I determined based on the strain gage readings at the non-optimal location $r_3 = 50\,\text{mm}$ $(> r_{\max})$ is as high as 13.5%. Since the other optimal strain gage location $r_2 = 35\,\text{mm}$ which is very close to $r_{\max}$, slightly more error can be noticed at this location as compared to the gage location at r_1. However, this error is still within the acceptable limits. These experimental observations clearly verify the existence of optimal gage locations and their use in determination of accurate values of mode I SIFs. It should be noted that these optimal and non-optimal gage locations have been decided based on the Eq. (6) for which $r_{\max}$ is required for a configuration. Thus, the experimental results in Table 5 also substantiate the efficacy of methodology proposed by Sarangi et al. [12, 13] for determination $r_{\max}$ and its importance in deciding the optimal strain gage locations for accurate determination of mode I SIF. Moreover, the results in Table 5 clearly show the importance of $r_{\max}$ for selection of optimal strain gage locations.

5. Conclusions

The present investigation examines the experimental verification of optimal strain gage locations and their importance in accurate determination of mode I SIFs. This examination also validates the methodology for determination of maximum permissible strain gage radial location $r_{\max}$ proposed by Sarangi et al. [12, 13] and its use in locating the optimal strain gage locations for accurate determination of SIFs using the DS technique. The results of the present investigation clearly demonstrate that very accurate mode I SIFs can be determined using the DS technique if the strain gages are placed within the $r_{\max}$ value i.e., optimal locations. The results also show that the experimentally obtained SIFs using the strain gages placed at non-optimal locations (i.e., beyond $r_{\max}$ value of a specimen) contain significant errors.

Acknowledgements

Authors gratefully acknowledge financial support from the Naval Research Board (NRB), Ministry of Defence, India, under grant number NRB-167/MAT/08-09.

References

[1] K. Ravi-Chandar, Fracture Mechanics, in: W.N. Jr. Sharpe (Ed.), Springer Handbook of Experimental Solid Mechanics, Springer Science + Business Media, New York, 2008, pp. 125-158.

[2] J.W. Dally, R.H. Sanford, Strain gage methods for measuring the opening mode stress intensity factor. Exp Mech, 27 (1987) 381–388.

[3] J.H. Kuang, L.S. Chen, A single strain gage method for K_I measurement. Eng Fract Mech, 51 (1995) 871–878.

[4] J. Wei, J.H. Zhao, A two-strain-gage technique for determining mode I stress-intensity factor. Theor Appl Fract Mech, 28 (1997) 135–140.

[5] J.W. Dally, D.B. Barker, Dynamic measurements of initiation toughness at high loading rates. Exp Mech, 28 (1988) 298–303.

[6] A. Shukla, B.D. Agarwal, B. Bhushan, Determination of stress intensity factor in orthotropic composite materials using strain gages. Eng Fract Mech, 32 (1989) 469–477.

[7] L. Parnas, O.G. Bilir, Strain gage methods for measurement of opening stress intensity factor. Eng Fract Mech, 55 (1996) 485–492.

[8] S. Rijal, H. Homma, Dimple fracture under short pulse loading. Int J Impact Eng, 24 (2000) 69-83.

[9] J.F. Kalthoff, A. Burgel, Influence of loading rate on shear fracture toughness for failure mode transition. Int J Impact Eng, 30 (2004) 957-971.

[10] S. Shirley, H. Homma, Approach to dynamic fracture toughness of GFRP from aspect of viscoelastic and debonding behaviors. J Solid Mech Mat Eng, 1 (2007) 275-286.

[11] S. Swamy, M.V. Srikanth, K.S.R.K. Murthy, P.S. Robi, Determination of the mode I stress intensity factors of the complex configurations using the strain gages. J Mech Mater Struct, 3 (2008) 1239–1255.

[12] H. Sarangi, K.S.R.K. Murthy, D. Chakraborty, Radial locations of strain gages for accurate measurement of mode I stress intensity factor. Mater Des, 31 (2010) 2840-2850.

[13] H. Sarangi, K.S.R.K. Murthy, D. Chakraborty, Optimum Strain gage location for evaluating stress intensity factors in single and double ended cracked Configurations. Eng Fract Mech, 77 (2010) 3190-3203.

[14] W. Yang, L.B. Freund, Transverse shear effects for through-cracks in an elastic plate. Int J Solids Struct, 21 (1985) 977-994.

[15] J. Rosakis, K. Ravi-Chandar, On crack-tip stress state: An experimental evaluation of three-dimensional effects. Int J Solids Struct, 22 (1986) 121–134.

[16] T.M. Maccagno, J.F. Knott, The fracture behaviour of PMMA in mixed modes I and II. Eng Fract Mech, 34 (1989) 65-68.

Analysis of Crack Retardation Effects and Crack Path in Ship Structure Members on Different Routes

Fredhi Agung Prasetyo[1,*], **Wengang Mao**[2], **Tomohei Kobayashi**[1], **Naoki Osawa**[1], **Jonas W Ringsberg**[2]

[1] Department of Naval Architecture & Ocean Engineering, Osaka University, Suita Osaka 5650871, Japan
[2] Department of Shipping and Marine Technology, Chalmers University of Technology, Gothenburg, Sweden
* Corresponding author: Fredhi_Agung@naoe.eng.osaka-u.ac.jp

Abstract The ship size has been rapidly increased in recent years. Consequently, many aspects of ship structural safety have been concerned, i.e. fatigue strength. Since fatigue cracks are found in the early stage of a ship's service life, it might be that the classical cumulative fatigue rule is insufficient to consider the effects of many uncertain factors, such as variable wave environment loads. The wave load history hinges on the short-sea history. It means that the accuracy of fatigue assessment is affected by the used wave model. There are several established wave models, which could be used to simulate wave load history as in the real ocean conditions. In this paper, wave load histories of a 2800TEU container ship are generated by two different wave models. It is used for crack propagation analysis in the changing routes and trades. The result in the simulated crack propagation lives is examined and discussed.

Keywords fatigue crack propagation, fatigue damage sensor, hindcast data, ship structures

1. Introduction

Fatigue is an important issue for maritime industry. Large ship designers must consider the fatigue strength of ship structures. The traditional ship fatigue assessment is conducted by using a simplified method, in which Palmgren-Miner linear cumulative law and S-N curves are used. In this method, all parameters are provided by classification societies' rules. A comparative study shows that this method gives wide scatter of fatigue life predictions [1]. Thus, fatigue cracks are observed much earlier than expected, challenge the safety of structural integrity and final failure in shipping. This is caused by many uncertain factors, e.g. chosen S-N parameters, load spectrum range, fatigue assessment method, etc.

The solving alternately starts from how to get the structural stress history for various sea-states. A sea-state is characterized by its energy spectra, which is a function of significant wave height (*Hw*) and mean wave period (*Tw*). The transfer function of structural stress response, also known as RAOs, is obtained from a direct calculation by considering wave loads for all loading conditions, ship speeds, and heading angles. It can be combined with the wave energy spectrum of a sea state to compute the stress spectrum. The fatigue crack propagation theory is capable to predict fatigue crack propagation length in a real service voyage [1][2].

The accuracy of fatigue propagation analysis hinges on the load sequence's reproducibility of the actual sea-state history. Ship owners' concern about fatigue damage is growing, and the ship operation / route is changed constantly according to the weather condition. The load sequence obtained from the wave scatter diagram in classification society rules may be different from that of the actual load [3]. This may affect the accuracy of the crack propagation analysis.

Recently, many sources of wave data, i.e. hindcast, satellite measurement, and onboard measurement can be utilized for load history simulation. In this study, the effect of the wave environments encountered by a 2800TEU container ship in North Atlantic Ocean on the fatigue crack propagation life is discussed. The crack propagation analyses are conducted by using stress histories simulated from the ship's encountered sea-state history. In these simulations, two stochastic wave models are utilized, and the difference in the simulated crack propagation lives is examined.

2. The two established wave models

This section explains the capability and reliability of two wave models in load sequence and fatigue damage estimation. These wave models are developed based on statistical analysis of ocean wave measurements. The first model is the 'Spatio-temporal wave model' developed by using satellite wave data [5]. The other model is the '3G-storm model' developed by using the hindcast data [7]. The target ship is a 2800TEU container ship. The sea-states were measured onboard on this ship, and the onboard data are used as a reference. The ship sailed on the North Atlantics routes in the first half-year of 2008 as shown in Fig. 1. Details of this target ship are described in [4].

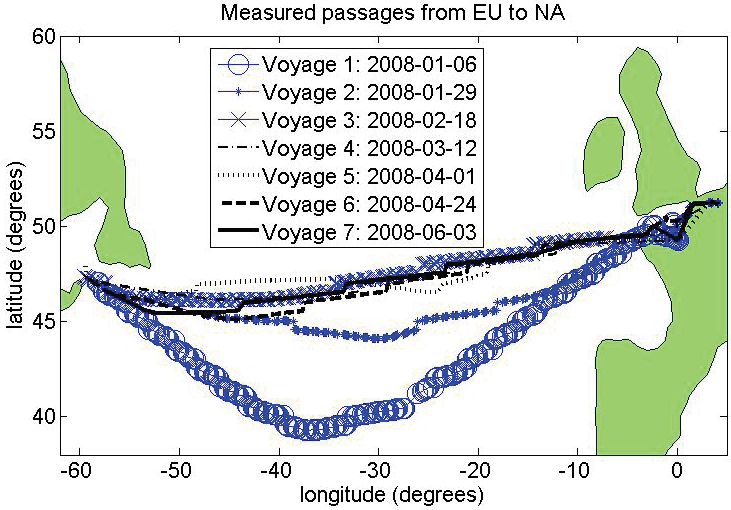

Figure 1. Voyage from EU to USA of 2800TEU container ship along first semester of 2008 (the arrival date of each voyage is indicated in the legend) [3].

2.1 The spatio temporal wave model

The significant wave height *Hw* at position ***p*** and time *t* is accurately modeled by means of lognormal cumulative distribution function (cdf). Let $X(\mathbf{p},t) = ln(Hw(\mathbf{p},t))$ denote a field of logarithms of significant wave height that evolves in time. For a fixed *t*, the local field $X(\mathbf{p},t)$ is assumed to be homogeneous Gaussian with covariance changes for the location ***p***. The Gaussian field $X(\mathbf{p},t)$ is assumed to have a mean that varies annually due to the periodicity of the climate. In the model, the mean value of the Gaussian field is assumed as:

$$\mu(t) = E\left[\mathrm{X}(p,t)\right] = \beta_0 + \beta_1 \cos(\phi t) + \beta_2 \cos(\phi t) + \alpha t \tag{1}$$

where $\phi = 2\pi/365.2$ is chosen to give an annual cycle for time in days. The parameters in Eq. (1)

can be computed from the satellite measurements.

Suppose t_0 be the starting date of a voyage, and the position on the planned route is given as $\boldsymbol{p}(t) = (x(t), y(t))$, for the time period $[t_0, t_1]$, and the ship's velocity as $v(t) = (v_x(t), v_y(t))$. For a given route let $z(t) = X(\boldsymbol{p}(t),t)$ be the encountered logarithms of Hw. (The encountered significant wave height is $Hw(t) = exp(z(t))$.) Obviously it will be different for $\boldsymbol{p}$ close to the coast and for $\boldsymbol{p}$ in the middle of the ocean. Hence, the encountered process $z(t)$ will be Gaussian but non-stationary.

In principle, the mean value and variance of the Gaussian field are needed in order to compute the distribution of Hw along the route. The covariance structure should also be provided if the variance of fatigue damages is required. In general, the data from both satellites and buoys are necessary to get the parameters of the covariance structure in the model. The median value of Hw in February and August in the spatio-temporal model is shown in Fig. 2. Further description of the model can be referred to [5].

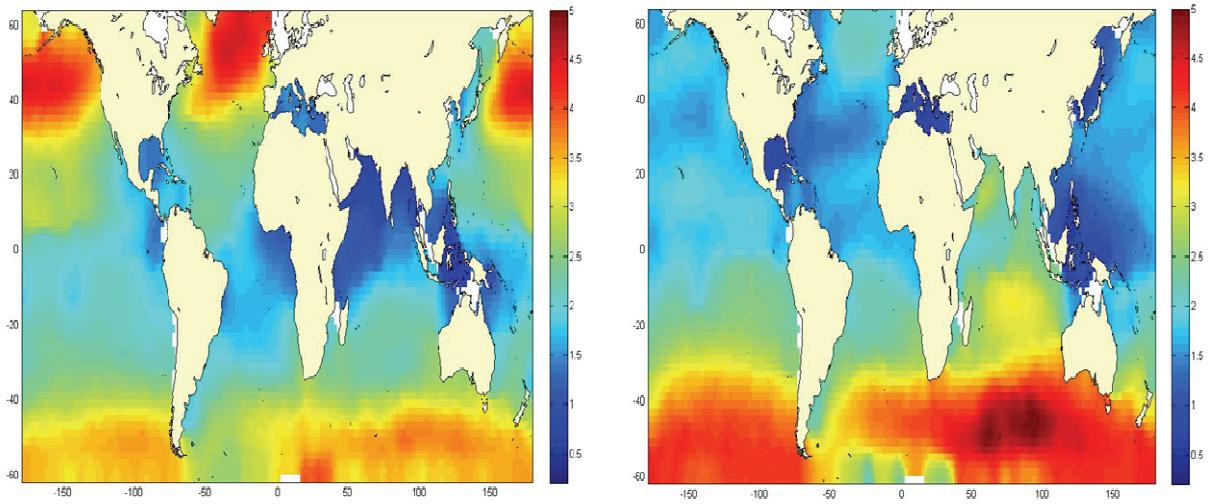

Figure 2. The median value of Hw (meters) in February (left) and in August (right).

2.2 The 3G-storm model

In order to simulate load sequences in the real oceans, Tomita [6] proposed the storm model. It was assumed that ocean conditions could be classified into either calm-sea or storm. Calm-seas are modeled as time-independent random waveforms, while storms are modeled as individual wave sequences with crescendo de-crescendo amplitude waveforms. Tomita's storm model was modified by Prasetyo and Osawa [7] so that the correlation between Hw and Tw and the variance of storm duration can be taken into account. This modified model is called '3G-storm model'. Storm profiles are determined by assuming that the long-term probability distribution of Hw obeys Weibull distribution [6]. The detail and procedure to determine storm profile parameters is described in [7]. Once Hw is determined, Tw is determined by using a wave scatter diagram (a joint probability distribution of Hw and Tw, $P(Hw,Tw)$).

2.3 Comparison of the two wave models

Figure 3 shows the comparison of probability density function (pdf) of *Hw* simulated by using the spatio-temporal wave model and the 3G-storm model along the North Atlantic voyages of Fig. 1. In this figure the pdf of H_w from the onboard measurement and that provided in DNV recommendation [8] are also presented. This figure shows that both wave models give more frequent mid-range waves (2m < *Hw* < 4m) than the onboard measurement and the DNV recommendation. The fatigue damage accumulated during 7 voyages of Fig. 1 is compared and presented in Table 1. Two wave models give about 25% overestimation comparing with the total rainfall damages which is computed using the recorded stress signals. Generally speaking, for each voyage, the difference of fatigue damage is negligible except the voyage 2008-06-03. It means that the two wave models could be used for the design purpose to generate *Hw* history and fatigue damage estimation.

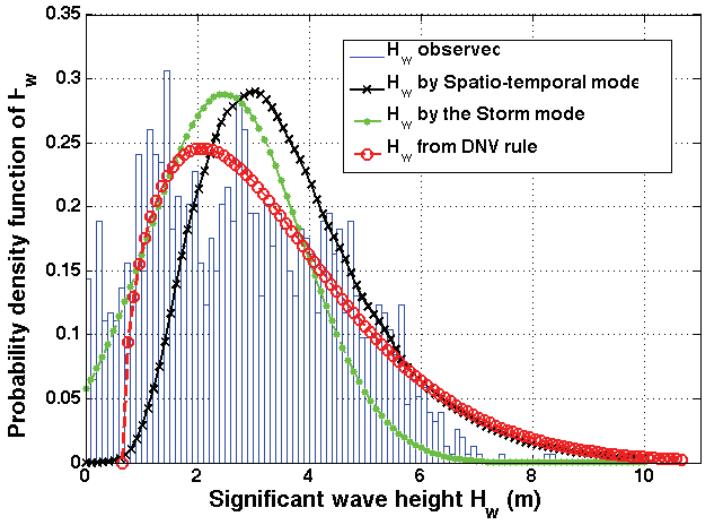

Figure 3. Probability density function (PDF) of *Hw*.

Table 1. Calculated Fatigue damage by using *Hw*, that generate from both wave models and rain-flow damage of observed voyage.

Voyage	Observed voyage	Spatio-temporal model	3G-storm model
Voy. 2008-01-06	0.0080	0.0077	0.0078
Voy. 2008-01-29	0.0057	0.0075	0.0073
Voy. 2008-02-18	0.0045	0.0067	0.0063
Voy. 2008-03-12	0.0014	0.0032	0.0028
Voy. 2008-04-01	0.0032	0.0041	0.0030
Voy. 2008-04-24	0.0027	0.0019	0.0029
Voy. 2008-06-03	0.0007	0.0010	0.0026
Sum:	0.0262	0.0321	0.0325

3. Fatigue crack propagation analysis

3.1 Comparison of stress history

Sea-state histories (*Hw*, *Tw*) can be simulated by the 3G-storm model. Once a sea-state is simulated, the stress history can be generated by using the wave spectrums and the transfer function of ship

structural stress, known as RAO. Once (*Hw*, *Tw*) are given, the power spectral densities of wave, $S(\omega)$, is determined. Ocean wave spectrums such as JONSWAP spectrum, modified Pierson-Moskowitz (ISSC) spectrum [9] are utilized in this analysis. In the stress calculation, the history of the ship's heading angle to the wave, χ, is needed because the RAO depends on not only *Hw* and *Tw* but also χ. Once *Hw*, *Tw* and χ are given, the power spectral densities of stress is determined as the cross spectrum, then the individual stress waveform is generated by assuming that the stress amplitude follows Rayleigh distribution whose parameter are determined from the cross spectrum.

The cdf of *Hw* is estimated by the spatio-temporal wave model at a given time and point. Once the probability distribution of *Hw* is given, the energy spectrums of wave and stress response can be computed by using ocean wave spectrums and RAOs for stress response. It is known that for fatigue assessment, the ship structural stresses can be assumed to Gaussian distributed. For one stationary sea-state, the Gaussian stresses are fully defined by its spectral density and the mean value. Hence, one could also simulate the stress signal from the obtained stress spectral density for each sea-state; see Fig. 4 for an example.

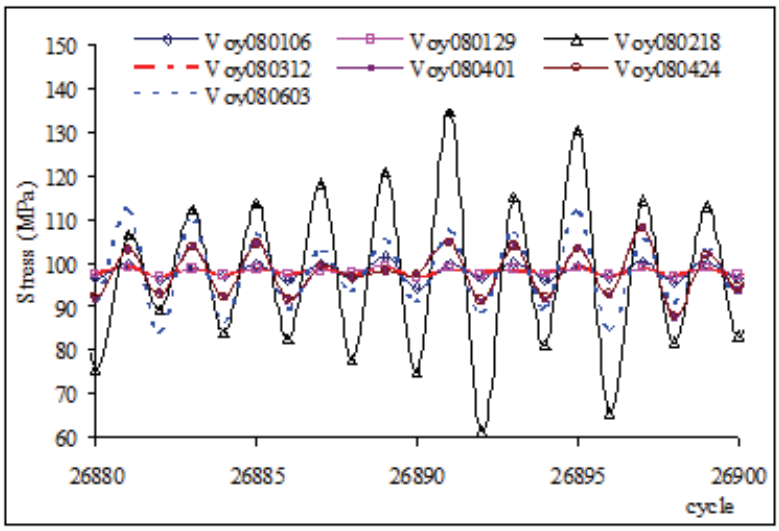

Figure 4. Examples of simulated stress histories of the 2800TEU container ship for different voyages from EU to USA using the 3G-storm model' in a certain cycle.

In the following discussion, the stress history generated by 3G-storm model is called 'model 1', and that generated by the spatio-temporal wave model is called 'model 2'. In order to make the maximum stress amplitude of two histories to be of almost equal level, the simulated stresses are normalized by a correction factor. Figure 5 shows the relation between the stress amplitude S_a and the occurrence frequency. The S_a threshold of crack propagation for the given initial crack size, $S_{a,th}$=49.5MPa, is presented in this figure. It is shown that the occurrence frequency of S_a derived from Spatio temporal model is larger than that of 3G-stom model for cases where $S_a > S_{a,th}$.

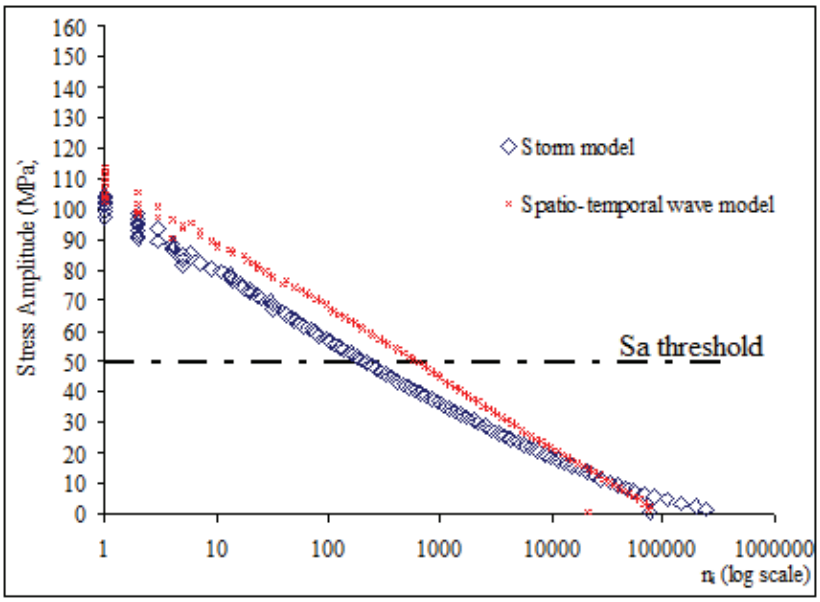

Figure 5. The relation between the stress amplitude S_a and the occurrence frequency of stress histories generated by the 3G-storm and spatio-temporal wave models.

3.2 Fatigue crack propagation model and analyses

Fatigue crack propagation analysis might concern some uncertainty factors on its computation [1]. Analyses results depend on crack growth formula and the accuracy of stress intensity factor (SIF) calculation. In this study, crack propagation is computed by FASTRAN II [12], which is based on cohesive yield model and crack closure concept. The software was developed using crack closure concept [11][12]. Details of the background theory of this code are described by Newman [11][12]. In this study, the crack propagation of a surface crack in a weld of ship structural member is analyzed. SIF range ΔK is calculated by using the modified Newman-Raju formula [10], given as:

$$\Delta K = K_s . M_k . \left(\Delta\sigma_m . F_m \left(c, a, t \right) + \Delta\sigma_b . F_b \left(c, a, t \right) \right) \sqrt{\pi a} \tag{2}$$

where, K_s is the stress concentration factor of structural detail, and it can be calculated by FE direct calculation or by using the engineering formula provided by classification society rules. M_k F_b and F_m are correction factor for weld bead and finite plate size, and they are presented in [10]. The parameters a and c are the depth and surface length of a semi elliptical surface crack defined in Fig. 6 and t is the thickness of the main plate.

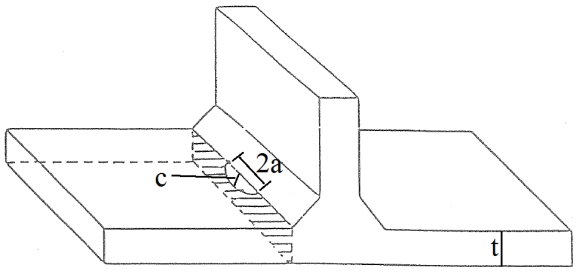

Figure 6. Typical semi-elliptical surface crack on weld toe of fillet weld joint.

The crack growth rate is calculated by modified Paris-Elber law (Eq.3):

$$\frac{da}{dN} = C\left\{\left(\Delta K_{eff}\right)^m - \left(\left(\Delta K_{eff}\right)_{th}\right)^m\right\} \tag{3}$$

where C and m are the material parameters. ΔK_{eff} and $\left(\Delta K_{eff}\right)_{th}$ are the effective SIF range and its threshold.

3.3 Results: fatigue propagation analyses

The crack propagation analysis of two stress histories (model 1 and model 2) is conducted. The initial surface crack length is 0.2 mm, and the initial aspect ratio is 1/2. The propagation analyses are continued until the crack depth exceeds 8 mm or the surface length exceeds 10 mm. Crack growth is computed by using Eq. (3). The material parameters, C and m are 1.45e-11m/cycle and 2.75, respectively. Let Sa_{th} be the threshold of stress range so that the initial crack can growth. The threshold of the stress intensity $\left(\Delta K_{eff}\right)_{th}$ is equal to 2.45MPa.m$^{1/2}$ and Sa_{th} is about 49.5MPa. The stress history is simulated 15 trials in order to provide statistical data of crack propagation analysis and the mean stress is chosen to be 98.0MPa.

The statistics of propagation lives analyzed is presented in Table 2. Figure 7 shows the comparison of the relationship between the growth rate and SIF range for the cases with the shortest propagation life as listed in Table 2. In this table, it is shown that the model 1 leads to longer lives than those of model 2 in most voyages while fatigue damages derived from these two models are almost equal (see Table 1). The model 2 leads to rapid crack growth rate for the cases with same SIF range (i.e. 14MPa.m$^{1/2}$ ≤ SIF ≤ 17MPa.m$^{1/2}$) than the model 1 as seen in Fig. 7.
It is supposed that the retardation of crack growth rate for the cases of model 1 is caused by the excessive load of the generated storm state in Hw history. This shows that the loading sequence of the excessive load affects to crack propagation behavior.

Table 2. Calculated crack propagation life of stress history that it is computed using the 3G-storm model and the spatio-temporal model.

Voyage		Model 1 Crack propagation life (1e6 cycles)				Model 2 Crack propagation life (1e6 cycles)			
No	Arrival Date	Mean	Max.	Min.	Std.Dev	Mean	Max.	Min.	Std.Dev
1	20080106	2590	8034	782	1694	568	1768	137	498
2	20080129	1019	2244	305	506	1805	18807	99	4794
3	20080218	1181	3030	386	675	679	1856	209	542
4	20080312	11658	37885	2269	8431	2033	13120	71	4429
5	20080401	8320	17411	1285	4776	438	1494	146	385
6	20080424	11537	30086	2769	9188	8218	56415	264	14740
7	20080603	7901	30192	1848	7447	18215	54144	170	19633

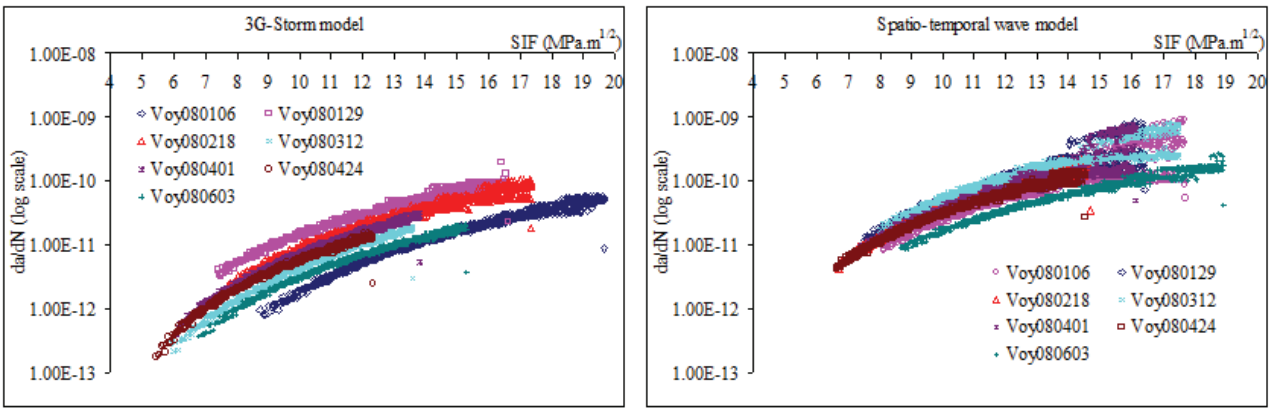

a) 3G-storm model b) Spatio-temporal wave model

Figure 7. Computed crack growth related with stress intensity factor by using the 3G-storm model and the Spatio-temporal wave model for the cases with the shortest propagation life as listed in Table 2.

4. Conclusions

Wave environment loads could be simulated based on different wave models for the fatigue strength assessment. In this study, two different wave models (the spatio-temporal wave model and the 3G-storm model) are compared with the onboard measurement of a 2800TEU containership. The comparison shows that the two wave models give the same probability density function of *Hw* along these measured routes. Subsequently, the generated stress history could be obtained for different routes, but there is some difference in occurrence frequency of stress amplitude computing from stress spectra.

Retardation and acceleration of crack growth is shown by optimizing different routes with simulated load sequence of two wave models. The crack propagation analysis can be utilized in ship design to be more realistic.

Acknowledgements

The authors are greatly thanks to Research Initiative for Ocean Going Ship (RIOS) Osaka university for providing and permission JWA hind-cast data used in this study.

References

[1] W Fricke, W Cui, H Kierkegaard, D Kihl, M Koval, T Mikkola, G Parmentier, M Toyosada, J-H Yoon, Comparative fatigue strength assessment of a structural detail in containership using various approach of classification societies, Marine Structures 15 (2002), pp.1-13.
[2] W Cui, F Wang, X Huang, A unified fatigue life prediction method for marine structures, Marine Structures 24 (2011), pp.153-181.
[3] W Mao, F A Prasetyo, J W Ringsberg, N Osawa, A comparison of two wave models and their influence on fatigue damage in ship structure, to be presented on Proceeding of 32nd OMAE conference 2013.
[4] W Mao, Fatigue assessment and extreme prediction of ship structures, PhD dissertation, Chalmers University of Technology, Gotheburg, Sweden (2010).
[5] A Baxevani, S Caires and I Rychlik, Spatio-temporal statistical modelling of significant wave height. Environmetrics, Vol. 20 (2009), pp.14–31.

[6] Y Tomita, M Matoba, H Kawabe, Fatigue crack growth behaviour under random loading model simulating real encountered wave condition, Marine Structures 8, (1995), pp.407-422.
[7] F A Prasetyo, N Osawa, T Kobayashi, Study on Preciseness of Load History Generation based on Storm model for fatigue assessment of ship structures members, Proceeding of 22nd ISOPE conference IV, pp.
[8] DNV [Det Norske Veritas] (2010). "Classification Note No. 30.7 Fatigue Assessment of Ship Structure". July 2010. Det Norske Veritas, ed.
[9] W H WARNSINK, Report of Committee 1 on Environmental conditions, Proceedings 2nd International Ship Structures Congress (ISSC), (1964).
[10] Panel SR219, Annual report of panel SR219, The Shipbuilding research association of Japan (1996), in Japanese.
[11] J C Newman Jr, A crack closure model for predicting fatigue crack growth under aircraft spectrum loading, Methods and Models for predicting Fatigue crack growth under random loading, ASTM STP 748 (1981), pp. 53-84.
[12] J C Newman Jr, FASTRAN II – a fatigue crack growth structural analysis program, NASA Technical Memorandum 104159 (1992).

A Weight Function for Zr-2.5Nb Pressure Tube Burst Test Specimens

(DRAFT FOR REVIEW)

Steven X. Xu*, Douglas A. Scarth

Structural Integrity and Risk Assessment, Kinectrics Inc., Toronto M8Z 5G5, Canada
* Corresponding author: steven.xu@kinectrics.com

Abstract Based on a literature review, the weight function for an axial through-wall crack in a cylinder has not been reported in the open literature. A weight function for an axial through-wall crack in a cylinder that is applicable to the pressure tube burst test specimens has been developed and is described in this paper. Three-dimensional finite element analyses were performed to calculate the stress intensity factors corresponding to line loads on the crack face. The calculated stress intensity factors were used to develop a weight function for the pressure tube burst test specimens based on regression analysis and engineering judgment.

Keywords Weight function, Stress intensity factor, Axial through-wall crack, Pressure tube, Burst test

1. Introduction

In CANDU® nuclear reactors, the primary containment for the uranium dioxide fuel is provided by thin-walled Zr-2.5Nb pressure tubes, which are nominally 6.3 m long, 103 mm in diameter, and 4.2 mm thick [1, 2]. During operation, the pressure tubes undergo corrosion with the heavy water coolant, D_2O. A portion of the deuterium (D) released by the corrosion reaction is absorbed by the pressure tube and its accumulation over time represents a primary integrity concern. Technical requirements for in-service evaluation of Zr-2.5Nb pressure tubes in CANDU reactors are provided in the CSA Standard N285.8 [3], including evaluation of service conditions for protection against fracture of operating pressure tubes, as well as defense-in-depth demonstration of leak-before-break. Evaluation procedures for protection again fracture and demonstration of leak-before-break are based on use of the fracture toughness versus temperature relationship. Fracture toughness measurements from pressure tube burst tests have shown that hydrides associated with high levels of hydrogen equivalent concentrations can have a significant effect on reducing the fracture toughness at reactor operating temperature during reactor warm-up and cool-down [4]. To support safe operation of pressure tubes at late life where the projected hydrogen equivalent concentrations are of high levels, there has been an initiative in CANDU industry in Canada to gain mechanistic understanding of the effect of levels of hydrogen equivalent concentrations on fracture toughness. A cohesive-zone based engineering fracture toughness model is being developed to assess the effect of zirconium hydrides on the fracture toughness of Zr-2.5 Nb pressure tubes. The knowledge of weight function is required in the calculation of crack opening displacement in the cohesive-zone modeling. Based on a literature review, the weight function for an axial through-wall crack in a cylinder has not been reported in the open literature. A weight function for an axial through-wall crack in a cylinder that is applicable to the Zr-2.5Nb pressure tube burst test specimens have been developed and is described in this paper.

2. Considerations for Development of Weight Function for Burst Test Specimens

A schematic illustration of the pressure tube burst test specimen is given in Figure 1. Three-dimensional finite element analyses were performed to calculate the stress intensity factors corresponding to line loads on the crack face. The calculated stress intensity factors were used to develop a weight function for the burst test specimens based on regression analysis and engineering

® CANDU is a registered trademark of Atomic Energy of Canada Ltd.

judgment**.** The following considerations for the development of a weight function for the burst test specimens were identified.

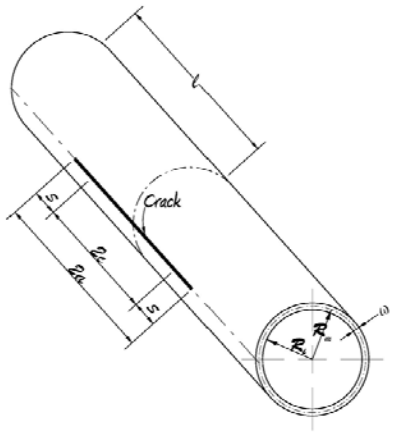

Figure 1. Illustration of pressure tube burst test specimen

(1) Consideration was given to ranges of dimensions for the burst test specimens. Variations in inner radius R_i and wall thickness w of pressure tube burst test specimens are insignificant. The dimension ranges for pressure tube inner radius and wall thickness were not considered. A representative inner radius R_i = 52 mm and wall thickness w = 4.0 mm were used in the weight function development. The initial crack length of a burst test specimen, $2c$, is typically 55 mm. An axial through-wall crack with length $2a$ of 50 to 75 mm was considered in the weight function development.

(2) Consideration was given to the crack model as one dimensional. The axial through-wall crack was treated as one dimensional, and the crack geometry was characterized by the crack length. The treatment of a one-dimensional crack in the axial direction of the pressure tube is considered to be reasonable since the ratios of pressure tube radius to wall thickness of burst test specimens exceed ten. The overall behavior of a pressure tube burst test specimen is expected to be representative of a plane stress state. This assumption was verified through finite element calculations as described in Section 3.

(3) Consideration was given to characterization of the crack-tip singularity. It was assumed that a through-wall axial crack in a pressure tube and a through-wall crack in a flat plate have the same type of singularity. This assumption forms the basis for the proposed format for the weight function for the burst test specimens. Using the notation as illustrated in Figure 2, one format of the weight function for a through-wall crack in an infinite flat plate, $m_0(x,a)$, is given by Eq. 1 [5].

$$m_0(x,a) = \frac{2}{\sqrt{\pi a}} \frac{1}{\sqrt{1-\left(\frac{x}{a}\right)^2}} \tag{1}$$

where x is x-coordinate relative to the crack center in an infinite plate.

(4) Consideration was given to the format of the weight function for the burst test specimens. Further to the consideration in (3), it was assumed that the weight function for an axial through-wall crack in a pressure tube, $m(x,a)$, can be written in terms of the weight function for a through-wall crack in an infinite flat plate with a modification coefficient. It is assumed that the modification coefficient is a function of the location parameter x/a, and the geometry parameter $a/\sqrt{R_m w}$, as expressed in Eq. 2. This assumption is based on engineering judgment. As discussed later in Sections 4 and 5, finite element calculation results provided support for this assumption.

$$m(x,a) = m_0(x,a)\, F\left(\frac{x}{a}, \frac{a}{\sqrt{R_m w}}\right) \tag{2}$$

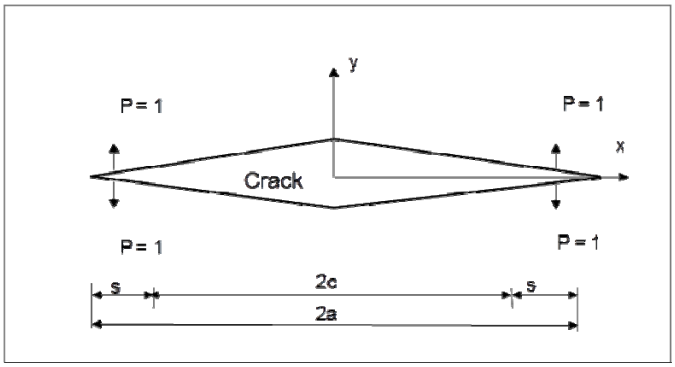

Figure 2. Weight function notation for a central through-wall crack in a flat plate or an axial crack in a pressure tube

3. Confirmation of Thickness Averaged Behavior of Plane Stress State

Three-dimensional elastic finite element analyses were performed to calculate the stress intensity factors for an axial through-wall crack in an internally pressurized long cylinder. The geometry of a representative burst test specimens was used. The inner radius of the cylinder was R_i = 52 mm and wall thickness was w = 4.0 mm. Two cases of crack length were considered, $2a$ = 50 mm and $2a$ = 75 mm. The length of the cylinder was set to 50 times crack length in the finite element model. Crack face pressure loading was included. Only one quarter of the cylinder was modeled and analyzed due to the symmetry consideration. The fracture mechanics specific three-dimensional finite element mesh generation tool FEACrack was used [6]. The generated three-dimensional finite element mesh for a 50 mm long axial through-wall crack is shown in Figure 3. The mesh contains 107,246 nodes and 24,360 20-node brick elements. Twenty one elements were used across the wall thickness near the crack-tips. The spider-web mesh design was used with concentric rings of elements focused towards the crack tips. The element edge length for the first ring elements was 5 μm. The mid-side nodes at the crack-tips were move to the one-quarter points. The crack-tip nodes were tied together. A similar mesh was used for the case of a 75 mm long crack. The mesh for the 75 mm long crack contains 119,446 nodes and 26,985 20-node brick elements. Elements around the crack-tips were essentially the same as in the case of 50 mm long crack.

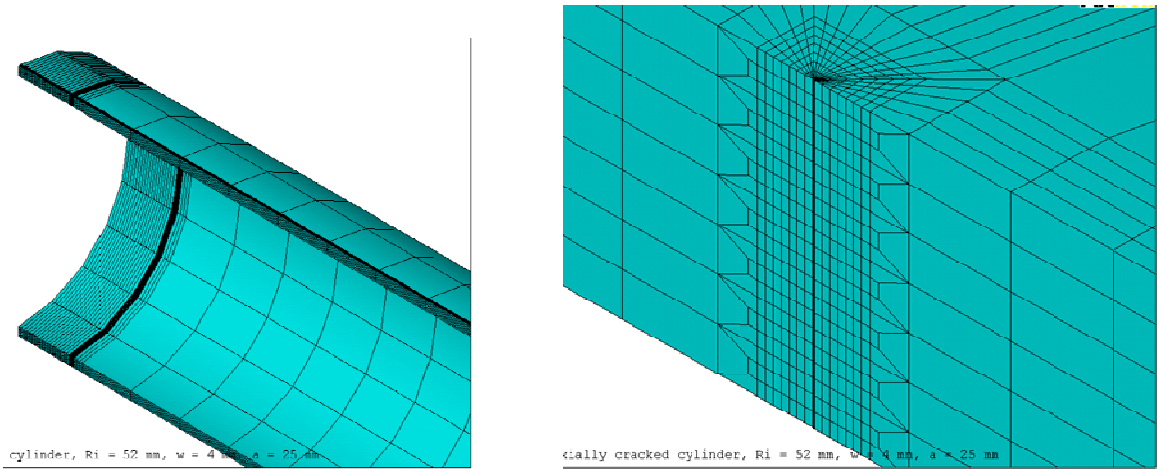

Figure 3. Three-dimensional finite element mesh of one quarter of a pressure tube burst test specimen

Two cases of Poisson's ratio were considered, $\upsilon = 0.3$ and $\upsilon = 0.4$. Finite element analyses were performed using ANSYS [7]. Stress and strain data obtained from ANSYS were read to FEACrack for calculation of the J integral. The path independence of J integral results was confirmed. Forty-three values of the J integral were obtained along the wall thickness for each case of crack depth and Poisson's ratio. Each value of J was converted to a stress intensity factor, K_I, using either plane stress or plane strain conditions. An internal pressure of p = 100 MPa was used in the calculation, with inclusion of crack face pressure. Since the calculations are based on linear elastic material behavior, the level of internal pressure is arbitrary in the context of development of weight functions. The thickness averaged K_I results for crack length $2a$ of 50 and 75 mm for plane stress and plane strain conditions, when Poisson's ratio $\upsilon = 0.3$ was used in the finite element calculations, are listed in Table 1. The mid-thickness K_I results are also listed for comparison. In addition, the K_I results calculated based on the commonly used bulging factor are listed in Table 1 [3]. The bulging factor is based on the shallow shell theory and calculated K_I results correspond to plane-stress conditions [8, 9, 10]. It is seen that the thickness averaged K_I results for plane stress conditions are in reasonable agreement with the K_I results calculated based on the bulging factor. The mid-thickness K_I results also generally agree with K_I results calculated based on the bulging factor, but the agreement is not as good as the thickness averaged K_I results. Similarly, the thickness averaged K_I results and the mid-thickness K_I results when Poisson's ratio $\upsilon = 0.4$ was used in the finite element calculations are listed in Table 2. The K_I results calculated based on the bulging factor are also listed in Table 2. Again, it is seen that the thickness averaged K_I results for plane-stress conditions are in reasonable agreement with the K_I results calculated based on the bulging factor.

The above observations from Tables 1 and 2 confirm that the thickness averaged behavior of the pressure tube is of a plane stress state. This average over the wall thickness approach was subsequently used to extract stress intensity factor results from three-dimensional finite element results for the development of the weight function for the burst test specimens as described in Sections 4 and 5.

Another observation from Tables 1 and 2 is that the effect of Poisson's ratio on the thickness averaged K_I results for plane-stress conditions is insignificant. In Table 1 with $\upsilon = 0.3$, the thickness averaged K_I are 854 and 1406 MPa√m for crack lengths $2a$ = 50 and 75 mm, respectively. In Table 2 with $\upsilon = 0.4$, the corresponding K_I are 849 and 1398 MPa√m for crack lengths $2a$ = 50 and 75 mm, respectively. This observation provides additional support for using the wall thickness averaged result when extracting three-dimensional finite element results for the development of the weight function for burst test specimens.

Table 1. Stress intensity factors for an axial through-wall crack in a pressure tube with internal pressure of 100 MPa, Poisson's ratio of 0.3 used in finite element calculation

METHOD TO CALCULATE STRESS INTENSITY FACTOR		STRESS INTENSITY FACTOR, K_I (MPa√m)	
		$2a$ = 50 mm	$2a$ = 75 mm
Averaged result over thickness based on 3-D FE results	Plane stress	854 MPa√m	1406 MPa√m
	Plane strain	895 MPa√m	1474 MPa√m
Mid-thickness result based on 3-D FE results	Plane stress	874 MPa√m	1441 MPa√m
	Plane strain	917 MPa√m	1511 MPa√m
Result based on the bulging factor [3]		834 MPa√m	1409 MPa√m

Table 2. Stress intensity factors for an axial through-wall crack in a pressure tube with internal pressure of 100 MPa, Poisson's ratio of 0.4 used in finite element calculation

METHOD TO CALCULATE STRESS INTENSITY FACTOR		STRESS INTENSITY FACTOR, K_I (MPa√m)	
		$2a$ = 50 mm	$2a$ = 75 mm
Averaged result over thickness based on 3-D FE results	Plane stress	849 MPa√m	1398 MPa√m
	Plane strain	927 MPa√m	1526 MPa√m
Mid-thickness result based on 3-D FE results	Plane stress	882 MPa√m	1455 MPa√m
	Plane strain	962 MPa√m	1587 MPa√m
Result based on the bulging factor [3]		834 MPa√m	1409 MPa√m

4. Finite Element Calculation of Weight Function for Burst Test Specimens

A one-dimensional weight function can be interpreted as the stress intensity factor for a pair of opposing unit line loads acting on the crack faces of a three-dimensional cracked body. Three-dimensional finite element analyses were performed to calculate the stress intensity factors for a line load on the crack faces, or discrete values of the weight function, for pressure tube burst test specimens.

As discussed in Considerations (3) and (4) in Section 2, it was assumed that the normalized weight function for the pressure tube burst test specimen, $m(x,a)/m_0(x,a)$, does not contain any singularity, where $m_0(x, a)$ is the weight function for a through-wall crack in an infinite flat plate. It was also assumed that the normalized weight function $m(x,a)/m_0(x,a)$ is a function of the location parameter x/a and the geometry parameter $a/\sqrt{R_m w}$.

Table 3. Finite element calculation matrix for development of weight function for burst test specimen

CALCULATION SET	CRACK LENGTH, $2a$ (mm)	LOAD LOCATION, x/a
I	12 values distributed between [2, 100]	0
II	50	10 values distributed between [0, 1)
III	75	10 values distributed between [0, 1)

The finite element calculation matrix for the development of a weight function for the burst test specimens is listed in Table 3. The pressure tube inner radius R_i of 52 mm and wall thickness w of 4.0 mm were used in all cases. Poisson's ratio $\upsilon = 0.3$ was used. Based on the discussion in Section 3, the effect of Poisson's ratio on the wall thickness averaged K_I values for plane-stress conditions has been confirmed to be insignificant. Three sets of finite element calculations in Table 3 were chosen based on parameter combinations of load location and crack length. In calculation Set-I, the load was always applied on the crack center line, *i.e.* $x/a = 0$. Discrete values of the weight function from calculation Set-I were used to characterize the trend of the weight function with the geometry parameter $a/\sqrt{R_m w}$. In calculation Set-II, the crack length was fixed to $2a$ = 50 mm, and pressure load was applied to lines located at ten different locations between crack centers and crack-tips.

Calculation Set-III is similar to Set-II, except that the crack length was $2a$ = 75 mm. The finite element mesh design was the same as described in Section 3. An example of a crack-tip zoomed-in view of the three-dimensional finite element mesh of one quarter of a burst test specimen with line load of pressure applied on the crack face is given in Figure 4.

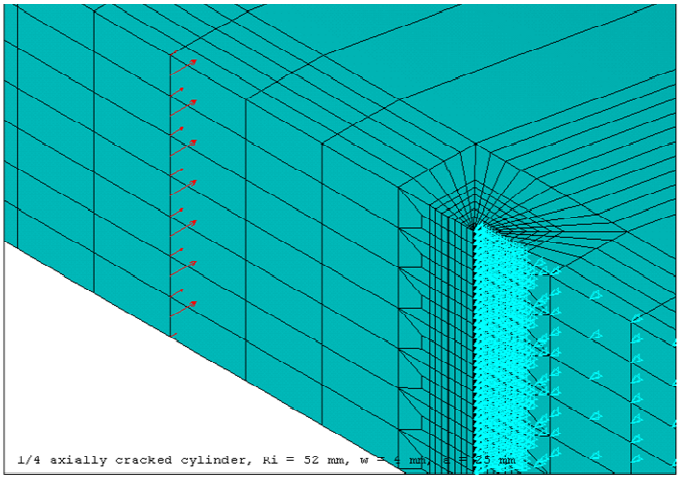

Figure 4. Crack-tip zoomed-in view of three-dimensional finite element mesh of one quarter of a pressure tube burst test specimen with inner radius of 52 mm, wall thickness of 4 mm, and 50 mm long axial through-wall crack, line load of pressure applied on crack face (denoted by red arrows)

The wall thickness averaged K_I results for plane-stress conditions, or the discrete values of weight function $m(x, a)$, were extracted from the three-dimensional finite element results. The normalized weight functions $m(x,a)/m_0(x,a)$ were obtained for the calculation Sets-I, II and III, respectively.

5. Regression Fit and Proposed Weight Function

The wall thickness averaged finite element results of normalized weight function obtained in Section 4 were fitted to an engineering equation using TableCurve2D [11], in conjunction with engineering judgment.

The discrete values of normalized weight function at the crack center for the calculation Set-I in Table 3 were found to fit well with the following simple equation.

$$\frac{m(0,a)}{m_0(0,a)} = \sqrt{1+3.696\frac{a^2}{R_m w}} \tag{3}$$

The R^2 coefficient of variation was 0.999, the fit standard error was 0.0612, and F-statistic was 11570. The comparison of finite element data and the fitted equation is plotted in Fig. 5. The maximum fitting error was 2.1%.

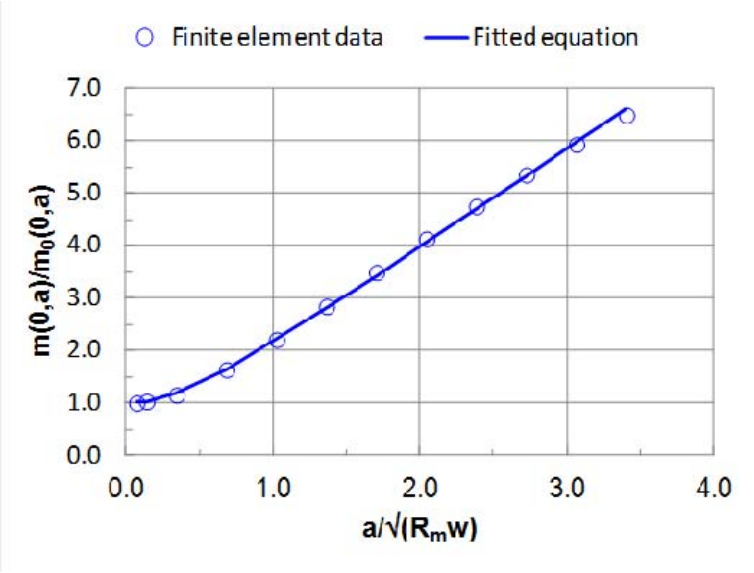

Figure 5. Finite element results and fitted equation of normalized weight function for the calculation Set-I for an axial through-wall crack in a pressure tube

The trend of normalized weight function with the location parameter *x/a* was investigated using the finite element data for the calculation Set-II and Set-III in Table 3. The discrete values of normalized weight function $m(x,a)/m_0(x,a)$ for a crack length of $2a$ = 50 mm for the calculation Set-II were fitted as a function of *x/a*. A separate fit was performed for the data for the calculation Set-III for a crack length of $2a$ = 75 mm. It was found that the equation format of Eq. (4) fits well to the data for both calculation sets. For the case of the 50 mm long crack, the fit standard error was 0.0371, and the *F*-statistic was 3635. For the case of the 75 mm long crack, the fit standard error was 0.0478, and the *F*-statistic was 6160.

$$\frac{m(x,a)}{m_0(x,a)} = C_1 + C_2\left(\frac{x}{a}\right)^2 \tag{4}$$

where C_1 and C_2 are fitting coefficients.

The fitting of C_1 and C_2 in Eq. (4) were used to determine the appropriate functional form of $m(x,a)/m_0(x,a)$, and were not used in the final form of the weight function. In the absence of using a three-dimensional fitting tool and with limited finite element data, engineering judgment was applied to establish an engineering equation using equation formats of Eqs. (3) and (4). The engineering equation is written as

$$\frac{m(x,a)}{m_0(x,a)} = M - (M-1)\left(\frac{x}{a}\right)^2 \tag{5}$$

with

$$M = \sqrt{1 + 3.696\frac{a^2}{R_m w}} \tag{6}$$

The comparison of finite element data for the calculation Set-II and Sec-III and the engineering equations of Eqs. (5) and (6) is plotted in Figure 6. The maximum fitting error was 4.2% for the data for the calculation Set-II, and 6.7% for the data for the calculation Set-III. These fitting errors were considered to be acceptable. An improved equation fit might be obtained if a proper three-dimensional fitting tool was used in the fitting process. Generating additional finite element data for crack lengths other than $2a$ = 50 and 75 mm may be necessary for improvement in the equation fit.

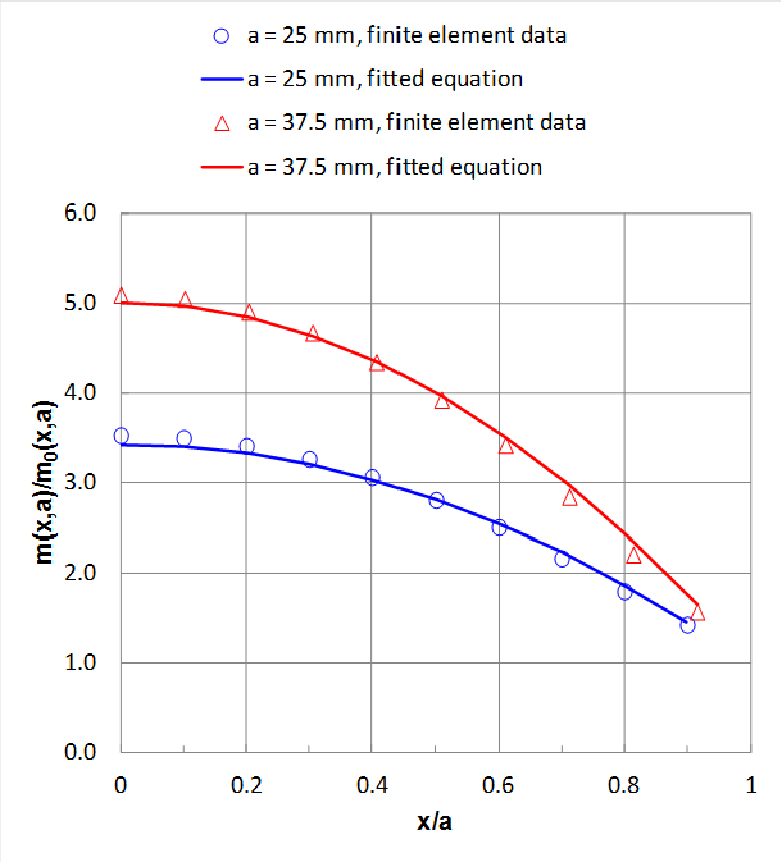

Figure 6. Finite element results and fitted equation of normalized weight function for calculation Set-II and Set-III for an axial through-wall crack in a pressure tube

The proposed weight function for the burst test specimen is given by

$$m(x,a) = \frac{2}{\sqrt{\pi a}} \frac{1}{\sqrt{1-\left(\frac{x}{a}\right)^2}} \left[M - (M-1)\left(\frac{x}{a}\right)^2 \right] \tag{7}$$

where the parameter M is given by Eq. (6).

It is reasonable to expect that, when loading on the crack face is uniform, the stress intensity factor calculated using the developed weight function is consistent with the conventional calculation approach based on the bulging factor for an axial through-wall crack. This consistence was checked. When the internal pressure is p, the stress intensity factor for the burst test specimen using the

bulging factor M_b, $K_I(M_b)$, is written as Eqs. (8) and (9).

$$K_I(M_b) = p\frac{R_i}{w}M_b\sqrt{\pi a} \tag{8}$$

with

$$M_b = \sqrt{1+1.255\frac{a^2}{R_m w}-0.0135\left(\frac{a^2}{R_m w}\right)^2} \tag{9}$$

With the use of the weight function approach, the stress intensity factor for the burst test specimens, $K_I(m)$, is written as

$$K_I(m) = \int_0^a m(x,a)\, p\frac{R_i}{w}dx \tag{10}$$

Substitution of Eq. (7) into Eq. (10) results in

$$K_I(m) = p\frac{R_i}{w}\left(\frac{M+1}{2}\right)\sqrt{\pi a} \tag{11}$$

The numerical values of $K_I(M_b)$ and $K_I(m)$ were compared for four cases of crack length, $2a$ = 50, 60, 75 and 100 mm. The percentage differences between $K_I(M_b)$ and $K_I(m)$ are within 5%.

Acknowledgements

This work was funded by the CANDU Owners Group.

References

[1] W.J. Langford, L.E.J. Mooder, Fracture behaviour of zirconium alloy pressure tubes for Canadian nuclear power reactors. International Journal of Pressure Vessels and Piping, 6 (1978) 275–310.
[2] P.H. Davies and R.S.W. Shewfelt, Link Between Results of Small- and Large-Scale Toughness Tests on Irradiated Zr-2.5Nb Pressure Tube Material, in: E.R. Bradley and G.P. Sabol (Eds.), Zirconium in the Nuclear Industry: Eleventh International Symposium, ASTM STP 1295, American Society for Testing and Materials, 1996, 492-517.
[3] Canadian Standards Association, Technical Requirements for In-service Evaluation of Zirconium Alloy Pressure Tubes in CANDU Reactors, CSA Standard N285.8-10, Toronto, 2010.
[4] S. St Lawrence, unpublished work, 2012.
[5] G. Glinka and G. Shen, Universal Features of Weight Functions for Cracks in Mode I. Engineering Fracture Mechanics, 40 (1991) 1135-1146.
[6] FEACRACK, 3D Finite Element Software for Cracks, Version 3.2.16, Quest Reliability, Boulder, CO, U.S.A., 2012.
[7] ANSYS, General Purpose Finite Element Software, ANSYS Mechanical, Version 14.0, Ansys, Canonsburg, Pennsylvania, U.S.A., 2012.
[8] E.S. Folias, An Axial Crack in a Pressured Cylindrical Shell. International Journal of Fracture Mechanics, 1 (1965) 104-113.
[9] R. Ehlers, Stress Intensity Factors and Crack Opening Areas for Axial Through Cracks in Hollow Cylinders under Internal Pressure Loading. Engineering Fracture Mechanics, 25 (1986) 63-77.
[10] J.F. Kiefner, W.A. Maxey R.J. Eiber and A.R. Duffy, Failure Stress Levels of Flaws in Pressurized Cylinders. ASTM STP 536, 1973, 461-481.
[11] TableCurve 2D, Automated Curve Fitting Software, Version 5.01, SYSTAT Software Inc., Richmond, CA, U.S.A., 2002.

Study on CTOD and microstructure in flash welded joints for 630-730 MPa grade mooring chains

Shuwei Leng[1,*], Zhangmu Miao[1], Ping Sun[2] and Xuelian Yao[1]

[1]School of Transportation of Wuhan University of Technology, Wuhan, 430063,P.R.China;
[2]Foshan Marine Anchor Chain Ltd, Foshan, 528132, P.R.China.
* Corresponding author: shuweileng1987@yahoo.com.cn

Abstract Three kinds of welding and heat treatment procedures are commonly used to make mooring chains for offshore structure in this paper. In order to determine the toughness, several specimens extracted from the welded joints and base metals are subjected to mechanical testing by means of Crack Tip Opening Displacement (CTOD) tests. Considering the data obtained, it can be recommended that the materials are safe enough in toughness to construct engineering structures (higher than the acceptable value specification by DNV).M2 tempered with 640℃ (for 60 minutes) presents the highest CTOD and yield strength, followed by M3 tempered with 650℃. M1 tempered with 600℃ presents the lowest CTOD and yield strength. That means tempering at 640℃ can obtain best toughness together with yield strength. The fracture surface and microstructure of the samples are characterized using scanning electron microscopy. Quantitative examinations including grain size analysis and carbide content measurements are carried out. The fracture parameter CTOD is correlated with the fracture surface and microstructures. The carbide contents of M2 and M3 are greater than those of M1 and the greater the carbide content is, the higher the CTOD value will be. And the grain size has the same trend.

Keywords Offshore,Welded joint, Mooring chain, CTOD, Microstructure

1. Introduction

As one of the most important components, mooring chain is playing a key role in the marine structure. When the operating depth becomes deeper, the higher demand is required especially when under the depth of 1000m. In the deep sea, the temperature of water is low and the environment is corrosive, so cracks easily occurs (especially for stud link chains).In the welding process, weld metal is heated to melt, and it experiences crystallization and solid transformation when it cools down; various parts of the weld joints are subjected to different thermal cycles which bring about the differentiation and heterogeneity. Toughness is the ability to resist crack initiation and propagation under external loads and the ability to absorb energy in deformation process. It is a comprehensive performance of the strength and plasticity. Compared with the materials with bad toughness, the good ones can prevent the procedure from micro-crack to macro-crack from happening therefore. to avoid the disaster . Because of the bad toughness, the micro-cracks in the weld joint shown in Fig.1 [1] may easily turn into macro-cracks, and the whole structure may break down suddenly.

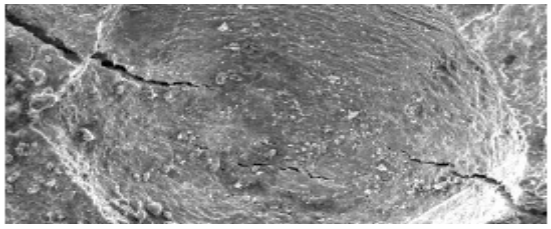

Fig.1.Micro-cracks of weld joints

Crack Tip Opening Displacement (CTOD) test is widely used to evaluate the toughness of steel structures especially the marine steel. There have been some studies about the relationship between toughness and microstructure in the past years [2, 3]. This paper aims at a further study of this issue and seeks for some ways to improve the microstructure to make the toughness and strength better.

Then the cracks will not initiate and propagate. As is known that the strength and toughness are contradicted, when the toughness becomes higher, the strength normally goes down. There are three types of mooring chains in this study, the first one is weak in both toughness and strength but the last two have better performance. Some reasons can be found in the microstructure for this phenomenon.

2. Tests procedure

2.1. Material

There are three types of mooring chains in this study: M1 with the diameter of 160mm, M2 with 124mm and M3 with 125mm. The mooring chains are provided by Foshan Marine Anchor Chain Ltd. and the flash butt welding is adopted. The production process is shown as follows: Cutting bars → Induction preheating→ Bending→ Flash butt welding→ Pressing→ Continuous heat treatment→ Mechanical tests. Table1 and Table2 have shown the Chemical composition of M1 (with the specimens 62-66), M2 (with the specimens 11-13) and M3 (with the specimens 1-3).

Table1. Chemical composition of M1（R3）

C	Si	Mn	P	S	Cr	Mo	Ni	Nb	Cu	Alt
0.27	0.15	1.40	≤	≤	≤	≤	≤	≤	≤	0.020
-0.33	-0.35	-1.90	0.025	0.025	0. 25	0.08	0.30	0.05	0.20	-0.050

Table2. Chemical composition of M2 and M3 (R3S)

C	Si	Mn	P	S	Cr	Mo	Ni	Nb	Cu	Alt
0.23	0.15	1.15	≤	≤	0.45	0.20	0.10	0.02	≤	0.020
-0.31	-0.30	-1.65	0.025	0.025	-0.75	-0.50	-0.20	-0.06	0.20	-0.050

2.2. CTOD and Charpy impact test

Three-point bending CTOD test was performed in accordance with BS7448:part2 [4] and EN 10225:2009[5] with WAW-1000kN tester controlled by computer, the testing temperature is -20℃. The schematic illustrations of CTOD test set-up is shown in Fig.3. According to the DNV's standard [6]: the specimen location is shown in Fig.2. The weld side specimen is named A specimen and the non-weld side one is named B specimen.

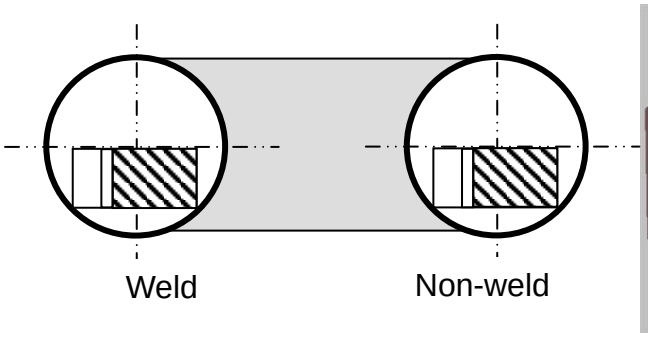

Fig.2. Location of CTOD test specimens

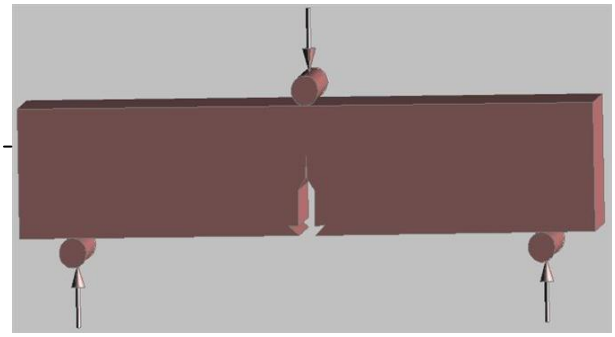

Fig.3. schematic illustrations of CTOD test set-up

The specimens are prepared perpendicular to the rolling direction and the weld bead. The facility to make fatigue pre-crack is JXG-200kN computer controlled high-frequency fatigue tester. The position of machining notch has been figured out in Fig.3. In order to reduce the effect of the weld residual stress on the fatigue pre-cracking, the fatigue pre-cracking is divided into two steps according to BS7448 Part 2 and each step uses different fatigue stress ratios (R). For the first step, the stress ratio R=0.1 is used until the fatigue pre-crack has grown to a length of about 2.5 mm .In

the second step, R is 0.7 and the fatigue pre-crack grown to 0.5mm. All the specimens are pretreated by local compression before pre-cracking. According to FV curve and other obtained data, CTOD value δ can be calculated referring with Eq. 1.

$$\delta = \delta_e + \delta_p = \left[\frac{FS}{BW^{3/2}} \cdot f(\frac{a_0}{W})\right]^2 \frac{(1-\mu^2)}{2\sigma_s E} + \frac{r_p(W-a_0)}{r_p(W-a_0)+a_0+z} \cdot V_p \qquad \text{Eq. 1}$$

Charpy impact was carried out according to DNV's standard, the testing temperature is -20℃. The samples were extracted through thickness notches, transverse to the weld bead and notched at the weld position. The average value of the three test results meets the specified requirement，no individual value is below the minimum average value specified.

2.3. Micro-analysis

The samples for metallographic and fracture analysis are extracted from the rupture specimens which have Conducted the CTOD fracture toughness tests. Positions to extract samples for microanalysis and sample geometry are presented in Fig.4. Samples A perform metallographic analysis. Other kinds of samples contain fracture surface and microstructure next to the cross-section are samples B. Samples B are along with the crack propagation direction and perpendicular to the crack surface.

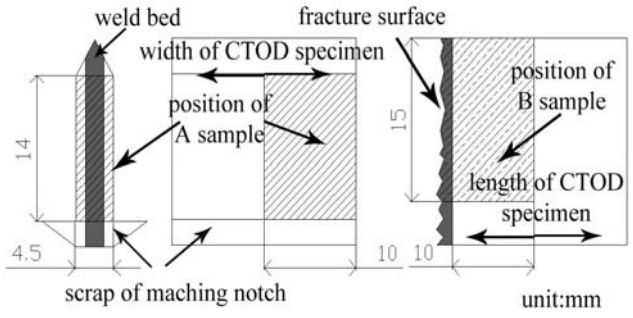

Fig.4. Position to extract samples for microanalysis

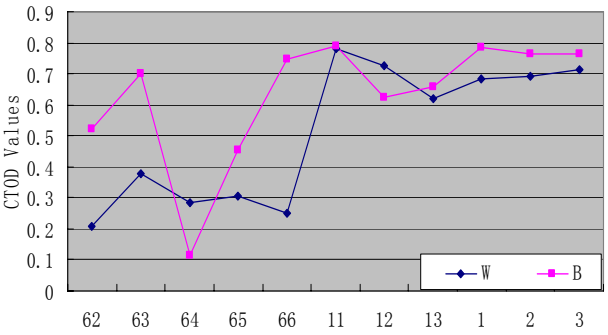

Fig.5.Tendency of CTOD values

The samples used to analyze microstructure should be grinded, polished and etched with 4% alcohol solution of nitric acid at first. Both the fracture surface and microstructure of samples were characterized using Scanning Electron Microscopy (SEM).

3.Test Results and Discussions

3.1. CTOD and Charpy impact test results

Through the CTOD test, Vp and a0 are measured, then referring to equation1, the δ is obtained and listed in Table5 and Table6. CTOD values of M1 specimens (with the number 62-66) are greater than those of M2 and M3 (with the number 1-3 and11-13). Fig.5 shows the tendency of CTOD values and table 7 gives the Charpy impact energy of different specimens.

Table5. CTOD values of weld specimens

Specimen	W62	W63	W64	W65	W66	W11	W12	W13	W1	W2	W3
δ_u(mm)	0.210	0.379	0.285	0.307	0.252	-	-	-	-	-	-
δ_m(mm)	-	-	-	-	-	0.781	0.728	0.620	0.685	0.690	0.713

Specimen	B62	B63	B64	B65	B66	B11	B12	B13	B1	B2	B3

δ_u(mm)	0.524	-	0.114	0.454	-	-	-	-	-	-	-
δ_m(mm)	-	0.701	-	-	0.749	0.789	0.625	0.657	0.786	0.765	0.764

Table6. CTOD values of base metal specimens

Table7.Charpy impact energy of values of weld specimens

Specimen	W62	W63	W64	W65	W66	W11	W12	W13	W1	W2	W3
akv (J)	43	61	40.5	39.5	36.5	144	140	146	99	91	110

From Fig.6, some features can be found from the macro section: There are both stable and unstable cracks in the specimens of all; The crack propagation of M1（with the specimens 62-66）is unstable，large parts of the crack face of both base metal and weld. Lots of parts of the crack of base metal are grey and the bright parts are not straight, it experiences some plastic deformation with obvious signs of tearing; the cracks of weld specimens are bright without any obvious signs of tearing.

Fig.6. fracture cross-section of different CTOD specimens

All of these phenomena conform to the tendency of CTOD values. Both the crack propagation of base metal and weld of M1 and M2 are unstable, the rupture areas of the base metal are smooth with obvious 45°shear lip.

3.2. Microstructure Analysis Results

Through the micro test using SEM, something about the microstructure can be obtained. Metallographs of the center of the weld and base metal of sample A in specimens (W62,W63,W66) of M1 are obtained. From the microstructure of base metal in W62A shown in Fig.7.a, ferrite and a small amount of martensite are presented. Fig.7.b shows the ferrite and cementite on the grain boundaries in the center of weld of W62A. The lath martensite, ferrite, sorbite and cementite on the grain boundaries are distinguished as is shown in Fig.7.c Carbide, sorbite and a little ferrite are found in Fig.7.d There are some ferrite, cementite and a little sorbite in Fig.7.e and Fig.7.f.

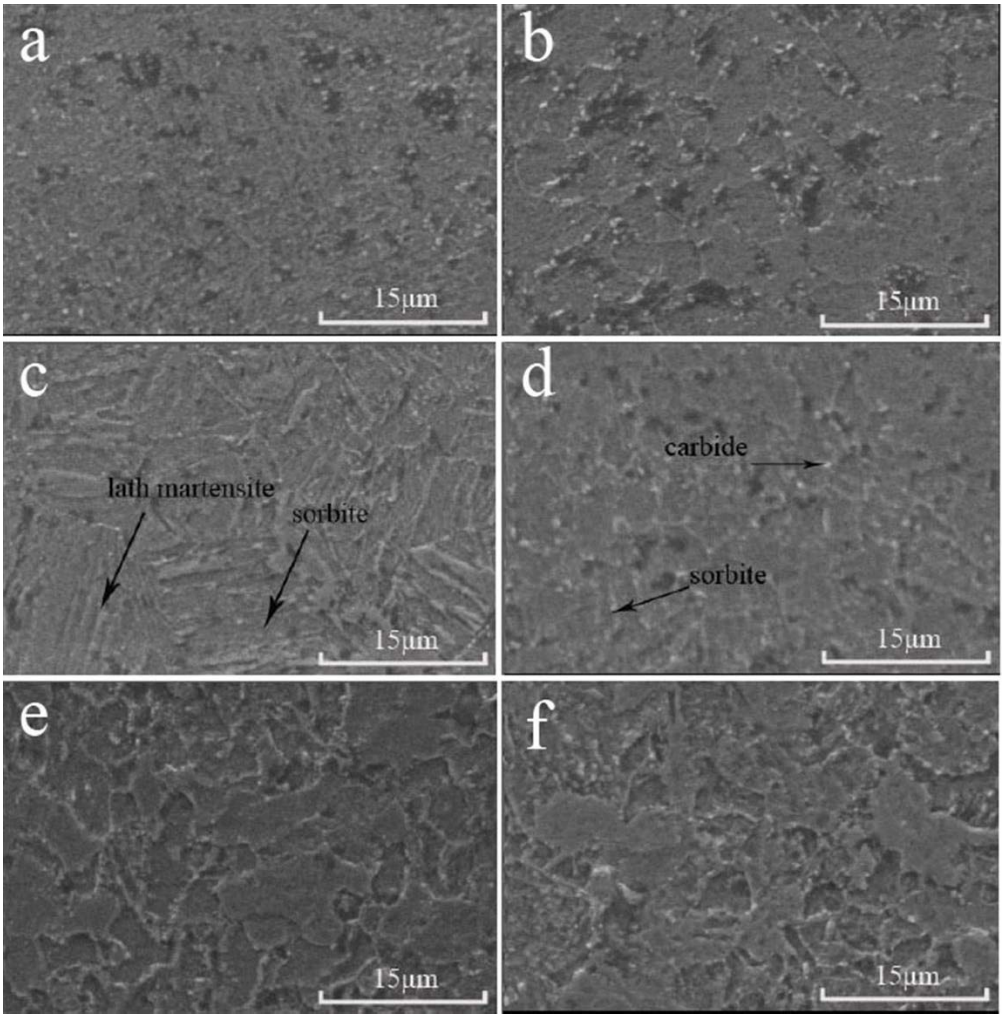

Fig.7. Microstructure of sample W62A,W63A and W66A
a.Base metal of W62A; b.Weld center of W62A; c.Base metal of W63A;
d.Weld center of W63A; e.Base metal of W66A; f.Base metal of W66A

The micro-morphology near the crack face is listed in Fig.8. Fig.8.a shows the microstructure near the crack of W62B: the grains have distinct directivity caused by plastic deformation and the elongated direction parallel to the crack face; Fig.8.b shows the secondary cracks, large inclusions, Carbide and ferrite near the fracture edge: The crack is caused by mixed influence of stress and inclusion; Fig.8.c shows the microstructure of W63B: there are lath martensite and sorbite without any deformation; Fig.8.d shows some inclusions but no secondary crack; Grains in Fig.8.e have obvious directivity and elongated direction perpendicular to the crack face. Secondary crack in Fig.8.f is classic facing a 45 ° angle with the main crack and the microstructure is ferrite and fine carbide.

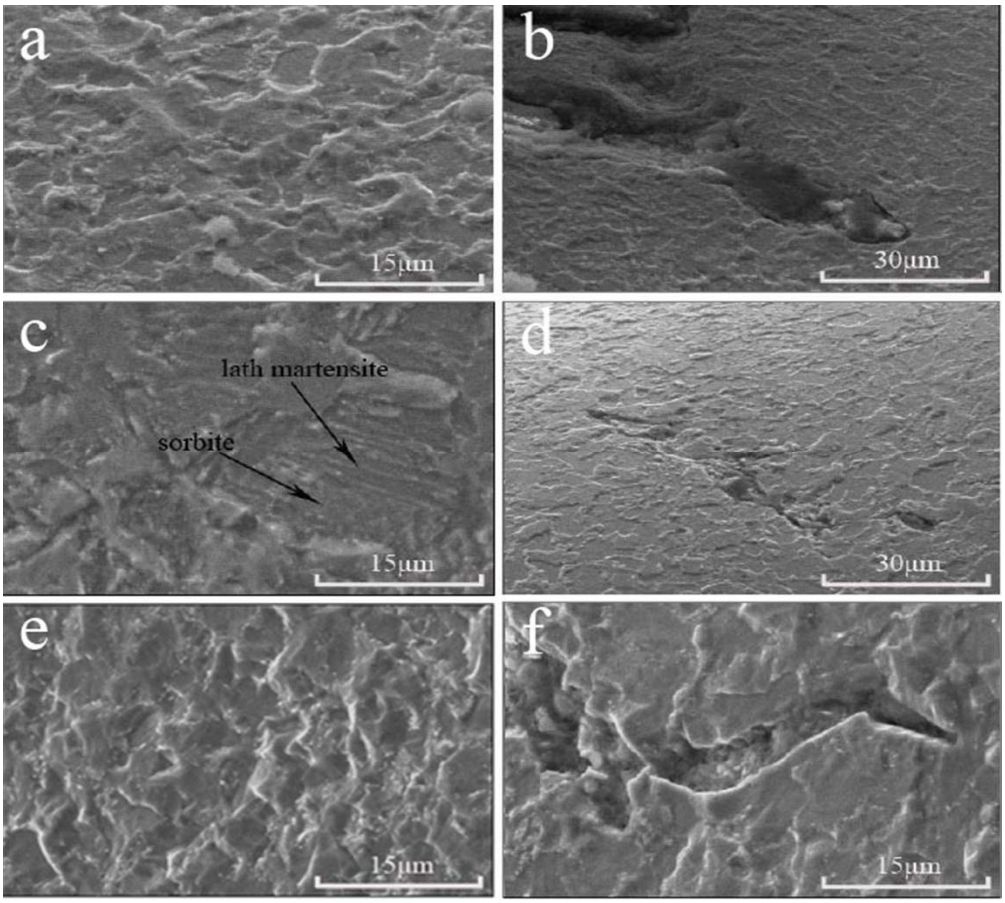

Fig.8. Microstructure of sample W62B,W63B and W66B
a.Near crack edge in W62B; b.Secondary crack of W62B; c.Near crack edge in W63
b.d.Inclusion in W63B; e. Near crack edge in W66B; f.Secondary crack of W66B

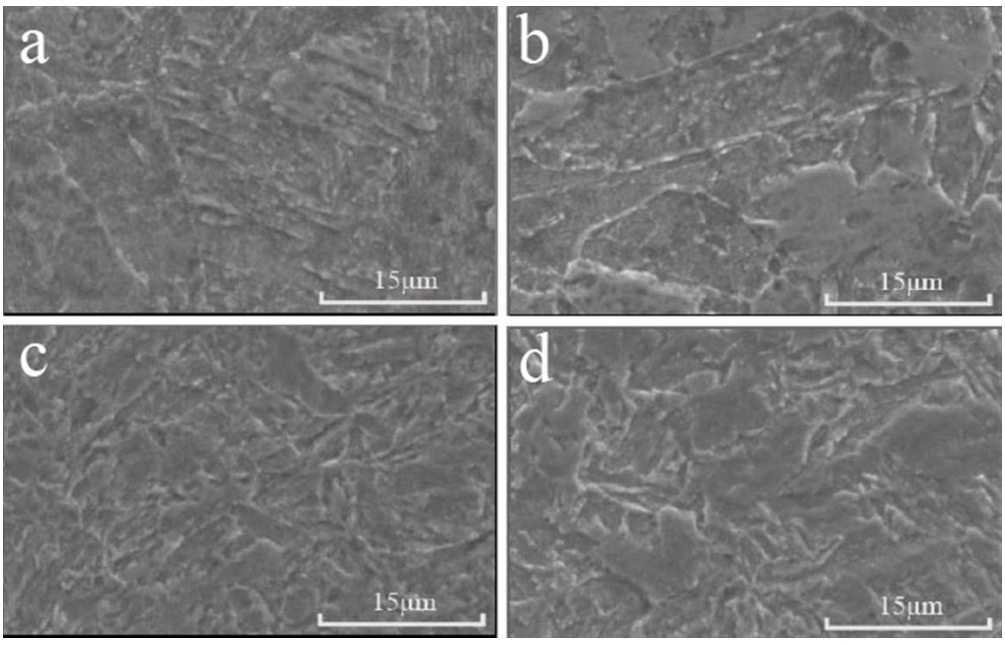

Fig.9. Microstructure of sample W3A and W13A
a.Base metal of W3A; b.Weld center of W3A; c.Base metal of W13A； d.Weld center of W13A

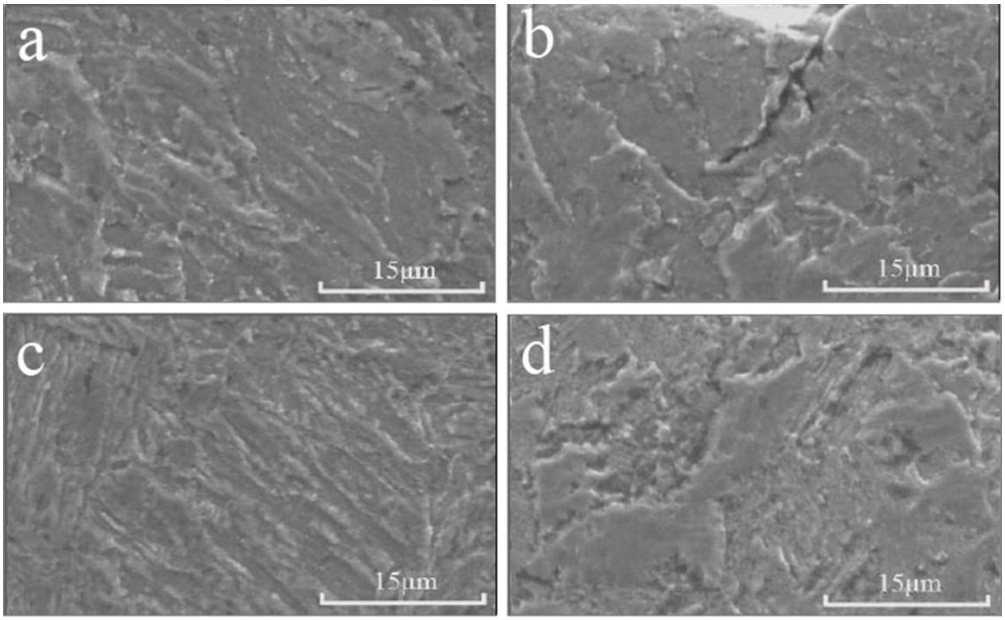

Fig.10. Microstructure of sample W3B and W13B
a.Near crack edge in W3B; b.Secondary crack of W3B;
c.Near crack edge in W13B; d.Cavity near crack edge in W13B

Fig.9 and Fig.10 show the microstructure of W3 and W13 coming from M2 and M3 respectively. Fig.9.a shows some lath martensite and ferrite; Fig.9.b shows ferrite and sorbite; the grains in the microstructure of base metal in W13A shown in Fig.9.c are so fine and disorganized. There are sorbite and ferrite in Fig.9.d; Fig.10.a shows some sorbite, a small amount of martensite and a small amount of carbide precipitation on the edge of fracture face in W3B; Fig.10.b shows the secondary cracks caused by small holes near the fracture edge of W3B and the crack is smaller than that in Fig.8.b and Fig.8.f. The crack direction is approximately perpendicular to the cross-section. There are martensite and sorbite in Fig.10.c and ferrite and sorbite in Fig.10.d.

3.3. Discussions about the results

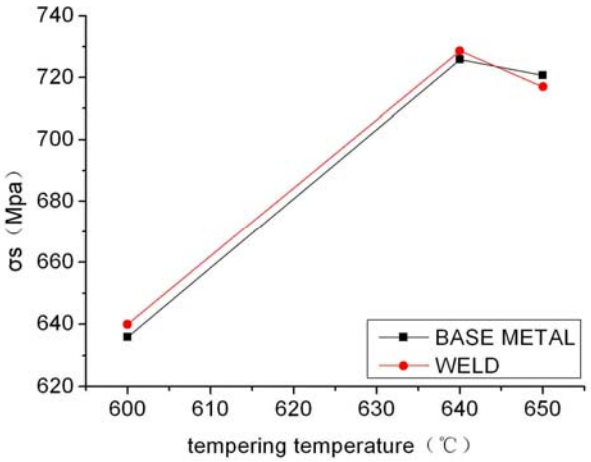

Fig.11.CTOD-tempering temperature

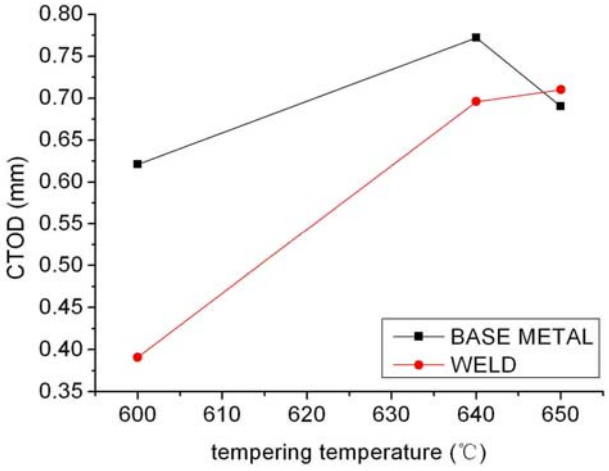

Fig.12. σs-tempering temperature

Some studies have shown that the large inclusions and the secondary cracks caused by them are bad for the toughness [7]. Compared with the W13 and W3, there are more secondary cracks and

inclusions in the microstructure and micro-fracture photographs of W62, W63 and W66 while the CTOD values conform to the rule. The sharp crack tips of the secondary crack in W62B, W63B and W66B indicate that it is relatively easy to expand compared with that of W3B and W13B. At the same time, the toughness conforms to this phenomenon. Grains of martensite and sorbite near the fracture face with small deformations may be caused by the content of carbide. There are mainly martensite in the base metal and sorbite in the weld center. The content of carbide particle between the spaces of α-phase in the weld and base metal of M1 is more than that of M2 and M3.

The relationship between tempering temperature and CTOD values and between tempering temperature and yield strength are shown in Fig.11 and Fig.12. The specimens tempered with 640℃(for 60 minutes) show the highest CTOD values and yield strength from the figures. That means tempering at 640℃ can obtain good toughness together with yield strength. This result is different with related reference [8,9]: increasing of tempering temperature (at 600-650 ℃) will makes the toughness worse.

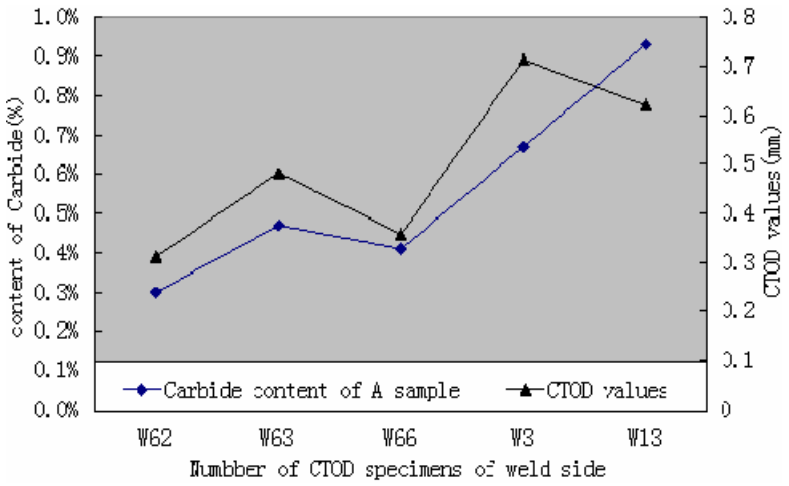

Fig.13. Variations in CTOD values and carbide content

According to the law of Dreiser, the quantitative measurements of content of carbide and grain size grade of weld center and the base metal in W62A, W63A, W66A, W3A, and W13A have been presented through using computer image processing system on scanning electron microscope images. Distribution of the content of carbide and the relationship with the CTOD are shown in Fig.13.The distribution of grain size grade and relationship with CTOD are shown in Fig.14.

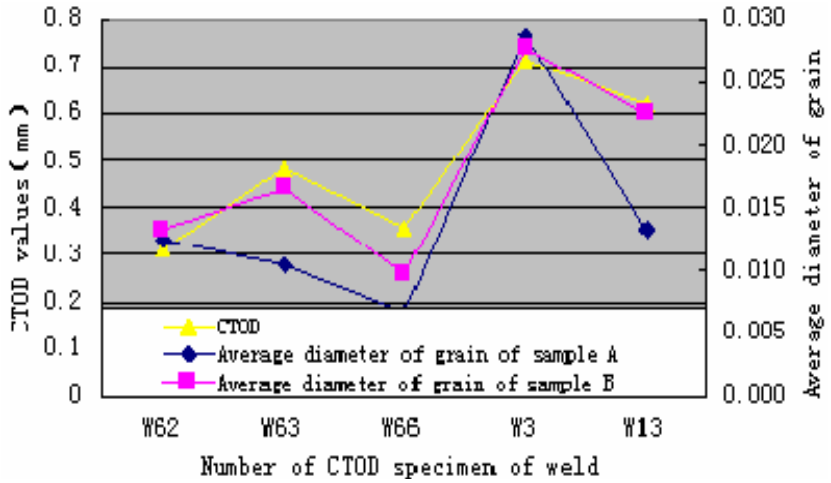

Fig.14. Variations in CTOD values and Grain size grade

Fig.13 shows that the carbide contents of M2 and M3 are greater than those of M1 and the greater the carbide content is, the higher the CTOD value will be. This situation conforms to the reference [10]. The grain size grades vary with the positions of the samples: weld center, base metal or near the edge of fracture face. The higher the grain sizes grade are， the lower the CTOD values will become, which is contrary to the common law. The specific reasons can be summarized as follows: 1. The CTOD values of M2 and M3 are all very large (all greater than 0.6 mm) and all the CTOD values are highly discrete. All the CTOD values are higher than the acceptable value 0.15 specified by DNV. That means the materials are safe enough in toughness for constructing engineering structures. However, the CTOD（toughness）is a macro concept and reflects the mechanical properties of the macro-structure. Samples for microscopic analysis are only taken from a small part of the macro-structure and the microscopic image is just a small part of the sample. Because of the existence of one-sidedness, it cannot reflect the overall situation of the organization. 2. The analysis of the forms of the grains (for the lath martensite in base metal, the strength is determined by the carbon content, but substructure plays an important role in toughness. It can be organized as follows: The compositions of microstructure in the weld center are mainly sorbite, ferrite and cementite mixture. Carbides are mainly distributed in the ferrite in the weld of M1, but those of M2 and M3 are fine and distributed on the grain boundaries. This is the reason why the specimens have better toughness and higher strength in M2 and M3. 3. From the contrast of alloy elements in Table 2 and Table 3, the contents of Cr and Mo in M2 and M3 are higher than those of M1. According to reference [10], the high content of Cr and Mo is good for strength but bad for toughness when the Mn content is near 1.6%.

4.Conclusions and Further studies

Through the results and discussions，some conclusions can be drawn as follows:

1. M2 tempered with 640℃ (for 60 minutes) presents the highest CTOD and yield strength, followed by M3 tempered with 650℃. M1 tempered with 600℃ presents the lowest CTOD and yield strength. That means tempering at 640℃ can obtain good toughness together with yield strength.

2. The fracture parameter CTOD is correlated with the microstructures. The carbide contents of M2 and M3 are greater than those of M1 and the greater the carbide content is, the higher the CTOD value will be. The grain size has the same trend .

In the discussions of this paper， limitations and one-sidedness also have been put forward in the study of the relationship between CTOD toughness and microstructure. More experimental and theoretical analysis is needed in the further studies.

Acknowledgements

The authors would like to thank the supporter, the Ministry of Industry and Information Technology (P.R.China). The study is supported by the program“Research of Key Points of Whole Fabrication and Installation of Deep-Sea Semisubmersible Drilling Platform” ([2009] No382).

References

[1] Miao Zhangmu, Miao Ting, Qiu Fuxiang, Leng Shuwei, Niu Lina: Applied Mechanics and Materials.Vols. 117-119 (2012) pp 1597-1601

[2] Leng Shuwei, Miao Zhangmu, Qiu Fuxiang, Niu Lina, Miao Ting: Applied Mechanics and Materials Vols. 117-119 (2012) pp 1867-1873
[3] J.J. Coronado and C. Cerón: Theoretical and Applied Fracture Mechanics.53 (2010) 145-152
[4] BS7448:Part2: Method for Determination of KIC, Critical CTOD and Critical J Values of Welds in Metallic Materials. London: British Standard Institution, 1997
[5] BS EN 10225: Weldable structural steels for fixed offshore structures — Technical delivery conditions. London: British Standard Institution, 2009
[6] DNV-OS-E302: OFFSHORE MOORING CHAIN AND ACCESSORIES.Norway: DET NORSKE VERITAS, 2010
[7] Debdulal Dasa, Rajdeep Sarkarb, Apurba Kishore Duttac ,Kalyan Kumar Rayd: Materials Science and Engineering A 528 (2010) 589–603
[8] Fawad Tariq • Nausheen Naz ,Rasheed Ahmed Baloch • Ashraf Ali:J Mater Sci (2010) 45:1695–1708
[9] Li Hong-ying, Zeng Cui-ting，Wang Fa-yun: TRANSACTIONS OF MATERIALS AND HEAT TREATMENT, Vol .32 No.3 March 2011
[10] Yin Shike, welding material and microstructure and property of weld joints. Beijing: Chemical Industry Press, 2011

Fracture mechanics model for predicting fracture strength of metallic alloys containing large second phase particles

Uwe Zerbst* and Mauro Madia

BAM-Federal Institute for Materials Research and Testing, 9.1
D-12205 Berlin, Germany
* Corresponding author: uwe.zerbst@bam.de

Abstract An analytical fracture mechanics model for predicting the finite life fatigue strength of components is presented which combines a number of well established and newly developed approaches such as Murakami's and McEvily's approach for describing the transient behaviour of crack closure of short cracks, the analytical (long) crack closure function of Newman, the R6 procedure modified by a method for improving the ligament yielding correction proposed by the authors and other elements. Basic assumption is the preexistence of initial flaws such that the crack initiation or nucleation stage is small and can be neglected. The application of the model is demonstrated for small tension plates of aluminium Al 5380 H321 with artificial initial defects generated by FIB technology, the size of which was fixed on the basis of fractographic investigations on broken, smooth specimens.

Keywords fatigue strength, S-N curve, fracture mechanics, crack propagation, short cracks

1. Introduction

The lifetime of a cyclically loaded component can be roughly subdivided into three stages: crack initiation, fatigue crack propagation and fracture. Frequently the crack initiation stage is defined such that it covers nucleation and early crack propagation until the crack reaches some tenth of a millimetre at surface. However, a closer look reveals that this phase can be subdivided in a number of sub-stages (e.g. [1]):

(a) The crack initiation sub-stage in a narrower sense which is characterised by the accumulation of microscopic plastic deformation sometimes occurs at the smooth surface but more frequently it happens at scratches, pores, inclusions and similar defects which act as micro-notches and/or due to strain concentration zones caused by different stiffness properties of defect and matrix material. In the case of very high cycle fatigue (fracture after 10^8 loading cycles or more) initiation takes place subsurface but also at material defects [2].

(b) Subsequent to crack initiation the crack size is in the range of micro-structural features such as the grain size. Its propagation is characterised by a irregular crack front and alternating phases of acceleration and retardation or even crack arrest. The arrest of the largest of a number of initially growing cracks is associated with the fatigue limit phenomenon [3].

(c) With the increasing crack size the effect of the microstructure on local fatigue crack propagation diminishes and the propagation rate becomes rather steady. When the crack size reaches the order of mechanical discontinuities such as the plastic zone size or a notch stress field the crack is designated as mechanically short. Its propagation, in principle, can be described by classical fracture mechanics, however not by the linear elastic ΔK concept. As the micro-structurally short crack also the mechanically short one can be arrested under constant applied loading due to the gradual build-up of the plasticity-induced crack closure phenomenon.

(d) Long cracks propagate above a crack-size independent long-crack threshold ΔK_{th}. Their growth can be described by the da/dN-ΔK curve concept when the crack closure phenomenon is taken into account. The long crack propagation is terminated by the fracture of the component.

The crack initiation sub-stage in the narrower sense frequently is very limited for many engineering materials. Instead of a detailed discussion a statement of Polak in Elsevier's"Comprehensive Structural Integrity" shall be cited here: "Numerous studies have shown that in the majority of materials and under normal loading conditions, the period of crack initiation in smooth specimens without defects amounts to less than 5-20% of the fatigue life. In materials containing defects, the fraction of life spent in crack initiation is even lower. The major part of the life is spent in the growth of cracks, namely in the growth of short cracks." [1]. This fact allows to model metallurgical defects as initial cracks without yielding over-conservative lifetime predictions.

2. Model Proposed for Predicting Finite-life Fatigue Strength and Lifetime

The observation that the essential part of fatigue lifetime of many engineering materials is covered by short crack growth requires a fracture mechanics model which is able to describe this stage in an adequate manner. The authors proposed such a model in [4] where the reader can also find a more detailed description as it is possible here due to limited space. The model, for a number of partial aspects, uses and combines otherwise established approaches because of which there exist similarities with alternative models (e.g. [5-8]) which also cannot be discussed here in any detail. Instead, the reader is referred to [4]. Fig. 1 summarises the input and model parameters and the analysis steps of the present procedure. In the following the analysis steps shall be exemplarily explained for tension plates of aluminium alloy Al 5083 H 321. This will then be added by validation exercises on two more aluminium alloys the data of which were taken from the literature.

2.1 Initial crack size

For the present study fracture surfaces of cyclically tension loaded flat plates were fractographically analysed. A fracture surface containing an initial defect is shown along with a micrograph section and statistics of the defect sizes found on all specimens in Fig. 2. In Fig. 2(d), following a proposal of Murakami (e.g. [2]), the initial crack size is given as the square root of its area, $\sqrt{\text{area}}$, with the index "i" standing for "initiation". The statistical upper bound of the initial defect depth was found to be in the order of 50 μm which is quite typical for aluminium alloys [9].

2.2 Material properties

The material properties needed as input parameters of the proposed model comprise the da/dN-ΔK curve for the stress ratio $R = K_{min}/K_{max}$ of interest (in the present case R = 0.2), the long crack fatigue threshold ΔK_{th} for the same R, the intrinsic threshold (no plasticity-induced crack closure) and the stabilised cyclic stress-strain curve. The Paris range of the da/dN-ΔK curve was experimenttally determined for R = 0.2 on four specimens. The average value of C was $C = 4.05 \cdot 10^{-12}$ (ΔK in $\text{MPa}\sqrt{\text{mm}}$; da/dN in mm/loading cycle) for an n assumed as n = 3. The threshold values for R = 0,2 und $R \rightarrow 1$ (intrinsic value) were 1.5 $\text{MPa}\sqrt{\text{m}}$ and 0.925 $\text{MPa}\sqrt{\text{m}}$ respectively.

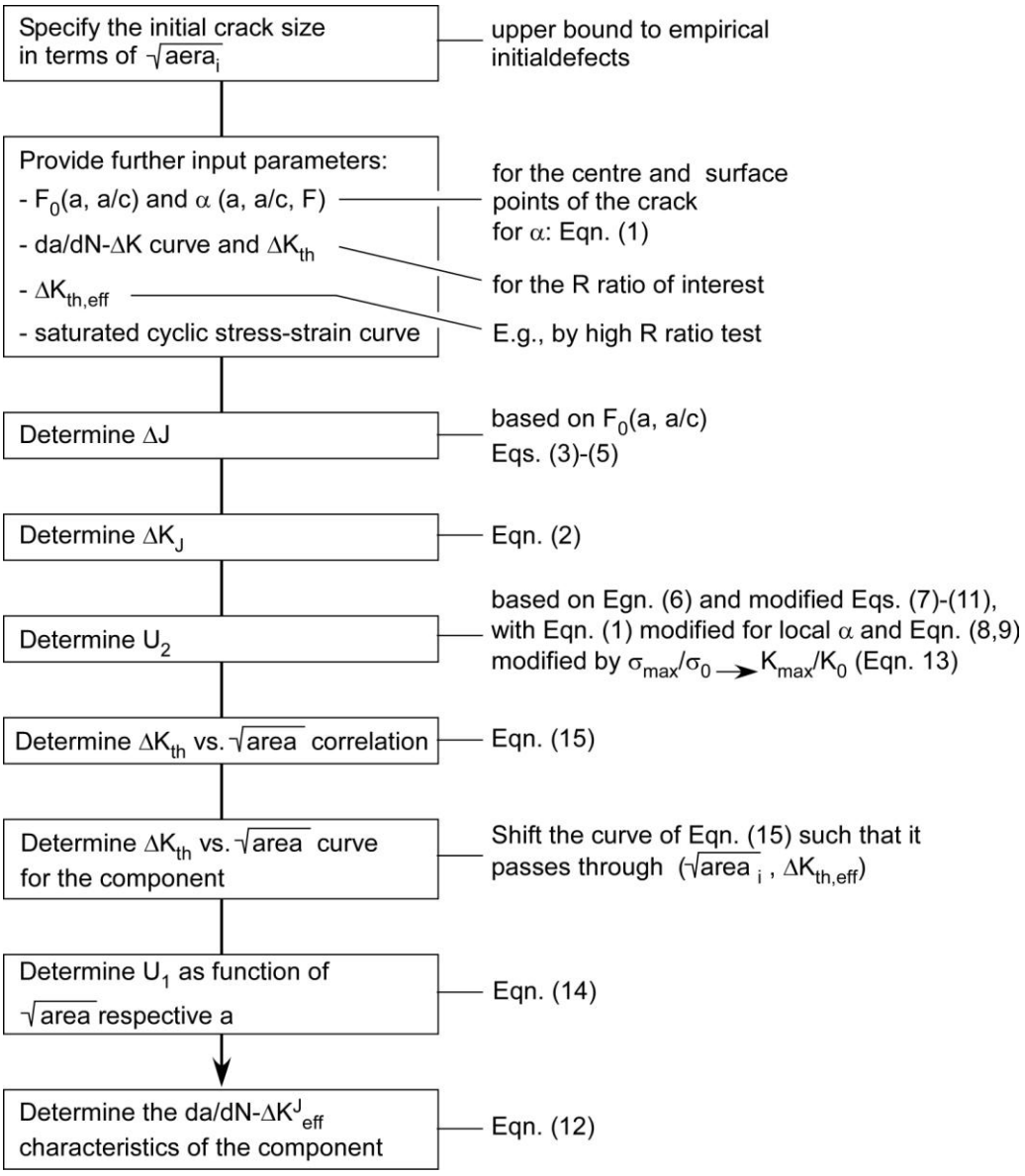

Fig. 1: Input and model parameters and steps of the fracture mechanics model presented here.

2.3 Model parameters

The model parameters of the analysis are the linear elastic stress intensity factor K for the deepest and the surface points at the crack front which were obtained by the solution of Raju and Newman [10] and confirmed by finite elements.

Following a proposal of the authors in [11] the reference load F_0 replaces the limit load in assessment procedures such as R6 [12] or SINTAP [13]. It is defined as that load at which the ligament plastification $L_r = F/F_0 = 1$. This may be different for different positions at the crack front.

A local constraint parameter α was determined instead of the global value according to Newman [14] the latter being given by Eqn. (1):

$$\alpha_g = \frac{1}{A_T} \sum_{m=1}^{M} \left(\frac{\sigma_{yy}}{\sigma_0} \right)_m A_m \qquad (1)$$

(A_m = projected area of a yielded element m on the uncracked ligament, σ_{yy}/σ_0 = normalized crack opening stress for the element m, A_T = total projected area of all elements (M) which have yielded)

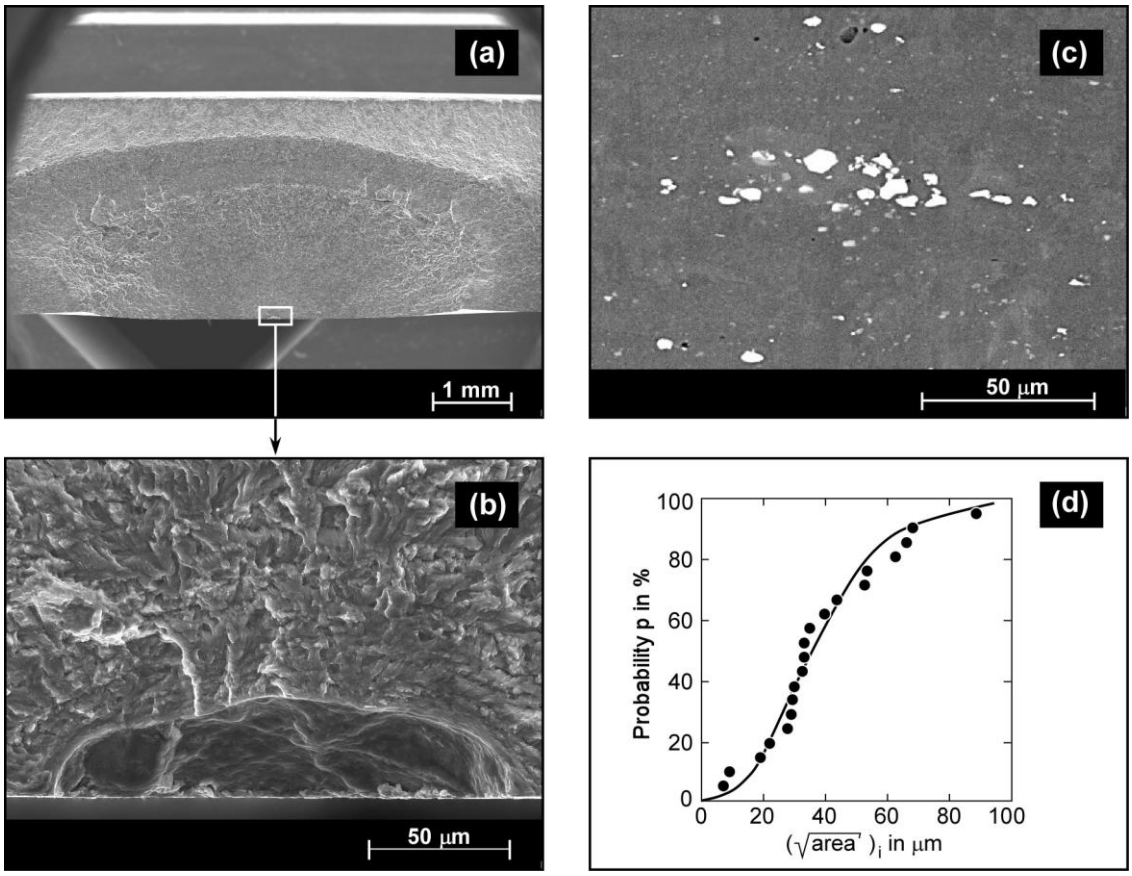

Fig. 2: Initial defects in the material AL5380 H321, fractographic and metallographic investigations: (a) and (b) example for an initial defect; (c) a cluster of inclusions with increased concentration of manganese, iron and nickel; (d) statistical distribution of the initial crack depth.

The parameter has been obtained by finite elements as a local parameter separately for the deepest and surface points of the semi-elliptical surface crack by modifying Eqn. (1) such that the total area of the plastic zone ahead of the crack, A_T, is replaced by local areas around the two points of interest. A more detailed description of the concrete realisation is found in [15].

2.4 Crack driving force of mechanically short cracks

The considerations in this paper mainly focus on short crack propagation (see Section 1). This is no problem insofar as the maximum initial defect sizes found at the fracture surfaces (see Fig. 2d) were sufficiently large not to be micro-structurally short cracks any more. It has already been mentioned that mechanically short cracks cannot adequately been described by the ΔK concept since the size of the plastic zone ahead of the crack is in the same order as the crack length. In order to address the local yielding effect ΔK is replaced by a ΔK^J which is formally obtained as

$$\Delta K^{J} = \sqrt{\Delta J \cdot E'}$$

$$E' = \begin{cases} E & \text{plane stress} \\ E/\left(1-\nu^2\right) & \text{plane strain} \end{cases} \tag{2}$$

With respect to a discussion of the cyclic J integral, ΔJ, the reader is referred to [4]. Within this paper a (slightly modified) approach of McClung [16,17] is applied by which ΔJ is determined by

$$\Delta J = \frac{\Delta K^2}{E'} \cdot \left[f \;\; \Delta L_r \right]^{-2} \tag{3}$$

with $$\Delta L_r = \frac{\Delta F}{2F_Y} = \frac{\Delta \sigma_{ref}}{2\sigma_Y} . \tag{4}$$

and $$L_r = F/F_0 . \tag{5}$$

2.5 Modelling the plasticity-induced crack closure pheneomenon

With respect to modelling the crack closure effect it has to be distinguished between long cracks (the effect is completely build-up) and short cracks (the effect is still gradually developing). Crack closure is described by a parameter U (U_1 – short crack; U_2 – long crack). For the long crack the so-called NASGRO equation is used which is based on results obtained by applying the modified strip yield model of Newman [18]:

$$U_2 = \frac{\Delta K_{eff}}{\Delta K} = \frac{1-f}{1-R} \tag{6}$$

$$\text{with } f = \frac{\sigma_{open}}{\sigma_{max}} = \begin{cases} A_0 + A_1 R + A_2 R^2 + A_3 R^3 & \text{for } R \geq 0 \\ A_0 + A_1 R & \text{for } -2 < R < 0 \end{cases} \tag{7}$$

The coefficients A_i are given by

$$A_0 = \; 0.825 - 0.34\alpha_g + 0.05\alpha_g^2 \left[\cos\left(\frac{\pi/2 \cdot \sigma_{max}}{\sigma_0} \right) \right]^{1/\alpha_g} \tag{8}$$

$$A_1 = \; 0.415 - 0.071\alpha_g \; \frac{\sigma_{max}}{\sigma_0} \tag{9}$$

$$A_2 = 1 - A_0 - A_1 - A_3 \tag{10}$$

$$A_3 = 2A_0 + A_1 - 1 \tag{11}$$

For the present model Eqs. (8) to (11) have been modified in several aspects:

(a) The ΔK parameter is replaced by ΔK^J. The determination of the parameter is as described above. The complete modified crack propagation equation is then:

$$\frac{da}{dN} = C\ \left(\Delta K^J_{eff}\right)^n = C \begin{cases} U_1 \Delta K^J{}^n & a_i < a < a^* \\ U_2 \Delta K^J{}^n & a_i \geq a^* \end{cases} \tag{12}$$

(b) Originally the f function in Eqn. (7) has been obtained for centre-cracked plates subjected to uniform tension. The question arises whether it can also be applied to other configurations, for example bending geometries. McClung at al. [19] (see also [17]) carried out extended finite element investigations on M(T) center-cracked plates in tension, SE(T) single-edge-cracked plates in tension, SE(B) single-edge-cracked plates in bending and pure bending geometries and concluded that the f-function and, as a consequence, the crack opening stress σ_{open} (or K_{op}) are more accurately correlated by the K_{max}/K_0 ratio than by σ_{max}/σ_0 in Eqs. (8) and (9). They proposed to substitute the latter by K_{max}/K_0:

$$\frac{K_{max}}{K_0} = \frac{Y\sigma_{max}\sqrt{\pi a}}{\sigma_0\sqrt{\pi a}} \tag{13}$$

Other authors [20,21] have also found K_{max}/K_0 to be a superior parameter. Therefore, it is adopted in the present study too.

(c) The constraint parameter α in Eqs. (8) and (9) is not used as a fixed parameter as in the NASGRO approach but determined by finite element analyses based on Eqn. (1), but determined as local parameter for points A and C of the crack.

(d) The reference stress σ_0 in Eqs. (8), (9) and (13) is not chosen as the average of the quasi-static yield and tensile strength as in NASGRO but as the cyclic yield strength.

With respect to the gradual build-up of the plasticity-induced crack closure effect for the short crack stage the model assumes that the latter is mirrored in the development of the short crack fatigue threshold (as e.g. in [6]). The parameter U_1 can then be determined by

$$U_1 = \frac{U_2}{\Delta K_{th}\ \ a\ \big/ \Delta K_{th,lc}} \tag{14}$$

with the index „lc“ designating the long crack. The ΔK_{th}-crack depth function is described by an approach of McEvily et al. [22]

$$\Delta K_{th} = \Delta K_{op} + \Delta K_{th,eff} = \left[1 - e^{-k\cdot\ a - a_0}\ \right] \cdot \Delta K_{op,max} + \Delta K_{th,eff} \tag{15}$$

but modified by replacing the crack depth a by an equivalent crack depth $\sqrt{area}$ as introduced above. In Eqn. (15) k is a fit parameter which describes how the crack closure effect develops as a function of $a\text{-}a_0$ or $\sqrt{area} - \sqrt{area_0}$ respectively. Since Eqn. (15) includes two fit parameters, k and a_0

or $\sqrt{area_0}$, a minimum of two conditional equations is necessary. The first one is ΔK_{th} = 0 für $\sqrt{area}$ = 0; the second on is given by $\Delta K_{th} \propto \sqrt{area}^{1/3}$ for an arbitrary crack size. For steels, according to [2], this can be realised by an estimate

$$\Delta K_{th} = 3{,}3 \cdot 10^{-3} \ \ HV + 120 \ \Big/ \ \sqrt{area}^{1/3} \tag{16}$$

with HV being the Vickers hardness. However, for the aluminium alloy investigated in this study no similar solution exists. Therefore, an alternative solution had to be found which will be described in Section 3.

As assumed in [22] the threshold ΔK_{th} is subdivided into an intrinsic value, $\Delta K_{th,eff}$, and an additional amount due to the crack closure effect, $\Delta K_{th,op}$. The intrinsic term is a lower bound which exists even if no crack closure effect occurs (therefore the designation "eff"). It can, e.g., be determined by experiments at different R ratios and extrapolation for R → 1 as realised in the present paper. Because the state of the initial defect is characterised by both, the intrinsic threshold $\Delta K_{th,eff}$ and the initial crack area (respective its square root $\sqrt{area}_i$ the curve according to Eqn. (15) has to be shifted to pass through this point such as shown in Figure 3. The prediction of the ΔK_{th} versus crack size curve in the component is then provided by the un-dotted dark line. The transition between short and long crack propagation occurs at $\sqrt{area}^*$, where the ΔK_{th} according to the (shifted) Eqn. (15) curve intersects the long crack threshold value.

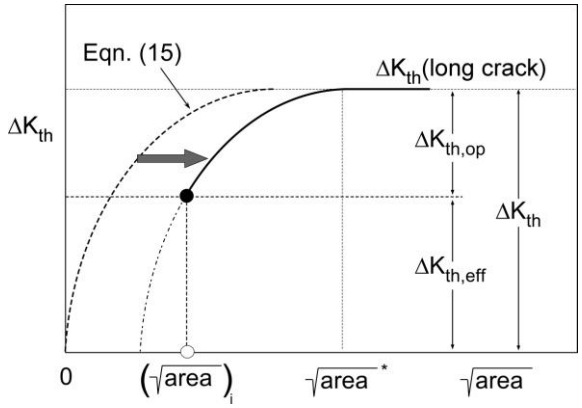

Fig. 3: Proposed method for determining the ΔK_{th}-crack size correlation for short cracks in the present model.

3. Validation on AL5380 H321 specimens

The validation of the model was performed with specimens prepared with artificial initial defects. Using the FIB (Focus Ion Beam) technology notches with a notch width of 6 μm, a depth of a = 37.4 μm and a length at surface 2c = 101.25 μm were generated.[1)]

[1)] The authors wish to thank Dr. Erica Lilleodden, HZG Geesthacht, who prepared the FIB cracks.

The notch dimensions were identical for all validation specimens. With an area of 3230 μm^2 or $\sqrt{\text{area}}_i \approx 57$ μm the size of these artificial defects referred to the upper tail of the statistical distribution of the natural defects found on the fracture surfaces as shown in Fig. 2(d). The prepared specimens were then used to generate an S-N curve. The tests were interrupted when cracks of about 2c = 3 mm were visible at the specimen surfaces. The stress-strain data of the material were: cyclic proof strength $R_{p0.2,cyc}$ = 341 MPa and cyclic modulus of elasticity E_{cyc} = 68.4 GPa.

It has already been mentioned in Section 2.5 that Eqn. (16) was not applicable to the aluminium alloy investigated. Therefore, an alternative second conditional equation had to be used. This is given by a general form

$$\Delta K_{th} = 3.3 \cdot 10^{-3} C_0 \left(\sqrt{\text{area}}\right)^{1/3} \tag{17}$$

with $\sqrt{\text{area}}_i$ referring to the size of the artificial initial defect and C_0 being a material constant which, according to Murakami [2], correlates with the fatigue limit σ_e (in the present case the fatigue strength at 10^7 loading cycles) by

$$C_0 = \frac{1}{1.43} \sigma_e \left(\sqrt{\text{area}}\right)^{1/6}. \tag{18}$$

With σ_e = 80 MPa and $\sqrt{\text{area}}_i$ = 56.85 the parameters in Eqn. (15) have finally been determined as $\sqrt{\text{area}}_0$ = 20.86 μm, k = 0.0652 μm^{-1} and $\sqrt{\text{area}}^*$ = 140 μm. As mentioned above Eqn. (15) curve had to be shifted such that it passed through the point ($\sqrt{\text{area}}_i$, $\Delta K_{th,eff}$). This is realised in Fig. 4.

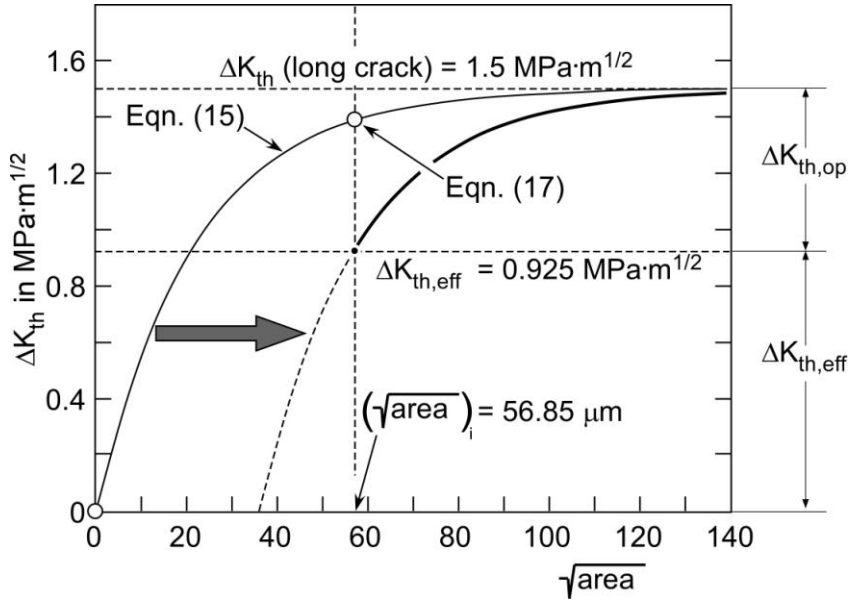

Fig. 4: Application of the model of Figure 3 to the present example.

As the final result the fatigue strength for finite life was predicted as shown in Fig. 5. The analyses were performed for each individual specimen. In addition the predicted and experimental values of the crack size, a and 2c, at test end, are compared in Fig. 5. It shows up that all experimental data were predicted with satisfying accuracy.

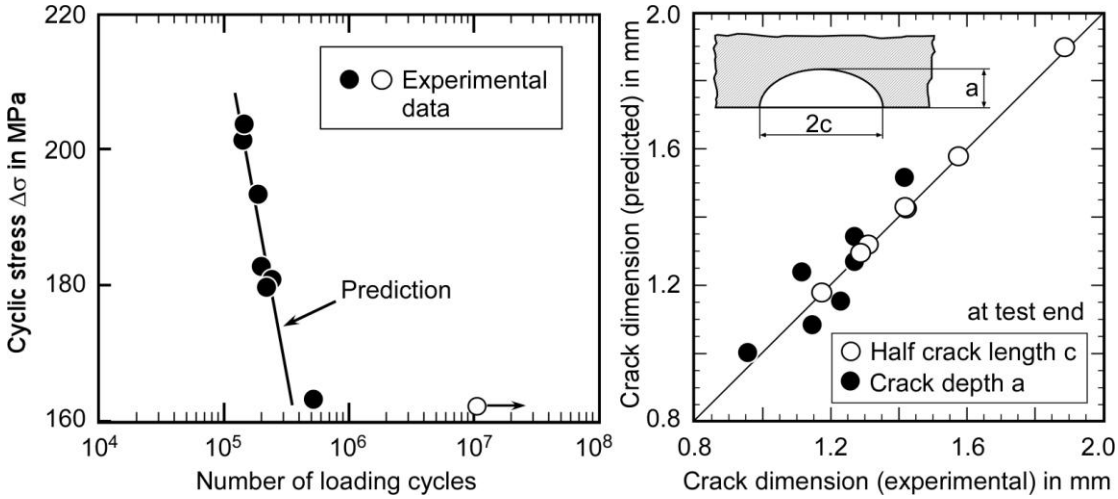

Fig. 5: S-N curve obtained for the tensile plates with artificial (FIB) cracks. Comparison between the experiments and the predictions with the present model.

4. Validation on further aluminium alloys (literature data)

Further validation of the model has been conducted using short crack propagation data from the literature which are available for aluminum alloys commonly used in the aerospace field. In particular, two different alloys have been considered: Al 2024-T3 and Al 7075-T6. An extensive collection of data for these materials is provided in [23] and [24]. Figure 6 shows the S-N lines used for validation. In case of the Al 2024-T3, experimental test data were available for two different load ratios (R = 0, -1) whereas the Al 7075-T6 has been tested at R = 0 only. The specimens did show almost no stress concentration which allowed the use the stress intensity factor and reference load equations already applied to the validation example of section 3. Since no finite element calculations have been conducted for the constraint factor α, such as above, Schijve's equation [25]

$$U = 0.55 + 0.33 \cdot R + 0.12 \cdot R^2 \tag{19}$$

has been used to determine the effective stress intensity factor range for long cracks.

The analytical simulation for the Al 2024-T3 has been performed for a suggested initial crack size of a_i = 20 μm, which resulted from an approximation of the experimental S-N data for both R = 0 and -1. In case of the Al 7075-T6, two different crack sizes have been employed in order to show the impact of a different starting crack size on the calculated number of cycles to failure. Figure 6b shows slightly conservative results a_i = 20 μm which were, however, improved when fractographic data of a_i = 6 μm were used. All simulations have been stopped when the crack reached a final depth of 80% the plate thickness.

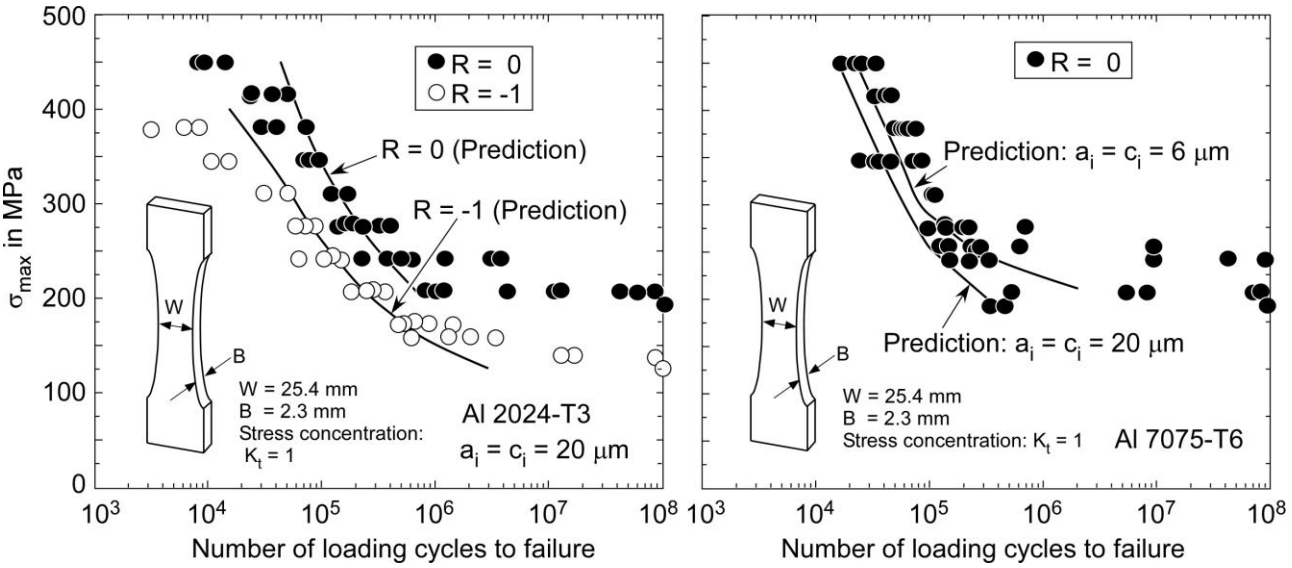

Fig. 6: S-N curves obtained for the tensile plates of two aluminium alloys compared with predictions based on the present model. S-N data taken from [23,24].

5. Summary and Outlook

An analytical fracture mechanics model for predicting the finite life fatigue strength range of the S-N curve was developed. Its application was demonstrated for tension loaded small plates made of different aluminium alloys. The results were promising.

The model is based on a number of assumptions:

(a) In engineering materials fatigue crack propagation initiates at pre-existing material defects such as welding flaws, pores, inclusions etc.

(b) The crack initiation sub-stage in a narrower sense during which a crack develops from the pre-existent defect is typically rather limited. Therefore, a fracture mechanics based lifetime prediction (which per definition is a residual lifetime prediction) yields conservative but not over-pessimistic lifetimes. Note, however, that this has not to be the case for any material.

(c) The initial crack size has been determined by fractographic investigation of fracture surfaces of cyclically loaded specimens.

(d) Since the major part of lifetime belongs to short crack propagation specific issues such as the transient behaviour of crack closure of short cracks and local ligament plasticity effects had to be taken into account.

(e) The presented model is limited to the propagation of mechanically short cracks and not applicable to micro-structurally short ones.

(f) Fracture mechanics based determination of fatigue strength provided significant potential as compared to and in addition to classical fatigue strength concepts because it takes parameters such as weld geometry, residual stresses etc. explicitly into account.

6. References

[1] Polak, J. (2003): Cyclic deformation, crack initiation, and low-cycle fatigue. In: Ritchie, R.O. and Murakami, Y. (Eds.): Comprehensive Structural Integrity; Volume 4: Cyclic loading and Fracture; Elsevier, 1-39.

[2] Murakami, Y. (2003): High and ultrahigh cycle fatigue. In: Ritchie, R.O. and Murakami, Y. (Eds.): Comprehensive Structural Integrity; Volume 4: Cyclic loading and Fracture; Elsevier, 41-76.

[3] Miller, K.J. and O'Donnel, W.J. (1999): The fatigue limit and its elimination. Fatigue & Fracture of Engng. Mater. & Struct. 22, 545-557.

[4] Zerbst, U., Madia, M. und Hellmann, D. (2011): An analytical fracture mechanics model for estimation of S-N curves of metallic alloys containing large second particles. Engng. Fracture Mech. 82, 115-134.

[5] Ishihara, S. and McEvily, A.J. (2002): Analysis of short crack growth in cast aluminium alloys. Int. J. Fatigue 24, 1169-1174.

[6] Bruzzi, M.S. and McHugh, P.E. (2002): Methodology for modelling the small crack fatigue gehaviour of aluminium alloy. Int. J. Fatigue 24, 1071-1078.

[7] McClung, R.C., Chell, G.G., Lee, Y.-D., Russel, D.A. und Orient, G.E. (1997): A practical methodology for elastic-plastic fatigue crack growth. ASTM STP 1296, 317-337.

[8] Eufinger, J., Heinrietz, A., Bruder, T. und Hanselka, H. (2010): Bruchmechanisch basierte Schwingfestigkeitsanalyse von Gusseisen unter Berücksichtigung der Gefügeeigenschaften. 43. Tagung des DVM-Arbeitskreises "Bruchvorgänge, DVM-Bericht 243, 203-213.

[9] White, P. (2006): Review of methods and approaches for the structural risk assessment of aircraft. Australian Defence Science and Technology Organisation, Victoria, Australia, http://www.dtic.mil/cgi-bin/GetTRDoc?Location=U2&doc=
GetTRDoc.pdf&AD=ADA462955

[10] Raju, I.S. and Newman, J.C., Hr. (1979): Stress-intensity factors for a wide range of semi-elliptical surface cracks in finite-thickness plates. Engng,. Fracture Mech. 11, 817-829.

[11] Zerbst, U., Ainsworth, R.A. und Madia, M. (2011): Reference load versus limit load in engineering flaw assessment: A proposal for a hybrid analysis option. Engng. Fracture Mech., upcoming.

[12] R6, Revision 4 (2009): Assessment of the Integrity of Structures Containing Defects. British Energy Generation Ltd (BEGL), Barnwood, Gloucester.

[13] Zerbst, U., Schödel, M., Webster, S. and Ainsworth, R.A. (2007): Fitness-for-Service Fracture Assessment of Structures Containing Cracks. A Workbook based on the European SINTAP/FITNET Procedure. Elsevier.

[14] Newman, J.C., Jr. (1984): A crack opening stress equation for fatigue crack growth. Int. J. Fracture 24, R131-R135.

[15] Beretta S., Carboni, M. and Madia, M. (2006): Fatigue Strength in Presence of Inhomogeneities: Influence of Constraint. Journal of ASTM International. Vol. 3, No. 4.

[16] McClung, R.C., Chell, G.G., Lee, Y.-D., Russel, D.A. und Orient, G.E. (1997): A practical methodology for elastic-plastic fatigue crack growth. ASTM STP 1296, 317-337.

[17] McClung, R.C., Chell, G.G., Lee, Y.-D., Russell, D.A. and Orient, G.E. (1999): Development of a practical methodology for elastic-plastic and fully plastic fatigue crack growth. NASA Report NASA/CR-1999-209428.

[18] Newman, J.C., Jr. (1984): A crack opening stress Equation for fatigue crack growth. Int. J. Fracture 24, R131-R135.

[19] McClung, R.C (1994): Finite element analysis of specimen geometry effects on fatigue crack closure. Fatigue Fracture Engng. Mat. Struct. 17, 861-872.

[20] Liu, J.Z. and Wu, X.R. (1997): Study of fatigue crack closure behaviour for various cracked geometries. Engng. Fracture Mech. 57, 475-491.

[21] Kim, J.H. and Lee, S.B. (2000): Fatigue crack opening stress based on the strip-yield model. Theor. Appl. Fracture Mech. 34, 73-84.

[22] McEvily, A.J., Endo, M. and Murakami, Y. (2003): On the $\sqrt{\text{area}}$ relationship and the short fatigue crack threshold. Fatigue Fracture Engng. Mat. Struct. 26, 269-278.

[23] Newman, J.C., Jr., Phillips, E.P. and Swain, M.H. (1999): Fatigue-life prediction methodology using small-crack theory. International Journal of Fatigue 21, 109-119.

[24] Edwards, P.R. and Newman, J.C., Jr. (1990): AGARD-R-767: Short-crack behaviour in various aircraft materials. AGARD.

[25] J. Schijve, J. (2001): Fatigue of Structures and Materials. Kluwer Academic Publishers. Dordrecht.

Strain gage radial locations for the accurate determination of mode I stress intensity factors

H. Sarangi[1,*], K.S.R.K. Murthy[2], D. Chakraborty[2*]

[1] Research Scholar, Department of Mechanical Engineering, IIT Guwahati Guwahati 781039, India
[2] Faculty of Department of Mechanical Engineering, Indian Institute of Technology Guwahati, Guwahati 781039, India
* Corresponding author: chakra@iitg.ernet.in

Abstract Strain gage based methods for experimental determination of stress intensity factors (SIFs) are equally powerful as compared to the other methods such as photoelasticity and caustics. However, a major problem with the strain gage methods is the lack of practical recommendations for appropriate radial locations for strain gages for accurate measurement of SIFs. Determination of valid gage locations is thus an open problem. In order to obviate this important problem, a finite element based approach has been suggested in the present investigation for determination of valid or optimal strain gage locations for determination of the mode I SIFs. The proposed approaches are strongly supported by the theory. The present work attempts to estimate the maximum permissible radial distance r_{max} for strain gages (from the crack tip) using the proposed finite element based approaches. This r_{max} of a configuration in turn can be used to obtain the valid locations for strain gages for accurate determination of mode I SIFs. The results of the present investigation show that very accurate values of r_{max} can be obtained using the proposed approach. Dependence of r_{max} on crack length to width ratio has also been investigated in the present work.

Keywords Strain gage, Stress intensity factor, Radial location, Fracture

1. Introduction

The most important parameter in linear elastic fracture mechanics (LEFM) is the stress intensity factor (SIF) as its limiting value decides whether an existing crack in a component grows or not. It is a measure of severity of the crack tip and is frequently used in control of fracture and in life prediction estimations. Accurate values of SIFs are necessary for correct application of LEFM principles in predicting and preventing fracture of the engineering components. Three approaches are currently used to estimate stress intensity factors viz., analytical, numerical and experimental methods. Analytical methods are generally restricted to the simple configurations and collection of such solutions of SIFs can be found in various handbooks [1, 2]. Numerical and experimental techniques are widely used in relatively complex situations [3].

Most widely used experimental techniques for the measurement of SIFs are caustics [4, 5], compliance method [6, 7], photoelasticity [8, 9] and strain gage techniques [10-14]. Among the experimental techniques, strain gage techniques are relatively simple and easy for the determination of SIFs due to direct measurement of strains near the crack tip. Irwin [15] first suggested the use of strain gages for the determination of SIF. However, factors such as the local yielding, high strain gradients, three dimensional state of stress at the crack tips and finite size of the gages strongly affected against the development of strain gage techniques.

To eliminate the above difficulties, Dally and Sanford [10] developed a practically feasible strain gage technique (DS technique) for measuring the static mode I SIF (K_I) in two dimensional

isotropic single ended cracked bodies. A truncated strain series (based on the generalized Westergaard approach [16]) consisting of three unknown coefficients for the representation of the strains has been employed in their technique. A major advantage of their approach is that, only a single strain gage is sufficient to determine mode I SIF and it can be located at a distance sufficiently away from the crack tip. However, no suggestions were made by them on the valid gage locations.

Wei and Zhao [11] proposed a different strain gage method based on the two parameter strain equation which requires two strain gages for measuring the mode I SIF. However, the suggested radial locations of gages necessitate *a priori* knowledge about the plastic zone size which depends on the unknown SIF.

Kuang and Chen [12] employed the asymptotic strain expressions for the measurement of mode I SIF. They suggested that gages could be placed at distances greater than half the thickness of the specimen from the crack tip in spite of the fact that at large distances the measured strains could not be accurately represented by asymptotic equations alone.

It could be seen from the literature that DS technique has been more widely used as compared to other strain gage techniques. While there are some recommendations available for radial locations of strain gage techniques developed by Wei and Zhao [11] and Kuang and Chen [12], no method has been presented until recently for determination of appropriate radial location of strain gages corresponding to the DS technique in experimental determination of the mode I SIFs. Due to uncertainty over the radial location of strain gage in DS technique, very limited amount of work has been published using this technique for corroborating the analytical or numerical SIFs [14]. Determination of valid gage locations for DS technique is thus an open problem.

The present paper aims at development of an efficient finite element based approach for accurate and consistent evaluation of the maximum permissible radial distance $r_{\max}$ for strain gages (from the crack tip) for accurate measurement of mode I SIFs in configurations with single ended cracks. This $r_{\max}$ of a configuration in turn can be used to obtain the valid locations for strain gages for accurate determination of mode I SIFs. Another objective of the present work is to study the dependence of $r_{\max}$ on crack length to width ratio of a given configuration. The proposed numerical methodology is well supported with theory.

2. Theoretical Background

This section describes the background theory for the estimation of $r_{\max}$ value for accurate measurement of mode I SIF using Dally and Sanford [10] single strain gage technique. According to this technique the region around a crack tip is divided into three zones viz. zone I, zone II and zone

III as shown in Fig. 1. Zone I is close to the crack tip and first term of the strain series (singular term) is sufficient to represent the strains within this zone. However, it is not a valid zone for accurate measurement of strains as the stress state in this region is three dimensional [10, 17] and the measured strains will be severely affected by plasticity effects.

Zone III is again not suitable for measurement of strain data because, very large number of terms in the strain series is required to yield accurate results. Therefore, the intermediate region or zone II is favorable and optimum zone for accurate measurement of the surface strains. This is defined as a zone in which a singular term and a small number of higher order terms will accurately describe the strain field.

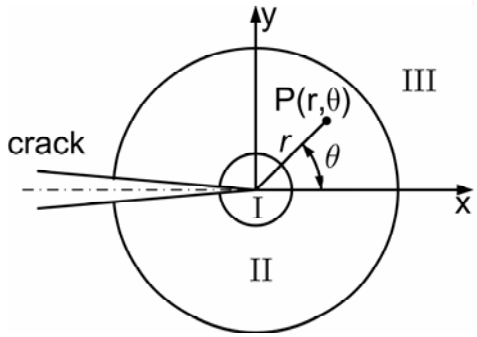

Figure 1. Different zones at the crack tip

The generalized Westergaard approach can be employed to obtain the expressions of different strain components within the zone II. The modified Airy stress function in this approach is given by [16]

$$\phi = \mathrm{Re}\,\overline{\overline{Z}}(z) + y\,\mathrm{Im}\,\overline{Z}(z) + y\,\mathrm{Im}\,\overline{Y}(z) \tag{1}$$

where

$$\frac{d\overline{\overline{Z}}}{dz} = \overline{Z}, \quad \frac{d\overline{Z}}{dz} = Z, \text{ and } \quad \frac{d\overline{Y}}{dz} = Y \tag{2}$$

and the complex analytic functions $Z(z)$ and $Y(z)$ are defined as

$$Z(z) = \sum_{n=0}^{\infty} A_n\, z^{n-\frac{1}{2}} = \frac{K}{\sqrt{2\pi z}} + \sum_{n=1}^{\infty} A_n\, z^{n-\frac{1}{2}} \tag{3}$$

$$Y(z) = \sum_{m=0}^{\infty} B_m\, z^m = \frac{\sigma_{0x}}{2} + \sum_{m=1}^{\infty} B_m\, z^m \tag{4}$$

which are series type functions (in terms of complex variable $z = x + iy$) containing infinite number of coefficients ($A_1, A_2, ..., A_\infty$; $B_1, B_2, ..., B_\infty$). The strain field in the zone II can be sufficiently represented by the three parameter series with unknown coefficients A_0, A_1 and B_0 [10] which depend on boundary conditions. Assuming plane stress conditions, the three term representation of strain field in this zone is therefore,

$$
\begin{aligned}
2G\,\varepsilon_{xx} &= A_0\, r^{-1/2}\cos\frac{\theta}{2}\left[\kappa-\sin\frac{\theta}{2}\sin\frac{3\theta}{2}\right]+\frac{2B_0}{(1+\nu)}+A_1\, r^{1/2}\cos\frac{\theta}{2}\left[\kappa+\sin^2\frac{\theta}{2}\right]\\
2G\varepsilon_{yy} &= A_0\, r^{-1/2}\cos\frac{\theta}{2}\left[\kappa+\sin\frac{\theta}{2}\sin\frac{3\theta}{2}\right]-\frac{2\nu B_0}{(1+\nu)}+A_1\, r^{1/2}\cos\frac{\theta}{2}\left[\kappa-\sin^2\frac{\theta}{2}\right]\\
2G\,\gamma_{xy} &= A_0\, r^{-1/2}\left[\sin\theta\cos\frac{3\theta}{2}\right]-A_1\, r^{1/2}\left[\sin\theta\cos\frac{\theta}{2}\right]
\end{aligned}
\tag{5}
$$

where $\kappa=(1-\nu)/(1+\nu)$ and A_0, A_1 and B_0 are unknown coefficients which can be determined using geometry of the specimen and loading conditions. Using the definition of K_I it can be shown that

$$K_I=\sqrt{2\pi}\,A_0 \tag{6}$$

The strain component ε_{aa} at the point *P* located by r and θ (Fig. 2) is given by

$$
\begin{aligned}
2G\varepsilon_{aa} &= A_0\, r^{-1/2}\left[\kappa\cos\frac{\theta}{2}-\frac{1}{2}\sin\theta\sin\frac{3\theta}{2}\cos 2\alpha+\frac{1}{2}\sin\theta\cos\frac{3\theta}{2}\sin 2\alpha\right]\\
&+A_1\, r^{1/2}\cos\frac{\theta}{2}\left[\kappa+\sin^2\frac{\theta}{2}\cos 2\alpha-\frac{1}{2}\sin\theta\sin 2\alpha\right]+B_0\left(\kappa+\cos 2\alpha\right)
\end{aligned}
\tag{7}
$$

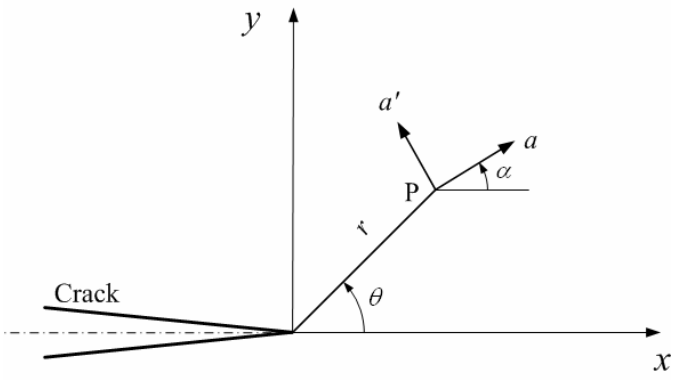

Figure 2. Strain gage orientation and location

The coefficient of B_0 term in Eq. (7) can be eliminated by selecting the angle α such that

$$\cos 2\alpha=-\kappa \quad =-\frac{1-\nu}{1+\nu} \tag{8}$$

Similarly coefficient of A_1 can also be made zero if the angle θ is selected as

$$\tan\frac{\theta}{2}=-\cot 2\alpha \tag{9}$$

Thus by placing a single strain gage (Fig. 2) with α and θ as defined by Eqs. (8) and (9) the

strain ε_{aa} can be measured which in turn is related to K_I by

$$2G\varepsilon_{aa} = \frac{K_{\mathrm{I}}}{\sqrt{2\pi r}}\left[\kappa\cos\frac{\theta}{2} - \frac{1}{2}\sin\theta\sin\frac{3\theta}{2}\cos 2\alpha + \frac{1}{2}\sin\theta\cos\frac{3\theta}{2}\sin 2\alpha\right] \tag{10}$$

It should be noted that the above equation accurately determines ε_{aa} upto a radial distance say $r_{\max}$ and it can be written as

$$\varepsilon_{aa} = \frac{1}{\sqrt{r}}\left[\frac{K_{\mathrm{I}}}{G\sqrt{8\pi}}\left(\kappa\cos\frac{\theta}{2} - \frac{1}{2}\sin\theta\sin\frac{3\theta}{2}\cos 2\alpha + \frac{1}{2}\sin\theta\cos\frac{3\theta}{2}\sin 2\alpha\right)\right] \tag{11}$$

For a given configuration, applied load, Young's modulus E and Poisson's ratio ν the expression within the square bracket on the right hand side of Eq. (11) is a constant. Therefore,

$$\varepsilon_{aa} = \frac{C}{\sqrt{r}} \tag{12}$$

where C is a constant. Taking logarithm on both sides of Eq. (12)

$$\ln(\varepsilon_{aa}) = -\frac{1}{2}\ln(r) + \ln(C) \tag{13}$$

Eq. (13) is valid along the line given by Eq. (9) for $r \le r_{\max}$. Thus a plot of Eq. (12) on log-log axes depicts a straight line of slope equals to – 0.5, with an intercept of $\ln(C)$. Theoretically, the straight line property will break beyond $r > r_{\max}$ as more than three parameters are needed in Eq. (7) to estimate the ε_{aa}. Using the straight line property exhibited by Eq. (13), the value of $r_{\max}$ can be accurately estimated from the log-log plots of ε_{aa} and r.

Several experimental and numerical studies have established that 3D effects prevailed up to a radial distance equal to half the thickness of the plate from the crack tip [17]. It was reported that the state of stress is neither plane stress or plane strain within this distance [10, 17]. Therefore, the minimum radial distance $r_{\min}$ for strain measurements on the free surface should be grater than half the thickness of the plate. As a consequence, the optimal or valid radial location r for strain gage in DS technique can now be given as

$$r_{\min}\left(=\frac{1}{2}\text{thickness of plate}\right) \le r \le r_{\max} \tag{14}$$

3. Results and Discussion

In this section, $r_{\max}$ is determined for a single-ended cracked plate using the theoretical formulation described in Section 2. For this purpose, edge cracked plates (Fig. 3(a)) with $a/b=0.1-0.8$ (in steps 0.1) and subjected to uniform tensile stress are considered in this study. Due to symmetry only half of the domain as shown in Fig. 3(b) is employed for FEA. Width $b=1200\,\text{mm}$ and $h/b=3.0$ are considered for this example. Poisson's ratio $\nu=1/3$, and Young's modulus $E=200\,\text{GPa}$ have been assumed. The applied stress σ is set to 100 MPa. Plane stress conditions have been assumed.

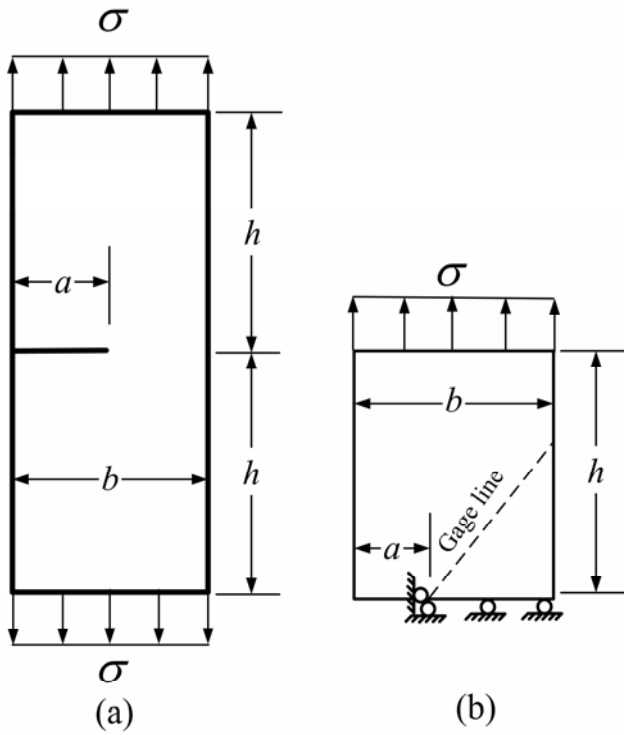

Figure 3. (a) A typical edge cracked plate (b) solution domain for edge cracked plate

To determine the $r_{\max}$ value of the above configurations, a typical finite element mesh for one half of the plate is shown in Fig. 4 (a). The mesh (Fig. 4(a)) is so designed that nodes of several elements are made to lie along the gage line which makes an angle of θ with the axis of crack (Eq. 9). In all the meshes, this line (gage line) begins at the crack tip and terminates at the outer boundaries of the cracked plate. According to DS technique, a single strain gage is required to be placed at an appropriate location on the gage line in the direction of α (Eq. 8) in order to measure the linear strain ε_{aa}. The strains calculated in global coordinate along the gage line are then transformed into linear strain ε_{aa} in the direction α. The radial distances (r) of each of the nodes on the gage line from the crack tip are then computed.

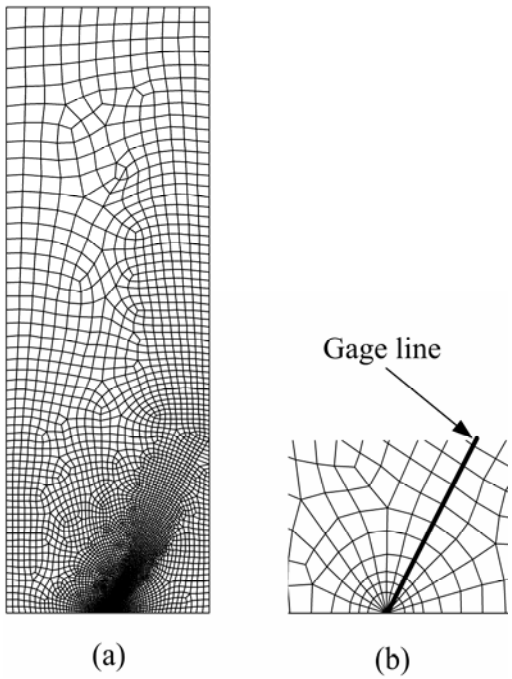

Figure 4. (a) Typical mesh used for edge cracked plate (b) enlarged view at the crack tip corresponding mesh

Following the procedure described in section 2, plot of $\ln(\varepsilon_{aa})$ versus $\ln(r)$ for all values of a/b is shown in Fig. 5. Crack tip point is not plotted as the radius of this point is zero. It is interesting to notice from Fig. 5 that, each plot consists of distinguishable linear portion followed by nonlinear portion (in logarithmic scale) as predicted by theory (section 2). The linear trend distinctly exists up to a certain radial distance and thereafter gradually turns to the nonlinear portion. This can be observed in plots for all values of a/b of edge cracked plate.

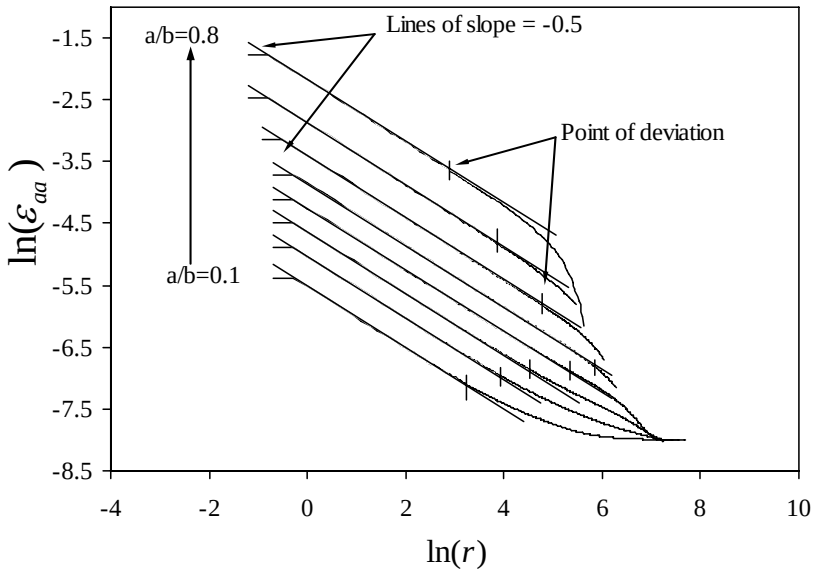

Figure 5. Variation of $\ln(\varepsilon_{aa})$ with $\ln(r)$ along the gage line for the edge cracked plates

As discussed earlier, the initial linear part is due to the dominance of the three parameters and nonlinear part is due to the presence of more than three parameters in the expression in equation for ε_{aa} (Eq. 7). The end point of the linear portion of the plots in Fig. 5 clearly indicates the extent of the three parameter strain series which is the upper bound for strain gage locations i.e. $r_{\max}$ according to the proposed theory.

For determination of $r_{\max}$, straight lines having slope of -0.5 are superposed onto the all plots of $\ln(\varepsilon_{aa})$ versus $\ln(r)$ in Fig. 5. It is interesting to notice from Fig. 5 that both the initial straight line portion of the plots and superposed lines are congruent to each other up to a certain radial distance for all a/b values and the numerical results deviate from the superposed line thereafter due to the dominance of coefficients other than A_0, A_1 and B_0 in Eq. (7). The estimated values of maximum permissible radial distance $r_{\max}$ or the extent of validity of the three parameter zone are marked in Fig. 5 as per the procedure described in [18]. The corresponding numerical values of the $r_{\max}$ are presented in Table 1. A plot of variation of $r_{\max}$ with a/b is also presented in Fig. 6.

It can be seen from the results of Table 1 and Fig. 6 that as the crack length is increased, the value of $r_{\max}$ increases initially until it reaches a maximum value around $a/b = 0.5$ ($r_{\max}$ = 505.34 mm) and thereafter it decreases with the increase of the crack length.

Table 1 Variation of the $r_{\max}$ with crack length a/b

a/b	a (mm)	$r_{\max}/b$
0.1	120	0.021
0.2	240	0.043
0.3	360	0.077
0.4	480	0.174
0.5	600	0.290
0.6	720	0.101
0.7	840	0.040
0.8	960	0.015

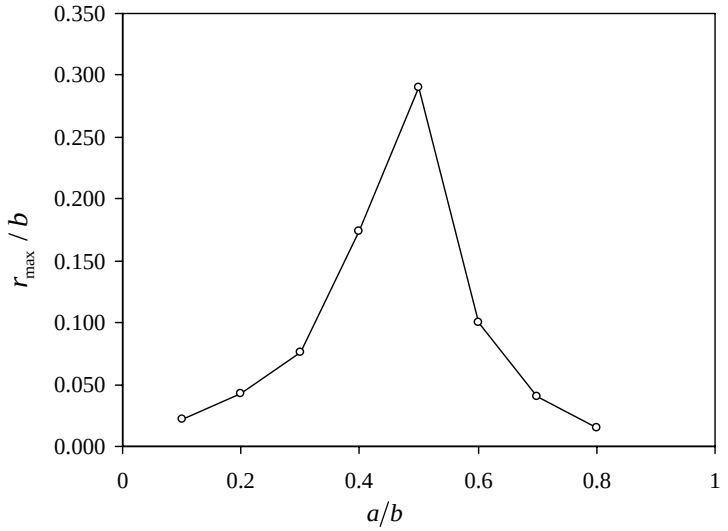

Figure 6. Graph of the r_{max} as a function of a/b (0.1-0.8) for the edge cracked plate.

4. Conclusions

In this paper, a finite element based approach is presented for determination of the valid or optimal radial location of strain gages corresponding to DS technique. The proposed approach is based on efficient computation of the maximum permissible radial distance r_{max} of a strain gage. The existence and determination of the r_{max} is shown theoretically. To demonstrate the proposed approach single ended cracked configurations have been analyzed. Variation of the computed strains in the direction of strain gage along the gage line is as per the theoretical predictions. The results of present investigation show that the maximum permissible radial distance (r_{max}) increases initially with the increase in a/b and decreases with further increase in a/b values. The present method will be extremely useful in placing strain gages for accurate experimental determination of the SIF using DS technique.

Acknowledgements

Authors gratefully acknowledge financial support from the Naval Research Board (NRB), Ministry of Defence, India, under grant number NRB-167/MAT/08-09.

References

[1] H. Tada, P.C. Paris, G.R. Irwin, The stress analysis of cracks handbook. ASME, New York, 2000.

[2] Y. Murakami, Stress intensity factors handbook, Pergamon, England, 1987.

[3] R.J. Sanford, Principles of fracture mechanics, Prentice Hall, NJ, 2003.

[4] K. Konsta-Gdoutos, Limitations in mixed-mode stress intensity factor evaluation by the method of caustics. Eng Fract Mech, 55 (1996) 371–382.

[5] P.S. Theocaris, Local yielding around a crack tip in Plexiglas. J Appl Mech, 37 (1970) 409–415.

[6] R.M. Bonesteel, D.E. Pipers, A.T. Davinroy, Compliance and calibration of double cantilever beam (DCB) specimens. Eng Fract Mech, 10 (1978) 425–428.

[7] J.C. Jr Newman, Stress-intensity factors and crack-opening displacements for round compact specimens. Int J Fract, 17 (1981) 567–578.

[8] E.E. Gdoutos, P.S. Theocaris, A photoelastic determination of mixed-mode stress intensity factors. Exp Mech, 18 (1978) 87–96.

[9] T.H. Hyde, N.A. Warrior, An improved method for determination of photoelastic stress intensity factors using the Westergaard stress function. Int J Mech Sci, 32 (1990) 265–273.

[10] J.W. Dally, R.J. Sanford, Strain gage methods for measuring the opening mode stress intensity factor. Exp Mech, 27 (1987) 381–388.

[11] J. Wei, J.H. Zhao, A two-strain-gage technique for determining mode I stress-intensity factor. Theor Appl Fract Mech, 28 (1997) 135–140.

[12] J.H. Kuang, L.S. Chen, A single strain gage method for measurement. Eng Fract Mech, 51 (1995) 871–878.

[13] J.R. Berger, J.W. Dally, An overdeterministic approach for measuring using strain gages. Exp Mech, 28 (1988) 142–145.

[14] S. Swamy, M.V. Srikanth, K.S.R.K. Murthy, P.S. Robi, Determination of the mode I stress intensity factors of the complex configurations using the strain gages. J Mech Mater Struct, 3 (2008) 1239–1255.

[15] G.. R. Irwin, Analysis of stresses and strains near the end of a crack traversing a plate. J Appl Mech, 24 (1957) 361- 364.

[16] R.J. Sanford, A critical re-examination of the Westergaard method for solving opening-mode crack problems. Mech Res Comm, 6 (1979) 289–294.

[17] J. Rosakis, K. Ravi-Chandar, On crack-tip stress state: An experimental evaluation of three-dimensional effects. Int J Solids Struct, 22 (1986) 121–134.

[18] H. Sarangi, K.S.R.K. Murthy, D. Chakraborty, Optimum Strain gage location for evaluating stress intensity factors in single and double ended cracked Configurations. Eng Fract Mech, 77 (2010) 3190-3203.

Effect of the pearlite content of ferritic cast iron material on the crack resistance behaviour under dynamic load

Peter Trubitz[1], Hans-Peter Winkler[2,], Roland Hüggenberg[2], Annette Ludwig[1,*], Gerhard Pusch[1]**

[1]Technical University Bergakademie Freiberg, Freiberg, Germany
[2]Gesellschaft für Nuklear-Service mbH, Essen, Germany
[*]Corresponding author: ludwig@ww.tu-freiberg.de
[**]Corresponding author: hans-peter.winkler@gns.de

Abstract
The factor of safety against rupture of castings subject to high-strength loads, such as transport and pressure vessels as well as windmill components, is assessed taking into account fracture mechanical characteristic values for the static, cyclic and dynamic load condition. The experimental investigation of dynamic crack initiation values with regard to cast iron-specific aspects was the subject of a contribution at the 12th ICF in Ottawa.

Continuing the examination, the contribution on hand describes the effect of the microstructure on the mechanical and fracture-mechanic properties of ferritic and ferrite-pearlite cast iron materials at low temperatures. The strength and sensibility to brittle fracture are conventionally evaluated by applying the characteristic values of the tensile test or the notched bar impact test. During the recording of the notched bar impact work-temperature curves in the temperature range of 180 °C to -60 °C, the transition temperature curves are defined by comparing various criteria. The dynamic crack initiation values at -40 °C are determined via the recording of cracking resistance curves (J integral concept). In addition, via the determination of the crack arrest toughness K_{Ia} at 50 mm thick CCA samples, the crack arrest behaviour is controlled in the temperature range of -40 °C to -80 °C.

Keywords Cast iron, perlite content, crack resistance behavior, dynamic loading

1 Introduction

Resulting from various solidification and cooling conditions, microstructures may develop distinguishing themselves clearly with regard to the graphite morphology and pearlite content. Using the example of ferritic or ferrite-pearlite ferritic cast iron materials, the contribution on hand describes their effect on the mechanical and fracture-mechanic properties at low temperatures.

2 Materials

The examinations were performed on ductile ferritic cast iron materials with various pearlite content (Fig. 1), designated in the following GJS (4) and GJS (29).

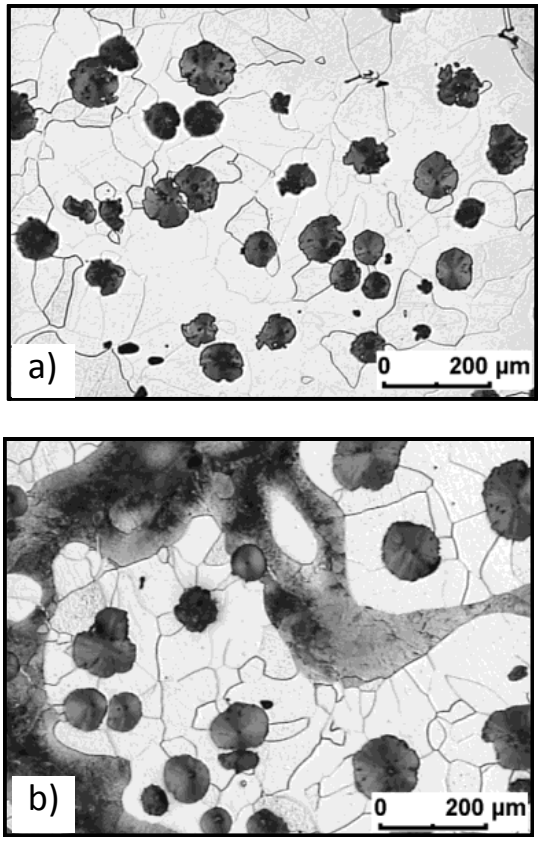

Microstructure parameters:

Diameter of the graphite particles: 63 µm
Ferrite grain size: 62 µm
Particle separation: 88 µm
Form factor: 0.71
Number of particles: 47 mm^{-2}

Pearlite content: 4 %

Microstructure parameters:

Diameter of the graphite particles: 69 µm
Ferrite grain size: 62 µm
Particle separation: 102 µm
Form factor: 0.74
Number of particles: 32 mm^{-2}

Pearlite content: 29 %

Figure 1: Microstructure and microstructure parameters a) GJS (4), b) GJS (29)

3 Mechanical characteristic values

The characteristic values of the tensile test were always determined on three tensile tests according to DIN EN 10 002 at RT and taking into account the special application at -40 °C (Tab. 1).

Table 1: Mechanical characteristic values and hardness values

Material	Temperature °C	$R_{p0.2}$ MPa	R_m MPa	A %	Z %	E GPa	ν	HBW 2.5/187.5
GJS(4)	RT	245	367	12	13	172	0.28	137
	-40	273	393	10	11			
GJS(29)	RT	284	424	11	12	174	0.28	163
	-40	315	427	5	5			

The notched bar impact test according to DIN EN 10 045-1 was performed with ISO-V samples (10x10x55 mm) using a 300 J pendulum striking mechanism in a temperature range of 180 °C to -60 °C, whereby at each temperature three samples were tested. Following the determination of the notched bar impact work used KV and the lateral expansion LE the approximation of the KV-T or LE-T-curves is performed according to Eq. 1

$$KV, LE = X + Y \tanh \frac{T - T_0}{Z} \quad (1)$$

The transition temperature T_t was determined by calculating the KV-T or LE-T curves at 0.5 (KV_{max} + KV_{min}) or 0.5 (LE_{max} + LE_{min}), Tab. 2.

Table 2: Characteristic values of the notched bar impact test

	Parameter equation (1)				KV (RT)	KV (-40 °C)	T_t^{KV}
Material	T_0 °C	X -	Y -	Z -	J	J	°C
GJS (4)	-2.2	10.54	6.14	28.30	17	5	-2
GJS (29)	66.6	12.44	8.24	42.56	7	5	67
Material	T_0 °C	X -	Y -	Z -	LE (RT) mm	LE (-40 °C) mm	T_t^{LE} °C
GJS (4)	3.3	0.27	0.25	38.03	0.43	0,10	3
GJS (29)	66.6	0.32	0.27	55.54	0.18	0,07	67

The differently determined transition temperatures show a good correlation.

4 Fracture mechanical characteristic values

The static fracture mechanical characteristic values of the J integral concept at -40 °C (Tab. 3) were determined at 20% side grooved SENB-samples (10x20x120 mm) according to ESIS P2-92 applying the compliance method, and the J_R curves approximated with the extended power approach, Eq. 2

$$J = A(\Delta a + B)^C \quad (1)$$

The physical crack initiation values $J_{i/BL}$ are determined with the J_R curve at the point of intersection of the blunting line according to Eq. 3

$$J = 3.75 \cdot R_m \cdot \Delta a \quad (2)$$

The technical crack initiation values $J_{0.2}$ are determined at Δa = 0.2 mm (Fig. 2). The conversion of the J values into the respective characteristic values of the K concept is performed via the elastic constants according Eq. 4 to.

$$K(J) = \left[\frac{J \cdot E}{1 - \nu^2}\right]^{1/2} \quad (4)$$

Apart from the determination of the crack initiation values, the increase in the cracking resistance curve distinguishes the material resistance against a constant crack propagation, which can be defined as T module (tearing modulus) according to Eq. 5

$$T^J = \frac{dJ}{da} \cdot \frac{E}{\left(R_{p0.2}\right)^2} \quad (3)$$

Here, the T^J module is quantified during the applied nonlinear curve adjustment according to the Eq. 5 via the increase of the secant in the range of Δa = 0.2 mm to Δa = 1 mm.

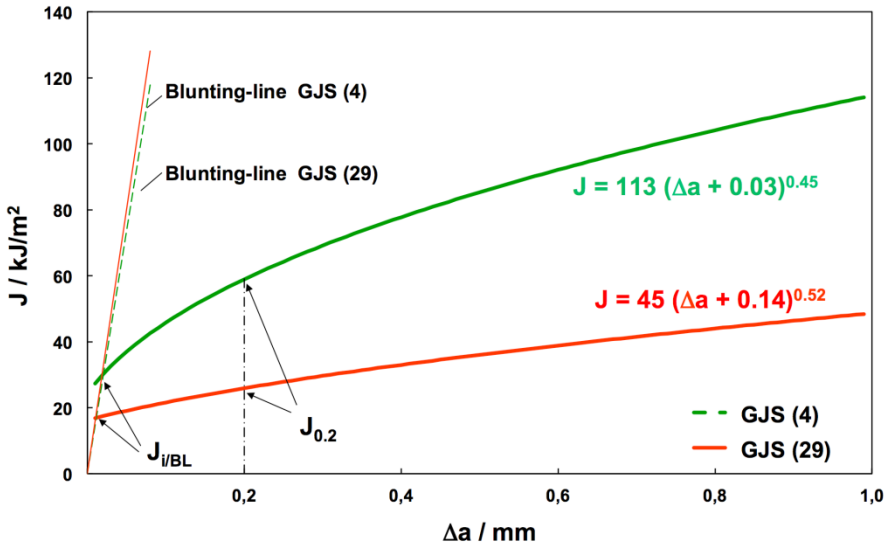

Figure 1: Static J_R curves at -40 °C

Table 3: Static fracture toughness characteristic values of the J integral concept at -40 °C

Material	A -	B -	C -	$J_{i/BL}$ kJ/m²	$J_{0.2}$ kJ/m²	K ($J_{i/BL}$) MPa√m	T^J
GJS (4)	113	0.03	0.45	28	59	73	162
GJS (29)	46	0.14	0.52	16	26	55	50

The experimental investigation of the dynamic cracking resistance curves of the J-integral-concept (J_{dR}-curves) was carried out on 20 % side-grooved SENB samples (10x10x55 mm) with fatigue cracking according to the "low-blow"-technique using an instrumented pendulum. Thereby, six to eight samples in the range $2.8 \cdot 10^4$ MPa√m/s ≤ $\dot{K}$ ≤ $5.7 \cdot 10^4$ MPa√m/s were stressed, the J_d values were determined via the calculated dynamic force-distance diagrams and the Δa values were determined on the fracture surfaces of the samples. Testing procedure and evaluation were performed in adaptation to ESIS P2-92. Contrary to the static load, the stable ductile crack propagation for the dynamic load is replaced with a stable cleavage-faced crack propagation. The resulting material-specific aspects with regard to recording, evaluation and definition of the dynamic crack initiation values have been described in [1] and [2]. The determined J_{dR}-curves or the characteristic values derived from these are shown in Fig. 3 and Tab. 4. Occurring "pop-in"-effects can be attributed to pearlite islands or graphite degenerations. For GJS (29) no experimental determination of a J_d-Δa-curve was possible at -40 °C, since only "pop-in" effects occurred. They are to be attributed to the increased pearlite content and are shown in Table 4 as J_{dc} values. The range of the J_{dc} values corresponds with the size and/or the number of the pearlite islands in front of the crack tip.

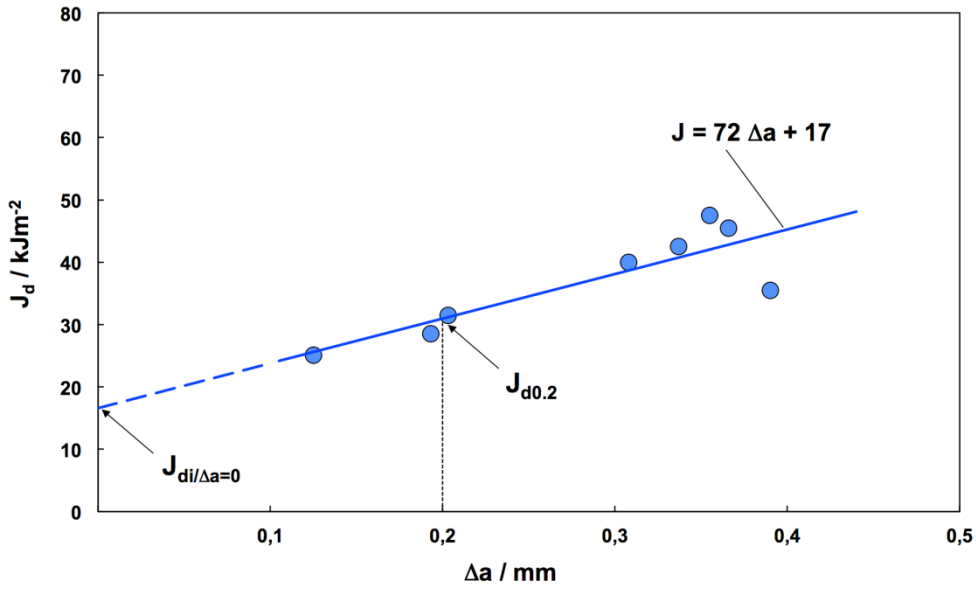

Fig. 2: Dynamic J_{dR} curve of the GJS(4) at -40 °C

Table 4: Dynamic fracture toughness characteristic values of the J integral concept at -40 °C

Material	$J_{di/\Delta a=0}$ kJ/m²	$J_{d0.2}$ kJ/m²	$K(J_{di/\Delta a=0})$ MPa√m	T_d^J	J_{dc} kJ/m²	$K(J_{dc})$ MPa√m
GJS (4)	17	31	56	64	22[1)]	64
GJS (29)	-	-	-	-	10[2)]	34

[1)]…Mean value of 6 samples with J_{dc}^{min} = 16 kJ/m² and J_{dc}^{max} = 27 kJ/m²
[2)]…Mean value of 10 samples with J_{dc}^{min} = 6 kJ/m² and J_{dc}^{max} = 14 kJ/m²

While the dynamic fracture toughness distinguishes the material resistance against instable crack propagation for impact load, the crack arrest toughness K_{Ia} evaluates the ability of the material to trap a crack propagating at high speed. A crack arrest presents a special case of an instable crack propagation aiming to secure components with high requirement on the safety against fracture on the material and / or load side so that instably propagating cracks as a result of overstress and / or embrittlement on the material side are trapped again before a catastrophic failure occurs. The crack arrest toughness K_{Ia} is determined according to ASTM E 1221-06 on 50 mm thick CCA-samples in the temperature range of -40 °C to -80 °C.

A temperature equalisation is possible via the cooling system of the base plate, on which the CCA-sample rests. After setting the test temperature, the sample is loaded with 5 to 10 mm/min via a wedge firmly connected to the crosshead of the testing machine. Thus, this is pressed into the divided jaws located in the bore, and the sample is loaded until, starting at the notched welding bead, instable crack propagation occurs (Fig. 4).

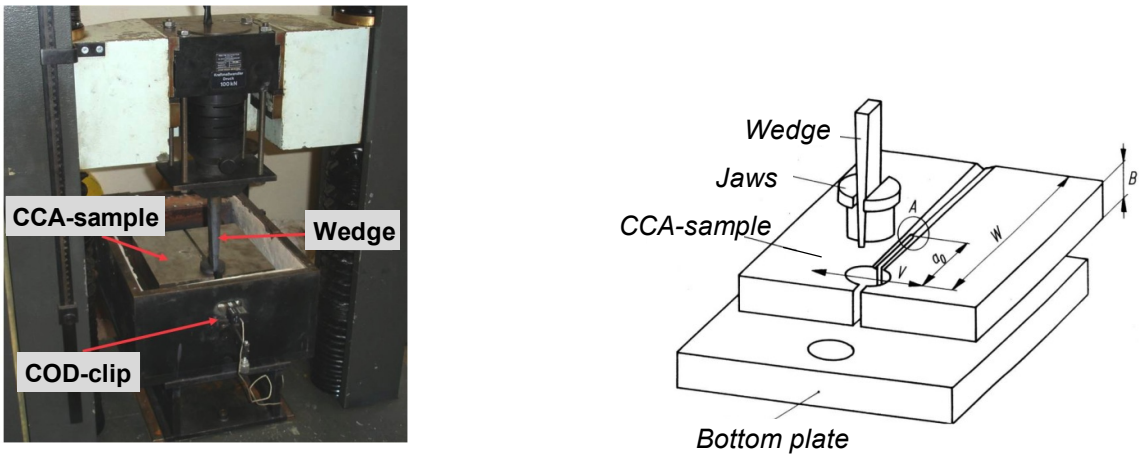

Fig. 3: Test set-up and transversal wedge load of the CCA-samples according to ASTM E 1221-06 (A: brittle build-up welding with notch)

During the test, the force and the notch opening (COD clip) are registered. An abrupt notch opening with a simultaneous reduction of force indicates an instable crack propagation. Details on the test evaluation are specified in ASTM E 1221-06. To this end, with regard to the validity criteria concerning the minimum and maximum crack length as well as the verification of the required minimum sample thickness B implementing the level elongation state according to

$$B \geq 2.5 \left(\frac{K_{Ia}}{R_{dp0.2}} \right)^2 \tag{6}$$

It must be taken into account that this requires knowledge of the dynamic yield strength $R_{dp0.2}$. The determination of $R_{dp0.2}$ for ferritic cast iron materials is possible via the Arrhenius equation (Eq. 7) describing the dependence of the dynamic yield strength of the elongation rate $\dot{\varepsilon}$ and the temperature according to

$$R_{dp0.2} = \sigma_i + \sigma_0^* \left[1 - \frac{k \cdot T \cdot ln \, {\dot{\varepsilon}_0}/{\dot{\varepsilon}}}{\Delta G_0} \right]^m \tag{7}$$

The parameters of the Arrhenius equation ($\dot{\varepsilon}_0 = 8.68 \cdot 10^8$/s, σ_i = 212 MPa, σ_0^* = 621 MPa, $\Delta G_0 = 2.2 \cdot 10^{-19}$ J, m = 3.43) determined within extensive examinations [3] of 15 batches at T = -80 °C and $\dot{\varepsilon}$ = 1/s result in a value for $R_{dp0.2}$ = 422 MPa. The specified elongation rate corresponds with $\dot{K} = dK/dt$ values between 10^4 MPa√m/s and 10^5 MPa√m/s existing during impact bending tests determining dynamic K_{Id} values. For ferrite-pearlite cast iron materials, the value $R_{dp0.2}$ = 385 MPa determined in [4] for $\dot{\varepsilon}$ = 1/s and -40 °C can be used. The crack-arrest tests performed on 50 mm thick CCA-samples in the temperature range of -40 °C to -80 °C show that due to the failure to achieve the "minimum crack length" required by the standard, at -40 °C

and -60 °C no valid K_{Ia} values can be determined. The cause is the still available high crack initiation toughness. This also applies to the ferritic as well as the ferrite-pearlite cast iron. The conditions for the check of the level elongation state are only met at -80 °C, and valid K_{Ia} values can be determined, which are in the range 44 MPa√m ≤ K_{Ia} ≤ 61 MPa√m. The crack propagation occurs at -80 °C, also within the fracture surface area of the crack-arrest, exclusively cleavage-faced, whereby crack trapping can be attributed material-specific to the energy-dissipative effect of the graphite particles.

5 Summary

A summarising evaluation of the effect of the pearlite content on the mechanical and fracture mechanical characteristic values is performed based on a graphical representation of the characteristic values determined (Fig. 5 to Fig. 7). In addition to the expected work-hardening with declining temperature and higher pearlite content, only with higher pearlite content and -40 °C a significant decrease of the plasticity occurs, i.e. a more than 50 % decrease of the fracture elongation A or the percentage reduction of fracture Z (Fig. 5).

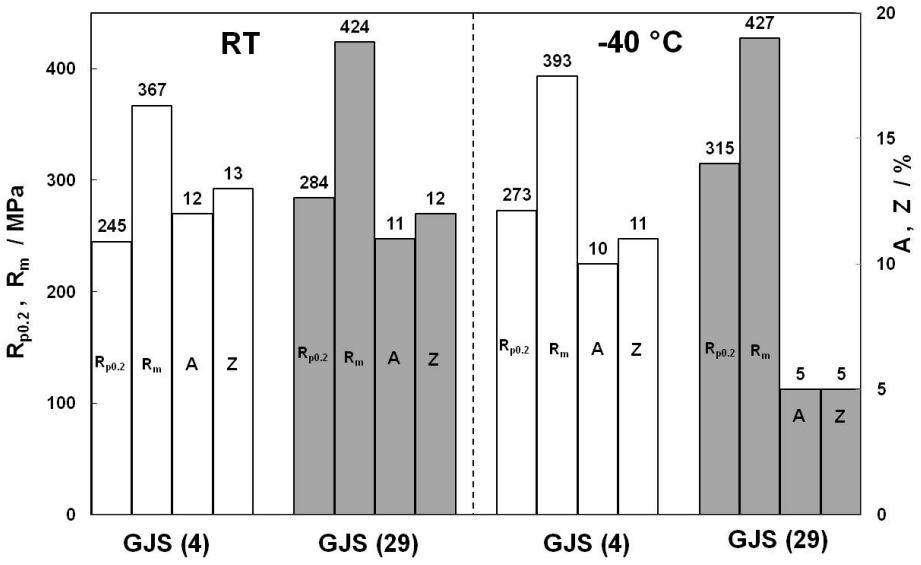

Figure 5: Mechanical characteristic values of the tensile test

With a sudden load, the increased pearlite content leads to a significant decrease in toughness, as resulting from the course of the KV-T curves (Fig. 6a) and the notched bar impact work used KV at RT as well as the transition temperature T_t (Fig. 6b). At -40 °C, both materials are located in the lower position of the KV-T-curve.

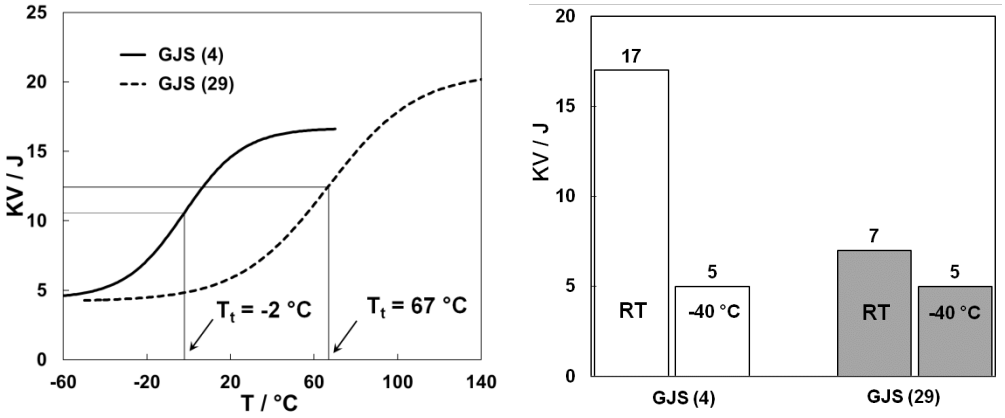

a) KV-T curves b) KV values (RT and -40 °C)

Figure 4: Mechanical characteristic values of the notched bar impact test

It results from the comparison of static fracture-toughness values at -40 °C that the increased pearlite content leads to a significant reduction of the material resistance against crack initiation ($J_{i/BL}$, $J_{0.2}$) and ductile stable crack propagation (T^J). As the dynamic fracture-toughness values of the GJS (4) show, a shock load at this temperature leads, due to the cleavage-faced stable crack propagation, to a significant decrease of the crack resistance behaviour (Fig. 7). With these loading conditions, the effect of the pearlite becomes also apparent with the occurrence of "pop-in"-effects, occasionally with GJS (4) and exclusively with GJS (29).

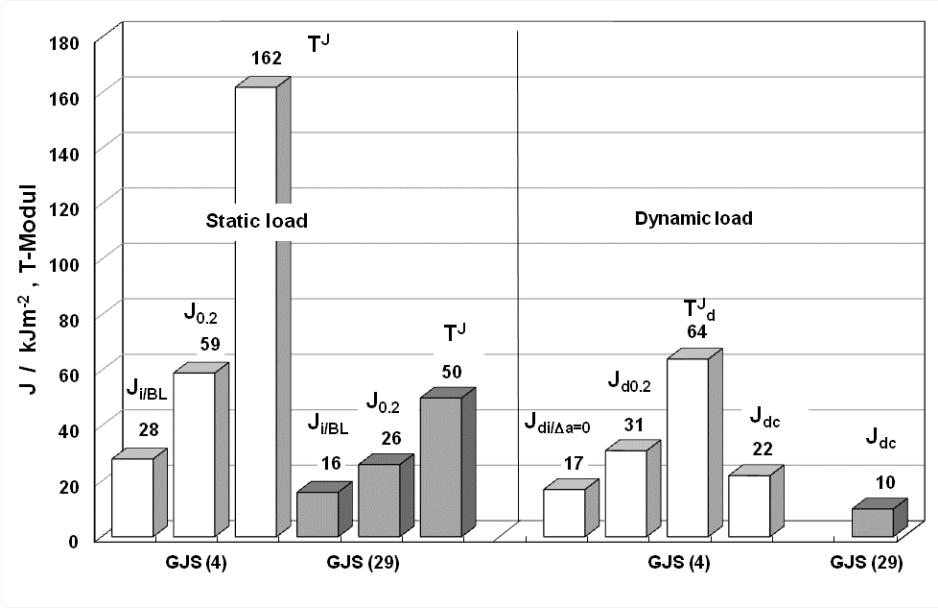

Fig. 5: Fracture mechanical characteristic values for static and dynamic load (-40 °C)

The K_{Ia} values determined at -80 °C are evaluated via the allocation to the reference curve on hand (lower-bound curves) to the temperature-dependent course of the K_{Ia} values (Fig. 8). There only tends to be an effect noticeable with regard to the increased pearlite content.

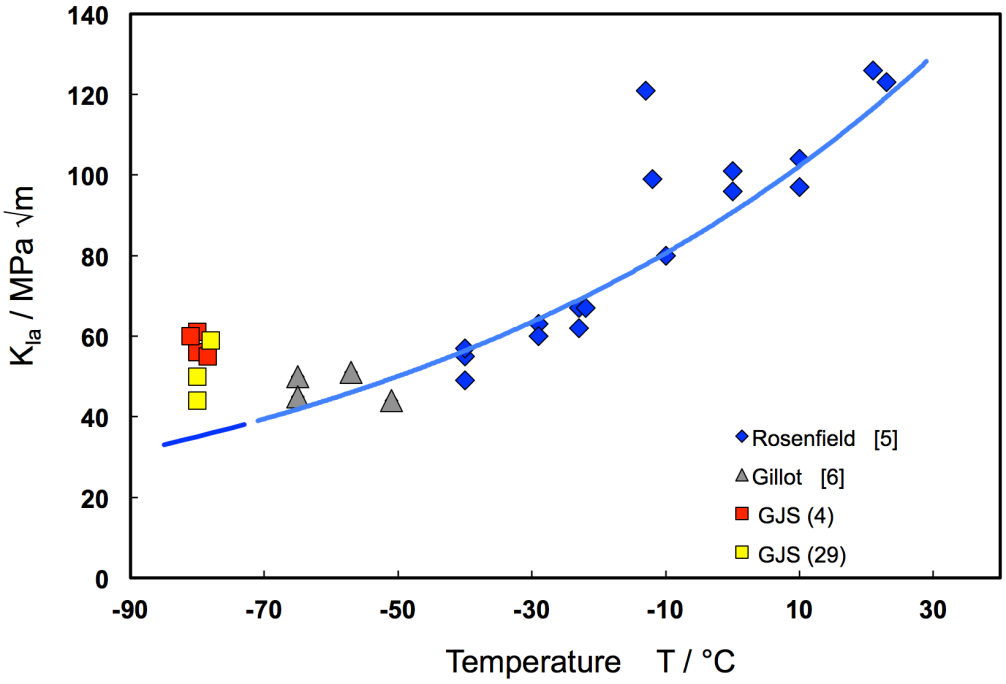

Figure 6: K_{Ia}-values for ferritic cast iron as a function of the temperature

According to [5], the determination of valid K_{Ia} values at ferritic cast iron in the temperature range of -40 °C to 20 °C is only possible by means of a duplex-arrest sample, to which a hardened steel (AISI 4340) as the crack starter is connected via a work intensive heat-treated electron-beam welded connection with the GJS-400 test specimen. In this combination, the crack does not start in a brittle build-up welding according to (Fig 4), but inside the hardened steel and runs into the cast iron at high speed. Thus, the determination of the K_{Ia} values can be implemented even at the higher temperatures specified in Fig. 7. The temperature-dependent course of the K_{Ia} values integrates the values listed in [6] as well as the K_{Ia} values determined here at -80 °C. Based on the temperature-dependent course of the K_{Ia} values, an estimation of the crack-arrest capacity after the crack initiation is possible with the knowledge of the stress intensity factor K_I dependent on the component geometry and fault type or size.

6 References

[1] Winkler, H.-P.; Hüggenberg, R.; Ludwig, A.; Pusch, G.; Trubitz, P.: Determination and definition of fracture toughness of dynamically loaded ductile cast iron. 12th International Conference on Fracture, Juli 2009, Ottawa

[2] Ludwig, A.; Pusch, G.; Trubitz, P.; Winkler, H.-P.; Hüggenberg, R.: Ermittlung und Definition dynamischer Bruchzähigkeitswerte. Giesserei-Praxis 2012, Ausgabe 1/2, S. 10-13

[3] DYNTEST: Bestimmung dynamischer Rissinitiierungswerte für duktiles Gusseisen (DCI), Interner Bericht, TU Bergakademie Freiberg, Institut für Werkstofftechnik, 2008

[4] Baer, W.; Häcker, R.: Werkstoffcharakterisierung von Gusseisenwerkstoffen mit Kugelgraphit. MP Materialprüfung, 47 (2005) 1-2, S. 34-44.

[5] Rosenfield, A. R.; Ahmad, J.; Cialone, H. J.; Landow, M. P.; Mincer, P. N. and Papaspyropoulos, V.: Crack arrest toughness of nodular iron. In: Nuclear Engineering and Design 116 (1989), S. 161-170

[6] Gillot, R.: Experimentelle und numerische Untersuchungen zum Rissstopp-Verhalten von Stählen und Gusseisenwerkstoffen. Techn.-wiss. Ber. MPA Stuttgart (1988) Heft 88-03

Study of Fracture Mechanics Assessments in Industrial Applications

Bartolomeus Irwanto[1,*], Thorsten Prothmann[1]

[1] Alstom, Zentralstrasse 40, 5242 Birr, Switzerland
* Corresponding author: bartolomeus.irwanto@power.alstom.com

Abstract
Fracture mechanics has been widely used for mechanical integrity assessment in industrial applications. Different approaches in the fracture mechanics assessment have been developed to achieve more accurate prediction of component lifetime. This paper describes fracture mechanics assessments by applying the 2D and 3D crack growth analyses of a real mechanical component under cyclic load as an example from the power industry. In 2D crack growth analysis, both an appropriate equivalent geometry as well as the original geometry with an explicit crack model are investigated. A limitation of 2D crack growth analysis in the example is to consider load redistribution, which follows from the local stiffness change attributed to the cyclic crack growth. This can be overcome by 3D crack growth analysis with an explicit crack model. Comparison between 2D and 3D assessment results are given. The concept of local limit load and failure assessment diagram (FAD) are reviewed and studied by using finite element (FE) analysis.

Keywords fracture mechanics, crack growth, load redistribution, limit load

1. Introduction

Industries have been challenged to come up with better and less costly products within shorter development cycles. Thus, product development processes have also needed to be improved. This has lead to a tremendous challenge for engineers, to continuously develop improved approaches including fatigue life time assessment of a component. In the lifetime assessment it is important to consider both crack initiation and crack propagation. Fatigue failure is caused by microscopic damage in the material that after continued cycling develops into a crack that may finally lead to a component failure. Generally the design should avoid the initiation of fatigue cracks during the design life time. However one has to assume the existence of initial flaws in the raw material, e.g. forgings. In order to determine criteria for the non-destructive testing of forgings, appropriate investigations of crack propagation are required. This paper focuses on these numerical crack propagation investigations.

In this paper, the application of fracture mechanics for mechanical integrity assessment is shown in industrial applications. Different approaches in the fracture mechanics assessment have been developed to achieve more accurate prediction of component lifetime. This paper describes fracture mechanics assessments by applying the 2D and 3D crack growth analyses of a real mechanical component under cyclic load as an example from the power industry. Some limitations in the application of crack growth simulation in 3D analysis and the potential use of a failure assessment diagram (FAD) are discussed.

2. Mechanical model

In the shaft trains of large steam turbine generator sets, the mechanical integrity of each component of the shaft train has to be verified. The rotating parts such as generator and steam turbine rotor

have to be particularly verified with accurate lifetime assessment methods. In this work, a generator rotor is taken as an example for fracture mechanics assessment. Figure 1 shows the FE-model of a generator rotor and one example of analysis results by using ANSYS [8]. A generator rotor has complicated geometries and components such as insulation, conductors and wedges. The calculation of a complete 3D rotor model is very time consuming. Therefore, a 2D model can be used to reduce the computational efforts. In 2D crack growth analysis, a stress analysis should be performed beforehand. A 2D model of generator rotor is depicted in Fig. 2. The corresponding 2D elements in ANSYS are applied in the mesh generation.

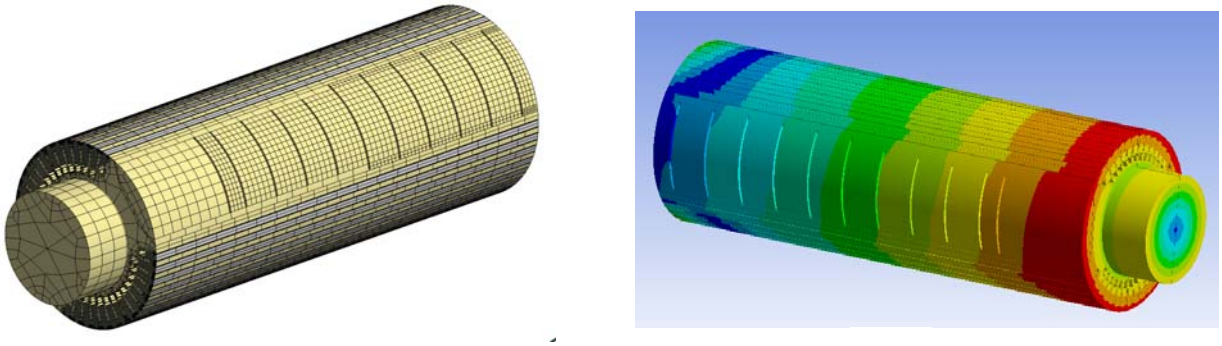

(a) (b)

Figure 1. FE model (a) and displacement results (b) of a complete 3D generator rotor

The dominating load in a generator rotor is due to centrifugal forces, i.e. the main contribution for cyclic rotor loading is related to the start/stop cycles of the shaft train. The number of design start/stop cycles is specified in IEC 60034-3. Thus, the centrifugal load at rated speed is considered for stress analysis. For 3D crack growth analysis, a simplified 3D model is created as shown in Fig. 3, where a rotor tooth is modeled. The influence of conductors and wedges is replaced with equivalent pressure applied at the rotor tooth flank.

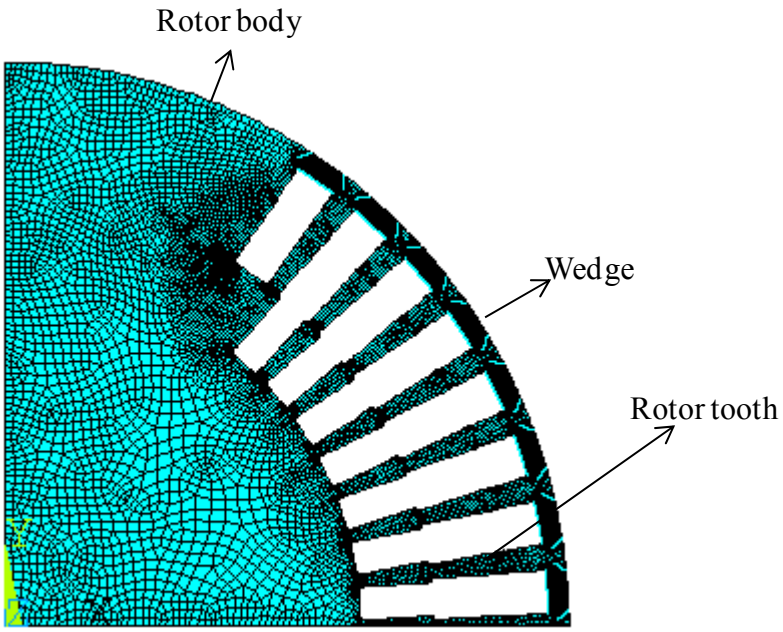

Figure 2. 2D FE model of generator rotor

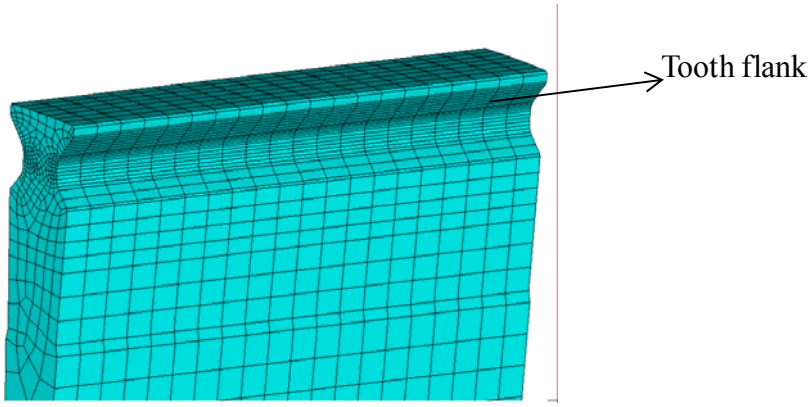

Figure 3. Simplified 3D FE-model for calculation and crack growth analysis

3. Crack growth analysis

3.1. 2D crack growth calculation

To calculate 2D crack growth the program AFGROW [1] is used in this example. AFGROW is an analytical fatigue crack growth prediction program initially developed in AFRL for airframe applications and based on the principles of Linear Elastic Fracture Mechanics (LEFM) [1]. AFGROW calculates fatigue crack growth by considering known stress intensity solutions for a particular geometry, under an applied stress field. A stress intensity solution has the following general form:

$$K = \beta\sigma\sqrt{\pi a} \tag{1}$$

in which 'K' is the stress intensity factor, 'a' is a characteristic crack length, 'σ' is the applied stress, 'β' is the geometrical factor. As the stress intensity solutions are dependent on the geometry of the components, AFGROW provides certain standard predefined geometries (crack models) for predicting crack propagation.

To create the initial crack, a surface crack model is selected as shown in Fig. 4. As input data, the corresponding model geometry and dimensions should be defined. The crack growth rates are expressed in the form of the Walker equation, which is simplified to a Paris equation. In AFGROW the stress gradient can be included in the analysis. The analytical solution for this crack model is described in [2], which is implemented in AFGROW. It is assumed that the first principal stress is always normal to the crack plane. The calculated first principal stress from the 2D finite element model described previously is shown in Fig. 5, where the stress path can be seen. Using the stress gradient along the stress path, the crack growth calculation is performed and the normalized results are depicted in Fig. 6. The crack size 'a' corresponds to the crack growth in the circumferential direction and crack size 'c' to the axial direction.

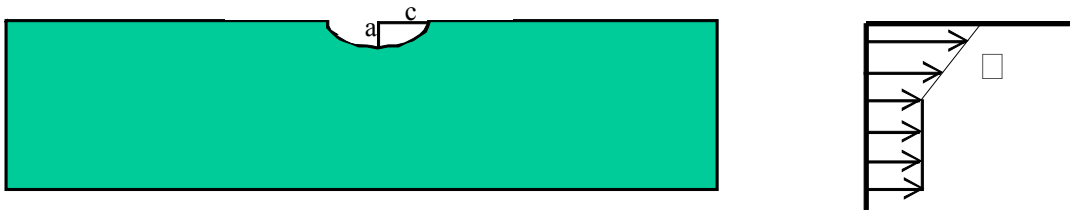

Figure 4. Crack model in AFGROW and stress gradient (schematic)

The application of the crack model has to satisfy a limit that the ratio of crack size 'a' and plate thickness 't' must be less than or equal to 0.8 ($a/t \leq 0.8$). The reason of this limitation is according to Glinka that the reference solutions used for the derivation of the weight function were valid for this range (see also [2]). Further investigation shows that the reference solution is related to the local limit load which causes local crack-ligament yielding somewhere along the crack front [5]. The local limit load will be further discussed in the next section.

2D crack growth analysis is a straight-forward approach, where the FE results can be used directly in the crack growth calculation. Its numerical effort is also acceptable. However, 2D crack growth analysis is limited by the fact that for larger crack extension compared to the geometrical dimension of the analyzed component possible load redistribution cannot be considered. The load redistribution occurs as the local stiffness around the crack changes more significantly as the crack becomes larger. Moreover, the assumption that the 1st principal stress is always normal to the crack plane may lead to a conservative result. The load redistribution may have a significant impact as demonstrated in the next section with the results of the 3D crack growth analysis of the same component.

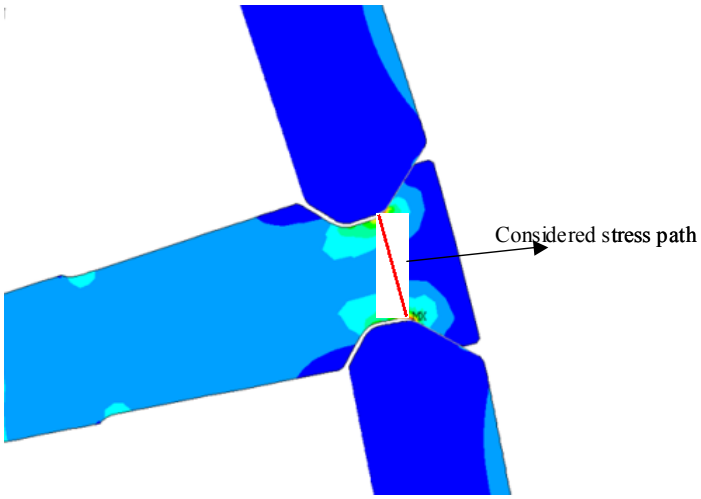

Figure 5. 1st principal stress distribution of rotor due to centrifugal load

3.2. 3D crack growth calculation

A critical issue in 3D crack growth calculation is the mesh generation. In general cases, the use of a

standard FE program faces time-consuming challenges such as:

- Component geometries are complex and time consuming to model, where cracks can occur at geometrically difficult locations, e.g. chamfers, corners.
- Initial cracks of the correct size and shape must be inserted in the component at the correct location.
- After several load cycles and depending on the loading, initial planar crack may develop into a non-planar crack.

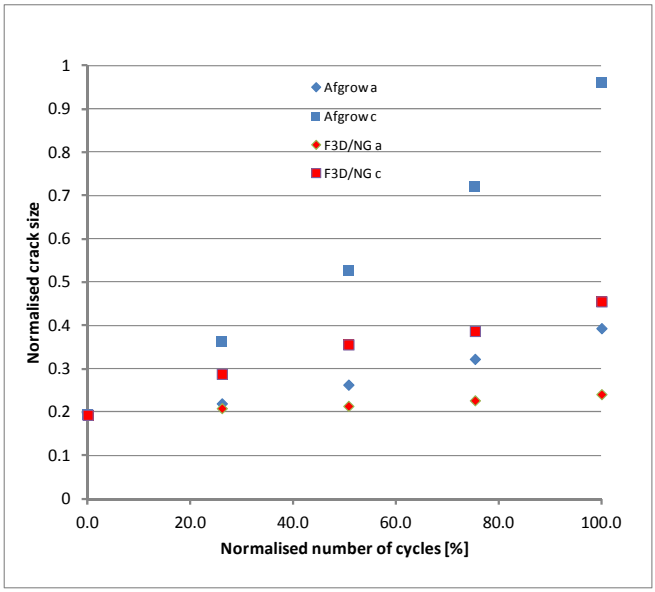

Figure 6. 2D and 3D crack growth calculations and their comparison

To alleviate the above challenges, there are several programs existing that allow users to generate/insert a crack into the FE model. In this work, the program FRANC3D/NG (short name F3D/NG) version 4.0 has been used. The methodology of F3D/NG has been documented in [3]. In F3D/NG the stress and displacement fields in the structure of interest are obtained from a Finite Element program such as ANSYS or ABAQUS [9].

The results of the FE analysis as well as geometry are read directly into F3D/NG in a text format. The F3D/NG program uses the FE program as solver to obtain the stresses and displacements after growing the crack at a user defined step size. Hence, by updating the stresses and displacements for each crack growth step with the FEA method, the simulation can more closely represent the crack's influence on the structure. The crack insertion and all re-meshing are carried out within F3D/NG in the submodel created before by using the FE program. The F3D/NG will produce a neutral format file that can be read back into the FEA code and re-analysed.

In F3D/NG the stress intensity factors of Mode I, II and III are calculated by using M-Integral (interaction integral) for isotropic and anisotropic materials [3, 4]. F3D/NG can also compute stress intensity factors using a displacement correlation approach. In this approach, the calculated displacements for nodes on the crack faces are substituted into the theoretical expressions for the crack-front displacement fields as functions of the stress-intensity factors. The applied propagation direction criterion is based on the maximum stress criterion. In this method, depending upon user's choice, the mode I and mode II with/without mode III values are combined to yield both magnitude

and direction of the propagation at the various discrete points along the crack front.

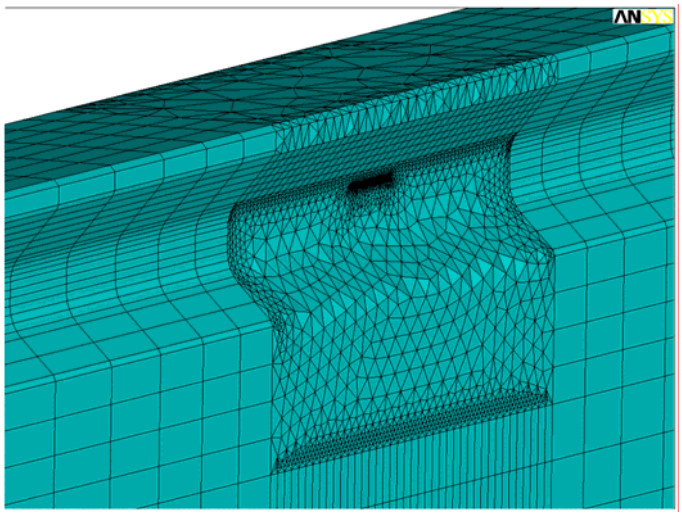

Figure 7. Example showing the submodel with finer mesh and inserted crack

Fig. 7 shows the global model and the submodel having finer mesh and inserted crack. The applied element type is an element with a quadratic shape function. The calculated equivalent stress field is shown in Fig. 8. By using the same parameter for the Paris equation as for 2D crack growth, 3D crack simulation with the same initial crack size is carried out. Small size steps and other meshing options are defined in order to get optimal results. The calculated crack sizes in both directions are presented in Fig. 6. It is clearly observed from Fig. 6 that there is a significant difference in the results from the 2D and 3D crack growth calculation yielding an overestimation of the cyclic crack growth with the 2D model. This demonstrates that the influence of load redistribution as well as the stress direction to the crack plane is significant for crack growth analysis.

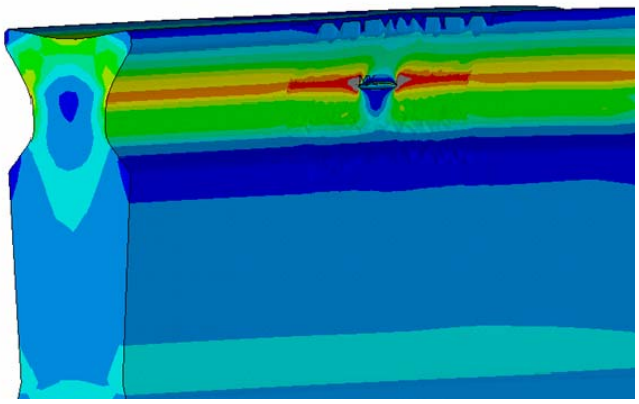

Figure 8. Stress field of model with a crack

Conventional limit load analysis computes the global (net-section) limit load, at which displacements become unbounded. However, the global limit load might be taken conservatively for a part-through crack. Thus, local limit load is proposed and defined as the load needed to cause a local crack-ligament yielding somewhere along the crack front [5]. In the paper, the local limit load is derived by finite element analysis of a plate with surface crack. In order to check the local limit

load of the rotor, elastic-plastic analysis with ideal plastic material behavior is performed on the model with sequentially increased crack sizes. The result analysis shows that the local load limit is achieved at a/t=0.8. Strain distribution at ligament yields that the limitation of up to a/t=0.8 is also valid for the component assessment.

3.3. Failure Assessment Diagram (FAD)

The failure assessment diagram (FAD) method is the broadly accepted methodology for the analysis of components containing a crack-like flaw. The FAD method is described in the engineering code, for example API 579 and FKM guideline for fracture mechanics [6]. The FAD method uses brittle fracture ratio (K_r) and plastic collapse ratio (L_r). In a FAD the non-dimensional ratio L_r is on the horizontal-axis and K_r (brittle fracture ratio) on the vertical-axis. The plastic collapse ratio is a parameter measuring the proximity to plastic collapse. The brittle fracture ratio is a parameter comparing the stress intensity factor at the crack and the fracture toughness of the material. The FAD curve can be computed if the stress-strain curve exists. In this case, the plastic collapse ratio is determined by using the reference stress, which can be computed using the J-integral results from the elastic-plastic analysis. The brittle fracture ratio is computed from the crack front stress intensity, obtained by an elastic analysis.

Fig. 9 shows a graph of FAD and the evaluation point for the example calculated in the previous section, where the ratio a/t is less than 0.5. In Fig. 9, the evaluation point inside the FAD curve indicates an acceptable crack. The evaluation point represents the quasi static condition of a crack/flaw at certain size and loading. The FAD curve is not created by using a specific structural component and a stress-strain curve. The FAD curve is derived from the following equations [6]:

$$F1(L_r) := \begin{cases} \left(1 + \frac{L_r^2}{2}\right)^{\frac{-1}{2}} & \text{if } L_r < 1 \\ \left(\lambda + \frac{1}{2\lambda}\right)^{\frac{-1}{2}} & \text{if } L_r = 1 \\ \left[\left(\lambda + \frac{1}{2\lambda}\right)^{\frac{-1}{2}} \cdot L_r^{\frac{N-1}{2N}}\right] & \text{if } L_{rmax} > L_r > 1 \\ 0 \text{ if } L_r \geq L_{rmax} \end{cases} \quad (2)$$

in which λ and N are parameters given in [6], which depend on material yield strength as well as ultimate tensile strength. The above equations are based on basic level assessment, which is more conservative than the use of stress-strain curve in FAD. However, the computed FAD curve with stress-strain curve can provide a better representation of the particular material effect and the particular structural component geometry.

If the evaluation point is above the FAD curve, the crack is unacceptable and this can indicate a predicted structural failure. The evaluation point can be updated as the crack grows to determine the end of life when the evaluation point reaches the FAD curve. Thus, an evaluation point on the FAD curve can be useful to determine predicted critical crack sizes.

4. Conclusions

This paper demonstrates the application of fracture mechanics in industrial practice. 2D crack growth analysis provides significantly less computational effort but can yield over conservative results, since the load redistribution and the actual stress state are not taken into account.

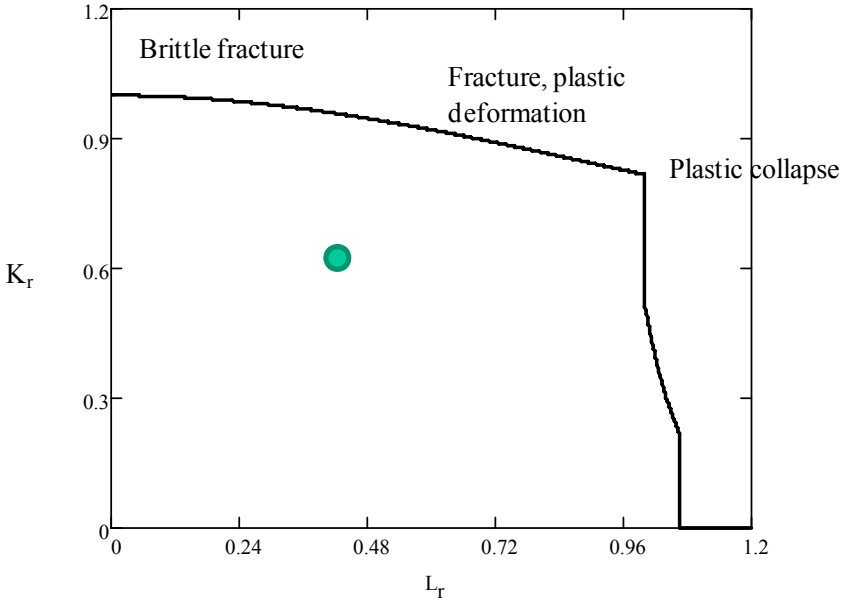

Figure 9. Calculated FAD showing the acceptable evaluation point

These weaknesses can be overcome by 3D crack growth analysis but it requires significant computational efforts. The use of submodelling in 3D crack growth analysis may reduce the computational time; however, from the practical point of view it is still a big challenge to use this method for fast development projects. Application of XFEM in the 3D crack growth calculation might offer an opportunity to extend the use of 3D crack growth analysis in lifetime assessment. However, the use of commercial XFEM code should be reviewed critically due to the result accuracy. Different strategies are currently developed for damage calculation to improve the accuracy and convergence rate of XFEM. Instead of re-meshing in the region of crack tip elements, a higher order element approach, different enrichment functions and integration rules can be applied (see e.g. [7]). Finally, the FAD assessment can be used to ensure that a component with a certain crack/flaw size is acceptable for the design load.

Acknowledgements

The authors would like to thank Alstom for allowing this publication.

References

[1] James A. Harter, AFGROW User Guide and Technical Manual, Air Force Research Laboratory, June 2006.
[2] G. Shen, A. Plumtree, G. Glinka, Weight function for the surface point of semi-elliptical surface crack in a finite thickness plate, Engineering Fracture Mechanics, Vol. 40 (1), 167-176, 1991.
[3] Fracture analysis consultants, FRANC3D/NG Reference Manual, 2007.
[4] P. A. Wawrzynek et al., Advances in Simulation of Arbitrary 3D Crack Growth using FRANC3D/NG, ICF 12, Ottawa, 2009.

[5] I. Sattari-Far, P. Dillström, Local limit load solutions for surface cracks in plates and cylinders using finite element analysis, International Journal of Pressure Vessels and Piping 81, 57-66, 2004.
[6] FKM guideline Fracture mechanics proof of strength for engineering components, 3th Edition, 2006.
[7] E. Sala-Lardles, et al.: Optimally convergent high order X-FEM for problems with voids and inclusions, ECCOMAS 2012, Vienna.
[8] ANSYS Inc., ANSYS User's Guide, 2007.
[9] Dassault Systèmes, Abaqus/CAE User's Manual, 2012.

Safety Assessment and Fatigue Life analysis of Aged Crane Structures

Kai Qi[1]*, Weixiong Wang[1], Xinhua Wang[1], Aihua Jiang[1], Boqing Liu[1], Zhongliang Guo[1], Jin Liu[1]

[1] Guangzhou academy special equipment inspection & testing, Guangzhou, 510180 China
* Corresponding author: kqichina@163.com

Abstract The fatigue life of crane steel structure will inevitably decrease in the course of work, which directly affects the work of crane. So the correct safety assessment and fatigue life evaluation is necessary. According to the results of stress testing and non-destructive examination, a framework of assessing remaining fatigue life of crane metal structures is built in this paper based on crack propagation theory. Moreover, in order to descript the analysis process, an example about fatigue life estimation of a shipbuilding gantry crane whose maximum hoist 100 ton was shown.

Keywords Crane, steel structure, fatigue life, crack propagation

1. Introduction

Crane is one kind of mechanics which is of significant characteristics such as repetitive, cycle, frequent brake and large impact load etc. . Especially, there is about 70-80% metal failure accident which is associated with fatigue. So it is very necessary to research the fatigue life estimation of metal structure. When metal structure of a crane reaches its allowable safe life, it must be retired from service. One of the most important life prediction approaches is the stress-life approach [1-2]. As parts of the damage accumulation calculations, rain flow algorithm and Miner's rule were used. However, with no cracks, this could be the ultimate tensile strength or yield strength, depending upon the failure criteria chosen. As a crack forms and grows under cyclic loading, the residual strength decreases. This decrease as a function of crack size is dependent upon material, environment, component and crack configuration, location and mode of crack growth. Considering the crack, a new analysis method based fatigue crack growth is introduced. Compared to the conventional S-N fatigue analysis, crack detection methods, using several different nondestructive inspection techniques and standard procedures, have been developed [3-6]. This paper will present a framework of assessing remaining fatigue life of in-service crane.

2. Principles of fatigue life analysis

2.1. Conventional S-N fatigue analysis

S-N fatigue analysis is a conventional approach which touches on the relationship between applied stress and expected life. And the relationship is characterized by means of the S-N curve so that fatigue life can be predicted (Fig. 1). “S” stands for the cyclic stress range while “N” represents the number of cycles to failure. The core idea of this method is stress change is the main reason of fatigue failure of materials. Of course, the S-N curve is the inherent property and is derived from

tests on samples of the material to be characterized (often called coupons) where a regular sinusoidal stress is applied by a testing machine which also counts the number of cycles to failure. The applied stress used to calculate fatigue life can be obtained by tested strain or stress analysis via finite element method.

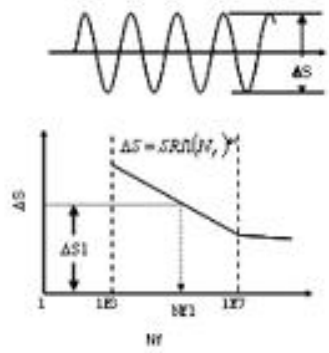

Figure 1. S-N fatigue curve

It should be noted that there are several short comings of S-N fatigue data. First, the conditions of the test specimens do not always represent actual service conditions. For example, components with surface conditions, such as pitting from corrosion, which differs from the condition of the test specimens will have significantly different fatigue performance. Furthermore, there is often a considerable amount of scatter in fatigue data even when carefully machined standard specimens out of the same lot of material are used. Since there is a considerable scatter in the data, a reduction factor is often applied to the S-N curves to provide conservative values for the design of components.

2.2. LEFM based fatigue crack growth analysis

The greatest significance in fatigue crack growth analysis in comparison to the conventional method is the existence of a crack. Cracks can form due to fatigue, or they can exist as a consequence of manufacturing processes such as deep machining marks or voids in welds and metallurgical discontinuities such as foreign particle inclusions. In fatigue life estimation process of metal structure of crane, linear elastic fracture mechanics (LEFM) is introduced to describe and predict fatigue crack growth life and fracture under the basic assumption that material conditions are predominantly linear elastic during the fatigue process. For crack growth or fracture conditions that violate this basic assumption, elastic-plastic fracture mechanics approaches are used to describe the fatigue and fracture process.

In order to perform the life estimation or prediction, several key items are needed: stress intensity factor, maximum and minimum stresses, fracture toughness (KIC), and initial crack size. Of course, environmental conditions, load history, statistical aspects, and safety factors must be incorporated in this methodology for remaining fatigue life assessment.

During the fatigue life estimation process, load history can be finished by the survey of crane usage

and statistical analysis. Nondestructive technologies such as magnetic particle testing (MT), ultrasonic testing (UT), penetrate testing (PT) and so on are usually used to detect the size of crack or flaw on the surface of structure. At the same time, the fatigue crack growth behavior is also inspected by these technologies. After idealizing the detected defection, relevant stress intensity factor will be gained via calculation or fatigue handbook. And maximum and minimum stresses can be determinated by means of finite element stress analysis. Certainly, both of them can be tested after typical load test. Furthermore, material properties such as young modulus, tensile strength, yield strength and fracture tough and so on can be obtained via tests. The issued handbooks can also be utilized if common material used in assessing structure. Finally, fatigue analysis can be performed based on measured strains and calculated stresses via finite element method. Prediction of fatigue remaining life can be carried on using professional software.

3. Interpreting methodology for remaining fatigue life assessment

As discussed previously, LEFM is one of the methodologies for remaining fatigue life assessment of metal structure of crane based on fatigue crack growth analysis. The following example shows how the procedures work.

In this example, we researched a shipbuilding gantry crane whose maximum hoist is 100 ton (Fig. 2). Then actual load history data was extracted while referring to the crane usage record. Fig. 3 shows the raw data about one week. Additionally, strains were measured at stress concentration positions, for example, cantilever and boom system. Fig. 4 shows one of the strain measure points at cantilever. All the data was used as the basic input during the estimating residual life process.

Figure 2. The photo of aged crane

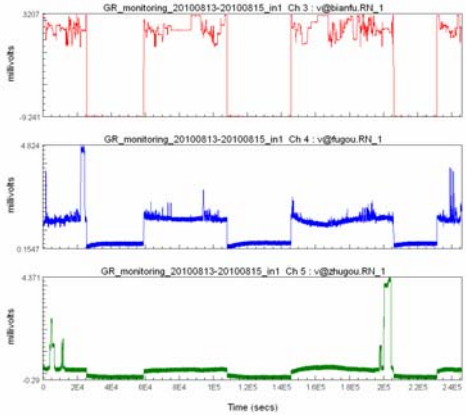

Figure 3. Actual data of load history of crane in less than one week

Finite Element stress analysis provided the primary stress concentration components of the crane. That is, cantilever and boom system. The results can be identified in Fig. 5.

Figure 4. Strain measurement point on cantilever

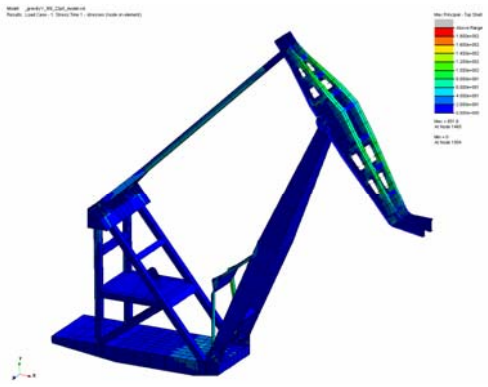

Figure 5. Stress contours of model when lifting 95 ton weight

Nondestructive inspection technology allows parts and materials to be inspected and measured without damaging them. Because LEFM is based on the fatigue crack growth analysis, the technology plays a critical role in inspecting crack or flaw of metalwork structure. During the nondestructive inspection procedure, several defections were found on the cantilever by ultrasonic phased arrays. Defections were inspected by ultrasonic phased arrays such as shown in Fig. 6. Subsequently, these defections were idealized as single edge crack of long atrip and input the fatigue analysis software. The calculation flow can be seen in Fig. 7. The remaining fatigue life of the crane was about 26 years in terms of present damage situation or structural integrity.

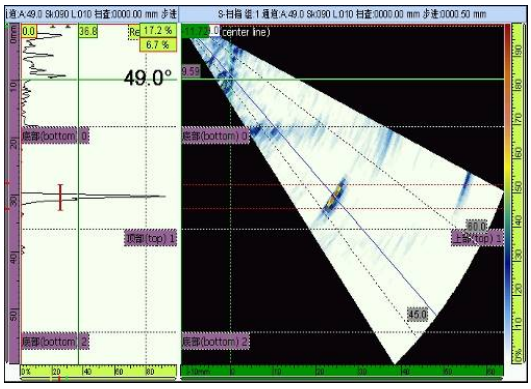

Figure 6. Defection on cantilever via ultrasonic phased arrays

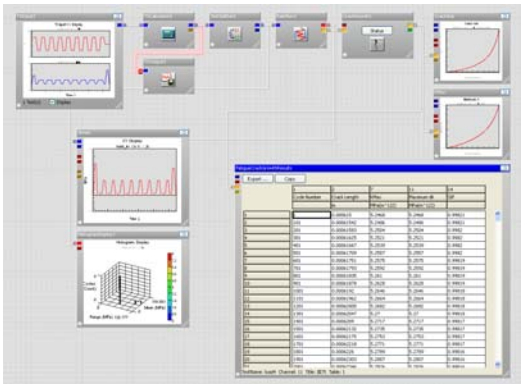

Figure 7. Calculation flow of fatigue life.

4. Conclusions

Based on fatigue crack growth analysis, linear elastic fracture mechanics (LEFM) is introduced to describe and predict fatigue crack growth life and fracture in fatigue life estimation process of metal structure of crane. Especially, the methodology is more suitable for aged crane, which exists some crack or flaw positively. The following example also shows how the procedures work.

Acknowledgments

The paper is fully supported by General Administration of Quality Supervision, Inspection and Quarantine of the People's Republic of China funded project 2010QK081 and 2010QK086.

References

[1] P. Paris, F. Erdogan, A critical analysis of crack propagation laws, Journal of Basic Engineering, Transactions of the American Society of Mechanical Engineers. (1963) 528-534.
[2] D. Radaj, Review of fatigue strength assessment of nonwelded and welded structures based on local parameters. International Journal of Fatigue, 18 (1996) 153-170.
[3] M. Euler, U. Kuhlmann, Crane runways-fatigue evaluation of crane rail welds using local concepts. International Journal of Fatigue, 33 (2011) 1118–1126.
[4] Zeljko Domazet, Lovre Krstulovic-Opara, Mladen Stupalo, Fatigue cracks and failures in cement industry, shipbuilding and power plant facilities. Engineering Failure Analysis, 12 (2005), 819–833.
[5] Ozden Caglayan, Kadir Ozakgul, Ovunc Tezer, Erdogan Uzgider, Fatigue life prediction of existing crane runway girders. Journal of Constructional Steel Research 66 (2010) 1164-1173.
[6] Shana Pang, Shiyang Zhou, Zhijing Zhang, Research on fatigue life of overhead traveling crane based on damage tolerance design. Energy Procedia 13 (2011) 9430 – 9434.

Local fracture behavior and integrity assessment of a dissimilar metal welded joint in nuclear power systems

Guozhen Wang*, Haitao Wang, Fuzhen Xuan, Shantung Tu

Key Laboratory of Pressure Systems and Safety, Ministry of Education, East China University of Science and Technology, Shanghai 200237, China
* Corresponding author: gzwang@ecust.edu.cn

Abstract In this paper, fracture tests and microscopic observations were conducted on an Alloy52M dissimilar metal welded joint (DMWJ) between A508 ferritic steel and 316L stainless steel in nuclear power systems. The local fracture behavior in the DMWJ was investigated, and the significance of using local fracture resistance in integrity assessment of the DMWJ was analyzed. The results show that the local fracture resistance in the DMWJ is determined by the local fracture behavior, and which is mainly related to the microstructure and local strength mismatch of materials at the crack locations. The crack growth always deviates to the materials with lower strength, and the crack path deviations are mainly controlled by the local strength mismatch. If the local fracture resistance properties could not be obtained and used for cracks in heat affected zone (HAZ), interface and near interface zone, the use of the J-resistance curves of base metals or weld metals following present codes will unavoidably produce non-conservative (unsafe) or excessive conservative assessment results. In most cases, the assessment results will be potentially unsafe. Therefore, it is recommended to obtain and use local mechanical and fracture resistance properties in the integrity assessment of DMWJs.

Keywords Local fracture behavior, Dissimilar metal welded joint, Integrity assessment, Strength mismatch, Crack growth path

1. Introduction

In primary water systems of pressurized water reactors (PWRs)，low alloy ferritic steel is specifically selected to manufacture the nuclear pressure vessels for its high toughness and economical interest, while austenitic stainless steel is selected to make primary pipes for its proper strength and good corrosion resistance. In order to join the ferritic steel pipe-nozzles of the pressure vessels to the austenitic stainless steel pipes well, a transitional stainless steel safe-end pipe is usually introduced. A dissimilar metal welded joint (DMWJ) is usually utilized to join the pipe nozzle with the safe end pipe, as shown in Fig.1. Nevertheless, the welds were indicated to be vulnerable components from the international surveys, owing to their proneness to different types of flaws. Axial and circumferential defects within DMWJs caused by stress corrosion or fatigue have been found in the nuclear power plants (NPPs) in many countries [1-2]. In addition, serious leakage events on such DMWJs have also been reported [3-4]. Thus, maintaining integrity of such joints in case of defect presence and structure overloading is critical to ensure their safe service. To do this, an accurate structural integrity assessment for such DMWJ structure is very important.

Understanding local fracture behavior on the critical regions of such welded joints is essential for conducting an accurate integrity assessment and design. However, due to highly inhomogeneous nature across the DMWJ in terms of microstructure, mechanical, thermal and fracture properties, it is difficult to conduct analytical or experimental fracture investigations on the DMWJs. Only there are limited studies on the fracture behavior of the DMWJs in the literature[5-8]. In addition, in the integrity assessment methods for weld joints in existing codes, such as R6[9], SINTAP and FITNET FFS [10], the weld joints are often simplified as a sandwich composite composed of base metal and weld metal, and the effects of the interface fusion regions between different materials and heat affected zones (HAZs) are usually ignored. In fact, defects in welded structures can occur anywhere, such as in the fusion zone, HAZ, weld, near weld, interface region, base metal, etc. The use of adequate and precise material input parameters (based on the experimental observation of the local damage and fracture process in the joint area) is particularly essential to describe and predict the

critical condition in welded structures [10]. Therefore, the local fracture behavior of the DMWJs should be investigated and understood.
In this study, the local fracture behavior in a real Alloy52M dissimilar metal welded joint between A508 ferritic steel and 316L stainless steel in NPPs were investigated by using the single-edge notched bend (SENB) specimens. The significance of using the local fracture properties in integrity assessment of DMWJs was analyzed.

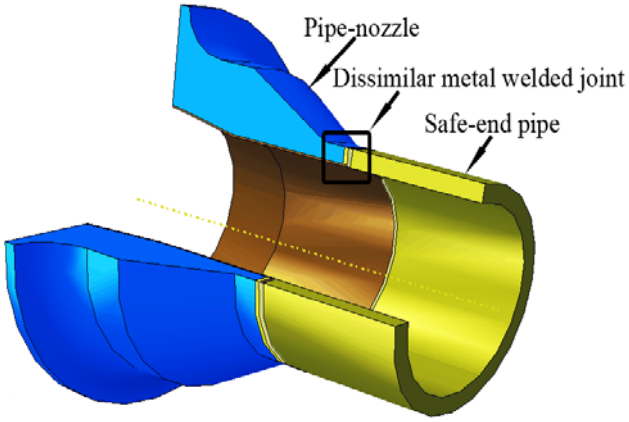

Figure 1. The DMWJ structure for connecting the pipe-nozzle of a reactor pressure vessel to safe-end pipe

2. Experimental procedures

2.1 Materials and fabrication of the DMWJ

A full scale mock up of the DMWJ was fabricated by Shanghai Company of Nuclear Power Equipment in China. The pipe-nozzle material is ferritic low-alloy steel (A508), and the safe end pipe material is austenitic stainless steel (316L). The weld was manufactured by applying a buttering technique and the buttering material as well as weld material is the same nickel-base alloy (Alloy52M), but their manufacture procedures were different. The buttering layer was deposited through an Alloy52M welding wire by automatic gas-tungsten arc welding (GTAW) on the ferritic nozzle face. Then a heat treatment was conducted on the buttering to relieve the residual stress. This buttering layer material is denoted as Alloy52Mb. After buttering, welding was carried out between the buttering layer and the austenitic safe-end pipe by using the GTAW, and the Alloy52M welding wire was also used. Here, this weld metal material is denoted as Alloy52Mw.

2.2 Specimen geometry and crack locations

The single-edge notched bend (SENB) specimen was used for measuring the local fracture properties and observing fracture mechanism in the DMWJ. The SENB specimens with different crack locations were extracted by electric discharge machining from the DMWJ. The initial crack locations and specimen orientation are shown in Fig.2. The cracks 1 and 13 are located in the base metal A508 and 316L, respectively. The cracks 5 and 9 are located in the center of the butter Alloy52Mb and weld Alloy52Mw, respectively. Other cracks are mainly located in the interface regions between materials with complex metallurgical microstructures and inhomogeneous mechanical properties. The interface region cracks include the HAZ cracks in base metals (cracks 2, 6 and 12), interface cracks at fusion lines (cracks 3, 7 and 11), and the near interface zone (NIZ) cracks in weld metals (cracks 4, 8 and 10). The distance of the HAZ and NIZ cracks from the interfaces is 1.5mm. The SENB specimen geometry, size and loading method are typically shown in Fig.3 for the crack 4 specimen.

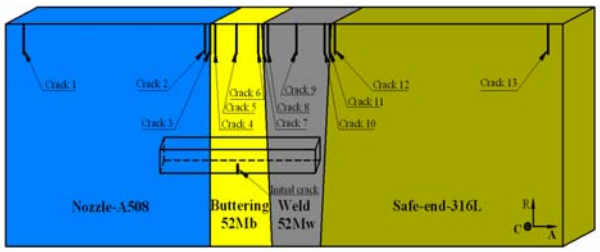

Figure 2. Schematic diagram showing initial crack positions and SENB specimen orientation in the DMWJ (C: circumferential, R: radial direction, A: axial direction)

2.3 Experiments and observations

The fracture tests of the SENB specimens were performed by an Instron screw-driven machine at room temperature. One specimen was tested for every crack location. The quasi-static loading was conducted by displacement controlled mode at a cross-head speed of 0.5mm/min. The load-load line displacement curves were automatically recorded by a computer aided control system of the testing machine. The single specimen method and the normalization technique conforming the ASTM E1820 procedure [11] were used to obtain the J-resistance curve for each specimen. After testing, the tested specimens with a certain crack growth length were sectioned at the mid-plane. One of the cut pieces was polished and etched to reveal damage and fracture patterns in microstructure ahead of the crack tip, which was observed by an optical microscope (OM) and a scanning electron microscope (SEM). Another piece was broken, and the initial crack length and the final crack growth length were measured and the fracture surfaces were observed with the SEM to understand the failure mechanism.

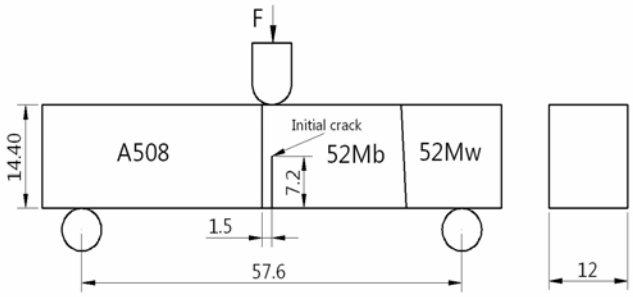

Figure 3. The SENB specimen geometry, size and loading method typically shown by the crack 4 specimen

3. Results and discussion

3.1 Local fracture properties of the DMWJ

The J-resistance curves of the SENB specimens with various crack positions are given in Fig.4. These J-resistance curves reflect local crack growth resistance of different material regions in the DMWJ. It can be seen that the three cracks (cracks 1-3) in A508 region and the two cracks (cracks 9 and 10) in weld Alloy52Mw region have lower crack growth resistance, and which represents local weak zones for fracture in the DMWJ. The fracture resistance of crack 3 at A508/Alloy52Mb interface is lowest. The J-resistance curves of crack 5 in the center of buttering Alloy52Mb and crack 13 in the base metal 316L are highest, and they represents the highest fracture resistance zones in the joint. The J-resistance curves of other cracks (cracks 4, 6, 7, 8, 11 and 12) are located

between the lower crack growth resistance curves (cracks 1,2,3,9 and 10) and the highest crack growth resistance curves (cracks 5 and 10). The cracks 6, 7 and 12 have similar resistance curves. The resistance curves of cracks 4, 8 and 11 are also basically the same, but they are lower than those of the cracks 6, 7 and 12. The local crack growth resistance in the DMWJ is determined by fracture mechanism occurring ahead of the crack tip, and which is mainly related to the microstructure and local strength mismatch of materials at the crack location. This will be analyzed in the following sections.

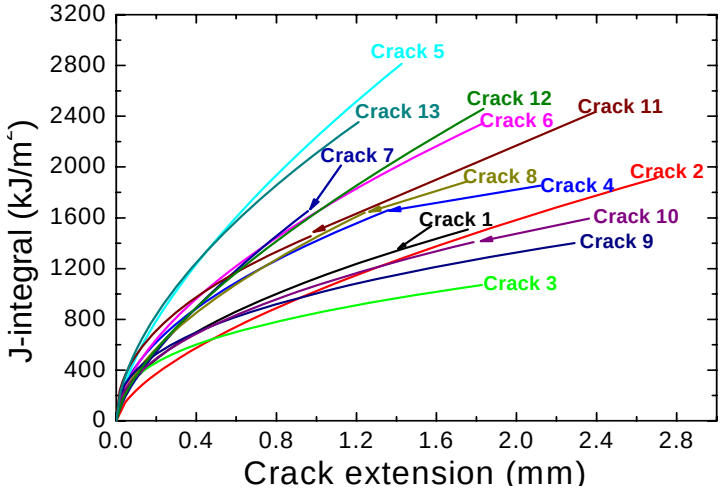

Figure 4. J-resistance curves for the 13 cracks in the DMWJ

3.2 Fracture behavior of typical cracks in the DMWJ

Because of the microstructual and mechanical heterogeneities along the DMWJ, the cracks located in different regions in the DMWJ will have different fracture behavior and leads to different local fracture properties. This can be analyzed as follows.

Fig.5 shows the fracture surface and crack growth path of the A508 HAZ crack 2. Fig.5(a) shows an overview of the fracture surface. In the area A marked in Fig.5(a) in front of initial fatigue precrack, the brittle flat fracture appearance can be seen, as shown by Fig.5(b). This indicates that local brittle fracture initiats and propagates from the the initial fatigue pre-crack tip. In the area B marked in Fig.5(a), a large amout of shollow dimples can be seen, as shown by Fig.5(c). This shows that local ductile fracture has occurred there. Because the area B is behind the area A, this implies that the fracture mode in the crack 2 specimen firstly is brittle fracture, and than changes into ductile fracture. This change in fracture mode also can be observed from the crack growth path shown in Fig.5(d). On the first crack growth length of about 1mm, edges of the crack path are flat, and this is a characteristic of brittle fracture. On the later crack growth path, irregular crack edges can be seen, and this is a characteristic of ductile fracture. This crack path deviation also can be seen by the change of fracture surface from flat (zone I) to rough (zone II) in Fig.5(a). Fig.5(d) also shows that the crack 2 has a deviation path towards A508 base metal (away from the A508/Alloy52Mb interface). The initial brittle fracture of crack 2 is related to the dominated martensite microstructure with higher strength in A508 HAZ. The high strength martensite microstructure generally has low fracture toughness, and the brittle fracture tends to occur under higher crack-tip opening stress. In addition, the A508 HAZ has steep strength gradient, as shown in Fig.6. The left side of crack 2 is near the A508 base metal, and has lower strength (Fig.6). The local higher plastic strain and stress triaxiality will occur at the left side of crack 2, which will induce the crack 2 to grow towards its left side [10]. This crack path deviation may promote the change of fracture mode from the brittle fracture to the ductile fracture. This comes from two factors. One factor is that the crack path

deviation makes the mode I crack change into mixed crack of mode I and II, and this reduces the driving stress for brittle fracture (crack-tip opening stress). Another factor is that the crack path deviates to the material with lower strength (may have higher toughness), and larger plastic deformation may relax local crack-tip opening stress, which can promote development of ductile fracture process. The mixed mechanism of brittle and ductile fracture in the crack 2 specimen leads to the lower fracture resistance curve (Fig.4). In this case, the resistance curve only reflects apparent fracture resistance of A508 HAZ due to the change of fracture mechanism and crack growth path deviation which is mainly related to the local strength mismatch.

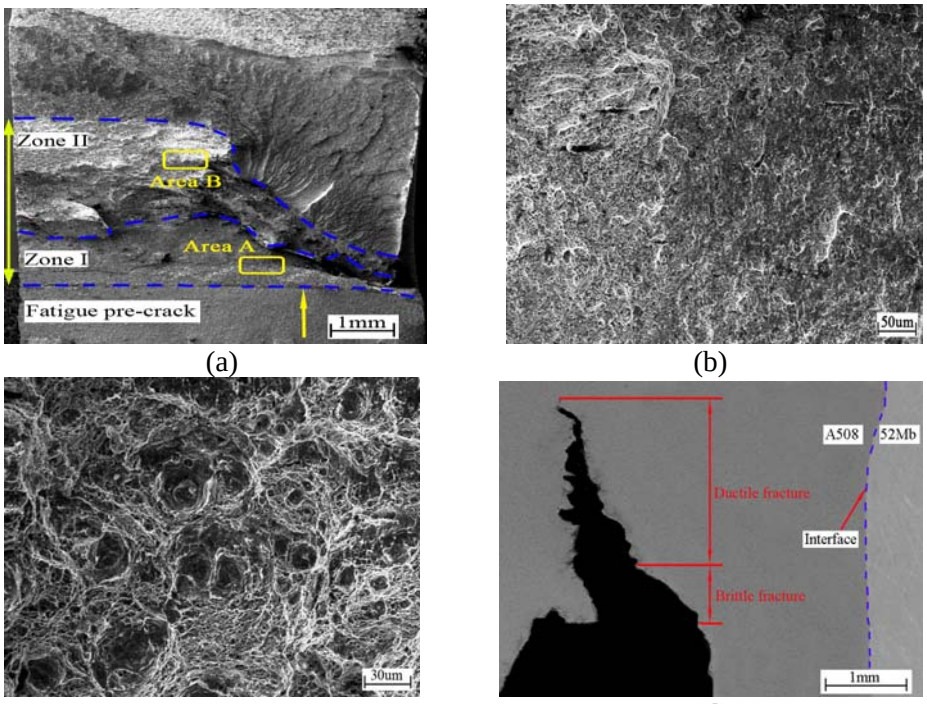

Figure 5. SEM images show fracture mechanism of the A508 HAZ crack 2. (a) overview of fracture surface, (b) higher magnification of area A in (a), (c) higher magnification of area B in (a), (d) crack growth path.

Fig.7 shows the crack growth path and fracture surface of A508/52Mb interface crack 3. It can be observed from Fig.7 (a) that the crack path deviates to the side of 52Mb with lower strength (Fig.6). The fracture surface in Fig.7 (b) displays a large amount of brittle facets with some shallow dimples. This implies that the fracture mechanism of A508/52Mb interface crack 3 is mixed brittle and ductile fracture, but is dominated by brittle fracture. This predominantly brittle fracture may result from two factors. One factor is the local strength mismatch of materials at two sides of crack 3. The essence of the strength mismatch lies on the crack tip plasticity development and effect of the strength difference between different local regions on the deformation pattern ahead of the crack tip [10]. The strength mismatch affects the constraint conditions and stress levels near the crack tip, hence affects the fracture mechanism and crack growth path inevitably. For the A508/52Mb interface crack 3, the Alloy52Mb side has lower strength than the A508 side (Fig.6). During loading the crack 3 specimen, the plastic deformation will firstly appear in the Alloy52Mb material near the interface, and higher stress triaxiality, opening stress and plastic strain will be induced in the Alloy52Mb side with increasing applied load. This has been confirmed by the finite element analyses in the Ref. [13]. The higher stress triaxiality and opening stress will promote development of the brittle fracture with little ductility, and make the crack path deviate towards the Alloy52Mb side. Another factor for producing the predominantly brittle fracture is the predominant martensite microstructure with high strength and low toughness in the A508/52Mb interface region. It can be concluded that the predominantly brittle fracture mechanism causes the lowest J-resistance curve of

the A508/52Mb interface crack 3 (Fig.4). The A508/52Mb interface region is the weakest zone for failure in the DMWJ.

Typical damage patterns ahead of crack tips for the cracks in Alloy52Mb and 52Mw are shown in Fig.8. It can be found that there are a lot of voids distributed on the grain boundarys of columnar crystals near crack, and some grain boundary cracks also have been formed by coalescence of voids. It is believed that the grain boundarys are weak zones for damage and fracture in the weld metals. The crack growth direction is approximately perpendicular to the transverse columnar crystals in buttering Alloy52Mb, but it is approximately parallel to the lognitudinal columnar crystals in weld Alloy52Mw. Fig.8(a) shows that the crack in Alloy52Mb propagtes across the transverse columnar crystal boundary, while Fig.8(b) shows that the crack in Alloy52Mw propgates along the lognitudinal columnar crystal boundary. The columnar crystal orientation relative to crack growth direction apparently affects fracture mechanism and crack growth resistance. For the cracks in buttering Alloy52Mb, the direcrion of the maximum crack-tip opening stress is parallel to columnar crystal boundaries, and the stress normal to the grain boundaries is too low to drive damage and fracture along weak grain boundaries. It needs much high driving force to propagate a crack across columnar crystals, thus the crack growth resistance is high. But for the cracks in weld Alloy52Mw, the direcrion of the maximum crack-tip opening stress is perpendicular to columnar crystal boundaries, and it is ease to drive damage and fracture developing along weak grain boundaries, thus the crack growth resistance is low.

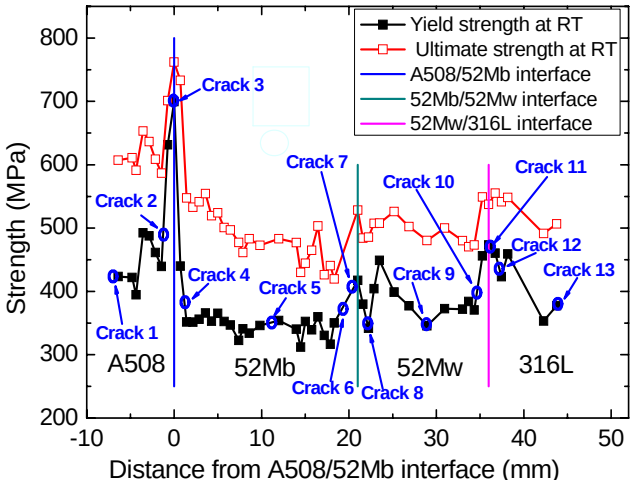

Figure 6. The strength distributions [12] and crack positions across the DMWJ.

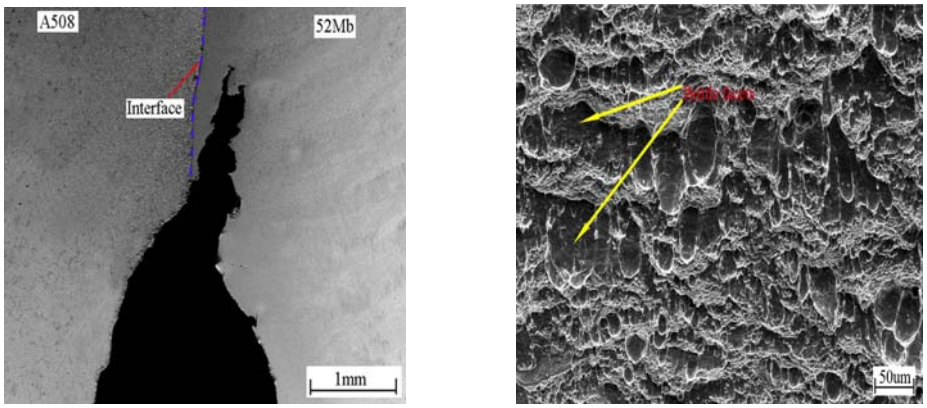

(a) (b)

Figure 7. Crack growth path (a) and fracture surface (b) of A508/52Mb interface crack 3

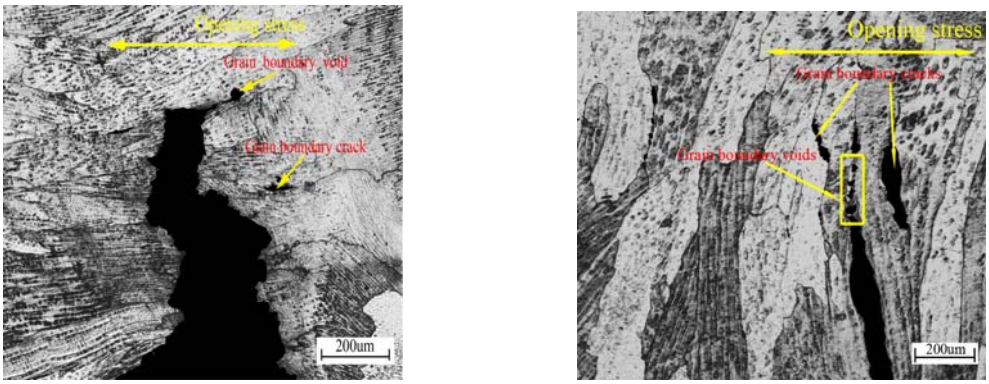

(a) (b)

Figure 8. Typical damage patterns ahead of crack tips for the cracks in Alloy 52Mb (a) and 52Mw (b)

3.3 Integrity assessment for the DMWJ structure

Although there are many methodologies for structural integrity assessment, the failure assessment diagram (FAD) is extremely simplified and convenient which is in the realm of elastic-plastic fracture mechanics. However, the use of the FAD for the DMWJ structure in nuclear power plants is a challenge due to the highly heterogeneous microstructure, mechanical and fracture properties along the joint. When the initial cracks are located at different positions (such as base metal, buttering, weld, interfaces region, HAZ, NIZ, etc.), the crack-tip plastic deformation, damage and further crack growth can occur in any materials and even the crack growth path may change from one material to the other, as shown in Figs. 5(d) and 7(a). In these cases, the crack-tip fracture parameter and plastic deformation behavior of the structure is difficult to define due to the complex strength mismatch effect in the DMWJ, thus the general FADs in current codes cannot be directly and accurately used. It has been found that the strength mismatches in similar metal weld joints have significant effects on the crack driving force, limit load and failure assessment curve [14, 15]. At present, simplified engineering integrity assessment methods have been developed for treating the problem of weld joints, and the concept of equivalent material properties is utilized so that the integrity assessment method for single material can be used for the joints [16-18]. However, the effects of the crack locations and related local strength mismatches in the DMWJ on the local fracture resistance, crack growth paths, failure assessment curves and structural deformation behavior have not been completely understood and accurately taken into account in FADs, and no specific accurate methods exist for the integrity assessment of the complex DMWJ.

In the integrity assessment methods for weld joints in existing codes, such as R6[9], SINTAP and FITNET FFS [10], the joints are often simplified as a sandwich composite composed of base metal and weld metal, and the effects of the interface region, HAZ and NIZ are ignored. In fact, defects in welded structures can occur anywhere, including in base, weld, near weld, HAZ, fusion zone, interface region, etc. The selection of strength and toughness values to be used in the integrity assessment of welded structures has significant implications on the outcome of the analysis. The use of adequate and precise input parameters (based on the experimental observation of the local damage and fracture process in the joint area) is particularly essential to describe and predict the critical condition in such structures [10]. According to the present codes, in the integrity analysis and assessment for the DMWJ structure, the DMWJ will be simplified as a composite composed of four materials (A508 steel, buttering Alloy52Mb, weld Alloy52Mw and 316L stainless steel). For the cracks located in various positions in the DMWJ, only the mechanical and fracture properties of the four materials are used. For the HAZ, interface region and NIZ cracks, if only the mechanical and fracture properties of base metals (A508, 316L) or the weld metal (buttering Alloy52Mb, weld Alloy52Mw) are used, non-conservative (unsafe) or excessive conservative results will then be potentially produced. This can be analyzed as follows for the DMWJ.

To conduct the ductile tearing assessment and leak-before-break (LBB) analysis, a ductile crack growth instability evaluation based on elastic-plastic fracture mechanics should be performed under a maximum loading condition, and a ductile crack growth resistance curve of a material is needed. For the cracks in A508 region, it can be estimated from Fig.4 that if the J-resistance curve of the A508 base metal (crack 1) is used to assess the A508 HAZ crack 2 and the A508/Alloy52Mb interface crack 3, slight non-conservative and unsafe result will be produced, respectively. This is due to that the J-resistance curve of cracks 2 and 3 is slight lower and lower than that of the A508 base metal crack 1, respectively. For the cracks in buttering Alloy52Mb region, it can be judged from Fig.4 that if the J-resistance curve of the buttering Alloy52Mb (crack 5) is used to assess the interface crack 3, NIZ crack 4, HAZ crack 6 and interface crack 7, non-conservative (unsafe) results will be produced due to the highest J-resistance curve of the buttering Alloy52Mb. Especially for the A508/Alloy52Mb interface crack 3 with local crack growth into the Alloy52Mb, the use of the J-resistance curve of the Alloy52Mb will lead to the extreme unsafe result. For the cracks in weld Alloy52Mw region, it can be predicted from Fig.3 that if the J-resistance curve of the weld Alloy52Mw (crack 9) is used to assess the interface crack 7, NIZ crack 8 and interface crack 11, it will lead to excessive conservative assessments. While the use for the NIZ crack 10 will be reasonable due to the similar J-resistance curve of cracks 9 and 10. For the cracks in 316L region, it can be estimated from Fig.4 that if the higher J-resistance curve of the base metal 316L (crack 13) is used to assess the interface crack 11 and HAZ crack 12 with lower J-resistance curve, non-conservative (unsafe) results will be obtained.

In general, the analyses described above demonstrate that without considering the local fracture resistance properties of narrow HAZ, interface region and NIZ , the use of the J-resistance curves of base metals (A508 and 316L) or the weld metals (buttering Alloy52Mb and weld Alloy52Mw) will unavoidably produce non-conservative (unsafe) or excessive conservative assessment results. In most cases, the assessment results are potentially unsafe. A recent study [19] has shown that the resistance to crack initiation and growth is greatly affected by the heterogeneity of the weldment, and the importance of the HAZ for fracture behavior of welded joints was also emphasized. Therefore, in the integrity assessment for the DMWJ structure, it is recommended to obtain and use local mechanical and fracture resistance properties of all regions of the joint if the complex local mismatch situation is a concern. The new integrity assessment methods based on local damage and fracture models also need to be developed for the DMWJs.

4. Conclusion

(1) The local fracture properties in the DMWJ are determined by fracture mechanism occurring ahead of the crack tip, and they are mainly related to the microstructure and local strength mismatch of materials at the crack locations.

(2) The fracture mechanism of A508 HAZ crack 2 and A508/52Mb interface crack 3 is a mixed brittle and ductile fracture, which is related to strength mismatch and predominant martensite microstructure. This fracture behavior leads to the lower crack growth resistance.

(3) The columnar crystal orientation relative to crack growth direction apparently affects fracture behavior and crack growth resistance of cracks in buttering Alloy52Mb and weld Alloy52Mw. The cracks in Alloy52Mb propagate across columnar crystals in a ductile mode, thus higher crack growth resistance is produced. While the cracks in weld Alloy52Mw mainly propagate along columnar crystal boundaries with low resistance in a brittle mode, which leads to lower crack growth resistance.

(4) The crack path deviations are observed for most cracks in the interface regions, HAZs and NIZs. The cracks always deviate to the materials with lower strength, and the crack path deviations are mainly controlled by strength mismatch.

(5) If the local fracture resistance properties could not be used for the heat affected zone (HAZ),

interface and near interface zone cracks, the use of the J-resistance curves of base metals (A508 and 316L) or the weld metals (buttering Alloy52Mb and weld Alloy52Mw) will unavoidably produce non-conservative (unsafe) or excessive conservative assessment results. In most cases, the assessment results will be potentially unsafe.

(6) In the integrity assessment for the DMWJ structure, it is recommended to obtain and use local mechanical and fracture resistance properties of all regions of the joint if the complex local mismatch situation is a concern. The new integrity assessment methods based on local damage and fracture models also need to be developed for the DMWJs.

Acknowledgement

This work was financially supported by the Projects of the National Natural Science Foundation of China (51075149), the National High Technology Research and Development Program of China (2012AA040103), and the Fundamental Research Funds for the Central Universities of China.

References

[1] C. Jang, J. Lee, J.S. Kim, Mechanical property variation within Inconel 82/182 dissimilar metal weld between low alloy steel and 316 stainless steel. Int J Press Ves Pip, 85(2008) 635–646.

[2] J.W. Kim, K. Lee, J.S. Kim, Local mechanical properties of Alloy 82/182 dissimilar weld joint between SA508 Gr.1a and F316 SS at RT and 320℃. J Nual Mater, 384(2009) 212–221.

[3] PWR Material Realiability Project, Interim Alloy 600 Safety Assessment for U.S. PWR Plants, Part 1: Alloy82/182 pipe butt welds. EPRI Report TP-1001491, 2001.

[4] R. Celin, F. Tehovnik, Degradation of a Ni-Cr-Fe alloy in a pressurised water nuclear power plant. Mater Technol, 45(2011)151-157.

[5] K.H. Schwalbe, A. Cornec, D. Lidbury, Fracture mechanics analysis of the BIMET welded pipe tests. Int J Pres Ves Pip, 81(2004)251-277.

[6] C. Faidy, G. Martin, N. Taylor. Nuclear science and technology. Assessment of Aged Piping Dissimilar Metal Weld Integrity (ADIMEW) final report. European commission. 2008. Eur23315.

[7] M.K. Samal, M. Seidenfuss, E. Roos, K. Balani, Investigation of failure behavior of ferritic-austenitic type of dissimilar steel welded joints. Eng Fail Anal, 18(2011) 999-1008.

[8] A. Laukkanen, P. Nevasmaa, U. Ehrnsten, R. Rintamaa. Characteristics relevant to ductile failure of bimetallic welds and evaluation of transferability of fracture properties. Nucl Eng Des, 237(2007)1-15.

[9] R6, Assessment of the integrity of structures containing defects, Procedure R6-Revision 4. Gloucester: Nuclear Electric Ltd. 2007.

[10] M. Kocak. Structural Integrity of welded structures: Process-Property-Performance (3P) Relationship. 63rd Annual Assembly & International Conference of the International Institute of Welding. 2010, Istanbul, Turkey.

[11] ASTM E1820-08a. Standard test method for measurement of fracture toughness. Philadelphia: American Society for Testing and Materials, 2008.

[12] H.T. Wang, G.Z. Wang, F.Z. Xuan, C.J. Liu, S.T. Tu. Local mechanical properties and microstructure of Alloy52M dissimilar metal welded joint between A508 ferritic steel and 316L stainless Steel. Adv Mater Res, 509(2012)103-110.

[13] H.T. Wang, G.Z. Wang, F.Z. Xuan, S.T. Tu. Numerical investigation of ductile crack growth behavior in a dissimilar metal welded joint. Nucl Eng Des, 241(2011)3234-3243.

[14] M. Zhang, Y.W. Shi, X.P. Zhang. Influence of strength mis-matching on crack driving force and failure assessment curve of weldment. Int J Pres Ves Pip, 70(1997)33-41.

[15] T.K. Song, Y.J. Kim, J.S. Kim, T.E. Jin. Mismatch limit loads and approximate *J* estimates for tensile plates with constant-depth surface cracks in the center of welds. Int J Fract, 148(2007)343-360.

[16] K.H. Schwalbe, U. Zerbst, The Engineering treatment model. Int J Pres Ves Pip, 77(2000) 905–918.
[17] Y.J. Kim, K.H. Schwalbe, Mis-match effects on plastic yield loads in idealized weldments. Engng Fract Mech, 68(2001)163–182.
[18] I.A. Khana, V. Bhasin, An estimation procedure to evaluate limit loads of bi-metallic specimens. Int J Pres Ves Pip, 81(2004)451–462.
[19] B. Younise, A. Sedmak, M. Rakin, Micromechanical analysis of mechanical heterogeneity effect on the tearing of weldments. Mater Des, 37(2012)193-201

AE monitoring and structural modeling of the Asinelli Tower in Bologna

Alberto Carpinteri[1], Giuseppe Lacidogna[1,*], Stefano Invernizzi[1], Amedeo Manuello[1]

[1] Department of Structural, Geotechnical and Building Engineering, Politecnico di Torino, 10129, Torino, Italy.
* Corresponding author: Giuseppe.lacidogna@polito.it

Abstract The Acoustic Emission (AE) technique was used to assess the structural stability of the Asinelli Tower, the tallest building in the city of Bologna, which, together with the nearby tower, named Garisenda, is the renowned symbol of the city. AE is a passive, non-destructive structural evaluation technique based on the spontaneous emission of pressure waves by evolving fracture processes. The monitoring program was carried out with the aid of a USAM tool, which is part of the equipment used at the Fracture Mechanics Laboratory of the Department of Structural Engineering at the Politecnico di Torino. This tool makes it possible to conduct a complete analysis of AE signals, acquire a huge quantity of data from on site monitoring, and identify the microcracks triggering the damage processes in a structure.
In the second part of the paper, the results from a preliminary linear analysis are presented, in order to assess the structural behavior of the tower. The cracking and crushing strengths of the masonry have both been compared with the calculated stresses. The numerical analysis gives a valuable picture of the modal response of the tower, providing useful hints for the prosecution of structural monitoring.

Keywords Acoustic emission, monitoring, finite element method, modal analysis, structural assessment.

1. Introduction

For some years, the authors have been conducting research through the application of a material and structure control method based on the spontaneous emission of pressure waves from evolving defects. With the Acoustic Emission (AE) monitoring technique, the ultrasound signals emitted by damage phenomena are received by wide-band piezoelectric (PZT) sensors, i.e., sensors calibrated for a frequency range of between 50 and 800 kHz. The AE technique is non-invasive and non-destructive and therefore is ideally suited for use in the assessment of historic and monumental structures that are subjected to high, long-term loads or cyclic loads, or, more generally, are exposed to seismic risk. Having to identify the fractured or damaged portion of a structure, it is possible to evaluate its stability from the evolution of damage, which may either gradually come to a halt or propagate at an increasingly fast rate. Moreover, if the position of the defects is not known to begin with, it can be located by making use of a multiplicity of sensors and by triangulation, prior to assessing the stability of a structure based on the evolution of damage phenomena. Using the AE technique, the authors have acquired considerable experience in the monitoring of medieval masonry towers and other significant historic buildings [1-5].
The AE technique is ideally suited to control the evolution of structural damage caused by pulse phenomena, such as wind and seismic actions. In this study − a significant zone of the masonry structure to be analysed having been identified − the AE count obtained during the monitoring period was correlated with the frequency of seismic events in the areas around the city of Bologna. The data were used to assess the critical phenomena taking place in the structure with the aim to predict the evolution of damage over time.

2. Structural description of the tower

The authors of the various histories of the city of Bologna all agree in dating the Asinelli and Garisenda Towers to the early twelfth century, but with some minor discrepancies as to the year of construction, as pointed out by Ludovico Savioli in discussing the Asinelli Tower in his *Annali*

Bolognesi, written around the end of the eighteenth century: *"Our chronicles do not converge around the time when it was perfected, some mentioning the year 1111, others the years 1117 and 1119; a majority of them indicate the year 1109"* [6,7].

The Asinelli Tower rises to a height of 97.30 m above the ground. It has a square cross-section, tapering along its height, the sides measuring ca 8.00 m at the base and 6.50 m at the top. From the structural standpoint, the tower can be subdivided into four segments, depending on type of masonry. The thickness of the walls varies from 3.00 m at the foundations to 1.00 m at the top. The first segment, at the base of the tower, is made entirely of selenite blocks. It starts at a depth of ca 1.70 m below ground level and rises to 3.00 m above ground. The substructure of the tower is nearly square, with sides approx. 10.50 m long. The second segment, with sides tapering from 8.15 m to 7.70 m, rises to a height of 34.20 m. The third segment, which constitutes the upper part of the tower and contains the merlons added in the fifteenth century, has sides that gradually decrease in size to ca 6.50m at a height of 81.25 m above ground level. The masonry of the second and third segments is a sacco, i.e., consists of an outer and an inner face, 90 cm and 45 cm thick respectively, enclosing a mixture of rubble, bricks and mortar – and is characterised by an overall thickness of 2.80 m. At the base, up to a height of 8.00 m, the tower is surrounded by an arcade built at the end of the fifteenth century.

The studies conducted in the early twentieth century by F. Cavani [8] revealed that the Asinelli Tower leaned westward by 2.25 m; this is the reason why it is known as the tallest leaning tower in Italy. The latest measurements, made in 2009 by Prof. A. Capra by laser scanning, on behalf of the municipality, showed an overall inclination of 1.51 degrees and a deviation from verticality of 2.38 m. Thus we find that the deviation increased by 13 cm in the course of approx. one century, that is to say at an average rate of 1.30 mm/year. Figure 1 shows the Asinelli Tower and the adjacent Garisenda Tower in the city centre of Bologna. Figures 2 and 3 show the front elevations and the cross-section of the Asinelli Tower and a plan view indicating the zone of application of the AE sensors.

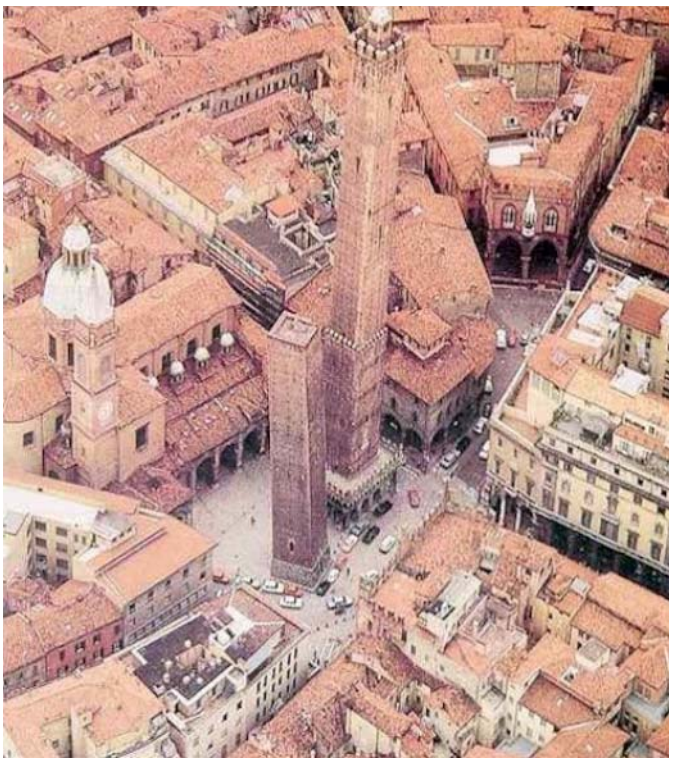

Figure 1. The Asinelli Tower and the Garisenda Tower in the city center of Bologna.

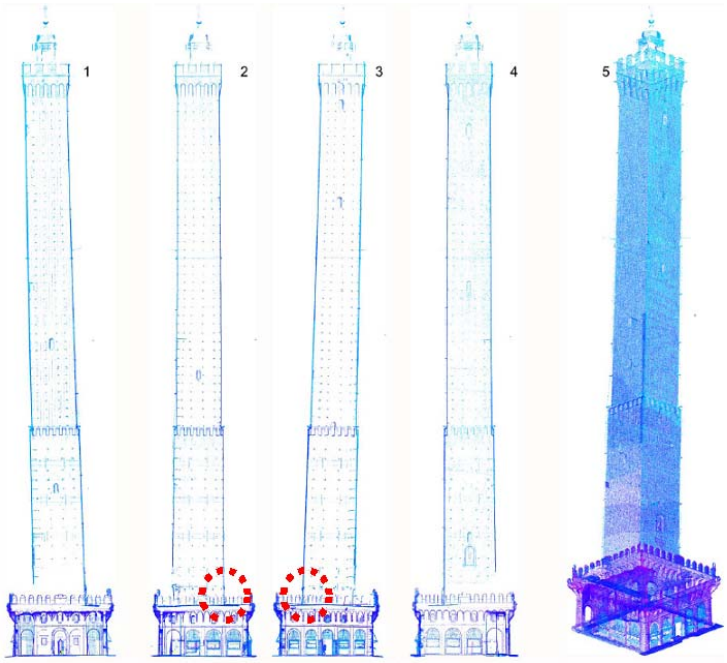

Figure 2. Front views and axonometric view of the Torre degli Asinelli. These views, supplied by the Municipality of Bologna, are taken from the measurements of the exterior of the structure made by Prof. Alessandro Capra by laser scanning. Faces (1) South; (2) East; (3) North; (4) West; (5) Axonometric view. The transducers were applied to the north-east corner of the tower, in the zones marked with a circle.

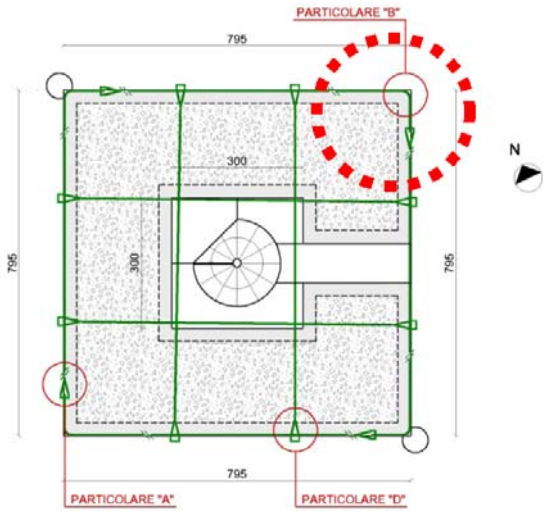

Figure 3. Cross-section of the tower at a height of ca 10 m above ground. Drawing supplied by the Municipality of Bologna. The corner where the sensors were applied is marked with a circle.

3. Monitoring with the Acoustic Emission technique

Only a limited number of sensors were available and hence the AE devices were positioned in a zone that would be both significant for monitoring purposes and easy to reach. In particular, six AE sensors were applied to the north-east angle of the tower at an average height of ca 9.00 m above ground level, immediately above the terrace atop the arcade. In this area, the double-wall masonry has an average thickness of ca 2.45 m (see Figs. 2 and 3). AE monitoring began on 23 September 2010 at 5:40 PM, and ended on 28 January 2011 at 1:00 PM. It was carried on for ca 2915 hours, corresponding to 122 consecutive days. The arrangement of the AE sensors, shown in the photos in Fig. 4, corresponds to the scheme illustrated in Fig. 5. The sensors were glued to the outer surface of the masonry with cold set silicone based adhesives, selected on account of their good ultrasound

signal transmission capacity, resulting in reduced damping at the interface between the masonry and the sensors.
The coordinates of the sensor application points are given in Table 1. The origin of the coordinate system of reference, as can be seen in Fig. 5, is at the bottom corner of the masonry at the intersection with the outer surface of the terrace surrounding the tower.

Figure 4. Photos of the AE data acquisition system on the monitoring site.

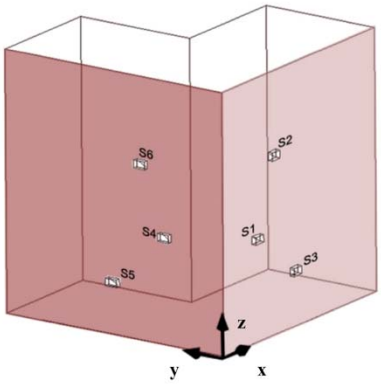

Figure 5. Axonometric scheme of the points of application of the AE sensors at the north-east corner of the tower.

Table 1: Coordinates (in cm) of the points of application of the sensors

Sensors	x	y	z
S1	51.50	0.00	98.00
S2	78.00	0.00	171.0
S3	110.00	0.00	53.00
S4	0.00	63.50	102.00
S5	0.00	121.06	50.00
S6	0.00	89.00	167.00

measurements in cm

4. Results of the Monitoring

The data collected during the monitoring period were analysed to evaluate crack growth and correlate it with the other phenomena considered, e.g., earthquake frequency in the areas around the city, and wind effects on the tower.
In AE analysis, the signals received by the transducers are analysed by means of a threshold detection device that counts the signal bursts exceeding a certain electric tension (measured in volts (V)). Then, cumulative curves are plotted reflecting the number of bursts recorded in a continuous manner during the testing period. This method of analysis, known as Ring-Down Counting, is widely used for defect detection purposes. As a first approximation, in fact, the total count number, N, can be compared with the amount of energy released during a monitoring period based on the

assumption that N grows proportionally to the growth of the damage zone. Needless to say, this assumption will apply only to a slowly progressing damage process. [9].
Figure 6 shows a plot of the cumulative AE count obtained on the basis of the number of events detected per monitoring day. The curve was plotted starting from the date of application of the sensors to the time the sensors were permanently removed. Throughout the monitoring period, the threshold level for the detection of the input signals coming from the PZT transducers was kept at 100 mV. Based on the authors' experience, in fact, this level is the most significant for the detection of AE signals from damage processes in non-metallic materials such as concrete and masonry [1,2,5,9].
From the curve in Fig. 6 it can be seen that the masonry is actually undergoing a damage process. The plot of the cumulative AE count, in fact, is characterised by jumps reflecting sudden increases in N that are seen to occur at certain time intervals. The discontinuities in the cumulative AE count curve denote the critical moments during which the release of energy from the microcrack formation process is greatest.
The AE count hourly distribution chart over a 24 hour time span, as determined for the entire monitoring period, is shown in Fig. 7.

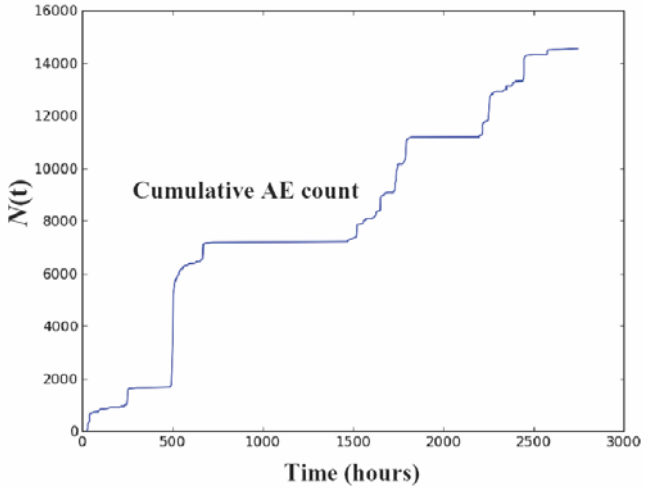

Figure 6. Cumulative AE count based on the data collected at the northeast corner of the tower, from 5:40 PM of 23 September 2010, to 1:00 PM of 28 January 2011.

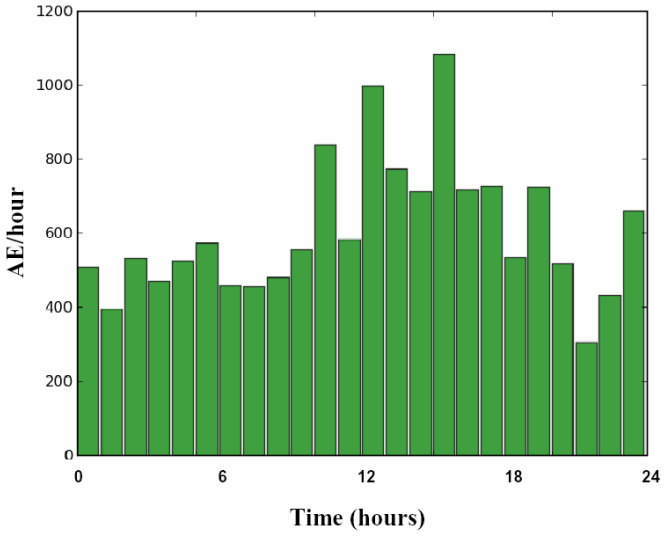

Figure 7. AE count hourly distribution chart over a 24 hour time span, as determined for the entire monitoring period.

4.1. AE and earthquakes

During the monitoring period, frequent seismic activities were recorded in the area around the city of Bologna. Earthquake data were taken from the website of the Istituto Nazionale di Geofisica e Vulcanologia (INGV). From among all the seismic events, only those that might have affected the stability of the tower were taken into account. In particular, the following seismic events were considered: the two strongest quakes –i.e., the one that hit the Rimini area on 13 October at 11:43 PM (4.1 Richter magnitude), and the one recorded in the Modena Apennines on 21 November at 4:10 PM (3.4 Richter magnitude)– and the earthquakes with a magnitude of over 0.5 that occurred within a radius of ca 20 km from the centre of the city.
The chart in Fig. 8 shows the AE count rate per hour, the earthquakes recorded within a 20-km radius from the city centre, and the two strongest quakes that hit the region. All the quakes, the two most important ones (denoted with red dots) and the weaker ones (blue dots), are shown as a function of time of occurrence and magnitude.
Fig. 8 reveals a *correlation between the AE events recorded experimentally and the seismic events.* As can be seen, in fact, the energy peaks measured through the AE count rate almost invariably occurred during a seismic event. In particular, the highest AE count peak (ca 500) was detected on 13 October, at 11:43 PM, when the Rimini area was hit by the 4.1 magnitude quake. Hence, this seismic event is the pulse phenomenon that resulted in the highest damage effect on the tower.
The second strongest earthquake, i.e., the 3.4 magnitude quake that hit the Modena Apennines on 21 November at 4:10 PM, does not introduce any significant change to the chart shown in Fig. 8, since the AE activity detected during this event was rather limited.

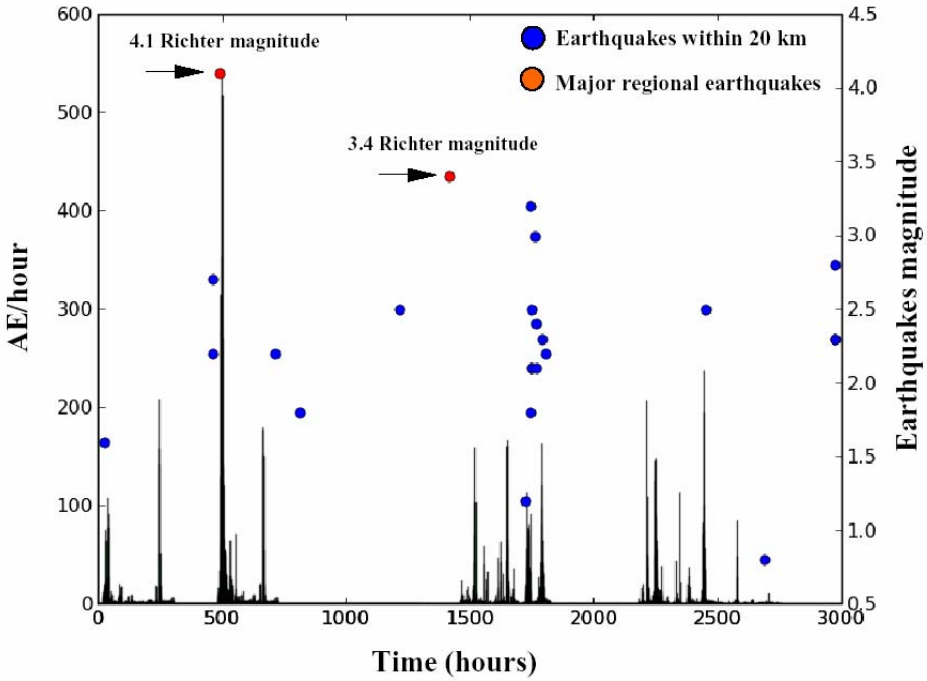

Figure 8. Historic series of the AE differential count and the earthquakes detected within a 20-km radius from the Bologna city centre. The chart also shows the two strongest regional earthquakes, which occurred in Rimini area and in the Modena Apennines. This chart refers to the entire monitoring period.

4.2. AE and wind

Further analyses were also conducted with a view to correlating the intensity of the wind acting on the tower with the AE data recorded during the monitoring period, but no clear correlation has been identified as yet. The measurements of wind velocity were obtained from data acquired by wind

velocity sensors applied at the height of 78 m on the monitored tower, and averaged for each hour. The wind velocity intensities measured during the monitoring period were comprised between 1 and 7 m/s. These velocities were unable to generate sensible aerodynamic loads on the structure.
In the chart of Fig. 9 are represented in detail the AE count rate and the wind velocity in a time window of 30 hours just after the earthquake that hit the Rimini area on 13 October 2010. The graph shows that the peaks in the AE count rate do not correspond with those of the wind velocity.
Moreover, the chart of Fig 10 relates the wind velocities and the AE count rate obtained during all the monitoring period (2915 hours). This graph makes more clear that the two phenomena are completely statistically unrelated.

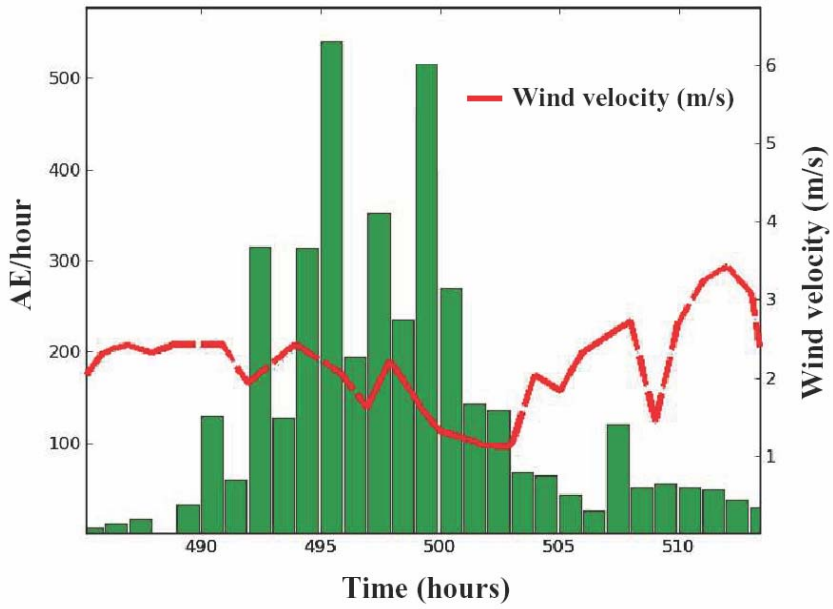

Figure 9: AE rate and wind velocity measurements during the monitoring period in a time window of 30 hours just after the earthquake of 13 October 2010.

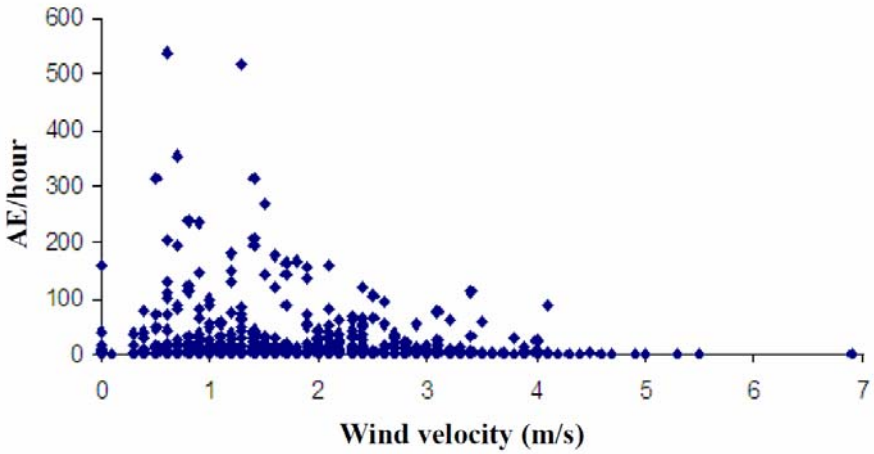

Figure 10: Chart relating the wind velocity and the AE count rate during all the monitoring time, the two time series seem to be statistically unrelated.

7. Preliminary Finite Element Analysis

A preliminary linear elastic finite element analysis has been carried out in order to assess the stress level in the tower, together with the main dynamic characteristics. The finite element model accounts for the three-dimensional geometry of the tower, and is composed of nearly 15300 wedge

and pyramid elements connecting almost 9000 nodes. The mass of the masonry and of the stone in the foundation has been assumed equal to 1800 kg/m^3. A mean value for the young modulus, accounting for the fact that up to a certain height the tower presents three leafs walls with internal filling, has been assumed equal to 5 MPa.
The preliminary linear elastic analysis considered only the self-weight of the tower (Fig. 11a). It was possible to assess that the elastic deformation of the tower is about 8 cm, which is about 1/30 of the present total deviation from verticality.
The level of stress in the masonry of the tower (Fig. 11b) is generally low, although in proximity of the monitored area, the level of vertical stress approach 2.1 Mpa, which can be critical in case of very poor masonry.
The preliminary modal analysis showed that the first mode is bending in the west-east plane, with a resonance frequency of 0.357 Hz (Fig. 11c). The second mode is bending in the orthogonal plane, with an eigen-frequency equal to 0.365 Hz (Fig 11d). The third eigen-frequency is 1.75 Hz, and the fourth is 1.78 Hz. The fifth mode is torsional (Fig. 11e) with an eigen-frequency of 3,07 Hz. Those results agree quite well with more detailed dynamic analyses carried out by other Authors [11].
The maximum vertical stress in the tower is compatible with the acquire rate of acoustic emissions from the monitored region. The fact that the first modal shape tends to increase the stress in the same area agrees well with the increase of acoustic emissions connected with seismic events.

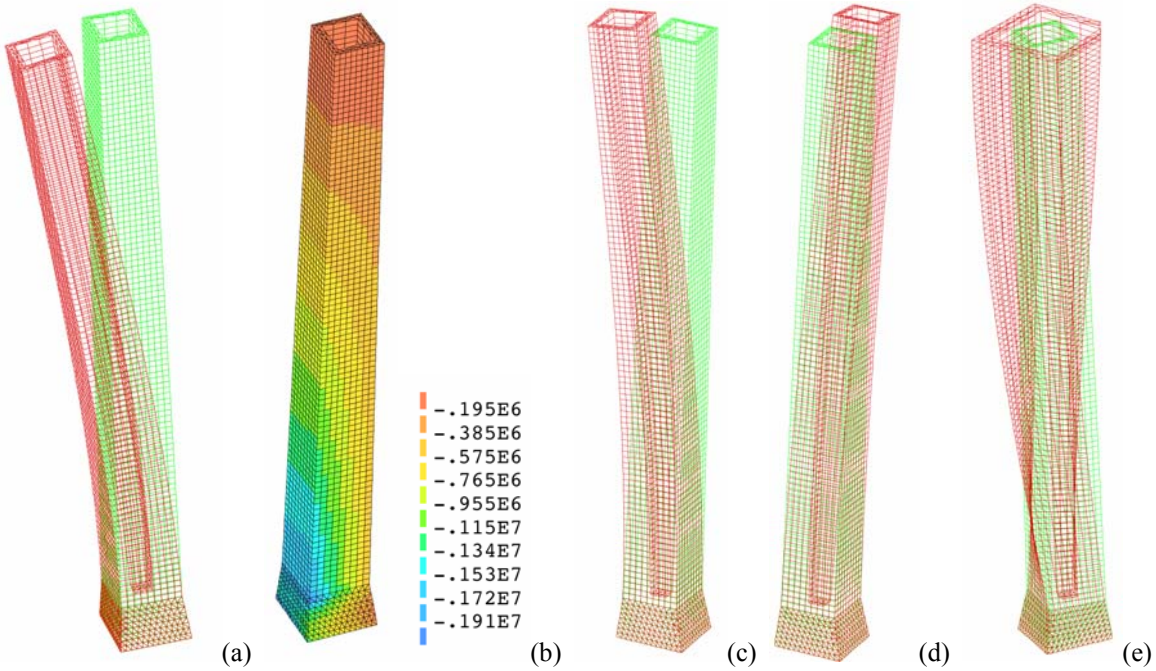

Figure 11. Deformation due to the effect of gravity (a); vertical stress expressed in MPa (b); first modal shape (c); second modal shape (d); fifth modal shape (e).

6. Conclusions

From the monitoring process carried out on a significant part of the *Torre degli Asinelli* it was possible to evaluate the incidence of seismic activity and wind action on the progress of fracture and damage phenomena within the structure.
During the monitoring period a correlation between peaks of AE activity in the structure and regional seismicity is found. The tower, in fact, as in the case of other monitored historical structures built in seismic territory [1,2,5,10], behaved as sensitive earthquake receptor.
Finally, during the monitoring, no statistical correlation was found between wind and acoustic emission.

The presented study suggests that the AE structural monitoring coupled with local earthquake activity can be a tool of crucial importance in damage mitigation of the structure.
In order to arrive at a more comprehensive and objective evaluation of the structural conditions of the tower, the results obtained with the AE technique −that analyses the ultrasound signals coming from microcracks in the masonry− should be supplemented with data obtained on other zones of the structure subject to different stress-strain conditions.
Moreover, earlier studies conducted by the authors with the AE technique on the stability of historic buildings made of stone or brick masonry have shown that the damage process is characterised by appreciable size effects on dissipated energy density. The multiscale aspect of energy dissipation can be addressed with statistical and fractal criteria in order to predict the onset of critical conditions in an actual structure [1,2].
By adopting these methods it becomes possible to introduce an appropriate energy parameter for the assessment of damage propagation in structural elements. This parameter is based on the correlation between the cumulative AE count in an actual structure and the corresponding AE activity measured on different size specimens obtained from the structure and tested up to failure [1,2]. Accordingly, if an opportunity arose to take test specimens from the tower (small cores, 2.5 to 10 cm in diameter, according to a minimally invasive approach), or if it were possible to carry out on-site double-jack tests while acquiring the AE signals, the safety and residual life of the structural parts monitored could be evaluated more effectively.
Additional significant data −as was done in [12] for the Medieval Towers of Alba− are obtained with a FEM numerical modeling of the structure that is able to capture the static effects on damage phenomena of permanent loads and the dynamic effects of seismic events and wind-structure interaction.

Acknowledgements

The financial support provided by the Regione Piemonte (Italy) RE-FRESCOS Project, is gratefully acknowledged. The authors wish to thank the Municipality of Bologna and Eng. R. Pisani for allowing this study on the Asinelli Tower.

References

[1] Carpinteri, A. and Lacidogna, G., “Structural monitoring and integrity assessment of medieval towers”, Journal of Structural Engineering, ASCE, 132 (2006) 1681–1690.
[2] Carpinteri, A. and Lacidogna, G., “Damage evaluation of three masonry towers by acoustic emission”, Engineering Structures, 29 (2007) 1569–1579.
[3] Carpinteri, A. and Lacidogna, G. (Editors), Earthquakes and Acoustic Emission, Taylor & Francis, London 2007.
[4] Carpinteri, A., and Lacidogna, G. (Editors), Acoustic Emission and Critical Phenomena: From Structural Mechanics to Geophysics, CRC Press, Boca Raton 2008.
[5] Niccolini, G., Carpinteri, A., Lacidogna, G. and Manuello, A., ”Acoustic emission monitoring of the syracuse athena temple: Scale invariance in the timing of ruptures”, Physical Review Letters, 106 (2011) 108503/1–4.
[6] Savioli, L. V., Annali Bolognesi, Vol. 3, Bassano, Remondini e figli, Bologna 1784–1795.
[7] Bertocchi, E. and Trussardi, D.C., “Studio delle vicende storiche e dei quadri fessurativi di torri in muratura per la valutazione della loro sicurezza sotto carichi ciclici e di lunga durata”, Degree Thesis, Politecnico di Milano, Supervisors Binda, L. and Anzani, A. 1996.
[8] Cavani, F., “Sulla pendenza e sulla stabilità della Torre degli Asinelli di Bologna”, Accademia delle Scienze, Bologna 1912.
[9] Carpinteri, A. and Lacidogna, G., “Damage monitoring of an historical masonry building by the acoustic emission technique”, Materials and Structures, 39, (2006) 161–167.
[10] Carpinteri, A., Lacidogna, G and Niccolini, G., “Acoustic emission monitoring of medieval

towers considered as sensitive earthquake receptors", Natural Hazards and Earth System Sciences, 7 (2007) 1–11.

[11] Riva P., Perotti F., Guidoboni E. & Boschi E., "Seismic analysis of the Asinelli Tower and earthquakes in Bologna", Soil Dynamics and Earthquake Engineering 17 (1998) 525–550.

[12] Carpinteri, A., Invernizzi S. and Lacidogna, G., "In situ damage assessment and nonlinear modelling of a historical masonry tower", *Engineering Structures*, 27 (2005) 387–395.

Multiscale monitoring of interface failure of brittle coating/ductile substrate systems: a non-destructive evaluation method combined digital image correlation with acoustic emission

Weiguo Mao [1, 2, *] Duojin Wu [1, 2] Wangbin Yao [1, 2] Meng Zhou [1, 2]
Yichun Zhou [1, 2] Chunsheng Lu [3]

[1] Key Laboratory of Low Dimensional Materials and Application Technology, Ministry of Education, Xiangtan University, Hunan 411105, China
[2] Faculty of Materials, Optoelectronics and Physics, Xiangtan University, Hunan 411105, China
[3] Department of Mechanical Engineering, Curtin University, Western Australia 6845, Australia
* Corresponding author: wgmao@xtu.edu.cn and ssamao@126.com

Abstract In this paper, we proposed a non-destructive evaluation method combined digital image correlation (DIC) with acoustic emission (AE) techniques, which was used to *in-situ* monitor interface failure and internal damage of brittle coating/ductile substrate systems under different size scales by bending tests. Measurements of full/local field strain fields by DIC in the segmented coating clearly show typical heterogeneous failure process and successfully clarify several controversial assumptions introduced in theoretical models. AE results effectively reveal the damage evolution of cracking nucleation, propagation and coating spallation of the ceramic coating by combining wavelet transform with traditional parameter analysis under external loads. The conclusions show that there is a good relationship between digital image correlation and acoustic emission signals with the aid of test time during the coating failure, which can be applied to judge cracking formation and coating delamination, and to obtain the most important critical experimental data. As an example, several crucial mechanical properties of a thermal barrier coating system including fracture strength, fracture toughness and shear strength were determined.

Keywords Digital image correlation, Acoustic emission, Brittle coating/ductile substrate, Mechanical properties, Thermal barrier coating

1. Introduction

A system consisting of ductile substrate with functional brittle film/coating layers has been ubiquitous in a variety of applications such as micro-electronics, ferroelectric actuators, thermal and abrasion resistance.[1-4] Owing to mismatch of thermo-mechanical properties between film/coating and substrate, however, such a system is always subjected to residual stresses, which would eventually lead to a structural degradation of coating near interfacial regions. Therefore, how to evaluate the interface adhesion performance of a system and predict its reliability has attracted ever-increasing attention in recent years. To realize optimal design, it is necessary to measure the variation of full/local strain fields, cracking nucleation, propagation and spallation of a coating/film system during tests. However, it is difficult and inconvenient to accurately obtain information at small size scales with conventional strain gauges, displacement and force sensors, and optical microscopes. Recently, several advanced experimental techniques have been available in the investigations of coating failure and delamination. Atomic force microscopy provides a means of accurate mapping of changes in coating sub-surface that are related to the evolution of debonding.[5] Ultrasonic force microscopy was used to identify the locations of decohesion, which is sensitive to the local variation in mechanical compliance.[6] Scanning electron microscope and thermograph have been utilized to detect the damage evolution.[7,8] Unfortunately, these techniques can only be applied to qualitatively characterize the microstructure variation and cracking morphology of coating. It is difficult to provide *in-situ* quantitative stress/strain information and other detailed damage features to study interfacial properties of a coating/film system. Thus, it is urgent to

develop a real-time reliable method to monitor the microscopic failure process of a brittle coating/ductile substrate system and to provide the criteria of coating delamination.

The digital image correlation (DIC) technique, which measures strain fields by tracking random speckle patterns on specimen surface,[9-11] is suitable for continuously detecting micro/nano-scale deformations.[12,13] In addition, accompanied with cracking and coating fracture, the locally stored elastic energy is released in the form of acoustic emission (AE) signals. AE is a passive non-destructive testing technique that relies upon the detection of stress waves propagated through a solid as it undergoes strain. Thus, it is appropriate for monitoring the internal damage evolution of a material.[14,15] In previous works, DIC and AE techniques have been simultaneously applied to study the crack profile, localized plastic strain evolution and full/local strain fields of bulk materials, especially metal alloys with different scales.[16-20] However, precise matches have not been established between AE and DIC techniques to elucidate failure mechanisms of alloys. On the other hand, strain fields and crack profiles of brittle coating/ductile substrate systems are much more complicated than that of bulk materials. To the best of our knowledge, there have been few studies where both DIC and AE techniques are applied to monitor the failure process of multiple coating/film systems.

In this paper, we proposed a combined experimental method of DIC and AE techniques to realize *in-situ* tests of the failure process of brittle film/coating systems under bending tests. The main attention was on how to accurately judge the time and location of cracking formation and coating delamination by synthetically analyzing DIC, AE, and universal testing machine data. A relationship between DIC and AE techniques was established to elucidate interfacial failure mechanisms of brittle coating/ductile substrate systems at small size scales.

2. Experimental

An air plasma sprayed as-received thermal barrier coating (TBC) was selected as a typical brittle coating/ductile substrate system. Well-polished and cleaned SUS304 stainless steel plates of 40 × 20 × 2 mm^3 were used as substrate, on which a Ni–20Cr–10Al–1Y bond coat with thickness of 100 μm and an 8 wt % Y_2O_3 top coating with thickness of 300 μm were deposited, respectively, by air plasma sprayed technique. The experimental set-up is illustrated in Fig. 1. The total of 10 TBC and 5 uncoated substrate specimens were tested under three-point bending at a speed of 0.1 mm/min using the universal testing machine (REGER 2000), DIC instrument (ARAMIS), and AE equipment (SWAE-5) at room temperature. Prior to DIC testing, stochastic patterns were prepared by spraying a thin layer of black and white paint with airbrush guns. A 1624×1236 pixels charge coupled device camera equipped with a lens of 50 mm focal length was used to *in-situ* measure the macroscopic morphology and strain evolution of a region with a sampling rate of 2 images per second. DIC was performed on an image of 4 × 2 mm^2 to determine local strain fields during loading, as shown with a dashed frame in Fig. 1. The facet size was defined to be 90 × 90 μm^2 during tests. Post-processing was achieved with the commercially available DIC software (Aramis) to obtain strain data. The measuring error of strain is less than 0.05%.[9,16]

An AE sensor probe with the resonance of 70–400 kHz was located on the side of substrate, which was utilized as a *real-time* continuous monitor to record signal waves released from fracture

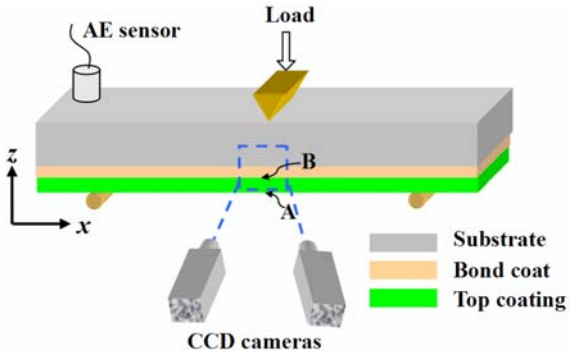

Figure 1. Schematic of three-point bending tests with DIC and AE techniques. The rectangle with dashed blue lines was defined as a region for DIC monitoring.

sources. The AE sampling rate was set to be 1 MHz. The amplitude distribution of AE signals was in the range of 0–100 dB. For TBC tests, we chose 40 dB as the amplitude threshold to avoid the influence of noise and substrate deformation. AE data were analyzed by combining wavelet transform with traditional parameter analysis. The corresponding energy coefficient was calculated by using MATLAB programs with "db8" wavelet.[14] Similarly, the scale was restricted to 5 and all signals were decomposed into 6 levels with the frequency range of D1, D2, D3, D4, D5 and C5.[14] It is found that the peak value of the energy ratio of different frequency bands corresponds to the different failure type, which is similar to the results by Seong *et al.*.[21] Therefore, according to the maximum energy ratio among the frequency bands of AE data, the dominant failure or cracking patterns can be determined with the aid of DIC observations. It is worth noting that, however, all experimental apparatus should be *synchronously* performed to validly judge crack nucleation, propagation and delamination of coating.

3. Results and discussion

3.1 AE features of uncoated substrate

To consider the influence of uncoated substrate deformation on AE signals of TBCs, the characteristics of AE events and load-deflection-time curve are shown in Fig. 2. It is seen that the amplitude and number of AE signals are weak and small even though substrate experiences elastic and plastic deformation under bending. The wavelet analysis indicates that the dominant frequency band of AE signals is D3 for substrate deformation and its corresponding energy ratio is 0.55.

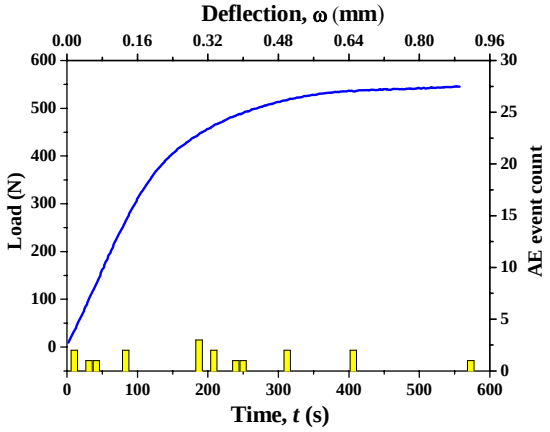

Figure 2. The distribution of AE events of uncoated substrate versus test time and the corresponding loading-deflection curve during bending.

3.2 *In-situ* monitoring of interface strain during bending

As shown in Fig. 1, the brittle coating was located underneath substrate, where fracture occurs first due to undertaking the maximum tensile or bending stress. Thus, the subsurface and interface regions were monitored and denoted with A and B, respectively. Based on the analysis of DIC data, three special points L1, L2 and L3 are extracted and marked in the curve of Fig. 3, corresponding to cracking nucleation and coating delamination. For each point, its maps of lateral strain ε_{xx} and longitudinal strain ε_{zz} are displayed and inset in Fig. 3. When the deflection ω is small, strain maps of ε_{xx} and ε_{zz} represent a homogeneous distribution behavior at the early stage (point L1). When ω increases up to 0.38 mm (point L2), the monitor of DIC shows that three apparent strain concentration regions appear close to coating subsurface. With the increase of ω, micro-cracks rapidly propagated towards the coating/substrate interface and other strain concentration regions continued to initiate near the coating subsurface region, as indicated in inset of strain maps at ω_3 = 0.68 mm (point L3). The DIC micro-observations clearly reveal that vertical cracks firstly form near the coating subsurface and then propagate to the coating/substrate interface as bending load increases. Once arriving at the interface, they gradually deflect into interface cracks and start to propagate within coating along the interface direction. Eventually, the number of surface vertical cracking stops increasing and goes into a saturation state. Partial interface cracks result in coating delamination and subsequent spallation. Thus, there are two main types of cracking patterns: surface vertical cracks and interface cracks (see inset in Fig. 3).

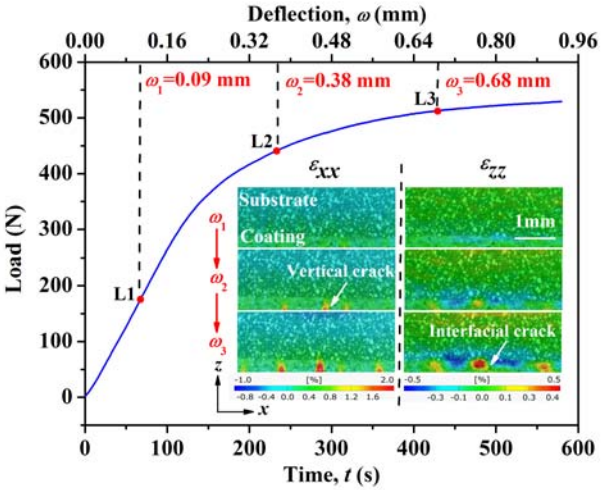

Figure 3. A typical loading-deflection-time curve of TBCs under bending. A series of strain map insets show the evolution of lateral and longitudinal strains in monitored area with the increase of ω, as shown in Fig. 1(a). Here, ω at three points L1, L2 and L3 are equal to, respectively, 0.09, 0.38 and 0.68 mm.

3.3 Failure modes and AE measurements during bending tests

The local stored elastic energy in coating would release due to cracking formation and coating fracture. The evolution of local strain and AE data of two regions A and B were extracted and re-plotted in Figs. 4(a) and (b), respectively. For region A, the magnitude of ε_{xx} gradually increases with the increase of ω. The result of a randomly selected AE signal before coating cracking shows that the dominant frequency band of AE signals is D3 and the corresponding energy

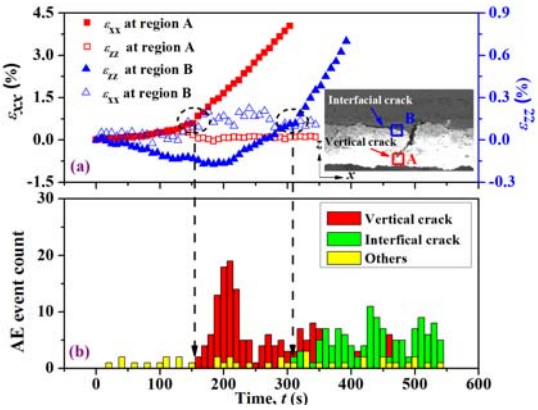

Figure 4. The evolution of local strain and AE signals as a function of loading time during bending tests. (a) The variations of ε_{xx} and ε_{zz} with test time provided by DIC, and (b) the distributions of three different kinds of AE signals with test time corresponding to different failure types.

ratio is 0.55, as presented in Figs. 5(a) and (b), respectively, which means that AE signals are mainly ascribed to substrate deformation before cracking nucleation. It is interesting to observe an abrupt transition at ε_{xx} = 0.75% when the loading time t = 152 s, which implies a surface vertical crack formation in region A. The wavelet analysis of recorded AE data indicates that AE signals change from a single type into two completely different modes (see Fig. 4(b)). The related dominant frequency band of AE signals changes from D3 into D1 and its energy ratio is 0.62, as shown in Figs. 5(c) and (d). It clarifies that before t = 152 s, AE signals are substrate deformation, as marked with yellow in Fig. 4(b). But after t = 152 s, two AE signals are composed by surface vertical cracks and substrate deformation. The new AE events are labeled by red in Fig. 4(b). It is obvious that the amplitude and energy of cracking AE signals are much more than that of substrate deformation. When ω increases, similar surface vertical cracks occur close to coating subsurface and then propagate toward the coating/substrate interface. It is observed from DIC data that the evolution of ε_{zz} in region B displays an apparent excursion and changes from compressive to tensile states at t = 312 s. The reason may be that, after the first vertical crack in region A reaches at the coating/substrate interface (region B), it transformed into a new interface crack. Simultaneously, the analysis of AE signals indicates that there appears another new kind of AE events marked with green in Fig. 4(b). In this phase, the dominant frequency band of AE signals turns from D1 into D2 and the corresponding energy ratio is 0.75, as shown in Figs. 5(e) and (f), respectively. Finally, as ω increases, brittle coating may break into a few small segmented coatings when different interface cracks link with each other. Based on the wavelet transform with traditional parameters and DIC micro-observations, the major features of AE signals of TBCs can be divided into three different phases, including no cracking, surface vertical cracks and interface cracks. Therefore, the related border lines can be determined by these special test time points, as shown in Fig. 4(b). The correlation between DIC and AE data as a function of test time can be established, which is utilized to accurately judge cracking formation and coating delamination of coating/film systems. More importantly, such a method can be used to obtain critical experimental data near transition points,

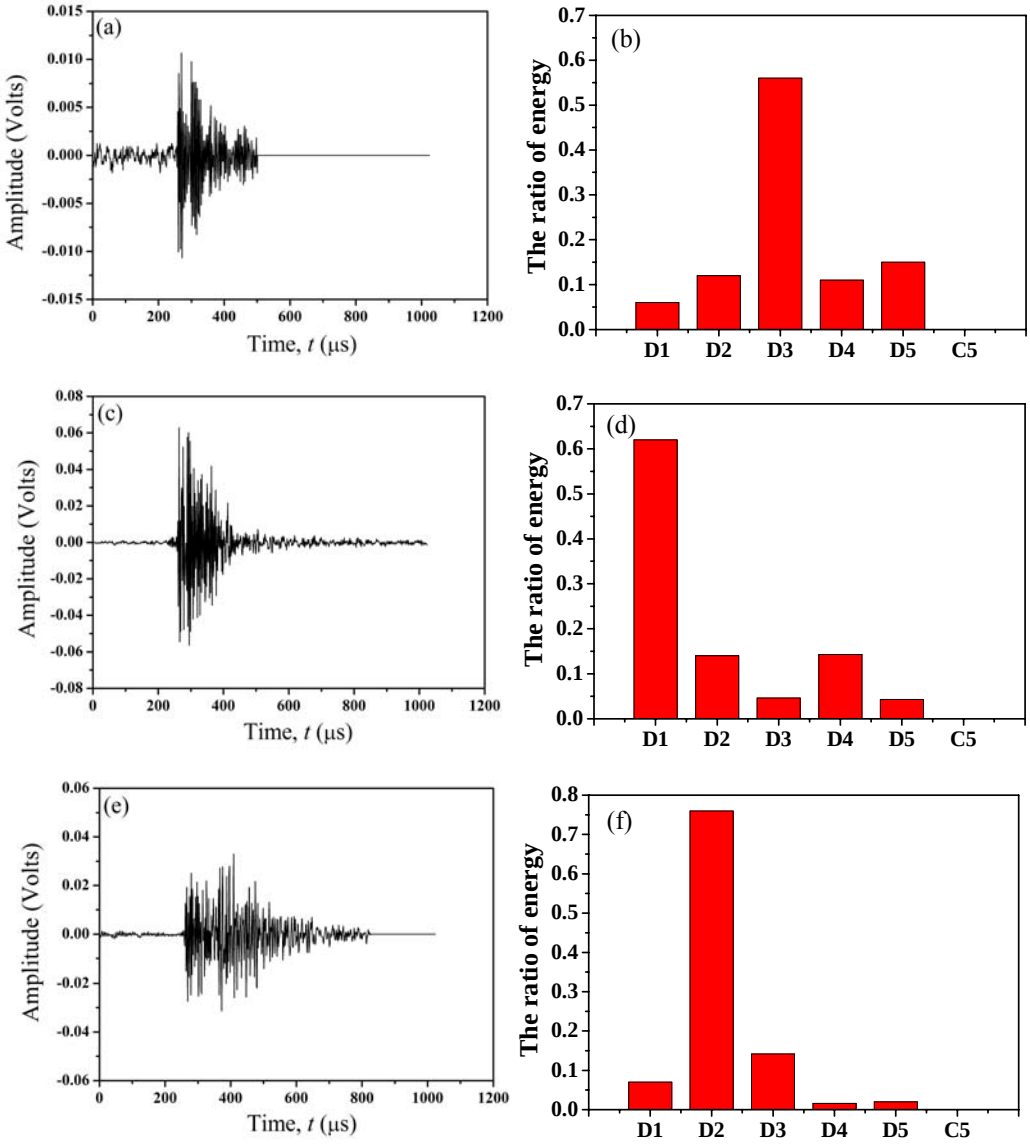

Figure 5. Three typical AE waveforms extracted from different test time points in Fig. 4(b), i.e. (a) primary phase, (c) t = 152 s and (e) t = 312 s, respectively. Figures (b), (d) and (f) are their energy coefficient ratios after wavelet analysis.

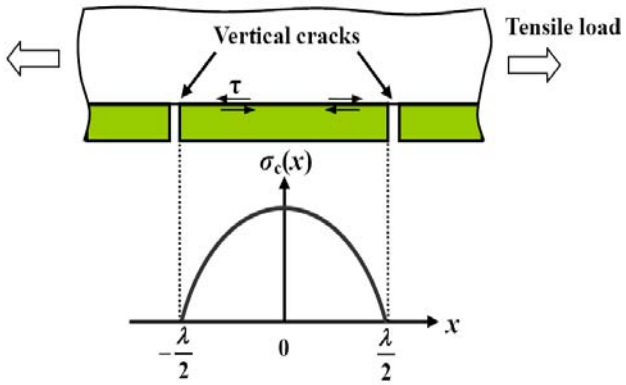

Figure 6. Schematic of the shear lag model for a segmented coating

which are crucial to deduce mechanical properties of coating/film systems, such as interface adhesion strength, fracture toughness and energy release rate.

3.4 Evaluation of interface fracture toughness

Using the critical experimental data obtained above, a shear-lag model was introduced to estimate the fracture toughness of TBCs.[22,23] In our tests, deflection is currently restricted within a very small range. Assumed that the segmented coating mainly undertakes tensile stress,[24] as illustrated in Fig. 6, the stress distribution in a coating segment can be written as [25]

$$\sigma_c(x) = E_c\varepsilon_s\left[1-\frac{\cosh(x/\xi)}{\cosh(\lambda/2\xi)}\right] \tag{1}$$

where λ and $\sigma_c(x)$ are length and tensile stress of the segmented coating, respectively, ε_s is average tensile strain in substrate, and ξ is defined as $\xi=\sqrt{E_c d_1 d_2/G_i}$. Here, E_c is Young's modulus of coating and G_i is shear modulus of interlayer, and d_1 and d_2 are thicknesses of coating and interlayer, respectively. The strain energy accumulated in the coating segment per unit length under tensile stress can be approximated by

$$U=\int_{-\frac{\lambda}{2}}^{\frac{\lambda}{2}}\frac{\sigma_c^2(x)d_1}{2E_c}\mathrm{d}x \tag{2}$$

Inserting Eq. (1) into Eq. (2), the strain energy is

$$U=\frac{E_c\varepsilon_s^2 d_1}{2}\left[\lambda+\frac{\lambda}{1+\cosh(\lambda/2\xi)}-3\tanh(\lambda/2\xi)\right] \tag{3}$$

As the length a of interface delamination grows, the length of bonded part is reduced as $\lambda=\lambda_o-2a$, where λ and λ_o denote the current and initial lengths of the bonded coating. For simplicity, it is assumed that only the strain energy in coating drives delamination.[26] Then, the energy release rate G associated with interface delamination can be written as

$$G=-\frac{\partial U}{\partial a}=\frac{E_c\varepsilon_s^2 d_1}{2}\left\{2+\frac{2}{1+\cosh\left[(\lambda_o-2a)/\xi\right]}-3\sec h^2\left(\frac{\lambda_o-2a}{2\xi}\right)+\frac{2(\lambda_o-2a)\sinh\left[(\lambda_o-2a)/\xi\right]}{\xi\left[1+\cosh\left[(\lambda_o-2a)/\xi\right]\right]^2}\right\} \tag{4}$$

Thus, the interface fracture toughness G_c can be deduced based on the delamination onset strain $\varepsilon_{\mathrm{crit}}$ at $a=0$. For an as-received TBC system, E_c = 10 GPa [27], G_i = 4.5 GPa, d_1 = 300 μm, d_2 = 100 μm, λ_o = 0.83 ~ 1.16 mm, and $\varepsilon_{\mathrm{crit}}$ = 0.64 − 0.72 % by DIC measurements. The interface fracture toughness of TBCs was estimated to be 103−129 J/m^2 by Eq. (4), which are agreement well with available results.[28,29]

4. Conclusions

The interface failure characteristics of TBCs were studied by bending tests with the aid of DIC and AE techniques. An important correlation between DIC and AE was established as a function of test time, which can be used to judge cracking nucleation and coating delamination of TBCs. Compared with traditional strain measurements and crack observation methods, this non-destructive measurement method has an advantage in dynamically monitoring the coating/film failure and assessing their reliabilities at different size scales. Using crucial experimental data, the fracture

toughness of top coating/bond coat interface was estimated to be 103−129 J/m^2 by a shear-lag model. For tensile tests, according to the dominant frequency bands and SEM observations, the correlations between AE signals, fracture types and failure mechanisms can be successfully established. Such a method can be also applied in non-destructive *real-time* evaluation of mechanical characteristics of bulk and coating/film materials at high temperatures.

Acknowledgments

This work has been supported by the National Natural Science Foundations of China (Nos. 11102177, 51172192 and 11002122), the Natural Science Foundation of Hunan Province for Innovation Group (No. 09JJ7004), and the Program for Changjiang Scholars and Innovative Research Team in University (No. IRT1080).

References

[1] N. P. Padture, M. Gell, E. H. Jordan, Thermal barrier coatings for gas-turbine engine applications. Science, 296 (2002) 280-284.

[2] S. Gupta, Q. Zhang, T. Emrick, A. C. Balazs, T. P. Russell, Entropy-driven segregation of nanoparticles to cracks in multilayered composite polymer structures. Nat Mater, 5 (2006) 229-233.

[3] N. Holten-Andersen, G. E. Fantner, S. Hohlbauch, J. H. Waite, F. W. Zok, Protective coatings on extensible biofibres. Nat Mater, 6 (2007) 669-672.

[4] X. L. Zhong, J. B. Wang, L. Z. Sun, C. B. Tan, X. J. Zheng, Y. C. Zhou, Improved ferroelectric properties of bismuth titanate films by Nd and Mn cosubstitution. Appl Phys Lett, 90 (2007) 012906.

[5] M. George, C. Coupeau, J. Colin, J. Grilhe, Atomic force microscopy observations of successive damaging mechanisms of thin films on substrates under tensile stress. Thin Solid Films, 429 (2003) 267-272.

[6] A. P. McGuigan, B. D. Huey, G. A. D. Briggs, O. V. Kolosov, Y. Tsukahara, M. Yanaka, Measurement of debonding in cracked nanocomposite films by ultrasonic force microscopy. Appl Phys Lett, 80 (2002) 1180-1182.

[7] E. P. Busso, L. Wright, H. E. Evans, L. N. McCartney, S. R. J. Saunders, S. Osgerby, J. Nunn, A physics-based life prediction methodology for thermal barrier coating systems. Acta Mater, 55 (2007) 1491-1503.

[8] L. H. Qian, S. J. Zhu, Y. Kagawa, T. Kubo, Tensile damage evolution behavior in plasma-sprayed thermal barrier coating system. Surf Coat Technol, 173 (2003) 178-184.

[9] D. J. Wu, W. G. Mao, Y. C. Zhou, C. Lu, Digital image correlation approach to cracking and decohesion in a brittle coating/ductile substrate system. Appl Surf Sci, 257 (2011) 6040-6043.

[10] P. Luo, Y. Chao, M. Sutton, W. Peters, Accurate measurement of three-dimensional deformations in deformable and rigid bodies using computer vision. Exp Mech, 33 (1993) 123-132.

[11] T. C. Chu, W. F. Ranson, M. A. Sutton, Applications of digital-image-correlation techniques to experimental mechanics. Exp Mech, 25 (1985) 232-244.

[12] C. C. Aydiner, D. W. Brown, N. A. Mara, J. Almer, A. Misra, In situ x-ray investigation of freestanding nanoscale Cu--Nb multilayers under tensile load. Appl Phys Lett, 94 (2009)

031906.

[13] A. Fedorov, W. P. Vellinga, J. T. M. D. Hosson, Effects of tensile and compressive in-plane stress fields on adhesion in laser induced delamination experiments. J Appl Phys, 103 (2008) 103523.

[14] L. Yang, Y. C. Zhou, W. G. Mao, C. Lu, Real-time acoustic emission testing based on wavelet transform for the failure process of thermal barrier coatings. Appl Phys Lett, 93 (2008) 231906.

[15] S. A. Catledge, Y. K. Vohra, S. Woodard, R. Venugopalan, Structural and mechanical properties of nanostructured metalloceramic coatings on cobalt chrome alloys. Appl Phys Lett, 82 (2003) 1625-1627.

[16] H. Louche, K. Bouabdallah, P. Vacher, T. Coudert, P. Balland, Kinematic fields and acoustic emission observations associated with the Portevin Le Châtelier effect on an Al-Mg alloy. Exp Mech, 48 (2008) 741-751.

[17] H. Jiang, F. A. Garcia-Pastor, D. Hu, X. Wu, M. H. Loretto, M. Preuss, P. J. Withers, Characterization of microplasticity in TiAl-based alloys. Acta Mater, 57 (2009) 1357-1366.

[18] S. V. Panin, A. V. Byakov, V. V. Grenke, I. V. Shakirov, S. A. K. Yussif, Multiscale monitoring of localized plastic strain evolution stages in notched aluminum AA 2024 alloy tension specimens by acoustic emission and television-optical techniques. Phys Mesomech, 13 (2010) 203-211.

[19] X. Sun, K. S. Choi, W. N. Liu, M. A. Khaleel, Predicting failure modes and ductility of dual phase steels using plastic strain localization. Int J Plast, 25 (2009) 1888-1909.

[20] J. Kovac, C. Alaux, T. J. Marrow, E. Govekar, A. Legat, Correlations of electrochemical noise, acoustic emission and complementary monitoring techniques during intergranular stress-corrosion cracking of austenitic stainless steel. Corros Sci, 52 (2010) 2015-2025.

[21] S.-H. Seong, S. Hur, J.-S. Kim, J.-T. Kim, W.-M. Park, U.-C. Lee, S.-K. Lee, Development of diagnosis algorithm for the check valve with spectral estimations and neural network models using acoustic signals. Ann Nucl Energy, 32 (2005) 479-492.

[22] S. Frank, U. A. Handge, S. Olliges, R. Spolenak, The relationship between thin film fragmentation and buckle formation: Synchrotron-based in situ studies and two-dimensional stress analysis. Acta Mater, 57 (2009) 1442-1453.

[23] X. C. Zhang, B. S. Xu, H. D. Wang, Y. X. Wu, Analytical modeling of edge effects on the residual stresses within the film/substrate systems. II. normal stresses. J Appl Phys, 100 (2006) 113525.

[24] X. F. Zhu, B. Zhang, J. Gao, G. P. Zhang, Evaluation of the crack-initiation strain of a Cu-Ni multilayer on a flexible substrate. Scripta Mater, 60 (2009) 178-181.

[25] A. P. McGuigan, G. A. D. Briggs, V. M. Burlakov, M. Yanaka, Y. Tsukahara, An elastic-plastic shear lag model for fracture of layered coatings. Thin Solid Films, 424 (2003) 219-223.

[26] S. Tarasovs, J. Andersons, Y. Leterrier, Estimation of interfacial fracture toughness based on progressive edge delamination of a thin transparent coating on a polymer substrate. Acta Mater, 58 (2010) 2948-2956.

[27] W. G. Mao, Q. Chen, C. Y. Dai, L. Yang, Y. C. Zhou, C. Lu, Effects of piezo-spectroscopic coefficients of 8 wt.% Y_2O_3 stabilized ZrO_2 on residual stress measurement of thermal barrier coatings by Raman spectroscopy. Surf Coat Technol, 204 (2010) 3573-3577.

[28] Y. Yamazaki, A. Schmidt, A. Scholz, The determination of the delamination resistance in thennal barrier coating system by four-point bending tests. Surf Coat Technol, 201 (2006) 744-754.

[29] S. S. Kim, Y. F. Liu, Y. Kagawa, Evaluation of interfacial mechanical properties under shear loading in EB-PVD TBCs by the pushout method. Acta Mater, 55 (2007) 3771-3781.

Interfacial mechanics of fiber push-out test: nano-indention technique and cohesive element modeling

Xi Li, Qingsheng Yang *, Zhiyuan Liu

Department of Engineering Mechanics, Beijing University of Technology, Beijing 100124, China
* Qingsheng Yang: qsyang@bjut.edu.cn

Abstract The fiber push-out test is a basic method to probe the mechanical properties of the fiber/matrix interface of a fiber-reinforced composite. In this paper, the interfacial mechanical properties of carbon fiber/epoxy composites are analyzed effectively combing nano-indention technique with cohesive element modeling. Based on the load-displacement curve obtained from the nano-indention experiments, the interfacial shear strength is calculated about 13.7MPa. Furthermore, the finite element method (FEM) model of a fiber-reinforced composite is built in software ABAQUS, in which cohesive zone model is chosen to represent of carbon fiber/epoxy composites interface. The computed results are consistent with experiment data.

Keywords Nano-indentation, Cohesive element, Fiber push-out test, Interfacial shear strength

1. Introduction

Due to the superb properties of high stiffness, high modules, high strength and low thermal, carbon fiber-reinforced composites material are widely used in many fields such as aerospace, electronic and medical engineering [1]. The carbon fiber-reinforced composite is consisting of three components, ie. fiber, matrix and interface. A good interfacial bonding is important to the effective load transfer from matrix to fiber, which helps reducing stress concentrations. Besides, fracture toughness and fatigue life of fiber-reinforced composites also rely on their interfacial properties. Therefore, research on the interface between fiber and matrix can help designing fiber-reinforced composites material with improvement of the above properties [2].

In recent decades, three main methods are used to analysis interfacial bonding strength, namely, single fiber pull-out, single fiber push-out and fiber fragmentation (Figures1-3). The fiber push-out test is the most effective measure method to quantify the in situ characterization of interfacial properties of the fiber-reinforced composite. Nowadays, most experimental investigations of the fiber push-out debonding are based on universal testing machine (UTM), in which the fiber diameter is chosen larger than the one used in actual composites. However, compare to UTM, nano-indentation push-out test has higher precision, in which mechanical properties of interface is investigated under micro-nanoscale, A.Urena[3]studied the interfacial mechanical properties of AA6061(aluminum alloy) reinforced by short carbon fibers coated with different metallic films using the nano-indentation technique and presented the load-displacement curve. In order to obtain accurate interfacial parameter, combined experimental and numerical studies of carbon fiber/polymer composites are more used in this paper. Cohesive zone in finite element analysis (FEA) is a common method to build the interfacial model, which was proposed by Barenblatt[4]and Dugdale[5]. Afterwards, many studies pay attention to mode Ⅰ fracture failure by using cohesive zone simulation. For example, cohesive finite element method (CFEM) is employed by X. Guo [6] to investigate the paradox of a brittle nano-structured interface (nano-grained interface layer) and a ductile layered stainless steel. However, less attention has been paid to cohesive modeling of fiber push-out test. In our work, the interface is built by zero thickness cohesive elements in ABAQUS

software.

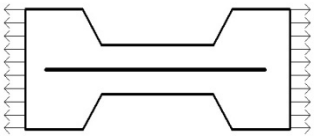

Figure 1. Fiber fragmentation

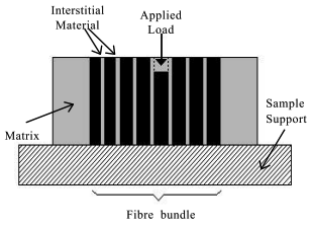

Figure 2. Fiber push-out

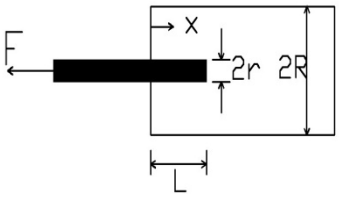

Figure 3. Fiber pull-out

2. Experiment details

Push-out tests were performed on carbon fiber-reinforced epoxy composite material where the fiber volume fraction is about 0.6. The specimens were cut from the original composite by wire cutting machine and the uniform size is 20mm in length, 18mm in width and 10mm in thickness. Afterwards, the specimens are polished by using Sic abrasive paper with 2500 grain size, a thickness 100μm can be obtained. In order to make sure that fiber has enough space to be pushed out, we designed a sample table (as shown in Figure4). There is a circle hole in the centre of sample table; the specimens cut-well were glued on the top face. Besides, the direction of fiber layer should be perpendicular to the sample table.

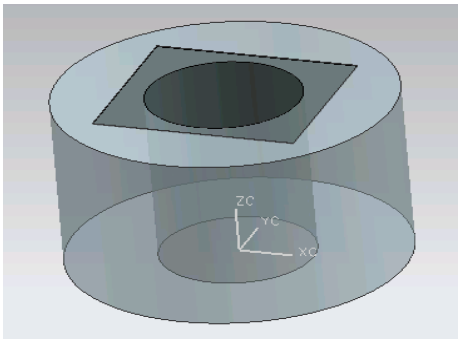

Figure 4. Sample for fiber push-out

The load-displacement curve of a single fiber push-out process is measured by nano-indention instrument and illustrated in Figure 5. It is shown that the whole process can be divided into three stages. In the first stage, fiber displacement is increased linearly with the applied load; and in the second stage, fiber begins to slide from the matrix and crack start to propagate in the interface, until interfacial failure, both the maximum load of fiber debonding and maximum displacement can be achieved in this stage. At last stage, because of indenter contact the matrix, the load continues to grow with the growth of the displacement, this stage means the end of push-out test.

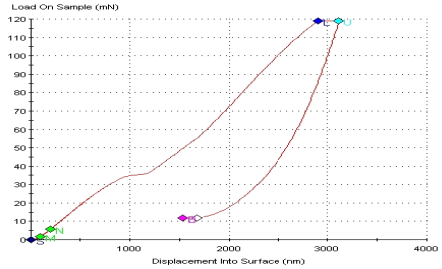

Figure 5. Load-displacement curve of fiber push-out test

In this paper, single fiber nano-indentation push-out tests were performed by using a spherical indenter with a contact diameter of 10μm.The applied load on the fiber was increased at a constant rate of 0.05μm/s. The load-displacement curve was obtained in which the maximum load is 32-35mN and the related displacement is about 1μm.It is assumed that the shear stress was uniform distribution at the interface, so the interface shear strength can be calculated as equation (1).

$$\tau_{max} = \frac{p_{max}}{2\pi RL} \quad (1)$$

where P_{max} indicates the maximum load, R represents fibre radius, L denotes the thickness of the sample, the calculated shear strength is about 13.7MPa.

3. Numerical simulation

3.1 FEM model and material parameters

Currently there are three main kinds of interface element: represented-line spring element [7], represented-Contact element [8] and CFEM. Particularly in CFEM, the damage variable can be specified by an initiation criterion and evolution law, thus the CFEM has been widely used for interface failure and debonding study [9-11].

In this paper, the FEM model is built by commercial software ABAQUS, which consists of carbon fiber, epoxy matrix, and interface (Figure6). Four-node axi-symmetric plane element (CAX4R) is used for both fiber and matrix and four-node axi-symmetric plane cohesive element (COHAX4) is used for interface between them. In total, there are 4097 CAX4R elements and 250 COHAX4 elements. Moreover, the material properties of fiber and matrix are listed in tables 1 and 2.

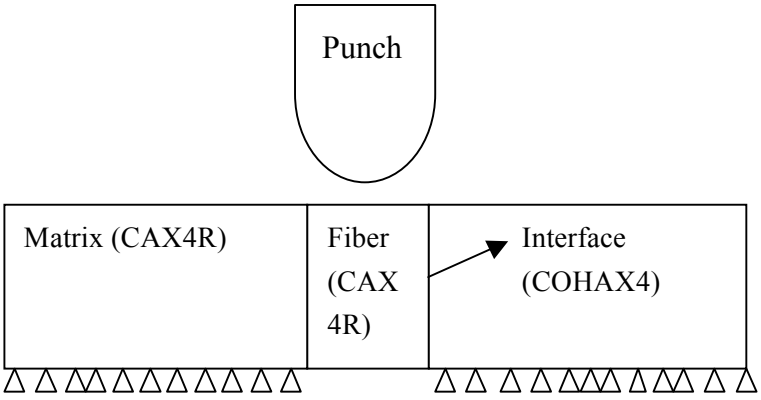

Figure 6 . FEM model

Table 1. Mechanical properties of carbon fiber [1]

Parameter	Carbon fiber(T300)
Transverse modulus (GPa)	15
Axial modulus (GPa)	230
Axial shear modulus (GPa)	27
Transverse shear modulus (GPa)	7
Axial Poisson's ratio	0.013
Fiber radius (μm)	3.5

Table 2. Mechanical properties of epoxy [1]

Parameter	Epoxy 3501
Modulus (GPa)	4.3
Poisson ratio	0.3

3.2 Cohesive zone traction-separation law

In addition, a traction-separation law is implemented to describe the interface cohesive elements between the fiber and the matrix for FEM simulation as shown in Figure 7. The debonding in push-out process is a pure mode II fracture problem. At first, the stress of crack tip in cohesive zone increases linearly with the separation displacement until the displacement reaches the initiation point of damage δ_{init} at where the crack begins to propagate. Afterwards, the tensile stress of crack will be decreased linearly with the displacement. When the stress is reduced to zero at the point of δ_{fail}, the crack is extended along the whole interface surface which leads to the interface failure of the material.

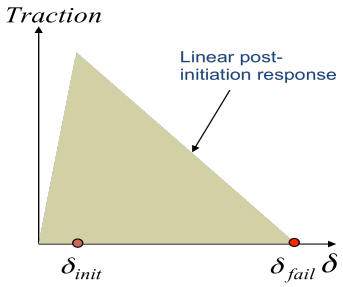

Figure 7. Traction-separation law proposed for interface fracture modeling

The interfacial shear stress τ_{is} can be expressed as equation (2) where τ_{max} is the interfacial crack initiation stress under shear loading condition

$$\tau_{is} = \begin{cases} \frac{\tau_{max}}{\delta_{init}}\delta & 0 \le \delta \le \delta_{init} \\ \frac{\tau_{max}}{\delta_{fail}-\delta_{init}}(\delta_{fail}-\delta) & \delta_{init} \le \delta \le \delta_{fail} \end{cases} \tag{2}$$

Correlating to energy-based fracture toughness and load-displacement curve, the fracture energy can be calculated as equation (3):

$$G_{IIC} = \frac{1}{2}\tau_{max}\delta_f \tag{3}$$

The cohesive element stiffness equal to the material stiffness .The uncoupled elastic constitutive relation is written as equation (4):

$$T = \begin{pmatrix} T_n \\ T_s \end{pmatrix} = \begin{bmatrix} K_{nn} & K_{ns} \\ K_{ns} & K_{ss} \end{bmatrix} \begin{pmatrix} \varepsilon_n \\ \varepsilon_s \end{pmatrix} = \begin{pmatrix} \delta_n \\ \delta_s \end{pmatrix} \tag{4}$$

The damage and fail law of the cohesive elements is according to the traction-separation relation, while the traction-separation relation was defined by the initiation and evolution. Damage initiations rely on the beginning of stiffness degradation. In our work, the linear maximum nominal stress criterion was used. Damage is initiated when the maximum nominal stress ratio reaches unity [10].

$$\max\left[\frac{T_n}{T_n^0}, \frac{T_S}{T_S^0}\right] = 1 \tag{5}$$

where T_n^0, T_S^0 represent the peak nominal and shear stress, the damage evolution law describes the rate at which the effective material stiffness degrades after damage initiation.

4. Numerical results

By numerical simulation, a typical fiber push-out load-displacement curve can be obtained. The whole process a divided into three stages that can be shown in Figure 8, the first stage of curve is mainly fiber elastic deformation occurs. The second stage of curve is a nonlinear relationship, due to the punch increase load on interface characterized by cohesive element damaged and failure, Led to the separation between fibers and matrix. The third stage, the fiber and matrix lose bonding; there is only friction between them.

Compared with previous experimental curve, the reason why the experimental curve different with Simulation curve was attributed to that our work was not consider the contact between punch and fiber, the effect of contact with matrix is meaningless. While debonding force and failure displacement from the simulation and experimental are the same value.

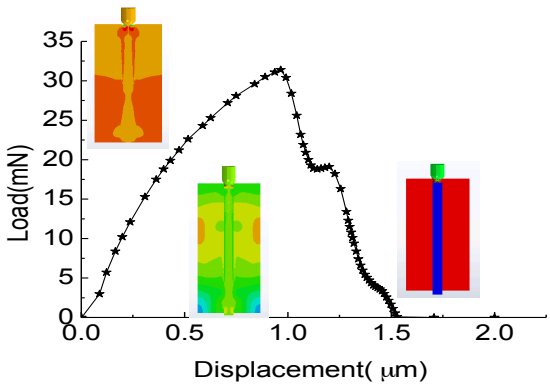

Figure 8. Load-displacement curve of numerical simulation

As the lateral friction will be produced when punch contact fiber, the numerical simulation which fully considered. The coefficient of friction in simulation are 0、0.3、0.6、0.9. The results are shown in Figure 9.

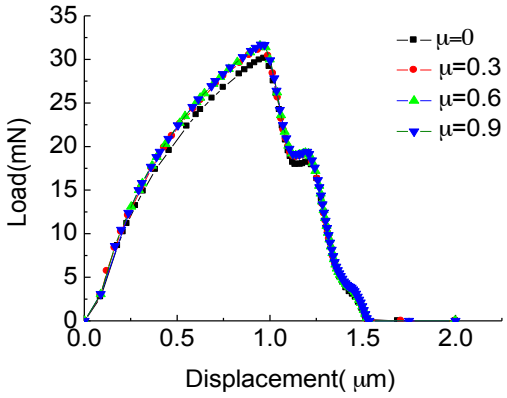

Figure 9. Variation of load with push-out displacement of carbon fibers with different fiction coefficients

Because the interface characterized by cohesive element, wherein the relationship exists between modulus, strength and fracture energy release, therefore, fracture energy release rate is important parameters, its impact is shown in Figure 10.

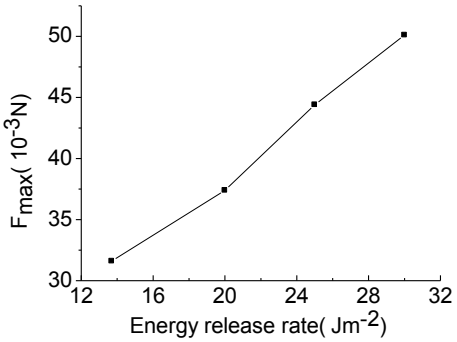

Figure 10. Relation of fracture energy release and maximum debonding force

5. Conclusions

In this paper, the interfacial shear strength of carbon fiber-reinforced composite was investigated by nano-indentation experiment. The interface was also simulated by cohesive element in software ABAQUS. The conclusions are as follows.

(1) The load-displacement curve of carbon fiber push-out derived from experiments is different with the one obtained from the simulation. However, the debonding force and failure displacement are the same from the simulation and experiment as the contact between punch and fiber is ignored.

(2) The effect of lateral friction between punch and fiber can be ignored due to its slight effect on the experimental results.

(3) The maximum debonding force is related to the fracture energy release of cohesive elements and increases with the interfacial strength.

Acknowledegement
The financial support form the from the NSFC under grant #11172012 is gratefully acknowledged

References

[1]Y.Y.Jia,W.Y.Yan.Carbon fiber pull out under the influence of residual thermal stresses in polymer matrix composites. Computational Materials Science. 62(2012)79–86

[2]A.Godara, L.Gorbatikh, G.Kalinka. Interfacial shear strength of a glass fiber/epoxy bonding in composites modified with carbon nanotubes. Composites Science and Technology. 70 (2010)1346–1352

[3]A.Urena,J.Rams,M.D.Escalera, M.Sanchez. Characterization of interfacial mechanical properties in carbon fiber/aluminium matrix composites by the nanoindentation technique. Composites Science and Technology. 65(2005)2025–2038

[4]G.Barenblatt. The mathematical theory of equilibrium cracks in brittle fracture [J]. Advances in Applied Mechanics. 7(1962) 55–129.

[5]D.Dugdale. Yielding of steel sheets containing slits. Journal of the Mechanics and Physics of Solids .8(1960)100–104

[6]X.Guo, G.J.Weng, A.K.Soh. Ducility enhancement of layered stainless steel with nanograined interface layers. Computational Materials Science. 55(2012)350-350

[7]N.Chandra,C.R.Ananth. Analysis of interfacial behavior in MMCS and IMCS by the use of thin slice push-out tests. Composites Science and Technology. 54(1995)87-92

[8]V.T.Bechel, N.R.Sottos, A comparison of calculated and measured debond length from fiber push-out tests. Composites Science and Technology. 58(1998)1727-1739.

[9]G.Lin, G.Geubelle, P.H. Sottos, N.R. Simulation of fiber debonding with frictionin a model composite push-out test. International Journal of Solids and Structures. 38(2001)8547–8562.

[10]J.H.You, W. Lutz. Fiber push-out study of a copper matrix composite with an engineered interface: Experiments and cohesive element simulation. International Journal of Solids and Structures. 46 (2009)4277–4286

[11]R. Sharma, P. Mahajan. Fiber bundle push-out test and image-based finite element simulation for 3D carbon/carbon composites. Carbon. 50(2012)2717–2725

Interfacial Delamination of SMA Reinforced Composite under Low Velocity Impact

Jun Luo[1,*], Dongjie Liang[1]

[1] Department of Mechanics , Huazhong University of Science and Technology, Wuhan 430074, China
* Corresponding author: luojun.l@gmail.com

Abstract Former studies shows that the impact resistance of composite can be significantly enhanced by insterting shape memory alloy (SMA) fibers. The interfacial delamination behavior of SMA reinfored composite plate is numerically studied with the cohesive zone model. Our results indicate that the interfacial damage of SMA reinforced composite plate is apparently decreased compared with traditional composite plates.

Keywords Interfacial delamination, SMA, Composite, Low velocity impact

1. Introduction

As is well known, fiber reinforced compoistes (FRC) are prone to impact damage. The scientific community has sought different ways to improve the impact performance of FRC. Shape memory alloys such as NiTi alloys, have long been known as a class of smart materials, which possess pseudoelastic behavior and shape memory effect, depending on the temperature of the enviroment. When the SMAs display pseudoelastic behavior, the recovery strain can reach 8%. A large amount of deformation energy can be absorbed in a loading cyclic. This special character of SMAs has importatn potential applications to improve the mechanical performance of FRCs.

The idea of inserting SMA fibers into FRC was initilized by Paine and Rogers in 1994 [1]. They revealed by experiments that the damage of the composites can be largely reduced by inserting SMA fibers. A large amount of the deformation energy was absorbed by the SMAs during the deformation process. Jia et al.[2] further studied the impact behavior of SMA reinforced composites. Their study also shows that the impact behavior of the composites is largely enhanced due to the pesudoelastic behavior of the SMA fibers. Lau [3] and his collabrators studied the interfacial delamination behavior of SMA reinforced composites both experimentally and theoretically. Again, the beneficial effects of the inserting SMA fibers were identified. This paper studies the interfacial delamination of SMA reinforced composites by finite element analysis. The cohesive zone modelling is adopted to simulate the delamination behavior of the composite laminates. The influences of the position of the inserted SMA fibers and the enviroment temperature on the delamination behavior of the composites under low velocity impact are systematically studied.

2. FEM Models and Simulations

Former studies have shown that matrix fracture and interfacial delamination are two main damage modes of fiber reinforced composites. In order to see how the SMA fibers enhance the delamination behavior of the composite laminates, we adopt the FEM model shown in Figure 1.. In Figure 1., eight layers of composite laminates are considered. For the upper four layers, the fibers are along

the zero degree direction while for the lower four layers, the fibers are along the 90 degree direction. Inbetween the middle two layers, the cohesive elements are inserted to simulate the interfacial delamination.

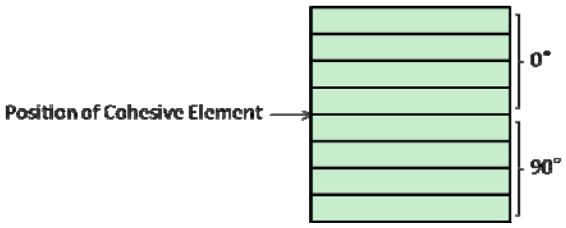

Figure 1. The numerical model to simulate the interfacial delamination.

A cylindrical projectile with a spherical head is adopted to introduce the low velocity impact. The velocity of the projectile is calculated according to the impact energy and the mass of the projectile. We assume the the cross section of the SMA fibers is of rectangular shape. The thickness of of the SMA fiber is the same as that of the laminate. In the simulation, we assume the projectile is rigid. In the impact zone, the mesh of the FE model is refined. The mesh of the FE model is shown in Figure 2.. The simulation was conducted on the finite element software ANSYS/LS-DYNA.

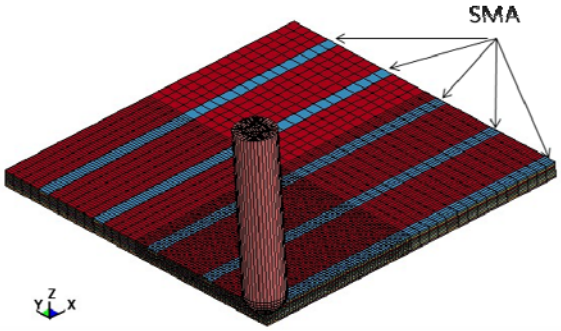

Figure 2. The mesh of the FE model.

In order to simulate the pseudoelastic behavior of NiTi SMA, we adopt the constitutive equation given by Kim et. al. [4]. The constitutive relation of the NiTi SMA is dependent upon the environment temperature. As only limited experimental results are available, only three temperatures are adopted, i.e., 350K, 370K and 390K, as shown in Figure 3..

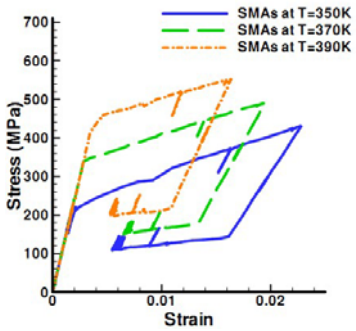

Figure 3.The constituve behavior of SMA under different temperatures [4].

3. Results and Discussions

In order to validate our simulation, we assume there are no SMA fibers inserted in the FE model. The shape of the delaminated zone is then recorded. The simulated results show that the shape of the delaminated zone is consistent with the experimental measurements, which implies that the FE model is reliable to simulate the interfacial delamination of the composite laminates. After that, the influences of the SMA fibers on the delamination behavior is further studied.

Figures 4 and 5. compares the delamination area and maximum deflection of the laminate during the impact process. In these two figures, the SMA fibers are inserted into the third and sixth layers respectively. From these two figures, we can see that the delamination behavior of the composite laminates can be largely enhanced by inserting the SMA fibers.

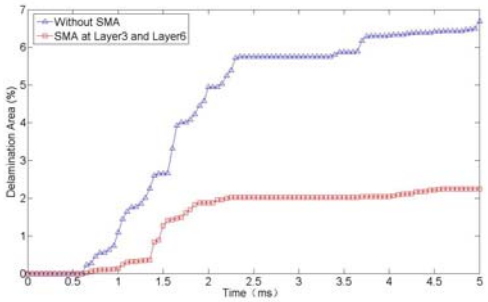

Figure 4. The time history of the delamination ratio. The impact energy is 4J.

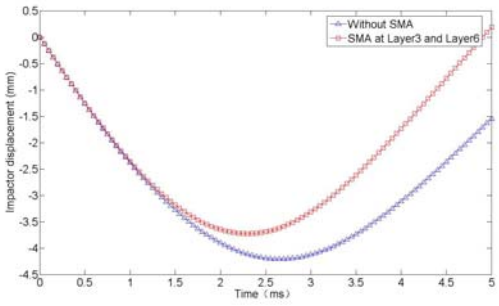

Figure 5. The deflection of the compoiste plate. The impact energy is 4J.

The delamination behavior of the composite laminates under different temperatures are also simulated, as shown in Figure 6.. From Figure 6., we can see that the delamination area under different temperatures doen't change much. This is due to the fact that the mechanical behavior of the SMA fibers in the temperature range 350K-390K doesn't change significantly. It is believed that the temperature will influence the delamination behavior more significantly when the temperature changes in a larger range.

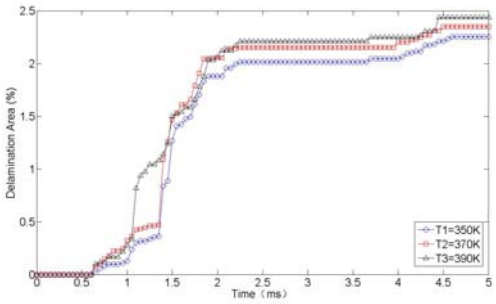

Figure 6. The delamination ratio under different temperatures. The impact energy is 4J.

In Figure 7, the position of the inserted SMA fibers are studied. In Figure 7., the SMA fibers are inserted in the sixth, seventh and eighth layer respectively. We can see that as the position of the SMA fibers is further from the impact point, the beneficial effects of the SMA fibers to prevent delamination become more pronounced.

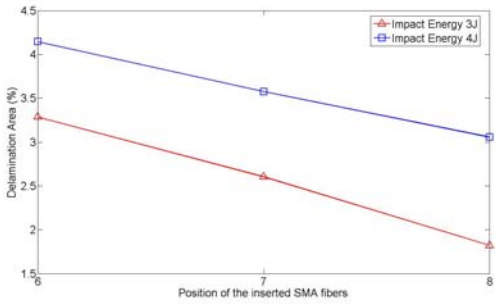

Figure 7. The influence of the position of the SMA fibers on the delamination ratio.

References

[1] J.S.N. Paine and C. A. Rogers, The Response of SMA Hybrid Composite Materials to Low Velocity Impact. J Intellig Mater Sys Struct, 5 (1994) 530-535.

[2] H.Y. Jia, L. F. Ellis, R. L. Rogers. Impact energy absorption of shape memory alloy hybrid composite beams. Collection of Technical Papers, AIAA/ASME/ASCE/AHS/ASC Structures, Structural Dynamics & Materials Conference, 1997, 917-926.

[3] K.T. Lau, H. Y. Ling, L. M. Zhou, Low velocity impact on shape memory alloy stitched composite plates. Smart Mater Struct, 13 (2004) 364-370.

[4] E.H. Kim, I. Lee, I.H. Roh, I.H. Choi, K.N. Koo, Effects of Shape Memory Alloys on Low Velocity Impact Characteristics of Composite Plate. Composite Struct, 93 (2011) 2903-2909.

ECCI and EBSD Study of Subsurface Damages in High Speed Turning of Inconel 718 under Different Tools and Machining Parameters

Zhe Chen[1,*], Ru Lin Peng[1], Jinming Zhou[2], Johan Moverare[1], Volodymyr Bushlya[2], Sten Johansson[1]

[1] Division of Engineering Materials, Linköping University, 58183 Linköping, Sweden
[2] Division of Production and Materials Engineering, Lund University, 22100 Lund, Sweden
* Corresponding author: zhe.chen@liu.se

Abstract Inconel 718 is a Ni-based superalloy that can perform excellently at elevated temperatures. However, surface and subsurface damages in the form of microstructural and property changes and tensile residual stresses are common in a machined Inconel 718 component because of its poor machinability. Such damages have a significant influence on performance and the life time of the part. To characterise microstructural damages and understand how they are correlated to machining conditions are not only important for the evaluation of surface integrity but also for the optimization of machining operations to minimise effects from the machining process. This paper uses the ECCI (electron channelling contrast imaging) and EBSD (electron back scatter diffraction) methods to study the effect of cutting tools and cutting speeds on subsurface plastic deformation of machined Inconel 718. When turning at 200 m/min, a comparable level of plastic deformation was found under the surface machined with uncoated cubic boron nitride (CBN), titanium nitride coated CBN and whisker reinforced alumina (WRA). With an increase in cutting speed, the plastic deformation depth increased, and uncoated CBN tools showed superior performance in term of subsurface microstructure alterations compared to the other tool materials.

Keywords Inconel 718, High speed turning, Surface integrity, Plastic deformation, EBSD

1. Introduction

Superalloys which can maintain high performance at elevated temperatures are widely used in aerospace, automotive, and power industries. Ni-based superalloys are outstanding members in this big family because of their high resistance to corrosion, mechanical and thermal fatigue, mechanical and thermal shock, and creep at high temperatures [1, 2]. However, Ni-based superalloys are difficult-to-cut materials due to their superior mechanical properties and the low thermal conductivity. High cutting heat tends to generate in the contact area between cutting tools and the component during machining processes. The high temperature which can be in excess of 1200 °C leads to rapid tool wear because of softening of tool materials [3, 4]. These characterizations consequently result in surface damages, and eventually affect the mechanical performance and service life of final products. In industries, the finish machining of Ni-based superalloys is generally performed by using traditional cemented carbide tools at low cutting speeds (30-90 m/min) to maintain a reasonable tool life [5]. However, in recent years, more aggressive cutting conditions, such as higher cutting speeds, are promoted for the purpose of increasing production efficiency and reducing manufacturing costs. These accelerate the application of new tool materials like whisker reinforced ceramics (WRC) and cubic boron nitride (CBN) [3, 6, 7]. WRC tools can maintain a high hardness at elevated temperatures and the toughness is dramatically improved by adding whiskers of silicon carbides. The achievable cutting speed varies from 200 m/min to 750 m/min, depending

on the hardness of the superalloy [8]. Compared to WRC tools, CBN tools have a better strength and resistance to fracture but poorer chemical stability [7, 8]. By applying coatings, a diffusion barrier forms which can suppress the chemical wear of CBN tools [9].

During high speed machining operations, the alloy will be exposed to high thermal and mechanical fields which can lead to microstructure alterations near the surface, such as plastic deformation, phase transformation and recrystallization [10-12]. These alterations play a significant role in determining the final fatigue strength of the machined component [13]. Therefore, the surface integrity provided by using these novel machining tools should be investigated in order to predict the quality of machined components. The aim of this study is to evaluate and compare microstructure alterations with focus on the plastic deformation under the machined surface produced with uncoated CBN, coated CBN and WRC tools at high cutting speeds.

2. Experimental details

Solution annealed and aged Inconel 718 with 45HRC hardness was chosen for this study. The chemical composition is given in Table 1. A bar with 70 mm diameter and 200 mm in length was machined at finishing turning conditions. Cutting tools consisted of uncoated CBN (UCBN), titanium nitride-coated CBN (CCBN) and whisker reinforced alumina (WRA). UCBN and CCBN tools have low CBN contents (approximately 50% vol.). The thickness of the titanium nitride coating was 2 μm. Whisker reinforced alumina inserts with honed cutting edge and 0.1×20° chamfer were employed. The insert was mounted in the tool holder provided 6° inclination and -6° rake angle. Coolant was used throughout all cutting tests. Two cutting speeds, v_c =200 m/min and 350 m/min, were selected. The cutting feed rate f =0.1 mm/rev and the cutting depth a_p =0.3 mm, were constant for all tests. Cutting forces in the cutting, feed and radial directions were measured with a force dynamometer, Kistler 9121.

Table 1. Chemical composition (wt. %) of Inconel 718

Ni	Cr	Nb	Mo	Ti	Al	C	Si	Fe
53.8	18.1	5.5	2.9	1	0.55	0.25	0.04	Balance

The ECCI (electron channelling contrast imaging) technique is based on variations of the collected backscattered electrons intensity, and observed channelling contrast is attributed to lattice misorientations introduced during fabrication or deformation processes [14]. The EBSD (electron back scatter diffraction) technique can be used to quantitatively measure the extent of plastic deformation beneath the machined surface by offering grain orientations as well as information about intragranular misorientations [15]. In this study, ECCI and EBSD techniques were used to characterize microstructure and measure the deformation intensity and depth. All these studies were conducted on a Hitachi SU-70 FED electron scanning microscope installed with an EBSD set-up. Results of the density of low angle grain boundaries were obtained using the Channel-5 software from HKL technology.

3. Results and discussions

3.1 Subsurface microstructure

Typical microstructure alterations introduced during the machining process are presented in Fig. 1a. Based on the observed morphology, four obvious zones can be identified in the machined subsurface region [16]. The very thin layer (less than 1 μm) close to the top surface is the heat affected zone. The microstructure was strongly affected by the heat generated during the cutting process, as a consequence of the high cutting speed. The high resolution image shows that the structure in the heat affected zone is highly refined with nano-scaled grain size which is much smaller than the grain size of the bulk material (Fig.1b). This ultrafine nanostructure corresponds to the white layer often found after high speed cutting [17]. The formation of the white layer is generally attributed to a high cutting temperature followed by rapid cooling or severe plastic deformation [18]. Beneath the heat affected zone, the severe deformation can be characterized by bending and elongation of grains, grain boundaries and slip bands towards the cutting direction. This morphology varies as the depth increases. In the slight deformation zone, only some slip bands can be observed. The intensity of the plastic deformation declines following the temperature and mechanical load gradient from the surface to the bulk material.

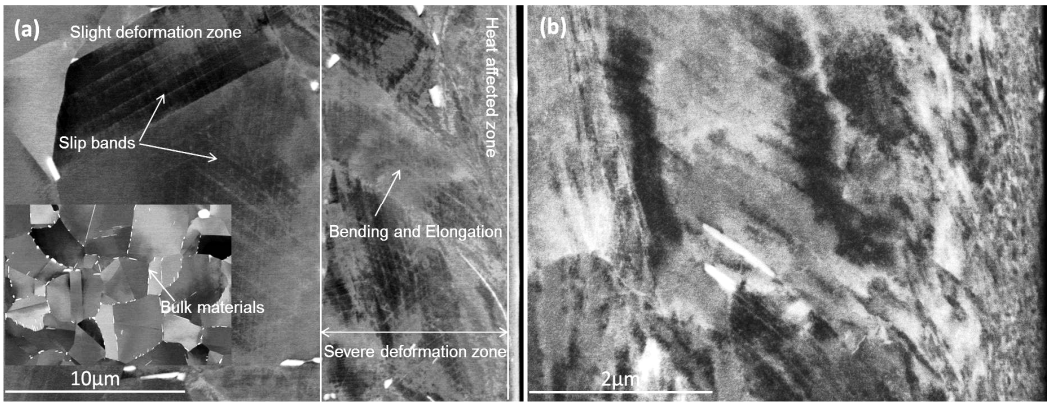

Figure 1. Typical microstructure of (a) machined surface and subsurface layers (b) the heat affected zone (CCBN tools, 350 m/min)

Figs. 2a and b show the effect of cutting speeds on the plastic deformation beneath the surface machined with WRA tools. When the cutting speed was increased from 200 m/min to 350 m/min, more distinguishable bending and slip bands were observed and the whole deformation area in the subsurface layer became much larger. Since the cutting force components of WRA tools were found to slightly decrease with the increased cutting speed (Fig. 3a), it may be concluded that the increased cutting temperature at the higher cutting speed is responsible for the greater level of the plastic deformation in the subsurface zone [19]. The same influence of cutting speeds was observed in the machined surface produced by UCBN tools and CCBN tools (Fig. 2c-f). Besides cutting speeds, the type of cutting tools is also an essential parameter affecting the plastic deformation in the machined subsurface. At 350 m/min, the most severe and deeper plastic deformation was found in the subsurface machined with WRA tools (Fig. 2b). It was also found that cutting with CCBN

tools resulted in a larger extent of plastic deformation in the machined subsurface compared with UCBN tools (Figs. 2d and f). These observed differences in the plastic deformation level can be explained by the increased cutting forces (Fig. 3b). The highest force level found for WRA tools leads to the largest plastic deformation under the machined surface. For the case of CBN tools, the higher cutting forces given by CCBN tools are responsible for the greater level of subsurface plastic deformation. It is expected that CCBN tools should show a lower cutting force than UCBN tools due to a lower friction coefficient and thermal conductivity of the titanium nitride coatings [20]. The opposite result is mainly due to the different tool microgeometry. Simulation and experimental results indicated that cutting forces increase as the tool radius increases [21, 22]. In this study, the edge radius r_β is 15-18 μm for UCBN tools, 20-22 μm for CCBN tools, 25-28 μm for WRA tools. At the higher cutting speed, the cutting tools had a strong influence on the subsurface plastic deformation level. However, when cutting at 200 m/min, comparable plastic deformation was found in Figs. 2a, c and e, and no obvious differences can be distinguished in the microstructure images for the different tools.

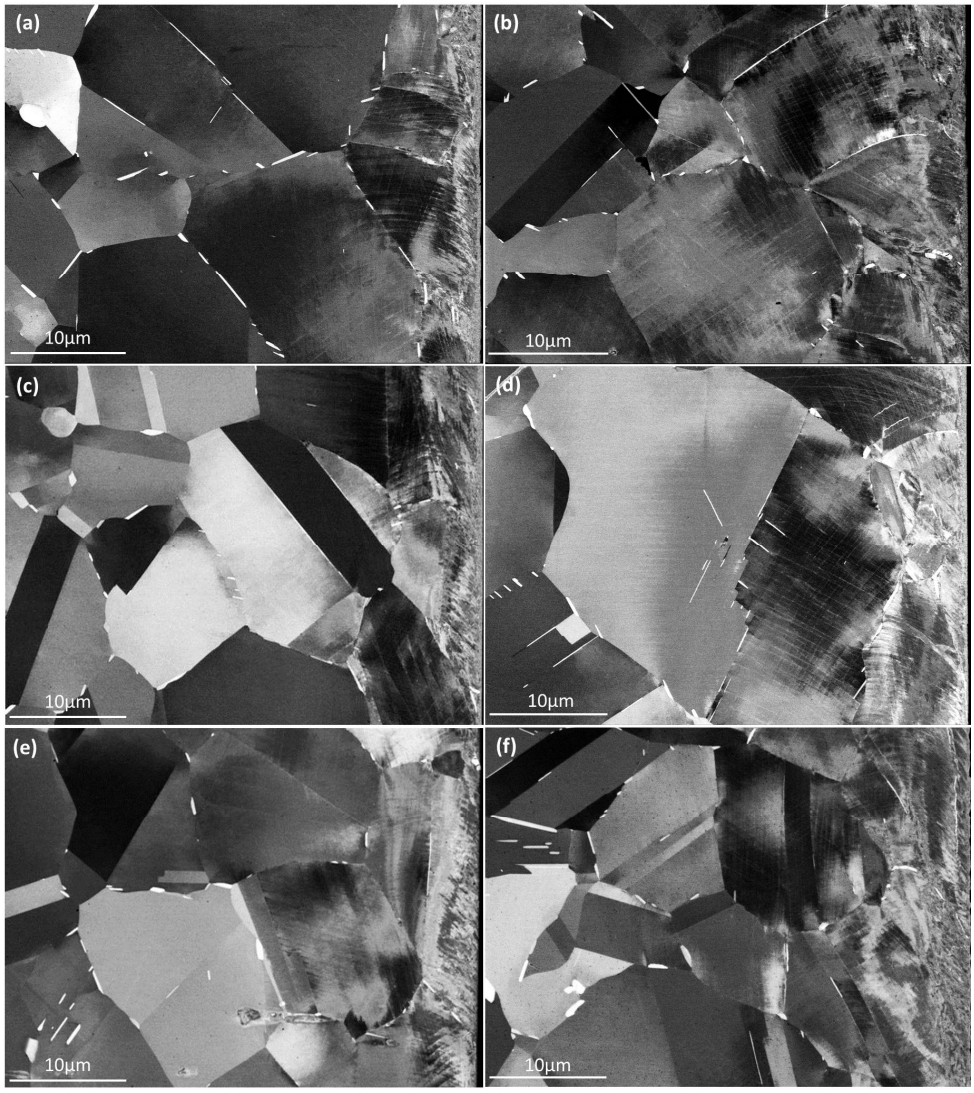

Figure 2. Microstructure images showing surface and subsurface deformation (loaded on the right side)
(a) WRA tools, v_c =200 m/min (b) WRA tools, v_c =350 m/min (c) UCBN tools, v_c =200 m/min
(d) UCBN tools, v_c =350 m/min (e) CCBN tools, v_c=200 m/min (f) CCBN tools, v_c =350 m/min

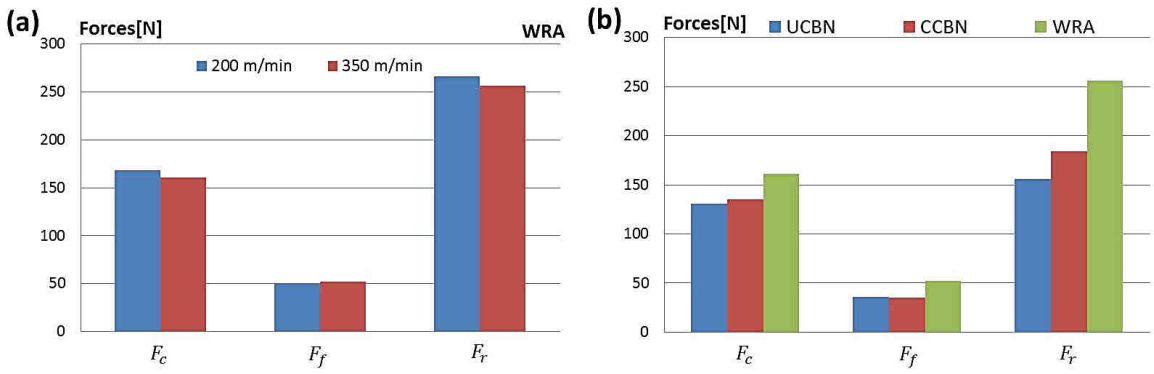

Figure 3. Comparison of cutting (F_c), feed (F_f) and radial (F_r) force components for (a) WRA tools, v_c =200 m/min and v_c =350 m/min (b) UCBN, CCBN and WRA tools, v_c =350 m/min

3.2 EBSD measurement

The EBSD maps were scanned with a step size of 1 μm in both vertical and horizontal direction from the surface. The crystallographic orientation of each measured point was collected according to the Kikuchi pattern and then the crystallographic misorientation associated with plastic deformation between each two points was calculated. A misorientation angle within the range of 1° and 10° was defined as a low angle grain boundary. The EBSD maps in Fig. 4 reveal the subsurface plastic deformation induced by turning using WRA tools. Areas where the value of the misorientation angle is within the range of 1° and 5° are marked by white lines, and those within the range of 5° and 10° are marked by red lines. The red lines were found to concentrate in the top surface showing a greater level of plastic deformation in this area. Meanwhile, when moving away from the surface into the bulk material, a general decrease of the white lines can be observed which shows the decrease of the plastic deformation. This tendency is corresponding to the microstructure variation from the heat affected zone to the undeformed zone. By calculating statistical data obtained in five random areas under the machined surface, misorientation variations versus the depth were delineated to demonstrate the plastic deformation level and depth beneath the machined surface (Fig. 4c). The increase of subsurface plastic deformation at the higher cutting speed was confirmed by the higher density and the greater depth of the misorientation. The EBSD results combined with the microstructure observation demonstrate that the higher cutting speed tends to result in a larger level of plastic deformation in the subsurface area

Microstructure observations in Section 3.1 have proven that the choice of cutting tools had an effect on the subsurface plastic deformation level, but this effect highly depends on the cutting speed. Fig. 5b confirmed the increase of plastic deformation for the machined surface from UCBN tools, CCBN tools and WRA tools at 350 m/min. This increase is strongly related to the increased cutting force level. However, at the lower cutting speed of 200 m/min, although the cutting forces for WRA tools still maintain the highest level compared with UCBN and CCBN tools (Fig. 5c), the plastic deformation generated during machining operations with WRA tools shows a slightly lower level instead (Fig. 5a). Such a significant change is probably attributed to the lower cutting temperature at a relatively low cutting speed. The coherency strain hardening has been reported to be the principal strengthening mechanism in aged Inconel 718 [23]. The major strengthening phase in Inconel 718 is

the γ'' phase. When the cutting temperature is below the γ'' solvus temperature, due to the strain hardening, the further plastic deformation is restricted. Therefore, at the lower cutting speed, the cutting forces had a limited effect on determining the plastic deformation in the machined subsurface. UCBN, CCBN and WRA tools give a similar plastic deformation level.

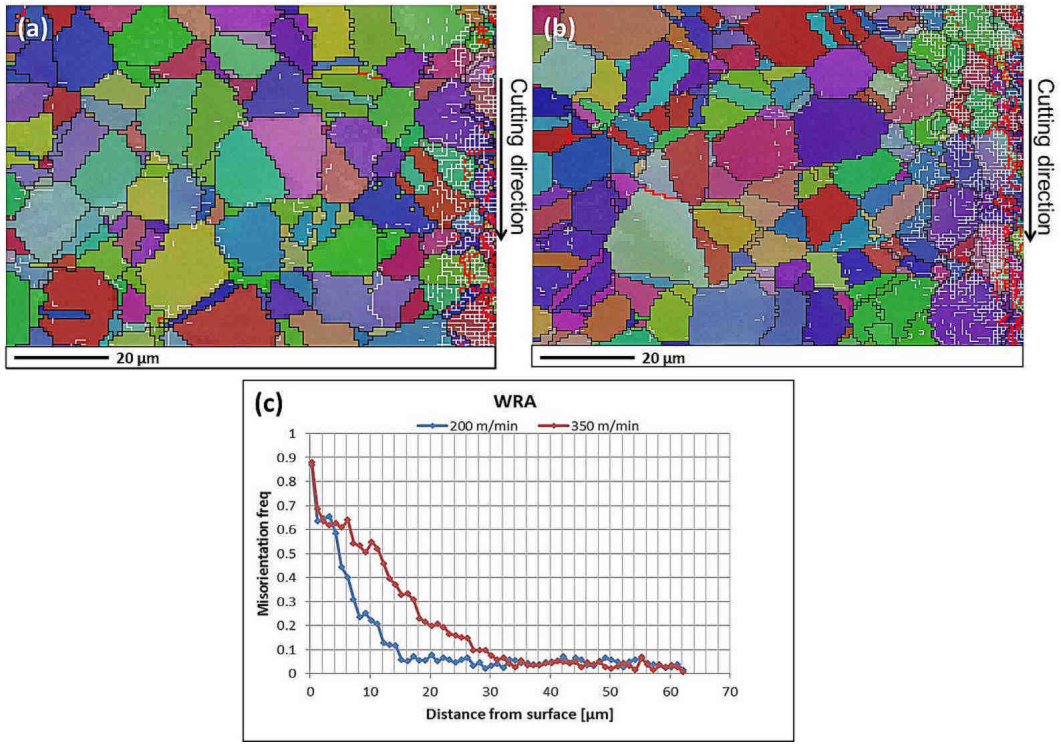

Figure 4. EBSD maps of subsurface deformation (a) WRA tools, v_c =200 m/min (b) WRA tools, v_c =350 m/min (c) Misorientation within grains beneath the surface machined with WRA tools

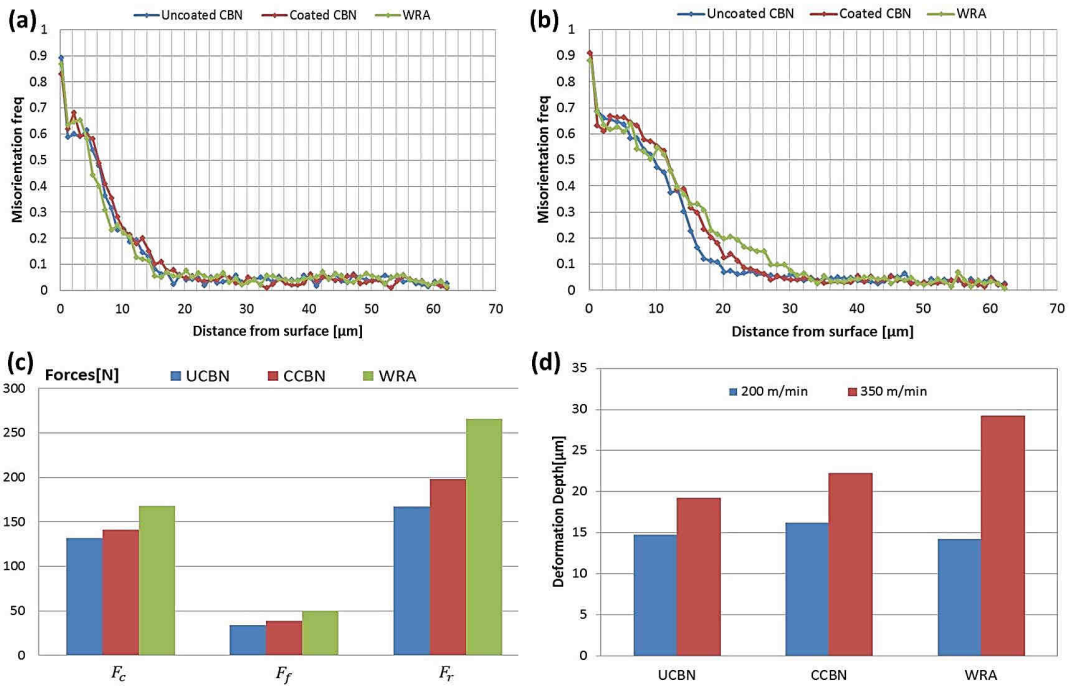

Figure 5. Misorientation within grains beneath the surface machined at (a) 200 m/min (b) 350 m/min (c) Cutting force components at 200 m/min (d) Deformation depth under different cutting conditions

Deformation depth is an essential parameter to assess the damage in form of structural alterations produced by mechanical machining processes. Fig. 5d summarises the influence of cutting conditions on the plastic deformation depth. It reveals that a higher cutting speed can significantly increase the plastic deformation depth under the machined surface. This tendency is more obvious for WRA tools, suggesting that the performance of WRA tools is much more sensitive to the cutting speed. Comparing the effect of the three cutting tools, the plastic deformation depth varies within a small range of 2-3 μm at the lower speed. However, when cutting at the higher speed, a noticeable increase of the deformation depth from UCBN tools, CCBN tools and WRA tools was found.

4. Conclusions

Microstructure alterations of Inconel 718 machined with UCBN, CCBN and WRA tools at two different cutting speeds have been investigated using ECCI and EBSD techniques. An attempt has been made to characterize the performance of the three advanced cutting tools in high speed machining in terms of influence on the subsurface microstructure. The results reveal an obvious alteration of subsurface microstructure associated with the gradient of mechanical forces and temperature along the depth direction for all the cutting conditions. The cutting speed was found to have a significant influence on subsurface plastic deformation with a larger plastic deformation level at higher cutting speeds. For the effect of cutting tools, comparable plastic deformation was observed under the surface machined with UCBN, CCBN and WRA tools at the lower cutting speed. However, at the higher cutting speed, the UCBN tools outperformed the other two types of cutting tools. Hence, for the cutting conditions studied in the current work, UCBN tools should be considered when a higher cutting speed is required in order to increase the production efficiency.

Acknowledgements

The authors of this paper express their sincere thanks to Mrs Annethe Billenius for her help with the sample preparation. The scholarship provided by the China Scholarship Council for Mr Zhe Chen is also greatly appreciated.

References

[1] E.O. Ezugwu, Key improvements in the machining of difficult-to-cut aerospace superalloys. Int. J. Mach. Tool Manuf., 45 (2005) 1353-1367.

[2] D. Ulutan, T. Ozel, Machining induced surface integrity in titanium and nickel alloys: A review. Int. J. Mach. Tool Manuf., 51 (2011) 250-280.

[3] T. Kitagawa, A. Kubo, K. Maekawa, Temperature and wear of cutting tools in high-speed machining of Inconel 718 and Ti6Al6V2Sn. Wear., 202 (1997) 142-148.

[4] F. Pusavec, H. Hamdi, J. Kopac, I. Jawahir, Surface integrity in cryogenic machining of nickel based alloy- Inconel 718. J. Mater. Process. Technol., 211 (2011) 773-783.

[5] R. M'Saoubi, T. Larsson, J. Outeiro, Y. Guo, S. Suslov, C. Saldana, S. Chandrasekar, Surface integrity analysis of machined Inconel 718 over multiple length scales. CIRP Ann. Manuf. Technol., 61 (2012) 99-102.

[6] R. Arunachalam, M.A. Mannan, Machinability of nickel-based high temperature alloys. Mach. Sci. Technol., 4 (2000) 127-168.

[7] J.P. Costes, Y. Guillet, G. Poulachon, M. Dessoly, Tool-life and wear mechanisms of CBN tools in machining of Inconel 718. J. Mach. Tool Manuf., 47 (2007) 1081-1087.

[8] I.A. Choudhury, M.A. El-Baradie, Machinability of nickel-base super alloys: a general review. J. Mater. Process. Technol., 77 (1998) 278-284.

[9] S.A. Khan, S.L. Soo, D.K. Aspinwall, C. Sage, P. Harden, M. Fleming, A. White, R. M'Saoubi, Tool wear/life evaluation when finish turning Inconel 718 using PCBN tooling. Procedia CIRP, 1 (2012) 283-288.

[10] D.G. Thakur, B. Ramamoorthy, L. Vijayaraghavan, Machinability investigation of Inconel 718 in high-speed turning. Int. J. Adv. Manuf. Technol., 45 (2009) 421-429.

[11] M. Imran, P.T. Mativenga, S. Kannan, Evaluation of the effects of tool geometry on tool wear and surface integrity in the micro drilling process for Inconel 718 alloy. Int. J. Mach. Mach. Mater., 11 (2012) 244-262.

[12] J. Li, M. Umemoto, Y. Todaka, K. Tsuchiya, A microstructural investigation of the surface of a drilled hole in carbon steels. Acta Mater., 55 (2007) 1397-1406.

[13] D. Novovic, R.C. Dewes, D.K. Aspinwall, W. Voice, P. Bowen, The effect of machined topography and integrity on fatigue life. Int. J. Mach. Tool Manuf., 44 (2004) 125-134.

[14] S. Kaboli, J. Su, R. Gauvin, Comparison of electron channeling contrast imaging (ECCI) and electron back scattered diffraction (EBSD) using Hitachi SU8000 FE-SEM. Microsc. Microanal., 18 (2012) 700-701.

[15] R. M'Saoubi, L. Ryde, Application of the EBSD technique for the characterisation of deformation zones in metal cutting. Mater. Sci. Eng. A, 405 (2005) 339-349.

[16] J.M. Zhou, V. Bushlya, R.L. Peng, S. Johansson, P. Avdovic, J. Stahl, Effects of tool wear on subsurface deformation of nickel-based superalloy. Procedia Eng., 19 (2011) 407-413.

[17] S. Veldhuis, G. Dosbaeva, A. Elfizy, G. Fox-Rabinovich, T. Wagg, Investigations of white layer formation during machining of powder metallurgical Ni-based ME 16 Superalloy. J. Mater. Eng. Perform., 19 (2010) 1031-1036.

[18] B.J. Griffiths, Mechanisms of white layer generation with reference to machining and deformation processes. J. Tribol., 109 (1987) 525-530.

[19] N. Narutaki, Y. Yamane, K. Hayashi, T. Kitagawa, K. Uehara, High-speed machining of Inconel 718 with ceramic tools. CIRP Ann. Manuf. Technol., 42 (1993) 103-106.

[20] B. Zou, M. Chen, C. Huang, Q. An, Study on surface damages caused by turning NiCr20TiAl nickel-based alloy. J. Mater. Process. Technol., 209 (2009) 5802-5809.

[21] K.W. Kim, W.Y. Lee, H.C. Sin, A finite-element analysis of machining with the tool edge considered. J. Mater. Process. Technol., 86 (1998) 45-55.

[22] Y. Yen, A. Jain, T. Altan, A finite element analysis of orthogonal machining using different tool edge geometries. J. Mater. Process. Technol., 146 (2004) 72-81.

[23] J.M. Oblak, D.F. Paulonis, D.S. Duvall, Coherency strengthening in Ni-base alloys hardened by DO_{22} gamma double prime precipitates. Metall. Trans., 5 (1974) 143-153.

Modelling of molecular bonding with a cohesive zone model strategy

R. Estevez[1,*], G Parry[1], P. Mc Garry[2]

[1] Université de Grenoble, SIMaP, UMR CNRS 5266, Grenoble-INP, UJF, 1130 rue de la piscine, BP75, F-38402 St Martin d'Hères cedex, France
[2] College of Engineering and Informatics, Mechanical and Biomedical Engineering National University of Ireland, Galway, University Road, Galway, Ireland
* Corresponding author: Rafael.Estevez@simap.grenoble-inp.fr

Abstract Molecular or direct bonding is an emerging technique to assemble directly two silicon wafers or metal parts. In vaccum, the two surfaces are free to bond perfectly if their lattice orientation is coincident. When defects have to be considered like a misorientation or when bonding is processed in air, a slowdown of the bonding velocity is observed and its efficiency in term of adhesion energy decreased. The aim of this project is to gain insight in the bonding process and to investigate the influence of the bonding characteristics. A specific strategy based on a non linear contact mechanics scheme is adopted to describe the bonding process: the methodology is shown to provide enough flexibility to account for the normal and tangential interactions. These latter are described with Traction-Opening displacement laws that are first derived from interactomic potential. the influence on the bonding characteristic on the bonding wavefront is investigated to attempt deriving local information of the bonding mechanism.

Keywords Cohesive model, molecular bonding, finite element simulation

1. Introduction

Molecular bonding is nowadays used in the microelectronics industry to assemble directly parts with no use of a gluing layer. The technique is based on the natural adhesion between clean surfaces that come close to each other. The technique is shown efficient when performed in vacuum (see for instance the review by Prössl and Kräuter [1] and references therein). One of the challenges for improving this technique is to perform the bonding in air instead of vacuum which induces problems related to the air wedge generated in the vicinity of the process zone (see for instance Rieutord et al. [2]). Among the features that need to be to be handled carefully is the estimation of the adhesion energy and the stress induced by the processing in the wafer. Wedge tests are performed to measure the interface energy with the so called Maszara configuration (see [3] for a review). An alternative to the Maszara test, which is not so easy to handle, is to adopt an inverse approach based on the observation of the bonding wavefront during the adhesion process. The present study focuses on this aspect. The goal is to identify the adhesion energy from the observation of the bonding wavefront profile and its velocity. To this end, a modelling of the molecular bonding is presented here that is based on a cohesive description of the molecular interactions between two Silicon wafers. The work is restricted to bonding in vaccum. The cohesive description is first postulated but could be atomistically informed with molecular dynamics simulations as reported by Kubair et al. [4] for instance.

We first describe the modelling strategy and next, present a typical simulation of molecular bonding performed with the finite element package abaqus [5]. The approach is shown able to capture qualitatively observations reported in the literature. This work precedes a parametric study currently under progress.

2. Modelling and simulation the continuum scale

2.1 Problem formulation

The two wafers are modeled as circular plates, of diameter 200 mm and thickness 0.7 nm. A linear elastic constitutive law is chosen, with values of Young's modulus E=100 GPa and Poisson's ration $\upsilon = 0.22$, typical from Si. The geometry and boundary conditions of the system are depicted in Fig.1, where only the top wafer is represented. A symmetry boundary condition is imposed along a diameter. The two wafers are originally distant from a few nanometers. A pressure is applied over an area along the edge of the upper wafer. By pushing the two wafers together, they are coming in sufficiently close contact to activate the attraction between the two surfaces. A bonding wave is hence triggered from this area, spreading all along the interface between the wafers.

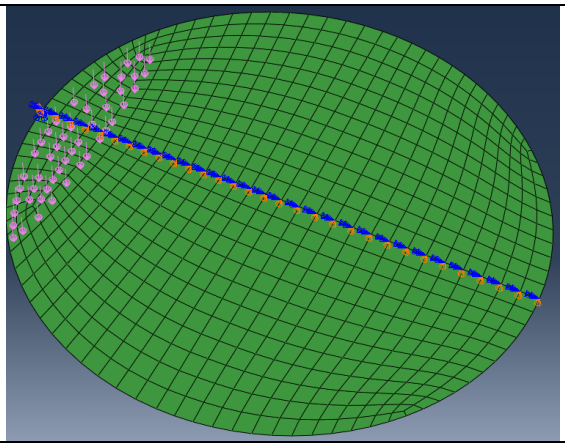

Figure 1: schematic description of the boundary conditions prescribed on the top wafer. Symmetry boundary conditions are enforced along one diameter. A pressure is applied on a small area along one edge in order to trigger the bonding process.

It is critical to model properly the interaction between the two surfaces. The Xu and Needleman (XN) cohesive model [6] is used to describe the interface behaviour. This formulation show a Traction-Separation similar to that reported in Kubair et al. [4] and therefore adopted for the case reported here. It is based on the definition of an interface potential,$\emptyset$, representing the work done when two opposing surfaces at an interface undergo a relative separation $\underline{\Delta}$The resulting tractions are given by;

$$\underline{T}(\underline{\Delta}) = \partial\emptyset(\underline{\Delta})/\partial\underline{\Delta} \tag{1}$$

The interface potential is given by;

$$\emptyset\,(\Delta_n, \Delta_t) = \emptyset_n + \emptyset_n exp\left(-\frac{\Delta_n}{\delta_n}\right)\left[\left\{1 - r + \frac{\Delta_n}{\delta_n}\right\}\left(\frac{1-q}{r-1}\right) - \left\{q + \left(\frac{r-q}{r-1}\right)\frac{\Delta_n}{\delta_n}\right\} exp\left(-\frac{\Delta_t^2}{\delta_t^2}\right)\right] \tag{2}$$

Coupling in this model is controlled through the parameters q and r;

where, $q = \emptyset_t/\emptyset_n$ $\quad r = \Delta_n^*/\delta_n$

$\emptyset_n$ and $\emptyset_t$ are the work of normal and tangential separation respectively. The normal and tangential components of the interface separation vector, $\underline{\Delta}$, are Δ_n and Δ_t respectively. The normal and tangential interface characteristic lengths are δ_n and δ_t respectively and Δ_n^* is the value of Δ_n after complete tangential separation takes place under the condition of normal tension being zero (T_n= 0).

Using equations (1) and (2), the interfacial tractions are obtained as follows;

$$T_n = \frac{\partial \emptyset}{\partial \Delta_n} = \left(\frac{\emptyset_n}{\delta_n}\right) exp\left(-\frac{\Delta_n}{\delta_n}\right)\left\{\frac{\Delta_n}{\delta_n} exp\left(-\frac{\Delta_t^2}{\delta_t^2}\right) + \frac{1-q}{r-1}\left[1 - exp\left(-\frac{\Delta_t^2}{\delta_t^2}\right)\right]\left[r - \frac{\Delta_n}{\delta_n}\right]\right\} \tag{3}$$

$$T_t = \frac{\partial \emptyset}{\partial \Delta_t} = 2\left(\frac{\emptyset_n}{\delta_n}\right)\left(\frac{\delta_n}{\delta_t}\right)\frac{\Delta_t}{\delta_t}\left\{q + \left(\frac{r-q}{r-1}\right)\frac{\Delta_n}{\delta_n}\right\} exp\left(-\frac{\Delta_n}{\delta_n}\right) exp\left(-\frac{\Delta_t^2}{\delta_t^2}\right) \tag{4}$$

The characteristic lengths δ_n and δ_t are given by;

$$\delta_n = \emptyset_n / \left(Tn_{max} exp(1)\right) \tag{5}$$

$$\delta_t = \emptyset_t / \left(Tt_{max}\left(0.5\, exp(1)\right)^{0.5}\right) \tag{6}$$

Where Tn_{max} is the maximum normal traction without tangential separation and Tt_{max} is the maximum tangential traction without normal separation. Typical shapes of the tractions are depicted in Fig. 2. It is worth noting that this constitutive law managing the interactions between the two surfaces is strongly nonlinear.

Practically, we have used q=1 and r=0, a maximum traction of 1GPa and characteristic opening δ_n=δ_t=1nm. The traction-opening profiles are reported in Fig. 2.

A viscosity term has been added according to [7] in order to avoid instability problems during the decay in the traction with opening (see Fig. 2), in the event of a strong drop in stiffness during loading (e.g. a snap-through).

The calculation are carried out using the finite element code ABAQUS [5]. The interaction between the two surfaces is accounted for through a non linear contact mechanics algorithm. The tractions representing the bonding are taken from (3-4) and implemented in Abaqus in a User INTERface routine (UINTER). The non linear contact scheme is implemented using a user subroutine linked to the implicit FEM solver. The methodology is shown to provide enough flexibility to account for the

normal and tangential interactions. Unlike the cohesive elements methods, it is easy to start in a configuration where the two plates are distant. It is also possible to activate the shear only when the distance between the two plates is smaller than $6\delta_n$, which is typically when the interaction between the two surfaces can be considered as non negligible according to the XN model. For the simulations, $Tn_{max} = 1GPa$ and $\delta_n = 1nm$. The shear interaction has been set to zero in the first place.

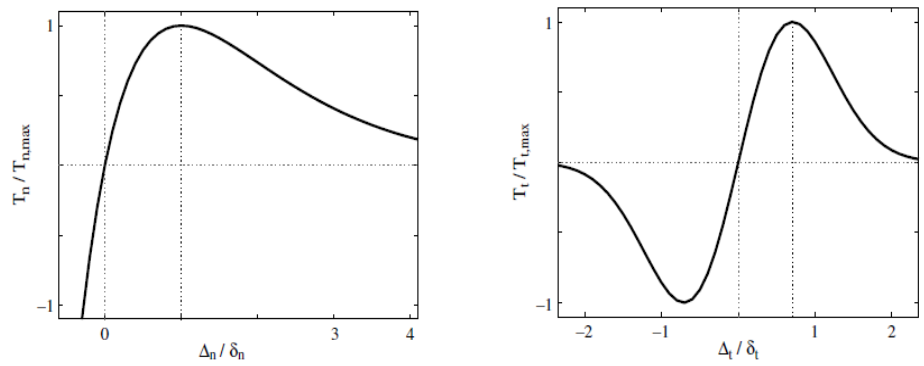

Figure 2. Description of the traction versus separation interaction between the two wafers (Eqs. 3 for normal traction and 4 for shear separation).

2.2 Results

Fig. 3 shows a typical experimental observation of the wavefront bonding observed with an InfraRed camera during the molecular bonding of two silicon wafers (top in Fig. 3). The bright zone corresponds to the bonded region, the darker to the area that is not bonded yet. On the top-left picture, the bonding is initiated on the left of the wafer. Initiation consists of applying a short pressure to trigger the process. Once the bonding propagation is initiated, the wave front runs from left to right. Due to the initiation of the bonding process, the wavefront show initially an almost circular contour but its curvature increases as the bonding extends across the interface.

In the bottom of Fig. 3, we present the results of the finite element simulations. The distribution of the displacement normal to the wafer surfaces is reported. The blue/darker corresponds to the bonded area, and the green-red area (brighter region) to the surface that is not bonded yet. The area where an initial pressure is prescribed to trigger the bonding process is more extended in the simulation compared to the experimental data reported in Fig. 3. Therefore, the curvature of the initial bonding wavefront is larger curvature. During the wavefront propagation, its curvature increases as the bonding extends, toward the middle of the wafer. When the second half of the wafer bonds; the radius of curvature of the bonding wavefront decreases until complete bonding.

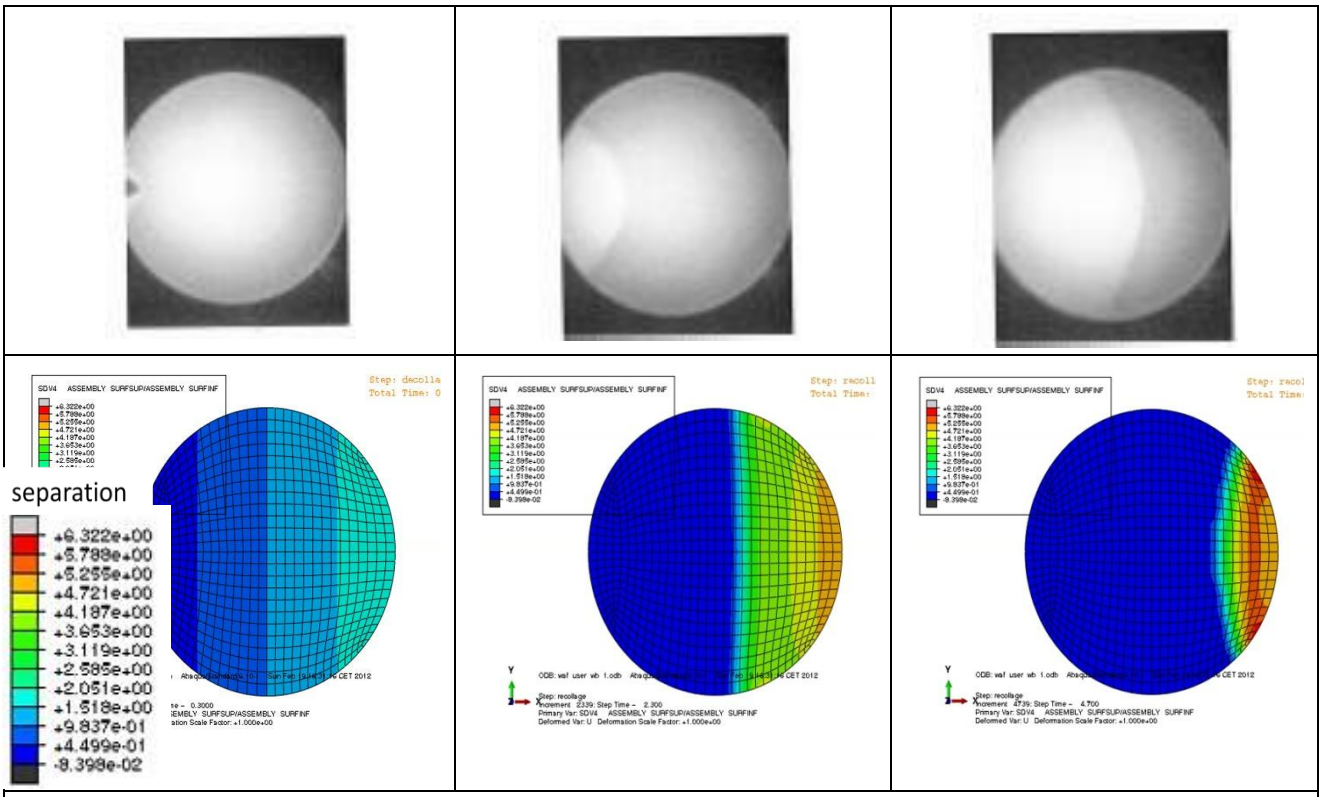

Figure 3: experimental observation (top) and numerical simulation (bottom) of the bonding front. In both cases, the bonding wave is propagating from left to right. In the simulation, the contour lines indicate the normal separation in nm. The wafers are lightly tilted at the beginning. Blue indicates a bonded area.

4. Discussion and Conclusion

We have presented a modeling of the natural bonding between two interactive surfaces by accounting for realistic adhesion interactions, at least qualitatively. The wavefront propagation predicted in our simulations is qualitatively consistent with available data of this problem.The methodology of using a contact mechanics approach to handle the cohesive interaction is found suitable for this problem. We here postulated the cohesive interaction between the two plates but some information can be extracted from the molecular dynamics calculations, in the spirit of a recent work by Kubair et al. [4] for instance. The influence of the cohesive parameters and in particular the magnitude of the maximum traction and that of the adhesion energy are currently under progress. How these could modify the wave front profile and the stress distribution in the plates will be investigated.

References

[1] A. Prössl and G. Kräuter, Wafer direct bonding: tailoring adhesion between brittle materials, Materials Science and Engineering, R25, (1999), 1-88

[2] F. Rieutord, B. Bataillou and H. Moriceau, Dynamics of a bonding wavefront, Phys Rev Lett. 94, (2005),236101

[3] O. Vallin, K. Jonsson, U. Lindberg, Adhesion quantification methods for wafer bonding, Materials Science and Engineering, R50, (2005), 109-165.

[4] D.V. Kubair, D. J. Cole, L. C. Ciacchi, and S M. Spearing, Multiscale mechanics modeling of direct silicon wafer bonding, Scripta Materiala, 60, (2009), 1125-1128

[5] Abaqus, finite element package, v6.10, Simulia, Dassault Systems

[6] X.P. Xu and A. Needleman, Numerical simulations fast crack growth in brittle solids, Journal Mechanics Physics Solids, 42, (1994), 1397-1434.

[7] Y.F. Gao and A.F. Bower, A simple technique for avoiding convergence problems in finite element simulations of crack nucleation and growth on cohesive interfaces, Modell. Simul. Mat. Sci. Engng, 12, (2004), 453-463

Contact Fracture Mechanism of Electroplated Ni-P Coating on Stainless Steel Substrate

Akio Yonezu[1,*], **Michihiro Niwa**[1]

[1] Department of Precision Mechanics, Chuo University, Tokyo 112-8551, Japan
* Corresponding author: akioyonezu.31x@g.chuo-u.ac.jp

Abstract The contact fracture property and mechanism of electroplated Ni-P coating on stainless steel substrate were investigated using ball indentation testing, through a comprehensive experimental and numerical approach. First, the elastoplastic properties of both coating and substrate were evaluated using micro indentation tests. Next, ball indentation test with large contact force was performed, such that the brittle coating on ductile substrate suffers from cracks, including ring crack (propagates circumferentially) and radial cracks (propagates radially), owing to the coating bending effect. The fracture nucleation process was investigated using the acoustic emission technique (AET). In addition, finite element method (FEM) with cohesive zone model (CZM) was carried out to compute stress field and simulate crack initiation around the impression during the test. By using the comprehensive experimental/computational framework, the nucleation process (mechanism) of such a complicate crack system was clarified. The present technique and fracture mechanism may be applicable to the analysis of structural integrity of other brittle coatings.

Keywords Electroplated Ni-P coating, Contact fracture, Ball indentation

1. Introduction

Hard thin films or surface coatings on ductile metallic substrates are often used for contact and slide wear protection. Therefore, the characteristics and mechanism of their contact fracture are critical for ensuring their mechanical performances. Many hard coatings are deposited using the electroplate technique, which may achieve massive production with low cost and large area/ thick deposition (even when the substrate geometry is complicated) [1-5]. Among the electroplated hard coatings, Ni–P material possesses high hardness, high strength and other superior mechanical properties, providing excellent performance (such as wear and corrosion resistance) for metallic ductile substrate/components [2, 6-9]. Thus, characterizing the contact fracture properties of Ni–P coatings is the most important issue regarding structural integrity and application.

Indentation method is convenient way to simulate contact fracture against foreign object. Such a contact loading sometimes shows complicate fracture morphology, such as radial crack, ring crack and lateral crack [13, 14]. These differences are dependent on coating thickness, geometry of indenter, elastoplastic properties of both coating and substrate [15-17], which dictates various types of stress field and the maximum value that are responsible for coating fracture. One of the critical challenges lies in an understanding of the process how several different types of cracks occurs. It may require reliable method to monitor the crack propagation and fracture processes in-situ during indentation test, as well as to effectively analyze the stress field upon indentation loading and during crack propagation.

In this study, ball indentation test was carried out to simulate contact fracture of electroplated Ni-P coating on stainless steel substrate. Acoustic emission technique was utilized to monitor the timing of coating cracks. Stress field upon indentation was computed by finite element method (FEM), where the cohesive element was used to simulate crack nucleation. The comprehensive experimental/numerical approach helps to clarify stress criterion of complicate coating crack system.

2. Materials

In this study, Ni-P alloy was electroplated onto SUS304 in the plating bath. The electrolysis condition is described elsewhere [10]. The coating thickness is about 180 μm. After electroplating, heat treatment of 350°C was performed for one hour in vacuum. According to the reference [9, 10], post-heat treatment is crucial for the mechanical properties of the coating. Initially, the element of P (phosphorus) is a solution in the matrix of Ni, and then NiP_3 (having high hardness) gradually precipitates during post-heat treatment; when the post-heat treatment temperature is between 300 and 350°C, the maximum hardness (*HV*=800 - 1000) is achieved [9, 10] for wear protection, whereas the fracture toughness exhibits the lowest value [9]. Therefore, the investigation of crack morphology and cracking resistance due to contact loading is a critical issue for the Ni-P electroplated coating.

To evaluate mechanical properties (elastoplastic properties) of both Ni-P coating and steel substrate, micro indentation tests against the cross section were performed as shown in Fig. 1(a). Berkovich indenter was used with the maximum force of 100 mN. The representative *F-h* curves were plotted by solid lines in Fig. 1(b). Based on the *F-h* curves, the elastic properties (Young's modulus) were

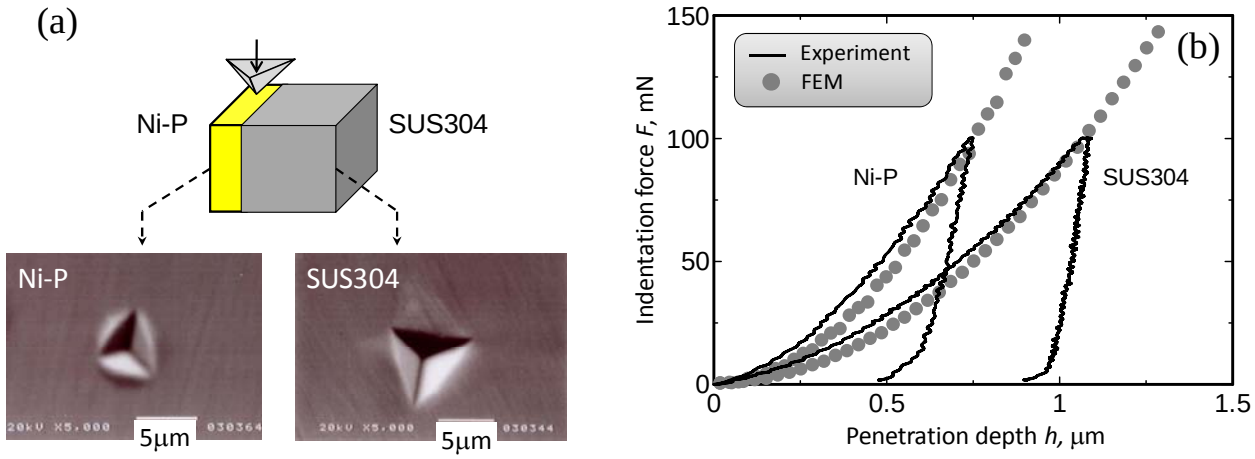

Fig.1 (a) Micro indentation method for cross-section of Ni-P coating and SUS304, and their impressions. (b) Their indentation curves combined with computational ones using finite element method.

Table 1 Mechanical properties of electroplated Ni-P coating and SUS304 substrate.

Material	Young's modulus *E* GPa	Poisson's ratio ν	Hardness H GPa	Yield stress σ_y GPa	Work hardening exponent *n*
Ni-P coating	217	0.37*	7.51	2.40	0.05
SUS304 substrate	175	0.3	3.49	0.22	0.47

* Morikawa et al. The Iron and Steel Institute of Japan (ISIJ), Vol.82, pp.935-940, 1996

estimated by Oliver-Pharr method [18, 19]. Here, the Poisson's ratio of coating is referred to be 0.37 obtained by the surface acoustic wave (SAW) technique [10]. The Young's modulus of coating/substrate shows similar values, i.e. Ni-P coating is 217 GPa, and SUS304 is 175 GPa. Subsequently, the plastic properties (stress - strain relationship) of coating and substrate were estimated by using the reverse analysis ([20, 21]). Here, the plastic properties were assumed with power-law constitutive equation, involving yield stress σ_Y and work hardening exponent n. The estimated results were shown in Table 1. To verify the estimation, finite element simulation (employing these estimated properties) of the micro indentation test was carried out and the resulting indentation curve (F-h) was shown in Fig. 1(b). The simulated results (as indicated by grey circle) agreed well with experimental data for both coating/substrate. This suggested that the estimated elastoplastic properties were robust, and can be employed for stress analysis and crack nucleation subjected deep ball indentation (see Section 5.1). Noted that, according to the reference [9], there might be internal residual stress of Ni-P coating. By using X-ray diffraction, the stress was measured to be almost zero for the present coating (with heat treatment temperature of 350C^o) [9]. Thus, we consider the internal stress-free coating.

3. Experimental Method

Ball indentation tests were performed using an electro-hydraulic testing machine equipped with a ball indenter and two eddy current sensors. The diameter of indenter ball d is 10 mm. The indentation force F gradually increases with the rate of dF/dt = 1 N/s up to the maximum indentation force F_{max} (=1000 N or 2000 N), and sustains the constant value in 50 s, and gradually decreases with the same dF/dt until the force of zero. During the test, acoustic emission (AE) signals were monitored in order to identify the timing of crack nucleation. Four small AE sensors were mounted on the side surfaces of a specimen.

4. Experimental Results

Figures 2 show the micrographs of specimen surface after the test of F_{max}=2000 N. Although the test of F_{max}=1000 N shows no clear crack (however, some friction/ wear tracks were observed), the test of F_{max}=2000 N (Fig. 2) shows complicated coating crack morphology: one type is circumferential crack, namely "ring crack", and the other type initiates from the ring crack and propagate radially, namely "radial crack". There is no delamination (coating spalling) thanks to the strong adhesive strength of the coating/substrate system. The present study therefore focuses on the formation mechanisms of ring crack and radial crack, which may provide useful insights for the mechanical/material design of coating/substrate system.

Figure 3 shows indentation curve of the test with F_{max}=2000 N. The detected AEs were plotted as triangles on the F-h curve in this figure. It is found that the first AE was detected at about F=1200 N and several AEs were subsequently monitored up to about F=1500 N. Furthermore, the unloading process was found to start AE generation from F=1600 N during unloading. Therefore, it is expected that the coating cracks occur during both loading and unloading. Based on these experimental evidences, the stress field is investigated by finite element method in the next section, so as to further clarify the contact cracking behavior.

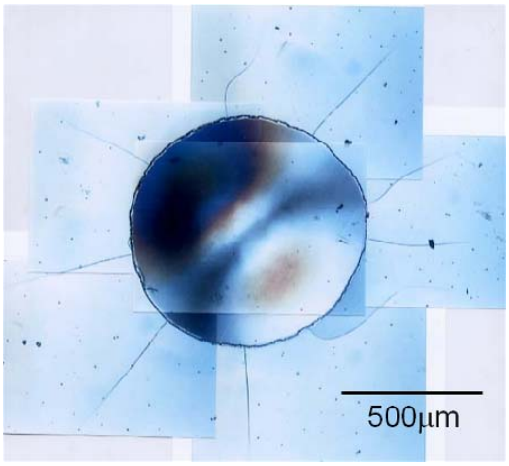

Fig.2 Micrographs of impressions tested with 2000 N.

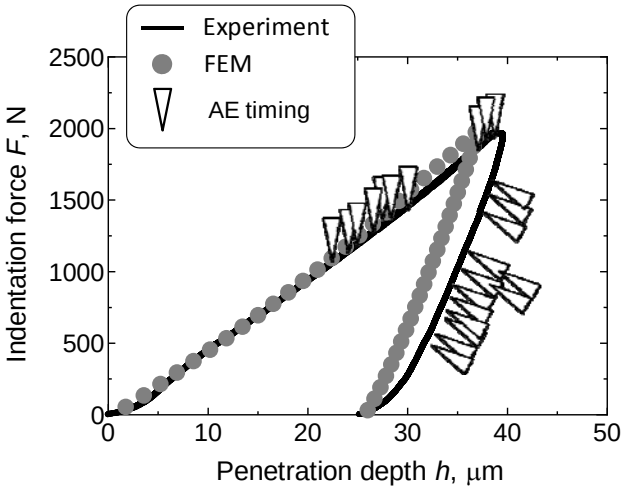

Fig.3 Indentation curve obtained by the test with maximum force of 2000 N. Triangle on the curve indicates the timing of AE generation. In addition, grey circle indicates the simulated indentation curve with finite element method.

5. Discussion

5.1 Crack initiation

By taking advantage of symmetry, an axisymmetric model is established for FEM analysis with the commercial code MARC and MENTAT. The material parameters are taken from Table 1, for both coating and substrate. A rigid ball indenter with radius d=10 mm is employed as a close analog to that used in experiment. To verify both the present FEM model and measured material property, the computed indentation curve is plotted as symbols (grey circle) in Fig. 3, showing reasonable agreement with the experimental curve.

Figure 4 represents a contour map of the indentation stress field computed by FEM simulation when the first AE was detected (as discussed in Fig.3). Fig. 4 (a) shows the map for the radial stress component (σ_{rr}), which is responsible for ring crack, and Fig. 4(b) is the circumferential component ($\sigma_{\theta\theta}$) for radial crack. For σ_{rr}, a large tensile stress (up to about 1.8 GPa) occurs outside the contact region, where the ring crack may be produced if such a tensile stress is sufficiently high. Indeed, such a prominent tensile stress is contributed by the large local bending curvature of the film, assisted by the extensive plastic deformation of the substrate [12, 15, 16]. On the other hand, $\sigma_{\theta\theta}$ (in Fig. 4(b)) is relatively small (less than about 1.0 GPa which is quite lower than the σ_{rr} component). Therefore, the first detected AE should be from ring crack, suggesting that the ring crack initiated first.

The surface distribution of σ_{rr} as a function of the indentation force is given in Fig.5. As expected, the maximum tensile stress increases and shifts outwards with increase in indentation force (deeper penetration), which is associated with the increased coating bending curvature outside the contact zone. When the indentation force reaches the critical value (F = 1200 N), the location of the maximum stress (r = 390 μm) roughly coincides with the radius of the ring crack (as indicated by dashed vertical lines) observed in experiment (see Figs. 2). Thus, we can obtain the critical fracture strength of the coating, σ_C=1.8 GPa. Note that, this value of σ_C is seemed to be the intrinsic strength of the coating (since the present Ni-P coating does not have large internal stress [9], Section 2).

From the above investigations, it is revealed that when a ball indenter makes deep contact with the

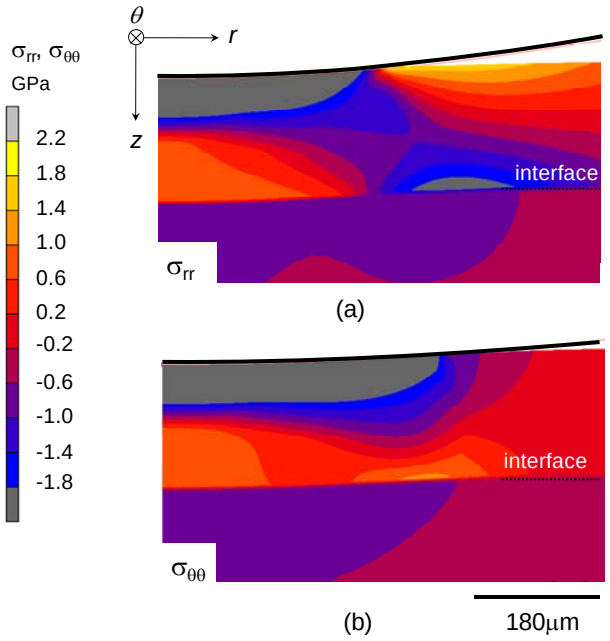

Fig.4 Counter map of stress distribution when the first AE was detected (see Fig.6). (a) normal stress along radial direction, σ_{rr}, and (b) normal stress along circumferential direction, $\sigma_{\theta\theta}$.

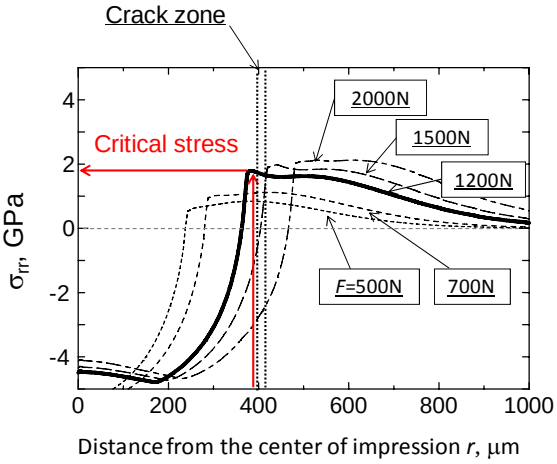

Fig.5 Radial stress σ_{rr} distribution as a function of distance r, with the increases in indentation force. The thick line corresponds to the critical indentation force of 1200 N, when first AE is detected (see Fig.6).

Fig.6 Contour map of CZM damage for ring crack nucleation, when indentation force is about 1200 N.

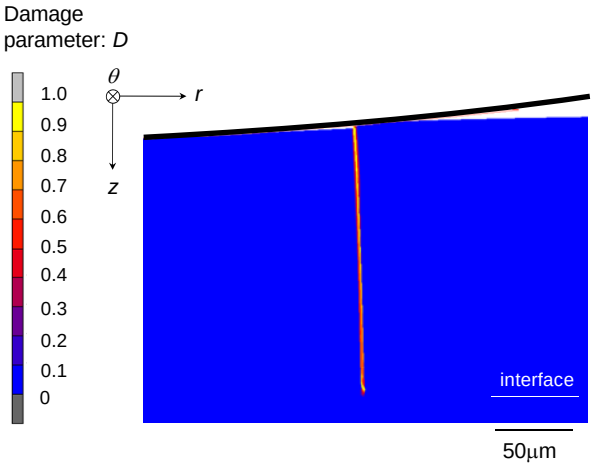

surface of brittle coating, the steel substrate undergoes extensive plastic deformation, which bends the coating and leads to large tensile stress, producing ring crack. Thus, the next question is how the radial crack initiates after the ring crack formation.

5.2 Subsequent crack initiation

To investigate how radial crack forms, the existence of ring crack must be incorporated with stress analysis during indentation. Thus, we employed the cohesive zone model (CZM) in the FEM to compute the stress field in conjunction with ring crack formation.

The CZM is applicable to both ductile and brittle materials [23-29]. The CZM essentially models the fracture process zone in a plane ahead of the crack tip. The zone is assumed to be subjected to cohesive traction. The model usually describes the gradual degradation of the adhesion between two regions along the crack propagation plane. The mechanical response of the cohesive zone obeys a

traction–separation law that yields the relationship between the separation distance v of the two material faces at an interface and the traction stress σ acting between them. Although numerous traction–separation laws for the cohesive zone element have been proposed, this study employed an exponential law (called the Smith-Ferrante type [24]) due to its simplicity. This exponential law requires two independent materials parameters, i.e. the maximum stress σ_{max} and the crack growth resistance K_C. Since the σ_{max} roughly corresponds to the critical stress (fracture strength), σ_{max} is set to be 1.8 GPa from Fig. 5. However, the other parameter K_C is unknown. Thus, several values (0.5, 1.0 and 5.5 MPa $m^{1/2}$) were employed to simulate ring crack formation.
To compute the stress field involving ring crack formation, we introduced CZM element into FEM model. Here, the CZM elements are implemented at the location where the ring crack forms (r=400 μm in Fig.2 and Fig.5). Figure 6 shows the contour map of damage parameter D around the impression (when D becomes one, crack completely forms [22, 24]). When K_c=5.5 MPa $m^{1/2}$, as shown in Fig.6, the ring crack (due to σ_{rr} component) propagates from the surface to the interface. In fact, actual crack was found to propagate up to the interface from the cross sectional observation. (Note that the choice of Kc value does not affect the subsequent stress field after crack propagation.)

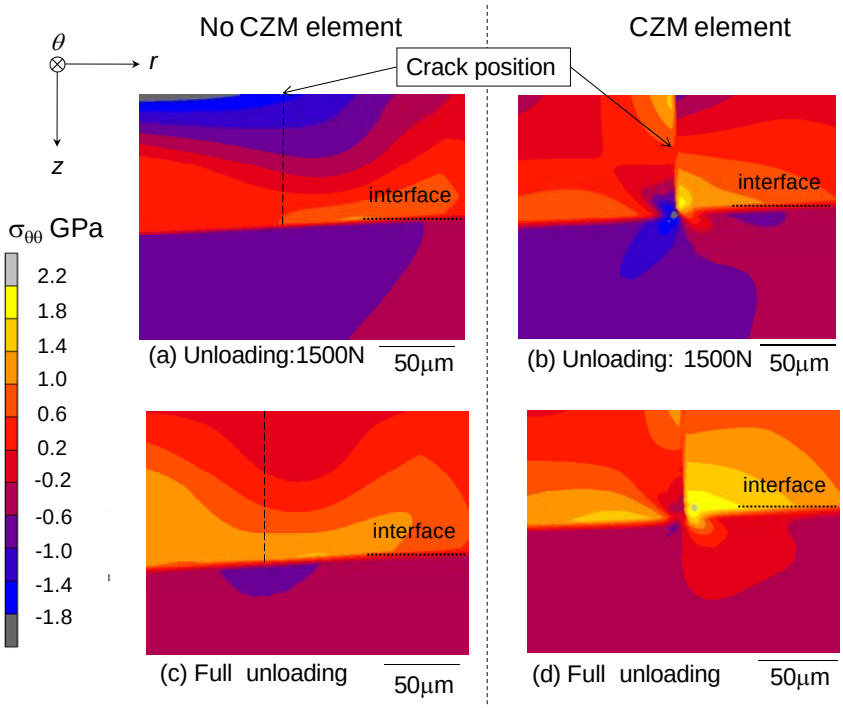

Fig.7 Contour map of stress $\sigma_{\theta\theta}$ distribution around the impression during indentation loading: homogenous model with no CZM element ((a),(c)) and model with CZM element ((b),(d)). (a) and (b) shows the map at F= 1500 N (F/F_{max}=0.75), while (c) and (d) is at the maximum force (F_{max}=2000 N). 1200 N.

5.3 Mechanism of cracking system

Figure 7 shows the snapshot of the normal stress $\sigma_{\theta\theta}$ distribution during the loading process. Fig. 7 (a) and (b) show the stress field at F=1500 N, whereas Fig. 7 (c) and (d) show the result at the maximum indentation force (2000 N). For comparison, the model with no cohesive zone element was also computed, as shown in Fig. 7(a) and (c). This model simulates the stress field due to

indenter contact, and does not induce any crack formation. Thus, $\sigma_{\theta\theta}$ (in Figs.7(a)(c)) does not show large tensile stress, which is the same trend with Fig.4(b). On the other hand, the model with CZM element in Figs.7(b)(d) exhibits different $\sigma_{\theta\theta}$ stress field, owing to the ring crack formation. In particular, possible area for large tensile $\sigma_{\theta\theta}$ develops near the interface.

Figures 8 shows a snapshot of $\sigma_{\theta\theta}$ distribution during unloading process, in a similar fashion with Fig.7. In Figs.8 (a) and (c), without the CZM element model there is no large $\sigma_{\theta\theta}$ distribution, whereas with the CZM element, the significant larger $\sigma_{\theta\theta}$ develops at the right side of crack path near interface, and its magnitude increases during the unloading process and reaches the maximum value upon full unloading. Therefore, it is found that ring crack formation significantly changes the subsequent stress field during the indentation, in particular the large $\sigma_{\theta\theta}$ upon unloading, and the radial crack is seemed to initiate at the right side of crack path.

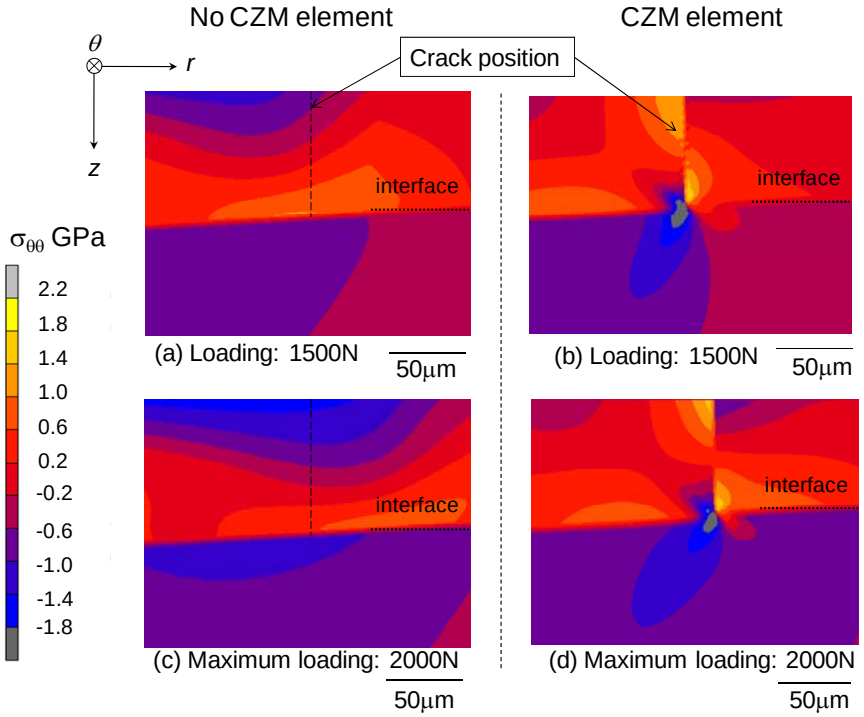

Fig.8 Contour map of stress $\sigma_{\theta\theta}$ distribution around the impression during indentation unloading: homogenous model with no CZM element ((a),(c)) and model with CZM element ((b),(d)). (a) and (b) shows the map at F=1500 N (F/F_{max}=0.75), while (c) and (d) is at the full unloading (F=0 N).

Figure 9 shows the stress $\sigma_{\theta\theta}$ distribution along the crack path with respect to the distance from coating surface to interface. The four curves indicate the results of 1500 N and 2000 N (loading) and 1500 N and 0 N (unloading). While the overall $\sigma_{\theta\theta}$ magnitude increases during the unloading process, the position of the maximum $\sigma_{\theta\theta}$ does not change (at about 175 μm below the surface). Finally, the change in the maximum $\sigma_{\theta\theta}$ value is investigated as a function of the indentation force (during unloading process) in Fig.10. As expected, the maximum $\sigma_{\theta\theta}$ increases with decreasing indentation force. Referring to Fig.3, the AE occurrence was seen at about F=1600 N under unloading. In Fig.10, this force (F=1600 N) corresponds to $\sigma_{\theta\theta}$ = 1.82 GPa, which is reasonably agreement with the critical stress σ_{rr} for ring crack in Fig.5. Therefore, it is found that radial crack is produced by $\sigma_{\theta\theta}$, which develops near the interface and ring crack path, suggesting that ring crack formation (during loading) is crucial for subsequent radial crack nucleation during unloading.

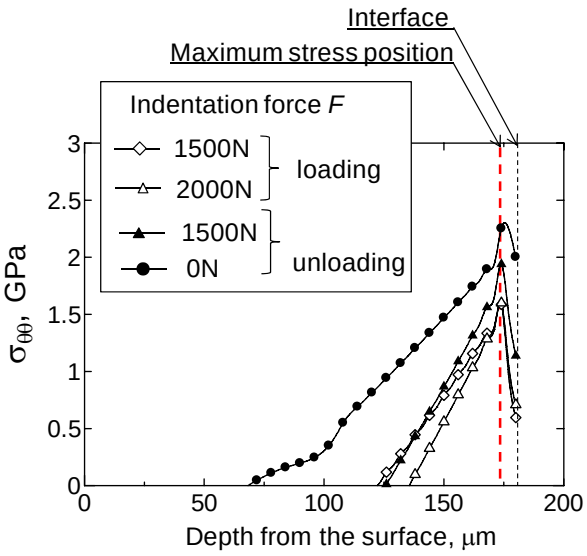

Fig.9 Stress $\sigma_{\theta\theta}$ distribution along the ring crack path (the depth from coating surface to interface). Four lines with various symbols indicate the results of 1500 N and 2000 N (loading process) and 1500 N and 0 N (unloading process).

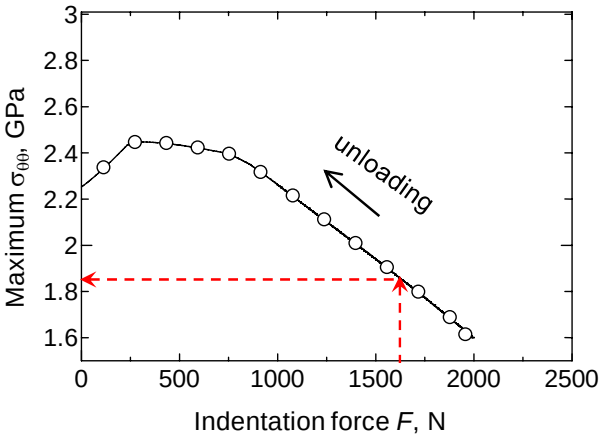

Fig.10 Changes in maximum stress $\sigma_{\theta\theta}$ (in Fig.9) as a function of indentation force during unloading.

6. Conclusion

This study investigated the contact fracture property of electroplated Ni-P coating on stainless steel substrate, which is important for its application as contact/sliding member for wear resistance. Ball indentation test with large contact/indentation force produces two types of cracks in the coating, namely the ring crack and radial crack. To elucidate the fracture process, acoustic emission technique (AET) was employed to identify the timing of crack initiation during the test. In addition, finite element method (FEM) was carried out to compute the stress field around the impression during the test. The cohesive zone modeling (CZM) was embedded with FEM to simulate the crack interaction. It is found that the ring crack first initiates during loading process, due to tensile radial stress (owing to the coating bending effect). Subsequently, radial crack nucleates from ring crack path (i.e. near ring crack tip at interface) due to the large circumferential stress developed upon unloading.

By using the comprehensive experimental/computational indentation framework (combined with AE and FEM), the mechanism of the complicate coating crack system is clarified, and the stress criterion for each cracking system is quantified. Based on these findings, further systematic study may suggest how to control or prevent the coating cracks. This will become useful guidance for material design in coating industry. The comprehensive experimental/computational framework is also applicable to other coating/substrate systems.

Acknowledgements

The work of A.Y. is supported in part of Grant-in-Aid for Young Scientist of (B) (No. 22760077) of

the Ministry of Education, Culture, Sports, Science and Technology, Japan, and Research Grant for Science and Technology of SUZUKI Foundation

References

[1] K.-H. Hou, M.-C. Jeng, M.-D. Ger, Wear 262 (2007) 833-844.
[2] H. Tian, N. Saka, E. Rabinowicz, Wear 142 (1991) 51-85.
[3] Z. Ping, J. Yuan, Y. He, X. Li, Acta Metall. Sin. (Engl. Lett.) 22 (2009) 225-232.
[4] Y. D. He, H. F. Fu, X. G. Li, W. Gao, Scri. Mater. 58 (2008) 504-507.
[5] P. Peeters, G. Hoorn, T. Daenen, A. Kurowski, G. Staikov, Electrochim. Acta 47 (2001) 161-169.
[6] S.-H. Kim, Mater. Lett. 61 (2007) 3589-3592.
[7] W. Sha, J.-S. Pan, J. Alloys Compds. 182 (1992) L1-L3.
[8] W. Sha, P. J.-S., J. Less-Common Metals 166 (1990) L11-L13.
[9] T. Yashiki, T. Nakayama, J. Kato, The Iron and Steel Institute of Japan 81 (1995) 48-53.
[10] Y. Morikawa, H. Cho, T. Nakayama, M. Takemoto, The Iron and Steel Institute of Japan 82 (1996).
[11] A. Yonezu, B. Xu, X. Chen, Mater. Sci. Eng. 507 (2009) 226-235.
[12] A. Yonezu, B. Xu, X. Chen, Thin Solid Films, 518 (2010) 2082–2089.
[13] R. F. Cook, G. M. Pharr, J. Am. Ceram. Soc. 73 (1990) 787-817.
[14] X. Chen, J. W. Hutchinson, A. G. Evans, J. Am. Cer. Soc. 88 (2005) 1233-1238.
[15] B. R. Lawn, Y. Deng, P. Miranda, P. Pajares, H. Chai, D. K. Kim, J. Mater. Res. 17 (2002) 3019-3035.
[16] H. Chai, B. R. Lawn, J. Mater. Res. 19 (2004) 1752-1761.
[17] A. Yonezu, H. Cho, T. Ogawa, M. Takemoto, Sci. Tech. Adv. Mater. 7 (2006) 97-103.
[18] W. C. Oliver, G. M. Pharr, J. Mater. Res. 7 (1992) 1564-1583.
[19] W. C. Oliver, G. M. Pharr, J. Mater. Res. 19 (2004) 3-20.
[20] N. Ogasawara, N. Chiba, X. Chen, Scripta Materialia 54 (2006) 65-70.
[21] A. Yonezu, X. Chen, Dia. Relat. Mater.19 (2010) 40-49.
[22] Marc, Marc 2010, Theory and User's Manual A 2010.
[23] N. Chandra, H. Li, C. Shet, H. Ghonem, Int J Solids Struct 39 (2002) 2827-2855.
[24] B. A. E. Hal, R. H. J. Peerlings, M. G. D. Geers, O. Sluis, Microelectronics Reliability 47 (2007) 1251-1261.
[25] Z. Xia, W. A. Curtin, B. W. Sheldon, Acta Mater. 52 (2004) 3507-3517.
[26] V. Tvergaard, J. W. Hutchinson, J. Mech. Phys. Solids 40 (1992) 1377-1397.
[27] G. I. Barenblatt, Advances in Applied Mechanics 7 (1962) 56-129.
[28] V. Olden, C. Thaulow, R. Johnsen, E. Østby, T. Berstad, Eng. Fract. Mech. 75 (2008) 2333-2351.
[29] A. Yonezu, T. Hara, T. Kondo, H. Hirakata, K. Minoshima, Mater. Sci. Eng. A 531 (2012) 147–154

Influence of Interface Roughness on the Fatigue Life of Thermal Barrier Coatings

Robert Eriksson[1,*], Sören Sjöström[1], Håkan Brodin[1,2], Sten Johansson[1], Lars Östergren[3], Xin-Hai Li[2]

[1] Department of Management and Engineering, Linköping University, Linköping SE-58183, Sweden
[2] Siemens Industrial Turbomachinery AB, Finspong SE- 61283, Sweden
[3]GKN Aerospace Engine Systems, Trollhättan SE-46181, Sweden
* Corresponding author: robert.eriksson@liu.se

Abstract Thermal barrier coatings (TBC) are coating system comprising a heat insulating ceramic coating deposited on top of a oxidation resistant metallic coating. During thermal cycling, cracks grow in the metal/ceramic interface which causes the coating system to fail. In order to model such crack growth by finite element (FE) modelling, accurate interface models must be developed. The presented research studies the influence of interface roughness on the thermal fatigue life of TBCs, and suggests how interface models can be derived from interface roughness parameters. High interface roughness was found to promote longer fatigue lives. Interface models were derived from the roughness parameters Rc, Ra, RSm and Rdq and used for FE modelling of crack growth in the interface. The calculated stress intensities, KI and KII, increased with increasing interface roughness and thereby did not predict a slower crack growth with higher interface roughness as was observed experimentally.

Keywords Thermal barrier coating, Interface, Roughness, Fatigue

1. Introduction

Thermal barrier coating (TBC) systems are coating system containing a heat resistant ceramic top coat (TC), and an oxidation resistant metallic bond coat (BC) [1-4]. Such TBC systems are widely in use in gas turbines to provide heat insulation and oxidation protection for structural parts in the combustor and turbine sections; thereby prolonging the life of structural parts, as well as increasing efficiency by enabling higher combustion temperatures [1-4].

During operation, the TBC system is subjected to thermal fatigue. Thermal loads arise from the difference in coefficient of thermal expansion (CTE) of the ceramic top coat and the metallic bond coat [5-7]. Failure of TBCs often occurs close to the BC/TC interface where fatigue cracks grow under a stress field influenced by: the mismatch in CTE, the BC/TC interface roughness and the growing layer of thermally grown oxides (TGO) that form in the interface [5-7].

Predicting TBC life is a matter of great concern and several approaches to the subject exist; one of which is a fracture mechanical approach involving finite element (FE) modelling of crack growth in the BC/TC interface [5,6]. To perform such FE modelling, the BC/TC interface must be accurately modelled. The sine wave has emerged as a common interface model with amplitudes and wavelengths roughly in the intervals 5–20 μm and 20–150 μm respectively [7-13]. However, an in-depth study of the actual BC/TC interface roughness, and its influence on fatigue life, is still missing. Among the few attempts on the subject, Casu et al. [9] can be mentioned, who performed FE modelling for an interface geometry derived from an actual BC/TC interface.

The current research studies the interface characteristics by the means of common surface roughness parameters, and suggests how these can be used to create interface models. TBC coated specimens with various interface roughness were thermally cycled until failure, cross-sectioned and image analysis was used to obtain the interface roughness. The interface roughness parameters were

then used to create interface models. FE modelling of a crack growing in the interface was performed to test whether interface geometries derived in such a way would capture the experimental results from thermal fatigue testing.

1.1. Roughness parameters

The roughness parameters used in this paper are explained by Fig. 1 and Eq. (1)–(4); for further information about roughness parameters see, for example, Gadelmawla et al. [14]. In summary, it may be said that *Rc* and *Ra* are *amplitude parameters* (i.e. they contain information about profile height), *RSm* is a *spacing parameter* (i.e. contains information about profile spacing) and *RΔq* is a *hybrid parameter* (i.e. contains information about both profile height and spacing).

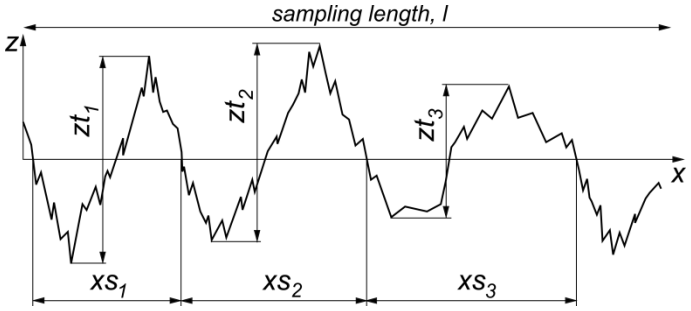

Figure 1. Generic roughness profile.

$$Rc = \frac{1}{n}\sum_{i=1}^{n} zt_i \tag{1}$$

$$Ra = \frac{1}{l}\int_0^l |z(x)|dx \tag{2}$$

$$RSm = \frac{1}{n}\sum_{i=1}^{n} xs_i \tag{3}$$

$$R\Delta q = \sqrt{\frac{1}{l}\int_0^l \left(\frac{dz}{dx}\right)^2 dx} \tag{4}$$

2. Experimental

2.1. Thermal cycling fatigue

Four TBC coated specimens with varyingly coarse BC/TC interfaces were put through thermal cycling until failure. The specimen substrates were cut from 5 mm thick Haynes 230 sheet material in 30x50 mm rectangles. The substrates were coated by 200 µm of NiCrAlY deposited by vacuum plasma spraying, and 350 µm of 7%-yttria partially-stabilised zirconia deposited by atmospheric plasma spraying (APS). The variation in BC/TC roughness was accomplished by using different feedstock powder sizes during spraying of the bond coat.

The specimens were thermally cycled in a furnace until failure. The cycle included heating to 1100 °C for 1 h, and cooling to 100 °C by forced airflow; the specimens reached 100 °C after about 10 min of cooling. After failure, which was considered to occur when more than 20 % of the top coat had spalled, the specimens were infiltrated in epoxy, cross-sectioned and polished for microscopy.

2.2. Interface roughness measurement

The interface roughness was measured on cross-sectioned specimens with an image analysis routine outlined in Fig. 2. The method involves the following steps: 1) Thresholding of the grayscale image to get a binary image, see Fig. 2 a) and b). 2) Acquisition of the interface roughness profile by simulating a profilometer stylus tip, see Fig. 2 c). 3) Filtering of the profile and establishing the mean line, see Fig. 2 d). 4) Cropping the profile to a suitable *sampling length*, see Fig. 2 e).

The results from image analysis were compared with results from a profilometer for some BC coated specimens (no top coat). This comparison was done to validate the accuracy of the image analysis derived surface roughness parameters, and to find a suitable magnification at which to perform the routine. Fig. 3 shows the results from this comparison; it can be seen that the results from the image analysis compares well to the results from the profilometer and that the lower magnification, with a resolution of 1.074 μm/pixel, was sufficient.

The setup used for image analysis can be summarised as: Roughness parameters were established and averaged from 65 interface roughness profiles with sampling lengths of 800 μm, thus resulting in a total examined length of about 5 cm which was considered enough to generate reliable mean values. The obtained profiles correspond to the BC/TGO interface. The simulated stylus tip had a radius of 5 μm. All wavelengths larger than the sampling length and smaller than two times the stylus tip radius were removed by Gaussian filtering.

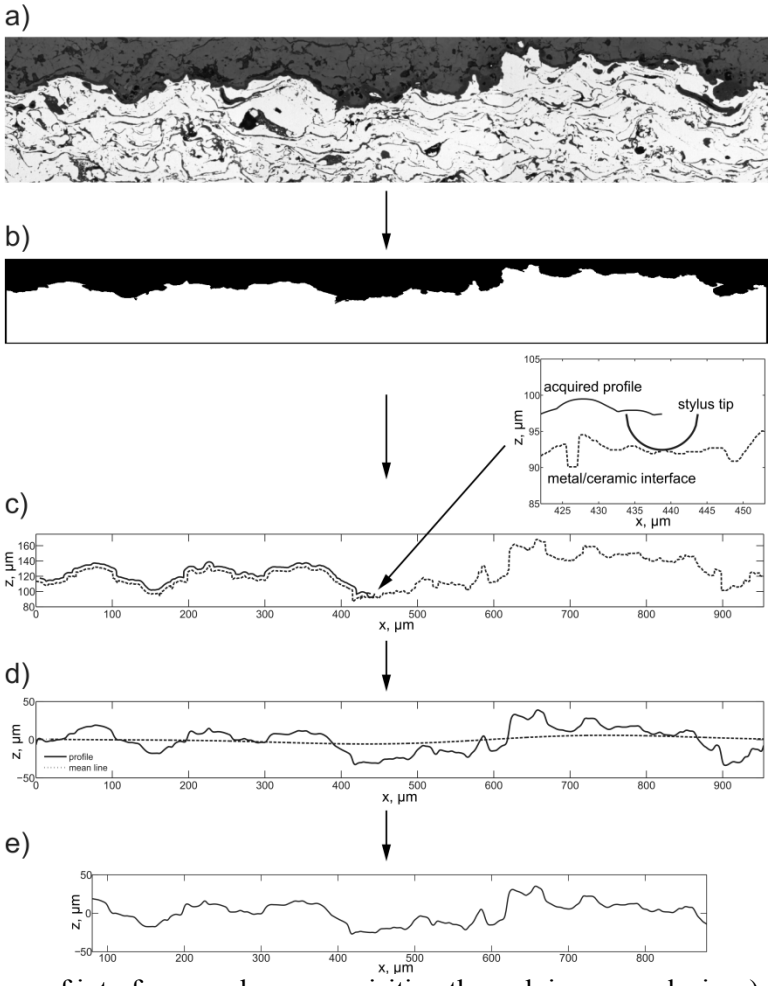

Figure 2. The process of interface roughness acquisition through image analysis: a) grayscale image b) binary image c) simulation of stylus tip d) filtering and mean line calculation e) final profile.

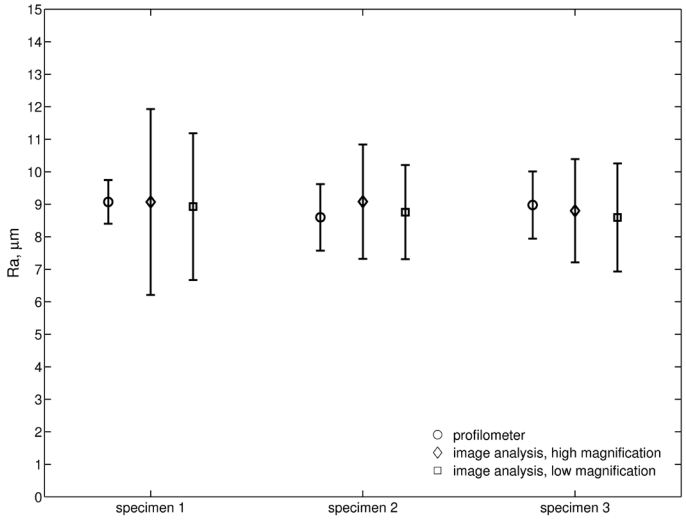

Figure 3. Comparison between the results from a profilometer and results obtained by image analysis performed on images with two different magnifications.

3. Results

3.1. Influence of interface roughness on the thermal fatigue life

The measured *Ra* and *Rc* of the specimens are presented in Fig. 4 as a function of the number of thermal cycles the specimens withstood until failure. There is a clear tendency for higher roughness (higher *Ra* and *Rc*) to give longer fatigue lives.

Fig. 5 shows the measured *RSm* and *RΔq* versus cycles to failure. *RSm* contains information about (wave)length, and *RΔq* contains information about both length and height. For *RΔq* a correlation with fatigue life exists where higher *RΔq* gives longer life. The same cannot be said for *RSm*, however, since the *RSm* value appears to be roughly equal for all specimens; the variation between the specimens is less than ± 5 % of the mean value of 232 µm.

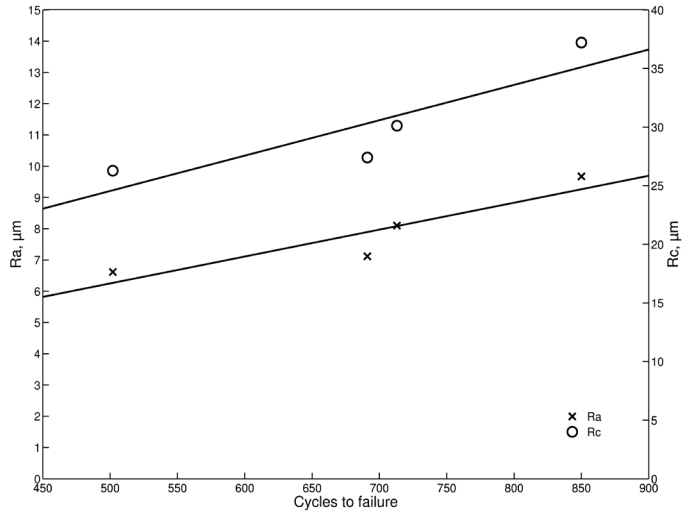

Figure 4. The influence of *Ra* and *Rc* on the thermal fatigue life.

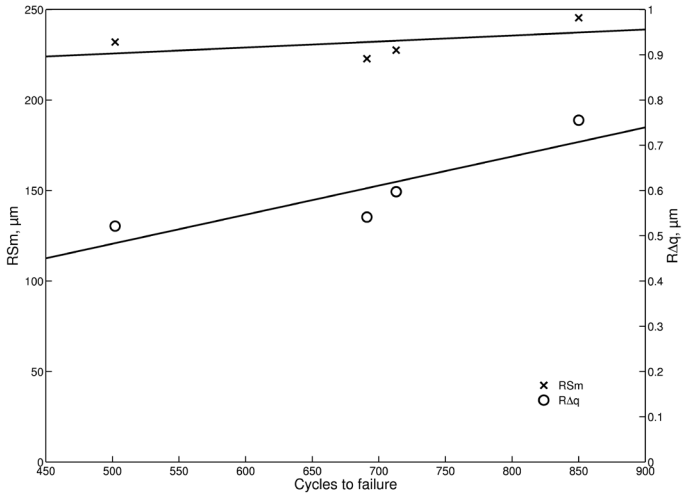

Figure 5. The influence of *RSm* and *RΔq* on the thermal fatigue life.

3.2. Interface models

In order to derive usable interface models, several assumptions have to be made. 1) Basing the model on measured interface roughness parameters will cause it to capture the main features of the actual interface. 2) Interface parameters that show a correlation with fatigue life (such as *Ra* and *Rc*) are appropriate to use as a base for model formulation. 3) For simplicity, the interface needs to be modelled as a periodic function.

Two models are presented here; they are both based on sine waves, see Eq. (5), as this is a commonly used shape for interface models in TBCs. The amplitude A and wavelength λ can then be derived from the interface roughness parameters as shown in Table 1.

$$z = A\sin\left(\frac{2\pi}{\lambda}x\right) \tag{5}$$

Model 1, see Table 1, is roughly the equivalence of measuring the height and wavelength directly in a micrograph. This model is based on *Rc* and *RSm* where *Rc* is twice the amplitude and *RSm* is the wavelength. Model 2 is derived from *Ra* and *RΔq*. It is obtained by entering Eq. (5) into Eq. (2) and its derivative into Eq. (4). Using the equations from Table 1 with Eq. (5) and values from Fig. 4 and 5, the amplitudes and wavelengths can be calculated and are listed in Table 2. For the remaining paper, only the specimen with lowest roughness (shortest life) and highest roughness (longest life) will be considered.

Table 1. Equations for the interface models.

Model	Amplitude	Wavelength
1	$A = Rc/2$	$\lambda = RSm$
2	$A = \frac{\pi Ra}{2}$	$\lambda = \frac{\pi\sqrt{2}}{R\Delta q}A$

Table 2. Amplitudes and wavelengths calculated from roughness parameters.

Specimen	Model	Amplitude, μm	Wavelength, μm
low roughness	1: *Rc*- and *RSm*-based	13.1	232
low roughness	2: *Ra*- and *RΔq*-based	10.4	89
high roughness	1: *Rc*- and *RSm*-based	18.6	245
high roughness	2: *Ra*- and *RΔq*-based	15.2	89

3.3. FE crack modelling

The two interface models were used for further FE modelling of crack growth under thermal stress. A fracture-mechanical analysis was done of a crack advancing along a sine-shaped interface of an idealised TBC. The analysis was done on a least representative cell of the TBC, as shown in Fig. 6 b), using the FE code Abaqus. The least representative cell was assumed to have a symmetry boundary on the left, and on the right hand boundary a kinematic boundary condition was applied causing the right boundary to remain plane. Crack growth was modelled both in the BC/TGO interface and the TGO/TC interface.

Fig. 6 shows the vertical stress component around a crack growing from a peak towards a valley in the TGO/TC interface. Fig. 7 shows the corresponding energy release rates, G, and stress intensity factors, K_I and K_{II}; the values in Fig. 7 are plotted versus *interface damage* where damage is defined as the horizontal length of the crack divided by half the wavelength, i.e. the damage is 1 when the crack reaches the valley. The K_I and K_{II} were obtained from Eq. (9) by post-processing of the results as demonstrated in the appendix. For both models, the specimen with high roughness gave higher G, K_I and K_{II} for most part of the crack growth; this was observed for both BC/TGO and TGO/TC cracks.

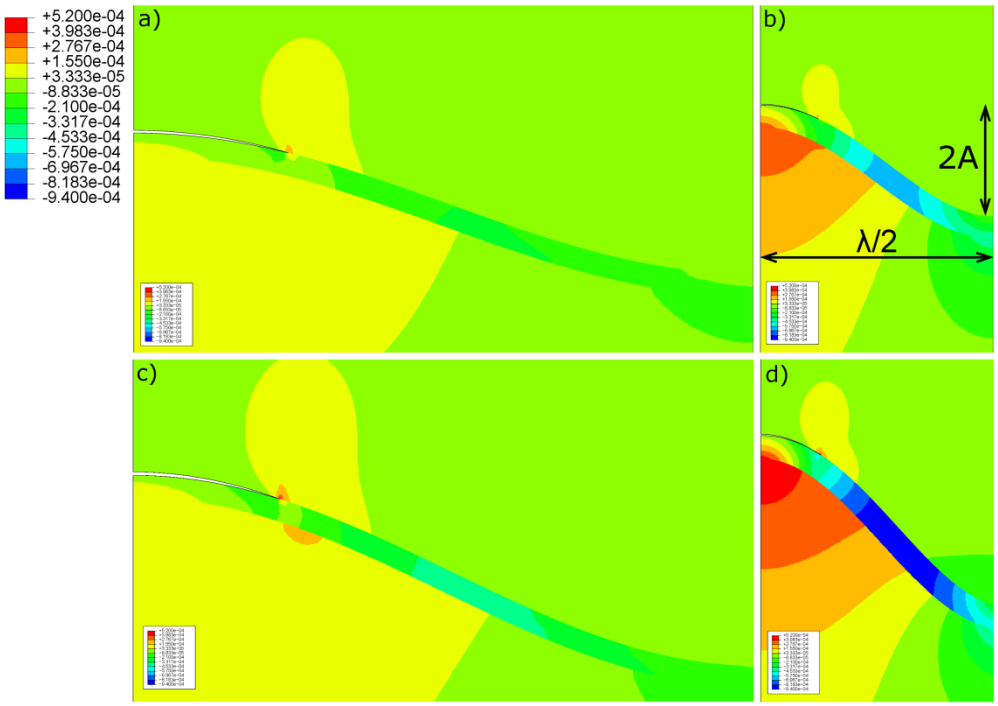

Figure 6. Vertical stress in the interface for: a) low roughness, model 1; b) low roughness, model 2; c) high roughness, model 1; d) high roughness, model 2.

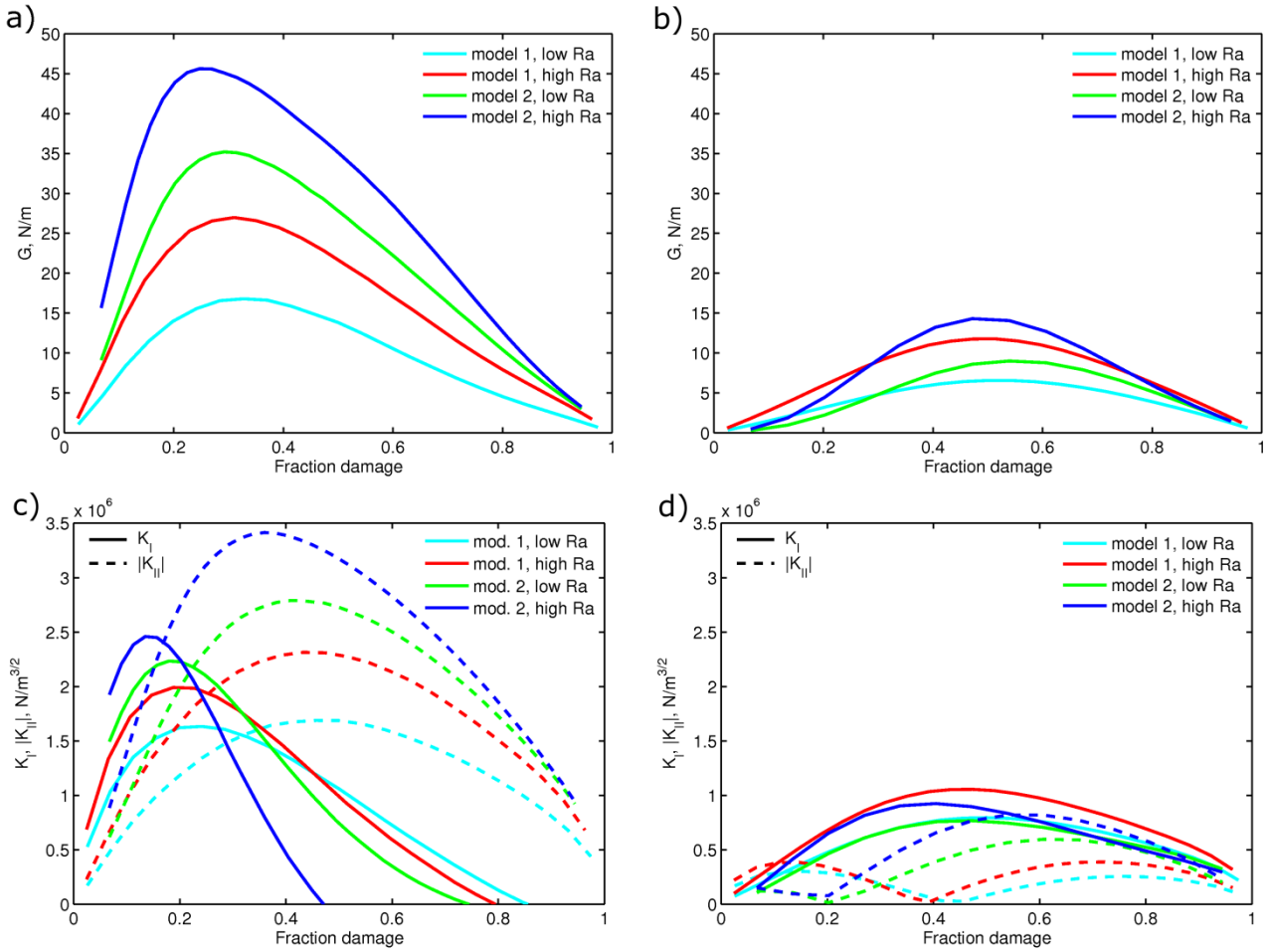

Figure 7. The calculated energy release rate, G, and stress intensity factors, K_I and K_{II} for a BC/TGO crack, a) and c), and a TGO/TC crack, b) and d).

4. Discussion

The large variation in fatigue life caused by different BC/TC interface roughness accentuates the importance of accurate interface models during FE modelling of crack growth in TBCs. Also other researchers have found the roughness to influence properties such as coating adhesion [8]. While earlier studies have investigated the influence of amplitude and wavelength on the stress field in TBCs by FE modelling [6,10-13], very little effort has been put on trying to derive those amplitudes and wavelengths from actual interfaces.

Both the suggested models were chosen so that they would agree well with the roughness parameters of the actual interfaces. Because of this, the models surely capture some of the characteristics of the interface. It is worth noting that the wavelength derived from $R\Delta q$ is the same for both specimens; also the *RSm* values indicate that the wavelengths of the specimens are in fact very similar. Casu et al. [9] argued that the wavelength could be correlated to the powder size during spraying; however, that is not the case for the specimens presented here.

The performed FE modelling may serve as a tool for evaluation of the relative behaviour of crack growth in the suggested interface models. Both model 1 and 2 showed an unexpected behaviour in that the G, as well as the K_I and K_{II}, increased with higher roughness; higher roughness was experimentally shown to increase fatigue life. Neither model 1 or 2 thus capture the experimentally observed tendency for higher interface roughness to promote longer fatigue lives.

Several explanations for this discrepancy exist, among them:

- The sine wave may be an inappropriate shape for modelling the interface.
- The increase in mechanical adhesion caused by the rougher interface may outweigh the detrimental effects of higher stresses in the interface.
- Cracks may grow in different ways than modelled here.

It is evident that further work remains before an FE model can accurately capture the experimentally observed tendency for higher interface roughness to promote longer fatigue life.

5. Conclusions

The bond coat/top coat interface roughness was shown to largely influence the thermal fatigue life of TBCs where higher roughness gave longer lives. Various roughness parameters were calculated from the interface roughness profiles, which were obtained by image analysis. *Ra*, *Rc* and *RΔq* were found to have a correlation with fatigue life where higher values gave longer life. The spacing parameter *RSm* was essentially the same for all specimens and could not have had an effect on the fatigue life. These parameters were used to establish two sine shaped interface models which were applied to FE modelling of crack growth in the specimens with shortest and longest life. The K_I and K_{II} were compared for the two specimens. Neither of the suggested models appeared to capture the experimentally observed tendency for increased life with higher roughness; the K_I and K_{II} increased with higher roughness for both suggested models. This study resulted in two interface models which were directly derived from the actual interface, but also showed that much work remains before accurate interface models can be formulated.

Acknowledgements

This research has been funded by the Swedish Energy Agency, Siemens Industrial Turbomachinery AB, GKN Aerospace Engine Systems, and the Royal Institute of Technology, through the Swedish research programme TURBO POWER, the support of which is gratefully acknowledged.

References

[1] J.T. DeMasi-Marcin, D.K. Gupta, Protective Coatings in the Gas Turbine Engine, Surf. Coat. Technol. 68/69 (1994) 1–9.

[2] H.E. Evans, M.P. Taylor, Oxidation of high-temperature coatings, Proc. IMechE, J. Aerospace Engineering. 220 (2006) 1–10.

[3] G.W. Goward, Progress in coatings for gas turbine airfoils, Surf. Coat. Technol. 108/109 (1998) 73–79.

[4] M.J. Pomeroy, Coatings for gas turbine materials and long term stability issues, Mater. Des. 26 (2005) 223–231.

[5] S. Sjostrom, H. Brodin, Thermomechanical fatigue life of TBCs - experimental and modelling aspects, Ceram. Eng. Sci. Proc. 31 (2010) 23–39.

[6] M. Jinnestrand, S. Sjostrom, Investigation of 3D FE simulations of delamination crack initiation in TBC caused by alumina growth, Surf. Coat. Technol. 135 (2001) 188–195.

[7] H. Brodin, R. Eriksson, S. Johansson, S. Sjostrom, Fracture mechanical modelling of a plasma sprayed TBC system, Ceram. Eng. Sci. Proc. 30 (2010) 113–124.

[8] A. Nusair Khan, J. Lu, H. Liao, Effect of residual stresses on air plasma sprayed thermal barrier coatings, Surf. Coat. Technol. 168 (2003) 291–299.

[9] A. Casu, J. Marques, R. Valien, D. Stover, Numerical simulation of crack growth mechanisms occurring near the bondcoat surface in air plasma sprayed thermal barrier coatings, Ceram. Eng. Sci. Proc. 27 (2007) 115–126.

[10] M. Ahrens, R. Vafien, D. Stover, Stress distributions in plasma-sprayed thermal barrier coatings as a function of interface roughness and oxide scale thickness, Surf. Coat. Technol. 161 (2002) 26–35.

[11] M. Baker, J. Rosler, G. Heinze, A parametric study of the stress state of thermal barrier coatings, Acta Mater. 53 (2005) 469–476.

[12] Y. Liu, C. Persson, J. Wigren, Experimental and Numerical Life Prediction of Thermally Cycled Thermal Barrier Coatings, J. Therm. Spray Technol. 13 (2004) 415–424.

[13] J. Aktaa, K. Sfar, D. Munz, Assessment of TBC systems failure mechanisms using a fracture mechanics approach, Acta Mater. 53 (2005) 4399–4413.

[14] E.S. Gadelmawla, M.M. Koura, T.M.A. Maksoud, I.M. Elewa, H.H. Soliman, Roughness parameters, J. Mater. Process. Technol. 123 (2002) 133–145.

[15] J.W. Hutchinson, Z. Suo, Mixed Mode Cracking in Layered Materials, Advances in Applied Mechanics. 29 (1991) 63–191.

Appendix: Mechanics of the interface crack

From the FE solution, the energy release rate G and the crack flank displacements $u_1^{(u)}$, $u_1^{(l)}$, $u_2^{(u)}$ and $u_2^{(l)}$ at a number of nodes along the crack flank are used.

For a description of the theory of an interface crack see, for instance, [15].
The relation between G, K_I and K_{II} is given by

$$G = \frac{1}{H}(K_I^2 + K_{II}^2) \tag{6}$$

in which

$$H = \frac{2\cosh^2(\pi\epsilon)}{\frac{1}{E_1^*} + \frac{1}{E_2^*}}$$

$$\epsilon = \frac{1}{2\pi}\ln\frac{\frac{1+\nu_2}{E_2} + \kappa_1\frac{1+\nu_1}{E_1}}{\kappa_2\frac{1+\nu_2}{E_2} + \frac{1+\nu_1}{E_1}}$$

$$\kappa_i = \begin{cases} 3-4\nu_i \text{ ; plane strain} \\ \dfrac{3-\nu_i}{1+\nu_i} \text{ ; plane stress} \end{cases} ; i = 1,2$$

$$E_i^* = \begin{cases} \dfrac{E_i}{1-\nu_i^2} \text{ ; plane strain} \\ E_i \text{ ; plane stress} \end{cases} ; i = 1,2$$

Using the general fracture-mechanical solution for an interface crack, $\delta_1 = u_1^{(u)} - u_1^{(l)}$ and $\delta_2 = u_2^{(u)} - u_2^{(l)}$ are then given by

$$\begin{bmatrix}\delta_1 \\ \delta_2\end{bmatrix} = \Psi \cdot \begin{bmatrix}\sin(\epsilon\ln r) - 2\epsilon\cos(\epsilon\ln r) & 2\epsilon\sin(\epsilon\ln r) + \cos(\epsilon\ln r) \\ 2\epsilon\sin(\epsilon\ln r) + \cos(\epsilon\ln r) & -\sin(\epsilon\ln r) + 2\epsilon\cos(\epsilon\ln r)\end{bmatrix}\begin{bmatrix}K_I \\ K_{II}\end{bmatrix} \tag{7}$$

where

$$\Psi = \frac{1}{2}\left(\frac{1}{E_1^*} + \frac{1}{E_2^*}\right)\cdot\frac{8}{(1+4\epsilon^2)\cosh(\pi\epsilon)}\cdot\left(\frac{r}{2\pi}\right)^{\frac{1}{2}}$$

Eq. (7) is only used for establishing an expression for $\beta = K_I/K_{II}$:

$$\beta = \frac{K_I}{K_{II}} = \frac{[\sin(\epsilon\ln r) - 2\epsilon\cos(\epsilon\ln r)]\cdot\delta_1 + [2\epsilon\sin(\epsilon\ln r) + \cos(\epsilon\ln r)]\cdot\delta_2}{[2\epsilon\sin(\epsilon\ln r) + \cos(\epsilon\ln r)]\cdot\delta_1 - [\sin(\epsilon\ln r) - 2\epsilon\cos(\epsilon\ln r)]\cdot\delta_2} \tag{8}$$

By combining Eq. (6) and (8) we finally get

$$\begin{cases} K_I = \sqrt{\dfrac{GH}{1+\dfrac{1}{\beta^2}}} \\ K_{II} = \sqrt{\dfrac{GH}{1+\beta^2}} \end{cases} \tag{9}$$

Experimental and Numerical Investigation into the Adhesion of PVD Coatings on Minting Dies

Jason Tunis[1], Xin Wang[1,*] and Xianyao Li[2]

[1] Department of Mechanical and Aerospace Engineering, Carleton University,
Ottawa, Ontario, K1S 5B6, Canada
[2] Corporate Engineering, Royal Canadian Mint, 320 Sussex Drive,
Ottawa, Ontario, K1A 0G8, Canada
*Corresponding author: xwang@mae.carleton.ca

Abstract This paper reports on the adhesion characterization of a PVD coating deposited onto mirror polished and laser frosted minting die surfaces. Experimental and numerical methods are both used to study the adhesion of the PVD coating. Stepped Rockwell-C indentation testing method is used to experimentally examine the coating adhesion. Finite element analyses of the stepped indentation adhesion tests are performed using critical loads determined from experimental testing. The analyses are performed to determine the stresses produced at the coating-substrate interface prior to coating adhesion failure and characterize the coating adhesion. The indentation simulations found that large compressive, shearing, and opening stresses were present at the coating-substrate interface in the regions where coating delamination was observed during experimental testing. The value of the compressive, opening, and shear critical stresses are found during finite element simulation of the indentation. These stress components provide good quantification of the coating adhesion strength.

Keywords PVD coating, adhesion, indentation tests, critical stresses

1. Introduction

Advances in the minting of coinage have led to the use of highly specialized die coatings. These coatings, in the form of thin hard films, are applied to die surfaces to improve their surface performance and increase their service life. The Royal Canadian Mint (RCM) uses a Cr-Ti-N based physical vapour deposition (PVD) coating applied to a hardened tool steel using magnetron sputter ion plating [1].

Coin forming is achieved by the striking of a blank disc between two dies. A collar surrounding the blanks circumference limits radial expansion of the blank during striking. The forming process produces large stresses in the die coating and steel substrate. The coating is expected to survive thousands to multiple hundreds of thousands of these impacts. To achieve long die life, the coating must be well adhered to the tool steel substrate and for this reason it is very important to ensure that adequate adhesion is achieved.

In recent years, laser engraving and frosting has started to be used on minting dies prior to coating to produce highly detailed coins with new surface finishes. Limited research has been completed in examining the effect of these new surface finishes on coating adhesion.

Many test methods exist for examining the adhesion between the coating and substrate. Among them are the indentation and the scratch adhesion tests, both of which are commonly used for testing the adhesion of thin hard coatings. These adhesion tests can be used to characterize the coating adhesion semi-quantitatively and with added analyses quantitatively [2].

Recently, the combination of experimental testing and numerical simulation has been used by several researchers to quantify coating adhesion. Indentation adhesion tests have been used together with finite element simulations to quantify the adhesion of thin hard coatings, see Pachler et al. [3], Nygards et al. [4], Xu et al. [5] and Sun et al. [6], for examples.

In this paper, the combination of experimental testing and finite element simulations of indentation tests is used to quantify the adhesion of the PVD coating used by the RCM. The adhesion to a mirror polished surface and to several laser frosted surfaces are examined. The critical loads determined during experimental testing are used in the finite element simulations. The maximum opening stress, maximum shear stress and maximum compressive stress values at the coating-substrate interface determined from finite element simulations are used to characterize the adhesion strength.

2. Background

In this section, an examination of the adhesion of thin-film systems and the testing of their adhesion are summarized. A detailed review of the use of experimental adhesion testing combined with numerical simulations to quantify the stresses produced during testing is presented for the indentation tests.

2.1. Adhesion of Thin-Film Systems

Depositing a thin hard film onto a softer substrate is only beneficial if the film has good adhesion and does not fail during normal operation. For this reason, coating adhesion must be closely examined and well understood.

Adhesion is defined as an attractive process between dissimilar materials which brings two compounds into direct contact. The strength of adhesion is difficult to quantify, but can be determined qualitatively, semi-quantitatively, and under certain scenarios quantitatively using various adhesion tests. The adhesion measurement between two materials estimated during experimental testing is generally dependent on the test method employed to determine it. For this reason, adhesion test results must be stated with the method used to determine them. Common adhesion test methods are the indentation test, scratch test, peel test, tape test, blister test, self loading test, beam bending test, pull test, and laser spallation test [2]. The indentation adhesion tests are reviewed below. Indentation adhesion tests will be used in this paper to quantify the adhesion strength of the PVD coating.

2.2. Indentation Adhesion Test

Indentation testing was first developed to quantify the hardness of materials. By applying a specific load using a standardized indenter, the hardness of a material can be determined by measuring the size of the resultant indentation crater and/or the vertical displacement of the indenter. Several varieties exist and the following is a list of the most common indentation tests: Brinell hardness test, Rockwell hardness test, Vickers hardness test, and Knoop hardness test. Corresponding ASTM standards can be found for these various tests.

Indentation tests can also be used to test the adhesion of coatings. The procedure is very similar to indentation tests completed to determine hardness except instead of measuring the indentation size, the damage caused to the coating is examined. A schematic of an indentation adhesion test is shown in Figure 1 and the apparatus used for testing in this paper is shown in Figure 2. The advantages of this test method are:

- sample preparation is minimal
- the test equipment is readily available (cost effective)
- test standards are well established
- semi-quantitative or quantitative results can be achieved

2.3. Finite Element Simulation of Indentation Adhesion Testing

In order to further understand the causes of coating failures during indentation adhesion testing, the stress state in the coating can be determined using finite element analysis. Radial and circular cracking the coatings has been studied by examining the tangential and radial stresses induced during indentation. This provides insight into through thickness coating failure. Delamination along the coating-substrate interface (adhesion failure) has been studied by examining the shear and opening stresses at the interface. Compressive stress in the coating are also be studied if buckling failure of the coating is present in experimental testing.

In this paper, indentation adhesion tests will be performed to obtain the critical load at which adhesion failure occurs for the PVD coating on each die surface. These loads will then be used in finite element analysis. The corresponding maximum opening, shear, and compressive stresses at the coating-substrate interface will be used to quantify the coating adhesion.

3. Experimental Testing of Coating Adhesion

The experimental setup, procedure, and results of the adhesion testing completed on the hard PVD coating used by the RCM are presented in this section. Eight dies were prepared and the adhesion of the coating to a mirror surface and to four laser frosted surfaces was investigated using a stepped variation of the Rockwell-C indentation adhesion test.

3.1. Sample Preparation

The dies used for testing were machined from a soft annealed bar stock of a tool steel. The bar stock was first cut to length and the top and bottom surface were machined flat using a lathe. The machined substrates were then heat treated using a vacuum heat treatment furnace. The top surface of the substrates was then polished to a mirror surface. In total eight test dies were manufactured. Four of the eight dies were laser frosted on three quarters of their surface, each with a different surface frosting (termed as Bullion, Glass Bead, Four-to-One, and Aluminum Oxide, respectively) as shown in Figure 3. The remaining four were not laser frosted. After preparing the die surface, the hard PVD coating was applied using a Teer UDP650/4 magnetron sputter ion plating system. The thickness of the Cr-Ti-N PVD coating is controlled to between two and three μm.

3.2. Stepped Indentation Adhesion Test

The stepped indentation adhesion test is a variation on the Rockwell-C indentation adhesion test. The indentation load is increased in steps and the produced indentation craters are examined for signs of coating failure. Coating delamination was defined as the failure criteria and the highest loading case which causes no coating delamination was examined for each coated die surface. The maximum survivable load provides a semi-quantitative measurement of the PVD coating adhesion and will also be used later in section 4 during finite element simulations. The maximum survivable load will be the indentation load used in simulations of indentation tests examining the stress state at the coating-substrate interface prior to coating adhesion failure.

The experimental apparatus is the same as that used for the Rockwell-C indentation adhesion tests, but for this test multiple loading conditions were used. The available weight options were 15, 30, 45, 60, 100, 150 kg_f and all were used.

3.3 Experimental Results

Multiple indentation tests were performed on each different die surface to determine the maximum load each respective coating-substrate systems could withstand. More tests were performed at loadings where the coating changed from a pass to a fail. The stepped indentation tests for the PVD coating on the mirror surface and laser frosted surfaces are conducted, in this manner. The following subsections provide observations for each die surface.

PVD coating deposited on a mirror surface

A summary of the results for the stepped indentation test of the PVD coating deposited on a mirror surface is shown in Figure 4. The indentation tests using a 45 kg_f load caused a delamination for half of the 14 tests and the tests performed using a 30 kg_f load only caused one delamination out of 14 tests. The typical results for indentations of 30 kg_f can be seen in Figure 5. Cracking is visible around the circumference of the indent crater and small radial cracks are also visible. The typical results of indents using 60, 100, and 150 kg_f were also obtained. Small delaminations are visible around the edge of the craters and the cracking is no longer radial. The 30 kg_f load was found to be the maximum load the coating could reliably survive without coating delamination.

PVD coating deposited on a Bullion type laser frosted surface

The Bullion test results show that the coating failed all three 45 kg_f and passed all three 30 kg_f. Figure 6 shows typical results for 30 kg_f loading conditions. For loads at 30 kg_f loading condition only causes cracking, while the higher loading condition causes cracking and delamination. Therefore, the 30 kg_f loading was found to be the maximum survivable indentation load for the Bullion laser frosted surface.

PVD coating deposited on a Glass Bead type laser frosted surface

The Glass Bead test results show that the maximum safe load is 15 kg_f. Typical results are shown in Figure 7 for 15 kg_f loading conditions. The 15 kg_f loading condition only causes cracking, while the 30 kg_f loading condition causes cracking and delamination. The 15 kg_f loading case was found to be the maximum survivable load for the Glass Bead laser frosted surface.

Note the other two types of laser frosted surfaces (four-to-one, and aluminum oxide), the surface roughness makes the finding of coating failure difficulty, therefore, from now on, only Bullion and Glass Bead laser surfaces are further studied together with mirror finished surface.

4. Finite Element Simulation of Indentation Adhesion Testing

This section presents the two-dimensional axisymmetric finite element simulation of indentation adhesion tests using ABAQUS [7]. The simulations are used to determine the stress state at the coating-substrate interface prior to coating failure. Focus is placed on the opening stress, the shear stress, and compressive stress at the interface since these stress components are the likely cause of delamination growth. The maximum survivable indentation loads estimated using the stepped indentation adhesion tests in Section 3 are used as indentation loads in the simulations. Simulations are completed using 15 and 30 kg_f indentation loads. The 15 kg_f simulation represents the PVD coating deposited on the Glass Bead laser frosted surface and the 30 kg_f represents the PVD coating deposited on the mirror surface and Bullion laser frosted surface.

The finite element model geometry, boundary conditions, material properties, and mesh design will be outlined below, followed by a presentation of the computed stress state at the coating-substrate interface. The opening, shear, and compressive stresses at the coating-substrate interface will provide a quantification of the PVD coating adhesion strength to the mirror surface and Glass Bead and Bullion laser frosted surfaces.

4.1 FEM Model Setup, Geometry, and Boundary Conditions

The indentation adhesion test is axisymmetric and therefore a simplified axisymmetric finite element model was used to simulate the test. ABAQUS/Standard version 6.8 [7] was used for the finite element analysis. The indentation adhesion test consists of three steps, first the indenter is lowered to the die surface and then load is applied and ramped up to the maximum load. Finally the load is removed and the indenter is raised off the die surface. The indentation test was modeled as quasi-static and all time-dependant effects were neglected. The indenter and die geometry and the boundary conditions are presented below.

Indenter Geometry

The indenter geometry used is that of a Rockwell-C cone indenter as defined by ASTM E18-8b [8]. The indenter has a 200 μm radius cone tip and 60° half angle. The axisymmetric indenter model was defined as presented in Figure 8 and the geometry was fixed to a reference point. Displacements and loads are applied to the indenter by moving or loading the reference point.

Die Geometry

The die geometry used is shown in Figure 9. An axisymmetric boundary condition is placed on the axis of symmetry and vertical displacement is fixed at the bottom of the model. The PVD coating thickness used by the RCM is controlled to be between two and three microns. The average of the thickness range, 2.5 μm, was selected for the model. The overall size of the die segment modeled was one millimetre by one millimetre and was selected after testing different model sizes. Multiple model sizes were tested and the model size selected was chosen since it minimized the model size while not affecting the stress values at the coating-substrate interface.

4.2 Material and Interface Properties

Indenter Properties

The Rockwell-C indenter tip is made of diamond which is significantly harder than the die substrate. The deflection of the diamond indenter during loading up to the maximum indentation load used, 30 kg_f, is negligible and therefore it was modeled as an analytical rigid body.

Substrate Properties

The substrate of the die samples used for experimental testing was a tool steel and it was modeled as an elastoplastic material with isotropic strain hardening. The material properties used during indentation simulations are shown in Table 1. The elastic modulus and yield strength values were taken from a tool steel material datasheet [9]. The Ramberg-Osgood stress strain relationship was used to define the materials strain hardening as follows:

$$\varepsilon = \frac{\sigma}{E} + \alpha \frac{\sigma_y}{E} \left(\frac{\sigma}{\sigma_y} \right)^n \quad (1)$$

where α is the yield offset and n is the strain hardening exponent. Assuming an industry standard strain value of 0.2 % was used when defining the yield strength of the tool steel, α can be calculated to be 0.18.

The strain hardening exponent was determined using a numerical and experimental approach as described by J. Yan et al. [10]. A strain hardening exponent value (n) of 15 was found to agree well with the experimental data and therefore n = 15 was used as the strain hardening exponent for the substrate.

Coating Properties

The material properties used for defining the Cr-Ti-N based hard PVD coating are shown on Table 2. The elastic modulus, yield strength, and Poisson's ratio values for the PVD coating were determined using nano-indentation testing completed by McLean [11]. As recommended by Piana et. al [12], Ramberg-Osgood strain hardening parameters of α = 1 and n = 100 were chosen to produce a material with minimal strain hardening.

Interface Properties

The loading conditions used during the indentation test simulations are below the failure load of the coating-substrate interface, therefore the interface between the coating and substrate was modeled as being in perfect adhesion.

The interaction between the indenter and the coating surface was defined using the "Interaction Module" built into ABAQUS [7]. A contact pair was defined, with indenter being the master surface and the coating surface being the slave surface. The indenter is ideal for the master surface because it is an analytical rigid body and is accurately defined without discretization using an arc and a line. To complete the interaction definition the tangential and normal behaviour between the two surfaces must be defined. The tangential behaviour was defined as frictionless as recommended by Piana et al. [12]. Neglecting friction has an insignificant effect on the results of indentation test simulations [12]. The normal behaviour was defined as "hard contact", which does not allow the coating top surface nodes to pass through the indenter geometry. Separation after contact was permitted to allow for unloading of the indenter.

4.3 Mesh Design

The mesh was refined towards the indentation location to properly model the large deformation and steep stress gradient. Due to the large deformation in the region of the indentation, it is important to enable nonlinear geometry in ABAQUS [7]. The finite element models were discretized using 4-node bilinear axisymmetric quadrilateral elements, which are defined as CAX4R in the ABAQUS element library [7]. This element type is a first order continuum element and uses reduced integration. Reduced integration lowers the number of constraints introduced by the elements, thus decreasing the CPU time and storage requirements and also preventing volumetric locking. The "hourglass control" is enabled to address the potential zero energy deformation modes (hourglass modes) introduced when using reduced integration [7]. The mesh design of the

coating-substrate system is shown in Figure 10. The shown model uses 4 element layers to discretize the coating, 8, 16 and 25 layered meshes were also used for mesh refinement analysis. A node set is defined along the coating-substrate interface for easy retrieval of displacement and stress data during post processing.

4.4. FEA results

Stress Transformation

In order to properly evaluate the stresses at the coating-substrate interface, the global stress components obtained from ABAQUS [7] must be transformed into local coordinate stress components. Figure 11 shows how the global coordinates axes (x-y-z) relate to the local coordinates axes (x'-y'-z'). The x' local coordinate axis is parallel to the coating-substrate interface and the y' local coordinate axis is perpendicular to the coating-substrate interface. The following equations show how the global stress components were transformed into local stress components [13]:

$$\sigma_{x'x'} = \frac{\sigma_{xx}+\sigma_{yy}}{2} + \frac{\sigma_{xx}-\sigma_{yy}}{2}\cos 2\theta + \tau_{xy}\sin 2\theta \quad (2)$$

$$\sigma_{y'y'} = \frac{\sigma_{xx}+\sigma_{yy}}{2} - \frac{\sigma_{xx}-\sigma_{yy}}{2}\cos 2\theta - \tau_{xy}\sin 2\theta \quad (3)$$

$$\sigma_{z'z'} = \sigma_{zz} \quad (4)$$

$$\tau_{x'y'} = \frac{\sigma_{xx}-\sigma_{yy}}{2}\sin 2\theta + \tau_{xy}\cos 2\theta \quad (5)$$

Going forward, $\sigma_{x'x'}$, $\sigma_{y'y'}$, $\sigma_{z'z'}$, and $\tau_{x'y'}$ will be called the radial stress, the opening stress, the hoop stress and the shear stress. Note that the stress component ($\sigma_{x'x'}$) named radial stress is not perfectly radial once x' is not aligned with x, but the name is still used for simplicity. The two out of plane shear stress components, τ_{xz} and τ_{yz}, are zero due to the problem being axisymmetric.

Results

The stress state at the coating-substrate interface was examined at two times during the simulations, first when the maximum indentation load is applied and second after unloading of the indenter. Von Mises stress, radial stress ($\sigma_{x'x'}$), hoop stress ($\sigma_{z'z'}$), opening stress ($\sigma_{y'y'}$), and shear stress ($\tau_{x'y'}$) along the coating-substrate interface for both the maximum load and after unloading states are obtained. The stress in the coating material and substrate material at the interface are both included in the presented stress results.

Von Mises Stress Results

Von Mises stress contour plots are shown in Figure 12 (maximum load case) and Figure 13 (after unloading) for the 30 kg_f indentation case. At maximum load, large von Mises stresses occur in the coating under the indenter and extend outward past the indentation radius. After unloading, the von Mises stress is significantly reduced inside the crater region, but large values are still present outside the indentation radius. Very low von Mises stress gradients are present near the bottom and right edges of the model, which shows that the model was properly sized. Results for 15 kg_f are also obtained.

The maximum von Mises stress experienced in the coating is 8.31 GPa and 8.39 GPa for the 15

and 30 kg_f loading conditions respectively. The maximum von Mises stress experienced in the substrate is 3.10 GPa and 3.23 GPa for the 15 and 30 kg_f loading conditions respectively. All the maximum von Mises stresses occur at the maximum load condition.

Results of Stress Components

The opening stress ($\sigma_{y'y'}$) distribution along the interface is obtained for (15 kg_f) and (30 kg_f). The coating and substrate opening stress distribution match very well as expected due to stress equilibrium perpendicular to the interface [14]. The maximum opening stress occurs near the indentation crater edge after unloading with values of 0.896 GPa (coating) and 0.872 GPa (substrate) for the 15 kg_f loading case and of 1.18 GPa (coating) and 1.16 GPa (substrate) for the 30 kg_f loading case. These simulated opening stresses provide a measure of the coating adhesion strength for the mirror surface and Bullion and Glass Bead laser frosted surface.

To satisfy equilibrium conditions along the coating-substrate interface, the shear stress ($\tau_{x'y'}$) in the coating and substrate materials must be equal and the results agree well with this equilibrium condition [14]. The difference between the coating and substrate shear stress value is minimal except near the indentation crater edge where a nearly 20% difference occurs. The maximum shear stress values along the interface are 1.89 GPa (coating) and 1.67 GPa (substrate) for the 15 kg_f loading case and of 2.16 GPa (coating) and 1.78 GPa (substrate) for the 30 kg_f loading case. These maximum shear stress values occur at maximum loading of the indenter and provide a measure of the coating adhesion strength for the simulated surface types.

The radial stress ($\sigma_{x'x'}$) distributions along the coating-substrate interface for the 15 and 30 kg_f loading cases are obtained. The maximum compressive radial stress occurs at maximum loading, the values for the 15 and 30 kg_f loading conditions are 11.29 GPa and 12.69 GPa. Table 3 summarised the maximum values of these stress components.

5. Conclusions

The stress state at the coating-substrate interface during 15 and 30 kg_f indentation tests has been simulated. Peak stress values were found in the region near the indentation crater edge, which is where failure was observed during experimental testing. Using finite element simulations, the PVD coating deposited on a mirror surface and Glass Bead and Bullion laser frosted surfaces was found to be capable of surviving the loads corresponding to stress values presented in Table 3. The peak opening and shear stresses at the coating-substrate interface provide a characterization of the coating adhesion strength since these two stress components are capable of directly causing delamination growth and coating adhesion failure. Significant compressive radial stress is present in the coating outside the indentation crater. In the presence of coating adhesion defects, this compressive stress can lead to coating buckling and spallation.

The three stress components (opening, shear, and radial compressive) reach their peak near the indentation crater edge, which is the location where coating delamination occurred during experimental testing at higher loads. Now that the stress state at the coating-substrate interface produced during indentation adhesion tests has been simulated and analyzed, a similar process can be performed for the scratch adhesion tests and the results can be compared.

Acknowledgements

The authors gratefully acknowledge the financial supports from the Ontario Centres of Excellence (OCE), Royal Canadian Mint and the Natural Sciences and Engineering Research Council (NSERC) of Canada. Thanks also go to Hibbit, Karlsson and Sorensen, Inc. for making ABAQUS available under an academic licence to Carleton University.

References

[1] Bodor, S., (2010). Personal interview at Royal Canadian Mint, Sept. 28 2010.

[2] Lacombe, R. (2006). Adhesion measurement methods: Theory and Practice. *CRC Press*, pp. 7-73.

[3] Pachler, T., Souza, R. M., Tschiptschin, A. P. (2007). Finite element analysis of peak stresses developed during indentation of ceramic coated steel. *Surface and Coating Technology*, Vol. 202, pp. 1098-1102.

[4] Nygards, C. M., White, K. W., Ravi-Chander, K. (1998). strength of HVOF coating-substrate interfaces. *Thin Solids Films*, Vol. 332, pp. 185-188.

[5] Xu, M., Li, L., Liu, Y., Cai, X., Chen, Q., Chu, P. K. (2007). Experimental tests and numerical simulation studies on nano-indenation of TiN film deposited on N+-implanted aluminum. *Surface and Coatings Technology*, Vol. 201, pp. 6707-6711.

[6] Sun, X., Liu, W. N., Stephens, E., Khaleel, M. A. (2008). Determination of interfacial adhesion strength between oxide scale and substrate for metallic SOFC interconnects. *Journal of Power Sources*, Vol. 176, pp. 167-174.

[7] ABAQUS (2008). ABAQUS Analysis User's Manual. ABAQUS *Online Documentation, Dassault Systèmes*, Version 6.8.

[8] ASTM E18-8b (2008). Standard Test Methods for Rockwell Hardness of Metallic Materials. *ASTM International.*

[9] Bohler Uddeholm (Novembe 15, 2010). Plastic Mold Steel. Retrieved November 15, 2010, from Bohler Uddeholm Web site: http://www.bucorp.com/plastics.htm

[10] Yan, J., Karlsson, A. M., Chen, X. (2007). Determining plastic properties of a material with residual stress by using conical indentation. International Journal of Solids and Structures, Vol. 44, Issue 11-12, pp. 3720-3737.

[11] McLean, D. A. (2010). The characterisation and performance of magnetron sputter coatings on minting dies. Department of Mechanical and Aerospace Engineering, Carleton University. Ottawa, Canada.

[12] Piana, L. A., Pérez, R. E., Souza, R. M., Kunrath, A. O., Strohaecker, T. R. (2005). Numerical and experimental analyses on the indentation of coated systems with different mechanical properties. *Thin Solid Films*, Vol. 491, pp. 197-203.

[13] Benham, P. P., Crawford, R. J., Armstrong, C. G. (1996). Mechanics of Engineering Materials, Prentice Hall, 2nd Ed., pp. 292-521.

[14] Ramalingam, S., Zheng, L. (1995). Film-substrate interface stresses and their roles in the tribological performance of surface coatings. Tribology International, Vol. 28, No. 3, pp. 145-161.

Table1 Material properties of the simulated substrate

Property	**Symbol**	**Value**
Elastic Modulus	E_s	213 GPa
Yield Strength	σ_{ys}	2.35 GPa
Poisson's Ratio	ν_s	0.3
Strain hardening exponent	n_s	15
Yield offset	α_s	0.18

Table 2 Material properties of the simulated coating

Property	**Symbol**	**Value**
Elastic Modulus	E_c	300 GPa
Yield Strength	σ_{yc}	8.2 GPa
Poisson's Ratio	ν_c	0.15
Strain hardening exponent	n_c	100
Yield offset	α_c	1

Table 3 Stress component values for coating adhesion strength characterisation

Stress Component *[material]*	**15 kg_f (Glass Bead)**	**30 kg_f (Mirror and Bullion)**
Maximum Opening stress (GPa) *[average of coating and substrate value]*	0.884	1.17
Maximum Shear stress (GPa) *[average of coating and substrate value]*	1.78	1.97
Maximum Compressive stress (GPa) *[coating value]*	-11.3	-12.7

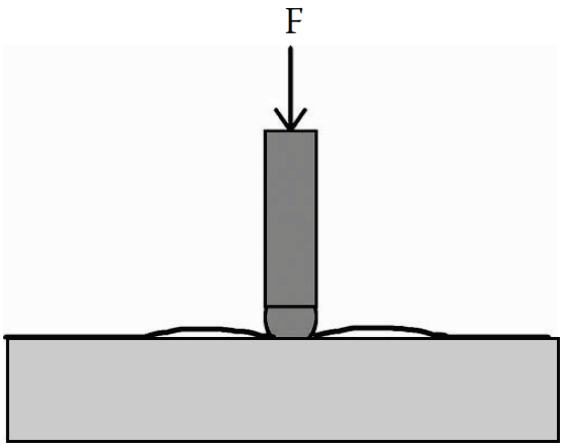

Figure 1. Schematic of indentation test causing coating adhesion failure [2]

Figure 2. Wilson Rockwell 3TT Twin Hardness Tester

Figure 3 Test dies with three-quarter laser frosted surfaces

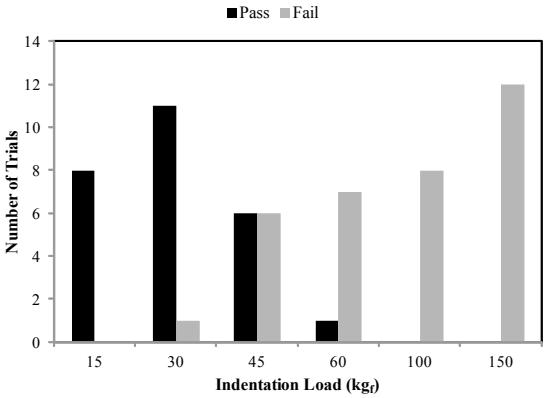

Figure 4 Distribution of the stepped indenation results for the PVD coating on a mirror surface

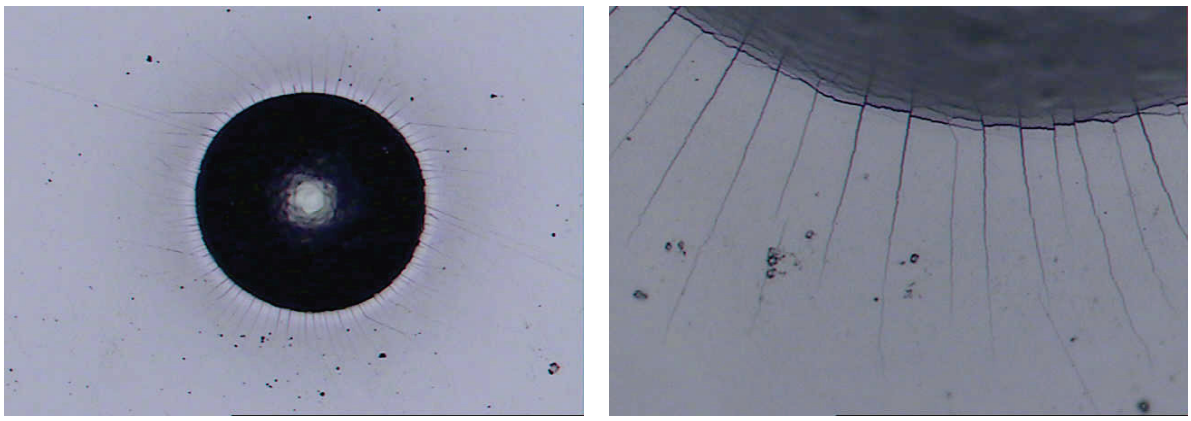

(10X) (50X)

Figure 5 Typical results for the Rockwell-C indentation of the PVD coating on a mirror surface for load 30 kg_f

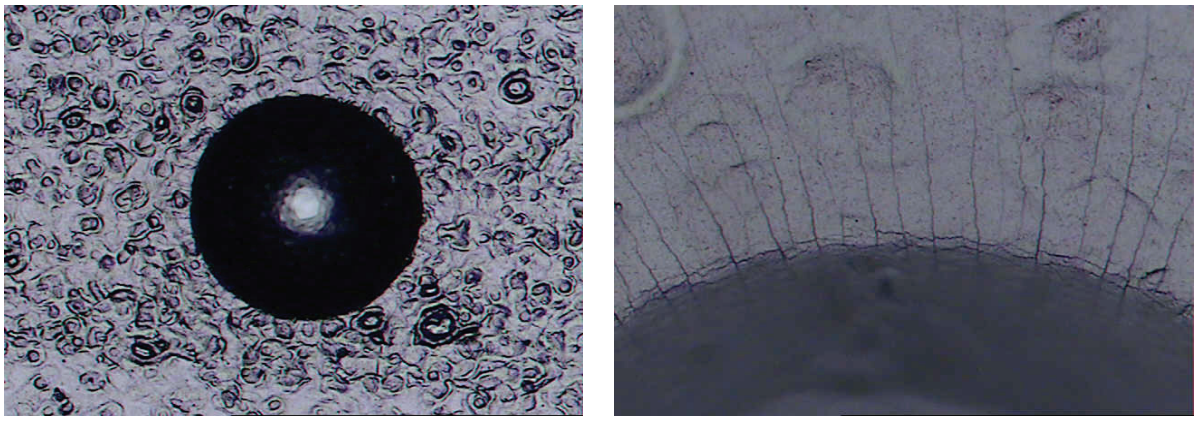

(10X) (50X)

Figure 6 Typical results for Rockwell-C indentation of the PVD coating on a Bullion laser frosted surface for loads of 30 kg_f

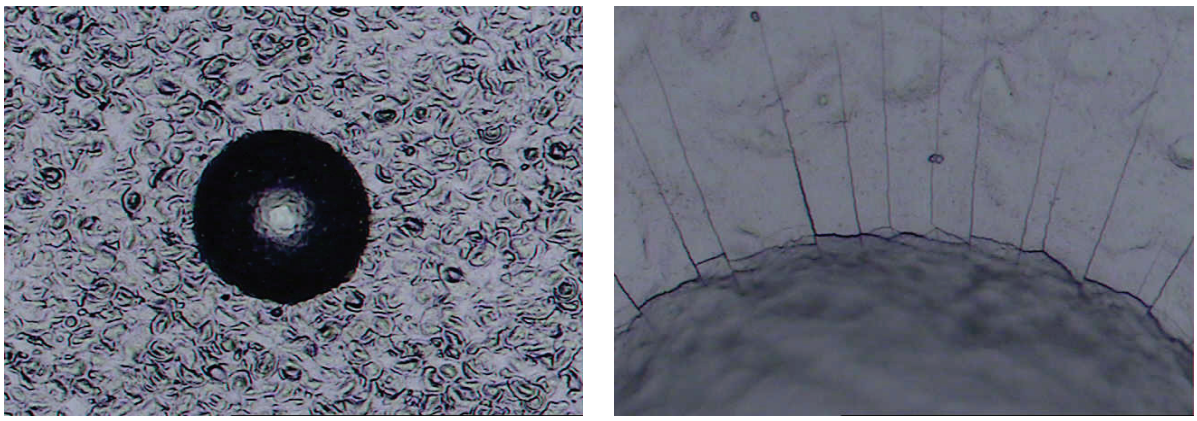

(10X) (50X)

Figure 7 Typical results for Rockwell indentation of the PVD coating on a Glass Bead laser frosted surface for loads of 15 kg_f

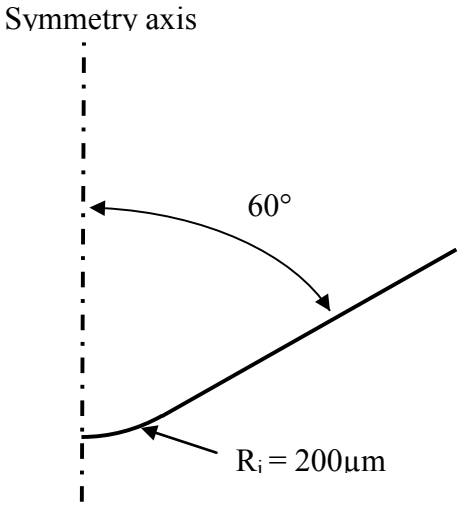

Figure 8 Rockwell C indenter tip geometry

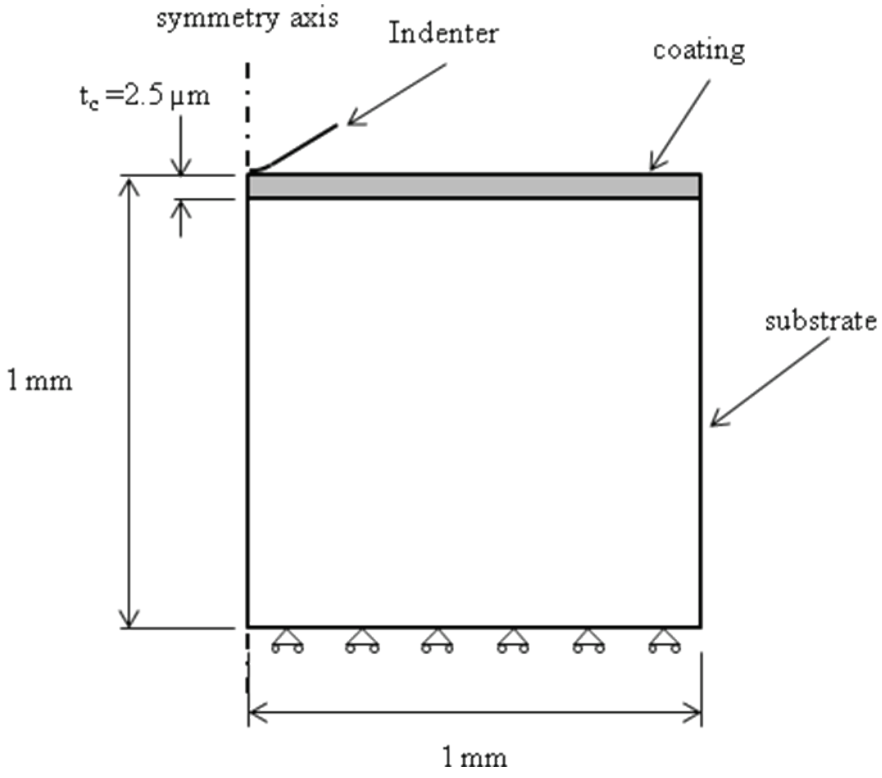

Figure 9 Die geometry and boundary conditions (not to scale)

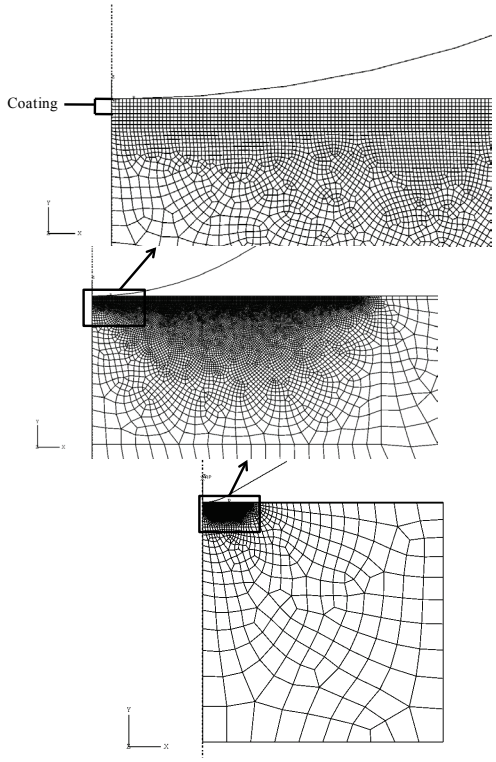

Figure 10 Coating substrate mesh design, 4 element layer coating

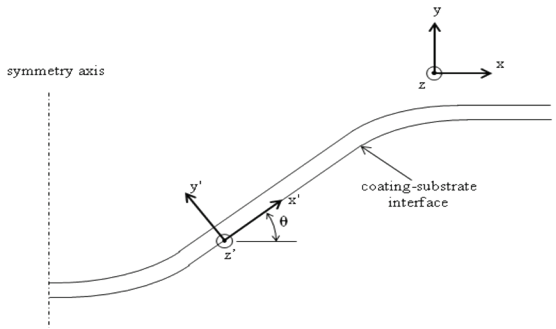

Figure 11 Local coordinate system at the coating-substrate interface

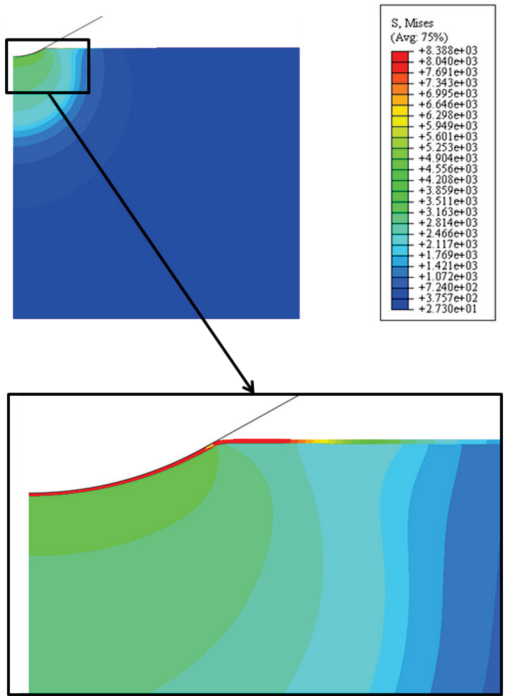

Figure 12 von Mises Stress contour at the 30 kg_f loading condition

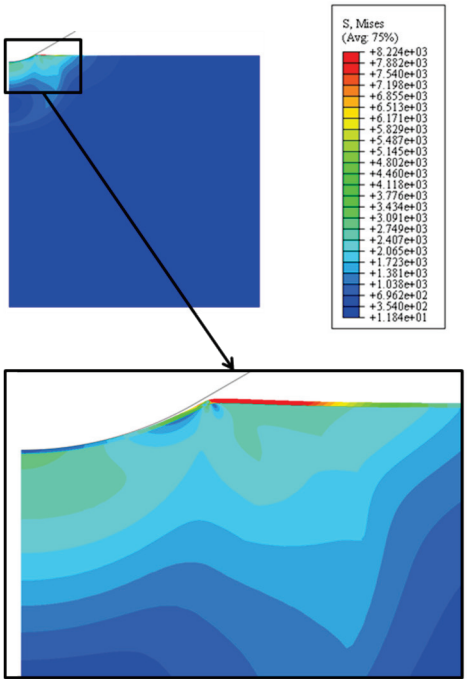

Figure 13 von Mises Stress contour after unloading the 30 kg_f load

Experimental study of the influence of thermal shock on mechanical properties of ceramic coating systems

Xiaona Li[1,*], Lihong Liang[1], Hua Wei[2], Yueguang Wei[1]

1 LNM, Institute of Mechanics, Chinese Academy of Sciences, Beijing, 100190, China
2 Institute of Metal Research, Chinese Academy of Sciences, Shenyang, 110016, China
* Corresponding author: lixiaona@lnm.imech.ac.cn

Abstract In this work, the change of Young's modulus, hardness, and bending strength of air plasma sprayed ceramic coating systems after different thermal shock was investigated by nanoindentation tests and three-point bending tests. The results of these tests show that the Young's modulus and hardness of nanostructured coatings and the bending strength of nanostructured coating-substrate systems fluctuate relatively slightly as the thermal shock temperature difference increases, while the Young's modulus and hardness of micro-structured coatings and the bending strength of micro-structured coating-substrate systems increase with the thermal shock temperature difference monotonously. Therefore, in the temperature range we studied, the mechanical properties of nanostructured coatings are less sensitive to the change of temperature and more stable than micro-structured coatings.

Keywords Ceramic coating systems, Thermal shock, Young's modulus, Bending strength

1. Introduction

Ceramic coatings are widely used because of their excellent thermal insulation, wear resistance and corrosion resistance [1, 2]. In the service condition of ceramic coatings, thermal shock frequently occurs. Therefore, in-depth understanding of the influence of thermal shock on mechanical properties of ceramic coating systems becomes significant. Some relevant studies on the effect of thermal shock on ceramic coatings have been reported. Bo Liang et al. [3] investigated the thermal shock resistances of nanostructured and conventional zirconia coatings deposited by atmospheric plasma spraying, and found that the nanostructured as-sprayed coating possessed better thermal shock resistance than the conventional coating. Chunxia Zhang et al. [4] studied the influence of thermal shock on insulation effect of nano-multilayer thermal barrier coatings, and acquired the change of thermal conductivity and impedance as function of thermal shock number. Moreover, some researches have shown that thermal shock could obviously affect the mechanical properties of Si-SiC coated C/C composites [5], fiber concrete [6], alumina–mullite–zirconia and alumina–mullite refractory materials[7]. However, there are few reports on the influence of thermal shock on mechanical properties of ceramic coating systems. Therefore, in this work, we studied the change of elastic modulus, hardness, and bending strength of air plasma sprayed ceramic coating systems by nanoindentation tests and three-point bending tests.

2. Experimental procedure

2.1. Specimen preparation

The ceramic coating system used in this study consists of YSZ (8 wt.% Y2O3 stabilized ZrO2) top coat prepared with atmospheric plasma spraying (APS), NiCrAlY (25.42wt.%Cr-5.1wt.%Al-0.48wt.%Y) bond coat prepared with high velocity oxygen fuel (HVOF) process and Ni-based superalloy substrate. The thickness of the top coat, bond coat and substrate is approximately 0.1 mm, 0.05 mm, and 1.35 mm separately. In our study, two kinds of ceramic coating layers were prepared---nano-scale and micro-scale microstructure, respectively.

2.2. Thermal shock tests

In the thermal shock tests, the specimens were heated with a rate of 20℃/min up to a preset temperature T_m (200 ℃, 500 ℃, and 800 ℃, respectively) and held at T_m for 20 min [8]. After that, the heated specimens were quickly placed into water at the ambient temperature (25 ℃) for quenching and maintained for 10 min [8]. Therefore, the thermal shock temperature difference ΔT is 175 ℃, 475 ℃, and 775 ℃, respectively. The mechanical property was then measured using nanoindentation and bending tests at room temperature.

2.3. Nanoindentation tests

The grinded and polished coatings were analyzed by nanoindentation tests in which the Agilent Technologies Nano Indenter G200 System was used. All indentations were done with a triangular pyramid Berkovich diamond indenter. The total number of measurement points for each sample was chosen to be 10. The indentation depth was 300 nm and the maximum load was 12 mN in the tests. The typical distance between two neighboring sites is above 50 μm aiming to avoid possible interference of measurements. During the indentation test，the indentation load and depth are measured by load cell and gap sensors.

2.4. Three-point bending tests

The three-point bending tests were done with a computer control electronic universal testing machine RG2000-5. The nominal dimensions of each specimen for the three-point bending test are 3 mm wide, 1.5 mm high and 15 mm long. The span length of the support is 10 mm. The tests were carried out under constant displacement rates 0.1 mm/min at the loading point. Consequently, we could acquire a series of load-displacement curves in the loading process.

3. Results and discussion

3.1. Influence of thermal shock on Young's modulus and hardness of ceramic coatings

In the temperature range of 25-800℃，the results of these tests show that the Young's modulus E and hardness H of nanostructured coatings fluctuate relatively slightly as the thermal shock

temperature difference ΔT increases, while that of micro-structured coatings increase with ΔT monotonously, as shown in Fig. 1. For the as-spayed coating, the Young's modulus of nanostructured coating $E_c = 161.2$ GPa and micro-structured coating $E_c = 101.4$ GPa, which are in good general agreement with former reports [9] [10] ; the hardness of nanostructured coating $H_c = 11.6$ GPa and micro-structured coating $H_c = 5.4$ GPa, which are close to some data in the literatures[2, 10] [11]. After the thermal shock test, we carefully examined the microstructure of specimens and found that the porosity of micro-structured coatings reduces relatively obviously with the increase of ΔT, while that of the nanostructured coatings changes a little. From the literature[12], for porous materials, the Young's modulus E can be described empirically by $E = E_0 \exp(-ap)$, where E_0 is the zero-porosity Young's modulus, p is the porosity, and a is an empirical constant. Therefore, the Young's modulus will increase as the porosity decreases, and our test results agree with this theoretical model.

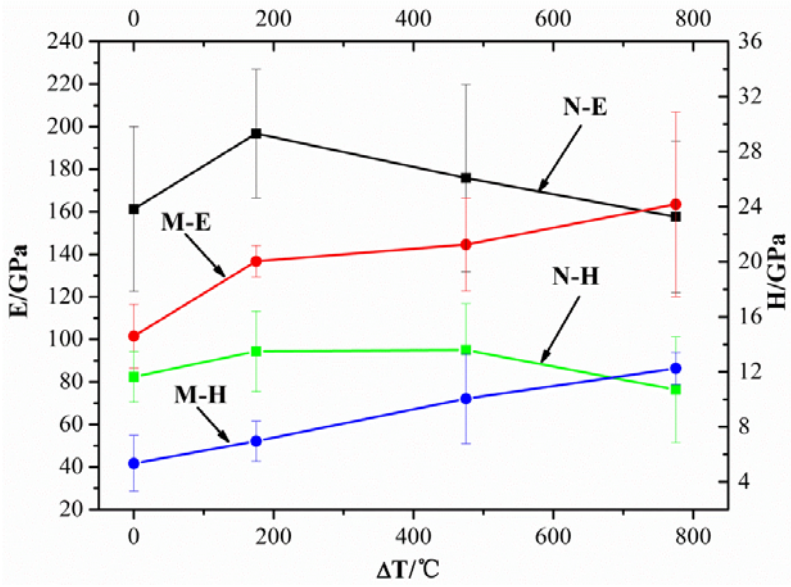

Figure 1. The change of Young's modulus and hardness of coatings with different thermal shock temperature difference ΔT (N-nanostructured coatings, M-micro-structured coatings).

3.2. Influence of thermal shock on bending strength of coating-substrate systems

One of the curves of the load F and loading point displacement w in our experiments is shown in Fig. 2. The maximum load was considered as the failure load and used to calculate the bending strength of coating-substrate systems.

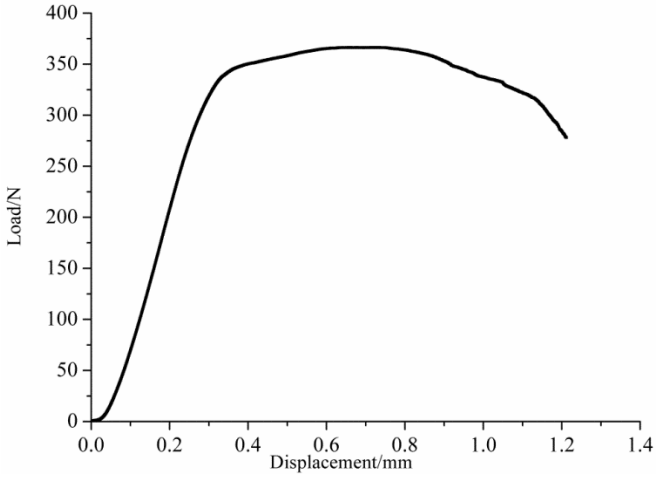

Figure 2. The load-displacement curve in three-point bending test.

During the three-point bending test, the largest normal stress at the failure load was considered to be the bending strength σ_b, which can be determined by Eq. (1) [13] as following:

$$\sigma_b = 0.8 \cdot (1 - \frac{4h}{3\pi l}) \cdot \frac{P_f l}{4} \cdot \frac{1}{M_0} \cdot \frac{E_c(h_c + \varsigma)}{E_s(h_s - \varsigma)} \qquad (1)$$

Where *l* and *h* are the span length of support and the height of specimens respectively, P_f is the failure load, h_c and h_s are the thickness of the coating and substrate respectively, E_c and E_s are the Young's modulus of coating and substrate respectively, ς is the distance between the neutral axis and the interface of the layered specimen, and M_0 is the resultant moment of the cross section. The values of ς and M_0 can be determined by $\varsigma = \frac{E_s h_s^2 - E_c h_c^2}{2(E_s h_s + E_c h_c)}$ and $M_0 = \frac{b}{3(\varsigma - h_s)}(h_s^3 - 3h_s^2\varsigma + 3h_s\varsigma^2) + \frac{E_c}{E_s}\frac{b}{3(\varsigma - h_s)}(h_c^3 + 3h_c^2\varsigma + 3h_c\varsigma^2)$, respectively, where *b* is the width of the specimen. The bending strength of all specimens obtained by Eq. (1) is presented in Fig. 3. It is worth mentioning that (1) the top coat and bond coat are considered as one layer, i.e. the coating, considering that Young's modulus of the bond coat is about 155 GPa [10, 14] which is close to that of the top coat, and the top coat and bond coat bind well according to our experimental observation, (2) the value of E_c is obtained from Fig. 2, and (3) the value of E_s is assumed constant and taken as 200 GPa [10] [15].

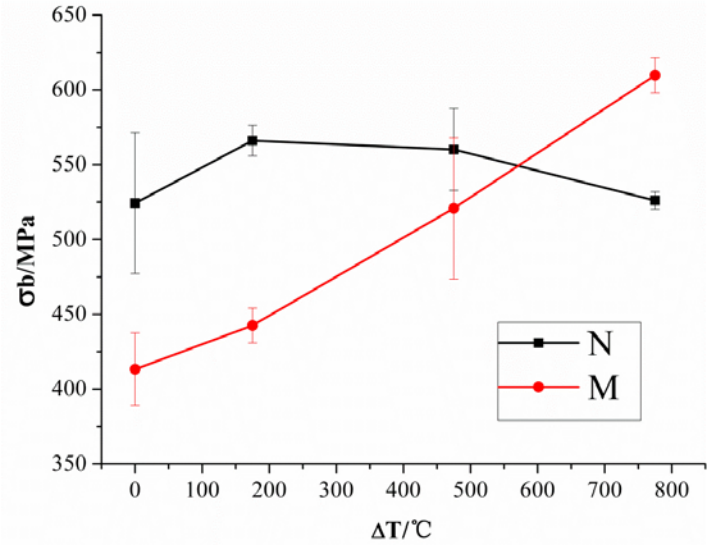

Figure 3. The change of bending strength of coating-substrate systems with different thermal shock temperature difference ΔT (N- nanostructured coatings, M- micro-structured coatings).

From Fig. 3, we can see that like the change of Young's modulus and hardness of coatings with different thermal shock temperature difference ΔT, the bending strength of nanostructured coating-substrate systems fluctuate relatively slightly as ΔT increases, while that of micro-structured coating-substrate systems increase monotonously with ΔT.

The bending strength of coating-substrate systems is determined by the strength of coating and substrate, and the interfacial bonding strength. In the temperature range of 25-800℃, the yield strength of the substrate is considered as constant[16]. Therefore, the main parameters are the strength of coating and the interfacial bonding strength. For porous materials, like the relationship between Young's modulus and porosity, the strength can be empirically described by $\sigma = \sigma_0 \exp(-kp)$ [17], where σ_0 is the zero-porosity strength, p is the porosity, and k is an empirical constant. Therefore, the strength will increase as the porosity decreases. Besides, according to our experimental observation, for micro-structured coating-substrate systems, the interfacial bonding strength decreases as the thermal shock temperature difference increases, while that of the nanostructured coating-substrate systems changes a little. Since the strength of coating-substrate systems is obviously influenced by the interfacial bonding strength, and weakening of interfaces helps to increase the bending strength of coating-substrate systems, [5] we can see that it is the combined effect of porosity of the coating and interfacial bonding strength of the coating-substrate that leads to the result of our tests.

4. Conclusions

In this work, the change of elastic modulus, hardness and bending strength of air plasma sprayed ceramic coating systems after different thermal shock was investigated by nanoindentation tests and three-point bending tests. The results of these tests show that (1) since the porosity of

micro-structured coatings reduces relatively obviously, while that of the nanostructured coatings changes a little with the increase of thermal shock temperature difference, the Young's modulus and hardness of nanostructured coatings fluctuate relatively slightly, while that of the micro-structured coatings monotonously increase as the thermal shock temperature difference increases. (2) Apart from the difference in porosity of the coating, the interfacial bonding strength of micro-structured coating-substrate systems decreases as the temperature increases, while that of the nanostructured coating-substrate systems changes a little. Therefore, the bending strength of nanostructured coating-substrate systems fluctuates relatively slightly, while that of micro-structured coating-substrate systems monotonously increases as the thermal shock temperature difference increases. In conclusion, in the temperature range we studied, the mechanical properties of nanostructured coatings are less sensitive to the change of temperature and more stable than micro-structured coatings.

Acknowledgements

This work was supported by the National Basic Research Program of China (2012CB937500), the National Natural Science Foundation of China (10802088, 10832008, and 11023001), and the Opening Fund of LNM.

References

[1] P.F. Zhao, C.A. Sun, X.Y. Zhu, F.L. Shang, C.J. Li, Fracture toughness measurements of plasma-sprayed thermal barrier coatings using a modified four-point bending method, Surf. Coat. Technol., 204 (2010) 4066-4074.

[2] N.P. Padture, M. Gell, E.H. Jordan, Thermal barrier coatings for gas-turbine engine applications, Science, 296 (2002) 280-284.

[3] B. Liang, C. Ding, Thermal shock resistances of nanostructured and conventional zirconia coatings deposited by atmospheric plasma spraying, Surf. Coat. Technol., 197 (2005) 185-192.

[4] C. Zhang, C. Zhou, H. Peng, S. Gong, H. Xu, Influence of thermal shock on insulation effect of nano-multilayer thermal barrier coatings, Surf. Coat. Technol., 201 (2007) 6340-6344.

[5] Q.G. Fu, H.J. Li, Y.J. Wang, K.Z. Li, L. Wei, Influence of Thermal Shock on the Mechanical Behavior of Si-SiC Coated Carbon/Carbon Composites, J. Mater. Sci. Technol., 25 (2009) 251-253.

[6] G.-F. Peng, S.-H. Bian, Z.-Q. Guo, J. Zhao, X.-L. Peng, Y.-C. Jiang, Effect of thermal shock due to rapid cooling on residual mechanical properties of fiber concrete exposed to high temperatures, Constr. Build. Mater., 22 (2008) 948-955.

[7] C. Aksel, Mechanical properties and thermal shock behaviour of alumina–mullite–zirconia and alumina–mullite refractory materials by slip casting, Ceram. Int., 29 (2003) 311-316.

[8] F. Song, S. Meng, X. Xu, Y. Shao, Enhanced Thermal Shock Resistance of Ceramics through Biomimetically Inspired Nanofins, Phys. Rev. Lett., 104 (2010).

[9] G. Soyez, J.A. Eastman, L.J. Thompson, G.R. Bai, P.M. Baldo, A.W. McCormick, R.J. DiMelfi, A.A. Elmustafa, M.F. Tambwe, D.S. Stone, Grain-size-dependent thermal conductivity of nanocrystalline yttria-stabilized zirconia films grown by metal-organic chemical vapor deposition, Appl. Phys. Lett., 77 (2000) 1155-1157.

[10] J.-Y. Kwon, J.-H. Lee, Y.-G. Jung, U. Paik, Effect of bond coat nature and thickness on mechanical characteristic and contact damage of zirconia-based thermal barrier coatings, Surf.

Coat. Technol., 201 (2006) 3483-3490.
[11] J.A. Thompson, T.W. Clyne, The effect of heat treatment on the stiffness of zirconia top coats in plasma-sprayed TBCs, Acta Mater., 49 (2001) 1565-1575.
[12] R.M. Spriggs, Expression for Effect of Porosity on Elastic Modulus of Polycrystalline Refractory Materials, Particularly Aluminum Oxide, J. Am. Ceram. Soc., 44 (1961) 628-629.
[13] H. Deng, H. Shi, S. Tsuruoka, Influence of coating thickness and temperature on mechanical properties of steel deposited with Co-based alloy hardfacing coating, Surf. Coat. Technol., 204 (2010) 3927-3934.
[14] Z.B. Chen, Z.G. Wang, S.J. Zhu, Tensile fracture behavior of thermal barrier coatings on superalloy, Surf. Coat. Technol., 205 (2011) 3931-3938.
[15] N. Zotov, M. Bartsch, G. Eggeler, Thermal barrier coating systems — analysis of nanoindentation curves, Surf. Coat. Technol., 203 (2009) 2064-2072.
[16] L.Z. He, Q. Zheng, X.F. Sun, G.C. Hou, H.R. Guan, Z.Q. Hu, Low ductility at intermediate temperature of Ni–base superalloy M963, Mater. Sci. Eng., A, 380 (2004) 340-348.
[17] D. W., Discussion of Ryshkewitch paper, J. Am. Ceram. Soc., 36 (1953) 68.

Asymptotic solutions for buckling delamination induced crack propagation in the thin film- compliant substrate system

Tongqing Lu, T. J. Wang*

State Key Lab for Strength and Vibration of Mechanical Structures, School of Aerospace Engineering,

Xi'an Jiaotong University, Xi'an 710049, P.R. China

* Corresponding author: wangtj@mail.xjtu.edu.cn

Abstract In a thin-film substrate system in-plane compressive stress is commonly generated in the film due to thermal mismatch in operation or fabrication process. If the stress exceeds a critical value, part of the film may buckle out of plane along the defective interface. After delamination buckling, the interface crack at the ends may propagate. In the whole process, the compliance of the substrate compared with the film plays an important role. In this work, we study a circular film subject to compressive stress on an infinitely thick substrate. We study the effects of compliance of the substrate by modeling the system as a plate on an elastic foundation. The critical buckling condition is formulated. The asymptotic solutions of post-buckling deformation and the corresponding energy release rate of the interface crack are obtained with perturbation methods. The results show that the more compliant the substrate is, the easier for the film to buckle and easier for the interface crack to propagate after buckling.

Keywords buckling delamination, interface crack, film-substrate system, post-buckling

1. Introduction

The thin film-substrate system is widely used in various of applications, such as thermal barrier coatings and micro-electronics [1-4]. In operation or fabrication process, in-plane compressive stress is commonly generated in the film due to thermal mismatch. If the stress exceeds a critical value, part of the film may buckle out of plane along the defective interface. Delamination buckling is considered as one of the most important failure modes in thin-film substrate system. Delamination buckling on a stiff substrate is well studied in the literature [5-7]. If the substrate is compliant, the critical buckling load and the energy release rate of the interface crack can be significantly affected[8]. Yu and Hutchinson analyzed the effects of compliance of substrate by introducing compliance coefficients [9]. After delamination buckling happens, the film and the substrate are detached. In this work we study the effects of compliance of the substrate by modeling the system as a plate on an elastic foundation. We use perturbation method to obtain the asymptotic solutions of post-buckling deformation and calculate the mode-adjusted energy release rate of the interface crack after buckling happens. Analysis of a plate on a foundation is a classical problem in mechanics, which can be an effective model of analyzing film-substrate system.

2. Governing equations

2.1. A circular plate on an elastic foundation

We study the delamination buckling of the thin film as buckling of a thin plate on an elastic foundation. To focus on the effects of the compliance of the substrate we study a simple configuration, a circular plate on an infinitely thick foundation, as shown in Fig. 1. We use the linear Wrinkler foundation model

$$F = Kw, \tag{1}$$

where w is the deflection, K the stiffness of the foundation, F the effective reaction force.

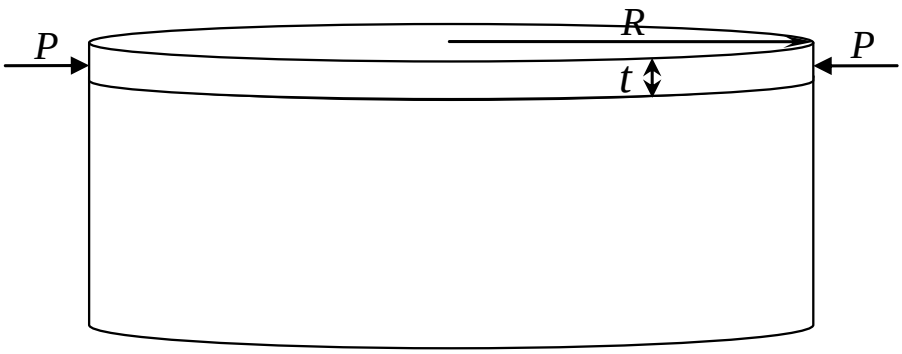

Fig.1. Schematics of a circular plate on an elastic foundation.

The equations of post-buckling of a thin plate on a linear Wrinkler foundation are [10]

$$\dddot{w}+\frac{2\ddot{w}}{r}-\frac{\ddot{w}}{r^2}+\frac{\dot{w}}{r^3}-\frac{12}{t^2}\left(\dot{u}+\frac{\dot{w}^2}{2}+\nu\frac{u}{r}\right)\ddot{w}-\frac{12}{t^2}\left(\nu\dot{u}+\nu\frac{\dot{w}^2}{2}+\frac{u}{r}\right)\frac{\dot{w}}{r}+\frac{P}{D}\left(\ddot{w}+\frac{\dot{w}}{r}\right)+\frac{K}{D}w=0, \quad (2)$$

$$\ddot{u}+\frac{\dot{u}}{r}-\frac{u}{r^2}+\dot{w}\ddot{w}+\frac{(1-\nu)\dot{w}^2}{2r}=0, \quad (3)$$

where u is the in-plane displacement, ν the Poisson's ratio, t the thickness of the plate, D the bending stiffness of the plate, P the in-plane load, $\dot{w}$ denotes derivative with respect to r. The deformation is assumed to be axisymmetric. A material point at location r in deformed state is fully described by deflection $w(r)$ and in-plane displacement $u(r)$.

We normalize the quantities as the following: radius of a material point $x=r/R$, deflection $\overline{w}=w/t$, in-plane displacement $\overline{u}=uR/t^2$, in-plane load $\overline{P}=PR^2/D$, foundation stiffness $\overline{K}=KR^4/D$. The normalized governing equations are

$$\dddot{\overline{w}}+\frac{2\ddot{\overline{w}}}{x}-\frac{\ddot{\overline{w}}}{x^2}+\frac{\dot{\overline{w}}}{x^3}-12\left(\dot{\overline{u}}+\frac{\dot{\overline{w}}^2}{2}+\nu\frac{\overline{u}}{x}\right)\ddot{\overline{w}}-12\left(\nu\dot{\overline{u}}+\nu\frac{\dot{\overline{w}}^2}{2}+\frac{\overline{u}}{x}\right)\frac{\dot{\overline{w}}}{x}+\overline{P}\left(\ddot{\overline{w}}+\frac{\dot{\overline{w}}}{x}\right)+\overline{K}\overline{w}=0, \quad (4)$$

$$\ddot{u}+\frac{\dot{u}}{r}-\frac{u}{r^2}+\dot{w}\ddot{w}+\frac{(1-\nu)\dot{w}^2}{2r}=0, \quad (5)$$

where $\dot{\overline{w}}$ denotes derivative with respect to x.

2.2. Strain energy release rate

In the film-substrate system, the interface crack may propagate after delamination buckling happens. The strain energy release rate is given in [11]

$$G=\frac{6(1-\nu^2)}{Et^3}\left(M^2+t^2\Delta N^2/12\right), \quad (6)$$

where E is the Young's modulus, M is the bending moment at the delamination edge, ΔN is the change of the in-plane force. The normalized form of these quantities are $\overline{M}=MR^2/(Dt)$, $\Delta\overline{N}=\Delta NR^2/D$, $\overline{G}=\overline{M}^2+\Delta\overline{N}^2/12$.

The crack is in a mixed mode of Mode I and Mode II. Define phase angle of mixture ψ. In this configuration the phase angle of mixture can be calculated as

$$\tan\psi=\frac{\sqrt{12}M\cos\omega+t\Delta N\sin\omega}{-\sqrt{12}M\sin\omega+t\Delta N\cos\omega}, \quad (7)$$

where $\omega=\omega(\phi,\varphi)$ is the phase factor, ϕ and φ are Dundur's elastic mismatch parameters. In the calculation, we set Poisson's ratio $\nu_{film}=\nu_{substrate}=1/3$. The details of value of ω can be found in the literature [11].

Considering the effects of mode mixture, the strain energy release rate is adjusted as

$$\bar{G}_{\psi}=\frac{\bar{G}}{f(\psi)}, \tag{8}$$

where the function $f(\psi)$ can be experimentally fitted. One of the common forms of $f(\psi)$ is

$$f(\psi)=1+(1-\lambda)\tan^2\psi, \tag{9}$$

where λ is the fitting parameter. In the calculation we set $\lambda=0.3$.

3. Asymptotic solutions

The perturbation method is an effective way of solving problems of plate undergoing large deflection[12]. We expand the displacement and load as

$$\bar{w}(x)=sw_1(x)+s^2w_2(x)+s^3w_3(x)+\ldots, \tag{10}$$

$$\bar{u}(x)=su_1(x)+s^2u_2(x)+s^3u_3(x)+\ldots, \tag{11}$$

$$\bar{P}=P_c+sP^{(1)}+\frac{1}{2}s^2P^{(2)}+\ldots, \tag{12}$$

where s is the perturbation parameter.

Inserting Eqs. (10)-(12) into Eqs. (4) and (5) we obtain the decoupled equations of coefficients in the order of s, s^2, s^3. The out-of-plane equations are

$$\dddot{w}_1+\frac{2\ddot{w}_1}{x}-\frac{\ddot{w}_1}{x^2}+\frac{\dot{w}_1}{x^3}+P_c\left(\ddot{w}_1+\frac{\dot{w}_1}{x}\right)+\bar{K}w_1=0, \tag{13}$$

$$\dddot{w}_2+\frac{2\ddot{w}_2}{x}-\frac{\ddot{w}_2}{x^2}+\frac{\dot{w}_2}{x^3}-12\left(\dot{u}_1+\nu\frac{u_1}{x}\right)\ddot{w}_1-12\left(\nu\dot{u}_1+\frac{u_1}{x}\right)\frac{\dot{w}_1}{x}+P_c\ddot{w}_2+P^{(1)}\ddot{w}_1+\bar{K}w_2=0, \tag{14}$$

$$\begin{aligned}&\dddot{w}_3(x)+\frac{2\ddot{w}_3(x)}{x}-\frac{\ddot{w}_3(x)}{x^2}+\frac{\dot{w}_3(x)}{x^3}\\&-12\left(\dot{u}_1(x)\dot{w}_2(x)+\dot{u}_2(x)\dot{w}_1(x)+\frac{\dot{w}_1(x)^2\ddot{w}_1(x)}{2}+\nu\frac{u_1(x)\ddot{w}_2(x)+u_2(x)\ddot{w}_1(x)}{x}\right)\\&-12\left(\nu\frac{\dot{u}_1(x)\dot{w}_2(x)+\dot{u}_2(x)\dot{w}_1(x)}{x}+\nu\frac{\dot{w}_1(x)^2\dot{w}_1(x)}{2x}+\frac{u_1(x)\dot{w}_2(x)+u_2(x)\dot{w}_1(x)}{x^2}\right)\\&+P_c\left(\ddot{w}_3(x)+\frac{\dot{w}_3(x)}{x}\right)+P^{(1)}\left(\ddot{w}_2(x)+\frac{\dot{w}_2(x)}{x}\right)+\frac{1}{2}P^{(2)}\left(\ddot{w}_1(x)+\frac{\dot{w}_1(x)}{x}\right)+\bar{K}w_3(x)=0\end{aligned}, \tag{15}$$

The in-plane equations are

$$\ddot{u}_1+\frac{\dot{u}_1}{x}-\frac{u_1}{x^2}=0, \tag{16}$$

$$\ddot{u}_2+\frac{\dot{u}_2}{x}-\frac{u_2}{x^2}+\dot{w}_1\ddot{w}_1+\frac{(1-\nu)\dot{w}_1^2}{2x}=0, \tag{17}$$

$$\ddot{u}_3+\frac{\dot{u}_3}{x}-\frac{u_3}{x^2}+\dot{w}_1\ddot{w}_2+\dot{w}_2\ddot{w}_1+\frac{(1-\nu)\dot{w}_1\dot{w}_2}{x}=0, \tag{18}$$

The edge is clamped. The boundary conditions are

$$u\big|_{x=0}=0,\quad \dot{w}\big|_{x=0}=0,\quad \left(\ddot{w}-\frac{\dot{w}}{r}\right)\Big|_{x=0}=0, \tag{19}$$

$$u\big|_{x=1}=0,\quad w\big|_{x=1}=0,\quad \dot{w}\big|_{x=1}=0, \tag{20}$$

We use the central deflection w_0 as the perturbation parameter. We have additional condition $w_1(0)=1$; $w_j(0)=0 \quad j\neq 1$. Inspecting the six equations (13)-(18) together with boundary conditions (19) and (20), we can easily obtain solutions $u_1=0, w_2=0$ and $P^{(1)}=0$. Therefore, only three equations (13), (15) and (17) are to be solved. The general solution of Eq.(13) is

$$w_1(x)=C_1J_0(\alpha x)+C_2J_0(\beta x), \tag{21}$$

where $\alpha=\left(\frac{P_c-\sqrt{P_c^2-4\bar{K}}}{2}\right)^{1/2}$, $\beta=\left(\frac{P_c+\sqrt{P_c^2-4\bar{K}}}{2}\right)^{1/2}$.

Inserting boundary conditions into Eq. (21) we obtain

$$C_1J_0(\alpha)+(1-C_1)J_0(\beta)=0, \tag{22}$$

$$\alpha C_1J_1(\alpha x)+\beta(1-C_1)J_1(\beta x)=0, \tag{23}$$

Once the foundation stiffness $\bar{K}$ is given, we can obtain P_c and C_1 by solving Eqs. (22) and (23). Subsequently we use Eq. (17) to solve u_2. A simple way to obtain u_2 is expanding Bessel function into Taylor series. Once w_1 and u_2 are known, we use Eq. (15) to solve $P^{(2)}$. We multiply $w_1(x)x$ on both sides of Eq. (15) and integrate from 0 to 1. Using the feature of Bessel function, the solving process can be simplified. Similar process can be iterated to obtain more accurate solution by expanding displacement fields to higher order terms and solving higher order equations. Once the displacement fields are known, the bending moment at the edge, the change of in-plane force and the energy release rate can be obtained.

4. Results and discussions

The critical buckling load P_c at different value of foundation stiffness $\bar{K}$ is plotted in Fig. 2. It can be seen that as the foundation become stiffer, the critical buckling load increases. Using the way of normalization in this work, the relation between P_c and $\bar{K}$ is approximately linear. This result is consistent with the literature, where different normalized quantities are used to plot [13].

The post-buckling path of central deflection is plotted in Fig. 3. The horizontal axis σ/σ_c is the in-plane stress over the critical buckling stress. Note that, the critical buckling stress σ_c at different foundation stiffness is different. But for the aid of comparison, we plot them into the same figure. The curve with $\bar{K}=0$ reduces to classical post-buckling path of a thin circular plate without foundation. It is found that stiff foundation lowers the central deflection, especially in the initial stage of post-buckling.

The mode-adjusted energy release rate G_ψ given by Eqs. (6)-(9) is plotted in Fig. 4. The displacement fields solved with perturbation method are relatively accurate, while the bending moment and in-plane force are not especially when the post-buckling stress is high. Therefore, in

Fig. 4 we plot the post-buckling stress up to $\sigma / \sigma_c \approx 4$. It can be seen that the more compliant the substrate is, the easier for the interface crack to propagate after buckling.

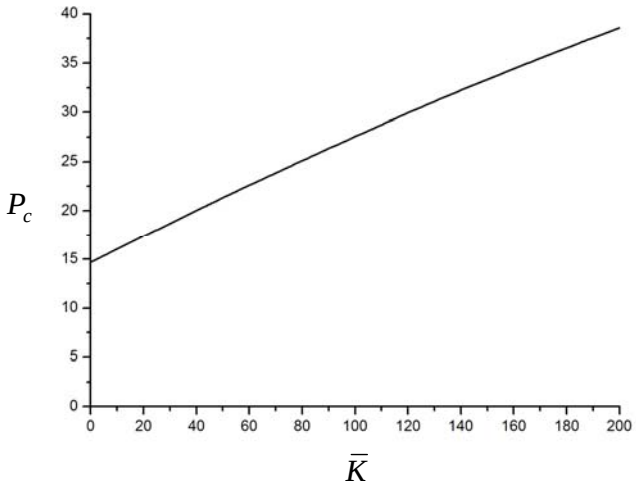

Fig. 2. Critical buckling load at different foundation stiffness.

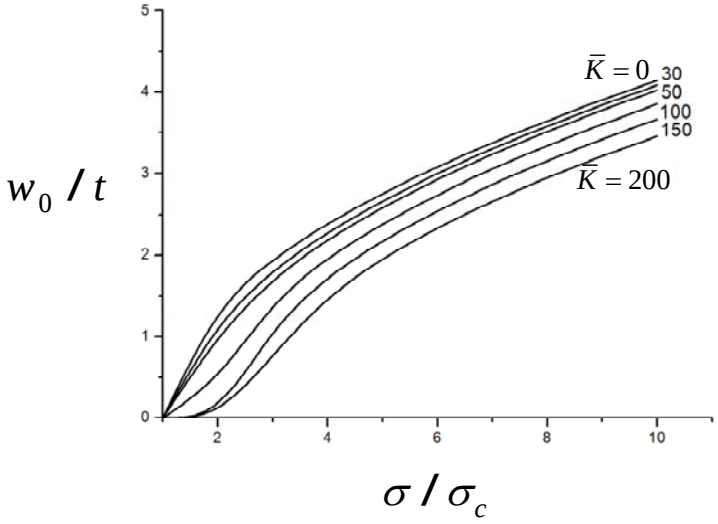

Fig. 3. Post-buckling path with different foundation stiffness.

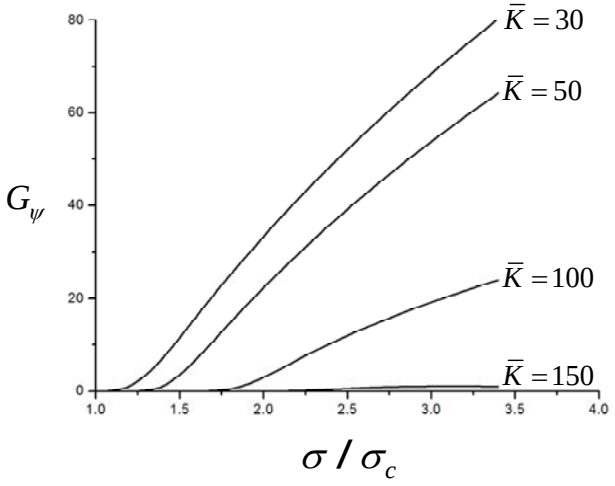

Fig. 4. Mode-adjusted energy release rate of interface crack with different foundation stiffness.

5. Conclusion

In the thin film-substrate system, compressive stress in the film can induce delamination buckling. We study the effects of compliance of the substrate by modeling the system as a plate on an elastic foundation. We use perturbation method to obtain the asymptotic solutions of post-buckling deformation and calculate the mode-adjusted energy release rate of the interface crack after buckling happens. The results show that the more compliant the substrate is, the easier for the film to buckle and easier for the interface crack to propagate after buckling.

Acknowledgements

This work was supported by the state 973 program of China (2013CB035701), NSFC(11021202) and MOE fund.

References

[1] N. P. Padture, M. Gell, H. Jordan, Thermal barrier coatings for gas-turbine engine applications. Science, 296 (2002) 280-284.

[2] T. Q. Lu, W. X. Zhang and T. J. Wang, Strain energy release rate of buckling derived delamination crack in thin film-substrate system incorporating surface effect. International Journal of Engineering Science, 49 (2011) 967-975.

[3] X.L. Fan, R. Xu, W.X Zhang and T.J. Wang, Effect of periodic surface cracks on the interfacial fracture of thermal barrier coating system. Applied Surface Science, 24 (2012) 9816-9823.

[4] X.L. Fan, W.X Zhang and T.J. Wang, The effect of thermally grown oxide on multiple surface cracking in air plasma sprayed thermal barrier coating system. Surface and Coatings Technology, 208 (2012) 7-13

[5] A. G. Evans, D. R. Mumm, J. W. Hutchinson, G. H. Meier, F. S. Pettit, Mechanisms controlling the durability of thermal barrier coatings. Progress in Materials Science, 46 (2001) 505-553.

[6] J. S. Wang, A. G. Evans, Measurement and analysis of buckling and buckle propagation in compressed oxide layers on superalloy substrates. Acta Materialia, 46 (1998) 4993-5005.

[7] A. G. Evans, J. W. Hutchinson, On the mechanics of delamination and spalling in compressed films. International Journal of Solids and Structures, 20 (1984) 455-466.

[8] B. Cotterell, Z. Chen, Buckling and cracking of thin film on compliant substrates under compression. International Journal of Fracture, 104 (2000) 169-179.

[9] H. H. Yu, J. W. Hutchinson, Influence of substrate compliance on buckling delamination of thin films. International Journal of Fracture, 113 (2002) 39-55.

[10] S. R. Li, W. S. Yu, Thermal post-buckling and the critical buckling mode transition of heated elastic circular plates on elastic foundation. Engineering Mechanics, 24 (2007) 63-67

[11] J. W. Hutchinson, Z. Suo, Mixed mode cracking in layered materials. Advances in Applied Mechanics, 29 (1992) 63-191.

[12] W. C. Qian, K. Y. Ye, On the problem of circular plate undergoing large deflection. Acta Physica Sinica, 10 (1954).

[13] C. Y. Wang, On the buckling of a circular plate on an elastic foundation. Journal of Applied Mechanics, 72 (2005) 795-796.

A Simplified Approach for the Evaluation of Nearly singular integrals in Boundary Element Method

Yu Miao[1,*], Jiahe Lv[1]

[1] School of Civil Engineering and Mechanics, Huazhong University of Science and Technology, Wuhan 430074, China
* Corresponding author: my_miaoyu@163.com

Abstract The accurate and efficient evaluation of nearly singular integrals is one of the major concerned problems in the implementation of the boundary element method. Among the various commonly used nonlinear transformation methods, the distance transformation technique seems to be a promising method to dealing with various orders of nearly singular integrals both in potential and elasticity problems. In this paper, some drawbacks of the conventional distance transformation, such as the sensitivity to the position of projection point, are investigated by numerical tests. And a general distance transformation technique is developed to circumvent these drawbacks, which is aimed to remove or weaken the limitations of the projection point. Numerical examples are presented for curved line elements to validate the accuracy and efficiency of our method.

Keywords Boundary element method, Nearly singular integrals, Numerical integration, Distance transformation technique.

1. Introduction

The nearly singular integrals arise when the source point is very close to but not on the integration element in the implementation of boundary element method (BEM). The conventional Gauss quadrature becomes inefficient or even inaccurate to evaluate such integrals. The accurate and efficient evaluation of nearly singular integrals plays an important role in many cases, especially involving problems of thin or shell-like structures [1-3], the unknowns around crack tips [4], the contact problems [5] and the sensitivity problems [6].

Various numerical techniques have been proposed to remove the near singularities, such as the element subdivision technique [7], the rigid body displacement solutions [8], global regularization method [9, 10], semi-analytical and analytical algorithms [11, 12], and the nonlinear transformation method [13-25]. The element subdivision technique is simple but not recommended because of its inefficient. The closer the computing point is to the integration element, the more subdivisions are needed, which consumes great computation effort and may increase the accumulative error. The rigid body displacement method constructs a nearly zero factor in the denominator of kernel function by the zero factor in density function using the regularization ideas, but the accuracy of the results are not satisfactory. The analytical and semi-analytical algorithms are effective but only limited to linear or planar elements. Curved elements must be divided into a large number of linear or planar elements, thus losing efficiency and accuracy. At present, the most widely used methods are various nonlinear transformations, such as the cubic polynomial transformation [13], the bi-cubic transformation [14], the sigmoidal and semi-sigmoidal transformation [15, 16], the coordinate optimization transformation [17], the attenuation mapping method [18], the rational transformation [19], the PART method [20], and the sinh transformation [21]. The basic ideas of the above transformations can be generalized into two categories: one is removing the nearly zero factor in the denominator of the kernels using zero factor, the other is converting the nearly zero factor in the denominator of the kernels to be part of the numerator. However, most nonlinear transformations are limited to certain order of singularities or specific boundary element. The distance transformation method [22-25], which has been proposed by Ma, is a general strategy to deal with nearly singular integrals in BEM. This promising method is derived from Guiggiani's excellent work for dealing with singular boundary integrals [26]. It has been applied to two- and

three-dimensional nearly singular integrals with various orders both in potential and elasticity problems, and attractive results have been presented.

However, as the definition of the projection point, finding the projection point is essential for each computation, which may lower the efficiency of the method. And numerical tests in Section 4.1 show that the local coordinate of the projection point must be calculated accurately, otherwise undesirable results will be obtained. Moreover, if the projection point is located on the tangential line through the projection point, the method failed and another transformation should be taken. In this paper, a general distance transformation is developed to circumvent these drawbacks.

The paper is organized as follows. The general form of nearly singular integrals is described in Section 2. The conventional distance transformation is briefly reviewed in Section 3. The drawbacks for conventional distance transformation are presented by some numerical tests，and a general distance transformation is developed in the Section 4. Some illustrative numerical examples are given to verify the efficiency and accuracy of presented method in Section 5. The paper ends with conclusions in Section 6.

2. Statement of the problem

Considering the description of 2D potential problems in the domain Ω enclosed by boundary Γ, the two basic integral equations are written in terms of the flux q and the potential u on the boundary as follows:

$$c(\mathbf{y})u(\mathbf{y}) = \int_\Gamma q(\mathbf{x})u^*(\mathbf{x},\mathbf{y})\mathrm{d}\Gamma(\mathbf{x}) - \int_\Gamma u(\mathbf{x})q^*(\mathbf{x},\mathbf{y})\mathrm{d}\Gamma(\mathbf{x}) \tag{1}$$

$$c(\mathbf{y})u_k(\mathbf{y}) = \int_\Gamma q(\mathbf{x})u_k^*(\mathbf{x},\mathbf{y})\mathrm{d}\Gamma(\mathbf{x}) - \int_\Gamma u(\mathbf{x})q_k^*(\mathbf{x},\mathbf{y})\mathrm{d}\Gamma(\mathbf{x}) \tag{2}$$

where $\mathbf{y}$ and $\mathbf{x}$ are the source and the field points, respectively. c is a coefficient depending on the smoothness of the boundary at the source point $\mathbf{y}$. $u^*(\mathbf{x},\mathbf{y})$ represents the fundamental solution for 2D potential problems expressed as

$$u^*(\mathbf{x},\mathbf{y}) = \frac{1}{2\pi}\log(\frac{1}{r}) \tag{3}$$

and $u_k^*(\mathbf{x},\mathbf{y})$, $q^*(\mathbf{x},\mathbf{y})$ and $q_k^*(\mathbf{x},\mathbf{y})$ are the derived fundamental solutions

$$u_k^*(\mathbf{x},\mathbf{y}) = \frac{\partial u^*(\mathbf{x},\mathbf{y})}{\partial x_k}, \quad q^*(\mathbf{x},\mathbf{y}) = \frac{\partial u^*(\mathbf{x},\mathbf{y})}{\partial \mathbf{n}}, \quad q_k^*(\mathbf{x},\mathbf{y}) = \frac{\partial q^*(\mathbf{x},\mathbf{y})}{\partial x_k} \tag{4}$$

where r denotes the Euclidean distance between the source and the field points and $\mathbf{n}$ is the unit outward normal on the boundary Γ.

To evaluate the boundary integrals numerically, the boundary Γ is discretized into a number of linear or quadratic elements and then the boundary integrations are performed on each element. When the source point is very close to but not on the integration element, nearly singular integrals arise with different orders.

In this paper, we deal with these boundary integrals with nearly singularity of the following forms:

$$\mathrm{I} = \int_{-1}^{1} O(1/r)\, f(\xi)\phi_i(\xi)G(\xi)\mathrm{d}\xi \tag{5}$$

where $O(1/r)$ represents the nearly singular integral kernels, $\log(1/r)$ for nearly weak singular integrals, $1/r$ for nearly strong singular integrals and $1/r^2$ for nearly hyper-singular integrals. $f(\xi)$ is a bounded function for local coordinate ξ, $\xi \in [-1,1]$. $\phi_i(\xi)$ denotes the shape functions and $G(\xi)$ is the Jacobian of the transformation from $\mathrm{d}\Gamma$ to $\mathrm{d}\xi$. As the singular integrals over linear elements can be computed analytically, only quadratic elements are discussed

in this paper.

3. Conventional distance transformation

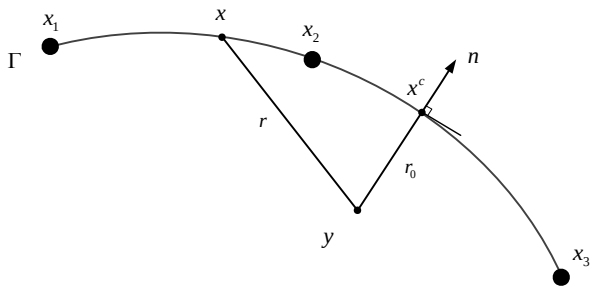

Figure 1. Definition of the projection point $\mathbf{x}^c$

In this section, we review the definition of the conventional distance function and the variable transformation technique. As shown in Fig. 1, the minimum distance r_0 from the source point to the boundary element is defined perpendicular to the tangential line, through the projection point $\mathbf{x}^c$ and the source point $\mathbf{y}$. By employing the first-order Taylor expansion in the neighborhood of the projection point, we have

$$x_k - y_k = x_k - x_k^c + x_k^c - y_k = \frac{\partial x_k}{\partial \xi}|_{\xi=c}(\xi - c) + r_0 n_k(c) + O(|\xi - c|^2) \tag{6}$$

where c is the local coordinate of the projection point $\mathbf{x}^c$. The real distance can be expanded to the following form:

$$\begin{aligned} r^2(\xi) &= (x_k - x_k^p)(x_k - x_k^p) \\ &= r_0^2 + \frac{\partial x_k}{\partial \xi}\frac{\partial x_k}{\partial \xi}|_{\xi=c}(\xi - c)^2 + 2r_0\frac{\partial x_k}{\partial \xi}|_{\xi=c} n_k(c)(\xi - c) + O(|\xi - c|^3) \\ &= r_0^2 + G_c^2(\xi - c)^2 + O(|\xi - c|^3) \\ &= G_c^2 g^2(\xi) + O(|\xi - c|^3) \end{aligned} \tag{7}$$

where G_c stands for the Jacobian at point c and $g(\xi)$ is the distance function defined as

$$g(\xi) = \sqrt{\alpha^2 + (\xi - c)^2} \tag{8}$$

This definition represents the distance in the local parametric plane and $\alpha = r_0 / G_c$. When the projection point is inside of the boundary element, the integration span is split into two parts at point c, taking the following one-order transformation pairs for the integration variable:

$$\eta(\xi) = \log[g(\xi) + (\xi - c)] \tag{9}$$

$$\xi(\eta) = \frac{1}{2}[\exp(\eta) - \alpha^2 \exp(-\eta)] + c \tag{10}$$

Substituting Eq. (9) and (10) into Eq. (5) yields

$$\begin{aligned} \mathrm{I} &= \int_{-1}^{1} O(1/r)\, f(\xi)\phi_i(\xi) G(\xi)\mathrm{d}\xi \\ &= \int_{\eta(-1)}^{\eta(c)} O(1/r)\, f[\xi(\eta)]\phi_i[\xi(\eta)] G[\xi(\eta)] g[\xi(\eta)]\mathrm{d}\eta \\ &+ \int_{\eta(c)}^{\eta(1)} O(1/r)\, f[\xi(\eta)]\phi_i[\xi(\eta)] G[\xi(\eta)] g[\xi(\eta)]\mathrm{d}\eta \end{aligned} \tag{11}$$

It is easily can be seen that the distance function $g(\xi)$ and the Jacobian of transformation play the role of damping out the nearly singularity of the kernels. For the possibility of unifying and simplifying the computer code, the one-order transformation is used for various orders of singularity, which can obtain an acceptable result even for the hyper-singular kernel [23].

4. General distance transformation

4.1. Sensitivity to the position of projection point

As we know, finding the accurate position of the projection point is an essential step for the successful implementation of the distance transformation method when dealing with nearly singular integrals. The Newton's method is widely used to finding approximate position of the projection point and an inevitable error will be produced. In this section, we investigate the influence of the position of the projection point on the accuracy of the distance transformation method. Here we assume the source point is fixed and the local coordinate ξ_a^c of the approximate projection point is determined by an offset parameter k with the following equation:

$$\xi_a^c = \xi^c + k\xi^c \tag{12}$$

where ξ_c is the accurate local coordinate of the projection point and k indicates the offset caused by the error during finding the projection point. Obviously, the approximate projection point is coincident with the accurate one when $k = 0$.

Considering the first example in Ref. [23], the relative distance describing the closeness of the near singular point to the boundary is taken as 10^{-4} and ten points Gauss quadrature is used for all the computations. The integrals with kernel u^* and q^* corresponding to different offset values of k have been computed using the conventional distance transformation and the reference value are obtained by subdivision method with enough subelements. Numerical results are shown in Fig. 2 and Fig. 3, and it can be easily seen that the results obtained with conventional distance transformation is very sensitive to the position of the projection point and poor results can be obtained even with a very little deviation of the position of the projection point. Besides, the results get much worse for high order singular integrals.

Now the drawbacks of the distance transformation method are very obvious: the computation of the position of the projection point should be very rigorous and the process of finding the projection point is time-consuming but essential for each source point, which may lower the computational efficiency. Is the projection point really essential? The work presented later is tried to overcome the shortcomings of the conventional distance transformation method.

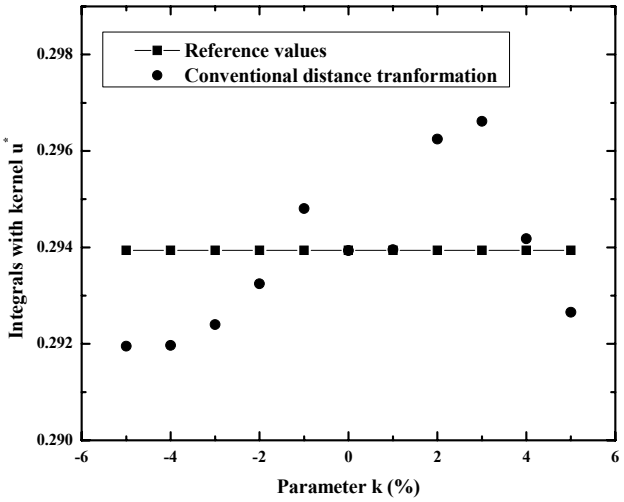

Figure 2. Various integrals with kernel u^*

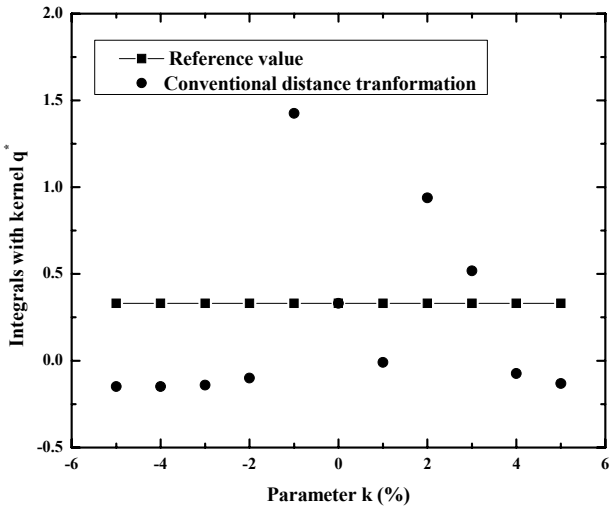

Figure 3. Various integrals with kernel q^*

4.2. Definition of general distance function

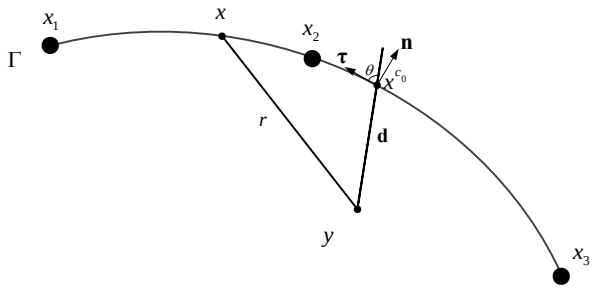

Figure 4. General definition of the projection point $\mathbf{x}^c$

In this section, a general projection point $\mathbf{x}^{c_0}$ is defined to construct a new distance function as shown in Fig. 4. The general projection point $\mathbf{x}^{c_0}$ can be located inside the integration element or on one node of the element. $\boldsymbol{\tau}$ and $\mathbf{n}$ are the unit tangential and outward normal vector, respectively. A new vector $\mathbf{d}$ from the source point $\mathbf{y}$ to the general projection point $\mathbf{x}^{c_0}$ is defined additionally, which is not required to be perpendicular to the tangential line through $\mathbf{x}^{c_0}$. By applying the first-order Taylor expansion in the neighborhood of point $\mathbf{x}^{c_0}$, we have

$$x_k - y_k = x_k - x_k^{c_0} + x_k^{c_0} - y_k = \frac{\partial x_k}{\partial \xi}|_{\xi=c_0}(\xi - c_0) + d_k + O(|\xi - c_0|^2) \tag{13}$$

where c_0 is the local coordinate of the general projection point $\mathbf{x}^{c_0}$, and d_k is one of the components of $\mathbf{d}$. The real distance can also be expanded to the following form:

$$\begin{aligned} r^2(\xi) &= (x_k - y_k)(x_k - y_k) \\ &= d_k^2 + \frac{\partial x_k}{\partial \xi}\frac{\partial x_k}{\partial \xi}|_{\xi=c_0}(\xi - c_0)^2 + 2d_k\frac{\partial x_k}{\partial \xi}|_{\xi=c_0}(\xi - c_0) + O(|\xi - c_0|^3) \end{aligned} \tag{14}$$

Noted that

$$2d_k\frac{\partial x_k}{\partial \xi}|_{\xi=c_0}(\xi - c_0) = 2G_{c_0}(\mathbf{d}\mathbf{g}\boldsymbol{\tau}) = 2G_{c_0}d\cos\theta \tag{15}$$

where G_{c_0} stands for the Jacobian at point c_0 and θ is the angle between $\mathbf{d}$ and $\boldsymbol{\tau}$, which is only related to the position of $\mathbf{x}^{c_0}$ and $\mathbf{y}$.The real distance can be rewritten as

$$\begin{aligned} r^2(\xi) &= d^2 + G_{c_0}^2(\xi - c_0)^2 + 2G_{c_0}d\cos\theta(\xi - c_0) + O(|\xi - c_0|^3) \\ &= G_{c_0}^2[\alpha^2 + (\xi - c_0)^2 + 2\alpha\cos\theta(\xi - c_0)] + O(|\xi - c_0|^3) \\ &= G_{c_0}^2 g^2(\xi) + O(|\xi - c_0|^3) \end{aligned} \tag{16}$$

where $g(\xi)$ is the general distance function defined as follows:

$$g(\xi) = \sqrt{\alpha^2 + (\xi - c_0)^2 + 2\alpha\cos\theta(\xi - c_0)} \tag{17}$$

with α being d / G_{c_0}. $g(\xi)$ represents the distance in the local parametric plane as shown in Fig. 5, which can be proved using the cosine law.

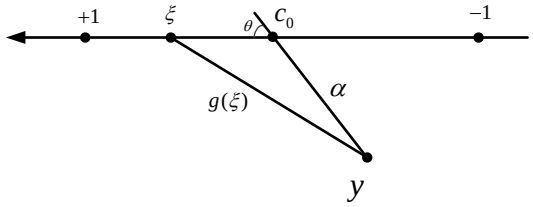

Figure 5. The distance function $g(\xi)$ in the local parametric plane

Now we introduce a similar pair of transformations for the integration variable, which is expressed as

$$\eta(\xi) = \log[g(\xi) + (\xi - c_0) + \alpha\cos\theta] \tag{18}$$

$$\xi(\eta)=\frac{1}{2}e^{-\eta}[(e^{\eta}-\alpha\cos\theta)^2-\alpha^2]+c_0 \tag{19}$$

After splitting the integration element into two parts at point $(c_0-\alpha\cos\theta)$, which is unnecessary if the general projection point is located at the vertex of the integration element, we can obtain the distance-transformed form of the near singular boundary integrals as Eq. (20). Now the nearly singular integrations with various orders can be computed accurately even if $\mathbf{x}^{c_0}$ is a little far away from the conventional projection point.

$$\begin{aligned}
\mathrm{I}&=\int_{-1}^{1}O(1/r)\phi(\xi)G(\xi)\mathrm{d}\xi\\
&=\int_{-1}^{c_0-\alpha\cos\theta}O(1/r)\phi(\xi)G(\xi)\mathrm{d}\xi+\int_{c_0-\alpha\cos\theta}^{1}O(1/r)\phi(\xi)G(\xi)\mathrm{d}\xi\\
&=\int_{\log[g(c_0-\alpha\cos\theta)]}^{\log[g(-1)+(-1-c)+\alpha\cos\theta]}O(1/r)\phi(\xi(\eta))G(\xi(\eta))g(\xi(\eta))\mathrm{d}\eta\\
&+\int_{\log[g(c_0-\alpha\cos\theta)]}^{\log[g(+1)+(1-c)+\alpha\cos\theta]}O(1/r)\phi(\xi(\eta))G(\xi(\eta))g(\xi(\eta))\mathrm{d}\eta
\end{aligned} \tag{20}$$

5. Numerical examples

In this section, numerical examples for curved lines are presented to validate the accuracy and efficiency of our method. The relative distance is given in terms of r_0/l to describe the influence of the nearly singular integrals over each element, where r_0 is the minimum distance as shown in Fig.1 and l stands for the length of the element. For the purpose of error estimation, the relative error is defined as follows:

$$error=\frac{I_{num}-I_{ref}}{I_{ref}} \tag{21}$$

where the subscripts num and ref refer to the numerical and reference solutions, respectively. The reference solutions are obtained by subdivision method with enough subelements. Ten Gauss points are used in all cases for the convenience of comparisons.

The numerical example in Ref. [23] is taken as the second example. The example is computed over a curved boundary element with the node coordinates of (2.0, 0.0), (1.0, 1.0), and (0.0, 0.5). The local coordinate of the conventional projection point c is set outside of the element interval and $c=1.01$. The relative error of nearly singular integrals using general and conventional distance transformation is presented in Table 1. The local coordinate of the general projection point c_0 is located at 0.0. For results obtained with the conventional distance transformation, the precision will decline as the range of r_0/l. The results using the general distance transformation can keep high precision in a wide range of r_0/l, far better than results obtained by conventional distance transformation.

Table 1 Relative error of nearly singular integrals using general and conventional distance transformation

	r_0/l	10^{-1}	10^{-2}	10^{-3}	10^{-4}	10^{-5}	10^{-6}
	Reference	-0.08013504	-0.07159177	-0.07055153	-0.07044348	-0.07043263	-0.07043155
$\phi_1 u^*$	General	-1.3931E-07	-4.8909E-08	-3.7454E-08	-3.4041E-08	-3.3901E-08	-3.3889E-08
	Conventional	-2.7597E-06	6.2638E-05	8.6432E-07	-3.7262E-07	-1.7228E-05	2.1675E-03
$\phi_1 u_1^*$	Reference	0.03240507	0.03656118	0.03868258	0.03896392	0.03899269	0.03899557

	General	-2.9928E-06	-2.9649E-07	-5.0784E-06	-3.8277E-06	-3.6064E-06	-3.5835E-06
	Conventional	2.9397E-06	-3.4924E-04	-6.5327E-04	-6.5951E-04	-6.7930E-04	1.8681E-03
	Reference	-0.01156755	-0.02226277	-0.02430147	-0.02448001	-0.02449723	-0.02449894
$\phi_1 u_2^*$	General	-4.1133E-05	8.0888E-07	2.1044E-06	6.5314E-06	6.8976E-06	6.9330E-06
	Conventional	-1.5371E-05	-3.5901E-04	-9.5886E-05	-8.7302E-05	-9.4695E-05	8.8743E-04
	Reference	-0.04679418	-0.04497265	-0.04301120	-0.04278013	-0.04275696	-0.04275464
$\phi_1 q^*$	General	8.2062E-06	-2.3720E-07	2.6763E-06	2.4552E-07	-4.2287E-08	-7.1289E-08
	Conventional	5.2246E-06	-2.3952E-04	-4.5426E-04	-4.6333E-04	-4.7736E-04	1.2603E-03

The influence of the location of the general projection point is also studied for curved boundary element. As the general projection point moves along the element, computations for nearly singular integrals with r_0 / l being 10^{-4} are performed and the relative error is given out in Table 2. As the general projection point is located at the middle of the element, best results can be got compared with other locations. The results are also acceptable relative to those obtained with the conventional distance transformation.

Table 2 Relative error of nearly singular integrals with various general projection points

c_0	-1.0	-0.5	0.0	0.5	1.0	Conventional
$\phi_2 u^*$	-3.1992E-03	-5.8251E-04	-3.9583E-07	1.8035E-05	3.1392E-03	3.1624E-03
$\phi_2 u_1^*$	2.1904E-03	7.7142E-04	2.4198E-06	1.2023E-04	1.7605E-04	1.7676E-04
$\phi_2 u_2^*$	4.3266E-03	1.4958E-03	4.2367E-06	2.2400E-04	1.9356E-04	1.9587E-04
$\phi_2 q^*$	-4.4855E-05	-3.7130E-05	-4.1349E-07	-1.6025E-05	2.4758E-04	2.4803E-04

As the local coordinate of the conventional projection c changes from 1.1 to 1.000001, the source point $\mathbf{y}$ becomes increasingly closer to the element, which may lead to poor results during computation of nearly singular integrals. Here we consider $c_0 = 0$ and $r_0 / l = 10^{-4}$ to verify the effectiveness of the conventional and general distance transformation. The results with kernel u^* as c varies from 1.1 to 1.000001 are listed Table 3. It can be easily seen that our method is less sensitive to different values of c and better results can be obtained than the conventional distance transformation.

Table 3 Relative error of weakly singular integrals with different values of c

c		1.1	1.01	1.001	1.0001	1.00001	1.000001
$\phi_1 u^*$	General	-3.7832E-08	-3.4041E-08	7.3708E-07	1.1750E-06	1.2146E-06	1.2184E-06
	Conventional	-3.0558E-06	-3.7262E-07	-2.1542E-03	-1.0368E-02	-1.4545E-02	-1.5049E-02
$\phi_2 u^*$	General	-5.1030E-08	-3.9583E-07	-4.0356E-05	-6.7932E-05	-7.0701E-05	-7.0970E-05
	Conventional	-1.5179E-06	3.1624E-03	4.2508E-02	2.1993E-01	3.1620E-01	3.2782E-01
$\phi_3 u^*$	General	2.3404E-07	-9.6050E-07	-3.9180E-04	-1.3210E-03	-1.5231E-03	-1.5434E-03
	Conventional	-6.9787E-06	1.0358E-04	6.6305E-04	4.0438E-03	5.5950E-03	5.7729E-03

6. Numerical examples

In this paper, the drawbacks of the conventional distance technique, such as the sensitivity to the position of projection point, are investigated by numerical tests. A general distance transformation technique is developed to remove or weaken the limitations of projection point, which is based on a more general definition of the projection point. The presented method has been verified through numerical examples with different kernel functions and relative distances.

References

[1] T. A. Cruse, R. Aithal, Non-singular boundary integral equation implementation, International journal for numerical methods in engineering 36 (2) (1993) 237–254.
[2] G. Krishnasamy, F. J. Rizzo, Y. J. Liu, Boundary integral equations for thin bodies, International Journal for Numerical Methods in Engineering 37 (1) (2005) 107–121.
[3] Y. J. Liu, Analysis of shell-like structures by the boundary element method based on 3-d elasticity: formulation and verification, International Journal for Numerical Methods in Engineering 41 (3) (1998) 541–558.
[4] M. H. Aliabadi, D. P. Rooke, Numerical fracture mechanics, Vol. 8, Springer, 1991.
[5] G. Karami, Boundary element analysis of two-dimensional elastoplastic contact problems, International journal for numerical methods in engineering 36 (2) (1993) 221–235.
[6] D. Zhang, F. J. Rizzo, T. J. Rudolphi, Stress intensity sensitivities via hypersingular boundary integral equations, Computational mechanics 23 (5) (1999) 389–396.
[7] U. Eberwien, C. Duenser, W. Moser, Efficient calculation of internal results in 2d elasticity bem, Engineering analysis with boundary elements 29 (5) (2005) 447–453.
[8] H. B. Chen, P. Lu, M. G. Huang, F. W. Williams, An effective method for finding values on and near boundaries in the elastic bem, Computers & structures 69 (4) (1998) 421–431.
[9] V. Sladek, J. Sladek, M. Tanaka, Regularization of hypersingular and nearly singular integrals in the potential theory and elasticity, International Journal for Numerical Methods in Engineering 36 (10) (1993) 1609–1628.
[10] Y. J. Liu, T. J. Rudolphi, New identities for fundamental solutions and their applications to non-singular boundary element formulations, Computational mechanics 24 (4) (1999) 286–292.
[11] Z. R. Niu,W. L.Wendland, X. X.Wang, H. L. Zhou, A semi-analytical algorithm for the evaluation of the nearly singular integrals in three-dimensional boundary element methods, Computer methods in applied mechanics and engineering 194 (9) (2005) 1057–1074.
[12] H. L. Zhou, Z. R. Niu, C. Z. Cheng, Z. W. Guan, Analytical integral algorithm applied to boundary layer effect and thin body effect in bem for anisotropic potential problems, Computers & Structures 86 (15) (2008) 1656–1671.
[13] J. C. F. Telles, A self-adaptive co-ordinate transformation for efficient numerical evaluation of general boundary element integrals, International Journal for Numerical Methods in Engineering 24 (5) (2005) 959–973.
[14] M. Cerrolaza, E. Alarcon, A bi-cubic transformation for the numerical evaluation of the cauchy principal value integrals in boundary methods, International journal for numerical methods in engineering 28 (5) (1989) 987–999.
[15] P. R. Johnston, Application of sigmoidal transformations to weakly singular and near-singular boundary element integrals, International journal for numerical methods in engineering 45 (10) (1999) 1333–1348.
[16] P. R. Johnston, Semi-sigmoidal transformations for evaluating weakly singular boundary element integrals, International journal for numerical methods in engineering 47 (10) (2000) 1709–1730.
[17] V. Sladek, J. Sladek, M. Tanaka, Optimal transformations of the integration variables in computation of singular integrals in bem, International journal for numerical methods in

engineering 47 (7) (2000) 1263–1283.
[18] A. Nagarajan, S. Mukherjee, A mapping method for numerical evaluation of two-dimensional integrals with 1/r singularity, Computational mechanics 12 (1) (1993) 19–26.
[19] Q. Huang, T. A. Cruse, Some notes on singular integral techniques in boundary element analysis, International journal for numerical methods in engineering 36 (15) (1993) 2643–2659.
[20] K. Hayami, Variable transformations for nearly singular integrals in the boundary element method, Publications of the Research Institute for Mathematical Sciences 41 (4) (2005) 821–842.
[21] P. R. Johnston, D. Elliott, A sinh transformation for evaluating nearly singular boundary element integrals, International journal for numerical methods in engineering 62 (4) (2005) 564–578.
[22] H. Ma, N. Kamiya, A general algorithm for accurate computation of field variables and its derivatives near the boundary in bem, Engineering analysis with boundary elements 25 (10) (2001) 833–841.
[23] H. Ma, N. Kamiya, Distance transformation for the numerical evaluation of near singular boundary integrals with various kernels in boundary element method, Engineering analysis with boundary elements 26 (4) (2002) 329– 339.
[24] H. Ma, N. Kamiya, A general algorithm for the numerical evaluation of nearly singular boundary integrals of various orders for two-and three dimensional elasticity, Computational mechanics 29 (4) (2002) 277–288.
[25] H. Ma, N. Kamiya, Nearly singular approximations of cpv integrals with end-and corner-singularities for the numerical solution of hypersingular boundary integral equations, Engineering analysis with boundary elements 27 (6) (2003) 625–637.
[26] M. Guiggiani, A. Gigante, A general algorithm for multidimensional Cauchy principal value integrals in the boundary element method, Journal of Applied Mechanics 57 (4) (1990) 906–915.

Evaluation of the Strength of Thin Metallic Films Coated on Brittle Materials by using an Indentation Fracture Method

Yuzo Nakamura [1], Takashi Kawabata [2, 3], Shinya Ishigami [2, 4]
Jun Wakiyama [1], Yoshikazu Maeda [1]

[1] Department of Mechanical Engineering, Graduate School of Science and Engineering
[2] Department of Nanostructure Advanced Materials, Graduate School of Engineering, Kagoshima University, Kagoshima 890-0065, Japan
[3] Present address: Kobe Mashinery Center, Kobe Steel Ltd., Takasago 676-8670, Japan
[4] Present address: NIDEC Co., Kyoto 601-8205, Japan
* Corresponding author: nakamura@mech.kagoshima-u.ac.jp

Abstract Nanoindentation techniques are poplar methods which are used for the evaluation of the hardness and elastic modulus of very thin films. However, since the plastic and elastic regions formed underneath the indenter are much larger than its penetration depth, the thickness of films, which can be used for the nanoindentation measurement, is limited to a certain value. In the present study, microcracking caused by micro-Vickers indentation was applied to the evaluation of the tensile properties of very thin metallic films coated on brittle materials. For this purpose, gold films with the thicknesses ranging from 23 nm to 227 nm were coated on glass substrates, and the lengths of radial cracks before and after coating were measured. The crack opening displacements in uncoated glass were also measured to assess the stress intensity factor at crack tips. In the case of 34 nm thick gold film, a fracture mechanics analysis based upon the crack-tip stress intensity factor led to the yield strength of about 620 MPa and the fracture toughness of 2.0 MPa·m$^{1/2}$. The evaluation of mechanical properties of thicker films, however, became more difficult, since the elongation in thicker films are considered to become comparable with the crack opening displacement.

Keywords Thin film, Indentation fracture, Mechanical properties, Stress intensity factor, crack opening displacement

1. Introduction

The Young's modulus, yield strength, ultimate tensile strength, work hardening exponent, elongation to failure and fracture toughness, are key factors which should be measured in order to guarantee the structural integrity of metallic materials. It is well known that the hardness can be related with the tensile properties of metals [1, 2]. According to contact mechanics, especially the analysis of Love [3] given for the elastic contact of a conical indenter with a semi-infinite body, the Young's modulus of the body can be estimated from the relation of the load with the contact area. This situation is realized by measuring the load-depth curve of elastic recovery which occurs during the unloading of indentation testing. Following this principle, a nanoindetation technique using the Berkovich indenter with a sharp apex has been developed currently, since a systematic study of Oliver and Pharr [4]. Nanoindentation shows its great applicability, in measuring the hardness and elastic modulus of very thin films to which normal tensile tests or hardness tests cannot be applied.
Hill [5] proposed a cavity theory, which treats the elastic-plastic stress problem around an internally pressurized cavity in an infinite body. The cavity theory has also been shown to be applicable in the analysis of the elastic-plastic stress fields around indent. According to Johnson [6], the radius, b, of plastic zone formed underneath a conical indenter with a half apex angle of ψ_c is given by

$$b = a[E\cot\psi_c/\{6(1-\nu)\sigma_y\} + 2(1-\nu)/\{3(1-2\nu)\}]^{1/3}, \quad (1)$$

where a is the radius of contact area, and E, ν and σ_y are is the Young's modulus, the Poisson's ratio and the yield strength, respectively. As for a conical indenter having the same projected hardness H and penetration depth h as those of the Vickers indenter, ψ_c becomes 70.3° and the radius of contact area is given by $a \approx 2.8h$. When $\nu = 0.3$, thus, equation (1) gives the value of b/h ranging from 2.8

to 26 for the change of E/σ_y from 100 (ultrahigh strength steels) to 10000 (annealed metals). Nearly the same values are obtained for b/h of the Berkovich indenter. One can see from this simple estimation that the penetration depth of the indenter, should be smaller by a factor of about 30 than the thickness of film, when its mechanical properties are not known. It should be also noted that, even if this requirement is satisfied, the elastic deformation of substrates on which the films are coated influences the penetrating behavior of indenter, leading to the change of measured hardness with penetration depth, as is demonstrated by Han *et al* [7]. On the other hand, as the load is lowered, the deformation mechanism underneath the indenter changes from the one representing the bulk properties to the one reflecting the generation of dislocations and their development to surrounding. Dietiker *et al*. [8] have shown that the critical penetration depth where this transition occurs is about 10 nm in single-crystalline Au films coated on NaCl substrates, when the Berkovich indenter is used. Accordingly the interpretation of hardness measured by nanoindentation becomes more complicated in thinner films than 200 nm. In addition to these problems, since the films are compressed by indentation, there is the possibility that the measured hardness does not represent their tensile properties, which are strongly affected by defects like small cavities introduced during synthesis.

It is well known that when an indenter is impressed on the surface of a ceramic material, cracks are formed around the indent at loads higher than a critical load [9]. Among such cracks, radial cracks with a half-penny shape formed by the Vickers indentation are frequently used to measure the fracture toughness of ceramic materials. The crack opening displacement (COD), δ_{tip}, very close to the tip of a radial crack with a radius of C can be approximately expressed as

$$\delta_{tip} \approx \delta_o \sqrt{\frac{2x}{C}} \text{ , where } \delta_o = \frac{4(1-\nu^2)K_{tip}\sqrt{C}}{\sqrt{\pi}E}, \tag{2}$$

which will be mentioned later. Here x is the distance from the crack tip toward the interior of crack and K_{tip} is the stress intensity factor (SIF) at the crack tip. Eq. (2) can be easily verified to hold true for any stress state acting on a circular crack in an infinite body. However the COD profile given by this equation deviates considerably from the one which is measured at distance far from the crack tip. Fett [10] proposed a sophisticated model of COD profile for the Vickers indentation crack by computer calculation, while Burghard *et al*. [11] used a polynominal equation of $x^{1/2}$ to fit it to the measured COD profiles. When we introduce a radial crack in a brittle substrate coated with very thin film of ductile metal, it is expected that the film be elongated at the crack mouth emerging at the film/substrate interface. The elongation changes with the COD along the crack, and its magnitude is considered related with the COD profile of the substrate. Despite that this microscopic elongation test by means of microcracking is dynamical and localized, we can obtain the information on the tensile properties of the film.

In the present study, microcracking by means of the Vickers indentation is used as a nanoscale tensile testing of thin metallic films coated on brittle substrates, and a fracture mechanics model to estimate the tensile properties of the films is proposed. In order to check the validity of the model, gold film and glass substrate are used as a model film/substrate system. The Young's moduli of these materials are nearly equal so that we can ignore the misfit in elastic behavior between the film and substrate. The Vickers indentation cracks are introduced in Au film/glass substrate systems (hereafter called Au/glass) by varying the film thickness and changing the indentation load. The indent size, crack size and COD profile in uncoated glass as well as in Au/glass are measured, and the yield strength, plastic work and fracture toughness of Au films are evaluated based upon the proposed model.

2. Modeling

2.1 SIF and COD

Lawn *et al.* [11, 12] showed, by using glass, that small circular cracks were first formed underneath the Vickers indenter during loading, and then the cracks grew into semi-circular ones during unloading. Thus the driving force for the development of the radial cracks, observed after the Vickers indentation, is substantially provided by the residual pressure remaining in the plastic zone formed underneath the indent. Assuming that the stress field around the plastic zone is represented by the cavity theory [5, 6], the circumferential stress around the plastic zone is given by

$$\sigma_\theta = p_r b^3/2r^3, \tag{3}$$

Here r is the distance from the center of indent and p_r is the residual pressure within the plastic zone. The stress intensity factor (SIF) of the radial crack with a radius C is then expressed as

$$K = \frac{2\alpha Y_s Y_c}{\sqrt{\pi C}} \int_b^C \frac{\sigma_\theta r dr}{\sqrt{C^2 - r^2}}, \tag{4}$$

by applying the SIF given for a circular crack in an infinite body [13]. Here the coefficients, Y_s and Y_c, are correction factors arising from the effects of surface and crack interaction, respectively, and α is a correction factor, which modifies the deviation from the assumed cavity theory as well as the assumed half-penny shape of radial cracks. By inserting Eq. (3) into Eq. (4) and integrating it, one can obtain the following formula.

$$K = \chi P / C^{3/2} \sqrt{1 - (b/C)^2}, \tag{5}$$

where P is the indentation load and χ is a parameter that correlates the SIF due to load P with that of stress σ_θ. , *i.e.*, $\chi = \alpha Y_s Y_c p_r b^2/\pi^{1/2}/P$. It should be noted here that this equation does not involve the pressure within the plastic zone, which acts as the force to close the crack in the zone [10]. When the crack is larger by a factor of more than three than the plastic zone, *i.e.*, $C \geq 3b$, $\{1-(b/C)^2\}^{1/2} \approx 1$ so that the above equation is approximately written as

$$K = \chi P / C^{3/2}. \tag{6}$$

The condition $C >> b$ also enables us to ignore the closing effect of pressure within the plastic zone. There have been many formulae that relate χ with the properties of materials and the characteristics of indent [13]. In the present analysis, we use the formula, $\chi = 0.016(E/H)^{1/2}$, which was proposed by Anstis *et al.* [14]. Here the projected hardness is defined by $H = 2P/d^2$, where d is the diagonal length of Vickers indent.

The COD at a distance of r from the center of indent is given by [15]

$$\delta(r) = \frac{4(1-\nu^2)}{\sqrt{\pi} E} \int_r^C \frac{\sqrt{C'} K(C') dC'}{\sqrt{C'^2 - r^2}}. \tag{7}$$

The insertion of Eq. (6) into Eq. (7) and the use of the formula of integral [16] lead to

$$\delta(r) = \delta_o \frac{\arccos(r/C)}{r/C}. \tag{8}$$

This equation does not cover the COD profile over the whole crack length. However, it reproduces the COD profile at longer distances from the crack tip than Eq. (2) does. Thus Eq. (8) is satisfactory and its simple form is very useful in the present analysis of COD, as will be mentioned below. One can also see that Eq. (7) approaches Eq. (2) irrespectively of the form of K, when $x << C$.

2.2 Evaluation of yield strength of metallic films

When a ductile film deposited on a brittle substrate does not have large enough strength to close the crack mouth in the substrate, the film is considered to be elongated at the crack mouth, as is shown in Fig. 1. Since the film thickness, t_o, considered here is much smaller than the radial crack size, it is assumed that the film is elongated only at the crack mouth. It is anticipated that the film fails, when the COD exceeds the elongation to failure of the film which is isolated from the substrate. Hence the half crack length C_f observed at the surface of film/substrate system is expected to be smaller

than the half crack length C of uncoated substrate. It is also postulated that the plastic work done until the failure of the film is much larger than the surface energy of the film so that we can ignore the term related with the surface energy. Assuming that the film is a rigid-plastic body having the yield strength of σ_y, the plastic work done in an element between x an $x + dx$ is given by

$$dW_p = \sigma_y \int_0^\delta t dx d\delta , \tag{9}$$

where t is the thickness at the distance of x. The film thickness changes with δ. Assuming that plastic deformation in the film is constrained at the film/substrate surface, it is considered that the shear displacement through thickness takes place at the angles of ±45° from the surface, as shown in Fig. 2, following the maximum shear stress theory [5]. The geometrical condition of this constraint deformation leads to

$$t(\delta) = -\delta/2 + \sqrt{\delta^2/4 + {t_o}^2} . \tag{10}$$

Consequently the plastic work done in the plastic zone of the film becomes

$$W_p = \sigma_y V(R) , \tag{11}$$

where $V(R)$ implies the volume of plastic zone and is given by

$$V(R) = \int_0^R \int_0^\delta t(\delta) d\delta dx . \tag{12}$$

Here R is the distance of plastic zone in the film and is given by the difference in half crack size between the substrate and film, *i.e.*, $R = C - C_f$. The integration of $t(\delta)$ with regard to δ in the above equation leads to

$$T(\delta) = \int_0^\delta t(\delta) d\delta = \frac{\delta\sqrt{\delta^2 + 4{t_o}^2} - \delta^2}{4} + {t_o}^2 \ln\left[\tan\left(\frac{\pi}{4} + \frac{1}{2}\arctan\frac{\delta}{2t_o}\right)\right]. \tag{13}$$

On the other hand, the film/substrate system increases its fracture toughness due to the reduction in crack size. Assuming that the SIF in the film is expressed by Eq. (6), the elastic energy in the film,

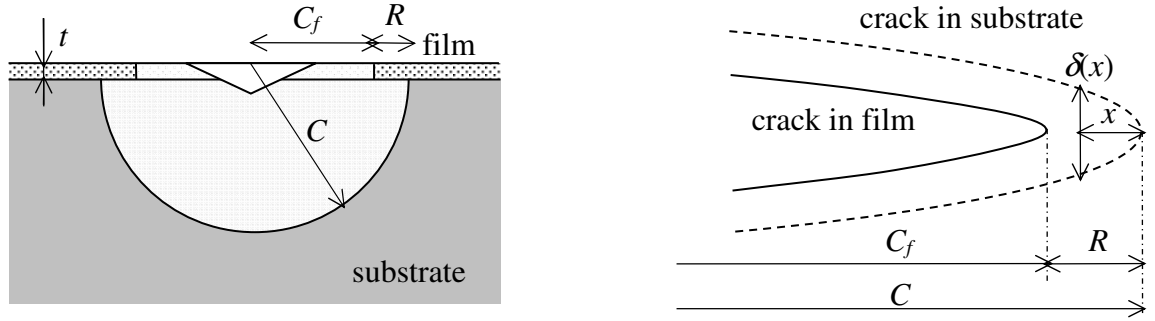

(a) Cross-sectional view. (b) Top view near crack tip.

Fig. 1. Film/substrate crack in which the crack tip is discontinuous at the film/substrate interface.

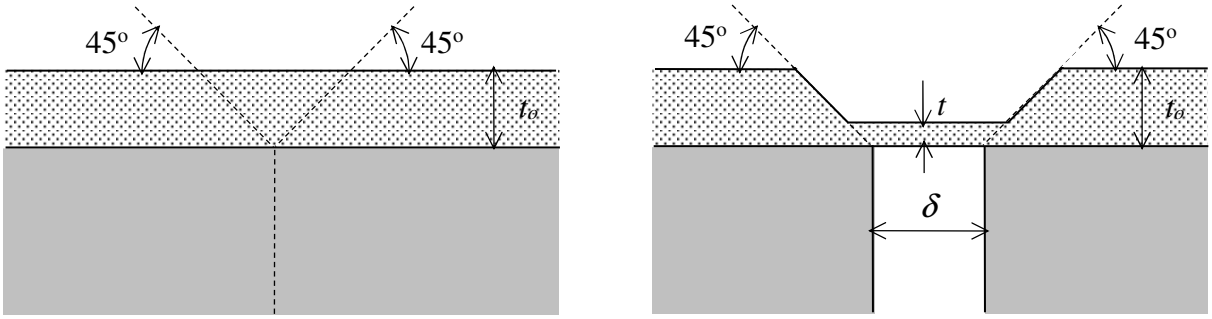

(a) Before cracking. (b) After cracking.

Fig. 2. Assumed mechanism of plastic deformation in film.

which is required to reduce the crack size from C to Cf, is written as follows.

$$U_e = \int_{C_f}^{C} \frac{K(C')^2}{E_f} t_o dC' = \frac{K_C{}^2 t_o}{2E_f} \frac{CR(2C-R)}{(C-R)^2}. \quad (14)$$

where E_f is the Young's modulus of the film. By equating U_e with W_p, the yield strength of the film is given by

$$\sigma_y = \frac{K_C{}^2}{E_f t_o} \frac{CR(2C-R)}{V(R)(C-R)^2}. \quad (15)$$

Since the elongation of the film increases with increasing the distance from crack tip in the substrate, the plastic work per unit area consumed in the plastic zone of the film is also expected to increase with distance from the crack tip in the substrate. Accordingly the local plastic work per unit area can be defined as follows.

$$\gamma_p(x) = \frac{dW_p}{t(x)dx} = \frac{\sigma_y T(\delta)}{t(\delta)}. \quad (16)$$

We can evaluate the profile of local plastic work as a function of x by using the dependence of δ on x. The maximum value of local plastic work is obtained at $x = R$, which corresponds to the plastic work done to failure. Accordingly the fracture toughness of the film is given by

$$K_{fC} = \sqrt{E_f \gamma_p(R)}. \quad (17)$$

It should be noticed, that the effect of residual stress in the film is not taken into account in the present analysis, since yield strength is not affected significantly by isotropic stress.

3. Experimental procedures

Slide glass with a thickness of 1.2 mm ~ 1.5 mm and cover glass with a thickness of 0.12 mm ~ 0.17 mm were used as substrate material. Table 1 shows the chemical composition of the glass obtained by X-ray fluorescence analysis (Rigaku ZSX-100e). The Young's modulus and Poisson's ratio of these glasses are 71.3 GPa and 0.22, respectively. The thicker glass plates were used for the Vickers indentation with large loads, which formed cracks with radii larger than 50 μm. The glass plates were annealed at 723 K for 3.6 ks in order to remove pre-existing residual stresses. The films of 99.9% purity Au were deposited on the surfaces of these glass plates by using a DC sputtering machine (Eiko Engineering, IB-2). The film thickness was evaluated from the change in weight before and after the sputter-deposition, and the thickness of very thin films was measured by using atomic force microscopy. The film thickness ranged from 23 nm to 227 nm. The Vickers indentation was conducted at room temperature. The load changed from 1.96 N to 4.9 N for thinner glass substrates and from 1.96 N to 19.6 N for thicker glass substrates. The indentation tests were carried out twenty times for each load. The half-lengths of radial cracks which developed only in the diagonal directions of indent were measured by using an optical microscope (OM) and a field-emission scanning electron microscope (SEM, Hitachi S-4100H). The COD profiles of some cracks, in uncoated glass were also measured by the SEM.

Table 1. Chemical composition of glass substrate (mass%)

SiO_2	B_2O_3	Al_2O_3	Na_2O	K_2O	TiO_2	ZnO	P_2O_5	Fe_2O_3	Sb_2O_3
60.9	11.1	4.17	7.03	7.08	4.26	5.28	0.018	0.0176	0.0918

4. Results and discussion

4.1 Uncoated glass

Fig. 1 shows an example of radial cracks formed around the Vickers indent in uncoated glass. At light loads ranging from 0.98 N to 2.94 N, some cracks deviated from the diagonal directions of indent or very short cracks were formed in the diagonal direction, as is shown in this figure. These cracks were excluded in the measurement. The values of COD were measured in the direction normal to the crack propagation, as shown in Fig. 1(b). Fig. 2 shows typical examples of COD profiles measured at 2.94 N and 9.8 N. These COD profiles are similar in shape to those in soda-lime glass which were measured at the same load range by us, and those at larger loads (9.1 N - 98 N) by Burghard *et al* [14]. Solid curves in Fig. 2 are fitting curves which are obtained by applying Eq. (8) to the COD values in the range of $C/2 \le r \le C$. One can see that the solid curves agree fairly well with the measured COD profiles in this range. The values of δ_o estimated by the solid curves are 67.5 nm at 2.94 N and 92.7 nm at 9.8 N, providing 0.32 MPa·m$^{1/2}$ for the value of K_{tip} independently on the crack size or load. Broken curves in Fig. 2 are the COD profiles, which are obtained by inserting the values of δ_o into Eq. (2). The coincidence of the COD profiles predicted by Eq. (2) with the measured ones is limited to a distance of about 10% from the crack tips. As a result, the accurate determination of δ_o by using Eq. (2) is very difficult at small loads, since the measurement error as well as the scatter of COD become relatively large compared to the small COD values near the crack tips.

Table 2 shows the average values of d, C, H and K_C and γ_s in uncoated glass, where the surface energy of glass is given by $\gamma_s = K_C^2/(2E)$. All of the values of d and C listed in this table are measured by SEM observation. It should be noted here that the OM measurement yielded 6.4 GPa and 0.65 MPa·m$^{1/2}$ for H and K_C, respectively, as will be shown in Table 3. On the other hand, the SEM observations leads to slightly higher hardness and smaller fracture toughness compared to those measured by OM observation. It is considered that this discrepancy in H and K_C arises from the fact that SEM images do not have such a large sensitivity to the change in the height of surface

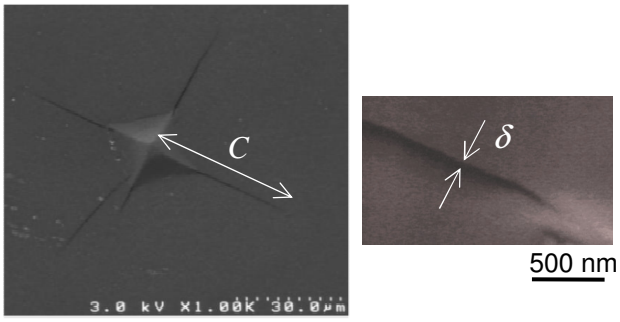

(a) Indent and radial cracks. (b) Crack tip.

Fig. 1. SEM photographs of radial cracks in uncoated glass (P = 2.94 N).

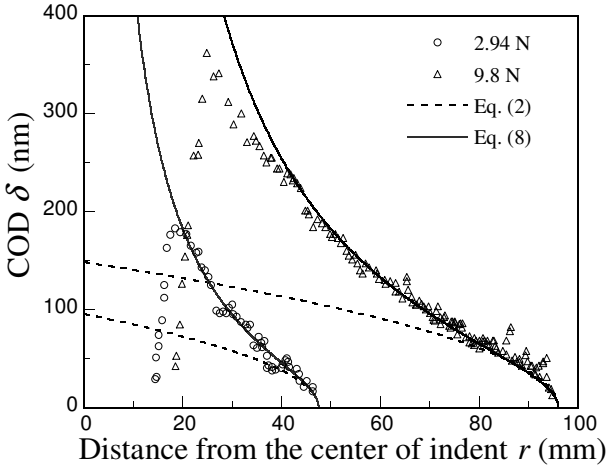

Fig. 2. COD profiles in uncoated glass at 2.94 N and 9.8 N.

Table 2. The values of d, C, H, K_C and γ_s evaluated by SEM observation.

P (N)	d (mm)	C (mm)	H (GPa)	K_C (MPa·m$^{1/2}$)	γ_s (J/m^2)
0.98	17.1	19.7	6.70	0.585	2.40
1.96	24.0	30.2	6.81	0.612	2.62
2.94	29.3	38.2	6.85	0.643	2.90
4.90	38.3	56.0	6.68	0.611	2.62

as OM images provides, while OM observation do not give as high a resolution in the measurement of crack size as that of SEM observation. In the evaluation of the mechanical properties of thin films, we will use the data measured by SEM observation in order to avoid the systematic error arising from a difference in measurement method.

4.2 Apparent hardness and apparent fracture toughness of Au/glasss

Fig. 3 shows the OM and SEM images of 23 nm thick Au/glass indented at a load of 2.94 N. The Au film is translucent to light at this thickness, so we can estimate the crack size in glass substrate underneath the film. Table 3 shows the values of d and C in uncoated glass and 23 nm thick Au/glass, which were measured by OM observation. It is obvious that the crack size is nearly equal between these specimens, while the indent size of the Au/glass is slightly larger than that of the uncoated glass. As a result, the apparent hardness, H_A, of the Au/glass is lowered slightly compared to that of the uncoated glass. The value of χ in the Au/glass increased only by 6.5% so that its apparent fracture toughness, K_A, is close to that of the uncoated glass. On the other hand, secondary electrons in SEM are emitted from a very shallow surface layer within a depth of a few nm. Accordingly we can observe the morphology of cracks formed only in the Au film. Fig. 3(c) shows the enlarged SEM micrograph of a crack front shown highlighted by the square in Fig. 3(b). One can see from this figure, that the crack front in the Au film has a faintly dark contrast; and its length is about 1.8 μm. Comparing this result with the crack size measured by OM observation, it is considered that the Au film is elongated over this distance from the crack front in the underlying substrate.
Fig. 4 shows the load-dependence of the hardness (H) of uncoated glass and the apparent hardness (H_A) of Au/glass. The apparent hardness decreases when increasing the thickness of Au film, and the difference between H and H_A tends to increase with lowering the load. The decrease in the apparent hardness of Au/glass is brought by the plastic deformation of the Au film, which is evidenced by the morphology of the indented surface of 227 nm thick Au/glass shown in Fig 5. When the film thickness is 227 μm, radial cracks were not observed at loads less than 9.8 N. The

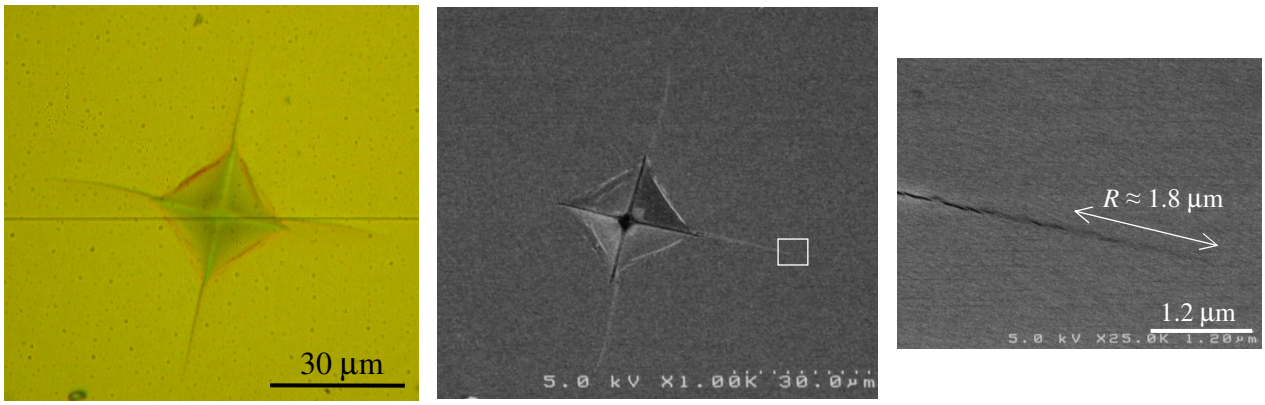

(a) OM photograph. (b) SEM micrograph. (c) SEM micrograph of crack front.

Fig. 3. Cracks formed around the Vickers indent in 23 nm thick Au/glass (P =2.94 N).

Table 3. The values of d, C, H, H_A, K_C and K_A evaluated by OM observation.

Crack system	d (μm)	C (μm)	H , H_A (GPa)	K_C, K_A (MPa·m$^{1/2}$)
Glass	29.2	38.2	6.38	0.645
23 nm thick Au/glass	31.2	38.7	5.62	0.675

maximum COD of uncoated glass is 182 nm at 2.94 N and 360 nm at 9.8 N (Fig. 2). Thus it is obvious that when the film thickness is larger than the maximum COD, cracks are not formed in the film. The apparent fracture toughness of Au/glass evaluated by using $\chi_A = 0.016(E/H_A)^{1/2}$ in Eq. (6) increased about twice at a thickness of 40 nm and about four times at 100 nm in comparison with the fracture toughness of uncoated glass.

4.3 Analysis of 34 nm thick Au/glass

As mentioned in sections 4.1 and 4.2, the COD profiles for $C/2 \le r \le C$ in uncoated glass obey those predicted by Eq. (8), and the Au/glass crack systems investigated here show their discontinuity at the film/substrate interfaces. As a case study, the mechanical properties of 34 nm thick Au film coated on glass substrate are evaluated here. The apparent hardness of the Au/glass decreases by about 0.5 GPa, but its apparent fracture toughness increases by a factor of about 1.8, in comparison with the hardness and fracture toughness of uncoated glass (Fig. 6). The value of R increases with load, and the ratio, R/C, is 30 - 35% irrespectively of load, as is shown in Fig. 7.

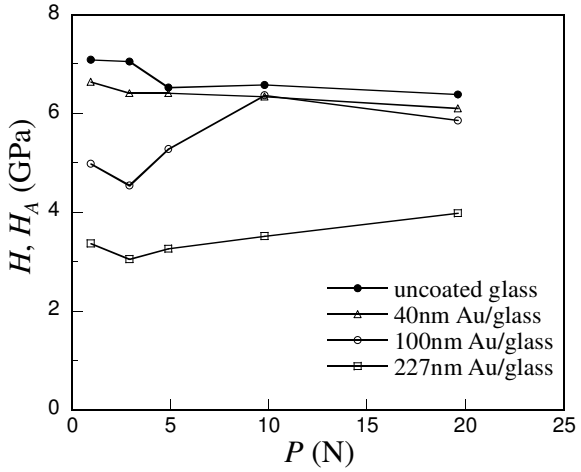

Fig. 4. Load-dependence of hardness in uncoated glass and Au/glass.

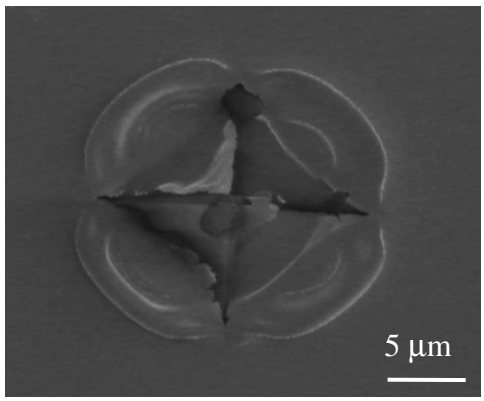

Fig. 5. Indent formed on 227 nm thick Au/glass (P = 2.94 N)

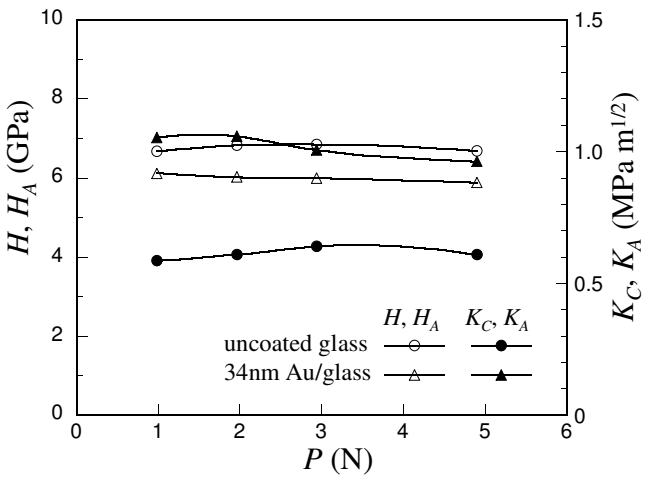

Fig. 6. Load-dependence of apparent hardness and fracture toughness in 34 nm thick Au/glass.

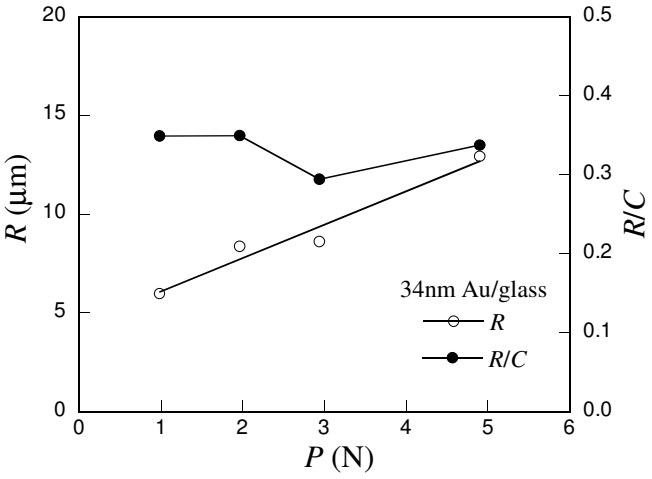

Fig. 7. Load-dependence of R and R/C in 34 nm thick Au/glass.

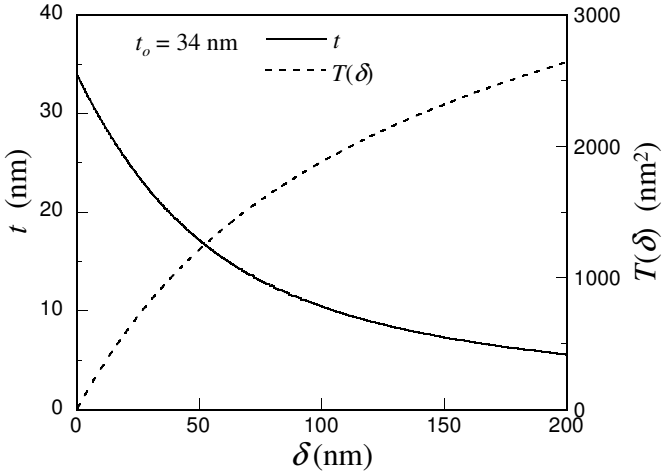

Fig. 8. The change in film thickness and $T(\delta)$ with COD in 34 nm thick Au film.

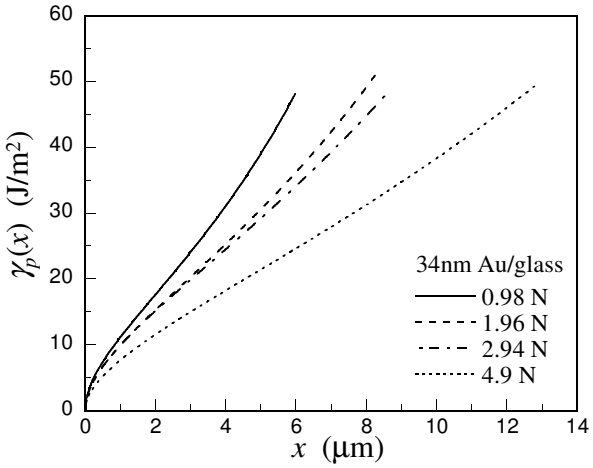

Fig. 9. The profiles of local plastic work per unit area in 34 nm thick Au film.

Table 4. Parameters and mechanical properties evaluated for 34 nm thick Au film.

P (N)	δ_o (nm)	R (μm)	$V(R)$ (x10^6 nm^3)	σ_y (MPa)	$\gamma_p(R)$ (J/m^2)	K_{fC} (MPa·m$^{1/2}$)
0.98	42.8	5.98	4.52	695	48.2	1.94
1.96	52.9	8.38	7.11	633	51.9	2.01
2.94	59.6	8.62	7.17	639	48.4	1.94
4.9	72.1	12.93	12.58	499	49.9	1.97

Therefore we can use Eq. (8) to estimate the COD profile in the substrate. Fig. 8 shows the changes of t and $T(\delta)$ as a function of δ, which are calculated by inserting Eq. (8) into Eq. (10) and Eq. (13) and using the value of δ_o determined by K_{tip} = 0.32 MPa·m$^{1/2}$.

The values of σ_y at 0.98 N - 4.9 N obtained by setting the Young's modulus of Au as 78 GPa [20] are listed with other parameters in Table 4. The average yield strength of 34 nm thick Au film evaluated in the present study is 620 MPa, which is comparable with about 400 MPa in 2.7 μm thick Au film [21] and about 600 - 900 MPa in 0.85 μm and 1.76 μm thick Au films [22]. However, it has been shown that the mechanical properties of thin Au films depend on the thickness [22, 23], temperature [21, 22] and strain rate [22]. One of the most available data to be compared with the present result may be the mechanical properties of 20 nm thick Au films examined by Olliges *et al* [24]. They elongated such very thin Au films deposited on polyimide substrates and measured the stress in the films by using synchrotron X-ray. They reported that the yield strength of the films ranged from 700 MPa to 875 MPa at room temperature, which is in a good accordance with the yield strength obtained for 34 nm thick Au film. The local plastic energy $\gamma_p(x)$ of 34 nm thick Au film increases with the distance from crack tip and its shape resembles the COD profile near the crack tip, as is shown in Fig. 9. The maximum value of COD, however, does not depend on the value of R or load. Consequently the maximum plastic work and fracture toughness of the Au film is about 50 J/m^2 and 2.0 MPa·m$^{1/2}$, respectively (Table 4).

5. Summary

In the present study, microcracking induced by the Vickers indentation was applied to the evaluation of the mechanical properties of very thin films of ductile metals. For this purpose, a simple expression was proposed for the estimation of the COD of radial cracks in brittle substrates, which agreed very well with the COD profiles measured in uncoated glass in the range of $C/2 \le r \le C$. The

comparison of the OM and SEM images of 23 nm thick Au/glass crack fronts clearly showed that the film was elongated to failure at the crack mouth of the substrate. However, when the film thickness exceeded the COD of the substrate, radial cracks were not formed in the film. These results suggest the validity of assumptions used in the present analysis of the mechanical properties of very thin metallic films. The yield strength of 34 nm thick Au film was evaluated to be about 620 MPa, which is comparable with the yield strength of very thin Au films given in literature. The maximum plastic work and fracture toughness of 34 nm thick Au film were also evaluated to be 50 J/m^2 and 2.0 $MPam^{1/2}$, respectively.

Acknowledgement

We thank the staff of Division of Intrumental Analysis, NSCRE, Kagoshima University for their great help.

References

[1] D. Tabor, Hardness of Metals, Oxford University Press, New York, 2000.
[2] G. Dieter, Mechanical Metallurgy, 3rd Ed., McGraw-Hill, New York, 1986.
[3] A.E.H. Love, Quat J Math, 10 (1939) 161−175.
[4] W.C. Oliver, G.M. Pharr, J Mater Res, 7 (1992) 1564−1583.
[5] R. Hill, The Mathematical Theory of Plasticity, Oxford University Press, Oxford, 1950.
[6] K.L. Johnson, Contact Mechanics, Cambridge University Press, Cambridge, 1985.
[7] S.M. Han, R. Saha, D. Nix, Acta Mater, 54 (2006) 1571−1581.
[8] M. Dietiker, R.D. Nyilas, C. Solenthaler, R. Spolenak, Acta Mater, 56 (2008) 3887−3899.
[9] B.R. Lawn, Fracture of Brittle Materials, 2nd Ed., Cambridge University Press, Cambridge, 1993.
[10] T. Fett, Report FZKA 6757, Forschungszentrum Karlsruhe, Karlsruhe, 2002.
[11] Z. Burghard, A. Zimmermann, J. Rödel, F. Aldinger, B.R. Lawn, Acta Mater, 52 (2004) 293−297.
[12] T. Fett, G. Rizzi, Report FZKA 6907, Forschungszentrum Karlsruhe, Karlsruhe, 2003.
[13] B.R. Lawn and A.G. Evans, J Mater Sci, 12 (1977) 2195−2199.
[14] D.B. Marshall and B.R. Lawn, J Mater Sci, 14 2001 (1979).
[15] H. Tada, P.C. Paris, G.R. Irwin, The Stress Analysis of Cracks Handbook, 3rd Ed., ASME, 2000.
[16] I.J. McColm, Ceramic Hardness, Prenum Press, New York, 2010.
[17] G.R. Anstis, P. Chantikul, D.B. Marshall and B.R. Lawn, J Am Ceram Soc, 64 533 (1981).
[18] H. Miyamoto, Three Dimensional Elasticity, Shokabo, Tokyo, 1967 (in Japanese).
[19] I.S. Gradshteyn, I.M. Ryzhik, Tables of Integrals, Series, and Products 5th Ed., Academic Press, San Diego, 1994.
[20] T.H. Courtney, Mechanical Behavior of Materials, McGraw-Hill, New York, 1990.
[21] A.A. Volinsky, N.R. Moody, W.W. Gerberich, J Mater Res, 19 (2004) 2650−2657.
[22] K. Jonnalagadda, N. Karanjgaokar, I. Chasiotis, J. Chee, D. Peroulis, Acta Mater, 58 (2010) 4674−4684.
[23] H.D. Espinosa, B.C. Prorok, B. Peng, J Mech Phys Sol, 52 (2004) 667−689.
[24] S. Olliges, S. Frank, P.A. Gruber, V. Auzelyte, H. Solak, R. Spolenak, Mater Sci Eng A, 528 (2011) 6203−6209.

Crack and defect formation in diamond films

Duosheng Li[1,2*], Qing H. Qin[2], Yi Xiao[2], Dunwen Zuo[3], Wenzhuang Lu[3]

[1] College of Material Science and Engineering, Nanchang Hangkong University, Nanchang 330063, China
[2] Research School of Engineering, Australian national University, Canberra, ACT 2601, Australia
[3]College of Mechanical and Electrical Engineering, Nanjing University of Aeronautics and Astronautics, Nanjing 210016, China
*duosheng.li@anu.edu.au or ldscad@163.com

Abstract In this paper, mechanisms of defect and crack initiation in a diamond film prepared at substrate temperatures are investigated using direct current plasma chemical vapor deposition method. The study is by way of X ray diffraction (XRD), optical microscope (OM), and scanning electron microscopy (SEM) and reveals that initiation of defects and cracks during the growth of diamond films depends strongly on substrate temperature. The defects and impurities formed in high substrate temperatures include mainly residual stresses, and non-diamond phase such as graphite and amorphous carbon, which result in forming crack and microscopic hole in diamond film. X ray diffraction, optical microscope and SEM have been used to examine the temperature dependence of various defect inductions. It is found that cracks in diamond film are generally derived at grain boundary. In general, diamond films prepared in high temperature substrate will result in high residual stress at the interface between the diamond film and the substrate

Keywords Diamond film, Defect, Crack, Substrate temperature, Residual stress

1. Introduction

Due to its excellent physical and chemical properties, diamond film prepared using chemical vapor deposition (CVD) is becoming a popular material in many engineering applications such as infrared optical window, coating cutting tools, biomaterials, micromechanical, and thermal heat sink materials [1-3]. Diamond film can grow on hetero-epitaxial substrates, such as Si, Mo, Ti, and Ta substrates. It should be mentioned that diamond film deposited on the substrates mentioned above may induce some defects and impurity due to lattice mismatch and residual stress. Takeuchi et al. [4] analyzed surface defect status of diamond by photoelectron emission yield experiments; Ikeda et al. [5] investigated facture shape of polycrystalline diamond film through indentation test. Shames et al. [6] studied the localization and nature of defects for powder and compact diamond film samples. Stiegler et al. [7] investigated the impurity and defect incorporation in diamond films deposited from a carbon-hydrogen-oxygen gas system at substrate temperatures between 560 and 345 ^{o}C. Jeong et al. [8] explored mechanisms of cracking in the CVD films was investigated experimentally and theoretically. Qin and Kang et al [9, 10] investigated experimentally the effect of film thickness and size on fracture toughness. In the recent years, diamond films become popular and commercial diamond wafers are successfully used for some important fields. However, crack and defect problems reported in the literature are for large size diamond wafer only [11, 12]. For diamond film deposited on curved surface, (for example convex substrate), and it was very difficult to keep a uniform temperature on a convex substrate. It induces often cracks and defects due to non-uniform temperature distribution over the substrate surface. Crack problems for such a thin film seem not being reported in the literature. In this study, we select Mo as substrate material for depositing diamond film because of its low lattice mismatch between the diamond and the underlying Mo substrate. The mechanisms of crack and defect generation during the depositing process of the diamond film are investigated. It should be mentioned that a new substrate cooling system presented in [13] was used to ensure nearly uniform temperature over the substrate surface.

2. Experimental

The deposition system used in the present work for the growth of diamond films by direct current plasma jet CVD (DCPJCVD) is similar to that described in [14]. Using the deposition system, diamond films are prepared on convex molybdenum (Mo) substrate. The reaction gas employed is a mixture of methane (CH_4) and hydrogen (H_2), which are fed into a reaction chamber. Argon (Ar) gas is subsequently ignited by high frequency system to generate DC plasma. The anode and cathode are made of metal Mo and W, respectively. The substrate temperature is controlled by regulating the flow rate of the cooling water and the discharge current density. Typical experimental conditions for the growth of diamond film by DCPJCVD are given as follows: Source gases used are CH_4, H_2 and Ar; H_2 flow rate is 450 sccm, CH_4 flow rate is 3500 sccm; the total pressure of reaction chamber is approximately 43KPa, and CH_4 concentration is about 2.15 %. The substrate temperature is measured by an IR pyrometer and can be adjusted within the range of 830-1050℃. The diamond films are characterized by optical microscope, scanning electron microscopy, X ray diffraction with regard to surface morphology or defect, crack and their incorporation.CH_4

3. Results and discussion

As mentioned above, diamond films are prepared on Mo substrate by DCPCVD in this work. The substrate temperature is about 900-940 ℃ and the other growth conditions for the deposition process of the diamond films are kept constant or nearly constant. To illustrate the temperature distribution along radial direction, six points on the substrate surface labeled in O, A, B, C, D E as Fig. 1 and the temperatures at these points are measured on line using IR pyrometer.

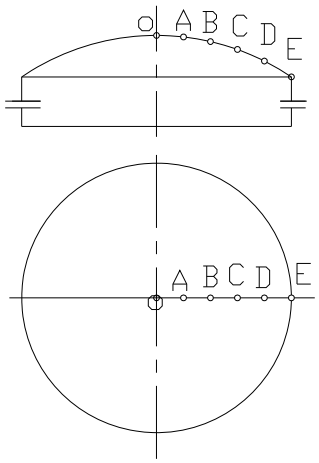

Fig. 1 Schematic diagram of radial direction of substrate

Fig. 2 shows the variation of temperature at the six points with deposition time. As expected, Fig. 2 shows that the highest temperature of the diamond film occurs at central point O and the lowest temperature presents at edge point E.

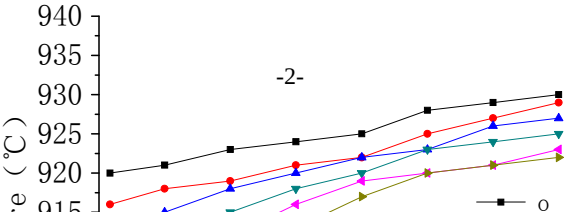

Fig. 2 Temperature distribution of diamond films at different deposition time: from 3 to 21 hours

It is also found from Fig. 2 that diamond temperature increases with the increase in deposition time. Temperature difference along the radial direction is not obvious and the maximum is about 15 ^{o}C only as Fig. 2. It is also found that surface temperature of the diamond film decreases along the outward radial direction. The temperature difference (or temperature fluctuation) on surface of substrate may significantly affect the quality of the diamond film. It is found that, when temperature difference was under 1-2% of the maximum, it has a negligible negative effect on the growth of diamond film.

When diamond film was prepared on a hetero-epitaxial substrate, some defects and impurity in diamond film may be inevitably induced due to lattice mismatch and residual stress. It is observed from the experiment that the residual stress is the main defect in diamond film, which depends strongly on the substrate temperature.

In this paper, four diamond film samples had been prepared and tested under substrate temperatures of 870, 940, 980 and 1050 ^{o}C respectively. The other growth parameters are kept the same in all experiments. The residual stress in diamond film is measured using X-ray diffraction (XRD), and the corresponding results are listed in Fig. 3.

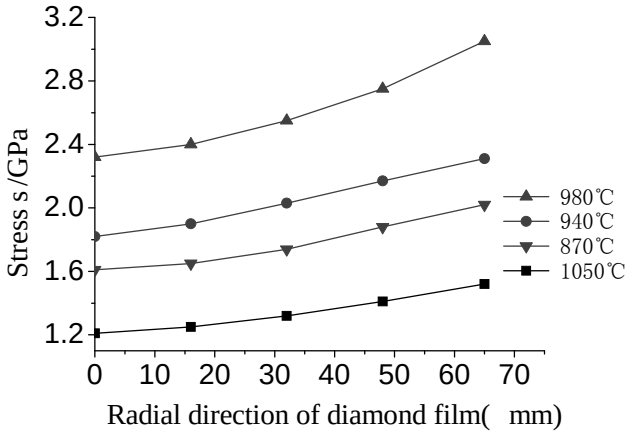

Fig. 3 Residual stress of diamond film

It is observed from Fig. 3 that the residual stress of the diamond film increases along with an increase in the substrate temperature when substrate temperature varied in the range 870-980 ^{o}C, Tensile stresses vary in range of 1.4 GPa - 3.0 GPa. It is interesting to note that the residual stress decreases significantly when the substrate temperature reaches 1050 ^{o}C. The mechanism for inducing this phenomenon should be further investigated.

It should be mentioned that, when the substrate temperature is in a higher, value, the nucleation process of some microcrystals of the original diamond film will speed up which causes the other microcrystals to slow down their emerging and growing process. As a consequence, in the thin film will be in low nucleation density and larger grain size. Noted that the coefficient of thermal expansion (CTE) of Mo substrate is higher than that of diamond, It may induce significant residual stress in diamond film when the film is cooling from a relatively high temperature, which will degrade its mechanical property [15]. If the internal stress of diamond film is greater and more than fracture strength of the diamond film, it may induce microcracks and even fracture.

To investigate further the formation mechanism of microcracks in diamond film, experimental testing using Optical microscope (OM) has been conducted. The OM photograph of diamond film is shown in Fig. 4.

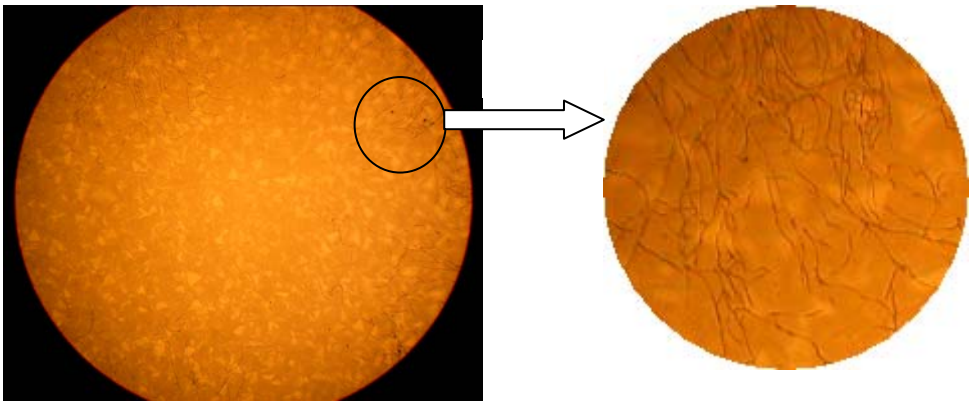

Fig.4. Optical microscope photograph of diamond film, (a) whole (30×), (b) an enlarged scale (100×)

It can be seen from Fig. 4 (a) that, in a low amplification, the size of the diamond crystals is approximately uniform and clear grain boundary appears. Fig. 4b shows an enlargement of microstructures of the diamond film. It is found that some radial microcracks penetrates the surface of diamond film and extends to the center area of the diamond film. Thus, when the substrate temperature is as high as 1050 ℃, some radial microcracks are created in the diamond and extend to the whole surface. Partial residual stress in diamond film is released with the creation of microcracks which is in agreement with the results shown in Fig. 3. Crack and defects cause significantly damage of physical and mechanical properties of the diamond film, including dimensional stability, mechanical stiffness, optical properties, and thermal conductivity.

The mechanism of defect formation in the thin diamond can also be explained as follows. Diamond film prepared on the substrate with curve surface usually accompanies some defects such as crack, non-diamond impurity, and microscopic hole due to inappropriate growth process. These defects like microcracks can extend to the surface of diamond film from somewhere inside. This is the major factor to cause diamond rupture. Fig. 5 shows a diamond film with some microcracks and non-microcrack.

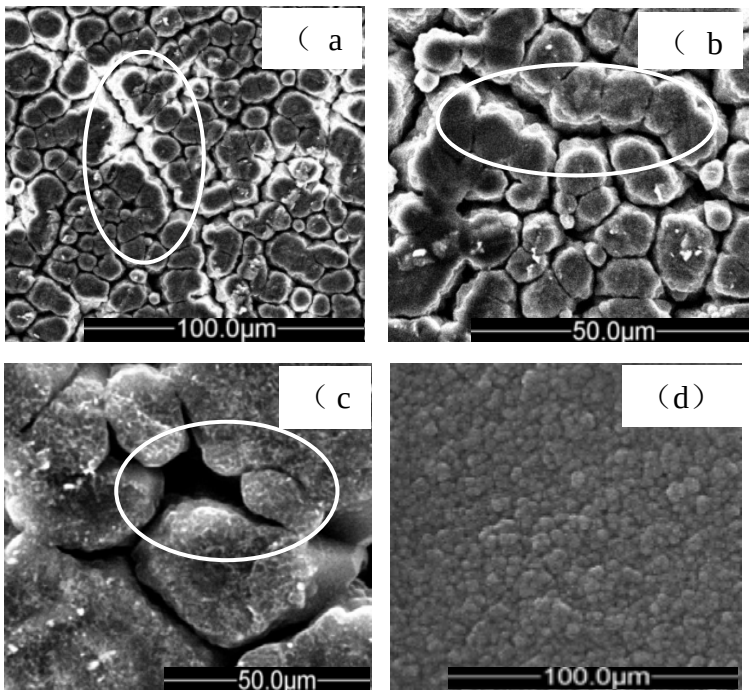

Fig.5. SEM photograph of diamond film, (a) little microcrack, (b) microcrack extending, (c) microscopic hole, (d) non-microscopic,

It is observed from Fig.5 that there exist some defects in the diamond film. In particular, some microcracks appeared in diamond film as shown in Fig. 5(a). When these microcracks further converge and accumulate, it may become a visible crack as shown in Fig. 5(b). Due to improper growth processes such as high or low substrate temperature, high CH_4 concentration and high growth rate, diamond film deposited with competitively columnar way, diamond film deposited may also contain some microstructure defects including amorphous carbon, graphite and microscopic hole as Fig.5c. It is also found from Fig. 5 that microcracks in diamond film generally appearing at grain boundary. These defects may cause sharply degrading in terms of physical and mechanical performance of diamond film.

CVD method, the process of synthetic diamond film has undergone the course of nucleation and growth. During the nucleation stage, the carbon-containing gas source under appropriate process parameters on the deposition substrate to form a certain number of isolated diamond nucleation. Growth stages of diamond nucleation continue to grow and even become one, to cover the entire surface of the substrate, and then grew along the vertical direction of the substrate; at last, it grew a certain thickness of the diamond film. While the nucleation density is usually less than 10^{12} cm^{-2} on the non-diamond substrate [16], which probably lead to a gap between the grain and the grain of the nucleation surface, so that the formation of the diamond film and the substrate are not entirely brought into close contact, and the presence of tiny non-contact area, these tiny non-contact area in the diamond film into an even cover the entire surface of the substrate still exists, leaving microvoids in the film based interface. Especially when the substrate temperature increases or high CH_4 concentration, this phenomenon is more obvious last microvoids evolved into micro-cracks as Fig. 5(a)-(c). The presence of micro-voids and microcracks weakening the binding of the diamond film and the substrate, between the interface of the diamond and the properties of diamond film, the crystal grains of the diamond film is formed the initial crack. Under external force, where the initial crack first cause stress concentration at the crack tip region caused by crack propagation, triggered coating breaking off. However, through the control of

the diamond film growth temperature, the concentration of carbon source and the substrate surface temperature uniformity optimization, we are able to prepare a high-quality, without micro-cracks diamond film, as shown in Fig.5 (d).

4. Results and discussion

The formation of defects and crack represents an intrinsic problem in fabricating diamond film structures. In this work, of the study on diamond film deposited at different substrate temperature, through combination use of XRD, OM and SEM shows that some defects rapidly increases along with an increase in the substrate temperature. XRD analysis testifies that high temperature result in high residual stress in diamond film when the substrate temperature is less than 980 ℃. When the substrate temperature exceeds 1050 ℃, diamond film prepared has very low residual stress due to having more cracks in the film and most residual stress being released. OM and SEM results reveal that some radial cracks penetrates surface of diamond film and extends to center of diamond film. When those cracks gathered and grow up, they may induce microscopic hole and even cause local fracture in diamond film.

Acknowledgements

DL acknowledges the financial support of Education Science Foundation of Jiangxi Province (GJJ09188), Fund for the Doctoral Program of NCHU (EA200901168) and Natural Science Foundation of China (50605032).

References

[1] D. Li, D. Zuo, W. Lu, R. Chen, B. Xiang, M. Wang, Effects of methane concentration on diamond spherical shell films prepared by DC-plasma jet CVD. Solid State Ionics, 179 (2008) 1263-1267.
[2] D.M. Trucchi, C. Scilletta, E. Cappelli, P.G. Merli, S. Zoffoli, G. Mattei, P. Asearelli, Optimization of the performance of CVD diamond electron multipliers. Diam Relat Mat, 15 (2006) 827-832.
[3] N. Jiang, S. Kujime, I. Ota, T. Inaoka, Y. Shintani, H. Makita, A. Hatta, A. Hiraki, Growth and structural analysis of nano-diamond films deposited on Si substrates pretreated by various methods. J Cryst Growth, 218 (2000) 265-271.
[4] D. Takeuchi, C.E. Nebel, S. Yamasaki, Surface defect states analysis on diamond by photoelectron emission yield experiments. Diam Relat Mat, 16 (2007) 823-825.
[5] R. Ikeda, M. Hayashi, A. Yonezu, T. Ogawa, M. Takemoto, Fracture observation of polycrystalline diamond film under indentation test. Diam Relat Mat, 13 (2004) 2024-2030.
[6] A.I. Shames, A.M. Panich, S. Porro, M. Rovere, S. Musso, A. Tagliaferro, M.V. Baidakova, V.Yu. Osipov, A.Ya. Vul', T. Enoki, M. Takahashi, E. Osawa, O.A. Williams, P. Bruno, D.M. Gruen, Defects localization and nature in bulk and thin film utrananocrystalline diamond. Diam Relat Mat, 16 (2007) 1806-1812.
[7] J. Stiegler, A. Bergmaier, J. Michler, Y. von Kaenel, G. Dollinger, E. Blank, Impurity and defect incorporation in diamond films deposited at low substrate temperatures. Diam Relat Mat, 7 (1998) 193-199.
[8] J.H. Jeong, S.Y. Lee, W.S. Lee, Y.J. Baik, D. Kwon, Mechanical analysis for crack-free release of chemical-vapor-deposited diamond wafers. Diam Relat Mat, 11 (2002) 1597-1605.
[9] Y.L. Kang, Z.F. Zhang, H.W. Wang, Q.H. Qin, Experimental investigations of the effect of thickness on fracture toughness of metallic foils. Mat Sci Eng A-Struct 394 (2005) 312-

319.
[10] H.W. Wang, Y.L. Kang, Z.F. Zhang, Q.H. Qin, Size effect on fracture toughness of metallic foil, Int J Fracture, 123 (2003) 177-185.
[11] C.S.J Pickles, The fracture stress of chemical vapour deposited diamond. Diamond and Related Materials, 11 (2002) 1913-1922.
[12] D. Zuo, D. Li, W. Lu, R. Chen, Y. Sun, Methods and devices of uniform substrate temperature in preparing spherical diamond film. Chinese Patent No. 200810024384.5, 2010.
[13] D. Li, D. Zuo, R. Chen, B. Xiang, W. Lu, M. Wang, Growth of high quality spherical diamond film by DC plasma jet CVD. Synthesis and Reactivity in Inorganic Metal-Organic and Nano-Metal Chemistry 38 (2008) 325-328.
[14] O. Durand, R. Bisaro, C.J. Brierley, P. Galtier, G..R. Kennedy, J.K. Krüger, J. Olivier, Residual stresses in chemical vapor deposition free-standing diamond films by X-ray diffraction analyses. Materials Science and Engineering a-Structural Materials Properties Microstructure and Processing, 288 (2000) 217-222.
[15] C. Li, H. Li, D. Niu, F. Lu, W. Tang, G. Chen, H.Zhou, F. Chen, Effects of residual stress distribution on the cracking of thick freestanding diamond films produced by DC arc jet plasma chemical vapor deposition operated at gas recycling mode. Surface & Coatings Technology, 201 (2007) 6553-6556.
[16] D. Dai, K. Zhou, Diamond film deposition preparation process and application, Beijing, Metallurgical Industry Press, 2001.

Mechanics of Graphene Bubbles

Peng Wang, Wei Gao, Kaimin Yue, Zhiyi Cao, Kenneth M. Liechti, Rui Huang*

Department of Aerospace Engineering and Engineering Mechanics, University of Texas, Austin, TX 78712, USA
* Corresponding author: ruihuang@mail.utexas.edu

Abstract Pressurized graphene bubbles have been observed in experiments, which can be used to determine the mechanical and adhesive properties of graphene. A nonlinear plate theory is adapted to describe the deformation of a graphene monolayer subject to lateral loads, where the bending moduli of monolayer graphene are independent of the in-plane Young's modulus and Poisson's ratio. A numerical method is developed to solve the nonlinear equations for circular graphene bubbles, and the results are compared to approximate solutions by analytical methods based on membrane and linear plate theories. The adhesion energy of mechanically exfoliated graphene on silicon oxide is extracted from two reported data sets. The strain distribution of the graphene bubbles and transport of gas molecules among the bubbles are discussed. Moreover, the effect of van der Waals interactions between graphene and its underlying substrate is analyzed, including large-scale interaction for nanoscale graphene bubbles subject to relatively low pressures.

Keywords Graphene, Adhesion, van der Waals interactions

1. Introduction

Graphene bubbles have been observed in experiments. Stolyarova et al. [1] observed nanoscale bubbles when mechanically exfoliated graphene flakes were placed on top of a silicon substrate covered with a thermally grown silicon oxide layer and exposed to proton irradiation. Much larger graphene bubbles were observed when the graphene flakes were exposed to vapors of hydrofluoric acid (HF) and water. In both cases, gas was released from the silicon oxide and trapped underneath the impermeable graphene, resulting in formation of the bubbles. More recently, Georgiou et al. [2] reported that bubbles are regularly found at the silicon oxide/graphene interface in large flakes obtained by mechanical cleavage. They observed graphene bubbles with diameters ranging from tens of nanometers to tens of microns and a variety of shapes (circular, triangular, and diamond). Bubbles have also been observed in graphene grown on metals such as Pt (111) [3] and Ru (0001) [4]. While the origin of graphene bubbles has not been fully understood and may depend on the material systems and experimental conditions, several potential applications of the graphene bubbles have emerged. Using highly strained graphene nanobubbles, Levy et al. [3] demonstrated enormous pseudo-magnetic fields and suggested strain engineering as a viable means of mechanical control over electronic structure of graphene. Georgiou et al. [2] demonstrated controllable curvature of graphene bubbles by applying an external electric field, which may be used as optical lenses with variable focal length. Zabel et al. [5] used graphene bubbles to study the Raman spectrum of graphene under biaxial strain. A well-controlled pressurization method was developed by Bunch et al. [6] to form graphene bubbles (or balloons) on patterned substrates, which was used to demonstrate the impermeability of graphene to gas molecules and to measure elastic properties of graphene. Following a similar approach, Koenig et al. [7] measured the adhesion energy between graphene and silicon oxide. On the other hand, Zong et al. [8] used intercalation of nanoparticles to generate graphene blisters on silicon surface and thereby provided a measurement of the graphene adhesion.

The present study focuses on the mechanics of graphene bubbles in order to establish a theoretical relationship between the morphology of graphene bubbles and the mechanical as well as interfacial properties of graphene. We present a nonlinear plate theory, adapted for the in-plane and bending properties of monolayer graphene. A numerical method is developed to solve the nonlinear

equations for circular graphene bubbles, subjected to gas pressure and van der Waals interactions. The numerical results are compared to the approximate solutions obtained by analytical methods. We show that, with known elastic properties of graphene, the adhesion energy between graphene and its substrate can be determined from the measurable dimensions of a graphene bubble (e.g., diameter and height). We confirm that the strain of graphene is non-uniform, varying from an equibiaxial strain at the center of the bubble to a uniaxial strain at the edge. The magnitude of the strain depends on the adhesion energy. The mechanics of graphene bubbles is extended to discuss transport of gas molecules among graphene bubbles of different sizes and the coalescence of graphene bubbles from a thermodynamics perspective.

2. A Nonlinear Plate Theory for Monolayer Graphene

The mechanical behavior of a graphene monolayer can be described by a mixed continuum mechanics formulation mapping a two-dimensional (2D) plane to a three-dimensional (3D) space [9]. Under the assumption of relatively small deformation but with moderately large deflection, a set of nonlinear equations can be used, which closely resemble the von Karman equations for an isotropic elastic thin plate. The only notable difference lies in the bending moduli of graphene. Unlike classical plate theory, the bending moduli of monolayer graphene are not directly related to the in-plane Young's modulus and Poisson's ratio. Instead, they are determined from atomistic modeling as independent properties [10-14]. As discussed in a previous study [13], the physical origin of the bending moduli of the monolayer graphene is fundamentally different from those in classical plate theory. In particular, we note that it is unnecessary to define a thickness for the graphene monolayer in the 2D continuum formulation.

Consider a circular graphene membrane subjected to axisymmetric loading. The displacements expressed in polar coordinates are: $u_r = u(r)$, $u_\theta = 0$, and $w = w(r)$. The corresponding in-plane strain components are:

$$\varepsilon_r = \frac{du}{dr} + \frac{1}{2}\left(\frac{dw}{dr}\right)^2, \tag{1}$$

$$\varepsilon_\theta = \frac{u}{r}. \tag{2}$$

The radial and circumferential membrane forces are

$$N_r = \frac{E_{2D}}{1-\nu^2}\left(\frac{du}{dr} + \nu\frac{u}{r} + \frac{1}{2}\left(\frac{dw}{dr}\right)^2\right), \tag{3}$$

$$N_\theta = \frac{E_{2D}}{1-\nu^2}\left(\nu\frac{du}{dr} + \frac{u}{r} + \frac{\nu}{2}\left(\frac{dw}{dr}\right)^2\right), \tag{4}$$

where E_{2D} is the 2D Young's modulus of graphene and ν is Poisson's ratio. The in-plane force equilibrium equation reduces to a nonlinear displacement equation

$$\frac{d^2u}{dr^2} + \frac{1}{r}\frac{du}{dr} - \frac{u}{r^2} = -\frac{1-\nu}{2r}\left(\frac{dw}{dr}\right)^2 - \frac{dw}{dr}\frac{d^2w}{dr^2}. \tag{5}$$

The bending moments are:

$$M_r = D\frac{d^2w}{dr^2} + \left(D - D_G\right)\frac{1}{r}\frac{dw}{dr}, \tag{6}$$

$$M_\theta = (D - D_G)\frac{d^2w}{dr^2} + \frac{D}{r}\frac{dw}{dr}, \tag{7}$$

where D and D_G are the two bending moduli corresponding to the mean curvature and the Gaussian curvature, respectively. The moment equilibrium equation leads to another nonlinear displacement equation

$$D\left(\frac{d^3w}{dr^3} + \frac{1}{r}\frac{d^2w}{dr^2} - \frac{1}{r^2}\frac{dw}{dr}\right) - \frac{E_{2D}}{1-\nu^2}\frac{dw}{dr}\left(\frac{du}{dr} + \nu\frac{u}{r} + \frac{1}{2}\left(\frac{dw}{dr}\right)^2\right) = \frac{1}{r}\int_0^r qrdr, \tag{8}$$

where q is the lateral loading intensity (e.g., pressure). In the present study, the lateral load intensity consists of a constant pressure (p) and the van der Waals (vdW) force between graphene and the substrate, i.e., $q = p - \sigma_{vdW}$, where $\sigma_{vdW} > 0$ for attractive force. By a simple model of vdW interactions [15], the vdW force is written as a function of deflection:

$$\sigma_{vdW}(w) = \frac{9\Gamma}{2\delta_0}\left[\left(\frac{\delta_0}{w+\delta_0}\right)^4 - \left(\frac{\delta_0}{w+\delta_0}\right)^{10}\right], \tag{9}$$

where δ_0 is the equilibrium separation and Γ is the interfacial adhesion energy. For monolayer graphene on SiO_2, experimental measurements have reported values from 0.4 to 0.9 nm for δ_0 [16-18] and from 0.09 to 0.45 J/m^2 for Γ [7, 8]. In the present study, we take $\delta_0 = 0.6$ nm and $\Gamma = 0.1$ J/m^2. For monolayer graphene bubbles, we use E_{2D} = 345 N/m, ν = 0.16, and D = 1.5 eV (or equivalently, 0.238 nN-nm). The radii of the graphene bubbles ranges from 10 to 1000 nm, and n = 1000 is used for the finite difference discretization.

3. Analytical Methods

Several approximate solutions for graphene bubbles were presented in a previous study [19]. They are briefly reviewed here for comparison with the numerical results.

3.1. Linear plate solution

For the linear plate analysis, the in-plane strain is assumed to be negligible, and Eq. (8) reduces to

$$D\left(\frac{d^3w}{dr^3} + \frac{1}{r}\frac{d^2w}{dr^2} - \frac{1}{r^2}\frac{dw}{dr}\right) = \frac{1}{r}\int_0^r qrdr. \tag{10}$$

Subjected to a uniform lateral load ($q = p$) and clamped boundary condition at the edge (i.e., $w = dw/dr = 0$ at $r = a$), Eq. (10) can be solved analytically by

$$w = h\left(1 - \frac{r^2}{a^2}\right)^2, \tag{11}$$

where a is the bubble radius and $h = \frac{pa^4}{64D}$ is the center deflection (bubble height).

3.2. An approximate membrane solution

For a membrane analysis, it is assumed that the bending stiffness is negligible. The nonlinear membrane equations however cannot be solved analytically. An approximate solution was developed by the energy method assuming the displacements [19]:

$$w = h\left(1 - \frac{r^2}{a^2}\right), \tag{12}$$

$$u = u_0 \frac{r}{a}\left(1 - \frac{r}{a}\right), \tag{13}$$

where $h = \left[\phi(\nu) pa^4 / E_{2D}\right]^{1/3}$ and $u_0 = \left[\psi(\nu) p^2 a^5 / E_{2D}^2\right]^{1/3}$, with $\phi(\nu) = \frac{75(1-\nu^2)}{8(23+18\nu-3\nu^2)}$ and $\psi(\nu) = \frac{45(3-\nu)^3(1-\nu^2)^2}{8(23+18\nu-3\nu^2)^2}$. A more accurate membrane analysis was developed by Hencky [20], which included 7 terms in the polynomial expansion of the deflection profile (as opposed to the two terms in Eq. 12) with the coefficients determined numerically for specific Poisson's ratios. In particular, for $\nu = 0.16$, the center deflection by Hencky's solution is: $h = 0.687\left(pa^4 / E_{2D}\right)^{1/3}$.

3.3. An approximate nonlinear plate solution

An energy method was used to develop an approximate solution to the nonlinear plate equations by assuming a deflection profile in form of (11) along with the radial displacement [19]

$$u = r(a-r)(c_1 + c_2 r). \tag{14}$$

Minimization of the potential energy leads to

$$c_1 = \frac{179 - 89\nu}{126}\frac{h^2}{a^3}, \tag{15}$$

$$c_2 = \frac{13\nu - 79}{42}\frac{h^2}{a^4}, \tag{16}$$

$$p = 64\eta(\nu)\frac{E_{2D}h^3}{a^4} + 64\frac{Dh}{a^4}, \tag{17}$$

where $\eta(\nu) = \frac{7505 + 4250\nu - 2791\nu^2}{211680(1-\nu^2)}$. It was shown that the approximate solution converges to the linear plate solution when the bubble height is small (h < 0.1 nm) but considerably underestimates the pressure when h > 1 nm.

4. A Numerical Method

A numerical method is developed to solve the coupled nonlinear equations, (5) and (8). For convenience we define an effective thickness, $h_e = \sqrt{\frac{12(1-\nu^2)D}{E_{2D}}}$, and re-write the equations in a dimensionless form

$$g = \frac{d^2\bar{u}}{d\bar{r}^2} + \frac{1}{\bar{r}}\frac{d\bar{u}}{d\bar{r}} - \frac{\bar{u}}{\bar{r}^2} + \frac{1-\nu}{2\bar{r}}\theta^2 + \theta\frac{d\theta}{d\bar{r}} = 0, \tag{18}$$

$$f = \frac{d^2\theta}{d\bar{r}^2} + \frac{1}{\bar{r}}\frac{d\theta}{d\bar{r}} - \frac{\theta}{\bar{r}^2} - 12\theta\left(\frac{d\bar{u}}{d\bar{r}} + \nu\frac{\bar{u}}{\bar{r}} + \frac{\theta^2}{2}\right) - \frac{1}{\bar{r}}\int_0^{\bar{r}} \bar{q}\bar{r}d\bar{r} = 0, \tag{19}$$

where $\theta = \frac{dw}{dr}$, $\bar{r} = \frac{r}{h_e}$, $\bar{u} = \frac{u}{h_e}$ and $\bar{q} = \frac{qh_e^3}{D}$. The equations are discretized by the finite difference method and solved by the Newton-Raphson method. At each iteration, the residuals are calculated and a correction vector is calculated as

$$\begin{pmatrix} \Delta\boldsymbol{\theta} \\ \Delta\bar{\mathbf{u}} \end{pmatrix} = -\begin{bmatrix} \dfrac{\partial \mathbf{f}}{\partial \boldsymbol{\theta}} & \dfrac{\partial \mathbf{f}}{\partial \bar{\mathbf{u}}} \\ \dfrac{\partial \mathbf{g}}{\partial \boldsymbol{\theta}} & \dfrac{\partial \mathbf{g}}{\partial \bar{\mathbf{u}}} \end{bmatrix}^{-1} \begin{pmatrix} \mathbf{f} \\ \mathbf{g} \end{pmatrix}, \tag{20}$$

where $\Delta\boldsymbol{\theta}$ is a vector of n-1 components ($\Delta\theta_k$, k = 1 to n-1) and same for $\Delta\mathbf{u}$, $\mathbf{f}$, and $\mathbf{g}$. The Jacobian matrix on the right-hand side of (20) consists of four square blocks, each with a rank of n-1. For the convergence criterion, we require that the L2-norm of the relative correction vector is smaller than a specified tolerance, namely

$$|\mathbf{R}| = \left[\sum_{k=1}^{n-1}\left(\Delta\theta_k^2/\theta_k^2 + \Delta u_k^2/u_k^2\right)\right]^{1/2} < \tau \sim 10^{-4}. \tag{21}$$

If not satisfied, the iteration procedure repeats with a new approximation, $\theta_k^{(i+1)} = \theta_k^{(i)} + \Delta\theta_k$ and $\bar{u}_k^{(i+1)} = \bar{u}_k^{(i)} + \Delta u_k$. Once converged, we calculate the deflection at each node by numerical integration:

$$\bar{w}_k = -\frac{\bar{a}}{2n}\sum_{m=k}^{n-1}\left(\theta_m + \theta_{m+1}\right). \tag{22}$$

for k = 0 to n-1, and the center deflection is then obtained as $h = w_0$. Moreover, we calculate the strain components at each node according to (1) and (2).

5. Results and Discussions

Using the numerical method in Section 4, we calculated the deflection profiles, $w(r)$, for graphene bubbles of various radii. Figure 1(a) shows the normalized deflection for a graphene bubble of radius a = 10 nm subject to increasing pressure (without van der Waals interaction). The deflection is normalized by the center deflection, $h = w_0$. In comparison, the analytical deflection profiles in (11) and (12) from the linear plate solution and the approximate membrane analysis are both independent of the pressure after the normalization. The numerical result agrees well with the linear plate solution at low pressures. As the pressure increases, the deflection profile approaches the membrane solution. Apparently, (12) is a reasonably good approximation for the deflection profile at high pressures. A more accurate membrane analysis [20] would yield a better approximation but also require a numerical method. Therefore, the analytical solutions in (11) and (12) may be considered as the lower and upper bounds for the deflection profiles.

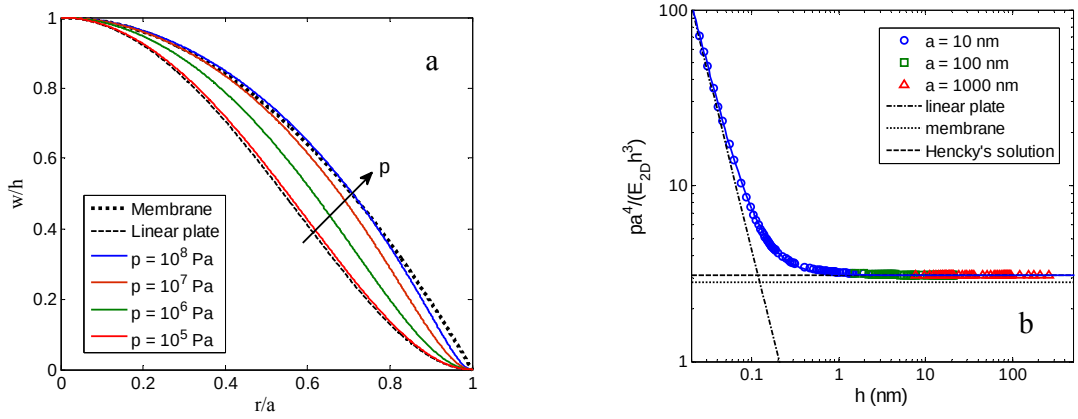

Figure 1. (a) Normalized deflection profiles of a graphene bubble (a = 10 nm) subject to increasing pressure; (b) Normalized pressure as a function of the center deflection.

The center deflection of a graphene bubble is a function of the pressure and the bubble radius. The linear plate solution predicts that the center deflection increases linearly with pressure ($h \propto p$). On the other hand, from the membrane analysis, the cube of the center deflection increases linearly with pressure ($h^3 \propto p$). We plot the center deflection versus a dimensionless group, $pa^4/(E_{2D}h^3)$, as shown in Fig. 1(b). In such a plot, the numerical results for different bubble radii collapse onto one master curve. When h > 1 nm, the numerical results agree closely with Hencky's membrane solution, while the simple membrane analysis in Section 3.2 underestimates the normalized pressure. It is found that the numerical results can be fitted by a single function that is a simple sum of the linear plate solution and the membrane solution:

$$\frac{pa^4}{E_{2D}h^3} = A(\nu) + B(\nu)\left(\frac{h_e}{h}\right)^2, \tag{23}$$

where A and B are two dimensionless functions of Poisson's ratio. From the membrane solution, $A = 1/\phi(\nu)$, which equals 2.825 for $\nu = 0.16$. On the other hand, Hencky's solution yields $A = 3.09$ for $\nu = 0.16$. From the linear plate solution, $B = \dfrac{16}{3(1-\nu^2)}$. The effective thickness, $h_e = \sqrt{\dfrac{12(1-\nu^2)D}{E_{2D}}}$, defines a length scale for the monolayer graphene. Therefore, the transition from the linear plate solution to the membrane solution depends on the ratio h/h_e. For relatively large bubbles (e.g., a > 100 nm), since the center deflection is typically much greater than h_e, the second term on the right-hand side of (23) is negligible and Hencky's membrane solution is sufficient.

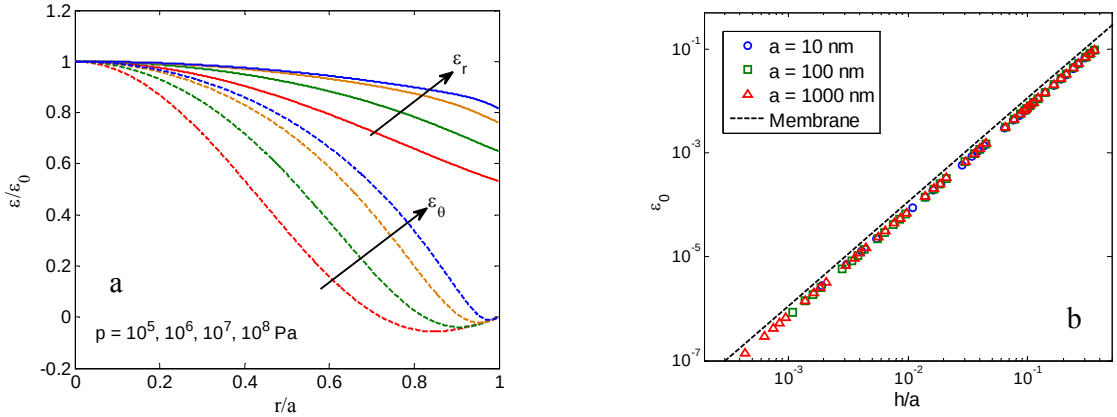

Figure 2. (a) Strain distributions in graphene bubbles (a = 10 nm) subject to increasing pressure; (b) Center strain versus h/a.

The strain distribution is important for strain engineering as a potential approach to manipulating the electronic properties of graphene [3, 4]. Figure 2(a) shows the strain distribution in graphene bubbles. By the symmetry and boundary conditions, the strain is equi-biaxial at the center (r = 0) and uniaxial at the edge ($r = a$). However, the strain distribution in between is very different from the prediction by the simple membrane analysis in Section 3.2. By inserting (12) and (13) into (1) and (2), the circumferential strain ε_θ would decrease linearly from the center to the edge, while the radial strain ε_r first decreases and then increases [19]. Moreover, the analytical membrane solution predicts that the normalized strain distribution should be independent of the pressure or the bubble radius. However, the numerical results clearly demonstrate that the strain distribution (after normalization) depends on both the pressure and the bubble radius. The difference in the strain

distribution between the numerical and the analytical solutions can be traced back to the difference in the deflection profiles as shown in Fig. 1(a). Furthermore, the in-plane radial displacement obtained by the numerical method differs from the analytical assumption in (13). Notably, the radial displacement becomes negative near the edge, resulting in compressive circumferential strain ($\varepsilon_\theta < 0$).

The equi-biaxial strain at the center ($\varepsilon_r = \varepsilon_\theta = \varepsilon_0$) is plotted in Figure 3(b) as a function of the normalized pressure. Noting that the center strain $\varepsilon_0 \propto (h/a)^2$ in both analytical solutions, we plot the numerical results as a function of *h*/*a* in Fig. 2(b). Indeed the numerical results for different bubble radii collapse onto one line with the slope 2 in the log-log plot. Therefore, the center strain may be written as

$$\varepsilon_0 = C(\nu)\left(\frac{h}{a}\right)^2, \tag{24}$$

where $C(\nu)$ is a dimensionless functions of Poisson's ratio. By the membrane solution in Section 3.2, $C(\nu) = \psi^{1/3}/\phi^{2/3}$, which equals 1.136 for $\nu = 0.16$. The numerical results can be fitted approximately by taking $C(\nu) = 0.76$. Therefore, the analytical membrane solution overestimates the center strain considerably.

Based on the membrane analysis, the adhesion energy of between graphene and its substrate can be determined from the measurements of the equilibrium bubble size (*a* and *h*) [19]. With the number of gas molecules (*N*) fixed inside the bubble, the potential energy is obtained as a function of the bubble radius

$$\Pi(a, N) = \frac{Nk_BT}{4} - Nk_BT \ln\left[\frac{p_0 a^{5/2}}{(Nk_BT)^{3/4} E_{2D}^{1/4}}\right], \tag{25}$$

where p_0 is the ambient pressure outside the bubble and k_B is Boltzmann constant. The first term on the right hand side of (25) is the strain energy in graphene, which is independent of the bubble size under the condition of constant *N*. The second term is the potential energy of the gas, relative to the reference state in the ambient condition. As the bubble radius *a* increases, the total potential energy decreases. Meanwhile, the interfacial energy increases as part of the graphene is detached from the substrate. The equilibrium bubble radius is attained when the potential energy of the bubble is balanced by the adhesion energy (Γ) of the graphene/substrate interface, which gives rise to the adhesion energy

$$\Gamma = -\frac{1}{2\pi a}\left(\frac{\partial \Pi}{\partial a}\right)_N = \frac{5Nk_BT}{4\pi a^2} = \frac{5E_{2D}h^4}{8\phi a^4}. \tag{26}$$

Combining (24) and (26), we have $\varepsilon_0 \propto (\Gamma / E_{2D})^{1/2}$. Therefore, the magnitude of the strain depends on the adhesion energy. This suggests that strain measurement could be used as an alternate approach for determining the adhesion energy [19]. On the other hand, to achieve a relatively large strain (> 5%) for strain engineering to manipulate the electronic properties of graphene [3, 4], the adhesion energy must be sufficiently high.

Georgiou et al. [2] measured the cross-sectional profile of a graphene bubble on an oxidized silicon substrate by atomic force microscope (AFM) in tapping mode. The bubble radius and central deflection were determined as $a = 1183$ nm and $h = 132$ nm. Using these values in (26), we obtain the adhesion energy Γ = 0.097 J/m^2. The data set from Koenig et al. [7] puts the adhesion energy in the range between 0.25 and 0.43 J/m^2, with an average value of 0.33 J/m^2. These values

are lower than the reported value (0.45 J/m^2) for monolayer graphene on silicon oxide [7]. The difference is partly attributed to the approximations made in the present membrane analysis as opposed to Hencky's solution used by Koenig et al. [7]. The scattering of the adhesion energy from these data suggest that the adhesion energy could be non-uniform due to the statistical nature of the surface roughness [21].

Stolyarova et al. [1] observed coalescence of graphene bubbles during annealing, which can be understood as a result of the transport of gas molecules along the interface driven by the different pressures in bubbles of different sizes. The membrane analysis predicts that the pressure inside the graphene bubble is inversely proportional to the bubble radius [19]. Consequently, the pressure is higher in the smaller bubbles and the pressure difference drives the gas molecules to diffuse from smaller bubbles to larger bubbles. The diffusion process is kinetically mediated and is enhanced by thermal annealing so that the large bubbles grow larger while the small bubbles disappear, similar to the Ostwald ripening process in thin film growth. The coalescence of graphene bubbles may also be understood from an energy consideration. It can be shown that the free energy of two small bubbles is greater than the free energy of one large bubble with the same total number of gas molecules [19]. Therefore, there exists a thermodynamic driving force for the two small bubbles to coalesce so that the total free energy is reduced. In other words, while each graphene bubble is in a thermodynamically equilibrium state, the system with a group of graphene bubbles is not in equilibrium. Since the graphene is impermeable [6], the kinetic pathways for the transport of gas molecules may include the graphene/substrate interface and the substrate bulk.

Figure 3(a) shows the deflection profiles of a graphene bubble (a = 10 nm) under the effect of vdW interaction. When the pressure is relatively low, the deflection is reduced considerably by the attractive vdW force. On the other hand, when the pressure is high, the effect of vdW force on the deflection is negligible. As shown in Fig. 3(b), the distribution of vdW force is non-uniform and depends on the pressure. In the spirit of nonlinear fracture mechanics [22], we may define an interaction zone where the vdW force is appreciable in comparison with the pressure, e.g., $\sigma_{vdW} > p/10$. Subject to a low pressure, the interaction zone spans the entire area underneath the bubble, indicating large-scale bridging from a fracture mechanics perspective. At a higher pressure level, the interaction zone is much smaller, where the condition of small-scale bridging prevails. Consequently, in the presence of vdW interactions, the relationship between the center deflection and the pressure becomes nonlinear at low pressures.

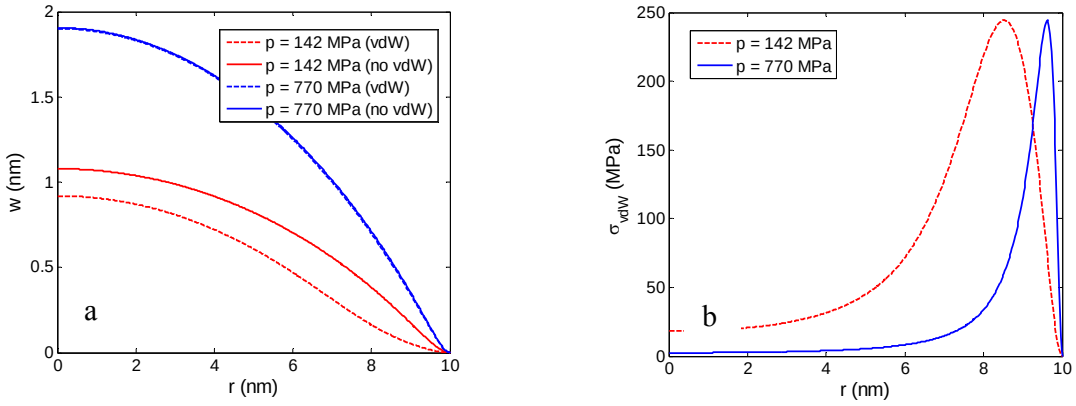

Figure 3. (a) Effect of the vdW interaction on the deflection profile of a graphene bubble (a = 10 nm); (b) Distributions of the vdW force intensity.

6. Summary

A nonlinear plate theory is adapted to describe the deformation of a graphene monolayer subject to lateral loads. A numerical method is developed to solve the nonlinear equations for circular graphene bubbles. In comparison to approximate solutions by analytical methods, it is found that the deflection profile and the strain distribution are generally not well described by the analytical solutions. Based on the numerical results, approximate formulae for the center deflection and center strain are suggested. We show that, with known elastic properties of graphene, the adhesion energy between graphene and its substrate can be determined from the measurable dimensions of a graphene bubble (e.g., diameter and height). The mechanics of graphene bubbles is extended to discuss transport of gas molecules among graphene bubbles of different sizes and the coalescence of graphene bubbles from a thermodynamics perspective. Moreover, the effect of van der Waals interactions between graphene and its substrate is found to be significant when the center deflection is relatively small due to large-scale adhesive interactions.

Acknowledgements

The authors gratefully acknowledge financial support of this work by the National Science Foundation through Grant Nos. CMMI-0926851 and CMMI-1130261.

References

1. Stolyarova, E., et al., 2009, "Observation of graphene bubbles and effective mass transport under graphene films", Nano Lett. 9, 332-337.
2. Georgiou, T., et al., 2011, "Graphene bubbles with controllable curvature," Appl. Phys. Lett. 99, 093103.
3. Levy, N., et al., 2010, "Strain-induced pseudo-magnetic fields greater than 300 Tesla in graphene nanobubbles," Science 329, 544-547.
4. Lu, J., Castro Neto, A.H., Loh, K.P., 2012, "Transforming moire blisters into geometric graphene nano-bubbles," Nature Communications 3: 823.
5. Zabel, J., et al., 2012, "Raman spectroscopy of graphene and bilayer under biaxial strain: bubbles and balloons" Nano Lett. 12, 617-621.
6. Bunch, J. S., et al., 2008, "Impermeable atomic membranes from graphene sheets," Nano Lett. 8, 2458-2462.
7. Koenig, S. P., Boddeti, N. G., Dunn, M. L., Bunch, J. S., 2011, "Ultrastrong adhesion of graphene membranes," Nature Nanotechnology 6, 543-546.
8. Zong, Z., Chen, C.-L., Dokmeci, M. R., Wan, K.-T., 2010, "Direct measurement of graphene adhesion on silicon surface by intercalation of nanoparticles," J. Appl. Phys. **107**, 026104.
9. Lu, Q. and Huang, R., 2009, "Nonlinear mechanics of single-atomic-layer graphene sheets," Int. J. Applied Mechanics **1**, 443-467.
10. Kudin, K. N., Scuseria, G. E., and Yakobson, B. I., 2001, "C_2F, BN, and C nanoshell elasticity from ab initio computations," Phys. Rev. B, **64**, 235406.
11. Arroyo, M., and Belytschko, T., 2004, "Finite crystal elasticity of carbon nanotubes based on the exponential Cauchy-Born rule," Phys. Rev. B, **69**, 115415.
12. Huang, Y., Wu, J., Hwang, K. C., 2006, "Thickness of graphene and single-wall carbon nanotubes," Phys. Rev. B, **74**, 245413.
13. Lu, Q., Arroyo, M., Huang, R., 2009, "Elastic bending modulus of monolayer graphene," J. Phys. D: Appl. Phys. **42**, 102002.
14. Koskinen, P., and Kit, O. O., 2010, "Approximate modeling of spherical membranes," Phys. Rev. B **82**, 235420 (2010).
15. Aitken, Z. H., and Huang, R., 2010, "Effects of mismatch strain and substrate surface corrugation on morphology of supported monolayer graphene," J. Appl. Phys. **107**, 123531.
16. Ishigami, M., Chen, J. H., Cullen, W. G., Fuhrer, M. S., Williams, E. D., 2007, "Atomic structure of graphene on SiO_2," Nano Lett. **7**, 1643-1648.
17. Gupta, A., Chen, G., Joshi, P., Tadigadapa, S., and Eklund, P. C., 2006, "Raman scattering from high-frequency phonons in supported n-graphene layer films" Nano Lett. **6**, 2667-2673.

18. Sonde, S., Giannazzo, F., Raineri, V., and Rimini, E., 2009, "Dielectric thickness dependence of capacitive behavior in graphene deposited on silicon dioxide," J. Vac. Sci. Technol. B **27**, 868-873.
19. Yue, K., Gao, W., Huang, R., Liechti, K.M., 2012, "Analytical methods for the mechanics of graphene bubbles," J. Appl. Phys., **112**, 083512.
20. Hencky, H., 1915, *Zeitschrift fur Mathematik und Physik* 63, 311–317.
21. Gao, W., and Huang, R., 2011, "Effect of surface roughness on adhesion of graphene membranes" J. Phys. D: Appl. Phys. **44**, 452001.
22. Hutchinson, J. W., and Evans, A. G., 2000, "Mechanics of materials: top-down approaches to fracture," Acta Materialia **48**, 125–135.

Crack Healing Behavior of SiN/SiC Nano-Laminated Films

Masanori Nakatani[1,*], Junki Nishimura[2], Satoshi Hanaki[1], Hitoshi Uchida[1]

[1] Department of Mechanical Engineering, University of Hyogo, Himeji, 671-2280, Japan
[2] Graduate Student, Department of Mechanical Engineering, University of Hyogo, Himeji, 671-2280, Japan
* Corresponding author: nakatani@eng.u-hyogo.ac.jp

Abstract We investigated the self−crack−healing behavior of SiN/SiC nano-laminated film. Moreover, we discussed the healing condition including heating temperature and heating time. The films were deposited on a silicon substrate using an ion-beam-assisted deposition. The SiN/SiC nano-laminated film was fabricated with alternating layers of SiN and SiC. After the deposition, a pre-crack was introduced using a Vickers indentor. Then, the cracked samples were heated using an electric furnace in an air atmosphere at the temperature of 600 °C to 1200 °C.
In the case of the SiN and SiC monolayer films, the crack was poorly healed after heating irrespective of the temperature. This was because the size of the crack opening increased after heating. On the other hand, slight crack healing occurred at the temperature of 600 °C. Crack healing improved with an increase in the heating temperature and time. From these results, we concluded that SiN/SiC nano-laminated film has a superior self-crack-healing ability.

Keywords Self-healing, Thin film, Crack, High temperature, Oxidation

1. Introduction

Ceramic thin films are one of the key materials in micro-electro-mechanical systems (MEMS) such as sensors and micronozzles. Ceramic thin films are superior to metals in terms of strength, heat resistance, and corrosion resistance. However, the sensitivity of these thin films to defects is extremely high and their fracture toughness is much lower than those of metals. The reliability of ceramic thin films decreases significantly once a crack is initiated. Therefore, defects that occur during the deposition and etching process significantly affect the strength and life of MEMS.

For use in MEMS employed under severe conditions such as high temperature or a corrosive environment, ceramic thin films are required to be made more reliable. Self-healing is an important concept for improving the reliability and lifetime of the mechanical components. Recently, various self-healing materials such as polymers, concrete, composites, and coating have been developed by researchers [1–4]. If this ability can be applied to ceramic thin films, then minor defects can be tolerated and cracks caused from the defects during service can be healed before the entire system breaks down.

In bulk materials, certain kinds of structural ceramic composites exhibit self-crack-healing behavior at high temperatures [5–8]. One such composite is silicon nitride (Si_3N_4) reinforced by silicon carbide (SiC) nanoparticles. When a cracked Si_3N_4 composite is heated to a temperature over 800 °C in air, the SiC particles exposed on the crack plane thermochemically react to form silicon dioxide (SiO_2). As this reaction proceeds, the crack is filled by SiO_2, because the volume of SiO_2 expands as compared with that of SiC. The additional SiC plays an important role in the crack healing because of its low reaction enthalpy [8]. Other research groups have reported that a TiC/Al_2O_3 composite coating fabricated by plasma spraying also exhibits self-crack-healing by oxidation in the same manner as that in Si_3N_4 ceramic composites [9].

On the basis of the above reports, it is thought that carbide composite thin films may also exhibit a self-crack-healing ability at high temperatures. In general, thin films for MEMS are fabricated by

chemical vapor deposition (CVD) or physical vapor deposition (PVD). However, it is difficult to control the precipitation and dispersion of carbide in these methods. Nanolaminated structures are effective for increasing the crack-growth resistance. Moreover, the crack healing is always induced because a crack can pass the carbide layer surely. In this study, we investigated the self-crack-healing ability of SiN/SiC nano-laminated films at high temperatures. Cracked samples of SiN/SiC nano-laminated films were heated under various heating conditions in air to clarify the factors influencing the self-crack-healing ability of the thin films. In addition, the healed crack was observed and analyzed using scanning electron microscopy (SEM), a focused ion beam system (FIB), and Auger electron spectroscopy (AES) to further analyze the crack healing behavior.

2. Experimental procedures

SiN/SiC nano-laminated films were deposited on Si(100) substrates by ion-beam-assisted deposition (IBAD) [10]. The substrates were cleaned by successive rinsing in ultrasonic baths of acetone. After cleaning, the Si substrates were placed on a water-cooled holder. After the placement of the substrates, the chamber was evacuated to a base pressure of 3×10^{-4} Pa. Prior to deposition, the substrates were sputtered using a nitrogen ion beam at an acceleration voltage of 2 keV for 15 min.

The SiN/SiC nano-laminated films were fabricated with alternating layers of SiN and SiC. The deposition conditions for SiN and SiC are shown in Table 1. The SiN layer was obtained by an electron beam evaporation of silicon (purity: 99.99%) and the simultaneous bombardment of a nitrogen ion beam. The SiC layer was deposited by electron beam evaporation of silicon and simultaneous bombardment of argon ion beam under an ethylene atmosphere at a partial pressure of 2.0×10^{-2} Pa [11]. The fabricated laminated films consisted of four layers and the top layer was SiN. The bilayer thickness was 500 nm. Monolayer films of SiN and SiC were also fabricated in order to compare their properties with those of the SiN/SiC nano-laminated films. The total thickness of all the films was 0.9–1.2 μm.

After the film deposition, a small artificial crack was introduced using a Vickers indenter at a load of 2.0 N. Figure 1 shows an example of the indentation and crack, as observed by field-emission scanning electron microscopy (FE-SEM). A radial crack occurred from the corner of the indentation, as shown in Fig. 1. The cracked samples were heated using an electric furnace in an air atmosphere. It has been reported that the self-crack-healing behavior is dependent on various factors such as heating temperature, heating time, and atmosphere [5]. In this study, the self-crack-healing behavior of the nano-laminated films was investigated systematically by changing the heating temperature

Table 1. Deposition conditions.

	SiN	SiC
Arc voltage (V)	80	
Ion beam	Nitrogen	Argon
Gas flow rate (sccm)	4.0	1.5
Acceleration voltage (keV)	2.0	0.3
Deceleration voltage (keV)	0.3	1.0
Acceleration current (mA)	14.0	15.0
Atmosphere gas	-	Acetylene
Vapor rate (nm/s)	0.2	0.1

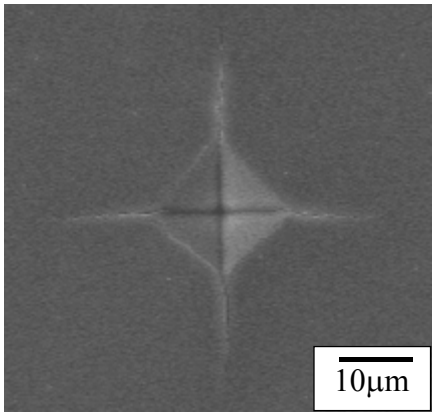

Figure 1. FESEM image of indentation and cracks on SiN film.

(T_h = 600–1200 °C) and time (t_h = 24 h, 48 h, 72 h).

The surface morphology and cross section of the samples were examined by FE-SEM. The chemical composition was analyzed by X-ray photoelectron spectroscopy (XPS). AES was used to observe the distribution of the oxides generated by crack healing. Before both analyses, Ar ion sputtering at an acceleration energy of 3 keV was conducted for 10 s to remove any contamination.

3. Results and discussion

3.1 Film morphology

Figure 2 shows the FE-SEM images of the surface and cross section of the deposited films. All films had an extremely smooth morphology. Although the interface between SiN and SiC can be observed, a columnar structure was not observed. Moreover, X-ray diffraction peaks could not be observed. On the basis of these results, it is suggested that the SiN and SiC films fabricated in this study were amorphous.

3.2 Chemical composition

The average chemical compositions obtained by XPS analysis are summarized in Table 2. Both films contained some oxygen atoms. It is postulated that the water vapor evaporated during the heating with the electron beam might have been entered the film. Therefore, it is suggested that the SiN and SiC films include some oxide compounds, most probably, SiO_2.

3.3 Crack healing behavior

3.3.1 Effect of film structure

Figure 3 shows the FE-SEM images of the indentation and crack after heating the samples at a temperature of 800 °C for 24 h. In the case of the SiN and SiC monolayer films, the crack was poorly healed after heating, as shown in Figs. 3(a) and (b), respectively; however, a slight crack healing did occur near the crack tip. Moreover, the size of the crack opening increased after heating. When SiN_x and SiC are heated in air, oxidation occurs by the following chemical reactions:

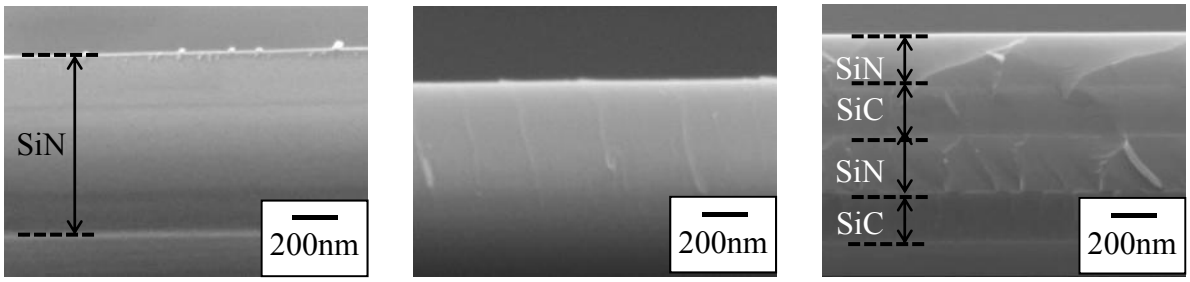

(a) SiN film (b) SiC film (c) SiN/SiC film

Figure 2 FE-SEM images of cross section of thin films.

Table 2. Chemical composition of SiN and SiC film.

Film	Si	N	C	O
SiN	59.6	25.1	–	15.3
SiC	62.7	–	16.2	21.1

$$2SiN_x + 2O_2 \rightarrow 2SiO_2 + xN_2 \quad (1)$$
$$SiC + 3/2O_2 \rightarrow SiO_2 + CO \quad (2)$$

These chemical reactions results in volume expansion, and thereby, crack healing. In the case of the SiN and SiC monolayer films, it was concluded that the crack healing did not occur sufficiently because the volume of the crack-opening region was larger than the volume expansion due to the oxidation reaction.

On the other hand, the cracks in the SiN/SiC nano-laminated films were healed without an increase in crack opening, as shown in Fig. 3(c). The laminated structure probably decreases the residual stress. Delamination was observed around the indentation, which occurred during the heating because the delamination cross section was covered with oxidation products.

Figure 4 shows the FE-SEM image of the cross section of the healed crack. The cross section was achieved using a focused ion beam system. The crack reached the substrate through the film. It was found that the crack in the film was also healed internally. Moreover, the laminated structure was still preserved, which suggests that the oxidation reaction occurred only on the crack plane exposed to air.

The oxide distribution around the indentation and cracks after heating was analyzed using AES. Figure 5 shows a mapping image of oxygen around the indentation and cracks. The Auger electron counts for oxygen were high along the healed crack. It is suggested that the oxidation reaction induced crack healing similar to the healing of bulk Si_3N_4/SiC composites. These results indicate

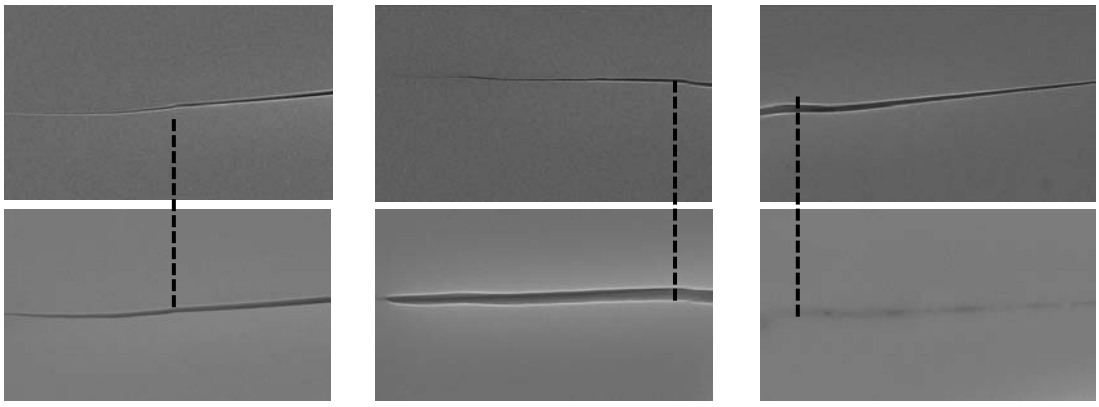

(a) SiN film (b) SiC film (c) SiN/SiC film

Figure 3. FE-SEM images of crack tip before and after heating. The upper and below images indicate crack before and after heating, respectively. The dotted lines indicate the same points before and after heating.

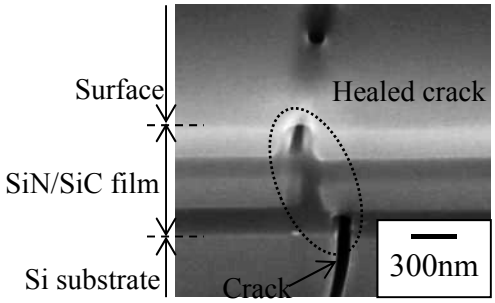

Figure 4. FE-SEM image of cross section of healed crack.

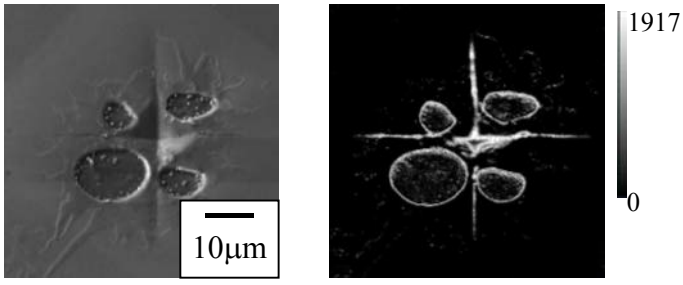

(a) SEM image (b) Oxygen mapping image

Fig. 5 SEM and AES mapping image of oxygen after heating.

that the self-crack-healing ability of a SiN/SiC nano-laminated film is superior to that of a monolayer film.

3.3.2 Effect of heating temperature

The influence of heating temperature on the self-crack-healing behavior was investigated. The heating temperature was varied from 600 °C to 1200 °C and the heating time was fixed at 1 h. Figure 6 shows the FE-SEM images of the indentation and cracks after heating. Slight crack healing occurred at the temperature of 600 °C. Crack healing improved with an increase in the heating temperature, and heating at 1000 °C healed the crack perfectly. However, at 1200 °C, observation of the cross section and analysis of the chemical composition revealed that even though the crack was healed, the laminated structure disappeared because of oxidation. This indicates that the crack healing ability also disappears once the SiN/SiC nano-laminated film is heated to temperatures over 1200 °C.

3.3.3 Effect of heating time

The influence of heating time on the self-crack-healing behavior was also investigated. The heating time was varied from 24 h to 72 h at the heating temperature of 600 and 800 °C. Figure 7 shows the FE-SEM images of the indentation and cracks after heating. At 600 °C, crack healing improved with an increase in the heating time. However, at temperatures over 800 °C, the influence of heating

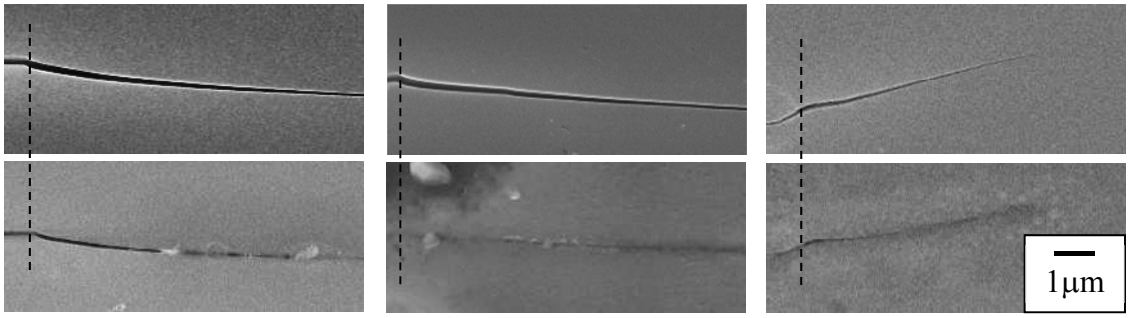

(a) 600 °C (b) 1000 °C (c) 1200 °C

Figure 6. Influence on heating temperature on the crack healing. The upper and below images indicate crack before and after heating respectively. The dotted lines indicate the same points before and after heating.

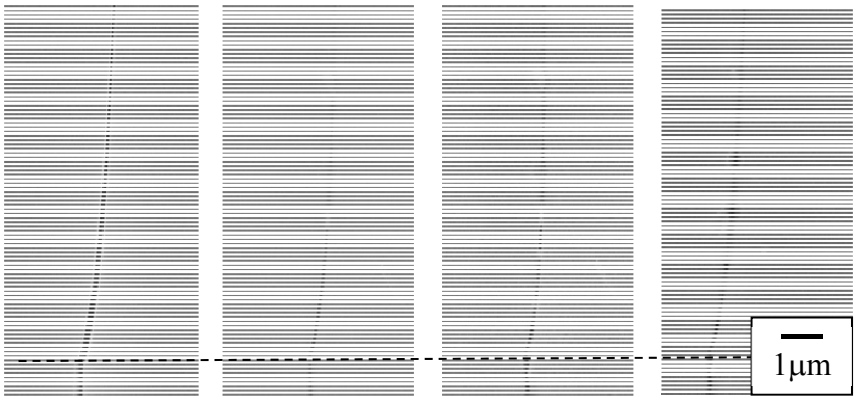

(a) Before heating (b) After 24h (c) After 48h (d) After 72h

Figure 7. Influence on heating time on the crack healing. The dotted lines indicate the same points before and after heating.

time on the crack healing was not observed clearly. It was postulated that the oxidation reaction on the crack plane was almost completed at 24 h at temperatures over 800 °C because the crack plane exposed to air is extremely small in the case of a thin film.

4. Conclusions

In this study, we investigated the self-crack-healing ability of SiN and SiC monolayer films and SiN/SiC nano-laminated thin films subjected to high temperatures in an air atmosphere. We also analyzed the influence of heating temperature and heating time on the healing ability of the nanolaminated thin films. The investigation yielded the following conclusions:

1. In SiN and SiC monolayer films, cracks were poorly healed because the size of the crack opening increased significantly during heating. On the other hand, SiN/SiC nano-laminated films exhibited a superior self-crack-healing ability.
2. Around the healed crack, the oxygen concentration was found to be high. This indicates that crack healing was achieved by oxidation.
3. Crack healing was promoted by an increase in the heating temperature and time. However, at temperatures over 1200 °C, the laminated structure disappeared and the film was subjected to oxidation overall.

Acknowledgements

The authors acknowledge financial support from JSPS KAKENHI Grant Number 23656091.

References

[1] S. R. White, N. R. Sottos, P. H. Geubelle, J. S. Moore, M. R. Kessler, S. R. Sriram, E. N. Brown, S. Viswanathan, Autonomic Healing of Polymer Composites, Nature 409 (2001) 794–797.

[2] V. C. Li , E.-H. Yang, Self healing in concrete materials, in: S. van der Zwaag (Ed.), Self Healing Materials–an Alternative Approach to 20 Centuries Materials Science, Springer, The Netherlands, 2007, pp. 161–194.

[3] A. Kumara, L. D. Stephenson, J. N. Murray, Self-healing coatings for steel, Progress in Organic Coatings, 55 (2006) 244–253.

[4] F. Miccichè, H. Fischer, R. Varley, S. van der Zwaag, Moisture induced crack filling in barrier coatings containing montmorillonite as an expandable phase, Surf Coat Tech, 202 (2008) 3346–3353

[5] S. R. Choi, V. Tikare, Crack healing behavior of hot pressed silicon nitride due to oxidation, Scripta Metall Mater, 26 (1992) 1263–1268.

[6] K. Houjou, K. Ando, S.-P. Liu, S. Sato, Crack-healing and oxidation behavior of silicon nitride ceramics, J Euro Ceram Soc, 24 (2004) 2329–2338.

[7] A. M. Thompson, H. M. Chan, M. P. Harmer, Crack healing and stress relaxation in Al_2O_3-SiC nanocomposites, J Am Ceram Soc, 78 (1995) 567–571.

[8] Y.-S. Jung, Y. Guo, W. Nakao, K. Takahashi, K. Ando, S. Saito, Crack-healing behaviour and resultant high-temperature fatigue strength of machined Si_3N_4/SiC composite ceramic, Fatigue Fract Engng Mater Struct, 31 (2008) 2–11.

[9] J.-F. Gao, J.-P. Suo, Proposal of self-healing coatings for nuclear fusion applications, Surf Coat Tech, 204 (2010) 3876–3881.

[10] J. K. Hirvonen, Ion beam assisted thin film deposition, Mater Sci Rep, 6 (1991) 215–274.

[11] Z.-G. He, S. Inoue, G. Carter, H. Kheyrandish, J. S. Colligon, Ion-beam-assisted deposition of Si-carbide films, Thin Solid Films, 260 (1995) 32–37.

Mechanical Properties and Fracture Behavior of Poly(vinylidene fluoride)-Polyhedral Oligomeric Silsesquioxane Nanocomposites by Nanotensile Testing

Fanlin Zeng[1,*], Yizhi Liu[1], Yi Sun[1]

[1] Department of Astronautic Science and Mechanics, Harbin Institute of Technology, Harbin, China
* Corresponding author: zengfanlin@hit.edu.cn

Abstract The key static and dynamic mechanical properties and fracture behavior of nanocomposite films composed of a poly(vinylidene fluoride) (PVDF) matrix and different contents of polyhedral oligomeric silsesquioxane (FP-POSS) were researched by nano-tensile testing. The Young's modulus, storage modulus, loss modulus, loss tangent, yield strain, yield strength, tensile strength, fracture strength, fracture strain, fracture toughness and fracture deformations of all different nanocomposite systems were obtained. The influence of FP-POSS and its contents on the mechanical properties of PVDF was analyzed. Results showed that both the stiffness and toughness of PVDF were enhanced at some specific FP-POSS content and further additions of FP-POSS brought dramatic enhancements in toughness while associated with a decline in stiffness. Dynamical mechanical properties showed that FP-POSS increased the viscosity of PVDF. The mechanism of the effects of FP-POSS on PVDF was analyzed from the unique nano scale organic-inorganic molecular structure of FP-POSS and the micro structures of the nanocomposite films

Keywords Poly(vinylidene difluoride), Polyhedral oligomeric silsesquioxanes, Nano-tensile, Mechanical properties, Fracture

1. Introduction

Poly(vinylidene difluoride) (PVDF) is a kind of semicrystalline polymer and widely used in smart structure sensors, actuators, and soft/thin transducers since it exhibits excellent piezoelectric and pyroelectric properties which derive from the two polar phases β and γ of PVDF [1, 2]. But unfortunately, neat PVDF can not completely meet the mechanical, thermal, and oxidation resistance property requirements of some harsh environments [3, 4]. Many efforts have been taken to improve the properties of PVDF. For example, incorporation of organic polymer or inorganic fillers into the PVDF matrix to produce composites has been extensively studied with the objective of further improving its properties [5-7]. However, few materials are miscible when melted with PVDF, and their improvement in one property is always accompanied by a deterioration in others. Over the past decade, Polyhedral oligomeric silsesquioxanes (POSS) have been widely known as a unique class of organic-inorganic hybrid materials which exhibits many superior thermomechanical properties in terms of wearability, thermal stability, oxidation resistance and high strength [8-10] because of the robust inorganic cage-like core structure with the Si-O atoms, while at the same time they perform very good bonding capability with polymeric base matrixes because of the alterable organic branches on the corners of the core. For a polymer matrix, it is widely accepted that inorganic fillers tend to improve in stiffness while organic ones in toughness. But as a kind of organic-inorganic hybrid compounds, how will fluorinated POSS influence the mechanical properties and fracture behaviors of PVDF needs to be researched. Our previous work has been proved that fluorinated POSS compounds and PVDF are fully miscible at any temperature and the miscibility is derived from the polar C-F bonds and the electrostatic interactions in the POSS and PVDF molecules [11]. The molecular dynamics simulation results show that the glass transition temperature of PVDF was significantly improved with (3, 3, 3- trifluoropropyl)$_8$Si$_8$O12 (FP-POSS) [12] and the moduli of PVDF were improved and the improvement effect, in general, nearly decreased with the increase of the mass ratio of FP-POSS [13]. However, simulation results need to be verified from experiments. And in addition, some other key mechanical properties, especially the fracture properties can only be effectively obtained by this means.

As a standard mechanical test method, the tensile test has been widely used to determine some important mechanical properties such as Young's modulus, fracture toughness and yield stress of materials. But a traditional tensile test is not capable of a sample with nano scale size, where a very small tensile load and very precise measure equipments are needed. In recent years, the nano-tensile test has been developed and used to characterize the tensile behaviors of very small samples such as the nanotubes, silk, fibers and so on [14-16]. The nano-tensile test is also used to determine some dynamic mechanical properties by adding a very small harmonic force with specific frequency on the sample [17]. In this work, the PVDF/FP-POSS nanocomposites were firstly prepared by the solvent evaporation method. And then the nano-tensile testings were carried out. Although similar work has been performed and some valuable results have been given [18, 19], the focus of this work is on the tensile properties of PVDF/POSS at a relative high strain rate and the fracture behaviors were analyzed in detail from the experimental data and microscopy images.

2. Experimental

2.1. Materials and sample preparation

The detailed solvent evaporation method to prepare the neat PVDF and its FP-POSS nanocomposites can be found in Ref. [18, 19]. The mass ratios of FP-POSS added to the PVDF matrix were 0%, 3%, 5%, and 8%, and nanocomposites with different FP-POSS contents are denoted as PVDF-FPi% (i = 0, 3, 5 and 8), which has the morphology of film with the thicknesses around 70~110 μm. In addition, the films were white and translucent, with the exception of neat PVDF, which appeared to be transparent. With increased percentage of FP-POSS, the transparency of the films declined. The images of PVDF-FP$_i$% (i = 0, 3, 5 and 8) films are shown as figure 1. Samples for nano-tensile testing were cut from these films. The size of the samples is about ~100um×~10mm (shown as figure 2, but not exactly the same size in each test).

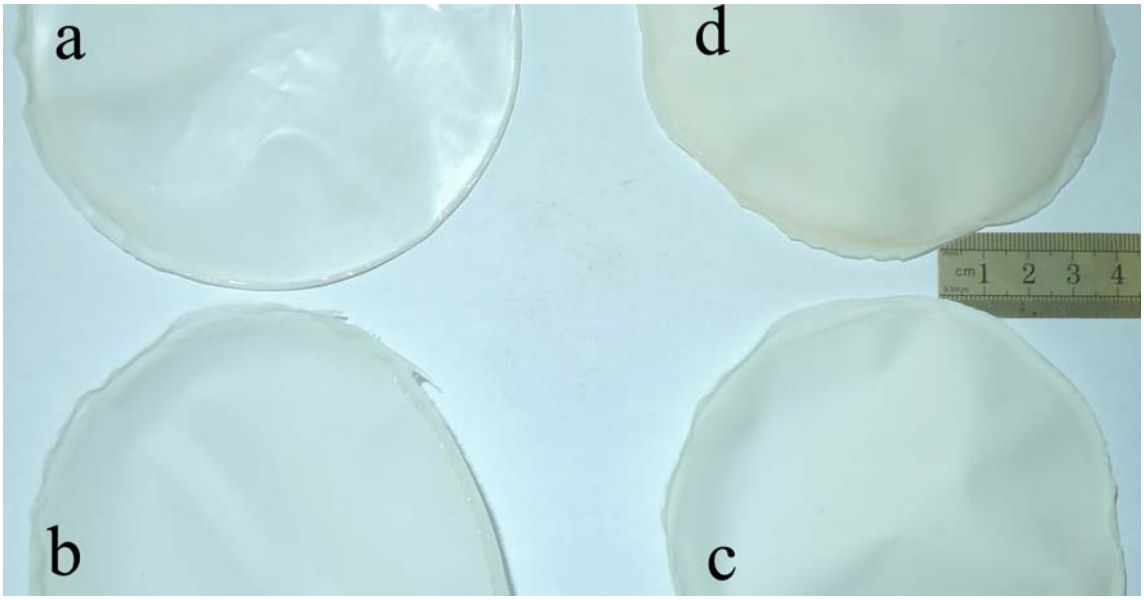

Fig. 1 Films of PVDF-FP$_i$% obtained by solution, i= (a) 0, (b) 3, (c) 5 and (d) 8.

2.3. Morphology and structure characterization

Optical microscopy was performed on the nanocomposite films to observe the fracture morphologies by using a VHX 600E digital microscope (Keyence Company) with a real-time depth composition, two/three-dimensional functions, and 20× to 5000× zoom. Scanning probe microscopy

(SPM) was performed using a SPM9500J2 microscope (Shimadzu Company) for images processing and profile analysis. The detailed results about the mciro structures and the crystallization of all the samples have been analyzed in Ref. [18].

2.3. Nano-tensile testing

A commercial nano-tensile testing system (Nano UTMTM Universal Testing System T150, Agilent Technologies, Inc.) with the method of UTM-Bionix Standard Toecomp CDA was used to conduct the tensile test in this paper. Detailed information and the image of the instrument were introduced in Ref. [18]. The samples were cut from PVDF-FP$_i$% films and seem like slender belts as shown in Fig. 2. The length and height of the belt like samples were measured by a caliper and screw micrometer, and the width was measured by the VHX 600E optical microscopy. Three individual samples have been prepared and tested in each category. The tensile strain rate was set as 1.0×10^{-2} s^{-1} here, which is ten times that of 1.0×10^{-3} s^{-1} in Ref. [18].

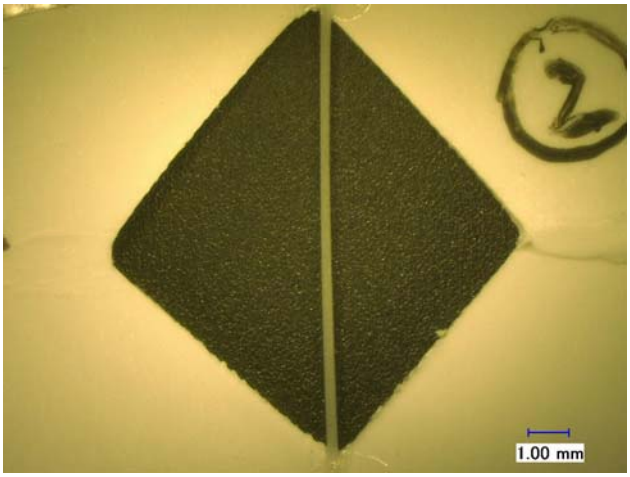

Fig.2. The image of the sample for the nano-tensile testing measured by optical microscopy.

3. Results and Discussion

3.1. Engineering stress-strain response

The engineering stress-strain responses for PVDF-FP$_i$% as obtained from the nano-tensile testing are shown in Fig. 3. The key points in these curves, such as the offset yield strain (0.2% offset), peak stress and break point, have been labeled as letters Y, P and B, respectively. The subscript numbers point out which sample these values belong to. The full stress-strain curves can be divided into three regions: (1) the elastic region (from the start point to Y), in which recoverable (elastic) deformation happens and the Hooke's law is satisfied between the stress and strain thus the Young's modulus can be computed. The stress at the offset yield strain point (σ_y) is called the tensile yield strength [20]; (2) the strain hardening region (Y→P), in which the stress is no longer proportional to strain and permanent nonrecoverable (plastic) deformation occurs. The stress at the maximum on the engineering stress–strain curve (point P) is defined as the tensile strength or ultimate strength [21]; (3) the unstable failure region (P→B), in which a small constriction or neck begins to form at some point, and fracture ultimately occurs at the neck. The fracture strength [20] corresponds to the stress at fracture and the area under the stress-strain curve up to the point of fracture is used to detect the fracture toughness, which is a measure of the ability of a material to absorb energy up to fracture and always used to delineate the brittleness or ductility of a material. All these key mechanical properties, for PVDF-FP$_i$% in the three regions are listed in table 1.

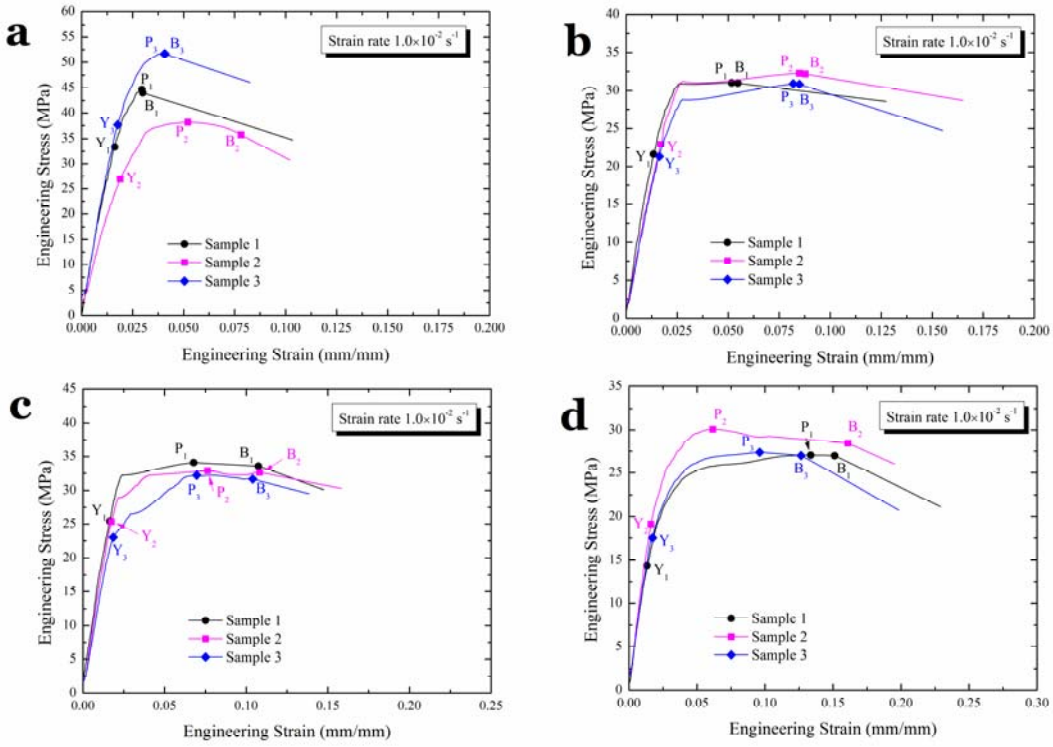

Fig. 3. Engineering stress-train response for PVDF-FP$_i$%, i= (a) 0, (b) 3, (c) 5 and (d) 8 at strain rate of 1.0×10^{-2} s^{-1}. The letters Y, P and B locate the positions of offset yield strain, peak stress and break point, respectively.

The Young's modulus of PVDF-FP$_{i\%}$ follows the orders PVDF-FP$_{0\%}$ > PVDF-FP$_{3\%}$ > PVDF-FP$_{5\%}$ > PVDF-FP$_{8\%}$. This means that the addition of FP-POSS reduced the modulus values of PVDF, which is quite different from the results in Ref. [13, 18]. This is probably resulted from two factors: (1) the much higher tensile strain rate, which is ten times that in Ref. [18]. A higher strain rate in tensile testing tends to achieve higher Young's modulus values. Thus nearly all the moduli of PVDF-FP$_{i\%}$ are greater than those obtained at the strain rate of 1.0×10^{-3} s^{-1} [18] except PVDF-FP$_{3\%}$; (2) the thinner film of PVDF-FP$_{0\%}$ (as shown in Fig.1, the film of PVDF-FP$_{0\%}$ is much thinner than the three other ones), which will bring the so called size effect during the tensile test and make the modulus value of PVDF-FP$_{0\%}$ become higher. But anyway, it is obvious that the elastic modulus of PVDF was weakened by further additions of FP-POSS at high strain rate. The values of yield strength (Y_S), tensile strength (T_S), and fracture strength (F_S) show a similar trend and indicate the FP-POSS contents have the similar effect on the strength of PVDF. The values of offset yield strain (ε_y) are almost the same for PVDF-FP$_{5\%}$ and PVDF-FP$_{0\%}$ and a little higher for PVDF-FP$_{3\%}$ and PVDF-FP$_{8\%}$, shows there is no obvious rule to describe the effect of FP-POSS on the elastic deformation range of PVDF at high strain rate.

The elongation at break (fracture strain) and fracture toughness values reveal an undoubtedly influence of FP-POSS on PVDF. The fracture strain and fracture toughness increase with the increasing content of FP-POSS. The value of εf increases from 4.9 % to 14.62 %, giving PVDF-FP$_8$% the toughness ~200 % higher than that of neat PVDF. Dramatic enhancements in fracture toughness can be observed when the FP-POSS content reaches to some extent. The content of 3 wt.% FP-POSS only brings a 26 % increase of the fracture toughness to PVDF (1.99 MPa vs. 1.58 MPa). However, when the content of FP-POSS reaches to 8 wt.%, the enhancement in fracture toughness will increase sharply to 130 % (3.63 MPa vs. 1.58 MPa). The similar mechanism to the toughness enhancements at high strain rate can be deduced from the microstructures of neat PVDF and its FP-POSS nanocomposites that have been detected [18]. The effect of FP-POSS in PVDF has

been proved to form bigger PVDF particles. FP-POSS act like the nucleating agents in PVDF mixtures and make more PVDF molecules be nucleated around them. Thus the particles are more separate and the domain size of the particles becomes larger with the increasing of the FP-POSS content. In contrast to the neat PVDF, more separate and less cross-linked particles in PVDF nanocomposites (especially in PVDF-FP_5% and PVDF-FP_8%) lead to a structure much more conductive to plastic flow under applied stress and result in a more efficient energy-dissipation, thereby reducing crack formation [22].

Table 1. The Young's modulus (E), offset yield strain (ε_y), yield strength (Y_S), tensile strength (T_S), fracture strength (F_S), fracture strain (ε_f) and fracture toughness (K_c) of PVDF-FP_i% (i = 0, 3, 5 and 8) as obtained from stress-strain responses and hardness values.

FP-POSS (wt.%)	E (GPa)	ε_y (%)	Y_S(MPa)	T_S (MPa)	F_S (MPa)	ε_f (%)	K_c (MPa)
0	2.17(0.46)	1.73(0.12)	32.14(6.21)	44.83(6.76)	44.18(7.75)	4.90(2.40)	1.58(0.80)
3	1.65(0.21)	1.53(0.21)	21.99(0.85)	31.41(0.74)	31.35(0.72)	7.58(1.83)	1.99(0.53)
5	1.64(0.19)	1.73(0.15)	24.59(1.36)	33.04(0.96)	32.61(0.97)	10.66(0.22)	3.05(0.24)
8	1.27(0.11)	1.56(0.21)	16.98(2.43)	28.17(1.67)	27.47(0.83)	14.62(1.78)	3.63(0.65)

Note: Values in parentheses indicate (±) standard deviations.

3.2. Dynamic mechanical properties

There is a sensitive spring installed in T150 which can provide a very small harmonic force with specific frequency on the sample thus the dynamic mechanical properties of PVDF-FP_i%, such as the storage modulus, loss modulus and loss tangent can also be obtained during the tensile procedure. To viscoelastic materials, the storage modulus measures the stored energy, representing the elastic portion; and the loss modulus illustrates the energy dissipated as heat, representing the viscous portion ; the loss tangent is defined as the ratio of viscous to elastic portion and would change with the storage and loss modulus. The value of loss tangent is important to measure the viscoelastic properties of a material. A value of 0 means that a material is fully elastic while a high value represents a material with high viscosity. Dynamic mechanical properties are helpful to understanding and confirming the energy-dissipation mechanism for PVDF-FP_i% as analyzed previously.

Table 2 lists the values of storage modulus (G'), loss modulus (G'') and loss tangent (tan δ) for PVDF-$FP_{i\%}$ (i = 0, 3, 5 and 8) obtained from the nano-tensile testing at the harmonic force of 4.5 mN and the frequency of 20 Hz. It can be observed that all the values of storage modulus are higher than the corresponding values of Young's modulus as obtained from the elastic portion of stress-strain responses (listed in table 1). This is not surprising since the storage modulus is averaged within the whole range of stress-strain responses, in which modulus with higher values is keeping after the yield strain due to a full elastic deformation. Loss modulus values for PVDF-$FP_{i\%}$ (i = 3, 5 and 8) show that the addition of FP-POSS obviously increases the viscosity of PVDF since they are much higher than that of the neat PVDF. Compared with the storage and loss modulus, loss tangent is more reliable to measure viscoelastic properties because it is the ratio of loss to storage modulus thus less influenced by the uncertain factors in measuring or some unpredictable defects in materials. The values of loss tangent in table 2 show an evidently viscosity increasing with the increasing content of FP-POSS. Compared with the loss tangent values obtained at the strain rate of 1.0×10^{-3} s^{-1} [18] (from 0.089 of neat PVDF to 0.113 of PVDF-$FP_{8\%}$), the values increase more obviously at the strain rate of 1.0×10^{-2} s^{-1} in this article (from 0.075 of neat PVDF to 0.151 of PVDF-$FP_{8\%}$), which shows the perspicuous effect of the strain rate on the viscosity of PVDF and its nanocomposites.

Table 2. The storage modulus (G'), loss modulus (G'') and loss tangent (tan δ) of PVDF-FP$_i$% (i = 0, 3, 5 and 8) as obtained from nano-tensile testing at a harmonic force of 4.5 mN and a frequency of 20 Hz.

FP-POSS (wt.%)	G' (GPa)	G'' (MPa)	tan δ
0	2.40(0.31)	169.2(78.5)	0.075(0.046)
3	1.86(0.17)	176.9(73.1)	0.097(0.065)
5	1.74(0.15)	186.0(74.9)	0.107(0.043)
8	1.43(0.18)	203.7(93.5)	0.151(0.099)

Note: Values in parentheses indicate (±) standard deviations.

3.3. Fracture appearance analysis

The fracture appearance of PVDF-FP$_i$% (i = 0, 3, 5 and 8) are shown in Fig.4. These images were obtained by VHX 600E with a real-time depth composition, three-dimensional functions at 500× or 1000× zoom. It can be found very clearly that the image of neat PVDF (Fig. 4 (a)) is quite different from the others. Compared with the three other ones, the fracture appearance of neat PVDF is more regular and the boundary is clear, shows only a small area near the fracture surface was obviously influenced during the fracture procedure. On the contrary, the fracture appearance of PVDF-FP$_i$% (i = 3, 5 and 8) (Fig. 4 (b), (c) and (d)) are irregular and the boundaries of the fracture surfaces are not obvious. These results have undoubtedly proved that the brittleness of neat PVDF is higher than its FP-POSS nanocomposites and the viscosity of PVDF will be increased by the addition of FP-POSS. Another important phenomenon is that the fracture regions of PVDF-FP$_i$% (i = 3, 5 and 8) are different. As shown in Fig. 4, the area of the fracture regions increases with the content of FP-POSS in PVDF, reveals that the brittleness drops and the viscosity rises when FP-POSS is mixed into PVDF. And more FP-POSS was mixed, more obvious this effect was displayed, which is in good agreement with the variation trend of the loss tangent values in section 3.2 and the fracture toughness values in section 3.1.

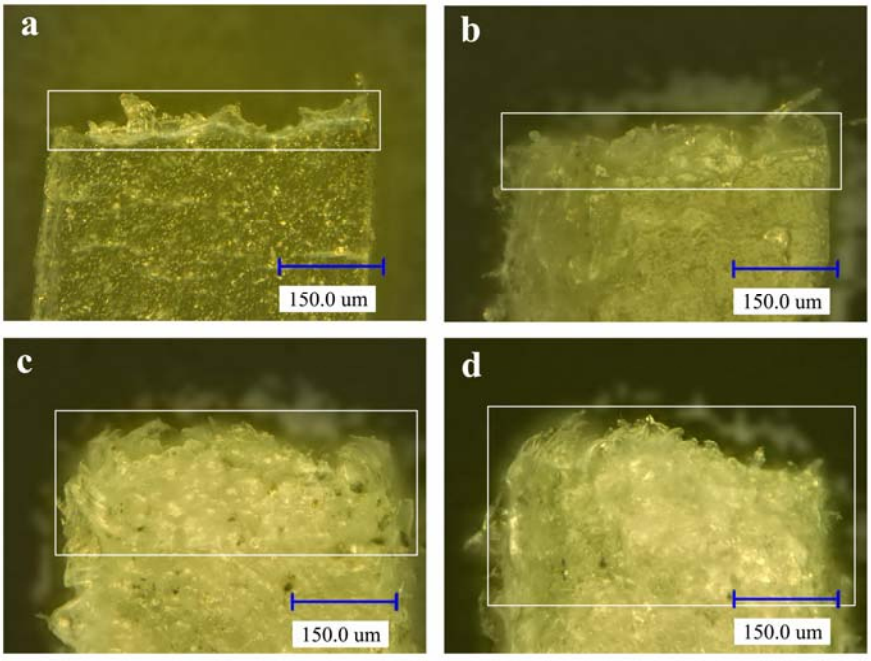

Fig. 4. Optical microscopy images of the fracture appearance for PVDF-FP$_i$% obtained by VHX 600E, i= (a) 0, (b) 3, (c) 5 and (d) 8. The square boxes locate the fracture regions.

4. Conclusions

PVDF/FP-POSS nanocompostites can be prepared by solvent evaporation method. Nano-tensile testing results at the strain rate of 1.0×10^{-2} s^{-1} showed the toughness of PVDF were enhanced by FP-POSS and further additions of FP-POSS brought surprisingly enhancements in toughness of the nanocomposites while associated with a decline in stiffness. Dynamical mechanical properties indicated the viscosity of the nanocomposites increased with the increasing FP-POSS contents in PVDF-$FP_{i\%}$. Fracture appearance analysis results showed that the fracture appearance of neat PVDF was regular and the boundary was clear, while PVDF-$FP_{i\%}$ (i = 3, 5 and 8) are irregular and not obvious. And the fracture regions increased with the content of FP-POSS in PVDF, which provided the visual evidence for the conclusions obtained from the data analysis. The great improvement effects on toughness and the increasing viscosity resulted from further additions of FP-POSS should be derived from the more separate and less cross-linked particles in the nanocomposities and the nano scale size of POSS compounds, which made the materials, are more easy to form plastic flow and more efficient on energy-dissipation.

Acknowledgements

The authors would like to thank the Science and Technology Innovation Talents Special Fund of Harbin (Grant No. 2012RFQXG001), the National Natural Science Foundation of China (11102053) and the Fundamental Research Funds for the Central Universities (Grant No. HIT. NSRIF. 2010070) for the financial support of this research.

References

[1] Seminara Lucia, Capurro Marco, Cirillo Paolo. Electromechanical characterization of piezoelectric PVDF polymer films for tactile sensors in robotics applications. Sensors and Actuators A-Physical, 169(1) (2011) 49–58.

[2] Kerur SB, Ghoshy A. Active vibration control of composite plate using AFC actuator and PVDF sensor. International Journal of Structural Stability and Dynamics, 11(2) (2011) 237–255.

[3] Dargaville TR, Celina M, Chaplya PM. Evaluation of Piezoelectric Poly(Vinylidene Fluoride) Polymers for Use in Space Environments. I. Temperature Limitations. Journal of Polymer Science Part B: Polymer Physics, 43 (2005) 1310–1320.

[4] Dargaville TR, Celina M, Martin JW, et al. Evaluation of Piezoelectric Pvdf Polymers for Use in Space Environments. II. Effects of Atomic Oxygen and Vacuum Uv Exposure. Journal of Polymer Science Part B: Polymer Physics, 43 (2005) 2503–2513.

[5] Xu HP, Dang ZM, Jiang MJ, Yao SH, Bai J. Enhanced dielectric properties and positive temperature coefficient effect in the binary polymer composites with surface modified carbon black. Journal of Materials Chemistry, 18 (2008) 229–234.

[6] Li YJ, Shimizu H. Conductive PVDF/PA6/CNTs nanocomposites fabricated by dual formation of cocontinuous and nanodispersion structures. Macromolecules, 41(14) (2008) 5339-5344.

[7] Malmonge LF, Langiano SD, Cordeiro JMM, et al. Thermal and Mechanical Properties of PVDF/PANI Blends. Materials Research-Ibero-American Journal of Materials, 13(4) (2011) 465–470.

[8] Fu BX, Gelfer MY, Hsiao BS, Phillips S, Viers B, Blanski R, P Ruth. Physical gelation in ethylene–propylene copolymer melts induced by polyhedral oligomeric silsesquioxane (POSS) molecules. Polymer, 44(5) (2003) 1499–1506.

[9] Deng J, Polidan JT, Hottle JR, Farmer-Creely CE, Viers BD, Esker A. Polyhedral Oligomeric Silsesquioxanes: A New Class of Amphiphiles at the Air/Water Interface. Journal of the American Chemical Society, 124(51) (2002) 15194.

[10] Fu BX, Hsiao BS, White H, Rafailovich M, Mather PT, Jeon HG, Phillips S, Lichtenhan J,

Schwab J. Nanoscale reinforcement of polyhedral oligomeric silsesquioxane (POSS) in polyurethane elastomer. Polymer International, 49(5) (2000) 437–440.
[11] Zeng FL, Sun Y, Zhou Y, Li QK. Molecular simulations of the miscibility in binary mixtures of PVDF and POSS compounds. Modelling and Simulation in Materials Science and Engineering, 17, (2009) 075002.
[12] Mabry JM, Vij A, Iacono ST, Viers BD. Fluorinated Polyhedral Oligomeric Silsesquioxanes (F-POSS). Angewandte Chemie International Edition, 47(22) (2008) 4137–4140.
[13] Zeng FL, Sun Y, Zhou Y, Li QK. A molecular dynamics simulation study to investigate the elastic properties of PVDF and POSS nanocomposites. Modelling and Simulation in Materials Science and Engineering, 19 (2011) 025005.
[14] Tan EPS, Ng SY, Lim CT. Tensile testing of a single ultrafine polymeric fiber. Biomaterials, 26 (2005) 1453–1456.
[15] Kiuchi M, Matsui S, Isono Y. Mechanical characteristics of FIB deposited carbon nanowires using an electrostatic actuated nano tensile testing device. Journal of Microelectromechanical Systems, 16(2) (2007) 191–201.
[16] Seydel T, Knoll W, Greving I, etal. Increased molecular mobility in humid silk fibers under tensile stress. Physical Review E, 83(1) (2011) 016104.
[17] Chang WY, Fang TH, Lin YC. Thermomechanical and optical characteristics of stretched polyvinylidene fluoride. Journal of Polymer Science Part B: Polymer Physics, 46(10) (2008) 949–958.
[18] Fanlin Zeng, Yizhi Liu, Yi Sun, Enlai Hu, Yu Zhou. Nanoindentation, Nanoscratch and Nanotensile Testing of Poly(vinylidene fluoride)-Polyhedral Oligomeric Silsesquioxane Nanocomposites. Journal of Polymer Science Part B: Polymer Physics, 50(23) (2012) 1597–1611.
[19] Liu Yizhi, Sun Yi, Zeng Fanlin, etal. Morphology, crystallization, thermal and mechanical properties of poly(vinylidene fluoride) films filled with different concentrations of polyhedral oligomeric silsesquioxane. Polymer Engineering & Science, DOI: 10.1002/pen.23398.
[20] William D, Callister Jr. Materials Science and Engineering An Introduction (7th ed). John Wiley & Sons, United States of America, 2006.
[21] Dowling N E. Mechanical Behavior of Materials (2nd ed). Prentice Hall PTR, Paramus, NJ, 1998.
[22] Shah D, Maiti P, Gunn E. Dramatic enhancements in toughness of polyvinylidene fluoride nanocomposites via nanoclay-directed crystal structure and morphology. Advanced Materials, 16(14) (2004) 1173–1177.

Fracture behavior of thin aluminum films on soft substrate

Dan Wu, Huimin Xie*, Yajun Yin
AML, Department of Engineering Mechanics, Tsinghua University, Beijing 100084, China
* Corresponding author: *xiehm@mail.tsinghua.edu.cn

Abstract
Thin metal films on soft substrate are conventional in flexible electronics and flexible devices. Thermal stress often exists in the thin metal films due to thermal mismatch during the physical vapor deposition (PVD) process, which leads to the fracture failure of metal films. Theoretical analysis and numerical simulations have predicted that the cracking of a thin stiff layer on a soft substrate depend on the relative stiffness and thickness of the film and the substrate. However, few experimental results reported support the hypothesis.
In this paper, An experimental investigation is conducted to study the fracture behavior of the aluminum films on soft Polydimethylsiloxane(PDMS) substrate during physical vapor deposition. It has been found that when the thickness of the aluminum film is relatively smaller, surface wrinkling is induced to accommodate the mismatched strain between the substrate and the film. When the thickness of the aluminum film is relatively larger, cracking of the film occurs.
Keywords Aluminum film, PDMS substrate, PVD process, Fracture behavior

1. Introduction

Films/substrate structures have been widely researched for the extensive application of this structure. Thin stiff film including metal film and non-metal film on soft substrate are exploited for the use of flexible electronics and devices [3,8-10,13,14]. Several ways have been applied to fabricate the relatively thin solid film on the flexible substrate forming flexible structures. Transferring the thin silicon film onto the pre-stretched soft PDMS substrate leading to the waving surface structures is a frequently used process [4]. Casting the viscous PDMS on the metal foils, and then conducting a photolithography process to obtain the structure is another means[16]. Evaporation and sputtering are two deposition means forming several nanometers to micrometers thick film on the substrate [6,11,15]. During the deposition process, the temperature on the surface of the substrate will rise and leads to thermal expansion of the substrate. The PDMS substrate is heated when the gold film is deposited onto the substrate [1]. Because the thermal expansion coefficient is several times larger than the gold film. When the surface temperature cools down, a thermal mismatch will be produced. From former observation [1], this thermal mismatch will lead to wrinkling of the film on the soft substrate, which is generally produced in other experiments [7].
In this paper it is found wrinkles will be formed on the film when the thickness of the film is the range of several hundred nanometers. When the thickness of the film exceeds this confine, approximate orthogonal cracks occur on the film. The detailed illustration of this difference is given out from the experimental results.

2. Experimental details

In our experiment, aluminum films with different thickness have been fabricated on the PDMS substrate. The PDMS is formed by mixing Sylgard 184 silicone elastomer with the curing agent at ratio 10:1 (by weight) and then the uncured mixture is spread on the glass substrate, which is placed in a vacuum drying oven at temperature 70℃ for an hour later. The cured PDMS have the same smooth surface with the glass substrate. The thickness of the PDMS substrate is in the range of 1-2mm. Pure aluminum is deposited on the PDMS substrate by E-beam evaporation at pressure of 5 ×10-5 torr. The elastic modulus of the PDMS substrate is 2.2 Mpa [7]. The elastic modulus and

Possion's ratio of the aluminum film are 72Gpa and 0.33 respectively. During the deposition process, the surface temperature of the substrate will rise and this leads to a thermal expansion of the substrate. When the deposition finished, the surface temperature cools down. Because the thermal expansion coefficient of the PDMS substrate is several times larger than that of the aluminum film, a thermal mismatch will be produced between the substrate and the film. This strain mismatch will lead to the surface wrinkles of the specimen when the thickness of the deposited aluminum film is in the range of several hundred nanometers. But when the thickness exceeds that confine, cracks will occur generally on the aluminum film. Aluminum film with thickness 40nm, 150nm, 200nm, 260nm and 700nm are fabricated on the PDMS substrate. Different experimental phenomena reflecting different mechanical behavior are observed after the deposition of the film under the microscopy.

3. Experimental results and discussions

During the deposition of the aluminum, the cooling of the aluminum steam on the surface of the PDMS substrate leads to the temperature elevating. After deposition, the temperature cools down. And this change leads to a deformation mismatch due to the distinct difference of the thermal coefficient of these two materials. The induced compressive stress in the film can be expressed as [1]:

$$\sigma = \frac{E_f(\alpha_f - \alpha_s)(T_D - T)}{(1-\upsilon_f)} \tag{1}$$

In the expression, the subscripts *f* and *s* represent the film and substrate respectively. T_D represents the deposition temperature and *T* corresponds to the cooled down temperature. α represents thermal coefficient of the film and the substrate respectively. υ is the Possion's ratio of the film. The thermal coefficient of the PDMS substrate and the aluminum film is about 300×10^{-6} and 20×10^{-6}. For the aluminum film with thickness of several hundred nanometers, wrinkles occur to accommodate the deformation mismatch.

For the film with thickness of 40nm, no surface wrinkles are found under the microscopy. This can be understood that the surface temperature during the deposition of the 40nm thick film is below the critical buckling temperature. For the film with thickness of 150nm, disordered wrinkles (Fig.1) can be observed under the microscopy. The measured wavelength for the wrinkles is about 10 μm. The overall estimation of the wavelength of the buckled wrinkles is [5]:

$$\lambda_c = 2\pi h\left[\frac{E_f(1-\upsilon_s^2)}{3E_s(1-\upsilon_f^2)}\right]^{1/3} \tag{2}$$

According to the theoretical solution, the wavelength of the film with thickness 150nm is about 20 μm, two times of the experimental result. This discrepancy comes mainly from two aspects: the simplification of the theoretical model and the neglecting of the change of the surface elastic modulus of the PDMS substrate [1].

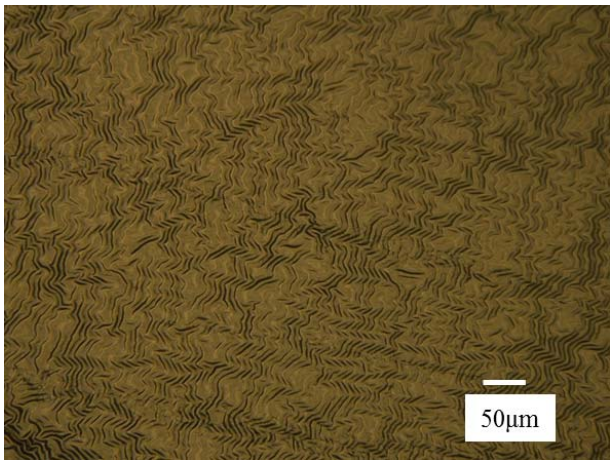

Figure 1. Wrinkling surface of the aluminum film with thickness 150nm on the PDMS substrate

The wavelength of the wrinkles of the film with thickness 200nm and 260nm are about 12 μm and 17.5 μm respectively (Fig.2). From Eq.2, it can be seen that the buckling wavelength only rely on the thickness of the film for the aluminum film on PDMS substrate. But this is not the real case. The deposition temperature varies with the thickness of the film. So the elastic modulus of the PDMS substrate changes to a certain extent. The wavelength does not simply rely on the thickness of the film, but also the surface temperature which may alter the surface elastic modulus of the PDMS substrate.

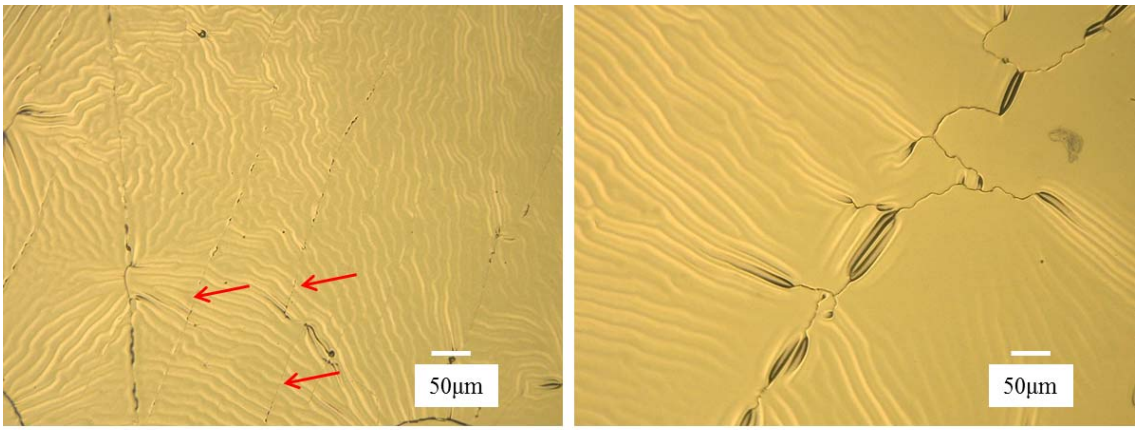

Figure 2. Wrinkled surface of the aluminum film with thickness 200nm and 260nm on soft PDMS substrate

From the observation, the wrinkles are mostly initiated from a flaw, which may induce stress concentration. There are some cracks occurring in the aluminum film (marked by red arrow in Fig.2 (a)). This can be understood that the wrinkles occurring vertical to the maximum compressive stress and. In the direction vertical to the maximum compressive stress, the tensile stress may be induced, which leads to cracking of the film in the direction vertical to the wrinkles.

For the aluminum film with thickness of 700nm, there are definitely no wrinkles formed on the film. Instead of this, approximate vertical cracks appear in the aluminum film (Fig.3). In former report, wrinkles formed on the PDMS substrate have been researched from experiments and finite element modeling. But few reports concern the cracking behavior of the stiff film on the PDMS substrate. This is mainly because the film thickness in former research work is relatively small. For film with relatively large thickness, cracking may be induced for mismatched strain. In this experiment,

aluminum film is found cracking on the PDMS substrate with thickness of 700nm.

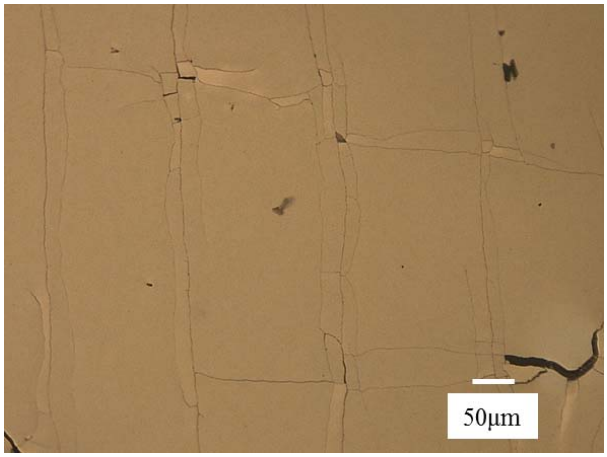

Figure 3. Cracking of the aluminum film on the PDMS substrate

Cracking substitutes wrinkling for the aluminum film with relatively larger thickness. In theoretical analysis, the bending equilibrium equation of the wrinkles formed on the thin stiff film is [12]:

$$\frac{E_f I}{1-\upsilon_f^2}\frac{d^4 w}{dy^4} + F\frac{d^2 w}{dy^2} + Kw = 0 \tag{3}$$

Where w is the displacement of the film in z direction (Fig.4), the expression of w has been obtained from both theory and experiment, which can be expressed by [2]:

$$w(y) = A(1+\cos\frac{2\pi y}{\lambda}) \tag{4}$$

Where λ is the buckling wavelength and A is buckling amplitude of the wrinkles.
$I=h^3/12$ is the second bending moment of the film around the x axis per unit width. F is the compressive force provided by the substrate in the film. K reflects the influence of the underlying substrate expressed by [2]:

$$K = \frac{E}{1-\upsilon^2}\frac{\pi}{\lambda} \tag{5}$$

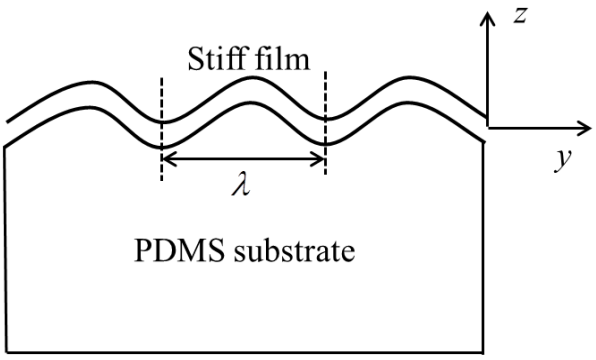

Figure 4. A schematic of the surface wrinkling on stiff film/soft substrate

F is derived from Eq.3-5 and expressed by [12]:

$$F = E_f I\left[\frac{4\pi^2}{(1-\upsilon_f^2)\lambda^2} + \frac{E}{4\pi(1-\upsilon_f^2)E_f I}\lambda\right] \tag{6}$$

In Eq.6, it can be seen that the compressive force in the film is in proportion to the thickness of the film. For the overall mechanical behavior of the film/substrate, the compressive stress is in linear with the thickness of the film. In local, the tensile stress at the crest induced by bending of the film is in the same increasing rate with the compressive stress in the film. When the tensile stress at the crest exceeds the tensile strength of the aluminum film, the film will crack instead of wrinkle to accommodate the mismatched strain. Fractured ribbons are induced during the cracking of the film (marked by red arrows). The fractured ribbons released the compressive force of the film. And the stress in the isolated fractured fragment is insufficient to lead to wrinkling of the film. The buckling and wrinkling behavior of the film transfer into the fracture behavior of the film when the thickness of the film is relatively larger.

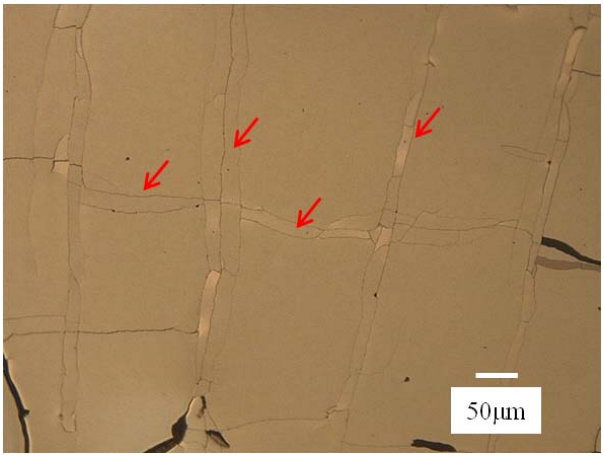

Figure 5. Approximately vertical cracking of the film and fractured ribbons (marked by red arrows)

4. Conclusions

In this paper, wrinkling and cracking behavior of the aluminum film on the PDMS substrate have been studied from experimental results. For aluminum film with smaller thickness (less than several hundred nanometers), wrinkling is mostly likely to happen due to the mismatched strain. When the thickness of the aluminum film is relatively larger, cracking substitutes the wrinkling to accommodate the mismatched deformation between the film and the substrate. The reason of this transformation lies in the increasing of the tensile stress with the thickness of the film. When the tensile stress in the film exceeds the tensile strength of the aluminum film, cracking behavior of the film predominates.

Acknowledgements

The authors are grateful to the financial supported by the National Basic Research Program of China (“973” Project) (Grant No.2010CB631005, 2011CB606105), the National Natural Science Foundation of China (Grant Nos.90916010, 11172151，11232008, 11227801) Specialized Research Fund for the Doctoral Program of Higher Education (Grant No.20090002110048), Tsinghua University Initiative Scientific Research Program.

References

[1] N. Bowden, S. Brittain, A.G. Evans, J.W. Hutchinson, G.M. Whitesides,Spontaneous formation of ordered structures in thin films of metals supported on an elastomeric polymer. Nature 393 (1998) 146-149.

[2] Y.-P. Cao, X.-P. Zheng, F. Jia, X.-Q. Feng,Wrinkling and creasing of a compressed elastoplastic film resting on a soft substrate. Computational Materials Science 57 (2012) 111-117.

[3] Z.H. Cao, K. Hu, X.K. Meng,Strain rate sensitive stretchability and fracture behavior of

nanocrystalline Cu films on flexible substrate. Materials Science and Engineering: A 536 (2012) 244-248.
[4] X. Feng, B.D. Yang, Y. Liu, Y. Wang, C. Dagdeviren, Z. Liu, A. Carlson, J. Li, Y. Huang, J.A. Rogers,Stretchable Ferroelectric Nanoribbons with Wavy Configurations on Elastomeric Substrates. Acs Nano 5 (2011) 3326-3332.
[5] F. Jia, Y.-P. Cao, T.-S. Liu, Y. Jiang, X.-Q. Feng, S.-W. Yu,Wrinkling of a bilayer resting on a soft substrate under in-plane compression. Philosophical Magazine 92 (2012) 1554-1568.
[6] Z. Jia, C. Peng, J. Lou, T. Li,A map of competing buckling-driven failure modes of substrate-supported thin brittle films. Thin Solid Films 520 (2012) 6576-6580.
[7] H. Jiang, D.-Y. Khang, H. Fei, H. Kim, Y. Huang, J. Xiao, J.A. Rogers,Finite width effect of thin-films buckling on compliant substrate: Experimental and theoretical studies. Journal of the Mechanics and Physics of Solids 56 (2008) 2585-2598.
[8] H. Jiang, Y. Sun, J.A. Rogers, Y. Huang,Mechanics of precisely controlled thin film buckling on elastomeric substrate. Applied Physics Letters 90 (2007) 133119.
[9] D.Y. Khang,A Stretchable Form of Single-Crystal Silicon for High-Performance Electronics on Rubber Substrates. Science 311 (2006) 208-212.
[10]W. Qinghua, X. Huimin, L. Zhanwei, L. Xinhao, W. Jianfeng, X. Kewei, Z. Zhaohui, L. Jianhui, G. Changzhi,Residual stress assessment of interconnects by slot milling with FIB and geometric phase analysis. Optics and Lasers in Engineering 48 (2010) 1113-18.
[11]G.-D. Sim, Y. Hwangbo, H.-H. Kim, S.-B. Lee, J.J. Vlassak,Fatigue of polymer-supported Ag thin films. Scripta Materialia 66 (2012) 915-918.
[12]A.L. Volynskii, S. Bazhenov, O.V. Lebedeva, N.F. Bakeev,Mechanical buckling instability of thin coatings deposited on soft polymer substrates. Journal of Materials Science 35 (2000) 547-554.
[13]Q.-H. Wang, H.-M. Xie, X. Feng, Z. Chen, F.-L. Dai,Delamination and Electromigration of Film Lines on Polymer Substrate Under Electrical Loading. Ieee Electron Device Letters 30 (2009) 11-13.
[14]D. Wu,Micro-scale delaminating and buckling of thin film on soft substrate. Journal of micromechanics and microengineering (2012). Received.
[15]C. Yu, K. O'Brien, Y.-H. Zhang, H. Yu, H. Jiang,Tunable optical gratings based on buckled nanoscale thin films on transparent elastomeric substrates. Applied Physics Letters 96 (2010) 041111.
[16]H. Yung-Yu, M. Gonzalez, F. Bossuyt, F. Axisa, J. Vanfleteren, I. De Wolf,The effects of encapsulation on deformation behavior and failure mechanisms of stretchable interconnects. Thin Solid Films 519 (2011) 2225-34.

Self-patterning through thin film buckling

Jean-Yvon Faou[1,*], Guillaume Parry[2], Sergey Grachev[1], Etienne Barthel[1]

[1] Surface du Verre et Interfaces, UMR 125 CNRS/Saint-Gobain,
39 Quai Lucien Lefranc, F-93303 Aubervilliers, Cedex, France
[2] SIMAP, Institut National Polytechnique de Grenoble Domaine Universitaire
1130 Rue de la Piscine, 38 402 St Martin d'H`eres Cedex France
* Corresponding author: jean-yvon.faou@saint-gobain.com

Abstract Thin films may spontaneously form buckles if the residual stresses are compressive and large and if adhesion is weak. Buckling driven delamination leads to periodic patterns, such as the telephone cord morphology which has been studied for decades. Until recently the role of adhesion in the formation of buckling patterns was rather poorly understood. The difficulties are: 1. buckling is a non-linear phenomenon 2. Adhesion is a complex process involving mode mixity at the crack tip. Here coupling buckling and mixed-mode adhesion in a FEM model, we investigate the influence of film thickness, adhesion and residual stresses on the final buckle morphology. In particular, we show that it is possible to control the delamination front to create branching morphologies. Such morphologies remain periodic and can cover large areas. Experimentally, we show how the relevant conditions can be achieved for multilayer stacks of thin films deposited by magnetron sputtering. In particular we demonstrate self-organized hexagonal networks of buckles at the 10 micron scale. We anticipate that these patterns can be scaled from the micron-scale to the nano-scale.

Keywords Buckling, Adhesion, Mode mixity, Patterning,

1. Introduction

Thin films may spontaneously form buckles[1,2] if the residual stresses are compressive and large and if adhesion is weak. Buckling driven delamination leads to periodic patterns, such as the telephone cord morphology which has been studied for decades. Until recently the role of adhesion in the formation of buckling patterns was rather poorly understood. The difficulties are: 1. buckling is a non-linear phenomenon 2. Adhesion is a complex process involving mode mixity at the crack tip. Here coupling buckling and mixed-mode adhesion in a FEM model, we investigate the influence of film thickness, adhesion and residual stresses on the final buckle morphology. We then use the results as a guideline for experiments

2. Numerical simulation

2.1. Model

In order to analyze the growth of the blister, we use a numerical model coupling finite elements with cohesive zone modeling. It is essential to use a nonlinear plate model to capture the buckling equilibrium. The surface of the plate is defined as the (O,x,y) plane and the out-of-plane displacement is $w(x,y)$. In order to take into account the presence of a purely rigid substrate, the unilateral contact condition $w(x,y)>0$ is introduced. The calculations are made for large displacements w, using the Green Lagrange strain tensor. When w is large, the strain tensor reduces to

$$\begin{cases} e_{xx} = \dfrac{\partial u}{\partial x} + \dfrac{1}{2}\left(\dfrac{\partial w}{\partial x}\right)^2 \\ e_{yy} = \dfrac{\partial u}{\partial y} + \dfrac{1}{2}\left(\dfrac{\partial w}{\partial y}\right)^2 \\ e_{xy} = \dfrac{1}{2}\left(\dfrac{\partial u}{\partial y} + \dfrac{\partial v}{\partial x}\right) + \dfrac{1}{2}\dfrac{\partial w}{\partial x}\dfrac{\partial w}{\partial y} \end{cases} \quad (1)$$

In Eq. (1) the terms which are non-linear in w are responsible for a third order term in the thin plate equilibrium equations and it is this non-linearity which is essential to capture the post-buckling evolution of the blisters (e.g. see [3]).

The second key point is the description of adhesion rupture for which a cohesive zone model (CZM) [29–32] is used. Detailed description of the model can be found in [4]. Cohesive elements are inserted at the interface. A bilinear softening behavior is used in order to take into account for the mode mixity of the interfacial toughness. The interfacial toughness Γ^c is defined as a function of the mode mixity angle ψ, see Fig.1, which is the relative proportion of shear and normal traction applied at the interface:

$$\tan\psi = \frac{K_{II}}{K_I} \quad (2)$$

We use for the definition of $\Gamma^c(\psi)$ the one proposed by Hutchinson in [5] and based on experimental data[6].

$$\Gamma^c(\psi) = \Gamma_I^c\left(1 + \tan^2 \eta\psi\right) \quad (3)$$

Where Γ_I^c is the mode I interfacial toughness, and η a dimension-less parameter to adjust the level of the mode II interfacial toughness Γ_{II}^c.

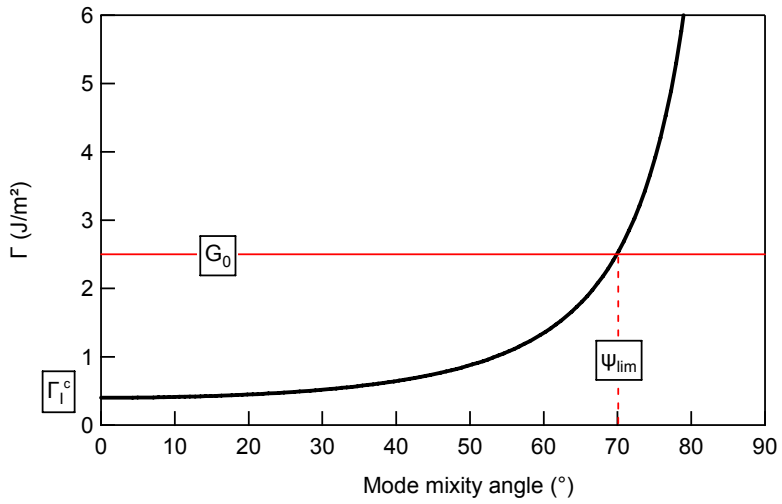

Figure 1 : Dependence of the interfacial toughness as a function of the mode mixity angle.

Thin film is modeled by a plate of thickness h, elastic modulus E and Poisson ratio ν. In-plane

stress σ_0 is introduced by a thermal expansion.

2.2. Results

We fix the materials parameters of the film to *E*=329 GPa and υ=0.31. The interfacial toughness is kept constant choosing $\Gamma_I^c = 0.4 J.m^{-2}$ and $\eta = 0.95$. The morphology of the delamination is then studied as a function of loading, which is given by the couple $(h;\sigma_0)$. It is convenient to define the total energy per unit area stored in the film due to the in-plane stress.

$$G_0 = \frac{1-\nu}{E} h {\sigma_0}^2 \tag{4}$$

We also define the limit for the mode mixity above which the interface cannot be fully separated. In case where the energy release rate is close to G_0 then

$$\psi_{\lim} = \frac{1}{\eta} \tan^{-1} \sqrt{\frac{G_0}{\Gamma_I^c} - 1} \tag{5}$$

It should be noted that $\psi_{\lim}$ is attained at the side of the blister as the film sags[4] and the mode mixity reaches pure mode II, $\psi = \pi/2$. However the interface is not fully separated at all angles above $\psi_{\lim}$.

Changing level of loading with $\psi_{\lim}$, we observe different morphologies, from no delamination to complete delamination of the film and draw a phase diagram $\psi_{\lim}$ is a relevant parameter for the instability of the blister and is equivalent to the loading ratio σ_0/σ_c of the blister. In case of the straight sided blister, the critical buckling stress σ_c corresponds to the stress needed to enter in the post-buckling regime.

$$\sigma_c = \frac{\pi^2}{12} \frac{E}{1-\upsilon^2} \left(\frac{h}{b}\right)^2 \tag{6}$$

Secondary buckling instability computation on the sides of a straight sided blister by Jensen [7], and on the collapse of a circular blister by Hutchinson [8] show that such destabilization is solely a function of G_0 and therefore $\psi_{\lim}$.

3. Experiments

We aim to study morphologies of the delamination experimentally. We use the superlayer method to make blisters [9]. A compressive stressed layer of molybdenum is deposited on top of a weak interface to provide elastic energy for buckling. The residual stress in the Mo layer before buckling is around 3GPa. The stress can be tuned changing the deposition conditions of the Mo layer during sputtering [10]. The thickness is varied from 100nm to 200nm. We here use a silver layer to create the weak interface with the substrate.

Both control over the residual stress and the thickness enable scanning different loading conditions and therefore variation of ψ_{lim}. Experimentally we observe several morphologies, from the telephone cord like blister to complete delamination, see Fig.2. Those morphologies can be compared to the numerical results and placed in a phase diagram.

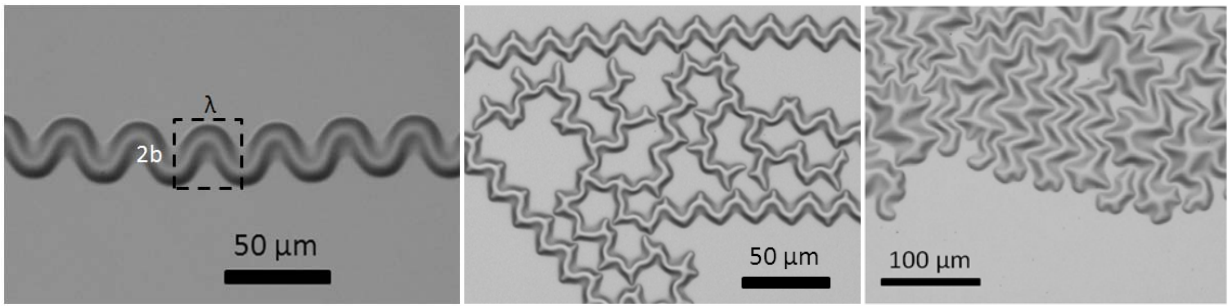

Figure 2: Evolution of the delamination morphology for Si/Ag interface for different layer of molybdenum.

In particular we use numerical simulations to demonstrate that a self-organized network of buckles can be generated and that the conditions to generate such a network experimentally can be achieved with the superlayer method.

4. Conclusions

We present a numerical model to explore the morphology of the buckling driven delamination pattern as a function of interfacial properties and loading conditions. Confronting the experimental data with the simulation, we find relevant parameters for patterning of large surfaces.

References

[1] G. Gilles and B. Rau, Thin Solid Films 120, 109, 1984.
[2] E. Spiecker, A.K. Schmid, A. M. Minor, U. Dahmen, S. Hollensteiner, and W. Jäger, Phys. Rev. Lett. 96, 086401, 2006.
[3] L. D. Landau and E. M. Lifshitz, Theory of Elasticity, Butterworth Heinemann, 1986.
[4] J-Y. Faou, G. Parry, S. Grachev and E. Barthel, Physical Review Letters, 108, 116102, 2012
[5] J.W. Hutchinson and Z. Suo, Adv. Appl. Mech. 29, 63, 1991.
[6] K. M. Liechti and Y. S. Chai, J. Appl. Mech. 59, 295, 1992.
[7] H. M. Jensen, Acta metall, mater. Vol. 41, No. 2, 1993, pp. 601-607
[8] J.W. Hutchinson, M. D. Thouless, and E. G. Liniger, Acta Metall. Mater. 40, 1992, pp. 295
[9] S. Grachev, A. Mehlich, J.-D. Kamminga, E. Barthel, and E. Sondergard, Thin Solid Films 518, 6052, 2010.
[10] J-Y. Faou, E. Barthel, S. Grachev, Stress tuning in sputter-deposited MoO_x films, Thin Solid Films, 2012, 10.1016/j.tsf.2012.11.053

Towards interface toughness measurement in nanometric films

Guillaume Parry[1,*], Jean-Yvon Faou[2], Sergey Grachev[2], Etienne Barthel[2]

[1] SIMAP, Institut National Polytechnique de Grenoble,
Domaine Universitaire, 1130 Rue de la Piscine, 38 402 St Martin d'Hères Cedex France
[2] Surface du Verre et Interfaces, UMR 125 CNRS/Saint-Gobain,
39 Quai Lucien Lefranc, F-93303 Aubervilliers, Cedex, France
* Corresponding author: guillaume.parry@simap.grenoble-inp.fr

Abstract Thin films deposited on substrates are usually submitted to large residual compression stresses, causing delamination and buckling of the film into various patterns. This phenomenon has been widely investigated in the past few decades, both experimentally and with nonlinear plates models. Nevertheless, the formation of the most commonly observed pattern, the "telephone cord blister", has only be understood recently, with FEM models coupling post-buckling studies and mixed-mode adhesion. Here, relying on these models, we show remarkable properties of these wavy blisters, in particular we show that the wavelength of the telephone cord patterns scales linearly with a parameter depending on the stress level in the film, the thickness and the adhesion energy. This result has an important practical application. As a matter of fact, since it is experimentally possible to control the stress level and the film thickness during elaboration, the measurement of this wavelength can indirectly lead to a measurement of the interface toughness, even in very small films.

Keywords Buckling, Adhesion, Mode mixity, Patterning,

1. Introduction

Compressively stressed thin films with low adhesion frequently buckle and delaminate simultaneously into various patterns, amongst which the so called "telephone cords" pattern is very often observed [1,2]. Although these buckles have been studied for decades, no complete understanding of their propagation had been presented until recently. As a matter of fact, the post-buckling equilibrium shapes of the blisters require the use of non-linear plates theory (e.g. see [3]). Furthermore adhesion is a complex process involving mode mixity at the crack tip. A nonlinear plate deformation model has been coupled with a cohesive zone model to simulate the kinematics of a propagating telephone cord buckle in very close agreement with experimental observations. Proper inclusion of the dependence of an adhesion upon the mode mixity proved to be central to the success of the approach. The clarification of the mechanism allows for a better understanding of buckle morphologies and highlights remarkable properties of these wavy blisters. In particular it is shown that the wavelength of the telephone cord patterns scales linearly with a parameter depending on the stress level in the film, the thickness and the adhesion energy. This result has an important practical application: since it is experimentally possible to control the stress level and the film thickness during elaboration, the measurement of this wavelength can indirectly lead to a measurement of the interface energy, even in very small films.

2. Mechanical model for blisters propagation

2.1. Model

A nonlinear plate model is used to capture the buckling equilibria. As a matter of fact, the blisters morphologies are characterized by very large out-of-plan displacements, meaning that the equilibria are located very far in the post-critical buckling regime compared to the flat (i.e. unbuckled)

equilibrium. The thin film is modeled by a plate of thickness h, made of linear elastic material characterized by a Young's modulus E and Poisson's ratio ν. The surface of the plate is defined as the *(O,x,y)* plane and the out-of-plane displacement is denoted *w(x,y)*. In order to take into account the presence of the substrate, the unilateral contact condition *w(x,y) ≥ 0* is introduced. The calculations are made for large displacements *w*, using the Green Lagrange strain tensor. As only *w* is large, the strain tensor reduces to

$$\begin{cases} e_{xx} = \dfrac{\partial u}{\partial x} + \dfrac{1}{2}\left(\dfrac{\partial w}{\partial x}\right)^2 \\ e_{yy} = \dfrac{\partial u}{\partial y} + \dfrac{1}{2}\left(\dfrac{\partial w}{\partial y}\right)^2 \\ e_{xy} = \dfrac{1}{2}\left(\dfrac{\partial u}{\partial y} + \dfrac{\partial v}{\partial x}\right) + \dfrac{1}{2}\dfrac{\partial w}{\partial x}\dfrac{\partial w}{\partial y} \end{cases} \tag{1}$$

In Eq. (1) the terms which are non-linear in *w* are responsible for a third order term in *w* the thin plate equilibrium equations and it is this non-linearity which is essential to capture the post-buckling evolution of the blisters.

The second key point is the description of adhesion rupture between the film and the substrate. A cohesive zone model (CZM) is introduced for this purpose between the elastic film and the rigid substrate. The tractions developed in the cohesive zone at the edges of the buckle provide boundary conditions for the buckled plate. The blister extends its boundary by forcing the separation along the delaminated edge as it buckles under large in-plane compression. Details of the cohesive zone model are given in [4]. A bilinear softening traction versus separation law is used, with a damage variable d increasing monotonically with the separation. The most important feature of this cohesive zone model is the mode mixity dependence of the interfacial toughness G^c. The relationship proposed by Hutchinson in [5] and based on experimental data[6] is used :

$$G^c(\psi) = G_I^c\left(1 + \tan^2 \eta\psi\right) \tag{2}$$

where ψ is the mode mixity angle defining the ratio between shear traction and normal traction at the interface ($\tan\psi = \dfrac{T_t}{T_n}$, with T_t the shear traction and T_n the normal traction. Hence, pure normal traction is obtained for ψ=0° whereas pure shear traction is obtained for ψ=90°). The definition given in Eq. (2) is meant to take into account that it is all the more difficult to break the interface that the proportion of shear is higher at the interface. Fig.1 describes both shapes of the traction versus separation law and of the toughness. Note that the quantity G_0, which is the energy per unit area stored in the film in its plane fully adherent state, has been introduced. G_0 is defined by:

$$G_0 = \frac{1-\nu}{E} h \sigma_0^{\,2} \tag{3}$$

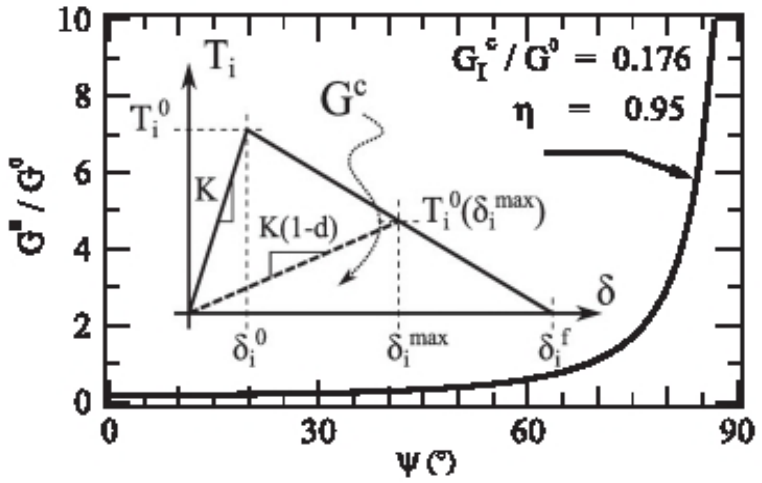

Figure 1 : From [4], Mixed-mode dependence of the work of adhesion at the film-substrate interface and bilinear traction vs separation law (Inset: i = n for mode I and t for mode II).

Finally, the thin film loading consists of an eigenstrain $\varepsilon_0 > 0$ uniformly applied to the plate ($\varepsilon_{xx} = \varepsilon_{yy} = \varepsilon_0$, $\varepsilon_{xy} = 0$). Since the film is relying on a rigid substrate, this is generating an equibiaxial stress state in the film ($\sigma_{xx} = \sigma_{yy} = -\frac{E}{1-\upsilon}\varepsilon_0 = \sigma_0, \sigma_{xy} = 0$). This loading is applied in the initial state. An explicit scheme is used for the calculation.
In order to trigger delamination, a small defect is created. This defect consists of an adhesion-free area. The blister is nucleated in this area.

2.2. Results

This model has been implemented in the finite element code ABAQUS [7]. As it has been described in [4], this model has been able to demonstrate the mechanism of propagation of the telephone cord blister. The specificity of this propagation comes from the pinning of the buckle front in mode II. As a matter of fact, as crack front is expanding in a circular shape with an increasing radius, a configurational instability occurs on the outer edge of the buckle front followed by the development of a strong mode II area. As G_c is much higher in mode II, the propagation is stopped in this area, which forms the pinning point responsible for the inversion of the curvature of the buckle and finally the wavy shape since the front has to go around this point for further propagation of the blister.
By varying the parameters of the model in the simulation, it is possible to obtain a wide variety of telephone cords buckles. Besides, the buckles are also obtained experimentally, with a setup allowing the control of the different parameters (film thickness h, residual stress σ_0, interface toughness G_I^c). The samples are molybdenum coatings deposited by magnetron sputtering on 30 µm thick silicon wafers. The deposition of a thin silver layer onto the substrate allows varying the adhesion (depending on the silver layer thickness). Immediately following, a 120 nm thick layer of

partially oxidized molybdenum, obtained by adding 2 sccm of O_2, is deposited. Controlling the oxygen content in the film leads to a fine tuning of the residual stress.
For the simulations, the elasticity parameters for the films are E=329 GPa and υ=0.31. The mode I interfacial toughness G_I^c is a variable, whereas $\eta = 0.95$. The calculations are carried out for different values of the film thickness h and the residual stress σ_0. Comparison between calculations results and experimental observations are reported in Fig. 2. Depending on the parameters, different aspect ratios (i.e. ratios between the wavelength and the width of the telephone cord) can be observed in the simulations. These ratios are usually observed to be ranging between 0.9 and 1.4, both in the simulations and in the experiments. Two cases are reported in Fig. 2: one large aspect ratio and one short aspect ratio.

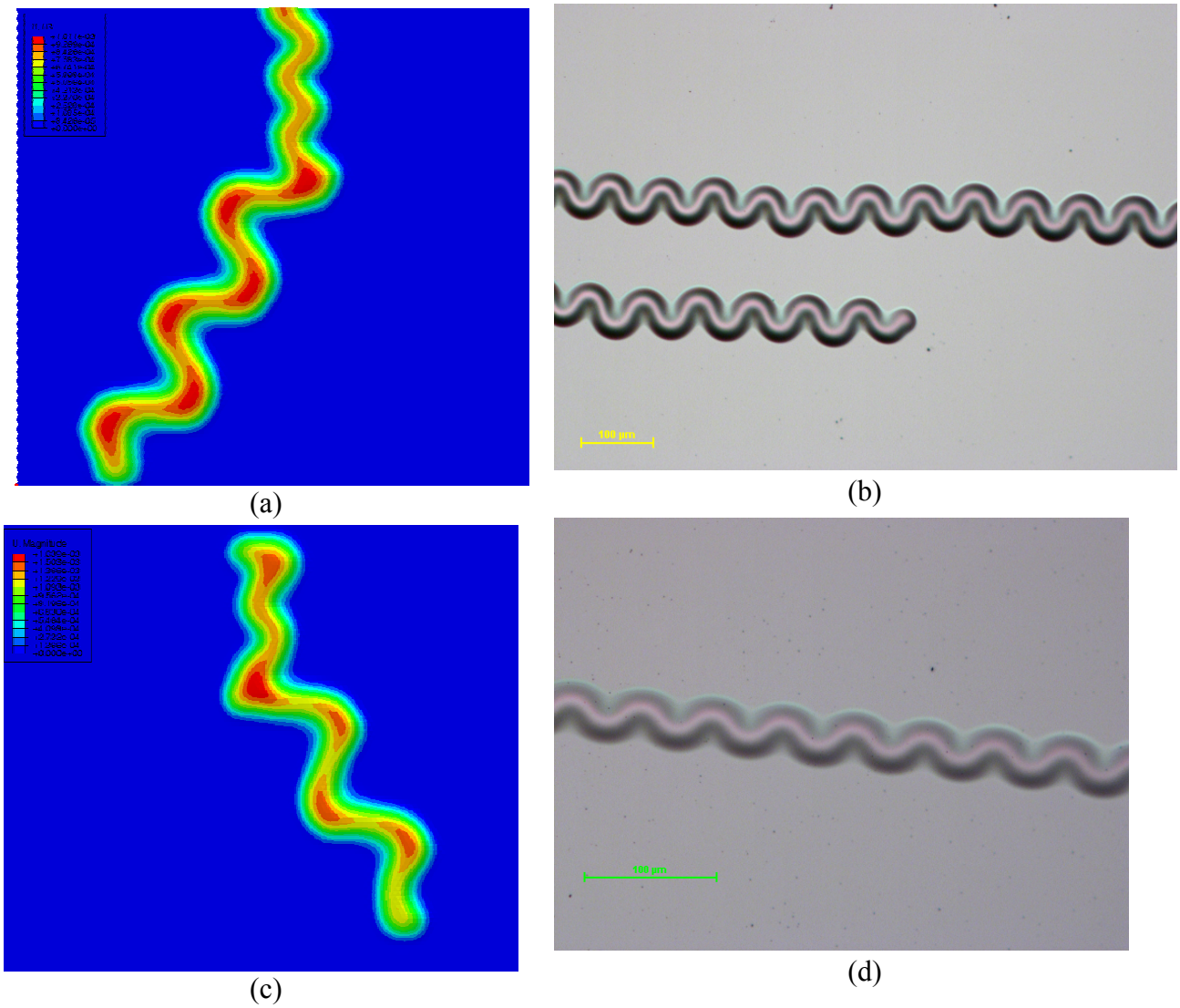

(a) (b) (c) (d)

Figure 2 : Comparison between telephone cords simulations (a and c) and experimental observation on Mo thin films deposited on silicon wafers (b and d). The two upper cords are showing short aspect ratios (i.e. wavelength over width), whereas the two bottom cords have large aspect ratio.
(a): $h = 225nm$, $G_I^c = 1.35J/m^2$, $\sigma_0 = 2.9GPa$, aspect ratio 1. (b): 600nm thick MoOx, potential -75V, aspect ratio 1. (c): $h = 300nm$, $G_I^c = 2.83J/m^2$, $\sigma_0 = 3GPa$, aspect ratio 1.36. (d) 600nm thick MoOx floating potential, aspect ratio 1.2.

3. Scaling of the wavelength

A relationship between the wavelength λ of the telephone cords and the other parameters have been found. In order to express this relationship, it is convenient to introduce a limit mixity angle, denoted $\psi_{\lim}$. It corresponds to the mode mixity above which the interface cannot be fully separated. This is the case when the interface toughness is exceeding the stored energy ($G^c \geq G_0$), so the limit case is $G^c = G_0$. In this case, using Eq. (2) yields:

$$\psi_{\lim} = \frac{1}{\eta}\tan^{-1}\sqrt{\frac{G_0}{G_I^c}-1} \tag{4}$$

It should be noted that $\psi_{\lim}$ is attained at the side of the blister as the film sags[4] and the mode mixity reaches pure mode II, $\psi = \pi/2$. However the interface is not fully separated at all angles above $\psi_{\lim}$.

By similar arguments that can be found in [8], it is possible to show that the following non dimensional relationship is verified among the telephone cords equilibria.

$$\frac{\sigma_0}{\overline{E}}\left(\frac{\lambda}{h}\right)^2 = f\left(\psi_{\lim}\right) \tag{5}$$

So whatever the shape of the telephone cord, the wavelength can be expressed as $\lambda = h\sqrt{\frac{\overline{E}}{\sigma_0}}f\left(\psi_{\lim}\right)$. The function f is determined numerically, giving the remarkable result exposed Fig. 3. It appears that λ is proportional to the quantity L defined as:

$$L = h\sqrt{\frac{\overline{E}}{\sigma_0}}\frac{1}{\sqrt{\tan\psi_{\lim}}} \tag{6}$$

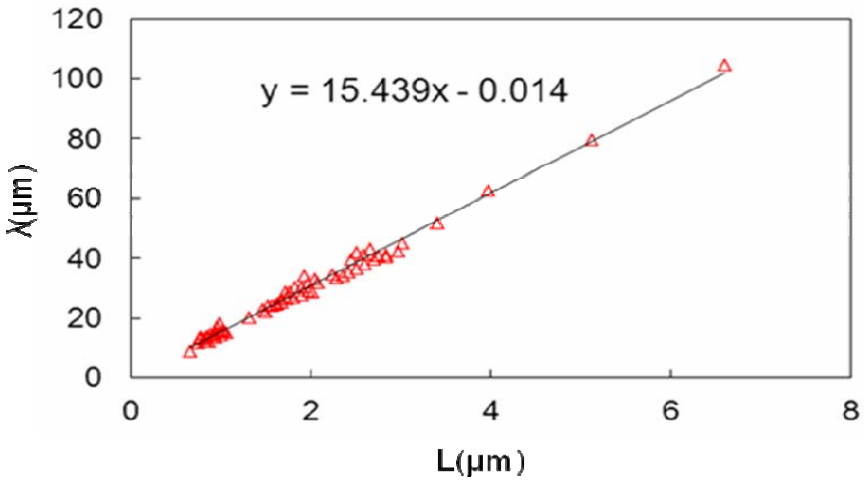

Figure 3 : Linear relationship between the telephone cord wavelength λ and the non dimensional quantity $L = h\sqrt{\frac{\overline{E}}{\sigma_0}}\frac{1}{\sqrt{\tan\psi_{\lim}}}$.

Once the relationship between λ and L is determined numerically, it is possible to find G_I^c from the experiments by measuring λ, assuming that σ_0, $\overline{E}$ and h are known, which is the case in our experiments.

4. Conclusions

We have a numerical model capable of describing the mechanisms of buckling driven delamination. A lot of patterns can be modeled, all observed in experiments. We have here emphasized the case of the telephone cords buckles, which is very often observed in experiments. The analysis of the telephone cords formation using the model has allowed for uncovering a very interesting relationship between the telephone cords wavelength, the stress level in the film, the thickness and the interface toughness. This result has an important practical application. When controlling the stress level and the film thickness during elaboration, the measurement of this wavelength can indirectly lead to a measurement of the interface toughness, even in very small films.

References

[1] G. Gilles and B. Rau, Thin Solid Films 120, 109, 1984.
[2] E. Spiecker, A.K. Schmid, A. M. Minor, U. Dahmen, S. Hollensteiner, and W. Jäger, Phys. Rev. Lett. 96, 086401, 2006.
[3] L. D. Landau and E. M. Lifshitz, Theory of Elasticity, Butterworth Heinemann, 1986.
[4] J-Y. Faou, G. Parry, S. Grachev and E. Barthel, Physical Review Letters, 108, 116102, 2012
[5] J.W. Hutchinson and Z. Suo, Adv. Appl. Mech. 29, 63, 1991.
[6] K. M. Liechti and Y. S. Chai, J. Appl. Mech. 59, 295, 1992.
[7] ABAQUS Manuals Collection, Dassauly Systèmes Simulia Corp., Providence, RI, USA (2010).
[8] G. Parry, A. Cimetière, C. Coupeau, J. Colin and J.Grilhé, Phys. Rev. E 74, 066601 (2006).

SDUDY OF THE CREEP DAMAGE PROPERTIES OF ASPHALT MIXTURE UNDER STATIC LOAD

Zhou Zhigang，Feng Lin，Yuan Xiuxiang，Xiong Hua

(Changsha University of Science & Technology, Key Laboratory of Road Structure & Material, Ministry of Transport of PRC, Hunan Changsha 410004)

Abstract: Asphalt concrete AC-13 and SMA-13 are designed to study their viscoelastic and damage properties under uniaxial pressure. The results indicate that the flow deformation of viscosity of asphalt mixture doesn't unlimitly increase with the loading time. As time goes by, the increment of flow deformation of viscosity decreases gradually and causes the flow deformation of viscosity to incline a stable value ultimately, which is so-called 'consolidation effect'. Moreover, under the same conditions, SMA has a stronger anti-deformation ability than AC. According to the flow characteristics of asphalt mixture, it is proposed a comparatively desirable and useful creep compliance model and visco-elastic-plastic creep model. Based on the static creep test results, the parameters concerned of the models are determined by using a constrained optimization method.

Key words: Asphalt mixture; Creep; Viscoelasticity; Damage; Model

Introduction

Asphalt mixture is thermoviscoelastic material with flow characteristics, the physical and mechanical properties is closely related to the effects of temperature and loading time. The load conditions often exhibit obvious nonlinear viscoelastic properties. The mechanical analysis generally focused on the linear viscoelastic category. In practical applications, using asphalt mixture is in non-compliance with infinitesimal deformation of the linear theory assumptions, when the deformation exceeds a certain range; linear superposition is no longer effective, so nonlinear viscoelastic theory of more universal. In recent years, road researchers have made some studies on the general nonlinear, elastic-plastic, creep, viscoelasticity of asphalt mixture [1]-[13]. As the two branch of the viscoelastic theory, liner viscoelastic theory is already quite mature, nonlinear viscoelastic theory also made a series of research results, but because of its difficulties in testing and mathematical theory, is still in development and perfected.

Damage mechanics as a subject branches is nearly 20 years. The classic nonlinear viscoelastic material constitutive theory does not consider initial defect and in actual engineering, creep failure of various loads and environmental conditions, may belong to the creep damage, more likely to be the initial defect evolution and the crack initiation and propagation. The study for the establishment of asphalt mixture viscoelastic damage constitutive model and its engineering applications is still small [14]-[25].

Therefore, based on the contrast test of AC-13 and SMA-13 two kinds of asphalt mixture road performance, focus on them under uniaxial pressure static creep damage behavior. Through the static creep test of different temperature, pressure, study the creep deformation of the characteristics and the law of variation. To reflect the creep deformation characteristics of the asphalt mixture creep deformation, establish nonlinear viscoelastic creep model and the creep damage model as the permanent deformation analysis and the high temperature stability of asphalt mixture and pavement which provides theoretical and experimental basis for evaluation.

1 Asphalt mixture design and road performance

1.1 Raw materials performance and mixture ratio design

Raw material of the test is modified asphalt, stone, mineral powder and fiber. The technical Specifications refer to references [27], which meet the technical specification for construction of highway asphalt pavement [27] requirements. Through the results of Marshall test, based on the method of technical specification for construction of highway asphalt pavements [27], AC-13 and SMA-13 asphalt mixture optimum asphalt content is 4.8%, 5.95%.

1.2 Pavement performance of asphalt mixture

The result of high temperature stability, low temperature crack resistance and water stability of two kinds of asphalt mixture according to the high-temperature rutting test, low-temperature bending test, freeze-thaw splitting test and immersion Marshall test are shown in Table 1. the results are shown in Table 2 when carried out fatigue tests under the control of stress.

Table 1 The test results of two kinds of asphalt mixture high temperature stability, low temperature crack resistance and water stability

Material type	High temperature stability	Low temperature crack resistance	Water stability	
	Dynamic stability（times/mm）	Bending limit strain(10-6)	Freeze-thaw cleavage strength (%)	Residual stability (%)
AC-13	4624	2478	87.1	90.9
Regulatory requirements [27]	≥1000	≥2000	≥75	≥80
SMA-13	5886	2645	91.0	92.1
Regulatory requirements [27]	≥2800	≥2500	≥80	≥85

Table 2 The test results of Asphalt mixture fatigue

Mixture	Temperature（℃）	Stress level σ0（MPa）	Fatigue Fracture Life Ncr（time）
AC-13	25	0.1	2986
		0.2	1836
		0.3	1248
		0.7	654
SMA-13	25	0.1	3628

		0.2	2156
		0.3	1452
		0.7	800

As the results shown, the high temperature stability and low temperature crack resistance and water stability of two kinds of mixture meet the technical standard value, and the performance of SMA-13 asphalt mixture is significantly better than ordinary asphalt mixture AC-13.

2 Creep test and analysis of static load of asphalt mixture

According to the standard test methods of bitumen and bituminous mixtures for highway engineering, the cylinder specimen for the static pressure method is controlled by the density of the Marshall test. The specimen size: diameter 100mm, height 100mm. Considering the performance of the high-temperature creep tests reflect asphalt mixture, select the test temperature is 25 ° C, 40 ° C, 60 ° C; applied three stress levels: 0.05, 0.1 and 0.2 MPa; loading time 5000s in order to facilitate the deformation full recovery. Put the sample in the environmental case for 4 hours before the test, and then after installing the servo-hydraulic materials testing machine HYD-25 applied preload 0.002Mpa, preload three minutes to prevent eccentric compression. Then loaded on specimen and the time data collected every 2 seconds. Static creep test results are shown in Figure 1 to Figure 3.

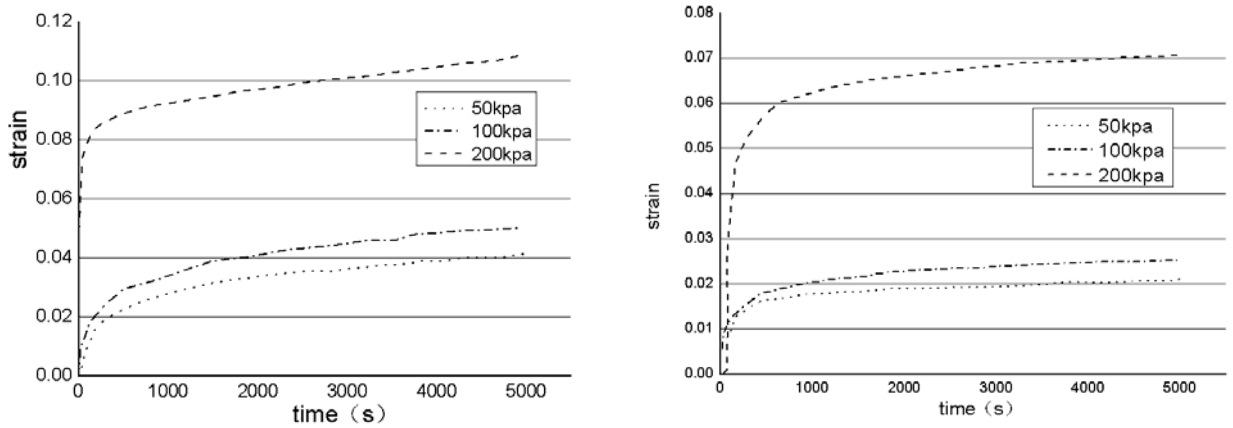

AC-13 SMA-13

Fig 1 The static creep curves at 25 ℃

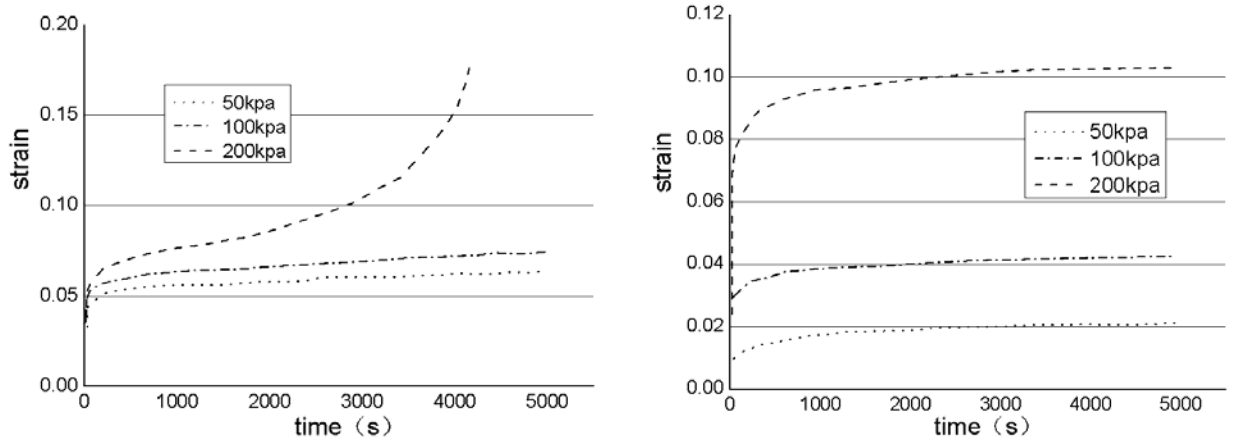

AC-13 SMA-13

Fig 2 The static creep curves at 40 ℃

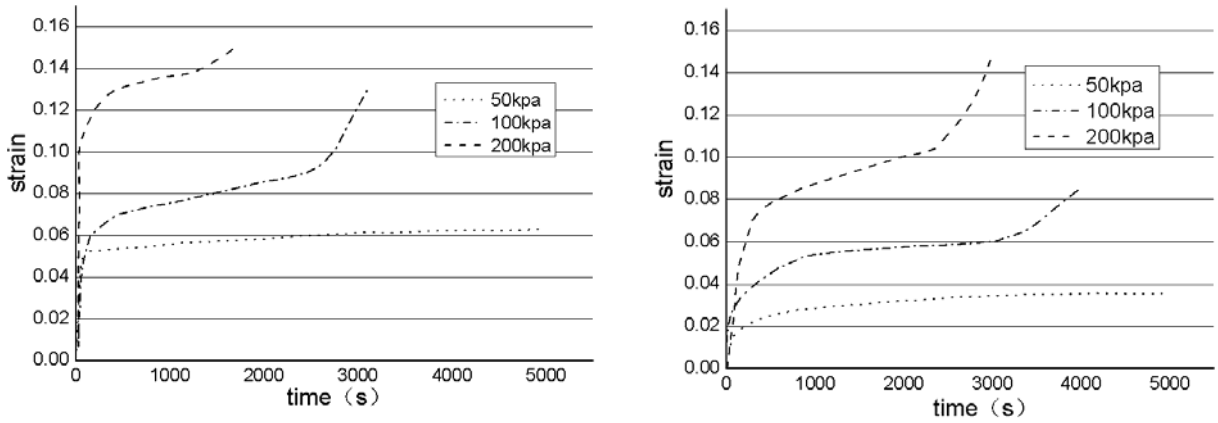

AC-13 SMA-13

Fig 3 The static creep curves at 60 ℃

Contrast Figures 1 to 3 static creep curves:

①Asphalt mixture at low stress levels, with the loading time, creep curve slope from large to small gradually stabilized, which shows that asphalt mixture increases the deformation resistance, resulting in further deformation is more difficult, the viscous flow of asphalt mixture with the load deformation does not affect the extension of time with load and increase infinitely, the increment decreases, finally tends to a stable value, is called the‘consolidation effect’.

②At the same temperature, high stress levels, the asphalt is too late to produce viscous and flow along with the mineral aggregate elastic deformation, with time goes on ,the start of viscous flow, VMA further reduce ,the mineral aggregate embedded squeeze more and more obvious, strain rate tend to stable, mineral aggregate porosity is further reduced, the viscous flow decreases with increasing time. But with time goes by, because of greater stress, mineral aggregate begin to slip, viscous flow of asphalt also been further extended. Therefore, the specimen is not immediately destroyed and to produce an accelerated deformation rate, which has a direct relationship with the load and temperature. Then specimen’s void ratio and clearance rate increased with increasing time and then continue to increase as the deformation, the specimen eventually completely destroyed.

③Under the same conditions, SMA has stronger deformation resistance than ordinary asphalt concrete(AC). Because the composition of SMA, coarse aggregate accounted for more than

70%,there is a lot of the mutual contact surface between coarse aggregate, and part of the stone mastic asphalt fill the gap among the coarse aggregate,. In high temperatures and loads, the coarse aggregate mutual good interlocking role, so that the mixture has better resistance to deformation. Under the condition of high temperature, stone mastic asphalt viscosity decrease which reduces the impact of the ability of resistance to deformation.

④The temperature of asphalt mixture has a great effect on deformation resistance ability, the higher the temperature, deformation resistance decreased more quickly, 2 times the deformation of high temperature of 60 ℃ to 40 ℃.Because the asphalt and asphalt mixture is a typical viscoelastic materials, these materials exhibit mechanical behavior of deformation is obviously dependent on temperature.

3 Representation to rheological model analysis of asphalt mixture viscoelastic properties

3.1 Representation to rheological model of asphalt mixture viscoelastic properties

In order to fully describe the rheological properties of the asphalt mixture under complex stress state, it is necessary to re-establish a better creep model. The first analysis of a plurality of Kelvin composite model units (as shown in Figure 4), the creep compliance is [29]

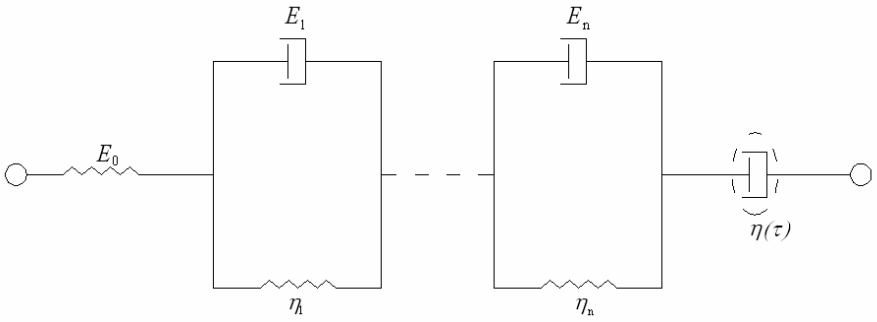

Fig 4 Several Kelvin unit composite models

$$J(t-t') = \frac{1}{E_0} + \sum_{i=1}^{n} q_i[1-e^{-\lambda_i(t-t')}] \qquad (1)$$

Where: $q_i = 1/E_i$, $\lambda_i = E_i/\eta_i$, t' is the starting moment loads. The model reflects the instantaneous elastic deformation, recoverable viscoelastic deformation and “consolidation effect", but does not reflect the unrecoverable viscous flow deformation. Therefore, the equation (1) is suitably supplemented as follows:

$$J(t-t') = \frac{1}{E_0} + \sum_{i=1}^{n} q_i[1-e^{-\lambda_i(t-t')}] + \sum_{i=1}^{m} p_i e^{-\gamma_i t'}[1-e^{-\gamma_i(t-t')}] \qquad (2)$$

Eq. (2) in the third term on the right side means that the viscous flow deformation, while it does not destroy the Eq. (1) with “consolidation effect" characteristic. Eq. (2) there is two summations. The more number of terms in summation, the more accurately express the stress and deformation characteristics of materials. But it involves too many parameters; the actual application is not conducive to the model. A simple model only considered here, each sum of only one, so the Eq. (2)

is simplified as:

$$J(t-t') = \frac{1}{E_0} + q[1-e^{-\lambda(t-t')}] + pe^{-\gamma t'}[1-e^{-\gamma(t-t')}] \quad (3)$$

There are five parameters in Eq (3), which can be determined by creep test curve.

3.2 Determination of asphalt mixture rheological model parameters

According to the creep test curves（Figure 1 to Figure 3）, the five parameters in the asphalt mixture rheological model of Eq. (3) can be constrainer optimization method (Levenberg-Marqurdt global optimization method) to determine. The model parameter values obtained at three different temperatures as shown in Table 3 below.

Table 3-1 Model parameters simulation results under 0.05MPa pressure

Types of asphalt mixture	Test temperature（℃）	E0（MPa）	q（10-4MPa）	λ（10-4s）	p（10-4s）	γ（10-4s）	Correlation coefficient R2
SMA-13	25	1620	6.86(1458)	8.44	8.46	8.12	0.9456
AC-13		1260	9.48	12.85	12.86	6.20	0.9686
SMA-13	40	1300(0.20)	11.20(893)	13.06	13.70	5.85	0.9861
AC-13		1010	13.52	19.80	19.53	5.76	0.9675
SMA-13	60	760(0.53)	14.80(676)	28.46	27.82	4.53	0.9770
AC-13		600	18.45	37.40	32.20	4.08	0.9687

Table 3-2 Model parameters simulation results under 0.1MPa pressure

Types of asphalt mixture	Test temperature（℃）	E0（MPa）	q（10-4MPa）	λ（10-4s）	p（10-4s）	γ（10-4s）	Correlation coefficient R2
SMA-13	25	1780	6.96	7.86	8.24	7.80	0.9566
AC-13		1360	8.60	12.84	12.45	5.68	0.9642
SMA-13	40	1380(0.22)	9.80	13.08	13.80	4.94	0.9712
AC-13		1120	10.67	16.50	18.46	5.12	0.9513
SMA-13	60	820(0.54)	13.90	26.45	26.48	4.40	0.9824
AC-13		680	16.88	35.81	31.80	3.96	0.9780

As we can see from table 3-3:

①Under the same condition, E0 of SMA-13 is bigger than AC-13's, and with the higher the temperature , the relative proportions of the tendency is to diminish. Under the conditions of 25℃,

40℃, 60℃ with 0.2MPa，E0 of SMA-13 are respectively higher by 29.23%, 25.71% 23.44% than AC-13's.

②In different stress but the same other conditions, the parameters variation of Model 5 is small.

4 Analysis to Nonlinear viscoelastic creep damage model for asphalt mixture

The static creep deformation reflected in Figure 1~Figure 3 usually can be divided into three stages: migration period, strain increases rapidly, but the strain rate gradually decreases with time increasing; stable period, strain steady growth, but the strain rate is essentially unchanged; Period of destruction, strain, and strain rate increases rapidly until failure increases with time. In the deformation of asphalt mixture, the modulus of the existence of a first increased and then decreased with the process, is also a first strengthened after the weakening of the process, the creep strain of asphalt mixture can be used as a nonlinear spring and a viscoplastic unit series, namely:

$$\varepsilon = \varepsilon_e + \varepsilon_{vp} \tag{4}$$

For the total strain where non-destructive condition can be expressed as:

$$\varepsilon = \frac{\sigma}{at^2 + bt + c} + [\frac{B}{A}(n+1)]^{\frac{1}{n+1}} \sigma^{\frac{m}{n+1}} t^{\frac{1}{n+1}} \tag{5}$$

In the one-dimensional problem, effective stress can be expressed as:

$$\sigma = \frac{\sigma_0}{1-\omega} (\sigma \geq 0) \tag{6}$$

Where: ω is damage factor.

Kachanov [31] uses the Norton formula obtained law of creep damage Kachanov:

$$\dot{\omega} = [\frac{\sigma_0}{C(1-\omega)}]^k \tag{7}$$

Where: *C, k* are material parameters.

Using the fully coupled method to consider the coupling effect of creep and damage of asphalt mixture, can be obtained by the constant stress damage of asphalt mixture under creep deformation equation.

$$\varepsilon = \frac{\sigma_0}{(1-\frac{t}{t_r})^{\frac{1}{K+1}}(at^2+bt+c)} + [\frac{B}{A}(n+1)]^{\frac{1}{n+1}} (1-\frac{t}{t_r})^{-\frac{m}{(K+1)(n+1)}} \sigma^{\frac{m}{n+1}} t^{\frac{1}{n+1}} \tag{8}$$

$$t_r = \frac{1}{K+1}(\frac{\sigma_0}{C})^{-K} \tag{9}$$

Where: $\frac{B}{A}(n+1) = O$, $\frac{1}{n+1} = P$, $\frac{m}{n+1} = Q$.

Fitting of Figure2,the AC-13 at 40℃,0.2MPa under load data manipulation the Levenberg-Marqurdt and the global optimization method, can obtain a creep damage model parameters, such as shown in Table 4.The comparison between creep test values calculated and creep damage model is shown in

Figure 5. The result shows, the creep damage model proposed (Eq. (9)) with high precision, can well simulate the creep damage of asphalt mixing material.

Table 4 Values of parameters in creep damage model of asphalt concrete AC-13

a(MPa)	b(MPa)	c(MPa)	t_r(s)	K	O	P	Q
3764.57	1511.66	258.66	4399.98	6.18	4.61	0.07	2.03

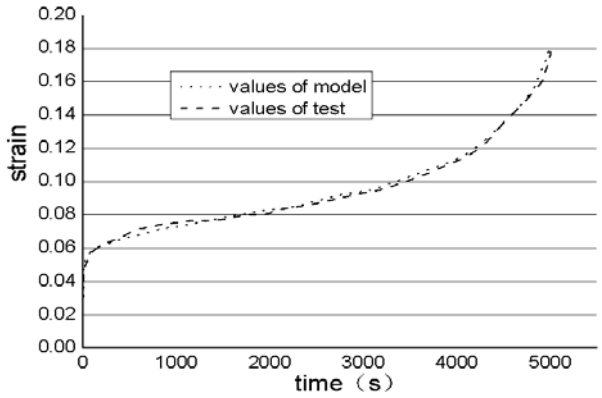

Figure 5　The AC-13 asphalt mixture creep test and creep damage model comparison under 40 ℃, 0.2MPa

5 Conclusions

（1）The results of test show that , the high temperature stability, water stability and low temperature crack resistance of the asphalt mixture of AC-13 and SMA-13 which this paper designed can meet the requirement of the construction technology, various performance indicators of SMA-13's are better than AC-13 .

（2）A　creep test is implemented on the two kinds of asphalt mixture under different temperatures and uniaxial pressure load ,and the result show that: ①The viscous flow deformation tends to a stable value after long period of loading at low stress levels which call this phenomenon as 'consolidation effect'. ②under the same level of temperature and high stress, the strain rate tends to be stable as time goes on, there will be accelerated distortion, and the rate of deformation has a direct bearing on the load and temperature. With the increase of deformation, the specimen will be destroyed completely. ③The temperature of asphalt mixture has a great effect on deformation resistance ability, the higher the temperature, the more quickly the deformation resistance decrease. ④SMA has a stronger ability to resist deformation than AC under the same conditions.

（3）A relatively ideal and practical creep model was established according to the rheological characteristics of asphalt mixture, which can express the asphalt mixture 'consolidation effect', and can reflect the permanent deformation of asphalt mixture after unloading, and also can represent rheological characteristics such as the instantaneous elastic deformation, And the effectiveness of this model was verify by comparing with the test results.

（4）A model about asphalt mixture viscoelasticity creep damage was established, and the asphalt mixture creep damage was analyzed and simulated via global coupled and the parameters of the

model were determined.

References

[1] C.L. Monishmith, G.A. Secor, Temperature induced stresses and deformations in asphalt concrete. Proceeding of the Association of Asphalt Paving Technologists，1965,(34)：248-285

[2] C.L.Monismith, R.L.Alexander, K.E.Secr. Rheologic behavior of asphalt concrete .Proceedings of the Association of Asphalt Paving Technologists，1966, (35)：400-450

[3] G.L.Dehlen. The effect of non-linear material on the behavior of pavements subjected to traffic loads.Ph.D.Dissertation. University of California，1969，(4):45-48

[4] Schapearyra. Models for damage growth and fracture in nonlinear viscoelastic particulate composite.Proc 9th U S Nat Congr Appl Mech.ASME，1982，237～245.

[5] Zhang Nanlu, Hou Xiaosong, Li Lihan.Study on deformation behaviour of domestic asphalt mixtures for heavy traffic road. Petroleum Processing and Petrochemicals, 1990，(2)：74-76.

[6] Zhang Xiaoning, Pan Dalin, Zhu Xiiing. One dimensional non-liner viscoelastic constitutive equation of bituminous mixture. Acta Mechanical Sinica, 1992, 24(6):81-83.

[7] Xu Shifa, Zhu Zhaohong. Prediction of rutting in asphalt pavement of high-class road. China Civil Engineering Journal, 1993，26(6)：28~36.

[8] M.G. Bouldin, R. Dongre,G.M.Rowe. Predicting thermal cracking of pavements from binder properties：theoretical basis and field validation . Proceeding of the Association of Asphalt Paving Echnologists，2000,(69)：455-488.

[9] A. R. Abbas., A. T. Papagiannakis.,E. A. Masad. Linear and nonlinear viscoelastic analysis of the microstructure of asphalt concretes. Journal of materials in civil engineering ，2002,(4)：506-510.

[10] Wang Houyu ,Zhu Keshan ,Yan Zhixin , Ling Tianqing .A practical creep compliance model of asphalt mixture and its application. Chinese Journal of Solid Mechanics, 2002, 23(2):232-236.

[11] Zhou Zhigang, FuBofeng. Applying the theory of viscoelasticity to evaluate thermal stability of asphalt mixture. Journal of Highway and Transportation Research and Development, 2005,22(11)：54-56.

[12] Zhang Xiaoning. Principle and application of asphalt and asphalt mixture viscoelasticity.Bei Jing,China Communications Press,2006：45-48.

[13] Qian Guoping, Zheng Jianlong, Zhou Zhigang, Tian Xiaoge. Incremental thermalviscoelastic constitutive relation of asphalt mixtures. Chinese Journal of Applied Mechanics, 2006,23(3)：338-343.

[14] Tang Xuesong, Jiang Chiping, Zheng Jianlong. Stress strain constitutive relation and damage evolution equation for elastic damaged materials. Journal of Transport Science and Engineering, 1999, 15(9):8-14.

[15] Tang Xuesong, Jiang Chiping, Zheng Jianlong. Damage mechanical analysis for fatigue failure process of bituminous mixtures.Chinese Journal of Applied Mechanics, 2000，17(4)：92-98.

[16] Zhou Zhigang.A research on the fatigue damage cracking in asphalt pavement under traffic load [A Dissertation Submitted for the Degree of Doctor of Philosophy].Chang Sha,Central South University, 2003.

[17] Guan Hongxin.A research on viscoelastic fatigue damage model of asphalt mixture[A Dissertation Submitted for the Degree of Doctor of Philosophy].Chang Sha,Central South University, 2005.

[18] Li Xiaojun, Zhang Xiaoning, Wu Jianmin.Internal structure discrimination of asphalt mix with X-ray computerized tomography under repetitive uniaxial loadings. Journal of Harbin Institute of Technology, 2005，37(9)：1228-1230.
[19] Ying Ronghua, Chen Xiao,Zhang Zhiyong.Damage model analysis of SBS modified asphalt mixture. Journal of Transport Science and Engineering, 2006，22（1）：42-47.
[20] Guan Hongxin, Zheng Jianlong, Zhang Qisen.Viscoelastic fatigue damage model of bituminous mixture.Mechanics in Enginerring, 2007，29（2）：50-53.
[21] Guan Hongxin, Zheng Jianlong.The Viscoelastic fatigue damage developing of asphalt pavement. Journal of Hunan University of Science & Technology(Natural Science Edition), 2008,23（3）：54-57.
[22] Wu Kuanghuai,Yang Guoliang,Zhang Xiaoning.A fatigue damage model of asphalt mixture considering stress relaxation. Journal of Shenzhen University Science and Engineering, 2008，25 (4):345-350.
[23] Yong Ye, Xinhua Yang, and Chuanyao Chen. Modified Schapery's model for asphalt sand. Journal of engineering mechanics, 2010,136（4）：448-453.
[24] Jaeseung Kim, Hyung Suk Le e, and Namho Kim. Determination of shear and bulk moduli of viscoelastic solids from the indirect tension creep test. Journal of engineering mechanics, 2010,136（9）：1067-1075.
[25] Chien-Wei Huang, Rashid K. Abu Al-Rub, Eyad A. Masad, and Dallas N. Little. Three-dimensional simulations of asphalt pavement permanent deformation using a nonlinear viscoelastic and viscoplastic model. Journal of materials in civil engineering, 2011,23（1）：56-68.
[26] Feng Lin.The research on the static and dynamic creep model of asphalt mixture under uniaxial pressure [A Dissertation Submitted for the Degree of Master].Chang Sha, Changsha University of Science & Technology 2008.
[27] Highway scientific research institute of Transport Department.The technical Specifications refer to references, Bei Jing, China Communications Press, 2004.
[28] Highway scientific research institute of Transport Department. The technical specification for construction of highway asphalt pavement, Bei Jing, China Communications Press, 2000.
[29] I.Suliciu. Some energitic properties of smooth solutions in rate-type viscoelasticity. International journal of nonlinear mechanics, 1984,19(6)：525-544.
[30] Mao Xueping,Liu Zongde,Yang Kun,An Jiangying,Pu Zelin.A study on creep damage behaviors of 30Cr1Mo1V. Proceedings of the CSEE, 2003,23 (7) :201~203.
[31] L.M.Kachanov. On the time to failure under creep condition. Izv Akad Nauk USSR Otd Tekhn Nauk,1958,(8)：26-31.

Analysis on Arithmetic and Application of Rigidity Distribution for Simply Supported Structure

Ling–bo WANG [1,*], Xin Kang [2], Pei–wen JIANG [3]

[1] Key Laboratory for Bridge and Tunnel of Shaanxi Province,Chang'an University, 710064, China
[2] Civil Engineering, Missouri University of Science and Technology, 65401, USA
[3] Basic Construction Project Quality Supervision Station , Shaanxi Provincial Transport Department,710075, China
* Corresponding author: nancywlb1984@163.com

Abstract Bridges under life–long service often suffered from invisible diseases which could cause the bridge stiffness decay (rigidity) and pose great threatening to human lives. This paper focused on studying the real stiffness distribution in a simple beam. The relationship between stiffness and deflection in a bridge segment has been established which is based on the material mechanics, numerical modeling, and reciprocal displacement theorem. The conversion of the deflection curve at mid span resulted from three axle vehicle and single unit load has been developed so that by measuring the deflection caused by low speed vehicle passing over the bridge, the real stiffness distribution of the bridge could then be obtained and the assessment of the bridge damage could be carried out. Compatible software was developed in accordance with the proposed stiffness calculation method. The software was found worked well in predicting the stiffness distribution and the test results supported that the proposed prediction method is applicable. The test results showed that the stiffness distribution in longitudinal direction varied significantly, which is due to the different degrees of damage. The analysis showed that it is not good to use the overall stiffness to evaluate the damage of the whole beam.

Key words: simple supported beam, longitudinal stiffness, invisible damage, damage assessment

1. Introduction

In recent decades, as the developing of our country, the number of highway bridges increased significantly, which in turn increased the number of bridges under life–long service. Due to the climate change, environment varies, temperature drops and wind and mechanical erodes, bridge aging becomes gradually a serious problem. Cyclic traffic loading could cause bridge elements to lose its mechanic properties and evolve into fatigue damage. Some bridges currently in service suffered from concrete crack, rebar erosion, and pre–stress relaxation, which could result in the overall stiffness decay and reduce its engineering performance. When the bridge stiffness decays, the bearing capacity would be greatly reduced which prohibited its service life and threatens the human lives[1]. Currently, there are two different ways to evaluate the bridge stiffness distribution, namely the direct way and indirect way. The indirect way is that to look over the outside of the bridge, for example, conduct a walk tour throughout the bridge, look for cracks, damage points and find out weak areas, which is very objective and cannot give a very accurate evaluation. The direct way is to carry out load test and measure the real stress strain response under different loadings. The load test can reflect the real stiffness of the bridge; however, it cannot indicate the damage degree of a bridge and show where the damage area is[2]. Therefore, to check the overall quality of a bridge, and evaluate the performance of the bridge and each segment has great significance in transportation engineering.

The assessment of the bridge stiffness and damage has been studied by many researchers. Zhao et al. [3] proposed to use bridge structure bilateral difference response model to analyze the integrity of the bridge in longitudinal and transverse directions, so that to study the stiffness in longitudinal directions. Yuan et al.[4] studied the erosion of Cl^- under freezing–thaw cycles. They have proposed a method to predict the expiration life of Cl^- under freezing–thaw cycles. Y.M. et al.[5] have proposed method to calculate the rotation when the top of the beam has cracks, and to predict the service life of the beam under such situation. Yao et al. [6] studied the bearing capacity of beams

that suffered from damage in longitudinal directions. Shan et al.[7] studied the detection of damage location and damage degree of highway bridges under the vibration of vehicles moving. Z. H. et al.[8] studied the bearing capacity of bridges under service by using the dual coding genetic algorithm. Yuan et al.[9] proposed a method to calibrate the stiffness matrix which based on the assumption that the finite element mass matrix and the stiffness matrix were asymmetry, and the mass matrix was given.

The previous studies have advanced the state of the art of the knowledge of stiffness decay damage of bridges; however, there are no effective methods in determining the damage inside the bridge (ex. The invisible concrete cracks, the rebar corrosion, and pre–stress relaxation). Those common diseases could result in heavily decay of the stiffness of the bridge elements, thus influencing the service life and posing failure the bridge. This paper focused on a simple beam structure to study the real stiffness distribution at each bridge segment. The stiffness prediction is based on the measured deflection from the mid span, and used proposed method to calculate the real stiffness distribution, so that the stiffness decay degree inside the bridge could be evaluated, the location of the damage area could be found, and the damage degree could be estimated.

2. The relationship between deflection influence line and stiffness in bridge segment

2.1 Finite element equation of single beam element

Simple bridge beam does not have axle force (the traffic loading cannot cause axle force). For a beam without axial force, the four degree of freedoms are: the vertical displacement at both sides of the beam, v_1 *and* v_2; and the rotation angles at both sides, θ_1 *and* θ_2 (Fig. 1).

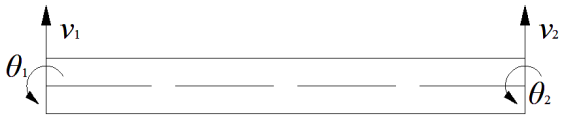

Figure 1.beam element without of axial force

According to finite element theory[9],the solution equation for a rigid beam element is:

$$K^e \cdot q^e = P^e \tag{1}$$

where: K^e is the stiffness matrix without axial force [10], K^e is the parameters in the matrix as shown in Eq.(2), E is the elastic modulus of the beam, I is the bending moment of inertia, and l is the length of the beam.

$$K^e = EI\begin{bmatrix} \frac{12}{l^3} & \frac{6}{l^2} & \frac{-12}{l^3} & \frac{6}{l^2} \\ \frac{6}{l^2} & \frac{4}{l} & \frac{-6}{l^2} & \frac{2}{l} \\ \frac{-12}{l^3} & \frac{-6}{l^2} & \frac{12}{l^3} & \frac{-6}{l^2} \\ \frac{6}{l^2} & \frac{2}{l} & \frac{-6}{l^2} & \frac{4}{l} \end{bmatrix} \tag{2}$$

q^e is the displacement matrix of the rigid beam at each nods, $q^e = \begin{bmatrix} v_1 & \theta_1 & v_2 & \theta_2 \end{bmatrix}^T$

P^e is the stress matrix, $P^e = \begin{bmatrix} P_1 & M_1 & P_2 & M_2 \end{bmatrix}^T$

2.2 Establish the relationship between deflection influence line and stiffness in bridge segment

Take simple beam as an example; divide the bridge into N segments in longitudinal direction. The deflection influence line could be achieved by superposition of the deflection resulted from each unit load that applied at the mid span of each bridge segment. From structure mechanics point of view, according to the reciprocal displacement theorem that in a rigidity beam, a force applied to point i, which caused the displacement at point j is equal to the same force that applied to j that caused the displacement that happened at i. Similarly, the unit force that applied in the mid－span of the N segment, where the resulted deflection is equal to the unit force that applied in the mid span where the resulted deflection happened at the N segment. Therefore, when the deflection influence line is known at mid span, the real stiffness is easily achieved. Because there are no element nods at the mid span, each bridge segment is subdivided into two sections, thus the overall segments become to 2N, and the computational model is shown in Fig. 2.

For the bridges under service, it is convenient to use moving vehicles passing through the bridge to collect the mid span deflection to predict the stiffness distribution (model 1),the conversion relationship between the moving vehicles and the single unit weight is shown in section 2. For the beams in laboratory and precast beams in field, the stiffness could be calculated based on the mid span loading condition (model 2).

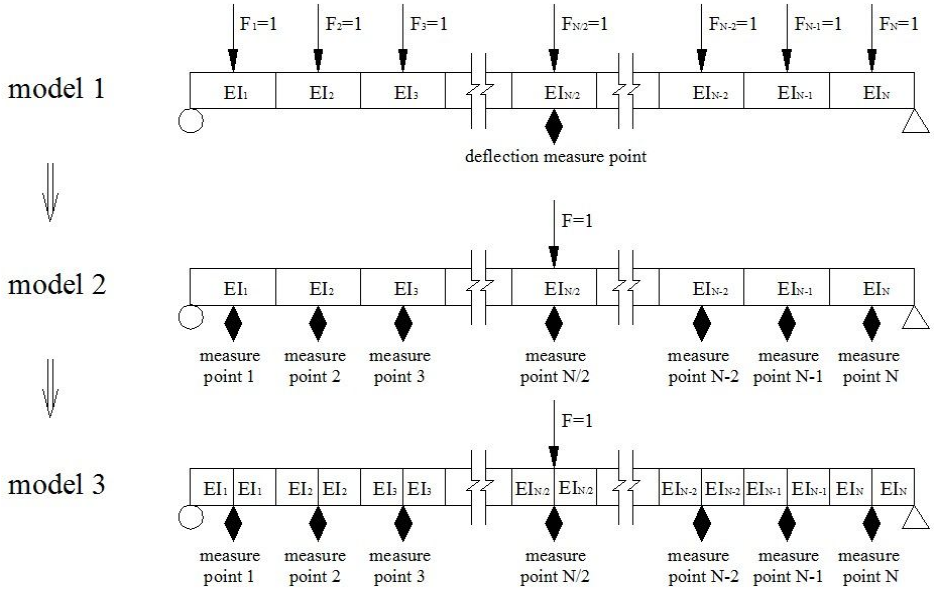

Figure 2.Computational Models

The relationship between load, deflection, and stiffness in model 3 are presented below:

$$
\begin{cases}
EI_1(\frac{12}{l_1^3}v_1+\frac{6}{l_1^2}\theta_1-\frac{12}{l_1^3}v_2+\frac{6}{l_1^2}\theta_2)=P_1 \\
EI_1(\frac{6}{l_1^2}v_1+\frac{4}{l_1}\theta_1-\frac{6}{l_1^2}v_2+\frac{2}{l_1}\theta_2)=M_1 \\
EI_i(-\frac{12}{l_i^3}v_i-\frac{6}{l_i^2}\theta_i+\frac{12}{l_i^3}v_{i+1}-\frac{6}{l_i^2}\theta_{i+1})+EI_{i+1}(\frac{12}{l_{i+1}^3}v_{i+1}+\frac{6}{l_{i+1}^2}\theta_{i+1}-\frac{12}{l_{i+1}^3}v_{i+2}+\frac{6}{l_{i+1}^2}\theta_{i+2})=P_{i+1} \\
EI_i(\frac{6}{l_i^2}v_i+\frac{2}{l_i}\theta_i-\frac{6}{l_i^2}v_{i+1}+\frac{4}{l_i}\theta_{i+1})+EI_{i+1}(\frac{6}{l_{i+1}^2}v_{i+1}+\frac{4}{l_{i+1}}\theta_{i+1}-\frac{6}{l_{i+1}^2}v_{i+2}+\frac{2}{l_{i+1}}\theta_{i+2})=M_{i+1} \\
EI_{2N}(-\frac{12}{l_{2N}^3}v_{2N}-\frac{6}{l_{2N}^2}\theta_{2N}+\frac{12}{l_{2N}^3}v_{2N+1}-\frac{6}{l_{2N}^2}\theta_{2N+1})=P_{2N+1} \\
EI_{2N}(\frac{6}{l_{2N}^2}v_{2N}+\frac{2}{l_{2N}}\theta_{2N}-\frac{6}{l_{2N}^2}v_{2N+1}+\frac{4}{l_{2N}}\theta_{2N+1})=M_{2N+1}
\end{cases}
\tag{3}
$$

where: EI_i is the stiffness of each bridge segment(i=1～2N), v_i is the vertical deflection at each

element nod(i=1～2N+1), θ_i is the rotation angle at each element nod(i=1～2N+1), P_i is the vertical load at each element nod(i=1～2N+1), M_i is the bending moment at each element nod(i=1～2N+1), l_i is the length of each element(i=1～2N), in summary, there are 12N+4 parameters.
In Eq. (3) there are some boundary conditions:

$$\left.\begin{aligned} & v_1 = v_{2N+1} = 0 \\ & P_{N+1} = 1 \\ & P_j = 0 \\ & M_i = 0 \\ & l_i = \frac{L}{2N} \\ & EI_i = EI_{i-1} \end{aligned}\right\} \tag{4}$$

where: L is the span of bridge($i = 1, 2, 3...2N$), P_j is the vertical load at each element nod when $j \neq N+1$ and $j \in i$.

2.3 Solution of the deflection stiffness equation

Maple is the most popular tool in Math and Engineering practice worldwide. Maple is also a good tool for symbolic operations, and very helpful in studying the mathematics models. In this research, therefore, Maple was adopted to solve the Eq. (3) and Eq. (4), and all the parameters (12N+4) in the equations. It is found that Maple could offer an analytic solution for those equations. The stiffness EI_i (i=1～2N)in each bridge section could be represented as follows:

$$EI_i = EI_{i+1} = \frac{L^3}{96N^4 \cdot B_i} \tag{5}$$

where: B_i is the i row in matrix $\mathbf{B}$ ($i = 1, 3, 5...2N-1$),the matrix $\mathbf{B}$ could be obtained by Eq. (6).

$$\mathbf{B} = \mathbf{A}^{-1} \cdot \mathbf{f} \tag{6}$$

In Eq. (6), $\mathbf{f}$ is the deflection at the mid span of each bridge segment, which is similar to the displacement matrix $v_i (i = 2, 4, 6...2N)$, however, matrix $\mathbf{A}$ is very complex, and the element in matrix $\mathbf{A}_{i,j}$ could be categorized into two groups according to their parity:
(1)When N is even:

$$\mathbf{A}_{i,j} = \begin{cases} (24j^2 - 24j + 8)(2N - 2i + 1) & (i > j \text{ and } j \le \frac{N}{2}) \\ (-24m^2 + 24m + 24mN - 12N - 8)(2N - 2i + 1) & (N > j > \frac{N}{2} \text{ and } i > j \text{ and } m = N - j + 1) \\ (-24m^2 + 24m + 24mN - 12N - 8)(2m - 1) - 6mN + 5N & (i = j > \frac{N}{2} \text{ and } m = N - i + 1) \\ \mathbf{A}_{N+1-i, N+1-j} & (i = j \le \frac{N}{2} \text{ or } j > \text{i}) \end{cases} \tag{7}$$

(2)When N is odd:

$$\mathbf{A}_{i,j}=\begin{cases}(24j^2-24j+8)(2N-2i+1) & (i>j \text{ and } j<\frac{N}{2})\\ (-24m^2+24m+24mN-12N-8)(2N-2i+1) & (N>j>\frac{N+1}{2} \text{ and } i>j \text{ and } m=N-j+1)\\ (-24m^2+24m+24mN-12N-8)(2m-1)-6mN+5N & (i=j>\frac{N+1}{2} \text{ and } m=N-i+1)\\ \mathbf{A}_{N+1-i,N+1-j} & (i=j<\frac{N}{2} \text{ or } j>\text{i})\\ 6N^2-3N & (i=N \text{ and } j=\frac{N+1}{2})\\ (6N^2-3N)(2N-2i+1) & (\frac{N+1}{2}<i<N \text{ and } j=\frac{N+1}{2})\\ 2N(3N^2-3N+1) & (i=j=\frac{N+1}{2})\\ \mathbf{A}_{N+1-i,j} & (i<\frac{N+1}{2} \text{ and } j=\frac{N+1}{2})\end{cases} \quad (8)$$

Based on Eq. (5) to Eq. (8), the stiffness EI_{i} (i=1～2N) of each bridge segment could be obtained from the known deflection values, hence the real stiffness of the whole bridge could be determined.

3. The Deflection Influence Line in Mid－Span

From section 1, it is known that when the mid span deflection influence line is given, the real stiffness distribution could be determined. However, it is hard to use a unit concentrated force to pass through the bridge, usually, the mobility of the load is similulated as a two axle or three axle vehicle passing over the bridge (speed at 5km/h), and measure the deflection at the mid span. The vehicle size and models are shown in Fig. 3. The conversion relationship of the resulted deflection curve in the mid span between common two axles or three axles vehicle and the unit load are achieved and showed in Eq. (9) to Eq. (12).

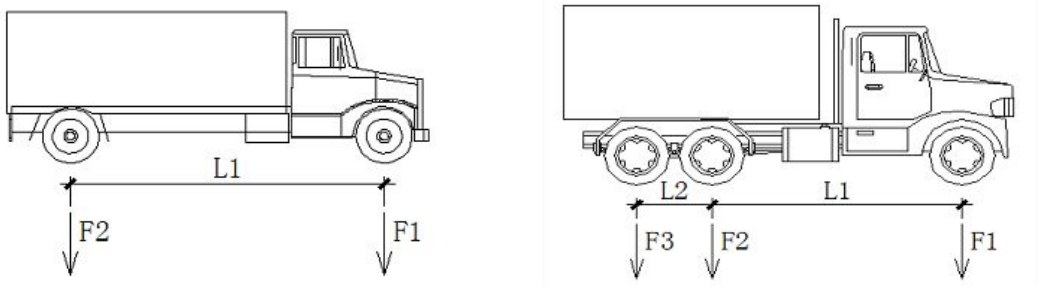

(a)Double axles vehicle (b)triple axles vehicle

Figure 3.Vehicle Models and Sizes

(1)Double axle vehicle

For the vehicle model in 3 (a), the single concentrated load F and vehicle length L after conversion are shown from Eq. (9) to Eq. (10).

$$F=F_1+F_2 \quad (9)$$

$$L=\frac{F_2L_1}{F_1+F_2} \quad (10)$$

(2)Triple axle vehicle

For the vehicle model in 3 (b), the single concentrated load F and vehicle length L after conversion are shown from Eq. (11) to Eq. (12).

$$F = F_1 + F_2 + F_3 \tag{11}$$

$$L = \frac{F_2 L_1 + F_3 (L_1 + L_2)}{F_1 + F_2 + F_3} \tag{12}$$

When the multiple axles loads have been converted to single concentrated unit load, use the linear relationship between concentrated load and unit load, the deflection at mid span caused by the vehicles could be converted into deflection influence line, so that to calculate the real stiffness distribution in the whole beam.

4. Case Study and the Development of the Compatible Software

When the deflection values D_1 to D_4 are known in model 1 or model 2 in Fig. 2, the real stiffness of a bridge in four segments at length of L could be obtained as presented below:
Based on Eq. (7) when N=4:

$$\mathbf{A} = \begin{bmatrix} 36 & 88 & 56 & 8 \\ 40 & 236 & 168 & 24 \\ 24 & 168 & 236 & 40 \\ 8 & 56 & 88 & 36 \end{bmatrix} \tag{13}$$

$$\mathbf{B} = \mathbf{A}^{-1} \cdot \mathbf{f} = 10^{-5} \begin{bmatrix} 4802D_1 - 1990D_2 + 308D_3 - 83D_4 \\ -949D_1 + 1263D_2 - 749D_3 + 201D_4 \\ 201D_1 - 749D_2 + 1263D_3 - 949D_4 \\ -83D_1 + 308D_2 - 1990D_3 + 4802D_4 \end{bmatrix} \tag{14}$$

From Eq. (5), the stiffness are shown below, for example, when i=1:

$$EI_1 = EI_2 = \frac{L^3}{96 \times 4^4 \cdot B_1} = \frac{L^3}{1180.1D_1 - 489.1D_2 + 75.7D_3 - 20.4D_4} \tag{15}$$

The Eq. (15) is the stiffness prediction equation that at the number of 4 bridge segments, the results were matched well with the published results in literature[10].

When N is large, the matrix $\mathbf{A}$ and $\mathbf{A}^{-1}$ are complex and hard to manipulate. In order to make it simple to carry out the stiffness prediction, windows based software was developed in accordance with the proposed equations and simple beam model. When the number of bridge segments, the length of the simple beam, and the influence line have been given, the real stiffness distribution could then be easily calculated, as shown in Fig. 4.

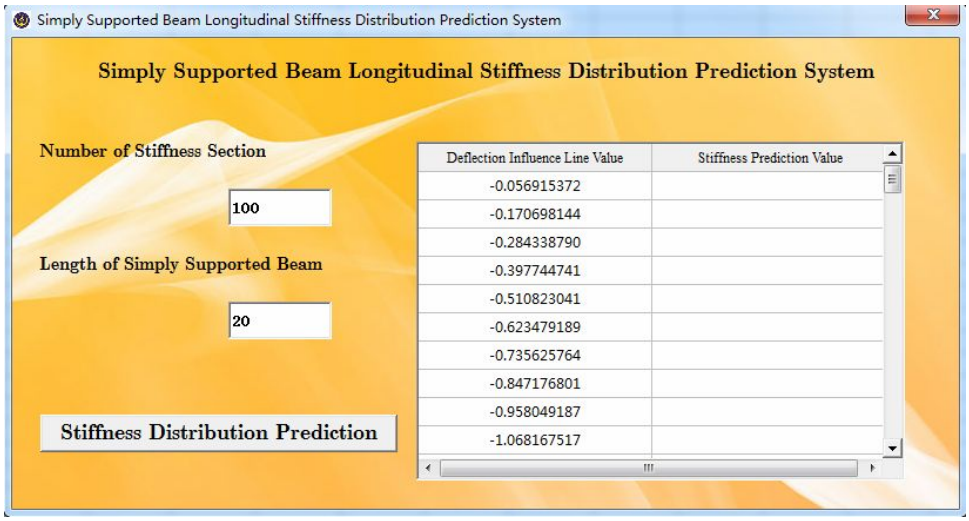

(a) Pretreatment

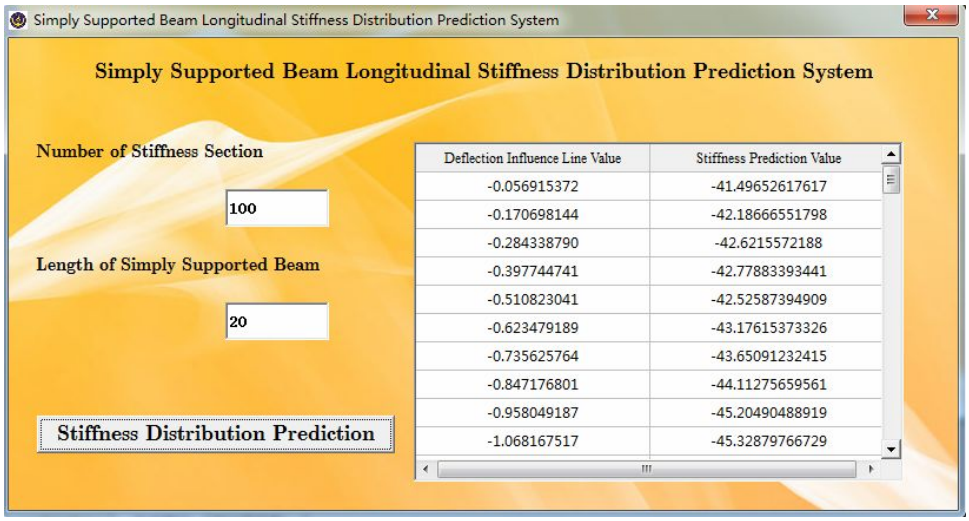

(b) post processing

Figure 4.the user interface

An old simple beam bridge, 20m in length, was adopted in the case study. The bridge was divided into 100 segments; the mid span deflection is tested by moving a two axle vehicle passing through the bridge at a low speed. The deflection influence line was calculated and shown in Fig. 5, and the stiffness distribution is shown in Fig. 6.

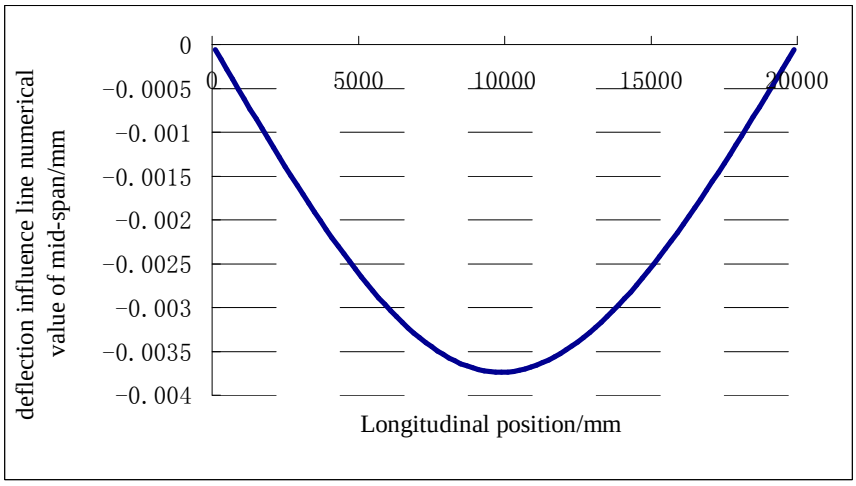

Figure 5.deflection influence line at the mid span

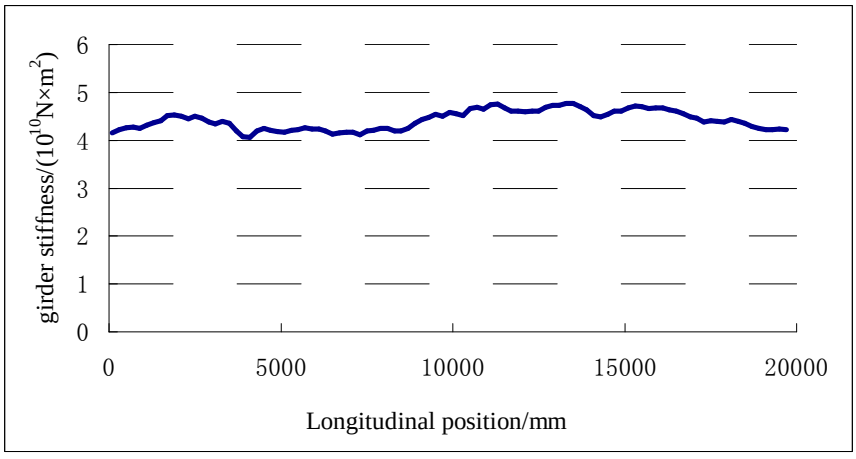

Figure 6.stiffness distribution curve

The calculation results showed that the proposed prediction methods worked pretty well, the bridge stiffness distribution could be calculated from the mid span deflection influence line. From the stiffness distribution curve the following features could be observed, the minimum stiffness is 4.09, maximum is 4.71, and the difference is 14%; significant stiffness decay happens at L/4, however, the stiffness decay was slightly at 3L/4. According to the stiffness distribution curve, the real working condition of the bridge could be evaluated, and thus helps the damage detection and bridge reinforcement work.

5. Conclusion

(1)This research is focused on the real stiffness distribution of simple beam structure in bridge engineering. The real stiffness distribution prediction equations were achieved based on the relationship between stiffness and deflection. The analysis results showed that there were analytical solutions for the stiffness distribution prediction equations, and it could be achieved from by measuring the deflection influence line in the mid span of each bridge segment.
(2)In order to simplify the measurement of the deflection in the field, the conversion method between two axles (three axles vehicles) and single unit concentrated loading condition was developed, so that to improve the measurement of the real deflection data in filed and help the prediction of the actual stiffness distribution.
(3)When calculating large numbers of bridge segments, for example, N is very large, the direct calculation work would be very heavy, therefore, a compatible software was developed to simplify the calculation work. A case study was carried out to check the workability of the software. The calculation results showed that the stiffness in each segments were slightly different. The developed software was found to actually predict the stiffness change of each segment in a bridge, estimate the decay area and decay degree, and help to improve the bridge and reinforcement work.

Acknowledgements

The thesis has got the support from the central university basic scientific research business special fund (Contract Number: CHD2011JC155).

Reference

[1] HE Dong–dong, SHAN Cheng–lin, Discussion on the evaluating method of bearing strength to existing bridge. Guangdong Highway Communications, 1 (2009) 36–39.
[2] Xu Wenping, Yang Zi, Study of Appraisal Standard for Carrying Capacity of Existing Concrete Bridges. Urban Roads Bridges & Flood Control, 10 (2010) 174–176.
[3] Zhao Hu, Pu Qian–hui, Shi Zhou, Study on Identification of Bridge Component Damage Based on Transverse Modal Difference. Railway Standard Design, 7 (2010) 77–81.
[4] YUAN Cheng–fang, NIU Di–tao1, GAI Qing–shan, SUN Cong–tao, Research on chloride penetration life prediction of reinforced concrete bridge with consideration of the damage caused by freeze–thaw cycles. Journal of Xi'an University of Architecture & Technology (Natural Science Edition), 42 (2010) 256–260.
[5] YANG Ming, HUANG Qiao, WANG De–jun, Equivalent bending stiffness of simply supported preflex beam bridge with variable cross–section. Journal of Harbin Institute of Technology, 17 (2010) 13–17.
[6] YAO Xiao–fei, XU Yue, FU Ying–chun, FENG Zhuo–de, Experimental study on ultimate bearing capacity of damaged concrete T–beam bridge systems. Journal of Guangxi University (Natural Science Edition), 34 (2009) 144–149.
[7] SHAN Deshan, LI Qiao, Damage Detection of Bridge Structures Based on Moving Vehicle Caused Vibration. Journal of Southwest Jiaotong University, 44 (2009) 60–65.
[8] Zhao Hongmei, Wang Huali, Jin Jun, Beam shaping with limited amplitude weight values for

satellite active phased array antenna. Engineering Sciences, 8 (2010) 62–66.
[9] Yuan Yongxin, Jiang Jiashang, A direct updating method for the stiffness matrix. Journal of Jiangsu University of Science and Technology (Natural Science Edition). 24 (2010) 193–196.
[10] WANG Ling–bo, HE Shuan–hai, ZHAO Yu, JIANG Pei–wen, A comprehensive evaluation method of damage in in–service girder bridges based on the finite element method. Journal of Guangxi University (Natural Science Edition), 36 (2011) 94–100.

Fatigue Safety Monitoring and Fatigue Life Evaluation for Existing Concrete Bridges

Chun-Sheng Wang[1,*], Mu-Sai Zhai[1], Yu-Jiao Wang[1]

[1] Key Laboratory for Bridge and Tunnel of Shaanxi Province,
College of Highways, Chang'an University, Xi'an, Shaanxi Province, China, 710064
* Corresponding author: wcs2000wcs@163.com

Abstract This paper firstly combines acoustic emission (AE) technique with monitoring of traffic loads and dynamic strain in healthy monitoring of concrete bridge structures. AE sensors and strain gauges were located on the web zone, deck plate and bottom plate of the box girder of Yaoxian Bridge, weigh-in-motion system (WIM system) was located in the pavement. Three monitoring systems clock was set synchronizedly, so they could monitor AE information, vehicles information and dynamic strain at the same time. Through the amplitude distribution and *b*-value analysis of AE signals, it finds the monitored bridge is in good service condition. The fatigue life of steel bars as well as strands in the box girders was calculated based on recorded data. Then, based on fatigue failure mechanism of concrete bridges, fatigue life evaluation approaches using S-N curves and fracture mechanics are presented. The evaluation results show that the fatigue life of the bridge is over 200 years, longer than the design service life. Finally, based on current study, it concludes that acoustic emission is an effective technique to evaluate existing concrete bridges.

Keywords existing concrete bridges, fatigue damage, fatigue load, acoustic emission, fatigue life

1. Introduction

Concrete bridges are widely used in China, accounting for 90 percent of all highway bridges. With the rapid development of highway transportation, traffic volume, vehicle weight and speed are constantly increasing, and overload phenomenon is difficult to eliminate, so fatigue damage caused by above problems cannot be neglected [1]. Current safety evaluation in China is mainly based on Code for Maintenance of Highway Bridges and Culverts and Specification for Inspection and Evaluation of Load-bearing Capacity of Highway Bridges. In order to evaluate the fatigue safety and remaining fatigue life of existing concrete bridges, emphasis should be laid on fatigue load monitoring, fatigue damage and fatigue life evaluation.

After World War II, some developed countries were beginning to research on fatigue fracture of concrete bridges, and corresponding design codes are gradually formed [2~5]. British scholar Tilly studied the reduction coefficient of fatigue strength of steel bars under different levels of corrosion [6], the result was used to evaluate durability and remaining life of concrete bridges; Schlafli and Bruhwiler of Swiss Federal Institute of Technology Lausanne have studied the basic method for fatigue evaluation of existing concrete bridges, and conducted fatigue safety evaluation of existing concrete bridges in Swiss [7].

With the development of non-destructive technique (NDT), real-time monitoring of the fatigue damage of existing bridges becomes possible [8]. Acoustic emission (AE) is a typical non-destructive technique, which can realize the effective monitoring of fatigue crack propagation in steel bridges. Nowadays some researches are trying to apply AE technique to

concrete bridges.

This paper combines weigh-in-motion (WIM) technique, dynamic strain monitoring technique with AE technique to evaluate a typical concrete bridge with box girders. Through fatigue life evaluation based on S-N curve and fracture mechanics, in combination with AE signals analysis, fatigue safety of the concrete bridge is comprehensively evaluated.

2. Fatigue Safety Monitoring Technique and Evaluation Methods

2.1 Weigh-in-motion Technique

HI-TRAC 100 is an advanced weighing system which includes two piezoelectric sensors, one induction coil sensor and a data acquisition unit (shown in Figure 1). When vehicles pass the bridge, the induction coil set in pavement picks up different responses, and the piezoelectric sensors send the information to the acquisition unit. Then the controlling unit can calculator the specific information of the passed vehicle and record the information. The system can record comprehensive information about the vehicles moving through, such as weight, speed, direction, axle number and so on.

Figure 1. TDC WIM system

2.2 Acoustic Emission Technique

AE signal is a transient elastic stress wave generated by sudden changes in materials like deformation, cracking and transformation [8~9]. Figure 2 shows the model of AE signal production and spreading, when structure or material is in the condition of tension, compression or impact, the internal crack tip of structure will lead to a transient release of stress that can produce stress waves. When the crack propagates, the stress waves spread in all directions. Then these stress waves could be picked up by AE sensors attached on the surface of structure.

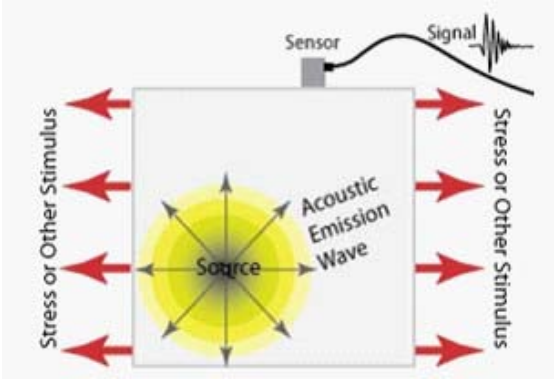

Figure 2. Model of AE production and spreading

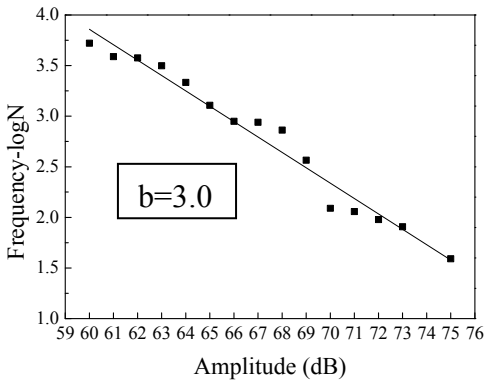

Figure 3. Example of calculation of *b*-value

Researchers began to apply AE technique to bridges monitoring in 1970s. Colombo developed *b*-value analysis method in 2003, and successfully evaluated the damage degree of reinforced concrete beam [9]. The analysis result shows that changing trend of maximum *b*-value reflects microcracks propagation; while minimum *b*-value reflects macrocracks development, which shows a good correlation with cracking process of reinforced concrete beam. Figure 3 shows *b*-value calculation method, while *N* stands for counts of different amplitude. Least-square fitting method is adopted to draw the line, the slope of the fitted line is -0.152, *b*-value is 3.04 according to the relationship between them.

2.3 Fatigue life evaluation method based on S-N curve and Miner law

According to Miner linear fatigue accumulative damage, fatigue damage can be calculated by Equation (1):

$$D = \sum_i D_i = \sum_i \frac{n_i}{N_i} \tag{1}$$

In each stress range level $\Delta\sigma_i$, the fatigue damage D_i was linearly proportional to n_i, where n_i is the number of cycles at σ_i, N_i stands for cycles under stress range level $\Delta\sigma_i$ and D is the total damage when fatigue failure occurs. Fatigue life Y can be calculated by Equation (2):

$$Y = \frac{D_{\mathrm{cr}}}{D_T} \times T \tag{2}$$

While D_{cr} stands for critical fatigue damage, T stands for monitoring time and D_T is fatigue damage during time T. Previous experiments show that, under random loading, D_{cr} is around 1, so the value of D_{cr} is taken as 1.

2.4 Fatigue life evaluation method based on fracture mechanics

In order to simulate the process of crack initiation, crack propagation to destruction in steel bars, assume the initial crack is semi-circle and the depth is a_0, so the crack propagation can be calculated by Paris formula (Equation 3).

$$\frac{\mathrm{d}a}{\mathrm{d}N} = C \cdot \Delta K^{\mathrm{m}} \tag{3}$$

While C and m are material constants; $\Delta K = Y \cdot \Delta\sigma \cdot \sqrt{\pi \cdot a}$, $\Delta\sigma$ is stress range and Y is a modified coefficient.

According to K criterion in linear elastic fracture mechanics, if $K_I \geq K_{IC}$, the steel bar tends to brittle fracture, the critical crack depth is a_{cr}; if the steel bar tends to yield dstruction along with the crack propagation, the critical crack depth is a_y. Thus the critical crack depth of fatigue failure of steel bar is a_{fr}=min (a_{cr}, a_y). Fatigue life can be calculated by Equation (4):

$$N = \int_{a_0}^{a_{fr}} dN = \int_{a_0}^{a_{fr}} \frac{1}{C \cdot \Delta K^m} da = \int_{a_0}^{a_{fr}} \frac{1}{C \cdot Y^m \cdot \Delta\sigma^m \cdot \pi^{m/2} \cdot a^{m/2}} da \tag{4}$$

3. Fatigue stress and traffic load monitoring

Accumulating fatigue damage caused by passing vehicles is needed for fatigue safety evaluation

of existing concrete bridges, but there is no fatigue vehicle spectrum in China, so it is important to acquire actual traffic load or fatigue stress.

Yaoxian Bridge (shown in Figure 4) is a key bridge of provincial road 305, from Tongchuan to Jiaopin in Shaanxi, China. It is an 8-span prestressed box girder bridge with span length of 30m. Since the bridge is near a coal mine, many coal-trucks pass the bridge everyday, so the bridge is under great fatigue stress. In this paper, the writer has conducted dynamic strain monitoring for 21 days. Figure 5 shows a typical dynamic strain curve.

Figure 4. Yaoxian Bridge

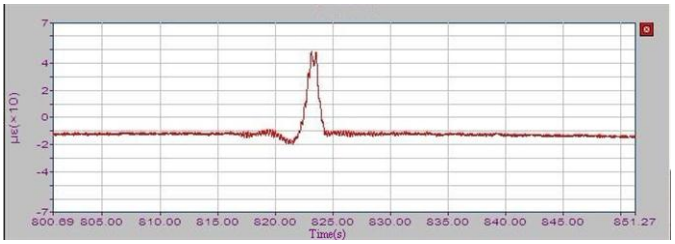

Figure 5. Example of dynamic strain curve

Through the analysis of recorded vehicles information, vehicle make-ups of every day are similar. Figure 6 is the vehicle load information of 4th September, 2011: passage time of full trucks is mainly from 9:00 to 13:00 and from 14:00 to 19:00; among all vehicles, weights of 1,12 and 33 tons are most, and there are more vehicles passing bridge in daylight than night. Full trucks of Tongchuan direction are mainly 30 tons to 40 tons, the maximum recorded weight is 55 tons; vehicle loads of Jiaoping direction are mainly around 1 tons and 12 tons.

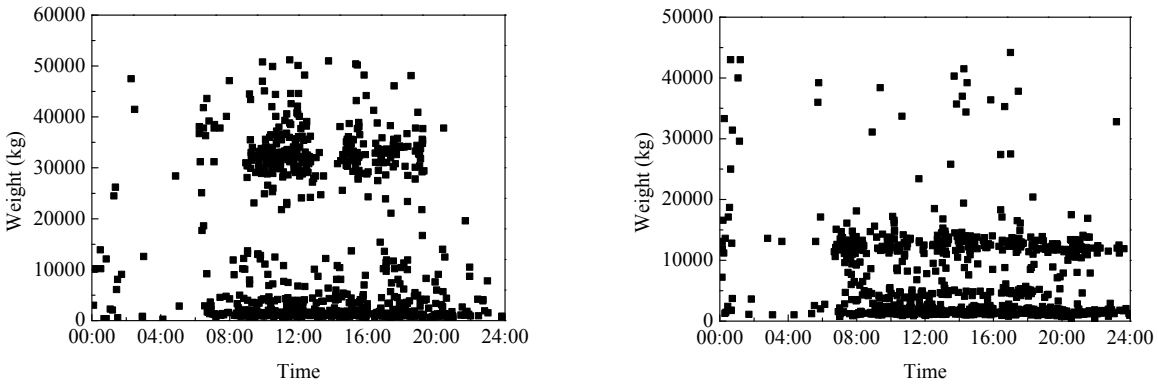

(a) Tongchuan direction (lane 1) (b) Jiaoping direction (lane 2)

Figure 6. Vehicle load information during a day

Figure 7 shows the vehicle load distribution of Yaoxian Bridge. Total monitoring time is 35 days, the total number of passing vehicles is 57802, and the average traffic volume is 1650 during a day. Cars accounts for 46.7 percent, trucks with 2 axles accounts for 19.8 percent, trucks with 3 axles accounts for 25.2 percent, other kinds are 8.3 percent. Maximum vehicle load is lighter than design loads, and no overloaded vehicle is recorded. Total weight and axle weight of all vehicles are lighter than fatigue vehicles in Europe Code, and there are less than 500 trucks in

every lane during a day, so during design service life fatigue damage caused by recorded vehicle loads is little.

4. AE monitoring and signals analysis

4.1 Site monitoring information

The AE monitoring was started in 23rd August, 2011, ended in 7th September, 2011, and the NO.2 and NO.3 box girder of the first span was chosen to be the monitoring region. In order to identify the different signal characteristics of different locations, sensor locations are on the every part of the box girder, as shown in the Figure 8: NO.7 and NO.11 sensors are on the deck plates; NO.2, 5, 9 and NO.13 sensors are on the bottom plates; other 10 sensors are on the webs.

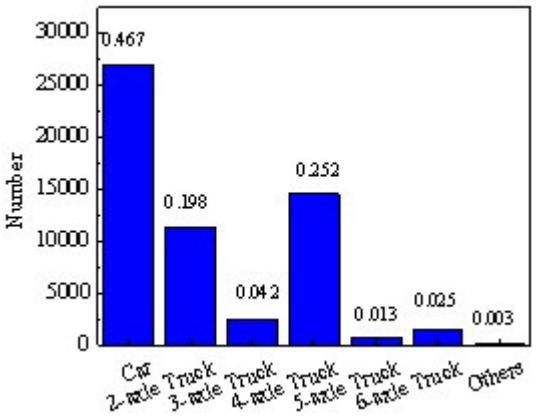

Figure 7. Vehicle load distribution

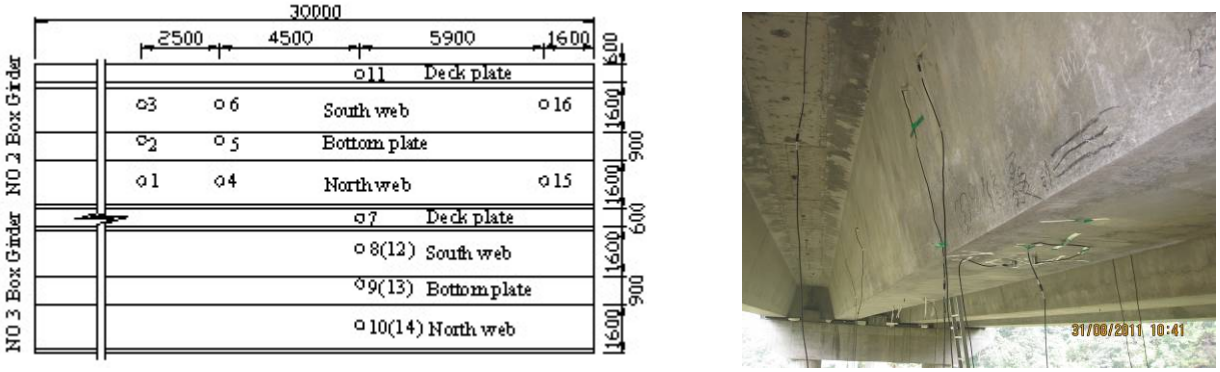

Figure 8. AE sensor locations (mm)

The acoustic emission equipment used in the bridge monitoring was made by Physical Acoustic Corporation, including an independent AE system: Micro-II, R3I and R15a sensors. R15a with 150 kHz-resonant-frequency was located at positions of NO.12, 13, 14, R3I with 30 kHz-resonant-frequency sensors are for the other monitoring positions. Based on the level of noise in the monitoring site, the threshold level was set at 50 dB.

4.2 Characteristics analysis of AE data

NO.2, 4, 7 sensors have recorded the most hits in 3 different locations respectively, so signals acquired by this 3 sensors were analyzed to evaluate the box girders. Figure 9 shows the analysis results of data acquired by NO.2 sensor on bottom plate: (a) is the amplitude distribution of 16 day's data, there are more than 70000 signals at 54dB, amplitudes of almost all signals are lower than 70dB; (b) is the *b*-value changing trend, the minimum *b*-value is 1.94, and the maximum is 3.90.

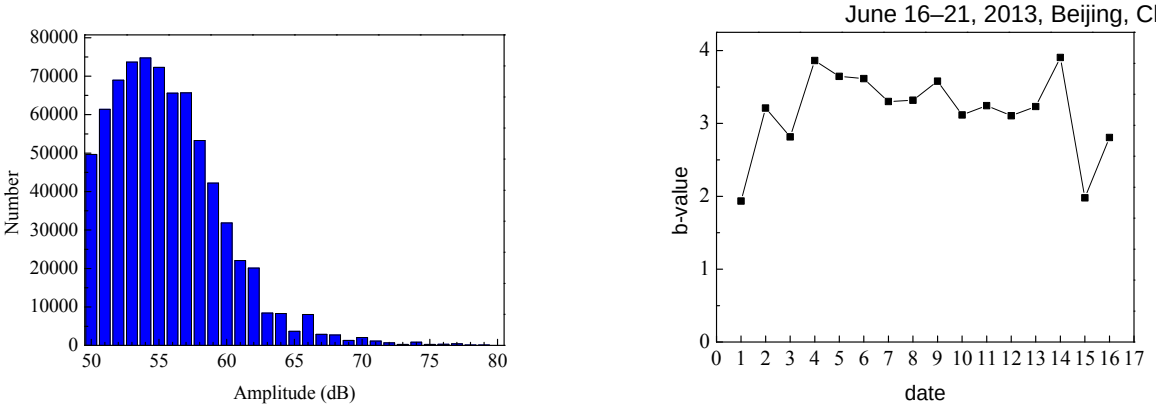

(a) Amplitude distribution (b) Changing trend of *b*-value

Figure 9. Data analysis of NO.2 sensor (23rd August, 2011 to 7th September, 2011)

Figure 10 shows the analysis results of data acquired by NO.4 sensor on web: (a) is the amplitude distribution of 16 day's data, there are more than 6000 signals at 57dB, amplitudes of all signals are lower than 75dB; (b) is the *b*-value changing trend, the minimum *b*-value is 1.83, and others are higher than 2.00.

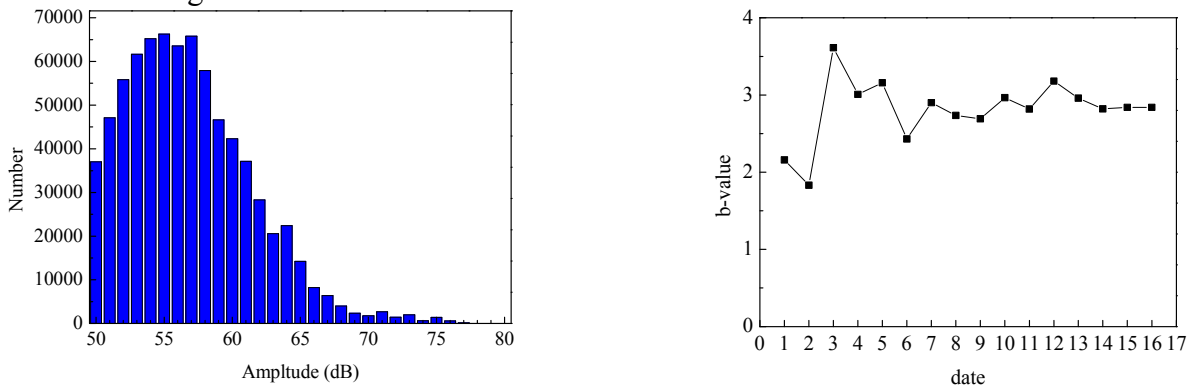

(a) Amplitude distribution (b) Changing trend of *b*-value

Figure 10. Data analysis of NO.4 sensor (23rd August, 2011 to 7th September, 2011)

Figure 11 shows the analysis results of data acquired by NO.7 sensor on deck plate, which acquired the most signals in all sensors: (a) is the amplitude distribution of 16 day's data, there are more than 14000 signals at 57dB, amplitudes of all signals are lower than 75dB; (b) is the *b*-value changing trend, the minimum *b*-value is 1.72 occurred in the 13rd day (4th September, 2011).

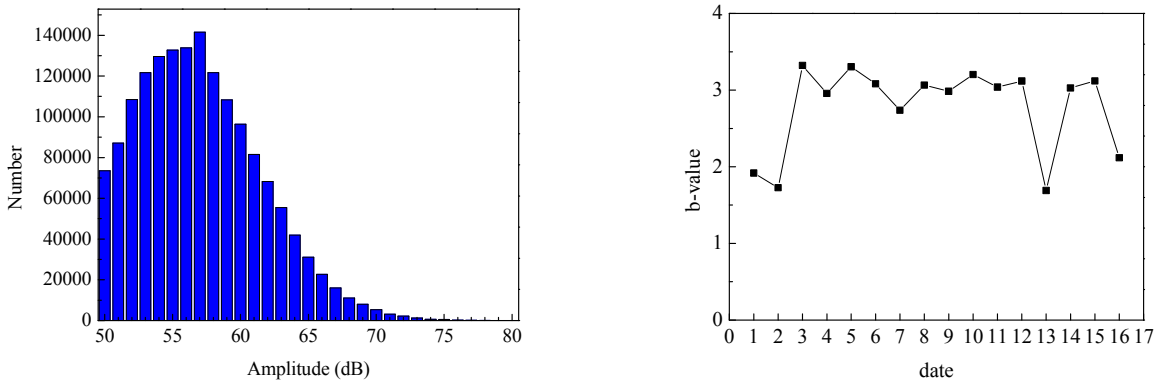

(a) Amplitude distribution (b) Changing trend of *b*-value

Figure 11. Data analysis of NO.7 sensor (23rd August, 2011 to 7th September, 2011)

From the amplitude distribution of 3 typical positions, it is easy to find sensor on deck plate acquired the most signals, and sensor on bottom plate acquired the least. Amplitudes of almost

all signals are lower than 70dB, and there are most signals at 57dB, so the noise level in site is around 57dB.

According to research by Colombo, changing trend of maximum *b*-value reflects the propagation of microcracks, and changing trend of minimum *b*-value reflects the propagation of macrocracks; when *b*-value is higher than 1.7, the structure is in period of microcracks propagation[9]. Figure 9 to Figure 11 shows the *b*-value changing trend of 3 locations, all *b*-values are higher than 1.7, and no macrocrack has been detected, and so Yaoxian Bridge is in the period of microcracks, it is in good working conditions.

5. Fatigue life evaluation

5.1 Fatigue life evaluation based on S-N curve

From all S-N curves of different fatigue details in research documents and specifications in different countries, S-N curve in European Institute of steel construction (ECCS) is adopted to evaluate the fatigue life of steel bars and strands in concrete bridges.

In this specification, fatigue strength of 2 million cycles is 80.0MPa, fatigue strength of constant stress range is 59.0MPa, and threshold of fatigue strength is 32.4MPa. The slope of curves changes from -3 to -5 when cycles are more than 5 million. Since most full trucks are on lane 1, 4 typical stain monitoring positions (shown in Figure 12) below lane 1 are chosen to evaluate the fatigue life of steel bars and strands in box girders of Yaoxian Bridge. The evaluation result is shown in Table 1: fatigue life of steel bars in deck plate (measure point BST2) is 3756 years; fatigue life of strands in bottom plate is longer than 1000 years. Therefore, it can be concluded that under the present fatigue load level, fatigue failure of Yaoxian Bridge will not occur during design service life.

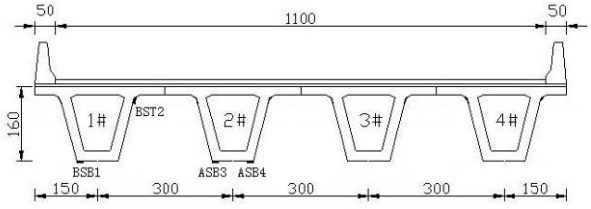

Figure 12. Strain measure points of Yaoxian Bridge.

Table 1. Fatigue life based on S-N curve

Measure point	*D* (10^{-6})	*Y* (year)
BSB1	12.16	1239
BST2	4.01	3756
ASB3	0.45	infinite
ASB4	40.31	1427

5.2 Fatigue life evaluation based on fracture mechanics

According to appearance detection, no crack was found on Yaoxian Bridge, so initial crack was assumed to evaluate the fatigue life. Fracture toughness of steel bar used in concrete bridge is $K_{IC} = 50\text{MPa}\cdot\sqrt{\text{m}}$. Fracture constants are $D = 2\times10^{-13}$ and $m = 4$ according to previous researches, threshold of crack propagation of steel bar is $\Delta K_{th} = 2.0\text{MPa}\cdot\sqrt{\text{m}}$. Fatigue life evaluation result based on fracture mechanics is shown in Table 2, under the present fatigue load level, fatigue failure of Yaoxian Bridge will not occur during design service life.

The above fatigue life evaluations are based on the present vehicle loads, with the development of transportation and other disadvantage influences, the fatigue life of concrete bridge will be far shorter.

Table 2. Fatigue life based on fracture mechanics

Measure point	Initial crack width a_0 (mm)	Maximum stress σ_{max} (MPa)	Critical crack length a_{fr} **Error! Reference source not found.**(mm)	Remaining life Y (year)
BSB1	0.1	185	7.57	245
BST2	0.1	67	10.12	1198
ASB3	0.5	47	10.49	5124
ASB4	0.1	97	9.54	578

6. Conclusions

This paper combines WIM, fatigue stress monitoring, AE with fatigue life evaluation techniques to give a comprehensively fatigue safety monitoring and fatigue life evaluation of a concrete bridge, the followings can be concluded:

(1) Using WIM and dynamic strain monitoring techniques, traffic loads monitoring for 35 days and fatigue stress monitoring for 21 days were conducted, influence of present traffic loads to concrete bridges fatigue life was studied.

(2) Fatigue safety and fatigue life evaluation model based on S-N curve and fracture mechanics is given.

(3) Through analysis of AE signals, it is found that noise level in site is around 57 dB; signals of deck is far more than of web and bottom plate of box girders, it indicates that the deck may have more fatigue damage of concrete bridges. From *b*-value analysis, Yaoxian Bridge is in period of microcracks propagation, no macrocracks was found.

(4) Fatigue life of Yaoxian Bridge based on S-N curve is 1239 years, fatigue life based on fracture mechanics is about 245 years, fatigue failure will not occur during design service life.

(5) Combination of different monitoring techniques can give comprehensive evaluation of concrete bridges.

Acknowledgements

The work described in this paper was partially supported by the Foundation for the Author of National Excellent Doctoral Dissertation of the P.R. China (Grant No. 2007B49), the Special Fund for Basic Scientific Research of Central Colleges of the P.R. China, Chang’an University (No.CHD2012ZD008), the Shaanxi Province Transportation Technology Research Projects (Grant No.07-04k) and the China West Transportation Development Research Projects (Grant No. 200831849404, 20113185191410).

References

[1] C.S. Wang, G. Li, X.H. Dong, L. Hao and J.H. Wang. Fatigue life evaluation of existing highway reinforced concrete bridges. Frangopol D M, Sause R and Kusko C S. The 5th International Conference on Bridge Maintenance, Safety and Management. London: CRC Press, Taylor & Francis Group, 2010:685-690.

[2] RILEM Committee 36-RDL. Long term random dynamic loading of concrete structures. Materials and Structures, 1984, 17(9): 1-28.
[3] A. Herwig. Reinforced Concrete Bridges under Increased Railway Traffic Loads—Fatigue Behavior and Safety Measures. Lausanne: Swiss Federal Institute of Technology Lausanne (EPFL), 2008.
[4] Q.F. Zha and J.Z. Xiao. An Overview of Domestic and Foreign Researches of Fatigue Behavior of Reinforced Concrete Beams, World Bridge.2004 (3):30-34.
[5] ECCS: Recommendations for the Fatigue Design of Steel Structures. Brussels: European Convention for Constructional Steelwork, 1985.
[6] G.P. Tilly. Durability of concrete bridges. Journal of Institute of Highways and Transportation, 1988, 35(2): 10-19.
[7] M. Schlafli and E. Bruhwiler. Fatigue of existing reinforced concrete bridge deck slabs. Engineering Structures, 1998, 20(11): 991-998.
[8] A. NAIR and C.S. CAI . Acoustic emission monitoring of bridges: Review and case studies. Engineering Structures, 2010, 32 (6):1704-1714.
[9] S. Colombo, G. Main and M.C. Forde. Assessing damage of reinforced concrete beam using "*b*-value" analysis of acoustic emission signals. Journal of Materials in Civil Engneering, 2003, 15(3): 280-286.

Application Research of Elastic-plastic Fracture Toughness Index CTOD in the Design of Railway Steel Bridge

Yuling Zhang[1,*], Jiyan Pan[1], Jiluan Pan[2]

[1]Railway Engineering Research Institute, CARS, Beijing 100081, China

[2]Department of Mechnical Engineering, Tsinghua University, Beijing 100084, China

*Corresponding author: zjzy2009@hotmail.com

Abstract Railway steel bridge belongs to large scale weld structures suffered with cyclic dynamic stress generated by train. In recent years, the section of bridge member becomes bigger, plate becomes thicker, connection form becomes more complicated, and steel bridge is applied to more districts even lower temperature environment. Fatigue and fracture problems become more serious. On the basis of Crack Tip Open Displacement (CTOD) test data of 372 specimens tested in different temperature, this paper discusses research work about fracture proof design that involved how to determine the criterion of Charpy V Notch (CVN) impact toughness by building the relationship between CTOD and CVN, how to prevent brittle fracture by stress control in railway steel bridge design based on COD design curve from test data, and how to do the fatigue design for railway steel bridge at -50 ℃ of design temperature in an easy way, The method of fatigue design at -50 ℃ environment has been used for railway steel bridge structure of Qinghai-Tinet Railway in China.

Keywords Railway steel bridge, Fracture proof design, Fatigue at low temperature, CTOD test, Toughness criterion

1. Introduction

Fatigue fracture is one of the most important contents in design of railway steel bridge that belongs to large scale weld structure suffered with heavy cyclic dynamic stress generated by train. In recent years, the section of bridge member becomes bigger, plate becomes thicker, connection form becomes more complicated, and steel bridge is applied to wider districts even in lower temperature environment, so as to meet the needs of construction development in China. Fatigue and fracture problems become more serious. Traditional design concept and method is just focused on building steel bridge in the south part of China with warm weather, without enough experience for using steel bridge in cold weather, so it is necessary to supplement special regulation or renew some research method. It were given by an engineering test research[1] that, fatigue strength is higher when specimen is at lower temperature than it is at room temperature in comparison tests. The conclusion were doubted[2] and is not reasonable either. With the cognition developed the idea that, elastic-plastic fracture toughness has to be applied to fracture proof design in railway steel bridge, formed and expected to obtain reasonable interpretation and solve the fatigue problems as well when the steel bridge serving in lower temperature. A series of Crack Tip Open Displacement (CTOD) tests were carried out in different temperature to the common bridge steel with the thickness of 12, 16, 24, 32, 44, 50 mm both for base metal and butt weld seam. The total numbers of specimen was 372, and the effective test data was 364. CTOD test was done by straight three point bending specimen. The regression data point for weld seam and the relationship between CTOD and

temperature after regression[3] are shown in Fig. 1 and Fig. 2.

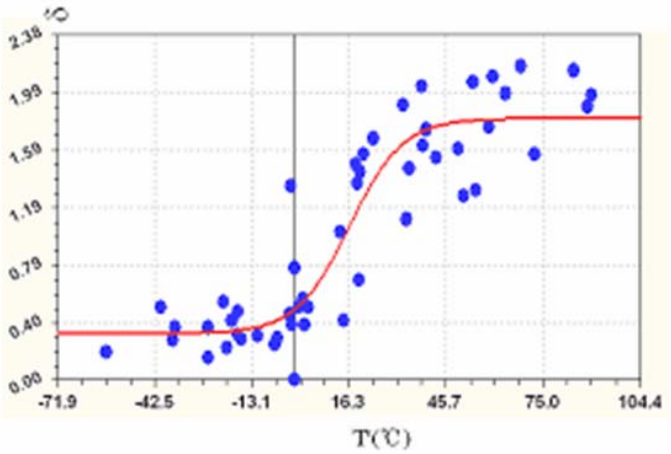

Figure 1. Statistics result of weld seam test data

Charpy V Notch (CVN) impact toughness is an important index proving toughness quality of steel material and weld joint. It is applied to engineering widely because of its simple and inexpensive test procedure compared with CTOD. In order to get the relationship between the two toughness indexes, 702 specimens of CVN impact test were also carried out in different temperature accordingly[4]. The regressed curve is shown in Fig. 3.

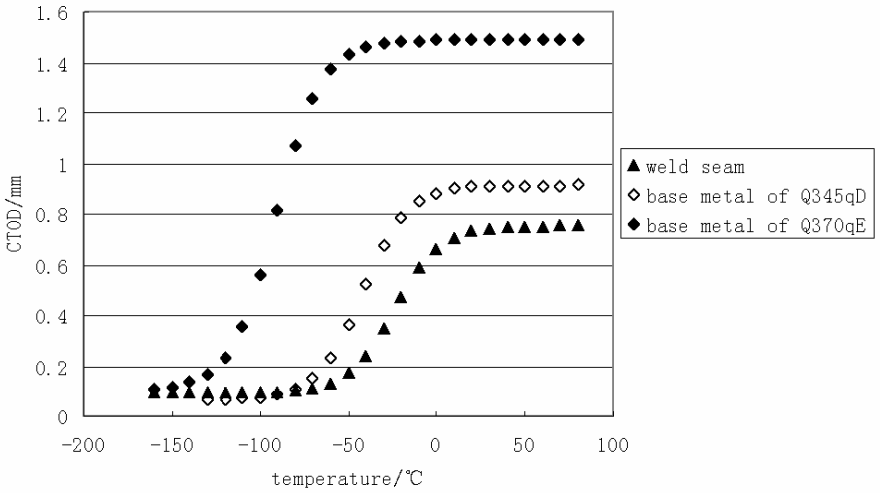

Figure 2. CTOD versus temperature of base metal and weld seam

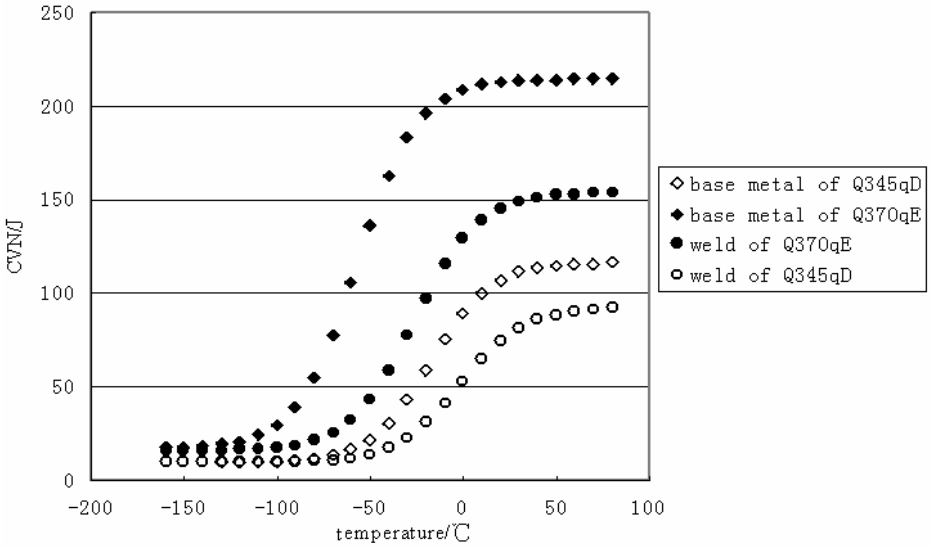

Figure 3. CVN versus temperature of base metal and weld

Three aspects of research are carried out around fatigue and fracture problem based on the test data of CTOD and CVN above: (1) to create the relationship between CTOD and CVN by absorption energy at the moment of specimen damaged in test, to find the basic CVN impact toughness of weld joint proof brittle fracture, and then to determine the toughness criterion that should be easy and practical. (2)find special stress calculation formula for railway steel bridge to check and control maximum stress level preventing from brittle fracture when the material and section of bridge member had be the fact. And (3) to determine the complementary requirement and provide method for fatigue design temperature at -50℃ to apply to Tsinghai-Tibet Railway line. The research result will be the reference of revising code later.

2. Weld toughness criterion

So far the major way to control toughness of steel material in engineering is to check the impact energy by CVN impact test. In bridge design, the first thing is to choose material and confirm the toughness criterion. Usually the lowest impact toughness criterion is determined by comparing with the similar bridge and accumulated experience. Which produce a lot of discussion and dispute. The better way to make sure the criterion is by means of CTOD test data, since it can be leant clearly that which situation would generate brittle fracture and which ductility damage. By this way it can guide to determine the toughness criterion. However, CTOD test is complicated comparatively and is unapt to inspect as normal way in engineering. Therefore, the absorption energy is taken as the instrumentality to establish the relationship between CTOD and CVN. The test record of vertical replacement at load point and loading value are utilized to get the basic absorption energy in CTOD test, and then it can be used to guide to work out basic CVN impact toughness criterion. The idea comes from the CTOD test data within temperature from room temperature to -70℃. It shows that the basic absorption energy provided by specimen is independent of test temperature when it gets to certain CTOD value. It also can leads to, on one side, the impact toughness for real bridge under the temperature from room to -70℃ should satisfy with basic absorption energy obtained from certain critical state in CTOD test. On the other side, the relationship also should be analyzed between loading velocity and character temperature for CTOD test, CVN impact test and service train passing bridge, by which the test temperature is confirmed for doing impact test. Consequently the reasonable impact toughness criterion with large amount of test basis can be prescribed.

Following regulation should be complied in analysis:：

(1) It is required for material to have the absorption energy ability that can suffer the destroy state with transition ability from brittle to ductility. In other words, when the structure gets to fracture, the maximum stress in member section would exceed yield strength, and the structure should have a certain deformation.
(2) Towards to safety direction, increasing 2 standard deviation to average value during statistics analysis.

2.1. Method to confirm basic toughness index

The step to determine the toughness criterion is followed by below items:

(1) Calculate integral to obtain the absorption energy by the test record of vertical replacement at load point and loading value;

(2) Analysis the loading model difference of CTOD test and CVN impact test, formulate the relation of energy between the absorption energy in CTOD test and impact energy in CVN test[5]. It is shown in formula (1).

$$A_{kv} = \frac{A_{CTOD}}{C_e} \tag{1}$$

where A_{CTOD} and A_{kv} = absorption energy in CTOD test and in CVN test, J; C_e = transition coefficient, $C_e = 0.32B$, B is the thickness of CTOD specimen.

(3) Sort the test data from CTOD test that were damaged at the transition situation from brittle and ductility, pick-up their absorption energy in list, and calculate the basic energy value that is corresponding to the specimen condition and is impossible to generate brittle fracture.

(4) Determine test temperature. It is shown from CTOD test that the basic absorption energy provided with a specimen when the crack tip in it open a certain displacement is independent of temperature when the thickness of specimen is certain. Meanwhile, in practical bridge the narrowest open displacement should be controlled mainly. Therefore it is no need to consider what temperature the CTOD test is done corresponding to absorption energy in step (3) above, just consider the difference of loading velocity in CTOD test and CVN impact test. It mainly affects the exact place at where the toughness-temperature character curve located on the temperature coordinate.

The analysis about temperature coordinate is shown below:

(1) As per the relation of character temperature point between fracture toughness stress intention factor K_{IC} that is tested by static or equivalently static loading and the loading velocity caused by service train, the character temperature of service train is equivalent to increase ΔT_1℃ by static K_{IC} test [6]. It can be shown by the following equation:

$$\Delta T_1 = (83 - 0.08\sigma_s)\varepsilon^{0.17} \tag{2}$$

Where: ε = loading strain velocity, s^{-1}.

(2) As per the relation of character temperature point between the loading velocity caused by service train and impact toughness test, the character temperature of service train is equivalent to decrease ΔT_2℃ from impact toughness test[7]. It can be shown by the following equation:

$$\Delta T2 = 70℉ = 39℃ \tag{3}$$

(3) The test character temperature replacement in impact test between loading slowly to and normal loading speed in engineering can be represented by ΔT_3 [8]:

$$\Delta T_3 = 120 - 0.121\sigma_s \quad (℃) \tag{4}$$

(4) As per the relation of character temperature point between fracture toughness CTOD that is tested by static or equivalently static loading and impact toughness test, the character temperature of CTOD test is equivalent to decreaseΔT_4℃ from impact toughness test according to the test in comparison above:

$$\Delta T_4 = 15 \sim 35 \quad (℃) \tag{5}$$

Taking bridge steel Q370qE as an example, the character temperature relationship above is summed up and drawn as Fig. 4.

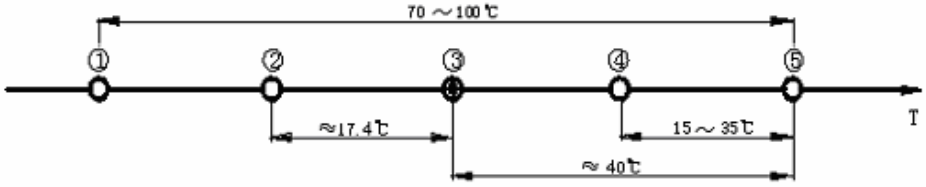

Figure 4. Comparative character temperature relation

Compared with the five situations in Fig. 4, the character temperature of CTOD test is higher than that under loading velocity caused by service train, even though it is static loading. It is understood that the loading way in CTOD test is three points bending, and the notch is sharp fatigue crack, which is very severe situation. As a result, the character temperature of service train is replaced by CTOD test temperature on the safe side, including the effect of temperature at bridge location and loading velocity. And then, the temperature replacement value from bridge site temperature to impact test is confirmed based on the character temperature relationship between CTOD and CVN test.

2.2. Analysis result and application

Followed by the steps above, the basic indexes of impact toughness proof brittle fracture are obtained in Table 1.

Table 1. Basic indexes of impact toughness

material		Thickness/mm	Environment temperature at bridge location /℃			
			-50	-40	-30	-20
Q370qE	Base metal	≤30	45J,-30℃	45J,-20℃	45J,-10℃	45J,0℃
		30-50	70J,-30℃	70J,-20℃	70J,-10℃	70J,0℃
	Weld		46J,-35℃	46J,-25℃	46J,-15℃	46J,-5℃
Q345qD	Base metal	≤32	43J,-30℃	43J,-20℃	43J,-10℃	43J,0℃
	Weld		34J,-35℃	34J,-25℃	34J,-15℃	34J,-5℃

The stipulation of steel material about the lowest impact toughness in national standard is classified by test temperature into 0℃, -20℃ and -40℃. The steel material used in railway steel bridge is the steel with -20℃ and -40℃ of requirement. Utilizing the curve equation of railway bridge steel regressed by CVN test (see Fig. 3), the equivalent index of the basic impact toughness in Table 1 are compared with the stipulation in national standard, and the commended toughness criterion for railway steel bridge is shown as Table 2-3.

Table 2. Commended lowest impact toughness criterion

material	Thickness/mm	Environment region and temperature at bridge location /℃	
		region E*	region D*

Q370qE	Base metal	≤30	41J,-40℃	41J,-20℃
		30-50	70J,-40℃	70J,-20℃
	Weld		41J,-40℃	41J,-20℃
Q345qD	Base metal	≤32	34J,-20℃	34J,-20℃
	Weld		30J,-20℃	30J,-20℃

*See Table 3.

Table 3. Region distribution for constructing bridge in China

Region mark	Name of territory	Extreme temperature in history/℃
E	Heilongjiang, Sinkiang, Inner Mongolia, Tibet, Jilin, Shanxi, Tsinghai	-40℃以下
	Liaoning, Gansu, Szechwan, Hebei, Shannxi, Ningxia	-30℃--40℃
D	Beijing, Tientsin, Shandong, Henan	-20℃--30℃
	Other	-20℃以上

3. Control stress prevent from brittle fracture

It is found by observing CTOD test process that, controlling action force on structure less than the force that would arouse brittle fracture can also prevent structure from brittle fracture. The purpose to research this subject is for exist bridges since their toughness situation had already been the fact. The controlling stress formula for railway steel bridge to prevent from brittle fracture can be deduced by means of the brittle fracture data in CTOD tests[3]. Formula (6) and (7) is for base metal, and (8) and (9) for weld seam:

$$\frac{\sigma}{\sigma_s} \le \frac{1}{1.12}\sqrt{\frac{E\delta}{2\pi a\sigma_s}} - 0.6 \tag{6}$$

$$\delta = \frac{a}{t}\left[0.1059 + \frac{1.383}{1+e^{-0.0778(T+90.666)}}\right] \tag{7}$$

$$\frac{\sigma}{\sigma_s} \le \frac{1}{1.12}\sqrt{\frac{E\delta}{2\pi a\sigma_s}} - 0.3 \tag{8}$$

$$\delta_W = \frac{a}{t}\left[0.0918 + \frac{0.6615}{1+e^{-0.0767(T+24.1927)}}\right] \tag{9}$$

Where: δ = base metal of Q370qE; δ_w = weld seam.

3.1. Analysis result

To base metal of Q370qE, elastic module $E = 2.1\times10^5\,MPa$, average yield strength $\overline{\sigma}_s = 385MPa$, and put them into Formula (6) and (7), then:

$$\sigma \le 3202.82\sqrt{\frac{1}{W}\left[0.2118+\frac{2.766}{1+e^{-0.0778(T+90.666)}}\right]}-206.25 \tag{10}$$

To weld joint, elastic module $E=2.1\times10^5 MPa$, average yield strength $\overline{\sigma}_s=377MPa$ (taking average value of base metal that is on safe side), and put them into Formula (8) and (9), then:

$$\sigma \le 3169.37\sqrt{\frac{1}{W}\left[0.1836+\frac{1.3229}{1+e^{-0.0767(T+24.1927)}}\right]}-101 \tag{11}$$

Calculating by the formula (10) and (11), the available maximum stress σ without occurring brittle fracture to different thickness of bridge member can be obtained.

3.2. Application

Suppose α is available stress coefficient, $\alpha=\sigma/\sigma_s$, the calculation results to steel bridge steel are shown in Table 4.

Table 4. The maximum available stress coefficient α

Material	Tem. ℃	Thickness of steel plate/mm									
		12	16	20	24	30	32	38	40	44	50
Base metal of Q370qE	-50	1	1	1	1	1	1	1	1	1	1
	-40 to 0	1	1	1	1	1	1	1	1	1	1
Base metal of Q345qD	-50	1	1	1	0.95	0.79	0.75	-	-	-	-
	-40 to 0	1	1	1	1	1	1	-	-	-	-
weld	-50	1	0.97	0.83	0.74	0.63	0.60	0.53	0.51	0.48	0.43
	-40	1	1	1	0.93	0.80	0.77	0.68	0.66	0.62	0.56
	-30	1	1	1	1	1	0.98	0.87	0.84	0.79	0.73
	-20	1	1	1	1	1	1	1	1	0.97	0.89
	-10	1	1	1	1	1	1	1	1	1	1
	0	1	1	1	1	1	1	1	1	1	1

Usually, the ratio of design stress to yield strength is 0.58. Compared with the values in Table 4, it can be concluded that when the weld is used at the temperature of -40℃ to -50℃, some available stress is less than its design stress. It means that even though those members with the weld suffered the action stress that is below the allowable value in design code, brittle fracture may happen at some moment. In this way, reducing working stress calculated by the method above can stop some brittle fracture.

4. Fatigue design method of steel bridge at low temperature

Tsinghai-Tibet railway line is located at high altitude and cold region in China, where the extreme lowest temperature is -45 ℃, with undeveloped traffic and atrocious environment. The length of

bridge within iced soil region exceeds 70 kilometers. In order to solve the problem of long time limit for constructing concrete bridge, the test investigation for steel-concrete composite bridge in Tsinghai-Tibet railway line were carried out. As per steel girder of composite bridge, the major effect under those bad conditions caused by the peculiar geography environment is the perennial cold weather. Low temperature would reduce toughness of steel and weld joint, make structure brittle, bring structure to a lower fatigue performance, and therefore reduce safety level of railway steel bridge suffered with very heavy live load. The current fatigue design parameter that is made and used to the structure at common temperature cannot meet the needs of Tsinghai-Tibet railway line.

4.1 Research Method

The test of fatigue crack propagation rate were carried out to 24mm thickness of Q370qD base steel and weld at -50℃ temperature. It indicated that, under -50℃ temperature the material coefficients of Paris equation in middle part of speed propagation region, $da/dN = C(\Delta K)^m$, have smaller 'C' and larger 'm', and have higher fatigue crack threshold ΔK_{th}, compared with room temperature. Furthermore, S-N curve at -50℃ is above the curve at room temperature, and its slope is even slightly from tests[1]. It leads the wrong direction that using common fatigue design method is good enough at low temperature.

However, CTOD tests indicate that, low temperature at -50℃ would reduce the critical crack open displacement, and increase the trend to brittle fracture. The average critical CTOD value at room temperature is 0.72mm, while it is only 0.14mm at -50℃.

Crack length can be expressed by Formula (12) at room temperature and Formula (13) at -50℃ according to the test result[3]:

$$a \le \frac{E\delta}{\pi(1.12\sigma + \sigma_s + 0.3\sigma_s)} \tag{12}$$

$$a \le \frac{E\delta\sigma_s}{2\pi(1.12\sigma + 0.3\sigma_s)^2} \tag{13}$$

Take $E = 2.1\times10^5 MPa$, $\delta = 0.72mm$ at room temperature and $\delta = 0.14mm$ at -50℃; $\sigma_s = 490MPa$ at room temperature[9] and $\sigma_s = 512MPa$ at -50℃[3]; $\sigma = 200MPa$ from allowable design stress in the code, the critical crack length are calculated by formula (12) and (13), that is, $a = 56mm$ at room temperature, and $a = 17mm$ at -50℃.

From Paris equation $\frac{da}{dN} = C(\Delta K)^m$, transform it into:

$$N = \int_{a_0}^{a_c} \frac{da}{C\Delta K^m} \tag{14}$$

where: $\Delta K = Y\Delta\sigma\sqrt{\pi a}$, Y= crack type coefficient. It can be taken as a destiny to bridge structure at both room and low temperature, then:

$$N = \frac{1}{CY^m \Delta\sigma^m \pi^{\frac{m}{2}} (\frac{m}{2} - 1)} \left(\frac{a_0}{\sqrt{a_0^m}} - \frac{a_c}{\sqrt{a_c^m}} \right) \tag{15}$$

4.2. Research Result

In formula (15), suppose original crack length $a_0 = 0.001m$, critical crack length $a_c = 0.056m$ at room temperature, and $a_c = 0.017m$ at -50℃. The coefficients of C and m are taken from the test data regressed with 97.7% probability, Y is taken for the most unfavourable situation in engineering when $a/W = 75\%$, and the life N is taken as the same cycles at both room and low temperature. The ratio of fatigue stress range between -50℃ and room temperature is 0.88.

This calculation result shows that, fatigue at low temperature should not be considered as a common fatigue problem. It is mainly because at low temperature, the critical fracture crack length shorten sharply. Consequently, the fatigue safety level drops, that can be noticed at the obvious intersection moving ahead between crack stable propagation region and sharp propagation region. The only way to solve the problem is to apply Fracture Mechanics theory and elastic-plastic CTOD test.

As a result, the allowable fatigue design stress range for steel bridge in Tsinghai-Tibet railway line is prescribed to 80% of the current fatigue design index. At the same time, the further requirement below should be followed:

(1) During design of bridge for Tsinghai-Tibet railway line, thinner steel plate should be preferred, so long as its local stabilization can be content.

(2) All of the steel material is required to fine microstructure by raising temperature during steel making to increase stopping-fracture ability.

(3) It should be taken into consideration to choose other kind of structure or connection style rather than to choose thicker plate when fatigue checking cannot pass the regulation at low temperature.

5. Conclusions

Fracture mechanics theory combined with the usual way for fatigue and toughness in railway steel bridge can solve the special problem when the environment is in low temperature. Three aspects of research can be concluded as below:

(1) It is important to select bridge steel that is both safe and economic. A reliable criterion can be made based on CTOD test. The recommended method this paper is easy to choose which steel category available.

(2) It is usually confused for engineer to check working stress for some bridge member with lower stress than allowable stress, impact toughness being above the normative value in the code, but the brittle fracture still happened. Additional method to check and control the stress level prevent from brittle fracture is suggested.

(3) The critical fracture crack length would be shorten sharply at low temperature. Fatigue at low temperature should not be considered as a common fatigue problem. As an example, the allowable fatigue design stress range for steel bridge in Tsinghai-Tibet railway line is prescribed to 80% of the current fatigue design value. The method is easy to be used for designer.

Acknowledgement

The authors would like to thank Mr. Wang Maoming from CARS for his help to do so large amount of tests in this project.

References

[1] Zhang Yuling, Liu Xiaoguang, Pan Jiyan, Tao Xiaoyan, Wang Maoming, Fatigue test research at low temperature for steel beam of concrete-steel combined railway bridge in Qinghai-Tibet Railway Line, Proceeding of Qinghai-Tibet Railway Line Symposia on Service Administration and Related Technology, China Science and Technology Press, 2005, pp. 77-83.

[2] Shul'ginov B S, Matveyev V V, Impact fatigue of low-alloy steels and their welded joints at low temperature. Int. J. Fatigue，1997，19(8-9), pp. 621-627.

[3] Zhang Yuling, Wang Maoming, Sun Zhenhua, Tao Xiaoyan, CTOD performance of railway bridge base steel and weld seams, Journal of Tsinghua University Science and Technology, Vol. 45, No. 5 (2005), pp. 585-588.

[4] Zhang Yuling, Dai Fuzhong, Tao Xiaoyan, Wang Maoming, Test Analysis of 14MnNbq and 16Mnq steel and the welding CVN impact toughness, China Railway Science, Vol. 26, No. 3 (2004), pp. 80-85.

[5] Zhang Yuling, Liu Xiaoguang, Pan Jiyan, Research on toughness criterion for bridge steel in railroad, China Railway Science, Vol. 26，No. 3 (2005) pp. 16-20.

[6] Qian Weiping, Liu Jiaju, Jiang Heshui, Report on safe fracture selecting rules of 14MnNbq for welded steel bridge components, Research Report, Science and Technology Developing and Planning Project of Wuhu Yangtze River Bridge, No. 96G35-F-05-01, China State Shipbuilding Corporation. 1999.

[7] AREMA Manual for Railway Engineering. Chapter 15 Steel Structures, American Railway Engineering and Maintenance-of-Way Association, USA, 2002.

[8] Fisher J W. Fatigue and fracture in steel bridges —— case studies, A Wiley-Interscience publication, USA, 1984.

[9] Manufactural techniques of girder of Wuhu Yangtze River Bridge, China railway engineering corporation, Wuhu Yangtze River Bridge Corporation, Beijing, Science Press, 2001.

Fatigue Strength and Fatigue Life Evaluation of National Cultural Relic Steel Bridges

Chun-Sheng Wang[1,*], Lan Duan[1], Shi-Chao Wang[1], Jing-Yu Hu[1]

[1] Engineering Research Center for Large Highway Structure Safety of Ministry of Education, College of Highways, Chang'an University, 710064, China
* Corresponding author: wcs2000wcs@163.com

Abstract This paper is regard with material mechanics, fatigue and fracture properties of Lanzhou Yellow River Iron Bridge, which is an old metal bridges built about 100 years ago. An original steel angel cut off from Lanzhou Yellow River Iron Bridge was used to carry out series of tests including material properties, fracture toughness and fatigue strength of riveted joints. The results have shown that the strength of the old steel is relatively equal to A3 steel in the old code, and the ductile-brittle transition temperature is nearly -23°C，which means that the structure is unsafe in winter due to the cold climate conditions of Lanzhou city. The main regression parameters of the fatigue crack growth rate are $C=7.88\times10^{-12}$m/cycle and m=3. According to the test result, the fatigue strength of tensional plate specimens with new drilling hole is similar to the category 140 in the EUROCODE. Based on the tested result, the remaining fatigue life of Lanzhou Yellow River Iron Bridge was evaluated using S-N curve and fracture mechanics method. It can be concluded that two kinds of adverse loading situations should be restricted including people loading only on half of bridge, and truck load over 120kN.

Keywords national cultural relic steel bridges, fatigue strength, fracture toughness, fatigue crack growth rate, fatigue life

1. Introduction

Until now lots of riveted old steel bridges are still in service in many countries. In recent years, traffic load and speed on both existing railway and highway steel bridges have increased, which is much higher than those originally designed load. With the great increase of load number and magnitude, these riveted bridges may close to the end of their service life. However, the work for replacement of these old riveted bridges takes time. So capacity calculation, safety assessment and remaining fatigue life calculation are essential for these ageing bridges, which is helpful to decide whether to demolish or retrofit these bridges.

To evaluate fatigue resistance of old steel and establish fatigue categories for riveted connections, this paper conduct series of fatigue behavior tests for old riveted steel bridge for Lanzhou Yellow River Iron Bridge, which is a simple supported truss bridge over Yellow River originally built in 1909. During 100 year's service time, several repair and rehabilitation were conducted for Lanzhou Yellow River Iron Bridge, and nowadays Lanzhou Yellow River Iron Bridge is the historical cite in Lanzhou City. Material properties were studied for steel used in Lanzhou Yellow River Iron Bridge, which is fabricated more than 100 years ago. From Lanzhou Yellow River Iron Bridge, standard compact specimens are cut and fabricated for fatigue crack growth rate test, and fatigue test were also conducted for specimens with newly drilled hole. Based on the tested result, the remaining fatigue life of Lanzhou Yellow River Iron Bridge was evaluated.

2. Material Properties of Old Steel

Material property is studied initially for steel of old riveted bridge. For Lanzhou Yellow River Iron Bridge, tensile specimens and toughness specimens were cut from a demolished chord to conducted material tensile test and Charpy V notch test.

2.1. Tensile test

The tensile test was conducted according to metallic materials-Tensile testing at ambient temperature (GB228-2002) [1]. Three ratio samples with same dimensions were manufactured according to the requirements of Chinese GB2975-1998 [2]. The strains in longitudinal direction are measured by strain gages for calculating the material properties. After the test, the mechanical indexes were calculated, such as elastic modus (E), yield stress (σ_s), ultimate stress (σ_b) and elongation.

The tensile test results are listed in Table 1. It can be concluded that the strength of the old steel is roughly equal to A3 steel in the old code, but the yield-strength ratio, σ_s/σ_b, is equal to 0.629, which is slightly higher than A3 steel(0.486~0.579).

Table 1. Results of tensile test

E(GPa)	σs(MPa)	σb(MPa)	Elongation(%)	Cross section reduction(%)
194.3	275.7	438	29.1	63.77

2.2. Toughness test

According to Chinese test standard for metallic materials-Charpy notch impact test (GB/T229-1994) , Charpy V toughness tests were conducted at different temperatures ranging from -53°C to 10°C [3]. 25 Charpy V notch (CVN) standard specimens were cut from one third of steel angle leg and the notch of specimen was perpendicular to rolling direction. The dimension of CVN specimen is shown in Table 2.

Table 2. Dimension of CVN specimens (mm)

Thickness	Width	Length
10	10	55

Toughness test was conducted at eight different temperatures, including -53 ℃，-43 ℃, -32.5℃, -26 ℃, -23 ℃, -21 ℃, 0℃ and 10 ℃. After test, the impact toughness energy (A_{kv}) was recorded and the crystallinity percentage of fracture surface was measured for each specimen, shown in Figure 1. Learn from Figure 1, A_{kv} in upper region is 146J at 10℃, A_{kv} in lower region is 7J at -53℃, and A_{kv} drops apparently from -15℃ to -28℃. At -23℃, the crystallinity percentage of fracture surface is approximately 50%. It can be concluded from the result of Charpy-V tests, the temperature of ductile-brittle of old steel used in Lanzhou Yellow River Iron Bridge is nearly -23℃. And the transition is very sharp. When the temperature drops to -23℃, steel in Lanzhou Yellow River Iron Bridge will exhibit clear brittleness instantly. Learn from test results, steel in old bridge usually exhibits both low strength and low toughness. Thus, safety of the structure should be take care especially when temperature is low, even if considering the contribution of riveted member redundancy.

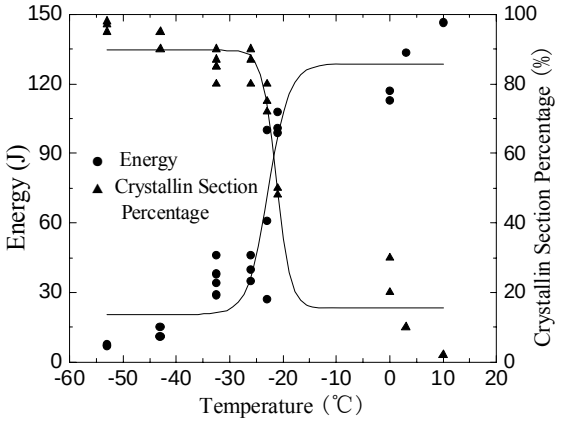

Figure 1. Toughness test result for old steel

3. Fatigue Crack Growth Rate Test of Old Steel

Fatigue crack growth rate (da/dN) tests were conducted for base steel in Lanzhou Yellow River Iron Bridge to determine its fatigue crack growth rate in region II according to requirement of ASTM E647-08 and Chinese GB/T 6398-2000 [4, 5]. da/dN tests were conducted for compact specimen [C(T)] with 11mm thick under load ratio of R=0.1, 0.5 and 0.8. The prefabricated crack for all the specimen is oriented perpendicular to the rolling direction of the steel plate (L-T). The dimension and specimen are shown in Figure 2 and Table 3.

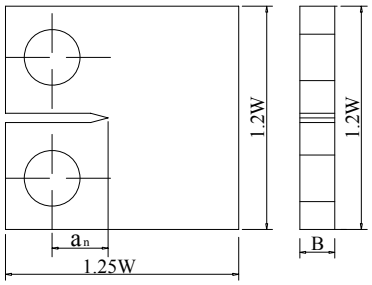

Figure 2. Compact specimen

Table 3. Specimens dimensions (mm)

B	$1.25W$	$1.2W$	a_n
11	62.5	60	12.5

After the test, the stress-intensity factor range ΔK_i under each crack length is calculated, according to Eq.1. The parameters are obtained including material constant m and C, and correlation coefficient. The da/dN test result for old steel in Lanzhou Yellow River Iron Bridge is shown in Figure 3. Learn from da/dN test result, with the increase of load ratio R, fatigue crack growth rate is increasing. Some researchers have conducted fatigue resistance behavior study for old steel. For example, the fatigue test result of Barson shows $C=6.89\times10^{-12}$ m/cycle and m=3, while Sedlacek found $C=1.26\times10^{-11}$ m/cycle and m=3 for old steel. The fatigue crack growth rate of Lanzhou Yellow River Iron Bridge is between the tested rate of Barson and Sedlacek, which serves test data for remaining fatigue life assessment of old steel bridge.

$$\Delta K = \frac{\Delta P}{B/W}\frac{(2+\alpha)}{(1-\alpha)^{3/2}}\cdot \\ (0.886+4.64\alpha-13.32\alpha^2+14.72\alpha^3-5.6\alpha^4) \tag{1}$$

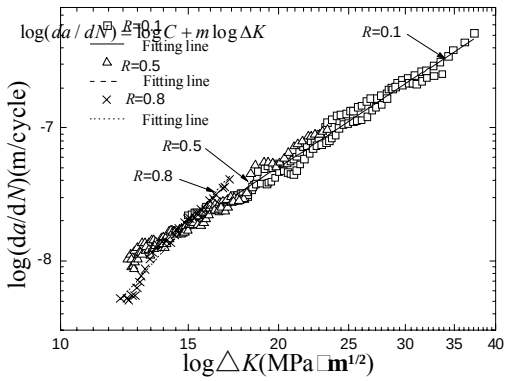

Figure 3. The da/dN~ΔK curve.

4. Fatigue Test for Drilled Specimen

3 fatigue specimens were cut from a chord of Lanzhou Yellow River Iron Bridge, and holds were newly drilled in the specimen. The dimension of fatigue specimens are shown in Figure 4 and Table 4. In order to observe the fatigue crack accurately, surface clean and polishing was conducted for each specimen. Strain gauge was located on the specimen before test. During testing procedure, the loading frequency is 15 Hz.

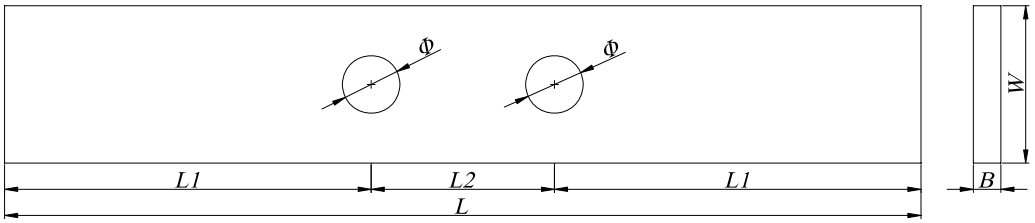

Figure 4. Dimension of fatigue specimen

Table 4. Dimension of fatigue specimen with drilled holes (mm)

Specimen	*B*	*W*	*Φ*	*L*	*L1*	*L2*
1	11	50	18	330	127	76
2	10.5	60	22	350	140	70
3	10.5	60	22	350	140	70

Fatigue test result is classified by fatigue details specified in AASHTO specification and Eurocode [6, 7]. Learning from Fig. 15 and 16, the fatigue detail of old steel with drilled hole is better than detail C in AASHTO specification and is higher than detail category 100 in Eurocode. The tested fatigue strength is greater than actual situation since two causes. Firstly, holes on specimens were newly drilled for fatigue test, avoiding fatigue crack initiate and corrosion during bridge service period over 100 years. Secondly, the surface of specimen was polished to observe and capture fatigue crack precisely, eliminating effect of surface defects.

5. Remaining Fatigue Life Evaluation

Based on the analysis of riveted steel bridge fatigue failure mechanism, the assessment model on the basis of S-N curve and fracture mechanics was applied to evaluate the remaining life of Lanzhou Yellow River Iron Bridge.

5.1. Evaluation methods

5.1.1. S-N curve and linear damage accumulation rule

Linear damage accumulation theory is based on fatigue damage D and assumes structural fatigue damage can be linearly accumulated if varying stresses spectrum was determined. The linear damage accumulation model described the sum of structure damage, D. The typical linear damage accumulation rule is Palmgren-Miner rule. It defined that D=1 indicated failure where D was the amount of damage degree in material. Sum of fatigue damage for all stress range levels is shown in Eq. 2. In Eq. 2, in which in each stress range level σ_i, the damage fraction D_i was linearly proportional to n_i, where n_i was the number of cycles at σ_i and D_i was the ratio of n_i/N_i. N_i is the total number of cycles that would cause failure under that stress range level. Loading sequence is not considered in Miner rules, but it has great affection when calculating fatigue life. The critical damage (D_{CR}) member is near 1 when failure occurs.

$$D = \sum_{i=1}^{n} D_i = \sum_{i=1}^{n} \frac{n_i}{N_i} \tag{2}$$

In this paper, detail category D in AASHTO is used during the evaluation, with reference to the riveted joint fatigue strength analysis of Lanzhou Yellow River Iron Bridge when it was built, and the fatigue tests results conducted nationally and internationally, as well as the fatigue test result of Lanzhou Yellow River Iron Bridge.

5.1.2. Fracture mechanics assessment mode

For riveted steel bridge, crack is usually propagating from edge of hole perpendicularly until member fracture. Two basic fracture mechanics modes are used in this paper. One is central crack tension (CCT) mode and another mode is double edge crack tension (DECT) mode.

Initial crack is assumed as $2a_i=D+2\times$detected value, in which D is diameter of riveted hole. With propagation of fatigue crack, the net section may be yield under loading and fracture failure may be occurred. The critical crack length (a_{cr}) can be calculated by Eq. (3) and Eq. (4). In Eq. (3) and (4), W is the width of member, R_{el} is yield strength and σ_{max} is maximum sum of dead stress and live stress.

CCT：
$$a_N = W(1 - \sigma_{max} / R_{el}) \tag{3}$$

DECT:
$$a_N = W\sqrt{2.25 + 4(1 - \sigma_{max} / R_{el})} - 1.5W \tag{4}$$

If stress intensity factor at crack tip (K_I) is greater than fracture toughness of steel (K_{IC}), fracture may be occurred. In this case, critical crack length (a_{cr}) is calculated by Eq. (5), in which Y is geometrical amend factor.

$$a_{cr} = \left(K_{IC} \Big/ Y\sigma_{\max} \right)^2 \Big/ \pi \tag{5}$$

The calculated critical crack length by Eq. (5) should be less than the max length that member can observe ($a_{\max}$). For steel angle, crack length should be no more than angle width. So, critical length is finally determined by Eq. (6).

$$a_f = \min(a_N, a_{cr}, a_{\max}) \tag{6}$$

A safety evaluation result will be obtained if is just considering $\triangle\sigma$ in Paris equation. However, threshold value relative to load ratio R (R=$\sigma_{\min}/\sigma_{\max}$) should be considered, shown in Eq. (7). When crack propagating from a_i to a_f, the remaining fatigue life is calculated by Eq. (8).

$$\frac{da}{dN} = \begin{cases} 0 & \Delta K \le \Delta K_{th} \\ C\left(\Delta K^m - \Delta K_{th}^m\right) & \Delta K > \Delta K_{th} \end{cases} \tag{7}$$

$$N = \int_{a_i}^{a_f} \frac{\mathrm{d}a}{C\left(\Delta K^m - \Delta K_{th}^m\right)} \tag{8}$$

5.2. Evaluation results

Remaining fatigue life of Lanzhou Yellow River Iron Bridge is evaluated by the following steps. Firstly, finite element mode of Lanzhou Yellow River Iron Bridge is established and influence lines for main truss members and cross beam are acquired. Secondly, traffic load survey is conducted to determine fatigue load using in fatigue life evaluation. Thirdly, stress spectrums are acquired using flow counting method when applying fatigue load on influence lines of members considering traffic load impact factor. Fourthly, considering corrosion effect and fatigue propagation rules for riveted detail, fatigue life for Lanzhou Yellow River Iron Bridge is assessed.

By the method of S-N curve, the remaining fatigue life evaluation of main truss and deck plate in Lanzhou Yellow River Iron Bridge are all more than 100 years, except inclined truss member L3 loaded by people load. When fracture mechanics method is used, only hanger member L2 in main truss structure has remaining fatigue life more than 100 years under varieties of fatigue loads. In other members, inclined member L3 has the shortest remaining fatigue life (17 years) under people load. Learn from calculation result, all members in main truss structure have infinite remaining fatigue life under fatigue load of small cars, while they have shortest remaining fatigue life under people load and truck load. As a result, to ensure the safety of bridge structure, two kinds of adverse loading situations should be restricted including people loading only on half of bridge, and truck load over 120kN.

6. Conclusions

This paper focused on study of the actual fatigue remaining life, service safety, maintenance intervals and the ultimate bearing capacity of old historical steel bridges to preserve their high cultural value. It can be concluded that: (1) the strength of the old steel is relatively equal to A3 steel in the old code, and the ductile-brittle transition temperature is nearly -23 ℃, which means that the structure is unsafe in winter considering the cold climate of Lanzhou city; (2) The main regression parameters of the fatigue crack growth rate are C=7.88×10^{-12} and m=3 for base steel; (3)through fatigue test for specimen with drilled holes, the fatigue property of Zhongshan Steel

Bridge is superior to detail C in AASHTO and detail D in BS5400 and higher than detail 100 in Eurocode; (4) according to the fatigue remaining life evaluation of main truss and deck plate in Lanzhou Yellow River Iron Bridge by the S-N curve and fracture mechanics method, two kinds of adverse loading situations should be restricted including people loading only on half of bridge, and truck load over 120kN.

Acknowledgements

The work described in this paper was partially supported by the National Natural Science Foundation of China (Grant No.51078039), the Foundation for the Author of National Excellent Doctoral Dissertation of the P.R. China (Grant No.2007B49), the Special Fund for Basic Scientific Research of Central Colleges of the P.R. China, Chang'an University (No.CHD2012ZD008).

References

[1] Metallic Materials Tensile Testing at Ambient Temperature(GB/T 228-2002) (China Plan Publications, Beijing 2002).
[2] Steel and Steel Products—Location and Preparation of Test Pieces for Mechanical Testing(GB2975-1998) (China Plan Publications, Beijing 1998).
[3] Metallic Materials-Charpy Notch Impact Test(GB/T 229-1994) (China Plan Publications, Beijing 1994).
[4] ASTM, E647-08. Standard test method for measurement of fatigue crack growth rates;2008.
[5] GB/T 6398-2000.Standard test method for fatigue crack growth rates of metallic materials. Beijing: China Plan Publications, 2000.
[6] AASHTO (American Association of State Highway and Transportation Officials).1990.Guide specifications for fatigue evaluation of steel bridges.Washington :AASHTO.
[7] Eurocode 3: design of steel structures-part 1-9: fatigue. Brussels: CEN. CEN,2005. EN 1993-1-9.